The Influence of the Active Surface on the Cathodic Reduction of MnO_2

N. C. Cahoon[1] and M. P. Korver

Research Laboratory, Union Carbide Consumer Products Company, Division of Union Carbide Corporation, Parma, Ohio

ABSTRACT

The surface area of samples of manganese dioxide is shown to be an important factor in influencing its behavior. Four samples of MnO_2 of widely different origins, electrolytic, activated, natural ore, and synthetic pyrolusite, with total surface area values of 52.8, 50.5, 7.4, and 1.6 m^2/g, respectively, are used as examples. The rates of the recuperation reaction at temperatures of 21°-50°C are shown to be related to the total surface area of the oxides by a complex relation, dependent on temperature and other factors. The product of the reaction MnOOH develops on the surface and in the pores of the original MnO_2 particle, thus increasing the diameter and resulting in reduced pore volume, respectively. The MnOOH made under these conditions, from all four starting materials, appears as rod-shaped units in electron micrographs.

A survey of the literature on manganese dioxide and its cathodic operation indicates that the field has received considerable attention and is well defined. However, the technologist in this area soon finds that he cannot consistently apply this background to correlate the properties of a particular sample of MnO_2 with actual electrochemical performance in a battery. Each technological advance aids in understanding the over-all problems involved, but in itself provides only a part of the solution. Studies of manganese dioxide by chemical methods (1), *p*H-potential measurements (2), utilization test (3), and reaction rate determinations (4) when combined with electrolyte studies (5) provide the major portion of the answer to the problem from the electrochemical and chemical viewpoints. The physical properties of manganese dioxide have been studied by many methods (6) including x-ray diffraction (7) to determine the significance of the various allotropic forms and their crystallinity. The size and shape of the MnO_2 particle have been studied for many years, most recently by the electron microscope (8). A previously little-recognized property, the surface area of the material, is now shown to be an important factor in correlating the performance of various MnO_2 samples used as battery cathodes.

Experimental

The sample of electrolytic MnO_2 used in this work was prepared by the electrolysis of a manganous sulfate solution as previously described (9). The activated MnO_2 was prepared by leaching Mn_2O_3, from thermal reduction of MnO_2 ore, in sulfuric acid solution (10). The ore sample was typical of that obtained from West Africa (Ghana) and generally available to the battery industry. The synthetic pyrolusite was obtained some time ago and was prepared by the thermal decomposition of manganous nitrate (11). Portions of these same samples were used in the recuperation reaction rate study previously described (4).

Chemical analyses of the four samples were made in the usual manner. Particle size distribution curves were obtained by subjecting the portion of the sample which passed a 200 mesh sieve to the micromerograph (12). Particle surface area values were calculated from these data using a method recommended by the makers of the instrument. Total surface area values were obtained with a conventional BET nitrogen sorption apparatus (13). Pore spectra on the various samples were made using the same apparatus and the method described by Barrett, Joyner, and Halenda (14).

Compositions and properties of these four samples are given in Table I.

Discussion

It has been established that the cathode reduction in the Leclanché dry cell can occur through a stepwise series of reactions (15). The first step is electrochemical in which Mn^{IV} is reduced to Mn^{II} as in reaction [1]. The second step is chemical and may follow one or both of the directions given in reactions [2] and [3[.

$$MnO_2 + 2NH_4^+ + 2NH_4Cl + 2ZnCl_2 + 2e \rightarrow MnCl_2 + 2ZnCl_2 \cdot 2NH_3 + 2H_2O \quad [1]$$

$$MnO_2 + Mn^{++} + 2(OH)^- \rightarrow 2MnOOH \quad [2]$$

$$MnO_2 + Mn^{++} + 4(OH)^- + Zn^{++} \rightarrow ZnO \cdot Mn_2O_3 + 2H_2O \quad [3]$$

Some years ago, it became increasingly clear that chemical reactions [2] and [3] were sufficiently slow to limit seriously the output of the Leclanché cell on many of the shorter time tests and heavy

[1] Battery Development Laboratory, Union Carbide Consumer Products Company, Division of Union Carbide Corporation, Cleveland, Ohio.

Table I. Composition and properties of four MnO_2 samples

Sample	% Mn	% MnO_2	% Peroxidation	% Free MnO_2	% Mn_2O_3	Total Mn oxides	Total* inactive material	Crystal type	Real density, g/cc
Electrolytic	58.07	87.43	95.18	83.02	3.99	87.01	12.99	γ	4.25
Activated	50.83	73.79	91.70	67.27	12.03	79.30	20.70	α	4.09
African ore	54.99	84.81	97.6	82.61	4.00	86.61	13.39	ρ	4.49
Synthetic pyrolusite	62.12	97.97	99.7	97.62	0.49	98.11	1.89	β	5.07

* This column was obtained by subtracting the total manganese oxide content from 100%.
The values shown include acid soluble and insoluble gangue, metallic oxides in small amounts, as well as both free and combined water.
The electrolytic sample contains a small amount of graphite.

drain applications. A concerted study of the conditions governing the chemical or recuperation reactions was, therefore, undertaken. The general findings and data obtained for specific examples were presented in a recent paper (4). The most important finding was that the synthetic MnO_2 samples, which give better battery performance than the natural ores, show this superiority in their characteristically greater recuperation rate. Since there has been a considerable amount of speculation as to why the synthetic oxides are so much more active, this paper offers an experimental analysis and a partial explanation for this situation.

In any chemical reaction between a solid and a salt dissolved in a medium in which the solid is suspended, there are a number of important considerations which influence the reaction rate. A number of these factors, such as temperature and electrolyte pH, was discussed previously (4). One important physical property of the solid particles must also be considered, namely, the area of the particle which is in contact with the reaction solution. Preliminary studies in this direction involved the calculation of what we have termed the particle surface area (PSA) from the particle size spectrum. The latter is determined by sieving and by measurements of the subsieve portions with the micromerograph. A comparison of the particle surface area values and the reaction rate at the half life of the reaction is given in Table II for the four typical samples of manganese dioxide previously described. Compositions and properties of the manganese samples are shown in Table I.

Table II. Relationship between the particle surface area of four samples of MnO_2 and the experimentally determined reaction rate

Sample	Particle sample area, m^2/g	Reaction rate: Log $\left\{\left[\frac{dz}{dt}\right]_{t=0.5} \times 10^5\right\}$ at pH 6.50 and 21°C
Electrolytic	0.47	2.130
Activated	0.40	2.380
African ore	0.18	0.660
Synthetic pyrolusite	0.47	0.013

Table III. Comparison of the total and particle surface area of four representative MnO_2 samples

Sample	Total surface area BET determination, m^2/g	Particle surface area sizing determination, m^2/g
Electrolytic	52.8	0.47
Activated	50.5	0.40
African ore	7.4	0.18
Synthetic pyrolusite	1.58	0.47

It is clear from the data in Table II that no simple relationship exists between the particle surface area data and the rate of the recuperation reaction for these specific samples. Since the particle surface area is calculated on the assumption that all the particles are spherical, it is apparent that some error would be introduced by the shape factor of the particle; however, the error is not large enough to influence this conclusion.

The MnO_2 samples differ in other respects besides particle shape and size. They differ in crystal type and, most importantly, they differ in their total surface area as determined by the BET method. Measurements of total surface area on the above four samples are compared with the particle surface area in Table III.

Surface Area of MnO_2 Samples

Previous authors (16-19) have noted differences in the BET surface area of various samples of MnO_2. The concept of increasing the surface area of a sample of MnO_2 by grinding the particles to smaller and smaller diameters has often been proposed. The effect of such treatment can be calculated by assuming that only solid spherical particles are produced by the grinding process. Figure 1 shows the relation

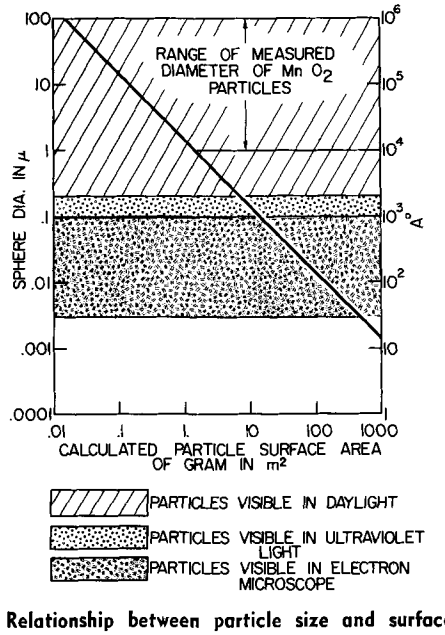

Fig. 1. Relationship between particle size and surface area.

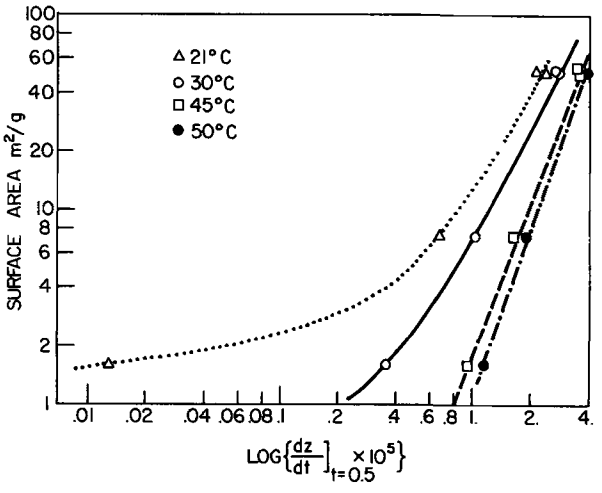

Fig. 2. Relationship between recuperation reaction rate and total surface area of four manganese oxides at pH 6.5 at a variety of temperatures.

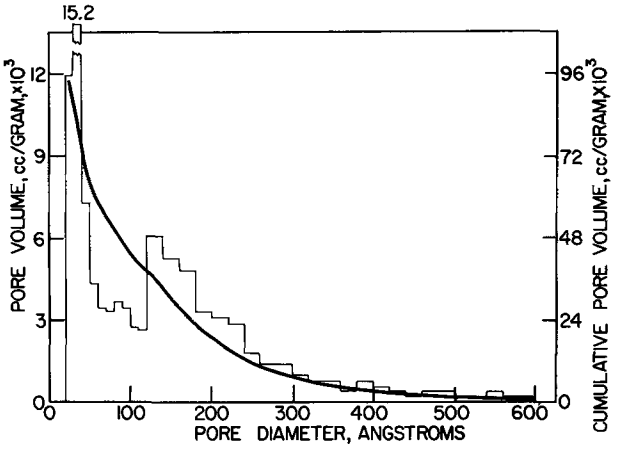

Fig. 3. Pore spectrum of electrolytic manganese dioxide.

between the particle diameter and the calculated surface area of a sample of MnO_2, assuming a real density of 4.54. From this chart, particles of MnO_2 of 200 mesh size (74μ diameter) are shown to have 0.019 m^2/g, and those of 325 mesh (44μ diameter) to have 0.033 m^2/g. Although these areas are considerably larger than those possessed by larger particles, on a unit weight basis, they fall far short of the actual measured surface areas given in Table III. Thus, a nominal 200 mesh ore which contains a considerable amount of finer material is found to have a total surface area of 7.4 m^2/g, of which 0.18 m^2 or about 2.4% represents the area present on the surface of the particles. Since the particle diameter and the total surface area are known, we must conclude that the difference in surface area between the total and calculated values resides in that area which is present in cracks, crevices, and pores in the MnO_2 particles. It is the surface area of this labyrinth that is effectively measured by the BET method. The alternative of grinding the MnO_2 to a particle size to produce a particle surface area 7.4 m^2/g is shown by Fig. 1 to require a particle diameter of 1900Å (0.19μ) or just about the limit of visibility with white light. Obviously, this particle size is not obtained nor is this method a practical or an economical procedure for commercial grinding operation.

Reaction rate values for a variety of temperatures from 21° to 50°C have been calculated from previous results (4). The relation of the total surface area to the reaction rates of the four MnO_2 samples at pH 6.5 at the above temperatures is shown in Fig. 2. A straight line relates the logarithm of the reaction rate to the logarithm of the total surface area at 45° and at 50°C. At other temperatures this relation departs significantly from a straight line. The change at the lower temperatures is caused by a large decrease in rate for the samples of lowest surface area. One important factor that should be considered is that the total surface values as measured on the individual samples of MnO_2 represent the combined surfaces of the MnO_2 itself, the Mn_2O_3, and the inert ingredients present. Since the latter can represent as much as 20% of the total weight of the sample (as may be seen from Table I), their contribution to the total surface area may be quite significant. Therefore, it is not surprising that the relation between the recuperation reaction rate and the surface area of the four samples is so complex. In view of the complexity, it appears impractical to attempt a direct correlation with actual battery test data.

Pore Spectrum of MnO_2 *Samples*

Having shown that some relationship exists between the total surface area of a depolarizer and reaction rate, it seems important to look for the reasons why. One attractive direction of study is to examine the dimensions of the pores in the MnO_2 particles which are responsible for the surface area. The pore structure of a sample of MnO_2 can be determined by established methods. The bar graph in Fig. 3 gives the distribution of the pores in a sample of electrolytic MnO_2 throughout the range of 20-600Å diameter, while the curve presents the cumulative pore volume present. When a sample of MnO_2 is exposed to a solution containing Mn^{++} under conditions where reaction [2] can occur, there is always the question as to how extensively does the reaction operate on the inside surfaces of the pores. The answer depends on many factors, including the availability of both the reaction Mn^{++} and the MnO_2 at the point of contact. One approach to this problem is to consider 1g of electrolytic MnO_2 with a total surface area of 52.8 m^2/g. If this were present as a thin flat plate of 26.4 m^2 area, its thickness could be calculated as 0.84×10^{-6} cm or 84Å. Each square centimeter of such a plate would weigh 3.78×10^{-6}g and, neglecting the minute area of the edge, it would have an exposed surface of 2 cm^2. According to reaction [2], 3.78×10^{-6}g MnO_2 would unite with 2.39×10^{-6}g Mn^{++} for complete conversion to MnOOH. This amount of Mn^{++} would be contained in a volume of 43.5×10^{-6} cc of a 1M solution which would be present in a layer 21.7×10^{-6} cm or 2170Å thick and 2 cm^2 in cross section. This rather involved calculation can be considered only a first and probably very rough approximation of the conditions present at the interface at which the MnO_2 contacts the electrolyte containing Mn^{++}. However, the result serves to emphasize one important fact. Since it requires a layer of electrolyte 2170Å thick to supply

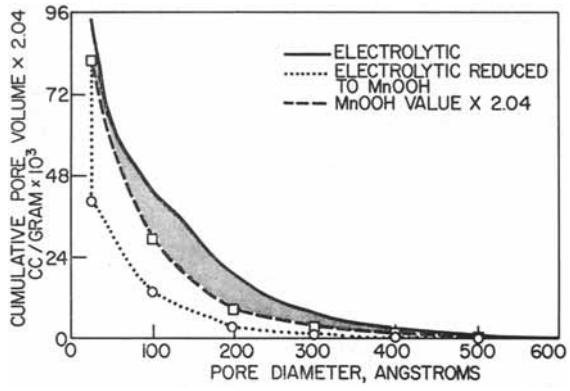

Fig. 4. Comparison of the cumulative pore volume of MnOOH and of the electrolytic manganese dioxide from which it was prepared.

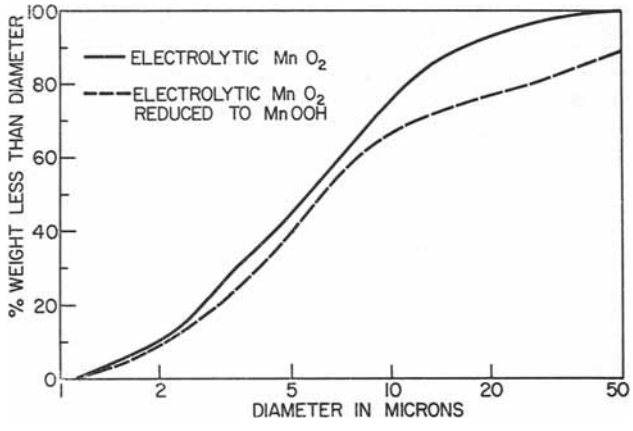

Fig. 5. Comparison of the particle size of MnOOH and of the electrolytic manganese dioxide from which it was prepared.

Mn^{++} at the initial 1M concentration to each square centimeter of MnO_2 plate or 2 cm^2 of MnO_2 surface area, it appears quite impossible to visualize any such complete reaction within the pores in the MnO_2 particle, since the pores are mostly below 400Å in diameter, and, therefore, cannot contain sufficient Mn^{++} in the initial solution absorbed for complete reduction of the MnO_2. Thus, we are forced to one or both of two conclusions: 1. the reaction between MnO_2 and Mn^{++} is initiated primarily on the outside of the particle, and 2, the reaction may occur in the pores of the MnO_2, but the replenishment of the Mn^{++} must be dependent on diffusion into the pores from the bulk of the electrolyte.

Pore Spectrum Measurements of MnOOH

To aid in assigning the proper significance to the above possibilities, some interesting evidence is provided by pore spectra determination data on electrolytic MnO_2 and on MnOOH prepared from it by the recuperation reaction. The initial value of 52.8 m^2/g obtained on the electrolytic MnO_2 is reduced to 27.4 m^2/g in a particular experimental run. According to reaction [2], 1g of the original MnO_2 thus provides 2.04g of the reaction product. Thus, the values on the cumulative pore volume curve obtained on 2.04g MnOOH should be compared with corresponding values obtained on 1g of the electrolytic MnO_2. These curves are shown in Fig. 4. The shaded area in this figure indicates the extent of the pore volume in the initial material that becomes filled with reaction product during the reduction. In the pore diameter range of 100-400Å, and even larger, from 1/3 to 1/2 of the original pore volume is filled, in general accord with the decrease in surface area cited above. This finding proves that the solution of Mn^{++} did diffuse into the pores of the MnO_2 particle to a considerable degree and deposit MnOOH therein. Microscopic examination of carefully sized particles showed that they increased in diameter during a recuperation reaction run. Particle size values were obtained on electrolytic MnO_2 and on MnOOH formed by the chemical reduction of this oxide in a recuperation test at a *p*H of 5.4 and a temperature of 43.95°C. The particle diameter distribution curves of the two materials are given in Fig. 5. From these data, it is apparent that the MnOOH particles are larger in diameter than those of electrolytic MnO_2 by an

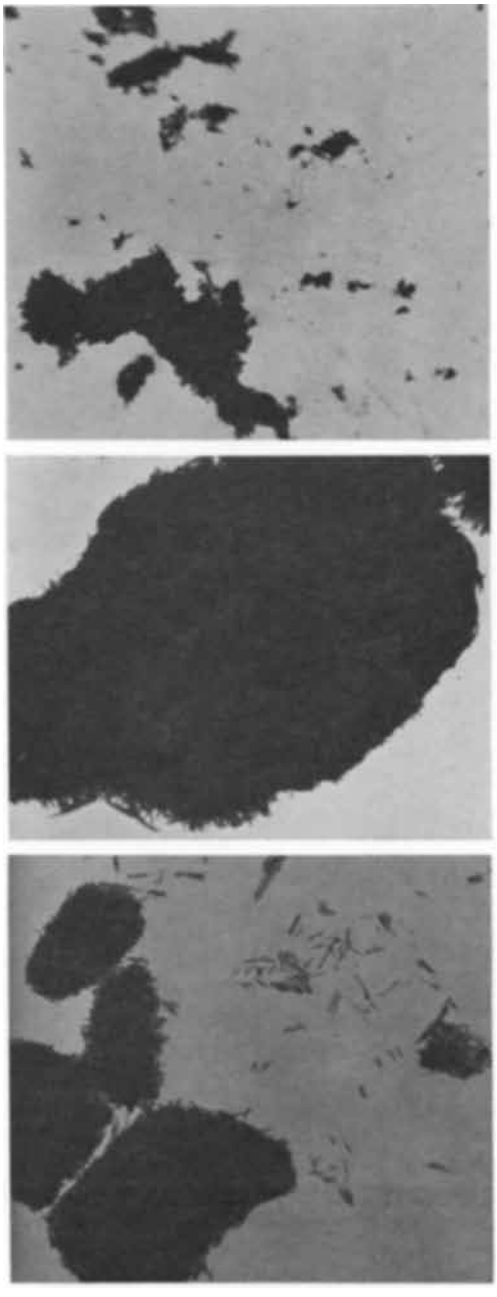

Fig. 6. Electron micrographs of electrolytic MnO_2 and MnOOH prepared therefrom. Top, Electrolytic MnO_2, magnification 7600X; center, MnOOH, magnification 6773X; bottom, MnOOH, magnification 7600X.

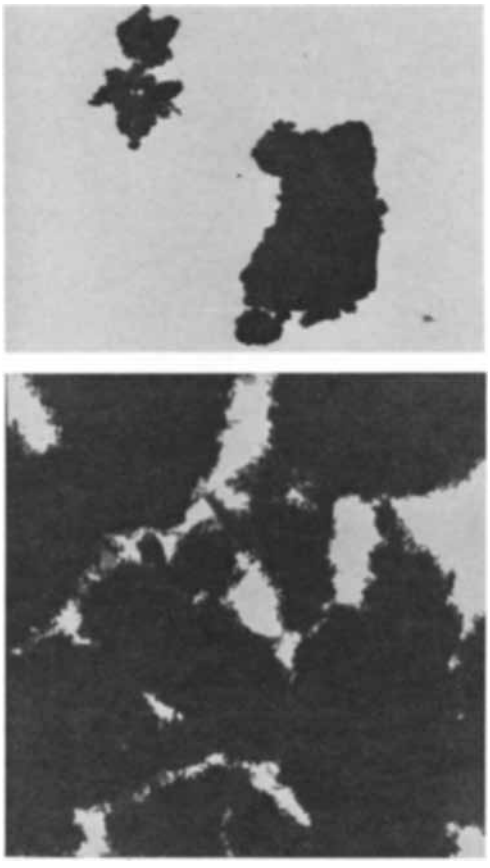

Fig. 7. Electron micrographs of african ore and the MnOOH prepared therefrom. Top, African ore, magnification 11,400X; bottom, MnOOH, magnification 11,400X.

amount varying from 0.5 to 40μ depending on the particle size fraction being considered. This finding emphatically indicates the formation of MnOOH on the external surface of the particle.

For many years, samples of cathode mix after reduction during battery discharge have been examined by all available means. Almost without exception the electron microscope pictures showed no significant characteristics that could be associated with the MnOOH present. The experiments described in this paper offered the opportunity to examine MnOOH prepared under conditions simulating battery discharge but without the carbon black present. Figures 6 and 7 show a comparison of the electron micrographs of two representative original MnO_2 samples and the MnOOH prepared from each. The electrolytic and activated MnO_2 samples (the latter not shown) were almost completely converted to MnOOH, i.e., 94.5 and 93.8%, respectively. The electron micrographs of the product from the electrolytic show in Fig. 6 characteristic rod-type particles approximately 0.4-0.6μ in length by 0.02μ in diameter. The African ore, which was reacted to only 50%, also shows in Fig. 7 the development of these rods of MnOOH on the surface of the lump is evident. In the case of the synthetic pyrolusite (not shown), which was reacted to the extent of 17% of its capacity, the beginnings of the rod formation on the MnO_2 particles are reasonably clear. The presence of the MnOOH in each of these products has been confirmed by both x-ray and electron diffraction.

Mechanism of the Recuperation Reaction

The mechanism of the recuperation reaction can now be visualized in the following manner. Under the conditions of the recuperation test the external surface of the MnO_2 particle is continually exposed to the solution of Mn^{++}. Furthermore, this solution probably enters most of the pores in the particle. The initial reaction must occur at the interface where MnO_2 and Mn^{++} meet, with the result that the product MnOOH forms at this point. Further reaction of Mn^{++} in the solution with the unreacted core of the MnO_2 particle probably occurs as the solution of Mn^{++} diffuses through the coating of MnOOH already formed on the external and pore surfaces. As shown in the electron micrographs, this layer consists of rod-shaped particles which adhere together to form a brush-heap type of layer. Since this is apparently quite porous, it probably does not slow down the diffusion process as much as though a solid barrier layer had formed. The reaction continues to proceed by diffusion of the solution of Mn^{++} through the MnOOH layer already formed with the result that the particle increases somewhat in size. In the course of this process a part of the pores in the initial particle becomes filled with MnOOH, thus reducing the internal surface area and establishing that diffusion does carry Mn^{++} into the pores of the MnO_2 particle to a considerable degree. Although the layer of MnOOH on the outside of the particle appears to consist of a myriad of rods of measurable size, the surface area actually found on the MnOOH product is considerably smaller (27.4 m^2/g) than that calculated for the equivalent amount of rods (48.4 m^2/g). Thus the interior of the MnOOH particle must be of a considerably denser structure than the external surface. We recognize that these conditions are analogous to, yet distinctly different, from those found in Leclanché cells during discharge. On this account, it becomes difficult to apply these findings more than a limited extent to practical applications.

Conclusions

From the data presented, it is apparent that the surface area of the sample of manganese dioxide, in the range studied, plays an important role in controlling the reaction rate between MnO_2 and Mn^{++}. It also appears significant that the recuperation rate of manganese dioxide samples of four different allotropic forms can be correlated with the surface areas which they possess. These findings suggest that some of the previous ideas on the importance of crystal structure may be explained, at least in part, by the surface area properties.

The pore structures of powdered samples of manganese dioxide and MnOOH are introduced in an effort to explore further the mechanism of the reaction between the solid MnO_2 and dissolved Mn^{++} to give a solid MnOOH product. The finding that the pore volume of the original MnO_2 particles is reduced to approximately half this level by conversion to MnOOH is supported by the observed reduction in the pore volume of approximately 1/3 to 1/2 in the pore diameter range of 100-400Å. This observation establishes that the recuperation

reaction occurred within these pores and proves that diffusion of electrolyte containing Mn^{++} is of considerable importance. Of equal significance is that the particles increase in size, and the product formed on the external surface is rod-shaped units of MnOOH. Thus the reaction site encompasses both the external surface of the particle and a considerable amount of the internal area of the pores.

The reaction conditions used in this work simulate those in a Leclanché cell during discharge but they differ in important aspects, *e.g.*, the concentration of the Mn^{++} used. On this account, these results should not be applied to battery problems without due consideration being given to the differences present.

Acknowledgment

The authors wish to acknowledge the contributions of the following individuals: R. S. Johnson for the experimental preparations used in this study; S. W. Glass for the pore spectra and surface area measurements; J. T. West for the Micromerograph and particle surface area data; and Richard Sprague for the electron microscope studies.

Manuscript received Nov. 28, 1960; revised manuscript received Sept. 25, 1961. This paper was prepared for delivery before the Houston Meeting, Oct. 9-13, 1960.

Any discussion of this paper will appear in a Discussion Section to be published in the December 1962 JOURNAL.

REFERENCES

1. O. D'Agostino, *Ricerca Sci.*, **9**, 1, 195 (1938).
2. N. C. Cahoon, *Trans. Electrochem. Soc.*, **68**, 177 (1935).
3. N. C. Cahoon, *This Journal*, **99**, 343 (1952).
4. M. P. Korver, R. S. Johnson, and N. C. Cahoon, *ibid.*, **107**, 7, 587 (1960).
5. N. C. Cahoon, *Trans. Electrochem. Soc.*, **92**, 159 (1947).
6. C. Drotschmann, *Chem. Ztg.*, **56**, 234 (1932); *C. A.*, **26**, 3734 (1932).
7. H. F. McMurdie, *Trans. Electrochem. Soc.*, **86**, 346 (1944).
8. H. F. McMurdie, *ibid.*, **86**, 313 (1944).
9. J. A. Lee, *J. (and Trans.) Electrochem. Soc.*, **95**, 2P (1949).
10. C. F. Burgess, U.S. Pat. 1,305,250, June 3, 1919.
11. M. L. Kaplan, U.S. Pat. 1,287,041 (1917); A. L. Fox, *et al.*, U.S. Bureau of Mines Tech. Paper No. 674, (1945).
12. F. S. Eadie and R. E. Payne, *Iron Age*, **174**, 10, 99 (1954).
13. S. Brunnauer, P. H. Emmett, and E. Teller, *J. Am. Chem. Soc.*, **60**, 309 (1938).
14. E. P. Barrett, L. G. Joyner, and P. P. Halenda, *ibid.*, **73**, 373 (1951).
15. N. C. Cahoon, R. S. Johnson, and M. P. Korver, *This Journal*, **105**, 296 (1958).
16. W. Buser and P. Graf, *Helv. Chim. Acta*, **38**, 810 (1955).
17. A. Kozawa, *This Journal*, **106**, 79 (1959).
18. W. C. Vosburgh, *ibid.*, **106**, 839 (1959).
19. J. Euler, *Electrochemica Acta*, **4**, 27 (1961).

Hydrogen Absorption by Zircaloy-2 and Some Other Alloys during Corrosion in Steam

B. Cox

Chemistry Division, United Kingdom Atomic Energy Authority, Atomic Energy Research Establishment, Harwell, Didcot, Berkshire, England

ABSTRACT

Results for hydrogen uptake by Zircaloy-2 during corrosion in steam are presented. The hydrogen absorption curve consists of three regions: in the first, covering the growth of the interference-color oxide film, about 30-50% of the hydrogen released by the corrosion reaction is absorbed; in the second, hydrogen absorption falls to a low value; and in the third, following the transition in the oxidation kinetics, it rises to 80-100% of the hydrogen released by the corrosion reaction during this period. A mechanism for the hydrogen absorption is offered based on the differing oxidation mechanisms in these three periods. The hydrogen absorption behavior of other alloys is similar for those alloys which show oxidation kinetics similar to Zircaloy-2.

It is known (1) that zirconium and its alloys absorb hydrogen during corrosion in water and steam. The amount of hydrogen absorbed usually is expressed as a fraction of the hydrogen released by the corrosion reaction (2-7). To assess the possibility of embrittlement of the metal by this hydrogen, it is the over-all hydrogen concentration in the metal which is important. In most instances the proposed service life is much longer than the longest experiments, and in order to extrapolate from these experiments the rate of hydrogen absorption, and not the integrated hydrogen content, is required. Data presented as the fraction of the corrosion hydrogen which has been absorbed at any point conceal variations in the instantaneous rate of absorption which may occur during the corrosion process.

Some recent results have been presented as the increase in weight of oxygen per unit area of surface versus the concentration of hydrogen in the

reaction occurred within these pores and proves that diffusion of electrolyte containing Mn^{++} is of considerable importance. Of equal significance is that the particles increase in size, and the product formed on the external surface is rod-shaped units of MnOOH. Thus the reaction site encompasses both the external surface of the particle and a considerable amount of the internal area of the pores.

The reaction conditions used in this work simulate those in a Leclanché cell during discharge but they differ in important aspects, *e.g.*, the concentration of the Mn^{++} used. On this account, these results should not be applied to battery problems without due consideration being given to the differences present.

Acknowledgment

The authors wish to acknowledge the contributions of the following individuals: R. S. Johnson for the experimental preparations used in this study; S. W. Glass for the pore spectra and surface area measurements; J. T. West for the Micromerograph and particle surface area data; and Richard Sprague for the electron microscope studies.

Manuscript received Nov. 28, 1960; revised manuscript received Sept. 25, 1961. This paper was prepared for delivery before the Houston Meeting, Oct. 9-13, 1960.

Any discussion of this paper will appear in a Discussion Section to be published in the December 1962 JOURNAL.

REFERENCES

1. O. D'Agostino, *Ricerca Sci.*, **9**, 1, 195 (1938).
2. N. C. Cahoon, *Trans. Electrochem. Soc.*, **68**, 177 (1935).
3. N. C. Cahoon, *This Journal*, **99**, 343 (1952).
4. M. P. Korver, R. S. Johnson, and N. C. Cahoon, *ibid.*, **107**, 7, 587 (1960).
5. N. C. Cahoon, *Trans. Electrochem. Soc.*, **92**, 159 (1947).
6. C. Drotschmann, *Chem. Ztg.*, **56**, 234 (1932); *C. A.*, **26**, 3734 (1932).
7. H. F. McMurdie, *Trans. Electrochem. Soc.*, **86**, 346 (1944).
8. H. F. McMurdie, *ibid.*, **86**, 313 (1944).
9. J. A. Lee, *J. (and Trans.) Electrochem. Soc.*, **95**, 2P (1949).
10. C. F. Burgess, U.S. Pat. 1,305,250, June 3, 1919.
11. M. L. Kaplan, U.S. Pat. 1,287,041 (1917); A. L. Fox, *et al.*, U.S. Bureau of Mines Tech. Paper No. 674, (1945).
12. F. S. Eadie and R. E. Payne, *Iron Age*, **174**, 10, 99 (1954).
13. S. Brunnauer, P. H. Emmett, and E. Teller, *J. Am. Chem. Soc.*, **60**, 309 (1938).
14. E. P. Barrett, L. G. Joyner, and P. P. Halenda, *ibid.*, **73**, 373 (1951).
15. N. C. Cahoon, R. S. Johnson, and M. P. Korver, *This Journal*, **105**, 296 (1958).
16. W. Buser and P. Graf, *Helv. Chim. Acta*, **38**, 810 (1955).
17. A. Kozawa, *This Journal*, **106**, 79 (1959).
18. W. C. Vosburgh, *ibid.*, **106**, 839 (1959).
19. J. Euler, *Electrochemica Acta*, **4**, 27 (1961).

Hydrogen Absorption by Zircaloy-2 and Some Other Alloys during Corrosion in Steam

B. Cox

Chemistry Division, United Kingdom Atomic Energy Authority, Atomic Energy Research Establishment, Harwell, Didcot, Berkshire, England

ABSTRACT

Results for hydrogen uptake by Zircaloy-2 during corrosion in steam are presented. The hydrogen absorption curve consists of three regions: in the first, covering the growth of the interference-color oxide film, about 30-50% of the hydrogen released by the corrosion reaction is absorbed; in the second, hydrogen absorption falls to a low value; and in the third, following the transition in the oxidation kinetics, it rises to 80-100% of the hydrogen released by the corrosion reaction during this period. A mechanism for the hydrogen absorption is offered based on the differing oxidation mechanisms in these three periods. The hydrogen absorption behavior of other alloys is similar for those alloys which show oxidation kinetics similar to Zircaloy-2.

It is known (1) that zirconium and its alloys absorb hydrogen during corrosion in water and steam. The amount of hydrogen absorbed usually is expressed as a fraction of the hydrogen released by the corrosion reaction (2-7). To assess the possibility of embrittlement of the metal by this hydrogen, it is the over-all hydrogen concentration in the metal which is important. In most instances the proposed service life is much longer than the longest experiments, and in order to extrapolate from these experiments the rate of hydrogen absorption, and not the integrated hydrogen content, is required. Data presented as the fraction of the corrosion hydrogen which has been absorbed at any point conceal variations in the instantaneous rate of absorption which may occur during the corrosion process.

Some recent results have been presented as the increase in weight of oxygen per unit area of surface versus the concentration of hydrogen in the

Table I. Analyses of Zircaloy-2 (Billet Z8006)

N_2 ppm	120
H_2 ppm	29 ± 1
O_2 ppm	—
Hf ppm	710
Al ppm	175
Ti ppm	75
Pb ppm	20
Si ppm	35
Co ppm	<10
W ppm	<10
Sn wt %	1.55
Fe wt %	0.172
Cr wt %	0.138
Ni wt %	0.057

specimen, and apparently lie on a straight line passing through the origin (8). This method of presentation is only valid where all the data are obtained on specimens of identical size. A preferable method is to plot both oxygen and hydrogen absorption as weight increases per unit area of surface. On such a plot the rate of hydrogen absorption can be assessed readily. When existing information (4) is plotted in this form the rate of hydrogen absorption in steam shows a sharp increase near the transition in the oxidation kinetics. The failure of other investigators to observe this appears to have been due only partly to the method of presenting results; the low total corrosion of specimens in some of the other studies probably has contributed also.

In the present work the hydrogen absorption curve for Zircaloy-2 is studied in greater detail, and an explanation of its features is proposed.

Experimental

Work was restricted initially to one billet of Zircaloy-2 (Z8006), available as sheet of 0.030 and 0.100 in. thickness. Its analysis is given in Table I. Specimens from the 0.030 in. sheet were used primarily to minimize the analytical scatter at low hydrogen contents. The blank hydrogen content was obtained on unoxidized corrosion specimens.

The specimens, approximately 3 x 1 cm, were abraded to 3/0 emery and pickled in nitric/hydrofluoric acid. They were corroded in steam at 1 atm pressure and 300°-600°C. The oxidation was carried out in the circulating steam loops described previously (9). The steam flow was maintained at a rate which prevented diffusion of air or hydrogen from the corrosion reaction back into the reaction chamber.

A further atmospheric pressure steam loop was built in which gases could be added to the steam on the inlet side of the furnace. The flow of these gases was determined at room temperature, using a "Rotameter." The steam flow rate was measured by the syphoning time of a known volume of condensate in the return arm of the loop. The values of these flow rates were adjusted to give approximately 50% by volume of the added gas at the temperature of the specimens. Additions of oxygen, air, nitrogen, ozonized air, hydrogen and nitric acid vapor were made at 500°C. Because of the short lifetime of O_3 at 500°C, ozonized air also was used at 350°C.

Some experiments, in water vapor at 1 cm pressure, on Sartorius "electrono" vacuum microbalances are reported, where the specimens subsequently have been analyzed for hydrogen content.

Hydrogen analyses were performed initially on specimens from which the oxide film had been removed. Difficulties in calculating the weight of the residual metal core in specimens showing high weight gains dictated a change to an analysis of specimens which still bore their oxide film. No change in the hydrogen uptake curves at high weight gains resulted from this change in procedure.

Results

The oxidation data from experiments in 1 atm steam are shown in Fig. 1-3. Hydrogen uptake by these specimens is shown in Fig. 4 and 5. The experimental weight gains in Fig. 1-3 have been corrected for the weight of hydrogen in the specimen before plotting in Fig. 4 and 5. The effect on the oxidation of Zircaloy-2 of gases added to the steam is shown in Fig. 6, and the hydrogen absorbed during these experiments in Fig. 7. Results obtained at 1 cm pressure are shown in Fig. 8 and 10 and the corresponding hydrogen contents in Fig. 9. Results for hydrogen uptake by Zircaloy-3 and a Zr-2% Nb-0.5% Sn alloy are shown in Fig. 11-13.

Discussion

The oxidation kinetics of Zircaloy-2 (billet Z8006) agree well with other work (11) and with our own work on other Zircaloy-2 billets. At temperatures of 500°C and above this billet shows shorter times to transition than some other billets. The signifi-

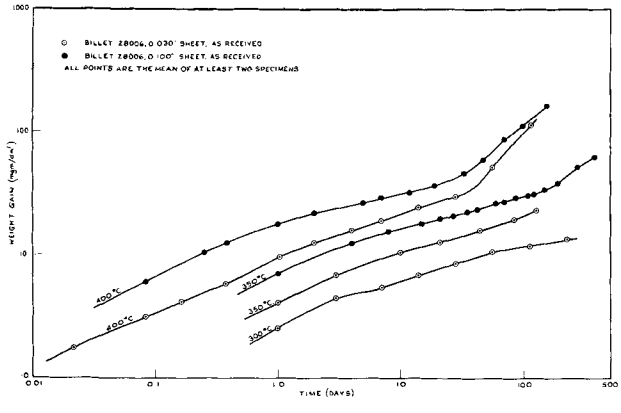

Fig. 1. Oxidation of Zircaloy-2 (billet Z8006) in steam at 300°-400°C, 1 atm pressure.

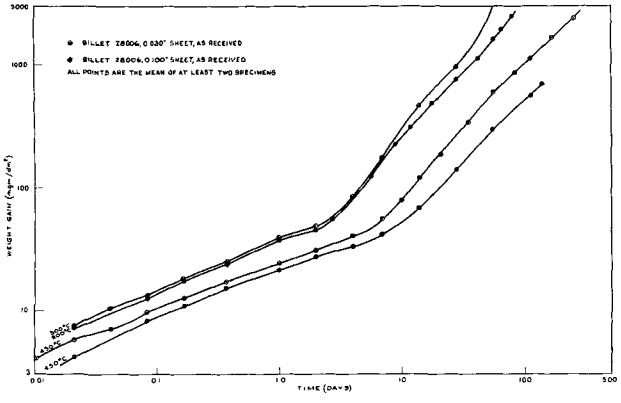

Fig. 2. Oxidation of Zircaloy-2 (billet Z8006) in steam at 450° and 500°C, 1 atm pressure.

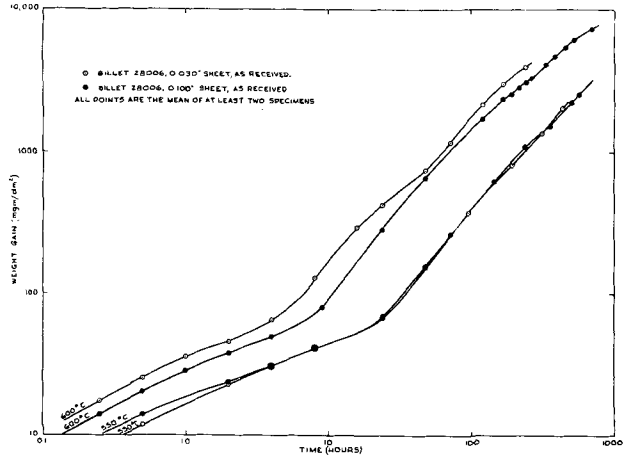

Fig. 3. Oxidation of Zircaloy-2 (billet Z8006) in steam at 550° and 600°C, 1 atm pressure.

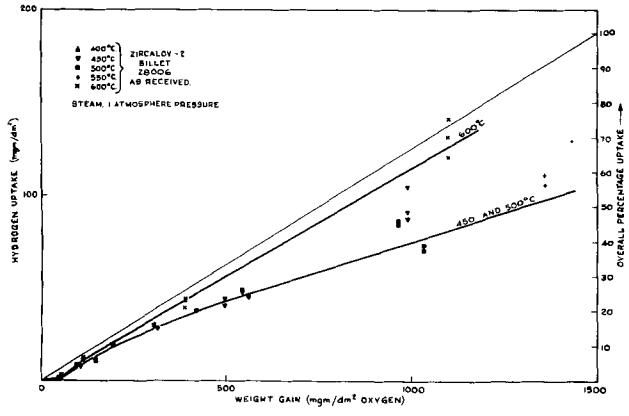

Fig. 4. Hydrogen uptake by Zircaloy-2 (billet Z8006) during oxidation in steam.

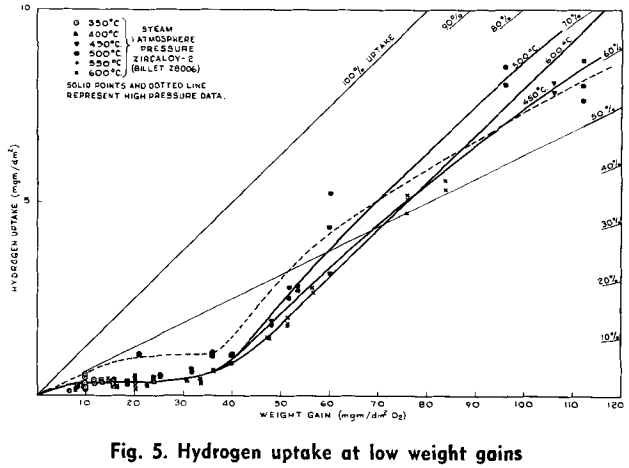

Fig. 5. Hydrogen uptake at low weight gains

cance of such small differences and of those between samples from the 0.030 and 0.100 in. sheets are not discussed here.

The curve for hydrogen uptake by Zircaloy-2 (Fig. 5) can be divided into three regions:

1. Region A covers the initial oxidation up to a weight gain of 8-10 mg/dm², where the oxide film is still showing interference colors;

2. Region B covers the oxidation from the end of region A up to the transition in the oxidation kinetics, during which a plateau in the hydrogen absorption curve is found;

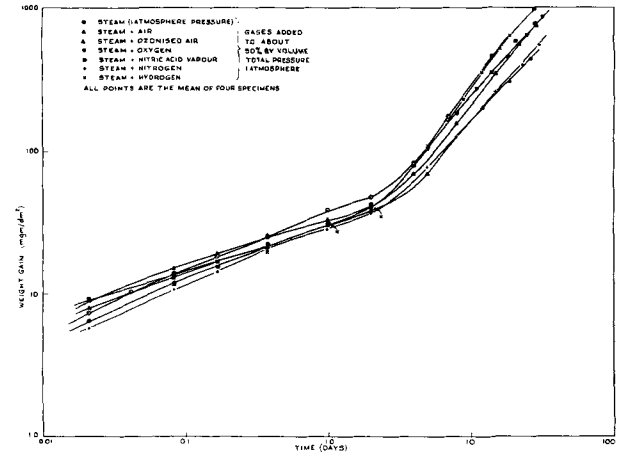

Fig. 6. Effect of added gases on the corrosion of Zircaloy-2 (billet Z8006) in steam.

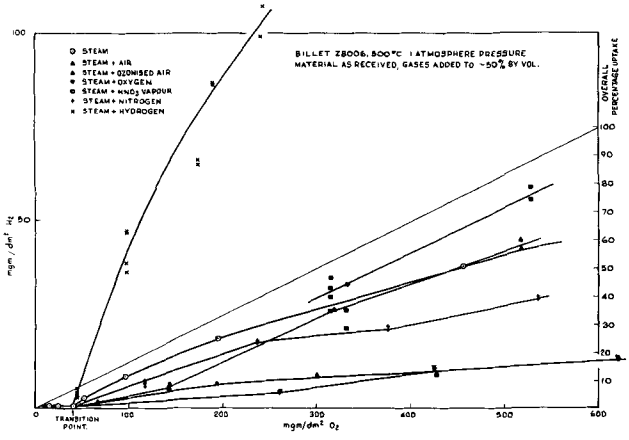

Fig. 7. Hydrogen uptake in steam plus added gases

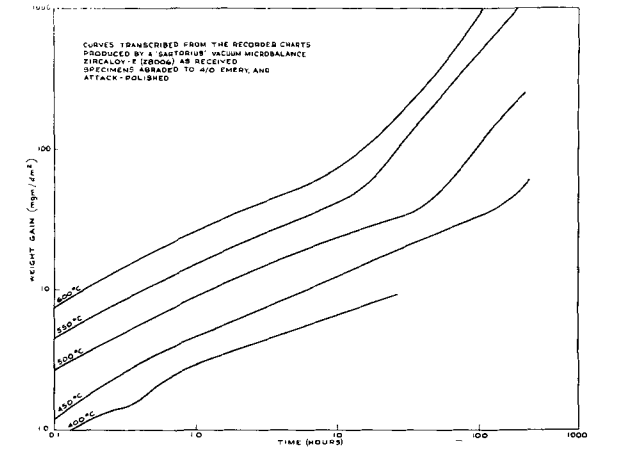

Fig. 8. Oxidation curves for Zircaloy-2 (Z8006) at 1.5 cm pressure in water vapor.

3. Region C commences near the transition in the oxidation kinetics and is marked by a rate of uptake close to 100%, in the early stages, falling to around 50% at high weight gains.

Oxidation Mechanism

Since the rate of hydrogen absorption changes along the oxidation curve, some knowledge of the oxidation mechanism in the above regions is needed before any interpretation of the hydrogen uptake curve is possible. The mechanisms, proposed in

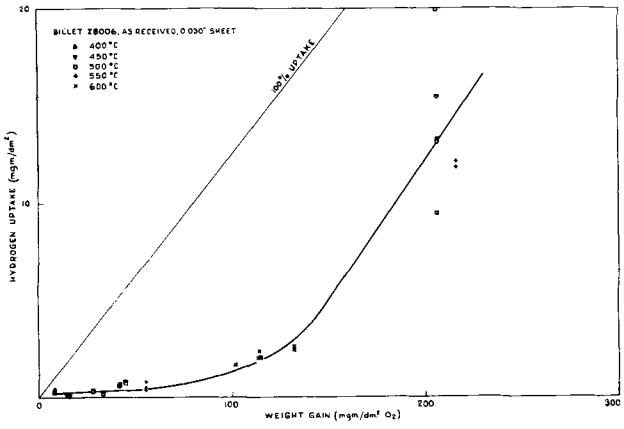

Fig. 9. Hydrogen uptake during oxidation in water vapor at 1.5 cm pressure.

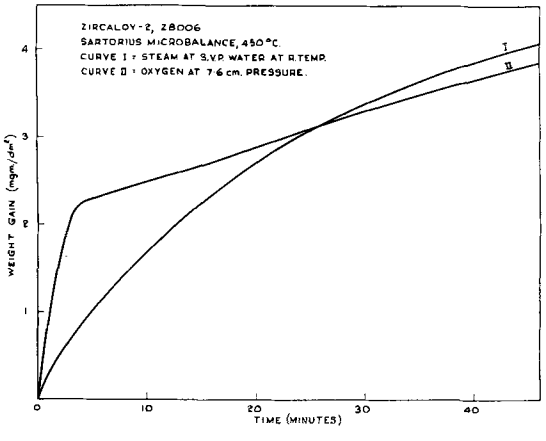

Fig. 10. Initial oxidation rates in steam and oxygen

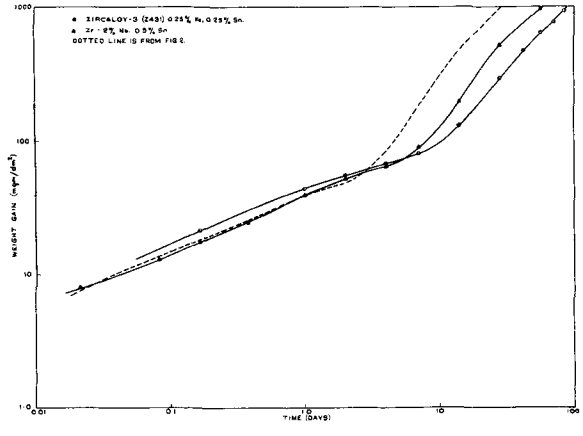

Fig. 11. Oxidation of Zircaloy-3 and Zr-2% Nb-1% Sn in steam at 500°C, 1 atm.

earlier reports, to explain these regions are recapitulated briefly:

1. Region A covers the growth of the interference-color oxide film which is thought to grow by transport of reactants down the potential gradient in the thin film, rather than by diffusion of reactants down a vacancy gradient. The rate law obeyed in the initial stages was thought to be logarithmic (12, 14).

2. Region B commences close to the point where the electric field has decreased until growth by the above mechanism is negligible. The transport of reactants by diffusion down easy paths in the oxide is thought to provide the principal method for film

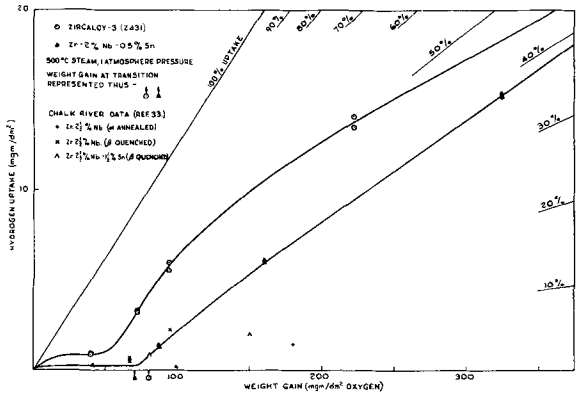

Fig. 12. Hydrogen uptake by Zircaloy-3 and Zr-2% Nb-0.5% Sn at low weight gains.

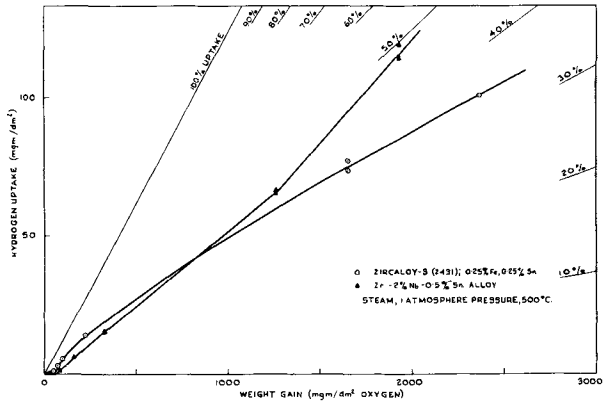

Fig. 13. Hydrogen uptake by Zircaloy-3 and Zr-2% Nb-0.5% Sn at high weight gains.

growth here. Transport through the uniform film continues in parallel with this mechanism. In Zircaloy-2 the easy paths for transport of reactant are distributed relatively uniformly and are thought to be associated with the oxidation of the intermetallic particles in the alloy and with grain boundaries in the metal. During this period the oxide film formed in region A persists as a surface layer (15) and the black film formed in region B grows underneath it.

3. Region C corresponds to the post-transition period of oxidation, where the black oxide film, formed in region B, is thought to have cracked due to stresses set up during its growth (13, 14). A decrease in the incidence of cracking (visible on the electron microscope), with increasing temperature of oxidation (16), suggests that cracking of the oxide film may be an effect of porosity, generated in some other manner, rather than its cause.

Hydrogen Uptake in Region A

If the rate of growth of the thin oxide film is determined by the electric field set up, then the process may be analogous to the growth of an anodic oxide film. The driving force would be provided by the chemical affinity of zirconium for oxygen. The rapid increase in the thickness of the anodic film, formed at a constant potential, with increasing temperature above 200°C (20) makes possible the growth of oxide films several thousand Ångstroms thick at the low potential available. Possible mechanisms by which hydrogen can pass through such a film are: (*a*) by the transport of OH′ ions through

the oxide under the influence of the applied field; and (*b*) by diffusion of the hydrogen down pores in the oxide film.

If the first mechanism applies then the hydrogen uptake should be approximately 50% of the theoretical yield, and higher values should not be possible. If the second mechanism holds, then hydrogen absorption in this region would not be restricted to 50% of that theoretically available, and addition of excess hydrogen to the system should result in increases in the rate of uptake. We have little knowledge of the physical nature of these thin films formed at high temperatures; however, it is known that anodic oxide films show variable porosity depending on the conditions of formation and on alloy composition (21-26).

Our results show that no points occur above the 50% line in this region (Fig. 5), and that no increase in uptake results from the addition of hydrogen to the steam (prior to the transition in the oxidation kinetics). These results support mechanism (*a*) and differences in the initial oxidation rates in oxygen and water vapor provide possible additional evidence for this mechanism for hydrogen uptake in region A (Fig. 10).

In water containing oxygen, with and without the addition of copper sulfate (4, 19), and in copper and cadmium sulfate solutions not containing oxygen (27), zero hydrogen uptake has been observed in this region. This may be evidence for the second mechanism, although it is possible that the reaction in sulfate solutions is with adsorbed sulfate ion and not with adsorbed water molecules. Variations with pressure in the amount of hydrogen absorbed in region A (Fig. 5 and 9) also suggest that microporosity in the oxide film may be partly responsible for hydrogen uptake here.

Specimens anodized at room temperature in N-H_2SO_4, N-$NaHSO_4$, and N-NaOH showed no increase in hydrogen content and did not resolve the above difference. Boyle and Kisiel's results in high-pressure steam plus hydrogen (37) support mechanism (*a*) for the uptake of hydrogen in this region, and it is considered that this mechanism is responsible for most of the hydrogen which enters the metal. Varying porosity of the oxide film, under varying conditions of formation, probably accounts for the apparent discrepancy between results obtained in steam and in water.

Hydrogen Uptake in Region B

In the previous section we have concluded that, in steam, access of hydrogen to the metal via porosity in the oxide film is unimportant. Capacitance measurements show that the oxide film or Zircaloy-2 is apparently porous before the transition point is reached. It seems probable, therefore, that there are some pores present in the oxide film during region B. Since the amount of hydrogen absorbed by the metal is unaffected by additions to the gas phase, these pores do not influence the absorption of hydrogen, prior to the transition in the oxidation kinetics.

During region B the electric field in the oxide is insufficient to transport ions through the film at a significant rate, and diffusion is the rate-controlling process. The hydrogen released in the oxidation reaction will probably be liberated first at surface sites. The probability of its recombining and being released as molecular hydrogen, before it can diffuse down the pores present is likely to be high. The observation of a plateau in the hydrogen uptake curve during region B, and the failure of oxygen and hydrogen additions to the gas to affect uptake prior to transition, can probably be explained on this basis.

In water there is some evidence, from the preceding section, that porosity in the oxide film plays a more significant part in the hydrogen uptake process. That high hydrogen uptakes, in water with added hydrogen, and the converse, with added oxygen, are found in region B (19) as well as in region A therefore is not surprising. There is no evidence for a threshold weight gain for increased hydrogen uptake, but there are indications of a threshold hydrogen concentration for increased absorption (19). The apparent discrepancy between Westinghouse data, in water containing a high concentration of hydrogen (1, 2, 29), and results obtained elsewhere (7, 36), with lower concentrations of hydrogen in solution, may be explained on this basis.

Hydrogen Uptake in Region C

In this region the oxide film is almost certainly porous, although at temperatures above 500°C it is not visibly cracked. The high percentage uptake is probably due to the release of the hydrogen at the bottoms of the pores. The hydrogen then may be unable to diffuse out of the pore, against the flow of the incoming reactants, before being absorbed by the metal. An initial rate of absorption, apparently greater than 100%, is not thought to result from hydrogen accumulating in the gas stream, but remains unexplained.

If the above mechanism for hydrogen absorption applies in region C, then a variation in the experimental conditions which increases the lifetime of the hydrogen atom at the bottom of the pore should increase the proportion of the available hydrogen which is absorbed by the metal. Adsorption on surfaces sites is a necessary preliminary to absorption by the metal, and the lifetime in such a state might be changed by the addition of gases to the steam which would compete for the surface sites. Additions of hydrogen to the steam would be expected to give increased absorption under these conditions, and additions of oxygen (either by surface recombination with the hydrogen or by competition) should reduce the amount of hydrogen absorbed. This is found to be the case (Fig. 7). The effect of nitrogen additions to the steam suggests that both recombination on the surface and competition for the surface sites are participating in the process. Additions of air, ozonized air, and nitric acid vapor result in hydrogen uptake curves not inconsistent with the above hypothesis.

In water vapor at 1 cm pressure the rate of hydrogen absorption, after the transition in the oxidation rate, is lower than at atmospheric pressure (Fig. 9), although it eventually rises to a rate of about 100%. The effect of pressure on the behavior in re-

gion C may result from a decrease with pressure in the ease of adsorption of hydrogen on surface sites.

Other Alloys

Data on other alloys are generally not sufficient to permit a treatment similar to that above. Discussion of the effect of alloying additions on hydrogen uptake, based on the over-all percentage, uptake at different points in the oxidation curve, is obviously invalid. In only a few instances is it possible to draw any conclusions.

Low-nickel alloys.—Hydrogen uptake by the low-nickel alloys, derived from Zircaloy-2 by removing the nickel (Zircaloy-4) and replacing it with the equivalent amount of iron (iron-replaced Zircaloy-4), has been reported (8, 30). The results were presented as the weight increase of oxygen versus the concentration of hydrogen. In other reports a low over-all percentage hydrogen uptake is quoted for alloys of the same type (31, 32). The highest weight gains in these experiments were not large, compared with the weight gain at the transition point, and any change in the rate of hydrogen absorption at the transition point may have been obscured.

Our results for Zircaloy-3 (0.25% Fe, 0.25% Sn, low-nickel) are illustrated in Fig. 11-13 and show an increased rate of hydrogen absorption following the transition in the oxidation kinetics. The maximum rate of absorption in region C is 70%, falling to about 30% at high weight gains. Thus estimates of the total hydrogen absorbed by low-nickel alloys, based on extrapolation of the results for regions A and B, are likely to be seriously in error.

Low-niobium zirconium-based alloys.—Zirconium alloys, containing 1-5 w/o Nb, are also reported to show low over-all percentage uptakes (33-35). Replotting some of these data (33) (Fig. 12) reveals evidence for an increase in the rate of uptake near the transition point in the oxidation curve. Results obtained here on a Zr-2% Nb-0.5% Sn alloy show that the rate of hydrogen absorption (in region C) is about 50% for this alloy (Fig. 11-13). Hence, extrapolation of the hydrogen content, on the basis of the low hydrogen uptake in regions A and B, would again lead to serious errors.

The relative merits of these alloys, for service in steam, may be assessed from the total hydrogen absorbed after corrosion for a given time. In Fig. 14 the hydrogen uptake by Zircaloy-2, Zircaloy-3, and the

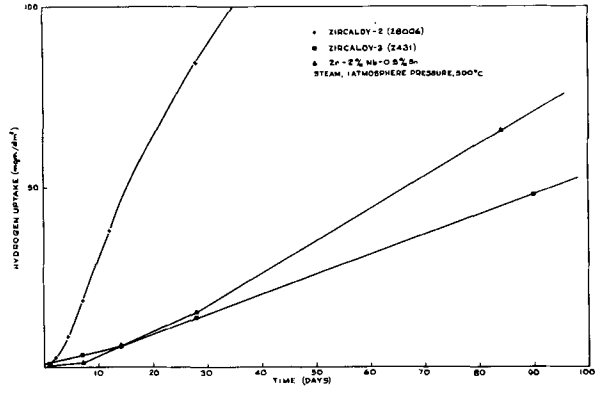

Fig. 14. Comparison of hydrogen absorbed by Zircaloy-2, Zircaloy-3, and Zr-2% Nb-0.5% Sn vs. time.

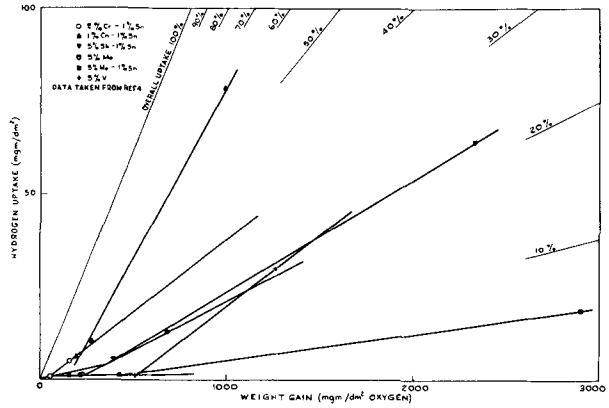

Fig. 15. Hydrogen uptake by some miscellaneous zirconium alloys

Zr-2% Nb-0.5% Sn alloy is plotted against time. Zircaloy-2 is seen to be inferior to the other two alloys (by a factor of ~7); and Zircaloy-3 is superior to the niobium alloy at long times The hydrogen contents of all three alloys at any time (in region C) will be higher than those calculated by the extrapolation of the pretransition data. Since, in practice, most calculations have used the (supposedly) conservative figure of 100% hydrogen uptake in estimating the service life of zirconium alloy components the conclusions reached in them are not invalidated by the work reported here.

Some earlier results (4) for other alloy systems have been replotted in Fig. 15. These show that insofar as a comparison of data obtained under different conditions is valid, increases in the rate of hydrogen absorption in region C are general. The final rates of absorption vary considerably with the alloying addition.

Conclusions

From this study of hydrogen-absorption by Zircaloy-2 it is concluded that the mechanism of absorption changes during the course of oxidation in steam. The processes taking place can be explained by considering the behavior in three regions of the oxidation curve:

1. Region A terminates with the disappearance of the interference-color oxide film. During this period transport of OH' ions through the oxide, under the influence of the electric field, provides the mechanism for the entry of hydrogen. Hydrogen absorption greater than 50% of that theoretically possible is not observed in steam. In water, variations in the porosity of the oxide film may influence the amount of hydrogen absorbed.

2. Region B extends from the point at which the interference colors disappear up to the transition in the kinetics of oxidation. The low percentage of hydrogen absorbed in this region is probably due to the release of hydrogen atoms at surface sites. These atoms recombine to form molecular hydrogen more rapidly than they can diffuse into the oxide.

3. Region C starts near the transition in the oxidation kinetics and is marked by a sharp increase in the rate of hydrogen absorption. In this region the hydrogen released by the corrosion reaction is liberated at the bottoms of pores, rather than at the outer surface of the oxide. Thus it has an increased change of diffusing through the film at the base of

the pore, before it can recombine and diffuse out of the oxide. The addition of oxygen to the steam suppresses the increase in the rate of uptake in region C; addition of hydrogen enhances it. The accelerated uptake following hydrogen additions is not evident during the previous periods, however. Other addition to the steam give results intermediate between those given by oxygen additions and those obtained with steam alone.

The shape of the hydrogen absorption curve, observed with Zircaloy-2, is found to hold for Zircaloy-3, and a Zr-2% Nb-0.5% Sn alloy and is probably general for zirconium alloys which follow oxidation curves in steam of similar form to that of Zircaloy-2. The rate of hydrogen uptake in the post-transition region (C) varies widely with alloying addition.

Acknowledgments

The assistance of T. Johnston and P. G. Chadd in the experimental work reported here is gratefully acknowledged. The author is indebted to A. Parker and his assistants at Woolwich Outstation for the hydrogen analyses. Discussions with J. N. Wanklyn, J. K. Dawson, J. H. O. Varley and with several American workers in the same field have proved valuable.

Manuscript received Feb. 20, 1961; revised manuscript received June 7, 1961.

Any discussion of this paper will appear in a Discussion Section to be published in the December 1962 JOURNAL.

REFERENCES

1. K. M. Goldman and D. E. Thomas, WAPD-MM-184 (1953).
2. G. J. Biefer, L. M. Howe, A. Sawatsky, and F. H. Krenz, CRMet-849.
3. W. E. Berry, D. A. Vaughan, and E. L. White, BMI-1380 (1959).
4. B. Cox, M. J. Davies, and A. D. Dent, AERE-621 (1959).
5. S. Lerner, D. Clark, and R. M. Lieberman, WAPD-IPC-1306 (1959).
6. W. W. Kirk, WAPD-NCE-607 (1958).
7. W. E. Berry, E. L. White, and F. W. Fink, BMI-1402 (1959).
8. W. W. Kirk, WAPD-ZH-21 (1960).
9. B. Cox and T. Johnston, AERE-R 3256 (1960).
10. E. Booth, F. J. Bryant, and A. Parker, *Analyst*, **82**, 50 (1957).
11. B. Lustman and F. Kerze, "Metallurgy of Zirconium," McGraw Hill Book Co., New York (1955).
12. B. Cox, AERE-R 2874 (1959); *Corrosion*, **16**, 380t (1960).
13. B. Cox, AERE-R 2931 (1959); *This Journal*, **108**, 23 (1961).
14. B. Cox, *Proc.* A.E.C., Euratom Conf. on Aqueous Corrosion of Reactor Materials, Oct. 1959, TID-7587
15. E. S. Sarsikov, N. T. Chebotarev, A. A. Nevzorova, and A. I. Zverkov, *Atomnaya Energiya*, **5**, 550 (1958.)
16. B. Cox, Unpublished data.
17. J. N. Wanklyn, *Proc.* 3me Colloque de Metallurgie, Saclay, p. 127 (1959).
18. D. R. Silvester and J. N. Wanklyn, AERE-R 3103 (1959).
19. B. Lustman, Personal communication.
20. R. D. Misch, ANL-6149 (1960).
21. A. Charlesby, AERE M/R 1014 (1952); *Acta Met.*, **1**, 340 (1953).
22. F. Keller, M. S. Hunter, and D. L. Robinson, *This Journal*, **100**, 411 (1953).
23. G. B. Adams, P. van Rysselberghe, and M. Maraghini, *ibid.*, **102**, 502 (1955).
24. M. Maraghini, G. B. Adams, and P. van Rysselberghe, *ibid.*, **101**, 400 (1954); AECU-2797 (1953).
25. G. B. Adams, M. Maraghini, T. S. Lee, and P. van Rysselberghe, AECU-3058 (1956).
26. L. Young, *Trans. Faraday Soc.*, **55**, 842 (1959).
27. R. D. Misch, Personal communication.
28. W. Yeniscavitch, R. A. Wolfe, and R. M. Lieberman, WAPD-T-912 (1958).
29. W. Yeniscavitch, R. A. Wolfe, and R. M. Lieberman, *J. Nucl. Materials*, **3**, 271 (1959).
30. W. W. Kirk, WAPD-ZH-24 (1960).
31. S. Kass and W. W. Kirk, WAPD-ZH-15 (1959).
32. S. Kass, *This Journal*, **107**, 594 (1960).
33. S. B. Dalgaard, CrMet 911 (1960).
34. D. L. Douglass and B. E. Dearing, KAPL-2071 (1960).
35. H. H. Klepfer, GEAP-3462 (1960).
36. D. W. Shannon, HW-55460 (1958).
37. R. F. Boyle and T. J. Kisiel, WAPD-BT-10 (1959).

Electrical Properties of Evaporated Aluminum Oxide Films

E. M. DaSilva and P. White

Thomas J. Watson Research Center, International Business Machines Corporation, Yorktown Heights, New York

ABSTRACT

Insulating films of aluminum oxide have been prepared by evaporation of aluminum in a partial pressure of 10^{-3} mm Hg of oxygen. On exposure to air both dielectric constant and dissipation factor increase to values similar to those observed for anodized films on bulk aluminum. The results can be understood if the initial insulating film is a suboxide similar to the postulated AlO which is normally unstable at room temperature in air or oxygen, decomposing to Al_2O_3.

In recent years anodic oxidation of metal surfaces has been a popular method of preparing thin film capacitors, and the techniques of anodizing various metals have been extensively investigated (1). The oxide dielectric films formed by these methods are generally in the thickness range of 200-500Å and appear to have comparatively high breakdown voltages.

More recently, a tantalum oxide capacitor has been prepared by sputtering tantalum in an inert

the pore, before it can recombine and diffuse out of the oxide. The addition of oxygen to the steam suppresses the increase in the rate of uptake in region C; addition of hydrogen enhances it. The accelerated uptake following hydrogen additions is not evident during the previous periods, however. Other addition to the steam give results intermediate between those given by oxygen additions and those obtained with steam alone.

The shape of the hydrogen absorption curve, observed with Zircaloy-2, is found to hold for Zircaloy-3, and a Zr-2% Nb-0.5% Sn alloy and is probably general for zirconium alloys which follow oxidation curves in steam of similar form to that of Zircaloy-2. The rate of hydrogen uptake in the post-transition region (C) varies widely with alloying addition.

Acknowledgments

The assistance of T. Johnston and P. G. Chadd in the experimental work reported here is gratefully acknowledged. The author is indebted to A. Parker and his assistants at Woolwich Outstation for the hydrogen analyses. Discussions with J. N. Wanklyn, J. K. Dawson, J. H. O. Varley and with several American workers in the same field have proved valuable.

Manuscript received Feb. 20, 1961; revised manuscript received June 7, 1961.

Any discussion of this paper will appear in a Discussion Section to be published in the December 1962 JOURNAL.

REFERENCES

1. K. M. Goldman and D. E. Thomas, WAPD-MM-184 (1953).
2. G. J. Biefer, L. M. Howe, A. Sawatsky, and F. H. Krenz, CRMet-849.
3. W. E. Berry, D. A. Vaughan, and E. L. White, BMI-1380 (1959).
4. B. Cox, M. J. Davies, and A. D. Dent, AERE-621 (1959).
5. S. Lerner, D. Clark, and R. M. Lieberman, WAPD-IPC-1306 (1959).
6. W. W. Kirk, WAPD-NCE-607 (1958).
7. W. E. Berry, E. L. White, and F. W. Fink, BMI-1402 (1959).
8. W. W. Kirk, WAPD-ZH-21 (1960).
9. B. Cox and T. Johnston, AERE-R 3256 (1960).
10. E. Booth, F. J. Bryant, and A. Parker, *Analyst*, **82**, 50 (1957).
11. B. Lustman and F. Kerze, "Metallurgy of Zirconium," McGraw Hill Book Co., New York (1955).
12. B. Cox, AERE-R 2874 (1959); *Corrosion*, **16**, 380t (1960).
13. B. Cox, AERE-R 2931 (1959); *This Journal*, **108**, 23 (1961).
14. B. Cox, *Proc.* A.E.C., Euratom Conf. on Aqueous Corrosion of Reactor Materials, Oct. 1959, TID-7587
15. E. S. Sarsikov, N. T. Chebotarev, A. A. Nevzorova, and A. I. Zverkov, *Atomnaya Energiya*, **5**, 550 (1958.)
16. B. Cox, Unpublished data.
17. J. N. Wanklyn, *Proc.* 3me Colloque de Metallurgie, Saclay, p. 127 (1959).
18. D. R. Silvester and J. N. Wanklyn, AERE-R 3103 (1959).
19. B. Lustman, Personal communication.
20. R. D. Misch, ANL-6149 (1960).
21. A. Charlesby, AERE M/R 1014 (1952); *Acta Met.*, **1**, 340 (1953).
22. F. Keller, M. S. Hunter, and D. L. Robinson, *This Journal*, **100**, 411 (1953).
23. G. B. Adams, P. van Rysselberghe, and M. Maraghini, *ibid.*, **102**, 502 (1955).
24. M. Maraghini, G. B. Adams, and P. van Rysselberghe, *ibid.*, **101**, 400 (1954); AECU-2797 (1953).
25. G. B. Adams, M. Maraghini, T. S. Lee, and P. van Rysselberghe, AECU-3058 (1956).
26. L. Young, *Trans. Faraday Soc.*, **55**, 842 (1959).
27. R. D. Misch, Personal communication.
28. W. Yeniscavitch, R. A. Wolfe, and R. M. Lieberman, WAPD-T-912 (1958).
29. W. Yeniscavitch, R. A. Wolfe, and R. M. Lieberman, *J. Nucl. Materials*, **3**, 271 (1959).
30. W. W. Kirk, WAPD-ZH-24 (1960).
31. S. Kass and W. W. Kirk, WAPD-ZH-15 (1959).
32. S. Kass, *This Journal*, **107**, 594 (1960).
33. S. B. Dalgaard, CrMet 911 (1960).
34. D. L. Douglass and B. E. Dearing, KAPL-2071 (1960).
35. H. H. Klepfer, GEAP-3462 (1960).
36. D. W. Shannon, HW-55460 (1958).
37. R. F. Boyle and T. J. Kisiel, WAPD-BT-10 (1959).

Electrical Properties of Evaporated Aluminum Oxide Films

E. M. DaSilva and P. White

Thomas J. Watson Research Center, International Business Machines Corporation, Yorktown Heights, New York

ABSTRACT

Insulating films of aluminum oxide have been prepared by evaporation of aluminum in a partial pressure of 10^{-3} mm Hg of oxygen. On exposure to air both dielectric constant and dissipation factor increase to values similar to those observed for anodized films on bulk aluminum. The results can be understood if the initial insulating film is a suboxide similar to the postulated AlO which is normally unstable at room temperature in air or oxygen, decomposing to Al_2O_3.

In recent years anodic oxidation of metal surfaces has been a popular method of preparing thin film capacitors, and the techniques of anodizing various metals have been extensively investigated (1). The oxide dielectric films formed by these methods are generally in the thickness range of 200-500Å and appear to have comparatively high breakdown voltages.

More recently, a tantalum oxide capacitor has been prepared by sputtering tantalum in an inert

gas atmosphere containing partial pressures of oxygen in the 1μ range (2). These capacitors have similar physical properties to those prepared by anodization. Attempts have been made to prepare metal oxide coatings by evaporating metals in pressures of oxygen in the 10-0.1μ range (3). These coatings are reported to have high mechanical strength and excellent optical properties, but no data exist on the electrical properties of oxides prepared in this manner.

This paper describes the preparation and electrical characteristics of aluminum oxide capacitors made up of thin films of aluminum oxide which were deposited between aluminum electrodes by evaporation techniques. The oxide dielectric was prepared by evaporation of aluminum in an oxygen atmosphere. The values of dielectric constant and dissipation factor of these films have been measured under a variety of conditions and are compared with the electrical properties of aluminum oxide films formed by anodization.

Experimental

There are two possible methods of preparing oxide films using evaporation techniques. The first of these, the direct evaporation of the bulk oxide, is difficult. Most metal oxides require relatively high temperatures for evaporation and often dissociate at or below this temperature. Products of this dissociation can then result in the contamination of the deposited layer. This method was not attempted. The second method is the evaporation of the metal in an oxygen atmosphere. Three possible mechanisms have been postulated for the oxide formation: (a) oxidation of the newly formed metal layer; (b) gas phase collisions between metal vapor and oxygen molecules; and (c) the formation of a suboxide on the source which, if sufficiently volatile, may evaporate. It has been reported (3) that tantalum oxide can be evaporated by mechanism (c). The films used in this study were prepared by the second method, but it was not determined which of the three mechanisms of oxide was operative.

Initially, experiments were performed to determine the resistivity of films evaporated from an aluminum source in various partial pressures of oxygen in the range 10^{-3} to 10^{-5} mm Hg. The pressure was controlled to $\pm 10\%$ by bleeding oxygen into the system through a needle valve and was measured on an ionization gauge mounted on the base plate of the belljar. In addition to controlling oxygen pressure in the system it was desirable to control the evaporation rate of the aluminum. This was not always possible since the presence of oxygen gas caused partial oxidation of the source. In general, three distinct types of film were obtained depending on the oxygen pressure and the evaporation rate of aluminum. Films deposited in an oxygen pressure range of 10^{-5} mm Hg were essentially metallic in appearance and had a low resistance. As the evaporation rate was decreased and the oxygen pressure increased, the resistivity of the film increased. Films deposited in an oxygen pressure of 1×10^{-3} mm Hg at a rate of 1-5 Å/sec exhibited the characteristics of an insulator having a resistivity of about 10^{14} ohm cm. Experimental results are summarized in Table I. The dielectric films for the capacitors discussed in this paper were prepared at low evaporation rates, 1-5 Å/sec, in an oxygen pressure of about 1×10^{-3} mm Hg.

All evaporations were carried out in an oil diffusion pumped high-vacuum belljar system capable of ultimate pressures in the low 10^{-5} mm Hg range. Inside the belljar, provision was made for two sources, each with a separate shutter for preliminary outgassing, arranged so that there was no contamination of one source by the other. Figure 1 illustrates this arrangement. Capacitors were made on a microscope slide by positioning a mask of the appropriate configuration in front of the slide for each of the three evaporations; first metal electrode, dielectric, and second metal electrode. Figure 2 shows the typical configuration of capacitors prepared. The metal electrodes were evaporated in a pattern such that contact was made with a silver painted area on the microscope slide. Copper wires previously soldered to these silvered areas were brought through the base plate of the belljar system and allowed the capacitor to be tested in vacuum in the belljar immediately after preparation.

Sinusoidal shaped sources constructed from stranded tungsten wire were used for evaporation of both pure metal and oxide dielectric. Two separate evaporations were required from the source used for preparation of the metal electrodes. Therefore, a large quantity of aluminum, approximately 0.5g, was

Table I. Resistivity of aluminum films deposited in various partial pressures of oxygen

Film No.	Average deposition rate, Å/sec	Pressure, mm Hg	Resistivity, ohm-cm	Appearance
7	50	4×10^{-5}	2.6×10^{-4}	Bright Metal
10	20	7×10^{-4}	1×10^{-1}	Black
19	1-5	1×10^{-3}	$>10^{14}$	Transparent

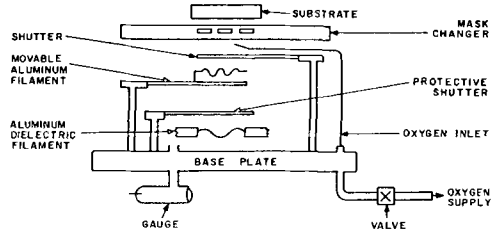

Fig. 1. Experimental assembly

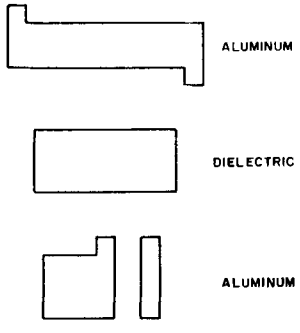

Fig. 2. Configuration of capacitors

distributed among the loops of the source. To achieve the evaporation rate control necessary for the preparation of the oxide dielectric, only one loop of the source was loaded with approximately 0.1g of aluminum. In this way the current input to the source was more stable, since deterioration of the filament was limited to the single loop containing the charge.

The preheat procedure for raising the aluminum charge to evaporating temperature was the same for each source. The temperature of the tungsten wire support was gradually increased within a 15-20 min period to 900°C in order to achieve some outgassing of the charge prior to the filament wetting. At this temperature aluminum was deposited at 15-20 Å/sec on a substrate placed 6.5 cm from the source. (During the preheat procedure the pressure increased from 1 x 10^{-5} to 6 x 10^{-5} mm Hg.) In this manner, metal electrodes, 5000Å thick, were deposited on the substrate.

The oxide dielectric film was prepared by raising the source temperature to 900°C and opening the oxygen leak valve to increase the pressure in the belljar from 6 x 10^{-5} to 1 x 10^{-3} mm Hg. At all times the pressure was maintained above 8 x 10^{-4} mm Hg. Under these conditions the source life was 8-10 min. Using this procedure, the rate of deposition of oxide film was between 0.5 and 1.0 Å/sec with a source-to-substrate distance of 17 cm.

Measurements of capacitance and dissipation factor of the test devices were made at 0.6, 1, and 2 kc, using a G.R. 716-C capacitance bridge. A signal of 1.5 v could be applied to the films at room temperature without adverse effects. Capacitance measurements were accurate to ±1% while dissipation factor varied within ±5% over the range 0.05-0.20. Measurements were made on the film immediately after preparation in the belljar at room temperature, after exposure to air at room temperature, at 78° and at 4.2°K.

Film thicknesses were measured by an optical interferometric method with an accuracy of ±100Å.

Results

The values of dielectric constant and dissipation factor measured immediately after preparation in vacuum and after exposure to air are shown in Table II for a number of aluminum oxide dielectric films. The large percentage change in dielectric constant on exposure to air seems to be about the same for each sample within experimental error. Figure 3 shows in a little more detail the behavior of a series of films. The changes in dielectric constant and dissipation factor are expressed as percentage changes of the values measured, in 10^{-5} mm Hg, immediately after preparation of the second metal layer. The capacitors were stored in the belljar for 24 hr at 10^{-3} mm Hg of oxygen and measured again. Immediately following this, measurements were made with film exposed to 1 atm pressure of nitrogen at 23°C and then with the film exposed to 1 atm pressure of oxygen at 23°C. There appears to be good reproducibility between the measurements on the different slides. The dielectric constant changes only slightly on being stored in vacuum, remains constant on admission of nitrogen to the sample, but increases considerably on subsequent exposure to air or oxygen. This change on admission of oxygen is not as rapid as that which takes place when the film has not been exposed to nitrogen; nevertheless the final values are about the same, *i.e.*, about twice the value of the film measured in vacuum. The values of dissipation factor on the other hand initially decrease on being stored in vacuum (10^{-3} mm Hg), remain constant on admission of nitrogen and then increase by a very large factor on admission of oxygen. The final values of dissipation factor were approximately the same as in the case when nitrogen was not admitted to the belljar prior to admission of oxygen.

The temperature dependence of both dielectric constant and dissipation factor of these films are shown in Fig. 4.

Table II. Values of dielectric constant and dissipation factor measured in vacuum and in air at room temperature

Film No.	Thickness, Å	Dielectric constant In vacuum	Dielectric constant In air	Dissipation factor In vacuum	Dissipation factor In air
28	500	6.0	12.0	0.23	0.29
32	700	6.2	10.3	0.04	0.10
35_A	875	6.95	12.90	0.10	0.27
35_B	875	7.02	12.95	0.10	0.28

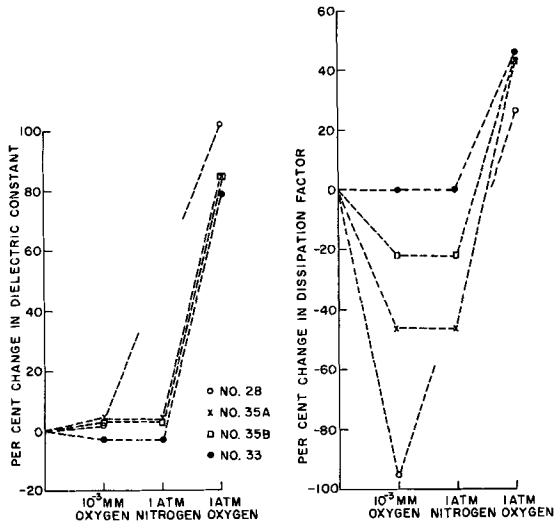

Fig. 3. Environmental dependence of dielectric constant and dissipation factor.

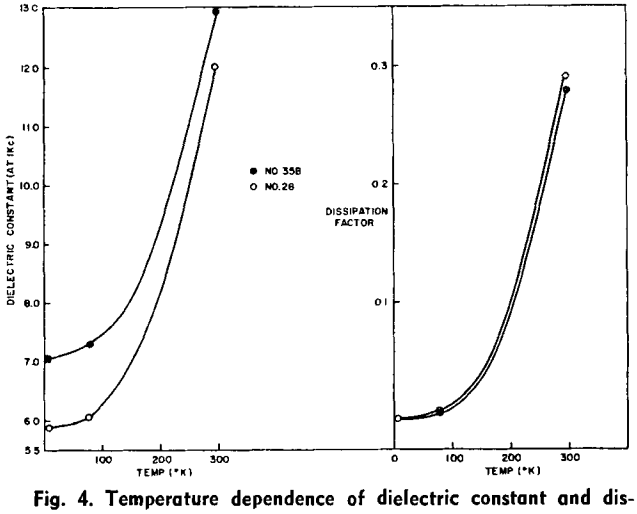

Fig. 4. Temperature dependence of dielectric constant and dissipation factor.

Discussion

After the aluminum oxide capacitor has been exposed to air, the values of dielectric constant at 1 kc and the values of the temperature variation of dielectric constant are similar to values which have been reported for anodized layers of aluminum (4). In spite of the difference between measured values of dissipation factor, it appears likely that the evaporated oxide after exposure to air is similar to bulk aluminum oxide, which has been reported to have a dielectric constant of about 11 (5). The insulating film formed by evaporation of aluminum in 10^{-8} mm Hg pressure of oxygen has a dielectric constant of about six and is apparently different from the bulk oxide.

A condition now exists in which the initial insulating film formed by evaporation in 10^{-8} mm Hg of oxygen is converted by exposure to 1 atm of oxygen gas into an insulating film having similar properties to those of the bulk oxide Al_2O_3. It may be inferred, therefore, that the film, as prepared, is a highly oxidized aluminum film with insufficient oxygen to form Al_2O_3, but which can react with excess oxygen to form a stable oxide similar to Al_2O_3. This type of behavior has been reported previously in the literature for aluminum oxide films prepared by thermal evaporation of aluminum oxide. (6). Both dielectric constant and dissipation factor of the suboxide are lower than the corresponding values of Al_2O_3. Two distinct interactions can be distinguished between oxygen and the suboxide as seen in Fig. 3: (*a*) exposure of the suboxide to pressures of 10^{-8} mm Hg of oxygen for a period of 24 hr accompanied by a slow increase in dielectric constant and a slow decrease in dissipation factor, and (*b*) exposure of the suboxide to 1 atm of oxygen accompanied by a sudden increase in both dielectric constant and dissipation factor.

The first of these is perhaps understandable in terms of an oxygen sorption mechanism. Table I shows that as the partial pressure of oxygen in the system was increased the resistance of the evaporated film increased, which was probably due to incorporation of oxygen in the aluminum lattice. Exposure of one of these films to a greater partial pressure of oxygen than that in which it was prepared, would undoubtedly lead to sorption of more oxygen with an accompanying increase in resistance similar to that observed in Table I.

If it is assumed that the change in dissipation factor caused by changes in polarization due to oxygen sorption is small, then the comparatively large decrease in dissipation factor may be related to an increase in resistivity of the suboxide. This increase in resistivity on sorption of oxygen is what might be anticipated as a result of the above discussion. Obviously, there must be a limit to this process.

It is well known that a variety of suboxides of aluminum are capable of existence, but all are unstable at room temperature in the presence of air or oxygen forming Al_2O_3. If, then, evaporation of aluminum in oxygen produces a suboxide, it might be expected that variation of oxygen pressure over a small range would cause a change similar to that observed above, but on exposure to air or oxygen a decomposition to Al_2O_3 should occur. The rate at which the decomposition takes place would be limited in this particular case by the geometry of the system since the aluminum oxide layer is covered almost completely by the aluminum electrodes.

Manuscript received May 22, 1961; revised manuscript received Sept. 19, 1961. This paper was prepared for delivery before the Indianapolis Meeting, April 30-May 3, 1961.

Any discussion of this paper will appear in a Discussion Section to be published in the December 1962 JOURNAL.

REFERENCES

1. L. Young, *Can J. Chem.*, **38**, 1141 (1960).
2. R. W. Berry and D. I. Sloan, *Proc. Inst. Radio Engrs.*, **47**, 1070 (1959).
3. W. Reichelt, U. S. Pat. 2,904,452 (1959).
4. F. Huber and W. Haas, *Proc. Inst. Radio Engrs.*, **48**, 1482 (1960).
5. A. vonHipple, "Dielectric Materials," J. Wiley & Sons, Inc., New York (1954).
6. A. R. Weinrich, U. S. Pat. 2,578,856.

Tin-Activated Magnesium Barium Pyrophosphate Phosphors

R. C. Ropp

Chemical and Metallurgical Division, Sylvania Electric Products Inc., Towanda, Pennsylvania

ABSTRACT

Although $Mg_2P_2O_7$ cannot be activated by tin, combination with $Ba_2P_2O_7$ (Ba <25 mole %) produces a very efficient phosphor, $(Mg,Ba)_2P_2O_7$:Sn, emitting at 3970Å. This last phase, combined with δ-$Ba_2P_2O_7$, forms a solid solution of limited stability, $(Ba,Mg)_2P_2O_7$:Sn, whose emission band appears at 5120Å when excited by 2537Å. A ternary phase can be formed $(Mg_{1.5}Ba_{0.5-x}Sr_x)P_2O_7$:Sn, whose ultraviolet emission peak changes with composition.

Many investigations have centered on the tin-activated orthophosphates (1, 2) and pyrophosphates (3) containing calcium, strontium, and barium, alone, or in combination. However, no tin-activated magnesium phosphate phosphors have been reported. The present work describes the preparation of the tin-activated magnesium barium pyrophosphates, their spectral characteristics, and the relationships among the members of the system. This study was part of a generic survey of phosphors emitting in the ultraviolet region of the spectrum.

Experimental Method

In general, methods of preparation and measurement of the phosphors were those described in a previous work (3). Ignition of $BaHPO_4$ and

Discussion

After the aluminum oxide capacitor has been exposed to air, the values of dielectric constant at 1 kc and the values of the temperature variation of dielectric constant are similar to values which have been reported for anodized layers of aluminum (4). In spite of the difference between measured values of dissipation factor, it appears likely that the evaporated oxide after exposure to air is similar to bulk aluminum oxide, which has been reported to have a dielectric constant of about 11 (5). The insulating film formed by evaporation of aluminum in 10^{-8} mm Hg pressure of oxygen has a dielectric constant of about six and is apparently different from the bulk oxide.

A condition now exists in which the initial insulating film formed by evaporation in 10^{-8} mm Hg of oxygen is converted by exposure to 1 atm of oxygen gas into an insulating film having similar properties to those of the bulk oxide Al_2O_3. It may be inferred, therefore, that the film, as prepared, is a highly oxidized aluminum film with insufficient oxygen to form Al_2O_3, but which can react with excess oxygen to form a stable oxide similar to Al_2O_3. This type of behavior has been reported previously in the literature for aluminum oxide films prepared by thermal evaporation of aluminum oxide. (6). Both dielectric constant and dissipation factor of the suboxide are lower than the corresponding values of Al_2O_3. Two distinct interactions can be distinguished between oxygen and the suboxide as seen in Fig. 3: (*a*) exposure of the suboxide to pressures of 10^{-8} mm Hg of oxygen for a period of 24 hr accompanied by a slow increase in dielectric constant and a slow decrease in dissipation factor, and (*b*) exposure of the suboxide to 1 atm of oxygen accompanied by a sudden increase in both dielectric constant and dissipation factor.

The first of these is perhaps understandable in terms of an oxygen sorption mechanism. Table I shows that as the partial pressure of oxygen in the system was increased the resistance of the evaporated film increased, which was probably due to incorporation of oxygen in the aluminum lattice. Exposure of one of these films to a greater partial pressure of oxygen than that in which it was prepared, would undoubtedly lead to sorption of more oxygen with an accompanying increase in resistance similar to that observed in Table I.

If it is assumed that the change in dissipation factor caused by changes in polarization due to oxygen sorption is small, then the comparatively large decrease in dissipation factor may be related to an increase in resistivity of the suboxide. This increase in resistivity on sorption of oxygen is what might be anticipated as a result of the above discussion. Obviously, there must be a limit to this process.

It is well known that a variety of suboxides of aluminum are capable of existence, but all are unstable at room temperature in the presence of air or oxygen forming Al_2O_3. If, then, evaporation of aluminum in oxygen produces a suboxide, it might be expected that variation of oxygen pressure over a small range would cause a change similar to that observed above, but on exposure to air or oxygen a decomposition to Al_2O_3 should occur. The rate at which the decomposition takes place would be limited in this particular case by the geometry of the system since the aluminum oxide layer is covered almost completely by the aluminum electrodes.

Manuscript received May 22, 1961; revised manuscript received Sept. 19, 1961. This paper was prepared for delivery before the Indianapolis Meeting, April 30-May 3, 1961.

Any discussion of this paper will appear in a Discussion Section to be published in the December 1962 JOURNAL.

REFERENCES

1. L. Young, *Can J. Chem.*, **38**, 1141 (1960).
2. R. W. Berry and D. I. Sloan, *Proc. Inst. Radio Engrs.*, **47**, 1070 (1959).
3. W. Reichelt, U. S. Pat. 2,904,452 (1959).
4. F. Huber and W. Haas, *Proc. Inst. Radio Engrs.*, **48**, 1482 (1960).
5. A. vonHipple, "Dielectric Materials," J. Wiley & Sons, Inc., New York (1954).
6. A. R. Weinrich, U. S. Pat. 2,578,856.

Tin-Activated Magnesium Barium Pyrophosphate Phosphors

R. C. Ropp

Chemical and Metallurgical Division, Sylvania Electric Products Inc., Towanda, Pennsylvania

ABSTRACT

Although $Mg_2P_2O_7$ cannot be activated by tin, combination with $Ba_2P_2O_7$ (Ba <25 mole %) produces a very efficient phosphor, $(Mg,Ba)_2P_2O_7$:Sn, emitting at 3970Å. This last phase, combined with δ-$Ba_2P_2O_7$, forms a solid solution of limited stability, $(Ba,Mg)_2P_2O_7$:Sn, whose emission band appears at 5120Å when excited by 2537Å. A ternary phase can be formed $(Mg_{1.5}Ba_{0.5-x}Sr_x)P_2O_7$:Sn, whose ultraviolet emission peak changes with composition.

Many investigations have centered on the tin-activated orthophosphates (1, 2) and pyrophosphates (3) containing calcium, strontium, and barium, alone, or in combination. However, no tin-activated magnesium phosphate phosphors have been reported. The present work describes the preparation of the tin-activated magnesium barium pyrophosphates, their spectral characteristics, and the relationships among the members of the system. This study was part of a generic survey of phosphors emitting in the ultraviolet region of the spectrum.

Experimental Method

In general, methods of preparation and measurement of the phosphors were those described in a previous work (3). Ignition of $BaHPO_4$ and

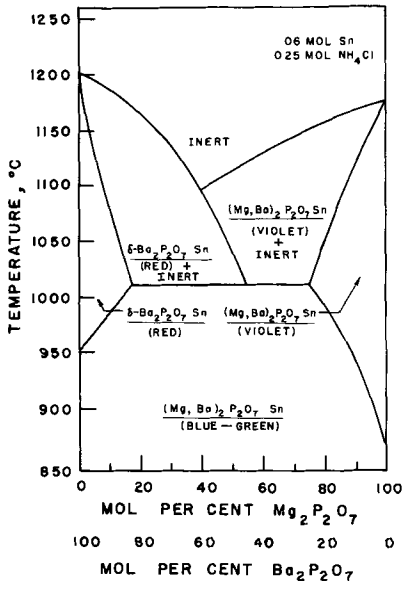

Fig. 1. Diagram of the tin-activated magnesium-barium pyrophosphate system.

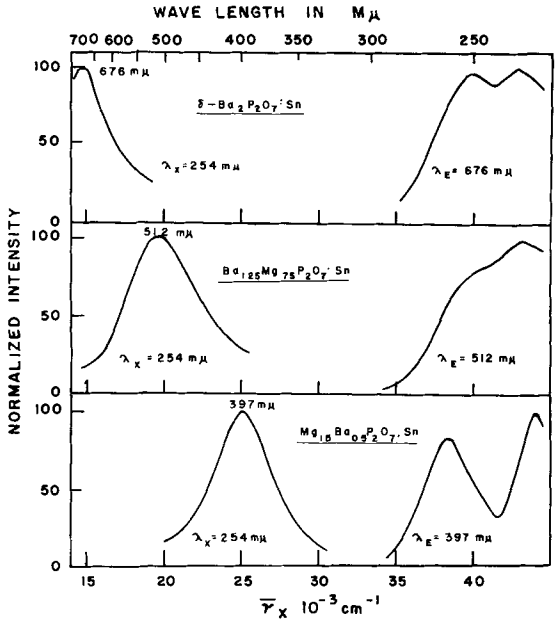

Fig. 2. Excitation-emission properties of the magnesium-barium pyrophosphates.

$MgNH_4PO_4 \cdot H_2O$ readily gave $Ba_2P_2O_7$ and $Mg_2P_2O_7$, respectively, although it was found in some cases that much brighter phosphors were obtained by utilizing the reaction:

$$2MgO + 2(NH_4)_2HPO_4 \rightarrow Mg_2P_2O_7 + 4NH_3 + 3H_2O$$

Precipitation of $BaHPO_4$ was accomplished by the addition of an aqueous solution of $(NH_4)_2HPO_4$ to a solution containing $Ba(NO_3)_2$. Both solutes were of high purity as was the solvent, water. The precipitation of $MgNH_4PO_4 \cdot H_2O$ followed the standard analytical procedure (4). In many cases, the use of NH_4Cl as a flux was found advantageous. Crystal structures were identified by x-ray powder diffraction patterns. The activator was added as SnO and concentrations between 0.01 mole Sn and 0.10 mole Sn per mole pyrophosphate did not change the luminescent properties.

Since tin functions as an activator in the reduced state, considered to be Sn^{+2}, formation of tin-activated phosphors must involve firing in a reducing atmosphere as part of the preparation process. Because excessive reduction can occur as well as undesired re-oxidation, control of the atmosphere during firing and cooling is vital.

Experimental Results

In order to define the luminescent phases present as a function of both firing temperature and composition, it was necessary to control the time of firing closely. An optimum firing time of 135 min gave maximum luminescence in most cases, as well as a single luminescent phase at a given composition.

A diagram is given in Fig. 1 outlining the regions of temperature and composition in which the luminescent phases discovered were stable. Three luminescent phases were found: a red-emitting phase whose x-ray diffraction pattern was similar to δ-$Ba_2P_2O_7$:Sn (5), a blue-green-emitting phase, $(Ba,Mg)_2P_2O_7$:Sn, whose x-ray diffraction pattern was in some respects comparable to α-$Ba_2P_2O_7$:Sn, and a violet-emitting phase, $(Mg,Ba)_2P_2O_7$:Sn. (The formulas are written so that the cation appearing first indicates that of greatest mole per cent composition.)

It was difficult to obtain a completely homogeneous blue-green-emitting phase in the presence of NH_4Cl flux unless the firing conditions were carefully controlled. Therefore, the preferred method of preparation for the blue-green phase involved prefiring in air and refiring in a reducing atmosphere (nitrogen-5% hydrogen). The red- and violet-emitting phases were more easily prepared in the presence of NH_4Cl (0.25 mole per mole pyrophosphate), which served as a flux, as well as a protective atmosphere, during firing. In the absence of flux, much higher temperatures were required to obtain the red- or violet-emitting phases.

The spectral properties of the three phases are given in Fig. 2 and are discussed below. X-ray diffraction powder patterns were employed for identification. Table I shows the *d* spacings and intensities measured for the three main lines and the innermost lines of all the phases discovered.

Table I. X-ray powder diffraction patterns of the magnesium-barium pyrophosphates

Phase	*d* spacings in A			
	Innermost	1	2	3
δ-$Ba_2P_2O_7$:Sn	5.29	3.88	2.81	2.10
$(Ba,Mg)_2P_2O_7$:Sn (blue-green)	7.10	3.72	2.99 (2.95)	2.17
$(Mg,Ba)_2P_2O_7$:Sn (violet)	7.05	6.30	3.36	3.00 (2.95)
$Mg_2P_2O_7$	6.3	3.00 (2.95)	2.52	2.10
α-$Ba_2P_2O_7$:Sn	3.6	3.56	2.13	1.94

Table II. Relative plaque brightness of the blue-green phase

Composition mole Ba	Composition mole Mg	% Plaque brightness (vs. barium titanium phosphate) Blue	Green
2.00	—	~3	~1 (estimated)
1.50	0.50	28	18
1.25	0.75	55	39
1.00	1.00	40	26
0.75	1.25	56	39
0.50	1.50	49	33

Barium-rich phases.—Only δ-$Ba_2P_2O_7$:Sn was found in barium-rich compositions when fired at 950°C or above, the minimum temperature depending on the amount of magnesium present. The luminescent properties described previously (3) include an emission band at 6760Å and excitation peaks at 2330Å and 2500Å. Although the magnesium was presumably incorporated within the lattice, as estimated by absence of lines due to MgO, $MgCO_3$ or $Mg_2P_2O_7$ in the x-ray diffraction pattern, magnesium apparently contributes little to the luminescent properties of the red-emitting phase.

The complexity of the diffraction patterns does not allow nor preclude the identification of $Mg_2P_2O_7$ as a separate phase.

The blue-green-emitting phase was stable over a wide range of composition below the critical temperature of 1010°C (see Fig. 1). The plaque response as compared to a standard phosphor is given in Table II.

The efficiency of the blue-green-emitting phase exceeded that of the low-temperature from α-$Ba_2P_2O_7$:Sn, by several-fold.

As shown in Fig. 2, $(Ba,Mg)_2P_2O_7$:Sn emits at 5120Å and has excitation peaks at 2320Å and 2520Å.

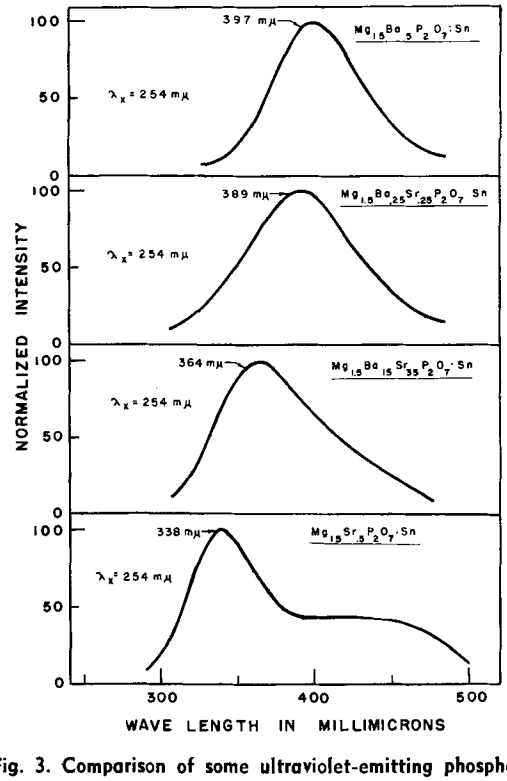

Fig. 3. Comparison of some ultraviolet-emitting phosphors

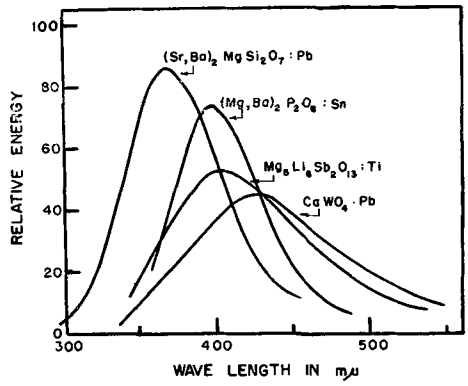

Fig. 4. Luminescent spectra of some ternary alkaline earth pyrophosphates.

The low-temperature form, α-$Ba_2P_2O_7$:Sn, which emits at 5050Å when excited by 2537Å radiation (3), is stabilized by the incorporation of magnesium, and the blue-green-emitting phase, $(Ba,Mg)_2P_2O_7$:Sn, is obtained at firing temperatures far in excess of those requisite for the low-temperature form, α-$Ba_2P_2O_7$:Sn. No difference in luminescent properties was noted between phosphors having the compositions $Ba_{1.25}Mg_{0.75}P_2O_7$:Sn and $Ba_{0.75}Mg_{1.25}P_2O_7$:Sn. However, the blue-green-emitting phase is unstable above 1010°C, and attempts to prepare the phosphor at higher temperatures always resulted in either the red-emitting phase, δ-$Ba_2P_2O_7$:Sn or the violet-emitting phase, $(Mg,Ba)_2P_2O_7$:Sn, depending on composition.

Magnesium-rich phases.—At the higher magnesium ratios, the violet-emitting phosphor was obtained. This phase emits at 3970Å, while two excitation peaks are found at 2270Å and 2600Å (see Fig. 2). In contrast, $Mg_2P_2O_7$ itself is not activated by Sn.

A comparison of the peak height response of four ultraviolet and blue-emitting phosphors to 2537Å irradiation is given in Fig. 3. The peak height of the violet-emitting phosphor is comparable to other more well-known phosphors (6, 7).

Tin content affected the emission peak only in intensity.

Ternary pyrophosphates.—The addition of Sr to the violet phosphor forms a homologous series of phosphors $Mg_{1.5}Ba_{0.5-x}Sr_xP_2O_7$:Sn, whose emission peaks change with the composition as shown in Fig. 4. Only single emission bands were found as the barium content approached zero, and no evidence for multiplicity was seen until the composition $Mg_{1.5}Sr_{0.5}P_2O_7$:Sn was reached. The emission at this point was then composed of an ultraviolet and a blue peak (3). The system $(Mg,Ba,Ca)_2P_2O_7$:Sn in contrast, shows no such effect, and only the violet emission due to $(Mg,Ba)_2P_2O_7$:Sn was seen.

Discussion

The emission colors noted in the tin-activated barium pyrophosphate-magnesium pyrophosphate system depend on the phase which is stable under the conditions of preparation. Considering each separately, it is difficult to relate one to another. The situation is further complicated by the fact that one of the end-members ($Mg_2P_2O_7$) is not activated by

tin. However, a satisfactory explanation may be given in terms of phase relationships.

The data in Fig. 1 represent a nonequilibrium diagram in which the colors and domains of stability of the phosphors are specified in terms of the optimum firing temperature and composition. However, the resemblance to a binary phase system which forms a solid solution over a limited range of composition is striking. In this case, the two phases are δ-$Ba_2P_2O_7$:Sn and $(Mg,Ba)_2P_2O_7$:Sn, which are red and violet emitters, respectively. They form a phase of limited temperature stability, $(Ba,Mg)_2P_2O_7$:Sn, whose emission lies between either parent. This phase seems to be the stable phase in the system at the lower firing temperature, but is not stable above 1010°C, decomposing to give one or the other of the parent phosphors, depending on composition. The inert or nonluminescent phase is probably a mixture of pyrophosphates, but no differences could be ascertained other than a lack of response to excitation, since the system as a whole was not at equilibrium in regard to phases present.

The violet phase is by far the most efficient of those found in the magnesium-barium pyrophosphate system. It has a single emission band in contrast to other binary tin-activated systems where in most cases two bands were found (3), and forms a ternary pyrophosphate phase whose peak emission changes with composition.

Of the known tin-activated systems, the violet phase, $(Mg,Ba)_2P_2O_7$:Sn, is the only one which emits in the 4000Å region. Strontium orthophosphate emits at 3700Å, but the intensity is low, whereas the violet phase possesses high efficiency.

Acknowledgment

The author gratefully acknowledges the assistance of Dr. C. W. W. Hoffman and T. J. Veleker for x-ray measurements and H. D. Layman and O. B. Bullock for some of the preparations.

Manuscript received June 12, 1961; revised manuscript received Aug. 16, 1961.

Any discussion of this paper will appear in a Discussion Section to be published in the December 1962 JOURNAL.

REFERENCES

1. K. H. Butler, *This Journal*, **100**, 250 (1953).
2. H. Koelmans and A. P. M. Cox, *ibid.*, **104**, 442 (1957).
3. R. C. Ropp and R. W. Mooney, *ibid.*, **107**, 15 (1960).
4. I. M. Kolthoff and E. B. Sandell, "Textbook of Quantitative Inorganic Analysis," p. 365, Macmillan Company, New York (1949).
5. P. W. Ranby, D. H. Mash, and S. T. Henderson, *Brit. J. Appl. Phys.* Supplement #4, S18 (1955).
6. R. W. Mooney, U. S. Pat. 2,865,862, Dec. 23, 1958.
7. H. A. Klasens, A. K. Hoekstra, and A. P. M. Cox, *This Journal*, **104**, 93 (1957).

Cathodoluminescent Characteristics of Mn-Activated $KMgF_3$

R. J. Kurtz[1]

Research Department, Westinghouse Electric Corporation, Bloomfield, New Jersey

ABSTRACT

The brightness, persistence, and maintenance of light output during life of cathode-ray excited $KMgF_3$:Mn phosphors were studied as a function of (*a*) Mn concentration, (*b*) K:Mg ratio, (*c*) ZnF_2 addition, and (*d*) firing conditions. The emission spectra and brightness-voltage and brightness-current characteristics of these samples are discussed. A cursory investigation of the cathodoluminescent characteristics of some other Mn-activated complex fluorides is also discussed.

Manganese-activated fluorides of zinc, magnesium, and zinc-magnesium have been investigated in the past from both practical and theoretical viewpoints. Because these fluorides are relatively long-persistence phosphors, they have been used in cathode-ray tubes for applications such as radar and loran display devices (1, 2). These phosphors have also been used by Williams (3-6) and his co-workers in the formulation of basic concepts of the luminescence process.

Other Mn-activated fluorides have, however, received scant attention. Fluorides of the alkali metals were found by Smith (7) to be poor phosphors, probably because in such phosphors there is a lack of suitable sites at which the manganese ions can function as activators. Smith further reported that attempts to prepare Mn-activated fluorides of strontium, barium, and cadmium resulted in nonluminescent samples of the first two and a weakly luminescent sample of the last. It is probable that the cations of these matrices are much too large to be replaced effectively by manganese.

Klasens (8) and his co-workers and Smith (7) have however reported on the preparation of a series of fairly efficient Mn-activated fluoride phosphors. These materials were all of the perovskite type structure. This family of phosphors has been reported (8) to have decay characteristics closely approximating those of ZnF_2:Mn and $(Zn,Mg)F_2$:Mn. Manganese-activated fluoride phosphors, however, in general display one notable disadvantage when compared to other cathodoluminescent phosphors, *i.e.*, they tend to deteriorate rapidly or "burn" during electron bombardment (9). Some of these phosphors have quite recently been found to be suitable for use in the form of transparent films for cathodolumines-

[1] Present address: Applied Research Laboratory, General Instrument Corp., Newark, N. J.

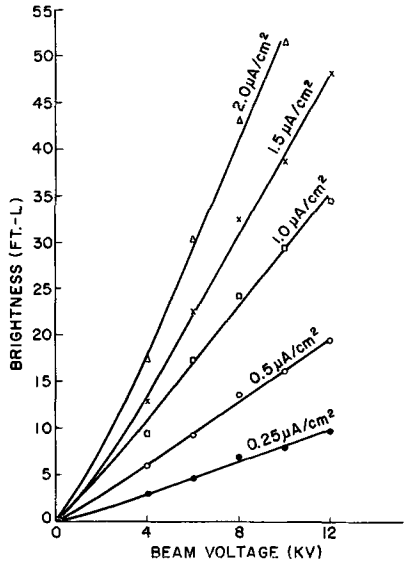

Fig. 1. Brightness-voltage characteristics for standard $KMgF_3$:Mn sample.

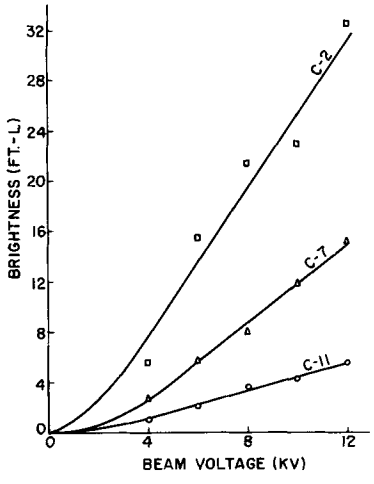

Fig. 2. Brightness-voltage characteristics for series C samples (current density = 1.0 $\mu a/cm^2$).

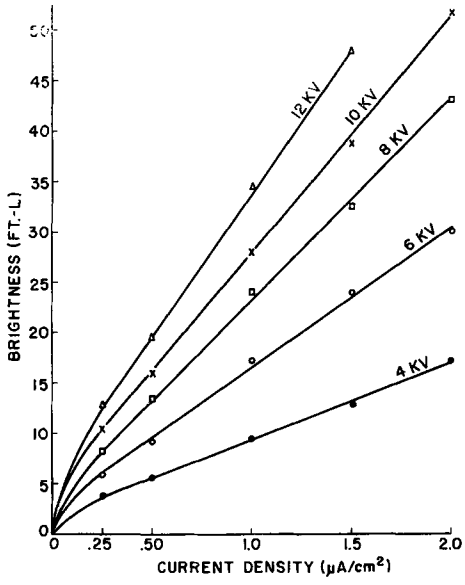

Fig. 3. Brightness-current characteristics for standard $KMgF_3$:Mn sample.

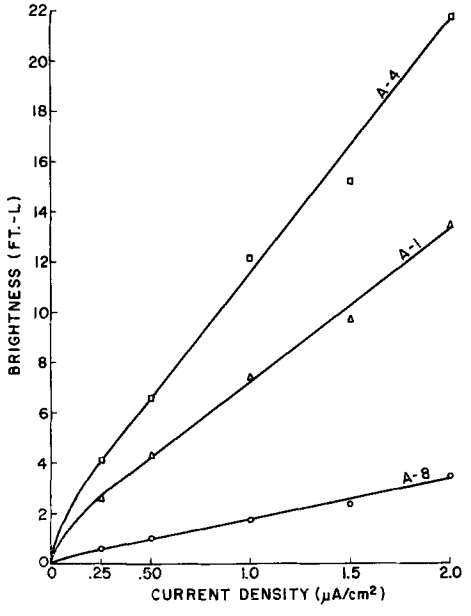

Fig. 4. Brightness-current characteristics for series A samples (beam voltage = 10 kv).

cent applications. This study of Mn-activated $KMgF_3$ is an outgrowth of work done to prepare better films of this material from the standpoint of brightness, persistence, and maintenance of light output during life.

Experimental Results

Three series of samples were prepared in order to determine the relationships between activator concentration and matrix composition and the following parameters: (*a*) brightness, (*b*) persistence, (*c*) maintenance of light output during life, (*d*) emission spectrum, (*e*) brightness-voltage characteristics, and (*f*) brightness-current characteristics. Series A samples were those in which the Mn concentration was varied, for a constant matrix composition. Series B samples were those into which small additions of ZnF_2 were introduced, at a fixed Mn concentration and at a fixed K:Mg ratio. Series C samples explored the effects of varying the K:Mg ratio for fixed Mn and ZnF_2 concentrations. (The manganese concentration, as may be noted later, is expressed in atoms Mn/atom Mg. Activator concentration expressed in this manner is probably more meaningful than weight % or mole %, for this type of compound, since manganese, in all likelihood, enters the lattice substitutionally at a Mg site.) Two additional series were also prepared to determine the effects of firing time and temperature on the aforementioned parameters.

For the preparation of each phosphor, the required quantities of the components, in the form of carbonates or fluorides, were mixed with hydrofluoric acid in platinum crucibles. The simple fluorides were then evaporated to dryness and fired in quartz tubes in a nitrogen atmosphere. For all series A, B, and C samples, firing was accomplished at 875°C for 1 hr. Following firing, each sample was ground lightly with a mortar and pestle. Preparation of the samples for examination in a demountable cathode-ray tube was done by settling a slurry of the phosphor powder onto 2 x 1 in. glass slides.

In measuring the brightness of each sample, data were taken at beam voltages from 4 to 12 kv, with

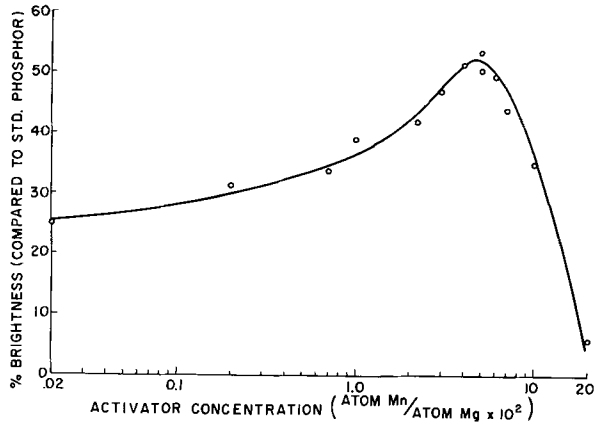

Fig. 5. Brightness as a function of Mn concentration (K:Mg = 0.79, no ZnF_2 added).

the current density ranging from 0.25-2.0 $\mu a/cm^2$. All data obtained are based on bombarded-side brightness. A commercial $KMgF_3$:Mn phosphor[2] was employed as a standard sample for brightness measurements. Brightness-voltage curves were obtained for series A, B, and C samples and also for the standard sample. Brightness-voltage relationships for the standard sample and some representative series C samples are shown in Fig. 1 and 2. Although not shown, similar curves were obtained for series A and B samples. It can be seen that for each series (and for the standard sample) the same characteristic linear relationship exists between brightness and beam voltage, except for a small "dead" voltage. From these curves we can conclude that changes in the phosphor composition do not have any effect on the screen charging properties of this material up to 12 kv. Isolated measurements up to 15 kv have also been made with no evidence of screen charging occurring.

Figures 3 and 4 show typical brightness-current density relationships obtained in measurements made on the standard sample and representative series A samples. Once again, similar relationships were observed for series B and C samples. Here it can be seen that in each series luminescence is proportional to the current density with no saturation effects observable; departure from linearity is observed, however, between zero and 0.25 $\mu a/cm^2$ and may be due to some type of current leakage in the demountable system itself.

Figure 5 presents a plot of the brightness as a function of the Mn concentration. For this series of samples no ZnF_2 was added. It is seen that the brightness reaches a maximum at 0.05 atoms Mn/atom Mg (or approximately 5 mole % with respect to $KMgF_3$) while quenching of the emission becomes pronounced at concentrations greater than 0.10 atoms Mn/atom Mg. It is interesting to note that previous investigation (10) has shown that this molar Mn concentration is close to the optimum for Mn-activated ZnS and ZnSe. Optimum brightness, however, for the other Mn-activated fluoride phosphors (10), such as ZnF_2 and MgF_2, has been found at 0.6 mole %. This apparent anomaly may be due to the fact that the lattice structure of $KMgF_3$ very closely

[2] Derby MF-767, obtained from United Mineral and Chemical Corp., New York, N. Y.

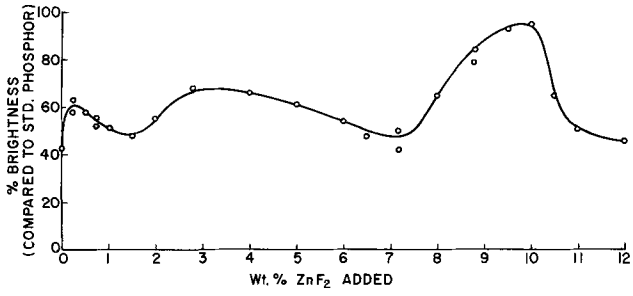

Fig. 6. Brightness as a function of ZnF_2 addition (K:Mg = 0.79, Mn:Mg = 0.026).

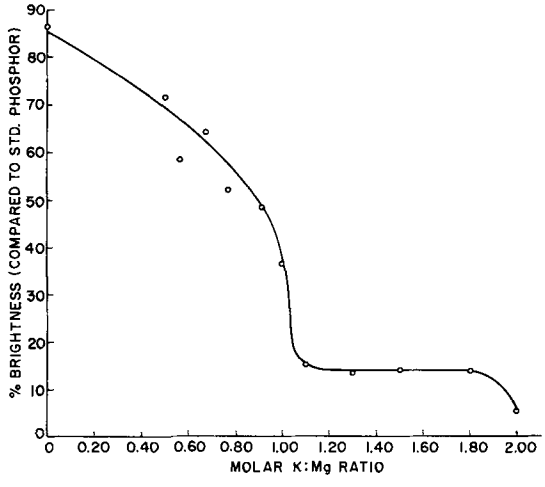

Fig. 7. Brightness as a function of K:Mg ratio (Mn:Mg = 0.026, 2.0 w/o ZnF_2 added).

resembles the cubic form of ZnS and ZnSe, while the other fluorides mentioned have tetragonal structures.

Figure 6 shows the effect on brightness of addition of ZnF_2 to the phosphor. The addition of this component to $KMgF_3$ in small quantities had been reported in the literature (11) as being beneficial in increasing the persistence. While this will be shown later to be so, here it is seen that a significant improvement in brightness also occurs as a result of such addition. The effect is marked even at low concentrations of ZnF_2, as evidenced by a substantial increase in brightness when as little as 0.25 w/o is added. The best brightness is obtained, however, in the region of 9-10 w/o. It should be noted that, although the curve in Fig. 6 displays a rather peculiar shape, the four check points plotted indicate the data to be fairly reproducible.

In Fig. 7 the effect of matrix composition on brightness is shown for a fixed Mn concentration and ZnF_2 concentration. It can be seen that maximum brightness occurs at a K:Mg ratio of zero, which, of course, corresponds to Mn-activated MgF_2. The brightness drops steadily to 43% of its maximum value at K:Mg = 1.0, remains constant at 15% for $1.1 \leq$ K:Mg ≤ 1.8, and then falls to 6% of maximum at K:Mg = 2.0. X-ray diffraction analysis of this series of samples shows the existence of $KMgF_3$ and MgF_2 in samples with molar K:Mg ratios of 0.5-1.0 and the presence of $KMgF_3$ and K_2MgF_4 at mole ratios from 1.1-2.0. Thus it seems that incorporation of Mn into an MgF_2 matrix results in more

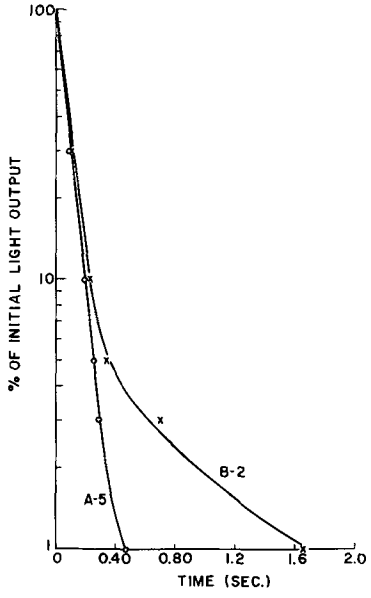

Fig. 8. Effect of ZnF_2 addition on persistence characteristics of $KMgF_3$:Mn (K:Mg = 0.79, Mn:Mg = 0.026).

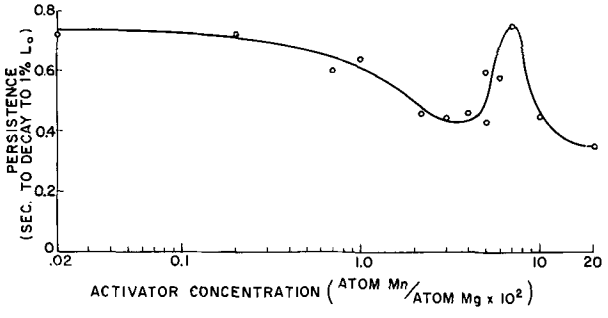

Fig. 9. Persistence characteristic as a function of Mn concentration (K:Mg = 0.79, no ZnF_2 added).

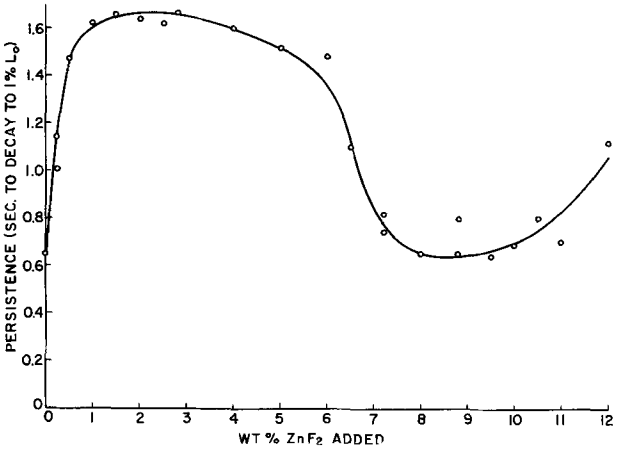

Fig. 10. Persistence characteristic as a function of ZnF_2 addition (K:Mg = 0.79, Mn:Mg = 0.026).

efficient luminescence than in $KMgF_3$, while incorporation of the Mn into K_2MgF_4 is far less efficient.

The phosphors in each series all exhibit a two-component type of decay; that is, initially the luminescence decays exponentially, then changes to a power-law type of decay. While the initial stages of the decay do not exhibit any clearly defined relationships as a result of variation of either activator concentration or matrix composition, very definite differences are discernible in the decay-tail region.

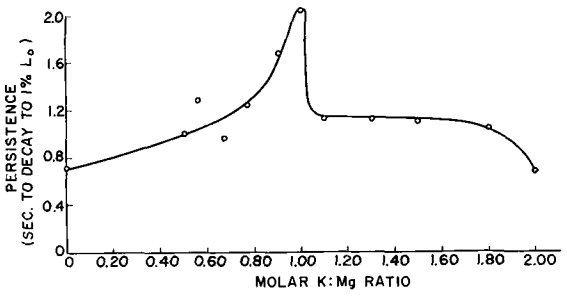

Fig. 11. Persistence characteristic as a function of K:Mg ratio (Mn:Mg = 0.026, 2.0 w/o ZnF_2 added).

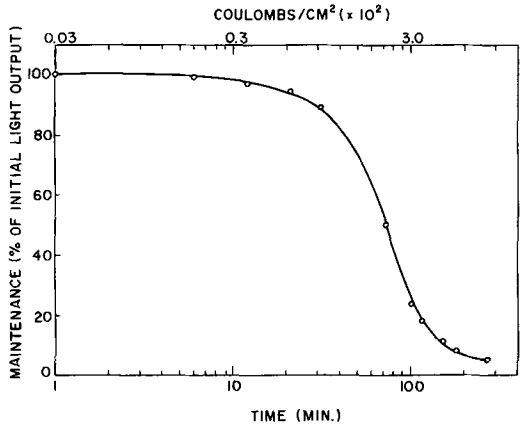

Fig. 12. Typical maintenance of light output curve for a $KMgF_3$:Mn phosphor (current density = 5.0 $\mu a/cm^2$).

The most significant difference is noted on addition of even a small per cent of ZnF_2 to the phosphor. In Fig. 8 this difference in the decay-tail characteristic of two samples is shown. Both samples have identical Mn concentration and K:Mg ratio. Sample B-2 has, however, in addition 2.8 w/o ZnF_2. Figure 9 shows the effect on the decay tail characteristic as a function of Mn concentration. Measuring the persistence as the time to decay to 1% of the initial light output, it was found that a maximum value is obtained at 0.07 atoms Mn/atom Mg. From the next curve (Fig. 10) it can be seen that an over-all improvement of the decay-tail characteristic occurs as a result of addition of varying amounts of ZnF_2 to the $KMgF_3$ matrix (11). The greatest improvement, however, occurs in the range of 0.5-6 w/o addition.

The decay-tail persistence as a function of K:Mg ratio is shown in Fig. 11. For these samples both the Mn and Zn concentrations have been held constant. Here it is seen that the persistence increases steadily to a maximum as the molar K:Mg ratio is increased from zero to 1.0. As the ratio is further increased, however, this decay-tail characteristic drops sharply and is essentially constant in the range of 1.1-1.8. A further decrease is noted as the ratio is further increased to 2.0.

Measurements of maintenance-of-light-output during life were obtained during sustained excitation of the samples in the demountable cathode-ray tube for periods of 2-3 hr at 5 $\mu a/cm^2$. The maintenance curve of a typical sample measured under these conditions is shown in Fig. 12. It seemed reasonable to use as a standard of comparison the per cent of initial light output reached after a given period of time, taking care to keep out of the regions near 0%

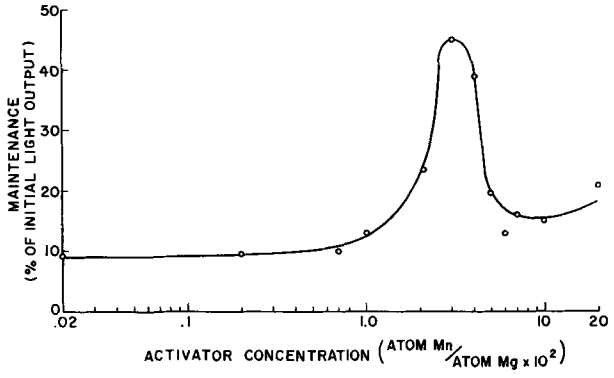

Fig. 13. Maintenance as a function of Mn concentration (K:Mg = 0.79, no ZnF_2 added).

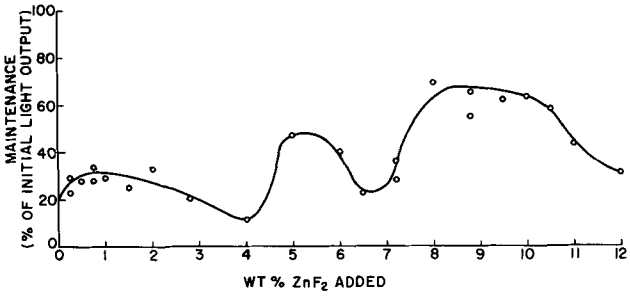

Fig. 14. Maintenance as a function of ZnF_2 addition (K:Mg = 0.79, Mn:Mg = 0.026).

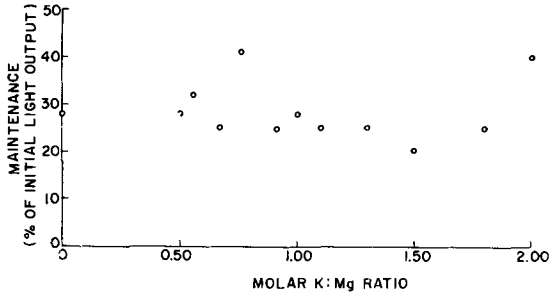

Fig. 15. Maintenance as a function of K:Mg ratio (Mn:Mg = 0.026, 2.0 w/o ZnF_2 added).

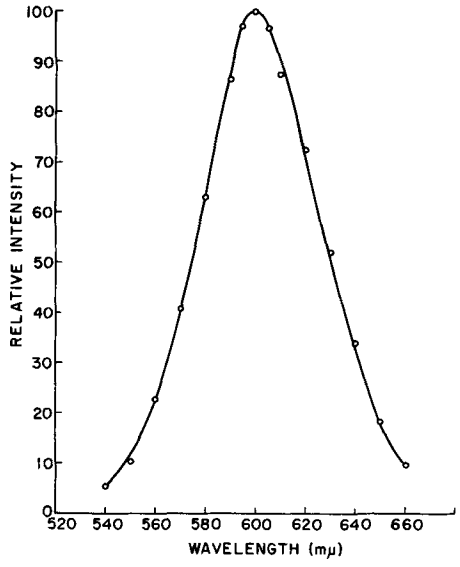

Fig. 16. Emission spectrum of typical $KMgF_3$:Mn phosphor

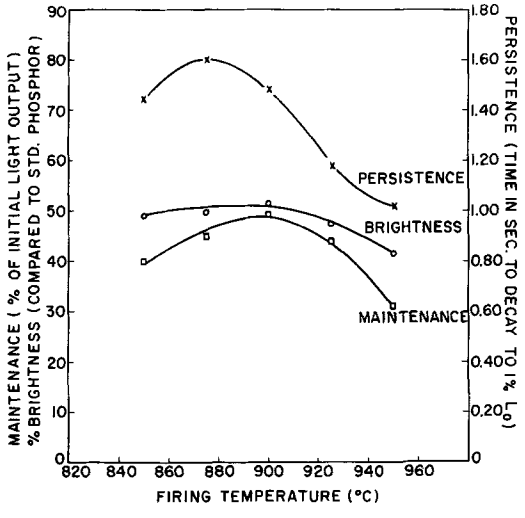

Fig. 17. Effect of firing temperature on cathodoluminescent characteristics of $KMgF_3$:Mn (firing time = 60 min; composition: K:Mg = 1.0, Mn:Mg = 0.02, 2.0 w/o ZnF_2 added).

and 100% of initial output. The figure of 100 min, which is equivalent to a charge of 3×10^{-2} coulombs/cm^2, was therefore selected.

This figure of merit for maintenance characteristics is plotted in Fig. 13 as a function of Mn concentration. Here a maximum is obtained in the region of 0.03 atoms Mn/atom Mg. Figure 14 shows that when this characteristic is plotted as a function of w/o ZnF_2 added, a somewhat ill-defined curve is obtained, similar in appearance to the curve in Fig. 6; the four checkpoints, however display the degree of reproducibility of the data. Highest maintenance is obtained in the region of 8-10 w/o ZnF_2. When this maintenance characteristic is plotted as a function of K:Mg ratio (Fig. 15), a series of scattered points results which might be interpreted as indicating an optimum ratio of 0.76.

The maintenance data plotted on these figures do not, however, represent the true maintenance of the material if measured in a sealed-off, well-evacuated cathode-ray tube. Pfahnl (12) has shown that maintenance is considerably poorer when measured in a demountable cathode-ray tube, in all probability as a result of increased ion damage to the phosphor. We have also found this to be true in our investigations. Measurement of a standard $KMgF_3$ phosphor in both a sealed-off tube and a demountable tube shows that the total charge necessary to reduce the light output to 50% of its initial value in the two cases differs by a factor of 10. It was also found, however, that as a result of always measuring the samples in the same demountable, at the same conditions of vacuum, fairly reproducible results could be obtained. Thus it appears that while the actual numbers obtained in demountable maintenance measurements are of no consequence themselves, the information obtained is still quite useful as a relative figure of merit.

Emission spectra were determined for all samples in each series. The data obtained show no shift in spectral emission peak and no change in band width as a result of either altering the phosphor composition or varying the beam voltage or current density. An emission spectrum of a typical sample is shown in Fig. 16. The emission peaks for these samples occur at 600 mμ.

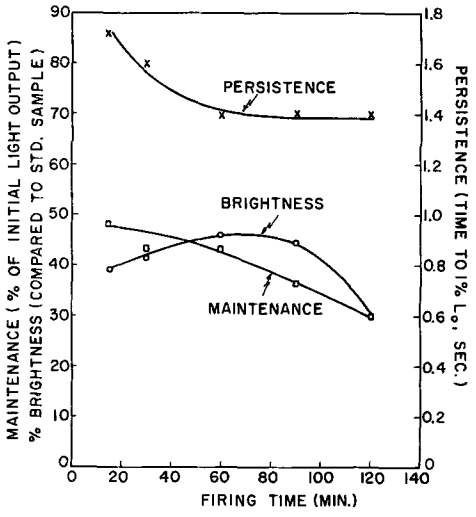

Fig. 18. Effect of firing time on cathodoluminescent characteristics of $KMgF_3$:Mn (firing temperature = 900°C; composition: K:Mg = 1.0, Mn:Mg = 0.02, 2.0 w/o ZnF_2 added).

As an additional part of the investigation, data were obtained to determine the effect of firing conditions on brightness, persistence, and maintenance. In Fig. 17 these characteristics are plotted as a function of firing temperature. The samples in this series were each fired for 1 hr. From the curves it can be seen that relatively little change in brightness occurs over this temperature range, but that persistence is optimum at 875°C, while best maintenance occurs for 900° firing. In Fig. 18 these characteristics are plotted as a function of firing time; all samples here were fired at 900°C. It is found that optimum brightness is obtained for 60-90 min firing, while best maintenance and longest persistence are obtained with a 15 min firing.

Because of the interest developed in $KMgF_3$:Mn as a starting material for the preparation of cathodoluminescent thin films, some additional investigation was done to determine the characteristics of other Mn-activated complex fluoride powder phosphors. While the study of these materials was only cursory, a summary of the characteristics determined seems worthwhile. Only three series of samples were prepared. In the first series Ca, Zn, Sr, or Cd were substituted for Mg in $KMgF_3$:Mn. In the second series, the elements Li, Na, Rb, and Cs were substituted for K in $KMgF_3$:Mn, while in the third series Mn-activated complex flourides were prepared with Zn as the divalent cation and either Li, Na, Rb, or Cs as the monovalent constituent. Control samples of $KMgF_3$:Mn were prepared with each series. For each sample the ratio of univalent cation:divalent cation was kept at 1.0, while the Mn concentration was held constant at 0.02 atom Mn/atom divalent cation. All samples were fired at 900°C for 1 hr. A summary of the brightness, persistence, maintenance, and spectral emission characteristics is shown in Table I. While not shown in Table I, the brightness-voltage and brightness-current characteristics were also measured and found to be linear for all samples (within the limits 4-15 kv and 0.25-2.0 $\mu a/cm^2$). The most promising of the materials investigated are $KCdF_3$ and LiF + ZnF_2, for brightness, and $RbZnF_3$ and $RbMgF_3$, for maintenance. Wherever brightness data for this series of samples could be compared with that compiled by Smith (7) or Klasens and his co-workers (8), it was found that best agreement was achieved with the results reported by the former.

Summary

While no attempt has been made to explain the results obtained, it can be seen that variation of phosphor composition in Mn-activated $KMgF_3$ can lead to materials with considerably improved maintenance characteristics (which of course is the strongest detriment of this class of materials). Improvement of brightness and persistence can also be made by composition change, but there appears to be no single optimum composition to encompass the best of all three characteristics.

An initial attempt to improve further on the cathodoluminescent characteristics of Mn-activated $KMgF_3$ by substitution of some Group IA, IIA, and IIB elements has resulted in some materials which show improved maintenance and brightness. Based

Table I. Summary of cathodoluminescent characteristics of some Mn-activated complex fluorides

Compound formed	Crystalline structure	Relative brightness[a]	Persistence,[b] sec		Relative maintenance	Emission peak, mμ
			to I_0/e	to 1% I_0		
$KMgF_3$	cubic	100	0.10	1.06	100	600
$KCaF_3$	cubic[d]	25.5	0.08	0.74	49	565
$KZnF_3$	tetragonal[d]	52.6	0.10	0.72	42	580
KF + SrF_2	KF + SrF_2[d]	0.3	not measured		not measured	420
$KCdF_3$	cubic[d]	129	0.10	0.83	98	588
LiF + MgF_2	LiF + MgF_2	73.1	0.10	0.56	135	590
$NaMgF_3$	cubic	45.8	0.10	0.49	122	593
$RbMgF_3$	cubic + hexagonal	49.3	0.07	0.98	168	580
$CsMgF_3$	cubic	1.9	0.005	0.14	not measured	430, 450
LiF + ZnF_2	LiF + ZnF_2	167	0.08	1.15	151	595
$NaZnF_3$[c]	—	—	—	—	—	—
$RbZnF_3$	tetragonal	35.5	0.07	0.37	170	575
$CsZnF_3$	mixture of many structures	2.9	0.035	0.34	106	600

[a] In each case the figure given represents the average of 25 readings taken under different conditions of beam voltage and current density.
[b] After raster presentation at 4 kv, 1.2 $\mu a/cm^2$.
[c] Sample ruined during firing.
[d] Samples not subjected to x-ray analysis; estimated structure shown is based on data by Klasens *et al* (8).

on these findings, a more thorough investigation of this family of compounds would seem worthwhile.

Acknowledgments

The author wishes to express his thanks to Messrs. L. J. McCloskey and W. J. Kmeta for their assistance in preparation and measurement of the samples, and to Dr. C. K. Lui-Wei for making the x-ray diffraction analyses. The author is further indebted to Dr. H. F. Ivey and Mr. P. M. Jaffe, of this laboratory, and Professor C. W. Carlson, Newark College of Engineering, for their helpful advice and encouragement, and to the U.S. Navy Bureau of Ships for supporting the work.

Manuscript received July 13, 1961. This paper was prepared for delivery before the Indianapolis Meeting, April 30-May 3, 1961. Work on this paper was supported by Government Contract NObsr-77582, and the paper was submitted in partial fulfillment of requirements for the M.S. degree to the Newark College of Engineering, Newark, N. J.

Any discussion of this paper will appear in a Discussion Section to be published in the December 1962 JOURNAL.

REFERENCES

1. W. B. Nottingham, in "Cathode-Ray Tube Display," p. 643, MIT Rad. Lab. Series, Vol. 22, T. Soller, M. A. Starr, and G. E. Valley, Jr., Editors, McGraw-Hill Publishing Co., New York (1948).
2. H. W. Leverenz, "Luminescence of Solids," p. 429, J. Wiley & Sons, Inc., New York (1950).
3. F. E. Williams, *J. Opt. Soc. Am.*, **37**, 302 (1947).
4. P. D. Johnson and F. E. Williams, *J. Chem. Phys.*, **18**, 323 (1950).
5. W. W. Parkinson, Jr. and F. E. Williams, *ibid.*, 534.
6. J. H. Crawford, Jr., and F. E. Williams, *ibid.*, 775.
7. A. L. Smith, *This Journal*, **101**, 189 (1954).
8. H. A. Klasens, P. Zalm, and F. O. Huysman, *Philips Res. Rept.*, **8**, 441 (1953).
9. G. F. J. Garlick, in "Advances in Electronics," Vol. II, p. 152, L. Marton, Editor, Academic Press, New York (1950).
10. H. W. Leverenz, "Luminescence of Solids," Table 5, J.Wiley & Sons, Inc., New York (1950).
11. C. G. A. Hill, *Brit. J. Appl. Phys.*, Suppl. No. 4, p. S6 (1955).
12. A. Pfahnl, Fifth National Conf. on Tube Techniques, New York City, Sept. 16, 1960.

Preparation, Stability, and Luminescence of Gallium Nitride

M. R. Lorenz and B. B. Binkowski

Research Laboratory, General Electric Company, Schenectady, New York

ABSTRACT

Gallium nitride has been prepared from gallium oxide and ammonia at temperatures from 600° to 1100°C. The emission of various preparations under cathode ray excitation has been investigated. Dissociation studies indicate the thermal instability of GaN at temperatures as low as 600°C. Observed emission spectra are discussed in terms of preparation temperature and dissociation.

In the search for new photo-, cathodo-, and electroluminescent phosphors, attention has been given recently to the higher band gap compounds of group III and V elements. The phosphides and nitrides of gallium, aluminum, and boron have been of particular interest, since their band gap would predict emissions in the visible or of shorter wavelength. The present investigation is concerned with methods of preparation, stability, and cathodoluminescence of GaN.

The preparation of GaN has been effected in a variety of ways using NH_3 as a common reactant (1-6). It is notable that direct nitriding with N_2 has been unsuccessful. GaN prepared at low temperatures (1), *i.e.*, in the range 350°-500°C, has been activated by incorporation of suitable impurities and yielded luminescent materials. The emission intensities are markedly affected by the annealing temperature except when activated with Li (1).

More recently, Addamiano (7) prepared GaN from GaAs and GaP. The reactions appeared attractive since both GaP and GaAs can be obtained with high purity.

Preparation.—Attempts at preparing GaN from the reaction of Ga with NH_3 at 1000°-1160°C resulted in a heterogeneous product exhibiting wide color variation. Preparation of the nitride from GaP as suggested by Addamiano (7) was unsatisfactory due to the difficulty in achieving quantitative conversion and the high temperatures involved, > 1000°C.

It was observed, however, that GaP crystals, partially hydrolyzed by grinding in moist air with resultant evolution of PH_3, rapidly reacted with NH_3 to yield GaN. This suggested the use of Ga_2O_3 as starting material and the reaction

$$Ga_2O_3 + 2NH_3 \rightarrow 2GaN + 3H_2O \qquad [1]$$

was studied as a function of preparation temperature. High-purity Ga_2O_3 (99.99%, Varlacoid Chemical Company) was heated in a stream of anhydrous NH_3 (purity > 99.99%, Matheson Company) at controlled temperatures. The products were checked by x-ray diffraction and chemical analysis. Table I shows the pertinent data where the length of reaction time indicated is not necessarily the minimum time required for complete conversion to GaN.

Dissociation.—On several occasions when GaN was heated to 1150°C in previously evacuated and sealed quartz tubes, explosions occurred. Since the quartz tubes were of relatively small diameters

Table I

Sample identification	Reaction temp, °C	Reaction time, hr	X-ray identification	Body* color
A	480	16	Ga_2O_3	Nearly white
B	550	4	Ga_2O_3	Yellowish white
C	600	24	GaN	Light yellow
D	700	16	GaN	Deep yellow
E	800	15	GaN	Yellow
F	1000	3	GaN	Tan yellow
G	1090	3	GaN	Light gray

* Pure Ga_2O_3 is white.

(⅜-¾ in.), pressures of several atmospheres would be necessary to cause explosions. This is particularly intriguing since GaN was prepared from Ga and NH_3 at temperatures as high as 1160°C at an ammonia flow pressure of 1 atm. Accordingly, the thermal stability of GaN was investigated.

GaN prepared by reaction [1] at 1000°C was placed in a graphite crucible and heated in a vacuum system. The samples could be isolated in a constant volume of approximately 600 cm^3 where any pressure buildup or decrease could be observed with a McLeod gauge and a mercury manometer. Samples were heated under pumped vacuum to various temperatures, then isolated and the pressure monitored as a function of time at a controlled temperature. Very slow rates of dissociation were observed which necessitated the introduction of N_2 pressure from an external source in order to show a pressure dependence of the dissociation rate. The effect of hydrogen on the dissociation rate was also investigated.

In Fig. 1 the observed pressure changes are plotted as a function of time. At 412°C no measurable dissociation occurs, but at 616°C, N_2 is generated slowly at a constant rate. With increasing temperature the rate of N_2 evolution increases. The dissociation at 812°C was monitored for 85 hr without observing any deviation in the rate of N_2 formation over the pressure range from less than 10^{-3} to 15 mm Hg pressure. At higher temperatures slight curvature is noted especially at low pressures. After N_2 is added to the system, note curves G and H, a lower rate is observed, but appears nearly constant over the measured pressure interval. The addition of H_2 does not alter the rate as evidenced in Fig. 1 by comparison of curve E to that of D at equivalent total pressures.

The results clearly indicate the thermal instability of GaN at temperatures as low as 600°C. The effect of this instability on the properties of GaN is discussed in detail later.

Cathodoluminescence.—The emission properties of GaN were studied with cathode-ray excitation. A demountable cathode-ray tube was used which included an attachment to permit sample excitation from 25°C to liquid N_2 temperatures. A grating spectrometer and a 1P21 photomultiplier detector completed the assembly. Samples were excited with 15 kv electrons at current densities of 1-4 $\mu a/cm^2$. The emission spectra at liquid N_2 temperature of various preparations and partially dissociated GaN are shown in Fig. 2. The spectra are corrected for the spectral sensitivity of the spectrometer. At low preparation temperatures, weak luminescence occurs with a peak at about 5200Å. With increasing preparation temperature the intensity of the broad 5200Å band decreases, going to zero, while a relatively sharp band centered at 3600Å appears. The relative intensity of this band rises sharply and reaches a maximum for the sample prepared at the highest temperature. It is interesting to compare the spectra of samples C and E. Both samples were prepared at 1000°C from Ga_2O_3 and C corresponds to this preparation. Part of it was heated in vacuum at 950°C and is listed as E. The nearly complete dis-

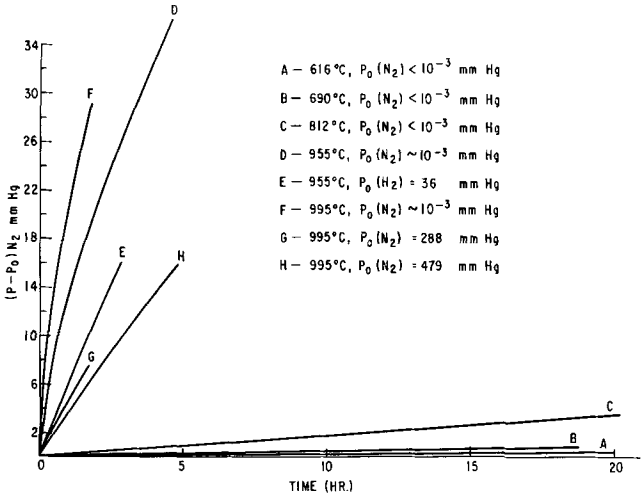

Fig. 1. Rates of GaN dissociation

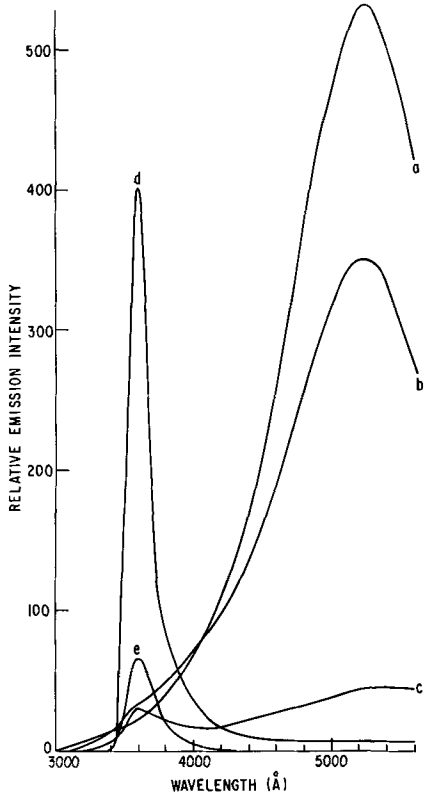

Fig. 2. Cathodoluminescence of GaN prepared at various temperatures, a, 800°; b, 900°; c, 1000°; d, 1090°; e, subjected to vacuum heating at 950°C. Intensities of a and b are reduced by a factor of 100 and c by a factor of 10, relative to d and e. Emission intensities are corrected for the spectral sensitivity of the spectrometer.

appearance of the 5200Å band and sharp rise in the 3600Å band are noteworthy.

Emission at 25°C is always weaker compared to low-temperature emission. A 50Å shift in the high energy peak position to longer wavelengths is observed, which correlates well with the expected band gap shift with temperature.

Discussion

It has been shown that GaN can be prepared from Ga_2O_3 at relatively low temperatures. However, all preparations in the range 600°-1100°C have some yellow body color with the products of the higher preparation temperature tending toward gray. According to Fig. 2, the fundamental absorption edge at 25°C would be expected near 3650Å or at an even shorter wavelength; therefore, the pure material should be white in appearance. The occurrence of discolored products can now be correlated with the thermal stability and cathodoluminescence studies.

The thermal dissociation of GaN proceeds in vacuum at temperatures as low as 600°C, as evident from Fig. 1. It also appears that at 1000°C GaN would dissociate completely in 1 atm of N_2 if given sufficient time. The slow and apparently constant rate suggests a diffusion-controlled dissociation process. Since the rate of dissociation is so low, reliable equilibrium pressures could not be obtained. However, the results explain the problems encountered in the preparation of pure GaN. It is apparent that two reactions are of concern, *i.e.*,

$$GaX + NH_3 \xrightarrow{k_1} GaN + \ldots \quad [2]$$

and

$$2GaN \xrightarrow{k_2} 2Ga + N_2 \quad [3]$$

where GaX may be metallic gallium or some of its compounds and k is the reaction rate constant. It is unnecessary to consider the back reaction of the latter equation since GaN could not be formed from Ga and N_2 at any temperature. From the dissociation studies it is evident that k_2 is relatively small; therefore, if k_1 is larger than k_2, GaN is produced. Since k_2 is not negligible, the products are always partially dissociated. The higher the preparation temperature, the greater the proportion of excess Ga, leading to gray material. This is in accord with the expected increase in the magnitude of k_2 with increasing reaction temperatures.

It is interesting to note that the only white GaN reported in the literature (1) was prepared at about 350°C, which is in agreement with the thermal stability reported here, *i.e.*, no measurable dissociation below 412°C.

The problem of instability also explains why crystal growth of GaN has been essentially unsuccessful. The preparation of the material at higher temperature is indeed possible only if the reaction leading to GaN is rapid. Under these conditions crystal growth is most unfavorable.

GaN prepared from the oxide at low temperatures shows weak luminescence in a broad band peaking at about 5200Å. With increasing preparation temperature this band disappears while at the same time a sharp band at 3600Å appears. The origin of the long wavelength band is uncertain. The only impurities found by emission spectroscopy were minute traces of Si and Fe. Although these may be responsible for the 5200Å band, it is felt that residual oxygen substitutions at nitrogen sites or interstitially are a more likely possibility. This is supported by the disappearance of the long wavelength band at higher preparation temperature or under vacuum heating. Either case enhances the out diffusion of oxygen, whereas it seems unlikely that Si and Fe are readily removed under these conditions. As the centers responsible for the 5200Å band are removed, the emission shifts to the 3600Å band. The latter has been observed by Grimmeis and Koelmans (2) and interpreted as edge emission.

It has been reported that GaN prepared and activated with various impurities below 600°C is luminescent (1). Annealing at temperatures of 600°C and above leads to a sharp decrease in luminescence intensity and eventually the material is nonluminescent when the annealing temperature reaches about 1000°C. The simultaneous decrease in luminescence with the onset of dissociation is more than accidental, and it is suggested that this decrease is indeed caused by the thermal instability of GaN. The mechanism by which the luminescence is quenched cannot be extracted with certainty from the present data, but is most probably a consequence of the formation of interstitial Ga or nitrogen vacancies.

In summary, it may be seen that the potential of GaN with regard to photo-, cathodo-, and electroluminescence is handicapped by its thermal instability at temperatures above 600°C. Accordingly, any effort in materials preparation and impurity activation should therefore be more fruitful at temperatures below 600°C.

Acknowledgment

The authors are indebted to Miss G. P. Lloyd for obtaining the emission spectra reported here and to Dr. J. S. Prener for valuable discussions.

Manuscript received May 18, 1961; revised manuscript received Aug. 30, 1961.

Any discussion of this paper will appear in a Discussion Section to be published in the December 1962 JOURNAL.

REFERENCES

1. H. G. Grimmeis, R. Groth, and J. Maak, *Z. Naturforsch.*, **15a**, 799 (1960).
2. H. G. Grimmeis and H. Koelmans, *ibid.*, **14a**, 264 (1959).
3. W. C. Johnson, J. B. Parsons, and M. Crew, *J. Phys. Chem.*, **36**, 2651 (1932).
4. R. Juza and H. Hahn, *Z. anorg. Chem.*, **244**, 111 (1940); *ibid.*, **244**, 133 (1940).
5. T. Renner, *ibid.*, **298**, 22 (1959).
6. G. A. Wolff, I. Adams, and J. W. Mellichamp, *Phys. Rev.*, **114**, 1262 (1959).
7. A. Addamiano, *This Journal*, **108**, 1072 (1961).

X-Ray Diffraction Microscopy Study of Imperfections in Silicon Single Crystals

G. H. Schwuttke

General Telephone and Electronics Laboratories Incorporated, Bayside, New York

ABSTRACT

The application of x-ray diffraction microscopy to the study and control of crystal perfection of silicon is discussed. The major significance of this technique in establishing standards by which the validity of other methods, such as etch-pit counting and decoration techniques, can be gauged is pointed out. The method previously used only for the mapping of dislocations in single crystals is now applied for the detection of impurities, segregation effects, cluster formation, and second phases. Segregation effects are studied in crystals containing oxygen. It is shown that, due to microsegregation of oxygen, the silicon lattice can become strongly anisotropic. The influence of such a lattice on the diffusion properties is shown. Precipitation effects are investigated in crystals containing copper precipitates. The results are verified by infrared microscopy. Experimental details of a method unique for the investigation of large crystal wafers are given.

It is impossible to characterize semiconductor crystals adequately without a fairly good knowledge of the imperfections present. The existence of as yet unexplained bulk variations encountered in semiconductors indicates the need for more complete studies. In view of the importance of such investigations, it seemed worthwhile to investigate the potentialities of x-ray diffraction microscopy techniques as recently developed for the mapping of dislocations in single crystals by Borrmann (1), Barth and Hosemann (2), Newkirk (3), and Lang (4) for imperfection studies in semiconductor single crystals.

In this paper we shall discuss x-ray diffraction microscopy by extinction contrast for the study and control of crystal perfection in silicon. Its major significance in establishing standards by which the validity of other methods, such as etch pit counting and decoration techniques, can be gauged will be pointed out, and its special importance in the detection of impurities, segregation effects, cluster formation, and second phases will be discussed. X-ray diffraction microscopy by anomalous transmission of x-rays will be covered in a separate paper.

Experimental

Technique.—The experimental technique selected to conduct our experiments is the transmission method as introduced by Lang (4). Silicon is almost ideal for transmission diffraction microscopic work. For hard radiation like Mo and Ag, the absorption coefficient is small, so that relatively thick wafers can be investigated. The optimum contrast can be determined by the thumb rule: the product of linear absorption coefficient and slice thickness is approximately equal to the order of unity; thus in the case of silicon, 1 to 2 mm in thickness can be tolerated.

No experimental details unique for the investigation of large crystal wafers have been published previously elsewhere;therefore they are given here. The experimental set-up, as sketched in Fig. 1, consists of an x-ray source and a diffractometer. The x-ray source, a standard diffraction tube, is placed at least 600 mm from the specimen with its line focus in the vertical position. A slit system in front of the anode is used to limit the effective source size as necessary.

The crystal wafer is mounted on a goniometer head on a diffractometer equipped with a Geiger counter to facilitate orientation for diffraction from various sets of diffracting planes. The slit S_1 in front of the specimen determines the effective beam width. A second slit S_2 behind the crystal wafer is adjusted so that the diffracted beam is allowed to pass while the direct beam is cut off. Slit S_1 consists of two metal plates, 25 x 25 mm in size, held at right distance by placing two metal foils between them. The photographic plate is placed close to the specimen behind S_2. The diffraction micrographs are recorded by moving the crystal wafer and photographic plate together while S_1 and S_2 are stationary.

Ilford x-ray film and Ilford nuclear plates, emulsion G-5, emulsion thickness 50μ, 100μ, and 200μ are used. For a slit width S_1 of 0.1 mm and a scanning width of 25 mm which corresponds to a recorded crystal area of 25 mm x 25 mm the exposure times are as follows: Mo radiation at 50 kv and 20 ma:

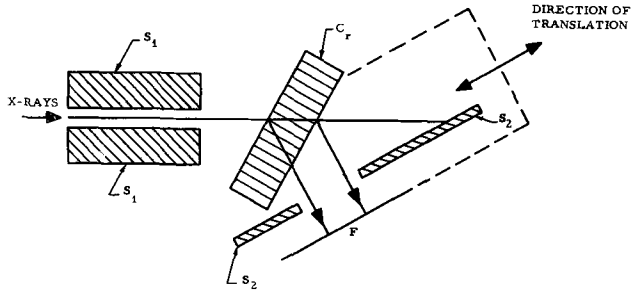

Fig. 1. Sketch of experimental setup: S_1 and S_2, slits; C_r crystal; F, photographic plate.

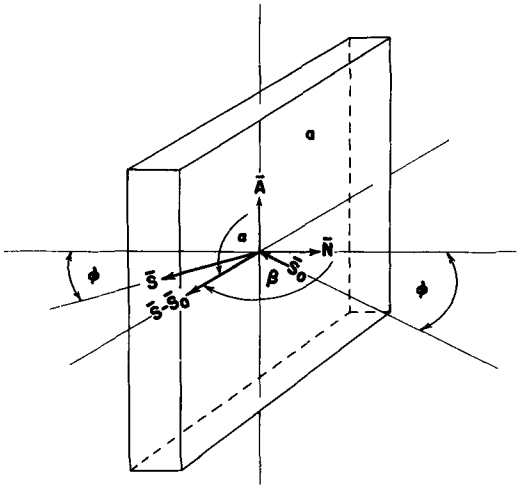

Fig. 2. Orientation of crystal wafer relative to x-ray beam and definitions of α and β.

Ilford x-ray film, 1-2 hr; Ilford nuclear plates 50μ, 10-14 hr; Ilford nuclear plates 100μ, 5-7 hr; Ilford nuclear plates 200μ, 2-4 hr.

Better resolution is obtained by using nuclear plates, but for many cases x-ray film is quite sufficient.

The nuclear plates are processed as follows: (*a*) soak in distilled water for 20 min at 20°C; (*b*) develop in Kodak Developer D 19 for 30 min; (*c*) transfer to 1% acetic acid as stop-bath at 20°C for 10 min, then remove surface fog by rubbing gently with cotton wool; (*d*) fix in 30% plain hypo for 50% longer than clearing time, then wash in running water, 50μ for 30 min, 100μ for 2 hr, 200μ for 4 hr.

It is expedient to describe different orientations of the crystal wafer with respect to the x-ray beam by introducing the angles α and β as shown in Fig. 2. According to this figure the largest lateral crystal face of the wafer is a, the main axis of the wafer is $\overline{A}$, and the normal to the crystal face a is called $\overline{N}$. If the direction of the incident beam is $\overline{S}_o$ and the direction of the diffracted beam $\overline{S}$, α is the angle between the diffraction vector $(\overline{S}-\overline{S}_o)$ and $\overline{A}$ and β is the angle between $(\overline{S}-\overline{S}_o)$ and $\overline{N}$. In our experiments the planes including $\overline{A}$ and $(\overline{S}-\overline{S}_o)$, respectively, $\overline{N}$ and $(\overline{S}-\overline{S}_o)$ are kept orthogonal to each other. Figure 2 is drawn for α and β equal to 90°.

Our experimental setup is such that the Bragg angle ϕ can be controlled with an accuracy of 1 sec of arc and the angle α with an accuracy of 1 min of arc. The photographic plate is placed perpendicular to the diffracted beam. All x-ray micrographs presented in this paper are taken on nuclear plates with the exception of Fig. 8, which is on x-ray film.

Specimen preparation.—Crystal wafers approximately 1.2 mm thick were cut from the bulk material. The lateral face (a in Fig. 2) is a low-index face such as (111), (110), (112), and is oriented optically better than one degree of arc (5). After cutting and lapping, the wafer is etched in a solution of 5 parts HNO_3, 3 parts HF, and 5 parts acetic acid for approximately 5 min to remove the surface layer. After etching the crystal thickness is approximately 1 mm.

General Observations

Diffraction microscopy of dislocations.—Figure 3 is a diffraction micrograph taken using (220) type planes; it shows dislocations lying in a (111) slip plane. Figure 4 explains how the wafer was cut from the bulk crystal. The slice is a 1.2 mm thick cut from a crystal grown in the [111] direction parallel to one of the three octahedral planes that make an angle of 19½° with the [111] growth direction. In cooling

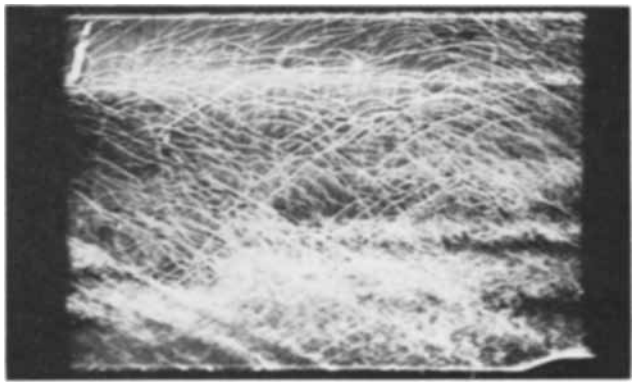

Fig. 3. Dislocations in octahedral plane; α = 90; β = 90. Magnification, 5X.

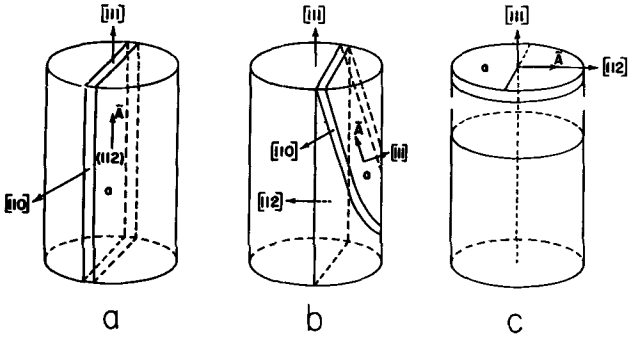

Fig. 4. Orientation of crystal wafers relative to bulk crystal

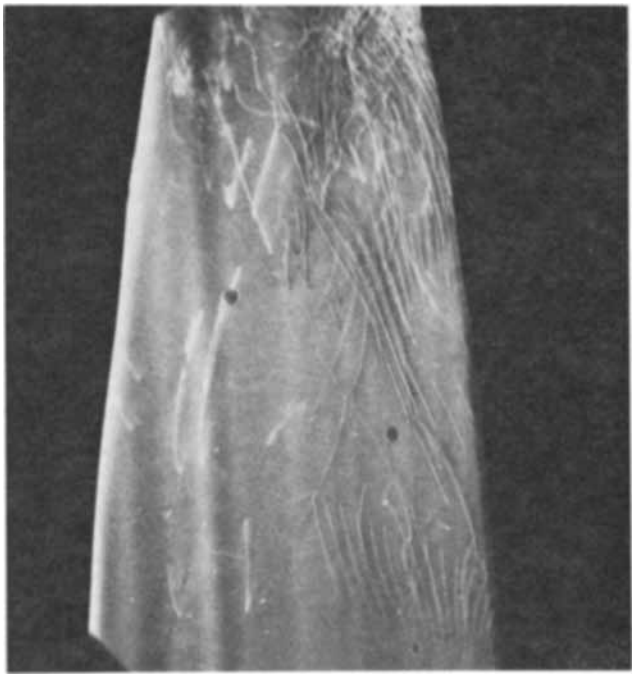

Fig. 5. Dislocations propagated by growth and dislocations introduced by plastic deformation; α = 90; β = 90. Magnification, 7X.

the crystal during growth, slip occurred in the octahedral planes introducing the dislocations seen in the micrograph.

Disclocations propagated by growth from the seed into the crystal (the seed was near the smaller end) are seen in Fig. 5. The wafer is a 1.2 mm thick cut parallel to a (112) plane containing the [111] growth axis as shown in Fig. 4a. The dislocations introduced through the seed grow out with the growing crystal. Some edge-type dislocation, generated by plastic deformation are also seen in the micrograph. The picture is a result of using (220) type planes for the reflection of x-rays.

The visibility of individual dislocation lines in the diffraction micrograph is determined by dislocation density and orientation of the dislocation line relative to the reflecting net plane. Dislocation lines are recorded photographically as lines of enhanced intensity. This is a consequence of the difference in the integrated intensity reflected by a "perfect" and an "imperfect" crystal area. Therefore the dislocation density must be low enough for these lines to be individually distinguishable, and low enough so that the regions between dislocations are sufficiently perfect to approximate the conditions of diffraction by a perfect crystal.

It has been found experimentally that for a dislocation density of 10^4 lines/cm^2 the imperfect region around a dislocation has a diameter of approximately 10μ (4). Bonse has calculated that the strain field around a single dislocation may even extend $50\text{-}80\mu$ (6). However, the extension of the strain field seems to depend on the dislocation density and decreases somewhat with increasing dislocation numbers. The maximum value for which single lines can still be recognized is approximately 10^5 to 10^6 lines/cm^2. For higher numbers the imperfect areas in the crystal begin to overlap. The photomicrograph shown in Fig. 6 is an x-ray transmission image of a crystal with a dislocation density of approximately 10^6 lines/cm^2.

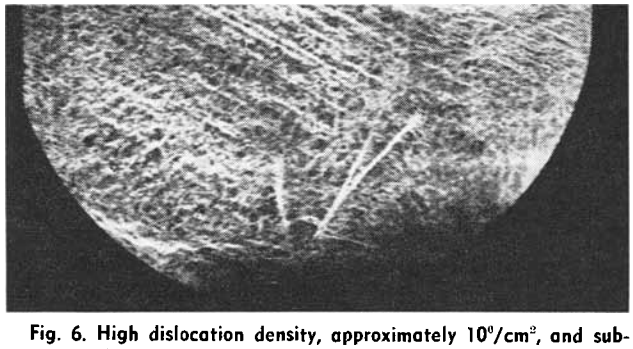

Fig. 6. High dislocation density, approximately 10^6/cm^2, and subboundary formation; $\alpha = 90$; $\beta = 90$. Magnification 10X.

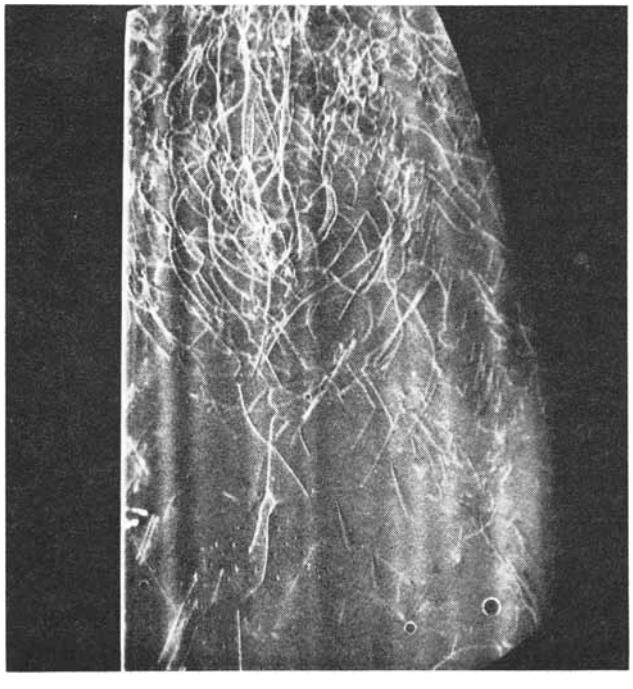

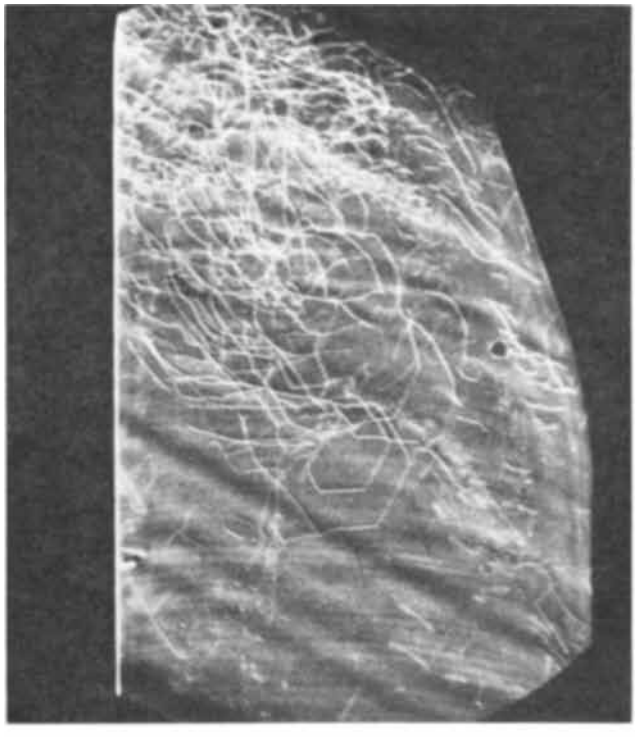

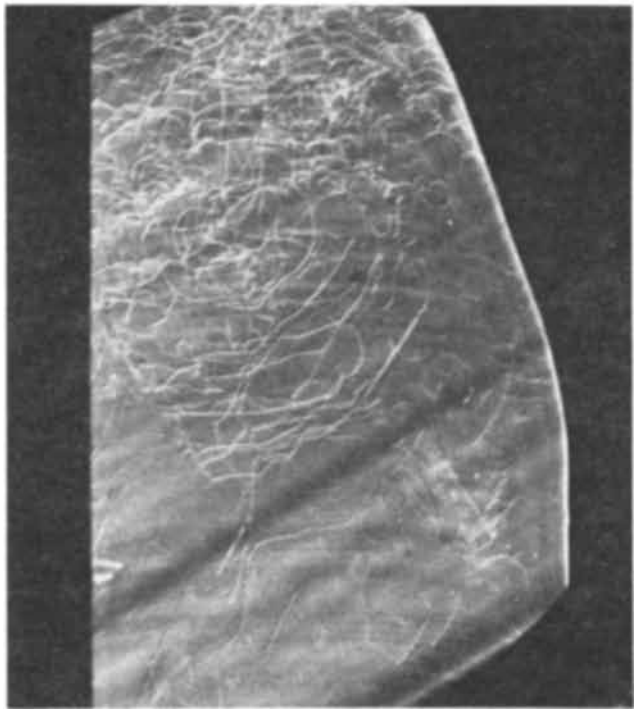

Fig. 7. Visibility of dislocation depending on different reflection: (a) (left) $\alpha = 90$; $\beta = 90$; (b) (top) $\alpha = 150$; $\beta = 90$; (c) (bottom) $\alpha = 210$; $\beta = 90$. Magnification, 7X.

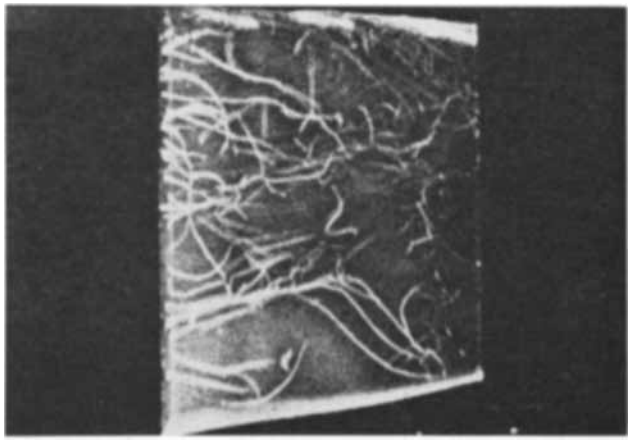

Fig. 8. Etch pits and dislocations: $\alpha = 90$; $\beta = 90$. On Ilford x-ray film. Magnification, 10X.

The slice was cut in accordance with Fig. 4c. In this picture sub-boundary formation is noticed. Formation of such dislocation arrays in silicon has been observed for dislocation densities larger than 10^5 lines/cm^2. The effective interaction distance between dislocations necessary to form such arrays can therefore be estimated to be approximately 10μ, correct to one order of magnitude, which is in good agreement with the radius of the strain field around dislocations as given in (4) and (6).

Dislocations produce a maximum of enhanced intensity in the x-ray image when the latter arises from Bragg reflection against a plane perpendicular to the Burger's vector (4). If the Burger's vector is parallel to the reflecting net-plane, the line is invisible or only very slightly visible in the image. In many cases one reflection is completely sufficient to determine the true dislocation density in a wafer. In cases of doubt a second or third reflection will provide enough evidence to obtain sufficient clarity. This is shown in Fig. 7 which represents three different {220} reflections of a silicon wafer cut in accordance with Fig. 4b. The change in contrast is especially distinct for the dislocation loops in the lower halves of the pictures. The spots are due to defects in the prints.

X-ray diffraction microscopy results are determined by changes in diffraction power due to disturbances in the crystal lattice; therefore, they can be used as standards to establish the validity of measurements obtained by indirect techniques. The x-ray micrograph shown in Fig. 8 is that of a 1-mm thick crystal wafer, cut as explained in Fig. 4a. The crystal thickness can be distinguished very clearly, especially on the left-hand side of the photograph where most of the dislocation lines are found to terminate in the plane of the side face. Before taking the x-ray picture, the wafer was slightly etched for dislocations. It can be seen that the ends of the dislocations at the left consist of small areas of enhanced contrast, similar to white specks. Each white speck represents a tiny etch pit, resulting in a one-to-one correspondence between etch pits and dislocation lines. The dislocation density can be counted easily. We discern approximately 32 dislocations counting those ending at the left-hand side of the wafer. Since the crystal is approximately 1 cm wide and 1 mm thick, we obtain 320 dislocations per cm^2. Another point is illustrated quite readily. Since most of the dislocation lines run from right to left in the picture, a cut through the crystal in this direction, for the purpose of etching the cut face for dislocations, would reveal considerably fewer dislocations. Etch pit counts at low dislocation densities can easily lead to wrong conclusions about crystal imperfection.

Previous investigations with silicon have shown that dislocation counts by decoration of dislocations with copper in general are quite accurate. Experiments with pure silicon crystals of 2000 ohm-cm resistivity and of low resistivity crystals containing varying concentration of oxygen impurities lead to the conclusion that accuracy in determining dislocation numbers is not influenced by the oxygen content of the crystal, which is contrary to results obtained by etching (7). If in addition to oxygen other impurities are present, interference with the copper decoration process may occur. Complicated solid-state reactions in such crystals have been observed (8). In the decoration of more than 100 silicon crystals we have found crystals that did not decorate in the usual way. The photomicrograph in Fig. 5 shows such a crystal. By evidence of this x-ray picture the wafer contains a relatively high dislocation density, especially close to the seed end. An inspection using the infrared microscope after decoration revealed dislocations only very faintly decorated and in addition precipitation, homogeneously distributed throughout the wafer. Due to the weak precipitation along the dislocation lines it was not possible to decide with certainty whether all lines visible in the x-ray image had been successfully decorated. It seems likely that the copper reacted with an unknown impurity in the crystal, thus the usual strong precipitation along the dislocation lines was not formed.

Diffraction microscopy of segregation and precipitation.—So far the use of x-ray microscopy has been reported only for the detection of dislocations. Another important application, which should be very useful for investigating semiconductor crystals, is the detection of segregation and precipitation in the lattice. In general, one expects that any change in lattice periodicity in a crystal will disturb the coherence of multiple reflections. Thus all localized imperfections will act as regions of imperfect crystal

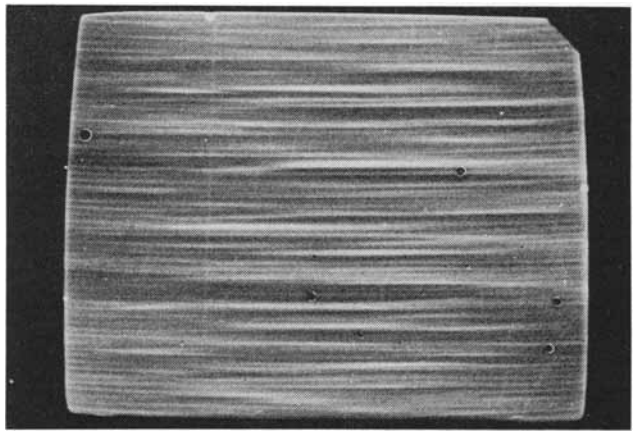

Fig. 9. Oxygen segregation in silicon: $\alpha = 180$; $\beta = 90$. Magnification, 7X.

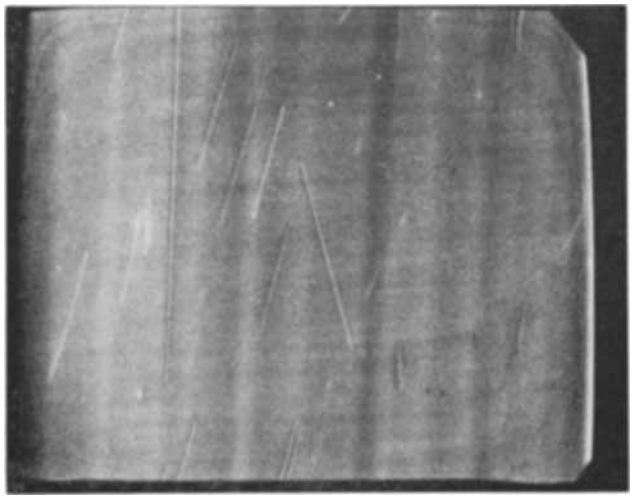

Fig. 10. Oxygen segregation in silicon, same wafer as Fig. 9 for $\alpha = 90$; $\beta = 90$. Magnification, 7X.

and, consequently, lead to an enhancement of diffracted intensity. The region of high strain surrounding areas of microsegregation and areas around precipitates fulfill the requirement for enhancement of diffracted intensity just as in the case of dislocations. Thus certain Bragg reflections can be used to record such imperfections in the same way that dislocations are recorded.

Segregation effects were studied in silicon crystals rotation-grown in a quartz crucible. These crystals are known to exhibit microsegregation of oxygen. The oxygen segregates perpendicular to the growth direction (9). It was found that microsegregation of oxygen can produce strong variations in the diffraction power and, accordingly, can be detected quite readily in the diffraction image (10). The sensitivity of this method is comparable to that of the 9-μ absorption method (11). Variations in oxygen concentration, computed from the absorption coefficient, of about 5 x 10^{16} cm^{-3} have been recorded in the x-ray image. The oxygen can be detected in crystals before and after heat treatment at 1000°C. The diffraction photomicrograph in Fig. 9 is a crystal wafer cut according to Fig. 3a, showing microsegregation of oxygen. The image was obtained by reflecting the x-rays from (111) net planes perpendicular to the growth direction. Figure 10 is a diffraction image of the same slice, but this time (220) type net planes containing the growth axis were used. It is interesting to observe that for the (220) type reflection the segregation stripes are only faintly visible. Several edge dislocation lines barely visible in the (111) reflection, show up much stronger in this picture because their Burger's vector is parallel to the (111) plane and perpendicular to the (110) plane used in these reflections.

For any other reflection, for instance (220) with $\alpha = 30$, $\beta = 90$, the segregation stripes appear stronger than in the (220) with $\alpha = 90$, $\beta = 90$. Maximum contrast was obtained for the reflection perpendicular to the growth direction. From this variation of contrast in the x-ray image with the type of reflection, one can conclude that, due to the segregation of oxygen, the silicon lattice has become strongly anisotropic. The influence of such a lattice on the diffusion properties is shown in the infrared photomicrograph, Fig. 11, which shows a silicon wafer containing oxygen segregation after copper was diffused. The copper is found to segregate and precipitate in the oxygen areas.

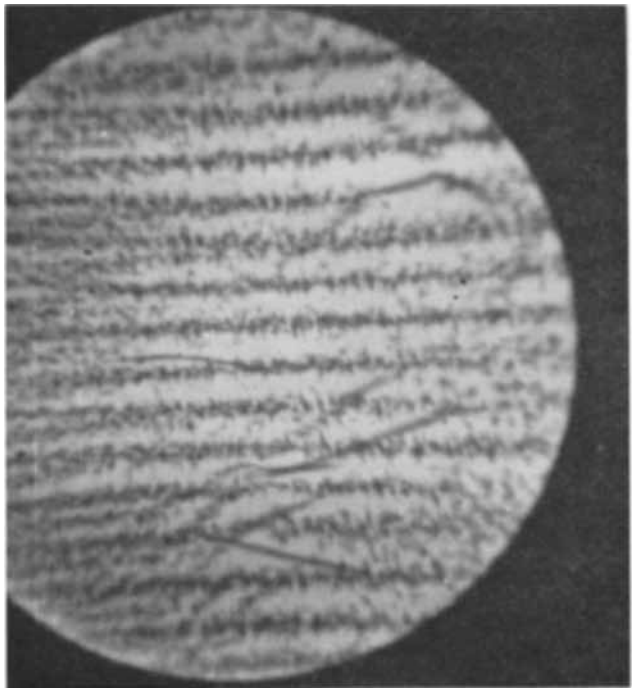

Fig. 11. Infrared micrograph showing copper precipitates in areas of oxygen segregation. Magnification, 25X.

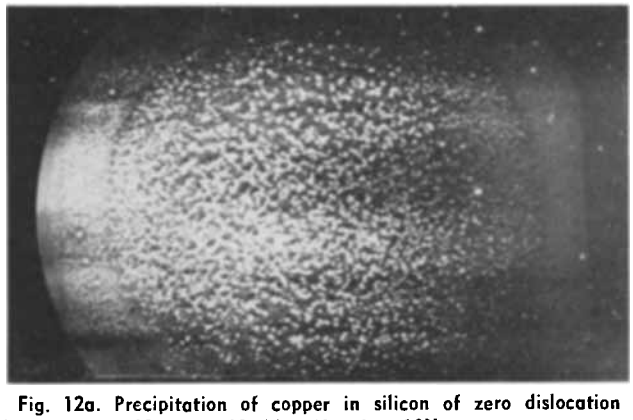

Fig. 12a. Precipitation of copper in silicon of zero dislocation density: $\alpha = 90$; $\beta = 90$. Magnification, 10X.

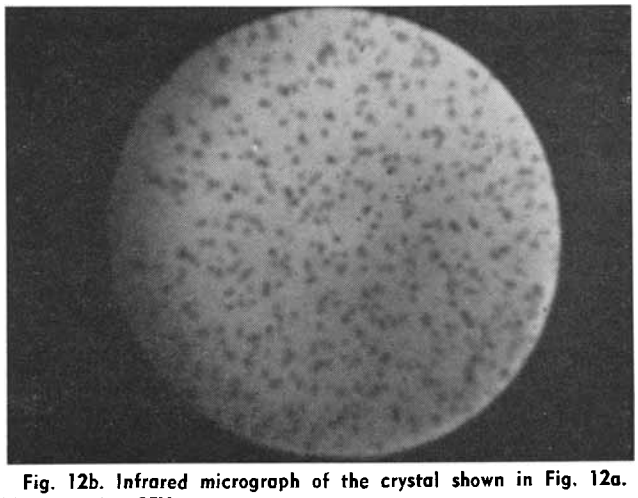

Fig. 12b. Infrared micrograph of the crystal shown in Fig. 12a. Magnification, 25X.

To investigate precipitation effects we selected silicon containing copper precipitates. For this case the x-ray results can be verified directly by infrared microscopy. The x-ray micrograph in Fig. 12a represents a silicon wafer having zero dislocation density. Copper was diffused into this wafer at 900°C for 15 min and then the sample was quenched to room temperature. The solubility of copper in silicon at 900°C is about 10^{17} atoms/cm^3 (12). Since no care was taken to obtain saturation, the concentration of copper in this sample is probably smaller than 10^{17} atoms/cm^3. Figure 12b is an infrared picture of the same wafer for comparison. Random precipitation is easily recognizable in both figures.

Another example of precipitation is shown in Fig. 13. This sample contains approximately 10^{18} atoms of copper/cm^3. The picture reveals a number of interesting details such as random precipitation, decorated dislocation lines, and decorated areas of oxygen precipitation. The precipitation is rather heavy, but the details revealed in the x-ray image in Fig. 13a are remarkably clear and sharp if compared with the infrared picture of the same wafer shown in Fig. 13b. For demonstrating this we chose a relatively large copper concentration. However, the method is sensitive enough to make precipitates directly visible if they are a few microns in size, or indirectly visible if they are much smaller than 1μ and are present in clusters or in clouds. The method is capable of trace analysis, and we have presented evidence that it is possible to find impurities in semiconductors even if their concentration is as small as 10^{15} atoms/cm^3 (13, 14).

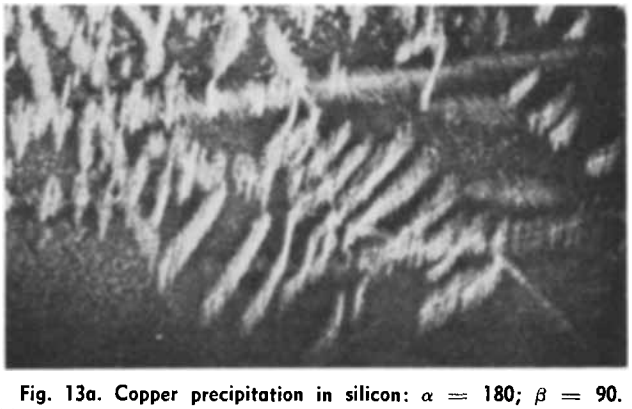

Fig. 13a. Copper precipitation in silicon: $\alpha = 180$; $\beta = 90$. Magnification, 12X.

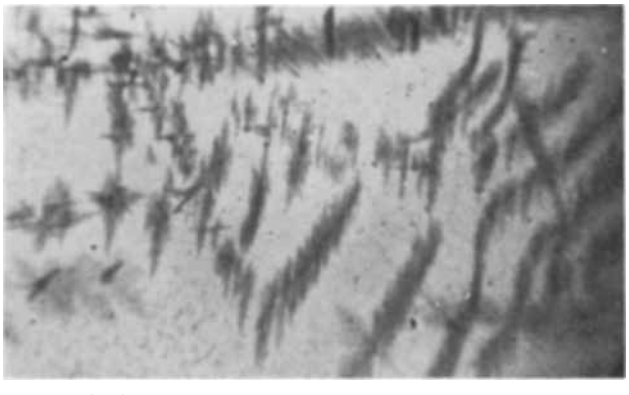

Fig. 13b. Infrared micrograph of the crystal wafer shown in Fig. 13a. Magnification, 25X.

Conclusions

X-ray diffraction microscopy by extinction contrast is a very useful technique for the investigation of structure defects in semiconductor crystals. An important feature of this method is its nondestructiveness to the sample. A correlation of electrical properties and imperfections for the same wafer is therefore possible. The methods can provide direct evidence for such crystal defects as dislocations, segregation, and precipitation effects. It should be a powerful tool for the investigation of such problems as the study of preferential segregation of impurities, which may lead to considerable resistivity changes due to core formation (15), the study of diffusion of impurities along dislocation lines and their subsequent precipitation (16), or the formation of metal precipitates in junctions (17). The method is applicable to all semiconductor materials if x-ray radiation of the proper wavelength is selected. The mass absorption coefficient of semiconductors is such that conveniently thick wafers can be investigated in transmission either by the K_α radiation of Mo or W. We have used the method successfully for studies of Ge, Si, GaAs.

Acknowledgment

The author gladly thanks Dr. P. H. Keck for advice and encouragement, Mr. E. Jungbluth and Mr. R. Modena for the help in performing the measurements, and Mr. P. K. Marshall for growing most of the silicon crystals.

The research reported in this paper was sponsored by the Electronics Research Directorate of the Air Force Cambridge Research Center, Air Research and Development Command, under Contract No. AF19(604)7313.

Manuscript received June 5, 1961; revised manuscript received Aug. 20, 1961. This paper was prepared for delivery before the Houston Meeting, Oct. 9-13, 1960.

Any discussion of this paper will appear in a Discussion Section to be published in the December 1962 JOURNAL.

REFERENCES

1. G. Borrmann, W. Hartwig, and H. Irmler, Z. *Naturforschung*, **13a**, 423 (1958).
2. H. Barth and R. Hosemann, *ibid.*, **13a**, 792 (1958).
3. J. B. Newkirk, *Phys. Rev.*, **110**, 1465 (1958).
4. A. R. Lang, *J. Appl. Phys.*, **29**, 597 1958).
5. G. H. Schwuttke, *This Journal*, **108**, 163 (1961).
6. U. Bonse, Z. *Physik*, **153**, 978 (1958).
7. G. H. Schwuttke, *This Journal*, **106**, 315 (1959).
8. C. S. Fuller, F. H. Doleiden, and K. Wolfstirn, *J. Phys. Solids*, **13**, 187 (1960).
9. G. H. Schwuttke, O. Weinreich, and P. H. Keck, *This Journal*, **105**, 706 (1958).
10. G. H. Schwuttke, Paper presented at Semiconductor Sym. of Electrochem. Society, Chicago (1960).
11. W. Kaiser, P. H. Keck, and C. F. Lange, *Phys. Rev.*, **101**, 1264 (1956).
12. J. D. Struthers, *J. Appl. Phys.*, **97**, 1560 (1956).
13. G. H. Schwuttke, Symposium on Ultrapurification of Semiconductor Materials, Boston, Mass., (April 1961).
14. G. H. Schwuttke, AIME Symposium on Direct Observation of Imperfections, St. Louis, (March 1961).
15. J. A. M. Dickhoff, *Solid State Electronics*, **1**, 202 (1960).
16. R. Bullough, R. C. Newman, J. Wakefield, and J. B. Willis, *J. Appl. Phys.*, **31**, 707 (1960).
17. A. Goetzberger and W. Shockley, *ibid.*, **31**, 1821 (1960).

Etching Ge with Mixtures of $HF-H_2O_2-H_2O$

J. Bloem and J. C. van Vessem

Semiconductor Development Laboratory, N. V. Philips' Gloeilampenfabrieken, Nijmegen, Holland

ABSTRACT

Etch rate *vs.* composition of the etchant ($HF-H_2O_2-H_2O$) was studied, together with the surface structures after etching Ge single crystals. Conclusions concerning the orientation dependence and the kinetics of the etching process are given. The ratio of the etch rate on different faces depends on the value of C_{H_2O}/C_{HF} in the etchant independent of the H_2O_2 concentration, whereas visible oxide films are formed for a $C_{H_2O_2}/C_{HF}$ ratio smaller than the stoichiometric ratio given by the over-all reaction:

$$Ge + 2H_2O_2 + 6HF \leftrightharpoons H_2GeF_6 + 4H_2O$$

Much work has already been done on the etching of Ge single crystals with mixtures of $HF-H_2O_2$ and H_2O (1-9). This work has been extended by studying the etch rates on (111) oriented Ge crystals at room temperature as a function of etchant composition and by a study of the surface structures after etching.

The Ge pellets used (dimensions 3 x 3 x 0.25 mm, 2-3 ohm-cm N-type) were cut along (111) planes to within 0.5 degree, the surfaces were polished with No. 500 carborundum abrasive powder. Etching was performed in a polyethylene vessel, rotating in a constant temperature bath (25°C). The vessel was inclined in order to be sure of adequate stirring. About 50 crystals at a time were etched in 250 cc of etchant.

After etching the etchant was quenched with water and poured off After washing and drying the thickness of the pellets was measured to within 1μ. Etching times were used to give a total decrease in thickness of about 100μ in each case. This procedure essentially follows that during fabrication, and the influence of damaged surface layers on the etch rate is small. The etch rate has been defined as that on a single surface in μ/min, thus half the decrease in thickness per unit time.

Etch Rates

The results are plotted in a tri-axial diagram (Fig. 1), where the basic components in the three corners correspond to pure water, concentrated HF (50%), and H_2O_2 (30%), respectively. The concentrations are expressed volume percent. Each composition corresponds to a certain point in the diagram to which in turn the appropriate etch rate can be attached. In Fig. 1 contour lines of equal etch rates, at room temperature, on a single Ge surface are given.

Maximum etch rates are found for about equal volume parts of HF and H_2O_2; on dilution with water the etch rate decreases. As the HF contains 28.8 moles HF/l and the H_2O_2 used 9.8 moles/l, equal volume parts of both compose a nearly stoichiometric etchant according to the over-all reaction:

$$Ge + 2H_2O_2 + 6HF \leftrightharpoons H_2GeF_6 + 4H_2O \qquad [1]$$

Figure 1 also shows that for low H_2O_2 or HF concentrations the etch rates vary proportional to this H_2O_2 or HF content.

The etch rates are strongly temperature dependent; a plot of log R over $1/T$ shows that for the stoichiometric etchants a variation in etch rate of about 6% per degree at room temperature is found (activation energy of 10.7 kcal/mole). It is quite possible that with less H_2O_2 or HF another activation energy is obtained, as other reaction steps may then become rate limiting. The experimental results at room temperature can be described by the following empirical formula

$$R = \frac{C_1C_2}{2.4C_1 + 1.0C_2 + 0.2C_3}\ \mu/\text{min}$$

where R is the etch rate in μ/min on a single (111) oriented surface, and C_1, C_2 and C_3 the concentrations of H_2O_2, HF, and H_2O, respectively, in volume per cents of the added reagents. For the higher etch rates (greater than 10-15 μ/min on a single surface) an exponential increase appears over the calculated values, even with good stirring, due to an inevitable temperature rise at the reacting surfaces.

Surface Structures

As to the surface structures after etching, in most cases the (111) surface is covered with small tri-

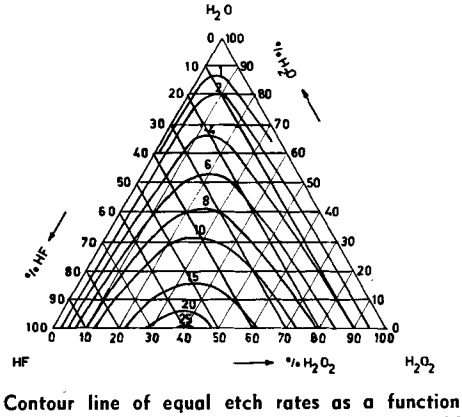

Fig. 1. Contour line of equal etch rates as a function of the composition of the etchant (volume parts of 50% HF, 30% H_2O_2, and water). The numbers in the figure refer to etch rates on a single surface of the crystal in μ/min.

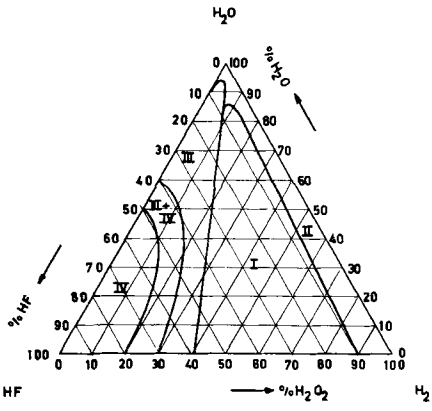

Fig. 2. Regions of different surface structures after etching: I, shiny surface with etch triangles; II, dull surface with etch triangles; III, thin oxide layer under which there are etch triangles; IV, thick oxide layer on top of amorphous surface structure.

angular etch figures. These figures are not related to the presence of dislocations, but arise from the original surface roughness (2, 3).

The surface structures after etching are indicated in Fig. 2. Four regions can be distinguished: (I) the etch triangles are well developed, the crystals having a shiny appearance; (II) the HF deficiency gives rise to somewhat dull surfaces in which the triangular pits are still present; (III) after etching a slight oxide film becomes visible (2). This film is readily soluble in H_2O_2; underneath the film small etch triangles are present; (IV) gives thicker oxide layers after etching, also soluble in H_2O_2. Underneath this film etch triangles can no longer be found, the surface is dull (1).

Growth of etch pits.—In the regions where etch triangles are found the growth rate of these triangles on prolonged etching also depends on the etchant composition. In general, the greater the water content the greater the size of the pits for the same decrease in thickness. For a number of etchants the growth of the pits was followed as a function of the decrease in thickness; initially the whole surface was covered with tiny pits; on prolonged etching the pits grow and overlapping occurs. Some results are

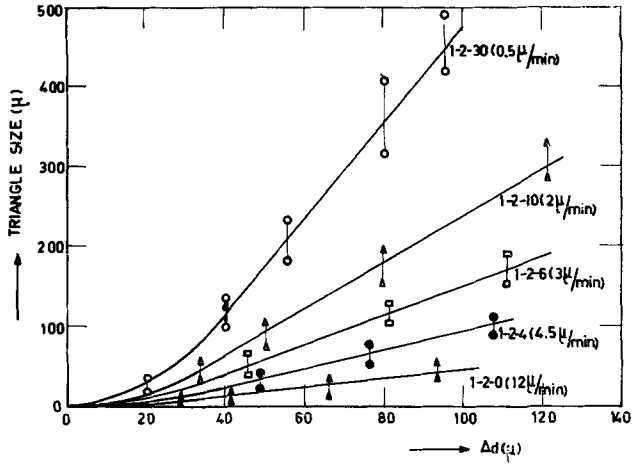

Fig. 3. Growth of the sides of etch triangles vs. decrease in thickness during etching. The greater growth rates are found for the slower etchants (e.g., the composition 1-2-30 indicates the number of volume parts of HF-H_2O_2 and H_2O in the etchant, respectively).

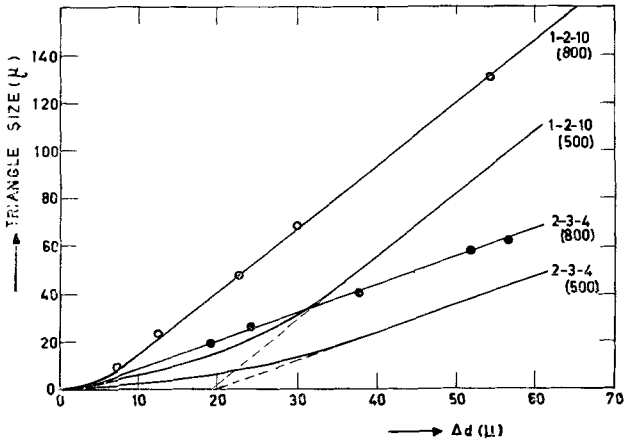

Fig. 4. Growth of etch triangles for Ge crystals lapped with No. 500 and No. 800 carborundum powder (mean grain size 32 and 14μ, respectively). The ultimate slopes are the same, the initial part, *i.e.*, the thickness of the worked layer, is different.

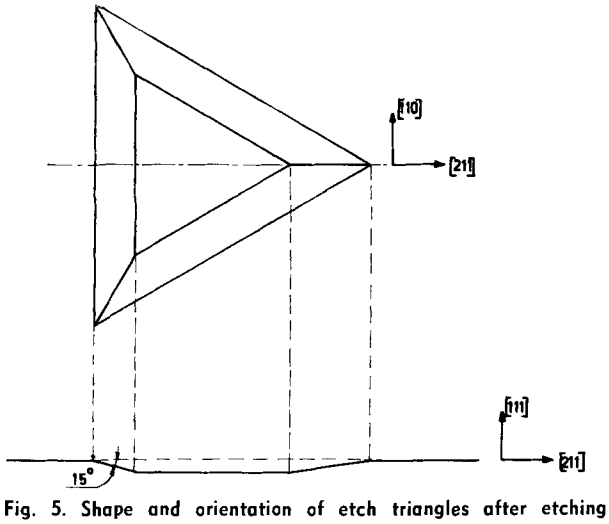

Fig. 5. Shape and orientation of etch triangles after etching (111) oriented Ge crystals.

given in Fig. 3 and 4. After an initial period in which the lapped layer is removed, the triangles begin to grow, the faster the lower the etch rate. Closer inspection of the etch figures (Fig. 5) reveals that the bottom of the pits is formed by a (111) plane, the sides of the pits making an angle of about 15° with the (111) surface. These sides are close to (322) planes. According to Battermann (3) this has to be expected as this orientation shows a relative maximum in etch rate compared with neighboring orientations in the (110) zone. As pointed out in ref. (3) the pits originate from the original surface roughness, as on the concave parts of the surface the slow etching (111) face is exposed, forming the bottom of the pits, whereas on the convex parts of the surface the fast etching (322) facets are stable, giving the sides of the etch triangles.[1]

Etch rates on (111) and (322) faces.—Since the sides of the pits consist of fast etching (322) planes

[1] Similar arguments can be used to explain why on wetting and alloying, e.g., In on Ge, alloy pits are found which tend to be triangular with an orientation different from those of the etch triangles. In this case the first rapid dissolution of Ge in the In pellet does not show any orientation dependency (10), and a hollow shaped cavity is formed. With prolonged alloying the rate of attack decreases because of the higher Ge content of the In; now the orientation begins to show its influence. As the pit already has a concave shape only the slow dissolving (111) faces are exposed, giving the pit a semi-triangular pattern which is rotated 60° if compared with the etch triangles on the same surface, bounded by (322) facets. The difference between normal alloy pits and etch triangles thus is found in the sides of the pits originating from a different mode of attack.

Table I. Etch rates (R), growth rate of etch triangles vs. decrease in thickness (exp. slopes) and the calculated value of the ratio of the etch rates on the sides and on the bottom of the pits (R_s/R_{111}) for various etchants

Etchant (HF-H_2O_2-H_2O)	R (μ/min)	Exp. slope	R_s/R_{111} (calc.)
1-2-0	12	0.60	1.06
1-2-2	6.5	0.85	1.09
1-2-4	4.5	1.2	1.14
1-2-6	3.2	1.9	1.24
1-2-10	2.0	3.0	1.40
1-2-30	0.5	6.0	1.86
1-6-0	5.0	0.60	1.06
1-6-3	3.5	0.90	1.10
1-6-13	1.7	3.0	1.40
1-6-23	1.0	4.5	1.63
2-1-0	25	0.9	1.10
2-1-10	2.0	1.9	1.24
2-1-30	0.55	4.0	1.56
1-1-0	20	0.50	1.03
1-1-2	7.5	1.12	1.13
1-1-4	4	1.75	1.22
1-1-8	1.6	2.3	1.30
1-1-18	0.6	3.8	1.54
1-1-28	0.3	5.4	1.77

and the bottom of the slow etching (111) plane, the growth of the pits *vs.* the decrease in thickness of the (111) oriented crystal is a function of the ratio of the etch rate on the (322) and (111) faces (R_s/R_{111}). The ratio R_s/R_{111} was calculated from the slopes of experimental curves given in Fig. 3 (see appendix A). Some examples are given in Table I.

Battermann (3) experimentally found a ratio $R_s/R_{111} = 1.2$ for an 1-1-4 etchant which value has to be compared with the calculated value of 1.22 given in Table I. From Table I it can be seen that in general a greater water content (low etch rate) will give values of R_s/R_{111} near to 2; for rapid etchants this ratio is about 1. Apart from this general trend a closer analysis shows that actually the ratio of the water and the HF content determines this value of R_s/R_{111}, independent of the peroxide concentration. Figure 6 shows this empirical relationship[2] which can be expressed as follows

$$\frac{R_s}{R_{111}} = 1 + 0.014\,\frac{C_{H_2O}}{C_{HF}} \text{ (concentration in moles/l)} \quad [2]$$

Discussion

From the relations found in the preceding section some conclusions can be drawn regarding the kinetics of the orientation dependent etching. In general (322) and (110) faces etch fast, while (100) and (111) are slower (1, 3). It has been shown above that such differences may disappear for higher etch rates (high HF and low H_2O content). By way of explanation it is worth noting that the fast and the slow etching faces have characteristic differences in atomic surface structures (Fig. 7). The former [(110) type] have surface atoms (bearing unsaturated "dangling" bonds) bonded directly to other surface atoms whereas the latter [(111) type] have Ge surface atoms bonded only to deeper lying "normal" Ge atoms.

[2] As the added H_2O_2 and HF also contain water, in Fig. 6 the ratio C_{H_2O}/C_{HF} is not determined from the amount of added reagents, but the total amount of H_2O and HF is expressed in moles per liter.

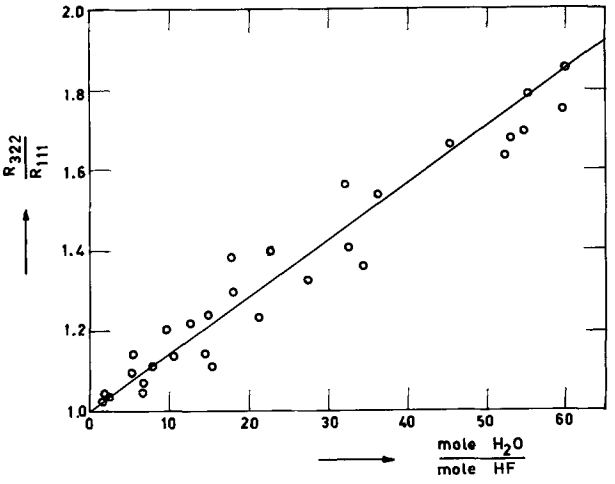

Fig. 6. The ratio of etch rates on the sides and bottom of the etch pits (R_{322}/R_{111}) for various etchants, plotted vs. the ratio of water and HF content in the etchant used, e.g., the higher the water content the faster the growth rate of the etch pits.

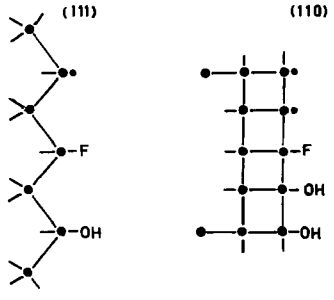

Fig. 7. Two types of surface structures, the (111)-type has surface atoms bonded only to deeper lying normal atoms; for the fast etching (110)-type the surface atoms are interconnected mutually.

It is postulated now that the Ge-Ge- bond of the slow etching (111) faces can be broken readily by H_2O_2 only if the surface atom carries the strongly electronegative F atom; the reaction rate is appreciably smaller if an OH group is attached to this surface atom. For the fast etching orientations of the (110) type this difference will be smaller as on each side of the bond the surface atoms carry electronegative atoms or groups (see Fig. 7).

The first reactions of the dangling bonds with the etchant will lead to the formation of [GeF]- and [GeOH]- groups (11). An "equilibrium"

$$[GeOH] + HF \leftrightharpoons [GeF] + H_2O$$

could be present giving

$$\frac{N_{OH}}{N_F} = K \cdot \frac{C_{H_2O}}{C_{HF}} \quad [3]$$

where N_{OH} and N_F denote the number of surface sites per unit area carrying an OH group or F atom, respectively. If this step is rate determining, which is possible for small HF and large H_2O concentrations, then the orientation dependent reaction rate could be proportional to the number of sites where the first H_2O_2 attack can be effectuated successfully, hence:

$$\frac{R'}{R''} = \frac{k'(N'_F + K'N'_{OH})}{k''(N''_F + K''N''_{OH})} \quad ; \quad (K'' << K' < 1) \quad [4]$$

Here a single prime indicates a property of the (110) and (322) type of surface and a double prime indi-

cates a (111) or (100) property. For the (111) type it is assumed that reactions at (OH) sites are much slower than on (F) sites; thus $K'' << N''_F/N''_{OH}$ then:

$$\frac{R'}{R''} = \frac{k'}{k''}\left(\frac{N'_F + K'N'_{OH}}{N''_F}\right)$$

With Eq. [3] this leads to

$$\frac{R'}{R''} = \frac{k'}{k''}\left(\frac{N'_F}{N''_F} + K'K\frac{N'_F}{N''_F}\cdot\frac{C_{H_2O}}{C_{HF}}\right)$$

$$= \frac{k'N'_F}{k''N''_F}\left(1 + K'K\frac{C_{H_2O}}{C_{HF}}\right) \quad [5]$$

Comparison with [2] shows that the observed relationship could be explained with the additional assumption that $k'N'_F \sim k''N''_F$, which means that the reaction rates on (F) sites for both the (110) and (111) type of surface are about the same.[3]

Conclusion

It seems reasonable to assume that in regions where the etch triangles are formed the orientation dependent etch rates are governed by the first steps in the reaction mechanism where the ratio C_{H_2O}/C_{HF} determines the differences in reaction rate on various crystal faces. This ratio will influence the amount of OH groups and F atoms bonded to the surface Ge atoms. This gives a slow etching (111) or (100) face if only Ge atoms carrying a F group can be oxidized easily on this type of surface. This is in contrast to the (110) and (322) type of surface where oxidation can be successful on Ge atoms bonded to OH or F radicals.

This will be the case especially for the lower etch rates where the water content is relatively high. For the more concentrated, faster etching mixtures the orientation dependence vanishes and a diffusion limited reaction rate could be predominant eventually.

Also for a low peroxide concentration no orientation dependence is found, and visible oxide films are present after etching. In this case it is possible that the oxidation potential near the Ge surface is so low that the oxidation of surface atoms from the divalent to the tetravalent state becomes more difficult, leading to the intermediate formation of GeO films.

[3] The reviewer of this paper has drawn the author's attention to an interesting comparison of the derived and empirical equations. Since $KK' = 0.014$ and $K' < 1$ (according to the hypothesis), then K must be fairly large (~ 1), i.e., the ratio $N_{OH}/N_F \sim C_{H_2O}/C_{HF}$.

Manuscript received July 14, 1961; revised manuscript received Sept. 1, 1961. This paper was prepared for delivery before the Houston Meeting, Oct. 9-13, 1960.

Any discussion of this paper will appear in a Discussion Section to be published in the December 1962 JOURNAL.

APPENDIX A

It can be shown that on etching the outward displacement p of the side of an etch pit per unit time is given by

$$p = \frac{R_s/\cos\alpha - R_{111}}{\tan\alpha}$$

where R_{111} is the etch rate on the original (111) surface, R_s the etch rate on the side of the etch pit, and α the angle between (111) and side of the pit (about 15°). Thus the triangle widens as $R_s/\cos\alpha > R_{111}$ with a rate of p μ/min. The increase in size of the edges of the triangle then is given by $2\sqrt{3}\ p$ μ/min. The ratio of the increase in size of the edges to the decrease in thickness can be given as

$$\frac{r}{\Delta d} = \frac{2\sqrt{3}\ (R_s/\cos\alpha - R_{111})t}{2R_{111}\tan\alpha\cdot t}$$

$$= 1.72\left(\frac{R_s}{R_{111}\cos\alpha} - 1\right)\cot\tan\alpha$$

A mean value for α of 15° gives

$$\frac{r}{\Delta d} = 6.4\left(\frac{R_s}{0.96R_{111}} - 1\right)$$

In Fig. 3, $r/\Delta d$ is found as the slope of the experimental curves for $\Delta d > 20\mu$.

REFERENCES

1. P. J. Camp, *This Journal*, **102**, 586 (1955).
2. S. G. Ellis, *J. Appl. Phys.*, **28**, 1262 (1957).
3. B. W. Battermann, *ibid.*, **28**, 1236 (1957).
4. D. Geist and E. Preuss, *Z. angew. Phys.*, **9**, 526 (1957).
5. P. Wang, *Sylvania Technol.*, **9**, 50 (1958).
6. P. J. Holmes, *Acta Met.*, **7**, 283 (1959).
7. B. A. Irving, *J. Appl. Phys.*, **31**, 109 (1960).
8. W. Riessler, *Z. angew. Phys.*, **12**, 433 (1960).
9. F. C. Frank and M. B. Ives, *J. Appl. Phys.*, **31**, 1996 (1960).
10. B. Goldstein, *RCA Rev.*, **18**, 213 (1957).
11. M. Michelitsch, *Z. angew. Phys.*, **12**, 180 (1960).

Controlled Etching of Silicon in the HF-HNO_3 System

D. L. Klein and D. J. D'Stefan

Bell Telephone Laboratories, Incorporated, Murray Hill, New Jersey

ABSTRACT

Some of the important factors that affect the degree of reproducibility of desired dimensions, flatness, and surface finish of chemically etched silicon have been investigated. The etching rate of single crystal silicon in hydrofluoric and nitric acids was studied as a function of the ratio of the concentrated acids, temperature, and stirring rate. These variables were found to be related to the etching rates over the ranges studied. No difference in etch rate was observed for n, p and n-p junction silicon, ranging in resistivity from 0.05 to 78 ohm-cm. The etch rate appears to be dependent on the diffusion of the fluoride species to the silicon surface in the nitric acid-rich region. The controlled etching technique has been applied to the etch-cutting of wafers from selectively masked silicon slices. Preliminary investigation has shown that this method is applicable for the preparation of slices for diffusion processing.

With the more sophisticated semiconductor devices now under development, dimensional control is becoming increasingly important. Regulation of the flatness and surface finish as well as the size of wafers and mesas require close dimensional control.

Silicon shaping processes now generally employ abrasive cutting and polishing techniques which are known to introduce surface damage. Therefore, devices must be etched following abrasive shaping to remove this damage. Final control of dimensions must then logically lie in the regulation of the etching process. Direct etch-cutting makes it possible to produce devices with surfaces approaching the degree of perfection inherent in the bulk material.

In order to achieve control of chemical etching, it is necessary to understand the important variables involved and their effects on the kinetics of silicon dissolution. The variables investigated and reported in this paper include etch composition, temperature, and stirring as they were observed on n, p, and junction-containing material over wide resistivity ranges. Additionally, some factors which affect the degree of roughness and the flatness of surfaces were examined.

The most commonly employed etches for silicon contain nitric and hydrofluoric acids together with one or more additives, such as acetic acid, bromine, iodine, and silver or mercuric nitrates (1). These additives are employed to modify the rate of reaction, the finish of the etched surface, or to cause preferential etching of certain crystallographic planes. However, to simplify the kinetics, the present study was limited to the concentrated hydrofluoric-nitric acid system.

Experimental Procedure

The etching was carried out in a specially constructed apparatus. This apparatus provided a close control of the etchant temperature as well as a means for stirring the solution and rotating the silicon samples at a constant rate. The etching solution was contained in a 400 ml polyethylene beaker sealed into a metal water jacket. Water was circulated through this jacket from an external constant temperature bath to control the temperature of the contents of the beaker to within $\pm 0.5°C$.

The samples to be etched were held in a slotted Teflon post by means of a Teflon set-screw. This post was fastened in the center of a flat Teflon disk surrounded by four Teflon blades which served as stirring paddles. The plastic disk assembly was held above the etching beaker by a movable bracket on which the stirring motor was also mounted. This movable bracket permitted the assembly to be lowered into and raised from the etching beaker. An electrical braking system stopped the stirring motor whenever the assembly was withdrawn from the beaker. In this manner the reaction could be quenched safely in less than 2 sec after withdrawal from the etch by immersing the assembly in a beaker of deionized water. Motor speeds were varied between 11 and 88 rpm.

The silicon used in this experiment was cut from single crystal ingots. The n- and p-type samples were cut perpendicular to the <111> and the n-p grown-junction samples were cut parallel to the <100>. All of the samples were cut so that their final dimensions were approximately 0.76 mm thick by 6.3 mm wide with lengths between 1.2 and 4 cm. The bulk resistivity of the material used was: n-type, 0.05-8.0 ohm-cm; p-type, 12.0-78.0; and the n-p samples averaged 0.3 ohm-cm on the n-side while the p-side averaged 5.0 ohm-cm.

Reagent grade nitric acid (69.9% assay) and reagent grade hydrofluoric acid (49.2% assay) were used for all mixtures reported herein as volume percentages.

Some consideration was given to the effects that long time storage might have on the reproducibility of prepared etches. No difference was observed in etch rate between batches of etch used within ½ hr of mixing and batches stored for as long as three months.

Etch rates, reported in microns per minute, were derived from weight loss measurements. Weight

losses were at least ten times the sensitivity of the balance (±0.2 mg).

Changes in thickness of all the samples were also determined directly with a micrometer having a vernier capable of being read to 0.0001 in. to verify the results of the weight loss method.

The flatness of several typical surfaces was determined by measuring differences of thickness across the width of the samples with a dial micrometer gauge. The accuracy of the gauge used was ±0.0001 in. Values for surface roughness were obtained by means of a Brush Surface Analyzer, Model BL103.

Results and Discussion

The rate of silicon dissolution in the HF-HNO_3 system has been examined over the entire composition range. In the concentration interval from 2 to about 65% HF the etch rate was found to increase with HF content. Between 65 and 70% HF the etch rate was observed to reach a maximum. Beyond the maximum, the rate was found to decrease until the dissolution reaction ceased in pure HF. The curve representing these data is shown as an insert in Fig. 1.

Staining of the silicon samples was encountered in etches containing less than 30% HNO_3 (2). Due to the stains, rate measurements based on weight loss or the change in thickness were difficult to make with a high degree of precision. In addition, the HF-rich portion of the system has a higher etch-rate dependence on the minority component than is found in the HNO_3-rich region. From a practical standpoint, therefore, etch-rate control is best achieved in etches containing less than 65% HF. For these reasons, only the nitric acid-rich region of the binary system was studied in detail.

Between 10 and 50% HF, the logarithm of the etch rate was found to be related linearly to the HF concentration while below 10% HF the rate was found to be directly proportional to the HF concentration. This observed change in the rate dependence below 10% HF possibly may result from an association of the HF with HNO_3. Association could reduce the effective concentration or the mobility of the reactive fluoride species required for the dissolution process.

Temperature.—The effect of temperature on the reaction rate was determined between 0 and 60°C for several etch compositions. Essentially, over this small temperature interval and for etch compositions containing between 2 and 50% HF, the reaction rates were found to increase linearly with temperature. When the data were plotted in a form suitable for the application of the Arrhenius equation ($1/T$ in degrees K *vs.* log reaction rate), the curves were found to have the same slope. This suggests that despite the change in the reaction rate slope at 10% HF (Fig. 1), the activation energy remains constant from 2 to at least 30% HF, the highest composition studied in determining this value. Using the Arrhenius equation, the activation energy was found to be 3.9 kcal/mole. This value compares favorably with the value of 4.1 kcal/mole reported by Schwartz and Robbins (3). Activation energies of this order of magnitude are recognized as indicating that the rate-determining step of the system is diffusion dependent. This point is considered in detail in a later section.

From a technological standpoint, the temperature dependence of the reaction rate is most important whenever a high degree of dimensional control must be considered. An illustration of the importance of temperature control was demonstrated when a sample of 10 cm^2 area was placed in 25 ml of a 30% HF-70% HNO_3 etch contained in a Teflon beaker. A wax-coated thermocouple placed within the beaker indicated a temperature rise of 70°C in 10 min. Within this period of time the reaction rate had more than doubled due to the temperature rise. Thus, with moderately fast etches, operating under essentially adiabatic conditions, there is little chance for good control of the etching rate due to thermal runaway. By employing large volumes of slow-acting etches (etches low in HF concentration) with constant agitation, however, the system can be operated under essentially isothermal conditions. In this way it has

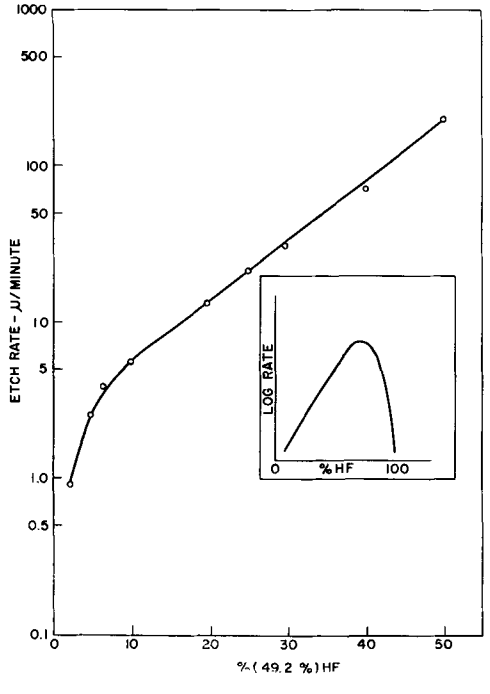

Fig. 1. Rate of reaction with respect to etch composition. Each experimental point is the mean of the values determined for n- and p-type samples; temperature 30°C; rotation, 88 rpm.

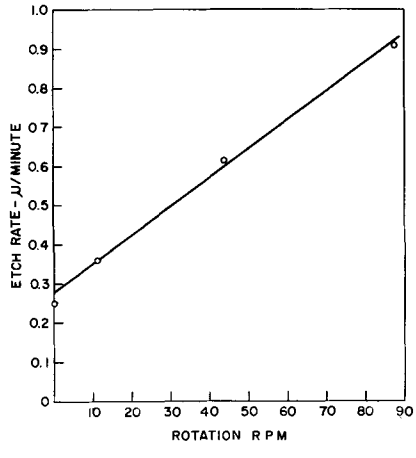

Fig. 2. Effect of rotation on etch rate. Temperature, 30°C; etch composition, 2% (49%) HF—98% (70%) HNO_3.

been found possible, with a slow etch, to limit the maximum temperature rise in an unthermostated system to 3°C in an etching bath operating at an ambient temperature of 25°C.

Rotation.—The rate of reaction was found to be directly related to the speed of sample rotation at constant temperature for etch compositions between 2 and 50% HF. A typical curve is shown in Fig. 2. An interesting relationship exists between the etch rate at various speeds of rotation and the HF concentration of the etch. If a plot is made of

$$\log r = Ra/Rb \qquad [1]$$

where r is the coefficient of rotation, Ra the etch rate at 88 rpm, and Rb the etch rate at 0 rpm with respect to the etch composition, a linear dependence was obtained as shown in Fig. 3. The increase in rotation-rate dependence with decreasing HF concentration will be used later to show that the dissolution of silicon is diffusion dependent with respect to HF in HNO_3-rich etches. Based on practical considerations, it might be thought that etch compositions in the range of the maximum etch rate (about 65% HF) might be advantageous since there is so little rotation dependence. Unfortunately, this apparent advantage is of no real value since the reaction rates are so fast that a high degree of control would be extremely difficult to achieve. In addition, rotation is important in order to prevent convection stirring of the etchant. Convection stirring will cause local temperature differentials to develop across the surface of the sample and will result in an increase in the average surface roughness. This is due to the increased etch rates on those areas of higher temperature.

Dissolution mechanisms.—According to Turner (4), the dissolution of silicon in HF-HNO_3 may be thought of as an electrolytic action wherein local anodic and cathodic sites develop on the surfaces of the semiconductor. Feuillade, Marette, and Dumontier (5) have also proposed an electrolytic mechanism for the corrosion of silicon. In addition to the electrolytic attack, they also have suggested that a localized consecutive chemical reaction can take place on the surface of the semiconductor.

The electrolytic attack described by Feuillade, Marette, and Dumontier may be shown diagrammatically:

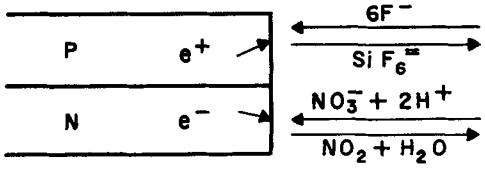

and written:

$$4e^+ + Si + 6F^- \rightarrow SiF_6^= \qquad [2]$$

$$4e^- + 8H^+ + 4NO_3^- \rightarrow 4NO_2 + 4H_2O \qquad [3]$$

This type of reaction would preferentially remove p-type sites. The local chemical attack is a reduction-oxidation reaction followed by the dissolution of the silicon dioxide formed. These reactions can be written

$$Si + 4HNO_3 \rightarrow SiO_2 + 4NO_2 + 2H_2O \qquad [4]$$

$$SiO_2 + 6HF \rightarrow H_2SiF_6 + 2H_2O \qquad [5]$$

Although NO_2 must be formed in the etching process as evidenced by the appearance of the brown fumes of the NO_2 dimer, N_2O_4, it is possible that NO also results from the reduction of the nitric acid according to the reaction

$$3e^- + 3H^+ + HNO_3 \rightarrow NO + 2H_2O \qquad [6]$$

Turner (4) has pointed out that the ratio $[HF]/[HNO_3] = 4.5$, corresponding to the stoichiometry of the reaction

$$3Si + 4HNO_3 + 18HF \rightarrow 3H_2SiF_6 + 4NO + 8H_2O \qquad [7]$$

is very close to the ratio of the molar acid concentrations that occur at the maximum etch rate observed in the HF-HNO_3 system. This is cited as support for the formation of NO as the major reduction product of HNO_3.

If, in the absence of a junction, the etching of silicon proceeds through a stepwise process, the etch rate might be expected to be diffusion controlled except when $[HF]/[HNO_3]$ approaches 4.5. It should be understood that the molar ratio $[HF]/[HNO_3] = 4.5$ is significant in supporting a diffusion-controlled mechanism only if the diffusion and temperature coefficients of the active species of both the hydrofluoric and nitric acid are the same. Since these active species have not yet been identified, the values of the coefficients have not been determined. It is further assumed for this argument that both the molecular oxidation to SiO_2 and the molecular reaction of SiO_2 to form H_2SiF_6 are essentially instantaneous. For etches low in HF, the surface of the silicon will be covered with an oxide film, probably SiO_2, whenever the reactive fluoride species arrives at the etch-semiconductor interface, due to abundance of the oxidizing agent. Under this condition the rate of silicon removal will be rate-dependent on the arrival of HF at the SiO_2 surface. If the HF is consumed immediately at this surface by reaction [5], the surface concentration of HF will be zero. In this manner, a concentration gradient of HF will develop from the silicon interface back into the bulk of solution. For a given HF concentration, the rate of arrival of HF at the interface will be directly related to the thick-

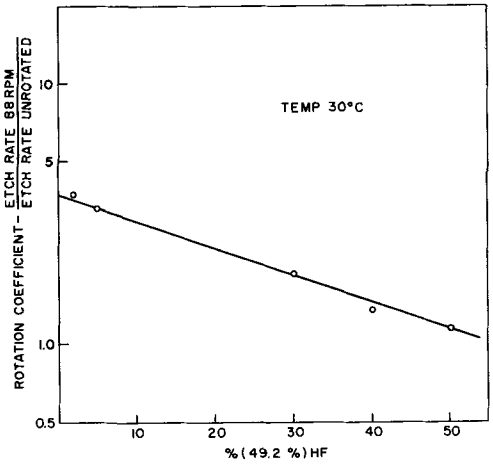

Fig. 3. Decrease in etch rate dependence on the rotation velocity with increasing HF content of the etchant; temperature 30°C.

ness of the diffusion layer. The thickness of diffusion layers of this type is known to be related inversely to the velocity of the interface with respect to the bulk of the solution (6). Thus, with increased rotation of the surface under attack, the thickness of the concentration gradient will decrease so that the diffusion time for an HF molecule to traverse this gradient will become smaller. This effect, that the etch rate does increase with increasing speed of rotation of the sample, has been observed as shown in Fig. 2. As expected, when the HF concentration in the etch was increased, the dependence of etch rate with rotation speed did become smaller (Fig. 3). The extrapolated value of about 60% HF, where the etch-rate dependence on rotation vanished, corresponds closely to the $[HF]/[HNO_3] = 4.5$ value expected. As mentioned previously, the relatively small activation energy of 3.9 kcal/mole measured for the dissolution process supports the contention that the reaction is diffusion controlled in the nitric acid-rich portion of the system.

The electrolytic attack proposed by Feuillade, Marette, and Dumontier should also show diffusion dependence with respect to the minority acid species present in the etch. In this situation, because of the necessity of charge balance, the concurrent oxidation-reduction reaction can occur at a rate no faster than the arrival at the surface of the minority reactant.

The electrolytic mechanism of silicon corrosion was clearly observed when p-n grown junction samples were etched. At distances greater than about 0.025 mm from the junction, the etch-rate was found to proceed at the same rate on the p- and on the n-sides of the junction. At these points, the reaction is believed to proceed through the nondifferentiating consecutive-type of local chemical attack. However, in the immediate vicinity of a junction with a large built-in electric field, the reaction changes abruptly to include an electrolytic attack which produces preferential etching of the p-side of the junction. This effect is shown for a typical sample in Fig. 4. In this case the etch rate in the immediate vicinity of the p-side of the junction was found to be about 60% greater than the remainder of the surface. The n-type silicon close to the junction exhibited a decrease in etch rate of the same magnitude. On the

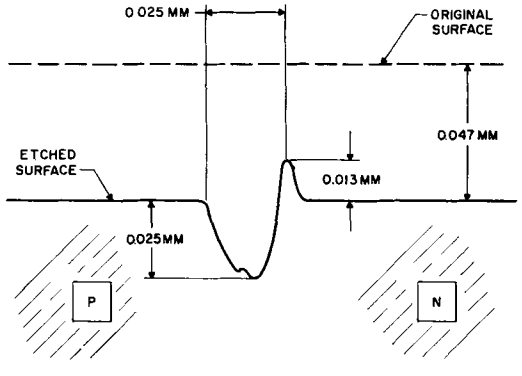

Fig. 4. A cross-section profile of a grown p-n junction after etching. The actual junction probably occurs close to the bottom of the trough. Temperature, 20°C; rotation, 88 rpm; etch composition, 2% (49.2%) HF-98% (70%) HNO_3. (Drawn to scale).

p-side, Eq. [2] is applicable and silicon is removed as H_2SiF_6. On the n-side, the cathodic reduction of the HNO_3 must take place. This reaction does not involve the corrosion of silicon and, therefore, the unattacked silicon is left as a small raised portion on the surface of the n-side of the junction.

For samples of single conductivity, the etch rate was found to be constant and reproducible (±5%), independent of the conductivity type and resistivity (0.05-78 ohm-cm) in etches containing between 2 and 50% HF. Also, no difference was observed between samples cut perpendicular to the <111> axis and those cut parallel to the <100> axis.

The absence of any detectable difference in etch rate between p- and n-type samples in nitric acid-rich etches suggests that the consecutive-type reaction, described in Eq. [4], [5], and [7] takes place. According to Dewald (7), the dissolution of germanium involves the diffusion of 2 electrons away from and 2 holes toward the interface. For silicon this type of reaction can be written

$$Si + 2e^+ \rightarrow Si^{+4} + 2e^- \qquad [8]$$

In the HF-HNO_3 system, the nitric acid serves as the electron acceptor. The holes must be supplied from the bulk of the silicon sample. So long as the electron acceptor, nitric acid, is present in large excess and the diffusion time for the HF to reach the interface is greater than the time necessary for either holes or electrons to diffuse to the surface, the etch rate will be independent of the conductivity type of the silicon. In etches of low HF content, the diffusion velocity of holes or electrons to the silicon surfaces can be expected to be faster than the diffusion of the fluoride species through the solution. As long as the reaction rate is diffusion dependent on the supply of HF to the surface, no differentiation of the etch rate will be observed between n- and p-type samples. With etch rates close to the maximum that occurs at about 65% HF this condition may not be satisfied, and it is possible that the etch rate of p-type material will be higher than n-type silicon.

Surface roughness and flatness.—A mechanically worked surface will etch at a faster rate than the undamaged body of a sample (8). This effect is due, in part, to the increased area of an abraded surface compared to a polished surface. Additionally, the faster rate probably is brought about by the formation of sites whose potential is markedly different from the average crystal value. The relative difference in potential between these sites and the adjacent surface would permit the electrolytic mode of corrosion to occur. As this mode probably operates at a generally higher etch rate than the local consecutive chemical attack, the surface will be consumed at a faster rate than would be observed for a surface with uniform potential.

For the critical removal of small amounts of silicon from samples which were previously lapped, some knowledge of the accelerated etch rate due to mechanical damage would be required. The rate of etching of the damaged surface produced by an 1800 mesh Al_2O_3 lap, after 0.5 min was determined to be about 3 times the steady-state etch rate of the sample. From the data, the average depth of damage appears

to correspond to approximately half of the diameter of the particle size of the abrasive. For 1800 mesh Al_2O_3 this is equivalent to 6μ of damaged material. This agrees closely with the value previously reported by Buck (8). In practice, when the amount of silicon to be removed is an order of magnitude greater than the depth of damage, the initially faster etch rate is of little importance.

The flatness of several typical surfaces was determined by measuring differences of thickness across the width of the samples. In 5 vol. % HF, it was observed on unrotated samples that edges were attacked faster than the faces and resulted in rounded edges of approximately 0.6 mm radius. In the same HF concentration, rotation of the samples increased the radius of curvature of leading diagonally opposite edges to approximately 0.9 mm, due to streaming of the etchant. The faces of the samples that had been rotated were found to be planar to within $\pm 12\mu$.

Surface roughness was determined by means of a Brush surface analyzer. The original surface of the lapped samples had an average roughness of 2.2μ. The average surface roughness after removal of 50μ of material from the surface with nitric acid-rich etches was found to be 0.40μ. The 5% HF etch consistently yielded the lowest surface roughness (0.29μ average). This does not seem to be due to the slowness of the etch since 2% HF etches always yielded rougher surfaces (0.45μ average).

During the course of repeated etching of a sample, it was observed that the surface roughness increased with each additional etch. Samples etched to a given depth in a single etching operation were found to have an average surface roughness one-third that of samples etched and quenched 15 times, with the same amount of silicon removed in each case. Careful observation showed that small droplets of the etch adhered to the samples after withdrawal from the etch container. The slight depressions etched into the surface, during the 1-2 sec before quenching, became preferential sites for droplets of the etch the next time the sample was withdrawn from solution. This progressive roughening of the surface could be eliminated if the etching reaction was quenched by dilution of the etch with either water or nitric acid, instead of quenching the reaction after withdrawal of the samples.

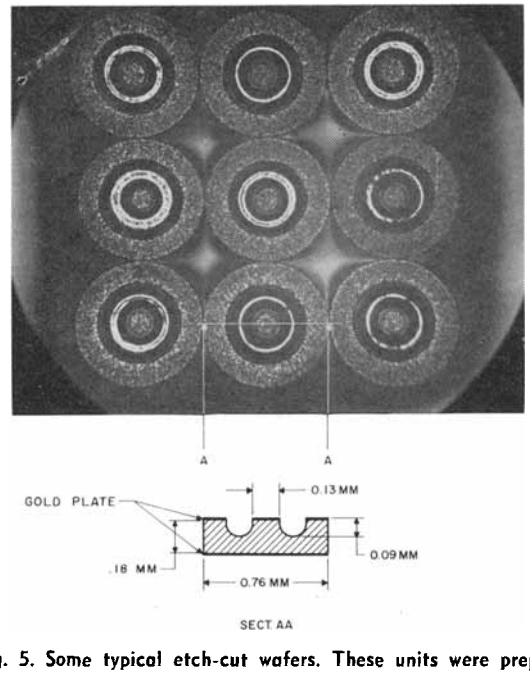

Fig. 5. Some typical etch-cut wafers. These units were prepared in a single operation which produced the mesas and separated the wafers simultaneously. The distortion of the diameters noticeable in all but the center sample is caused by photographic abberation.

Etch-cutting.—Controlled etching by this technique has been applied to the cutting of devices from slices of semiconductor material. The slices to be etched were contained in a platinum mesh basket supported and rotated in the experimental apparatus. Figure 5 shows a group of typical devices produced by this method. These wafers were produced from slices of silicon whose surfaces were masked by selective patterns of electrodeposited gold. The gold served as a mask while the slices were etched. In addition to serving as a mask, the gold provided a direct ohmic contact for the completed devices. Many geometries have been produced by this method. Several thousand devices of 0.76 $\pm$0.064 mm OD containing 0.13 mm diameter mesas have been made. Electrical characteristics of these have been equal to those made by ultrasonic grinding, diamond sawing, scribing and etching, and scribing and breaking processes which were followed by chemical etching.

A major advantage of etch cutting over abrasive techniques is the freedom from damage introduced into the semiconductor material by abrasive cutting action. Since this damage is generally undesirable the usual procedure is to remove it by chemical etching. Direct chemical etch cutting eliminates the damage producing step and greatly simplifies the cutting procedure.

The etching techniques were also evaluated by observing the electrical characteristics of devices made from slices of zone-leveled and pulled-single crystal silicon. These slices were approximately 2.5 cm in diameter and had been lapped with 1800 mesh Al_2O_3. The basic data gathered using small-size silicon samples appear to be completely applicable to the larger surface area slices which are often used for diffusion processing. The reproducibility in final thickness after removing approximately 0.185 mm from one surface of the slices was found to be better than $\pm$5%. The electrical characteristics of PNPN switching devices made from this material have equaled or exceeded the characteristics of similar units prepared by utilizing abrasive operations. The average saturation current of these units was found to be an order of magnitude lower than the control samples prepared by mechanical polishing.

Preliminary investigations indicate that slices of silicon can be controllably etched to thicknesses of less than 0.025 mm. To do this both sides must be etched to remove the mechanical strains introduced by the lapping process.

Summary

By employing nitric acid-rich HF-HNO_3 etches, together with temperature and rotation control, the dimensions of silicon samples can be etched reproducibly to within $\pm$5% of those desired. The applica-

tion of low rate and controlled etches has been used to etch cut complete devices from slices of silicon. In particular, the technique has been successfully employed in the preparation of several thousand mesa diodes of small dimensions. The major advantages gained by employing this technique are the simplicity of the method and the elimination of the damage produced in semiconductors by mechanical cutting.

The degree of control of thickness and surface finish achieved by this method has resulted in etch-polished slices which were found to equal or exceed the requirements for diffusion-doped devices.

Manuscript received June 5, 1961; revised manuscript received Aug. 19, 1961. This paper was prepared for delivery before the Chicago Meeting, May 1-5, 1960.

Any discussion of this paper will appear in a Discussion Section to be published in the December 1962 JOURNAL.

REFERENCES

1. P. Wang, *Sylvania Technologist*, **11**, [2], 50 (1958).
2. C. S. Fuller and J. A. Ditzenberger, *J. Appl. Phys.*, **27**, 544 (1956).
3. B. Schwartz and H. Robbins, *This Journal*, **108**, 365 (1961).
4. D. R. Turner, *ibid.*, **107**, 810 (1960).
5. M. G. Feuillade, S. Marette, and L. Dumontier, *L'Echo des Recherches*, **36**, 27 (1959).
6. H. A. Laitinen and I. M. Kolthoff, *J. Phys. Chem.*, **45**, 1061, 1079 (1941).
7. J. F. Dewald, "Semiconductors," N. B. Hannay, Editor, p. 733, Rheinhold Publishing Corp., New York (1959).
8. T. M. Buck, "The Surface Chemistry of Metals and Semiconductors," H. C. Gatos, Editor, p. 107, John Wiley & Sons, Inc., New York (1960).

The Effect of Organic Molecules on the Adsorptive Properties of Platinum Electrodes

M. W. Breiter

Research Laboratory, General Electric Company, Schenectady, New York

ABSTRACT

The effect of the addition of organic substances (amyl alcohol, caprylic acid, and diphenyl amine) to 1M $HClO_4$ on hydrogen and oxygen adsorption and in the double layer region of smooth platinum was studied by impedance measurements and quasistationary potentiostatic current potential curves in the potential range between hydrogen and oxygen evolution. Hydrogen adsorption is inhibited. The double layer capacity decreases with increasing amyl alcohol concentration between +0.3 and +1.5v. The degree of coverage with molecules was computed between +0.3 and +1.2v from the capacity decrease. An oxidation of the organic substance occurs at potentials where the oxygen coverage is formed simultaneously. Amyl alcohol molecules are adsorbed before the oxidation. Their oxidation goes over an intermediate and takes place to a large extent on surface sites free of oxygen.

The adsorption of organic molecules and ions has been studied mainly on mercury electrodes because mercury behaves like an ideally polarizable electrode in a wide potential range and has an easily reproducible surface of known size. Little work has been done on solid electrodes. Borisova, Ershler, and Frumkin (1) observed a capacity peak, which is characteristic for the desorption of organic molecules or ions on mercury, on a zinc electrode in 1*N* KCl if amyl alcohol was added. Kheifets and Krasikov (2) found capacity peaks on smooth platinum in the presence of caprylic acid and diphenyl amine in 2*N* H_2SO_4 and of sodium caprylite in 0.5*N* Na_2SO_4 and in 0.5*N* NaOH in the potential range between hydrogen and oxygen evolution. Franklin and Sothern (3) investigated the adsorption of different nitrides in 2*N* H_2SO_4 on platinized platinum at the potential of the hydrogen electrode. They assumed that the observed decrease of the amount of adsorbed hydrogen is due solely to a replacement of hydrogen atoms by nitride molecules.

As is well known, three distinct regions can be distinguished for the platinum electrode in the potential range between hydrogen and oxygen evolution. In perchloric acid hydrogen is adsorbed between 0 and +0.4v, the potential being measured against a hydrogen electrode in the same solution. Neither hydrogen nor oxygen is adsorbed between +0.4 and +0.8v in the so-called double layer region where platinum behaves as an ideally polarizable electrode. The chemisorption of oxygen takes place between +0.8 and +1.6v. In the present paper the influence of organic molecules on the adsorptive properties of the platinum electrode in the three regions was studied. Extensive measurements at room temperature were made in 1M $HClO_4$ with addition of amyl alcohol. A few experiments were run in 1M $HClO_4$ with caprylic acid and diphenyl amine. The capacity of the interphase smooth platinum/electrolyte was determined as a function of potential, frequency (5-105 cps) and time in 1M $HClO_4$ with different amounts of amyl alcohol (0.01-0.1M). Quasistationary current potential curves were obtained on smooth platinum in 1M $HClO_4$ with different amounts of amyl alcohol, in 1M $HClO_4$ with 10^{-3} or 10^{-4}M caprylic acid and in 1M $HClO_4$ with 10^{-5}M diphenyl amine by applying potentiostatically a potential which changed periodically and linearily with

time between +0.05 and +1.6v. The current potential curves were measured at different voltage speed.

Experimental

Figure 1 shows a schematic diagram of the circuit for the impedance measurements. The platinum wire with 0.03 cm ϕ was in the axis of a palladium wire spiral which formed a cylindrical counter electrode. The palladium wire with 0.1 cm ϕ was kept at the potential of the α- β-phase transition (ca + 0.05v). The surface of the counter electrode was about ten times larger than that of the test electrode. The impedance of a palladium electrode at the said potential is very small (4). The potential of the platinum electrode was changed with the aid of the potentiometer P and measured against a hydrogen electrode in 1M $HClO_4$. As the measurements were made in solutions saturated with nitrogen by intensive bubbling, the potential of the palladium electrode remained practically constant during the experiments. The resistor between A and B was a suitable one of a set of standard resistors. The a-c signal across the cell never exceeded 5 mv. The a-c voltage across AB was applied to the input of one of the two differential amplifiers of the dual beam oscilloscope Tektronix 502, the a-c voltage across CD to the other. The sweep was adjusted according to the frequency. A photograph was taken. The amplitudes of the two voltages and their phase shift were determined from enlargements of the photographs, and the impedance of the interphase was computed. This method allows fast measurements with an accuracy of 3-5%. It has the advantage that the d-c circuit need not be separated from the a-c circuit by an inductance in the low-frequency range used here.

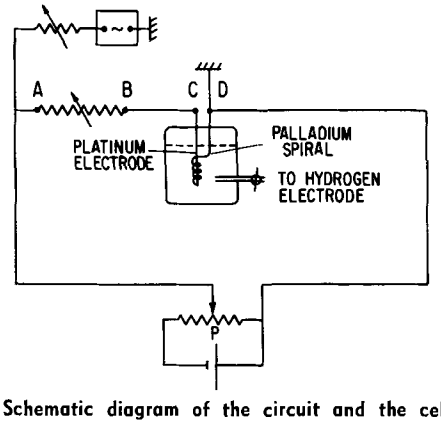

Fig. 1. Schematic diagram of the circuit and the cell for impedance measurements.

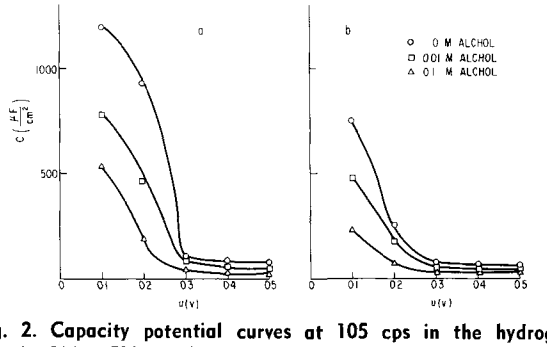

Fig. 2. Capacity potential curves at 105 cps in the hydrogen region in 1M $HClO_4$ with different amounts of amyl alcohol: a, after 2 min of polarization at constant potential; b, after 30 min of polarization at constant potential.

To measure the quasistationary current potential curves the circuit between A and C was connected to the electronic potentiostat and triangular wave generator described and used by Will and Knorr (5). The sine wave generator and the potentiometer P were disconnected. The reference electrode (hydrogen electrode in 1M $HClO_4$) was in a compartment separated from the test vessel by a closed stop cork, as with the impedance measurements. The palladium spiral served as counter electrode. The measurements were made in a resting solution, saturated with nitrogen by intensive bubbling before the experiments.

Preliminary runs showed that the a-c impedance of the platinum electrode changed with time. So the measurements were made in the following way to obtain comparable initial values. The platinum electrode was cleaned in chromic acid, rinsed with distilled water, and pretreated intermittently, cathodically and anodically in 1M $HClO_4$ in another vessel before any run in the test vessel. Then the electrode was transferred to the test vessel and the capacity was determined at constant potential as a function of time for 30 min in the frequency range 5-105 cps. The capacity became nearly time-independent after 30 min. The platinum electrode was subjected to the same pretreatment before taking any current potential curve.

Experimental Results

The capacity of the interface platinum/solution is plotted in Fig. 2a and 2b for different solutions as a function of potential in the region of hydrogen adsorption and in part of the double layer region. The interface was considered as a series circuit of a resistor and a capacitor C. As the measurements at frequencies between 5 and 105 cps yielded the same form of the capacity potential curves, only the curves at 105 cps are plotted in Fig. 2a and 2b. Figure 2a represents the values measured after 2 min of immersion and polarization in the test solution at a given potential. Figure 2b shows the capacity obtained at the same potential after 30 min of uninterrupted polarization.

Capacity potential curves for different solutions are plotted in Fig. 3a and 3b in the double layer region and in the region of oxygen chemisorption. The values in Fig. 3a correspond to 2 min, the values in Fig. 3b to 30 min of polarization at constant potential.

Quasistationary current potential curves in 1M $HClO_4$ with different amounts of amyl alcohol are

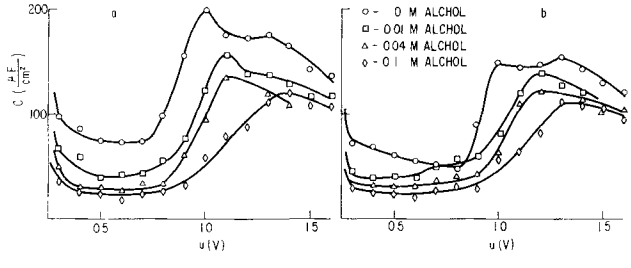

Fig. 3. Capacity potential curves at 105 cps in the region of the double layer and of the oxygen coverage in 1M $HClO_4$ with different amounts of amyl alcohol: a, after 2 min of polarization at constant potential; b, after 30 min of polarization at constant potential.

shown in Fig. 4a, 4b, and 4c. The concentration of amyl alcohol increases in the order of the lettering a, b, c, d, e and is given in the figure caption. The curves in Fig. 4a were measured at 0.2 v/sec, in 4b at 1 v/sec and in 4c at 10 v/sec. No time dependence of the current potential curves was observed within 15 min of observation if the applied potential

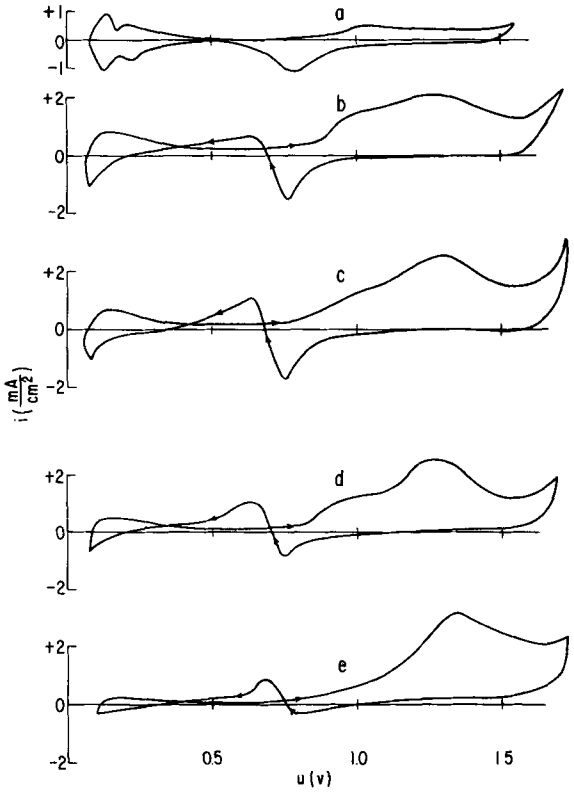

Fig. 4a. Quasistationary current potential curves at different voltage speed in 1M $HClO_4$ with different amounts of amyl alcohol, 0.2 v/sec: curve a, OM $C_5H_{11}OH$; curve b, 0.01M $C_5H_{11}OH$; curve c, 0.02M $C_5H_{11}OH$; curve d, 0.04M $C_5H_{11}OH$; curve e, 0.1M $C_5H_{11}OH$.

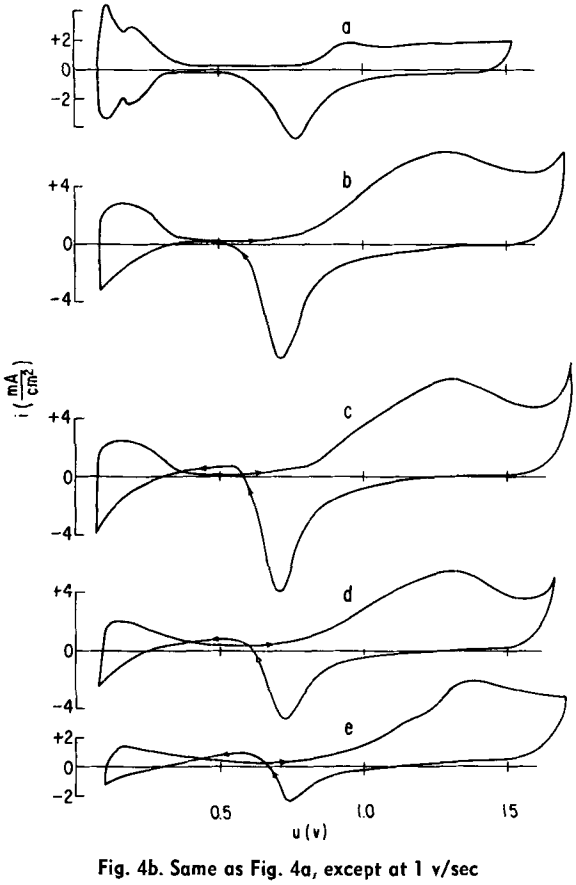

Fig. 4b. Same as Fig. 4a, except at 1 v/sec

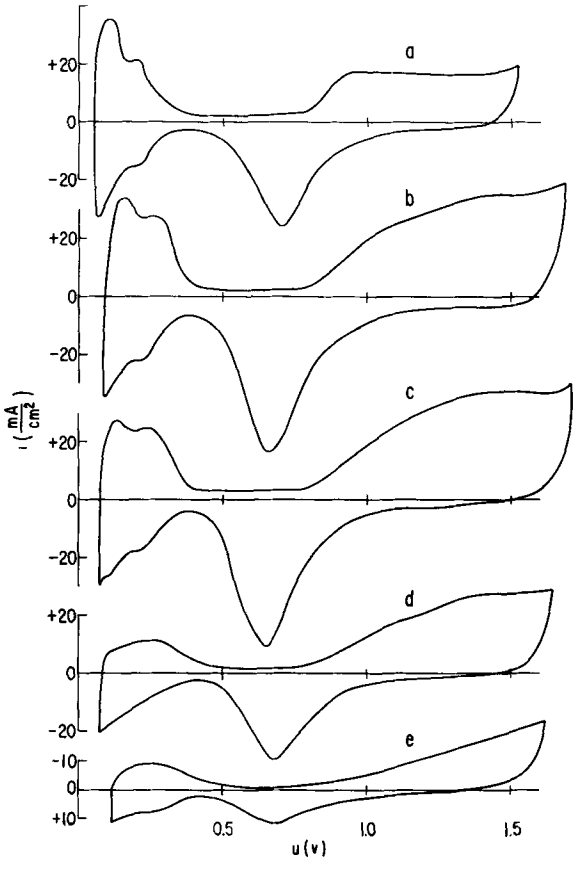

Fig. 4c. Same as Fig. 4a, except at 10 v/sec

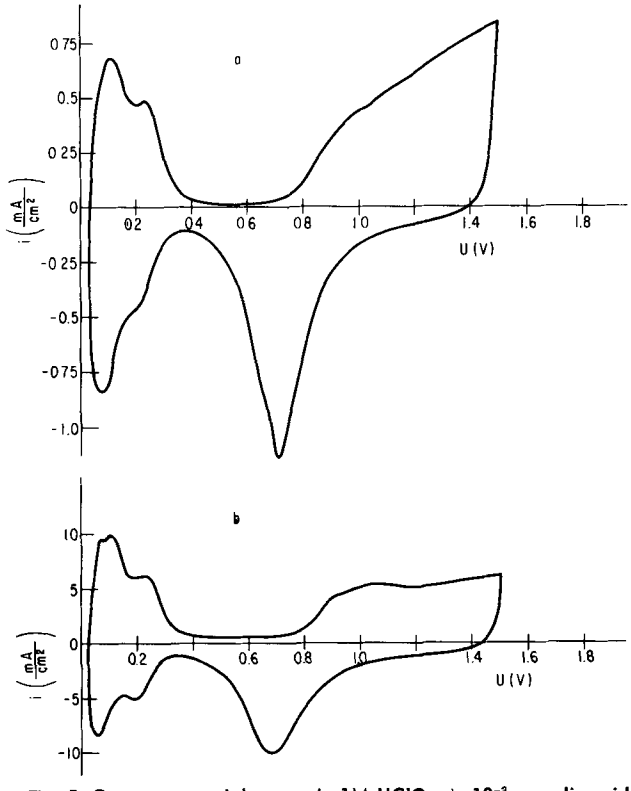

Fig. 5. Current potential curves in 1M $HClO_4$ + 10^{-3} caprylic acid at two different voltage speeds: curve a, 0.6 v/sec; curve b, 6 v/sec.

changed periodically between +0.05 and +1.6v. If the periodic potential sweep covered the range +0.05-+0.5v only, the current at the same potential decreased strongly with time in accordance with the time dependence of the capacity in the region of hydrogen adsorption.

Current potential curves in 1M $HClO_4$ with 10^{-4} caprylic acid are plotted in Fig. 5a and 5b. The voltage speed was 0.6 v/sec for Fig. 5a and 6 v/sec for Fig. 5b. The time dependence was similar to the one observed during the experiments in 1M $HClO_4$ with amyl alcohol.

Discussion

Capacity measurements in 1M $HClO_4$ *with amyl alcohol in the region of hydrogen adsorption.*—The capacity potential curve in 1M $HClO_4$ has the characteristic form described and discussed in earlier papers (6-8). The capacity increases with decreasing potential due to the adsorption of hydrogen atoms. The fine structure of the capacity potential curve (7, 8) in the hydrogen region cannot be seen from Fig. 2a because there are too few points.

The addition of amyl alcohol to 1M $HClO_4$ leads to a decrease of the capacity with increasing alcohol concentration at a given potential in the whole range. The surface area which is available for the adsorption of hydrogen atoms becomes smaller with increasing concentration of alcohol. A large part of this effect is due to the adsorption of organic molecules at surface sites which are covered with hydrogen atoms in 1M $HClO_4$. The beginning of hydrogen adsorption is shifted toward less positive potentials with increasing alcohol concentration. Specifically adsorbed anions have a similar effect on the hydrogen adsorption (9-11).

A computation of the number of adsorbed organic molecules in the case of simultaneous adsorption of hydrogen atoms and molecules from the capacity decrease in the hydrogen region is difficult because little is known about the interaction between the two types of adsorbed particles. The basic assumption of Franklin and Sothern (3), that hydrogen atoms are replaced quantitatively by molecules, *i.e.*, according to a linear relationship between the decrease of the amount of adsorbed hydrogen and the number of adsorbed molecules, requires an experimental verification.

The comparison between Fig. 2a and 2b shows a marked decrease of capacity with time in the hydrogen region. It cannot be said that this decrease is solely due to a slow displacement of hydrogen atoms by organic molecules, since the capacity also decreases with time at constant potential in 1M $HClO_4$. The decrease in 1M $HClO_4$ could be attributed to a decrease of the surface roughness within the first 20 min after the anodic pretreatment (11). Therefore, at least two effects overlap, and conclusions should only be deduced from the results in Fig. 2a and 3a where the time effect is small.

Capacity measurements in 1M $HClO_4$ *with amyl alcohol in the region of the double layer and of oxygen adsorption.*—The capacity potential curve in 1M $HClO_4$ (see Fig. 3a) has a characteristic form which was described in earlier papers (12-15). The measured capacity represents the double layer capacity in this region. It remains practically independent of potential in the double layer region and begins to increase with potential between +0.7 and +1.0v when the formation of a chemisorbed oxygen layer starts. There is a peak at +1.05v and a second one at +1.3v. The form of the capacity potential curve and the location of the peaks depends strongly on the composition of the electrolyte (12). The curves differ in 1*N* $HClO_4$ and 2*N* H_2SO_4. This suggests that the increase of the capacity is due to an increase of the Helmholtz capacity of the double layer with oxygen coverage. Llopis and Colum (15) and Laitinen and Enke (14) interpret the capacity increase as resulting from surface dipoles (polarized oxygen atoms or other intermediates). Generally the capacity of the ionic double is in series with the capacity of the oxide layer in such a model. Thus a decrease of the measured capacity is expected as found by Vermilyea (16) during the formation of an oxide film on tantalum. A decrease in capacity was observed before attainment of a monolayer. Based on this model of the interface, the observed capacity increase on platinum can be better interpreted by an increase of the capacity of the Helmholtz layer. The interpretation of Llopis and Colum (15) and of Laitinen and Enke (14) implies that the capacity of the ionic double layer is considerably larger than the measured value (20 to 60μF/cm^2 for Laitinen and Enke, 75-200 μ/Fcm^2 in the present work). A value of 00 to 600 μF/cm^2 or 750-2000 μF/cm^2, respectively, for the ionic double layer appears too high. Another possible interpretation is that the capacity increase is due to a kinetic effect such as with the desorption peaks of organic ions and molecules (17). The latter possibility may be ruled out because the reduction and formation of the oxygen layer are too irreversible for any contribution.

Figure 3a and 3b show that the capacity decreases with increasing concentration of amyl alcohol at constant potential in the whole range. The intersection of the curve for 0.04M and 0.1M alcohol at +1.4v in Fig. 3a may be due to a different effectiveness of the pretreatment. The capacity decreases with time at constant potential. The capacity potential curves for 0.04M and 0.1M alcohol in Fig. 3a are very close in the double layer region. This suggests that the surface is covered with a monolayer of adsorbed molecules. The form of all the curves is similar in the region of oxygen chemisorption. A simultaneous adsorption of molecules and oxygen takes place. The oxygen coverage grows more slowly with anodic potential if the concentration of alcohol increases. The capacity at +1.6v differs only slightly in all solutions. This indicates that the organic molecules are desorbed to a large extent from the surface when the evolution of molecular oxygen starts. The same conclusion cannot be made for the beginning of hydrogen evolution (see Fig. 2a). Capacity peaks which are due to the desorption of the organic particles in a small potential range, such as on mercury, were not found for amyl alcohol on platinum. The capacity potential curves indicate a gradual desorption of the alcohol on both sides of the double layer region.

An approximate computation of the degree of coverage θ with organic molecules was carried out for

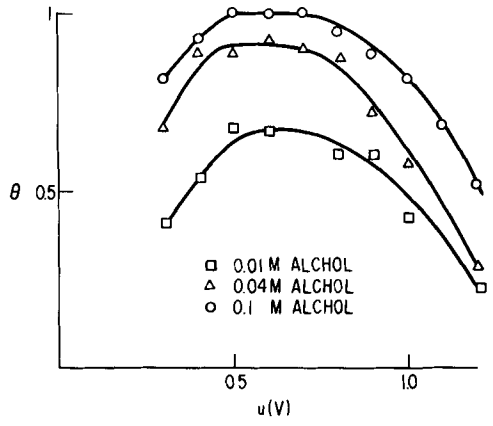

Fig. 6. Degree of coverage θ as a function of the potential and the concentration of amyl alcohol in 1M $HClO_4$ as basic electrolyte.

the potential range +0.3-+1.2v on the basis of Frumkin's model (18) of the double layer

$$C = C_{\theta=1} \cdot \theta + C_{\theta=0} (1 - \theta) \qquad [1]$$

The measured double layer capacity is assumed to be composed additively of a part due to the completely covered surface and a part due to the free surface. $C_{\theta=1}$ is the differential capacity of the surface completely covered with molecules at a given potential, $C_{\theta=0}$ is the capacity of the surface free of molecules at the same potential. An investigation of the adsorption of amyl alcohol on mercury showed that formula [1] is a satisfactory approximation at potentials between the adsorption peaks (19). As platinum behaves as an ideally polarizable electrode in the potential range +0.3-+1.2v with respect to impedance measurements and as no desorption peaks are observed, the application of formula [1] should give approximate θ values. It is possible that the range for the applicability of formula [1] extends anodically only to +1.0v where the oxygen coverage is still moderate. The θ values at +1.2v may be linked with a higher error.

Figure 6 shows the coverage as a function of potential and alcohol concentration. The values in Fig. 3a were used for the computation of θ with the aid of Eq. [1]. $C_{\theta=1}$ was taken equal to 24 μF/cm^2, the value of the double layer capacity in 1M $HClO_4$ + 0.1M amyl alcohol in the double layer region. It was assumed that $C_{\theta=1}$ is nearly independent of the potential at potentials more positive than +0.8v. The error made with this assumption cannot be too large as a look at the capacity potential curve in Fig. 3a shows. $C_{\theta=0}$ was set equal to the capacity in 1M $HClO_4$. The curves in Fig. 6 are similar to the respective curves on mercury (19). The coverage decreases on both sides of the double layer region. It is nearly independent of potential in the double layer region. The capacity potential curves indicate that the decrease of coverage in the cathodic direction is continued at a slower rate with decreasing potential in the hydrogen region than between +0.5v and +0.3v. The experiments on platinum suggest that the cause for the desorption of amyl alcohol is different on mercury and platinum. The potential drop across the interphase mercury/solution finally becomes so great on both sides of the electrocapillary maximum that organic molecules are replaced by water molecules (18, 20). On platinum the desorption is obviously caused by the formation of an oxygen layer at the positive side of the double layer region and probably by the adsorption of hydrogen atoms on the negative side. The coverage potential curves in Fig. 6 represent the behavior of an electrode with the same history of the surface. Therefore the θ values cannot be used for a quantitative kinetic discussion of the current potential curves in Fig. 4a, 4b, and 4c. However, the general tendency of the platinum electrode for the adsorption of amyl alcohol is given by them.

Current potential curves in 1M $HClO_4$ *with amyl alcohol.*—The impedance measurements yield information about the adsorption of the organic molecules in the three potential regions on a platinum electrode. They do not indicate if the molecules undergo oxidation. Therefore current potential curves were taken in the way described previously.

Curves a in Fig. 4a, 4b, and 4c were obtained on platinum in 1M $HClO_4$ at different voltage speeds. The curves show the typical form discussed by Will and Knorr (5) in detail. The three potential regions are clearly recognizable. The current potential curves are practically symmetrical to the abscissa in the hydrogen region during the anodic and cathodic sweep. The ionization and formation of adsorbed H-atoms occurs with a very small hindrance. The current is small in the double layer region. It increases between +0.8 and +1.0v and remains nearly constant between +1.0 and +1.5v during the anodic sweep when an oxygen layer is formed. The reduction of the oxygen layer is an irreversible process and takes place at less positive potentials than the formation.

If amyl alcohol is present, the current potential curves have a different form. The form depends on the alcohol concentration and the voltage speed. Current potential curves at 0.2 v/sec are plotted for different alcohol concentrations in Fig. 4a. The hydrogen adsorption is reduced with increasing alcohol concentration. The two current peaks which show the existence of two types of surface sites with different heat of adsorption for hydrogen (11, 21) disappear. The current is larger in the presence than in the absence of alcohol in the region of oxygen coverage during the anodic sweep. The current peak which is characteristic for the reduction of the oxygen layer is recognizable in all curves during the cathodic sweep. Curves b and c show practically no flow of current between +1.5 and +1.0v; curves d and e exhibit a small anodic current there. The curves have an additional anodic peak in the double layer region during the cathodic sweep. The height of this peak increased if the solution was stirred by nitrogen bubbling. Curves b, c, and d have two humps between +0.8 and +1.6v during the anodic sweep.

It can be concluded from results in Fig. 4a that the molecules of amyl alcohol undergo an anodic oxidation in the potential region where the oxygen layer is formed simultaneously. A large portion of the current is used for the oxidation of the alcohol in this range. The appearance of the anodic current peak in the double layer region during the cathodic sweep

can be interpreted as the oxidation of an intermediate which was formed during the preceding anodic sweep. The intermediate is oxidized at a less positive potential than the alcohol. Such a situation is often observed for the oxidation of an alcohol and the respective aldehyde. The oxidation of the intermediate requires a surface free of chemisorbed oxygen. The reduction of the oxygen coverage and the oxidation of the intermediate overlap. The effect of stirring and the investigations of the coverage show that the intermediate comes from the solution. Obviously part of the intermediate diffuses away after the anodic formation and diffuses back to the surface during the cathodic sweep. The decrease of the anodic current after the peak at about +1.3v is obviously produced by the increasing oxygen coverage which is paralleled by a decreasing coverage with molecules (compare Fig. 6). This suggests that the oxidation occurs on the oxygen-free surface only. The lack of an essential anodic current between +1.5 and +1.0v during the cathodic sweep supports this view. The small bump at about +0.95v of curves b, c, and d disappears at the highest concentration of alcohol. It is probably connected with a reaction between molecules and adsorbed oxygen and does not appear in curve e because the oxygen coverage at +1.0v is small in that case. The current of curve e starts to rise during the anodic sweep at a potential where the surface is practically covered with a monolayer of molecules. It is concluded from this result that the molecules are adsorbed before their oxidation.

An increase in voltage speed changes the ratio of the partial currents which are used for the oxidation of the alcohol and the formation of the oxygen layer in favor of the surface oxidation (see Fig. 4b and 4c). This is probably the reason why the oxidation of the intermediate is no longer strongly pronounced in the curves of Fig. 4b and disappears in Fig. 4c. In general the form of a curve in Fig. 4b is similar to that of the curve at the same alcohol concentration in Fig. 4a. The curves at a relatively high voltage speed of 10 v/sec in Fig. 4c exhibit new phenomena. The two characteristic current peaks in the region of hydrogen adsorption appear in curve b and c. The voltage speed is sufficiently large that the surface area for hydrogen adsorption is not diminished by blocking sites through molecules at the two lower concentrations of amyl alcohol. The average current efficiency for the oxidation of amyl alcohol is 45% for curve b and 60% for curve c under the plausible assumption that the integration of the cathodic current potential curves between +1.5 and +0.4v yields the electricity for the reduction of the oxygen coverage. Curves d and e indicate that the oxygen coverage is not completed to a monolayer at the large alcohol concentrations and high voltage speed. Part of the surface remains covered with molecules during the anodic and cathodic cycle under these conditions, so the area for hydrogen adsorption is reduced. The average current efficiency for the alcohol oxidation increases to 83% for curve d and 88% for curve e. It is difficult to give a more detailed picture of the oxidation mechanism on the basis of the results of this paper.

Current potential curves in 1M $HClO_4$ *with caprylic acid.*—A comparison between curve a in Fig. 5 and curve a in Fig. 4a or 4b shows that oxidation of the caprylic acid occurs at the low voltage speed during the anodic cycle. Oxidation and formation of the oxygen coverage takes place simultaneously. At the higher speed oxidation is not observed (see curve b). The current of the anodic curve b is nearly independent of the potential between +1.0 and +1.5v while this "plateau" is not present in curve a. The current potential curves in 1M $HClO_4$ + 10^{-5}M caprylic acid have a similar form. The characteristic shape of the curves in the hydrogen region is maintained at voltage speeds between 0.2 and 10 v/sec for a concentration of 10^{-5} and 10^{-4}M caprylic acid. However, the amount of hydrogen adsorbed between +0.05 and +0.4v is somewhat smaller in the presence (2.10^{-4} to 3.10^{-4} coul/cm^2) than in the absence (4.10^{-4} coul/cm^2) of caprylic acid. If the applied potential changes periodically between +0.05 and +0.5v only, a decrease of the current at the same potential with time is observed. The relative decrease in 5 min is 20% in 1M $HClO_4$ + 10^{-4}M caprylic acid and 25% in 1M $HClO_4$ + 10^{-5}M. These effects indicate that caprylic acid is adsorbed simultaneously with hydrogen atoms. On the whole the effect of caprylic acid on the adsorptive properties of platinum is small.

Kheifets and Krasikov (2) reported a capacity potential curve on platinum at 50 cps in 2*N* H_2SO_4 + 5.10^{-5}M caprylic acid with a peak at +1.3v and one at +0.2v (measured against a hydrogen electrode in the same solution). The double layer capacity between the two peaks is lower than the capacity in 2*N* H_2SO_4 within the same potential range. Their curves indicate that the hydrogen adsorption in the presence of caprylic acid does not start at a potential more positive than the potential of the hydrogen electrode. The capacity values in the vicinity of the peak at +1.3v are larger in 2*N* H_2SO_4 with caprylic acid than without. Otherwise the capacity potential curve in 2N H_2SO_4 + 5.10^{-5}M caprylic acid lies below that in 2*N* H_2SO_4 in the region of oxygen coverage. The latter effect is peculiar as the capacity potential curves on mercury in the presence of organic molecules used to be above the curve in the absence of molecules at potentials more positive than the left capacity peak.

The results of Kheifets and Krasikov (2) are not in agreement with the results of Fig. 5. If a strong influence of caprylic acid exists, it should be pronounced in the current potential curves of Fig. 5, too. An explanation of the discrepancy is difficult as Kheifets and Krasikov do not give information on the pretreatment of the platinum electrode, the sequence of the measurements, and the time effect.

Current potential curves in 1M $HClO_4$ *with* 10^{-3}M *diphenylamine.*—The current potential curves in 1M $HClO_4$ + 10^{-3}M diphenylamine are not shown in this paper. A current peak in the region of oxygen adsorption and a change of the curves in the hydrogen region were observed if platinum was polarized periodically between +0.05 and +1.5 v/sec. at 1.5 v/sec. The peak changed very much with time. The peak current was too large to attribute it to changes

of the doubler layer capacity. It is caused by the oxidation of diphenylamine. Kheifets and Krasikov (2) used a diphenylamine concentration which was 100 times smaller. The one capacity peak in the presence of diphenylamine was observed by Kheifets and Krasikov at the potential of the current peak of the current potential curves. Therefore it is suggested that the capacity peak is due to the oxidation of the diphenylamine. Owing to the small concentration of diphenylamine, Kheifets and Krasikov found Faradaic a-c currents of the magnitude of capacitive currents.

Manuscript received June 6, 1961. This paper was prepared for delivery before the Indianapolis Meeting, April 30-May 3, 1961. The experimental work was carried out in the Institute of Physical Chemistry and Electrochemistry of the Technical University, Munich, and supported by Dechema and Deutsche Forschungsgemeinschaft.

Any discussion of this paper will appear in a Discussion Section to be published in the December 1962 JOURNAL.

REFERENCES

1. T. I. Borisova, B. V. Ershler, and A. N. Frumkin, *Zhur. fiz. Khim.*, **22**, 925 (1948).
2. V. L. Kheifets and B. S. Krasikov, *Doklady Akad. Nauk*, **94**, 101 (1954).
3. T. C. Franklin and R. D. Sothern, *J. Phys. Chem.*, **58**, 951 (1954).
4. M. Breiter, H. Kammermaier, and C. A. Knorr, *Z. Elektrochem.*, **58**, 702 (1954).
5. F. Will and C. A. Knorr, *ibid.*, **64**, 258, 270 (1960).
6. P. Dolin and B. Ershler, *Acta Physiochim. U.R.S.S.*, **13**, 747 (1940).
7. A. Eucken and B. Weblus, *Z. Elektrochem.*, **55**, 114 (1951).
8. M. Breiter, H. Kammermaier, and C. A. Knorr, *ibid.*, **60**, 37 (1956).
9. A. Frumkin and A. Slygin, *Acta Physiochim. U.R.S.S.*, **5**, 819 (1936).
10. B. Ershler, *ibid.*, **7**, 327 (1937).
11. M. Breiter and B. Kennel, *Z. Elektrochem.*, **64**, 1180 (1960).
12. M. Becker and M. Breiter, *ibid.*, **60**, 1080 (1956).
13. K. Franke, C. A. Knorr, and M. Breiter, *ibid.*, **63**, 226 (1959).
14. H. Laitinen and C. Enke, *This Journal*, **107**, 773 (1960).
15. J. Llopis and F. Colum, "Proceedings of the International Committee on Electrochemical Thermodynamics and Kinetics, Eighth Meeting, 1958," pp. 414-427, Butterworths, London.
16. D. A. Vermilyea, *This Journal*, **101**, 389 (1954).
17. A. N. Frumkin and V. I. Melik-Gaikazyan, *Doklady Akad. Nauk. S.S.S.R.*, **77**, 855 (1951); V. I. Melik-Gaikazyan, *Zhur. fiz. Khim.*, **26**, 560 (1952).
18. A. N. Frumkin, *Z. Physik*, **35**, 792 (1926).
19. M. Breiter and P. Delahay, *J. Am. Chem. Soc.*, **81**, 2938 (1959).
20. J. A. V. Butler, *Proc. Roy. Soc. (London)*, **A122**, 399 (1929).
21. W. Böld and M. Breiter, *Z. Elektrochem.*, **64**, 897 (1960).

Electrodeposition of Gallium on Liquid and Solid Gallium Electrodes in Alkaline Solutions

J. O'M. Bockris and M. Enyo

John Harrison Laboratory of Chemistry, University of Pennsylvania, Philadelphia, Pennsylvania

ABSTRACT

A galvanostatic short time transient method has been used to examine deposition and dissolution on gallium electrodes in alkaline solutions of gallic chloride. The cathodic metal deposition current was distinguished from the total current by current efficiency determinations in steady state.

Behavior on the liquid electrode is consistent with a charge-transfer controlled mechanism in all current density regions, and the rate-determining step is probably $H_2GaO_3^- + e^- \rightarrow HGaO_2^- + OH^-$.

On the solid electrode, the rate constants of the transfer reaction are nearly those of the liquid electrode. However, the behavior in the low current density regions is qualitatively different from that on the liquid. Analysis of phenomena in this region suggests that surface diffusion begins to control the rate of the over-all deposition process on the solid cathode. Rate constants of the surface diffusion process evaluated from the low current density region are semiquantitatively applicable to deviations from the Tafel equation which occur on the solid at high current densities (surface diffusion controlled limiting current). The results provide support for the existence of rate-controlling surface diffusion in metal deposition and dissolution reactions.

In studies on the kinetics of the deposition and dissolution of monolayers of metals in aqueous solutions, it has been shown that the most important partial reactions which determine the rate of the over-all processes are charge transfer and the surface diffusion of adions on the electrode surface (1-6). There exists, however, a quantitative disagreement on the relative importance of these partial reactions in determining the over-all rate. Thus, according to the work of Mehl and Bockris (1), in the deposition and dissolution of Ag in $AgClO_4$ + $HClO_4$ solution, the charge transfer process becomes rate determining at higher current densities [cf. Despic and Bockris (2)]. According to other authors

(3-5), however, the charge transfer process is less important than the crystal building process in rate control for metal deposition and dissolution. It is desirable therefore to devise experiments in which crystal building steps (including surface diffusion) in metal deposition can be tuned out of the possibilities concerning rate control and the current-potential characteristics examined in the absence and presence of possible crystal building rate controlling steps.

A possible approach to this problem is by means of measurements on amalgams. There exist, however, difficulties in inferring the rate of charge transfer on the corresponding solid electrodes from measurements with amalgams. Thus, it is easy to show that

$$\frac{i_{o,\mathrm{am}}}{i_{o,\mathrm{solid}}} = \frac{k_1'}{k_1}\alpha_c/z \qquad [1]$$

where i_o is the exchange current density, [M] the concentration of the amalgam, k_1' and k_1 are the forward rate constants for the transfer reaction on the amalgams and on the solid, respectively, α_c the cathodic transfer coefficient, and z the ionic charge of the metal ion concerned.

If $k_1 = k_1'$, Eq. [1] shows that the charge transfer i_o value for a solid metal should be much greater than that observed experimentally on amalgam electrodes. Such conclusions cannot be made, however, because k_1' may differ greatly from k_1.

In comparison of k_1 and k_1', it is only necessary to consider the potential energy of the final state in the forward transfer reaction. The determining factors are the work function of Hg, and of the metal concerned, and the "heat of sublimation" of the metal atom from its own lattice or from that of the amalgam. If the latter is considerably increased in the amalgam compared with that of the pure substance, then k_1' may be much greater than k_1. These matters indicate the difficulties of inferences from amalgams.

Measurements on solid and liquid Hg are not suited to a comparison of deposition rates on solids and liquid because the temperature of fusion demands either nonaqueous or very concentrated aqueous solutions, and the i_o values for metal exchange involving Hg are very high and thus difficult to determine. Hence, the electrodeposition process of gallium from an alkaline gallate solution onto both solid and liquid electrodes was studied.

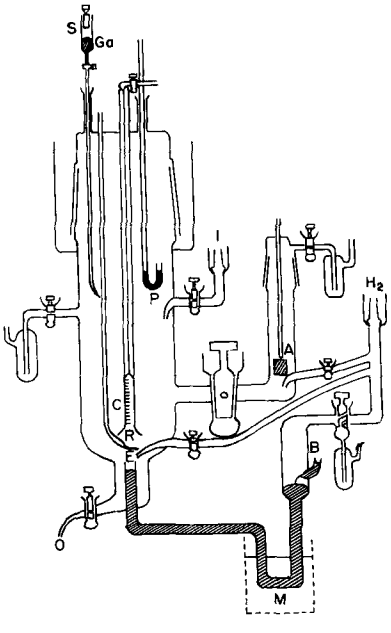

Fig. 1. Experimental cell used for studies on the gallium deposition. A, anode (Pt); B, Pt contact to Ga; C, glass tube to measure volume of hydrogen evolved; E, test electrode (Ga); I, solution inlet; M, cooling mixture (ice water); O, solution outlet; P, pre-electrolysis electrode (Ga); R, reference electrode (Pt); S, supply of Ga metal.

Experimental

Electrode construction and cell.—A cup-type electrode with a Pt wire contact was unsatisfactory, since the solution frequently contacted the wire. This type was employed therefore only for pre-electrolysis. The arrangement used is shown in Fig. 1. The temperature was controlled to ±0.5°C.

Reagents.—Gallium metal was 99.999% and gallic chloride 99.95% pure.

Procedure.—A solution of NaOH was prepared by the amalgam method (7), and the concentration was determined before mixing with $GaCl_3$. Hydrogen gas was purified using heated platinized asbestos (6, 8), charcoal traps (liquid air temperature), etc. Water was prepared by distilling conductance water into the cell in an atmosphere of hydrogen.

The cell was cleaned (8), and the system set up, including the container of NaOH solution already prepared. Air was removed by hydrogen flow, and 5 ml of NaOH solution taken into the cell. $GaCl_3$ then was distilled from I (Fig. 1) in a hydrogen [or helium similarly purified (8)] atmosphere by a weak torch flame (approximately half of the original amount was used). A further amount of NaOH solution was added to make up the final solution to 50 ml. Finally, gallium metal in S (Fig. 1) was taken through a thin glass capillary (9) into the U-tube portion, and the meniscus at E adjusted by hydrogen pressure in B, so that it came about 3 mm below the top of the tube at E. The gallate concentration was determined after the experiment (10).

Pre-electrolysis.—The solution was pre-electrolyzed at 3 ma cm^{-2} for 12-18 hr.

Measurements.—(*a*) *Current efficiency.*—The current efficiency was determined by collecting H_2 in the 1 ml pipette tube over the electrode (C in Fig. 1). The volume of the gas observed was of the order of a few hundredths of a milliliter. The current efficiency measurements were tested by measuring the H_2 produced on Pt electrodes in alkaline solution previously saturated with hydrogen. The result was 100 ±2%.

(*b*) *Polarization.*—The galvanostatic transient method was used (6). To compensate for the static potential difference between the test and counter electrodes, which caused difficulty in obtaining a suitable galvanostatic condition, an auxiliary potentiometer circuit was used between the pulse generator and the cell. The duration of the pulse was 3 msec-1 sec, with current densities of 10^{-5}-10^{-2} amp cm^{-2}. Measurements were mostly cathodic. Anodic dissolution produced films when the galvanostatic pulses were sufficiently long.

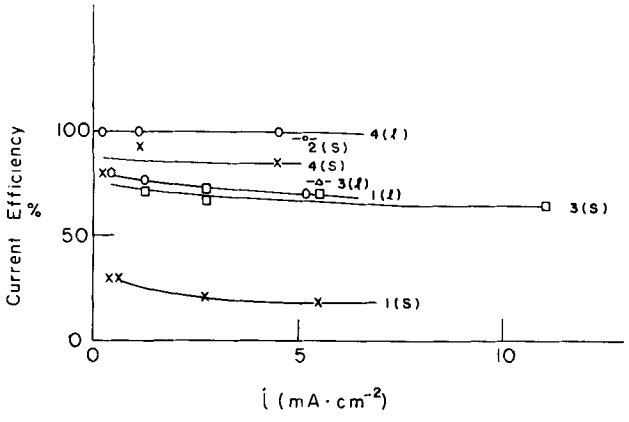

Fig. 2. Current efficiency as a function of current density; l, liquid electrode; s, solid electrode.

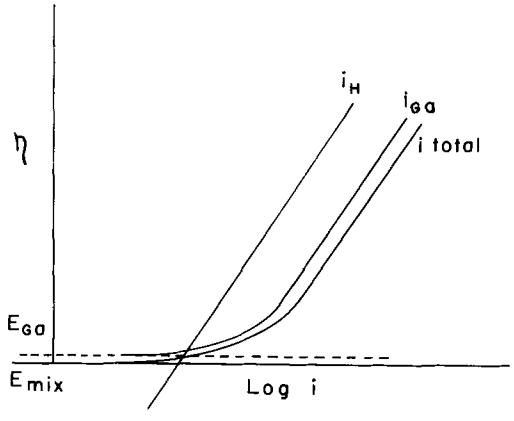

Fig. 3. Current efficiency corrections for gallium deposition (schematic). i_{total}, total current; i_H, hydrogen evolution current estimated from i_{total} and current efficiency; i_{Ga}, gallium deposition current $= i_{total} - i_H$; E_{mix}, mixed potential; E_{Ga}, equilibrium potential of Ga electrode, after correction of i_H.

Fusion and solidification of gallium.—Gallium has a tendency to supercool (11), and solidification occurred below 10°C, if the metal was not agitated. To ascertain whether the gallium is solid or liquid, a cathodic current was applied for a few seconds and the surface observed. For the liquid, the current causes slight deformation of the electrode due to electrocapillary effects.

Results

Current efficiency.—Current efficiencies (C.E.) are summarized in Fig. 2. C.E. decreases with increasing i, and is smaller on solid than on liquid electrodes. The apparently anomalous values from the system "1s" (Fig. 2) would cause, if corrected to the mean of the other C.E. values, a shift in the η-log i relation by about 0.3 log i units to increasing log i values (Fig. 3).[1]

Current efficiency corrections.—Overpotential was measured in the minutes-long polarizations used in the C.E. determinations. Values were in agreement (±10 mv) with those of the transient method for $[GaCl_3] > 0.1$ mole/l, and 30-50 mv higher at lower concentrations. The overpotentials from transient and steady-state methods gave linear Tafel lines.

[1] There is no critical current density below which no hydrogen ions discharge. Even at more anodic potential (downward in Fig. 3) than E_{mix}, there should be a finite amount of i_H, though it is negligible.

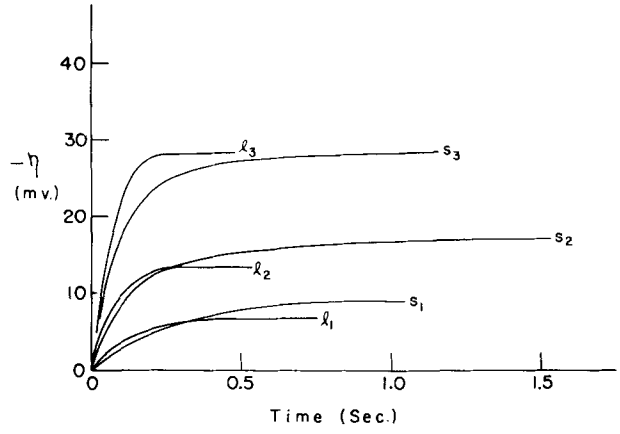

Fig. 4. Typical cathodic —t transients; l, liquid electrode; s, solid electrode.

The gallium deposition current, i_{Ga}, was obtained from

$$(i_{Ga})_\eta = (i_{total})_\eta - (i_H)_\eta \qquad [2]$$

For low overpotentials, i_H was calculated from the extrapolated Tafel line for the hydrogen evolution reaction.

The potential at the intersection of the linear η-log i_H line and the η-log i_{total} line, whose $i_{Ga} = 0$, corresponds to the reversible potential of the gallium electrode process and amounted expectedly to 2-10 mv more negative than the experimental corrosion potential.

Current efficiency corrections were usually less than 0.1 unit in the log i scale. Their reproducibility was ±3%.

Overpotential-time transient.—The rise-time of the η-t transient was 3-4 times longer on the solid than on the liquid electrodes at low current densities (Fig. 4).

The transients on the solid electrodes at low current densities were analyzed by the theory of surface diffusion of adions,[2] by a method already described (1, 2). The results on the equilibrium surface diffusion flux, $v_{ad,o}$, are shown in Fig. 5 as a function of current density. The equilibrium adion concentration was independent of the concentration of the solution or of the current density and the mean value was 5 (±2) x 10^{-11} mole cm^{-2}, which corresponds to 1-2% of the electrode surface coverage, assuming (8, 9) a roughness factor of 1.6.

Steady-state overpotential.—Clear cathodic Tafel relations were obtained on liquid electrodes (b = 130 mv). On solid electrodes, the lines were steeper, and the linearity less clear (Fig. 6 and 7, Table I). At low current densities, the rates of deposition at the same potential were much smaller on the solid than on the liquid electrodes.

[2] In the analysis of the $\eta - t$ transients on solid electrodes, the amount of electricity, Q_x, required to change the concentration of the intermediate state of the charge-transfer controlled mechanism, $HGaO_2^-$ (*cf.* Discussion part), from that at equilibrium to that at certain overpotential is neglected because: (i) The time at which the above-mentioned current appears on liquid electrode is much shorter than the time region concerned in the following analysis (by 10 times at low overpotentials). (ii) Q_x (~10^{-5} coulomb cm^{-2} at low cathodic overpotentials) (8) is much smaller than the variation in c_{ad} values, which is given by

$$(c_{ad} - c_{ad,o})/c_{ad,o} = (-i)/zFv_{ad,o} \text{ (cf. Eq. [18])}$$

and approximate value is $10c_{ad,o}$ at $i = 5 \times 10^{-4}$ amp cm^{-2}, or the numerical value is 10^{-4} coulomb cm^{-2}.

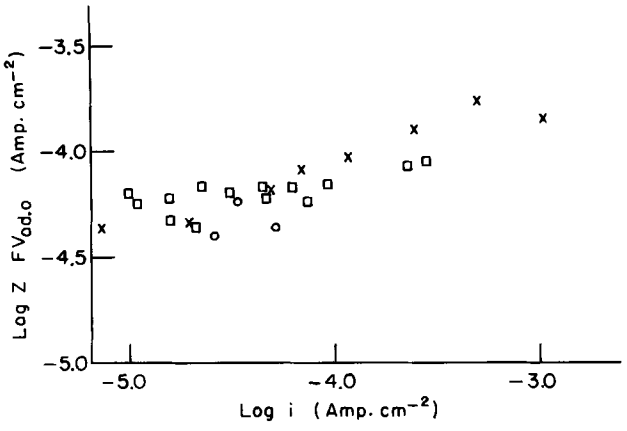

Fig. 5. $V_{ad,o}$ as a function of current density on solid electrode. □, X, ○ = different electrodes.

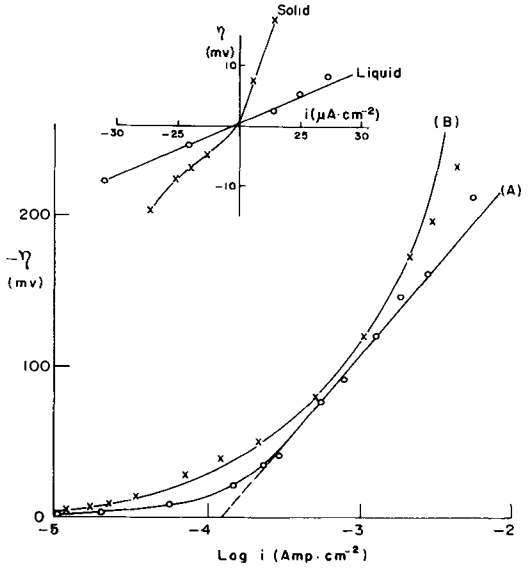

Fig. 6. Typical η vs. log *i* curves (cathodic). X, solid electrode, 28°C; ○, liquid electrode, 30°C; A, theoretical curve for charge transfer only; B, theoretical curve for Eq. [19].

Concentration dependence of exchange current density.—d log i_o/d log [$H_2GaO_3^-$] was about 0.7 ±0.2 (Fig. 8).

Discussion

Current efficiency corrections do not affect the values of log $i_{o,Ga}$ by more than about 0.1 unit. In agreement with the validity of i_{Ga} values is the fact that $i_{o,Ga}$ increases with increase of [$GaCl_3$]; $i_{o,H}$ would be expected to behave conversely (8).

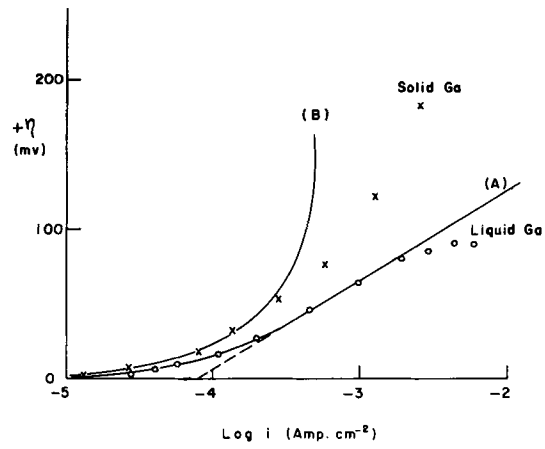

Fig. 7. Typical η vs. log *i* curves (anodic). X, solid electrode, 28°C; ○, liquid electrode, 30°C; A, theoretical curve for charge transfer only; B, theoretical curve for Eq. [19].

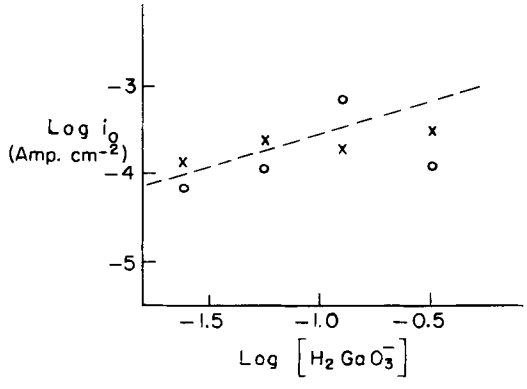

Fig. 8. Concentration dependence of i_o. [$H_2GaO_3^-$] in mole/l. X, solid electrode, 28°C; ○, liquid electrode, 30°C.

Nonsteady State

Overpotential-time transient on solid electrodes.—In Fig. 5, the equilibrium surface diffusion flux, $v_{ad,o}$ is seen to be almost independent of the current density. [The slight increase indicated at high current density concerns a region for which $-\eta > RT/F$, and the surface diffusion equations from which $v_{ad,o}$ is calculated become inaccurate (1, 2).] Recently a model has been developed (12) in which the relation between $v_{ad,o}$ and the dependence of the density of active growth sites upon current density has been evaluated. The constancy of $v_{ad,o}$ recorded in Fig. 5 implies that the density of active growth sites does not increase significantly with current density on solid gallium. Since the experimental temperature

Table I. Electrode kinetic parameters in the electrodeposition and dissolution of gallium*

	Liquid Ga (30°C)					Solid Ga (28°C)		
[$GaCl_3$]	$i_{o,c}$	$i_{o,a}$	$i_{o,\eta\to 0}$	α_c	α_a	$i_{o,c}$	$i_{o,a}$	α_c
0.32	130 ± 35	100 ± 35	120 ± 35	0.44 ± 0.03	1.4 ± 0.2	(450)	60	0.35 ± 0.05
0.123	(500)	—	(500)	0.48 ± 0.05	—	(200)	—	0.32 ± 0.05
(0.05)	110 ± 40	—	100 ± 10	0.47 ± 0.02	—	(250)	—	0.35 ± 0.02
0.24	70 ± 15	50 ± 10	70 ± 10	0.46 ± 0.02	(1.1)	(170)	—	0.30 ± 0.04
				0.45 ± 0.03	1.3 ± 0.3			0.33 ± 0.04

* Concentration in mole/l, i_o in 10^{-6} amp cm^{-2}. $i_{o,c}$ and $i_{o,a}$ are obtained by extrapolating cathodic and anodic Tafel lines respectively. α_c and α_a are from those slopes. $i_{o,\eta\to 0}$ is obtained from a linear plot of overpotential against current density near equilibrium.

Table II. Certain Hypothetical Mechanisms in the Deposition of Gallium and Expected Tafel Slopes*

Steps	Cathode Tafel slope	Anodic Tafel slope	$\alpha_c + \alpha_a$
(A) [4] [5] and [6]	$-RT/\beta F$	$RT/(3-\beta)F$	3
(B) [4] [5] and [6]	$-RT/(1+\beta)F$	$RT/(2-\beta)F$	3
(C) [4] [5] and [7]	$-RT/\beta F$	$RT/(2-\beta)F$	2
(D) [4] [5] and [8]	$-RT/\beta F$	RT/F	$1+\beta$

* Rate-determining step is underlined. β is the cathodic symmetry factor of the rate-determining elementary step with one-electron transfer (here it is assumed to be 0.5).

was close to the melting point, the metal would be in a well annealed state, *i.e.*, would have a relatively small number of surface dislocations, and hence a large portion of the dislocations are already "active" even at low current densities. [For $N_{active}/N_{total} = \exp(-k N_{total})$, where N is the number of surface dislocations and k a constant, k would be smaller on solid gallium than on Cu or Ag, because of the much lower surface tension values of Ga compared with these metals (12).]

Steady State

Mechanism of charge transfer process.—The clear Tafel lines observed on liquid electrodes may be interpreted only in terms of a charge-transfer controlled mechanism. The stable ionic species of trivalent gallium in an alkaline solution (13) is $H_2GaO_3^-$. The over-all deposition reaction will be

$$H_2GaO_3^- + H_2O + 3e_o^- = Ga + 4\,OH^- \quad [3]$$

The following steps may be considered

$$H_2GaO_3^- + e_o^- \rightarrow HGaO_2^- + OH^- \quad [4]$$

followed by

$$HGaO_2^- + e_o^- \rightarrow GaO^- + OH^- \quad [5]$$

and

$$GaO^- + H_2O + e_o^- \rightarrow Ga + 2\,OH^- \quad [6]$$

Or, since univalent gallium ion is unstable with respect to decomposition into trivalent gallium and metallic gallium (13)

$$3GaO^- + 2H_2O \rightarrow 2Ga + H_2GaO_3^- + 2\,OH^- \quad [7]$$

or

$$HGaO_2^- + GaO^- + H_2O \rightarrow Ga + H_2GaO_3^- + OH^- \quad [8]$$

Tafel slopes expected for various rate determining steps involving the above reactions are given in Table II.

According to the experimental results, $d\eta/d \log i_c = 130$ mv and $d\eta/d \log i_a = 45$-55 mv. (A) and (B) are not admissable; since the experimental conditions were such that there could not be anodic passivation during short time polarization, the observed anodic value is too largely different to be consistent with (A) (which requires 24 mv at 30°C assuming the cathodic symmetry factor, β, to be 0.5), (B) is not consistent with the cathodic value. Mechanism (D) is preferred over mechanism (C) because:

1. Reaction [7] in (C) is likely to involve reaction [8] in (D), and [8] is more probable than [7], since the concentration of the divalent state, $HGaO_2^-$, would be much higher than that of the univalent state, GaO^-.

2. A closer fit of $i_{o,c}$ and the corresponding i_o, $\eta \rightarrow 0$ is obtained if, in calculating the latter, the value of $\alpha_c + \alpha_a$ used is 1.5 [cf. (D) in Table II].

3. Better agreement between experimental and calculated overpotential was obtained in the non-linear Tafel region on the liquid electrode with $\alpha_c + \alpha_a = 1.5$ than if it is taken as 2.

Adding [5] and [8], the mechanism (D) can be rewritten as

$$H_2GaO_3^- + e_o^- \rightarrow HGaO_2^- + OH^- \text{ (slow)} \quad [4]$$

$$2HGaO_2^- + e_o^- + H_2O \rightleftharpoons Ga + H_2GaO_3^- + 2\,OH^- \text{ (fast)} \quad [9]$$

Thus, the cathodic partial current density is

$$i_c = -k_1 [H_2GaO_3^-] \exp[-\beta FV/RT] \quad [10]$$

and the anodic one

$$i_a = k_2 [HGaO_2^-]_V \exp[(1-\beta)FV/RT] \quad [11]$$

where V is the electrode potential measured from a suitable reference point. From [9]

$$[HGaO_2^-]_V = k_3 [H_2GaO_3^-]^{1/2} \exp(FV/2RT) \quad [12]$$

The final equation for i is ($\eta = V - V_R$)

$$i = i_o \left[\exp\left(\frac{\left(\frac{3}{2} - \beta\right) F\eta}{RT} \right) - \exp\left(-\frac{\beta F\eta}{RT} \right) \right] \quad [13]$$

The over-all reaction [3] is obtained from [4] and [9] . The reversible potential, V_R, can be obtained as follows. From [10], [11], and [12] at equilibrium

$$i_o = k_1 [H_2GaO_3^-] \exp\left(-\frac{\beta FV_R}{RT} \right)$$

$$= k_4 [H_2GaO_3^-]^{1/2} \exp\left(\frac{\left(\frac{3}{2} - \beta\right) FV_R}{RT} \right) \quad [14]$$

which gives

$$V_R = V_{R,o} + \frac{RT}{3F} \ln [H_2GaO_3^-] \quad [15]$$

in agreement with [3].

Rate of deposition on liquid gallium electrode.—Using $\beta = 0.5$, the η-log i relation can be calculated and may be compared with the experimental values. In the cathodic region [Fig. 6 line (A)] the agreement over the entire overpotential region is satisfactory. In the anodic region [Fig. 7 line (A)], the experi-

mental values are lower than those calculated at high current densities. This may be due to an increased concentration of the Ga^+ state at high anodic overpotentials, which would shift the mechanism from (D) to (C), whereupon α_a becomes 1.5 instead of 1.0, *i.e.*, the slope would tend to decrease from 60 to 40 mv.

Concentration dependence of exchange current density on liquid gallium electrode.—Substitution of [15] into [14] gives

$$\frac{d \ln i_o}{d \ln [H_2GaO_3^-]} = 1 - \frac{\beta}{3} = 0.83 \left(\beta = \frac{1}{2}\right) \quad [16]$$

Agreement with experimental value (0.7 ± 0.2, Fig. 8) is fair.

Overpotentials on solid gallium electrode.—The deviations between the cathodic Tafel lines on liquid and solid can be discussed in terms of the surface diffusion of adions.

The rate expression, when the changes in the adion coverage is taken into account for both cathodic and anodic partial currents, may be written as

$$i = i_o \left[\frac{c_{ad}}{c_{ad,o}} \exp\left(\frac{\alpha_a F \eta}{RT}\right) - \frac{G - c_{ad}}{G - c_{ad,o}} \exp\left(-\frac{\alpha_c F \eta}{Rt}\right)\right] \quad [17]$$

where G is the total number of metal atoms on the surface (mole cm^{-2}). At the steady state (1, 2)

$$\frac{c_{ad}}{c_{ad,o}} = 1 + \frac{(-i)}{zFv_{ad,o}} \quad [18]$$

[17] and [18] give

$$i = \frac{i_o \left[\exp\left(\frac{\alpha_a F \eta}{RT}\right) - \exp\left(-\frac{\alpha_c F \eta}{RT}\right)\right]}{1 + r \exp\left(\frac{\alpha_a F \eta}{RT}\right) + \theta' r \exp\left(-\frac{\alpha_c F \eta}{RT}\right)} \quad [19]$$

where

$$r = i_o / zFv_{ad.o} \quad [20]$$

and

$$\theta' = c_{ad,o}/(G - c_{ad.o}) \quad [21]$$

Approximate forms of [19] for various conditions of overpotentials can be obtained using the following numerical values (cathodic region).

$$i_o = 1.4 \times 10^{-4} \text{ amp cm}^{-2} \quad \text{(Fig. 6)}$$

$$zFv_{ad,o} = 5.5 \times 10^{-5} \text{ amp cm}^{-2} \quad \text{(Fig. 5)}$$

$$c_{ad,o} = 5 \times 10^{-11} \text{ mole cm}^{-2}$$

and

$$G = 4 \times 10^{-9} \text{ mole cm}^{-2} \text{ (roughness factor 1.6[9])}$$

thus

$$r = 2.5 \qquad \theta' = 0.013 \quad [22]$$

1. $-\eta << RT/F$ [19] and [20] give

$$\eta = \frac{RT}{(\alpha_c + \alpha_a)} \frac{i}{F} \left[\frac{1}{i_o} + \frac{1}{zFv_{ad,o}}\right] \quad [23]$$

using the above numerical values, and $(\alpha_c + \alpha_a) = 1.5$, the slope of the $\eta - i$ plot, $(d\eta/di)_{\eta \to o}$, is about 410 ohms cm^2, which is in fair agreement with the average experimental value, about 300 ohms cm^2.

2. $-\eta \simeq RT/F$

$$i = i_o \exp\left(-\frac{\alpha_c F \eta}{RT}\right) \Big/ \left[1 + r \exp\left(\frac{\alpha_c F \eta}{RT}\right)\right] \quad [24]$$

where $r \exp(\alpha_a F\eta/RT)$ is of the order of 0.1, *i.e.*, the relation between i and η is fairly close to that expected from the charge-transfer controlled mechanism.

3. $-\eta >> RT/F$

$$i = i_o \exp\left(-\frac{\alpha_c F \eta}{RT}\right) \Big/ \left[1 + \theta' r \exp\left(-\frac{\alpha_c F \eta}{RT}\right)\right] \quad [25]$$

This tends to yield a limiting current under the condition

$$1 << \theta' r \exp\left(-\frac{\alpha_c F \eta}{RT}\right) \quad [26]$$

which may be expected at $-\eta > 300$ mv according to [25], with the numerical value of the limiting current of [cf. (22)]

$$i_{lim} \simeq \frac{zFV_{ad,o}}{\theta'} \simeq 4 \times 10^{-3} \text{ amp cm}^{-2} \quad [27]$$

if there is no increase of $zFv_{ad,o}$ with i (but see Fig. 5 and 6).

For test of Eq. [19], i values are calculated at various values of η using the numerical values of [22]. The agreement is fairly satisfactory in the cathodic region [Fig. 6 line (B)].

In the anodic region, the value of $zFv_{ad,o}$ obtained from transients was less well reproduced, as it was not in good accord with that from cathodic experiments (10 times larger). The $\eta - i$ relation was calculated from [19] using this larger value and i_o of 8×10^{-5} amp cm^{-2} [Fig. 7, line (B)]. The experimental values deviate from the calculated line at high overpotentials, but the qualitative shape and the quantitative agreement at low overpotentials are acceptable. Thus, the concave shape of the η-log i curve on the solid gallium electrode is consistent with the development of a limiting current density due to surface diffusion control. The rate constant for this behavior is consistent with that obtained from the interpretation of the deviation from a charge-transfer controlled mechanism at very low current densities. The deviation of the experimental curve from that calculated at very high overpotentials is probably due to a small increase in the number of active growth sites, arising by the mechanism discussed (12).

Acknowledgments

The authors are indebted to the American Electroplaters Society for financial support and to the Supervising Committee of this Society's Project 16 for stimulating discussion. They wish to thank Mr. H. Kita for carrying out a number of confirmatory calculations with the material. One of them (M. E.) is grateful to Professor J. Horiuti for permission to take study leave to carry out this work.

Manuscript received April 25, 1961; revised manuscript received July 19, 1961.

Any discussion of this paper will appear in a Discussion Section to be published in the December 1962 JOURNAL.

REFERENCES

1. W. Mehl and J. O'M. Bockris, *J. Chem. Phys.*, **27**, 818 (1957); *Can. J. Chem.*, **37**, 190 (1959).
2. A. Despic and J. O'M. Bockris, *J. Chem. Phys.*, **32**, 389 (1960).
3. H. Gerischer, *Z. Elektrochem.*, **62**, 256 (1958).
4. H. Gerischer and R. P. Tischer, *ibid.*, **58**, 819 (1954); **61**, 1159 (1957).
5. H. Gerischer and M. Krause, *Z. physik. Chem. (N.F.)*, **10**, 264 (1957).
6. E. Mattsson and J. O'M. Bockris, *Trans. Faraday Soc.*, **55**, 1586 (1958).
7. M. A. V. Devanathan, J. O'M. Bockris, and W. Mehl, *J. Electroanal. Chem.*, **2**, 143 (1960).
8. M. Enyo, Dissertation, Univ. of Pennsylvania, Philadelphia (1960).
9. F. P. Bowden and E. A. O'Connor, *Proc. Roy. Soc.*, **A128**, 317 (1930).
10. R. Belcher, A. J. Nutten, and W. I. Stephen, *J. Chem. Soc.*, 2438 (1952).
11. A. Defrain, I. Epelboin, and M. Erny, *Compt. rend.*, **248**, 1486 (1959).
12. H. Kita, M. Enyo, and J. O'M. Bockris, *Can. J. Chem.*, **39**, 1670 (1961).
13. W. M. Latimer, "Oxidation Potentials," 2nd ed., p. 159, Prentice-Hall, New York (1953).

Unit Cell Volume Effects in Some Isomorphous Ferroelectric Systems

Thomas G. Dunne and Gerald Burns

Research Center, International Business Machines Corporation, Yorktown, New York

ABSTRACT

By examining published data, a linear relationship between unit cell volume and ferroelectric Curie point is found for a number of isomorphous systems. The meaning of this is discussed, and for the KH_2PO_4 system it is shown how one can extend Slater's theory qualitatively so that this relationship and the deuteration effect can be understood simultaneously. Several other systems of isomorphous compounds are discussed.

There are few adequate microscopic model theories of ferroelectrics. Often, new mechanisms are proposed when a new group of ferroelectric compounds is discovered. Phenomenological theories have met wider success.

In this paper a relationship between unit cell volume and Curie point is pointed out. This relationship seems to occur generally within isomorphous groups of ferroelectrics. It is not implied that volume itself is the important parameter that determines the ferroelectric behavior. For example, if electronic polarizability is the important parameter, a large electronic polarizability normally will mean larger ionic size, which means larger volume, or if hydrogen bond lengths are the important parameters, then again volume will be the convenient measurable parameter. It is hoped consideration of the relationships pointed out here will help make the transition from phenomenological to model theories and extend model theory. In the case of the KH_2PO_4(KDP) series of ferroelectrics, it is shown how one can extend Slater's model theory qualitatively so that alkali substitution effects and deuteration effects can be understood.

Perovskite System

Merz[1] originally pointed out that the decrease in the Curie temperature T_c of $BaTiO_3$ with increasing pressure is similar to the decrease in T_c as the unit cell volume decreases on substitution of Sr^{+2} in place of Ba^{+2}. Using recent data for T_c *vs.* composition in the (Ba, Sr) TiO_3 system (2) and elastic constants of $BaTiO_3$ (3), one obtains $\Delta T_c/\Delta V = +115°C/A^3$ for compression and $\Delta T_c/\Delta V = +70°C/A^3$ for Sr^{+2} substitution. The fact that these slopes should have similar values has been given some theoretical justification by Triebwasser (4). However, $PbTiO_3$ with a smaller unit cell and higher Curie point doesn't fit the relationship found for (Ba, Sr)TiO_3 (5). This may be due to the fact that

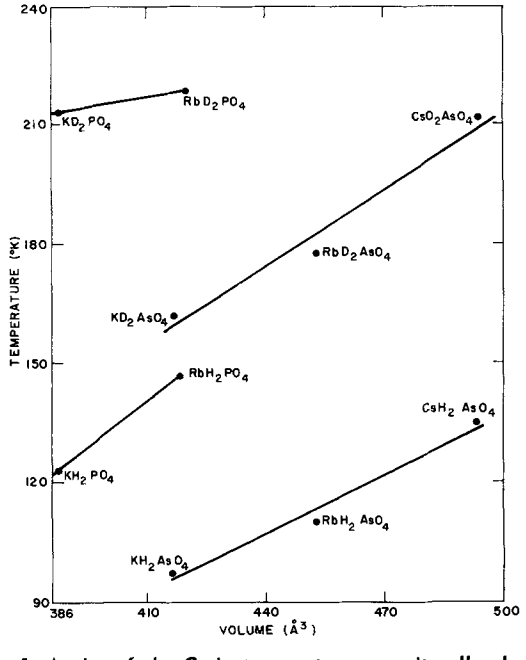

Fig. 1. A plot of the Curie temperature vs. unit cell volume for KDP-type compounds.

Pb is in a different group of the periodic table and tends to bond differently. In this paper hydrogen bonded systems are discussed.

KDP Systems

Using published data (6, 7) and lattice constants of RbH_2AsO_4 and CsH_2AsO_4 determined by Stemple (8), T_c *vs.* volume is plotted in Fig. 1. It is seen that both addition of a larger alkali ion and deuteration increases T_c.

One can connect these effects qualitatively by extending Slater's model (9). Slater derives the expression $\epsilon = k\ T_c \ln 2$ where ϵ is the energy difference between two configurations of the $(H_2PO_4)^-$ group, the lower energy configuration occurring when the protons associated with the PO_4^{-3} group are arranged so that the dipole moment μ of the $(H_2PO_4)^-$ group is parallel to the ferroelectric c axis. One can understand then the effects noted in Fig. 1 by the following reasoning:

1. O-O (the distance between the hydrogen bonded oxygen atoms) increases on substitution of a larger alkali ion. This is a reasonable assumption to make since all the macroscopic dimensions increase on substitution of a larger alkali ion.
2. O-H (the shortest hydrogen bond distance) decreases as O-O increases. This is what one finds in general for hydrogen bonding (10).
3. The decrease of the O-H distance will cause an increase in the induced dipole moment of the PO_4^{-3} group. This change in the dipole moment will further increase the energy difference between the two configurations.

Thus, as one increases the size of the alkali ion, O-O will increase causing O-H to decrease, causing the induced μ to increase, causing ϵ to increase. From Slater's theory T_c should then increase which is what occurs (see Fig. 1). This reasoning also explains the deuteration effect since, on deuteration, one generally observes that the O-O increases (11), which again would cause an increase in T_c, as observed.

Spontaneous polarization data, available for but a few KDP isomorphs, indicate that this quantity is fairly independent of unit cell volume.

Guanidine Aluminum Sulfate Series

The compounds of this isomorphous series are ferroelectric up to the temperature region in which decomposition takes place, so the volume dependence of the transition temperature cannot be investigated. However, the spontaneous polarization does show a consistent increase as the cell volume is increased by isomorphous substitution (12-15) as can be seen in Fig. 2.

The volume effect caused by compression has been obtained using published pressure and elastic constant data (16, 17). It is seen that in this case, spontaneous polarization increases with decreasing volume in contrast to the opposite effect in isomorphous substitution. However, one must be careful in comparing the two because the shape of the unit cell is changed in a different way by hydrostatic compression than by isomorphous substitution. This is well illustrated by comparing the ratio of lattice

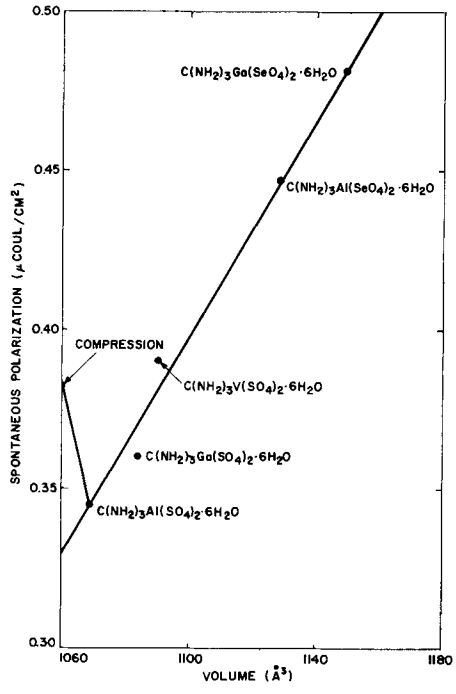

Fig. 2. A plot of the room temperature spontaneous polarization *vs.* unit cell volume for GASH-type compounds. Results of a compression experiment are also included.

constant increments, $\Delta c/\Delta a$ for the two processes. For compression $\Delta c/\Delta a \cong 4$ for GAlSH, GAlSeH, G GaSH, and G Ga SeH. However, in the case of isomorphous substitution, $\Delta c/\Delta a = 4.52$, 2.61, 0.44, and 0.36 for the substitution of Ga^{+3} for Al^{+3} in GAlSH, Ga^{+3} for Al^{+3} in GAlSeH, SeO_4^{-2} for SO_4^{-2} in GAlSH, and SeO_4^{-2} for SO_4^{-2} in G GaSH, respectively. Thus, compression and substitution change the lattice constants in a different way, and it is not surprising that the two processes have different effects on the spontaneous polarization.

However, in the tryglycine sulfate and isomorphous compounds, rough unit cell data (18, 19) indicate that the pressure effect (20) is in the same direction as the isomorphous substitution.

Alums

Ferroelectric behavior in a large number of the cubic alums has been observed (21, 22). In the series (listed in order of increasing unit cell volume) $NH_4M(SO_4)_2 \cdot 12H_2O$ where M= Al, Ga (23), Cr, Fe, V, and In the transition temperature increases approximately linearly with volume. Also for the three compounds with the larger volumes, Fe, V, and In, the transition is to a ferroelectric phase. While for the compounds with the smaller volume, Al, Ga, and Cr, the transition is to another paraelectric phase. Yet the transition temperature of both types fit on the same T_c *vs.* volume line. Also, the spontaneous polarization P is approximately the same ($\sim$ 0.1 μcoul./cm^2) for the two compounds of largest volume (M = In and V). For M = Fe, the compound with the lowest ferroelectric transition temperature, P is considerably smaller ($\sim$ 0.03 μcoul./cm^2).

For the $CH_3NH_3M(SO_4)_2 \cdot 12\ H_2O$ alums (where M stands for the same ions as in the previous case) T_c and P have values of approximately 170°K and

0.1 μcoul./cm^2, respectively, and are roughly independent of volume.

Thus, one often observes a relationship between the ferroelectric properties and the unit cell volume. This relationship can be extended sometimes to include compression experiments and, in the case of KDP systems, it is shown how one can qualitatively extend the present model theory to account for the observed effects.

Manuscript received June 26, 1961; revised manuscript received Sept. 8, 1961.

Any discussion of this paper will appear in a Discussion Section to be published in the December 1962 JOURNAL.

REFERENCES

1. W. Merz, *Phys. Rev.*, **78**, 52 (1950).
2. S. Kisaka, S. Ikagami, and H. Sasaki, *J. Phys. Soc. Japan*, **14**, 1680 (1951).
3. E. J. Huibregtse, W. H. Bessey, and M. E. Drougard, *J. Appl. Phys.*, **30**, 899 (1959).
4. S. Triebwasser, *Phys. Rev.*, **114**, 63 (1950).
5. W. Kanzig, "Ferroelectrics and Antiferroelectrics," Solid State Physics, Vol. 4, p. 23, Academic Press, New York (1957).
6. *Ibid.*, p. 14
7. Wykoff, "Crystal Structures," Vol. 2, Interscience Publishers, Inc., New York (1953).
8. N. Stemple, Private communication.
9. J. C. Slater, *J. Chem. Phys.*, **9**, 16 (1941).
10. G. C. Pimentel and A. L. McClellan, "The Hydrogen Bond," p. 259, W. H. Freeman, San Francisco (1960).
11. A. H. Ubbelhode and K. J. Gallagher, *Acta Cryst.*, **8**, 71 (1955).
12. N. Stemple, Private communication.
13. Z. I. Ezhkova, G. S. Zhadnov, and M. M. Umonskii, *Knistallografiya*, **3**, 231 (1958) [English Translation, *Soviet Phys.—Cryst.*, **230**, 3 (1958)].
14. A. N. Holden, W. J. Merz, J. P. Remeika, and B. T. Matthias, *Phys. Rev.*, **101**, 1 (1956).
15. J. P. Remeika and W. J. Merz, *ibid.*, **102**, 295 (1956).
16. W. J. Merz, *ibid.*, **103**, 565 (1956).
17. S. Haussuhl, *Z. Krist.*, **111**, 21 (1959).
18. B. T. Matthias, C. E. Miller, and J. P. Remeika, *Phys. Rev.*, **104**, 849 (1957).
19. R. Pepinsky, Y. Okaya, and F. Jona, *Bull. Am. Phys. Soc.*, Series II, 220 (1957).
20. F. Jona and G. Shirane, *Phys. Rev.*, **111**, 139 (1959).
21. F. Jona, T. Mitsui, and R. Pepinsky, To be published.
22. F. Jona and G. Shirane, "Ferroelectric Crystals," Pergamon Press, in press.

Ionic Transport Entropy in Nonisothermal Molten Silver Chloride Cells

S. Senderoff and R. I. Bretz

Parma Research Laboratory, Union Carbide Corporation, Parma, Ohio

ABSTRACT

The determination of the emf of the nonisothermal cells Ag/AgCl(1)/Ag and Cl_2/AgCl(1)/Cl_2 is used to estimate the magnitude of the transport entropy terms in the general equation for thermogalvanic potentials. The emf's were determined over the temperature range 500°-900°C with temperature differentials ranging from 40° to 400°C. The limits of accuracy of the measurement are established by reference to accurately known reversible thermodynamic quantities; the irreversible quantities are demonstrated to be small, but not negligible as they were reported to be in solid electrolyte cells; and the Seebeck coefficient's independence of the transport numbers in the system was experimentally confirmed.

When a temperature difference exists between the electrodes of a chemically symmetrical cell (*i.e.*, electrode | electrolyte | electrode in which the two electrodes are identical), an emf is developed which has frequently been called a thermogalvanic potential, or more briefly, a thermopotential. The nonisothermal cell which produces this emf is usually called a thermocell, and its emf is a special case of the very general thermoelectric effect which is associated with the contacts between dissimilar electrical conductors in a thermal gradient. By analogy with the metallic thermocouple, the electrodes represent one conductor, the electrolyte the second conductor, and the two electrode-electrolyte interfaces the hot and cold junctions. Figure 1 shows this analogy pictorially, and the theoretical equivalence of these systems has been discussed by Wagner (1), Lange (2), and others.

When considering the details of the general theory, however, an important difference between the thermocell and the metallic thermocouple emerges. In the latter only electrons flow in the circuit with no net transfer of material, while in the former, matter is transferred from one electrode to the other as a result of the electrochemical reactions at the junctions and ionic transport in the electrolyte. Consequently, the detailed theoretical treatment of these systems includes chemical entropies of classical thermodynamics and entropies of transport of ions.

Eastman (3) and Wagner (1) have presented a detailed theory of thermocells, and in recent years the methods of the thermodynamics of irreversible processes have been applied with great effectiveness to this subject by Holtan (4), Mazur (5), de Groot (6), and others. Excellent reviews of the subject

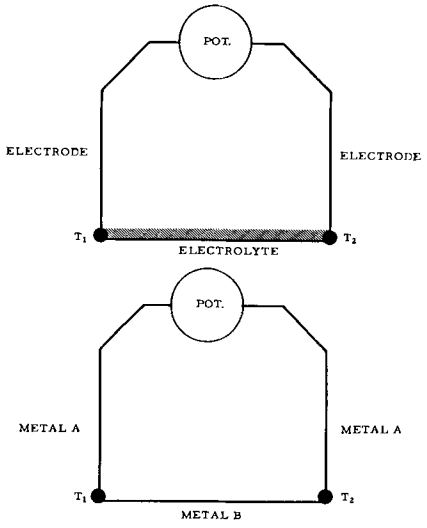

Fig. 1. Pictorial representation of thermocell as thermocouple

have been published by de Bethune (7) and by Agar (8).

Theory

The derivation of the general equations for thermocells has been presented frequently and adequately elsewhere (5-8) and will not be repeated here. Following Holtan (4), one may start with the expression for the emf of the thermocell,

$$\mathbf{F}(dE/dT) = -\sum_{k=1}^{n}(t_k/z_k)\overline{\overline{S}}_k - \overline{\overline{S}}_{el} - \Delta S + \sum_{k=1}^{n}(t_k/z_k)\overline{S}_k + \overline{S}_{el} \quad [1]$$

where $\mathbf{F}$ is the Faraday constant, dE/dT the Seebeck coefficient or thermopotential per degree of temperature difference between the electrodes (v/degree), t_k the transport number of substance, k, z_k the valence of substance, k (sign included), $\overline{\overline{S}}_k$[1] the transported entropy of k, $\overline{S}_k$ the partial molar entropy of k, $\overline{\overline{S}}_{el}$ the transported entropy of an electron in the electrode, $\overline{S}_{el}$ the partial molar entropy of an electron in the electrode, and ΔS the entropy change per equivalent associated with the electrochemical reaction at the electrodes.

It should be noted that all terms of the general equation associated with concentration gradients in the cell have been omitted since concentration gradients cannot exist when the electrolyte is a pure binary salt, molten or solid.

Again following Holtan, Eq. [1] may be separated into a part containing entropies of classical thermodynamics (or thermostatics) and a part containing the transported entropies. Properties of single ions appear only in the latter part. Thus,

$$\mathbf{F}(dE/dT) = \mathbf{F}(dE/dT)_c - \sum_{k=1}^{n}(t_k/z_k)\overline{\overline{S}}_k - \overline{\overline{S}}_{el} \quad [2]$$

where

$$\mathbf{F}(dE/dT)_c = -\Delta S + \sum_{k=1}^{n}(t_k/z_k)\overline{S}_k + \overline{S}_{el} \quad [3]$$

[1] The symbol and definitions used are those of Agar (8). $\bar{\bar{S}}_i \equiv S_i^*$, the latter being the symbol used by Holtan and others of the de Groot school. They define this as "entropy of transfer of i." S_i^* as used by Agar has another meaning. $\bar{\bar{S}}_i = Q_i/T^* + \bar{S}_i$ where Q_i^* is the heat of transfer of i.

It will be seen below that this separation was unfortunate when applied to the study of single binary electrolytes because it obscured the fact that with such an electrolyte the Seebeck coefficient is independent of the transport number. Nevertheless, in studying a large number of cells with solid electrolytes, Holtan made the discovery that in all cases $dE/dT = (dE/dT)_c$ within experimental error; or stated differently, there was no experimental evidence that the sum of the terms involving the transported entropy and single ion quantities was anything but negligible.

Holtan also investigated some solutions and molten salts and found in a number of cases that $dE/dT \neq (dE/dT)_c$, but this did not unambiguously establish that the sum of the transported entropy terms was not negligible since he did not know transport numbers in some cases and could not identify the significant species, *i.e.*, hydrate, complex ion, etc., in any case, as pointed out by Mazur (5) and by Holtan himself. As will be seen below, molten silver chloride is a particularly suitable substance to study to remove this ambiguity.

Silver chloride is also a particularly suitable substance for a measurement which establishes the limits of accuracy of the measured Seebeck coefficient with great certainty and, thus, the magnitude of the inequality, $dE/dT \neq (dE/dT)_c$, necessary to be considered as significant. Consider the thermocells:

$$\mathrm{M}|\mathrm{MX}|\mathrm{M} \qquad \text{I}$$

$$\text{graphite, } \mathrm{X_2}|\mathrm{MX}|\mathrm{X_2}\text{, graphite} \qquad \text{II}$$

and the isothermal cell:

$$\mathrm{M}|\mathrm{MX}|\mathrm{X_2}\text{, graphite} \qquad \text{III}$$

It can be shown that (5)

$$(dE/dT)_{II} - (dE/dT)_{I} = (dE/dT)_{III} - \epsilon_{M,\ graphite} \quad [4]$$

where $\epsilon_{M,\ graphite}$ is the Seebeck coefficient of the M, graphite thermocouple.

Since $(dE/dT)_{III}$ can be measured with considerable accuracy either directly by an emf determination or indirectly by a determination of the entropy of formation of MX, and since $\epsilon_{M,\ graphite}$ is usually less than 1% of $(dE/dT)_{III}$ when MX is a molten salt, a means is provided for checking the measured Seebeck coefficient of the thermocells without complication by the transport entropy

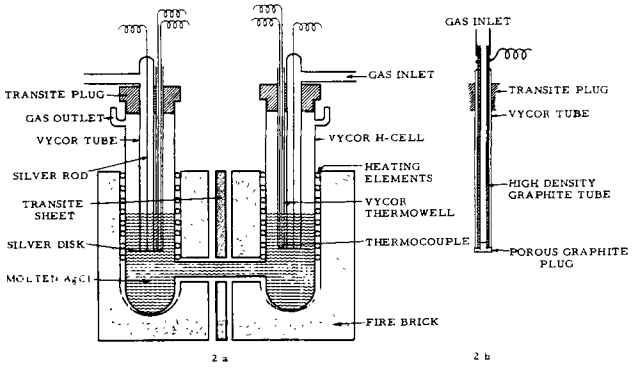

Fig. 2. Apparatus for determination of Seebeck coefficient: a, arrangement with silver electrodes for measurements on cell I; b, Chlorine electrode assembly for measurements on cell II.

and single ion quantities. In the case of silver chloride, cell III has been measured by a number of workers with good agreement, and cells I and II, involving highly reversible electrodes, are amenable to reasonably accurate measurements.

Experimental

The experimental arrangement of measuring the Seebeck coefficients of cells I and II is shown in Fig. 2. In Fig. 2a, the cell is shown with silver electrodes for the measurements on cell I. Measurements on cell II are made by removing the silver electrode assembly from each leg and replacing it with the chlorine electrode assembly shown in Fig. 2b. Two semicylindrical heating elements (Hevi Duty No. 7H-KS) are placed each around a leg of a Vycor H-cell and the assembly is insulated with a few layers of suitably shaped fire brick.

The H-cell is made by joining two Vycor test tubes (12 in. in length, 25 mm in diameter) with a 3 in. length of 13 mm Vycor tubing, the join being about ½ in. above the bottom of the test tubes. Two small tubes were attached near the top of the test tubes to serve as gas outlets.

When the cell is in place a piece of transite is interposed between the legs of the H-cell to maximize the thermal insulation of one leg from the other. The temperature of each of the legs is individually controlled with a controlling pyrometer fed by a Chromel-Alumel thermocouple in the electrolyte in each leg. The temperature of each leg is measured with the same two thermocouples by putting their output across an L&N thermocouple potentiometer (Catalog No. 8657-C).

Electrodes for the measurement of cell I are made by welding a silver disk, ⅝ in. diameter and 0.01 in. thick, to a ⅛ in. silver rod so that the disk is in a horizontal position in the melt. The rod is sheathed with a 9 mm Vycor tube which extends down to the disk. A slow stream of purified argon passing through the Vycor sheath keeps the electrolyte out of contact with the rod so that the emf is characteristic of the temperature of the horizontal disk. Since it is rather difficult to maintain a large isothermal region vertically in nonisothermal cells such as these, but much simpler to maintain a thin isothermal wafer, placement of a thermocouple in a Vycor thermowell as nearly as possible (within 2 mm) in contact with the horizontal disk was sufficient to give satisfactory temperature measurements.

Electrodes for the measurement of cell II were made by sealing a plug of porous graphite (National Carbon grade No. 60) 6 mm in diameter and ¼ in. thick to the end of a high density graphite tube, and purifying the electrode by heating to 2400°C, holding at temperature for 1 hr, and cooling, all in a chlorine atmosphere. The electrode was covered with a tightly fitting Vycor sheath with only the flat surface of the porous plug at the bottom and a few inches at the top to make electrical contact exposed. A seal of carbonaceous cement (National Carbon grade C-9) at the bottom effectively kept the electrolyte out of contact with the tube except at the face of the porous plug. Chlorine gas was passed through a drying tower, down the tube and out through the

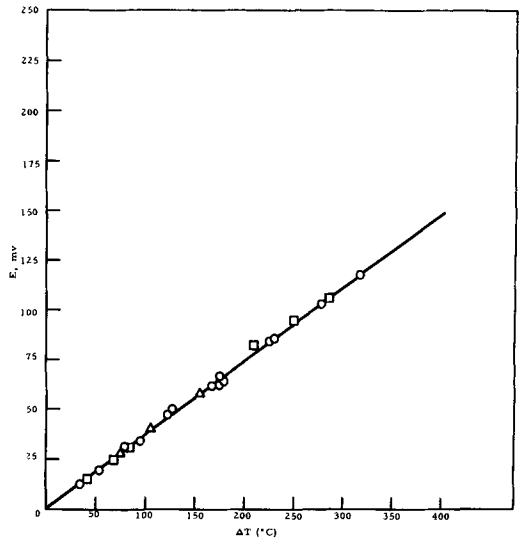

Fig. 3. EMF of thermocell, Ag/AgCl/Ag (cell I) as a function of ΔT, the temperature difference between the electrodes. Cold leg temperature: ○ 490°-524°C; □ 525°-549°C; △ 550°-600°C.

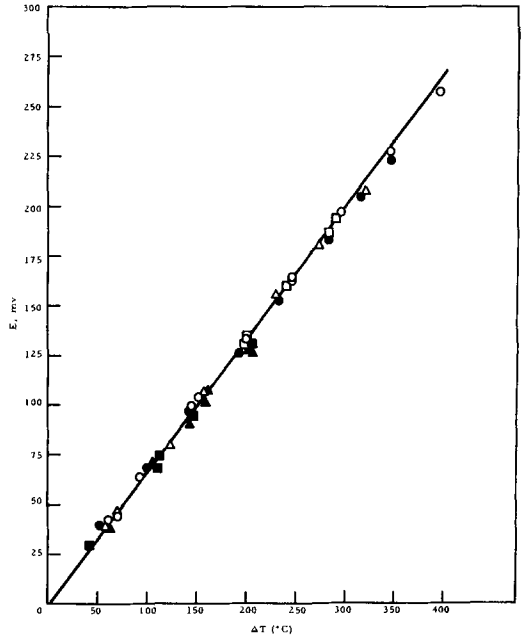

Fig. 4. EMF of thermocell, graphite, Cl_2/AgCl/Cl_2, graphite, (cell II) as a function of ΔT, the temperature difference between the electrodes. Cold leg temperature: ○ 475°-499°C; □ 500°-524°C; △ 525°-549°C; • 550°-600°C; ■ 600°-650°; ▲ 650°-700°C.

submerged porous plug. The thermocouple in its Vycor sheath was within 2 mm of the plug.

The cell was charged by adding enough reagent grade silver chloride to both legs to give a depth of about 2 in. when molten. The liquid was passed back and forth through the bridge to eliminate entrapped gas bubbles, by applying slight gas pressure to one of the outlets at the top of the H-cell.

Well-fitting transite plugs with holes to accommodate the electrode sheath and thermowell were placed on top of the two legs of the H-cell, gas lines were connected to the electrode (cell II) or a sidearm on the sheath of the electrode (cell I), and electrical leads were drawn from the electrodes to a Rubicon potentiometer (Catalog No. 2780). Thermocouples were inserted in the thermowells and con-

Table I. Seebeck coefficients of thermocells and temperature coefficient of the emf of the isothermal cell

$(dE/dT)_I$				$(dE/dT)_{II}$	
−0.375	−0.40	−0.42	−0.398	−0.664	
500-900	450-650	487-590		500-900	Temp. range, C°
This paper	ref. (4)	ref. (9)	Avg.	This paper	Source

$(dE/dT)_{III}$				mv/C°	
−0.289	−0.264	−0.244	−0.266	(calc.)	
−0.26	−0.289	−0.29	−0.23	−0.267 (meas.)	
500-900	480-900	450-600	500-800		Temp. range, C°
ref. (10)	ref. (11)	ref. (12)	ref. (13)	Avg.	Source

nected to the two controlling pyrometers, which were set at the desired temperature for each leg. When the temperatures became steady, the emf of the cell and of each of the thermocouples was measured at the same time, and the controllers reset for other temperatures. These measurements were made at temperatures between 500° and 900°C and temperature differentials ranging from 40° to 400°C. The temperatures of both cold and hot legs were varied widely within this range.

Results

The results of the measurements of the emf of cell I are shown in Fig. 3 and of cell II in Fig. 4. The emf is plotted against the temperature difference between the electrodes for various cold leg temperatures. A least squares straight line through the points in each yields a value of the Seebeck coefficient for cell I (Ag|AgCl|Ag) of −0.375 with a standard deviation of ±0.01 mv/C° and a value for cell II (graphite, Cl_2|AgCl|Cl_2, graphite) of −0.664 with a standard deviation of ±0.02 mv/C°. The negative sign indicates that the hot electrode is the negative pole of the cell. It will be noted that there is no significant variation of the Seebeck coefficient with either the mean temperature or the temperature difference in the range studied.

The accuracy of the Seebeck coefficients can now be estimated by application of Eq. [4]. In Table I are shown the values from various sources for the Seebeck coefficient of the two thermocells, and for the temperature coefficient of the emf of the isothermal cell, Ag|AgCl|Cl_2, graphite. By substituting, in turn, the three values of $(dE/dT)_I$ and the value of $(dE/dT)_{II}$ in Eq. [4], the calculated values of $(dE/dT)_{III}$ are 0.289, 0.264, and 0.244 mv/C°. These may be compared with the measured values of 0.26 and 0.289. Although there is reason to believe that the value of 0.42 for $(dE/dT)_I$ and that of 0.23 for $(dE/dT)_{III}$ are the least reliable of those cited and one would be justified in ignoring them, if no values are rejected and the mean of the three $(dE/dT)_I$ values, 0.398, is used in Eq. [4], the $(dE/dT)_{III}$ thus calculated, 0.266, agrees with the mean of the four values of $(dE/dT)_{III}$, 0.268. It has, thus, been demonstrated that the values of the Seebeck coefficients determined from the data in Fig. 3 and 4 are probably not in error by more than 0.02 to 0.03 mv/C°, equivalent to approximately 0.5 entropy unit.

Table II. Molar entropies at 1000°K (cal/ deg)

Ag	18.00
Cl_2	63.74
AgCl	43.30

These values may now be used to estimate the magnitude of the terms in Eq. [1] which contain transport entropy and single ion quantities. If one defines[2] $\tau \equiv \sum_{k=1}^{n} (t_k/z_k)\overline{\overline{S}}_k + \overline{\overline{S}}_{el}$, Eq. [2] becomes for a cell with a molten silver chloride electrolyte:

$$\mathbf{F}(dE/dT) = -\tau - \Delta S + t_+\overline{S}_{Ag^+} - (1 - t_+)\overline{S}_{Cl^-} + \overline{S}_{el} \quad [5]$$

since in a binary electrolyte $(t_-) + (t_+) = 1$.

The electrode reaction of cell I, $Ag \rightarrow Ag^+ + e$, involves an entropy change,

$$\Delta S = S_{Ag^+} - S_{Ag} + S_{el} \quad [6]$$

Substituting Eq. [6] into [5] gives:

$$\mathbf{F}(dE/dT)_I = -(t_-)S_{AgCl} + S_{Ag0} - \tau \quad [7]$$

and rearranging yields,

$$\tau = -\mathbf{F}(dE/dT)_I + S_{Ag0} - (t_-)S_{AgCl} \quad [8]$$

Similarly, the entropy change for the electrode reaction of cell II:

$$Cl^- \rightarrow \tfrac{1}{2}\, Cl_2 + e$$

$$\Delta S = \tfrac{1}{2}\, S_{Cl_2} + S_{el} - S_{Cl^-} \quad [9]$$

is substituted into Eq. [5] to obtain on rearrangement:

$$\tau = -\mathbf{F}(dE/dT)_{II} - \tfrac{1}{2}\, S_{Cl_2} + (t_+)S_{AgCl} \quad [10]$$

Table II gives the values of the molar entropies at 1000°K (14) required in Eq. [8] and [10]. Substituting these values, together with the Seebeck coefficients from Fig. 3 and 4, into Eq. [8] and [10] yields, respectively,

$$\tau = 23.07 \times 0.375 + 18.0 - 43.3\,(t_-)$$

or

$$\tau = 26.7 - 43.3\,(t_-) \quad [11]$$

and

$$\tau = 23.07 \times 0.664 - 31.87 + 43.3\,(t_+)$$

or

$$\tau = -16.6 + 43.3\,(t_+) \quad [12]$$

A plot of Eq. [12] is shown in Fig. 5.

[2] τ is not exactly the same for cells I and II, since $\overline{\overline{S}}_{el}$ refers to the electron in silver for cell I and in graphite for cell II. $\tau_{II} - \tau_I = \epsilon_{Ag,\,graphite}$, and since τ is the same order of magnitude as the Seebeck coefficients of the thermocells (as will be seen below) ϵ is less than 1% of this value and will be ignored.

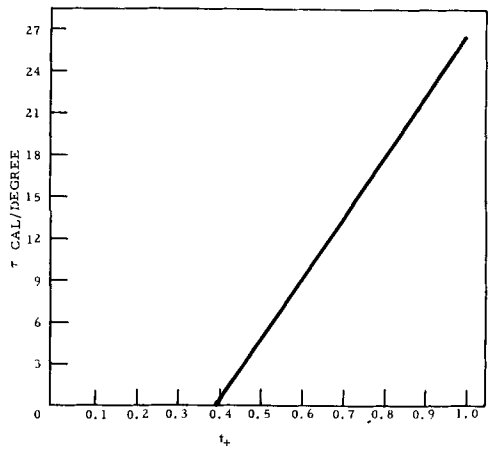

Fig. 5. τ as a function of transport number

Discussion

It is immediately obvious that τ, the sum of terms involving the transported entropies and single ion quantities, must be different from zero. For $\tau = 0$, the chloride ion must carry most of the current (*i.e.*, $t_+ = 0.384$). However, in the solid state, the silver ion is the only carrier ($t_+ = 1$), and measurements of the transference number in molten AgCl indicate that at 850°C t_+ is 0.83 (15), corresponding to $\tau = 19.4$ cal/deg. Even if t_+ were as low as predicted by the radius ratio calculation (16), *i.e.*, 0.59, τ would still be 8.9 cal/deg, and there is reason to believe that the radius ratio calculation is not applicable here.

Having established in the case of molten silver chloride that the transported entropy and single ion terms are not negligible, there remains only to demonstrate that there is little or no ambiguity of the components as in the case of other liquids.

Since in a pure molten salt there is no solvation or reaction with other components, one need only consider self-complexing as represented by $[Ag_2Cl]^+$, $[AgCl_2]^-$, etc. It is unlikely that any appreciable concentration of such clusters exists in molten AgCl at temperatures up to 900°C because silver ion, when it does form complexes, almost always has a coordination number of two and forms linear complexes based on the sp hybrid orbital, a notably weak bonding type. A number of investigations involving thermodynamic measurements such as emf (11, 17, 18) of mixtures of AgCl with other alkali halides show that in all cases the solutions are ideal or very nearly so. The largest reported departures are those in LiCl-AgCl mixtures in which the activity coefficient at 0.585 mole fraction AgCl is 1.10 and at 0.0286 mole fraction AgCl the activity coefficient is 2.23. These very small deviations from ideality with such a large disparity in cation sizes would preclude appreciable self-complexing in molten silver chloride. The high conductivity of molten silver chloride compared with other molten salts (4.5 compared with 2.6 ohm^{-1} cm^{-1} for KCl at 1000°K) also indicates little probability of clustering into large ions with consequent reduction in the number and mobility of carriers.

In view of the special character and well-known properties of silver chloride one can, with confidence, conclude that the sum of terms involving the transported entropies and single ion quantities is not only of the same order as, but larger than $(dE/dT)_c$, the sum of terms involving only classical thermodynamic entropies. Using the value of $t_+ = 0.83$, for which $\tau = 19.4$ cal/deg, $(dE/dT)_c$ for cells I and II are, respectively, 10.7 and 4.1 cal/deg.

Although the quantities τ and $(dE/dT)_c$ in which Holtan was interested depend on the transport number, the Seebeck coefficient of the thermocell is independent of transport number when the electrolyte is a single binary salt, as shown by Pitzer's (19) equation:

$$\mathbf{F}(dE/dT)_{\mathrm{I}} = S_{\mathrm{Ag}} - \overline{\overline{S}}_{\mathrm{Ag^+}} - \overline{\overline{S}}_{\mathrm{el}} \qquad [13]$$

If one separates some of the $\overline{\overline{S}}_k$ terms of Eq. [7] into their components, $\overline{S}_k + Q^*_k/T$, and writes it in the form:

$$\mathbf{F}(dE/dT)_{\mathrm{I}} = -(t_-)S_{\mathrm{AgCl}} + S_{\mathrm{Ag}} - \overline{\overline{S}}_{\mathrm{Ag^+}} + (t_-)(\overline{S}_{\mathrm{Ag^+}} + \overline{S}_{\mathrm{Cl^-}}) + (t_-)\frac{Q^*_{\mathrm{Ag^+}} + Q^*_{\mathrm{Cl^-}}}{T} - \overline{\overline{S}}_{\mathrm{el}} \qquad [14]$$

one notes that since $\overline{S}_{\mathrm{Ag^+}} + \overline{S}_{\mathrm{Cl^-}} = S_{\mathrm{AgCl}}$ Eq. [14] reduces to Eq. [13] if $\dfrac{Q^*_{\mathrm{Ag^+}} + Q^*_{\mathrm{Cl^-}}}{T} = \dfrac{Q^*_{\mathrm{AgCl}}}{T} = 0$. Pitzer asserts that $(Q^*_{\mathrm{Ag^+}} + Q^*_{\mathrm{Cl^-}})$ is, indeed, zero, since the process to which it refers is the bulk displacement of the liquid.

An equation similar to Eq. [13] may be written for cell II, *viz.*

$$\mathbf{F}(dE/dT)_{\mathrm{II}} = -\tfrac{1}{2}\,S_{\mathrm{Cl_2}} + \overline{\overline{S}}_{\mathrm{Cl^-}} - \overline{\overline{S}}_{\mathrm{el}} \qquad [15]$$

With the values of Table II in Eq. [13] and [15] and ignoring[3] (as previously) $\overline{\overline{S}}_{\mathrm{el}}$, one directly obtains the values of the transported entropies of the ions at 1000°K, $\overline{\overline{S}}_{\mathrm{Ag^+}} = 26.7$ eu and $\overline{\overline{S}}_{\mathrm{Cl^-}} = 16.6$ eu, and their sum, 43.3 eu, is seen to be identical with the absolute entropy of AgCl, 43.3 eu, thus confirming that within experimental error $(Q^*_{\mathrm{Ag^+}} + Q^*_{\mathrm{Cl^-}}) = 0$. It is interesting to note that previous workers (4, 20) have assumed transport numbers of unity when dealing with single binary electrolytes. This assumption is not necessary since Eq. [13] and [15] are independent of transport number. The terms in the general equation containing transport numbers cancel out without assumptions regarding transport mechanism.

If one takes an approximate value of the partial molar entropy of a single ion obtained from (19) $\overline{S}_A = 1/2(S_{AB} + 3/2\,R \ln M_A/M_B)$, where M is the atomic weight, one calculates the following values of the partial molar entropies and entropies of transfer for Ag^+ and Cl^- in AgCl at 1000°K.

Cl^-	Ag^+	
20.0	23.3	$\overline{S}$ (eu)
−3.4	3.4	Q^*/T (eu)

Since the entropy of transfer is small compared to the partial molar entropy of the ion, $(dE/dT)_{\mathrm{II}}$ should not differ very much when the electrolyte of the thermocell is any chloride whose absolute entropy is not very different from that of AgCl. CuCl is one such salt, its absolute entropy at 1000°K differing from that of AgCl by only 1 eu. In a recent study

[3] $\overline{\overline{S}}_{\mathrm{el}}$ in copper has been estimated to be approximately 0.1 eu at 800°K (20) and in silver about 0.03 eu at 400°K (21).

of molten cuprous chloride thermocells (20), cell II could not be measured because of the oxidation of CuCl by Cl_2 at the temperature of interest. However, $(dE/dT)_{II}$ was calculated from measurements of $(dE/dT)_{I}$, and extrapolated thermal data for the isothermal cell III. The agreement between the values of the Seebeck coefficient for cell II in the CuCl (calculated) and AgCl (measured) system, 0.65 mv/°C and 0.664 mv/°C, respectively, is remarkable.

Another interesting comparison can be made between the entropy of transfer, 3.4 eu, and the entropy of activation for conduction in molten AgCl. A small extrapolation of the conductivity measurements of Spooner and Wetmore (22) gives an entropy of activation at 1000°K of 1.3 eu. Considering the many approximations, this can be considered confirmation of the suggestion of Pitzer that the entropy of transfer should be of the order of the entropy of activation for conduction.

Acknowledgment

The authors appreciate the valuable discussions with J. K. Wilmshurst and G. E. Blomgren of this Laboratory which were of great assistance to them during the course of this work.

Manuscript received June 29, 1961. This paper was presented at the IUPAC Conference in Montreal in August 1961.

Any discussion of this paper will appear in a Discussion Section to be published in the December 1962 JOURNAL.

REFERENCES

1. C. Wagner, *Ann. Physik*, **3**, 629 (1929).
2. E. Lange, *Z. Physik Chem.*, **209**, 162 (1958).
3. E. D. Eastman, *J. Am. Chem. Soc.*, **48**, 1482 (1926); **50**, 283, 292 (1928).
4. H. Holtan, Jr., *Proc. Kon. Ned. Akad. v. Wet., Amsterdam*, **B56**, 498, 510 (1953).
5. P. Mazur, *J. Phys. Chem.*, **58**, 700 (1954).
6. H. Holtan, Jr., P. Mazur, and S. R. de Groot, *Physica*, **19**, 1109 (1953).
7. A. J. deBethune, *This Journal*, **107**, 829 (1960); **106**, 616 (1959).
8. J. N. Agar, "The Structure of Electrolytic Solutions," W. J. Hamer, Editor, Chap. 13, John Wiley and Sons, Inc., New York (1959).
9. B. F. Markov, *Doklad. Akad. Nauk U.S.S.R.*, **108**, 115 (1956).
10. S. Senderoff and G. W. Mellors, *Rev. Sci. Inst.*, **29**, 151 (1958).
11. M. B. Panish, R. F. Newton, W. R. Grimes, and F. F. Blankenship, *J. Phys. Chem.*, **63**, 668 (1959); **62**, 1325 (1958).
12. E. J. Salstrom, *J. Am. Chem. Soc.*, **55**, 2426 (1933).
13. W. J. Hamer, M. S. Malmberg, and B. Rubin, *This Journal*, **103**, 8 (1956).
14. L. L. Quill, Editor, "Chemistry and Metallurgy of Miscellaneous Materials," McGraw-Hill Book Co., New York (1950).
15. F. R. Duke, A. L. Bowman, E. Wolf, and H. Garfinkel, *Ann. N. Y. Acad. Sci.*, **79**, 1023 (1960).
16. F. R. Duke and B. Owens, *This Journal*, **105**, 548 (1958).
17. R. Suchy, *Z. anorg. Chem.*, **27**, 165, 193 (1901).
18. S. Senderoff and A. Brenner, *This Journal*, **105**, 31 (1954).
19. K. S. Pitzer, *J. Phys. Chem.*, **65**, 147 (1961).
20. A. R. Nichols, Jr. and C. T. Langford, *This Journal*, **107**, 842 (1960).
21. B. R. Sundheim and J. Rosenstreich, *J. Phys. Chem.*, **63**, 419 (1959).
22. R. C. Spooner and F. E. W. Wetmore, *Can. J. Chem.*, **29**, 777 (1951).

Technical Notes

The Electrodeposition of Iridium

E. L. MacNamara

Research and Development Group, United States Army Ordnance Arsenal, Frankford, Philadelphia, Pennsylvania

Interest in the development of protective coatings which are stable at high temperature has focused attention on the platinum group metals. Iridium is of particular interest because it is a very hard, dense metal having a high melting point (2454°C) and excellent resistance to high-temperature oxidation.

Examination of the literature revealed that iridium had not been of particular interest to the electrochemist. A few electrochemical constants were published before 1935 (1-8). Several patents (9-13) covering deposition methods for platinum metals included iridium in the claims. Through the early fifties theoretical studies pertinent to iridium deposition began to appear together with the reported attempts at deposition (19). Withers and Ritt (20) were able to deposit a uniform, adherent coating of iridium from a fused cyanide bath. Further studies on suitable electrolytes (21-22) especially those for depositing protective coatings of iridium on molybdenum were reported (23-24). A satisfactory method for the deposition of iridium from aqueous solution had not been developed.

Experimental

An aqueous solution of chloriridic acid[1] was chosen for study in our work. A compound contain-

[1] Available from J. H. Bishop Co., Platinum Works, Malvern, Pa.

ing 48% iridium was used. Present as impurities were 0.3% platinum and 0.15% each of palladium and rhodium. Readily soluble in water, chloroiridic acid ionizes as $H^+ + (IrCl_6)^=$, the resultant solutions being very acid.

Initial experiments were conducted in 50 ml volumes using copper wire cathodes, 0.040 in. in diameter and anodes of perforated platinum sheet, 1 × 3/16 in. The cathode area used for the electrolysis was approximately twice the area of the platinum anode. The anode was not soluble.

In the preliminary studies, the concentration of iridium in the electrolyte ranged from 1-5 g/l, and the solutions were at room temperature. Although there was some evidence of reaction at the electrodes there were no metallic deposits. The iridium concentration was increased to 120 g/l. Dark films were obtained over a current density range of 0.02-2.2 amp/dm², from room temperature to 50°C. When the temperature was increased to 90°C, a black metallic deposit was obtained at a current density of 4.4 amp/dm². Rinsing of the electrodes had diluted the bath at this point enough to decrease the metal concentration to 90 g/l. By increasing the current density to 6.6 amp/dm², a silvery-white deposit was produced. Bright, adherent, metallic deposits were identified spectrographically as iridium containing trace amounts of platinum, rhodium and palladium.

During the course of the work, deposits were obtained throughout a concentration range of 1-120g of metal per liter, within the range of current density of 2.2-10.8 amp/dm². However, as is shown in Table I, the deposition is temperature dependent. At a current density of 3.3 amp/dm² only the solution containing 10g of metal per liter produced a deposit at room temperature. Using the same current density, solutions containing approximately 40 g/l or more required minimum temperatures of 40°C while the solution containing 5 g/l did not produce a coating below 50°C. The lowest concentration (1.4 g/l) required a temperature of 70°C before deposition occurred.

Depending on the temperature, current density showed a marked effect on the appearance of the deposits produced from a bath of a metal content of 10 g/l. At room temperature and current density of 2.2 amp/dm², the cathode area was not completely covered; at 11 amp/dm², the coating was bright but nonuniform. The best appearing coating at room temperature was produced at 6.6 amp/dm².

Table I. Temperature concentration dependence
current density, 3.3 amp/dm²

Concentration, g/l	Temperature, °C						
	30	40	50	60	70	80	90
1.4	-	-	-	-	*	*	*
5.0	-	-	*	*	*	*	*
10.0	*	*	*	*	*	*	*
44.0	-	*	*	*	*	*	*
73.0	-	*	*	*	*	*	*

* Deposition occurred.
\- Deposition did not occur.

Table II. Cathode efficiency, %

Current density, amp/dm²	20°C	60°C
2.2	3	14
6.6	2	6
8.8	1	2

At 60°C, a current density of 2.2 amp/dm² produced a coating of slight nonuniformity while satisfactory coatings were produced at 6.6 amp/dm² and above. At 90°C no difference could be detected in the coatings produced at various current densities. The optimum conditions based on the data obtained from the various experimental baths appeared to be a metal content of the bath of 10 g/l, bath temperature, 60°C, and current density 6.6 amp/dm². The *p*H of the solution was approximately 2. These conditions did not produce the highest cathode efficiency, however. At the stated temperature, but at lower current density, 2.2 amp/dm², the cathode efficiency is 14% (see Table II). It decreased to 2% when the current density was increased to 8.8 amp/dm². It was consistently lower at lower temperature.

Deposits were obtained from sodium and potassium chloroiridates and bromoiridates as well as from chloriridic acid, but could not be obtained from the trichloride and tetrachloride or the tri- and tetrabromides of iridium.[2] The platinum-anode-copper cathode system was used predominantly in the experimental work. However, other materials which served suitably as cathodes were nickel, low carbon steel flash coated with electroless nickel, and polished molybdenum which was first etched in a solution of potassium ferricyanide and potassium hydroxide. There were no deleterious effects when carbon anodes were used.

Iridium, in either +3 or +4 valence state, forms many stable complex ions in solution. The tetravalent iridium complexes are extremely stable. The electrolytes from which iridium was deposited experimentally were aqueous solutions of complexes containing tetravalent iridium. These complexes, similar to those of other platinum metals, are of the inner orbital type, having octahedral configuration, with iridium in the ion having a net negative charge. Inner orbital complexes of most other metals possess such a high energy of coordination that the metal complex is more difficult to discharge than the hydrogen ion in aqueous solution. As has been indicated by Lyons (24), the platinum group metals generally do not follow this, and some of the platinum metals have been deposited with low cathode efficiency from complexes of this type.

The results so far support the premise that iridium (IV) complexes are necessary for successful deposition from aqueous solution. Further studies, using other iridium complexes, are being carried out, to determine the effect of the net charge of the iridium complex on deposition.

[2] Compounds prepared in this laboratory.

Acknowledgment

The author wishes to express appreciation to the Ordnance Corps for permission to publish this work.

Manuscript received July 20, 1961; revised manuscript received Oct. 6, 1961. This paper was prepared for delivery before the Houston Meeting, Oct. 9-13, 1960.

Any discussion of this paper will appear in a Discussion Section to be published in the December 1962 JOURNAL.

REFERENCES

1. R. Luther and F. J. Brislee, *Z. Phys. Chem.*, **45**, 216 (1903).
2. E. Newbery, *J. Chem. Soc.*, **109**, 1066 (1916).
3. A. Thiel and W. Hammerschmidt, *Z. anorg. u. allgem. Chem.*, **132**, 15 (1923).
4. E. G. Weischede, Dermstadt, 1927, Electroltische Bestimmung un Trennung der Plotinmetalle Pt, Ir, Os.
5. H. Terrey and H. C. Baker, *J. Chem. Soc.*, **1930**, 2593, Part II.
6. E. O. Hulbert, *Rev. Sci. Instr.*, **5**, 85 (1934).
7. A. D. Garrison and J. F. Liller, *Trans. Electrochem. Soc.*, **65**, 171 (1934).
8. I. I. Zhukov, *J. Gen. Chem., U.S.S.R.*, **3**, 958 (1933).
9. E. M. Wise (to INCO), U. S. Pat. 1,970,950, Aug. 21, 1934.
10. F. Zimmermann and E. F. Zechiegner (to Baker and Company, Inc.) U. S. Pat. 2,057,636, October 1936.
11. E. M. Wine and R. F. Vines (to INCO), U. S. Pat. 2,335,831, Nov. 30, 1934.
12. E. M. Wine and R. F. Vines (to INCO), U. S. Pat. 2,457,021, December 1948.
13. G. Jernstedt (to Westinghouse Electric Co.), U. S. Pat. 2,451, 240, Oct. 12, 1948.
14. E. H. Lyons, *This Journal*, **101**, 363, 410 (1954).
15. J. P. Hoare and S. Schuldiner, *J. Chem. Phys.*, **25**, 786 (1956).
16. J. Van Muylder and M. Pourbaix, CEBELCOR Rappt. Tech. No. 62 (1958).
17. M. Pourbaix, J. Van Muylder, and N. deZoubov, *Platinum Met. Rev.*, **3** [2], 47 (1959).
18. A. I. Lewin and B. A. Pankratov, *Zhur. Prikl. Khim.*, **32**, 1787 (1959).
19. P. J. Ovenden, *Nature*, **179**, 39 (1957).
20. J. C. Withers and P. E. Ritt, *Tech. Proc.*, Am. Electroplaters' Soc., *44th Ann. Conv.*, **124** (1957).
21. E. A. Parker, *Plating*, **47**, 621 (1959).
22. E. M. Wise, *Metal Finishing*, **57**, 94 (1959).
23. R. R. Freeman, Climax Molybdenum Co., Tech. Notes, September 1958.
24. Battelle Memorial Inst., Defense Metals Info. Center, Rpt 109, Mar. 6, 1959.

Junction Delineation in Silicon

Harry Robbins[1]

Hughes Semiconductors, Newport Beach, California

Junction delineation techniques are based on the fact that a surface chemical reaction can be influenced by the nature of the doping in the bulk of the semiconductor. In the presence of a p-n junction, differences in the rate of the reaction on the opposite conductivity types of the semiconductor may manifest themselves visually as a stain or deposit of metal that extends on one conductivity type up to the position of the junction. However, the reactions involved are often erratic and nonreproducible. It is often found that the reaction is difficult to induce. The reaction may also proceed preferentially on either of the conductivity types, thus making uncertain the identification of the conductivity type even in instances where the junction is sharply delineated. Situations are also encountered where the reaction takes place promiscuously over the entire surface and gives no indication of the location of the junction.

It has been found that one can achieve better control over the reaction in the presence of strong illumination. Under these conditions, Iles and Coppen (1) have postulated that an electrolytic cell is set up, powered by the conversion of the incident light into a photovoltage of such polarity that the n-side of the junction is the cathode, and the discharge of cations from the solution then proceeds selectively on the n-side of the junction. The results of Whoriskey (2), who found that the stain appeared on the p-side of the junction under the influence of light, are consistent with this theory, since the stain is probably caused by the oxidation of the semiconductor, and this reaction should take place on the anode of the electrolytic cell.

The author has found that it is also possible to obtain reproducible delineation in the absence of strong illumination, provided the reactions are carried out in the presence of strong HF. In the absence of substantial amounts of HF, it is possible that an oxide film on the surface may interfere with the reaction. This is indicated by the fact that most investigators employed relatively concentrated solutions of cations in their delineation work. For example, Iles and Coppen (1) used a solution of AgF that was 10% of saturated, which is approximately 18.0 g/l, and Silverman and Benn (3) used solutions containing 10 g/l of $KAg(CN)_2$. On the other hand, we have found that in a solution containing 30 vol. % HF (30 ml conc. HF diluted to 100 ml), concentrations of gold chloride in excess of 2 mg/ml produced indiscriminate plating on both sides of the junction, whereas lesser concentrations produced selective plating, fairly adherent, and invariably on the p-side of the junction. Similar results were obtained with other cations. The threshold concentration for chloroplatinic acid was found to be in the range of 2 mg/ml of 30 vol. % HF; for copper chloride, 0.25 mg/ml of concentrated HF; for silver acetate, 0.25 mg/ml of concentrated HF; and for palladium chloride, 2 mg/ml of 30 vol. % HF. In all instances plating was selective on the p-side of the junction. The threshold concentration

[1] Present address: Bell & Howell Research Center, 360 Sierra Madre Villa, Pasadena, California.

of cation necessary for selective plating varies with the amount of HF in the solution, since we have found that a concentration of less than 1 mg/ml of gold chloride in concentrated HF often gives nonselective plating.

In view of the above, it seems that the two mechanisms postulated by Iles and Coppen (1), namely, the electrolytic mechanism and the displacement mechanism, are oppositely directed. The electrolytic mechanism is directed so that the n-side of the junction is the cathode, whereas the displacement reaction in strong HF is preferential on the p-side. In the absence of strong HF (Iles and Coppen used solutions containing only one drop of HF to 5 ml of solution) the displacement reaction may possibly be influenced by the state of the surface as well as by the underlying bulk properties. This is indicated by the large concentration of cations necessary in the absence of HF and by the erratic preferentiality observed. The role of the surface is further indicated by the fact that Silverman and Benn (3) found it necessary to abrade their surfaces in order to obtain good delineation, and Turner (4) has found that it is possible to get delineation between abraded and nonabraded semiconductor of the same conductivity type.

The opposite directivity of the two mechanisms suggest the desirability of selecting conditions so as to suppress one or the other of these mechanisms. Iles and Coppen (1) have done this by reducing the concentration of AgF when they employed strong illumination, and Whoriskey (5) has done the same by deleting HNO_3 from the staining solution. The staining reaction of Fuller and Ditzenberger (6) may be looked on as a displacement of hydrogen ions by silicon, which causes the liberation of hydrogen selectively on the p-side, and results in the oxidation of the silicon to an insoluble, transparent film which is rendered visible and colored by optical interference. The growth of this film may be observed by noting the change in color through the spectrum, and several orders of interference may be observed. The role of the nitric acid may be either to participate in the selective oxidation of the silicon, or perhaps to act as a depolarizer to remove the hydrogen that is formed. Whereas Whoriskey (5) has found that the electrolytic reaction can be favored by deleting the nitric acid, we have found that the displacement reaction can be enhanced by the use of a trace of sodium nitrite, which catalyzes the oxidation of the silicon. A preferred method is to add oxides of nitrogen in the form of red fuming HNO_3, and a recommended formula is 1-2 drops of red fuming HNO_3 to 10 ml of concentrated HF. We have found that by this technique the reliability of the method has been considerably improved.

Manuscript received Dec. 27, 1960; revised manuscript received Sept. 16, 1961.

Any discussion of this paper will appear in a Discussion Section to be published in the December 1962 JOURNAL.

REFERENCES

1. P. A. Iles and P. J. Coppen, *J. Appl. Phys.*, **29**, 1514 (1958).
2. P. J. Whoriskey, Private communication.
3. S. J. Silverman and D. R. Benn, *This Journal*, **105**, 170 (1958).
4. D. R. Turner, *ibid.*, **106**, 701 (1959).
5. P. J. Whoriskey, *J. Appl. Phys.*, **29**, 867 (1958).
6. C. S. Fuller and A. J. Ditzenberger, *ibid.*, **27**, 550 (1956).

Problems Associated with Distribution Coefficient and Solid Solubility Determinations Using Crystal Growth Techniques

W. Bardsley, D. T. J. Hurle, and J. B. Mullin

Ministry of Aviation, Royal Radar Establishment, Great Malvern, Worcestershire, England

In a recent paper, Trumbore *et al.* (1) have described the use of a solvent evaporation technique (2) to grow single crystals of silicon from melts heavily doped with antimony. From measurements made on these crystals, they have calculated the distribution coefficient (k) at various temperatures and levels of doping. The possibility that {111} facets may have developed on the solid-liquid interface of the crystals during growth and modified the solute incorporation [the "facet effect" (3, 4)] and, hence, the measured value of k was considered. They concluded that their measured values of k were near the equilibrium values: in particular they obtained substantial agreement between values of k determined for growth in the three directions <111>, <110>, and <100>.

It is the purpose of this note to point out some of the conditions related to the solvent evaporation technique, under which the solid-liquid interface can become faceted and which can occur for any growth orientation. One such condition is the presence of a gradient of solute concentration in the melt ahead of the interface which, unless the temperature gradient in the melt is appropriately steep, gives rise to constitutional supercooling of the melt (5). Expressions have been derived (6) for the onset of constitutional supercooling and the magnitude of the supercooling when it exists, in a stirred melt. Work in this laboratory has shown (7-9) that, under conditions of constitutional supercooling, the solid-liquid interfaces of germanium and indium antimonide crystals are cellular, the

cells being made up of small {111} facets. This is likely to be the case for all diamond cubic and zinc blende-type semiconductors including silicon.

The laminar interface structure shown in Fig. 1a of ref. (1) is very similar in appearance to the cellular structure seen on the interfaces of [110] oriented germanium or indium antimonide single crystals grown under conditions of constitutional supercooling, where the cells are elongated in the $[1\bar{1}0]$ direction in the plane of the interface (7, 9). The principal faces of the cells are the two {111} planes inclined at 35° 16' to the plane of the interface. In general, the cellular morphology is determined by the direction of growth, the faces of the cells being composed of the {111} planes nearest the plane of the interface.

In the presence of a cellular interface there are three known effects which can result in a solute concentration in the solid which is different from that where the interface is not cellular or faceted:

(i) The facet effect (3, 4), *i.e.*, a difference in the interface distribution coefficient k^* (4) on and off a facet of magnitude appropriate to the particular system. In the case of indium antimonide grown from an indium rich melt, in such a way that constitutional supercooling occurs, the {111} facets which develop show this change in k^* when tellurium is present in the melt (9).

(ii) The lateral component of diffusion produced by segregation at the cell faces leads to an enhanced ($k < 1$) or depleted ($k > 1$) solute concentration at the re-entrant corners formed by the cells. The solute concentration in the re-entrant corners can, in some circumstances, exceed the solubility limit resulting in the precipitation of a second phase (8, 9).

(iii) Evidence has been obtained (8) which indicates that, when the crystal is rotated, the formation of the first cells on the solid-liquid interface produces turbulent flow over the whole interface which modifies the cellular morphology and hence the solute incorporation.

There are other conditions under which growth can be faceted, such as growth into a thermally supercooled melt when, in the absence of the appropriate twin planes, the crystal assumes a polyhedral form bounded by {111} planes (10, 11), or growth with a {111} plane tangential to the melt isotherm (3).

In general, thermal supercooling leads to a few large facets while constitutional supercooling leads to a large number of small facets. However, in both cases, the indications are that a facet, however formed, will show the facet effect. In the case of constitutional supercooling there is the additional inhomogeneity due to the intercellular segregation.

The determination of equilibrium distribution coefficients by growing crystals from heavily doped melts requires a very slow growth rate and a steep temperature gradient in the melt. The problem with the Czochralski technique is that, to promote growth at constant crystal diameter, the power supplied to the melt must be periodically lowered because the accumulation or depletion of solute in the melt ($k \leftrightharpoons 1$, respectively) continually lowers the liquidus temperature of the melt. These power changes cause transient increases in growth rate and lead to the transient formation of a cellular structure with its consequent inhomogeneities. This effect becomes very pronounced at the slowest growth rates (8). The advantage of the solvent evaporation technique in this respect is that the power supplied to the melt is kept constant and no mechanical pulling is employed. Its disadvantage is that it is a nearly isothermal process, *i.e.*, the temperature gradient in the melt is small, and hence constitutional supercooling of the melt readily occurs. To utilize the advantages of the technique a steep temperature gradient in the melt is required.

Trumbore and Porbansky (2) claim the isothermal nature of the process to be its chief advantage since it should yield homogeneous material. While, at present, little is known about the factors controlling cell size it may be possible to grow crystals by the isothermal process under conditions of constitutional supercooling in such a way that the crystal itself forms a "single cell" and the interface is bounded by a single set of low index planes with no re-entrant corners. In this case the material should be homogeneous although its impurity content will depend on the magnitude of k^* on the facets.

The above comments are not intended as a serious criticism of the experimental results of Trumbore *et al.* (1). The consistency of their results indicates that the influence of the effects described above was probably small in their experiments. However, in those alloy systems which exhibit a large facet effect, determination of the equilibrium distribution coefficients cannot be accomplished by the use of an isothermal process.

This note is published by permission of the Controller, H.B.M. Stationery Office.

Manuscript received Sept. 13, 1961.

Any discussion of this paper will appear in a Discussion Section to be published in the December 1962 JOURNAL.

REFERENCES

1. F. A. Trumbore, P. E. Freeland, and R. A. Logan, *This Journal*, **108**, 458 (1961).
2. F. A. Trumbore and E. M. Porbansky, *J. Appl. Phys.*, **31**, 2068 (1960).
3. K. F. Hulme and J. B. Mullin, *Phil. Mag.*, **4**, 1286 (1959).
4. J. B. Mullin and K. F. Hulme, *J. Phys. Chem. Solids*, **17**, 1 (1960).
5. J. W. Rutter and B. Chalmers, *Can. J. Phys.*, **31**, 15 (1953).
6. D. T. J. Hurle, *Solid State Electronics*, **3**, 37 (1961).
7. W. Bardsley, J. M. Callan, H. A. Chedzey, and D. T. J. Hurle, *ibid.*, **3**, 142 (1961).
8. W. Bardsley, J. M. Callan, H. A. Chedzey, and D. T. J. Hurle, To be published.
9. D. T. J. Hurle, O. Jones, and J. B. Mullin, *Solid State Electronics*, in course of publication.
10. R. S. Wagner, *Acta Met.*, **8**, 57 (1960).
11. S. G. Ellis, *J. Appl. Phys.*, **26**, 1140 (1955).

Unusual Ternary Behavior of Transition Metal Borides

J. M. Leitnaker, N. H. Krikorian, and M. C. Krupka

University of California, Los Alamos Scientific Laboratory, Los Alamos, New Mexico

During the course of a variety of experimental work on transition metal borides (1-3), unusual behavior was found in heated mixtures of the Group IVa metal diborides with tungsten and molybdenum. [Experimental methods are described in detail in ref. (1).]

All three of the diborides were found to behave differently when mixed with tungsten powder and heated. TiB_2 formed what appeared to be a ternary compound with W (at roughly 50-50 mole %). The compound could be indexed in orthorhombic symmetry, by its close analogy to TaB, and had lattice parameters of $a_o = 3.180 \pm 0.008$Å, $b_o = 8.462 \pm 0.006$Å, and $c_o = 3.071 \pm 0.003$Å. HfB_2, when heated with tungsten powder, does not easily attain equilibrium, or at least the quenched samples when examined by x-ray never indicated that equilibrium had been attained. A ternary compound appeared to form, however, but was either of low symmetry or the sample contained a mixture of two ternary phases.

In contrast, ZrB_2 forms no intermediate phases with tungsten. A 3-day heating of an intimate mixture of ZrB_2 and W at 2100°C showed only the sharpening of x-ray lines in the film and elimination of faint impurity lines. Heatings at lower temperatures with about 1% iron as a sintering aid also produced no extra phases.

All three diborides react with molybdenum. X-ray films of quenched samples of ZrB_2-Mo and HfB_2-Mo showed nearly identical patterns with those of HfB_2-W. The behavior of TiB_2 with Mo is nearly identical with the TiB_2-W reaction. Lattice parameters for the orthorhombic phase were $a_o = 3.185 \pm 0.007$Å, $b_o = 8.475 \pm 0.010$Å, and $c_o = 3.075 \pm 0.003$Å.

The ternary compound of TiB_2 with Mo was found to form as low as 1600°C. Steinitz (4) has shown that MoB has a high-temperature modification which is isomorphous with TaB. Hence, instead of a ternary compound, the intermediate one-phase region can be viewed possibly as a solution of TiB in β-MoB with a consequent lowering of the β-MoB transition temperature. The situation with the TiB_2-W system is similar. Whether the high-temperature MoB (or WB) phase can be stabilized down to room temperature is, of course, uncertain.

Examination of the six pseudobinary systems has been only cursory. It would seem that the unusual behavior is of more than passing interest and certainly deserves more attention.

Manuscript received Aug. 24, 1961.

Any discussion of this paper will appear in a Discussion Section to be published in the December 1962 JOURNAL.

REFERENCES

1. J. M. Leitnaker, Los Alamos Scientific Laboratory Report No. LA-2402, 1960.
2. J. M. Leitnaker, N. H. Krikorian, and M. G. Bowman, "High Temperature Poisons," To be published.
3. M. C. Krupa, Unpublished work.
4. R. Steinitz, I. Binder, and D. Moskowitz, *J. Metals*, **4**, 983 (1952).

Floating Zone Refining of Boron Using Electron Beam Melting

C. B. Hood and M. O. Thurston

Electron Device Laboratory, The Ohio State University, Columbus, Ohio

The use of electron beam zone refining in the purification of refractory metals was discussed by Davis, Calverley, and Lever (1). The advantages they found in this technique made it attractive for use with boron. They had, however, mentioned difficulties with high resistivity materials, and there was thus a question whether the high resistance of a boron rod near room temperature would permit sufficient beam current to flow at a reasonable voltage for the beam to melt a zone.

In practice it was found that the resistance of the rod is almost immaterial. The current flow in the rod is very slight, the predominant current being the secondary electron emission current from the bombarded zone. The secondary electrons complete the circuit by flowing to the grounded case of the vacuum furnace. The bombardment process could be started with the boron rod cold, and the zone could be brought to the melting point in a minute or less. This contrasts with the r.f. induction heating method, in which a boron rod must be preheated in order to reduce its resistivity sufficiently to allow effective electrical coupling to the heating coil.

Some of the details of the preparation of the materials, the operation of the equipment, and preliminary results obtained are described next. More complete studies of the electrical properties of boron are in progress and will be reported later.

Experimental Techniques

The boron rods used in these experiments were prepared by the reduction of boron trichloride on a 25μ diameter heated tantalum filament, suspended horizontally in a reaction chamber consisting of a Vycor tube with water-cooled copper end flanges and electrodes. Reaction temperatures varied from 1350° to 1450°C as measured with an optical pyrometer. The reaction chamber was connected to a Pyrex gas supply system as shown in Fig. 1. The vapor pressure of boron trichloride at the ice point is such that a stream of hydrogen passed through the liquid at this temperature gave an approximately stoichiometric mixture to feed to the reaction chamber. The spent gas from the chamber passed to the condenser, where unreacted boron trichloride was condensed and recycled. The feed gas was regulated in such a way that only 25-30% reduction took place, thus maintaining fairly uniform concentrations throughout the reaction chamber, giving rods of fairly uniform diameter. The system was operated at atmospheric pressure.

The rods obtained in this process were dark gray, with a fine-grained crystalline appearance, and were quite dense. Approximately 2½ hr were required to grow a rod 6 mm in diameter, which is the largest obtainable with our present power supply. The yield of boron was about 75% of theoretical. All the rods showed evidence of strains by undergoing some cracking when cooled through the 900°-1100°C range. The least amount of cracking seemed to take place when the rods were cooled rapidly by merely shutting off the heater current. By this means, pieces 7-15 cm long (with no apparent cracks) were obtained.

High-purity boron trichloride, obtained from the American Potash and Chemical Company, was used for this preparation. The impurity content, calculated from their analysis, assuming all the impurities entered the rod, is as follows:

Carbon	0.055%
Silicon	0.002%
Tantalum	0.015%
Total	0.072% by weight

The electron beam zone refiner is similar to the one described by Davis (1). It was constructed with a stationary filament assembly, through which the sample rod, supported on a frame, can be moved vertically. There was no provision for rotation of the sample. The entire filament and frame assembly was hung inside a water-cooled vacuum chamber, with an external gear-driven lifting mechanism to provide the vertical motion. The filament arrangement consisted of a tungsten strip 3/32 in. wide by 0.003 in. thick, formed to a 3-cm circle, surrounding the boron rod. Tantalum focusing plates, with 2.5-cm holes in them, were placed about 6 mm above and below the filament. This arrangement gave a molten zone about 6 mm in width. The electron beam current was about 0.15 to 0.20 amp at 3000v. Vertical motion of the rod was 12-18 cm/hr.

The emission of boron vapor from the molten zone was very slight, as evidenced by film formation on the chamber window. However, it was sufficient to contaminate the tungsten filament, reducing its emission, and distorting its shape. This difficulty, which limits the filament life to about 1 hr, seems to be the principal limitation of the filament structure described. An electron gun design in which the filament was not directly exposed to the boron might be expected to minimize this difficulty.

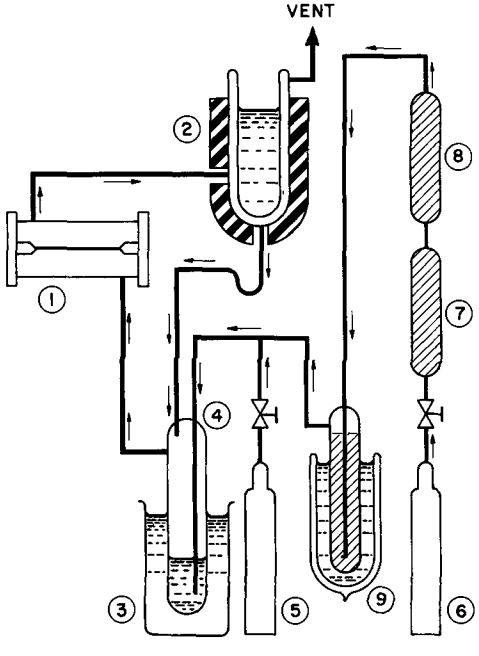

Fig. 1. Boron reduction apparatus. 1, Hot wire reaction chamber; 2, BCl_3 condenser using dry ice-acetone refrigerant; 3, ice bath for BCl_3 bubbler; 4, BCl_3 bubbler or mixer; 5, BCl_3 cylinder; 6, H_2 cylinder; 7, deoxo catalytic purifier; 8, silica gel dryer; 9, silica gel purifier with liquid N_2 refrigerant.

Experimental Results

Although no single crystal rods have been obtained, the zone refined specimens contain crystals 2-3 mm in size, as determined by observations on etched slices.

The electron beam furnace was also used to prepare doped samples of boron by fusing short sections of rod with impurities inserted. Rods were doped with nickel and carbon by this method.

Resistance measurements were made on the various samples of boron over a wide range of temperature. Electrical connections were made to the samples with tungsten wire, using a small amount of platinum as an alloying or bonding agent. The contacts were tested on an oscilloscope and found to be ohmic. The boron samples were not precisely cut, but were of such dimensions that the resistance values are numerically within 3-7 times the absolute resistivity in ohm centimeters.

Figure 2 shows resistance as a function of reciprocal temperature for freshly prepared boron, zone refined samples, and doped samples. Apparent band gaps, calculated for these samples from the average slopes of the curves at the higher temperatures, are as follows: zone refined sample (3 passes), 1.35 ev; unmelted samples, 1.2 ev; nickel doped sample, 1.2 ev; carbon doped sample, 1.2 ev.

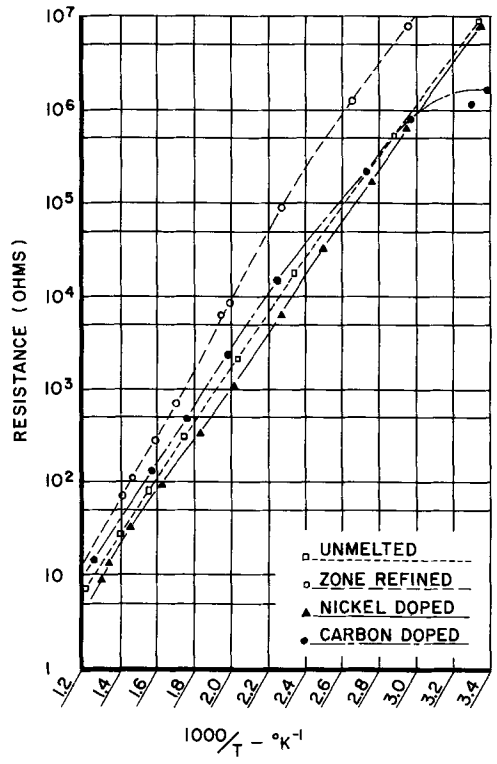

Fig. 2. Resistance of various boron samples as functions of the reciprocal of the absolute temperature.

The band gap, measured by this method, has been reported by various investigators (2-6), giving values ranging from 0.30 to 1.60 ev. Our values agree most closely with those of Greiner and Gutowski (5). These authors (6) also reported reduced resistivity with phosphorus doping, but of the two dopants selected by us, only carbon shows indication of reduced resistivity at room temperature.

Measurements at lower temperatures would be required to determine the energy level structure for impurities, but could not be made with the equipment available for these first tests.

The zone refining produces a definitely measurable increase in slope at the higher temperatures, but not necessarily an increase in resistivity over the entire temperature range.

Thermoelectric power measurements on all the samples studied so far indicate that they are p-type, although one might expect the carbon doped sample to be n-type due to the extra electrons in the lattice contributed by the carbon atoms.

Acknowledgment

The authors wish to acknowledge the cooperation and technical help provided by Mr. C. Powell and Mr. J. M. Blocher of Battelle Memorial Institute in connection with the preparation of boron rods for this work. This work was sponsored by the Air Force Office of Scientific Research of the Air Research and Development Command under Contract AF49(638)-424.

Manuscript received June 22, 1960; revised manuscript received Oct. 1, 1961.

Any discussion of this paper will appear in a Discussion Section to be published in the December 1962 JOURNAL.

REFERENCES

1. M. Davis, A. Calverley, and R. F. Lever, *J. Appl. Phys.*, **27**, 195 (1956).
2. L. W. Friedrich and V. P. Jacobsmeyer, *Phys. Rev.*, **91**, 492 (1953).
3. L. J. Badar and V. P. Jacobsmeyer, *ibid.*, **94**. 808 (1954).
4. W. C. Shaw, D. E. Hudson, and G. C. Danielson, *ibid.*, **107**, 419 (1957).
5. E. S. Greiner and J. A. Gutowski, *J. Appl. Phys.*, **28**, 1364 (1957).
6. E. S. Greiner and J. A. Gutowski, *ibid.*, **30**, 1842 (1959).

Brief Communications

An Electrochemical Method for the Preparation of AuSn and Its Possible Application to Other Intermetallic Compounds

T. Granville Carver and Henry Leidheiser, Jr.

Virginia Institute for Scientific Research, Richmond, Virginia

The purpose of this communication is to describe a simple electrochemical method for the preparation of the intermetallic compound AuSn and to suggest its applicability to other intermetallic compounds.

When gold electrodes were polarized in boiling 2M HCl containing 0.001M Sn(II) to potentials 10-100 mv more noble than that of tin in the same medium, a uniform deposit formed very rapidly on the gold.[1] The resulting deposit, as identified by electron and x-ray diffraction analysis, was AuSn(3). In a typical experiment in which the gold was polarized to a potential approximately 15 mv more noble than the potential of tin in this medium (−605 mv *vs.* the saturated calomel electrode), 8.7 mg

[1] Deposits on gold samples in contact with tin in solutions containing Sn(II) were reported as early as 1873 by Raoult (1). Later workers, such as Tammann and Wiederholt (2) studied the rate of change of potential of electrodes when polarized in the presence of less noble metal cations.

of AuSn was formed in 1000 min on a gold cylinder exposing approximately 2 cm^2 of surface.

Similar experiments carried out using evaporated gold films approximately 200Å in thickness resulted in the apparent complete transformation within 15 min of gold to AuSn on those fragments of the film which adhered to the glass substrate and remained in electrical contact with the polarization source. This conclusion was based on transmission electron diffraction studies.

In the majority of experiments, a single plateau was observed in the potential-time curve when the polarizing potential was removed. This plateau was approximately 150 mv more noble than the potential of tin in solutions containing 0.0001, 0.001, 0.01, and 0.1M Sn(II). In experiments carried out for long times in solutions 0.1M in Sn(II) and in experiments in which the gold electrode was charged briefly to a potential sufficient to electrodeposit tin, a second plateau was observed at a potential approximately 80 mv more noble than the potential of tin in these solutions. Attempts to identify the compound responsible for the second plateau by diffraction analysis were unsuccessful. It is suggested that this compound may be either $AuSn_2$ or $AuSn_4$ on the basis of the phase diagram for the Au-Sn system.

When a palladium electrode, exposing a surface area of 1.5 cm^2, was polarized in boiling 2M HCl containing 0.001M Sn(II) to a potential several mv more noble than the corrosion potential of tin, a deposit weighing 6 mg formed on the palladium in 24 hr. X-ray diffraction analysis indicated that the major constituent was $PdSn_4$.[2] The potential decay curve exhibited a plateau lasting 15 min at a potential approximately 25 mv more noble than that of tin in the same medium. Two smaller plateaus were also observed at more noble potentials.

Based on the results reported above and preliminary studies on other systems, it appears that intermetallic compounds of tin, lead, and cadmium with noble metals may be prepared by a reaction of the type, $xM + yM'^{+z} + yz\ e^- \longrightarrow M_xM'_y$, where M is the noble and M' is tin, lead, or cadmium.

Acknowledgment

The assistance of W. Roger Buck, III, Lucille B. Garmon, Calvin O. Tiller, and Richard S. Southworth is gratefully acknowledged. This research was supported by the Atomic Energy Commission.

Manuscript received Sept. 11, 1961.

Any discussion of this paper will appear in a Discussion Section to be published in the December 1962 JOURNAL.

REFERENCES

1. F. M. Raoult, *Compt. rend.*, **76**, 156 (1873).
2. G. Tammann and W. Wiederholt, *Z. anorg. u. allgem. Chem.*, **125**, 67 (1923).
3. H. E. Swanson, N. T. Gilfrich, and M. I. Cook, Natl. Bur. Standards Circular 539, vol. 7, p. 19 (1957).
4. K. Schubert and U. Rösler, *Z. Metallkunde*, **41**, 298 (1950).

[2] This analysis was based on a knowledge of the diffraction pattern for $PtSn_4$ (ASTM X-ray diffraction card No. 4-0744) and the fact that $PdSn_4$ is isotypic with $PtSn_4$ (4).

Niobium Solid Electrolyte Capacitors

H. W. Ling and T. L. Kolski

Pigments Department, E. I. du Pont de Nemours & Company, Wilmington, Delaware

Use of niobium as an anode material for solid electrolyte capacitors is arousing considerable interest. Previous reports (1-3) have indicated the feasibility of preparing niobium solid electrolyte capacitors with satisfactory life under load up to 20v. However, these same reports have shown that fabrication of devices of the 35-v class was unsuccessful because of total failure during life tests. This communication contains test results on 35-v niobium solid electrolyte capacitors which were shown to last longer than 1000 hr when tested at 85°C.

In an earlier communication (4) we indicated the means whereby niobium sintered pellets could be anodized to 200v. Briefly, the conditions involved forming at room temperature in 0.01% aqueous H_3PO_4 electrolyte at a current density of 50 ma/g, and maintaining at formation voltage for 2 hr to allow healing of the anodic film. Porous pellets weighing approximately 0.5g were anodized in this manner, and a counter electrode of MnO_2, graphite, and metal was applied to each using the conventional art. A cathode lead wire was attached to the metal coating of each device, but the units were not hermetically sealed or otherwise isolated from the atmosphere.

With no prior curing period under load, leakage current was measured after 5 min of electrification, using an RCA WV-48B ultrasensitive d-c microammeter. Potential was increased to 35v within a period less than 45 sec; the electrical leakage measured 5 min after reaching 35v was about 25% lower than the 2-min value. Capacitance and dissipation factor were measured on a General Radio Type 1611-B Capacitance Bridge at 35v d-c bias using a 120 cps, 1v a-c signal. After initial characterization, low impedance life testing was carried out at 85°C using wet cells as the d-c source.

A summary of the results is presented in Table I. Comparison of post-life test properties with initial dry properties shows that in the majority of cases capacitance and equivalent series resistance decreased, yielding lower dissipation factors. Absolute electrical leakage increased in most specimens. In general, variations in initial capacitance reflect the use of powders varying in particle size distribution, whereas differences in initial electrical leakage result from differing purity among several powder batches employed.

In previous publications (1, 3), it was stated that partial crystallization of the oxide film during for-

Table I. Niobium solid electrolyte capacitors

Initial dry properties at 35v, 25°C				Life test 1000 hr, 37v, 85°C	Post-life test properties at 35v, 25°C			
Capacitance, μf/g	Dissipation factor 120 cps, %	Absolute leakage, μa/pellet	Leakage, μa/μf v	Final hot leakage, μa/pellet	Capacitance, μf/g	Dissipation factor 120 cps, %	Absolute, leakage, μa/pellet	Leakage, μa/μf v
13.28	1.60	0.083	0.0004	2.00	11.54	1.26	0.290	0.0015
13.06	1.64	0.165	0.0008	6.60	11.54	2.66	0.740	0.0039
13.33	2.00	0.092	0.0004	4.65	11.64	1.04	0.555	0.0029
9.22	1.54	1.30	0.0085	4.70	8.02	0.70	0.490	0.0037
8.22	4.52	0.044	0.0003	2.70	8.15	3.16	0.310	0.0023
6.50	7.44	0.047	0.0004	5.40	6.65	3.18	0.470	0.0042
7.56	1.74	0.840	0.0066	4.70	7.36	5.68	0.460	0.0037
14.17	1.88	0.200	0.0008	12.5	12.26	1.28	1.45	0.0070
14.33	1.86	0.265	0.0011	13.5	12.42	1.38	3.30	0.0158
13.79	1.96	0.135	0.0006	7.65	11.99	1.60	0.465	0.0024
5.80	3.20	0.075	0.0008	2.45	5.82	1.76	0.240	0.0025
6.30	3.58	0.089	0.0008	3.05	6.14	1.76	0.265	0.0026
11.30	6.86	0.570	0.0030	20.0	10.10	5.70	1.20	0.0071
9.80	5.96	0.591	0.0036	12.5	8.78	3.38	1.05	0.0072
12.23	1.36	1.50	0.0076	37.5	10.10	0.80	2.45	0.0150
11.34	8.08	0.425	0.0022	15.0	9.88	4.76	1.00	0.0060
12.59	7.06	3.80	0.0193	24.0	11.50	5.48	0.920	0.0051

mation limited the voltage ratings of niobium solid electrolyte capacitors. Further, it was proposed that successful formation to voltages higher than 100-125v would have to await a niobium powder of higher purity and/or a more suitable electrolyte for anodization than those used previously. We agree that the feasibility of 35v niobium solid electrolyte capacitors demonstrated by the present data results from the ability to anodize to 200v and higher, which in turn depends on use of a high-purity niobium powder and dilute aqueous H_3PO_4 as an appropriate electrolyte.

Manuscript received Sept. 1, 1961.

Any discussion of this paper will appear in a Discussion Section to be published in the December 1962 JOURNAL.

REFERENCES

1. D. A. McLean, N. Schwartz, J. K. Werner, and M. Gresh, Final Report No. 25309-E Contract DA 36-039 sc-74996, Bell Telephone Laboratories, Inc. Jan. 15, 1960.
2. A. Shtasel and H. T. Knight, *This Journal*, **108**, 343 (1961).
3. N. Schwartz, M. Gresh, and S. Karlik, *ibid.*, **108**, 750 (1961).
4. R. B. Hand, H. W. Ling, and T. L. Kolski, *ibid.*, **108**, 1023 (1961).

Epitaxial Silicon-Germanium Alloy Films on Silicon Substrates

K. J. Miller and M. J. Grieco

Bell Telephone Laboratories, Incorporated, Murray Hill, New Jersey

Silicon-germanium alloys with up to 30 at. % germanium have been deposited epitaxially on silicon substrates by the simultaneous vapor phase reduction of $SiCl_4$ and $GeCl_4$. Silicon has also been epitaxially deposited on these alloys.

The method of deposition used was similar to that reported (1) for deposition of silicon films on silicon substrates. Hydrogen carrier gas was bubbled through a thermostated solution of $SiCl_4GeCl_4$ and carried these halides to the R.F. heated sample in a quartz reaction chamber. The temperatures of deposition were kept close to the alloy melting points. Different epitaxial alloy film compositions were obtained by varying the proportions of $SiCl_4$ and $GeCl_4$ in the solution with resulting variation of their vapor pressures in the reaction chamber. For example, at a 1200°C temperature of deposition a 25 at. % germanium alloy film required partial pressures of 1.3 mm for $GeCl_4$ and 5 mm for $SiCl_4$. Films were analyzed for germanium by x-ray fluorescence after a calibration curve was obtained. Epitaxy was established by Laue back-reflection x-ray diffraction and by electron diffraction which indicated the films had a high degree of crystal perfection.

Surfaces of alloy deposits appear macroscopically to be highly reflective and were smooth and of uniform thickness. Alloy films etched with the Dash etch (2) have surfaces which appear microscopically to have an incomplete triangle dislocation array when deposited on (111) and (110) silicon substrates, and on (100) substrates these films frequently have an incomplete square dislocation array. The (111) films have surfaces which appear microscopically as striae, presumably caused by microscopic variation of germanium composition in the film. The striae are especially evident on films deposited on highly doped substrates, such as the

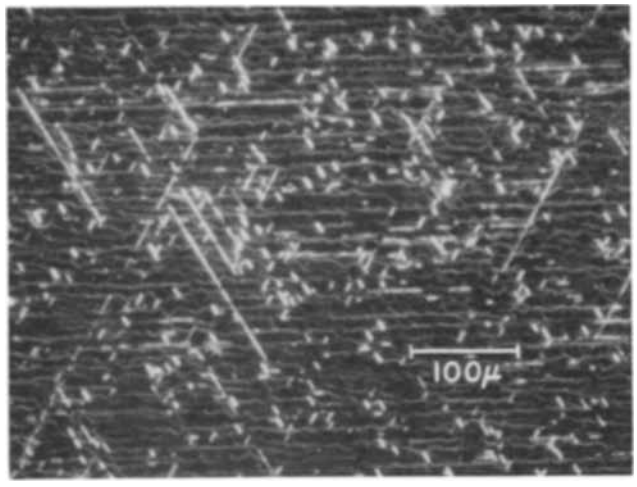

Fig. 1. Etched surface of epitaxial 14 at. % germanium, silicon-germanium alloy film deposited on (111) silicon substrate.

$10^{19}/cm^3$ phosphorus-doped substrate on which the film shown in Fig. 1 was deposited. The striae are fine, parallel lines at low germanium content and become broader and wavy in appearance with increasing germanium content. Figure 1 shows the surface of a 14 at. % germanium film after etching with the Dash etch, showing the striae and the triangular dislocation pattern. Goss *et al.* (3) have noted a similar striae pattern for a (111) 6 at. % silicon, germanium-silicon alloy grown from the melt. Films deposited on (100) and (110) substrates did not have a striae pattern over the entire composition range to 30 at. % germanium. Films of 13 at. % germanium composition, deposited on (110), (111), and (100) substrates had an average random dislocation etch pit density of $5 \times 10^6/cm^3 - 10^7/cm^3$ as revealed by a silver dislocation etch (4). Alloy films with compositions above approximately 30 at. % germanium were usually two-phase and inhomogeneous. Surfaces of epitaxial silicon films deposited on silicon-germanium alloy films appear the same as silicon single crystal film deposits on silicon substrates.

This method of silicon-germanium alloy preparation is simple and provides a means of preparing semiconductor material with properties which can be varied by changing the material composition.

Manuscript received Oct. 9, 1961. This paper was prepared for delivery before the Detroit Meeting, Oct. 1-5, 1961.

Any discussion of this paper will appear in a Discussion Section to be published in the December 1962 JOURNAL.

REFERENCES

1. H. C. Theuerer, *This Journal*, **108**, 649 (1961).
2. W. C. Dash, *J. Appl. Phys.*, **29**, 705 (1958).
3. A. J. Goss, K. E. Benson, and W. G. Pfann, *Acta Met.*, **4**, 332 (1956).
4. R. H. Wynne and C. Goldberg, *Trans. Am. Inst. Mining Met. Engrs.*, **197**, 436 (1953).

Oxidation of Silicon by High-Pressure Steam

Joseph R. Ligenza

Bell Telephone Laboratories, Incorporated, Murray Hill, New Jersey

ABSTRACT

The oxidation of silicon by high-pressure steam was studied at temperatures between 773° and 1123°K and pressures from 25 to 500 atm. Within a certain range of pressure and temperature a uniform film of amorphous silicon dioxide forms. At moderate pressures the film growth is linear in time and directly proportional to the steam pressure. At higher pressures the kinetics for film formation are complicated by the volatility of silica in steam, and, above a certain large pressure for any temperature, no film will grow. In the linear range, the rate depends on the orientation of the silicon surface and is greater for silicon that is phosphorus doped near the degenerate range than for high-purity material.

There is much current interest in passivating the surface of silicon devices by means of thick silica films grown at moderate temperatures in high-pressure steam (1). It is the purpose of this study to investigate the conditions of steam pressure and temperature which lead to the formation of amorphous silica films on high-purity silicon crystals and to determine the time dependency for film formation. A rather narrow temperature range was selected for study, and particular emphasis was placed on those pressures which would not cause the silica to volatilize. The silicon was oxidized in small bombs, and oxide film thicknesses were determined gravimetrically. Oxidation kinetics for film formation and the factors affecting the oxidation rate are discussed in terms of a model for the oxidation process based on the present experiments and others which have been presented in earlier papers.

Experimental Methods

The procedure followed in an oxidation run was to place a number of bombs, each containing a silicon specimen and water, into a hot furnace, in some sequence. A bomb will reach the furnace temperature in about 5 min during which time all of the water has passed into the gas phase. After the oxidation, the bombs are removed from the furnace, and the oxide film thickness is calculated from the weight of the oxide film. The growth of the films with time, at any fixed temperature and pressure, was found by using ten bombs, each of which was kept in the furnace for a different time. Runs at different temperatures and pressures provided the necessary data to evaluate the dependency of the oxidation rate on these parameters.

The silicon specimens were cut from n- and p-type single crystals of resistivities ranging from 0.5 to 10 ohm-cm, in the form of wafers with a geometric area of 1 cm^2. No attempt was made in the present study to use specimens of known orientation. The wafers were lightly etched in a 10-1 HNO_3-HF mixture to produce a mirror smooth surface. Prior to an oxidation the silicon and bombs were cleaned by boiling in nitric acid followed by at least three rinses in boiling water. All water used in rinsing and in oxidation was prepared by a double distillation in a silica still.

The bombs were made of Inconel X and the interiors were lined with gold. They were designed to support a pressure of 5000 atm at room temperature and 100 atm at 1123°K. The bombs are cylinders 6.5 cm long, 1.5 cm in diameter with a wall thickness of 0.3 cm, and an internal volume of about 0.6 cm^3. They were sealed by means of a screw cap which bore on a plug and compressed a gasket of heavy gold foil to the gold lining. The amount of water placed in the bomb for any desired temperature and pressure was calculated from PVT data for water above the critical temperature and was delivered to the bomb by means of a pipette with an accuracy of 0.5%. The furnace core consists of a nichrome cube, heated on each of its sides by independently controlled flat heating elements. This cube has ten holes located circumferentially on a radius into which the bombs are put. By placing thermocouples at the six faces of the cube, and one in its interior, the block can be easily kept at a uniform temperature of ±1° at any temperature up to 1223°K when the appropriate individual power adjustments are made with the six heating elements. The bomb volumes are known, at the oxidizing temperature, to 0.2% Accordingly, the pressure in the bomb is known to 1%. The drop in steam pressure in the bomb due to reaction with silicon is negligible when compared to the accuracy with which the pressure is known for most of the film thicknesses formed in this study.

A quartz microbalance was used to determine the oxide film thickness. The silicon was weighed before and after oxidation and after removing the film with aqueous HF. The geometric areas of the silicon specimens averaged 1 cm^2, and the balance sensitivity was 8.63×10^{-7}g. Thus the film thickness could be calculated to a precision of ±50Å by

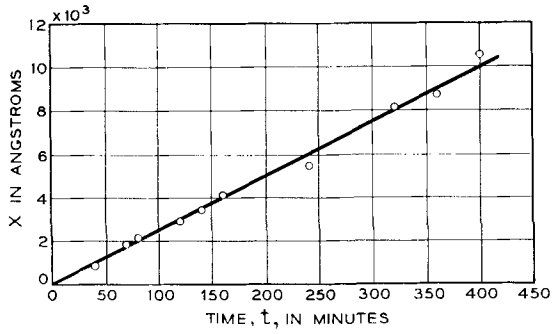

Fig. 1. Oxidation of silicon by steam to form amorphous SiO_2 at 923°K and 50 atm. The oxidation rate is 25.7 ± 0.8 Å/min.

using a weight of 7.85 × 10^{-8}g SiO_2/cm^2 for 3.57Å of the oxide. The latter values were calculated from an oxide density of 2.20 g/cm^3 for amorphous silica. Independent measurements of the film thickness by optical techniques and by capacitance measurements agreed with the gravimetric values within 5%. Electron diffraction reflection studies of the oxide have yielded no evidence of any crystallinity: the oxide films are amorphous SiO_2. When checking the film thickness optically and by capacity measurements, the values used for the refractive index and dielectric constant were those of silica.

Experiments and Results

The growth of silica films on silicon in high-pressure steam proceeds linearly in time. Figure 1 shows the results of an oxidation at 923°K and 50 atm. The line drawn through the experimental points has a slope which is the average value calculated from the points. The rate of growth here is constant to 10,000Å. Other experiments demonstrated that the growth is linear up to 70,000Å at this temperature and pressure. Experiments at temperatures from 773° to 1123°K and pressures from 25 to 400 atm, for times ranging from ½ to 8 hr all gave linear kinetics.

The rate of film formation is directly proportional to the steam pressure. The constant $dx/dt \cdot 1/P$ (Å min^{-1} atm^{-1}) is given in Table I where the results of all the experiments are presented. An average of ten different pressures was used to obtain the results in this table.

Film growth under conditions of relatively high pressure for long periods occurs at rates that are nonlinear. Furthermore, these rates are always smaller than those found at the lower pressures or for short time oxidations at the high pressures. This behavior is due to the "solubility" of the oxide in the steam (2). It has been known for some time that steam at pressures of 100 atm and above can dissolve the various forms of silicon dioxide. Booth and Bidwell (3) give solubility values for silica and quartz at a variety of pressures, but at temperatures lower than those used here. The over-all trend is that the solubility increases with temperature and pressure and that silica is more soluble than quartz. No data were given for the rates of solution. No precise statements can be made at present about the conditions that cause a departure from linearity. With the bomb volumes used here (0.6 cm^3) smaller rates occur at 923°K and 120 atm at times greater than 3 hr. At temperatures greater than 923°K deviations from linearity will occur at pressures above 75 atm and times greater than 2 hr. Less work has been done at temperatures below 923°K, but here pressures of 300 atm and periods up to 8 hr can be used without going outside the range of linearity.

Above certain pressures, the silica film does not grow. This effect results in an etching of silicon to produce a surface approximating the appearance of a lapped surface. This etching has been found to occur at a definite pressure at a given temperature. A number of experiments were done to determine just what these minimum pressures for etching were. The results of these experiments are given in Table II. Supporting evidence for the solubility of silica in steam is provided by the observation that the bomb interiors were uniformly coated with a white deposit after experiments at and above the pressures in Table II. This material must have precipitated from the gas phase when the bomb was cooled.

Although no detailed attention has been paid in this study to the role of silicon orientation on the rates of oxidation, the following effect was observed. A twinned crystal of 200 ohm-cm resistivity was oxidized at 923°K and 105 atm for 1 hr. The resulting film was divided into two regions of different thicknesses, one 2500Å thick, the other 3500Å thick. These regions corresponded to two different orientations resulting from the twinned growth. An analysis of the surface orientation of the bar by electron diffraction disclosed a 610 type plane 1° from the surface (100-type plane 10° from surface) under the 2500Å film and a 541-type plane 2° from the surface (110-type plane 14° from the surface) under the 3500Å film. The difference in rate between the two regions is 35%. Work is being carried on currently to measure the kinetics as a function of orientation. The results to date are consistent with those obtained on the twinned crystal.

Table I. Rate of silica film formation on silicon in high-pressure steam at various temperatures

T, °K	Pressure range, atm	$dx/dt \cdot 1/P$, A min^{-1} atm^{-1}
773	100-400	0.039 ± 0.014
848	50-400	0.19 ± 0.03
923	50-300	0.19 ± 0.04
973	25-80	1.14 ± 0.03
1123	20-60	4.00 ± 1.10

Table II. Steam pressures P_m and temperatures at which only etching of silicon will occur

T, °K	P_m ±50, atm
773	500
848	500
923	400
1023	200
1123	150

Another factor which can influence the rates to an even greater extent than the orientation is the doping level in the silicon. A piece of silicon which had been phosphorus diffused to a surface concentration of 10^{21} P atoms/cm^3 was oxidized at 923°K and 120 atm for about 1 hr. The film thickness was 20,000Å. Under the same conditions, only 3500Å would have grown on high resistivity material. This film was also amorphous. Subsequent oxidations of similar silicon specimens have yielded equivalent results.

Discussion

The rate-limiting step in the oxidation of silicon by high-pressure steam has been found by Ligenza and Spitzer (4) to occur at the interface between the silica and silicon. Films were prepared using O^{16} and O^{18} water and infrared absorption measurements of oxides prepared by successive isotropic oxidations showed that oxygen exchange took place. If, for example, a 7000A SiO_2^{16} film, grown either in oxygen or steam, is oxidized in 90% O^{18} steam at 923°K and 120 atm for 10 min, the O^{18} oxygen in the resulting oxide is found to be distributed uniformly throughout the thickness of the oxide. The conversion amounted, in this case, to 30%, uniformly distributed, although only 500Å of additional oxide was formed. Such results can be accounted for by assuming that a mobile oxygen species, having a very large diffusion constant, diffuses into the film from the silica-gas interface and distributes itself uniformly in the oxide film during the oxidation, while exchanging with the silica oxygens at a rate slower than it diffuses. Spitzer and Ligenza (5) also made a study of the exchange of oxygen between high-pressure steam and silica and found that the rate of exchange is directly proportional to the steam pressure. It was concluded that the diffusing oxygen species responsible for the exchange is interstitial water, the water in the silica film in equilibrium with water in the gas phase. The mechanism postulated for the exchange was a rapid reaction between the interstitial water molecules and a silicon-oxygen bridge to form a pair of silanol groups (Si—O^{16}H + HO^{18}—Si), followed by a slow condensation reaction by the pair to reform an interstitial water molecule and a silicon-oxygen bridge with exchanged oxygens.

On the basis of these experiments, the mechanism for the linear growth of silica films on silicon by oxidation in high-pressure steam is assumed to be the following. At high pressures and moderate temperatures water dissolves in the silica film. The diffusion constant for water in silica is sufficiently large[1] for the water to be uniformly distributed throughout the oxide film during oxidation. The interstitial water in the film is then in equilibrium with water in the gas phase, and the concentration of water in the film depends only on temperature and steam pressure. We shall assume that the oxidation step is the reaction between a water molecule in the silica phase and a silicon-silicon bond at the oxide-silicon interface to form a silicon-oxygen bridge and a hydrogen molecule. The reaction is

$$H_2O_i\ (SiO_2) + Si - Si \xrightarrow[N]{} \overset{HOH}{Si - Si} \rightarrow Si - O - Si + H_2\ (SiO_2) \quad [1]$$

where C_i is the concentration of water molecules in the oxide in molecules/cm^3 and N is the concentration of silicon bonds in bonds/cm^2. The oxidation rate is

$$\Omega \frac{dx}{dt} = kC_i N e^{\frac{\Delta E}{RT}} \quad [2]$$

where Ω is a conversion factor, k is the rate constant for oxidation, and ΔE is the activation energy for oxidation. If we assume the water in the film obeys Henry's law, the concentration of water in the silica film will be

$$C_i = \frac{PN_o}{RT} e^{\frac{\Delta S}{R}} e^{-\frac{\Delta H}{RT}}$$

where N_o is Avagadro's number, R is the gas constant, and ΔS and ΔH are the entropy and enthalpy of solution of water in silica, respectively. The final equation for the oxidation rate is

$$\Omega \frac{dx}{dt} = \frac{kN_o e^{\frac{\Delta S}{R}}}{R} \cdot \frac{PN}{T} e^{-\frac{(\Delta H + \Delta E)}{RT}} \quad [3a]$$

$$\frac{dx}{dt} = k' \frac{PN}{T} e^{-\frac{(\Delta H + \Delta E)}{RT}} \quad [3b]$$

where $k' = kN_o e^{\frac{\Delta S}{R}}/\Omega R$. The form of Eq. [3b] is in agreement with the experimental data. The oxidation rate is constant in time, proportional to the pressure, and is dependent on the orientation through the parameter N.

The parameter N will in general be determined by the bond density, the specific configuration of the silicon bonds at the interface, and by the fact that the effective diameter of the water molecule is large enough when in reacting position on a silicon bond to preclude reaction on adjacent bonds. The greater the available bond density, the larger the oxidation rate, provided that the activation energy ΔE for the different orientations remains unchanged. A detailed analysis of this effect, along with the appropriate experiments, will be published at a later date (6).

The values of the pre-exponential constant $k'N$ and the apparent activation energy $(\Delta H + \Delta E)$ for the data presented here can be determined by applying Eq. [3b] to the experimental rates given in Table I. However, these values will be of questionable accuracy since no attempt was made, while cutting the specimens from the crystals, to obtain but one surface orientation. Undoubtedly, more than one orientation has been used, and this will affect the precision as well as the accuracy of the

[1] Preliminary results on the diffusion of water into silica have been obtained by Ligenza and Spitzer. The diffusion constant appears to be independent of pressure in the range of 35 to 120 atm, and has a value of 1.0×10^{-9} cm^2/sec at 923°K.

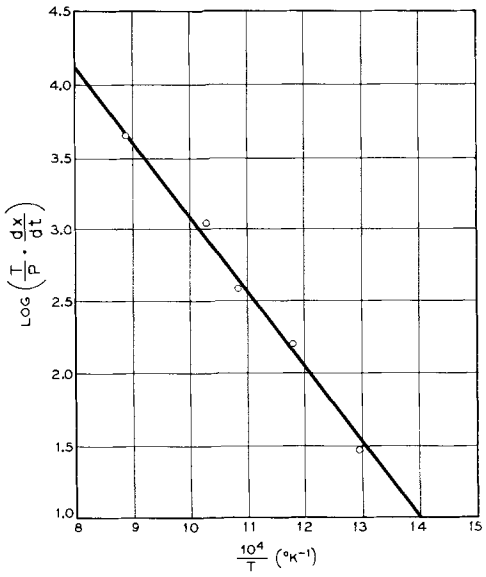

Fig. 2. Arrhenius plot of the steam oxidation data. The slope is the apparent activation energy $(\Delta H + \Delta E)/2.303R$, with $\Delta H + \Delta E = 23{,}800 \pm 920$ cal/mole. The intercept is log $k'N$ with $k'N = 1.90 \times 10^9$ Å °K min^{-1} atm^{-1}.

results. The parameters $k'N$ and $(\Delta H + \Delta E)$ are obtained by plotting $\log\left(\frac{T}{P} \cdot \frac{dx}{dt}\right)$ *vs.* $\frac{1}{T}$. The plot is shown in Fig. 2. The apparent activation energy is $\Delta H + \Delta E = 23{,}800 \pm 900$ cal/mole and $k'N$ is 1.9×10^9 Å °K min^{-1} atm^{-1}.

Acknowledgments

The author wishes to express his appreciation to Miss R. E. Cox for doing the measurements and to the late B. J. McNally who constructed the bombs and furnace.

Manuscript received May 2, 1961; revised manuscript received Sept. 5, 1961.

Any discussion of this paper will appear in a Discussion Section to be published in the December 1962 JOURNAL.

REFERENCES

1. M. M. Atalla, "Proceedings of the Conference on Elemental and Compound Semiconductors," H. Gatos, Editor, Interscience Publishers, New York (1960).
2. G. R. B. Elliott, University of California, Radiation Lab. UCRL-1831 (1952); E. L. Brady, *J. Phys. Chem.*, **57**, 706 (1953); A. S. Berezhnoi, "Silicon and Its Binary Systems," Consultants Bureau, New York (1960).
3. H. S. Booth and R. M. Bidwell, *Chem. Rev.*, **44**, 477 (1949).
4. J. R. Ligenza and W. G. Spitzer, *J. Phys. Chem. Solids*, **14**, 131 (1960).
5. W. G. Spitzer and J. R. Ligenza, *ibid.*, **17**, 196 (1961).
6. J. R. Ligenza, *J. Phys. Chem.*, to be published.

The Electrochemical Behavior of Uranium

John W. Ward and James T. Waber

University of California, Los Alamos Scientific Laboratory, Los Alamos, New Mexico

ABSTRACT

The potential behavior of uranium was studied in both oxidizing and non-oxidizing media. A low critical anodic current and a very high critical potential for passivity were observed. In the presence of oxygen especially interesting behavior was noted. Oxygen, while passivating the corroding electrode, was reduced to form hydrogen peroxide. At steady state the potential of the passive electrode was found to be slightly more active than that for the reversible oxygen-peroxide couple. Under these conditions, changing the partial pressure of oxygen caused potential shifts in accordance with the Nernst equation.

Stern (1-3) has described in both general and specific terms the mechanism for passivation. An interesting special case is the electrochemical behavior of uranium, which may be adequately interpreted by using the concepts developed by Stern. Since uranium appears to react by anionic diffusion (4), even the "active state" involves what must be considered a protective film, and results must be viewed with the realization that no measurable quantity of uranium ever enters solution. Most of the potentials recorded in this study were open-circuit values in neutral solution, and, as such, relate to the spontaneous corrosion behavior of uranium.

General Concepts

Uranium exhibits active-passive behavior similar to that of stainless steel and titanium. A typical anodic polarization curve for this type of behavior is shown in Fig. 1. Such a curve is obtained by holding the potential constant and measuring the current, and will describe the anodic polarization and passivation of an originally active metal. Stern (1) has shown that the addition of passivating inhibitors (oxidizing agents) produces a mixed potential dependent on the redox potential, exchange current, Tafel slope, and limiting diffusion current of the oxidizing inhibitor. This behavior is attributed to the production of a local-action current which acts to polarize the metal anodically. Whether or not passivity is attained will then depend on parameters exhibited by the metal, primarily the critical anodic current and the critical potential for passivity.

The general behavior of the composite system is shown in Fig. 2. Oxidizing inhibitor A is not present in sufficient concentration to passivate the metal.

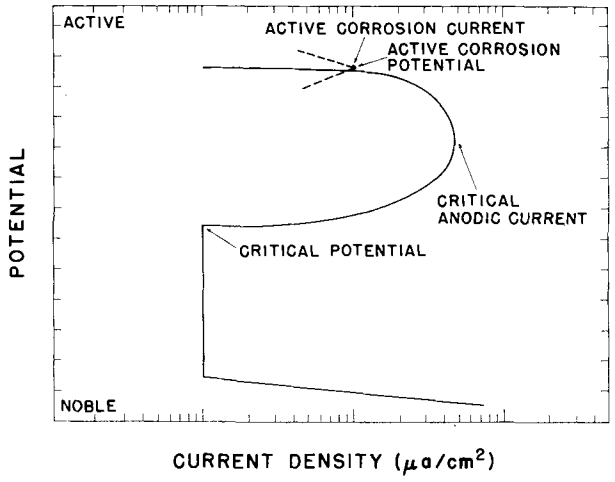

Fig. 1. Anodic polarization curve for a metal exhibiting active-passive behavior.

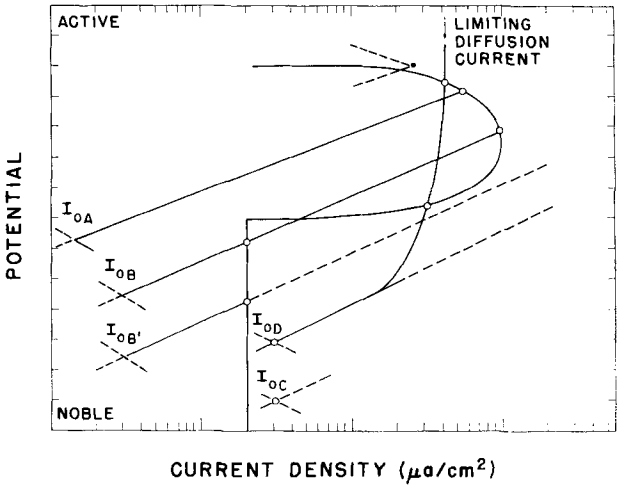

Fig. 2. Anodic polarization diagram, showing mixed potential produced by the addition of oxidizing agents of various concentrations and redox exchange currents.

Inhibitor B produces a situation whereby two possible potentials may exist, one active and one passive. Under these conditions it is possible for the metal to oscillate between active and passive states. Inhibitor B′ (at a higher concentration than B) produces stable passivity. Inhibitor C, whose redox exchange current I_{oD} is greater than the passive corrosion current, produces a mixed potential slightly more active than the reversible redox potential of the inhibitor. The value for this mixed potential will be related to the current that is produced through reduction of the inhibitor, and which is equal to the sum of the currents produced due to oxidation of the metal and oxidation of the reduced form of the inhibitor. Finally, inhibitor D, normally capable of passivating the metal, exhibits concentration polarization under certain experimental conditions as, for example, when the concentration of D is low, and the limiting diffusion current can bring the mixed potential into a non-passive region. Figure 2 was constructed to illustrate the manner in which high concentrations of an inhibitor and high redox exchange currents both favor passivity.

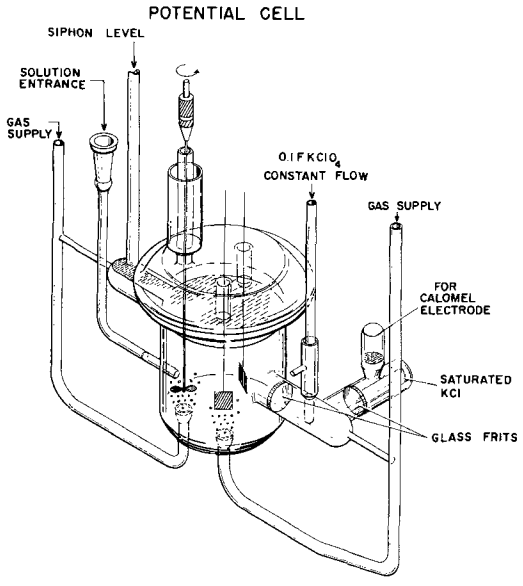

Fig. 3. Sketch of the potential cell used

It will be shown that uranium, under appropriate experimental conditions, will exhibit electrochemical behavior interpretable by the situations A through D described above.

Experimental

Apparatus.—The apparatus, shown in Fig. 3, consisted essentially of a glass vessel, 90 mm in diameter, with a ball joint cap through which the electrodes were suspended. Gas was bubbled into the solution through frits in the bottom of the chamber. By rotating the cap, the electrodes could be placed directly over the gas stream, or removed a distance from it. It was found, however, that stirring the solution by use of an impeller, rather than bubbling the gas directly past the specimen as was done in earlier work, improved the reproducibility immensely and also shifted the observed potential with oxygen in the noble direction. One explanation for this effect is that a surface partially covered by bubbles is not homogeneous; another is that under these conditions the supply of oxygen to the surface is not constant. Stirring should in general provide a more constant thickness of the stagnant layer.

Operation of the cell should be evident from Fig. 3. Since chloride ion was found to affect the study adversely, the 0.1F $KClO_4$ compartment was interposed between the saturated KCl electrode compartment and the main chamber. The siphon arrangement connected to the main chamber was used to maintain a constant level of solution, as a small amount of evaporation occurred during several days run time. The cell was immersed in a large thermostatically controlled bath, maintained at 35° ± 0.01°C.

Potentials were measured against a saturated calomel electrode, by using a Rubicon No. 2780 potentiometer in conjunction with a L&N 2430-D galvanometer having a sensitivity of 0.00045 μa/mm. Currents were measured with a Brown No. 15038G electrometer and strip-chart recorder.

Materials.—Carbon electrodes were made according to a technique outlined by Berl (5).

Solutions of electrolytes were prepared and stored in glass-stoppered volumetric flasks. Distilled water (specific conductivity 0.5 micromhos) was produced by means of a Comroe Laboratories, Inc. "Quikpure" ion-exchange water purifier and was used in making up all solutions. The pH of this water was 7.0.

Six different gases were used: pure oxygen, air, and four argon-oxygen mixtures having oxygen concentrations from 10 to 0.1 v/o (volume per cent). These mixtures were made by diluting commercially pure oxygen with welding grade argon. It had been found in other work that satisfactory mixing could be achieved in large cylinders by first admitting the diluent gas to the cylinder in high-pressure spurts to cause turbulence, and then heating a lower edge of the inclined cylinder. For the present work the oxygen mixtures were made up in H-size cylinders, and mass spectrographic analysis confirmed the accuracies of compositions. The concentration of dissolved oxygen at each partial pressure was calculated from studies by MacArthur (6) and the work of Shirley, Pachucki, and Lobos (7).

Procedure.—A given solution was admitted to the cell, and the gas (either pure argon, or an oxygen mixture, depending on the experiment) was then bubbled through the frits. The impeller was turned on and the cell was then maintained in this manner for 4 hr before the electrodes were immersed in the solution and measurements made. Because of the design of the cell, the equilibrium pressure over the solution was always 1 Los Alamos atmosphere (~590 mm). Atmospheric pressure was noted before, during, and after each experiment. A fixed flow rate, used for all studies, was achieved by using a Brooks Rotameter.

Uranium electrodes were prepared as follows: 1.6 x 1.9 cm depleted uranium specimens were polished through 600 grit paper and then spot-welded to a uranium wire that had been polished in similar fashion. This uranium wire was in turn spot-welded to a platinum wire which passed through the cell cap. Quick-setting epoxy resin was used to mask the wire to below solution level. All of the above operations were performed in an argon atmosphere. The electrodes were then inserted into the cell, which was already at bath temperature, and saturated with gas of the given composition. Potential recording was begun immediately. Steady-state potentials were usually achieved within 12 hr (with several exceptions, which will be noted). A potential value was accepted after five identical readings were obtained over a 2-hr period. Most of the work was done in 0.1F $KClO_4$, which was chosen as a noncomplexing neutral salt.

Behavior in Oxygen-Free Water

Uranium is an electropositive metal capable of releasing hydrogen from water. In boiling H_2O the net reaction is

$$U + 2H_2O \rightarrow UO_2 + 2H_2\uparrow \qquad [1]$$

It was assumed in this study that essentially the same reaction occurs at room temperature, although the amount of corrosion is too small to allow measurement of the evolved hydrogen in the apparatus used for these studies. The reasons for this assumption will become evident.

The first potential observation taken after the electrodes were immersed in the argon-saturated water gave a value of about −0.3v *vs.* SCE. The potential rose quickly at first to more active values and over a 3-hr period attained a steady value of −1.1012v *vs.* SCE. This potential was observed for both distilled water and 0.1F $KClO_4$. The value was not changed by using basic or acidic salts, but adding larger amounts of H^+ or OH^- ions caused competing side reactions to occur.

No pH change was observed during this corrosion reaction even after several days of exposure. Therefore it was assumed, as indicated above, that the primary reaction results in the evolution of hydrogen.

An adherent film was formed on the electrode and was dull gray-black in appearance. Broad x-ray diffraction peaks indicated that the film had a fine-grained structure. Under microscopic examination the oxide appeared dense and granular. The film could not be removed from the electrode by rubbing with a cloth.

The very active potential value reached by the electrode certainly indicates that the metal was in the active state although corrosion was limited or controlled by anionic diffusion through the oxide layer. The large rise in potential indicates the production of a powerful reducing agent in the oxide film, which is logically tri-positive uranium in some form. A likely oxidation reaction for the active region is the metal first going to the positive three state, in line with Stern's suggestion (1) that a metal corroding in the active state produces ions of lower valence than the same metal does when passivated.

$$U + H_2O \rightarrow UO^+ + H_2 + e^- \text{ (fast step)} \qquad [2]$$

$$UO^+ + H_2O \rightarrow UO_2 + H_2 - e^- \text{ (slow step)} \qquad [3]$$

$$U + 2H_2O \rightarrow UO_2 + 2H_2 \text{ (net equation)}$$

This set of equations predicts the existence of an excess of the tri-positive state at any given instant, as well as pH independence. Both predictions agree with the experimental observations. Since only UO_2 is found by x-ray analysis, the excess must be small, and therefore the electrode should be passivated easily.

Anodic polarization does passivate the electrode quickly, as does the addition of certain oxidizing inhibitors. Both these situations will be discussed. Under anodic polarization the oxide gradually becomes glossy, and thereafter the electrode apparently cannot easily return to the active state. This suggests that the oxide formed under active conditions (oxidation in oxygen-free water) may be somewhat porous.

Behavior with Inhibitors

The addition of oxidizing agents to the solution caused changes in behavior that were dependent on the concentration, redox potential, and exchange

Table I. Effect of various oxidizing agents on the corrosion potential of an active uranium electrode

Oxidizing agent	Formal concentration	Final potential, v
None	(0.1F $KClO_4$)	—1.1012
$NaNO_2$	0.0005	—1.04
$NaNO_2$	0.005	—0.94
$NaNO_2$	0.05	—0.54
$NaNO_2$	0.5	—0.11
$NaNO_3$	0.1	+0.03
Na_2CrO_4	0.066	—0.66
Na_2MoO_4	0.001	—0.84
Na_2WO_4	0.001	—0.82

current, as illustrated in Fig. 2. Results are presented in Table I.

Figure 4 shows the potential-time behavior of the nitrite and nitrate solutions. The 0.0005F $NaNO_2$ curve is suggestive of case A of Fig. 2. The potential was shifted only slightly in the noble direction. With 0.005F and 0.05F $NaNO_2$ note the uncertainties exhibited by the potentials, and indeed the violent oscillation between active and passive values with the 0.005F concentration before a steady but still active potential was reached. These two curves aptly illustrate case B. Case B′ is shown in the curve for 0.5F $NaNO_2$; after an initial small rise, the potential falls to a steady passive value. The behavior of 0.1F $NaNO_3$ is also similar to case B′.

Surprisingly, nitrate ion appears to be a better inhibitor for uranium than does nitrite ion. Also, the molybdate and tungstate solutions are not as dramatically effective with uranium as they appear to be with titanium and iron. The addition of oxygen to any of the solutions listed in Table I produced immediate passivity.

Addition of salts with complexing anions (Cl^-, Br^-, CNS^-, etc.) caused destruction of the protective film and rapid corrosion of the specimen. This behavior was actually accentuated by the addition of oxygen.

Behavior with Oxygen

Nature of the reaction.—By far the most interesting results of this study were obtained while using 0.1F $KClO_4$ solutions saturated with oxygen and oxygen mixtures of various concentrations. The

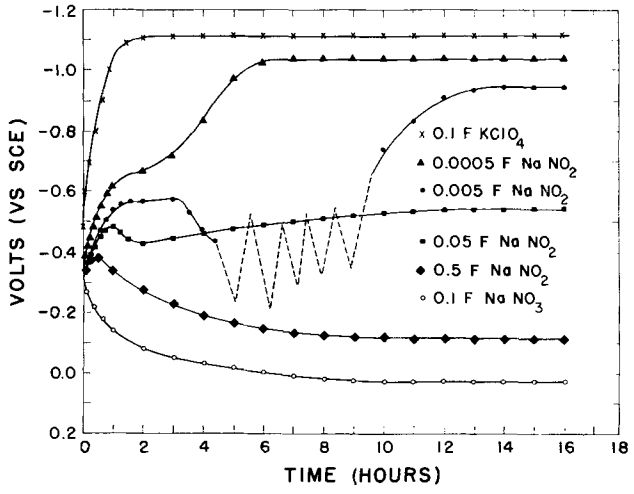

Fig. 4. Potential-time behavior of a uranium electrode in sodium nitrite and sodium nitrate solutions.

oxide that was formed in the presence of oxygen and oxidizing agents, which produced passivation, exhibited bright interference colors. X-ray diffraction patterns of the oxide were sharp, and microscopic examination showed that it had a smooth, nongranular surface.

The potential of the electrode in oxygen-saturated solution decreased over a period of about 6 hr to a steady value of + 0.1432 ± .0002v *vs.* SCE. Solution samples taken after this steady-state potential was reached gave a positive PbS test for hydrogen peroxide, indicating an equilibrium concentration of 1×10^{-6} moles per liter or greater. The *pH remained* at 7.0. The potential of an active carbon electrode in this solution was + 0.145v *vs.* SCE, indicating that the uranium electrode was about 2 mv more active than the reversible oxygen-peroxide redox couple in this solution. From the concentration of oxygen, the *p*H, and the observed potential, the equilibrium concentration of peroxide was calculated by means of the Nernst equation. A value of 9×10^{-6} moles per liter was obtained, which agrees well with the qualitative result of the PbS test.

The behavior of the uranium electrode with oxygen is a good example of case C in Fig. 2. The redox exchange current, I_{oc}, is evidently somewhat greater than the passive corrosion current, and the metal potential is slightly more active than the reversible redox potential. It is also clear that the uranium-uranium oxide electrode must exhibit a surface on which the oxygen-peroxide exchange current is relatively high, and that the catalytic decomposition of peroxide is not effected (or is effected very slowly) on this surface.

Delahay (8) has pointed out that the reduction of oxygen to water is usually easier than the reduction of oxygen to hydrogen peroxide, but that under irreversible conditions this conclusion may not hold. Churchill (9) has shown that hydrogen peroxide is formed during the corrosion of a number of metals (Zn, Sn, Pb, Ag, Hg, Cu, Al); furthermore, he reported that freshly abraded specimens gave a strong Russell effect, but that well-aged specimens did not. Of special interest was his observation that the process was cathodic and probably involved direct oxidation of atomic hydrogen by O_2. Such a process could produce the result observed with the uranium electrode (H_2O_2 production with no *p*H change) since atomic hydrogen must be formed at the oxide-solution interface before released as molecular hydrogen. If this is the actual mechanism, then hydrogen peroxide is formed, both from the O—+3 step (Eq. [2]) and the +3—+4 step (Eq. [3]), as hydrogen is released during the corrosion of uranium. A *p*H-independent net equation could then be written as

$$U + 2H_2O + 2\ O_2 \rightarrow UO_2 + 2H_2O_2 \qquad [4]$$

Under these conditions the basic corrosion mechanism might still be the reaction of uranium with water, with no direct intervention by oxygen. The formation of the entirely different passive film in the presence of oxygen is not so easily explained, however. The film normally formed by reaction

with water is clearly healed in some unspecified manner.

Effect of oxygen concentration.—Equilibrium potentials were measured for pure oxygen, air, and four mixtures of oxygen and argon: 10, 3, 1, and 0.1 v/o oxygen. It was found that the values for air, 10, and 3 v/o oxygen were as reproducible as that for pure oxygen (± 0.2 mv), but that deviations were somewhat larger for the 1 and 0.1 v/o oxygen mixtures. It is thought that this result was due, at least partly, to the slow approach to equilibrium. The more dilute the oxygen mixture, the longer was the time necessary to achieve a steady-state potential. Whereas 6 hr was sufficient time for pure oxygen, almost 30 hr were needed for the 1 v/o mixture. With both the 1 and the 0.1 v/o mixtures the potential began to rise to active values when the fresh electrode was inserted, unless the electrode was first exposed for several hours to a higher oxygen concentration to establish the passive film. Once this film was established, a steady value in (or close to) the passive region could be achieved. It is clear, however, that the passive-type film must be present.

Changing oxygen mixtures after an electrode had reached a steady value produced interesting results. Switching to higher oxygen concentrations caused fairly rapid shifts (~2 hr) to the potential associated with the higher value. Changing to a lower oxygen concentration, however, caused only a very slow shift toward the potential associated with that mixture. Indeed, the shift from the 1 v/o value to that for 0.1 v/o would probably have taken several days to effect, but the supply of mixed gas was not sufficient for such a long-term study.

Stern (1) has pointed out that, when the potential is in the passive region, changing the concentration of oxidizing agent should cause the reversible redox potential to shift according to the Nernst equation. At equilibrium, the current produced by oxidation of uranium and oxidation of peroxide is equal to the current produced due to the reduction of oxygen. If it is assumed that a steady-state concentration of peroxide, which is a function of the corrosion rate of uranium, exists under these conditions, the potential shift due to a change in the oxygen concentration may be calculated. Subtracting the Nernst equations for two different oxygen concentrations, we get

$$\Delta E = RT/n\mathbf{F} \ln(O_2)_1/(O_2)_2 \qquad [5]$$

where T is 308°K, and n, the number of electrons transferred, is 2.

The potentials measured for the several gas mixtures at 590 mm Hg, along with the values calculated for these concentrations (Eq. [5]),are listed in Table II. The first potential used for the calculations was + 0.1432v, the value for pure oxygen. The other calculated values were then obtained from this starting value.

The data of Table II are plotted in Fig. 5. As can be seen, the calculated values closely approximate the measured values from pure oxygen through the 3 v/o mixture. The slight variations are probably due to errors in estimating solubilities. Deviations become noticeable, however, for the 1 v/o mixture and become large with the 0.1 v/o mix. It is believed that these deviations are due to concentration polarization. This situation, then, is similar to case D of Fig. 2, where the limiting diffusion current due to the starved oxygen supply at the surface produces a potential more active than is expected.

Table II. Potentials as a function of the concentration of oxygen in 0.1F $KClO_4$

Composition of gas mixture	Oxygen concentration, g/l	Observed potential,* v	Calculated potential,* v
Pure O_2	2.455×10^{-2}	0.1432	0.1432†
Air	5.2×10^{-3}	0.1230	0.1227
10 v/o O_2	2.455×10^{-3}	0.1127	0.1127
3 v/o O_2	7.365×10^{-4}	0.0962	0.0974
1 v/o O_2	2.455×10^{-4}	0.0793	0.0822
0.1 v/o O_2	2.455×10^{-5}	0.0408	0.0516

* Potentials referred to a SCE at 35°C.
† Base value.

Other Measurements

Anodic polarization measurements were made on the active electrode in 0.1F $KClO_4$ saturated with argon. As indicated earlier, a small amount of anodic current brought the electrode into the passive region. Since no potentiostatic equipment was available, only an "orthodox" polarization measurement could be made. The critical current break occurred at only 2.2 $\mu a/cm^2$.

The first potential observed when a uranium electrode was immersed in a particular solution was close to −0.3v *vs.* SCE. This value was observed regardless of the solution media. Potentials then either rose to more active values, or fell to passive values from this −0.3v point, depending on the media. Therefore, −0.3v was chosen as a reasonable estimate of the critical anodic potential.

In the situation with oxygen present, addition of judiciously small concentrations of H^+, OH^-, and H_2O_2 produced potential shifts qualitatively in accordance with the Nernst equation. Addition of much larger quantities, however, caused drastic potential changes, formation of uranium peroxide, etc. It was concluded that the existence of the rever-

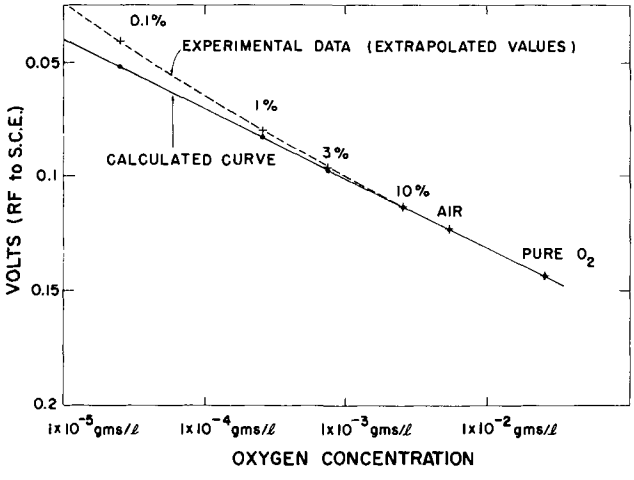

Fig. 5. Comparison of measured potentials with values calculated using the Nernst equation.

sible oxygen-peroxide couple on the uranium electrode is a delicately balanced situation.

Conclusions

Uranium has been shown to exhibit active-passive corrosion behavior similar to that observed with stainless steel and titanium. The uranium surface presents a low exchange current for establishing the redox potentials of a number of oxidizing agents, the most interesting of which is the oxygen-peroxide system. A value of −0.3v *vs.* SCE was estimated for the critical anodic potential, and a value of 2.2 μa/cm^2 was obtained for the critical current.

The electrochemical behavior of uranium in the presence of oxidizing agents and with oxygen illustrates many of the general points made by Stern (1). Data that show the production of a lower valence state during active corrosion have been cited, and examples have been given which illustrate the effect of oxidizing agents of different concentrations and redox exchange currents on the anodic polarization curve of uranium.

The corrosion of uranium in the presence of oxygen has been shown to generate hydrogen peroxide. The resulting equilibria that were established produced an electrode reversible with respect to oxygen concentration, reproducible, and predictable with respect to the Nernst equation, over a fair concentration range.

Because uranium reacts by anionic diffusion, the interesting situation has been observed whereby both the active and passive states involve the build-up of adherent UO_2 films, which are of entirely different natures. It has been shown that the passive film, once formed, is extremely stable, and furthermore, that this film must be present in order for passive potentials to occur.

Of interest is the absence of a *p*H shift for the spontaneous process, both at oxygen-free and oxygen-saturated electrodes, and the possible clue this gives to the generation of peroxide. The vigorous corrosion produced by complexing anions, especially in the presence of oxygen, was also noted.

Manuscript received Dec. 29, 1959; revised manuscript received Sept. 30, 1961. This paper was prepared for delivery before the Columbus Meeting, Oct. 18-22, 1959. The work on this paper was performed under the auspices of the U. S. Atomic Energy Commission.

Any discussion of this paper will appear in a Discussion Section to be published in the December 1962 JOURNAL.

REFERENCES

1. M. Stern, *This Journal*, **105**, 638 (1958).
2. M. Stern and H. Wissenberg, *ibid.*, **106**, 755 (1959).
3. M. Stern, *ibid.*, **104**, 600 (1957).
4. J. G. Schnizlein, J. D. Woods, J. D. Bingle, and R. C. Vogel, *ibid.*, **107**, 783 (1960).
5. W. G. Berl, *Trans. Electrochem. Soc.*, **83**, 253 (1943).
6. C. G. MacArthur, *J. Phys. Chem.*, **20**, 495 (1916).
7. E. L. Shirley, C. F. Pachucki, and L. K. Lolos, AECU-3795.
8. P. Delahay, *This Journal*, **97**, 198 (1950).
9. J. R. Churchill, *Trans. Electrochem. Soc.*, **76**, 341 (1939).

Anodic Polarization Studies in Neutral and Alkaline Solutions Containing Corrosion Inhibitors

I. NaOH-NaCl System

K. S. Rajagopalan, K. Venu, and K. Balakrishnan

Central Electrochemical Research Institute, Karaikudi, India

ABSTRACT

In neutral and alkaline solutions containing both inhibitive and corrosive constituents corrosion becomes localized and weight loss measurements are of little value in finding out when solution becomes corrosive. Points of attack also vary considerably at border line concentrations. An elegant method of finding out at what concentration of corrosive constituents such solutions become corrosive is described. The method is based on anodic polarization measurements over as short a period as 5 min and takes into account the mechanism of passivation of metal surfaces in such solutions.

Anodic polarization studies by galvanostatic and potentiostatic methods in acid solutions have been shown to be a powerful tool for elucidating the mechanism of passivation of metal surfaces (1-3). Their application to the behavior of neutral and alkaline solutions containing corrosion inhibitors as well as corrosive constituents is lacking. Mayne and Hancock (4) have recently shown that the corrosive or inhibitive character of neutral and alkaline solution containing corrosion inhibitors can be predicted by anodic polarization measurements involving application of a fixed current and following the changes in potential with time. They have studied several systems containing inhibitive and corrosive constituents by anodic polarization measurements at a fixed current density of 10 μa/cm^2. A detailed investigation into the applicability of Mayne's method with NaOH—NaCl system reveals that Mayne's choice of 10 μa/cm^2 is arbitrary and that a rise in potential to the passivation potential on application of this current cannot be a sufficiently reliable criterion for the inhibitive character of a

solution. A more elegant and sensitive method is presented. The present study is of considerable practical importance in relation to the understanding of the corrosion behavior of steel embedded in concrete.

Experimental

Metal: 1.25 cm diameter m.s. rods from the same stock were used in all the tests. The rods were cut into 5 cm pieces, scale and rust removed on grinding machine, and a smooth finish given by abrasion with 120 emery wheel. This was followed by solvent cleaning in trichloroethylene. A thin stem was screwed to the rod, and the joint was insulated from solution by fixing a glass sleeve and sealing the joint with a thin film of paraffin wax.

Solutions: NaOH solution in the normality range 0.0001-0.1*N* and containing varying concentrations of sodium chloride were used. The solutions were aerated before test.

Procedure: The test solution was taken in a 600 ml beaker, the specimen suspended in the solution and made anode. A mild steel sheet cut into the form of a cylinder and lining the wall of the container was made cathode. Current was applied to the cell from a battery source and the potential measured by null method, with reference to a saturated calomel electrode connected to the test solution with a saturated KCl-agar bridge. All experiments were carried out at 35°C ± 0.5°C.

Results

Potential time curves of NaOH—NaCl *solutions at 12 μa/cm².*—In his experiments Mayne (4) considered various current densities in the range 5-100 μa/cm² and concluded that 10 μa/cm² was a suitable current density to be applied to the system. Potential-time curves of test specimens immersed in 0.04*N* NaOH containing seven concentrations of chloride and 12 μa/cm² applied after 24 hr immersion in the test solution are given in Fig. 1. There is considerable similarity between these curves and

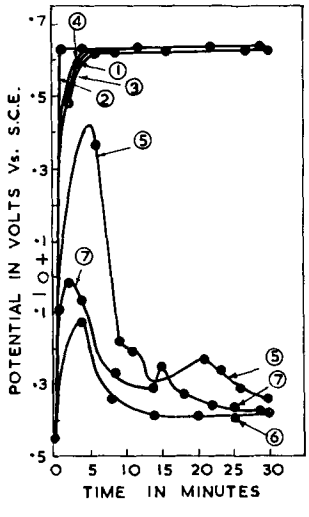

Fig. 1. Potential time curves of mild steel in NaOH-NaCl solutions when anodically polarized at 12 μa/cm². Concentration of NaOH 0.04*N* and concentrations of NaCl: 1, 0.001%; 2, 0.01%; 3, 0.02%; 4, 0.03%; 5, 0.05%; 6, 0.07%; and 7, 0.1%. Polarization carried out 1 day after immersion.

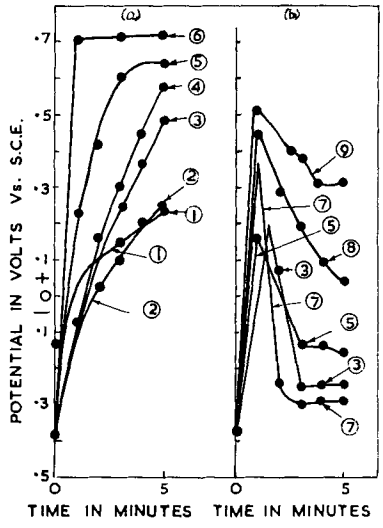

Fig. 2. Effect of current density on potential-time curves in 0.04*N* NaOH containing (a) 0.001% and (b) 0.05% NaCl. Current densities are: 1, 4.8; 2, 9.6; 3, 14.4; 4, 19; 5, 24; 6, 290; 7, 33.6; 8, 2156; and 9, 4800 μa/cm². Polarization carried out immediately after immersion.

those obtained by Mayne, and it is also seen that when a concentration of 0.05% NaCl is reached the potential-time curve first rises followed by a steep fall, while at lower concentrations the potential rises to a steady value of +0.65v (*vs.* SCE) at which oxygen evolution can take place in this medium. The rise in potential diminishes to a negligibly small value at the highest chloride concentration employed.

Potential-time curves at six different current densities in 0.04N NaOH *containing 0.001% and 0.05%* NaCl, *respectively.*—Unlike the potential-time curves given in Fig. 1, the curves given in Fig. 2 were obtained immediately after immersion of the test specimen in the medium which condition was presumably also employed by Mayne. It is now seen that the potential rises slowly at most of the current densities, and a steep rise is observed only at the highest current density (290 μa/cm²) in the case of 0.001% NaCl solution. The potential of oxygen evolution is obtained within 5 min at this current density. The curves in 0.05% NaCl solution are quite different from the curves in 0.001% NaCl solution. In 0.05% solution all the curves show a rapid fall after rising. The potential rises above +0.3v, the potential to which rise should take place according to Mayne, at the higher current densities. The potential values, in fact, show considerable variation at such high applied current density values.

Applied current density vs. NaCl *concentration.*—The data given in Fig. 1 and 2 show that with some of the solutions the potential rises steeply to the potential of oxygen evolution and remains steady there, while in some other solutions, although the potential rises initially, it falls subsequently. It is also seen that the value of applied current decides how quickly the potential of oxygen evolution is reached in different solutions. In every solution, as has been observed, it is possible to reach a given potential at sufficiently high current densities within the duration of test, namely, 5 min. It is also seen that at

Table I. Current density required to raise the potential of M.S. Rod in 0.04N NaOH-NaCl solutions to (a) + 0.3v (SCE) and (b) + 0.6v (SCE) in the course of 5 min when anodically polarized

NaCl concentration, %	Applied current density (ma/cm²)			
	Immediately after immersion		48 hr after immersion	
	(a)	(b)	(a)	(b)
0.001	0.014	0.024	0.007	0.019
0.01	0.014	0.024	0.0096	0.014
0.03	9.6	14.4	9.6	12.0
0.05	4.8	9.6	4.8	9.6
0.1	14.4	19.2	9.6	9.6
0.5	33.6	48.0	14.4	19.2

the same current density and in the same solution the potential rises steeply in the case of the specimen exposed to solution for 24 hr, but this does not take place immediately after immersion (compare Fig. 1 and 2).

The current densities at which the potential rises to +0.3 and +0.6v immediately after immersion in the solution and when polarized 48 hr after immersion are given in Table I. It is seen from the table that the current density decreases in the case of specimen polarized 48 hr after immersion as compared to specimens polarized immediately after immersion. Similarly the current density to raise the potential to +0.6v is always higher than the current density to raise it to +0.3v. In Fig. 3, the log current density is plotted against log NaCl concentration in all cases. It is seen from the figure that a S-shaped curve is obtained for both +0.3v and +0.6v, the range of potential over which the passivation of metal surface is likely to take place, and the two curves coincide. The curves also show that the current at which a jump in potential above +0.3v will take place shows a steep rise after a certain chloride concentration is reached. The chloride concentration and current density corresponding to the middle point appear to divide the solutions as well as the current densities into two broadly distinguishable groups, one in which the current density requirement is low and the other in which the current density requirement is very much higher. Practically the same values are obtained for the current density and the NaCl concentration for the curves relating to

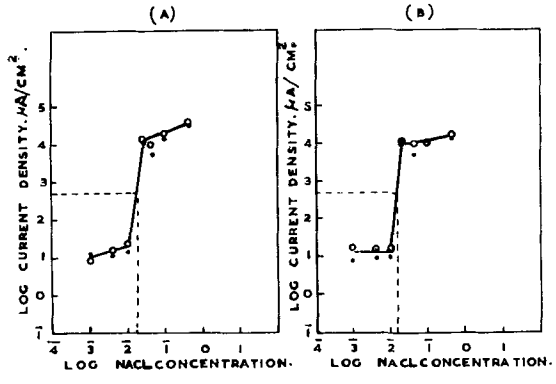

Fig. 3. Applied anodic current density vs. sodium chloride concentration: (A) immediately after immersion of specimen to get +0.3v (SCE) (●—●—●—●) and +0.6v (SCE) (O—O—O—O); (B) 48 hr after immersion in solution to get +0.3v and +0.6v (SCE).

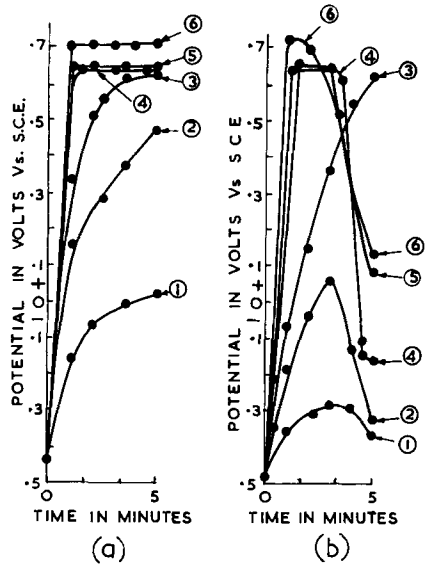

Fig. 4. Potential-time curves of mild steel in 0.04N NaOH containing (a) 0.02% and (b) 0.03% at various applied current densities: 1, 2.4; 2, 12; 3, 24; 4, 72; 5, 144; and 6, 290 μa/cm².

specimens polarized immediately after immersion and those polarized after immersion in solution for 48 hr. The current density and the NaCl concentration corresponding to the middle point are 290 μa/cm² and 0.02% NaCl, respectively. Since the local cell current that can be generated in the absence of applied anodic current will be only of the order of the current densities indicated in the first portion of the curve, it may also be concluded that chloride concentrations below that corresponding to the middle point perhaps do not make the solution corrosive. The current density corresponding to the middle point is then the appropriate current density to apply for distinguishing the two types of solutions. In Fig. 4 the potential-time curves for two solutions on either side of the middle point are considered at various current densities. The interesting observation is made that the solution above the concentration corresponding to the middle point always shows a fall of potential within the duration of the test, and the solution having a concentration below the middle point does not show such a fall. This seems to be a characteristic difference between the two types of solutions. Further, at the current density corresponding to the middle point and at some lower current densities, the rise of potential takes place very steeply in both types of solutions. Hence, the two solutions cannot be distinguished on the basis of whether the potential rises to a given value within the duration of the test. On the other hand, at very low current densities the potential does not rise appreciably in both solutions. Subsequent behavior after the rise, therefore, seems to be more important than the initial change, and the subsequent behavior is brought out in an unambiguous manner by application of the current density corresponding to the middle point.

Anodic polarization behavior at 290 μa/cm² of solutions containing varying ratios of NaOH *and* NaCl. —In Fig. 5, the NaOH concentration is maintained at 0.04*N* and NaCl concentration is changed. It is seen from the figure that solutions having NaCl concen-

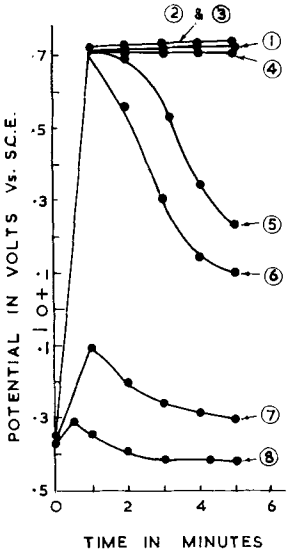

Fig. 5. Potential-time curves of mild steel in 0.04*N* NaOH containing: 1, 0.001%; 2, 0.005%; 3, 0.01%; 4, 0.02%; 5, 0.03%; 6, 0.05%; 7, 0.1%; and 8, 0.5% NaCl when anodically polarized at 290 $\mu a/cm^2$.

tration above 0.02% show the characteristic fall referred to earlier, while at this concentration and below the fall is not observed. These observations confirm the conclusions earlier arrived at from Fig. 3. In Fig. 6, the chloride concentration is kept constant at 0.02%, but normality of NaOH solution varies. It is observed that only in one solution containing 0.1*N* NaOH the potential rises to +0.65v (SCE) and remains constant there. In Fig. 7, both NaOH and NaCl concentrations vary. It is now observed that only one solution is able to show behavior similar to what is observed in 0.04*N* NaOH at NaCl concentration below the middle point of Fig. 3.

Effect of stirring and deaeration during the test on the polarization behavior at 290 $\mu a/cm^2$.— It was shown earlier that in a 0.04*N* NaOH solution containing 0.02% NaCl, the potential rises steeply to +0.6-0.7v and remains constant. The experiment was repeated after deaerating the solution by bubbling nitrogen before and during test. It is seen that no important difference is observed between the two conditions (Fig. 8). The effect of stirring the medium on the behavior of 3 solutions containing 0.02%, 0.03%, and 0.04% NaCl, respectively, are also considered in this figure. It is seen that when the solution is stirred the fall in potential is not observed in 0.03% within the duration of the test, but this was observed at 0.04% NaCl. Apparently the increased availability of oxygen brought about by stirring appears to have some effect, although variation should have been observed on deaeration also in that case.

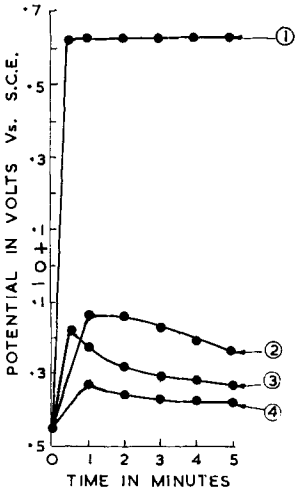

Fig. 6. Potential-time curves of mild steel in 0.02% NaCl containing: 1, *N*/10; 2, *N*/100; 3, *N*/1000; and 4, *N*/10000 NaOH anodically polarized at 290 $\mu a/cm^2$.

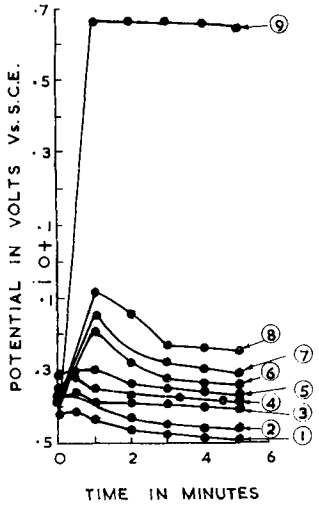

Fig. 7. Potential-time curves of mild steel when anodically polarized at 290 $\mu a/cm^2$ in the following solutions:

	NaOH	NaCl
1.	0.01*N*	0.09*N*
2.	0.02*N*	0.08*N*
3.	0.03*N*	0.07*N*
4.	0.04*N*	0.06*N*
5.	0.05*N*	0.05*N*
6.	0.06*N*	0.04*N*
7.	0.07*N*	0.03*N*
8.	0.08*N*	0.02*N*
9.	0.09*N*	0.01*N*

All the experiments mentioned earlier have been confined to a test period of 5 min. It is of interest to consider the behavior over longer periods although, from the point of view of application as test method, shorter test periods will be preferred. Potential-time curves for two concentrations of NaCl in 0.04*N* NaOH are given in Fig. 9. It is seen that even in solutions below 0.03% NaCl, the potential falls after a sufficiently long period. But it is also observed that this time appears to increase exponentially. It is, therefore, concluded that, for all practical purposes, it will be justified to carry out the experiments for a period of 5 min.

Discussion

Kabanov and Leikis (5, 6) showed that if iron previously reduced in hydrogen atmosphere was subjected to anodic polarization in 2*N* NaOH solutions, three arrests were obtained which were characteristic of ferrous hydroxide formation, ferric hydroxide or oxide formation, and oxygen evolution, respectively. Mayne, Menter, and Pryor (7) found that these arrests were not observed in the case of iron carrying an oxide film formed during exposure to air. They, therefore, observed a sharp rise in anodic polarization at a current density of 15 $\mu a/cm^2$ to the potential of oxygen evolution. Subsequently

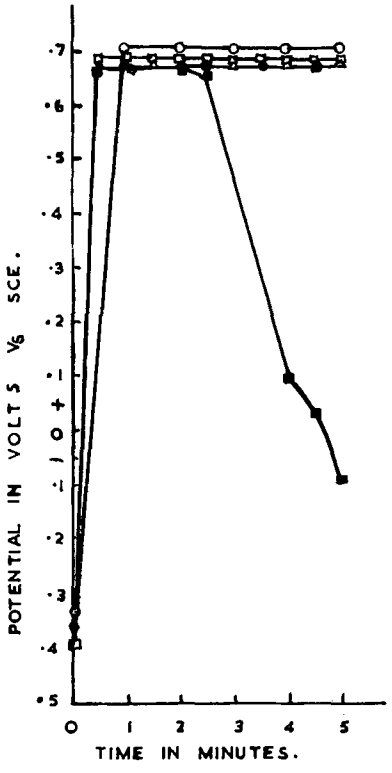

Fig. 8. Potential-time curves of mild steel in 0.04*N* NaOH containing NaCl when anodically polarized at 290 μa/cm^2.
O—O—O—O 0.02% NaCl
□—□—□—□ 0.02% NaCl solution, stirred
△—△—△—△ 0.02% NaCl solution, deaerated 15 min before experiment by bubbling nitrogen through the solution
●—●—●—● 0.03% NaCl solution, stirred
■—■—■—■ 0.04% NaCl solution, stirred.

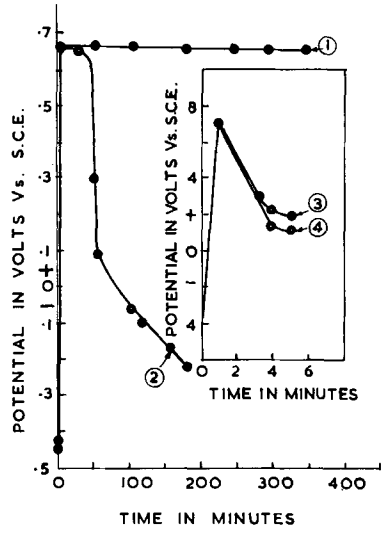

Fig. 9. Potential-time curves when anodically polarized at 290 μa/cm^2 in 0.04*N* NaOH containing 1, 0.01%; 2, 0.02%; 3, 0.03%; and 4, 0.05% NaCl.

Mayne and Hancock (8) showed that the current density at which the potential rose to the potential of oxygen evolution varied depending on the nature of the anion present. They showed that corrosion inhibitive anions such as acetate, benzoate, borate, etc., polarize the metal surface to the oxygen evolution potential at low current densities while the current density was very much higher in the case of sulfate and perchlorate solutions. They could not polarize in chloride solutions. On the basis of the detailed analysis of the polarization curve obtained with iron from which the air-formed oxide film was completely removed, as was done by Kabanov and Leikis, they concluded that the significant potential is the potential at which the second arrest correspond to the reaction:

$$2Fe + 6\,OH^- \rightarrow Fe_2O_3 + 3H_2O + 6e$$

is observed.

A solution which requires a very high current density in order to reach such a potential at which the dissolution reaction will give place to the reaction leading to film formation is obviously not likely to generate sufficient current in the corrosion process itself to reach the state of passive film formation. It is apparently from this point of view that the current density of 10 μa/cm^2 is employed in Mayne's studies. On comparing Fig. 1 and 2, it is seen that the same current density causes much less change on a freshly immersed specimen as compared to the specimen which had been left in solution for 24 hr. It is also readily seen from the typical S-shaped curves which are obtained in anodic polarization studies with metals which form passive films that the current density required to maintain the passive state is much smaller than the initial current to reach the passive state. Therefore, it is concluded that a corroding system must, if the analogy is correct, generate in the first instance sufficient current to reach the potential at which oxide film formation takes place. This potential is also referred to as "flade-potential" (9, 10) although flade-potential originally meant the resting potential before film breakdown occurred.

It is seen from Fig. 2 that in two different solutions like (*a*) 0.04*N* NaOH + 0.001% NaCl and (*b*) 0.04*N* NaOH +0.05% NaCl steel can be polarized to the potential of oxygen evolution within a few minutes by choosing the appropriate current density. If the time of measurement is increased, the current density may perhaps be reduced in the case of solution (*a*), but this is immaterial in the present discussion. It is, therefore, possible to find out, for the same time of measurement, at which current densities the different solutions containing increasing concentration of chloride are polarized to reach either the potential of oxide film formation or of oxygen evolution. When this was done and the log current density was plotted against chloride concentration, the curve shown in Fig. 3 is obtained. Despite the different conditions considered in Fig. 3, it is seen that a characteristic behavior is also indicated in Fig. 3, namely, in all cases the current density makes a jump after a particular chloride concentration is reached. Further, the current density and chloride concentration corresponding to the middle point are practically the same in all cases. Application of such a current density corresponding to the middle point should distinguish between a corrosive and inhibitive solution. Apparently, the jump should indicate the vast change in the current requirement for passivation to be brought about after a certain chloride concentration is reached. Solutions having

higher chloride concentration could not be polarized by the current density corresponding to the middle point. But solutions having chloride concentration corresponding to the region before the jump could be quickly polarized because they show this behavior at lesser current densities also.

The polarization behavior of the two solutions on both sides of the chloride concentration corresponding to the middle point are given in Fig. 4. As already pointed out, the time over which a certain potential is reached is a function of the current density. It is seen from the figure relating to a chloride concentration on the high side of the middle point that, although the potential rises to start with, there is a subsequent fall which is not observed in the case of the curves corresponding to the chloride concentration on the low side of the middle point. This is significant. When the metal is made positive, the field produced attracts the chloride ions to the metal surface. Adsorption of Cl^- on the metal-oxide film is facilitated by such conditions. If the chloride concentration is such that the rate of breakdown of the oxide film is higher than the rate of formation of the oxide film, then passive conditions will not be maintained. In this sense, the absence of a fall of potential may be said to be more characteristic of the inhibitive system than the rise to the particular potential. However, at the instant at which current is applied, in view of the well-known affinity of OH^- for metal surface and the presence of OH^- in much larger concentration at the vicinity of the electrode, conditions may be favorable for the potential to rise as is observed in Fig. 4 in both cases. However, when the field is maintained, adsorption of Cl^- will be facilitated, and the chloride concentration should not be such as to breakdown the oxide film. In a system in which no external current is applied, the same situation is expected to arise over a longer period of time.

The polarization curves for various chloride concentrations in Fig. 5 show that below a certain concentration the potential is maintained constant after the initial rise, but at higher concentrations the potential falls back. The highest concentration at which the potential remains constant and the lowest concentration at which the potential begins to fall are on the two sides of the middle point, as is to be expected. When the concentration of OH^- is changed, this behavior is also changed, which is to be expected. At concentrations lower than 0.01*N*, 0.02% NaCl cannot be tolerated. The method is also helpful in picking out the inhibitive system when both NaOH concentration and chloride concentration are varied. It is seen from Fig. 7 that out of the 9 concentrations only one is able to maintain the potential after the initial rise. In Fig. 9, the implications of such an approach are examined. On increasing the duration over which the observations are made, we get the interesting results that at concentrations of chloride lower than that corresponding to the middle point, there appears to be an exponential increase in the time over which the fall can be observed. The exact relationship, however, requires further study. If the corrosion current is considered to be less than 10 $\mu a/cm^2$, application of 290 $\mu a/cm^2$ may be said to accelerate the test more than 30 times.

Table II. Changes in potential with time in the absence of applied current of steel specimen immersed in 0.04*N* NaOH-NaCl solution

Concentration of NaCl, %	Potential in millivolts *vs.* SCE					
	1 hr	2 hr	3 hr	4 hr	1 day	2 days
0.001	—243	—237	—228	—231	—380	—460
0.01	—250	—250	—245	—250	—302	—302
0.02	—286	—279	—280	—284	—311	—331
0.03	—295	—293	—280	—268	—325	—354
0.04	—297	—306	—323	—306	—395	—
0.05	—320	—337	—354	—366	—402	—
0.1	—430	—470	—416	—416	—446	—454

The experiments with deaerated solutions shows that the extent of variation is not critical with regard to present study. Similarly, stirring appears to bring about only a minor change in the results obtained.

A comparison of the potential measurements in the absence of applied current with the polarization experiments can be made with the help of Table II.

It is seen from the table that in all cases the potential tends to become more negative with time. Further, as the chloride concentration is increased, the potential becomes more negative. These can hardly be useful criteria for distinguishing between the two types of solutions. It was earlier put forward (11) in connection with the potential changes following pretreatment of the metal surface that the potential will not change when both anodic and cathodic areas are increased or diminished and that diminution of the cathodic area as well as increase of anodic area can shift the potential in negative direction. Thus the

Table III. Total immersion tests, visual observations

Specimen: 3 × 2 in. mild steel panels; Test Solution: 0.04*N* NaOH solutions containing NaCl; room temperature.

NaCl concentration, %	When visible rust appeared on specimen after immersion	Appearance of the specimens at the end of two months
0.001	—	Unattacked
0.005	—	Unattacked
0.01	12th day	A tiny spot of rust formed at the top corner of one specimen. One spot at the edge of the second specimen; otherwise unattacked.
0.02	6th day	One elongated patch of rust on one side of one specimen. Three spots of rust on edge, one at the corner and suspension hole on the second specimen. Otherwise unaffected.
0.03	6th day	3 elongated patches of rust on the one specimen; and one elongated patch on the second specimen, otherwise unaffected.
0.05	1 day	Several elongated patches on both specimens.
0.1	4 hr	Widely attacked.
0.5	4 hr	Widely attacked covering almost the whole surface.

interpretation of changes in potential in the negative direction does not lend itself to an unambiguous explanation. It is not unlikely that with exposure to the medium the oxide film undergoes a certain amount of thickening in the inhibitive solutions which reduces the area over which cathodic reduction can take place and that the fall in potential is not indicative of corrosive conditions introduced. The visual observations made in direct corrosion tests for a period of two months, Table III, confirms this view.

Only at a concentration above 0.01% does the surface of the metal become susceptible to attack. The shift in potential in the negative direction in these cases is presumably due to the product of anodic areas where attack can take place.

Conclusions

The corrosive or inhibitive character of the neutral and alkaline solutions containing both corrosive and inhibitive constituents can be evaluated quickly by anodic polarization measurements at fixed current density. The criterion on which the current density should be chosen is indicated. The corrosive character is brought about by not maintaining the potential of the metal so that only reactions which do not involve dissolution can take place. It is likely that this method lends itself for application in the case of other systems where anodic inhibition takes place.

Acknowledgment

The authors wish to express their gratitude to Dr. K. S. G. Doss, Director, Central Electrochemical Research Institute, Karaikudi, for his keen interest in the study.

Manuscript received Feb. 27, 1961; revised manuscript received Aug. 7, 1961.

Any discussion of this paper will appear in a Discussion Section to be published in the December 1962 JOURNAL.

REFERENCES

1. T. P. Hoar in "Modern Aspects in Electrochemistry," Chap. IV, J. O'M. Bockris, Editor, Academic Press, New York (1954).
2. U. R. Evans, "The Corrosion and Oxidation of Metals," Edward Arnold & Co., London (1960).
3. Internationales Kolloquium uber die Passivatat der Metalle, Heilegenberg (1957).
4. P. Hancock and J. E. O. Mayne, *J. Appl. Chem.*, **7**, 700 (1957).
5. Kabanov and Leikis, *Acta Physico Chem. USSR.*, **21**, 769 (1946).
6. Kabanov, Burnstein, and Frumkin, *Discussions*, Faraday Soc., **1**, 259 (1947).
7. J. E. O. Mayne, J. W. Menter, and M. J. Pryor, *J. Chem. Soc.*, **1950**, 3229.
8. P. Hancock and J. E. O. Mayne, *J. Appl. Chem.*, **9**, 345 (1959).
9. U. F. Franck, *Z. Naturforschung*, **4A**, 378 (1949).
10. M. Stern, *This Journal*, **105**, 638 (1958).
11. K. S. Rajagopalan, *ibid.*, **106**, 112 (1959).

Dissolution of Zirconium in HCl-Methanol

J. R. Aylward and E. M. Whitener

Atomic Energy Division, Phillips Petroleum Company, Idaho Falls, Idaho

ABSTRACT

The dissolution of zirconium in HCl-methanol was studied potentiostatically as a function of HCl concentration and temperature. At low overvoltages the reaction is activation controlled and the rate independent of HCl concentration. In this region preferential grain boundary attack results in etching and separation from the electrode of finely divided particles of α-zirconium. At overvoltages above 0.5v a limiting current density is observed and the metal surface electropolished at HCl concentrations above 1.5M. The current for electropolishing decreases with increasing HCl concentration. The energy of activation at overvoltages of 0.0 and 1.0v (corrosion and electropolishing reactions) was found to be 16.5 and 7.7 kcal/mole, respectively.

The need to reprocess nuclear reactor fuel elements has given impetus to the study of the dissolution of zirconium, aluminum, and stainless steel. The present paper is concerned with the dissolution of zirconium, one of the more chemically resistant fuel element materials. The chemical inertness of zirconium is due to its strong affinity for oxygen and the resulting formation of protective oxide films. Of the anions, only fluoride forms a stronger bond with zirconium than oxygen, so that in aqueous systems zirconium readily dissolves in hydrofluoric acid. Because of the undesirable properties of this reagent in subsequent reprocessing steps, other media not containing fluoride were investigated.

Since the affinity of zirconium for anions decreases in the order $F^- > O^= > Cl^-$, a chloride system appeared to be the logical alternate. The formation of soluble zirconium compounds with chloride may be effected in two ways; (*a*), by changing the potential across the metal/solution interface; (*b*), by using nonaqueous systems. A preliminary investigation indicated that electrolytic dissolution in HCl-methanol [a combination of (*a*) and (*b*)] showed promise for dissolving zirconium as well as other reactor fuel element materials.

Potentiostatic determinations of the potential-current density relationship for zirconium in HCl-methanol solutions were undertaken to define the factors affecting the dissolution, the reactions taking place, and their mechanisms.

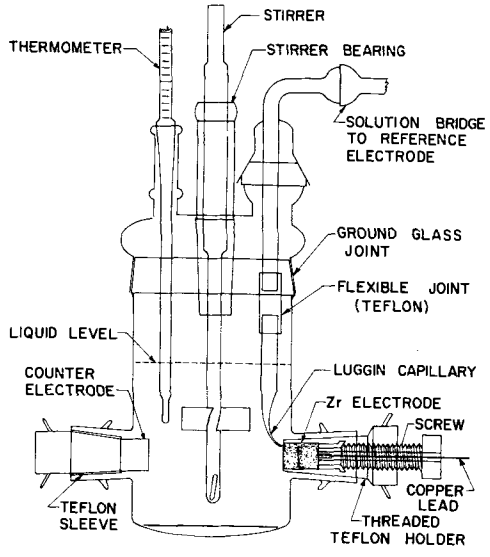

Fig. 1. Electrolysis cell

Experimental

The cell and electrode design used in this work are shown in Fig. 1. Vacuum annealed reactor grade zirconium rod was machined to fit tightly in the Teflon holder so that 1 cm² of electrode surface would be exposed to the solution. A 12-gauge copper wire was inserted into a nipple on the zirconium and crimped. In all cases the resistance from the electrode surface to the end of the copper lead was less than 0.002 ohm. A stainless steel screw mechanism facilitated removal of the zirconium from the Teflon holder on completion of an experiment. The holder was cut with a 19/38 standard taper (T) and provided with stainless steel hooks to give a leak proof fit in the polished T 19/22 glass joint of the cell. The counter electrode was machined from Hastelloy C (Ni 54.6%, Mo 16.0%, Cr 15.5%, Fe 5.5%, W 3.8%, Co 2.5%, Si and Mn 1.0%) to fit the other T 19/22 polished glass joint and a tapered Teflon sleeve used to prevent leaking. A solution bridge with a Luggin capillary connected the cell to a saturated calomel reference electrode (S.C.E.). The absence of appreciable error from IR drop and shielding effects with this capillary was confirmed by the use of interrupter techniques.

The solutions were freshly prepared by saturating absolute methyl alcohol with anhydrous hydrogen chloride gas at 15°C and diluting this with methanol to the desired concentration. Solution concentrations were determined by titration with sodium hydroxide. No attempt was made to eliminate atmospheric gases from the cell because any current resulting from the reduction of dissolved oxygen would be negligible compared to the lowest current density investigated (10^{-4} amp/cm²).

During a given experiment the solution temperature was controlled to within ± 1°C and the stirring speed maintained at 140 ± 10 rpm. Prior to each experiment, the exposed surface of the zirconium electrode was refaced by machining under an argon atmosphere. The resulting work-hardened surface was removed by dissolution at a high current density in an HCl-methanol solution of the same concentration as used in the ensuing experiment.

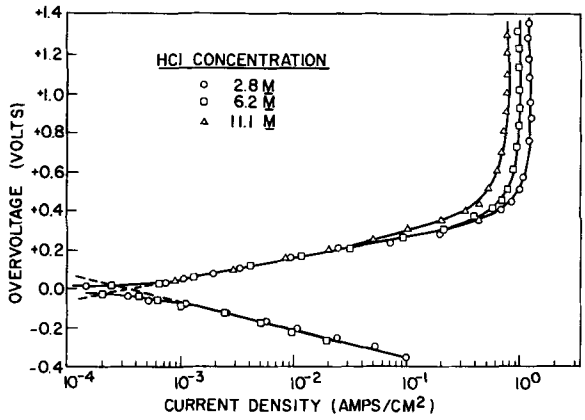

Fig. 2. Overvoltage at a zirconium electrode as a function of HCl concentration at 20°C.

An electronic potentiostat was used to obtain the potential-current density curves. Measurements were initiated at the steady-state mixed potential (approximately −0.54v with respect to the S.C.E.). The potential was increased in 50 mv increments to +1.0v, then decreased stepwise back to the steady-state mixed potential. The cathodic potential-current density curve was measured after completion of the anodic measurements.

This procedure was repeated three times for each run, and the current found to be reproducible to within ±10%. Duplicate experiments were also carried out for each temperature and HCl concentration to check the over-all reliability of the data.

Results

The anodic and cathodic overvoltage[1]-current density relationships for a zirconium electrode in HCl-methanol solutions are shown in Fig. 2 as a function of HCl concentration at 20°C. At low overvoltage values a Tafel relationship is obtained indicating that both the anodic and cathodic reactions are activation controlled. The Tafel slopes at 20°C are 0.115 and 0.15v, respectively. It can be seen that the current density at constant overvoltage in this region is independent of HCl concentration. The corrosion rate, as given by the intersection of the Tafel lines extrapolated to zero overvoltage, is also independent of HCl concentration within the limits of reproducibility (3 to 5×10^{-4} amp/cm²). The reproducibility of the steady-state mixed potential (−0.54v *vs.* S.C.E. for 6.0M HCl) was in the order of ± 10 mv. Because of this, it was difficult to determine with any accuracy the variation of the steady-state mixed potential as a function of solution composition. However, there appeared to be a trend toward more positive values with increasing HCl concentration (30 mv in going from 1M to 10M HCl).

Zirconium dissolution in the Tafel region (from zero to approximately +0.4v) results in an etched surface and is accompanied by the separation of a finely divided black residue from the electrode

[1] Overvoltage is defined in this case as the difference between the potential at any current density and the steady-state mixed potential.

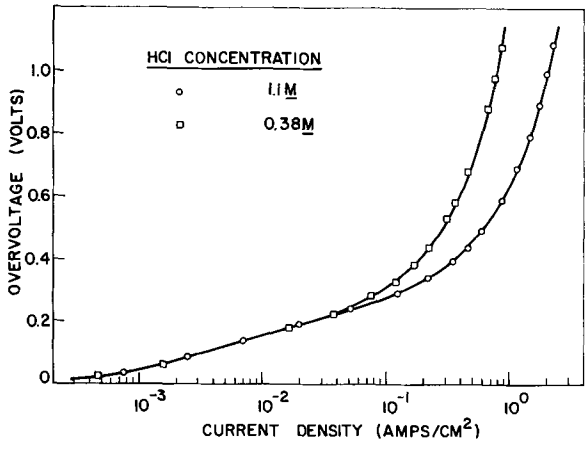

Fig. 3. Anodic overvoltage of a zirconium electrode in dilute HCl-methanol solutions at 20°C.

which is pyrophoric and gives an x-ray pattern corresponding to alpha-zirconium. This zirconium residue is quite passive in HCl-methanol solutions in contrast to bulk zirconium which corrodes at a rate of 3.4×10^{-4} amp/cm². The amount of residue formed decreases with increasing overvoltage.

At high anodic overvoltages ($> +0.5$v) the current density is independent of potential, and the value of this limiting current density decreases with increasing HCl concentration. Also, in this region, the zirconium surface is electropolished and complete dissolution is attained (no undissolved residue).

As shown in Fig. 3, the anodic behavior of zirconium in more dilute HCl-methanol solutions (<1.5M) is different at high overvoltages in that the limiting current density is not well defined and its value at constant overvoltage decreases with decreasing HCl concentration. In this case the surface at high overvoltages is etched (as opposed to electropolished), but the over-all surface is brighter than the etched surface obtained at low overvoltages.

A comparison of the different surface features obtained under the various dissolution conditions mentioned above is shown in Fig. 4. In A and B

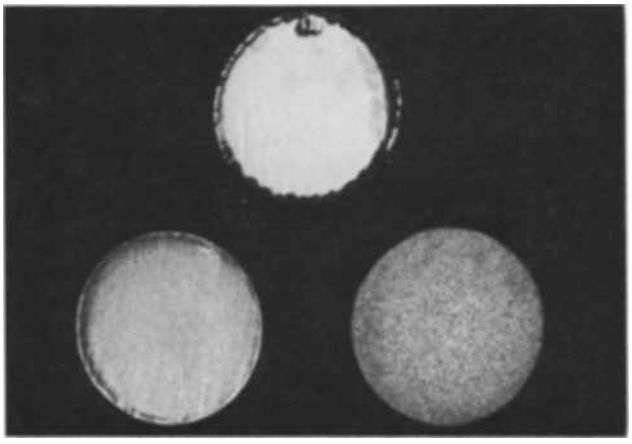

Fig. 4. Electrode surface obtained under various dissolution conditions: A. (top) 6.0M HCl, +0.8v overvoltage, ≈1 amp/cm²; B. (left) 1.0M HCl, +0.8v overvoltage, ≈1 amp/cm²; C. (right) 6.0M HCl, +0.3v overvoltage, ≈100 ma/cm².

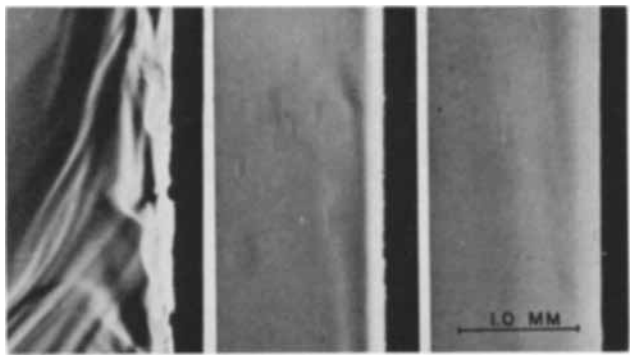

Fig. 5. Schlieren photographs of metal/solution interface during dissolution in HCl-methanol: A (left), 6.0M HCl, 1 amp/cm²; B (center) 1.0M HCl, 1 amp/cm²; C (right) 6.0M HCl, 100 ma/cm².

of Fig. 4 the effect can be seen of a higher dissolution rate at the electrode boundary. This is due to the presence of a considerable product concentration gradient which plays a predominant role in controlling the reaction rate in the limiting current density region. The fact that the gradient is larger at the electrode edge results in a higher dissolution rate at this point. In the region where the reaction is activation controlled an even dissolution rate is observed over the whole surface (electrode C of Fig. 4). Schlieren photographs of the metal/solution interface under conditions corresponding to A, B, and C of Fig. 4 are shown in Fig. 5A, B, and C, respectively. The light areas represent regions of higher refractive index (dissolution product concentration). In Fig. 5A the streaming off of the viscous layer is characteristic of electropolishing, while in B a quiescent concentration gradient typical of concentration polarization is evident. Both A and B were taken at the same current density (≈1 amp/cm²). Figure 5C obtained at approximately 100 ma/cm² (activation-controlled region) shows no significant concentration gradient.

Figure 6 shows the effect of temperature on the anodic overvoltage curves in 6.0M HCl-methanol. As is to be expected, the reaction rate in the activation and electropolishing region increases as the temperature is raised. From these data the energy of activation at overvoltages of zero and 1.0v corresponding to the corrosion and electropolishing

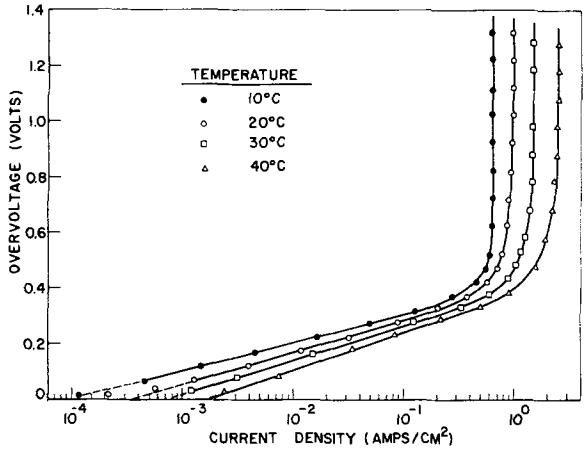

Fig. 6. Effect of temperature on the anodic overvoltage of zirconium in 6.0M HCl-methanol.

reactions was calculated to be 16.5 and 7.7 kcal/mole, respectively.

Discussion

When zirconium is placed in an HCl-methanol solution, dissolution of the metal takes place at a very slow rate to give as products hydrogen gas and a mixture of the various chlorozirconium methoxides. This over-all reaction is shown in [1] where x has values from 0 to 4.

$$Zr + (4-x)HCl + xCH_3OH \rightarrow ZrCl_{(4-x)}(OCH_3)_x + 2H_2 \quad [1]$$

Evidence for this reaction is supported by the identical optical spectra of dissolver solutions and solutions prepared by adding zirconium tetrachloride to methanol. Reaction [1] is believed to take place in two principal steps. First, zirconium reacts with hydrogen chloride to form zirconium tetrachloride and hydrogen gas at the metal/solution interface.

$$Zr + 4HCl \rightarrow ZrCl_4 + 2H_2 \quad [2]$$

The next step [3] takes place primarily in the bulk of the solution (at HCl concentrations >1M) and has little if any effect on the dissolution rate.

$$ZrCl_4 + xCH_3OH \overset{K_x}{\rightleftharpoons} ZrCl_{(4-x)}(OCH_3)_x + xHCl \quad [3]$$

At low HCl concentrations (<1M) and high overvoltage there is some indication that chlorozirconium methoxides may be formed directly at the metal/solution interface. This possibility will be discussed later.

The equilibrium constants K_x for reaction [3] were determined by Simmons and Hansen (1), ($pk_1 = 1.62$, $pk_2 = 5.18$, $pk_3 = 10.4$, and $pk_4 = 18.2$). From these data it is obvious that $ZrCl_4$ and $ZrCl_3OCH_3$ are the main species in solution.

Reaction [2] can be divided into two half reactions; one representing an oxidation [4] and the other a reduction [5]

$$Zr + 4Cl^- \rightarrow ZrCl_4 + 4e \quad [4]$$

$$4H^+ + 4e \rightarrow 2H_2 \quad [5]$$

In reaction [4] it is not to be construed that the reactive species is the chloride ion as such because molecular HCl is present at a higher concentration and may serve just as well. However, if the equilibration $HCl \rightleftharpoons H^+ + Cl^-$ is rapid the two would be kinetically equivalent.

When reactions [4] and [5] are activation controlled their respective rates i_a and i_c expressed in terms of current density are given by

$$i_a = i_0' \exp\left(\frac{1}{b_a}\eta\right) \quad [6]$$

and

$$i_c = i_0' \exp\left(-\frac{1}{b_c}\eta\right) \quad [7]$$

where η is the overvoltage, b_a and b_c constants, and i_0' the reaction rate at zero overvoltage. At zero overvoltage the anodic [4] and cathodic [5] rates are equal and, therefore, i_0' is the corrosion rate (reaction [2]). The cell current density, I, will be given by the difference in the rates of reaction [4] and [5]. Thus,

$$I = i_a - i_c = i_0'\left[\exp\left(\frac{1}{b_a}\eta\right) - \exp\left(-\frac{1}{b_c}\eta\right)\right] \quad [8]$$

This particular form of the equation gives negative values for the cell current when zirconium is the cell cathode and positive when it is the anode.[2]

Under circumstances where a limiting current density is observed, *e.g.*, in the electropolishing region, it can be shown (2, 3) that the equation expressing the current density as a function of overvoltage takes the form

$$I = \frac{i_a - i_c}{1 + i_a/i_l} = \frac{i_0'\left[\exp\left(\frac{1}{b_a}\eta\right) - \exp\left(-\frac{1}{b_c}\eta\right)\right]}{1 + i_0'/i_l \exp\left(\frac{1}{b_a}\eta\right)} \quad [9]$$

where i_l is the limiting current density for electropolishing. From the experimental data the corrosion current and the limiting current density (for electropolishing) are given by

$$i_0' = \exp\left[\, 20.09 - \Delta H_0^+/RT\right] \quad [10]$$

$$i_l = C^{-0.462} \exp\left[\, 14.02 - \Delta H_l^+/RT\right] \quad [11]$$

where C = HCl concentration, $\Delta H_0^+ = 16.5$ kcal/mole and $\Delta H_l^+ = 7.7$ kcal/mole. Equation [9] reduces to the usual Tafel relationship when $\eta > \pm 50$ mv and $i_a \leqq i_l/10$.

The stoichiometric number ν for the anodic reaction can be calculated from the equation

$$\nu = \frac{b_a n\mathbf{F}}{2RT} \quad [12]$$

where n is the number of electrons transferred during one act of the over-all process (equal to four from reaction [4]) and the other terms have their usual significance. Equation [12] assumes a symmetrical energy barrier. The stoichiometric number calculated from the average experimental anodic Tafel slope ($2.3\ b_a = 0.115 \pm 0.005$v) and Eq. [12] is 3.96 ± 0.16. From this it is concluded that the rate-determining step in the activation-controlled region for the anodic process represented by Eq. [4] must take place four times for each act of the over-all reaction. However, the behavior of the steady-state mixed potential and the corrosion rate with changing HCl concentration cannot easily be associated with any simple sequence of reaction steps for the over-all process. The change in the steady-state mixed potential of approximately 30 mv in going from 1*M* to 10*M* HCl is not of real significance because of possible changes in the liquid junction potential (HCl methanol | | KCl

[2] In Fig. 2 this sign convention is disregarded.

aqueous) with HCl concentration. Unfortunately, the Ag, Ag_2Cl_2 electrode was found to be unsuitable as a reference in concentrated HCl-methanol because of the high solubility of Ag_2Cl_2.

The independence of the corrosion rate on HCl concentration can possibly be explained by assuming complete coverage of the zirconium surface with specifically adsorbed Cl^-. This adsorption step could be rapid at the potentials and HCl concentrations involved (4). The next step would then result in the formation of a positively charged zirconium chloride species which could react further with chloride ion or methanol in the double layer to form a soluble product. Thus, the reaction may be divided into three parts:

$$M\text{-}Zr + pCl^- \rightarrow M\text{-}ZrCl_p^{-p} \quad [13a]$$

$$M\text{-}ZrCl_p^{-p} \rightarrow M\text{-}ZrCl_p^{+(4-p)} + 4e \quad [13b]$$

$$M\text{-}ZrCl_p^{+(4-p)} + (4-p)Cl^- \rightarrow M + ZrCl_4 \quad [13c]$$

The stoichiometric number of four indicates that the rate-determining step may be associated with the formation of the zirconium chloride species of [13b].

Under conditions of electropolishing it is generally believed that a solid film is formed on the metal surface which in the steady state is dissolving as fast as it is formed (5, 6). The rate-determining step is, in this case, the "physical" dissolution of the film and, therefore, independent of electrode potential. Increasing the potential merely increases the steady-state film thickness. Since the film is the controlling factor in the dissolution, the differing rates of removal of cations from the metal lattice due to their special positions within the lattice are no longer of significance. On the other hand, in the nonelectropolishing region preferential attack at grain boundaries, etc., results in etching and the separation of small bits of metal from the surface. (The reason for the passivity of this undissolved residue in HCl-methanol solutions is not apparent.) Fedot'ev and Grilikhes (6) attribute electropolishing to the formation of oxide films rather than salt films. This may be true for the most part in aqueous systems, but we do not believe it to be the general case in nonaqueous solutions. It is difficult to see how increasing the HCl concentration would decrease the dissolution rate of an oxide film (see Fig. 2), but this effect is conceivable if the film were a chloride of zirconium.

At low HCl concentrations and high current densities the transport of HCl to the electrode surface becomes rate determining (concentration polarization), and the value of the limiting current density decreases as the HCl concentration is decreased (see Fig. 3). Under these conditions the electrode surface cannot be completely covered with adsorbed Cl^- so that it becomes possible for the solvent (methanol) to play a direct part in the dissolution mechanism with the resulting formation of chlorozirconium methoxides at the metal/solution interface. This, combined with the fact that the rate of transport of Cl^- to the metal surface would increase with increasing potential (in the absence of supporting electrolyte), may explain the ill-defined limiting current density observed at low HCl concentrations.

Acknowledgment

The authors wish to thank Dr. G. L. Booman for designing the potentiostat used in this work and Dr. H. T. Hahn for helpful discussions. This work was done under the auspices of the U.S. Atomic Energy Commission.

Manuscript received July 3, 1961; revised manuscript received Sept. 27, 1961.

Any discussion of this paper will appear in a Discussion Section to be published in the December 1962 JOURNAL.

REFERENCES

1. C. R. Simmons and R. S. Hansen, *J. Phys. Chem.*, **59**, 1072 (1955).
2. J. O'M. Bockris, "Modern Aspects of Electrochemistry," No. 1, Chap. 4, Butterworth, London (1954).
3. W. A. Mueller, *This Journal*, **107**, 157 (1960).
4. Ja. M. Kolotyrkin, *ibid.*, **108**, 209 (1961).
5. T. P. Hoar, "Modern Aspects of Electrochemistry," No. 2, Chap. 4, J. O'M. Bockris, Editor, Academic Press Inc., New York (1959).
6. N. P. Fedot'ev and S. Ya. Grilikhes, "Electropolishing, Anodizing and Electrolytic Pickling of Metals," Translated by A. Behr, Robert Draper Ltd., Teddington (1959).

Effect of Partial Dissolution of the Oxide Film on the Aqueous Corrosion Resistance of Zircaloy-2

S. Kass and D. B. Scott

Bettis Atomic Power Laboratory,[1] Pittsburgh, Pennsylvania

ABSTRACT

The aqueous corrosion resistance of corrosion-tested Zircaloy-2 was found to decrease markedly after vacuum heating to dissolve the oxide film partially. Although a complete explanation of the accelerated corrosion is not proposed, several possible mechanisms are presented.

During the fabrication of Zircaloy-2 components for pressurized water reactors, it is occasionally desirable to remove the oxide film formed by various corrosion tests to ascertain that the corrosion resistance has not been reduced by processing methods. A potential method for accomplishing this utilizes zirconium's high affinity for oxygen. The components are vacuum annealed for sufficient time to dissolve the oxide film into the metal completely and to minimize the oxygen gradient in the vicinity of the surface. Although the feasibility of the process has been demonstrated (1), the work described herein was performed to determine the corrosion resistance of previously corrosion tested Zircaloy-2 which was improperly vacuum annealed and produced only partial dissolution of the oxide film.

Experimental

Specimens of Zircaloy-2,[2] measuring 1.5 x 0.5 x 0.1 in. prepared from one section of strip, were corrosion tested for 3 or 14 days in 360°C water using techniques and precautions previously noted (2). After the weight change measurements were recorded, specimens were annealed in vacuum (dynamic system, less than 0.1μ Hg pressure) for 40 or 60 min at 590°C or for 60 or 80 min at 700°C. All specimens were then returned for corrosion testing in 360°C water. Weight gains were determined periodically during the final corrosion exposure. The corrosion product was not removed after the vacuum treatment or during the subsequent corrosion exposure.

Vacuum annealing times and temperatures were selected in accordance with ref. (1) to produce incompletely dissolved oxide films.

Results

Corrosion test results depicted graphically in Fig. 1 and 2, show that Zircaloy-2 corrodes at an accelerated rate when the oxide film formed during the initial corrosion exposure is partially dissolved in the base metal by thermal treatment. Re-examination of the data when plotted in the conventional manner on logarithmic scales (Fig. 3) shows the influences of annealing times and temperature. Coupons annealed at 590°C after the initial corrosion test showed little or no variation of weight gain with variation in annealing time. Similarly, little or no dependence of corrosion kinetics on annealing time is noted for coupons treated at 700°C. Large differences in the corrosion behavior as functions of annealing temperature, however, are apparent. Coupons which were tested for 3 days at 360°C and subsequently annealed at 590°C showed weight gains of 9-12 mg/dm^2 in the first 3 days of re-exposure. In comparison, coupons which were not vacuum annealed showed weight gains of only 4 mg/dm^2 after 3 days of re-exposure. The same general trends are noted for specimens tested for 14 days, vacuum annealed at 700°C, and re-cor-

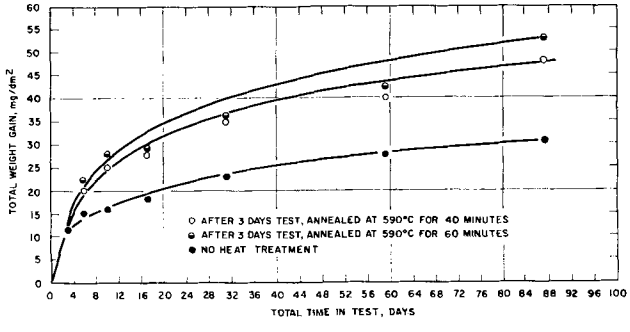

Fig. 1. 360°C water corrosion of Zircaloy-2 after vacuum annealing at 590°C.

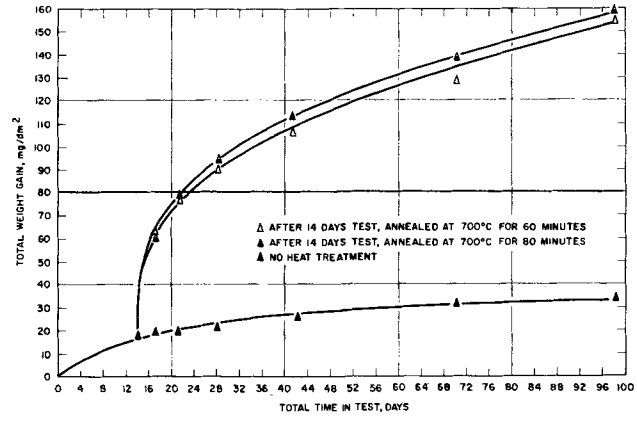

Fig. 2. 360°C water corrosion of Zircaloy-2 after vacuum annealing at 700°C.

[1] Operated for the U. S. Atomic Energy Commission, Bettis Atomic Power Laboratory, Westinghouse Electric Corporation.

[2] A zirconium base alloy containing 1.5% Sn, 0.14% Fe, 0.10% Cr, and 0.05% Ni. U. S. Patent No. 2,772,964.

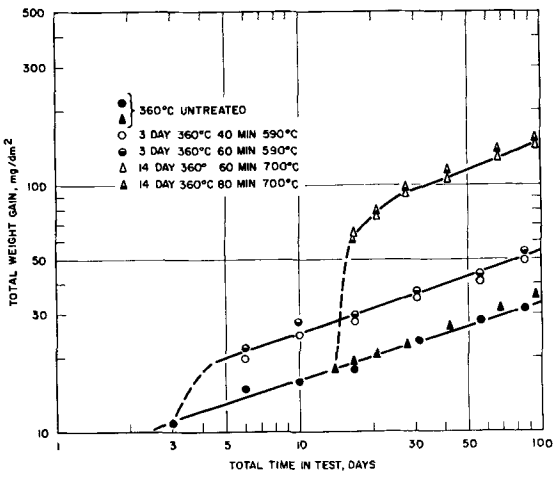

Fig. 3. Logarithmic plot of 360°C water corrosion of Zircaloy-2 after vacuum annealing at 590° and 700°C.

rosion tested. Treated specimens showed weight gains of 41-45 mg/dm^2 after 3 days of re-exposure, while those not treated showed gains of only 1-2 mg/dm^2.

Corrosion films on the coupons tested for 3 days and treated at 590°C were black throughout the test; those treated at 700°C were gray-black. No evidences of spalling or flaking were observed. It should be noted that the weight changes of the specimens not vacuum annealed agree with previously reported Zircaloy-2 curves (2-4).

Discussion

It is not believed that the heating alone causing modifications in the material microstructures produced the higher corrosion rates as it has been shown that the corrosion resistance of Zircaloy-2 does not vary with heat treatment provided temperatures are maintained below 815°C (5).

Chirigos and Thomas observed that the oxide grows by the inward diffusion of oxygen ions through the film and that new oxide is produced at the metal-oxide interface (5). The corrosion initially follows a quasi-cubic relationship with time, and the rate decreases as the oxide film thickens. As vacuum-annealing treatments reduce the oxide film thickness through the mechanisms of oxygen diffusion into the metal (6), the oxygen uptake rate during subsequent corrosion should increase. This explanation appears to be an oversimplification of the phenomena observed if Fig. 2 is re-examined. During the first 14 days of corrosion, where the specimens were initially in the bright etched condition (unoxidized surfaces), an average weight gain of 18 mg/dm^2 was obtained. Three days of corrosion exposure after heating the oxidized samples in vacuum produced an additional weight gain of 44 mg/dm^2, a value far in excess of what would be expected if complete oxide film dissolution was caused by the thermal treatment.

Another factor which must be considered is the oxygen enrichment of the metal at the metal-oxide interface. Calculations of the oxygen uptake and gradient in the metal produced by the treatments have shown the 700°C specimens to contain in excess of (2 w/o) oxygen at the interface and for some distance below, while values for the 590°C specimens approximate 0.1 w/o. Since Rubenstein and co-workers have shown that oxygen enriched Zircaloy-2 corrodes more rapidly than normal material (7), it is suggested that after subsequent corrosion exposure the vacuum annealed specimens should initially corrode more rapidly than specimens not containing an oxygen-rich area at the interface. This explanation is untenable if the growth of the oxide film is controlled by the diffusion of oxygen through the film. The explanation is reasonable (*a*) if marked changes in film characteristics occurred during the vacuum anneal, or (*b*) if the growth of the oxide film is controlled by other factors in addition to simple diffusion.

The suggested change in kinetics and accelerated corrosion rates may be explicable on the basis of the memory effect noted by Thomas and Kass (4) in experiments where Zircaloy-2 was initially tested in steam at 400°C and then transferred to water at 360°F. Specimens showed a peculiar tendency for the corrosion rate characteristics of the high temperature to persist for considerable times after transfer to the lower temperature. The memory phenomenon appeared to be explicable on the basis of anion diffusion as the oxide film is believed to grow by the diffusion of ions via oxygen ion vacancies from the water/oxide interface to the metal/oxide interface. It was expected that an oxide film of a given thickness formed at a higher temperature would have a greater oxygen ion vacancy gradient than when formed at a lower temperature. It was not surprising, then, that on returning the specimens to the lower temperature an initially higher corrosion rate operated until the excess anion vacancy gradient was removed. Analogous behavior is noted here. In the case of the 3-day test (Fig. 1) it is seen that the untreated specimens gained about 4 mg/dm^2 (an increase of 36%) while the 60 min, 590°C treatment produced weight gains of 11 mg/dm^2 (an increase of 100%) after the return to corrosion test. The accelerated corrosion rate associated with the excess vacancy gradient must also result in a continued rapid rate in the generation of vacancies. Thus the passage of many vacancies is required before the corrosion rate decays to normal. It is noted in Fig. 1 and 2 that times in excess of 84 days are required before the corrosion rate of the heat-treated specimens approaches the rate of the untreated specimens.

The authors agree with Misch and Gunzel (6) who studied the effects of vacuum heating and electrical conductivity of the oxide films formed on zirconium that more evidence concerning the ZrO_2 structure, diffusion rates, and electrical properties is desirable.

Manuscript received May 11, 1961; revised manuscript received Oct. 12, 1961. This paper was prepared for delivery before the Detroit Meeting, Oct. 1-5, 1961.

Any discussion of this paper will appear in a Discussion Section to be published in the December 1962 JOURNAL.

REFERENCES

1. S. Kass and D. B. Scott, "Dissolution of Zircaloy-2 Oxide Oxide Films," AEC Report, Zirconium Highlights, ZH-4 (1958).

2. S. Kass, *Corrosion*, **19**, 93t (1960).
3. B. Lustman and F. Kerze, Jr., "The Metallurgy of Zirconium," McGraw-Hill Book Co., Inc., New York (1955).
4. D. E. Thomas and S. Kass, *This Journal*, **103**, 478 (1956).
5. J. G. Goodwin, L. S. Rubenstein, and F. L. Shubert, "Symposium on Newer Metals," American Society for Testing Materials, pp. 123-142 (1960).
6. J. P. Pemsler, *This Journal*, **105**, 317 (1958).
7. L. S. Rubenstein, J. G. Goodwin, and F. L. Shubert, *ASM Transactions Quarterly*, 1 (1961).
8. R. D. Misch and F. H. Gunzel, Jr., *This Journal*, **105**, 15 (1959).

Physical and Dielectric Properties of the Metal-Silicon Dioxide-Silicon System

J. L. Sprague, J. A. Minahan, and O. J. Wied

Research Laboratories, Sprague Electric Company, North Adams, Massachusetts

ABSTRACT

Thin film capacitors using silicon dioxide as the dielectric material have been prepared by the thermal oxidation of silicon. The physical and optical characteristics of the oxide dielectric are given, and the permittivity and loss tangent of the capacitors are shown as functions of a-c frequency and d-c bias. The dielectric properties are seen to be functions of the conductivity type and resistivity of the substrate silicon.

It is possible to fabricate a capacitive device with silicon dioxide as the dielectric material by thermally oxidizing silicon at high temperatures. This paper describes the results of physical measurements made on the dielectric film, presents new dielectric measurements on the metal-silicon dioxide-silicon system, and gives a qualitative explanation for the shape of the observed dielectric curves.

The measured capacitance *vs.* applied d-c bias curves are similar to those reported by Moll (1), except that at low frequencies we have observed a unique capacitance minimum in many cases. Such a minimum was found by Brown (2) in measurements of the differential surface capacitance of a germanium sample, and predicted by Pfann and Garrett (3) for the more general case of the metal-insulator-semiconductor system. In each of these studies a change in the character of a space-charge region at the semiconductor surface was given as the reason for the observed capacitance variations. This mechanism is similar to that described by Uhlir (4) to explain the operation of the nonlinear p-n junction capacitor. In addition to the variation of capacitance with d-c bias, we have observed distinct dispersion effects in the frequency range studied. These effects are due, it is believed, to charge exchange between the bulk of the silicon and surface states or an inversion region at the surface of the semiconductor. Such charge exchange has been discussed by Lehovec (5).

Experimental Techniques and Results

Physical characteristics of the silicon dioxide film.—All measurements were made on films formed by the thermal oxidation of silicon at 950°C. Disks, 0.6 cm diameter, of single crystalline, noncompensated silicon were first cleaned by briefly etching them in a hydrofluoric acid-nitric acid solution followed by a series of recirculating hot deionized water, cold deionized water, and methyl alcohol rinses. The disks were then oxidized in a furnace in which steam was introduced at atmospheric pressure by passing argon through a heated deionized water bubbler.

The dielectric constant of the films was determined as follows. First, the capacitance of a parallel-plate capacitor consisting of optically polished low resistivity n-type silicon as one electrode, the thermally grown silicon dioxide film as the dielectric, and an evaporated metal plate as the counter-electrode was measured. Then the oxide thickness was determined by multiple-beam interferometry, and the permittivity of the silicon dioxide layer calculated using the standard parallel-plate capacitance formula. By this method, a relative permittivity of 3.82 $\pm$ 0.02 was found. For comparison, Von Hippel (6) found a value of 3.78 for several different samples of fused silica and quartz.

Silicon dioxide films were stripped from the silicon substrate by etching with hydrogen bromide (7). This method is similar to one described by Tannenbaum (8), except that the bromide is used as the etching agent rather than chlorine. The films showed an absence of crystalline structure when studied by means of x-ray diffraction and optical microscopy and gave an infrared absorption spectra identical to that of fused silica. The absorption spectra, in the u.v. and visible regions, of films which had been irradiated with u.v. light, high energy x-rays, and gamma rays were also studied. These spectra showed an absence of anion vacancy absorption, indicating that, as expected, the films were of very high purity.

Finally, the index of refraction of the films was found to be equal to 1.458 by matching them *vs.* different solutions of normal-amyl-phthalate and carbon disulfide. Comparing with other forms of noncrystalline silicon dioxide, opaline silica ($SiO_2 \cdot X\ H_2O$) has an n = 1.40 — 1.46 which increases

with decreasing hydration, while lechatelierite, a natural glassy form of silica, has an index of refraction of 1.458—1.462. Therefore, we conclude that the thermal oxide film formed was a high-purity form of amorphous or glassy silica, similar to "dry" opal or lechatelierite.

Dielectric properties of the metal-silicon dioxide-silicon system.—Dielectric measurements were made on a standard General Radio 716-C Schering bridge with a Rhode and Schwarz Tunable Detector and Dumont Type 347 Oscillator. Included in the bridge circuit was a network which permitted a known d-c voltage to be applied across the sample. The capacitors measured were constructed as follows: 0.6 cm diameter disks of single crystalline noncompensated silicon were oxidized for 5 hr at 950°C by the method outlined above. This gave an oxide film thickness of around 1.14 x 10^{-4} cm. Then the oxide was removed from one side of each disk by lapping or sandblasting and metal plates were evaporated, one directly onto the silicon as an ohmic contact and one onto the oxide film as a counter electrode. The capacitive area of the devices was determined by the area of the metal plates which was 0.178 cm^2.

Figures 1 and 2 show the frequency dependence of capacitance and loss angle, measured at zero d-c bias, for n- and p-type capacitors, respectively. The capacitance of n-type capacitors is seen to be frequency invariant while the loss angle increases with increasing resistivity indicating that there is an ohmic contribution due to the bulk silicon. The reason why the 1 ohm-cm and 20 ohm-cm loss angle curves in Fig. 1 cross is not clearly understood, but this may be due to different resistance values for the ohmic contacts on the two samples. The p-type units, on the other hand, show a strong

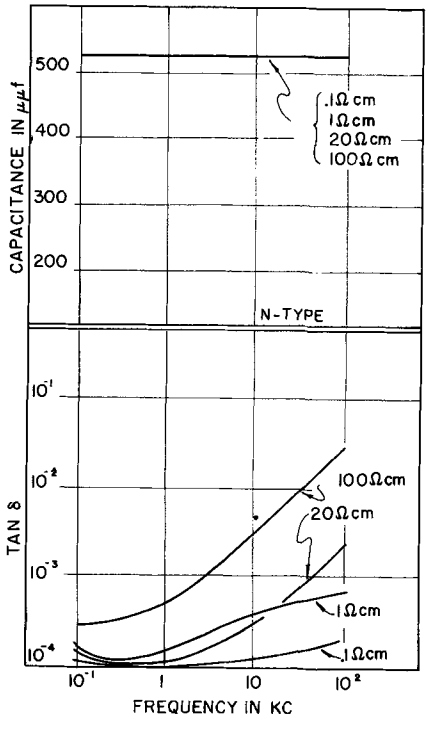

Fig. 1. Frequency dependence of capacitance and loss angle, at zero bias, of n-type capacitors.

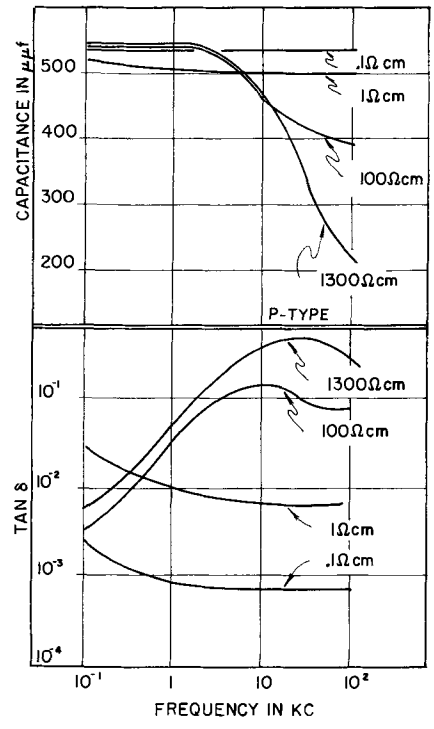

Fig. 2. Frequency dependence of capacitance and loss angle, at zero bias, of p-type capacitors.

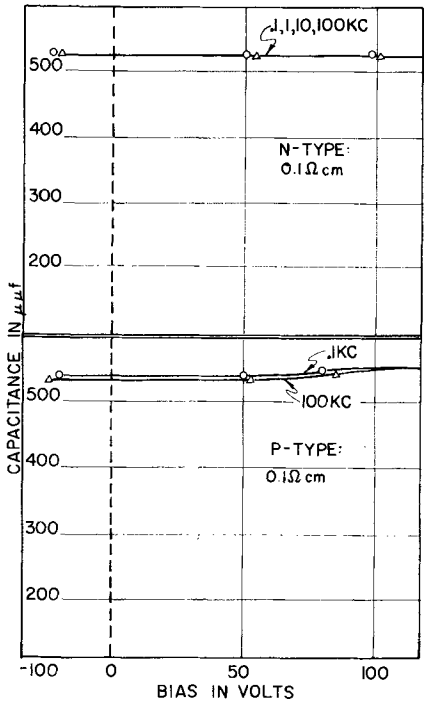

Fig. 3. Bias and frequency dependence of capacitance of 0.1 ohm-cm capacitors.

capacitance variation, particularly with the higher resistivity material, and the over-all dielectric response indicates a relaxation type phenomenon. It appears, in Fig. 2, that the relaxation frequencies for the 0.1 ohm-cm and 1 ohm-cm material are lower than the lowest measured frequency of 10^{-1} kc. This would account for the intersection of the 100 and 1300 ohm-cm curves with those for the 0.1 and 1 ohm-cm material.

Figure 3 shows the bias and frequency dependence of capacitance for capacitors made from 0.1

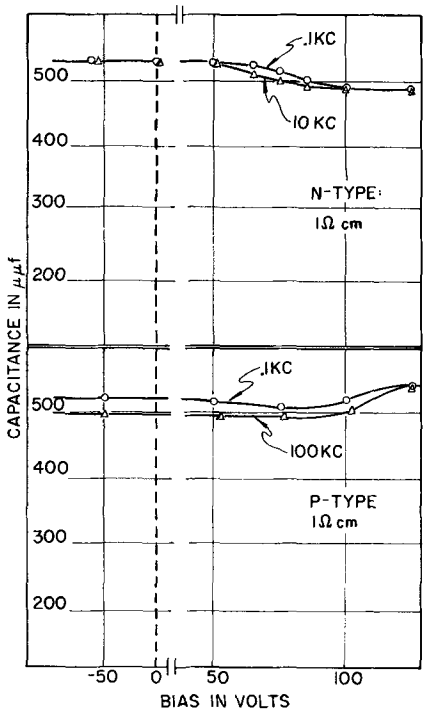

Fig. 4. Bias and frequency dependence of capacitance of 1 ohm-cm capacitors.

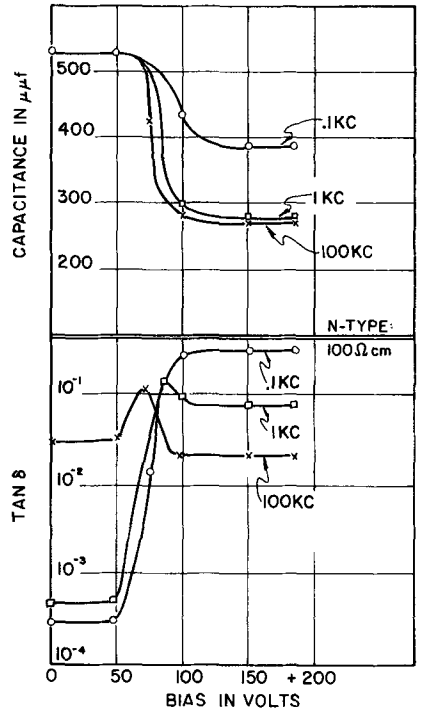

Fig. 5. Bias and frequency dependence of capacitance and loss angle for 100 ohm-cm n-type capacitors.

ohm-cm silicon. The sign of the potential indicates the polarity of the d-c voltage applied to the ohmic silicon contact. As is seen, with n-type silicon capacitance is bias and frequency independent, while with the p-type material there is a slight frequency dispersion and increase in capacitance starting around 70v. As Fig. 4 shows, these effects are amplified with 1 ohm-cm material, both types of capacitors demonstrating a bias and frequency dependence. However, whereas the capacitance of n-type units decreases with increasing bias, that of p-type capacitors increases at high positive bias.

Figures 5 and 6 show the bias effects on capacitance and tangent δ for 100 ohm-cm material, n- and p-type, respectively. Here the bias and frequency sensitivity is considerable, and there is evident a certain mirror-image symmetry between the two types of capacitors. While no capacitance minimum was observed with these particular n-type units, others have shown such a minimum in the lower frequency curves (see Fig. 8B). The loss

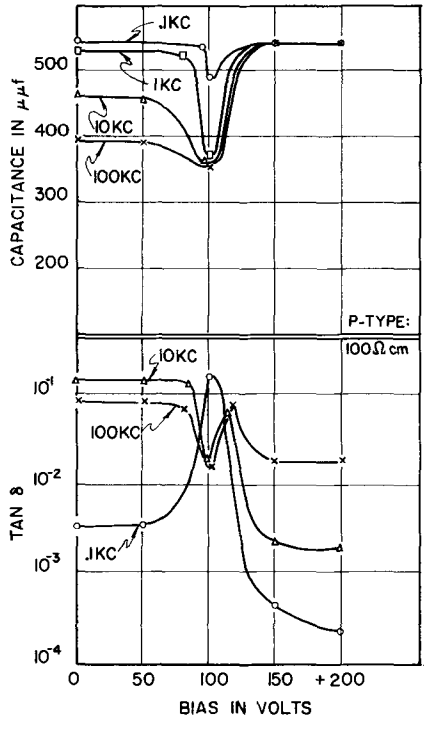

Fig. 6. Bias and frequency dependence of capacitance and loss angle for 100 ohm-cm p-type capacitors.

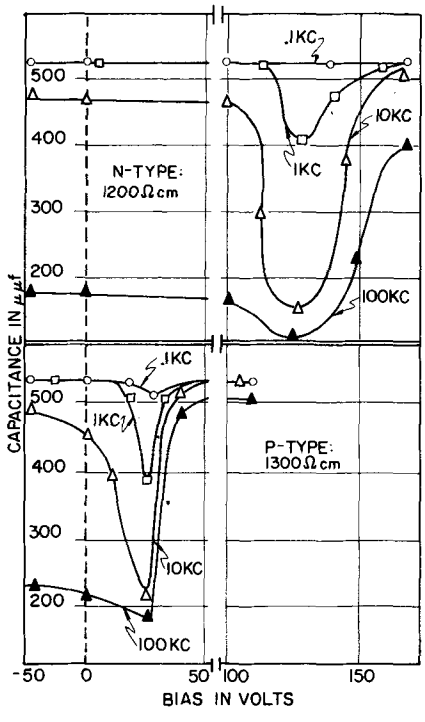

Fig. 7. Bias and frequency dependence of capacitance of 1000 ohm-cm capacitors.

angle curves are seen to be exceedingly complex, and the exact cause of these complexities is not clearly understood at this time, as is pointed out below.

As would be expected, these effects are even greater with 1000 ohm-cm material. This is seen clearly in Fig. 7. Interestingly, however, the 1200 ohm-cm n-type curve shows that this material has been converted to p-type during the oxidation process. This was possibly due to the introduction of boron into the system from Pyrex glassware associated with the quartz furnace tube. This phenomena has been encountered by Law (9) during his studies on the surface properties of vacuum cleaned silicon.

Theoretical Discussion

The capacitance *vs.* d-c bias p-type curves at high frequencies and the corresponding n-type curves which have been discussed so far are similar to those of Moll (1). That is, they show an increasing or decreasing capacitance, respectively, as bias is increased and the absence or near absence of a capacitance minimum. On the other hand, the lower frequency p-type curves all show a definite capacitance minimum, as was encountered in the work of Brown (2) and predicted by Pfann and Garrett (3). It is evident, therefore, that the dielectric response of the metal-silicon dioxide-silicon system is strongly dependent on the measurement frequency, and this fact must be taken into consideration in evolving any theoretical model for the system.

Figure 8A shows a theoretical curve, after Garrett and Brattain (10), of capacitance *vs.* surface potential for an oxide capacitance of 287 $\mu\mu$f in series with the space charge capacitance of 100 ohm-cm n-type silicon. Figure 8B shows, for comparison, experimental curves of capacitance *vs.* bias for the metal-silicon dioxide-silicon system in which the oxide capacitance is also 287 $\mu\mu$f, and the bulk starting material was 100 ohm-cm n-type silicon. These latter curves differ from the experimental n-type curves in Fig. 5 only in that the oxidation time was longer (19 hr) and therefore the oxide formed thicker (2.06×10^{-4} cm), and that here a capacitance minimum was observed. The theoretical and lower frequency experimental curves are seen to be similar in shape.

The shape of the theoretical curve is due to the fact that, with n-type silicon, as one goes from a strongly positive to strongly negative surface potential the space charge at the surface of the semiconductor goes from an accumulation to a depletion and finally into an inversion region. The capacitance minimum is caused by decreasing accumulation and depletion capacitances followed by an increasing inversion capacitance as Y goes from strongly positive to strongly negative. The expressions used in calculating the theoretical curve are given in the appendix at the end of the paper.

Figure 9 shows a proposed equivalent circuit for the metal-silicon dioxide-silicon system. In it, C_o is the oxide capacitance, C_d is the depletion region capacitance, C_a is the accumulation region capacitance, r_{si} is the bulk silicon resistance, and Σ is a

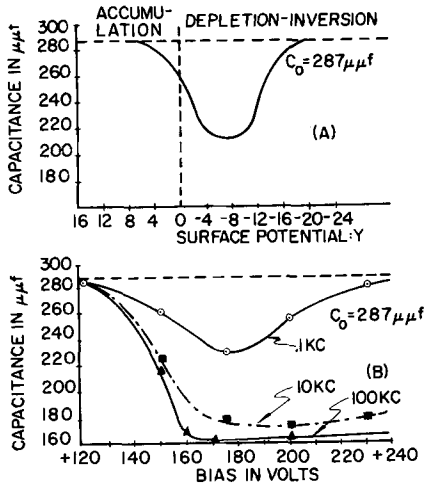

Fig. 8A. Theoretical curve of capacitance vs. surface potential for oxide capacitance in series with space charge capacitance for 100 ohm-cm n-type silicon.

Fig. 8B. Bias and frequency dependence of capacitance of metal-silicon dioxide-silicon (100 ohm-cm, n-type) system.

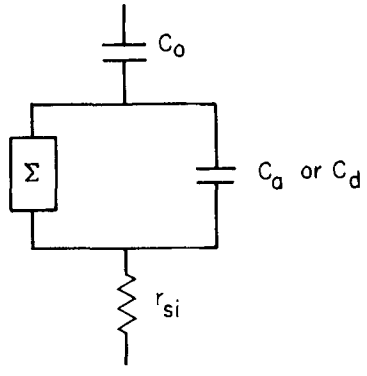

Fig. 9. Equivalent circuit for metal-silicon dioxide-silicon system

complex admittance. Σ has contributions from an inversion region capacitance, from charge leakage through the space charge region, and from charge exchange between the semiconductor bulk and surface states at the silicon-silicon dioxide interface or an inversion region at the silicon surface. Using this equivalent circuit, one can explain the shape of the curves in Fig. 8B as follows. It is postulated that there is sufficient positive charge, at zero bias, in donor type surface states to cause an accumulation region on the semiconductor surface. At very low frequencies one approaches a bias independent capacitance corresponding essentially to C_o. This is due to the fact that the impedance of Σ is much less than that of C_d or C_a at these frequencies and they are essentially shunted by it. At higher frequencies, for example at 0.1 kc, one observes a curve with a capacitance minimum similar in shape to the theoretical curve. Here as one increases the potential on the silicon, the space charge goes from an accumulation to a depletion to an inversion region. Finally, at high frequencies, one sees only the series combination of C_o and C_d or C_a due to the high relative impedance of Σ. In the experimental n-type curves where a capacitance minimum has not been observed (for example, Fig. 4 and 5) apparently there was insufficient d-c potential to form an inversion region.

With p-type silicon the effect is reversed. Here the positively charged surface states cause an inversion region to be formed on the semiconductor, and increasing the potential on the silicon causes the space charge region to go from inversion to depletion and finally to accumulation. Thus, the mirror symmetry between n- and p-type capacitors.

The decreasing amount of capacitance change with bias as the silicon resistivity decreases is readily explained by the fact that as bulk doping increases, C_a and C_d increase also. At a high enough doping level they become so large that one only observes the series oxide capacitance. On the other hand, the position of the capacitance minimum is determined by the charge density in the donor-type surface states. The complex form of the loss angle curves and frequency dispersion of capacitance are due to Σ. The exact form of Σ is presently not completely understood. It is believed, however, that the frequency dispersion in the inversion capacity region is due to the relaxation effects involved in minority carrier exchange between the inversion layer and bulk of the semiconductor through the depletion region, while dispersion in the depletion or accumulation region is due to minority and majority carrier exchange through the space charge region between the bulk silicon and surface states at the silicon-silicon oxide interface. A complete understanding of Σ should make it possible to interrelate curves of capacitance *vs.* total charge and *vs.* space charge in a similar manner to the way in which conductance change and charge are related in field effect studies. In the present studies, if one assumes that at high frequencies only an accumulation or depletion capacitance is observed in series with C_o, then from the curves in Fig. 8 one can calculate the surface state charge as a function of Y for the accumulation and depletion conditions. Such calculations have been made by Lehovec for 100 ohm-cm n-type silicon (5). Ultimately, simultaneous capacitance and field effect measurements should serve as the best check of the model.

Conclusions

The dielectric response of the metal-silicon dioxide-silicon system is strongly dependent on the resistivity and conductivity type of the substrate silicon. This is due to the presence of a space charge region at the surface of the semiconductor underneath the oxide. When low resistivity silicon (0.1 ohm-cm n-type or lower resistivity p-type) is used, the observed dielectric response is essentially that of the silicon dioxide film. Capacitors made using such material exhibit the excellent dielectric properties of high-purity amorphous silica: bias and frequency insensitivity, high insulation resistance, high power factor, low temperature coefficient, radiation resistance, and high stability. On the other hand, as the resistivity of the silicon is increased one observes an increasing dielectric contribution due to the space charge region in the silicon. When high resistivity material, such as 100 ohm-cm, is used, considerable capacitance change with both bias and frequency is observed. The present difficulty in using such capacitors in varactor applications is in reproducibly controlling the charges in the silicon surface states and therefore controlling the position of the capacitance minimum. This problem is probably not insolvable, however.

When the exact relationships between dielectric response and the nature of the silicon surface are understood, measurements of the type described in this paper should become a valuable tool in studying silicon surfaces.

Acknowledgment

The authors are grateful to K. Lehovec of our laboratories for many helpful discussions and suggestions during the course of this work.

Manuscript received Aug. 28, 1961; revised manuscript received Oct. 27, 1961. This paper was prepared for delivery before the Indianapolis Meeting, April 30-May 3, 1961.

Any discussion of this paper will appear in a Discussion Section to be published in the December 1962 JOURNAL.

REFERENCES

1. J. L. Moll, *I.R.E. Wescon Conv. Rec.*, Part 3, Electron Devices, 32 (1959).
2. W. L. Brown, W. H. Brattain, C. G. B. Garrett, and H. C. Montgomery, "Semiconductor Surface Physics," R. H. Kingston, Editor, p. 111, University of Pennsylvania Press, Philadelphia (1956).
3. W. G. Pfann and C. G. B. Garrett, *Proc. I.R.E.*, **47**, 2011 (1959).
4. A. Uhlir, *ibid.*, **46**, 1099 (1958).
5. K. Lehovec, J. Minahan, A. Slobodskoy, and J. Sprague, Report on Twenty-First Annual Conference on Physical Electronics (M.I.T.), p. 80 (March 29-31, 1961).
6. A. R. Von Hippel, Editor, "Dielectric Materials and Application," John Wiley & Sons, New York (1954).
7. J. L. Sprague and O. J. Wied, to be published.
8. E. Tannenbaum, *J. Appl. Phys.*, **31**, 940 (1960).
9. J. T. Law, *J. Phys. Chem. Solids*, **14**, 9 (1960).
10. C. G. B. Garrett and W. H. Brattain, *Phys. Rev.*, **99**, 376 (1955).

APPENDIX

Symbols

C_a, accumulation capacitance $= A[e^2\epsilon\epsilon_o n_o/2kT]^{1/2}\, e^{Y/2}$, farad
$C_{F.B}$, space charge capacitance at $Y = 0$ $= A[e^2\epsilon\epsilon_o\, n_i(n_o/n_i + n_i/n_o)/kT]^{1/2}$, farad
C_d, depletion capacitance $= A[e\epsilon\epsilon_o\, n_i(n_o/n_i - n_i/n_o)/2(-V_s)]^{1/2}$, farad
C_i, inversion capacitance $= A[e^2\epsilon\epsilon_o\, n_i^2/2n_okT]^{1/2}\, e^{-Y/2}$, farad
A, area, cm^2
e, electronic charge, coulomb
ϵ, relative permittivity of silicon
ϵ_o, permittivity in free space, farad/cm
n_o, concentration of electrons in body of semiconductor, cm^{-3}
k, Boltzmann constant, volt-coulomb/°K
T, temperature, °K
Y, surface potential $= e(\psi_s - \psi_o)/kT = e\,V_s/kT$
ψ_s, electrostatic potential at surface of semiconductor
ψ_o, electrostatic potential in bulk of semiconductor
n_i, intrinsic carrier concentration, cm^{-3}

Properties of Evaporated Film Capacitors

F. S. Maddocks and R. E. Thun

IBM Command Control Center, Federal Systems Division, Kingston, New York

ABSTRACT

The preparation of film capacitors by evaporation is described utilizing the following dielectric materials: silicon monoxide, silicon dioxide, magnesium fluoride, lanthanum fluoride, cerium fluoride, cerium dioxide, and zinc sulfide. The dielectric constants and loss tangents of these materials are presented as functions of the deposition parameters, and the contribution of the lead and condenser plate losses to the apparent loss tangents is shown. The necessary evaporation conditions are discussed for optimizing the dielectric properties of the chosen insulator material. For cerium fluoride, a deposition method utilizing a controlled partial decomposition is described yielding dielectric constants up to $\epsilon/\epsilon_0 = 300$ without an undue increase of the capacitor losses.

In the field of microelectronics, development of component and interconnector networks produced by the vacuum evaporation of metals, dielectrics and, to a more limited degree, semiconductors has made rapid progress during recent years. Dielectrics serve two purposes in these "thin film" circuits: they are used as insulating layers between crossing or superimposed conductor patterns and as capacitor dielectrics. In both cases, uniformity, good adhesion to substrates and other film materials, high electric breakdown strength, and low dielectric losses are desirable. The requirements regarding the permittivity, however, differ to a certain extent: a low dielectric constant is preferable for insulation films, a high dielectric constant for capacitor dielectrics.

The choice of dielectric film materials is usually limited to inorganic compounds, since dielectric films are often deposited jointly with materials requiring high deposition or annealing temperatures. The selection of suitable dielectric materials has been hampered, however, by the lack of data on the electrical and mechanical properties of most inorganics evaporable without decomposition. In view of this situation, this study was aimed at the compilation of data on the electrical and mechanical properties of the most common dielectric film materials and the development of a suitable capacitor dielectric of high permittivity, *e.g.*, $\epsilon/\epsilon_0 \geq 100$.

Deposition Techniques

A New York Air Brake vacuum system of the type R2H with an 18-in. glass bell jar was used for film deposition. Its 6-in. diffusion pump yields a vacuum of 1×10^{-5} torr or better in less than 1 hr. The depositions were performed between 10^{-6} and 10^{-5} torr.

Dielectric film thickness was monitored during deposition by recording the change of optical reflectance at a wavelength of 4358Å with an optical densitometer (Welch Densichron) coupled to a L&N millivolt recorder. Metal capacitor plate and land thicknesses were controlled by monitoring their resistance. Tolansky's multiple interference method was used to obtain the accurate film thickness after removal of the samples from the bell jar.

The coating chamber was equipped with a mask changer to permit deposition of the capacitor array shown in Fig. 1 without breaking the vacuum. In this mask changer (Fig. 2), two 1×3-in. substrates are positioned over a rotatable disk with apertures for four masks. Two masks yield the upper and

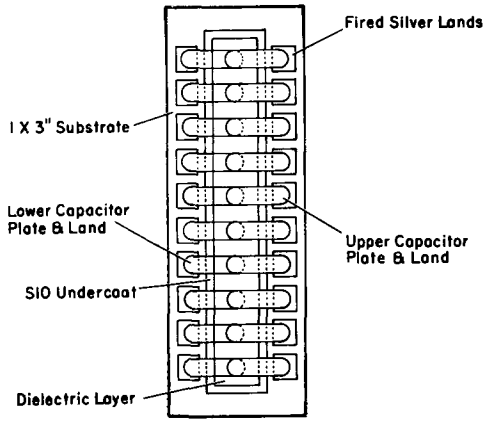

Fig. 1. Evaporated capacitor array

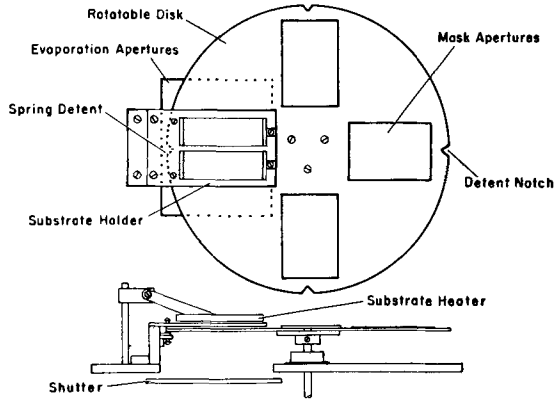

Fig. 2. Mask changer

lower metal capacitor plates, one a silicon monoxide undercoat and a protective top layer, and the fourth the dielectric film to be studied. The geometric registration is accurate to ±0.002-in. The substrate can be heated to a temperature of 400°C, measured by thermocouple. A source changer permits evaporation of the different layers from a single source location for a more uniform thickness distribution. It consists of a turntable with outside drive and rubber-sealed feedthrough.

Graphite crucibles have been used successfully for the evaporation of aluminum, but better results were obtained with boron nitride-titanium diboride crucibles made by the National Carbon Company. The dielectrics have been evaporated from a number of different source arrangements. Except as noted later, best results were achieved with a high-purity aluminum oxide crucible (Morganite "Triangle RR"[1] recrystallized alumina) covered with an aluminum oxide aperture plate with an orifice diameter of 0.25 in. The installation of such an aperture plate creates a space of more nearly saturated vapor over the evaporating surface and reduces thereby the decomposition of the evaporant. The crucible is heated by radiation from an enclosing graphite crucible, which in turn is induction heated. The source temperature was monitored by an optical pyrometer.

Substrate Requirements

Early attempts to evaporate capacitors on cleaned, but otherwise unprepared microscope slides yielded a large number of film pinholes, accompanied by electrical shorts between the capacitor plates. Microscopic examination of the glass slides showed extended areas of increased surface roughness which probably represented recrystallization zones. By applying an undercoat of silicon monoxide, however, a sufficiently smooth surface could be obtained to eliminate pinhole formation.

The yield of short-free capacitors was further increased by a proper choice of the metal used for the capacitor plates. Metals of high evaporation temperature such as chromium, nickel, germanium, and iron resulted in a higher percentage of failures, probably due to penetration of the dielectric by the highly energized metal atoms. Gold, an obvious choice because of its low evaporation temperature and high conductivity, also gave poor results. Its high mobility may have caused shorts by grain-boundary diffusion. Of all metals investigated, aluminum yielded the fewest shorts. This can probably be explained by its low evaporation temperature combined with a decreased surface mobility caused by the affinity of aluminum for oxide bonds. Copper, another obvious choice, was not investigated due to the known poor adherence of copper films when not backed by thin chromium layers. With aluminum plates and lands, a 95-100% yield of short-free capacitors could be obtained with most dielectrics investigated. In all cases, the same substrate cleaning procedure was followed, using detergent, water, and alcohol washes under ultrasonic agitation.

[1] Trademark of Morganite, Incorporated.

Electrical Measurements

The dielectric constants and loss tangents of the capacitor samples were measured in the frequency range from 120 cps to 5 mc on two different commercial capacitor bridges. At 120 cps, 1 kc and 10 kc, an ESI Universal Impedance Bridge with adaptors gave capacitance and loss tangent directly. From 30 kc to 5 mc, a Wayne-Kerr 601 Bridge, using a Rhode and Schwarz SBF Signal Generator and USVH Null Detector, yielded the capacitance and the effective parallel resistance, from which the loss tangent was calculated. The dielectric constant was calculated from the capacitor plate area and the thickness of the dielectric without correcting for edge effects, which are small compared to the experimental error.

Film Structure Determination

The crystallographic investigation of the film structures was performed by electron diffraction and x-ray diffraction. Samples for electron diffraction and electron microscopy were prepared on freshly cleaved rock salt substrates which were first coated with a thin amorphous silicon monoxide layer to prevent a preferential crystal growth of the dielectric films.

The optical constants n (refractive index) and k (absorption coefficient) were obtained from reflectance and transmittance measurements of separately prepared dielectric samples on a Beckman DK-2 spectrophotometer, covering the wavelength region from 3000 to 10,000Å.

In cases where the purity of the deposited dielectric films was questionable, samples were submitted to an analysis by x-ray fluorescence and emission spectroscopy.

Dielectric Losses at High Frequencies

The dielectric constant and loss tangent values were measured on layers forming the dielectric of vacuum deposited capacitors. To separate the ohmic lead and plate losses from the true dielectric losses, the electric resistance of leads and plates must either be kept negligible or be independently determinable. In the study of dielectric films, no completely satisfactory experimental solution exists for either approach.

Attempts to obtain low-resistance capacitor plates were not successful. On test capacitors consisting of an optically flat copper electrode coated with the dielectric and a second electrode in contact with the first, the remaining surface irregularities often caused electrical shorts. In addition, the air film at the second dielectric-metal interface caused errors in the electrical measurements. Increasing the thickness of evaporated capacitor plates and leads by electroplating was also unsuccessful, since the surface roughness of thick platings resulted in electrical shorts.

Better results were obtained by determining lead and plate losses with a method given by McLean

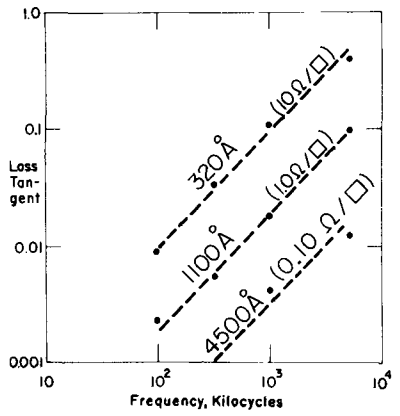

Fig. 3. Loss tangent vs. frequency for evaporated capacitor plates and leads of various thickness in series with a loss-free 1000 pfd air capacitor. The "ohm per square" values given indicate the resistivities of the films, whose dimensions were ⅛ x ⅜ in. (3 squares).

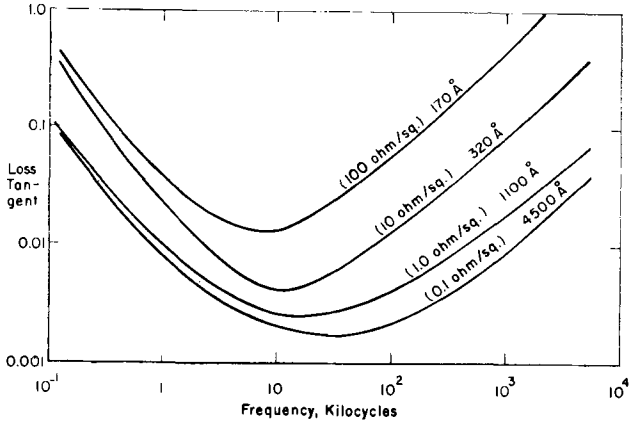

Fig. 4. Loss tangent vs. frequency for an evaporated magnesium fluoride 1000 pfd capacitor with plates and leads of various thicknesses.

(1). The loss tangent of a series capacitance-resistance network is given by

$$\tan \delta = \omega C \, (R_s + R'_s) \qquad [1]$$

where R_s is the "effective series resistance" of the dielectric, and R'_s is the ohmic resistance of the leads and plates. At high frequencies, R_s becomes small against the ohmic resistance R'_s, and the slope of the loss tangent curve approaches 45° in a log log plot. This has been shown by placing evaporated leads and plates, with no dielectric layer, in series with a loss-free air capacitor and comparing the loss tangent curve obtained (Fig. 3) with the one obtained using identical leads and plates containing an evaporated magnesium fluoride dielectric layer (Fig. 4). Figures 3 and 4 also show the dependence of the capacitor losses on the thickness of the leads and plates.

Equation [1] can be solved simultaneously at two points on the 45° slope of the loss tangent curve yielding R'_s, since it can be assumed that $\omega C R_s$ is approximately constant over this interval. With the R'_s values obtained, the loss tangent curve is then corrected point by point to yield the loss tangent of the dielectric itself as a function of frequency. The dielectric losses given in Fig. 6 have been obtained by this method.

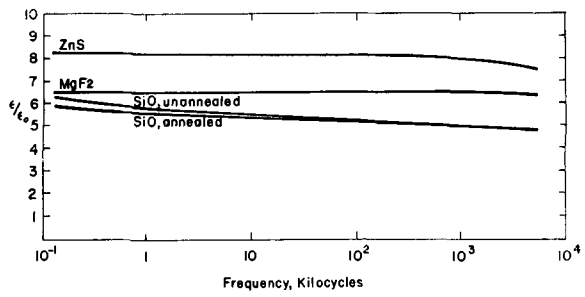

Fig. 5. Dielectric constant vs. frequency for evaporated dielectric materials.

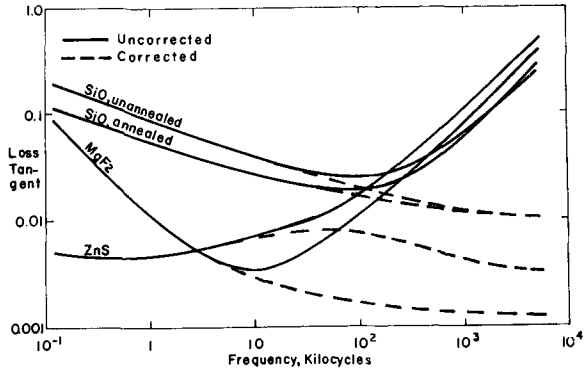

Fig. 6. Loss tangent vs. frequency for 1000 pfd evaporated capacitors. The solid line indicates the loss tangent measured on the evaporated capacitors, the dashed line the corrected loss tangent of the dielectric obtained by the method outlined in the text.

Experimental Results

Dielectrics of low dielectric constant.—The following dielectric materials have been studied: cerium dioxide, cerium fluoride, lanthanum fluoride, magnesium fluoride, silicon dioxide, silicon monoxide, and zinc sulfide.

Several of these materials were found to be unsatisfactory as capacitor dielectrics. Cerium dioxide decomposed strongly when evaporated from aluminum oxide crucibles. Its behavior when evaporated from metal crucibles will be discussed later. Lanthanum fluoride and silicon dioxide films were hygroscopic. These silicon dioxide films were produced by evaporating silicon monoxide in oxygen at a pressure of 5×10^{-4} torr.

The remaining materials all were satisfactory to a greater or lesser extent. Their dielectric constants as a function of frequency are shown in Fig. 5, and their loss tangents as a function of frequency in Fig. 6. Silicon monoxide has been previously used as a capacitor dielectric (2). Its dielectric constant of 6.0 could be reproduced only to about ±10%, due to the strong dependence of the film composition on the deposition parameters. However, its d-c breakdown strength of 2×10^6 v/cm is excellent, even exceeding that of mica (4×10^5 v/cm). This fact and the low dielectric constant make silicon monoxide an excellent choice for an insulation material.

Zinc sulfide yielded the comparatively high dielectric constant of 8.2, good reproducibility (± 5%), and small low-frequency losses when deposited from an aperture source. However, its d-c

breakdown strength of 2×10^5 v/cm is an order of magnitude lower than that of silicon monoxide.

Magnesium fluoride, with a dielectric constant of 6.5, good reproducibility, excellent d-c breakdown strength (2×10^6 v/cm), and very low d-c leakage current (less than 1 μa at 2×10^6 v/cm) exhibited the best dielectric properties of the materials tested. These values were achieved with films evaporated on room temperature substrates. The films were hard and durable, even in thicknesses up to 2μ.

A limited amount of accelerated life test data is available for one of these materials, silicon monoxide. These data indicate that the dielectric material itself is unaffected by thermal stress (—55° to 100°C), relative humidity (20-95%), and power dissipation (0 to 10 w/in.^{2}). However, corrosion of the metal plates and leads causes failure if not protected against excess humidity in combination with the other stresses.

Dielectrics of high dielectric constant.—In a certain range of deposition conditions, cerium dioxide, cerium fluoride, and lanthanum fluoride yielded films exhibiting a thickness dependent dielectric constant much higher than normal. Because of the ease of preparation, cerium fluoride was the most extensively investigated of these compounds. When evaporated from a tantalum crucible at 1450°C, cerium fluoride films have an apparent dielectric constant at 1 kc varying from $\epsilon/\epsilon_0 = 52$ at 1100Å to $\epsilon/\epsilon_0 = 280$ at 5900Å, as shown in Fig. 7. Powder x-ray diffraction measurements made from these films show the structure of bulk cerium fluoride, and measurements of the refractive index yield, in agreement with previously published data (3), a value for the dielectric constant of 2.7 at optical frequencies. Cerium fluoride films evaporated from aluminum oxide crucibles under otherwise identical conditions exhibit a nonthickness dependent dielectric constant of 8.2 at 1 kc.

Careful x-ray diffraction measurements obtained directly from the evaporated films show that films evaporated from oxide crucibles are amorphous, while the metal crucibles yield polycrystalline films, with the c-axis oriented in the plane of the substrate, and the a- and b-axes randomly oriented. Cerium fluoride has a hexagonal cell (a = 7.112Å, c = 1.279Å). Since no significant change in the degree of orientation could be observed with increasing film thickness, the thickness behavior of the dielectric constant cannot be explained by assumptions based on crystalline anisotropy. Ferroelectricity is also ruled out, since it too does not explain the observed thickness dependence of the dielectric constant.

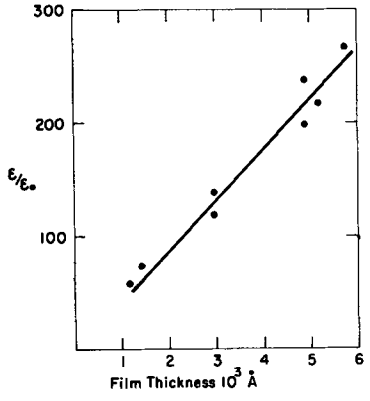

Fig. 7. Apparent dielectric constant vs. dielectric thickness at 1 kc for cerium fluoride evaporated from refractory metal crucibles.

A decomposition of the deposit leading to the formation of metallic grains imbedded in the dielectric could yield a high dielectric constant (4). However, in order to explain the large effect observed, the percentage of conducting material would have to be so high that the films would be optically opaque, and insulation would almost certainly not be achieved. For a 5900Å film having an apparent dielectric constant of 280 at 1 kc, the equivalent dielectric thickness would be 150Å and conductor thickness 5750Å.

As a mechanism for this thickness dependence, the possibility of the presence of Schottky barrier layers at the metal-dielectric interfaces was therefore investigated. Parker and Wasilik (5) have found the presence of barrier layers at the electrode-crystal interfaces of a single crystal of rutile and could thereby explain the high, thickness-dependent dielectric constant at low frequencies.

The Schottky barrier layer is formed at the interface of materials of different surface work functions. Equalization of the Fermi levels of the two interface materials results in a carrier depletion in the slightly semiconducting dielectric, forming the barrier layer. The depth of the layer D is determined by the difference in work functions θ, by the applied voltage V, and the carrier density N:

$$D = \left[\frac{2\epsilon(\theta - V)}{eN}\right]^{1/2} \qquad [1]$$

ϵ being the static dielectric constant of the semiconducting dielectric and e the electron charge.

A slight catalytic decomposition of the cerium fluoride at the metal crucible walls is probably causing the formation of charge carriers necessary to obtain the proposed barrier layers in the investigated rare earth compounds.

The equivalent circuit of an evaporated capacitor having barrier layers at the electrode-dielectric interfaces is shown in Fig. 8. C_1, R_1 and C_3, R_3 represent the capacitance and resistance of the barrier layers, and C_2, R_2 that of the dielectric layer. When a voltage is applied in a forward direction for the barrier layer (C_3, R_3), the resistance R_1 becomes much larger than R_2 and R_3, and the capacitance is given by:

$$C_1 = \epsilon A/D_1 \qquad [2]$$

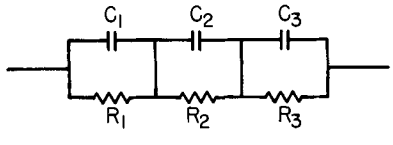

Fig. 8. Equivalent circuit of a capacitor having barrier layers at electrode-dielectric interfaces.

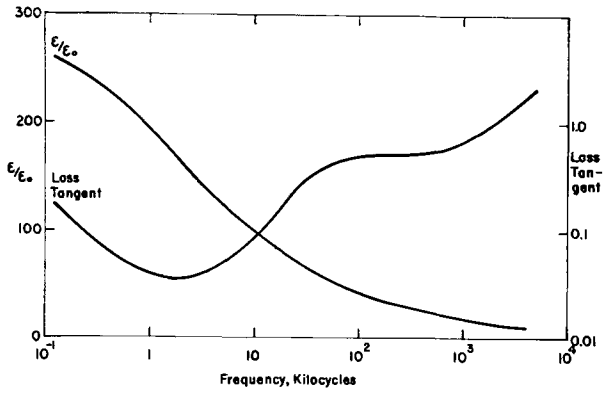

Fig. 9. Apparent dielectric constant and loss tangent vs. frequency for a 2300Å cerium fluoride capacitor.

where D_1 is the thickness of the barrier layer C_1, R_1. The capacitance of this condenser, at low frequencies, is therefore independent of the dielectric thickness and is determined solely by the area and the barrier layer thickness. Using the value for ϵ of 7.2×10^{-11} farad per m measured on amorphous cerium fluoride films, a barrier layer thickness of about 150Å is indicated.

As a further proof of the presence of barrier layers, a capacitor was made having a silicon monoxide layer at one metal-dielectric interface about 200Å thick. Ohmic contact was not achieved, but the barrier layer characteristics were changed so that rectification occurred. Although the resistance was very high ($> 10^6$ ohms) a front-to-back ratio of about 5-to-1 was observed.

As would be expected, losses are associated with such as mechanism, Fig. 9 shows the loss tangent and apparent dielectric constant of a 2300Å cerium fluoride film with respect to frequency. The dielectric constant remains high throughout the audio frequency range. The loss tangent at 1 kc is lower than that of silicon monoxide and remains acceptably low in the audio frequency range.

In spite of the small barrier layer thickness, the breakdown voltages of 20-30v and leakage resistances of the order of 10^6 ohms or higher make these capacitors well suited for applications in evaporated circuits. Storage of unprotected capacitors in air at room temperature for over a year has not altered their electrical properties.

Manuscript received July 17, 1961; revised manuscript received Sept. 28, 1961. This paper was prepared for delivery before the Indianapolis Meeting, April 30-May 3, 1961.

Any discussion of this paper will appear in a Discussion Section to be published in the December 1962 JOURNAL.

REFERENCES

1. D. A. McLean, *This Journal*, **108**, 48 (1961).
2. G. Siddall, *Vacuum*, **9**, 274-287, No. 5/6, Nov. '59/Jan. '60.
3. G. Hass, J. B. Ramsey, and R. E. Thun, *J. Opt. Soc. Am.*, **49** [2], 116 (1959).
4. "Handbuch der Physik," **17**, p. 132, Springer, Berlin (1956).
5. R. A. Parker and John H. Wasilik, *Phys. Rev.*, **120** [5], 1631 (1960).

Some Effects of the Electric Contact in Films of Electroluminescent ZnS:Cu,Cl

W. J. Harper

Electronics Department, Research Laboratories, Westinghouse Electric Corporation, Pittsburgh, Pennsylvania

ABSTRACT

A low-conductivity layer placed between a conducting electrode and a film of evaporated electroluminescent ZnS:Cu,Cl phosphor has a pronounced effect on the properties of the cell. The logarithm of the integrated brightness varies inversely as the voltage or as the square root of the voltage, or their combination, depending on the electric contact and on the conditions of excitation. Three brightness peaks may be obtained in each half cycle of alternating voltage, one substantially in phase, the other two delayed. The in-phase brightness peak is accompanied by some rectification of current. The direction of greater current is determined by the nature of the contact and the conditions of excitation.

In the electroluminescence (EL) of ZnS phosphor powders embedded in a dielectric the nature of the electrode plays a minor role (1-3). Greater attention has been given to the electric contact in the EL of single crystals where some correlation has been reported between different electrode metals, the method of applying them, and the resulting cell properties (4-11). For EL thin films Halsted and Koller (12) used an evaporated metal while Koller (13) applied a thin nonconductor prior to the metal. Vlasenko and Popkov (14) observed some effects of an insulating film on a ZnS:Mn phosphor, while Thornton (15) evaporated Al directly on phosphor films with various activators.

The dependence of EL brightness on voltage may be represented by

$$L = L_o \exp(-a/V) \quad [1]$$

or by

$$L = L_o \exp(-b/V^{1/2}) \quad [2]$$

where L is the brightness, V the voltage, and L_o, a, b are constants. These relationships, among

others, have been proposed by earlier authors. Most EL cells of phosphor powders and of films follow [2] quite well, although Lehmann (16) found that [1] represented results for some single particles and selected thin films of ZnS:Cu,Cl.

Generally, the brightness-voltage and the brightness-frequency relationships have not been correlated with the electric contact by previous authors. In the work reported here it was found that the nature of the electric contact to ZnS:Cu,Cl EL phosphor films has a pronounced effect on the brightness and its relationship to voltage, frequency, and efficiency.

Experimental Results

Electric contact.—The films were prepared by evaporating a phosphor onto a glass coated with tin oxide and were then heat treated. They are substantially similar to those reported by Thornton (15). The tin oxide on glass forms one electric contact and also the transparent electrode. A variation in the properties of EL is obtained by varying the other electric contact, which is usually an evaporated metal with or without a film of insulating material between the phosphor and the metal. In this report only electric fields normal to the plane of the phosphor are considered. The phosphor thickness is 1-3μ and appears to be a single-crystal thickness with the diameter of the crystals about the same dimension as the thickness of the film. The layer of low-conductivity material applied between the phosphor and the metal will be referred to as an insulator although in very thin layers it may conduct current appreciably.

It was found that if the metal electrode is evaporated directly on to the phosphor layer, EL may be obtained with the metals Al and Mg, but not at all or very poorly with some other metals such as Ag, Cu, In, Zn, Sn, Fe, Pt. The latter metals directly on the phosphor give a low resistance contact and a substantially ohmic current-voltage relationship for the cell. Thus the tin oxide apparently also forms a low resistance contact. However, all the metals give a high resistance contact and EL from ZnS:Cu,Cl films when excited by an alternating voltage if an insulating layer is placed between the metal and the phosphor. The thickness of the insulator required depends on the identity of the metal and the insulator. Occasionally any metal alone may give EL, but it is thought that in such instances effective insulating layers may be produced by the mechanical or chemical treatment of the ZnS surface or by some interaction between the phosphor and the metal. This conclusion is reached because the properties of the resulting cells are similar to those obtained with Al or Mg electrodes. However, there are additional factors involved since some metals such as Au, Pd, Ni, Bi, Pb yield luminescence and cell properties somewhat different from those obtained with Al.

This paper describes the type of properties obtained with Al electrodes with and without an insulator. The Al is evaporated from a tungsten filament at a pressure greater than 10^{-5} mm Hg. It is believed that the Al oxidizes on exposure to the atmosphere. There may also be some effect due to electrical forming since usually an initially higher voltage and current must be applied to Al and Mg contacts before EL can be obtained at lower voltages.

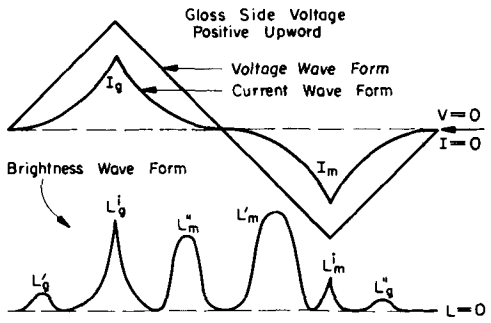

Fig. 1. Schematic diagram of the voltage, current, and brightness wave forms. Symbols shown for current and brightness are used to identify the peaks and also as their maximum amplitude.

Brightness wave form.—The brightness wave form of EL films forms a convenient reference for explaining and correlating other properties. Three brightness peaks are usually obtained in each half-cycle of sine or triangular voltage. In the films described here the brightness peaks in one half-cycle of voltage are much greater than those in the other half. Of the three peaks, one is substantially in phase with the voltage and the other two are delayed. Figure 1 shows a schematic diagram of the brightness and current wave forms obtained with a triangular voltage wave form. A triangular rather than a sine voltage is used in order to distinguish the in-phase peaks more readily. The brightness peak is denoted by subscript "g" (or "m") if it begins when the glass (or metal) side electrode is going positive. Superscripts "i," double prime, and prime are used for the in-phase, secondary, and primary peaks, respectively. Sometimes there are small peaks which cannot be identified as one of the above six. Figure 2 shows voltage, brightness and current wave forms for an evaporated Al electrode with and without a 10 mμ insulating layer of SiO_2. Brightness values given in this and the following figures should be considered as approximations.

The magnitude of the in-phase peaks, L_g^i and L_m^i, depend on the amount and type of low-conductivity material between the metal electrode and the phosphor and on the conductivity of the phosphor itself. Frequently, L_m^i is about equal to L_g^i, but because it is often overlapped by L_m', it does not appear prominently. Both peaks are absent if the metal electrode is insulated sufficiently. The amplitude of these peaks at low-frequency alternating voltage is about the same as for the equivalent direct voltage. With a-c excitation the maximum of the in-phase peaks follows the voltage and current maxima by an interval of about a millisecond. The interval decreases as the voltage or frequency is increased.

Narrow band optical filters indicate that the in-phase peaks L_g^i and L_m^i have a strong blue compo-

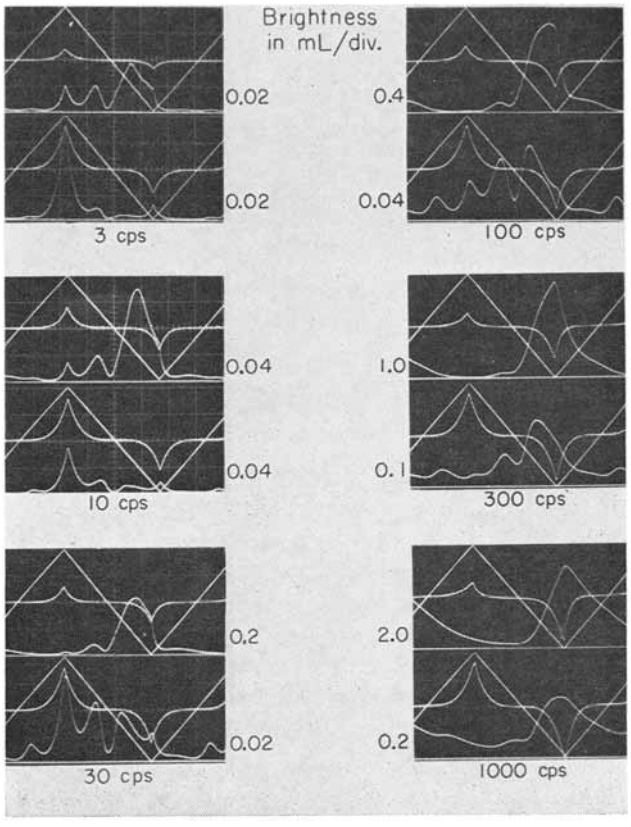

Fig. 2. Voltage, current, and brightness wave forms from an EL ZnS:Cu,Cl layer of thickness 1.5μ at six frequencies. The top half of each photograph is for a cell area with an Al electrode on 10 mμ of SiO_2; the bottom half is for another area of the same specimen with Al alone. The triangular voltage was held constant at 20v peak. Positive voltage on the glass side is to the top of the picture. Brightness zero is shown at the bottom of the picture. The brightness magnitude is given in millilamberts per division (major). The current magnitude is 25 ma/cm^2 per division. The phosphor layer is one of comparatively low conductivity.

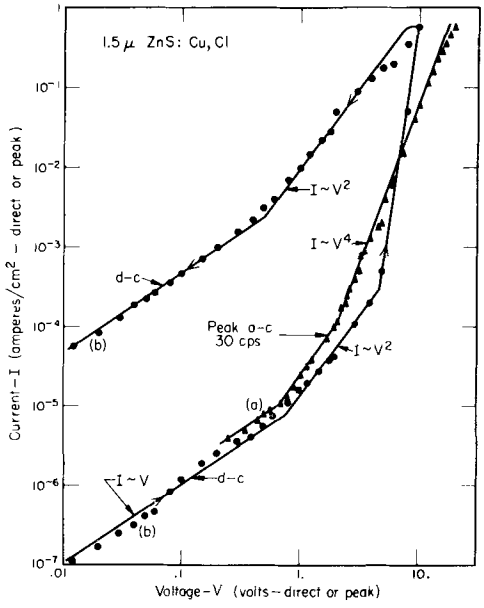

Fig. 3(a). Peak current variation with peak triangular voltage at 30 cps. Fig. 3(b). Steady-state d.c. with the Al electrode negative for increasing voltages starting with a de-excited phosphor, and for decreasing voltages.

nent. The peaks L_m' and L_m'' are of the same quality green at frequencies of 1-10 cps, but possess a more blue characteristic at 100-1000 cps.

A buildup in the initial several cycles, well known in EL powders, occurs in the peaks L_m' and L_m'', but the in-phase peaks do not have a buildup.

Current relations.—The current wave forms are also affected by the nature of the electric contact. With thick insulators the capacitive property of the cell dominates the current wave form. If high resistance Mg or Al contacts are used, the instantaneous current I varies approximately as the square of the voltage, V, as may be seen in Fig. 2. If prominent in-phase peaks are present, the current may be somewhat rectified. The direction of greater current is usually the glass side positive at low voltages, low frequencies, and high temperatures. If the small differences due to current rectification are neglected, the amplitude of the current peaks at low frequencies varies roughly as the second to the fourth power of the voltage [Fig. 3(a)].

If a direct voltage, V, is applied in steps to a cell with an Al contact and the current, I, is allowed about 1 min to reach a steady state, the current is proportional to V up to about 0.5v, varies as V^2 from about 1 to 8v and approximately as V^4 or a higher power up to breakdown. At voltages above about 8v the current must be limited to prevent destruction of the cell. The polarity of the applied voltage or whether it is being increased or decreased does not change the shape of the I-V relationship greatly. However, the history of the cell and other unknown factors often have large effects on the magnitude of the current at low voltages. For example, as shown in Fig. 3(b), the initial current through a de-excited phosphor layer is much lower than in the same cell after it has been recently excited.

Effect of voltage.—The dependence of integrated brightness on voltage for a ZnS:Cu,Cl layer may range from Eq. [1] to Eq. [2], depending on the electric contact, frequency of excitation, temperature, and the conductivity of the phosphor. Equation [2] is favored by phosphor films with high conductivity, with very thin insulators, and at low frequencies. With more insulation, Eq. [1] is followed quite well in the audio frequency range. Combination of the two forms are usually obtained. Frequently, at very low voltages, the fit is not good to either of the equations.

Whether Eq. [1] or [2] is followed by the variation of integrated L with V is determined by the dominant brightness wave forms. The amplitude of the peaks L_g', L_m', and L_m'' follow [2]; the peaks L_m' follow [1] fairly well. When the logarithms of L_g' and L_m'' are plotted against $V^{-1/2}$, the slopes of the lines are approximately equal as shown in Fig. 4. In all the figures showing amplitude of brightness peaks, the maximum was measured from zero brightness, and no correction has been made for overlap of peaks. The relative magnitude of the brightness peaks depends on the resistance of the contact, preparation of the phosphor, and conditions of excitation.

The peak L_m' may consist of two superposed peaks, suggested by the following evidence. At high voltages its amplitude may become greater or less than that given by [1], and this is accompanied by the narrowing or broadening of the peak. At high volt-

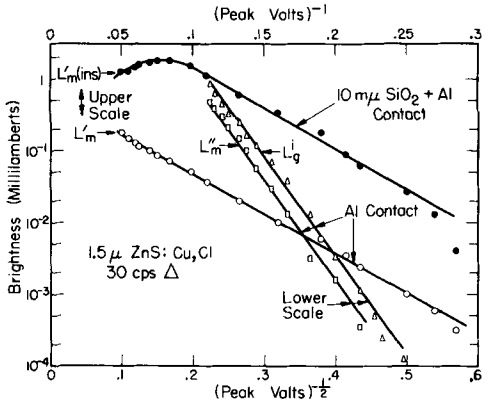

Fig. 4. Amplitude of brightness peaks as a function of voltage

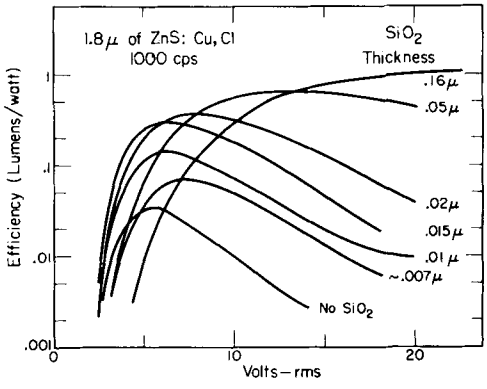

Fig. 6. EL efficiency for different thicknesses of silica insulator as a function of voltage.

ages and with high positive bias on the metal electrode, L_m' may develop two overlapping peaks. In the first few cycles after a voltage is applied, the amplitude sometimes decreases while the width broadens. These properties of L_m' occur even when L_m^i and L_m'' are distinctly separated from it. However, in this report, L_m' will be treated as a single peak.

The voltage relationship between the three peaks may also be shown by adding a small direct voltage, positive on the glass side, to an alternating voltage. Peaks L_g^i and L_m'' increase approximately the same amount, while peak L_m' remains unchanged. This indicates that L_m' depends more on the peak-to-peak voltage than on either of the two peak voltages.

Effect of thickness of insulator.—As the thickness of the insulating layer between the metal contact and the phosphor is increased beyond about 5 mμ, the conductance of the cell is decreased, while the brightness at moderate voltages and frequencies is increased. Thus the efficiency is increased substantially by the use of the insulating layer.

Figure 5 shows how the brightness-voltage relationship is affected by increasing the thickness of SiO_2 under Al electrodes. Up to a point the slope remains constant while the brightness increases. Then, as more insulation is added, the slope increases by pivoting on a point of constant L_o. The latter property is similar to that found for cells of phosphor powders embedded in a dielectric.

For the phosphor layer used, the optimum brightness at a given voltage corresponds to an SiO_2 layer of about 10 mμ. Optimum efficiency is obtained with greater thicknesses of insulation. Figure 6 shows how the efficiency varies with voltage as the SiO_2 layer is increased in thickness. At 1000 cps and moderate voltages the equivalent parallel capacitance of the contact 'C' in Fig. 5 is about 10 nf/cm^2 and the a-c conductance is 100 μmhos/cm^2.

Effect of frequency.—The nature of the electric contact also determines the relation of brightness to frequency. Again, a correlation with the brightness wave form is possible. The amplitude of the peaks L_g^i and L_m^i is almost independent of frequency. The base of the in-phase peaks retains the same fraction of each cycle as the frequency is varied. Thus the integrated brightness of the in-phase peaks is almost independent of frequency up to about 500 cps. Beyond this frequency the amplitude of the peaks diminishes and their identity is lost. An example is shown in Fig. 7. At room temperature the in-phase peaks dominate the total brightness up to frequencies of about 3 cps. The films described were prepared for a-c excitation. Films may be prepared to have the in-phase peaks dominant to higher frequencies. Such films are more suitable for d-c excitation.

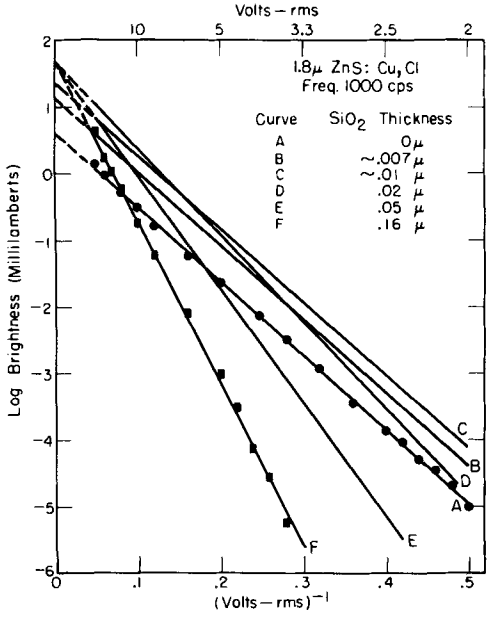

Fig. 5. Dependence of integrated brightness on thickness of silica insulator under an evaporated Al metal electrode as a function of voltage.

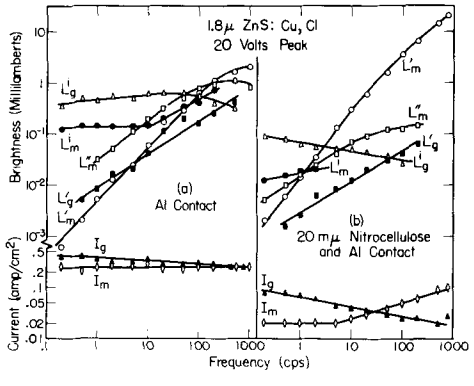

Fig. 7. The variation with frequency of the amplitude of brightness and current peaks, (a) with an Al contact, (b) with 20 mμ nitrocellulose under the Al. No correction is made for the overlap of brightness peaks. The phosphor layer is relatively more conducting than the specimen in Fig. 2.

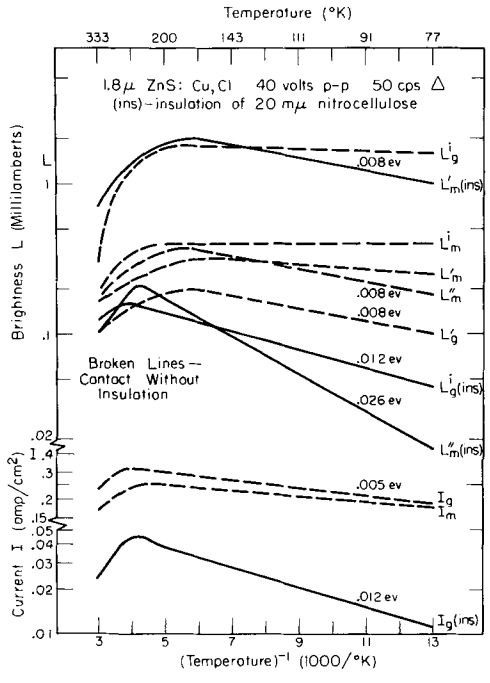

Fig. 8. Amplitude of brightness and current peaks as a function of temperature. The slope of the straight line portions of the curves is indicated in terms of electron volts.

The amplitude of peaks L' and L'' increases with frequency and hence the integrated light does also, if the delayed peaks dominate the brightness wave form. In the films described here the integrated light at moderate voltages is constant up to a frequency of about 3 cps, then increases with frequency up to about 5000 cps where it levels off.

Effect of temperature.—Each of the brightness peaks is affected by temperature somewhat differently. Figure 8 shows the amplitude of some peaks for a layer with 20 mμ of nitrocellulose plus Al and the corresponding peaks for the same phosphor with Al contacts only. In the figure it may be noted that curve L_m'', rather than L_m', for the Al-contact peak has the same slope as the peak L_m'(ins) for the insulated contact. This correlation occurs quite frequently. The range of temperature where these two curves are parallel seems to decrease with decreasing voltage and frequency. The magnitude of the brightness peaks and their dependence on temperature vary considerably for specimens which are substantially alike so that the values given in the example cannot be considered representative of the phosphor.

The integrated brightness curves for layers with insulated contacts have the same slope as those for the corresponding amplitudes of L_m'. In the specimens examined activation energies of 0.005-0.03 ev were obtained. The integrated brightness for layers with Al contact only is usually flat from 77°K to about 250°-300°K where it drops off rapidly.

Discussion

A common interpretation of EL in ZnS is that a barrier provides a high field region which may give rise to collision processes. An exhaustion layer of the Mott-Schottky type has been proposed by Piper and Williams (17). An insulator at the barrier contact has been considered by Zalm (18) and suggested by others (19, 20). Froelich (21) deduced from experimental observations that Al_2O_3 is associated with the formation of barriers in EL Zn(Al)S:Cu phosphor powders. Larach and Shrader (22) showed that a surface phase of CuZnS plays an important role in the EL of ZnS powders.

The results of the present work indicate that a low conductivity layer at an electrode is one method of inducing EL in single-layer thin films of ZnS:Cu,Cl when the voltage is applied normally to the plane of the films.

It is believed that the contact of the metal electrode and the insulating layer results in the accumulation of electrons in the insulator. Skinner (23) has shown that such an accumulation in depth occurs for a suitable choice of metal and insulator. The contact between the insulator and the phosphor probably results in a depletion or exhaustion layer in the phosphor, thus providing a high resistance and a local high field. Harrick (24) has shown that an insulator of thickness about 10 mμ facilitates charge injection and extraction. In the present work it was found that, with favorable conditions, about 5 mμ of SiO_2 plus a high-resistance Al evaporated electrode resulted in greater current at moderate voltages than with silica thickness somewhat greater or none at all. Charge carriers penetrating the insulating layer provide current for the in-phase peaks. When the insulator is thicker, an accumulation of electrons at the interface between the phosphor and the insulator may provide electrons for the delayed peaks. When the glass side electrode is positive, electrons from the insulator or, if the latter is thin enough, from the metal electrode are accelerated and may produce excited and ionized luminescent centers. Some of the electrons are trapped in the phosphor, forming a space charge. A field resulting from the space charge accelerates electrons toward the metal electrode. As the field due to the applied voltage is reduced, electrons thermally released could recombine with empty activator centers and produce the secondary peak L_m''. If a thick insulator is present, the latter action is subdued. As the field due to the external voltage reverses, electrons released from traps and the injected electrons are transported into the region of the crystal having ionized centers and the primary peak L_m' results. The peak L_m' may be due to the field resulting from the superposition of an external voltage and the space charge or polarization voltage. The effect of a small bias voltage mentioned above is used to support this interpretation. The presence of a polarization voltage has been previously reviewed and described by Haake (25).

The asymmetry of the brightness peaks L_m' and L_m'' with respect to the halves of the voltage cycle indicates that they depend on the barrier or junction at the metal electrode. The substantial symmetry of the in-phase peaks indicates that they are not very sensitive to the nature of the contacts. Changing the voltage, temperature, or frequency can reverse the direction of the current rectification and the relative intensity of the peaks, L_m^1 and L_g^1. Since both peaks have similar blue components in their spectrum, the peak L_m^1 does not depend on the "blue" centers created in the previous half cycle. It is concluded

that, in each half cycle, the in-phase peaks are due either to the electrons ionizing "blue" centers with which other electrons later combine, or the current results in the capture of holes by luminescent centers by some other process. Hole injection may be a part of the latter, but seems unlikely in view of the asymmetry of the electric contacts.

If the direct voltage I-V relationship of Fig. 3 is used with the space-charge-limited current relations developed by Lampert (26) and others (27, 28), what may be interpreted as the trap-filled-limit voltage leads to a calculated defect density of 10^{16} cm^{-3}. This appears to be another example of the type of compensation reported by Allen (29).

The dependence of emission intensity on the applied voltage has been reviewed by several authors (5, 16, 30). In particular, Zalm (18) has calculated that the L-V relationship [2] can be due either to the excitation probability or to the supply of primary electrons. If L_m'' were determined by the supply of electrons, then, when it is suppressed and presumably the released electrons are available to L_m', the $L_m'' - V$ characteristic should be superposed on L_m'. There is a little evidence at high voltages in some specimens of such superposition. Since both L_m' and L_m'' depend on the excitation when the metal electrode is negative, their difference in voltage relationship must depend on the conditions during recombination. Using relations developed by Rose (31), Alfrey and Taylor (32) associated single depth traps with Eq. [2] and trapping states distributed in energy with [1]. The present work gives some support to their suggestion since the field release of electrons may be predominantly from deeper trapping states distributed in energy.

The following may pertain to the form of the L-V relationship for the different peaks. During the emission of peaks L^1 and L'', the field within the crystal is the resultant of two opposing fields, one due to a space charge, the other due to a potential applied externally. During the emission of L', the external voltage reinforces the potential due to space charge in the portion of the crystal where emission takes place. The position and density with respect to time of the two space charge layers, one at the insulator and the other in the phosphor near the glass electrode, would determine the degree of validity of this interpretation.

The increase of efficiency with thickness of the insulating layer indicates that EL is more efficient when charge carriers move only within the crystal and much less efficient when they pass through the crystal. It may also indicate a greater accumulation of charge as the insulation thickness is increased.

The frequency effect is also related to the transport of carriers. The in-phase peaks are due to carriers passing through the crystal and hence do not vary with frequency. The delayed peaks are due to carriers oscillating within the crystal, so that, if the same charge transfer prevails for each cycle, their brightness increases with frequency.

The effect of temperature on the brightness peaks indicates that thermally released electrons from shallow traps are made use of by the peak L_m'' when the insulating layer is very thin, but by the peak L_m' when the insulating layer is thicker. With a thick insulator, the peak L_m'' is reduced, and a small peak often appears approximately where L_g'' would be expected. This evidence also suggests that the peak L_m' arises from two sources. The dependence of the peaks L_m^1 and L_g' on temperature, shown in Fig. 8, is not well established since there was considerable variation in them in the specimens examined. The activation energies (0.005-0.03 ev) obtained from the slopes of the curves of primary peaks are similar in magnitude to those obtained by Haake (33) for powders.

Variations in current amplitude with temperature, frequency, and voltage may be partly due to the nature of the conduction at the metal-insulator contact as explained by Fisher and Giaever (34). Two competing processes, the electrons tunnelling through the barrier and those passing over the potential barrier, could cause reversals in the direction of greater current.

Acknowledgments

The author is indebted to Dr. W. A. Thornton for the method of preparing EL films and for much fruitful association, to Dr. H. L. Cox for the design of a low-frequency amplifier, and to G. D. Ondo and K. A. Rumon for a great deal of the experimental work.

Manuscript received Aug. 21, 1961.

Any discussion of this paper will appear in a Discussion Section to be published in the December 1962 JOURNAL.

REFERENCES

1. G. Destriau, Brit. *J. Appl. Phys.*, **6**, Suppl. S49 (1955).
2. G. Destriau, *Illum. Eng.*, **51**, 197 (1956).
3. W. A. Thornton, *Phys. Rev.*, **113**, 1187 (1959).
4. W. W. Piper and F. E. Williams, *ibid.*, **87**, 151 (1952).
5. W. W. Piper and F. E. Williams, "Solid State Physics," **6**, p. 95, Academic Press, New York (1958).
6. D. R. Frankl, J. L. Birman, G. F. Neumark, and M. A. Lempicki, *J. Phys. Rad.*, **17**, 731 (1956).
7. G. Diemer, *Philips Research Repts.*, **10**, 194 (1955).
8. R. W. Smith, *Phys. Rev.*, **100**, 760 (1955).
9. G. F. Alfrey and I. Cooke, *Proc. Phys. Soc.*, **70B**, 1096 (1957).
10. H. Fujisaki, T. Matsumura, and Y. Tanabe, *Bull. Res. Inst. for Sci. Meas.*, Tohoku Univ., **7**, (Dec. 1958); SLA Translation 59-17899, John Crerar Library.
11. S. Narita, *J. Phys. Soc. Jap.*, **15**, 128 (1960).
12. R. E. Halsted and L. R. Koller, *Phys. Rev.*, **93**, 349 (1954).
13. L. R. Koller, U.S. Pat. 2,709,765, May 31, 1955.
14. N. A. Vlasenko and I. A. Popkov, *Optics and Spectroscopy*, **8**, 39 (1960).
15. W. A. Thornton, *J. Appl. Phys.*, **30**, 123 (1959).
16. Willi Lehmann, *This Journal*, **107**, 20 (1960).
17. W. W. Piper and F. E. Williams, *Phys. Rev.*, **98**, 1809 (1955).
18. P. Zalm, *Philips Research Repts.*, **11**, 353, 416 (1956).
19. L. Burns, *This Journal*, **100**, 572 (1953).
20. John F. Waymouth and Francis Bitter, *Phys. Rev.*, **95**, 941 (1954).
21. H. C. Froelich, *This Journal*, **100**, 496 (1953).
22. S. Larach and R. E. Shrader, *J. Phys. Chem. Solids*, **3**, 159 (1957).
23. S. M. Skinner, *J. Appl. Phys.*, **26**, 498, 509 (1955).

24. N. J. Harrick, *Phys. Rev.*, **115**, 876 (1959).
25. C. H. Haake, *J. Appl. Phys.*, **28**, 117 (1957).
26. M. A. Lampert, *Phys. Rev.*, **103**, 1648 (1956).
27. M. A. Lampert, A. Rose, and R. W. Smith, *J. Phys. Chem. Solids*, **8**, 464 (1959).
28. G. T. Wright, *Proc. Inst. Elec. Eng.*, **106B**, 915 (1959).
29. J. W. Allen, *Nature*, **187**, 403 (1960).
30. G. Destriau and H. F. Ivey, *Proc. I. R. E.*, **43**, 1911 (1955).
31. A. Rose, *Helv. Phys. Acta*, **29**, 199 (1956).
32. G. F. Alfrey and K. N. R. Taylor, *ibid.*, **30**, 206 (1957).
33. C. H. Haake, *This Journal*, **104**, 291 (1957).
34. J. C. Fisher and I. Giaever, *J. Appl. Phys.*, **32**, 172 (1961).

Luminescence of Copper-Activated Orthophosphates of the Type $ABPO_4$ (A = Ca, Sr, or Ba and B = Li, Na, or K)

W. L. Wanmaker and H. L. Spier

Light Division, N. V. Philips' Gloeilampenfabrieken, Eindhoven, Netherlands

ABSTRACT

Activation of orthophosphates of the type $ABPO_4$ with copper gives an efficient phosphor in some cases. The brightest phosphors found are $SrLiPO_4$-Cu and $BaLiPO_4$-Cu, with an emission peak (with 2537Å excitation) at 4150 and 4600Å, respectively. The properties of orthophosphates of the type $ABPO_4$ with two kinds of alkali earth or alkali metal ions, respectively, were also studied. X-ray diagrams of the compounds investigated are given.

During the past few years several papers concerning copper-activated phosphors have been published. Uehara, Kobuke, and Masuda (1) described the preparation and luminescent properties of copper-activated calcium orthophosphates and related phosphors, and Wanmaker and Bakker (2) investigated modified strontium orthophosphates. The properties of copper- and tin-activated halophosphates were given in a paper published by Hunt and McKeag (3).

Thorium phosphate activated with copper shows a yellow-orange emission when excited by 2537Å radiation (4). In a subsequent patent the application of this phosphor in low-pressure mercury discharge lamps is given, with the addition of diammonium phosphate or phosphoric acid (5).

Moreover, some papers were published concerning the more fundamental properties of this kind of phosphor. The configurational coordinate curve for the copper center in calcium orthophosphate was reported by Maeda (6). Uehara (7) has given a quantitative interpretation of the luminescent properties of the same phosphor.

The quantum efficiency of many copper-activated phosphors is high, *e.g.*, we found a quantum efficiency of 0.87 for strontium magnesium orthophosphate. Uehara and co-workers give a value of 0.91 for β-$Ca_3(PO_4)_2$-Cu with 2537Å excitation (8).

In this paper we deal with the preparation and luminescent properties of a new type of copper-activated phosphors, $ABPO_4$, in which A = Ca, Sr, or Ba and B = Li, Na, or K. Although we did not succeed in obtaining as high a quantum efficiency as that of the modified strontium orthophosphates, some phosphors of rather good efficiency were made, *e.g.*, $SrLiPO_4$-Cu with an emission peak at 4150Å and $BaLiPO_4$-Cu with an emission peak at 4600Å, both with 2537Å excitation.

Several phosphors with this type of host crystal have already been mentioned in the literature. Kröger (9) reports the luminescence of manganese-activated $CaLiPO_4$, $MgLiPO_4$, $ZnLiPO_4$, and $CdLiPO_4$. More recently Smith (10) studied manganese luminescence in the system $Zn_3(PO_4)_2$-Li_3PO_4 or Na_3PO_4 and $Cd_3(PO_4)_2$-Li_3PO_4 or Na_3PO_4. In the first system, formation of $ZnLiPO_4$ and $ZnNaPO_4$ was found, whereas in the second system more complicated structures are formed. Activation with cerium renders an u.v. emission (11) with very short decay time (smaller than 0.1 μsec.). From this group of phosphors $BaNaPO_4$-Ce (emission peak at 3600Å with cathode-ray excitation) may be used for excitation of other phosphors in order to determine their decay times (12).

The quantum efficiency of the cerium-activated phosphors, studied by Kröger, decreases in the sequence B = Li, Na, K. The highest values were obtained with $SrLiPO_4$-Ce (0.88) and $CaLiPO_4$-Ce (0.81). The copper-activated phosphors studied by us showed a similar difference in brightness with variation of the alkali ions.

Concerning other activator ions, a faint green emission (u.v. excitation) is reported for $MgNaPO_4$-U (13). $CaKPO_4$-Tl, excited with 2537Å radiation, gives an emission peak at 3150Å and was studied by Clapp and Ginther in connection with its possible use in sun-tan lamps (14).

Method of Phosphor Preparation

The ingredients used in the firing mixtures were reagent grade $CaHPO_4$, $SrHPO_4$, $BaHPO_4$, Na_2CO_3, Li_2CO_3, K_2CO_3, $(NH_4)_2HPO_4$, $CuSO_4$, Al_2O_3, and $MnNH_4PO_4$. The required amounts of the dry materials were thoroughly mixed and subsequently fired in a way already described (2). In some cases a prefiring in air at about 1100°C was carried out, followed by a second firing in a slightly reducing atmosphere at about 700°C. This procedure often gives a more homogeneous product.

Chemical Composition

In nearly all phosphors the brightness generally depends strongly on the ratio between the basic and the acidic constituents of the compound, the optimum brightness being found mostly at the stoichiometrical composition. In the phosphors investigated in this paper, however, we found the optimum brightness with a slight excess of cations, *e.g.*, in $SrLiPO_4$-Cu the optimum brightness is reached with a molar ratio $Me/P_2O_5 = 3.05$ (Me being $A^{II}O + B^{I}_2O$). The molar ratios are derived from the added amounts of ingredients, so the actual molar ratio of the fired phosphors may be different; *e.g.*, it may be possible that part of the alkali or earth alkali carbonate added does not react with the phosphate added, giving rise to an actual Me/P_2O_5 ratio being lower than the molar ratio derived from the added amounts of ingredients.

As regards the ratio of the alkali earth metal ions to the alkali metal ions, an optimum brightness was found with an excess of alkali ions of about 5 mole %.

In accordance with our previous results, we found that simultaneous addition of Cu and Al enhances the brightness of the phosphors prepared. This effect is probably due to a facilitation of the incorporation of Cu^+ in the $A^{II}B^{I}PO_4$ lattice, two A^{II} ions being substituted by a Cu^+ and an Al^{3+} ion.

A minimum amount of copper is necessary in order to absorb the u.v. radiation. With a high amount of copper added, however, in most cases a certain percentage of this copper is not incorporated into the crystal lattice, and the resulting copper-oxides give rise to grayish colored products with a low brightness.

With $SrLiPO_4$-Cu we achieved the best results with the following composition: $P_2O_5 = 1$; $SrO + Li_2O = 3.05$; $Li_2O = 1.05$; $CuO = 0.01$; $Al_2O_3 = 0.04$. It will be clear that this optimum composition is also a function of the firing conditions and the primary ingredients used.

Fluorescence of Copper-Activated Orthophosphates of the Type $ABPO_4$

In this survey only the luminescence with 2537Å excitation is considered, as the quantum efficiency with long wavelength u.v. excitation is very low.

A = Ca.—$CaLiPO_4$-Cu shows an u.v. emission with a peak at 3600Å. Moreover, a blue emission is observed in many cases at 4800Å, as may be seen from Fig. 1. The relative intensity of the two bands varies with the firing conditions, the u.v. peak being more pronounced at a lower firing temperature.

Several explanations for the occurrence of two emission bands in $CaLiPO_4$-Cu are possible; *e.g.*, one may suppose that two crystal forms are present. X-ray diffraction analysis, however, showed that the unactivated $CaLiPO_4$ has the same crystal structure at firing temperatures ranging from 500° to 1300°C. Because at a firing temperature below 900°C the primary ingredients will not react completely, these preparations were made by refiring the product prepared at a temperature of 900°C at the required lower temperatures. $CaLiPO_4$-Cu has the olivine structure, this structure possessing two kinds of cation sites (15, 16). According to Dachille (17) the olivine (Mg_2SiO_4) structure is built of SiO_4 tetrahedra joined together by O-Mg-O bands. One half of the Mg^{2+} is in a position of symmetry between two tetrahedra, the other half sharing oxygen of four tetrahedra, although all Mg^{2+} ions are surrounded by six oxygens. It is questionable whether the occurrence of these two kinds of cation sites explains the presence of two emission bands in $CaLiPO_4$-Cu.

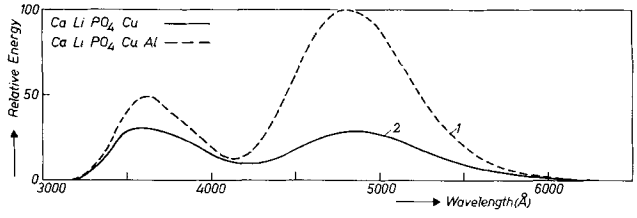

Fig. 1. Spectral energy distribution curves of the emission of $CaLiPO_4$-Cu, with Al added (curve 1) and without Al (curve 2). $Cu/P_2O_5 = 0.01$ (curve 1) and 0.015 (curve 2). $Al/P_2O_5 = 0.08$ (curve 1).

Perhaps the explanation of the problem may be found in the following direction. One cannot know for certain where the copper ions (ionic radius of Cu^+ — 0.96Å) are to be found, on a Ca^{2+} (ionic radius 1.06Å) or on a Li^+ site (ionic radius 0.78Å). On increasing the amount of aluminum, however, one would expect a tendency for the Cu^+ to occupy a Ca^{2+} site (two Ca^{2+} ions being replaced by a Cu^+ and an Al^{3+} ion). Comparing the spectral energy distribution curves of these types of phosphors, the actual amount of Cu^+ and Al^{3+} in the phosphors should be known, as in many cases a rather large proportion of the copper added is not incorporated into the host crystal lattice (as follows from the grayish body color of the fired products). Comparing phosphors with about the same body color, we found that increasing the amount of Al increases the relative intensity of the blue emission peak as illustrated in Figure 1.

One might conclude therefore that a Cu^+ ion on a Li^+ site gives the u.v. emission band and on a Ca^{2+} site the blue emission band. More work is required to elucidate this interesting problem, *e.g.*, investigating the effect of quenching on the intensities of the two peaks, and the effect of the firing atmosphere, as there are some indications that the hydrogen pressure also influences the relative intensity of the two emission peaks of $CaLiPO_4$-Cu.

Normally, copper-activated phosphors have a rather narrow emission peak. With the type of phosphors studied by us, we found in some cases a broader emission band, *viz.*, with $CaNaPO_4$-Cu, $CaKPO_4$-Cu, $SrNaPO_4$-Cu, $BaNaPO_4$-Cu, and $BaKPO_4$-Cu.

Probably these emission bands are caused by the simultaneous occurrence of two crystal forms, as it is known from the literature (18, 19) that several compounds investigated occur in two crystal forms. *E.g.*, we found, from x-ray diffraction analysis the high- and low-temperature form of $CaNaPO_4$-Cu, which phosphor has a broad emission peak located at 4400Å (Fig. 2). Although it was not possible to judge from x-ray analysis whether the $CaKPO_4$-Cu sample investigated contains both the α- and β-form (due to the small difference in the x-ray diagram of the two forms), we do conclude from the spectral distribution curve that the two crystal forms are present (Fig. 2). The emission peak of the second crystal

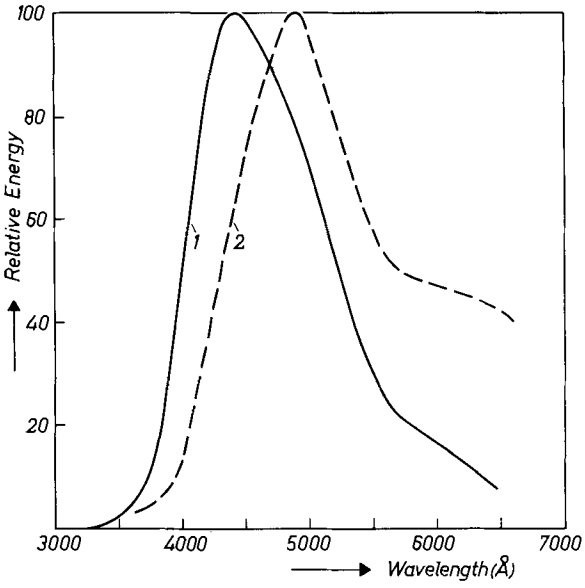

Fig. 2. Spectral energy distribution curves of the emission of $CaNaPO_4$-Cu (curve 1) and of $CaKPO_4$-Cu (curve 2). Cu/P_2O_5 = 0.01 and Al/P_2O_5 = 0.08.

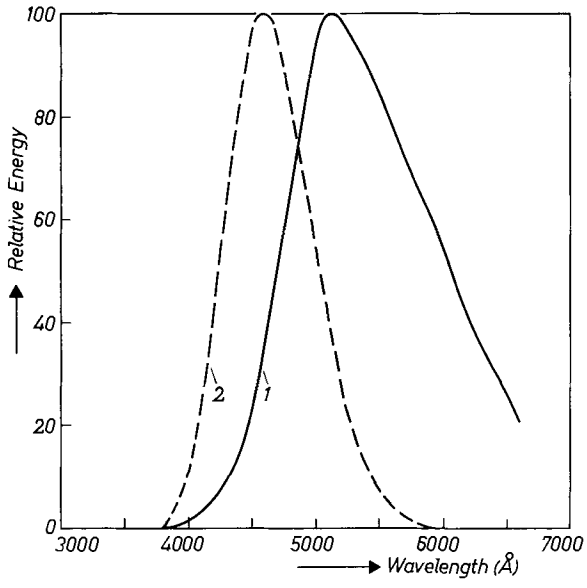

Fig. 4. Spectral energy distribution curves of the emission of $SrNaPO_4$-Cu (curve 1) and of $BaLiPO_4$-Cu (curve 2). Cu/P_2O_5 = 0.01 (curve 1) and 0.016 (curve 2). Al/P_2O_5 = 0.08 (curve 1) and 0.016 (curve 2).

structure can be found at a wavelength of about 5400-5700Å. Perhaps broadness may be due to a situation similar to the one proposed for $CaLiPO_4$, the two peaks lying close together.

A = Sr.—From Fig. 3 and 4 it may be seen that the emission peaks of $SrLiPO_4$-Cu and $SrNaPO_4$-Cu are to be found at 4100Å and at 5150Å, respectively. In $SrLiPO_4$-Cu addition of Al has only a small influence on the location of the emission peak. With the introduction of manganese, a second emission peak arises at 6100Å, as illustrated in Fig. 3. $SrLiPO_4$-Cu has a rather high brightness and is of potential interest for the application in blue-printing lamps, as the emission curve of this phosphor fits closely to the absorption curve of widely used types of diazotype papers. $SrNaPO_4$ shows a broad emission band with a maximum at 5000-5250Å (see Fig. 4, curve 1). As already discussed, $SrNaPO_4$-Cu probably contains two crystal forms. So, according to expectation, it was found that chemical composition and firing temperature have an influence on the position of the emission peak. Probably Al promotes the formation of the high-temperature form, because both with an increase of the Al content and with a higher firing temperature, the emission peak broadens, the high-temperature emission peak lying at about 5600Å. $SrKPO_4$-Cu gives a narrow emission peak of a low intensity, located at 4600Å.

A = Ba.—The emission peak of $BaLiPO_4$-Cu lies at 4600Å, as illustrated in Fig. 4. $BaNaPO_4$-Cu and $BaKPO_4$-Cu give an emission at about 4600 and 4900Å, respectively.

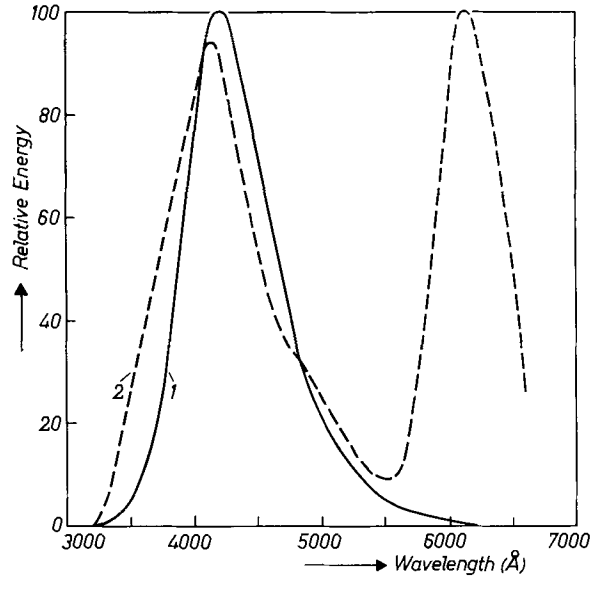

Fig. 3. Spectral energy distribution curves of the emission of $SrLiPO_4$-Cu (curve 1) and of $SrLiPO_4$-Cu.Mn (curve 2). Cu/P_2O_5 = 0.01, Al/P_2O_5 = 0.08, and Mn/P_2O_5 = 0.04 (curve 2).

Ternary Orthophosphates

Next to the binary orthophosphates of the type $ABPO_4$, described in the foregoing, some ternary orthophosphates were prepared with two kinds of alkali or earth alkali ions. Probably due to the fact that several binary orthophosphates have two crystal structures, the change in emission colors of the substituted orthophosphates is complicated.

Substituting sodium for lithium in $CaLiPO_4$-Cu causes the visible emission to shift gradually from 4800 to 4400Å, whereas the u.v. emission disappears when equal amounts of Na and Li are added. Although $SrLiPO_4$-Cu gives a single emission band only, a small amount of sodium gives a green emission band (5100Å) next to the deep blue emission band of the pure $SrLiPO_4$. On increasing the amount of Na, both bands move to shorter wave lengths, until at a high percentage of sodium the broad emission band of $SrNaPO_4$ appears at 5100Å. The location of the emission peaks in $Sr(Li,Na)PO_4$ are illustrated in Fig. 5.

Substitution of the earth alkali ions in the orthophosphates of the type $ABPO_4$ also gives rise to shifts in the location of the emission peak, as may be seen

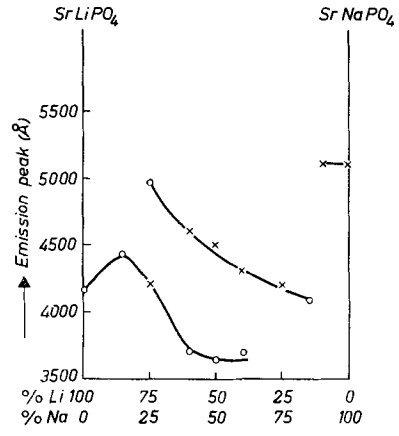

Fig. 5. Location of the emission peaks in Sr(Li,Na)PO_4-Cu. Cu/P_2O_5 = 0.01; Al/P_2O_5 = 0.08. o, main peak; x, secondary peak.

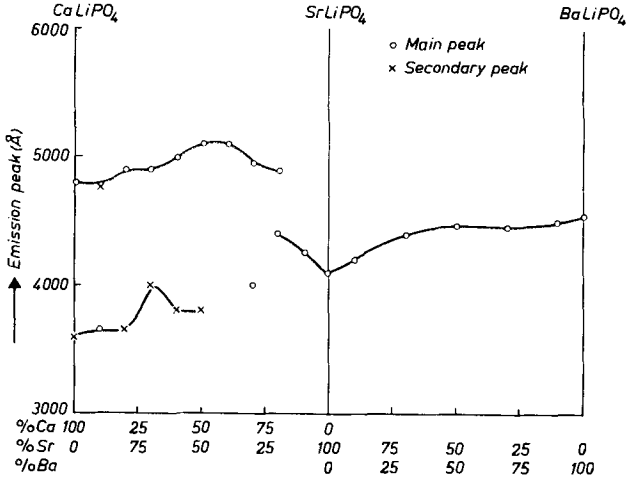

Fig. 6. Location of the emission peaks in (Ca,Sr)$LiPO_4$-Cu and (Sr,Ba)$LiPO_4$-Cu. Cu/P_2O_5 = 0.016; Al/P_2O_5 = 0.016.

from Fig. 6. Substituting Sr for Ca in $CaLiPO_4$-Cu shifts the blue emission peak to longer wavelengths, until a peak is obtained at 5100Å with equimolar amounts of Ca and Sr. With a still higher proportion of Sr this peak is moved to shorter wavelengths, and finally above about 75% of $SrLiPO_4$, the emission peak of $SrLiPO_4$-Cu is gradually reached. The u.v. peak of $CaLiPO_4$-Cu disappears with about 50% of the Ca being replaced by Sr. Substituting Ba for Sr in $SrLiPO_4$-Cu the emission peak shifts gradually from 4100 to 4600Å, as may be seen from Fig. 6.

Reflection and Excitation Spectra

Figure 7 shows the reflection spectra of the most important phosphors investigated, *viz.*, $SrLiPO_4$-Cu and $BaLiPO_4$-Cu. In order to determine the influence of the copper addition, the reflection spectra of the unactivated compounds are also given. It may be seen that the introduction of the copper ions produces an increase in absorption of the u.v. radiation. In the visible region of the spectrum an appreciable absorption still takes place, probably due to a certain amount of metallic copper or copper-oxides produced during the firing process. It is superfluous to say that this absorption decreases the brightness of the phosphors considerably.

The excitation spectra of $SrLiPO_4$-Cu and $BaLiPO_4$-Cu may be found in Fig. 8. From this figure

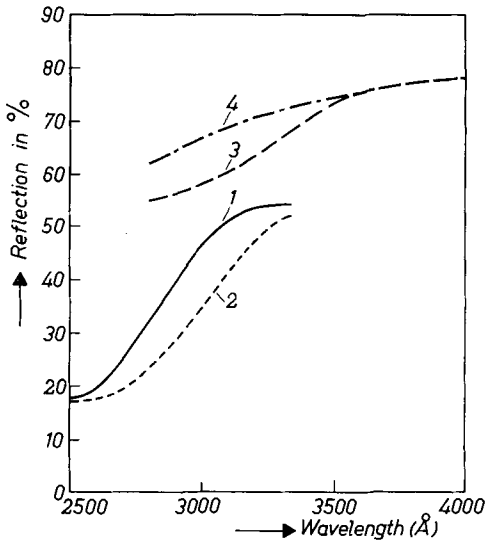

Fig. 7. Reflection spectra of $SrLiPO_4$-Cu (curve 1), $BaLiPO_4$-Cu (curve 2), $SrLiPO_4$ (curve 3) and $BaLiPO_4$ (curve 4). Cu/P_2O_5 = 0.01; Al/P_2O_5 = 0.08; Li_2/P_2O_5 = 1.05. Me (= earth alkali metal + alkali metal)/P_2O_5 = 2.90.

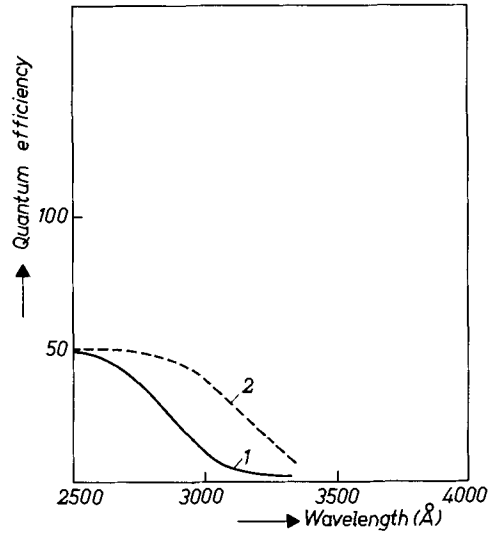

Fig. 8. Excitation spectra of $SrLiPO_4$-Cu (curve 1) and of $BaLiPO_4$-Cu (curve 2). Molar ratios as given in Fig. 7.

it may be seen that the phosphors investigated have a quantum efficiency of about 0.50 by excitation with the 2537Å mercury resonance line. Thus this new type of phosphor might be suitable for use in low-pressure mercury discharge lamps, were it not for the difficulties encountered with the application of these phosphors, as already reported in a previous paper (2).

X-ray Analysis

In our investigation, the x-ray diffraction of the phosphors was determined by conventional x-ray diffraction techniques using CuKα radiation from a Philips Norelco Unit.

The x-ray diffraction data of the compounds investigated are given in Tables I and II. The samples investigated have the theoretical chemical composition and are double fired for 3 hr at 900°C. No copper and aluminum were added in order to avoid any influence of these ions on the crystal structure, although we did not find a difference in the x-ray

Table I. X-ray diffraction data for $CaLiPO_4$, $CaNaPO_4$, $CaKPO_4$, $SrLiPO_4$, and $SrNaPO_4$

$CaLiPO_4$		$CaNaPO_4$				$CaKPO_4$				$SrLiPO_4$		$SrNaPO_4$	
I*		Bredig α		I		Bredig α		I		I		I	
d (Å)	I/I_o	d (Å)	Int.	d (Å)	I/I_o	d (Å)	Int.	d (Å)	I/I_o	d (Å)	I/I_o	d (Å)	I/I_o
6.11	10	3.815	m.	5.40	8			4.06	4	4.39	44	8.67	7
5.87	5	3.510	w.	4.62	7			4.02	4	4.33	89	5.12	10
4.95	10	2.780	v.st.	3.82	42			3.98	4	4.11	11	4.72	5
4.75	11	2.620	v.st.	3.78	28	3.800	m.	3.77	15	3.86	39	4.19	7
3.90	5	2.170	w.	3.40	7	2.990	v.st.	2.98	46	3.83	80	3.90	15
3.82	23	1.913	st.	3.10	5			2.96	47	3.69	10	3.66	8
3.71	16	1.770	w.	2.886	5			2.93	50	2.98	>114	3.62	17
3.63	38	1.542	m.	2.822	5			2.830	4	2.92	60	3.47	15
3.47	8	1.514	m.	2.772	8	2.790	v.st.	2.755	100	2.731	4	3.31	8
3.34	13	1.461	m.	2.739	100	2.310	m.	2.275	12	2.698	11	2.89	100
3.16	19	1.314	m.	2.690	49			2.253	10	2.593	13	2.875	>130
3.11	19			2.644	82	2.050	st.	2.027	22	2.501	100	2.763	15
3.00	5	$CaNaPO_4$ β		2.416	5			1.997	21	2.436	46	2.723	>130
2.92	49	d	Int.	2.321	8	1.900	w.	1.888	6	2.392	11	2.607	15
2.88	23	5.52	w.	2.264	15	1.650	m.	1.637	9	2.321	11	2.550	7
2.805	38	4.66	v.w.	2.196	36	1.610	m.			2.196	14	2.436	8
2.739	23	3.86	m.	2.166	8	1.570	m.			2.166	21	2.385	12
2.698	13	3.43	v.w.	2.108	7	1.395	m.			2.142	54	2.264	42
2.667	100	3.12	v.w.	2.058	5	1.263	w.			2.099	21	2.253	37
2.578	10	2.755	v.st.	2.027	10	1.224	w.			2.058	36	2.176	10
2.550	25	2.675	v.st.	2.013	31	1.149	v.w.			2.013	7	2.099	14
2.462	5	2.435	v.w.	1.933	14	1.119	w.			1.945	20	2.053	10
2.436	6	2.335	w.	1.918	38	1.060	w.			1.941	20	2.040	10
2.404	8	2.275	w.	1.896	10	1.048	w.			1.918	71	2.001	12
2.338	8	2.200	m.	1.765	5					1.859	44	1.989	39
2.275	5	2.126	v.w.	1.737	8					1.695	4	1.981	69
2.216	6	2.034	st.	1.704	8					1.640	20	1.859	10
2.161	8	1.928	st.	1.698	10							1.831	10
2.122	5											1.817	10
2.085	13											1.810	8
2.036	5											1.791	5
1.957	8											1.740	8
1.949	21											1.701	8
1.899	8											1.686	8
1.852	23												
1.810	6												
1.778	10												
1.734	5												
1.728	10												
1.701	8												
1.675	5												

* I, present investigation.

Table II. X-ray diffraction data for $SrKPO_4$, $BaLiPO_4$, $BaNaPO_4$, and $BaKPO_4$

$SrKPO_4$		$BaLiPO_4$		$BaNaPO_4$		$BaKPO_4$	
d (Å)	I/I_o	d (Å)	I/I_o	d (Å)	I/I_o	d (Å)	I/I_o
5.87	10	4.39	36	4.02	52	6.11	5
5.10	45	4.27	6	2.90	91	4.93	27
4.04	5	3.91	14	2.805	100	3.86	5
3.26	74	3.15	7	2.607	6	3.38	37
3.07	16	3.07	100	2.417	22	3.05	100
2.92	>135	2.780	6	2.303	35	2.866	37
2.772	>135	2.585	6	2.237	9	2.831	37
2.585	6	2.550	26	2.161	6	2.564	4
2.514	8	2.528	14	2.018	52	2.488	16
2.423	19	2.226	6	1.831	24	2.298	5
2.380	47	2.211	13	1.784	13	2.281	12
2.292	22	2.196	27	1.701	11	2.226	5
2.222	27	2.151	12	1.642	24	2.186	27
2.191	14	1.969	17			2.118	4
2.161	16	1.937	17			2.076	44
2.122	62	1.675	6			2.036	11
2.013	100	1.650	10			1.934	15
1.953	24					1.873	5
1.866	16					1.798	12
1.842	14					1.725	4
1.824	16					1.707	12
1.810	16					1.672	10
1.722	24					1.642	5
1.686	10						
1.645	32						

diagram between activated and unactivated phosphors.

According to Thilo (15) $CaLiPO_4$ should be isotypical with Monticellite $CaMgSiO_4$, both having the olivine (Mg_2SiO_4) crystal structure. The crystal structure of $CaNaPO_4$, $SrNaPO_4$, and $BaNaPO_4$ and of the corresponding potassium compounds were given by Klement and Steckenreiter (18). Bredig described in more detail the crystal structures of the α and β form of $CaNaPO_4$ and $CaKPO_4$ (19). We found no references concerning the crystal structure of $SrLiPO_4$ and $BaLiPO_4$.

Bragg and Brown (16) described the olivine structure extensively. According to these authors the oxygen atoms are hexagonal, closed packed, whereas the magnesium is octohedrically and the silicon tetrahedrically surrounded by oxygen.

Concerning $CaNaPO_4$, Bredig found two crystal structures with a transition temperature of 680°C. As may be seen from Table I, our unactivated sample is a mixture of the α and β structure, the amount of β being greater than that of α. This may explain the broad emission band observed in $CaNaPO_4$-Cu.

According to Bredig $\alpha CaKPO_4$ is transformed into $\beta CaKPO_4$ at a temperature of 705°C, the α-form hav-

ing a hexagonal structure [glaserite type = $(K,Na)_2SO_4$] and the β-form being rhombic with a pseudohexagonal cell. From Table I it may be seen that our figures fit closely with those of Bredig. As the d-values of α and $\beta CaKPO_4$ differ only when d is greater than about 1.60Å, and the differences are very small, moreover, it cannot be concluded from our figures whether α or $\beta CaKPO_4$ are present. From the spectral energy distribution of the phosphors, however, it follows that presumably two crystal forms are present. Our x-ray data of $SrNaPO_4$, $SrKPO_4$, $BaNaPO_4$, and $BaKPO_4$ correspond to the low-temperature form of the figures given by Klement and Steckenreiter.

Acknowledgments

The authors wish to express their thanks to Dr. A. Bril for the measurements of the quantum efficiency, the reflection, the emission and the excitation spectra of the phosphors; to Mr. J. G. Verlijsdonk and Mr. A. A. L. Sleutjes for preparing the phosphors; and to Mr. W. Parchen for carrying out the x-ray analysis.

Manuscript received July 3, 1961; revised manuscript received Oct. 17, 1961. This paper was prepared for delivery before the Indianapolis Meeting, April 30-May 3, 1961.

Any discussion of this paper will appear in a Discussion Section to be published in the December 1962 JOURNAL.

REFERENCES

1. Y. Uehara, Y. Kobuke, and I. Masuda, *This Journal*, **106**, 200 (1959).
2. W. L. Wanmaker and C. Bakker, *ibid.*, **106**, 1027 (1959).
3. B. E. Hunt and A. H. McKeag, *ibid.*, **106**, 1032 (1959).
4. British Pat. 827,967 (1960).
5. British Pat. 834,024 (1960).
6. K. Maeda, *J. Phys. Soc. Japan*, **14**, 478 (1959).
7. Y. Uehara, *ibid.*, **15**, 612 (1960).
8. Y. Uehara, I. Masuda, and Y. Kobuke, *This Journal*, **107**, 1 (1960).
9. F. A. Kröger, "Some Aspects of the Luminescence of Solids," p. 270, Elsevier Publishing Co., Amsterdam, New York (1948).
10. A. L. Smith, Enlarged Abstracts, Electronics Division, p. 46, Chicago Meeting, Electrochem. Soc., (1960).
11. F. A. Kröger, Unpublished report.
12. A. Bril, H. A. Klasens, and P. Zalm, *Philips Res. Repts.*, **8**, 393 (1953).
13. M. K. Slattery, *J. Opt. Soc. Am.*, **19**, 175 (1929).
14. R. H. Clapp and R. J. Ginther, *ibid.*, **37**, 355 (1947).
15. E. Thilo, *Naturwiss.*, **16**, 239 (1941).
16. W. L. Bragg and G. B. Brown, *Z. Kristallograf.*, **63**, 538 (1926).
17. F. Dachille, Thesis, p. 55, Pennsylvania State University (1959).
18. R. Klement and F. Steckenreiter, *Z. anorg. u. allgem. Chem.*, **245**, 236 (1940).
19. M. A. Bredig, *J. Phys. Chem.*, **46**, 747 (1942).

Surface Concentration of Indium in Germanium from Gaseous Diffusion

Karl M. Busen, Earl L. Meeks, and George A. Shirn

Sprague Electric Company, North Adams, Massachusetts

ABSTRACT

In order to measure surface concentrations C_o of indium, indiffused from the vapor phase into germanium, a new closed system was designed. Numerical values for C_o as a function of the diffusion temperature and the temperature of the liquid source, which is in equilibrium with its vapor, are given. The surface concentration, which depends mostly on the concentration of the indium vapor, is proportional to the concentration of the indium vapor with a "segregation coefficient" of about 10^{-7}.

Electrical devices made from semiconductive single crystals usually require the formation of p- and n-type regions within that crystal. One technique to obtain such regions is gaseous diffusion. It is performed by exposing, at an elevated temperature, the surface of a semiconductor doped homogeneously with an impurity to the vapor of a second impurity of opposite conductivity type.

After completion of the diffusion process a concentration distribution of the second impurity has been formed which extends from the surface toward the inner part of the semiconductor.

Where the concentration of the second impurity becomes equal to the concentration C_B of the first impurity, a boundary or junction between p-type and n-type regions is formed. The distance, x_j, of this junction from the surface and the concentration of the indiffused impurity at the surface, C_o, are important parameters for device design and fabrication. C_o is one of the parameters determining the junction depth; it also determines the "base" resistance of a graded base transistor. For mesa-type transistors where the emitter is plated and micro-alloyed on the surface, C_o is the impurity concentration adjacent to the emitter which is of great significance for the emitter capacitance and emitter breakdown voltage.

It is the purpose of this paper to discuss the surface concentration of indium resulting from indiffusion into antimony doped germanium. In the following, the apparatus which was used for the experiments is

described, and the surface concentrations resulting from the experiments are presented. A discussion of the results concludes the paper.

Apparatus Design and Experimental Procedures

A general method for diffusion of an impurity into a semiconductor is to expose the solid semiconductor to the vapor of the diffusing impurity. The temperature of the semiconductor and the vapor pressure of the diffusing impurity must be well controlled to obtain reproducible concentration distributions. One way to control the vapor pressure is to have equilibrium conditions between vapor and liquid phase of the diffusing impurity in a closed system. The pressure will then depend on the temperature of the liquid phase provided that the liquid phase is at the lowest temperature of the closed system. This requirement imposes the condition that, if the system has a closure, this closure must be at or above the temperature of the liquid phase. If the vapor pressure of the impurity is relatively low (in the order of 10^{-6} mm Hg) it is convenient to evacuate the system prior to the evaporation of the impurity. This means that the closure must have the properties of a high vacuum valve. If, furthermore, the liquid phase is at a relatively high temperature (over 500°C), most of the known vacuum valves will not perform satisfactorily.

A popular solution to this problem is to seal the impurity and germanium in an evacuated quartz tube and to introduce this tube into a two zone furnace. There are several disadvantages to this method: the necessity of a glass-blower to seal off for each run; introduction of impurities from the quartz in sealing the tubes; use of new quartz for each run which introduces an additional parameter to be taken into consideration in the evaluation of results. There are several other solutions known which overcome the problem of the valve. For convenience and best possible control of the vapor pressure a new apparatus was designed which is shown in Fig. 1.

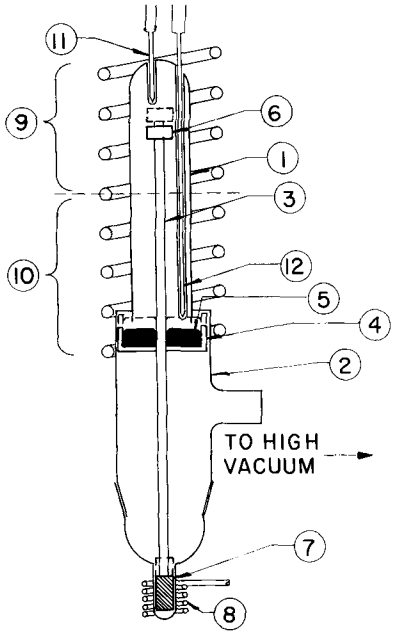

Fig. 1. Apparatus used for the diffusion experiments

This apparatus requires no glass blowing after initial construction and may be used repeatedly for many runs. It may also be cleaned and baked out under high vacuum at temperatures in excess of temperatures intended for the experimental work. This eliminates the aforementioned disadvantages of the sealed quartz tube. The apparatus consists of two vertical quartz tubes, 1 and 2, of different diameter which are concentrically arranged. A part of the upper quartz tube is inserted into the lower one and both quartz tubes are sealed together. Through the opening of the lower quartz tube a quartz rod, 3, is introduced which bears a trough, 4, for the impurity, 5, and a holder, 6, for the semiconductor. An iron slug, 7, is connected to the end of the quartz rod. The slug, together with the rod, can be moved up and down by means of an electromagnet, 8. The quartz tubes are surrounded by two independently controlled furnaces, 9 and 10. Two thermocouples, 11 and 12, are inside the upper quartz tube. For an experiment the trough, 4, is filled with indium, 5, and the holder, 6, is loaded with germanium. The rod, 3, is in its lowest position. First the quartz system is pumped down to a pressure of about 10^{-6} mm Hg. Then the two furnaces are heated. The upper furnace, 9, heats the germanium and determines the diffusion temperature. The lower furnace, 10, heats the indium, which is liquified. As long as the furnaces are not on their predetermined temperature care is taken that the germanium always has a higher temperature than the indium in order to prevent condensation of indium on the germanium. When both furnaces have the right temperature, the rod is lifted by means of the magnet, 8, into a position (see dotted line) such that the rim of the upper quartz tube is immersed into the liquid indium, which acts now as a valve against the pumping system. This indium valve at the same time acts as a source which builds up a saturation vapor pressure corresponding to the temperature of the liquid indium. The moment the indium valve is closed, the diffusion process starts. When the diffusion is to be terminated, the rod is lowered by means of the magnet, thus opening the indium valve. The pressure of the indium vapor drops and the diffusion process is stopped. Care was taken that the cooling time of the furnace was short compared to the diffusion time. Therefore, no correction was necessary.

Methods of Evaluation for the Experiments

The surface concentration, C_o, of indium, indiffused into germanium, has been obtained by the following measurements: (*a*) measurements by four-point-probe; (*b*) measurement of the absorption of infrared light; (*c*) measurement of junction depth: (i) by copper plating, (ii) by dielectric powder deposition, (iii) by thermoelectric probe.

Measurements by the four-point probe.—For the evaluation of the surface concentration, C_o, four-probe measurements (1) were made on the diffused samples. C_o was determined from

$$\rho_o = \frac{V}{I}\lambda\frac{\pi^{1/2}}{\ln 2} = \frac{V}{I}\lambda \times 2.56 \text{ ohm-cm} \qquad [1]$$

where $\lambda = 2(Dt)^{1/2}$ and V/I was measured by the

four-probe. The formula is derived from the relation (2, 3)

$$G = \bar{\sigma} x_j = e \int_0^{x_j} \mu(C) \left[C_o \operatorname{erfc} \frac{x}{\lambda} - C_B \right] dx \quad [2]$$

where x_j is the junction depth, G is the total conductance between surface and junction, $\bar{\sigma}$ is the average conductivity, C is the concentration and C_o the surface concentration of the indiffused impurity, C_B is the concentration of the n-type impurity (background concentration), and e is the electronic charge. With the assumptions that

$$\left.\begin{aligned} &\mu(C) = \mu(C_o) = \text{constant} \\ &\int_{x_j}^{\infty} \operatorname{erfc} \frac{x}{\lambda} dx \approx 0 \\ &C_B << C_o \end{aligned}\right\} \quad [3]$$

Eq. [2] yields

$$\bar{\sigma}^* = \lambda \frac{e\mu(C_o)}{x_j} \frac{1}{\pi^{1/2}} C_o \quad [4]$$

If the space between the probes is much larger than the junction depth and if the junction area is considered as a nonconducting bottom, the sheet conductivity of the diffused layer is given by (4)

$$\bar{\sigma} = \frac{\ln 2}{\pi x_j} \frac{I}{V} \quad [5]$$

Defining $\bar{\sigma} = g\,\bar{\sigma}^*$, combining Eq. [4] and [5] and observing $C_o = 1/e\rho_o\mu(C_o)$ results in

$$\rho_o = g \frac{V}{I} \lambda \frac{\pi^{1/2}}{\ln 2} \quad [6]$$

The functional relation between ρ_o and C_o as given by Hunter (5) is

$$C_o = \frac{3.47 \times 10^{15}}{\rho_o} \text{ for } 10 > \rho_o > 1 \text{ ohm-cm}$$

$$C_o = \frac{3.47 \times 10^{15}}{(1 + 0.33 \log \rho_o)} \text{ for } \rho_o \leq 1 \text{ ohm-cm}$$

This relation, which is in agreement with Prince (6) and Trumbore and Tartaglia (7) enables the evaluation of Eq. [6].

For our measurements, g was chosen unity. The error introduced by this choice and by the assumptions [3] was determined by comparison of the two surface concentrations C_o^* and C_o which were derived from the conductances G^* (where $\mu = \mu(C_o) = \text{const.}$ and $g = 1$) and G(where $\mu = \mu(C)$ and $g = \bar{\sigma}/\bar{\sigma}^*$). The conductances were obtained from graphical integration with the assumption that $C_B = 10^{15}$ and $x_j/\lambda = 2$. A comparison of C_o^* and C_o shows that the surface concentrations differ (in only a few cases) at the most by a factor of 1.4. This is well within the experimental error and can therefore be disregarded. The values for the diffusion coefficient D used in the calculations were taken from a paper by Bösenberg (8). When the concentration distribution, C, the diffusion coefficient, D, and the time, t, are known, the total number of atoms diffused into a sample after time t is given by

$$s = q \int_0^{\infty} C dx \text{ total number of atoms} \quad [7]$$

Dividing both sides of Eq. [7] by q, the cross section through which the diffusion took place gives

$$\frac{s}{q} = \int_0^{\infty} C dx \text{ atoms/cm}^2$$

If $C = C_o \operatorname{erfc} x/\lambda$, then $\int_0^{\infty} C dx = C_o\lambda/(\pi)^{1/2}$ so that

$$\frac{s}{q} = C_o \frac{\lambda}{(\pi)^{1/2}} \quad [8]$$

By determining C_o by the four-probe s/q can be easily derived by means of Eq. [8].

Infrared absorption measurements.—The method is described by several papers (9-11). The set-up for the absorption measurements is shown in Fig. 2. The quartz plate together with the n-type germanium act as a filter which passes a band of light with wave lengths between 2 and 4μ. When d is the thickness of the specimen, α is the coefficient of absorption, I_o is the intensity of the incident light beam, and R is the fraction which is reflected (for germanium $R = 0.36$), then taking into account all transmitted components and the absorption, the transmitted radiation can be obtained as

$$I_t = I_o \frac{(1 - R)^2 \exp[-\alpha d]}{1 - R^2 \exp[-2\alpha d]} \quad [9]$$

By means of the thermocouple the voltages for the combinations:

1. filter and specimen (intensity of transmission), V_1
2. filter without specimen (intensity of the incident light beam), V_2, are measured. Because the voltage is proportional to the intensity,

$$\frac{V_1}{V_2} = \frac{I_t}{I_o} = \frac{(1 - R)^2 \exp[-\alpha d]}{1 - R^2 \exp[-2\alpha d]}$$

From a calibration curve, where I_t/I_o is plotted *vs.* αd, α can be obtained when d is measured. Because α is proportional to the number of holes per cm^3 (9) it can be written $\alpha = AC$, $\alpha d = A \int_0^d C dx$, or

$$\frac{\alpha d}{A} \approx \int_0^{\infty} C dx \text{ number of atoms/cm}^2 \quad [10]$$

where A is a constant. For the measurements reported here the constant A was determined to be

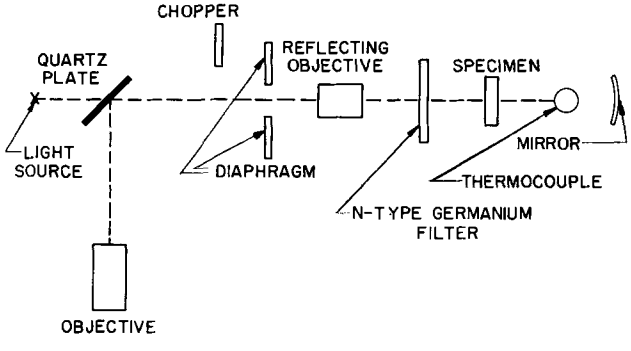

Fig. 2. Schematic diagram of the apparatus setup for infrared absorption.

$A = 1.124 \times 10^{-16}$ cm²/atoms. Furthermore, the expression $R^2 \exp[-2\alpha d]$ was neglected against 1. Thus the number of holes per cm² is obtained simply by dividing the determined expression αd by the constant A.

Measurements of junction depths.—Evaluations of surface concentrations from junction depth measurements require knowledge of the concentration distribution of the indium, the net ionized antimony concentration, and the diffusion coefficient. Difficulties were encountered when values had to be assigned to the net ionized antimony concentration. A detailed discussion of this problem is presented below. In order to be sure that the junction depths determined by junction delineations were reliable in several cases, three different delineation procedures were applied to the same sample.

The first procedure, described, for example, by Bond and Smits (12) and Glang (13) consisted of plating copper on the p-type area of a lapped bevel. After plating, an interference picture was taken in order to obtain the junction depth by counting the interference fringes. Figure 3 shows a typical sample which has been copper plated. Another junction delineation procedure was the dielectric powder deposition. The technique is described by Valdes and Smith (14), for example. The powder used consisted of $BaTiO_3$ which was ground in a mortar. The powder was suspended in trichlorethylene, and the suspension was regarded as satisfactory when it stayed cloudy for several hours after shaking. The thermoelectric probe (12) was applied as a final procedure. The probe was run over a bevel which made a 1° angle with the original surface. The place where p-type changed to n-type was an indication of the junction.

Discussion and Conclusions

The temperatures investigated were: 775°, 837°, and 900°C for the germanium, and 600°, 650°, 700°, and 750°C for the indium. The surface concentrations obtained from these experiments are based on four-probe measurements and are shown in Fig. 4.

The three different germanium temperatures give three sets for the number pair: absolute temperature of the indium, surface concentration. If for a set the log of the surface concentration is plotted *vs.* the inverse absolute temperature of the indium source, the graph through these points can be approximated rather well by a straight line which may be described by the equation

$$C_o = \exp\left[-\frac{m}{T} + p\right] \qquad [11]$$

Figure 4 shows the three straight lines a, b, and c which have been obtained from the application of the method of least squares to the sets of points which belong to the germanium temperatures 900°, 837°, and 775°C, respectively.

The numerical values for the constants m and p, as determined from the lines a, b, and c are listed in Table I. The spreading of the points around line b is indicated by line segments. The numbers on top of these segments give the numbers of points measured at the corresponding temperature. The spreading of points for lines a and c is similar to the spreading for line b. For the benefit of clearness no line segments are given for a and c.

The dashed line gives the log of the concentration of indium vapor in (atoms/cm³) x 10^7. The factor 10^7 was applied to the actual values in order to place the line in the vicinity of the other three. The concentration of the indium vapor was obtained from vapor pressure data (15).

From Fig. 4 it can be seen that the lines a, b, c are close together and nearly parallel to each other. This shows that the surface concentrations depend mostly on the concentration of the indium vapor and are less dependent on the temperature of the germanium. The slope of line a differs most from the slope of the indium vapor line. We think that this does not in-

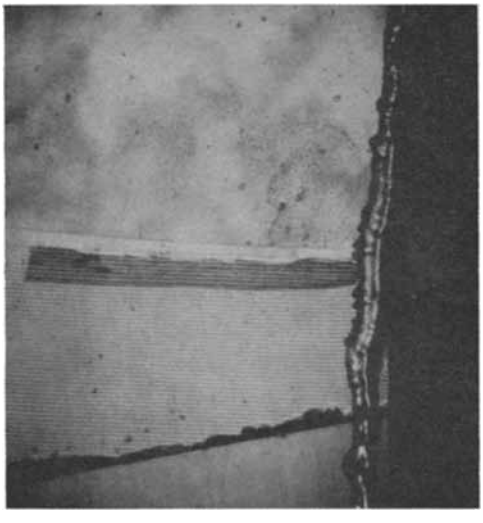

Fig. 3. A junction delineated by copper plating

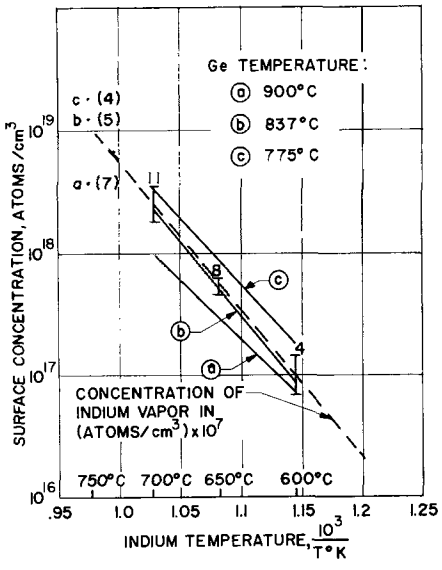

Fig. 4. Surface concentration *vs.* indium temperature for germanium temperatures of 775°, 837°, and 900°C.

Table I. Constants for Eq. [11]

Ge temp, °C	m	p
775	2.50×10^4	68.3
837	2.77×10^4	70.8
900	2.25×10^4	69.4

Table II. Impact rate of indium atoms at different temperatures

Ge temp, °C	In temp, °C	Indium vapor pressure, mm Hg	Impact rate, atoms/sec cm²
900	600	2.0×10^{-6}	1.91×10^{14}
	650	7.0×10^{-6}	6.70×10^{14}
	700	3.3×10^{-5}	3.15×10^{15}
837	600	2.0×10^{-6}	1.96×10^{14}
	650	7.0×10^{-6}	6.85×10^{14}
	700	3.3×10^{-5}	3.23×10^{15}
775	600	2.0×10^{-6}	2.02×10^{14}
	650	7.0×10^{-6}	7.07×10^{14}
	700	3.3×10^{-5}	3.34×10^{15}

dicate a special phenomenon but that the slope comes from two points which we did not want to omit but which were off from the bulk of the other points. While the rate of impacts of indium atoms on the germanium sample decreases with increasing temperatures at the same vapor pressure, the variation of the surface concentration with the germanium temperature is much stronger and cannot be explained by this effect. Table II lists numerical data which were obtained from the formula $\nu = 3.513 \times 10^{22}\ (P/(MT)^{1/2})$, where P is the vapor pressure of the indium in mm Hg, M is the molecular weight of indium, and T is the temperature of the germanium (16).

The lines a, b, and c in Fig. 4 are nearly parallel to the dashed line. Therefore, the quotient: indium vapor concentration ÷ surface concentration is nearly constant and about 10^{-7}, which may be named the distribution coefficient of indium between solid germanium and indium vapor.

For the establishment of the lines a, b, c it was observed that points were used where the limit of solid solubility of indium in germanium was not exceeded. The values for the solid solubilities were taken from Trumbore (17) and are listed in Table III. Thus, one should expect that according to Table III and line a in Fig. 4 for a germanium temperature of, for example, 900°C, the solid solubility limit is exceeded when the indium temperature is higher than 740°C. It was interesting to note that for all germanium temperatures the surface concentrations, which were derived from four-probe measurements, continue rather smoothly into a range where the solid solubility is exceeded. This is demonstrated in Fig. 4 where the three single points a, b, c at 750°C represent centers of gravity for 7, 5, and 4 points, measured at germanium temperatures of 900°, 837°, and 775°C, respectively.

Special experiments were carried out to confirm that the surface concentration is independent of diffusion time. Indium being at 600° and 650°C was indiffused into germanium at 837°C for different times. Table IV shows that the surface concentration is constant with time within tolerable limits.

Table III. Solid solubilities for indium in germanium (17)

Temperature, °C	Solid solubility, atoms/cm³
775	4.0×10^{18}
837	3.5×10^{18}
900	2.0×10^{18}

Table IV. Time dependence of the surface concentration of indium (indiffused at 837°C)

Temp of the indium source, °C	Diffusion time, hr	Surface concentration by four-point-probe, atoms/cm³
600	9.0	8.0×10^{16}
	16.0	9.5×10^{16}
650	2.5	4.0×10^{17}
	10.5	5.5×10^{17}
	16.0	3.5×10^{17}
	22.0	4.6×10^{17}

Table V. Comparison between four-probe and infrared absorption measurements

Sample No.	Ge temp, °C	In temp, °C	No. of indiffused indium atoms, atoms/cm² four-point probe	infrared absorption
1	775	750	2.4×10^{15}	2.5×10^{15}
2	775	750	2.4×10^{15}	1.6×10^{15}
3	775	750	2.4×10^{15}	2.4×10^{15}
4	837	750	1.8×10^{15}	1.9×10^{15}
5	837	750	5.6×10^{14}	8.1×10^{14}
6	900	700	1.8×10^{15}	1.8×10^{15}
7	900	725	7.6×10^{14}	6.3×10^{14}
8	900	750	1.5×10^{15}	1.9×10^{15}

The evaluations of four-probe and of infrared absorption measurements both lead to the number of p-type carriers/cm² indiffused into the germanium. Making measurements by both methods on some samples and using Eq. [1], [8], and [10] for the evaluation of s/q, the data of Table V result. The good agreement between the s/q values of this table indicates the reliability of the four-probe measurements.

All samples to which the four-point-probe method was applied underwent a junction delineation, which has already been described. However, in early experiments it was found that the surface concentrations derived from the junction depths scattered considerably in spite of the fact that the various delineation methods were in good agreement. Junction depths obtained from copper plating and dielectric powder deposition for the same sample were in nearly all of the cases within an error of about 0.25μ. Similar results were obtained by the thermoelectric probe. But because of the probe width the limits of error were greater.

For the evaluation from junction depth measurements, the value of the net ionized antimony concentration must be known because the surface concentration is given by

$$C_o = \frac{C(x_j,t)}{\operatorname{erfc} \frac{x_j}{\lambda}} \qquad [12]$$

where $C(x_j,t)$ is the net ionized antimony concentration at the junction.

The initial concentration, C_B, of the antimony is determined by the doping and is uniform throughout the whole piece of germanium. During the experiment outdiffusion and thermal conversion can take place. Outdiffusion would lead to concentrations near the surface which are smaller than C_B, and thermal

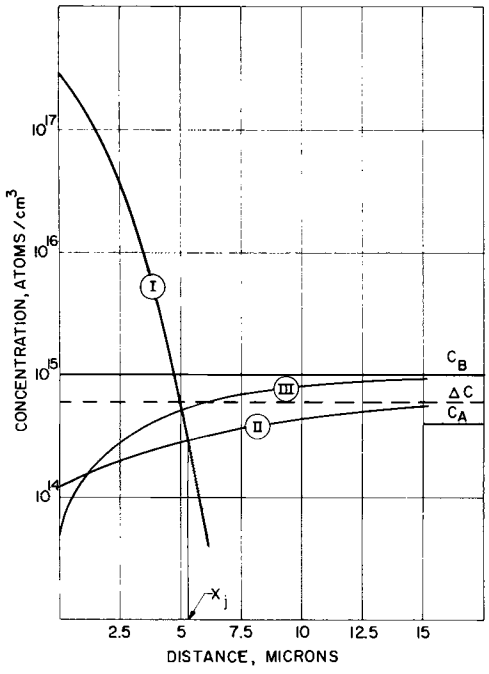

Fig. 5. Typical p- and n-type concentration distributions

conversion would result in a uniform bulk concentration C_A which is smaller than C_B. The concentration distribution after an outdiffusion time of t seconds is given by (18)

$$C_{out} = C_B \left\{ \operatorname{erf} \frac{x}{2(Dt)^{1/2}} + \exp\left[K\frac{x}{D} + K^2\frac{t}{D} \right] \operatorname{erfc}\left[K\left(\frac{t}{D}\right)^{1/2} + \frac{x}{2(Dt)^{1/2}} \right] \right\} \quad [13]$$

where D is the diffusion coefficient for antimony in solid germanium and K is a constant, the surface evaporation velocity.

The above-mentioned concentration distributions are shown in Fig. 5. The curves shown here are typical for many samples.

The concentration of the indiffused indium is plotted *vs.* the distance from the surface and is represented by curve I, which is a graph of $C = C_o \operatorname{erfc} x/\lambda$. Curves II and III are graphs of Eq. [13] and show the concentration distribution of the antimony (for $t = 16$ hr and $T = 837°C$) after the experiment has been completed. For both curves II and III the values of K are from a paper of Miller and Smits (19). The value for the diffusion coefficient of curve II has been taken from Bösenberg (8) and for the diffusion coefficient of curve III from Blakeslee (20).

After each experiment 25μ were lapped off the nonpolished side of the sample, and the bulk resistivity was measured with the four-probe. A change from C_B to C_A due to thermal conversion could be observed for almost all of the samples. The difference $C_B - C_A = \Delta C$ is equivalent to p-type centers introduced by thermal conversion and therefore represents a p-type level. For each sample it was tried to determine the net ionized antimony concentration $C(x_j,t)$ in such a way that the concentration profile I, which met $C(x_j,t)$ at x_j matched a surface concentration which was close to the surface concentration observed from four-probe measurements. Several possible cases were considered for the determination of $C(x_j,t)$:

1. $C(x_j,t) = C_A$
2. $C(x_j,t) = C_{out,II}$
3. $C(x_j,t) = C_{out,II} - \Delta C$
4. $C(x_j,t) = C_{out,III}$
5. $C(x_j,t) = C_{out,III} - \Delta C$

The best result was found for case 2, for which nearly half of the surface concentrations were within a factor of 3 or less in agreement with the surface concentrations from the four-probe measurements.

This led us temporarily to the assumption that thermal conversion measured for the bulk is negligible for a thin surface layer. In the light of new findings for the value of the diffusion coefficient of antimony in germanium (20) however, cases 4 and 5 have to be considered. Case 4 offers no good agreement, whereas case 5 gives a good fit for nearly a third of the samples. The other cases lead to inconclusive results. Therefore, for the present time we have no explanation why the junction delineations are so far off. For a better understanding of the whole situation it would be important to determine the net ionized antimony concentration at the junction by direct measurements, *e.g.*, by capacitance measurements.

It was observed that at higher indium temperatures the surface concentrations derived from junction depth measurements were higher by a factor of 10-10^3. The possibility that field-aided diffusion (21) was responsible for the inconclusive results could be excluded because the condition that the intrinsic carrier concentration was much smaller than the surface concentration was not fulfilled in any run. It seems as if the large disagreement between the surface concentrations from resistivity measurements and junction delineation starts when solid solubility values, given by Trumbore (17), are exceeded. This indicates that the assumed error-function distribution no longer holds. It is, therefore, surprising enough that the resistivity measurements still give consistent values (see points a, b, and c in Fig. 4).

Summary

1. Numerical values for the surface concentration of indium diffused into germanium at 775°, 837°, and 900°C are given.

2. The surface concentrations depend mostly on the concentration of the indium vapor and only to a small extent on the germanium temperature.

3. The surface concentrations are proportional to the concentration of the indium vapor phase with a "distribution coefficient" of about 10^{-7}.

4. Resistivity measurements, which are in good agreement with infrared absorption measurements, give the most consistent values for surface concentrations.

Acknowledgment

The authors want to thank Dr. Kurt Lehovec for helpful discussions and advice and Dr. Hans Reinheimmer for the infrared absorption measurements.

Manuscript received April 5, 1961; revised manuscript received July 20, 1961. This paper was pre-

pared for delivery before the Chicago Meeting, May 1-5, 1960.

Any discussion of this paper will appear in a Discussion Section to be published in the December 1962 JOURNAL.

REFERENCES

1. L. B. Valdes, *Proc. I.R.E.*, **42**, 420-427 (1954).
2. G. Backenstoss, *Bell System Tech. J.*, **37**, 699 (1958).
3. R. Glang and W. B. Easton, *This Journal*, **107**, 758 (1960).
4. F. M. Smits, *Bell System Tech. J.*, **37**, 711 (1958).
5. L. P. Hunter, "Handbook of Semiconductor Electronics," 1st ed., p. 7-5, McGraw-Hill Book Co., New York (1956).
6. M. B. Prince, *Phys. Rev.*, **92**, 681 (1953).
7. F. A. Trumbore and A. A. Tartaglia, *J. Appl. Phys.*, **29**, 1511 (1958).
8. W. Bösenberg, *Z. Naturforsch.*, **109**, 285 (1955).
9. H. B. Briggs and R. C. Fletcher, *Phys. Rev.*, **91**, 1342 (1953).
10. N. J. Harrick, *ibid.*, **103**, 1173 (1956).
11. N. J. Harrick, *J. Phys. Chem. Solids*, **14**, 60 (1960).
12. W. L. Bond and F. M. Smits, *Bell System Tech. J.*, **35**, 1209 (1956).
13. R. Glang, *This Journal*, **107**, 356 (1960).
14. L. B. Valdes and K. D. Smith, "Transistor Technology," vol. I, H. E. Bridges, J. H. Scott, and J. N. Shive, Editors, p. 290-292, D. Van Nostrand Co., Inc., New York (1958).
15. R. E. Honig, *RCA Rev.*, **18**, 195 (1957).
16. S. Dushman, "Vacuum Technique," fourth printing, p. 17, John Wiley & Sons, Inc., New York (1958).
17. F. A. Trumbore, *Bell System Tech. J.*, **39**, 205 (1960).
18. K. Lehovec, K. Schoeni, and R. Zuleeg, *J. Appl. Phys.*, **28**, 420 (1957).
19. R. C. Miller and F. M. Smits, *Phys. Rev.*, **107**, 65 (1957).
20. A. E. Blakeslee, Paper presented at Chicago 1960 Meeting of The Electrochemical Society, Abstract No. 106.
21. A. D. Kurtz and R. Yee, *J. Appl. Phys.*, **31**, 303 (1960).

The Chemical Polishing of Germanium

B. A. Irving

Research Laboratory, Associated Electrical Industries, Aldermaston Court, Aldermaston, Berkshire, England

ABSTRACT

The mode of action of the components of the polishing solution CP4 has been elucidated. The initiation of dissolution is dependent on the state of the germanium surface and the concentration of bromine. The final etch rate is limited by the diffusion of hydrofluoric acid to the germanium surface and even though the oxidizing agent, nitric acid, is in excess, the surface is free of detectable oxide. A difference in reactivity between ground and chemically polished surfaces has been demonstrated. Certain observations relevant to the practice of etching are made.

An important step in the manufacture of devices such as diodes and transistors from germanium single crystals is the chemical polishing of cut slices, usually with C.P.4[1] to produce clean surfaces free from cutting damage to which alloy contacts can subsequently be made. A similar treatment is used in the assessment of crystal quality and in the preparation of crystals for electrical measurements such as the lifetime of minority carriers. In the present investigation the chemical significance of each component of the polish was determined.

Experimental

The surfaces of the crystals were prepared by grinding (600 grade carborundum paper) and in some cases followed by chemical polishing. Etch rates were determined from the weight loss of slices etched for a measured time. Weight losses were determined for several different times in the same etchant so that any change of rate in the course of etching became apparent. The surface area of the slices was estimated from their weight and thickness (determined with a micrometer) and did not change significantly during the course of several etch rate measurements. Results were calculated in terms of weight loss (mgm) per square centimeter, and this quantity was plotted against time. The slope of the plots gives the etch rate. Slices of several crystals were used, but when a specific comparison was required, for instance between a ground surface and a chemically polished surface, adjacent slices of the same crystal were used.

The following etching technique was employed and gave reasonable reproducibility (about ±5%). A ring of polythene was cut from a 1/16 in. sheet so that it was somewhat smaller in internal diameter than the width of a slice. The ring was put round the slice so that the latter rested in a polythene beaker at about 45° to the horizontal. Both sides were thus attacked simultaneously when the slice was covered with etchant. After a measured time the etching was stopped by flooding with a large quantity of distilled water (at least 10 times the capacity of the beaker) poured through a polythene funnel which dipped into the etchant. A fresh portion of etchant was used for each measurement.

The potential differences between ground and chemically polished surfaces under etching and non-etching conditions were measured with the aid of a recording millivoltmeter. For these, a slice of germanium was ground on one side and gold plated with a standard cyanide solution using a brush plating

[1] The recipe for C.P.4 is: 25 ml nitric acid (conc); 15 ml hydrofluoric acid (conc); 15 ml acetic acid (glacial); 0.3 ml bromine. The bromine is first dissolved in the acetic acid and the other acids added. C.P. 8 is C.P.4 without bromine.

Table I. Ageing of C.P.4 and C.P.8

Time, min	C.P.4 Etch rate, mg/cm²/min Initial	Final	C.P.8 Etch rate, mg/cm²/min Initial	Final
0	1.7	7.1	7.1	
15	0.6	7.0	7.0	
30	0.8	7.7	6.5	6.8
45	1.2	7.9	6.9	
60	1.0	7.7		
75	1.8	7.5		
90	1.8	6.6		
Mean	1.3	7.3	6.9	6.8

Initial etch rate: measurements taken within the 1st minute of etching.
Final etch rate: measurements taken between 2nd and 4th minute of etching.

technique. The slice was cut in two and each half had a wire fixed to the gold plating with silver paste. The joint was cemented with epoxy resin and the specimen, except for the front face, was sealed into polythene. The faces of both specimens were ground and one was chemically polished.

Etchants were made up from Analar reagents. A stock solution of 5% bromine in acetic acid was used to prepare etchants with intermediate bromine concentration. For some experiments nitric acid was freed from lower nitrogen oxides by refluxing in a stream of nitrogen already saturated with nitric acid fully oxidized by ceric nitrate. Urea was added to an etchant by dissolving a small quantity (~¼g) in the acetic acid used.

Results

The following experiments were performed. The etch rate of previously polished germanium surfaces was determined in both C.P.4 and C.P.8 immediately after these had been made up and at 15-min intervals. Results are given in Table I. In addition a slice showed the same rate when etched with a C.P.8 mixture used immediately or stored in a closed polythene bottle for 5 days.

The variation in etch rate during the course of etching was measured for both ground and polished surfaces in C.P.4 and in C.P.8. Results are given in Tables II and III and are plotted in Fig. 1. This variation was further examined for a series of etchants

Table II. Variation of etch rate with degree of etching

Time, min	Chemically Polished Surface Wt loss, mg/cm² C.P.4		C.P.8	
1	1.1	0.6	7.7	7.0
2	5.9	7.3	14.1	14.6
3	14.3	13.6	23.1	23.2
4	21.4	21.9	29.8	27.8

Table III. As Table II but with initial surface ground

	C.P.4	C.P.8
1	8.4	1.8
2	15.2	7.1
3	22.4	14.9
4	28.6	—

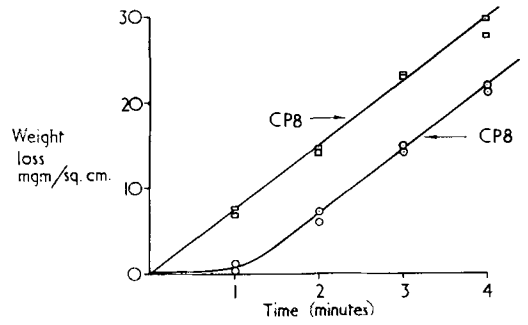

Fig. 1. Weight loss of a chemically polished surface of germanium in CP4 and CP8.

with intermediate bromine concentrations (0.01, 0.04, and 0.1% approx.), and Table IV gives the results. A considerably reduced bromine concentration gave more uniform attack on ground surfaces. A small quantity of hydrobromic acid (equivalent to about 0.5% Br_2) was added to a C.P.8 etchant. This, used immediately, behaved as normal C.P.8 on a polished surface and as C.P.4. on ground surfaces; neither surface showed an accelerating period. However, the etchant oxidized the hydrobromic acid to bromine. Bromine in acetic acid solution was injected into a beaker containing a slice being etched by C.P.8. It did not affect the weight loss or the apparent course of the reaction: bromine must therefore be present before the etching starts if it is to show its characteristic effects.

The etch rate of polished surfaces was determined for a series of etchants in which the amount of hydrofluoric acid was varied. The compositions of the etchants and the results are listed in Table V. A similar series in which the nitric acid concentration was varied was carried out and the compositions and results are given in Table VI and Fig. 2. A few experiments were performed in which the acidity was increased by using perchloric acid in place of acetic and/or nitric acid. Rates were similar to those with high nitric acid concentration, *i.e.*, replacing 5 ml of acetic acid by perchloric acid had similar effect to adding 5 ml of nitric acid in place of acetic acid.

A C.P.8 etchant made up with purified nitric acid gave the same etch rate as etchant with the usual nitric acid, demonstrating that the initial presence of nitrous acid is not essential for avoiding the accelerating period.

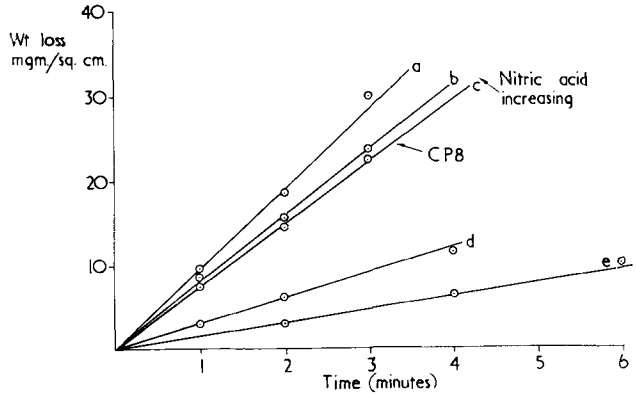

Fig. 2. Variation of weight loss (mg/cm²) with concentration of nitric acid.

Table IV. Variation of weight loss with bromine concentration

	Bromine concentration	Wt loss, mg/cm²				
		0 (C.P.8)	0.01	0.04	0.1	0.5 (C.P.4)
	Time					
Polished surface	1½ min	11.2	8.2	4.5	3.8	3.0
	3 min	22.5	19.7	16.4	—	14.5
Ground surface	1½ min	3.5	13.0	12.5	11.2	11.2
	3 min	15.0	23.2	24.4	24.2	22.5

Table V. Variation of weight loss with hydrofluoric acid concentration

		Wt loss, mg/cm²					
		C.P.8					
	Vol. hydrofluoric acid, ml	25	20	15	10	5	Nitric acid = 25 ml
Time	Vol. acetic acid, ml	5	10	15	20	25	
1 min		9.2	10.4	6.9	4.1	1.5	
2 min		23.0	26.0	15.1	7.6	2.8	
3 min		43.7	41.7	22.8	11.2	4.3	
4 min		—	—	30.5	14.9	—	
Final mean rate/min		~21	~16	7.5	3.8	1.4	

Table VI. Variation of weight loss with nitric acid concentration

		Wt loss, mg/cm²					
		C.P.8					
	Vol. nitric acid, ml	35	30	25	20	15	Vol. hydrofluoric acid, 15 ml
Time	Vol. acetic acid, ml	5	10	15	20	25	
1 min		9.5	8.5	7.7	3.1		
2 min		18.6	15.4	14.5	6.2	3.2	
3 min		30	23.8	22.4	—	—	
4 min					11.7	6.4	
6 min						10.1	
Final mean rate/min		~9.4	7.9	7.5	3.0	1.6	

The rate with an etchant containing urea was considerably lower than the normal rate. Urea reduces the nitrous acid available during etching.

A C.P.8 etchant already used for polishing germanium until a brown color due to reaction products persisted behaved as C.P.4. on a ground slice.

The potential difference between ground and polished surfaces of between 25 and 30 mv (ground surface more active) was recorded in an etchant made up with perchloric acid in place of nitric acid. In C.P.8. the difference in mixed potential decayed in about 1 min. Reversing the crystal preparations gave similar results, which could therefore be directly attributed to surface preparation.

Discussion

The results of the above experiments established certain facts which are summarized as follows.

There is no ageing effect with C.P.4. or C.P.8.

The etch rate of C.P.4. on a polished surface and C.P.8 on a ground surface builds up for about 1 min. The rate eventually reached is the same as that observed immediately for C.P.4 on a ground surface and C.P.8 on a polished surface.

The accelerating period is absent on a ground surface even when the bromine concentration is as low as 0.01%. At reduced concentrations of bromine on a polished surface the accelerating period is reduced, but is still nearly ½ min at 0.01% bromine.

The addition of hydrobromic acid to C.P.8 did not alter its etching characteristics provided it was used immediately after making up. The etchant slowly oxidized hydrobromic acid to bromine.

At hydrofluoric acid concentration lower than in C.P.8 etch rates on a polished surface were reduced, but were constant with time. At increased hydrofluoric acid concentration, etch rates increased as etching proceeded.

At reduced nitric acid concentration, etch rates on a polished surface were likewise reduced. Increased nitric acid concentration increased the etch rate only slightly, but caused considerable increase in bubbling.

Nitric acid free from lower oxides did not alter the etching of polished surfaces.

Etchants containing urea had lower rate on polished surfaces.

The presence of reaction products removed the accelerating period of C.P.8 on ground surfaces.

Potential measurements indicate that a ground surface is more reactive than a polished one.

The above facts conform to the following interpretation. The results at intermediate bromine concentration indicate that evaporation of bromine from C.P.4 is responsible for the alleged "ageing" of the etchant. These results also indicate that bromine adsorbs strongly onto polished surfaces and inhibits dissolution at low etch rate.

The constant rate exhibited by both C.P.4 and C.P.8 indicates that the rate of reaction is limited by the diffusion of hydrofluoric acid to the surface. The results of the experiments in which hydrofluoric acid and nitric acid concentrations were varied confirm this. The rates at high nitric acid concentration or when perchloric acid was added were rather more variable than most results, and this is attributed to the change in reduction product normally encountered with nitric acid. This produced excessive bubbling and turbulence and resulted in uneven surfaces. (Nitric acid can be reduced by metals or other reducing agents to nitric oxide or nitrogen dioxide depending on its concentration.)

This conclusion is in some ways surprising. The oxidizing agent, nitric acid, is in excess, but the surface produced by etching is free from any appreciable oxide layer. Holmes and Newman (1) failed to detect any oxide on chemically polished germanium by an electron diffraction method which could detect down to a monolayer. No visible oxide film was formed even at the lowest hydrofluoric acid concentration used. It would seem that the hydrofluoric acid participates in the oxidation reaction although it is not itself an oxidizing agent. (The situation is similar to that in some electropolishing processes. The rate of reaction is controlled by the diffusion of a reactant, although the anodic potential is theoretically great enough to cause extensive oxidation. A frequent, although by no means entirely satisfactory, explanation invokes a solid layer on the electrode surface in addition to the diffusion layer in the electrolyte.)

The oxidation of germanium by nitric acid has been investigated by Cretella and Gatos (2). The present etchant results are in substantial agreement with the mechanism they propose. However, their autocatalytic factors would seem unimportant in many instances, and a constant etch rate is established very quickly even though the nitric acid used in the etchant is free from lower oxides. The reduced rate in the presence of urea (which reacts with nitrous acid but not nitric acid $2HNO_2 + CO(NH_2)_2 \rightarrow 2N_2 + CO_2 + 3H_2O$) indicates the importance of nitrous acid to the etching. It is not certain that the urea removed all the nitrous acid produced by the reaction, but the rate of reaction of germanium with undissociated nitric acid must be appreciable. Usually a high surface concentration of nitrous acid is rapidly established by reduction of nitric acid, and the rate is then limited by the availability of hydrofluoric acid. The action of bromine is best understood in terms of the difference between ground and polished surfaces. The potential measurements indicate that the ground surface is more active and the value of 25-30 mv is quite large enough to change the reduction product of nitric acid from nitrous acid to nitric oxide (3). Nitric oxide and bromine react in the presence of water to give nitrous acid and bromide ion. Therefore bromine can promote the autocatalysis, due to nitrous acid, even though the ground surface produces only nitric oxide. In addition it was observed that bromide is oxidized to bromine by the etchant or at least the nitric acid it contains. Therefore bromine is regenerated and has its effect even though present in very small quantity.

In addition, the behavior of bromine-containing etchants on already polished surfaces suggests that it is adsorbed onto the surface. The adsorption increases the availability of bromine at the surface for reaction with nitric oxide. It also inhibits attack, and this can give rise to uneven attack at high bromine concentration even on ground surfaces. The absence of an accelerating period with C.P.8 containing reaction products, including nitrous acid, on ground surfaces is also in accord with this scheme.

Certain observations and deductions relevant to the practice of etching have emerged from this work. (*A*) Provided care is taken to avoid loss of bromine and hydrofluoric acid this type of chemical polish is stable and free from ageing effects. (*B*) The quantity of bromine in C.P.4 etchant can be reduced to about 1/50 that normally recommended to give a more even initial attack. (*C*) Bromine can be added more conveniently in the form of hydrobromic acid. The etchant oxidizes this to bromine. (*D*) Chemical polishing at a reduced rate takes place at lower hydrofluoric acid concentrations and produces a good surface. This modified etch would be useful for controlled thinning of specimens.

Manuscript received June 2, 1961; revised manuscript received Oct. 11, 1961.

Any discussion of this paper will appear in a Discussion Section to be published in the December 1962 JOURNAL.

REFERENCES

1. P. J. Holmes and R. C. Newman, *Proc. Inst. Elect. Engrs.*, **106B**, (Suppl. 15) 287 (1959).
2. M. C. Cretella and H. C. Gatos, *This Journal*, **105**, 487 (1958).
3. W. M. Latimer, "The Oxidation States of the Elements and their Potentials in Aqueous Solutions," 2nd ed., p. 93, Prentice-Hall, New York (1952).

The Stabilization of Germanium Surfaces by Ethylation

I. Chemical Treatment

G. W. Cullen, J. A. Amick, and D. Gerlich

RCA Laboratories, Radio Corporation of America, Princeton, New Jersey

ABSTRACT

It is proposed that the termination of each germanium surface atom in a (111) plane with an ethyl group should provide stabilization of the chemical composition of the surface, chemical stabilization being a prerequisite for the stabilization of electrical properties. The germanium surface is first activated with hydrogen chloride and chlorine gases and then ethylated by exposure to ethyl magnesium bromide. Evaluation by various methods indicates that ethyl groups are reproducibly and strongly bound to the surface in a ratio very close to one ethyl group for each surface atom. Details of the electrical and chemical evaluation are included in the following two papers.

The objective of the work described in this series of papers has been to gain further insight into the relationship between the electrical characteristics of a semiconductor surface and the chemical constituents bonded directly to the surface, and thus to learn better how to deal with the problems of control and stabilization of semiconductor surface properties.

The most common approach to surface stabilization has been to inhibit interaction between the surface and the ambient by application of a barrier over an etched surface. The chemical nature of such surfaces is not sufficiently well controlled to provide information on the relationship between the chemical and electrical nature of the surface since the species present subsequent to the inherently irreproducible etching processes are variable, and the nature of bonding at the surface is not defined.

Growth of oxide layers on silicon surfaces has provided more control over the species present on the surface (1), but the type of bonding at the surface is not clear cut since the substrate is crystalline while the oxide covering is amorphous (2).

It should be possible to prepare a chemically well-defined surface by choosing a material as a surface covering which bonds to each surface atom independently without imposing the requirements of a crystalline structure. These considerations have led to the proposal to terminate each surface atom with a saturated carbon chain. The preparation and evaluation described here is specifically concerned with the termination of each germanium surface atom in a (111) plane by an ethyl group. Ideally such a surface should exhibit the following characteristics:

1. A relatively nonabrupt transition from substrate to protective surface layer: The bonding in germanium is similar to that in carbon, thus the Ge-C bond at the interface should resemble the Ge-Ge bonds of the substrate and the C-C bond of the barrier. This should provide a more gradual transition of bond character than that, for instance, at the germanium-germanium oxide interface.

2. Termination of all the surface germanium atoms: Each carbon chain extending from a germanium surface atom is essentially independent of the carbon chain on the adjacent germanium atom; the cross section of the ethyl group is large enough to fill nearly the entire surface, but small enough to permit termination of each surface atom.

3. Chemical inertness: Germanium tetraethyl is an extremely stable compound which is not hydrolyzed by moist air. This stability indicates that the Ge-ethyl bond is strong and suggests that the ethylated surface should not be attacked by ambient constituents.

4. Insulating surface covering: Germanium tetraethyl is transparent to visible light and nonconducting. One may infer from this that the alkyl groups on the surface should also be nonconducting and thus should inhibit surface channeling.

Preparative Procedure

Ethylation of germanium surfaces is achieved by carrying out reactions at the surface which are analogous to well-known bulk reactions. The surface is activated by reacting the (hydrated) germanium oxide layer on the surface with hydrogen chloride and by reacting the underlying germanium with chlorine. The chlorinated surface is then exposed to ethyl magnesium bromide (a Grignard reagent) which replaces the chlorine atoms at the surface with ethyl groups in a manner analogous to the reaction

$$GeCl_4 + 4C_2H_5MgBr \rightarrow Ge(C_2H_5)_4 + 4MgBrCl$$

Very nearly quantitative yields have been realized in the preparation of tetraethyl germane by this procedure (3).

The ethylation process is described in the following sections. The treatment is designed to offer the greatest assurance of obtaining the desired surface,

and the complexity of the preparative procedure is of secondary importance.

In order to provide the greatest possible latitude in the initial preparative techniques, the stabilization of simple wafers, rather than of devices, was attempted. In particular, the (111) surfaces of both n- and p-type germanium were ethylated.

Sizing and cleaning of the sample.—The sample is cut from a single crystal and ground on a 240 grit wheel. Approximately 3 mils of material are removed from each surface by lapping with AO-305[1] abrasive. At least an additional 2 mils are removed from each surface with a fast etch ($2HNO_3$:1HF) to remove the mechanically worked layer left by the lapping operation.

It is essential to avoid the presence on the surface of strongly adsorbed ions which might interfere with subsequent steps in the reaction sequence. Fluoride ions are therefore carefully excluded from the surface at this point. If fluoride ions remain on the surface throughout the surface treatment, they may strongly influence the electrical characteristics of the final surface. For this purpose an etch free of hydrogen fluoride is used subsequent to the fast etch to act as a surface cleaning agent. The cleaning etch consists of 30% hydrogen peroxide saturated with oxalic acid dihydrate. The acid is added because it has been found that, in hydrogen peroxide solutions, the rate of dissolution of germanium increases rapidly with a decrease in *p*H below 5 (4). Oxalic acid, which is one of the strongest organic acids ($K_1 = 6.5 \times 10^{-2}$), provides a means of lowering the *p*H of the solution without adding ions which are diffcult to remove later. Oxalic acid is readily removed from the germanium surface following the etch, since it is decomposed by heat (186°C) or hot hydrogen peroxide into carbon dioxide and water, and it sublimes at 100°C. This treatment removes approximately 0.3 mil of material from the surface which carries with it strongly adsorbed contaminants remaining from the HNO_3-HF etch. Mass spectrometric data (5) show that, on heating, less gaseous material is released from a hydrogen peroxide-oxalic acid etched germanium surface than is released from germanium surfaces treated with other etching mixtures. The quantity of the gases evolved is taken as an indication of the total amount of material adsorbed on the surface.

Activation of the germanium surface.—The sample is activated and ethylated in the apparatus pictured in Fig. 2. The germanium is mounted in a glass clip on the end of a Trubore[2] rod which serves to center the specimen in the heating tube and provides for the rapid transfer of the sample into the various temperature zones. The two zones A and B are maintained at the proper temperatures with automatic controllers.

The sample is exposed for 15 min to pure argon at 144°-147°C and 1 atm pressure to drive off adsorbed moisture. The argon is first passed through type 5A Molecular Sieve[3] cooled to −78°C. The

[1] American Optical Co., Philadelphia, Pa.
[2] Ace Glass Co., Vineland, N. J.
[3] Linde Co., Union, N. J.

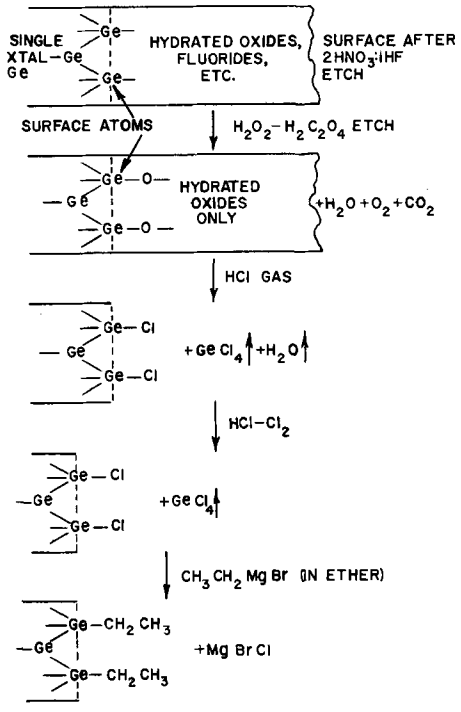

Fig. 1. Alkylation procedure, sequence of steps

sample is then exposed to hydrogen chloride gas at 144°-147°C for 20 min to remove all hydrous germanium oxide present. The water and germanium tetrachloride [bp 83.1 (6)] which form are volatile at this temperature.

The sample is lowered into zone B where the temperature is maintained at 87°-90°C, and an equal amount of chlorine (by volume) is then added to the HCl gas stream. The lower temperature is employed because above 100°C, in the presence of chlorine, an unidentified haze often forms on the germanium surface. At 87°-90°C in 20 min the chlorine removes approximately 0.2μ (by weight loss) from the surface. By removal of a small amount of germanium all impurities should be purged from the surface and each surface atom should then be occupied with a chlorine atom. Both tank gases and gases generated *in situ* (and dried with calcium sulfate and concentrated sulfuric

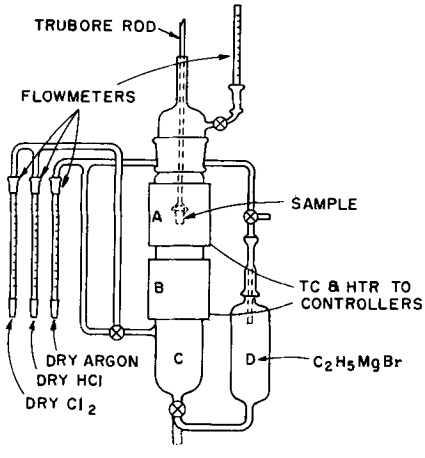

Fig. 2. Alkylation apparatus

acid) have been employed. The source of the gases does not appear to affect the final surface characteristics.

Ethylation.—The chlorine-hydrogen chloride gas mixture is flushed from the apparatus with dry argon, and the sample is lowered into zone C which is at room temperature. Ethyl magnesium bromide which has been prepared and stored in chamber D is forced into the reaction chamber. A stream of argon is allowed to flow into the apparatus at all times to maintain a positive pressure. The sample is allowed to remain immersed in the ethyl magnesium bromide for 15 min although radio tracer studies show that the surface alkylation reaction is essentially instantaneous (7). The excess ethyl magnesium bromide is then forced back into the storage chamber. When the sample is exposed to the atmosphere the ethyl magnesium bromide clinging to the surface immediately hydrolizes. The alkaline hydrolysis products are removed with slightly acidic aqueous ammonium chloride solution followed by distilled water. At this time the germanium surface is strongly hydrophobic.

Preparation of the ethyl magnesium bromide.—The ethyl magnesium bromide is prepared by reaction of ethyl bromide with magnesium turnings in dry ether. Details of the preparation may be found in organic texts (8). The reagent is made as concentrated as possible while avoiding solidification (approximately 5M at room temperature). Moisture and carbon dioxide are rigorously excluded during preparation of the reagent by carrying out the reaction in flamed glassware under an atmosphere of dry argon. The reagent is transferred to the storage chamber D in a completely closed system under argon.

Results and Discussion

The preparative procedure outlined above was developed from more primitive techniques in accordance with results from radio tracer analyses and electrical measurements. The procedure was modified, using these measurements as a control, until reproducibility and complete monolayer coverage with strongly bonded ethyl groups was achieved. These measurements are discussed in detail in the following two papers of this series.

The two major preparative uncertainties are the completeness of surface coverage and the effect of reagent impurities. Unfortunately, both of these factors may be only approximately evaluated by macroscopic chemical analysis due to the minute amount of material associated with a surface monolayer. More explicit information must be inferred from the surface electrical characteristics. A strong surface inversion layer (approx. 4 kT) is observed on ethylated n-type germanium. This may be an unanticipated characteristic of a completely ethylated surface or it may be associated with either of the preparative uncertainties mentioned above.

Occupation of a surface atom with an ethyl group may affect the chemical reactivity of adjacent surface atoms, and steric hindrance at a chlorinated atom surrounded by ethylated atoms may also play a role in the degree of surface coverage. It has been observed, however, that exposure of a chlorinated surface to lithium ethyl, which is an even more vigorous alkylating agent than ethyl magnesium bromide (9, 10), yields a surface with essentially the same electrical characteristics as that achieved with the ethyl magnesium bromide. If low reactivity of a partially ethylated surface were an important factor, one would anticipate that the use of ethylating agents of different reactivity would yield surfaces having different electrical properties.

The above observation also suggests that one may rule out the possibility that the surface electrical properties are strongly affected by adsorbed magnesium and lithium ions. It is anticipated that magnesium ions would have a different influence on the electrical properties than lithium ions.

Every effort has been made to exclude contaminants from the system prior to ethylation. The purity of the chlorine and hydrogen chloride gases is probably the most difficult factor to control. It was found that surface electrical properties were not altered if tank gases rather than gases generated in an all-glass apparatus with pure reagents were employed in the chlorination step. Moisture traps were used for the tank gases, the vapor pressure of the possible metal chlorides from tank gases is very low at room temperature, and surface adsorption of such contaminants as carbon dioxide or monoxide would be prevented by the more reactive major constituents. It is therefore assumed that the chlorination step does not introduce unknown impurities.

Since the electrical characteristics of an ethylated surface are essentially independent of the alkylating agent used and the source of the hydrogen chloride and chlorine gases, the origin of the surface inversion layer is not clear. This, as well as other questions presented in the subsequent papers, will be the subject of further investigation. All measurements available at this time, however, indicate that the procedure outlined above is effective in reproducibly preparing a surface essentially completely occupied with strongly held ethyl groups.

Acknowledgment

The authors are grateful to J. Baglio and J. Bacskai for their assistance in the preparation of the ethylated surfaces.

Manuscript received May 31, 1961; revised manuscript received Oct. 26, 1961. This paper was prepared for delivery before the Indianapolis Meeting, April 30-May 3, 1961.

Any discussion of this paper will appear in a Discussion Section to be published in the December 1962 JOURNAL.

REFERENCES

1. M. M. Atalla, E. Tannenbaum, and E. J. Scheibner, *Bell System Tech. J.*, **38** [3], 749 (1959).
2. *Loc. cit.*, p. 764.
3. C. A. Kraus and E. A. Flood, *J. Am. Chem. Soc.*, **54**, 1636 (1932).
4. This Laboratory, unpublished.
5. S. M. Fainshtein and V. I. Fistul, *J. Tech. Phys.*

(USSR), 26, 19 (1956). English Translation p. 2099.
6. H. S. Booth and W. C. Morris, *J. Am. Chem. Soc.*, **58**, 92 (1936).
7. J. A. Amick, G. W. Cullen, and D. Gerlich, *This Journal*, **109**, 127 (1962).
8. E. G. Rochow, D. T. Hurd, and R. N. Lewis, "The Chemistry of Organometallic Compounds," p. 86, John Wiley & Sons, Inc., New York (1957).
9. O. H. Johnson and W. H. Nebergall, *J. Am. Chem. Soc.*, **71**, 1720 (1949).
10. H. Gilman and R. N. Clark, *ibid.*, **68**, 1675 (1946).

The Stabilization of Germanium Surfaces by Ethylation

II. Chemical Analysis

J. A. Amick, G. W. Cullen, and D. Gerlich

RCA Laboratories, Radio Corporation of America, Princeton, New Jersey

ABSTRACT

Radiotracer techniques and mass spectrometry have been employed in analyzing ethylated germanium surfaces; the results from these two analytical techniques are in good agreement. The number of ethyl fragments on a treated (111) germanium surface is the same as the number of surface germanium atoms, within experimental error. The surfaces are stable at temperatures below 200°C in vacuum and in air, but begin evolving C_1 and C_2 fragments above 200°C. At higher temperatures, additional hydrocarbon fragments are seen mass spectrometrically. Using wafers having labelled ethyl groups, it has been found that the treated surfaces are stable to immersion in common chemical solvents.

As a result of research on the preparation of stable and reproducible semiconductor surfaces, a chemical treatment has been developed for germanium which is designed to bond ethyl groups to all surface atoms (1). Electrical measurements made on these surfaces show that they are unusually stable and insensitive to ambients (2).

To confirm the presence of ethyl groups on the treated surfaces and to enable a correlation of the electrical properties of the surface with its chemical composition to be made, suitable analytical techniques were required. For wafers of a few cm^2 total area, the number of surface fragments will be no greater than about 10^{15} for monolayer coverage. Both radiotracer studies and mass spectrometry were used in this investigation since they possess the required sensitivity, and since the two techniques give complementary information.

Radiotracer Studies

(111) wafers of germanium having labelled ethyl groups were first prepared by procedures more primitive than that described in the first report of this series (1). For the synthesis of the Grignard reagent, tritium labelled ethyl bromide was employed. The activity of the treated surfaces was used as a guide for modifying the treatment, leading finally to an ethylation procedure giving reproducible results and monolayer coverage. The consequences of exposing these treated surfaces to heat and to chemical solvents was then determined.

Materials and Equipment

The Grignard reagent used in preparing the ethylated surfaces, was synthesized from labelled ethyl bromide supplied by New England Nuclear Corporation. Tritium, rather than carbon, was chosen as the labelling atom since it can be obtained in much higher specific activity and can therefore be detected at lower concentrations than can C^{14}. With a half life of 12 years, the activity is essentially constant over a period of one or two months. Standard precautions were followed in the preparation and handling of Grignard reagent.

The apparatus used in the ethylation of germanium surfaces, was essentially a duplicate of that described earlier (1). Samples were counted in a 2π windowless gas flow counter[1] whose efficiency was found to be 0.670 using tritium labelled stearic acid films deposited on polished copper surfaces (3).

Concentration of Ethyl Groups on the Surface

The radio-ethyl bromide was supplied as Ethyl-1-H^3 Bromide in sealed vials containing 40 mg each, with a specific activity given as 27.7 millicuries per millimole. Each vial was specified to contain 10 millicuries. Before use, this material was diluted 1:100 with inactive ethyl bromide, making the ratio of labelled to unlabelled molecules 9.19×10^{-6}.

Corrections for back scattering and for counter efficiency were made on raw data. A factor of two correction is required because the counter detects radiation over only a 2π rather than a 4π solid angle. The number of ethyl groups on a treated surface can thus be calculated from:

$$N = \frac{C\,(1\text{-}0.275)\,(2)}{0.672\,A\,\lambda\,R}$$

where N is the number of ethyl groups per cm^2; C is the activity of the sample in counts per minute; 0.275 is the fraction of the radiation back scattered; 0.672 is the counter efficiency; A is the area of the sample in cm^2 = 0.816 cm^2; λ is the disintegration constant for tritium = 1.09×10^{-7} min^{-1}; R is the ratio of active to inactive ethyl bromide molecules.

[1] Nuclear Measurements Corp. Continuous gas flow proportional counter plus a Baird Atomic 132 Scaler.

Table I.

Sample	Average net cpm	Ethyl groups/cm² (±5% estimated)	Number of ethyl groups per surface Ge atom
1	117.8	3.12×10^{14}	0.43
2	105.9	3.1	0.43
3	134	4.08	0.56
4	29	0.75	0.10
5	212	5.62	0.77
6	211	5.59	0.77
7	234	6.20	0.85
8	234	6.20	0.85
9	254	6.73	0.92
10	282	7.47	1.0

The number of surface germanium atoms per cm² (111 plane) is given by Handler (4) as 7.3×10^{14}/cm².

Influence of Ethylation Procedure on Ethyl Group Concentration

The steps in the original ethylation procedure consisted of (*a*) an etch in CP-8 (HF-HNO_3) to remove any mechanically worked surface, (*b*) an oxalic acid hydrogen peroxide etch to remove undesirable ions from the surfaces (1), (*c*) chlorination in an HCl/Cl_2 mixture at 85°C, (*d*) without exposure to air, immersion in Grignard reagent for a few minutes, (*e*) rinsing with saturated ammonium chloride solution, then with water, and, finally, (*f*) drying in air at room temperature.

The influence of modifying the procedure may be seen in Table I. Samples 1 and 2 were treated according to the steps outlined above. Samples 3 and 4 were treated similarly except that the chlorination step (c) was omitted. Sample 3 has a reasonably large concentration of ethyl groups, but subsequent heat treatment showed that the surface was no longer heat stable. The concentration of ethyl groups on sample 4 is seen to be only 10% of that on sample 10. From this it is inferred that chlorination is an essential step in the surface treatment procedure. Samples 5 and 6 were heated in nitrogen at 120°C for 1½ hr following chlorination and preceding Grignard treatment. Samples 7 and 8 were similarly heated in nitrogen both preceding and following chlorination. Samples 9 and 10 were cycled three times between nitrogen heat treatments at 120°C and chlorination at 85°C prior to Grignard treatment.

With the cyclic treatments in nitrogen and HCl/Cl_2 mixtures, the number of ethyl groups on the surface was increased, presumably due to more complete chlorination of the germanium surface prior to Grignard treatment. Subsequent work has shown that equivalent results can be obtained by treatment in pure HCl at 144°-147°C and this has been incorporated into the standard ethylation procedure (1).

Sample 5 was allowed to stand in contact with the Grignard reagent overnight [step (*d*)]. The surface concentration of ethyl groups is seen to be about the same as for sample 6 which was in contact with the Grignard reagent for only a few minutes. Reaction of the chlorinated germanium surface is therefore presumed to be nearly instantaneous.

Following ethylation, the number of ethyl groups present on the germanium surface is seen to be very nearly one for each surface germanium atom (Table I, samples 9, 10). This is the ratio which would be expected using the simple conceptual model of a germanium surface in which each surface atom has a bond directed outward (normal to the surface) to which an ethyl group is covalently attached. Although the calculation assumes an atomically smooth surface, the statement would still be true, within experimental error, as long as the number of surface atoms is not increased by more than a few per cent because of surface roughness. For the germanium wafers used in this work, this seems a reasonable hypothesis.

If a thick hydrated oxide surface layer were "esterified" by this treatment, and if the structure were sufficiently porous to allow penetration of reagents into the layer, it is anticipated that more than one ethyl group would be present for each surface germanium atom. If ethane or some other hydrocarbon molecule were physically adsorbed on the surface, it would be surprising if exactly one molecule were present for each surface germanium atom.

Results of Exposure to Heat and Ambient

The Grignard treated surfaces appear stable to heating in air to about 200°C. Above this temperature they decompose and the radioactivity present on the surface decreases rapidly. This behavior may be seen in Fig. 1 where the activity on the surface, in counts per minute, is plotted as a function of time for sample 5 held at 335°C and for sample 6 held at 200°C. At 335°C the activity drops more than an order of magnitude in the first hour. After 4 hr at 200°C the activity has dropped to only about ½ the initial value. In Fig. 2, similar data for sample 9 (improved treatment) is presented. At 200°C the activity drops by about 10% and then remains constant during a 2-hr heat treatment during which the temperature is allowed to rise to 230°C. When the temperature is subsequently raised to 260°C the activity immediately begins to decrease. No loss in activity is observed for a sample kept in a vacuum for periods up to a day at room temperature, for a sample heated in a vacuum at 100° for 18 hr, or for a sample heated in a vacuum at 147°C for 5 hr.

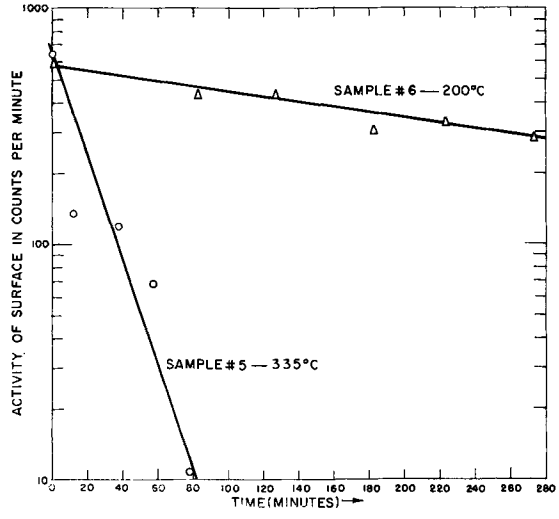

Fig. 1. Loss of radioactivity from ethylated germanium wafers during heating in air. Ethyl groups labelled with tritium.

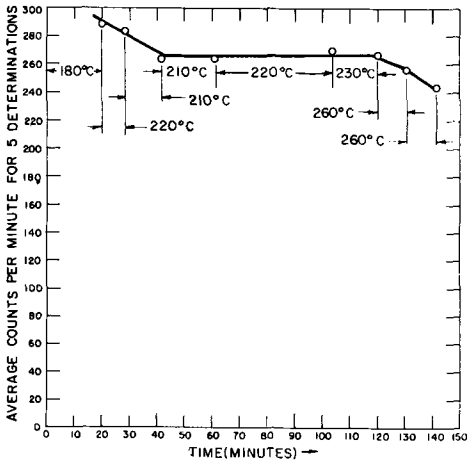

Fig. 2. Loss of radioactivity from an ethylated germanium surface during heating in air. Surface has one monolayer of ethyl groups, within experimental error. Ethyl groups labelled with tritium.

Results of Immersion in Common Chemical Reagents

The effect on the treated surface of immersion in some of the more common chemical reagents was determined in the following manner. A tritium labelled ethylated wafer was first placed in a beaker containing the reagent, and the solution was mechanically stirred for 3-5 min. The wafer was then removed, rinsed in water, dried, and counted. Results of these tests are shown in Table II. It will be noted that the surface is unaffected by immersion in the organic solvents tested, that small changes are observed when the surface is immersed in dilute acids, but that concentrated acids, and bases in all strengths, remove most of the activity from the treated surface.

From these experiments it is concluded that the labelled atoms are not present in molecules adsorbed on the surface. Adsorbed molecules should desorb in one or more of the solvents listed in the first column of Table II and should also desorb when the surface is heated moderately in vacuo.

Mass Spectrometry

To obtain analyses of the surface composition by mass spectrometry, it is first necessary to remove fragments from the surface. This has been done for the ethylated germanium surfaces by two techniques: (*a*) by sputtering with rare gas ions and (*b*) by heating *in vacuo*. The sputtering technique has the advantage that the temperature of the sample can be kept low and therefore rearrangement of fragments on the surface is minimized. The rare gas ions, however, introduce strong peaks of their own at the parent mass and at submultiples of the parent mass. This makes the detection of other radicals having masses in these regions difficult. Direct heating of the surface *in vacuo* is a very simple way of producing desorption of surface fragments. The surface may act as a catalyst at higher temperatures, however, and form new species not present originally. The interpretation of the spectra must therefore be made with caution.

Table II.

No change (within statistical error) (±3%)	Small changes (<10% removed)	Large changes (>10% removed)
Acetone	Ethyl bromide	0.1M NaOH 1.5M NH_4OH 3.0M NH_4OH
Amyl acetate Ether Ethyl alcohol	1.8M H_2SO_4 0.7M HNO_3	
Oleic acid Water Xylene		1M HCl 3.6M HCl 5M H_2SO_4 7.5M HNO_3

Spectra Obtained by Heating the Ethylated Surface

For analysis of the fragments desorbed by simple heating, a Diatron[2] 20 mass spectrometer was available. This instrument has several major advantages: The total volume is small. Thus, the absolute amount of gas needed for an analysis is a minimum and the sensitivity is high. The resolution is about 20; thus mass 20 is completely resolved from mass 21. The useful m/e range is 1-50 which is satisfactory for the present work. The instrument has been modified so that it is completely bakeable (5), which allows background pressures of 10^{-9} mm Hg to be obtained readily.

For the present work, the instrument was modified in two ways. A quartz sample tube wrapped with a heating tape was connected to the mass spectrometer through a Granville-Phillips[3] high vacuum valve. Secondly, a flap valve was included between the mass spectrometer and the diffusion pump. The fragments desorbed from the germanium surface are thus retained in the mass spectrometer chamber and their concentration increases as the heating proceeds. The temperature of the sample was monitored with an iron constantan thermocouple and a K-3 potentiometer.[4]

The entire system, including the quartz sample tube and the mass spectrometer, is first baked out at 350°C for several hours. After cooling, base pressures of 10^{-8} mm Hg are usually obtained. The mass spectrometer is then closed off from the sample area by means of the high vacuum valve. The sample tube is next cracked open and the sample is inserted. The sample tube is then sealed back onto the system, and the quartz section only is baked out at 500°C while the sample is kept in the Pyrex portion of the system at room temperature.[5] After a week of pumping the pressure is usually down to about 3×10^{-9} mm Hg.

In beginning a run, the ion gauge is turned off to prevent the pumping of fragments released by the surface, the flap valve is closed and a background spectrum is taken. The sample is then heated slowly until the surface begins to release hydrocarbon frag-

[2] Consolidated Electrodynamics Corp., Pasadena, California.

[3] Granville-Phillips Company, Pullman, Wash.

[4] Leeds and Northrup Co., Philadelphia, Pa.

[5] Initially, the sample tube was removed and resealed using a gas/oxygen flame. A test experiment showed, however, that during this sealing process, methane, carbon dioxide, carbon monoxide, and water were adsorbed on a clean, de-ethylated germanium sample, *i.e.*, one which had been baked out in the mass spectrometer at 400°C overnight. A new sample tube was consequently designed which would permit resealing without exposing the inner walls of the sample tube to the hot flame gases (Fig. 3). Hydrogen/oxygen flames were also used in order to minimize the presence of hydrocarbon impurities. With these precautions, impurities were reduced by an order of magnitude, but were not completely eliminated.

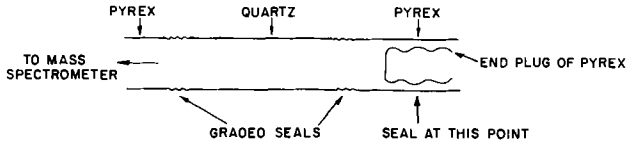

Fig. 3. Sample tube used for the thermal desorption of fragments from an ethylated germanium surface, showing the shape of the plug used for sealing the sample wafer into the system.

ments. Spectra are recorded continuously, each spectrum (m/e 12 through 44) requiring about 8 min. The current through the heating tape was usually increased stepwise in such a way that the temperature of the quartz tube approached 150°, 225°, and 400°C in sequence, spectra being recorded during each step.

Results

Typical spectra obtained from an ethylated germanium surface are shown in Fig. 4 and 5. The first spectrum Fig. 4a, corresponds to the background fragments which appear even when the sample is kept at room temperature. The major peak is 28 and consists of both CO and N_2. Also present are water, carbon dioxide, and methane. This background spectrum was obtained with the quartz sample tube at 163°C.

The ethylated sample was inserted in the heated tube, and after a 10-min interval the second spectrum, Fig. 4b, was taken. The C_1 peaks have continued to increase as have the CO/N_2 and water peaks. Peaks in the C_2 region at 25, 26, and 30 are just becoming detectable.

When the quartz sample tube is heated to 211°C, the C_2 peak heights rise by almost two orders of magnitude while the C_1 and water peaks remain almost unchanged, Fig. 4c. As the heating of the sample to

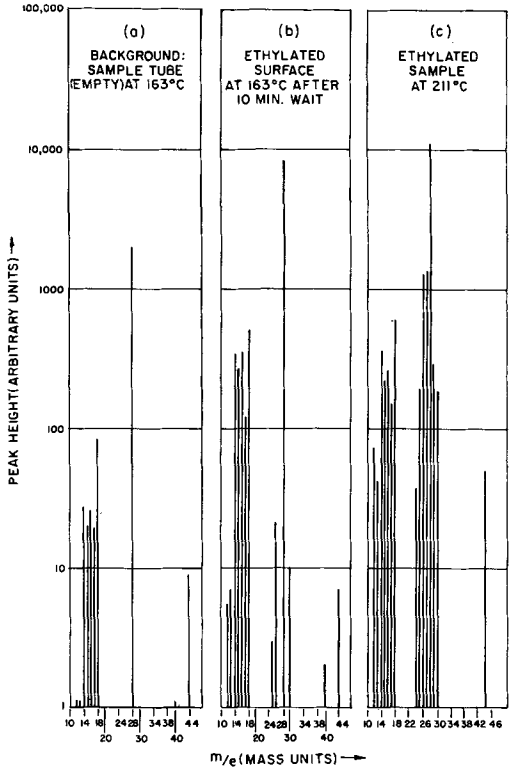

Fig. 4. Mass spectra of the fragments released from ethylated germanium surfaces by heating.

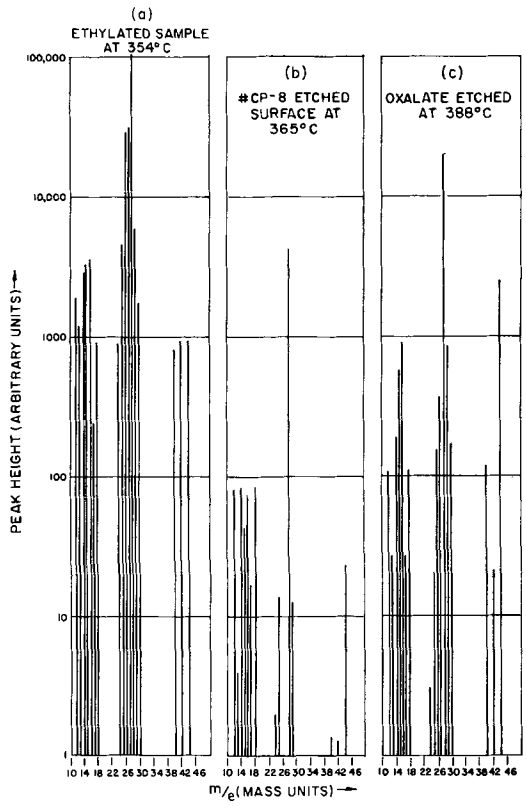

Fig. 5. Mass spectra of the fragments released from the germanium surfaces by heating. (a) ethylated surface at 354°C, (b) CP-8 etched surface, (c) oxalate etched surface.

successively higher temperatures continues, the pressure finally rises to the point where abnormal spectra having very broad peaks are obtained. This is apparently due to a continuous discharge occurring within the mass spectrometer. At this point, therefore, the temperature is held constant while the flap valve is opened for ½ to 1 min to pump out the accumulated gases. The valve is then closed and the heating continued.

Finally, the sample is heated to 354°C and the spectrum shown in Fig. 5a is obtained. The C_2 peak heights are much larger than in Fig. 4c, and new peaks, corresponding to C_3 fragments, are observed.

For comparison, the spectra obtained from a CP-8 etched wafer and from an oxalic acid-hydrogen peroxide etched wafer are also included in Fig. 5. These were obtained at temperatures greater than 350°C since it is only at these high temperatures that reasonable peak heights can be obtained. The CP-8 etched sample contains almost no C_2 or C_3 fragments. At temperatures up to 300°C, no C_2 or C_3 fragments can be detected on the oxalate etched wafer either. Even at the high temperatures, however, the C_2 peak heights are 100 times less intense than those obtained from an ethylated surface. It can thus be concluded that the C_2 peaks in the spectra of the ethylated surfaces are due to molecular fragments present on these surfaces before insertion into the mass spectrometer.

With the help of standard spectra taken under nearly equivalent conditions (6), it is possible to determine the composition of the gases resulting from vacuum heating. These are ethane, ethylene, acetylene, and methane, all of which would be expected

in the spectra of ethylated germanium surfaces. The ethane probably results from rearrangement of fragments on the hot quartz walls surrounding the sample.

Although no observation of the mass 1 or mass 2 peaks for hydrogen was made, an analysis of the average hydrogen to carbon ratio for the observed hydrocarbons was carried out. This ratio was 2.7 for the sample heated at 211°C, 2.3 for the sample heated at 354°C. If all of the hydrocarbons originated from ethyl groups on the surface, and if the desorption of hydrogen as H or H_2 were negligible, the ratio should be 2.5. This analysis is therefore consistent with the hypothesis of an ethylated germanium surface.

The stability of the surface at temperatures below about 200°C is also in agreement with the observations made on the tritium labelled surfaces, as is the occurrence of decomposition above 200°C. When an ethylated sample is heated to a given temperature, say 250°C, for the first time, and then pumped at that temperature for a period of several hours, the evolution of gas gradually ceases. If the sample is now heated above this temperature, say to 300°C, rapid evolution begins with the spectra having peaks at the same masses as obtained at the lower temperature. This behavior is characteristic of chemisorption where the binding energy of the groups on the surface depends on coverage.

Concentration of Surface Groups

The number of surface groups originally present on an ethylated surface can be estimated from (*a*) the surface area of the wafer, (*b*) the volume of the mass spectrometer and sample chamber, and (*c*) the pressure reached after most of the fragments have been removed from the surface. This estimate is only approximate because of the crudeness of the measurements involved, but should be good to within a factor of 10.

The ion gauge cannot be used directly to measure the pressure because of its strong pumping action for the hydrocarbon fragments. Although the reasons are not understood, this action is much less pronounced for water vapor and for nitrogen. The deflection of the chart recorder pen can thus be calibrated against the ion gauge during a background run where only water and nitrogen appear. Higher pressures of hydrocarbons can then be estimated using this calibration.

The total pressure can be estimated as the sum of the partial pressures of the major components present in the spectrum. In a spectrum such as Fig. 5a, the major peaks are 26, 27, and 28. Assuming that these are C_2 fragments which originated from ethyl groups on the surface, the total deflection can be taken as the sum of the individual deflections for these three masses only. For a typical spectrum, this leads to a surface concentration of ethyl groups of 10^{15} per cm^2, estimated accurate to within a factor of 10. This figure is in good agreement with the number of surface atoms per cm^2 in the (111) plane of germanium, 7.3×10^{14}. This calculation is thus in agreement with the radiotracer results which indicate that ethyl groups are present, within experimental error, in the ratio one for each surface germanium atom, and indicates that contaminating hydrocarbon layers, *e.g.*, of grease, are absent.

Although the sensitivity of the mass spectrometric technique is extremely high, no unusual impurities were detected. If fluorine or HF were present in small quantities (from the etching step), they would probably react rapidly with the quartz or the glass and would not appear in the mass spectrometer. Fragments which are not volatile, *e.g.*, Na or K ions, would not appear either and could only be detected in sputtering experiments. No oxygen containing fragments are observed except CO and CO_2 which are probably due to background. The only fragments which might be considered impurities are the higher hydrocarbon fragments, *e.g.*, C_3,C_4. These might be present in the original ethyl bromide in the concentrations observed on the surface, or they may result from rearrangement on the surface.

Spectra Obtained by Sputtering the Ethylated Surface

With a larger, higher resolving power mass spectrometer having a suitable sputtering source (7), several ethylated germanium wafers have been examined. In this instrument, the germanium wafer is mounted inside the ionization chamber of the mass spectrometer so that fragments released from the surface immediately become part of the ion beam. Rearrangement and loss of the fragments on the walls are therefore avoided. Although the argon ions are accelerated to 400v, the sputtering current is so low that the sample temperature is not perceptibly above room temperature.

Those fragments released from the surface as positive ions are recorded in Table III. Those fragments released from the surface as neutrals and ionized subsequently with an electron beam are recorded in Table IV.

Since the surface is partially decomposed during alignment of the source, it is not possible to obtain quantitative estimates of the species present. It is

Table III. Bombardment of ethylated germanium wafer by A^+ ions (400 ev): positive ions released from surface
Data from R. E. Honig (8)

Mass	Species	Intensity
15	CH_3	40
27	C_2H_3	100
29	C_2H_5	40
36-43	C_3H	Interference
51	C_4H_3	8
53	C_4H_7	15
74	Ge	1000
89	$GeCH_3$	20
91	GeOH	30
99	GeC_2H_1	6
101	GeC_2H_3	2
103	GeC_2H_5	1
113	GeC_3H_3(GeK?)	10
127	GeC_4H_5	3
129	GeC_4H_7	3
131	GeC_4H_9	2
146	Ge_2	16
162	Ge_2O	21

For simplicity, only those germanium peaks originating from the most abundant isotope, 74, are included. In the original spectrum, the normal isotopic distribution for germanium is observed.

Table IV. Bombardment of ethylated germanium wafer by A^+ ions (400 ev): neutrals released from surface
Data from R. E. Honig (8)

Mass	Species	Intensity
12	C	220
13	CH	70
14	CH_2	110
15	CH_3	220
16	CH_4	300
24	C_2	40
25	C_2H	150
26	C_2H_2	640
27	C_2H_3	280
28	CO, C_2H_4	1900
29	C_2H_5	60

(m/e = 30 not seen)

Because of ionization of argon in the electron beam, interference in the m/e = 40 region is severe. Peaks above m/e = 45 are too weak to be detected.

significant, however, that fragments consisting of an ethyl group attached to a germanium atom are observed, (Table III) whereas fragments consisting of an ethyl group, a germanium atom, and an oxygen atom are not observed. Further, $C_2H_5^+$ appears with a reasonably high intensity whereas $C_2H_5O^+$ is entirely absent. Since the oxygen containing fragments GeOH and Ge_2O do appear,[5] it can be deduced that the number of C_2H_5 groups bonded to the surface via an oxygen "bridge" is less than a few per cent of the number of C_2H_5 groups present. This observation is supported by the very weak intensity of the O^- peak seen in the spectrum of negatively ionized fragments released from the surface (8). Since no mass 30 peak is observed in the spectrum, the C_2H_5 groups cannot be present as adsorbed ethane. These observations therefore confirm the hypothesis that ethyl groups are bonded directly to germanium atoms in the surface. They also rule out such alternative possibilities as that the C_2H_5 groups are present as adsorbed ethane or ethyl alcohol or that an "ethyl germanate" surface results from the ethylation procedure.

Although the primary peaks for chlorine, 35 mass unit region, are masked by argon, no fragments consisting of a germanium atom or an ethyl group bonded to a chlorine are observed. The absence of chlorine containing fragments is taken as evidence that the reaction between the Grignard reagent and the chlorinated germanium surface is essentially complete.

Summary

Estimates of the number of surface groups per unit area, as obtained from the mass spectrometric data, agree well with the number obtained from radiotracer studies. This number corresponds, within experimental error, to one ethyl group for each surface germanium atom in a (111) plane. Ethyl groups are seen in the mass spectra of fragments sputtered from the surface, but no ethane is observed. Fragments consisting of ethyl groups attached to a germanium atom are also observed in these spectra, but no fragments containing chlorine and no fragments consisting of a germanium atom, a carbon atom, and an oxygen are detected.

Mass spectrometric analyses and radiotracer studies show that ethylated surfaces are stable in air and in vacuum below about 200°C. They are also stable to immersion in common organic solvents and in water. This supports the hypothesis that the surface layer consists of groups chemically bound to the surface rather than molecules adsorbed on the surface.

From these observations it is concluded that the treatment described in the first report of this series results in a (111) germanium surface in which an ethyl group is chemically bonded to each of the surface germanium atoms.

[5] The Ge-OH and Ge_2O peaks probably result from reaction of the bombarded germanium surface with background water. These peaks are relatively strong because reaction occurs continuously during sputtering, whereas the surface hydrocarbon monolayer is rapidly removed and is not regenerated. These peaks are in the same intensity ratio to the primary germanium peak (74) as for a bombardment cleaned (unethylated) germanium surface.

Acknowledgment

The radiotracer data on the ethylated germanium surfaces were obtained by Mrs. M. Tiner under the supervision of Dr. D. A. Ross at the Industrial Reactor Laboratories, Plainsboro, New Jersey. The mass spectrometric data on the sputtered germanium surfaces were obtained by Dr. R. E. Honig who also kindly made available the Diatron 20 mass spectrometer for the thermal desorption studies. The authors would also like to acknowledge the technical assistance of Mrs. J. Bacskai and Mr. J. Baglio.

Manuscript received May 31, 1961; revised manuscript received Oct. 26, 1961. This paper was prepared for delivery before the Indianapolis Meeting, April 30-May 3, 1961.

Any discussion of this paper will appear in a Discussion Section to be published in the December 1962 JOURNAL.

REFERENCES

1. G. W. Cullen, J. A. Amick, and D. Gerlich, *This Journal*, **109**, 124 (1962).
2. D. Gerlich, G. W. Cullen, and J. A. Amick, *ibid.*, **109**, 133 (1962).
3. M. R. Tiner and D. A. Ross, Private communication.
4. P. Handler, "Semiconductor Surface Physics," p. 25 ff, R. H. Kingston *et al.*, University of Pennsylvania Press, Philadelphia (1956).
5. R. E. Honig, "Vacuum Technology Transactions—Proceedings of the Sixth National Symposium New York," p. 20 ff, Pergamon Press, New York (1960).
6. Catalog of mass spectral data from American Petroleum Institute Project 44 obtained by Consolidated Engineering Corp., Pasadena, California, spectra No. 1—methane, No. 2 ethane, No. 128 ethylene and No. 192 acetylene.
7. R. E. Honig, *J. Appl. Phys.*, **29**, 549 (1958).
8. R. E. Honig, presented at the Mass Spectrometry Conference at Oxford University, September, 1961. To be published in *Proceedings, Joint Conference on Mass Spectrometry*, Oxford, September 1961.

The Stabilization of Germanium Surfaces by Ethylation

III. Electrical Measurements

D. Gerlich, G. W. Cullen, and J. A. Amick

RCA Laboratories, Radio Corporation of America, Princeton, New Jersey

ABSTRACT

Measurements of both the trapped charge density in the fast states and the surface recombination velocity as a function of the surface potential are reported for ethylated germanium surfaces. Measurements have been made at room temperature on n- and p-type wafers. The surface potential was varied over a range of 0.15v by the application of an a-c electric field normal to the surface. In the region of surface potentials examined, the charge distribution can be approximated by two discrete sets of surface states. The surface formed by ethylation have a concentration of fast states of the order of 5 x 10^{11} cm^{-2}. On n-type material a strong p-type inversion layer is formed; on p-type material the bands are nearly flat at the surface. Ethylated samples have also been examined by the large signal surface photovoltage technique and by observation of the slow states conductivity relaxation. Measurements on several samples and repeated measurements on the same sample in a series of different gaseous ambients show the surface structure to be reproducible, stable, and insensitive to ambients.

Extensive research has been carried out during the last several years on the electrical properties of germanium surfaces (1), and a fairly good concept of the electrical structure of these surfaces has evolved as a result of these investigations. Most of this work, however, has been done on germanium surfaces etched in CP-4 or some similar etch containing hydrofluoric acid. The chemical and structural features of the surfaces prepared in this manner are ill-defined, and it is therefore difficult to correlate the electrical properties of these surfaces with their chemical composition. It is desirable, therefore, to prepare a surface by a well-defined chemical treatment and correlate its electrical properties to its chemical composition.

At this laboratory, the approach to this problem was to create an active surface free of mechanical damage as far as possible on a germanium wafer and to react this surface with a chemical reagent which would bond ethyl groups to each surface atom (2). To monitor changes in the chemical procedure and to determine the influence which the chemical treatment has on the electrical properties of the wafer, electrical measurements were carried out on these surfaces. These included measurements of the large signal field effect, surface recombination velocity, large signal surface photovoltage and slow states conductivity relaxation on a number of different samples and in a series of different gaseous ambients. These measurements furnish information about the surface potential and the electronic structure of the surface states on the treated samples. Thus, hopefully, one will be able to correlate the chemical composition of these surfaces with their electronic structure.

Experimental Method

The germanium samples used in all measurements except the surface photovoltage were in the form of right parallelopipeds with the approximate dimensions of 0.03 x 0.4 x 1.2 cm^3, with ohmic tin contacts soldered to their ends. These were placed between two metal sheets which served as electrodes for the applied electric field, two Mylar[1] sheets of 0.0005 in. thickness serving as insulating spacers. The total capacity between the plates and germanium sample was of the order of 60 $\mu\mu$F. The quantities actually measured were the filament lifetime, τ_f, and the filament resistance, R_f, as a function of a 60 cps electric field which varied in amplitude from zero to a few hundred volts. The frequency was chosen so as to eliminate the relaxation effects of the slow states, while still being low compared to the response of the fast states (3-5).

τ_f was measured by means of a double bridge described in detail elsewhere (6, 7). The bulk lifetime of all the samples investigated was high enough (several hundred microseconds or more) so that effectively only surface recombination was active in the annihilation of the excess minority carriers. Thus the surface recombination velocity s could be determined directly from τ_f (8). R_f was measured by a modified Montgomery and Brown circuit (9). The changes in the measured R_f values are used to evaluate the changes in the surface conductance, and from these the surface potential ϕ_s is determined, ϕ_s being defined as $E_F - E_i$ where E_F is the Fermi level, E_i the intrinsic Fermi level at the surface. This is done by matching the observed and theoretical minimum of the surface conductance [as this minimum is independent of the surface states configuration, being determined solely by E_F (10)]. A modified Schrieffer correction for the surface mobility (11, 12) was used for computing the theoretical surface conductance *vs.* ϕ_s curve. s is thus determined at each ϕ_s value. Fin-

[1] DuPont registered trade mark.

ally from the voltage and the known capacity between the electrodes and the germanium sample, the total induced charge density can be determined. Subtracting from the latter the space charge density estimated theoretically (10-13), the trapped charge density in the fast states, Q_{fs}, is obtained.

The surface photovoltage was determined in a set up equivalent to that described by Johnson (14). The samples were in form of circular plates, about 1 cm in diameter and 3-4 mm thick. The back surface of each wafer was sandblasted after the chemical treatment, the photovoltage being measured on the front surface under high intensity light injection.

The slow states conductivity relaxation was measured with the same apparatus and on the same samples used for field effect studies. The only difference is that the applied field is d.c., and the off balance signal is followed with a recording potentiometer instead of an oscilloscope.

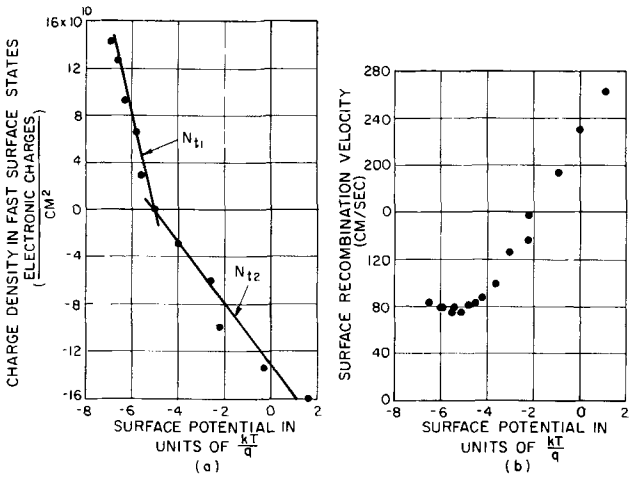

Fig. 1. Trapped charge density (a) and surface recombination velocity (b) *vs.* surface potential for an ethylated surface of an n-type sample, 15 ohm-cm resistivity in dry nitrogen (run 5 in Table I).

Results

Repeated runs of Q_{fs} and s *vs.* $q\phi_s/kT$ (q being the electronic charge) at room temperature were taken in a series of gaseous ambients over a period of several weeks. Usually the surface was exposed at least 24 hr to the ambient before making the measurement.

Figure 1 shows typical results for an n-type sample, resistivity 15 ohm-cm, (111) crystallographic plane, 6 days after ethylation, the sample having been kept in dry nitrogen all the time (run 5 in Table I). The circles in Fig. 1(a) represent the measured values of Q_{fs} *vs.* $q\phi_s/kT$. (Actually, Q_{fs} is the excess charge over and above the charge in the fast states at the quiescent surface potential, *i.e.*, the surface potential at zero applied field). The ultimate aim of the analysis of such results is to determine the energy E_t and concentration N_t of the fast states giving rise to this distribution. In principle this can be done by fitting the experimental curve with a Fermi distribution of the form

$$Q_{fs} = N_t \{1 + (1/2) \exp [(E_t - E_i - q\phi_s)/kT]\}^{-1} \quad [1]$$

or a sum of such terms, N_t and E_t are treated as parameters to be determined by the best fit, and the states are assumed to be spin degenerate. But since such a fit is not completely unambiguous (7), only an approximate analysis is carried out here. The experimental curve is approximated by two straight line segments, each of them attributed to a discrete fast state. The slope of the straight line determines the concentration of the state, being equal to $\frac{2}{9} N_t$ while the range in ϕ_s over which the particular segment extends determines the range in which E_t is to be found. Analyzing the curve in Fig. 1(a) in this manner, one can distinguish two states in these results; one closer to the valence band with a concentration N_{t1} of 4.0 x 10^{11} cm^{-2} and an energy $E_{t1} - E_i < -5kT$; the second state is closer to the conduction band with a concentration N_{t2} of 1.3 x 10^{11} cm^{-2} and an energy $E_{t2} - E_i > -5kT$. Another fact revealed by Fig. 1(a) is that the quiescent surface potential ϕ_{so} is about $-5kT/q$, *i.e.*, a strong p-type inversion layer of about 0.12v is formed on the ethylated surface, in contrast to CP-4 etched surfaces which usually tend toward forming an accumulation layer.

Figure 1(b) shows the complementary results of s *vs.* $q\phi_s/kT$ which were measured simultaneously with the field effect. As a result of the limited swing in ϕ_s due to the high concentration of the fast states and the strong inversion layer only a limited part of the extreme left branch of the $s(\phi_s)$ curve could be covered, and very little information can be drawn from it. Figure 2 shows similar results on the same filament, but in a gaseous ambient of dry oxygen (run 6 in Table I). The analysis is carried out in a completely analogous manner to

Table I. Values of characteristic fast states parameters for an ethylated surface on an n-type sample, 15 ohm-cm resistivity in dry nitrogen and oxygen

Run	Ambient	Time	$N_{t1} \times 10^{-11}$ cm^{-2}	$\frac{E_{t1} - E_i}{kT}$	$N_{t2} \times 10^{-11}$ cm^{-2}	$\frac{E_{t2} - E_i}{kT}$	$\frac{q\phi_{so}}{kT}$
1	dry N_2	0(0)	4.0	<—5	1.4	>—5	—4.6
2	dry N_2	1(1)	3.2	<—5	1.6	>—5	—4.6
3	dry N_2	4(4)	4.1	<—5	1.7	>—5	—4.5
4	dry N_2	5(5)	4.0	<—5	1.3	>—5	—4.6
5	dry N_2	6(6)	3.0	<—5	1.3	>—5	—5.0
6	dry O_2	1(7)	4.8	<—5.5	1.3	>—5.5	—5.3
7	dry O_2	2(8)	4.6	<—5	1.3	>—5	—5.5
8	dry O_2	5(11)	4.5	<—5	1.1	>—5	—4.2

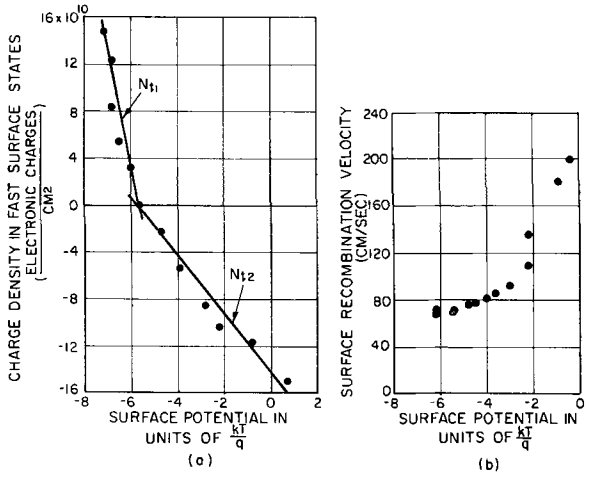

Fig. 2. Trapped charge density (a) and surface recombination velocity (b) *vs.* surface potential for an ethylated surface of an n-type sample, 15 ohm-cm resistivity in dry oxygen (run 6 in Table I).

the previous case. The Q_{fs} results show also in this case the presence of two states with concentrations $N_{t1} = 4.8 \times 10^{11}$ cm^{-2} and $N_{t2} = 1.3 \times 10^{11}$ cm^{-2}, and energies $E_{t1} - E_i < -5.5kT$ and $E_{t2} - E_i > -5.5kT$, respectively. Also here the surface exhibits a strong p-type inversion layer, and the $s(\phi_s)$ curve is similar in shape to that obtained with the nitrogen ambient.

Figures 1 and 2 are typical examples of a large number of runs on the same sample from immediately after ethylation to 11 days later. These runs are summarized in Table I, where the energies E_{t1} and E_{t2}, the concentrations N_{t1} and N_{t2} of the two states, as well as the quiescent surface potential $q\phi_{so}/kT$ are given. The column "time" shows the number of days during which the surface was exposed to the same ambient, while the numbers in parenthesis show the time elapsed since ethylation. The most striking feature of Table I is the stability and insensitivity of the ethylated surface structure to the different ambients, as contrasted to etched surfaces. The changes from run to run are well within the experimental error which is rather large due to the high concentration of fast states, the limited swing in surface potential, and the difficulty of using the $s(\phi_s)$ curves for the analysis of the surface structure. The quiescent surface potential is virtually clamped at -4 to $-5kT/q$ during the whole cycle, which shows that the Brattain-Bardeen gaseous cycle could not possibly have been used in the investigation of these surfaces.

Table II. Values of characteristic fast states parameters for an ethylated surface on an n-type sample, 30 ohm-cm resistivity in dry oxygen

Run	Time, days	$N_{t1} \times 10^{-11}$ cm^{-2}	$\frac{E_{t1} - E_i}{kT}$	$N_{t2} \times 10^{-11}$ cm^{-2}	$\frac{E_{t2} - E_i}{kT}$	$\frac{q\phi_{so}}{kT}$
1	0(0)	5.4	<-3			-4.1
2	1(1)	4.8	<-3			-3.8
3	2(2)	4.5	<-3			-3.8
4	3(3)	5.0	<-4	2.2	>-4	-4.4
5	4(4)	4.7	<-4	2.6	>-4	-4.2
6	6(6)			2.0	>-4	-5.5

Table III. Values of characteristic fast states parameters for an ethylated surface on an n-type sample, 16 ohm-cm resistivity in room temperature

Run	Time, days	$N_{t1} \times 10^{-11}$ cm^{-2}	$\frac{E_{t1} - E_i}{kT}$	$N_{t2} \times 10^{-11}$ cm^{-2}	$\frac{E_{t2} - E_i}{kT}$	$\frac{q\phi_{so}}{kT}$
1	0(0)	6.5	<-5	2.8	>-5	-4.8
2	1(1)	6.5	<-4	?	?	-4.2
3	2(2)	5.5	<-4	1.2	>-4	-4.7
4	4(4)	6.4	<-5	1.3	>-5	-5.2

Table II gives similar results for an n-type sample of 30 ohm-cm resistivity and (111) crystallographic plane, the sample having been kept in dry nitrogen during the whole course of the measurements. Table III shows similar results for an n-type sample, resistivity 16 ohm-cm, (111) crystallographic plane, the sample having been exposed to room atmosphere all the time. The results presented in both Tables II and III are extremely similar to those given in Table I, which shows that the ethylation forms a reproducible electronic structure which is very insensitive to changes in ambients ranging from dry nitrogen through dry oxygen to room atmosphere.

In order to check whether this particular surface structure is determined by the ethylation process or is due to some other factor, the same measurements were carried out on an n-type sample, resistivity 31 ohm-cm crystallographic plane (111) which has undergone only the oxalate etching process (2), and not the chlorination and ethylation steps. The results are shown in Fig. 3. As is readily seen, the structure which results is completely different from that of the ethylated surfaces. The undisturbed surface shows an accumulation layer, and the character of the $s(\phi_s)$ curve is completely different from the case of the alkylated surfaces.

Similar measurements have also been carried out on p-type material. Figure 4 shows typical results of Q_{fs} *vs.* $q\phi_s/kT$ for a p-type sample, 22 ohm-cm resistivity, (111) crystallographic plane, immediately after ethylation, the surface being exposed to dry nitrogen (run 1 in Table IV). It is evident that

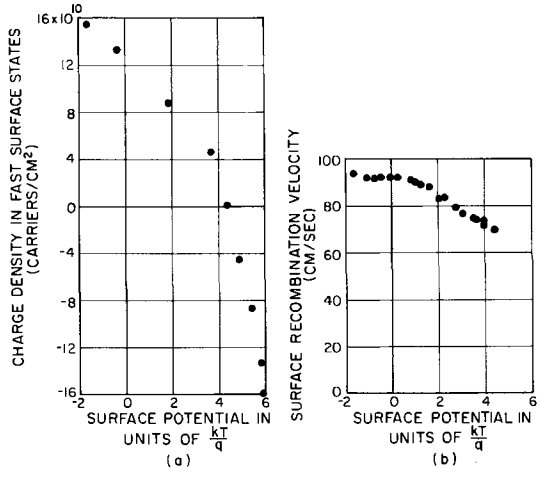

Fig. 3. Trapped charge density (a) and surface recombination velocity (b) *vs.* surface potential for an oxalate etched surface of an n-type sample, 31 ohm-cm resistivity in room atmosphere.

Table IV. Values of characteristic fast states parameters for an ethylated surface on p-type material, resistivity 22 ohm-cm in different gaseous ambients

Run	Ambient	Time, days	$N_{t1} \times 10^{-11}$ cm^{-2}	$\frac{E_{t1} - E_i}{kT}$	$N_{t2} \times 10^{-11}$ cm^{-2}	$\frac{E_{t2} - E_i}{kT}$	$\frac{q\phi_{so}}{kT}$
1	dry N_2	0(0)	10	<-3	3.0	>-3	-2.5
2	dry N_2	1(1)	8.4	<-2	4.7	>-2	-1.9
3	dry N_2	4(4)	8.2	<-3	4.1	>-3	-2.7
4	dry N_2	5(5)	10	<-3	4.6	>-3	-2.5
5	dry O_2	1(6)	7.0	<-2	3.8	>-2	-1.4
6	dry O_2	3(8)	7.2	<-2	3.4	>-2	-1.6
7	dry O_2	7(12)	?	?	3.2	>-2	-1.3
8	wet N_2	1(13)	3.2	<3	7.0	>3	2.9
9	wet N_2	3(15)	?	?	5.8	>3	3.3
10	dry N_2	0(15)	5.6	<-1	4.8	>-1	-0.4
11	dry N_2	3(18)	8.6	<-2	3.3	>-2	-1.8
12	dry N_2	4(19)	6.3	<-2	3.1	>-2	

the essential characteristics of the surface structure are the same as in the case of n-type material. The Q_{fs} results presented in Fig. 4 can also be explained by the presence of two levels, one closer to the valence band with a concentration $N_{t1} = 1.0 \times 10^{12}$ cm^{-2} and energy $E_{t1} - E_i < -3kT$, the second closer to the conduction band with a concentration $N_{t1} = 3.0 \times 10^{11}$ cm^{-2} and energy $E_{t1} - E_i > -3kT$. In this case the quiescent surface potential is close to the flat band position.

Table IV summarizes the results of a whole series of runs in different ambients on the sample described previously during a period of three weeks. Again one notes the similarity with the results for n-type material. Neither the fast states densities nor the quiescent surface potential changes appreciably in the different dry ambients. There is a change in these quantities in the measurements performed in wet nitrogen (100% relative humidity), a point which will be taken up later.

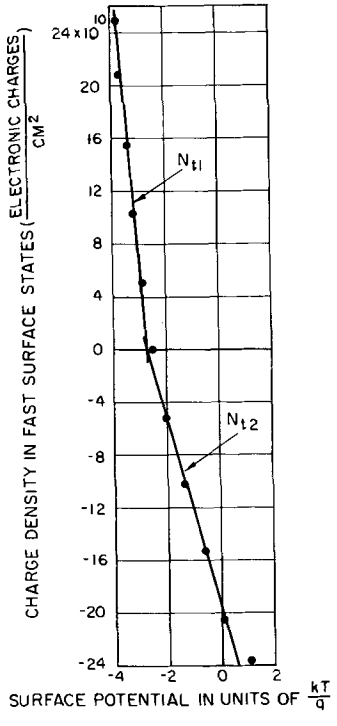

Fig. 4. Trapped charge density vs. surface potential for an ethylated surface of a p-type sample, 22 ohm-cm resistivity in dry nitrogen (run 1 in Table IV).

Preliminary measurements of the slow states conductivity relaxation were also carried out on the ethylated surfaces. Usually a d-c field of ± 800v was switched on and off, the conductivity variation being recorded continuously as a function of time. These relaxations are usually very long, of the order of hours. Apparently a highly insulating film has formed on the surface which slows down appreciably the leakage of charge from the space charge region and the fast states to the slow states. However, the surface relaxes back to its original state if one waits long enough, *i.e.*, all the charge initially induced in the fast states has looked to the slow states indicating that the latter are much more numerous than the fast states, and that there has been no permanent chemical change affecting the fast states during the cycle. Since the temperature stability of the system over extended periods was not good enough, no qualitative results concerning the slow states could be deduced.

Photovoltage measurements on ethylated wafers were carried out for both n- and p-type material. Table V lists the results of the photovoltage in units of kT/q (0.025 volts at room temperature) for an n-type sample, 15 ohm-cm resistivity, (111) crystallographic plane, in a series of gaseous ambients.

Table VI presents similar results for a p-type sample, 22 ohm-cm resistivity, (111) crystallographic plane. The measured photovoltage is given as such. It has been shown (14) that for complete saturation, the photovoltage is equal to $\phi_s - \phi_b$, where $\phi_b = E_F - E_i$ in the bulk, E_F being the Fermi level. Since in our case complete saturation has not been reached, the measured photovoltages are somewhat smaller than $\phi_s - \phi_b$. However, the meas-

Table V. Photovoltage for an ethylated surface on an n-type material, 15 ohm-cm resistivity in different gaseous ambients

Run	Ambient	Time, days	Photovoltage $\left(\frac{kT}{q}\right)$	Surface type
1	dry N_2	0(0)	-2.2	p
2	dry O_2	0(0)	-2.2	p
3	wet O_2 (100% relative humidity)	0(0)	-1.9	p
4	dry O_2	0(0)	-2.1	p

Table VI. Photovoltage for an ethylated surface on a p-type material, 22 ohm-cm resistivity in different gaseous ambients

Run	Ambient	Time, days	Photovoltage $\left(\frac{kT}{q}\right)$	Surface type
1	dry N_2	0(0)	−0.9	p
2	dry N_2	1(1)	−0.8	p
3	dry O_2	0(1)	−0.9	p
4	room atmosphere	3(4)	−0.4	p
5	wet O_2 (100% relative humidity)	0(4)	−0.4	p
6	wet N_2 (100% relative humidity)	0(4)	−0.4	p
7	wet N_2 (100% relative humidity)	1(5)	−0.5	p
8	dry N_2	0(5)	−0.5	p

urements are in agreement with the observation made with the field effect technique. Furthermore, these measurements show that the quiescent surface potential is not affected even by wet ambients; it remains essentially unchanged during the whole cycle of different ambients.

Discussion

Several conclusions concerning the ethylated surfaces can be drawn from the results presented above. The surfaces produced by this treatment are reproducible; completely different crystals yield essentially the same surface structure after ethylation. The quiescent surface potential is not affected appreciably by the whole gaseous cycle ranging from dry oxygen to wet nitrogen. This strongly suggests that the slow states on these surfaces are quite inert, being unable to absorb or desorb chemical species from or to the ambient. The character of the $Q_{fs}(\phi_s)$ and $s(\phi_s)$ curves is essentially the same for the different gaseous ambients, which indicates that the fast state structure stays constant. It can therefore be inferred that the ethylation treatment yields a reproducible and stable surface, one which does not change chemically in various gaseous ambients.

In contrast, for CP-4 etched surfaces, the quiescent surface potential will usually change over a range of 12 kT/q during the gaseous cycle (15-17), some changes in the fast states structure will occur due to exposure to different gaseous ambients (7, 18), and slow states conductivity relaxation is of the order of minutes (19).

The discrepancy between the photovoltage and the field effect measurements for the case of the wet ambients is probably due to irreversible changes caused by the action of the high electric fields on the surface in the presence of the wet ambient, on the surface. Such effects on etched surfaces have also been reported by other investigations (20-22) and might be due to ionic movement in a water film on the surface.

A puzzling feature of the ethylation treatment is the high concentration of fast states and the strong p-type inversion layer formed on n-type material. If one assumes that all the dangling bonds at the surface are occupied by ethyl groups, an assumption which is corroborated by tracer analysis and mass spectroscopy (23), then such a structure should, conceptually, be nearly electrically neutral. It is therefore difficult to conceive where the states observed on the ethylated surfaces can arise. On the other hand, the number of "dangling bonds" on a (111) germanium surface is of the order of 10^{14} cm^{-2} (24) so that, if only 1% were not saturated, they could account for the concentrations of the fast states appearing in our experiment. Incidentally the density of the fast states on ethylated surfaces is of the same order of magnitude as the density of fast states for etched surfaces (7, 9, 18). It is also possible that the fast states appearing on these surfaces are associated with distortions of the bonds connecting the ethyl groups to the germanium atoms, or with structural defects in the germanium layer beneath the ethyl groups, defects which have not been removed by etching prior to ethylation. Another possibility is that other groups besides ethyl are bound to the surface in small quantities during the treatment, and that these are responsible for the appearance of the fast states.

All these questions require further investigation before a complete understanding of the surface ethylation treatment can be achieved.

Acknowledgment

The authors wish to thank Mr. E. Margerum for his technical assistance and Mr. J. Baglio for his help in the ethylation treatment.

Manuscript received May 31, 1961; revised manuscript received Oct. 26, 1961. This paper was prepared for delivery before the Indianapolis Meeting, April 30-May 3, 1961.

Any discussion of this paper will appear in a Discussion Section to be published in the December 1962 JOURNAL.

REFERENCES

1. Two recent review articles on surface properties of semiconductors in which extensive literature is cited are: (*a*) J. T. Law, "Semiconductor Surfaces," in Semiconductors, N. B. Hannay, Editor, Reinhold Publishing Corp., New York (1959); (*b*) R. H. Kingston, *J. Appl. Phys.*, **27**, 101 (1956).
2. G. W. Cullen, J. A. Amick, and D. Gerlich, *This Journal*, **109**, 124 (1962).
3. R. H. Kingston and A. L. McWhorther, *Phys. Rev.*, **98**, 1191 (1955).
4. H. C. Montgomery, *ibid.*, **106**, 441 (1957).
5. G. Dousmanis, *ibid.*, **112**, 369 (1958).
6. A. Many, *Proc. Phys. Soc. (London)*, **B67**, 9, (1954).
7. A. Many and D. Gerlich, *Phys. Rev.*, **107**, 404 (1957).
8. W. Shockley, "Electrons and Holes in Semiconductors," D. Van Nostrand Co., Inc., New York (1950).
9. H. C. Montgomery and W. H. Brown, *Phys. Rev.*, **103**, 865 (1957).
10. C. G. B. Garrett and W. H. Brattain, *ibid.*, **99**, 376 (1955).
11. J. R. Schrieffer, *ibid.*, **97**, 741 (1955).
12. R. F. Greene, D. Frankl, and J. N. Zemel, *ibid.*, **118**, 967 (1960).
13. R. H. Kingston and S. F. Neustadter, *J. Appl. Phys.*, **26**, 718 (1955).
14. E. O. Johnson, *Phys. Rev.*, **111**, 153 (1958).
15. W. H. Brattain and J. Bardeen, *Bell System Tech. J.*, **32**, 1 (1953).

16. J. Bardeen and S. R. Morrison, *Physica*, **20**, 873 (1954).
17. W. H. Brattain and C. G. B. Garrett, *Bell System Tech. J.*, **35**, 1019 (1956).
18. S. Wang and G. Wallis, *Phys. Rev.*, **105**, 1459 (1957); **107**, 947 (1957).
19. S. R. Morrison, *ibid.*, **99**, 1655 (1955).
20. J. T. Law and T. S. Meigs, *J. Appl. Phys.*, **26**, 1265 (1955).
21. V. G. Litovchenko and V. I. Lyashenko, *Soviet Physics-Solid State*, **1**, 1470 (1960).
22. Y. Margoninski and H. E. Farnsworth, *Phys. Rev.*, **123**, 135 (1961).
23. J. A. Amick, G. W. Cullen, and D. Gerlich, *This Journal*, **109**, 127 (1962).
24. P. Handler, "Semiconductor Surface Physics," University of Pennsylvania Press, Philadelphia (1957).

Method for Analyzing Volatile Silicon Compounds

W. J. McAleer, M. A. Kozlowski, P. I. Pollak, and R. G. Denkewalter

Electronic Chemicals Research Department, Research Laboratories, Merck Sharp & Dohme, Rahway, New Jersey

ABSTRACT

A technique has been developed for the detection of donor impurities in volatile silicon compounds. The method consists of depositing a thin layer of elemental silicon from the silicon-containing vapor on to a single crystal wafer of high-resistivity silicon. Electrical measurements on the freshly deposited layer yield information about the effective concentration of total donor or acceptor impurities present in the volatile compound. The method is sensitive to at least 1 ppb of contaminating substance.

The use of Si in solid state electronic devices has produced the need for Si of an unusually high degree of purity. Many of the methods currently in use for producing ultrapure Si involve thermal or reductive decomposition of volatile Si compounds. It is important therefore to develop means of preparing the Si compounds in a highly purified state and to have an analytical method of extreme sensitivity for detecting electrically active impurities in the volatile semiconductor precursors. This work describes such an analytical technique based on the electrical behavior of impurities in the semiconductor itself.

The method developed in our laboratory consists of the deposition of a thin layer of Si from a vapor containing the volatile Si compound to be analyzed onto a single crystal wafer of high-purity Si. Examination of the type and resistivity of the freshly deposited layer can in an empirical manner reveal the type and quantity of the electrically active impurities present in the volatile compound.

It is important to note that, since the measurement employed shows only the final resistivity state of the Si, an integrated or net n- or p-concentration is determined. Thus, if the freshly deposited layer is found to be low resistivity, n-type Si, the volatile precursor compound contains a significant concentration of donor impurities. Conversely, if the volatile compound was contaminated with high levels of acceptor impurities, a p-layer of low resistivity would be formed. When lower levels of donors or acceptors are present, higher resistivity layers will result.

Analyses described here were carried out on trichlorosilane; however, the method is equally applicable to other volatile Si compounds and in principle could be used to analyze the volatile precursors of any semiconductor material.

Apparatus

The apparatus consists of a quartz reaction tube 18 mm in diameter and 30 cm long. The bottom (inlet) is tapered to receive 5 mm (ID) polyethylene tubing, and the top terminates in a 24/40 standard tapered quartz joint. A 24/40 ground glass (Pyrex) adapter is inserted in the top and extends, via Tygon tubing, to an oil bath bubbler through which the exiting gases are discharged into a fume hood. The gases are introduced into the reactor at the bottom through the vapor train sketched in Fig. 1.

The interior assembly consists of a quartz disk with a handle on top and a small hook on the bottom. The disk is of a diameter large enough to rest on indentations in the quartz reactor inserted just below the quartz joint. Suspended from the hook is a thin quartz rod (2 mm diameter and 12 cm long) on which the single crystal Si substrate is mounted horizontally. The Si is then virtually free of contact with the reactor.

An RF coil is fitted rather snugly around the wall of the quartz reactor to provide for the heating of the Si wafer. The coil, issuing from the RF generator on flexible leads, is mounted on a laboratory jack which permits easy raising and lowering of the coil in the vicinity of the wafer. RF heating is preferred since it allows the walls of the reactor to be cooler than the Si substrate, effectively eliminating deposi-

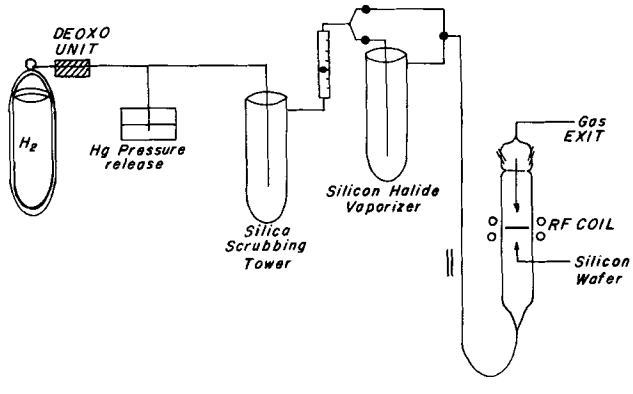

Fig. 1. Diagram of vapor train

tion of Si on the walls and decreasing the transfer of impurities from quartz to Si.

Operation

Silicon wafers 16 x 14 x 2 mm are cut from high-resistivity,[1] uncompensated (~1000 ohm-cm), zone-refined single crystals, and a 3 mm hole is drilled just off-center of the wafer. The Si piece is suspended from the thin quartz rod (described above) by slipping it over the hook at the top and sliding it down until it rests on a bead at the bottom. The wafer must lie approximately horizontally in the reactor to provide sufficient surface for RF coupling. If the crystal hangs perpendicularly, insufficient coupling occurs and the wafer cannot be raised to the proper temperature when an induction heater with a capacity of 5 kw operating at 4 megacycles is used.

The wafer, suspended on the quartz rod, is etched in 30 ml of warm (60°C) 50% potassium hydroxide solution for 5 min. High-resistivity (≧16 megohm) water is poured into the beaker to produce a more dilute solution (3:1), and the wafer is treated for an additional 15 min in this solution. The wafer is removed from the bath and washed copiously with the high-resistivity water. Finally, the piece is sprayed with reagent grade acetone and air dried.

The rod and wafer are attached to the inner assembly and the whole inserted into the reaction tube from above. The Pyrex adapter is fixed in place and a stream of hydrogen passed through the reactor for 15 min, at 0.8 liter/min, to purge it of air. The vaporizer line is also purged with hydrogen to insure complete removal of oxygen from all parts of the assembly before the Si wafer is heated. The total free volume in the system is approximately 250 cc; thus, at a plug flow rate of 0.8 l/min, the time required to displace the air with hydrogen is approximately 20 sec.

To effect RF coupling to the high-resistivity Si (which will not couple at room temperature) the wafer is heated to a red glow by warming the reactor wall immediately around the wafer with a hand torch burning a gas-oxygen mixture. As the Si piece glows red, torch heating is discontinued, and the RF coil, which has been held several inches below the wafer region, is cranked into place and the RF generator turned on to activate the coil. Coupling occurs immediately, and the wafer is brought to 1150°C (unconnected) by adjusting the power control on the RF generator to the proper setting. An optical pyrometer, accurate to ±2.5% in this temperature range, is used to check the temperature of the wafer.

When the desired temperature has been established, the hydrogen flow is continued for approximately ½ hr to effect a final *in situ* removal of SiO_2 from the substrate surface before deposition of Si is begun (1). The hydrogen stream is then diverted to pass through the vaporizer line and carry the trichlorosilane into the reactor. The hydrogen flow is held at 500 cc/min, and the trichlorosilane is at room temperature. Vaporization is carried out for 30 sec, and the stream of hydrogen is readjusted immediately by means of the two-way stopcock to allow pure hydrogen to pass through the reactor, purging it of residual trichlorosilane. Finally, the RF generator is turned off and the wafer allowed to cool to room temperature in a stream of hydrogen. Blank runs are carried out in identical fashion with the trichlorosilane step omitted.

[1] Although high resistivity Si was used throughout this work, lower resistivity material could be used since the requirement of nonconducting surfaces (cf. Measurement Section) is provided by the p-n junction.

Measurements

The thickness of the deposited n-layers is determined by angle lapping. The specimen is lapped in a jig of the sort described by Fuller (3), thus exposing the junction. The p and n areas are clearly delineated by applying the $HF \cdot HNO_3$ staining etch described by the same authors, and from the angle of a lap and a direct measurement of the exposed n zone the thickness can be calculated from the relationship: $X = d/\sin\theta$, where d is the horizontal distance across the stained surface. Following the deposition conditions given above, layers 1.0 mils in thickness are obtained.

The resistivity of the deposited Si layers is determined with a four-point probe apparatus (2). For a crystal of infinite thickness the resistivity ρ_o is given by the formula $\rho_o = (V/I)\,2\pi S$, where I is the current (amp) supplied to the crystal through the two outer probes, V is the potential difference (v) between the inner two probes, and S is the spacing between the probes (cm) where all spacings are made equal. For a finite geometry (*i.e.*, very thin layer) with nonconducting surfaces the necessary correction to the resistivity formula is given by the function $(\rho/\rho_o) = F(W/S)$, where W is the thickness of the layer and ρ_o the measured resistance. For values of $W/S << 1$ the factor reduces to $(\rho/\rho_o) = 0.72\ W/S$.

In measuring the resistivity of the deposited layers, we have assumed that the p-n junction acts as an insulating plane (3) and that the correction for finite geometry with a nonconducting surface can be applied. The resistivities given in the following tables have been corrected by multiplying the observed resistivities (ρ_o) by $0.72\ W/S$, since W is 0.0025 cm and $S = 0.1$ cm in our system.

A standard curve for the effect of various levels of phosphorus on the freshly deposited layers was ob-

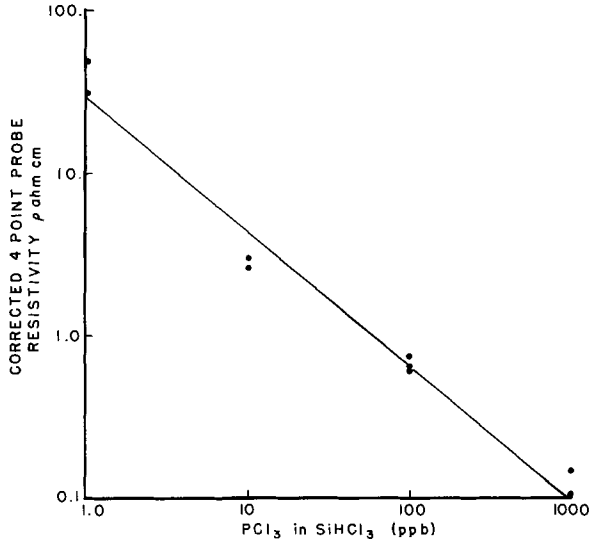

Fig. 2. Plot of resistivity vs. concentration of PCl_3

Table I.

Charge	Observed resistivity,* ohm-cm	Calculated** resistivity	Type
$SiHCl_3$ + 1000 ppb PCl_3	0.10, 0.15	0.22	n
$SiHCl_3$ + 100 ppb PCl_3	0.60, 0.75	2.40	n
$SiHCl_3$ + 10 ppb PCl_3	3.00, 2.60	24.0	n
$SiHCl_3$ + 1 ppb PCl_3	50.0, 32.0	240	n
H_2	00‡		p

* Duplicate runs at the various PCl_3 levels indicated an accuracy of ~25%. The resistivities have been corrected for layer thickness.

** The calculated resistivity values are obtained by assuming 100% cracking and incorporation of phosphorus from the PCl_3. A 10% yield of Si from the trichlorosilane is used in the calculation based on data obtained by Allegretti (4) for the reductive cracking of $SiHCl_3$ in flow system of the type used here. Finally, the mobilities used were from a compilation by Conwall (5).

‡ Wafers heated in hydrogen alone acquire a very thin film of high-resistivity p material. Immediately below this layer one detects the original 1000 ohm-cm Si unchanged.

Table II.

Material	Resistivity, ohm-cm	Type
Commercial $SiHCl_3$	6.0, 8.0, 7.5, 7.0, 5.5, 6.7	n
Distillation fractions		
Cuts 4 and 5	46.0, 45.0, 46.0	n
Late cut—cut 8	12.0, 16.0	n
Residue	0.60	n

Table III.

Material	Resistivity, ohm-cm	Type
Forerun	300	n
Center cut	160	n
Residue	1.0	n

tained by adding successively higher charges of phosphorus trichloride (from 1 ppb to 1 ppm based on grams of PCl_3 added to grams of $SiHCl_3$) to high-purity trichlorosilane and cracking aliquots of these known solutions on wafers. The results are shown in Table I. A plot of resistivity *vs.* concentration of PCl_3 in $SiHCl_3$ reveals a nearly linear relationship between the added PCl_3 and the observed resistivity of the deposited layer (cf. Fig. 2).

A series of analyses were carried out on samples of commercial trichlorosilane and fractions obtained from several distillations of this material. The results of these analyses are presented in Tables II and III.

Both distillations were carried out in all-quartz stills with quartz ring packing with an efficiency of approximately 14 plates. In the first distillation a reflux ratio of 5 to 1 was used while in the second distillation a 10 to 1 ratio was employed. The distillation covered in Table II was performed on approximately 17 liters of trichlorosilane. A 0.5 liter forerun and 8 cuts of 1.8 liter each were taken, leaving a residue of 2 liters. Analyses were performed on cuts 4 and 5, cut 8, and the residue. The very low resistivities resulting from the distillation residues are evidence of the fact that a donor impurity is concentrated in that fraction; furthermore, the higher resistivities obtained with fractions from the 10 to 1 ratio distillation show that improved distillation conditions can yield higher purity trichlorosilane.

Fitting the data obtained for the commercial trichlorosilane and the distillation cuts derived therefrom to the plot in Fig. 2, one could conclude that the commercial material contains approximately 10 ppb donor impurity. Fractional distillation is capable of reducing this well below the 1 ppb level in the overhead cuts while the concentrations in the residue go up to ~110 ppb. This, of course, assumes that the donor impurity in $SiHCl_3$ is behaving like PCl_3. In any event, it is possible with this method to follow the reduction of electrically active impurities in volatile Si compounds with a sensitivity not available by any other analytical technique.

Manuscript received June 13, 1961; revised manuscript received Oct. 13, 1961.

Any discussion of this paper will appear in a Discussion Section to be published in the December 1962 JOURNAL.

REFERENCES

1. R. C. Sangster, E. F. Maverick, and M. L. Croutch, *This Journal*, **104**, 317 (1957).
2. L. P. Hunter, "Handbook of Semiconductor Electronics," 1st ed., pp. 20-4, 20-6, McGraw-Hill Book Co., Inc., New York (1956).
3. C. S. Fuller and J. A. Ditzenberger, *J. Appl. Phys.*, **27**, 544 (1956).
4. J. Allegretti, Private communication.
5. E. M. Conwell, *Proc. I.R.E.*, **46**, [6], 1287 (1958).

Measurement of the Depth of Diffused Layers in Silicon by the Grooving Method

B. McDonald and A. Goetzberger

Shockley Transistor, Unit of Clevite Transistor, Palo Alto, California

ABSTRACT

A technique for the determination of the depth of diffused layers presented first by Happ and Shockley in 1956 is evaluated and compared with conventional methods. The process involves cutting a groove of cylindrical shape into a diffused specimen, delineating the junction by standard techniques, and, under magnification, measuring two variables which can be substituted into a simple equation to calculate the thickness of the diffused layer. The regularity of the groove contour is evaluated from measurements with interference fringes. Diffused layers as thin as 0.2μ can be measured with a deviation of $\pm$ 0.04μ over an entire slice.

It is the purpose of this paper to evaluate a technique of junction depth determination described in 1956 by Happ and Shockley (1). The technique discussed here lends itself particularly well to the measurement of very thin diffused layers which are difficult to measure accurately by the commonly used methods such as angle lapping (2) or breaking along crystal planes (3). Since extreme care in sample preparation is not required for this technique, measurements of diffused layers may be made conveniently and with a high degree of accuracy. This technique involves cutting a cylindrical groove into the silicon surface, staining the layers by conventional methods, and, under magnification, without the necessity of interference fringes, making simple linear measurements from which the depth of the diffused layer can be easily calculated.

Sample preparation.—A low melting, readily soluble wax, such as Apiezon wax, is melted on the top of a stainless steel mounting block (labeled 2 in Fig. 1) in a very thin layer. If the sample to be measured is thin, a glass cover plate (5 in Fig. 1) is then placed on the wax to provide a smooth flat surface on which to mount the sample. Additional wax is melted in a thin layer on the cover plate to hold a small piece of silicon broken from a diffused sample. The excess wax is removed and the mounting block is placed as shown in Fig. 1. The grooving cylinder, which may be made from a highly polished cast semisteel such as meehanite,[1] is held in a small lathe. The sample is held against the cylinder by a spring (labeled 4 in Fig. 1), and the cylinder is rotated over the sample by the lathe in the presence of an extremely fine abrasive (such as "Linde B") suspended in a light oil. This process cuts a groove into the silicon. (The accuracy of locating a groove in a particular area of the sample surface is determined by the capabilities of the lathe being used.) The abrasive suspension is cleaned off, and the sample is ready to be stained. It is possible to use any of the conventional methods for diffused layer delineation; however, the staining method which was found to be fastest and most reproducible is that described by Fuller and Ditzenberger (2). This stain consists of ½ H_2O, ½ HF (49%), and 0.1% HNO_3 (67%). A drop of this stain is placed on the groove and, with an illumination of approximately 850 f.c. from a tungsten filament lamp, the diffused layer can be nicely delineated in about 1 min.

Measurement.—The mathematics of the grooving technique are as follows. Figure 2 shows a schematic cross section of a groove in the surface of a silicon sample. X_j represents the depth of the diffused layer, R is the radius of the grooving cylinder, D is the cylinder diameter, and x and y are the distances one would measure looking at the groove from the top.

[1] Product (process) of the Meehanite Corp.

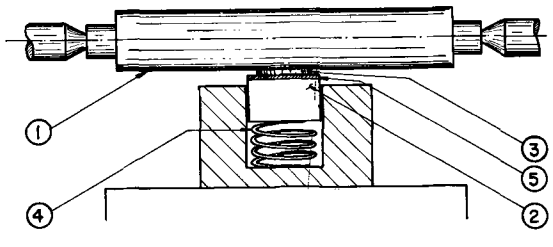

Fig. 1. Grooving apparatus: 1, grooving cylinder; 2, mounting block; 3, silicon slice; 4, spring; 5, glass cover plate.

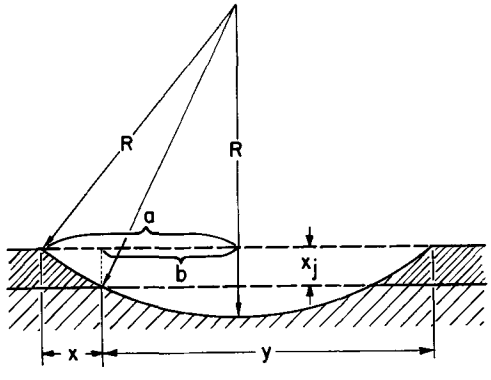

Fig. 2. Groove cross section

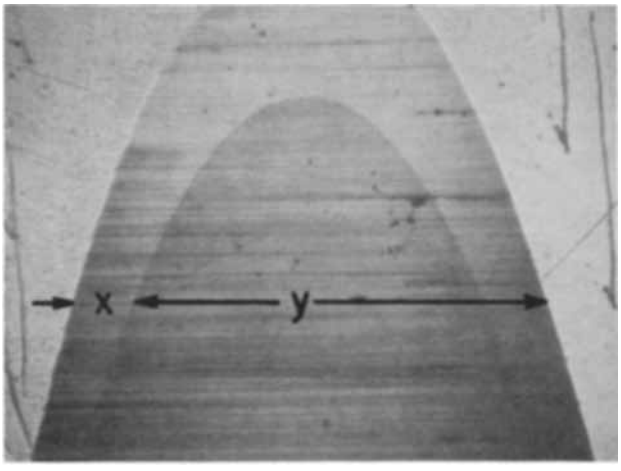

Fig. 3. Diffused n-layer

From Fig. 2,

$$x = a - b,$$

$$y = a + b,$$

and

$$X_j = \sqrt{R^2 - b^2} - \sqrt{R^2 - a^2}$$

$$= R\left[\sqrt{1 - \frac{b^2}{R^2}} - \sqrt{1 - \frac{a^2}{R^2}}\right]$$

When $b << R$

$$X_j \approx R\left[1 - \tfrac{1}{2}\frac{b^2}{R^2} - 1 + \tfrac{1}{2}\frac{a^2}{R^2}\right]$$

$$= \tfrac{1}{2}\frac{a^2 - b^2}{R}$$

$$= \tfrac{1}{2}\frac{(a+b)(a-b)}{R}$$

$$= \tfrac{1}{2}\frac{xy}{R} = \frac{xy}{D}$$

The grooved and stained sample will appear as in Fig. 3, which shows an n + layer delineated. (The surface of the sample is in the plane of the photograph. In this case, the axis of the grooving cylinder was at an angle to the surface). The values x and y are then measured along a continuous straight line, divided by the magnification of the optical system, and the simple calculation is made for X_j.

Evaluation of the Technique.—In order to evaluate the process more fully, several investigations were made, the first being a study of the groove contour. This was done by observing the groove with an interference objective and a filar eyepiece (Fig. 4). The number of fringes were counted between regular increments in the filar eyepiece and the number of fringes plotted against the number of increments to obtain the derivative of the curve. If the contour was of regular curvature, one would expect a plot displaying a straight line, such as is shown in Fig. 5. (These points were taken from the groove shown in Fig. 4.) Proof of a regular contour was obtained on all samples evaluated in this manner.

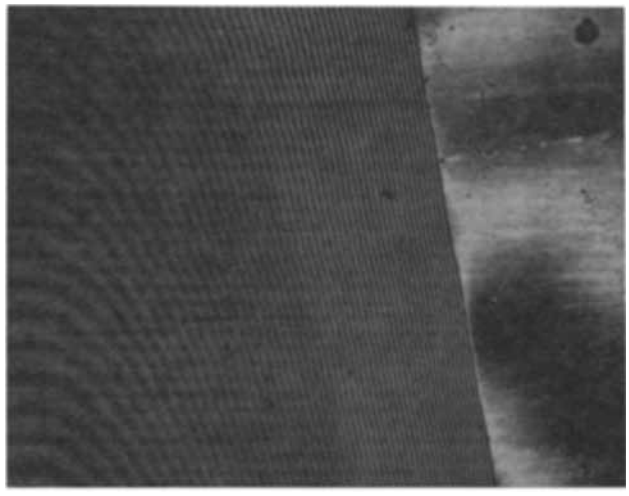

Fig. 4. Groove with interference fringes

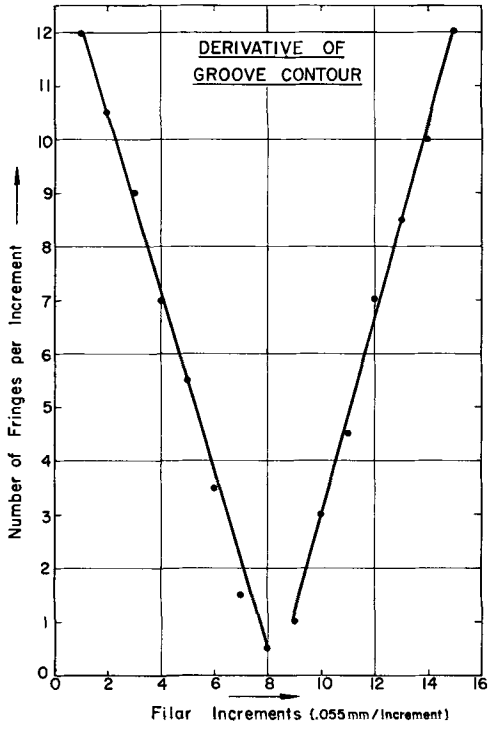

Fig. 5. Derivative of groove contour

The contour produced by the grooving technique has several qualitative advantages over the sloping surface produced by the conventional angle lapping method. For some undetermined reason, the diffused layer can be more easily delineated (using the same staining solution) with greater reproducibility. Since the angle of the silicon surface with respect to the axis of the cylinder is not critical within a few degrees, the sample may be mounted without extreme care, and there is no problem of maintaining the sample in a specific orientation while the operation is being performed. The advantages of the grooving method become particularly apparent when applied to very thin layers. The rounding which occurs at the edge of the lapped angle does not appear at the edge of the groove because the system is maintained securely in position and the abrasive action occurs only in one direction. This eliminates a very large source

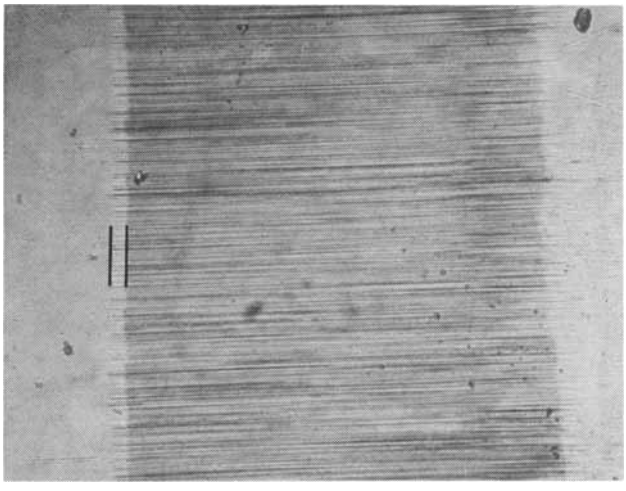

Fig. 6. Thin diffused layer (0.27μ)

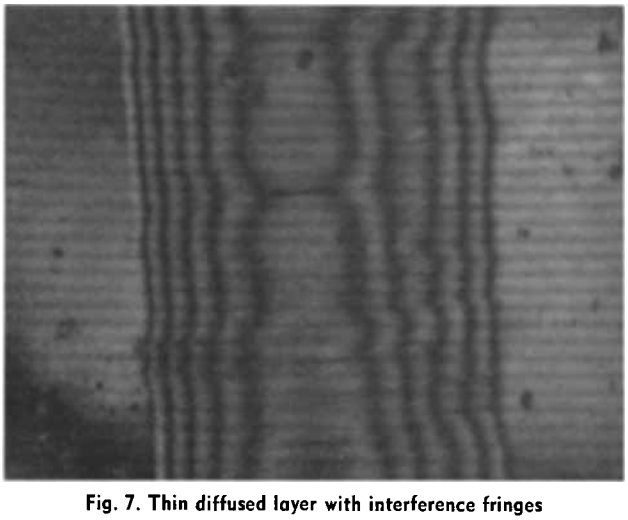

Fig. 7. Thin diffused layer with interference fringes

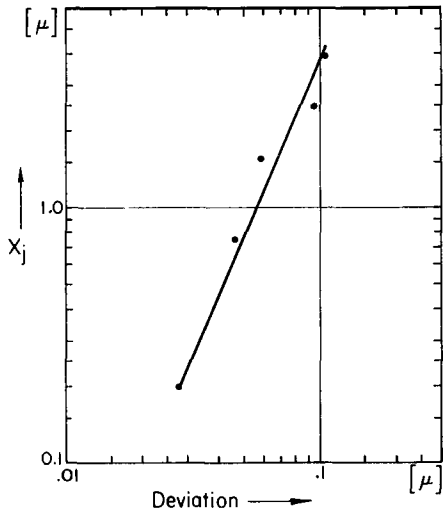

Fig. 8. Layer thickness (X_j) vs. deviation

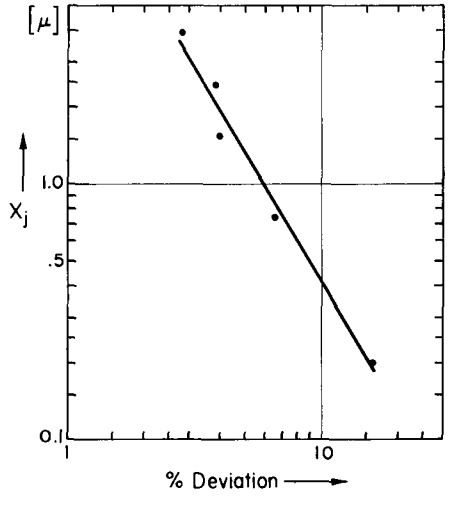

Fig. 9. Layer thickness (X_j) vs. % deviation

of error in measuring thin layers. Another advantage of the grooving method is that it is not necessary to measure a very small angle accurately. The only quantity that has to be known is the diameter of the grooving cylinder.

In measuring the delineated layer by conventional methods, either a probe or an interference objective is generally used. Probing for the depth is an extremely time-consuming and exacting procedure requiring delicate and precise equipment, especially in measuring shallow layers of less than 0.5μ. The estimated accuracy is $\pm$ 0.1μ. The use of an interference objective is also limited in accuracy when applied to extremely shallow layers, an example of which is shown in Fig. 6 and 7. Figure 6 shows a layer in a grooved sample which, measured by employing the technique previously described, was found to have a depth of 0.27μ. Figure 7 shows the same layer under illumination from a sodium vapor lamp with the fringe plates of an interference objective in contact with the sample. The edge of the delineated layer lies somewhere under the first fringe and cannot be seen at all. Even with a deep layer, as in Fig. 4, the interfringe distance with sodium vapor is 0.2945μ. The measurement can at best be approximated to $\pm$ 0.1μ. In contrast, measurements of diffused layers can be made down to depths as shallow as the order of 0.2μ, using the grooving technique, with an accuracy of $\pm$ 0.04μ.

In order to evaluate the reproducibility of the grooving technique, measurements were made on several grooves in the same specimen. This was repeated for specimens having diffused layer thicknesses between 0.195 and 3.92μ. The deviation of the measurements, which was taken as the average of the difference between the mean and measured values, and the per cent deviation are shown plotted against the diffusion depth in Figures 8 and 9. These results indicate a high degree of reproducibility and also point out that, while the absolute deviation increases with increasing layer thickness, the relative deviation decreases.

As a final check on the accuracy of this method, samples were sectioned anodically (4, 5) until the junction was reached. In all cases evaluated in this manner, the sum of the thicknesses removed down to the junction came with 200Å of the layer depth as measured by the grooving method.

Conclusion

The grooving technique described in this paper offers a convenient and accurate method for determining the depth of diffused layers in silicon. In this laboratory, the technique has been found to be

indispensable when it is necessary to determine accurately the depth of a very shallow layer.

Manuscript received Sept. 25, 1961. This work was supported in part by the Air Force Cambridge Research Laboratory AF 19(604)8060.

Any discussion of this paper will appear in a Discussion Section to be published in the December 1962 JOURNAL.

REFERENCES

1. W. W. Happ and W. Shockley, *Bull. Am. Phys. Soc.*, Ser. II **1**, 382 (1956).
2. C. S. Fuller and J. A. Ditzenberger, *J. Appl. Phys.*, **27**, 544 (1956).
3. B. Jansen, *Solid State Electronics*, **2** [1], 14 (1961).
4. B. McDonald and F. C. Collins, *Bull Am. Phys. Soc.*, Ser. II **6**, 106, (1961).
5. E. Tannenbaum, *Solid-State Electronics*, **2** [2/3], 123, March (1961).

Vapor Pressure of Gallium, Stability of Gallium Suboxide Vapor, and Equilibria of Some Reactions Producing Gallium Suboxide Vapor

C. N. Cochran and L. M. Foster

Alcoa Research Laboratories, Physical Chemistry Division, Aluminum Company of America, New Kensington, Pennsylvania

ABSTRACT

Vapor pressures of gallium in the literature are too high because $Ga_2O(v)$ formed in the reaction of gallium with the quartz effusion cells used for the measurements. Gallium was found to be less reactive with alumina than with quartz. Measurements in an alumina effusion cell gave vapor pressures for gallium that obey the expression

$$\log P \text{ (atm)} = -14{,}900/T - 0.515 \log T + 7.34$$

Values for $\Delta H_{f\,298[Ga_2O(v)]}$ of -17.4 ± 0.7 and -19.7 ± 0.7 kcal/mole were found for the reaction of gallium with quartz and magnesium oxide, respectively. The latter value was employed to calculate the equilibria in forming $Ga_2O(v)$ from the following pairs of reactants: gallium-gallia, graphite-gallia, tin-gallia, gallium-alumina, and gallium-water vapor. The vapor pressures of silver and tin were determined and compared with literature values to check the constants of the system.

Previous measurements (1, 2) of the vapor pressure of gallium employed the Knudsen method with quartz effusion cells. However, a mass spectroscopic study of Antkiw and Dibeler (3) showed that considerable concentrations of $Ga_2O_{(v)}$ formed from reaction of gallium with a quartz crucible at 865°-1025°C. This indicates that the reported vapor pressure data for gallium are too high.

In the present work an alumina effusion cell was used to measure the vapor pressure of gallium. Additions of quartz or magnesium oxide were made to the gallium in the cell to form gallium suboxide. The differences in the effusion rates with and without quartz or magnesium oxide are used to derive the heat of formation of gallium suboxide vapor.

Experimental

A single sintered alumina (99+% pure) effusion cell, 15 mm ID, 30 mm deep, with an orifice 0.90 mm in diameter and 0.37 mm thick, was employed in obtaining all of the data. Reactions between the charge materials and the alumina cell were negligible. The weight loss of the cell in an effusion experiment was always considerably less than 1% of the total weight loss. A cell constant of 0.00098 and a Clausing factor of 0.71 were calculated for the orifice.

In two experiments where silver was employed in the cell, the orifice was covered with a tight fitting cover of sintered alumina. By comparing the loss in this case with that when the orifice was uncovered, $46 \pm 5\%$ of the total loss with the orifice uncovered was found to occur through the lapped seal between the removable cover and the body of the cell. With this "leakage" taken into account, the following relationship between pressure and effusion losses from the cell was obtained

$$\text{Pressure}_{(atm)} = \frac{0.00075 \text{ (effusion rate in g/hr)} T^{1/2}}{\text{(molecular weight vapor)}^{1/2}}$$

The rates of weight loss were determined with an automatic, recording, vacuum analytical balance, modeled after the microbalance described elsewhere (4). Only data from the linear portions of the weight loss-time plots were used. This practice eliminated errors in effusion rate determination caused by outgassing of the cell and its contents as steady-state conditions were approached. Usually, steady-state conditions were reached within ½ hr after reaching temperature.

Temperatures were regulated to within ±1°C by a Foxboro Recorder-Controller, Model 8253-201R, with the control thermocouple located between windings of the furnace element at a position corresponding to the midpoint of the cell. The relationship between the temperature of the control couple and the

Table I. Gallium vapor pressure data
$Ga_{(l)} \rightleftarrows Ga_{(v)}$

°K	Effusion rate, mg/hr	Gallium vapor pressure, atm	No quartz present $-\Delta\frac{F°_T - H°_{298}}{T}$	$\frac{\Delta F°_T}{T}$	$\frac{\Delta H°_{298}}{T}$	$\Delta H°_{298}$	$\frac{68,960}{T}$	$P_{calc.}$, atm	Quartz added Effusion rate, mg/hr	Apparent gallium vapor pressure, atm*
1179	0.050	1.53×10^{-7}	27.03	31.17	58.20	68,620	58.49	1.3×10^{-7}	0.126	3.9×10^{-7}
1231	0.15	4.69×10^{-7}	26.96	28.94	55.90	68,810	56.02	4.4×10^{-7}	0.39	1.2×10^{-6}
1280	0.38	1.21×10^{-6}	26.90	27.06	53.96	69,070	53.88	1.3×10^{-6}	1.21	3.9×10^{-6}
1332	1.07	3.47×10^{-6}	26.84	24.97	51.81	69,010	51.77	3.5×10^{-6}	3.7	1.2×10^{-5}
1357	1.56	5.11×10^{-6}	26.81	24.20	51.01	69,220	50.82	5.6×10^{-6}	6.7	2.2×10^{-5}
1383	2.64	8.75×10^{-6}	26.78	23.14	49.92	69,040	49.86	9.0×10^{-6}	11.6	3.8×10^{-5}
						Avg. 68,960 ± 190				
2300			26.00				29.99	0.134		
2400			25.94				28.74	0.244		
2500			25.88				27.59	0.421		
2676			25.77				25.77	1.00		

* Effusion of $Ga_2O_{(v)}$ and $Ga_{(v)}$ from cell treated as being entirely $Ga_{(v)}$.

cell was determined with a second thermocouple in a separate experiment.

Materials

Alcoa GA-6 grade, 99.9999+% pure gallium, Tadanac Brand (Consolidated Mining and Smelting Company of Canada, Ltd., Trail, B. C.) 99.9999% silver, and Fisher Scientific Company's 99.97% tin were employed in this work. In the Ga-SiO_2 and Ga-MgO experiments, the gallium was covered with a bed of 4 to 8-mesh chips of ordinary fused quartz, and pellets (⅛ in. in diameter and ⅛-¼ in. long) of Fisher Scientific Company's 99.93% magnesium oxide, respectively.

Vapor Pressure of Gallium

Vapor pressures calculated from the effusion data for gallium are given in Table I and compared with literature values in Fig. 1. The values from the present work range from fourfold lower at 1100°C to fivefold lower at 900°C than the values selected by Stull and Sinke (5) from previously published data.

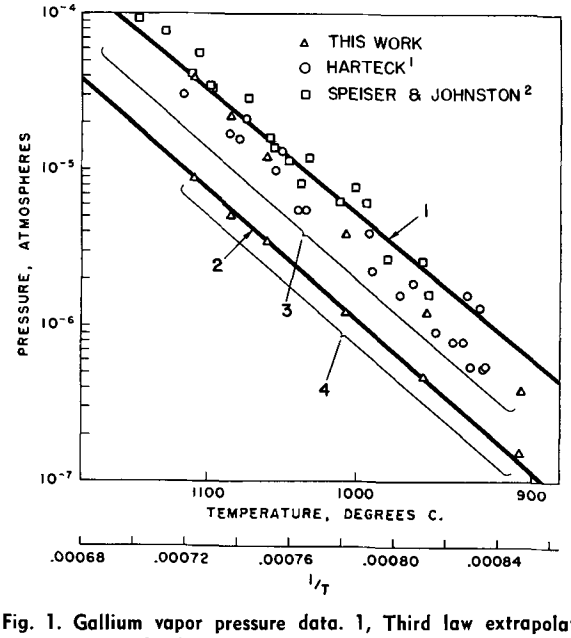

Fig. 1. Gallium vapor pressure data. 1, Third law extrapolation of previous data by Stull and Sinke (5), $\Delta H°_{v\,298}$ = 65.00 kcal/mole; 2, third law extrapolation of data from this work, $\Delta H°_{v\,298}$ = 68.96 kcal/mole; 3, measured in presence of quartz; 4, measured in an alumina effusion cell.

With the vapor considered as being monatomic, as indicated in mass spectroscopic studies (3,6), log $P = -14,900/T - 0.515 \log T + 7.34$, $\Delta H°_{v\,298} = 68.96 \pm 0.19$ kcal, and the boiling point is 2676°K. Stull and Sinke (5) chose $\Delta H°_{v\,298}$ = 65.00 kcal and a boiling point of 2510°K.

Drowart and Honig (6) found the heat of vaporization of gallium from beryllia and graphite crucibles to be 59 ± 4 kcal/mole by second law treatment of ion intensities in a mass spectroscopic study. It is recognized that their procedure might give only approximate results.

Apparent monatomic gallium pressures were calculated from the gallium-quartz effusion data and also plotted in Fig. 1. These data were found to fall within the band of pressures reported by the previous workers who vaporized gallium from quartz. These values show the same systematic deviation from the third law extrapolation line of Stull and Sinke (5) as do the data of the previous workers. This deviation is another proof, as noted by Drowart and Honig (6), that these data cannot be represented simply by vaporization of monatomic gallium.

Stability of Ga_2O Vapor

Before information on the stability of $Ga_2O_{(v)}$ could be obtained from the effusion data with quartz or magnesium oxide added to the gallium, the most favorable of the possible reactions had to be determined. This was accomplished in each case by finding the reaction that resulted in the least negative value of $\Delta H°_{f\,298[Ga_2O_{(v)}]}$ and that showed no systematic deviation of this quantity with temperature. Using these criteria, the steady-state reaction between quartz and gallium is

$$2Ga_{(l)} + SiO_{2(c)} \rightleftarrows SiO_{(v)} + Ga_2O_{(v)} \qquad [1]$$

However, calculations showed that the initial reaction of quartz with gallium produces silicon (reaction [2])

$$4Ga_{(l)} + SiO_{2(c)} \rightleftarrows Si_{(in\ Ga)} + 2Ga_2O_{(v)} \qquad [2]$$

This dissolves in the gallium until its activity is large enough that any further silicon produced will react with the quartz to produce $SiO_{(v)}$ (reaction [3]) and give the same over-all reaction as [1].

Table II. Calculation of ΔH°_{298} for the reactions and $\Delta H^\circ_{f\,298}$ for $Ga_2O_{(v)}$

$2Ga_{(l)} + SiO_{2(c)} \rightleftarrows SiO_{(v)} + Ga_2O_{(v)}$

°K	Total effusion rate, mg/hr	Correction for Ga evaporation, mg/hr	Ga_2O loss, mg/hr	SiO loss, mg/hr	P_{Ga_2O}, atm	P_{SiO}, atm	K	$\frac{\Delta F^\circ_T}{T}$	$-\Delta\left[\frac{F^\circ_T - H^\circ_{298}}{T}\right]$	$\frac{\Delta H^\circ_{298}}{T}$	ΔH°_{298}
1179	0.126	0.043	0.065	0.018	1.3×10^{-7}	6.9×10^{-8}	9.0×10^{-15}	64.25	79.63	143.88	169,630
1231	0.39	0.14	0.195	0.055	4.1×10^{-7}	2.2×10^{-7}	9.0×10^{-14}	59.67	79.31	138.98	171,080
1280	1.21	0.40	0.63	0.18	1.3×10^{-6}	7.2×10^{-7}	9.4×10^{-13}	55.01	79.02	134.03	171,560
1332	3.7	1.1	2.0	0.57	4.4×10^{-6}	2.3×10^{-6}	1.0×10^{-11}	50.31	78.71	129.02	171,860
1357	6.7	1.7	3.9	1.1	8.6×10^{-6}	4.5×10^{-6}	3.9×10^{-11}	47.61	78.56	126.17	171,210
1383	11.6	2.7	6.9	2.0	1.5×10^{-5}	8.2×10^{-6}	1.2×10^{-10}	45.37	78.41	123.78	171,190
										Avg. ΔH°_{298} =	171,070 ± 690

At 298°K, $\Delta H^\circ_{f\,Ga_2O} = \Delta H^\circ_{reaction} + \Delta H^\circ_{f\,SiO_{2(c)}} - \Delta H^\circ_{f\,SiO_{(v)}} = 171{,}070 - 209{,}900 + 21{,}411 = -17{,}420 \pm 690$ cal/mole

$2Ga_{(l)} + MgO_{(c)} \rightleftarrows Mg_{(v)} + Ga_2O_{(v)}$

°K	Total effusion rate, mg/hr	Correction for Ga evaporation, mg/hr	Ga_2O loss, mg/hr	Mg loss, mg/hr	P_{Ga_2O}, atm	P_{Mg}, atm	K	$\frac{\Delta F^\circ_T}{T}$	$-\Delta\left[\frac{F^\circ_T - H^\circ_{298}}{T}\right]$	$\frac{\Delta H^\circ_{298}}{T}$	ΔH°_{298}
1179	0.100	0.043	0.049	0.0077	1.0×10^{-7}	4.0×10^{-8}	4.0×10^{-15}	65.86	68.60	134.46	158,530
1231	0.85	0.14	0.18	0.028	3.8×10^{-7}	1.5×10^{-7}	5.7×10^{-14}	60.58	68.31	128.89	158,660
1280	0.89	0.40	0.42	0.066	9.0×10^{-7}	3.6×10^{-7}	3.2×10^{-13}	57.15	68.05	125.20	160,260
1332	2.9	1.1	1.6	0.25	3.5×10^{-6}	1.4×10^{-6}	4.9×10^{-12}	51.78	67.78	119.51	159,190
1383	7.2	2.7	3.9	0.62	8.7×10^{-6}	3.5×10^{-6}	3.0×10^{-11}	48.13	67.51	115.64	159,930
										Avg. ΔH°_{298} =	159,310 ± 680

At 298°K, $\Delta H^\circ_{f\,Ga_2O} = \Delta H^\circ_{reaction} + \Delta H^\circ_{f\,MgO_{(c)}} - \Delta H^\circ_{f\,Mg_{(v)}} = 159{,}310 - 143{,}700 - 35{,}330 = -19{,}720 \pm 680$ cal/mole

$$Si_{(in\ Ga)} + SiO_{2(c)} \rightleftarrows 2SiO_{(v)} \quad [3]$$

Similar calculations show that the steady-state reaction of gallium with magnesium oxide is

$$2Ga_{(l)} + MgO_{(c)} \rightleftarrows Mg_{(v)} + Ga_2O_{(v)} \quad [4]$$

Gallium saturates rapidly with magnesium from the reaction to achieve a steady-state condition.

The effusion data from experiments where quartz and magnesium oxide were added are listed in Table II. After correcting the effusion losses for metal vaporization, the remaining weight losses were divided stoichiometrically between the gaseous products according to the reaction equations. Partial pressures and equilibrium constants were calculated and converted to free energy changes. These in turn were converted to values of ΔH°_{298} with the aid of free energy function data discussed in a later section. Values of ΔH°_{298} were used together with values of $\Delta H^\circ_{f\,298}$ for the other reactants and products to calculate values of −17.4 ± 0.7 and −19.7 ± 0.7 kcal/mole for $\Delta H^\circ_{f\,298[Ga_2O_{(v)}]}$ from the quartz and magnesium oxide reactions, respectively.

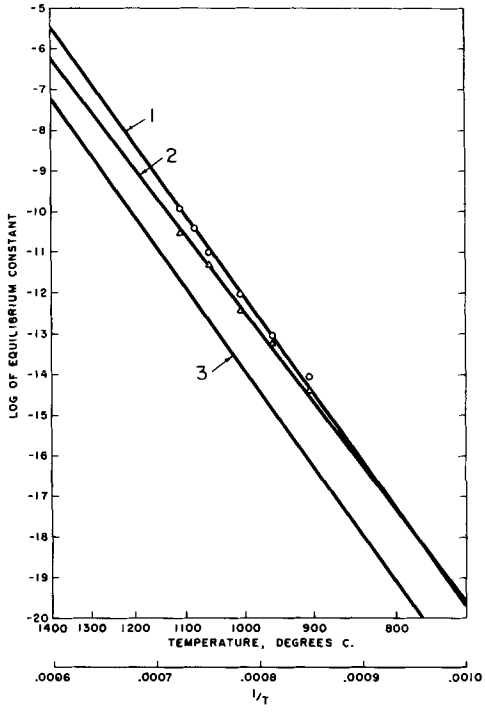

Fig. 2. Equilibrium constants for reaction of gallium with quartz and with magnesium.
1. $2Ga_{(l)} + SiO_{2(c)} \rightleftarrows SiO_{(v)} + Ga_2O_{(v)}$, ΔH°_{298} = 171.1 kcal
2. $2Ga_{(l)} + MgO_{(c)} \rightleftarrows Mg_{(v)} + Ga_2O_{(v)}$, ΔH°_{298} = 159.3 kcal
3. $4Ga_{(l)} + SiO_{2(c)} \rightleftarrows Si_{(c)} + 2Ga_2O_{(v)}$, ΔH°_{298} = 175.1 kcal

Other workers have found evidence recently that the presently accepted heat of formation for silica used in this work may be too positive. Taylor (7) and co-workers believe that the error in this value may be about 4.5 kcal/mole. A tentative calculation by Good (8) places the error at between 6-8 kcal/mole. If all of the difference in the values of $\Delta H^\circ_{f\,298[Ga_2O_{(v)}]}$ obtained from the quartz and magnesium oxide experiments in this work is assigned to an error in $\Delta H^\circ_{f\,298[SiO_2]}$, the error becomes 2 x 2.3 = 4.6 kcal/mole. (The difference of 2.3 kcal is multiplied by two because the heat of formation of SiO that is employed will become 2.3 kcal more negative at the same time.) The value of $\Delta H^\circ_{f\,298[Ga_2O_{(v)}]}$ calculated from the gallium-magnesium oxide experiments will be employed in all further calculations because of the good agreement between the 4.6 kcal/mole error in the value of $\Delta H^\circ_{f\,298[SiO_{2(c)}]}$ that we calculated using it and the 4.5 kcal/mole that Taylor and co-workers calculated.

The fit of all of the effusion data to the third law extrapolation of these data is shown in Fig. 2. The equilibrium constants for reaction [2], are also shown in Fig. 2. These equilibrium constants are the

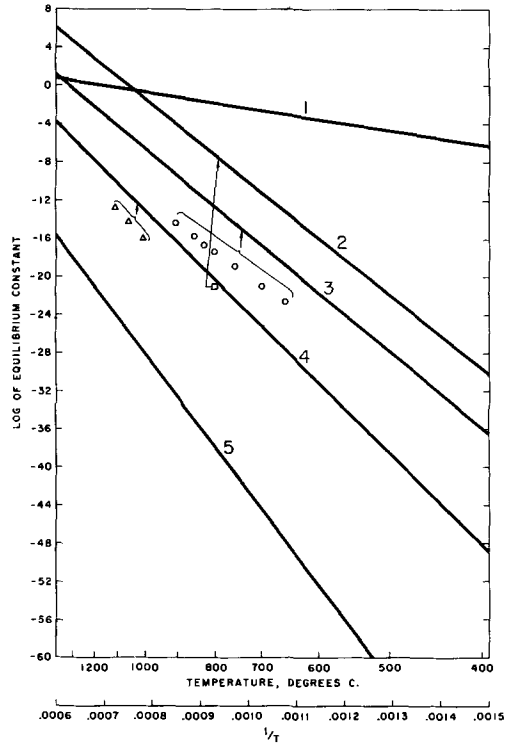

Fig. 3. Equilibrium constants of some reactions forming gallium suboxide based on $\Delta H^\circ_{f\,298[Ga_2O_{(v)}]}$ = —19.7 kcal

1. $H_2O_{(v)} + 2Ga_{(l)} \rightleftarrows Ga_2O_{(v)} + H_2O_{(v)}$, $\Delta H^\circ_{298} = 38.1$ kcal
2. $2C_{(c)} + Ga_2O_{3(c)} \rightleftarrows Ga_2O_{(v)} + 2CO_{(v)}$, $\Delta H^\circ_{298} = 185.5$ kcal
3. $4Ga_{(l)} + Ga_2O_{3(c)} \rightleftarrows 3Ga_2O_{(v)}$, $\Delta H^\circ_{298} = 198.9$ kcal
4. $2Sn_{(l)} + Ga_2O_{3(c)} \rightleftarrows 2SnO_{(v)} + Ga_2O_{(v)}$, $\Delta H^\circ_{298} = 236.3$ kcal
5. $4Ga_{(l)} + Al_2O_{3(c)} \rightleftarrows Al_2O_{(v)} + 2Ga_2O_{(v)}$, $\Delta H^\circ_{298} = 321.6$ kcal

Points represent apparent equilibrium constants calculated from Knudsen effusion experiments in which equilibrium was not attained.

same whether they are calculated from the uncorrected heat of formation of quartz and the heat of formation of gallium suboxide from the gallium-quartz experiments or from the corrected value for quartz and the value for gallium suboxide from the gallium -magnesium oxide experiments.

Equilibria of Some Other Reactions Producing $Ga_2O_{(v)}$

Calculated equilibrium constants are shown in Fig. 3 for a number of other reactions that produce $Ga_2O_{(v)}$. The small equilibrium constants calculated for the reaction of gallium with alumina are substantiated by the low reactivity between gallium and alumina found in this work. The equilibria of the reaction of gallium with water vapor will be employed along with the equilibria of the quartz-gallium reactions in the following paper dealing with implications of these reactions in the synthesis of gallium arsenide in quartz systems.

The reactions of tin, graphite, and gallium with gallia, shown in Fig. 3, were employed in other attempts to measure the stability of $Ga_2O_{(v)}$. However, equilibrium was not achieved in these cases. The apparent equilibrium constants that were obtained from the effusion rates were always less than the corresponding equilibrium constants calculated with the $\Delta H^\circ_{f\,298[Ga_2O_{(v)}]}$ from the magnesium oxide-gallium experiments.

The chief cause of poor approach to equilibrium in these cases is evident from the effusion data. The

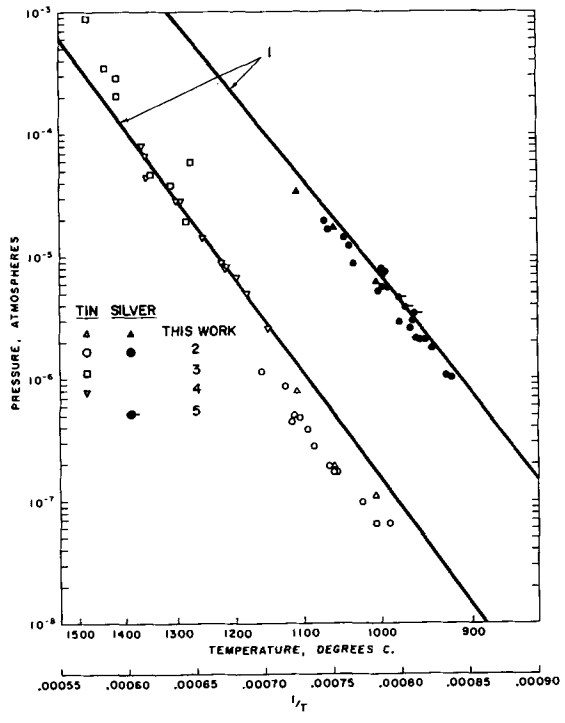

Fig. 4. Vapor pressures of silver and tin. 1, Third law extrapolations of previous data by Stull and Sinke (5); 2, Harteck (1); 3, L. Brewer and R. F. Porter, *J. Chem. Phys.*, 21, 2012 (1953); 4, A. W. Searcy and R. D. Freeman, *J. Am. Chem. Soc.*, 76, 5229 (1954); 5, C. L. McCabe and C. E. Birchenall, *AIME Trans.*, 197, 707 (1953).

average increases in the effusion rates on adding gallia to tin, gallium, and graphite were, respectively, 150-fold, 2000-fold, and an undetermined large factor. These compare to average increases of two to fourfold on adding quartz and magnesium oxide to gallium. If the reaction between the oxide and the metal involves mainly metal vapor rather than liquid metal, the ease of achieving equilibrium in the effusion cell will be related to the ratio of the equilibrium pressure from the reaction to the equilibrium metal vapor pressure. If this ratio is large, equilibrium will be difficult to achieve, especially as this ratio approaches the ratio of the metal surface area to the area of the effusion hole.

Reaction between metal vapor and the oxide would be expected to be the predominant reaction in the effusion cells because gaseous products formed at submerged sites where the liquid metal and oxide are in contact would have difficulty in escaping from under the head of molten metal at these low pressures. With the quartz and magnesium oxide added to the gallium, the increase in pressure was small enough that the gases in the effusion cell were probably at equilibrium.

Gershenzon and Mikulyak (9) reported that Frosch and Thurmond of Bell Telephone Laboratories, Inc. of Murray Hill, New Jersey, have measured gallium suboxide pressures of 0.2 mm at 800°C

Table III. Silver and tin vapor pressure data

	Ag		Sn	
°K	Effusion rate, mg/hr	Pressure, atm	Effusion rate, mg/hr	Pressure, atm
1280	2.38	6.1×10^{-6}	0.044	1.1×10^{-7}
1332	6.31	1.7×10^{-5}	0.076	1.9×10^{-7}
1383	14.5	3.9×10^{-5}	0.308	7.8×10^{-7}

Table IV. Values of $-\left[\frac{F^\circ_T - H^\circ_{298}}{T}\right]$ and $\Delta H^\circ_{f\,298}$ employed in calculations from Janaf Interim Thermochemical Tables (11) unless otherwise noted

	°K	$Si_{(c)}$	$H_{2(v)}$	$C_{(c)}$	$Al_2O_{3(c)}$	$Al_2O_{(v)}$	$SiO_{2(c)}$	$H_2O_{(v)}$
	700	5.912	33.153	2.166	18.549	64.730	13.579	47.406
	800	6.361	33.715	2.449	20.656	65.672	14.728	48.089
	900	6.795	34.250	2.736	22.533	66.584	15.879	48.749
$-\left(\frac{F^\circ_T - H^\circ_{298}}{T}\right)$	1000	7.212	34.758	3.020	24.434	67.459	16.999	49.382
	1100	7.610	35.240	3.300	26.261	68.295	18.064	49.991
	1200	7.989	35.696	3.573	28.012	69.093	19.077	50.575
	1300	8.352	36.130	3.839	29.689	69.855	20.041	51.136
	1400	8.698	36.543	4.098	31.295	70.582	20.961	51.675
	1500	9.028	36.937	4.348	32.835	71.276	21.840	52.196
	1600	9.345	37.314	4.591	34.311	71.940	22.681	52.698
$\Delta H^\circ_{f\,298}$		0	0	0	−400.4	−39.4	−209.9	−57.798

	°K	$SiO_{(v)}$	$MgO_{(c)}$	$Mg_{(v)}$	$Co_{(v)}$	$Ga_2O_{3(c)}$[1]	$SnO_{(v)}$[1]	$Ga_2O_{(v)}$[2]
	700	52.634	9.263	36.892	49.182	25.63	57.56	73.03
	800	53.257	10.130	37.291	49.759	27.38	58.26	74.07
	900	53.858	10.969	37.670	50.314	29.07	58.95	75.08
$-\left(\frac{F^\circ_T - H^\circ_{298}}{T}\right)$	1000	54.432	11.775	38.029	50.845	30.71	59.54	76.04
	1100	54.980	12.546	38.368	51.351	32.30	60.13	76.96
	1200	55.502	13.283	38.688	51.834	33.82	60.63	77.83
	1300	55.999	13.986	38.991	52.295	35.24	61.17	78.66
	1400	56.473	14.658	39.278	52.736	36.65	61.56	79.46
	1500	56.926	15.301	39.550	53.158	37.98	62.14	80.22
	1600	57.358	15.916	39.809	53.562	39.23	62.61	80.96
$\Delta H^\circ_{f\,298}$		−21.411	−143.7	−35.330	−26.417	−258.0 (12)	−1.9	—

[1] Calculated from $\Delta H^\circ_{f\,298}$ (12) and $\Delta F^\circ_{f\,T}$ and free energy function for the component elements (5).
[2] Estimated by method described in text.

and 10 mm at 1000°C for a 4-1M mixture of gallium and gallium suboxide. From Curve 3 in Fig. 3, the corresponding pressures calculated for this reaction are 0.091 mm and 8.6 mm. This good agreement supports the choice of −19.7 kcal/mole for the value of $\Delta H^\circ_{f\,298[Ga_2O_{(v)}]}$.

Vapor Pressures of Silver and Tin

In order to obtain an independent check on the effusion cell constants employed in this work, the vapor pressures of silver and tin were determined. These are given in Table III and are compared with literature values in Fig. 4. There is good agreement with the results of Harteck (1) who employed quartz cells. These values average 22% to 46% lower than the values chosen by Stull and Sinke (5) from data obtained mostly in graphite cells. It appears that diffusion through graphite cell walls was not considered in most of the earlier work.[1]

Sources of Thermodynamic Data

Except for the free energy functions for liquid and gaseous Ag, Sn, and Ga which were obtained from Stull and Sinke (5), all of the free energy functions and heats of formation employed are listed with their sources in Table IV.

Estimated values of the free energy functions for $Ga_2O_{(v)}$ are also listed in Table IV. This quantity is a function of heat capacities alone and, therefore, can be estimated for gases quite accurately from heat capacity data for molecules of similar structure and molecular weight. A value of 69.54 was estimated for $S^\circ_{298[Ga_2O_{(v)}]}$ from a correlation of molecular weights with values of S°_{298} for other triatomic gaseous molecules. Heat capacities for $Ga_2O_{(v)}$ above 298°K were taken to be the same as for $CTeS_{(v)}$ from the Bureau of Mines Bulletin 584 (13).

The described free energy functions were used to calculate the free energy function changes for the reaction at 100°K intervals. Free energy function changes for the desired temperatures were obtained by graphical interpolation.

[1] Fujishiro and Gokcen (10) found that the amount of titanium vapor permeating the walls of a cell made from a very dense, impervious graphite ranged from 45 to 77% of the total effusate in the 2383°-2593°K range.

Manuscript received June 28, 1961.

Any discussion of this paper will appear in a Discussion Section to be published in the December 1962 JOURNAL.

REFERENCES

1. P. Harteck, *Z. physik. Chem.*, **134**, 1 (1928).
2. R. Speiser and H. L. Johnston, *J. Am. Chem. Soc.*, **75**, 1469 (1953).
3. S. Antkiw and V. H. Dibeler, *J. Chem. Phys.*, **21**, 1890 (1953).
4. C. N. Cochran, *Rev. Sci. Instr.*, **29**, 1135 (1958).
5. D. R. Stull and G. C. Sinke, "Thermodynamic Properties of the Elements," American Chemical Society, Washington, D. C. (1956).
6. J. Drowart and R. E. Honig, *Bull soc. chim. Belges.*, **66**, 411 (1957).
7. D. A. R. Kay and J. Taylor, *Trans. Faraday Soc.*, **56**, 1372 (1960); J. D. Baird and J. Taylor, *Trans. Faraday Soc.*, **54**, 526 (1958).
8. W. D. Good, Bureau of Mines, Bartlesville, Oklahoma, Private communication.
9. M. Gershenzon and R. M. Mikulyak, *This Journal*, **108**, 548 (1961).
10. S. Fujishiro and N. A. Gokcen, *J. Phys. Chem.*, **65**, 161, (1961).
11. JANAF Interim Thermochemical Tables, Thermal Laboratory, Dow Chemical Company, Midland, Michigan, Dec. 31, 1960.
12. J. P. Coughlin, Bulletin 542, U. S. Bureau of Mines (1954).
13. K. K. Kelley, Bulletin 584, U. S. Bureau of Mines (1960).

Reactions of Gallium with Quartz and with Water Vapor, with Implications in the Synthesis of Gallium Arsenide

C. N. Cochran and L. M. Foster

Alcoa Research Laboratories, Physical Chemistry Division, Aluminum Company of America, New Kensington, Pennsylvania

ABSTRACT

The reaction of gallium with quartz to produce gallium suboxide, Ga_2O, and silicon is shown by equilibrium calculations to be a mechanism by which gallium arsenide can become contaminated with silicon, and possibly oxygen, when synthesized in quartz systems. The contamination of gallium arsenide with silicon by this reaction is governed by the rate at which the gallium suboxide vapor is removed. The silicon content commonly observed in GaAs (up to a few ppm) can be accounted for by this mechanism. Suggestions for minimizing the attack are given. The apparent transport of GaAs in a system containing traces of water vapor can be explained by reaction of water with gallium in the hot zone to form Ga_2O and hydrogen, which react with arsenic in the cold zone to produce GaAs and regenerate the water.

A current problem in the production of gallium arsenide for use in semiconducting devices is contamination of the product with silicon. This silicon is thought to be formed by the reaction of gallium with its container during synthesis, which is carried out in a quartz boat or crucible contained in a sealed quartz envelope. In this operation, some part of the quartz envelope contains solid arsenic at about 610°C in equilibrium with arsenic vapor at 1 atm pressure. This is slightly greater than the arsenic decomposition pressure of 0.9 atm from gallium arsenide at the melting point (1237°C) (1, 2).

A mass spectroscopic study (3) had shown the presence of significant quantities of Ga_2O vapor when gallium was heated with quartz at 865°-1025°C. This Ga_2O vapor was formed in the same reaction that produces the silicon that contaminates the gallium or gallium arsenide; thus,

$$4Ga_{(l \text{ or from GaAs})} + SiO_{2(c)} \rightleftarrows Si_{(\text{in Ga or GaAs})} + 2Ga_2O_{(v)} \quad [1]$$

Knudsen effusion studies were employed by the authors to determine the equilibria of the reactions of gallium with quartz and gallium with magnesium oxide in the 900°- 1100°C range (4). A reaction heat of 175.1 kcal at 25°C for reaction [1] was used from this work to calculate the equilibrium of reaction [1] at 1250°C, the temperature of synthesis of GaAs.

Gallium Activity in Gallium Arsenide

The activity of gallium in gallium arsenide at 1250°C in 1 atm of arsenic vapor must be known before the equilibria of the reactions with quartz can be calculated. The arsenic decomposition pressure at the melting point of gallium arsenide reveals nothing about the gallium activity without additional information about the stability of GaAs.

Drowart and Goldfinger (5), in a combined Knudsen effusion-mass spectroscopic experiment, measured the decomposition pressures and identified the vapor species from gallium arsenide at temperatures from 758° to 863°C. The phase diagram of the gallium-arsenic system (6) shows that the gallium content of the gallium-rich liquid phase produced in decomposition over this temperature range would increase from 91 to 94 at. %. These compositions would correspond in the simple ideal case to gallium activities ranging from 0.82 to 0.88, since GaAs is the only compound in the system. Presumably, Drowart and Goldfinger took this into account when they calculated the median values of $\Delta F°_f$ and $S°$ for gallium arsenide at 808°C (1081°K) given on the following page, although this was not made clear in their paper. (If they assumed instead that the liquid dissociation product was pure gallium with unit activity, the value of $\Delta F°_{f\,1081}$ would be only 0.3-0.4 kcal more positive.)

$$\Delta F°_{f1081} = -15.34 \text{ kcal (calculated from the } As_2 \text{ component of the vapor)}$$

$$S°_{1081} = 34.4 \text{ cal/deg}$$

Using Stull and Sinke's (7) heat capacity data for diatomic arsenic vapor and liquid gallium, and assuming that $C_P = 12$ for gallium arsenide and the $\Delta F_{\text{fusion }1523} = 0$, ($\Delta F$ is actually zero at the fusion temperature of 1510°K), the free energy change and equilibrium constant for formation from $As_{2(v)}$ and Ga were calculated for molten gallium arsenide as follows:

$$Ga_{(l)} + \tfrac{1}{2}\, As_{2(v)} \rightleftarrows GaAs_{(l)} \quad [2]$$

$$\Delta F°_{f\,1523} = -5.40 \text{ kcal}$$

$$\log K_{1523} = \frac{5{,}400}{(4.576)(1523)} = +0.77$$

$$= -\log a_{Ga} - \tfrac{1}{2} \log P_{As_{2(v)}}$$

For self-consistency, Drowart and Goldfinger's value for the heat of dissociation of arsenic tetramers to dimers ($\Delta H°_{298}$ = 71.8 kcal) was employed to calculate the partial pressure of $As_{2(v)}$ in 1 atm of arsenic vapor at 1250°C. Using free energy function data for $As_{2(v)}$ and $As_{4(v)}$ from Stull and Sinke, the equilibrium constant for the dissociation of arsenic tetramers (reaction [3]) at 1250°C (1523°K) was calculated:

$$As_{4(v)} \rightleftarrows 2As_{2(v)} \qquad [3]$$

$$\frac{\Delta F°}{T} = 2\left[\frac{F° - H°_{298}}{T}\right]_{As_{2(v)}} - \left[\frac{F° - H°_{298}}{T}\right]_{As_{4(v)}} + \frac{\Delta H°_{298}}{T}$$

$$\log K_{1523} = \frac{-9.35}{4.576} = -2.044$$

$$K_{1523} = 0.0090 = \frac{(P_{As_2})^2}{P_{As_4}}$$

$P_{As_2} = 0.090$ atm when $P_{As_4} = (1\text{-}0.090) = 0.91$ atm

With an $As_{2(v)}$ pressure of 0.090 atm substituted in the expression for the equilibrium constant for reaction [2], the gallium activity in gallium arsenide at 1250°C is 0.56.

The activity of gallium in gallium arsenide in equilibrium with 1 atm of arsenic vapor must also be known at lower temperatures for some of the calculations to be made later in this paper. The activity at 808°C is calculated to provide a basis for obtaining the activities at temperatures between 808° and 1250°C, by graphical interpolation. The As_2 pressure in 1 atm of arsenic vapor becomes 0.00084 atm at 808°C, and the corresponding gallium activity in gallium arsenide in equilibrium with 1 atm of arsenic vapor becomes 0.027.

Course of the Reaction of Gallium with Quartz

According to calculations in the preceding paper (4), gallium and quartz can react in two ways, the favored reaction depending on the silicon content of the gallium. If the gallium or gallium arsenide contains no silicon initially, Eq. [1] is favored. The silicon activities vs. Ga_2O pressures from this reaction, using log K_{1523} = −9.24 from that paper, are shown in Fig. 1 for pure gallium (curve I) and for gallium arsenide (curve II). As the silicon activity increases in the gallium or gallium arsenide, the equilibrium Ga_2O pressure decreases.

As reaction [1] proceeds, silicon monoxide, $SiO_{(v)}$, is simultaneously produced from the reaction of quartz with the silicon product, thus

$$Si_{(\text{in Ga or GaAs})} + SiO_{2(c)} \rightleftarrows 2SiO_{(v)} \qquad [4]$$

and its pressure increases with increasing silicon activity in the gallium or gallium arsenide. For reaction [4], log $K_{1523} = -5.82$, by combination of the equilibrium constant of reaction [1] and that of [5], below [see preceding paper (4)]. The silicon activity from reaction [1] increases eventually to a point where the SiO pressure from reaction [4] equals the Ga_2O pressure from reaction [1].

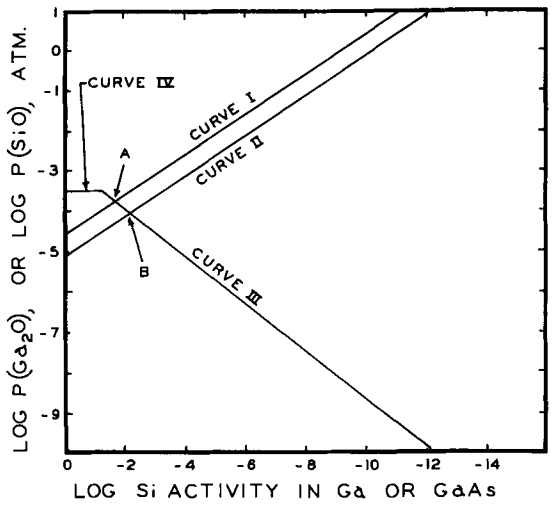

Fig. 1. Equilibrium partial pressures of $Ga_2O_{(v)}$ and $SiO_{(v)}$ from reaction of gallium with quartz at 1250°C; point A, where reactions for curve I and curve III occur concurrently, a_{Si} = 0.019; point B, where reactions for curve II and curve III occur concurrently, a_{Si} = 0.0061.

Curve I
$4Ga_{(l)} + SiO_{2(c)} \rightleftarrows Si_{(\text{in Ga})} + 2Ga_2O_{(v)}$
Curve II
$4Ga_{(\text{in GaAs})} + SiO_{2(c)} \rightleftarrows Si_{(\text{in GaAs})} + 2Ga_2O_{(v)}$
Curve III
$Si_{(\text{in Ga or GaAs})} + SiO_{2(c)} \rightleftarrows 2SiO_{(v)}$
Curve IV
$Si_{(\text{in Ga or GaAs})} + SiO_{2(c)} \rightleftarrows 2SiO_{(c)}$

Further reaction of gallium with quartz will not produce additional silicon but only $Ga_2O_{(v)}$ and $SiO_{(v)}$ by the composite reaction [5].

$$2Ga_{(l \text{ or from GaAs})} + SiO_{2(c)} \rightleftarrows Ga_2O_{(v)} + SiO_{(v)} \qquad [5]$$

Log $K_{1523} = -7.53$ for reaction [5] from the preceding paper (4).

The silicon activity that has been attained when reaction [5] takes over is 0.019 for the reaction of pure gallium and 0.0061 for the reaction of gallium arsenide (obtained as the intersection of curve III with curves I or II).

Removal of Reaction Products

Once the high-temperature zone containing the reacting gallium and quartz has been saturated with the equilibrium partial pressures of the gaseous products, the contamination reaction can proceed further only if the vapors are removed. Removal can occur by $Ga_2O_{(v)}$ dissolving in the gallium arsenide or diffusing to a colder zone where it can react with arsenic vapor, as follows

$$3Ga_2O_{(v)} + 2As_{2(v)} \text{ (or } As_{4(v)}) \rightleftarrows Ga_2O_{3(c)} + 4GaAs_{(c)} \qquad [6]$$

The solubility of gallium suboxide in gallium arsenide is unknown, and therefore only removal of vapors by diffusion (the case that results in the minimum amount of contamination) will be considered.[1]

The temperatures at which reaction [6] occurs to deposit crystalline GaAs and Ga_2O_3 are shown in

[1] Removal of $Ga_2O_{(v)}$ by dissolving in the quartz or by reacting with the quartz to form gallium silicate are two additional possibilities which, however, cannot be treated.

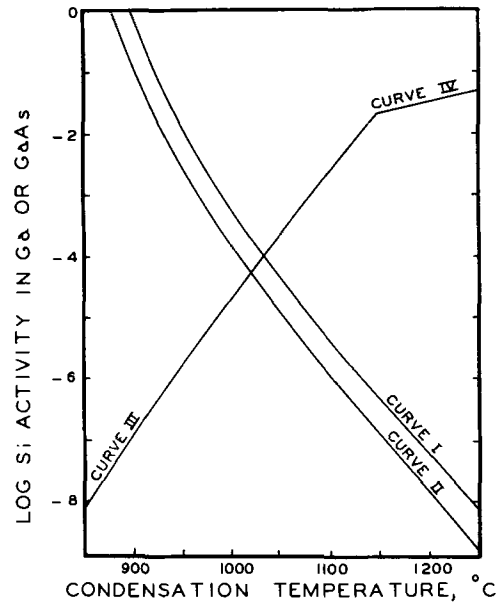

Fig. 2. Condensation temperatures of gaseous products from reaction of gallium with quartz at 1250°C in 1 atm of arsenic vapor.

Curve I
$3Ga_2O_{(v)}$ (from Ga + SiO_2) + $As_{(v)} \rightleftarrows Ga_2O_{3(c)} + 4GaAs_{(c)}$
Curve II
$3Ga_2O_{(v)}$ (from GaAs + SiO_2) + $As_{(v)} \rightleftarrows Ga_2O_{3(c)} + 4GaAs_{(c)}$
Curve III
$2SiO_{(v)} \rightleftarrows Si_{(c)} + SiO_{2(c)}$
Curve IV
$SiO_{(v)} \rightleftarrows SiO_{(c)}$

Fig. 2. These calculations employed the previously calculated activities of gallium in gallium arsenide in 1 atm of arsenic vapor, together with equilibrium constant data for the disproportionation of gallium suboxide to gallium and gallia from the preceding paper (4).

The reaction zone will also be saturated with the equilibrium partial pressure of silicon monoxide. Further transfer of silicon can occur only if there is diffusion of the silicon monoxide to a colder region where it can condense. Figure 2 also shows the temperatures at which the SiO vapors will deposit by disproportionation for different silicon activities in the Ga or GaAs. At silicon activities near one tenth (the break in the SiO curve), the SiO pressure becomes large enough for it to condense without disproportionation, according to the free energy of vaporization data given by Schick, (8) as follows:

$$\Delta F_{\text{vaporization}} = 77{,}530 - 34.94T$$

$$\log P_{SiO} = -\frac{77{,}530}{4.576T} + \frac{34.94}{4.576} = -\frac{16{,}950}{T} + 7.639$$

This expression was used to correct the $SiO_{(v)}$ curves of Fig. 1 and 2 for formation of condensed SiO at high silicon activities.

Klemm (9) reported a condensed phase from gallium suboxide vapors that contained no gallium by x-ray diffraction and only traces of gallia. However, this phase is probably unstable with respect to gallium and gallia at any of the temperatures of this work.

Rate of Silicon Formation

Assuming that the actual reaction of gallium with quartz is not rate-determining, the rate at which the silicon activity approaches the limiting activities shown in Fig. 1 ($a_{Si} = 0.019$ from reaction of pure gallium, and $a_{Si} = 0.0061$ from reaction of GaAs, determined by the point at which reaction [5] takes over to maintain the constant silicon level) will depend on the rate of removal of the gaseous products from the reaction zone.

Nothing is known about the solubility or rate of solution of $GaO_{(v)}$ in the gallium arsenide, but the rate of diffusion of $Ga_2O_{(v)}$ from the 1250°C zone can be considered. This rate will likely be proportional to the $Ga_2O_{(v)}$ pressure which, in turn, varies inversely as the square root of the silicon activity (from the equilibrium constant expression for reaction [1]). As a result, the rate of silicon production should decrease continually as the reaction proceeds and become zero at the limiting silicon contents given by the intersection of the curves in Fig. 1.

The rate of $Ga_2O_{(v)}$ removal in vacuum can be rapid, particularly in the proximity of a cold condensing surface, and relatively large quantities of silicon can be introduced. Figure 3 shows, at two magnifications, silicon single crystals deposited on a quartz vessel that had contained high-purity gallium at 1100°C for ½ hr in a vacuum of better than 10^{-5} mm. The gallium was heated inductively and was covered by a cold quartz condenser situated about 1 cm above the surface.

Figure 4 illustrates the attack of gallium on the surface of a quartz beaker heated to 1175°C for 3½ hr in vacuum below 5 x 10^{-6} mm. The curved border between the etched and unetched areas corresponds to the outer periphery of the gallium globule that rested on the quartz. Attack of the quartz underneath the gallium was negligible because the first Ga_2O vapor formed was slow in escaping from this area. However, gallium vapor

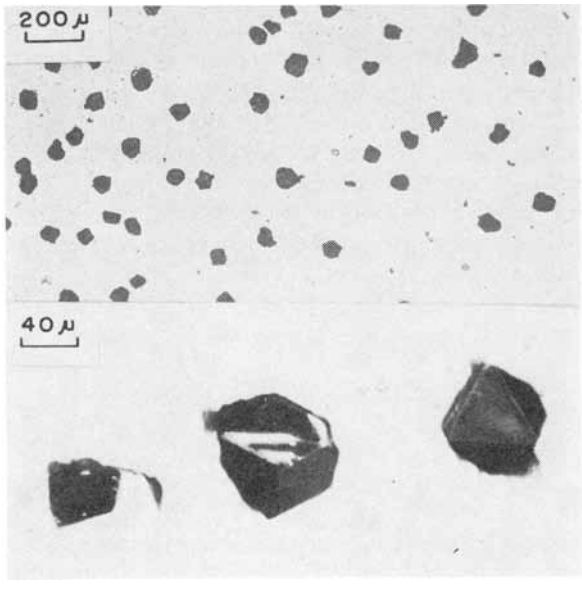

Fig. 3. Silicon crystals from reaction of gallium and quartz, growing on quartz surface.

Fig. 4. Micrograph showing vapor vs. liquid phase attack of gallium on quartz.

from the globule etched the quartz beside the globule because the $Ga_2O_{(v)}$ that formed there was free to escape into the vacuum.

The silicon contamination of the gallium can easily go undetected in such experiments unless great care is taken in sampling. Silicon is completely insoluble in gallium at room temperature, and it precipitates out and adheres to the quartz as shown, or floats to the top of the metal. In the experiments shown in Fig. 3, the quartz container lost 0.03g.

Heating of gallium in the presence of quartz at high temperature in high vacuum is certainly to be avoided. In the presence of the atmosphere of arsenic vapor employed during the synthesis of GaAS, the diffusion of gaseous products from the reaction zone will be much slower than in vacuum.

If the solubility of $Ga_2O_{(v)}$ in GaAs should prove to be insignificant, it should be possible to suppress the gallium-quartz reaction by saturating the 1250°C zone with a sufficiently high $Ga_2O_{(v)}$ pressure from the reaction of gallium with gallia or with water vapor. This presupposes that oxygen contamination is not a problem, however, and one would hesitate to recommend the deliberate addition of oxygen-containing species.

Clearly, if the gallium could be contained in a completely nonreactive boat, the entire situation would be changed. There would be no need to maintain the free volume around the gallium at 1250°C since there would be no volatile products that would condense at lower temperatures. In fact, it would be desirable in this case to maintain the entire quartz envelope just above the condensation temperature of arsenic, and heat only the gallium to 1250°C.

Examples of Contamination

The information that has been obtained can be used to estimate the extent of contamination by silicon under various circumstances. The relationship for making this estimate is derived as follows.

The equation for curve I of Fig. 1 is

$$\log P_{Ga_2O_{(v)}} = -\tfrac{1}{2} \log a_{Si \text{ in } Ga} - 4.62 \qquad [7]$$

Assuming an ideal solution of silicon in gallium, the activity of silicon in the dilute range is given by the following expression:

$$a_{Si} = \frac{M_{Ga}}{M_{Si}} W \qquad [8]$$

where M is the atomic weight and W is the weight fraction of silicon.

Since two molecules of gallium suboxide are produced for each atom of silicon formed, the partial pressure of suboxide, $P_{Ga_2O_{(v)}}$, can be expressed in terms of W and V, the ratio of the free volume in the 1250°C zone to the volume of gallium using a value of 6 g/ml for the density of liquid gallium.

$$P_{Ga_2O_{(v)}} = \frac{53{,}500W}{V} \qquad [9]$$

The weight fraction of silicon is solved for by combining Eq. [7], [8], and [9] to give

$$\log W = -6.365 + 2/3 \log V$$

The corresponding expression for GaAs is

$$\log W = -6.701 + 2/3 \log V$$

It can be seen that, in the case of the reaction of arsenic-free gallium and quartz, if the free volume of the 1250°C zone is five times the volume of the gallium in the boat, the silicon content of the gallium will reach 1.3 ppm (or 0.6 ppm based on the final GaAs) just in saturating this zone with Ga_2O vapor. If the free volume of the hot zone is ten times the volume of the gallium, the silicon content will reach 2.0 ppm (or 1.0 ppm based on the final GaAs). Somewhat lower silicon contents would result if the equilibria shown by curve II of Fig. 1 were determining.

Reaction at the Quartz Envelope

Thus far, only reaction at the gallium-containing boat has been considered. Gallium could also react with the quartz envelope to produce gaseous products that could diffuse back to the boat and be a source of contamination. Reaction [5] would predominate, since there is no gallium sink in which the silicon would dissolve at low activity.

In an atmosphere of arsenic vapor, the equilibrium gallium activity in the gas phase is the same as that in gallium arsenide ($a_{Ga} = 0.56$ at 1250°C, from an earlier section). In early stages of the synthesis, reaction of gallium vapor with the quartz envelope will be suppressed by the high pressure of Ga_2O that is more easily produced by reaction of unreacted gallium (or gallium-arsenic solutions) in contact with the quartz boat. Ultimately, when synthesis is complete, the equilibrium will

be the same whether the reaction is with the boat or the walls.

Solubilities and Activities

The activity coefficients of silicon in gallium and gallium arsenide are not known and are assumed to be unity for purposes of the present calculations. The usual concepts of solid solubilities and activities undoubtedly do not hold in the extremely dilute ranges that are of interest in semiconductor applications. The activity coefficient of silicon on cation sites in gallium arsenide might be different from that when it is on anion sites, for example.

The activity of silicon in more concentrated ranges can be predicted qualitatively from information obtained from phase diagrams of the Ga-As (5), Ga-Si (10, 11), and Si-As (12) systems. The high solubility (40 w/o) of silicon in gallium at 1250°C, with no compound formation, and the close correspondence between the measured heat of solution of silicon in gallium and the known heat of fusion of silicon both indicate that the activity coefficient of silicon in gallium at 1250°C may be near unity.

Two compounds, SiAs and $SiAs_2$, have been reported, and the activity coefficient of silicon in molten GaAs might be considerably less than unity.

The solid solubility limit of Si in GaAs at high temperatures has not been reported. If it is low, there exists the possibility that a silicon-rich phase could precipitate and become occluded in the GaAs during cooling. This has not been considered in the calculations.

The observed amounts of silicon contaminating the gallium arsenide that is currently being produced are of the same order of magnitude as the values predicted in this work for saturating the 1250°C zone with Ga_2O vapor.

Other Factors which May Affect the Reaction of Gallium with Quartz

Effect of oxide films.—Workers in other organizations, as well as in these Laboratories, have noted that etching of the quartz is promoted if the gallium is not initially heated in vacuum or flowing inert gas at low temperatures (600°-700°C). This treatment removes gallia films and their adsorbed water, or water of hydration, in the form of gallium suboxide, water, and hydrogen. A frequent observation is that if the gallium is not thus treated there might be general etching of the quartz but preferential attack at quartz-gallium interfaces where oxide films were known to be trapped.

This action is difficult to understand because the reaction of gallium with gallia or water vapor in these areas should form sufficient pressures of $Ga_2O_{(v)}$ to suppress the gallium-quartz reaction in the early stages of the attack. Apparently the quartz surface is sensitized in some manner, perhaps as a result of etching by the vapor species, so that it is more susceptible to further attack.

Effect of water vapor.—Frosch and Derick (13) demonstrated that about one hundred times more gallium was transported in flowing wet hydrogen at 950°C than in dry hydrogen. They explained that the water reacts with the gallium to form gallium suboxide and hydrogen. Weisberg (14) has observed the "distillation" of large quantities of GaAs with traces of water vapor.

In a test of these reactions at the authors' Laboratories, each of two identical quartz boats, 12 mm wide and 45 mm long, was placed near one end of separate, 15 cm long 37 ml volume, quartz tubes. One of the tubes with its boat was outgassed for 16 hr at 1000°C in a pressure of about 10^{-6} mm Hg. Vacuum was broken with argon and 6g of 99.9999+% gallium, weighed to ±0.05 mg, was added to each boat. The tubes were re-evacuated, and the tube that had been carefully outgassed was heated again to approximately 1000°C in high vacuum. A pressure of 19 mm of dry argon was admitted to this tube before sealing it off. A quantity of 0.0008g of water was introduced into the second tube before it was sealed off. These quantities of water and argon were such that the total pressure would be the same in both tubes at temperature.

The sealed tubes were placed side by side in a furnace in such a position that there was a temperature gradient along their length. The temperature at the end of the tubes containing the gallium was 1060°C. The temperature at the other end was 1020°C. Heating was continued for 48 hr.

In the tube containing argon, 0.0034g of gallium distilled to the ends, compared to 0.3259g, or 96 times as much, that distilled to the ends of the tube containing added water vapor. Nearly all of this gallium distilled to the end nearest the boat, even though this end was probably no more than 5° cooler than the gallium in the boat, whereas the other end, 7 in. away, was 40° colder.

The equilibrium constant derived for the reaction of gallium with water (4) becomes less favorable as the temperature is lowered so that gallium suboxide and hydrogen formed at one temperature will back-react partially to liquid gallium and water vapor at a lower temperature, other conditions remaining constant. The same water vapor can then diffuse back to the gallium at the higher temperature to form gallium suboxide and hydrogen, which can repeat the action.

If the water pressure is too high, some gallia will form in the distillate. This will not occur if the initial pressure of water vapor is reduced to the point where the pressure of gallium suboxide vapor forming at the higher temperature is too low for gallia to form by disproportionation at the lower temperature.

In principle, the transport of gallium from the hot to the cold end of the two tubes could be calculated from information on the equilibria between gallia, gallium, hydrogen, and water given in the previous paper (4). An approximate calculation showed that about a thousandfold difference in transport would be predicted for the two cases if vapor transport were accomplished by convection alone, one tube were completely free of moisture, and the temperature of the condenser were exactly

known. This is about tenfold greater than the observed ratio. However, diffusion transport may be of equal or greater importance, and the temperature of the actual site of condensation was not determined. Moreover, it is not possible to prevent accumulation of some trace of water vapor in a heated closed quartz tube even after careful outgassing.

Because of these uncertainties detailed treatment of the data is not warranted. A refined experiment would yield much interesting information about this transport process.

Distillation of gallium from gallium arsenide could also occur by the same transport mechanism, with the arsenic recombining with the gallium at a colder zone. This would seem to have interesting implications in the epitaxial growth of gallium arsenide, since there is no apparent mechanism for the transport of GaAs, *per se*.

Recommendations

It is interesting to speculate on modifications of the conventional horizontal GaAs synthesis apparatus that should lessen the attack on quartz and thus reduce the silicon contamination in the product.

An obvious precaution to observe is to separate any cold surface as far as possible from the reaction zone, *i.e.*, extend the 1250°C zone as near as possible to the arsenic boiler. Although extending the hot zone might enhance undesirable diffusion of gaseous products out of the reaction zone, such diffusion would be impeded by the countercurrent diffusion of arsenic into the reaction zone. This could be accentuated by reducing the diameter of the quartz tubing that joins the 1250°C zone to the 610°C zone. In the limiting case, this connection might even be a capillary tube.

The volume of "free space" in the 1250°C zone should be as small as possible, since this space will be filled with the gaseous reaction products whether or not there is a cold surface available.

Figure 5 is a sketch of the conventional apparatus and a suggested system that incorporates these recommendations. These recommendations might be met also in the conventional synthesis system by encapsulating the gallium in a quartz ampoule with a small hole at one end to admit the arsenic vapor. Such arrangements have not actually been employed in the synthesis of gallium arsenide to our knowledge.

Crucible synthesis and crystal pulling by the Czochralski technique seems to incorporate a number of undesirable features in the light of our present knowledge. The free space around the crucible is large in this case and, since induction heating is generally employed, a large area of cold condensing surface is close at hand. These features combine to present the worst situation from the standpoint of sustained reaction with the quartz. The

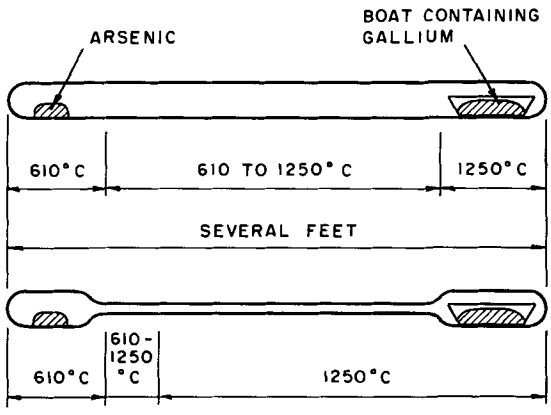

Fig. 5. Conventional top, and suggested, bottom of synthesis systems for GaAs.

fact that the carrier mobility in Czochralski grown GaAs is generally lower than in boat grown material, in spite of greater crystal perfection, seems to bear this out. Clearly the situation would be reversed if a completely nonreactive crucible material were available. In this case, the outer quartz envelope should be kept as near the arsenic condensation point as possible.

Only equilibrium calculations have been attempted here. Obviously, if the attainment of equilibrium can be delayed or prevented, lesser contamination should result. Carrying out the synthesis in the shortest possible time and at the lowest possible temperature are indicated.

Manuscript received June 28, 1961.

Any discussion of this paper will appear in a Discussion Section to be published in the December 1962 JOURNAL.

REFERENCES

1. J. van den Boomgaard and K. Schol, *Philips Research Repts.*, **12**, 127 (1957).
2. O. G. Folberth, *Phys. and Chem. Solids*, **7**, 295 (1958).
3. S. Antkiw and V. H. Dibeler, *J. Chem. Phys.*, **21**, 1890 (1953).
4. C. N. Cochran and L. M. Foster, *This Journal*, **109**, 144 (1962).
5. J. Drowart and P. Goldfinger, *J. chim. phys.*, **55**, 721 (1958).
6. W. Köster and B. Thoma, *Z. Metallk.*, **46**, 291 (1955).
7. D. R. Stull and G. C. Sinke, "Thermodynamic Properties of the Elements," American Chemical Society, Washington, D. C. (1956).
8. H. L. Schick, *Chem. Rev.*, **60**, 311 (1960).
9. W. Klemm and I. Schnick, *Z. anorg. u. allgem. Chem.*, **226**, 353 (1936).
10. W. Klemm, L. Klemm, E. Hohmann, H. Volk, E. Orlamünder, and H. A. Klein, *Z. anorg. Chem.*, **256**, 239 (1948).
11. P. H. Keck and J. Broder, *Phys. Rev.*, **90**, 521 (1953).
12. W. Klemm and P. Pirsher, *Z. anorg. u. allgem. Chem.*, **247**, 211 (1941).
13. C. J. Frosch and L. Derick, *This Journal*, **105**, 695 (1958).
14. L. R. Weisberg, R.C.A. Laboratories, Private communication.

Electrochemical and Adsorption Measurements on Single Crystals: The Germanium-Iodide Solution System

W. W. Harvey, W. J. LaFleur, and H. C. Gatos

Lincoln Laboratory,[1] Massachusetts Institute of Technology, Lexington, Massachusetts

ABSTRACT

An apparatus for simultaneous electrochemical and adsorption studies on single crystals is described. The electrode surface can be cleaned and characterized after mounting in position, the composition of the electrolyte can be altered, and repeated adsorption measurements can be made without removing the electrode. By employing the radioactive tracer I^{131} the adsorption of iodide was determined as a function of electrode potential and orientation in 0.1*N* Na_2SO_4 solutions of various *p*H containing small amounts of KI (5.0×10^{-6} to 2.5×10^{-4}*N*). Reversible multilayer adsorption on the {111} surface was observed, with a distinct maximum near the rest potential. Desorption of iodide occurred at strongly anodic and cathodic potentials. In addition to reversible adsorption of iodide, incorporation of iodide into an anodically formed surface compound was observed in the case of the {100} surface over a limited range of *p*H and iodide concentration.

Direct measurements of adsorption on solids from liquids can be made by tagging the adsorbing species with a radioactive tracer and determining the radioactivity on the surface. In such measurements the solid is usually removed from the liquid and freed from the mechanically adhering liquid before counting. The extent of adsorption on smooth electrodes can also be determined from the decrease in radioactivity in the solution, provided one employs extremely low adsorbate concentrations (1). If powders of large surface area are to be studied, direct adsorption measurements can be carried out by monitoring the adsorbate concentration in the liquid (2). A method has been reported for the continuous measurement of monolayer adsorption from solutions, using a thin film of the solid evaporated onto the window of a Geiger tube (3).

The methods outlined above are not generally suitable for performing simultaneous and continuous electrochemical and adsorption measurements on solids; they are particularly unsuited for single-crystal electrodes and relatively high concentrations of adsorbate. In order to overcome some of these limitations, an apparatus was developed recently and submitted to preliminary evaluation (4). This apparatus has been extensively modified for the present study and employed in an investigation of the adsorption of iodide ions onto germanium single crystals at controlled electrode potentials.

The adsorption of iodide on germanium has not been measured hitherto. However, the maxima observed in the rate of germanium dissolution in oxygen-saturated solutions as a function of Cl^-, Br^-, or I^- concentration were attributed to specific adsorption of the anion with charge transfer (5). Recently, it was reported (6, 7) that the limiting anodic current of n-type germanium in 0.1*N* HCl was increased by the presence of 0.1*N* KI. In contrast to the behavior of oxalate ion, which similarly increased the limiting anodic current, iodide ion was not oxidized at the n-type germanium anode. It was postulated that iodide is oxidized in an intermediate step of the anodic process, "injecting" electrons into the germanium, and that the iodine formed is subsequently reduced electrochemically with the injection of holes. Whether or not this explanation is correct, sufficient interest is attached to the system Ge-I^-(aq.) to warrant a direct study of the adsorption characteristics.

[1] Operated with support from the U. S. Army, Navy, and Air Force.

Experimental Techniques

Apparatus.—Details of the present shielding and counting arrangement are shown in Fig. 1. The ad-

Fig. 1. Adsorption cell and counting arrangement. A, Teflon gasket; B, electrode; C, gold foil for electrical contact; D, polyethylene insulator; E, steel plate for transmitting pressure (side arms prevent shearing); F, pressure applying screw; G, scintillation crystal; H, light source; I, photomultiplier tube; J, cell support; K, lead shield; L, brass fastening plate; M, lead cover; N, brass plate; O, reference vial; and P, lead plug.

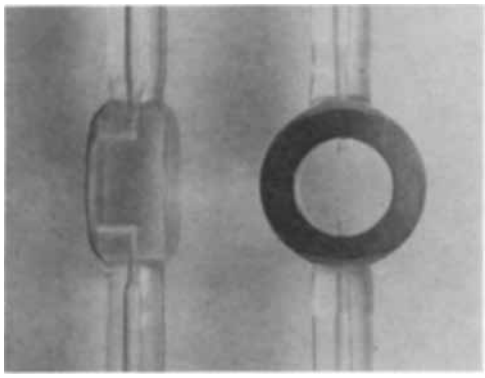

Fig. 2. Side and top view of Pyrex adsorption cell; Teflon coating is shown; diameter of recess 1.13 cm; diameter of capillary bore 1 mm.

sorption cell (Fig. 2) is of the same construction as that originally reported, except that a coating of Teflon replaces the Teflon gasket shown in Fig. 1; the coating has proved completely reliable in preventing leakage of radioactive solution out of the cell. Additional shielding within the lead pig and the use of a smaller scintillation crystal essentially restrict detection of radioactivity to that contained in the cell recess and in the immediately adjacent portions of the side arms. Illumination of the electrode surface is provided by a small lamp located between the cell and the scintillation crystal. More efficient circulation of the solution has resulted from replacing the thermal convection arrangement with a gas lift (Fig. 3); further modifications in the glass apparatus are evident on comparison of Fig. 3 with Fig. 1 of ref. (4).

The adsorption cell (capacity 0.05 ml) employed in this study has a recess 0.05 cm deep and 1.13 cm in diameter, allowing an exposed electrode area equal to 1.00 cm^2. With radioactive solution circulating through the cell, it was found that the counting rate, exclusive of that due to adsorption, corresponds to 0.10 ml of solution, *i.e.*, a factor of two greater than the volume of solution in the cell recess. Considering the large volume of solution contained in the glass apparatus, (approximately 130 ml, not including any solution in the reservoir) it is evident that the shielding arrangement is very effective, making for optimum sensitivity. The upper limit of radioactive solute concentration reported earlier (4), namely 10^{-4}M, applies to the detection of monolayer coverage; at this concentration the counting rate of the solution corresponds to 6 x 10^{15} atoms of the adsorbed species, or roughly six monolayer equivalents. At lower concentrations, small fractions of a monolayer equivalent can be detected.

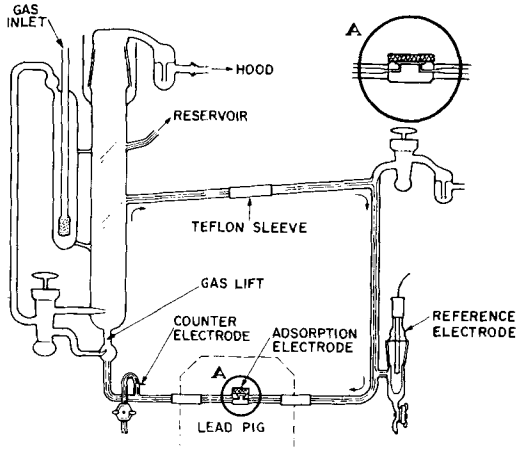

Fig. 3. Apparatus for radiotracer adsorption and electrochemical studies on single crystals.

Adsorption measurements.—The adsorbed activity is measured through a thin layer of solution in contact with the electrode and through some thickness of glass. Thus, the chemical species whose adsorption behavior is to be studied is tagged preferably with a gamma-emitting isotope, in this case I^{131} (half-life 8.14 days).

The contribution of the solution to the total observed counting rate is most conveniently established by comparing the counting rate of a 1.00-ml aliquot of the solution, contained in a suitable positioned vial (see Fig. 1), with that of the solution in the cell; for this measurement the specific activity of the adsorbing species is made so low that the adsorbed radioactivity is completely negligible. The ratio of solution counting rate (r_{soln}) to vial counting rate (r_{vial}) is a constant (R_{soln}) for a particular cell and counting arrangement. Once this "geometry" factor has been determined, the contribution of the solution in the apparatus to the observed counting rate is readily ascertained in an actual run by inserting the vial and measuring the increase in counting rate.

The difference between the observed counting rate, corrected for background, and the counting rate due to the solution in the apparatus is the counting rate of the adsorbed species. To proceed from this quantity to the amount of material adsorbed, use is again made of the counting rate of 1.00 ml of the test solution in the vial as follows: in a separate experiment the counting rate (r_{surf}) of a given quantity of radioactive material deposited on the surface of the electrode is compared with the counting rate (r_{vial}) of the same quantity of radioactive material contained in 1.00 ml of solution in the vial. The ratio $R_{surf} = r_{surf}/r_{vial}$, like the ratio R_{soln}, is a constant for the geometry employed. Having performed the necessary calibration, it becomes possible to evaluate the amount of material adsorbed from the observed counting rate, r_{obs} (corrected for background), the counting rate of the vial, r_{vial}, and the adsorbate concentration in the solution in contact with the electrode. Thus, for example, the number of adsorbed iodide ions $(I^-)_{ads}$ is given by:

$$(I^-)_{ads} = \frac{r_{obs} - R_{soln}\, r_{vial}}{R_{surf}\, r_{vial}} [I^-] \qquad [1]$$

where $[I^-]$ is the number of I^- ions per ml of solution. A distinct advantage in counting an aliquot of the solution is the fact that no explicit correction for radioactive decay need be made. Furthermore, this technique does not necessitate a determination of the absolute specific activity of the tagged species.

Characterization of the germanium electrodes.—Two types of electrochemical characterization were employed: (*a*) charging curves (8, 9), *i.e.*, plots of electrode potential *vs.* time (or number of coulombs) with a constant current passing through the cell, and (*b*) current-potential curves. An electronic con-

stant-current source having an equivalent source voltage of 500v was used for the charging curves; an apparent current density of 0.02 ma/cm² was generally employed. Current-potential characteristics were obtained by employing a potentiostat. Generally, the current employed did not exceed 0.1 ma. The varying efficiency of circulation in different parts of the recess posed no problem for the measurements reported here since the solutions used did not attack the electrode and since relatively long times were required for counting.

A limitation inherent in the method of counting adsorbed activity through a thin layer of solution is that the current density is not entirely uniform over the exposed surface of the electrode; in particular, the current density is greatest at the portions of the surface opposite the capillary orifices of the cell as revealed by prolonged anodic etching. In the present apparatus, a portion of the cell current flows in the direction of circulation (Fig. 3), so that a small IR drop is included in the potential of the adsorption electrode measured *vs.* the saturated calomel electrode. The virtual elimination of this small extraneous voltage is largely a matter of redesigning parts of the glass apparatus. Finally, it should be pointed out that the formation of gaseous reaction products on the electrode surface is to be avoided, since even very small bubbles constitute an appreciable fraction of the volume of the recess and are, moreover, difficult to dislodge.

Preparation of electrodes.—The electrodes were cut to the desired orientation from p-type germanium single crystals (resistivity about 10 ohm-cm) and had the nominal dimensions 2 x 2 x 0.8 cm. The large faces were ground precisely parallel and were chemically polished before mounting. Preliminary rinsing with distilled water circulating through the cell was followed by electrolytic cleaning in the solution to be studied (but containing no radioactivity); *i.e.*, the electrode was charged alternately anodically and cathodically until the characteristics of the charging curves did not change with time. Whenever some contaminant was present on the surface, it was readily detected as shown, for example, by the anodic portion of the initial charging curves in Fig. 4. Such contamination could be removed in a short time by the procedure described. A second portion of inert solution was employed for the electrochemical characterization of the electrode-solution system, both by charging curves and by current-potential curves. The characterization was repeated in the radioactive solution to insure that no chemical contamination was introduced along with the radioactivity. Occasionally, contamination was detected at this stage, and it was necessary to repeat the entire experiment. Electrochemical characterization, where applicable, is clearly an essential preliminary to reliable adsorption measurements.

Preparation of solutions.—All of the solutions employed in this study were 0.1*N* Na_2SO_4 containing various concentrations of H_2SO_4 and KI. Reagent grade anhydrous Na_2SO_4 was used to prepare a large volume of 1.0*N* stock solution; stock solutions of H_2SO_4 were prepared from Acculute volumetric standards. Since iodide in acid solutions is slowly oxidized by free oxygen, special consideration was given to the preparation of the KI solutions. First, weighed quantities of reagent grade KI were added to a dry volumetric flask containing a magnetic stirring bar. The air in the flask was then displaced by purified nitrogen; subsequently, the nitrogen in the flask was displaced by thoroughly deoxygenated distilled water, which was allowed to fill the flask to the brim. The solution in the completely filled and stoppered flask was then stirred magnetically. This stock KI solution was added last in making up Na_2SO_4/H_2SO_4/KI solution in the reservoir and only after oxygen had been removed from the solution by bubbling purified nitrogen.

The usual commercial form of carrier-free I^{131}, obtained from fission products, is in the form of NaI in alkaline sulfite solution. Since, however, sulfite participates in germanium electrode processes, sulfite-free solutions were specially procured from the Oak Ridge National Laboratory. Occasionally, these solutions contained peroxide and could not be used for adsorption measurements (see Fig. 4).

Results and Discussion

Current-potential characteristics. — Current-potential curves were obtained at various pH values and iodide concentrations. Some results are shown in Fig. 5 and 6. It is seen (Fig. 5) that in acid solutions of $10^{-4}N$ KI with 0.1*N* Na_2SO_4 supporting electrolyte,

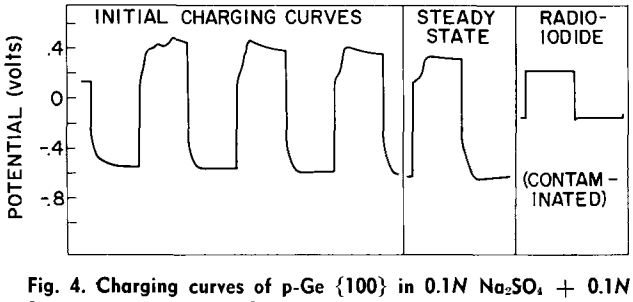

Fig. 4. Charging curves of p-Ge {100} in 0.1*N* Na_2SO_4 + 0.1*N* H_2SO_4 containing 5 x $10^{-6}N$ KI, showing removal of surface contamination present and detection of peroxide contamination in the radioiodide. Apparent current density 0.020 ma/cm²; charging intervals 60 sec.

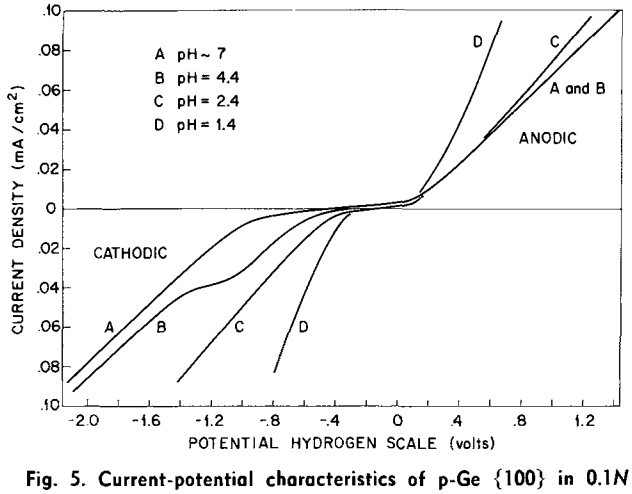

Fig. 5. Current-potential characteristics of p-Ge {100} in 0.1*N* Na_2SO_4 containing $10^{-4}N$ KI plus H_2SO_4 as follows: A, zero; B, $10^{-4}N$; C, $10^{-2}N$; D, $10^{-1}N$. Figure also shows convention used throughout this paper in plotting cathodic and anodic currents; 24°C.

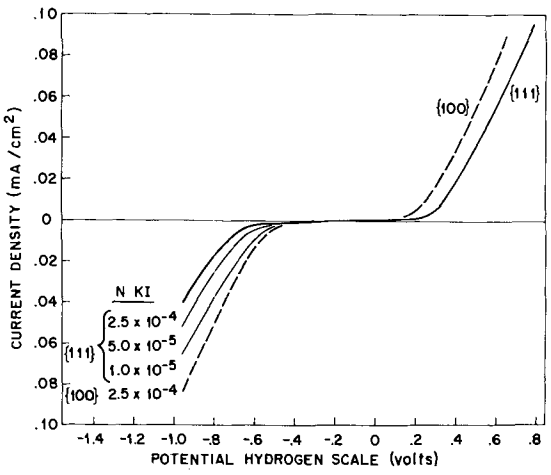

Fig. 6. Comparison of current-potential characteristics of the {100} and {111} surfaces of p-Ge in 0.1*N* Na_2SO_4 + 0.1*N* H_2SO_4 containing the indicated concentrations of KI; 24°C.

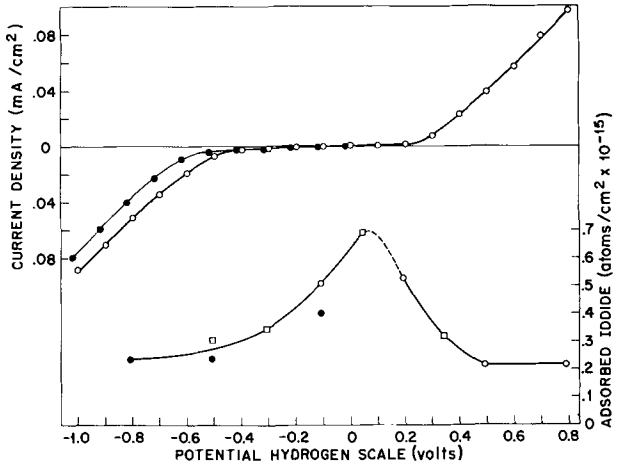

Fig. 7. Current-potential curves and iodide adsorption on {111} p-Ge from 0.1*N* Na_2SO_4 + 0.1*N* H_2SO_4 containing I^{131}-tagged 5 x 10^{-6}*N* KI. Measurements made with increasing (o) and decreasing (•) potential. Squares show adsorption measurements made on a subsequent day; 24°C.

both the germanium dissolution reaction (anodic branch) and the hydrogen ion discharge reaction (cathodic branch) become increasingly polarized with increasing pH. Since the primary interest in the present study is in adsorption behavior, and since the current density distribution is not entirely uniform, as pointed out earlier, a detailed discussion of these curves will not be attempted. It should be stated, however, that the inflection in the cathodic portion of curve B is reproducible; it may indicate the advent of strong iodide adsorption as the germanium electrode potential is changed in the positive direction. In the nearly neutral solution, current-potential characteristics at various lower KI concentrations were virtually superposable on curve A. This result is attributable to the fact that appreciable concentrations of hydroxide ion inhibit the adsorption of iodide, direct evidence for which will be presented later.

At pH 1.4, the hydrogen overvoltage on the {111} surface increases with iodide concentration (Fig. 6). By contrast, the {100} surface is characterized by an appreciably lower hydrogen overpotential at the highest iodide concentration and, in the same concentration range, iodide decreases the hydrogen overpotential. The latter effect is small, however, and is not shown in the figure. Evidently, no generalization can be made concerning the effect of iodide on the hydrogen overpotential on a germanium electrode. As is shown below, the {111} and {100} surfaces also differ considerably in their adsorption behavior.

Adsorption measurements.—The most characteristic feature of the adsorption data is the occurrence of a sharp adsorption maximum at the rest potential or at somewhat more positive potentials. Figure 7 shows the results obtained with the {111} electrode at the lowest KI concentration studied. Assuming a roughness factor of 1.5, the unit 10^{15} cm^{-2} approximates the calculated number of iodide ions in 1 cm^2 of a close-packed monolayer. Results obtained with increasing and decreasing potential are also shown in the figure. The data are somewhat atypical in that (*a*) the cathodic polarization curves taken with increasing and decreasing potential do not more nearly coincide, and (*b*) the calculated amount of adsorbed iodide does not fall to zero on either side of the maximum. The general features of the adsorption behavior, however, were duplicated at iodide concentrations up to 2.5 x 10^{-4}*N* KI. The data are summarized in Table I.

It is seen from the table that iodide is desorbed at potentials more positive than 0.4v. This behavior is consistent with the fact that the steady-state anodic reaction in these solutions is germanium dissolution. On the other hand, the ready removal of adsorbed iodide by cathodic polarization contrasts with earlier results obtained by Kolotyrkin (1), who estimated that adsorption of iodide on silver and lead begins at potentials near −1.0v. The contrast is even greater than it appears since a substantial portion of an applied cathodic potential may reside in the space charge region of a p-type germanium electrode (10, 11).

At potentials close to maximum adsorption, the amount of adsorbed iodide increases with iodide concentration over the entire range investigated. The adsorption isotherm taken at −0.11v, *i.e.*, approximately at the rest potential, shows no sign of leveling off even though the adsorption attained very high values, *e.g.*, 25 x 10^{15} atoms/cm^2 for the 2.5 x 10^{-4}*N* KI solution. Comparably large iodide adsorption was measured by Balashova (12) on smooth platinum. In

Table I. Adsorption of I^{131}-tagged iodide[a] on a {111} germanium surface at various potentials[b]

Iodide concentration, gram ions/liter	Adsorbed iodide in units 10^{15}/cm^2				
	−0.41v	−0.21v	−0.01v	+0.19v	+0.39v
1.0 × 10^{-5}	0.02	0.22	2.9	0.27	0.05
2.5 × 10^{-5}	0.07	1.0	7.3	0.42	0.22
5.0 × 10^{-5}	0.01	2.4↑[c]	3.8↓	6.8↓	0.10↓
1.0 × 10^{-4}	0.10	3.2	7.9	5.3↓	—
2.5 × 10^{-4}	0.07	1.7↑	9.3	8.5	0.53

[a] In 0.1*N* Na_2SO_4 + 0.1*N* H_2SO_4, 24°C.
[b] Rest potential = −0.10v.
[c] Arrows indicate that the amount of radioactivity was slowly increasing (↑) or slowly decreasing (↓) at the time of the measurement.

our case, autoradiograms showed no evidence of accumulation of iodide at active sites such as at the termination of dislocations, and the adsorption appeared to be uniform over small regions of the surface. Adsorption to the extent of many monolayer-equivalents cannot reasonably be described as specific adsorption, since contact with the surface is not possible for the majority of adsorbed atoms. Moreover, there must be coadsorption of cations in order to provide counter charges in sufficient numbers. A convenient alkali metal iodide for studying coadsorption might be RbI tagged with Rb^{86}; by measuring adsorption of both I^- and Rb^+, it could be determined whether HI is adsorbed in significant amounts.

The data of Fig. 7 and Table I were obtained with the same electrode by displacing a given solution with one containing a higher concentration of iodide. Repeated treatment of the electrode was unnecessary since the adsorption was completely reversible, *i.e.*, adsorbed activity was removed (by exchange) when the radioactive solution was replaced by a solution of inert (nonradioactive) iodide. The adsorbed activity could also be removed by circulating water or an iodide-free solution through the apparatus. A time-dependent irreversible adsorption as found, for example, by Balashova (12) for iodide on platinum was not observed in the present system. No attempt was made in our experiments to measure rates of exchange of iodide between surface and solution, although such measurements can be carried out with the present apparatus provided the times involved are not too short.

In some instances illumination effects were looked for, but no significant changes in the amount of adsorbed iodide were noted. However, for the electrodes and solution compositions employed, the photopotentials were not large. In order to observe photoadsorption and desorption on germanium, one would need to employ an electrode having bulk electrical properties such as to result in a large permanent photopotential (13) in the given electrolyte solution and in a region of electrode potential where the amount of adsorption depends strongly on potential.

Orientation effects.—Polarization and adsorption characteristics for the {111} and the {100} surfaces are compared in Fig. 8 for $10^{-4}N$ KI in $0.1N$ Na_2SO_4 + $0.1N$ H_2SO_4. It is seen from Fig. 8 that, in addition to the smaller anodic and cathodic overvoltages on the {100} surface (see also Fig. 6), iodide ions are adsorbed on the {100} surface to a much smaller extent than on the {111} surface. For the {100} surface, the amount of iodide adsorbed at the maximum, near zero volts on the hydrogen scale, is close to that observed for the {111} surface at the same potential, but at one twentieth of the iodide concentration (Fig. 7).

Another significant feature of the adsorption behavior of the {100} surface in the solution of Fig. 8 is the appearance of a second and larger adsorption maximum at a potential more positive than that of the first. Unlike the reversibly adsorbed iodide, the iodide in this case is associated with an anodically formed surface compound. Effects related to the presence of an anodically formed compound containing iodide are transient except within a fairly narrow range of solution composition as discussed below. An example of a transient effect of this nature is shown in Fig. 9 (lower curve). The hysteresis indicated by the dashed line was recorded by using the inert solution, but was not found subsequently by using the radioactive solution; otherwise, the curves for the two solutions are identical. The principal significance of Fig. 9 is a comparison of iodide adsorption at low and high pH. The extent of adsorption at the maximum is smaller by a factor of seventeen in the alkaline solution in which the concentration of hydroxide ion exceeds that of iodide ion by a factor of forty.

For the {100} electrode, effects associated with an anodic film (surface compound) were observed repeatedly in $10^{-4}N$ KI + $10^{-3}N$ H_2SO_4 + $0.1N$ Na_2SO_4, *i.e.*, at the same pH as for Fig. 9, but at a higher KI concentration. Thus, following anodic polarization, an extended step appeared in the cathodic charging curve, as shown in Fig. 10. By allowing various times to elapse between anodic and cathodic charging (see Fig. 10), it was determined that at least two hours are required for the complete dissolution (without external polarization) of the anodically formed sur-

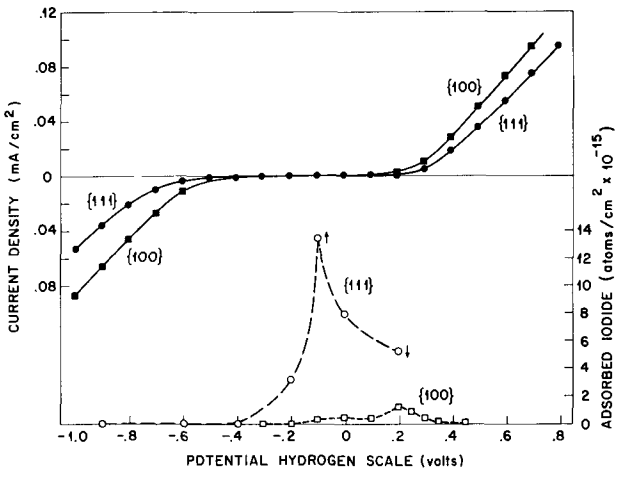

Fig. 8. Comparison of polarization and iodide adsorption characteristics of the {111} and {100} surfaces of p-Ge in $0.1N$ Na_2SO_4 + $0.1N$ H_2SO_4 containing $10^{-4}N$ KI; 23°C.

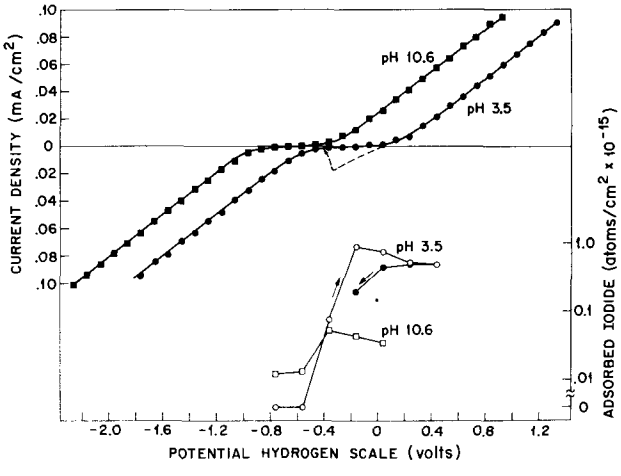

Fig. 9. Effect of pH on the polarization and iodide adsorption characteristics of {100} surface of p-Ge in $0.1N$ Na_2SO_4 containing 1 x $10^{-5}N$ KI + $10^{-3}N$ NaOH (pH 10.6, 26°C) or $10^{-3}N$ H_2SO_4 (pH 3.5, 24°C).

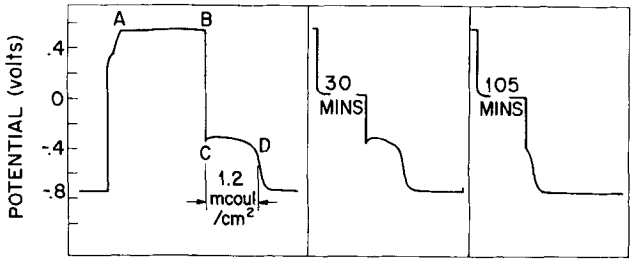

Fig. 10. Charging curves for {100} p-Ge in 0.1*N* Na_2SO_4 + 10^{-3} H_2SO_4 containing $10^{-4}N$ KI; apparent current 0.020 ma/cm².

face layer. For short anodic charging times, the width of the cathodic step $\overline{CD}$ is approximately equal to the length of the horizontal portion $\overline{AB}$ of the anodic curve. The thickness of the anodically formed layer does not increase indefinitely, however; if, for example, $\overline{AB}$ is made twice as great as for Fig. 10, $\overline{CD}$ is increased by about 40%. The steady-state anodic reaction, in other words, is still germanium dissolution. The steady-state thickness of the anodic surface layer at a current density of 20 μa/cm² is about 11 monolayer-equivalents, assuming that 10^{15} atoms/cm² constitutes one monolayer-equivalent and that one electron is transferred for each atom incorporated into the surface film. On the other hand, adsorption measurements revealed that 17 monolayer-equivalents of iodide present in the anodically formed surface layer are removed cathodically (Fig. 11). This observation is significant with regard to the chemical composition of the film in that it indicates that not all of the incorporated iodide is in good electrical contact with the substrate.

In the solution of Fig. 10 and 11, a pronounced hysteresis occurred in the current-potential curves when measurements were made fairly rapidly. However, the cathodic potential at which the anodically formed surface compound appears to be suddenly reduced is not critical, but depends on the rapidity of the measurements. In taking the adsorption data, roughly 20 min elapsed between settings of the electrode potential; consequently, although the current density followed the hysteresis curve for a time, the abrupt removal of the surface film occurred at a potential more positive by 0.54v (compare upper and lower parts of Fig. 11).

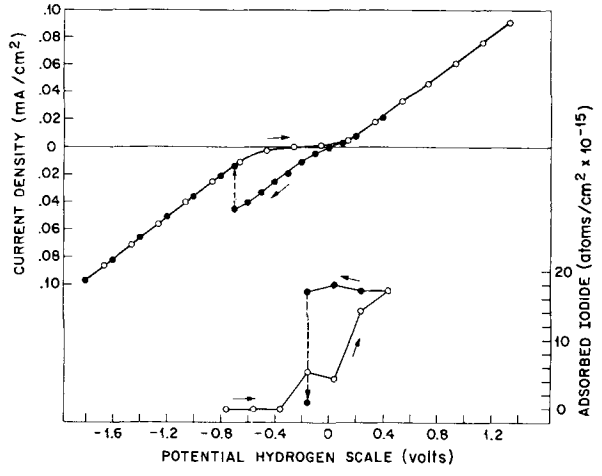

Fig. 11. Hysteresis in the polarization and adsorption behavior of the {100} surface of p-Ge resulting from the anodic formation of a surface compound. Solution composition as in Fig. 10; 25°C.

The adsorption data of Fig. 11 may be compared to those for the {100} electrode in Fig. 8. As a result of increasing the *p*H by two units, the amount of iodide adsorbed from $10^{-4}N$ KI solution was increased from 0.43 to 5.5, and the amount of iodide incorporated into the anodically formed surface layer was increased from 1.2 to 17.2, in units of 10^{15} cm⁻². However, there is reason to believe that at still higher *p*H's the amount of adsorbed iodide will decrease as for the $10^{-5}N$ KI solution (Fig. 9).

Summary

The capabilities and limitations of the apparatus and technique for the simultaneous measurement of adsorption and electrochemical properties of single-crystal electrodes were assessed in a study of the system germanium-iodide solution. In the absence of a significant amount of irreversible adsorption, the same electrode can be used repeatedly, without intermediate treatment of the surface. Electrochemical characterization (charging curves as well as current-potential curves) proved indispensable both as an aid in interpreting the adsorption data and as a sensitive means of detecting contamination of the surface or of the solution.

The practical upper limit of adsorbate concentration (about $10^{-4}N$ for monolayer adsorption) is orders of magnitude higher than that attainable by other techniques using solid electrodes and determining adsorption *in situ* by differences in radioactivity of the solution. In the case of multilayer adsorption, as observed in the present work, correspondingly higher adsorbate concentrations can be investigated. Owing to the necessity of counting through a thin layer of solution, IR drops in the solution result in nonuniform current distribution over the surface, with attendant uncertainties in the significance of the potentials measured. It was partly for this reason that relatively low current densities were employed in this work.

Iodide ion is reversibly adsorbed on the {111} surface of germanium, leading to an increase in the hydrogen overpotential. The adsorption exhibits a maximum near the rest potential; virtually complete desorption can be accomplished both by cathodic and anodic polarization at readily attainable potentials. At *p*H 1.4, the extent of adsorption increases with concentration in the range 5 x $10^{-6}N$ to 2.5 x $10^{-4}N$ KI, reaching many monolayer-equivalents in the more concentrated solutions. The nature of the observed multilayer adsorption must be such as to involve the coadsorption of cations; alternatively, the adsorbed species may be HI. Evidently it will be necessary to look for specific adsorption of iodide ions at KI concentrations well below 5 x $10^{-6}N$.

The {100} surface of germanium differs from the {111} surface in its polarization and adsorption behavior. The effect of iodide on the hydrogen overpotential is smaller than for the {111} surface and is in the opposite direction. Where comparisons were made at the same solution composition, the amount of reversibly adsorbed iodide was found to be an order of magnitude less on the {100} surface. In addi-

tion, in certain solutions the charging and current-potential characteristics revealed the anodic formation and cathodic removal of a surface compound containing substantial amounts of iodide as shown by adsorption measurements.

In a 0.1*N* Na_2SO_4 supporting electrolyte containing $10^{-4}N$ KI, reversibly adsorbed iodide on the {100} surface amounted to 0.4 and 5.5 monolayer-equivalents when the solution was made 0.1 and $10^{-3}N$, respectively, in H_2SO_4. At higher *p*H's the trend is reversed, and adsorption of iodide is small in alkaline solutions. The anodic surface compound is formed within fairly well-defined composition limits. Thus, aside from transient effects, evidence for its formation in 0.1*N* Na_2SO_4 containing $10^{-4}N$ KI was obtained at *p*H 3.4, but not at *p*H 2.4, and also not at *p*H 3.4 when the KI concentration was decreased to $10^{-5}N$.

In conclusion, it can be stated that the apparatus described previously and modified for the present work is admirably suited for extensive adsorption and polarization studies carried out *in situ* using solid electrodes. The capabilities of the technique with respect to electrochemical characterization and absolute measurements of adsorption have been demonstrated in a study of germanium electrodes in contact with solutions containing iodide ion.

Acknowledgment

The authors are pleased to acknowledge helpful discussions with Mr. J. A. Kafalas in developing the procedure for the calibration of the adsorption cell and his assistance with instrumentation.

Manuscript received Aug. 9, 1961. This paper was prepared for delivery before the Indianapolis Meeting, April 30-May 3, 1961.

Any discussion of this paper will appear in a Discussion Section to be published in the December 1962 JOURNAL.

REFERENCES

1. Ya. M. Kolotyrkin, *Trans. Faraday Soc.*, **55**, 455 (1959).
2. L. R. Scharfstein and C. V. King, *J. Phys. Chem.*, **58**, 180 (1954).
3. H. D. Cook, *Rev. Sci. Instr.*, **27**, 1081 (1956).
4. J. A. Kafalas and H. C. Gatos, *ibid.*, **29**, 47 (1958).
5. W. W. Harvey and H. C. Gatos, *This Journal*, **107**, 65 (1960).
6. E. A. Efimov and I. G. Erusalimchik, *Doklady Akad. Nauk S.S.S.R.*, **128**, 124 (1959).
7. E. A. Efimov and I. G. Erusalimchik, *Zhur. Fiz. Khim.*, **35**, 543 (1961).
8. D. R. Turner, *This Journal*, **103**, 253 (1956).
9. W. W. Harvey, S. Sheff, and H. C. Gatos, *ibid.*, **107**, 560 (1960).
10. W. H. Brattain and C. G. B. Garrett, *Bell System Tech. J.*, **34**, 129 (1955).
11. K. Bohnenkamp and H. J. Engell, *Z. Elektrochem.*, **61**, 1184 (1957).
12. N. A. Balashova, *Zhur. Fiz. Khim.*, **32**, 2266 (1958).
13. W. W. Harvey and H. C. Gatos, *J. Appl. Phys.*, **29**, 1267 (1958).

Transient Potentials of the Mercury-Aqueous Solution Interface

Carl D. Spear,[1] Melvin A. Cook, and Milton E. Wadsworth

Department of Metallurgy, Institute of Metals and Explosives Research, University of Utah, Salt Lake City, Utah

ABSTRACT

Methods of studying transient electrode potentials produced by expanding a mercury-aqueous KCl solution interface at constant rate are described and results obtained in studies of the expanding mercury electrode-aqueous chloride ion system presented. Correlations with available potential, overpotential, and electrocapillarity data for this system permit one to determine the variables which control the transient potentials for such a system. The transient potential produced by expansion of this metal-aqueous solution interface is thereby shown to be associated with a finite rate of reformation of the diffuse part of the electrical double layer.

Studies of strain potential transients of metals were stimulated by the development of the electrolytic theory of corrosion. Andrews (1) in 1894 investigated the potential between cold-worked and annealed steels. Researchers who have more recently studied the effect of stress on electrode potentials for solid metals are Nikitin (2), Zaretskii (3), Gautam and Jha (4), Coffin and Simon (5), McFadden (6), Dudley, Elliot, McFadden, and Shemilt (7), Fryxell and Nachtrieb (8), Coffin and Tingley (9), and Wernick (10).

More recently, Eyring *et al.* made experimental studies of strain induced electrode potentials as a function of electrode material, *p*H, nature and concentration of electrolyte, dissolved gases, etc. (11-14) using as the reference of potential the corresponding unstrained electrode. A model based on electrode kinetics was proposed (11) in which the electrode strain potentials were explained in terms of reactions that transfer charge across the electrical double-layer.

Also early investigators (2) ascribed transient potentials of stretching wires to heat produced by internal strain; however, more recent ones have indicated that surface reactions are responsible (3, 8, 11).

In order to demonstrate experimentally whether or not internal strain is necessary for the development of transient potentials of this sort the liquid metal mercury was chosen because its surface can

[1] Present address: Research and Development Division, Corning Glass Works, Corning, New York.

be expanded without developing internal strain and surface irregularities. For this purpose a cell and pump system was designed which permitted the mercury-aqueous solution interface to be expanded at a constant rate analogous to elongating a metal wire in contact with an aqueous solution at a constant rate.

Further advantages of mercury for studying transient potentials are that the extensive information concerning the electrical double-layer given by electrocapillarity and overpotential studies, and the large volume of standard electrode potential data permit one to establish a quantitatively steady-state potential ($dV/dt = 0$) as functions of the appropriate independent solution and variables.

Apparatus and Procedures

The equipment consisted of two parts: (a) a pump for the liquid mercury suitable for pumping the mercury at a constant rate into a cell permitting the mercury surface to expand the mercury-aqueous solution interface at a constant rate; and (b) an electronic device to measure and record automatically the voltages produced.

The mercury pump was constructed from a 100 ml hypodermic syringe and a screw and nut system which drove a plunger into the syringe cylinder. The screw was driven by an electric motor with a low rpm gear box and pulleys so that various expansion rates of the interface from 1.0 cm²/sec to 5.2 cm²/sec were achieved.

In determining the cell geometry it was necessary to design the cell so that the mercury-solution interface expanded at a constant rate when a constant volume of mercury was pumped into the cell $(dV/da) = k$.

The cell was constructed from three sheets of ¼-in. thick plexiglas cemented together with a plastic cement. It was connected to the pump with stainless steel tubing (2 mm ID) with a joint as shown in Fig. 1.

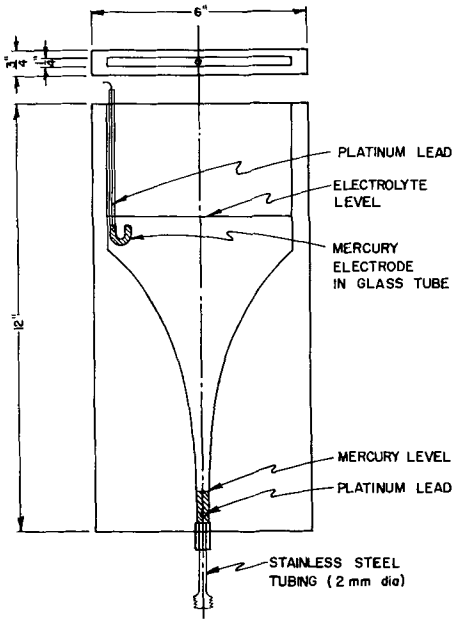

Fig. 1. Mercury cell which gives constant expanding interface between mercury and electrolyte.

The electrodes used to measure the potential developed in the cell are also shown in Fig. 1. The electrode for the expanding surface was simply a platinum wire passing through the cell wall into the mercury at the bottom of the cell. Either a saturated calomel cell or mercury itself was used as the reference electrode. The mercury electrode was made of a glass tube (3 mm ID) with a U bend situated just above the limiting position that the expanding mercury surface was capable of reaching. The U bend was filled with mercury and a platinum electrode placed in contact with the mercury. The two electrodes were connected to a high impedance L&N No. 7664 *p*H indicator for amplification. The output from the *p*H amplifier was modified by a variable voltage divider to actuate a Varian strip-chart potentiometer G11A recorder. A calibration voltage was displayed on the chart by means of the standardization control on the *p*H indicator.

The electrolyte was deaerated with N_2. The flow of gas was measured with a flowmeter which measured the pressure difference across a capillary constriction. A cellophane tape lid, with openings for the reference electrode and gas bubbler, maintained the desired gas composition. The bubbler with a sintered glass bottom was made using simply a glass rod long enough to reach to the bottom of the cell. A pyrogallol-sodium hydroxide solution trap was introduced into the nitrogen line to remove traces of oxygen, and a water trap kept the dry gases from depleting the water in the cell and changing the electrolyte concentration.

The spent mercury was first cleaned in a mercury oxifier. The clean mercury was then distilled in a Cenco vacuum mercury still. Fresh mercury prepared in this manner was used in each separate run.

In carrying out a run the hypodermic syringe (the pump) was first filled with mercury and connected to the cell by a coupling through a stainless steel tube. The mercury was then brought to a certain fixed level at the bottom of the cell, and a platinum wire in contact with the mercury at this point served as the lead for the expanding mercury electrode. The electrolyte was then poured into the cell and a mercury electrode or a saturated calomel reference electrode placed in it. The leads from the expanding mercury electrode and reference electrode were connected to the *p*H millivoltmeter. To remove dissolved oxygen the electrolyte was then deaerated with nitrogen. After deaeration for about 1 hr, the glass tube was removed and the pump motor switched on. The transient potential began to rise the instant the mercury surface started to expand.

Experimental Results

The potential-transient traces shown in Fig. 2 are typical of the results obtained with an inert electrolyte such as potassium chloride. Initially the potential rose sharply to a maximum and then remained essentially constant except for a slight dip in the curve caused by a tendency toward over-

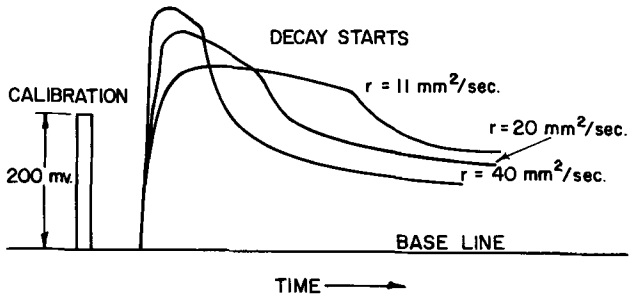

Fig. 2. Varian recorder trace in Hg-1M KCl system

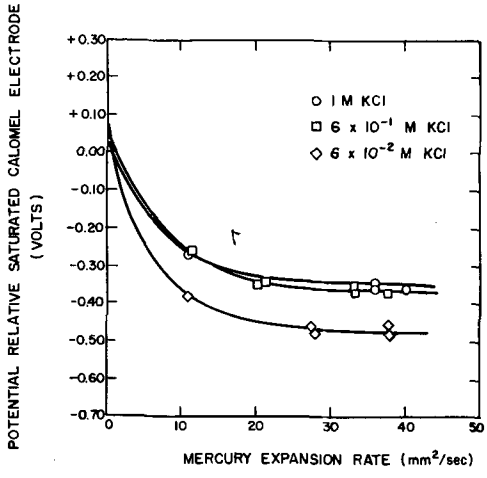

Fig. 3. Expansion rate vs. potential developed for KCl system in the absence of O_2.

shoot. When expansion was stopped the potential underwent characteristic exponential type decay. As may be seen from Fig. 2 the fastest expansion rate produced the greatest potential and the most rapid decay when expansion was stopped.

Figure 3 presents plots of the steady-state potential (maximum potential, $dV/dt = 0$) against the rate of expansion r for solutions of three different concentrations. For a given concentration of electrolyte the voltage approached a plateau as the expansion rate increased. Figure 4 presents graphically the steady-state potentials against electrolyte concentration for various expansion rates. The potential was linear in log $[Cl^-]$ at high concentrations. At 6×10^{-2}M KCl, the potential-concentration curves reached the most negative value. Significantly, this corresponds to the point where the potential of the expanding electrode reached the potential of the electrocapillary maximum. The potential then followed the electrocapillary maximum curve which varies with the concentration of the electrolyte. This occurred because the expanding interface was then essentially depleted of its charge. The dropping mercury electrode confirms this since its steady-state voltage is coincident with the electrocapillary maximum. The curves in Fig. 4 also show that at a given concentration the potential approached the electrocapillary maximum more and more as the expansion rate was increased.

For concentrations lower than 6×10^{-2}M KCl the voltages were nonreproducible. A probable reason for this was the presence of impurities in the electrolyte. While these impurities were always present their effects were negligible at high chloride ion concentrations. Hence, only the average values are shown in Fig. 4. The standard deviation was about 70 mv at potentials of 400 mv in this region, corresponding to an experimental error of about ±20%. This is contrasted with the high concentration region where the experiments were reproducible to within ±5%.

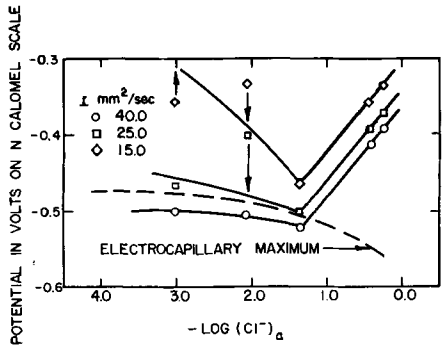

Fig. 4. Log $[Cl^-]_a$ vs. potential of an expanding mercury electrode for oxygen free electrolytes.

The logarithm of the expansion rate against potential plot was linear as shown in Fig. 5.

Discussion

The expanding mercury surface gave essentially the same type of potential-time trace described previously for elongating metal wires (see Fig. 2). The fact that the potential-time traces for mercury and the ones for metal wires were closely analogous indicates that the generation of active surface sites by internal strain may not be necessary for the development of transient potentials of stretching or expanding metals in aqueous solutions. The similarity of the traces cannot, of course, exclude the possibility that active surface sites play a role in transient potential phenomena for solid metal wires. However it appears that the important considerations are: when a metal is strained, interfacial conditions are disrupted and surface reactions result which tend to restore the wire-aqueous solution interface to its original condition. The reactions cause charge to flow into or from the electrical double-layer or possibly in some cases of chemical reaction to cross it, depending on the nature of the electrode and its environment.

Because of the practically ideal polarization characteristics of mercury in contact with aqueous

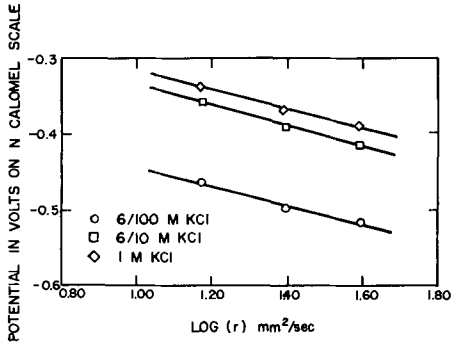

Fig. 5. Log (r) vs. potential of an expanding mercury electrode for oxygen free KCl electrolytes.

potassium chloride it is necessary only to account for the flow of ions into the reforming electrical double-layer following exposure of new surface in order to account for the transient potential developed when the electrode expands. The following reaction is postulated for the absorption of Cl^- at the mercury-aqueous chloride solution interface.

$$| \text{Hg} + \text{Cl}^- \rightarrow | \text{Hg Cl}^- \qquad [1]$$

Letting θ equal the fraction of the surface covered with adsorbed chloride ions and $(1-\theta)$ the fraction of uncovered mercury surface | Hg, the velocity of the chloride ion adsorption on the surface might be expected to be proportional to $(1-\theta)$, to the activity of the chloride ions $(Cl^-)_a$, and to the rate k_1 of reaction [1] in the forward direction. The rate k_1 is a function of the potential across the metal-solution interface and therefore a relationship of the following form can be written (1):

$$k_1 = k'_1 e^{\frac{\pm Z_i \alpha_i e V}{kT}} \qquad [2]$$

where V is the potential difference between electrode and solution and k'_1 the rate at zero potential or charge. The parameter α_i is usually considered to be a fraction which depends on the symmetry of the energy barrier. In a symmetrical barrier $\alpha_i = 1/2$. The sign of the exponential factor is either positive or negative depending on whether the reaction is anodic or cathodic, respectively. Here $e = 4.80 \times 10^{-10}$ esu and the number of electronic charges transported by a single ith process is Z_i. The rate of loss of chloride ions from the mercury surface is proportional to θ and to the rate k_2 of the desorption reaction, which for a freshly expanded surface might be expected to be negligible relative to the reformation of the electrical double-layer. It would not be negligible as the equilibrium conditions are again approached. Also, expansion decreases the surface coverage. Hence, the uncovered surface changes with time as follows:

$$\frac{d(1-\theta)}{dt} = \beta r - (1-\theta)\,[\text{Cl}^-]_a\, k'_1\, e^{\frac{-\alpha VF}{RT}} + \theta k'_2 e^{\frac{\alpha' VF}{RT}} \qquad [3]$$

where, as above r is the expansion rate and β is a proportionality constant. If θ is small, which is the case when the potential is approaching the electrocapillary maximum or the point of zero charge, and if the rate k_2 for chloride ions leaving the mercury-aqueous solution interface is small compared to the expansion rate, the term $\theta k'_2 e^{\alpha' VF/RT}$ may be neglected. At the maximum voltage the slope of the potential-time curve (see Fig. 2) is zero. The change in the uncovered interface with time will then also be zero because the amount of the interface covered with charge determines the potential at any given time. Hence $[d(1-\theta)/dt = 0]$ and Eq. [3] becomes

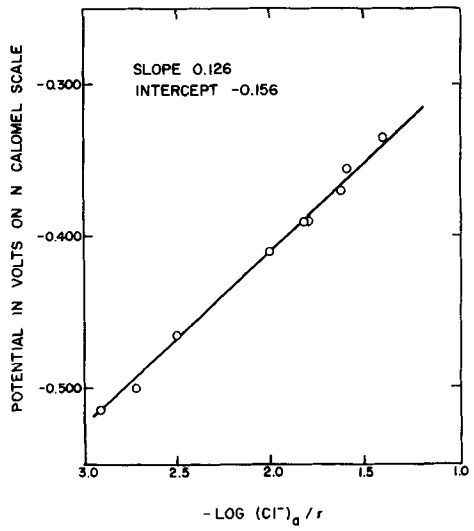

Fig. 6. Correlation of chloride ion concentration and the expansion rate r of the mercury with the steady-state potentials developed for an expanding mercury electrode.

$$\beta r - (1-\theta)\,[\text{Cl}^-]_a\, k'_1 e^{\frac{-\alpha VF}{RT}} = 0 \qquad [4]$$

Solving for V results in the expression

$$V = -\frac{RT}{\alpha \mathbf{F}} \ln \frac{\beta r}{(1-\theta)\,[\text{Cl}^-]_a\, k'_1} \qquad [5]$$

Now it is assumed that the fraction θ is proportional to the charge q on the interface divided by the total charge that occupies the interface ($\theta \sim q/Q$) when it is fully covered. Thus, q is small because, as the mercury surface is expanded, the potential approaches the point of zero charge and therefore $\theta << 1$. Equation [5] then becomes

$$V = 2.303 \frac{RT}{\alpha \mathbf{F}} \log \frac{[\text{Cl}^-]_a}{r} + 2.303 \frac{RT}{\alpha \mathbf{F}} \log \frac{k'_1}{\beta} \qquad [6]$$

In Fig. 6 $\log [(Cl^-)_a/r]$ is plotted against the potential. Note the good correlation of the data. Moreover, from the observed slope (0.126) one obtains for α the value 0.43 which is in good agreement with theoretical value 0.5 based on symmetry of the reaction barrier.

Summary

1. Based on results obtained with mercury, it may be concluded that internal strain or the production of active sites by the generation of dislocations in a metal is not requisite for the development of transient potentials for an expanding metal-aqueous solution interface.

2. Considering the variables which control the transient potentials of an expanding mercury-aqueous solution interface under the conditions approaching perfect polarization the transient potential was found to obey the equation

$$V = 2.303 \frac{RT}{\alpha \mathbf{F}} \log \frac{[\text{Cl}^-]}{r} + \text{K}$$

in the case of aqueous potassium chloride. The correlation held until the transient potentials reached

the electrocapillary maximum or point of zero surface charge. Then the potential followed that of the electrocapillarity maximum.

Acknowledgments

This research was supported in part by a grant from the Petroleum Research Fund administered by the American Chemical Society. The remainder of the financial support was provided by the Atomic Energy Commission under Contract Number AF(11-1)-82. The authors gratefully acknowledge these sources of support.

Manuscript received May 8, 1961; revised manuscript received Oct. 12, 1961.

Any discussion of this paper will appear in a Discussion Section to be published in the December 1962 JOURNAL.

REFERENCES

1. T. Andrews, *Proc. Inst. Civil Engrs., London,* **118**, 3561 (1894).
2. *a.* L. V. Nikitin, *C. A.,* **35**, 61917 (1941); *b.* **33**, 76689 (1939); *c.* **32**, 28454 (1938).
3. E. M. Zaretskii, *C. A.,* **47**, (1953).
4. L. R. Gautam and J. B. Jha, *Proc. Ind. Acad. Sci.,* **18A**, 350 (1953).
5. F. D. Coffin and S. L. Simon, *J. Appl. Phys.,* **24**, 1333 (1953).
6. W. H. McFadden, Masters Thesis, Columbia University (1951).
7. R. S. Dudley, R. Elliott, W. J. McFadden and L. W. Shemilt, *J. Chem. Phys.,* **23**, 585 (1955).
8. R. E. Fryxell and N. H. Nachtrieb, *This Journal,* **99**, 495 (1952).
9. C. C. Coffin and I. I. Tingley, *J. Chem. Phys.,* **17**, 502 (1953).
10. J. H. Wernick, Ph.D Thesis, Pennsylvania State University (1954).
11. A. G. Funk, J. C. Giddings, C. J. Christensen, and H. Eyring, *Proc. Nat'l. Acad. Sci.,* **43**, 421 (1957).
12. A. G. Funk, D. J. Chakravarty, H. Eyring, and C. J. Christensen, *Z. Physik. Chem. Neue Folge,* **15**, 64 (1958).
13. A. G. Funk, J. C. Giddings, C. J. Christensen, and H. Eyring, *J. Phys. Chem.,* **61**, 1179 (1957).
14. J. C. Giddings, A. G. Funk, C. J. Christensen, and H. Eyring, *This Journal,* **106**, 91 (1959).

Technical Notes

Birefringence Studies in Electroluminescent Zinc Sulfide

F. J. Baum and F. J. Darnell

Central Research Department, E. I. du Pont de Nemours and Company, Wilmington, Delaware

Several investigators have found correlation between electroluminescent activity in ZnS crystals and the extent of stacking disorder as evidenced by x-rays (1, 2) and optical birefringence (3-5). Microbeam x-ray studies (50μ diameter beam) on ZnS crystals in these laboratories have also shown electroluminescent activity to occur predominantly in regions of mixed hexagonal and cubic structure, with little activity in perfect cubic or perfect hexagonal regions. The majority of our crystals, which were grown from the vapor (6), appear in the form of prisms containing both wurtzite and sphalerite with the hexagonal [00·1] and cubic [111] directions along the prism axis. Stacking faults of planes perpendicular to this axis give rise to layered regions of differing structure. Electroluminescence, viewed normal to the axis, occurs in streaks parallel to these layers (6), in agreement with observations of others (3-5, 7, 8). The present experiments make use of birefringence to study the layered structure on a scale smaller than is possible with x-rays, and to correlate structure with electroluminescent activity.

The optical method involves the fact that ZnS in the sphalerite structure exhibits a single index of refraction, while in the wurtzite or other noncubic structures it has different indices for light polarized normal or parallel to the hexagonal axis. The amount of hexagonal structure in an element of a zinc sulfide crystal can then be determined by the degree of birefringence provided stacking sequences are regular, *i.e.*, definite polytypes exist, for distances along the prism axis comparable to the light wavelengths. There exists also the possibility that one-atom layer displacements of the type postulated by Strock (9) will lead to changes in birefringence.

A crystal to be examined was placed on a microscope stage between crossed polaroids with the axis of the crystal perpendicular to the microscope optic axis and at 45° to the polarizing direction of each polaroid. The magnified image of the crystal, made visible in high order colors, was projected onto the slit of a medium Hilger spectrograph equipped with glass optics. Interference between the ordinary and extraordinary rays created channel spectra which could then be photographed. Measurement of the wavelengths λ_i at which extinctions occurred, together with measurement of the crystal thickness, d, then allowed determination of the birefringence from the relation (10)

$$\Delta n \equiv n_o - n_E = \frac{1}{d} \frac{\Delta N}{\left(\frac{1}{\lambda_1} - \frac{1}{\lambda_2}\right)}$$

where ΔN is the difference in extinction orders which take place at wavelengths λ_1 and λ_2. Correlation of electroluminescence with the birefringence so observed was accomplished by exciting electro-

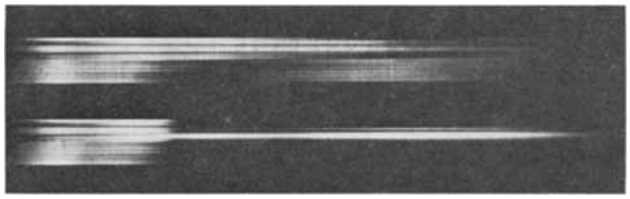

Photograph of birefringence channel spectra and electroluminescence in the visible region. Horizontal axis is wavelength, and vertical axis is 28μ distance along [00·1] direction of ZnS crystal. Upper image is birefringence only; lower image shows same birefringence filtered to pass only the red end of the spectrum, with electroluminescent image superposed. Birefringence exposure 3 sec; electroluminescence exposure 40 hr.

luminescence in the crystal as mounted and projecting this through the spectrograph onto the same photographic plate to make a double exposure. Since the intensity of the electroluminescence was low, 16-40 hr exposures with ASA film speed of about 2000 were necessary. A typical photograph of birefringence and electroluminescence is shown in Fig. 1. The superposed spectra, arising in one case from localized occurrences of electroluminescence and in the other from the varying magnitudes of birefringence, permitted a structurally sensitive characterization of those regions exhibiting electroluminescence.

All crystals were found to have a layered structure with layers lying perpendicular to the hexagonal c axis (prism axis). From the spectrographic plates, the birefringence of regions as small as 5μ in dimension along the crystal axis could be determined; regions as small as 1μ could be differentiated, but not accurately measured.

Many individual regions were characterized by discrete birefringence values ranging from zero to 0.036 at a mean wavelength of 5000Å, while other regions showed continuous variations. A few absolute values of birefringence were checked with an eight-order Babinet eyepiece-compensator, in order to check the largest value in this region of the spectrum. The zero value corresponds to cubic structure, the intermediate values presumably to polytypes (11-13) or faulted structures, and the maximum value to perfect hexagonal structure. Birefringences from 0.003 to 0.028 have been reported by Strock, Brophy, and Peters (5), with wavelength unspecified, but probably for Na D light. Careful measurements of the two indices of refraction as functions of wavelength on three ZnS single crystals have been made by Piper, Marple, and Johnson (14), who find a broad birefringence maximum in the visible region. Their largest value is $\Delta n = 0.024$. According to Smith (13), a detailed x-ray study of natural zinc sulfide mineral yielded no crystals possessing perfectly hexagonal structure. It is possible that the present narrow layers having the highest birefringence correspond to perfect hexagonal structure.

It was found that electroluminescent activity occurred only in crystal volumes that were characterized by varying structure. No structure in which electroluminescence occurred persisted for more than 2μ. The resolution of the technique unfortunately was not sufficient to determine whether activity occurred in regions of a fixed structure or in the transition plane between structures. There was no indication of a relation between occurrence of electroluminescence and any particular value of birefringence.

Acknowledgments

The authors wish to thank Dr. W. W. Piper of the General Electric Research Laboratories for making available the original optical data of ref. (14).

Manuscript received Aug. 11, 1961. Contribution No. 705, Central Research Department.

Any discussion of this paper will appear in a Discussion Section to be published in the December 1962 JOURNAL.

REFERENCES

1. A. H. McKeag and E. G. Steward, *This Journal*, **104**, 41 (1957).
2. D. W. G. Ballentyne, *ibid.*, **107**, 807 (1960).
3. M. S. Short, E. G. Steward, and T. B. Tomlinson, *Nature*, **177**, 240 (1956).
4. L. W. Strock, *Acta Cryst.*, **10**, 840 (1957).
5. L. W. Strock, V. A. Brophy, and T. E. Peters, Enlarged Abstracts, Electronics Div., New York Meeting, Electrochem. Soc., p. 61 (1958).
6. J. L. Gillson, Jr. and F. J. Darnell, *Phys. Rev.*, (to be published).
7. G. Diemer, *Philips Res. Repts.*, **10**, 194 (1955).
8. P. Zalm, *ibid.*, **11**, 353 (1956).
9. L. W. Strock, *Illum. Eng.*, **55**, 24 (1960).
10. See, *e.g.*, F. A. Jenkins and H. E. White, "Fundamentals of Optics," p. 528, McGraw-Hill Book Co., New York (1950).
11. L. W. Strock and V. A. Brophy, *Am. Mineral.*, **40**, 94 (1955).
12. D. C. Buck and L. W. Strock, *ibid.*, **40**, 192 (1955).
13. F. G. Smith, *ibid.*, **40**, 658 (1955).
14. W. W. Piper, D. T. F. Marple, and P. D. Johnson, *Phys. Rev.*, **110**, 323 (1958).

Junction Delineation in GaSb by Differential Chemical Etch Rate

S. J. Silverman

Research Laboratory, General Electric Company, Schenectady, New York

Etching to delineate p-n junctions in semiconductors is a useful tool in detecting impurity striations incorporated during the course of crystal growing and also in revealing single or multiple junctions produced by various device processing techniques. There is extensive literature on the subject concerning elemental semiconductors such as Ge or Si, a few examples of which are given in the bibliography (1, 2). Less information is available on III-V compounds. Whereas Cunnell (3), Schell (4), and more recently Haisty (5) refer to several such etches to detect junctions in GaAs, little has been recorded about GaSb other than Detwieler's (6) unspecified concentration ratio for the

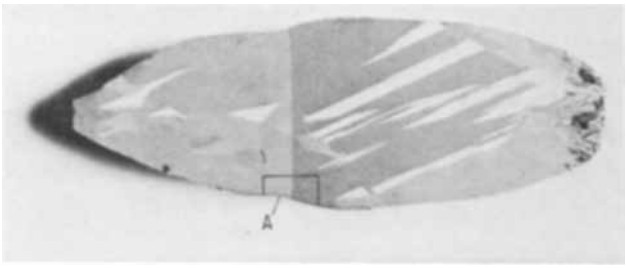

Fig. 1. GaSb ingot etched 12% HF:25% HNO_3:60% H_2O to delineate grain boundaries as well as the p-n junction; p-type, left; n-type, right. Magnification approximately 1½X.

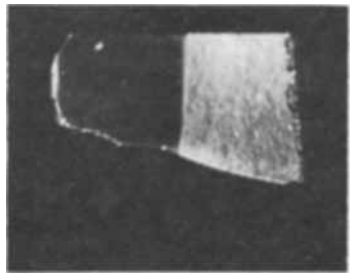

Fig. 2. Single crystal section cut from area (A) of ingot in Fig. 1 and etched in 15% HF:35% HNO_3:50% H_2O; p-type, left; n-type, right. Magnification 5X.

$HCl:HNO_3$ system. This paper deals with the HF: HNO_3:H_2O system and its successful application to the delineation of n-p junctions in GaSb.

Experimental

T. J. Soltys, of this Laboratory, in the course of growing GaSb by the Czochralski technique, produced a grown junction by doping the melt with Te. The resultant ingot, J-75, was cut longitudinally along the growth axis. Single crystal bars taken from the Te-doped section were investigated at room temperature by Hall, resistivity, and mobility measurements. The results of these measurements indicated a net carrier concentration of 2×10^{17}/cc, n-type and a Hall mobility of 3000 cm^2/v sec. The undoped p-type region was similarly studied and found to contain 2×10^{17} carriers/cc with a Hall mobility of 500 cm^2/v sec. The position of the junction was determined independently by obtaining resistivity and thermal emf profiles along the length of the ingot. The ingot was then prepared for etching to show that the position of the junction could be correlated with the previous measurements as well as the observations on the doping during crystal growth, as indicated by an abrupt change in crystal diameter seen in Fig. 1.

From a preliminary study it was soon realized that the etch composition was primarily instrumental in the success or failure of junction detection. Consequently a series of etches with different ratios of the components was evaluated to determine optimum compositions required. The same specimen was used by freshly preparing the surface prior to each exposure to a new solution. The surface preparation involved lapping with 600 mesh carborundum, thorough rinsing in running H_2O, and air drying. The specimen was then placed in a 25 cc polyethylene container. Care was taken not to contaminate the surface by improper handling techniques, which might otherwise lead to spurious patterns. The solution for each etch was freshly prepared immediately prior to use, and in each case was 10 cc in volume. The etching period was standardized to a 2-min exposure for each solution. At the end of this period the excess acid was decanted, leaving a smaller amount which still covered the specimen but which could be quickly flushed with running water from the tap. In this manner the formation of oxide films was minimized.

Some of the compositions were equally effective in portraying grain boundaries as well as a junction, as seen in Fig. 1. A single crystal section containing the junction was cut from the original ingot to eliminate the possibility of any competing differential etching action at the grain boundaries. An example of the junction delineation on such a single crystal region is shown in Fig. 2.

A summary of the compositions and their effects is given in Table I. If one were to average the compositions of solutions 1 and 2, then the etch having 15% HF:35%HNO_3:50%H_2O would be typical of a fast reaction solution, producing moderate gas evolution. Under these conditions a disk of GaAs having a diameter of 0.4-in. and thickness of 40 mils had an etch rate of 2 mil/min. This action resulted in a differential etching rate at the junction, leaving the p-type side with a smoother, more lustrous surface than the n-type side, as seen in Fig. 2. From microscopic observation at 100X, it was estimated that the p-type side was about 10μ lower than the n-type side. This action is analogous to that for a Si n-p junction where the p-type side etches faster than the n-type side in either an alkaline solution or a 3%K MnO_4:95% HNO_3 solution. The mechanism of this etching action appears to be similar to that discussed by Turner (7) who describes the etching phenomenon for Si or Ge in the HF-HNO_3-H_2O system as being electrochemical in nature. Semiconductor material goes into solution by forming water soluble complexes with the

Table I. Comparison of etch compositions and the effects on GaSb junctions

Solution	Composition in vol %			Effect
	HF	HNO_3	H_2O	
1	10	40	50	(a) moderate gas evolution (b) rapid junction delineation by differential etch rate
2	20	30	50	(c) p-type surface shiny
3	19	19	62	(a) little gas evolution (b) slow delineation by differentially reflected light
4	12	29	59	(a) little gas evolution
5	13	20	67	(b) rapid delineation by differentially reflected light
6	6	31	63	(a) no gas evolution (b) complete surface blackening
7	31	6	63	No apparent reaction

F^- anion on the anodic p-type side while the oxidizing agent, HNO_3, is reduced on the cathodic n-type side of the junction.

The etch rate could be significantly reduced with increased water dilution. Solutions 4, 5, and 6 were typical of the slower reaction rate which was accompanied by very little gas evolution. A difference in the reflected light intensities on either side of the junction was observed within the specified etching period. In this connection the apparent variation in reflected light intensity was reminiscent of the stain etch described by Fuller (8) and the Au chemiplating (9) on Si p-n junction discussed by the author, in which a photovoltaic effect was attributed to the differential staining or plating action. Fresh solutions similar to 4 through 6 were used to etch the specimen under the light of a 60-w tungsten source as well as in the dark. Under both conditions the junctions were reproducibly delineated so that this effect was not considered to be significant in this case. The present case is not to be confused with a stain which has been attributed to the presence of an oxide layer on the p-type side of the junction in Si (7). Furthermore, when a Si specimen so stained is viewed under a low-power microscope using oblique light, the apparent color contrast remains invariant with specimen rotation. This is not the case for GaSb etched in slowly reacting solutions such as 4 to 6. Upon rotating the specimen the contrast in the light intensity can be obliterated or reversed depending on the angle of incidence of the light as well as the angle in the plane of specimen rotation. This is exactly similar to the differential reflectivity from different facets on an abraded single crystal or from different grain orientations on polycrystalline specimens. However, in this case the crystal orientation is the same, but the impurity content is different.

The contrast in reflected light intensities from the specimen surface was enhanced as one increased the ratio of HNO_3 to HF, producing an easily delineated junction as seen in Fig. 1 until one approached conditions in solution 6 where a blackening of the entire surface, presumably due to oxidation by excessive HNO_3 and H_2O, completely obscured the junction. Reversing this ratio to a high concentration of HF, as in solution 7, leads to a condition of no apparent reaction.

It is of interest to note that in contrast to solution 5, if one substitutes glacial acetic acid for water as the diluent, rapid etching occurs, and the entire surface is left with a shiny luster which reveals neither junctions nor grain boundaries.

Conclusion

From the foregoing discussion, it can be seen that GaSb p-n junctions can be revealed readily by two different rates of differential chemical attack. The first is a rapid differential etch rate in which the p-type region etches faster than the n-type region. A representative composition is 15% HF: 35% HNO_3: 50% H_2O. For applications where the etch rate is very small, but differential reflectivity is desired, a typical composition 12% HF: 25% HNO_3: 63% H_2O will suffice.

It has been shown that by a judicious choice of the composition of the HF: HNO_3: H_2O system, n-p junctions and differently oriented grains in polycrystalline specimens can be revealed and delineated by a simple, straightforward etching technique.

Acknowledgment

The author wishes to acknowledge the assistance of G. D. Brower with the experimental work.

Manuscript received Sept. 11, 1961.

Any discussion of this paper will appear in a Discussion Section to be published in the December 1962 JOURNAL.

REFERENCES

1. R. W. Jackson, *J. Appl. Phys.*, **27**, 309 (1956).
2. P. J. Woriskey, *ibid.*, **29**, 1514 (1958).
3. F. A. Cunnell, J. T. Edmond, and W. R. Harding, *Solid State Electronics*, **1**, 97 (1960).
4. H. A. Schell, *Z. Metalk.*, **48**, 18 (1957).
5. R. W. Haisty, *This Journal*, **108**, 790 (1961).
6. D. P. Detwieler, *Phys. Rev.*, **97**, 1575 (1955).
7. D. R. Turner, *ibid.*, **107**, 810 (1960).
8. C. S. Fuller and J. A. Ditzenberger, *J. Appl. Phys.*, **27**, 544 (1956).
9. S. J. Silverman and D. R. Benn, *This Journal*, **105**, 170 (1958).

Polarization Capacitance Determinations of Surface Roughness[1]

M. R. Turpin and M. K. Testerman

Graduate Institute of Technology, University of Arkansas, Little Rock, Arkansas

Experimental measurements of the polarization capacitance of the electrical double layer at a metallic surface in a nonaqueous electrolytic solution were undertaken at this laboratory as a part of an evaluation survey of various methods of measuring irregularities in metallic surfaces. Results from tests using potassium iodide as the electrolyte and formamide as the nonaqueous solvent (0.25M KI-$HCONH_2$) suggest that this system could be employed, with some modification in technique, to determine roughness factors for metallic surfaces.

The polarization capacitance was measured as an impedance, using a modification of Grahame's bridge circuit (1). The electrolytic medium, 0.25M-KI-$HCONH_2$, was prepared from reagent grade chemicals and subsequently flushed with helium for 24

[1] A detailed report of these experiments is available from the University of Arkansas Technology Campus, Little Rock, in report number WADC-TR-60-97.

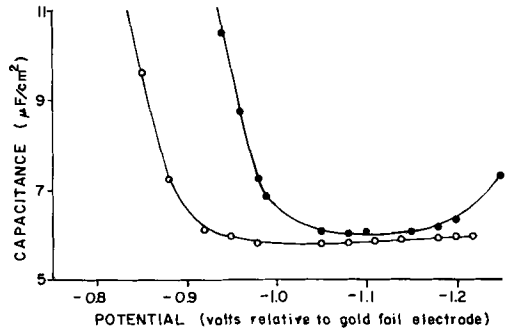

Fig. 1. Mercury and amalgamated copper polarization capacitance: solid circle, mercury; open circle, amalgamated copper.

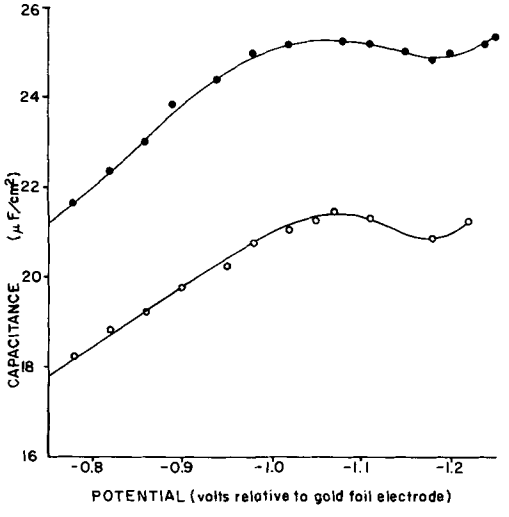

Fig. 2. Copper polarization capacitance: solid circle, "rough" electrode; open circle, "smooth" electrode.

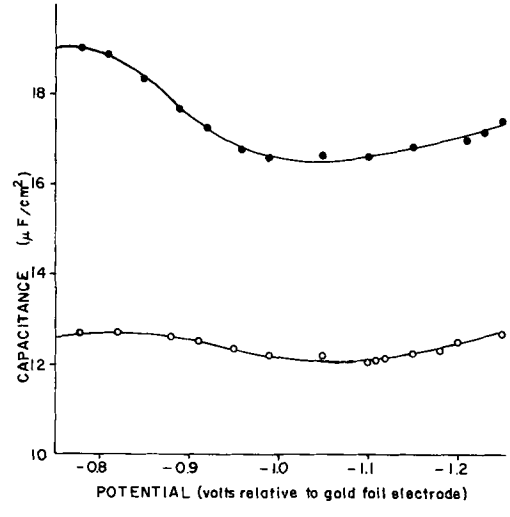

Fig. 3. Stainless steel polarization capacitance: solid circle, "rough" electrode; open circle, "smooth" electrode.

hr preceding polarization experiments. A helium atmosphere was maintained in the 300 ml Pyrex test cell during experiments. A large-area gold-foil cylinder was employed as a nonpolarizable electrode. All voltages were read relative to this gold-foil electrode.

The metals used in these tests were mercury, amalgamated copper, copper, stainless steel, aluminum, and titanium. The design of the mercury pool electrode holder was similar to that described by McMullen and Hackerman (2), consisting of a

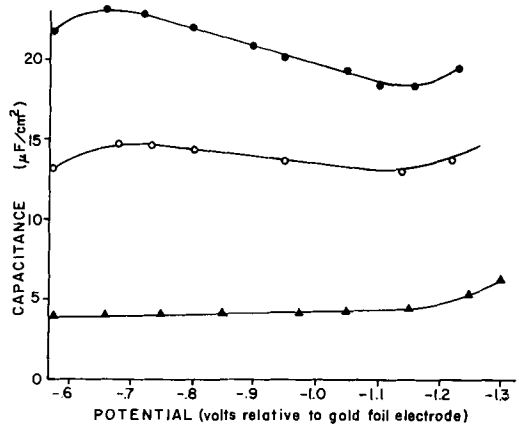

Fig. 4. Aluminum polarization capacitance: solid circle, "rough" pretreated electrode; open circle, "smooth" pretreated electrode; triangle, untreated electrode. (Note: Differences in polarization capacitance between "rough" and "smooth" untreated electrodes were too small to show on graph.)

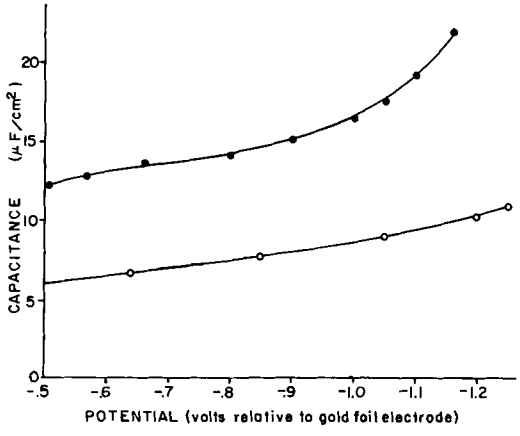

Fig. 5. Titanium polarization capacitance: solid circle, "rough" pretreated electrode; open circle, "rough" untreated electrode.

Teflon cup attached to a length of Pyrex tubing. The amalgamated copper electrode was prepared by first electroplating mercury on copper and then dipping into metallic mercury. The solid metal electrodes consisted of small cylinders, each sealed to a Pyrex tube whose outer diameter equalled that of the metal cylinder. For each solid metal, two electrodes were prepared, one of which was abraded with 320-grit sandpaper for a "rough" surface and the other with 800-grit sandpaper for a relatively "smooth" surface. The surfaces were rinsed with doubly distilled water to remove any foreign particles present after the abrasion process. The apparent surface area of each electrode was 1 cm². Figures 1-5 show typical polarization capacitance curves using these electrodes.

Surfaces of aluminum and certain other metals (*e.g.*, tantalum, titanium) are normally covered by a naturally occurring oxide film. This film is considered to be the cause of the abnormally low polarization capacitance usually exhibited by these metals. Various film removal methods have been attempted with some success, but they have proved to be largely unreproducible. A 10% trisodium phosphate bath immediately before polarization in the formamide solution will deoxidize an aluminum surface sufficiently to give reproducible polarization

capacitance readings of the same order of magnitude as those of the other metals tested (Fig. 4). In this treatment the aluminum is: (*a*) immersed in a hot (65°C) bath of Na_3PO_4 until effervescence of hydrogen infolds the surface completely; (*b*) transferred to an acetone bath until gas evolution is complete; (*c*) rinsed in doubly distilled water to displace any residual Na_3PO_4; (*d*) rinsed again in a separate solution of the electrolyte before being placed in the polarization cell. Reoxidation-pretreatment-polarization cycles were repeated several times with the aluminum electrodes. Capacitance readings were consistently within ± 0.05 $\mu F/cm^2$ of the initial values obtained using this method.

A titanium electrode pretreated in this same manner responded with a rise in capacitance (Fig. 5).

The results of these experiments indicate that this system offers a reliable and comparatively simple method of obtaining relative roughness factors for metallic surfaces.

Manuscript received Sept. 13, 1960; revised manuscript received Sept. 22, 1961.

Any discussion of this paper will appear in a Discussion Section to be published in the December 1962 JOURNAL.

REFERENCES

1. D. C. Grahame, *J. Am. Chem. Soc.*, **68**, 301 (1946).
2. J. J. McMullen and Norman Hackerman, *This Journal*, **106**, 341 (1959).

Brief Communication

The Effective Duration of a Linear Slow-Cool

Daniel Richard Killoran

Michigan State University, East Lansing, Michigan

In the diffusion of impurities into low-quality semiconductor material, annealing is often practiced to avoid the undesirable effects of thermal shock. When the annealing is done at a constant temperature, the effective duration is simple to calculate, but if the temperature is allowed to vary, trial and error methods have been relied upon. This paper examines the popular method of allowing the temperature to fall linearly with time. In particular we wish to find what length of time, at the initial temperature, will produce the same diffusion as an indefinitely prolonged slow-cool.

Given the diffusion equation

$$\frac{\partial C}{\partial t} = D\{\theta\}\frac{\partial^2 C}{\partial x^2} \qquad [1]$$

where C is the impurity concentration, θ is the temperature, t is the actual physical time, x is the distance from the surface, and D is the diffusion constant, we define a new variable (τ) by the relation

$$d\tau = D(\theta\{t\})\, dt \qquad [2]$$

We shall assume linear dependence of temperature on time.

$$\theta_o - \theta = Rt \qquad [3]$$

where (θ_o) is the initial temperature, and R is the rate at which temperature is falling with time.

For most diffusion processes

$$D = D_o \exp\{-k/\theta\} \qquad [4]$$

where k and D_o are constants.

Inserting [3] and [4] into [2] and integrating

$$\tau = \int_o^t D_o \exp\left\{-\frac{k}{\theta_o - Rs}\right\} ds \qquad [5]$$

where s is used as the integration variable.

Letting

$$x = \frac{k}{\theta_o - Rs} \qquad [6]$$

we have

$$\tau = \frac{k D_o}{R}\left[\int_{k/\theta_o}^{\infty} \frac{e^{-x}}{x^2}\, dx - \int_{k/(\theta_o - Rt)}^{\infty} \frac{e^{-x}}{x^2}\, dx\right] \qquad [7]$$

Now define

$$K(y) = \int_y^{\infty} \frac{e^{-x}}{x^2}\, dx \qquad [8]$$

Integrating [8] by parts, we have

$$K(y) = \frac{e^{-y}}{y^2} + Ei(-y) \qquad [9]$$

where $Ei\{-y\}$ is the well-known exponential integral function. (See the Handbook of Chemistry and Physics for tables).

For a long slow-cool, the second term in [7] is small, so we have approximately

$$\tau \approx \frac{k D_o}{R} K\left(\frac{k}{\theta_o}\right) \qquad [10]$$

However, the exponential integral is not commonly tabulated for the range of values of the argument in which we are interested, so we integrate [8] by parts and obtain

$$K(x) = \frac{e^{-x}}{x^2}\left\{1 - \frac{1\cdot 2}{x} + \frac{1\cdot 2\cdot 3}{x^2} - + \cdots\right\} \quad [11]$$

Using a more convenient form for the exponential,

$$K(x) = \frac{1 - 2/x + 6/x^2 - + \cdots}{x^2 \text{ antilog}_{10}(0, 43\ x)} \quad [12]$$

In the special case of seeking the effective time at the initial temperature, the exponential cancels when we insert [4] into [10] and we have simply

$$t_{\theta_o} = \frac{\theta_o^2}{k\,R}\left\{1 - 2\left(\frac{\theta_o}{k}\right) + 6\left(\frac{\theta_o}{k}\right)^2 - + \cdots\right\} \quad [13]$$

Example: Boron is diffused into silicon for 5 hr at 1200°C. Then the temperature is decreased at a rate of 2°/min to room temperature.

If the diffusion were to be done at a constant temperature of 1200° instead of slow-cooling it, how long a diffusion is needed?

Solution: We are given $R = 2°/\text{min}$, $\theta_o = 1200°\text{C} + 273 = 1473°\text{K}$. And for boron in silicon, $k = 40{,}800°\text{K}$.

Therefore

$$t_{\theta_o} \cong \frac{\theta_o^2}{k\,R} = \frac{(1473)^2}{2 \times 40{,}800}\ \text{min} = 27\ \text{min}$$

is the effective length of the slow cool, with an error of less than 10%.

Consequently, to obtain the same diffusion we must leave the silicon at 1200°C for 5 hr + 27 min = 5.45 hr.

Manuscript received Oct. 16, 1961.

Any discussion of this paper will appear in a Discussion Section to be published in the December 1962 JOURNAL.

The AgO-Ag_2O Electrode in Alkaline Solution

Thedford P. Dirkse

Department of Chemistry, Calvin College, Grand Rapids, Michigan

ABSTRACT

The standard potential of the $AgO/Ag_2O/OH^-$ electrode has been found by direct measurement against a hydrogen electrode to be 0.599 ± 0.001v at 25°C. The value appears to vary slightly with KOH concentration. Furthermore, dE/dT values appear to change with KOH concentration as well as with temperature. Voltages measured with pellets of AgO and Ag_2O show that the voltage is determined by the materials present at the grid.

It became evident while doing a literature search on silver(II)oxide that very little work has been done to determine the standard electrode potential of the silver(I)oxide-silver(II)oxide couple in alkaline solutions. Some careful work has been done with the Ag^{++}-Ag^+ couple in acid solutions (1), but the literature shows nothing corresponding to this in alkaline solutions. Nor is there much thermodynamic data from which the potential of this couple could be calculated.

Some of the earliest work in this area was that of Luther and Pokorny (2). They followed the oxidation of silver in 1*N* NaOH and measured the potential difference between that electrode and a $HgO/Hg/OH^-$ electrode in the same solution. Their results give the potential of this couple on the hydrogen electrode scale as 0.57v, and they suggested that this value was independent of OH^- concentration. They observed also that the difference between the potential of the $AgO/Ag_2O/OH^-$ and the $Ag/Ag_2O/OH^-$ couples was 0.23v. These results were confirmed by others (3).

Later Hickling and Taylor (4) measured the potential of the $AgO/Ag_2O/OH^-$ couple in 1*N* NaOH against a calomel electrode and obtained a value of 0.63v instead of the value reported by Luther and Pokorny. Hickling and Taylor prepared their electrode by making a slurry of the two oxides. Electrical contact was made by means of a platinum wire dipped into the mixture. This matter of the construction of the electrode may be significant as will be pointed out later.

Still other results on the potential of this couple were reported (5), but in only one case has an attempt been made to determine E° for this couple (6). Bonk and Garrett found this E° value to be 0.604v by measuring the voltage of the cell

$$Pt, Ag_2O(s), Ag(s) \,|1M\ NaOH|\, AgO(s), Ag_2O(s), Pt$$

They also measured dE/dT for this cell and from this calculated various thermodynamic values for AgO. Previous to this, the only thermodynamic data determined independently was that of Jirsa *et al.* (7), who measured the heat of reaction of AgO with hydrazine and the heat of solution of AgO both in perchloric acid and in nitric acid. From this they concluded that the heat of formation of Ag_2O_2 is close to 5400 cal/mole. This corresponds to 2700 cal/mole using the more generally accepted formula, AgO.

There are several difficulties to be overcome in making emf measurements with the AgO/Ag_2O couple. There is, *e.g.*, the matter of the preparation of the electrode. It was found in our work that when a slurry of AgO and Ag_2O was prepared and a platinum wire was used to make electrical contact, the measured emf was fairly steady, but it gave a value of about 0.4v on the hydrogen electrode scale. Other workers, however, have been more successful with this type of electrode (6). Using only a slurry of AgO, a somewhat lower value was obtained. A similar difficulty has been pointed out with respect to the Ag/Ag_2O couple (8). For this latter couple the difficulty was resolved by insuring intimate contact between the two solid phases in the electrode.

Another possible difficulty arises from the fact that not all methods suggested for the preparation of silver(II)oxide yield the same product (9). This work of Schwab and Hartmann raises some question about the oxide produced by anodizing a silver nitrate solution between platinum electrodes and then boiling the product with water. The AgO used by Hickling and Taylor (4) was prepared in this manner.

The purpose of this work was to determine the standard potential of the $AgO/Ag_2O/OH^-$ electrode by direct measurement against the hydrogen electrode.

Experimental

The cell used in this work can be represented as follows

$$Pt, H_2(g) \,|KOH(aq)|\, AgO(s), Ag_2O(s), Pt$$

The construction of the cell, the method of preparing and storing the electrolyte, the procedure used in making a run, the method for analyzing the electrolyte, and the train used to purify the hydrogen have all been described previously (10). A new hydrogen electrode was prepared for each run.

Several methods were used to prepare the AgO/Ag_2O electrodes. Some were prepared by pasting moist AgO on a Pt screen about 1 cm^2 and folded

Table I. Electrolyte concentrations and cell voltages at 25°C for the cell
Pt, H_2 | KOH(aq) | AgO, Ag_2O, Pt

E_{cell}, v	P_{bar}, mm	$E_{j\,max}$, v	Solutions: H_2 electrode m	H_2 electrode a_{H_2O}	AgO electrode m	AgO electrode a_{H_2O}	Electrode	$E°_{calc}$, v
1.4251	738	0.0000	0.199*	0.994	0.200*	0.994	A	0.5979
1.4248	744	—0.0002	0.251	0.992	0.248	0.992	C	0.5973
1.4278	742	—0.0003	0.396	0.987	0.391	0.987	A	0.5998
1.4268	746	0.0000	0.580	0.980	0.579	0.980	C	0.5990
1.4278	744	—0.0002	0.742	0.974	0.737	0.974	C	0.6000
1.4276	748	—0.0002	1.031	0.963	1.024	0.963	C	0.5994
1.4270	743	0.0000	1.056	0.962	1.056	0.962	C	0.5991
1.4278	739	0.0000	1.750	0.934	1.750	0.934	C	0.5995
1.4278	746	—0.0001	2.023	0.922	2.020	0.922	C	0.5991
							Average	0.599

* NaOH was used as the electrolyte in this cell.

to make a trough. The AgO used was that commercially available from Merck and Co. and also from the M. Ames Chemical Works. These electrodes were allowed to stand in water and in a dilute KOH solution for several weeks to age them and to produce a film of Ag_2O on the surface (11). The results obtained with two such electrodes are given in Table I, and the results obtained by using a third one are shown on Fig. 1.

Another electrode was prepared by pasting an aqueous slurry of Ag_2O on a 40 mesh nickel screen and then treating this anodically for 24 hr in a KOH solution. After making a series of measurements with this electrode, shown on Fig. 1, it was placed in a 14% KOH solution and kept in the dark for a week. Then this KOH solution was boiled, with the electrode still in it, for 15 min and set aside for another day, at which time another series of measurements was made with this electrode. These last results agreed within a millivolt with those determined earlier for this same electrode. This was done to get an estimate of the stability of the electrode.

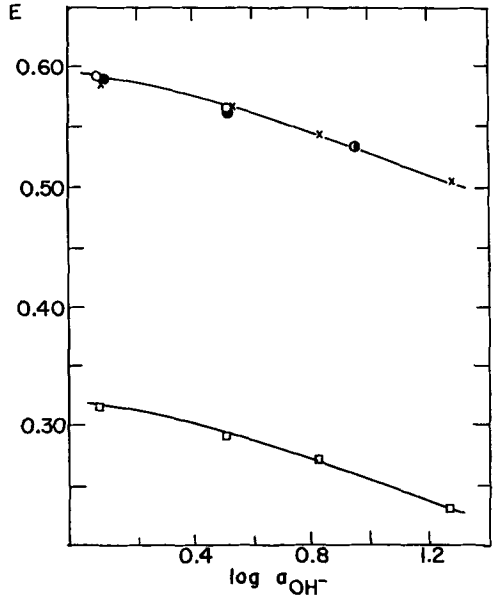

Fig. 1. Electrode potential of silver oxide electrodes vs. the hydrogen electrode: ○, electrolytically prepared AgO on nickel screen grid; ●, chemically prepared AgO on Pt screen grid; X, $AgO_{1.5}$ on Pt screen grid; □, Ag/Ag_2O electrode on Pt screen grid.

A third type of electrode was prepared by pasting an aqueous slurry of Ag_2O on a 40 mesh Pt screen. This was reduced thermally to Ag and then the electrode was treated anodically at a constant potential, about 350 mv above the reversible Ag/Ag_2O/OH^- potential, in a 21% KOH solution for 7 weeks. It was then soaked in distilled water, dried in a stream of N_2 at room temperature, and placed in a desiccator for at least a day. Assuming the weight gained by this electrode to be due solely to oxygen added during the oxidation process, this electrode had a composition that can be represented as $AgO_{1.5}$. Measurements with this electrode gave values that were in agreement with those of the other electrodes, Fig. 1. The x-ray diffraction pattern of this electrode had peaks identical to those obtained from AgO.

Figure 1 shows that the electrodes prepared by these various methods all have the same electrode potential value.

The cell was immersed in a constant-temperature bath kept at 25° ± 0.05°C. This was measured with a thermometer which had been calibrated by the National Bureau of Standards. A Rubicon portable potentiometer was used to make the voltage readings. It was checked from time to time against a National Bureau of Standards calibrated standard cell, and could be read to 0.1 mv. A run was considered acceptable only if the total variation of cell voltage readings was less than 0.5 mv over a 3-hr period. Furthermore, the results were rejected if there was a constant although small drift in voltage during this time. Little difficulty was experienced in getting a stable H_2 electrode. In one case cell voltages were constant within a millivolt for 48 hr. Some cells were also run at 45° ± 0.2° and 0° ± 1°C.

Results

The reaction for the Ag/Ag_2O/OH^- electrode is given in Eq. [1].

$$Ag_2O + H_2O + 2e = 2Ag + 2\ OH^- \qquad [1]$$

The variation of the potential of this couple with OH^- and solvent activity is the same as that of the AgO/Ag_2O/OH^- electrode in the same solution, Fig. 1. This indicates that the contribution of H_2O and OH^- is the same for both these electrode reactions,

and the reaction of the latter electrode is then taken to be

$$2AgO + H_2O + 2e = Ag_2O + 2\ OH^- \quad [2]$$

Table I lists the results of cell voltage measurements and the analysis of the solutions in the electrode compartments. The electrode reactions were assumed to be Eq. [2] and [3].

$$H_2 + 2\ OH^- = 2H_2O + 2e \quad [3]$$

The equilibrium electrode potentials for each of these reactions as written is, at 25°C,

$$E_{Ag} = E^\circ_{AgO/Ag_2O} - 0.05916 \log a_{OH^-} + 0.02958 \log a_{H_2O} \quad [4]$$

$$E_H = 0.8282 - 0.05916 \log a_{H_2O} + 0.05916 \log a_{OH^-} + 0.02958 \log a_{H_2} \quad [5]$$

The activity of the OH^- ions was calculated from the data of Akerlof and Bender (12). The activity of the solvent at 25°C was calculated from this same work while the values at 0° and 45°C were calculated using the treatment described by Lewis and Randall (13). The a_{H_2} was taken to be equal to

$$(P_{bar}\ mm - a_{H_2O} \cdot 23.76\ mm)/760\ mm \quad [6]$$

As a first approximation, the cell voltage at equilibrium is

$$E_{cell} = E_{Ag} + E_H \quad [7]$$

This assumes no junction potential. Table I shows that in some instances the solutions in the two electrode compartments did not have exactly the same composition. Consequently, the possibility of a junction potential must be considered. Since the solutions in the electrode compartments differed only in concentration, the junction potential may be considered as due to the transfer of ions across the junction. Its value then is given by Eq. [8].

$$E_j = (2t^- - 1) \cdot 0.05916 \log a_{OH^-_{Ag}}/a_{OH^-_H} \quad [8]$$

where $a_{OH^-_{Ag}}$ and $a_{OH^-_H}$ refer to the hydroxide ion activities in the silver and hydrogen electrode compartments, respectively. To estimate the maximum value of this junction potential t^-, the transference number of the OH^- ions, is assumed to be unity. Equation [8] then becomes

$$E_{j\,max} = 0.05916 \log a_{OH^-_{Ag}}/a_{OH^-_H} \quad [9]$$

Equation [9] has been used to calculate the $E_{j\,max}$ values given in Table I.

The E°_{AgO/Ag_2O} values in Table I are calculated from Eq. [4], [5], and [6] and are based on the assumption of zero junction potential. A summary of the maximum uncertainties introduced into these calculated E° values by the various experimental operations is given in Table II.

Table II. Maximum uncertainties introduced into E°_{calc} of Table I

	mv
Potentiometer reading	±0.2
Activity of solute	±0.1
Activity of solvent	±0.02
Activity of hydrogen	±0.05
Total	±0.37

The E° value of 0.599v is larger than that given by Latimer (14) based on the work of Luther and Pokorny (2), but smaller than that found by Bonk and Garrett (6). Using the value 0.599v, ΔF°_{298} for reaction [2] is −27.63 kcal. From this and other accepted free energy values (8, 15) ΔF°_{298} for the formation of AgO is 3200 cal/mole.

The value of 0.604 for E° of the AgO/Ag_2O/OH^- couple reported by Bonk and Garrett (6) was determined by measuring the difference in potential between this couple and the Ag/Ag_2O/OH^- couple in the same solution. This difference was 0.262v, and E° for the latter couple was taken to be 0.342v. The difference between the E° reported in this paper (0.599) and that reported earlier (10) for the Ag/Ag_2O/OH^- couple by direct measurement *vs.* a hydrogen electrode (0.338) is 0.261v, practically the same as the difference reported by Bonk and Garrett.

There seems to be some dependence of this E° value on the electrolyte concentration, Fig. 2. The lower values at the low concentrations are not due to permanent changes in or damage to the electrode. Each of these low values was obtained with a different electrode. One of these electrodes was later used in more concentrated KOH solutions and then gave the higher voltage value obtained with other electrodes in such solutions. It appears that these low voltage values are associated with the strength of the alkali solution, and this may indicate a change in electrode reaction or mechanism. If the two lowest points on Fig. 2 are excluded, then E° for the AgO/Ag_2O/OH^- electrode at 25°C is 0.5994 ± 0.0003v.

To obtain further thermodynamic data, the temperature coefficient of the electrode potential for reaction [2] was measured. Figure 3 shows the temperature variation of this potential. Three different temperatures were used. From these data a plot of E *vs.* T can be made for various OH^- activities, Fig. 4. The temperatures are too far apart to permit a determination of dE/dT values at a specific temperature. The results do suggest that dE/dT varies with KOH concentration as well as with temperature. This also may indicate that the electrode reaction or mechanism is not the same under all the conditions described here. The possibility

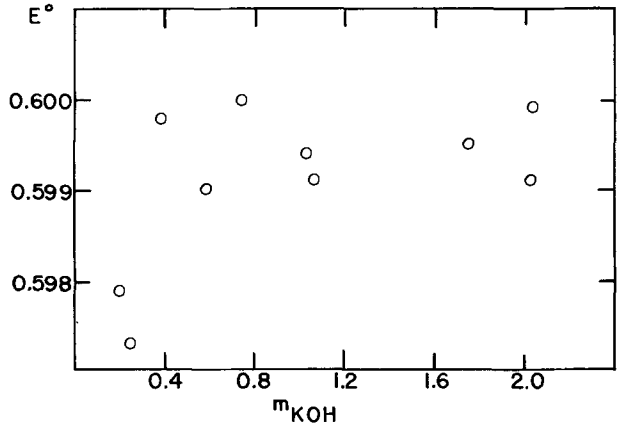

Fig. 2. Variation of E° for the AgO/Ag_2O/OH^- electrode with KOH concentration.

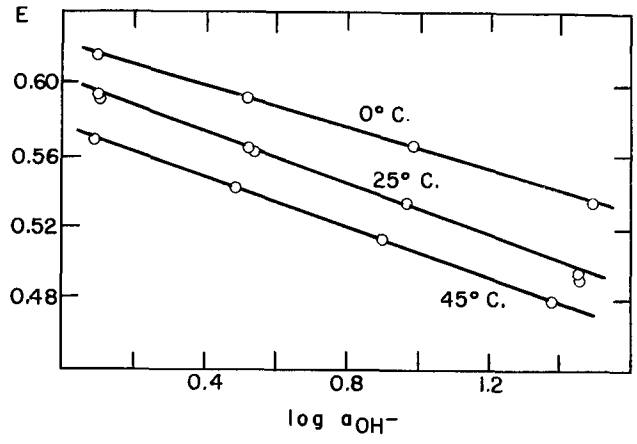

Fig. 3. Potential of the $AgO/Ag_2O/OH^-$ vs. the hydrogen electrode as a function of temperature and OH^- activity.

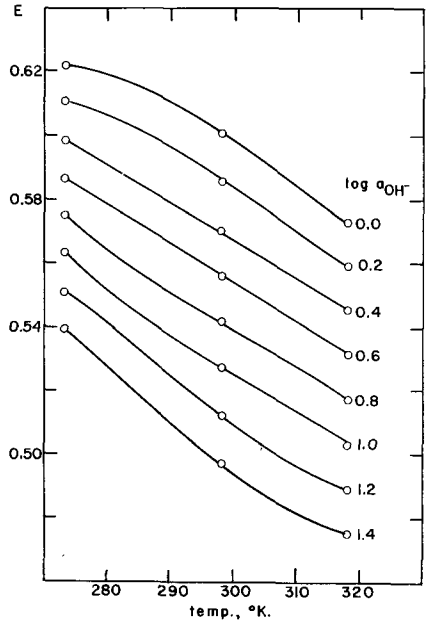

Fig. 4. Variation of the potential of the $AgO/Ag_2O/OH^-$ electrode vs. the hydrogen electrode at various OH^- ion activities.

of a mixed potential seems to be ruled out because only two solid species are present, AgO and Ag_2O.

Bedwell (16) found difficulty in getting reproducible voltage values above 30°C for a cell similar to that used by Bonk and Garrett (6). However, she did not attribute these difficulties to either electrode as against the other. Her voltage values for this cell from 0 to 25°C were linear and fairly reproducible. Assuming that the values on Fig. 4 are linear from 0 to 25°C, then they are in agreement with those of Bedwell as far as comparisons can be made.

An attempt was made to relate the values reported here to the silver-zinc-alkali cell. The open-circuit voltages (ocv) of this system are usually 1.85 and 1.60v, corresponding, it is believed, to the presence of the AgO/Ag_2O and the Ag/Ag_2O couple, respectively. These are about the values expected assuming E° values of 0.599 and 0.338, respectively, for these two couples in alkaline solutions.

To check this, pellets of Ag_2O and AgO were prepared and used in a cell described previously (17). The pellets were 2.5 cm in diameter and about 1

Table III. Open-circuit voltages of silver oxide pellets

Electrode pellet	Metal backing	Open-circuit voltage vs. zinc: At start	After charge	After discharge
Ag_2O	Ag	1.80	1.95 1.89	1.67 1.82
Ag_2O	Pt	1.89	2.18 1.96	1.66
AgO	Ag	2.13 1.79	1.95	1.67
AgO	Pt	2.05 1.93	1.95	1.66

mm thick. They were made from commercially available material and were pressed at 5000 lb. The opening between the pellet and the electrolyte was 6 mm diameter. The electrolyte was 30% KOH to which a small amount of ZnO had been added. The ocv's were measured by a General Radio d-c electrometer having an input resistance of 10^{10} ohms. The output from this electrometer was fed into a recorder. A sheet of zinc served as the negative electrode. Electrical contact to the pellets of silver oxide was made by means of a platinum or silver foil clamped against the pellet.

The ocv was measured over a period of several hours. Then the electrode was charged at 10 ma for about 30 min, and the ocv was again measured for an hour. Finally the electrode was discharged at 10 ma for an hour or more, and the ocv was again measured over a period of an hour or so. Results are shown in Table III. "Metal backing" refers to the metal foil used to make electrical contact with the pellet, and the multiple values refer to the fact that the ocv varied from the first to the second during the time the measurements were being made.

The ocv of the fresh pellets does not correspond to the potential for either reaction [1] or [2]. The ocv of the fresh Ag_2O pellet was steady but considerably higher than that of the Ag_2O/Ag electrode even when Ag foil was used as the backing. These ocv's are likely those of a nonequilibrium system and/or those of a solid-electrolyte interface even though they approximate the values associated with the presence of AgO.

The ocv of the fresh AgO pellets was unsteady, starting at a high voltage and falling rapidly at first. With the Ag foil as backing no steady ocv was obtained. Probably the AgO reacts with the electrolyte to form Ag_2O (11) so that Ag_2O and AgO are present at the Ag foil. This may give a mixed potential or it may prevent attainment of equilibrium. With Pt foil as backing the reaction of AgO with the electrolyte produces Ag_2O giving an AgO/Ag_2O electrode on a Pt surface. This decomposition takes place rapidly. The ocv then corresponds to that of the $AgO/Ag_2O/OH^-$ electrode and is 1.93v in the 30% KOH. This is substantially the same as the ocv obtained after the Ag_2O pellet had been charged on a Pt foil backing. In the case of the AgO pellets, the small charge did not oxidize all the Ag_2O that had been formed previously on stand so that the ocv after charge was still that of the $AgO/Ag_2O/OH^-$ electrode.

The ocv corresponding to the Ag/Ag_2O electrode is obviously 1.67v under these conditions, as seen from the last column in Table III. The reduction of

the Ag_2O pellet on a Ag foil backing gave an ocv of 1.67v, but this later increased to 1.82v. This no doubt is due to reactions at the Ag foil which could have resulted from the dissolving of some Ag_2O in the electrolyte, or some change in contact of the backing with the pellet.

With the partial discharge of the AgO pellets only a small amount of reduction could take place because of the small quantity of current withdrawn. At the end of this discharge the pellet was largely AgO. What discharge there was appeared to have taken place at the backing. Spots of reduced Ag were observed there and only there. It appears then that the potential of the electrode is determined solely by the materials present at the grid and not by the bulk composition of the pellet. Here the ocv corresponded to that of Ag_2O/Ag even though the bulk of the pellet was AgO.

These results show, among other things, that ocv's of silver-zinc cells in the neighborhood of 1.66v correspond to the presence of the $Ag/Ag_2O/OH^-$ system in the silver electrode, and those near 1.93v correspond to the presence of the $AgO/Ag_2O/OH^-$ system. However, the ocv's are determined by the materials present at the backing and give no indication of the composition of the electrode active material.

Intermediate potentials or voltages have been observed (18), and these probably are mixed potentials due to the presence of AgO, Ag_2O, and Ag. This is likely also true of ocv values in the neighborhood of 1.85v.

Acknowledgment

The author wishes to express his appreciation and thanks to the Office of Naval Research for a grant in support of this work, to the M. Ames Chemical Company and to Merck and Company for supplying the oxides used in this work, to Dr. W. J. Hamer for his helpful comments and suggestions, and to Dr. J. De Vries for help with the experimental work.

Manuscript received Aug. 9, 1961; revised manuscript received Nov. 20, 1961. This paper was prepared for delivery before the Detroit Meeting, Oct. 1-5, 1961.

Any discussion of this paper will appear in a Discussion Section to be published in the December 1962 JOURNAL.

REFERENCES

1. A. A. Noyes and A. Kossiakoff, *J. Am. Chem. Soc.*, **57**, 1238 (1935); A. A. Noyes, D. De Vault, C. D. Coryell, and T. J. Deahl, *ibid*, **59**, 1326 (1937).
2. R. Luther and F. Pokorny, *Z. anorg. u. allgem. Chem.*, **57**, 290 (1908).
3. F. Jirsa and J. Jelinek, *ibid.*, **148**, 130 (1925).
4. A. Hickling and D. Taylor, *Discussions Faraday Soc.*, **1**, 277 (1947).
5. P. Jones, H. R. Thirsk, and W. F. K. Wynne-Jones, *Trans. Faraday Soc.*, **52**, 1003 (1956).
6. J. F. Bonk and A. B. Garrett, *This Journal*, **106**, 612 (1959).
7. F. Jirsa, J. Jelinek, and J. Srbek, *Z. anorg. u. allgem. Chem.*, **158**, 33 (1926).
8. W. J. Hamer and D. N. Craig, *This Journal*, **104**, 206 (1957).
9. G. Schwab and G. Hartmann, *Z. anorg. u. allgem. Chem.*, **281**, 183 (1955).
10. T. P. Dirkse, *J. Chem. Eng. Data*, **6**, 538 (1961).
11. P. Rüetschi and R. F. Amlie, *This Journal*, **108**, 813 (1961).
12. G. Akerlof and P. Bender, *J. Am. Chem. Soc.*, **70**, 2366 (1948).
13. G. N. Lewis and M. Randall, "Thermodynamics," p. 269, McGraw-Hill Book Co., Inc., New York (1923).
14. W. M. Latimer, "Oxidation Potentials," 2nd ed., p. 190, Prentice-Hall, Inc., New York (1952).
15. "Selected Values of Chemical Thermodynamic Properties," National Bureau of Standards Circular 500 (1952).
16. M. E. Bedwell, "Thermodynamics of the Zinc-Silver Oxide Cell," Report No. Chem. 515, Feb. 1958, Royal Aircraft Establishment, Farnborough, England.
17. T. P. Dirkse, *This Journal*, **107**, 862 (1960).
18. C. P. Wales, *ibid.*, **108**, 395 (1961).

Electrode Potentials and Thermal Decomposition of Alpha- and Beta-PbO_2

R. T. Angstadt, C. J. Venuto, and P. Rüetschi

The Carl F. Norberg Research Center, The Electric Storage Battery Company, Yardley, Pennsylvania

ABSTRACT

Electrode potentials of α- and β-PbO_2 were measured in solutions containing fixed amounts of SO_4^{--} ions or ClO_4^- ions, as a function of pH. Oxygen overvoltage and ease of electrochemical reduction are correlated with anion adsorption and true surface area of the two oxide modifications. A method for synthesis of α-PbO_2 by chemical means is described. Differences in the solid-state properties between α- and β-PbO_2 are revealed by thermal degradation to the intermediate oxide PbO_x, with $1.42 < x < 1.58$. The unit cell of PbO_x was determined to be orthorhombic with $a_0 = 7.76$Å, $b_0 = 10.98$Å, and $c_0 = 15.31$Å.

The electrochemical and solid-state properties of lead dioxide have been studied extensively in recent years, with particular emphasis on the polymorphism of the substance (1-19). Both modifications, the orthorhombic α-PbO_2 and the tetragonal β-PbO_2, are good conductors of electricity (20-23), but until recently little quantitative data were available on their physical properties. Results with nuclear and electron resonance techniques (24-26) are consistent with the concept that PbO_2 behaves

as a metal. The Knight shift in the PbO_2 resonance is dependent on the density of conduction electrons near the top of the Fermi distribution and is therefore a qualitative measure of conductivity. From the relative chemical shifts of α- and β-PbO_2 (0.48 for α and 0.62 for β), it appears that α-PbO_2 might be a slightly better conductor. The conductivity of both modifications seems to be due to a nonstoichiometry, related to the oxygen deficiency. The α modification often tends to show a lower oxygen content.

If the oxygen content of β-PbO_2 is decreased by thermal decomposition below $PbO_{1.94}$, a new chemical compound starts to appear in the reaction product (2,27-29); a compound with the composition PbO_x with $x \cong 1.5$, is formed. The corresponding N M R absorption (25) indicates an increase in the Knight shift relative to the metal which corresponds to a decrease in conductivity.

The present paper presents new results of electrochemical and solid-state measurements with α- and β-PbO_2. In particular, thermal decomposition was studied with improved techniques and with special consideration of the polymorphism of PbO_2.

Although a large amount of work has been done on thermal degradation of PbO_2 by earlier investigators, a lot of previous results are inconclusive and in disagreement with each other. This is in part due to the fact that earlier investigators did not know of the polymorphism of PbO_2. The decomposition products reported by these investigators range from Pb_3O_4, Pb_2O_3, Pb_5O_8, Pb_7O_{11}, to intermediate oxides with variable oxygen content, called PbO_x. The crystal structures reported for these compounds range from face-centered cubic (28) to tetragonal (28) to orthorhombic (27) to monoclinic (27). In the present paper the decomposition products were analyzed chemically and by x-ray techniques.

Equilibrium electrode potential studies and kinetic measurements on oxygen evolution and electrochemical reduction to $PbSO_4$ were performed with improved experimental techniques and with particular emphasis on the influence of the lattice polymorphism on these electrochemical parameters.

Experimental

Electrode potentials of α- and β-PbO_2 were measured using a new type of electrode construction, illustrated in Fig. 1. A thin platinum wire was sealed into a U-shaped glass tube forming an open cup at one end (electrode to the left). The platinum wire extending into the cup was electroplated with the particular modification of PbO_2 to be studied (electrode in the middle). The plating procedures for α- and β-PbO_2 have been reported earlier (3). By plating tht platinum wires, the exposure of any platinum to the electrolyte was prevented, and by surrounding the plated wires with powdered PbO_2 a very high degree of stability of electrode potentials could be achieved. The cup was subsequently filled with powdered PbO_2 of the same modification as electroplated (electrode to the right).

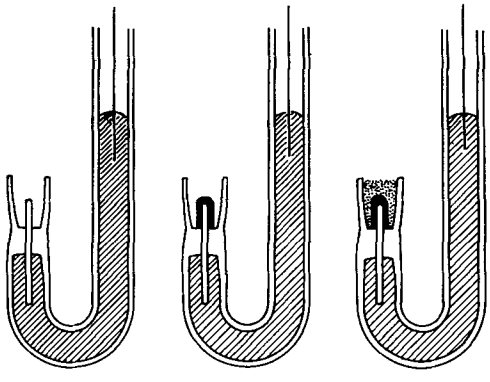

Fig. 1. Powder-type PbO_2 electrodes for potential measurements. At the left the Pt-wire seal into the glass cup is illustrated. In the middle, the Pt-wire extending into the cup is shown electroplated with PbO_2. At the right, the cup is filled with powdered PbO_2.

The α-PbO_2 powder was synthesized by ammonium persulfate oxidation of lead acetate in a strongly ammoniacal solution of ammonium acetate (1), according to the reaction

$$4NH_4OH + PbAc_2 + (NH_4)_2S_2O_8 \rightarrow \alpha PbO_2 +$$

$$2NH_4Ac + 2(NH_4)_2SO_4 + 2H_2O$$

A quantity of 250g $(NH_4)_2S_2O_8$ was added to 250 cc of water and 1 liter of saturated ammonium acetate solution; a saturated solution of 325g of $PbAc_2$ in water was then added slowly, simultaneously with 300 cc of 58% NH_4OH. The reaction proceeded at a very low rate. After 6 hr an additional amount of 50g $(NH_4)_2S_2O_8$ was added. The mixture was stirred for 24 hr and then heated to 70°C to drive off excess NH_3 and to dissolve any divalent lead compounds. The precipitate was filtered on a Buchner filter, washed with NH_4Ac and distilled water, and dried at room temperature.

The β-PbO_2 powder was reagent grade Merck PbO_2 whose crystal structure was confirmed by x-ray diffraction.

Electrode potentials were measured as a function of pH in solutions containing constant amounts of either SO_4^{--} or ClO_4^- ions. In solutions containing SO_4^{--} ions, the electrode potentials were measured with Hg/Hg_2SO_4 reference electrodes up to pH 4, and with Hg/HgO electrodes above pH 10. These solutions were saturated with $PbSO_4$. The potentials were checked also against hydrogen electrodes. For these checks lead sulfate saturation was omitted in the hydrogen electrode cells to prevent poisoning of the hydrogen electrodes. Several thousand measurements were made on several hundred different electrodes of the type shown in Fig. 1 over a period of two years.

In solutions containing ClO_4^-, a constant lead ion concentration of 1/1000M was maintained for all experiments. In this system, the electrode potentials were measured against a hydrogen electrode in a separate compartment, containing the same electrolyte, but without the lead ions being present. The reference electrode compartment was separated by a microporous plug.

Kinetic measurements were performed with electroplated rod-shaped electrodes, 20 mm long and 1.3 mm in diameter. The electrodes were prepared according to the procedure described earlier (3). Smooth, adherent deposits about 1 mm in thickness were obtained using a plating current of 1 ma/cm^2 for 168 hr, at 30°C.

These electrodes were transferred to 4.00M H_2SO_4 solution and anodized at 10 μa at 30°C over extended periods of time, prior to taking measurements.

For all electrochemical measurements the solutions were prepared with triple distilled water. Equilibrium electrode potentials were measured with a Minneapolis-Honeywell/Rubicon-Instrument Potentiometer, Model No. 2780S and galvanometer.

For the kinetic measurements constant current was obtained with electronic instrumentation described previously (1). Changes in electrode potential were followed using a Keithley model 610 electrometer, with an input impedance of better than 10^{14} ohm, driving a ¼ sec Minneapolis-Honeywell recorder. In this manner electrode potentials were measured with a precision of 1 mv and with a response of better than 1 mv in 20 msec (30).

All the electrochemical measurements were made in Pyrex glass vessels, thermostated to ± 0.02°C using an infrared lamp as a heater, controlled by a mercury contact-thermometer, and an electronic relay.

For the thermal decomposition experiments the starting materials were α-PbO_2 prepared by the persulfate oxidation method described in the experimental part, and β-PbO_2 in the form of reagent grade Merck PbO_2. Samples of 1g were placed in 8 mm Pyrex tubes, 70 cm long, and inserted in a tube furnace at constant temperature for 23 hr. The temperature was controlled by setting a regulated (0.25%) a-c voltage with a Variac. Two samples in separate tubes were heated simultaneously. One tube was maintained at 47 mm pressure of O_2, and the other at 2280 mm O_2 pressure. At the end of the 23-hr period the tubes were removed from the furnace, air cooled, and samples subjected to x-ray diffraction, and analyzed iodometrically for active oxygen content.

The 47 mm O_2 pressure regulation during thermal decomposition was achieved by a mercury-glass check valve simliar to the one described by Smith *et al.* (31). The sample tube was attached to the high-pressure side of a fritted glass disk, which was barely immersed on the opposite side into a mercury pool. The low-pressure side was attached to a vacuum pump. The regulation of the oxygen pressure to 2280 mm Hg was achieved by a special regulator valve on an oxygen tank and a controlled leak. The latter was necessary because of the oxygen generated by the thermal degradation reaction.

The decomposition products were analyzed with x-ray techniques using nickel-filtered copper radiation. The diffraction unit was a GE-XRD-5. Slow and fast scanning was used and the reflections were indexed by analytical methods.

Results

Electrode potentials measured with cup-type electrodes in solutions 1M and 1/10M in SO_4^{--} ions at 30°C are shown in Fig. 2 and 3. The variation in *p*H at constant SO_4^{--} ion concentration was achieved by mixing appropriate amounts of NaOH and H_2SO_4 (except the first point at negative *p*H,

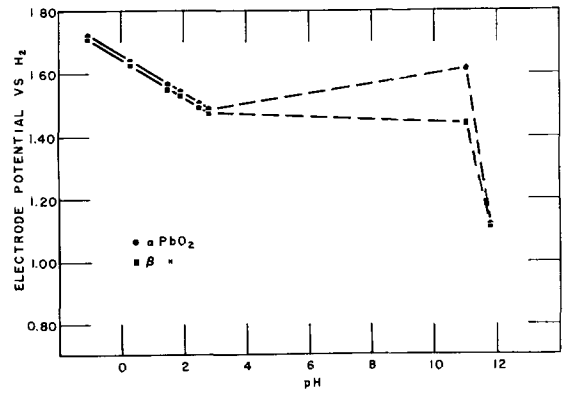

Fig. 2. Electrode potentials (vs. H_2 in the same solution) of α- and β-PbO_2 electrodes in solutions containing SO_4^{--} ions at 1 mole/liter as a function of *p*H at 30°C.

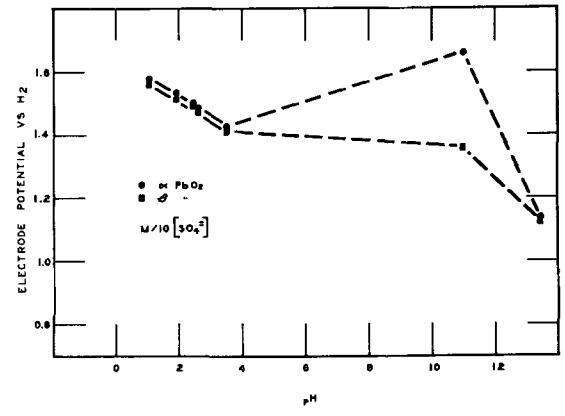

Fig. 3. Electrode potentials (vs. H_2 in the same solution) of α- and β-PbO_2 electrodes in solutions containing SO_4^{--} ions at 1/10 mole/liter as a function of *p*H at 30°C.

which was obtained in 4M H_2SO_4). Each point is an average of about 100 measurements on several different electrodes. At low *p*H values the electrode potential followed the theoretically expected behavior, changing about 60 *mv* per *p*H unit (*vs.* H_2 in the same solution). At *p*H values above 4, the potentials tended to become independent of *p*H. In this region the electrode did not readily establish stable values. Very long time periods, up to many days, were required to approach steady potentials, and the measurements were quite tedious.

The electrolyte system H_2SO_4-Na_2SO_4 is naturally a very poor buffer at *p*H values above about 4. Because of our interest in relating our studies to phenomena in lead-acid batteries, we preferred not to introduce an anion of a weaker acid and not to buffer the system between *p*H 4 and 10, but rather to measure the potentials as accurately as possible in the SO_4^{--} system.

It must be pointed out that the important *p*H region with regard to conclusions on lead-acid batteries is the one at low *p*H values. The striking result here is that both the α- and β-PbO_2 electrode show the thermodynamically expected response to the hydrogen ion concentration. This confirms that also the α-PbO_2 electrode is able to establish an electrochemical equilibrium in acid solution (3, 8).

One can calculate (32) that in solutions containing SO_4^{--} ions of activity 1, $PbSO_4$ should be the stable divalent lead phase up to *p*H 8.4, monobasic

lead sulfate between 8.4 and 9.6, tribasic sulfate between 9.6 and 14.7, and PbO above this value. In solutions containing SO_4^{--} ions of activity 10^{-4} only, the $PbSO_4$ phase is stable up to *p*H 6.4, then between *p*H 6.4 and 7.4 monobasic lead sulfate is stable and above 7.4 tribasic lead sulfate, and finally above *p*H 12.7 lead oxide. As long as a solid divalent phase of some kind is present, the electrode potentials in these regions are due to couples between PbO_2 and the corresponding basic sulfates or PbO.

The slopes of potential-*p*H plots should therefore decrease successively from 0.059 to zero toward the higher *p*H ranges, if the potentials are measured *vs.* hydrogen in the same solution. Delahay, Pourbaix, and Rysselberghe, in their *p*H-potential diagram, neglected the presence of solid basic lead sulfates and concluded that independence of *p*H begins at *p*H 9 if the electrode potential is measured against a hydrogen electrode in the same solution. Experimentally, it was found here that the potentials tended to become *p*H-independent at considerably lower *p*H values.

As pointed out, the hydrogen ion concentration was not stabilized above *p*H 4. Nevertheless, several thousand measurements on over 100 different electrodes were made above this *p*H value. Although reproducibility was not as good as in the low *p*H region, it must be pointed out that these measurements gave consistently higher electrode potential values than one would have expected theoretically. The average values of the observed potentials are indicated with dotted lines in Fig. 2 and 3.

The result that the α-PbO_2 electrode in acid solution has an electrode potential 7-10 mv higher than the β-PbO_2 electrode (2, 3, 12) is strongly corroborated in Fig. 2 and 3. On the other hand, these new results do now show the crossover of electrode potentials between *p*H 1 and 2, as reported earlier (3). The apparently reproducible crossover was observed with rod-shaped electrodes of very limited surface area. The present measurements with powder-type electrodes are considerably more accurate.

While Fig. 2 and 3 show potentials at constant SO_4^{--} ion concentration, Fig. 4 shows the *p*H dependence of the PbO_2 electrode at constant ClO_4^- ion (1/10M) and constant lead ion (1/1000M) concentration. The results show that also in this system, the potential of the α-PbO_2 electrode is higher than that of the β-PbO_2 electrode. Again, there is a region of ill-defined *p*H in which the potentials appear independent of *p*H. In the acid region the potential dependence confirms the expected behavior, the slope being just slightly higher than theoretical.

The temperature dependence of the α- and β-PbO_2 electrode potentials in 3.90M (4.62M) H_2SO_4 is illustrated in Fig. 5. It is interesting to note that the α-PbO_2 potential decreases more rapidly with temperature than the β-PbO_2 potential. A crossover is observed at about 50°C. It seems that above this point α-PbO_2 becomes the more stable modification.

From the equations defining the electrochemical equilibria

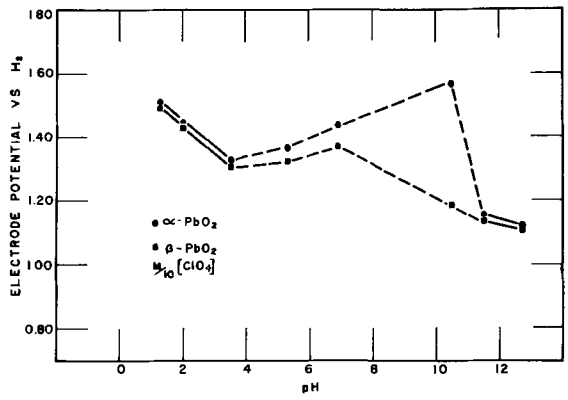

Fig. 4. Electrode potentials (vs. H_2 in the same solution) of α- and β-PbO_2 electrodes in solutions containing 1/10 mole/liter of ClO_4^- ions and 1/1000 mole/liter of divalent lead, as a function of *p*H at 30°C.

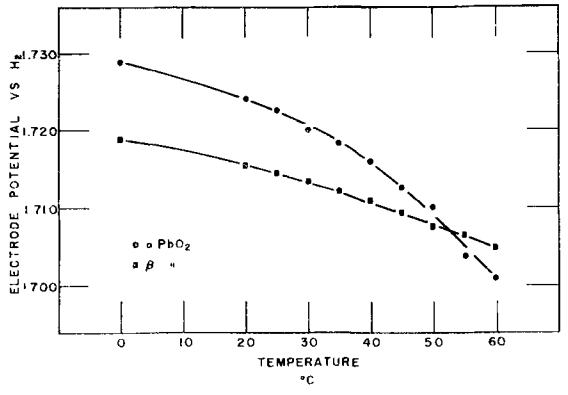

Fig. 5. Electrode potentials of α- and β-PbO_2 in H_2SO_4 (3.90 moles/liter) as a function of temperature.

$$\beta\text{-}PbO_2 + H_2\ (1\ atm) + H_2SO_4\ (4.62M) \rightleftarrows PbSO_4 + 2H_2O\ (\text{in. } 4.62M\ H_2SO_4)\quad E = 1.713 \text{ at } 25°C \quad [1]$$

$$\alpha\text{-}PbO_2 + H_2\ (1\ atm) + H_2SO_4\ (4.62M) \rightleftarrows PbSO_4 + 2\,H_2O\ (\text{in. } 4.62M\ H_2SO_4)\quad E = 1.722 \text{ at } 25°C \quad [2]$$

with the corresponding free enthalpy equations $\Delta G_\beta = -nFE_\beta$, and $\Delta G_\alpha = -nFE_\alpha$ one obtains for the free enthalpy difference between α- and β-PbO_2 at 25°C

$$\alpha\text{-}PbO_2 \rightleftarrows \beta\text{-}PbO_2 \qquad \Delta G = -0.4 \text{ kcal}$$

The data of Fig. 5 are the most precise ones obtained to date for α- and β-PbO_2 electrodes in sulfuric acid. Earlier results for electrode potentials of the two modifications were obtained with electroplated rod-type electrodes (3), which had a limited surface area. The present results for both modifications are 5 to 6 mv higher than the values reported earlier (3). From the data of Hamer (33) one obtains, for an acid concentration of 4.62*M* at 25°C, a potential of 1.707v, while from Fig. 5 the corresponding value for β-PbO_2 is 1.713v. The temperature dependence of the electrode potential for β-PbO_2 checks very accurately with the values of Hamer:

$$\alpha\text{-}PbO_2 : \left(\frac{\partial E\alpha}{\partial T}\right)_p =$$

-0.36 mv/°C at 25°C, 4.62*M* H_2SO_4

$$\beta\text{-}PbO_2 : \left(\frac{\partial E\beta}{\partial T}\right)_p =$$

-0.20 mv/°C at 25°C, 4.62M H_2SO_4

$$PbO_2 \text{ Hamer (33)} : \left(\frac{\partial E}{\partial T}\right)_p =$$

-0.20 mv/°C at 25°C, 4.62M H_2SO_4

These temperature dependences of the electrode potentials of α- and β-PbO_2 permit a calculation of the enthalpy difference between the two modifications at 25°C. With

$$\Delta H_\beta = -nFE_\beta + nFT\left(\frac{\partial E\beta}{\partial T}\right)_p$$

$$\Delta H_\alpha = -nFE_\alpha + nFT\left(\frac{\partial E\alpha}{\partial T}\right)_p$$

for Eq. [1] and [2] one obtains for the difference of the ΔH's between α- and β-PbO_2

$$\alpha\text{-}PbO_2 \rightleftarrows \beta\text{-}PbO_2 \qquad \Delta H = -2.6 \text{ kcal at } 25°C$$

Kinetic studies on α- and β-PbO_2 electrodes were performed with electroplated rod-type electrodes of reproducible surface area, prepared by electroplating under identical conditions of current density, temperature, electrolyte composition, and mass transport (3). Figures 6 and 7 show buildup of oxygen overvoltage at constant current in 4.00M H_2SO_4 on α- and β-PbO_2, respectively. Charging currents as indicated were switched on only after prolonged (several days) anodization at 10 μa/cm² in order to prevent the presence of $PbSO_4$ and changes in surface area. The charging curves are linear with time initially. From the slopes one can conclude that α-PbO_2 had a larger adsorption capacity per total electrode surface. From unpublished work in this laboratory, indications are that α-PbO_2 also has a larger "specific" capacity (per unit of "true" surface area). The "true" total surface area of the α-PbO_2 electrodes was smaller than that for the β-PbO_2 electrodes. In general, α-PbO_2 tends to develop larger crystals than β-PbO_2 (9).

The Tafel slopes for the oxygen evolution on the two modifications, obtained from the steady-state oxygen overvoltage values of Fig. 6 and 7, agree well with the data reported earlier (3). It appears that the difference in Tafel slopes can be best interpreted as follows. On electrodes of β-PbO_2, SO_4^{--} ions are adsorbed to a larger degree and contribute to the charge of the double layer. This increase of the double layer charge, due to SO_4^{--} ions, increases the electrode potential for a given current, or a given number of reacting oxygen species on the surface. The Tafel slope of the α-PbO_2 electrode, however, would possibly be characteristic for an oxygen evolving electrode with decreased adsorption of these SO_4^{--} species.

To study the difference in the kinetics of the discharge reaction between α- and β-PbO_2

$$2e + PbO_2 + 4H^+ + SO_4^{--} \rightarrow PbSO_4 + 2H_2O \quad [3]$$

about 30 electrodes of each type described in ref. (3) were discharged in 1M H_2SO_4 solution. The discharge curves at 1 ma/cm² are shown in Fig. 8 (β-PbO_2) and Fig. 9 (α-PbO_2). The discharge time for the β-PbO_2 electrodes average 2000 sec, while the average time for α-PbO_2 electrodes was about 800 sec. The remarkable difference must be

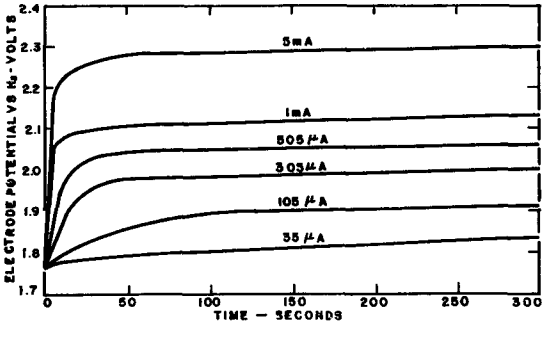

Fig. 6. Buildup of oxygen overvoltage on β-PbO_2 in H_2SO_4 (4.00 moles/liter) at constant current at 30°C.

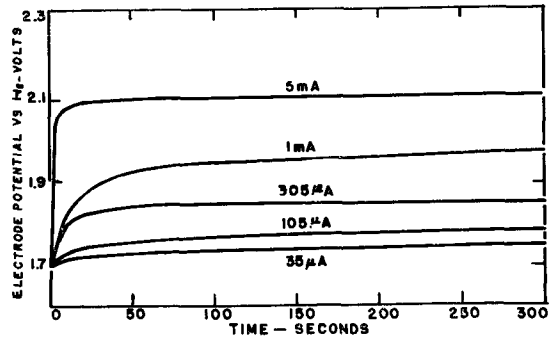

Fig. 7. Buildup of oxygen overvoltage on α-PbO_2 in H_2SO_4 (4.00 moles/liter) at constant current at 30°C.

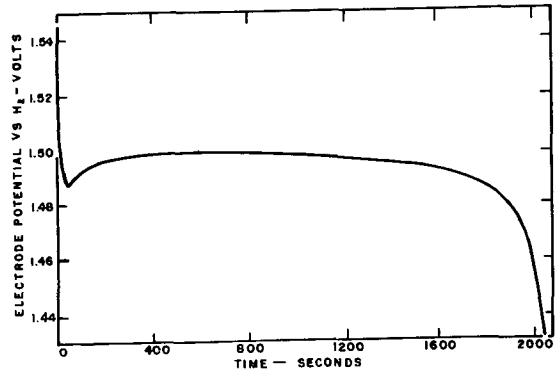

Fig. 8. Discharge of electroplated β-PbO_2 electrode at constant current in H_2SO_4 (1 mole/liter) at 1ma/cm² at 30°C.

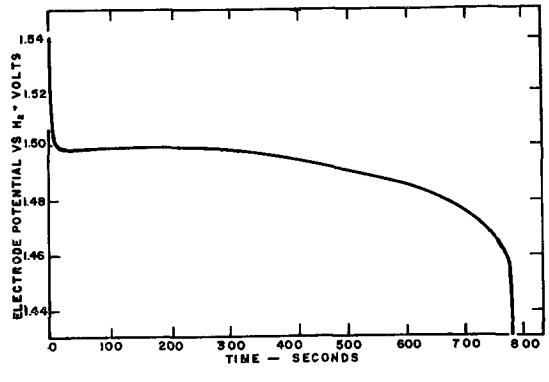

Fig. 9. Discharge of electroplated α-PbO_2 electrode at constant current in H_2SO_4 (1 mole/liter) at 1 ma/cm² at 30°C.

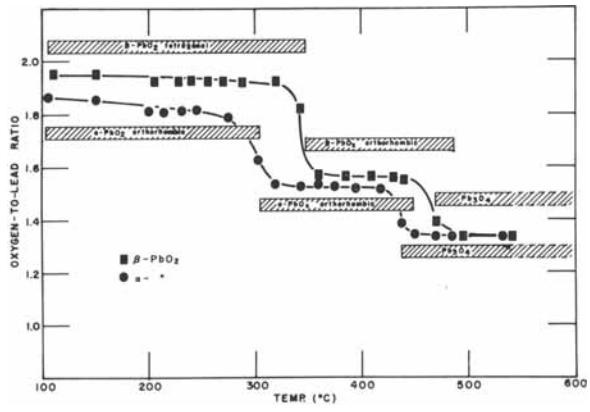

Fig. 10. Oxygen content and x-ray analysis of reaction products from thermal decomposition of α- and β-PbO_2 at 2280 mm O_2 pressure.

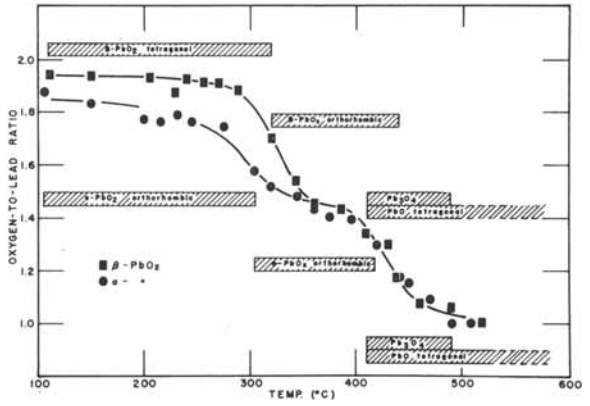

Fig. 11. Oxygen content and x-ray analysis of reaction products from thermal decomposition of α- and β-PbO_2 at 47 mm O_2 pressure.

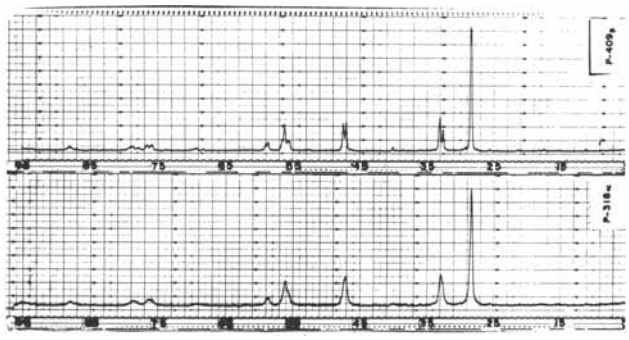

Fig. 12. Typical fast-scan x-ray patterns for α- and β-PbO_x materials. The chart marked P 318 α was obtained with a sample produced at 318°C from α-PbO_2 at 2280 mm O_2 pressure. The chart marked P 409 is for a sample produced at 409°C at the same pressure from β-PbO_2.

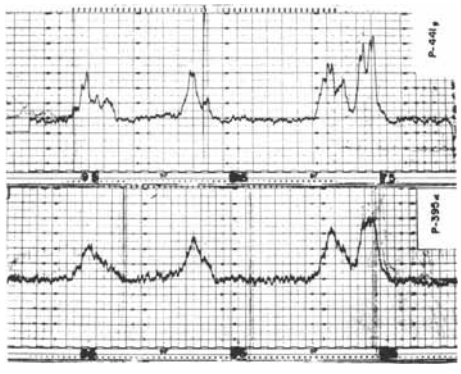

Fig. 13. Typical slow-scan x-ray patterns α- and β-PbO_x. The α-PbO_x (P 395 α) was obtained at 395°C from α-PbO_2 at 2280 mm O_2 pressure, the β-PbO_x (P441 β) is for a sample produced from β-PbO_2 at 441°C at the same pressure.

attributed largely to difference in the true surface area. The apparent areas were identical. Only a very thin surface layer of PbO_2 reacted on both electrodes, with a depth in the order of 10^{-4} cm in agreement with Ikari *et al.* (15).

The results of the behavior of α- and β-PbO_2 during thermal decomposition are illustrated in Fig. 10 to 13. In Fig. 10 and 11 the lead to oxygen ratios determined iodometrically are plotted *vs.* the decomposition temperature for two different partial oxygen pressures. The regions of appearance of different reaction products, as determined by x-ray diffraction (shown by the hatched areas), correlate well with the plateaus of the chemical analysis data.

At 2280 mm partial oxygen pressure (Fig. 10) three plateaus are observed. The three plateaus correspond to PbO_2, PbO_x (with $x = 1.52$ to 1.58) and Pb_3O_4. The PbO_x materials seem to have a somewhat variable oxygen content. The decomposition of α-PbO_2 to PbO_x occurs at a lower temperature than that of β-PbO_2. The PbO_x compounds produced from α- and β-PbO_2 are called here α- and β-PbO_x, respectively.

At 47 mm partial oxygen pressure (Fig. 11) the plateau corresponding to the PbO_x materials is still apparent. However, the Pb_3O_4 plateau has disappeared, although some Pb_3O_4 was detected by x-ray analysis of the reaction products formed between 415° and 485°C. Above 490°C, PbO (tetr.) is the sole reaction product. A comparison of Fig. 10 and Fig. 11 reveals the drastic influence of the partial oxygen pressure on the stability of Pb_3O_4 at temperatures above 400°C. A further transition, not shown in Fig. 11, was observed at approximately 610°C from tetragonal to orthorhombic PbO.

Since considerable discrepancies concerning the PbO_x materials exist in the literature, it was decided to study the crystallography of these compounds in greater detail with x-ray techniques. A comparison of fast scan x-ray charts of α- and β-PbO_x illustrates a close similarity of the crystal structure of these two lead oxides (Fig. 12). The well resolved multiple peaks in the β-PbO_x pattern have their counterparts in the α-PbO_x pattern, where they appear as more diffuse, single peaks. The diffuse composite single peaks of α-PbO_2 occur at the same average 2θ values as the equivalent double peaks of β-PbO_x.

Detailed slow scans, as shown in Fig. 13, of the two PbO_x materials substantiate and emphasize the similarity of the two patterns. It can be seen that the broad diffuse peaks in the α-PbO_x pattern have their well-defined equivalents in the β-PbO_x pattern at the same 2θ angles. The x-ray data obtained for α- and β-PbO_x with slow scanning are summarized in Tables I and II.

The reflections were indexed by analytical methods using the $\sin^2\theta$ relationship for the orthorhombic system.

Table I. X-ray powder diffraction data α-PbO_x

hKl	d-Å	hkl	d-Å
024	3.137	080	1.369
040	2.728	258	1.355
204	2.708	268	1.251
240	2.413	552	1.248
400	1.926	622	1.243
008	1.918	3·0·11	1.225
064	1.647	614	1.214
228	1.636	644	1.116
440	1.573	2·4·12	1.109
048	1.568	628	1.049
		4·2·12	1.044

Table II. X-ray powder diffraction data β-PbO_x

hKl	d Å	hkl	d Å
100	7.893	080	1.373
003	5.081	258	1.356
103	4.425	620	1.260
104/202	3.467	268	1.250
220	3.148	0·2·12	1.237
024	3.129	545/527	1.234
005	2.948	3011	1.225
040	2.738	630	1.215
204	2.708	2·0·12	1.212
240	2.244	086	1.210
400	1.928	644	1.119
008	1.913	2·4·12	1.109
064	1.647	700	1.107
228	1.635	0·10·4	1.0549
440	1.584	628	1.0494
434	1.541	4·2·12	1.0437
		705	1.0249

Table III. Lattice constants for α- and β-PbO_x

α-PbO_x, Å	β-PbO_x, Å
$a_0 = 7.72$	$a_0 = 7.76$
$b_0 = 10.98$	$b_0 = 10.98$
$c_0 = 15.31$	$c_0 = 15.31$

$$\sin^2\theta_{hkl} = h^2\frac{\lambda^2}{4a^2} + k^2\frac{\lambda^2}{4b^2} + l^2\frac{\lambda^2}{4c^2}$$

where θ is the diffraction angle, hkl are the indexes of the reflecting plane, λ is the wavelength (copper radiation), and *abc* are the dimensions of the unit cell. All the observed reflections were indexed. Table III presents the data for the unit cell of α- and β-PbO_x; both unit cells were determined to be orthorhombic.

It is concluded from the similarity of the x-ray powder patterns and the unit cell dimensions that α- and β-PbO_x are identical materials. It appears that β-PbO_x is simply a more perfectly ordered structural equivalent of α-PbO_x. This accounts for the well-defined multiple peaks in the β pattern, and some smaller peaks, not observed in the α pattern.

These crystallographic results agree well with the data of Bystrom (27). The two sets of data are compared in Table IV. The agreement is particularly good for the β-PbO_x pattern. The unit cell turned out to be a multiple of Bystrom's cell. With the unit cell chosen here, it was possible to *index satisfactorily all the observed reflections of both the α- and β-PbO_x materials.* It should be pointed out that Bystrom prepared the PbO_x materials differently, "α-PbO_x" by thermal decomposition of β-PbO_2 at 400°C for 11 hr, or by hydrothermal treatment with NaOH at 290°C; β-PbO_x by thermal decomposition of β-PbO_2 at 400°C for 37 hr. Bystrom suggests for α-PbO_x a monoclinic unit cell with $\beta = 88.68°$, $a_0 = 7.72$Å, $b_0 = 10.81$Å, $c_0 = 11.48$Å. However, he expresses some concern about the purity of his α-PbO_x sample and admits that his data may not be accurate due to the very diffuse nature of the reflections at the high angles. Also, his value of $\beta = 88.68°$ is so close to 90° (and the orthorhombic system) that no conclusive distinction can be made on the basis of powder data. The same conclusion was recently reached by Reuter (29).

Table IV. Comparison between Bystrom's data (27) and results of the present paper (ESB)

α-PbO_x Bystrom	β-PbO_x Bystrom, Å	β-PbO_x Multiple Bystrom, Å	β-PbO_x ESB, Å
7.72Å	3.89	7.78	7.76
10.81Å	5.49	10.98	10.98
11.48Å	3.82	15.28	15.31
β-88.68°			

Manuscript received May 1, 1961; revised manuscript received Oct. 24, 1961. This paper was prepared for delivery before the Houston Meeting, Oct. 9-13, 1960.

Any discussion of this paper will appear in a Discussion Section to be published in the December 1962 JOURNAL.

REFERENCES

1. P. Rüetschi and B. D. Cahan, *This Journal*, **104**, 406 (1957).
2. P. Rüetschi and B. D. Cahan, *ibid.*, **105**, 369 (1958).
3. P. Rüetschi, R. T. Angstadt, and B. D. Cahan, *ibid.*, **106**, 547 (1959).
4. P. Rüetschi and B. D. Cahan, *ibid.*, **106**, 1079 (1959).
5. N. Kameyama and T. Fukumoto, *J. Soc. Chem. Ind. (Japan)*, **49**, 154 (1956).
6. A. I. Zaslavski, Yu. Kondrashev, and S. Tolkachev, *Doklady Akad Nauk.*, **75**, 4, 559 (1950).
7. R. Weiss and R. Faivre, *Compt, rend.*, **245**, 1629 (1957).
8. I. G. Kiseleva and B. N. Kabanov, *Doklady Akad, Nauk, SSSR*, **122**, 1042 (1958).
9. I. I. Astachov, I. G. Kiseleva, and B. N. Kabanov, *ibid.*, **126**, 1041 (1959).
10. H. Bode and E. Voss, *Z. Elektrochem*, **60**, 1053 (1956).
11. M. Fleischmann and M. Liler, *Trans. Faraday Soc.*, **54**, 1370 (1958).
12. S. J. Bone, Symposium on Batteries, Signal Research and Development Establishment, Ministry of Supply, Christchurch, Hants. England, Oct. 1958.
13. J. Burbank, *This Journal*, **104**, 693 (1957).
14. J. Burbank, *ibid.*, **106**, 369 (1959).
15. S. Ikari, S. Yoshizawa, and S. Okada, *J. Electrochem. Soc. Japan*, **27**, E-223 (1959).
16. S. Ikari, S. Yoshizawa, *ibid.*, **27**, E-247 (1959).
17. W. Feitknecht, *Z. Elektrochem.*, **56**, 595 (1958).
18. D. Spahrbier, Dissertation Technische Hochschule Stuttgart, April 1960.
19. V. H. Dodson, *This Journal*, **108**, 401, 406 (1961).
20. N. Palmaer, *Z. Elektrochem.*, **29**, 415 (1923).
21. U. B. Thomas, *This Journal*, **94**, 42 (1948).
22. A. Kittel, Dissertation Techn. Hochschule Prag, Czechoslovakia, 1944.
23. H. J. Schuster, *Chem. Ing. Techn.*, **28**, 654 (1956).

24. L. H. Piette and H. E. Weaver, *J. Chem. Phys.*, **28**, 735 (1958).
25. D. A. Frey and H. E. Weaver, *This Journal*, **105**, 930 (1960).
26. J. Rocard, M. Bloom, and L. Robinson, *Can. J. Phys.*, **37**, 522 (1959).
27. A. Bystrom, *Arkiv for Kemi, Mineralogi och Geologi*, **20A**, [11], 1 (1945).
28. G. Butler and J. L. Copp, *J. Chem. Soc.*, **1956**, 725.
29. B. Reuter and W. Töpfer, *Angewandte Chemie*, **71**, 137 (1959).
30. B. D. Cahan and P. Rüetschi, *This Journal*, **106**, 543, (1959).
31. H. A. Smith, J. C. Posey, and C. O. Thomas, *Rev. Sci, Instr.*, **30**, 202 (1959).
32. H. Bode and E. Voss, *Electrochemica Acta*, **1**, 318 (1959).
33. W. J. Hamer, *J. Am. Chem. Soc.*, **57**, 9 (1935).

Oxide Films on Aluminum

I. Ionic Conduction and Structure

Michael J. Dignam[1]

Aluminium Laboratories Ltd., Kingston, Ontario, Canada

ABSTRACT

Films formed on superpurity aluminum and certain of its binary alloys were studied employing anodic polarization and electron transmission microscopy. Specimens were prepared by electropolishing followed by either oxidation in dry oxygen, anodic oxidation, or anodic oxidation followed by high-temperature annealing. The nucleation and growth of gamma alumina crystallites during oxidation at 450°C and the inhibiting effect of copper and particularly silicon on this process was explained by assuming that an 0.001% magnesium impurity was responsible for the nucleation. The change in ionic conduction of anodic oxide films on annealing was interpreted as arising primarily from a decrease in the number of aluminum ions which can become current carriers, rather than a change in activation energy or activation distance. Annealed anodic films and "amorphous" films formed in dry oxygen could not be distinguished. The observations in general, are consistent with Wilsdorf's model for the "amorphous" oxide films, randomly oriented "molecular" groups.

It has been known for some time that films formed on aluminum in dry oxygen above about 500°C exhibit the structure of gamma alumina, whereas for films formed below about 500°C x-ray diffraction analysis yields only diffuse halos characteristic of either amorphous material or material composed of extremely small crystals (1-9). From an examination of the literature (10-12) it can be concluded that anodic oxide films formed at room temperature and low current densities in a nonsolvent electrolyte also give rise to diffuse halo x-ray diffraction patterns.[2] The original reason for undertaking this investigation was to compare the ionic conduction of films formed in dry oxygen with that of films formed by anodic oxidation. This information was desired in order to adapt an electrometric method developed by Hunter and Fowle (13) for determining anodic oxide film thicknesses, to the measurement of thicknesses of oxide films formed in dry oxygen. The completed investigation, however, was more general in scope. It provides information concerning the nature of the so called "amorphous" films, the difference in properties between anodic oxide films and those formed in oxygen at elevated temperatures, and the nucleation process associated with the appearance of gamma alumina crystallites in the oxide film.

[1] Present address: Department of Chemistry, University of Toronto, Toronto, Ontario, Canada.

[2] Stirland and Bicknell (11) imply that the applied voltage is the fundamental parameter which determines whether the film is "amorphous" or crystalline. It is more likely, however, that the anodic current density (or field strength) is the fundamental parameter (10), the voltage, for fixed cell and circuit geometry, merely limiting the maximum current obtained.

The bulk of the data was obtained from anodic polarization measurements made in an aqueous boric acid solution on aluminum and aluminum alloy specimens. These specimens were treated previously by anodizing, by anodizing followed by annealing in helium at temperatures of 250° and 450°C, and by exposure to dry oxygen at temperatures of 250°, 350°, and 450°C. In addition electron transmission micrographs were taken of films stripped from certain aluminum specimens in order to elucidate oxide crystallization effects.

Apparatus

The vacuum furnace assembly was designed to permit the simultaneous thermal treatment of a number of specimens. Samples could be moved by a magnetic counterweight arrangement from the furnace zone proper into a water-cooled head piece while the apparatus was under vacuum (or controlled atmosphere).

The cylindrical resistance furnace had three windings controlled by two independent thermocouple activated pyrometric controllers. The temperature was maintained uniform and constant to ±0.5°C over at least 14 in. of the furnace. (Specimens never exceeded 6 in. in length.) Specimens required about 10 min to reach thermal equilibrium when lowered into the furnace in 5 mm Hg pressure of helium and, on removal, cooled from 350° to 300°C in 30 sec and from 300° to 250°C in 60 sec.

The vacuum system was of conventional design. A liquid air trap was placed between the specimens and the rest of the system to prevent mercury

contamination. Helium was purified, as required, by passage through a bright metallic sodium column. Oxygen was purified by passing it through Ascarite, phosphorus pentoxide, then distilling it from a liquid air trap retaining the middle fraction in a storage volume.

Experimental Procedure

Materials.—Experiments were carried out on 0.020 gauge sheet rolled from ingot of superpurity and superpurity base binary alloys containing 0.19% Ga; 0.01 or 0.06% Fe; 0.24 or 1.78% Si; 0.53 or 2.20% Mn; 0.08, 0.19, 1.51 or 6.0% Cu. The major impurities in the superpurity metal were 0.003% Fe, 0.001% Cu, 0.001% Mg, and 0.001% Si.

Sample preparation.—Samples 0.25 × 8 in. were cut from the 0.020 gauge sheets and formed into symmetrical "hair pin" shapes. After vacuum annealing for 1 hr at 543°C (this temperature was chosen as the highest safe temperature for annealing Al + 6% Cu), the samples were electropolished for 1 min at about 15°C and 17v (~ 0.5 amp/cm^2) in a bath containing 1 part 71% perchloric acid to 5 parts anhydrous methanol by volume. Immediately after polishing, a sample was rinsed 15 sec in absolute methanol, 45 sec in a jet of distilled water, then dried in a clean, dry, air blast and stored in a desiccator over activated alumina.

Oxide formation.—To form high-temperature oxide films, the electropolished samples were placed on the furnace sample holder and the system evacuated and kept at $< 10^{-6}$ mm Hg pressure for about 20 hr with the furnace at temperature and the samples in the cold furnace head. The samples were then lowered into the hot zone in 5 mm Hg pressure of helium. After 0.5 hr, 0.2 atm of purified oxygen was introduced. When the desired oxidation period had elapsed, the samples were raised into the cold furnace head, allowed to cool, removed, and stored in a dry desiccator until required.

Anodic oxide annealing.—Certain electropolished superpurity samples were anodized to various voltages at a constant current density of about 70 μa/cm^2. This was achieved by increasing the voltage at a steady rate of 1.75 v/min. The anodizing bath consisted of an aqueous ammonium bicarbonate solution (40 g/l, pH ≃ 7.5) held at 30°C. Sets of anodized samples were evacuated 20 hr in the cold furnace head as above then annealed in purified helium for the desired period, cooled, removed, and stored in a dry desiccator until required. Ammonium bicarbonate was used so that any of the salt which might remain on the samples would largely be removed during the subsequent vacuum treatment.

Electron micrographs.—Electron transmission micrographs were made of certain of the oxide films formed during high-temperature oxidation. The films were isolated by dissolving the metal in a 2% bromine-methanol solution.

Polarization measurements.—Polarization measurements were made employing one half a "hair pin" sample as anode suspended within a cylindrical wire gauze platinum cathode (surface area ~ 40 cm^2). The electrolyte, which was maintained at 30.0°C, consisted of an aqueous solution, 0.67M in boric acid and neutralized to pH 6 with ammonia. The cell was supplied with a d-c potential increasing steadily at the rate of 1.75 v/min, the selection of this rate being arbitrary to a large extent. The cell current was recorded with a strip chart recorder.

Providing that the cathodic overpotential and iR drop in the electrolyte and external circuit can be neglected, it is apparent that the anodic overpotential, V, is given by $V = V' + E$ where E is the reversible emf for the cell reaction, $2Al + 3H_2O = Al_2O_3 + 3H_2$ and V' is the applied potential (all terms taken as positive). In the present case, for anodic current densities up to 11 μa/cm^2 or more, both these terms were found to be less than 10 mv and hence negligible. The voltage values reported, therefore, are $V = V' + E$, where E was calculated to be 1.42v from the thermodynamic data compiled by Thompson (14). Provided that space charges at the metal-oxide and oxide-electrolyte interface are small, for current densities less than about 11 μa/cm^2, V will represent within about 10 mv the voltage drop across the oxide film.

Experimental Results

Polarization curves.—Figures 1 to 6 are a selection of tracings from the original polarization curves. The curves were quite reproducible in shape, although the peak heights and steady-state currents were reproducible only to about 10% because of lack of careful control of the sample area exposed during measurement.

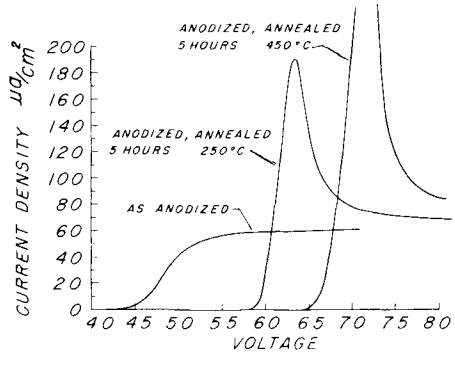

Fig. 1. Influence of annealing on the polarization curve for anodized superpurity.

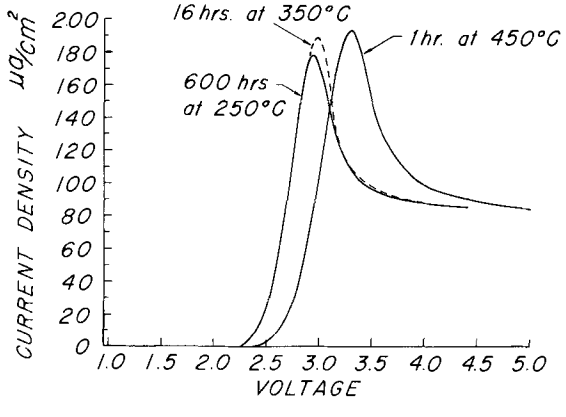

Fig. 2. Influence of oxidation temperature on the polarization curve for superpurity.

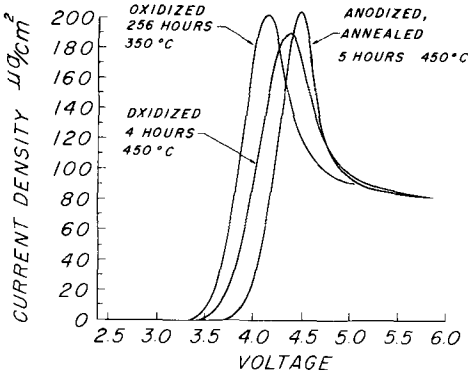

Fig. 3. Comparison of polarization curves for superpurity treated by anodic oxidation and annealing, with those for superpurity treated by oxidation in oxygen.

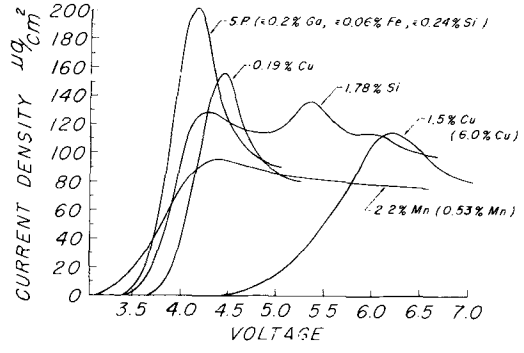

Fig. 4. Influence of alloying additions on the polarization curve for specimens oxidized 256 hr at 350°C. (Alloys with the compositions shown in brackets have polarization curves the same as the one illustrated.)

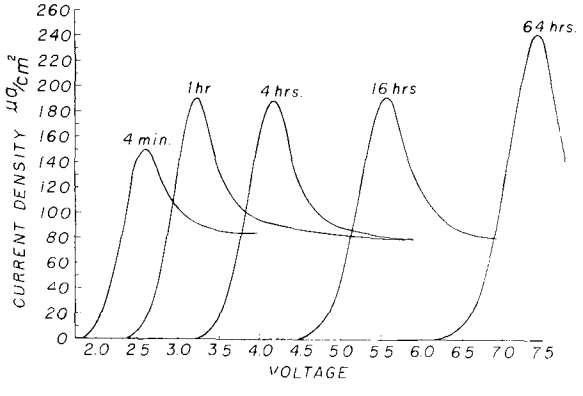

Fig. 5. Influence of oxidation time at 450°C on the polarization curve for superpurity + 0.24% silicon.

Electron transmission micrographs.—Figure 7 represents a selection of the micrographs obtained for electropolished samples oxidized in 0.2 atm of oxygen.

Annealing results.—The results obtained from polarization measurements on the anodized samples and the annealed anodized samples are presented in Fig. 8. The "barrier voltage" values are anodic overpotentials obtained in the following way. For a sample anodized to about 1 v, the potential was read at a point on the polarization curve corresponding to a current density of about 1 $\mu a/cm^2$, those anodized to 6v, at 6 $\mu a/cm^2$, and so on. This procedure was adopted in anticipation of the interpretation of the results. The slopes of the resulting straight lines in barrier volts per anodizing volt

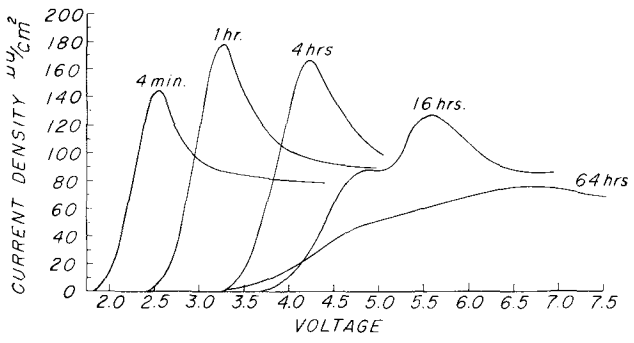

Fig. 6. Influence of oxidation time at 450°C on the polarization curve for superpurity.

are 0.83 for freshly anodized samples, 1.08 and 1.11 for samples annealed 1.5 and 5 hr at 250°C, and 1.18 and 1.20 for samples annealed 0.5 and 5 hr at 450°C.

Interpretation of Results

Oxide nucleation phenomena.—From electron transmission micrographs, conduction measurements, and weight gain data, it is apparent that the oxide film on superpurity aluminum undergoes a discontinuous change in properties during oxida-

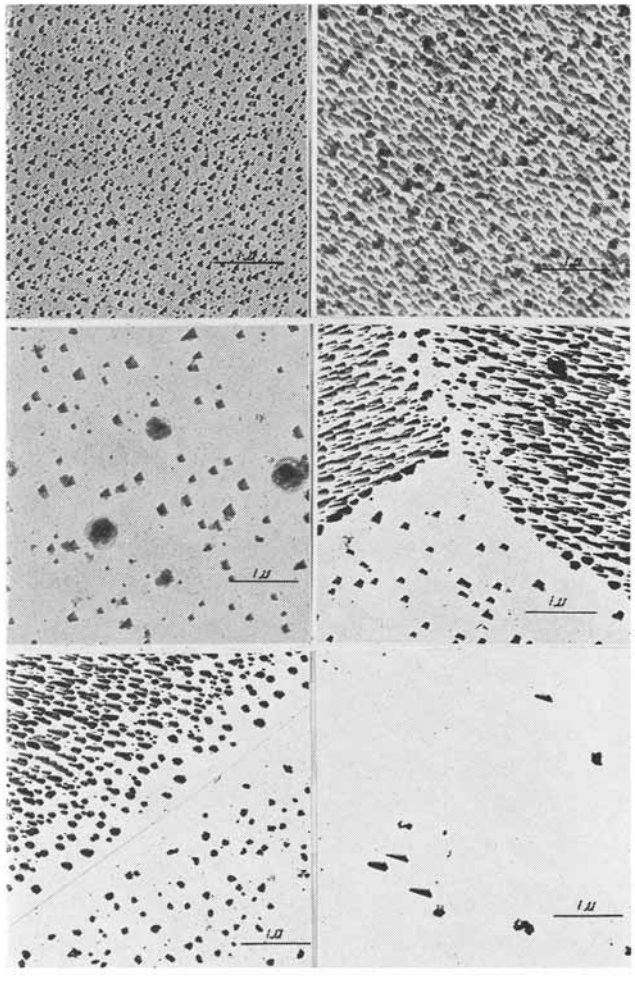

Fig. 7. Electron transmission micrographs of oxide films formed on aluminum at 450°C. (a) (top left) superpurity oxidized 16 hr, (b) (top right) and (c) (center left) superpurity oxidized 64 hr, (d) (center right) superpurity + 0.06% Fe, oxidized 64 hr, (e) (bottom left) superpurity + 0.53% Mn, oxidized 64 hr, and (f) (bottom right) superpurity + 0.24% Si, oxidized 64 hr.

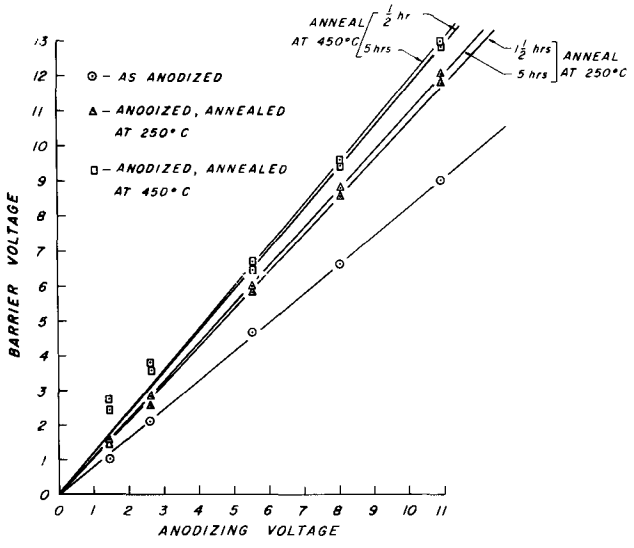

Fig. 8. Influence of annealing on the "barrier voltage" values for anodic films.

tion in pure oxygen at 450°C. Between 4 and 16 hr at 450°C, the oxidation rate is found to increase somewhat, falling off once again beyond 16 hr (15). Polarization curves for superpurity samples oxidized at 450°C for 16 or 64 hr show distinct anomalies not present for samples oxidized for 4 hr or less (Fig. 6) or oxidized at lower temperatures (Fig. 2). It is known (1-9) that sufficiently prolonged oxidation of aluminum at a temperature of about 450°C will lead to the formation of gamma alumina; x-ray diffraction measurements on films formed at appreciably lower temperatures or for sufficiently short oxidation periods yield only diffuse patterns. There is little doubt, therefore, that the decorations apparent in the transmission micrographs (Fig. 7a, b, and c) represent crystallites of gamma alumina which have nucleated from the thin base "amorphous" film. No evidence of these crystallites could be found for oxidation periods of 4 hr or less at 450°C, or for oxidation periods up to 256 hr at 350°C or 600 hr at 250°C. A surface discoloration was observed to accompany the formation of these crystallites, a bluish haze or bloom, which varied in shading from one metal grain to the next.

The regular orientation of the oxide crystallites within a metal grain and the change in orientation across a grain boundary (Fig. 7) suggest an epitaxial relationship between the crystallites and the metal. Although such a relationship is by no means certain, the postulate is strengthened by evidence that nucleation of the crystallites takes place near the metal-amorphous oxide interface. This evidence is provided by the observed variation from grain to grain of the surface concentration of the crystallites, implying preferred metal planes for nucleation. The above observations are only consistent with nucleation near the metal oxide interface, unless long range order in the amorphous film, a contradiction of terms, is assumed. (The amorphous films are ~ 40Å thick). Crystal nucleation at the metal-oxide interface was found by Vermilyea (10) during high field anodizing of tantalum.

The nucleation sites do not appear to be related to general impurities, since additions of 0.53% Mn, 0.06% Fe, or 0.2% Ga cause no observable change in the nucleation behavior. The presence of copper, and to a greater extent silicon, was found, however, to have a very appreciable affect on the induction period for crystal nucleation during oxidation at 450°C. From a series of polarization curves (curves not shown) the induction periods were estimated to be about 7 hr for superpurity, and 10 hr and 20 hr for the 0.2 and 1.5% Cu alloys, respectively. Copper was also found to affect the conduction properties and rate of growth of the amorphous oxide film; this effect will be discussed later. The presence of 0.24% silicon, however, appears to have no appreciable effect on the amorphous oxide or oxidation behavior except to increase the induction period for crystal nucleation. From Fig. 7f, and on comparing Fig. 5 and 6, it is apparent that little or no crystal nucleation has taken place on this alloy after 64 hr oxidation at 450°C.

It has been observed by Brouckère (1) that addition of magnesium to aluminum decreases the temperature at which gamma alumina first becomes apparent on oxidation in dry oxygen. That the presence of magnesium should promote nucleation of gamma alumina is not at all surprising, since gamma alumina is isomorphous with spinel, $MgAl_2O_4$ (16). It is reasonable to suggest, therefore, that in the present experiments the nucleation sites are in some way related to the 0.001% magnesium impurity. The observations may be explained qualitatively if it is assumed that clusters of magnesium atoms trapped by vacancy-like defects at the metal-oxide interface form the nucleation sites. The attraction of the grain boundaries for vacancies and impurities would tend to deplete the areas adjacent to the grain boundaries of such nucleation sites, which agrees with the observations (see particularly Fig. 7e). Preferred planes for nucleation would of course be expected. Again, soluble impurities which could compete with the trapping sites for magnesium atoms would be expected to reduce the probability of formation of a nucleation site. Thus the influence of copper and silicon can be explained. The attraction of copper and magnesium atoms for one another would be expected since copper atoms are smaller, while magnesium atoms are larger than the host atoms, aluminum. The greater influence of silicon can be attributed to weak chemical bonding between magnesium and silicon atoms. (Magnesium silicide is a moderately stable intermetallic compound.)

Ionic Conduction—General

The most striking feature of the polarization curves (Fig. 1 to 6) is the high current peak which occurs for all films formed or annealed at high temperatures. Polarization curves for identically anodized samples, as anodized, and annealed at 250° and 450°C, respectively, are compared in Fig. 1. Annealed samples exhibit a current peak, and the "barrier voltage" is increased over that for an unannealed sample. For polarizing potentials greater than about 12v, the current densities for the samples

illustrated in Fig. 1 become the same within experimental error. Also, the total charge passed in the three cases (determined by integration under the curves) on anodizing to say 12v, is very nearly the same. The suggestion is, therefore, that the change brought about in the film by annealing is reversed by further anodizing. Although some such effect would be predicted by the theory of transient ionic conductivity proposed by Bean, Fisher, and Vermilyea (17), the very long observed decay times for the transients (> 1 min) is far more consistent with the postulate of a more major change in the film, perhaps a rearrangement of the amorphous film structure.

A comparison of polarization curves for samples with films of about the same thickness formed by oxidation at 250°, 350°, and 450°C is presented in Fig. 2. The three curves are, within experimental error, identical in shape. A similar comparison for films formed by oxidation at 350° and 450°C, and by anodizing and annealing at 450°C is presented in Fig. 3. Again, the three curves are nearly identical in shape. The conduction properties and hence film structure are therefore apparently the same for samples oxidized in the range 250°-450°C and for samples anodically oxidized and annealed at 450°C. Anodic films annealed for 5 hr at 250°C do not exhibit quite the same conduction properties as the above group. It is possible, however, that on prolonged annealing, agreement would be obtained, since films formed by oxidation at 250°C conform to this group.

It has been suggested to the author that annealing anodic films results in the loss of water which is assumed to have been incorporated into the oxide structure during the formation of the film. This explanation for the observed change in conduction properties on annealing, however, appears rather unlikely. This is so because on further anodizing an annealed sample, the conduction properties of the film return to those of a freshly anodized sample, implying a re-hydration of the anhydrous film if the postulate mentioned is accepted. It is difficult to conceive of a mechanism by which this re-hydration could take place during anodizing in a few minutes at room temperature. The transport number for the hydroxyl ion would be expected to be insignificant compared to that for the aluminum ion, and protons would hardly diffuse against a potential gradient of about 10^7 v/cm, the field strength present in the film during anodizing. It has been assumed, therefore, that these anodic oxide films are essentially anhydrous, differing only slightly from films formed in dry oxygen.

Figure 4 illustrates the effect of certain alloying additions on the polarization curves. Small additions of Ga, Fe, Si, or Cu appear to have little or no effect on the conduction properties of the film formed during oxidation. The effects observed for the 1.78% Si alloy and the manganese alloys are probably due to the presence in the metal of a substantial second phase, rather than a change in the film properties. This view is supported in the case of the 0.54% Mn alloy by the fact that weight gain data for oxidation of this alloy at 450°C does not differ from that for superpurity aluminum (15). On the other hand there is little doubt that copper effects a pronounced change in the conduction properties of the oxide films. In the following paper (15) it is concluded from a comparison of weight gain and barrier voltage data for the oxidation at 450°C of superpurity and superpurity plus 1.5% Cu that the ratio of film thickness to barrier voltage for the 1.5% Cu alloy is about 2.5 times that for superpurity aluminum. This indicates that the specific ionic conductivity for the amorphous film on this alloy is substantially greater than that for the amorphous film on superpurity. Such an effect would be expected providing ionic conduction through the amorphous film can be considered as involving an interstitial cation (or pseudo interstitial cation) transport mechanism. The substitution of divalent copper for trivalent aluminum ions in the oxide would then lead to an increase in the equilibrium concentration of interstitial cations. It is of interest to note that, of the alloying elements studied, only copper gives rise to an ion of radius close to that for aluminum, but differing from it in valency.

A comparison of the polarization curves for samples of superpurity and superpurity + 0.24% Si oxidized at 450°C is of interest. At 16 or 64 hr oxidation, the superpurity samples have developed oxide crystallites, whereas those of superpurity + 0.24% Si have not to any appreciable extent. The first current peak for the superpurity sample oxidized 16 hr is very likely due, therefore, to conduction through the crystallites. The second peak, falling in the same position as that for the 0.24% Si alloy, is undoubtedly due to conduction through the remaining amorphous film. After 64 hr oxidation, this second peak is very much reduced in agreement with the observed reduction in the proportion of the original amorphous film remaining (*cf.* a and b, Fig. 7).

Accepting the above interpretation it follows that the specific ionic conductivity of the crystallites is considerably higher than that for the amorphous film. (Electronic contribution to the measured current was shown experimentally to be small.) The fact that the crystallites grow to a greater thickness than does the amorphous film (see Fig. 7) also suggests a higher ionic transport coefficient for the crystallites.

According to the views of Ervin (18), the structure of gamma alumina in all its modifications differs from spinel, $MgAl_2O_4$, only in that 8 cations must be distributed among sites occupied by 9 cations in the spinel lattice. These various crystal modifications, resulting from different cation distributions, would not be expected to have greatly differing cationic diffusivities or conductivities. Also the observed effect of copper on the ionic conductivity of the amorphous film can only be expected if ionic conductance in the film is by interstitial cations. Ionic conductance in gamma alumina would be expected to be by cation vacancies, since it possesses as an essential part of its structure one vacancy per 9 cation sites. It seems unlikely, therefore, that the amorphous oxide has a proper gamma

alumina type structure. A high cationic transport coefficient for gamma alumina is to be expected because of the high vacancy concentration. It is, however, difficult to conceive a crystalline structure, metastable with respect to gamma alumina, yet having a much lower transport coefficient. Perhaps this difficulty can be resolved by considering the amorphous film to be made up of randomly oriented "molecular" units, as suggested by Wilsdorf (9).[3]

Ionic Conduction—Interpretation of Annealing Effects

The interpretation of the results illustrated in Fig. 8 has been based on the high field ionic conductance theory of Bean *et al.* (17) as this theory appears to provide the best explanation for ionic conductance effects in amorphous films on tantalum and aluminum (19). Only an outline of the development given by Dewald (19) is presented here. It is assumed that during anodic oxidation, metal ions are the mobile species and that the rate-controlling step is the passage of ions through the film. In the bulk of the film, every lattice ion[4] is a potential source of an ion-vacancy pair, the rate of production of ion-vacancy pairs being given by

$$\frac{dn^+}{dt} = \frac{dm^+}{dt} = (N_o - m)\nu \exp - (W - E\lambda q)/kT \qquad [1]$$

where n is the carrier concentration, m vacancy concentration, N_o concentration of lattice sites, ν frequency of atomic vibration, 10^{12} sec^{-1}, W activation energy for the creation of an ion-vacancy pair, λ the distance from the equilibrium to the position of the maximum in the potential energy diagram of an ion around a lattice site, q charge of the interstitial ion, E electric field in the film, k Boltzmann constant, and T absolute temperature.

It is further assumed that whenever an interstitial ion passes within an area, σ, in the vicinity of an immobile vacancy, it will be captured by that vacancy; the rate of annihilation of ion-vacancy pairs is therefore given by

$$\frac{dn^-}{dt} = \frac{dm^-}{dt} = \frac{i'\sigma m}{q} \qquad [2]$$

where i' is the current density in the oxide film. The conduction through the film is assumed to depend exponentially on the field strength according to Eq. [3]

$$i' = 2qa\nu n \exp - (U - Eaq)/kT \qquad [3]$$

where U is the activation energy for diffusion of an ion through the oxide, and a is the activation distance associated with U.

Neglecting space charge in the film and current associated with charging the electrolyte-oxide-metal capacitor, and assuming $n \cong m < No$, Eq. [1], [2], and [3] become

$$\frac{dn}{dt} = N_o \nu \exp - (W - E\lambda q)/kT - i\sigma n/q \qquad [4]$$

and

$$i = 2qa\nu n \exp - (U - Eaq)/kT \qquad [5]$$

where i is the external, observed current density.

The solution of Eq. [4] and [5] for the case of a linearly increasing applied voltage (the conditions obtaining during a polarization measurement) is very complicated; a useful solution can be obtained, however, for certain limiting conditions. For amorphous films either formed or annealed at high temperatures, the concentration of interstitial ions and vacancies will be small due to the high recombination rate caused by thermal diffusion of the ions within the film. During the early stages of a polarization measurement, the rate of annihilation of ion-vacancy pairs may therefore be neglected by comparison with their rate of formation, giving:

$$\frac{dn}{dt} = N_o\nu \exp - (W - E\lambda q)/kt \qquad [6]$$

Substituting $E = V/\delta$ and $t = V/R$ (where V is the voltage across the film, δ the film thickness, and R the rate of voltage rise, a constant) and integrating assuming δ independent of time (which is a good approximation provided that the total charge passed is small compared to the film thickness) the following equation is obtained:

$$n - n_o = \frac{N_o \nu kT\delta}{R\lambda q}(\exp - W/kT)\left(\exp\frac{V\lambda q}{\delta kT} - 1\right) \qquad [7]$$

where n_o is the concentration of interstitial ions at $t = V = 0$. As soon as an appreciable current is flowing, n will be $> n_o$, and $\exp V\lambda q/\delta\, kT >>> 1$. To a first approximation, therefore, n is given by:

$$n = \frac{N_o \nu kT\delta}{R\lambda q}\exp - (W - V\lambda q/\delta)/kT \qquad [8]$$

Substituting this value for n into Eq. [5], the following relation is obtained:

$$V = \frac{kT\delta}{(\lambda + a)q}\ln\left(\frac{R\lambda \exp (W + U)/kT}{2a\nu^2 N_o kT}\frac{i}{\delta}\right) \qquad [9]$$

The logarithm term has a value of about 100; a factor of 10 error in the value of n resulting say from the use of Eq. [8], will therefore cause an error of only about 2.5% in V, calculated using Eq. [9]. It should be emphasized that Eq. [9] will be valid only for the initial current rise portion of polarization curves for samples with amorphous films formed or annealed at high temperatures. It predicts a linear relationship between the barrier voltage, V, and the film thickness, δ, where the voltage measurements are made at current densities

[3] Such a postulate does not preclude the possibility that the "intermolecular" order in the amorphous film is essentially the same as the short range order in gamma alumina. It would be expected that inter atomic forces within sufficiently small "crystals" would differ considerably from those within macro crystals.

[4] Dewald (19) defines, for an amorphous solid, a lattice cation as a cation whose charge is locally compensated, an interstitial cation as one whose charge is not locally compensated, and a cation vacancy as a region of negative charge which is not locally compensated.

such as to maintain (i/δ) approximately constant. This is in agreement with the experimental dependence shown in Fig. 8, since the film thickness is proportional to the anodizing voltage (20). (It is believed that the high barrier voltage values for the samples anodized to 2.5v and less and annealed at 450°C were caused by oxidation during annealing, arising from the presence of adsorbed oxygen or water.) Provided annealing is carried out under such conditions as to reduce n sufficiently (*i.e.*, make n_o sufficiently small) Eq. [9] clearly predicts the barrier voltage *vs.* thickness curves to be independent of annealing conditions, which is contrary to the experimental results.

Vermilyea (21) concludes from conduction measurements on tantalum oxide films annealed under various conditions that the conductance theory by Bean *et al.* is inadequate. Dewald (19), however, studying transient conduction effects during anodic oxidation of tantalum at 25°C and over a moderate range of current densities, obtained excellent confirmation of the theory. It appears to be reasonable to assume, with Vermilyea, that the structure of the oxide film modifies on annealing. Dewald's results, however, suggest that the theory of Bean *et al.* is applicable, providing the measurements are made on films all of which have the same structure. Some support for this notion is also provided by the results in Fig. 8. The variation in the observed slopes (Fig. 8) for samples annealed at different temperatures can perhaps be explained, therefore, in terms of a difference in structure of the oxide films and hence different values for the parameters of Eq. [9]. In the following calculation an attempt is made to determine which of the parameters is primarily responsible for the change in conduction properties observed on annealing.

Re-arranging Eq. [9], the following is obtained:

$$q(\lambda + a)/2 = \frac{\delta}{V}\frac{kT}{2}\ln\frac{R(i/\delta)\lambda}{kT/2\,\nu^2 a N_o} + \frac{\delta}{V}\frac{(W+U)}{2} \qquad [10]$$

For films annealed 5 hr at 450°C, δ/V is calculated from the value 12.7 Å/v (22) for converting barrier voltage to film thickness for the as-anodized samples and from the slopes obtained from Fig. 8. Thus $\delta/V = 12.7 \times 0.83/1.20 = 8.8$ Å/v. $kT = 0.0261$ ev at 30°C, the temperature at which polarization measurements were made. $R = 2.92 \times 10^{-2}$ v/sec, and $i/\delta = 1.0$ μa/cm^2 per anodizing volt $= 7 \times 10^{19}$ electrons cm^{-3} sec^{-1}, the current density to film thickness ratio used to obtain the barrier voltage values, $(W + U)/2 = 1.76$ ev, from kinetic measurements on the oxidation of aluminum in the temperature range 250°-450°C (15). The use of this value appears to be justified, first, because the air oxidation kinetics are in agreement with Eq. [4] and [5], and second, because the conduction properties of annealed anodic and high temperature air-formed films appear identical, as discussed earlier. $\Omega\nu(2N_o\, a/\sigma)^{1/2} = 7.5 \times 10^{-2}$ cm-sec^{-1}, from kinetics of air oxidation (15). Ω is the volume per metal ion in the oxide and is 2.34×10^{-23} cm^3 for Al_2O_3 of density 3.6g cm^{-3}. $\sigma/\lambda = 10^{-7}$ cm, a value estimated from the results of Dewald (19) and Vermilyea (21) on tantalum and aluminum. An error of a factor of 10 in this estimate will introduce an error of less than 2.5% in the calculated value of $q(\lambda + a)/2$.

On making the above substitutions, the result $q(\lambda + a)/2 = 11.3$ eÅ is obtained.

In order to make a similar calculation for $q(\lambda + a)/2$ for the as-anodized films, a somewhat different expression must be used, since the assumptions made in deriving Eq. [10] are not applicable in this case. The solution of Eq. [4] and [5] for steady state conditions (*i.e.*, $dn/dt = 0$) can be written as follows:

$$q(\lambda + a)/2 = \frac{kT}{2E}\ln\left(\frac{i^2(\sigma/a)}{q^2\nu^2 2N_o}\right) + \frac{W+U}{2E} \qquad [11]$$

During the formation of the anodic films under discussion, steady state conditions prevailed, permitting the use of Eq. [11]. The samples were anodized at a constant current density of about 7×10^{-5} amp/cm$^2 = i$. By comparing the voltage to which the samples were anodized with the corresponding barrier voltage (Fig. 8) and employing the value 12.7Å per barrier volt, one obtains $1/E = \delta/V = 0.83 \times 12.7 = 10.5$ Å/v. Since the activation energy for anodic oxidation of aluminum determined by Charlesby (20), 1.6-1.8 ev, is the same within experimental error as the value for high-temperature oxidation, the value $(W + U)/2 = 1.76$ ev was used for this calculation as well. Setting $N_o = 4.27 \times 10^{22}$, the concentration of aluminum ions in Al_2O_3 of density 3.6 g/cm^2, $\sigma/a = 10^{-7}$ cm (an estimate), $\nu = 10^{12}$ and $kT = 0.026$ ev, one obtains $q(\lambda + a)/2 = 10.5$ eÅ.

Vermilyea (21) obtained values of $q(\lambda + a)/2$ for aluminum oxide formed by anodizing. His film thickness measurements were based on a dielectric constant for the oxide films of 10. Since the present film thickness measurements are based on the results of van Geel and Schellen (22) (*i.e.*, their value 12.7 Å/barrier volt was employed) before comparing the present values with those of Vermilyea, his results were recalculated using van Geel and Schellen's value for the dielectric constant, 8.7. Vermilyea's results then become $q(\lambda + a)/2 = 9.2$ eÅ and 10.5 eÅ for films formed at current densities of about 2 and 0.2 ma/cm^2, respectively, as compared to the present values of 10.5 eÅ for films formed at 0.07 ma/cm^2, and 11.3 eÅ for films annealed at 450°C. The agreement between these results is quite amazing and probably somewhat fortuitous. In addition to the values for films formed at low current densities agreeing so well, the trend of increasing $q(\lambda + a)/2$ for increasing order in the film structure is preserved. (It is assumed that films formed at high current densities would be the most disordered, those formed at low current densities the next, and annealed films the most ordered.) From the results of Bernard and Cook (23), obtained from room temperature anodic oxidation measurements, one can calculate a mean value for $q(\lambda + a)/2$ of 12.5 eÅ ± 7%. Comparing

this value with the value of 12.2 Å/v obtained from their results for films formed at 0.07 ma/cm², it can be seen that the ratio of these numbers is in excellent agreement with the ratio of the corresponding values reported herein (*i.e.*, 10.5 eÅ and 10.5 Å/v at 0.07 ma/cm²), indicating once again excellent agreement apart from the scale of thickness.

From these calculations most of the change in conduction properties which accompany the annealing of anodic oxide films on aluminum can be ascribed to the pre-exponential factor, rather than to either the effective activation energy, $(W + U)/2$ or the effective activation distance $(\lambda + a)/2$. For films formed by anodizing at 0.07 ma/cm², No appears to be nearly equal to the total number of aluminum ions in the film, that is about 4×10^{22} ions/cm³. On the other hand for the annealed films N_o is equal to about 10^{11} ions/cm³ (from $\Omega\nu(2N_oa/\sigma)^{1/2} = 7.3 \times 10^{-2}$ cm sec). Annealing, therefore, appears to reduce greatly the number of lattice sites which are potential sources of ion-vacancy pairs, or more generally, it appears to decrease the conductivity of the film by reducing the number of potential current carriers. It can be shown that this conclusion is substantially independent of the particular conduction mechanism assumed.

Wilsdorf's model for the amorphous oxide can once again provide an explanation of the results. In a randomly oriented molecular array one would expect certain cations to be in relatively high potential energy sites. It would be these ions, presumably, that could be excited into interstitial positions, leading to cationic conductivity. On annealing the film, some ordering of the molecular groups could take place, causing a reduction in the number of cations in high potential energy sites, hence a reduction in the number of cations which can become current carriers, in agreement with the interpretation of the results. The high ionic current imposed during re-anodizing of an annealed sample could cause, initially, rearrangement of the molecular groups, leading to an increase in the concentration of ions in high potential energy sites. This, in turn, would lead to an increase in the conduction ion concentration and hence to a current overshoot during a polarization measurement. Ultimately, the properties of the film would be expected to return to those of a freshly anodized sample, as observed. A more quantitative appraisal of these ideas is at the moment not possible.

Manuscript received Nov. 7, 1960; revised manuscript received June 5, 1961. This paper was prepared, in part, for delivery before the Ottawa Meeting, Sept. 8-Oct. 2, 1958.

Any discussion of this paper will appear in a Discussion Section to be published in the December 1962 JOURNAL.

REFERENCES

1. L. De. Brouckère, *J. Inst. Metals*, **71**, 131 (1945).
2. E. A. Gulbransen and W. S. Wysong, *J. Phys. & Coll. Chem.*, **51**, 1087 (1947).
3. G. Hass, *Z. anorg. Chem.*, **254**, 96 (1947).
4. G. Hass, *Optik*, **1**, 134 (1946).
5. G. Hass, *Verhandl. deut. physik, Ges.*, **22**, 1 (1941).
6. G. Hass and H. Kehler, *Kolloid-Z.*, **97**, 27 (1941).
7. G. D. Preston and L. L. Bircumshaw, *Phil. Mag.*, **22**, 654 (1936).
8. A. Steinheil, *Ann. Physik*, **19**, 465 (1934).
9. H. G. F. Wilsdorf, *Nature*, **168**, 600 (1951).
10. D. A. Vermilyea, *This Journal*, **104**, 542 (1957).
11. D. J. Stirland and R. W. Bicknell, *ibid.*, **106**, 481 (1959).
12. R. A. Harrington and R. H. Nelson, *Trans. AIME*, **137**, 62 (1940).
13. M. S. Hunter and P. Fowle, *This Journal*, **101**, 481 (1954).
14. M. de Kay Thompson, "The Total and Free Energies of Formation of the Oxides of Thirty-two Metals," American Electrochemical Society, New York (1942).
15. M. J. Dignam, *This Journal*, **109**, 192 (1962).
16. E. J. Verwey, *Z. Krist.*, **91**, **65**, 317 (1935).
17. C. P. Bean, J. C. Fisher and D. A. Vermilyea, *Phys. Rev.*, **101**, 551 (1956).
18. J. R. Guy Ervin, *Acta Cryst.*, **5**, 103 (1952).
19. J. F. Dewald, *J. Phys. Chem. Solids*, **2**, 55 (1957).
20. A. Charlesby, *Proc. Phys. Soc.*, **B66**, 317 (1953).
21. D. A. Vermilyea, *This Journal*, **104**, 427 (1957).
22. W. Ch. van Geel and R. J. J. Schellen, *Philips Res. Repts.*, **12**, 240 (1957).
23. W. J. Bernard, and J. W. Cook, *This Journal*, **106**, 643 (1959).

Oxide Films on Aluminum

II. Kinetics of Formation in Oxygen

Michael J. Dignam[1]

Aluminium Laboratories Ltd., Kingston, Ontario, Canada

ABSTRACT

The reaction rates in oxygen of electropolished samples of superpurity aluminum and certain of its binary alloys were investigated in the temperature range 250°-450°C, employing anodic polarization[2] and weight gain measurements. The rate of formation of "amorphous" oxide was not affected by small alloying additions of Fe, Mn, or Ga, and was found to be in good accord with the Cabrera-Mott[3] theory for the formation of very thin films. A modified version of this theory is preferred, however, since the rate appears to be controlled within the film, rather than at the metal-oxide interface. At 450°C and presumably above, the nucleation and initial growth of gamma alumina crystallites was found to coincide with a region of approximately constant oxidation rate, providing a qualitative explanation for the latter. The presence of copper was found to have an appreciable effect on the oxidation behavior. This effect can be explained by assuming that the presence of copper ions in the oxide film increases the concentration of conducting aluminum ions substantially.

The kinetics of formation of the oxide film on aluminum and its alloys at low temperatures where a so-called limiting oxide film thickness is obtained has not been studied in any detail. The data of Hass (3), Gulbransen and Wysong (4), Smeltzer (5), and Aylmore, Gregg, and Jepson (6) indicate that a limiting oxide film thickness is obtained on aluminum for oxidation below about 400°C, and, while the results of Obrist (7) and Cabrera and Hamon (8) indicate a somewhat lower temperature, anodic polarization studies of Hunter and Fowle (9) tend to confirm this value. It might reasonably be expected, and indeed the present results show, that the rate of oxidation of aluminum in this low-temperature range is of the form predicted by Cabrera and Mott (2) for the growth of very thin oxide films on metals.

Most of the data consist of "barrier voltage" values determined using a modification of the anodic polarization measurement technique employed by Hunter and Fowle (10), although some weight gain data were also obtained. Samples oxidized for various times at temperatures of 250°, 350°, and 450°C were anodically polarized and the barrier voltage determined as described in the foregoing paper. For superpurity aluminum the film thickness may then be taken to be proportional to the barrier voltage. Until the present work, the validity of this method had only been demonstrated for the case of nonporous anodic films (10). In the foregoing paper, however, it was shown that for superpurity the barrier voltage is proportional to film thickness for annealed anodic films; also, the room temperature ionic conduction properties of films formed by oxidation at 250°, 350°, or 450°C could not be distinguished from those of anodic films annealed at 450°C; it appears likely, therefore, that for films formed on superpurity aluminum by oxidation in the range 250°-450°C, the barrier voltage is proportional to the oxide thickness, the value of the proportionality constant being the same as that for anodic films annealed at 450°C, namely, 8.8 Å/v (1).

The main advantages in this method of film thickness determination are the following. First, the barrier voltage is independent of sample area to a first approximation, in contrast to weight gain or capacitance measurements. For example, a roughness factor of 2, if not taken into account, will lead to an error in the film thickness calculated from the barrier voltage of less than 1% (cf. Eq. [9], (1)). Second, absolute film thickness can in principle be obtained from polarization measurements, whereas only changes of film thickness can be obtained from weight gain measurements. Finally, the barrier voltage value is not affected appreciably by flaws or fissures in the oxide film, in contrast to the film capacitance. The main disadvantage of the method is that it is by no means absolute, requiring, therefore, careful calibration. Its application depends on the properties of the particular oxide-metal system in question. The same relation between barrier voltage and film thickness cannot be assumed, *a priori*, for samples other than those with identical oxide-metal interface and identical oxide form. Techniques for obtaining the thickness of films on aluminum, similar to the one employed herein, have been used by some workers rather indiscriminately, without experimental or theoretical justification for its application to the system under study.

The present investigation was undertaken to determine the oxidation mechanism of aluminum and the effect of small alloying additions of gallium, iron, manganese, silicon, and copper on the oxidation behavior. Alloy additions were kept small in

[1] Present address: Department of Chemistry, University of Toronto, Toronto, Ontario, Canada.

[2] See ref. (1).

[3] See ref. (2).

order to avoid having to consider the oxidation properties of phases rich in alloying element, where such phases existed. The above alloys were included in an attempt to further elucidate the oxidation mechanism of pure aluminum. Certain of the alloys studied are heterogeneous at one or more of the oxidation temperatures. However, copper was the only alloying addition found to have an observable effect on the growth rate of the amorphous oxide film on an aluminum rich phase. Alloy heterogeneity is of consequence therefore only in the case of the data for oxidation of the 1.5% Cu alloy at 350° and 250°C, where the solubility limit is about 0.8% and 0.3%, respectively. As other limitations of these data exist, very little weight is attached to them. Accordingly, conclusions concerning the effect of copper are based on the behavior of the 1.5% copper alloy at 450°C, where it is homogeneous, and on the behavior of alloys containing less than 0.3% Cu.

All the alloys studied except the alloy containing 1.5% Cu have been shown to exhibit oxidation kinetics consistent with the Cabrera-Mott theory of oxidation. A modified version of this theory is preferred, however, since the rate appears to be controlled within the film rather than at the metal-oxide interface. In contrast, the results for the 1.5% Cu alloy suggest that the rate-determining step in this case could very well be controlled at the metal-oxide interface. The results for this alloy for oxidation at 450°C are in accordance with a direct logarithmic law.

Experimental Procedure

Samples of superpurity aluminum and superpurity base binary alloys of composition, purity, and dimensions given in the foregoing paper, were oxidized in 0.2 atm of purified oxygen at temperatures of 250°, 350°, and 450°C, as previously described (1). Polarization measurements were then made on the samples from which "barrier voltage" values were obtained (1). A new set of samples was used for each oxidation period, since a polarization measurement changes the thickness and conduction properties of the oxide film (1). Comparison of the behavior of different alloys was of primary interest; one sample of each alloy was therefore oxidized in the multiple sample furnace at one time in order that random variations of the furnace temperature might influence the oxidation rate of all alloys equally. Each sample permitted duplicate determinations of the barrier voltage to be made.

Weight gain measurements for oxidation at 450°C were made on superpurity and superpurity base binary alloys containing 0.01% Fe, 0.24% Si, 0.54% Mn, or 1.51% Cu. Samples 1 × 12 in. were cut from the 0.020 in. thick sheets, and vacuum annealed for 1 hr at 543°C. They were then electropolished for 30 min at 30v (~ 25 ma/cm²) in a bath at about 10°C containing 27.7% by volume of 71% perchloric acid, 8.3% by volume of water, and 64.0% by volume of acetic anhydride. The perchloric acid-methanol electropolishing bath (1) could not be used for these large samples because of the high currents that would have been required. The samples were rinsed 30 sec in absolute methanol and 1 min in running distilled water, then dried in a clean, dry air jet. They were then folded over a quartz hook and suspended from the furnace sample holder. The degassing and oxidation procedure was the same as that described previously (1). The samples were weighed on a Mettler chemical microbalance, correcting the observed weighings for atmospheric conditions. After weighing, the samples were returned to the furnace for further oxidation.

Experimental Results

The results obtained from polarization and weight gain measurements are presented in Tables I and II, respectively. The barrier voltage values are reported with reference to the hypothetical reversible aluminum electrode (1). Each voltage entry is the result of averaging duplicate determinations, which agreed in general to about 0.04v. The accuracy of the weight gain measurements was estimated to be about ± 4 μg.

Table I. Barrier voltage results for superpurity-base alloys oxidized at 250°, 350°, and 450°C

Oxidation temp.	Time, hr	Barrier volts											
		S.P.	Ga	Fe		Si		Mn		Cu			
	(per cent)		0.2	0.01	0.06	0.24	1.78	0.53	2.2	0.011	0.08	0.19	1.51
450°C	0.0667	1.78	1.83	1.81	1.96	1.98	2.07	1.84	1.83	1.80	1.89	2.22	3.55
	0.25	2.20	2.36	2.50	2.17	2.39	2.43	2.06	2.08	2.24	2.27	2.39	3.79
	1.0	2.47	2.51	2.42	2.42	2.58	2.54	2.38	2.43	2.51	2.50	2.69	3.73
	4	3.29	3.47	3.11	2.97	3.42	3.23	3.11	3.13	3.25	3.36	3.50	4.27
	16	3.66	3.34	3.45	3.55	4.44	3.98	3.57	3.53	3.38	3.68	3.95	4.83
	24	2.89	2.70	3.21	3.05	6.09	4.37	2.96	3.53	2.92	2.95	3.75	4.50
350°C	1.0	1.70	1.78	1.78	1.84	1.86	1.83	1.74	1.73	1.74	1.76	1.86	2.90
	4	2.04	1.93	2.03	2.10	2.26	2.28	2.07	2.06	2.08	2.22	2.39	3.22
	16	2.34	2.36	2.34	2.46	2.35	2.38	2.30	2.30	2.34	2.44	2.67	4.02
	64	2.83	2.72	2.70	2.81	2.70	2.70	2.54	2.52	2.72	2.99	3.23	4.10
	256	3.36	3.38	3.32	3.32	3.34	3.36	3.13	3.14	3.36	3.62	3.70	4.29
250°C	1.0	1.33	1.36	1.34	1.38	1.47	1.49	1.36	1.38	1.38	1.49	1.51	1.92
	5	1.62	1.66	1.65	1.63	1.71	1.72	1.63	1.64	1.64	1.71	1.76	2.41
	24	1.75	1.75	1.76	1.80	1.80	1.85	1.86	1.70	1.78	1.88	1.94	2.91
	120	2.02	2.04	2.03	2.13	2.06	2.11	2.00	1.89	2.00	2.07	2.13	3.19
	600	2.37	2.34	2.35	2.41	2.30	2.45	2.31	2.02	2.36	2.41	2.65	3.53

Table II. Weight Gain Results for Superpurity Base Alloys Oxidized at 450°C

Oxidation time, hr	Weight gain in μg per 24 in.² for S.P. base alloys				
	S.P.	0.01% Fe	0.24% Si	0.53% Mn	1.51% Cu
0.0667	0	0	0	0	0
0.25	23	39	19	18	43
1.0	41	49	43	41	84
4	63	68	62	67	116
16	151	143	109	137	158
64	347	231	155	386	263

Interpretation of Results

Examination of the results in Tables I and II indicates that, within experimental error, all of the alloys except the copper bearing alloys oxidize at the same rate at temperatures of 250°C, 350°C and for oxidation periods up to 4 hr at 450°C.[4] Oxidation results for the aluminum copper alloys are therefore treated separately, those for the remaining alloys being treated as a unit.

Figure 1 illustrates the effect of silicon on the oxidation of aluminum at 450°C. The weight gain data was converted to oxide thickness, expressed in barrier voltage units, by choosing the value of the initial weight of the film and the relation between film weight and barrier voltage (25.8 μg/dm² per barrier volt) which gave the best agreement between the two sets of data. The agreement between the two measurement techniques is considered quite good for the 0.24% Si alloy, and for oxidation periods up to 4 hr or so for superpurity as well. Choosing a value for the oxide density of 3.6 g/cm³ and using the value 8.8Å per barrier volt for the conversion factor, 25.8 μg/cm² per barrier volt implies a roughness factor for the weight gain samples of 1.65. This is considered a reasonable value since these samples, although bright after electropolishing, were not smooth on a macro scale.

The divergence of the weight gain and barrier voltage data for superpurity after 4-16 hr oxidation at 450°C is undoubtedly caused by the onset of crystal nucleation in the oxide film in accordance with the results and discussion of the foregoing paper.

If the rate-determining step for the oxidation of aluminum were controlled at the metal-oxide interface, as assumed by Cabrera and Mott, it would be expected that the oxidation rate would vary considerably from one sample to the next because of variations in the nature of the interface which are bound to exist. To an even greater extent, one would expect large impurity concentrations in the metal to affect the oxidation rate. However, the polarization data fall on smooth curves (see Fig. 1 and 2) indicating consistency, since each point is obtained from a separate sample. Also, with the exception of the high copper bearing alloys, the polarization and weight gain data indicate little influence of alloying conditions on the oxidation rate of aluminum. In addition, the electron transmission micrographs of the foregoing publication (1) show no variation in the thickness of the amorphous film with metal grain orientation. It seems probable, therefore, that the rate-determining step is controlled in the bulk of the oxide rather than at the oxide-metal interface.

The 0.24% Si alloy behaves the same at all temperatures as superpurity except for the oxide crystallization phenomenon at 450°C; this alloy rather than superpurity, therefore, was used to test the modified Cabrera-Mott theory, since it provides more data for calculation.

Oxidation of superpurity + 0.24% silicon.—The barrier voltage and weight gain data for this alloy are illustrated in Fig. 2.

The Cabrera-Mott theory of oxide film growth in the very thin film region is based on the assumption that equilibration of electrons between the metal and the adsorbed oxygen is established in a time short compared with that required for ions to be transported across the oxide film. The resulting constant voltage, V, established across the film causes the metal ions to be transported across a barrier which is assumed to be at the metal oxide interface, the rate of transport depending exponentially on the field strength. In interpreting the present data, this theory was modified by assuming

[4] This conclusion may be reached from the barrier voltage data as well as from the weight gain data despite the fact that barrier voltage values were calibrated in terms of film thickness only in the case of superpurity aluminum. This is so since the only alternative conclusion is extremely improbable, namely, that the film thicknesses are different for these alloys, but that the conduction properties of the films also differ in just such a way as to give the same barrier voltage values for oxidation at all three temperatures.

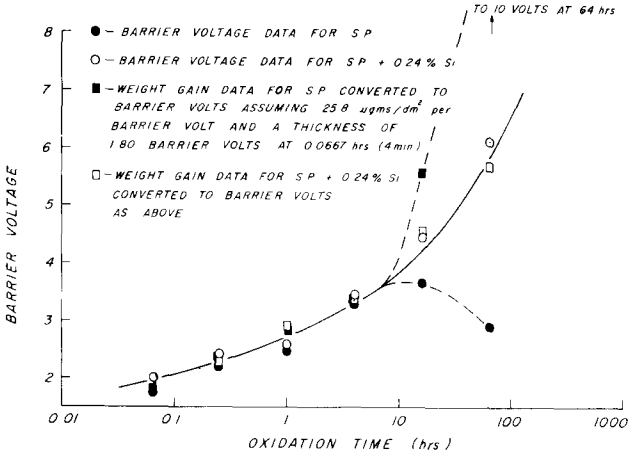

Fig. 1. Influence of silicon on the oxidation of aluminum at 450°C.

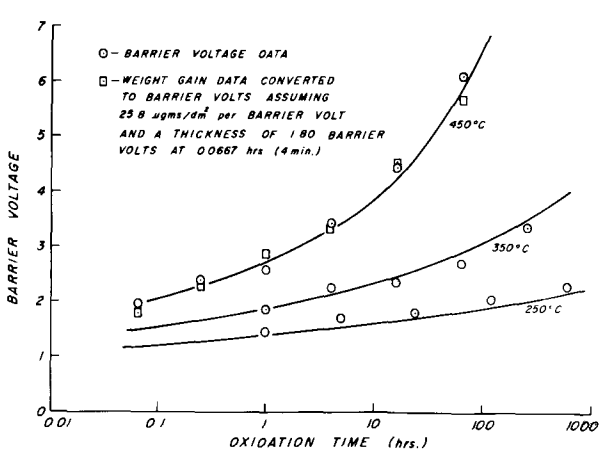

Fig. 2. Influence of temperature on the oxidation of superpurity aluminum + 0.24% silicon.

the rate-controlling process to be site to site diffusion of the metal ions within the oxide film in accordance with the ionic conductance theory of Bean *et al.* (1, 11).

From the 450°C oxidation results, at 4 min, the oxidation rate (or oxidation current) changes by less than 0.4% per sec. At longer oxidation times, or lower temperatures, the rate of change is much slower, being, for example, 0.05% per sec at 15 min at 450°C. From this, it can reasonably be concluded that for oxidation times of 4 min or more at 450°C or less, transient effects will be of only secondary importance. The steady-state relation between current density and field strength is obtained from Eq. [4] and [5] of the foregoing paper (1) by eliminating n for the condition that $dn/dt = 0$. The resulting equation is:

$$\frac{d\delta}{dt} = \Omega\nu\left(\frac{2N_o a}{\sigma}\right)^{1/2} \exp - \left[\frac{W+U}{2} - \frac{Vq(\lambda+a)}{2\delta}\right]/kT \quad [1]$$

where the field strength, E, has been replaced by V/δ, δ being the film thickness, and the units have been changed from current density to rate of growth of film thickness, Ω being the volume per metal ion in the oxide. This equation is formally the same as that by Cabrera and Mott.

Equilibration of electrons between the metal and the adsorbed oxygen, which is assumed to establish the potential V across the film, can only take place if the electrons can pass freely through the film. Vermilyea (12), in discussing this problem, concludes that for a film 100Å thick and a concentration of electrons in the conduction band of the oxide of only 10^8 cm^{-3}, a potential difference of the order of a volt would be established across the oxide in 1 sec. Since the films presently being discussed were not more than 55Å thick, it seems likely that essentially the full equilibrium potential would be established, particularly in view of the extremely slow rate of growth of the thicker films.

The following method was used to fit the barrier voltage data to Eq. [1], which can be written

$$\frac{d\delta}{dt} = A \exp B/\delta \quad [2]$$

where A and B, constants for a given temperature, are given by $A = \Omega\nu(2N_o a/\sigma)^{1/2} \exp - (W+U)/2kT$, and $B = Vq(\lambda+a)/2kT$. The integrated form of Eq. [2] can be written

$$\ln t/\delta^2 = -B f(B/\delta)/\delta - \ln AB \quad [3]$$

where $f(B/\delta)$, a function of B/δ only, approaches unity for large values of B/δ. $f(B/\delta)$ was calculated as a function of B/δ by comparing Eq. [3] with the following integrated form of Eq. [2]

$$\frac{At}{B} = \int_o^{\delta/B} \exp - B/\delta \, d(\delta/B) \quad [4]$$

and from numerical values of the above integral.

An approximate value for B at 450°C, B_3, was obtained by plotting log t/δ^2 *vs.* $1/\delta$, the slope of the resulting straight line being approximately $-B_3/2.303$. The data for the three temperatures were then plotted for several assumed values of B_3 (which settled the values for B at 350° and 250°C, B_2 and B_1, since $B_1 : B_2 : B_3 : : 1/T_1 : 1/T_2 : 1/T_3$) plotting log t/δ^2 *vs.* $f(B/\delta)/\delta$ and drawing the best straight lines of slopes B_1, B_2, and B_3 with intercepts approximately linear in $1/T$ (since $-\log AB = -\log[\Omega\nu(2N_o a/\sigma)^{1/2} \; Vq(\lambda+a)/2kT] + (W+U)/4.606kT$). The term $Vq(\lambda+a)/2$ was then calculated from the best value for B_3. From the values of the intercepts and of B, log A was plotted against $1/T$, and $(W+U)/2$ and $\Omega\nu(2N_o a/\sigma)^{1/2}$ obtained from the resulting slope and intercept. The values of the parameters obtained in this way for the oxidation of the 0.24% Si alloy are:

$$\Omega\nu(2Noa/\sigma)^{1/2} = 3.0 \times 10^9 \text{ (barrier volts) hr}^{-1} = 7.3 \times 10^{-2} \text{ cm sec}^{-1}$$

$$(W+U)/2 = 1.76 \text{ ev}$$

$$Vq(\lambda+a)/2 = 0.935\, e\text{(barrier volts)} = 8.2 \text{ eÅ v}$$

The solid curves in Fig. 2 were calculated using the above values. Although the average deviation of the points from the lines is only about ±0.13v (or ±1.2Å), there does appear to be a small systematic deviation of the experimental points from the best fit calculated curves. It can be shown that this systematic deviation could have arisen as a result of small variations with temperature and film thickness of V, in accordance with the theory presented by Grimley (13). Small differences in the conduction properties of the oxide films formed at the different temperatures might also have been responsible. This discrepancy, however, is not considered to be very significant.

The value for the activation energy, 1.76 ev, compares favorably with the values 1.6 and 1.8 ev calculated by Charlesby (14) from steady-state anodic oxidation measurements on aluminum. From $\Omega\nu(2N_o a/\sigma)^{1/2} = 7.3 \times 10^{-2}$ cm sec^{-1} and setting $\Omega = 2.34 \times 10^{23}$ cm^{-3}, $\nu = 10^{12}$ sec^{-1}, $a = 10^{-8}$ cm, and $\sigma = 10^{-15}$ cm^2, the result $N_o = 5 \times 10^{11}$ cm^{-3} is obtained which is to be compared with a value of about 4×10^{22} cm^{-3} for the concentration of aluminum ions in the oxide lattice. An interpretation of this result would be that of the aluminum ions in the oxide lattice, only 1 in 10^{11} is a potential source of an ion-vacancy pair for films formed by oxidizing between 250° and 450°C. This phenomenon has been discussed in the foregoing paper.

By making the very reasonable assumption that the mechanism of air oxidation and anodic oxidation are the same for samples with the same film structure, it is possible to calculate the value of the voltage, V, established across the film during oxidation. From the foregoing paper, a study of ionic conduction through films with apparently the same conduction properties are those formed during air oxidation led to the value $q(\lambda+a)/2 = 11.3$ eÅ. Comparing this with the present results, $Vq(\lambda+a)/2 = 8.2$ eÅ, the result $V = 0.73$v is obtained. This compares favorably with the value 0.7v estimated by Vermilyea (12) for the oxidation of tantalum between 50° and 300°C.

In the light of the present results and those presented in the foregoing paper, it is of interest to investigate the results obtained by Smeltzer (5), and more recently by Aylmore, Gregg, and Jepson (6), on the oxidation of aluminum between 400° and 650°C. Both these sets of data were obtained from weight gain measurements on samples of superpurity abraded with emery. A typical curve of weight gain *vs.* time can be divided, for purposes of discussion, into three regions; an initial region in which the rate falls off rapidly, an intermediate region of nearly constant oxidation rate, and a final region in which the rate decreases once again. The present data for oxidation of superpurity at 450°C, when plotted on a linear time scale, indicate an initial region in which the rate decreases rapidly with time. This region persists somewhat beyond 4 hr. Between 4 and 16 hr oxidation, during which time crystallites of gamma alumina are known to be forming (1), the oxidation rate actually increases, falling off once again from about 16 hr to 64 hr oxidation or more. The general features of this curve, although not the same as those obtained by Smeltzer and by Aylmore *et al.*, strongly suggest that their initial region is associated with the formation of amorphous oxide in accordance with the mechanism proposed herein, the second approximately linear region with the nucleation and rapid initial growth of gamma alumina crystallites, and the final region with the coalescence of the crystallites and continued growth of a film composed entirely of such crystallites. Smeltzer's data at 450°C exhibits a linear oxidation rate between about 2 and 16 hr oxidation, confirming the above thesis. In other areas of comparison, however, the data of Smeltzer and of Aylmore *et al.* do not agree with the present results. Thus for oxidation at 450°C of samples possessing films formed at room temperature the weight gains per unit area reported by Aylmore *et al.* are higher than those presented herein by factors of about 22, 13, and 4 for oxidation periods of 64, 4, and 0.25 hr, respectively. Some of this enormous discrepancy could perhaps be explained by a difference in roughness factor, but the major difference almost certainly arises because of the different methods employed for preparing the surface.

An emery abraded surface will most probably be rough on a very fine scale, giving rise to cracking and buckling of the oxide film during oxidation, exposing fresh metal, and leading to excessively high weight gains. This oxide cracking must take place if the surface roughness is on a small enough scale such that the radii of curvature of peaks and edges on the surface are of the same order of magnitude as the thickness of the oxide film formed. Under these conditions, as oxidation proceeds, it can be demonstrated that the surface area of the metal will decrease appreciably in the neighborhood of the sharp edges and peaks in much the same fashion as occurs during the electropolishing of metals (15). Since the oxide grows by transport of aluminum through the film, however, the surface area of the oxide in contact with the metal will not change, leading eventually to rupture of the oxide film.

In addition to this roughness effect it has been demonstrated by Aziz (16) that emery abrasion leaves a very high concentration of emery particles in the surface of the metal. The abrading material is revealed after metallographic polishing of the abraded surface.

In the study of any surface reaction, the type of surface treatment used is all important. Although no type of surface treatment is without fault, it is felt that abrasion is a poor choice in many instances. The state of emery abraded surfaces is ill defined, and consequently results pertaining to such surfaces, although undoubtedly of practical interest, may often be of little theoretical consequence in respect to the elucidation of the basic reaction mechanisms.

The effect of vacuum annealing in reducing the subsequent oxidation rate, as observed by Smeltzer and by Aylmore *et al.* can be explained either by one of several hypothesis arising from the foregoing discussion, or from a consideration of the process of nucleation of gamma alumina. It is not considered worthwhile at present to discuss this in detail.

In contrast to the poor correlation with results obtained from abraded samples, the present results are in quite good agreement with those obtained by Hass (3) on evaporated aluminum films. For oxidation periods of 2 hr at 20°, 150°, 300°, 400°, and 450°C Hass obtained total film thickness values of 10, 12, 17, 25, and 42Å, respectively. From the present results, total film thicknesses corresponding to these same oxidation conditions were calculated to be 7.5, 10, 14.5, 21, and 26Å, respectively. Excluding the values at 450°C, the two sets agree very well, differing by a constant factor of about 1.2. The lack of such good agreement for oxidation at 450°C is probably related to the phenomenon of oxide crystallization.

Oxidation of superpurity-copper alloys.—The influence of copper on the barrier voltage values for the oxidation of aluminum is illustrated in Fig. 3. The data indicate an increase in barrier voltage for increasing copper content. The influence is minor, however, for copper additions up to 0.2%. The data for these alloys can still be represented, within experimental error, by the Cabrera-Mott theory, whereas those for the 1.5% Cu alloy cannot. The change in oxidation behavior on adding 0.2% copper to superpurity aluminum can be explained equally well, within experimental error, by a change in the

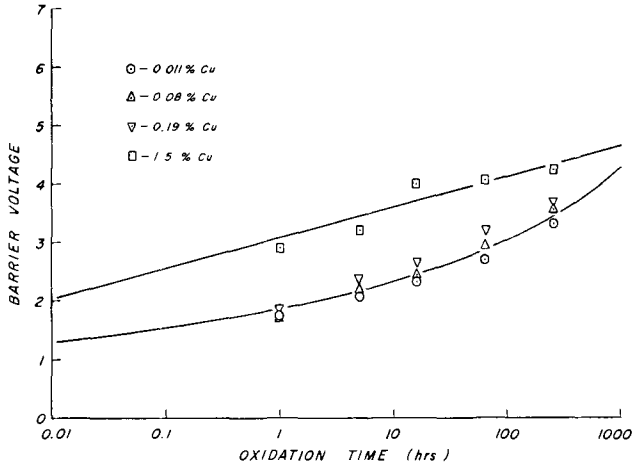

Fig. 3. Influence of copper on the barrier voltage values for the oxidation of aluminum at 350°C.

pre-exponential factor, activation energy, or activation distance. Thus the addition of 0.2% Cu could cause a factor of 6.3 ±1.6 increase in N_o, or a (12 ± 4) % increase in $V(\lambda + a)$, or a decrease in the activation energy, $(W + U)/2$, of 0.05 ± 0.004 *eV*, or some combination of all three changes.

There is no doubt that the addition of 1.5% copper causes a fundamental change in the reaction mechanism. The weight gain data for the oxidation of this alloy at 450°C indicate adherence to a direct logarithmic oxidation law (δ linear in log t), and are quite inconsistent with the Cabrera-Mott theory. A relation between weight gain and barrier voltage change for the oxidation at 450°C of this alloy can be obtained in the same way as was that for the 0.24% silicon alloy. The ratio 52.6 $\mu g/dm^2$ per barrier volt obtained for this alloy is to be compared with the result 25.8 $\mu g/dm^2$ per barrier volt obtained for superpurity and the other superpurity base alloys. Assuming the same roughness factors for these alloys, the relation between barrier voltage and film thickness, 21.3Å/barrier volt, may be deduced. It is doubtful, however, that this value also applies to the films formed on this alloy at 350° and 250°C, since there is no very convincing evidence that the films formed at the three temperatures have the same conduction properties.

Assuming copper increases the ionic conductivity of the amorphous film by introducing interstitial aluminum ions into the oxide (1), it is of interest to consider what effect this might have on the kinetics of air oxidation. If the equilibrium concentration of aluminum ions is not too large, but large compared to the concentration of ion-vacancy pairs, it can be shown that oxidation will still proceed in accordance with an equation of the same form as Eq. [1], although with somewhat different parameters. This is apparently not the case for the 1.5% Cu alloy. If the interstitial aluminum ion concentration is increased sufficiently, it is entirely possible that the rate-controlling process will no longer be the transport of aluminum ions through the film, but rather the transport of aluminum ions, or perhaps electrons, across the metal-oxide interface. Some evidence to support the supposition that the oxidation rate of the 1.5% Cu alloy is controlled at the metal-oxide interface is found in the lack of reproducibility of the polarization data for this alloy as compared to that for superpurity. Also, some results obtained for the oxidation of a 6% Cu alloy at 450°C (in which a second phase would be present) were highly erratic, although conforming more or less to those for the 1.5% Cu alloy.

Uhlig (17) has derived a rate equation, assuming the rate-controlling process to be transport of electrons across a rectifying metal-oxide interface. The process is assumed to be aided by the "apparent positive potential at the metal surface created by the growing oxide," and hindered by the opposing field arising from a uniform concentration of negative space charge in the film. A major difficulty presented by the application of Uhlig's theory to the 1.5% Cu alloy is that it requires that the metal work function be greater than the electron affinity of the adsorbed oxygen, whereas the Cabrera-Mott theory, or its modification, requires the opposite. It is very difficult to understand how the introduction of copper could cause such a large change in these properties.

As an alternative to Uhlig's theory, it is possible to obtain a direct logarithmic oxidation law of the same form from the Cabrera-Mott (2) theory for the formation of very thin oxide films, by including the possibility of space charge in the oxide. If the rate-controlling process has shifted from metal ion transport within the film to transport across the interface, in the manner proposed, it can be shown that under steady-state conditions a negative space charge must be present near the metal-oxide interface. If beyond this negative space charge region, a positive space charge region is assumed to exist, such that the total negative space charge in the film decreases linearly with film thickness, the desired oxidation law will result. Although the application of this theory to the results does not lead to any obvious contradictions, the space charge concentrations required are very high indeed ($\sim 10^{20}$ e/cm^3). Also, in common with Uhlig's theory, it is difficult to account entirely for the space charge distributions required. Further experimental investigation must be made before a definite conclusion can be reached.

General Discussion

In conjunction with those results of the foregoing paper pertaining to oxide crystallization, the present results provide a reasonable explanation for the oxidation behavior of aluminum in dry oxygen. Below about 450°C, and initially at higher temperatures, a very thin, amorphous film is formed. The observed kinetics are in agreement with a mechanism in which a nearly constant potential difference of 0.73v is established across the film by means of electron transport from the metal to oxide surface levels. The resulting field causes metal ion transport through the film in accordance with an exponential field strength relationship. The rate of formation of this film appears to be unaffected by metal grain orientation in conformity with the above mechanism.

After a suitable induction period, for oxidation temperatures above about 450°C, nucleii of crystalline gamma alumina form and initially grow rapidly. The weight gain data for this region conform approximately to a linear oxidation law. The induction period is effected by impurities, and the surface concentration of crystal nucleii by metal grain orientation; each of these factors would therefore be expected to have considerable influence on the film growth during this period of oxide crystallization, and perhaps also on the subsequent growth of the all-crystalline film, as they might influence the distribution of crystal orientation in the final polycrystalline film.

It is not possible, on the basis of the data presented herein, to suggest a mechanism for the growth of the crystalline oxide; it is apparent, however, that the rate does decrease with increasing film thickness. In view of the fact that the crystalline film is nucleated at the metal-oxide interface, its rate of growth is probably dependent on the orientation of the underlying metal, irrespective of whether the oxidation

rate is controlled at the metal-oxide interface or within the film.

The effect of impurities, both surface and bulk, on the general oxidation behavior is of interest. On the basis of the interpretation presented herein, only those impurities which can introduce defects into the oxide film would be expected to affect the rate of formation of the amorphous film, and then only if the concentration of defects introduced is of the same order of magnitude or larger than the concentration of defects assumed to be introduced by the electric field, in accordance with the theory of Bean *et al.* It appears likely, therefore, that the rate of formation of amorphous oxide for ultra high-purity aluminum would not differ from that for superpurity reported herein. It is apparent, however, that very small traces of impurities could have a profound effect on the nucleation of gamma alumina, and consequently on the subsequent oxidation rate. The time and temperature required to initiate growth of gamma alumina may be affected by trace impurities whether or not these appear in the film itself.

Acknowledgments

The author wishes to express his appreciation for the invaluable assistance given him by his former colleagues of Aluminium Laboratories Limited, particularly Drs. H. P. Godard and P. M. Aziz.

Manuscript received Nov. 7, 1960; revised manuscript received June 5, 1961. This paper was prepared, in part, for delivery before the Ottawa Meeting, Sept. 28-Oct. 2, 1958.

Any discussion of this paper will appear in a Discussion Section to be published in the December 1962 JOURNAL.

REFERENCES

1. M. J. Dignam, *This Journal*, **109**, 184 (1962).
2. N. Cabrera and N. F. Mott, *Rep. Prog. Phys.*, **12**, 163 (1949).
3. G. Hass, *Z. Anorg. Chem.*, **254**, 96 (1947).
4. E. A. Gulbransen and W. S. Wysong, *J. Phys. Coll. Chem.*, **51**, 1087 (1947).
5. W. W. Smeltzer, *This Journal*, **103**, 209 (1956).
6. D. W. Aylmore, S. J. Gregg, and W. B. Jepson, *J. Inst. Metals*, **88**, 205 (1961).
7. A. Obrist, Thesis, Tech. School in Zurich (1944).
8. N. Cabrera and J. Hamon, *Compt. rend.*, **224**, 1713 (1947).
9. M. S. Hunter and P. Fowle, *This Journal*, **103**, 482 (1956).
10. M. S. Hunter and P. Fowle, *ibid.*, **101**, 481 (1954).
11. C. P. Bean, J. C. Fisher and D. A. Vermilyea, *Phys. Rev.*, **101**, 551 (1956).
12. D. A. Vermilyea, *Acta Met.*, **6**, 106 (1958).
13. T. B. Grimley, *Discussions Faraday Soc.*, **28**, 223 (1959).
14. A. Charlesby, *Proc. Phys. Soc.*, **B66**, 317 (1953).
15. P. A. Jacquet, *Met. Rev.*, **1**, 2, 157 (1956).
16. P. M. Aziz, Internal Report, Aluminium Laboratories Ltd., Kingston, Canada, No. K-RR-622-57-28 (1957).
17. H. H. Uhlig, *Acta Met.*, **4**, 551 (1956).
18. L. De. Brouckère, *J. Inst. Metals*, **71**, 131 (1945).

Fission Fragment Recoil Effects on Zirconium Oxidation

W. C. Yee and G. H. Jenks

Oak Ridge National Laboratory, Oak Ridge, Tennessee,
Operated by the Union Carbide Nuclear Company for the United States Atomic Energy Commission

and E. E. Stansbury

University of Tennessee, Knoxville, Tennessee

ABSTRACT

Fission fragment recoil effects on zirconium oxidation in pure oxygen were studied at 1 atm pressure and 250°C. Specimens were oxidized under the following conditions: (*a*) reactor radiations including recoils, (*b*) reactor radiations in the absence of recoils, and (c) no radiation. Irradiation experiments were conducted in a maximum thermal neutron flux of 8.5 x 10^{11} neutrons/cm^2-sec. Specimen surfaces subject to fission fragments were exposed to an estimated average recoil intensity of 6 x 10^8 particles/cm^2-sec, the average particle energy being about 32 Mev or ~40% of the initial energy. It was concluded from electron and optical microscopy studies of the specimens that the normal oxide film on surfaces exposed to recoils had undergone a phase transformation with fine particle size, although the possibility that the normal oxide had developed a fine particle size of random orientation could not be ruled out. From estimates of oxide thickness based on interference colors and from a limited amount of weight gain data, it was concluded that the oxide film on surfaces exposed to fission fragments was thicker than surfaces exposed to reactor radiation alone. The amount of corrosion as indicated by the oxide thickness and weight data was at least a factor of ten less than that expected in a solution of uranyl sulfate producing an equivalent recoil intensity. However, the data obtained do not provide sufficient information to establish the mechanism of the effects of fission fragment recoils on zirconium oxidation.

It has been shown that under radiation the corrosion rate of Zircaloy-2 and zirconium in uranyl sulfate solutions is appreciably greater than in similar control experiments run in the absence of radiation. Jenks (1, 2) has summarized the results of these experiments to date.

Several mechanisms have been proposed to explain this increase in corrosion rate. These involve

the effects of irradiation on (*a*) the dilute uranyl sulfate solution, and (*b*) the metal and/or its oxide film. For aqueous solutions, it has been reported (3) that the initial products of irradiation are hydrogen peroxide and the free radicals H and OH. Although these provide a possible means of influencing the corrosive properties of the liquid, Jenks (1) has reported that the results of radiation studies of Zircaloy-2 and zirconium in uranyl sulfate solutions have indicated that the increased corrosion rate is not directly due to changes in the solution itself.

The alternate interpretation proposes that the damage is due to fission fragment recoil effects on the metal and/or its oxide film. Mechanisms which have been advanced to explain the loss in protective qualities of the oxide film include (*a*) increased rate of solution of the oxide exposed in aqueous environments (1), (*b*) production of easy diffusion paths along the tracks of the fission fragments (4, 5), and (*c*) conversion of the oxide film to a different phase (monoclinic to cubic) (6).

Another approach considers the consequences of fission fragment recoils on the metal itself. This model proposes (2) that recoils produce defects within the metal which increases its activity. For zirconium, in particular, it has been suggested (7) that the normal oxidation reaction occurs at the metal-oxide interface. Because of these defects in the metal, the rate of reaction at the interface is increased.

Since the study of the aqueous corrosion of zirconium under irradiation involves the resolution of several variables, it was thought that experimental data on the effects of fission fragment recoils on the gaseous oxidation of zirconium would be of aid in interpreting the aqueous radiation corrosion results. Specifically, this information might be helpful in separating the effects in the oxide and/or metal due to radiation *per se* from those due to changes in the aqueous environment.

Equipment

The experiments were designed to provide for the gaseous oxidation of zirconium under the following conditions: (*a*) reactor radiation including fission fragment recoils, (*b*) reactor radiation in the absence of fission fragment recoils, and (*c*) no radiation.

Each of the experiments was conducted in an especially designed autoclave unit which had three main components: (*a*) a water-cooled stainless steel holder containing the fission fragment recoil source, (*b*) a hollow cylindrical heater unit, and (*c*) a specimen holder. The source was placed in one end of the hollow cylinder. Inserted in the other end was the holder containing specifically located zirconium specimens. Figure 1 is a schematic diagram which locates the specimens and source within the autoclave unit. The components of the autoclave are shown in Fig. 2.

The recoil source was prepared by powder metallurgy techniques (8). A binary powdered mixture of enriched uranium dioxide (93.2% U-235) and stainless steel, 36 w/o UO_2, was sintered and

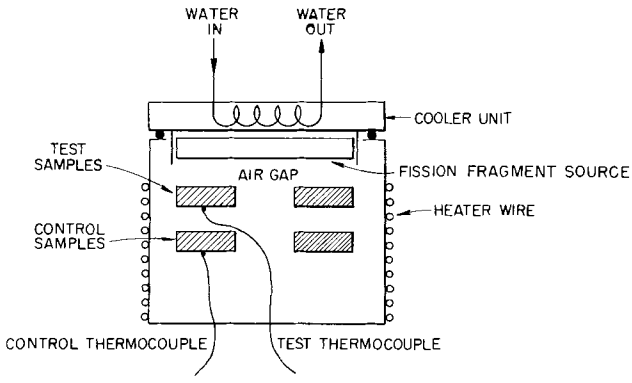

Fig. 1. Schematic diagram of assembled autoclave unit

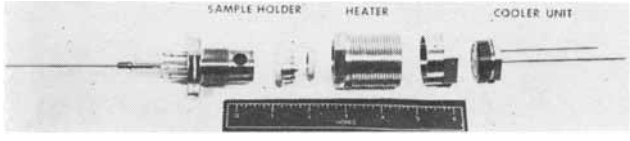

Fig. 2. Components of autoclave

then bonded to a cooler unit to dissipate heat generated by uranium fission.

The specimen holder held four zirconium specimens in position. One pair was placed approximately 1 mm away from the recoil source thus permitting one surface of each specimen to be exposed to recoil bombardment. These specimens, designated as test specimens, were maintained at 250°C by the heater unit. The remaining two specimens, the control specimens, were located in back of the test specimens, and except for the fission fragment recoils, were exposed in approximately the same radiation and oxidation environment. The control specimens operated at about 265°C.

The temperatures were measured by attaching 30-gauge iron-constantan thermocouples to the back side of one of the test and one of the control specimens. From the symmetrical arrangement of the specimens and their essentially identical mass, it was assumed that the experimental conditions for the weighed specimen were identical to the conditions for the matching specimen to which the thermocouple had been attached. This experimental arrangement was chosen to provide a means whereby the temperature of the test and control samples could be accurately established and still permit a reasonable evaluation of the magnitude of weight changes.

A third thermocouple was peened to the exterior wall of the heater section. This served as a detector for temperature control.

At the conclusion of the series of experiments, a comparison of the test and control specimens, both irradiated and nonirradiated, was made on the basis of weight change and individual surface characteristics.

Experimental

The zirconium specimens were made from crystal bar stock furnished in the form of a cold-rolled sheet, 0.025-in. thick. This metal had the following nominal spectrographic analysis: 100 ppm hafnium, 200-500 ppm iron, 200 ppm nickel, and less than 100 ppm each of titanium, aluminum, and silicon.

Samples in the form of half disks were machined from this sheet. Each specimen weighed approximately 0.4g and each side of the half-disk had a surface area of 1.2 cm^2.

The surfaces of all zirconium specimens were chemically polished in a solution of 50% distilled water, 45% concentrated nitric acid, and 5% hydrofluoric acid (48%). Each disk was alternately put into polish solution for 1 or 2 min and then in distilled water until the surfaces appeared visually to be smooth and bright. In order to achieve uniform polishing, the specimen had to be manually agitated even though the polish solution was magnetically stirred. Quick transfer of the disk to vigorously boiling distilled water removed trace quantities of polishing solution. This was followed by successive rinses in ethyl alcohol, ethyl ether, and petroleum ether. After shaking off excess solvent, the remaining thin film on the surface was evaporated rapidly by a jet of oxygen.

Each assembled autoclave unit, including zirconium specimens, was oxidized in an oxygen atmosphere at 250°C for 48 hr as part of a reliability test prior to irradiation.

Four irradiation experiments (Table I) were performed in Hole 16 of the ORNL Graphite Reactor where the maximum thermal neutron flux is 8.5 x 10^{11} nv. Three of these experiments contained a fission fragment source; one was exposed for two weeks and two were exposed for one week. The fourth in-pile test, exposed for one week, contained no source in order to establish any effects on the specimens due to fast neutron flux alone. Another test was a control experiment run out-of-pile for two weeks.

Table I. Experimental summary

Run	Time, weeks	Conditions
Z-5	1	Source—irradiated
Z-6	1	Source—irradiated
Z-8	2	Source—irradiated
Z-7	1	No source—irradiated
Z-9	2	Source—out-of-pile

Irradiated experiments: Hole 16 of ORNL graphite reactor
$\phi_{th\,max} = 8.5 \times 10^{11}$ neutrons/cm^2-sec

Table II. Nuclear conditions—irradiated experiments

	Average of 3 exps. with source	One exp.—no source
Thermal flux—Zr samples (neutrons/cm^2-sec)	4.7×10^{11}	4.9×10^{11}
Thermal flux—Source (neutrons/cm^2-sec)	$\sim 4.2 \times 10^{11}$	
Calc'd fission fragment intensity at Zr sample surface (particles/cm^2-sec)	5.9×10^8	
Fast flux—2 Mev energy—at Zr samples (neutrons/cm^2-sec)	2×10^{14}*	$\sim 10^{11}$ (>2 Mev)

* Calculated Zr atomic displacement rate due to recoils expressed in terms of fast flux.

An estimate of the fission fragment intensity impinging on the exposed test sample surfaces was obtained (9) from the prevailing thermal neutron flux conditions (Table II). The actual thermal neutron flux in the vicinity of the zirconium samples and source was determined experimentally by activation analysis of the exposed specimens themselves. For the geometry of this experiment, it was estimated that the flux in the source was depressed to about 90% of this value due to its high thermal neutron absorption cross section. From this flux in the source, a fission rate was approximated for a depth equal to the fission fragment range in the UO_2-stainless steel mixture (7μ). The number and total energy of fission fragments bombarding the exposed sample surface were calculated to be 25% and 10% of the number and total energy generated in the 7μ layer. For the nuclear conditions of these experiments, the fission fragment intensity at the sample was estimated to be 6 x 10^8 particles/cm^2-sec.

The potential damage rate at the fission fragment irradiation intensity can be estimated (9) to be several orders of magnitude greater than that of the prevailing fast neutron flux by comparing the atomic displacement rate due to recoil absorption in a thin surface layer of zirconium with the fast neutron flux (2 Mev neutrons) which would cause an equivalent displacement rate. Assumptions made for this comparison included (*a*) Ozeroff's calculated value (10) of 10^5 displacements in uranium per 80 Mev fission fragment applies in zirconium, and (*b*) although a spectrum of fission fragment energies exists in the incident particle flux on the specimen, 10^5 displacements occurred for each 80 Mev of energy in these particles.

The volume of zirconium considered for this comparison was 2 x 10^{19} atoms/cm^2 or a thickness of about 60% of the maximum range of recoils in zirconium. Calculations indicate that the potential damage rate by recoils could have been 2 x 10^{13} zirconium atoms displaced/cm^2-sec. The data of Kinchin and Pease (11) were employed to find a fast neutron flux which could approximate this rate of damage. They estimated that, after exposing copper to an integrated neutron dose of 10^{19} $(nvt)_{fast}$, about 10% of these atoms are displaced. Assuming these estimates apply also to zirconium, it was found, by proportion, that a fast neutron flux of about 2 x 10^{14} nv would cause an atomic displacement rate equivalent to that for the estimated fission recoil intensity.

The actual flux of neutrons with energies greater than 2 Mev was approximately 10^{11} nv for these experiments, about 10% of the thermal flux. Thus the probable rate of production of atomic displacements by neutrons in this experiment was about a factor of 10^2-10^3 less than that due to fission recoils.

Results

At the conclusion of each run, the zirconium specimens were studied by a number of techniques. Listed according to explicitness of result, these were microscopic examination of the surfaces at both high and low magnification using normal and

polarized light, low angle electron diffraction studies for possible identification of the structure of the oxide film on the surface seeing fission fragment recoils, study of surface topography of replicas of sample surfaces by electron microscopy, and visual comparison of surface interference colors. Weight change data were obtained also whenever possible.

Visually, almost a whole range of interference colors was seen on surfaces subject to recoils. All surfaces not subject to recoils had more uniformly colored surfaces. Figure 3 shows the scheme used to identify the various specimen surfaces. Unfortunately it is not possible to produce photographs which would show, satisfactorily, the detailed characteristics of the surface. However, some of the gross features are shown in Fig. 4, which compares the surfaces of specimens irradiated for two weeks in-pile with a source to those irradiated one week in-pile without a source, an out-of-pile oxidized specimen and a chemically polished specimen.

Microscopic examination of the specimens under bright field illumination showed a consistent difference between those surfaces facing the fission fragment source and those exposed to neutron flux only. As shown in Fig. 5, the recoil effects were particularly evident on comparison of the protected edge (due to the shoulder of a metal ring holding the specimen in place) and the unprotected center of the test specimen surface facing the source. Assuming the blue blotches appearing at the shielded edge result from first order interference, it was possible to observe the entire second order interference color band and finally a mixture of gold and red-purple of third order on the main surface. The oxide thickness of the directly exposed area was estimated (9) to be 2500-3000Å.

No other surface exhibited this feature along its periphery. The opposite surface of the test specimen was a uniform yellow field intermixed with blue and reddish purple (1500-1600Å). Test sample surfaces of run Z-7, which involved no recoils, had a uniform array of similar interference colors while run Z-9, which was out-of-pile, had a blue field with light yellow and purple spots (700-800Å).

Microscopic examination of the specimens under polarized light showed pronounced differences between surfaces that were exposed to fission fragment recoils and all other surfaces examined. Only the surfaces seeing recoils were inactive to polarized light. All of the other specimen surfaces, when examined, were responsive to polarized light as the specimen was rotated 180°. Figure 6 shows again the periphery of the same surface exposed to fission fragment recoils as in Fig. 5, but this time under polarized light. A line of demarcation divides the surface into two distinct regions: the featureless region corresponds to the surface area that saw fission fragment recoils while the contrasting region is the surface area that was shielded from recoils by the metal ring holder. Figure 7 is a picture of the opposite surface of the same specimen. Here, resolvable areas are uniformly distributed over the whole surface area exactly as under the shielded edge in Fig. 6.

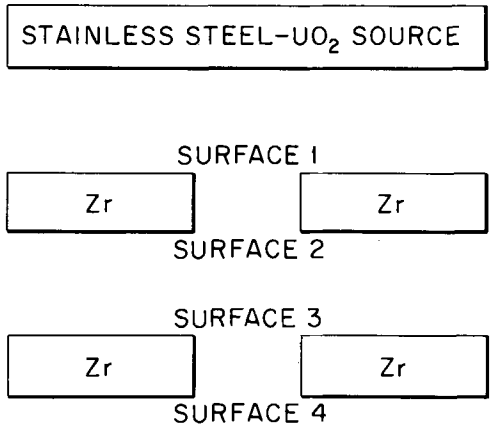

Fig. 3. Configuration of typical fission fragment recoil experiment

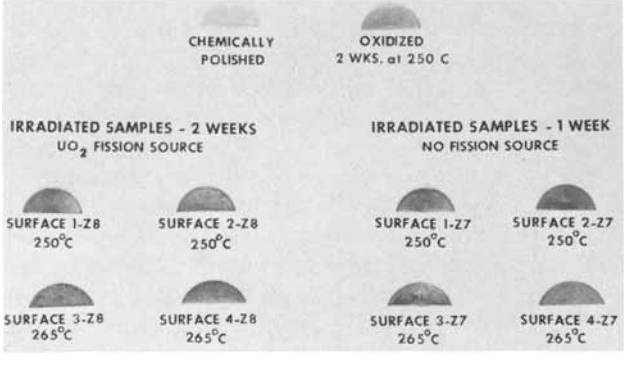

Fig. 4. Effect of neutron flux and fission recoils on the oxidation of zirconium (average neutron flux at samples 4.6 x 10^{11} neutrons/cm^2-sec).

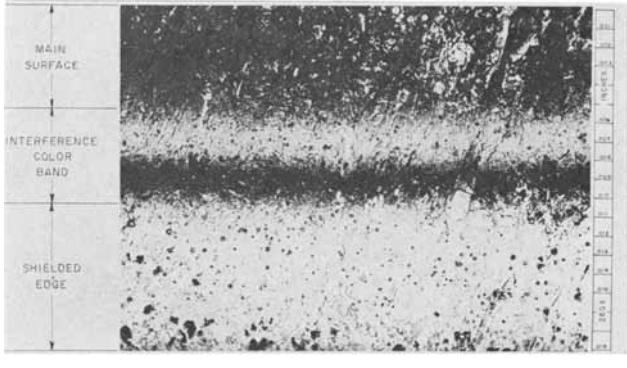

Fig. 5. Periphery of zirconium test specimen surface exposed to fission fragment recoils, normal illumination.

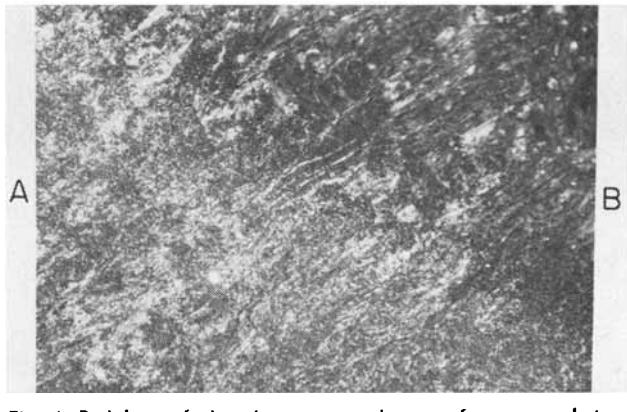

Fig. 6. Periphery of zirconium test specimen surface exposed to fission fragment recoils, polarized light (250X). A, Main surface; B, shielded edge.

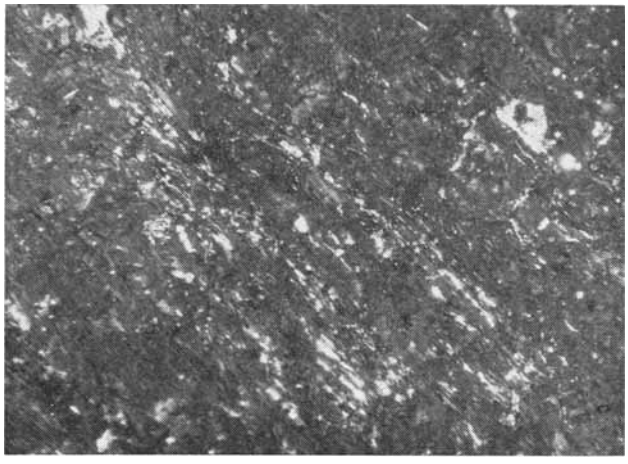

Fig. 7. Periphery of zirconium test specimen surface opposite to side seeing fission fragment recoils (exposed in neutron flux only), polarized light.

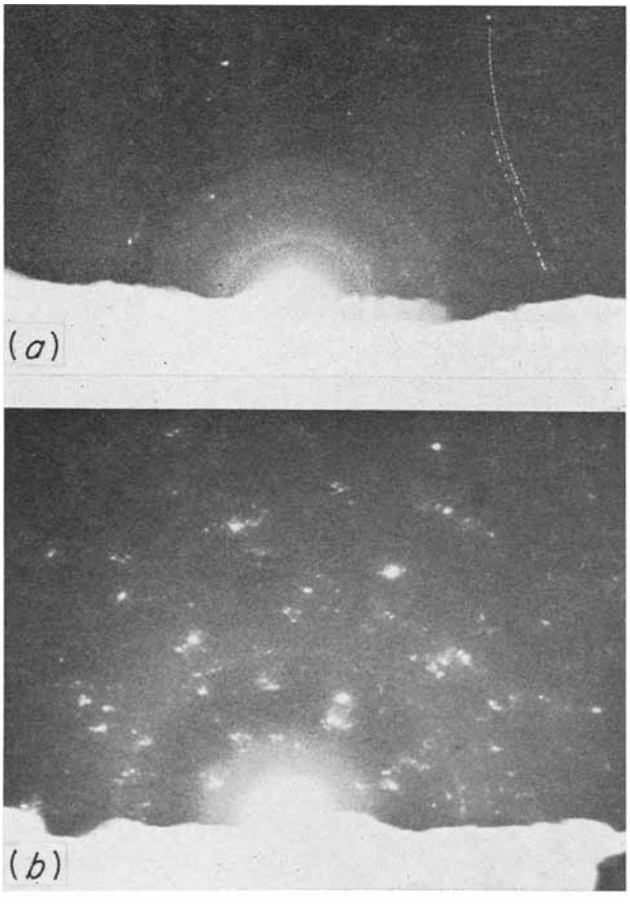

Fig. 8. Low angle electron diffraction patterns of each surface of a zirconium test specimen: (a) surface facing fission fragment recoil surface; (b) surface opposite to side facing fission fragment recoil surface.

Low angle electron diffraction patterns of the side exposed to fission fragment recoils appeared to be composed of very diffuse rings. In contrast, the opposite surface showed a pattern of a relatively large number of spotty rings. The two types of patterns described are shown in Fig. 8.

Palladium shadowed carbon replicas were made of the surfaces of all specimens used in this series of experiments. Fifteen areas were photographed on the surfaces seeing fission fragment recoils. These electron micrographs in all but two cases indicated a rough mottled surface, an example of which is shown in Fig. 9. The size of the mounds seen in the figure was in the order of 0.5μ. The surfaces not seeing fission fragment recoils were consistently much smoother as shown in Fig. 10. The size of the pebbles observed was about an order of magnitude smaller than the mounds seen in Fig. 9.

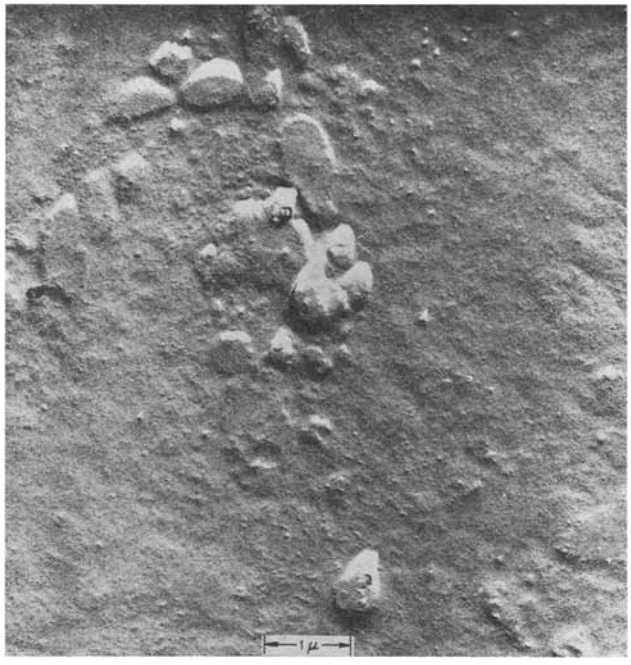

Fig. 9. Surface of zirconium test specimen exposed to fission fragment recoils (Pd shadowed carbon replica).

Unfortunately it was not possible to obtain weight change data on all of the samples. From the data available, however, it was possible to observe a trend which was not inconsistent with the other results. For the single experiment exposed in-pile for two weeks, the weight gain of the test and control sample was 0.10 and 0.11 mg, respectively. For the single experiment run out-of-pile for two weeks, the corresponding increases in sample weights were 0.02 and 0.04 mg, respectively. A comparison of these data indicate that (*a*) the weight gain of the in-pile samples was significantly greater than the out-of-pile samples, and (*b*) both samples of the in-pile experiment gained about the same amount of weight.

The latter observation suggests that the fission fragment recoils had no effect on the weight gains. However, it was observed that the control sample was at 265°C which compares to 250°C for the test sample. Thus, it is possible that a fission recoil effect was masked by the difference in temperature.

Sample surface studies under bright field illumination of the two week in-pile experiment lend support to this possibility. As estimated from observed interference colors, the test sample surface exposed to fission fragments had an oxide film thickness of about twice (2500-3000Å) that of the unexposed surface (1500-1600Å), while both surfaces of the control sample had about the same film thickness (2100-2200Å). The calculated weight gains, equivalent to the estimated oxide thicknesses, were

Fig. 10. Surface of zirconium test specimen opposite to side seeing fission fragment recoils (exposed in neutron flux only; Pd shadowed carbon replica).

found to be about 0.07-0.09 mg for both the test and control samples, which compares favorably with the corresponding measured weight gains.

Discussion and Conclusions

Polarized light and electron microscopy studies show that surfaces exposed to fission fragments either (*a*) had undergone a phase transformation or (*b*) had developed a fine particle size. Based on recently published information, the authors are more inclined toward the first possibility. Wittels and Sherrill (12, 13) have found that pure monoclinic ZrO_2 is stable to an integrated neutron flux of $\sim 10^{20}$ $(nvt)_{fast}$, but transforms to the cubic phase under the action of fission fragments at a rate of $\sim 10^{8}$ transformations per fission recoil. Adam and Cox (14, 15) have reported that the oxide on certain alloys of zirconium exposed to 10^{19} $(nvt)_{fast}$ will either partially or completely change to the cubic phase when there is uranium impurity in the presence of fission fragments. Based on the data of Wittels and Sherrill, the exposure time for the zirconium specimens ($\sim 10^{6}$ sec) was $\sim 10^{2}$ sec greater than that needed for complete transformation of the oxide to the cubic phase. This estimate assumes a fission fragment intensity of 6×10^{8} particles/cm^2-sec and an oxide film thckness of about 4000Å or less. An appreciable transformation would also be expected on the basis of the findings of Dawson *et al.* (4) for oxide on a Zr-5% V alloy under fission recoil irradiation.

Although retaining their optical activity to polarized light, surfaces exposed to reactor radiation, but not to fission fragments, appeared to have an oxide thickness intermediate between that formed on surfaces oxidized out-of-pile and surfaces exposed to recoils. Film thickness estimates, based on interference colors, in radiation run Z-8 and out-of-pile run Z-9 are typical of the data obtained. For run Z-8, the test sample surface, controlled at 250°C and not exposed to recoils, had an oxide thickness of 1500-1600Å. This is a factor of about two greater than that observed on out-of-pile oxidized surfaces (700-800Å) and a factor of two less than surfaces exposed to recoils (2500-3000Å). Irradiated control specimens in run Z-8, operating at 265°C, had an oxide thickness of 2100-2200Å, about a factor of two greater than corresponding specimens oxidized out-of-pile (1100Å). Thus it appears that test sample surfaces exposed to recoils had an oxide film three to four times as thick as the corresponding out-of-pile test sample, but only twice as thick as surfaces exposed to reactor radiation only. The corrosion of the surface exposed to recoils, as indicated by the oxide thickness, was at least a factor of ten less than that expected in uranyl sulfate solution at the same recoil intensity as that assumed in this report (this is equivalent to a solution fission power density of about 12 watts/ml) (2).

There is evidence that some oxide was lost from the recoil irradiated surfaces and, as a consequence, the actual corrosion may have been greater than that estimated from oxide thicknesses and sample weights. This is based on a subsequent experiment, not reported here, in which zirconium samples were irradiated for one week at 300°C in the presence of a fission recoil source. Spectrographic analysis of surface scrapings from the exposed source gave qualitative evidence of zirconium being present. Unfortunately, surfaces of the sources reported in this paper were not analyzed for the presence of zirconium. Hence, the magnitude of an error that might be introduced in this way is not known.

From the experimental results and the above discussion the following conclusions can be stated:

1. The oxide film of the surfaces that saw fission fragment recoils did not show optical anisotropy as determined by examination under polarized light with the microscope employed (750X). This indicates that these oxide films either underwent a phase transformation or developed randomly oriented grains of a size too small to resolve the optical activity with an optical microscope. All other oxide surfaces remained highly oriented and showed resolvable areas of optically active oxide.

2. The low angle electron diffraction study revealed that the surface subjected to recoil bombardment had a structure which produced a diffuse ring pattern while the opposite surface, exposed to a neutron flux only, produced a pattern of relatively large numbers of spotty rings. Since the diffuse rings could not be interpreted in terms of a crystal structure, it is not possible to state whether or not the fine particles are those of a transformed oxide or merely fine particles of the normal oxide.

3. It was found from interference color-oxide thickness estimates and a limited amount of weight gain data that the oxide film of surfaces exposed to fission fragments was thicker than surfaces exposed to reactor radiation in the absence of fission fragments. In turn, the oxide film of these latter

surfaces was thicker than surfaces oxidized out-of-pile. Thus it is concluded that fission fragment recoils do, in fact, have an effect on the oxidation rate. However, the amount of corrosion as indicated by the oxide thickness and weight data was at least a factor of ten less than that expected in a solution of uranyl sulfate producing an equivalent recoil intensity.

4. The electron micrographs gave evidence of a difference in the surface that had been subjected to recoil bombardment. Most of the photographs of these surfaces showed mounds on the surface in the order of 0.5μ in size. In comparison, most of the other surfaces that were either in a neutron flux or were oxidized out of radiation revealed a pebbly surface with the size of each pebble being about an order of magnitude smaller than the mounds.

5. The data obtained do not provide sufficient information to establish the mechanism of the effects of fission fragment recoils on the oxidation of zirconium.

6. The experimental technique that has been developed is one which can be effectively used to study the fission fragment recoil effects on other metals or alloys.

Acknowledgment

The authors wish to express their appreciation to J. V. Cathcart and M. L. Picklesimer for the helpful discussions on the interpretation of the results; to E. L. Long, Jr. and W. H. Bridges and their groups for the detailed optical and electron microscopy studies of the specimen surfaces; and to A. R. Olsen and his group for the remote disassembly of each radioactive experiment.

Manuscript received Jan. 23, 1961; revised manuscript received Sept. 20, 1961.

Any discussion of this paper will appear in a Discussion Section to be published in the December 1962 JOURNAL.

REFERENCES

1. G. H. Jenks, in "Fluid Fuel Reactors," J. A. Lane, H. G. MacPherson, and F. Maslan, Editors, pp. 232-245, Addison-Wesley Publishing Co., Inc., Reading, Mass. (1958).
2. G. H. Jenks, USAEC Report ORNL-3039, Oak Ridge National Lab. (July 6, 1961).
3. H. W. Dewhurst, A. H. Samuel, and J. L. Magee, *Radiation Research*, **1**, 62 (February 1954).
4. J. K. Dawson *et al.*, *Proceedings of the Second United Nations International Conference on the Peaceful Uses of Atomic Energy, Reactor Technology*, **7**, 22 (1958).
5. B. Cox, K. Alcock, and F. W. Derrick, *This Journal*, **108**, 129 (1961).
6. J. R. Johnson, *AIME Trans.*, **212**, 13 (1958).
7. D. E. Thomas, in "Metallurgy of Zirconium," B. Lustman and F. Kerze, Jr., Editors, National Nuclear Energy Series Division VII 4, 1st ed., p. 635, McGraw-Hill Book Co., Inc., New York (1955).
8. D. T. Bourgette and R. J. Beaver, USAEC Report ORNL-CF-12-1-31, Oak Ridge National Lab. (December 1958).
9. W. C. Yee, USAEC Report ORNL-2742, Oak Ridge National Lab. (April 29, 1960).
10. Reported by H. Brooks in "Nuclear Radiation Effects in Solids," *Ann. Rev. Nuclear Sci.*, **6**, 215 (1956).
11. G. H. Kinchin and R. S. Pease, *Repts. Prog. in Phys.*, **18**, 1 (1955).
12. M. C. Wittels and F. A. Sherrill, *J. Appl. Phy.*, **27**, 643 (1956).
13. M. C. Wittels and F. A. Sherrill, *Phys. Rev. Letters*, **3**, 176 (1959).
14. J. Adam and B. Cox, *J. Nuclear Energy, Part A*, **A11**, 31 (1959).
15. J. Adam and B. Cox, *Phys. Rev. Letters*, **3**, 543 (1959).

Oxidation of Zirconium and Zirconium-Oxygen Alloys at 800°C

K. Östhagen and P. Kofstad

Central Institute for Industrial Research, Blindern, Oslo, Norway

ABSTRACT

Oxidation of zirconium and zirconium-oxygen alloys in oxygen at 800°C has been studied. The studies include gravimetric oxidation rate measurements and metallographic and x-ray diffraction studies of oxidized specimens. The initial oxidation conforms with an approximate cubic oxidation rate, after which a breakaway oxidation is observed. The initial cubic period becomes shorter and the rate of breakaway oxidation becomes faster with increasing oxygen concentration up to 12-15 at. % oxygen. The oxidation is interpreted in terms of simultaneous oxide formation and oxygen dissolution in the metal.

Oxidation of zirconium constitutes oxide scale formation and oxygen dissolution in the metal (1-9). In the temperature range 300°-900°C the rate data of the initial oxidation of zirconium in oxygen appear to be best fitted by an approximately cubic oxidation rate (3, 5, 8). After an initial period, alterations in the kinetics have been observed, and for alloys this has in many cases been found to result in a "breakaway" oxidation (7, 8). This change in kinetics has been suggested to be a result of a mechanical breakdown of the scale, a change in ZrO_2 modification or to be associated with the oxygen dissolution in the metal. So far no clear correlation appears to have been established. In general there appears to be no satisfactory interpretation of the oxidation mechanism of zirconium.

Oxidation of metals which may dissolve relatively large amounts of oxygen appear to have several fea-

tures in common (7, 9-12). Depending on the temperature the oxidation of titanium, niobium, and tantalum involves initial stages which are to a large extent associated with oxygen dissolution in the metal. These initial stages are followed by a more rapid rate of oxidation, a "breakaway" oxidation, which primarily involves heavy oxide formation (9-12). For titanium the change in kinetics has been found to take place when the oxygen concentration in an outer layer of the metal reaches a composition of approximately $TiO_{0.85}$ (11). It does not appear unreasonable that similar considerations may apply for zirconium. At any rate, for an understanding of the oxidation mechanism of zirconium the relative importance of and the interplay between oxide formation and oxygen dissolution have to be considered. In the present work the effect of dissolved oxygen on the oxidation of zirconium at 800°C has been studied.

Materials and Methods

Zirconium metal in the form of rolled plates of 0.5 mm thickness was obtained from Johnson, Matthey & Co. Ltd., England. Spectrographic analysis of impurities gave the following estimates of metallic impurities: Al, 0.01%; Mn, Pb, Si, Mg, and Fe, each 0.001%. Neutron activation analysis showed that 2.4% Hf was also present in the material. Metallographic examinations of the as-received material indicated zirconium carbide inclusions in the metal. No analysis was made of the carbon content or of gaseous impurities in the metal. The hardness of the as-received cold-rolled plates was 197 VHN (10 kg).

The zirconium metal was cut into specimens with dimensions 10 x 20 x 0.5 mm. Specimens with varying concentrations of oxygen were prepared by oxidation at 1200°C at oxygen pressures $<10^{-1}$ torr and with subsequent high-vacuum anneal at 1200°C in high vacuum for 18 hr. Microhardness indentation studies indicated no oxygen gradient in the specimens after this treatment. The zirconium was oxidized in commercial oxygen dried over phosphorus pentoxide.

The rate of oxidation was measured gravimetrically by means of a quartz helix type apparatus. Prior to start of each run the apparatus was evacuated overnight to a pressure of 10^{-5} torr. A more detailed description of both the apparatus and the procedure employed has been given elsewhere (13).

Experimental Results

Oxidation rate measurements.—The results of oxidation of as-received zirconium at 800°C in oxygen at atmospheric pressure are shown in Fig. 1, where the weight gain is plotted *vs.* time and $(\text{time})^{1/3}$. As seen, the oxidation conforms with an approximate cubic rate during the first 300 min, after which an increase in the rate of oxidation is observed. Annealing of the as-received material in high-vacuum at 1200°C for 1 hr did not change the kinetics of the oxidation. The results were reproducible to within 5%.

Zirconium specimens containing from 2 to 17 at. % oxygen were oxidized under the same conditions. The results of these studies are shown in Fig. 2 where the weight gain is plotted as a function of time. During the very initial oxidation all specimens oxidized at approximately the same rate. In later stages, however, the rate of oxidation increased with increasing oxygen concentration. Above approximately 12-15 at. % oxygen there was no increase in oxidation rate with oxygen concentration. Furthermore, the time period until the transition to a faster breakaway oxidation became shorter with increasing oxygen concentration.

X-ray diffraction and metallographic studies of oxidized specimens.—X-ray diffraction studies of the oxide scale after various lengths of oxidation showed that the oxide in all cases consisted of monoclinic ZrO_2. Micrographs of metallographic cross sections of oxidized specimens of unalloyed zirconium suggested the presence of a single oxide layer on the surface. During initial periods the oxide scale had an even thickness, while with increased oxidation a more uneven attack of the metal surface was observed. The results suggest a more localized oxidation associated

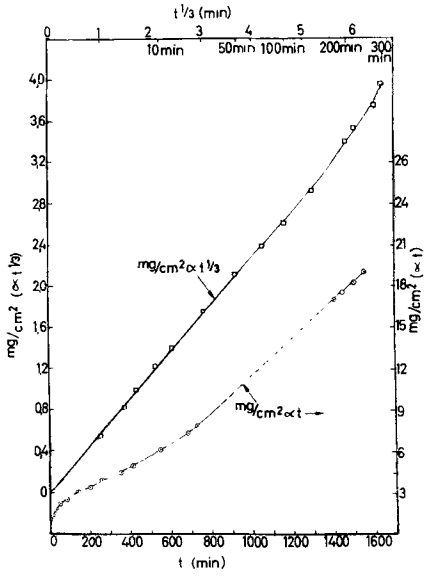

Fig. 1. Oxidation of zirconium at 800°C and 1 atm oxygen. Weight gain as a function of time and $(\text{time})^{1/3}$.

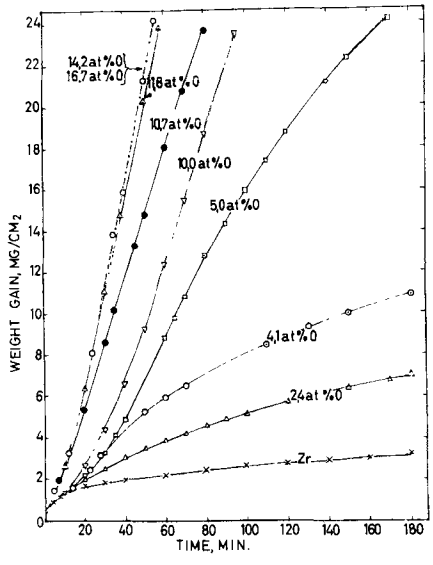

Fig. 2. Oxidation of zirconium and zirconium-oxygen alloys at 800°C and 1 atm oxygen. Weight gain as a function of time.

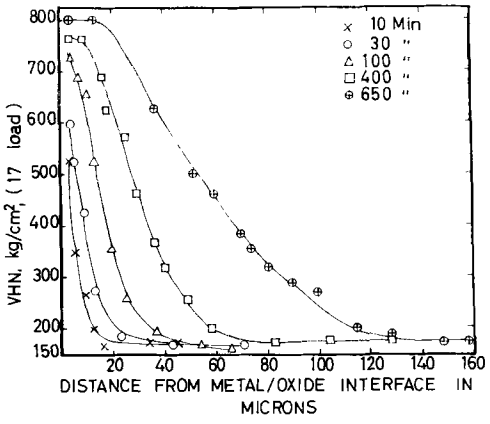

Fig. 3. Microindentation hardness studies on zirconium specimens oxidized for various lengths of time at 800°C and 1 atm oxygen.

with the individual grains in the metal. In addition the micrographs also showed evidence of an oxygen-enriched zone in the metal beneath the surface oxide.

Microindentation hardness studies on specimens of unalloyed zirconium oxidized for various lengths of time clearly showed an increased oxygen penetration into the metal with time. These measurements are shown in Fig. 3. Assuming that the hardness increases with increasing oxygen concentration, the results suggest that the oxygen in an outer layer of the metal reaches a "saturation" value.

Examinations of metallographic cross sections of oxidized zirconium-oxygen alloy specimens showed an uneven oxidation of the metal surface after the breakaway oxidation. Specimens containing relatively large concentrations of oxygen also exhibited an appreciable grain growth during oxidation.

Discussion

The present results confirm that the oxidation of zirconium involves both oxygen dissolution and oxide scale formation. Furthermore, the rate and kinetics of oxidation have been shown to be greatly dependent on the oxygen concentration in the metal.

From the present study it is difficult to calculate accurately the relative importance of oxygen dissolution in the metal. Estimates of the oxide thickness from metallographic cross sections suggest that approximately 10 and 20% of the reacted oxygen has dissolved in the zirconium metal after 100 and 300 min of oxidation, respectively.

Assuming a diffusion-controlled oxygen dissolution in the metal, an estimate of the amount of dissolved oxygen may also be made from the diffusion coefficient and the appropriate diffusion equation (22). Taking $D = 5.2 \exp(-51000/RT)$ (6) and assuming the oxygen concentration in the metal at the surface to be 29 at. % (solubility limit), the amount of dissolved oxygen after 300 min at 800°C is calculated to about 1 mg/cm². As seen from Fig. 1 this is about 25% of the observed weight gain. The calculation of course neglects oxide scale formation.

The results clearly suggest that the cubic oxidation rate reflects a combined result of oxygen dissolution and oxide scale formation. A resultant, approximate cubic oxidation may be a result of two-part processes obeying approximate logarithmic and parabolic time dependences, respectively. However, at present any considerations of the mechanism of the cubic oxidation may be only speculative due to the lack of detailed knowledge as to the part processes and their interplay. It is commonly assumed, possibly partly by analogy with TiO_2, that ZrO_2 is an n-type semiconductor and that its defect structure involves oxygen vacancies (3, 14, 15). However, the only studies known to the authors of the electrical conductivity of ZrO_2 as a function of oxygen pressure at high temperature (900°-1000°C) show that the electrical conductivity is approximately proportional to $p_{O_2}^{+1/5.2}$ (16). This relationship suggests that ZrO_2 is a p-type conductor and possibly that the defect structure involves interstitial oxygen ions.

With regard to oxygen dissolution in the metal, studies of oxygen diffusion in zirconium indicate that grain boundary diffusion predominates at 800°C and lower temperature (17), and that volume diffusion only becomes appreciable at about 1000°C. Grain boundary diffusion would result in a different time dependence than for the parabolic volume diffusion. According to Fisher's (18) model for grain boundary diffusion, the amount of oxygen dissolved would in this case be proportional to $t^{1/4}$.

From the above considerations it is evident that further studies of the relative importance and interplay of oxygen dissolution and oxide formation and studies of the defect structures of ZrO_2 are needed for an elucidation of the mechanism of the cubic oxidation of zirconium.

Studies of oxidation of zirconium and zirconium alloys by Porte *et al.* (8) indicate no change to a faster oxidation rate during the initial 400 min of oxidation at 800°C and an oxygen pressure of 200 torr. In the present case such a change is observed after approximately 300 min of oxidation. This may possibly be affected by presence of carbon impurities, as such have been shown to increase the tendency for breakaway oxidation (8). However, the present results also clearly demonstrate the effect of dissolved oxygen on the oxidation behavior of zirconium. The rate of oxidation is found to increase with increasing oxygen content up to 12-15 at. % above which no further increase in oxidation rate is observed. Furthermore, the time periods until the change in kinetics become shorter with increasing oxygen content up to 12-15 at. %.

If one assumes, as is suggested for titanium (11), that heavy oxide formation (breakaway oxidation) begins to take place after the oxygen concentration in an outer layer of the metal reaches a "saturation" value, the time lag until the change in kinetics occurs will be shorter the higher the oxygen concentration in the starting material. This is in accord with the present results. The fact that the time lag decreases until the oxygen concentration of the Zr-O alloys reaches 12-15 at. % may suggest that the "saturation" limit corresponds to this concentration range. Zirconium may dissolve up to 29 at. % oxygen, and it is not altogether clear why the "'saturation" value does not correspond to this solubility limit. A possible explanation may be that relatively large structural changes take place in zirconium-oxygen solid solutions at concentration of oxygen of 12-15 at. %. Such changes may affect the rate of oxygen dissolu-

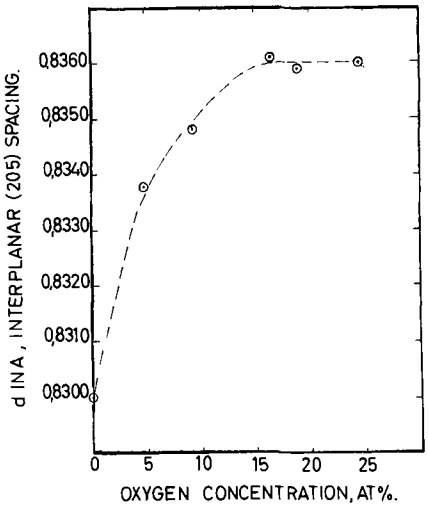

Fig. 4. The d-value of the interplanar (205) spacing as a function of oxygen content in zirconium-oxygen solid solutions.

tion, and further dissolution of oxygen may lead to large stresses and strains which partly results in cracking of this layer, and with a subsequent more rapid oxidation. Titanium solid solutions corresponding to approximately Ti_6O (14.3 at. % oxygen) have been found remarkably volatile possibly because of the relative large stability of individual Ti_6O octahedra (19-21). Corresponding effects may be found in zirconium-oxygen solid solutions. To study this, samples of zirconium oxygen-solid solutions were prepared by argon arc melting of mixtures of Zr and ZrO_2 and subsequently studied by x-ray diffraction. The results are given in Fig. 4, which shows the interplanar (205) spacing as a function of oxygen concentration. As seen, a transition in the effect of the oxygen content on the interplanar spacing is at approximately 15 at. % oxygen, in agreement with the arguments presented above.

The increased rate of oxidation with oxygen content is suggested to reflect a competition and interplay between oxygen dissolution and oxide formation. As proposed for oxidation of titanium, niobium, and tantalum (10-12), the rate of oxide formation is suggested to be governed by the rate of nucleation and rate of growth of oxide nuclei during breakaway oxidation.

An additional or alternative interpretation may be made in terms of considerations of the zirconium-oxygen phase diagram (23). Zirconium-oxygen alloys prepared at 1200°C containing less than 4 at. % oxygen will be homogeneous beta alloys; alloys containing between 4 and 12 at. % are in the alpha-plus-beta region; and alloys above 12 at. % are homogeneous solid solutions of the alpha alloy. The rapid increase in the oxidation rate in the region between 4 and 5 at. % may be due to the presence of grains of alpha alloy. Alloys above 12 at. % oxygen consist entirely of alpha alloy and this may give rise to an apparent "saturation" limit. Metallographic studies of oxidized alloy specimens showed a mixture of two phases up to about 10 at. % oxygen, while above this value only one phase was observed.

The present study clearly establishes the great importance of oxygen dissolution and dissolved oxygen on the oxidation of zirconium. For an elucidation of the mechanism of oxidation of zirconium further studies of the relative importance and interplay between oxide formation and oxygen dissolution are needed. This will form the subject of future studies of oxidation of zirconium in this laboratory.

Manuscript received June 19, 1961; revised manuscript received Sept. 13, 1961.

Any discussion of this paper will appear in a Discussion Section to be published in the December 1962 JOURNAL.

REFERENCES

1. E. A. Gulbransen and K. F. Andrew, *Trans. Am. Inst. Mining Met. Engrs.*, **185**, 515 (1949).
2. D. Cubiciotti, *J. Am. Chem. Soc.*, **72**, 4138 (1950).
3. J. Belle and M. W. Mallett, *This Journal*, **101**, 339 (1954).
4. E. A. Gulbransen and K. F. Andrew, *Trans. Am. Inst. Mining Met. Engrs.*, **209**, 394 (1957).
5. R. G. Charles, S. Barnartt, and E. A. Gulbransen, *ibid.*, **212**, 101 (1958).
6. J. P. Pemsler, *This Journal*, **105**, 315 (1958).
7. G. R. Wallwork and A. E. Jenkins, *ibid.*, **106**, 10 (1959).
8. H. A. Porte, J. G. Schnizlein, R. C. Vogel, and D. F. Fisher, *ibid.*, **107**, 506 (1960).
9. T. Hurlen, *J. Inst. Metals*, **89**, 273 (1961).
10. P. Kofstad, 1st International Congress on Metallic Corrosion, London, April 1961.
11. P. Kofstad, P. B. Anderson, and O. J. Krudtaa, *J. Less-Common Metals*, **3**, 89 (1961).
12. P. Kofstad, "Oxidation of Tantalum in the Temperature Range 500-700°C" ARDC Final (Technical) Report, Central Inst. for Industrial Research, Oslo, Norway, April 1961, to be published.
13. P. Kofstad, K. Hauffe, and H. Kjöllesdal, *Acta Chem. Scand.*, **12**, 239 (1958).
14. M. W. Mallett and W. M. Albrecht, *This Journal*, **102**, 407 (1955).
15. S. Aronson, *ibid.*, **108**, 312 (1961).
16. J. Rudolph, *Z. Naturforsch.*, **14a**, 727 (1959).
17. G. Sainfort, R. Jacqueson, and P. Laurent, "Diffusion of Oxygen in Zirconium," Symposium on Solid State Diffusion, Saclay 1958, North Holland Publishing Co.
18. J. C. Fisher, *J. Appl. Phys.*, **22**, 74 (1951).
19. P. Ehrlich, *Z. anorg. u. allgem. Chem.*, **247**, 53 (1941).
20. S. Anderson, B. Collén, U. Kuylensticerna, and A. Magnéli, *Acta Chem. Scand.*, **11**, 1641 (1957).
21. T. Hurlen, H. Kjöllesdal, J. Markali, and N. Norman, "Oxidation of Titanium," ARDC-report Contract No. AF 61(514)-892, Central Institute for Industrial Research, Oslo, Norway, April 1958.
22. L. S. Darken and R. W. Gurry, "Physical Chemistry of Metals," p. 445, McGraw-Hill Book Co., New York (1953).
23. J. P. Pemsler, Private communications.

Solution and Diffusion of Corrosion Oxide Film in Zircaloy

R. M. Treco

United Nuclear Corporation, New Haven, Connecticut

ABSTRACT

In Zircaloy-2 processing, an oxide surface film is formed during the water corrosion test. Removal by vacuum annealing is an economical and rapid method. The effects of heating on the distribution of oxygen in the Zircaloy were reviewed, and it is shown that subsequent pickling is desirable to remove the surface layer of diffused oxygen.

During the fabrication of Zircaloy-2 for reactor cores, a corrosion test is required which forms a black oxide film on the surface. Since the Zircaloy-2 is further processed, it becomes necessary to remove the tightly adherent film. The oxide film is not readily removed by the usual chemical methods, and its elimination poses a problem.

One method which has been used successfully has been to anneal at a sufficiently high temperature to dissolve the oxide film in the Zircaloy. This method is most desirable from the economic standpoint since it involves few processing steps and the annealing treatment involved is required for other reasons as well. Removal of the film by annealing has been objected to because the dissolved oxygen adversely affects the mechanical properties, particularly in relation to surface crack susceptibility. However, it is usual to pickle the surface at a subsequent step of the process, and this has been thought sufficient to remove most of the dissolved oxygen. Pickling removes from 0.001 to 0.002 in. of the surface. A second method of removing the film is mechanical, involving sand or vapor blasting. This method has the disadvantages that the thin film is difficult to remove evenly thereby maintaining the dimensional tolerance requirements, and it is an additional step requiring additional equipment.

Since experimental data were available for the purpose, an analysis has also been made of the contribution of the corrosion film in adding oxygen to the Zircaloy. A further analysis has been made of the annealing process and its effect on the oxygen concentration in the Zircaloy-2. The losses due to these processes have been compared with the losses due to pickling.

Zirconium Oxide Corrosion Film Formation

The rate of oxide film formation on Zircaloy-2 has been well established. For the case involved, namely, 3 days in 680°F water, the weight gain in mg/dm^2 is found from the equation,

$$\log \Delta m = 0.76 + 0.38 \log t \qquad [1]$$

where t is in days. Thus the weight gain in 3 days at 680°F is 8.7 or 9 mg/dm^2. Corresponding values are 15.7 mg/dm^2 for 14 days at 680°F and 29.3 mg/dm^2 for 14 days in 750°F steam.

The oxide film consists of monoclinic zirconium oxide ZrO_2, having a density of 5.6 g/cc and consisting of 26 w/o oxygen. From this it is easily shown that a weight gain after 3 days of 0.09 mg/cm^2 is equivalent to a film thickness on one surface of the Zircaloy of 62 x 10^{-6} cm or 24 x 10^{-6} in. The corrosion film thickness is based on the assumption that all of the oxygen weight gain stays on the surface, an assumption which is shown to be justified in a later section where the diffusion rate of oxygen in the corrosion test is examined.

Diffusion Constants for Oxygen in Alpha Zirconium

To study the effect of surface oxide solution, it is necessary to establish the diffusion rate of oxygen in alpha zirconium. Experimental work has established three separate equations for the diffusion of oxygen in zirconium as a function of temperature.
These equations are summarized below.

1. Pemsler (3), for the temperature range, T = 400° — 585°C:

$$D = 9.4 \exp (-51{,}780 \pm 220/RT) \qquad [2]$$

2. Misch (2), for the temperature range, T = 450° — 600°C:

$$D = A \exp (-43{,}500/RT) \qquad [3]$$

3. Mallett, Albrecht, and Wilson (4) for the temperature range, T = 1000° — 1500°C:

$$D = 0.196 \exp (-41{,}000 \pm 1500/RT) \qquad [4]$$

where D is the diffusion constant in cm^2/sec, R the universal gas constant, and T the temperature in degrees Kelvin. Of the three values given, the first two, those of Pemsler and Misch, were determined by studies of the dissolution rate of the oxide in the metal. The third equation was determined as a study of the rate of diffusion of oxygen in alpha and beta zirconium in the alpha solid solution range of the phase diagram. It will be apparent that the activation energies given by Eq. [3] and [4] are in reasonably good agreement and somewhat lower than the value determined by Pemsler (Eq. [2]). Despite this fact there appears to be little significant difference in the choice of the diffusion equation. Since Misch did not put his values in the form of a specific diffusion constant, the values of Pemsler and Mallet *et al.* were used. The temperature of interest for film dissolution in this study is 750°C, a temperature not covered specifically by either of these investigators. It was therefore necessary to extrapolate upward in the case of the Eq. [2] constant and downward in the

case of Eq. [4]. A comparison of the two values at 750°C shows that, if the higher limit of activation energy is used in Eq. [4], the diffusion rate from this relation will be in the ratio of approximately 2 to 1 to the diffusion constant according to the Pemsler relation. Thus the respective values for the diffusion constant at 750°C are D (Eq. [2]) = 8.07×10^{-11} and D (Eq. [4]) = 16.42×10^{-11} cm²/sec. In determining the oxygen gradient as a function of time during the 750°C anneal, an average value for the diffusion constant based on Eq. [2] and [4] was used, as follows:

$$D_{ave} = 12.24 \times 10^{-11} \text{ cm}^2/\text{sec} \quad (T = 750°\text{C})$$

In considering diffusion at temperatures lower than 585°C the Pemsler values were used. In particular, for the corrosion temperature of 680°F (360°C), the diffusion constant according to Eq. [2] is equal to 11.41×10^{-18} cm²/sec.

All values of the diffusion constant have been determined for oxygen in zirconium. It is assumed that the same values may be applied to Zircaloy-2 without substantially altering the conclusions, since it is known that oxygen reactions with Zircaloy-2 are almost identical with those of zirconium.

Solution of Corrosion Film in Zircaloy-2

Quantity of Oxygen.—From Eq. [1] it was shown that the weight gain in corrosion after 3 days at 680°F in water is 0.09 mg/cm². It is interesting to calculate the thickness of the oxide film from the oxygen weight gain and the following relation:

$$L = \frac{\Delta m}{(\rho \times \text{w/o } O_2)_{ZrO_2}} \qquad [5]$$

where Δm is weight gain in mg/dm² and ρ the density of ZrO_2 in mg/dm³. From this it can be shown that the thickness of the film is equivalent to 6180Å or 24.3×10^{-6} in. In view of the small value of L, the diffusion calculations have been made with no allowance for film thickness in the penetration curve.

If the entire weight gain of the oxygen in the film were to be dissolved and diffused uniformly throughout the Zircaloy-2, it would increase the average oxygen concentration by 270 ppm. Since the average oxygen level in wrought Zircaloy is approximately 1000 ppm, the total oxygen becomes about 1300 ppm. However, the oxygen does not diffuse in this way under normal conditions, and it is necessary to consider further, not the over-all average oxygen, but the maximum concentration at any particular point in the Zircaloy. In other words, it is necessary to examine the diffusion penetration curve.

Diffusion penetration during corrosion.—The possibility of oxygen diffusion from the film during the time of the corrosion test must be considered since, if the additional oxygen supplied by the film diffuses inward appreciably, it will have an effect on the concentration gradient after annealing. To examine this effect the Pemsler diffusion constant value was used rather than the average constant used at higher temperatures. Referring to Fig. 1, we have a representative diagram of the cross section of a corrosion coupon showing the ZrO_2 film. Since the diffusion constant does not take into account the physical phenomena involved in the dissociation of ZrO_2 which

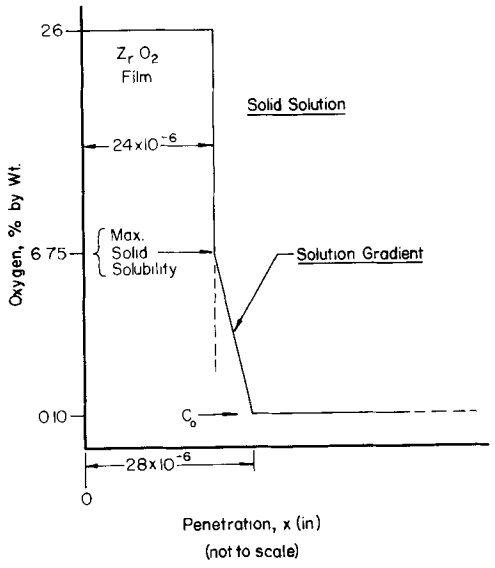

Fig. 1. Distribution of oxygen in Zircaloy-2 after 3 days in 680°F water.

supplies oxygen atoms for diffusion, the oxygen differential which is the driving force for the diffusion, *i.e.*, the boundary conditions, must be established. The maximum concentration of oxygen C_s is the maximum solid solubility of oxygen in Zircaloy and is equal to 6.75 w/o. Initial oxygen content C_o was taken equal to 1000 ppm, corrosion conditions are 3 days at 680°F (360°C), and the diffusion constant for this temperature equals 11.41×10^{-18} cm²/sec. Under these conditions the expression for concentration *vs.* distance penetrated is given by Darken and Gurry as

$$(C - C_o)/(C_s - C_o) = 1 - \text{erf } (X/2\sqrt{Dt}) \qquad [6]$$

where C is O_2 concentration after time t, C_o is initial concentration of O_2, C_s is max solid solubility of O_2 in Zircaloy-2, erf is error function, D is diffusion constant, t is time (sec), and X is penetration (in.). In this case it is sufficient to determine the depth of penetration at which the oxygen concentration is reduced to the initial level of the material. From Eq. [6] it can be shown that the quantity $(X/2\sqrt{Dt})$ equals 6.0, from which the penetration, X, can be calculated as 4.05×10^{-6} in. This amount of penetration is negligible and is therefore ignored in the later calculation of diffusion during the annealing at 750°C. Figure 1 shows the distribution of oxygen after the corrosion test.

Solution of the corrosion film.—The time required for complete solution of the film is obtained by using the proper boundary conditions in the following relation adapted from Barrer:

$$C_f - C_o = \frac{Q}{(\sqrt{\pi D_T t})\rho_{solv}} \quad \text{for } X = 0 \qquad [7]$$

To determine the time required for the film to be completely dissolved and uniformly distributed throughout the Zircaloy-2, the boundary conditions are:

$$C_f = 1270 \text{ ppm}$$
$$C_o = 1000 \text{ ppm}$$
$$Q = 9 \times 10^{-5} \text{ g/cm}^2$$
$$D_T = (D_{ave})\ 750°\text{C} = 12.24 \times 10^{-11} \text{ cm}^2/\text{sec}$$
$$\rho_{solv} = 6.55 \text{ g/cc}$$

Substituting and rearranging,

$$t = \frac{(9 \times 10^{-5})^2}{\pi(12.24\times10^{-11})[(1270-1000)(10^{-6})]^2(6.55)^2}$$

from which $t = 1.87 \times 10^2$ hr $= 7.8$ days. It is apparent that this time is much too long to be economical. It is therefore of more significance to determine the annealing time required to make the corrosion film just disappear from the surface. In this case, and using the same relation, the boundary conditions are $C_f = 0.0675$ (*i.e.*, maximum solid solubility) and $C_o = 1000$ ppm as before. Substituting in Eq. [7] and solving, the time required for the oxide film to just disappear is 0.03 hr or 1.8 min. Laboratory tests under ideal conditions have confirmed that this short time is correct for film disappearance. Since this time is shorter than the normal process anneal of 4 hr, it is apparent that further diffusion of the oxygen will take place. However, if only film disappearance is required, an anneal of 20-30 min is indicated.

Diffusion penetration during process anneal.—As noted previously, a common process anneal is 4 hr at 750°C *in vacuo*. During this annealing the oxide film disappears from the surface of the Zircaloy and is distributed by diffusion. The distribution of oxygen after the 4-hr anneal requires that the diffusion equation be solved for the condition where the surface concentration does not remain constant, but decreases with time. The following equation has been adapted from Barrer to fit the conditions for Zircaloy-2 during annealing and the appropriate boundary conditions:

$$C - C_o = \left(\frac{Q}{\rho_{solv}\sqrt{\pi D_T t}}\right) \exp(-X^2/4D_T t) \quad [8]$$

where Q is the quantity of oxygen dissolving (g/cm^2),

$$\rho_{solv} = 6.55 \text{ g/cc}$$

$$D_T = (D_{ave})750°C = 12.24 \times 10^{-11} \text{ cm}^2/\text{sec}$$

t is time (sec), and X is penetration (cm). Substituting appropriate values, the concentration as a function of time and penetration at 750°C is then

$$C - C_o = \left(\frac{0.7}{\sqrt{X}}\right) \exp(-1.32 \times 10^{+10} X^2_{in}/t) \quad [9]$$

For an annealing time of 4 hr

$$C - C_o = 5.83 \times 10^{-3} \exp(-9.16 \times 10^{+5} X^2_{in.}) \quad [10]$$

Solving for $(C - C_o)$ from Eq. [10] for various appropriate values of X, results in the following values:

X, in.	C, ppm
0	6830
1.5×10^{-4}	6710
5.0×10^{-4}	5640
1.0×10^{-3}	3300
1.25×10^{-3}	2394
1.5×10^{-3}	1780
2.0×10^{-3}	1150
3.0×10^{-3}	1002
4.0×10^{-3}	1000

The diffusion gradient thus obtained has been plotted in Fig. 2 (solid curve). It is apparent that in order to reduce the surface oxygen to a value equivalent to that of the Zircaloy, it is necessary to remove

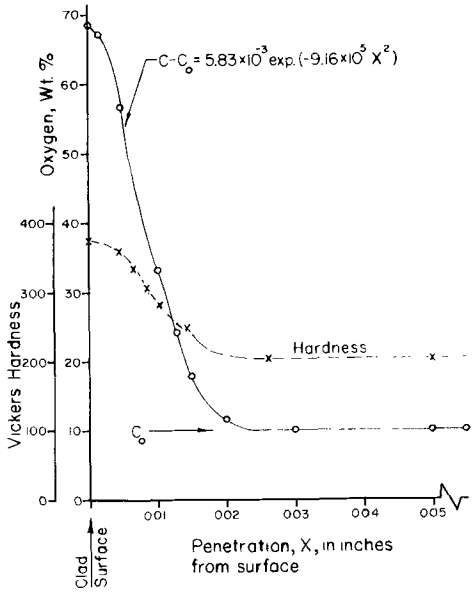

Fig. 2. Diffusion gradient after annealing 4.0 hr at 750°C

0.002 in. from the surface. If a lesser amount of metal is removed, it is then necessary to consider the effect of the residual surface oxygen on the Zircaloy properties. For example, if only 0.001 in. is removed, there will be approximately 0.33 w/o of oxygen in solution at the surface of the Zircaloy. However, it is apparent that all of the oxygen added by solution and diffusion of the 3-day corrosion film can be removed by pickling 0.002 in. from the surface.

Recorrosion Testing

Occasionally it becomes necessary to submit Zircaloy to a second corrosion test. In this case the Zircaloy must be prepared so as to have a clean surface for recorrosion testing. To do this, the initial corrosion film from the first test must be completely removed. While the film can be removed by mechanical means, it is often more convenient to dissolve the film by vacuum annealing as described above. A simple and obvious procedure for preparing the surface is to anneal the Zircaloy at 750°C for just the amount of time required to dissolve the film completely. It has been shown above that the dissolution time is 1.8 min at this temperature. Assuming that a 30-min anneal is used for convenience, we must consider how deep the oxygen penetrates in this time. Knowing the penetration, a decision can be made as to how much to pickle from the surface in order to restore the Zircaloy to its initial condition. To determine the concentration gradient curve, the same boundary conditions are used as those for the 4 hr anneal with the exception that the time is now reduced to 30 min. The diffusion equation is then

$$C - C_o = 0.0165 \exp(-7.33 \times 10^{+6} X^2) \quad [11]$$

where X is in inches. Values for total oxygen as a function of distance penetrated are shown below.

Penetration, X, in.	Total O_2, ppm
1×10^{-6}	17,500
1×10^{-5}	17,500
1×10^{-4}	16,350
5×10^{-4}	3,640
1×10^{-3}	1,011

The results of this calculation show that the total oxygen concentration is reduced to the residual value of the Zircaloy at a penetration of 0.001 in. It is therefore apparent that in order to restore the Zircaloy to its original condition after a 3-day, 680°F water corrosion test, the Zircaloy should be annealed *in vacuo* at 750°C for 30 min followed by a pickling operation to remove 0.001 in. per surface. This may be done as many times as required, subject to maintaining final dimensions. If less than 0.001 in. per surface is removed, consideration must be given to the retained oxygen. For example, removal of only 0.0005 in. per surface leaves approximately 3600 ppm at the surface in solution.

Conclusions

It has been shown above that the oxygen film accumulated during a 3-day, 680°F water test diffuses into the Zircaloy-2 during the process anneal at 750°C. The effect of this additional oxygen is primarily one of increasing hardness although other properties are also affected (8). The hardening effect of oxygen in Zircaloy-2 has been discussed by Rubenstein (9), and it can be shown that the Vickers hardness is a function of oxygen concentration as follows:

$$\text{VHN} = 333(\text{w/o O}_2)^{1/2} + 97.5 \qquad [12]$$

A hardness-penetration curve has been plotted from this relation in Fig. 2 (dashed line) from which it may be seen that the hardness is almost doubled at the surface after the 4-hr anneal. It is apparent that the removal of 0.0015-0.002 in. by pickling is sufficient to reduce the hardness to an acceptable level. Furthermore, the hardening effect is considerably reduced at elevated temperatures and in addition the notch sensitivity of Zircaloy-2 has been shown by fatigue tests to be very low. These factors substantiate the original assumptions that the Zircaloy is not damaged by the solution treatment to remove oxide if the surface is subsequently pickled.

Manuscript received Aug. 14, 1961.

Any discussion of this paper will appear in a Discussion Section to be published in the December 1962 JOURNAL.

REFERENCES

1. S. Kass and D. B. Scott, *Zirconium Highlights*, WAPD-ZH-4, pp 23-26 (February 1958).
2. R. D. Misch, *Acta Met.*, **5**, 179 (1957).
3. J. P. Pemsler, "The Diffusion of Oxygen in Zirconium and Its Relation to Oxidation and Corrosion," NMI-1177, p. 25 (May 1957).
4. M. W. Mallett, W. M. Albrecht, and P. R. Wilson, *This Journal*, **196**, 181 (1959).
5. R. M. Barrer, "Diffusion in and through Solids," Cambridge University Press, London (1951).
6. L. S. Darken and R. W. Gurry, "Physical Chemistry of Metals," pp. 441-445, McGraw-Hill Book Co., Inc., New York (1953).
7. B. Lustman and F. Kerze, "The Metallurgy of Zirconium," p. 634, McGraw-Hill Book Co., Inc., New York (1955).
8. R. M. Treco, *Trans. Am. Soc. Metals*, **45**, 872 (1953).
9. L. S. Rubenstein, *Zirconium Highlights*, 1-4, WAPD-ZH-17 (May 1959).

An Electron Optical Study of the Effect of Temperature and Environment on the Growth of Oxide Whiskers on Cold-Rolled and Annealed Copper

William R. Lasko and Warren K. Tice

Research Laboratories, United Aircraft Corporation, East Hartford, Connecticut

ABSTRACT

A systematic electron microscope study comparing the effect of temperature and environment on the formation of oxide crystal growths on high-purity, cold-rolled, and preannealed copper sheet is presented. Changes in size, shape, and rate of whisker growth in environments of dry air and oxygen occurred only during critical temperature intervals, clearly differentiating the phenomena of whisker-type growth from simple oxide film thickening. Whisker growth examinations of the preannealed copper specimens at some temperatures, both in air and oxygen, revealed increased whisker growth over that exhibited by specimens which were initially cold-rolled. Generally, the oxide crystal growths obtained on the preannealed material were longer and thinner than those observed on the preworked material.

In recent years a great deal of emphasis has been given to the propagation of oxide whiskers on metal surfaces (1-3). The formation of oxide whiskers is unique in itself, but still of greater interest is the relationship between whisker growth and metallic oxidation (4). The latter point of view has not received the attention it deserves in the past literature. This was one of the reasons for the comprehensive research effort undertaken to determine the effect of temperature and environment on the growth of oxide whiskers with particular attention being directed at determining the relationship between whisker growth and oxidation.

Despite the large amount of work performed (5-7) on the oxidation behavior of copper, little is still known at what critical temperatures oxide whisker growth is initiated in environments such as air and oxygen and the effect of these localized growths on

the kinetics of oxidation. Recent work by Gulbransen, Copan, and Andrew (8) has indicated that whisker growths, although of interest as a natural phenomena, do not have an appreciable effect on the oxidation kinetics. However, information is still lacking concerning the effects of deformation and subsequent annealing on the crystal nature of oxide whiskers and the correlation of these growth effects with current concepts on dislocation density changes during annealing. The purpose of this paper is to present the results of a careful and precise electron microscope investigation of the effects of temperature, treatment, and environment on the crystal habit of copper oxide whiskers. The ultimate goal is to arrive at a better understanding of the mechanism of whisker formation and its ultimate relationship to various metallurgical processes and phenomena such as cold-rolling, annealing, and oxidation.

Experimental Procedure

High-purity (99.999%) copper rod[1] was cold-rolled to a sheet thickness of 0.003 cm, and 0.3 cm disks with a V-slot were punched out using a special jig. The disks were slotted in order to make an area near the center of the disk which would be parallel to the electron beam so that the nature and shape of the outgrowths emanating from the slotted area could be directly observed. After punching, the V-slot disks were degreased, hand polished using conventional techniques, and immediately subjected to environmental study to avoid the buildup of contamination. Annealed specimens were prepared by heat treating the cleaned V-slotted disks in argon at 450°C for 4 hr. These are referred to as condition B specimens to differentiate them from the nonannealed (cold-rolled) or condition A specimens. This differentiation was made since it was realized that, once the specimens were exposed to temperature during growth, they could no longer be strictly referred to as cold-rolled or annealed.

Reaction environments studied included dry air and laboratory pure (99.995%) oxygen. The gases were passed through a drying chamber containing Drierite (anhydrous calcium sulfate) and glass wool prior to flowing over the samples supported in porcelain boats. A tubular furnace was designed and equipped with a chromel-alumel thermocouple element to monitor the temperature within ±2°C. A reaction time of 1 hr at 100°C intervals was employed for temperature ranges from 100° to 800°C.

The Hitachi HU-11 electron microscope was used to examine the surface growths. Normal bright-field images, using the 75-kv electron beam were taken at 3000X and enlarged optically to 6000X.[2] In specific instances, especially at the higher temperatures, where the growths were extensive, the magnification was reduced to accommodate the whole field. Specimens were examined in all phases of growth, but only selected micrographs necessary for clarity are illustrated.

Both x-ray and selected area diffraction techniques were applied to a number of the A and B specimens to determine changes in structure brought about by the environment. Under the conditions studied gross oxide formation (whiskers and base oxide) were identified by x-ray diffraction methods to be a mixture of $Cu_2O + CuO$, while selected area diffraction analysis of individual whiskers alone showed CuO. No differences in structure between the A and B specimens could be detected in either air or oxygen.

Whisker length measurements and density counts were taken from the original negatives of the various samples. Both determinations were made directly on the viewing glass window of a Jones and Lamson comparator by enlarging the negatives from 3000X to 30,000X employing a 10X objective. Whenever possible approximately 50 whiskers were measured to ensure obtaining a good statistical average. To aid in obtaining accurate whisker determinations, a grid network consisting of small squares was drawn on the comparator viewing window, and the ends and lengths of the whiskers located in each square for a designated vertical and horizontal area were counted and measured. As a further precautionary measure, to ensure obtaining counts and length measurements representing a random distribution of the whiskers, the determinations were made in arbitrary areas of the negatives for each of the samples.

Results

A summary of the observations which were made is presented in Table I. Since it is extremely difficult to describe quantitatively or measure each of the specimens with respect to such salient features as whisker shape, density, length, width, etc., particularly at the higher whisker densities, the descriptions given in Table I are semiquantitative estimations of the average whisker length and density for the conditions indicated. As a result, in the descriptions of the electron micrographs to follow, the discussions are confined primarily to revealing gross changes in growth rather than to describing particulars.

Table I. Summary of observations on whisker growth

Temp, °C	Condition*	Environment and time of exposure** Dry air—1 hr Fig. 1-2 Avg. density/cm²	Length-μ	Oxygen—1 hr Fig. 3-4 Avg. density/cm²	Length-μ
100	A	No growth		No growth	
	B	No growth		No growth	
200	A	No growth		No growth	
	B	No growth		No growth	
300	A	2.2×10^6	0.3	1.5×10^7	1.2
	B	No growth		8.2×10^6	1.6
400	A	1.4×10^7	1.8	1.1×10^7	2.6
	B	1.7×10^7	1.0	2.1×10^7	3.2
500	A	4.0×10^6	2.5	8.0×10^6	6.3
	B	2.0×10^7	3.2	1.1×10^7	7.2
600	A	4.0×10^6	4.6	4.4×10^6	4.0
	B	1.9×10^7	9.3	3.4×10^6	3.3
700	A	3.8×10^6	5.2	3.8×10^6	6.4
	B	2.6×10^6	3.2	3.4×10^6	7.2
800	A	Few whiskers		3.2×10^6	8.0
	B	Few whiskers		2.4×10^6	13.0

* A refers to the specimen that was cold-rolled while B refers to preannealed specimen heat treated at 450°C in argon.
** All treated at atmospheric pressure.

[1] American Smelting & Refining Co., Research Department, South Plainfield, N. J. No impurities detected by standard spectrographic methods.
[2] Reduced ~½ for publication.

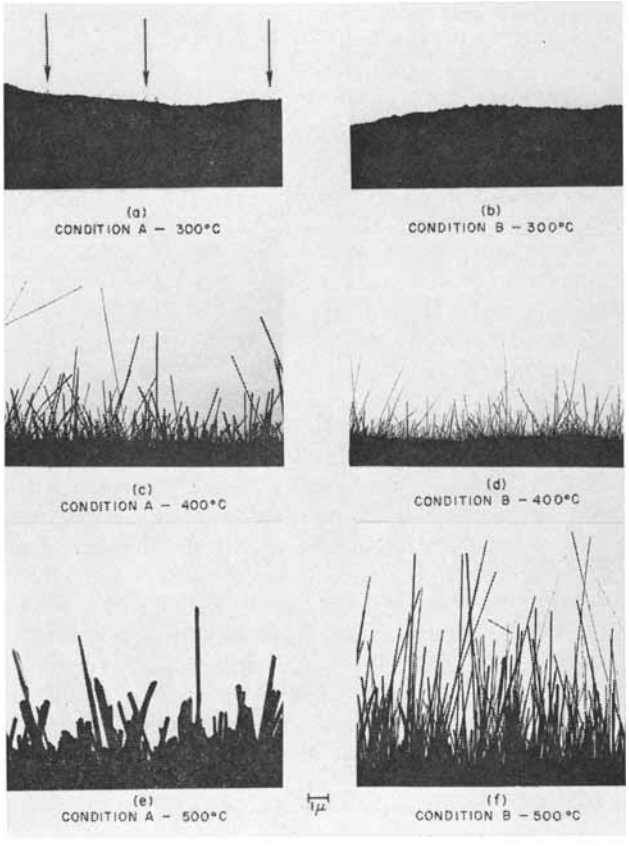

Fig. 1. Effect of temperature on the growth of oxide whiskers on pretreated copper in dry air. Magnification approx. 3000X.

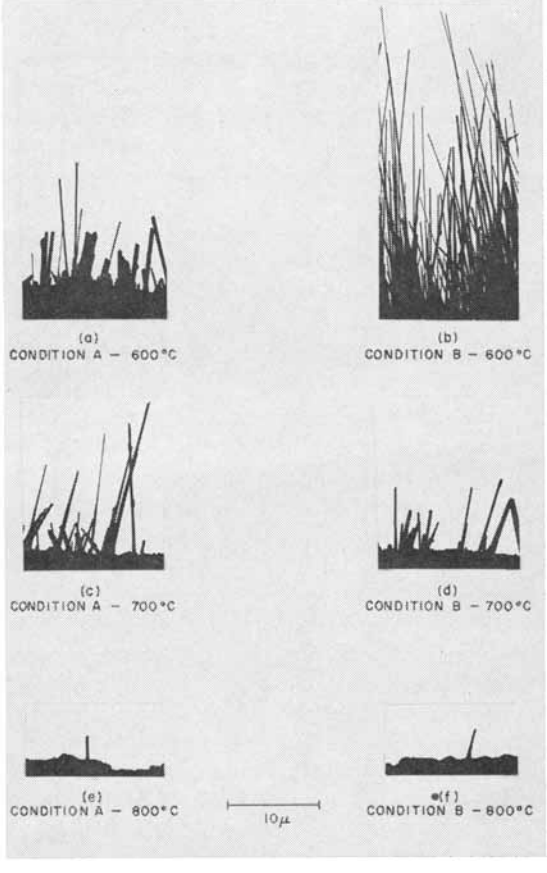

Fig. 2. Effect of temperature on the growth of oxide whiskers on pretreated copper in dry air. Magnification 1300X.

Dry air.—Some whisker-type growths (shown by arrows on Fig. 1a) were observed after exposure for 1 hr at 300°C for condition A (cold-rolled) specimens and at a slightly higher temperature for condition B (annealed) specimens. At higher temperatures more whiskers were formed on both the A and B specimens, but in general, thinner, longer and a higher density of whiskers formed on B specimens than on A specimens treated under identical conditions. Whisker growths reached a maximum at about 600°C. As the temperature was increased to 700°C, the differences in whisker growth between the pretreated specimens (cold-rolled and annealed) were less pronounced. At 800°C whisker growth had virtually ceased; no differences could be detected between the A and B specimens, but a general surface roughening had occurred.

Oxygen.—Whisker growth began at about 300°C. At this temperature, more thin whiskers apparently formed on the A specimen than on the B specimen. At 400° and 500°C, the same pattern was observed as for those specimens treated in air, namely, more thin long whiskers on the B disks than on the A disks. Comparing the micrograph of Fig. 3 with that of Fig. 1, it is also apparent that whisker growth is greater in oxygen than in air. The same trend of more thin whiskers on the B specimen than on the preworked or A specimens persisted to the highest reaction temperature studied, but as the temperature was raised, the whiskers became coarser and as a result, the density was decreased. In an oxygen atmosphere, whisker formation did not completely cease at the highest temperature (800°C) as it did on those specimens exposed to air (compare Fig. 2e and f with Fig. 4e and f).

Observations

The pertinent trends which have been observed from these experiments on copper disks can be summarized as follows:

1. At the lowest whisker formation temperature in dry atmospheres (300°C), whiskers occur more profusely on the specimens which were initially cold-worked (A specimens) than on the preannealed samples (B specimens) (Fig. 1a *vs.* 1b, 3a *vs.* 3b).
2. In direct contrast to the previous observation for the initiation of growth, at the higher temperatures the whiskers which form on the preannealed specimens appear to be more profuse, longer, and thinner than on the specimens which were initially in the cold-rolled condition.
3. In an air environment, there was a temperature at which growth reached a maximum. This temperature was always in the neighborhood of 500° or 600°C. At temperatures much in excess of this, no whisker formation was observed.
4. Oxygen enrichment of the reacting atmosphere accentuated whisker growth.
5. In general, whisker formations on the specimens which were initially cold-rolled were coarser than those observed on the preannealed specimens.

Discussion

It has been found from these experiments that many variables (reaction temperature and time, atmospheric composition, pretreatment, etc.) affect the

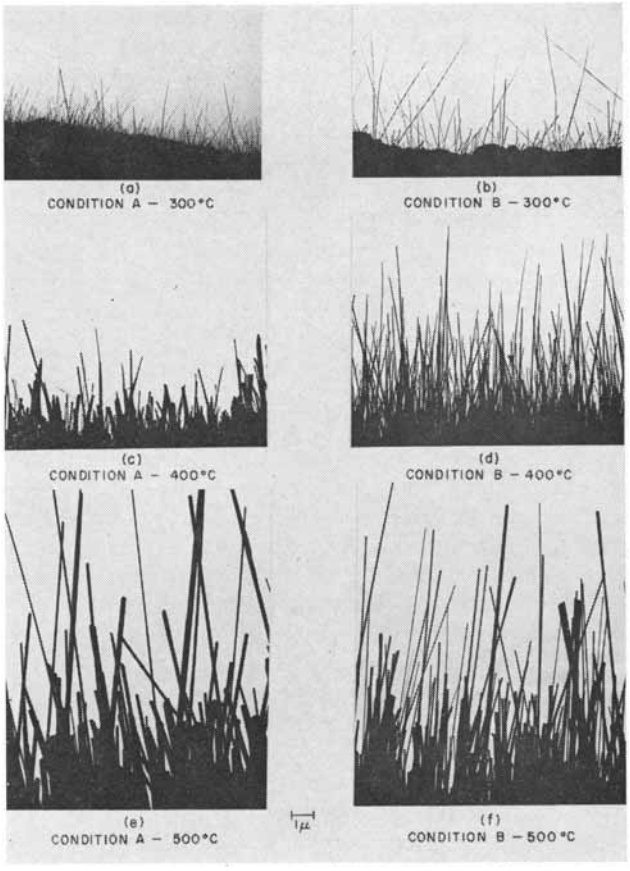

Fig. 3. Effect of temperature on the growth of oxide whiskers on pretreated copper in dry oxygen. Magnification approx. 3000X.

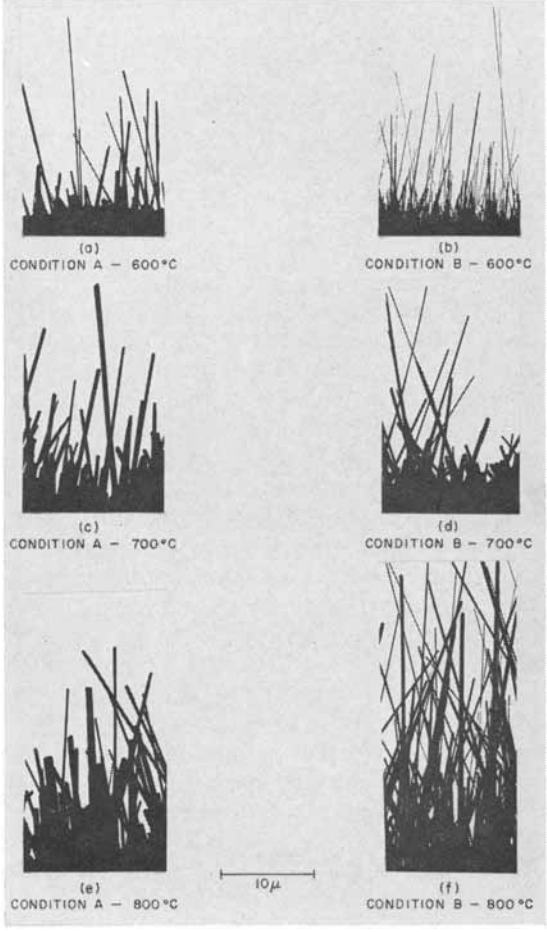

Fig. 4. Effect of temperature on the growth of oxide whiskers on pretreated copper in dry oxygen. Magnification 1300X.

formation of whiskers and that many parameters (number, length, width, shape, crystallography, etc.) are required to describe a whisker formation. It is apparent that any theory of whisker formation in air or oxygen must account for the observations given in this paper. Many of the concepts (3, 9) on oxide whisker growth have revealed that whiskers originate from a defect site such as a screw dislocation and that the energy required to form the whisker is supplied by surface oxidation. Two theories have been developed to establish the rate at which whiskers grow, namely, by diffusion of material at the whisker base (growth from the base) or by surface diffusion to the growth step at the whisker tip (growth from the tip). Undoubtedly, the development of whisker growth is a common phenomena, but the exact mechanism whereby this growth occurs is still quite obscure. Nevertheless, it is believed that valid rationalizations can be made on some of the features of whisker growth based on the relative ease of dislocation mobility and surface diffusion. It is on this basis that an attempt will be made to account for the differences in growth behavior obtained under the experimental conditions reported herein. The whisker density would then be related to the number of dislocations which have penetrated the oxide layer, while whisker growth would be associated with the rate of surface diffusion of material to a spiral growth step at the whisker tip.

In comparing the gross changes in whisker density between the cold rolled and preannealed samples in air and oxygen from Table I, it is apparent that the whisker density counts are generally greater for whiskers grown on the preannealed material than for those grown on the cold worked samples. A possible explanation for this difference is that the dislocations in the cold-rolled samples are restricted in movement by opposing dislocation stress fields and barriers instituted by the cold rolling process. On the preannealed samples the stress fields have been sufficiently reduced to permit the remaining dislocations to move more readily which would account for the increased whisker density. The effect of the cold-rolling process is also delineated in the whisker shape. Broader whiskers were obtained on the cold-rolled than on the preannealed samples, indicating a rearrangement or elongation of the initial growth sites by the cold-rolling process.

A strong dependency of whisker growth on temperature is indicated for both the cold-rolled and preannealed samples in air and oxygen. The temperature dependency may be considered on the basis of the rate of material diffusion, that is, an increase in temperature results in an increase in the rate of diffusion accounting for the increase in whisker growth length observed at the higher temperatures. The effect of temperature on whisker density is not clearly delineated, but may be partially explained on the basis of stress relieving and metal purity. At temperatures below 300°C, it would appear that the dislocations are still quite immobile and difficult to move accounting for the lack of whisker growth. At a temperature of 300°C and above, it would be reasonable to assume that the dislocation stress fields and lattice faults induced by the cold-rolling process

have been sufficiently reduced, in the case of the cold-rolled sample, to permit the dislocations to move more easily, accounting for the growth. The lack of any gross changes in whisker density, after 300°C indicates that the metal is of high purity. Only in impure metals would it be reasonable to expect a gross variation in whisker density at a critical temperature range resulting from a sudden release of dislocations where barriers of the Cottrell type are released by impurity atoms. The reduction in whisker densities obtained at the highest temperature studied (800°C) has been previously explained by other workers on the basis of sintering of the surface oxide layer.

The increase in whisker lengths obtained in an oxygen environment over that typified in air may be explained on the basis of increased availability of oxygen for surface reaction, perhaps by the process of surface diffusion to the spiral dislocation growth step at the whisker tip. Undoubtedly, the explanations described herein are not without some limitations, and close inspection will reveal some inherent discrepancies, particularly the observation that an oxide whisker emerges from a defect site such as a dislocation. To date, this observation has not been rigorously demonstrated. However, it is believed that, through the use of thin foils subjected to controlled oxidation, the role of specific dislocations could be unambiguously correlated with whisker formations. In particular this would apply in establishing a correlation between the nature of the growth site and the points at which dislocations emerge. It is further believed that application of this technique should clarify the effect of environment and pretreatment on the shape of the growth site. Further emphasis using this approach is underway.

Manuscript received Sept. 25, 1961; revised manuscript received Nov. 20, 1961.

Any discussion of this paper will appear in a Discussion Section to be published in the December 1962 JOURNAL.

REFERENCES

1. S. E. Koonce and S. M. Arnold, *J. Appl. Phys.*, **25**, 365 (1953).
2. G. Pfefferkorn, *Naturwiss.*, **40**, 551 (1953).
3. G. Pfefferkorn, *Z. Metallkunde*, **46**, 204 (1955).
4. M. Matyas, *J. Phys.*, **5** [2], 24 (1955).
5. A. Goswami and Y. N. Trehan, *Trans. Faraday Soc.*, **52**, 358 (1956).
6. B. Lustman and R. F. Mehl, *Trans.* AIME, **143**, 246 (1941).
7. D. W. Bridges, J. P. Baur, and W. M. Fassell, *This Journal*, **103**, 475 (1956).
8. E. A. Gulbransen, T. P. Copan, and K. F. Andrew, *ibid.*, **108**, 119 (1961).
9. J. Franks, *Acta Met.*, **6**, 103 (1958).

Cell and Thermoelectric Effects of Tantalum Electrolytic Capacitors

Jack M. Law[1] and William C. Richards

Fansteel Metallurgical Corporation, North Chicago, Illinois

ABSTRACT

A voltage is normally present across the terminals of electrically isolated electrolytic tantalum capacitors. The magnitude, cause, and source impedance of this voltage were investigated. Wet-electrolyte units generate a small, high-impedance, cell emf between the tantalum anode and the silver case. This emf increases with film thickness to a maximum of 3v at elevated temperatures. Solid-electrolyte units generate a small, high-impedance emf, apparently thermoelectrically, normally not exceeding a few millivolts, but on some units, reaching a few hundred millivolts. Larger voltages are generally due to a residual charge from previous electrification, either from a slow decay rate or from dielectric hysteresis.

A voltage, although it may be small, is normally found to be present when an electrically isolated tantalum capacitor is tested with a voltmeter having a high internal impedance. In some applications for which tantalum capacitors are used, the magnitude of this voltage and its variation with temperature are important design considerations.

This paper reports the investigation that was made of the emf at the terminals and the causes for it. The two types of tantalum capacitors tested were solid electrolyte and wet electrolyte, both containing porous anodes of large surface area covered with a dielectric film of Ta_2O_5. The solid-electrolyte type has a layer of thermally decomposed MnO_2 covering the Ta_2O_5 film. The MnO_2 is electrically connected to the case and the cathode lead through a layer of graphite, silver paint, and solder. In the wet-electrolyte type, the anode is immersed in a liquid electrolyte which is contained in a sealed silver case. The cathode lead is soldered to the case.

The possible causes for the voltage were thought to be (*a*) an internally generated voltage such as a cell emf or a thermoelectric output, (*b*) an undecayed charge from previous electrification, (*c*) dielectric hysteresis, or (*d*) an electrostatic or electromagnetic charge. That wet-electrolyte electrolytic capacitors have a cell emf with a very large internal impedance was reported by Guntherschulze (1), but no values were given for tantalum.

[1] Present address: Rheem Semiconductor Corporation, Mountain View, California.

Several papers have reported cell potentials for tantalum (2, 3), but the measurements are not directly applicable to a commercial-type tantalum capacitor, where a formed anode and a silver case are the electrodes.

Dielectric hysteresis of aluminum electrolytic capacitors was investigated by van Geel and Pistorius (4), and the amount of dielectric hysteresis was found to increase with temperature and with the thickness of the oxide layer.

Methods of Testing

Voltages were measured with a 10-megohm meter (SIE Model R-2) and a 10^{11} ohm electrometer using a chopper and an a-c amplifier (Brown Recording Electrometer).

For d-c leakage measurements, the voltage drop across a 100-ohm series resistor was measured (the conventional manner of testing). However, unusual results were obtained under certain conditions of testing if the leakage current was less than 1 μa. When a d-c amplifier-type electrometer was used in combination with a d-c supply containing some ripple, a reversed voltage reading was obtained, indicating a negative leakage current, as though the capacitor was generating a larger voltage than the applied working voltage. The reversed voltage reading was not taken to be a true reading because a normal reading was obtained under the same conditions using the chopper-type a-c amplifier electrometer. Therefore, the latter meter and a lead battery voltage supply were used for all d-c leakage measurements.

For dielectric hysteresis tests, the working voltage was applied for 15 min, after which the unit was shorted through a 100-ohm resistor for 5 sec. The open-circuit terminal voltage was then measured at suitable intervals.

Wet-Electrolyte Capacitors

Voltages at room temperature were measured at the terminals of a number of wet-electrolyte capacitors. To minimize the possibility of a residual charge being present, a group of capacitors was used that had been at room ambient temperature and had not been electrified for six months or longer. The temperature was then increased in increments. Because of the extremely slow charge decay rate usually present in these capacitors, precautions were taken that the voltage at a given temperature was not affected by a residual charge from a previous temperature where the voltage had been higher. This was done by short circuiting the anode and cathode leads together for 1 min. The voltage at each temperature was found to be unstable at first, slowly changing, but normally reaching equilibrium within 4 hr. The voltage readings were recorded after equilibrium was reached.

Figure 1 shows the average terminal emf readings for several of these units over the temperature range of −55° to 125°C. The emf from −55° to +25°C is a few millivolts, changing from slightly negative to positive within this temperature range.

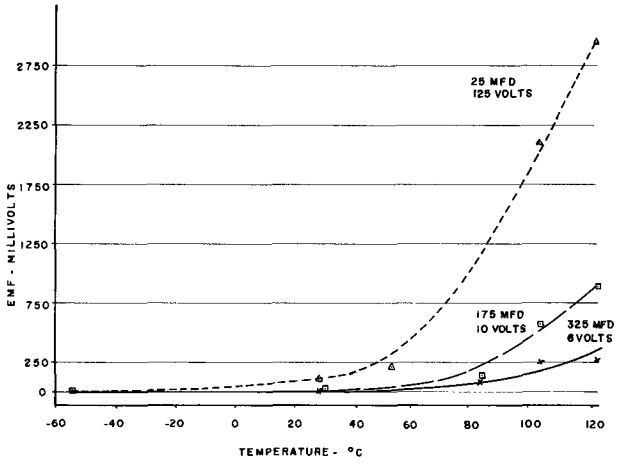

Fig. 1. Change of emf with temperature of wet-electrolyte capacitors. Values are for equilibrium conditions.

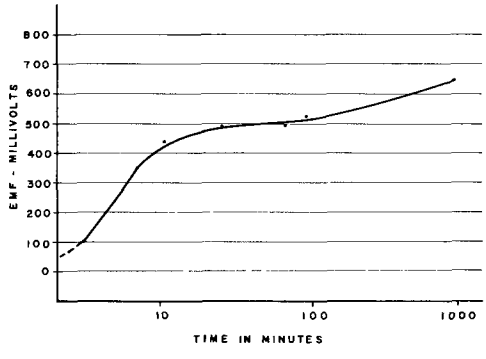

Fig. 2. Change in emf with time of a wet-electrolyte 25 μf/125v capacitor heated from 25° to 125°C, as measured on a voltage recorder.

Above room temperature the voltage increases to a maximum at 125°C. The emf reaches the highest value, 3v, on the 25 μf/125v units with the thickest film (and largest voltage rating).

To determine if the results would be similar if the temperature was increased immediately to 125°C instead of stepwise as in the preceding test, the voltage was recorded on a 25 μf/125v unit as it was placed in a 125°C oven, Fig. 2. The voltage increases fairly rapidly during the first 10 min and then levels off. No violent fluctuations or reversals in voltage are noted.

The small emf on the terminals of the capacitors shown in Fig. 1 and 2 are assumed to be due to a cell effect. To investigate the cell emf further, a capacitor was fabricated with an unformed tantalum anode, a silver case, and 40% sulfuric acid electrolyte. Figure 3 shows how the emf varies with temperature and reaches −190 mv at 125°C in contrast to the formed anodes that had a positive voltage. That the presence of an oxide causes tantalum to become more electropositive in oxidation-reduction potential was noted by Vermilyea (5). The unfilmed anode has a thin oxide film from contact with air that gives a potential different than that obtained with pure tantalum. If the half-cell potential of tantalum is more negative than the silver, Ta_2O_5 tends to form and the tantalum electrode is negative. If a film of Ta_2O_5 is present and the half-cell potential is more positive, silver tends

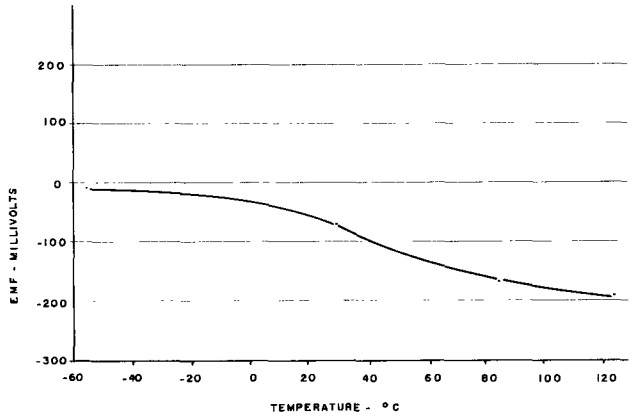

Fig. 3. The change of emf with temperature of wet-electrolyte capacitors containing an unformed tantalum anode. Average values for two units for equilibrium conditions.

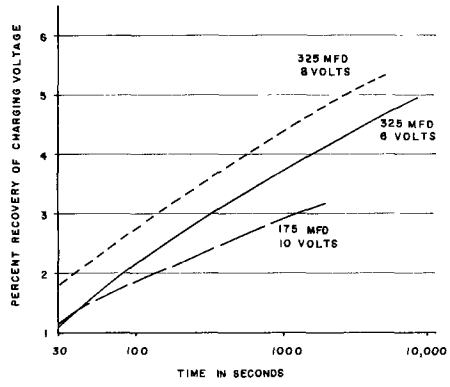

Fig. 4. Dielectric hysteresis of low-voltage wet-electrolyte capacitors, measurements at 25°C.

to dissolve and the silver electrode is negative. Some of the possible half-cell reactions are:

$$5H_2O + 2Ta = Ta_2O_5 + 10H^+ + 10e^- \quad E^\circ = -0.81v \qquad [1]$$

$$Ag = Ag^+ + e^- \quad E^\circ = 0.7991v \qquad [2]$$

$$2Ag + SO_4^{--} = Ag_2SO_4 + 2e^- \quad E^\circ = 0.653v \qquad [3]$$

There are many variables that can affect the cell potential of a tantalum capacitor including the activities of the various ions in the electrolyte and the thickness of the Ta_2O_5 film, and the emf can undoubtedly vary from one type to another.

The internal impedance was measured using a 1-megohm load to determine if these capacitors are a good source of emf. The impedance was determined by taking the open-circuited emf (no load) minus the emf with the load, and dividing by the current flowing through the load.

$$Z = \frac{E_{NL} - E_L}{I_L} \qquad [4]$$

The results are shown in Table I. The currents were extremely small, varying from 2 to 7 mμa. It will be noted that the internal impedance increases as the thickness of the tantalum oxide film increases. The computed resistivity of Ta_2O_5 based on a thickness of 18.5 Å/v (6) compares with previously reported values of 10^{12} to 10^{15} ohm-cm (7-9). The internal impedance is due, therefore, primarily to the resistivity of the Ta_2O_5.

Because the available current is in the milli-microampere range and the voltage is a few millivolts with a 1-megohm load, these devices are not too practical as batteries.

Voltages from External Sources

A voltage on a capacitor can be due to dielectric hysteresis from prior electrification (4) even though the capacitor has been completely discharged at one time. For example, Fig. 4 shows three capacitors that were charged to their working voltage and then discharged according to the procedure previously outlined. After 3 hr the terminal voltage of one 325 μf/6v capacitor is 5% of the charging voltage and is still increasing. The emf from dielectric adsorption could be mistaken for an internally generated voltage, particularly if the capacitor has a very slow decay rate.

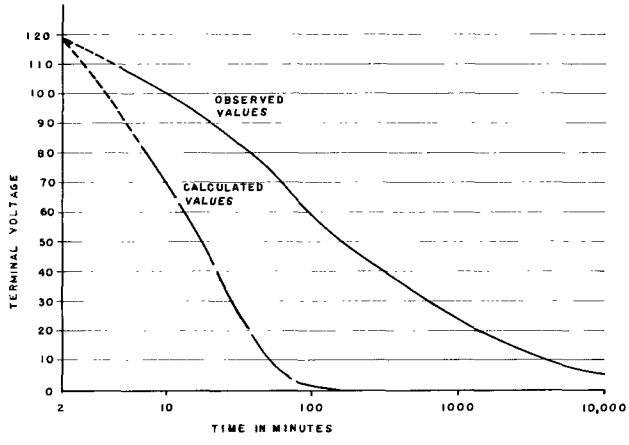

Fig. 5. Decay in charge on a high-voltage wet-electrolyte capacitor after the removal of the working voltage compared to the theoretical, (25 μf/125v capacitor); measurements were made at 25°C.

To determine how long a charge can be held if a capacitor is not discharged after the working voltage is applied for 15 min, voltage readings were taken at intervals on a 25 μf/125v capacitor as shown in Fig. 5. Internal leakage paths which are responsible for d-c leakage when a steady voltage is applied would also be the discharge paths for a charged capacitor. The resistance of the internal leakage paths can be approximated from

Table I. Internal impedance of wet-electrolyte capacitors as cells

Capacitor rating	Temperature of test, °C	No load emf, mv	emf with load, mv	Current with load, mμa	Internal impedance, megohms	Thickness of Ta_2O_5, Å	Resistivity of Ta_2O_5, ohm-cm
325 μf/6v	85	56	2	2	27	185	5×10^{15}
175 μf/15v	85	161	2	2	80	425	7×10^{15}
25 μf/125v	125	2100	7	7	300	3700	3×10^{15}

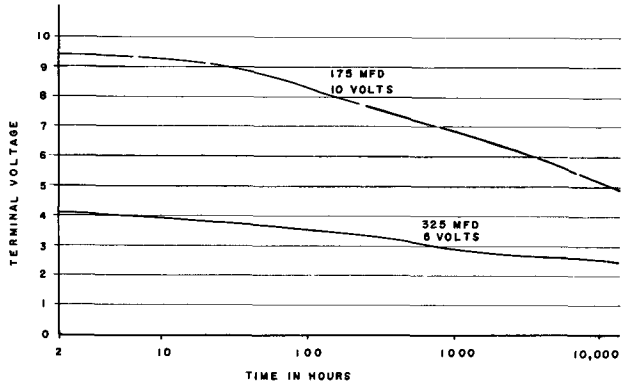

Fig. 6. Decay in charge on low-voltage wet-electrolyte capacitors after removal of the charging voltage, (10v and 4.3v); measurements were made at 25°C.

the d-c leakage current. The discharge rate should follow the formula for an R-C combination:

$$E = E_o e^{\frac{-T}{RC}} \qquad [5]$$

where E is the voltage at time, T, in seconds, E_o is the initial charging voltage, RC is the time constant, R is the resistance in megohms, and C is the capacitance in microfarads. The theoretical values do not agree too well with the observed values. The calculated internal resistance is 62.5 megohms, but the apparent resistance during discharge from 125 to 46v (which is 37%, or $1/e$, of 125v) is ten times greater (640 megohms). The apparent resistance from 46v to 17v shows a further increase by a factor of eight (5100 megohms). Therefore, it is evident that the internal resistance increases as the voltage decays.

Figure 6 shows the observed decay rates for two low-voltage units. The 325 μf/6v capacitor had been charged to 4.3v initially and the 175 μf/10v capacitor had been charged to 10v. After 18 months, the 6v part still has 57% of the initial charge and the 10v capacitor, 48.5%.

The exact explanation for the retention of such a large charge for such a long time is not known. That a cell emf causes the voltage does not seem likely; uncharged units have not been found to approach these values. The effective internal resistance, which has been shown to increase with a decay in voltage, might reach a sufficiently large magnitude in thin film units to cause the very slow decay rate.

Several factors can contribute to an increase in effective internal resistance. The resistivity of the Ta_2O_5 film can vary with a change in space charge and also with the direction of current flow. The current flow caused by cell action in a capacitor is opposite in direction to the current flow due to a decay in charge. The current that is flowing due to cell action with the tantalum positive is such that the electrons flow internally from the tantalum through the Ta_2O_5. The current that is flowing when an isolated capacitor is discharging internally is such that the electrons flow through the Ta_2O_5 to the tantalum. The resistance of Ta_2O_5 is known to be considerably less for the former case than for the latter. This might be the reason for the difference in the internal impedance calculated for the capacitors as cells in Table I as compared to the higher effective internal resistance shown by the charge decay rate. In the latter case, the resistivity of Ta_2O_5 might be considerably greater than 10^{15} ohm-cm.

The effective internal resistance of liquid-electrolyte capacitors can also be increased by the presence of double layers at both the Ta_2O_5 and the silver case surfaces, which would add series resistance. Gaseous layers causing an overvoltage can also have an effect on the retaining of a charge. A comparison of a thick-film, 125v capacitor in Fig. 5 with the thin-film capacitors in Fig. 6 shows that the former does not hold a charge as efficiently as the latter. The 125v capacitor continued to discharge at a faster rate and reached lower voltages than the thin-film capacitors. Young (10) has found evidence that the buildup of thicker Ta_2O_5 films on rough tantalum surfaces tends to create stresses as the tantalum is used up from protuberances under the film. Finally the Ta_2O_5 cracks, forming fissures down to the tantalum metal. Such fissures would result in more imperfections in thicker Ta_2O_5 films and would help to explain why such capacitors do not hold a charge as well as thin-film units.

Solid-Electrolyte Capacitors

The voltage present on a solid-electrolyte capacitor can be expected to be different than a wet-electrolyte capacitor. The solid electrolyte does not conduct current by ions. Therefore no cell emf should be present. Two semiconductors, MnO_2 and Ta_2O_5, are present. These capacitors appeared to be more sensitive to electrostatic charge pick-up than the wet units, and particular care was taken to keep them electrically insulated during testing, especially from contact with the hands. Even approaching the units with the hands can cause widely fluctuating electrometer readings, which subside upon withdrawing the hands.

The emf at the terminals of several typical 68 μf/10v capacitors over a temperature range is shown in Fig. 7. When the temperature was changed, the capacitors were discharged by shorting the leads together for 5 min to eliminate any residual charge. The results are similar to the wet

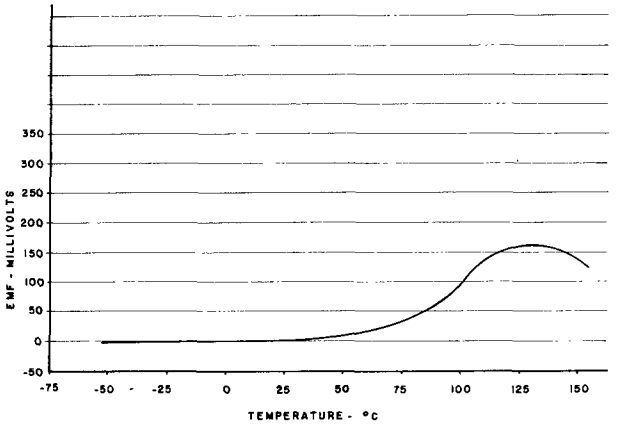

Fig. 7. Change of emf with temperature of 68 μf/10v solid-electrolyte capacitors. Values are for equilibrium conditions.

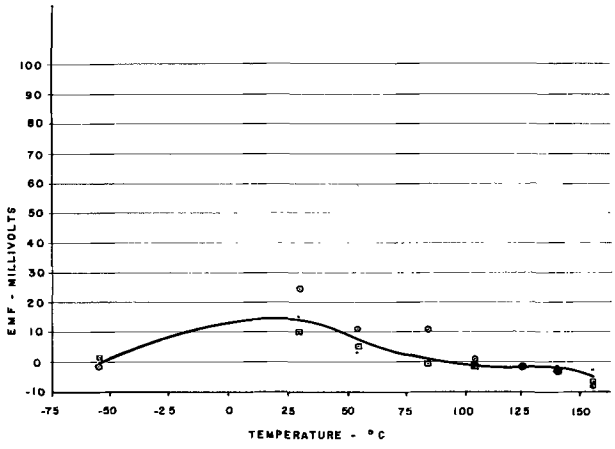

Fig. 8. Change of emf with temperature for 22 μf/35v solid-electrolyte capacitors. Values are for equilibrium conditions.

units except that the voltage decreases at higher temperatures (over 130°C). The explanation for this is presumed to be the decrease in internal resistance above the maximum operating temperature and the bleeding off of the charge.

The voltage-temperature relationship for three 22 μf/35v units is shown in Fig. 8. The emf drops to values between zero and —10 mv. The emf stayed in this region when the units were annealed at 155°C for days. Figure 9 shows the results on three smaller-size capacitors. The 6-volt units show a decrease above 130°C, as was previously noted for 68 μf/10v units. The two units with higher voltage ratings are similar to each other, both being slightly negative over the entire temperature range. Figure 10 shows the emf for two large intermediate-voltage units. Here, the 15-volt unit shows a continuous increase in voltage at higher temperatures, whereas the 20-volt unit shows very little output over the entire temperature range.

Figure 11 shows the daily variation in emf on capacitors of three different voltage ratings and sizes at 155°C. The two groups with higher voltage ratings have an emf close to zero, particularly the 100 μf/20v units. The 6-volt units have a somewhat more negative voltage, but are quite stable.

Figure 12 shows the effect on open-circuit terminal voltage of placing a room-temperature 68

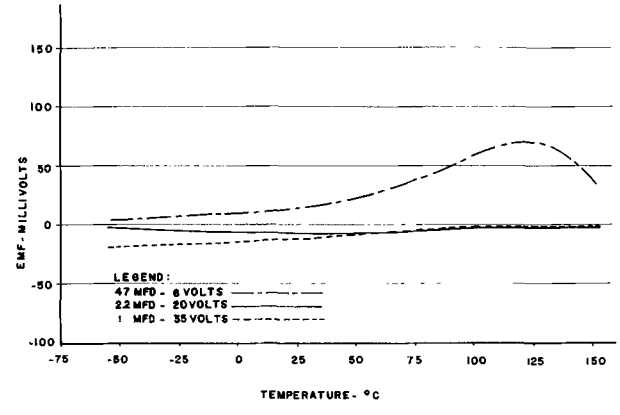

Fig. 9. Change of emf with temperature for three ratings of small solid-electrolyte capacitors. Values are for equilibrium conditions.

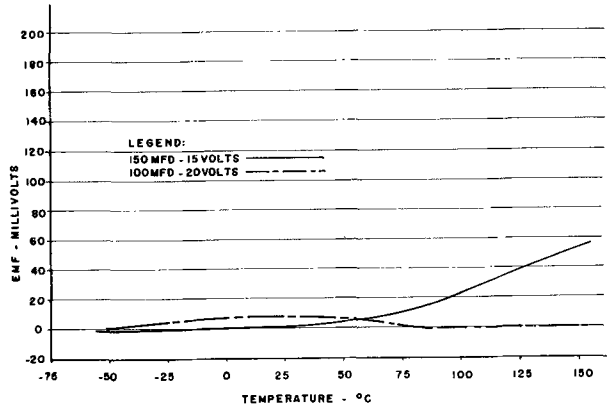

Fig. 10. Change of emf with temperature for two ratings of large capacitance solid-electrolyte capacitors. Values are for equilibrium conditions.

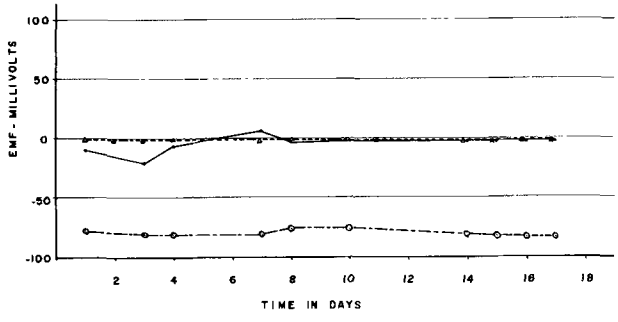

Fig. 11. Open-circuit terminal emf from day to day of solid-electrolyte capacitors stored at 155°C. - - - -, 100 mfd, 20v; ————, 1.0 mfd, 35v; — - — - — -, 47 mfd, 6v.

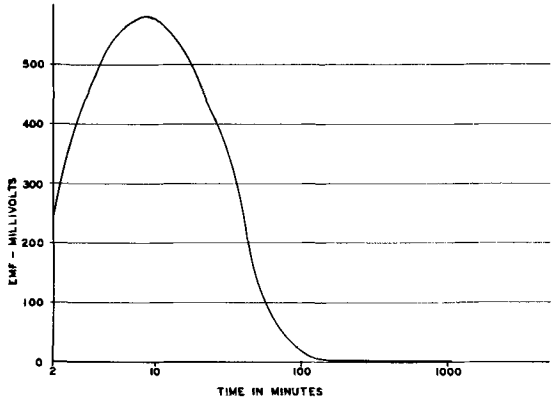

Fig. 12. Change of emf with time of a solid-electrolyte 68 μf/10v capacitor heated from 25° to 155°C, as measured on a voltage recorder.

μf/10v unit in a 155°C oven. Here again, the capacitor was shorted for 5 min before being placed in the oven. The emf reaches 580 mv after 8 min, then gradually decreases to zero at about 1000 min. This curve shows evidence of what appears to be a thermoelectric effect due to the thermal gradient between the inside and outside of the device during the short time required to reach thermal equilibrium. Such an emf could leave a residual voltage on a capacitor.

Mechanisms for the internal voltage generation were investigated by assembling various combinations of the elements normally found in a solid unit. For example, the MnO_2 electrolyte was placed over the surface of an unfilmed tantalum anode and a cathode contact was made with solder. No

emf reading was detected. A graphite coating was placed over the MnO_2 with no change. A conductive silver coating was placed over the graphite, making a complete capacitor except for the Ta_2O_5 film. No emf can be detected from any combination of components as long as unfilmed tantalum is used. That is, there appears to be no thermoelectric or Seebeck effects in action as long as the temperature is held constant. When graphite was placed directly over a 90v tantalum oxide film with no MnO_2 present, an emf of about —12 mv was noted over a 22-day series of measurements at 155°C. No emf was detectable at 145°C or below. Thus, apparently the presence of the MnO_2 is not necessary for such voltage, but the tantalum oxide is required.

The internal impedance of a number of solid-electrolyte capacitors was measured. On groups of 68 μf/10v and 22 μf/35v units, the voltage decreased to such low values (less than 10 μv) that it was very difficult to obtain measurements having any real meaning. It can only be said that the internal impedance appears to be extremely high on these devices.

Voltages from External Sources

Dielectric hysteresis was investigated on these units. Figure 13 shows the curve for a typical 22 μf/35v unit. The voltage reaches a peak of 1.2% of the original applied voltage 3 min after the shunt is removed and then decreases very rapidly. A 68 μf/10v unit reached the peak of 3% of the applied voltage also in 3 min and decreased rapidly after that. Thus, it appears that dielectric hysteresis in the solid capacitor contributes very little to any terminal emf.

Charge decay rates were also investigated for solid units. They were found to be much more rapid than for the wet devices. Figure 14 shows the calculated and observed decay rates for a 120 μf/10v unit. The internal resistance is 23.8 megohms, computed from the d-c leakage at 10v. The apparent internal resistance for a decay in voltage to 3.68v (1/e) is 360 megohms, as calculated from the actual decay rate. The apparent internal resistance for a further decrease to 1.33v is 1470 megohms, showing that the apparent internal resistance again increases as a charge decays, as it did for the wet devices, probably due to a change in resistance of the Ta_2O_5 with a change in space charge. Figure 15

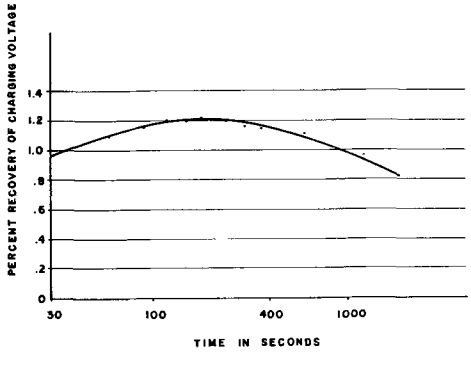

Fig. 13. Dielectric hysteresis of a 22 μf/35v solid-electrolyte capacitor, measurements at 25°C.

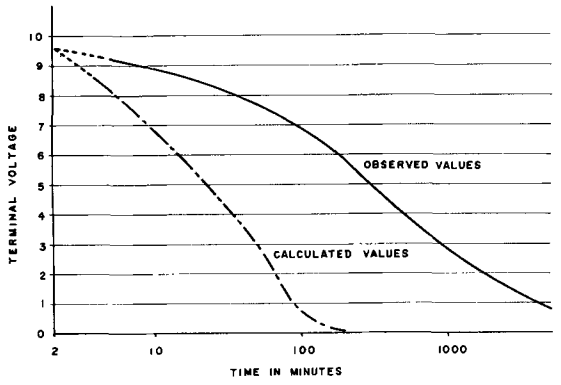

Fig. 14. Decay in charge on a 120 μf/10v solid-electrolyte capacitor after the removal of the working voltage compared to the theoretical; measurements were made at 25°C.

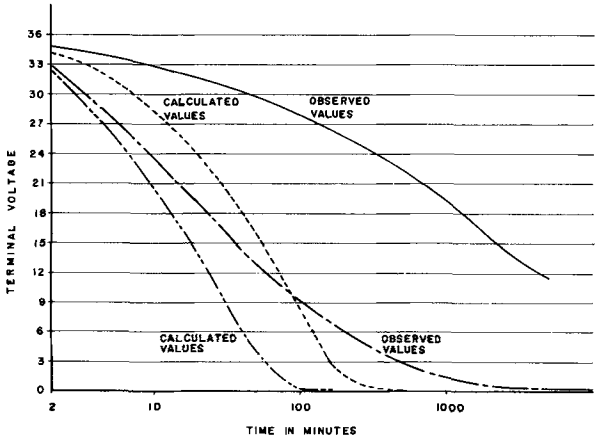

Fig. 15. Decay in charge for two 22 μf/35v solid-electrolyte capacitors after the removal of the working voltage compared to the theoretical; measurements were made at 25°C.

shows the observed and theoretical curves for two 22 μf/35v units. Again, the decay rate is much slower than if the apparent internal resistance at the operating voltage, as determined by the leakage current, holds constant. The apparent internal resistance for a voltage decay to 1/e of 35v (13v) is 10,000 megohms, which is substantially higher than the previous low-voltage unit.

The internal resistance paths, both series and parallel, of solid-electrolyte capacitors are undoubtedly a very important factor in determining what emf values can be sustained and how fast these will decay. Variations in these resistances probably account for a considerable part of the differences noted in the observed open-circuit emf's.

Conclusions

A high-impedance cell emf can be present across the terminals of an open-circuited wet-electrolyte tantalum capacitor and can be as high as 3v on a 25 μf/125v unit at 125°C. Other ratings are generally found to have only a few hundred millivolts.

An emf can also be present on the terminals of solid-electrolyte tantalum capacitors. These are generally only a few millivolts, but can be as high as a few hundred millivolts.

No forward current flow is found for either wet- or dry-electrolyte units when measuring d-c leak-

age using a series resistor if a proper d-c source and voltage-sensing instrument are used.

Voltages remaining due to the extremely slow charge decay rates of tantalum capacitors can be readily mistaken for internally generated voltages.

Manuscript received May 17, 1961; revised manuscript received Oct. 6, 1961. This paper was prepared for delivery before the Chicago Meeting, May 1-5, 1960.

Any discussion of this paper will appear in a Discussion Section to be published in the December 1962 JOURNAL.

REFERENCES

1. A. Guntherschulze, *Arch. tech. Messen*, **210**, 165 (1953).
2. M. Haissinsley, *Metaux et Corrosion*, **23**, 15 (1948).
3. E. M. Khairy and M. Kamal Hussein, *Chem. Soc. Japan Bull.*, **30**, 944 (1957).
4. W. Ch. van Geel and C. A. Pistorius, *Philips Research Rpts.*, **11**, 471 (1956.)
5. D. A. Vermilyea, *This Journal*, **101**, 388 (1954).
6. W. Ch. van Geel, C. A. Pistorius, and P. Winkel, *Philips Research Rpts.*, **13**, 265 (1956).
7. R. L. Taylor and H. E. Haring, *This Journal*, **103**, 611 (1956).
8. D. A. Vermilyea, *Acta Met.*, **6**, 166 (1958).
9. P. Alley, *Western Electronic News*, **26** (March 1958).
10. L. Young, *Acta Met.*, **5**, 711 (1957).

Gas Permeation Study and Imperfection Detection of Thermally Grown and Deposited Thin Silicon Dioxide Films

S. W. Ing, Jr., R. E. Morrison, and J. E. Sandor[1]

Semiconductor Products Department, General Electric Company, Syracuse, New York

ABSTRACT

Methods have been developed to measure gas permeation through thin thermally grown and deposited silicon dioxide films. From the data collected it is shown that pores and microchannels (orders of magnitude smaller than pores) are formed in these films, and permeation through them is the main diffusion mechanism involved. The existence of imperfections in the oxides is demonstrated by using a chlorine etching technique. An important result from this work is that insufficient surface cleaning is an important factor in the production of relatively large pores in the oxide. Channel size approaching atomic dimensions could be obtained in these films by being extremely careful in the preoxidation or predeposition cleaning of the silicon. Some oxide films show the presence of crystalline structures considered to be caused by a nucleation phenomena due to the presence of foreign particles on the silicon surface.

Measurements of the permeation rate of gases through thin films (10,000-40,000Å) of thermally grown and pyrolytically formed silicon dioxide have been made to determine quantitatively the imperfections existing in these films. Moreover, the procedures and techniques developed may be applied to permeation measurements of thin films of other materials.

A survey of the techniques used for permeation studies of glasses and crystalline material indicates that most classical approaches are not adaptable for studying very thin films, and in particular, most methods require large areas of material. The early permeation studies for silica and glasses, done by Urry (1, 2), Barrer (3), Rayleigh (4, 5) and others (6), utilize a form of double-bulb cell in which the inner bulb is blown from the material being studied. More recent techniques developed for permeation studies of sheet organic polymers (7, 8) satisfy the requirements for this investigation more closely; however, many modifications are still necessary due to the extreme fragility of the silica films and the limited size attainable.

From the existing published permeation studies reviewed, the device and procedures used by Park (7) seemed to satisfy thin film requirements provided gas permeation rate through the film is comparatively high. The device measures the volume of the permeated gas under conditions of constant pressure and temperature while a pressure difference is maintained across the film.

Park obtained ±5% accuracy with this procedure and could measure a flow rate of 2.3×10^{-3} cm³/min (permeation constant of 1×10^{-9} cc-cm/sec-cm²-cm Hg) with excellent reproducibility.

Initial permeability studies were begun by employing this volume change procedure, but as some permeability constants of below 1×10^{-14} cc-cm/sec-cm²-cm Hg were anticipated for these silicon dioxide films, ultimate values were expected to be obtained by using mass spectrometer. However, the semimicro film holder and volume increase measurement procedure proves an excellent method for screening films and collecting information.

Apparatus and Procedure

Semimicro film holder and volume increase measurement procedure.—The film holder, which is a slight modification of Park's device, is shown in Fig. 1. It is constructed of brass with an aluminum tightening ring. The high-pressure side is constructed with a set-screw-ball and socket valve to flush air from the upstream side prior to testing.

[1] Present address: Fairchild Semiconductor Corporation, Palo Alto, California.

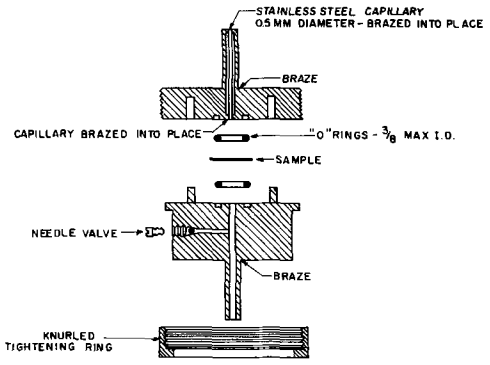

Fig. 1. Cross-sectional view of film holder for permeability measurement.

The volume on the low-pressure half of the device is minimized by brazing a 0.5 mm stainless steel capillary into place. Rubber "O" rings, recessed into the face of the device, provide a gastight seal with the sample when the unit is assembled and the tightening ring is applied. To insure against torsional tearing forces on the sample, three positioning pins are placed on the device halves.

The silicon dioxide films tested range in thickness from 10,000 to 40,000Å. These films are extremely fragile, and it would be impossible, as it is with plastic materials, to simply place the sheet between the device "O" rings and tighten. The film must be mounted or supported on a rigid frame, which will bear all the pressure of the "O" ring contact, and yet the film must lie completely flat on this support surface and adhere tightly about the periphery of the hole drilled into the support.

Many attempts were made to float a stripped silica film onto a polished quartz plate that had a hole of known diameter. Water, alcohol, and acetone were used; however, in most cases the film either wrinkled or would lift around the periphery of the hole creating possible error in the area considered for permeation study. Some success was attained by heat-sealing a sheet of film between two sheets of polyvinyl chloride containing drilled windows. However, this method proved unfeasible as the film cracked readily in most cases due to differences between the thermal properties of the film and the polymer.

Eventually, two satisfactory methods were developed for rigidly mounting the films for testing,

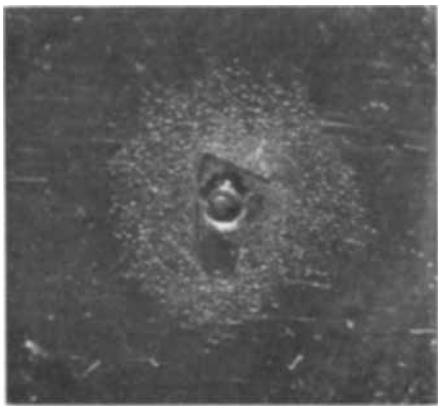

Fig. 2. Stripped film glass-brass sandwich; film 15,000Å

the oxide window method and the stripped film sandwich (see Fig. 2).

For the oxide window method a silicon wafer (3 cm^2) is completely oxidized on both sides. The surfaces are then completely masked with wax except for a circular area on one side of approximately 1 mm diameter. The silica is removed from this nonmasked area by etching with HF; the surface is washed with distilled water, and all wax removed with solvent. The wafer is then placed-silicon exposed side up–in a dry chlorine gas stream at 900°C for 2 min. In this period a neat vertical channel is cut through the silicon substrate, with very little horizontal undercutting, until the silica film on the opposite side of the wafer is reached. In this method, the silicon itself acts as support for the "O" ring contact, and the permeation area can be measured accurately as the film lies flat over the window area and is, of course, tightly adhered to the silicon substrate.

The stripped-film sandwich method was also used many times with success. Here, a silicon wafer covered with oxide is completely masked on one side with wax. All oxide on the opposite side is etched off with HF leaving the silicon clean and exposed. The wax is removed with solvent, and the wafer is placed silicon side up in a dry chlorine gas stream at 900°C for 10 min. In this period, all the silicon reacts and volatilizes leaving a flat transparent sheet of silicon dioxide.

This film is laid down on a clean, mechanically polished piece of brass which has a drilled hole of known diameter. A very light coating of silicone grease provides a tight seal. Next, a lightly greased glass plate with a matching hole, slightly larger in diameter, is placed on top of the silica-brass making a glass-silica-brass sandwich. "O" ring contact on this assembly gave a tight seal when pressure was applied on the permeation device with the tightening ring. The stripped film sandwich had the advantages of ease of handling and less film breakage; however, if the film does wrinkle or lift from the brass plate, an error is introduced into the assumed area measurement for permeation.

Both methods, however, provide a good film support for insertion into the permeation device.

In operation, the supported silicon dioxide film is placed horizontally on one half of the film holder. The holder is assembled and tightened as hard as possible with hand pressure. The film holder, is then placed between two three-way-stopcocks held flush with the holder with Tygon tubing. The test gas is slowly applied until a constant pressure is reached on the manometer. The entrapped air on the upstream side of the film holder is bled off several times through a needle valve.

A glass capillary containing an approximate 2 mm slug of methyl isobutyl ketone is next attached flush to a stopcock with Tygon tubing. A millimeter scale is adjusted to measure accurately the progression of the slug with volume increase.

During a run, the gas pressure is fixed and the rate of displacement of the organic capillary slug

Table I. Experimental results

Film No.	Gas used	Film mounting method	Film thickness, Å	Means of measurement	P, cm³ cm / sec-cm²-cm Hg
1	Air	PVC* sandwich	16,000	Volume displacement	8.5×10^{-8}
1	Air	PVC sandwich	16,000	Volume displacement	8.9×10^{-8}
2	Hydrogen	Glass-brass sandwich	22,000	Volume displacement	3.7×10^{-7}
2	Argon	Glass-brass sandwich	22,000	Volume displacement	1.98×10^{-7}
2	Air	Glass-brass sandwich	22,000	Volume displacement	2.18×10^{-7}
3	Air	Glass-brass sandwich	22,000	Volume displacement	1.98×10^{-7}
3	Argon	Glass-brass sandwich	22,000	Volume displacement	1.67×10^{-7}
3	Hydrogen	Glass-brass sandwich	22,000	Volume displacement	4.39×10^{-7}
4	Hydrogen	Glass-brass sandwich	22,000	Volume displacement	$<10^{-10}$
4	Air	Glass-brass sandwich	22,000	Volume displacement	$<10^{-10}$
5	Air	Oxide window	21,000	Volume displacement	$<10^{-10}$
6	Helium	Stripped film	38,000	Mass spectrometer	3×10^{-9}
6	Hydrogen	Stripped film	38,000	Mass spectrometer	3.2×10^{-9}
6	Oxygen	Stripped film	38,000	Mass spectrometer	5.6×10^{-10}
6	Xenon	Stripped film	38,000	Mass spectrometer	7.4×10^{-10}
6	Argon	Stripped film	38,000	Mass spectrometer	2.9×10^{-10}
7	Argon	Oxide window	35,000	Mass spectrometer	3×10^{-4}
8	Argon	Oxide window	35,000	Mass spectrometer	6×10^{-5}
9	Argon	Glass-brass sandwich	15,000	Volume displacement	$<10^{-10}$

* Polyvinyl chloride.

is noted over a set 3 cm distance. Repeated determinations on the same piece of film are made by one closing stopcock and gently sucking the slug back to the starting position, again observing the time intervals required to progress the successive sections of the 3 cm distance.

In general, with an exposed film area of approximately 0.01 cm², a range of gas pressure difference across the film can be used without puncturing the film varying from 200 mm Hg for 5000Å thickness to well over 760 mm Hg for 15,000Å.

Since the capillary slug movement is affected by changes in ambient temperature, as much care as possible should be taken to provide a constant ambient temperature.

Mass spectrometer measurement apparatus.— Both oxide window and stripped silicon dioxide films are used. The film is mounted between the polished ends of two capillary glass tubes, 1 mm bore, and is sealed tightly with apiazon wax. The assembly is then incorporated into the mass spectrometer vacuum system. A fraction of a millimeter Hg gas pressure differential is generally applied across the film. The film temperature can be varied by using a heater placed around the film assembly.

Results

For all films investigated, there was no evidence of an initial induction period. In the case of volume change permeation measurements, the rate of displacement of the liquid slug seemed to reach a steady state very readily after the start of each run.

The experimental results of permeation of various gases through different silicon dioxide films are presented in Table I. All films were thermally formed by steam oxidation with the exception of film No. 5, which was formed with oxygen bubbling through a room temperature water supply. *P*, the permeability, is defined as the cc of gas at normal temperature and pressure passing through a film 1 cm thick, per second, per cm² area with 1 cm Hg pressure difference across the film.

Discussion of Permeation Results

As can be seen from the tabulated data, the permeation constants for these thin silicon dioxide films not only vary using the same gas, e.g., air, 2.18×10^{-7} to $< 10^{-10}$ and argon 3×10^{-4} to $< 10^{-10}$, but also the lower values obtained are several orders of magnitude higher than those anticipated (9).

From the spread of permeation results, a proposed spectrum of values is suggested according to the degree of imperfections within the silicon dioxide films. Breaking the values down into permeation ranges, one might categorize the results as follows for a gas like argon or oxygen.

A. 10^{-3} to 10^{-5} — Flow through microcracks, pores, and crystalline portion boundaries.

B. 10^{-7} to 10^{-10} — Flow through micro-channels.

C. $\sim 10^{-15}$ — True diffusion and permeation (9).

If a film contains a crack due to handling or insertion into the film holder, it is readily detected by the rapid progression of the capillary slug. On microscopic examination the crack can usually be observed.

The higher rates of 10^{-4} and 10^{-5} are obtained on films in which many fine crystal-like growths appear. These crystals very closely resemble those described by other authors (10) and are probably also cristobalite. The average diameter of these crystals vary from 4×10^{-4} cm to 3.3×10^{-3} cm (see Fig. 3). It is noted sporadically that this phenomenon occurs independent of the oxidation technique although the standard preoxidation cleaning treatment is used. In advanced stages this "crystallization" can give a milky cast to the oxide, even while still on its silicon substrate, and often after etching away such a film, the silicon surface is noticeably pitted in regions where these "crystals" were observed. This phenomenon seems to be pre-

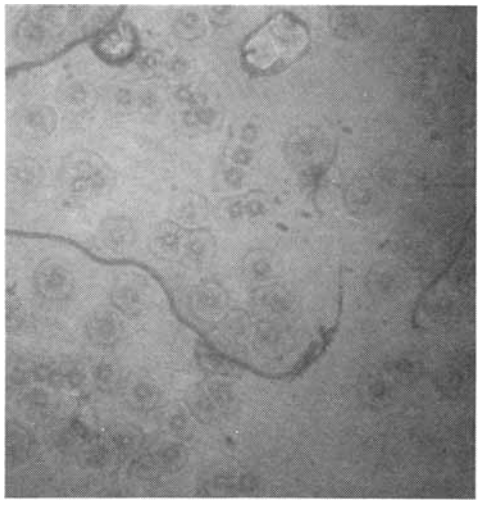

Fig. 3. "Crystalline" growth in stripped thermal oxide film. Magnification 150X.

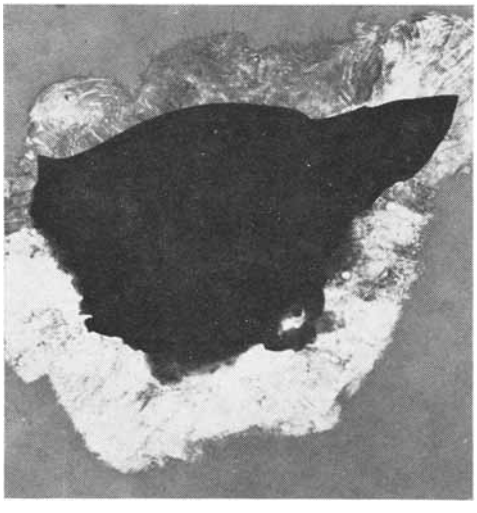

Fig. 4. SiO_2 crystallization around foreign particle; note: produced during electron microscope observation.

dominant in cases in which the amorphous silica can nucleate about a foreign material such as might be found on an insufficiently cleaned silicon surface. Figure 4 illustrates this crystallization phenomenon. This transition occurred while scanning a stripped silica film under the electron microscope. While the photographed area was being observed, some unknown foreign material landed on the silica, and immediately the surrounding silica crystallized.

The bulk of the results fall into the 10^{-7}-10^{-10} permeation range. It is felt that this range indicates permeation through microchannels rather than through the membrane by solubility for several reasons. First, a steady-state flow is immediately observed on starting a run either by mass spectrometer or by volume displacement. Solubility type of permeation should show an initial time lag. Second, mass spectrometer measurement shows H_2 and He are about equal in rate, and H_2 should be approximately 1/10 the rate of that of He for fused silica (9). Third, the temperature dependence is not found to be exponential. Argon was used in the mass spectrometer with a pressure differential of 6 mm Hg. Permeation measurements were made at 29° and 59°C, and the rates were found to be approximately the same with, perhaps, a 3% higher rate for the higher temperature. As a rough approximation with a P of 5×10^{-10} for oxygen it is estimated that using a test area of 3×10^{-2} cm^2 the total "channel area" would be 3.65×10^{-10} cm^2. If this entire area is assumed to be one pore, this would correspond to a pinhole of approximately 2×10^{-5} cm in diameter in a test area of 0.2 cm diameter. The electron microscope failed to detect any pores in several films over the limited field observed, even with a resolution down to 50Å, so channels should be numerous and extremely small in size.

The rates obtained with hydrogen and helium (see Table I) approach the values found by other authors using fused silica (11) by one or two orders of magnitude. Leiby and Chen (12) studied the permeation of various gases through Vycor glass, and report permeation constants in the range of 10^{-10} to 10^{-11} cm^3-cm/sec-cm^2-cm Hg for He at room temperature, which is again one or two orders lower than is found with the least permeable thermally grown oxide. The permeation constant of He in Vycor glass was found to be both a square root and an exponential function of temperature. The square root temperature dependence was considered to indicate the existence of a molecular streaming process through extremely small voids and/or channels of near molecular dimension. If this is the case, then the channels existing in some of these thermally grown oxide films also could not be too much larger than molecular size.

The runs which gave values below 10^{-10} were obtained by the volume displacement method, but this value is certainly the extreme upper limit measurable by this procedure due to time factor and effects of external surroundings such as temperature. For values less than 10^{-9} mass spectrometer is the most accurate and most sensitive method, for with the present system, a permeability for oxygen in the order of 10^{-15} could have been detected if these films were free of imperfections and if permeation occurred through the silica by solubility.

Detection of Film Imperfections

Basically, the films studied for imperfection detection are prepared by either of three methods: (*a*) thermal oxidation of silicon with oxygen, (*b*) thermal oxidation of silicon with steam, and (*c*) pyrolytic decomposition of an organic-oxy-silane onto a silicon crystal surface. The state of the surface prior to oxidation or deposition appears to affect the quality of the resulting film greatly, as undesirable foreign materials on the silicon surface will produce a poor oxide. In general, few physical differences are noted in the oxides prepared by these three methods. All are amorphous by x-ray and electron diffraction. The films deposited pyrolytically, however, appear to be under considerably more stress than the thermally oxidized films, so an annealing step must be introduced to get them to lie flat and continuous (see Fig. 5). Of course, the reaction kinetics and the preparation tempera-

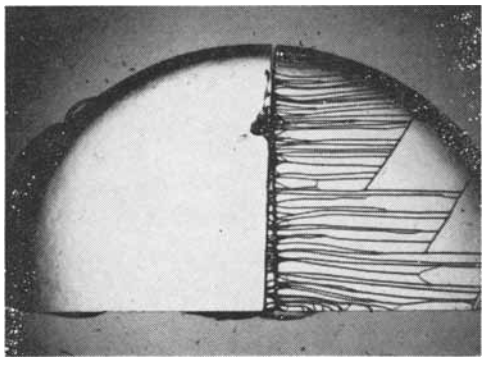

Fig. 5. Effect of annealing on pyrolytic film; left, annealed; right, unannealed; both after 1 min Cl_2 at 900°C.

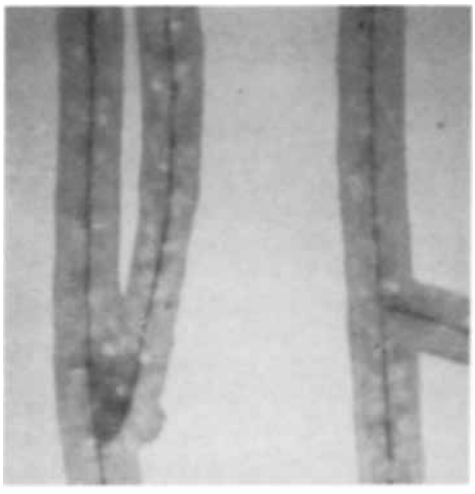

Fig. 6. Unannealed pyrolytic film cracking defined by chlorine etching. Original oxide crack and chlorine channel shown. Magnification 100X.

tures of these three preparation methods are quite different.

A method is developed by which films and silicon preoxidation cleaning processes could be evaluated qualitatively in relation to the imperfections introduced into the silicon dioxide film. Chlorine etching proves to be a very effective method for qualitatively screening films for cracks and pores. A test oxide must still be on its silicon substrate, whether thermally grown or deposited, and the silicon must be completely covered including its edges. Gross film imperfections, even those not visible with the eye, are easily detected after placing the sample in a dry Cl_2 stream at 900°C for 1-2 min. If the sample oxide contains large visible cracks, this time will be almost sufficient to attack the silicon completely, leaving fragments of oxide film.

A 2-min, 900°C Cl_2 etch finely brings out microcracks in oxide films as the chlorine attacks through the discontinuities and slowly undercuts along into the silicon (see Fig. 6). Microscopic examination of the etched areas always discloses the crack in the oxide.

However, to reveal some of the pores previously discussed, at least 30 minutes in Cl_2 at 900°C are required to undercut the silicon sufficiently for observation.

Chlorine etching tends to indicate that there is little difference in the three preparation methods

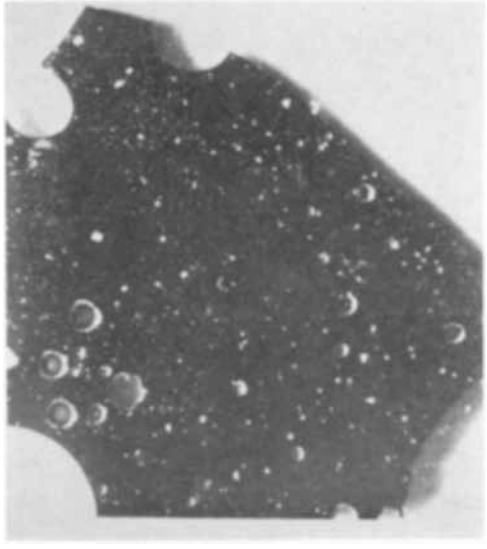

Fig. 7. Effect on oxide by chlorine etching insufficiently cleaned silicon; 10,000Å oxide by dry O_2 at 1200°C.

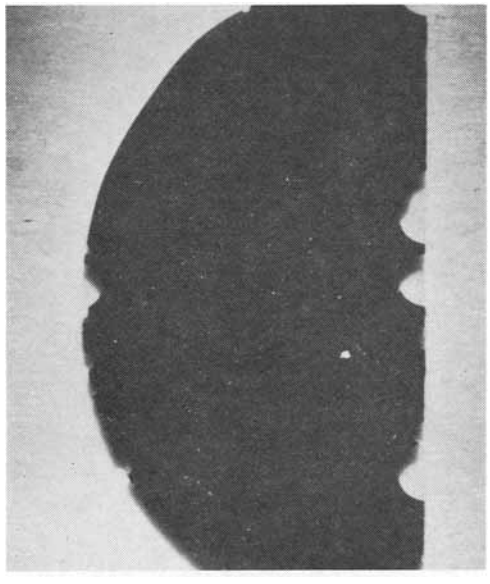

Fig. 8. Effect on oxide by chlorine etching chemically cleaned silicon; 6000Å oxide by steam at 1200°C.

in their relative susceptibility to film imperfections. All are basically equivalent in regard to number of pinholes; however, unannealed pyrolytically deposited oxides do tend to crack more readily in thicknesses over 15,000Å. The factor which appears most critical for imperfection reduction is silicon pretreatment and cleanliness prior to oxidation or deposition (see Fig. 7 and 8).

Conclusions

Methods have been developed to measure gas permeation through thin silicon dioxide films. From the data collected it is shown that pores and microchannels (orders of magnitude smaller than pores) are formed in these films, and permeation through them is the main diffusion mechanism involved.

The existence of imperfections in the oxides is demonstrated by using a chlorine etching technique.

An important result from this work is that surface contamination is an important factor in the production of pores in the oxide. Channel size ap-

proaching atomic dimensions could be obtained in these films by being extremely careful in the preoxidation cleaning of the silicon.

Some oxide films show the presence of crystalline structures considered to be caused by a nucleation phenomena due to the presence of foreign particles on the silicon surface.

Acknowledgments

The authors wish to express their appreciation to Dr. Frank J. Norton, General Electric Research Laboratory, Schenectady, for making mass spectrometer measurements and also to Dr. William C. Dash, General Electric Research Laboratory, Schenectady, for electron microscope photography.

Manuscript received Sept. 14, 1961.

Any discussion of this paper will appear in a Discussion Section to be published in the December 1962 JOURNAL.

REFERENCES

1. U. Urry, *J. Am. Chem. Soc.*, **54**, 3887 (1932).
2. U. Urry, *ibid.*, **55**, 3242 (1933).
3. R. M. Barrer, *J. Chem. Soc. London*, 378 (1934).
4. Rayleigh, *Proc. Royal Soc. (London)*, **A156**, 350 (1936).
5. Rayleigh, *ibid.*, **A163**, 377 (1937).
6. T. F. Newkirk and F. V. Tooley, *J. Am. Ceramic Soc.*, **32**, 272 (1949).
7. W. R. R. Park, *Anal. Chem.*, **29** [12], 1897 (1957).
8. D. W. Brubaker and K. Kammermeyer, *Anal. Chem.*, **25** [3], 424 (March 1953).
9. F. J. Norton, *J. Am. Ceramic Soc.*, **36** [3] (March 1953).
10. L. A. D'Asaro, Solid-State Electronics, **1** [1], 3 (March 1960).
11. R. M. Barrer, "Diffusion in and through Solids," University Press, Cambridge (1951).
12. C. C. Leiby, Jr. and C. L. Chen, *J. Appl. Phys.*, **31** [2], 268 (1960).

Preparation of Solid Solutions of GaP and GaAs by a Gas Phase Reaction

Frank A. Pizzarello

Chemical Physics Department, Semiconductor Materials Section, Hughes Research Laboratories, Newport Beach, California

ABSTRACT

Homogeneous solid solutions of gallium phosphide and gallium arsenide were synthesized. The synthesis involves the transport of the constituents of the solid solution to a cool substrate by means of a complex reaction with iodine under near-equilibrium conditions. The homogeneity of the samples prepared was demonstrated by x-ray, microscopic, and optical absorption measurements.

Among the first to describe the synthesis of the III-V compounds by a gas phase reaction were Antell and Effer (1). These workers demonstrated that GaAs, GaP, and InP can be successfully synthesized from a mixture of a group III halide and an element of group V. At present, a great deal of work is being devoted to the epitaxial growth of silicon (2) and germanium (3). In these epitaxial growth systems transport of silicon and germanium halides to a substrate occurs either by mixing with a flowing gas or under the influence of a thermal gradient. The substrate temperature is so fixed that deposition takes place by the disproportionation of the silicon and germanium halides.

The technique described in this paper uses the general approach of transport of halides by means of a thermal gradient. The principle advantages of this method of synthesis is that high temperatures, high pressures, and long periods of equilibration are not required to form homogeneous solid solutions.

A mechanical mixture of gallium arsenide and gallium phosphide, together with a measured quantity of iodine, is sealed in a quartz tube that is heated in a furnace of a known temperature gradient. The gallium phosphide-gallium arsenide mixture is placed in the high-temperature zone of the furnace. Material is transported to the cooler zone and deposits on the quartz wall of the reaction vessel as a homogeneous solid solution of gallium phosphide-gallium arsenide. Microscopic examination, x-ray analysis, and optical measurements were made to verify the homogeneous nature of the deposited material.

The net chemical reactions involved in the process can be represented by the following equations:

High-temperature region: Source material

$$4GaP\ (S) + 2I_2\ (g) \rightarrow 4GaI\ (g) + P_4\ (g) \quad [a]$$

$$4GaAs\ (S) + 2I_2\ (g) \rightarrow 4GaI\ (g) + As_4\ (g) \quad [b]$$

Cooler temperature region: substrate

$$4GaI\ (g) + (1-x)P_4\ (g) + (x)As_4\ (g) \rightarrow 4GaAs_xP_{(1-x)}\ (S) + 2I_2\ (g) \quad [c]$$

Reactions [a] and [b] occur at the high source temperature. The gallium iodide, phosphorus, and arsenic formed are transported to the cooler region of the tube by thermal convection. In the cooler region $GaAs_xP_{(1-x)}$ deposits on the walls of the tube as indicated by reaction [c].

Experimental

Mechanical mixtures are prepared by grinding measured quantities of gallium phosphide and gal-

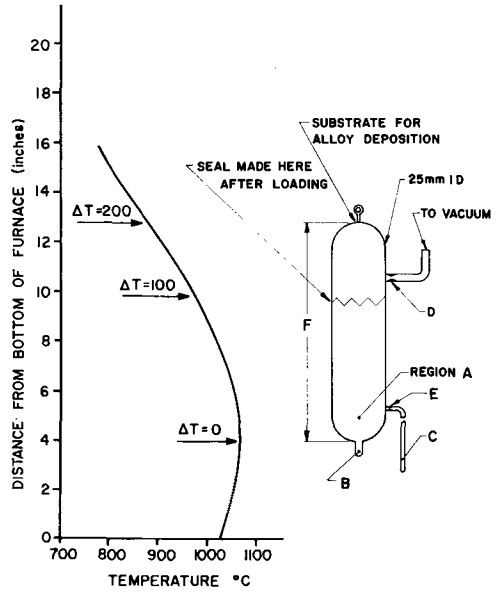

Fig. 1. Composite view of the quartz apparatus and the thermal gradient used in these experiments.

lium arsenide together in an agate mortar. Two grams of the desired mixture are placed in region A of the quartz reaction tube shown in Fig. 1.

One tenth of a gram of iodine is placed in tubulation B. The assembly is evacuated to 10^{-6} mm Hg. In earlier experiments, the tubulation B was immersed in liquid nitrogen during evacuation to avoid loss of iodine. It was found, however, that small quantities of water introduced into the system by this procedure produced undesirable effects. This contamination is avoided through use of cuprous iodide, placed in tubulation C, as an iodine source. The system is evacuated and thoroughly degassed at 100°C. The cuprous iodide is then decomposed at approximately 400°C and the liberated iodine condensed at B. The quartz tube is degassed by heating with an oxygen-hydrogen torch, and then sealed off at the constriction D. This is followed by sealing off tubulation C at constriction E.

The assembly is placed in a vertical furnace with the thermal distribution shown in Fig. 1. Any desired temperature difference, t, can be imposed on the system by adjusting the length, F, of the quartz tube. In these experiments, the temperature differences used were 100° and 200°C.

Results

Figure 2 illustrates a typical gallium phosphide-gallium arsenide deposit. These deposits are densely packed, adherent masses of crystallites, ranging in size from 1 mm to 10^{-2} mm on an edge. The largest crystallites are found in the center portion of the deposit. Microscopic examination reveals well-formed tetrahedral outcroppings, indicating preferential growth on (111) faces.

X-ray powder patterns show the deposits to be homogeneous solid solutions with a crystal structure of the zinc-blende type. A plot of the lattice parameter *vs.* mole fraction of gallium arsenide is given in Fig. 3. This plot shows that Vegard's law is approximated, a result which is in agreement with that of Flicker and Herkart (3). The scatter in the data shown in Fig. 4 is due, in part, to the inaccuracy of

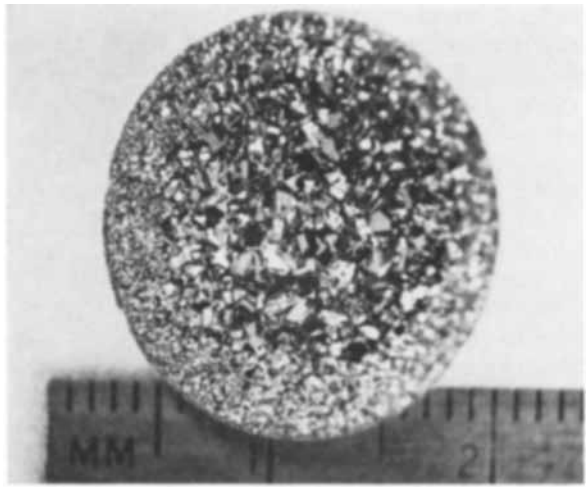

Fig. 2. Photograph of a typical solid solution deposition

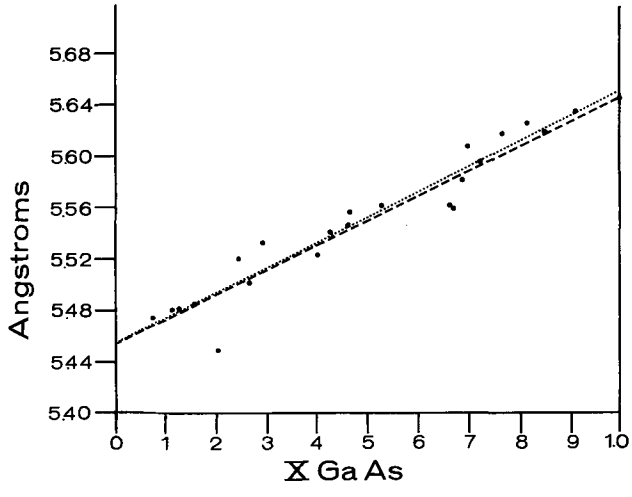

Fig. 3. Lattice parameter *vs.* mole fraction of gallium arsenide

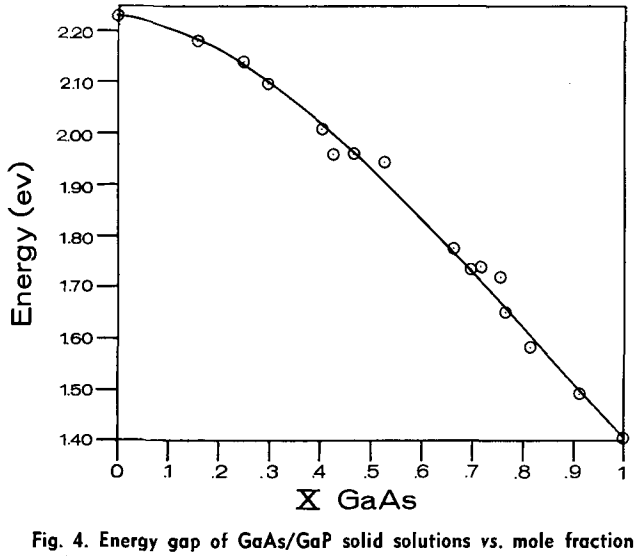

Fig. 4. Energy gap of GaAs/GaP solid solutions *vs.* mole fraction of gallium arsenide.

the analytical chemical technique used for the determination of concentration. The accuracy of the chemical analysis technique used was determined to be 6%. X-ray and microscopic examinations revealed the inclusion of a second phase in the deposition. An x-ray powder pattern of this material was identified as $Ga(PO_4)$. The amount of this material was reduced below the level of detection by microscopic and x-ray

techniques by using the cuprous iodide thermal decomposition technique, which assured the exclusion of oxygen and water from the system.

Optical absorption measurements on polished polycrystalline samples of gallium phosphide-gallium arsenide solid solutions were performed. Results are given in Fig. 4. Values of energy gap were determined from a plot of transmission *vs.* energy at a point on the energy axis where the transmission is 30% of the maximum transmission. Comparison of this optical data with similar data published by Folberth (4) shows agreement within a maximum deviation of 6%. Optical samples containing less than 0.50 mole fraction of gallium arsenide are transparent to visible light. Visual and microscopic examination of these samples revealed uniformly colored material containing a random mosaic pattern of crystallites. Samples not prepared by the cuprous iodide technique show a maximum transmission less than that calculated from reflectance data. This effect is probably due to the presence of occluded gallium phosphate acting as light scattering sites.

Since the nature of this system is such that many factors may have an effect, the four parameters, concentration of the mechanical mixture of gallium phosphide-gallium arsenide, temperature difference between source and substrate, pressure of arsenic, and pressure of phosphorus, were independently varied. A composite graph of the experimental results is given in Fig. 5. The term "excess pressure" used in the legend of Fig. 5 refers to the partial pressure of phosphorus or arsenic developed at the temperature of deposition in excess of the pressure developed by the decomposition of the gallium arsenide or gallium phosphide. This excess pressure is determined by the quantity of phosphorus or arsenic added to the mechanical mixture. Curve a (no excess phosphorus or arsenic used) shows a simple proportional relation between mechanical mixture concentration and deposition concentration. Curves b and c, 0.25 atm excess pressure of arsenic and 0.48 atm excess of phosphorus respectively, show a more complicated relationship between the mechanical mixture concentration and deposition concentration at the end portions of the curves. An interesting consequence of the study is that a wide range of concentrations was synthesized by using mixtures of gallium arsenide-red phosphorus and gallium phosphide-arsenic. Figure 6 shows the variation of concentration of deposition with excess phosphorus pressure when gallium arsenide-red phosphorus mixtures are used.

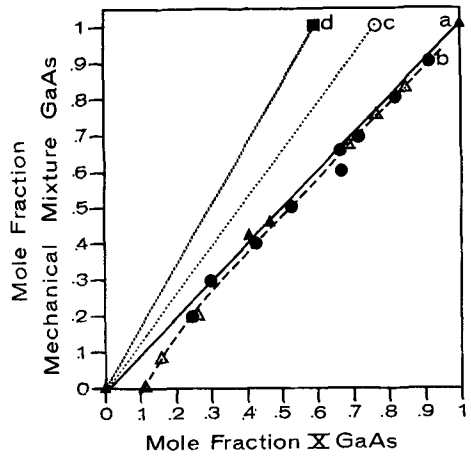

Fig. 5. Mole fraction of a mechanical mixture of gallium arsenide in gallium phosphide *vs.* mole fraction of deposited GaAs/GaP alloy; curve a-▲, no excess As_4 or P_4 pressure; △*t*-200°C; curve b-△, 0.25 atm excess As_4 pressure, △*T*-200°C; curve b-●, 0.25 atm excess As_4 pressure, △*T*-100°C; curve c-⊙, 0.48 atm excess P_4 pressure, △*T*-200°C; curve d-□, 0.72 atm excess P_4 pressure, △*T*-200°C.

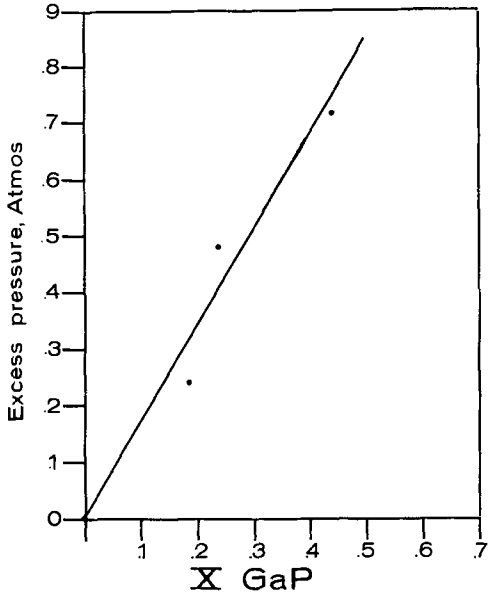

Fig. 6. Excess pressure of phosphorus *vs.* mole fraction of gallium phosphide in gallium arsenide.

Discussion

The Gibbs free energy of the net equilibrium reaction

$$4\,GaI(g) + (1-x)\,P_4(g) + X\,As_4(g) \rightarrow 4\,GaAs_x\,P_{(1-x)}\,(s) + 2I_2(g)$$

is given by

$$\Delta F_1 = -RT_1 \ln \frac{P^2_{I_2}}{P^4_{GaI}\,P_{P_4}^{1-x}\,P^x_{As_4}} \qquad [1]$$

where P_{I_2} is the total iodine pressure, P_{GaI} is the total gallium iodide pressure, P_{P_4} is the total phosphorus pressure, P_{As_4} is the total arsenic pressure, T_1 is the substrate temperature, and x is the mole fraction of gallium arsenide. Rearranging terms Eq. [1] can be put in the form.

$$x = \frac{\frac{\Delta F_1}{RT_1} + 2\ln P_{I_2} - 4\ln P_{GaI} - \ln P_{P_4}}{\ln P_{As_4} - \ln P_{P_4}} \qquad [2]$$

At the source region of the system, the net chemical equilibrium reactions postulated are:

$$4GaAs\ (S) + 2I_2\ (g) \rightarrow 4GaI\ (g) + As_4\ (g)$$
$$4GaP\ \ (S) + 2I_2\ (g) \rightarrow 4GaI\ (g) + P_4\ \ (g)$$

The Gibbs free energy for these reactions are:

$$F_2 = -RT_2 \ln \frac{P^4_{GaI}\,P_{As_4}}{P^2_{I_2}} \qquad [3]$$

$$F_3 = -RT_2 \ln \frac{P^4_{GaI}\,P_{P_4}}{P^2_{I_2}} \qquad [4]$$

where T_2 is the source temperature.

From Eq. [3] and [4] it can be seen that for a given temperature, T_2, the total pressures of arsenic, phosphorus, gallium iodide, and iodine in the closed system are independent of the relative proportions of GaAs and GaP in the solid phase. Consequently one expects x, as given by Eq. [2], to be single valued when the substrate and source temperatures are fixed. This conclusion is in direct contradiction to the data shown in Fig. 5 where it is seen that the alloy composition is varied by changes of mixture composition at the source region. No exact mechanism has been devised to explain the observed data. This anomaly, however, is resolved by postulating a complex solid phase reaction between GaAs and GaP at the source temperature which forms gallium arsenide-gallium phosphide solid solutions of composition dependent on the concentration of the mechanical mixture introduced. This postulate is partially supported by the observation that GaAs is preferentially transferred to the substrate when GaAs and GaP is used as the source in an unmixed state.

Acknowledgments

The author wishes to thank Mr. J. Vuoto for his support in the experimental work, Mr. D. Thrasher for the performance of the chemical analysis, and Dr. J. B. Bryden for the x-ray work needed.

Manuscript received Aug. 9, 1961; revised manuscript received Nov. 6, 1961.

Any discussion of this paper will appear in a Discussion Section to be published in the December 1962 JOURNAL.

REFERENCES

1. G. R. Antell and D. Effer, *This Journal*, **106**, 509 (1959).
2. I. C. Marimace, *I.B.M. J. of Research and Development*, **4**, [3], 248 (1960).
3. E. S. Wajda, B. W. Keppenhan, W. H. White, *ibid.*, **4**, [3], 288 (1960).
4. H. Flicker and P. G. Herkart, *Bull. Am. Phys. Soc.*, **8** II, [6], 407 (1960).
5. O. G. Folberth, *Z. Naturforsch.*, **10a**, 502 (1955).

Study of Aluminum Fusion into Silicon

Tchang-Il Chung

Semiconductor Division, Hughes Aircraft Company, Newport Beach, California

ABSTRACT

The wettability of silicon by aluminum, the spreading diameter of aluminum on silicon, and the depth of penetration of aluminum into silicon are analytically and experimentally studied as a function of the fusion temperature, the fusion time, and the aluminum spherical diameter. Graphs are provided to estimate these factors quantitatively during the fusion process and to predetermine the configuration of an alloyed junction. A method is also derived to calculate the penetration depth of aluminum in silicon.

In the manufacture of some semiconductor devices, the p-n junctions are prepared by alloying acceptor-type material such as aluminum to a homogeneous silicon crystal. The formation of alloy junctions is principally determined by the wetting of the silicon by the aluminum and subsequent solubility of the silicon into the aluminum. In order to increase the reproducibility of the process, it is often necessary to understand the causes which affect the values of diode parameters.

The purpose of this paper is to study, in detail, the phenomena occurring during the fusion of semiconductor devices.

Wettability of Silicon by Aluminum

On heating in an inert atmosphere, aluminum will wet the silicon and spread out to the shape of a section of a sphere. The wetting is dependent, in part, on the surface tension of the molten aluminum and affects the junction shape. The degree of wettability (1) of silicon by an aluminum liquid is characterized by the contact or wetting angle θ and the spreading diameter of the aluminum as indicated (2, 3) in Fig. 1, where γ_{SG} is the interfacial tension of the solid silicon-gas, γ_{SL} is the interfacial tension of solid silicon-liquid aluminum, γ_{LG} is the interfacial tension of liquid aluminum gas, and D_s is the spreading diameter of the aluminum. These interfacial tensions can also be represented as force vectors as shown in Fig. 2.

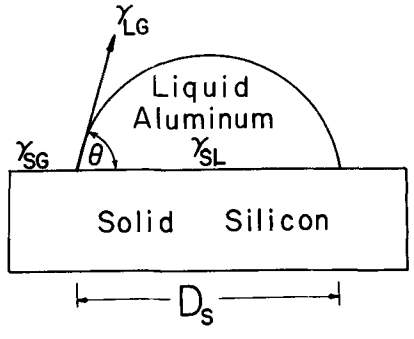

Fig. 1. Angle of contact θ of a liquid aluminum with a solid silicon surface, considered in terms of interfacial tensions.

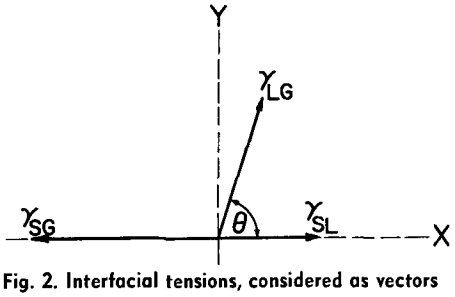

Fig. 2. Interfacial tensions, considered as vectors

For the equilibrium along the contact line, these three forces must balance each other. This gives when the gravitation is neglected

$$\gamma_{SG} = \gamma_{SL} + \gamma_{LG} \cos\theta \quad [1]$$

therefore,

$$\cos\theta = \frac{\gamma_{SG} - \gamma_{SL}}{\gamma_{LG}} \quad [2]$$

From this expression it is noted that the contact angle varies directly as the tension at the liquid aluminum-gas interface and the tension at the solid silicon-liquid aluminum interface.

For most materials, however, the surface tension of liquid decreases approximately linearly from very low temperature to a few degrees below the critical temperature where it becomes almost zero. If γ_L is surface tension of the liquid at the temperature T, its value is approximately given by (3)

$$\gamma_L = \gamma_o \left(1 - \frac{T}{T_c}\right)^{11/9} \quad [3]$$

where T_c is the critical temperature and γ_o is a quantity independent of temperature but characteristic for every substance.

According to Eq. [2] and [3] the contact angle θ is a function of temperature. The contact angle depends on the fusion temperature, time, and the gaseous medium in which the wetting occurs. It should be noted (1), however, that when aluminum is fused into silicon, the silicon is not only wetted but also dissolves in the aluminum and when the fusion temperature increases, the composition of the wetting liquid varies.

Penetration Depth of Aluminum into Silicon

The depth of penetration is determined by the solubility of silicon into the aluminum, and it depends on the fusion temperature, time, and the relative weight of the alloyed components (4). The aluminum-silicon phase diagram (5) (Fig. 3) is one way of describing the solubility of one component in another as a function of temperature. When the fusion temperature increases (6), the silicon concentration in the melt increases and the liquid will penetrate into the interior of the silicon slowly, gradually approximating an equilibrium value.

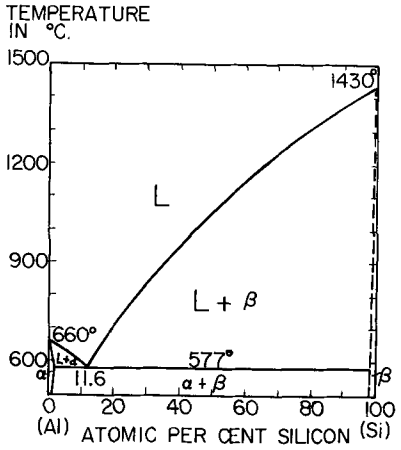

Fig. 3. Aluminum-silicon phase diagram

To calculate (6) the penetration depth of aluminum into silicon, let the ratio of silicon atoms to the total number of atoms in a melt at certain temperature be S. Then

$$V_{Si} = V_{Al} \frac{S}{1-S} \frac{\text{Density of Aluminum}}{\text{Density of Silicon}} \frac{\text{Atomic Weight of Silicon}}{\text{Atomic Weight of Aluminum}} \quad [4]$$

Since S is a function of temperature as given by the aluminum-silicon phase diagram, this can be rewritten as (6)

$$V_{Si} = F(T)\, V_{Al} \quad [5]$$

where $F(T)$ is a function of temperature and is plotted against temperature in Fig. 4. This figure has been prepared from the aluminum-silicon phase diagram shown in Fig. 3. When a small amount of aluminum sphere is heated on a flat silicon surface, it (6) will wet the silicon and spread out to the shape of a spherical segment, and at the same time it dissolves some silicon in a limited volume. The dissolved silicon volume is assumed to be in the shape of the frustum of a cone, one of whose base area is that of the contact area of the aluminum and the other is the area of transition and whose height x is the depth of penetration (see Fig. 5).

Substituting the aluminum and silicon dissolved volumes in Eq. [5],

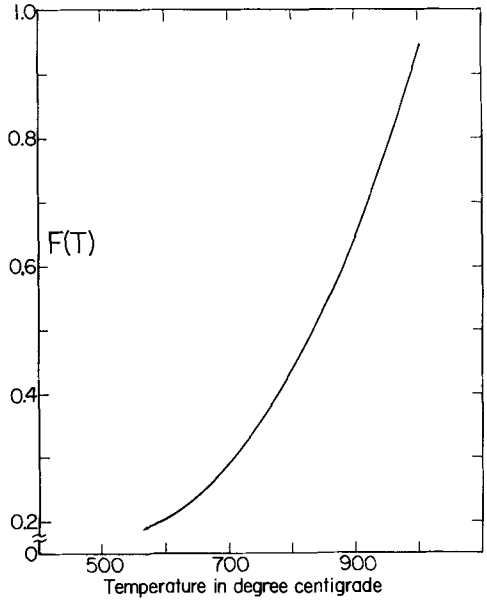

Fig. 4. Volume solubility of silicon in aluminum *vs.* temperature

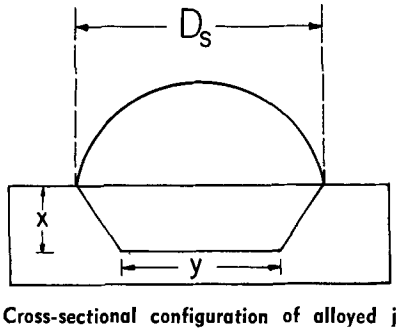

Fig. 5. Cross-sectional configuration of alloyed junction

$$\frac{\pi}{12} x(D_s^2 + D_s y + y^2) = F(T) \frac{\pi}{6} D^3$$

$$x = F(T) \frac{2D^3}{D_s^2 + D_s y + y^2} \qquad [6]$$

This is the general equation to calculate penetration depth of alloying, x, as a function of temperature, $F(T)$, diameter of aluminum sphere, D, spreading diameter, D_s, and diameter of transition, y.

Fusion Technique (1, 7)

A pure aluminum sphere is fused to the silicon dice cut from the slices of crystal to form a rectifying junction.

The procedure is to place a controlled amount of pure aluminum sphere on the surface of silicon dice and heat the crystal above the silicon-aluminum eutectic point which is 577°C in an inert atmosphere. The aluminum first melts, allows the alloy to wet the surface and dissolve some silicon in a limited area. When the silicon-aluminum liquid solution becomes saturated at fusion temperature, the fusion comes to attain an equilibrium position. However, the aluminum atoms are still diffusing into the solid silicon at the interface and convert the immediately adjacent region to p-type. If we now cool the sample under controlled cooling conditions, the saturated silicon-aluminum liquid solution, which has become p-type, regrows on the original crystal, as a continuation of the single crystal, to form the rectifying p-n junction. Both the diffusion converted and the regrown region play important factors in the device properties. The remaining aluminum liquid crystallized to form an ohmic contact to the p-region.

The entire heating and cooling cycles take place while the crystals are in an inert atmosphere, so that all the possibilities of any contamination of active elements during the fusion operation have been eliminated.

Experimental and Discussion

A fusion study was made on n-type silicon. Silicon slices were first ground using carborundum No. 280. Ground samples were polished in a mixture of hydrofluoric, nitric, and acetic acids, taken in the ratio of 1:1:1 for 6 sec at 30°C. The semipolished surface, with no scratches, dust or grease on it, was fused as described in fusion technique. Resistivity of silicon varied from 7 to 15 ohm-cm.

Contact angle.—The dependence of the contact angle on the wetting of silicon by aluminum was investigated in the temperature range of 700°-960°C. The results are shown in Fig. 6. It is evident that the contact angle decreases rapidly up to a temperature of 800°C as expected, then decreases very slowly up to a temperature of 900°C, and remains almost constant with an increase in the temperatures. The results are also illustrated by the photographs of cross sections in Fig. 7. As predicted in the theory, the surface tension of the fused aluminum decreases with an increase in the temperature. Besides, depending on the temperature, the contact angle must depend on the fusion time. In order to investigate this dependence, a fusion time of from 18 to 180 sec at the peak temperature was used. The time was measured from the instant at which the specimen reaches the preheated peak temperature. As can be seen in Fig. 8, the contact angle decreases as the fusion time at the peak temperature of 800°C increases. The result is also illustrated by the photographs of cross sections in Fig. 9.

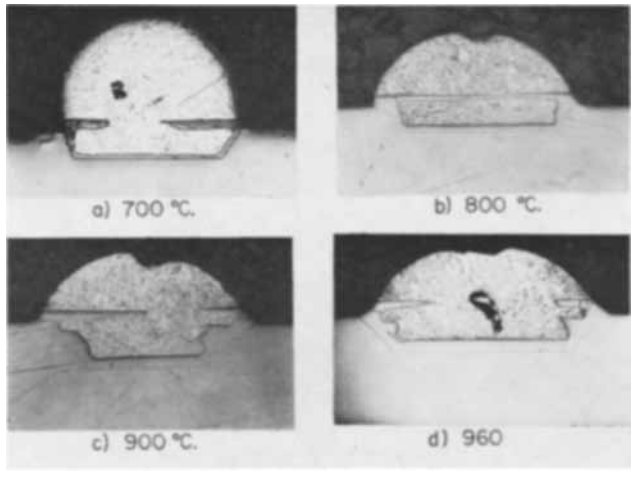

Fig. 7. Cross-sectional shapes of 12 mils aluminum drops at various temperatures.

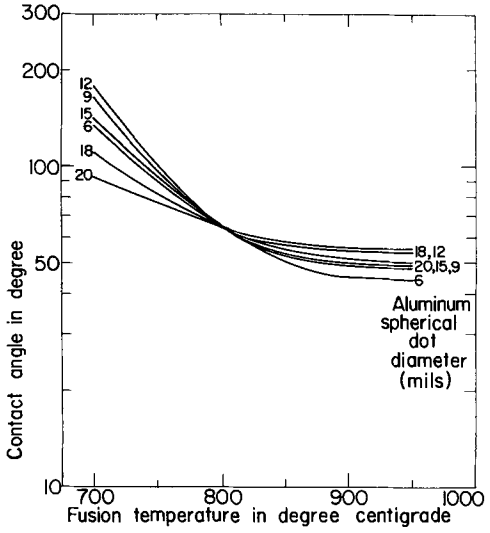

Fig. 6. Contact angle on fusion temperature and aluminum dot size (fusion time, 180 sec).

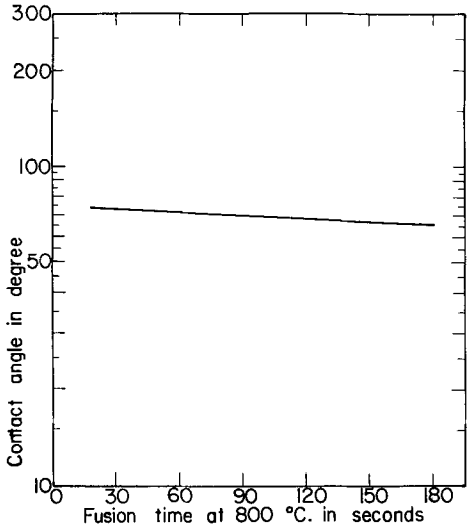

Fig. 8. Contact angle on fusion time at 800°C

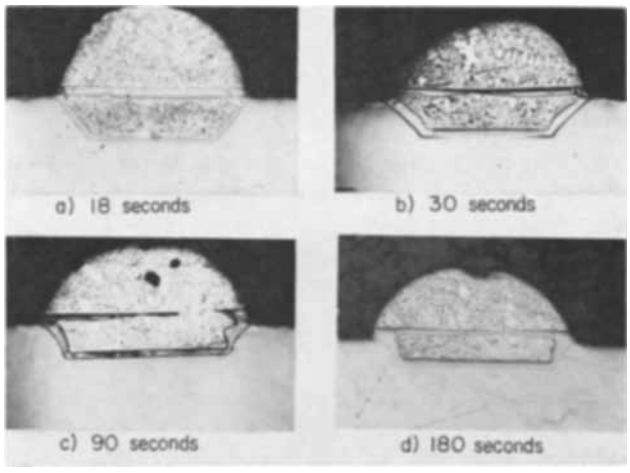

Fig. 9. Cross-sectional shapes of 12 mils aluminum drops at various fusion times at 800°C.

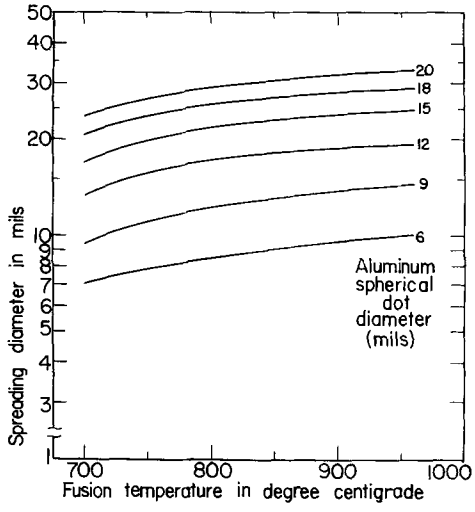

Fig. 10. Spreading diameter of the aluminum on fusion temperature and aluminum dot size (fusion time, 180 sec).

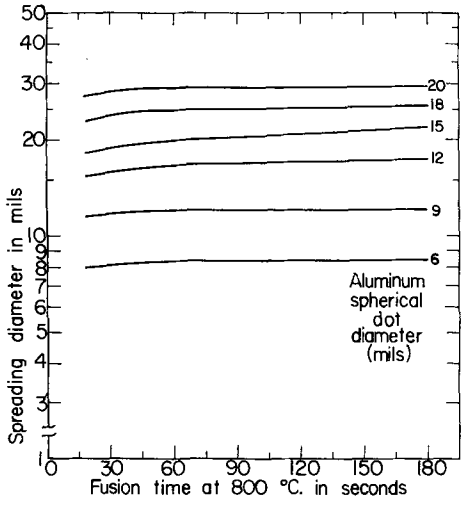

Fig. 11. Spreading diameter of the aluminum on fusion time at 800°C and aluminum dot size.

Spreading diameter.—The dependence of the spreading diameter for the wetting of silicon by aluminum was investigated in range 700°-960°C. The results are shown in Fig. 10. The spreading diameter of the aluminum dot increases rapidly up to a temperature of 800°C, and then increases slowly as the temperature increases. The spreading diameter (D_s in Fig. 1) was also investigated on the fusion time at 800°C as shown graphically in Fig. 11. The spreading diameter attains its equilibrium value during a period of 60-90 sec and remains constant for further heating. The wetting can be accelerated by exerting mechanical pressure on the aluminum liquid during alloying which helps overcome the surface tension. This method aids particularly a uniform penetration of the alloy junction area. Further wetting during alloying can be prevented by tight jig construction around the aluminum liquid.

Depth of penetration.—The dependence of the depth of penetration of aluminum into silicon was investigated in the temperature range 700°-960°C. The results on the temperature dependence of the depth of penetration of aluminum into silicon are shown in Fig. 12. The limit of the alloying depth is closely dependent on the solidus curve in the silicon-aluminum phase diagram in Fig. 3. Elementary considerations indicate that the higher the temperature, the greater will be the penetration. The depth of penetration is a function of temperature, as predicted in the theory, and also depends linearly on the relative amount of aluminum or aluminum spherical diameter. The rate of penetration will be essentially characteristic of pure aluminum dissolving pure silicon at the fusion temperature. If there is little aluminum,

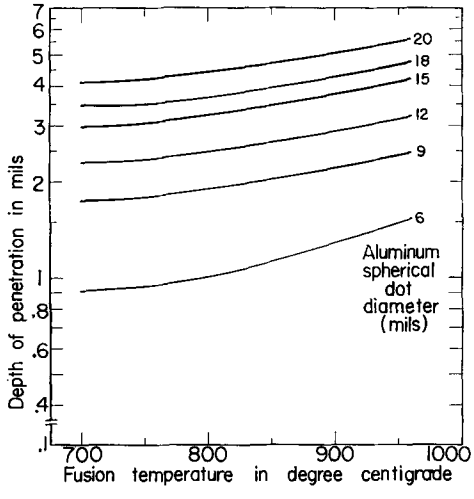

Fig. 12. Depth of penetration on fusion temperature and aluminum dot size (fusion time, 180 sec).

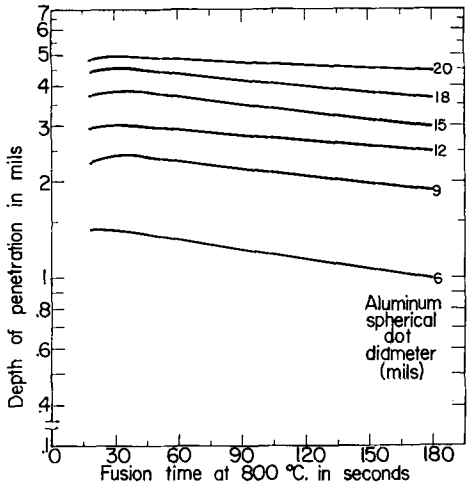

Fig. 13. Depth of penetration on fusion time at 800°C and aluminum dot size.

the silicon will saturate the aluminum rapidly and the rate of penetration must decrease rapidly. The depth of penetration of aluminum into silicon on temperature and aluminum spherical diameter, which is shown in Fig. 12, was obtained experimentally for the constant period of fusion time at peak temperature in question. In this regard, the dependence of the depth of penetration on the fusion time was also investigated and, as obtained at a temperature of 800°C, is shown in Fig. 13. The rate of penetration increases up to a fusion time of 30 sec and decreases as increasing the fusion time. It is the author's opinion that, when heated in 30 sec, the depth of penetration attains its equilibrium value on cooling. When heated beyond 30 sec, however, the aluminum melt spreads rapidly; this is caused by decreasing liquid surface tension before the depth of penetration attains its equilibrium value. The depth of penetration is determined by the temperature, aluminum spherical diameter, and time; therefore, when aluminum is fused into silicon it is not practical to prolong the heating process beyond 30-40 sec. It is also not practical to limit the fusion time to less than 20-30 sec.

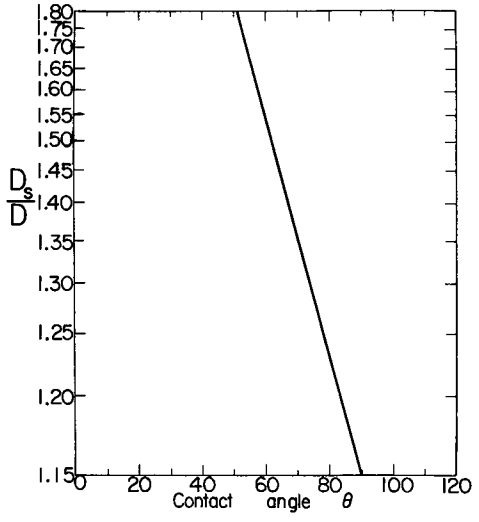

Fig. 14. Contact angle vs. spreading ratio

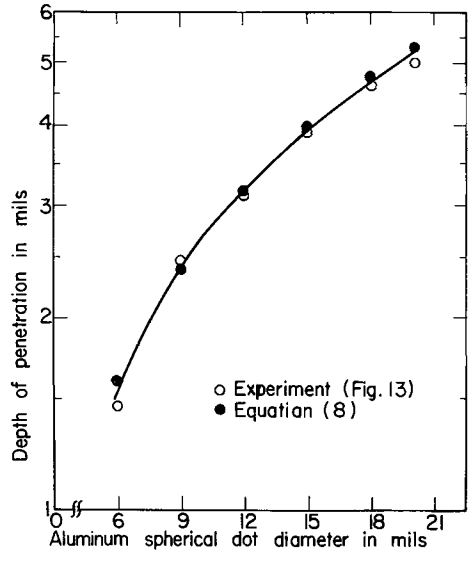

Fig. 15. Depth of penetration on aluminum dot size at 800°C for 30 sec.

Throughout this experiment, it was observed that the contact angle is closely related to the spreading diameter, since both relate to the surface tensions. This relationship gives the curve of Fig. 14 in which D_s/D is called the spreading ratio. As the result of this experiment, it has been found that $D_s/D = 1.4$ as a median value for pure aluminum fusion into the clean silicon in an argon atmosphere. Substituting the value of $D_s/D = 1.4$ into Eq. [6]

$$x = F(T)\frac{2D^3}{1.96D^2 + 1.4Dy + y^2} \qquad [7]$$

Let us suppose that $y = \frac{2}{3}D$, Eq. [7] becomes

$$x = F(T)\ (0.6\,D) \qquad [8]$$

This equation was then used in preparing the curve of Fig. 15, which has closely agreed with experimental values in Fig. 13. Equation [8] is applicable only for the calculation of maximum depth of penetration at given temperature. The value of spreading ratio, $D_s/D = 1.4$, is not always to be expected, since the spreading diameter of aluminum, D_s, has a tendency to spread beyond the value of $D_s/D = 1.4$ for the prolonged fusion time beyond 30 sec.

When an aluminum sphere 12 mils in diameter, for example, is heated on a pure silicon surface at 800°C, the cross-sectional configuration of fused junction can be predicted, as shown in Fig. 16.

Shape of the p-n transition.—The typical shapes of the transitions which were observed in this experiment are shown in Fig. 17. Figure 18 shows the approximate locations of photographs in Fig. 17. The "isosceles" effect on triangle is due to slight polishing angle.

Since silicon is normally grown in the direction (111) and dice used for making devices are cut from the crystal at right-angles to the growth axis, the author was interested mainly in the revealing of fusions on the (111) plane. However, he also studied plane (100), shown in Fig. 19. Figure 20 shows the approximate locations of photographs in Fig. 19. The

$F(T) = F(800°C) = 0.44$ (Fig. 4)

maximum penetration depth:
$x = (0.6)(12)(0.44) = 3.17$ mils (Eq. 8)

median spreading diameter:
$D_s = 1.4D = 16.8$ mils (Fig. 14)

minimum transition diameter:
$y = \frac{2}{3}D = 8$ mils

median high of aluminum melt:
$V_{al} = \frac{\pi}{6}D^3 = \frac{\pi}{6}(h^3 + \frac{3}{4}D^2h)$
$\therefore h = 6.73$ mils

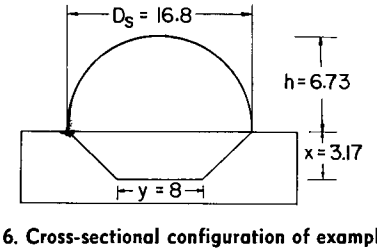

Fig. 16. Cross-sectional configuration of example

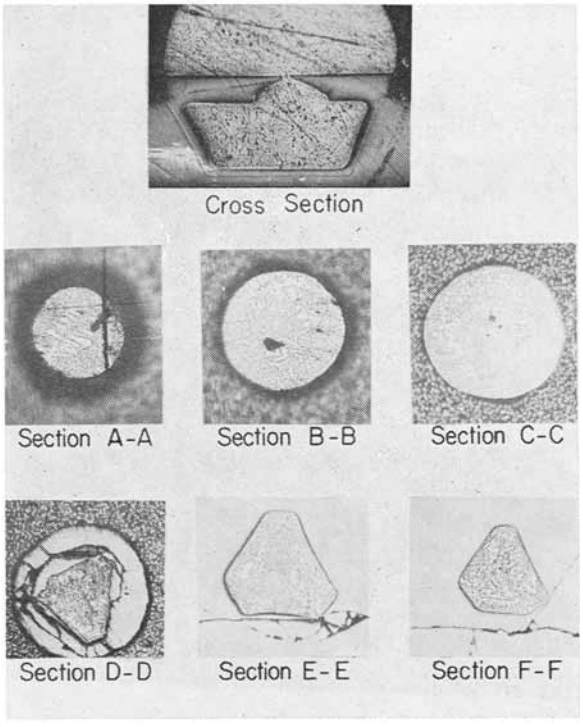

Fig. 17. Photographs illustrating planes parallel to crystal 1-1-1 plane (see Fig. 18 for sections).

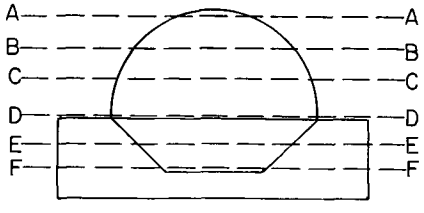

Fig. 18. Approximate locations of photographs in Fig. 17

trapezoidal effect noted in sections "E-E" and "F-F" is due to a slight polishing angle. At the tip "G-G", the p-n transition tends to approach a spherical shape.

Conclusions

The work described in this paper has been concerned with an investigation, analytically and experimentally, of the influence of fusion temperature, time, and aluminum sphere dot size on aluminum fusion into silicon. For calculating the depth of penetration of aluminum into silicon, Eq. [8] is analytically derived and verified by the experiment in Fig. 15. Figures 12 and 13 are prepared to predetermine the penetration depth of aluminum into silicon for various aluminum spheres, fusion temperatures, and time. Control of all phases of the process would make very uniform junction formation. The amount of aluminum and the heating and cooling cycles affect the junction area and the penetration of regrown region; therefore, its capacitance and the forward characteristics. Moreover, the perfection of junction formation affect on the over-all characteristics of device.

Acknowledgment

The author wishes to express sincere thanks to Mrs. P. Wilson for carrying out the experimental work. Thanks are also extended to personnel in the Metallurgical Laboratory for their valuable time on sectioning, measurement, and photographing of samples.

Manuscript received Sept. 14, 1961; revised manuscript received Nov. 24, 1961.

Any discussion of this paper will appear in a Discussion Section to be published in the December 1962 JOURNAL.

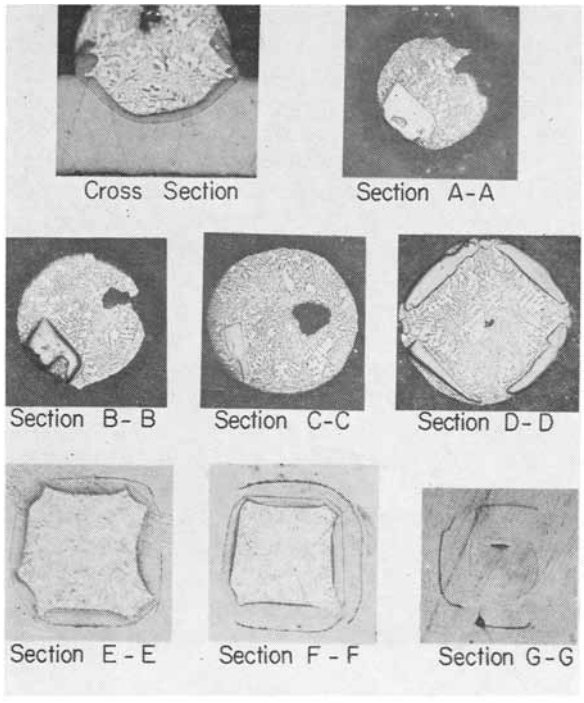

Fig. 19. Photographs illustrating planes parallel to crystal 1-0-0 plane (see Fig. 20 for sections).

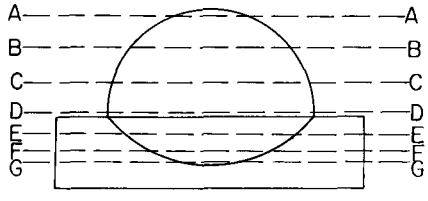

Fig. 20. Approximate locations of photographs in Fig. 19

REFERENCES

1. A. P. Viatkin, "The Problem Which Is Involved In Determining The Causes Which Give Rise To The Spread In the Values Of Transistor Parameters," Siberian Physics—Engineering Institute, Tomsk, 1957
2. J. J. BiKerman, "Surface Chemistry—Theory and Applications," p. 340, Academic Press Inc., New York (1958).
3. W. D. Kingerg, "Property Measurements At High Temperatures," p. 362, John Wiley & Sons, Inc., New York (1959).
4. D. A. Jenny, *Proc. IRE*, p. 1728 (December 1953).
5. "Alpha Semiconductor Materials Data Sheets," Alpha Metals, Inc., Jersey City, Chicago, Los Angeles.
6. L. Pensak, "Calculations of Alloying Depth of Indium In Germanium," Transistors I, RCA Laboratories, 1956.
7. "Reliability Assurance Program For Silicon Diodes," Continental Device Corporation, Hawthorne, Calif.
8. S. J. Gregg, "The Surface Chemistry of Solids," Chapman & Hall Ltd., p. 183, London (1951).

The Average Conductivity and Hall Effect of Diffused Layers on Silicon

O. N. Tufte

Honeywell Research Center, Hopkins, Minnesota

ABSTRACT

The relation between the average conductivity and Hall coefficient of a diffused layer on silicon and the surface concentration of the layer has been calculated for a complementary error function impurity distribution. The results show that the Hall coefficient is almost completely determined by the surface concentration of the layer and is only a very weak function of the mobility values used in the calculation. An experimental comparison of the surface concentration values obtained by the two methods is made.

The mathematical form of the impurity distribution in a diffused layer is determined by the boundary conditions of the diffusion process. If the mathematical form of the impurity distribution is known, the diffused layer may be completely described by a knowledge of the surface concentration and the concentration of impurities at a given distance from the surface. By knowing the concentration of electrically active impurities in the silicon before diffusion and by diffusing in electrically active impurities of the opposite conductivity type, the concentration of impurities at a given depth can be determined by measuring the location of the resulting p-n junction. Also, the p-n junction electrically isolates the diffused layer from the base silicon and allows electrical measurements to be made on the diffused layer. The general problem in the evaluation of diffused layers by this method is to relate some electrical property of the diffused layer to the surface concentration. It has previously been shown that for silicon (1, 2) and germanium (3-5) the surface concentration can be obtained by measuring the average conductivity of a diffused layer if the impurity distribution and the carrier mobilities are known for all concentrations of impurities found in the layer. Recently, Hall coefficient measurements have also been used by Subashchiev and Poltinnikov (6) to determine values of surface concentration.

In the present work, a calculation of the relation between the average conductivity and Hall coefficient of a diffused layer and the surface concentration is given for a complementary error function distribution of impurities. The results for several values of the impurity concentration in the base silicon are shown graphically. An experimental comparison of the values of surface concentration obtained by the two methods is made for n- and p-type layers on silicon.

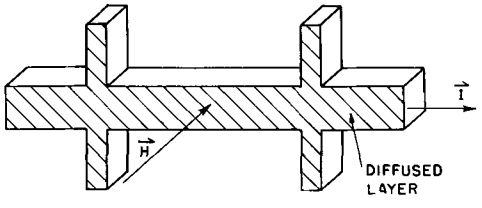

Fig. 1. Arrangement considered in the calculation of the average Hall coefficient of a diffused layer.

Method of Calculation

The arrangement considered here for the measurement of the Hall coefficient has the magnetic field perpendicular to the surface of the diffused layer as shown in Fig. 1. This arrangement has the advantage that the deflection of the carriers by the magnetic field is in a plane parallel to the surface of the layer so that the carriers are not deflected to regions of different mobility. Also, this method allows the use of the side-arm technique for making Hall effect contacts to the sample.

For the arrangement shown in Fig. 1, the expressions for the average conductivity and Hall coefficient of a surface layer in which the carrier concentration and mobility vary continuously with x, the distance from the surface area, are (7)

$$\sigma = \frac{|e|}{x_o} \int_0^{x_o} n(x)\, \mu(x)\, dx \qquad [1]$$

and

$$R = \frac{e x_o \int_0^{x_o} n(x)\, \mu^2(x)\, dx}{[|e| \int_0^{x_o} n(x)\, \mu(x)\, dx]^2} \qquad [2]$$

In these expressions $n(x)$ is the density of charge carriers at position x, $\mu(x)$ is the mobility of these carriers, e the charge of the carriers, and x_o the thickness of the layer. In Eq. [2] the assumption is made that the Hall mobility is equal to the drift mobility. It is also assumed that the diffused surface layer is completely isolated from the bulk so that the bulk is neglected in the calculation. Thus the layer thickness x_o is equal to the measured pn junction depth. Only one type of charge carrier is assumed to be present in the diffused layer. This assumption is questionable near the pn junction, but for the cases discussed here, the contribution to the integrals from the region near the pn junction is very small so that no significant error results.

For the complementary error function impurity distribution, the $n(x)$ in Eq. [1] and [2] is replaced by

$$n(x) = N_s \left(1 - \operatorname{erf} \frac{x}{2\sqrt{Dt}}\right) - N_o \qquad [3]$$

where N_o is the bulk impurity concentration of the base silicon, N_s the surface concentration, x the distance from the surface, and Dt the diffusion coefficient-time product. The values of the carrier mobilities used by Backenstoss (1) are used here. His relations for n-type silicon are

$$\mu_n = 300(19\text{-}\log N) \quad \text{for } 10^{16} < N < 5 \times 10^{18} \text{ cm}^{-3}$$
$$\mu_n = 80 \quad \text{for } 5 \times 10^{18} < N < 10^{21} \text{ cm}^{-3} \quad [4]$$

and for p-type silicon,

$$\mu_p = 180(18.2\text{-}\log N) \quad \text{for } 10^{16} < N < 8 \times 10^{17} \text{ cm}^{-3}$$
$$\mu_p = 40 \quad \text{for } 8 \times 10^{17} < N < 10^{21} \text{ cm}^{-3} \quad [5]$$

where N is the concentration of donor or acceptor atoms. For impurity concentrations of less than 10^{16}, the nearly constant mobilities appropriate to lightly doped silicon were used. The mobilities given in Eq. [4] and [5] are effective mobilities defined by

$$\mu = \frac{1}{e\rho N}$$

where ρ is the resistivity. This takes into account the incomplete ionization which occurs in doped silicon.

By making use of Eq. [3] one can rewrite Eq. [1] as

$$\sigma = \frac{|e|}{x_o} \int_o^{x_o} \mu(N) \left[N_s \left(1 - \text{erf} \frac{x}{2\sqrt{Dt}} \right) - N_o \right] dx \quad [6]$$

where $\mu(N)$ is given by Eq. [4] or [5]. At this point it is convenient to make a change of variable in Eq. [6] by letting $x = ax_o$, where a is a number between 0 and 1 and $w = x_o/2\sqrt{Dt}$. Equation [6] may then be written

$$\sigma = |e| \int_o^1 \mu(N) \left[N_s(1 - \text{erf } wa) - N_o \right] da \quad [7]$$

By making the same substitutions for the Hall coefficient in Eq. [2], one finds that

$$R = \frac{e \int_o^1 \left[N_s(1 - \text{erf } aw) - N_o \right] \mu^2(N)\, da}{\left[|e| \int_o^1 \left[N_s(1 - \text{erf } aw) - N_o \right] \mu(N)\, da \right]^2} \quad [8]$$

The expression in the denominator of Eq. [8] is the conductivity given by Eq. [7] and thus, if the conductivity for a given set of conditions has been calculated, only the numerator of Eq. [8] must be calculated to determine the Hall coefficient.

The value of w in Eq. [7] and [8] is determined by the values of N_s and N_o used in the calculation. Since intrinsic carriers are neglected when a is unity, $n(a)$ must be zero so that

$$w = \text{erf}^{-1} \left(1 - \frac{N_o}{N_s} \right)$$

The value of w depends only on N_o and N_s and not on the diffusion coefficient or time.

The integrals in Eq. [7] and [8] were evaluated numerically using Simpson's rule.

Results and Discussion

The results of this calculation for n- and p-type layers are shown in Fig. 2 through 5. The various curves in each figure are for different values of N_o, the impurity concentration in the base silicon. Three

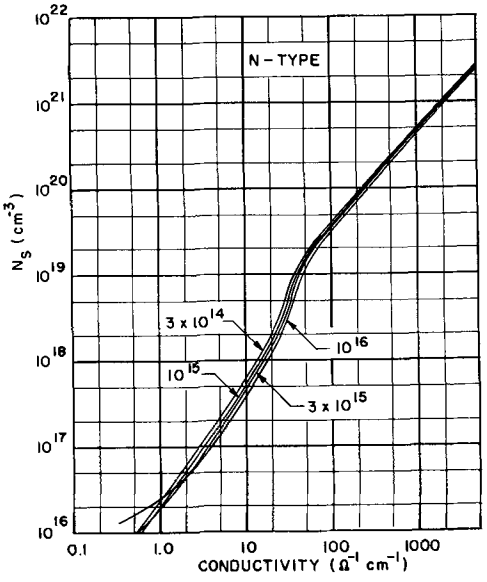

Fig. 2. Surface concentration N_s vs. average conductivity for an n-type diffused layer on silicon.

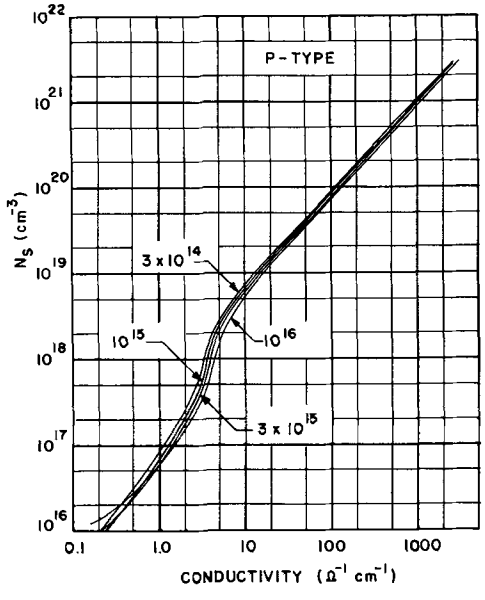

Fig. 3. Surface concentration N_s vs. average conductivity for a p-type diffused layer on silicon.

points per decade were used for each curve. The conductivity curves shown in Fig. 2 and 3 compare very well with the ones given by Backenstoss (1) for surface concentrations below 10^{18} cm^{-3}. However, for conductivities corresponding to concentrations above about 10^{18} cm^{-3}, the present curves give surface concentration values between two and three times larger due to a systematic error present in Backenstoss' curves.

The Hall effect curves for n- and p-type layers shown in Fig. 4 and 5 are very nearly identical. To show this better the curves for n- and p-type layers on silicon having a bulk impurity concentration of 3×10^{14} cm^{-3} are replotted in Fig. 6. Also shown in this figure is the Hall coefficient curve obtained by assuming the mobility is independent of impurity concentration, *i.e.*, $R = 1/\overline{N}e$ where $\overline{N}$ is the average impurity concentration. The curves in Fig. 6 show that the Hall coefficient in both n- and p-type dif-

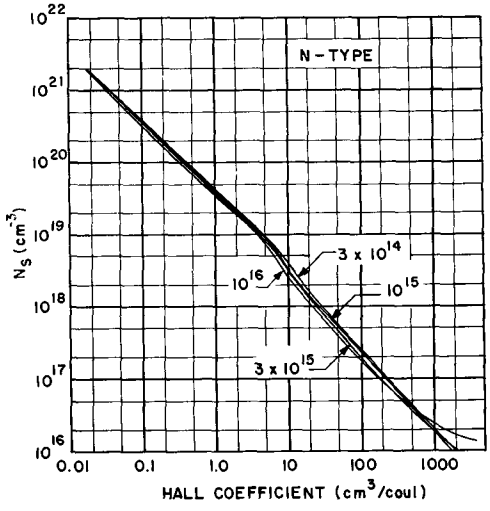

Fig. 4. Surface concentration N_s vs. average Hall coefficient for an n-type diffused layer on silicon.

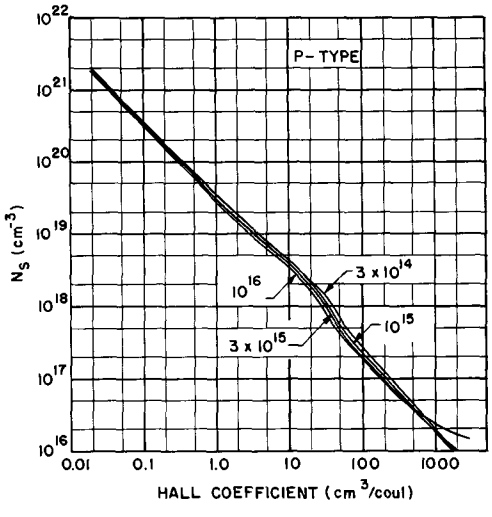

Fig. 5. Surface concentration N_s vs. average Hall coefficient for a p-type diffused layer on silicon.

fused silicon layers is very nearly a measure of the average carrier density and only a weak function of the mobility. Thus the accuracy of the surface concentration values obtained by the Hall effect method can be much greater than the accuracy to which the mobility values are known. This would make the Hall effect method especially useful for diffusion studies on less well-known semiconductor materials.

Comparison of surface concentration values obtained by average conductivity and Hall effect measurements.—Hall effect and conductivity measurements were made on diffused silicon layers to compare the values of surface concentration obtained by the two methods. Samples having two sets of side arms for Hall and conductivity measurements were ultrasonically cut from high resistivity (~300 ohm-cm) silicon. Both a pn junction and high resistivity base material were used to minimize leakage of current from the diffused layer. The samples were placed in an open-tube diffusion apparatus, and a diffused layer was formed on all sides of the samples. The thickness of the diffused layer was measured by angle lapping and staining (8) a monitor sample to determine the pn junction depth. The diffused layer is made sufficiently thick that the resistance of the

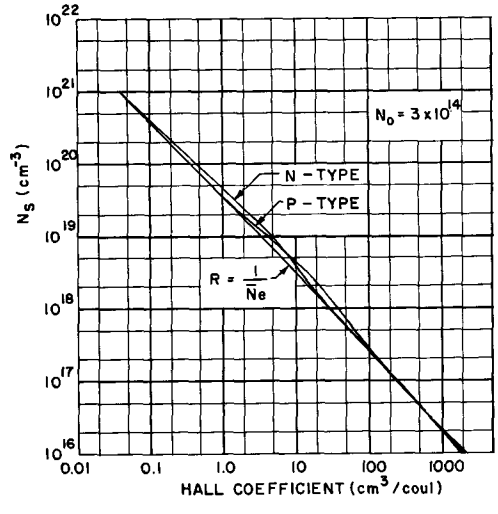

Fig. 6. Comparison of the surface concentration N_s vs. average Hall coefficient curves for n- and p-type diffused layers on silicon along with the mobility independent Hall coefficient curve.

layer is less than 2% of the resistance of the silicon in parallel with it. On one sample, the sides were etched after diffusion leaving a diffused layer only on the front and back surfaces such as shown in Fig. 1. The measured conductivity and Hall coefficient were the same before and after etching, indicating that the diffused layer on the sides of the sample is not introducing any spurious effects. Boron or gallium were used for p-type layers, and phosphorus or antimony were used for n-type layers.

The results for several n- and p-type layers having a wide range of surface concentrations are given in Table I. The agreement between the surface concentration values obtained by the two methods is very good at the higher concentrations. The largest discrepancies occur at the lower surface concentrations and can be attributed mostly to the insensitivity of the conductivity to surface concentration at concentrations near 10^{18} cm^{-3}. In this region a variation of ±10% (the accuracy of the layer thickness measurement) in the conductivity will result in a change of a factor of two in the surface concentration. Also, the uncertainty in the mobility values used in the calculation of the conductivity and deviations of the impurity distribution from a complementary error function can lead to a variation in the surface concentration values measured by the two methods. Conductivity values are corrected for incomplete ionization of the impurities by means of the mobility values used in the calculation. Since the calculated Hall coefficient values are nearly independent of the

Table I. Results for several n- and p-type layers

	Sample	N_s (conductivity) cm^{-3}	N_s (Hall coefficient) cm^{-3}
p-type	251A	2.0×10^{21}	2.0×10^{21}
	254A	7.0×10^{20}	7.7×10^{20}
	1021A7	2.7×10^{20}	2.4×10^{20}
	C595	6.6×10^{19}	5.9×10^{19}
	C593	1.3×10^{19}	0.7×10^{19}
	C594	3.5×10^{18}	5.6×10^{18}
n-type	3153	3.2×10^{20}	3.8×10^{20}
	KG1	3.0×10^{19}	5.2×10^{19}
	3151	1.8×10^{18}	0.8×10^{18}

mobility, these values are not corrected for incomplete ionization. However, for the impurities used, this correction is significant only in p-type layers and at an impurity concentration near 10^{18} cm^{-3}. Experimentally, the Hall effect method does not give consistently lower surface concentration values. This indicates that any errors due to incomplete ionization are smaller than the discrepancy between the surface concentration values obtained by the two methods.

Acknowledgments

The author wishes to thank Mrs. E. Swedberg for her assistance with the numerical calculations and Mr. E. Stelzer and Mr. J. Zoellmer for their assistance with the experimental work. Thanks are also due to Dr. D. Long for helpful discussions and for reviewing the manuscript.

Manuscript received Aug. 21, 1961; revised manuscript received Dec. 5, 1961. This paper was prepared for delivery before the Detroit Meeting, Oct. 1-5, 1961.

Any discussion of this paper will appear in a Discussion Section to be published in the December 1962 JOURNAL.

REFERENCES

1. G. Backenstoss, *Bell System Tech. J.*, **37**, 699 (1958).
2. M. F. Lamorte, *Solid State Electronics*, **1**, 164 (1960).
3. R. Glang and W. B. Easton, *This Journal*, **107**, 758 (1960).
4. H. S. Veloric and W. J. Greig, *R.C.A. Review*, **21**, 437 (1960).
5. D. B. Cuttriss, *Bell System Tech. J.*, **40**, 509 (1961).
6. V. K. Subashchiev and S. A. Poltinnikov, *Soviet Physics Solid State*, **2**, 1059 (1960).
7. R. L. Petritz, *Phys. Rev.*, **110**, 1254 (1958).
8. C. S. Fuller and J. A. Ditzenberger, *J. Appl. Phys.*, **27**, 548 (1956)

Effects of Copper on Fast Surface States of Etched Germanium

D. R. Frankl

General Telephone & Electronics Laboratories, Inc., Bayside, New York

ABSTRACT

Copper contamination is found to influence the fast surface states of Ge. The nature of the effect depends on the previous surface treatment: (*a*) on an etched surface, which is hydrophobic, the copper has little immediate effect, but enhances the growth of the density of recombination centers in oxidizing atmospheres; (*b*) on a KOH-treated surface, which is hydrophilic, the copper immediately produces a large concentration of recombination centers. In general, there is no apparent correlation between surface recombination and charge trapping in fast states.

In recent years there have been a number of studies (1-9) of the influence of the preparation and treatment procedures on the resulting fast surface states on germanium surfaces. One of the primary objectives of such studies has been to associate the surface states with specific physicochemical entities existing at or near the surface. In further pursuit of this objective, the present work deals with the effects of a deliberately added contaminant, copper, on the fast states of germanium, both freshly etched and aged in various gases. Copper was chosen for this study because of its known activity in the bulk and because it had already been shown (8) to influence certain surface properties.

Experimental Procedures

Measurements of the large-amplitude a-c field effect in the dark and under illumination were made on samples cut to the shape illustrated in Fig. 1. This geometry obviates the necessity of masking the contacts during etching, since the sample is dipped into the etchant only about half way up the legs. Thus, there is no possibility of contamination of the surface by matter dissolved from the masking material.

Figure 1 also shows the arrangement of the two field plates (one transparent) and mylar spacers. An important feature is that, in contrast with the usual arrangement, the spacers are cut out over the active portion of the sample. This promotes uniformity of the surface in two ways: (*a*) the ambient gas has free access to all portions of the surface; and (*b*) the capacitance variations arising from surface roughness are minimized. It is true that the applied field is limited by breakdown to about 10^6 v/cm, which is only about one-tenth as large as can be applied with a full dielectric spacer, so that the accessible range of surface potential is reduced by several kT/e. However, since the work of Rzhanov *et al.* (4), as well as some preliminary experiments in this laboratory, have shown that higher a-c fields can significantly increase the fast state density, it is not certain that this restriction is a serious one.

Most of the measurements were made on a 10.8 ohm-cm p-type germanium sample about 8 mils thick with surfaces parallel to [111] planes. The bulk lifetime was not known precisely, but was certainly >150

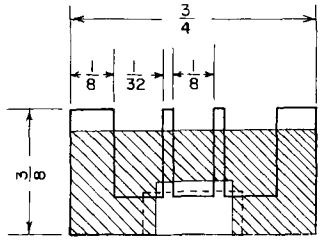

Fig. 1. Sample geometry. Heavy outline = die-cut Ge sample, dimensions in inches; hatched area = 1 mil mylar spacers; dashed outline = field plates, one transparent. The sample thickness is ~ 0.010 in.

μsec, so that the recombination was nearly always strongly dominated by the surface.

Two types of etchant were principally employed: (*a*) a "standard etchant" (600 cc HNO_3, 1200 cc acetic acid, 100 cc HF, 25 mg KI) that gave slow uniform dissolution, and (*b*) HF followed by hot KOH. The reasons for the use of the latter rather unconventional treatment will be given later. After etching, the sample was quickly plunged into a large volume of deionized water, rinsed copiously in flowing water (about 1 megohm-cm), rinsed again in recirculating water (5 to 10 megohm-cm), and dried with absolute ethanol. When copper was to be applied, the sample was dipped in a 1 ppm $Cu(NO_3)_2$ solution before the ethanol.

The prepared sample was mounted in a holder with field plates and spacers, the latter being swabbed with cotton dampened with trichloroethylene to remove dust. This usually assured that the capacitances to the two field plates agreed within 2 or 3%. The total time for preparation, mounting, and capacitance measurement amounted to about 10 min. Thereafter, the assembly was kept under controlled conditions in a copper box immersed in a water bath thermostatted to 27.00° ± 0.01°C. Nitrogen or oxygen, dried with "molecular sieve" or bubbled through water, was circulated through the box at about 0.1 liter/min after passing through a long copper coil in the water bath, and was taken out through a dew-point apparatus and a silicone oil trap. Dew points of the dried gases were usually below −75°C. The nitrogen was first de-oxygenated with a vanadyl sulfate solution (10). The oxygen could be ozonized by sparking with a Tesla coil.

Measurements were begun as soon as the temperature was stabilized, using the circuit shown in Fig. 2. The bridge is first balanced with switch SW open, adjusting R_G and the C_1's to obtain a single horizontal trace on the X-Y oscilloscope. Then, with SW closed and with light chopped at a nonsynchronous frequency, directed onto the sample through the transparent field plate, the oscilloscope displays both the "light" and "dark" field-effect curves. Auxiliary zero-field measurements of dark resistance and lifetime provide the factors necessary to obtain surface potential and trapped charge in fast states as usual (11) from the "dark" curve, and surface recombination velocity from the vertical difference between the two curves.

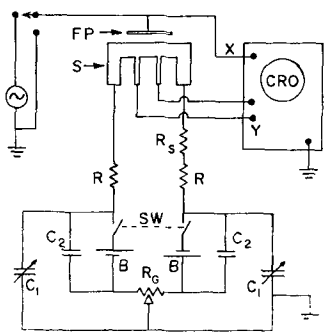

Fig. 2. Circuit diagram. S = sample; FP = field plates, one each side, one transparent; R = 300 kΩ; R_s = 1 kΩ standard resistor for measurement of sample current; B = 45-v battery; C_2 = 1 mfd; C_1 = 6-100 pf; R_G = 20 kΩ; SW = DPDT switch.

Several precautions are necessary to obtain valid results with this method. First, the sample current must be small enough to prevent sweepout of minority carriers when inversion layers are present. This requires $t_{tr} >> \tau$, where t_{tr} is the transit time of minority carriers across the region between probes, and τ the sample lifetime. Thus, the current was limited to about 0.15 ma, and a sensitive preamplifier (Tektronix Type 53/54G) used in the oscilloscope. Second, as discussed by several authors (13, 14) the light intensity must be low enough to produce little shift in the surface potential yet (necessarily) large enough to obtain measurable photoconductance. In the present work it was sometimes impossible to satisfy both of these requirements completely, particularly when the lifetime varied widely with field. It is estimated that shifts of as much as $(1/2)kT/e$ may occasionally have occurred under extreme conditions. For the most part, however, they were much smaller, and no attempt was made to correct the data. A third precaution is that the field frequency should be chosen to minimize hysteresis in the curves. In this respect, the present method has the advantage over point-by-point methods (1) that hysteresis, if present, is clearly evident. Two principal types can occur: one, due to the presence of "slow" states with fairly small time constants, can usually be minimized by increasing the frequency; the other, due to a "lifetime" effect (15), can be minimized by decreasing the frequency. Occasionally, due to one or both of these effects, single-valued curves are not obtained. In that event, the mean of the two branches is assumed to represent the correct curve provided the spread is not too large.

Results

Surfaces prepared with standard etchant.—Graphs of the surface recombination velocity s and trapped charge density Σ_{tr} as functions of the normalized surface potential u_s are shown in Fig. 3a and 3b, respectively, for the initial runs following six standard etch preparations, three with and three without copper treatment. The experimental points in these and all subsequent figures were computed without any mobility correction (16) for diffuse surface scattering. The reason for omitting this correction was that some of the oscillograms were, as was also found by Millea and Hall (17), too steep to be accountable by completely diffuse scattering. There are, of course, the possibilities that the surface scattering was partially diffuse and that the degree of diffuseness varied with the preparation and/or aging. Thus, the detailed shapes of the computed curves at extreme u_s values must be regarded as somewhat uncertain.

The s-curves (Fig. 3a) may be compared with the familiar theoretical expression (1) for a single type of recombination center, viz.

$$s = s_M \frac{\cosh(u_s - u_o) + 1}{\cosh(u_t - u_o) + \cosh(u_s - u_o)} \text{ (cm/sec)} \quad [1]$$

where $u_s = (E_F - E_i)/kT$, E_F = Fermi level, E_i = intrinsic Fermi level at the surface. $u_t = (E_t - E_i)/kT$, E_t = energy level of the center. $u_o = 1/2 \ln (C_p/C_n)$; C_p and C_n are the capture probabilities (cm³/sec) of the center for holes and electrons, respectively.

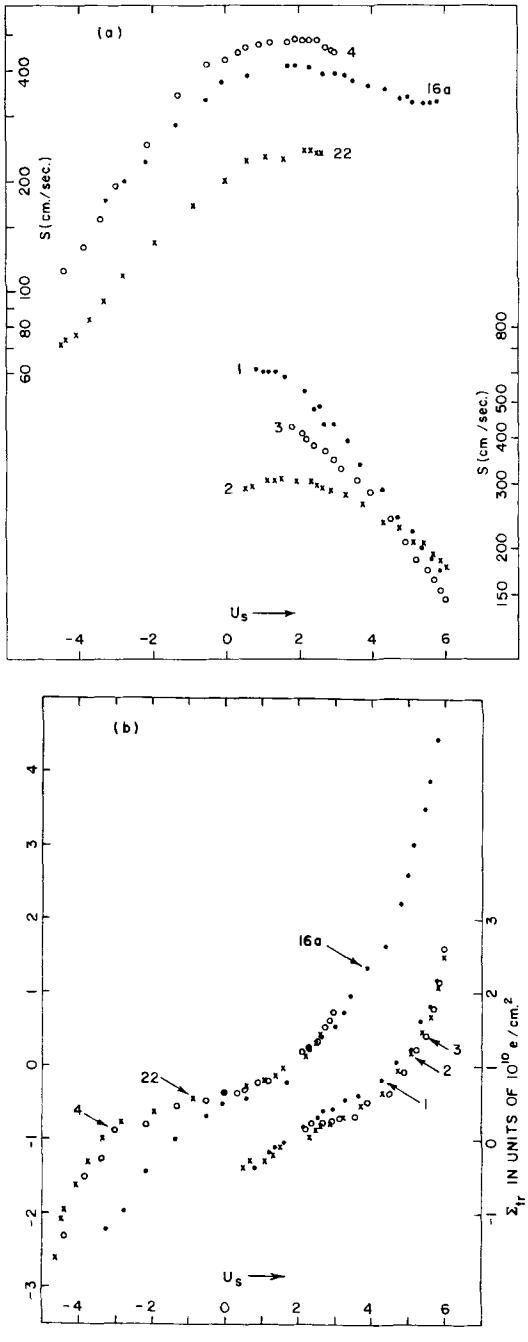

Fig. 3. First measurements after standard etches No. 1, 2, 3 (no copper added) 4, 16a, 22 (copper added). Note shift of ordinate scales.

$$s_M = \frac{N_t (C_p C_n)^{1/2} (n_o + p_o)}{2n_i[\cosh(u_t - u_o) + 1]}$$

$= \text{maximum value of } s$

$N_t = \text{surface density of centers (cm}^{-2})$

The present results are in fair agreement with the commonly observed values (1-7, 9) $u_o \sim 1$ to 2, $u_t \sim 5$, although curves 2 and 16a clearly indicate the presence of additional centers with larger u_o values. However, most striking is the rather large variation of s_M without a corresponding variation in trapped charge density in the range $u_s > 2$. Indeed, the copper treatment appears, if anything, to lower s_M slightly, but roughly to double Σ_{tr}. Thus, there appear to be recombination-ineffective states in the same energy range as the recombination centers. A

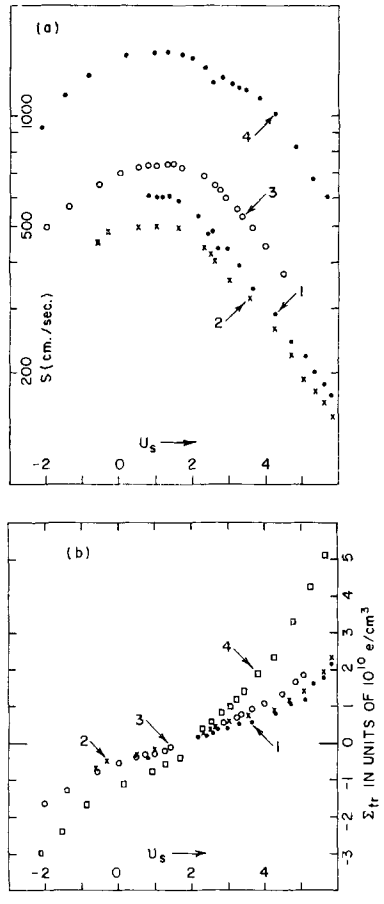

Fig. 4. Aging effects after etch No. 1 (no copper added). 1, initial run after 24 hr in dry N_2 (same data as in Fig. 3). 2, 48 hr in dry N_2. 3, 24 hr in dry O_2. 4, 16 hr in dry O_2 following 15 sec in ozonized O_2.

similar result was found by Arnold (13) on ion-bombarded surfaces, and further examples will be cited below.

As is evident from Fig. 3, the surfaces prepared without copper were quite strongly n-type at zero field. Indeed, initially the n-type bias was so strong that the conductance minimum could not be reached, and it was necessary to wait several hours (24 hr in the case of etch No. 1) while the surface drifted toward p-type. The copper treatment, however, made the surfaces more p-type (8), and measurements were commenced at once.

Some effects of oxygen and of brief (15 sec) exposure to ozone are illustrated in Fig. 4 and 5. The effects of the ozone could only be measured after some hours of "recovery" during which an appreciable hysteresis effect slowly diminished. These treatments increased both s_M and Σ_{tr}, as had been previously found, in whole or in part, by some authors (2, 4, 5, 12).

A new result, however, is the fact that the increases in s_M are considerably greater for the copper-treated than for the untreated surface. Furthermore, although Σ_{tr} at $u_s \sim 5$ changes roughly proportionally to s_M for the untreated surface, there is very little change in this range with copper. This again illustrates the lack of correlation between s_M and Σ_{tr}.

An attempt was made to ascertain whether the aging effects on the untreated surface were connected with accidental copper contamination, by rinsing the

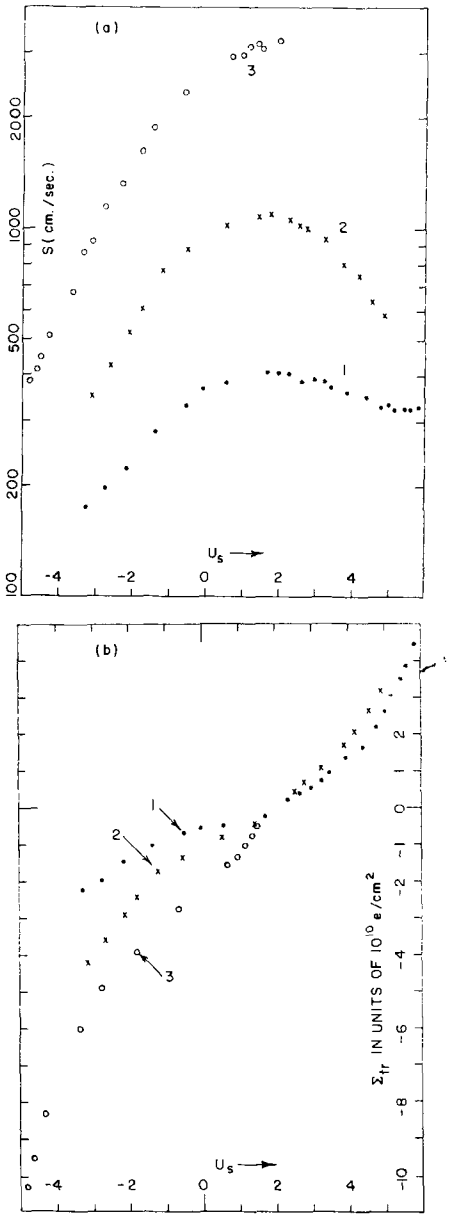

Fig. 5. Aging effects after etch 16a (copper added). 1, initial run after 30 min in dry O_2 (same data as in Fig. 3). 2, 24 hr. in dry O_2. 3, 16 hr in dry O_2 after 15 sec in ozonized O_2.

sample in KCN after etching. The surface was then, however, highly sensitive to the a-c field (*i.e.*, the "dark" oscilloscope curve changed markedly, indicating an increase in Σ_{tr}, within a few seconds after applying the field) and no reliable data were obtained.

Surfaces prepared with HF *and* KOH.—In the course of the work described in the preceding section, it became clear that the standard etch procedure suffered two major deficiencies: (*a*) the initial strong n-type bias described above; and (*b*) the initial, familiar (18), strongly hydrophobic character of the surface, which cast doubt on the efficacy of the rinsing procedure.

Accordingly, an extensive series of variations of the preparation procedure was undertaken, with results, in brief, as follows:

1. Careful drying (copious amounts of absolute ethanol) and crude drying (blotting) produced essentially the same results. Hence, the initial n-type bias was not due to residual water, as was first conjectured.

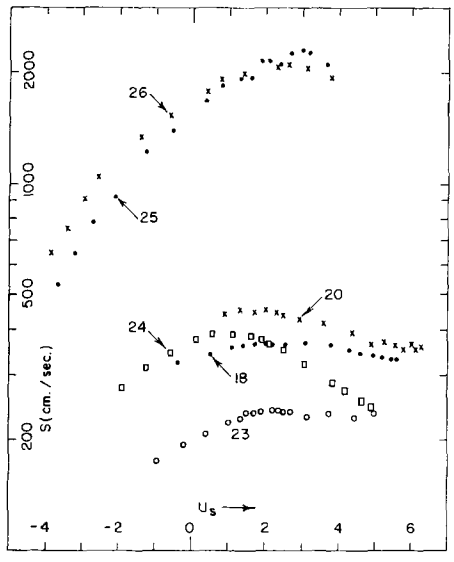

Fig. 6. Initial runs following treatment with 48% HF (1 min) followed by hot KOH (1 min). Nos. 18, 23, 25: 1% KOH; Nos. 20, 24, 26: 0.1% KOH; Nos. 25, 26: copper added. Measurements made about 30 min (in dry N_2) after treatment.

2. HF, alone or followed by acetic acid, produced essentially the same results as the standard etch, though with perhaps slightly higher s_M.

3. On one occasion, dipping the sample in 5% NH_4OH about 4 hr (in dry N_2) after a standard etch immediately removed the n-type bias. This experiment had been prompted by the thought that the bias might be due to an adsorbed layer of protons remaining from the strong acid etchant. The initial result appeared to bear this out, but later it was found that NH_4OH solutions up to 30% concentration applied immediately after etching, either in the standard etchant or in HF, left the surface still strongly n-type. Therefore, it appeared plausible that, if protons were indeed the surface donors giving rise to the n-type bias, they were initially protected from chemical neutralization by a hydrophobic film. The well-known (18) disappearance of the hydrophobicity with time would then account for the observation of neutralization by dilute NH_4OH after some hours.

4. Two of the writer's colleagues, P. Goldberg and D. H. Baird, made the valuable suggestion that the supposed film might be a hydrated oxide of germanium and that it might be soluble in a caustic solution. This treatment proved to reduce both the hydrophobicity and the n-type bias greatly, and the remainder of this paper is devoted to measurements on the resultant surfaces. In detail, the treatment was as follows: 1 min in 48% HF at room temperature; plunge, then rinse copiously in 1 megohm-cm water; 1 min in hot (~90°C) KOH (0.1-10%); rinse as before; rinse in 5-10 megohm-cm water; 15 sec in 1 ppm $Cu(NO_3)_2$ when desired; dry with absolute ethanol.

Figure 6 shows the initial *s* curves after several surface treatments of this type. The copper now greatly increases s_M, presumably by introducing additional recombination centers. If the above hypotheses concerning the hydrophobic film are cor-

rect, then removal of this film by KOH permits the copper ions to interact much more strongly with the germanium surface.

The additional centers due to copper appear either to be of several kinds or to possess several energy levels, since the differences in s between the copper-treated and untreated surfaces cannot be fitted by a single expression of the form (1). Fitting near the maximum indicates $u_o \sim 2.8$, $| u_t - u_o | \sim 3.5$, with additional levels having $u_o < -4$, but these values should be regarded as highly tentative.

The trapped charge curves corresponding to Fig. 6 showed, unfortunately, a great deal of variation, hence will not be discussed in detail. As before, however, there was no apparent correlation between Σ_{tr} and s.

Some preliminary aging results were also obtained following etches 20 and 26. In the former (no copper), s_M increased to about 700 cm/sec in N_2, 800 in O_2 and 1100 after ozone. In the latter, s_M changed relatively little in N_2, but decreased to 1400 cm/sec in O_2 and remained at about that value after ozone. In both cases, Σ_{tr} increased in both O_2 and ozone.

Discussion

The major results of the preceding section may be summarized as follows:

1. Copper (and presumably many other contaminants) influences the fast surface states; the nature of this influence depends on the previous surface treatment.

2. On the hydrophobic surface produced by at least one etchant, the copper effect is relatively slight initially, but the growth in density of recombination centers in oxidizing atmospheres is enhanced.

3. On the hydrophilic surface resulting from hot KOH treatment, the copper immediately produces recombination centers with indications of complex level structure.

4. There is, in general no correlation of s with Σ_{tr}. This means that the recombination center energy level cannot be used validly in the fitting of the Σ_{tr} *vs.* u_s curve by a sum of Fermi functions. It is for this reason that no attempt has been made in the foregoing to deduce trap state energies or concentrations.

A qualitative comparison with previous work may, however, be obtained by comparison of the minimum slopes of the trapping curves. For fresh surfaces, we obtain $(d\Sigma_{tr}/du_s)_{min} \sim 3 \times 10^9$ cm^{-2}, which is comparable to the results of Montgomery and Brown (11), Wallis and Wang (5), Rzhanov *et al.* (2), and Litovchenko and Lyashenko (19). Harnik and Margoninski (6), on the other hand, found minimum slopes about three to ten times greater, comparable with the results on "aged" surfaces of Many and Gerlich (1) and Margoninski and Farnsworth (9) and to those on ozone-treated surfaces of Rzhanov *et al.* (2), Flietner (12), and the present work. Presumably this reflects some subtle difference in surface preparation and may be connected with their finding (6) that s_M was sometimes decreased by ozone treatment, as in the present copper-treated KOH-prepared surfaces.

Another point of comparison concerns the use of HF alone as an etchant. Margoninski (7) finds that this "greatly increases the surface recombination velocity" whereas here little or no change was found. The latter result is the more "desirable" since it permits many repeated etches of the same sample without serious geometrical distortion. The conflicting results, however, strongly emphasize again the sensitivity of surfaces to minute variations in the preparation procedures.

Finally, mention should be made of the very interesting recent work of Boddy and Brattain (20), who found that on germanium surfaces in contact with especially purified electrolytes addition of trace amounts of Cu^{++} to the solution introduces appreciable numbers of surface recombination centers. This again demonstrates that copper can produce quite drastic effects if allowed to come into intimate contact with the surface.

Acknowledgments

Sincere thanks are due to A. Feuersanger for assistance and suggestions in setting up the measurements, and to P. Goldberg and D. H. Baird for extremely helpful discussions.

Manuscript received Oct. 5, 1961. This paper was prepared for delivery before the Detroit Meeting, Oct. 1-5, 1961.

Any discussion of this paper will appear in a Discussion Section to be published in the December 1962 JOURNAL.

REFERENCES

1. A. Many and D. Gerlich, *Phys. Rev.*, **107**, 404 (1957).
2. A. V. Rzhanov, Yu. F. Novototskii-Vlasov, and I. G. Neizvestnyi, *J. Tech. Phys. (USSR)*, **27**, 2440 (1957). [Translation, *Sov. Phys. Tech. Phys.*, **2**, 2274 (1958).]
3. Same authors, *Fiz Tverdogo Tela*, **1**, 1471 (1959). [Translation, *Sov. Phys. Solid State*, **1**, 1349 (1960).]
4. A. V. Rzhanov, N. M. Pavlov, and M. A. Selezneva, *J. Tech. Phys. (USSR)*, **28**, 2645 (1958). [Translation, *Sov. Phys. Tech. Phys.*, **3**, 2419 (1958).]
5. G. Wallis and S. Wang, *This Journal*, **106**, 231 (1959).
6. E. Harnik and Y. Margoninski, *J. Phys. Chem. Solids*, **8**, 96 (1959).
7. Y. Margoninski, *J. Chem. Phys.*, **32**, 1791 (1960).
8. S. R. Morrison, *J. Phys. Chem. Solids*, **14**, 214 (1960).
9. Y. Margoninski and H. E. Farnsworth, *Phys. Rev.*, **123**, 135 (1961).
10. L. Meites and T. Meites, *Anal. Chem.*, **20**, 984 (1948).
11. H. C. Montgomery and W. L. Brown, *Phys. Rev.*, **103**, 865 (1956).
12. H. Flietner, *Ann. Physik*, **3**, 414 (1959).
13. S. R. Arnold, ASTIA Document No. AD 210 839 (March 20, 1959).
14. A. V. Rzhanov, *Fiz Tverdogo Tela*, **2**, 2431 (1960). [Translation, *Sov. Phys. Solid State*, **2**, 2166 (1961).]
15. D. R. Frankl, Paper 121, presented at Electrochem. Soc. Mtg., Detroit (October 1961).
16. J. R. Schrieffer, *Phys. Rev.*, **97**, 641 (1955). R. F. Greene, D. R. Frankl, and J. Zemel, *ibid.*, **118**, 967 (1960).
17. M. F. Millea and T. C. Hall, *Phys. Rev. Lett.*, **1**, 276 (1958)
18 S. G. Ellis, *J. Appl. Phys.*, **28**, 1262 (1957).
19. V. G. Litovchenko and V. I. Lyashenko, *Fiz. Tverdogo Tela*, **1**, 1609 (1959). [Translation, *Sov. Phys. Solid State*, **1**, 1470 (1960).]
20. P. J. Boddy and W. H. Brattain, Paper No 114, presented at Electrochem Society Mtg, Detroit (October 1961).

Double Layer Capacities of Single Crystals of Gold in Perchloric Acid Solutions

G. M. Schmid and Norman Hackerman

Department of Chemistry, The University of Texas, Austin, Texas

ABSTRACT

The electrical double layer differential capacity has been measured by single pulse technique on single crystal gold electrodes exposing the (100) and (110) crystal plane in 0.001-1*N* $HClO_4$ between about —0.9v (15 ma/cm² maximum cathodic current) and +1.4v *vs.* SCE. A capacity maximum at +0.9 to +1.3v, depending on concentration, is attributed to "oxygen" adsorption. This showed strong hysteresis, the corresponding desorption peaks being as much as 500 mv more negative. Some evidence for adsorption of a second "oxygen" species is presented. A maximum occurring at +0.4v has been ascribed to slight specific ClO_4^- adsorption. A "hydrogen" adsorption peak is observed only on the (100) electrode at —0.2v. The complete absence of a profile during actual H_2 evolution is taken as evidence that recombination of H atoms is not the rate-determining step. A capacity minimum appears at the (110) electrode in $10^{-3}N$ $HClO_4$ at 0.0v and between two small maxima at the (100) electrode at —0.05v. These minima have been tentatively identified as the zero point of charge. The difference of 50 mv is reflected in an equal difference in the oxygen adsorption peaks. The zero point of charge potentials agrees satisfactorily with values interpolated from work function data.

The metal/electrolyte system is of interest to both the surface chemist and the electrochemist, mainly because it allows variation of the potential drop across the metal/electrolyte interface by applying a bias in an electrochemical cell. According to the theory of electrocapillarity (1), measurements of the interfacial tension as a function of potential permit calculation of the electronic charge on the metal at any potential and the determination of the zero point of charge (2). This information can be used to calculate the amount of cationic and anionic charge adsorbed at the solution side of the interface (1).

Surface tension measurements of the required accuracy are limited to liquid metals, *i.e.*, at room temperature, to mercury, some amalgams, and gallium. High-temperature data on molten metals are available (3). Attempts to replace surface tension by other properties, for example friction (4), repulsion of two wires of equal potential (5), have been made recently with some success in the latter case.

Complementary to surface tension data, and in principle not restricted to liquid metals, are measurements of the interfacial differential capacity, which constitutes the second derivative with respect to potential of the surface tension-potential function. On mercury, excellent agreement was found between properties of the interface calculated from surface tension data and from differential capacity measurements (1).

Differential capacity measurements can be made with an impedance bridge using sine wave alternating current (a.c.) (6), or with charging techniques using square wave currents (7, 8) or single constant current pulses (9, 10). The data are interpreted on the basis of simple circuit analogs, *e.g.*, a capacitor and a resistor in series, or in parallel.

On electrodes other than mercury, electrochemical reactions frequently take place. These find their expression in a more or less pronounced dependence of the capacity on the frequency of the bridge a.c. (11), or in an increasingly curved potential-time function when using a charging technique (7). At least part of the charge supplied to the electrode by the measuring signal flows across the interface, rather than only up to it as in the case of an ideally polarizable electrode (12). For a given electrochemical reaction the charge crosses the interface at a rate which is dependent on the frequency of the a.c., or on the time elapsed after application of the constant current signal. It is only at high frequencies, or at times in the order of microseconds, that this part of the total supplied charge becomes negligible and true double layer capacities are measured. "Pseudocapacities" obtained with low frequency a.c. on nonideally polarized electrodes should be interpreted on the basis of reaction parameters rather than properties of the electrical double layer.

The impedance of a given interface becomes smaller and smaller with increasing frequency of the a-c measuring signal. Thus, the limit of practicality for this type of measurement is set at about 200 kc (13). On the other hand, single pulses of 1 μsec duration are easily available today, corresponding in fundamental frequency to values with which a-c impedance measurements can be made only with difficulty.

Solid electrodes present some special problems. The unknown true area of the electrodes makes un-

certain the absolute magnitude of the parameters of the electrical double layer. Moreover, roughening of the electrode during the experiment should lead to time dependence. The electrode surface cannot be renewed constantly, as in the case of the dropping mercury electrode. Therefore extreme purity has to be achieved and maintained. Due to the difference in work function of single crystal faces (14), a difference in their electrical double layer parameters can be expected (15). In other words, two electrodes of the same material in the same solution may behave quite differently, depending on which crystal plane is predominantly oriented in the surface.

This investigation was undertaken to elucidate the influence of crystal orientation on the capacity of the electrical double layer. Gold was selected because of its availability in single crystals. Perchloric acid solutions were taken as electrolyte, ClO_4^- being the anion with the least likelihood of specific adsorption (1). The capacities were measured with a single pulse technique and equipment recently developed (10). The method is based on a circuit analog for the electrical double layer of a single resistor and capacitor in parallel.

Experimental

Materials.—The single crystals of gold, oriented by x-ray analysis, were obtained from Monocrystals Company, Cleveland, Ohio. They were pressure sealed into short pieces of Kel-F at 200°C, so that the (100) or (110) face was exposed. This method was adopted after attempts to obtain a good seal with Teflon as described by Breiter and Hoffman (16) failed, probably because of the rather irregular surface of the single crystal rods. A threaded brass rod, nut, and Teflon washers allowed the Kel-F mold to press tightly against a Pyrex glass holder, giving a water-proof seal and providing electrical contact with the gold. The apparent electrode area was about 0.09 cm^2. To obtain minimum roughness, electropolishing was tried at first, but had to be abandoned because of preferential attack at the edges. For the experiments reported here, the electrodes were etched in aqua regia, washed in conductivity water, and degreased with acetone in a soxhlet. The roughness factor was estimated to be 1.5.

Solutions, 1 to $10^{-3}N$ $HClO_4$, were made up from stock 70% $HClO_4$ and water from a Barnstead conductivity still ($\sim 2 \times 10^{-7}$ ohm^{-1} cm^{-1}). The solutions were pre-electrolyzed between Pt electrodes for 48 hr at 10-100 ma, and degassed with a steady stream of Grade A He for an additional 12 hr.

Cell and method.—The all-Pyrex glass cell contained a large platinized Pt wire gauze as polarizing electrode. Polarizing current was supplied by the pulse generator, or by a potentiometer and a large SCE whenever the total required current was less than 1 μa (from about $-0.2 + 1.4$v). The potentials were measured with a second SCE and a Haber-Luggin capillary, using a Keithley electrometer. They are reported with respect to SCE. A rapid stream of He served as stirrer and to remove gases evolved during the experiments. The cell had a jacket which contained $K_2Cr_2O_7$ solution, thermostated at 30°C. When connected to ground, the jacket gave an efficient shield for the cell.

The single pulse method and equipment used here has been described elsewhere (10). The differential capacity, C, was calculated with

$$C(t = 0) = \Delta Q'(0)/\Delta e'(0) \qquad [1]$$

[Eq. 10a in ref. (10)], where $\Delta Q'(0) = I_2 - I_1$, with I_1, the current density at time $t < 0$ (before the pulse) and I_2 the current density at $t > 0$ (during the pulse). $\Delta e'(0)$ is the change in slope of the potential-time curve at $t = 0$. A resistor and a capacitor in parallel were taken as the circuit analog for the electrical double layer in this analysis. The potential-time function of the test electrode was displayed on a Tektronix Type 545 oscilloscope using a Type-D preamplifier. The trace was photographed with a Dumont Polaroid oscilloscope camera.

Equation [1] requires obtaining the slope of a curve at one point ($t = 0$). Taking slopes with a ruler involves at least two points, and the measurement becomes more accurate the straighter the portion of the curve between the two points and in the limit of a straight line, the greater the distance between the two points. Therefore, the horizontal sweep of the scope was set so that a linear portion over at least 5 cm was obtained. In most cases, 5 μsec/cm served the purpose, but during H_2 evolution a sweep speed of 1 μsec/cm was necessary. The amplitude of the pulse was selected so that a vertical deflection of 2-4 cm over the horizontal screen width was obtained (1-0.1 ma). The scope amplifiers are linear to within 3% only, thus limiting the precision of the capacity measurement. The agreement between successive runs also was within 3%.

A run was started at about -1.0v (15 ma/cm^2 cathodic for $1M$ $HClO_4$). A capacity measurement was taken 10 min after the potential became steady. The electrode potential was then gradually made more noble, in steps of approximately 50 mv every 10 min. In most cases, the capacities had reached a stable value after 5 min. Experiments in which the time to obtain a final value exceeded 10 min were discarded. At $+1.4$v the direction of the potential change was reversed. Data taken this way were more reproducible than data from runs started at $+1.4$ v.

Results

During H_2 evolution the capacities of both the (100) and the (110) electrode are of the order of 10

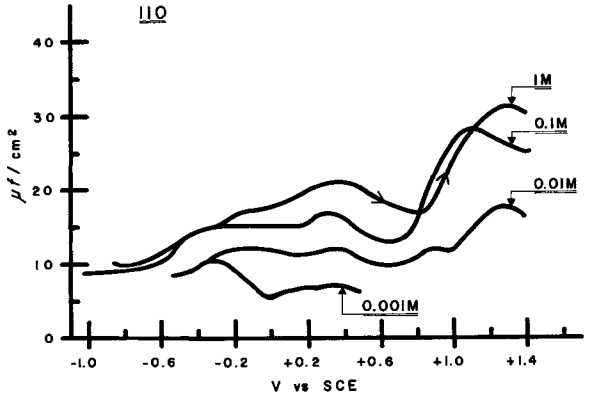

Fig. 1. Differential capacities of a (110) single crystal gold electrode in perchloric acid.

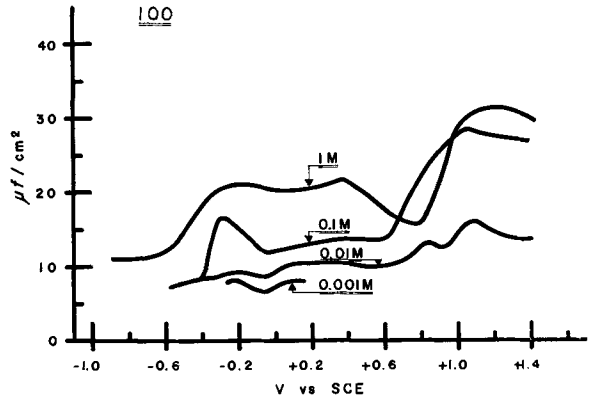

Fig. 2. Differential capacities of a (100) single crystal gold electrode in perchloric acid.

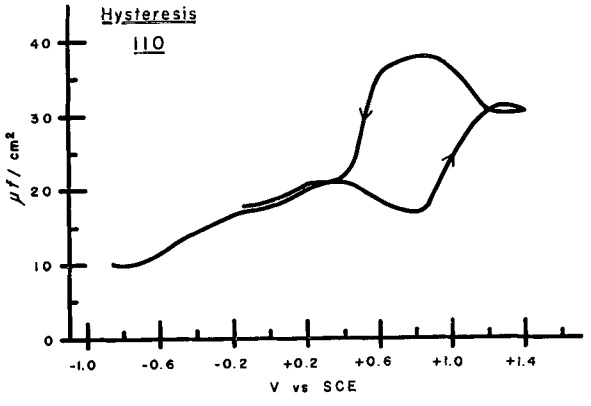

Fig. 4. Differential capacities of a (110) single crystal gold electrode in 1M perchloric acid.

$\mu f/cm^2$ (Fig. 1 and 2). The curves are flat and show no significant variation of capacity with potential between —0.6 and —0.9v (15 ma/cm^2 maximum cathodic current).

At the (110) face (Fig. 1) the capacity begins to increase at less negative potentials leading to a maximum positioned at +0.4v, independent of concentration. In 10^{-3}M $HClO_4$ this increase is interrupted by a minimum at 0.0v. A second maximum, found at +1.3v for 1M solutions, shifts about 200 mv per tenfold concentration decrease to less positive values. There is a third maximum at +1.25v in 10^{-2}M $HClO_4$ and some evidence of a third maximum beyond +1.4v in 1M and 0.1M $HClO_4$. The reproducibility becomes very poor beyond +1.4v, probably due to oxide film formation and a thorough investigation has not been possible.

The (100) electrode (Fig. 2) shows an additional maximum at —0.2v. The minimum that follows is at —0.05v. The maximum at +0.4v did not change position compared to the (110) electrode. The maxima at the far anodic side are 50 mv more negative for the (100) electrode than the corresponding maxima at the (110) electrode (Fig. 3).

Both electrodes show pronounced hysteresis when going from +1.4v to more negative potentials (Fig. 4). The maximum previously found at +0.9-+1.3v is displaced by as much as 500 mv to more active values. The maximum capacities are larger than any of the previous maximum values. The maximum itself is rather flat and drops off sharply toward negative potentials. At about +0.2v the hysteresis disappears.

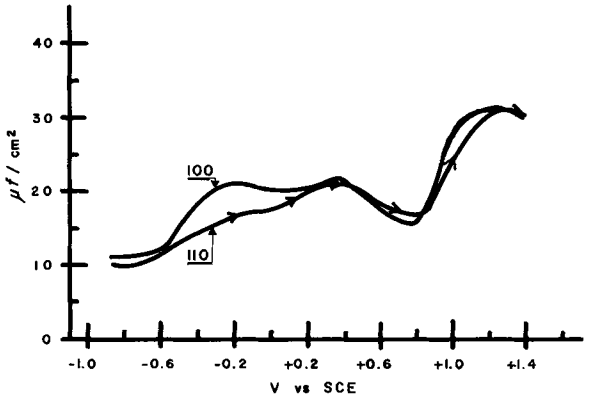

Fig. 3. Differential capacities of a (100) and a (110) single crystal gold electrode in 1M perchloric acid.

Discussion

The differential capacity is defined as (1)

$$C = \delta q/\delta\psi \qquad [2]$$

where q is the electronic charge on the metal side of the interface, and ψ the potential drop across the electrode/electrolyte interface. Thus, the value of the differential capacity gives a measure of the change of electronic charge on the metal with potential. According to the principle of electroneutrality, this change of electronic charge is compensated by an equal change of ionic charge with potential at the solution side of the interface. Thus, at any given potential, the absolute magnitude of the differential capacity gives a direct measure of the change with potential in the amount of adsorbed charged species. It has to be kept in mind, however, that changes in ionic charge density or adsorption of neutral organic molecules also lead to changes in differential capacities. This becomes apparent if the electrical double layer is considered as a plate condenser.

At present there is no clear-cut way to distinguish between the two effects. In the absence of adsorbable neutral organic substances and the presence of maxima and minima in the capacity potential curve we prefer the former view. In this case the occurrence of maxima cannot be explained by changes in ionic charge densities, unless one wants to assume complete saturation of the electrical double layer at the potential of the maximum.

In agreement with this interpretation, the appearance of the maximum at +0.9-+1.3v can be explained as being due to adsorption and/or chemisorption of oxygen (or some oxygen containing species). This explanation is prompted and confirmed by results obtained with a potential sweep method (17) and by cathodic stripping experiments (18). The high overpotential necessary for "oxygen" desorption (400-500 mv) (17) is again pointed out by the pronounced hysteresis in the capacity-potential curves.

Integration of the "oxygen" adsorption peak between +0.8 and +1.4v gives 6 μcoul/cm^2 for the (110) electrode in 1M $HClO_4$, or about 4×10^{13} electronic charges/cm^2. This is equivalent to 4 electronic charges per 100 surface atoms at +1.4v. The

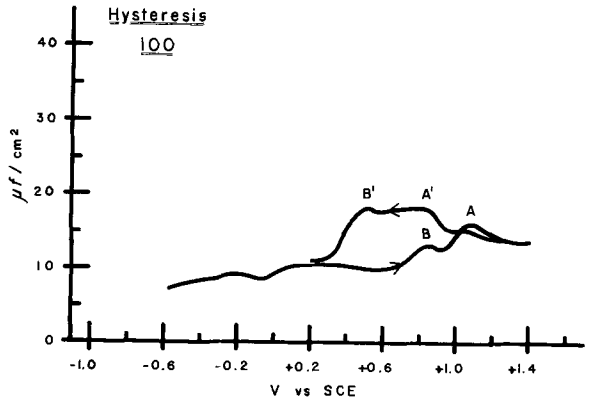

Fig. 5. Differential capacities of a (100) single crystal gold electrode in 10^{-2}M perchloric acid.

integration includes only part of the peak, as may be seen from Fig. 1. The 6 μcoul/cm² found in this way have to be confronted with a coverage equivalent to 800 μcoul/cm² as determined by cathodic stripping experiments (18) and 650 μcoul/cm² as measured with a triangular potential sweep method (17). It must be kept in mind, however, that the 6 μcoul/cm² represents a net charge, the excess of anionic charge over cationic charge. Further analysis, *e.g.*, a separation of positive and negative charges, requires $(\Delta C/\Delta a)_E$ data (a = activity) (19), involving high precision measurements for which our method is not suitable as yet.

Beyond a potential of +1.5v permanent changes seem to take place at the gold electrode. Therefore, no attempt was made to obtain data beyond +1.4v. Some indication for a second "oxygen" adsorption maximum above +1.4v was found, and this becomes apparent in 10^{-2}M $HClO_4$, where the shift with concentration brings this second peak down to about +1.2v (Fig. 5). Here the first "oxygen" adsorption maximum is represented by the little hump at about +0.9v, as can be seen from the hysteresis curve.

Measurements in 10^{-3}M $HClO_4$ could be made only in a narrow potential region. The high solution resistance tends to overdrive the scope amplifier, which leads to erroneous potential time curves.

The appearance of a small capacity maximum at +0.4v may be identified with the occurrence of some slight ClO_4^- adsorption. Evidence for specific adsorption of ClO_4^- on mercury has quite recently been found by Delahay and co-workers (20). The expected shift in position of the maximum by 60 mv/tenfold concentration change was not observed, however. Adsorption of a species like OH^-, on the other hand, should lead to the same shift in the opposite direction. The maximum in question does not shift either way with concentration. This discrepancy has not been solved so far.

The method of electrode preparation used here causes some faceting. The (110) and (100) electrode are therefore surfaces with a predominantly rather than complete (110) or (100) character. Nevertheless, some distinct differences can be detected. A capacity maximum at about −0.2v was found at the (100) face, but not at the (110) face. In view of the potential at which this maximum appears we ascribe this peak to hydrogen adsorption.

At the (100) electrode, the minimum between the maxima at −0.2 and +0.4v is found at −0.05v. At the (110) electrode a minimum appears at 0.0v. These two minima may be tentatively identified with the zero point of charge of the (100) or (110) face of gold, respectively. These zero point of charge potentials agree fairly well with values interpolated from work function data although this amounts only to an estimate at best. According to Frumkin (15), the difference in work function of two metals coincides with the difference in the zero point of charge potentials. Taking 4.5 ev and −0.45v, respectively, for mercury, and 4.9 ev for gold (21), one obtains 0.0v for the zero point of charge of gold. The difference between (110) and (100) of 50 mv is reflected in a difference of 50 mv in the position of the oxygen adsorption peaks of the two electrodes (Fig. 1 and 2). There is, of course, a liquid junction potential between a saturated KCl solution and $HClO_4$ involved.

The present capacity data are considerably lower than the 110 μf/cm² (22), 150 μf/cm² (23), and 200 μf/cm² (17) previously reported for gold in acid. This is probably due to the influence of Faradaic processes in the methods used by these authors. Quite recently, Laitinen and Chao (18) measured the capacity of gold, oriented predominantly with the 111 plane in the surface, in $HClO_4$, using a pulse technique. There is good agreement with our values in position and magnitude of the "oxygen" adsorption maximum (~35 μf/cm² at +1.30v). The agreement is not so good at other potentials (60 *vs.* 22 μf/cm² at +0.40v), although considerably better than with data obtained by others. A Δt of 200 μsec used by Laitinen and Chao may already be too long a time to eliminate the possibility of Faradaic processes completely and cause the capacity values to be too high. Our "oxygen" peaks and hysteresis effects are much more pronounced and seem perhaps more reasonable in view of other available oxygen adsorption data (17). On the other hand, Laitinen and Chao observe a shift of the maximum of 60 mv/pH unit, which is closer to expectations than the 200 mv/tenfold concentration change observed by us.

The magnitude of the capacities found in this work may seem to be too low. Frequently, the metal/electrolyte interface is assumed to have a capacity of 20 μf/cm², especially just before H_2 evolution (24). Apparently this assumption has its roots in the findings on mercury (1). In view of our interpretation, values considerably lower than 20 μf/cm² should be acceptable and, of course, have been found. The complete absence of an adsorption peak during actual H_2 evolution (up to 15 ma/cm²) on the (110) face is remarkable. This suggests that there is no buildup of hydrogen at the surface in this case, and recombination of hydrogen atoms cannot be the rate-determining step.

Summary

Electrical double layer differential capacities have been measured, using a single pulse technique, on

single crystal gold electrodes exposing the (110) or (100) crystal plane. 1*N* to 10^{-3}*N* $HClO_4$ solutions were used as electrolyte. The effectiveness of fast pulse techniques for the measurement of "true" double layer capacities is demonstrated for cathodic current densities up to 15 ma/cm^2.

The observed maxima and minima in the capacity potential curve have been interpreted on the basis of adsorption and desorption processes. Thus, a maximum occurring at +0.9 to +1.3v, depending on $HClO_4$ concentration has been attributed to adsorption of oxygen-containing species. This peak shows strong hysteresis and is displaced on desorption up to 500 mv to more negative values. Some evidence of adsorption of a second oxygen species is presented. A peak at +0.4v has been attributed to slight ClO_4^- adsorption, but does not show the expected concentration dependence. A maximum observed at −0.2v at the (100) electrode only was identified with "hydrogen" adsorption.

The absence of an adsorption peak during actual H_2 evolution up to 15 ma/cm^2 is taken as evidence for the nonexistence of a rate-determining recombination step.

A minimum occurring in dilute solutions at the (110) electrode at 0.0v, and between two slight maxima at the (100) electrode at −0.05v has been tentatively identified as the zero point of charge. The potentials agree fairly well with values obtained by interpolation of work function data. The difference of 50 mv between the crystal faces is reflected by an equal difference in the "oxygen" adsorption peaks.

Acknowledgments

The authors take this opportunity to express their appreciation for financial help to the Robert A. Welch Foundation of Houston, Texas, and to the Office of Naval Research under Contract Nonr 375(02) and 375(15).

Manuscript received Nov. 3, 1961. This paper was prepared for delivery before the Detroit Meeting, Oct. 1-5, 1961.

Any discussion of this paper will appear in a Discussion Section to be published in the December 1962 JOURNAL.

REFERENCES

1. For review see D. C. Grahame, *Chem. Revs.*, **41**, 441 (1947), A. N. Frumkin, *This Journal*, **107**, 461 (1960).
2. M. G. Lippmann, *J. Phys. Radium*, [2] **2**, 116 (1883); *Ann. Chim. Phys.*, [5] **5**, 494 (1875).
3. S. Karpachev and A. Stromberg, *J. Phys. Chem., USSR*, **18**, 47 (1944).
4. J. O'M. Bockris and R. Parry-Jones, *Nature*, **171**, 930 (1953).
5. T. N. Voropaeva, B. V. Deryagin, and B. N. Kabanov, *Proc. Acad. Sci. USSR* (English Translation), **127**, 829 (1959).
6. D. C. Grahame, *J. Am. Chem. Soc.*, **63**, 1207 (1941).
7. J. J. McMullen and Norman Hackerman, *This Journal*, **106**, 341 (1959).
8. B. D. Cahan, J. B. Ockerman, R. F. Amlie, and P. Rüetschi, *ibid.*, **107**, 725 (1960).
9. F. P. Bowden and E. K. Rideal, *Proc. Roy. Soc., London*, **120A**, 80 (1928).
10. J. S. Riney, G. M. Schmid, and Norman Hackerman, *Rev. Sci. Instr.*, **32**, 588 (1961).
11. K. Franke, C. A. Knorr, and M. Breiter, *Z. Elektrochem.*, **63**, 226 (1959).
12. F. O. Koenig, *J. Phys. Chem.*, **38**, 111, 339 (1934).
13. W. Lorenz, *Z. Phys. Chem. (NF)*, **19**, 377 (1959).
14. See f.e. H. E. Farsworth and R. P. Winch, *Phys. Rev.*, **58**, 812 (1940).
15. A. N. Frumkin, *Colloid Symposium Annual*, **7**, 89 (1930).
16. M. Breiter and K. Hoffmann, *Z. Elektrochem.*, **64**, 462 (1960).
17. F. G. Will and C. A. Knorr, *ibid.*, **64**, 270 (1960).
18. H. A. Laitinen and M. S. Chao, *This Journal*, **108**, 726 (1961).
19. D. C. Grahame and B. A. Soderberg, *J. Chem. Phys*, **22**, 449 (1954).
20. K. Asada, P. Delahay, and A. K. Sundaram, *J. Am. Chem. Soc.*, **83**, 3396 (1961).
21. R. H. Fowler, *Phys. Rev.*, **38**, 45 (1931).
22. G. Armstrong, F. R. Himsworth, and J. A. V. Butler, *Proc. Roy. Soc., London*, **143A**, 89 (1934).
23. A. Hickling, *Trans. Faraday Soc.*, **47**, 522 (1946).
24. C. Wagner, *This Journal*, **97**, 72 (1950).

Preparation of Lanthanide and Actinide Monosulfides by Fused Salt Electrolysis

R. Didchenko[1] and L. M. Litz[2]

Parma Research Center, Union Carbide Corporation, Parma, Ohio

ABSTRACT

The monosulfides of the metals in the lanthanide and actinide series may be prepared by the electrolytic reduction of the higher sulfides in an oxygen-free, fused salt medium that contains the chloride of the metal in question.[3] A detailed description of the preparation of CeS and ThS is given, and possible reaction mechanisms are discussed.

The monosulfides of thorium, uranium, and of the lanthanide elements are highly refractory materials with the NaCl structure. Most of them exhibit high electrical conductivity of the metallic type, but some are semiconductors. The first synthesis by Eastman and Brewer (1, 2) was based on the reaction $2CeH_3 + 2Ce_2S_3 \rightarrow 6CeS + 3H_2$ and required for completion heating above 2000°C at 10^{-4} mm Hg, rather extreme conditions. The method of Flahaut and Attal (3) circumvents the need for CeH_3, which

[1] Parma Research Laboratory of Union Carbide Corporation.
[2] Research Laboratory of National Carbon Company, Division of Union Carbide Corporation.
[3] Patent applied for.

is difficult to handle, and instead utilizes aluminum metal as the reducing agent in the reactions

$$9\ Ce_2S_3 + 2\ Al \xrightarrow{1000\text{-}1200^\circ C} 6\ Ce_3S_4 + Al_2S_3$$

$$3\ Ce_2O_2S + 3\ Ce_3S_4 + 2\ Al \xrightarrow{1200^\circ C} 15\ CeS + 2\ Al_2O_3$$

The sulfide and oxide of aluminum are stated to be removed by vacuum distillation at 1500°C and 10^{-2} mm Hg. The evaporating oxide species is most likely Al_2O (4). The reduction of cerium dioxide with sulfur in a hydrogen sulfide atmosphere claimed by Samsonov (5) and coworkers could not be repeated in our Laboratory.

The purpose of this paper is to describe a new method which is particularly suitable for large-scale preparations and which may be applied to synthesize the subsulfides of many other transition metals. It is based on the electrolytic reduction of the sulfide of a metal in its higher oxidation state, suspended in a molten salt bath which may conveniently consist of alkali metal chlorides and the chloride of the metal in question. The reduction is followed by vacuum distillation of the salts and electrolysis by-products at 1000°C. The higher sulfide used as one of the starting materials may be prepared either separately or *in situ*. In the latter case, an alkali sulfide, preferably Na_2S, may be added to the melt containing a calculated excess of the metal chloride beyond the requirements of the electrolytic bath.

Experimental

A typical preparation of CeS and ThS is described in detail to illustrate the experimental procedures based, respectively, on a higher metal sulfide and on an alkali sulfide as one of the starting materials.

Preparation of the starting materials.—1. The NaCl-KCl eutectic (mp 658°C) was prepared by mixing 44 weight % (w/o) NaCl and 56 w/o KCl in a graphite crucible, placing it inside a vertical quartz tube, flushing with purified argon and heating to 800°-850°C. Purified argon was then bubbled through the melt for 1 hr. The last traces of chemically bound water were eliminated most effectively by electrolyzing the melt at 1.8-2.0v with the crucible acting as anode and a graphite rod immersed in the melt as the cathode. Thus, electrolysis was conducted until the current through the melt became constant and very small ($\simeq$ 0.1 amp). The solidified cake was removed from the crucible in a good dry-box and ground to a coarse powder.

2. Cerium sesquisulfide, Ce_2S_3, was prepared by prolonged treatment of cerium dioxide with hydrogen sulfide gas in a graphite crucible at 1000°-1100°C (6).

3. Cerium trichloride, $CeCl_3$, was prepared either from cerium sesquisulfide or from the dioxide. In the first case, dry chlorine was passed over the sulfide while raising the temperature slowly. At around 300°C, a strongly exothermic reaction set in and proceeded very rapidly. In order to achieve complete conversion, it was necessary finally to raise the temperature above the melting point of cerium trichloride (822°C) and to bubble chlorine through the melt. When cerium dioxide was the starting material, it was treated with S_2Cl_2 (7) while slowly increasing the temperature from 400° to 750°C. After the main bulk of the oxide was converted into the chloride, the temperature was raised to 850°C and a chlorine stream charged with S_2Cl_2 bubbled through the melt. A new method for dehydrating commercial cerium and thorium chlorides also was developed in the course of this investigation (8). All these methods gave pure anhydrous cerium trichloride which crystallized from the melt in large, pure white needles that dissolved rapidly in absolute alcohol forming completely clear solutions. The latter is a very sensitive test for the absence of undesirable oxychloride which, when present even in small amounts, produces a cloudy solution. Anhydrous cerium trichloride is extremely hygroscopic and should be handled only in a good dry-box.

4. Anhydrous sodium sulfide is easily prepared in small quantities by elemental synthesis in liquid ammonia (9). For larger scale preparations the method of Koenig (10) based on the reaction $Na_2CO_3 + H_2S \rightleftharpoons Na_2S + CO_2 + H_2O$ was found suitable although tedious.

Electrolytic cell.—The cell is shown in Fig. 1. The crucibles (55 mm OD, 45 mm ID, 90 mm high) were made from ATJ grade graphite (National Carbon Company). Graphite could not be used as the cathode material because it disintegrated during the electrolysis, ostensibly due to the formation of laminar compounds with alkali metals. Therefore, the cathode shaft and paddle were made of molybdenum and were protected from attack by anodically produced chlorine by an alumina sleeve projecting above the melt. Electrical contact to the cathode was made by means of a spring-loaded carbon brush which permitted rotation of the cathode during the electrolysis. Alundum extraction thimbles (Norton, RA 98) 34 mm diameter, 100 mm high, were used as catholyte container and diaphragm.

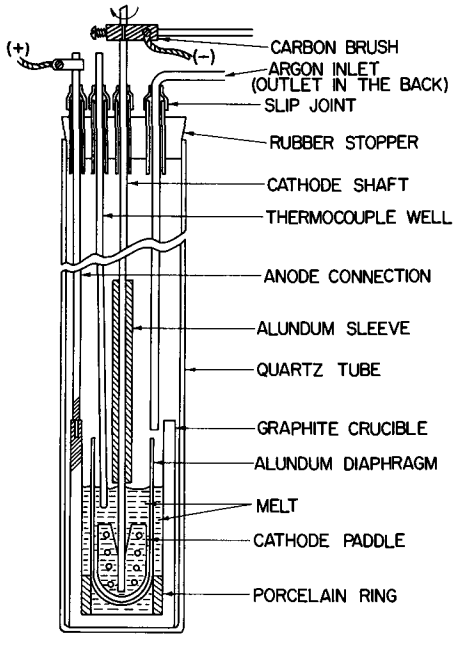

Fig. 1. Electrolytic cell

The electrolysis.—A typical preparation of cerium monosulfide was conducted in the following manner. Cerium sesquisulfide (35g) and cerium trichloride (35g) were mixed together and put into the Alundum diaphragm cup. The NaCl-KCl eutectic prepared as described above was charged loosely into the bottom part of the cell until it covered the porcelain support ring. The Alundum cup then was fitted into the ring and more eutectic charged into the cell with constant tapping to make sure that both anode and cathode compartments were tightly filled with salt. The total charge of the eutectic mixture was 225g. The cell was lowered into the quartz envelope previously flushed with argon and closed (by the rubber stopper) with the cathode in the proper position. All above operations were performed in the dry-box. The cell was then heated electrically to 800°C in a pot furnace while maintaining a slow flow of argon (2-3 l/min) through the tube. The cathode was set in rotation at 60-80 rpm, with the blades 2-3 mm above the bottom of the Alundum cup, centered in such a manner that no scraping of the walls occurred.

For the first 45 min the melt was "pre-electrolyzed" in order to eliminate any moisture and oxygen which may have found their way into the cell during the loading and transfer operations. In the course of this pre-electrolysis the applied voltage ran from 0.6 to 2.1v, which is just below the decomposition voltage of cerium trichloride in these melts (11), and the current fell from 0.3 to below 0.1 amp. The back-emf, *i.e.*, the open-circuit voltage between the cathode and the anode an instant after interrupting the current, reached the value of 2.0v indicating the presence of cerium metal at the cathode. The voltage then was raised to 5.0v and maintained close to this value during the entire electrolysis. The current decreased from a peak value of 6.3 amp to about 5.5 amp after 3 hr while the back-emf remained constant at 2.4v for the first hour, rose to 3.0v within the next 30 min and remained at this value, which corresponds to the decomposition voltage of NaCl, until the end of the electrolysis (Fig. 2). Sixteen ampere-hours of current passed through the cell, *i.e.*, twice the amount needed to produce sufficient cerium metal to convert the sesquisulfide to the monosulfide. After continuing the stirring without current for 1 hr, the cathode was lifted above the melt and the cell allowed to cool under argon. The solidified melt was easily separated from the graphite crucible; the

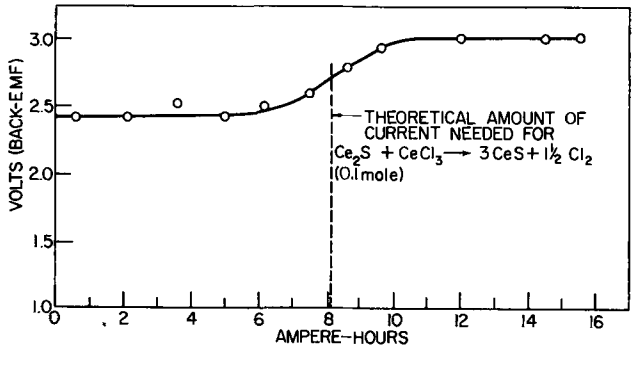

Fig. 2. Plot of back emf *vs.* current passed through the cell

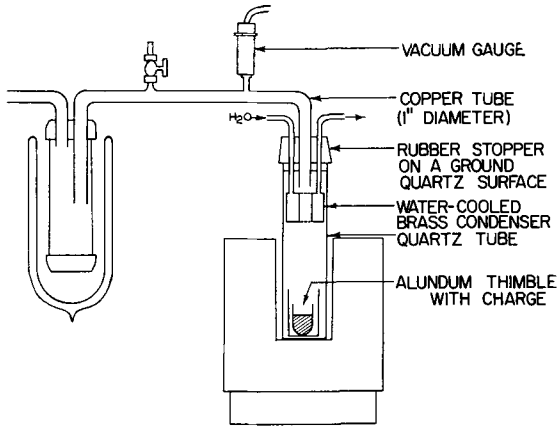

Fig. 3. Vacuum distillation apparatus

thimble was broken exposing at the bottom a large golden-brown button of cerium monosulfide, embedded in the salts.

Vacuum distillation of the salts.—The salts above the cerium monosulfide in the diaphragm thimble were mechanically removed as well as possible. The thimble, inside of a Vycor cup, was then placed in the quartz tube of the distillation apparatus shown in Fig. 3. After repeatedly evacuating and purging the entire assembly with purified argon, the thimble was heated in the course of 2-3 hr to about 1000°C at a few microns pressure. The distilled salt condensed on the cold baffle together with alkali metals and some cerium metal. These finely divided metals reacted immediately after exposure to air, often sparking and flaming. The light-brown cake of CeS, which remained in the thimble, was easily removed and broken up into a crystalline powder of about 200 mesh.

Purification and sintering of cerium monosulfide.—The powder was placed in a molybdenum crucible and heated inductively in a vacuum furnace. Between 1000° and 1500°C, some residual salts and cerium metal distilled off while the pressure decreased from 10^{-3} to 10^{-5} mm Hg. The sulfide was then heated at this pressure to 1800°-1900°C for 15-30 min and cooled, first *in vacuo*, then in purified helium atmosphere. After this treatment, the monosulfide was found to be sintered to a bright golden ingot which weighed 42g. When occasionally the product was contaminated with small amounts of higher sulfides and oxysulfide, these impurities tended to separate on the outside of the ingot as a black skin. They were removed by breaking up the ingot into a coarse powder and heating it again in the vacuum furnace with approximately 5% by weight of cerium metal.

Preparation of thorium monosulfide and other monosulfides.—The only modification in the preparation of ThS was in the original charge. Thus, 37.4g (0.1 mole) of anhydrous thorium tetrachloride and 7.8g (0.1 mole) of anhydrous sodium sulfide were mixed together and put in the diaphragm cup. The cell was then filled with the salt eutectic and assembled as described above. An electrolytic current of 4-6 amp at 4.4-5.0v was passed through the cell for 150 min which amounted to 11.0 amp-hr or twice the theoretical requirement for the reduction

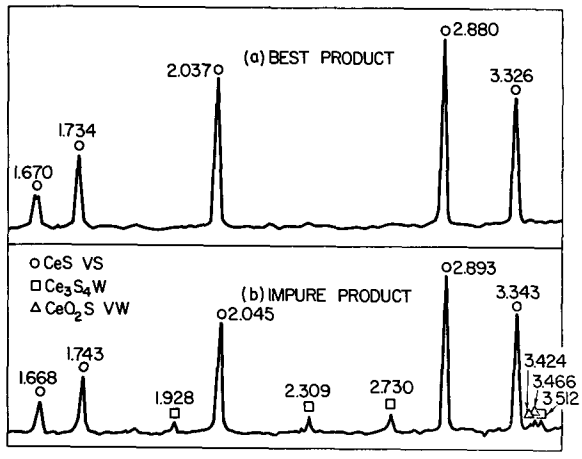

Fig. 4. X-ray patterns of electrolytic CeS

of all the thorium in the melt from tetrapositive to dipositive ion. The product was vacuum-distilled in the same manner as the cerium monosulfide. Twenty-one grams of thorium monosulfide were obtained, a yield of 78% based on the amount of thorium added as the tetrachloride.

The monosulfides of lanthanum, gadolinium, ytterbium, and uranium were prepared in a manner analogous to that described for CeS. It was also possible, starting with "didymium" oxide, converting it to mixed trisulfides and trichlorides and electrolytically reducing the latter, to obtain a mixture of monosulfides of lanthanum, cerium, neodymium, praseodymium, samarium, and other rare earths.

Discussion

The yields of monosulfide varied from 80 to 90% based on the conversion of the sulfur in the original trisulfide. Therefore, the over-all reaction must be: $Ce_2S_3 + CeCl_3 \rightarrow 3\,CeS + 1\frac{1}{2}\,Cl_2$. The back-emf curve shown in Fig. 2 is typical for all electrolyses; it shows a rather abrupt change in voltage at the number of ampere-hours necessary to produce just the amount of cerium metal needed for the reduction of the trisulfide. The back-emf values do not necessarily represent equilibrium potentials at the very high current densities used. It is then reasonable to expect that, along with the cerium metal, alkali metals also are formed to some extent from the onset of electrolysis, contributing to the total polarization voltage of the cell. The break in the curve occurs at a point where the major "depolarization" reaction, *i.e.*, reduction of Ce_2S_3 with cerium metal, is completed.

In further support of this reaction mechanism, it has been shown repeatedly that complete conversion of the trisulfide is greatly facilitated if cerium trichloride is present in the melts at least in 1.5-fold excess over the above stoichiometric equation. Since cerium metal dissolves in the melts containing cerium trichloride (12, 13) its reducing action would thus be enhanced. In this context it is also important that cerium monosulfide can be obtained without the electrolysis by simply adding cerium metal to a suspension of cerium trisulfide in a melt composed of NaCl-KCl eutectic and cerium trichloride and stirring the latter for several hours. Although this heterogeneous reaction appears most straightforward, different homogeneous mechanisms are also possible. The authors have established that cerium trisulfide is slightly soluble in cerium trichloride. Mellors and Senderoff (14) consider likely the existence of the species Ce^{I} $[Ce^{III}\ Cl_4]$ in solutions of cerium metal in cerium trichloride. It seems possible, therefore, that the reduction of the trisulfide in electrolyzed melts also can involve the interaction in solution between Ce^{+} and some species derived from dissolved cerium trisulfide.

The monosulfides obtained by this method are usually metal-rich and analyze $MeS_{0.95-1.00}$. The major impurities are silica and iron if these are present in the starting material (oxide). They occur in total concentrations of up to 1%, but do not seem to affect the properties of the monosulfide in any noticeable manner in contrast to oxygen which easily forms oxysulfides. The oxysulfides form solid solutions with the monosulfides and, even in small quantities, change their golden color to dark brown or black and reduce their melting point considerably. For this reason a rigid exclusion of moisture and oxygen from the electrolytic melt is necessary. The best products obtained by fused salt electrolysis give the x-ray pattern of pure CeS as shown in Fig. 4a. When incompletely reduced and when small amounts of oxysulfide are present, there is obtained a pattern as shown in Fig. 4b. The vacuum treatment with cerium converts pattern b into pattern a due to the reduction of Ce_3S_4 to CeS, whereas Ce_2O_2S is eliminated by the reaction: $Ce_2O_2S + Ce \rightarrow CeS + 2\,CeO_{(volatile)}$.

Manuscript received Aug. 4, 1961; revised manuscript received Dec. 6, 1961.

Any discussion of this paper will appear in a Discussion Section to be published in the December 1962 JOURNAL.

REFERENCES

1. E. D. Eastman L. Brewer, *et al.*, *J. Am. Chem. Soc.*, **72**, 2248 (1950).
2. E. D. Eastman, L. Brewer, *et al.*, *ibid.*, **72**, 4019 (1950).
3. J. Flahaut and E. Attal, *Compt. rend.*, **238**, 682 (1954).
4. G. DeMaria, J. Drowart, and M. G. Inghram, *J. Chem. Phys.*, **30**, 318 (1959).
5. G. V. Samsonov, N. M. Popova, and L. I. Tikhomirova, *Zhur. Prikl. Khim.*, **31**, 153 (1958).
6. M. Picon, *ibid.*, **195**, 957 (1932); Bull Soc. Chim. France, **49** [4], 703 (1941).
7. F. Bourion, *Compt. rend.*, **145**, 62 (1907).
8. R. Didchenko, *Trans. Met. Soc. AIME*, **215**, 492 (1959).
9. See f.i.: G. Brauer, "Handbuch der preparativen anorganischem Chemie," p. 279, Stuttgart (1954).
10. H. T. J. Koenig, USP 2, 106, 952 (Feb. 1938).
11. S. Senderoff, G. W. Mellors, R. I. Bretz, *Ann. N. Y. Acad. Sci.*, **79**, 878 (1960).
12. D. Cubiccioti, *J. Am. Chem. Soc.*, **71**, 4119 (1949).
13. G. W. Mellors and S. Senderoff, *This Journal*, **105**, 224 (1958).
14. S. Senderoff and G. W. Mellors, *J. Phys. Chem.*, **63**, 1110 (1959).

Electroosmosis in Cation-Selective Collodion Matrix Membranes of Graded Porosity

Charles W. Carr, Ruth McClintock,[1] and Karl Sollner

Department of Physiological Chemistry, University of Minnesota Medical School, Minneapolis, Minnesota, and Laboratory of Physical Biology, National Institute of Arthritis and Metabolic Diseases, National Institutes of Health, Bethesda, Maryland

ABSTRACT

Electroosmosis was studied in a series of highly charged cation-selective collodion matrix membranes varying in porosity from fairly dense permselective membranes (9% water content) to highly porous membranes (75% water content). In all membranes the amount of water transported per faraday was independent of the current density in the tested range, 0.05-0.80 ma/cm². There was a parallelism between the water content of the membrane and the moles of water transported per faraday. In the presence of KCl the moles of water transported per faraday varied from 3 to 50 for the series of membranes tested, and with LiCl from 6 to 90. With all membranes the values with LiCl were about twice those obtained with KCl. This is in conformity with current theories of the transport process, according to which the water transport is higher the greater the friction between water and the permeating ions. Accordingly, the lower mobility of the lithium ion in the membrane (and in aqueous solution) is associated with a higher transport per faraday across the membrane. Exclusively anion permeable membranes gave analogous results.

The collodion matrix membranes developed in our laboratories (1-5) have recently been used in studies of the relative rates of electromigration of two ions of the same charge across a membrane (6), and of anomalous osmosis (7). In this connection, the electroosmotic behavior of the membranes is of importance. Accordingly, the present report is concerned with the electroosmosis across permselective membranes and across a series of membranes of graded porosity prepared by swelling permselective membranes in various concentrations of ethanol (8).

In our permselective membranes, which in the concentration range explored in these experiments are essentially permeable to ions of one sign only, the current is carried virtually exclusively by the counter ions of the charged (ionic) groups which are located in the pore system of the membrane and constitute an integral part of the latter. Thus the number of counter ions in the membrane is determined by the number of fixed charges on the pore walls and is independent of the concentration of the external solution. For all concentrations in which the membranes are of extreme ionic selectivity one would therefore predict that the ratio of current to rate of water transport is constant. With more porous membranes (as well as with permselective membranes and solutions of rather high concentrations) nonexchange electrolyte enters the pores; its concentration depends on the external concentration. In this case, the nonexchange electrolyte carries a part of the current. Consequently, the number of moles of water transported per faraday under these conditions should depend to some extent on the concentration of the external solution.

Several recent papers are concerned with the electroosmotic transport of water across ionic membranes (9-20), prompted in part by the technical use of such membranes for saline water conversion. Some of the data were obtained under conditions in which the membranes were not exclusively permeable to ions of one sign only and therefore cannot readily be compared with our observations on permselective membranes. Some of the data however are comparable; first, those obtained with truly permselective membranes; second, those obtained with solutions of low concentration in which the transport number of the preferred ion in the membrane is close to unity, the membrane acting almost like a truly permselective membrane; and third, those in which the water transported per ion was obtained by measurement of both the quantities of preferred ion and of water moved. Winger, Ferguson, and Kunin (14) obtained 7.0 ± 1 moles of water per faraday with K^+ and 13.5 ± 1 with Li^+, values which were independent of the electrolyte concentration. For Na^+, Stewart and Graydon (17) reported 4-15 and Oda and Yawataya (13) 8-19 moles per faraday. The latter groups both observed a lower water transfer at higher concentrations and a parallelism between the water content of the membrane and the quantity of water transferred.

Experimental Procedure

Most of the permselective membranes used were cation-selective collodion matrix membranes prepared with different concentrations of polystyrene sulfonic acid (PSSA) to obtain membranes of different resistances (and water contents) (3). Their

[1] Present address: Department of Physiology, The George Washington University, School of Medicine, Washington, D. C.

Table I. Properties of a series of polystyrene sulfonic acid collodion matrix membranes of graded porosity

Designation of membrane	Concentration potential, 0.1/0.01M KCl, mv	Water content, vol %	Smallest molecule held back
Alc 0	55	≃15	Urea (60)
Alc 80	51	23	Glucose (180)
Alc 90	44	30	Salmine (3000-6000)
Alc 95	28	55	Serum albumin (70,000)
Alc 97	19	75	Edestin (310,000)

resistances in 0.1*M* KCl and their approximate water contents are given below with the experimental results.

Membranes of graded porosity were prepared by swelling permselective membranes in solutions of 80, 90, 95, and 97% ethanol (8). The membranes of this series, including an unswelled one, vary in porosity from a permselective membrane to membranes with porosities corresponding to conventional dialyzing membranes. A membrane swelled in 95% ethanol is designated an Alc 95-Membrane, a membrane that has not been swelled, an Alc 0-Membrane, etc. A summary of the properties of this series of membranes is given in Table I. Column 2 gives the concentration potential in 0.1/0.01*M* KCl, which indicates the degree of ionic selectivity of the membrane (3); column 3 lists the water content in per cent by volume (3,21); column 4 gives the smallest molecule which does not move across the membrane to any significant extent (the molecular weights are given in parentheses) (8).

The apparatus for the measurement of the electroosmotic water transport consisted essentially of a test-tube shaped membrane, 25 x 100 mm, with a similarly shaped electrode on either side, a calibrated tube for measuring the volume change of the solution in the inside compartment, and a beaker for the outside compartment (Fig. 1). The membrane was tied to a glass ring in which was mounted a rubber stopper carrying a three-way stopcock connected with the calibrated tube, made from a 1-ml graduated pipet, and a side-arm for filling. In some experiments with permselective membranes, a 0.1-ml graduated pipet was substituted to facilitate the measurement of small volume changes. The silver screen electrodes were electrolytically coated with thin layers of silver chloride. The entire assembly was mounted in a rubber plate and placed in the beaker. The electrical circuit included a source of direct current, a variable resistance, a milliammeter, and the electroosmosis apparatus.

Currents of 2.5-60 ma were employed, which, with the total membrane area of approximately 50 cm², gave current densities of about 0.05-1.2 ma/cm². The external resistance was adjusted periodically so that the current did not vary by more than ± 2% during an experiment. The volume changes, measured over intervals of about 5-15 min, were 4-40 μl. The experiments were carried out in an air-conditioned room so that volume changes due to fluctuations in temperature were insignificant.

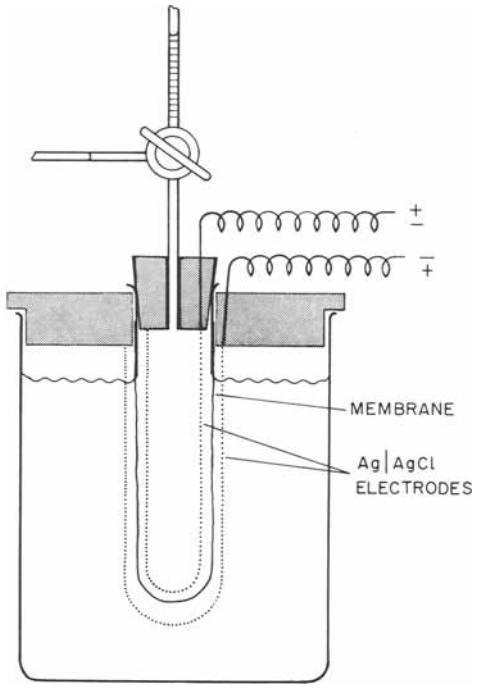

Fig. 1. Apparatus for measuring electroosmosis across test-tube shaped membranes.

Because the height of the solution in the calibrated tube was 20-30 cm above the solution in the beaker, there was a slow downward movement of the meniscus when no current was flowing. The rates of water movement with the current on and with the current off were measured repeatedly. The difference between the average rates was considered as the true rate of electroosmotic water movement; it was independent of the direction of the current. The results were expressed in terms of moles of water transferred per faraday.[2] The reproducibility was ordinarily within ± 10%, except with the very densest membranes, where the error might be somewhat larger.[3]

Results

Measurements made at several current densities with unswelled (permselective) and swelled membranes showed that the water transport per faraday is independent of the current strength, at least at current densities of about 1 ma/cm² or lower. Table II gives representative data for both groups of membranes obtained with 0.02*M* KCl.

[2] With the two densest permselective membranes, the movement of water began slowly with an initial lag after the current was started; it continued, often with a sudden spurt, for a short time after the current was stopped. The final spurt just equalled the initial lag. The curves of water moved *vs.* time were similar to those reported by Oda and Yawataya (13). The values for the rate of electroosmosis were taken from the linear portions of the curves, omitting the small initial and final effects.

[3] Mackay and Meares (20) have recently pointed out that, in determining the rate of electroosmotic flow through a membrane, volume changes occurring at the electrodes should be taken into account. If the cation transport number is unity and one faraday of electricity is passed through the cell, then the increase in volume in the compartment with the cathode, ΔV, is (in the case of a KCl solution)

$$\Delta V = W\bar{V}_{H_2O} + \bar{V}_{KCl} + \bar{V}_{Ag} - \bar{V}_{AgCl} \qquad [1]$$

The $\bar{V}$'s are the partial molal volumes, and W is the number of moles of water transported per faraday. $\bar{V}_{KCl}$ (in 0.2*M* solution) is 27.5, $\bar{V}_{Ag}$ is 10.3 and $\bar{V}_{AgCl}$ is 25.8 so that $W\bar{V}_{H_2O} = \Delta V - 12.0$. The increase in the cathode compartment, which is equal to the decrease in volume in the anode compartment, is 12 ml per faraday or about 0.7 mole per faraday. For LiCl the correction is 0.1 mole per faraday. Such corrections would be insignificant with nearly all the data reported below. Only in the case of the permselective membranes with solutions of KCl (Table III) would they be significant; however, they would not be large enough to change the meaning of our results.

Table II. Electroosmosis across PSSA collodion matrix membranes of different porosities with 0.02M KCl at varying current densities

Designation of membrane	Moles of H_2O transported/faraday 0.05 ma/cm²	0.10 ma/cm²	0.20 ma/cm²	0.40 ma/cm²	0.80 ma/cm²
Alc 0	—	11.8	11.2	—	11.9
Alc 90	23.8	23.5	22.4	23.5	20.9
Alc 97	44.7	50.6	47.6	49.9	47.0

Table III. Electroosmosis across permselective PSSA collodion matrix membrane with 0.2M KCl and 0.2M LiCl

Membrane Resistance, ohm-cm²	Water content,* vol %	Moles of H_2O transported/faraday 0.2M KCl	0.2M LiCl
420	9.3	3.2	6.4
140	10.2	3.5	7.4
25	15.0	11.5	16.0

* Estimated from the data of Neihof (3).

Having established that the water transport per faraday is independent of the current strength, we proceed to the influence of (*a*) water content of the membranes; (*b*) nature of the permeating or preferentially permeating ion; and (*c*) concentration of the solutions.

With both groups of membranes the higher the water content the more water moved with each ion through the membrane. Table III gives the results for a group of permselective membranes; Figures 2 and 3 show that at any given concentration the same holds true for a series of membranes of higher porosities.

Likewise, with both groups of membranes more water was transported with Li^+ than with K^+ (Table III and Fig. 2 and 3). Figure 4 shows a direct comparison of the results obtained with solutions of KCl and LiCl as well as with NaCl, for a membrane of high water content, 75% by volume.

The lowest curves in Fig. 2 and 3 show that with low resistance permselective membranes of relatively high water content (15% by volume) there is a variation of about 20% in the quantity of water transportation per faraday over the concentration range 0.001-0.50*M*. It might be added that with permselective membranes of lower water contents the concentration of the solutions has no

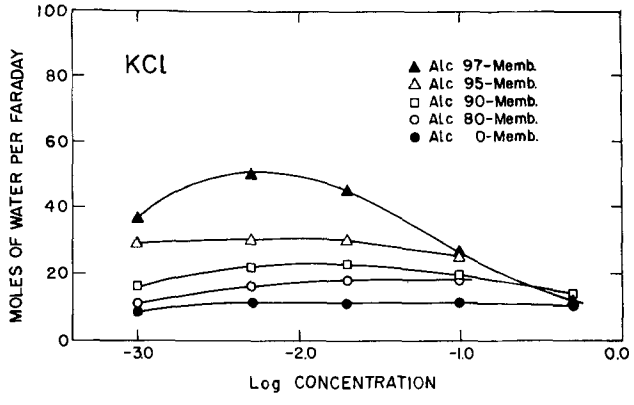

Fig. 2. Electroosmosis across PSSA collodion matrix membranes with KCl solutions.

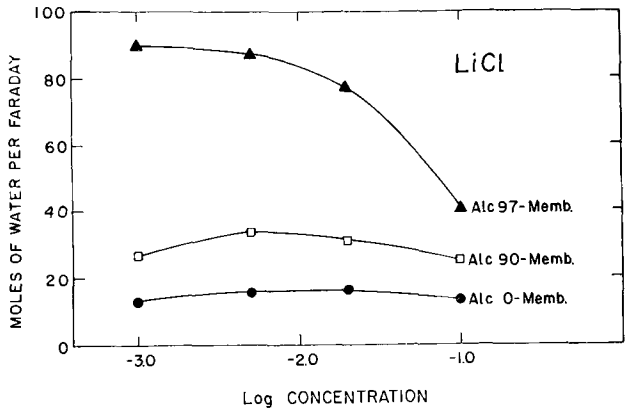

Fig. 3. Electroosmosis across PSSA collodion matrix membranes with LiCl solutions.

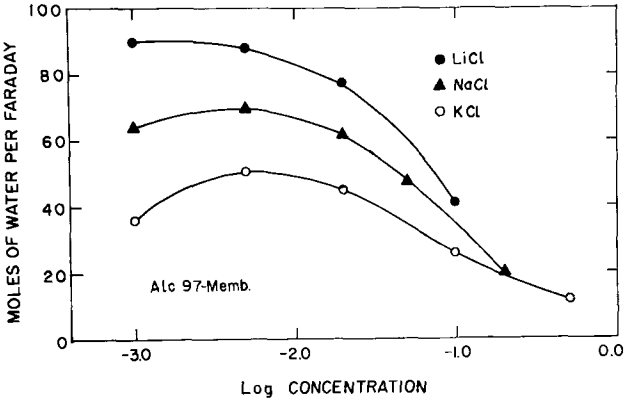

Fig. 4. Electroosmosis across an Alc 97-PSSA collodion matrix membrane with KCl, NaCl, and LiCl solutions.

significant influence on the quantity of water transported. With membranes of higher water content, 23-75% by volume (Alc 80- to Alc 97-Membranes) the influence of the concentration tends to be more pronounced the higher the water content (Fig. 2 to 4).

A few experiments were performed with anion permeable permselective membranes with various concentrations of KCl, KI, and KAc. These membranes are similar in their electroosmotic behavior to the cation permeable ones with respect to the amounts of water transported, to the correlation of water transport with the water content of the membrane, to the dependence on the species of permeating ion, and to the absence of a concentration effect.

Discussion

The values for electroosmotic transport with the permselective collodion matrix membranes (Table III) are in the same range as those obtained by Winger, Ferguson, and Kunin (14) for K^+ and Li^+, and by Stewart and Graydon (17) and Oda and Yawataya (13) for Na^+ with membranes made of ion exchange materials. The electrolyte concentration has little influence on the rate of electroosmotic water transport as anticipated on the basis that in the concentration range studied, (0.001-0.5*M*), the number of movable counter ions in the membrane is practically independent of the concentration of the external solution. This is also in agreement with the observations of Winger, Ferguson, and

Kunin (14) on membranes of sulfonated polystyrene cross-linked with 4-15% divinylbenzene.

In the case of the ethanol-swelled membranes, the most porous of which are similar in porosity to dialyzing membranes, the expected decrease in the electroosmotic water movement at higher concentration is clearly seen (Fig. 2-4). This decrease was also observed by Oda and Yawataya (13) and by Stewart and Graydon (17). Entirely unexpected, however, was the fact that the water transport per faraday is in many instances less at low (0.001*M*) concentration than in an intermediate concentration range. An explanation for this phenomenon, based on the uncoiling of entrapped polyelectrolyte at low ionic strength, has been suggested by Caplan of this laboratory. This topic will be developed in a later publication concerning the preparation of polyacrylic acid collodion matrix membranes (22).

With both the unswelled, permselective membranes and the swelled membranes of graded porosity, the electroosmotic transport parallels the water content, as shown in Table III for permselective membranes and in Fig. 2 and 3 for more porous membranes. For example, the ratio of the water contents (Table I) of the Alc 97- and Alc 0-Membranes in Fig. 2 is 5.0, and the ratio of the moles of water transported electroosmotically at the optimum electrolyte concentration is also about 5. Similarly, for the Alc 90- and Alc 0-Membranes the ratio of water contents is 2.0 while the ratio of the quantities of water transported is 2.2. The correlation is much poorer at higher salt concentrations. The observed parallelism between water content and electroosmotic water transport is in agreement with the data of Oda and Yawataya (13) and Stewart and Graydon (17) obtained with membranes of commercial ion exchange materials. A somewhat different relationship was found by Winger, Ferguson, and Kunin (14) with membranes of different degrees of cross-linking; while the water transported was greater across membranes of higher water content there was not a direct proportionality.

The lowest values we have obtained (3.2 moles of water per faraday for K^+ and 6.4 moles of water per faraday for Li^+) indicate that under these conditions the ions carry only a little more than what is believed to be the tightly held water of hydration. According to a recent review by Bell (23) the most probable hydration numbers are about 1 for K^+ and about 3 for Li^+. Thus, in the denser permselective membranes not more than 2 or 3 water molecules are being swept along electroosmotically.

The ratio of the quantities of water transported electroosmotically per faraday at any given concentration with KCl solutions and with LiCl is fairly independent of the water content of the membranes. For instance, in the two densest membranes with water contents of about 10 v/o (volume per cent), where only a few molecules of water are transported per ion (Table III), the water moved with K^+ is about 50-60% of that transported with Li^+; the same ratio is also found with the Alc 97-Membrane containing 75% water by volume across which up to 90 molecles of water per faraday are transported in LiCl solutions (Fig. 4). It is of interest that the work of Ballou (24) with kaolinite showed that, in an even more open structure than our most porous membranes, lithium is much more effective than other monovalent cations in electroosmotic water transport.

The resistances of ion exchange bodies in general, including ion exchange membranes, are higher when equilibrated with ions of low electrolytic mobility, such as Li^+, than with ions of higher mobility, such as K^+. In fairly open exchangers, such as the resins studied by Heymann and O'Donnell, the ratio of the resistances in the K^+ and Li^+ states, 1:1.86, is nearly the same as that of the reciprocals of the ionic mobilities of these two ions in free solution, 1:1.95 (25). Similar results were reported by Jakubovic, Hills, and Kitchener (26). The resistances of earlier types of low charge density collodion matrix membranes were shown to be 1.3-3.7 times higher in LiCl than in KCl solutions in the concentration range 0.001-0.1*M* (27). Thus it is apparent that the twin factors of higher electroosmotic water transport and higher resistance of the membranes in the lithium form are linked with the lower mobility of the lithium ion in free solution, as compared with the potassium ion.

A clear understanding of these observations emerges from the treatment of membrane transport recently given by Spiegler (19). The balance of forces is evaluated for the steady state of flux, the retarding forces being represented quite generally as simple frictional interactions between the four components: counter-ions, co-ions, water, and solid matrix. No specific structure is postulated for the membrane. A large frictional interaction between an ion and the surrounding water implies a large transference of momentum from the ion to the water. Consequently, such an ion moves more slowly, and drags water along with it more efficiently. The quantitative analysis of this situation with regard to electroosmosis leads to a straightforward relationship between water transport and friction. For the case of a membrane in which the concentration of nonexchange electrolyte is negligibly small, and in which the counter-ion is M^+, this relation can be written:

$$W = H + \frac{1}{\frac{c_{M^+}}{c_{H_2O}} + \frac{X_{H_2O\text{-matrix}}}{X_{M^+\text{-}H_2O}}} \qquad [2]$$

where W represents the total moles of water transported per faraday, H is the counter-ion hydration (moles H_2O/mole M^+), c_{M^+} and c_{H_2O} represent the concentrations of counter-ion and "free" water, respectively, and X denotes a friction coefficient between the components given in the subscripts. From this it is readily seen that, *ceteris paribus*, the higher the friction coefficient $X_{M^+\text{-}H_2O}$ the higher the value of W. Furthermore, the parallelism found between W and c_{H_2O} is obviously to be expected. An additional consequence is that in membranes of increasing porosity, where much of the water is at a distance from the matrix and the friction coefficient $X_{H_2O\text{-matrix}}$ becomes relatively small, W approaches in

value the ratio c_{H_2O}/c_{M^+} (provided the concentration of nonexchange electrolyte remains negligible). This implies that in the limit, when zero friction occurs between water and matrix, the water migrates in the membrane with the same velocity as the counter-ions. For permselective membranes this cannot, of course, be the case.

The concept of uniform migration velocity forms the basis of the classical Helmholtz electrokinetic theory, which is only applicable to membranes having relatively large pore radii, in contact with very dilute solutions. A theory based on a model can be developed which relates the electroosmotic permeability of a membrane and its conductivity, despite the assumptions and simplifications involved. More realistic models than the classical have been proposed by Schmid (28) and Meares (29), although they too assume uniform migration velocity. Schmid considers the space charge due to the counter-ions to be uniformly distributed within the pores, and arrives at the following relation:

$$V = \frac{F^2 A r^3}{8\eta\kappa} \qquad [3]$$

where V is the volume of solution transported per faraday, A the equivalents of fixed charges per unit volume of pore liquid, the latter being taken to have a viscosity η and a conductivity κ, and r is the radius of the pores. Equation [3] is consistent with our conclusions on the basis of Eq. [2] and is also relevant to situations where significant quantities of nonexchange electrolyte enter the membrane. To the extent that nonexchange electrolyte enters the pores (without significant change in viscosity), the conductance of the membrane increases and the quantity of water transported per faraday is decreased accordingly, this effect being most conspicuous with the most porous membranes (Fig. 2-4).

Equation [3] may also be interpreted in terms of the quantity of electrical energy used in the process of electroosmosis. If the resistance of a membrane is doubled by using another electrolyte at the same concentration, twice the voltage is required to obtain the same current; therefore, twice the energy is expended in the work of moving the ions and the water.

Acknowledgment

The authors wish to thank Dr. S. R. Caplan for stimulating discussions which were most helpful in the critical interpretation of the data.

One of the authors (C.W.C.) would like to express his appreciation to the Lalor Foundation for a Summer Fellowship in 1956 during which time part of this work was carried out, and to the National Institute of Health for providing laboratory facilities.

Manuscript received July 3, 1961.

Any discussion of this paper will appear in a Discussion Section to be published in the December 1962 JOURNAL.

REFERENCES

1. C. W. Carr and K. Sollner, *J. Gen. Physiol.*, **28**, 119 (1944); H. P. Gregor and K. Sollner, *J. Phys. Chem.*, **50**, 53 (1946); K. Sollner and H. P. Gregor, *ibid.*, **50**, 470 (1946); **51**, 299 (1949); *J. Colloid Sci.*, **6**, 557 (1951).
2. C. W. Carr, H. P. Gregor, and K. Sollner, *J. Gen. Physiol.*, **28**, 179 (1943); H. P. Gregor and K. Sollner, *J. Phys. Chem.*, **50**, 88 (1946); K. Sollner and H. P. Gregor, *ibid.*, **54**, 325, 330 (1950); *J. Colloid Sci.*, **7**, 37 (1952).
3. K. Sollner and R. Neihof, *Arch. Biochem. Biophys.*, **33**, 166 (1951); R. Neihof, *J. Phys. Chem.*, **58**, 916 (1954).
4. M. H. Gottlieb, R. Neihof, and K. Sollner, *ibid.*, **61**, 154 (1957).
5. M. Lewis and K. Sollner, *This Journal*, **106**, 347 (1959).
6. R. McClintock, R. Neihof, and K. Sollner, *ibid.*, **107**, 315 (1960).
7. K. Sollner and I. Abrams, *J. Gen. Physiol.*, **24**, 467 (1941); E. Grim and K. Sollner, *ibid.*, **40**, 887 (1957); **44**, 381 (1960); C. W. Carr and K. Sollner, in preparation.
8. C. W. Carr, D. Anderson, and I. Miller, *Science*, **125**, 1245 (1957).
9. I. Abrams and K. Sollner, *J. Gen. Physiol.*, **26**, 369 (1943).
10. G. Scatchard, *J. Am. Chem. Soc.*, **75**, 2883 (1953).
11. A. G. Winger, G. W. Bodamer, R. Kunin, C. J. Prizer, and G. W. Harmon, *Ind. Eng. Chem.*, **47**, 50 (1955).
12. W. R. Walters, D. W. Weiser, and L. J. Marck, *ibid.*, **47**, 61 (1955).
13. Y. Oda and T. Yawataya, *Bull. Chem. Soc., Japan*, **28**, 263 (1955); **29**, 673 (1956); **30**, 213 (1957).
14. A. G. Winger, R. Ferguson, and R. Kunin, *J. Phys. Chem.*, **60**, 556 (1956).
15. J. G. McKelvey, Jr., K. S. Spiegler, and M. R. J. Wyllie, *This Journal*, **104**, 387 (1957).
16. N. W. Rosenberg, J. H. B. George, and W. D. Potter, *ibid.*, **104**, 111 (1957).
17. R. J. Stewart and W. F. Graydon, *J. Phys. Chem.*, **61**, 164 (1957).
18. G. Schmid, *J. Chim. Phys.*, **55**, 163 (1958).
19. K. S. Spiegler, *Trans. Faraday Soc.*, **54**, 1408 (1958).
20. D. Mackay and P. Meares, *ibid.*, **55**, 1221 (1959).
21. C. W. Carr and K. Sollner, *J. Gen. Physiol.*, **27**, 77 (1943).
22. S. R. Caplan, in preparation.
23. R. P. Bell, *Endeavour*, **17**, 31 (1958).
24. E. V. Ballou, *J. Colloid Sci.*, **10**, 450 (1955).
25. E. Heymann and I. J. O'Donnell, *J. Colloid Sci.*, **4**, 405 (1949).
26. A. O. Jakubovic, G. J. Hills, and J. A. Kitchener, *Trans. Faraday Soc.*, **55**, 1570 (1959).
27. K. Sollner and H. P. Gregor, *J. Colloid Sci.*, **6**, 557 (1951).
28. G. Schmid, *Z. Elektrochem.*, **54**, 424 (1950); **55**, 229 (1951); **56**, 181 (1952).
29. P. Meares, *J. Polymer Sci.*, **20**, 507 (1956).

On the Mechanism of the Hydrogen Reaction

A. C. Makrides[1]

Metals Research Laboratory, Union Carbide Metals Company, Niagara Falls, New York

ABSTRACT

Two simple reaction schemes for hydrogen evolution, the Volmer-Tafel and Volmer-Horiuti mechanisms, are discussed. The results are applied to hydrogen evolution on nickel from alkaline solutions.

Criteria for various possible mechanisms for the hydrogen reaction, $2H^+ + 2e^- \rightleftharpoons H_2$, have been discussed in a number of articles (1-6). Of particular interest are the slope of the Tafel line and the stoichiometric number. Characteristic values of these quantities are in dispute (3-6). Some of the controversy involves the interpretation of experimental results for the hydrogen reaction on nickel (7-11). We discuss here two simple reaction schemes, the Volmer-Tafel and Volmer-Horiuti mechanisms, and apply our results to nickel cathodes.

The stoichiometric number was introduced by Horiuti and Ikusima (1). They started from the relation

$$\frac{\vec{i}}{\overleftarrow{i}} = f(\eta) = e^{\lambda\eta} \qquad [1]$$

where $\vec{i}$ and $\overleftarrow{i}$ are the velocities in amperes/cm^2 of $2H^+ \rightarrow H_2$ and $H_2 \rightarrow 2H^+$, η is the overpotential in units of RT/F,[2] and λ a constant. In the current literature the stoichiometric number, $\nu = 2/\lambda$, is used generally.

From Eq. [1] we have by differentiation with respect to η

$$\frac{f'(\eta)}{f(\eta)} = \lambda = 2/\nu \qquad [2]$$

Since $f(o) = 1$, ν is given by

$$\nu = 2/f'(o) \qquad [3]$$

The net cathodic current i_c is given by

$$i_c = \vec{i} - \overleftarrow{i} = \overleftarrow{i}\,[f(\eta) - 1] \qquad [4]$$

Differentiating Eq. [4] and evaluating the derivative at $\eta = 0$ we also find

$$\nu = 2\, i_o/(\partial i_c/\partial\eta)_{\eta=0} \qquad [5]$$

where $i_o = \vec{i} = \overleftarrow{i}$ at $\eta = 0$

An alternative definition of ν has been given by Parsons (3). It is assumed in ref. (3) that the rate of the whole reaction is determined by the rate of some intermediate step. The stoichiometric number is then the number of times the rate-determining step must be repeated for the over-all process to occur once. Parsons also derives Eq. [5] using this definition and the activated complex reaction rate theory.

[1] Present address: Field Research Laboratory, Socony Mobil Oil Company, Dallas, Texas.

[2] We follow Frumkin's convention for the sign of η and consider it positive for cathodic polarization ($\eta = E_o - E$ where E_o is the reversible potential and E the potential at some current i_c).

Reaction Mechanisms

We consider two mechanisms suggested frequently (1-6):

(i) Volmer-Tafel Mechanism		(ii) Volmer-Horiuti Mechanism
$e^- + H^+ \underset{U_2}{\overset{U_1}{\rightleftharpoons}} H_{ads}$	(I)	$e^- + H^+ \underset{U_2}{\overset{U_1}{\rightleftharpoons}} H_{ads}$
$H_{ads} + H_{ads} \underset{U_6}{\overset{U_5}{\rightleftharpoons}} H_2$	(II)	$e^- + H^+ + H_{ads} \underset{U_4}{\overset{U_3}{\rightleftharpoons}} H_2$

[6(i, ii)]

We assume the electrode surface to be homogeneous and neglect any interaction between adsorbed hydrogen atoms. We also neglect the ψ-potential effect. With these assumptions we may write for the rates in a solution of fixed composition (4-6)

$$\begin{aligned} U_1 &= k_1(1-\theta) &&= k_1^{\circ} e^{\alpha_1\eta}(1-\theta) \\ U_2 &= k_2\theta &&= k_2^{\circ} e^{-\beta_1\eta}\theta \\ U_3 &= k_3\theta &&= k_3^{\circ} e^{\alpha_2\eta}\theta \\ U_4 &= k_4(1-\theta) &&= k_4^{\circ} e^{-\beta_2\eta}(1-\theta) \\ U_5 &= k_5\theta^2 &&= k_5^{\circ}\theta^2 \\ U_6 &= k_6(1-\theta)^2 &&= k_6^{\circ}(1-\theta)^2 \end{aligned} \qquad [7(a\text{-}f)]$$

The rate of the over-all reaction is $\vec{R} = -\frac{1}{2}\frac{d[H^+]}{dt} = \frac{d[H_2]}{dt} = \frac{i_c}{2}$. The k's are rate constants in electrical units (amp/cm^2) and θ is the fraction of the electrode surface occupied by adsorbed hydrogen atoms.

Mechanism (i) [Volmer-Tafel].—The rates of the forward and reverse reactions are

$$\vec{i} = \frac{2U_1U_5}{U_2 + 2U_5} \quad \text{and} \quad \overleftarrow{i} = \frac{2U_2U_6}{U_2 + 2U_5} \qquad [8a, b]$$

From Eq. [8] together with ($\alpha + \beta = 1$) we have

$$f(\eta) = \frac{\vec{i}}{\overleftarrow{i}} = \frac{U_1U_5}{U_2U_6} = \frac{k_1^{\circ}k_5^{\circ}}{k_2^{\circ}k_6^{\circ}}\, e^{\eta}\, \frac{\theta}{1-\theta} \qquad [9]$$

and

$$f'(\eta) = f(\eta) + \frac{k_1^{\circ}k_5^{\circ}}{k_2^{\circ}k_6^{\circ}}\, e^{\eta}\, \frac{\partial\theta/\partial\eta}{(1-\theta)^2} \qquad [10]$$

From the steady-state condition, $d\theta/dt = 0$, we find

$$\theta = \frac{K \pm [K^2 - 8(k_6^\circ - k_5^\circ)(k_1^\circ e^{a_1\eta} + 2k_6^\circ)]^{1/2}}{4(k_6^\circ - k_5^\circ)} \quad [11a]$$

with

$$K = k_1^\circ e^{a_1\eta} + k_2^\circ e^{-\beta_1\eta} + 4k_6^\circ \quad [11b]$$

Differentiating Eq. [11], setting $\eta = 0$, and using the relation $(k_2^\circ)^2 k_6^\circ = (k_1^\circ)^2 k_5^\circ$, which can be derived from the conditions of equilibrium ($U_1 = U_2$, $U_5 = U_6$) we find

$$(\partial\theta/\partial\eta)_{\eta=0} = \frac{k_1^\circ k_2^{\circ\,2}}{(k_1^\circ + k_2^\circ)[k_2^\circ(k_1^\circ + k_2^\circ) + 4k_1^\circ k_5^\circ]} \quad [12]$$

Substituting Eq. [12] into Eq. [10] and noting that $(1 - \theta^\circ)^2 = [k_2^\circ/(k_1^\circ + k_2^\circ)]^2$ we find

$$f'(0) = 1 + \frac{k_2^\circ(k_1^\circ + k_2^\circ)}{k_2^\circ(k_1^\circ + k_2^\circ) + 4k_1^\circ k_5^\circ} \quad [13]$$

Designating by $i_{o\mathrm{I}}$ and $i_{o\mathrm{II}}$ the velocities of steps I and II at equilibrium, we have

$$i_{o\mathrm{I}} = k_2^\circ\theta^\circ = k_1^\circ k_2^\circ/(k_1^\circ + k_2^\circ)$$
$$i_{o\mathrm{II}} = 2k_5^\circ(\theta^\circ)^2 = 2(k_1^\circ)^2 k_5^\circ/(k_1^\circ + k_2^\circ)^2$$

Their ratio γ is

$$\gamma = i_{o\mathrm{I}}/i_{o\mathrm{II}} = k_2^\circ(k_1^\circ + k_2^\circ)/2k_1^\circ k_5^\circ \quad [14]$$

Substituting Eq. [14] into [13] and using Eq. [3] we have for the stoichiometric number

$$\nu = \frac{\gamma + 2}{\gamma + 1} \quad [15]$$

The stoichiometric number for this mechanism has the extreme values 1 ($\gamma >> 1$) and 2 ($\gamma << 1$). Thus, when there is a rate-determining step, ν gives the number of times this step must be repeated for the over-all process to occur once. For other values of γ, ν falls between 1 and 2. For example, $\nu = 1.50$ when $\gamma = 1$.

The net cathodic current is

$$i_c = U_1 - U_2 = 2(U_5 - U_6) \quad [16]$$

From Eq. [4], [8], and [9],

$$i_c = \frac{2(1-\theta)k_1^\circ k_5^\circ[k_2^\circ\theta e^{a_1\eta} - k_1^\circ(1-\theta)e^{-\beta_1\eta}]}{k_2^\circ(2k_5^\circ\theta + k_2^\circ e^{-\beta_1\eta})} \quad [17]$$

At $\eta >> 1$ (*i.e.*, where U_2 and U_6 are negligible) Eq. [17] reduces of course to

$$i_c = k_1^\circ(1-\theta)e^{a_1\eta} = 2k_5^\circ\theta^2 \quad [18]$$

where θ is given by Eq. [11].

Mechanism (ii) [Volmer-Horiuti].—The rates of the forward and reverse reactions are (5)

$$\vec{i} = \frac{U_1U_3}{U_2 + U_3} + U_3 \quad \text{and} \quad \overleftarrow{i} = \frac{U_2U_4}{U_2 + U_3} + U_4 \quad [19]$$

From the condition of equilibrium, $k_1^\circ k_3^\circ = k_2^\circ k_4^\circ$. From the steady-state condition ($d\theta/dt = 0$)

$$\theta = \frac{k_1 + k_4}{k_1 + k_2 + k_3 + k_4} \quad [20]$$

Using these relations and Eq. [7] and assuming $\alpha_1 = \alpha_2$, $\beta_1 = \beta_2$, we find[3]

[3] Equations [19], [21] and [24] are given by Frumkin (5).

$$f(\eta) = \frac{2(k_2^\circ/k_3^\circ)e^\eta + 1}{2(k_2^\circ/k_3^\circ)e^{-\eta} + 1} \quad [21]$$

The velocities of steps I and II at equilibrium are given by

$$i_{o\mathrm{I}} = k_2^\circ\theta^\circ = k_1^\circ k_2^\circ/(k_1^\circ + k_2^\circ)$$
$$i_{o\mathrm{II}} = k_3^\circ\theta^\circ = k_1^\circ k_3^\circ/(k_1^\circ + k_2^\circ) \quad [22a, b]$$

and

$$\gamma = i_{o\mathrm{I}}/i_{o\mathrm{II}} = k_2^\circ/k_3^\circ \quad [23]$$

Substituting [23] into [21] we find for $f(\eta)$,

$$f(\eta) = \frac{2\gamma e^\eta + 1}{2\gamma e^{-\eta} + 1} \quad [24]$$

and

$$f'(0) = 4\gamma(1 + 2\gamma)$$

or

$$\nu = 1 + \frac{1}{2\gamma} = 1 + \frac{i_{o\mathrm{II}}}{2i_{o\mathrm{I}}} \quad [25]$$

The stoichiometric number of this mechanism has a bound of 1 for large values of γ, but increases continuously as γ approaches zero. Thus, when the discharge step is much slower than the electrochemical desorption step, ν no longer represents the number of times the rate-determining step must be repeated for the over-all reaction to occur once. We discuss this point below.

The net cathodic current is

$$i_c = \left[\frac{U_2U_4}{U_2 + U_3} + U_4\right]\left[\frac{2\gamma e^\eta + 1}{2\gamma e^{-\eta} + 1} - 1\right] \quad [26]$$

from which, upon substitution for the U's, we find

$$i_c = 2k_1^\circ(1-\theta)e^{a\eta}\frac{1 - e^{-2\eta}}{1 + \gamma e^{-\eta}} \quad [27]$$

Equation [27] reduces at sufficiently large η to

$$i_c = 2k_1^\circ(1-\theta)e^{a\eta} = 2k_3^\circ\theta e^{a\eta} \quad [28]$$

where θ is given by Eq. [20].

General Discussion

The two mechanisms discussed above have been treated by a number of authors (1-5). Frumkin discussed the stoichiometric number of the Volmer-Horiuti mechanism using the method adopted here. Equations [19], [21], and [24] are identical with those given in ref. (5). However, our conclusions on the value of the stoichiometric number differ from those in ref. (5). Frumkin states that ν increases without limit when $i_{o\mathrm{I}} >> i_{o\mathrm{II}}$ in mechanism (ii). The discrepancy arises from an algebraic oversight in substituting for γ in Eq. [11] of ref. (5). If this equation and the discussion in the following paragraph of ref. (5) are modified to take into account this slip, they coincide with ours.

A form of Eq. [27] was derived by Vetter (4) for the case $\theta << 1$ using a different procedure from the one employed here. The assumption $\theta << 1$ at all $|\eta|$ is not applicable to most systems. It is particularly inappropriate when $\gamma \sim 1$ since θ in this case varies by at least an order of magnitude between $\eta = 0$ and $\eta = 10$, *i.e.*, over the range usually accessible in practice. Vetter (4) discusses the stoichiometric numbers for both the Volmer-Tafel and the Volmer-Horiuti mechanisms. His discussion correctly ap-

plies to "apparent stoichiometric numbers" (see below), but not to stoichiometric numbers obtained from Eq. [3].

Bockris and collaborators (6, 8, 12, 13) arrive at different conclusions although they use the same basic set of rate equations, *i.e.*, Eq. (7a-f). Bockris and Mauser (6) assume a rate-determining step and let ν be 1 or 2 corresponding to its happening once or twice in the course of a unit act the over-all reaction. They evaluate ν from Eq. [5] above, obtaining $(\partial i_c/\partial\eta)_{\eta=0}$ from the rate expression and i_o by extrapolation from large $|\eta|$. They find that Eq. [5] yields the assumed ν's.

The argument of Bockris and Mauser (6) follows essentially that of Parsons (4) who introduced this definition and procedure.

The different results of Bockris and Mauser (6) arise from the ambiguous meaning of the term i_o as used in ref. (6). The exchange current which appears in Eq. [5] is the total rate in the forward or reverse direction at equilibrium as is shown by the Horiuti and Ikusima (1) derivation reproduced above (Eq. [1]-[5]). It can be determined, at least in principle, by an isotopic experiment. It has therefore definite operational meaning. This exchange current may or may not coincide with the exchange current determined by extrapolation from large $|\eta|$. We shall denote this last quantity by $(i_o)_{extr}$. We discuss below the Bockris and Mauser (6) procedure in detail. We shall use the Volmer-Horiuti mechanism as an example. The Volmer-Tafel mechanism will be discussed for the hydrogen reaction on nickel.

Apparent stoichiometric numbers.—Frumkin (5) has shown that a variety of ν's can be obtained for the Volmer-Horiuti mechanism if the exchange current is determined by extrapolation.

Let us first consider Eq. [24] and [25]. As noted above, ν can attain any value as i_{oI} becomes negligible in comparison to i_{oII}. This result may seem surprising at first since in other cases, *e.g.*, the Volmer-Tafel mechanism, ν approaches a small integer when one step in the mechanism is rate determining. The lack of an upper bound of ν for $\gamma << 1$ is not inconsistent with its definition by Eq. [1]. The only restrictions imposed by classical thermodynamics on any electrochemical reaction are (14)

$$\frac{\vec{i}}{\overleftarrow{i}} = 1 \text{ at } \eta = 0, \qquad \frac{\vec{i}}{\overleftarrow{i}} > 1 \text{ at } \eta > 0 \qquad [29]$$

If there are no discontinuities in the region of equilibrium, for sufficiently small values of η we have

$$i_c = \vec{i} - \overleftarrow{i} = \lambda i_o \eta \qquad [30]$$

since the net reaction rate, i_c, and η vanish together at equilibrium. Equation [1] satisfies Eq. [29] and [30] for any finite value of λ. A coincidence of λ with the reciprocal of the number of times a rate-determining step is repeated is not necessary and must be examined separately for each mechanism.

Large values of ν in the case of the Volmer-Horiuti mechanism when $\gamma << 1$ are brought about by step II which, at equilibrium yields H_2 independently of step I, but has no influence on the net rate of hydrogen evolution away from equilibrium. In Frumkin's (5) terms, a large (total) exchange current does not insure a small polarizability in this case. This is true of all mechanisms which incorporate the scheme $A \overset{e^-}{\rightleftharpoons} C$, $A + C \overset{e^-}{\rightleftharpoons} P$, where A is the reactant, C an intermediate, and P the product.

To examine the conclusions of Bockris and Mauser (6), we formulate first their procedure in the terms used here. For the sake of simplicity of exposition we restrict our discussion to $\theta << 1$, the case discussed by Vetter (4). Results for the more general case where $(1-\theta)$ is not approximated by 1 are given in the table below.

If $(1-\theta)\sim 1$, Eq. [27] reads

$$i_c = 2k_1^\circ e^{a\eta}\frac{1-e^{-2\eta}}{1+\gamma e^{-\eta}} \qquad [31]$$

The net anodic current is given by $i_a = \overleftarrow{i}\,[1-f(\eta)]$ with the approximation $(1-\theta)\sim 1$. It is:

$$i_a = 2k_1^\circ e^{-\beta\eta}\frac{1-e^{2\eta}}{\gamma+e^{\eta}} \qquad [32]$$

Bockris and Mauser assume that $\gamma << e^\eta$ at all $|\eta|$ and simplify Eq. [31] and [32] to

$$i_c = 2k_1^\circ e^{a\eta}, \qquad i_a = 2k_1^\circ e^{-(1+\beta)\eta} \qquad [33]$$

In this range of $|\eta|$, *i.e.*, for sufficiently positive overpotentials on cathodic polarization and sufficiently negative on anodic, $i_c = \vec{i}$ and $i_a = \overleftarrow{i}$. Bockris and Mauser then extrapolate i_c and i_a to the neighborhood of equilibrium and write for all η

$$\vec{i} = 2k_1^\circ e^{a\eta} \qquad \text{and} \qquad \overleftarrow{i} = 2k_1^\circ e^{-(1+\beta)\eta}$$

from which they derive

$$i_c = 2k_1^\circ e^{a\eta} - 2k_1^\circ e^{-(1+\beta)\eta} \qquad [34]^4$$

and

$$(\partial i_c/\partial\eta)_{\eta=0} = 4k_1^\circ \qquad [35]$$

The exchange current, given by Eq. [33] with $\eta = 0$, is $2k_1^\circ$. With these values substituted in Eq. [5], they find $\nu = 1$.

The crucial difference between the present development and the Bockris and Mauser (6) argument outlined above is in the meaning of the exchange current. The extrapolated current, $(i_o)_{extr} = 2k_1^\circ$, does *not* coincide with $\vec{i}$ at $\eta = 0$. The exchange current is actually given by Eq. [7], [19], and [20] [with the approximation $(1-\theta)\sim 1$] by

$$i_o = \frac{2k_1^\circ + k_4^\circ}{1+\gamma} = \frac{2k_1^\circ(1+\tfrac{1}{2}\gamma)}{1+\gamma} \qquad [36]$$

Since $(\partial i_c/\partial\eta)_{\eta=0} = 4k_1^\circ/(1+\gamma)$, Eq. [36] together with Eq. [5] yield $\nu = 1 + (\tfrac{1}{2}\gamma)$ as before instead of $\nu = 1$. We call the quantity obtained from Eq. [5] when i_o is set equal to the extrapolated exchange current the apparent stoichiometric number and denote it by ν' (5). The apparent stoichiometric number depends on the approximations made in selecting

[4] This step is not justified nor is it valid generally. The net cathodic current is not necessarily the difference between the *extrapolated* cathodic and anodic currents.

Table I. Volmer-Horiuti mechanism

$\gamma = i_{oI}/i_{oII}$
(Extrapolated i_o from cathodic polarization curve)

	γ	ν	ν'	
(Slow electrochemical desorption)	$\gamma >> 1$	1	1	with $(i_o)_{extr}$ from range $\gamma e^{-\eta} >> 1$
			$1 + \gamma$	with $(i_o)_{extr}$ from range $\gamma e^{-\eta} << 1$
—	$\gamma = 1$	1.5	2	
(Slow discharge)	$\gamma << 1$	$1 + (\frac{1}{2}\gamma)$	1	

the linear section of the polarization curve. It also depends on whether the extrapolated exchange current is found from the anodic or cathodic polarization curve. The two extrapolated currents do not always coincide as can be shown easily from Eq. [31] and [32].

The exchange current is generally determined by extrapolation of the cathodic curve in the case of the hydrogen reaction. The apparent stoichiometric number is

$$\gamma' = \gamma \frac{(i_o)_{extr}}{i_o}$$

If $\gamma >> 1$ in the Volmer-Horiuti mechanism, there are two segments of the cathodic polarization curve [log i_c *vs.* η] which approximate a straight line. If a range of η is selected such that $\gamma e^{-\eta} >> 1$, then $(i_o)_{extr} = 2k_1^\circ/\gamma$ and $\nu' = 1$. If, on the other hand, the range of η is chosen for which $\gamma e^{-\eta} << 1$, then $(i_o)_{extr} = 2k_1^\circ$ and $\nu' = 1 + \gamma$. Therefore ν' attains any value as i_{oI} becomes much larger than i_{oII}. This last result was obtained by Vetter (4). Frumkin (5) finds $\nu' = 1$ for $\gamma >> 1$ making the approximation $\gamma e^{-\eta} >> 1$. We summarize our discussion in Table I. The values shown hold also for the general case where $(1 - \theta)$ is *not* approximated by 1.

The hydrogen reaction on nickel.—The mechanism of the hydrogen reaction on nickel is in dispute (8-10). Of particular interest are alkaline solutions where side reactions are negligible. Bockris and Potter (8) concluded that discharge of water is the slow step while Horiuti and collaborators (9) found the combination of two hydrogen atoms to be rate-determining. We have made extensive measurements, to be discussed in a later communication, which suggest that the Volmer-Tafel mechanism is operative. Equations [7] through [18] are applicable therefore, except that in alkaline solution H_2O must be substituted for H^+.

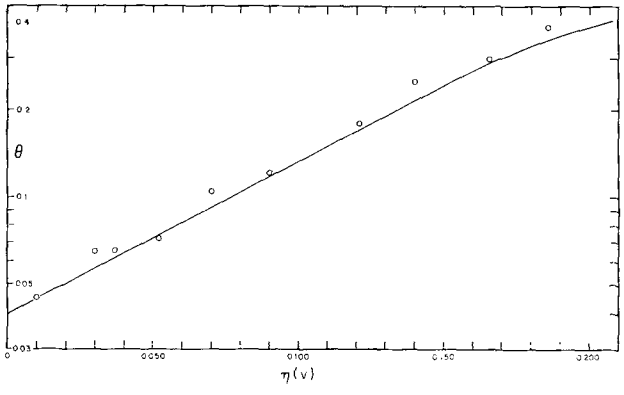

Fig. 1. Fractional surface coverage by adsorbed hydrogen atoms as a function of overpotential for nickel in 2*N* NaOH. The solid line was calculated from Eq. [11] with $k_1^\circ = 1.0 \times 10^{-5}$ amp/cm², $k_3^\circ = 3.15 \times 10^{-3}$ amp/cm², and $\theta^\circ = 0.04$. Circles give the experimental values of Devanathan and Selvaratnam (11).

Devanathan and Selvaratnam (11) recently determined θ on nickel cathodes in 2*N* NaOH. Their analysis suggested to them that discharge from water molecules is the rate-determining step. Their conclusion was based essentially on a value of 2 for the stoichiometric number. The previous controversy (9) also revolved around the proper value for the stoichiometric number. We examine therefore the Devanathan and Selvaratnam results in detail.

If the Volmer-Tafel mechanism is operative, according to Eq. [18] plots of $\log[i_c/(1-\theta)]$ *vs.* η and of i_c *vs.* θ^2 should yield straight lines as found by Devanathan and Selvaratnam. The intercepts of these plots give, respectively,

$$k_1^\circ = 1.0 \times 10^{-5} \text{ amp/cm}^2 \quad [38]$$

and

$$k_5^\circ = 3.15 \times 10^{-3} \text{ amp/cm}^2 \quad [39]$$

The slope of the log $[i_c/(1-\theta)]$ *vs.* η curve gives $\alpha = 0.67$ and, therefore, $\beta = 0.33$.

The value of θ at $\eta = 0$ is according to ref. (11),

$$\theta^\circ = 0.04 \quad [40]$$

From Eq. [7] for $\eta = 0$, we find

$$k_2^\circ = 2.5 \times 10^{-4} \text{ amp/cm}^2 \quad [41]$$

and

$$k_6^\circ = 5.4 \times 10^{-6} \text{ amp/cm}^2 \quad [42]$$

If the Volmer-Tafel mechanism is operative under the assumptions made above, θ should be given as function of η by Eq. [11] with the k°'s given by Eq. [38]-[42]. Figure 1 gives $\theta = \theta(\eta)$ calculated from Eq. [11] together with the experimental values. The agreement between calculated and observed θ is within experimental error.

The exchange currents for step I and II are

$$i_{oI} = k_1^\circ(1 - \theta^\circ) = k_2^\circ\theta^\circ = 1.0 \times 10^{-5} \text{ amp/cm}^2$$

$$i_{oII} = 2k_5^\circ(\theta^\circ)^2 = 2k_6^\circ(1 - \theta^\circ)^2 = 1.0 \times 10^{-5} \text{ amp/cm}^2$$

Consequently

$$\gamma = i_{oI}/i_{oII} = 1.0$$

The stoichiometric number is from Eq. [5] and [15]

$$\nu = 2i_o/(\partial i_c/\partial\eta)_{\eta=0} = 1.50$$

However, the apparent stoichiometric number is given by

$$\nu' = 2(i_o)_{extr}/(\partial i_c/\partial\eta)_{\eta=0}$$

Consequently

$$\nu' = \nu\frac{(i_o)_{extr}}{i_o} = \nu\frac{(i_o)_{extr}}{(i_{oI}/2)} = \nu\frac{(i_o)_{extr}}{5\times10^{-6}}$$

Devanathan and Selvaratnam give no details of their calculation of the stoichiometric number besides stating that it was 2. Data in the range $\eta << 1$ from which $(\partial i_c/\partial\eta)_{\eta=0}$ was presumably calculated are not given. If $(i_o)_{extr}$ is obtained from a plot of log i_c vs. η, then $(i_o)_{extr} = 8\times10^{-6}$ and $\nu' = 2.4$. If $(i_o)_{extr}$ is obtained from a plot of log $[i_c/(1-\theta)]$ *vs.* η, then $(i_o)_{extr} = i_{oI}$ and $\nu' = 3.0$. In any case, a value of ν' in the neighborhood of 2 does not prove that the discharge step is rate determining. Devanathan and Selvaratnam's results actually show that there is no rate-determining step, the exchange currents for discharge and combination being equal.

The calculation of $\theta = \theta(\eta)$ also gives the current at any η via Eq. [17]. To our knowledge, this is the first time that a complete description (including the variation of θ with overpotential) of the experimental cathodic curve for the hydrogen reaction is possible in terms of simple expressions involving only three independent constants. It is surprising that the simple Volmer-Tafel mechanism fits these results so well (see Fig. 1). Both the assumption of a homogeneous surface and the neglect of interactions between adsorbed hydrogen atoms appear *a priori* to be unlikely. However, nickel electrodes subjected to anodic-cathodic cycling, the procedure used in ref. (11), are probably covered by a layer of chemisorbed hydroxyl ions as we show elsewhere (17). Such surfaces should be essentially homogeneous for adsorption of hydrogen. A hydroxyl covered surface, in contrast to a nickel surface, is expected to adsorb hydrogen weakly. This agrees with the small coverage ($\theta^0 = 0.04$) found at equilibrium by Devanathan and Selvaratnam (11). Lateral interactions between adsorbed atoms are predominantly isolated pair interactions at low coverages. They apparently do not contribute significantly to the total heat adsorption for $\theta < 0.4$.

Manuscript received July 13, 1961; revised manuscript received Oct. 26, 1961.

Any discussion of this paper will appear in a Discussion Section to be published in the December 1962 JOURNAL.

REFERENCES

1. J. Horiuti and M. Ikusima, *Proc. Imp. Acad. Tokyo*, **15**, 39 (1939); J. Horiuti, *J. Res. Inst. Catalysis*, **1**, 8 (1948).
2. P. D. Lukovtsev, *J. Phys. Chem., Moscow*, **21**, 589 (1947).
3. R. Parsons, *Trans. Faraday Soc.*, **47**, 1332 (1951).
4. K. J. Vetter, *Z. Elektrochem.*, **59**, 435 (1955).
5. A. N. Frumkin, *Doklady Akad. Nauk SSSR*, **119**, 318 (1958).
6. J. O'M. Bockris and H. Mauser, *Can. J. Chem.*, **37**, 475 (1959).
7. J. Horiuti and G. Okamoto, *Bull. Chem. Soc., Japan*, **13**, 216 (1938).
8. J. O'M. Bockris and E. C. Potter, *J. Chem. Phys.*, **20**, 614 (1952).
9. J. Horiuti and H. Sugawara, *J. Res. Inst. Catalysis*, **4**, 1 (1956).
10. P. D. Lukovtsev and S. Levina, *J. Phys. Chem., Moscow*, **21**, 599 (1947).
11. M. A. V. Devanathan and M. Selvaratnam, *Trans. Faraday Soc.*, **56**, 1820 (1960).
12. J. O'M. Bockris in "Modern Aspects of Electrochemistry" J. O'M. Bockris, Editor, pp. 200-210, Butterworth, London (1954).
13. J. O'M. Bockris and E. C. Potter, *This Journal*, **99**, 169 (1952).
14. A. C. Makrides, *ibid.*, **104**, 677 (1957).
15. J. Horiuti, *Proc. Japan Acad.*, **29**, 160 (1953); J. Horiuti and S. Enomoto, *ibid.*, **29**, 164 (1953).
16. J. Horiuti and T. Nakamura, *Z. Physik. Chem.*, **11**, 358 (1957).
17. A. C. Makrides, to be published.

Transport Numbers in Pure Fused Zinc Chloride

Arnold Lundén[1]

Institute for Atomic Research and Department of Chemistry, Iowa State University, Ames, Iowa

ABSTRACT

The radioactive tracer method differs in two aspects from other methods used to determine transport numbers in fused salts. First, four different tracer experiments can be designed: two with cation and two with anion tracer. Second, due to nonideal conditions at the disk separating catholyte and anolyte, there is a tendency that the measured transport numbers are too low. This second property should be most pronounced in salts with low self-diffusion coefficients, such as the zinc halides.

The transport numbers have been measured for both cation and anion in molten zinc chloride. The tendency to give too low values for t^+ and t^- became stronger as the current density increased in the cell. An extrapolation to zero current density, *i.e.*, infinite running time, gives $t^+ = 0.6 \pm 0.1$ for the region from 420° to close to the boiling point. No current transport by complex ions could be detected.

In recent years a number of experiments have been designed for measuring transport numbers in pure molten salts (1). However, the interpretation of the experiments has been questioned, and it has even been stated that the whole concept of transference has little significance in pure molten salts (2). The aim of the present work is to examine

[1] On leave from the Department of Physics, Chalmers Institute of Technology, Gothenburg, Sweden.

critically some factors that might influence the results of the experiments. The general discussion is exemplified by measurements on zinc chloride.

Consider first the general experimental arrangement with two compartments separated by a membrane. Both compartments are at least partly filled with a melt, either a pure salt or a mixture of several components. The membrane can consist of a fritted disk of sufficiently fine porosity (such as in most "transport number" experiments), a separation column (a packed column of some 20 cm length used in isotope enrichment experiments) (3), an electrophoresis strip (4, 5), or some similar arrangement. Transport of salt through the membrane can be due to a hydrostatic pressure gradient, diffusion and, in the presence of an electric field, electroosmosis and transference. The distinction between the two latter entities is obvious if a quasi-lattice model (6-8) for the melt is considered,[2] in which case electroosmosis causes a bulk transport of salt relative to the walls of the capillaries of the membrane, and transference refers to the migration of individual ions in the "lattice." Transference should thus solely be a property of the melt (at the temperature, pressure (9), and chemical composition in question), and it should be independent of external conditions such as the type of material used for the construction of the membrane. For transference, the transport number, *e.g.*, for a cation, can be defined as $t_t^+ = v^+/w^+$, where v^+ is the velocity of the cation measured relative to the "lattice," while w^+ is measured relative to the anions (10). The question arises: Is this theoretically defined transport number t_t identical with, or can it be determined from, the experimentally measured "transport number" t_m?

Of the four entities contributing to the transport through a membrane, the hydrostatic effect can be measured in an arrangement with a sufficient head of the melt on one side of the membrane. Harrington and Sundheim (11) have thus measured leakage rates through membranes of five different types, for which the electrical resistance was also measured in order to determine if the membranes could be useful for transference experiments. It might be mentioned in this connection, that there need not be a close correlation between leakage and resistance, *e.g.*, two membranes should be expected to have nearly the same electrical resistance if the total geometrical cross section of their pores is the same, but if one of these membranes has a great many pores of a small diameter while the other one has a few pores with relatively large diameter, the leakages should, according to Poiseuille's law, be considerably higher in the latter case. The hydrostatic flow through a membrane should increase if an electric current passes through the melt, since local heating is likely to give an appreciable decrease in the viscosity of the melt within the pores. The hydrostatic flow of salt through a membrane might well be disturbed by "stickiness" (12) between the melt and parts of the apparatus, which in turn can be due to surface tension effects or to chemical reactions taking place (giving oxides or other reaction products, which might change the properties of the original surfaces).

The diffusion through a membrane can be estimated, if the self-diffusion coefficient is known for the ion in question, since a "cell constant" can be determined by measuring the electrical resistance. It is, however, worth remembering that studies of aqueous solutions (13) and melts in separation columns (14) have shown that the "electrical free space," calculated from measuring the resistance when the column is filled with a liquid of known conductivity, is of the order of 75% of the "geometrical free space," determined by weighing the packing in the column. There might thus be reason to expect that the cell constants are not identical for diffusion and conductivity.

Electroosmosis and transference are both proportional to the field strength (6), which makes it very difficult to distinguish between these two entities when interpreting "transport number" experiments. It is possible to introduce a formal transport number for electroosmosis, t_{os}, by using the following definition:

$$t_{os} = V_{os}/V_{eq} \qquad [1]$$

V_{eq} is the equivalent volume of a liquid, and V_{os} is the volume transported by electroosmosis through a surface perpendicular to the electrical field if the transported charge is 1 Faraday.[3] If we choose to define V_{os} as positive for transport toward the cathode, the following relations hold:

$$t_m^+ = t_t^+ + t_{os} \qquad [2]$$

$$t_m^- = t_t^- - t_{os} \qquad [3]$$

Thus $t_m^+ + t_m^- = 1$, independent of the magnitude of t_{os}. However, one of the t_m will be > 1 and the other negative, unless

$$-t_t^+ \leqq t_{os} \leqq t_t^- \qquad [4]$$

Sundheim (2) has claimed that t_t can be calculated for each experimental setup from the conservation of momentum within the melt. In this case the experiments actually should give not only t_m but also t_{os}. However, Sundheim has recently modified his theory (15)[4] so that, due to friction within the melt, momentum can be transferred from the melt to the membrane.

It might be mentioned for completeness that the contribution from electroosmosis can change with time if the properties of the surfaces within the membrane change due to chemical reactions between melt and membrane. Such changes might be of importance, *e.g.*, for lithium salts, if the running times are several hours (6, 17).

It is obvious that t_m is the only measurable entity, *e.g.*, in the indicator bubble (18), electrode

[2] A way to picture the situation is to consider the melt as containing minute crystallites or aggregates held in place by the membrane. For our discussion there is no difference between this view and the quasi-lattice model.

[3] In the assumed formalism, V_{os} is proportional to a zeta potential and the dielectric constant of the liquid, and inversely proportional to the viscosity and conductivity of the liquid, *cf*, *e.g.*, F H. MacDougall, "Physical Chemistry," p. 690, MacMillan, New York (1943).

[4] This new theory has not been available for study while preparing this paper, and it is thus not possible to consider it in detail. For this reason it is not clear if there are any contradictions between the results of Sundheim's theory and those of a recent theory by Klemm (16).

displacement (19, 20) and moving boundary (21) experiments, but the situation is not quite the same for the radioactive tracer method (22), since one might say that the movement of individual ions is followed. Thus, if the two electrode compartments were separated by an ideal membrane with a thickness of the same order of magnitude as the average interatomic distance in the melt, *i.e.*, if an ion had to make only a few "jumps" (perhaps only one jump) in the quasi lattice structure in order to pass from one compartment to the other, there would be reason to expect that electroosmosis could be detected even if restriction [4] were fulfilled. However, in all practical arrangements the thickness of the membrane is at least 10^6 times the average interatomic distance, and the measured transport is an average over the displacement of the individual ions, *i.e.*, also in this experiment t_m is the only measurable entity.

So far no experiments with molten salts have given results in contradiction with the limits for t_{os} set in [4]. The situation is different in molten metals, where studies of the Haeffner-effect (isotope effect in electromigration) have shown that the transport number for the metal ions (equivalent to our t_t^+) is of the order of 10^{-4} (23). Klemm (16, 24) has recently found for mercury that the electroosmotic mobility is about 17 times higher than that of transference.

It has usually been assumed for the performed experiments on transport numbers, that the contribution from electroosmosis is negligible in comparison with the transference, *i.e.*, $t_{os} \simeq 0$. This assumption has been supported by the fact that within experimental error, with perhaps one exception, the same transport numbers have been obtained regardless of the membrane material or the method employed. $PbCl_2$ has been studied by the indicator-bubble method with different membranes (18, 25), a moving boundary method (21), and with radioactive tracers (22). For $NaNO_3$, the transport number determined by the volume-change method (26) agrees with what can be calculated from Arnikar's electrophoresis experiments (5, 27), but very careful measurements with the indicator-bubble method (28) seem to show a slight dependence of t_m on the material used for the membrane. The original electrode-displacement method (19) did not give agreement with the indicator-bubble method (18, 12), but after a modification of the former method agreement has been obtained for $AgNO_3$ (20). When considering this indirect evidence for $t_{os} \simeq 0$, it might be worthwhile to remember that electroosmosis of molten mercury is found to be independent of the chosen capillary (glass, Fe, Pt, or Ge) (24). Thus experiments performed with different membranes need not rule out the possibility that t_{os} is of importance in molten salts.

In the above discussion we have assumed that the more or less complete dissociation of the salt has given only simple ions. The situation would be different if complex ions with a long life time were formed. For salts such as alkali halides or nitrates, complete dissociation generally is assumed, but for divalent halides it has been questioned (22, 29) whether the primary dissociation dominates or if complete dissociation takes place. In the case of zinc halides there is much evidence for the presence of complex ions (30, 31) or associations (32). Consider a divalent halide MX_2 where the following reactions take place in the melt:

$$MX_2 \rightleftarrows MX^+ + X^- \quad [5]$$

$$MX^+ \rightleftarrows M^{2+} + X^- \quad [6]$$

$$MX_2 + X^- \rightleftarrows MX_3^- \quad [7]$$

Thus, we have the ions M^{2+}, X^-, MX^+, and MX_3^- to which the transport numbers t^+, t^-, t_c^+, and t_c^- can be ascribed.

Four experiments can be performed with radioactive tracers:

I. Tagged M in the anolyte can pass through the membrane as M^{2+} or MX^+, giving $t^+ + t_c^+$ (see below).

II. Tagged M in the catholyte can pass through the membrane as MX_3^- giving t_c^-.

III. Tagged X in the anolyte can pass through the membrane as MX^+, giving t_c^+.

IV. Tagged X in the catholyte can pass through the membrane as X^- or MX_3^-, giving $t^- + t_c^-$.

As an example of the evaluation consider Experiment I, where Z equivalents of charge are passed through the cell. Thus, t^+Z equivalents of M^{2+} ions and t_c^+Z equivalents of MX^+ ions pass through the membrane toward the cathode, while t^-Z equivalents of X^- ions and t_c^-Z equivalents of MX_3^- ions pass through toward the anode. After the run, the weight of the salt in the anolyte is W_A g, and in the catholyte, W_c g. Depending on the method used for measuring the radioactivity, either the total activity, I_A counts/min, or the specific activity C_A (counts/min)/g, is determined for the anolyte and for the catholyte, I_C and C_C. (The measured activities are corrected for diffusion.) The equivalent weight of the salt MX_2 is M. Because the specific activity is the same in the migrating $(t^+ + t_c^+)Z$ equivalents of salt as in the anolyte, we have

$$\frac{I_C}{(t^+ + t_c^+)Z} = \frac{I_A}{W_A/M}$$

$$t^+ + t_c^+ = \frac{1}{Z}\frac{I_C}{I_A}\frac{W_A}{M} = \frac{1}{Z}\frac{C_C}{C_A}\frac{W_C}{M} = \frac{1}{Z}\frac{I_C}{C_A}\frac{1}{M} \quad [8]$$

since $I_C = C_C W_C$ and $I_A = C_A W_A$.

If there is reason to suspect that complex ions are responsible for part of the current transport, it is necessary to perform at least three experiments, II, III and either I or IV, to determine the transport numbers in a melt. Thus, a complete study requires that suitable tracers are available for both cation and anion.

The question arises if t_t can be determined indirectly from other types of experiments than those discussed above, which all give t_m. In developing a theory for the isotope effect of electromigration in molten salts (and aqueous solutions), Klemm (7, 10) finds that the transport number t_t is a constant of proportionality in the expression for $\Delta w/w$,

the relative difference in velocity for the ions of two isotopes of an element. In Klemm's model there are also a couple of other parameters for which certain assumptions need to be made, if transport numbers are to be calculated from available data on isotope effects. However, it cannot be expected that such estimations made from the measured isotope effects for zinc and lead halides ($ZnCl_2$, $ZnBr_2$, $PbCl_2$, and $PbBr_2$, where all eight isotope effects have been measured) (33), will give more than, at best, very approximate values for t_t. The accuracy would not be good enough to estimate t_{os} from a comparison with t_m.

Experimental

Materials.—Inactive anhydrous zinc chloride was prepared by letting a stream of chlorine gas pass over zinc metal at 500°-750°C and collecting the distilled zinc chloride in tubes that were sealed off from the apparatus. Zinc chloride tagged with radioactive zinc (Zn^{65}, half-life 245 days) was made in the same way as the inactive salt.

For the zinc chloride tagged with radioactive chlorine (Cl^{36}, half-life of 4×10^5 years) another method was needed because the above method would require special arrangements to recover the excess chlorine after it had passed over the zinc metal. The radioactive chlorine was available as a solution of hydrochloric acid from which silver chloride was precipitated. After drying, the silver chloride was mixed with slightly more than twice the equivalent amount of zinc metal (34), and the mixture was slowly heated to about 800°C, whereby zinc chloride was distilled off. Since the product contained considerable amounts of zinc metal, it was purified by redistillation (35).[5] However, for most of the runs with radioactive zinc chloride, this was prepared by letting molten anhydrous zinc chloride flow down into a tube containing a small amount of silver chloride of high specific activity. The salt was kept molten long enough to be sure that the mixture of $ZnCl_2$ and AgCl was homogeneous. The radioactive salt thus obtained contained about 0.3 w/o silver chloride.

Apparatus.—Because $ZnCl_2$ is a very hygroscopic salt, it was considered best to work under a nitrogen atmosphere, and since the salt is fairly volatile at the higher working temperatures the cells were designed as shown in Fig. 1. The cells were made of Pyrex glass or of quartz. The disks were treated as described elsewhere (22, 36) in order to reduce the porosity. In the runs with tagged zinc, the anode consisted of a carbon rod, but when working with tagged chloride, an anode of a droplet of zinc metal was used to prevent liberation of radioactive chlorine gas, which otherwise could penetrate over to the compartment with inactive salt. In all runs at temperatures above 420°C, the melting point of Zn, the metal was merely deposited at a tungsten cathode, but when this cathode was used at lower temperatures, the deposited metal grew as dendrites which punctured the disk, thus short-circuiting the cell. For the lowest temperature region, mercury metal was used as a cathode in the hope that the zinc would form an amalgam at the same rate as it was deposited. For the temperature region 356°-420°C, molten lead was tried as the cathode, but there was little success because the lead-zinc alloy was not formed fast enough to prevent the growth of zinc dendrites.

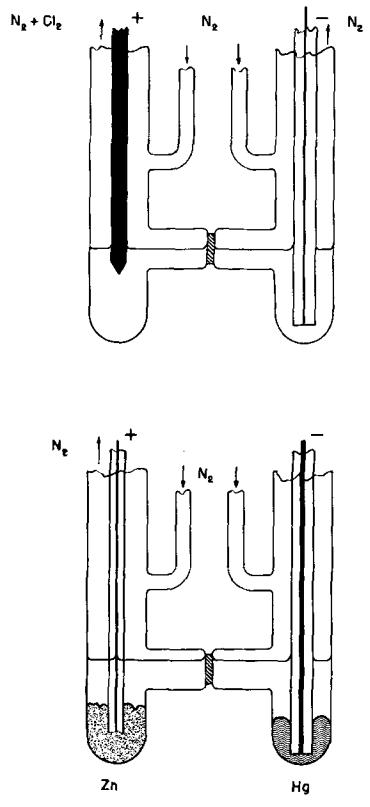

Fig. 1. Designs of cells

The power supply was a rectifier capable of giving up to 500v dc. The transported electrical charge was measured with a silver coulometer.

Runs at temperatures below 420° were performed in a temperature-stabilized salt bath, while the other runs were made in a vertical oven, which also was temperature stabilized. In the latter runs the cell temperature was measured by means of a Pt, Pt-Rh thermocouple, which was wound around the cell as close to the disk as possible.

Procedure.—For each run one batch of inactive and one of radioactive zinc chloride were selected, cut open, and lowered into the hot part of the cell, through which nitrogen gas had been flowing during the entire heating-up period. When the salt had melted, the empty holders were pulled out of the cell and the electrodes were inserted; meanwhile, the temperature of the oven was raised to the desired height. The temperature of the cell was measured before the run, at frequent intervals during the run, and also some ten minutes after the electrolysis current had been shut off. As expected, the heat generated in the disk was sufficient to raise the temperature of the cell some 3°-20°C above the temperature in the oven. Due to the fact that the conductivity of $ZnCl_2$ increases rapidly with temperature (37), the current drifted considerably the first seconds after each adjustment of the applied voltage, but in nearly all runs the current was very steady most of the time. The real exception

[5] This procedure was worked out by J. P. Cook.

to this was in those runs below 420°C, where dendrites of Zn metal penetrated through the disk. Obviously the dendrites were formed and then dissolved or broken at frequent intervals, thus causing current fluctuations. Simultaneous measurements of the current and the voltage across the cell gave an approximate figure for the resistance. The resistance would vary considerably from cell to cell, evidently because the porosity of the individual disk was not the same.

The electrolysis time was chosen such that the transported charge was of the order of 150-200 coulombs in each run. After the run the cells were lifted out of the oven to check whether the melt had been at equal heights on both sides of the disk. The cell was quenched and then divided into two samples, catholyte and anolyte, the disk being included with the part to which the radioactivity had been added.[6] Samples were dissolved and then treated in two slightly different ways depending on whether Zn^{65} or Cl^{36} had been used as tracer.

When working with radioactive zinc the total activity of liquid sample was measured with a scintillation well counter. For the runs with radioactive chlorine, on the other hand, the specific activity was measured for a solid sample of silver chloride (36). The zinc chloride in the samples was determined by an EDTA titration with naphthyl azoxine as indicator (38).

In all runs with a tungsten cathode the deposited zinc was collected and either weighed or determined by an EDTA titration. In this way we had a check on the transported electrical charge as determined with a silver coulometer. As an additional check, the average current was always found to be in agreement with readings during the run.

A couple of auxiliary experiments were also performed. Thus, it was found that a considerable exchange of zinc takes place in the molten state between metal and salt. The effect of a hydrostatic head was studied at 512°C by letting a cell stand for 10 hr with a height difference of about 25 mm between the salt in the two compartments. The leakage was found to be 0.4%. Self-diffusion of zinc ions was measured in a run at 674°C.

[6] In a few cases the disk and part of the horizontal tube formed a third sample, which also was analyzed. The remaining sample from the low activity side (catholyte in type I) had a normal specific activity, which proved that convection flow gave a homogeneous distribution of the activity within each compartment.

Results and Discussion

As seen from the data summarized in Table I, the runs covered a wide range of temperature and current settings. Of the resistances calculated from

Table I. Transport number experiments on molten $ZnCl_2$

Run No.	Temp, °C	Approx. temp increase, °C	Time, sec	Transported charge, coulombs	Mean current, ma	Approx. resistance, ohms	t_+	Remarks
				I. Runs with Zn^{65} in the anolyte				
1	435	30	10800* (2200)	125	11.6 (35)	2100-65 k	0.51	
2	440	20	1800	177	98.2	450	0.36	
3	443	4	6000	137	22.9	1600	0.58	
4	457	0	6000	131	21.8	785	0.28	
5	465	60	1200	177	148	380-875	0.46	
6	470	10	4000	161	40.1	975	0.52	
7	475	45	1200	153	128	380-1740	0.52	
8	506	5	6000	122	20.3	950	0.58	
9	510	15	2400	189	78.6	350	0.36	
10	533	5	6000	131	21.9	1260	0.57	
11	648	12	3000	215	71.7	300	0.49	Quartz cell
12	673	0	6000	147	24.6	100	0.55	Quartz cell
13	434	0	68800	7.7	0.1	400 k-5M	0.10	Disk was fused
14	327	—	10800* (4800)	49	4.5 (10)	12 k-200 k	0.19	Hg cathode
15	343	—	6000	149	25	4.5 k-33 k	0.12	Hg cathode
16	343	—	10200* (7500)	196	19.2 (26)	5 k-250 k	0.36	Hg cathode
17	332	—	5640* (3600)	115	20.3 (31)	1 k-500 k	0.30-1	W cathode; dendrites
18	332	—	7500* (5500)	173	23.0	1 k-200 k	0.23-0.63	W cathode; dendrites
19	393	—	10800	182	16.8	910-3.3 k	0.11-0.37	Pb cathode; dendrites
				II. Runs with Zn^{65} in the catholyte				
20	490	9	6000	214	35.7	570	—	$t_c^- < 0.0004$
21	343	—	7500	226	30.1	4 k-166 k	—	$t_c^- < 0.0004$; Hg cathode
22	660	0	6000	254	42.4	140	—	$t_c^- \simeq 0$; see text
				III. Runs with Cl^{36} in the anolyte				
23	465	10	6000	274	45.6	700	—	$t_c^+ < 0.002$
24	343	—	6000	162	26.9	3500	—	$t_c^+ < 0.0005$
				IV. Runs with Cl^{36} in the catholyte				
25	426	2	7500	154	20.5	900	0.85	$t^- = 0.15$
26	434	6	6000	140	23.4	950	0.75	$t^- = 0.25$
27	475	10	6000	190	31.7	900	0.66	$t^- = 0.34$
28	475	45	1800	187	103.8	450	0.72	$t^- = 0.28$
29	477	5	6000	129	21.5	700	0.61	$t^- = 0.39$
30	342	—	10800	222	20.6	4500	0.78	$t^- = 0.22$; Hg cathode

* The resistance was very high during the first part of the run, but it dropped suddenly to a normal value. The run was continued for the time given in parentheses.

the frequent measurements of current and voltage during the runs, either one typical value or the extreme limits are given in Table I. In a few runs (No. 1, 14, 16, 17, and 18) the resistance was very high in the beginning, but after a while there was a sudden change to "normal" conditions. Since this only happened at lower temperatures where the viscosity of zinc chloride is high (39), the plausible explanation is that it took some time before enough salt had penetrated into the disk to establish a good contact between the two compartments. For these runs, Table I gives both the mean current calculated for the whole running time and, in parentheses, an estimated value for the second part of the run.

The current and voltage measurements were also used as a basis for calculating the wattage, which of course varied very much from run to run (and also, in some cases, during a run), with typical values from 0.4-8.3w. (The high-temperature runs in quartz cells used 0.1-1.5w.) We could also make a crude estimation of the total cross section of the "capillaries" in the disk and of the current density in these capillaries, since

$$A_{eff} = L/R\kappa \qquad [9]$$

$$\beta = \frac{L}{f A R\kappa} \qquad [10]$$

and

$$i = I R\kappa/L \qquad [11]$$

where A is the geometrical cross section of membrane, f the fraction of disk covered by the melt, L the length of the "capillaries,"[7] A_{eff} the total cross section of the "capillaries," 100 β the free area, percentage, κ the conductivity of zinc chloride (37), R the resistance in the membrane, approximately equal to total cell resistance, I the current, and i the current density.

All the disks had a diameter of 1 cm, thus A = 0.79 cm^2. Since it is difficult to determine the average path length through the membrane, we found it sufficient merely to use the thickness of the disks, approximately 1.5 mm, as L in our calculations. Since the conductivity of zinc chloride is extremely temperature dependent (37), the calculations are very sensitive to errors in estimating the temperature *in* the capillaries.[8] For this reason the uncertainty in the β and i obtained was considered greatest for the runs at low temperatures or with high currents. Although in one run an extreme value of 1.6% was found for β, the runs with currents less than 30 ma gave values between 0.2 and 0.5%. Further considerations showed that the most likely free area of a disk was 0.3-0.4%. The limits for the current densities in our runs with Pyrex cells were found to be 5 and 25 amp/cm^2. For one of the runs with a quartz cell the current density was found to have been 47 amp/cm^2. For previous work with similarly prepared membranes (22, 36) no measurements of the current density have been reported, but it might have been of the order of 100 amp/cm^2.

The transport numbers were calculated according to Eq. [8] and corresponding equations. For the runs with Zn^{65} in the anolyte (Type I), the activity I_c measured for the catholyte was corrected for the activity in the deposited zinc. The amount of deposited metal was too small to allow any accurate measurement of its activity, but from our exchange experiment (see above) we concluded that the specific activity of the deposited metal could be considered as approximately 0.75 C_c.

The above-mentioned diffusion experiment at 674°C confirmed that the known self-diffusion coefficient for zinc in $ZnBr_2$ could be used in our estimations (40). It was assumed from measurements in other salts (41, 42) that the chlorine and zinc self-diffusion coefficients were of the same order of magnitude. The contribution from self-diffusion was of importance only when calculating the transport numbers at higher temperatures. For the run at 673°C (No. 12), 5-10% of the activity was transported by diffusion.

Of the runs for measuring t_c^- and t_c^+ (Type II and III), the four runs in Pyrex cells showed such a small transport of activity through the membrane that it was difficult to distinguish from the background. Estimations gave the result that self-diffusion alone was more than sufficient to account for the whole transport, and the measured t_c^- (runs 20 and 21) and t_c^+ (runs 23 and 24) are to be considered as upper limits, likely to be at least an order of magnitude too high. The run at 660°C (No. 22) gave an uncorrected value for t_c^- of 0.036, which, however, was due to self-diffusion and a hydrostatic head of about 3 mm. Thus, also in this run t_c^- is very small, and we can conclude that no transport by complex ions has been detected in any part of the investigated temperature range, and that t_c^+ and t_c^- can be neglected in comparison with t^+ and t^- when interpreting the runs of Type I and IV. If complex ions exist in molten $ZnCl_2$, their life time must be considerably less than the time it takes for an ion to traverse the membrane.

Regarding the measured t^+ and t^-, it is obvious that the spread in the obtained results is considerably higher than what can be expected from the statistical error of the chemical, electrical, and radioactivity measurements. Most runs have probable error of about ± 0.02, while the extreme values for t^+ (runs 3 and 8, resp. 4) differ by a factor of 2. The variations from run to run could be suspected to be due to hydrostatic effects, but the head was less than 1 mm for more than half of the runs, and for the remaining runs there was no correlation be-

[7] The pores in the disks consist of a number of cavities connected with each other by small openings. This whole irregular system is for this estimation considered as equivalent to a series of parallel capillaries.

[8] It is obvious that the temperature distribution is very inhomogeneous in the disks, since the heat production is concentrated to the salt-filled "capillaries." The heat is then transported through the disk to the other parts of the cell. The heat conductivity of molten $ZnCl_2$ is not known, but it is possible to make some very crude estimations of existing temperature gradients by assuming that the heat production is homogeneous throughout the disk, and that heat conduction in the axial direction dominates. The heat conductivity of Pyrex glass can be estimated to be approximately 0.015w cm^{-1} degree^{-1}, *cf. e.g.*, Morey, "The Properties of Glass," 2nd ed., p. 220, New York, (1954). The difference in temperature between the center of the disk and the ends would then be 1.6°C for 1w and 13°C for 8.3w dissipated in the disk. Due to the concentration of the heat production to the capillaries the actual temperature differences are likely to be higher. Because of the lack of information on the actual temperatures in the disks, the conductivity at the measured cell temperature was used when calculating β and i. The systematic error introduced in these latter entities by using a low value for η is counteracted by the fact that a low value has been used also for L, see above.

tween t^+ (or t^-) and the occurrence of a head of a couple of millimeters on either side of the disk. Neither would this be expected from a comparison with the above-mentioned check run at 512°C.

The most striking result of the runs is that the t^+ values obtained as $1 - t^-$ from the runs with Cl^{36} do not agree with the t^+ values of the runs with Zn^{65}. The division in two groups is significant, since, in spite of the great spread within both groups, not a single result falls among the data obtained with the other method. The unexpected result that $t_m^+ + t_m^- < 1$ can only be obtained with the radioactive tracer method, while for all other methods $t_m^+ + t_m^- = 1$ by definition. To explain the discrepancy between the runs with Zn^{65} and Cl^{36}, it is to be noticed that there are strong indications that the transport numbers depend on the current or, perhaps rather, the duration of the run. Thus the four highest values for t^+ (runs 3, 8, 10, and 12) were all obtained in 6000 sec runs, and these do not differ more than by the experimental error, since, due to the considerable contribution from self-diffusion at higher temperatures, run 12 has an experimental error of $\pm$ 0.06 instead of $\pm$ 0.02. However, the remaining 6000 sec t^+ run (No. 4) is far off. The shorter runs (1200-4000 sec) show much more of a spread in the obtained t^+. The highest t^- value is obtained in a 6000 sec run. It might be noticed that among the long t^- runs (all runs except No. 28) there is a tendency that t^- increases with temperature, and also that the low-temperature t^+ runs give low transport numbers. (Runs 17-19 are uncertain due to dendrites, but this disturbance did not occur in the runs with a Hg cathode.)

The time-dependent process in the experiments is diffusion, *i.e.*, the exchange of ions due to self-diffusion in the melt. The distribution of concentration by diffusion depends on $(Dt)^{1/2}$, where D is the diffusion coefficient and t the time (43). Thus for $D \approx 10^{-6}$ cm^2/sec and $t \approx 3000$ sec very little material is transported further than 1 mm from the original position. Diffusion should be of importance inside the disk as well as in the surface layer on both sides of the disk. If the disk were to be considered as an ideal membrane with only straight channels open in both ends, the transport would depend only on the electrical field strength, and an ion would traverse the disk in something like 50 sec, *i.e.*, a time that is short compared to our running times. However, in the disks there are many blind channels and other cavities, containing salt which is gradually exchanged by diffusion. Once an ion has been transported through the disk, it might stay a certain time in a thin salt layer close to the surface. Since the field strength outside the disk is roughly 0.3% of what it was in the channels in the disk, a diffusion process should be responsible for the transport of the ion out into the bulk of salt, where, again, transport is rapid, since a considerable convection flow takes place here (as was checked by dividing some cells into three parts, see above). If the tracer concentration is higher in a thin surface layer, which adheres to the disk when the cell is cut apart than it is in the bulk of salt, the obtained transport numbers will be too low. This systematic error should increase with decreasing running time and with decreasing temperature. This seems to be the case in the present experiments.

When discussing the existence of a surface layer through which diffusion is the main mode of transport, it might be worthwhile remembering that, due to the heat dissipation at the high current densities in the disk, the salt within the disk and immediately on its surface will be at a higher temperature than the bulk of salt. Regarding zinc halides, even rather small temperature gradients mean considerable changes in physical properties such as viscosity and conductivity. These differences between individual salt layers will be accentuated with increasing current density in the disk, but we cannot distinguish between current and time effects in the present experiments, since it was necessary to transport about the same charge in each run.

Since there is a tendency for obtaining low values for the transport numbers, it is suitable to make an extrapolation to zero current density, *i.e.*, infinite running time. For both t^+ and t^- the limiting value is close to $t_m^+ = 0.6$. For ideal conditions we can thus expect a transport number of $t^+ = 0.6 \pm 0.1$. This result is in agreement with the very recent experiments by Fischer and Klemm (44), who used a new method. Due to their better precision, they were able to detect a slight dependence on temperature (θ). Thus they found $t^+ = 0.716 - 3.07 \times 10^{-4} \times (\theta - 318)$.

The question arises if the discussed diffusion effects have caused systematic errors in previous measurements with the radioactive tracer method, where only one tracer, Cl^{36}, was used (22, 36). In general, this need not be the case, since the self-diffusion coefficient is higher and much less temperature dependent for $PbCl_2$ and the alkali halides than it is for $ZnCl_2$. For $PbCl_2$ the result is in agreement with what was obtained by other methods. However, for AgCl the radioactive tracer method (45) has given much lower values than another method (25). Thus it seems wise always to check the results by using both anion and cation tracers.

Summarizing, we find that the shortcomings of the radioactive tracer method are accentuated by the rather special properties of the chosen salt, but that even in this case it is possible to use the method if suitable precautions are taken, such as using two tracers. A final valuation of the merits of this method relative to other ones will require further measurements on several salts.

Acknowledgments

The author is much indebted to Professor F. R. Duke and Mr. J. P. Cook for stimulating discussions during the experiments and to the former also for valuable criticism of the manuscript.

Manuscript received Feb. 20, 1961; revised manuscript received Dec. 11, 1961. Work was performed in the Ames Laboratory of the U.S.A.E.C.

Any discussion of this paper will appear in a Discussion Section to be published in the December 1962 JOURNAL.

REFERENCES

1. G. J. Janz, C. Solomons, and H. J. Gardner, *Chem. Rev.*, **58**, 480 (1958).

2. B. R. Sundheim, *J. Phys. Chem.*, **60**, 1381 (1956).
3. A. Neubert and A. Klemm, *Z. Naturforsch.*, **16a**, 685 (1961).
4. M. Chemla, *J. Chromatography*, **1**, 2 (1958); C. Mangalo, H. J. Arnikar, and M. Chemla, *Compt. rend.*, **244**, 2796 (1957).
5. H. J. Arnikar, *Compt. rend.*, **244**, 2241 (1957).
6. A. Lundén, E. U. Monse, and N. G. Sjöberg, *Z. Naturforsch.*, **11a**, 75 (1956).
7. A. Klemm, "Physikertagung Wiesbaden," p. 73 (1955).
8. R. W. Laity, *J. Chem. Phys.*, **30**, 682 (1959).
9. S. D. Hamann, "Physico-Chemical Effects of Pressure, p. 119, Butterworths, London (1957).
10. A. Klemm, *Proc Symp. Isotope Separation*, p. 275, Amsterdam (1957).
11. G. Harrington and B. R. Sundheim, *J. Phys. Chem.*, **62**, 1454 (1958).
12. M. R. Lorenz and G. J. Janz, *ibid.*, **61**, 1683 (1957).
13. A. K. Brewer, S. L. Madorsky, *et al.*, *J. Research Nat. Bur. Standards*, **38**, 137 (1947).
14. A. Lundén, Thesis, Göteborg, p. 55 (1956).
15. B. R. Sundheim, Private communication.
16 A. Klemm, *Z. Naturforsch.*, **13a**, 1039 (1958).
17. A. Lundén, S. Christofferson, and A. Lodding, *Trans. Chalmers Univ., Technol., Gothenburg*, No. 221 (1959).
18. F. R. Duke and R. Laity, *J. Phys. Chem.*, **59**, 549 (1955).
19. H. Bloom and N. J. Doull, *ibid.*, **60**, 620 (1956).
20. H. Bloom and D. W. James, *ibid.*, **63**, 757 (1959).
21. F. R. Duke and J. P. Cook, *ibid.*, **62**, 1593 (1958).
22. F. R. Duke and R. A. Fleming, *This Journal*, **106**, 130 (1959).
23. A. Klemm, *Z. Naturforsch.*, **9a**, 1031 (1954).
24. H. Knof and A. Klemm, *ibid.*, **14a**, 1020 (1959).
25. I. G Murgulescu and L. Marta, *Acad. rep. populare Romine, Studii cercetari chim.*, **8**, 375 (1960).
26. F. R. Duke and B. Owens, *This Journal*, **105**, 548 (1958).
27. A. Lundén, *Z. Naturforsch.*, **14a**, 801 (1959).
28. V. A. Lamb and R. J. Labrie, Private communication.
29. F. R. Duke and M. L. Iverson, *J. Phys. Chem.*, **62**, 417 (1958).
30. W. Bues, *Z. anorg. u. allgem. Chem.*, **279**, 104 (1955); M. A. Bredig and E. R. Van Artsdalen, *J. Chem. Phys.*, **24**, 478 (1956).
31. S. N. Flengas and T. R. Ingraham, *Can. J. Chem.*, **35**, 1254 (1957).
32. R. Laity, *Ann. N. Y. Acad. Sci.*, **79**, 997 (1960).
33. A. Lundén and G. Blomqvist, *Z. Naturforsch.*, **15a**, 950 (1960).
34. For phase diagram see Landolt-Börnstein, "Zahlenwerte u. Funktionen," 6th ed., Vol. II: 3, p. 13, Berlin (1956).
35. For similar methods, see Gmelins "Handbuch der Anorganischen Chemie," 8th ed., 32 Erg. band, p. 847, Weinheim (1956).
36. F. R. Duke and A. L. Bowman, *This Journal*, **106**, 626 (1959).
37. F. R. Duke and R. A. Fleming, *ibid.*, **104**, 251 (1957).
38. J. S. Fritz, W. J. Lane, and A. S. Bystroff, *Anal. Chem.*, **29**, 821 (1957).
39. J. D. Mackenzie and W. K. Murphy, *J. Chem. Phys.*, **33**, 366 (1960).
40. L. E. Wallin and A. Lundén, *Z Naturforsch.*, **14a**, 262 (1959).
41. A Lundén, *Trans. Chalmers Univ. Technol., Gothenburg*, No. 241 (1961).
42. J. O'M. Bockris and G. W. Hooper, *Discussion Faraday Soc.*, in press.
43. W. Jost, "Diffusion in Solids, Liquids, Gases," p. 20, Academic Press, New York (1952).
44. W. Fischer and A. Klemm, *Z. Naturforsch.*, **16a**, 563 (1961).
45. F. R. Duke, A. L. Bowman, E. Wolf, and H. Garfinkel, *Ann. N. Y. Acad. Sci.*, **79**, 1023 (1960).

Technical Notes

Vapor-Phase Doping of Silicon with Arsenic Trichloride

E. J. Mehalchick and P. K. Marshall

Chemical and Metallurgical Division, Sylvania Electric Products Inc., Towanda, Pennsylvania

With the advent of Esaki diodes, fast-switching electronic devices, and epitaxial devices, a need for very low resistivity crystals became very important.

Low resistivity silicon monocrystals are available commercially, but methods of production are not reported. Backenstoss (1) has reported values of 0.001 ohm-cm, arsenic-doped, melt-grown silicon crystals. Trumbore (2) gives a solubility limit of arsenic in silicon, most probably by diffusion, of 1.2×10^{21} atoms/cm^3 below 1375°C, corresponding to about 2×10^{-4} ohm-cm. Goorissen and VanRun (3) reported constant resistivities of about 0.01 ohm-cm by gas-phase doping with a phosphine-hydrogen mixture in float-zoned silicon crystals.

An easier method of growing arsenic-doped silicon crystals with uniform resistivity profiles ranging from 1.0×10^{-3} to 5.0×10^{-2} ohm-cm has been developed. The procedure involves passing an arsenic trichloride-helium mixture into a crystal-growing apparatus. Upon reaching the hot zone, the arsenic trichloride is reduced by the molten silicon, producing arsenic and silicon halides. A fraction of the arsenic is dissolved in the silicon. The evaporation rate of arsenic is sufficiently slow that it is possible subsequently to grow the crystal in pure helium and yet maintain a constant displacement of arsenic atoms from the liquid to the solid.

Experimental Details

The silicon used in the experiments was prepared by deposition on a silicon substrate by the hydrogen reduction of silicon tetrachloride. The boron concentration of this material after six passes in a semiautomatic floating-zone refiner was calculated

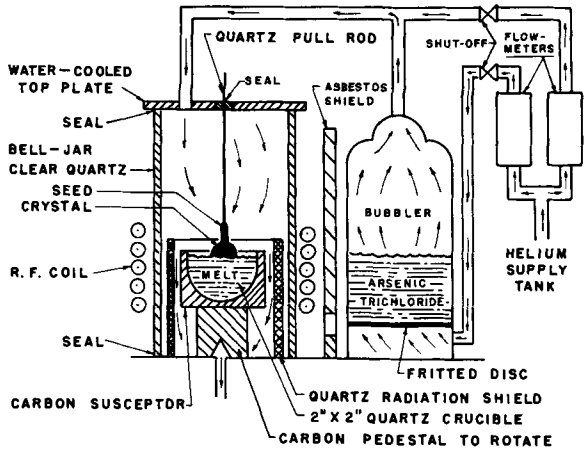

Fig. 1. Crystal puller

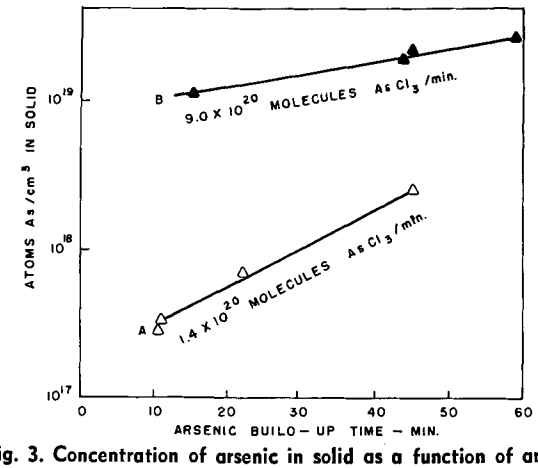

Fig. 3. Concentration of arsenic in solid as a function of arsenic buildup in the melt.

to be 1.1 ppb based on resistivity measurements. All resistivity measurements were made with a two-point probe.

A diagram of the crystal-growing apparatus is shown in Fig. 1. The experimental procedure first involved melting a charge of silicon in a vitreous silica crucible in an atmosphere of pure helium. Arsenic trichloride was introduced by metering a known volume of helium through a saturator containing the arsenic trichloride at 25°C. The exact supply rate was determined by weighing the arsenic trichloride before and after the experiment and by recording the times The gas mixture was then admitted to the crystal-growing apparatus and was allowed to pass over the molten silicon for 45 min, permitting a sufficient quantity of arsenic to be dissolved in the melt. The crystal was then grown in the same gas mixture.

During the crystal-growing operation, the supply rate of arsenic trichloride, the total gas-flow rate, and the growth rate were carefully kept constant to provide a constant supply of impurity atoms to replace those being incorporated into the solid.

Results and Discussion

The feasibility of the method depends on the existence of an equilibrium in which the net number of impurity atoms captured by a unit volume of the liquid per unit time is equal to the net number incorporated into a unit volume of the solid in the same period.

Several arsenic-doped silicon crystals were grown, and the concentration in the solid was found to be a function of the arsenic trichloride supply rate and/or the arsenic build-up in the melt.

The following conditions were held constant in the experiments performed: growth rate, 0.152 cm/min; total gas-flow rate, 66 l/min; pot charge, 150g; crystal diameter, 22-28 mm; pot rotation, 6 rpm; arsenic buildup time, 45 min. The results of these experiments are given in Fig. 2.

Variations in the preceding method were carried out to study the effect of growing in a neutral atmosphere after some initial buildup period in the melt. The lowest possible supply rate of arsenic trichloride (1.4×10^{20} molecules $AsCl_3$ per minute) was kept constant and the buildup period was varied from 11 to 45 min. All other conditions were the same as in the preceding section. The results of these experiments are given in Fig. 3 (curve A).

A series of experiments using a higher arsenic trichloride supply rate (9×10^{20} molecules $AsCl_3$ per minute) with other conditions the same as in the preceding section yielded a maximum arsenic concentration of 2.5×10^{19} atoms/cm³ after 1.0 hr. In all experiments the arsenic carrier density was determined from the resistivity measurements made on the crystal. The results of these experiments are given in Fig. 3 (curve B).

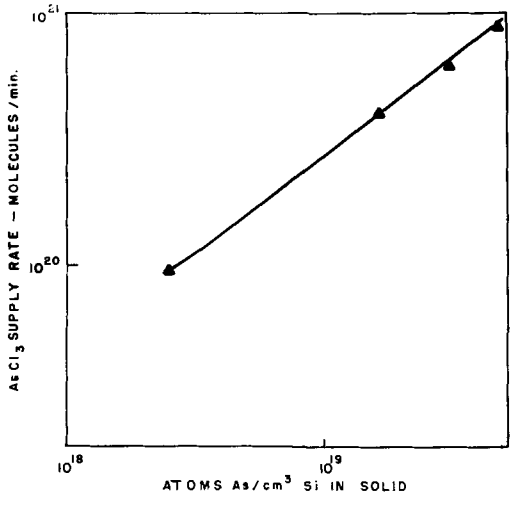

Fig. 2. Concentration of arsenic in solid as a function of $AsCl_3$ supply rate.

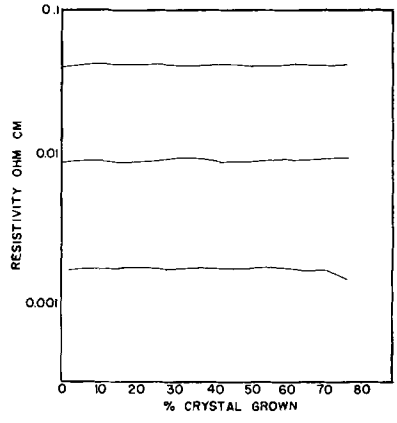

Fig. 4. Axial resistivity distribution obtained by vapor phase doping of silicon.

The axial resistivity profiles of the silicon crystals were quite level. It appears then that the evaporation of arsenic atoms from the liquid is nearly in equilibrium with the number of atoms rejected by the freezing solid. Figure 4 shows some typical plots of resistivity *vs.* the percentage crystal pulled for crystals grown by the vapor-phase technique and doped with arsenic trichloride.

A few experiments using higher arsenic trichloride-supply rates and longer buildup periods of arsenic in the melt, produced crystals with resistivities not lower than 0.0009 ohm-cm. It appears that saturation of arsenic in the melt occurs after 45-60 min, limiting the carrier concentration of arsenic in the crystal to a maximum value of 3×10^{19} atoms/cm^3.

Summary

Arsenic-doped, melt-grown silicon crystals with level resistivity profiles, ranging from 1×10^{-3} to 5×10^{-2} ohm-cm, were obtained by passing an arsenic trichloride-helium mixture into a silicon crystal grower. The desired resistivity could be obtained by varying the arsenic trichloride supply rate and/or by varying the arsenic buildup period in the melt.

Acknowledgments

The authors wish to thank J. M. Demangone and W. S. Shaw, both of this laboratory, for evaluating the crystals.

Manuscript received Sept. 29, 1961.

Any discussion of this paper will appear in a Discussion Section to be published in the December 1962 JOURNAL.

REFERENCES

1. G. Backenstoss, *Phys. Rev.*, **108**, 1416 (1957).
2. F. A. Trumbore, *Bell System Tech. J.*, **39**, 205 (1960).
3. J. Goorissen and A. M. J. G. VanRun, The Institute of E. E., Paper No. 3022E, March 1960.

Controlled Chemical Etching in the Production of Semiconductor Dice

P. J. A. McKeown

Transistor Division, Standard Telephones & Cables Ltd., Footscray, Kent, England

In the production of some kinds of semiconductor device, a key process is the etching of single crystal dice to remove mechanical damage and to clean the surface in preparation for the next operation. It is desirable to remove an appreciable thickness of material and to require the etched dice to have a small spread of thicknesses. An investigation of the process has led to the development of improved means of control. The dice used in this work were 2.25 mm square and were n-type single crystal germanium of {111} orientation.

The main factors which influence the amount removed are: (*a*) lapping damage, since the etching rate of a mechanically damaged surface is higher than that of undamaged material; (*b*) etching time, since this is usually less than a minute and therefore timing errors introduced by an operator can be significant; (*c*) the temperature at which etching takes place. This is made up of two terms, the average temperature of the etchant bath, and the local temperature rise at the semiconductor surface due to the heat of the reaction. The heat of solution of germanium in a typical etchant containing nitric and hydrofluoric acids was measured and found to be about 2000 cal/g. From this it has been calculated that the temperature of an isolated die together with liquid layers 100μ thick, would increase at about 200°C/sec.

Temperature control obviously requires that the local dice temperature should be kept close to that of the bulk etchant. This was achieved by means of an apparatus which used a stationary polythene beaker 7 cm in diameter with a conventional mechanical stirrer near the bottom and a special baffle to provide the necessary flow pattern. The stirring was adjusted so that all dice 150μ thick were kept in suspension in the etchant, and yet the breakage rate for dice 50μ thick was only 0.25% per min.

The temperature of the bulk etchant was controlled by means of a heat exchanger made from 4 mm diameter platinum/rhodium tubing. This was made into a 10 turn spiral 2.1 cm in diameter. The spiral was bent to form almost one complete turn about the stirring shaft. This heat exchanger also acted as the baffle to improve dice agitation. All gaps between beaker, coil, and stirrer were such that dice could not wedge nor be caught between moving parts.

Water at a controlled temperature flowed through the heat exchanger at 18 cc/sec. The temperature was regulated by means of three heaters. The first heater automatically kept the temperature of water leaving it about 4° below the required etchant temperature. Heater No. 2 raised the temperature of the water by an amount such that its effect on the etchant temperature was approximately equal to the heat produced by etching. This heater was switched off a few seconds before etching so that it ceased to influence the etchant temperature just as the etching began. The third heater was controlled by a thermocouple in the etchant and corrected any small errors in temperature.

The bottom of the beaker was perforated by 185 holes each 1.4 mm in diameter, but during etching a solenoid-operated sealing plate prevented loss of etchant. Etching was started by automatic injection of dice, and the reaction was stopped by draining the etchant and at the same time adding a large volume of deionized water. All operations were con-

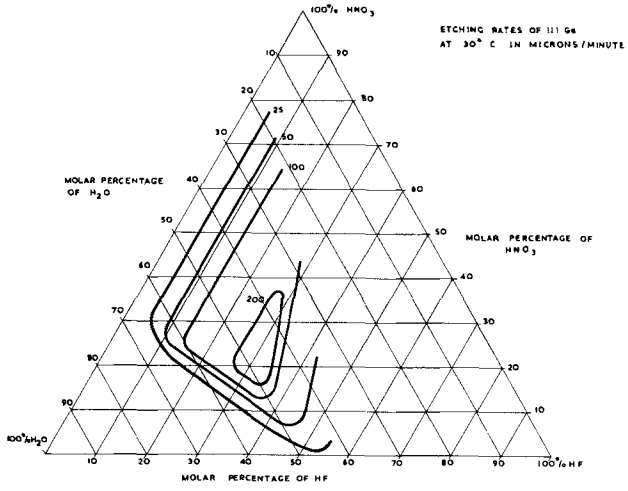

Fig. 1. Etching rates of {111} germanium at 30°C in microns per minute.

trolled by timers and the etching time could be preset with accuracy of ¼ sec.

It was found that 200 dice could be etched at a time so that the mean scatter in thickness introduced by etching was less than 0.3 of a micron. The reproducibility from batch to batch was ± 0.7μ, and thicknesses of etched dice could therefore be predicted.

The machine has also been used for the accurate measurement of etching rates. Figure 1 shows a triangular plot of etching rates for the HNO_3-HF-H_2O system. It refers to 2 ohm-cm dice with a dislocation density of 5000/cm^2. It should be noted that the etching rates plotted differ by factors of 2, and so a wide separation of contour lines indicates an insensitivity to etchant composition. The activation energy of the reaction is 14.5 kcal for solutions containing 15 molar % HF and increases to 40 kcal for solutions in which the molar ratio $HF/HNO_3 = 3$. These values are higher than those reported by Schwartz and Robbins (1) for silicon.

Other factors which have a slight effect on etching rates are dice thickness, resistivity, and dislocation density. For an etchant removing 1.25 μ/sec, the etching rate was found to be a minimum for dice 50μ thick. Thicker dice etched slightly faster because of the increased flow of etchant over their surfaces, and thinner dice did so because their low thermal inertia permitted temperature fluctuations. Resistivity appeared to have little effect on etching rate within the narrow range investigated. Seven ohm-cm material etched about 1% faster than 1 ohm-cm. Dislocation density had more effect, a minimum etching rate being obtained at a dislocation density about 1000/cm^2, 20,000 dislocations/cm^2 increased the rate by about 3%, and in the absence of dislocations the rate increased by 10%. This may be because both dislocations and lattice vacancies promote attack by acting as nuclei.

Some fast etchants have been observed to produce pits at dislocations. This was traced to the etching which occurs during the fraction of a second required to quench by the addition of water. Very rapid quenching such as is obtained with the machine described above keeps this pitting to a minimum.

Acknowledgments

This note is published by kind permission of Standard Telephones and Cables Ltd., London. The author is indebted to Mr. J. A. E. Wilkinson and other colleagues in the Transistor Division, Footscray for their assistance in this work.

Manuscript received May 2, 1961; revised manuscript received Nov. 10, 1961. This paper was prepared for delivery before the Indianapolis Meeting, April 30-May 3, 1961.

Any discussion of this paper will appear in a Discussion Section to be published in the December 1962 JOURNAL.

REFERENCE

1. B. Schwartz and H. Robbins, *This Journal*, **108**, 365 (1961).

Alloying to III-V Compound Surfaces

L. Bernstein[1]

Alloys Unlimited, Incorporated, Long Island City, New York

Because of the interest in using the III-V intermetallic semiconductor compounds for making semiconductor devices, it was felt that a greater understanding of the alloying nature of these materials would be helpful. To this end, a program to determine the condition under which the indium and gallium antimonides, arsenides, and phosphides alloy with some of the common bonding materials was instituted.

Alloy bonds may be required either for ohmic contact or p-n junction formation. Impurities in Group II of the periodic chart (Zn and Cd) act as acceptors in the III-V compounds, whereas those in Group VI (S, Se, and Te) act as donors. In addition, however, materials like Ge, Si, Pb, Sn, Cu, or Mn, which may be used in bonding to III-V surfaces, also act as donors or acceptors. Usually, however, they have low doping efficiency compared with the II-VI elements. Small quantities of II or VI group impurities may, therefore, be added when necessary to give the appropriate doping.

The III-V compounds used in this investigation were in the form of dice 0.100 x 0.100 x 0.020 in. thick. All alloying was done on material cleaned using the etchants shown in Table I. Except for a few alloys studied for feasibility in producing p-n junctions, the bulk of this investigation was concerned with large surface area ohmic contact covering the complete die. In the case of Au alloying, the material used was 0.2 to 0.5 mil gold clad material on suitable substrate (1). All other alloys

[1] A portion of this work was done by the author while with Hughes Semiconductor Products.

studied were 0.5 to 1.0 mil foil or clad on the same substrate material.

All of the etchants shown in Table I produced shiny, clean surfaces. The etch was followed by a wash in distilled water and finally an acetone rinse before alloying.

Table II describes the results of some bonding experiments run during this investigation. Approximate eutectic temperatures and preferred bonding temperature ranges are shown. Additional results with other alloys are shown in the body of the report. In addition, the type of doping is indicated with the appropriate literature references.

Thermal expansion measurements on these III-V compounds were reported in a previous publication (1).

Au-Sn *bonding.*—From previous experience in bonding to Si and Ge, it was learned that Au-Sn alloyed to their surfaces at lower temperatures and under much less critical atmosphere conditions than did pure gold. With the III-V compounds, however, this was not the case; therefore, there seems to be no advantage in its use over pure gold, other than those cases where the doping effects of tin are required.

Au-Ge *bonding.*—No eutectic formations were noted in these systems at all. Very little solution of the intermetallic took place as much as 100°C above the melting points of the gold-germanium eutectic, but in all cases good alloy bonds were formed. Much less penetration was noted compared with pure gold. The antimonides are apparently more sensitive to cracking than all the other compounds; therefore, Au-Ge is not recommended for use with them.

Au-Si *bonding.*—Again, no eutectic formations were observed. Similar to the Au-Ge system, solubilities and penetrations were low. In all cases, except for InSb, bonds formed were excellent.

Pb *bonding.*—Alloying with pure lead was very reproducible and simple. No eutectic formation was observed. Solubility and penetration (in most cases approximately 5-10μ) was low at temperatures as high as 300°C above the melting point of Pb. No cracking was observed at all.

Pb-Sn *eutectic bonding.*—Again, no eutectic formation or cracking was observed. At necessary bonding temperatures, however, there was more penetration and solubility than with pure Pb. Small additions of In or Sb had no effect on the wetting properties.

Table I. Etching of III-V compounds

III-V Compound	Etching solution	Etching time in sec
InSb	2HF/1HNO_3 diluted with an equal volume of H_2O	10-15
InAs	Conc. HCl	12-15
InP	Conc. HCl	3-6
GaSb	2HF/1HNO_3 diluted with an equal volume of H_2O	10-15
GaAs	2HF/1HNO_3 diluted with an equal volume of H_2O	10-15
GaP	2HF/1HNO_3	10-15

Sn *bonding.*—No eutectic formation or cracking was observed. Alloying with tin produced the lowest temperature bonds so far possible (see Table II). Small additions of gallium, contrary to results experienced in other systems, inhibited good wetting.

Ni, Cu, *and* Ag *bonding.*—In all these systems eutectic formations were observed. With nickel they were in the 700°-800° range; with copper 350°-500°C; with silver 400°-680°C. No bond was formed to InSb or GaSb with Ni below their melting points (523° and 702°C, respectively). No cracking was observed, except in the case of copper alloying to GaAs, and even in this system, no fracture occurs if the bond is formed above 650°C. The microstructure of bonds made at these elevated temperatures indicates a possible phase transformation to a more ductile form.

Bonding with Al *and* Al/Si *eutectic.*—Bonding to all six intermetallic compounds was accomplished with aluminum below 650°C. However, no eutectic structure was noted. Even in cases where fusions were made as high as 700°C, penetration was extremely shallow, much less than 5μ, indicating low solubility of the compounds in Al. This fact may be used to advantage in making contacts to shallow diffused regions. Al/Si bonds to III-V compounds were unsuccessful.

Cd *and* In *bonding.*—These bonds require temperatures in a range of 600°-800°C. Little if any eutectic formation is noticeable, and the penetration is extremely shallow as compared with other alloy bonds, except aluminum, made in a similar fashion. With Cd, some eutectic seems to form at a very low III-V concentration and only a few degrees below its melting point. Indium bonds with these elements were successfully made to all the intermetallics.

A number of alloys were studied for possible p-n junction formation on the III-V compounds. Binary alloys, where the major alloying element was In, Ag, Sn, Pb, Cd, or Au, were were fused on to all of the III-V surfaces. In a simple-type phase system such as exists in the Al-Si or In-Ge systems, the semiconductor bulk material, which has been dissolved at some elevated temperature, recrystallizes out on its original surface after cooling. These regions are sometimes referred to as regrown regions. They can be delineated by metallographic etching on a cross-section sample. If a pseudobinary phase diagram, using the III-V compound as one component and one of the binary alloys as the other, was of the two-component system type without intermediate compounds or solid solutions (similar to the Al-Si or In-Ge systems), one would expect to see some regrown region crystallizing out on the original III-V surface. Although all of the alloys mentioned, when doped appropriately, exhibited rectification properties after fusion, only the Sn and Au alloys showed any regrown regions. In all the other systems, at least one other unidentified phase was observed to have crystallized out of solution, and no regrown regions were observed. One ternary alloy composed of Sn, Cd, and Zn gave the appearance of a double junction formation when fused

Table II. Temperatures of alloy fusions to III-V surfaces

MP	Material °C (2)	Au 1063 Approx. eutectic temp, °C	Au 1063 Preferred bonding temp range, °C	Au 1063 Type dopant*	Au-Sn eutectic 280 Approx. eutectic temp, °C	Au-Sn eutectic 280 Preferred bonding temp range, °C	Au-Sn eutectic 280 Type dopant*
InSb	523	350	375/400			350/375	N[4]
InAs	936	<450	600/700			400/600	N[4]
InP	1060	450	600/700		None Ob-	400/500	N[4]
GaSb	702	300	325/350	O[3]	served	350/450	P[4]
GaAs	1280	<450	600/700			500/600	N[5]
GaP	>1300	450	600/700			>700	

MP	Material °C (2)	Au-Ge eutectic 356 Approx. eutectic temp, °C	Au-Ge eutectic 356 Preferred bonding temp range, °C	Au-Ge eutectic 356 Type dopant*	Au-Si eutectic 370 Approx. eutectic temp, °C	Au-Si eutectic 370 Preferred bonding temp range, °C	Au-Si eutectic 370 Type dopant*
InSb	523		375/450	P[4]			
InAs	936		400/450	N[4] [7]		375/380	N[7]
InP	1060	None Ob-	425/475	N[4]	None Ob-	375/425	
GaSb	702	served	375/450	P[4]	served	375/425	P[3]
GaAs	1280		400/450	N[4] [6]		400/425	N[6]
GaP	>1300		400/450			400/425	

MP	Material °C (2)	Pb 327 Approx. eutectic temp, °C	Pb 327 Preferred bonding temp range, °C	Pb 327 Type dopant*	Pb-Sn eutectic 183 Approx. eutectic temp, °C	Pb-Sn eutectic 183 Preferred bonding temp range, °C	Pb-Sn eutectic 183 Type dopant*
InSb	523		350/400	O[4]		300/325	
InAs	936		400/500	O[4]		450/500	
InP	1060	None Ob-	500/550	O[4]	None Ob-	450/550	See Pb &
GaSb	702	served	500/550	O[4]	served	500/550	Sn
GaAs	1280		500/600	N[6]		500/600	
GaP	>1300		550/650			600/650	

MP	Material °C (2)	Sn 232 Approx. eutectic temp, °C	Sn 232 Preferred bonding temp range, °C	Sn 232 Type dopant*	Ni 1455 Approx. eutectic temp, °C	Ni 1455 Preferred bonding temp range, °C	Ni 1455 Type dopant*
InSb	523		250/350				
InAs	936		250/350		700/750	750/800	
InP	1060	None Ob-	300/350	See	700/750	750/800	
GaSb	702	served	350/450				
GaAs	1280		400/500	Au-Sn	700/800	700/800	
GaP	>1300		500/600		750/800	750/800	

MP	Material °C (2)	Cu 1083 Approx. eutectic temp, °C	Cu 1083 Preferred bonding temp range, °C	Cu 1083 Type dopant*	Ag 960 Approx. eutectic temp, °C	Ag 960 Preferred bonding temp range, °C	Ag 960 Type dopant*
InSb	523	350	400/450		400	400/450	
InAs	936	400	450/500	N[9]	400/450	450/550	
InP	1060	400/500	525/600		400/455	550/600	
GaSb	702	450	450/500	P[3]	450	450/525	O[3]
GaAs	1280	500	>650	P[10]	650	700/725	
GaP	>1300	500	525/600		680	700/800	

* "O" Means neutral.

to Ge or In arsenide. This could be occurring by the post alloy diffusion mechanism. Sn behaves as a donor while Cd and Zn behave as acceptors, making an npn structure possible.

Manuscript received Oct. 19, 1961.

Any discussion of this paper will appear in a Discussion Section to be published in the December 1962 JOURNAL.

REFERENCES

1. L. Bernstein and R. J. Beals, *J. Appl. Phys.*, **32**, 122 (1961).
2. D. A. Jenny, *Proc. IRE*, **46**, 959 (1958).
3. K. Smirous, *Czech. J. Phys.*, **6**, 39 (1956).
4. O. G. Folberth and E. Shillman, *Z. Naturforsch.*, **12a**, 943 (1957).
5. S. Stopek, Private communication.
6. D. A. Jenny and R. Braunstein, *J. Appl. Phys.*, **29**, 596 (1958).
7. E. Shillman, *Z. Naturforsch.*, **11a**, 463 (1956).
8. J. McCaldin, Private communication.
9. C. Hilsum, *Proc. Phys. Soc.*, **73**, 685 (1958).
10. C. S. Fuller and J. M. Whelan, *J. Phys. Chem. Solids*, **6**, 173 (1958).

Kinetics and Mechanism of Nickel-Sulfur Reaction

Lucjan Czerski, Stanislaw Mrowec, and Teodor Werber

Department of General and Coal Chemistry, School of Mining and Metallurgy, Crakow, Poland

ABSTRACT

Kinetics and mechanism of the reaction between nickel and sulfur vapors were investigated in the temperature range 480°-640°C under atmospheric pressure. The sulfurization of nickel has been found to follow, under these conditions, the parabolic rate law. The activation energy of this process amounts to 22 kcal/mole. The examination of x-ray patterns of the scale formed on the surface of the metal has demonstrated that this scale layer is composed almost entirely of NiS. Morphologic investigations show that the scale is composed of two distinct layers. The outer layer, constituting the main part of the whole scale, is compact, polycrystalline, and exhibits an ordered growth texture. The inner layer is porous and does not exhibit any growth texture. The investigations carried out with the aid of the radioactive sulfur isotope ^{35}S have demonstrated that the sulfide scale on nickel is formed exclusively by the outward diffusion of the metal.

The confrontation of experimental data with the results obtained by Dravnieks (1) leads to the assumption that the mechanism of the sulfide scale formation on nickel does not depend on the state of aggregation of the oxidizing medium.

Dravnieks (1) and Wagner and Lichter (2) have demonstrated that the sulfurization of nickel in molten sulfur in the temperature range 205°-445° follows the parabolic rate law. On the other hand Hauffe and Rahmel (3), as well as Pfeiffer (4), stated that if the reaction was carried out in sulfur vapor at 630° under a pressure not exceeding 1 mm Hg the course of the reaction could be described with a linear rate law.

It was thereby stated that the sulfide scale formed on nickel is composed exclusively of the NiS-phase independently of the state of aggregation of the oxidizing medium and of the temperature. The scale is built up of two distinct layers; the outer one is compact, and the other, inner layer, is porous. Arkharov and Blankova (5), Czerski (6), Mrowec and Werber (7), Pfeiffer (4), and Hauffe (3) suppose that the formation of these two layers of the same reaction product can be explained by assuming simultaneous diffusion of both reactants through the scale layer in two opposite directions.

However, according to the opinion of Pines and Tchaikowskij (8), the sulfide scale layer on nickel grows exclusively because of the inward diffusion of sulfur.

From the literature data given above it can be seen that the mechanism of sulfurization of nickel is not yet definitively cleared up and more experimental work must still be done. The aim of the present work was therefore to investigate the kinetics and mechanism of sulfurization of nickel in sulfur vapor under atmospheric pressure in the temperature range 480°-640°C.

Experimental

The measurements were carried out on specimens containing 99.85% Ni. By means of spectral analysis the presence of the following impurities Fe, Mn, Cu, Mg, Si, Co, Al, and traces of Ag, Zn, Ca has been shown. The metal was melted *in vacuo* (10^{-4} mm Hg) and cold rolled to sheets 0.1 cm thick. The sheets were annealed for 100 hr at 750°C in helium atmosphere and subsequently cut into samples of dimensions 3 x 2 x 0.1 cm. The surface of the samples was polished with emery paper (including No. 4/O) and washed with water, acetone, and methanol. The process of sulfurization was carried out in a modified apparatus of Wagner (2) enabling continuous gravimetric measurements of the reactions kinetics (9) (Fig. 1). The apparatus (Fig. 1) consisted of two electrical furnaces into which a quartz tube containing molten sulfur was inserted. The lower furnace controlled the temperature of the molten sulfur at the bottom of the quartz tube and

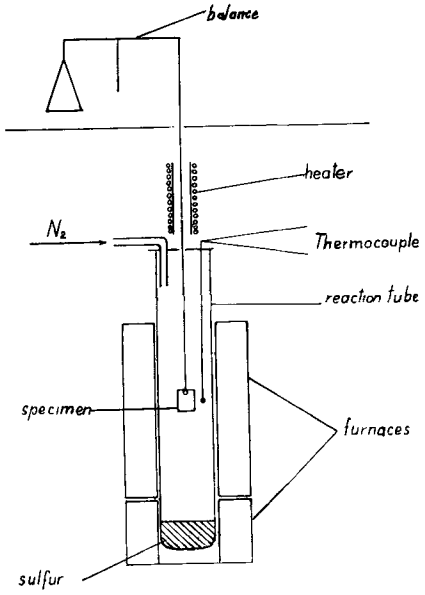

Fig. 1. Apparatus for kinetic measurements of sulfurization of metals in sulfur vapor under atmospheric pressure by the continuous gravimetric method.

the upper furnace controlled the temperature of the sulfur vapor in the reaction chamber. The temperature of sulfur vapor in the reaction tube was controlled automatically by an electronic compensator with an accuracy of ± 3°C. The thermocouple was introduced into the reaction tube on the specimen level at a distance from the tube wall equal to that of the specimen. Purified nitrogen was introduced into the upper, nonheated part of the quartz tube in order to avoid penetration of oxygen into the reaction zone. Traces of sulfur escaping with nitrogen from the reaction tube were directed into a corresponding trap with the aid of an appropriate exhauster. The specimen suspended in the reaction tube was fastened with a nichrome wire to an arm of an analytical balance. The wire was preliminarily oxidized in air at 1000°C for 100 hr to protect it against the attack of sulfur. In order to eliminate the possibility of condensation of sulfur on the wire in the upper, nonheated part of the tube the wire itself was heated to 600°C with an additional heater which maintained its temperature above 450°C. Preliminary investigations have shown that the mass of the wire did not change much during the reaction (the variation amounted to ± 1.0 mg). These variations can be explained by the convection flow of air and sulfur vapor around the wire. The increase in weight of the sulfurized nickel specimens was of the order of 100 mg; the mass of the wire on which the specimen was suspended therefore could be considered to be practically constant. The sulfurization rate could be measured continuously by determining the weight increase of the sample. The investigations were carried out in the temperature range 480°-640°C. This restriction of the temperature range resulted from the necessity of investigating the process at temperatures above the boiling point of sulfur and below the melting point of the eutectic Ni-NiS (645°C). The results of the sulfurization rate measurements are given in Fig. 2 and 3. The figures show the $(\Delta m/q)^2$ values plotted against t where Δm is the weight gain of the sample, q the surface area of the sample, and t the reaction time. Surface area q was assumed to be constant during the sulfurization process and equal to the initial surface area of the metal specimen. It is clear that this surface decreases during the process, but owing to the particular geometric form of specimens used the maximum changes in the surface area of metal did not exceed 2-3% of the initial value in the investigated ranges of temperature and reaction time.

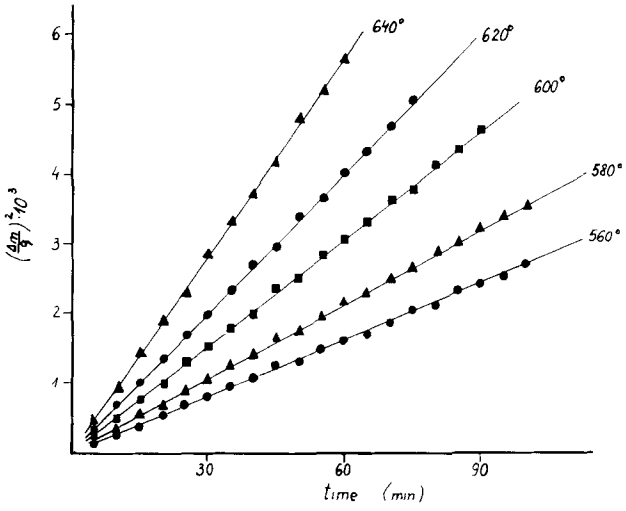

Fig. 3. Weight gain plot for the temperature range 560°-640°C

As can be seen, the experimental data in these coordinates fit a straight line independent of the reaction temperature. This means that in our experimental conditions the scale formation process follows the parabolic rate law:

$$\left(\frac{\Delta m}{q}\right)^2 = k'' \cdot t \qquad [1]$$

where k'' is the parabolic rate constant of the sulfurization process. Measurements of the sulfurization rate could be reproduced with an accuracy of ±5%. Table I contains the parabolic rate constants calculated from our data. The relation between the rate of sulfurization and the reaction temperature is illustrated by Fig. 4 in which log k'' is plotted *vs.* $1/T$. As can be seen from the figure this relation is linear. Activation energy for the sulfurization of nickel as calculated from these figures amounts to **22 kcal.**

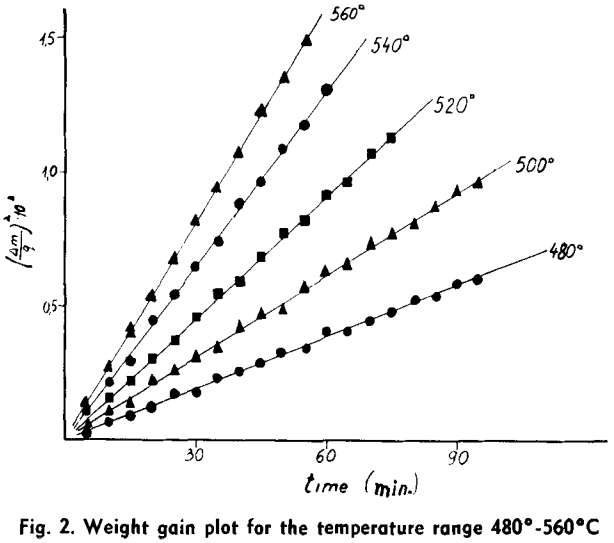

Fig. 2. Weight gain plot for the temperature range 480°-560°C

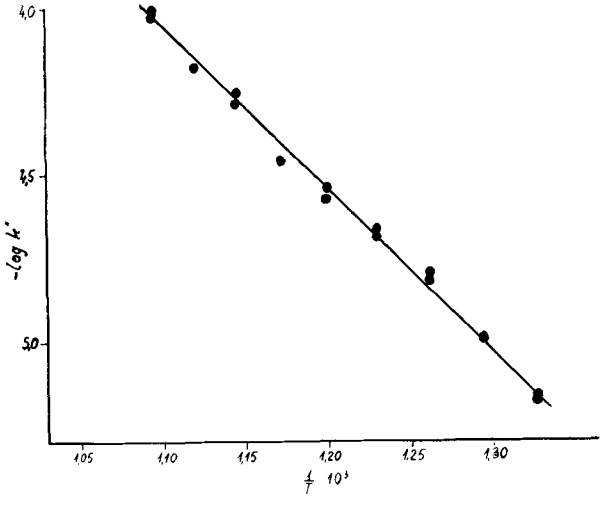

Fig. 4. Change of the parabolic rate constant for the NiS formation with temperature.

Table I. Parabolic rate constants

No.	Temp, °C	k'' (g^2 cm^{-4} sec^{-1})
1	480	$1.05 \cdot 10^{-7}$
2	500	$1.65 \cdot 10^{-7}$
3	520	$2.60 \cdot 10^{-7}$
4	540	$3.50 \cdot 10^{-7}$
5	560	$4.65 \cdot 10^{-7}$
6	580	$5.92 \cdot 10^{-7}$
7	600	$8.75 \cdot 10^{-7}$
8	620	$11.2 \cdot 10^{-7}$
9	640	$15.7 \cdot 10^{-7}$

Morphologic investigations have demonstrated that, independent of the reaction temperature, the sulfide scale growing on nickel is composed of two layers. The outer layer, constituting the main part of the scale, is compact, polycrystalline, and exhibits an ordered growth texture (5). The thinner, inner layer is porous and composed of very small crystals of sulfide. In this layer no growth texture could be detected. According to the results of the x-ray analysis both scale layers are built up of the same phase of the reaction product which was identified as the high-temperature form of NiS (stable above 300°C) (10). The mean chemical composition of the scale corresponded to the nonstoichiometric formula $Ni_{0.91-0.92}S$ and was practically independent of the temperature of the reaction.

As proved by detailed microscopic observations the ratio of the thicknesses of the two scale layers depends on the temperature of the sulfurization process and the time of the reaction. The relative mass of the porous inner layer has been found to decrease with increasing reaction temperature. On the other hand, the ratio of thicknesses of both scale layers observed on various samples at the same temperature has been found not to be constant, but to vary with increasing duration of the experiment (the porous inner layer is growing faster). Corresponding photomicrographs of the cross sections through the scale formed at 600°C are shown in Fig. 5. The boundary between the layers of the scale can be seen easily on these micrographs; the growth of the scale is accompanied by a distinct growth of the relative thickness of the porous inner layer. On the micrographs one can also see a thin platinum wire marker wrapped primarily around the metal sample and situated nearly at the boundary between both layers of the scale.

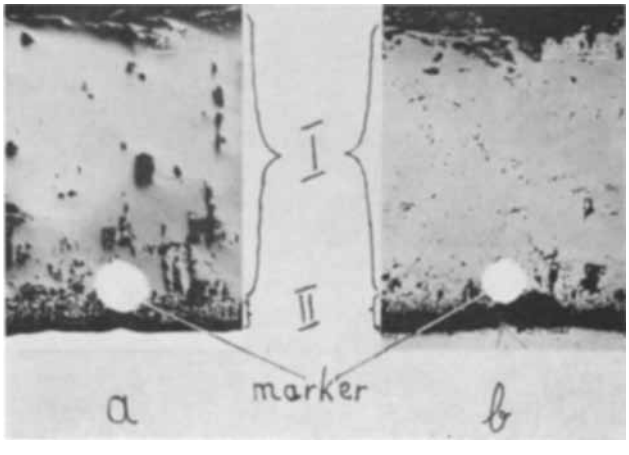

Fig. 5. Cross section through specimens sulfurized at 600°C: a, 1 hr; b, 4 hr. I. The outer layer is compact. The dark regions result from the mechanical process of the metallographic preparation of the scale. II. The inner layer is porous. The platinum wire marker was artificially retouched for greater clarity of the micrograph.

According to the conventional interpretation such position of the marker (11, 12) is taken as proof that the scale grew because of the diffusion of both reactants, nickel and sulfur, migrating simultaneously in two opposite directions. The compact outer layer formed because of the outward diffusion of the metal; the thinner, porous inner layer formed because of the inward diffusion of sulfur.

Recent investigations by two of the present authors (13-15) and Rickert (16) on Cu-S and Ag-S systems have shown however that the position of the marker in the scale does not definitively explain the mechanism of observed double-layer scale formation. Thus, contrary to the results obtained by the marker method, the formation of a double-layer sulfide scale on copper and silver was found not to depend on the diffusion of both reactants in the opposite directions. The scale was formed exclusively because of the outward diffusion of the metal (15, 17). The formation of the porous inner layer is bound up, in this case, with secondary processes occurring within the scale during its growth (17, 18). From the morphologic point of view the structure of the two-layer sulfide scale on nickel is analogous to the structure of the sulfide scale formed on copper and silver. Therefore it can be supposed that the mechanism of both sulfurization processes is also analogous, and the process develops exclusively owing to the outward diffusion of nickel. In order to verify this assumption Brückman, Mrowec, and Werber carried out a new series of measurements (19) using the isotopic method described in previous papers (13, 15). These investigations were carried out at 600°C in an apparatus shown in Fig. 1. Nickel plates of the same dimensions as those in the kinetic investigations were preliminarily sulfurized in a medium not containing the radioactive sulfur isotope until a scale layer was formed thick enough to absorb fully the radiation emitted by the isotope ^{35}S. The radioactive sulfur isotope in the form of a pellet was then introduced into the reaction chamber and the sulfurization was continued. After various periods of time the process was stopped by removing the specimens from the sulfurizing medium and by cooling them in air. The scale layer was separated from the metal and the activity of both scale surfaces was measured with the aid of a G.M. counter.

The inner surface of the scale (which had been in contact with the metal during the sulfurization) was found to be practically inactive independent of the time of the sulfurization carried out in the radioactive medium. The results obtained for different reaction times are given in Table II. It can be seen that the radioactivity at the inner surface does not exceed 2% of the activity measured at the outer surface of the scale. The activity at the inner surface of the scale has been shown not to increase with increasing time of sulfurization in the active

Table II. Radioactivity at the surfaces

No.	t_1, min	t_2, min	t_2/t_1	A_1, imp. min^{-1}	A_2, imp. min^{-1}	$\frac{A_2}{A_1}100$
1	15	15	1	3080	20	0.6
2	15	45	3	4500	90	2.0
3	15	75	5	3270	31	0.9
4	15	105	7	4620	60	1.3
5	15	135	9	6220	82	1.3

t_1, time of sulfurization in the nonactive medium; t_2, time of sulfurization in the medium containing the radioactive sulfur isotope; A_1, activity of the outer scale surface (which was in contact with the oxidizing agent); and A_2, activity of the inner scale surface (which was in contact with the metal).

medium containing the ^{35}S-isotope. If the inward diffusion of sulfur were to participate in the growth of the scale, an appreciable radioactivity could be expected to appear at the inner scale surface after relatively short periods of sulfurization carried out in the radioactive medium. The results described above can then be considered to prove that the inward diffusion of sulfur does not practically participate in the formation of the sulfide scale on nickel. The insignificant activity revealed at the inner surface of the scale can be explained probably by the inevitable contamination of this surface with traces of the sulfide formed primarily on the outer surface of the scale. The inner surface becomes contaminated during the operations of cutting the fragile scale layer and separating it from the metal.

Discussion

The sulfurization of nickel in the temperature range 480°-640° under atmospheric pressure has been shown to follow the parabolic law. With the aid of the radioactive sulfur isotope it could be found that sulfurization occurs in these conditions exclusively owing to the outward diffusion of the metal. This conclusion concerning the mechanism of nickel sulfurization has been fully confirmed by the recent investigations carried out by Mrowec and Rickert (28) with aid of the well-known Wagner pellet method. On the basis of obtained results it can be stated that the outward diffusion of the metal being the slowest partial process determines the rate of sulfurization of nickel. Taking into account the deviation from the stoichiometric composition in the case of NiS (metal deficit) (10, 20) it can be assumed that the metal, in conformity with the theory given by Wagner (21), diffuses in the form of ions and electrons through the cation vacancies and electron holes in the crystal lattice of NiS.

From the considerations given above it follows that the sulfide scale formed on nickel ought to be compact and composed of a single layer only. It has been found, however, that the scale is built up of two layers of the same reaction product. The formation of the porous inner layer can be explained on the basis of the following assumptions concerning the mechanism of the reaction: during the initial stage of the reaction a thin, compact, and adherent scale layer is formed. Since the scale is formed owing to the outward diffusion of the metal, *i.e.*, at the phase boundary scale/sulfur, the contact between the growing layer of the reaction product and sulfurized metal could be easily cut off if the plastic flow of the scale toward the surface of the metal would not take place. The extent of this plastic flow is limited by the dimensions and the size of the specimen. For geometrical reasons the deformations of the scale are not observed at edges and curved parts of the sample (2, 15, 22, 23). At some critical scale thickness which depends on the temperature of the reaction, on the plasticity of the scale, and on the geometry of the sulfurized metal specimen the decrease in the volume of the metal cannot be further compensated by the plastic flow of the scale; the contact between the scale layer and the metal becomes partially broken and longitudinal cracks are formed. The formation of the cracks begins at the edges of the specimen where the plastic flow of the scale is limited in its extent by geometrical factors.

Before the crack has been formed the gradient of the chemical potential responsible for the outward diffusion of the substrate is distributed in the scale in the following manner.

The chemical potential of the metal attains its highest value at the phase boundary scale/metal. This value is approximately equal to the value calculated for virtual thermodynamic equilibrium between the metal and the scale.

Conditions at the phase boundary scale/sulfur do not deviate very much from the conditions of the thermodynamic equilibrium between NiS and sulfur; in the vicinity of this phase boundary the chemical potential of the metal attains its minimal value.

When the contact between the metal and the scale gets partially broken the chemical potential of the metal in the scale tends to attain at the phase boundary scale/crack a value corresponding to the equilibrium state between sulfur and nickel sulfide. Correspondingly, the sulfur vapor pressure in the void space must increase. At the metal surface the process of secondary NiS formation begins; the pressure of dissociation of the nickel sulfide remaining in contact with the metal is lower than the dissociation pressure of the detached scale consisting of the same phase. The secondary process of the sulfide layer formation at the metal surface results in decreasing the vapor pressure within the crack and in shifting the equilibrium of the system scale/crack: the scale dissociates in order to replace the sulfur deficit in the crack. Nickel ions and electrons formed in this process migrate through the NiS lattice vacancies toward the surface of the scale and recombine there with sulfur. The existing gradient of the sulfur vapor pressure enables the migration of the sulfur molecules toward the surface of the metal or NiS grains adjacent to the metal and participate there in the formation of the porous inner layer of the scale. Owing to this process the contact between the scale and the metal is partially maintained. In accordance with the mechanism described above, formation of the two-layer scale does not involve the diffusion of both reactants through the layer of the reaction product in two opposite directions, but is conditioned by secondary processes which depend on the conditions of the experiment-limited size of sulfurized specimens.

Such a mechanism of the two-layer scale formation was first proposed by Dravnieks and McDonald (24). It was proved experimentally in a recent investigation of Mrowec and Werber who had used the radioactive sulfur isotope in investigations of the mechanism of two-layer scale formation on copper (13, 15, 17) and silver (15, 25).

Rickert, who investigated the mechanism of the sulfurization of copper and silver using a modified Wagner-Tubandt pellet method, came to analogous results (16). An analogous mechanism of the two-layer scale formation on Fe has also been proposed by Birchenall (26).

The rate of sulfurization is considerably influenced by the formation of the porous inner layer. In view of the fact that nickel can be transported only through the volume of the sulfide, the cross section available for diffusion in the porous inner layer is smaller than in the case of the compact outer layer. The fact that the process of sulfurization of nickel can be described in the initial stage of reaction with the parabolic law indicates that, in this case, the porosity of the inner layer is small and remains practically constant in the course of the reaction. This means that the secondary processes mentioned above and resulting in filling the longitudinal cracks between the metal and the compact scale layer occur sufficiently fast to compensate to a considerable degree the loss of the metal. The absolute values of the parabolic rate constants given in Table I must be considered, therefore, regarding the formation of the porous inner layer, to be only approximate values and to characterize the formation of NiS in given conditions only in a rough manner. These values cannot therefore be used for the evaluation of the self-diffusion coefficients with the aid of the well-known Wagner relation (27). Much more reliable results may be obtained with the help of the pellet method (15) enabling the elimination of all secondary processes resulting in the formation of the inner porous layer of the scale (16, 28).

The investigations carried out by Dravnieks (1) have demonstrated that the sulfurization of nickel in molten sulfur can be described also with the parabolic law. The energy of activation calculated for this process from data obtained in the temperature range 324°-444° (when the high-temperature modification of NiS is formed) amounts to 20 kcal. Considering the analogy between processes of sulfurization in molten sulfur and in sulfur vapor and taking into account the equality of energies of activation it can be assumed that the mechanism of this reaction does not depend on the state of aggregation of the oxidizing medium.

On the other hand, investigations carried out by Hauffe and Rahmel (3) and by Pfeiffer (4) proved that the sulfurization of nickel in sulfur vapor at low pressures (<1 mm Hg) and at 600°-630°C can be described with the linear rate law. This shows that it is not the outward diffusion of the metal but the chemical reaction occurring at the phase boundary scale/metal or scale/sulfur which must be considered as a rate-determining step. According to Pfeiffer the transition of nickel in form of ions and electrons through the phase boundary scale/metal is the slowest partial process which determines the rate of sulfurization.

The investigations carried out by the present authors have demonstrated, however, that the sulfurization of nickel carried out at the same temperature but under a higher sulfur vapor pressure can be described with the parabolic rate law. These results indicate that the mechanism of the sulfurization is influenced by the pressure of sulfur vapor.

If the rate of sulfurization were controlled, as postulated by Pfeiffer, by the transition of nickel atoms from the metal in to the scale, this rate should not be dependent on the pressure of sulfur vapor. Such dependence is, however, strongly suggested from the comparison of Hauffe's and Pfeiffer's low-pressure experiments with our high-pressure experiments. According to our opinion it is rather the chemical reaction at the phase boundary scale/sulfur that is the rate-controlling process. Evidently it must be preceded by chemisorption of sulfur at the outer surface at the scale. At low pressures of sulfur and correspondingly low surface concentration of S-atoms or molecules chemical reaction may be slow even in comparison with the solid-state diffusion; at higher pressures of sulfur vapor and higher surface concentrations of adsorbed sulfur the chemical reaction may become faster than the diffusion of nickel.

Summary

The sulfurization of nickel in sulfur vapor under normal pressure at temperatures between 480°-640°C has been found to follow the parabolic law. In the sulfide scale layer formed in these conditions and built up of NiS (with stoichiometric deficiency of the metal) two different sublayers can be clearly distinguished: the outer compact sublayer and the inner porous one.

With the aid of the radioactive tracer method it has been demonstrated that sulfurization can proceed exclusively owing to the outward diffusion of nickel. The porous sublayer, therefore, can be formed exclusively as the result of secondary processes occurring within the layer of the reaction product and consisting of the formation of a "crack" between the scale and the metal in the course of the reaction. This crack becomes filled with fine-crystalline nickel sulfide formed as a result of interaction between the metal and the sulfur supplied to the metal surface by the dissociation of the compact scale layer. Relative thicknesses of these two sublayers depend on the temperature of sulfurization, on the duration of this process, and on the geometry of specimens under investigation.

In view of formation of the porous sublayer, the rate constants, which can be determined experimentally, must be considered to characterize the reaction rate in the Ni-S system in given conditions only in an approximate manner.

Acknowledgment

This investigation was sponsored by the Polish Academy of Sciences Commission of Technical Sciences in Cracow. Special appreciation is due to Dr. J. Nedoma for his helpful discussions.

Manuscript received June 19, 1961.

Any discussion of this paper will appear in a Discussion Section to be published in the December 1962 JOURNAL.

REFERENCES

1. A. Dravnieks, *This Journal*, **103**, 435 (1955).
2. B. D. Lichter and C. Wagner, *ibid.*, **107**, 168 (1960).
3. K. Hauffe and A. Rahmel, *Z. phys. Chem.*, **199**, 152 (1952).
4. I. Pfeiffer, *Z. Metallkunde*, **49**, 267 (1958).
5. W. I. Archarow and E. B. Blankova, *Fiz. Metal. i Metallovied.*, **8**, 452 (1959).
6. L. Czerski, *Arch. Gornictwa i Hutnectwa* PAN, **2**, 3 (1954).
7. S. Mrowec and T. Werber, *Naturwiss.*, **46**, 73 (1959).
8. B. Ja. Pines and E. F. Tchaikowskij, *Fiz. Metall. i Metallovied.*, **9**, 369 (1960).
9. S. Mrowec and T. Werber, Chemia Analityczna (in press).
10. M. Laffitt, *Bull. Soc. Chim. France*, **1959**, 1211.
11. K. Sachs, *Metallurgia*, **54**, 11 (1956).
12. L. Czerski, S. Mrowec, and T. Werber, *Arch. Gornictwa i Hutnictwa PAN*, **3**, 37 (1958).
13. J. Mikulski, S. Mrowec, I. Stronski, and T. Werber, *Z. phys. Chem. NF*, **22**, 20 (1959).
14. S. Mrowec, *Z. phys. Chem. NF*, **29**, 47 (1961).
15. S. Mrowec, *Arch. Hutnictwa*, **6**, 61 (1961).
16. H. Rickert, *Z. phys. Chem. NF*, **23**, 355 (1960).
17. S. Mrowec and T. Werber, *Acta Met.*, **7**, 696 (1959).
18. S. Mrowec and T. Werber, *Fiz. Metal. i Metallovied.*, **10**, 572 (1960).
19. A. Brückman, S. Mrowec, and T. Werber, *Nucleonika (Warszawa)*, **6**, 17 (1961).
20. W. Biltz, *Z. anorg. u. allgem. Chem.*, **228**, 275 (1936).
21. C. Wagner, *Z. phys. Chem.*, **21B**, 25 (1933); **32B**, 447 (1936).
22. J. Moreau and M. Cagnet, *Rev. Met.*, **55**, 1091 (1958).
23. H. J. Engell, *Acta Met.*, **5**, 695 (1957).
24. A. Dravnieks and H. J. McDonald, *This Journal*, **94**, 139 (1948).
25. S. Mrowec, J. Mikulski, and T. Werber, *Bull. Acad. Polon. Sci. Ser. chim.*, **7**, 734 (1959).
26. C. Birchenall and R. Meussner, *Corrosion*, **13**, 677t (1957).
27. C. Wagner, "Diffusion at High Temperature Oxidation of Metals" in "Atom Movements," p. 153, American Society of Metal, Cleveland (1952).
28. S. Mrowec and H. Rickert, *Z. phys. Chem. NF*, **28**, 422 (1961).

Oxidation of Iron-Nickel Alloys

V. Influence of H_2O in Oxidizing Gas

R. T. Foley[1]

General Engineering Laboratory, General Electric Company, Schenectady, New York

ABSTRACT

The oxidation of three iron-nickel alloys nominally 30%, 41%, and 78% Ni was investigated over the temperature range of 600°-1000°C in controlled O_2/N_2 atmospheres with partial pressures of H_2O of 0.32 mm, 5.81 mm, and 26.3 mm. The gross effect of H_2O in the oxidizing atmosphere is to increase the oxidation rate (up to 13-fold for the 30% alloy at 1000°C). In addition, at higher temperatures and higher p_{H_2O}, the rate-determining diffusion process changes from the first half to the second half of the 60-min reaction. The observed rates for the 30% and 41% alloy during the second phase are higher, while the second-phase rate for the 78% alloy is lower. The Arrhenius plots for these alloys are not linear over the 600°-1000°C range. Below 800°C a low apparent activation energy, 30-40 kcal, is calculated, while above 800° a value in the 60 kcal range is obtained.

The results are interpreted in terms of changes in the physical condition of the oxide film as caused by H_2O which enhances surface migration of ions and promotes solid-state reactions.

Several previous reports from this laboratory have dealt with the oxidation of iron-nickel alloys (1-4). Alloys of these two elements have found many engineering applications because of their magnetic properties, their ability to participate in glass-to-metal seals, and their thermal expansion characteristics. Therefore, it is important to know quite completely the behavior of these alloys in various environments such as oxidizing atmospheres at high temperature.

The present investigation is concerned with the oxidation of alloys, nominally 30, 41, and 78% Ni, in the range 600°-1000°C. In an earlier report (3) the kinetics of oxidation in two atmospheres, laboratory air and a 21.7% O_2-78.3% N_2 mixture, was established. An inspection of the rates in the two atmospheres does not allow any good generalization to be made relative to the oxidizing potential of these two atmospheres. The observed reaction rate in the laboratory air was greater, less, or equal to that in the controlled atmosphere depending on the alloy and the reaction temperature. Certain conclusions could be drawn from the rate data however. The first had to do with the precision of the measurements. While two runs made during the same day in laboratory air were quite precise (within 3% of an average value) runs made several weeks or months apart might vary by 60%. The second conclusion was that, while the reaction rate for oxidation in the controlled atmosphere followed the parabolic law quite well, in laboratory air there were real deviations. Moreover, the deviation was not always in the same direction.

[1] Present address: Melpar, Inc., Falls Church, Virginia.

While not the only "contaminant" in the atmosphere it is highly probable that water vapor is the significant one. The k[1] laboratory air is free of exhaust fumes, sulfur oxide gases, and such compounds that have been demonstrated to have an accelerating effect on the corrosion of metals. Thus, to explain these results it was necessary to learn the role of H_2O on the mechanism and kinetics of oxidation.

The role of H_2O in high-temperature oxidation is an extremely important item despite the fact that it has been often overlooked. The development of general principles which would define its part in the oxidation process would be a significant contribution to oxidation theory. Further, knowing the role of H_2O in the oxidation process would help to interpret much of the "practical" oxidation data in the literature in comparison with well-controlled experiments. A final contribution to basic oxidation theory is the over-all objective of this series of papers, the complete description of the kinetics and mechanism of oxidation of iron-nickel alloys.

Experimental

Alloys.—The composition of the alloys, the heat treatment prior to oxidation, and the technique of surface preparation have already been described (2, 3). It has been pointed out that the preferred method of surface preparation involves chemical etching because, following proper etching, electron diffraction patterns of the alloy itself were obtained whereas abrasion and polishing techniques sometimes gave patterns difficult to interpret.

Oxidation studies.—The Chevenard thermobalance employed in this work is capable of operation up to 1050°C. The instrument furnace has a quartz tube liner which allows the introduction of special atmospheres into the oxidation zone. The oxidizing atmospheres flowing at a rate of 263 ml/min consisted of a mixture of 21.7% oxygen and 78.3% nitrogen (by volume) with three different H_2O contents. These atmospheres were: (*a*) the gas mixture without any intentional addition of H_2O with a dewpoint of −20°F [vapor pressure H_2O = 0.32 mm (5)]; (*b*) the gas mixture to which H_2O was added by passing the gas stream through a fritted glass plug and water held at about 0°C. The measured dewpoint of this gas was +38°F [vapor pressure H_2O = 5.81 mm (5)]; (*c*) the gas mixture to which H_2O was added by passing the gas stream through a fritted glass plug and water held at room temperature. The measured dewpoint of this gas was +80°F [vapor pressure H_2O = 26.3 mm (5)].

In each case the dewpoint of the gas was measured with a General Electric Dew Point potentiometer with a precision of ±3°F. At least duplicate experiments were run at 600°, 700°, 800°, 900°, and 1000°C in each atmosphere, each run being of 60 min duration.

Treatment of data.—The oxidation rate for these iron-nickel alloys may be represented by a parabolic rate equation.

$$(\Delta m)^2 = b + k_p t \qquad [1]$$

where Δm is gain in weight in g/cm² of a sample oxidized for t seconds; k_p is the parabolic rate constant ($g^2\ cm^{-4}\ sec^{-1}$); b is a constant (g^2cm^{-4}). The data for certain experiments were represented over the entire run by a linear plot, Eq. [1]. In other cases, notably those at higher temperatures and higher H_2O vapor pressure, the plot was not linear over the whole 60 min duration. These data could be represented in either of two ways. The first would be by using two parabolic equations, one for the early part of the run and a second for the later part of the run. Alternatively the data could be represented over the entire time interval by using an equation wherein the (Δm) exponent fell somewhere between 1.5 and 2.5. On theoretical grounds the use of two parabolic equations for separate time intervals seems more justified.

The temperature dependence for reactions of this type is usually described by an Arrhenius type equation:

$$k_p = Ae^{\frac{-\Delta E^*}{RT}} \qquad [2]$$

in which ΔE^* is termed the apparent energy of activation and A the frequency factor. The exact significance of ΔE^* has not been satisfactorily established insofar as high-temperature oxidation is concerned and can only be considered a guide to the type of oxidation process. Some of the difficulties in the interpretation of ΔE^* have been discussed (3). Further, where the reaction product film is composed of more than one species it would be suspected that ΔE^* would not be constant over an extended temperature range. This was the situation encountered in this study.

Electron diffraction examination of oxide films.—Electron diffraction analyses by the reflection technique were made of the oxide films with a General Electric electron diffraction instrument. This instrument is equipped with a furnace attachment enabling one to study the oxidation products at the temperature of reaction. The detailed description and interpretation of the patterns obtained in these special atmospheres have been reported (4).

Results

The parabolic rate constants, k_p in Eq. [1], for the 30% Ni alloy are listed in Table I. Only average values for the several runs are given, the precision of these data having been discussed (3). The values given for the $p_{H_2O} = 0.32$ mm run were taken from this earlier paper. These data are plotted in Fig. 1. At 600° there is a moderate increase in rate while at 700° the rate constant is insensitive to H_2O additions to the gas stream; at 800° the rate doubles over the p_{H_2O} range investigated here; at 900° and 1000° the rate increases by a factor of 5 and 14, respectively, the "initial" rate being compared in the last two cases. The influence of water vapor in the oxidizing gas has a second effect at 900° and 1000°. At these temperatures it is necessary to use two parabolic equations to represent the experimental data. The first equation holds for the initial 30 min, the second (solid circles on Fig. 1) for the 30-60 min part of the reaction. This in-

Table I. Parabolic rate constants for 30% Ni alloy

t °C	k_p (g² cm⁻⁴ sec⁻¹) p_{H_2O} = 0.32 mm	p_{H_2O} = 5.81 mm	p_{H_2O} = 26.3 mm
600	1.27×10^{-12}	1.74×10^{-12}	2.14×10^{-12}
700	1.46×10^{-11}	1.65×10^{-11}	1.50×10^{-11}
800	8.5×10^{-11}	1.24×10^{-10}	1.85×10^{-10}
900	5.2×10^{-10}	(a) 1.42×10^{-9} (0-30 min)	2.73×10^{-9} (0-30 min)
		(b) 1.75×10^{-9} (30-60 min)	4.28×10^{-9} (30-60 min)
1000	3.3×10^{-9}	(a) 1.10×10^{-8} (0-36 min)	4.48×10^{-8} (0-30 min)
		(b) 1.53×10^{-8} (36-60 min)	10.8×10^{-8} (30-60 min)

crease in rate for the second part of the reaction itself increases with p_{H_2O}. At p_{H_2O} = 5.81 the second parabolic reaction rate constant increases by about 30% over the first, while at p_{H_2O} = 26.3 mm the rate during the second half of the reaction approximately doubles.

The temperature dependence of the reaction is given by the Eq. [2] type of plot in Fig. 2.[2] The curves labeled A and D, B and E, and C and F represent data at 0.32 mm, 5.81 mm, and 26.3 mm vapor pressure H_2O, respectively. The apparent activation energies derived from the slopes of these lines are:

A = 41.2 kcal
B = 41.2
C = 41.5

D = 55.2
E = 60.6
F = 73.7

It is very obvious that a single linear plot does not represent the data over the entire temperature range. Above 800° the slope increases to yield activation energies considerably higher than the "normal" 41,200 cal.

The parabolic rate constants representing the

[2] Note that in Fig. 2, 4, and 6, decreasing rate constants are plotted in the vertical direction.

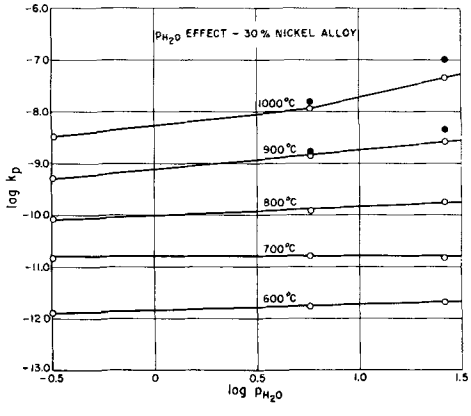

Fig. 1. Oxidation rate of 30% Ni alloy as a function of vapor pressure H_2O. O, 0-30 min kinetics, •, 30-60 min kinetics.

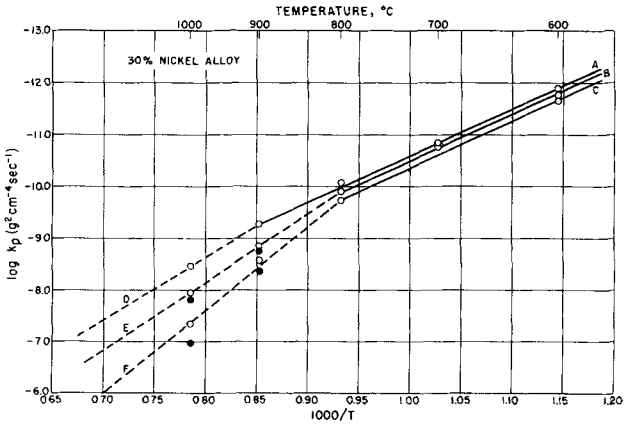

Fig. 2. Temperature dependence of oxidation rate for 30% Ni alloy; A, D, p_{H_2O} = 0.32 mm; B, E, p_{H_2O} = 5.81 mm; C, F, p_{H_2O} = 26.3 mm.

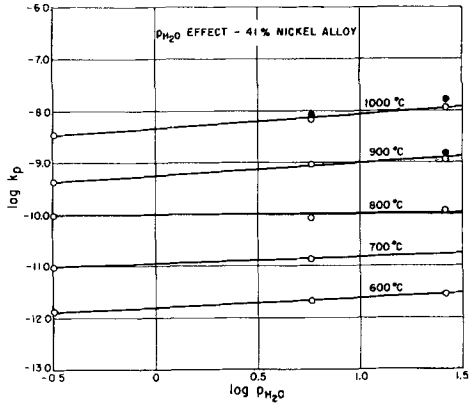

Fig. 3. Oxidation rate of 41% alloy as a function of vapor pressure H_2O. O, 0-30 min kinetics; •, 30-60 min kinetics.

oxidation kinetics of the 41% alloy in the three different atmospheres are listed in Table II and plotted in Fig. 3. In the oxidation of the 41% Ni alloy the effect of H_2O is evidenced at 600° and 700° with increased rates; at 800° there is practically no effect, and at 900° and 1000° the rates are increased approximately threefold over the p_{H_2O} range studied. The necessity to represent the data by two

Table II. Parabolic rate constants for 41% Ni alloy

t °C	k_p (g² cm⁻⁴ sec⁻¹) p_{H_2O} = 0.32 mm	p_{H_2O} = 5.81 mm	p_{H_2O} = 26.3 mm
600	1.27×10^{-12}	2.20×10^{-12}	2.88×10^{-12}
700	9.8×10^{-12}	1.37×10^{-11}	
800	9.3×10^{-11}*	8.33×10^{-11}	1.18×10^{-10}
900	4.05×10^{-10}	8.92×10^{-10}	(a) 1.10×10^{-9} (0-30 min)
			(b) 1.58×10^{-9} (30-60 min)
1000	3.51×10^{-9}	(a) 6.90×10^{-9} (0-30 min)	(a) 1.20×10^{-8} (0-30 min)
		(b) 8.00×10^{-9} (30-60 min)	(b) 1.71×10^{-8} (30-60 min)

* Corrected from typographic error in (3).

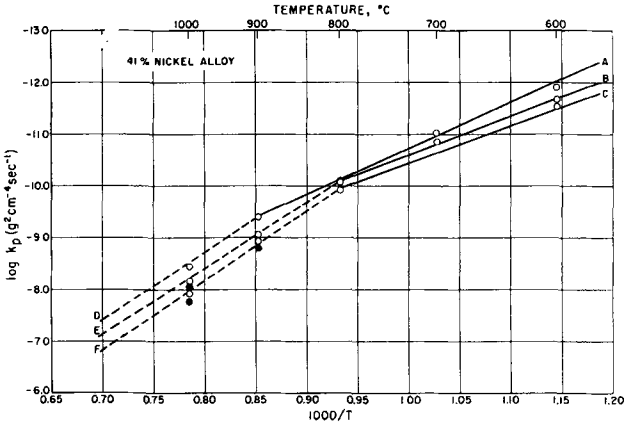

Fig. 4. Temperature dependence of oxidation rate for 41% alloy; A, D, p_{H_2O} = 0.32 mm; B, E, p_{H_2O} = 5.81 mm; C, F, p_{H_2O} = 26.3 mm.

parabolic equations rather than one is observed at 900° in the 26.3 mm p_{H_2O} atmosphere and at 1000° in both the 5.81 mm and the 26.3 mm p_{H_2O} atmospheres. The rate during the second phase of the reaction increases by about 43% over the first half of the reaction.

The temperature dependence of the reaction is given in Fig. 4. Again, the Arrhenius plot is not linear, but deviates because of higher reaction rates above 800°. In each of the three atmospheres, a low apparent activation energy is observed in the 600°-800° range and a high value in the 800°-1000° range. The activation energies corresponding to the slopes are as follows:

A	40.8 kcal
B	33.9
C	32.7
D	59.3
E	58.3
F	61.3

The parabolic rate constants which describe the oxidation behavior of the 78% alloy in the three

Table III. Parabolic rate constants for 78% Ni alloy

t °C	k_p (g² cm⁻⁴ sec⁻¹) p_{H_2O} = 0.32 mm	p_{H_2O} = 5.81 mm	p_{H_2O} = 26.3 mm
600	7.2×10^{-12}		2.13×10^{-12}
700	3.01×10^{-12}	6.56×10^{-12}	8.59×10^{-12}
800	1.70×10^{-11}	3.34×10^{-11} (a)	3.65×10^{-11} (0-36 min)
			(b) 2.47×10^{-11} (36-60 min)
900	7.5×10^{-11}	1.16×10^{-10} (a)	1.69×10^{-10} (0-30 min)
			(b) 1.08×10^{-10} (30-60 min)
1000	(a) 6.4×10^{-10} (0-30 min)	7.85×10^{-10} (a)	1.49×10^{-9} (0-30 min)
	(b) 5.5×10^{-10} (30-60 min)		1.16×10^{-9} (30-60 min)

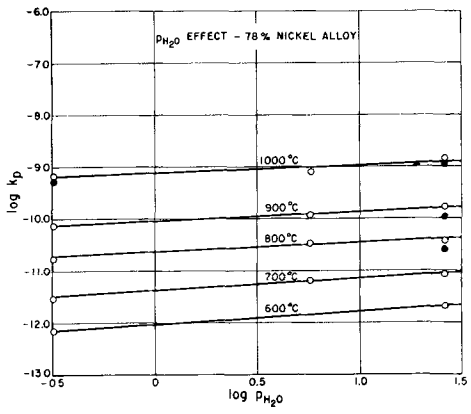

Fig. 5. Oxidation rate of 78% alloy as a function of vapor pressure H_2O. O, 0-30 min kinetics; •, 30-60 min kinetics.

atmospheres are given in Table III and the log k_p — log p_{H_2O} plot in Fig. 5. Here the over-all effect of increased H_2O vapor pressure is one of increased rate. The effect is not as pronounced as is the case with the 30% and 41% alloy, but rather a consistent doubling or tripling over the whole p_{H_2O} range. The other effect observed was seen in the high p_{H_2O} run and in the temperature range of 800°-1000°. Under these experimental conditions the oxidation kinetics is represented by two parabolic rate constants, the second k_p less than the first.

Figure 6 gives the temperature dependence of the rate. The apparent activation energies corresponding to the slopes are as follows:

A	= 35.5
B	= 33.6
C	= 33.4
D	= 66.0
E	= 60.4
F	= 66.0

Discussion

Experimental observations indicate that certain broad conclusions may be drawn as to the influence of moisture in the oxidizing gas on the oxidation kinetics of these alloys. The most conspicuous effect

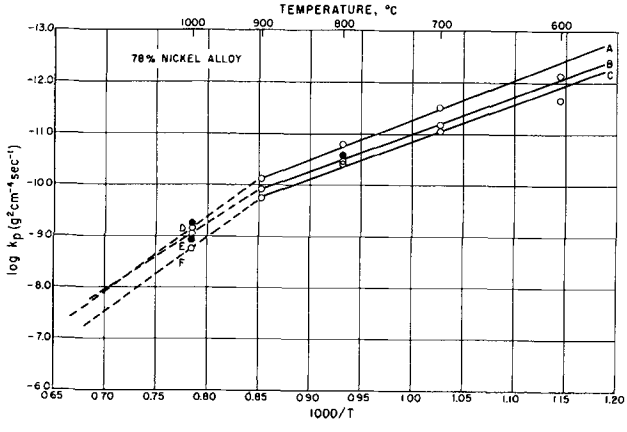

Fig. 6. Temperature dependence of oxidation rate for 78% alloy; A, D, p_{H_2O} = 0.32 mm; B, E, p_{H_2O} = 5.81 mm; C, F, p_{H_2O} = 26.3 mm.

is to increase the rate as expressed by the parabolic rate constants. This holds with few exceptions (700°C with the 30% alloy, 800° with the 41% alloy). With respect to the 30% alloy this increase is considerable, over 13-fold over the p_{H_2O} range considered. The second effect is demonstrated at the higher temperatures and higher partial pressure of H_2O. Under these conditions the oxidation reaction over the 60-min duration must be represented by two parabolic equations rather than a single one. The inference is that different processes operate during different phases of the reaction. In the case of the 30% and 41% alloys the reaction rate accelerates during the second half of the reaction, whereas with the 78% alloy the parabolic rate constant is less. For each of the three systems it is quite obvious that the conventional "Arrhenius" plot is not linear over the entire 600°-1000°C range. This nonlinearity is emphasized with the increase in p_{H_2O}. Recognizing this nonlinearity over the whole temperature range it is still possible to calculate two values of apparent activation energy for each alloy. One value would hold below 800°, and this would be a low activation energy process, 30-40 kcal. A second would hold for experiments above 800°, a high activation energy, of the order of 60 kcal. A final effect of moisture in the oxidizing gas, namely, the production of an enlarged lattice parameter in the oxide product, has already been discussed in connection with the electron diffraction examination (4) of the films formed under these experimental conditions. A major reaction product on alloys containing 30% and 41% Ni is a spinel of the $Ni_xFe_{(3-x)}O_4$ type in which the Ni and Fe content can vary with distance from the metal-oxide interface. $NiFe_2O_4$ has an a_o value of 8.33Å; and usually the a_o value for the spinel formed on this type of alloy falls in the range 8.33-8.40 depending on the Ni content (6). The spinel formed in the higher p_{H_2O} atmospheres had observed a_o values of 8.60Å and 8.58Å for the 30% and 41% alloy, respectively. The structure of the oxide film formed on the 78% alloy apparently was not influenced by H_2O vapor in the oxidizing gas within the limitations of the electron diffraction technique.

Thus the influence of moisture is revealed in both reaction kinetics and oxide film structure with the 30% and 41% alloy and in reaction kinetics with the 78% alloy.

With few exceptions, these occurring at 600° and 700°C, the oxidation rates observed previously in laboratory air (3) can be explained on the basis that the oxidizing atmosphere contained moisture equivalent to a few millimeter partial pressure which varied from day to day. The few exceptions to this semiquantitative explanation are rates that were lower in laboratory air than in the controlled atmosphere. These deviations at the lower temperatures fall almost within experimental error and, as discussed below, the influence of moisture should be more pronounced at the higher temperatures. The present results also explain the need to use two parabolic plots to represent data for the 30% alloy and the 78% alloy in laboratory air at 1000°, accounting for the higher later phase kinetics of the 30% and the lower later phase kinetics of the 78% alloy.

In attempting to explain the observed results the first consideration should be one of the thermodynamics involved. From free energy calculations on Fe-Ni alloys of these compositions it would be concluded that Fe would react with H_2O vapor at these temperatures while Ni would not. Experimentally this appears valid as discussed by Kubaschewski and von Goldbeck (7) who found the Fe-Ni system to be almost ideal. Thus at the start it would be expected that the reactions that take place by moisture additions to the oxidizing atmosphere would involve mainly Fe and the oxides of Fe rather than Ni and NiO. This was confirmed by the only structural changes observed. The 78% alloy contained 3.8% Mo which would be expected to react with H_2O and lead to a higher rate.

Considering the reaction product formed on the 30% and 41% Ni alloy, the interpretation of the enlarged lattice parameter constitutes a critical point as the rate-determining step for oxidation of these alloys is most likely the diffusion of cations through a spinel of variable nickel content. The possibility of this parameter being due to the incorporation of Mn in the lattice was discussed (4), and it was pointed out that Mn in the amount present in our alloys had been observed to have a profound effect on the oxidation rate of heater alloys by Gulbransen *et al.* (8, 9) and actually detected by Yearian and co-workers on chrome steels (10). However, the possibility also exists that the lattice parameter is a measure of the physical condition of the film. Spinels with lattice parameters in the 8.5-8.7Å range were observed by Hickman and Gulbransen (11) in their early oxidation studies, for example, a spinel of a_o = 8.66Å was observed on an 18-8 stainless steel after oxidation at 700°C. These investigators considered this high value as being associated with a stressed condition which in time could lead to cracking. Pande also observed oxide lattice parameters during electron diffraction studies that were 0.60% higher than x-ray measurements and discusses these in terms of the particle size of crystals (12). That water vapor can have a profound effect on nucleation, lateral growth, and morphology of oxide films was clearly demonstrated by Gulbransen and Copan (13) in experiments carried out with pure Fe at 450°C for 48 hr. Fine oxide whiskers grew in a dry O_2 atmosphere (dewpoint −79°C) as contrasted with blades grown in a 10% H_2O-90% argon atmosphere. Their experiments led to the conclusion that H_2O facilitates nucleation, promotes surface diffusion, and expands reaction sites. This would imply that the general effect of moisture in the absence of specific reactions (*e.g.*, hydroxide formation) would be to increase reaction rate, and this would explain the over-all general effect. Thus, while there may exist compositional variation in oxide films formed in atmospheres of varying dewpoint which have gone undetected it seems more logical that the kinetic changes observed reflect changes in the physical condition of the films.

The morphology of the oxide films which would normally be grown on the 30% and 41% alloys would be governed to a large extent by solid-state reactions that would occur as the component oxides attempt to achieve equilibrium structures as established by Brabers and Birchenall (14). These solid-state reactions would be enhanced by the presence of moisture. Reported observations on the kinetics of such reactions and the influence of moisture on the kinetics leads one to conclude that such solid-state reactions must be given consideration in establishing the mechanism of oxidation of binary or ternary alloys that contain more than one oxidizable metal. The reaction between NiO and Fe_2O_3 to form nickel ferrite commences at about 650°C and is rapid above 800°C (15, 16). For example, at 900°C the reaction is over 70% completed in 30 min as shown by Turnbull (16) in his review and interpretation of the kinetics of this reaction. Fe_2O_3 is observed on the surface layers of oxides formed on the 30% and 41% alloys in low dewpoint atmospheres but not in the higher dewpoint runs, suggesting that under the latter conditions cation diffusion occurred to establish a spinel with lower nickel content (less protective). Water vapor has the effect of promoting such solid-state reactions. Wickert and Wiehr (17) observed that water vapor lowered the temperature at which solid-state reactions would occur between CuO and Fe_3O_4 and increased the rate of reaction as compared to that in neutral atmosphere. Bénard (18) concludes from sintering experiments with oxides that in certain situations water vapor increases rate of reaction by promoting surface diffusion of ions. Certainly the possibility of these solid-state reactions occurring exists, and certainly such reactions would alter the morphology of the oxide films, but with the available experimental evidence one can only speculate as to whether these changes would account for the increased rate observed in the three systems.

The nonlinearity of the Arrhenius plot may be explained on the basis of different rate-determining mechanisms holding in the two temperature ranges. It seems reasonable that any change in the rate-determining mechanism would be gradual rather than abrupt, so any discussion of "low temperature activation energy" and "high temperature activation energy" is quite arbitrary. The activation energy value derived for the 30% and 41% alloys in the 600°-800° range is interpreted as representing diffusion through a spinel structure varying in composition from $NiFe_2O_4$ (near the metal-oxide interface) to Fe_3O_4.

This diffusion process is considered to involve an activation energy of about 41.5 kcal, and lower values are interpreted in terms of this diffusion process being enhanced by surface migration as suggested by Bénard. Considering the way in which these activation energies are established, more precise interpretation would be questionable. In the 800°-1000° range the rate is accelerated, but the slope of the Arrhenius plots would indicate a high activation energy, characteristic of some other process. The higher activation energy was common with all three alloys and would support the hypothesis which explained the moisture influence in terms of the physical condition of the film.

There is evidence that would lead one to expect that, if one dealt with an oxidation involving a single diffusion process, and further, if the oxide film remained compact and continuous during the oxidation run, then a linear Arrhenius plot would indeed be observed. Obviously such conditions were not achieved in these experiments, but were by Paidassi (19) who obtained linear temperature dependence plots for the oxidation of iron over the range of 700°-1250°C. His micrographs show a uniform, compact, and continuous oxide film, and his kinetics indicate diffusion through an FeO layer. On the other hand if there was no change in reaction mechanism, but there was change in the physical condition of the film, a nonlinear Arrhenius plot would result. Thus the temperature dependence plots of Gulbransen and Andrew (20) on the oxidation of Ni over the 750°-1050°C range yielded a heat of activation of 41,200 cal below 900°C and 68,300 cal above, with the explanation probably lying in cracking and change in the physical condition of the film. Studies on film structure similar to those conducted by Brabers and Birchenall (14) would be very illuminating here.

Several investigators have employed models which utilize the defect structure of the oxide as altered by the moisture in the oxidizing atmosphere (21). Presumably the decomposition of water vapor at these elevated temperatures would supply hydrogen or oxygen to alter the concentration of defects. It would not appear that such models would apply in view of our experimental conditions. The percentage decomposition of H_2O is low and would alter in a negligible way the total oxidizing potential of the atmosphere.

Manuscript received Sept. 5, 1961.

Any discussion of this paper will appear in a Discussion Section to be published in the December 1962 JOURNAL.

REFERENCES

1. R. T. Foley, J. U. Druck, and R. E. Fryxell, *This Journal*, **102**, 440 (1955).
2. R. T. Foley, C. J. Guare, and H. R. Schmidt, *ibid.*, **104**, 413 (1957).
3. R. T. Foley and C. J. Guare, *ibid.*, **106**, 936 (1959).
4. R. T. Foley, *ibid.*, **108**, 216 (1961).
5. Lange's "Handbook of Chemistry," Handbook Publishers, Sandusky, Ohio (1956).
6. H. J. Yearian, H. E. Boren, Jr., and R. E. Warr, *Corrosion*, **12**, 561t (1956).
7. O. Kubaschewski and O. von Goldbeck, *Trans. Faraday Soc.*, **45**, 948 (1949).
8. E. A. Gulbransen and W. R. McMillan, *Ind. Eng. Chem.*, **45**, 1734 (1953).
9. E. A. Gulbransen and K. F. Andrew, *This Journal*, **106**, 941 (1959).
10. H. J. Yearian, E. C. Randall, and T. A. Longo, *Corrosion*, **12**, 515t (1956).
11. J. W. Hickman and E. A. Gulbransen, *Trans. AIME*, **171**, 344 (1947).
12. A. Pande, *J. Sci. Industr. Res.*, **17B**, 205 (1958).
13. E. A. Gulbransen and T. P. Copan, *Nature*, **186**, 959 (1960).
14. M. J. Brabers and S. E. Birchenall, *Corrosion*, **14**, 179t (1958).

15. H. Kedesdy and A. Tauber, *Trans. AIME (J. Metals)*, **209**, 1140 (1957).
16. R. C. Turnbull, *J. Appl. Phys.*, **32**, 380S, (1961).
17. K. Wickert and H. Wiehr, *Werkstoffe u. Korrosion*, **7**, 13 (1956).
18. J. Benard, Private communication.
19. J. Paidassi, *Acta Met.*, **6**, 184 (1958).
20. E. A. Gulbransen and K. F. Andrew, *This Journal*, **104**, 451 (1957).
21. D. Caplan and M. Cohen, *J. Metals*, **4**, 1057 (1952).

Oxidation of Refractory Metals as a Function of Pressure, Temperature, and Time: Tungsten in Oxygen

J. N. Ong, Jr.

Research Laboratories, Aeronutronic, A Division of Ford Motor Company, Newport Beach, California

ABSTRACT

By regarding the kinetics of oxidation of tungsten as occurring by the consecutive reactions: $W + O_2 \rightarrow WO_2$; $WO_2 + \frac{1}{2}O_2 \rightarrow WO_{3(s)}$; $WO_{3(s)} \rightarrow 1/n(WO_3)_{n(vap)}$ and by expressing the rate in terms of conventional chemical kinetic quantities, it is shown that the results of three investigations may be correlated in the temperature range 500°-1300°C and pressure range 0.0013-20.8 atm of oxygen. A good approximate form for the rate of attack of metallic tungsten above 700°C is shown to have the form: Rate $= d(m/A)/dt = 5.89 \times 10^6 \exp(-12{,}170/T)\ P^{1/2}$ mg_W/cm^2 hr, where T is expressed in °K and P in atmospheres of oxygen.

Although there has been much work done on the kinetics of oxidation of tungsten as summarized recently (1), the basic understanding of the mechanism of oxidation has not as yet yielded to analysis. This is due in part to the complexity of the chemistry and in part to the fact that an entirely adequate theory for oxidation of metal oxygen systems has not heretofore been available. It has been fairly well established (2) that tungsten in the presence of oxygen reacts first to form a suboxide, which for present purposes may be assumed to be WO_2, according to: $W + O_2 \rightarrow WO_2$, followed by subsequent reaction to form WO_3: $WO_2 + \frac{1}{2}O_2 \rightarrow WO_{3(s)}$. The WO_3 then sublimes according to: $WO_3 \rightarrow 1/n\ (WO_3)_{n(vap)}$. There are minor changes in the stoichiometry of these oxides with temperature and pressure, but these may be considered incidental to the kinetic problem.

It is the purpose of the present paper to demonstrate the utility of a method of treatment of reacting metal-oxygen systems recently developed (3). The method will (*a*) correlate the results of the three principal experimental investigations (2, 4-6), (*b*) introduce the effect of pressure on the rate of oxidation, and (*c*) present the results in a form having practical utility.

Development of Rate Equations

It has been shown (3) that all metal-oxygen reactions are first order complex chain reactions whose rate is described by an equation of the form:

$$\text{Rate} = \frac{d\,m_{O_b}/A}{dt} = k_r C_i = k_r f(P) \qquad [1]$$

where m_{O_b}/A (g/cm²) is the weight change per unit area of a specimen caused by reaction with b atoms of oxygen, k_r is the reaction rate constant, C_i is the concentration of intermediate species controlling the rate of reaction, and $f(P)$ is a complex function of pressure relating pressure to the intermediate species concentration.

When the reaction rate is controlled at a phase boundary Eq. [1] can be written:

$$\text{Rate} = k_s C_{is} \qquad [2]$$

where C_{is} is the concentration of intermediate species at the phase boundary (g/cm²) and k_s is the specific reaction rate constant (sec^{-1}). This has been interpreted (7) as

$$k_s = \frac{kT}{h} \exp(\Delta S^{+}/R) \exp(-\Delta H^{+}/RT) \qquad [3]$$

where k is Boltzmann's constant (ergs/°K), T is absolute temperature (°K), h is Planck's constant (erg-sec), ΔS^{+} the entropy of activation (cal/g mole °K) and ΔH^{+} the enthalpy of activation (cal/g mole).

When the reaction is controlled by diffusion through an oxide phase, the rate equation may be written

$$\frac{d\,m_{O_b}/A}{dt} = \left\{\frac{D\Delta C \rho_{ox} M_{O_b/Me_aO_b}}{2}\right\}^{1/2} \frac{1}{t^{1/2}} \qquad [4]$$

where $\Delta C = C_{i\ o-g} - C_{i\ o-m}$, which is the concentration difference of diffusing species at the oxide-oxygen and oxide-metal interfaces, respectively, (g/cm³), ρ_{ox} is the density of the oxide film (g/cm³), D is the diffusion coefficient (cm²/sec), and M_{O_b/Me_aO_b} is

$$\frac{\text{weight of oxygen consumed } (b/2\ O_2)}{\text{weight of oxide formed } (Me_aO_b)}. \quad (g/g)$$

The diffusion coefficient may be written in its temperature dependent form:

$$D = D_o \exp\left(\frac{-\Delta H^{+}_d}{RT}\right) \qquad [5]$$

where D_o is the diffusion constant and $\Delta H^{\ddagger}_d$ is the enthalpy of activation of a diffusion process.

D_o may be further interpreted by the reaction rate theory of Eyring as (8)

$$D_o = \alpha d^2 q \frac{kT}{h} \cdot \exp\left(\Delta S^{\ddagger}_d / R\right) \qquad [6]$$

where α is a geometrical factor related to the arrangement of sites into which a diffusing species may jump, d is the lattice parameter, q is the number of equivalent diffusion paths and $\Delta S^{\ddagger}_d$ is the entropy of activation of the diffusion step.

For purposes of further analysis the following assumptions are made: (*A*) For every chemical product formed an equation may be written for its rate of formation. (*B*) The rate of formation of the inner oxide (WO_2) is diffusion controlled and Eq. [4] applies. (*C*) The rate of formation of the outer oxide (WO_3) is phase boundary controlled and is given by Eq. [2]. (*D*) The rate of volatilization of (WO_3) is also phase boundary controlled. (*E*) The rate of consumption of tungsten metal is unaffected by the volatility rate of WO_3. (*F*) The functions relating concentration to pressure are of the form of the Langmuir isotherm involving dissociation of oxygen molecules to atoms

$$C_{is} = C^{\circ}_{is}\left\{\frac{\exp(\Delta S_{is}/R)\exp(-\Delta H_{is}/RT)\,P^{1/2}}{1+\exp(\Delta S_{is}/R)\exp(-\Delta H_{is}/RT)\,P^{1/2}}\right\} \qquad [7]$$

where ΔS_{is} and ΔH_{is} are the entropy and enthalpy of adsorption of intermediate species at the phase boundary, and C°_{is} is a conversion factor relating mole fraction of adsorbed species to concentration of adsorbed species (g/cm²) and

$$\Delta C = \Delta C^{\circ}_d\left\{\frac{\exp(\Delta S_d/R)\exp(-\Delta H_d/RT)\,P^{1/2}}{1+\exp(\Delta S_d/R)\exp(-\Delta H_d/RT)\,P^{1/2}}\right\} \qquad [8]$$

where ΔS_d, ΔH_d, and ΔC°_d(g/cm³) are the corresponding quantities of Eq. [7] pertaining to the appropriate intermediate species in the diffusion process. Tentative evidence for this type of pressure dependency may be inferred from the low pressure work of Speiser and St. Pierre (9).

A great source of confusion, resulting in considerable misinterpretation of kinetic data, has arisen from failure to pay careful attention to the meaning of defined rate equations.

The defining equation is in terms of oxygen consumption, Eq. [1]. However, of greater importance in metal oxygen reactions is the rate of metal consumption, given by

$$-\frac{d(m_{Me}/A)}{dt} = \frac{1}{M_{O_b/Me_a}}\frac{d(m_{O_b}/A)}{dt} \text{ (g/cm}^2\text{ sec)} \qquad [9]$$

where M_{O_b/Me_a} is

$$\frac{\text{weight of oxygen consumed } (b/2\ O_2)}{\text{weight of metal reacted } (aMe)} \text{ (g/g)}$$

or

$$\frac{-dX_{Me}}{dt} = \frac{1}{M_{O_b/Me_a}\rho_{Me}}\frac{d(m_{O_b}/A)}{dt} \text{ (cm/sec)} \qquad [10]$$

where X_{Me} and ρ_{Me} are, respectively, the thickness and density of the metal.

Where volatile species are formed during reaction, it is necessary that care be taken that thickness or weight change measurements are properly related to oxygen or metal consumption.

The derivations which follow will be on the basis of oxygen consumption and will be modified to other convenient forms as necessary.

The reaction of tungsten with oxygen has been identified as a consecutive reaction and analyzed by Loriers (10) and Webb, Norton, and Wagner (6).

Using the present formulation, it is found that the rate due to the formation of the first oxide (WO_2) is given by:

$$\frac{d(m_{O_2}/A)}{dt} = \left\{\frac{D_b\,\Delta C_b\,\rho_b\,M_{O_2/WO_2}}{2}\right\}^{1/2}\frac{1}{t^{1/2}} - \frac{1}{M_{O_3/O_2}}k_{s_c}C_{is_c} \qquad [11]$$

where m_{O_2} is weight change due to formation of WO_2 and subscripts b and c pertain to the quantities governing the formation rate of the oxides WO_2 and WO_3, respectively.

$\frac{d(m_{O_2}/A)}{dt}$ becomes zero at

$$t_m = \frac{D_b\,\Delta C_b\,\rho_b\,(M_{O_2/WO_2})\,(M_{O_3/O_2})^2}{2k^2_{s_c}C^2_{is_c}} \qquad [12]$$

The total amount of WO_2 formed can be found by $\int_o^{t_m}\frac{d(m_{O_2}/A)}{dt}$ which has the value:

$$(\Delta m_{O_2}/A)_{max} = \frac{D_b\,\Delta C_b\,\rho_b}{2k_{s_c}C_{is_c}}\cdot M_{O_2/WO_2}M_{O_3/O_2} \qquad [13]$$

The rate of formation of the second oxide, WO_3, is given by

$$\frac{d(m_{O_3}/A)}{dt} = k_{s_c}C_{is_c} \qquad [14]$$

where m_{O_3} is weight gain due to the formation of WO_3.

In graphical form Eq. [11] and [14] appear as represented in Fig. 1. The two processes combined are designated as "sum" in the figure and the arrow designates the value of t_m and $(\Delta m_{O_2}/A)_{max}$.

When the volatility rate becomes appreciable, an appropriate term must be subtracted from the sum of Eq. [11] and [14]. This rate may be represented by

$$\frac{-d(m_{WO_3}/A)}{dt} = k_{s_v}C_{is_v} \qquad [15]$$

where m_{WO_3} is the weight change due to WO_3 volatilization. The subscript v pertains to the quantities governing the weight loss due to the volatilization of WO_3. As illustrated in Fig. 2, the sum of the three terms takes different forms depending on the magnitude of the volatility rate.

A third type of weight change curve is encountered under the conditions where the molar evaporation rate of WO_3 exceeds the molar consumption rate of metal. Under these conditions an experimental weight change measurement represents the sum of oxygen pickup due to the formation of WO_2 and the

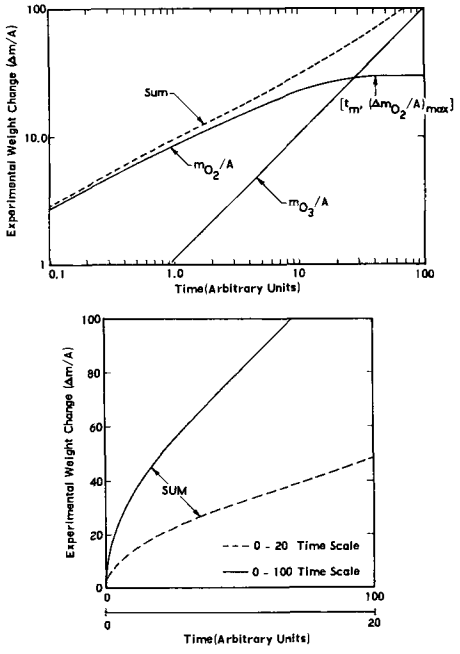

Fig. 1. Experimental weight change due to WO_2 and WO_3 formation, Eq. [11] and [14].

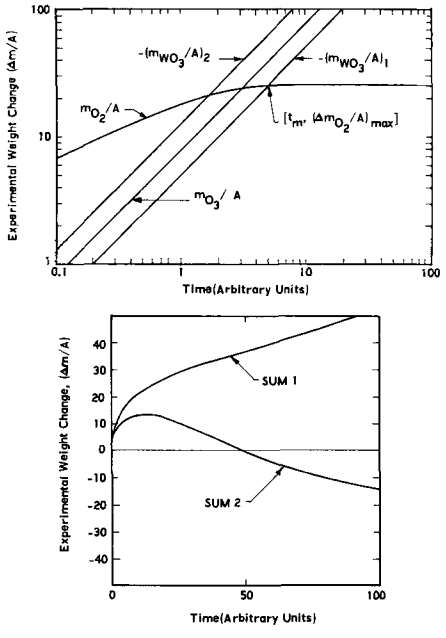

Fig. 2. Experimental weight change due to WO_2 and WO_3 formation and WO_3 volatilization, Eq. [11], [14], and [15].

metal loss due to volatilization of W in the form of $1/n(WO_3)_n$ as shown in Fig. 3. All three types of curves were obtained by Gulbransen in his extensive study (4, 5).

Analysis of Data

Equations [12] and [13] may be solved simultaneously to give the following equations:

$$k_{s_c} C_{t_{s_c}} = \frac{(\Delta m_{O_2}/A)_{max}}{t_m} \cdot M_{O_3/O_2} \qquad [16]$$

$$(D_b \Delta C_b \rho_b M_{O_2/WO_2}) = \frac{(\Delta m_{O_2}/A)^2_{max}}{t_m} \cdot \frac{2}{M_{O_3/O_2}} \qquad [17]$$

An overlay of experimental points was made and compared with a master plot of Eq. [11] and [14].

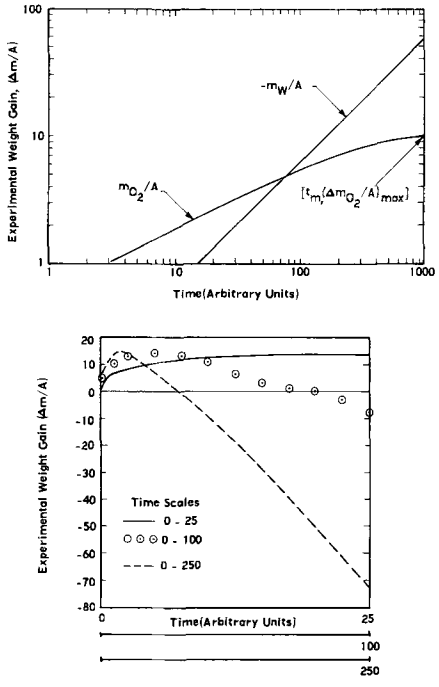

Fig. 3. Experimental weight change due to WO_2 formation and W metal loss, Eq. [11] and [20].

From this, values of t_m and $(\Delta m_{O_2}/A)_{max}$ could be obtained. From Eq. [16] and [17], values of $k_s C_{t_s}$ and $D_b \Delta C_b \rho_b M_{O_2/WO_2}$ could be directly calculated. The logarithm of these values were then plotted *vs.* $1/T$ to determine activation energies and *vs.* log P to determine pressure sensitivities. The results are presented in Fig. 4 through 7. From these plots it was determined that Eq. [7] and [8] represented reasonable pressure functions for both the diffusion controlled and phase boundary controlled reactions. Overheating is obtained at higher rates which accounts for the deviations of experimental points from the theoretical curves.

The simplest form of the equations governing the oxidation rate of tungsten is also the most directly practical, namely, by expressing it in terms of metal consumption.

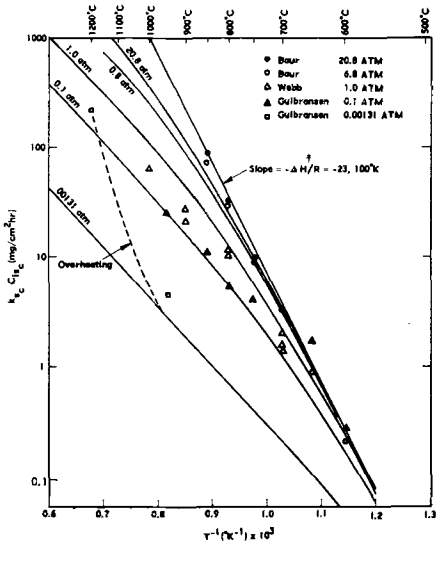

Fig. 4. Arrhenius plot of $k_{s_c} C_{t_{s_c}}$ isobars. Deviations from slope of $-\Delta H^{\ddagger}/R$ indicate pressure sensitivity.

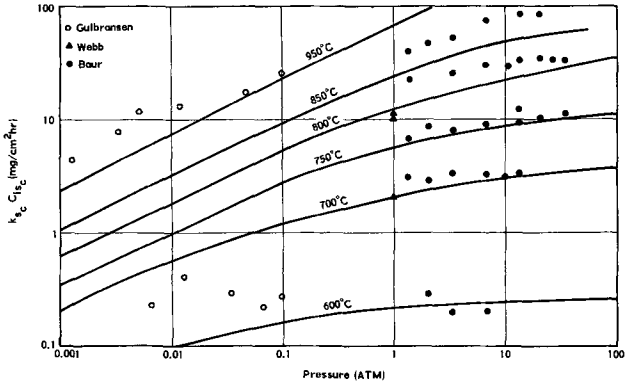

Fig. 5. Plot of $k_{s_c} C_{i_{s_c}}$ isotherms vs. pressure showing pressure dependency at high temperatures and low pressures.

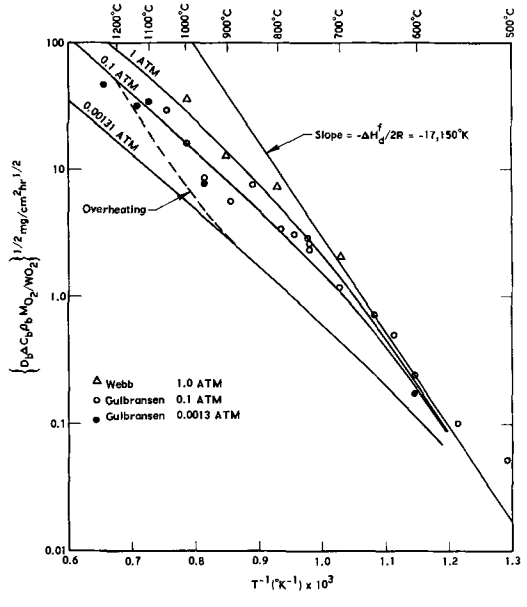

Fig. 6. Arrhenius plot of $\{D_b\ \Delta C_b\ \rho_b M_{O_2/WO_2}\}^{1/2}$ isobars. Deviations from slope of $-\Delta H^{\ddagger}/2R$ indicate pressure sensitivity.

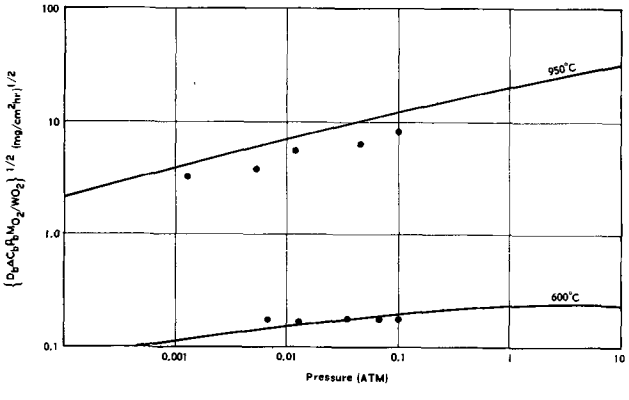

Fig. 7. Plot of $\{D_b\ \Delta C_b\ \rho_b M_{O_2/WO_2}\}^{1/2}$ isotherms vs. pressure for data of Gulbransen showing pressure dependency at high temperatures and low pressures.

The rate of metal loss due to the formation of WO_2 is, from Eq. [11] and [9]

$$\frac{-d(m_w/A)}{dt} = \frac{1}{M_{O_2/W}} \frac{d(m_{O_2}/A)}{dt}$$

$$= \frac{1}{M_{O_2/W}} \left[\left\{ \frac{D_b\ \Delta C_b\ \rho_b\ M_{O_2/WO_2}}{2} \right\}^{1/2} \frac{1}{t^{1/2}} - \frac{1}{M_{O_3/O_2}} k_{s_c} C_{i_{s_c}} \right] (\text{mg/cm}^2\,\text{hr}) \quad [18]$$

or

$$\frac{-dX_W}{dt} = \frac{1}{\rho_W M_{O_2/W}} \left[\left\{ \frac{D_b\ \Delta C_b\ \rho_b\ M_{O_2/WO_2}}{2} \right\}^{1/2} \frac{1}{t^{1/2}} - \frac{1}{M_{O_3/O_2}} \cdot k_{s_c} C_{i_{s_c}} \right] (\text{cm/hr}) \quad [19]$$

where ρ_W is the density of tungsten (g/cm³).

Each equation is to be integrated over the limits 0 to t_m determined by Eq. [12], as before.

The metal consumption rate due to the formation rate of WO_3 is given by

$$\frac{-d(m_W/A)}{dt} = \frac{1}{M_{O_3/W}} \frac{d(m_{O_3}/A)}{dt}$$

$$= \frac{1}{M_{O_3/W}} k_{s_c} C_{i_{s_c}} (\text{mg/cm}^2\,\text{hr}) \quad [20]$$

or

$$\frac{-d\,X_W}{dt} = \frac{1}{\rho_W M_{O_3/W}} k_{s_c} C_{i_{s_c}} (\text{cm/hr}) \quad [21]$$

Since the metal loss due to the formation of WO_3 reaches a limiting value, Eq. [20] and [21] may be used as a satisfactory approximation to describe the oxidation rate.

The values obtained by the above analysis for the appropriate quantities are presented in Table I. When these values are substituted into the appropriate equations, the experimental curves of three investigations (2, 5, 6) are adequately reproduced in the temperature range 500°-1300°C and pressure range 0.0013-20.8 atm.

For purposes of practical application, the rate of consumption of tungsten above 700°C may be expressed by the equations

$$\frac{-d(m_W/A)}{dt} = 5.89 \times 10^6 \exp(-12{,}170/T)\ P^{1/2}\ (\text{mg/cm}^2\,\text{hr}) \quad [22]$$

and

$$\frac{-d\,X_W}{dt} = 3.05 \times 10^2 \exp(-12{,}170/\text{T})\ \text{P}^{1/2}\ (\text{cm/hr}) \quad [23]$$

where T is to be expressed in °K and P in atmospheres of oxygen.

Discussion

Two recent investigations have reported a decrease in rate with temperature above 2000°C (11, 12). Referring to Eq. [12] and [13] and noting that the quantity $D_b\ \Delta C_b\ \rho_b\ M_{O_2/WO_2}$ increases more rapidly than $k_{s_c} C_{i_s}$ with increasing temperature, it is seen that both t_m and $(\Delta m_{O_2}/A)_{max}$, or $(\Delta X_{O_2})_{max}$ where X_{O_2} is the thickness increase due to WO_2 formation, will increase at higher temperatures and also at lower pressures. The resulting weight or thickness change measurements will then take the form of the curves of Fig. 3. Since the absolute weight change and zero time are not known experimentally, an arbitrary straight line through a series of points will give an

Table I. Values for rate equations

Phase boundary process	Diffusion process
$(3.6 \times 10^8) \cdot \frac{kT}{h} \cdot \exp(\Delta S^{\ddagger}/R) C^{\circ}_{ts_c}$	$(3.6 \times 10^9) D_b \rho_b M_{O_2/WO_2} \Delta C_b^{\circ}$
$= 7 \times 10^{10}$ (mg/cm^2 hr)	$= 7.15 \times 10^{15}$ (mg^2/cm^4 hr)
$\Delta H^{\ddagger} = 45.9$ (kcal/mole)	$\Delta H_d^{\ddagger} = 68$ (kcal/mole)
$\exp(\Delta S_{ts}/R) = 2.2 \times 10^{-5}$	$\exp(\Delta S_d/R) = 1.133 \times 10^{-6}$
$\Delta H_{ts} = -21.7$ (kcal/mole)	$\Delta H_d = -27.6$ (kcal/mole)

apparent rate which will always be lower than the rate of metal loss, and in general decrease with increasing temperature.

Manuscript received Oct. 20, 1961. This paper was prepared for delivery before the Detroit Meeting, Oct. 1-5, 1961.

Any discussion of this paper will appear in a Discussion Section to be published in the December 1962 JOURNAL.

REFERENCES

1. V. D. Barth and G. W. P. Pengstorff "Oxidation of Tungsten," DMIC Report 155, Battelle Memorial Institute, Columbus, Ohio, July 19, 1961.
2. J. P. Baur, D. W. Bridges, and W. M. Fassell, Jr., *This Journal*, **103**, 266 (1956).
3. J. N. Ong, Jr. and W. M. Fassell, Jr., Aeronutronic Publication No. U-1566, August (1961).
4. E. A. Gulbransen, K. F. Andrew, P. E. Blackburn, T. P. Copan, and H. Merlin, "Oxidation of Tungsten and Tungsten Based Alloys," WADC TR 59-575, February, 1960.
5. E. A. Gulbransen and K. F. Andrew, *This Journal*, **107**, 610 (1960).
6. W. W. Webb, J. T. Norton, and C. Wagner, *ibid.*, **103**, 107 (1956).
7. S. Glasstone, K. J. Laidler, and H. Eyring, "The Theory of Rate Processes," McGraw-Hill Co., New York (1941).
8. C. E. Birchenall, *Metallurgical Revs.*, **3**, [11] 247 (1958).
9. R. Speiser and G. R. St. Pierre, "Research on the Oxidation Behavior of Tungsten," Ohio State U. Research Foundation, Columbus, Ohio, Report 831-9, October, 1960, WADD Contract AF33(616)-5721.
10. J. Loriers, *Acad. Sci. Paris.*, **231**, 522 (1950).
11. J. A. Becker, E. J. Becker, and R. G. Brandes, *J. Appl. Phys.*, **32**, 411 (1961).
12. R. A. Perkins and D. D. Crooks, *J. Metals*, **13**, 490 (1961).

The Effect of Organic Compounds on the Codeposition of Hydrogen with Nickel

Thomas C. Franklin and Jack R. Goodwyn[1]

Chemistry Department, Baylor University, Waco, Texas

ABSTRACT

A coulometric method of analyzing for hydrogen was used to study the effect of a group of organic additives on the amount of hydrogen codeposited with nickel from a Watts-type bath. This technique indicated the presence of one form of hydrogen at the electrodes, and this was indicated to be hydrogen codeposited in the nickel. There was marked correlation between the hydrogen content of the nickel deposits and the current efficiency for the deposition of hydrogen. It was also observed that, in general, the brightest deposits occurred at the minimum in the hydrogen content curves.

Thon (1) studied the codeposition of hydrogen and nickel, but did not study the effect of additives. Yeager and co-workers (2) have also carried out this type of study. Brenner and co-workers (3) studied the effect of additives on this process, but found no definite relationship; however, the technique used in their study analyzed for both free and combined hydrogen in the deposit. The purpose of the work reported in this paper was to reinvestigate the effect of additives on the amount of hydrogen codeposited with nickel using a technique which analyzed only for the free hydrogen to see if there was a systematic variation.

[1] Present address: Texas Eastman Company, Longview, Texas.

At the same time, a study was made of the effect of the organic compounds on the current efficiency for nickel deposition.

Experimental Materials and Methods

Nickel wire electrodes were prepared by sealing 14 gauge nickel wire in glass tubing with 1.2-1.5 cm lengths exposed. The wire electrodes were mechanically polished and plated at a known current density for a definite time, usually 6.96 ma/cm^2 for 12 min. They were plated in a Watts-type plating bath consisting of $NiSO_4 \cdot 6H_2O$, 240 g/l; $NiCl_2 \cdot 6H_2O$, 45 g/l; and H_3BO_3, 30 g/l. After dissolving the components, nickel carbonate was added to raise the pH.

The solution was filtered and the pH lowered to 4.0 by adding dilute hydrochloric or sulfuric acid. Measured amounts of a solution of the organic additive in the Watts bath were added to the plating bath with a graduated pipette.

Hydrogen content studies.—After plating, the electrode was rinsed with distilled water, and the hydrogen was analyzed coulometrically by the procedure used by Franklin and Cooke (4). The electrode was oxidized polarographically in a cell filled with hydrogen-saturated 2*N* sodium hydroxide. The reference cell was mercury, mercuric oxide, 2*N* sodium hydroxide. A Sargent Model XXI polarograph was used to record the current-voltage curves. The area under the curves was used as a measure of the amount of hydrogen in the deposit. Most of the data recorded are differences between results obtained with and results obtained without additives present in the plating bath. Each of the hydrogen analyses was made at least in triplicate, and each complete curve reported was run at least twice. The ethanenitrile study (Fig. 3) was repeated by three different workers on a number of electrodes over a period of two years. Even though the total amount of hydrogen codeposited varied from one experiment to another, the differences using the same basic pretreatment method were the same within ±5%. All connections were standard taper or ball and socket ground glass joints.

The appearance of the deposit was also noted as the additive concentration was varied.

Current efficiency studies.—The apparatus used to determine current efficiencies is shown in Fig. 1. The coil cathode of 14 gauge nickel wire was attached to the iron shaft of the mercury sealed rotating electrode designed after that of Kolthoff and Lingane (5). The length of wire extending into the solution was 28 cm. The iron shaft of the stirrer was coated with ceresin wax. The stirring motor was rotated at 600 rpm, and the anode was made of nickel wire.

In a typical run, 35 ml of the plating solution were placed in the cathode compartment, and enough plating solution was placed in the anode compartment to equalize the liquid levels. The entire apparatus was immersed in a water bath maintained at 25° ± 0.1°C. After making preliminary runs until the amount of hydrogen evolved in a run became constant, measured amounts of a solution of the organic additive in the plating solution were added to the cathode compartment. After each addition, the electrode was plated for 12 min at a current density of 6.96 ma/cm^2. The amount of hydrogen evolved was indicated by the displacement of a drop of butyl phthalate along the capillary tube, the current was measured with a previously calibrated ammeter, and the time was measured with a timer. The current efficiency for nickel deposition or for hydrogen ion discharge was obtained from the number of coulombs passed and the volume of hydrogen evolved. All curves are the average of at least two runs. The same pretreatment technique was used in all experiments. The volumes of hydrogen were reproducible within ±3%.

In all experiments the inorganic chemicals were reagent grade, the water was triply distilled, and the organic chemicals were the purest grades available commercially. (In all cases except one this was either Spectrograde or Eastman White Label. The disodium 2,7-naphthalene disulfonate was technical grade. At a later date this chemical was purified somewhat, but the purification did not alter the general shape of the curve.)

Data and Results

Effect of organic compounds on the hydrogen content of electrodeposited nickel.—Along with this study of Watts nickel an investigation was made of the polarographic oxidation of palladium, black nickel, and iron electrodes. With all of these metals three peaks were observed that could be interpreted as being due to the oxidation of three forms of hydrogen. In the cases of palladium and platinum black all three forms could be observed by bubbling hydrogen over the electrode. However, it was necessary to generate hydrogen electrolytically or codeposit hydrogen with the metal in order to observe all three forms with black nickel and iron. These peaks were not observed unless hydrogen was generated, indicating that they were caused by the oxidation of hydrogen at the electrode. Hydrogen

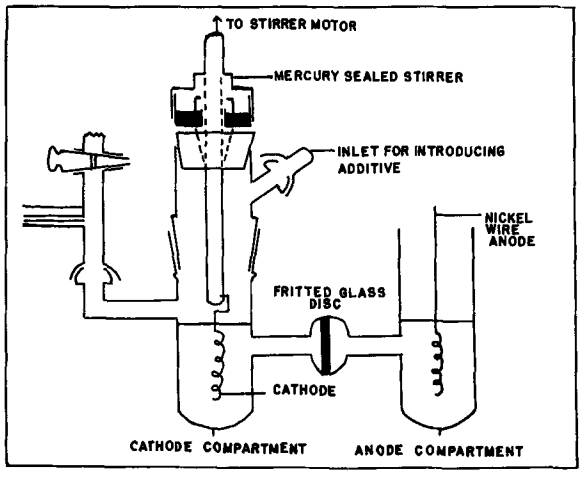

Fig. 1. Apparatus for measuring the hydrogen evolved during the plating process.

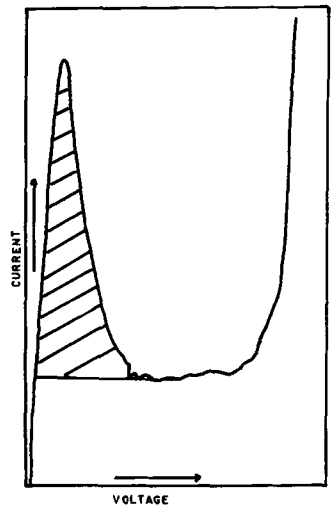

Fig. 2. Current-voltage curve for the oxidation of the hydrogen codeposited with Watts nickel.

was placed on the electrodes in one bath and then the polarograms were run in a hydrogen-free sodium hydroxide solution. This would make it unlikely that solution hydrogen was being oxidized.

Figure 2 shows a typical current voltage curve for the oxidation of the hydrogen present at a nickel electrode which has been plated in a Watts bath.[2] The peak is the middle peak observed in the oxidation of hydrogen on black nickel. Since hydrogen was not appreciably absorbed from solution into nickel it was not possible to make a study similar to that made of platinum (4). However, the hydrogen oxidized to cause this peak was concluded to be hydrogen in the interior of the nickel deposit. This was shown by dipping the freshly plated electrode in 1*N* potassium permanganate in 1*N* sulfuric acid. There was no change in the area under the oxidation curve. With black nickel the two other peaks decreased markedly. In addition when the electrode was plated, mechanically polished, then replated before oxidizing, the area under the curve was higher than the area obtained when the electrode was plated only one time. Both of these experiments indicate that the hydrogen being oxidized is in the interior of the nickel and not on the surface.

Figures 3 and 4 show the variation of the hydrogen content for ethanenitrile, propanenitrile, butanenitrile, and pentanenitrile. The visual appearance of the deposits is also indicated in these figures. Curves similar in shape were obtained for hexanenitrile, 3 hydroxypropanenitrile, butanedinitrile, m-aminophenol, 1 ethylquinolium iodide, and disodium 2,7 naphthalenedisulfonate. As will be noted in the curves there was considerable variation in the initial point. This was probably caused by differences in pretreatment of the electrode. Using the same pretreatment, one obtains results that agree within ±5%. For all of these compounds there was the same marked correlation between the hydrogen content and the appearance of the deposits that is seen in Fig. 3 and 4. The best deposits were always obtained at the minimum in the curve. However, in the cases of m-aminophenol and butanedinitrile the minimum hydrogen content did not correspond to the minimum in the curve as seen, for example, in Fig. 5. Of the compounds investigated only thiourea (Fig. 6) did not give a curve similar to those above. But, even here it can be seen that there

[2] The areas recorded in the figures correspond to the shaded area in Fig. 2. This is not the total hydrogen content since the residual current lies lower than the level portion of the curve. However, it was found that the residual was constant for each electrode; therefore, the total amount of hydrogen would be different, but the shape of the curve would be the same.

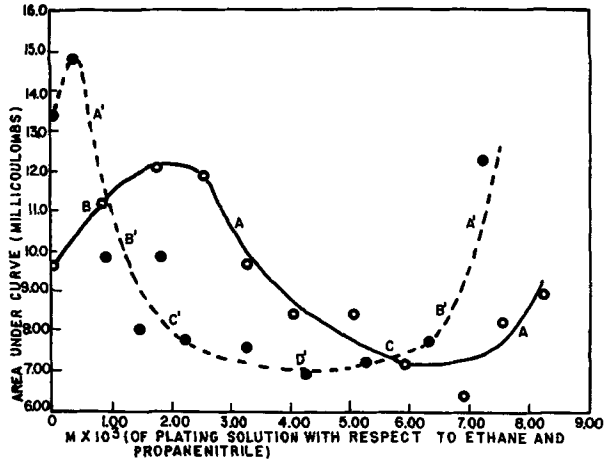

Fig. 3. Amount of codeposited hydrogen as a function of nitrile concentration. —○—○ Ethanenitrile; —●—● propanenitrile; A,A, dark streaked; B,B, dull; C,C, semi-bright.

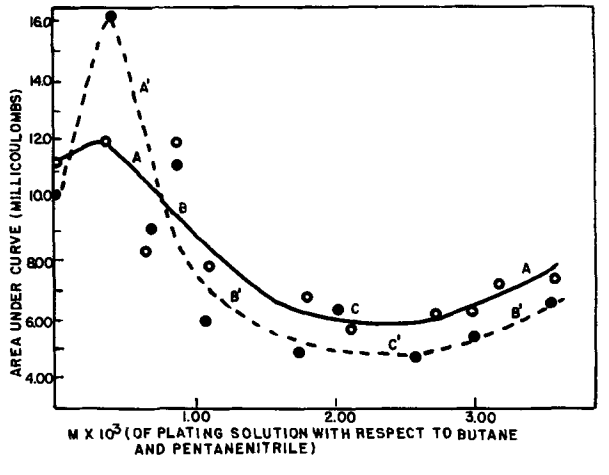

Fig. 4. Amount of codeposited hydrogen as a function of nitrile concentration. ○—○— Pentanenitrile; ●—● butanenitrile; A,A', dark streaked; B,B', dull; C,C', semi-bright; D,D', bright.

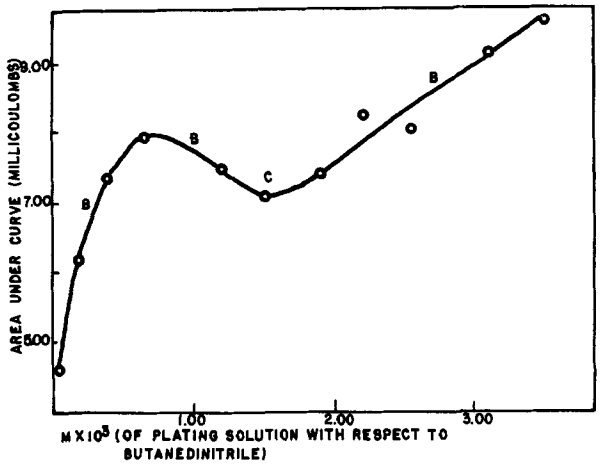

Fig. 5. Amount of codeposited hydrogen as a function of butanedinitrile concentration; B, dull; C, semi-bright.

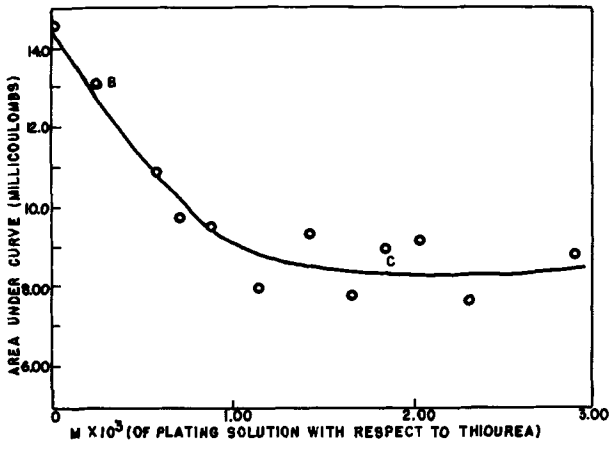

Fig. 6. Amount of codeposited hydrogen as a function of thiourea concentration; B, dull; C, semi-bright.

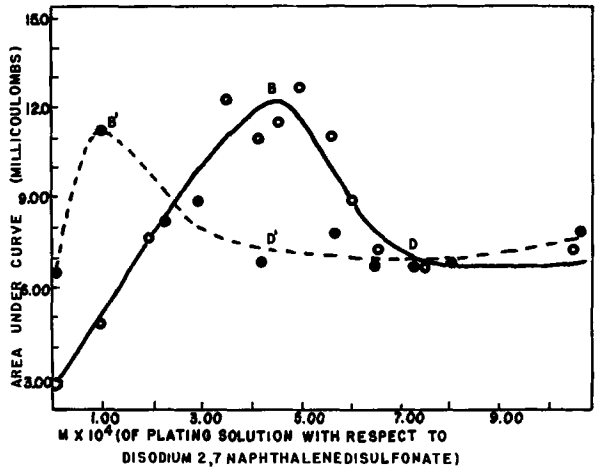

Fig. 7. Effect of stirring on the hydrogen content curves obtained with disodium 2,7-naphthalenedisulfonate; (a) stationary electrode, ——○——○——; (b) rotating electrode, — • — — — • —; B,B', dull; D,D', bright.

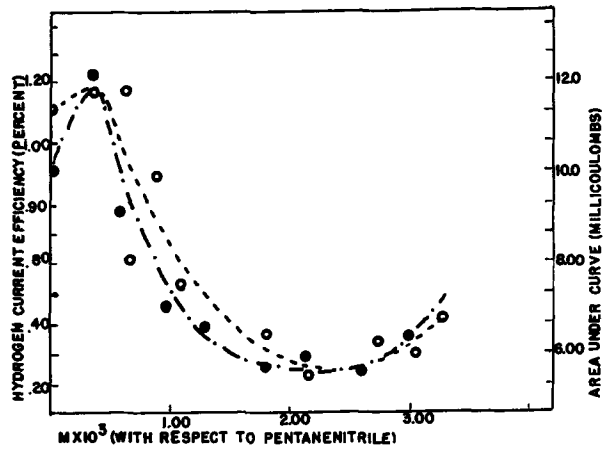

Fig. 9. Comparison of results for pentanenitrile; (a) hydrogen content, ——○——○——; (b) current efficiency, • — · — • — · — •.

is the same correlation between the appearance of the plate and the hydrogen content.

Effect of pressure on hydrogen content.—In a further investigation of the correlation between the appearance of the deposit and the amount of co-deposited hydrogen, a study was made of the effect of pressure on the codeposition of hydrogen and nickel. It was noted that there was a decrease in hydrogen content with a decrease in pressure and that the plates became smoother and more even, but not bright. In addition, it required only a concentration of 3.2 x 10^{-3}M propanenitrile to obtain the brightest deposits at 70 mm pressure compared to 4.5 x 10^{-3}M propanenitrile at atmospheric pressure.

Effect of stirring on hydrogen content curves.—Since some of the experiments were run in stirred solutions and some in nonstirred solutions, a study was made of the effect of stirring on the hydrogen content of the deposits. In the case of the nitriles, stirring had no effect on the hydrogen content curves. Figure 7 shows the effect of stirring on the hydrogen content curves for disodium 2,7 naphthalenedisulfonate. As can be seen, stirring causes a shift in the curve, but does not change the general shape of the curve.

Effect of organic compounds on the current efficiency of hydrogen deposition.—The observed variation of the hydrogen content could be due to variations in the current efficiency of the deposition process or it could be due to variations in the amount of hydrogen adsorbed at the surface of the electrode. In order to distinguish between these two possibilities the current efficiency in the Watts bath for the deposition of hydrogen was measured as a function of the concentration of the organic additive.

Figures 8, 9, and 10 show a definite correlation between the current efficiency for the deposition of hydrogen and of hydrogen content curves for propanenitrile, pentanenitrile, and disodium 2,7 naphthalene disulfonate, indicating that the cause of the variation in hydrogen content is a change in the current efficiency for the deposition process.

In summary, it has been shown that there is a marked correlation between the amount of hydrogen codeposited with nickel from a Watts bath containing various organic additives, the current efficiency for hydrogen deposition, and the appear-

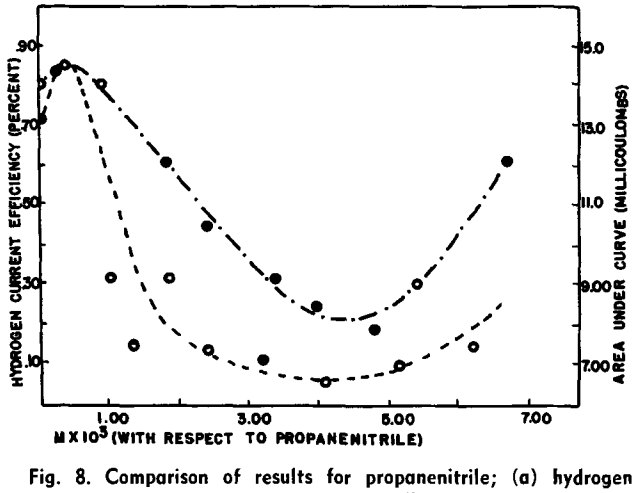

Fig. 8. Comparison of results for propanenitrile; (a) hydrogen content, ——○——○——; (b) current efficiency, • — · — • — · — •.

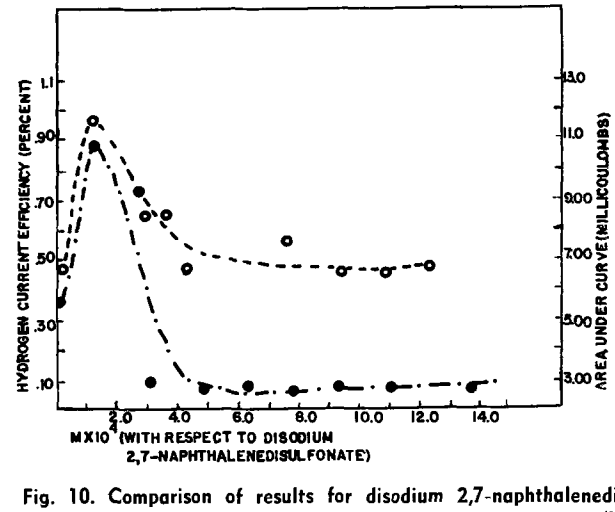

Fig. 10. Comparison of results for disodium 2,7-naphthalenedisulfonate; (a) hydrogen content, ——○——○——; (b) current efficiency, • — · — • — · — •.

ance of the deposit. All of these quantities vary in the same manner as a function of the concentration of the additive.

Acknowledgment

This work was sponsored by the Office of Ordnance Research, U. S. Army.

Manuscript received Jan. 13, 1961; revised manuscript received Dec. 4, 1961. This paper was prepared for delivery before the Houston Meeting, Oct. 9-13, 1960.

Any discussion of this paper will appear in a Discussion Section to be published in the December 1962 JOURNAL.

REFERENCES

1. N. Thon, D. G. Kelemen, and L. Yang, *Plating*, **38**, 1055 (1951).
2. J. Yeager, J. P. Cels, Ernest Yeager, and F. Hovorka, *This Journal*, **106**, 328 (1959).
3. V. Zentner, A. Brenner, and C. W. Jennings, *Plating*, **39**, 865 (1952).
4. T. C. Franklin and S. L. Cooke, Jr., *This Journal*, **107**, 556 (1960).
5. I. M. Kolthoff and T. J. Lingane, "Polarography," p. 440, Interscience Publishers, Inc., New York (1946).
6. C. C. Roth and H. Leidheiser, *This Journal*, **100**, 553 (1953).

Simultaneous Cataphoretic and Electrolytic Deposition of Nickel for Cathode Bases of Reliable Electron Tubes

Peter F. Váradi and Kitty Ettre

The Machlett Laboratories, Incorporated, Springdale, Connecticut

ABSTRACT

The combination of electrolysis and cataphoretic deposition of metal particles was used in the development of a porous nickel matrix layer for electron tube extended interface cathodes. The codeposition phenomenon was studied and the influence of the various parameters (time, temperature, concentration) on the deposited layer structure was shown. The technique may be used for preparing porous layers from metal mixtures and alloys.

The extended interface (matrix) cathode used in high voltage or high power electron tubes was described by Fisk *et al.* (1) and by Field (2). This cathode consists of a nickel base metal, which is coated by a porous nickel layer. This nickel layer is sintered to the base and thereafter the voids are filled with the standard emissive $(BaSrCa)CO_3$ coating material. The main advantages of the use of a porous nickel matrix layer as the base for oxide coated cathodes are: good heat and electrical conductivity, increase in the adherence of the emissive coating to the base metal, decrease in the interface resistance, and finally minimization of the detrimental effect of the high voltage sparking.

On considering the working mechanism of such a nickel matrix cathode, it is evident that the porous nickel matrix must have the following properties: (*A*) Adherence: A very good adherence to the base metal after sintering, to avoid peeling off of the matrix. (*B*) Pore size: The size of the voids must be several times larger than those of the carbonate grains. This means that the pores should be filled easily by the emissive materials. It is recommended, assuming a carbonate size of 2-5μ, to have a pore size of 25-50μ. (*C*) Reproducibility: Height, density, surface properties of the porous layer, and the dimensions and shape of the voids must be reproducible from sample to sample and lot to lot in mass production.

The most important part of this type of electron emitter is the uniformly porous nickel matrix layer. This layer can be prepared as described, utilizing painting (3, 4), spraying (4, 5), or press technique (3). The disadvantages of these methods are: it is difficult to get uniformly porous and reproducible structures, and the layer obtained might readily peel.

In order to develop a method to produce reproducible and reliable porous nickel matrix layers suitable for electron tube cathode purposes, we made experiments with a new process: simultaneous electrolytic and cataphoretic deposition. The two types of deposition can be performed from the same solution simultaneously, resulting in a porous nickel matrix deposit. In the following method, the influence of the various parameters on the layer structure and the mechanism of deposition are described.

Experimental Method

The experimental arrangement is shown in Fig. 1. The glass beaker (B) contained the plating solution with the added nickel metal powder. The

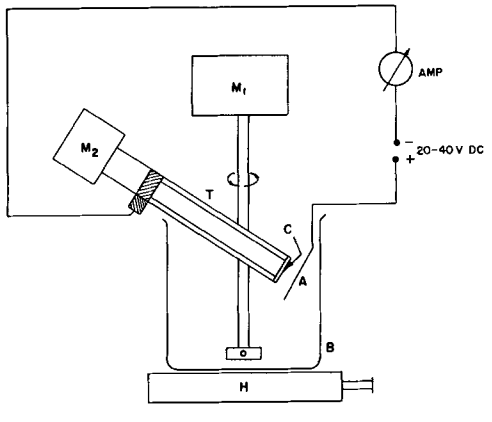

Fig. 1. Schematic drawing of the experimental setup

plating solution was a "hard nickel plating bath" containing 5% $NiSO_4$ and 2.3% $(NH_4)_2SO_4$ in deionized water. Carbonyl nickel powder of 325 mesh was mixed into the solution, and the mixture was agitated thoroughly by a Teflon stirrer (M_1). The sample to be coated (C) was mounted on a holder and was rotated by a slow (10 rpm) motor (M_2), and except for the round flat (0.5 cm^2) target surface, it was protected by a Teflon shield (T). The sample was attached to the negative side of a d-c power supply, while the positive side was attached to a flat nickel anode (A) spaced approximately 8-15 mm from the sample. The temperature of the slurry was maintained by a hot-plate (H) and was controlled in the solution.

The nickel samples to be coated were cleaned carefully before using. The samples were degreased in ether and rinsed in acetone and boiling water. Finally they were rinsed again in acetone and dried in air. After mounting the samples on the holder, the sample was immersed in the slurry, and a voltage of 25v d.c. was switched on. After the time required for obtaining the proper coating thickness had passed, the voltage was switched off, and the sample was removed from the solution and from its holder. It was rinsed in distilled water, then in acetone, and after drying it was examined.

Appearance and Characteristics Data of a Nickel Matrix

The general appearance of a nickel matrix cathode suitable for electron tube application is shown in a schematic drawing, Fig. 2. The drawing shows a cross section of the porous layer. The characteristic data of such a matrix can be defined by the height of the porous layer and by its roughness. The porous nickel layer was scratched with a pin across the center of the coated surface (before sintering). The height of the matrix is defined as the depth of this scratched groove from the bottom (base metal) to the top of the nickel peaks (see Fig. 2A). The roughness of the coating denotes the distance between the peaks and valleys of the matrix (see Fig. 2B). The height and roughness measurements were made with a Zeiss light section microscope. Another characteristic datum of the porous layer is the weight of the deposited nickel. The apparent density of the layer can be calculated from the above data and also the ratio of height/roughness. The ratio of height/roughness is most characteristic on the structure of the matrix layer, and it is affected by the different parameters as described below.

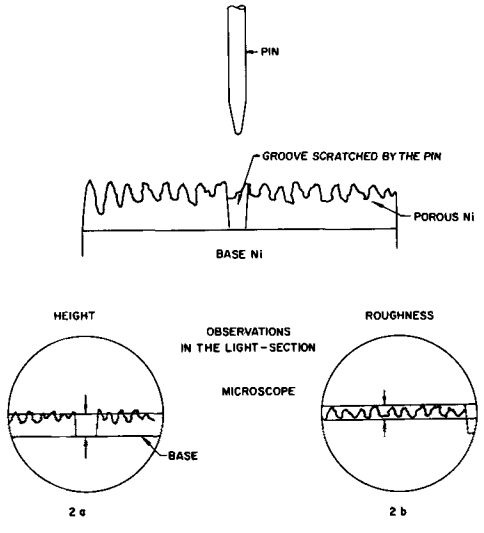

Fig. 2. Schematic drawing of the cross section of a deposited layer

Influence of Several Parameters on the Matrix Surface Structure

The characteristic data of a porous matrix, height, roughness, height/roughness ratio, depend on the following parameters: nickel powder concentration, temperature of the plating solution, coating time. Experiments were made on the influence of these parameters on the structure of a porous matrix layer. The voltage was kept constant at 25v.

Effect of the nickel powder concentration.—The effect of the nickel powder concentration of the solution on the porous layer structure is shown in Fig. 3. The data were taken at 70°C bath temperature and with 12 sec coating time. Two conclusions can be drawn from the experiment: (*a*) Height and roughness values increase with increasing amount of nickel powder and finally they reach a saturation; and (*b*) the ratio of height/roughness decreases considerably with increasing nickel powder concentration. The roughness increases much faster at higher nickel concentration than the height, which

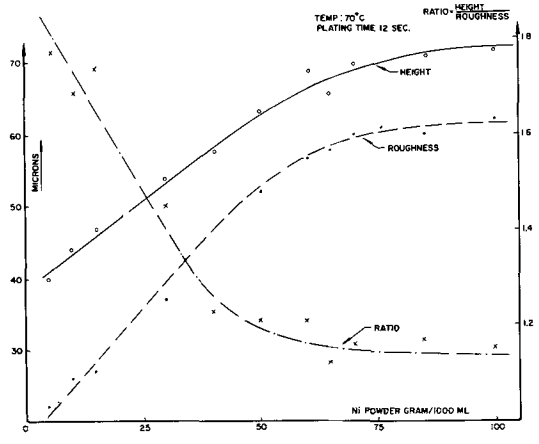

Fig. 3. Effect of the nickel powder concentration on the layer structure.

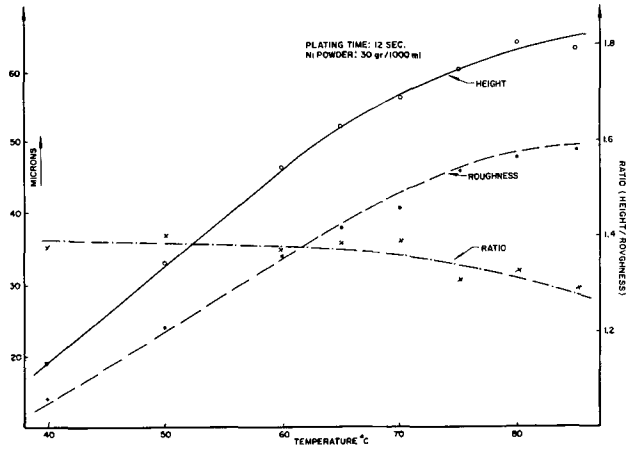

Fig. 4. Effect of the temperature on the layer structure

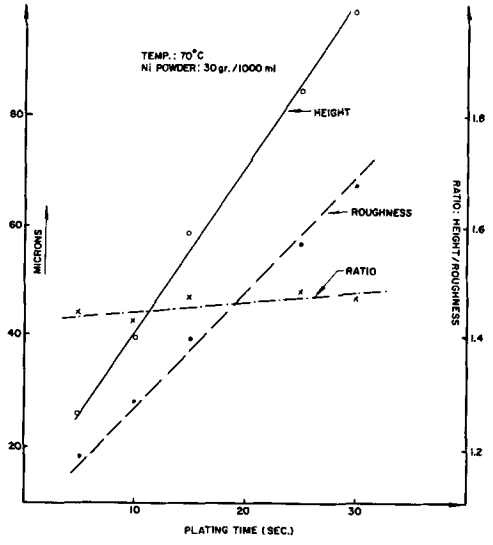

Fig. 5. Effect of the plating time on the layer structure (30 g/1000 ml nickel powder concentration in the solution).

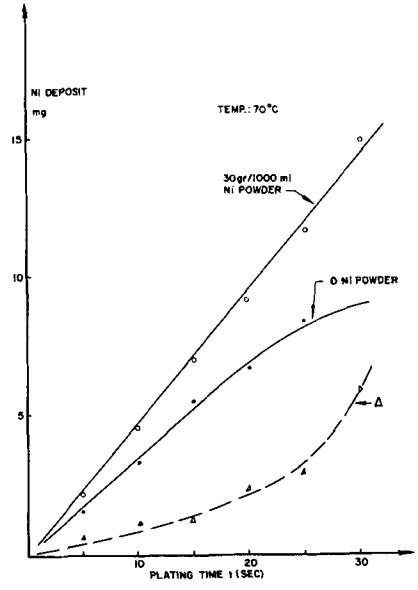

Fig. 6. Effect of the plating time on the deposited nickel quantity

means that the structure of the porous matrix layer changed considerably at higher nickel powder concentration.

Effect of bath temperature.—Figure 4 shows the effect of temperature on the structure of a matrix applying 30 g/1000 ml nickel powder concentration and 12 sec coating time. As can be seen (*A*) the height and roughness values increase with increasing temperature and tend to reach saturation above 75°C; (*B*) the ratio of height/roughness is not much affected by the temperature and it decreases only very slightly wtih increasing temperature.

Effect of coating time.—Figure 5 shows the effect of the coating time on the characteristic data of the matrix at 30 g/1000 ml nickel concentration and 70°C bath temperature. The results show that: (*a*) the height and roughness data increase with increasing coating time; (*b*) the ratio of height/roughness remains practically constant, *e.g.*, the structure of the layer does not change by increasing the coating time.

Simultaneous Electrolytic and Cataphoretic Deposition

The preceding experiments show that the structure of the porous layer is affected considerably only by the change in the nickel powder concentration in the plating solution. It is evident that a combined deposition process takes place: an electrolytic deposition process of nickel on the cathode from the plating solution, and simultaneously a cataphoretic deposition of the nickel particles from the slurry. The nickel quantity deposited purely by electrolysis, having no nickel particles in the solution, was measured, as was also the deposition from the combined process, having 30 g/1000 ml nickel powder concentration in the slurry. We made experiments varying the coating time but keeping the temperature constant at 75°C (Fig. 6). The addition of the nickel powder to the solution causes a considerable increase in the deposited amount indicating that the cataphoretic process also takes place. The deviation from the pure electroplating caused by the addition of nickel powder is indicated also in the figure denoted as Δ.

The current density during our measurements was approximately 4 amp/cm^2; it remained the same when nickel powder was added. There was a slight but definite trend of current increase over the plating period if nickel powder was present, which is normal for cataphoretic depositions. The current, however, remained constant during the plating experiments having no nickel powder in the solution.

From the above experiments we can conclude that by adding nickel powder to a regular nickel plating solution a combined electrolysis-cataphoresis process takes place. The cataphoretically deposited nickel powder is incorporated in the electrolytically deposited layer forming a very rough and highly porous nickel layer which is suitable for the extended interface (matrix) cathode purposes. This procedure can be used for deposition of a rough layer of any metal mixtures.

Deposition of Metal Mixtures

In certain types of electron tubes the emitter contains known amounts of additives in the nickel. This is necessary also for certain types of matrix cathodes. The technique described above is also useful in producing porous nickel matrixes with known amount of additives as magnesium, titanium, tungsten, aluminum, etc.

Metal powder mixtures.—We made experiments on depositing a mixture of nickel and titanium powder. The coating procedure described above was followed, except that a mixture of nickel and titanium (0.5%) powder was used. The resulting layer had the same structure as one without the titanium additive.

Chemical analyses were made on the original nickel and titanium metal powder mixture; the deposited coating was also analyzed. The original metal powder mixture contained 0.5% titanium, and the deposited porous coating contained only 0.26% titanium. These results were reproducible and indicate that metal particles different from nickel also can be deposited this way cataphoret-

ically. The chemical determination of titanium besides excess amount of nickel was performed by a modification of the colorimetric method described in Snell's book (6).

Nickel alloys.—Nickel alloy powder containing 3.6% tungsten was prepared. This powder was used in our experiments. The original powder and also the deposited layer were chemically analyzed. There was 3.5% tungsten in the original, while the tungsten content of the deposited layer was found to be 2.5%. The analysis of the tungsten content of the nickel was performed colorimetrically as described in Snell's book (6).

Sintering

The appearance of the resulting matrix layer, after deposition, is black, and it becomes metallically bright after sintering. The sintering was made in wet hydrogen at 1000°C for 10 min. The adherence of the sintered layer is excellent. Its removal from the base nickel after sintering is not possible.

Reproducibility

The reproducibility of the method (height, roughness values of the matrix layer) depends on how well the different parameters are kept constant during the preparation. With the simple equipment shown in Fig. 1 the values may be kept within ±4% deviation from the mean. By introducing a more advanced setup, this reproducibility can be improved greatly.

Experiments in Electron Tubes

Spraying.—The voids of the porous matrix body are filled with the standard emissive spray material by a "wet" spraying. The void structure of the co-deposited layer is such that no special solution or technique is required to fill the pores with the emissive material.

Electron tubes.—These were prepared utilizing this co-precipitated nickel matrix base cathode procedure. The pumping and processing of tubes with this type of cathode is similar to the standard sprayed oxide coated cathodes. Life and high voltage stability tests of electron tubes in which this type of matrix cathode was incorporated (under the trade name "Phormat cathodes") indicated high reliability and several thousand hour life. These experiments were made (7) in ML-7698 and ML-7815 tubes, tested in a grid-modulated amplifier circuit with a plate voltage of 3000v d.c. In the ML-7815 tube type in a hard tube modulator circuit, the Phormat cathode tubes withstood a field strength of 135 kv/cm. At this field strength standard sprayed cathodes were almost completely destroyed, while the Phormat type cathodes showed only a few arc marks.

Manuscript received Oct. 4, 1961; revised manuscript received December 15, 1961.

Any discussion of this paper will appear in a Discussion Section to be published in the December 1962 JOURNAL.

REFERENCES

1. J. B. Fisk, H. D. Hagstrum, and P. L. Hartman, *Bell System Tech. J.*, **25**, 167 (1946).
2. L. M. Field, U. S. Pat. 2,594,897 (April 29, 1952).
3. G. B. Collins, "Microwave Magnetrons," McGraw-Hill Co., New York (1948).
4. E. A. Thurber, U. S. Pat. 2,594,470 (Oct. 28, 1958).
5. L. Andersen, Rept. 20th Annual Conference Physical Electronics, M.I.T., pp. 24-29 (1960).
6. F. D. Snell and C. T. Snell, "Colorimetric Methods of Analysis," Vol. II, D. VanNostrand Co., New York (1957).
7. W. Brunhart, *Cathode Press*, **18**, (1961), To be published.

Electron-Microscopic Observations of the Structure of Electroplated Nickel

R. Weil and H. C. Cook

Department of Metallurgy, Stevens Institute of Technology, Hoboken, New Jersey

ABSTRACT

Nickel electrodeposits, of various thicknesses, were prepared from Watts' baths containing several addition agents to study the development of the surface structure. By electron-microscopic examinations of replicas, thin films, and electrolytically thinned bulk metal the reasons for the formation of several structural features, previously observed, were found. Selected-area diffraction was found to be the best method of measuring the grain size of the electrodeposits studied. Markings believed to be sites of lattice-included foreign substances were observed.

An earlier paper (1) dealt with the use of electron microscopy in the elucidation of certain structural phenomena observed in nickel electrodeposits from Watts' baths containing a variety of addition agents. The work described below is a continuation of this study. The purposes of the present work are to investigate the causes for the formation of the various structural features, the reasons for the fiber axes observed under certain plating conditions, and the location of the foreign substances known to exist in plated nickel. In order to accomplish these objectives, the growth of different structures was observed with electron microscopy using replicas as well as thin metal films.

Experimental Procedure

To study the effect of addition agents on the growth of electrodeposited nickel as independently

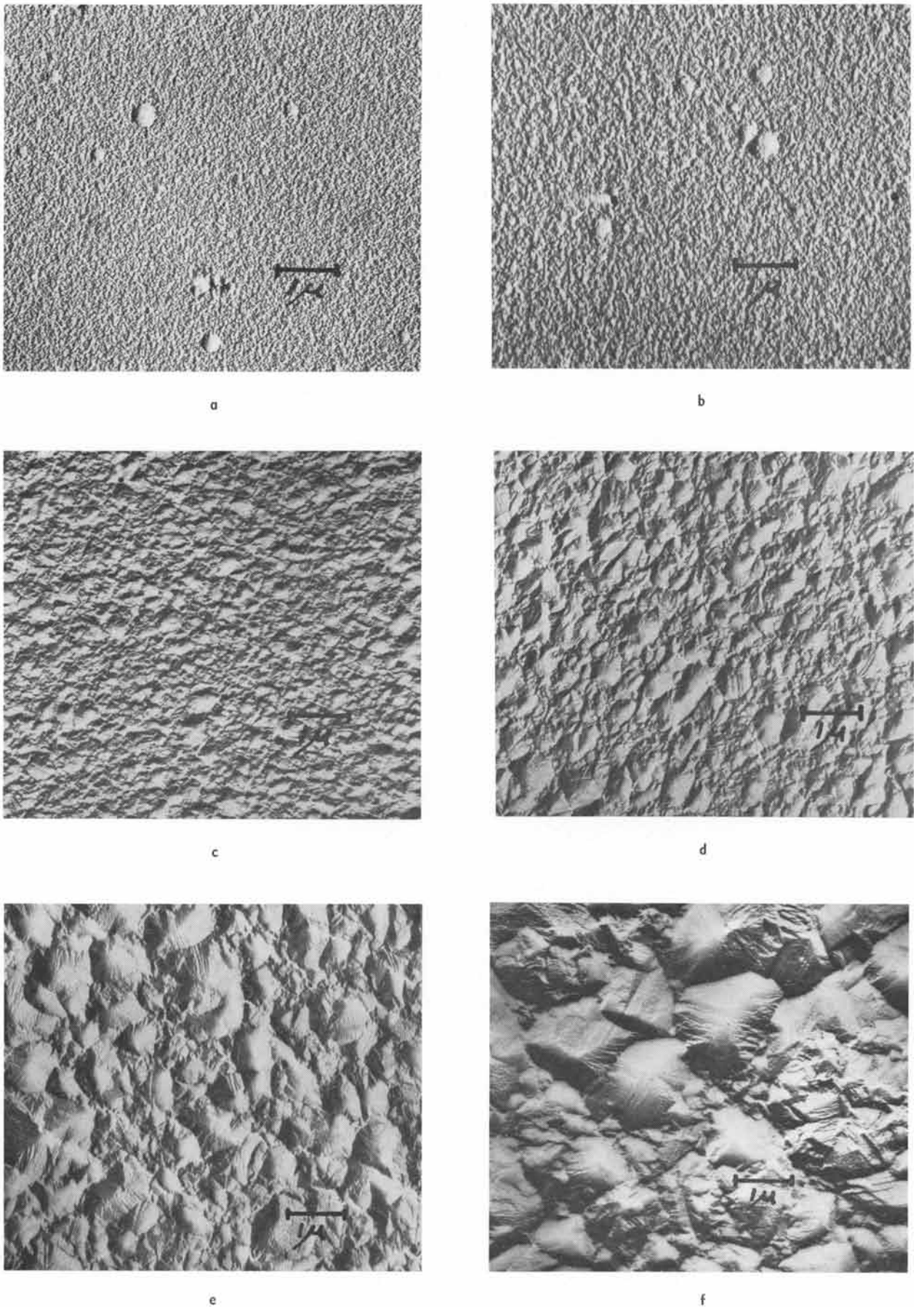

Fig. 1. Negative parlodion replicas of surface structures of nickel from plain Watts' bath plated for (a) 20 sec, (b) 40 sec, (c) 1 min 20 sec, (d) 2 min 40 sec, (e) 5 min 20 sec, (f) 10 min 40 sec.

Table I. Plating conditions and addition agents

Bath compositions: 400 g/l $NiSO_4 \times 6H_2O$, 45 g/l $NiCl_2 \times 6H_2O$, 45 g/l H_3BO_3.
Plating conditions: pH: 4.0; temperature: 50°C ± 2°C; current density: 5 amp/dm².
Addition agents in baths where nickel was plated for 5 sec to 42 min, 40 sec.

1. None
2. 0.03 g/l Coumarin
3. 0.05 g/l Coumarin
4. 0.1 g/l Coumarin
5. 0.15 g/l Coumarin
6. 0.02 g/l Thiourea
7. 0.07 g/l Thiourea
8. 0.2 g/l Thiourea
9. 0.3 g/l Thiourea
10. 0.25 g/l Aniline
11. 0.6 g/l 1-5 Naphthalene disulfonic acid + 0.2 g/l chloral hydrate

as possible of the substrate, special copper basis metal had to be prepared. This was done by vapor depositing copper on specular nickel or polished glass and then electroforming a piece of sufficient thickness to handle. After stripping, the copper surface which faced the nickel or the glass was specular and consisted of extremely fine, randomly oriented grains. Nickel was deposited on the specular copper from Watts' baths; the composition and plating conditions are listed in Table I. To study the growth, the plating time was increased in a geometric series from 5 sec to 42 min, 40 sec. The area deposited was 0.25 dm², while that of the anode was 0.4 dm². Otherwise the experimental apparatus was as previously (1) described. Thin nickel films were plated over thin copper on half the originally deposited area as in the earlier work.

The surfaces of the deposits were examined electron microscopically with negative parlodion replicas as before. When greater resolution was required, carbon replicas were made by first shadowing the specimen with palladium and then evaporating carbon. The replicas were removed by scoring the specimen to produce squares to fit the electron-microscope holder and then making the specimen anodic in an aqueous solution of 25% by volume H_2SO_4 with a stainless steel cathode. The current was slowly increased until the replica floated off. Thin films were also prepared by electropolishing. First the surface of the nickel was coated with an adherent plastic film. Then the copper basis metal was dissolved. The electropolishing method used was that described by Kelly and Nutting (2). Because of the plastic coating, the thin film came from a region near the surface.

Results and Discussion

The surface structures of the deposits from a plain Watts' bath plated for various times are shown in Fig. 1. Figure 1a shows that after 20 sec of plating a few grains grow faster than the others. There is some evidence from selected-area-diffraction studies of such grains in thin films that they have a (100) plane parallel to the surface. With increasing deposition time, these preferentially oriented grains grow over other grains and some new ones form

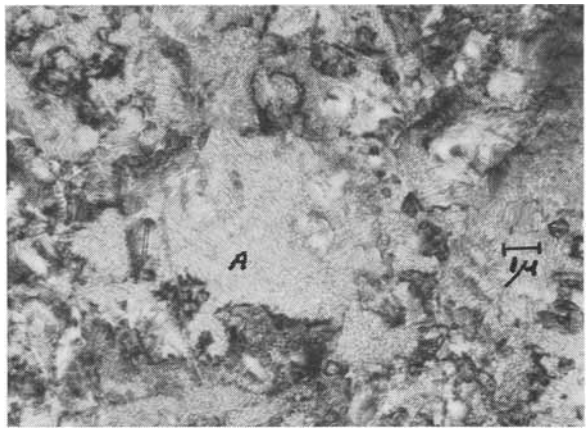

Fig. 2. Thin film of nickel deposit from plain Watts' bath

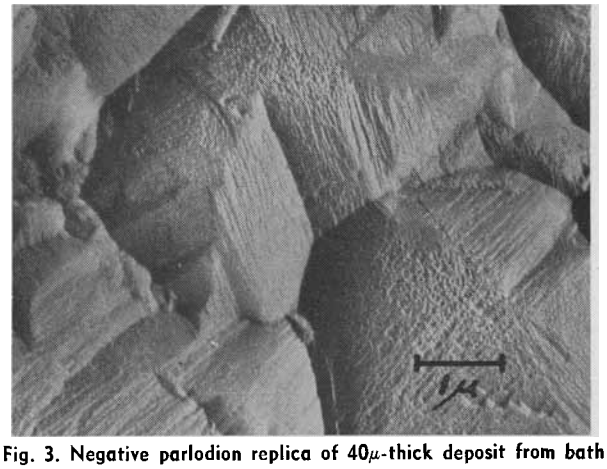

Fig. 3. Negative parlodion replica of 40μ-thick deposit from bath containing 0.03 g/l coumarin.

and start to develop until they occupy almost the entire surface. The growth layers become discernible at an early stage in the deposition and tend to become coarser probably by a bunching mechanism. The layers are not parallel, but inclined to the surface frequently resulting in a pyramid structure. In the thin nickel film, shown in Fig. 2, the growth steps and their orientations can be readily seen. An area such as that marked 'A' has a (100) direction perpendicular to the surface and a single-crystal pattern as determined by selected-area diffraction. It is thus possible to measure the grain size of the film by this method. Similar measurements using electrolytically thinned bulk material showed that the film is representative of the surface of the electrodeposit on which it was plated.

Some addition agents in Watts' baths do not change the fiber axis or decrease the grain size. An example of such a material is coumarin. Figures 3-5 show the effect of increasing coumarin concentrations in the bath on the structure of samples plated for 42 min 40 sec and which were about 40μ thick. Figure 3 represents the surface of a deposit from a solution containing 0.03 g/l coumarin. The difference between this deposit and one from a plain Watts' bath is that the height and distance between successive growth layers has decreased resulting in a flatter surface. The deposit from a bath with 0.05 g/l coumarin shown in Fig. 4 has more platelets growing parallel to each other, resulting in still larger areas which are flat. The degree of preferred

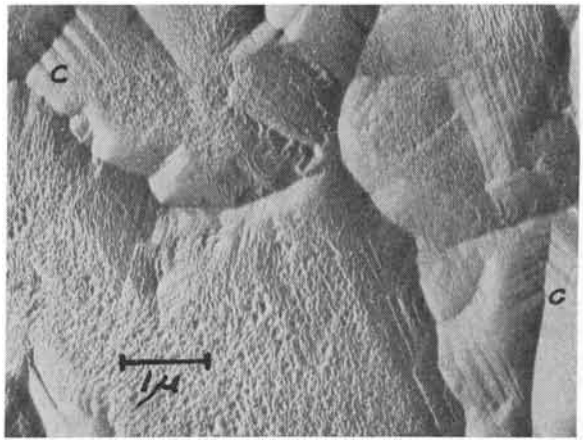

Fig. 4. Negative parlodion replica of 40μ-thick deposit from bath containing 0.05 g/l coumarin.

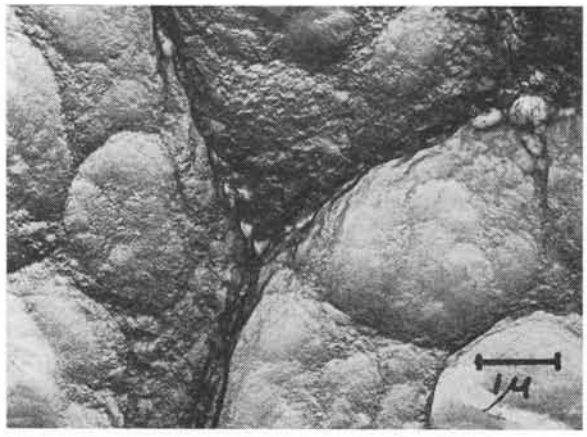

Fig. 6. Negative parlodion replica of 40μ-thick deposit from bath containing 0.02 g/l thiourea.

Fig. 5. Negative parlodion replica of 40μ-thick deposit from bath containing 0.15 g/l coumarin.

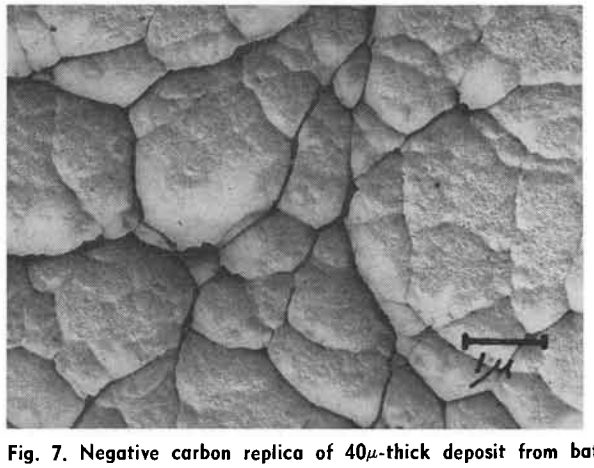

Fig. 7. Negative carbon replica of 40μ-thick deposit from bath containing 0.07 g/l thiourea.

orientation as determined by x-ray diffraction in the way previously (1) described did not change with the concentration of coumarin in the plating bath. The crevices between growth in different directions also have become shallower. It is also noticed that growth occurs simultaneously along two intersecting planes, probably of the same family in the areas marked 'C'. With a concentration of 0.15 g/l coumarin in the plating bath the deposit was quite bright. The reason for this is evident in Fig. 5 which shows very large areas of parallel-growing platelets with a few, relatively shallow crevices. It can thus be seen that one way of getting brighter nickel deposits is to cause growth to proceed along the same directions and to decrease the step height. The same features as were observed in the examination of the replicas were seen in thin films. Selected-area diffraction again showed that almost all grains large enough to give single-crystal patterns had a [100] direction perpendicular to the surface.

Almost specular deposits are obtained in a bath containing 0.6 g/l naphthalene disulfonic acid and 0.2 g/l chloral hydrate because the platelets are fine and only very few crevices or ridges form. As the development of the structure of deposits from such a bath with increasing time is followed, there is practically no coarsening of the platelet size with deposit thickness. The crevices which are present are chiefly due to stacking irregularities of the growth layers. In thin films from these samples, where such irregularities caused the stacking of the platelets to be somewhat coarser than average, the edges of the steps could be seen and were found to be along [100] directions.

An interesting feature observed in many structures is the formation of colonies, *i.e.*, a series of grains surrounded by a relatively deep crevice, which often resembles a grain boundary. Samples from baths containing thiourea and aniline exhibited this structural feature. With a concentration of 0.02 g/l thiourea very large colonies formed as seen in Fig. 6. With increasing thiourea concentrations, the colonies become smaller as do the growth steps. Figure 7 is a photograph of the surface of a deposit from a bath containing 0.07 g/l thiourea. Deposits from a bath containing 0.3 g/l thiourea have no crevices deeper than 0.4μ and are bright.

Examination of the surface structures at various stages in the growth of a deposit from a bath containing 0.07 g/l thiourea showed that they begin as very fine grains which tend to form groups with crevices between them. With increasing thickness, the crevices become deeper, but are not yet continuous as seen in Fig. 8. The actual grain size of the samples, even the one from the bath with 0.02 g/l thiourea, is quite small. This can be seen in Fig. 9 which is a transmission electron micrograph of a

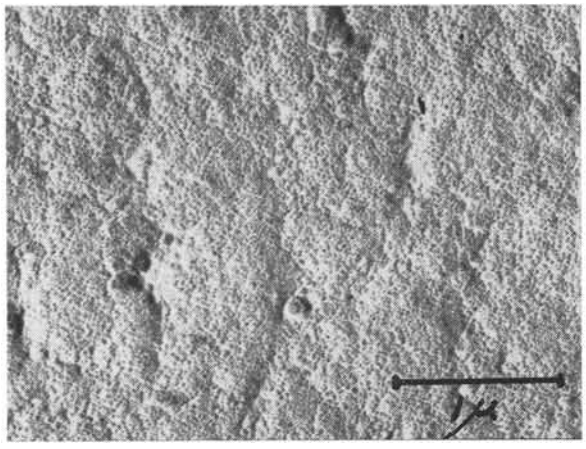

Fig. 8. Negative carbon replica of 1μ-thick deposit from bath containing 0.07 g/l thiourea.

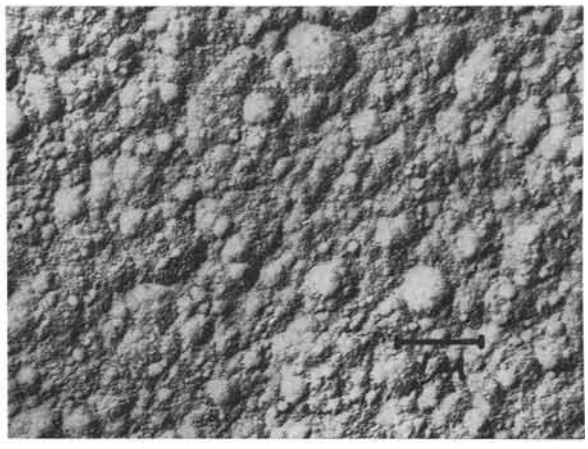

Fig. 10. Negative parlodion replica from 5μ-thick deposit from bath containing 0.25 g/l aniline.

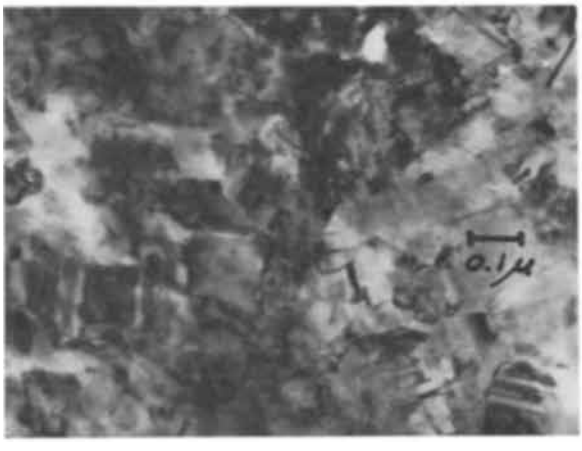

Fig. 9. Transmission micrograph of electrolytically thinned deposit from bath containing 0.02 g/l thiourea.

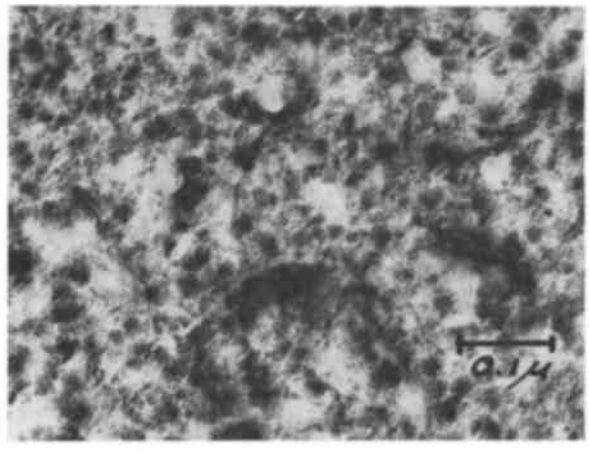

Fig. 11. Thin film of surface shown in Fig. 10

40μ-thick deposit from this bath. The sample was thinned by electropolishing.

The colony size in samples from baths containing other addition agents can be quite small as shown in Fig. 10, an electron micrograph of a replica from a deposit plated for 5 min, 20 sec in bath containing 0.25 g/l aniline. The extremely fine grain size of this sample can be seen from Fig. 11, a photograph of the corresponding thin film. Also with a selected-area-diffraction aperture of 1μ square, the pattern consisted of complete rings. This, plus the presence of all diffraction rings in what appeared to be normal intensities also indicates random orientation, a fact which the very irregularly oriented growth layers corroborates.

The location of codeposited material in electrolytically thinned films of copper deposits has recently been observed by Steinemann and Hintemann (3). Similar structural features were observed in nickel films. In Fig. 12 which represents a thin film from a 2μ-thick deposit from a bath containing 0.10 g/l coumarin, a large number of light markings are seen. These tend to be aligned along definite crystallographic directions. In a fully bright deposit from a proprietory bath shown in Fig. 13 they are more randomly distributed. To determine if these are the sites of codeposited foreign materials, the findings of Beacom and Riley (4) that foreign substances are preferentially codeposited at

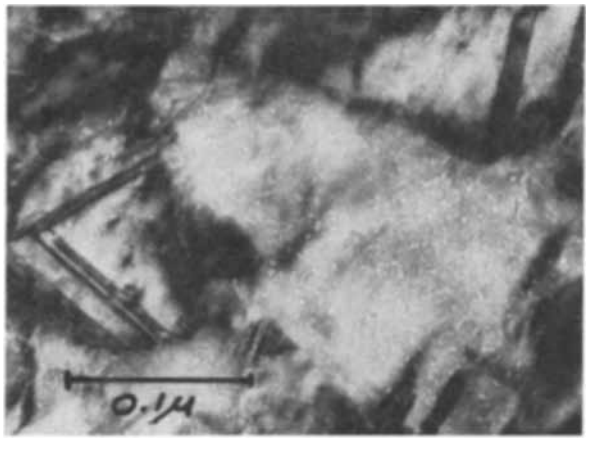

Fig. 12. Thin film showing markings in sample from bath containing 0.10 g/l coumarin.

protrusions in high-levelling baths, were utilized. Copper basis metal was prepared by vapor depositing on bright nickel having fine buffing scratches. The copper, copying the surface, therefore had tiny ridges. A photograph of the thin film plated on this surface and then stripped is shown in Fig. 14. A concentration of the light markings can be seen along the ridge. The plating bath, No. 11 in Table I was of the levelling type because the ridges could no longer be seen in a deposit 0.5μ thick. There is some evidence that the light markings represent sites where material has evaporated, as they tend

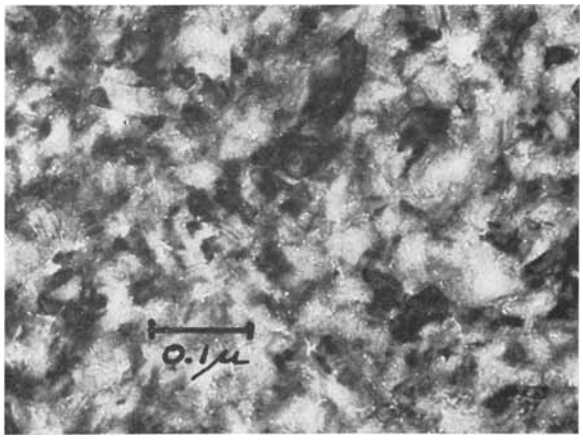

Fig. 13. Thin film showing markings in bright nickel deposit

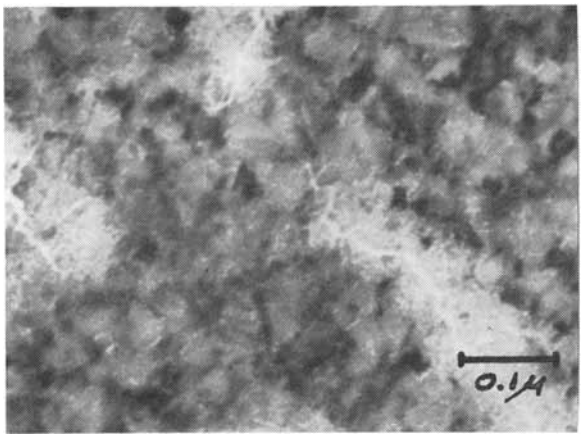

Fig. 14. Thin film showing markings lined up along ridges

to develop as a result of exposure to the electron beam. It is possible that some of the markings are due to electron bombardment. Such markings, however, tend to be randomly distributed and not lined up along certain directions. A few markings may be dislocations. However, in thin films, dislocations tend to extend from the top to the bottom surfaces. Most of the markings shown in the previous figures appear to be in a plane parallel to the surface. None of the markings were observed to move under the electron beam; dislocations often do. In a photograph taken as soon as an area is exposed to the electron beam there are dark markings and black areas lined up along the ridge.

The reasons for the formation of crevices, which have previously (1) been shown to be responsible for haziness in very fine-grained deposits and, depending on their size, can be a cause of dullness in general, have not yet been determined. On the basis of this study it is possible to make some suggestions. As previously indicated, irregularities in the height or spacing of the growth steps can cause crevices when the steps are inclined to the surface. A change in the growth direction of the platelet can result in a ridge or a valley. The crevices surrounding colonies may be caused, at least in part, by surface tension as suggested by the angles at their intersections. No crystallographic reasons have been found for their existence. The same diffraction patterns are observed on either side or on a crevice. Stresses may also cause regions to separate. There is a marked similarity between the dark areas seen on a ridge and crevices in fine-grained deposits which are hazy. This suggests that there may be some local adsorption of foreign material which hinders deposition and thereby causes a crevice. It is noteworthy that Watson and Edwards (5) observed negative levelling at the same concentration of thiourea where the deep crevices were formed. It is quite possible that crevice formation is a normal phenomenon in electroplating. Only under the right conditions for levelling are these crevices prevented from forming to noticeable depths so that a specular deposit results. These optimum conditions need not be the same as those which give best results with the relatively larger crevices used in levelling experiments. It has been shown by Garmon and Leidheiser (6), for example, that levelling is a function of the size and shape of the crevice.

The results of this study also permit further discussions about preferred orientations. Strong fiber axes were observed in samples showing relatively large grains and extended growth layers. It has been found by Pick, Storey, and Vaughan (7) that the surfaces of growth steps are usually low-index crystallographic planes. As the conditions which favor extended growth layers also favor continuation of the substrate orientation, layers will be formed nearly parallel to each other, resulting in large grains. As these grains grow from preferentially oriented nuclei, they tend to be aligned with a common direction of low indices perpendicular to the surface. Under conditions of growth inhibition, the layers are small and tend to be more randomly oriented with respect to one another because there is only a weak tendency to continue the immediate substrate orientation. Thus, fine-grained structures show generally only weak fiber axes or are randomly oriented.

The relative merits of using thin films plated on copper and stripped by removing the latter and those prepared by thinning bulk material became evident from this study. As the measurements of grain size and orientation obtained from both methods were the same, either is suitable for this purpose. For the examination of growth layers, crevices, and surface contours, the as-plated thin films are best suited as these features are no longer visible after electropolishing. Etching effects from the electropolishing solutions often occur in complicated structures. This again favors the first method. A slight etching effect has also been observed in the thin films due to the solution which dissolves the copper. The as-plated films can be made thinner, and they are more uniform in thickness than the thinned films. On the other hand, to study dislocations, subgrain formations, and annealing behavior, the thinned films are preferable. Dislocations are probably introduced in the as-plated thin films. Small changes in the lattice spacing, as occur in going from copper to nickel, can be easily accommodated under conditions of epitaxy by the introduction of dislocations.

Conclusions

Electron microscopy, especially using thin films in conjunction with replicas, has been usefully ap-

plied to the study of the very fine structure of electroplated nickel. Selected-area diffraction appears to be the only satisfactory method of measuring grain size of electrodeposits of the type used in this study as other means do not differentiate between colonies and grains or between microstress and microcrystals. An investigation of the interaction of dislocations with the sites of lattice-included, foreign material should be very helpful in elucidating the reason for the wide range of mechanical properties, as should also be a study of the effect of crevices acting as possible stress raisers.

Acknowledgment

This study was sponsored by the U. S. Army Research Office (Durham).

Mauscript received Oct. 19, 1961; revised manuscript received Jan. 5, 1962. This paper was prepared for delivery before the Detroit Meeting, Oct. 1-5, 1961.

Any discussion of this paper will appear in a Discussion Section to be published in the December 1962 JOURNAL.

REFERENCES

1. R. Weil and R. Paquin, *This Journal*, **107**, 87 (1960).
2. P. M. Kelly and J. Nutting, *J. Iron and Steel Inst.*, **192**, 246 (1959).
3. S. Steinemann and H. E. Hintemann, *Schweizer Archiv*, **26**, 202 (1960).
4. S. E. Beacom and B. J. Riley, *This Journal*, **106**, 304 (1959).
5. S. A. Watson and J. Edwards, *Trans. Inst. Metal Finishing*, **34**, 167 (1957).
6. L. B. Garmon and H. Leidheiser, Jr., *Plating*, **48**, 1003 (1961).
7. H. J. Pick, G. G. Storey, and T. B. Vaughan, *Electrochimica Acta*, **2**, 165 (1960).

Aging of Electrodeposited Chromium

I. Deposits from Chromic/Chromous Plating Baths

Kenneth A. Moon and Charles Levy[1]

Ordnance Materials Research Office, Watertown, Massachusetts

ABSTRACT

Deposits from the chromic/chromous plating baths used for the commercial electrowinning process lose about half their hydrogen and gain about 0.06 weight per cent (w/o) oxygen during about 100 days aging. The hydrogen loss does not occur in vacuum and is probably due to oxidation of elementary dissolved hydrogen. The remaining hydrogen is probably in hydrous oxide inclusions. The oxygen gain may be due to absorption in chromous oxide inclusions.

During studies of the nature and behavior of impurities in electrodeposited chromium, we have found that many deposits show pronounced aging effects during storage at room temperature. In this paper we report the results obtained with specimens deposited from chromic/chromous plating baths by the electrowinning process developed by the U.S. Bureau of Mines and the Union Carbide Metals Company (1). Studies of the aging of deposits from chromic acid plating baths are in progress (2) and will be reported later.

Materials and Procedures

Six deposit samples were used in this work. Deposits 1-5 were received from Union Carbide Metals Company in November 1959, and deposit 6 was received from the same source in March 1959. For these deposits, the usual heat-treatment in the plating plant to dry and dehydrogenate the material was omitted. The experimental specimens were given numbers which include the number of the deposit of which they were a portion, and a letter to distinguish between different specimens from the same deposit, *e.g.*, 1A, 1B, 2A, etc.

Dilatometric work was done with a Leitz Type HTV Universal Dilatometer, which produces a photographic curve representing specimen length *vs.* temperature. The slope of this curve, minus the slope of a curve on the same film made with the same specimen after complete annealing, multiplied by the appropriate calibration factors, gives the rate of shrinkage. The dilatometer furnace heating rate was 3°C/min, and the specimens were in an atmosphere of about 1 cm pure hydrogen gas up to about 550°C, and in vacuum thereafter. The purpose of the hydrogen gas was to increase heat transfer.

Hydrogen analyses were performed with a glass vacuum system in which the specimen was heated at 3°/min and the hydrogen evolved was collected in a known volume. Pressure of the hydrogen was measured with an oil manometer containing Dow Corning DC 703 silicone oil, and a Gaertner Scientific Corp. Model M300 cathetometer. To facilitate rate of evolution measurements, which require rapid manipulation, no Toepler pump was used, and the upper boundary of the known volume was the mercury vapor stream in the collector diffusion pump. Since this vapor stream retreats further into the pump as the pressure builds up, the known volume (511-561 cc) had to be calibrated as a function of pressure. It was established experimentally that loss of hydrogen by permeation through the silicone oil or by oxidation by mercury oxide in the pump was negligible, and also that no measurable hydrogen was evolved during the period of pumping which preceded the heating. Spot checks indicated that the gas collected in the known volume was essentially pure hydrogen. A liquid nitrogen trap was used between the specimen and the collector diffusion pump; the term "hydrogen content" as used in this paper does not include any

[1] Present address: Research Department, Gillette Safety Razor Company, Boston 6, Mass.

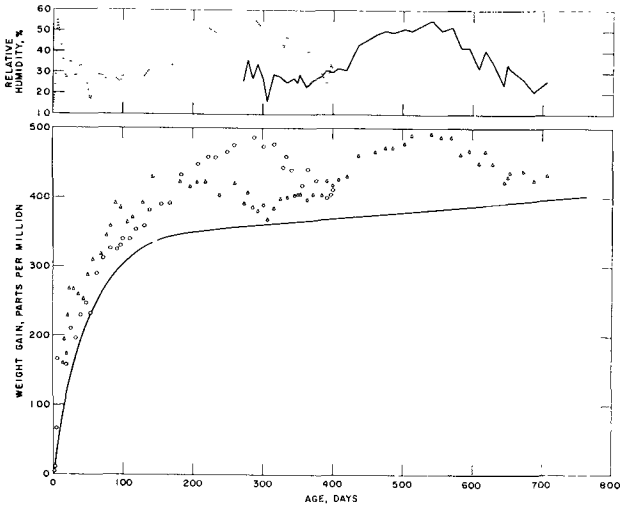

Fig. 1. Effect of age and humidity on the weight of specimens 1B (circles) and 6A (triangles). Weight gain is relative to the weight at age 1.3 days and 15% humidity. The curve represents the effect of age alone. See Fig. 2.

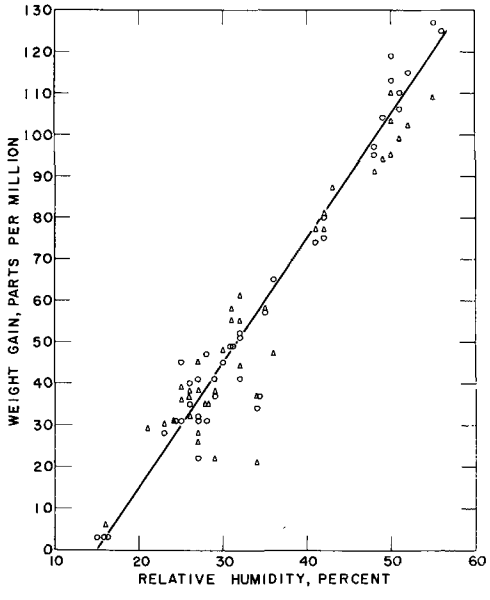

Fig. 2. Effect of humidity on the weight of specimens 1B (circles) and 6A (triangles). The ordinate of each point is the vertical distance between the corresponding point in Fig. 1 and the curve in Fig. 1.

hydrogen evolved from the specimens in the form of water vapor. Hydrogen content was calculated graphically from the rate-of-evolution data. In some cases rate measurements were not made, and hydrogen content could be calculated directly from the pressure/volume data; where cross checks were possible, the two methods gave identical results for hydrogen content.

Oxygen analyses by vacuum fusion and carbon analyses by combustion were performed by the Analytical Chemistry Branch of Watertown Arsenal Laboratories. In some cases we extracted the oxides from annealed specimens and submitted these to the Analytical Chemistry Branch for chromium analysis by standard procedures. The reported chromium content was then multiplied by the factor 48/104 to give the oxygen content. For extraction, a 1g specimen was placed in a solution of 10 ml bromine and 100 ml methanol. When solution of the metal was complete the mixture was filtered and the residue washed thoroughly with a solution containing 7g of ammonium bromide per 100 ml of methanol.

Results

Figure 1 shows how the weight of specimens 1B and 6A changed with age, age being reckoned from the time of removal of the deposit from the plating bath. The first weighing of specimen 1B was at age 1.3 days, and that of 6A, 14 days. To bring the two sets of measurements into conformity, a hypothetical 1.3-day weight was chosen for specimen 6A such that the two sets of data coincided as closely as possible. Spot checks with specimens 1G, 1H, and 1I gave agreement with the data for specimen 1B. The relative humidity of the laboratory atmosphere at the time of weighing is also shown in Fig. 1; for specimen 1B up to age 6 days direct humidity readings were not available, and the values shown were calculated from indoor temperature and outdoor dew point. These calculated values are probably a little low. It is clear that both age and

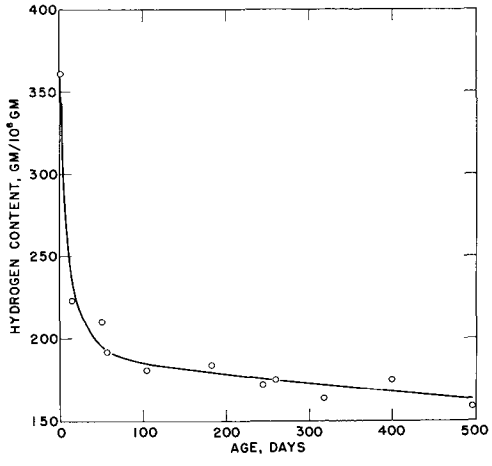

Fig. 3. Effect of age on hydrogen content. See also the data for specimens 1D and 2 P in Table I.

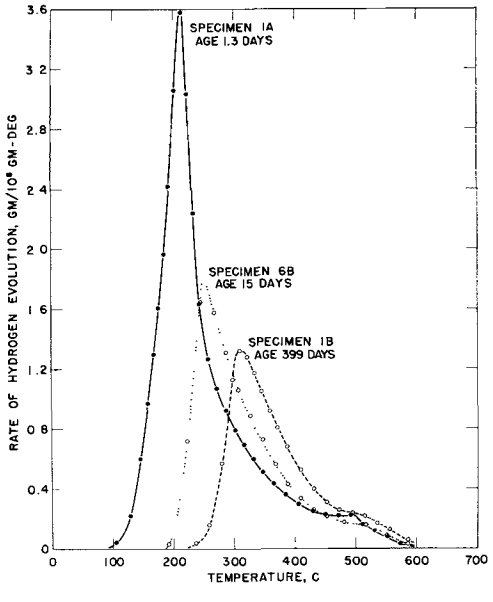

Fig. 4. Effect of age on hydrogen evolution during annealing at 3°/min.

Table I. Details of vacuum annealing experiments. In each case the specimen was pumped at room temperature for the time shown, and then annealed at 3°/min to the temperature shown. Annotations: a, days elapsed from removal of deposit from plating bath to beginning of pumping in the vacuum system; b, corrected for hydrogen recovered and to 15% humidity; c, by alcoholic bromine extraction; d, the specimen was not continuously in contact with normal air: see text; e, plus 30 min at 800°.

Specimen	Weight, g	Age[a], days	Pumping, hr	Anneal, °C	Wt loss[b], ppm	Hydrogen recovered, ppm	Oxygen content, w/o	Carbon content, ppm
1A	2.40	1.3	18	700	354	361	0.333	21
6B	0.89	15	17	1085	404	223		
2D	2.12	50	23	1000		210		
1H	0.80	56	19	700	235	192	0.396	28
1D	2.43	61d	2	800e	260	304	0.344	24
6E	2.06	86	18	1000			0.388c	
6H	2.40	104	22	650	118	181		
6R	1.98	107	3	915			0.410c	
6S	2.24	110	26	1019			0.379c	
6U	2.30	110	26	1019			0.401c	
6V	2.03	120	18	850			0.396c	
6X	2.56	120	18	850			0.383c	
2E	3.05	182	20	800	196	184	0.393c	
2P	1.05	190d	20	800		313	0.316c	
1I	0.91	244	22	600	—19	172		65
1M	0.91	259	21	650		175	0.399	
2L	2.22	301d	26	800	303	176	0.399	56
6I	1.87	317	22	800e	324	164	0.404c	
1E	2.27	329d	24	800	364	293	0.394	33
2B	2.33	333d	20	800	206	177	0.419	39
2N	3.48	341d	19	800	309	180		
2K	2.57	364d	24	830	191	176		
2A	0.99	391d	24	800	213	176		
1F	1.95	396d	23	800	186	171		
1B	3.80	399	24	800	199	175		
6J	1.94	496	20	600		159		

Table II. Summary of dilatometric experiments

Specimen	Length, cm	Age, days	Linear shrinkage when annealed at 3°/min To 1040° %	To 400° %
1J	4.38	1.4	0.708	0.140
1K	4.39	5	0.694	0.128
3A	5.04	57	0.664	0.100
6F	2.37	112	0.638	0.086
6G	2.72	113	0.637	0.080
3B	5.04	237	0.634	0.090
3D	5.97	313	0.623	0.085
3C	4.51	319	0.633	0.086
6K	5.44	575	0.608	0.061

humidity affect the weight, and the separate effects are shown by the curve in Fig. 1 and the line in Fig. 2.

Figure 3 shows how the hydrogen content changes with age, and Fig. 4 shows how age affects the details of the hydrogen-evolution process. Since aging produces a hydrogen loss but a weight gain, it follows that something is absorbed from the atmosphere during aging. If this material were lost during vacuum treatment, there should be a corresponding trend in the data for age *vs.* weight loss during vacuum treatment; the appropriate data from Table I are plotted in Fig. 5, and we see there is no such trend. When data for oxygen content *vs.* age are examined, however, as in Fig. 5, the correspondence between weight gain and increase in oxygen content is readily apparent. Thus, either oxygen or water vapor is absorbed during aging.

The easy access of oxygen and/or water to the interior of the deposits can be attributed to an inclusion system which forms a finely divided skeleton throughout the entire deposit. Conventional sectioning, polishing, and microscopy do not easily reveal this system, but by dissolving the metal in alcoholic bromine as described above, the skeleton is isolated in the form of a pseudomorph, of composition approximating Cr_2O_3, which under the microscope has a spongelike appearance with an average pore diameter of roughly 1μ. Annealing the specimen slightly (say 3°/min to 300°, which is too slight to give rise to any doubts as to whether the skeleton has been changed appreciably in size or shape by annealing) is necessary to obtain a good

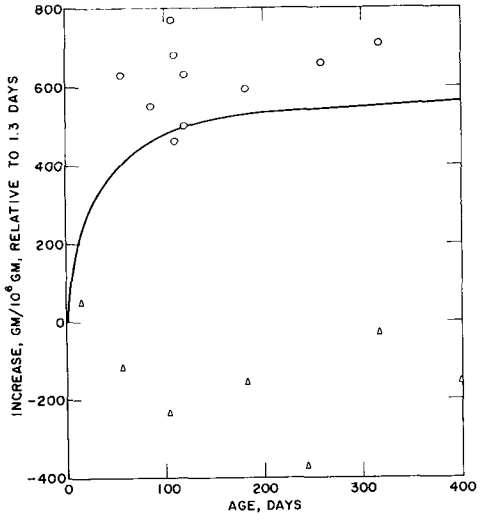

Fig. 5. Effect of age on oxygen content of annealed specimens (circles) and weight loss during annealing (triangles). Weight losses are corrected for hydrogen recovered and for humidity variations. The curve is the sum of weight gain and hydrogen loss, from Fig. 1 and 3. See also the data for specimens 1D and 2P in Table I.

pseudomorph. Very old unannealed specimens also gave good pseudomorphs; slightly aged unannealed specimens gave broken pseudomorphs; and it appears that a very fresh unannealed specimen would yield no pseudomorph at all.

Figure 6 shows the effect of age on the shrinkage characteristics of the deposits. The curves have been slightly idealized to eliminate random variations not related to age. The increase in the 300° peak from age 1.4 days to 60 days could be spurious. The other trends shown in Fig. 6 are qualitatively reliable. Figure 7 compares the observed decrease in length during aging with the observed loss, during aging, of capacity to shrink during annealing. The data for length *vs.* age were obtained by mounting specimen 4A, of length 4.15 cm, in a dial micrometer which could be read with a precision of 5 x 10^{-5} cm. It will be noted that there is a discontinuity at 5 or 6 days, preceded by five points of constant length. We believe that this was caused by sticking of the micrometer, and accordingly are reluctant to place too much reliance on Fig. 7. However, it does provide some indication that the oxygen or water absorbed during aging does not compensate dilatationally for the hydrogen lost during aging.

Some specimens were stored in special atmospheres and weight was followed as a function of time after returning the specimens to the normal atmosphere. Figure 8 shows one set of experiments in which specimens were placed in the special atmospheres at age 4 days and retrieved at some later age as indicated by the dotted lines. Figure 9 shows a second set of experiments in which the beginning of treatment in special atmospheres was at age 46 days. Because of the late start, the experiments in Fig. 9 were made with specimens which had been stored in an evacuated glass capsule from age 4 days to 42 days. With specimen 1E the carbon dioxide atmosphere was provided by storing the specimen in a bottle which was filled by gravity with carbon dioxide and then stoppered; presumably air was also present. In every other case a

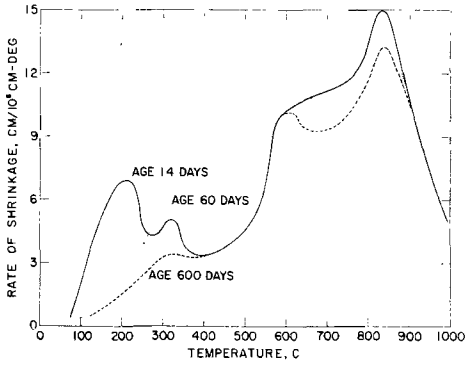

Fig. 6. Effect of age on shrinkage during annealing at 3°/min. Slightly idealized: see text.

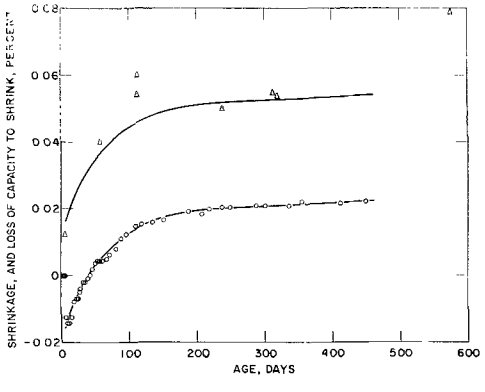

Fig. 7. Effect of age on the length and shrinkage capacity of deposits. Triangles show the loss in linear shrinkage during annealing at 3°/min to 400°, relative to specimen 1J of age 1.4 days. Circles show the loss in length of specimen 4A relative to 1.4 days. The two curves are identical except for vertical displacement.

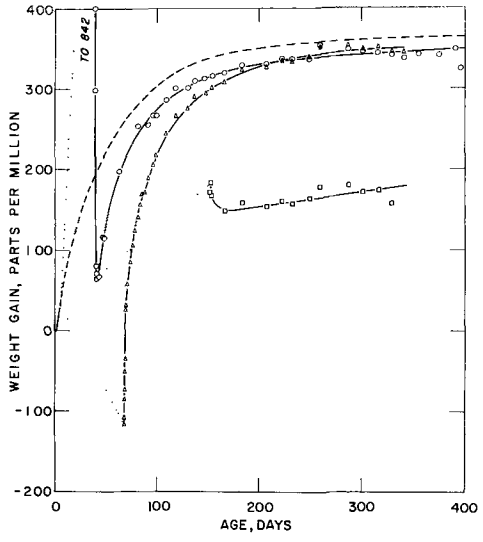

Fig. 8. Effect of storage in special atmospheres on the weight gain relative to age 1.3 days. Specimen 1F (circles) was in pure saturated water vapor from age 4 to 39 days; specimen 2N (triangles) was in an evacuated glass capsule from 4 to 68 days; specimen 1E (squares) was in a mixture of carbon dioxide and air from 4 to 151 days. The dashed line is the curve in Fig. 1. All weighings were corrected for humidity variations.

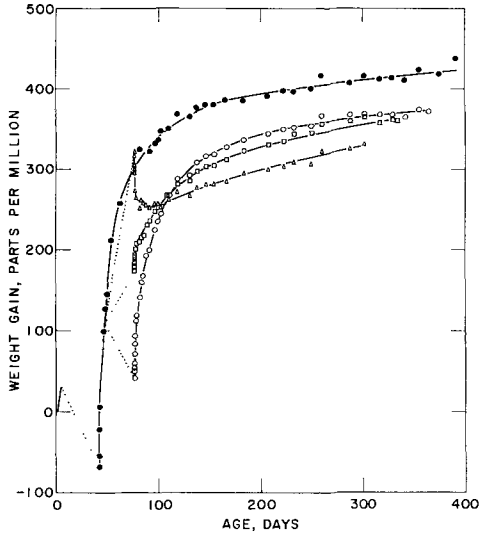

Fig. 9. Effect of storage in special atmospheres on the weight gain relative to age 1.3 days. Up to age 46 days, all four specimens were part of a single piece, which was in an evacuated glass capsule from 4 to 42 days. After the original piece was broken up, specimen 2A (solid circles) was left exposed to normal air; specimen 2K (open circles) was in 0.7 atm pure nitrogen from 46 to 76 days; specimen 2B (squares) was in 0.7 atm pure carbon dioxide from 46 to 76 days; specimen 2L (triangles) was in 0.7 atm pure oxygen from 46 to 76 days. All weighings were corrected for humidity variations.

glass capsule of volume about 100 cc was used, and air was pumped away with a high vacuum system before admitting the special gas and sealing by fusion of a constriction. The duration of pumping before admitting the special atmosphere was 1½ hr for specimens 2B, 2K, and 2L; 17 hr for 2A; and 20 for 2N. Observed weights were corrected for deviation of relative humidity from a standard value by means of the line in Fig. 2. For each specimen the standard value was chosen as the humidity prevailing at the time of opening the capsule, so that no humidity correction would have to be applied to the weight of the freshly retrieved specimen. The use of different standard humidity values for different specimens does not vitiate direct comparison of the curves in Fig. 8 and 9, because each curve is based on a reference weight which was also adjusted to the same standard humidity. The values of the standard humidities were 2L, 25%; 1E, 42; 2B, 25; 2N, 24; 2K, 25; 2A, 30; 1F, 32. The hydrogen content of each specimen was measured immediately after the last weighing shown in Fig. 8 or 9 and is listed in Table I.

The hydrogen content of two specimens was measured after a period of storage in sealed evacuated glass capsules. Specimen 2P was stored from age 4.3 days to 190 days, and its hydrogen content at 190 days was 313 ppm. In addition there was 9 ppm free hydrogen in the capsule. Specimen 1D was stored from 4.2 days to 60.05 days, and at 61.06 days its hydrogen content was 304 ppm.

Discussion

The results with specimens 1D and 2P strongly suggest that the hydrogen loss during aging takes place according to the reaction

$$4H(Cr) + O_2(gas) = 2H_2O(gas) \quad [1]$$

where H(Cr) represents hydrogen dissolved in the metal, presumably stabilized at imperfections or impurity atoms, since the true solubility of hydrogen in chromium is very small (3). Equation [1] is also supported by the experiment in which specimen 2L, after storage in pure dry oxygen, lost weight immediately after being returned to the normal atmosphere, whereas with specimens 2A, 2B, 2K, and 2N there was an initial rapid weight gain, followed in a day or so by a rather abrupt change (not clearly visible in Fig. 8 and 9 because of the small scale) to a slower rate of weight gain. This behavior suggests that the humidity in the capsule containing 2L was higher than that in the laboratory.

That accounts for about half the initial hydrogen content. It is reasonable to assume that the other half is in hydrous form, as a constituent of hydrous oxide inclusions (4). One plausible interpretation of the weight gain during aging and of the shift of hydrogen evolution to higher annealing temperatures as shown in Fig. 4 is based on the hypothesis that some or all of the chromium in the hydrous oxide inclusions is in the divalent state. Then on annealing

$$2CrO + H_2O(oxide) = Cr_2O_3 + H_2(gas) \quad [2]$$

$$2Cr + 3H_2O(oxide) = Cr_2O_3 + 3H_2(gas) \quad [3]$$

and during aging

$$4CrO + O_2(gas) = 2Cr_2O_3 \quad [4]$$

where the symbols CrO and H_2O(oxide) represent constituents of the hydrous oxide inclusions. Reaction [4], which is known to occur at room temperature (5), would account for the weight gain during aging, and perhaps also for the observation that the inclusions become more insoluble in alcoholic bromine as aging proceeds. From Fig. 5, reaction[4] would occur to the extent of 600 ppm oxygen. Thus reaction [2] would occur to the extent of 600 x 4/32 = 75 ppm hydrogen in fresh specimens, but not at all in old specimens. Correspondingly, reaction [3] would increase with aging by 75 ppm hydrogen. This would account for the shift of hydrogen evolution to higher annealing temperatures, as shown in Fig. 4, since reaction [2] is known (6) to occur rapidly in the vicinity of 100°, and reaction [3] probably occurs in the general vicinity of 300° (7). We have been attempting, so far without success, to prepare some hydrous chromous oxide by the method of Lux and Illman, in order to determine its behavior more precisely.

Other possible but less credible interpretations of the aging behavior have been discussed in ref. (2).

A puzzling feature of our results is the effect of carbon dioxide on the weight and hydrogen content of the deposits. The effect is both profound and sensitive to the details of the experimental conditions, perhaps to presence of oxygen or water vapor. These characteristics suggest that further study might prove very instructive. However, because of the difficulty of maintaining a supply of the fresh deposit, we do not at present have any plans for such a study.

Acknowledgment

The authors are grateful to the Union Carbide Metals Company and to Dr. R. M. Fowler for providing the chromium deposits.

Manuscript received Sept. 8, 1961; revised manuscript received Jan. 15, 1962.

Any discussion of this paper will appear in a Discussion Section to be published in the December 1962 JOURNAL.

REFERENCES

1. M. C. Carosella and J. D. Mettler, "Ductile Chromium," Chap. 6, American Society for Metals, Cleveland (1957).
2. K. A. Moon and C. Levy, Ordnance Materials Research Office, Watertown, Mass., MRL Report No. 97, August, 1961.
3. E. Martin, *Arch. Eisenhuttenw.*, **3**, 407 (1929).
4. A. Brenner, P. Burkhead, and C. Jennings, *J. Research Natl. Bur. Standards*, **40**, 31 (1948).
5. H. Lux and G. Illman, *Chem. Ber.*, **91**, 2143 (1958).
6. H. Lux and G. Illman, *ibid.*, **92**, 2364 (1959).
7. K. A. Moon and G. A. Consolazio, "Ductile Chromium," Chap. 17, Fig. 2, American Society for Metals, Cleveland (1957).

Thallium-Activated ZnS Phosphors

A. Wachtel

Research Department, Westinghouse Electric Corporation, Bloomfield, New Jersey

ABSTRACT

Firing of ZnS with Tl_2S + S in sealed tubes results in yellow photoluminescence peaked at 590μ as well as thermoluminescence and infrared-stimulated emission with the same color. In the presence of Cu or Ag, the photoluminescence is red and peaks at 835 mμ. This emission is excited at wavelengths where ZnS:Cu,Cl or ZnS:Ag,Cl, respectively, emit. The thermoluminescence and infrared-stimulated emission, at room temperature, of ZnS:Ag,Tl is yellow; in the case of ZnS:Cu,Tl, the stimulated emission contains yellow and red components.

Recent work in this laboratory has shown that Tl can be incorporated into ZnS. Because of lack of published data on Tl-activated ZnS (1)[1], an attempt was made to correlate the results of the present investigation with data on ZnS:Cu or ZnS:Ag coactivated by Al, Ga, or In (2-7), as well as ZnS activated by In alone (8).

Phosphor Preparation

Thallium salts are known to be quite volatile, and numerous samples of ZnS:Cu,Tl fired at atmospheric pressure indicated at best incomplete incorporation of the added Tl under such firing conditions. Because of the high limit of spectrographic detectability of Tl (100 ppm), it was also considered difficult to obtain accurate analytical data on such phosphors. A more practical approach, therefore, consisted of conducting all firings for 1 hr in sealed, evacuated silica tubes. Additions of Cu or Ag were made from aqueous solutions prior to a preliminary firing in H_2S at atmospheric pressure which, in such cases, is always necessary to enable the proper degassing of the sample during the subsequent evacuation. Quantitative incorporation of the added Tl was not proven, but at least extensive incorporation was assumed on the basis that no separate phase of Tl-sulfide was discernible[2] on the fired phosphors, except after additions as large as 10^{-3} g atoms Tl/mole ZnS. X-ray diffraction analyses showed that both firing temperatures of 950° and 1100°C resulted in essentially cubic phosphors which, moreover, had the same emission spectra. Therefore, the presence of Tl evidently favors the formation of the cubic phase.

All of the phosphors described in this paper were fired in sealed tubes. At this time, it should however be pointed out briefly that, depending on composition and firing schedules, some ZnS:Cu,Tl phosphors fired at atmospheric pressure displayed similar properties. With increasing Cu addition and firing temperature (decreasing Tl retention), green luminescence was obtained, however, without evidence of special properties such as deep traps which could be ascribed to the presence of Tl. For this reason as well as their necessarily uncertain composition,[3] they are not further described until such samples can be duplicated under more controlled conditions.

Results

Table I shows the compositions employed and the visually observed photoluminescence properties. Sample 1 was prepared by firing ZnS with TlCl (in the absence of S) in an effort to obtain Tl^{1+} acceptor centers. This was unsuccessful because the phosphor showed only the characteristics of self-activated

[1] Ballentyne's phosphor (1) was prepared with Tl, but was stated to contain no Tl after firing.

[2] Unavoidable temperature gradients always cause a separate phase with high vapor pressure to segregate in clearly visible form on one side of the tube.

[3] To avoid complete loss of Tl, firing in capped silica tubes was necessary in such cases. This, however, made it impossible to avoid the presence of some oxygen.

Table I. Visually observed luminescence of Tl-activated ZnS Phosphors

Sample No.	Phosphor-composition in g-atoms/mole ZnS Ag	Cu	Tl	Cl	77°K Photolumin.	77°K Infrared stimulation	77°K Thermolum. below r. t.	Room temperature Photolumin.	Room temperature Infrared stimulation	Room temperature Thermolum. above r. t.	About 400°K Photolumin.
1	0	0	10^{-3}	10^{-3}	s. blue	blue	blue	s. blue	none	none	v. w. bl.-gr.
2	0	0	3×10^{-5}	0	w. orange	w. orange	yellow	yellow	s. yellow	yellow	yellow
3	0	0	10^{-4}	0	s. orange	s. orange	s. yellow	s. yellow	s. yellow	s. yellow	s. yellow
4	0	10^{-4}	3×10^{-5}	0	w. lavender	yellow	w. yellow	w. orange	yellow	none	w. yellow
5	0	10^{-4}	10^{-4}	0	w. orange	v. w. orange	v. w. yellow*	or.-red	or.-yellow	none*	v. w. red
6	0	10^{-4}	3×10^{-4}	0	w. orange	v. w. orange	none	red	orange	none	v. w. red
7	0	10^{-4}	10^{-3}**	0	w. orange	v. w. orange	none	deep red	or.-red	none	v. w. red
8	10^{-4}	0	10^{-4}	0	v. w. orange	s. orange	none*	deep red	s. yellow	yellow	orange

* Glow curves show thermoluminescence but visible evidence is uncertain.
** Separate phase of a Tl-sulfide noted after firing.
s = strong, w = weak, v = very.

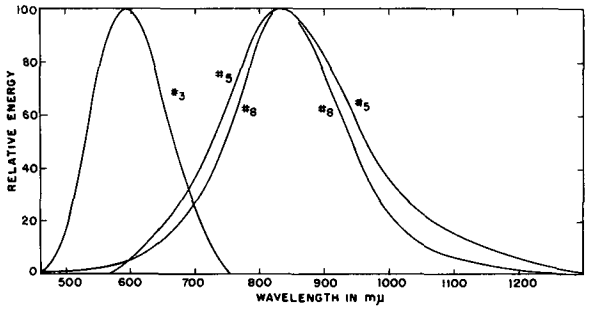

Fig. 1. Room-temperature emission spectra of phosphors. Excitation: 365μ. Perkin-Elmer Model 13-U Spectrometer.

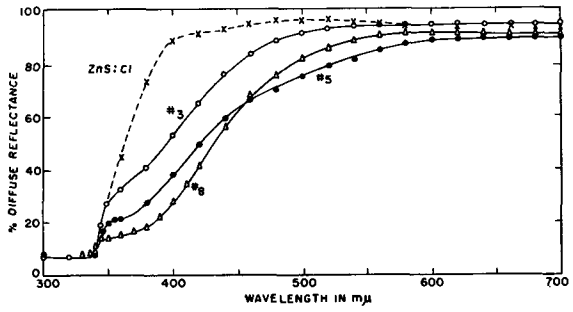

Fig. 3. Diffuse reflectance spectra of Tl-activated phosphors in comparison to ZnS:Cl. Beckman Model DU Spectrophotometer. Measurements relative to MgO.

ZnS:Cl. In all other samples, Tl was added as Tl_2S (absence of Cl) with a small excess of elementary S so as to favor the formation of Tl^{3+} centers. Measurements on sample No. 3 (ZnS:Tl), No. 5 (ZnS:Cu,Tl), and No. 8 (ZnS:Ag,Tl) are shown in Fig. 1 to 4. The numbers in the figures refer to the sample numbers in Table I.

The room temperature emission spectra (Fig. 1) indicate that each phosphor emits a single band. In the case of ZnS:Tl, the emission is peaked at 590 mμ[4] and has a band width of 0.38 ev, *i.e.*, nearly the same as that of the ZnS:Cu,Cl luminescence. The emission bands of ZnS:Cu,Tl and ZnS:Ag,Tl peak at 835 mμ with half widths of 0.43 and 0.33 ev, respectively. The narrower distribution of the latter is made apparent by a deeper red visual appearance of the photoluminescence. The accuracy of the difference between the band widths of the Cu- and the Ag-activated phosphors is questionable because of the low sensitivity of the detector (PbS) which was required to measure the long wavelength emission.

The excitation spectra (Fig. 2) show some interesting features: ZnS:Tl is excited primarily in the fundamental band, and in addition, there is excitation in the neighborhood of 370 and 380 mμ which is the region where excitation of blue ZnS:Cl emission has been noted (9). Excitation of the red emission of ZnS:Cu,Tl and ZnS:Ag,Tl is predominantly in the same bands where ZnS:Cu,Cl and ZnS:Ag,Tl are known to emit. A similar phenomenon has been noted in the excitation spectrum of ZnS:Cu,Li,Ti (10). The diffuse reflectance spectra, as shown in Fig. 3, indicate the presence of absorption in the neighborhood of 370-380 mμ and an additional absorption of the Cu-activated phosphor at longer wavelengths. Despite the poor resolution obtained in this type of measurement, there appears to be general agreement between the observed wavelengths for absorption and excitation. For comparative purposes, Fig. 3 also shows the diffuse reflectance spectrum of a typical blue emitting ZnS:Cl phosphor.

The yellow thermoluminescence of ZnS:Tl is very strong. Its glow curve (Fig. 4) shows two peaks above room temperature which are obtained more clearly by excitation at room temperature (filled points). In contrast, the thermoluminescence of ZnS:Cu,Tl is extremely feeble, and its color could not be observed with certainty. ZnS:Ag,Tl, however, showed a clearly visible yellow thermoluminescence at higher temperatures and in addition, one of the glow peaks (265°K) is also obtained with the Cu-activated phosphor. Unfortunately, agreement of the positions of glow peaks for ZnS:Tl with

[4] By means of sensitive equipment (RCA 7102 photomultiplier), an extremely weak band peaked at 915μ was also observed. This, however, could not be detected with the apparatus used to measure the spectra shown in Fig. 1, and its existence is therefore questionable.

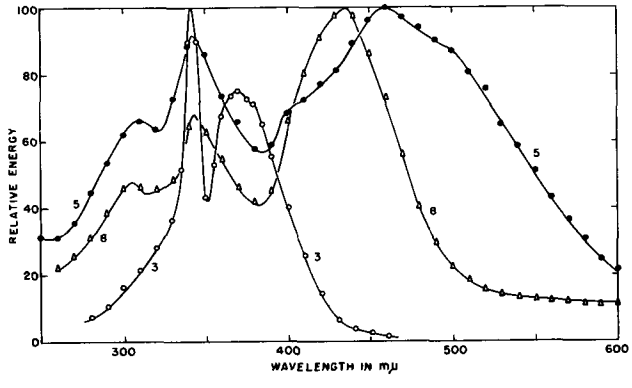

Fig. 2. Excitation spectra, corrected for equal number of quanta of exciting radiation. Thin powder layers, measured on side opposite to excitation. Below 420μ: Xe-lamp and RCA 1P21 photomultiplier. Above 400μ: W-lamp and RCA 7102 photomultiplier. B&L 500 mm Grating Monochromator.

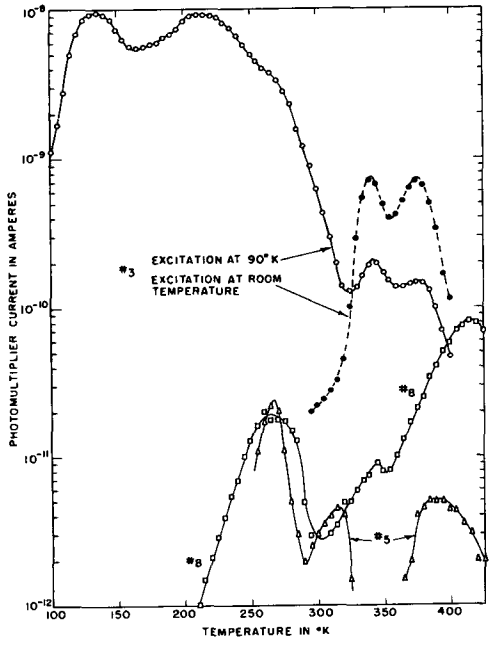

Fig. 4. Glow curves obtained after 365μ excitation and 10 min decay. Detector: RCA 1P22 photomultiplier. Heating rate: 10°/min.

those shown by ZnS:Cu,Tl and ZnS:Ag,Tl is uncertain. The visually observed emission colors, however, seem to be similar for all phosphors.

In this work, only visual observations were taken on infrared-simulated emission (Table I). The source of infrared was an incandescent lamp equipped with a Corning No. 2540 filter. The emission of ZnS:Tl is fairly strong and persistent during infrared irradiation and, at room temperature, of the same color as the ultraviolet-excited fluorescence. This phosphor also shows a persistent yellow phosphorescence. Introduction of 10^{-4} Cu results in decreased yellow and increased red emission, depending on the amount of Tl in the phosphor.[5] The effect of Cu on the emission color is weaker for the stimulated emission than for room temperature photoluminescence. The same holds true for the effect of Tl concentration, as seen in Table I.

Copper also quenches the room temperature phosphorescence and reduces the infrared-stimulated emission to a brief flash. The latter effect seems to differ very slightly for the two emission bands, and consequently, both yellow and red stimulated emission can be discerned side by side. In order to indicate the relative strength of the respective bands, Table I shows only the over-all color impression. It can be seen that it is always less red than that of photoluminescence; if the phosphor is excited simultaneously by ultraviolet and infrared and then the infrared is turned off, a distinct change to a deeper red color can be noted in all ZnS:Cu,Tl samples.

The effect of 10^{-4} Ag on the infrared stimulated emission seems to be less pronounced than that of Cu.[6] The emission is weaker than in ZnS:Tl, but still persistent and appears to contain no red component. The more greenish-yellow color obtained with Ag may be due to a weak blue band whose origin has not been ascertained. It could easily arise from contamination by traces of Cl. ZnS:Ag,Tl also showed no room temperature phosphorescence.

Careful heating of a mixture of CuS and Tl_2S with excess S resulted in a black product whose x-ray diffraction analysis is shown in Table II. The tetragonal structure, $a = 5.58$Å, $c = 11.16$Å ($c/a = 2.0$) is similar to that listed for $CuGaS_2$ (11). The substance is therefore likely to consist of $CuTlS_2$. Continued heating results in loss of S, followed by sublimation of Tl_2S. Therefore, no attempts to prepare phosphors at atmospheric pressure, analogous to ZnS:$CuGaS_2$ (4), seemed worthwhile. Nevertheless, the existence of this compound suggested the possibility of charge compensation of Cu^{1+} by Tl^{3+} in ZnS.

Discussion

Because of the position of Tl in the periodic table, it is tempting to seek an analogy between the present phosphors and the properties of phosphors coactivated by Al, Ga, and In as reported by others. The emission which may be associated with trivalent substituents in Cu-activated phosphors shifts to longer wavelengths with increasing atomic weight of the substituent; therefore, one should expect a further shift in the case of Tl. Figure 1 shows that this is the case. The narrower spectral distribution of the Cu- and Ag-activated phosphor, as compared to that reported for ZnS:Cu,In (7), may be explained by the absence of pronounced subsidiary emission bands such as are clearly shown in measurements reported by Melamed (6).

Table II. X-ray diffraction data for $CuTlS_2$

hkl	CuK_α radiation d (Å)	Intensity
	8.15	5
112	3.22	100
	3.11	3
	3.04	5
004, 200	2.79	15
201, 113	2.72	52
	2.04	4
220, 204	1.973	30
312, 115	1.685	17
224	1.614	5

A further analogy of ZnS:Cu,Tl in comparison to Al, Ga, and In coactivated phosphors may be desirable on the basis of systematically increasing trap depths as reported by Hoogenstraaten (12). Unfortunately in the present system, there is no definite evidence of thermoluminescence either in the long wavelength emission band characteristic for the Cu and Ag activated phosphors, or of green Cu (520μ) or blue Ag (445μ) emission. Therefore, the observed glow peaks may arise from processes which differ from those proposed for Al, Ga, and In coactivated phosphors. The same argument may be advanced with respect to the infrared-simulated emission of ZnS:Ag,Tl. It is felt that conclusions as to the nature of the trapping states in Tl-activated phosphors will require identification of the spectral distributions of thermoluminescence and stimulated emission, as well as measurements of the latter as a function of wavelength of infrared radiation. Further investigations will also be necessary on phosphors prepared with varying amounts of Ag and Cu.

The similarity of the blue luminescence of ZnS:Al and ZnS:Ga (2) with the blue emission band in ZnS:In (8) (470 mμ) suggests that the wavelength for this transition (which is generally associated with a Zn vacancy) is not strongly affected by the atomic weight of the donor. One should therefore expect that "self-activated" emission caused by Tl^{3+} should be similar, which was, however, not observed. The question as to whether the 590 mμ band of ZnS:Tl is caused by transitions proposed either for the 535 mμ band or the 620 mμ band in ZnS:In (8) is much more difficult. At this time, it is felt that the large polarizability of Tl, as well as its ability to exist in an additional (monovalent) state, adds to the complexity of this system.

Summary

The important results obtained in this investigation are: (*A*) The 590 mμ emission of ZnS:Tl which is also visually observed (although not identified) in thermoluminescence and infrared-stimulated

[5] No samples with Cu additions other than 10^{-4} were prepared.

[6] The comparison can be made only with ZnS:10^{-4} Cu, 10^{-4} Tl (sample No. 5). No ZnS:Ag phosphors with more than 10^{-4} Tl were prepared, and the possibility of stimulated red emission in such samples must be left open.

emission of the Cu and Ag activated phosphors. (*B*) The 835 mμ emission which is shown in the photoluminescence of the Cu- or Ag-activated phosphors, while at least in the case of Ag, it does not seem to appear during thermoluminescence of infrared-stimulated emission. (*C*) The fact that the 835 mμ luminescence of the Cu and Ag activated phosphors is at least nearly identical. (*D*) The fact the excitation spectra of the Cu- and Ag-activated phosphors are different and correspond to the emission bands of ZnS:Cu,Cl and ZnS:Ag,Cl, respectively. At present, no mechanism can be proposed to explain all of these observations.

Acknowledgments

The writer wishes to thank Miss I. Walinski for phosphor preparations, Mr. I. Meister for emission spectra, and Dr. C. K. Lui Wei for x-ray diffraction analyses. He also wishes to thank Dr. W. A. Thornton, Dr. H. F. Ivey, and Professor E. Banks for helpful discussions. This work was supported by Contract AF33(616)-7350 from the Wright Air Development Division, ARDC, U.S. Air Force.

Manuscript received Nov. 2, 1961.

Any discussion of this paper will appear in a Discussion Section to be published in the December 1962 JOURNAL.

REFERENCES

1. D. W. Ballentyne, *This Journal*, **107**, 807 (1960).
2. F. A. Kröger and J. A. M. Dikhoff, *Physica*, **16**, 297 (1950).
3. H. C. Froelich, *This Journal*, **100**, 496 (1953).
4. E. F. Apple, *ibid.*, **105**, 251 (1958).
5. E. F. Apple and F. E. Williams, *ibid.*, **106**, 224 (1959).
6. N. T. Melamed, *J. Phys. Chem. Solids*, **9**, 149 (1959).
7. W. van Gool, A. P. Cleiren, and H. J. M. Heijlingers, *Philips Research Repts.*, **15**, 254 (1960).
8. H. Koelmans, *J. Phys. Chem. Solids*, **17**, 69 (1960).
9. A. Halperin and H. Arbell, *Phys. Rev.*, **113**, 1216 (1959).
10. A. Wachtel, *This Journal*, **109**, 309 (1962).
11. H. Hahn, *et al.*, *Z. anorg. u. allgem Chem.*, **271**, 153 (1953).
12. W. Hoogenstraaten, *This Journal*, **100**, 356 (1953).

The Effect of Li and Ti on ZnS:Cu and ZnS:Ag Phosphors

A. Wachtel

Research Department, Westinghouse Electric Corporation, Bloomfield, New Jersey

ABSTRACT

ZnS:Cu,Li fired in H_2S or H_2 shows blue and green photoluminescence peaked at 443 and 510 mμ, respectively. Addition of Ti quenches this emission and causes red and infrared emission peaked at 730 and 830 mμ, respectively. Infrared radiation stimulates the red emission and also quenches the blue and green bands. ZnS:Ag,Li,Ti emits in the orange with a band peaked at 640 mμ and an infrared band peaked at 810 mμ. In the absence of Ti, ZnS:Ag,Li shows properties essentially similar to those of ZnS:Cu,Li, except for a weak orange-yellow infrared-stimulated emission.

Kröger (1) has shown that Li or Na can form activator centers in ZnS, provided that Cl is present. If the concentration of Cl is decreased sufficiently, the presence of Li then quenches the self-activated (blue) photoluminescence which can otherwise be observed. Recent work in this laboratory has shown that, in the presence of Cu and Li, blue and green photoluminescence is obtained even in the absence of halides. If the phosphor has been fired in H_2S or H_2 (preferably at 1100°C), it also shows a deep red photoluminescence which can be stimulated by infrared radiation either during or after excitation by 365 mμ u.v. (ultraviolet). At the same time, the blue and green emission is quenched. Spectrographic analyses of specimens with more pronounced red emission indicated the presence of Ti which was therefore investigated in more detail.

Phosphor Preparation

The samples were prepared in 10-g lots, fired in small open silica tubes in a current of purified H_2S at 1100°C for 1 hr. The raw materials were ZnS (RCA LM476) and solutions of $Cu(C_2H_3O_2)_2 \cdot H_2O$ or $AgNO_3$, $LiHCO_2 \cdot H_2O$, and Ti $[(CH_3)_2CHO]_4$, hydrolyzed in $(CO_2H)_2$ solution. The activator additions were kept at 3 x 10^{-5} g-atoms Cu or Ag, and 10^{-3} g-atoms Li per mole ZnS.[1] Owing to volatility, the concentration of Li in the fired phosphors was probably much lower, but was not determined. Any free Li_2S formed during the firing in H_2S was removed by washing in dilute acetic acid.

Results

Figure 1 shows room-temperature 365 mμ-excited emission spectra of phosphors prepared with or

[1] Preliminary experiments indicated that for red emission, the optimum Cu concentration is between 1 and 3 × 10^{-5}. The higher concentration was chosen in order to minimize the effect of any unwanted contaminations. The effect of Li addition was less marked; the amount chosen is nominal.

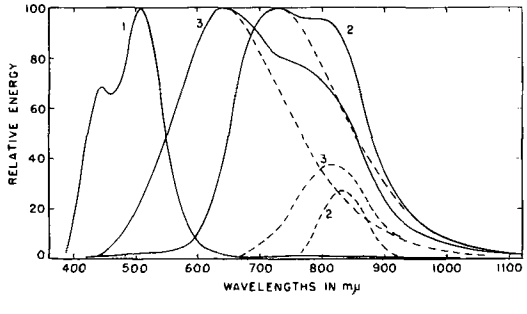

Fig. 1. 365 mμ-excited emission spectra of 1, ZnS:Cu,Li and Zns:Ag,Li; 2, ZnS:Cu,Li, 10^{-5} Ti; 3, ZnS:Ag,Li, 10^{-5} Ti. Perkins-Elmer Model 13-U Spectrometer.

without additions of 10^{-5} Ti. It should be noted that, except for intensity,[2] the spectral distributions of the blue and green emission bands of ZnS:Cu,Li and ZnS:Ag,Li were identical. Only in the presence of Ti did the Ag-activated phosphor show a different emission spectrum, the visual impression of this being orange. Moreover, the same blue and green emission bands remained unchanged in phosphors prepared with the addition of 3 x 10^{-5} Al (as well as Li). Therefore, the possibility that they are due to coactivation by Al (spectrographically detectable in the ZnS raw material) cannot be ruled out. On the other hand, the blue-green emission in ZnS:Cu,Na and ZnS:Cu,K as well as in ZnS:Cu (presumably caused by Al contamination) was much weaker. Samples prepared without Cu or Ag were nonluminescent.

The identity of the emission spectra of ZnS:Cu,Li and ZnS:Ag,Li suggests that the latter emits only by virtue of traces of Cu whose presence can rarely be avoided. This does not explain the absence of a distinct blue band in ZnS:Ag,Li (*i.e.*, different from that of the Cu-activated phosphor), even when fired with additional Al. The absence of any luminescence of ZnS fired only with Li also indicates that no significant contamination by Cu was likely. On the other hand, ZnS fired with Li and 1 x 10^{-6} Cu showed not only weak blue-green photoluminescence, but also a very weak orange (rather than red) IR-stimulated flash, similar to that observed on the 3 x 10^{-5} Ag-activated phosphor.

The excitation spectra for the blue-green emission of ZnS:Cu,Li and ZnS:Ag,Li (Fig. 2 filled points) show the same similarity, except for the shift of the short wavelength band of ZnS:Ag,Li to 325 mμ, corresponding to an energy appreciably more than the band gap of ZnS. No such discrepancy can be noted in the diffuse reflectance spectra as shown in Fig. 3. In all other cases, the fundamental excitation band (peaked at 338 mμ) is shown quite clearly. In the u.v., no additional band due to Ti (long wavelength emission, open points) can be observed; for the most part, the excitation bands for short and for long wavelength emission differ only in relative height. In the visible region, the excitation bands for the red and infrared emission of ZnS:Cu,Li,Ti (open circles) are conspicuous inasmuch as they appear to match the two emission bands (blue and green) of the same phosphor prepared without Ti. To facilitate this comparison, the emission spectrum of ZnS:Cu,Li (from Fig. 1) is reproduced in Fig. 2, dashed line. A similar effect was also noted with ZnS:Cu,Tl and ZnS:Ag,Tl phosphors (2). In the case of the orange and infrared emission of ZnS:Ag,Li,Ti (open triangles), the excitation peak at 415μ cannot be similarly correlated; the concept that it may correspond to a hypothetical distinct blue emission of ZnS:Ag,Li (which was not obtained experimentally) is too speculative to be of serious concern.

The pronounced influence of variations of the concentration of Ti on the blue-green and red photoluminescence of ZnS:Cu,Li,Ti is illustrated in Fig. 4. Addition of 1 x 10^{-6} Ti decreases the blue-green photoluminescence by a factor of 16. The increase in red emission obtained between the additions of zero and 1 x 10^{-6} is indeterminate because of the questionable validity of the point corresponding to "zero Ti", excited without infrared. The par-

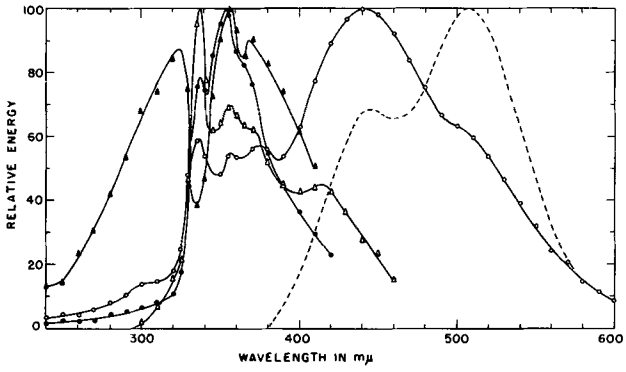

Fig. 2. Excitation spectra of phosphors, corrected for equal number of quanta of exciting radiation. Below 420 mμ: Xe lamp, measurements with RCA 1P21 photomultiplier. Above 400 mμ: W lamp, measurements with RCA 7102 photomultiplier. Phosphor powder layers veiwed on side opposite to excitation. B&L 500 mm Grating Monochromator. ●—● ZnS:Cu,Li (blue-green emission); ▲—▲ ZnS:Ag,Li (blue-green emission); ○—○ ZnS:Cu,Li, 10^{-5} Ti (red emission); △—△ ZnS:Ag,Li, 10^{-5} Ti (orange emission); - - - - emission spectrum of ZnS:Cu,Li from Fig. 1.

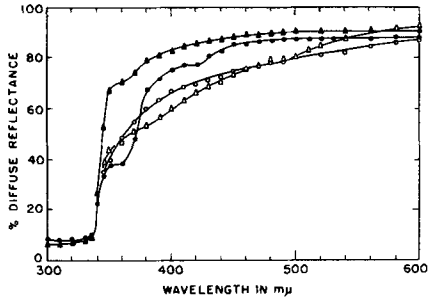

Fig. 3. Diffuse reflectance spectra of phosphors, relative to MgO. Beckman Model DU Spectrophotometer, ●—● ZnS:Cu,Li; ▲—▲ ZnS:Ag,Li; ○—○ ZnS:Cu,Li, 10^{-5} Ti; △—△ ZnS:Ag,Li, 10^{-5} Ti.

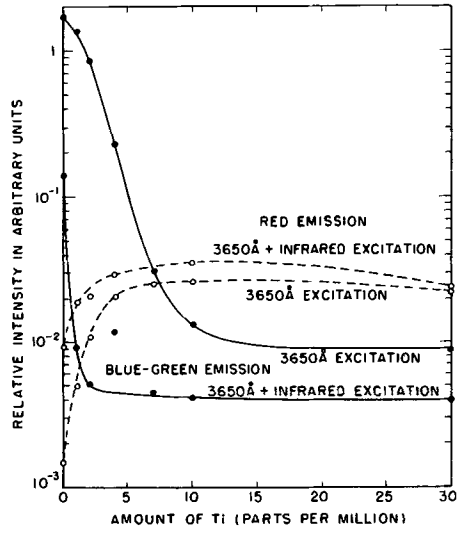

Fig. 4. Relative intensity of 365 mμ-excited photoluminescence of ZnS:Cu,Li,Ti as a function of Ti addition. Infrared obtained by W-lamp with Corning No. 2540 Filter. Measurements with Spectra Brightness Spot meter set on "Blue" and on "Open" with Corning No. 2030 Filter.

[2] The quantum yields under 365 mμ excitation of ZnS:Cu,Li, ZnS:Ag,Li, ZnS:Cu,Li,10^{-5} Ti, and ZnS:Ag,Li,10^{-5} Ti were measured to be 48, 29, 56, and 34%, respectively, of that obtained with ZnS:3 x 10^{-5} Cu,Cl.

ticular sample[3] on which it was measured is the same whose emission spectrum (Fig. 1) shows only a very weak long wavelength band.[4] Therefore, the measured value may incorporate a contribution from the long wavelength tail of the green band. The red flash which can be stimulated by infrared after u.v. excitation of this phosphor is, however, strong and unmistakable. Nevertheless, it is still an open question as to whether this is due to spectrographically undetectable traces of Ti, or an intrinsic property of ZnS:Cu,Li. In connection with Fig. 4, it may be mentioned that phosphors with higher Ti additions were also prepared. It was interesting to observe that with as little as 1 x 10^{-4} Ti, the red emission was appreciably quenched; at higher concentrations, it became very weak. Inasmuch as the same was observed with respect to Cu addition, this seems to be a system requiring unusually low activator concentrations.

Figure 5 shows the 365 mμ-excited intensities of blue-green and red emission of ZnS:Cu,Li as a function of wavelength of infrared radiation simultaneously incident on the phosphor plaque. All points represent differences between the measured intensities with and without u.v. excitation. The latter represents stray light from the monochromator (used as source of infrared) whose intensity was usually equal to or greater than that of the red radiation (open circles) to be measured. These points, therefore, show considerable scatter. Below 830 mμ, the reflected primary radiation from the monochromator dominated, and no meaningful differences could be obtained. In the case of ZnS:Ag,Li, no long wavelength emission could be measured. For blue-green emission, it can be seen that the dependence of the intensity on infrared wavelength shows considerable differences for the Cu- and Ag-activated phosphors.

An attempt was made to determine the influence of Ti by performing similar measurements on ZnS:Cu,Li,4 x 10^{-6} Ti (blue-green emission weak but still measurable). The results (inverted triangles, dashed curves) show that the quenching of blue-green emission (filled points) is shifted from 1150 to 1300 mμ, and that the red emission (open points) is stimulated at all wavelengths below 1700 mμ. Especially toward shorter infrared wavelengths, the interference from stray radiation was considerable, and no attempt was made to extend the curve into that region.

The glow curves or blue-green and red or orange emission are shown in Fig. 6 and 7, respectively. In the case of ZnS:Cu,Li and ZnS:Cu,Li,Ti, excitation was performed not only at 90°K[5] (open circles), but also at room temperature, followed by continued excitation during cooling (filled circles). In the latter case, one usually observes an intensification of the

[3] A selected sample with minimum infrared-stimulated red emission.

[4] The red bands became pronounced at 4 × 10^{-6} Ti. With 7 × 10^{-6} Ti, the peak heights of the green and red bands were equal.

[5] The lowest temperature obtainable with the equipment.

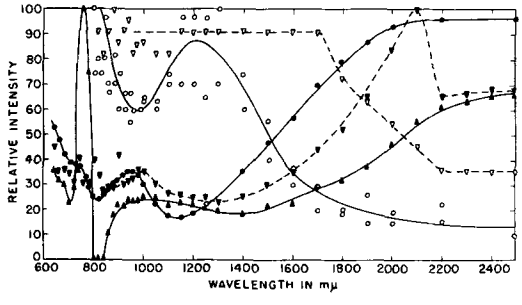

Fig. 5. Relative intensity of 365μ-excited photoluminescence as a function of wavelength of infrared radiation. Measurements as in Fig. 4. ●—● ZnS:Cu,Li, blue-green emission; ▲—▲ ZnS:Ag,Li, blue-green emission; ○—○ ZnS:Cu,Li, red emission; ▼—▼ ZnS:Cu,Li, 4 x 10^{-6} Ti, blue-green emission; ▽—▽ ZnS:Cu,Li, 4 x 10^{-6} Ti, red emission.

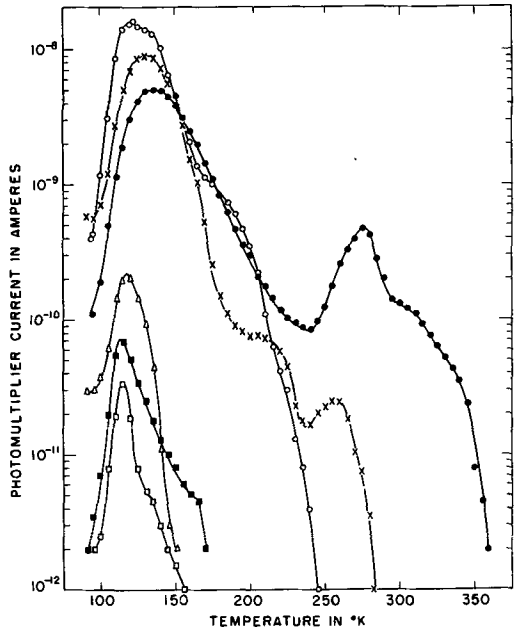

Fig. 6. Glow curves of blue-green emission of phosphors, measured through Corning No. 5433 Filter. Heating rate: 10°/min. ○—○ ZnS:Cu,Li, excited at 90°K only; ●—● ZnS:Cu,Li, excited at room temperature and at 90°K; □—□ ZnS:Cu,Li, 10^{-5} Ti, excited at 90°K only; ■—■ ZnS:Cu,Li, 10^{-5} Ti, excited at room temperature and at 90°K; △—△ ZnS:Ag,Li, excited at 90°K only; x—x ZnS:Cu,Li, 3 x 10^{-5} Al, excited at 90°K only.

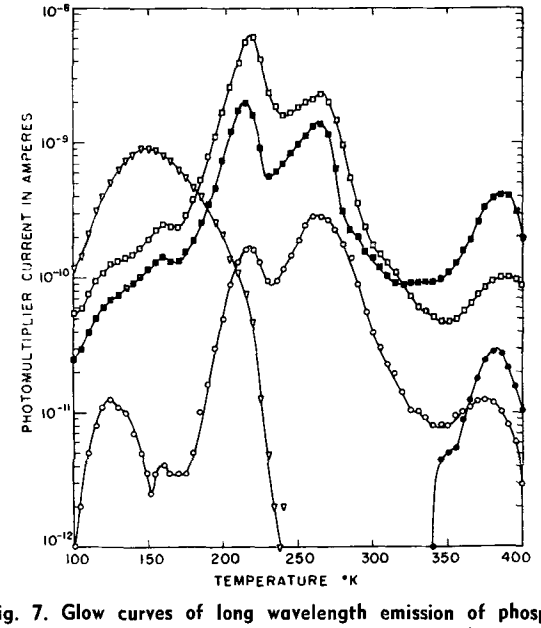

Fig. 7. Glow curves of long wavelength emission of phosphors, measured through Corning No. 2404 Filter. ○—○ ZnS:Cu,Li, excited at 90°K only, ●—● ZnS:Cu,Li, excited at room temperature and at 90°K; □—□ ZnS:Cu,Li, 10^{-5} Ti, excited at 90°K only; ■—■ ZnS:Cu,Li, 10^{-5} Ti, excited at room temperature and at 90°K; ▽—▽ ZnS:Ag,Li, 10^{-5} Ti, excited at 90°K only.

higher temperature glow peaks, as reported by Garlick and Mason for CaS:Bi (3). The present results show this effect especially for the 275°K peak for ZnS:Cu,Li (Fig. 6). This method of excitation of the same phosphor also prevents all red thermoluminescence below room temperature (Fig. 7), although the excitation was continued down to 90°K.

Except for intensity, the glow curve for blue-green emission of ZnS:Ag,Li does not significantly differ from that of ZnS: Cu, Li. The orange thermoluminescence of ZnS: Ag, Li, Ti (Fig. 7) is, however, distinct from the red thermoluminescence of the Cu-activated phosphors.

Particular attention should be drawn to the effect of Al on the glow curve of blue-green emission of ZnS:Cu,Li. It was mentioned earlier that 3×10^{-5} Al had no influence on the emission spectrum of this system. A critical comparison of the glow curve for ZnS:Cu,Li,Al shown in Fig. 6 with that of red emission of ZnS:Cu,Li (or ZnS:Cu,Li,Ti) in Fig. 7 shows that the two characteristic red glow peaks at 217° and 265°K seem to be reproduced, but now represent the short wavelength radiation.

Discussion

The complex nature of the system precludes definite conclusions as to the nature of the activator centers responsible for the phenomena observed. In order to avoid further complications at this time, no attempt has been made to differentiate between the blue and the green emission bands separately, although such investigations have proven to be fruitful in the case of single crystals of ZnS:Cu,Cl (4). Similarly, the infrared emission bands were not detected in the measurements described in Fig. 4 to 7. Therefore, one can only summarize those data which tend to suggest the occurrence of certain processes.

Regardless of which model for the blue and green emission of Cu in ZnS one wishes to accept, the presence of such emission requires the concept of some donor which is capable of compensating the single charge produced by Cu at a Zn site. In the present system, the only possibility seems to be interstitial Li. To support this, it may be pointed out that the sizes of the alkali metal ions are such that Li (strong emission observed), but not Na or K (little emission observed) can enter ZnS interstitially. The Cu-Li emission bands are displaced slightly to shorter wavelengths with respect to accepted values for hex. ZnS:Cu,Cl (5); the difference possibly arises from the influence of the different coactivator. Any simple analogy of this nature fails, however, because of the identical emission spectra observed in Cu-Li and Ag-Li activated phosphors.

Figure 5 shows that the infrared wavelength for maximum quenching of blue-green emission of ZnS:Cu,Li,Ti agrees with the value of 1300 mμ reported by Melamed for ZnS:Cu,Co (6). In the absence of Ti, there is, however, no agreement. Substitution of Cu by Ag causes a shift of one of the bands to longer wavelengths. It can probably be assumed that the mechanism of quenching involves electron capture, from the valence band, by ionized acceptor centers and the creation of a hole in the valence band (7). Inasmuch as the infrared band causing the quenching also stimulates the red emission, the latter evidently depends on the presence of such holes. Among different models which may be proposed, there seems to be none which satisfactorily explains all of the observed phenomena. The fact that the orange ZnS:Ag,Li,Ti emission band peaks at a shorter wavelength than the red ZnS:Cu,Li,Ti band suggests that the long wavelength transitions may occur from the conduction band to ionized Cu or Ag centers which, in association with Li or Ti, would have to occupy positions only 1.6 to 1.9 ev below the conduction band. If one wishes to avoid the concept of acceptor levels in those positions, transitions from highly associated donor levels may be visualized, such as proposed by Apple and Williams for the long wavelength emission in Ga- and In-activated phosphors (8).

It has been shown that in the absence of infrared radiation, efficient red emission depends on small but appreciable concentrations of Ti. The firing conditions (H_2S or H_2) suggest that Ti may be present in trivalent form and therefore acts as a donor, although not independently, *i.e.*, in the absence of Li. Accordingly, it should have no influence on the excitation spectra, as was observed. The shape of the glow curves shown in Fig. 7 indicates that red thermoluminescence originates from sites whose position is quite independent of Ti concentration[6] and may therefore not be associated with Ti. On the other hand, the lack of red thermoluminescence, below room temperature, of ZnS:Cu,Li after room temperature excitation, suggests that the number of electrons available for trapping at these sites was limited, evidently by lack of Ti. The concept of Ti as an auxiliary donor is involved and certainly requires further experimental evidence. Nevertheless, the fact that under simultaneous u.v. and i.r. excitation, the red emission of ZnS:Cu,Li was only 4 times smaller than the maximum obtained with Ti (see Fig. 4) indicates that Ti is not directly involved in this process. Qualitatively, its action rather resembles that of infrared radiation, *i.e.*, it facilitates the thermal filling of acceptor levels from the valence band. The mechanism by which this occurs has not been ascertained.

Acknowledgments

The writer wishes to thank Miss I. Walinski for phosphor preparations and Mr. I. Meister for determinations of emission spectra. He is also indebted to Dr. W. A. Thornton, Dr. H. F. Ivey, and Professor E. Banks for helpful discussions. This work was supported by Contract AF33(616)-7350 from the Wright Air Development Div., ARDC, U.S. Air Force.

Manuscript received Nov. 2, 1961.

Any discussion of this paper will appear in a Discussion Section to be published in the December 1962 JOURNAL.

REFERENCES

1. F. A. Kröger, *J. Opt. Soc. Am.*, **39**, 670 (1949).
2. A. Wachtel, *This Journal*, **109**, 306 (1962).
3. G. F. J. Garlick and D. E. Mason, *ibid.*, **96**, 90 (1949).
4. A. Halperin and H. Arbell, *Phys. Rev.*, **113**, 1216 (1959); **117**, 45 (1960).
5. F. A. Kröger, J. E. Hellingman, and N. W. Smit, *Physica*, **15**, 990 (1949).
6. N. T. Melamed, *This Journal*, **97**, 33 (1950).
7. H. A. Klasens, *ibid.*, **100**, 72 (1953).
8. E. F. Apple and F. E. Williams, *ibid.*, **106**, 224 (1959).

[6] The glow curves obtained on phosphors with 1, 2, 4, and 7 × 10^{-6} Ti were identical except for relative intensities.

Fabrication and Characteristics of Phosphorous-Diffused Silicon Solar Cells

J. Mandelkorn, C. McAfee, J. Kesperis, L. Schwartz, and W. Pharo

United States Army Signal Research and Development Laboratory, Fort Monmouth, New Jersey

ABSTRACT

Results of an experimental study of fabrication processes for making phosphorous-diffused silicon solar cells are presented. Solar cells having sheet resistance of 10 ohm/sq, high long-wavelength collection efficiency, and efficiencies above 10% were fabricated by diffusion at 975°C. Diffusions carried out at 875°C for ½ to 1 hr periods resulted in cells having high short- and long-wavelength collection efficiency. Gridded contacts applied to such cells to minimize effects of their comparatively high sheet resistance raised the efficiencies of the cells to values above 10%. Phosphorous-diffused cells in general have superior radiation resistance as compared to boron-diffused cells because of the slower rate of degradation of lifetime of minority carriers in p-type silicon as compared to n-type silicon under bombardment by atomic particles. The high short-wavelength collection efficiency of the 875°C diffused cells results in increased radiation resistance of these cells. Cells having efficiencies above 10% were made from 13-ohm-cm material and found to have higher radiation resistance than cells made from 1-ohm-cm material. Low junction reverse currents and contact resistances of approximately 0.2 ohm have also been achieved.

Until recently commercial silicon solar cells have been made by diffusion of boron into n-type silicon having a resistivity of 0.5 to 1 ohm-cm. Industrial efforts to improve the efficiencies and spectral response of silicon solar cells were concentrated on modification of boron-diffusion processes. A possibility completely overlooked was that phosphorous diffusion could be more successfully adapted to the creation of better solar cells.

The purpose of this paper is to present the results of a 2-yr study of phosphorous-diffused solar cells. The information will be presented in two sections. The first part deals with the diffusion conditions and processing methods that were found to yield phosphorus cells having desirable characteristics. The second part discusses the results obtained and the interrelationship of fabrication processes and solar-cell characteristics. The various characteristics considered are: (*a*) forward current-voltage behavior of the solar-cell diode, (*b*) contact resistance, (c) junction reverse current, (*d*) collection efficiency, (*e*) radiation resistance, and (*f*) temperature behavior.

Experimental

Material preparation.—Single-crystal silicon ingots were grown from transistor grade material, using the Czochralski technique, a necked down seed (1), a rotation rate of 14 rpm, and a pull rate of 4 in./hr. The melt was doped with a master boron-silicon alloy to produce p-type ingots with selected resistivities in the 0.2 to 40-ohm-cm range. Etch pit counts using the Dash etch (2) gave counts below 1000/cm^2 on wafers cut from several ingots. Typical counts were less than 100/cm^2.

Wafers cut from ingots were lapped with No. 1000 silicon-carbide abrasive in a planetary lapping machine and then given a finish lap with No. 3000 aluminum-oxide abrasive. After the wafers were thoroughly degreased and cleaned ultrasonically in organic solvents and distilled water, they were given a 5-min etch in a solution consisting of 20:12:2 parts of acetic acid, nitric acid, and hydrofluoric acid, respectively. Etching time was not found to be critical; however, prolonged etching (greater than 10 min) resulted in poor adhesion of subsequently plated nickel contacts to the surface of the wafers.

Diffusion.—After the wafers were etched, they were rinsed in distilled water, dried, and laid flat on a quartz-slab diffusion boat. The boat was inserted into a high-temperature zone of a laboratory-designed two-zone diffusion furnace, shown in Fig. 1. Dry oxygen, used as a carrier gas, was passed through the quartz diffusion tube at a flow rate of approximately 40 cc/sec. The constancy of wafer boat thermocouple readings indicated that the boat had reached temperature equilibrium. Following the attainment of equilibrium, a hollow quartz boat containing phosphorus pentoxide was moved forward in the source zone to a point that had been precalibrated for a temperature of 220°C. The phosphorous pent-

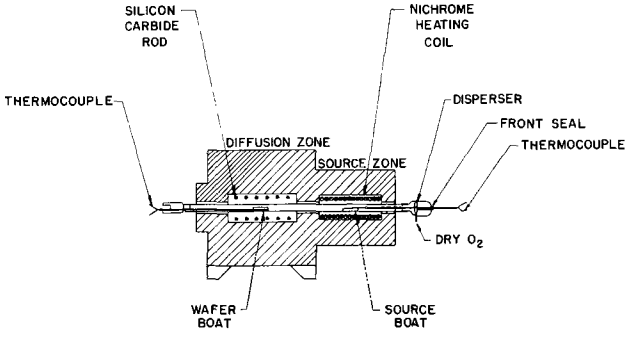

Fig. 1. Phosphorous-diffusion furnace

oxide vapors formed were transported to the diffusion zone by the carrier gas.

The establishment of a proper flow pattern of carrier gas and the degree of dryness of the carrier gas is critical. A silica-gel drying tube followed by two liquid-air traps removed water vapor from the carrier gas. The diffusion tube was sealed at its front end to prevent the entry of water vapor from the external environment. The diffusion process was terminated by withdrawal of the source boat and shutoff of power to the furnace. Carrier-gas flow was continued until the source vapors were removed from the system. The wafers were withdrawn from the furnace after they had cooled to a temperature of 600°C or less.

The process incorporates the following features that establish a flow pattern, yielding solar cells with very good junction characteristics: (*a*) the sequence of introduction of wafers, source vapors, and carrier-gas flow; (*b*) use of a moderate source temperature and a slow rate of carrier-gas flow; (*c*) a special fritted glass carrier-gas disperser, as shown in Fig. 1.

Application of contacts.—When the diffusion process was completed, the bottom surfaces of the wafers (those in contact with the quartz slab) were marked with acid-resistant paint. The surface layers formed on the wafers were removed by a 5-min soak in hydrofluoric acid, a 5-min treatment in boiling aqua regia, and a 1-min cleanup in hydrofluoric acid. The resultant surfaces were clean, without any traces of foreign films or discolorations, and presented a satin-smooth gray appearance.

A photoresist pattern was applied to mask the top surface. Nickel was plated in the form of a thin grid pattern with one wide stripe on the unmasked regions of the wafer by use of the electroless nickel-plating method (3). The bottom surface of the wafer was lapped to remove the nickel plating. The photoresist mask was removed from the top surface and Divco No. 335 Liquid Flux[1] brushed over the nickel-plated pattern on the top surface. The nickel-plated pattern was then covered with solder by dipping the wafer into a molten solder bath. The bottom of the wafer was lapped with No. 600 silicon-carbide abrasive and plated electrolytically with rhodium. Plating-current densities of 3-5 ma/cm^2 have yielded adherent low-resistance contacts.

Edge and surface finish.—The final fabrication steps consisted of dry-lapping the periphery of the wafers, using No. 600 silicon-carbide paper on a belt sander, and applying crystal-clear Krylon[2] over the active top surface to form an antireflective coating. The completed solar-cell structure is shown in Fig. 2.

Results

Diffusion.—A polished "control" wafer was diffused in each run to determine junction depths and sheet resistances. Junction depths were measured by angle lap and stain techniques (4). The estimated error of measurement is $\pm 0.1\mu$. Sheet resistances were calculated from 4-point probe measurements applying appropriate correction factors. Table I presents data typical of the results obtained using various diffusion temperatures and time periods for material of different resistivities.

[1] Trademark, Division Lead Co., Summit, Ill.

[2] Trademark, Krylon Inc., Norristown, Pa.

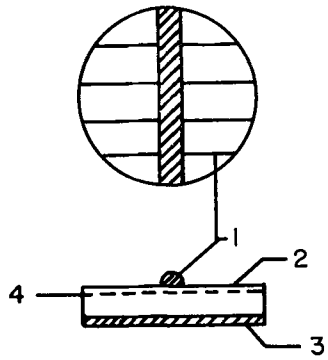

Fig. 2. Phosphorous solar-cell structure, active surface Krylon coated: 1, nickel plate, solder dip contact; 2, diffused layer-phosphorus; 3, contact-rhodium plate; 4, junction, 0.6μ deep.

No significant variation in junction depth with resistivity of material for equal temperatures and time periods of diffusion was detected. Sheet resistances for equal junction depths were found to depend primarily on carrier-gas flow pattern for investigated rates of flow between 10 cc and 40 cc/sec. Turbulent flow patterns introduced wide variation in sheet resistances of wafers diffused in the same run. Turbulence was decreased by use of a slower rate of carrier-gas flow, and better junctions were obtained. However, a flow rate of 40 cc/sec was necessary to achieve sheet resistances of less than 50 ohm/sq for 875°C ½-hr diffusions. The upper limit of 50 ohm/sq of sheet resistance was set by imposing a minimum efficiency requirement of 10% for cells made by the process. The 10 ohm/sq sheet resistance of 975°C diffused cells was sufficiently low to permit attainment of efficiencies above 10% without the use of gridded contacts. However, cells made by 875°C diffusion having sheet resistances above 50 ohm/sq were found to be limited to efficiencies below 10% even with the use of gridded contacts.

Calculations of surface concentrations were not made because of the anomalous characteristics of shallow phosphorous-diffused layers noted in this investigation and by other investigators (5).

Forward-diode characteristic.—The "n" value measurement is a nonconventional solar-cell measurement applied very successfully in this investigation to monitor diffusion processes. The n value as given in the modified ideal diode equation, $I = I_o(e^{qV/nkT} - 1)$, was determined from the slope of the log I *vs.* V plot of the solar-cell diode in the re-

Table I. Effects of diffusion temperature and time

ρ, ohm-cm	Temp, °C	Time, min	Junction depth, μ	ρ_s, ohm/sq
0.2	975	15	1.2	9
1	975	15	1.1	10
1	975	5	0.9	9
1	875	30	0.6	50
1	875	60	0.9	36
13	975	5	0.9	16
13	875	30	0.6	45
13	875	60	0.9	35

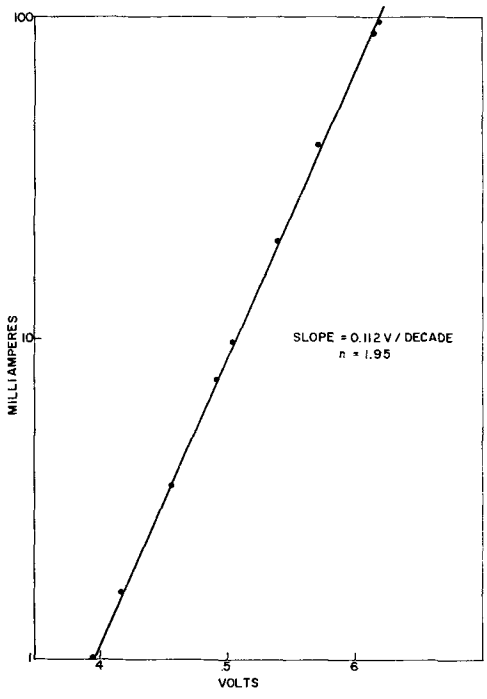

Fig. 3. Typical cell forward characteristic with n value below 2

gion of 1-100 ma of forward current. A typical n value characteristic showing a constant value of n over two decades of current is shown in Fig. 3.

The n value was found to be extremely fabrication dependent and a sensitive parameter for optimizing fabrication processes and controlling them. By the use of the process described, n values below 2 were normally obtained. High n values or increases in n value of cells made in particular runs have been related to the presence of excess water vapor during diffusion or turbulent flow patterns of carrier gas. The n value is directly related to junction reverse current and influences the open-circuit voltage and solar-cell junction impedance (6). Values of n of commercial boron cells and of boron cells made in this investigation (7) are generally well above 2. Often n values cannot be specified for boron-diffused cells because of the nonlinear relationship of log *I vs V* of such cells. The fact that the n value is fabrication dependent was further substantiated by the measurement of three selected boron-diffused cells that had n values below 2 and efficiencies in the range of 13 to 14.5%.

Contact resistance.—The slope of the solar-cell diode characteristic in the range of forward currents of 300-400 ma determines what is commonly referred to as the limiting diode forward resistance (LDFR). The LDFR depends primarily on contact resistance. This measurement was used in the investigation to determine the effects of various plating conditions and surface preparations on contact resistance. Typical values of LDFR presently obtained are in the 0.2-ohm range and this compares with values in the 1-ohm range common to commercial cells.

Instrumentation.—Monitoring of n value, LDFR, and junction reverse current was carried out rapidly by displaying "dark" cell voltage-current curves on the calibrated oscilloscope face of the Tektronix-575 Transistor Curve Tracer. Display of the illuminated solar-cell characteristic curve on the same instrument permitted rapid visual measurement of open-circuit voltage, short-circuit current, and comparative sheet resistance. Precise measurements of voltages and currents with a potentiometer and precision decade resistance box showed that the values obtained from oscilloscope readings are sufficiently accurate for evaluation of cell characteristics.

Where measurements in sunlight are indicated, these were made using a double-barrel narrow aperture system especially designed by the Eppley Laboratories for solar-cell measurements. The solar cell was mounted in one barrel while the incident radiation was monitored by a temperature-compensated thermopile in the other barrel. The system was mounted on an equatorial mount for tracking the sun.

Junction reverse current.—Dark cell reverse currents were measured for 0.6-v reverse bias. Reverse currents of 10-30 μa were commonly obtained. The only periphery treatment given the cells was dry belt sanding. The low junction reverse currents of these cells represent better than an order of magnitude improvement as compared to typical commercial boron-diffused cells and boron cells made in the investigation (7). The three selected boron cells previously mentioned had junction reverse currents of 10-20 μa.

Collection efficiency.—The ability of the process to preserve high values of lifetime in the base region of solar cells is evident from comparison of the integrated long-wavelength collection of the cells, as shown in Table II.

Table II gives the values of short-circuit current/cm^2, I_{sc}/cm^2, obtained by illuminating cells with light passed through a long-wavelength pass filter having a cutoff at 0.65μ. Under these conditions, hole-electron pairs were generated in the base well below the junction, and the integrated collection was an indication of lifetime of minority carriers in the base.

The equivalent collection values obtained for 975° and 875°C diffusions into material of the same resistivity indicated that the process preserved base lifetime equally well for both diffusion temperatures. The more than 10% higher collection obtained for the 13-ohm-cm cells represents a considerable difference in the lifetime in the base of these cells as compared to the lifetime in the base of the high-efficiency 1-ohm-cm cells. The reason for this is that collection

Table II. Comparison of integrated long-wavelength collection

1-ohm-cm base resistivity			13-ohm-cm base resistivity		
Cell	I_{sc}, ma/cm^2	Diff. temp, °C	Cell	I_{sc}, ma/cm^2	Diff. temp, °C
324-3D	7.4	975	331-1B	8.3	875
324-3E	7.6	975	331-1D	8.2	875
324-4B	7.3	975	331-2B	8.4	875
324-4C	7.8	975	331-2C	8.9	875
324-5B	7.5	975	331-2D	8.8	875
324-5C	7.3	975	331-3B	8.7	975
324-6B	7	875	331-3C	8.2	975
324-7B	7.5	875			
324-7C	7.3	875			

All cell surfaces bare.

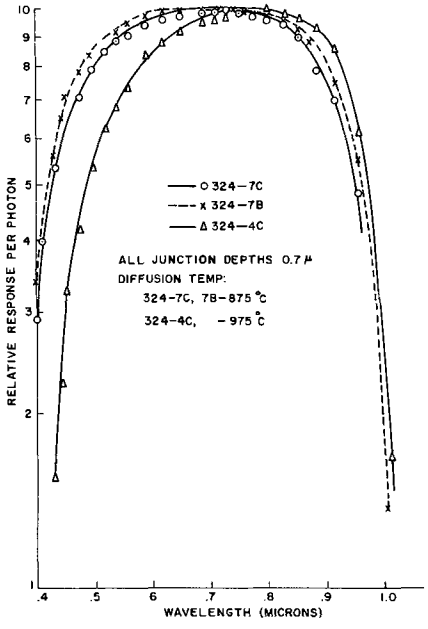

Fig. 4. Relative collection efficiency for 975° and 875°C diffusions (normalized to 10 at maximum).

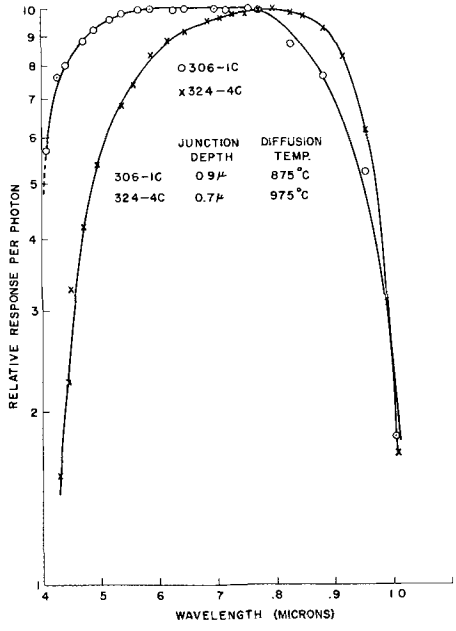

Fig. 5. Relative collection efficiency for a junction depth of 0.9μ (normalized to 10 at maximum).

increases slowly with increasing base lifetime for values of lifetime above 1 μsec.

Measurements of diffusion lengths of minority carriers generated in the base by electron bombardment revealed that lifetimes of 10-15 μsec were preserved in the 13-ohm-cm cells, whereas the lifetimes in the 1-ohm-cm cells were 3-5 μsec (8).

Although high long-wavelength collection can be achieved with diffusion temperatures of 975° or 875°C, high short-wavelength collection has only been obtained by 875°C diffusion. This is shown by the plots of relative collection efficiency *vs.* wavelength in Fig. 4. The curves are shown for cells having equal junction depths, and the only difference in fabrication is that the cells with the high "blue" collection were made by an 875°C diffusion. The curve for the 975°C cell (Fig. 4) is similar to that obtained for boron cells having "good blue" collection. High "blue" collection can also be obtained for comparatively deep junction depths (1-hr diffusion at 875°C), as shown in Fig. 5. Measurements of collection efficiency *vs.* wavelength of the USASRDL cells were made at several industrial laboratories, and the results agree with those presented here.

Table III. Comparison of short-circuit currents

13-ohm-cm base				1-ohm-cm base			
Cell	I_{sc}, ma/cm²	Diff. temp, °C	Time, min	Cell	I_{sc}, ma/cm²	Diff. temp, °C	Time, min
331-1B	33.5	875	30	324-4C	24.5	975	5
331-1C	32	875	30	324-6B	28	875	30
331-2B	30	875	30	324-7B	28	875	30
331-2C	34.4	875	30	324-7C	28.4	875	30
331-2D	32	875	30	13.5% Boron	31.2		
331-3B	28	975	5	14.5% Boron	31.4		
331-4B	26	975	5				
331-4C	27	975	5				

All measurements in sunlight.
Phosphorous cells Krylon coated; boron cells boron-diffusion coated.

The effects of high base lifetime and high "blue" collection on the short-circuit current of cells are shown in Table III.

Analysis of the data shows that an increase in short-circuit current per sq cm, I_{sc}/cm^2, of approximately 15% was obtained from the improved short-wavelength collection of 875°C diffused cells. An additional increase of 10% in I_{sc}/cm^2 was obtained from the higher long-wavelength collection of the high base lifetime 13-ohm-cm cells. The net increase results in values of I_{sc}/cm^2 of 13-ohm-cm 875°C cells above that obtained for a selected 14.5% boron-diffused cell. The referenced boron cell was the highest efficiency cell ever measured at this Laboratory.

The phosphorous-diffused cells were coated with Krylon, as indicated in Fig. 2. Cells of this type were sent to several industrial laboratories for application of more effective antireflective coatings. The short-circuit currents of the cells after coating with silicon monoxide were 8-10% higher than those obtained with Krylon coatings. The percentage increase in short-circuit current obtained by application of coatings, using the uncoated cell short-circuit current as a reference, is 15-20% for Krylon coatings and 30% for optimized silicon-monoxide coatings.

The efficiencies of the 13-ohm-cm cells were limited by sheet resistance and comparatively lower open-circuit voltages because of Fermi-level considerations. However, the very high short-circuit currents and low n values of these cells decreased their junction impedance, as shown in Fig. 6. The junction impedance is defined as $r_j = dV/dI$ under constant illumination.

Eleven per cent efficiencies were obtained for Krylon-coated high-resistivity cells (Table IV).

Application of optimum antireflective coatings should raise the short-circuit current of the cells by 8-10% and increase the efficiencies. Cells similar in characteristics to those shown in Table IV were made using 10-ohm-cm and 40-ohm-cm material.

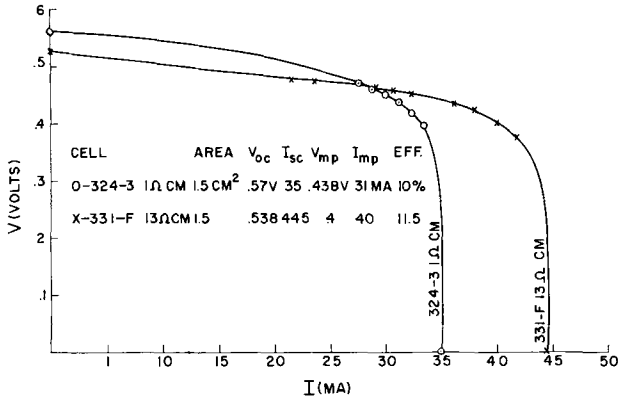

Fig. 6. Output characteristics of a 13 ohm-cm and a 1 ohm-cm cell.

Table V compares the characteristic "limits" of cells made in this investigation from material of several different resistivities.

It is difficult to obtain n values in the range of 2 and high open-circuit voltages in solar cells made from highly doped material. As shown in Table V, both open-circuit voltages and short-circuit currents are comparatively low for cells made from 0.2-ohm-cm material. The listed characteristics of the 1-ohm-cm base cells are similar to those of boron-diffused cells with the exception of the limiting diode forward resistance.

The high short-circuit currents obtained for cells made from high-resistivity material was a result of the high base lifetime and high short-wavelength collection of these cells.

Radiation resistance.—Analysis of collection efficiency *vs.* wavelength curves of solar cells before and after atomic bombardment revealed that the lifetime of minority carriers decreased more slowly in the p-type base material of phosphorous cells than in the n-type base material of boron cells (9-13). Direct measurement of base diffusion length degradation as a function of atomic bombardment was carried out for electron and proton bombardment over a wide range of bombarding particle energies (8). The collected data show that the phosphorous-diffused cell has superior radiation resistance compared to the boron-diffused cell.

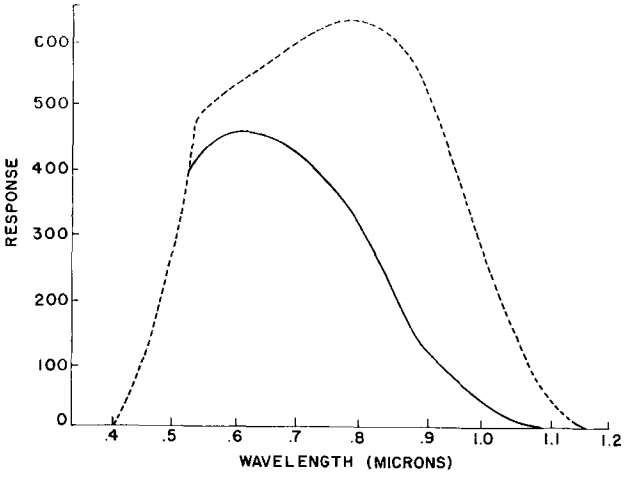

Fig. 7. Postbombardment collection degradation (absolute output in arbitrary units for equal photon input); - - - original; —— after bombardment.

Table IV. Characteristics of 13-ohm-cm 875°C cells

Cell	I_{sc}/cm², ma/cm²	V_{oc}	Temp, °C	Radiation, mw/cm²	Efficiency, %
331-A	25.8	0.538	30	85.5	11
331-B	27	0.538	30	86	11
331-C	25.9	0.536	30	86	10.8
Boron 14.5%	27.8	0.623	18	89.6	14.96
Boron 13.5%	27.6	0.620	18	89.6	13.96

All measurements in sunlight. Phosphorous-diffused cells gridded, Krylon-coated. Boron-diffused cells gridded, boron-diffusion coated.

Table V. Characteristics vs. resistivity of base material for typical solar cells

Resistivity, ohm-cm	V_{oc}, v	I_{sc}, ma/cm²	LDFR, ohm	Efficiency, %
0.2	<0.56	<22	0.2	<10
1	<0.60	<26	0.2	10-12
13	<0.55	<31	0.2	10-12

All cells measured in sunlight (intensity 88 mw/cm²).

The comparative radiation resistance of cells is also dependent on the short-wavelength collection efficiency. This dependency becomes stronger with increasing integrated bombardment flux. Measurements of absolute collection efficiency *vs.* wavelength showed that after bombardment which reduced the total "sunlight" short-circuit current of cells to 75% of their initial value, the collection at short wavelengths (0.6μ or less) had decreased by less than 5%. Figure 7 illustrates this effect for very heavy bombardment. Since approximately one-third of the short-circuit current of the 875°C phosphorous-diffused cells is obtained from short-wavelength collection, these cells have improved radiation resistance.

Further improvement in radiation resistance was obtained by fabricating cells with high-resistivity base material using 875°C diffusions. Table VI compares the short-circuit current degradation of cells in relation to diffusion temperature and base resistivity.

Although only small quantities of high-efficiency high-resistivity cells were subjected to bombard-

Table VI. Relationship of I_{sc}/I_{so} to ρ and diffusion temperature

Cell	ρ, ohm-cm	Diffusion temp, °C	$\frac{I_{sc}}{I_{so}}$, %
	1-Mev electron bombardment*		
326-2	1	875	73
331-1	13	875	81
331-2	13	875	81
331-4	13	875	81
	1.2-Mev proton bombardment**		
324-3	1	975	45
324-5	1	975	66
331-5	13	875	90

Cell original efficiencies >10% measurements in sunlight or equivalent. I_{so}, prebombardment value of I_{sc}.
* Based on measurements by Dr. W. Rosensweig and colleagues of BTL.
** Based on USASRDL measurements (13).

ment, it is significant that good consistency in results was obtained.

Temperature behavior.—The changes in open-circuit voltage, short-circuit current, and efficiency of phosphorous solar cells with increasing temperature in the 25°-125°C temperature range were found to be similar to those of boron-diffused cells (14).

Conclusions

The investigation resulted in a phosphorous-diffusion process that yields solar cells with the following desirable characteristics: 1, efficiencies above 10%; 2, n values of 2 or less; 3, junction reverse currents of 10-30 μa for reverse bias of 0.6v; 4, contact resistances in the range of 0.2 ohm; 5, high short-wavelength collection (1/3 of I_{sc} from short-wavelength collection); 6, very-high long-wavelength collection efficiency for high-resistivity base cells; 7, superior radiation resistance.

The 875°C diffusion process has already been adapted for production of solar cells for use in communications satellites (15). A recent outer space experiment has verified the superior radiation resistance of the phosphorous-diffused solar cell (16).

The most promising approach to further improvement of phosphorous-diffused cells is believed to be the study of effects of electrically inactive impurities in silicon on characteristics of solar cells. Another area requiring research is the interactions of impurities and imperfections in the region of the junction.

Acknowledgments

The authors wish to give special acknowledgment to F. M. Smits and his colleagues at the Bell Telephone Laboratories for their significant work in the study of radiation behavior of solar cells. Acknowledgment is also made to Joseph Wysocki, RCA, David Sarnoff Research Center, Princeton, New Jersey, for collection-efficiency measurements, and to Calvin Davidson and Margaret Palmateer, USASRDL, for preparation of material. The authors have been encouraged in this investigation by William R. Cherry, Chief, Semiconductor and Microelectronics Branch, USASRDL.

Manuscript received Aug. 15, 1961; revised manuscript received Dec. 11, 1961.

Any discussion of this paper will appear in a Discussion Section to be published in the December 1962 JOURNAL.

REFERENCES

1. W. C. Dash, *J. Appl. Phys.*, **29**, 736 (1958).
2. W. C. Dash, *ibid.*, **27**, 1193 (1956).
3. M. V. Sullivan and J. H. Egler, *This Journal*, **104**, 226 (1957).
4. C. S. Fuller and J. A. Ditzenberger, *J. Appl. Phys.*, **27**, 544 (1956).
5. E. Tannenbaum, *Solid State Electronics*, **2**, 123 (1961).
6. J. Mandelkorn *et al.*, "Junction Characteristics of Silicon Solar Cells," to be published.
7. J. S. Kesperis and R. S. Yatsko, *This Journal*, **107**, 11 (1960).
8. F. M. Smits, Bell Telephone Laboratories, Private communication.
9. "Investigation of High-Temperature Improved-Efficiency Photovoltaic Converter," Final Progress Report, RCA, David Sarnoff Research Center, Princeton, N. J., Signal Corps Contract DA36-039 sc-78184 (Cognizant Agency, USASRDL).
10. "Semiconductor Photovoltaic Conversion," Triannual Reports 1 and 2, RCA, David Sarnoff Research Center, Princeton, N. J. (Cognizant Agency, USASRDL).
11. "Radiation Damage to Silicon Solar Cells," Quarterly Reports 1-3, RCA, David Sarnoff Research Center, Princeton, N. J. (Cognizant Agency, National Aeronautics and Space Administration, Goddard Space Flight Center).
12. J. Mandelkorn *et al.*, "Phosphorus Solar-Cell Fabrication and Radiation Resistance Behavior," USASRDL Conference on Solar Cells, 8 Dec. 1960.
13. J. Mandelkorn *et al.*, "A New Radiation-Resistant Silicon Solar Cell," USASRDL Technical Report 2162.
14. J. Mandelkorn *et al.*, *Proc. Fourteenth Annual Power Sources Conf.*, 42-45 (1960).
15. F. M. Smits, K. D. Smith, W. L. Brown, *J. Brit. IRE*, **22** [2], 161 (1961).
16. Unpublished data—MIDAS III Solar Cell Experiment.

Purification of Tellurium by Distillation

Bruce D. Wedlock

Department of Electrical Engineering, Energy Conversion Laboratory, Massachusetts Institute of Technology, Cambridge, Massachusetts

ABSTRACT

A rapid method is described by which tellurium and materials of similar vapor pressures may be separated from less volatile impurities such as antimony and various oxides. The technique consists of multiple distillation under a continuously pumped vacuum. A mechanical arrangement has been devised which employs a reusable crucible, thereby increasing the speed of the operation. Evaluation indicates that one operation will produce tellurium with an electrically active impurity concentration of 4 x 10^{14}/cc from material with considerable surface oxides.

The increasing interest in thermoelectric energy converters during the past few years has resulted in a large research effort in the area of intermetallic semiconducting tellurides, notably bismuth telluride and lead telluride. In addition, mercury telluride, cadmium telluride, and molybdenum telluride also are receiving increased attention. As research in each of these materials progresses, it is necessary to produce crystals of the highest possible perfection, both chemically and crystallographically speaking, if de-

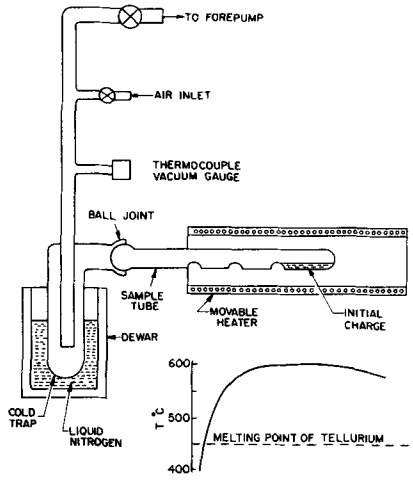

Fig. 1. Tellurium distillation apparatus

tailed experiments on their transport properties and band structure are to yield meaningful results. In an effort to produce such high-quality single crystals by both the Bridgman and Czochralski techniques, it was determined experimentally that the "high-purity" tellurium as commercially supplied[1] required further purification. Accordingly, the scheme of multiple distillation under a continuously pumped vacuum was employed with considerable success.

A system was designed to employ a reusable sample tube. This feature reduced the time required to purify a given sample inasmuch as glass blowing operations associated with individual sample tube preparation have been eliminated. At present, using a 25 mm tube the system has an output capability of approximately 35g of purified tellurium per hour.

System Description

A schematic diagram of the tellurium distillation apparatus is shown in Fig. 1. It consists of a sample tube, surrounded by a moveable heater and connected to a vacuum system by means of a ground-glass ball joint. The sample tube, made entirely of Vycor, consists of three sections formed by semicircular indentations of the tube wall. The tube is sealed at one end and provided with a Vycor ground ball-joint at the other. This ball-joint mates with a Pyrex ball-joint on the vacuum system, thereby eliminating the need for a graded seal. The heater power is controlled by a Variac, and the temperature is monitored by a thermocouple mounted on the inside wall of the heater.

The tellurium to be distilled is placed at the closed end of a clean, dry sample tube. The tube then is connected to the vacuum system and pumped down to a pressure of approximately 1μ. The movable heater is placed so that only the end section of the sample tube will be above the melting point of tellurium. The heater temperature is then brought up to approximately 500°C, whereby the molten tellurium condenses in the center section of the tube. The heater is then moved so that the center section is now included and the temperature raised to approximately 600°C. The tellurium then recondenses in the third section. It is important that a temperature profile similar to that shown in Fig. 1 be maintained along the sample tube. Otherwise, if the temperature of the right-hand section is allowed to drop below that of the center section, back-distillation will take place, with a resulting loss of some of the tellurium. Finally, the condensed tellurium in the third section is melted down by moving the heater to form an ingot, and the tube is cooled rapidly in air by retracting the movable heater. After the tube is cooled, the purified tellurium may be removed without breakage by rotating the tube and sliding the ingot past the last indentation and out through the ball joint. In this way, the tube may be reused.

[1] American Smelting and Refining Co., South Plainfield, N. J.; semiconductor grade, 99.999% pure tellurium.

Experimental Evaluation

In order to obtain some quantitative measure of the effectiveness of this method of purification, an evaluation program was proposed and executed. Considerable information is available (3, 4) on the effects of impurities on electrical conductivity in tellurium. Since these data established that most acceptors are nearly fully ionized down to liquid nitrogen temperature and for impurity concentrations less than 10^{20}/cc the mobility may be assumed constant at a given temperature, it was decided to employ electrical conductivity measurements as a measure of the purity of tellurium. In addition to measurements of improvement on commercially supplied "high-purity" tellurium, the effect on antimony impurity also was investigated.

Sample preparation.—In order to reduce the effect of anisotropy ($\sigma_{||}/\sigma_{\perp} = 2$) (4) in the conductivity measurements, samples were taken from large grain material and the current axis was chosen along the parallel direction. Samples measured approximately 0.2 x 0.2 x 1 cm. Current contacts were soldered with indium solder, and voltage probes were attached by welding fine gold wires. Samples were etched in dilute aqua regia momentarily prior to measurements.

Estimation of carrier concentration.—The dashed line in Fig. 2 represents an experimentally determined curve of hole concentration as a function of electrical conductivity at 167°K ($10^3/T = 6.0$). This relationship will be used to estimate the carrier concentrations quoted in the following sections. We believe that these estimations will be accurate within

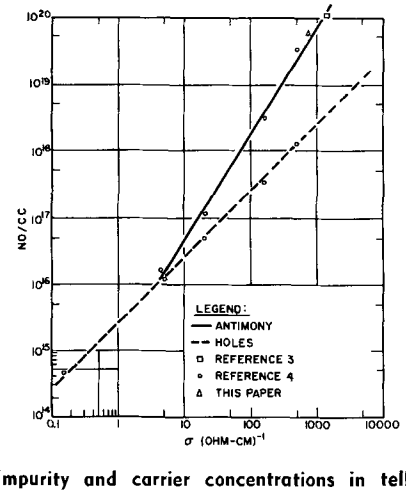

Fig. 2. Impurity and carrier concentrations in tellurium as a function of conductivity at 167°K.

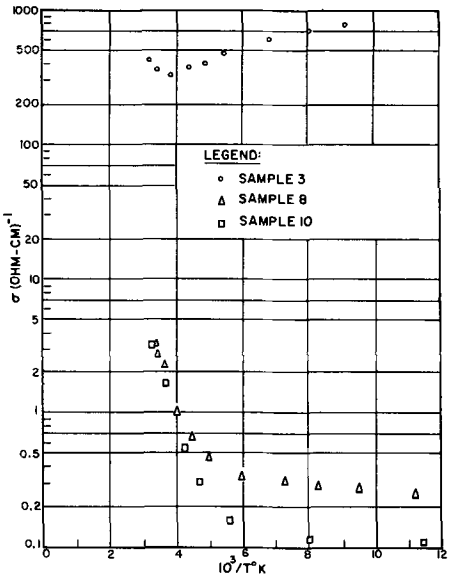

Fig. 3. Effect of distillation on commercial high-purity tellurium

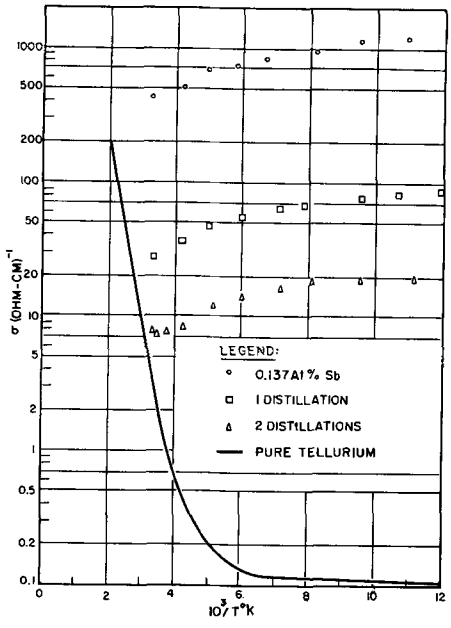

Fig. 4. Effect of distillation on antimony concentration in tellurium.

perhaps a factor of two and hence sufficient for this evaluation program.

Commercial high-purity tellurium.—It has been found that by distillation commercial high-purity tellurium can be further purified. This material as supplied consists of large lumps as well as small pieces and fine powder. Sample 8 was cut from a large piece of tellurium as received. Sample 3 was cut from an ingot produced by melting under vacuum small pieces and powder as received. Even though the tellurium is stored under vacuum, the small pieces and dust absorb a considerable amount of oxygen due to their large surface to volume ratio. From Fig. 2 and 3 we find that in the low-temperature extrinsic range sample 3 exhibits greater than 10^{18} holes/cc compared to 8 x 10^{14} holes/cc for sample 8. Sample 10 was produced by one distillation from a batch of small pieces and dust, special care being taken to keep the oxidized material out of the section where the final product is cooled. As usual, a sizeable quantity of white residue remained in the initial section of the distillation tube. The compositon of this residue is unknown, but certainly contains oxides of tellurium. The hole concentration at 167°K in sample 10 is on the order 4 x 10^{14}/cc. The conductivity curve for sample 10 represents the limit which has been achieved consistently for one distillation of commercial high-purity material. The carrier concentration in sample 10 agrees with the best materials prepared by Kronmuller *et al.* (4) and with tellurium which has been zone refined with 300 passes by Aigrain (1). This limiting value of carrier concentration may represent the best that can be obtained by distillation or zone refining or may be due to the large number of crystal imperfections introduced by even the most careful handling of the material.

Antimony doped tellurium.—Since the conductivity of tellurium is very sensitive to antimony doping and since at 600°C the vapor pressure of antimony is 10^3 less than that of tellurium, it was decided to attempt separation of antimony by distillation. A sample doped with 5 x 10^{19}/cc antimony atoms was distilled successfully and samples prepared. The results of this experiment are presented in Fig. 4. Using Fig. 2 it may be seen that one distillation reduced the antimony concentration to 6 x 10^{17}/cc and two distillations reduced it to 7 x 10^{16}/cc. A third distillation yielded essentially the same result as two distillations, indicating that an equilibrium situation was reached with two operations.

Conclusions

It has been shown that the quality of commercial high-purity tellurium can be improved substantially by a simple vacuum distillation technique. The success of this method has been measured directly by carrier concentration improvement as summarized in Table I, and indirectly by success in growing high quality single crystal material by both the Bridgman and Czochralski techniques. In the case of antimony, a limiting impurity level of 7 x 10^{16} was obtained after two distillations.

Acknowledgment

The research reported in this paper has been sponsored by the Electronics Research Directorate of the Air Force Cambridge Research Center, Air Research and Development Command, under contract

Table I. Summary of purification of tellurium by distillation

Impurity	Initial hole concentration No./cc T = 167°K	Number of distillations	Final hole concentration No./cc T = 167°K
Large lumps (oxides)	8 × 10^{14}	1	4 × 10^{14}
Small pieces and powder (oxides)	10^{18}	1	4 × 10^{14}
Antimony	5 × 10^{19}*	3	7 × 10^{16}*

* Antimony concentration.

AF19(604)-4153 wih the Energy Conversion Group, Department of Electrical Engineering, Massachusetts Institute of Technology. This paper, although based on work sponsored by the U.S. Air Force, has not been approved or disapproved by that Agency.

Manuscript received Nov. 3, 1961. This paper was presented at the Conference on the Ultrapurification of Semiconductor Materials, April 1961; and originally appeared in the conference proceedings published by the Macmillan Company, New York.

Any discussion of this paper will appear in a Discussion Section to be published in the December 1962 JOURNAL.

REFERENCES

1. P. Aigrain, Private communication.
2. C. H. Cartwright and M. Haberfield Schwartz, *Proc. Royal Soc.*, **148A**, 648 (1935).
3. T. Fukuroi, S. Tanuma, and S. Tobisawa, *Sci. Rep.* Res. Insts. Tohoku Univ., A4, 283 (1952).
4. Von H. Kronmuller, J. Jaumann, and K. Seiler, *Z. Naturforsch.*, **11A**, 243 (1956).

Sources of Contamination in GaAs Crystal Growth

L. Ekstrom and L. R. Weisberg

RCA Laboratories, Radio Corporation of America, Princeton, New Jersey

ABSTRACT

Current evidence indicates that the purity of GaAs is now limited by contamination during crystal growth, rather than by the purity of the starting materials. A careful study has been carried out to identify sources of such contamination in the preparation of GaAs. Vacuum baking of gallium at 650°C for several hours in a quartz boat to remove oxides was found to increase the copper content, but not the silicon or other spectrographically detectable impurities. Back diffusion of impurities from a contaminated high vacuum pump was observed to affect properties of GaAs even when pressures of 10^{-6} torr were maintained. Sealing under vacuum of large (20 mm) diameter quartz ampoules introduces significant quantities of silicon and copper onto the inner ampoule walls, which subsequently contaminate arsenic vapor when heated to above 1000°C. During growth, it was found that there is no appreciable diffusion of atmospheric gases through quartz at 1200°C. However, nearly 10^{18} molecules of gas are released due to outgassing of the walls. The most serious contamination, especially with silicon, occurs from the reaction between the GaAs melt and the quartz boat, and the reaction increases rapidly with increasing melt temperature.

The application of GaAs for transistors and transistor-like devices requires a material of extremely high purity in single crystal form. Past efforts to increase the purity of GaAs have centered on the purification of the component elements, gallium and arsenic, because of the existence of impurities that could not readily be removed from GaAs by zone refining. The impurity content of commercially available gallium and arsenic has now been reduced to the point where it is comparable to or below the amount of impurities introduced into GaAs by contamination during its preparation. The following evidence supports this conclusion.

First, emission and mass spectrographic analyses have detected impurities, such as silicon and copper, in GaAs in concentrations greater than that present in the starting materials. Second, series of GaAs crystals produced from the same lots of gallium and arsenic have had widely varying electrical properties. However, variations in the lots of gallium and arsenic have produced only minor changes in the electrical properties of the resulting GaAs. Third, special purification treatments carried out for gallium and arsenic have improved the properties of other compounds such as InAs, but have had little or no effect on the properties of GaAs.

For these reasons, this investigation was carried out to determine the sources of such contamination and thus provide guidance in devising improved methods of preparation. The investigation is specifically concerned with the horizontal Bridgman technique of crystal growth; however, the results are applicable to other methods of crystal growth. The details of the preparation of a GaAs growth ampoule for this growth technique are described in the following section. In subsequent sections each step in this procedure is carefully examined for possible sources of contamination. Throughout this paper, it is implicit that careful precautions were taken to remove the obvious contamination sources such as dust and similar foreign matter, to use gloves where required, etc.

Preparation of GaAs

The arsenic was received in chunks each weighing approximately a gram, sealed in a Pyrex ampoule in 50 or 100 g lots. After being opened, the Pyrex ampoule was stored under vacuum in a larger Pyrex ampoule, sealed by a vacuum stopcock. The gallium is received in a polyethylene bag as a large lump. To remove pieces, the gallium was cooled to liquid nitrogen temperature, placed in "Glassine" paper bags, and cracked by squeezing in a vise. It was subsequently stored in these bags within a closed glass jar inside an air tight cabinet.

The ampoule, shown in Fig. 1, consists of a quartz tube of 20 mm bore with a ball joint at each end and a breakseal dividing it into two chambers. All quartz ware, including the tube, growth boat, and slug for

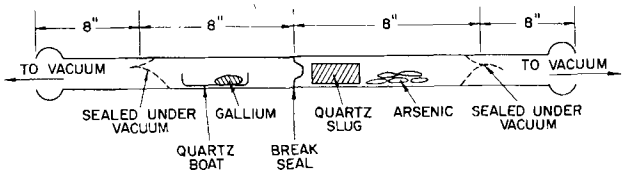

Fig. 1. GaAs growth ampoule

rupturing the breakseal, was cleaned by first washing it in a detergent such as "Alconox", then treating it with aqua regia, then etching with a 1:1 mixture of HF and HNO_3, and finally cleaning in a mixture of triple distilled HNO_3 and HCl. Each step was followed by extensive rinsing in triple distilled water, and after the final rinse, the water was removed using transistor-grade acetone which was drained, and the quartz allowed to dry in air. The quartz slug and the arsenic were loaded in air into one chamber of the tube, and the tube was then connected through a liquid nitrogen trap to a diffusion pump and evacuated. The arsenic was heated in a vacuum of below 10^{-6} torr for 1 hr at 300°C to remove surface oxides and then that section of the ampoule was sealed under vacuum after first collapsing the tube with a broad flame produced by a brass hydrogen-oxygen torch.

Next, the growth boat containing solid gallium was placed in the other chamber of the tube, which was then evacuated before the gallium was melted. A vacuum heat treatment of 3 hr at 650°C was given to remove oxides of gallium as Ga_2O, after which the gallium was refrozen and the ampoule sealed off using the same technique as for the arsenic section. The final ampoule is shown in Fig. 1.

After the breakseal was ruptured by causing the quartz slug to strike it, the GaAs was synthesized and grown into a crystal in a typical two zone horizontal Bridgman furnace (1). In synthesizing the GaAs, the entire system was brought up to the arsenic reservoir temperature of about 600°C, and then the temperature of the reaction zone containing the molten gallium was gradually raised to about 1260°C. The crystal was then grown by moving the entire furnace over the stationary quartz tube at a rate of about 1 cm hr^{-1} for a total period of 16 hr.

Effects of Cleaning and Handling Procedures

It was first determined whether the ordinary rinsing with distilled water is sufficient to remove the acids used for cleaning. This was found by measuring the resistivity of the water after each rinse. A 1:1 mixture of HCl-HNO_3 was placed in a quartz ampoule for 1 hr. This mixture was then discarded and replaced with deionized water, which remained in the ampoule for various times (usually 10 sec). After a number of rinses, the rinse water was also boiled in the ampoule. Typical results are shown in Table I. It can be seen that even ten rinsings with cold deionized water is not sufficient to remove all traces of impurities subsequent to acid cleaning. Instead, it is at least necessary to boil the water for a half hour in the vial.

Experiments were also carried out to determine if the cleaning procedure itself was adequate. Many

Table I. Effect of rinsing treatment on removal of acids from ampoules

Rinse No.	Conditions	Water resistivity, megohm-cm
0	Original water	2
4		0.035
5		0.2
6	All rinses through No. 10	0.3
7	in ampoule for 10 sec.	1.0
8		1.5
9		1.8
10		2
11	Boiled for ½ hr	0.8
12	10 sec	2
13	Boiled for 1-½ hr	1.8
14	10 sec	2
15	10 sec	2

variations were tested, such as treating different ampoules with HF only, HF followed by aqua regia, or aqua regia alone, using nondistilled acids, eliminating the acetone rinse, etc. It was noted that a scouring agent such as "Ajax" should be avoided since it is not dissolved by aqua regia. Variations were also attempted in the handling of the elements such as weighing out and transferring gallium as a liquid rather than a solid (2), the use of filter paper instead of "Glassine" paper, and plastic instead of stainless steel forceps. Despite all of these variations, no difference could be seen in the properties of the resulting GaAs. The conclusion can be drawn that the cleaning procedure used for quartz and the handling techniques for the elements are not significant variables compared to contamination sources described in the sections to follow.

Effects of Vacuum Baking and Sealing

During the vacuum annealing of the gallium and arsenic to remove oxides and the subsequent sealing of the evacuated ampoules, there are several ways in which contamination might occur. The three which have been investigated are back diffusion of impurities from the vacuum pump, reaction between gallium and the quartz boat during bakeout, and evolution of material from the quartz while it is being sealed.

Contamination from vacuum pumps.—Both oil and mercury diffusion pumps have been used in the preparation of GaAs ampoules, and no significant difference was noted in the purity of the resulting GaAs. On certain occasions, the vacuum pumps have been cleaned or new vacuum pumps have been used. In general, this has caused no improvement in the properties of the GaAs, except on one occasion (2). In this case, a series of crystals were produced with electron mobilities on the average below 4000 cm^2 v^{-1} sec^{-1}. Many variations were attempted, but the mobilities did not improve until the mercury diffusion pump was dismantled and cleaned. The resulting change in the mobility is shown in Fig. 2. The points with the attached bars indicate crystals of GaAs produced from the same lots of gallium and arsenic. Not all crystals grown are included in the graph, because some were doped or else grown under special conditions. The importance of a clean vacuum

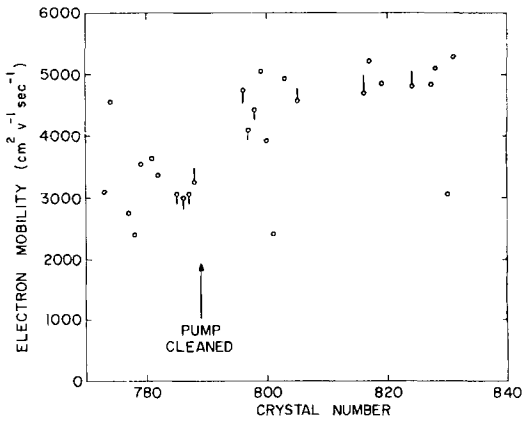

Fig. 2. Electron mobility of GaAs crystals before and after cleaning of the mercury diffusion pump.

system is manifest from these results. However, this result is somewhat surprising since the system was producing vacuums of the order of 10^{-6} torr both before and after the cleaning. At this pressure, the number of residual gas molecules in the ampoule is about 10^{13} while the change in properties corresponds to 10^{17} atoms or more. It would appear that material was continuously diffusing back from the pump through the trap and condensing on the walls.

In further tests of the effects of vacuum systems, the vacuum grease in the ball and socket joints used to attach the cold trap and growth ampoule to the vacuum system was replaced by black vacuum wax. This wax does not have a tendency to flow out of the joint into the system and reportedly has a vapor pressure of only 10^{-8} torr at room temperature. However, this substitution did not improve the purity of GaAs prepared with this vacuum system.

Vacuum baking of gallium.—The next possibility is that gallium might react with the quartz boat during the vacuum anneal and become contaminated, especially with silicon. Gallium is known to react with quartz readily at higher temperatures (3), so there was reason to suspect that this reaction might also be occurring a 650°C to a significant extent. To test this possibility, gallium samples were subjected to the same annealing conditions used in preparing an ampoule, except that the annealing time was increased to 12 hr from the usual 3 hr to exaggerate any effects. Changes in the impurity content of the gallium were determined by emission spectrographic analysis before and after the anneal. In each case, several samples were analyzed, and the reported impurity concentration is the geometric mean of the results. This averaging process was necessary, since the spectrographic analysis was semiquantitative and accurate to within only a factor of three. To differentiate between bulk contamination of the gallium and impurities which collect on, or segregate to the surface of the gallium, two types of samples were taken for analysis. The first consisted of pieces from the interior of a 5g ingot of gallium, obtained by fracturing the ingot. The other type was a piece of gallium small enough to be used directly in the spectrograph, thus including the entire original surface. The samples were treated simultaneously in a suitably compartmented boat. Table II shows the results

Table II. Impurities introduced during the vacuum baking of gallium in quartz

Gallium treatment	Type of sample	No. of samples	Spectrographic impurity content in ppm Si	Mg	Fe	Cu
As received	—	5	<0.1	0.3	2	<1
12 hr at 650°C, pressure of 3×10^{-6} torr	interior	2	<0.1	0.2	1	2
	exterior	3	<0.1	0.3	2	3
12 hr at 650°C, pressure of 5×10^{-5} torr (air leak)	interior	2	1	<0.1	2	<1
	exterior	3	5	0.5	3	1

of such a heat treatment on the gallium using both a tight vacuum system and one with a small air leak. It can be seen that no detectable silicon contamination occurs due to the baking process at 650°C provided there is no oxygen present. However, one of the oxides of gallium apparently attacks quartz at this temperature. It can also be seen that there is no evidence for iron and magnesium contamination, but that the copper content is increased. The copper could be leached from the quartz boat, since quartz is known to contain copper that easily diffuses out (4). Since copper has a small distribution coefficient in GaAs, this source of contamination has little effect on the electrical properties of the grown crystals.

Sealing of the ampoule.—During the sealing of the ampoule the quartz is heated above its softening point. The quartz vaporizes with some decomposition at these temperatures and redeposits in part on cooler portions of the quartz as manifested by the appearance of a rough white film. The decomposition products include oxygen (5) which could enter the ampoule, as could the gases from the oxy-hydrogen flame. Thus, the sealing procedure might first introduce gaseous impurities into the ampoule; second, directly contaminate gallium or arsenic within the ampoule; and third, contaminate the inner ampoule walls and thereby contaminate the arsenic vapor during growth.

The first possibility was investigated by attaching a thermocouple gauge to a quartz ampoule, which was subjected to the same cleaning and vacuum baking process used for growth ampoules. After sealing of the ampoule, the pressure in the ampoule was below the 10^{-3} torr detection limit of the gauge, indicating that a total of less than about 5×10^{15} gas molecules are trapped in the ampoule due to the sealing process. This represents a comparatively negligible amount of contamination in the GaAs crystal, which is usually about 4 cm^3 in volume.

The possibility of direct deposition of decomposition products onto the gallium was investigated by preparing an ampoule containing a compartmented boat with both large and small gallium samples similar to the experiment described in the previous section. After the usual vacuum baking and freezing, the quartz ampoule was sealed at a point beyond the boat and vacuum pump. Thus, if there were a flow of material toward the vacuum pump, it would enhance the effects of deposition. Subsequent to the sealing, the samples were spectrographically analyzed. Results are shown in Table III, which also includes re-

Table III. Impurities introduced during the sealing of an ampoule

Material and treatment	No. and type of sample	Spectrographic impurity content in ppm Si	Mg	Fe	Cu
Gallium (as received)	5	<0.1	0.5	3	<1
Gallium (after vacuum bake and sealing)	2 interior	<0.1	1	nd	1
	3 exterior	<0.1	1	1	1
Arsenic (as received)	3	0.1	<0.1	nd	nd
Arsenic (after vacuum bake and sealing)	3	<0.1	nd	nd	nd

sults for a similar experiment with arsenic. The analysis of the interior samples of gallium indicates that no accidental introduction of impurities occurred during the vacuum baking within the limits of error. It can be concluded, therefore, that direct deposition of impurities onto the elements is not a significant source of contamination.

The third experiment on the sealing of quartz tubing dealt with the possibility of the deposition of impurities on the ampoule walls from the sealing operation with subsequent contamination of the arsenic vapor during crystal growth. The procedure was again designed to duplicate the conditions prevailing in the growth of GaAs. A 20 mm bore quartz ampoule, cleaned in the usual manner, was degassed in vacuum for 2 or 3 hr at 700°C, cooled, and about 0.3g of arsenic was then introduced without breaking the vacuum. This amount of arsenic was calculated to be just sufficient for complete vaporization. After vacuum baking to remove arsenic oxides, the ampoule was sealed under vacuum and placed in a two-zone furnace for periods of about 16 hr with the sealed end held at 1220°C and the opposite end at 600°C. After this treatment, care was taken to cool the ampoule slowly and at the cooler end first. In this manner the arsenic condensed in the form of lumps, rather than as large area thin sheets. The condensed arsenic was recovered by breaking the ampoule. Changes in the impurity content of the arsenic were determined by spectrographic analyses before and after this exposure to quartz. In all cases, the arsenic starting material was found to contain only two impurities: copper at or below the detection limit of 1 ppm, and silicon at or below 0.2 ppm. For each run, four samples of arsenic were analyzed. The reported impurity concentration represents the geometric mean of the four results.

The typical contamination of arsenic that is observed due to the sealing is shown in the first two rows of Table IV for two separate runs. A large increase in both the silicon and copper content of the arsenic can be seen. To try to enhance this effect, several runs were made in which multiple seals were performed on the ampoule, each seal being made closer to the arsenic. The results of one such run using 6 seals is shown in the third row. The absence of a proportional increase in the contamination is probably caused by much of the vaporized material depositing very close to the seal, so that most of the contamination comes from only the last seal.

In the above experiments the possibility existed that the arsenic simply attacked the quartz walls, and the contamination was not related to the sealing process. To test this possibility, ampoules were constructed with the 20-mm bore quartz ampoule terminating with 6-mm bore tubing. Much less heating is required to seal 6-mm bore quartz tubing than 20-mm bore tubing so less quartz is vaporized. As shown in Table IV in the last two rows, this reduces the arsenic contamination to below the limits of detection.

Next, the effect of temperature on the above reaction was investigated. To exaggerate any effects so that they could be easily observable, four to five seals were made on the 20 mm bore tube for each run. The sealed end of the ampoule was held in different runs at 700°, 1000°, and 1220°C while the opposite end was held at 600°C. The improve reliability, separate runs were made two or three times at each temperature. The results in Table V represent geometric averages of 8 or 12 analyses. The usual contamination discussed previously is shown in the first row. It can be seen that reducing the temperature to only 1000°C is not sufficient to remove the contamination completely; and to do so, a temperature as low as 700°C must be employed.

Although contamination due to sealing of quartz has been demonstrated, no unambiguous effect of sealing has been noted on the electrical properties, indicating that other sources of contamination are more important.

Table IV. Effect of sealing quartz on contamination of arsenic after heating at 1220°C for 16 hr

No. of seals	Quartz bore, mm	Spectrographic analysis, ppm Si	Cu
1	20	3	4
1	20	4	9
6	20	10	7
1	6	0.05	<1
1	6	0.2	1

Contamination during Crystal Growth

Gaseous impurities from quartz.—In general, it is known that fused quartz can release considerable quantities of gases when heated, and is quite permeable to both helium (6) and hydrogen (7) at elevated temperatures. The latter fact suggests that atmospheric gases might also diffuse through the quartz ampoule at the melting temperature of GaAs. Therefore, the effect of both diffusion through and desorption from quartz has been investigated at temperatures used during GaAs crystal growth.

The literature on the diffusion of gases other than H_2 and He through fused quartz is conflicting, and does not include studies above 1000°C. T'sai and

Table V. Contamination of arsenic at various temperatures due to sealing of 20-mm bore quartz tubing

No. of runs	No. of seals	Temp, °C	Spectrographic analysis, ppm Si	Cu
3	5	1220	4	3
3	4	1000	1	1
2	4	700	0.1	1

Hogness (7) report no observable diffusion of air through quartz at 1000°C. Nevertheless, based on Barrer's (8) data, Dushman (9) calculates a permeability rate for N_2 at 1100°C high enough to allow over 10^{19} N_2 molecules to enter an ampoule during a routine crystal growth. However, Barrer's work failed to take account of the outgassing of quartz. In order to distinguish between diffusion and degassing as the source of this gas, experiments were conducted with an apparatus similar to that of T'sai and Hogness (7).

The present apparatus consisted of two fused quartz tubes, one inside the other and so connected that the outer one could be either evacuated or open to the atmosphere. The inner tube was connected to a thermocouple gauge and to a diffusion pump by means of a stopcock. After the inner tube was evacuated with the diffusion pump, the stopcock was closed and the rate at which the pressure increased in the inner tube was measured. Every 12 hr the stopcock was again opened, and the process repeated. In this way the rate at which gas collected in the inner tube was obtained when it was alternately surrounded by air and by vacuum for these 12-hr periods. A temperature of 1200°C was used throughout, because it is the maximum temperature to which an evacuated fused quartz tube can be heated in air for several hours without collapsing.

The typical results of one of these experiments are shown in Fig. 3. The units of the ordinate are chosen to correspond to the maximum area of fused quartz that is heated above the melting point of GaAs in a routine crystal growth. It can be seen that the rate at which gas is collected is independent of whether there is air or vacuum around the tube. Thus, the amount diffusing through the walls is below the detection limit of the experiment, which is estimated to be 2 x 10^{15} molecules hr^{-1}. Furthermore, the fused quartz used in these tests was about ½ as thick as that used in a standard growth ampoule. It is also noteworthy from Fig. 3 that the rate of evolution decreases exponentially with time, which is not to be expected for the general case of the permeation of gases through a wall from a relatively large source

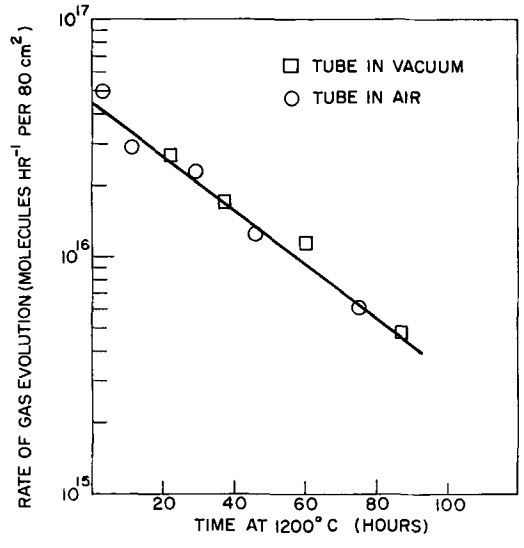

Fig. 3. Time dependence of the rate of gas evolution from fused quartz at 1200°C.

Table VI. Outgassing of quartz for 16 hr at indicated temperatures after various treatments

Prebaking treatment Time, hr	Prebaking treatment Temp, °C	Outgassing Temp, °C	Outgassing Total gas molecules
3	650	1200	7×10^{17}
1	350	650	2×10^{17}
40	1100	1200	3×10^{17}
40	1200	1200	2×10^{17}
80	1200	1200	8×10^{16}
100 hr at 1200°C, exposed to air at 25°C, then 3 hr at 650°C		1200	2×10^{17}

such as the atmosphere. Nevertheless, this type of behavior was always observed. Thus, the diffusion of gases through the quartz walls during crystal growth is not considered an important source of contamination of GaAs.

To determine the number of molecules entering the ampoule during the usual 16-hr growth period due to the desorption, apparatus similar to that previously described was used but with no outer tube. Results are shown in Table VI. In the first line is shown the number of gas molecules desorbed from the section of the ampoule containing the gallium. The second line gives the molecules desorbed from the arsenic end of the ampoule. Therefore, a total of nearly 10^{18} molecules of gases enter the growth ampoule, which could dope a 20g GaAs crystal to a level of roughly 3 x 10^{17} cm^{-3}.

The effect of predegassing at 1100° and 1200°C is shown by the data in the third and fourth lines in Table VI. It can be seen that predegassing is not very effective since the rate of degassing is quite slow, which is also indicated by the data in Fig. 3. As would be expected, predegassing at the higher temperature is always more effective. The fraction of the total degassing that is due to *ad*sorbed gases as compared to *ab*sorbed gases is indicated in the final two lines of Table VI. Prebaking the ampoule at 1200°C for 80 or 100 hr reduces the evolution of absorbed gases to below 10^{17} molecules. Subsequently, a short exposure to the air will introduce 2 x 10^{17} adsorbed molecules, which is a sizable fraction of the total number of molecules desorbed from quartz that has not been prebaked. Therefore, quartz ware that has been prebaked and subsequently exposed to air will still introduce significant contamination during GaAs growth.

A preliminary mass spectrometric analysis of the gases evolved from quartz *in vacuo* has been obtained by Honig (10). His results were reported as percentage of the total gas evolved at 600° and at 1150°C. The analysis at 1150°C was obtained after the quartz had been prebaked in vacuum at 1200°C for about 1 hr. The amount of helium evolved was not investigated. Results are given in Table VII. In accord with these results is the separate observation that most of the gas evolved at 600°C can be condensed at liquid nitrogen temperature, while very little of the gas evolved at 1200°C is thus condensible. Even if one assumes that hydrogen is not harmful to GaAs, there is still a total of 3 x 10^{17} molecules

Table VII. Composition of gases evolved from fused quartz *in Vacuo* at 600° and 1150°C

Component	Percentage at 600°C	Percentage at 1150°C
H_2O	68.7	17.5
CO	8.2	7.5
CO_2	5.5	3.0
H_2	5.0	71
HF	4.5	—
NO	2.2	—
N_2	2.0	0.8
O_2	1.6	0.2
HCl	1.4	—
BF_3	0.8	—
SiF_4	0.1	—

Table VIII. Impurities introduced into GaAs during crystal growth

Sample		Spectrographically det. imp., ppm Si	Mg	Fe	Cu
Gallium (as received)		<0.1	0.5	3	1
Arsenic (as received)		<0.1	0.1	—	1
GaAs	Front	3	1	—	1
	Middle	1	0.3	—	<1
	Tail	10	1	—	10

of water vapor and 7 x 10^{16} molecules of carbon monoxide introduced into the growth ampoule due to the desorption from both its sections. In addition, it has been found that the presence of arsenic in the reaction tube will increase by an order of magnitude the number of molecules of the major species of gaseous molecules found in the growth ampoule (11). To determine the effect of these impurities on the electrical properties, growth procedures must be devised to eliminate this source of contamination so as to provide control samples.

Contamination from the boat.—It has been previously found (1) that silicon is the main donor in GaAs, and tests have shown that the major source of silicon contamination is due to a reaction of molten GaAs with the quartz boat. The type of contamination that occurs is shown in Table VIII. The crystal was grown with a maximum temperature in the range 1265°-1275°C. It is seen that both copper and silicon are introduced; however, the copper segregates to the tail end of the crystal due to its small distribution coefficient. There is also some evidence for a little magnesium contamination.

The contamination shown in Table VIII is not due to the sealing process, since it depends strongly on relatively small variations of the growth temperature. The effect of the maximum temperature to which the melt is heated is shown in Table IX. It can be seen that higher growth temperatures simultaneously increase the electron (or silicon) concentration and decrease the electron mobility. The scatter in the data in Table IX is due in part to the use of nonuniform preparative techniques for all of the crystals. It should be remembered that in these tests 16-hr growth periods were used, so that the melt remained at or near the elevated temperatures for periods of several hours. An extremely rapid change in the stability of quartz at these temperatures is also manifest by the amount of devitrification of the

Table IX. Properties of n-type GaAs crystals grown at various temperatures

Maximum growth temp, °C	300°K n (cm^{-3})	300°K μ (cm^2v^{-1} sec^{-1})	78°K n (cm^{-3})	78°K μ (cm^2v^{-1} sec^{-1})
1265 to 1275	3.4×10^{17}	2210	2.8×10^{17}	2290
	2.5×10^{17}	3300	2.4×10^{17}	2880
	1.4×10^{17}	3500	1.1×10^{17}	3960
	1.6×10^{17}	3650	1.5×10^{17}	3950
	3.7×10^{17}	3790	2.5×10^{17}	3680
1255 to 1265	1.4×10^{17}	4100	1.3×10^{17}	4250
	2.6×10^{17}	3700	2.4×10^{17}	3700
	6.5×10^{16}	4000	5.0×10^{16}	5470
1250 to 1255	9.3×10^{16}	4550	7.5×10^{16}	5300
	4.1×10^{16}	4850	3.4×10^{16}	7250
	2.8×10^{16}	4320	2.1×10^{16}	7460*
	5.4×10^{16}	5300	4.3×10^{16}	7850*
	5.9×10^{16}	4550	4.8×10^{16}	5200

* Grown at higher speeds.

quartz ampoule. After a 16-hr run at 1270°C, the devitrification is so bad that the quartz becomes opaque; while at 1250°C devitrification causes only slight clouding. It can be concluded that reaction of the GaAs melt with the quartz boat constitutes the major source of contamination.

Conclusions

A study has been carried out of the contamination introduced during the preparation and growth of GaAs by the horizontal Bridgman technique in a quartz ampoule and quartz boat. The major source of contamination, especially with silicon, is due to reaction of the GaAs melt with the boat. Contamination with silicon and copper has also been observed during sealing of the quartz ampoules, with copper during vacuum baking of gallium, and with water vapor and carbon monoxide during growth due to outgassing of quartz. Contamination has also been observed to occur due to back diffusion of impurities from a vacuum system.

Atmospheric gases were not observed to diffuse through quartz at the growth temperature, and the cleaning procedures used for the quartz had no significant effect on the properties of GaAs. No direct reaction of gallium with the boat was observed during vacuum baking at 650°C.

To reduce the contamination of GaAs crystals, it is most important to control the reaction of the melt with the boat. As a first step in this direction, the melt temperature must be maintained as close as possible to the melting point and the crystal grown in a short time. In addition, other boat materials such as BN, AlN, BeO, etc., might prove to be more suitable than quartz if they can be made ultrapure and impervious. To minimize the outgassing of the quartz ampoule, the ampoule should be maintained well below 1000°C by employing heating methods such as r.f. induction. The high vacuum pumps used in processing the ampoules should be cleaned at regular intervals. Finally, alternative growth procedures might be investigated, in which lower temperatures are employed, such a growth from solution, or from the vapor phase.

Acknowledgments

The authors are grateful to Mr. E. A. Miller and Mr. E. J. Stofko for important technical assistance. They are indebted to Mr. H. H. Whitaker for the spectrographic analyses, and to Dr. F. D. Rosi for continued interest and encouragement throughout this work. This research has been sponsored by the Electronic Research Directorate of the Air Force Research Division, Air Research and Development Command under Contract No. AF19(604)-6152.

Manuscript received Sept. 1, 1961; revised manuscript received Nov. 24, 1961. This paper was presented at the Conference on the Ultrapurification of Semiconductor Materials, April 1961, and originally appeared in the conference proceedings published by the MacMillan Co., New York.

Any discussion of this paper will appear in a Discussion Section to be published in the December 1962 JOURNAL.

REFERENCES

1. L. R. Weisberg, F. D. Rosi, and P. G. Herkart, "Properties of Elemental and Compound Semiconductors," Metallurgical Society Conference, Vol. 5, p. 25, Interscience Publishers, Inc., New York (1960).
2. P. G. Herkart, Private communication.
3. L. M. Foster and R. A. Kramer, *This Journal*, **107**, 189C (1960).
4. J. T. Edmond and C. Hilsum, *J. Appl. Phys.*, **61**, 1300 (1960).
5. H. L. Schick, *Chem. Rev.*, **60**, 331 (1960).
6. D. E. Swets, R. W. Lee, and R. C. Frank, *J. Chem. Phys.*, **34**, 17 (1961).
7. L. S. T'sai and T. Hogness, *J. Phys. Chem.*, **36**, 2595 (1932).
8. R. M. Barrer, *J. Chem. Soc.*, **1934**, 378.
9. S. Dushman, "Scientific Foundations of Vacuum Technique," p. 534, J. Wiley & Sons, Inc., New York (1949).
10. R. E. Honig, Private communication.
11. S. Skalski and R. Foehring, Private communication.

Polarization Curves of Redox Systems Involving Consecutive Electron-Transfers: Some Theoretical Aspects

R. M. Hurd

Texas Research Associates, Austin, Texas

ABSTRACT

An equation, first worked out by Vetter, describing the complete polarization curves for redox systems involving two consecutive electron transfer steps, has been examined in detail by computer solutions. It is shown that quite wide variations in the values of the individual transfer coefficients have little effect on the shape of the theoretical curves. However, as the ratio of the individual exchange currents approaches 100:1, two definite linear-logarithmic regions appear in one branch of the curve. It is further shown that in many cases the diffusion current masks the true Tafel portion, leaving the "pseudo-Tafel" part as the only observable linear-logarithmic region.

In one of a series of papers (1, 2-9) describing the use of reaction order methods in determining mechanisms of electrode reactions in redox systems, Vetter derived an equation which describes the theoretical polarization curves for a redox system which proceeds by two consecutive electron transfer steps. The conditions and assumptions for the applicability of his equation are the usual constancy of activity coefficients, compression of the double layer to constant and nearly negligible zeta potential, suppression of the transference number of the reacting species, etc. Most of these conditions, it should be noted, are accomplished by addition of a large excess of inert electrolyte to the system. There is, however, one additional assumption in this particular case, *i.e.*, that the actual electrode reactions involve the transfer of only *one* electron between *individual* solution species. For an over-all electrode reaction $A+2e \rightleftarrows C$, the reaction scheme thus can be formulated:

$$A + e \rightleftarrows B \qquad [1]$$

$$B + e \rightleftarrows C \qquad [2]$$

Each of these reactions is characterized by its own transfer coefficient, α_1 or α_2, and by its own exchange current, $i_{o,1}$ or $i_{o,2}$.

This assumption excludes reactions which involve simultaneous electron transfer and molecular combination, such as

$$A + H^+ + e \rightleftarrows HA \qquad [3]$$

It does not exclude purely chemical equilibrium reactions involving any of the substances in Eq. [1] and [2], provided only that they are rapid equilibria. The over-all reaction can thus include other species which do not enter into the actual electron transfer processes. A notable example is the quinone/hydroquinone system, in which the over-all reaction involves hydrogen ion and a two electron transfer, while the electrode reactions, according to Vetter (10), involve single electron transfers in which hydrogen ion does not participate.

For the conditions as stated, then, the equation which describes the complete polarization curves for a system which proceeds by the two consecutive transfer steps 1 and 2 above is given by Vetter as

$$\frac{i}{2} = \frac{\exp(\alpha_1+\alpha_2)\frac{\mathbf{F}\eta}{RT} - \exp\left[-2+(\alpha_1+\alpha_2)\right]\frac{\mathbf{F}\eta}{RT}}{\frac{1}{i_{o,2}}\exp\alpha_1\frac{\mathbf{F}\eta}{RT} + \frac{1}{i_{o,1}}\exp\left[-(1-\alpha_2)\right]\frac{\mathbf{F}\eta}{RT}} \qquad [4]$$

In this equation i is the net external current and η the overvoltage. Both i and η are positive for anodic, negative for cathodic, polarization. It should be noted that the factor 2 (in $i/2$) does not appear in the original article (1), but was introduced as a correction in a subsequent note (11).

Vetter examined this equation in the four simplified forms to which it reduces when one assumes η "large and positive," η "large and negative," when $i_{o,1} = \infty$, and when $i_{o,2} = \infty$. From this examination he has drawn the following three conclusions, which may be used as criteria for the existence of two consecutive electron transfer steps in the reaction mechanism:

1. Since α_1 will not generally be equal to α_2, the slopes of the anodic and cathodic linear-logarithmic regions which occur at high overvoltages will not add up to 1, as they must for a single transfer step $[\alpha + (1 - \alpha) = 1]$.

2. Extrapolation of the linear-logarithmic regions to $\eta = 0$ will give two values of exchange current. Because of the factor 2 mentioned above, the values at the intercept are actually $2i_{o,1}$ from extrapolation of the cathodic branch and $2i_{o,2}$ from extrapolation of the anodic branch.

3. For either exchange current equal to infinity, the linear-logarithmic regions extrapolate to the exchange current characteristic of the slower step, but exhibit slopes which add up to 2 instead of 1.

In a research program designed to extend Vetters' reaction order methods to organic systems somewhat more complicated than the quinone-hydroquinone case, some of the experimental results (which will be presented in subsequent papers) led to the conclusion that an exchange current ratio in the range 1-1000 was a more practical case than a ratio of infinity. As a matter of fact, it seems reasonable that the large majority of electrode systems of this type will involve exchange current ratios up to perhaps only 100, from which it follows that a detailed examination of Eq. [4] in these regions is desirable. With the use of modern computers, such an examination is actually rather straightforward, and can even be extended to the general case of n electron steps with little additional effort.

Solutions of Eq. [4] at Intermediate Exchange Current Ratios

Visual examination of Eq. [4] reveals that, regardless of the magnitudes of the two exchange currents, there exists a value of η sufficiently large and positive to justify neglecting the second term in both numerator and denominator. The same holds true for the first terms for η large and negative. However, it is also apparent that the criterion for η sufficiently large in either direction to justify dropping of terms is dependent on the values of the exchange currents. The same reasoning process holds true for dropping either term in the denominator on the basis of a "sufficiently large" value of either exchange current.

The questions which can be answered, then, by complete solutions of the equation are:

1. For various magnitudes and ratios of the two exchange currents, what values of overvoltage are required to put one in the linear-logarithmic region, i.e., Vetter's limiting cases?

2. What is the character of the polarization curves in the intermediate overvoltage regions (40-300 mv) when the exchange current ratio is large, but not infinite?

A computer program was established to obtain values of i as a function of η as η ran the series 1, 2, 4, 7, 10, 20, 40, . . . *etc.*, mv. Solutions were cut off at 2v. Exchange current densities of various values and various ratios were used through the range 10^{-7} to 10^{-4} amp/cm^2. Transfer coefficients of 0.2, 0.4, 0.5, 0.7, and 0.8 were used in various combinations. Plots were made of log i *vs.* η for the complete polarization curves and of i *vs.* η in low overvoltage ranges (0-50 mv). Although literally dozens of such curves have been obtained (the limiting factor is the time required to plot the data), only the more significant are presented here.

Figure 1 shows the complete polarization curves for $\alpha_1 = \alpha_2 = 0.5$, with $i_{o,2}$ fixed at 10^{-4} amp/cm^2 and $i_{o,1}$ varying. Note that an average value for a diffusion limited current density in well stirred $10^{-2}N$ solutions (conditions used in the experimental work for this program) is about 10^{-2} amp/cm^2, which is indicated by the horizontal dashed line in the figure. The most interesting part of the curve is the progression on the anodic side as the cathodic exchange current decreases. At a ratio of $i_{o,1}/i_{o,2}$ of 100, a well-defined linear-logarithmic region covering nearly two orders of magnitude appears and becomes even more distinct and extended as the ratio increases. This branch of the curve thus contains two linear-logarithmic regions, the true Tafel region at values of overvoltage above about 250 mv, and a "pseudo-Tafel" region at the lower values. For $\alpha_1 = \alpha_2 = 0.5$ the slope of this pseudo-Tafel region varies between about 1.0 at the lowest ratio of exchange currents (50-100) at which it is observable, and 1.5 at the

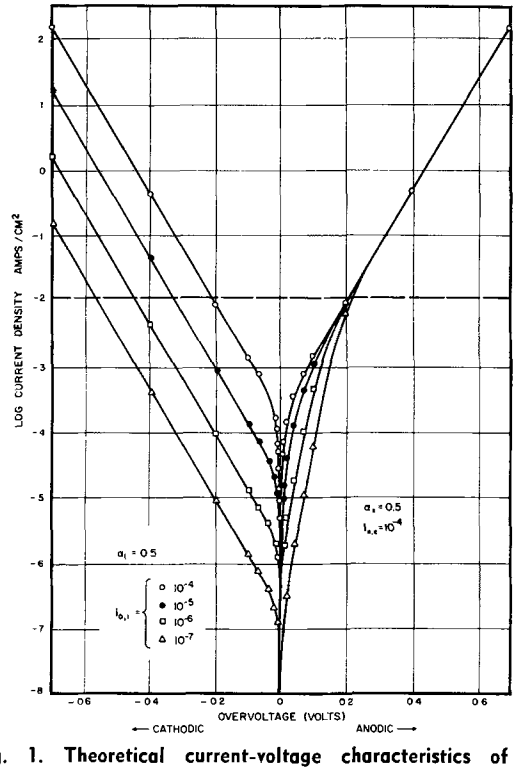

Fig. 1. Theoretical current-voltage characteristics of redox system with two consecutive electron transfers, varying $i_{o,1}$.

limiting case of one exchange current equal to infinity.

The difficulties to which the existence of this "pseudo-Tafel" region can lead are illustrated by Fig. 2 and 3. Figure 2 is a redrawn portion of Fig. 1 with the approaches to the limiting current densities sketched in as would be observed in an actual experiment. It is apparent that the true values of anodic exchange current and anodic transfer coefficient are completely obscured. Figure 3 is an actual experimental curve obtained with platinum electrodes in a 10^{-2}M toluquinone-10^{-2}M toluhydroquinone system. The measured cathodic α from these data is -0.49, an entirely reasonable value, but the measured slope of the well-defined linear-logarithmic region in the anodic curve corresponds to an apparent anodic α of 1.2. The similarity of these curves to the theoretical curves of Fig. 2 is not of itself sufficient proof of the existence of consecutive electron transfers and a "pseudo-Tafel" region. Curves which show *two* well-defined linear-logarithmic regions below the limiting current, plus agreement between the exchange current ratios and transfer coefficients would constitute unequivocal proof.

Curves obtained by using values of α_1 and α_2 other than 0.5 are quite similar to those of Fig. 1, except for the slopes in the true Tafel region. It is interesting to note that if from actual data one true Tafel slope and one exchange current are known, as will usually be the case, a fair prediction of the other exchange current and the other transfer coefficient can be obtained by comparison with the various theoretical curves. The accuracy of such a prediction is markedly dependent on the accuracy of the polarization data in the pseudo-Tafel region.

As in most electrode kinetic studies, additional information about the nature of the electrode reactions can be obtained from data very near the reversible potential. Differentiation of Eq. [4] with respect to η and determination of $(d\eta/di)_{i\to 0}$ yields

$$\frac{4F}{RT}\left(\frac{d\eta}{di}\right)_{i\to 0} = \left(\frac{1}{i_{o,1}} + \frac{1}{i_{o,2}}\right) \qquad [5]$$

Vetter denoted this quantity by $1/i_o$* and used it to check the values of individual exchange currents obtained by extrapolation in his quinone/hydroquinone paper.

Plots of the computer calculations in the low overvoltage regions (+20 to −20 mv) show that the curves pass through the origin at the slopes predicted by Eq. [5], and that variations in α values tend to spread the curves apart somewhat in this region, but probably not enough to make firm determinations of α. Figure 4 is a plot for $i_{o,1} = i_{o,2} = 10^{-4}$ amp/cm^2, and for five different combinations of α_1 and α_2. Figure 5 is a similar plot for $i_{o,1} = 10^{-4}$, $i_{o,2} = 10^{-5}$ amp/cm^2. It is notable that even at this small ratio of exchange currents, the plots possess a definite curvature at the

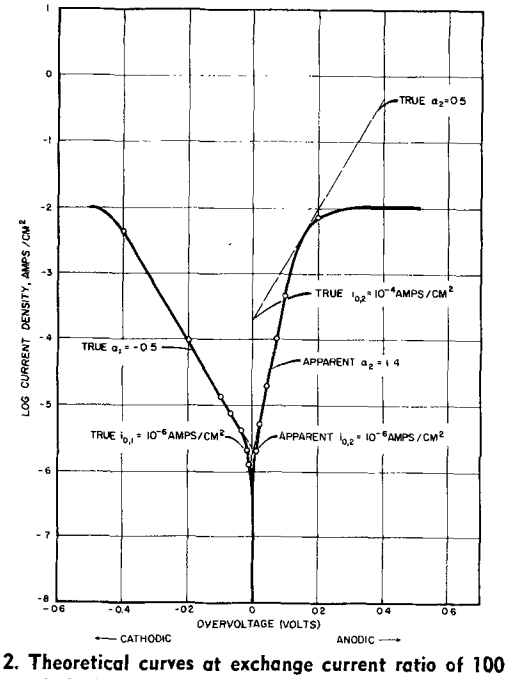

Fig. 2. Theoretical curves at exchange current ratio of 100 (from Fig. 1) with limiting diffusion current of 10^{-2} amp/cm^2 superimposed.

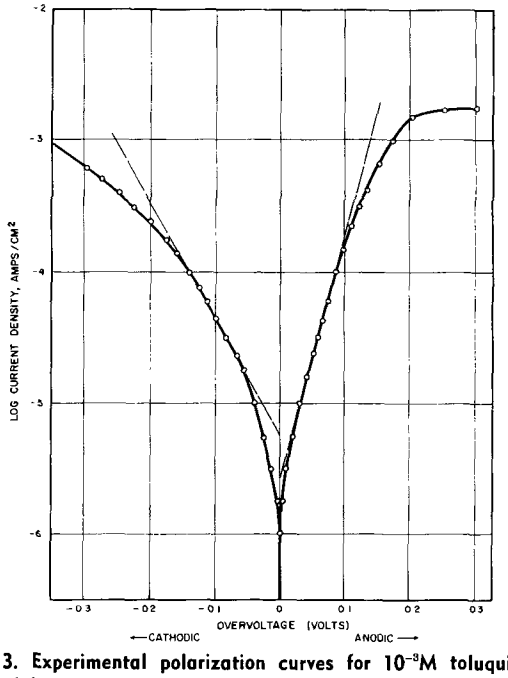

Fig. 3. Experimental polarization curves for 10^{-3}M toluquinone, 10^{-3}M toluhydroquinone.

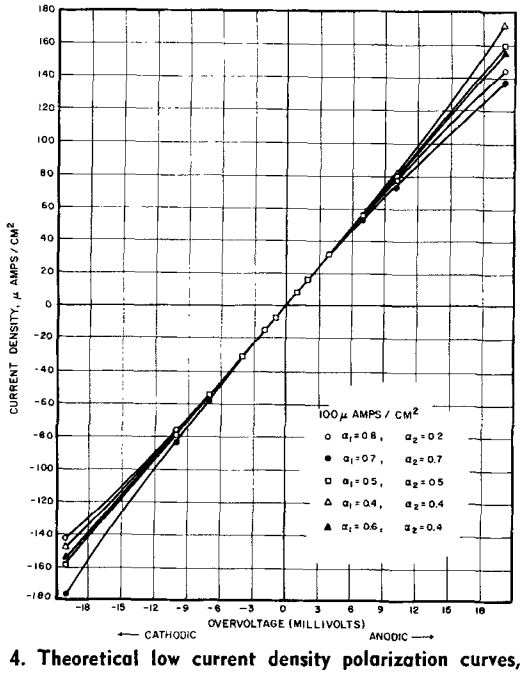

Fig. 4. Theoretical low current density polarization curves, two consecutive electron transfers, equal exchange currents.

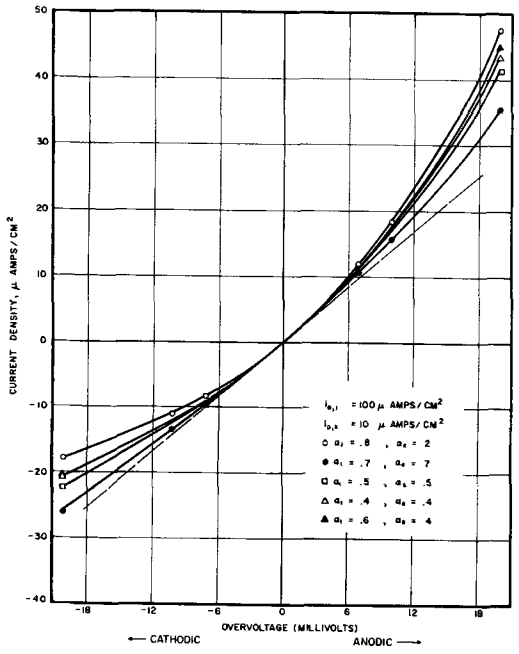

Fig. 5. Theoretical low current density polarization curves, two consecutive electron transfers, exchange current ratio equals ten.

origin, while at $i_{o,1} = i_{o,2}$ they pass through the origin in a straight line. This curvature persists at the higher ratios of exchange currents, but does not become significantly more pronounced. For values of $i_{o,2} > i_{o,1}$, the curvature is an exact mirror image of Fig. 5.

Examination of Eq. [5] reveals that the value of i_o* obtained from the slope at the origin can be obtained by many combinations of perfectly reasonable values of $i_{o,1}$ and $i_{o,2}$. If values of the individual exchange currents as obtained by extrapolation of Tafel regions combine in the manner of Eq. [5] to give close agreement with the measured i_o*, then certainly the extrapolated values merit a greater confidence. However, in those cases where one exchange current is about 100 times larger than the other (the condition, incidentally, which leads to the pseudo-Tafel region of Fig. 1 and 2), the larger exchange current no longer has any influence on i_o*. For cases of this type, the combination of curvature in the low-overvoltage region and a greater than usual slope in the linear-logarithmic region, or, even more convincing, two linear-logarithmic regions in one branch of the curve, will lead one to expect a large ratio of exchange currents. It would then be hoped that further experiments could be designed to ferret out the elusive electrokinetic parameters.

General Solution for *n* Consecutive Steps, with Some Solutions for the Three Electron Case

The solution for the general case of n consecutive electron transfer, represented as

$$S_1 + e \underset{k_2}{\overset{k_1}{\rightleftarrows}} S_2 \text{ - - - - - - with } \alpha_1 \text{ and } i_{o,1}$$

$$\vdots$$

$$S_i + e \underset{k_{2i}}{\overset{k_{2i-1}}{\rightleftarrows}} S_{i+1} \text{ - - - - - with } \alpha_i \text{ and } i_{o,i} \quad [6]$$

is obtained by solving simultaneously a group of equations of the form

$$\frac{i}{n} = k_{2i}\, C_{s_{i+1}} \exp \frac{\alpha_i \mathbf{F}\epsilon}{RT} - k_{2i-1}\, C_{s_i} \exp -\frac{(1-\alpha_i)\mathbf{F}\epsilon}{RT} \quad [7]$$

With the exchange current expression

$$i_{o,i} = k_{2i}\, \overline{C}_{s_{i+1}} \exp \frac{\alpha_i \mathbf{F}\epsilon_o}{RT} = k_{2i-1}\, \overline{C}_{s_i} \exp -\frac{(1-\alpha_i)\mathbf{F}\epsilon_o}{RT} \quad [8]$$

Equation [7] reduces to

$$\frac{i}{n} = i_{o,i}\left[\frac{C_{s_{i+1}}}{\overline{C}_{s_{i+1}}} \exp \frac{\alpha_i \mathbf{F}\eta}{RT} - \frac{C_{s_i}}{\overline{C}_{s_i}} \exp -\frac{(1-\alpha_i)\mathbf{F}\eta}{RT}\right] \quad [9]$$

The barred concentrations are the equilibrium concentrations (at the reversible potential) of the intermediate substances; the unbarred concentrations are those at the electrode surface during current flow. In the absence of concentration polarization, the ratios $C_{s_1}/\overline{C}_{s_1}$ and $C_{s_{n+1}}/\overline{C}_{s_{n+1}}$ are unity. Therefore $n-1$ variables exist besides i and η in the n equations. These $n-1$ variables can be eliminated by simple determinantal solution. To simplify expression of the determinant, let

$$F_1 \equiv n \exp \frac{\alpha_i \mathbf{F}\eta}{RT} \quad [10]$$

$$G_2 \equiv -n \exp -\frac{(1-\alpha_i)\mathbf{F}\eta}{RT} \quad [10']$$

$$X_i = C_{s_i}/\overline{C}_{s_i} \quad [11]$$

Equation [9] then forms a system of n linear equations with i and X_i as unknowns. The general solution for i can be written as

$$i = N/D$$

where

$$D = \begin{vmatrix} \frac{1}{i_{o,1}} & -F_1 & 0 & 0 & \cdots & 0 \\ \frac{1}{i_{o,2}} & -G_2 & -F_2 & 0 & \cdots & 0 \\ \frac{1}{i_{o,3}} & 0 & -G_3 & -F_3 & \cdots & 0 \\ \vdots & & & & & \\ \frac{1}{i_{o,n-1}} & & & & -G_{n-1} & -F_{n-1} \\ \frac{1}{i_{o,n}} & & & & 0 & -G_n \end{vmatrix}$$

AND

$$N = \begin{vmatrix} G_1 & -F_1 & 0 & \cdots & 0 \\ 0 & -G_2 & -F_2 & \cdots & 0 \\ 0 & 0 & -G_3 & \cdots & 0 \\ \vdots & & & & \\ 0 & & & -G_{n-1} & -F_{n-1} \\ F_n & 0 & & 0 & -G_n \end{vmatrix}$$

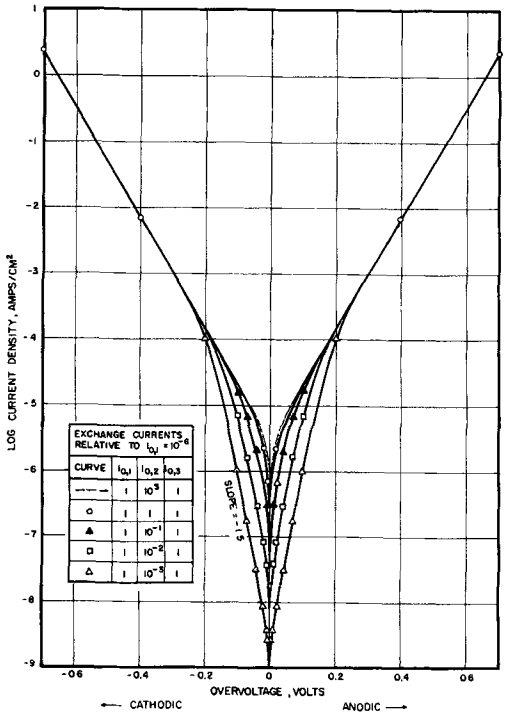

Fig. 6. Theoretical polarization curves—three consecutive electron transfer steps, $i_{o,2}$ varying.

Evaluating the indicated determinant and substituting back for F_i and G_i from Eq. [10] and [10′] gives the resulting general expression:

$$\frac{i}{n} = \frac{\exp\left(\sum_{j=1}^{n} \alpha_j\right)\frac{\mathbf{F}\eta}{RT} - \exp\left[-\left(n - \sum_{j=1}^{n}\alpha_j\right)\frac{\mathbf{F}\eta}{RT}\right]}{\sum_{k=1}^{n}\frac{1}{i_{o,k}}\exp\left[-\left\{(n-k) - \sum_{\substack{j=1\\ j\neq k}}^{n'}\alpha_j\right\}\frac{\mathbf{F}\eta}{RT}\right]} \qquad [12]$$

This equation can be put into many different forms, some of which are more convenient for examination of limiting cases and/or computation, by simply multiplying both numerator and denominator by appropriate exponential terms. One of these forms, which was used for the computer solutions of the three electron case is

$$\frac{i}{ni_{o,1}} = \frac{\left[1 - \exp -\frac{n\mathbf{F}\eta}{RT}\right]}{\sum_{j=1}^{n}\gamma_{o,j}\exp\left\{-\left[(n-j) + \alpha_j\right]\frac{\mathbf{F}\eta}{RT}\right\}} \qquad [13]$$

where $\gamma_{o,j} = \frac{i_{o1}}{i_{o,j}}$ with $\gamma_{o,1} \equiv 1$. This represents a normalization with respect to $i_{o,1}$, and eliminates many operations by introducing exchange current ratios directly.

Equation [13] was solved for $n = 3$, $\alpha_1 = \alpha_2 = \alpha_3 = 0.5$, and both $\gamma_{o,2}$ and $\gamma_{o,3}$ varying from 1 to 1000. The number of possible combinations of α values and exchange current ratios for $n = 3$ is so large as to make it impractical to examine the situation in detail, although again the limiting factor is the mere plotting of the data. However, examination of only a few of the more interesting cases reveals that much the same situation prevails here as with the two electron case, *i.e.*, the appearance of pseudo-Tafel regions at intermediate ratios of exchange currents, the slopes of which approach limiting values which sum to three when a single exchange current controls. This is illustrated by Fig. 6 in which the terminal exchange currents are fixed and equal while the center exchange current ranges from 10^3 to 10^{-3} of the terminal values. Essentially no effect is noted on the curves while the center reaction is faster or even of equal speed, but as it becomes slower the pseudo-Tafel regions appear and approach a slope of 1.5 on each branch. Further illustration is given by Fig. 7 in which $i_{o,2}$ and $i_{o,3}$ are increased until $i_{o,1}$ controls and by Fig. 8 in which $i_{o,3}$ is made progressively smaller until it alone controls. Note that in each of these last two figures one branch of the curve exhibits a true Tafel slope of ± 0.5, while the pseudo-Tafel slope approaches ± 2.5, so that in all three figures the limiting slopes sum to 3, although in different manners. Note also that in each limiting case, extrapolation of both the true and pseudo-Tafel regions yields the value of the smallest exchange current. Still it is entirely plausible that both linear-logarithmic regions may be observable in some experimental systems, thereby yielding sufficient information to solve the reaction parameters completely.

There are, of course, other interesting combinations of transfer coefficients and exchange currents for the three electron case, as well as for the higher n values, but those given are sufficient for the present paper. For those who desire to examine other cases, it need be noted only that the equations are

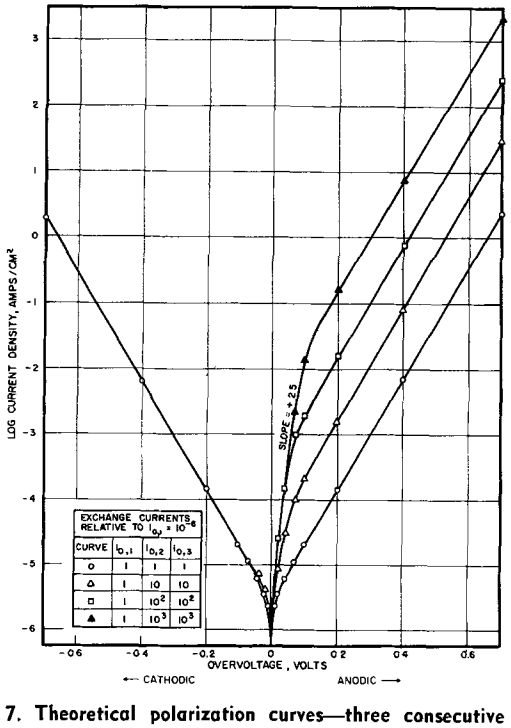

Fig. 7. Theoretical polarization curves—three consecutive electron transfer steps, $i_{o,2}$ and $i_{o,3}$ varying.

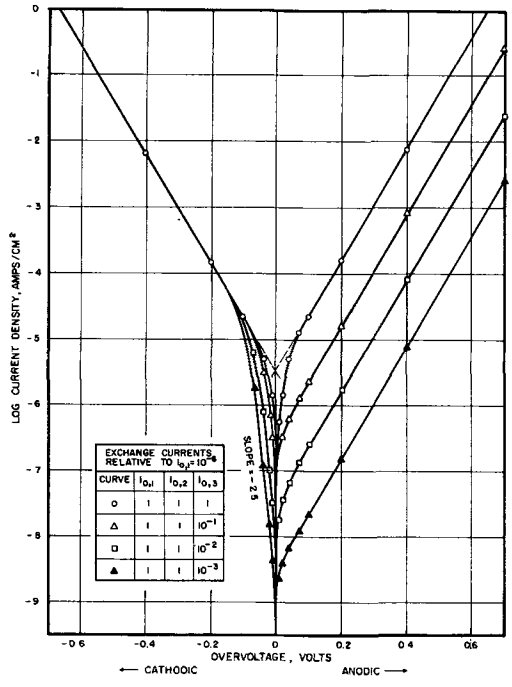

Fig. 8. Theoretical polarization curves—three consecutive electron transfer steps, $i_{0,3}$ varying.

solved readily in a matter of seconds on almost any modern computer, once a satisfactory program is established.

Conclusion

The use of complete solutions of equations describing the particular process of consecutive electron transfers can improve materially the interpretation of experimental data over the previously used methods of approximation and limiting cases. Certainly this is true in the majority of practical systems, where intermediate values of the kinetic parameters will be prevalent, and limiting cases not often encountered. The biggest drawback to the use of such complete solutions for interpretation lies in the fact that the experimental data need to be considerably more accurate to obtain full value from comparison with the theoretical curves. As a matter of fact, it is easy to see how one can be led to a false conclusion by data which are only a few per cent in error. Nevertheless, one can also be led (and probably more often) to a false conclusion by very accurate data if it is *not* realized that perfectly sound theoretical curves describing the data exist. As the procedures for obtaining data in electrode kinetics improve in accuracy, then, it is desirable to extend the use of computers and complete solutions of the kinetic equations into those areas where only approximations and limiting cases have been used previously.

Acknowledgment

The author wishes to acknowledge the invaluable help of Dr. A. F. Wittenborn of Texas Research Associates, who not only extended the equations to the general case of n consecutive steps, but also pointed out the various forms the equations could take, and selected the one for numerical computations.

This work was carried out under a research contract with Union Carbide Consumer Products Company as a part of their fundamental research program in organic electrochemistry.

Manuscript received July 31, 1961; revised manuscript received January 9, 1962. This paper was prepared for presentation at the Indianapolis Meeting, April 30-May 3, 1961.

Any discussion of this paper will appear in a Discussion Section to be published in the December 1962 JOURNAL.

REFERENCES

1. K. J. Vetter, *Z. Naturforsch.*, **7a**, 328 (1952).
2. K. J. Vetter, *Z. physik. Chem.*, **194**, 288 (1950).
3. K. J. Vetter and G. Manecke, *ibid.*, **195**, 270 (1950).
4. K. J. Vetter and G. Manecke, *ibid.*, **195**, 337 (1950).
5. H. Gerischer, *Z. Elektrochem.*, **54**, 366 (1950).
6. K. J. Vetter, *Z. physik. Chem.*, **196**, 360 (1951).
7. K. J. Vetter, *ibid.*, **199**, 22 (1952).
8. K. J. Vetter and D. Otto, *Z. Elektrochem.*, **60**, 1072 (1956).
9. K. J. Vetter and J. Bardeleben, *ibid.*, **61**, 135 (1957).
10. K. J. Vetter, *ibid.*, **56**, 797 (1952).
11. K. J. Vetter, *Z. Naturforsch.*, **8a**, 823 (1953).

Cathodic Oxygen-Evolution Reaction of the Peroxo Cobalt Complex $[(NH_3)_5CoO_2Co(NH_3)_5]^{5+}$

S. Barnartt and R. G. Charles

Research Laboratories, Westinghouse Electric Corporation, Pittsburgh, Pennsylvania

ABSTRACT

At a bright platinum cathode in H_2SO_4 solutions, the complex ion $[(NH_3)_5CoO_2Co(NH_3)_5]^{5+}$ is reduced quantitatively to $2Co^{2+}$ in a one-electron reaction, with evolution of one molecule of oxygen gas. The same products also are produced by chemical reduction with silver powder. A probable mechanism for the cathodic reduction is outlined and its applicability to chemical reduction described. A cell containing an acid solution of this cobalt complex and platinum electrodes evolves 1.25 O_2/F, and may be used as an oxygen generator or as a sensitive gas coulometer.

In the course of cathodic current efficiency measurements for the oxygen-dissolution reaction, some measurements were made using sulfuric acid solutions containing the pentavalent decammino-μ-peroxo dicobalt ion I.

$$[(NH_3)_5CoO_2Co(NH_3)_5]^{6+}$$

I

$$[(NH_3)_5CoO_2Co(NH_3)_5](SO_4)_2(HSO_4)\cdot 3H_2O$$

II

There has been considerable interest in this ion in the past due to the supposed tetravalency of one of the two cobalt atoms. Recent work has shown, however, that the single unpaired electron present in I is delocalized over the grouping CoO_2Co and that the two cobalt atoms are equivalent (1).

Solutions made by dissolving the corresponding sulfate, compound II, in molar sulfuric acid are relatively stable at ordinary temperatures. We have found that oxygen did not dissolve at a platinum cathode in these solutions, but instead oxygen was evolved. Preliminary experiments indicated that one mole of oxygen was liberated per Faraday. Since cathodic oxygen-evolution reactions are virtually unknown, we have investigated this reaction in some detail.

Experimental Procedures

Materials.—The preparation of $[(NH_3)_5CoO_2Co(NH_3)_5](SO_4)_2\cdot(HSO_4)\cdot 3H_2O$ was carried out by the method of Gleu and Rehm (2). The compound was recrystallized from 1M H_2SO_4 and air-dried at room temperature. Cobalt analysis gave a value of 17.8% (theoretical 17.77%).

Acid solutions containing II were moderately stable, but detectable changes in the visible and ultraviolet spectra occurred after long standing at room temperature (> 24 hr). Hence the solutions were prepared, without heating, immediately before use. Solid compound II was stored in a refrigerator and appeared to be stable indefinitely.

Measurements of current efficiency for oxygen evolution.—Figure 1 presents a diagram of the Pyrex glass electrolytic cell, which was designed for measurements of gas-evolution or gas-dissolution efficiency. For cathodic efficiencies the vertical plate a was made anode and the horizontal screen c was cathode. Both electrodes were of bright platinum. The former was suspended by a thin platinum wire; the latter, a screen of total geometrical area 10 cm^2, was held in place by means of a gold-plated clip and rod b, the latter being sealed through the cap of the cell. The cap was joined to the body of the cell with a standard taper rubber o-ring joint.

The catholyte was separated from the anolyte by a coarse fritted glass disk d, and was stirred magnetically by means of a Teflon-covered stirrer. Stopcocks e and f, attached to the cell with o-ring joints g, permitted the gas phase above the catholyte to be flushed and pressurized with oxygen or other gas.

A glass tube of uniform cross section was used for a 13 cm length of the anode compartment at and above the reference line, ref. Changes in the height h of anolyte level above catholyte level were restricted

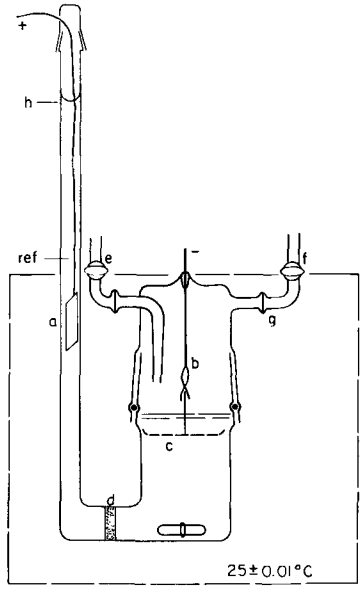

Fig. 1. Diagram of cell for measurement of gas-evolution or gas-dissolution efficiency.

to this region during a current efficiency measurement. The total volume of the cell up to the reference line was determined by filling the cell with water and weighing. In each experiment the volume of electrolyte was fixed at 50.0 ml, so that the gas volume in the cathode compartment was known for any value of h.

The cell was calibrated with 1M H_2SO_4 in an atmosphere of pure oxygen, with a current of 3.60 ma (0.36 ma/cm^2). A 1-hr period of cathodic pre-electrolysis was used to remove reducible impurities, after which the oxygen pressure was adjusted so that the solution level h was near the top of the uniform bore tube. The level was allowed to stabilize; then the screen electrode was made cathode again and the change of level Δh, for passage of a measured number of coulombs, was determined with a traveling microscope.

The number of moles Δn of gas dissolved or evolved is related to Δh through the relationship (see Appendix)

$$\Delta n = \frac{\Delta h}{RT}[A(P_i - P_s) + V_f d/13.5] \qquad [1]$$

Here A is the internal cross-sectional area of the anolyte tube. P_i is the initial pressure and V_f the final volume of the gas in the cathode compartment. P_s is the vapor pressure of the solution and d its density; for dilute solutions the corresponding values for the solvent may be used. When the atmospheric pressure changes during the determination, a correction to Δh is applied by use of Eq. [2], Appendix. Calibration of the cell involved determining A from an experimental measurement of Δh and the corresponding value of Δn, the latter derived from the number of Faradays passed. The value of A thus obtained for cathodic oxygen dissolution agreed with that similarly obtained from anodic oxygen evolution measurements within 1%.

For measurements on solutions of compound II, the cathode compartment was flushed and filled with pure argon. Otherwise the procedure used followed that of the calibration experiments, using the same current (3.60 ma) and the same pre-electrolysis period (1 hr) for each measurement.

Reduction of the μ-peroxo compound.—The number of moles of compound II reduced at the cathode per Faraday, as well as the reduction potential, were determined in a cell similar to that of Fig. 1 but with two modifications. (*A*) The cap of the cathode compartment contained an opening which permitted insertion of a saturated calomel electrode of the fiber-junction type. (*B*) The fritted disk was of very fine porosity; and the electrolyte level as well as the gas pressure (flowing argon above the catholyte, air above the anolyte) were the same on both sides. Thus diffusion of II between catholyte and anolyte was negligible.

The concentration of II in the catholyte was determined periodically by interrupting the current and removing a sample of the solution for analysis with a Cary recording spectrophotometer. The characteristic absorption peak at 6690Å (molar extinction coefficient = 880 for solutions in 1M H_2SO_4) was used for concentration measurements; none of the reduction products absorb significantly at this wavelength. Each sample was analyzed without dilution using an absorption cell of path length 0.20, 1.00, or 10.0 cm, as required The sample was returned as fully as possible to the electrolytic cell after measurement.

Cathode potential measurements, made with reference to the saturated calomel electrode, were converted to the hydrogen scale.

Determination of reduced cobalt-containing species.—Solutions which were analyzed for the quantity of II cathodically reduced also were subjected to cation-exchange chromatography to separate the cobalt-containing species. The ion-exchange column used (Bio-Rad AG 50W-X8 in the hydrogen form) and its effectiveness for acid solutions of some cobalt complexes have been described by the authors in a previous paper (3). The amount of eluted Co^{2+} was determined in acetate-buffered solutions by precipitation with 8-hydroxyquinoline (2). Since it was necessary to precipitate in the presence of a large amount of inert salts, which caused errors due to coprecipitation, simultaneous runs were carried out with standard $CoSO_4$ solutions containing similar salt concentrations. The latter results were used to apply corrections for coprecipitation.

Results and Discussion

Cathodic oxygen evolution.—A saturated solution of compound II in 1.00M H_2SO_4 was studied at 25.0°C (±0.01) in the cell of Fig. 1. An excess of II was added to the cell as a finely ground powder, and vigorous agitation was used. Hence the concentration of II remained close to the saturation value, 0.0035M, during cathodic reduction. Mass spectrometer analysis of the gas above the catholyte after electrolysis showed that only oxygen was evolved.

A typical curve showing the change in h (corrected for changes in atmospheric pressure) during reduction of II at constant current is presented in Fig. 2.

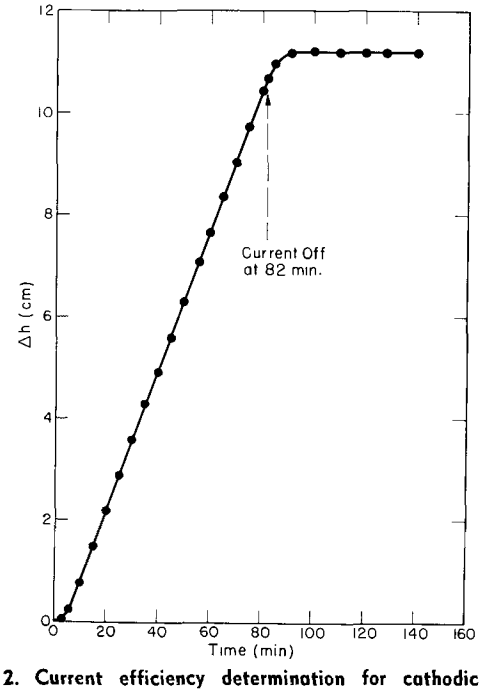

Fig. 2. Current efficiency determination for cathodic oxygen evolution from saturated solution of compound II in molar H_2SO_4, 25.00°C, 3.60 ma.

Table I. Experimental results for cathodic reduction of a saturated solution of $Co_2O_2(NH_3)_{10}(SO_4)_2HSO_4 \cdot 3H_2O$ in 1M H_2SO_4

	mole/Faraday	
$Co_2O_2(NH_3)_{10}(SO_4)_2HSO_4$ reacted	1.01,	1.00
O_2 evolved	0.99,	0.97
Co^{2+} produced	2.00,	1.99

The indicating level h exhibited an initial time lag, caused in part by the presence of the fritted disk in the cell. Cathodic oxygen evolution per Faraday calculated from the slope of the curve, however, was the same as that derived from the total Δh and total coulombs passed, within experimental error. It should be noted that oxygen also was evolved at the anode, but the rate of evolution and bubble size were sufficiently small that there was no difficulty in reading the meniscus level h with the traveling microscope.

The cathodic oxygen evolution from compound II was found to be one mole per Faraday, Table I.

Moles of compound II reduced per Faraday.—In the first type of experiment the current efficiency for reduction of II, as well as the cathode potential, were followed as a function of concentration, beginning with an unsaturated solution. The concentration of unreacted II was determined spectrophotometrically. The data, shown in Fig. 3, demonstrated that one mole of the compound was reduced per Faraday over the concentration range studied.

At concentrations below 0.3 mM the cathode potential was decreasing rapidly. Small amounts of a second cathodic reaction, such as oxygen reduction, could be expected in this region, but were not detectable within the accuracy of the data.

A more precise determination of the reduction efficiency was carried out in a second type of experiment in which the cathode compartment contained a saturated solution of II in 1M H_2SO_4, together with an excess of the powdered compound. After passage of 2.7×10^{-4} F, the contents of the cathode compartment (dissolved and undissolved) were removed. Sufficient 1M H_2SO_4 was added to effect complete solution and the resulting solution was analyzed spectrophotometrically to determine the quantity of II reduced. The results of duplicate experiments, included in Table I, show one electron per molecule of II reacted. There was evidently no simultaneous reduction of molecular oxygen (which would require 4 electrons per molecule) at the reduction potential, which was 0.82v in these experiments.

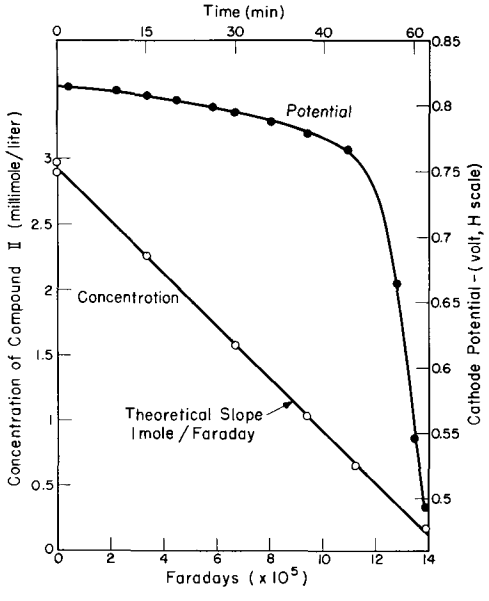

Fig. 3. Change in concentration and cathode potential during electrolysis of an unsaturated solution of compound II in 1M H_2SO_4, 3.60 ma, 22°C.

To test the possibility that a cathode surface of greater catalytic activity might give rise to a competing reaction, the latter type of experiment was repeated with a freshly platinized platinum screen in place of the bright platinum cathode. Results under these conditions were less reproducible but a lowered efficiency for reduction of II always resulted (moles II reacted per Faraday $\leqq 0.9$). Possibly the highly active platinized surface catalyzed the 5-electron reduction of II to Co^{2+} and water.

Cobalt-containing products.—Ion-exchange separation of cathodically reduced solutions of II in 1M H_2SO_4 yielded only one cobalt-containing product, Co^{2+} ion. Quantitative determination of Co^{2+} showed that two Co^{2+} ions were produced per electron (Table I). Under the conditions used, 8-hydroxyquinoline precipitates only Co^{2+} and does not interact with Co(III) species (2).

Reaction mechanism.—The above results establish unequivocally the over-all cathodic reaction

$$[(NH_3)_5CoO_2Co(NH_3)_5]^{5+} + 10H^+ + e \rightarrow O_2 + 2Co^{2+} + 10NH_4^+ \quad [3]$$

as well as the absence of side reactions.

The following reduction mechanism is proposed. The pentavalent ion is assumed to adsorb on the cathode with the peroxo group attached to the metal surface. Transfer of a single electron yields the adsorbed tetravalent ion III

$$M - - - \begin{bmatrix} & Co(NH_3)_5 & \\ O_2 & & \\ & Co(NH_3)_5 & \end{bmatrix}^{5+}$$

$$+ e \rightarrow M - - - \underset{\text{III}}{\begin{bmatrix} & Co(NH_3)_5 & \\ O_2 & & \\ & Co(NH_3)_5 & \end{bmatrix}^{4+}} \quad [4]$$

By means of the internal oxidation-reduction reaction [5], III decomposes to yield adsorbed molecular oxygen and an ammine complex of Co (II)

$$M - - - \begin{bmatrix} & Co(NH_3)_5 & \\ O_2 & & \\ & Co(NH_3)_5 & \end{bmatrix}^{4+}$$

$$\rightarrow M - - - O_2 + 2[Co(NH_3)_5]^{3+} \quad [5]$$

The latter is known to be unstable in acid solutions

$$[Co(NH_3)_5]^{2+} + 5H^+ \rightarrow Co^{2+} + 5NH_4^+ \quad [6]$$

Thus this simple mechanism is in complete accord with the observed over-all reaction [3].

Reaction [5] requires some justification in view of results reported previously (3) for decomposition of the ion $[(NH_3)_5CoO_2Co(NH_3)_5]^{4+}$ in H_2SO_4 solutions. This ion was found to decompose rapidly to yield at least eight cobalt-containing species. The data described in the previous paper (3) indicated that the first step in this decomposition involved attachment of a hydrogen ion to the peroxo group. From this it may be assumed that the attachment of the tetravalent ion III to the cathode surface prevents bonding of hydrogen ion and forces ion III to follow the simpler decomposition path of [5].

In a recent paper Vlcek (4), using a vibrating platinum cathode, showed that the reduction of $[(NH_3)_5CoO_2Co(NH_3)_5]^{5+}$ to $[(NH_3)_5CoO_2Co(NH_3)_5]^{4+}$ occurs reversibly in ammoniacal solutions. In ammonia, unlike acid, the tetravalent ion is relatively stable and can exist in the bulk of the solution in equilibrium with dissolved O_2 and Co (II) ammines. Thus the mechanism for cathodic reduction of I in ammonia differs from that in acid in that $[(NH_3)_5CoO_2Co(NH_3)_5]^{4+}$ can desorb from the cathode and accumulate in the ammoniacal solution.

The only other published investigation on reduction of I concerned chemical reduction with As_2O_3 in H_2SO_4 solutions, in the presence of OsO_4 as catalyst (2). A simple over-all reduction reaction was obtained. Oxygen was evolved, and Co^{2+} was the only cobalt-containing product. Incidental to the present work we studied a second, and more convenient, chemical reduction method. This involved merely shaking a mixture of powdered compound II and excess powdered silver metal with 1M H_2SO_4. The reaction proceeds quantitatively and relatively rapidly at room temperature in accordance with the over-all change

$$[(NH_3)_5CoO_2Co(NH_3)_5]^{5+} + Ag + 10H^+ \rightarrow O_2 + 2Co^{2+} + 10NH_4^+ + Ag^+ \quad [7]$$

Analytical results for Co^{2+}, O_2, and Ag^+ were all in good agreement with the theoretical values from [7].

That Co^{2+} is the only reduced cobalt species produced in acid by either chemical-reduction method is readily explained by generalizing the mechanism represented by [4] to [6]. For chemical reduction, the reductant [As(III) or Ag] becomes attached to the peroxo group of the pentavalent complex I. Following electron transfer the oxidized form of the reductant, which is still bonded to the peroxo group, prevents the hydrogen ion addition step which is needed to produce the more complex cobalt-containing products observed in our earlier work (3).

Possible applications.—The fact that oxygen is evolved at both cathode and anode in an acid solution containing II provides a novel and potentially useful method for electrolytically introducing known amounts of oxygen, uncontaminated by other gases, into closed systems. Electrolysis of solutions containing II also should find application in gas coulometers such as those described by Lingane (5). The sensitivity of the coulometer is increased by the use of II since 1.25 moles of gas (O_2) are evolved per Faraday, as compared with a total of 0.75 mole/**F** of hydrogen plus oxygen from the solutions commonly employed.

Conclusions

1. At a bright platinum cathode in H_2SO_4 solutions, the pentavalent complex $[(NH_3)_5CoO_2Co(NH_3)_5]^{5+}$ is reduced quantitatively to Co^{2+} in a one-electron reaction, with simultaneous release of the peroxo oxygen as oxygen gas.

2. Simple chemical reduction with silver powder was found to yield the same products quantitatively.

3. A probable reduction mechanism is outlined, based on the assumption that the reducing ion or metal surface atom becomes attached to the pentavalent complex at the peroxo group.

4. Electrolysis of an acid solution of the pentavalent complex between bright platinum electrodes provides a convenient electrolytic generator of pure oxygen. This system may also be used as a sensitive oxygen coulometer, yielding 1.25 O_2 per Faraday.

Manuscript received Sept. 8, 1961; revised manuscript received Nov. 29, 1961. This paper was prepared for delivery before the Los Angeles Meeting, May 6-10, 1962.

Any discussion of this paper will appear in a Discussion Section to be published in the December 1962 JOURNAL.

REFERENCES

1. E. A. Ebsworth and J. A. Weil, *J. Phys. Chem.*, **63**, 1890 (1959).
2. K. Gleu and K. Rehm, *Z. anorg. allgem. Chem.*, **237**, 79 (1938).
3. R. G. Charles and S. Barnartt, *J. Inorg. Nuclear Chem.*, in press.
4. A. A. Vlcek, *Coll. Czech. Chem. Comm.*, **25**, 3036 (1960).
5. J. J. Lingane, "Electroanalytical Chemistry," 2nd Ed., p. 452, Interscience Publishers, Inc., New York (1958).

APPENDIX

Relationship between Δn and Δh for the current-efficiency cell

Evolution of Δn moles of gas increases the gas volume above the catholyte by $A(\Delta h)$. It increases the pressure of the gas by $(\Delta h)d/13.5$ and its water content by $\Delta n_w = A(\Delta h)P_s/RT$. From $\Delta n + \Delta n_w = (P_fV_f - P_iV_i)/RT$, one obtains

$$\Delta n = \frac{\Delta h}{RT}[A(P_i - P_s) + V_f d/13.5] \quad [1]$$

Dissolution of Δn moles of gas decreases the volume, pressure and water content of the gas by the same quantities as above. Since Δh is now negative, Eq. [1] still applies without any change of sign. A negative value of Δn refers to gas dissolution, a positive one to gas evolution.

If atmospheric pressure changes during the measurement, a correction δh must be applied to the observed value of Δh in Eq. [1]. An increase in atmospheric pressure, p_a, corresponds to an increase in gas volume of $A(\delta h)$ and a net increase in gas pressure of $[p_a + (\delta h)d/13.5]$. By applying the approximation $\Delta P/P_f = -\Delta V/V_f$, one obtains, with sufficient accuracy

$$\delta h = -p_a[A\,P_f/V_f + d/13.5]^{-1} \quad [2]$$

Thus $|\delta h|$ must be added to Δh_{obs} where atmospheric pressure has increased, and vice versa.

Technical Notes

Conditions for the Formation of α or β Lead Dioxide During the Anodic Oxidation of Lead

Richard A. Baker

Bell Telephone Laboratories, Incorporated, Murray Hill, New Jersey

The work of Kiseleva and Kabanov (1,2) concerning the behavior of the α and β modifications of lead dioxide in sulfuric acid has led them to propose that the formation of the β form is a consequence of H_2SO_4 chemisorption on the PbO_2 formed during anodic oxidation of lead. This explanation is open to challenge since it implies that sulfate or bisulfate anions perform, at least in part, a vital function in determining the lead dioxide modification formed. Recent work performed in this laboratory as well as other well-known facts support the contention that it is hydrogen ion concentration which influences the nature of the PbO_2 deposit.

Methods for the preparation of α- and β-PbO_2 in the laboratory are well known. In this laboratory, β-PbO_2 has been readily prepared by electrodeposition from acidic solutions of lead nitrate, lead sulfamate, lead fluoborate, and lead perchlorate as well as by the anodic oxidation of lead in strong sulfuric acid. On the other hand, α-PbO_2 has been electrodeposited from neutral solutions composed primarily of lead nitrate and lead acetate, and by the anodic oxidation of lead in alkaline solution at high current densities. Published descriptions of electrodeposition methods have been given by Rüetschi, Angstadt, and Cahan (3) and by Thomas (4). These conditions for electrodeposition suggest strongly that it is the pH which is the major factor controlling the modification of lead dioxide formed.

To test further the relative importance of H^+, $SO_4^=$, and HSO_4^- ions, a lead electrode was anodized and cycled in solutions of 2M Na_2SO_4, 2M $KHSO_4$, and 2M H_2SO_4 at room temperature and the lead dioxide modification produced was identified by means of x-ray diffraction powder patterns. The electrode was Doe-Run lead 99.998% pure which was first etched, washed, dried, and after immersion in electrolyte, made cathodic for a short time to reduce residual oxide.

The anodic current density was 1.5 ma/cm^2 of geometric area while cathodic current density was 0.75 ma/cm^2. Periods of charge were of the order of 10 times the capacity of the lead dioxide formed and discharges were carried to reversal of potential sign referred to a Hg/Hg_2SO_4 reference electrode. The results are presented in Table I.

Table I.

Electrolyte	pH	Electrode treatment	PbO_2 Modification
2M Na_2SO_4	7.6-8.0	Anodic only	100% α
		Anodic + 5 charge-discharge cycles	100% α
2M $KHSO_4$	0.7	Anodic only	100% α
		Anodic + 5 charge-discharge cycles	30% α — 70% β to 60% α — 40% β
2M H_2SO_4	<0	Anodic only	~50% α ~50% β
		Anodic + 3 charge-discharge cycles	<10% α >90% β

It is significant that only α-PbO_2 was formed in neutral Na_2SO_4 solution. Initial anodic oxidation of lead resulted in the formation of β-PbO_2 only in 2M H_2SO_4. In $KHSO_4$ solution, β-PbO_2 was produced only after charge-discharge cycling. It may be concluded, therefore, that the modification of lead dioxide formed on anodic oxidation of lead and even subsequent cycling depends primarily on the pH of the electrolyte. The only function of the sulfate species present other than electrical neutrality and conductivity of the electrolyte is the limit its concentration places on the solubility of lead II ions present in the solution.

Kiseleva and Kabanov have proposed that the formation of β-PbO_2 is retarded by the addition of Co^{++} in the cell because the Co^{++} displaces H_2SO_4 which is chemisorbed on the oxide. The formation of the α modification in turn is supposed to provide better protection against the anodic oxidation of the underlying lead. Our work as reported here together with the other facts previously described

indicate that it must be the protons which are displaced by cobalt ions and not H_2SO_4 as such.

Acknowledgment

Acknowledgment is due to Mrs. Mildred H. Read of Bell Telephone Laboratories, Inc., who performed the x-ray diffraction analyses.

Manuscript received October 31, 1961.

Any discussion of this paper will appear in a Discussion Section to be published in the December 1962 JOURNAL.

REFERENCES

1. I. G. Kiseleva and B. N. Kabanov, *Akad. Nauk SSSR, Doklady*, **108**, 864 (1956).
2. I. G. Kiseleva and B. N. Kabanov, *ibid.*, **122**, 1042 (1958).
3. P. Rüetschi, R. T. Angstadt, and B. D. Cahan, *This Journal*, **106**, 547 (1959).
4. U. B. Thomas, *ibid.*, **94**, 42 (1948).

The Effect of Electropolishing on the Codeposition of Hydrogen with Nickel

Thomas C. Franklin and Archie Blackburn

Chemistry Department, Baylor University, Waco, Texas

A number of investigations have been made of the advantages of electropolishing as a pretreatment of the electrode in electrodepositions. These have been surveyed by Faust (1). As a part of an investigation of the effect of organic additives on the hydrogen content of nickel deposits (2), a short study was made of the variation in the amount of hydrogen codeposited with nickel as a function of the pretreatment of the electrode.

Experimental Procedure

Nickel wires were used as the basis metal for nickel plating. They were 14 gauge and 1.5 cm in length. They were prepared for plating by two procedures. In one procedure the wire was polished mechanically by hand with number 2/0 emery cloth. In the other procedure the wire was polished mechanically in the same way and then electropolished at a current density of 60 ma/cm^2 in a bath containing 50 ml water, 370 ml 85% phosphoric and 80 ml 98% sulfuric acid. Nickel was plated from a standard Watts bath for a period of 12 min at a current density of 6.96 ma/cm^2.

The hydrogen content of the deposits and the current efficiencies were measured in the manner previously reported (2). The codeposited hydrogen was oxidized electrolytically, and the number of coulombs necessary for the oxidation was a measure of the amount of hydrogen. Current efficiency was measured by measuring the volume of hydrogen evolved during the deposition.

Table I. Effect of pretreatment of electrode on amount of codeposited hydrogen

	Number of millicoulombs necessary to oxidize codeposited hydrogen		
Electrode	Mechanically polished electrode	Electropolished electrode	Remarks
1	6.25 ± 0.086	Not measurable	Plated 12 min, electropolished 2 min
2	3.12 ± 0.51	Not measurable	Plated 12 min, electropolished 2 min
2		Not measurable	Plated 60 min, electropolished 2 min
3	3.26	Not measurable	Plated 12 min, electropolished 5 min

Results and Conclusions

Table I summarizes the results of the measurements of the amount of codeposited hydrogen. The table shows clearly that electropolishing the electrode before plating cuts the amount of hydrogen codeposited down to the point where it was not measurable by this technique.

There are two possible explanations for these results: (*a*) the difference in strain in the surface could change the current efficiency of the deposition process; (*b*) the difference in surface strain and roughness could change the ability of the hydrogen to adsorb to the surface.

Table II shows that there is essentially no difference between the current efficiency on the mechanically polished and electropolished electrodes.

Apparently the difference lies in the ability of the mechanically polished electrode to adsorb hydrogen. This is further shown by Table III, in which is tabulated the hydrogen retained by the nickel electrodes when only hydrogen is electrically generated on the electrodes.

Table II. Effect of pretreatment of the electrode on the current efficiency for the evolution of hydrogen

	Current efficiency for the evolution of hydrogen on:	
Electrode	Mechanically polished electrode, %	Electropolished electrode, %
4	1.69	2.00
5	1.83	1.64
6	2.42	2.80

Table III. Number of millicoulombs necessary to oxidize hydrogen adsorbed on and absorbed in nickel electrodes

Electrode	Mechanically polished	Electropolished
1	4.05 ± 0.23	0.04
2	4.38	0.02
3	3.62 ± 0.03	Not measurable
4	2.65 ± 0.02	Not measurable

This work was sponsored by the Office Ordnance Research, U. S. Army.

Acknowledgment

Manuscript received Jan. 13, 1961; revised manuscript received Dec. 4, 1961.

Any discussion of this paper will appear in a Discussion Section to be published in the December 1962 JOURNAL.

REFERENCES

1. C. L. Faust, "Electroplating Engineering Handbook," p. 107-27, Reinhold Publishing Corporation, New York (1955).
2. T. C. Franklin and Jack Goodwyn, *This Journal*, **109**, 288 (1962).

Some Observations on Overpotential Variations During the Galvanostatic Electrodeposition of Copper

J. K. Prall and L. L. Shreir

Metallurgy Department, Corrosion Section, Battersea College of Technology, London, England

The variation in the activation overpotential with time, which has been observed by several workers during studies of the mechanism of electrode processes (1a-1h), is a factor which may result in irreproducibility of the value of the overpotential. During a study of the electrodeposition of copper from acid copper sulfate solutions it was observed that the conventional method of determining the activation overpotential (η_A), *i.e.*, allowing a predetermined time to elapse before recording the overpotential, did not always give reproducible results owing to the changing topography of the cathode surface during electrodeposition. As a result of these observations a reproducible substrate technique has been developed in which a platinum sheet is used as the cathode for each determination of η_A at each value of constant current. Removal of the copper deposit is effected by anodic dissolution before the next determination of η_A at another current. Full details of this apparatus and technique have been described in a previous publication (2).

Observations of the $\eta_A - t$ curves using this technique for a series of acid copper sulfate solutions (including some with addition agents) has led to the conclusion that these curves can be classified into three types. In the initial time interval, t_1, which may be a fraction of a second, the rapid rise in η_A is due principally to the establishment of the electrical double layer; t_1 is affected only slightly by variations in the substrate properties. If the surface topography of the substrate is unaffected by the electrode process, *e.g.*, a reduction of ions to a lower valency state or hydrogen evolution, the activation overpotential should remain constant with time. However, in the present study it was observed that during the next time interval t_2 (which could persist for several minutes), η_A could either increase or decrease immediately after the double layer was completely charged. The sign, magnitude, and duration of this change appeared to depend on the nature of the substrate (crystal orientation and size, crystal defects and thickness of deposit) and on the nature of the electrolyte (presence of co-depositable metallic impurities, active impurities such as chloride ions, concentration polarization, etc.). If the duration of t_2 is appreciable, then clearly the experimental time involved in obtaining $\eta_A - i$ plots will be unduly long and, in addition, other errors may be introduced by prolonged electrolysis.

A study has been made of the factors responsible for η_A changes during time t_2, and it has been established that the greater the amount of mechanical deformation applied to the platinum substrate (*e.g.*, by rolling or polishing) then the greater is the magnitude of $\Delta\eta_A$ and t_2. Figure 1 shows some $\eta_A - t$ curves which have been obtained using a platinum substrate, which had been subjected to different degrees of cold-rolling; before electrolysis the cathodes were lightly etched in boiling aqua regia for 10 sec.

It can be seen that the initial values of η_A differ according to the extent of cold-working of the platinum although the steady-state value is independent of any textural difference in the substrate which could have arisen during either cold-working or recrystallization. This indicates that the technique provides a sensitive method of detecting any effects caused by the structure of the substrate. It is relevant to observe that it has been previously postulated (3) that lattice building in electrocrystallization is accomplished by surface diffusion of transferred adions to edges, steps, or kinks; in the present study the number of these defects will be proportional to the degree of cold-work (4).

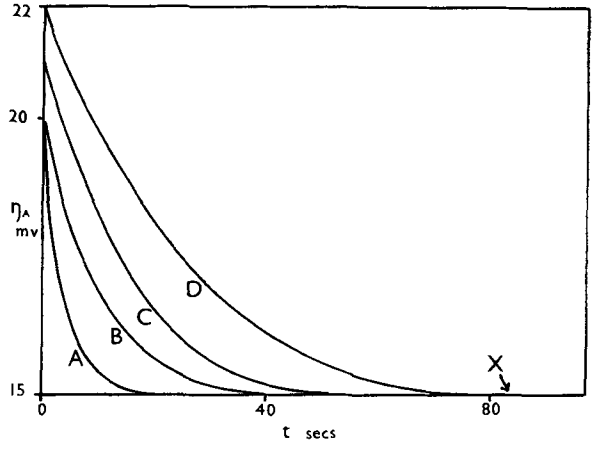

Fig. 1. Effect of metallurgical condition of the platinum substrate on the variation of η_A with time: electrolyte 0.5M $CuSO_4$ + 0.5M H_2SO_4, at 25°C and 0.25 amp/dm²: A,* V.P.N. 48, heat treatment continued to allow grain growth; B, V.P.N. 48; C, V.P.N. 72; D, V.P.N. 90. X, is the steady-state η_A.

* V.P.N. = Vickers Pyramid Hardness Number.

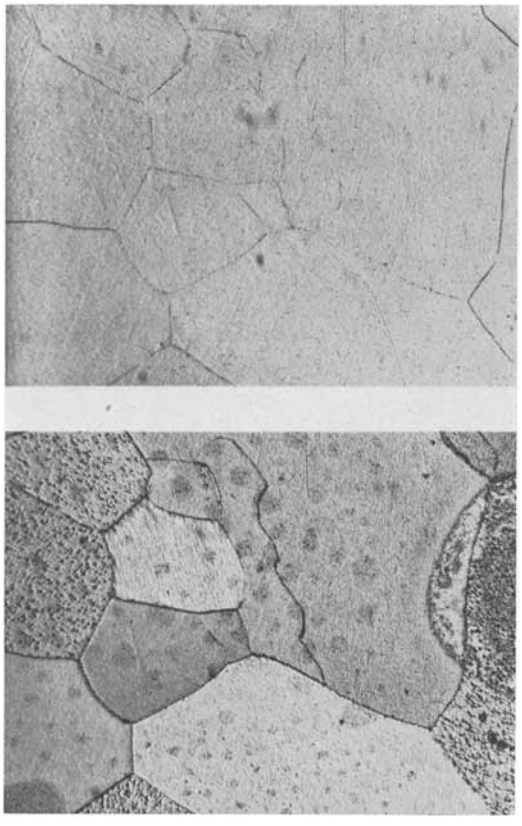

Fig. 2. A. (top) Platinum substrate surface, after light etching and prior to its being electroplated. Mag. 20X. B. (bottom) Localized growth of copper at the grain boundaries. Platinum substrate as described above, electroplated with copper and removed from plating solution when the steady η_A was reached.

Observations of the growth of thin layers of the deposits (Fig. 2A, 2B) show that deposition occurs preferentially at grain boundaries and in a direction which is perpendicular to the substrate. This would indicate that the more imperfect the substrate the greater will be localized deposition at imperfect sites (in this case crystal boundaries) and the greater the charge required to cover completely the platinum substrate. This is supported by the results shown in Fig. 1. In addition it has been observed that with any given substrate the $\eta_A - t$ curve can be reproduced after any time t (within the time t_2) without hysteresis during anodic and cathodic cycling. Further, it has been established that, irrespective of the current density, a constant charge is required to produce the same steady-state value of η_A.

The classical procedure (5) of allowing η_A to become constant at a given value of current is not always satisfactory owing to surface roughening of the deposit and other factors such as changes in concentration of active species in the electrolyte; such factors are insignificant in the reproducible substrate method owing to the very small charge used for each determination of η_A.

The present work has necessitated a study of the effect, and elimination, of adverse impurities in the electrolyte as it is well known that even trace amounts of impurities may have a very marked effect on η_A and the crystal form of the deposit (8). In particular, the effects of traces of chloride ions have been studied as, with normal reagents, this impurity is usually present in significant quantities and is difficult to remove by, for example, repeated recrystallization of $CuSO_4 \cdot 5H_2O$ (where 1-10 ppm Cl can still persist). Electrolytes, low in Cl^-, were prepared in solution by one of the following reactions, and in both cases the reagents can be prepared virtually free of chloride

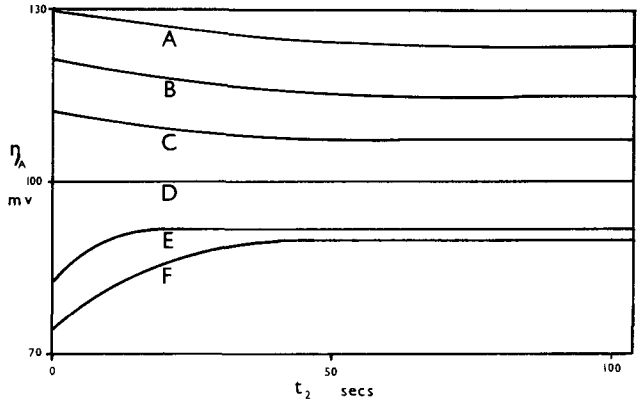

Fig. 3. Effect of chloride ions, added to a chloride-free electrolyte, on the variation of η_A with time: electrolyte 0.5M $CuSO_4$ + 0.5M H_2SO_4, at 25°C and 2.0 amp/dm^2: A, 0.00 ppm Cl^-; B, 0.08; C, 0.15; D, 0.60-5.00; E, 12.00; F, 40.00.

$$Ag_2SO_4 + Cu \rightarrow CuSO_4 \text{ aq.}$$

$$CuO + H_2SO_4 \rightarrow CuSO_4 \text{ aq.}$$

A further possibility of removing chlorides is by anodic oxidation at a platinum anode (6).

The effects of Cl^- on η_A are shown in Fig. 3, and it is evident that the amounts of chloride which are normally present, even in carefully prepared electrolytes, can markedly affect η_A.

The effect of Cl^-, on depolarization generally, has been attributed to their action in facilitating the transfer of electrons at the cathode surface (7). The reduction in t_2 with increasing chloride ion concentration may be explained on the basis that these ions encourage the electrodeposition of copper at otherwise unfavorable planar sites thereby resulting in a more rapid coverage of the platinum substrate.

It is considered from this preliminary study that the reproducible substrate technique may be of general application in studying the effect of the metallurgical condition of the substrate [providing that this is unaffected during electrolysis (2)] on electrocrystallization.

Manuscript received Nov. 10, 1961.

Any discussion of this paper will appear in a Discussion Section to be published in the December 1962 JOURNAL.

REFERENCES

1. a. T. Erdey-Gruz and M. Volmer, *Z. physik. Chem.*, **A157**, 182 (1931).
b. T. Erdey-Gruz and H. Wick, *ibid.*, **162**, 63 (1932).
c. A. G. Samartsev and K. S. Evstropev, *J. Phys. Chem. (U.S.S.R.)*, **5**, 854 (1934).
d. O. A. Esin, L. I. Antropov, and A. I. Levin, *ibid.*, **9**, 269 (1937).
e. L. D. Kopyl and V. A. Yuza, *ibid.*, **14**, 1074 (1940).

f. L. L. Shreir and J. W. Smith, *This Journal*, **99**, 2, 70 (1952).
g. L. L. Shreir and J. W. Smith, *Trans. Faraday Soc.*, **50**, 393 (1954).
h. V. V. Mikhailov, *Zhur. fiz. Khim.*, **28**, 1067 (1954).
2. J. K. Prall and L. L. Shreir, *Trans. Inst. Metal Finishing*, **38**, 9 (1961).
3. a. B. E. Conway and J. O'M. Bockris, *Proc. Roy. Soc.*, **248A**, 394 (1958).
b. B. E. Conway and J. O'M. Bockris, *Plating*, April, 371 (1959).
4. A. L. Titchenor and M. B. Beaver, "Progress in Metal Physics," p. 247, Pergamon, London (1958).
5. L. L. Shreir and J. W. Smith, *This Journal*, **98**, 193 (1951).
6. R. G. Wilkinson, *Platinum Metals Rev.*, **5** [4], 128 (1961).
7. E. H. Lyons, *This Journal*, **101**, 380 (1954).
8. a. S. C. Barnes, Ph.D. Thesis, Birmingham, 1960.
b. S. C. Barnes and G. G. Storey, *Trans. Inst. Metal Finishing*, **37**, 11 (1960).

Chemical Etching of Germanium in HF-HNO_3-H_2O Solutions

Thomas E. Burgess

Research Laboratories, Sprague Electric Company, North Adams, Massachusetts

The kinetics of etching of germanium in HF-HNO_3-H_2O solutions have been reported by several authors and proposals of etching mechanisms have been made (1-4). Camp (5) has shown that both activation and diffusion control of the etching rate of germanium exist in solutions of HF-H_2O_2-H_2O and similar systems. The work reported here is concerned with the etching of germanium in HF-HNO_3-H_2O solutions under isothermal conditions and gives the chemical etch rates of germanium over a wide range of solution composition and temperatures of the etching medium. The results indicate that diffusion control of the etching rate appears when the nitric acid concentration in the etchant is high. An abrupt shift to activation control appears at lower nitric acid concentration and holds over a wide concentration range.

Experimental

The etch rates of germanium in the HF-HNO_3-H_2O solutions were determined by measuring the loss in weight of germanium pieces which had been etched for given periods of time in solutions maintained at constant temperatures during the etching process. Pieces of germanium measuring 0.64x0.64x0.25 cm were cut from single crystal material with the 0.64x0.64 faces lying in the crystal plane. These pieces were weighed and then supported in the etchant with all faces except one 0.64x0.64 cm face masked with polystyrene cement. The polystyrene cement effectively masked all surfaces during the etching reaction with only very slight lifting occurring around the edges of this mask leading to an insignificant etching error. The etchant was maintained at a constant temperature during the reaction by placing the polyethylene reaction beaker containing about 30 cc of solution inside a glass cooling cell through which water circulated from a controlled temperature bath. Vigorous agitation of the etchant was maintained during the reaction by a magnetic stirrer in order that the surface temperature of the etching germanium would remain at a constant value. It had been previously determined, by cementing a thermocouple to the etching surface, that the surface temperature rose 30°-40°C above the bath temperature when stirring was omitted. After etching for 3 min the germanium was removed from the etchant, washed with water, and the mask removed by peeling off the cement. Following this, the germanium piece was washed in toluene to remove traces of the cement, dried under a heat lamp, and weighed. The amount of germanium removed from the pieces during etching varied from 1 to 30 mg, depending on the composition and temperature of the etch.

The etchants were prepared from reagent grade nitric acid (70%) and hydrofluoric acid (49%) and water was added to all mixtures to adjust its concentration to 33M, the concentration of water in the reagent hydrofluoric acid. Thus, the etching rates were made in solutions having a constant water concentration with varying concentration ratios of nitric acid and hydrofluoric acid.

Results

Table I lists the data obtained in etching 1 ohm-cm n-type {111} germanium crystals. The etch rates are given for four temperatures and each point is an average of four values.

A plot of the log etch rates *vs.* $1/T$ appears in Fig. 1 for some of the data in Table I. The activation energies calculated from the slopes of these curves are around 6 kcal for the mole ratios of HNO_3/HF greater than 4.9. Below this ratio the energies range from 19 to 12 kcal. Figure 2 shows a plot of these activation energies *vs.* mole ratio HNO_3/HF for the ratio range between 0.06 to 1.3.

Table I. Etching rates of germanium in HF-HNO_3 solutions at various temperatures

Mole ratio HNO_3/HF	Etch rate, μ/min 15°C	25°C	35°C	40°C	Activation energy* ΔE kcal
0.06	0.76	1.5	3.1	4.2	12.3
0.14	0.94	2.8	4.9	7.4	12.7
0.23	1.2	4.0	5.7	9.7	14.5
0.36	1.6	3.6	6.8	14	15.3
0.55	1.2	4.2	9.3	15	16.2
0.82	1.2	5.6	12	27	19.6
1.30	2.2	5.6	12	26	18.5
2.20	2.2	5.6	16	31	17.9
4.90	7.0	13	16	18	6.2
10.4	4.3	5.8	7.0	9.3	5.6

* Calculated from slope of the plot of log etch rate *vs.* $1/T$.

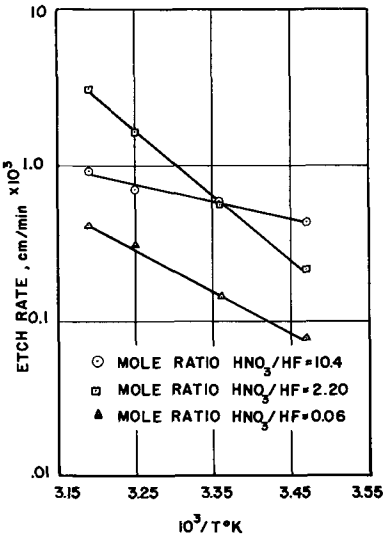

Fig. 1. Temperature dependence of the dissolution rate of germanium in HF-HNO_3-H_2O solutions.

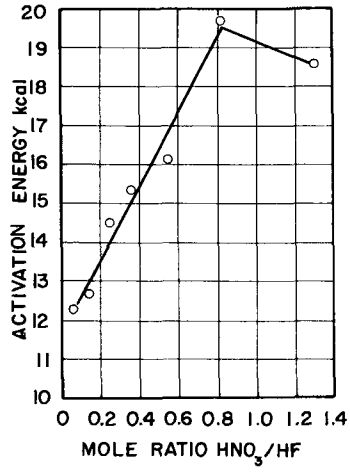

Fig. 2. Activation energy vs. mole ratio

Discussion

It is apparent from the activation energy curves shown in Fig. 1 that at higher concentrations of nitric acid the rate of etching is controlled by a transport process while at lower concentrations the controlling step is an activation process. This is to be expected since at high nitric acid concentrations the etch rate of germanium would be dependent on the ability of the hydrofluoric acid to diffuse to the oxide surface (probably the relatively insoluble GeO_2) where it would react with the oxide forming the soluble fluoride complex ion. As the concentration of hydrofluoric acid is increased there is a change to activation control and also an increase in the etching rate. At nitric acid concentrations below those reported there is probably again diffusion control, with the rate limited by transport of the oxidizing agent to the solid surface.

The region between these two extremes is complicated by the presence of a thin film found on the solid surface. This thin gold-colored film, which is visible on the etched surface when the molar ratio of HNO_3/HF is 0.36 or less (25°C), could possibly be caused by the formation of an amorphous germanium monoxide previously reported by Ellis (6) or by the formation of a polycrystalline germanium layer similar to that reported for silicon by Archer (7). The presence of this film accounts for the fairly low etch rate observed at the lower concentrations (Table I). It is interesting to note in the plot of activation energy *vs.* mole ratio (Fig. 2) that the activation energy increases linearly up to a mole ratio at about 0.8. This could possibly be an indication of the range of the film formation process.

If the film is amorphous germanium monoxide then it is conceivable that in this concentration range the dissolution of the germanium is a two-step reaction where the oxidation of germanium to the monoxide occurs at the surface with the subsequent solution and oxidation of this material to the tetravalent state followed by the function of the fluoride complex. The etch rate in this range would be dependent on the rate of solution of the monoxide. However, if the film is polycrystalline germanium then a mechanism similar to that proposed for silicon by Turner (8) may be involved where the divalent form of germanium would appear first, followed by disproportionation to polycrystalline germanium and germanium dioxide. The correct mechanism for the etching reaction could be determined possibly if an analysis of the reaction products including the film was made. Initial spectrographic analysis of a known weight of film removed from the germanium substrate by solution in 6*N* potassium hydroxide indicates that it is not pure germanium. This fact appears to support the germanium monoxide mechanism.

Manuscript received Oct. 13, 1961.

Any discussion of this paper will appear in a Discussion Section to be published in the December 1962 JOURNAL.

REFERENCES

1. M. C. Cretella and H. C. Gatos, *This Journal*, **105**, 487 (1958).
2. D. R. Turner, *ibid.*, **107**, 810 (1960).
3. R. L. Myuller, T. P. Markova, and S. M. Repinskii, *Vestnik Leningrad Univ. Ser. Fiz. i. Khim.*, 106 (1959).
4. W. W. Harvey and H. C. Gatos, *This Journal*, **107**, 65 (1960).
5. P. R. Camp, *ibid.*, **102**, 586 (1955).
6. S. G. Ellis, *J. Appl. Phys.*, **28**, 1262 (1957).
7. R. J. Archer, *J. Phys. Chem. Solids*, **14**, 104 (1960).
8. D. R. Turner, "The Surface Chemistry of Metals and Semiconductors," H. C. Gatos, Editor, p. 298, J. Wiley & Sons, Inc. (1960).

Brief Communications

Mechanism of Stress Corrosion Cracking in Stainless Steels

R. Stickler and S. Barnartt

Research Laboratories, Westinghouse Electric Corporation, Pittsburgh, Pennsylvania

Recently Forty (1) proposed a restricted-slip theory of stress corrosion cracking which may be used to predict the susceptibility or immunity of metals to this type of cracking. The theory presupposes cyclic chemical-mechanical propagation, as first clearly described by Keating (2). In this method of propagation a short period of relatively slow chemical attack, or electrochemical attack in the case of aqueous corrodents, leads to localized stress concentration and embrittlement. A microscopic crack results; then further chemical attack occurs at the tip of the crack, and the cycle repeats. Direct observations of periodic crack extension were made by Edeleanu (3) on the surface of an α-brass single crystal corroding in ammonia, and by Kirk, Beck, and Fontana (4) on commercial stainless steel surfaces in dilute NaCl solutions at 204°C. Hines (5), however, pointed out the need for other direct evidence, because it is possible for cracks growing smoothly in the bulk of the alloy to break through the surface periodically.

The chemical embrittlement process may be expected to vary with the type of corrodent and alloy involved. In studies on copper alloys, using the technique of electron transmission through thin films, Bassett and Edeleanu (6) and also Swann and Nutting (7) showed evidence for preferential chemical attack at or near stacking faults. They suggested that solute segregation at stacking faults may control the chemical embrittlement step, but as yet little is known of the embrittlement mechanism.

The restricted-slip theory refers to the mechanical-fracture step of the propagation cycle. According to this theory, when a crack is formed within the embrittled surface layer it will propagate into the underlying ductile metal only if dislocation movement is highly restricted. Propagation ceases when the crack enters a soft region, such as a preexisting slip band. Hence alloys which readily cross slip should be immune to this type of cracking.

Evidence that the restricted-slip theory may apply to copper alloys has been given by Swann (8). In the copper-zinc system, 3-37% Zn, it was shown that the stacking fault energy decreases with increasing zinc concentration, and a gradual change in dislocation distribution occurs. Pure copper has a high stacking fault energy, and the dislocation groups exhibit a cellular structure, which indicates that the dislocations can readily cross slip. As zinc is added the stacking fault energy decreases and cross slip becomes more difficult. The cell structure disappears and dislocations become confined to slip planes, indicating restricted slip. Alloys having 15-37% Zn, which are known to be highly susceptible to stress corrosion cracking, were found to have low stacking fault energy and exhibited highly restricted slip, in agreement with the theory.

Similarly with aluminum additions to copper, Swann showed that increasing aluminum content in the range 3.5-8% continuously lowered the stacking fault energy and restricted slip. Although no stress corrosion data were given for the particular alloys studied, others have reported Cu-4% Al to be apparently immune to stress corrosion cracking (9, 10) while alloys in the range 5 to 10% Al have cracked (10).

We have now tested the applicability of the restricted-slip theory to stainless steels. Both the stress corrosion behavior and the dislocation pattern have been determined in a pair of purified vacuum-melted 16 Cr-20 Ni steels. One of these was immune to stress corrosion cracking and the other susceptible. The immune alloy, E, has been shown in a previous paper (11) to remain uncracked in boiling 42% $MgCl_2$ under severe corrosion conditions. The susceptible alloy, K, has essentially the same composition except for the addition of 1.5% molybdenum, Table I. According to the theory, the molybdenum addition should have caused highly restricted

Table I. Alloy composition and stress corrosion behavior

Alloy designation:		E	K	M
Composition (%):	Cr	16.2	16.1	16.5
	Ni	19.9	19.9	19.9
	Mo	—	1.51	5.06
	C	0.013	0.013	0.013
	N	0.010	0.011	0.018
	Mn	—	—	1.44
	Si	—	—	0.45
	Al	—	—	0.059
	O	0.0015	0.027	0.018
	S	0.011	0.007	0.009
	P	0.003	0.003	0.002
Average time to fracture* (hr):		>250 (no cracks)	6	14

* Wires of 0.7 mm diameter, under constant tensile stress of 2800 kg cm^{-2} (40,000 psi), in 42% $MgCl_2$, 146°C.

dislocation movement. This was studied by electron transmission through thin films.

The thin films were prepared from annealed wire specimens (0.7 mm diameter) by first cold rolling the wires to 0.1 mm thick strips. The strips were annealed in vacuum (10^{-5} mm Hg) at 1065°C for 15 min and quenched by rapidly moving them to a cold section of the vacuum system. They were then deformed 15-20% by cold rolling; this amount of plastic deformation was approximately the same as that which occurred during initial loading of the wire specimens in stress corrosion cracking tests. An area 2 x 20 mm, the perimeter masked with lacquer, was electropolished under the following conditions until thin edges were produced: solution: H_3PO_4 (conc.)—60%, H_2SO_4 (conc.)—40% by vol; temperature: 60°C; anode current density: 2.5 amp cm^{-2}.

The thin areas thus produced, the order of 1000Å thick, were examined by transmission electron microscopy, and typical micrographs are shown in Fig. 1. In these micrographs dislocations appear as dark lines. Although the dislocation density is high, the general distribution is evident. In the purest alloy E (top micrograph) the dislocations form a "cell structure" consisting of light regions, which are relatively dislocation-free, and boundaries which contain high dislocation density. This distribution is characteristic of deformed face-centered cubic metals which allow easy cross-slip and which have high stacking fault energy (12). Alloy K (center micrograph) exhibits a dislocation distribution in which there is a definite tendency for the dislocations to be concentrated along parallel (slip) planes. This is characteristic of deformed face-centered cubic metals in which slip is restricted and the stacking fault energy is low (12). As shown in Table I the former alloy is not susceptible to stress corrosion cracking, while the latter with molybdenum added cracks readily. Thus the molybdenum addition has caused restricted slip in the metal and also made it susceptible to cracking, in agreement with Forty's theory.

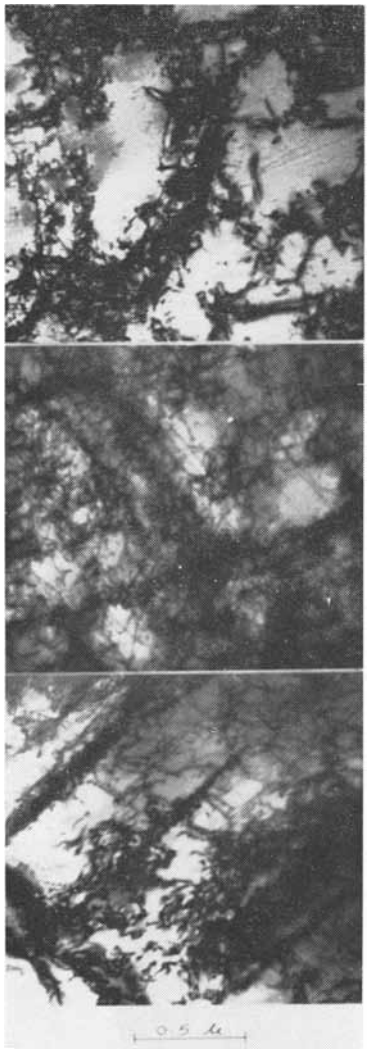

Fig. 1. Transmission electron micrographs of deformed 16 Cr-20 Ni stainless steels. Top, alloy E, no added element; center, alloy K, 1.5 Mo addition; bottom, alloy M, 5.06 Mo-1.44 Mn-0.45 Si-0.06 Al additions.

The only other data obtained with molybdenum addition to the 16-20 steel was for an air-melted alloy, M, containing 5% Mo plus smaller additions of Mn, Si, and Al (Table I). This alloy was susceptible to stress corrosion cracking, and the typical dislocation pattern found in the 20% cold-worked metal, Fig. 1 (bottom), again shows that restricted slip is associated with crack susceptibility.

The observations reported here all indicate that Forty's restricted-slip theory is applicable to these stainless steels. It is desirable to extend this work to include other single impurity additions to the purified 16-20 alloy, in order to isolate the effects of those which induce cracking and those which do not. In addition, direct measurements of stacking fault energy in stainless steels are needed for comparison with Swann's correlation of cracking in copper alloys having low stacking fault energy. These studies are now in progress.

Acknowledgment

Thanks are due to the Office of Naval Research, Metallurgy Branch, Washington, D.C., for partial support of this work.

Manuscript received Jan. 2, 1962.

Any discussion of this paper will appear in a Discussion Section to be published in the December 1962 JOURNAL.

REFERENCES

1. A. J. Forty in "Physical Metallurgy of Stress Corrosion Fracture," T. N. Rhodin, Editor, p. 99, Interscience Publishers, New York (1959).
2. F. H. Keating in "Symposium on Internal Stresses in Metals and Alloys," p. 311, Institute of Metals, London (1948).
3. C. Edeleanu, ref. (1), p. 79.
4. W. W. Kirk, F. H. Beck, and M. G. Fontana, ref. (1), p. 227.
5. J. G. Hines, ref. (1), p. 92.
6. G. A. Bassett and C. Edeleanu, ref. (1), p. 117.
7. P. R. Swann and J. Nutting, *J. Inst. Metals*, **88**, 478 (1960).
8. P. R. Swann, Thesis, University of Cambridge, England (1960).
9. D. H. Thompson and A. W. Tracy, *Trans. AIME*, **185**, 100 (1949).
10. M. Cook, ref. (2), p. 73.
11. S. Barnartt and D. van Rooyen, *This Journal*, **108**, 222 (1961).
12. P. B. Hirsch, *J. Inst. Metals*, **87**, 406 (1958-9).

Sealed Solid Method for Zone Melting Decomposable Compounds

F. K. Heumann

Research Laboratory, General Electric Company, Schenectady, New York

A number of procedures are used to crystallize materials containing or consisting of components volatile over the melt. Those in current use have limitations for achieving purification or for recovering material of uniform composition. Thus, the sealed tube Bridgman or directional freezing method results in general in ingots of varying composition along their length. Zone-melting in a boat or by floating zone requires that all of the sealed tube and hence the solid be heated by multiple furnaces at all times to control the partial pressures of the volatile components or impurities. With the solid always hot, movement of constituents in the solid either by diffusion in the solid or by a process of vapor transport and diffusion is possible. This can result in vitiating purification by zone melting or can result in inhomogeneous material if zone levelling is conducted. These problems can be overcome in a zone melting process in which there is no free volume for the movement of volatile constituents and in which the solid does not need to be maintained at an elevated temperature.

A schematic drawing of a sealed solid method of zone melting is shown in Fig. 1(b) in which the floating zone method is compared in (a). It has been found that many materials with volatile constituents can be weighed into a suitable tube, allowed to react, and cast without cracking the tube. Also, a narrow molten zone can be made to traverse the tube without causing cracking. If, as in Fig. 1(b), a molten zone is transported upward through the sealed cast ingot, the solid above and below the melt acts as the seal for vapor. Thus vapor transport does not occur. The last zone width to freeze is the only region that need lose volatile material. This amount may be kept small by keeping the volume above the casting small and/or by heating, and also by using a narrow zone. A narrow zone can be readily maintained because, without having to heat the solid, a sharp temperature gradient between melt and solid is realized. Since the solid cools rapidly toward room temperature after the passage of a molten zone, solid diffusion is kept to a minimum.

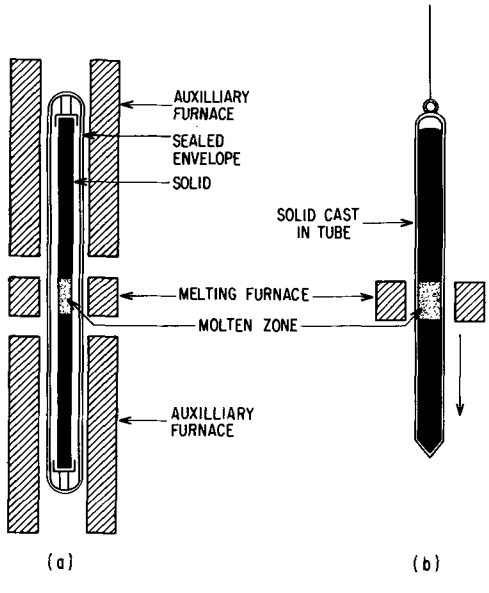

Fig. 1. Comparison of normal (a) and simple (b) zone melting of decomposable materials.

In the application of this method to the preparation of bismuth telluride alloys, for example, since material of uniform composition is desired, the process is conducted for zone levelling. The equipment used is simple. The melted zone is created by a narrow resistance furnace. The mechanism used to move the tube through the furnace can be simple as long as a constant rate can be maintained with the tube kept concentric with the furnace. A relatively rapid rate for the zone movement is used in order that the effective segregation coefficients of the constituents approach unity as nearly as possible. The limiting rate is that permitting good oriented crystal growth. Even in these materials with low thermal conductivity, rates of the order 6-8 cm/hr can be used since the thermal gradients can be kept large. Cracking of the tubes is not encountered when care is exercised to remove oxides from the materials. Ingots of 28 cm length have been made in quartz tubes using a single zone pass and a zone width of 1-2 cm. Typical electrical resistivity profiles for ingots of p- and n- type alloys were flat, with a deviation of less than 10% over 90% of the length. These profiles were used as one criterion of the homogeneity of the ingot. By comparison, ingots of the same alloys made by the Bridgman process showed variations in resistivity of a factor of almost two from one end to the other. The other thermoelectric parameters of the zoned ingots are similarly uniform, resulting in a variation for the figure of merit of less than $\pm 5\%$ of the average value obtained for a number of ingots.

A number of different materials, including I-VI, III-V, and V-VI compounds, have been successfully made by this process. Each compound may require a slightly different preparative technique in order to satisfy the requirement that the ingot be free to move in the tube before zoning. However, as long as the material does not react with

or stick to the crucible material, the method should work.

Acknowledgment

The author wishes to acknowledge the assistance of G. B. Gidley in the setup of the equipment and in the preparation of the compounds used in this work, and L. H. Rosen in carrying out the electrical measurements.

Manuscript received Dec. 21, 1961.

Any discussion of this paper will appear in a Discussion Section to be published in the December 1962 JOURNAL.

Electron Diffraction Study of the Ferrimagnetic Structure of Fe_3O_4

S. Yamaguchi

Institute of Physical and Chemical Research, Tokyo, Japan

It has been found possible to determine the orientation of magnetic induction in a magnetite crystal as described below.

A layer of a single crystal of magnetite (thickness about 5μ, area 2 x 1 mm^2) was prepared by mechanical polishing. This layer contained some pinholes with diameters of about 10μ. The specimen was magnetized in a thin and homogeneous field which was prepared at the sharp edges (thickness about 3μ) of two razor blades, whose remanence was about 2000 gauss. These two edges, separated by a narrow gap (ca. 1 mm), acted as magnetic poles (Fig. 1). A beam of electrons (diameter about 50μ) of well-defined wavelength was passed through, grazing one of the pinholes found in the specimen in order to give rise to a diffraction pattern. Here the incident electron beam runs nearly perpendicular to the face of the layer or to the lines of force (Fig. 1).

The diffraction pattern from the cold specimen, i.e., at 40°C, was first registered, and then that from the heated specimen at 300°C was superimposed. In this process, the positions of the specimen and of the photographic emulsion, and the well-defined wavelength of the incident electrons were kept fixed. The double diagram thus obtained is shown in Fig. 2. The incident electrons in Fig. 2 are parallel to the [$\bar{1}$10] zone axis of the Fe_3O_4 crystal. The temperature of the specimen was controlled by regulation of the electronic irradiation (1).

Figure 3 is a single diagram obtained from the specimen kept at the higher temperature, *i.e.*, at 300°C. It is noted in Fig. 2 that every diffraction spot is split, with a constant separation and in a definite direction, whereas such splitting is not found in Fig. 3. This phenomenon of splitting re-

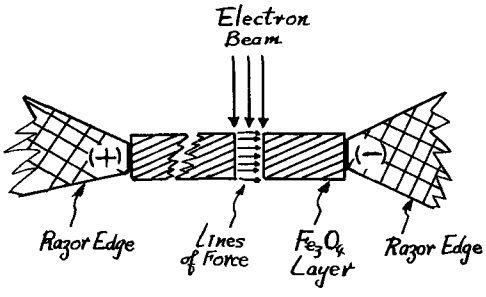

Fig. 1. Arrangement for the diffraction of electrons subjected to the magnetic lines of force in the Fe_3O_4 crystal. A photographic plate is situated perpendicular to the incident beam.

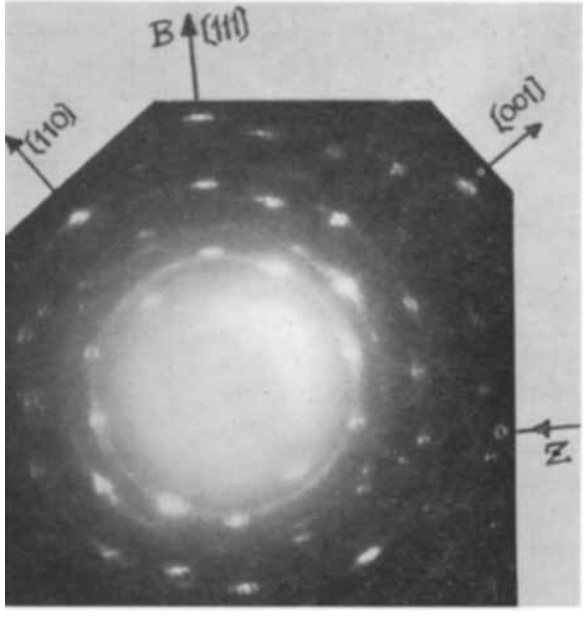

Fig. 2. Diffraction patterns of the cold specimen (40°C) and of the hot specimen (300°C) obtained by the double exposure process. The diffraction spots corresponding to these two temperatures are split as the result of the Lorentz effect. The direction of the splitting $\vec{Z}$ is perpendicular to the[111] axis, *i.e.*, to the induction $\vec{B}$. The incident beam is parallel to the[$\bar{1}$10] zone axis. Wavelength of the electrons: 0.0281Å; camera length: 495 mm. The positive enlarged 3.7 times.

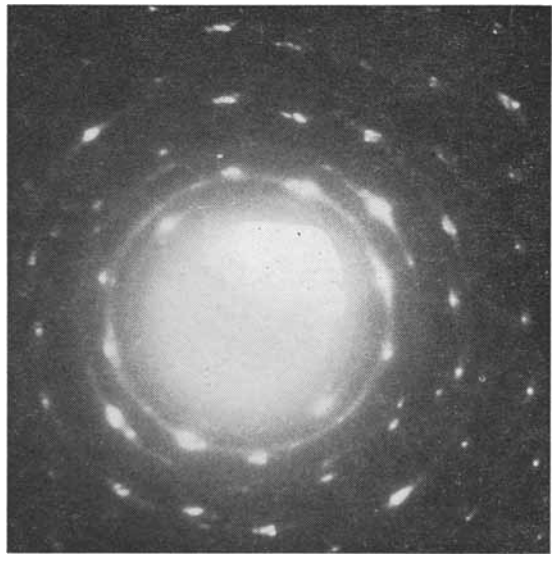

Fig. 3. A single diagram obtained from the specimen kept at 300°C.

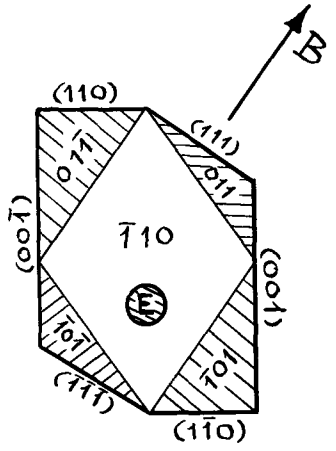

Fig. 4. Relations between the incident beam (E), the net planes of the Fe_3O_4 crystal and the induction (B). E and the (110), (111), and (001) planes are perpendicular to the paper face. B and the ($\bar{1}$10) plane are parallel to the paper face.

sults from the difference between the action of the Lorentz force of the specimen when hot and when cold, on the electron trajectories. The direction of the observed splitting $\vec{Z}$ is perpendicular to the crystallographic orientation of the magnetic induction found in the specimen, according to the Lorentz law. The direction of the induction $\vec{B}$ thus determined agrees with the [111] axis of the crystal of Fe_3O_4 (Fig. 2). It is concluded in this way that the ferrimagnetic electron spin planes are parallel to the (111) planes of the Fe_3O_4 crystal. This conclusion is in accordance with that reached by neutron diffraction (2). The relations between the incident beam (E), the orientation of the net planes, and the magnetic induction (B) are illustrated in Fig. 4.

Quantitative analysis of Fig. 2 results from a consideration of the Lorentz force F acting on an electron beam:

$$F = \frac{e}{c}[v\,B]$$

where e is the electron charge, c the velocity of light, v the velocity of the electrons, B the magnetic induction, and [ ] the vector product. From this expression we obtain a relation between the thermomagnetic splitting ΔZ of the diffraction spots in Fig. 2 and the induction change $\Delta I(\Delta B = 4\pi\,\Delta I)$ caused by the thermal perturbation under the experimental arrangement:

$$\Delta Z = \frac{eL\bar{l}}{mv} \cdot 4\pi\,\Delta I \qquad (L >> \bar{l})$$

$$= \frac{eL\lambda\bar{l}}{h} \cdot 4\pi\,\Delta I \qquad [1]$$

where m is the electron mass, v the velocity of the electrons, e the electron charge (1.6×10^{-20} emu), L the camera length (495 mm), λ the wavelength of the electrons (0.0281Å), h the Planck constant (6.6×10^{-27} erg-sec), and $\bar{l}$ the magnetic path of the electrons. We measure $\Delta Z = 0.348$ mm on Fig. 2. Therefore, we obtain according to Eq. [1], $\Delta I \cong 160$ gauss, if we assume $\bar{l}$ equal to the thickness of the specimen layer, 5μ (Fig 1). This ΔI value is plausible as the induction change of magnetite caused by the temperature change from 40° to 300°C.

Conclusion.—The present thermal perturbation procedure of electron diffraction is more to be recommended for the magnetic structure analysis of ferrites than neutron diffraction, especially when access to a nuclear reactor is not possible.

Manuscript received Sept. 26, 1961; revised manuscript received Dec. 15, 1961.

Any discussion of this paper will appear in a Discussion Section to be published in the December 1962 JOURNAL.

REFERENCES

1. S. Yamaguchi, *This Journal*, **107**, 1011 (1960).
2. G. E. Bacon, "Neutron Diffraction," p. 241, Oxford at the Clarendon Press (1955).

On the Polarization of the Manganese Dioxide Electrode

F. Kornfeil

U. S. Army Signal Research and Development Laboratory, Fort Monmouth, New Jersey

ABSTRACT

Experiments on the cathodic polarization and the potential recovery of γ-MnO_2 electrodeposited on platinum are described. It is shown that at low current densities and pH 7.5 the shape of the potential-time curves is in very good agreement with that predicted from the Coleman-Scott theory of concentration polarization involving the solid phase of the electrode.

The theoretical and experimental treatment of the discharge mechanism and the polarization of the manganese dioxide electrode has been of considerable interest to both theoretical electrochemists and battery engineers for some time (1-3). In 1946 Coleman (1) first advanced the idea that under certain conditions the overpotential associated with the cathodic polarization of the MnO_2 electrode and its subsequent decay after interruption of the polarizing current are determined by a diffusion process taking place in the solid phase of the electrode: At low current densities and in neutral or slightly alkaline electrolyte solutions the surface of the oxide is reduced to MnOOH ($Mn_2O_3 \cdot H_2O$ in the original publication)

$$MnO_2 + H^+ + e^- \rightarrow MnOOH \qquad [1]$$

The MnOOH remains part of the crystal structure, and the resulting "dilution" of the surface MnO_2 gives rise to a corresponding decrease of the electrode potential. Equalization of the concentrations of MnO_2 and MnOOH, and hence the recovery of the electrode potential, is effected by the diffusion of protons and electrons into the interior of the oxide particle. According to Coleman's theory we are therefore dealing with the phenomenon of concentration polarization involving the solid state. Mechanisms other than the diffusion of protons are possible, although less probable, *e.g.*, the diffusion of oxygen ions from the interior toward the surface, or the diffusion of Mn^{+++} ions from the surface into the interior of the oxide. These alternatives are of only minor concern here because the exact knowledge of the nature of the diffusing species is, fortunately, not required for a mathematical treatment of this problem.

To verify the correctness of Coleman's theory experiments were started in our laboratory to determine if the electrode potential observed during the periods of discharge and recovery is in agreement with the potential-time relation obtained from a quantitative treatment of the diffusion process as the rate-determining step of the electrode reaction.

It is quite obvious that an agreement between the observed and calculated values of the electrode potential, and indeed also the absence of such an agreement, can be meaningful only if certain experimental precautions are taken to insure the following conditions: (*a*) the reaction Eq. [1] is the only reaction occurring at the MnO_2 electrode at an appreciable rate. This was achieved by choosing a suitable electrolyte solution and by discharging the electrode at low current densities; in none of the experiments described below could Mn^{++} ions be detected in the electrolyte after discharge. (*b*) The sum of activation overpotential and concentration overpotential involving the electrolyte phase must be small compared to the total electrode polarization. Discharge at low current densities combined with vigorous stirring of the electrolyte alleviated this problem.

Preparation of Electrodes and Polarization Studies

Platinum electrodes (2 x 2 cm) were cut from Pt sheet, leaving in the center of one side an extension approximately 2 mm wide and 5 mm long which was then sealed into one end of a glass tube (10 cm long, 3 mm ID) so that only the square part of the electrode is exposed to the electrolyte. A copper wire and mercury provided the electrical contact with the platinum.

Manganese dioxide was deposited electrolytically onto these Pt electrodes from an aqueous solution of 50g $MnSO_4$ and 67g H_2SO_4 per liter, following essentially the procedure described by Ferrell and Vosburgh (5). Nickel sheet, arranged parallel to the surface of the platinum electrode, served as the cathode. The current density was maintained at 3.20 ma/cm^2 of platinum surface for 30 min. The electrolyte was mechanically stirred throughout the electrolysis and the bath temperature kept at 85°-90°C. After electrodeposition the electrodes were washed in running tap water for several days and then in frequently changed distilled water.

The manganese dioxide deposited in this manner is black in appearance and is formed as an extremely firmly adherent coating, particularly if the platinum electrodes are first given a dull finish by blasting with fine aluminum oxide. X-ray analysis, electron diffraction and electron microscopy characterized it as γ-MnO_2.

For the polarization experiments an MnO_2 electrode was positioned along the axis of a 400 ml cylindrical glass vessel, covered with a machined Teflon stopper through which holes had been drilled to accommodate the MnO_2 electrode, a saturated calomel electrode, a thermometer, stirrer, and a platinum lead connected to a platinum strip lining the inside of the vessel and serving as the anode. The electrolyte was a 1M aqueous solution of NH_4Cl

to which NH_3 had been added to raise the pH to 7.5. The electrolyte volume was sufficiently large (~ 350 ml) to render changes in the composition of the solution during discharge negligible. All experiments were made at 25° ± 0.5°C.

Each thoroughly washed electrode was allowed to stand in the electrolyte solution until its potential, measured against the calomel electrode, did not change by more than about 1 mv in 24 hr, two to three days normally being sufficient to attain this stability. To facilitate the uniformity among the electrodes necessary for a comparison of the potential-time curves with both polarizing current density and discharge time as the experimental variables, the MnO_2 was always deposited from the same solution simultaneously onto a pair of electrodes. The electrodes of each pair were then discharged at the same current density but for different lengths of time, and the potential recorded during the discharge and recovery periods. The current from a d-c power supply was regulated manually and the potential of the MnO_2 electrode measured with either a L&N K-3 potentiometer or with a Brown recording potentiometer.

Discussion

Knowledge of two factors is fundamental to the derivation of the potential-time relation. First, it is necessary to know the dependence of the MnO_2 electrode potential on the concentrations of MnOOH and MnO_2 at the electrode/electrolyte interface, and second, we must be able to calculate the change in these concentrations occurring during and after polarization at different current densities for different lengths of time.

Johnson and Vosburgh (6) found from measurements of the potential of electrodes of different compositions that the electrode potential ϵ, at 25°C and pH 7.5, is given by

$$\epsilon = \epsilon_o + k \log \frac{c_4}{c_3} \qquad [2]$$

where ϵ_o is a constant, c_3 and c_4 are the concentrations, in mole per cent, of MnOOH and MnO_2, respectively, and k equals 0.073v. The difference between the empirical factor k and the theoretical value of 0.059v is attributed to the use of concentrations rather than activities.

While our own polarization measurements were in progress, Scott (7) showed that a solution of the diffusion problem is possible, provided the following assumptions are made: (*a*) the effect of the gradient of the electrical potential on the migration of the ions through the solid is negligible compared to that of the concentration gradient (gradient of the chemical potential); (*b*) the diffusion coefficient D is constant; (*c*) the diffusion is linear and semi-infinite; (*d*) the MnOOH concentration $c_3 = 0$ at the start of the discharge ($t = 0$).

Scott realized that under these conditions the problem of the concentration changes occurring when the MnO_2 electrode is discharged at constant current density for a certain period of time, say τ, followed by recovery of the potential for a time t-τ, is mathematically identical with the problem of the temperature changes taking place when a flat heating element, immersed in an infinite medium of constant thermal conductivity, initially at zero temperature, is supplied with heat at a constant rate and then switched off. A solution of this heat transfer problem is available in the literature (8).

After making the necessary transformations from heat transfer to mass transfer, Scott obtained (in effect) the following expression for c_3 as a function of time t and distance x from the MnO_2 surface

$$c_3(x,t) = \frac{2\phi}{\sqrt{D}} \left(\sqrt{t}\ i\,\mathrm{erfc}\frac{x}{2\sqrt{Dt}} - \sqrt{t-\tau}\ i\,\mathrm{erfc}\frac{x}{2\sqrt{D(t-\tau)}} \right) \qquad [3]$$

where ϕ is the number of moles of MnOOH formed per unit area in unit time. At the surface Eq. [3] reduces to

$$c_3(0,t) = \frac{2\phi}{\sqrt{\pi D}} (\sqrt{t} - \sqrt{t-\tau}) \qquad [4]$$

Neglecting volume changes in the solid phase of the electrode, the sum of c_3 and c_4 is constant and the potential-time relation, therefore, is of the general form

$$\epsilon(t) = \epsilon_o + k \log \left(\frac{A}{\sqrt{t} - \sqrt{t-\tau}} - 1 \right) \qquad [5]$$

In Eq. [3] and [4] $\sqrt{t-\tau}$ is to be taken as zero for $t < \tau$, so that for the discharge period Eq. [5] is simply

$$\epsilon(t) = \epsilon_o + k \log \left(\frac{A}{\sqrt{t}} - 1 \right) \qquad [6]$$

The discharge and potential recovery curves for one representative pair of MnO_2 electrodes, discharged at 0.10 ma/cm² of apparent surface area, are shown in Fig. 1. One electrode was polarized for $\tau_A = 20$ min, the other for $\tau_B = 30$ min. A and B are the corresponding recovery branches of the potential-time curve. The solid lines in the diagram represent the observed values of the electrode potential.

A comparison of the experimental curves with the curves calculated from Eq. [5] can readily be made

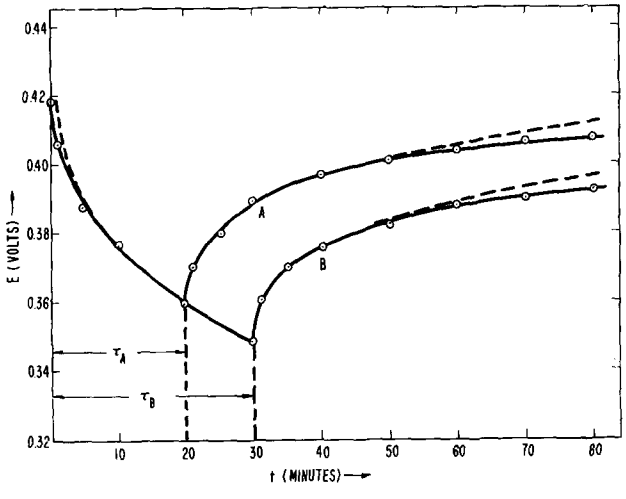

Fig. 1. Discharge and potential recovery curves for i = 0.10 ma/cm²; solid line observed; dashed line calculated.

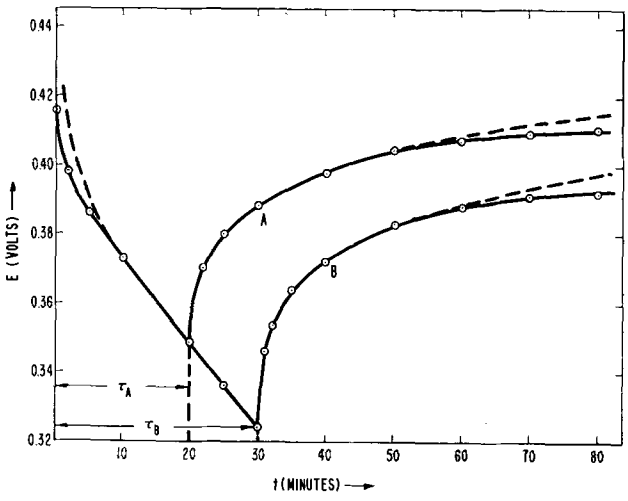

Fig. 2. Discharge and potential recovery curves for i = 0.15 ma/cm^2; solid line observed; dashed line calculated.

once the parameters ϵ_0, k, and A have been determined. These parameters can, in principle, be obtained from Eq. [6] and the values corresponding to three points on the discharge branch of the potential-time curve. However, because of the difficulties encountered in simultaneously solving three logarithmic equations with three unknowns, it is far more convenient to measure the slope of the discharge branch at two points.

Differentiation of Eq. [6] with respect to t gives the slope S

$$S = \frac{d\epsilon}{dt} = -0.434\, k \frac{A}{2t(A - \sqrt{t})} \qquad [7]$$

Having two corresponding values of S and t, it is easily seen that

$$A = \frac{\Delta(St\sqrt{t})}{\Delta(St)} \qquad [8]$$

ϵ_c and k can then be calculated by solving Eq. [6] and [7]. Using the foregoing method the parameters determined from Fig. 1 have the values: ϵ_0 = 0.352v, k = 0.068v, A = 10.25 min$^{1/2}$. Substitution of these figures in Eq. [5] yields the theoretical curves represented by the dashed lines in Fig. 1.

The same procedure was used to evaluate the parameters for the curves shown in Fig. 2. Here, the current density was 0.15 ma/cm^2, again for τ_A = 20 min., and τ_B = 30 min. Under these conditions the values of the parameters are: ϵ_0 = 0.370v, k = 0.068v, and A = 6.65 min$^{1/2}$. In both cases the agreement between the observed and calculated potentials is indeed very good, with deviations occurring only at the start of the polarization and after relatively extended periods of potential recovery. The deviations in the discharge branch are, of course, the result of the assumption of $c_s = 0$ at $t = 0$, making $\epsilon = \infty$ at the beginning of the discharge period. The deviations in the last part of the recovery branch are certainly due to the assumption of a semi-infinite diffusion, and are perhaps to some degree also the result of variations in D. The inconstancy of the diffusion coefficient can, however, be only small in view of the coincidence of the theoretical and experimental curves over such a wide range. It is therefore rather doubtful that the hypothesis of Scott (7) is correct, namely, that D should be proportional to the MnO_2 concentration. It seems quite conceivable that the mobilities of the protons and associated electrons are much the same in MnO_2 and MnOOH, the flux through a plane through the mixture being solely governed by the concentration gradient. It is interesting to note that the value of k = 0.068 is independent of the current density, as expected, and agrees well with k = 0.073, as determined by Johnson and Vosburgh (6) by an independent method. Since A is inversely proportional to ϕ, and therefore also to the current density, the ratio of A for i = 0.10 ma/cm^2 and i = 0.15 ma/cm^2 should be 1.50. The ratio of the two values of A presented in this paper is 1.54. There is little significance to the value of ϵ_0 since its only function is to shift the curves parallel to the ordinate.

Acknowledgment

The author wishes to express his appreciation to Mr. W. F. Nye for his help in the structural and morphological analyses of the MnO_2 deposits.

Manuscript received Nov. 9, 1961; revised manuscript received Jan. 12, 1962.

Any discussion of this paper will appear in a Discussion Section to be published in the December 1962 JOURNAL.

REFERENCES

1. W. C. Vosburgh, *This Journal*, **106**, 839 (1959).
2. W. C. Vosburgh and J. H. DeLap, *ibid.*, **107**, 255 (1960).
3. W. C. Vosburgh and Pao-Soong Lou, *ibid.*, **108**, 485 (1961).
4. J. J. Coleman, *Trans. Electrochem. Soc.*, **90**, 545 (1946).
5. D. T. Ferrell and W. C. Vosburgh, *This Journal*, **98**, 334 (1951).
6. R. S. Johnson and W. C. Vosburgh, *ibid.*, **100**, 471 (1953).
7. A. B. Scott, *ibid.*, **107**, 941 (1960).
8. H. S. Carslaw and J. C. Jaeger, "Conduction of Heat in Solids," p. 76, Oxford (1959).

Correction

In the paper by A. C. Makrides "On the Mechanism of the Hydrogen Reaction" in the March 1962 issue of the *Journal*, the unnumbered equation in column 1, page 259 should read

$$\nu' = \nu \frac{(i_o)_{extr}}{i_o}$$

Investigation of the Electrochemical Characteristics of Organic Compounds

IX. Pyrimidine Compounds

R. Glicksman

Semiconductor and Materials Division, Radio Corporation of America, Somerville, New Jersey

ABSTRACT

A study of the electrochemical characteristics of nitropyrimidine compounds as cathodes in $MgBr_2$ electrolyte, and amino and hydroxypyrimidine compounds as anodes in NaOH electrolyte, shows that the potentials of these compounds are dependent on the aromaticity of the pyrimidine ring, as well as the type and position of substituted groups on the ring. The effect of these factors on the anode and cathode potentials of the various pyrimidine compounds is interpreted in terms of the electron density distribution in the molecule. Half-cell potential data for the alloxan-dialuric acid oxidation-reduction system is also presented.

As part of a general investigation of the electrochemical characteristics of organic compounds, a study has been made of the effect of the presence and molecular position of various group types on the cathode potential of aromatic nitro compounds (1) and the anode potential of aromatic hydroxy and amine compounds (2). Various heterocyclic nitro compounds such as the pyridine, thiophene, and furan nitro derivatives have also been investigated (3).

In this paper, the electrochemical characteristics of pyrimidine compounds are presented. These compounds are considered both as oxidizing agents (*e.g.*, nitro and nitrosopyrimidines) and as reducing agents (*e.g.*, amino and hydroxypyrimidine compounds.)

Apparatus and Technique

A technique, previously described (2), has been used to measure the operating potential of the various pyrimidine compounds during current flow. This technique consists in discharging a 0.5-g sample of the pyrimidine compound mixed with 0.05g of Shawinigan acetylene black, at a constant current drain of 0.005 amp/g, in a large volume of electrolyte. The change in anode or cathode potential with time was measured with a L&N type K potentiometer using a saturated calomel reference electrode. The measured potentials were corrected for the IR drop associated with the apparatus and electrolyte by means of an oscillographic technique.

All half-cell potential data reported are referred to the normal hydrogen electrode and include a liquid junction potential. For most of the anode-potential measurements, an aqueous 1.44M NaOH solution ($a_{OH^-} = 1$)[1] was used as the electrolyte, and a manganese dioxide bobbin wrapped in cheesecloth served as the cathode. For the cathode half-cell potential studies, an aqueous magnesium bromide electrolyte was used with a magnesium anode.

[1] Calculated from the data given by Latimer (4).

Experimental Data and Discussion of Results

Nitropyrimidine compounds as oxidizing agents. —It has been shown previously that the cathode potential of aromatic nitro compounds increases with increasing ring aromaticity (3) in the order: 1-nitronaphthalene, nitrobenzene, and 2-nitropyridine. This order may be attributed to a lower electron density in the vicinity of the reducible nitro group of the more strongly aromatic pyridine compound.

Pyrimidine, a six membered ring containing two nitrogen atoms, can be represented by the usual Kekulé resonance possibilities.

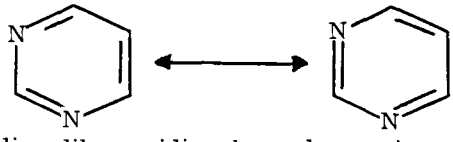

Pyrimidine, like pyridine, has a lower ring electron density than benzene, and thus nitropyrimidine compounds would be expected to operate at higher cathode potentials than their corresponding nitrobenzene derivatives. However, because of the general reluctance of pyrimidine to react with electrophilic reagents, simple nitropyrimidine compounds are not readily available; therefore, a comparison of the cathode potentials of these compounds with nitrobenzene compounds is difficult.

Pyrimidine derivatives with electron donor groups such as the hydroxy and amino groups undergo electrophilic substitution reactions with a variety of reagents to introduce substituents in the 5-position, and a number of 5-nitropyrimidine derivatives are available. This type of behavior is consistent with the electronic effects operating in the pyrimidine ring which produce electon deficient centers at the 2-, 4-, and 6-positions (5).

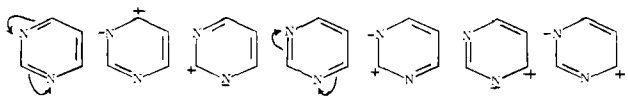

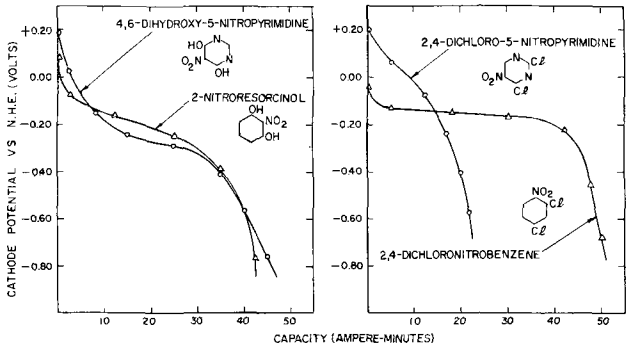

Fig. 1. Half-cell potential discharge curves of various nitropyrimidine and nitrobenzene compounds discharged at a rate of 0.005 amp/g in 250 g/l $MgBr_2 \cdot 6H_2O$ electrolyte.

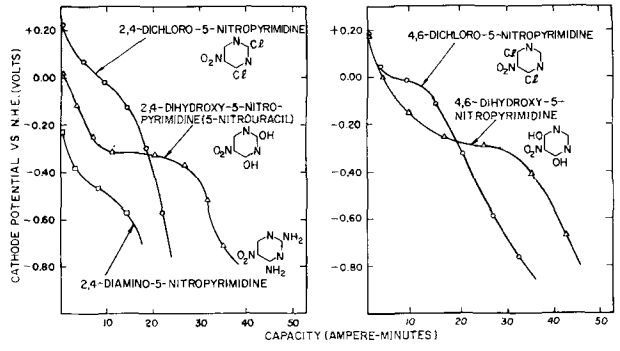

Fig. 2. Effect of substituted groups on the cathode potential of nitropyrimidine compounds discharged at a rate of 0.005 amp/g in 250 g/l $MgBr_2 \cdot 6H_2O$ electrolyte.

Half-cell potential discharge curves of 4, 6-dihydroxy-5-nitropyrimidine and 2,4-dichloro-5- nitropyrimidine compared with their corresponding nitrobenzene derivatives, 2-nitroresorcinol and 2,4-dichloronitrobenzene are shown in Fig. 1. These curves were obtained by discharging the compounds at a rate of 0.005 amp/g in a 250 g/l $MgBr_2 \cdot 6H_2O$ electrolyte. In agreement with theory, the 5-nitropyrimidine derivatives initially operate at higher cathode potentials than the nitrobenzene derivatives. Additional compounds were not available to compare the two classes of nitro compounds further.

In Fig. 2, the higher cathode half-cell potentials of 2,4-dichloro- and 4,6-dichloro-5-nitropyrimidine as compared to 2,4-dihydroxy- and 4,6-dihydroxy-5-nitropyrimidine illustrate the effect of substituted groups on the cathode potential of nitropyrimidine. As with the nitrobenzene derivatives, compounds containing electron attracting chloro groups operate at higher cathode potentials than compounds containing electron-repelling hydroxyl groups. The more strongly electron repelling amino group is more effective in reducing the cathode potential than the hydroxyl group, as evidenced by the low cathode potential of 2,4-diamino-5-nitropyrimidine during discharge.

The effect of substituted electron attracting (*e.g.*, $-COOC_2H_5$) and of electron repelling (*e.g.*, —OH) groups on the cathode potential of nitropyrimidine compounds is further evidenced by the half-cell potential discharge curves for 5-nitrouracil, 5-nitrobarbituric acid, and 2,4-dihydroxy-5-nitro-6-carboxyethyl-pyrimidine shown in Fig. 3. The effect of these substituent groups on the cathode potential of nitropyrimidine compounds is similar to that observed with nitrobenzene derivatives and can be readily explained in terms of the electron-density distribution in the molecule (1).

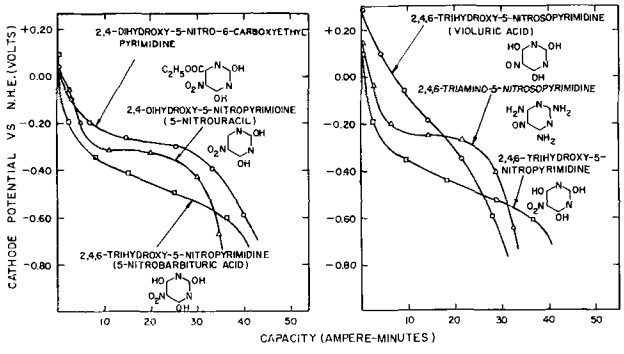

Fig. 3. Half-cell potential discharge curves of various 5-nitro and 5-nitrosopyrimidine derivatives discharged at a rate of 0.005 amp/g in 250 g/l $MgBr_2 \cdot 6H_2O$ electrolyte.

A comparison of the half-cell potential discharge curves of 2,4,6-trihydroxy-5-nitrosopyrimidine (violuric acid) and 2,4,6-trihydroxy-5-nitropyrimidine (5-nitrobarbituric acid) is also shown in Fig. 3. As with the benzene derivatives, the cathode potential of the nitrosopyrimidine compound is higher than that of the corresponding nitropyrimidine compound (6).

Theoretical capacity and electrode efficiency data for the nitro and nitrosopyrimidine compounds are given in Table I. The theoretical capacities were

Table I. Theoretical capacities and electrode efficiencies of various nitro and nitrosopyrimidine compounds

Compound	Theoretical capacity, amp-min/g	Experimental capacity,* amp-min/g	Electrode efficiency, %
2-nitroresorcinol	62.3	40.3	64.7
2,4-dichloronitrobenzene	50.3	46.8	93.0
2,4-dichloro-5-nitropyrimidine	49.8	19.9	40.0
4,6-dichloro-5-nitropyrimidine	49.8	27.3	54.8
4,6-dihydroxy-5-nitropyrimidine	61.4	41.9	68.2
2,4-dihydroxy-5-nitropyrimidine	61.4	33.6	54.7
2,4-diamino-5-nitropyrimidine	62.3	15.1	24.2
2,4-dihydroxy-5-nitro-6-carboxypyrimidine ethyl ester	42.1	40.2	95.5
2,4,6-trihydroxy-5-nitropyrimidine	55.8	35.7	64.0
2,4,6-trihydroxy-5-nitrosopyrimidine	40.9	27.9	68.2
2,4,6-triamino-5-nitrosopyrimidine	41.8	31.8	76.1

* Capacity calculated on the basis of a −0.40v end potential.

computed by means of Faraday's law assuming a 6 and 4 electron change for the nitro and nitroso group, respectively. The electrode efficiencies were calculated from the data in Fig. 1-3. A —0.40v end potential was used to compute the capacities. In general, the electrode efficiencies of the nitropyrimidine and nitrosopyrimidine compounds are not as high as those of the nitrobenzene and nitrosobenzene compounds previously studied.

Aminopyrimidine and hydroxypyrimidine compounds as reducing agents.—Because of the more strongly aromatic nature of the pyrimidine ring as compared to the benzene nucleus, pyrimidine compounds have a lower ring electron density; thus, the electron affinities of amino and hydroxypyrimidine groups should be greater than those of amino and hydroxy groups on a benzene ring. As a consequence, the amino and hydroxypyrimidine compounds should be weaker reducing agents and have lower anode potentials than their corresponding benzene compounds.

These characteristics are consistent with the half-cell potential discharge data of various amino and hydroxypyrimidine and amino and hydroxybenzene compounds shown in Fig. 4 and 5. These data were obtained by discharging the compounds as anodes in 1.44M NaOH at a rate of 0.005 amp/g. In agreement with theory, o- and p-phenylenediamine operate at higher anode potentials than 4,5-diaminopyrimidine and 2,5-diaminopyrimidine, respectively (Fig. 4), whereas phloroglucinol and resorcinol are stronger reducing agents than barbituric acid and uracil (Fig. 5). The lower anode potential of cyanuric acid as compared to barbituric acid indicates that an additional nitrogen atom in the nucleus further increases the ring aromaticity. Similarly, additional half-cell potential data show that melamine, the triamide of cyanuric acid, has a lower anode potential than 2,4,6-triaminopyrimidine (Fig. 7).

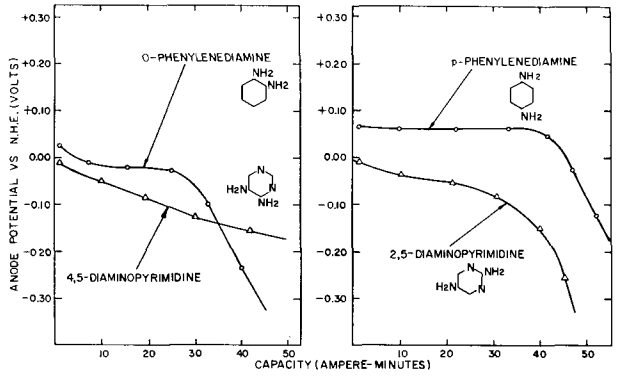

Fig. 4. Half-cell potential discharge curves of various diaminopyrimidine and diaminobenzene compounds discharged at a rate of 0.005 amp/g in 1.44M NaOH.

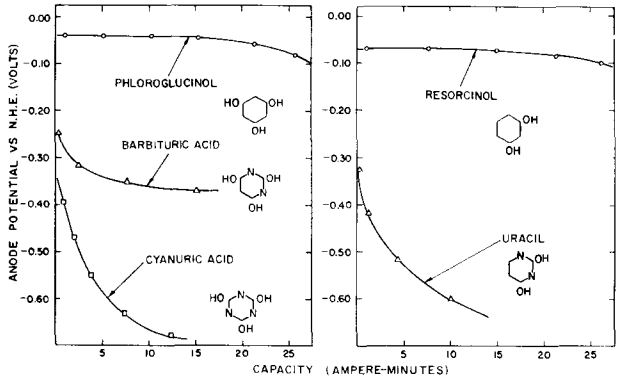

Fig. 5. Half-cell potential discharge curves of various hydroxypyrimidine and hydroxybenzene compounds discharged at a rate of 0.005 amp/g in 1.44M NaOH.

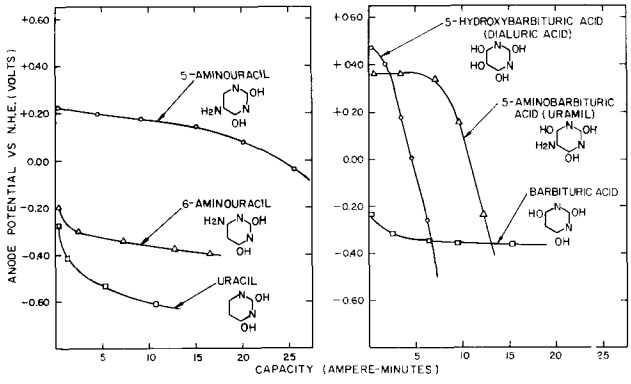

Fig. 6. Effect of substituted groups and their position on the anode potential of hydroxypyrimidine compounds discharged at a rate of 0.005 amp/g in 1.44M NaOH.

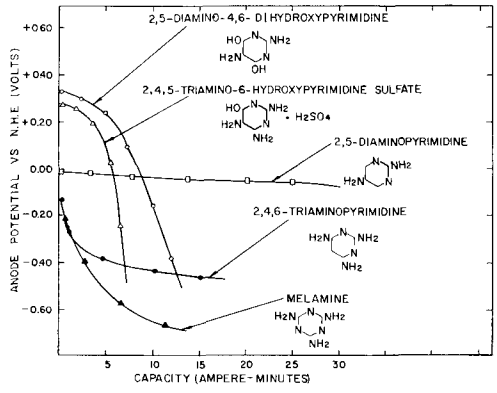

Fig. 7. Effect of substituted groups and their position on the anode potential of aminopyrimidine compounds discharged at a rate of 0.005 amp/g in 1.44M NaOH.

Figure 6 shows that the addition of substituted amino and hydroxy groups to uracil and barbituric acid results in compounds having higher anode potentials. This effect, which is in accord with previous results obtained with hydroxybenzene compounds (2), can be readily explained in terms of the effect of electron-repelling groups on the electron density in the vicinity of the oxidizable hydroxy groups. The higher potential of 5-aminouracil as compared to 6-aminouracil is believed to be due to the fact that, on oxidation, 5-aminouracil loses two hydrogen atoms and yields the corresponding quinoid compounds. Oxidation of this type is not possible for 6-aminouracil because no stable meta-quinoid structure can be written for this compound. The high anode potentials of uramil and dialuric acid can also be attributed to the same type of oxidation reaction.

Similarly, the 2,5-diaminopyrimidine compounds shown in Fig. 7, which have amino groups para to each other, operate at higher potentials than 2,4,6-triaminopyrimidine, which have the amino groups meta to each other. The higher anode potentials of 2,5-diamino-4,6-dihydroxypyrimidine and 2,4,5-

triamino-6-hydroxypyrimidine sulfate, as compared 2,5-diaminopyrimidine, are due to additional amino and hydroxy groups on the pyrimidine ring.

Alloxan-dialuric acid system.—The quinoid-benzenoid type of oxidation-reduction system in pyrimidine compounds is illustrated by the alloxan-dialuric acid system. Their structural formulas indicate that alloxan bears the same relationship to dialuric acid that quinone bears to hydroquinone.

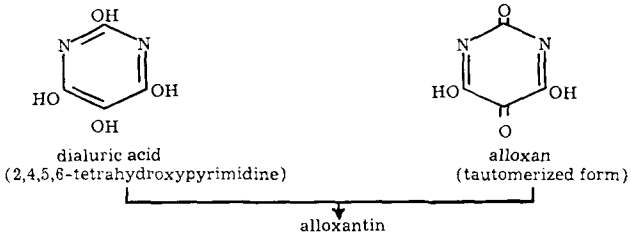

Alloxantin is an intermediate product in the reduction of alloxan as well as the oxidation of dialuric acid and bears a relationship to dialuric acid and alloxan similar to that which quinhydrone bears to hydroquinone and quinone (7).

Figures 8 and 9 show comparisons of the cathode half-cell potential discharge curves of p-benzoquinone, alloxan, quinhydrone, and alloxantin discharged in different electrolytes. Table II compares the theoretical capacities and electrode efficiencies in the same electrolytes. The data were obtained by discharging these compounds as cathode materials

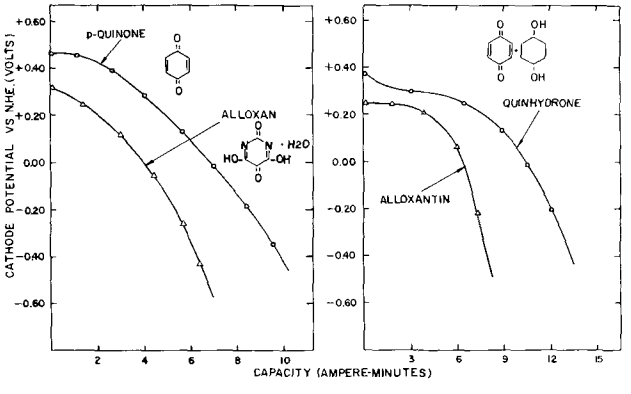

Fig. 8. Half-cell potential discharge curves of alloxan, alloxantin, and their corresponding quinone-type compounds discharged at a rate of 0.005 amp/g in 25% NH_4Cl—20% $ZnCl_2$—55% H_2O electrolyte.

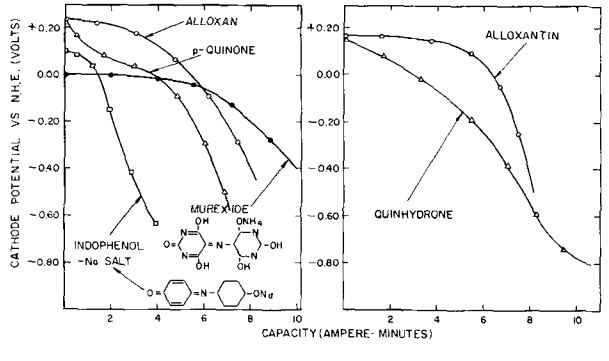

Fig. 9. Half-cell potential discharge curves of alloxan, alloxantin, murexide, and their corresponding quinone-type compounds discharged at a rate of 0.005 amp/g in 250 g/l $MgBr_2 \cdot 6H_2O$ electrolyte.

Table II. Theoretical capacities and electrode efficiencies of various pyrimidine derivatives and their corresponding benzene compounds

Compound	Theoretical capacity, amp-min/g	Electrode efficiency, %	
Cathode materials		NH_4Cl-$ZnCl_2$*	$MgBr_2$*
p-benzoquinone	29.8	33.2	21.5
alloxan	20.1	31.3	39.8
quinhydrone	14.7	90.5	49.0
alloxantin	10.0	79.0	79.0
indophenol-Na salt	14.6	—	19.2
murexide	11.3	—	87.6
Anode materials		NaOH**	
hydroquinone	29.2	>100	
dialuric acid	22.3	20.2	
quinhydrone	14.7	>100	
alloxantin	10.0	25.0	

* Electrode efficiencies calculated on the basis of a −0.40v end potential.
** Electrode efficiencies calculated on the basis of a 0.00v end potential.

in 25% NH_4Cl-20% $ZnCl_2$ (pH = 4.5) and 14% $MgBr_2$ (pH = 8.2) electrolytes at a rate of 0.005 amp/g. In acidic NH_4Cl-$ZnCl_2$ electrolyte, it is seen that p-quinone and quinhydrone operate at higher cathode potentials and yield greater capacities than alloxan and alloxantin, respectively. However, the reverse is true in weakly basic $MgBr_2$ electrolyte. The high cathode potential of alloxan in these electrolytes was to be expected on the basis of its ability to liberate iodine from iodides (7).

A comparison of the half-cell potential discharge curves of indophenol-sodium salt with that of a comparable pyrimidine compound, murexide, is also shown in Fig. 9. The pyrimidine compound is apparently more stable and less soluble than the indophenol salt, and it therefore operates at a much higher electrode efficiency in the magnesium bromide electrolyte.

The half-cell potential discharge data shown in Fig. 10 indicate the anodic characteristics of dialuric acid and alloxantin in 5.4% NaOH electrolyte in comparison to hydroquinone and quinhydrone. The high anode potential of dialuric acid as compared to hydroquinone is believed to be due to the additional hydroxyl groups on the pyrimidine nucleus, whereas

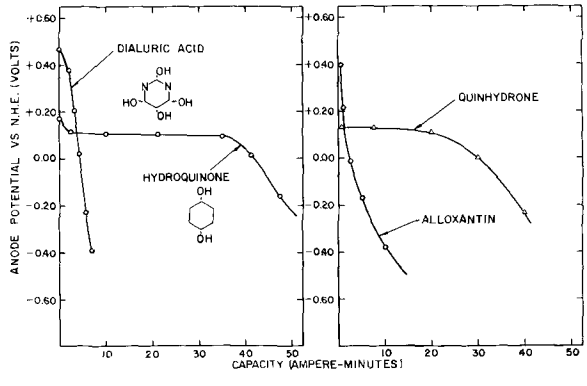

Fig. 10. Half-cell potential discharge curves of dialuric acid, alloxantin, and their corresponding hydroxybenzene compounds discharged at a rate of 0.005 amp/g in 1.44M NaOH.

its poor electrode efficiency is attributed to the fact that dialuric acid undergoes air oxidation readily. The high electrode efficiencies of hydroquinone and quinhydrone (in excess of 100%) have been shown to be due to a continued oxidation of the products of the initial oxidation reaction, *i.e.*, p-quinone itself is easily oxidized in alkaline electrolyte (2).

The electrochemical behavior of the alloxan-dialuric acid system, which has previously been studied polarographically (8), further emphasizes the aromatic nature of pyrimidine and the similarity of some of its derivatives to benzene compounds.

Acknowledgment

The author wishes to acknowledge the support of this research by the U.S. Army Signal Engineering Laboratories under Contract No. DA-36-039-sc-78048.

Manuscript received Nov. 27, 1961.

Any discussion of this paper will appear in a Discussion Section to be published in the December 1962 JOURNAL.

REFERENCES

1. R. Glicksman and C. K. Morehouse, *This Journal*, **105**, 299 (1958).
2. R. Glicksman, *ibid.*, **108**, 1 (1961).
3. R. Glicksman and C. K. Morehouse, *ibid.*, **107**, 717 (1960).
4. W. M. Latimer, "Oxidation Potentials," 2nd ed., p. 354, Prentice-Hall, Inc., Englewood Cliffs, N. J. (1952).
5. H. Gilman, "Organic Chemistry," Vol. IV, p. 875, John Wiley & Sons, Inc., New York (1953).
6. R. Glicksman and C. K. Morehouse, *This Journal*, **105**, 613 (1958).
7. F. C. Whitmore, "Organic Chemistry," 2nd ed., pp. 436-438, D. Van Nostrand Company, Inc., New York (1951).
8. G. Sartori and A. Liberti, *Ricerca Sci.*, **16**, 313 (1946).

Nickel-Cadmium Cells

I. Thermodynamics and X-Ray Studies

Alvin J. Salkind[1] and Paul F. Bruins

Department of Chemical Engineering, Polytechnic Institute of Brooklyn, Brooklyn, New York

ABSTRACT

Voltage decays of electrodes in sintered type nickel-cadmium cells were measured in cells stored at temperatures between —18° and 52°C. The heat of reaction of the cell was calculated to be —64 kcal/g mole. The solid reaction products of the cell were studied, *in situ*, by x-ray techniques, in special cells designed to fit on an x-ray diffractometer.

Recently, several careful studies on the crystal structure and reaction mechanisms of the active materials of the nickel-cadmium cell have been reported (1-7). In some of these (6, 7), references have been made to the work discussed in this paper, which was available only by private communication (8). This research, initiated in 1955 and completed in February 1958, attempted to clarify some of the points concerning the oxide or hydroxide states of the electrodes and their potential decays. This present condensation is presented because later works have not duplicated the experimental methods and because of the unavailability of the private report to most of those who have expressed an interest in it.

Experimental X-Ray Studies

In all previous experiments reported in the literature, except those of Falk (6) which were carried out after this investigation was concluded, the x-ray studies were conducted with electrodes isolated from electrochemical cells. Thus, it appeared that some of the conflicting data could have arisen from changes in the nature of the active materials during washing and drying. Procedures were designed so the x-ray examinations of the electrodes were carried out while the electrodes were *in situ* in electrochemical cells in electrolyte. The electrodes were supplied by the Sonotone Corporation and were standard sintered plates, 0.625mm thick, made by impregnating sintered nickel plaques with nickel nitrate and cadmium nitrate salts and then converting to the hydroxides. The plates used for the x-ray studies were from the same batch as the test cells (nominal 5 A.H. Sandia type) used in the potential studies.

The first procedure used to avoid washing and drying plates was to charge sintered nickel plates in open plastic cells, and, after the completion of charge and partial or complete discharge, the wet plates were cut into quarters, sealed in polyethylene bags, and mounted on x-ray equipment. This method was abandoned since it was difficult to determine by film methods the comparative intensity of reflections of the active materials in different stages of charge. In addition, since 3-8 hr exposures were necessary to get sufficient blackening of the films, any possible products present only immediately after charge would not be detected. This was particularly important because the nickel electrode was known to have a fast initial self-discharge rate. A special cell was then designed and constructed which could be mounted on an x-ray diffractometer, so that selected reflections could be watched continuously as the active materials were charged and discharged, and of course, in addition, complete patterns could be recorded. This cell was made from polymethyl methacrylate (Lucite) and is shown in

[1] Present address: The Carl F. Norberg Research Center, The Electric Storage Battery Company, Yardley, Pa.

Table IA. X-ray reflections from nickel electrodes

Pattern No. Charge state	A Uncharged	B 1/10	C 2/10	D 3/10	E 1/2	F 9/10	G Full	H Full charge	after (cycling)
	4.65 [18]	4.73-4.58 [14]	4.69 [14]	4.63-4.70 [6]	4.67 [9]	4.70 [9]	4.70 [9]	4.62-4.77 [7]	
	2.69 [15]	2.70 [15]	2.70 [15]	2.71 [16]	2.70 [6]	—	—	—	
	2.34 [18]	2.34 [20]	2.34 [18]	2.34 [16]	2.33 [7]	2.37 [9]	2.39 [9]	2.40 [6]	
	1.565 [13]	1.563 [13]	1.560 [12]	1.563 [9]	1.560 [6]	1.560 [2]	—	—	
	1.482 [8]	1.485 [8]	1.483 [8]	1.485 [7]	1.485 [3]	—	—	—	
						1.41 [3]	1.40 [2]	1.40 [1]	

Key: First numbers indicate "d" spacings in Angstrom units (Å). Numbers in brackets indicate comparative intensities of reflections. Reflections of nickel lines omitted from table.

Fig. 1. Small electrode plates were coated with polystyrene resin on all but the top surfaces so that the charge and discharge reactions had to take place on this surface, where they could be investigated with the diffractometer. Suitable electrical leads were potted in the plastic so that the cell could be charged or discharged, and the cell, with electrolyte, was covered with a polyester (Mylar) film during the x-ray examination. Twenty-one diffraction patterns were obtained on positive electrodes in various states of charge. The patterns were corrected using the reflections from nickel, and the reflections are listed in Tables 1A and 1B; reflections caused by nickel are omitted from this table. All intensities were corrected so that the value for the nickel 1.76Å reflection corresponded to 50. Few intensity corrections were necessary since almost all patterns were obtained with the same slit system on the x-ray machine and with the same amplification and recording constants in the electronic equipment. Duplicate patterns are not shown. The voltages of the electrodes were determined against mercury-mercuric oxide reference electrodes with a potentiometer, in many cases, immediately before the patterns were obtained. Diffractometer patterns A through G represent stages in the charge process for the same electrode. The uncharged active material gave a pattern which completely fitted the pattern

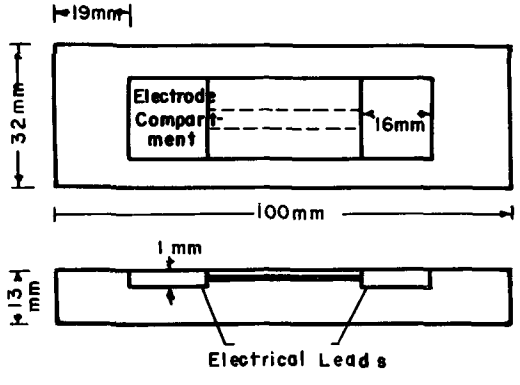

Fig. 1. Diagram of experimental nickel-cadmium cell used for x-ray studies.

for nickel hydroxide in the ASTM file. The charged active material gave patterns which fitted those associated by Glemser and Einerhand (8) with the structure of nickel III oxyhydroxide (β-NiOOH). Although several other of the higher nickel hydroxides have similar reflections, they may all be eliminated from consideration because they create additional strong reflections which were not present.

Early stages of charge were marked by the disappearance of lines in the patterns of $Ni(OH)_2$ rather than the creation of any new lines. In comparing patterns A through G it was seen that the 2.70, 1.56, 1.48, and 1.30Å lines gradually lost intensity as the charge progressed; the 4.60 and 2.33Å reflections shifted to larger d spacings. When the charge was nearly complete, the weak 1.40Å reflection of β-NiOOH appeared. Pattern H was obtained from an electrode which had been subjected to 5 charge-discharge cycles. The pattern obtained was similar to G, which was obtained on the first charge cycle. The failure of nickel hydroxide and β nickel hydroxide reflections to appear simultaneously, on charging, supports the conclusion that these materials are in a state of solid solution. This is confirmed by the evidence that the open-circuit electrode potential is a function of the state of charge. The sample prepared for pattern X, Table IB, was given a charge and severe overcharge at a high rate, the 1-hr rate, and then was dried free of electrolyte. In addition to the reflections attributed to β-NiOOH, the pattern obtained from this sample contained reflections of $Ni_2O_3 \cdot H_2O$. This material is stoichiometrically the same as NiOOH. The conditions used in the preparation of this sample would not normally be encountered in battery operation. Patterns O, I, J, K, P, L, and M represent decay and discharge states of nickel electrodes. As can be seen from patterns O, I, and J, no change in the pattern of NiOOH was obtained for the first 27 hr after charge when the electrodes were stored in the electrolyte at 24°C. After storing the nickel electrodes for 7 days at this temperature the 2.33Å line of $Ni(OH)_2$ appeared. When electrodes were stored for longer periods or were partially discharged the en-

Table IB. X-ray reflections from nickel electrodes

Pattern No. Charge state	O 1 hr after normal charge at 75°F	I 5 hr at 75°F	J 27 hr at 75°F	K 7 days at 75°F	P 10 days at 110°F	L 1/2 discharged	M 2/3	X Overcharged at high rate and dried
								6.92 [19]
	4.70 [10]	4.63 [7]	4.68 [9]	4.69 [9]	4.68 [9]	4.74-4.60 [7]	4.66 [7]	4.72 [22]
					2.76 [6]	2.70 [11]	2.70 [11]	3.45 [10]
				2.43 [5]	2.45 [5]	2.41 [2]		2.44 [15]
	2.40 [5]	2.39 [7]	2.38 [8]	2.33 [6]	2.33 [10]	2.33 [12]	2.34 [12]	2.40 [20]
					1.56 [3]	1.56 [10]	1.56 [7]	1.42 [8]
					1.485 [3]	1.48 [5]	1.49 [1]	1.40 [9]
	1.404 [4]	1.41 [2]	1.41 [2]	1.40 [1]	1.41 [2]	1.41 [1]		

tire $Ni(OH)_2$ pattern was obtained. Pattern E, obtained with a half-charged electrode, was almost identical with that of pattern L, obtained with a half-discharged electrode.

Cadmium electrodes were studied by rotating the previously prepared cells so that the negative electrode instead of the positive, was in the beam. The reflections from the nickel plaque were used to correct each pattern, as previously described. Patterns from partially charged plates included reflections from both cadmium and cadmium hydroxide. The peaks in these patterns were much sharper than those obtained with the nickel electrodes which indicates that the material was more crystalline. The charge process did not result in a gradual shift of reflections, but in the decrease in the intensity of the cadmium hydroxide reflections and the simultaneous increase in the intensity of the cadmium reflections. Reflections caused by cadmium hydroxides were found even in fully charged plates. Normal charge procedures were, therefore, not able to convert all the cadmium hydroxide to cadmium. The patterns were checked carefully for the reflections of cadmium oxide. The strongest reflection of cadmium oxide would be at 2.712Å, but this reflection was never observed on any of the patterns. The charge reaction of the cadmium electrode determined by x-ray examination is therefore cadmium hydroxide simply becoming cadmium. Thus, the data obtained by cycling electrodes *in situ* on x-ray apparatus confirms the earlier conclusion of Wynne-Jones and Briggs (2), obtained from washed and dried electrodes, and the later ones of Falk (6), obtained by a different *in situ* method. They are in agreement with the reaction mechanism later suggested by Kornfeil (4) in his very careful analysis of the charge-discharge process at the nickel electrode.

$$2\,NiOOH^* + 2H_2O + 2e^- \rightarrow 2\,Ni(OH)_2^* + 2\,OH^- + 1.16H_2O + 0.067KOH \quad [1]$$

where the asterisks indicate hydration.

Experimental—Voltage Decay Studies

The electrode potentials in sintered plate nickel cadmium cells (97 Sandia cells) were measured with potentiometers using mercury-mercuric oxide reference electrodes containing electrolyte of the same concentration as the cells. The variables studied were temperature, plate spacing, electrolyte composition, and separator material. Only the effects of temperature and electrolyte composition are discussed in this paper. The cells were stored at temperatures of —17.8°, 34.4°, 43.3°, and 51.7°C and were originally filled with 20 and 31% potassium hydroxide electrolytes. Potential determinations were usually made at 30-min intervals for the first few hours after charge. Thereafter they were made daily for two weeks, and then weekly for several months. The initial voltage of the cadmium electrode at the end of charging at the ½-amp rate was approximately —1.00v with reference to the standard hydrogen electrode (acid). This dropped immediately on opening the circuit approximately to —0.96v and then decayed rapidly and linearly with the logarithm of time to approximately —0.88v. The voltages of the cadmium electrodes in all the cells tested at 34°C were in the range of —0.88v ± 0.01v after a thousand minutes from the end of charge. They then stayed in this range for the duration of the runs (about six months). Data on the potentials of the Cd-$Cd(OH)_2$ and Hg-HgO couples measured directly *vs.* hydrogen in KOH solutions were later obtained by Rüetschi, Ockerman, and Salkind (10) and are given in Table II. These data show that the equilibrium potential of the cadmium electrode is above the potential of hydrogen at all temperatures and concentrations of electrolyte, and therefore the electrode cannot self-decay through the evolution of hydrogen.

Potential measurements of nickel electrodes in nickel cadmium cells were made at the previously mentioned temperatures. It was possible to estimate the nickel potential of other cells where only

Table II. Potentials of Cd-Cd(OH)$_2$ and Hg-HgO electrodes vs. hydrogen in KOH solutions

Temp, °C		Cd-Cd(OH)$_2$	Hg-HgO
25		+0.022 ± 0.002	+0.929 ± 0.001
35	18.1% KOH	+0.0195 ± 0.001	+0.928 ± 0.001
45		+0.015 ± 0.001	+0.926 ± 0.001
25		+0.023 ± 0.002	+0.931 ± 0.001
35	26% KOH	+0.020 ± 0.002	+0.9295 ± 0.001
45		+0.014 ± 0.001	+0.927 ± 0.001
25		+0.023 ± 0.002	+0.936 ± 0.001
35	34.7% KOH	+0.016 ± 0.002	+0.933 ± 0.001
45		+0.008 ± 0.002	+0.930 ± 0.001

the total voltage was determined by subtracting the stable value of the cadmium electrode discussed in the previous paragraph. The potential of the nickel electrode decayed immediately on opening the charging circuit. This decay, after a few minutes, was linear with the logarithm of time. When the voltage level of the nickel electrode was approximately 0.40v with respect to hydrogen, a slower rate of decay began. The second decay period started 4 or 5 days after the end of charge. This is shown in Fig. 2. Not all points on these curves are shown, for simplicity in viewing. All points are for cells with 31% KOH electrolyte. Capacity determinations on cells, as well as data from the Sandia Corporation, indicated that very little cell capacity was lost in the first period of decay. Although there were some small differences in the half-cell potentials of the individual cells, the rate of voltage decay was essentially constant in all cells at a given temperature and electrolyte concentration. The voltage levels of the nickel electrodes in the secondary decay periods show the negative coefficient of $\partial E/\partial T$ for the electrodes. The values calculated were −0.0004 V/°C ± 0.0001 for the nickel electrode and −0.0005 ± 0.0001 for the cells. The voltage decay confirms the conclusions drawn from the x-ray data that the active materials of the nickel electrode are in solid-state solution. The two linear regions were also later observed by Conway and Bourgault (5) and were accounted for, by them, by a charge-transfer reaction.

The standard method of calculating heats of reaction is the direct use of cell or electrode potentials in the Gibbs-Helmholtz equation

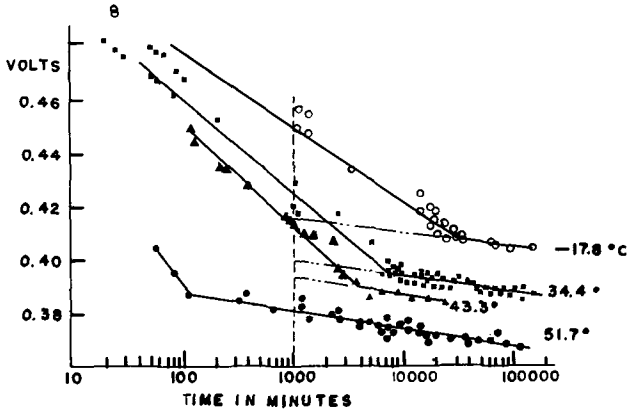

Fig. 2. Open-circuit voltage decay of nickel electrodes at different temperatures.

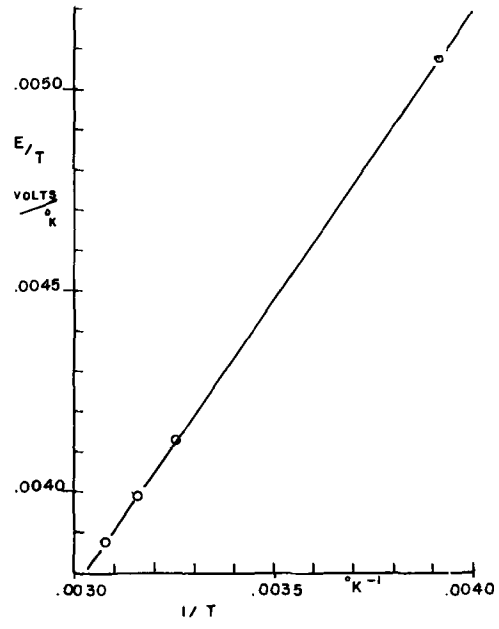

Fig. 3. Plot of E/T vs. $1/T$ for nickel-cadmium cells

$$\Delta H = -n\mathbf{F}E + n\mathbf{F}T\left(\frac{\partial E}{\partial T}\right)_p \qquad [2]$$

This can be rearranged to

$$\frac{E}{T} = -\frac{\Delta H}{n\mathbf{F}T} + \left(\frac{\partial E}{\partial T}\right)_p \qquad [3]$$

If we consider the coefficient of voltage change with temperature for nickel-cadmium cells to be constant over the range in question, then the slope of a plot of E/T vs. $1/T$ is $-\Delta H/n\mathbf{F}$. The ΔH thus obtained includes heat of hydration as well as heat of reaction. It is known, however, that the hydration energies of these particular electrodes are very low, as shown by the readiness with which CdO goes to Cd(OH)$_2$ and by the work of Rüetschi and Delahay (12).

The values used for electrode and cell voltages should be reversible electrode potentials. Since the nickel electrodes in the nickel-cadmium cells were never in thermodynamic equilibrium, an extrapolation method was used to obtain potentials which were approximately those of NiOOH at the beginning of the second decay period. The slopes of the decay curves in Fig. 2 were extrapolated or interpolated to a common time, 1000 min from the start of the open-circuit period. This represented close to the initial time in the experiment which ran six months. The potentials of cells and nickel electrodes given in Table III were used to prepare Fig. 3. From

Table III. Potentials of nickel electrodes and nickel-cadmium cells in the second decay period extrapolated to a common time (1000 min)

Temp, °K	Nickel electrode, in terms of S.H.E.	Ni-Cd cells, v
255.4	0.4112	1.295
307.6	0.3907	1.270
316.5	0.3861	1.203
324.9	0.3834	1.260

the slope of this line, the heat of reaction of nickel-cadmium cells was calculated to be −64 kcal/g mole. Another method of calculating heats of reaction, proposed by Othmer and Gilmont (9), gave a value of −62 kcal/g moles for this reaction.

A simplified reaction for the nickel-cadmium cell can be written as:

$$2\beta\,NiOOH + Cd + 2H_2O \rightleftharpoons 2Ni(OH)_2 + Cd(OH)_2 \quad [4]$$

The value −64 kcal/g mole, calculated for the heat of reaction, was used to estimate the approximate value for the heat of formation of β-NiOOH, since the values for all the other components in Eq. [4] were known (13). The value arrived at for the heat of formation of β-NiOOH was −164 kcal/g mole. This value was in close accord with the only value listed (13) for a valence three hydroxide of nickel, 162.1 kcal/g mole for $Ni(OH)_3$.

Acknowledgments

The authors would like to express their appreciation to Dr. G. Baumstark for his help in preparing the cells, to Mr. U. B. Thomas and Dr. R. Baker for their assistance and advice, especially in checking foreign references, to Dr. A. Fleischer, for his interest, and to Dr. E. Baars of Squire Signal Laboratories, Fort Monmouth, New Jersey, for the use of his laboratory in carrying out some low-temperature discharges. The authors are indebted to the Sandia Corporation for their support of this study and in particular to Dr. F. Thomas for his encouragement.

Manuscript received Jan. 11, 1960; revised manuscript received Nov. 25, 1961. This paper was prepared for delivery before the Columbus Meeting, Oct. 19-21, 1959. This paper was abstracted from the thesis of one of the authors (A.J.S.), submitted in partial fulfillment of the requirements for the Degree of D. Ch. E. at the Polytechnic Institute of Brooklyn.

Any discussion of this paper will appear in a Discussion Section to be published in the December 1962 JOURNAL.

REFERENCES

1. E. Jones and W. F. K. Wynne-Jones, *Trans. Faraday Soc.*, **52**, 1260 (1956).
2. G. W. D. Briggs and W. F. K. Wynne-Jones, *ibid.*, **52**, 1272 (1956).
3. R. Baker, Bell Labs Memorandum "X-Ray Diffraction Studies of the Nickel Electrode," Oct. 25, 1955. A private communication.
4. F. Kornfeil, "The Charge-Discharge Process of the Nickel-Oxide Electrode" Proc. Ann. Battery Research Development Conf., 12th, Fort Monmouth 1958, 18-22.
5. B. E. Conway and P. L. Bourgault, *Can. J. Chem.*, **37**, 292 (1959); **38**, 1557 (1960).
6. S. U. Falk, *This Journal*, **107**, 661 (1960).
7. L. Wilson, S. E. Voltz, and I. M. Schulman, U.S. Air Force Contract AF-04(647)476. Private communication.
8. O. Glemser and J. Einerhand, *Z. Elektrochem.*, **54**, 302 (1950).
9. D. Othmer and R. Gilmont, *Ind. Eng. Chem.*, **36**, 858 (1944).
10. P. Rüetschi, J. Ockerman, and A. J. Salkind, Private communication.
11. Glasstone, Textbook of Physical Chemistry, D. Van Nostrand Co., Inc., New York (1940).
12. P. Rüetschi and D. Delahay, *J. Chem. Phys.*, **23**, 556 (1955).
13. Selected Values of Chemical Thermodynamic Properties, Series I, National Bureau of Standards (1947).

The Thermal Runaway Condition in Nickel-Cadmium Cells and Performance Characteristics of Sealed Light Weight Cells

Alvin J. Salkind and Joseph C. Duddy

The Carl F. Norberg Research Center, The Electric Storage Battery Company, Yardley, Pennsylvania

ABSTRACT

The thermal runaway condition, sometimes called the vicious cycle, can be caused in almost any type of cell under certain conditions. The underlying causes of the runaway condition are discussed with specific application to sealed nickel-cadmium cells on constant potential overcharge. The discharge and overcharge performance characteristics of sealed nickel-cadmium cells with plastic electrodes are presented. These cells operated at high energy density levels on both a weight and volume basis and were more difficult to put in the runaway condition.

The thermal runaway condition, sometimes referred to as the "vicious cycle," can occur in cells of all types. It is of particular importance in the case of sealed nickel-cadmium cells because it is a more dangerous phenomenon where sealed cells are involved, and nickel-cadmium cells are not only commonly charged and discharged at high rates but are also subjected to continuous overcharge. Literature references to this phenomenon are both few and brief; the most complete was that of Earwicker (1) concerning aircraft batteries of the lead-acid, silver-zinc, and nickel-cadmium types.

Description of the "Runaway Condition"

Since oxygen overpotential is due to a slow stage in the ionic discharge process, it is evident and well established (2) that an increase of temperature will decrease the overpotential. In the particular case of the nickel-cadmium cell, not only does the overpotential decrease with increasing temper-

Table I. Values of dE/dT for nickel electrodes and nickel-cadmium cells

	Type	Charge state	Temp range, °C	Values, v/°C Nickel electrodes	Cells	Reference
1	Sintered	Half charged	−40 to +50	−0.00014	−0.00018	(3)
2	Sintered	Fully charged	−18 to +54		−0.0004	(4)
3	Pocket	Half charged	−40 to +50	−0.00006	−0.00030	(3)
4	Tubular (Edison)	10% discharged	−40 to +30 (av)	−0.0005	−0.0008	(5)
			20 30	−0.0005	−0.0004	
5	Plastic electrode	Fully charged	−18 to +38		−0.0005	This work

ature, but the temperature coefficient of the open-circuit potential is negative. The coefficients have been reported by Falk (3) for sintered plate and pocket-type cells, by Salkind and Bruins (4) for sintered plate cells, and by Hosono and Watanabe (5) for tubular nickel electrodes. The coefficient is not completely independent of the state of charge, but, in the application to the overcharge problem, the coefficient of interest is the one representing a completely charged nickel electrode with a partially charged cadmium electrode.

In Table I, are presented the voltage temperature coefficients reported in the literature, as well as new data obtained with plastic electrodes prepared by the method described by Duddy and Salkind (6). Cell and electrode voltages were measured in cells, of the A type later described, stored at minus 18°, 26°, and 38°C. The voltage decays were plotted on open-circuit decay, and the stable voltages at a common time, approximately 1500 min from the end of charge, were used to calculate the voltage coefficient. The number shown is only an approximate one; experiments are still in progress to achieve a more exact value.

There is some variation in voltage and voltage coefficient with the state of charge of all the nickel electrode types listed, but all coefficients reported were negative. It can be seen that there is also a wide variance in the values reported. Since the nickel electrode is unstable, the magnitude of the coefficient obtained changes with the method of obtaining and plotting data. The inclusion of iron in the negatives of the pocket type and of cobalt or lithia and other additives in the Edison type also affect the magnitude of the coefficient for these cells. However, in every case, the over-all coefficient reported for the cell was negative.

The minimum emf necessary to charge a cell is the summation of the polarization at the nickel electrode, the equilibrium voltage, and the potential drops across electrolytic and electronic resistances. Glasstone (2) has given an approximate value for the change of overpotential with temperature of 2 mv/°C, and we can assume that the polarization change will be in this order. If we assume for the second item, a value of 0.5 mv/°C, and that for nickel cadmium cells, the temperature coefficients of last items are small, the total change of impedance with temperature in potential terms is approximately 2.5 mv/°C.

The Onset of Runaway

When a sealed cell is in the overcharge state, the oxygen cycling balances the electrochemical charge, so that the negative electrode stays in a constant state of partial charge and the energy of overcharge is dissipated as heat. (This is referred to by Earwicker as the parisitic current.) A temperature rise which can occur because of an environmental change or the inability of the cell to radiate or transfer heat at the generating rate causes a reduction in the cell impedance and increases the charge current, if the charge source is of the constant potential type. The increase in current increases the internal temperature, which reduces the impedance again, etc., and the runaway has begun. Where the capacity of the charger is large in proportion to the cell capacity, it is possible for the charging current to increase to the level where the oxygen re-adsorption rate at the negative plate is insufficient to prevent the full charging of the cadmium electrode. Then, one gets excess oxygen pressure and the possibility of hydrogen as well.

It may be advisable to remind ourselves, at this point, that other electrochemical systems can also be put in the runaway condition. In the case of the lead acid battery, the change in equilibrium emf with temperature has been reported by Vinal (7) to be about +0.25 mv/°C in battery concentration electrolyte. However, in this case the electrolytic resistance is appreciable and decreases with a temperature increase. Of course, the change in overpotential is the paramount item. Runaways in silver-zinc cells have also been reported, in particular by Chapman (8). At the same meeting, Earwicker (9) commented on runaways in several different battery systems.

Buffering Effect of Dehydration

Both the charged and discharged forms of the hydroxides of nickel are believed to contain either chemically combined or adsorbed waters of hydration. Kornfeil (10) has made some clarification of this in his work. In Fig. 1 are shown the dehydration curves for nickelous hydroxide at various temperatures. The material used was the green hydroxide precipitate employed in pocket electrodes. The loss of water was determined by weighing ceramic boats stored at the various temperatures after they had cooled in a dessicator. X-ray patterns of the dried materials were also obtained. It was observed that the water loss leveled out at the lower temperatures at a point equal to ¼-½ of a mole of water of hydration, and there was no change of crystal structure observed with the x-ray patterns under these conditions.

However, at the higher series of temperatures, above 175°C, the formation of NiO (Bunsenite) was

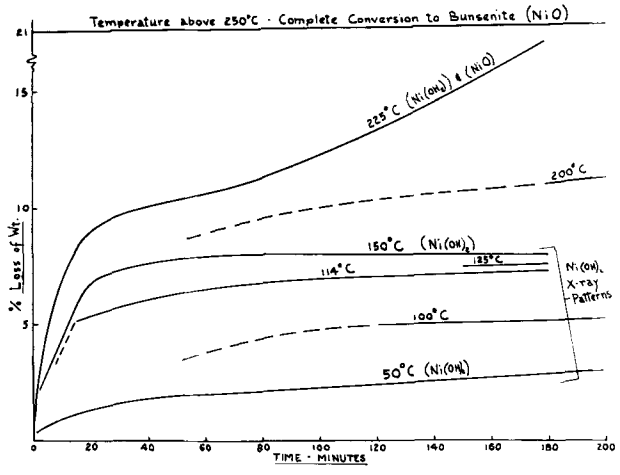

Fig. 1. Dehydration curves for nickelous hydroxide

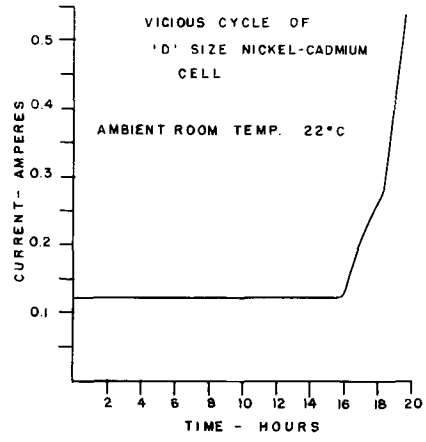

Fig. 2. Runaway charge of a 2.5 amp-hr cylindrical sealed nickel-cadmium cell with sintered electrodes.

observed with the loss of water and a blackening of the material; this was confirmed by x-ray analyses.

There are two buffering affects to the runaway condition which result from this dehydration. Under all temperature conditions the loss of water from the hydroxide crystal would dilute the electrolyte. The emf of nickel-cadmium cells is known to increase as the electrolyte concentration is decreased. The second buffering effect would take place when nickel oxide, Bunsenite, is formed. This material is an insulator, and its formation through dehydration increases the resistance of the nickel electrode on charge, because of the decrease in surface area as well as the straight-forward increase in electronic resistance. The exact amount of buffering that one obtains from these phenomena will depend on the geometry of the cell, but, in any case, will probably be quite small.

Aside from the peculiar usefulness of the conversion of nickel hydroxide to nickel oxide in this instance, in general it is a reaction very detrimental to cell performance. Our data indicate that it is irreversible, and that there is a permanent loss in cell capacity as well as the increase in electrode resistance. Probably it is mainly this reaction that precludes the high-temperature storage of nickel-cadmium cells. We believe that the conversion takes place at lower temperatures than those indicated in Fig. 1 over long periods of time, and experiments are in progress to determine this and the effect of storing in alkali.

Examples of Runaway Cells

Upstrom (11), Belove (12), and others in private communications have all reported observing runaway cells, and through their cooperation typical cycles are given. In Fig. 2 the charge of a 2.5 amp-hr cell at 1.40v and an ambient temperature of 22°C is shown. The cell was at an equilibrium current of 120 ma. The equilibrium was upset after 16 hr, and the charge current rose within 2 hr to over one-half an ampere, when the charge was interrupted. It has been suggested that this phenomenon will not occur if the charge voltage is below 1.40v, but no accurate data are available concerning the lower limit of potential which can cause the runaway condition.

In Fig. 3 another charge is shown; the battery in this case was a 24 cell unit, and the charge was at 36.0v. The rise in cell temperature was also recorded and is portrayed. The battery was cut off charge just after the charge current started to take a sharp rise.

General Performance Characteristics of Plastic Electrode Nickel-Cadmium Cells

Discharge and overcharge characteristics of some sealed cells constructed with high-energy density nickel and cadmium electrodes (6) were studied. The cells were designated as A, B, and C types. The A-type cell dimensions were 11 x 6 x 2.5 cm and were made with 11 positive and 10 negative plates. The types designated as B and C types had dimensions of 15 x 6.5 x 3 cm and 16 x 5.5 x 1.8 cm, respectively. The plates used in the latter two types were identical, with only the number of plates and the outer enclosure being varied The B type was made with 19 positive plates and 18 negative plates and had a nominal capacity of 18 amp-hr. The cell container used was extremely heavy and the energy density obtained was 28 whr/kg. The C type was made with 10 positive plates and 9 negative plates and delivered over 11.5 amp-hr to a 1.1v per cell cut-off. Since each cell weighed slightly over 400g, this corresponded to about 35 whr/kg. Most of the discrepancy in energy densities between the B and C types was attributable to the loss of positive

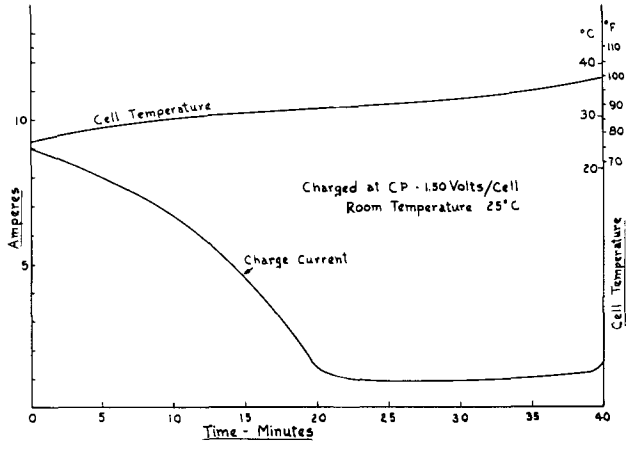

Fig. 3. Runaway charge of a 24-cell battery with sintered plate cells

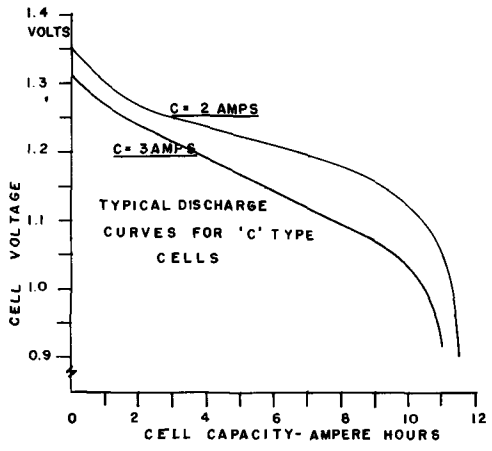

Fig. 4. Typical discharge curves for C-type cells at ambient room temperature, approximately 28°C.

electrode capacity in the B type because of prolonged heating during the case welding stage. Typical discharge curves for the C type cells are given in Fig. 4. The curves represent discharges at ambient room temperature, approximately 28°C. C-type cells were assembled into 4-cell batteries similar to those used for miner's lamps. The overcharge characteristics on constant current charging for such batteries are shown in Table II. These voltages are slightly higher than those reported for sintered plate cells; it has been shown (6) that these electrodes have Tafel curves with greater slopes than sintered electrodes.

In the C-type cells the most efficient charge was obtained by a two-stage constant-current charge. In the first stage, 75% of the capacity was replaced at the 5-hr rate, then the charge current was reduced and the cell kept on overcharge at the 20-hr rate.

Runaway of Nickel-Cadmium Cells with Plastic Electrodes

It has been possible to put the cells with plastic electrodes into the runaway condition with slightly more difficulty than conventional sintered plate cells. The ease with which a cell enters the runaway condition should depend on the total charging impedance, and the higher electronic resistance of the plastic nickel electrode acts as a buffer to cell runaway. Runaways in these cells were sometimes obtained at a charge voltage of about 1.44v or about 0.04v higher charge potential than that used to put some of the sintered plate cells into the runaway

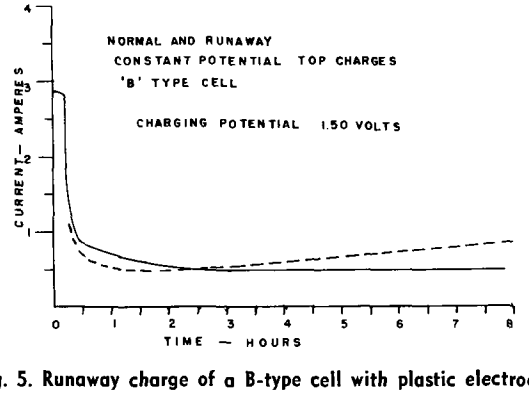

Fig. 5. Runaway charge of a B-type cell with plastic electrodes

Table II. Voltage as a function of overcharge current in Mine Lamp-type battery of 4 cells

Cur. amp	Voltage in overcharge v	per cell, v
0.3	5.55	1.38_8
0.4	5.62	1.40_5
0.5	5.78	1.44_5
0.6	5.86	1.46_5
0.7	5.90	1.47_5
0.8	5.94	1.48_5

condition. In Fig. 5 the runaway condition in a B-type cell is shown.

Discussion

We are entering an era where the use of sealed cells is likely to increase markedly. Many of the applications will be in space, but as Schulman (13) has pointed out, thermal runaways are unlikely in space applications because of the current limitations in the primary energy sources. However, many new applications are unfolding in portable appliances and tools. Although constant potential charging had been accepted in the past as one of the optimum methods of charging vented nickel-cadmium cells, it offers some hazards for sealed cells. It still provides a rapid method of charging, for most of the electrochemical capacity is restored before the nickel electrode begins to gas and, under normal conditions, the charge voltage can be set to restrict the charge current to a level the negative can accept for oxygen recombination.

However, where the danger of thermal runaways is likely, other provisions will have to be made. Lapuyade (15) and others have proposed voltage controls for the charger, based on the thermal condition of the battery. Earwicker (2) suggested polarized thermal relays, but cautioned that their use might lead to undercharging in warm conditions. Another solution is to match the maximum output of the charger to the current which the cell can accept in recombination.

A convenient limiter in laboratory applications is a common light bulb, for its resistance rises with both current and temperature. Modern design of batteries has resulted in a large increase in capacity with a reduction in internal resistance. This has been discussed by both Barak (14) and Earwicker (9). It may be possible to increase the heat dissipation of cells and therefore alleviate the runaway condition with better cell design. Since negative plates are usually much better electrical and thermal conductors than positive plates, future designs may ground the negatives to metallic outer cans in order to better dissipate the heat from the core, which is the hottest part of the cell stackup. In such designs, a series of parallel plates should dissipate heat faster than the common coiled cell design.

Manuscript received Oct. 25, 1961; revised manuscript received Jan. 17, 1962. This paper was prepared for delivery before the Detroit Meeting, Oct. 1-5, 1961.

Any discussion of this paper will appear in a Discussion Section to be published in the December 1962 JOURNAL.

REFERENCES

1. G. A. Earwicker, *Proc. Inst. Elec. Engrs.*, **103A**, Supplement No. 1 (1956).
2. S. Glasstone, "An Introduction to Electrochemistry," p. 466, D. Van Nostrand Co., Inc., New York (1942).
3. S. U. Falk, *This Journal*, **107**, 661 (1960).
4. A. J. Salkind and P. F. Bruins, "Investigation of the Sintered Plate Nickel-Cadmium Battery," Final Report, Feb. 28, 1958, Chemical Engineering Dept., Polytechnic Institute of Brooklyn.
5. T. Hosono and K. Watanabe, *J. Electrochem. Soc., Japan*, **19**, 14 (1951).
6. J. C. Duddy and A. J. Salkind, *This Journal*, **108**, 717 (1961).
7. G. W. Vinal, "Storage Batteries," 4th ed., p. 194, John Wiley & Sons, Inc., New York (1954).
8. C. L. Chapman, "Technical Problems Associated with the Silver-Zinc Battery and Its Use," Proceedings International Symposium on Batteries, Oct. 21-23, 1958; Signals Research and Development Establishment, Ministry of Supply, Christchurch, Harts, England.
9. G. A. Earwicker, "Heating Effects in Aircraft Batteries," same Proceedings as (8).
10. F. Kornfeil, "The Charge-Discharge Process of the Nickel-Oxide Electrode," Proc. Ann. Battery Research Development Conference, 12th, 18-22, Ft. Monmouth, N. J. (1958).
11. P. Upstrom; Private communication.
12. L. Belove; Private communication.
13. I. Schulman, Paper No. 1307-60 presented at the ARS Space Power Systems Conference, The Miramar Hotel, Santa Monica, Calif., Sept. 27-30, (1960).
14. M. Barak, "Fundamental Problems in the Development of Storage Batteries," same Proceedings as (8).
15. R. H. Lapayude, U. S. Pat. 2,957,117.

The "Vicious Cycle" in Secondary Batteries—A Mathematical Approach

W. G. Eicke, Jr.

National Bureau of Standards, Washington, D. C.

ABSTRACT

Equations relating voltage, temperature, heat capacity, time, and current have been derived for a cell on constant-potential charge. Assuming the cell to be fully charged and thermally isolated from its surroundings, thereby retaining all of the electrical energy supplied to it, the equations derived are

$$1/i = \frac{1}{i_o} - \left(\frac{(V_a - V_{\Delta H})(\Delta H^* - \alpha \mathbf{F} \eta)}{2RT_o^2 C_p} \right) t$$

and

$$1/T = \frac{1}{T_o} + \left(\frac{2R}{\Delta H^* - \alpha \mathbf{F} \eta} \left[\ln \frac{i_o}{i} \right] \right) t$$

where i is the current, t the time, T the absolute temperature, V_a the applied voltage, $V_{\Delta H}$ the voltage corresponding to the fraction of the electrical energy converted into chemical energy, ΔH^* the activation energy for the electrode reaction, α the transfer coefficient, η the activation overpotential, i_o and T_o the initial current and temperature, respectively, and C_p the heat capacity of the cell. The equations have been verified experimentally. The case where cooling occurs is also considered.

One problem that is encountered in secondary batteries is the tendency for them to go into a "vicious cycle" or "runaway" condition when they are charged at a constant potential especially at elevated temperatures. These terms apply to the phenomenon in which the charging current through a fully or nearly fully charged battery reaches destructive proportions because of the increase in battery temperature. Since the increase in battery temperature is caused by the charging current, the above terms are quite apt.

Whether a particular battery will go into a "vicious cycle" depends on the manner in which the temperature will vary with charging voltage, ambient temperature, rate of heat removal, the nature of the reactions taking place, and the physical construction of the cells and battery. In general, any of the present types of secondary batteries in use today can be made to go into a "vicious cycle" under the proper conditions.

It is the purpose of this paper to analyze mathematically the conditions that cause the "vicious cycle." However, before doing so, it will be desirable to review qualitatively the constant-potential charge.

Constant-Potential Charging

A constant-potential charge at normal and high temperature is characterized by a very high initial current which decays more or less exponentially with time as the cell becomes charged. Under ideal conditions the battery should become fully charged in 3-4 hr after which the current will be constant at a relatively low value. The charging potential is usually selected so that the cell can be fully charged in the minimum safe time. To accomplish this the charging potential is well above the re-

versible potential of the electrochemical reaction taking place. Woodbridge (1) reported that the variation of current with time could be approximated by the empirical equation,

$$i(t) = A \exp(-t) \quad [1]$$

where $i(t)$ is the instantaneous current at time t, and A is a constant. The above equation, however, does not adequately describe a normal constant-potential charge because it neither provides for a finite final charging current nor will one adjustable parameter satisfy all cases. A better approximation is

$$i(t) = i_f + A \exp(-kt) \quad [2]$$

where i_f is the final current after the cell is fully charged; A and k are adjustable parameters. At a constant temperature i_f would be constant and represents the current driving the overcharge reaction. The exponential term of Eq. [2] describes the current variation of the charging reaction. Equations [1] and [2] are represented graphically in Fig. 1 for the condition where a cell is held at a constant temperature.

If on the other hand the temperature of the cell is allowed to vary, as it normally does in service, the charging curve may be approximated by that shown in Fig. 2. It is assumed here that the cell does not lose any heat to the surroundings. If the charge is continued for sufficient time, the final current i_f will rise until it reaches destructive proportions as is shown by the dashed portion of the curve. This latter part of the curve is the region of "vicious cycle." If a typical curve were to be integrated, it would be found that the current will not begin to rise until the cell is either fully charged or nearly so. Since the "vicious cycle" does not normally occur until the cell is charged, the value of the second term in Eq. [2] will be zero or very nearly so. Therefore, any increase in current must be due to

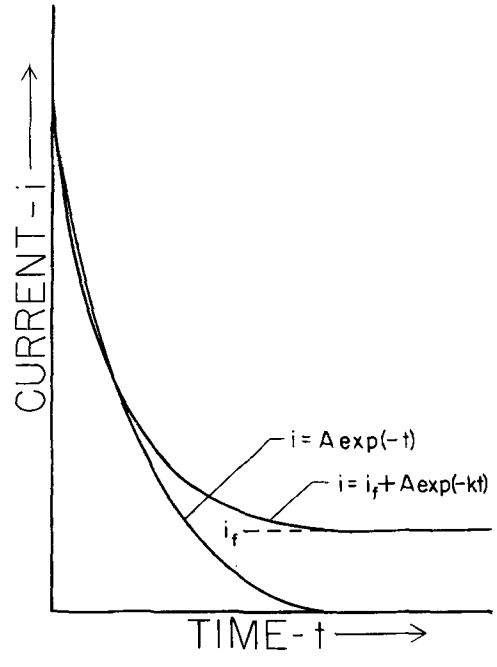

Fig. 1. Ideal constant-potential charging curves at constant temperature.

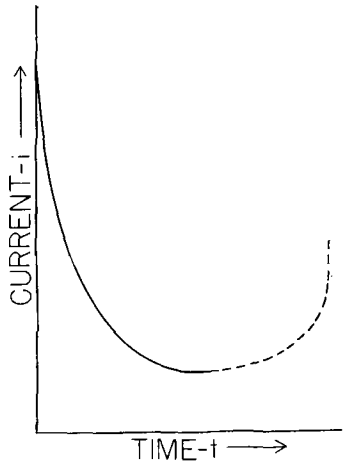

Fig. 2. Constant-potential charging curve for a cell that heats during the charge.

the effect of temperature on i_f, and it is this term that will be considered herein in some detail. An excellent discussion of the performance of several types of batteries on constant-potential charge is is given by Earwicker (2).

Assumptions and Idealized Model

As was stated earlier, the final charging current depends on a number of parameters which are often difficult to isolate and identify. To avoid the difficulty that would arise if an attempt were made to take them all into account in a mathematical analysis a simplified model will be used. This model is a cell, on charge at a constant potential, thermally isolated from its surroundings so that the only energy entering or leaving the system is the electrical energy being supplied by the charging current. It is also assumed that the cell is fully charged and all of the current is used to decompose water because in most open battery systems when fully charged most of the current is utilized to decompose water.

Mathematical Derivation

In general, the net rate at which the energy content of any system is changing is the difference between the rates at which energy enters and leaves the system. In the model just described no energy leaves the system, and the only energy being supplied the cell is the electrical energy. Therefore, the rate at which the energy content of the cell is increasing is

$$dU(t)/dt = V_a i(t) \quad [3]$$

where $dU(t)/dt$ is the rate at which energy being supplied at any time t, V_a the applied potential, and $i(t)$ the current at any time t.

The electrical energy is consumed in two ways. One is the electrochemical reaction and the other is the production of heat. As a result of the electrochemical reaction (the decomposition of water) the products of the reaction are in a higher energy state than the reactants by an amount of energy $-\Delta H/n\mathbf{F}$ energy units per coulomb. Assuming ΔH to be independent of temperature and hence time, the rate at which the electrical energy is converted to chemical energy $[dH(t)/dt]$ is

$$dH(t)/dt = (\Delta H/{}_{\eta}\mathbf{F})i(t) \quad [4]$$

where n is the number of equivalents for the electrochemical reaction and $\mathbf{F}$ the faraday. Defining $V_{\Delta H} = -\Delta H/n\mathbf{F}$ Eq. [4] can be rewritten as

$$dH(t)/dt = V_{\Delta H} i(t) \quad [5]$$

Since the rate at which the total energy supplied to the system is given by Eq. [3] and the rate at which electrical energy is converted to chemical energy is given by Eq. [5], the difference of these two equations gives the rate at which heat is being produced; hence

$$dQ(t)/dt = (V_a - V_{\Delta H}) i(t) \quad [6]$$

where $dQ(t)/dt$ is the instantaneous rate at which heat is being added to the cell at any time t. The heating of the cell can further be defined in terms of the temperature change of the cell, $dT(t)$, and its heat capacity, C_p. Assuming the latter is independent of temperature

$$dQ(t) = C_p dT(t) \quad [7]$$

Substituting Eq. [7] into Eq. [6] and rearranging

$$dT(t)/dt = (V_a - V_{\Delta H}) i(t)/C_p \quad [8]$$

In order to solve Eq. [8] it is necessary to establish a relationship between the current and the temperature. Such a relationship can be developed by considering the applied potential, V_a, which is made up of four components: the reversible potential (E), which is the potential of the H_2, O_2 couple, the activation overpotential (η), the ohmic overpotential (η_r) and the concentration overpotential (η_c). Hence

$$V_a = E(T) + \eta(T) + \eta_c + \eta_r = \text{constant}. \quad [9]$$

Both concentration and ohmic overpotential are small compared to the activation overpotential and can therefore be neglected. Furthermore the effect of temperature on $E(T)$ is negligible. Thus, for a constant-potential charge the activation overpotential will be constant, and in conjunction with the temperature it will control the current. The approximation that the current is determined by activation overpotential has been verified experimentally for the lead acid system by Vinal (3) and for the nickel-cadmium system by Duddy and Salkind (5). For both of these systems it was found that, on overcharge, plots of cell voltage, *vs.* log i are linear.

For any electrochemical reaction taking place at a single electrode the activation overpotential is given by

$$\eta = (RT/\alpha\mathbf{F}) \ln (i/i_e) \quad [10]$$

where α is the transfer coefficient and i_e the exchange current, which is given approximately by

$$i_e = K \exp -(\Delta H^*/RT) \quad [11]$$

where K is a constant whose value depends on the cell under consideration and ΔH^* is the activation energy for the electrode reaction. Since there are two reactions (one at each electrode) taking place, the total activation overpotential is the sum of the individual reaction overpotentials or

$$\eta = \eta_+ + \eta_- \quad [12]$$

where η_+ and η_- are given by

$$\eta_+ = (RT/\alpha_+ \mathbf{F}) \ln i - (RT/\alpha_+ \mathbf{F}) \ln [K_+ \exp - (\Delta H^*_+/RT)] \quad [13]$$

and

$$\eta_- = (RT/\alpha_- \mathbf{F}) \ln i - (RT/\alpha_- \mathbf{F}) \ln [K_- \exp - (\Delta H^*_-/RT)] \quad [14]$$

adding Eq. [13] and [14] and solving for i

$$i = \sqrt{K} \exp - [(\Delta H^* - \alpha\mathbf{F}\eta)/2RT] \quad [15]$$

where $K = K_+K_-$, $\Delta H^* = \Delta H^*_+ + \Delta H^*_-$, and α_+ and α_- are both approximately 0.5 for the decomposition of water.

For temperature changes that are small compared to the absolute temperature (as would be the case for room temperature and above) the current at any temperature (T) is given approximately by

$$i(T) = i_o \exp [(\Delta H^* - \alpha\mathbf{F}\eta)\Delta T/2RT_o^2] \quad [16]$$

where i_o and T_o are the initial current and temperature, respectively, and $\Delta T = T - T_o$. Differentiating Eq. [16]

$$di/dT = (\Delta H^* - \alpha\mathbf{F}\eta) i/2RT_o^2 \quad [17]$$

Solving Eq. [17] for dT and substituting in Eq. [8]

$$di(t)/i(t)^2 = \frac{(V_a - V_{\Delta H})(\Delta H^* - \alpha\mathbf{F}\eta)}{2RT_o^2 C_p} dt \quad [18]$$

Integrating Eq. [18] between the limits $t = 0$, $i = i_o$ and $t = t$, $i = i$,

$$1/i = 1/i_o - \left(\frac{(V_a - V_{\Delta H})(\Delta H^* - \alpha\mathbf{F}\eta)}{2RT_o^2 C_p}\right) t. \quad [19]$$

The variation of temperature with time can be evaluated using Eq. [19] and [16], thus

$$\frac{1}{T} = \frac{1}{T_o} + \left(\frac{2R}{\Delta H^* - \alpha\mathbf{F}\eta} \ln \frac{i_o}{i}\right) t \quad [20]$$

The last two equations have the empirical forms

$$1/i = A - Bt \quad [21]$$

and

$$1/T = C + D \ln(A - Bt) \quad [22]$$

Equations [19] and [20] define the variation of current and temperature with time for the ideal case in terms of measurable physical quantities, *i.e.*, the case where the only energy exchange between the cell and its surrounding is the electrical energy supplied for charging. These equations have certain limitations because of the simplifying assumptions made in their derivation and, therefore, should be considered only as limiting cases. The current or temperature predicted by the equations will be somewhat greater than would be realized in practice.

The Case Where Cooling Occurs

Above it was assumed that there was no heat exchange between cell and surroundings. It is also desirable to consider the case where the cell can lose heat to its surroundings since this situation is the one most frequently encountered in normal service.

When cooling occurs, the rate at which the heat leaves the cell is

$$dQ'(t)/dt = -k(T_c - T_a) \quad [23]$$

where $[dQ'(t)/dt]$ is the rate at which heat is being transferred from the cell to the ambient surround-

ings at any time t, T_c the cell temperature, T_a the ambient temperature, and k the heat transfer coefficient. Since the total rate at which heat is added to the cell is given by Eq. [6], the net rate of change of the heat content of the cell is the sum of Eq. [6] and [23] or

$$dQ_\eta(t)/dt = (V_a - V_{\Delta H})i(t) - k[T_c(t) - T_a] \quad [24]$$

Making use of Eq. [8] the net rate of temperature change of the cell is

$$C_p dT(t)/dt = (V_a - V_{\Delta H})i(t) - k[T_c(t) - T_a] \quad [25]$$

Setting $dT(t)/dt = 0$ Eq. [25] after rearranging becomes

$$(V_a - V_{\Delta H})\ i_{max} = k(T_{c_{max}} - T_a) \quad [26]$$

Since the current and cell temperature are related by means of Eq. [15], it is possible to solve Eq. [26] for either i_{max} or T_{max} in terms of the other parameters. Likewise, if i_{max} or $T_{c_{max}}$ are specified, it is possible to solve for either V_a, k, or T_a provided the other two are given.

Experimental Verification

Equations [19] and [20] were verified experimentally for a small lead acid cell and a nickel-cadmium cell. The charged test cell was placed in a Dewar flask at room temperature. To insure that it was fully charged the cell was charged at a low constant current for several hours before the experiment was started. The cell was then charged at a constant potential and the results recorded. The cell temperature was measured by a thermometer in the electrolyte and the current by an ammeter in series with the cell. The charging potential was held constant manually. Because of the heat loss through the electrical leads entering the Dewar and from the flask itself, it was necessary to use charging potentials greater than is considered normal in order to minimize these effects. The lead acid and nickel-cadmium cells were charged, respectively, at 2.60 and 1.60v. The results of these experiments are summarized in Fig. 3 through 6 in which the reciprocal of current and temperature are plotted as a function of time and log $(A - Bt)$, respectively. It can be seen that for both the lead acid and the nickel-cadmium the experimental data obey the empirical Eq. [21] and [22] except for longer times. As the

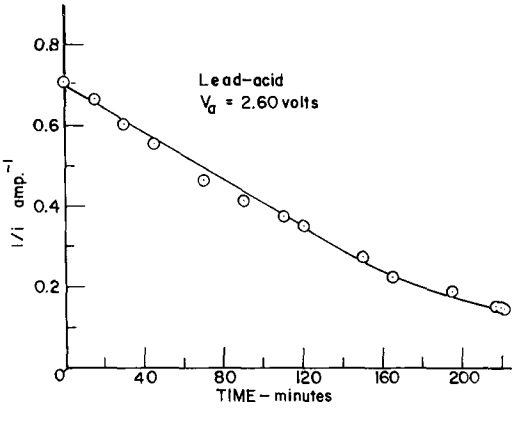

Fig. 3. Variation of current with time for a lead-acid cell on constant-potential charge.

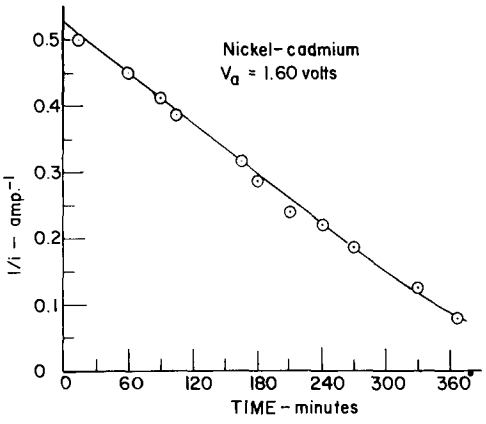

Fig. 4. Variation of current with time for a nickel-cadmium cell on constant-potential charge.

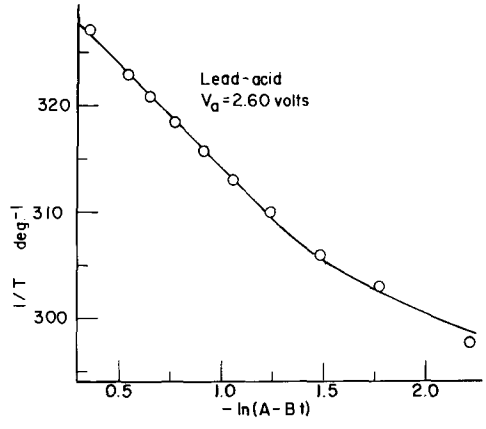

Fig. 5. Variation of temperature for the cell of Fig. 3

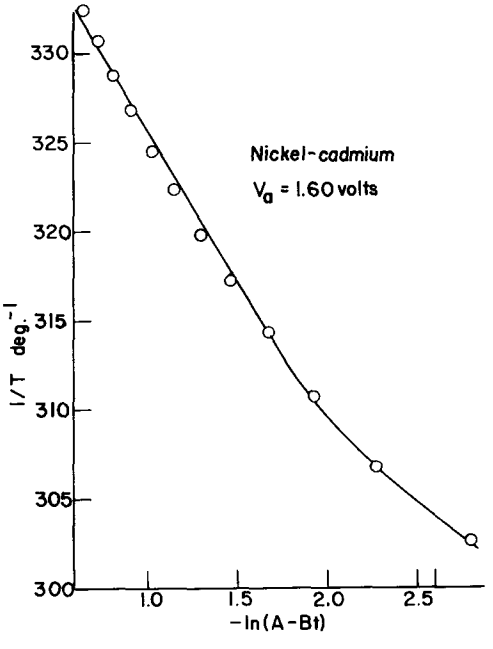

Fig. 6. Variation of temperature for the cell of Fig. 4

time increased, so did the temperature and consequently the heat loss. The deviations from expected behavior are in the correct direction to be accounted for by heat loss. For both types of cell the constants for the empirical equations were calculated from the figures and are summarized in Table I.

As a further verification of the derivation the activation energy, ΔH^* was calculated for the lead

Table I. Calculated constants for equations [21] and [22]

Cell	V_a, v	Constants A, amp^{-1}	$B \times 10^3$, amp^{-1} min^{-1}	$C \times 10^5$, deg^{-1}	$D \times 10^5$, deg^{-1}
Lead acid	2.60	0.700	2.95	330.4	17.8
Nickel-cadmium	1.60	0.523	1.40	343.2	16.6

acid cell. Using an estimated heat capacity of 233 cal/deg and the heat of formation of water to calculate $V_{\Delta H}$, ΔH^* was calculated to be 31.6 kcal/mole for the evolution of hydrogen and oxygen. This value agrees very well with that obtained from Glasstone and Bockris (4) and with the value calculated from Vinal's data (3). From these sources ΔH^* was found respectively to be 29 kcal/mole and 26.2 kcal/mole. The mean of the three is 28.9/kcal. This agreement adds confidence to the validity of Eq. [19] and [20]. Unfortunately, the heat capacity of the nickel-cadmium could not be estimated; however, from (4) ΔH^* was found to be 32 kcal/mole.

Acknowledgment

The author thanks Dr. W. J. Hamer and Miss E. H. Ostrander for their helpful discussion and suggestions.

Manuscript received Nov. 17, 1961; revised manuscript received Jan. 17, 1962. This paper was prepared for delivery before the Detroit Meeting, Oct. 1-5, 1961.

Any discussion of this paper will appear in a Discussion Section to be published in the December 1962 JOURNAL.

REFERENCES

1. J. L. Woodbridge, *Trans. Am. Inst. Elec. Engrs.*, **54**, 516 (1935).
2. G. A. Earwicker, *Proc. Inst. Elec. Engrs.*, **103**, 180 (1956).
3. G. W. Vinal, "Storage Batteries," 4th ed., p. 244, John Wiley & Sons, Inc., New York (1954).
4. J. O'M. Bockris, "Electrochemical Constants," pp. 252-260, National Bureau of Standards, Circular 524, (1953); S. Glasstone, "Introduction to Electrochemistry," p. 467, D. Van Nostrand Co., New York (1942).
5. J. C. Duddy and A. J. Salkind, *This Journal*, **108**, 717 (1961).

Tarnishing Reaction of Copper with Solutions of Thiourea and Derivatives. Study by Radiotracers

J. Llopis, J. M. Gamboa, L. Arizmendi, and F. Alonso

Instituto de Química Física "Rocasolano," Consejo Superior de Investigaciones Cientificas, Madrid, Spain

ABSTRACT

A tarnishing reaction takes place at the surface of copper when this metal reacts with thiourea or its derivatives, both in aqueous solutions and in organic solvents. In all cases coherent films of copper sulfide showing interference colors are formed. The kinetics of the film growth may be expressed by a quadratic equation, which leads to linear and parabolic laws as limiting cases. The kinetics will be linear with time if any of the interface reactions is the rate-determining step. This is the case for the reactions of dimethyl and diphenylthiourea in organic solvents, such as the hydrocarbon liquids. The remarkable influence of the dissolved O_2 has been widely studied. In aerated aqueous solutions of low concentration the reactivity decreases in the order thiourea > methylthiourea > dimethylthiourea, and the energy of activation amounts to 10 kcal/mole. In the case of dimethylthiourea the reactivity is smaller when anisole is used as solvent. Diphenylthiourea in xylene also shows a lower reactivity. In these cases the smaller reactivities lead to higher activation energy (14-20 kcal/mole). The research work has been carried out using radioactive tracers. In general, the compounds have been labeled with ^{35}S, but in the case of thiourea we also used ^{14}C, which permits the estimation of the proportion of molecules adsorbed at or occluded in the tarnishing film.

The study of the formation of sulfides on metallic surfaces by radiotracer methods, using ^{35}S labeled compounds, both in gaseous phase and organic solutions has been the subject matter of numerous publications during the last few years. This method is rapid, very sensitive, and accurate. A previous calibration permits the establishment of the activity-thickness ratio, according to which it is sufficient to measure the activity of a sample to know the sulfur content of the deposit formed.

Earlier results (1) suggested that a tarnishing reaction takes place at the surface of Cu, when this metal reacts with aqueous solutions of thiourea, forming a film of Cu_2S. This reaction yields coherent films showing interference colors. The kinetics of the film growth might be expressed by a quadratic relation such as

$$\frac{\Delta^2}{k_a} + \frac{\Delta}{k_r} = t \qquad [1]$$

where Δ is the deposit formed per unit area, usually expressed in μg of S per cm^2, t is the reaction time, and k_a and k_r are rate constants.

The research was extended to study the surface reaction of Cu with solutions of diphenylthiourea in xylene (2) and aqueous solutions of methylthiourea

(3). These reactions also give coherent films, and the remarkable influence of O_2 on their kinetics was established. If the O_2 is eliminated from the solution of methylthiourea, by passing pure N_2 before and during the reaction, the reactivity of this compound against Cu is very small.

Discussion of the results led us to conclude that molecules of thiourea, or its derivatives, are chemisorbed at the surface of the metal or at the outer interface of the tarnishing film. The access of O_2 to this interface seems to be essential for the splitting of the chemisorbed molecules, to form $S^=$ ions and cationic vacancies, which migrate toward the inner metal/sulfide interface. In this sense, the reaction involving the formation of surface sulfides will not proceed in the absence of O_2, and the following steps might be distinguished.

(*A*) The sulfide ions are formed at the outer ininterface (Cu_2S/H_2O + thiourea) through the action of O_2, which diffuses from the solution. Positive holes ($e\,\square$) and cationic vacancies ($Cu^+\square$) are formed, and they migrate from the outer interface to the metal. The reaction at the outer interface has been postulated as follows

$$\frac{1}{2}O_2 + \begin{matrix}RHN\\ \diagdown\\ \quad CS\\ \diagup\\ RHN\end{matrix} \longrightarrow \begin{matrix}RHN\\ \diagdown\\ \quad CO\\ \diagup\\ RHN\end{matrix} + S^= + 2Cu^+\square + 2e\square \qquad [2]$$

(*B*) Penetration of the metal in the Cu_2S film. This compound is deficient in metal, and therefore it has cationic vacancies which act as centers of effective negative charges. The electrical neutrality is preserved by the existence of positive holes near the lattice defects. The reaction taking place at the inner interface will then be:

$$Cu + Cu^+\square + e\,\square \longrightarrow Cu^+ \qquad [3]$$

according to which a Cu atom penetrates as Cu^+ ion into the Cu_2S lattice, filling a cationic vacancy and giving out an electron to a positive hole $e\,\square$ in the valence band of the sulfide.

(*C*) Transport of material through the tarnishing film. If this film is coherent, the transport takes place, for high temperatures and great thickness, by diffusion of Cu^+ ions through a concentration gradient of $Cu^+\square$ vacancies (Wagner's mechanism). For lower temperatures and small thicknesses, as may be the case for the processes here considered, the action of electrical fields, due to reactions [2] and [3], must be considered (Hauffe's boundary layers and mechanism of Mott and Cabrera). However, frequently, the films formed are no longer coherent, and the transport of matter is made easier, through pores, cracks, grain boundaries, etc., present in the film.

When none of the above processes (A, B, C) is the rate-determining step, it can be said that the "slowness" of the reaction (defined as the reciprocal of the reaction rate) is the sum of those corresponding to each of the partial processes (4, 5). These ideas lead to Eq. [1], where the term Δ/k_r accounts for the "slowness" due to the inner and outer interface reactions, being

$$\frac{1}{k_r} = \frac{1}{k_e} + \frac{1}{k_i} \qquad [4]$$

and the term Δ^2/k_d corresponds to that of the matter transport process.

The kinetic relation [1] leads as limiting cases to linear and parabolic kinetic laws. The kinetics will be linear ($\Delta = k_r\,t$) if any of the interface reactions is the rate-determining step. This implies that the transport of matter is rapid. For this transport it is essential to have a lattice with defects and high electrical conductivity. This is the case at the beginning of the formation of the surface films we are considering and especially in the case when Cu is attacked by thiourea derivatives in organic solvents. The parabolic term Δ^2/k_d appears as a curvature in the plot Δ *vs.* t. This curvature depends clearly on the experimental conditions.

All these considerations suggest a restudy in greater detail of the reaction of Cu with aqueous solutions of thiourea. The possibility of using this compound labeled alternatively with ^{35}S or ^{14}C permits the estimation of the proportion of thiourea molecules occluded as such in the deposit formed. On the other hand, since the dimethylthiourea is soluble in water and in anisole, the study of the reaction of Cu with this compound makes it possible to obtain information about the influence of the solvent. This paper describes results not yet published which we considered more relevant to our present discussion. Also, a general picture of the kinetics of this sulfuration process will be given especially regarding the influence of the various alkyl and aryl substituents of thiourea, the presence of O_2, and the nature of the solvent.

Experimental Technique

Preparation of labeled compounds.—In some cases labeled compounds of high specific activities have been obtained from radioisotope distribution centers (thiourea). In other cases the radioactive compounds have been prepared in our laboratory, either by an exchange reaction with high specific activity ^{35}S (diphenylthiourea) or by synthesis from other more simple compounds (methylthiourea and dimethylthiourea). In general, the compounds used were labeled with ^{35}S, but in some cases with ^{14}C. In both cases the activity is due to weak β radiation.

Counting equipment.—A Geiger-Müller tube was used for counting, and the necessary corrections were applied to the results. The uniformity of the deposits was checked by autoradiography. The samples were usually counted for a time long enough to have a statistical error of 1%.

Calculations of the specific activity of the labeled compounds.—Determination of counting efficiency.—To determine the efficiency of our counting system a thiourea reference source was used. It was supplied by the Radiochemical Center, Amersham, with a specific activity of 222 millicurie/g. With this source a solution was prepared containing 9.3 microcurie/ml and on the other hand another solution of inactive thiourea containing 100 mg/ml was

prepared. With these two solutions we could prepare solutions of varying concentration and varying specific activity.

The efficiency for solid samples was measured with circular Cu disks, identical with those used in the sulfuration experiments, of 2.5 cm diameter and 0.4 mm thickness, previously submitted to mechanical and electrochemical polishing. The efficiency for liquid samples was measured with flat bottom glass ashing dishes, 2.2 cm internal diameter and 7 mm deep.

Efficiency measurements for solid samples have been carried out by two procedures, denoted as evaporation and depletion method, respectively. In the first case solid samples were obtained by evaporation of thiourea solutions, containing known amounts of ^{35}S and distributed so that they occupy centered circles of increasing radius on the copper disks. The solutions are prepared so that both the sulfur content of the deposit expressed as μg of S per cm^2 and the total activity of the samples are kept constant. Therefore the specific activity of the deposit (microcurie/cm^2) will decrease with increasing radius. Countings corrected for coincidence, background, standard, and decay, are plotted *vs.* the radius of the samples, and the extrapolation to $r = 12.5$ mm of the graphically adjusted curve allows us to calculate the counting that would be obtained, should the deposit be uniformly distributed over the whole area of the disks.

Table I shows the results of experiments 1 to 4 carried out by evaporation procedure. In column 2 the deposits of S in $\mu g/cm^2$ are given; column 3 shows the absolute radioactivity of the samples; column 4 the activity measured in our equipment and column 5 the efficiency in percentage; column 6 shows the statistical weight given to the determinations.

In the depletion method the same experimental procedure as in the sulfuration experiments is used. Polished disks of copper are made to react with thiourea solutions until these are completely depleted; the concentration of each thiourea solution is such that a sulfide deposit of a certain thickness is obtained. The solution will be depleted when another disk, in the same conditions, does not show any reaction and its counting equals that of background. Table I shows the results of experiments 5 to 10 carried out by this procedure.

It can be seen in Table I that the counting efficiency is constant for the whole range of thicknesses of sulfide (Δ) studied, except for the experiments corresponding to negligible thickness carried out using the active thiourea solutions only. The value of the efficiency is higher in this case (9.5%), probably due to nonuniform distribution of the deposit which tends to accumulate at the center of the disks, during evaporation. The autoradiographs confirm this assumption. This result has been rejected in calculating the weighted mean value of the efficiency which is 7.0%.

For liquid samples the efficiency decreases with increasing density, due to a greater absorption of β particles. With aqueous solutions of thiourea, whose concentrations vary between 12 mg/l and 3 g/l (densities very nearly unity), an excellent proportionality between the disintegration rate and the counting rate is observed. The slope of the straight line thus obtained corresponds to an efficiency of 0.082%. Hence the ratio of efficiencies for solid and liquid samples is 85. This ratio is useful, because the higher precision of liquid sample counting avoids preparation of solid samples, where small variations in the uniformity of the deposit gives place to considerable errors.

Preparation of reacting solutions.—In each case the preparation of solutions with desired characteristics has been carried out by admixture, in appropriate proportion of the two stock solutions, one active and the other inactive.

Preparation of copper disks.—The disks were first mechanically polished, then degreased with benzene in a Soxhlet apparatus, followed by washing with acetone and distilled water. After further washing and electrochemical polishing in 60% H_3PO_4 solution, the disks were rapidly washed in distilled water. The polishing and subsequent washing were carried out immediately before the reaction experiments and, to minimize oxidation, the disks were introduced while still moist into the reactant solution.

When hydrocarbons or similar compounds are to be used as solvents the treatment of the copper disks was slightly modified. After electrochemical polishing the disks were washed again with distilled water and acetone and immediately submerged in dry benzene, xylene, etc. These manipulations were always carried out quickly and under the same conditions.

Performance of the experiments.—The experimental method consists in introducing the polished copper disks into the solution (30 ml) in such a

Table I. Counting efficiency for solid samples

Experiment No.	$\Delta\mu g/cm^2$	Disintegration rate $\times 10^{-3}$ dis/min	Activity $\times 10^{-4}$ cts/min	Effic., %	Statist. weight	Procedure
1	negligible	1.5	1.5	9.5	—	Evaporation
2	13.0	1.5	1.1	6.9	1	Evaporation
3	13.0	1.0	0.67	6.5	1	Evaporation
4	13.0	0.51	0.34	6.7	0.5	Evaporation
5	21.0	5.0	3.7	7.3	5	Depletion
6	10.0	2.5	1.8	7.3	3	Depletion
7	5.2	1.2	0.97	7.7	1	Depletion
8	2.6	0.62	0.41	6.6	2	Depletion
9	1.3	0.31	0.18	6.0	0.3	Depletion
10	0.64	0.15	0.09	6.0	0.2	Depletion

Table II. Corrections in calculations for two experiments done with aqueous solutions of thiourea—^{35}S at 35°C. Standard 5500 cts./min.

1	2	3	4	5	6	7	8	9	10	11	12	13
Disk No.	Conc. × 10^3M	Time, min	Cts/min	Cts/min correct. for coincid.	Back-ground cts/min	Cts/min correct. for back-ground	Stand. cts/min	Cts/min correct. for stand.	Cts/min correct. for decay	Spec. activ. cts/min / μg/cm²	Δ μg/cm²	Mean value μg/cm²
183	2.6	90	680	683	18	665	5900	619	998	875	1.1	1.1
183′	2.6	90	658	661	18	643	5900	599	981	875	1.1	
165	0.33	90	1246	1256	18	1238	5900	1145	1861	875	2.1	2.1
165′	0.33	90	1211	1221	18	1203	5900	1121	1808	875	2.1	

way that, by means of a slow rotating motor (60 rpm), they are moved up and down with simultaneous rotation, to obtain an efficient removal of the solution at the interface. During each experiment the temperature is kept constant. After a time the disk is rapidly removed, washed repeatedly either with distilled water or the solvent used in the experiment, then with acetone, and finally it is allowed to dry before counting.

Counting and calculation of film thicknesses.—Calculation by radioactivity measurements.—The radioactivity of the dried disk was then measured, taking into account corrections for coincidence, background, reference to standard, and decay of the nuclide. If the specific activity of the solution used is expressed as cts. $min^{-1}/\mu g\ cm^{-2}$, the original countings can be translated into amounts of sulfur in $\mu g\ cm^{-2}$ deposited at the surface. The thickness of the surface film can be calculated easily assuming a certain value for the density of the compound formed. Table II shows an instance of corrections and calculations performed for two experiments done with Cu and aqueous solutions of thiourea.

In Table II, column 5 shows the activities corrected for a paralysis time of 400 μ sec, fixed in our system of counting. In column 9 the activities are referred to a certain standard, while in column 10 account is taken of the correction for decay of nuclide. Column 12 gives the weights of sulfur per unit area, estimated from the activities given in column 10 and taking account of the specific activity given in column 11. If it is assumed that the product formed is Cu_2S, the thickness of the film can be estimated from its density 5.783 g/cm^3, whence 1 $\mu g\ cm^{-2}$ of sulfur deposited corresponds to a thickness of 85.9Å.

Thickness scale by visual observation of interference colors.—In the course of our experiments, it has been verified that the reaction of Cu with diphenylthiourea (2) leads to the formation of coherent sulfide films, showing suitable interference colors for establishing a scale relating colors with weights of deposited sulfur. This scale provides a convenient visual method of estimating the thicknesses of the surface films formed.

Dyess and Miley (6) determined by the coulometric method the thicknesses of sulfide films on Cu, corresponding to several interference colors in the first two orders. The success of a quantitative coulometric reduction of Cu_2S has been studied later on by Hoar and Stockbridge (7). Weighings of cathode and colorimetric determination of Cu in solution indicated that reduction was complete. Comparison of sulfur contents of films showing similar interference colors evidences satisfactory agreement between coulometric, colorimetric, and radiotracer estimation. This allows a greater reliability for estimating the thicknesses by visual observation of the disks during sulfuration.

Experimental Results with Aqueous Solutions of Thiourea

The reaction of Cu with aqueous solutions of thiourea is studied below in greater detail. The electrochemical behavior of this compound makes this study advisable. On the other hand, the availability of thiourea labeled with ^{35}S or ^{14}C allows one to draw new conclusions about the mechanism of this reaction.

Experiments with thiourea-^{35}S.—Experiments with aerated solutions.—In these solutions the O_2 concentration is determined by the partial pressure of this element in the air. Thus, the conditions prevailing in these experiments can be assumed to be similar to the actual conditions of corrosion phenomena.

With a constant O_2 concentration, the variables to be studied are the temperature and the concentration of thiourea. Figure 1 shows the results obtained for Δ *vs.* reaction time t, for a concentration 1.32 x 10^{-3} M and temperatures shown in the figure. It can be seen that the kinetic reaction law is quadratic [1], and plotting t/Δ *vs.* Δ the rate constants, k_d and k_r, for each value of concentration and temperature may be determined. To carry out this determination of rate constants the method of least squares has been applied in most cases.

The values of these rate constants from the whole series of experiments are shown in Table III, in which they are given in laboratory units (μg, cm^{-2},

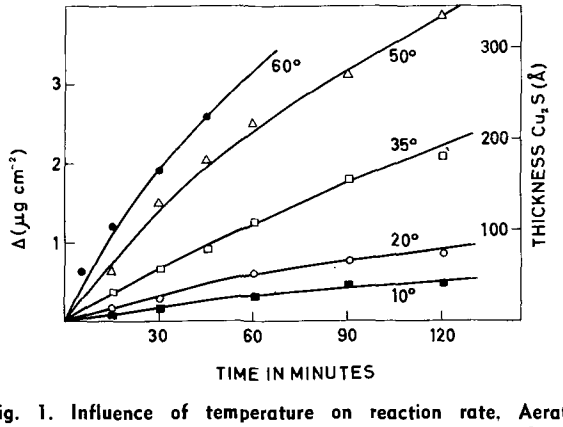

Fig. 1. Influence of temperature on reaction rate. Aerated aqueous solutions of thiourea—^{35}S, concentration 1.32 x 10^{-3}M.

Table III. Kinetic parameters for the whole series of experiments carried out with aerated aqueous solutions of thiourea—^{35}S

Conc. × 10^{-3}M	Temp, °C	$k_r \times 10^2$ $\mu g\ cm^{-2}min^{-1}$	$k'_r \times 10^{10}$ $g\ cm^{-2}sec^{-1}$	$k_d \times 10^2$ $\mu g^2\ cm^{-4}min^{-1}$	ΔH_r^* kcal/mole
0.33	50	5.0	8.3	72	
0.33	35	2.3	3.8	79	9.6
0.33	20	1.0	1.7	6.8	
0.66	50	10.0	16.6	50	
0.66	35	3.0	5.0	19	11.1
0.66	20	1.3	2.1	1.9	
1.32	60	11.4	19.0	29	
1.32	50	8.5	14.2	21	
1.32	35	2.6	4.3	12	10.9
1.32	20	1.2	2.0	3.7	
1.32	10	0.7	1.2	0.8	
2.64	50	5.5	9.2	20	
2.64	35	3.0	5.0	2.5	8.0
2.64	20	1.5	2.5	0.8	
5.28	50	6.5	10.8	13.6	
5.28	35	4.5	7.5	1.7	7.3
5.28	20	2.1	3.5	0.75	
7.92	50	6.4	10.7	12.8	
7.92	35	4.0	6.6	1.8	7.0
7.92	20	2.0	3.3	0.75	

min^{-1}) and in practical units (g, cm^{-2}, sec^{-1}). Figure 2 shows the plot log k_r *vs.* $1/T$ for the concentration 1.32 x 10^{-3}M. In all cases this plot allows one to draw straight lines from which the parameters in the Arrhenius equation may be calculated

$$k = A \exp(-\Delta H^*/RT) \qquad [5]$$

Values of ΔH_r^* are also given in Table III. The value $\Delta H_r^* = 10.9$ kcal/mole reported for the above concentration agrees well with that found for the same conditions in ref (1), which due to miscalculation should read 10.4 kcal/mole.

Figure 3 is a plot of k_r and k_d *vs.* thiourea concentration for the temperatures 20°, 35°, and 50°C. With regard to k_r it can be observed that the interface reaction rate passes through a maximum for a concentration 0.8 x 10^{-3}M. On the contrary, the values of k_d decrease at the beginning with increasing thiourea concentration, tending later to steady values nearly independent of the concentration. The study of the variations of both is discussed below.

Experiments carried out passing nitrogen and oxygen.—In order to check if the presence of dissolved O_2 is a decisive factor in the process of sulfuration

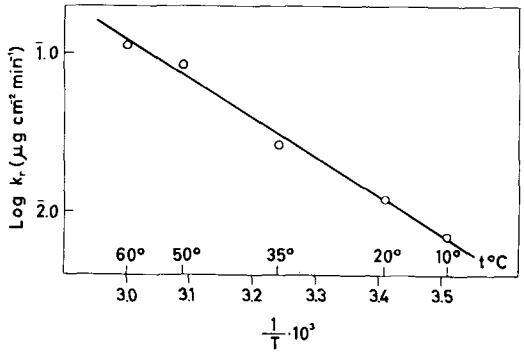

Fig. 2. Plot of log k_r vs. $1/T$ to determine the energy of activation. Concentration of thiourea 1.32 x 10^{-3}M.

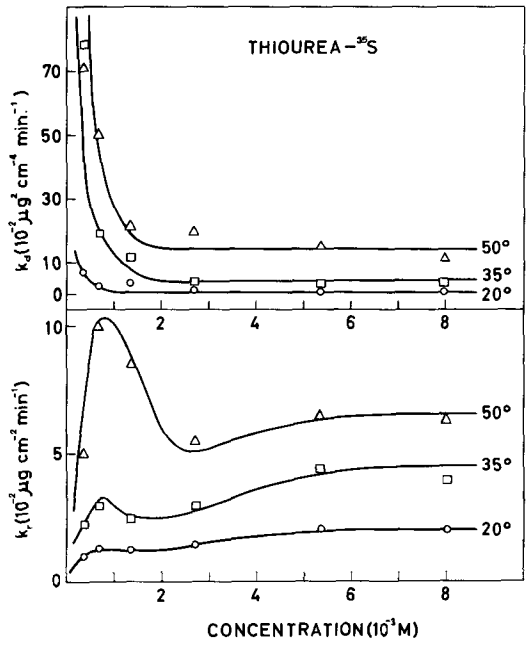

Fig. 3. Plots of k_d and k_r vs. concentration of thiourea for 20°, 35°, and 50°C. Aerated aqueous solutions of thiourea.

of Cu by thiourea, a series of experiments were carried out, eliminating the dissolved air in the solution by passing N_2 at a rate of 20 cm^3/min. Figure 4 shows the results thus obtained for a concentration 1.32 x 10^{-3}M and 35°C. It shows also the results for experiments carried out passing O_2 in the same conditions and those obtained with aerated solutions. From this series of experiments we may conclude that the reactivity of thiourea against Cu increases notably by passing O_2, while the elimination of this element by passing N_2 decreases the reactivity. This effect is more evident as the elimination becomes complete.

Experiments carried out with thiourea-^{14}C.—Using thiourea-^{14}C we have been able to determine the content of thiourea molecules in the tarnishing films, due to adsorption at the solid/liquid interface or inclusion in the bulk of the sulfide film. The results so obtained are expressed, as before, as deposited S in $\mu g/cm^2$ so that they can be easily compared with those obtained with thiourea-^{35}S. The experimental procedure is the same as above, except that in this case the decay correction given in column 10, Table II, does not apply. The specific

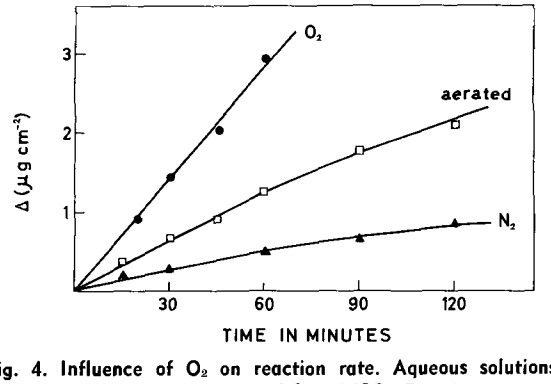

Fig. 4. Influence of O_2 on reaction rate. Aqueous solutions of thiourea, concentration 1.32 x 10^{-3}M, 35°C. Experiments carried out passing nitrogen, oxygen, and with aerated solutions, respectively.

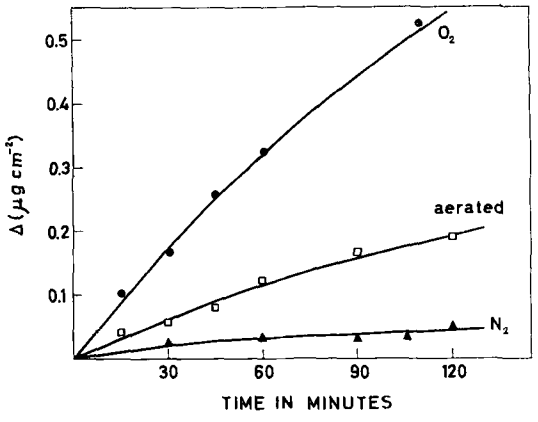

Fig. 5. Experiments carried out with aqueous solutions of thiourea—^{14}C. Concentration 1.32 x 10^{-3}M, 35°C.

activity to be given in column 11 is in this case 1.9 x 10^8 cts. $min^{-1}/\mu g\ cm^{-2}$.

The progress of the reaction is followed by observation of interference colors which should be identical, for the same experimental conditions, to those obtained with thiourea-^{35}S. The activity of the disks gives the contribution of thiourea molecules to the deposit formed. Figure 5 shows these contributions against time for a series of experiments carried out under similar conditions to those of Fig. 4. Comparing both figures it can be concluded that the contribution of thiourea molecules to the total thickness of the deposit considered as sulfide is approximately 14% in the experiments carried out passing O_2, 10% in those with aerated solution, and 6% when passing N_2. The influence of temperature has also been studied with aerated solutions of the above concentration, and the approximate contribution of thiourea molecules varied from 13% at 20°C to 10% at 35°C and 7% at 50°C.

Table IV. Kinetic parameters for the whole series of experiments carried out with aerated aqueous solutions of methylthiourea—^{35}S

Conc. x 10^3M	Temp. °C	k_r x 10^2 $\mu g\ cm^{-2}min^{-1}$	k'_r x 10^{10} $g\ cm^{-2}sec^{-1}$	k_d x 10^2 $\mu g^2 cm^{-4}min^{-1}$	ΔH_r^* kcal/mole
0.33	50	—	—	—	
0.33	35	5.25	8.7	—	
0.33	20	4.75	7.1	25	
0.66	50	7.1	12	—	
0.66	35	4.0	6.6	—	7.5
0.66	20	2.3	3.8	12.7	
1.32	70	8.3	14	—	
1.32	60	5.4	9.0	—	
1.32	50	4.7	7.8	—	7.3
1.32	35	2.5	4.2	—	
1.32	20	1.8	3.0	5	
1.98	50	4.1	6.8	30	
1.98	20	2.5	4.2	2.1	
2.64	50	5.3	8.8	6.7	
2.64	35	3.5	5.8	3.4	4.9
2.64	20	2.5	4.2	1.3	
3.96	50	7.0	12	4.0	
3.96	20	3.3	5.5	1.6	
7.92	50	8.4	14	6.8	
7.92	35	6.0	10	5.7	5.3
7.92	20	3.3	5.5	3.1	

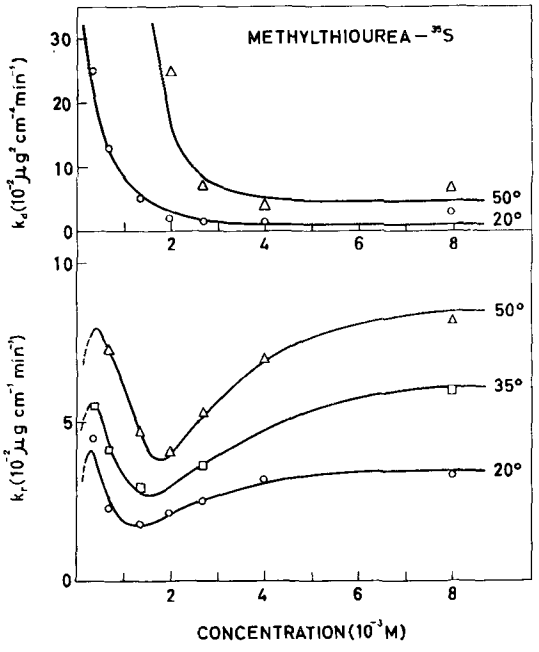

Fig. 6. Values of k_d and k_r vs. concentration of methylthiourea in aerated aqueous solutions.

Experimental Results with Aqueous Solutions of Methylthiourea

The surface reaction of Cu with aqueous solution of methylthiourea has been reported in another paper (3). However, a new consideration of those results obtained with aerated solutions of methylthiourea permits a more precise determination of the rate constants k_r and k_d. The results so obtained differ little from those published (3) and are summarized in Table IV, where in the last column the values of the activation energy for several concentrations are gathered.

Figure 6 shows the values of k_r and k_d *vs.* methylthiourea concentrations for three values of temperature (20°, 35°, and 50°C). The variation of k_r in the curve is similar to the one described for thiourea, but the maximum appears at lower concentrations, about 0.3 x 10^{-3}M. This fact is confirmed because of the presence of a minimum which is displaced to the left. The minimum reaches a lower level with methylthiourea. The value of k_d decreases rapidly at the beginning, tending later to steady values. In general lines the trend of these variations is similar to that observed in the case of thiourea.

Experimental Results with Aqueous Solutions of Dimethylthiourea

Dimethylthiourea presents the advantage of being soluble in water and in organic solvents; results obtained with aqueous solutions are described below. Radioactive dimethylthiourea was prepared from $^{35}S_2C$. The specific activity was determined by measurement of liquid samples and calculating the solid sample activities by the above mentioned ratio. Thus, we calculated for these experiments that 1 $\mu g/cm^2$ of S corresponds to 80.3 cts./min. The counting of the disks and the corresponding corrections are carried out in a form similar to that described for thiourea, except that in column 11 of

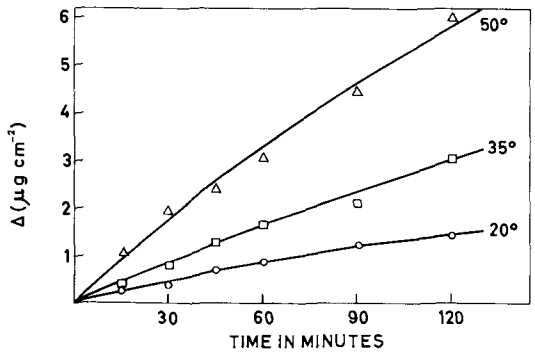

Fig. 7. Reaction curves for experiments carried out with aerated aqueous solutions of dimethylthiourea—^{35}S. Concentration 1.32 x 10^{-3}M.

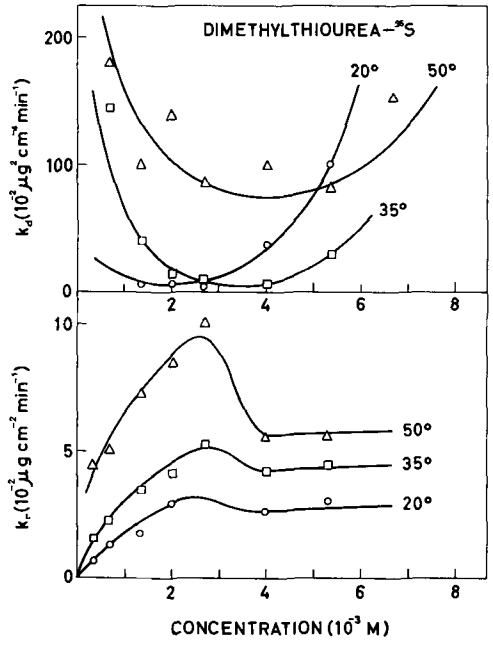

Fig. 8. Values of k_d and k_r vs. concentration of dimethylthiourea in aerated aqueous solutions.

Table II now appears the value 80.3 (cts. $min^{-1}/\mu g\ cm^{-2}$) for this activity-thickness ratio.

Experiments carried out with aqueous aerated solutions.—Figure 7 shows the reaction curves for three series of experiments carried out, respectively, at 20°, 35°, and 50°C and a concentration 1.32 x 10^{-3}M. As in the cases of thiourea and methylthiourea the results obtained in these experiments can be analyzed by the aforesaid quadratic law. The values of k_r, k_d, and ΔH_r^*, calculated in the same way as before for several concentrations and temperatures, are given in Table V.

In Fig. 8 the values of k_r and k_d are plotted against dimethylthiourea concentration for temperatures of 20°, 35°, and 50°C. The variation of k_r is similar to that observed for thiourea, except that the maximum lies displaced toward the concentration 2.5 x 10^{-3}M. The most noteworthy fact concerns in this case k_d, since this rate constant passes through a minimum with increasing concentration of dimethylthiourea. This minimum appears for smaller concentrations with decreasing temperature. Formally, this fact reflects itself in the plots of Δ *vs.* t, which, for a given temperature, tend to be again

Table V. Kinetic parameters for the whole series of experiments carried out with aerated aqueous solutions of dimethylthiourea—^{35}S

Conc. x 10^3M	Temp, °C	k_r x 10^2 $\mu g\ cm^{-2}min^{-1}$	k'_r x 10^{10} $g\ cm^{-2}sec^{-1}$	k_d x 10^2 $\mu g^2 cm^{-4}min^{-1}$	ΔH_r^* kcal/mole
0.33	50	4.5	7.5	—	
0.33	35	1.6	2.6	—	11.4
0.33	20	0.7	1.2	—	
0.66	50	5.1	8.5	181	
0.66	35	2.3	3.8	147	9.1
0.66	20	1.2	2.1	—	
1.32	50	7.3	12.1	100	
1.32	35	3.5	5.8	41	9.3
1.32	20	1.8	3.0	5.9	
1.98	50	8.5	14.1	140	
1.98	35	4.2	7.0	15.3	7.3
1.98	20	3.0	5.0	7.2	
2.64	50	10.0	16.6	85	
2.64	35	5.2	8.6	8.3	8.0
2.64	20	—	—	1.6	
3.96	50	5.6	9.3	100	
3.96	35	4.3	7.1	5.0	4.1
3.96	20	2.6	4.3	38	
5.28	50	5.7	9.5	83	
5.28	35	4.5	7.5	30	3.3
5.28	20	3.0	5.0	100	

linear for higher concentration. The interpretation of these facts is given below in the Discussion.

Experiments carried out passing nitrogen.—In several series of experiments carried out at 20°, 35°, and 50°C, with different concentrations, and passing N_2 at a rate of 20 cm^3/min, the results show in all cases that there is a considerable decrease of reactivity against Cu, due to removal of dissolved air.

Experimental Results with Solutions of Dimethylthiourea in Anisole

Experimental conditions are similar to those used in aqueous solutions. The copper disks, after mechanical and electrochemical polishing, were washed with distilled water, with acetone, and finally with anisole. After reaction the disks were washed with anisole, acetone, and allowed to dry before counting. Figure 9 shows the results obtained for a concentration 1.32 x 10^{-3}M and temperatures of 60°, 75°, 80°, and 90°C. It follows from these results that the reactivity is lower than in aqueous solutions, and for most of the experiments the kinetic law of the film growth was linear with time. The results

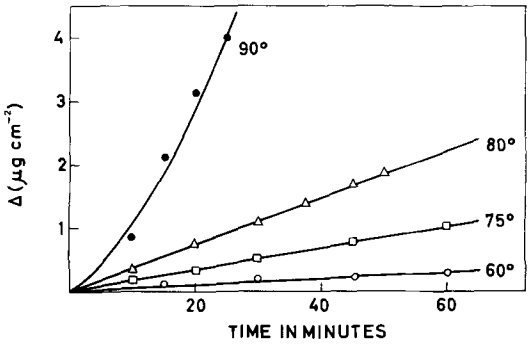

Fig. 9. Reaction curves for experiments with solutions of dimethylthiourea—^{35}S, in anisole. Concentration 1.32 x 10^{-3}M.

Table VI. Kinetic parameters for the whole series of experiments carried out with solutions of dimethylthiourea in anisole

Conc. $\times 10^{-3}$M	Temp, °C	$k_r \times 10^2$ μg cm^{-2}min^{-1}	$k'_r \times 10^{10}$ g cm^{-2}sec^{-1}	ΔH_r* kcal/mole
1.32	60	0.6	1.0	
1.32	75	1.8	3.0	21
1.32	80	3.8	6.3	
3.96	60	0.9	1.5	
3.96	75	2.8	4.6	21
3.96	80	5.6	9.0	
7.92	60	1.3	2.1	
7.92	75	4.0	6.6	21
7.92	80	9.2	15.3	

obtained for different values of temperature and concentration of dimethylthiourea are given in Table VI. A set of experiments was also carried out passing pure N_2 before and during the reaction of sulfuration. They showed a decrease of reactivity to a minimum.

Experimental Results with Solutions of Diphenylthiourea in Xylene

Results obtained in the study of the surface reaction of Cu with solutions of diphenylthiourea in xylene have been published elsewhere (3); this reaction also yields coherent films, showing interference colors. The reactivity in this case is much lower than that of thiourea in aqueous solution, and the kinetic law of the film growth is linear with time. A value of $\Delta H_r^* = 14.2$ kcal/mole for the energy of activation is obtained. In the discussion below these results are considered again in trying to establish a comparison with all the results obtained with different compounds.

Discussion

From the results described above concerning the formation of surface films of sulfides on Cu by thiourea and derivatives we conclude that these compounds supply the $S^=$ ions at the outer interface, by the action of the O_2 dissolved in the solution. If the O_2 is eliminated, the reactivity with Cu decreases notably, and if the elimination should be complete, the reaction could be reduced to a chemisorption of a thiourea monolayer on the Cu surface, the molecules anchoring through the groups S=C.

Recent work by Trivich *et al.* (8), in which thiourea-^{35}S was used to study the effect of this compound on electrodeposition of Cu, showed how the adsorbed molecules interfere with the growth of the crystals. However, if aerated solutions of thiourea are used, the splitting of these molecules at the cathode surface may play also a role in the inhibiting effect. This splitting of the molecule may explain the occlusion of S in the electrodeposits (9, 1). Likewise, the results obtained in the experiments carried out with thiourea-^{14}C show the presence of molecules adsorbed and partly occluded in the sulfide film. This effect is greater when the sulfuration process is more intense. These results, besides the use of thiourea as collector in the flotation of sulfide minerals (10) and the possibility of complex and chelate formation with Cu, indorse the hypothesis that the thiourea molecules are chemisorbed both at the metal surface, in the initial stage of the reaction, and at the external surface of the sulfide film during its growth.

On the other hand, chemisorption of oxygen on a p-type semiconductor such as Cu_2S seems to be associated with adsorbed oxygen atoms and neutral pairs formed by O^- ions and positive holes trapped at the surface lattice cations (11). However, if the adsorption takes place at a thin sulfide film on a metal, it may be modified by electron transfer from the metal to the surface level in such a way that adsorption as O^- ions will exceed that on bulk sulfides. The electrical field thus established will contribute furthermore to the migration of Cu^+ ions through the tarnishing film (12, 13).

The high reactivity of the chemisorbed oxygen is readily understandable (14, 15) being ascribed to the O^- ions formed at the surface. In this way once the molecules of oxygen and thiourea are chemisorbed, the oxidation of the latter may take place, but the mechanism of the reaction cannot yet be elucidated. Freundlich and Fischer (16) studied the oxidation of thiourea solutions in the presence of activated carbon, and they supposed that sulfur and Hector base ($C_2H_4N_4S$) were formed in the reaction. However, the experiments described show that, in the presence of O_2, all the sulfur contained in the thiourea or its derivatives can react with Cu. This has led to the use of reaction [2] at least as a working hypothesis.

The observed variation of k_r, in the experiments carried out with aqueous solutions of thiourea, would show that there exists at the beginning an increasing reactivity with concentration, followed by an inhibiting effect due to the same thiourea. On the other hand, the variation of k_d leads to a greater curvature in the plot Δ *vs.* t for thiourea concentrations greater than 10^{-3}M. Now, if the physical meaning of this rate constant is related to the transport of matter, this would mean a greater hindrance for this transport when using solutions of increasing concentration. In principle, we can assume that this hindrance is due, in a great part, to the thiourea molecules occluded in the deposit formed and whose percentage has been determined in the experiments carried out with thiourea-^{14}C.

These results have been confirmed, in general, in the experiments carried out with aqueous solutions of methyl and dimethylthiourea. In the last case, constant k_d goes through a minimum when the concentration increases, and this minimum appears at lower concentration with increasing temperature. This means that, for a given temperature, the permeability of the films is greater when the concentration of dimethylthiourea increases above a certain value, perhaps due to CuS formation, which favored lowering the temperature (17).

If the rate of the interface reaction is smaller than that of the matter transport through the surface film and hence it becomes the rate determining step for the whole tarnishing process, it can be expected that the kinetic law of the film growth be linear. This might be the case with solutions of di-

Table VII. General view of rate constants k_r and activation energies ΔH_r for the surface reactions here studied

Sulfurating agent	Solvent	Temp, °C	c = 0.66 × 10⁻³M $k_r \times 10^{10}$ g cm⁻²sec⁻¹	c = 0.66 × 10⁻³M ΔH_r^* kcal/mole	c = 1.32 × 10⁻³M $k_r \times 10^{10}$ g cm⁻²sec⁻¹	c = 1.32 × 10⁻³M ΔH_r^* kcal/mole	c = 5.28 × 10⁻³M $k_r \times 10^{10}$ g cm⁻²sec⁻¹	c = 5.28 × 10⁻³M ΔH_r^* kcal/mole	c = 7.92 × 10⁻³M $k_r \times 10^{10}$ g cm⁻²sec⁻¹	c = 7.92 × 10⁻³M ΔH_r^* kcal/mole
Thiourea	water	50	16.6		14.2		10.8		10.7	
Thiourea	water	35	5.0	11.1	4.3	10.9	7.5	7.3	6.6	7.0
Thiourea	water	20	2.1		2.0		3.5		3.3	
Methylthiourea	water	50	12.0		7.8				14	
Methylthiourea	water	35	6.6	7.5	4.2	7.3			10	5.3
Methylthiourea	water	20	3.8		3.0				5.5	
Dimethylthiourea	water	50	8.5		12.1		9.5		—	
Dimethylthiourea	water	35	3.8	9.1	5.8	9.3	7.5	3.3	—	—
Dimethylthiourea	water	20	2.1		3.0		5.0		—	
Dimethylthiourea	anisole	80			6.3				15.3	
Dimethylthiourea	anisole	75			3.0	21			6.6	21
Dimethylthiourea	anisole	60			1.0				2.1	
Diphenylthiourea	xylene	70			13.0				31.0	
Diphenylthiourea	xylene	60			6.5	14.2			15.0	14.2
Diphenylthiourea	xylene	50			3.5				9.0	

methylthiourea in anisole and diphenylthiourea in xylene.

With all the experimental data, a comparative study regarding the rate constants k_r and the activation energies ΔH_r^* can be made, taking into account the several compounds, concentrations, and temperatures used. The results shown in Table VII lead to the following considerations.

In aerated aqueous solutions, the reactivity with Cu decreases in the order thiourea > methylthiourea > dimethylthiourea for very small concentrations. However, if the concentration is greater than 3 x 10^{-3}M the reactivities become of the same order or perhaps they increase in reverse direction. The activation energies ΔH_r^* are of the order of 10 kcal/mole. In general, if it is assumed that the prevailing factor for the reactivity of these compounds is the splitting of the C=S bond that depends on the negative electronic density of the S atom and the positive of the C atom, the substitution of H in the amine group by CH_3 will not alter essentially the conditions comparing with thiourea, because the CH_3 group is a weak electron donor.

In the case of dimethylthiourea, the reactivity is less when anisole is used as solvent. Diphenylthiourea in xylene shows a reactivity of the same order as that of dimethylthiourea in anisole. In many cases it is observed that weaker reactivity leads to greater activation energy, when the sulfuration reaction with thiourea derivatives takes place in non-aqueous solutions.

Finally, it is to be pointed out that, in all cases, the microscope observation of the surfaces after reaction reveals the presence of a color mosaic that follows the grain structure of metallic base. In general, the film is of uniform color for each grain. The observed colors can be due either to different thickness of the films formed on each grain, or differences in refraction index or to both factors. If the film formed is anisotropic the refraction index depends on the orientation. However, the experiments of Kruger (18) concerning the oxidation of a Cu monocrystal submerged in an aqueous O_2 solution and the gravimetric measurements of Benard and Talbot (19, 20), in the sense that certain crystallographic planes of Cu are oxidized more rapidly than others, seem to show that the variation in the thickness of the film and not that of the refraction index is the reason for the differences in color observed for different grains after the sulfuration reaction.

However, it is to be pointed out that this influence on the reaction rate, due to the orientation of the base lattice, will tend to decrease as the thickness of the tarnishing film increases, the reaction at the outer interface becoming finally the rate-determining step.

Manuscript received July 17, 1961; revised manuscript received Jan. 21, 1962.

Any discussion of this paper will appear in a Discussion Section to be published in the December 1962 JOURNAL.

REFERENCES

1. J. Llopis, J. M. Gamboa, and L. Arizmendi, *Proc. CITCE*, **9**, 448 (1957).
2. J. Llopis, J. M. Gamboa, and L. Arizmendi, *Electrochim. Acta*, **3**, 75 (1960).
3. J. Llopis, J. M. Gamboa, and L. Arizmendi, *An. Real Soc. Esp. Fis. Quim.*, **46B**, 499 (1960).
4. K. Fischbeck, *Z. Elektrochem.*, **39**, 316 (1933).
5. M. Billy and G. Valensi, *J. Chim. phys.*, **53**, 832 (1956).
6. J. B. Dyess and H. A. Miley, Trans. AIME, **133**, 239 (1939).
7. T. P. Hoar and C. D. Stockbridge, *Electrochim. Acta*, **3**, 94 (1960).
8. B. Ke, J. J. Hoekstra, B. C. Sison, and D. Trivich, *This Journal*, **106**, 382 (1959).
9. H. Fischer, "Elektrolytische Abscheidung und Elektrokristallisation von Metallen," Springer, Berlin (1954).
10. A. M. Gaudin, "Flotation," McGraw Hill Book Co., New York (1957).
11. T. B. Grimley, *Discussions Faraday Soc.*, **28**, 223 (1959).
12. N. F. Mott, *Trans. Faraday Soc.*, **43**, 429 (1947).
13. N. Cabrera and N. F. Mott, *Rep. prog. Phys.*, **12**, 163 (1949).
14. W. E. Garner, T. J. Gray, and F. S. Stone, *Discussions Faraday Soc.*, **8**, 246 (1950).
15. T. Wolkenstein, *J. Chim. phys.*, **54**, 175, 183 (1957).
16. H. Freundlich and H. Fischer, *Z. phys. Chem.*, **114**, 413 (1925).

17. J. Llopis, J. M. Gamboa, and L. Arizmendi, *Electrochim. Acta*, **1**, 39 (1959).
18. J. Kruger, *This Journal*, **106**, 847 (1959).
19. J. Benard and J. Talbot, *Compt. rend.*, **225**, 441 (1947).
20. J. Benard and J. Talbot, *ibid.*, **226**, 912 (1948).
21. B. Le Boucher, C. Libanati, and P. Lacombe, "3rd Metallurgy Symposium on Corrosion," p. 205, Centre d'Etudes Nucleaire de Saclay, North Holland Pub., Amsterdam (1960).

On the Oxidation of Zirconium

Karl A. Sense[1]

Research Department, Atomics International, A Division of North American Aviation, Inc., Canoga Park, California

ABSTRACT

The rate law for the oxidation of zirconium was found to be initially intermediate to linear and parabolic, then parabolic, and then nearly cubic over the first 10-min interval at both 400° and 500°C. At 400°C the oxidation rate became parabolic for an oxide thickness of about 300Å. At 500°C the oxidation rate became nearly cubic at about 3300Å, the transition from one rate to another being gradual rather than sharp. The activation energy for the parabolic region was 29.3 kcal/mole and for the nearly cubic region approximately 42 kcal/mole. The results obtained were independent of the shape of the specimen and its surface preparation. An analysis shows that the high solubility of oxygen in zirconium is not a sufficient condition to account for a cubic rate law of oxidation for a concentration-independent diffusion constant.

This work is a by-product of the primary objective, namely the study of the diffusion of hydrogen through thin films of ZrO_2 on zirconium metal. Since it was easier to obtain the desired oxide thickness at a lower temperature because of lower oxidation rates, the oxidation of zirconium was carried out at only two temperatures, 400° and 500°C. Also, since only thin films were desired, all of the runs with one exception were of a very short duration. The diffusion of hydrogen through ZrO_2 being the primary study, the kinetics of the oxidation of zirconium were not analyzed until after the experimental program was terminated, thus leaving the oxidation study incomplete from the standpoint of longer runs and greater temperature spread. Nevertheless, it is felt that the findings presented here are of sufficient interest to stimulate further work.

Experimental

Method.—The reaction rate between oxygen and zirconium was measured gravimetrically with an Electrona II balance which could detect weight changes of 1 μg. The reaction tube was attached directly to the balance. The furnace used was a 12-in. Hevi-duty type. Temperatures were measured with a platinum-platinum-rhodium couple located on the surface of the reaction tube. This couple was calibrated with respect to another couple located at the site normally occupied by the specimen. The temperature was controlled by a proportioning photocell-activated controller.

Two kinds of specimens were used, rectangular and spherical. The rectangular specimens had a surface area of about 13 cm^2 and a thickness which varied from 0.015-0.022 cm. The diameter of the spherical specimens varied from 0.51 to 0.52 cm. All of the specimens were prepared from reactor grade hafnium-free zirconium. All of the spherical and some of the rectangular specimens were abraded by being treated successively with 1, 2/0, and 3/0 abrasive paper and then polished with diamond dust to a mirror finish. They were then cleaned with a soap solution followed by water, acetone, ether, and absolute alcohol rinse. The rectangular specimens which were not abraded were chemically polished with a bath having the composition 45% HNO_3 (conc) 45% H_2O, and 10% HF (48%). The oxygen used was Matheson Company's research grade, maximum impurities in mole per cent being given by the manufacturer as follows: carbon dioxide 0.1, carbon monoxide 0.01, argon 0.01, nitrogen 0.05, hydrogen 0.01, and water 0.0002.

The following procedure was adhered to in making runs. The rectangular specimen was suspended from a thin hooked silica rod which was attached to either another silica rod or a three mil tungsten wire which was attached to the balance. The length of the system was so adjusted that the temperature gradient across the specimen in the hot zone was least, about 2°C. The spherical specimens were placed in a small silica basket. Because of the small diameter of the spheres the temperature gradient across the specimen was less than 1°C. At the start of a run the whole system was evacuated to a pressure of 7×10^{-5} mm Hg or less. Once the desired run temperature was obtained oxygen was admitted, the pressure being determined by a mercury manometer. Pure gold foil was placed between the manometer and the system to prevent mercury vapor from contaminating it. Balance readings were taken as soon as possible, usually 20 sec after oxygen was first admitted, and at 10-sec intervals thereafter except for the 2-hr run at 500°C when readings were taken at longer intervals after about 8 min.

Spheres were used in this work because we wanted to eliminate edge effects in the study of the diffusion of hydrogen through ZrO_2 films. Since the weighing capacity of the Electrona II balance used

[1] Present address: Astropower, Inc., Costa Mesa, California.

Table I.

(a) Oxidation runs at 400°C

1. Rectangular zirconium specimens about 1.8 × 3.5 cm^2 with thickness of from 0.015-0.022 cm

Oxygen pressure, mm	Preparation of specimen	First & last readings taken at, sec	Oxidation rate law, n, of initial film	Change of oxidation rate law at: wt. gain, $\mu g/cm^2$	Change of oxidation rate law at: time, sec	New oxidation rate law, n	Further change of oxidation rate law at: wt. gain $\mu g/cm^2$	Further change of oxidation rate law at: time, sec	New oxidation rate law, n
12	Chem	20-190	1.35	4.5	67	1.90	—	—	—
22	Abraded	20-180	1.16	4.9	75	1.45	—	—	—
21	Abraded	20-420	1.44	4.2	77	2.14	—	—	—
19	Abraded	30-320	1.41	5.4	70	2.42	—	—	—
		Average:	1.34	4.75	72	1.98			
		2. Zirconium spheres with diameter of from 0.51-0.52 cm							
17	Abraded	20-510	1.51	4.6	66	1.73	11	300	2.7
58	Abraded	10-350	1.55	4.9	92	3.05	—	—	—
83	Abraded	40-290	1.05	4.2	79	1.39	—	—	—
61	Abraded	20-290	1.35	3.9	74	2.32	—	—	—
62	Abraded	20-290	1.20	4.9	106	1.60	—	—	—
61	Abraded	20-290	1.15	4.8	64	1.61	—	—	—
		Average:	1.30	4.55	80	1.95			
	Over-all average of 1 and 2:		1.32	4.63	77	1.96			
		(b) Oxidation runs at 500°C							
		Rectangular zirconium specimens about 1.8 × 3.5 × 0.015 cm^3							
25	Chem	60-260	—	<19.3	<70	2.05	—	—	—
19	Chem	20-240	1.49	20.2	95	1.87	—	—	—
16	Chem	20-7200	—	<12	<30	1.95	51	500	2.81
					Average:	1.96			

was 1g we were limited to the use of small zirconium spheres so that the surface area of the spheres was only 0.81-0.86 cm^2. As a result, the magnitude of weight change for a 10-sec interval reading was only about one-fifteenth of that for a rectangular specimen. Since the most sensitive scale had to be used to measure weight changes for the spheres, the data showed more scatter than for the rectangular specimens.

Oxidation rates are expressed by the general law $w^n = kt$ where w is the weight gain, t the time, and k a constant. In making log-log plots of the weight gain *vs.* time from the data obtained in this work to get the value of the exponent, n, we found interestingly enough that every run made at 400°C obeyed at least two different rate laws of oxidation. This is shown very clearly in Fig. 1 for an abraded rectangular specimen. Table Ia summarizes the results for spherical and rectangular abraded specimens including one which was chemically polished. It is noted that the average of the results obtained for the rectangular specimens agrees quite well with that of the spherical specimens. Hence, the results obtained for the rectangular specimens are as valid as those obtained for the spheres. Also, the results for the chemically polished specimen are in good agreement with those of the abraded specimens. This contradicts the data of Gulbransen and Andrew (1) who found that the reaction rate for abraded specimens was 2-3 times as great as for chemically polished specimens in the 400°-500°C temperature region. Porte *et al.* (2) found that mechanically polished specimens reacted somewhat faster than did chemically polished specimens at 400° and 500°C, but that there was no significant difference at 600° and 700°C.

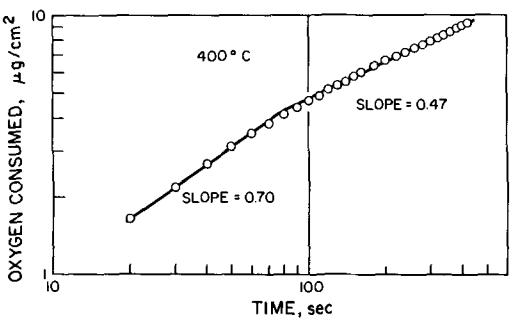

Fig. 1. Log-log plot of oxygen consumed *vs.* time at 400°C for a rectangular specimen.

Comparing the results of this work on the rate at which zirconium consumes oxygen with the results obtained by Pemsler (3) on the dissolution rate of anodically deposited ZrO_2 films we find that at 400°C the latter process is so much slower than the former that virtually all the oxygen consumed by zirconium can be considered to have gone into the formation of the ZrO_2 film. Hence, the critical film thickness at which the reaction rate becomes parabolic can be readily calculated. Using the conversion factor of 66.4Å/$\mu g/cm^2$ [2] this film thickness turns out to be about 307Å. One notes from Fig. 1 that the reaction rate changes gradually instead of sharply in the vicinity of the critical thickness. This behavior is true also for all the other runs and implies that one rate-controlling process takes over gradually from the other one as the oxide film gets thicker.

Of the runs made at 400°C only one had attained a sufficiently thick oxide film so that still another rate law could be observed. A plot of this run is shown in Fig. 2. We note that for a film thickness greater than about 730Å a new rate law prevails

[2] Obtained from an assumed density of 5.8 g/cm^3 for hafnium-free ZrO_2.

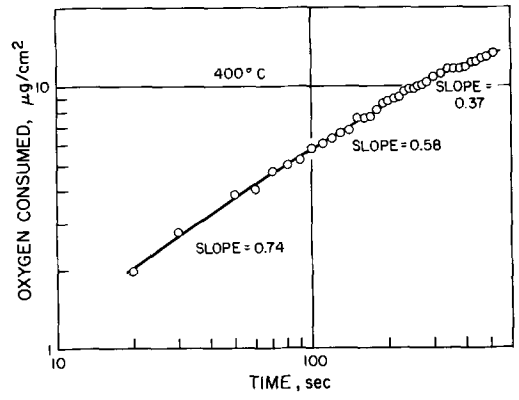

Fig. 2. Log-log plot of oxygen consumed vs. time at 400°C for a spherical specimen.

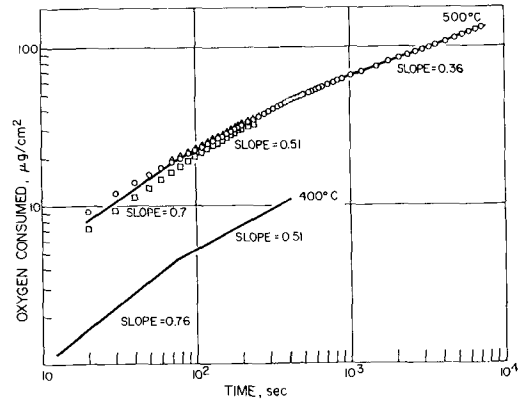

Fig. 3. Log-log plot of oxygen consumed vs. time at 400° and 500°C. Plot at 400°C represents composite of all runs made at that temperature up to 11 μg/cm² (see text).

which is nearly cubic, n having a value of 2.7. The scatter is greater here than in Fig. 1 because these data were obtained for a spherical specimen which has an unfavorable area-to-weight ratio, as pointed out above.

The results for the runs made at 500°C are summarized in Table Ib. A log-log plot of these runs is given in Fig. 3. This figure also shows a plot of the average of the results obtained from runs made at 400°C to a maximum oxide film thickness of 730Å. The change of slope occurring at 730Å as shown in Fig. 2 was not incorporated in this plot. The reason is that it occurs somewhat sooner in the one run shown than the average of all ten runs indicates (compare Fig. 2 and 3).

We note from Table Ib and from Fig. 3 that at 500°C the oxidation rate laws correspond to those observed at 400°C. The parabolic rate law starts when approximately 19 μg of oxygen have been consumed by 1 cm² of zirconium. This rate law continues until a weight gain of 51 μg/cm² has been attained after which the rate law becomes nearly cubic, n having a value of 2.81. From Pemsler's work (3) it is clear that in calculating the oxide thickness at 500°C correction must be made for the dissolution of the oxide film into the zirconium while the zirconium is being oxidized. Calculations then show that the parabolic rate law exists for an oxide thickness ranging very roughly from 1200Å to about 3300Å.

The rate law governing the initial oxidation of zirconium at 500°C is not nearly as well established as that at 400°C. We can only conclude that it is intermediate to linear and parabolic.

The reaction rate constants, k, for the parabolic portions of the 500° and 400°C curves were found to be 4.46 (μg/cm²)$^{1.86}$/sec and 0.261 (μg/cm²)$^{1.96}$/sec, respectively. Using these values the activation energy, ΔE, is determined from the equation $k = Ae^{-\Delta E/RT}$ where A is the frequency factor. ΔE turns out to be 29.3 kcal/mole, which is quite close to the value 28.6 kcal/mole obtained by Gulbransen and Andrew (1) who obtained a parabolic relationship for the temperature range of 525°-750°C using abraded rectangular specimens.

For the "cubic" region the reaction rate constants are 122.4 (μg/cm²)$^{2.8}$/sec and 2.16 (μg/cm²)$^{2.7}$/sec for 500° and 400°C, respectively. From these a ΔE value of 42 kcal/mole is obtained which is in agreement with the value of 42.7 kcal/mole found by Porte *et al.* (2) on the basis of a cubic relationship over the temperature range 400°-900°C. It must be pointed out that the data of this work in or near the "cubic" region show poorer agreement with those of Porte than might be assumed from the good agreement of the ΔE's. For example, at 500°C Porte shows weight gains of about 80 and 170 μg/cm² in 10 and 100 min, respectively. This is to be compared with weight gains of 55 and 123 μg/cm² found in this work for the same time intervals. At 400°C Porte shows a weight gain of about 28 μg/cm² after 5 min. For the corresponding time interval we obtain a value of 9.3 μg/cm² for the composite of all runs, or 11 μg/cm² for the single run (Fig. 2) for which a "cubic" rate law is observed.

Discussion

Whether the oxidation of zirconium obeys a parabolic or cubic rate law in the 400°-500°C temperature range has been disputed by various investigators (1, 2, 4-6). Gulbransen and Andrew (1) found furthermore that rectangular specimens such as used in this study obeyed the parabolic rate law when chemically polished and the cubic rate law when mechanically polished. The present study, on the other hand, finds that zirconium, regardless of the shape of the specimen or the manner of surface preparation, whether chemically polished or abraded, obeys both a parabolic and nearly cubic rate law depending on the thickness of the oxide coating. In fact, for about the first minute or so a nearly linear rate law seems to hold. It must be realized, of course, that the present investigation examines the initial oxidation critically, whereas other workers studied the oxidation rate over much longer times.

The formation of oxide films having a maximum thickness of several hundred Angstroms has been the subject of a theory by Mott (7) and Cabrera and Mott (8). The basis of their theory is that a contact potential difference exists between the chemisorbed oxygen and the metal resulting in the existence of an electric field across the oxide film. The cations move through this film under the influence of the electric field without much help from the temperature. For films of 50-100Å thickness Cabrera and Mott obtain a logarithmic law. In the case of an n-

type semiconductor Cabrera and Mott (8) obtain a parabolic law for films several hundred Angstroms thick. It turns out that ZrO_2 is an n-type semiconductor according to the work of Mallett and Albrecht (9) and should therefore obey the parabolic law.

Even at 400°C the rate of oxidation is sufficiently rapid that we cannot tell whether the logarithmic law is obeyed for a thickness of from 50-100Å. However, it is evident that the parabolic law is not obeyed until a thickness of about 300Å is attained. Hence, the theoretical results obtained by Cabrera and Mott (8) for thin films are not in agreement with the results obtained in this work.

The oxidation mechanism for film thicknesses greater than thin films but less than thick films (ca. 10,000Å) is imperfectly understood (8). For this intermediate range Wagner (10) states that an oxidation rate can be arrived at which is nearly logarithmic. Uhlig (11) finds that under certain circumstances a cubic equation can be obtained for oxide thicknesses up to several thousand Ångstroms. He bases his derivation on the consideration that the controlling step in the oxidation process is the electron flow from the metal. Still we find that in this work the rate law in the intermediate region is primarily parabolic.

The oxidation rate for thick films is found by Wagner (12) and Cabrera and Mott (8) to obey the parabolic law. However, Porte *et al.* (2) show that the oxidation of zirconium for thick oxide films follows the cubic law. The present work also shows that a nearly cubic rate law is obeyed for an oxide film about 8300Å thick (corrected for dissolution of the oxide film into zirconium). Until now there has been no satisfactory explanation as to why such thick films should obey a cubic oxidation rate law for n-type semiconductors. Kofstad and Hauffe (13) find that a cubic rate law exists also for the oxidation of titanium (TiO_2 also being an n-type semiconductor). They suggest that a cubic rate law could be the result of two factors, namely, the high solubility of oxygen in titanium and the dependence of the value of the diffusion "constant" on the oxygen concentration in titanium. The latter assumption is based on the work by Wasilewski and Kehl (14) who found indications that the value of the diffusion constant is concentration dependent. Since zirconium also has a high oxygen solubility (15), Kofstad and Hauffe assume that the cubic oxidation of zirconium can be explained in a similar manner.

Porte *et al.* (2) in attempting to follow Kofstad and Hauffe's explanation for the existence of a cubic rate law point out only the importance of the diffusion of oxygen through the layer of oxygen-enriched metal (having a high oxygen solubility). However, they fail to mention Kofstad and Hauffe's important hypothesis that, in addition, a concentration-dependent diffusion constant is necessary to arrive at a cubic rate law. The following analysis will show that high solubility of oxygen in metal is not a sufficient condition to account for a cubic rate law when the value of the diffusion constant is concentration-independent.

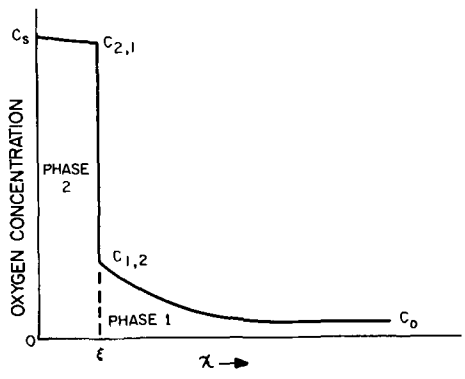

Fig. 4. Oxygen concentration as function of distance from the ZrO_2-oxygen interface ($x = 0$) as zirconium is reacting with oxygen (after Wagner).

Mallett and Albrecht (9) find that the oxidation of zirconium occurs by anion diffusion across the oxide layer to the zirconium-oxide interface to produce more ZrO_2. Hence, the problem falls under the general category of diffusion of oxygen into a homogeneous phase (oxygen dissolved in zirconium), a second phase (ZrO_2) developing from the surface.

Figure 4 is a plot of the oxygen concentration *vs.* distance from the oxide-oxygen interface at any time $t > 0$. C_s is the concentration of oxygen at the ZrO_2 surface. $C_{2,1}$ is the minimum oxygen concentration which can exist in the ZrO_2 phase. The difference between C_s and $C_{2,1}$ results from the presence of anion vacancies at $C_{2,1}$. $C_{1,2}$ is the maximum concentration of oxygen in zirconium metal at a given temperature. C_o is the initial concentration of oxygen in zirconium. The plane of discontinuity, ξ, is occasioned by the fact that a two-phase region separates phases 1 and 2.

For a concentration-independent diffusion constant, D, the diffusion processes are governed by Fick's second law.

$$\frac{\partial c}{\partial t} = D_1 \frac{\partial^2 c}{\partial x^2} \text{ for } \xi < x \qquad [1]$$

$$\frac{\partial c}{\partial t} = D_2 \frac{\partial^2 c}{\partial x^2} \text{ for } 0 < x < \xi \qquad [2]$$

The initial and boundary conditions are

$$c(x > 0, 0) = C_o \qquad c(0, t > 0) = C_s$$
$$c(\xi + \epsilon, t) = C_{1,2} \qquad c(\xi - \epsilon, t) = C_{2,1} \qquad [3]$$

Using these conditions one can follow Wagner's analysis as outlined by Jost (16) and obtain the following result

$$C_{2,1} - C_{1,2} = \frac{(C_s - C_{2,1}) \exp(-\gamma^2)}{\gamma\sqrt{\pi}\,\mathrm{erf}(\gamma)} - \frac{(C_{1,2} - C_o) \exp(-\phi\gamma^2)}{\gamma\sqrt{\pi\phi}\,[1 - \mathrm{erf}(\gamma\sqrt{\phi})]} \qquad [4]$$

where

$$\phi = \frac{D_2}{D_1} \quad \text{and} \quad \gamma = \frac{\xi}{2\sqrt{D_2 t}}$$

This result differs from that given in Jost's book only in the value of the exponent of the second term on the right side, the difference probably being due

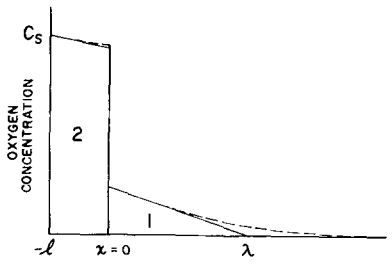

Fig. 5. Diffusion in two-phase system using "quasi-stationary state" approach. See text for explanation.

to a typographical error. Since it is not immediately obvious from Eq. [4] which rate law is being followed for a concentration-independent diffusion constant we shall try a different approach.

The diffusion processes resulting from the oxidation of zirconium can, to a good approximation, be considered to be in the "quasi-stationary state," and hence Eq. [1] and [2] can be set ≈ 0. For greater mathematical simplicity in this treatment the metal-oxide interface is considered to be the stationary boundary at $x = 0$ with the oxide-oxygen interface moving in the negative direction, and the initial oxygen concentration, C_o, in the metal taken to be zero. C_s is, as before, the concentration of oxygen at the ZrO_2 surface. Figure 5 shows the essentials. The dashed curves result from the exact solutions of Eq. [1] and [2] while the solid lines represent the solutions resulting from setting [1] and [2] equal to zero. The error involved by setting [1] and [2] equal to zero is given by the difference in the areas below the respective curves, the area below the straight line being about 90% of that below the error function curve in the case of phase 1.

Using this method we then have for

Phase 1:

$$\frac{\partial^2 c_1}{\partial x^2} \approx 0 \qquad [5]$$

Phase 2:

$$\frac{\partial^2 c_2}{\partial x^2} \approx 0 \qquad [6]$$

With solutions

$$c_1 = A_1 + B_1 x \qquad [7]$$

$$c_2 = A_2 + B_2 x \qquad [8]$$

and boundary conditions

$$c_1(\lambda) = 0 \qquad [9]$$

$$c_2(-l) = C_s \qquad [10]$$

The total amount of oxygen in phase 1 has come there by diffusion across the plane $x = 0$ during the time t. Hence, we have per unit cross section

$$\int_o^\lambda c_1 dx = \int_o^t J_1 dt = -\int_o^t D_1 B_1 dt \qquad [11]$$

where $J_1 = -D_1 B_1$ is the flux of oxygen across the interface $x = 0$, and D_1 the diffusion constant for phase 1. Similarly,

$$\int_{-l}^o c_2 dx = \int_o^t D_1 B_1 dt - \int_o^t D_2 B_2 dt \qquad [12]$$

First, we shall find a solution for λ. Using [7] and [9] we get

$$B_1 = -\frac{A_1}{\lambda} \qquad [13]$$

and

$$c_1 = A_1\left(1 - \frac{x}{\lambda}\right) \qquad [14]$$

Hence,

$$\int_o^\lambda c_1 dx = \int_o^\lambda A_1\left(1 - \frac{x}{\lambda}\right) dx = \frac{A_1\lambda}{2} \qquad [15]$$

From [11], [13], and [15] we also get

$$\int_o^t D_1 \frac{A_1}{\lambda} dt = \frac{A_1\lambda}{2} \qquad [16]$$

Differentiating [16] wih respect to t we get

$$\frac{D_1}{\lambda} = \frac{1}{2}\frac{d\lambda}{dt}$$

resulting in

$$\lambda = 2\sqrt{D_1 t} \qquad [17]$$

Next, we shall find a solution for l. From [8] and [10] we obtain

$$\int_{-l}^o c_2\, dx = \int_{-l}^o \left[A_2 + \left(\frac{A_2 - C_s}{l}\right)x\right] dx$$

$$= \frac{l}{2}(A_2 + C_s) \qquad [18]$$

Using [18] and [12] and differentiating with respect to t there results

$$\frac{A_2 + C_s}{2} \cdot \frac{dl}{dt} = D_1 B_1 - D_2 B_2$$

Using [8], [10], [13], and [17] we get

$$\frac{A_2 + C_s}{2} \cdot \frac{dl}{dt} = \frac{(C_s - A_2)D_2}{l} - \frac{A_1 D_1}{2\sqrt{D_1 t}}$$

Rearranging,

$$\frac{dl}{dt} - \frac{2(C_s - A_2)D_2}{(C_s + A_2)l} = -\frac{A_1\sqrt{D_1}}{(C_s + A_2)\sqrt{t}} \qquad [19]$$

Letting $l = \alpha\sqrt{t}$ we get

$$\frac{\alpha}{2\sqrt{t}} - \frac{2(C_s - A_2)D_2}{(C_s + A_2)\alpha\sqrt{t}} = -\frac{A_1\sqrt{D_1}}{(C_s + A_2)\sqrt{t}}$$

and

$$\alpha = -\frac{A_1\sqrt{D_1}}{C_s + A_2} + \sqrt{\left(\frac{A_1}{C_s + A_2}\right)^2 D_1 + \frac{4(C_s - A_2)D_2}{C_s + A_2}} \qquad [20]$$

From [20] it is noted that α is not a function of the time t. Therefore, since $l = \alpha\sqrt{t}$ we conclude that for a concentration-independent diffusion constant the parabolic law is observed for the growth of the oxide film as well as for the diffusion of oxygen into the metal and that this result is independent of the extent of oxygen solubility in the metal.

Acknowledgment

The assistance of Mr. Joseph Morreale in the laboratory and suggestions by Dr. Guy Ervin, Jr., who examined the manuscript in its final form are gratefully acknowledged. The author is particularly grateful to Dr. H. Reiss for the solution of the diffusion equations using the quasi-stationary approach. Work on this paper was performed under the auspices of the U. S. Atomic Energy Commission contract AT(11-1)-GEN-8.

Manuscript received May 12, 1961; revised manuscript received Jan. 9, 1962.

Any discussion of this paper will appear in a Discussion Section to be published in the December 1962 JOURNAL.

REFERENCES

1. E. A. Gulbransen and K. F. Andrew, *J. Metals*, **9**, 394 (1957).
2. H. A. Porte, J. G. Schnizlein, R. C. Vogel, and D. F. Fischer, *This Journal*, **107**, 506 (1960).
3. J. P. Pemsler, *ibid.*, **105**, 315 (1958).
4. E. A. Gulbransen and K. F. Andrew, *J. Metals*, **1**, 515 (1949).
5. J. Belle and M. W. Mallett, *This Journal*, **101**, 229 (1954).
6. R. G. Charles, S. Barnartt, and E. A. Gulbransen, Trans. AIME, **212**, 101 (1958).
7. N. F. Mott, *Trans. Faraday Soc.*, **36**, 472 (1940).
8. N. Cabrera and N. F. Mott, *Rept. Prog. Phys.*, **12**, 163 (1949).
9. M. W. Mallett and W. M. Albrecht, *This Journal*, **102**, 407 (1955).
10. C. Wagner, "Symposium on High Temperature Properties of Metals," p. 93, American Society for Metals, Cleveland (1950).
11. H. H. Uhlig, *Acta Met.*, **4**, 541 (1956).
12. O. Kubaschewski and B. E. Hopkins, "Oxidation of Metals and Alloys," pp. 120-130, Butterworths Scientific Publications, London (1953).
13. P. Kofstad and K. Hauffe, *Werkstoffe und Korrosion*, **7**, 642 (1956).
14. R. J. Wasilewski and G. L. Kehl, *J. Inst. Metals*, **83**, 94 (1954/5).
15. R. F. Domagala and D. J. McPherson, Trans. AIME, **200**, 238 (1954).
16. W. Jost, "Diffusion in Solids, Liquids, Gases," pp. 71-72, Academic Press Inc., New York (1952).

Effect of Surface Roughness on the Oxidation Rate of Iron

A. G. Eubanks and D. G. Moore

National Bureau of Standards, Washington, D. C.

and W. A. Pennington

Department of Metallurgy, University of Maryland, College Park, Maryland

ABSTRACT

An investigation was made of the effect of surface roughness on the oxidation rate of iron in air at 800°C. Specimens of ingot iron were grit blasted to give surfaces of different textures. The roughened specimens were found to oxidize more slowly than as-rolled ones, the difference in rate becoming greater with increasing roughness. The as-rolled specimens oxidized parabolically with a certain rate constant at the beginning; however, with continued oxidation, roughness developed on the metal surface, and a change in the rate constant occurred. Specimens of high-purity iron with smooth surfaces, on the other hand, not only remained smooth throughout a 3-hr oxidation period, but they also oxidized parabolically with a single rate constant. It was found that the reduction in rate due to roughening was not caused by surface contamination or by surface cold work, but by voids that form in the scale layers on roughened surfaces. These voids apparently act as diffusion barriers for iron ions and, thereby, lower the rate at which roughened specimens oxidize.

In practically all studies of the oxidation of metals, the area of the specimen is computed from its macroscopic dimensions. For specimens that are optically flat and which remain flat throughout the oxidation, this procedure is acceptable. However, such surfaces are exceptions, and in most cases a certain amount of surface roughness is either present initially or develops as the oxidation progresses. The presence of this roughness increases surface area which, in turn, might be expected to increase the over-all oxidation rate of the specimen.

Several investigations have indicated, however, that when iron is oxidized the expected increase in rate with increased roughness does not always occur. Moore, Pitts, and Harrison (1), for example, found that grit blasting of both ingot iron and a titanium-bearing, low-carbon steel reduced the amount of oxidation occurring in air after 2 min at 840°C by a factor of about four. Bénard (2) observed that, although electrolytically polished iron, when heated in air at 850°C for various times, oxidized at a slightly lower rate than iron abraded with various grades of emery paper, the difference was less than would be expected from the differences in surface area. Winterbottom (3) found that iron surfaces polished with alumina had slower oxidation rates than bright annealed surfaces.

In the investigations cited, the observation that the oxidation rate of iron was reduced in certain cases by roughening was incidental to the main purpose of the study, and the effect was not investigated systematically. In the present investigation, a more

complete study of the roughness effect was undertaken. The goals were twofold: i, to determine by controlled oxidation tests in air at a single temperature (800°C) if the oxidation rate of iron specimens could, in fact, be reduced by roughening of the surface, and ii, if such a reduction was observed, to arrive at the most probable explanation for the reduction. The 800°C temperature was used because the study was a phase of an investigation concerned with ceramic-metal systems in which this particular temperature was of primary interest.

Materials and Test Equipment

Ingot iron in the form of sheet 0.7 mm thick was used for most of the experiments. The nominal composition of this material is C < 0.02, Mn < 0.02, P-0.005, S-0.02, and Si-trace.

Very high-purity iron was also used in a few of the experiments. This material, which was furnished by Dr. G. A. Moore of the Thermal Metallurgy Group of the National Bureau of Standards, was in the form of sheet 0.5 mm thick. It was prepared initially by J. G. Thompson and H. E. Cleaves (4) who were then of the Bureau staff. A chemical analysis made at the time of preparation showed it to be 99.990% Fe. Copper, silicon, sulfur, and oxygen were present as trace impurities.

The specimens were roughened by grit blasting their surfaces under closely controlled conditions. Different degrees of roughness were obtained by using different types of grit. The grits used are listed in Table I.

Oxidation tests were made in a wire-wound tube furnace that rested on a pneumatic lift. Three independent heating coils connected to separate variable transformers were used to heat the furnace. Each coil was adjusted so that the metal specimen would be heated as uniformly as possible. The temperature in the hot zone was measured with a Pt, Pt-10% Rh thermocouple that had been calibrated by the Temperature Physics Section of the National Bureau of Standards. At 800°C the temperature variation over the specimen was not more than 3°C.

The specimen to be oxidized was suspended in the furnace by a platinum wire attached to the beam of an automatic recording balance (5) mounted above the furnace. The balance is designed to sense any weight change that occurs and to record the change on a strip chart. The balance was found to be accurate to within 0.5% of the weight change indicated at any given instant.

Tests were begun by stabilizing the furnace at the desired temperature and then quickly raising the furnace around the specimen. Temperature measurements made with a small-wire thermocouple attached to a specimen showed that the specimen reached furnace temperature in approximately 2 min. At the end of a test the furnace was lowered, and the specimen was allowed to cool in air.

Table I. Grits used for roughening specimens

Grit No.	Grit Type	Particle size, μ
1	Silicon[a]	177-840
2	Silicon Carbide[a]	177-420
3	Fused Alumina[a]	177-420
4	Ottawa sand[b]	297-840
5	Ingot iron[c]	250-840

[a] Commercial grade.
[b] Well-rounded grains of quartz.
[c] Formed into tiny cubes from the same sheet stock as that used for the oxidation specimens by a semi-automatic shearing operation.

All experiments were performed in air at atmospheric pressure. The water vapor content of the air during the testing period varied over the range 0.0072-0.0093 g/g of dry air. The order in which the specimens were tested was selected so as to minimize any effect that the variation in water vapor content might have on differences in the oxidation rates of specimens having surfaces of different roughness. Air flow was controlled by natural convection through small vents at the top and bottom of the furnace. The measured flow rate was 3.6 liters/min. Based on this flow rate, the oxygen partial pressure in the furnace cavity during the first few minutes of testing, for specimens with the highest oxidation rate, was computed to be 155 mm Hg.

Experiments with Grit-blasted Ingot Iron

Ingot iron specimens, 25 by 75 mm in size, were cleaned in acetone, annealed in dry hydrogen for 2 hr at 950°C, and finally vacuum annealed for 1 hr at 730°C at a pressure of 2×10^{-5} mm Hg. The specimens were then divided into six groups of five specimens each. The specimens in groups one through five were roughened, in turn, by the five grits listed in Table I. After each blasting treatment, the specimens were cleaned ultrasonically in acetone to remove loosely adhering particles. The specimens in all six groups were then re-annealed in hydrogen and in vacuum in the manner just described.

Measurements of surface area were made on two specimens of each group. This was done by first shearing each of the two specimens into smaller pieces; three randomly selected pieces from each specimen were then plated with nickel by an electroless process (6) to preserve the surface contour, and mounted and polished. The "surface area index" and "true surface area" were determined from these polished sections by the procedure outlined in the Appendix. Figure 1 shows some of these surfaces.

Weight gain measurements were made on the remaining specimens of each group. The results of these measurements are shown in Fig. 2 in which the square of the weight gain per unit area is plotted against time. Each curve represents the average for three specimens. The data for the three were in good agreement in all cases; the maximum deviation observed was 3.4%.

Data plotted in Fig. 2 were computed on the basis of the true surface areas obtained by multiplying the macroscopic area of each specimen by the appropriate surface area index (see Appendix). It will be noted that in every case roughening reduced the oxidation rate. The treatment with silicon gave the greatest reduction, the weight gain after 90 min being lower than that of unroughened specimens by

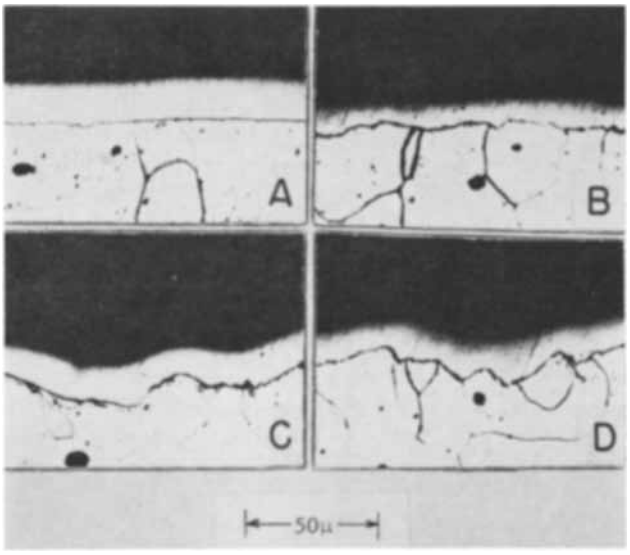

Fig. 1. Surface contours of specimens before oxidation; (A) as-rolled, (B) blasted with ingot iron grit, (C) blasted with silicon carbide and (D) blasted with fused alumina. White area above iron surface is nickel plate applied to preserve surface contour during polishing (2% nital etch).

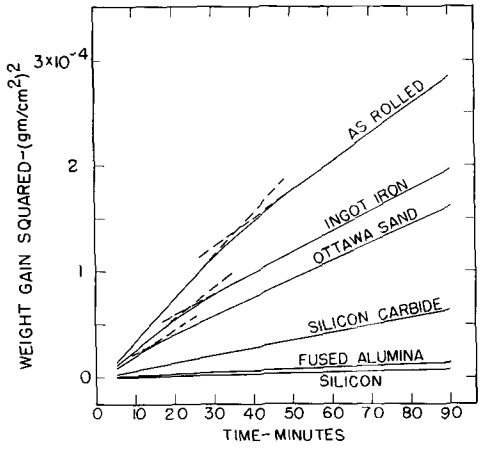

Fig. 2. Oxidation behavior at 800°C in air of ingot-iron specimens that had been grit blasted and then annealed. Weight gains are based on "true surface areas."

a factor of 6.2. The least reduction occurred when the specimens were roughened with ingot iron grit, the weight gain in this case being lower than that of the unroughened specimens by a factor of 1.2.[1]

In general the oxidation followed the parabolic rate law

$$w^2 = kt$$

where w is the weight gain per unit area, t the time, and k the rate constant.

The parabolic oxidation is indicated by the trend toward straight-line plots in Fig. 2. In the case of the specimens roughened with silicon carbide, fused alumina, and silicon, the plots are linear after the first few minutes. The curves for the as-rolled[2] specimens and for those roughened with Ottawa sand and ingot iron are more complex in that they consist of two linear portions rather than one.

[1] When these weight gains were computed on the basis of macroscopic area rather than true surface area the values differed by factors of 4.6 and 1.1, respectively.

[2] As-rolled refers to the surface that resulted from the final rolling operation in the steel mill.

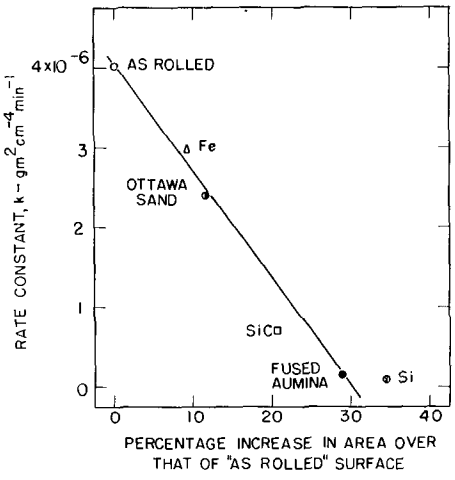

Fig. 3. Change in rate constant, k, with increase in computed surface area. Label for each point shows grit used for producing increased area of surface.

The rate constant, k, was obtained for each group of specimens by measuring the slopes of the straight lines in Fig. 2. For specimens that gave two different slopes, the rate constant assigned was that computed from the slope of the initial portion of the curve.

Figure 3 shows these rate constants plotted against the percentage increase in surface area produced by the various treatments. The points fall approximately on a straight line. This suggests that there is a direct relation between roughness, as measured by surface area, and the early stage oxidation rate. It also suggests that the reduction in rate is independent of the type of grit used for roughening.

That grit contamination was not a controlling factor in reducing the rate is shown by the results with ingot iron grit. In this particular case, the grit was made from the same material as the specimen; hence, it could not contaminate the specimen surface. Yet the point for the specimens roughened with ingot iron is below that for the as-rolled specimens.

Because the surface of the metal was cold worked during grit blasting, it was in a strained condition after the roughening treatments. If this strain were not relieved, it could conceivably affect the oxidation rate. However, since the temperature range in which iron recrystallizes is 200°-300°C the annealing treatments (2 hr in hydrogen at 950°C followed by 1 hr in vacuum at 730°C) that each specimen received after it was grit blasted very likely relieved any strain that was present. Even had the specimens not been annealed following the roughening procedure, the 800°C oxidation temperature is probably high enough to relieve the induced strain before it has any appreciable effect on the oxidation rate. In order to make certain that such was the case, however, the following experiment was carried out. Specimens were roughened by blasting with ingot-iron grit and oxidized without further treatment. These specimens were found to gain weight at the same rate as those that had been annealed after the grit-blasting. Such a result shows that any residual strain caused by cold working of the surface during the blasting had no influence on the oxidation behavior at 800°C. The same ex-

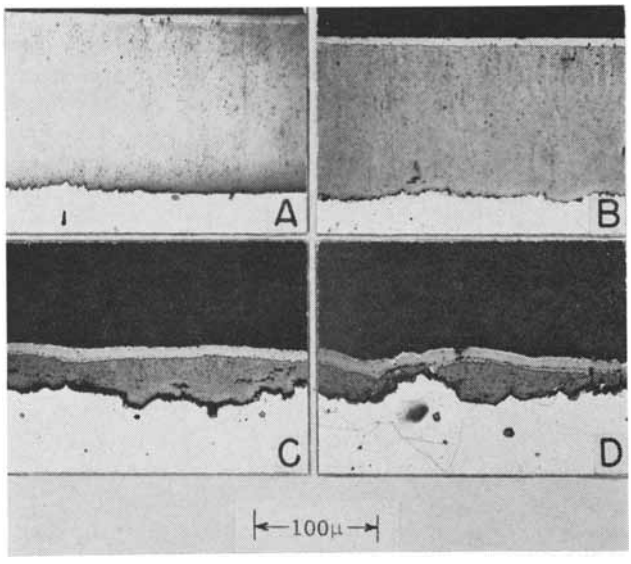

Fig. 4. Oxide layers formed on ingot iron after oxidation for 90 min in air at 800°C. Dark gray layer is wüstite (iron deficient FeO); lighter gray layer above it is magnetite (Fe_3O_4), while thin white layer at outer surface (visible in C and D only) is hematite (α-Fe_2O_3). Surface preparation was (A) as-rolled, (B) grit blasted with ingot iron, (C) grit blasted with alumina and (D) grit blasted with silicon. (2% nital etch).

periment also shows that any oxide that might have formed on the specimen surface during the blasting process had no effect on the subsequent oxidation rate.

Metallographic sections were prepared from many of the specimens after oxidation. The micrographs in Fig. 4 show the oxide scale and the interface between the oxide and the metal for four of these specimens. At temperatures above about 570°C the oxide scale on iron consists of three layers (7); the innermost layer is wüstite (iron deficient FeO), the center layer is magnetite (Fe_3O_4) and the outer layer is hematite (α-Fe_2O_3). The wüstite and magnetite layers are visible in Fig. 4; however, the outermost hematite layer is not clearly defined except in Fig. 4C and D.

Examinations of the sections showed that the over-all scale thickness decreased with increasing surface roughness. The examinations also showed that the relative thicknesses of the magnetite and hematite layers increased with increasing roughness while that of the wüstite layer decreased and that the relative thicknesses of the layers did not depend on the total scale thickness. The results of measurements of the relative thicknesses of the layers are listed in Table II.

Table II. Change of relative oxide layer thickness with increasing surface roughness after oxidation for 90 min in air at 800°C

Blasting medium	Surface area index	Rate constant, k[a] $gm^2\ cm^{-4}\ min^{-1}$	Relative thickness Wüstite %	Magnetite %	Hematite %
None	1.048	4.02×10^{-6}	95.5	3.5	1.0
Ingot iron	1.144	2.96	94.5	4.5	1.0
Ottawa sand	1.170	2.39	94.0	5.0	1.0
Silicon carbide	1.264	0.70	92.0	6.5	1.5
Fused alumina	1.350	0.15	65.0	32.0	3.0
Silicon	1.408	0.09	61.5	34.5	4.0

[a] Determined from the initial linear portion of the weight-gain squared curves for the as-rolled specimens and for the specimens roughened with ingot iron grit and Ottawa sand.

Another finding of interest was that the surface of the as-rolled specimens, and, to a lesser extent, the surfaces of specimens roughened with ingot-iron grit and Ottawa sand became rougher as oxidation proceeded. Also, voids began to appear in the wüstite layer quite close to the iron surface. Both the roughening effect and the void formation have previously been observed by Païdassi (8) on ingot iron that was electrolytically polished prior to oxidation. Micrographs of the oxide-metal interface of as-rolled specimens after various periods of oxidation are shown in Fig. 5. After 15 min of oxidation the surface was still relatively smooth. After 45 min the surface had become rougher, and voids were visible near the interface. In most instances these voids were not touching the metal. At 60 min the number of voids had increased considerably. From 60 to 90 min, however, the surface, although continuously changing, was found to have about the same degree of roughness, and the number and size of the voids remained fairly constant.

In the case of the specimens roughened with ingot-iron grit and Ottawa sand the oxidation time required to reach a condition of constant roughness was appreciably shorter. The oxide-metal interface of specimens that had been roughened by blasting with Ottawa sand are shown in Fig. 6. Voids are visible at the tips of asperities on the roughened surface after only 5 min at 800°C, and after 20 min numerous voids are visible in the oxide near the interface.

Experiments with Surfaces of Fixed Geometry

The experiments with grit-blasted ingot iron indicated that the geometry of the iron surface had an important influence on the subsequent oxidation rate. However, the grit blasting produced highly irregular interfaces (see Fig. 1), and it was believed that additional information could be obtained about the

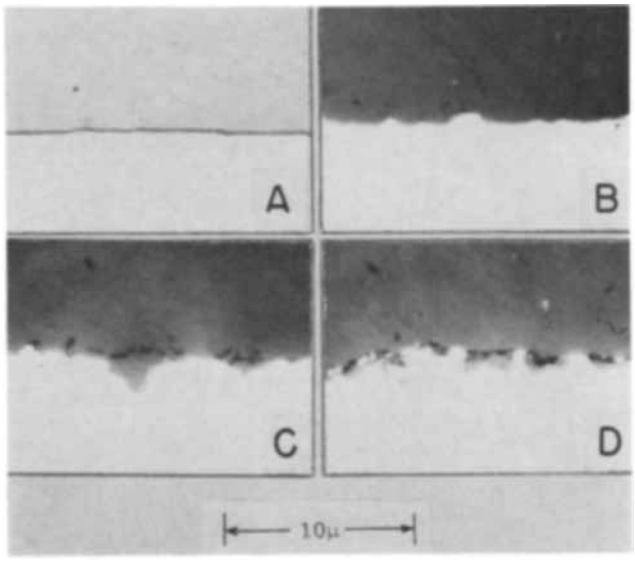

Fig. 5. Oxide-metal interface of as-rolled surface after oxidation at 800°C in air for (A) 0 min, (B) 15 min, (C) 45 min, and (D) 60 min. Gray area above iron surface in (A) is electroless nickel. Unetched.

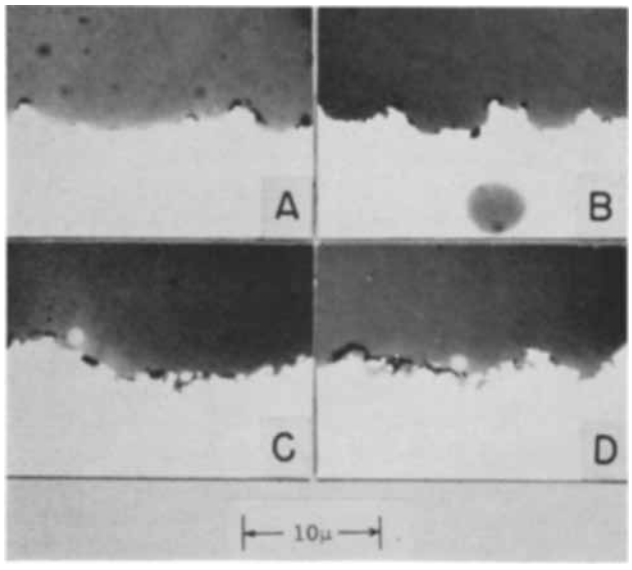

Fig. 6. Oxide-metal interface of surface roughened with Ottawa sand after oxidation in air at 800°C for (A) 5 min, (B) 10 min, (C) 20 min, and (D) 30 min.

oxidation-inhibiting mechanism, if tests were made with specimens that had surfaces of regular contour. Therefore, specimens were prepared by machining very small grooves into their surfaces. Some of the specimens had square grooves 0.004 in. deep and 0.006 in. wide spaced 0.003 in. apart. Others were prepared with V-shaped grooves approximately 0.004 in. deep and 0.008 in. wide. After being machined, the specimens were annealed in hydrogen and vacuum in the manner previously described and oxidized at 800°C in air.

Results of the tests with the grooved specimens are given in Fig. 7. Surface areas were computed from the dimensions of the grooves as determined from measurements made on polished cross sections. As seen in Fig. 7, the grooved specimens gained weight at a slower rate after the first 6-8 min than the as-rolled specimens. Here, as in the case of the specimens that were roughened by blasting, surface contamination is not considered to have played a significant role in the observed retardation of oxidation since the grooves were cut with a tool-steel saw on which no discernible wear was noted after the cutting operation.

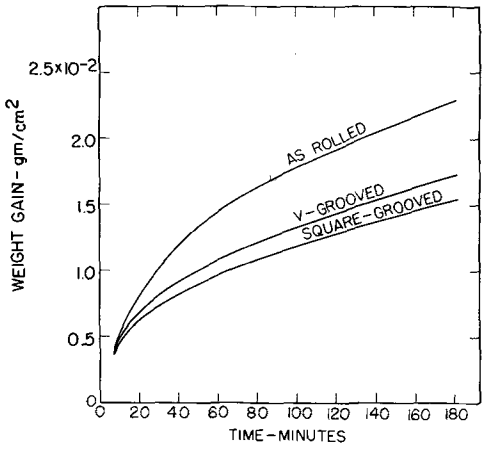

Fig. 7. Oxidation curves in air at 800°C for specimens with fixed surface geometry.

When grooved specimens that had been oxidized for various periods were mounted in cross section and examined microscopically they appeared as shown in Fig. 8. Separations between the oxide and metal were visible at the sharp corners of the square asperities and at the tips of the saw-toothed asperities after about 5 min. of oxidation at 800°C. The small voids which are concentrated above the asperities (some of which are indicated by arrows in Fig. 8) were first visible at high magnification on specimens that had been oxidized for about 15 min.

Experiments with High-purity Iron

In the tests with as-rolled ingot iron specimens, the oxidation rate was relatively high in the early stages. As oxidation progressed, however, the surface became roughened and the oxidation rate was lowered. This behavior suggested that, if the iron had remained smooth throughout the testing period, the specimens would have oxidized parabolically with only one rate constant. In this connection Collongues and Chaudron (9), while studying the high-temperature oxidation of iron in a mixture of hydrogen and water vapor, observed that the surface of ingot iron became rougher during the oxidation process while that of electrolytic iron did not. They attributed the roughening of the ingot iron to uneven oxidation of the surface as a result of localized variations in composition which did not exist in the case of the electrolytic iron.

It was believed that a high-purity iron might also oxidize without detectable roughening of the surface if the oxidation was done in air rather than in a mixture of hydrogen and water vapor. Consequently, specimens of the high-purity iron were cleaned by annealing in hydrogen and vacuum in

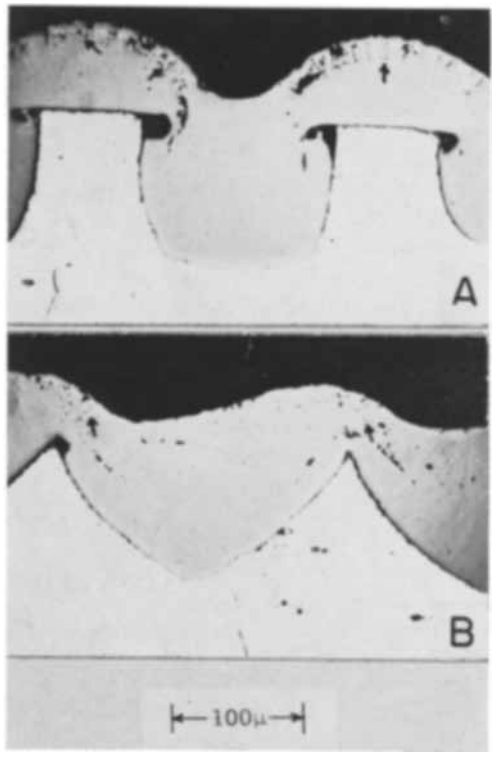

Fig. 8. Square-grooved and V-grooved specimens after oxidation in air at 800°C for 45 min.

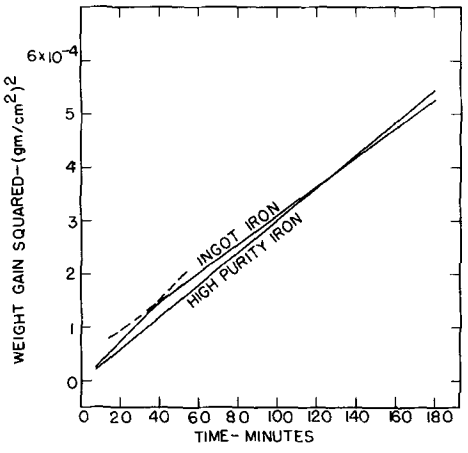

Fig. 9. Comparison of oxidation behavior in air at 800°C of high-purity (99.990 Fe) iron and ingot iron.

the manner previously described and oxidized for various periods at 800°C. The specimens were then mounted and polished for microscopic examination. The examination showed that the surface of the high-purity iron remained smooth even after 3 hr of oxidation and that no voids of any sort formed in the scale layer. Also, the weight-gain data, which is plotted against time in Fig. 9 along with similar data for ingot iron, showed that the high-purity iron oxidized with a single rate constant throughout the entire testing period.

Discussion of the Mechanism

The experiments described above show quite conclusively that the oxidation rate at 800°C in air of ingot-iron specimens with roughened surfaces was lower than that of specimens with smooth surfaces. That this reduction was not caused by surface contamination is indicated by the observation that the reduction in rate was a function of the roughness of the specimen surface and not of the type of grit that was used for the roughening treatment. Furthermore, the reduction occurred even when ingot-iron grit was used for the roughening operation. Other tests showed that strain in the surface layer caused by cold work had no measurable effect on the oxidation rate. Thus, some other but less obvious mechanism must be responsible.

In arriving at this mechanism, the decrease in the relative thickness of the wüstite layer which was observed on the grit-roughened specimens (see Table II) is considered to be especially significant. According to Païdassi (10) the oxide scale formed on iron in air at 800°C consists of approximately 95% wüstite, 4% magnetite, and 1% hematite. The relative thicknesses of the oxide layers on the as-rolled surface, as seen in Figure 4, and as listed in Table II, are in good agreement with these values. However, the relative amount of wüstite decreases markedly with increasing roughness.

It is of interest to consider how this change in the relative thicknesses of the layers could occur. Davies, Simnad, and Birchenall (11, 12) studied the mechanisms of growth of the three oxide layers and found that the growth of wüstite occurs nearly exclusively as a result of the outward diffusion of iron ions and that magnetite grows primarily, but not completely, by this same mechanism. The growth of hematite, however, was found to occur almost solely as a result of the inward diffusion of oxygen These investigators also concluded that above ; bout 620°C the rate of growth of the over-all layer s controlled by the growth of the wüstite. Taken to; ether, these results imply that the rate-controllin; process in the oxidation of iron at 800°C is the r :e at which iron ions diffuse through the wüstite la er. Thus, if this diffusion could be retarded in som- way, such as by creating separations between the iron and wüstite or by placing diffusion barriers of some sort in the layer, the growth rate of the over-all scale would be expected to decrease. Moreover, since the growth of the hematite is due almost solely to the inward diffusion of oxygen and the growth of the magnetite at least partially to the same mechanism, a decrease in the outward iron diffusion rate would bring about an increase in the relative amounts of these two outer layers at the expense of the wüstite. Table II shows that such an increase occurred for the roughened specimens.

Microscopic examinations showed that voids were present in the scale over rough iron surfaces, and it is believed that these voids act as barriers which partially block the diffusion of iron ions. The voids probably begin as tiny discontinuities in the iron oxide lattice and at the oxide-metal interface and eventually grow large enough to become visible under the microscope. The voids are found at three different places in the scale layer, and it is quite likely that they form at different times during the oxidation process. The places where the voids are found are (i) between the oxide and the metal at the tips of asperities (see Fig. 6A, 6B, and 8), (ii) in the wüstite layer close to the wüstite-metal interface over regions of the iron surface that are being, or have been, roughened by the oxidation process (see Fig. 5), and (iii) in the wüstite and magnetite layers above an asperity (examples are indicated by arrows in Fig. 8), but much further from the iron surface than (ii). For purposes of the discussion to follow the voids will be designated as type 1, type 2, and type 3.

Type 1 voids.—The voids that separate the iron from the scale layer at the tips of asperities (Fig. 6A, 6B, and 8) are similar to those observed by other investigators (13-15) at the corners of iron sheet specimens, and the explanation given in two of these studies (14, 15) for a corner separation applies in all essentials to one which forms at the tip of an asperity on a rough iron surface. Engell and Wever (15) demonstrated indirectly and MacKenzie and Birchenall (16) showed by actual experiment that wüstite will deform plastically at elevated temperature under a relatively low stress. Juenker, Meussner, and Birchenall (14) and Engell and Wever (15) concluded independently that on a flat surface this plasticity enables the wüstite layer to follow the iron surface as it recedes during oxidation, but that at a corner or an edge the mutual supporting effect of the oxide layers meeting at an angle hinders the flow, and eventually the receding iron breaks away from the oxide. Iron ions cannot dif-

fuse across this break, and as a result oxidation is retarded.

Type 2 voids.—The second type of void, which is observed in the wüstite layer near the ingot-iron surface over areas which have become roughened during the oxidation process, is probably formed by a mechanism somewhat similar to the one just described. The oxidation time which elapses before this type of void begins to form, however, is greater. It is possible that the voids are formed in the following way: At the beginning of the oxidation, the first thin layer of oxide has the same area as the ingot-iron surface. As oxidation proceeds the iron surface becomes roughened, and, as a consequence, its area increases. Since the wüstite layer grows at its upper surface, because outward iron ion diffusion is its growth mechanism, the portion near the oxide-iron interface cannot increase in volume to compensate for the increasing area of the iron surface. Therefore, plastic deformation must occur in such a way as to allow oxide from above to flow into the stressed regions, or, as an alternative, the wüstite must become porous near the iron surface. The ability of the wüstite to deform plastically at first permits it to maintain contact with the metal and still remain compact and continuous. Eventually, however, the plastic flow cannot keep pace and porosity occurs. It is this sort of porosity which is shown in Fig. 5.

Type 3 voids.—The third type of void is that found in both the wüstite and magnetite layers at some distance above asperities on the iron surface. In some cases, voids of this type tended to form radial patterns in the scale layer (Fig. 8) with no break in the pattern at the wüstite-magnetite interface. Similar voids have been observed in the oxidation of wires by Juenker, Meussner, and Birchenall (14), but no explanation was given as to their cause. These authors found that the time required for voids of this type to appear increased with increasing wire diameter. This is in agreement with the findings of the present investigation in which it was observed that in the oxidation of a surface with relatively large rounded protuberances the oxidation period required before the formation of voids began was greater than in the case of surfaces where the asperities were sharp.

Knowing that these three types of voids exist it is possible to explain the oxidation curves for the ingot-iron specimens as plotted in Fig. 2. In the case of specimens with smooth surfaces oxidation would occur parabolically until roughening developed and the type 2 voids began to form. The oxidation rate would then decrease continuously as the iron surface became rougher and more voids were formed until such time as a relatively stable degree of roughness had been reached and the number and size of the voids became constant. At this point a new and lower rate constant would prevail. As seen in Fig. 2 the behavior just described was followed by the as-rolled ingot-iron specimens.

In the case of surfaces that have been roughened prior to oxidation, type 1 voids would form very soon after oxidation began. The number and size of these voids, and consequently their effect on the oxidation rate, would depend to a large degree on the number and shape of the asperities present on the metal surface, the "rougher" the surface, the greater the number of voids. A short time later type 3 voids would also begin to form, contributing to the retardation of iron ion diffusion. The time at which the formation of type 3 voids began and the extent to which their formation occurred would also, as in the case of the type 1 voids, depend on the nature of the roughened surface.

The presence of type 1 voids on a roughened surface reduces the area of intimate contact between the iron surface and the wüstite layer. Since the interfacial area across which ion diffusion can occur is thus lessened, while the volume of oxide into which the diffusion occurs does not change appreciably, the ion flux across the contact areas between oxide and metal will be increased, and the metal surface in these areas will roughen more rapidly. As a consequence, the degree of roughness necessary for the formation of type 2 voids will be attained more quickly, and the time required for the surface to reach a stable roughness condition will be shorter, resulting in a shorter oxidation rate transition period which begins sooner. This type of behavior is seen to occur for the specimens roughened with the ingot-iron grit with the Ottawa sand.

In the case of severely roughened specimens such as those blasted with silicon carbide, fused alumina and silicon, such an abundance of type 1 and type 3 voids form at or near the oxide-metal interface that the area of metal surface which is suitable for the formation of type 2 voids is very small. Type 2 voids thus have a negligible effect on the oxidation rate, and as a consequence no transition region is detectable for these specimens.

Conclusions

The following conclusions appear to be justified from the results of an investigation of the effect of surface roughness on the oxidation behavior of iron specimens in air at 800°C.

1. Specimens that had been grit blasted oxidized at a slower rate than those with smooth surfaces. The reduction in rate was a function of the degree of roughening.

2. Specimens roughened by machining small grooves into their surfaces also oxidized at lower rates than those with smooth surfaces.

3. Experimental evidence indicated that the reduced oxidation rates on rough surfaces were not caused by (*a*) surface contamination during roughening, (*b*) residual strains due to cold work, or (*c*) formation of an oxide film during the blasting process.

4. Ingot iron specimens with smooth or mildly roughened surfaces oxidized parabolically in the early stages. However, with continued oxidation, roughness developed on the metal, and the rate constant began to change. After a transition period, the oxidation again became parabolic, but with a lower rate constant. High-purity iron, however, remained smooth throughout a 3-hr oxidation period. Also it oxidized parabolically with a single rate constant.

5. The relative thickness of the wüstite layer in the oxide scale decreased as the roughness of the iron surface increased. This behavior showed that there was a lowered diffusion rate of iron ions through the wüstite layer that formed on a rough surface.

6. The most likely reason for the lowered iron ion diffusion rate is the blocking of the diffusion path by small voids in the oxide scale that forms over rough surfaces. These voids, which were detected in the oxide layers on all roughened specimens, but not on smooth ones, act as barriers to ion diffusion and thereby lower the rate at which a roughened specimen oxidizes.

Acknowledgment

This investigation was supported in part by the U. S. Air Forces, Wright Air Development Division, under Contract No. AF (33-616) 58-19.

Manuscript received Sept. 22, 1961; revised manuscript received Jan. 26, 1962. This paper was taken in part from a Master's Thesis submitted by one of the authors (A.G.E.) in partial fulfillment of the requirements for a Master's Degree in Metallurgy at the University of Maryland.

Any discussion of this paper will appear in a Discussion Section to be published in the December 1962 JOURNAL.

REFERENCES

1. D. G. Moore, J. W. Pitts, and W. N. Harrison, *J. Amer. Ceramic Soc.*, **37**, 363 (1954).
2. J. Benard, *J. Met. Italiana*, **42**, 3 (1950).
3. A. B. Winterbottom, *J. Iron and Steel Inst., London*, **165**, 9 (1950).
4. J. G. Thompson and H. E. Cleaves, *J. Research Nat. Bur. Standards*, **23**, 163 (1939), RP 1226.
5. F. A. Mauer, *Rev. Sci. Instr.*, **25**, 598 (1954).
6. A. Brenner and Grace Riddell, *J. Research Nat. Bur. Standards*, RP 1835, **39**, 385 (1947).
7. O. Kubaschewski and B. E. Hopkins, "Oxidation of Metals and Alloys," p. 173, New York (1953).
8. J. Paidassi, *Bol. soc. chilena quim.*, **7**, 20 (1955).
9. R. Collongues and G. Chaudron, *Rev. met.*, **49**, 699 (1952).
10. J. Paidassi, *Acta Met.*, **6**, 184 (1958).
11. M. H. Davies, M. T. Simnad, and C. E. Birchenall, *Trans. AIME*, **191**, 889 (1951).
12. M. H. Davies, M. T. Simnad, and C. E. Birchenall, *ibid.*, **197**, 1250 (1953).
13. J. Paidassi, Discussion of Wrazej's paper, "Observation on Scaling of Iron," *ibid.*, **197**, 1570 (1953).

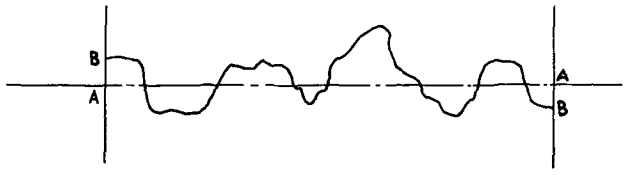

Fig. 10. Schematic drawing of metal surface contour illustrating method used to obtain the surface area index.

14. D. W. Juenker, R. A. Meussner, and C. E. Birchenall, *Corrosion*, **14**, 39t (1958).
15. H. Engell and F. Wever, *Acta Met.*, **5**, 695 (1957).
16. J. D. MacKenzie and C. E. Birchenall, *Corrosion*, **13**, 783t (1957).

APPENDIX

Determination of Surface Area

In making the surface area measurements, randomly selected interfaces of specimens that had been nickel plated, mounted, and polished (see Fig. 1) were projected at a magnification of 4000X on the ground-glass screen of a Bauch and Lomb model ILS metallograph. The contour of each projected interface was then traced on a clear sheet of plastic (see Fig. 10) from which a quantity termed the "surface area index," S_i, was computed.

The length of the contour line BB in Fig. 10 was determined with a map measurer; the straight line distance AA with a rule.

The surface area index was then taken as:

$$S_i = \left(\frac{BB}{AA}\right)^2$$

The average index for each roughening treatment was computed from 20 fields selected at random. With this number of fields it was found that the true mean was within 3% of the calculated mean on the 95% confidence level. The true surface area was obtained by multiplying the macroscopic area of the specimen by this index.

The procedure just described does not give the exact surface area of the specimens for two reasons. First, the highest magnifications obtainable by optical methods probably do not resolve the smallest surface deviations. For example, if useful magnifications of 50,000 or 100,000 diameters were possible, the measured surface areas would undoubtedly be different from those obtained at the magnifications selected for the present measurements.

Second, the method used for calculating the surface area is not mathematically rigorous. The surface contours are highly irregular and because of this irregularity, it is difficult, if not impossible, to apply an exact analysis. The selected method is believed, however, to give the best indication of surface area that is possible from measurements made with a microscope on polished sections.

The Effect of Pressure on the Electroless Deposition Process

J. S. Sallo, J. I. Swenson, and J. M. Carr

Minneapolis-Honeywell Research Center, Hopkins, Minnesota

ABSTRACT

The effect of changes in hydrostatic pressure on the electroless deposition system has been investigated. The results indicate that some of these systems are controlled by a diffusion process while others are controlled by the area of active catalytic surface which is hydrogen free. The effect of hydrostatic pressure is attributed to an effect on the volume of the hydrogen bubbles formed at the active surface.

Since the initial development of the electroless deposition process by Brenner and Riddell in 1946 (1), a large quantity of data has become available on this and related systems. Conflicting data have been reported on acid baths of this type. Brenner (2) reports the rate of deposition to be independent of the hypophosphite ion concentration. Gutzeit (3), utilizing a different type of acid bath, reports the reaction to be first order[1] in hypophosphite ion provided the area of the substrate is small relative

[1] It seems likely that the data really indicate a pseudo-first order reaction. The pH is known to alter the rate of the reaction, and pH was held constant during these kinetic studies.

to the volume of the solution. In addition, Brenner reports that the efficiency of the process (moles nickel reduced/mole hypophosphite consumed) varies with the ratio of the area of the catalytic surface to the volume of the solution. Gutzeit presents data to refute the importance of this factor (4). It appears that, although the two systems are similar in composition, the mechanisms of these reactions may be different.

Brenner has suggested (5) previously that the rate in the acid bath may be controlled by diffusion of hydrogen ion from the catalytic surface. This hypothesis explains the independence of the rate on the concentrations of the primary reactants and the increase in rate which is observed when the substrate is moved during deposition. If this is the case, it seems likely that the rate of hydrogen gas leaving the substrate will control the diffusion (or transport) rate due to the agitation effect. In order to determine which, if any, of these reactions are transport controlled, the reactions were studied under various pressures. The change in pressure may alter the volume of the evolved hydrogen and alter the rate of the transport controlled reaction.

Experimental

The following systems were studied: Bath 1: [Brenner (2)] $NiCl_2 \cdot 6H_2O$, 30 g/l; $NaH_2PO_2 \cdot H_2O$, 10 g/l; sodium acetate, 3 g/l; bath 2: [Gutzeit (3)] $NiSO_4 \cdot 6H_2O$, 17 g/l; $NaH_2PO_2 \cdot H_2O$, 24 g/l; sodium acetate, 41 g/l; acetic acid, 30 g/l.

All electrodes were flash-coated on both sides with nickel from a Watts bath and weighed. Prior to insertion in the bath, the electrode was given a quick dip in 1:1 HCl followed by a water rinse. This was necessary to insure reproducible initiation of nickel reduction. When this procedure was followed, hydrogen evolution always began within 5 sec of the insertion of the sample. The sample was entirely immersed in the solution. Deposition time was 20 min in all cases.

An all-glass system (system A) was used for runs between 740 mm Hg and 1140 mm Hg. Higher pressures could not be attained in this system. It consisted of a one-liter reaction kettle fitted through ground glass joints with a plug for holding the sample, a thermometer well, a water-cooled condenser, and an open end mercury manometer. For runs under pressure all fittings were held by clamps and pressure was introduced through the condenser opening. The system was thermostated at 85° ± 0.2°C in a constant temperature oil bath. Electrodes were 51.5 cm^2 sheets of phosphor bronze.

For some of the reactions, and particularly where higher pressures were desired, a glass pressure bottle was used (system B). The sample, prepared as before, was allowed to stand on the bottom of the cell. In this case, the volume of the solution was 300 cc, and the electrode had an active area of 12.9 $cm.^2$

The sonic unit was a 2000w (average) generator driving a magnetostrictive transducer at 15 kc. The entire apparatus (system A) including the oil bath, was placed in the sonic cell. The cell was filled with water to insure transmittal of the sound waves, and the presence of cavitation inside the reaction vessel was confirmed both with and without applied pressure through the use of a ceramic lead zirconate titanate transducer.

All results reported are the average of several runs.

Results

The results obtained when a series of plates were prepared from fresh baths at various pressures of either nitrogen or hydrogen in system A are shown in Fig. 1. The application of pressure to bath 1 caused a decrease in rate of nickel deposition (Fig. 1A). Experiments with pressure in the case of bath 2 (Fig. 1B) showed an increase in the rate with applied pressure. If the decrease in rate observed in bath 1 is due to diffusion control, the application of a sonic field should destroy the diffusion control. When the pressure experiment on bath 1 is performed in a sonic field, the results are similar to those observed in bath 2; an increase in rate with pressure is observed. The results are shown in Fig. 1C.

A series of runs were made from bath 1 at higher pressures using system B. In this case a plot of Ni

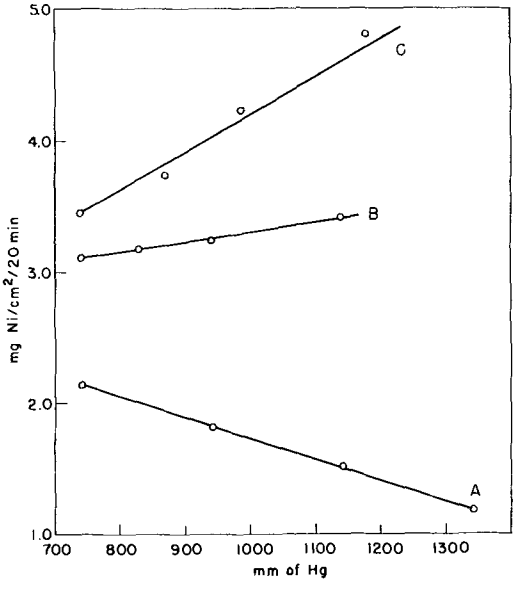

Fig. 1(A). Plot of mg $Ni/cm^2/20$ min vs. pressure for bath 1, system A; (B) Plot of mg $Ni/cm^2/20$ min vs. pressure for bath 2, system A; (C) plot of mg $Ni/cm^2/20$ min vs. pressure for bath 1 in the presence of ultrasonic cavitation, system A.

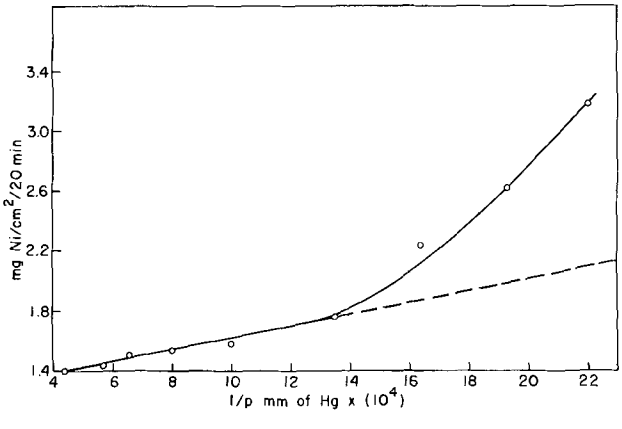

Fig. 2. Plot of mg $Ni/cm^2/20$ min vs. 1/pressure for bath 1, system B.

formed *vs.* pressure does not produce a linear relationship. A plot of Ni formed *vs.* I/P does produce a linear relationship. This is seen in the portion of Fig. 2 between 13.6 x 10^{-4}/mm Hg (atmospheric pressure) and 4.2 x 10^{-4}/*mm* Hg. As a further check, experiments were run in system B at less than atmospheric pressure. As expected, an increase in rate resulted. As is shown in Fig. 2, this increase is greater than is predicted by the I/P relationship (dashed line). This is probably due to an increase in the agitation effect caused by boiling of the solution at the lower pressures.

Discussion

Since nitrogen and hydrogen produce the same effect, it appears that the results are due to a true pressure effect rather than to a chemical effect. If the results were due to a chemical retardation of hydrogen formation, the results would be independent of nitrogen pressure. This limits any interpretation to purely physical effects independent of the chemistry of the process.

No rigorous interpretation of these results has been made; however, an explanation can be offered which fits the available data. This explanation is based on the decrease in the volume of the bubbles of hydrogen gas formed at the catalytic surface. When the system is under hydrostatic pressure, the hydrogen bubbles will be evolved at a lesser volume. Consequently, a less vigorous agitation effect will result. If the rate of nickel deposition is diffusion controlled, and if the diffusion rate is determined by the rate of agitation produced by hydrogen evolution, a decrease in rate is predicted as the result of hydrostatic presure. This is the case in Bath 1.

If this analysis is correct, the rate of deposition in a transport controlled system should vary with the volume of hydrogen evolved rather than with the applied pressure. Consequently the rate of nickel deposition should vary as I/P. Figure 2 shows this to be the case for pressures above atmospheric pressure. In Fig. 1A, due to the upper pressure limit of system A, a short segment of the I/P curve is seen and the apparent linear relationship with P results.

The rate of nickel deposition from bath 2 is increased by the application of hydrostatic pressure. In this case, the rate of nickel deposition must be controlled by factors other than diffusion control. As a check on this point, a series of deposits were prepared on rod substrates which could be rotated. Rotation of the rod served to double the rate of deposition from bath 1. Rotation of the rod caused only a very slight change in the rate of deposition from bath 2. This result further indicates that the rate of deposition from bath 1 is controlled by transport processes while the rate of deposition from bath 2 is controlled by other factors.

Under hydrostatic pressure the same quantity of hydrogen gas at the catalytic surface occupies less volume. Thus, in the case of a nontransport controlled system, the rate of nickel reduction may be increased because a larger area of active (hydrogen gas free) surface is available. If this conclusion is correct, the rate of nickel reduction is dependent on the area of the catalytic surface which is not covered by hydrogen. This result does not conflict with Gutzeit's claim that the rate is first order in hypophosphite since the active area probably remained constant during his work.

In the case of the experiments in the sonic field, the diffusion control in bath 1 is eliminated. It is then expected that the rate of deposition should be the same as that from bath 2 and that the application of pressure should lead to an increase in rate. In fact, the rate of deposition is greater than that observed in bath 2, and the increase of rate with pressure is greater than expected as seen from the slope of the curve in Fig. 1C.

The increase in over-all rate caused by sonics at atmospheric pressure and the increased effect of pressure on the rate in a sonic field are not surprising. Brenner (2) indicates that the rate of electroless deposition from alkaline solutions is not increased by agitation and that the rate is first order in hypophosphite. It therefore can be concluded that this system is not subject to transport control. Rich (6) has reported a large increase in the rate of electroless deposition from the alkaline system when ultrasonics are used. Ultrasonics must cause effects other than the elimination of diffusion control, and the increase in rate at atmopsheric pressure and the augmented effect of pressure in the presence of sonics must at present be attributed to unknown causes. The important conclusion is that ultrasonics reverses the effect of pressure in bath 1, leading to an increase in rate with increased pressure. This result is attributed to the elimination of transport control of the process.

It appears that increased hydrostatic pressure has the effect of decreasing the volume of evolved hydrogen. In the case where the system is transport controlled (bath 1), this results in a decrease in agitation which is proportional to the decrease in volume of evolved gas. The rate dependency on I/P results. In the case where the system is not transport controlled (bath 2 or bath 1 with sonics) the volume of evolved gas has no effect on the rate. In this case the rate is increased by the increase in hydrostatic pressure because the reduced volume of hydrogen gas at the surface leaves a greater area of exposed catalytic surface. In this case, no quantitative relationship between pressure and rate can be deduced from the available data.

The discrepancy over the area to volume ratio cannot be rigorously explained; however, when it is understood that the systems are different, this further difference is not unlikely. It is probable that the main difference between the systems studied in this work is that bath 2 is highly buffered and bath 1 is not. The buffer in bath 1 may be consumed in a local region of high hydrogen ion concentration. Thus, the rate of removal of hydrogen ion from the electrode region becomes rate controlling. In a system with a small area to volume ratio the entire system will not be agitated and a high hydrogen ion concentration will still exist near the electrode. This may explain the lower efficiency observed in this system.

Conclusions

It is concluded that the rate of nickel deposition from the Brenner bath is controlled by a transport

process. The rate of deposition from the Gutzeit bath is not transport controlled; however, the area of hydrogen free catalytic surface is rate controlling. If this area does not vary, other factors control the rate. Other factors also may control the rate if they control the active area. Hydrostatic pressure may control the rate in this way by an effect on the size of hydrogen bubbles or the quantity of gas contained by a bubble.

Acknowledgments

The authors are indebted to Dr. Cyril Solomons for his comments and suggestions. They also wish to acknowledge the assistance of the Honeywell Ceramics Laboratory, Golden Valley, Minnesota, for providing them with the ceramic transducer used in this work.

Manuscript received Oct. 9, 1961; revised manuscript received Jan. 11, 1962. This paper was prepared for delivery before the Detroit Meeting, Oct. 1-5, 1961.

Any discussion of this paper will appear in a Discussion Section to be published in the December 1962 JOURNAL.

REFERENCES

1. A. Brenner and G. E. Riddell, *J. Res. Nat. Bur. Standards*, **37**, 31 (1946).
2. A. Brenner and G. E. Riddell, *ibid.*, **39**, 385 (1947).
3. G. Gutzeit, *Plating*, **46**, 1158 (1959).
4. G. Gutzeit, *ibid.*, **46**, 1378 (1959).
5. C. H. de Minjer and A. Brenner, *ibid.*, **44**, 1297 (1957).
6. S. R. Rich, *ibid.*, **42**, 1411 (1955).

The Diffusion of Phosphorus in Silicon

I. M. Mackintosh*

Bell Telephone Laboratories, Murray Hill, New Jersey

ABSTRACT

A new process is described for the diffusion of phosphorus into silicon. The diffusions are carried out in a closed system, using as the diffusant source a glass consisting of phosphorus pentoxide and calcium oxide. This glass is shown to satisfy the various criteria which apply to such a source. The process is shown to be highly controlled. Sheet resistance values between 0.3 (±2%) and ~10,000 (±20%) ohms/□ can be obtained, and the junction depths are reproducible to about ±4%. Surface concentrations as low as about 10^{19} cm^{-3} and as high as 10^{21} cm^{-3} can be obtained with good reproducibility. The process is compatible with the oxide masking of layers with surface concentrations as high as 10^{21} cm^{-3}.

The high degree of process control, combined with the relative precision with which the measurable diffusion parameters have been determined, has revealed anomalies in the shape of the diffused impurity distributions. The general characteristics of these anomalous distributions are inferred and various mechanisms through which such effects might arise are discussed.

Data are presented for the effective diffusion coefficient and the effective activation energy for phosphorus in silicon as a function of temperature, surface concentration, and sample resistivity.

This paper describes a new process for the diffusion of phosphorus into silicon. The need for a new process has increased as the various older processes have become less able to meet the demand for ever-increasing reproducibility over wider and wider ranges of diffused distributions.

Various methods have been described for diffusing phosphorus into silicon.[1] One which has been used widely is the open-tube system (1), in which the diffusant molecules are carried from a P_2O_5 source to the silicon through the use of a moving gas. Such open-tube systems, however, suffer from a variety of disadvantages which tend to limit the reproducibility of the process. The principal problems are the necessity for controlling two temperatures, one for the silicon and one for the diffusant source, and the sensitivity of the process to the system geometry and to the rate of carrier gas flow. These problems largely could be avoided, however, by diffusing in a closed system, in which the silicon and diffusant source sit inside a closed box at a uniform temperature. Such a system has been used for boron diffusions (2) and has exhibited good process control. The efforts to improve the phosphorus diffusion situation were, therefore, focused on the development of a closed system, and it is such a process which is described below.

In the development of this process the philosophy of two-stage diffusion has been retained, as first suggested by C. J. Frosch and first described in detail by Howard (1). In the first (prediffusion) stage the silicon is heated in a saturated vapor pressure of the diffusant so that the surface concentration N_o depends only on the effective solid solubility of the impurity in the semiconductor. The junction depth x_j depends on both the temperature and time of prediffusion, but will, in general, be quite shallow. In the second (diffusion) stage the silicon is heated alone in order to redistribute the total number of prediffused impurity atoms $\bar{N}$ to the required final distribution.

The work is presented in the same general order: first, the prediffusion results, and then the diffusion results. The reproducibility of the process and the precision of the results has led to a further insight

* Present address: Westinghouse Central Research Laboratories, Pittsburgh 30, Pennsylvania

[1] For example, C. S. Fuller, U.S. Pat. 2,794,846, 1957.

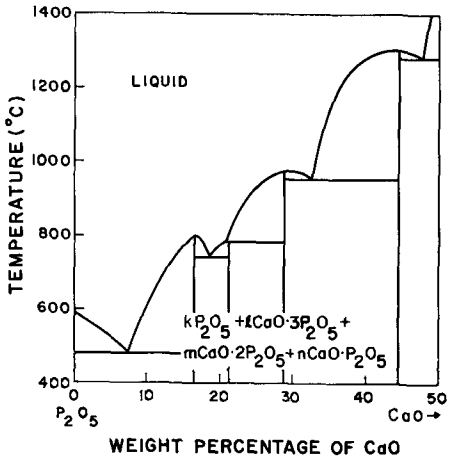

Fig. 1. Simplified phase diagram for system P_2O_5:CaO

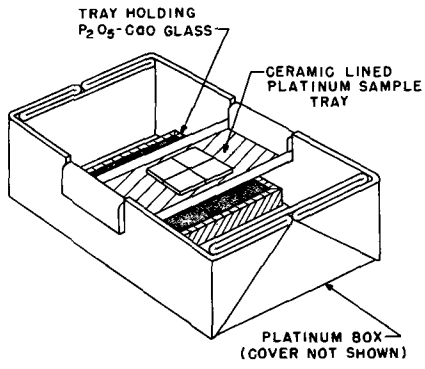

Fig. 2. Sketch of platinum diffusion assembly

into the nature of the diffused profiles, and this is discussed in detail in the last section.

Prediffusion Stage

Diffusant source.—Prediffusions in a closed system impose certain severe restrictions on the diffusant source. The essential properties of such a source can be stated as follows: (i) A source which is chemically complex must be molten over the desired range of prediffusion temperatures so that the diffusant vapor pressure is not affected by depletion effects at the surface of the source; (ii) the diffusant vapor pressure over a wide range of temperatures must be high enough so that the surface concentration is a function only of the solid solubility of the diffusant in silicon and is not limited by the rate of arrival of diffusant molecules at the silicon surface. In addition, the vapor pressure must not be so high as to cause deleterious effects (such as local alloying) on the silicon surface, nor to exhaust the source too rapidly; (iii) the source must evolve nothing which could impair the surface or the bulk properties of the silicon.

A phosphorus source which fulfills all of these requirements is the glass formed between phosphorus pentoxide and calcium oxide. A detailed phase diagram of this glass has been published (3) and a simplified portion of this is shown in Fig. 1. The solid section is composed of the compounds shown in the various proportions k, l, *etc.* It may be seen that the melting point of the glass can be made as low as about 500°C by suitably adjusting the proportions of the CaO and P_2O_5.

Other properties of this glass, plus evidence that the glass fulfills all of the above requirements are presented later. It should be mentioned, however, that none of the calcium phosphates (nor, indeed, any of the phosphorus compounds which have been considered) is suitable as a diffusant source. Their principal disadvantages are either a high melting point (thereby limiting the process to high temperatures) or decomposition at relatively low temperatures.

Manufacture of the glass is extremely simple. In this work the glass has been made by mixing together appropriate weights of P_2O_5 and CaO and firing these at about 900°C in dry nitrogen. The result is a clear, hard glass. The proportions of P_2O_5 and CaO used depend to some extent on the prediffusion temperature to be used, although it is shown later that the process is not sensitive to variations in these proportions.

Prediffusion equipment and procedure.—The prediffusion assembly used in the development of this process was the small platinum box depicted in Fig. 2. The glass was contained in the small tray and the silicon samples were laid on the ceramic-lined bridge. A close-fitting platinum lid is not shown in this figure. This assembly was inserted into the furnace on a quartz rod; the temperatures were monitored throughout every run by means of a standardized thermocouple and were controlled to ±1°C. A gas flow of about 1 liter/min was used throughout.

All the prediffusion runs were for 60 min, this being the time between insertion and withdrawal of the box. The average warm-up time for this system was about 11 min so that the assembly was at the actual prediffusion temperature for about 49 min. Prediffusion temperatures from 650° to 1300°C were used, with most emphasis on the range 700° to 1200°C. The material used was p-type silicon, polished on one side and lapped on the other; the diffusions were through the polished surface. The slices were in the form of ¼ in. x ¼ in. squares, approximately 0.012 in. thick, and four such slices were used in each run. Two resistivities were used; ~0.3 ohm-cm, corresponding to a background acceptor concentration N_B of about 10^{17} cm^{-3}, and ~25 ohm-cm, corresponding to about 5 x 10^{14} cm^{-3}. At least four different silicon ingots of each resistivity were used.

The silicon surfaces after prediffusion were almost invariably very good throughout the entire range of prediffusion temperatures used. There was no observable glass on the silicon, and a brief rinse in HF gave clean, polished surfaces.

Prediffusion results.—In order to assess the control limits of the process at least four runs were prediffused at 100° intervals throughout the range 700° to 1300°C. After each run the prediffusion sheet resistance r_p of all four samples was measured on an accurate four-point probe. To ensure precise knowledge of the geometrical factor used in computing r_p, the unknown diffused layer on the back of each slice was etched off prior to measurement. The values then were analyzed by standard

quality control techniques to determine the median value and the percentage control limits. One slice from each of these "control" runs was angle-lapped to determine the prediffusion junction depth x_{jp}, and an average value obtained from the four determinations. The measurement was made by means of a standard interference fringe technique. A few "single" runs (*i.e.*, one run of four samples) were made at various temperatures, but were not used to assess the process control. Their agreement with the control data, however, is a measure of the reproducibility of the process.

Figure 3 is a plot of r_p *vs.* the reciprocal of the prediffusion temperature T_p in degrees Kelvin. Points representing control runs and single runs, for both sample dopings used, are shown. Associated with each control point are the percentage control limits at that temperature. All the points lie satisfactorily on a smooth curve, the gradient of which increases with decreasing temperature, and no dependence of r_p on sample doping can be distinguished. The control limits increase from about 2% at high temperatures, to about 25% at 700°C. Prediffusions at 650°C do not appear on this figure because r_p was too high ($> 10^4$ ohm/□) to be meas-

The junction depth x_{jp} is plotted *vs.* $1/T_p$ in Fig. 4. The points represent the average of four determinations, one sample from each of the four control runs. In all cases the spread in the values was less than the measurement uncertainty, which was estimated to be a maximum of ± 0.005 mil and which is represented by the lines on the left of the figure. No values are available below 900°C because of the difficulty of measuring extremely thin layers.

In spite of the relatively large measurement uncertainty below about 0.2 mil the results clearly fall into separate straight lines according to sample doping, as expected. The precise location of the lines is uncertain; those shown represent the best

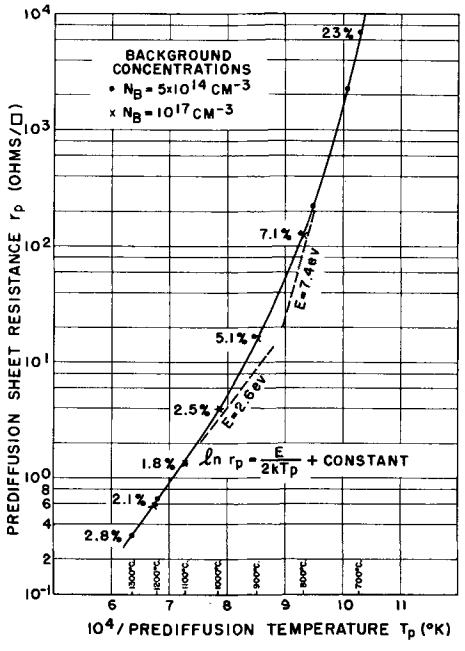

Fig. 3. Prediffusion sheet resistance *vs.* reciprocal prediffusion temperature.

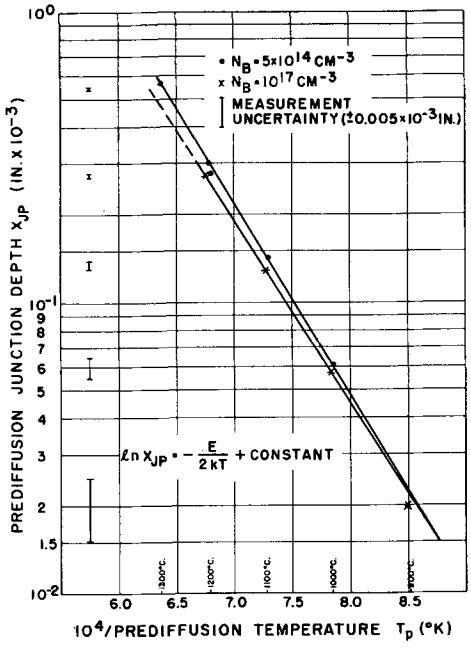

Fig. 4. Prediffusion junction depth *vs.* reciprocal prediffusion temperature.

fit. Note, however, that the separation of these lines is appreciably less than would be expected theoretically. The junctions were invariably flat and parallel to the surface.

From the experimental measurements of r_p and x_{jp}, the prediffusion surface concentration N_{op} can be inferred, assuming that the impurity distributions are complementary error function (erfc).[2] Values of N_{op} obtained in this way are shown plotted against T_p in Fig. 5, for temperatures ranging from 900° to 1300°C. It can be seen that N_{op} tends to saturate in the region 1100° to 1200°C at a value close to 10^{21} cm^{-3}. The apparent dependence of N_{op} on sample doping is not a real effect and is discussed in a later section.

Process criteria.—At this stage it is worthwhile considering how well the process satisfies the various criteria by which the usefulness of a diffusion

[2] These values of N_{op} were computed from diffusion curves calculated by I. M. Mackintosh and A. J. Siuta. Their curves are in agreement with the extensive diffusion data of Irvin (4)

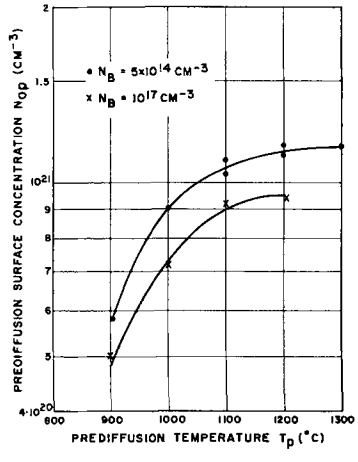

Fig. 5. Prediffusion surface concentration *vs* prediffusion temperature.

Table I. Oxide masking capabilities

Nonoxidized control sample				Oxidized test sample		
r_p (ohm/□)	x_{jp} (in. × 10^{-3})	N_{op} (cm^{-3})	SiO_2 (Å)	r_p (ohm/□)	x_{jp} (in. × 10^{-3})	N_{op} (cm^{-3})
0.69	0.244	$1.3 \cdot 10^{21}$	12,500		Masking successful	
0.71	0.244	$1.2 \cdot 10^{21}$	9,100		Masking successful	
0.68	0.255	$1.2 \cdot 10^{21}$	9,100		Masking successful	
0.69	0.267	$1.6 \cdot 10^{21}$	6,500	5.8	0.081	$4.4 \cdot 10^{20}$

All runs ~ 1200°C 60/min. All samples ~ 0.3 ohm-cm ($N_B \sim 10^{17}$ cm^{-3}).

process may be judged. These criteria, and the performance of the present process, are described below in some detail.

Process control.—In view of the capabilities of other known phosphorus diffusion processes the performance of this new process is very satisfactory. There is a general improvement in control, relative to other known processes, throughout the entire temperature range. In particular, control limits of better than 10% on sheet resistances of several hundred ohms significantly increase the range of phosphorus as a useful n-type impurity in silicon. The 1.8% limits on r_p at 1100°C effectively represent a temperature uncertainty of less than 1°C.

Compatibility with other device and process requirements.—No incompatibility with other processes or with specific device requirements has been exhibited by this process. Good alloy contacts have been made to silicon surfaces which had been diffused by this means. Lifetime-dependent devices have been made using the present process as one of the fabricating steps, and no unusual or adverse effects have been experienced.

It is pertinent to consider, however, the role of the calcium oxide in this process. After very long diffusion times at high temperatures the diffusant glass tends to disappear completely. This is strong evidence that the CaO is evaporating at a rate similar to that of the P_2O_5. No information is available, however, on the electrical behavior of calcium in silicon. This is apparently due to the fact that the solid solubility is extremely low (5). Moreover, the great stability of the CaO molecule inhibits its reduction and the subsequent diffusion into the silicon of metallic calcium (5). Thus the calcium, although present during the prediffusion treatment, is either electrically inactive in silicon or cannot get into the silicon in significant amounts.

Oxide masking capabilities.—Present-day device requirements demand from any silicon diffusion process with a claim to universality the ability to inhibit diffusion by the use of silicon dioxide layers on the silicon surface. By such masking techniques localized diffused regions of any desired shape can be obtained with ease.

The oxide masking capabilities of this process were investigated by prediffusing for 60 min at approximately 1200°C a number of slices (background concentration 10^{17} cm^{-3}) having different oxide thicknesses. Each run consisted of one completely oxidized slice (to determine the sheet resistance of the impurity layer, if any, which had been able to penetrate the oxide), and one control slice completely free of oxide (to ensure, through its sheet resistance, that the process was performing properly).

The results are shown in Table I. It can be seen that a layer of sheet resistance about 0.7 ohm/□ ($N_{op} \sim 10^{21}$ cm^{-3}) can be successfully masked by about 9000Å of SiO_2, a thickness which is compatible with photoresist etching techniques. Higher sheet resistance layers presumably can be masked by thinner oxides, although no data are available at this time.

Process simplicity.—Difficulties arise in any process involving the use of weighed quantities of a hydroscopic substance such as P_2O_5. For example, how can the water content be kept reproducibly low and, having weighed the powder, what fraction of the weight is due to the water content? If the process depends critically on these factors, it would probably be unsuitable for use in large-scale diffusion operations.

The sensitivity of the process to the method of manufacture of the glass was investigated in the following way. Without taking any special precautions, two samples of diffusant glass were made in ostensibly the same manner, but at different times. In each case the proportions of the weighed powders were approximately 15 parts P_2O_5 to 1 part CaO, by weight. These are described as 15:1 glasses. After being fired in identical ways (900°C for 30 min) the glasses were analyzed for P_2O_5 content and their approximate melting points were measured. The results are given in Table II. It can be seen that within the accuracy of the determinations the two glasses are essentially identical. It therefore is assumed that no major problem exists in the manufacture of the glass.

The sensitivity of the process to the glass proportions is also of great importance. To investigate this, glasses of widely differing proportions were

Table II. Reproducibility of diffusant glass

Glass sample	Weight ratio (P_2O_5:CaO)	Weight percentage of P_2O_5	Melting point, °C
A	15:1	87 ± 2	650 ± 50
B	15:1	89 ± 2	700 ± 50

Table III. Dependence of r_p on glass ratio

Temperature/time	No. of runs	Glass ratio	$\tilde{r}_p$
805°C/60 min	1	50:1	130
805°C/60 min	4	6:1	131
1000°C/60 min	2	50:1	4.04
1000°C/60 min	2	10:1	4.03

used for prediffusions at various temperatures. The results are shown in Table III, and it can be seen that there is no significant variation of the sheet resistance values with the glass ratio. Further confirmation of this propitious insensitivity is given by Fig. 3, in which the various points were obtained using a wide variety of glasses (6:1 to 50:1) without any noticeable effect. It is a safe assumption, therefore, that variations in the glass proportions will have an insignificant effect on the process, providing the ratio is high enough for the glass to be molten at the temperature of prediffusion.

Process simplicity is further improved if the necessity for frequent renewals of the loading or "charge" of the diffusant glass is avoided. In other words, the process is simpler the longer a given charge remains "active" and gives the correct results. The results of various investigations during the course of this work show that at 1200°C an average charge (~ 2g) will last at least 12 hr. At temperatures below 1000°C no charge renewal was found to be necessary.

Diffusion Stage

Diffusion equipment and procedure.—The diffusion of previously prediffused samples was carried out in the same general furnace system used for the prediffusion process, but using a clean furnace tube. The quartz push-rod was simply a long hollow rod with a flat platform at one end, on which the samples were laid. A standardized thermocouple was inserted into the rod so that it lay close to the samples, and the temperature was accurately measured and controlled during every diffusion run. A gas flow of 1000 cc/min of dry oxygen was used in all the diffusions.

In an attempt to obtain accurate information on the process (and on the value of the diffusion coefficient) at more than one temperature, each group of identically prediffused samples was divided into two subgroups, one being diffused for 16 hr at 1200°C, the other for 3 hr at 1300°C. These times were chosen so that the diffusion lengths for the two subgroups were approximately equal, thus permitting comparisons between the two sets of results.

Diffusion results.—No deterioration in the sample surfaces was observed after diffusion. A quick rinse in HF removed the oxide grown during diffusion and gave clean, bright surfaces. After each diffusion run measurements were made of the sheet resistance r_d and the junction depth x_{jd} of every sample, using the same techniques as used for the prediffusion measurements.

Figure 6 is a plot of r_d *vs.* the reciprocal prediffusion temperature, $1/T_p$. As with most of the diffusion results four point-symbols are used, representing the combination of sample resistivities and diffusion temperatures used. In this figure the symbols are separated from the actual points in order to avoid confusion. The points all lie satisfactorily close to a smooth curve and no systematic variation in r_d can be distinguished for either diffusion temperature or sample resistivity.

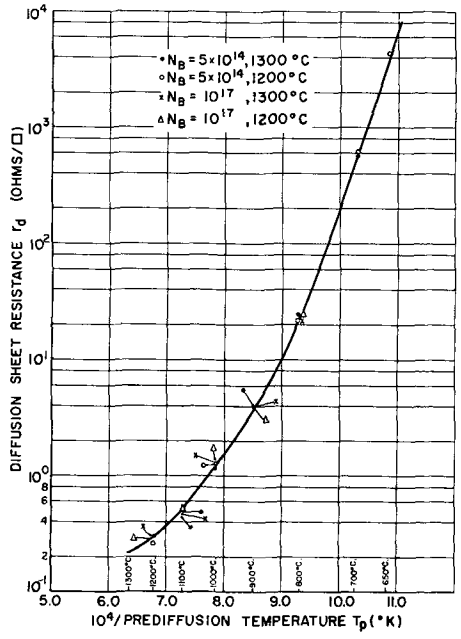

Fig. 6. Diffusion sheet resistance *vs.* reciprocal prediffusion temperature.

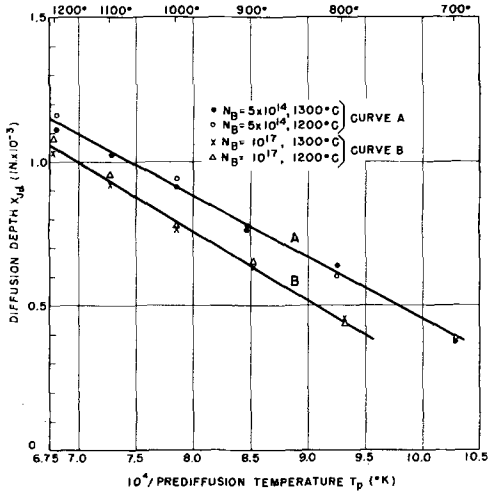

Fig. 7. Diffusion junction depth *vs.* reciprocal prediffusion temperature.

Precise information on the control of the diffusion process was difficult to obtain because of the small number of samples. This arose from the separation into two subgroups of the available prediffused samples. Roughly, however, the control limits seemed to be somewhat worse after diffusion; for example, ±3% after prediffusion, and about ±4% after diffusion. This is expected and reflects additional small randomizing effects during the diffusion runs.

The diffusion depth x_{jd} is plotted against T_p in Fig. 7. Here, as expected, the results separate according to sample resistivity. No further observable separation occurs since the diffusion lengths of the 1200° and 1300° runs are nearly equal. Measurement uncertainty in these values is quite small. The points represent average values and the spread was invariably less than ±4%. As with the prediffusion results, the separation of the two lines in Fig. 7 is

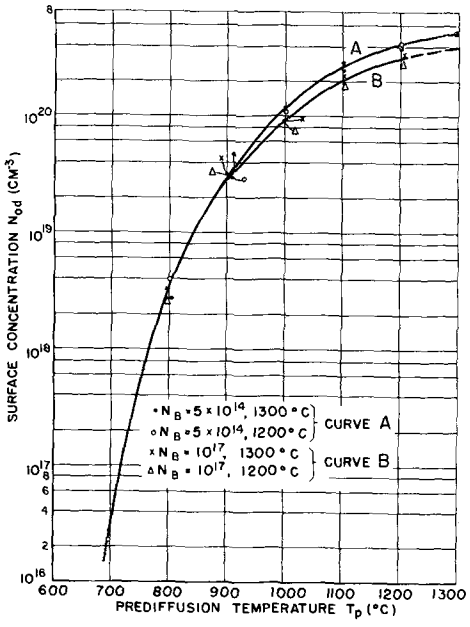

Fig. 8. Diffusion surface concentration *vs.* prediffusion temperature.

appreciably less than would be expected theoretically.

From the experimental measurements of r_d and x_{jd}, the diffused surface concentration N_{od} can again be inferred, assuming that the impurities have a purely Gaussian distribution.[3] Figure 8 shows a plot of N_{od} *vs.* T_p. The results separate into two curves above 900°C and, as for the prediffusion results, N_{od} is apparently higher for lower sample doping. The implications of this are discussed in the following section. It should be noted that surface concentrations as low as about 10^{16} cm^{-3} can be achieved with reproducibilities of about 20%.

Over-all process.—The successful use of two-stage processes necessitates good control in both stages of the process. For example, samples of identical r_p values, when identically diffused, should have the same values of r_d within close limits. That the present process fulfills this condition is established by Fig. 6.

[3] As for the prediffusion results, these values of N_{od} were computed from diffusion curves calculated by I. M. Mackintosh and A. J. Siuta, which are in agreement with the computed data recently obtained by Irvin (4).

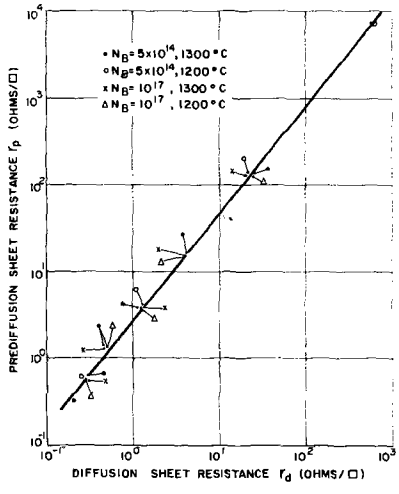

Fig. 9. Prediffusion sheet resistance *vs.* diffusion sheet resistance

In addition, it is very desirable to be able to predict with reasonable accuracy the prediffusion conditions necessary to give specific final distributions. An example of how well the present process achieves this desirable feature is shown in the plot of r_p *vs.* r_d in Fig. 9. A linear dependence of $\ln(r_d)$ on $\ln(r_p)$ is exhibited over at least five decades, and no dependence on sample resistivity or diffusion temperature is observed (a significantly different diffusion length, however, would change the shape of the plot). Thus, a required final value of r_d can be associated accurately with a required value of r_p; Fig. 3 then gives the necessary prediffusion temperature.

This pronounced linearity (on logarithmic scales) is somewhat surprising, but can be justified qualitatively on theoretical grounds.[4] The line can be represented by the equation

$$r_p = a\, r_d^{\,b} \qquad [1]$$

where $a = 2.8$ and $b = 1.3$. Now, by the use of several simplifying assumptions (see appendix) it can easily be shown that

$$r_p \approx r_d \frac{\bar{\mu}_d}{\bar{\mu}_p} \qquad [2]$$

where $\bar{\mu}_d$ and $\bar{\mu}_p$ are the effective average (constant) mobilities for the diffusion and prediffusion distributions, respectively. It also has been established (4) that over considerable ranges of impurity concentrations the mobility exhibits a dependence of the form

$$\mu = cN^{-d} \qquad [3]$$

where c and d are constants. Combination of Eq. [2] and [3] then can be shown to lead to a general relation between r_p and r_d of the form of Eq. [1]. The experimental values of the constants a and b are shown in this way to be theoretically reasonable but to depend (in a complicated manner) on the diffusion length L_d.

General Discussion

Shape of impurity distributions.—The results already presented have shown that this process performs in a controlled and reproducible manner over several orders of magnitude of sheet resistance. This reproducibility, and the relative precision with which the parameters r and x_j have been measured, raises the possibility of using these data to further the understanding of the diffusion process itself. Such an attempt is made in this section.

The curves shown in Fig. 5 and 8 suggest that the surface concentration N_o is a function of the background concentration N_B. Under the conditions imposed during these diffusions, however, there is no feasible mechanism by which such an effect could occur, particularly when N_o is many orders of magnitude greater than N_B. This is the primary anomaly through which an understanding of the true nature of the impurity profiles may be sought.

It is convenient at this stage to focus attention on the prediffusion results. The values of N_{op} were computed on the assumption that the impurity profiles were truly erfc distributions and, of course,

[4] A brief discussion of the appropriate diffusion theory is given in the appendix.

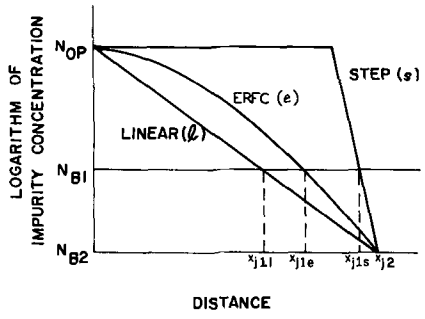

Fig. 10. Schematic of anomalous distributions

any departure from this theoretical distribution would lead to anomalous values for N_{op}. Departures from such a distribution can take two general forms, more convex or less convex on a logarithmic concentration plot.[5] In Fig. 10 these are represented in exaggerated form as step function (s) and linear gradient (1) distributions, respectively, on a plot of log (concentration) *vs.* distance. All three profiles have the same surface concentration and the same junction depth at the lower concentration N_{B2}.

Now it is well known that the sheet resistance of a diffused layer is primarily a function of the surface concentration, so that r_{pl}, r_{pe}, and r_{ps} (denoting the linear, erfc, and step profiles, respectively) will not be sensitive to changes in N_B. However, the form of the profile certainly affects the sheet resistance and it can be seen readily that $r_{pl} > r_{pe} > r_{ps}$. If the junction depths and sheet resistance values are now used to compute the apparent surface concentrations, assuming that each profile is an erfc distribution, then it is found that: (*i*) the linear gradient distribution gives apparent N_{op} values which lie below the true erfc values, and which increase with increasing N_B: (*ii*) the step function distribution gives apparent N_{op} values which lie above the true erfc values, and which decrease with increasing N_B. Since it is the latter trend which is observed experimentally (Fig. 5) then the actual profiles can be assumed to be more convex than the true erfc distribution. And, therefore, the true surface concentrations must lie on or below the lower curve shown in Fig. 5. This result gains additional support from the fact that the plots of x_{jp} *vs.* $1/T_p$ in Fig. 4 have a smaller separation than expected theoretically.

Diffused profiles which also exhibit this type of step function distribution have been observed (6) for zinc diffusion in gallium arsenide. One proposed explanation (6) is the increase in ionic radius of the Zn acceptor as it changes from an un-ionized state at heavy concentrations (Fermi level below the acceptor levels) to an ionized state at low concentrations, leading to a decrease in diffusion coefficient at these concentrations. This proposed mechanism cannot account for the present results because phosphorus is a donor in silicon and its decrease in ionic radius at low concentrations would lead to an increase in the diffusion coefficient.

Another proposal (7) to explain the anomalous Zn diffusion profiles in GaAs is based on the assumption that Zn can diffuse both substitutionally and interstitially with high and low diffusion coefficients, respectively. If most of the vacancies are surface-created (by the evaporation of As?) and themselves diffuse slowly, then it is readily seen that a step-function distribution would be obtained, the step occurring at the depth to which the surface-created vacancies have diffused. It is difficult, however, to envisage such an effect in silicon since the diffusion of vacancies in this material is commonly assumed (8) to be much faster than the diffusion of phosphorus.

Several other mechanisms can be postulated to account for this anomalous kind of impurity profile. Prominent among these are: (*i*) the presence of a strained surface layer (in which the diffusion coefficient might be abnormally high) due to mechanical polishing or other surface preparations; (*ii*) the simultaneous diffusion into or out of the silicon of a different species of impurity, chemical or electrical (*e.g.*, vacancy).

The first mechanism has been investigated experimentally by simultaneously prediffusing both mechanically and chemically polished samples which were otherwise identical. No significant difference in values of r_p and x_{jp} was observed between these samples thus suggesting that surface strain is not a cause of the observed anomalies.

The second mechanism is difficult to investigate experimentally. However, any impurity which could cause this effect must have a diffusion coefficient significantly less than that for phosphorus. This eliminates vacancies, oxygen, iron, gold, etc. from consideration. The fact that most of the crystals used in this experiment were boron-doped might be significant. Further work would be necessary before the importance of this could be checked.

The general conclusion that the prediffused impurity profiles[6] are more convex (on a logarithmic plot) than a true complementary error function distribution is confirmed by a recent detailed analysis of phosphorus-diffused layers in silicon (9). This method involves repeated room-temperature anodization of the silicon and measurement of the sheet resistance of the residual diffused layer, and is capable of yielding precise information about the distribution of ionized impurities.[6] The analysis indicates the existence of an upper limit to the concentration of electrically active phosphorus in silicon which is below the apparent surface concentrations shown in Fig. 5. Such a concentration limit would, of course, lead to a region close to the surface where the concentration of electrically active phosphorus was essentially constant, thus giving an impurity profile which was more convex than the error function complement.

The diffusion profiles, as considered through the curves of N_{od} in Fig. 8, exhibit similar anomalies for prediffusion temperatures above 900°C. In other words, the separation of the curves according to sample doping again leads to the conclusion that the diffusion profiles are more convex (on a logarithmic

[5] The terms "convex," "linear," etc., as used in this discussion refer to the shape of the distribution when plotted on semilog paper.

[6] Obviously, the measurement of sheet resistance will yield information on the density of electrically active impurities, not on the total density. Such limitation is implied during all of this discussion.

concentration plot) than the true Gaussian distribution. For prediffusion temperatures below 900°C there is no evidence (within experimental error) of a dependence of N_{od} on N_B, and it is therefore possible to assume the existence of Gaussian distributions for these cases. These conclusions are confirmed partially by the plots of x_{jd} in Fig. 7, since the separation of the two lines is quite close to the theoretical value at low values of T_p, but is considerably less than the theoretical separation at high values of T_p.

The situation therefore can be summarized as follows. Using only the measurement of sheet resistance and junction depth it has been established that, with the exception of samples having low-temperature prediffusions and relatively long diffusions, both the prediffused and diffused impurity profiles are more convex (on a logarithmic plot) than the theoretical error function and Gaussian distributions. The reason for this effect cannot be established with any certainty using these data, although it is possible to rule out some of the more likely causes. The precise nature of the impurity profiles can be investigated more easily using the anodization technique (9) mentioned previously, and it is from this work that a fuller understanding of the phenomenon can be expected to emerge.[7]

Evaluation of the diffusion coefficients.—In view of the existence of these anomalous distributions it is obvious that the value of the diffusion coefficient obtained from these results is not necessarily the true value. What emerges from the calculations is an effective value which represents the value the diffusion coefficient would have for a theoretically correct profile having the same sheet resistance, junction depth, etc. This effective diffusion coefficient is nevertheless of considerable interest since it represents the value which must be used in any practical diffusion experiment. For this reason various plots of the diffusion coefficient are presented in this section.

Figure 11 shows the value of the diffusion coefficient D, as calculated from the prediffusion results, plotted *vs.* $1/T_p$. The equations describing the prediffusion and diffusion conditions, and the methods for calculating the effective diffusion coefficients and activation energies are shown in the appendix. The points fall into two straight lines, according to sample doping, and have slightly different activation energies.

In calculating the diffusion coefficient from the diffusion results two additional complications arise. In the first place, the distributions can be truly Gaussian only when the prediffused layer can be regarded as a sheet source at the surface. This is certainly not a valid assumption for prediffusions above 900°C (where $x_{jp} = 0.02 \cdot 10^{-3}$ in.), but deviations from the true distributions already have been taken into account by calling the calculated value of D an "effective" coefficient. Second, the effective surface from which the diffusion depth should be measured lies inside the true surface by an amount which depends on the prediffusion conditions. In this work the penetration x'_{jp} of this effective surface is defined as that distance which, when multiplied by N_{op}, gives a total density of impurities equal to $\bar{N}_p$. In other words, the prediffusion profile is assumed to be a step function, the concentration falling from N_{op} to zero at a distance x'_{jp} from the surface such that

$$N_{op}\, x'_{jp} = \bar{N}_p = \frac{2L_p N_{op}}{\sqrt{\pi}} \qquad [4]$$

For the computation of the effective diffusivity, therefore, the depths shown in Fig. 7 have been corrected by their respective x'_{jp} value. This correction is a maximum of about 5% of the measured

[7] During the preparation of this paper for publication, a new study of phosphorus diffusion profiles by radioactive tracer techniques was published (10). The results of this recent study confirm the existence of anomalous impurity distributions of the kind described above.

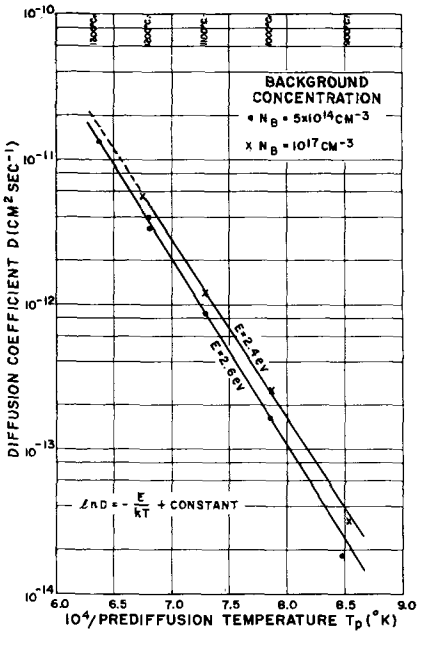

Fig. 11. Diffusion coefficient *vs.* reciprocal prediffusion temperature.

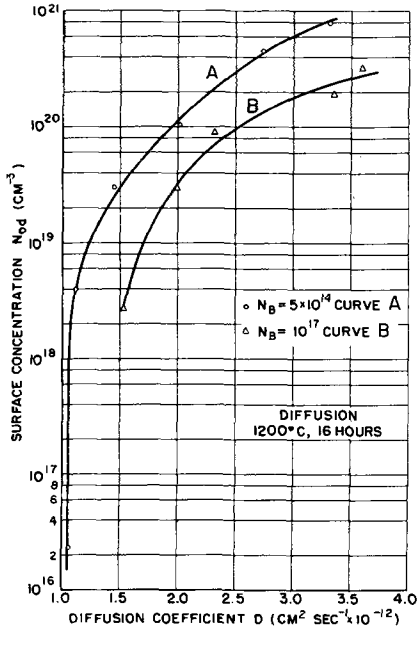

Fig. 12. Diffusion surface concentration *vs.* 1200°C diffusion coefficient.

diffusion depth for the high-temperature prediffusions.

Figure 12 shows a plot of N_{od} *vs.* D, calculated in the manner described above from the 1200°C diffusion results. D is a function of concentration because of the field-acceleration effect which occurs when N_o exceeds the intrinsic concentration n_i at the temperature of diffusion. It has been shown (11) that this effect can lead to a factor of two increase in D and that the effect in silicon first should be observed at some value of N_o less than about 10^{19} cm^{-3}. The figure confirms the latter aspect, but the fact that these results exhibit much more than a factor of two increase in D can be explained only by the presence of some other mechanism, as yet unknown.

Figure 13 shows the same kind of plot of N_{od} *vs.* D, but for the 1300°C diffusion runs. It serves to confirm that the effects observed in Fig. 12 are not special to 1200°C. Both of these figures demonstrate the dependence of this effective diffusivity on sample doping. This is not understood for samples prediffused below 900°C since Fig. 8 appears to confirm the existence of true Gaussian distributions (or very close to it) for these samples. Apparently it is not arising because of any peculiarity in the silicon samples since, as stated earlier, at least four different ingots of each resistivity range have been used in this work. No adequate explanation for this apparent effect has yet been found.

Values of D at 1200° and 1300°C for any specified N_{od} can be obtained from Fig. 12 and 13. By this means plots of D *vs.* $1/T$ have been obtained for three representative surface concentrations and are shown in Fig. 14. Also shown (dotted) are the values obtained from the prediffusion results (Fig. 11), corresponding to even higher surface concentrations. Figure 14 thus summarizes all of the present data on the effective diffusion coefficient as a function of temperature, surface concentration, and sample doping and may serve as a useful working chart.

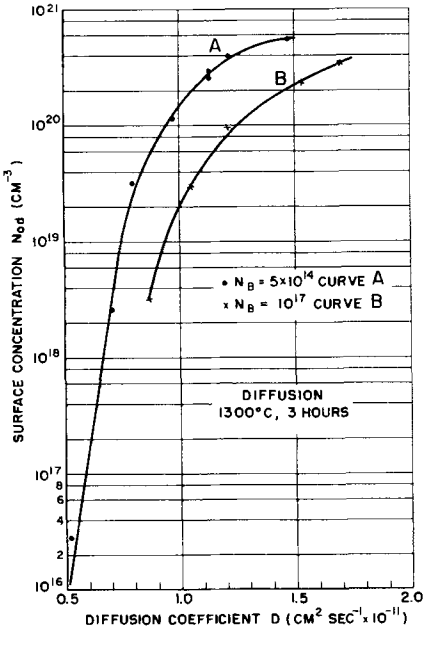

Fig. 13. Diffusion surface concentration *vs.* 1300°C diffusion coefficient.

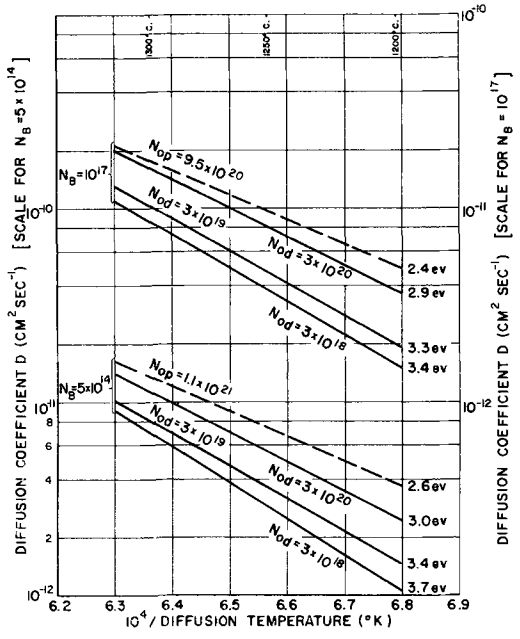

Fig. 14. Effective diffusion coefficient *vs.* reciprocal temperature

The dependence of the effective activation energy E on both N_{od} and N_B clearly emerges from this figure (14). Table IV summarizes all of the present data on E and a satisfactory degree of self-consistency is seen clearly. It should be noted, however, that these effective activation energies are significantly out of agreement with the results of earlier workers (1, 12).

Summary and Conclusions

A new process for the diffusion of phosphorus into silicon has been described which utilizes the inherent advantages of the closed system. The process is highly controlled and is capable of producing prediffused layers over at least five decades of sheet resistance. After diffusion, surface concentrations in the range 10^{16} to 5 x 10^{20} cm^{-3} can be obtained with good reproducibility. The various aspects of the process have been described in detail, and the diffusant glass has been shown to satisfy the several criteria which apply to such a source.

The high degree of process control, combined with the relative precision with which the measurable diffusion parameters (sheet resistance and junction depth) have been determined, has revealed an apparent dependence of surface concentration and diffusion coefficient on the background doping of the silicon samples. This effect has been shown to arise because of discrepancies between the actual impurity profiles and the distributions expected theoretically. Various possible causes of this effect have been discussed, but no satisfactory explanation has yet been found. Plots of the effective diffusion coefficient as a function of temperature, surface concentration, and sample doping have been presented. These represent the values which should be used in a practical diffusion experiment.

Acknowledgments

The author particularly wishes to express his gratitude and to acknowledge his debt to R. L. Brown, who carried out much of the experimental

Table IV. Effective activation energy

Method of determination	Effective activation energy (ev) $N_B = 5.10^{14}$	$N_B = 10^{17}$	Surface concentration, cm^{-3}	Temperature range, °C
From r_p (Fig. 3)	2.6	2.6	$\sim 10^{21}$	1100-1300
	7.4	7.4	$<<10^{21}$	700-800
From x_{jp} (Fig. 4)	~2.5	~2.5	$\sim 10^{21}$	1000-1300
From D (Fig. 11)	2.6	2.4	$\sim 10^{21}$	1000-1300
From D (Fig. 14)	2.6	2.4	10^{21}	1200-1300
	3.0	2.9	3.10^{20}	1200-1300
	3.4	3.3	3.10^{19}	1200-1300
	3.7	3.4	3.10^{18}	1200-1300
Fuller and Ditzenberger (12)	4.0 ev		—	950-1250
Howard (1)	4.4 ev		—	≤1100

work described in this paper. Gratitude also is expressed to Mrs. A. J. Siuta, who carried out the quality control analysis of many of the experimental results, and to those colleagues who contributed by deed or discussion to the completion of this investigation.

Manuscript received Nov. 13, 1961. This paper was prepared for delivery before the Chicago Meeting, May 1-5, 1960.

Any discussion of this paper will appear in a Discussion Section to be published in the December 1962 JOURNAL.

REFERENCES

1. B. T. Howard, Paper presented at the Buffalo Meeting of The Electrochemical Society, October 1957.
2. B. T. Howard, Paper presented at the Ottawa Meeting of The Electrochemical Society, October 1958.
3. W. E. Hill, G. T. Faust, and D. S. Reynolds, *Am. J. Sci.*, **242**, 469 (1944).
4. J. C. Irvin, B.S.T.J., In preparation.
5. C. D. Thurmond, Private communication.
6. J. W. Allen and F. A. Cunnel, *Nature*, **182**, 1158 (October 25, 1958).
7. J. M. Whelan, Private communication.
8. F. M. Smits, *Proc. I.R.E.*, **46**, 1049 (1958).
9. E. T. Handelman, *Solid State Electronics*, **2**, 123 (1961).
10. V. K. Subashiev, A. P. Landsman, and A. A. Kukharskii, *Sov. Phys.—Solid State*, **2**, 2406 (1961).
11. F. X. Hassion and L. J. Russo, Private communication.
12. C. S. Fuller and J. A. Ditzenberger, *J. Appl. Phys.*, **27**, 544 (1956).

APPENDIX

Simplified Diffusion Theory

Prediffusion.—Theoretically the prediffusion impurity profiles are described by the equation

$$N_B = N_{op} \operatorname{erfc} (x_{jp}/2\sqrt{Dt_p}) \qquad [A\text{-}1]$$

from which

$$x_{jp} = 2\sqrt{Dt_p} \operatorname{erfc}^{-1} (N_B/N_{op}) \qquad [A\text{-}2]$$

The diffusion coefficient is given by

$$D = D_o \exp (-E/kT) \qquad [A\text{-}3]$$

where E is the activation energy and k is Boltzmann's constant. Hence, over the range of temperatures in which (N_B/N_{op}) is effectively constant we get

$$\ln (x_{jp}) = -\frac{E}{2kT_p} + \text{constant} \qquad [A\text{-}4]$$

This is the equation represented in Fig. 4.

The expression for the prediffusion sheet resistance can be simplified in the present work to

$$r_p \simeq \sqrt{\pi}/q\bar{\mu}_p \, 2N_{op} \sqrt{Dt_p} \qquad [A\text{-}5]$$

where q is the electronic charge. Hence,

$$\ln r_p = \frac{E}{2kT_p} + \text{constant} \qquad [A\text{-}6]$$

which is the expression represented in Fig. 3.

The total concentration of impurities in the prediffused layers is given by

$$\bar{N}_p = \int_0^{x_{jp}} N(x)\, dx = \frac{2N_{op}\sqrt{Dt_p}}{\sqrt{\pi}} \qquad [A\text{-}7]$$

Diffusion.—Theoretically the diffusion impurity profiles are described by the Gaussian equation

$$N_B = N_{od} \exp (-x_{jd}^2/4Dt_d) \qquad [A\text{-}8]$$

from which

$$D = x_{jd}^2/4t \ln (N_{od}/N_B) \qquad [A\text{-}9]$$

This is the equation from which the values shown in Fig. 12 and 13 were calculated.

The expression for the diffusion sheet resistance can be simplified in the present work to

$$r_d \simeq 1/q\bar{\mu}_d \, N_{od} \sqrt{\pi Dt_d} \qquad [A\text{-}10]$$

from which

$$\ln r_d = \frac{E}{2kT_d} + f(t_d, N_{od}, \text{etc.}) \qquad [A\text{-}11]$$

This expression has not been used to obtain another estimate of the effective activation energy, however, because no experiments were made keeping t_d constant and varying only T_d.

The total concentration of impurities in the diffused layers is given by

$$\bar{N}_d = \int_0^{x_{jd}} N(x)\, dx = N_{od}\sqrt{\pi Dt_d} \qquad [A\text{-}12]$$

The expression shown in Eq. [2] (section on Over-all process) can easily be obtained from Eq. [A-5] and [A-10] using the assumption that $\bar{N}_p = \bar{N}_d$.

The Adsorption of Water Vapor by Porous Glass

Myron J. Rand

Bell Telephone Laboratories, Inc., Allentown, Pennsylvania

ABSTRACT

Porous glass is a good getter for water vapor in semiconductor devices. This article presents a fundamental study of the physical adsorption of water on multiform porous Vycor over the range 30°-150°C and 10^{-3} to 25 torr water vapor pressure, with surface coverages up to a third of a monolayer. The adsorption isotherms, for which a general equation is given, are of the Freundlich type. Differential heats and entropies of adsorption have been determined, and from the latter it is concluded that the film of adsorbed water is intermediate in nature between rigidly localized and completely mobile. Kinetic studies give the result that the amount adsorbed is proportional to $(\text{time})^{1/2}$. The effects of various drying procedures on the subsequent adsorptive capacity of the glass are considered in some detail and the mechanism of surface dehydration inferred.

The porous glass discussed in this paper is an intermediate in the manufacture of Vycor brand glassware by the Corning Glass Works, and is essentially a finely divided amorphous silica with a consolidated instead of loose powder structure. It may be precision-fabricated into a variety of shapes by multiforming techniques; typical properties are shown in Table I. As a moisture adsorbent in a semiconductor device enclosure such a material would have the paramount advantage of physical strength and attendant freedom from dusting, spalling, or particle-shedding. In this it is unique among high-surface-area adsorbents. There are in addition the advantages of cleanness, freedom from ionizing impurities and organic contaminants, and closely controlled and reproducible manufacture. As a consequence porous glass was tried by these Laboratories as a moisture getter for transistors before any fundamental data on its adsorptive behavior were known. The criterion for success, as usual, was the stability of certain electrical parameters during life-testing. The first public mention (1) of improved reliability of devices incorporating a porous glass getter was made in 1957, and subsequent work has provided abundant evidence of the superiority of gettered germanium transistors (2).

A fundamental investigation of the behavior of multiform porous glass (MPG) as a moisture adsorbent begins with the establishment of its adsorption isotherm for water vapor. The complete isotherm for 25°C is shown in Fig. 1, which is a synthesis of measurements from Bell Telephone Laboratories, Corning Glass Works (by T. H. Elmer), and published data (3). The ordinate is the weight of water adsorbed per unit weight of dry MPG (x/m), and the abscissa the relative humidity (r. h.). The large hysteresis loop beyond 60% r.h. is presumed due to capillary filling and has been reported for a large variety of adsorbents on porous glass.

Since the glass, the transistor unit, and the gas ambient (if any) are all carefully dried at the time of encapsulation, the region of interest for getter behavior is the extreme toe of the isotherm. The range above 5% r. h. is easy to study, using sulfuric acid solutions to control water vapor pressure, but there is no way to predict accurately the low humidity part of the curve by the shape of any other part. All the work reported here is in the range below 5% r.h., and measurements have been made down to $p/p_o = 10^{-4}$. Isotherms have been established at nominal temperatures of 30°, 60°, 100°, and 150°.

Table I. Properties of multiform porous glass (Corning 7930 glass)

Typical composition	
SiO_2	96.3%
B_2O_3	2.9
$R_2O_3 + RO_2$*	0.7
Na_2O	0.05
Physical properties	
Apparent specific gravity	1.5
Porosity	29%
Average pore diameter	30-40Å
Surface area	170-230 m^2/g

* Mostly Al_2O_3 and ZrO_2.

Apparatus and Materials

The apparatus used for the determination of the MPG adsorption isotherms is shown schematically

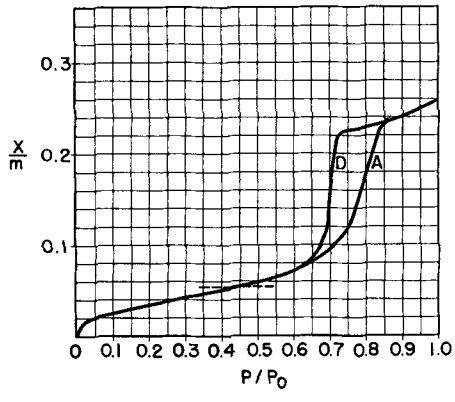

Fig. 1. Adsorption isotherm of porous glass at 25°C. D and A are desorption and adsorption branches. The dotted line indicates the monolayer.

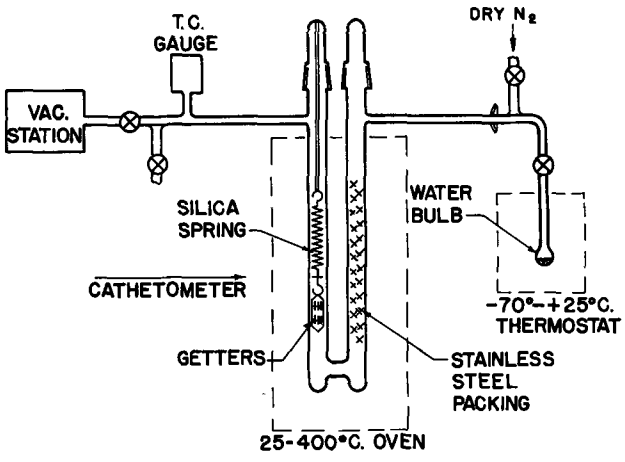

Fig. 2. Schematic diagram of sorption balance apparatus

in Fig. 2. This is a McBain-type sorption balance, with weight changes followed by observing the extension of a helical silica spring (4) with a cathetometer. The balance is designed for use in either vacuum or gas ambient, and the stainless steel packing in one arm of the adsorption cell aids in bringing flowing gas up to oven temperature before it reaches the sample suspended from the spring. The vacuum station includes a roughing pump, a three-stage oil diffusion pump, traps, and an ionization gauge. There is no trap between this gauge and the sorption balance. The thermocouple gauge continuously monitors the system pressure, but it is not relied on for accurate readings of the water vapor pressure. This is accomplished by maintaining a reservoir of pure water in the cryostat, whose temperature is controlled to ±0.1°C and read on a calibrated alcohol-filled thermometer. The water is degassed by several cycles of freezing, pumping, and melting.

The oven surrounding the adsorption cell is insulated heavily, with very narrow slots covered with plate glass serving as windows to follow the spring travel. Temperature is read on calibrated mercury thermometers. The elastic modulus of the spring is temperature-sensitive, and very close control is required: the temperature of the oven must be known to 0.1° to realize the ultimate sensitivity of the spring-cathetometer combination. The spring extension for a given weight change varies with the load also, and the spring must be calibrated accordingly. This was carried out over the range 30°-300° with gold weights placed in a silica bucket hung on the end of the spring. The micrometer-slide cathetometer, with a 20X eyepiece, read to 0.001 mm. With a spring of one-gram capacity and 10-cm stretch, the detection limit was a weight change fraction of 2×10^{-5}, corresponding to a sample surface coverage of 3×10^{-4} monolayer.

The MPG samples were from a standard production lot and are representative of those currently used as device getters. They are annular wafers about 8 mm OD x 0.8 mm thick, with a 2 mm diameter hole through the center; each weighs about 50 mg. Before use they were heated 16 hr at 150° in room air to drive off loosely held water. The "dry weight" (m of x/m) was taken on this basis; it does not differ from the activated weight, as determined below, by as much as 1%, and provides an invariant reference point. Fourteen getters were hung on the rods of a silica rack suspended from the spring.

In typical operation the spring and sample assembly are lowered into the adsorption cell with the oven already at the temperature chosen for activation of the MPG. After the ground joint is seated the apparatus is evacuated and the MPG pumped, most commonly at 200° for 12 hr. The pressure is read on the ionization gauge and weight changes may be observed if desired. At the end of the activation period the oven is cooled to the temperature at which the isotherm is to be measured, and the pumping station is closed off. The pressure at this point is below 10^{-5} torr; the apparatus can stand for several days with no change in the reading of the t.c. gauge, which is sensitive to 10^{-3} torr.

As soon as the balance reading for the activated condition is obtained, the water vapor source (which has been evacuated earlier) is opened to the cell and the weight gain followed. Equilibrium takes 2-12 hr, depending on conditions, and is considered attained when no detectable weight gain takes place in 1 hr. Equilibria could be approached also from the desorption side, but were reached more slowly.

The MPG had a surface area of 215 m^2/g by conventional B.E.T. methods (5). Assuming an adsorbed water molecule to occupy 10.8Å^2, the monolayer corresponds to $x/m = 0.06$, *i.e.*, a 6% weight gain. The range of x/m investigated here is from 5×10^{-4} to 2×10^{-2}, or $\theta = 0.01$ to 0.33.

Adsorption Isotherms

The moisture adsorption isotherms follow quite closely the Freundlich adsorption isotherm

$$x/m = k\, p^{1/n} \quad (n > 1)$$

This equation gives a straight line on a log-log plot, and the results are so presented in Fig. 3. Plotted as Langmuir isotherms ($p/(x/m)$ *vs.* p) the curves are concave toward the pressure axis; Temkin isotherms (x/m *vs.* log p) have opposite curvature (6).

A different group of samples was used for each isotherm. On several occasions a group used to establish one isotherm was used to fill in a point on a

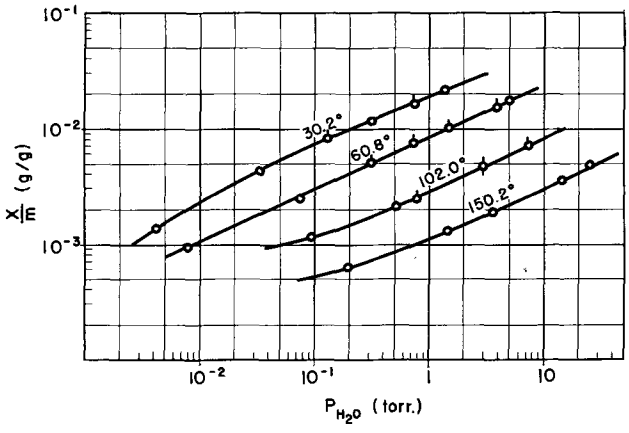

Fig. 3. Adsorption isotherms of water vapor on MPG. Activation 200°, 12 hr pump. Ó—second activation Ó third activation.

different isotherm. Often the samples were reactivated (particularly after standing over a weekend), and one group was reactivated twice; such points are indicated on Fig. 3. It is evident that the homogeneity of the MPG is good, and also that the adsorption is physical, at least in the sense that it is reversible, since weight gains were the same after reactivation. Sample surface areas and dry weights were found substantially unchanged after the measurements.

All the data of Fig. 3 are referred to initial activation conditions of 12-hr pumping at 200°. It is necessary to specify some standard activation since there is no readily definable zero point at which the glass may be said to be perfectly dry. At any temperature MPG *in vacuo* continues to release water for many hours. The 200° 12-hr activation was selected because these conditions should remove physically held water without appreciably dehydrating the silanol (SiOH) groups of the surface. This activation is hardly economical for device manufacture, however, and a study of the effect of various activation conditions is reported in the last section.

The isotherms have not been corrected for thermal transpiration (7) between the adsorption cell and the low-temperature water source. The correction can be calculated only rather empirically; the most generally useful discussion is that of Bennett and Tompkins (8). The thermal transpiration pressure ratio R has been calculated for a variety of temperature and pressure conditions; largely because the tubing connecting the points of temperature difference is 10 mm ID or more, the correction was so small as to be invisible on Fig. 3 except for the lowest pressure points of the 30° and 60° isotherms.

The exponent $1/n$ of the Freundlich isotherm equation appears as the slope of the log-log plots (Fig. 3). The value for the straight-line portions is 0.44, independent of temperature. The factor k is determined simply by reading it off the isotherm plot at $p = 1$, since here $k = x/m$. It happens that log k *vs.* $1/T$ is linear, and $k = 7.60 \times 10^{-7} \exp(3090/T)$. A general equation for the isotherms may now be written

$$x/m = [7.60 \times 10^{-7} \exp(3090/T)]\, p^{0.44}$$

where T is the absolute temperature and p the equilibrium pressure in torr. This equation describes a large range of behavior of MPG with an error not exceeding a few per cent, which is probably as good as the agreement among various manufacturing lots.

It should be remarked that over a 120° temperature range it is unusual for $1/n$ to be independent of temperature, and equally unusual to find a simple relationship between k and T. As an investigation of physical adsorption the work reported here is perhaps out of the ordinary in two respects: the surface coverages are low throughout, minimizing interactions between adsorbate molecules; and the adsorption is comparatively strong, probably involving forces beyond the usual van der Waals attractions.

Adsorption Thermodynamics

With equilibrium water vapor pressures over the MPG known at several temperatures, the isosteric differential heat of adsorption may be calculated from the Clausius-Clapeyron equation

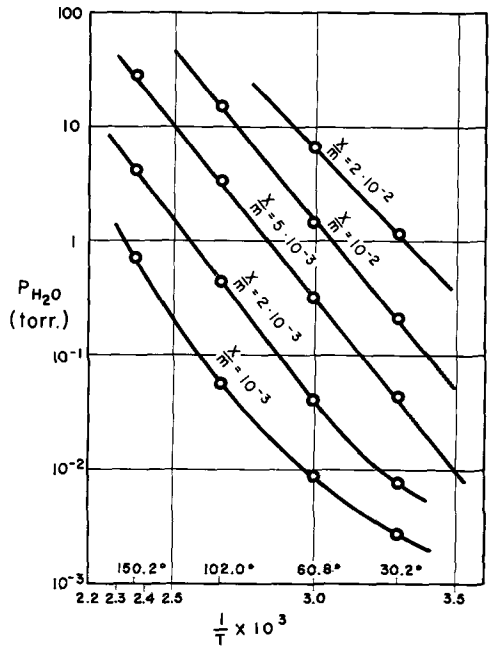

Fig. 4. Isosteres for water vapor adsorption on MPG

$$\left(\frac{\partial \ln p}{\partial T}\right)_\theta = \frac{\overline{\Delta H_a}}{RT^2} \qquad [1]$$

Figure 4 shows isosteres at θ's ranging from 0.017 to 0.33, plotted as log p *vs.* $1/T$. According to Eq. [1], assuming $\overline{\Delta H_a}$ independent of temperature, these should be linear, with slopes of $\overline{\Delta H_a}/2.303R$.

The isotherms also may be used to calculate an even more fundamental property, the entropy of adsorption, from which, by comparison with idealized models, some indication of the degree of mobility of the adsorbed film may be obtained. For this calculation it is necessary to choose a standard reference state; this is water vapor (ideal) at 1 atm throughout the discussion which follows. The free energy difference between this reference gas and the adsorbed molecules in equilibrium with water vapor pressure p is

$$\Delta G = RT \ln p \qquad [2]$$

with p in atmospheres. Experimental differential entropies then are calculated from

$$\Delta \bar{S}_a = \frac{\overline{\Delta H_a} - \Delta G}{T} \qquad [3]$$

It must be emphasized that $\Delta \bar{S}_a$ differs from ΔS_a, the change in entropy content of the system on adsorption of the gas. $\Delta \bar{S}_a$ is $(\partial S_a/\partial n)_{p,T,N}$ where n and N are amounts of adsorbate and adsorbent: the entropy change per mole accompanying infinitesimal adsorption at constant coverage, pressure and temperature, referred to the chosen standard state. The number of adsorption sites also is assumed constant. ΔS_a is always negative but $\Delta \bar{S}_a$ may take either sign.

Results for $\Delta \bar{H}_a$ and $\Delta \bar{S}_a$ are given in Table II. Since $\Delta \bar{H}_a$ is of the order of magnitude of the latent heat of liquefaction, the adsorption is physical. However, the

Table II. Results for $\Delta\bar{H}_a$ and $\Delta\bar{S}_a$

θ	T, °K	$-\Delta\bar{H}_a$, kcal/mole	Equil. p, atm	$-\Delta G$, kcal/mole	$-\Delta\bar{S}_a$, cal/mole^{-1} deg^{-1}
0.033	303	14.6	$1.0_0 \times 10^{-5}$	6.9_5	24.3
	334		$5.2_6 \times 10^{-5}$	6.5_4	
	375		$5.9_2 \times 10^{-4}$	5.5_5	
	423		$5.2_6 \times 10^{-3}$	4.4_1	
0.083	303	13.8	$5.5_2 \times 10^{-5}$	5.9_1	26.1
	334		$3.9_5 \times 10^{-4}$	5.2_0	
	375		$4.4_7 \times 10^{-3}$	4.0_4	
	423		$3.8_7 \times 10^{-2}$	2.7_4	
0.167	303	13.5_5	$2.7_5 \times 10^{-4}$	4.9_4	28.3
	334		$1.8_9 \times 10^{-3}$	4.1_6	
	375		$2.0_4 \times 10^{-2}$	2.9_1	
	423		$1.5_1 \times 10^{-1}$	1.5_7	
0.333	303	11.6	$1.5_4 \times 10^{-3}$	3.9_0	25.3
	334		8.8×10^{-3}	3.1_6	

result is close to the limit of $\Delta H_L + 5.5RT$ (= 13.8 kcal/mole) which Trapnell (9) will allow for pure physical adsorption. At $\theta < 0.01$ there may well be some chemisorption; the difficulty of removing the last traces of water during activation supports this belief.

To interpret $\Delta\bar{S}_a$, models of the two extremes of the adsorbate, perfectly mobile and rigidly localized, will be considered, and the differential entropy changes calculated for each. Because of numerous assumptions in both the models and the conventional entropy equations for various kinds of motion, such an approach cannot be pushed too far. Agreement to perhaps 3-5 e.u. between theory and experiment is all that may be expected.

In the gas phase at ordinary temperatures the significant contributions to the entropy are the translational and rotational motions. In the perfect gas the entropy is an extensive quantity and $(\partial S/\partial n)_{p,T}$ and $S(p,T)/n$ are identical. The conventional entropy equations thus give the differential entropy directly. The three-dimensional translational entropy is given by the Sackur-Tetrode equation, which after inserting all the constants, is

$$_3S_{tr} = 11.44 \log T + 6.33 \qquad [4]$$

for one mole of ideal water vapor at 1 atm. The results range from 34.7 to 36.4 e.u. The three-dimensional rotational entropy is given by

$$_3S_{rot} = \frac{3}{2}R + R \ln \frac{8\pi^2}{\sigma h^3} (8\pi^3 ABC)^{1/2} (kT)^{3/2}$$

where A, B, C are the moments of inertia and σ the symmetry number. For a water molecule $\sigma = 2$ and A, B, C are (10) 1.024, 1.920, and 2.947 x 10^{-40}g cm^2. After inserting all the constants the result is

$$_3S_{rot} = 6.86 \log T - 6.59 \qquad [5]$$

giving 10.4 to 11.4 e.u.

The model of the adsorbed film must be less exact. If it is perfectly mobile its rotational freedom remains essentially unrestricted; in place of three-dimensional translation there will be a restricted two-dimensional translation plus a weak vibration. For the differential entropy of the former Law (11) gives an equation which is equivalent to

$$_2\bar{S}_{tr} = R \ln \left[\frac{2\pi mkTa_o e}{h^2} \left(\frac{1-\theta}{\theta} \right) + 1 \right]$$

where a_o is the area occupied by an adsorbed molecule, here taken as 10.8 x 10^{-16} cm^2 for water. The expression reduces to

$$_2\bar{S}_{tr} = 4.58 \log \left[1.73T \left(\frac{1-\theta}{\theta} \right) + 1 \right] \qquad [6]$$

giving values ranging from 13.8 to 21.2 e.u. over the coverages and temperatures used.

The molar vibrational entropy per mode is given by

$$S_{vib} = \frac{Rx}{e^x - 1} - R \ln (1 - e^{-x}) \qquad [7]$$

where $x = hc\omega/kT = 1.439\ \omega/T$, with ω the vibration frequency in cm^{-1}. For ordinary chemical bonds with vibration frequencies in the infrared, say 1000-5000 cm^{-1}, x is of such size that S_{vib} is negligible. Unfortunately this is not true of the weak bond of a mobile film and the entropy can only be estimated roughly. On rather tenuous evidence (12) 3 e.u. will be assigned to $_2\bar{S}_{vib}$.

With a completely localized adsorbate all the entropy associated with the 3-dimensional translation will disappear. Most of $_3S_{rot}$ of 10-11 e.u. also will disappear, but there will remain the rotation of the hydrogen atoms around the axis passing through the oxygen atom and the center of mass, since it is probably the oxygen which is most closely bonded to the silica surface. The value of 2-3 e.u., depending on temperature, will be assigned to $_0\bar{S}_{rot}$.

For localized adsorption $_3\bar{S}_{vib}$ can be neglected. If the bond is like an OH bond ($\omega \sim 3500$ cm^{-1}) Eq. [7] gives $S_{vib} << 0.01$ e.u. If attachment is by an Si-O bond ($\omega \sim 1100$ cm^{-1}) the associated entropy is 0.2 e.u.

Finally there remains a configurational entropy term arising out of the fact that on a partially covered surface there are many ways to distribute the adsorbate molecules among the available surface sites. $\bar{S}_{config.}$ may be readily derived statistically by considering a system composed of n molecules and m sites (m a constant) so that $n/m = \theta$. The number of ways in which the m sites may be arranged into two groups of n occupied sites and $(m\text{-}n)$ empty sites is $m!/(m\text{-}n)!n!$ and the molecular entropy is $S = k \ln \dfrac{m!}{(m\text{-}n)!n!}$. The use of the Stirling approximation, followed by differentiation with respect to n, leads to

$$\bar{S}_{config} = 4.58 \log \left(\frac{1-\theta}{\theta} \right) \qquad [8]$$

with values of 8.1-1.4 e.u. over the coverages studied.

Thus for the localized adsorption model

$$-\Delta\bar{S}_a = {}_3S_{tr} + {}_3S_{rot} - {}_0\bar{S}_{rot} - \bar{S}_{config} \qquad [9]$$

whereas for mobile adsorption

$$-\Delta\bar{S}_a = {}_3S_{tr} - {}_2\bar{S}_{tr} - {}_2\bar{S}_{vib} \qquad [10]$$

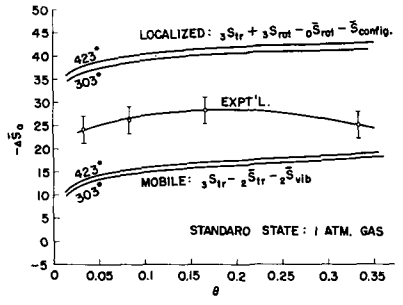

Fig. 5. Comparison of experimental values of $\Delta\bar{S}_a$ with those computed for extreme cases of fixed and mobile adsorbed film.

Values thus computed are nearly independent of temperature, so Eq. [9] and [10] are plotted *vs.* θ in Fig. 5, together with the experimentally determined $\Delta\bar{S}_a$ from Table II. It is evident that at coverages of 2-30% the adsorbed water on MPG is intermediate in nature between the two extreme models. The water molecules execute many vibrations in place, but presently they do hop to a neighboring site. There is some indication of greater mobility at coverages > 25%.

Law (11) found $\Delta\bar{H}_a = -14$ kcal mole^{-1} for the first layer of water on GeO_2 at ~300°K, and from entropy considerations he concluded that the adsorption was localized. For the multilayer region, however, the $\Delta\bar{H}_a$ fell toward −10 and the film, as expected, became mobile. At 30°C a monolayer of water on GeO_2 is completed at about 4 torr, at which MPG is only half covered. It is reasonable to conclude that dry MPG enclosed in a container with a GeO_2 surface cannot prevent the adsorption of some water vapor by the GeO_2 but definitely should prevent the formation of a film of water in which the molecules are mobile. Very probably a porous glass getter cannot hold surface recombination velocity at the optimum, nor can it prevent channel formation; but it should not permit any ionic conduction across the surface. This alone may be sufficient explanation for the improved performance of MPG-gettered devices, since without such a getter multilayer adsorption is easily possible.

Kinetics

In establishing the adsorption isotherms frequent readings of the weight change with time were made to study the approach to equilibrium, with the combination of low temperature (30°) and low pressure (~0.005 torr) being the slowest. Half the ultimate adsorption is reached in the order of ten per cent of equilibrium time. With gases other than water vapor present, *e.g.*, as in a device encapsulated in nitrogen, oxygen, etc., equilibrium will be reached much more slowly. In air at 1 atm, 25°C with p_{H_2O} = 1.2 torr (5% r.h.), MPG reaches equilibrium $x/m \sim 0.025$ in a week, with half the pickup occurring the first day.

Figure 6 presents typical data on the approach to equilibrium. Here the curves have been normalized by plotting θ/θ_{eq}, the fraction of the equilibrium coverage reached in time t. The curves are linear up to $\theta/\theta_{eq} = 0.75$. It is evident that the rate of approach to equilibrium is more sensitive to ambient

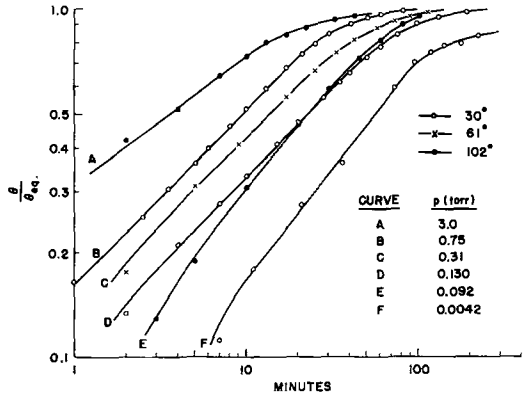

Fig. 6. Rate of approach to equilibrium during adsorption

pressure than to temperature; for example, curves D and E, which nearly coincide, are from runs 72° apart but with nearly the same pressure. Adsorption at higher temperatures does reach equilibrium somewhat sooner, but this is due almost entirely to more rapid approach above $\theta/\theta_{eq} = 0.8$.

There is some deviation from linearity in Fig. 6 at low coverages and low pressures. This probably reflects the heating effect of the initial rapid adsorption; heat transfer to the surroundings would be delayed not only by the low pressure but by the low thermal conductivity of MPG. For a typical case it was calculated that the heat liberated during the first minute of adsorption was sufficient to raise the entire adsorbent 3°, and doubtless even higher at the gross surface where the initial adsorption occurs.

It has been possible to find a general equation for the approach to equilibrium in much the same way as for the equilibrium isotherms. The slopes of the straight portions of the log-log plots are close to 0.5. If

$$\log \frac{\theta}{\theta_{eq}} = 0.5 \log t + \log k \qquad [11]$$

k may be determined for each run by observing t at some suitable θ/θ_{eq}. A temperature-independent relationship between k and pressure is shown in Fig. 7, where

$$1/k = 5.60 - 3.85 \log p$$

Then $\theta/\theta_{eq} = (x/m)/(x/m)_{eq} = t^{0.5}/(5.60 - 3.85 \log p)$, with t in minutes, p in torr, with no other gas present.

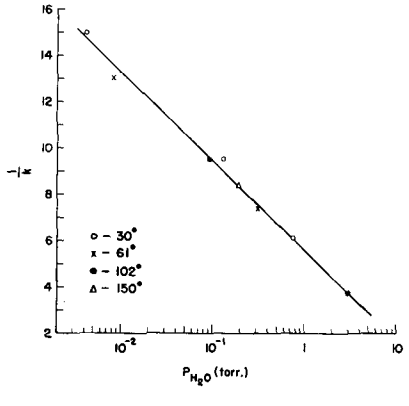

Fig. 7. Relation between k of Eq. [11] and pressure

Finally $(x/m)_{eq}$ from the general isotherm equation may be substituted, resulting in an equation of the form

$$\frac{x}{m} = \frac{Ae^{B/T}p^{C}t^{0.5}}{D - E\log p}, \quad 0.8 > \theta/\theta_{eq} > 0.1$$

with A, B, C, D, E all known constants. (D and E may change with getter geometry.) The equation states that at given conditions of pressure and temperature the cumulative weight gain $x/m = k_1\sqrt{t}$ and the rate of moisture pickup $\dfrac{d(x/m)}{dt} = k_2/\sqrt{t}$.

The treatment outlined above is not so successful for desorption. While the curves do have linear portions with similar slopes, the range of such correlation is limited not only in θ/θ_{eq} but in temperature also. Equilibrium is approached more slowly during desorption, probably because the activation energy for desorption is higher than that for adsorption.

Effect of Activation Conditions

When MPG which has been standing in room atmosphere is put into an oven a large part of the adsorbed water comes off in a rush during the first minute or two. Desorption continues, at a slower and slower rate, over a long period; the process may be accelerated by pumping. Desorption by vacuum bakeout has been followed up to 24 hr with the silica spring balance, but weight loss continues. There is no clearly definable point where it may be said that the MPG is "completely dry" or that it has been activated to a degree where no further treatment will improve its adsorptive capacity. It is generally believed that water can be liberated from silica surfaces in two ways: by desorption of physically adsorbed molecules and by interaction of adjacent silanol groups; but with MPG the two kinds of desorption apparently cannot be distinguished by weight changes.

The progress of vacuum desorption from the end of the first hour onward is shown in Fig. 8. An Elovich-type equation is followed: the weight loss is linear with log time (13). Such behavior usually is considered characteristic of chemisorption. Doubtless much of the water removed above 200° is chemically bound, *i.e.*, from SiOH groups, and largely irreversible, as will be shown; but it is still believed

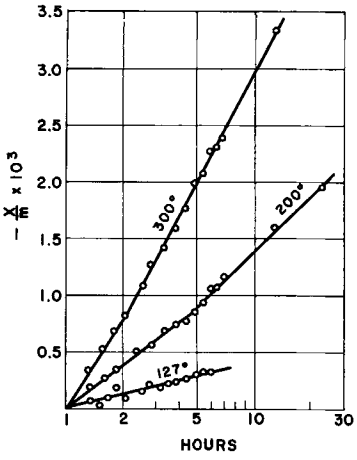

Fig. 8. Vacuum activation rates

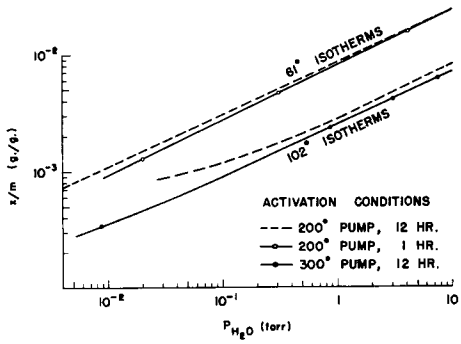

Fig. 9. Effect of vacuum bakeout conditions

that in MPG the rates are diffusion-controlled, and that the curves of Fig. 8 are more of practical rather than theoretical interest.

All the studies up to this point have employed 200° 12-hr vacuum activation. It remains to justify this choice, and also to investigate the effect of other activation conditions. The criterion is again the adsorption isotherm.

Two sets of experiments on pumping temperatures and times are summarized in Fig. 9. The dashed lines for the standard activation are taken from Fig. 3. When the pumping time is cut from 12 hr to 1 hr the 60.8° isotherm falls short of the standard one by a small and constant amount of $x/m = 0.3 \times 10^{-3}$. (On the log scale the isotherms appear to converge.) This is interpreted to mean that at 200° one hour is not sufficient to remove all the physically adsorbed (reversible) water. A few tenacious sites are still occupied, and the moisture pickup at a given pressure is then this much less.

Since the question now arises whether even the 12-hr activation is the optimum, a 300° 12-hr pump was next tested. Under these conditions removal of some chemically bound water is likely, but the literature is in conflict on the conditions and time required to reverse this reaction. To allow more opportunity for any rehydration to occur the 102° isotherm was determined for this activation. It is seen in Fig. 9 that a definite decrease in adsorptive capacity has occurred, and this time it is a constant proportion instead of a constant amount. The difference is about 12% and increases at $\theta < 0.02$. Here the inference is that some of the adsorption sites, and a disproportionate number of the more energetic ones, have been permanently removed. With this activation there was an irreversible 0.6% weight loss, [exactly the amount predicted (14) for amorphous silica from aquasols] whereas with 200° activation the getters showed essentially no dry basis weight change. While 300° activation is clearly deleterious, in all probability it could be tolerated if the time is restricted to an hour or less.

Experiments on the effect of dry nitrogen activation are summarized in Fig. 10. The dashed line is again the standard 60.8° isotherm from Fig. 3. The gas contained 8 ppm H_2O, at which the equilibrium adsorption at 61° is 0.87×10^{-3}. If this amount is subtracted from the isotherm over the entire range the dotted line results. This is the isotherm which would be predicted if (*a*) the gas flush activation is as effective as the standard one, and (*b*) after the activa-

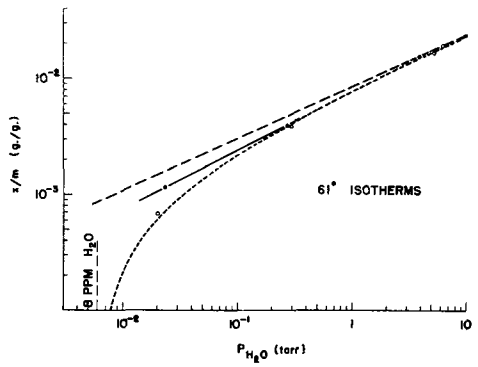

Fig. 10. Effect of hot gas activation. —— —— standard 200° 12 hr vacuum activation; -------- same, minus equilibrium adsorption at 61° from 8 ppm flushing gas; ○, *N* flush, 8 ppm H_2O, 200°, 12 hr, equilibrated with flushing gas at 61°; ●, *N* flush, 8 ppm H_2O, 300°, 30 min, incompletely equilibrated with flushing gas.

tion the MPG is permitted to come to equilibrium with the gas at the temperature at which the isotherm is determined. With the 200° 12-hr flush this latter requirement was met by allowing the getters to stand overnight in the gas before measurement. The resulting isotherm follows the predicted one closely. Thus condition (*a*) above is presumed true; nevertheless, a substantial loss in capacity at low pressures has resulted. This shows the folly of storing activated MPG at room temperature in dryboxes, which are usually far above 8 ppm moisture.

The 300° 30-min gas flush activation, shown also in Fig. 10, is a practical semiconductor device processing step. Here readsorption of moisture from the flushing gas was prevented as far as possible; the oven surrounding the sorption balance was cooled from 300° to 61° in 1½ hr and the isotherm measurements begun immediately. There is again a constant, but smaller, difference in the adsorptive capacity, since some readsorption cannot be avoided. However, in apparatus where the getters can be removed quickly from the activation chamber into sealed containers, or encapsulated immediately in devices, the 300° 30-min dry gas flush should be a quite satisfactory activation.

In all the gas flush experiments, the velocity of the nitrogen past the getters was about 20 cm/min. A higher velocity is desirable for the first few minutes if exposed getters are introduced into an oven already at temperature, to carry off the large initial burst of water vapor. Wet MPG should first be dried in a 150° air oven before any activation procedure.

The relative insensitivity of the 61° adsorption isotherm to the duration of 200° activation is significant. The adsorption is perfectly reproducible whether the sample has had one activation or three, even though the weight change continues in accord with the curve in Fig. 8. Between the end of the first and the twelfth hours of pumping a weight loss of 1.6×10^{-3} g/g occurs; yet the difference in the adsorption isotherms is only 0.3×10^{-3}. Water of constitution, *i.e.*, within the solid phase, cannot be removed at 200°; neither can the weight loss be due entirely to physically adsorbed water persisting past the first hour, since these tenacious sites would be the first to readsorb and the weight loss would be reversible. The 0.3×10^{-3} difference is ascribed to this kind of water, but the remainder can only represent silanol dehydration. A weight loss of 1.3×10^{-3} g/g represents removal of one hydroxyl in twenty, and if these hydroxyls were sites of physical adsorption of water molecules (by hydrogen bonding) the effect on the adsorption isotherm should be quite detectable at higher pressures. The absence of such an effect shows that the first hydroxyls to be removed are not adsorption sites, and indeed other work in these Laboratories has indicated that the MPG surface must be almost half dehydrated before moisture adsorption is significantly lower.

The futility of prolonged vacuum activation is thus demonstrated. The same is true of 200° dry gas activation, where both the weight loss over the second through twelfth hours (1.5×10^{-3} g/g) and the adsorptive capacity are virtually identical to those for vacuum activation. It is evident that the 200° 12-hr pump is the most effective activation procedure of all those tried, but any of the others can approach it with proper handling. Careless exposure first degrades the adsorption capacity at low equilibrium pressures, where device behavior may be very sensitive to moisture level. By and large there is no reason to believe, either from work reported here or from life-testing, that activation conditions are critical in the application of MPG to moisture gettering in devices.

Manuscript received Nov. 21, 1961; revised manuscript received Jan. 18, 1962. This paper was prepared for presentation before the Detroit Meeting, Oct. 1-5, 1961.

Any discussion of this paper will appear in a Discussion Section to be published in the December 1962 JOURNAL.

REFERENCES

1. T. R. Robillard and R. W. Westberg, *I.R.E. Wescon Convention Record*, pp. 14-16 (1957).
2. See, for example, D. S. Peck, "Semiconductor Reliability Predictions from Life Distribution Data," in "Semiconductor Reliability," pp. 51-67, Engineering Publishers, Elizabeth, N. J. (1961). Also G. A. Dodson and B. T. Howard, *Proc.* Seventh Nat. Symposium on Reliability and Quality Control in Electronics, pp. 262-272, Institute of Radio Engineers Inc., New York (1961).
3. C. H. Amberg and R. McIntosh, *Can. J. Chem.*, **30**, 1012 (1952).
4. Supplied by Worden Laboratories, Houston, Texas.
5. Determined by W. G. Guldner, Bell Telephone Laboratories, Murray Hill, N. J.
6. For a discussion of the theory and properties of the three types of isotherm see B. M. W. Trapnell, "Chemisorption," Chap. V; Butterworths Scientific Publications, London (1955).
7. M. Knudsen, *Ann. physik*, **31**, 205, 633 (1910).
8. M. J. Bennett and F. C. Tompkins, *Trans. Faraday Soc.*, **53**, 185 (1957).
9. Trapnell, *op. cit.*, p. 143.
10. G. Herzberg, "Molecular Spectra and Molecular Structure," p. 488, D. Van Nostrand Company, Inc., New York (1945).
11. J. T. Law, *J. Phys. Chem.*, **59**, 67 (1955).
12. C. Kemball, *Advances in Catalysis*, **2**, 233 (1950); D. Hadzi, *J. Chem. Phys.*, **34**, 1445 (1961).
13. For a discussion of the characteristics and applicability of Elovich equations see M. J. D. Low, *Chem. Rev.*, **60**, 267-312 (1960).
14. W. K. Lowen and E. C. Broge, *J. Phys. Chem.*, **65**, 16 (1961).

Etching of Abraded Germanium Surfaces with CP-4 Reagent

E. N. Pugh and L. E. Samuels

Department of Supply, Australian Defence Scientific Service,
Defence Standards Laboratories, Sydney, New South Wales, Australia

ABSTRACT

The dissolution of the damaged layer has been investigated by a metallographic taper-sectioning technique and by direct microscopical examination of the etched surfaces. It is shown that the reagent penetrated the damage cracks in abraded surfaces opening them into deep crevices. At the same time, the surface begins to be smoothed out, a characteristic cellular pattern being produced. A completely flat surface is not achieved until well after the damaged layer is removed. A critical comparison of certain methods of estimating the depth of the damaged layer is made in the light of these observations. It is concluded that metallographic methods are the most reliable.

A recent metallographic study established that the damaged layer in abraded germanium surfaces contains numerous cracks and that these cracks in fact constitute the damage; it also established that high densities of dislocations are not present (1). In practice, the damaged layer in semiconductor devices is removed by chemical etching, so that it was considered of interest to investigate the effects of the cracks on this dissolution process. Such a study is also desirable to investigate further the discrepancy found in the earlier work between the metallographic measurements of the depth of damage and values obtained by the photomagnetoelectric (PME) method developed by Buck and McKim (2).

Experimental Methods

The investigations were carried out on {111} surfaces of n-type germanium abraded unidirectionally, by hand, with silicon carbide abrasives. Most of the work was carried out with 220-grade abrasive, but experiments with other grades confirmed that the results had general application. The abrasives were used both in papers, using flowing water as lubricant, and in a water slurry on a glass plate. The abraded specimens were etched for various times with CP-4 reagent,[1] the etching being confined to rectangular areas, 1.0 x 0.5 cm, by protecting the remainder of the abraded surface with a suitable lacquer coating. In each case, an estimation of the depth removed was made by the standard weight-loss method.

After preliminary examination under the microscope, the surfaces were taper sectioned at a nominal angle of 5° 43′ (taper ratio 10 : 1), the section line being made approximately perpendicular to the direction of abrasion. During sectioning, the surface was protected by means of electrodeposited nickel coatings. The sectioned surfaces were polished metallographically and examined under the microscope. The sections showed two regions corresponding to the unetched abraded surface and the etched surface, respectively. The depth removed by etching could therefore also be estimated from the displacement of the section line between the two regions, measured by means of a travelling microscope. These measurements were made from the crests of the surface irregularities in both the unetched and etched regions, the preferentially attacked area immediately adjacent to the unetched portion of the surface being ignored.

[1] 50 ml nitric acid (69%), 30 ml acetic acid (100%), 30 ml hydrofluoric acid (48%), and 0.6 ml bromine.

Metallographic Observations

Examination of the taper sections.—The taper sections of lightly etched surfaces indicated that the CP-4 reagent penetrated rapidly along the cracks in the damaged layer. Etching was uniform over the contact area resulting in widening of the cracks and rounding of their tips (Fig. 1). Once the most severely shattered portions of the damaged layer had been removed, the surface irregularities began to smooth out. A typical sequence for a surface treated with abrasive papers is shown in Fig. 2-5; allowing for the initial difference in the distribution of the

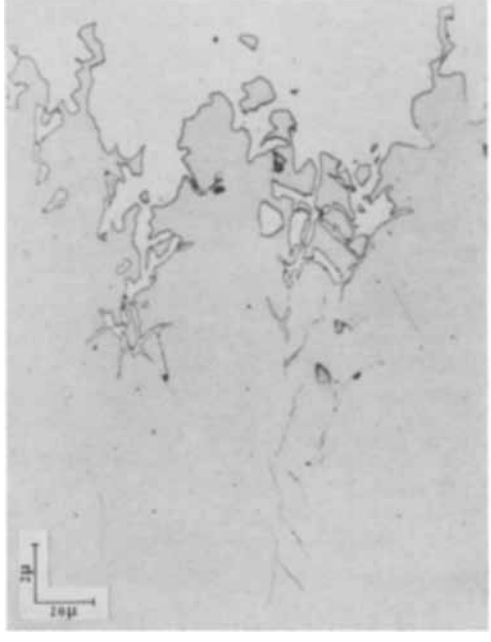

Fig. 1. Taper section of a germanium surface abraded with 220-grade silicon carbide paper and etched with CP-4 reagent to remove approximately 4μ. Taper section unetched.

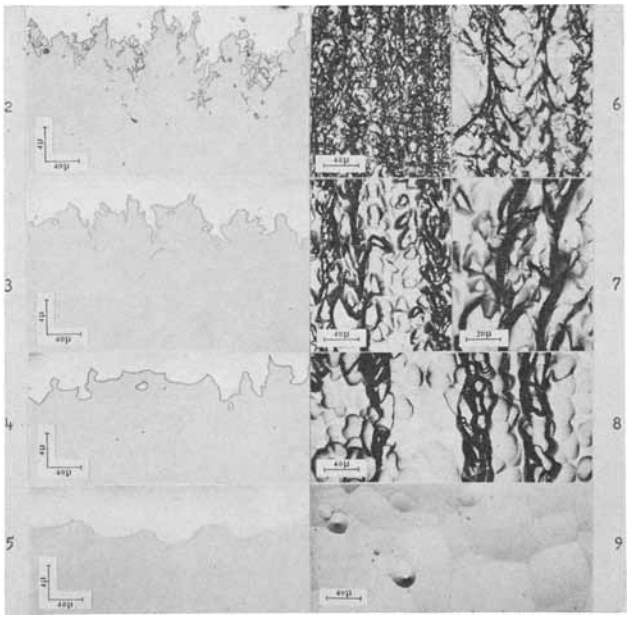

Fig. 2-9. Germanium surfaces abraded with 220-grade silicon carbide paper and etched with CP-4 reagent. Figures 2-5 are taper sections of the etched surfaces. Figures 6-9 show the appearance of the surface when examined directly by a metallurgical microscope.

Fig. No.	Depth removed by etching, μ
2, 6	4
3, 7	11
4, 8	18
5, 9	26

The last vestiges of damage cracks are present in three vertical bands in Fig. 8, but none are present in Fig. 9.

damage cracks (1), the behavior of surfaces abraded with a slurry was similar. The surface is still not completely smoothed even when the damaged layer has been removed completely (Fig. 5).

Direct examination of the etched surfaces.—Three distinct features were observed when successively etched surfaces were examined directly by optical microscopy, namely, cracks, a cellular structure, and etch pits.

Cracks.—In the early stages of etching, the cracks appeared as dark markings which mostly lay in directions consistent with their being {111} cleavage traces (Fig. 6 and 7). As expected from the earlier work (1), the cracks in surfaces abraded with abrasive papers formed regular patterns in the abrasion direction (Fig. 6-8). Those in surfaces abraded with an abrasive slurry were randomly arranged (Fig. 10-12). Further etching caused the cracks to broaden (cf. Fig 6 and 7), but they were still recognizable immediately before complete removal (Fig. 8 and 12).

The identification of the cracks at the early stages of etching was difficult because they tended to be obscured by the background structure. Indeed, Faust (3) was unable to distinguish them in a similar type of experiment. Their identification here was greatly assisted by the prior knowledge obtained from the examination of taper sections of the surfaces. Their presence was also confirmed by metallographically polishing the abraded surfaces until all the surface chipping had been removed, the surface subsequently being etched with CP-4 reagent as before. The confusing background did not then develop and the broadened cracks stood out clearly.

However, by using Fig. 6-9 and Fig. 10-13 as guides, there should now be no confusion in recognizing damage cracks in abraded and etched surfaces, particularly when the damaged layer had been almost completely removed; Figure 12 illustrates how clearly the last traces of the damage cracks can be distinguished. A simple yet reliable method of estimating the depth of damage can be based on this technique, the approximate depth removed when the last traces of the damage cracks disappear being estimated by the weight-loss method. The results obtained by this technique have been compared in a number of instances with those obtained by the original taper-sectioning technique (1), and in all cases the agreement was good. For example, the series illustrated in Fig. 10-13 for abrasion with 220-grade silicon carbide slurry indicated a depth of damage of 88μ. the value determined by taper sectioning was 85μ (1).

Cellular structure.—The cellular structure developed in the areas between the cracks; the cell diameter increased with increased etching (Fig. 6-9 and

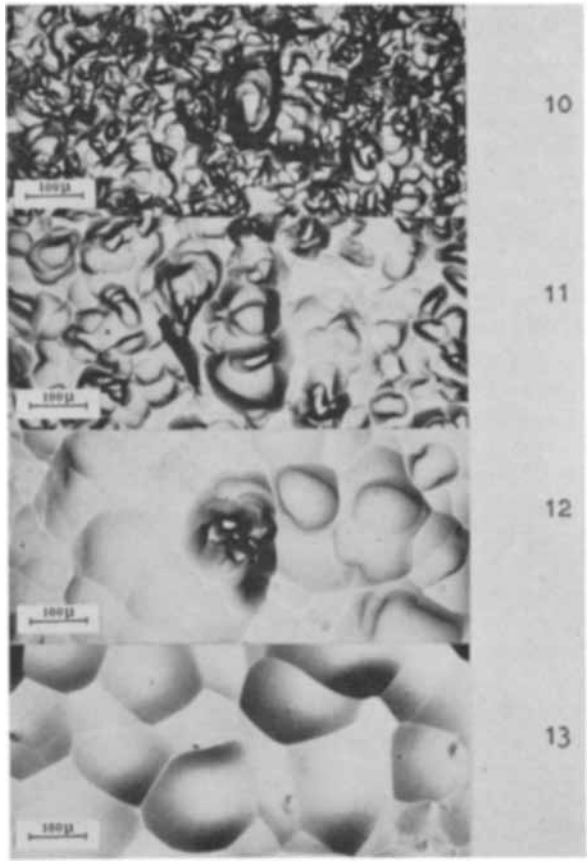

Fig. 10-13. Germanium surface abraded with 220-grade silicon carbide slurry and etched with CP-4 reagent.

Fig. No.	Depth removed by etching, μ
10	24
11	45
12	77
13	88

The last vestiges of damage cracks are present at the center of Fig. 12, but none are present in Fig. 13.

10-13) and was still prominent when the damaged layer had been removed completely (Fig. 9 and 13). Under otherwise comparable conditions, the cell diameter was smaller the finer the abraded finish; indeed, it did not develop at all if the surfaces were initially quite flat, as after complete metallographic polishing. Correlation with the taper sections (*e.g.*, Fig. 5) indicated that each "cell" consisted of a dish-shaped depression bounded by a comparatively sharp rim.

This structure is the so-called "first-order" network reported by Chang (4). The present observations confirm the findings of Noggle and Stiegler (5) that it results not from any substructure in the crystal itself but rather from the mechanical preparation of the surface. The cleavage pits in the original abraded surface are smoothed out into a series of dish-shaped depressions during etching. Some depressions then grow at the expense of the others, at the same time becoming progressively shallower. The pattern is no longer detectable when a layer some five times deeper than the damaged layer has been removed. Noggle and Stiegler (5) used the disappearance of the cellular pattern as a criterion for the complete removal of the damage, but the present observations indicate that there is no real relationship between the two.

Some confusion has resulted from the fact that Bonfiglioli *et al.* (6) have also used the term first-order network to describe a similar but much less pronounced cellular pattern produced by the etching of grown-in dislocations, which is considered in the following section. Both patterns result from the mechanism by which the CP-4 reagent smooths out depressions in the surface, but clearly different terms should be used for the two cases.

Dislocation etch pits.—During the formation of the cellular structure, classical dislocation etch pits of the type described by Pfann and Vogel (7) were also observed (several are present in the field shown in Fig. 9). The type of cellular pattern described by Bonfiglioli (6) developed when these dislocation etch pits were suitably grouped, but this pattern could always be distinguished from that due to the cleavage pits.

The density of the dislocation etch pits was about $10^8/cm^2$, which is of the order to be expected for grown-in dislocations. Faust (3) has reported observing dislocation etch pit densities as high as $10^6/cm^2$ in the damaged layer in a similar type of experiment. It is possible that Faust mistook an early development of the first-order network for dislocation etch pits, but this cannot be confirmed from his published micrograph.

Comparison between the Metallographic and Other Methods of Estimating the Depth of Damage

The earlier work (1) showed a considerable discrepancy between the results of the metallographic taper-sectioning method of estimating the depth of damage and the method based on the photomagnetoelectric (PME) effect developed by Buck and McKim (2). The metallographic method gave consistently higher results. The principle of the PME and most earlier methods of estimating the depth of damage is to remove successive layers from the damaged surface by etching and to determine some relevant property of the surface at each stage. The damaged layer is assumed to have been removed completely when this property reaches a constant base level, and the depth removed at that stage is estimated from the weight lost from a known area of surface.

The first possibility in accounting for the discrepancies between the two general methods is that the weight-loss method of depth measurement is unreliable because of the irregular topography of these surfaces. It was to check this point that the weight-loss method was compared with the metallographic method described above. The latter method indicated that the etched surfaces were irregular on a macro scale when the damaged layer was almost completely removed and frequently were not exactly parallel to the original surface. These irregularities develop mainly as a result of the general unevenness in the depth of the damaged layer itself and from the penetration of the etchant along the damage cracks. Consequently, this metallographic method of measuring the depth removed during etching, which measures a local depth, yielded a range of values which lay on both sides of the value given by the weight-loss method. This suggests that the latter is reliable in estimating the average value of the depth removed, although the exact significance of this figure is debatable. The early stages of etching, when the etchant penetrated along the cracks, are exceptional. The weight-loss method then grossly overestimates the depth removed, but this is not significant in the present context.

The original taper-section method of estimating the depth of damage (1) measures the maximum local depth from the crests of the surface irregularities to the extremities of the deepest cracks. This is necessarily greater than the average value determined by any of the methods depending on weight-loss measurements. It is doubtful, however, whether this would account for more than a small portion of the discrepancy between the two methods. The explanation must be sought in the characteristics of the methods used to detect the damage, and the present work does throw some light on two of the more important of these, namely, the PME method (2) and the etching rate method (8, 9).

The PME method determines the balance between the production of carrier pairs by the illumination of the surface and the recombination of these pairs in the damaged layer. The surfaces of the cracks now known to be present in the damaged layer provide extensive surfaces on which recombination can occur, and the forest of cracks must be a very efficient trap for the drifting carriers. The PME voltage consequently is initially very low. When the surface layers are removed by etching, the area of the recombination surface is reduced as also is the depth of the trap, so the PME voltage rises. However, the cracks are also opened out and, at some stage, the illumination may become incident on their sides and bases, in which event these surfaces now become

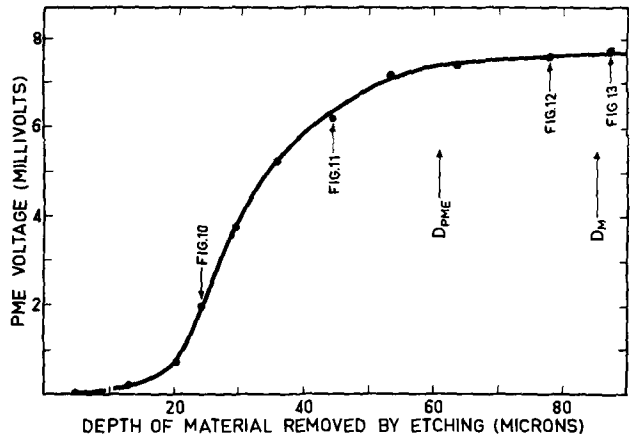

Fig. 14. Change of open-circuit PME voltage with etching, after abrasion on 220-grade silicon carbide slurry. D_{PME} and D_M indicate the depth of damage estimated from this curve and by the metallographic taper-sectioning technique (1), respectively. The arrows labelled Fig. 10-13 indicate the surfaces for which the micrographs shown in Fig. 10-13, respectively, are representative.

sources of carrier pairs. It seemed probable, therefore, that the PME voltage would reach a constant value before the original damaged layer had been removed completely.

To confirm this, a specimen used for the determination of the depth of damage by the PME method was examined microscopically at each successive stage in the etching process. The resulting PME curve is shown in Fig. 14, and representative fields of the surface at various stages are illustrated in Fig. 10-13. It can be seen that cracks are still visible in Fig. 12 although the PME curve indicated that all the damage had been removed at this stage. The stage at which all the cracks had actually been removed, as shown by microscopic examination (Fig. 13), is indicated in Fig. 14. It can be concluded that the original metallographic method (1) is more reliable in measuring the full extent of the crack-containing layer. However, it may be argued that the value determined by the PME method is adequate for practical purposes, since the residual crevices would not be expected to affect the electrical properties of the material significantly.

The etching rate method of measuring the depth of damage depends on the fact that the dissolution rate of abraded surfaces is initially very high and decreases as material is progressively removed until a constant rate is reached; the depth removed at the latter stage is taken as the depth of damage. Camp (8) attributed the increased etching rate merely to increased surface area, but Faust (10) has suggested that a high dislocation density in the damaged layer also contributes. It is now apparent that the damaged layer does not contain high densities of dislocations (1), so that the increase in etching rate must be attributed entirely to increase in surface area; the results described above leave little doubt that this factor can adequately account for an initially high dissolution rate of an abraded surface. On this basis, the etching rate should reach an approximately constant value when the surface area reaches an approximately constant value. Although a quantitative assessment has not been made of this factor, the observations made in the course of the present work clearly suggest that this stage would be reached before the original damaged layer had been removed completely.

Summary

The CP-4 reagent penetrates the damage cracks in abraded surfaces, opening them into deep crevices. At the same time, cleavage pits in the regions between the cracks are smoothed into dish-shaped depressions which, on further etching, result in the formation of a cellular structure. This structure persists for etching times considerably longer than those required to remove the damage cracks. The reagent also produces dislocation etch pits in the surface, but these are solely due to dislocations produced during growth of the crystal.

The complex manner in which the crack-containing layer is removed by CP-4 reagent introduces uncertainties into the measurement of its depth by methods involving changes in some surface property as the damaged layer is removed by etching. It is suggested that metallographic methods of measuring the depth of damage are the more reliable. The metallographic taper-sectioning technique is probably the most precise method, but a simpler approximate method adequate for many purposes would be to examine the surface microscopically after removal of successive layers by etching with the CP-4 reagent. The damage cracks can be recognized in the etched surface and the stage at which they have been completely removed can be determined, the approximate average depth removed by etching then being estimated by the weight-loss method. This microscopic method of examining etched surfaces to determine whether damage cracks have been removed could also be used in production control.

Acknowledgments

The assistance received from Mr. D. K. Sewell and Mr. M. B. McGirr in the PME determinations is gratefully acknowledged. This paper is published by permission of the Chief Scientist, Department of Supply, Australian Defence Scientific Service, Melbourne, Victoria, Australia.

Manuscript received Oct. 9, 1961; revised manuscript received Jan. 16, 1962.

Any discussion of this paper will appear in a Discussion Section to be published in the December 1962 JOURNAL.

REFERENCES

1. E. N. Pugh and L. E. Samuels, *This Journal*, **108**, 1043 (1961).
2. T. M. Buck and F. S. McKim, *ibid.*, **103**, 593 (1956).
3. J. W. Faust, Jr., in "The Surface Chemistry of Metals and Semiconductors," H. C. Gatos, Editor, p. 130, John Wiley & Sons, Inc., New York (1960).
4. R. Chang, *J. Appl. Phys.*, **28**, 385 (1957).
5. T. S. Noggle and J. O. Stiegler, *ibid.*, **30**, 1279 (1959).
6. G. Bonfiglioli, A. Ferro, and A. Mojoni, *ibid.*, **31**, 684 (1960).
7. W. G. Pfann and F. L. Vogel, *Acta Met.*, **5**, 377 (1957).
8. P. R. Camp, *This Journal*, **102**, 586 (1955).
9. J. W. Faust, Jr., Am. Soc. Testing Materials, Symposium of Cleaning of Electronic Device Components and Materials, *Special Tech. Publ.* 246 (1959).
10. J. W. Faust, Jr., Electrochemical Soc. Meeting, Buffalo, N. Y., Oct. 1957 (unpublished).

The Electrochemistry of V_2O_5 in LiCl-KCl Eutectic Melt

H. A. Laitinen and D. R. Rhodes[1]

Department of Chemistry and Chemical Engineering, University of Illinois, Urbana, Illinois

ABSTRACT

The electrochemistry of V_2O_5 in an LiCl-KCl eutectic melt has been investigated with the aid of several electroanalytical techniques. Independent measurements with voltammetry, chronopotentiometry, and constant current electrolysis indicate that V_2O_5 is reduced to a mixed lithium vanadium oxide (lithium vanadium bronze) on the electrode surface at a potential which is a function of V_2O_5 concentration. Lithium vanadates of limited solubility are also formed during the reduction. Lithium vanadium bronzes which were obtained by the thermal decomposition of Li_2CO_3 and V_2O_5 do not agree in chemical and x-ray analysis with those obtained by the electrochemical reduction of V_2O_5.

Although numerous papers have been published concerning the electrochemistry of metal chlorides in molten alkali metal chloride systems, relatively few investigations have been made of the electrochemistry of complex metal oxide systems in these solvents. In general, the electrochemical techniques which have been developed for simple metal ions should be useful for the study of complex metal oxide systems.

Vanadium (V) oxide in LiCl-KCl eutectic melt represents a complex system in which electrochemical and acid-base properties are interrelated. This system is of practical interest because of its use as a cathode in high-temperature batteries (1). Because V_2O_5 should act as a relatively strong acid in this solvent, the oxidizing strength of vanadium (V) will be a function of the basicity of the melt. The addition of electrons to V_2O_5 might be expected to cause the release of oxide ions which will react with V_2O_5 to form anionic species of vanadium (V).

The chemistry and electrochemistry of vanadium in molten salt systems has been partially studied by several groups. The standard potentials of V(II)/V(O) and V(III)/V(II) in an LiCl-KCl eutectic melt have been determined (2). Molina (3) has described the absorption spectra of V(II), V(III), VO^{+2}, and V_2O_5 and gave a detailed discussion of the effect of adding oxide ion and acidic species to a V_2O_5 solution in an LiCl-KCl eutectic melt. Van Norman and Osteryoung (4) found that metavanadate in an LiCl-KCl eutectic melt reacted with an excess Na_2CO_3 to form orthovanadate as determined from the evolution of CO_2.

Massive electrolysis of V_2O_5 in molten magnesium or lithium borates gave spinels of the formula, $MgO:V_2O_3$ or $Li_2O:2V_2O_3$ (5). Electrolysis of V_2O_5 in molten $AlBr_3$-KBr (6) yielded a deposit of VO_2 on the cathode, but electrolysis of V_2O_5 in $AlCl_3$-KCl gave no deposit. The electrolytic reduction of V_2O_5 in alkali phosphate melts gave, in general, VP in weakly alkaline melts, V_2O_3 in strongly alkaline melts in the presence of chloride, and VO in strongly alkaline melts in the absence of chloride (7, 8).

[1] Present address: California Research Corporation, Richmond, California.

Voltammetry, chronopotentiometry, potentiometry, and coulometry were used in this investigation to study the electrochemistry of V_2O_5 in an LiCl-KCl eutectic melt solution. These methods have been shown to be useful techniques to study molten salt systems (9).

Experimental

A eutectic mixture of 41 mole % KCl and 59 mole % LiCl (melting point 352°C) at a temperature of 450°C was used as the solvent system for these investigations. The method employed in the preparation of the solvent has been described in detail elsewhere (10). The purity of the melt was tested by taking residual current-voltage curves of the melt with a platinum microelectrode (0.8 mm^2 in area). Up to a potential of −2.0v *vs.* Pt(II) (1M)/Pt reference the residual current was of the order of 1μa.

The fused salt cell and related equipment was similar to that described previously (10). All electrodes and solutions were separated into compartments by means of fritted glass sealing tubes.

The reference electrode for this system was a platinum foil in contact with a Pt(II)-melt solution. This electrode is stable, reproducible, and nonpolarizable in the eutectic melt at 450°C (11). Unless otherwise noted, all potentials are given with reference to a Pt(II) (1M)/Pt electrode, which is defined as an arbitrary reference point of zero. The IUPAC sign convention (polarity refers to charge of metal phase for reduction half-reaction) is used.

Several types of indicator electrodes were used in this investigation. Platinum microelectrodes were prepared by sealing the appropriate gauge wire into a glass bead of Corning 010 G-164-EC glass and by sealing this glass bead to a 5 mm tube of lead glass (Corning 0120). The tip of the bead was ground to a flat surface with emery paper to expose a cross section of platinum wire and was then polished to a smooth surface with 4/0 emery paper.

Gold-plated microelectrodes were prepared by electrolyzing the appropriate gauge platinum microelectrode as a cathode in an aqueous gold-cyanide bath buffered with Na_2HPO_4 (12). A smooth gold plate, which was stable in the eutectic melt, could

be obtained by using a current density of 1-5 ma/cm² in a bath at 70°C. Residual current curves with gold microelectrodes in LiCl-KCl eutectic melt were similar to those obtained with platinum microelectrodes except for a positive shift of the anodic limit of about 0.1v.

Because platinum and, to a lesser extent, gold are oxidized by V_2O_5-melt solutions, a nonporous indicator electrode which was stable in a V_2O_5-eutectic melt solution was needed. Spectroscopic graphite rods gave ill-defined potentials because of their porosity. Recently, a special form of graphite called Pyrographite (13) or Pyrolytic Carbon (14) has been developed. This is a polycrystalline form of graphitic carbon, impervious to gases and liquids (13), which has been deposited from a carbonaceous vapor on a graphite substrate at temperatures above 2000°C.

The Pyrographite electrode (15) used as an indicator electrode consisted of a Pyrographite coating, 6-11 mils thick, on a ¼-in. graphite rod. The rod was threaded and attached to a ⅜-in. by 12-in. graphite rod. The surface of the electrode under 80 times magnification with a Leitz microscope had the appearance of a "blistered paint surface."

Where necessary, a ⅛-in. spectroscopic graphite rod, which had been previously cleaned in HCl and dried with heat under vacuum, was used as a counter or working electrode.

Potential measurements were made with several types of instruments. An adapted L&N student potentiometer with a sensitivity of 13 μv was used for high sensitivity and accuracy. For measurement of potential as a function of time, a MR Sargent Recorder or Tektronix, Type 502, oscilloscope was used. According to the instruction manual, the recorder is accurate to 0.1% or 20 μv, whichever is greater. The oscilloscope voltage scale and sweep rate are accurate to within 3% of full-scale deflection.

Current-voltage curves were obtained with either a L&N Electrochemograph, Type E, or a Sargent, Model XV, polarograph.

For chronopotentiometric measurements, an apparatus was constructed which was similar to that used by Laitinen and Gaur (15, 16). The potential of the indicator electrode during the transition time *vs.* a platinum reference electrode was followed with an oscilloscope and recorded on 35-mm Kodak Plus-X film. The measurements were made from 4-in. by 5-in. enlargements. A large Pyrographite electrode (1.2 cm²), a ⅛-in. spectroscopic graphite rod, and a Pt(II)/Pt electrode were used as the indicator, counter, and reference electrodes, respectively.

Constant current for coulometry was obtained from two sources. A Sargent coulometric current source, Model IV, provided an accurate and constant supply of current. When this was not available, current was obtained from a constant current-voltage source through a high resistance in the usual manner. The procedure for coulometry was to pass a constant current between the indicator electrode and a counter electrode in separate compartments and to measure the potential of the indicator electrode *vs.* a reference electrode as a function of time with a Sargent MR recorder. During electrolysis, the solution was stirred with a long glass rod connected to a stirring motor above the melt.

The solubility of V_2O_5 in an LiCl-KCl eutectic melt is unlimited. At higher concentrations, however, V_2O_5 reacts with the melt to form Cl_2 and some type of insoluble reduced vanadium compound (17). Since large additions of V_2O_5 to the melt would result in large localized concentrations, only small additions of V_2O_5 were made, and the solution was vigorously stirred to prevent any reactions.

Results and Discussion

Synthetic lithium vanadium oxides.—There exists some confusion in the literature concerning anionic species of vanadium oxides and their solubilities in LiCl-KCl eutectic melt. Molina (3) concluded that metavanadate ion is soluble and that orthovanadate is insoluble. Van Norman and Osteryoung (4) did not report the formation of any insoluble vanadates when they added Li_2CO_3 to metavanadate-eutectic melt solutions. Observations made in this laboratory indicate that several lithium vanadate species have limited solubilities. Attempts were made to measure their solubilities, but only qualitative results could be obtained.

Because the electrochemical reduction of V_2O_5 involves the formation of a mixed lithium vanadium oxide (lithium vanadium bronze), several attempts were made to prepare bronzes by thermal decomposition of Li_2CO_3 and V_2O_5 mixtures.

In a typical preparation, these substances in molar ratio of one were heated to the molten state in a platinum crucible. The molten mixture was left open to air for several hours and then slowly cooled. While the melt was cooling, dark blue-black crystals formed; but when the frozen mass was ground up for analysis, a brown phase was also observed to be present. The brown phase was removed by boiling the mixture in aqueous ammonia solution. The remaining blue-green precipitate was filtered, dried, and analyzed. Chemical analysis of two mixtures gave a stoichiometry of 2.6 ± 0.2 Li_2O:V_2O_4:4.8 ± 0.4 V_2O_5. The similarity between the x-ray powder diffraction patterns for the two mixtures is shown in Table I.

Chemical analysis of the thermally prepared bronzes does not fit the results of other authors. Flood and co-workers (18) prepared a number of

Table I. X-ray diffraction data of 2.6 Li_2O:V_2O_4:4.8 V_2O_5

Sample I		Sample II	
d	I/I°	d	I/I°
6.28	100	6.23	100
3.18	25	3.18	30
3.12	25	3.13	30
2.87	30	3.02	35
2.18	25	2.87	45
2.13	40	2.19	30
2.11	25	2.13	50
1.66	15	2.10	45
1.50	25		

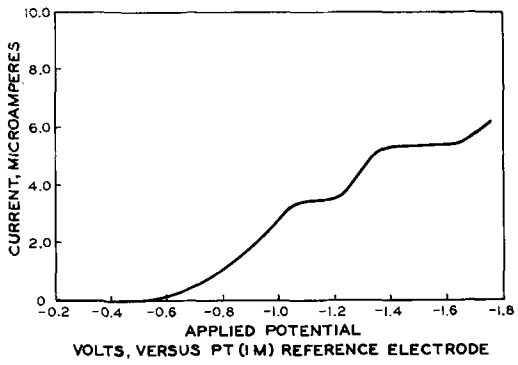

Fig. 1. Current-voltage curve of 10 mM $NaVO_3$ in LiCl-KCl eutectic melt at 450°C with a Pt microelectrode, 0.33 mm^2 in area.

bronzes by heating various ratios of Li_2CO_3 and V_2O_5. Ozerov (19) obtained a different bronze, 1.1 $Li_2O:V_2O_4:2.6$ V_2O_5, noting that the stoichiometry varied significantly with the experimental technique.

Voltammetry of $NaVO_3$ *and* V_2O_5.—In order to examine the course of the reaction involved in the reduction of V_2O_5, current-voltage curves of $NaVO_3$ and V_2O_5 solutions were obtained. A typical C-V curve of Na_2VO_3 taken with a Pt microelectrode in the forward or negative direction of polarization is shown in Fig. 1. The reproducibility of these curves was not good.

A definite reduction wave can be observed at —0.9v. The reverse C-V curve indicates the oxidation of a deposit on the electrode surface at a potential corresponding to the first reduction wave.

Above a concentration of about 10 mM $NaVO_3$, a light-tan colored precipitate was formed. However, the cathodic current still increased with each addition of $NaVO_3$. This would indicate that metavanadate equilibrates in solution to form orthovanadate and polyvanadate(s), some of which are insoluble in the melt.

The same general shape of current-voltage curves was obtained for V_2O_5 with a gold microelectrode except for the presence of a wave at more positive potential (—0.4v) for V_2O_5 (Fig. 2). This wave had poor shape and a rather diffuse limiting current region. This could have been caused by the slow oxidation of the gold microelectrode by V_2O_5. Current was roughly proportional to concentration, but meaningful measurements of current were difficult because of the formation of insoluble products with rapid changing surface area on the electrode surface.

Chronopotentiometry of V_2O_5.—In recent years much attention has been given to chronopotentiometry as a tool in elucidating reaction mechanisms for electrochemical reactions. Using a variety of boundary conditions, mathematic expressions have been derived for various reaction mechanisms (20). These have been recently summarized and extended by Reinmuth and co-workers (21-24).

Potential-time curves for chronopotentiometry of V_2O_5 melt solutions were obtained by applying a constant current between an indicator electrode and a counter electrode and by measuring the potential of the indicator electrode *vs.* a reference electrode as a function of time.

"Blank" chronopotentiograms of the melt with a large Pyrographite indicator electrode (1.2 cm^2) at a current of 500 μa indicated a short residual transition time of approximately 0.5 sec at —1.4v. Since these experiments involve transition times at more positive potentials, the results were not affected.

A typical chronopotentiogram of V_2O_5 with an applied current of 500 μa is shown in Fig. 3 with cathodic current and then with reversal of current at —0.7v for observation of the reverse process. A chronopotentiogram at higher current (800 μa) is shown in Fig. 4. No transition time was observed for the reduction at —0.94v even with a current of 1000 μa and over a period of 20 sec. The transition waves occur at about the same potential as the polarographic waves obtained from the voltammetry of V_2O_5.

Anodic chronopotentiometric curves are also shown in Fig. 3 and 4. For the ideal case of a reversible reduction to a soluble species followed by a reversible reoxidation, the ratio of the transition time for the cathodic wave to the transition time for the anodic wave is 3:1. If an insoluble species is formed, the ratio should be 1:1. If the reduction is reversible and the solution resistance is small, the $E_{1/4}$ for the cathodic wave should equal the $E_{1/4}$ for the anodic wave for either an insoluble or soluble species.

For the trace in Fig. 3, the current was reversed at what seemed to be the inflection point after the first transition time (about —0.7v). In Fig. 4, the cur-

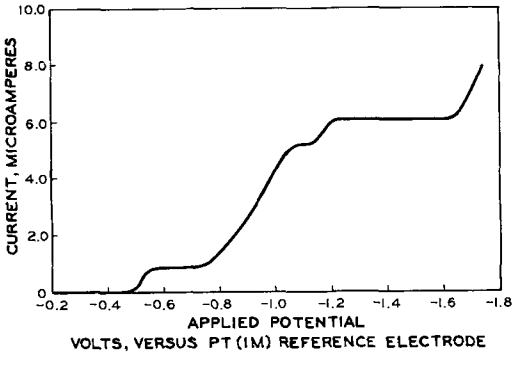

Fig. 2. Current-voltage curve of 8 mM V_2O_5 in LiCl-KCl eutectic melt at 450°C with a gold-plated Pt microelectrode, 0.8 mm^2 in area.

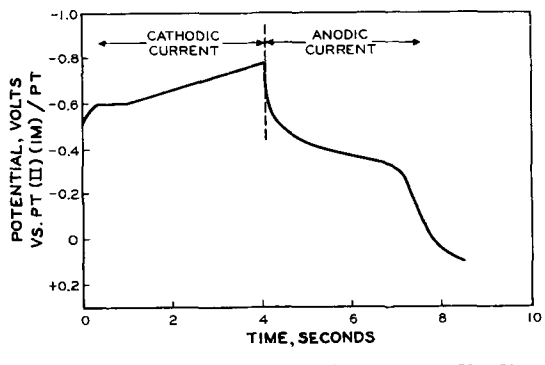

Fig. 3. Chronopotentiogram of 2.1 mM V_2O_5 in LiCl-KCl eutectic melt at 450°C with a Pyrographite indicator electrode. Area = 1.2 cm^2, current = 500 μa.

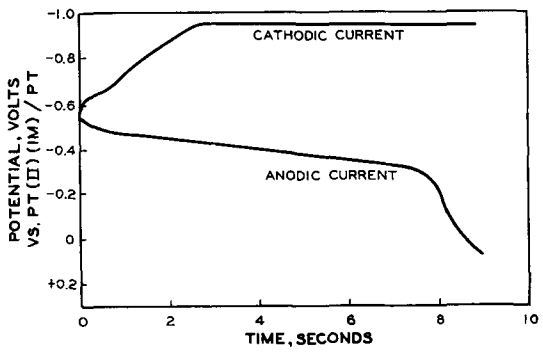

Fig. 4. Chronopotentiogram of 2.1 mM V_2O_5 in LiCl-KCl eutectic melt at 450°C with a Pyrographite indicator electrode. Area = 1.2 cm^2, current = 800 μa.

rent was reversed after the trace had reached the side of the oscilloscope (about —0.95v). In each case, the total time required for reduction and the transition time of reoxidation were about equal. These facts indicate the formation of one or more insoluble products for the reduction at —0.64v and at —0.94v. The reoxidation potential is the same for the reduction at —0.64v and —0.94v.

The results for different concentrations of V_2O_5 and currents are given in Table II. Because of the poorly defined character of the transition time curve, there was an error of measurement of ±5%.

For a semi-infinite linear diffusion controlled process, the following equation may be given:

$$\frac{\tau^{1/2} i}{C} = \frac{n \mathbf{F} A D^{1/2} \pi^{1/2}}{2} \qquad [1]$$

where i is the current (amp) applied to an electrode of area, A (cm^2), τ is the transition time (sec), C is the concentration of V_2O_5 (moles cm^{-3}), D is the diffusion coefficient (cm^2 sec^{-1}), and n, $\mathbf{F}$, and π have their usual significance. The left hand term in this equation, the transition time constant, should be independent of current or concentration for a simple reversible, linear diffusion controlled process. This constant has been calculated and is given in Table II. It seems to increase slightly with an increase in current or concentration, but the measurement error is too large for any definite conclusions.

Because a solid product is formed on the electrode during the first transition, the $E_{1/4}$ of the wave will be a function of the logarithm of V_2O_5 concentration.

$$\frac{dE_{1/4}}{d \ln C} = \frac{RT}{n\mathbf{F}} \qquad [2]$$

This equation can be used to calculate n without having to assume an electrode area and a diffusion coefficient for V_2O_5.

Table II. Chronopotentiometry of V_2O_5 Pyrographite indicator electrode, apparent geometric area = 1.24 cm^2

$[V_2O_5]$, moles/liter	I, $\mu a/cm^2$	$\tau^{1/2}$, $sec^{1/2}$	$\tau^{1/2}I/[V_2O_5]$, amp $sec^{1/2}$ / mole/cm	$E_{1/4}$, v
2.12×10^{-3}	403	0.73 ± 0.05	0.14 ± 0.01	—0.64
2.12×10^{-3}	323	0.79 ± 0.08	0.12 ± 0.01	—0.62
5.16×10^{-3}	968	0.87	0.16	—0.54
5.16×10^{-3}	1210	0.63 ± 0.04	0.16 ± 0.01	—0.52

For concentrations of 2×10^{-3}M V_2O_5 and 5×10^{-3}M V_2O_5, the observed $E_{1/4}$ potentials were —0.63 ± 0.01 and —0.54 ± 0.01v, respectively. By substitution into Eq. [2], n was calculated to be 0.6. Because there was a measurement error of about 20 mv, n fell within the range 0.5-0.7.

From this value of n and assuming that the electrode area was the apparent geometric area (1.2 cm^2), the diffusion coefficient for V_2O_5 was estimated to be 0.8×10^{-5} cm^2/sec.

For more precise chronopotentiometric results, a greater range of current and concentration should be used. However, several factors severely limit the range that can be investigated. Most important is the large area of the Pyrographite electrode; relatively large currents must be used for small concentrations of V_2O_5. Because of convection effects at these high temperatures, the transition time must be kept below 2 sec (16). These and other factors limited the concentration range of V_2O_5 to about 1×10^{-3}M to 6×10^{-3}M V_2O_5.

The following conclusions can be made from the above chronopotentiometric data: two steps, which are similar to those obtained with voltammetry, occur in the reduction of V_2O_5. Although rather poor in definition, the transition time of the first step may be determined. An insoluble product is reversibly formed on the electrode surface. The number of electrons per V_2O_5 is 0.6 ± 0.1. Therefore, the ratio of V_2O_4:V_2O_5 in the insoluble reduction product which forms on the electrode surface is probably within the limits of 1:2 to 1:3.

Coulometry of V_2O_5.—The most satisfactory method to substantiate the results obtained with voltammetry and chronopotentiometry is the coulometric reduction of V_2O_5 in LiCl-KCl. A constant current was applied between a Pyrographite cathode and a working anode which were in separate compartments. The potential of the cathode *vs.* a Pt(II)/Pt reference electrode was followed during the period of electrolysis. Because the current density was kept small and the solution was stirred, the only reduction process taking place should have been that with the most positive reduction potential. Since the potentials of the first and second reduction processes of V_2O_5 were known from chronopotentiometry and voltammetry, it was possible to follow the potential during electrolysis and to determine when the first process was completed. An estimation of the number of coulombs to the first potential break gave the number of electrons involved in the reduction. Analysis of the product formed on the electrode helped to characterize it.

At a current density of 10 ma/cm^2, two types of insoluble products formed in the V_2O_5 solution. Dark blue-green needles adhered to the surface of the electrode; a light tan precipitate, which was qualitatively identified as a lithium polyvanadate, was present in the bulk of the solution.

After 20% of the total number of coulombs needed to reduce V(V) to V(IV) had been passed, the electrolysis of the V_2O_5 solution was stopped, and the electrode and product were removed from the melt. The potential, which at the beginning of the elec-

Table III. X-ray diffraction data of $Li_2O \cdot 2V_2O_5 \cdot 4V_2O_5$ CuKα Source

d-Spacing, Å	Relative intensity, I/I_o	d-Spacing, Å	Relative intensity, I/I_o
8.5	35	2.70	20
5.1	100	2.37	20
4.50	20	2.24	10
4.46	20	2.09	30
3.25	40	2.06	10
3.13	15	1.94	20
3.06	45	1.80	10
2.79	25	1.52	10

trolysis was +0.27v *vs.* Pt(II) (1M)/Pt reference, slowly decreased to +0.18v at the end.

The dark blue-green product was boiled in water to remove all chlorides and water-soluble vanadates. After the sample had been dried, an x-ray powder diffraction pattern was obtained. The product was then boiled in 0.1M K_2CO_3 solution to remove V_2O_5 and less soluble vanadates and another x-ray pattern obtained (Table III). There was no significant difference between the two patterns.

The x-ray powder diffraction patterns did not resemble those of any known compound or compounds. The d-spacings did not compare with those obtained from the product of thermal decomposition of Li_2CO_3 and V_2O_5. The electrolysis experiment using the Pyrographite electrode was repeated; the x-ray patterns which were obtained were reproducible.

The product after being weighed was dissolved in 1M H_2SO_4 to analyze for Li^+, V(V), and V(IV). Lithium was determined by flame photometry, and V(V) and V(IV) were determined by addition of an excess of Ce(IV) and back-titrating with Fe(II) using a potentiometric end point determination.

Chemical analysis of the product gave a stoichiometry of $0.5Li_2O \cdot V_2O_4 \cdot 1.9V_2O_5$ suggesting the compound $Li_2O \cdot 2V_2O_4 \cdot 4V_2O_5$. This does not agree with a stoichiometry of $2.6Li_2O \cdot V_2O_4 \cdot 4.8V_2O_5$ obtained for the thermally prepared product.

A similar type of experiment was repeated, except in this case the electrolysis was continued until after a large change in potential of the Pyrographite electrode had taken place. The potential of the Pyrographite electrode *vs.* a Pt(II)/Pt reference electrode was followed with a Sargent MR recorder. At periodic intervals the electrolysis was stopped, and the steady-state potential was measured.

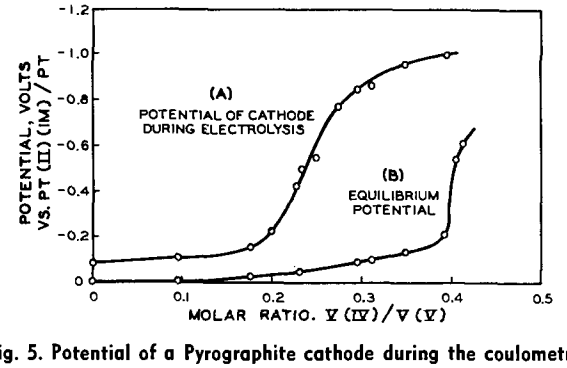

Fig. 5. Potential of a Pyrographite cathode during the coulometric reduction of V_2O_5 in LiCl-KCl eutectic melt at 450°C with a constant current density of 10 ma cm^{-2}.

The results are shown in Fig. 5. The potential of the Pyrographite electrode has been plotted as a function of the molar ratio of vanadium (IV) formed to vanadium (V) originally present in solution. These values were calculated on the basis of 100% current efficiency. The potential for curve A was obtained during electrolysis. If stirring of the V_2O_5-melt solution was sufficiently rapid to make the diffusion layer very thin, the rapid rise to more negative potentials may be taken as the point where V_2O_5 approaches extremely small concentrations. The inflection point of this curve occurs at about 0.25, corresponding to 25% of the total number of coulombs necessary to reduce vanadium (V) to (IV). The number, 0.25, corresponds to a value of 0.50 for the number of electrons needed for the reduction of a molecule of V_2O_5 in agreement with the chronopotentiometric value of 0.6 ± 0.1. Since the stoichiometry of the product which is formed on the electrode is $Li_2O \cdot 2V_2O_4 \cdot 4V_2O_5$ corresponding to 0.67 electrons per V_2O_5 molecule, the indication is that $2V_2O_5$ are involved in acid-base reactions.

Curve B in Fig. 5 was obtained by stopping the electrolysis at periodic intervals and allowing the potential to come to a steady-state value. After stopping or starting electrolysis, the potential would rapidly reach steady-state conditions in 1-5 min. This equilibrium potential showed a break at 0.4 V(IV)/V(V).

Potentiometry of V_2O_5.—The number of electrons needed per V_2O_5 (n) in the most positive reduction step of V_2O_5 in molten LiCl-KCl eutectic was determined, as discussed above, with chronopotentiometry using a form of the Nernst equation. This value was obtained in a dynamic situation with an electrode of rapidly changing surface area and with a diffusion layer of uncertain composition. In this section the determination of n from the Nernst equation using equilibrium conditions is discussed.

From the results in the preceding sections, the reduction of V_2O_5 at a potential of about −0.4v *vs.* a Pt(II) (1M)/Pt reference electrode may be written as follows:

$$6V_2O_5 + 2Li^+ + 4e \longrightarrow \underline{Li_2O \cdot 2V_2O_4 \cdot 4V_2O_5} + O^{-2}$$

The Nernst equation for this reaction may be given as

$$E = E^\circ + \frac{RT}{4F} \ln \frac{[V_2O_5]^6\,[Li^+]^2}{[O^{-2}]\ (\text{Solid})}$$

Because Li^+ has a constant activity in the solvent, the $[Li^+]$ term can be considered a constant and can be included in the E° term. Oxide ion will combine with V_2O_5 in acid-base reactions to form some type of vanadate ion. The particular species formed will depend on the relative concentrations of V_2O_5 and O^{-2}. If a sufficient amount of vanadate ion is present, lithium vanadate will precipitate out of solution. Because little is known at present concerning the complex equilibria between V_2O_5 and oxide ion in a LiCl-KCl eutectic melt, a complete solution of the Nernst equation is impossible at this time.

The solid lithium vanadate bronze in the Nernst equation is a semiconductor. Little is known about electromotive force properties of such a film in this

type of solvent. In this study, the solid has been assumed to act as a pure solid with an invariant thermodynamic activity. However, it is possible that the activity of this product is not constant and that its thermodynamic properties are a function of the concentration of V_2O_5 or base.

Several types of experiments were used to investigate the potentiometry of V_2O_5. In all cases, a coating of lithium vanadium bronze was formed on the electrode by partial reduction of a V_2O_5-melt solution. V_2O_5 was added to the melt in small known amounts, and the potential of the lithium vanadate bronze covered electrode *vs.* a Pt(II)/Pt reference electrode was determined with a potentiometer or Sargent MR recorder. Normally, stable potentials were obtained in 5 min.

Both gold and Pyrographite were used as a support for the bronze. In one type of experiment, potential measurements were made as a function of V_2O_5 concentration in the same compartment in which the bronze was prepared (Fig. 6, curve A). This meant that a small amount of vanadate ion existed in the solution. Curve B in Fig. 6 is a representative curve of potential as a function of log $[V_2O_5]$ for an electrode which had been covered with bronze in a separate compartment.

With a Nernst constant equal to 0.143 at 450°C, the slope of both of these curves gave a value of n equal to 0.85. The difference between the two curves on the potential axis is 0.02v.

The potential of a lithium vanadium bronze electrode was also measured as a function of the amount of K_2CO_3 added to a V_2O_5-melt solution. The procedure was to add K_2CO_3 in small amounts to a V_2O_5 solution and to measure the potential of the indicator electrode after attainment of steady-state potentials.

With each addition of K_2CO_3, CO_2 was given off and the solution became less intense in color. A light-tan precipitate formed in the solution throughout most of the titration. In Fig. 7 is shown a plot of potential of the bronze-covered electrode *vs.* the molar ratio of K_2CO_3 added to V_2O_5 originally present in solution. This plot has the general shape of a potentiometric titration curve with the inflection point occurring at a molar ratio of about one. However, the slope of the curve at the inflection

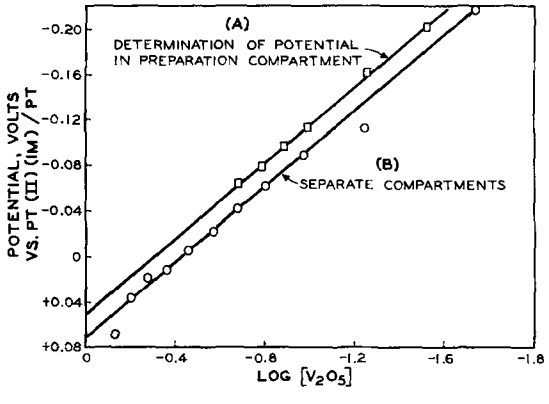

Fig. 6. Potential of $Li_2O \cdot 2V_2O_4 \cdot 4V_2O_5$ covered Pyrographite electrode as a function of V_2O_5 concentration in LiCl-KCl eutectic melt at 450°C.

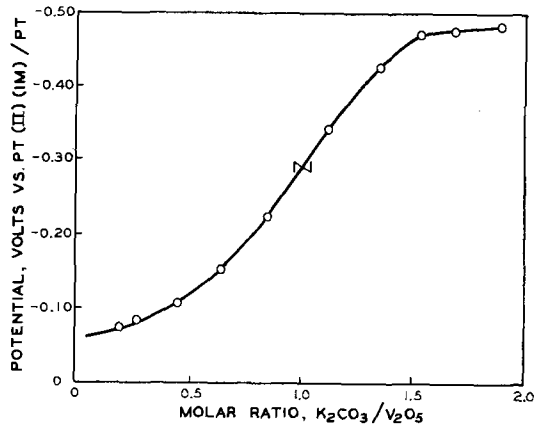

Fig. 7. Potentiometric titration of V_2O_5 with K_2CO_3 in LiCl-KCl eutectic melt at 450°C with a $Li_2O \cdot 2V_2O_4 \cdot 4V_2O_5$ on gold indicator electrode.

point is relatively small, and the inflection point would be difficult to determine for an unknown amount of V_2O_5 oxide concentration.

Because the inflection point occurs at one for the molar ratio, K_2CO_3/V_2O_5, it may be assumed that the following reaction occurs

$$V_2O_5 + CO_3^{=} \rightleftarrows 2VO_3^{-} + CO_2$$

The small slope of the curve at the inflection point indicates a relatively small equilibrium constant for this reaction. Also, this equilibrium was affected by the formation of a lithium vanadate precipitate.

Conclusions

In a LiCl-KCl eutectic melt at 450°C, V_2O_5 is reduced to an insoluble mixed lithium vanadium oxide at a potential which is a function of V_2O_5 concentration. Chemical analysis of the lithium vanadate bronze which was formed in the potential region 0.00-0.20v *vs.* Pt(II) (1M)/Pt reference electrode gave a compound with a stoichiometry of $Li_2O \cdot 2V_2O_4 \cdot 4V_2O_5$. With dynamic nonequilibrium conditions, electrochemical measurements indicated that the equivalent of 0.5-0.7 electrons (n) were required to reduce one V_2O_5 molecule, whereas n values of 0.85 and 0.8 were obtained from equilibrium electrochemical measurements.

For the Nernst equation which can be derived for the solid, $Li_2O \cdot 2V_2O_4 \cdot 4V_2O_5$, n cannot be larger than 0.67 electron per V_2O_5 regardless of the various possible equilibria between V_2O_5 and $O^{=}$ which can be considered.

One factor which could cause the discrepancy between dynamic and equilibrium values of n is the adsorption of V_2O_5 or vanadate ions into the surface of lithium vanadate crystals to change the surface composition. These crystals are composed of mixed metal oxides which could present active sites for the adsorption of acidic or basic species. Another factor, which was neglected because of the lack of necessary supporting information, was the electrochemical behavior of semiconductors.

Acknowledgment

The junior author would like to acknowledge the financial assistance of the Office of Ordnance Research. Special acknowledgment is given to Ray-

theon Company for supplying specially prepared Pyrographite rods.

Manuscript received Nov. 22, 1961.

Any discussion of this paper will appear in a Discussion Section to be published in the December 1962 JOURNAL.

REFERENCES

1. R. E. Panzer, Tech. Memo 44-7, U.S. Naval Ordnance Laboratory, Corona, Calif., October (1960).
2. H. A. Laitinen and J. W. Pankey, *J. Am. Chem. Soc.*, **80**, 1053 (1959).
3. R. Molina, *Bull soc. chim. France*, 301 (1961).
4. J. D. Van Norman and R. A. Osteryoung, *Anal. Chem.*, **32**, 398 (1960).
5. J. L. Andrieux and H. Bozon, *Compt. rend.*, **230**, 953 (1950).
6. V. A. Plotnikov and V. V. Lyulka, *Zapiski Inst. Khim., Akad. Nauk. (U.R.S.R.)*, **7**, 399 (1940).
7. H. Hartmann and W. Massung, *Z. anorg. u. allgem. Chem.*, **266**, 98 (1951).
8. P. N. Yocom, Ph.D. Thesis, University of Illinois (1958).
9. G. E. Blomgren and E. R. Van Artsdalen, *Ann. Rev. Phys. Chem.*, **11**, 273 (1960).
10. H. A. Laitinen, R. P. Tischer, and D. K. Roe, *This Journal*, **107**, 546 (1960).
11. H. A. Laitinen and C. H. Liu, *J. Am. Chem. Soc.*, **80**, 1015 (1958).
12. W. Blum and G. B. Hogaboom, "Principles of Electroplating and Electroforming," 3rd ed., p. 304, McGraw-Hill, Inc., New York (1947).
13. Raytheon Pyrographite Folder, p. 3, Raytheon Co., High Temperature Materials Dept., 57 Seyon St., Waltham 54, Mass.
14. National Carbon Co., Division of Union Carbide Corp.
15. D. R. Rhodes, Ph.D. Thesis, University of Illinois (1961).
16. H. A. Laitinen and H. C. Gaur, *Anal. Chim. Acta*, **18**, 1 (1958).
17. L. B. Johnson, "Differential Thermal Analysis Survey of the Fused Salt System, LiCl-KCl (Eutectic)-V_2O_5," University of Virginia, Report No. UVCS-4, Jan. 19, 1953.
18. H. Flood, T. Krog, and H. Srum, *Tids-Kjemi, Bergvesen Met.*, **6**, 59 (1946).
19. R. P. Ozerov, *Zhur. Neorg. Khim.*, **4**, 476 (1959).
20. Paul Delahay, "New Methods in Electrochemistry," pp. 179-216, Interscience, New York (1954).
21. W. H. Reinmuth, *Anal. Chem.*, **32**, 1515 (1960).
22. *Ibid.*, **33**, 322 (1961).
23. A. E. Testa and W. H. Reinmuth, *Anal. Chem.*, **33**, 1320 (1961).
24. *Ibid.*, **33**, 1324 (1961).

Improved Electrolytic Processes for the Production of Iodic Acid, Periodic Acid, and Their Salts Using a Special Lead Dioxide Anode

Yoshihiko Aiya and Shojiro Fujii

Sanwa Pure Chemicals Company, Limited, Tokyo, Japan

and Kiichiro Sugino and Kozo Shirai

Department of Industrial Chemistry, Tokyo Institute of Technology, Tokyo, Japan

ABSTRACT

A special type of lead dioxide anode was found to be the most suitable anode material to produce iodate from iodide, periodic acid from iodine, and also to regenerate periodic acid (periodate) from iodic acid (iodate). This anode could be used in the absence of sulfate with a very slight loss. The yields of the products were almost quantitative with good current efficiency. Improved processes for the production of periodic acid from iodine and iodate from iodide using this anode and also those concerning the regeneration of periodic acid (periodate) from iodic acid (iodate) are covered in this paper.

The increasing importance of periodic acid and its salt in the chemical industry prompted a study of the electrolytic process for the production of these compounds using a special lead dioxide anode[1] which was described previously (1).

It is known that lead dioxide is the best anode material for the oxidation of iodate to periodate. However, the so-called lead dioxide anode is truly a lead anode coated with lead dioxide. Preliminary experiments showed that this anode can be used in the oxidation of iodine to iodic and periodic acid only when the anolyte contains sulfate ion. But, even in this case, a certain amount of mud forms which shortens the electrode life and contaminates the product. Moreover, the presence of sulfuric acid or sulfate in the electrolyte seems to make the separation of the pure product difficult. These disadvantages led us to make this investigation using an anode consisting entirely of lead dioxide.

The electrolytic oxidation of iodine to periodic acid (periodate) or of iodic acid (iodate) to periodic acid (periodate) had been carried out by several investigators in both acid and alkali solution at anodes of platinum (2), nickel (2), lead dioxde on platinum (3), lead dioxide on lead (4), and lead dioxide (5). Among these, the following three processes are of practical interest: Willard and Ralston's (3) in which iodine in hydrochloric acid is converted to iodic acid at platinum and then to periodic acid at an electrodeposited lead dioxide layer on platinum; Mehltretter's (4) in which iodine in sodium hydroxide is oxidized directly to periodate at lead dioxide coated lead in the presence

[1] Manufactured by Sanwa Pure Chemicals Ltd.

of sulfate or borax; Torigai and Ishii's (5) for the direct production of periodic acid using a special lead dioxide anode of the same type as used in this study. They used hydrochloric acid as anolyte and reported conversion to periodic acid of 95% or more with about 70% current efficiency.

We conducted a series of experiments with the special lead dioxide anode for iodic acid, iodate, and periodic acid (periodate) production in both acidic and alkaline medium using various kinds of electrolytes. These results confirm that this electrode was the most suitable as an anode material for this purpose from the viewpoint of its effectiveness and its insolubility.

Experimental Results

Direct Production of Periodic Acid from Iodine

Dilute bromine water was used instead of hydrochloric acid as in (5).

The anolyte consisted of a suspension of iodine in 0.1-0.4*N* aqueous bromine solution. Iodine was dissolved gradually in the anolyte during electrolysis. All electrolyses were conducted until the formation of periodic acid was complete, as indicated by the disappearance of iodic acid.

The apparatus consisted of the simple cells shown in Fig. 1a, a', and b. A 6000 cc (Fig. 1a' 700 cc) and a 300 cc vessel served as the cell, respectively. In cell a, a porous cylindrical pot (unglazed earthenware) separated the anode chamber from the surrounding cathode space. In cell b, two porous pots encircled two cathodes and thus separated the cathode space from the anode chamber. The anode was a lead dioxide sheet of rectangular shape. Cell a was 50 mm wide, 7 mm thick, and 350 mm long, and cell a', b was 25 mm wide, 7 mm thick, and 150 mm long. It stood in the porous pot (cell a, a') or was placed in the center of the cell (cell b). A thermometer was inserted within the anode space. The anolyte was agitated by a glass or a magnetic stirrer.

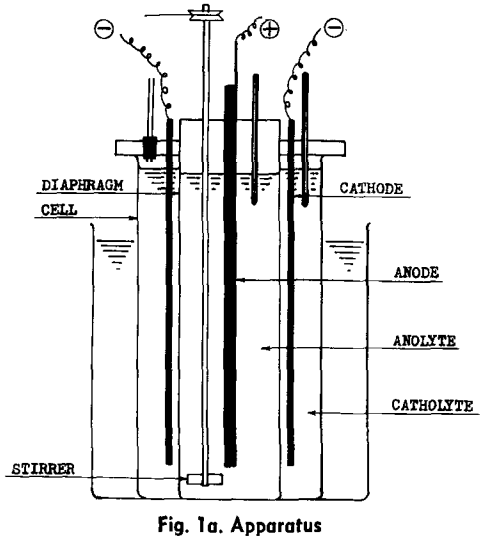

Fig. 1a. Apparatus

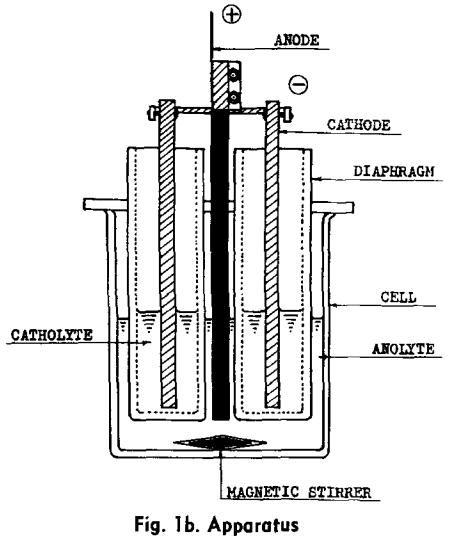

Fig. 1b. Apparatus

Operating conditions and results are shown in Table I.

Periodic acid and combined periodic acid and iodic acid were determined in the anolyte. The accuracy of the analysis was checked by direct recovery of periodic acid as crystals from 100 cc of the resulting anolyte and by the determination of its purity.

The yield of periodic acid was almost quantitative with 70-75% current efficiency. Except in run 1, a slight decrease of the yield resulted from the migration of anolyte to the cathode space and also the sublimation of iodine.

After electrolysis, the anolyte of two or three runs was combined, filtered to remove the small amount of mud, and concentrated at diminished pressure. Periodic acid crystallized out on cooling this solution. After removal of the crystals, the mother liquor was concentrated to a small bulk *in vacuo* and cooled. Almost all crude periodic acid was recovered by this procedure. It was purified by recrystallization from dilute nitric acid. About 70-80% of periodic acid produced could be obtained as pure crystals (purity 99%). When sulfuric acid was used as catholyte, it went into the anolyte making the crystallization of periodic acid difficult.

Anode losses averaged 0.07-0.15 g/100 amp-hr and indicated that the loss would amount to 15% of the original weight after the anode had been used for a year.

The results of separate runs using hydrochloric acid instead of bromine water also are shown in Table I. A slight decrease in yield and in current efficiency was observed in this case. The anode loss increased to 0.20-0.30 g/100 amp-hr, that is about twice the amount in bromine water. In addition, when electrolytically oxidizing iodine in hydrochloric acid, fine iodine powder should be used since it is only slightly soluble in dilute hydrochloric acid. Accordingly, here 0.4*N* solution is better from the viewpoint of iodine solubility even though anode loss increases with increasing concentration. However, according to the bromine water process, the above disadvantages can be eliminated due to high solubility of iodine in bromine water.

Production of iodic acid from iodine.—In this case, all electrolyses were stopped when the formation of iodic acid was complete. Results are shown in Table II.

Table I. Direct production of periodic acid from iodine

Cathode, graphite (run 1), copper (run 2-6); catholyte, 0.04 l (run 1), 3.5 l (run 2-6) 2*N* HNO_3; temp, 40°-50°C

Run No.	Anolyte: Iodine, g	Anolyte: Vol, l	Anolyte: Conc. of bromine water, *N*	Current, amp	Current density, amp/dm²	Cell voltage, v	Amount of current, amp-hr	Remarks
1	15	0.15	0.2	3	15	3.8-4.7	28.5	Cell b
2	97.5	1.2	0.1	29	14	3.7-5.5	184	Cell a
3	97.5	1.2	0.2	29	14	3.7-5.5	188	Cell a
4	97.5	1.2	0.4	29	14	3.6-5.5	188	Cell a
(Anolyte: dilute HCl)			Conc. of HCl, *N*					
5	100	1.2	0.2	29	14	4.0-5.5	207	Cell a
6	100	1.2	0.4	29	14	3.9-5.5	195	Cell a

Results

Run No.	Periodic acid present in anolyte, g	Yield, %	Current efficiency, %	Anode loss, g/100 amp-hr
1	25.8	96	75	0.10
2	163	91	73	0.07
3	167	93	73	0.15
4	167	93	73	0.15
5	157	88	63	0.20
6	164	91	69	0.28

Runs 10 and 11 in which hydrochloric acid was used as anolyte also are shown for comparison.

Analytical procedure was the same as in the previous experiments. Total iodic acid present indicates the amount of iodic acid after conversion of periodic acid to iodic acid by the procedure described below.

The following processes ($I_2 \rightarrow HIO_3$, $HIO_3 \rightarrow HIO_4$) seemed to take place successively; the resulting anolyte contained mostly iodic acid with a small amount of periodic acid. After electrolysis, the electrolyte was evaporated to desired concentration at ordinary pressure. Periodic acid was decomposed to iodic acid by the action of remaining hydrobromic acid or hydrochloric acid, so that crystals of iodic acid were obtained by procedures described in the recovery of periodic acid.

When 0.2*N* hydrochloric acid was used as anolyte (run 10), the formation of iodic and periodic acid occurred at the same time due to low iodine concentration.

Experiments with other anode materials.—The results at various anode materials are shown in Table III. All electrolyses were conducted within the stage of iodic acid formation because practically no periodic acid was formed at platinum or graphite as described later.

For the production of iodic acid from iodine, the special lead dioxide and lead, platinum, and graphite, each lead dioxide coated, proved effective. Some differences were seen in their current efficiencies, with the loss greatest at graphite. For the production of periodate, graphite and platinum showed their inefficiency as described later. It is obvious, therefore, that lead dioxide and lead dioxide coated lead are the best anode materials for periodic acid production from iodine. However, it should be pointed out that lead dioxide coated lead could be used only in the presence of sulfate ion. Even in this case, the loss amounted to about 2.5 g/100 amp-hr which is ten times larger than that at the special lead dioxide anode. Moreover, as mentioned above, the use of sulfuric acid as catholyte makes the separation of pure periodic acid from anolyte very difficult. On these bases, it is concluded that the special lead dioxide anode is the best material for both the production of iodic acid and periodic acid from iodine.

Table II. Production of iodic acid from iodine

Anolyte, 100 g iodine in 1,2 l dil. bromine water (run 7-9) or dilute HCl (run 10, 11); cathode, copper; catholyte, 3.5 l 2*N* HNO_3

Run No.	Conc. of bromine water, *N*	Current, amp	Current density, amp/dm²	Cell voltage, v	Amount of current, amp-hr	Remarks
7	0.1	29	14	3.7-4.2	108	Cell a
8	0.2	29	14	3.7-4.2	108	Cell a
9	0.4	29	14	3.6-4.2	107	Cell a
(Anolyte: dilute HCl) Conc. of HCl, *N*						
10	0.2	29	14	3.7-4.7	134	Cell a
11	0.4	29	14	3.7-4.5	110	Cell a

Results

Run No.	Amount of iodic acid and periodic acid present in anolyte: Periodic acid, g	Iodic acid, g	Total iodic acid present, g	Yield, %	Current efficiency, %	Anode loss, g/100 amp-hr
7	105	33	130	94	91	0.10
8	118	18	132	95	93	0.17
9	130	5	132	96	94	0.12
10	62	79	123	89	70	0.23
11	104	34	131	94	90	0.37

Table III. Experiments with various anode materials (Oxidation of iodine to iodic acid level)

Cell a', anolyte, 15g iodine in 150 cc 0.2*N* bromine water; cathode, copper or stainless steel (run 14 and 17); catholyte, 450 cc 2*N* HNO_3 or 2*N* H_2SO_4 (run 14 and 17)

Run No.	Anode	Current amp	Current density, amp/dm²	Amount of current, amp-hr	Iodic acid present in anolyte, g	Yield, %	Current efficiency, %	Anode loss, g/100 amp-hr
12*	PbO_2	4.8	12	15.9	18.8	91	90	0.15
13	Pb-PbO_2	4.0	10	8.0	—	—	—	120
14	Pb-PbO_2	4.5	10	20.3	15.3	74	58	2.5
15	Pt	4.8	12	15.9	17.0	82	82	None
16	Graphite	2.8	7	17.5	16.6	80	72	8.6
(Anolyte: 0.4*N* HCl)								
17	Pb-PbO_2	4.5	10	18.3	13.0	63	54	6.6

* Periodic acid (yield 9.0%) was formed in this case.

Production of Iodate from Iodine

In this process, sodium iodide solution was electrolyzed without diaphragm in the presence of 2 g/l sodium bichromate.

This process also can be useful in the production of periodate by combining it with the process described later. In regard to this electrolysis, no literature was found except Mehltretter's which used diaphragm to prevent cathodic reduction of iodate.

Apparatus.—A 700 cc beaker served as the cell. The anode was the lead dioxide of rectangular shape and was 25 mm wide, 7 mm thick, and 150 mm long. Two stainless steel cathodes were placed on either side of the anode.

A 500 cc aqueous solution containing 100g iodine, 40g sodium hydroxide (purity 94%), or 55g potassium hydroxide (purity 85%) and 1g $Na_2Cr_2O_7$ or $K_2Cr_2O_7$ was used as starting electrolyte. The *p*H of the electrolyte was adjusted within the range of 8.0-9.5. All electrolyses were conducted with 95% of the theoretical amount of current.

The results are shown in Table IV.

In this case, sodium iodate was recovered as crystals, and the amount of iodate in crude crystals and in solution was determined by analysis.

The current efficiency was almost 100% with 85-95% conversion. Lead dioxide losses were seen to be about the same order as in the electrolytic production of bromate from bromide at this electrode. That was about 50 mg/1000 amp-hr.

After electrolysis, the electrolyte was cooled to room temperature, and the crystals of sodium iodate were separated out by filtration. About 75% of sodium iodate produced was recovered as crystals. The mother liquor could be used for a new run by adding a suitable amount of iodine and alkali hydroxide to make up to the original concentration.

Following are the chemical specifications of the final product currently being produced: colorless crystal, $NaIO_3$ or KIO_3 assay, 99.9%, chloride, bromide 0.02% max., chlorate, bromate 0.02% max., sulfate 0.02% max., heavy metal (as Pb) 0.003% max., iron 0.002% max., iodide 0.03% max.

As reference, the results at various anode materials are shown in Table V.

In the case of lead dioxide coated lead or graphite, the current efficiency was almost quantitative with 80% conversion. However, losses averaged 1.9 g/100 amp-hr and 0.16 g/100 amp-hr, respectively. Moreover, lead dioxide coated lead must be used in the presence of sulfate. In the absence of sulfate, it could not serve as an insoluble anode. The presence of sulfate complicates the separation of pure iodate from the resulting solution. At graphite, the final product became slightly yellow and could not be decolorized easily. Therefore, these electrodes were considered inferior to the special lead dioxide anode.

Oxidation of Iodic Acid or Iodate to Periodic Acid

Electrolytic oxidation of iodic acid to periodic acid or iodate to periodate was studied with regard to the production of periodate from iodate obtained

Table IV. Production of iodate from iodine

Electrolyte, 100g iodine, 40g 94% NaOH (55g 85% KOH), 1g $Na_2Cr_2O_7$ or $K_2Cr_2O_7$ in 500 cc solution; cathode, stainless steel; temp, 50°-60°C; *p*H, 8.0-9.5

	Run No.	Current, amp	Current density, amp/dm²	Amount of current, amp-hr	Iodate produced, g (purity)	Iodate presented in solution, g	Yield, %	Current efficiency, %	NaI or KI unconverted, %	Insol. matter
										$Na_2H_3IO_6$
NaI	1	13	25	104	120 (99.2)	32	97	98	2.9	Trace
	2	13	25	102	116 (98.6)	32	94	98	5.9	None
	3	15	29	100	113 (99.3)	32	92	98	8.0	None
	4	11	21	90	102 (98.8)	29	84	99	16.1	None
	5	11	21	93	104 (99.0)	32	86	98	13.6	None
										KIO_4
KI	6	13	25	97	115 (98.6)	37	89	98	10.7	None
	7	12	24	97	113 (99.0)	37	88	96	11.6	None

Table V. Experiments with other anode materials

Iodate from iodine
Electrolyte, 99g NaI, 1g $Na_2Cr_2O_7$ in 500 cc solution; cathode, stainless steel; temp, 40°-50°C; pH 8.5-9.5

Run No.	Anode	Current, amp	Current density, amp/dm²	Amount of current, amp-hr	Iodate produced and present in solution g	%	Current efficiency, %	Anode loss, g/100 amp-hr	Remarks
8	Pb-PbO_2	2.7	5.5	10	—	—	—	dissolved	In the absence of sulfate
9	Pb-PbO_2	3.6	7.3	90	107	82	96	1.9	In the presence of sulfate
10	Graphite	10.0	16.6	90	107	82	97	0.16	
11	Magnetite	6.0	10.0	105	95	73	74	0.7	

by the above process and also the regeneration of periodic acid solution from spent oxidant solution containing iodic acid and its salt.

At a special lead dioxide anode several experiments were carried out varying the composition of both anolyte and catholyte. Material yields and current efficiencies in each experiment are shown in Table VI.

Analytical procedure was almost the same as in the previous experiments.

At the lead dioxide coated lead anode the same experiments were carried out by using the usual lead dioxide coated lead anode for comparison. Results are shown in Table VII.

At the graphite or platinum anode practically no periodic acid was obtained. Results are shown in Table VIII.

The lead dioxide and lead dioxide coated lead are the only practical anode materials for the oxidation of iodate to periodate. At these anodes, iodic acid or iodate was converted to periodic acid or periodate almost quantitatively. However, the special lead dioxide anode proved its superiority over ordinary lead dioxide coated lead as follows.

First, no loss was observed when a special lead dioxide anode was used for the oxidation of metal iodate. Even when used in iodic acid, the loss amounted to about one-tenth of that at lead dioxide coated lead.

Second, a current density as high as 5-15 amp/dm² could be used. At lead dioxide coated lead, a current density less than 2.5 amp/dm² had to be met to hold reasonable current efficiency.

As for the regeneration of periodic acid solution from the spent oxidant solution containing iodic acid and its salts, a process using metal iodate (containing some free acid) as anolyte and sodium hydroxide as catholyte (run No. 3-6) was seen to be the most advantageous. This produces periodic acid solution containing some periodate which is directly useful to the oxidation of organic substances.

Work on the mechanism of electrolytic oxidation of iodic acid (iodate) to periodic acid (periodate) at lead dioxide anode continues using polarographic method and techniques of constant potential electrolysis.

Acknowledgment

This investigation was promoted by a grant for fundamental scientific research from the Ministry

Table VI. Oxidation of iodic acid (iodate) to periodic acid (periodate)

(Regeneration of periodic acid from spent oxidant solution)
At a special lead dioxide anode

Cathode, graphite; volume of anolyte, 150 cc; volume of catholyte, 40 cc

Run No.	Sample in anolyte,	g	Catholyte	Current, amp	Current density, amp/dm²	Cell voltage, v	Amount of current, amp-hr	Temp, °C	Remarks
1	HIO_3	13.25	2*N* HNO_3	3	15	5.4	5.75	25-51	Cell b
2	HIO_3	13.25	2*N* H_2SO_4	3	15	5.2-5.8	5.45	30-40	Cell b
3	$NaIO_3$	14.85	5% NaOH	3.0-1.6	15-8	6.2-6.9	7.43	22-35	Cell b
4	$NaIO_3$	14.08	5% NaOH	2	10	6.3-7.9	5.55	24-45	Cell b
5	$NaIO_3$	14.08	5% NaOH	1	5	4.8-6.3	5.30	22-38	Cell b
6	$NaIO_3$	100.0	8% NaOH	20	10	7.0-8.0	33.7	35-43	Cell a

Results

Run No.	Periodic acid (periodate) g	%	Current efficiency, %	Anode loss, g/100 amp-hr
1	16.4	96	68	0.13
2	16.5	96	71	0.07
3	16.8	98	54	None
4	16.1	95	65	None
5	16.2	95	69	None
6	96.9	90	72	None

Table VII. Oxidation of iodic acid (iodate) to periodic acid (periodate)

At lead dioxide coated lead anode

Cell b; cathode, graphite; volume of anolyte, 150 cc; volume of catholyte, 40 cc

Run No.	Sample in anolyte,	g	Catholyte	Current, amp	Current density, amp/dm²	Cell voltage, v	Amount of current, amp-hr	Temp, °C
7	HIO_3	13.28	2*N* H_2SO_4	0.5	2.5	3.4-6.0	6.46	22-35
	H_2SO_4	0.75						
8	HIO_3	13.28	2*N* H_2SO_4	2.0	10	4.5-4.9	4.87	25-38
	H_2SO_4	0.75						
9	HIO_3	13.28	5% NaOH	0.5	2.5	4.3-7.5	6.12	25-36
	Na_2SO_4	2.14						
10	$NaIO_3$	14.22	5% NaOH	0.5	2.5	4.2-8.0	7.18	20-31
11	$NaIO_3$	14.72	5% NaOH	2.0	10	5.8-6.0	8.33	28-39
	Na_2SO_4	2.14						

Results

Run No.	Periodic acid (periodate) g	%	Current efficiency, %	Anode loss as lead, g/100 amp-hr
7	16.2	95	59	0.85
8	9.65	56	46	2.02
9	16.8	98	65	1.09
10	16.0	95	51	0.27
11	15.5	91	44	0.37

Table VIII. Oxidation of iodic acid (iodate) to periodic acid (periodate)

At graphite and platinum

Cell b; cathode, graphite; volume of anolyte, 150 cc; volume of catholyte, 40 cc

Run No.	Anode	Sample in anolyte,	g	Catholyte	Current, amp	Current density, amp/dm²	Cell voltage, v	Amount of current, amp-hr	Temp, °C
12	Pt	HIO_3	13.37	2*N* HNO_3	0.5	2.5	3.0-4.2	4.71	20-29
13*	Pt	$NaIO_3$	14.72	5% NaOH	2.0	10	5.4-6.2	8.00	26-32
14	Graphite	$NaIO_3$	14.24	5% NaOH	0.5	2.5	4.0	3.85	28-32

* pH of the anolyte was kept at 8-9.

Results

Run No.	Periodic acid (periodate) g	%	Current efficiency, %	Anode loss, g/100 amp-hr
12	0.34	2	1.7	—
13	1.30	8	4	—
14	0	0	0	25.4

of Education of Japan, for which the authors wish to express their deep appreciation.

Manuscript received May 22, 1961; revised manuscript received Nov. 5, 1961. This paper was prepared for delivery before the Second Seminar on Electrochemistry held at Central Electrochemical Research Institute, Karaikudi, India, Dec. 17-20, 1960. The same paper also was presented at the symposium on oxide electrode jointly sponsored by the Chemical Society of Japan and the Electrochemical Society of Japan held at the Tokyo Metropolitan University on Oct. 27, 1960.

Any discussion of this paper will appear in a Discussion Section to be published in the December 1962 JOURNAL.

REFERENCES

1. T. Osuga and K. Sugino, *This Journal*, **104**, 448 (1957).
2. A. Hickling and S. H. Richards, *J. Chem. Soc.*, **1940**, 256.
3. H. H. Willard and R. R. Ralston, *Trans. Electrochem. Soc.*, **62**, 239 (1932).
4. C. L. Mehltretter, U. S. Pat. 2,830,941 (1958). C. L. Mehltretter and C. S. Wise, *Ind. Eng. Chem.*, **51**, 511 (1959); V. F. Pfeifer, V. E. Sohns, H. F. Conway, E. B. Lancaster, S. Dabic, and E. L. Griffin, *ibid.*, **52**, 201 (1960).
5. E. Torigai and E. Ishii, *Bull. Osaka Ind. Research Inst.*, **7**, 195 (1956).

Reduction Mechanism of Chemisorbed Oxygen on Platinum Electrodes by Molecular Hydrogen

M. W. Breiter

Research Laboratory, General Electric Company, Schenectady, New York

ABSTRACT

Chemisorbed oxygen on platinum electrodes is reduced at open circuit in electrolytes in the presence of molecular hydrogen. It is shown that the rate of the chemical reaction between molecular hydrogen and the oxygen layer is small. The reduction occurs mainly by an electrochemical mechanism. The electrode is the seat of an anodic and a cathodic reaction. The anodic current of hydrogen dissolution on free sites is equal to the cathodic reduction current on the layer.

It is known that chemisorbed layers of oxygen or thin oxide layers on platinum, iridium, rhodium, and palladium are reduced at open circuit in electrolytes saturated with molecular hydrogen. The potential of a platinum electrode which was held potentiostatically at a value between +0.8v and +2.0v *vs.* a hydrogen electrode in the same solution decreases with time and tends toward the value zero after opening the circuit. The potential time curves at open circuit have arrests similar to those of cathodic charging curves at constant current which are taken from the same initial potential (1). The reduction of the oxygen layer occurs during the transition time of the first arrest after interruption. The transition time increases with increasing potential of interruption (1).

The net reaction of the reduction is

$$M - O + H_2 \rightarrow M + H_2O \qquad [1]$$

Here $M - O$ stands for the chemisorbed oxygen or an oxide. Two reduction mechanisms of different nature are conceivable. The hydrogen may interact chemically with the oxygen layer and reduce it. Many metal oxides are reduced in this way in the gaseous phase. A transfer of charges across the interphase platinum metal/solution is not involved in this case. The single steps of net reaction [1] in the gaseous phase are not yet known. As the knowledge of the single steps is not required here a detailed model of the chemical mechanism will not be given because of its tentative nature.

The second mechanism is electrochemical. After some free sites have been formed initially due to the chemical mechanism or due to a self-decomposition of the oxygen layer, the oxidation of molecular hydrogen occurs on these sites as an anodic electrochemical reaction. This reaction involves a splitting of the H_2 molecules in hydrogen atoms and the subsequent ionization of the adsorbed hydrogen atoms whose surface concentration is very small in the considered potential range. The anodic current of hydrogen oxidation is equal to the cathodic current of the electrochemical reduction of the oxygen layer. A mechanism for the electrochemical reduction was suggested and discussed recently (2). Then

on free sites: $$H_2 \xrightarrow{i_a} 2H^+ + 2e^- \qquad [2]$$

on layer: $$M + H_2O \xleftarrow{i_c} M - O + 2H^+ + 2e^- \qquad [3]$$

$$|i_a| = |i_c| \qquad [4]$$

The electrode is a bi-electrode (3) in this case. The purpose of this paper is to distinguish between the two mechanisms of reduction on the basis of experimental results. The experimental evidence presented so far in literature is not sufficient for the decision.

Experimental Results

The following technique was used to determine how the reduction proceeds with time. A potential of 1.25v or 1.5v, respectively, was applied potentiostatically from $U = 0$ (stationary open-circuit potential of the platinum electrode) and held there for 60 sec. Then the circuit was opened. This procedure gave fairly reproducible potential time curves (U-t-curves) at open circuit. When the decaying potential had reached a certain value, a cathodic current of 20 ma/cm² was impressed to the electrode by closing an auxiliary circuit (voltage supply and high resistor in series) with the aid of the Western Electric 275C Relay. Figure 1a shows the U-t-curves from +1.25v and +1.5v at open circuit. Some cathodic charging curves, obtained from different potentials during the decay of the upper curve in Fig. 1a, are represented in Fig. 1b. The charging curves are drawn only to $U = 0$. The continuation at negative potentials is not shown in Fig 1b. The smooth plati-

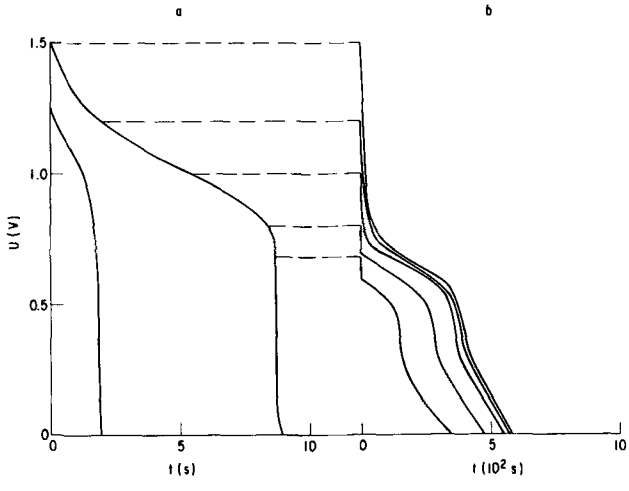

Fig. 1a. Potential decay with time from +1.5v or +1.25v respectively at open circuit on platinum in 1*N* $HClO_4$ with hydrogen stirring.

Fig. 1b. Cathodic charging curves taken with 20 ma/cm² from different potentials during the potential decay from +1.5v.

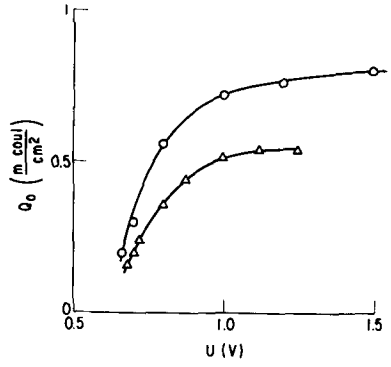

Fig. 2. Adsorbed amount of oxygen as a function of potential during the potential decay from +1.5v (upper curve) or +1.25v respectively (lower curve).

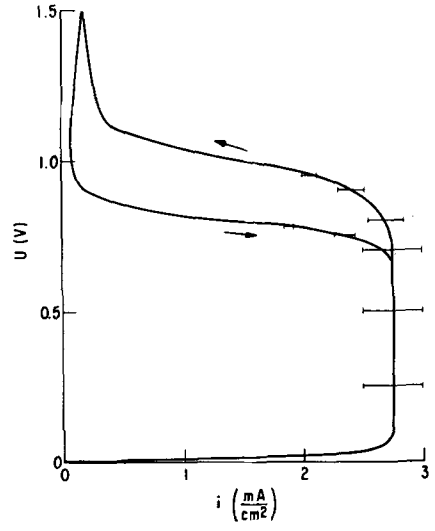

Fig. 3. Potentiostatic current potential curve, measured at 30 mv/sec in 1N $HClO_4$ with hydrogen stirring.

num wire electrode was in 1N $HClO_4$ at 30°C. The electrolyte was stirred with molecular hydrogen vigorously. The cathodic charging curves in Fig. 1b consist of the well-known three parts (oxygen region, double layer region, hydrogen region). The reduction of the oxygen layer occurs after a fast initial potential decay. In a first approximation, the transition time for reduction is equal to the time in which the potential decays from its original value to +0.4v. The electricity required for the double layer charging does not exceed 7% of Q_o under the experimental conditions here (1). Q_o is the number of coulomb/cm² necessary for the reduction of the oxygen layer. A layer of hydrogen atoms is formed during the potential decay between +0.4v and 0. The number Q_H of coulomb/cm² for the formation of the hydrogen coverage was 0.38 millicoulomb/cm² here. The double layer region which separates the hydrogen and oxygen region of anodic charging curves clearly overlaps with the oxygen region in the case of cathodic charging curves (1, 4). A thorough discussion of charging curves on platinum is given in the fundamental papers by Slygin and Frumkin (5).

Figure 2 shows Q_o as a function of U during the decay at open circuit. The upper curve is related to a starting potential of +1.5v, the lower curve to +1.25v. The oxygen coverage changes only slightly with potential between +1.5v and +1.0v. The main part of the reduction takes place between 1.0v and +0.6v.

Figure 3 represents a current potential curve which was measured potentiostatically. The potential was changed linearily with time between 0 and +1.5v with a voltage speed v = 30 mv/sec. The platinum electrode was in 1N $HClO_4$ at 30°C. The current fluctuations, due to irregular stirring with hydrogen, are marked. The limiting diffusion current of reaction 2 is observed between +0.1v and +0.7v. The current decreases gradually between +0.8v and +1.5v during the anodic sweep when the oxygen coverage is formed in this potential range (1). The inhibition of reaction [2] by adsorbed oxygen will be discussed in a subsequent paper. A very small current flows between +1.5v and +1.0v during the cathodic sweep. The time in which the potential changes from +1.5v to +1.0v is 16.6 sec. Below +1.0v the current reaches the limiting diffusion current in a relatively small potential range. A similar current potential curve was obtained with v = 3 mv/sec. Again the current was very small between +1.5v and +1.0v during the cathodic sweep.

Discussion

Although the potential decay between +1.25v and +1.0v or between +1.5v and +1.0v takes more than half the time of the potential decay from +1.25v to 0 or from +1.5v to 0 (see Fig. 1), only a small fraction of the oxygen coverage is reduced there (see Fig. 2). The average rate of reduction between +1.25v and +1.0v is 24 $\mu a/cm^2$. It is 15 $\mu a/cm^2$ between +1.5v and +1.0v. Probably these initial values represent the rate of the chemical mechanism. The rate of reduction i_r increases considerably with decreasing potential below +1.0v. It was determined according to

$$i_r = \frac{\Delta Q}{\Delta U} \cdot \frac{\Delta U}{\Delta t} \qquad [5]$$

for different potentials. A potential decay curve was taken with higher resolution to obtain $\Delta U/\Delta t$ between +1.0v and +0.6v. $\Delta Q/\Delta U$ is computed from the curves in Fig 2. Table I gives i_r at some potentials

Table I. Rate of reduction as a function of potential

U(v)	+1.0	+0.9	+0.8	+0.7	
$i_r \left(\frac{ma}{cm^2}\right)$	0.07	0.37	1.38	3.70	run +1.25v to 0
$i_r \left(\frac{ma}{cm^2}\right)$	0.02	0.045	0.30	1.64	run +1.5v to 0

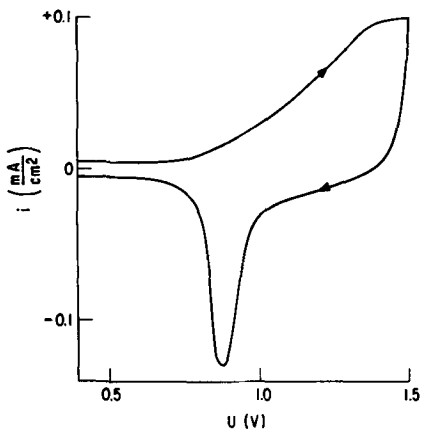

Fig. 4. Potentiostatic current potential curve, measured at 30 mv/sec in 1N $HClO_4$ with argon stirring.

below +1.0v. It follows from Table I that the rate of reduction grows considerably between +0.9v and +0.7v. This is the potential range where potentiostatic current potential curves in acidic solutions with nitrogen stirring show the electrochemical reduction of the oxygen layer during the cathodic sweep (4). Figure 4 represents part of such a current potential curve on platinum in 1N $HClO_4$ at 30°C with vigorous argon stirring. The voltage changed linearily with time with v = 30 mv/sec between 0 and +1.5v. The hydrogen region is omitted in Fig. 4. The cathodic current is counted negative, the anodic current is positive.

It can be concluded on the basis of the results in Fig. 2, Table I, and Fig. 4 that the reduction of the oxygen layer occurs according to electrochemical mechanism (Eq. [2], [3], and [4]). This conclusion is confirmed by the experimental result of Fig. 3 that the anodic current is relatively small between +1.2v and +1.5v during the anodic sweep and between +1.5v and +1.0v during the cathodic sweep. The oxygen coverage increases (1) from about 0.5 to 1 during the anodic sweep in the said potential range and remains practically equal to 1 between +1.5v and +1.0v during the cathodic sweep.[1] The above conclusion is in agreement with the results of a recent paper by Aikasyan (6) on the passivity of the platinum electrode.

It is suggested that the above conclusion can be transferred to smooth electrodes of iridium, rhodium, and palladium as these electrodes have a behavior similar to platinum. The potentiostatic current potential curves (4) have the same shape in the region of the oxygen coverage during the anodic and cathodic sweep and the oxygen coverage (2, 4) depends in a similar way on the potential. A similar situation exists for the reduction of an oxygen layer on platinum in the presence of some oxidizable organic substances like alcohols, aldehydes, or acids. There is no appreciable current during the cathodic sweep in the presence of CH_3OH, CH_2O, and CHOOH on platinum (6) as long as the surface remains partially covered with oxygen. An increase of the anodic current always is observed during the cathodic sweep in the potential range where the reduction of the oxygen layer takes place in the electrolyte without fuel.

Manuscript received Sept. 5, 1961; revised manuscript received Jan. 15, 1962.

Any discussion of this paper will appear in a Discussion Section to be published in the December 1962 JOURNAL.

REFERENCES

1. M. Becker and M. Breiter, *Z. Elektrochem.*, **60**, 1080 (1956).
2. W. Böld and M. Breiter, *Electrochim. Acta*, **5**, 145, 169 (1961).
3. E. Lange and P. V. Rysselberghe, *This Journal*, **105**, 420 (1958).
4. F. Will and C. A. Knorr, *Z. Elektrochem.*, **64**, 258, 270 (1960).
5. A. Slygin and A. Frumkin, *Acta Physicochim. URSS*, **3**, 791 (1935); **5**, 819 (1936).
6. E. Müller, *Z. Elektrochem.*, **33**, 561 (1927); E. Müller and S. Takegami, *ibid.*, **34**, 704 (1928); S. Tanaka, *ibid.*, **35**, 38 (1928).

[1] Unpublished measurements show that the oxygen coverage on platinum decreases with potential during the cathodic sweep in 1N $HClO_4$ at 30°C in practically the same way whether the electrolyte is stirred with hydrogen or argon.

Continuous Coulometric Analysis of Chlorine Bleach Solutions

Edgar L. Eckfeldt and Eugene R. Kuczynski

Research and Development Center, Leeds & Northrup Company, North Wales, Pennsylvania

ABSTRACT

An experimental coulometric system was devised for continuously and automatically titrating chlorine bleach solutions ranging in concentration from 20 ppm up to about 3%. The titrating reagent was produced cathodically, and the coulometric cell current at equivalence was a measure of concentration. The special cell construction provided about ±1% measurement accuracy throughout the concentration range. Difficulties in holding the titration solution at the required condition of equivalence were met by means of a function-generating circuit in the automatic control system.

A number of years ago a coulometric instrument was developed for continuously measuring low-level free chlorine concentrations (1-3). That instrument was intended primarily for water treatment applications and provided measurement ranges from 0 to 1 up to 0 to 20 ppm chlorine. Although the cell reactions used in that instrument appeared suitable for making measurements at high chlorine concentrations, the form of the equipment did not permit such measurements to be made. The continu-

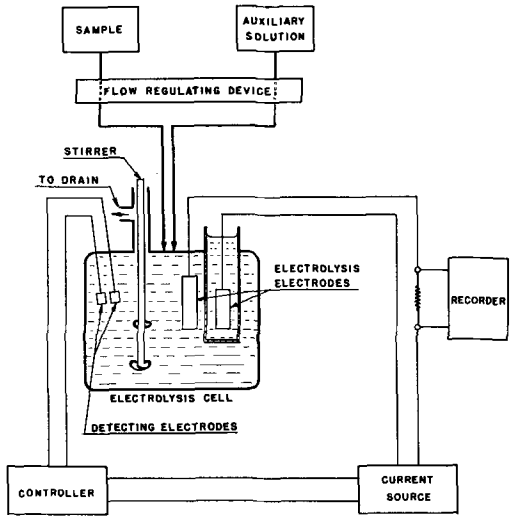

Fig. 1. Schematic diagram of continuous coulometric analysis system.

ous coulometric measurement of concentrated solutions poses certain basic problems. These problems have been surmounted in a newly devised system which is capable of making measurements throughout the concentration range from 20 ppm up to approximately 3% chlorine. It is a purpose of the present paper to describe this new measuring system. Although the equipment was of experimental character and was not tested in field applications, it is believed that potential applications for a measurement of this kind exist in the chlor-alkali industry and in industries that need to monitor and control chlorine in process solutions.

Principle of Operation

The measurement system is schematically shown in Fig. 1. The chlorine solution to be analyzed is metered into an electrolysis cell where it quantitatively reacts with ferrous ions that have been generated electrolytically from ferric ions. To provide a source of ferric ions, an auxiliary solution containing ferric iron and sulfuric acid is introduced into the cell. Detecting electrodes monitor the redox potential of the reacting solution and furnish a control signal to an electric control unit. The control unit automatically adjusts the electrolyzing current to the proper value to maintain a condition of equivalence in the cell solution. The chlorine concentration is given by the equation

$$N = I/96{,}500F \qquad [1]$$

where N is the chlorine concentration in equivalents per liter (normality), I is the generation rate in amperes, F is the flow rate of sample in 1/sec, and 96,500 amp-sec per equivalent is the Faraday constant.

The high chlorine concentrations in the present work made it difficult to maintain automatic control. Conditions in the cell changed rapidly, and large swings in potential were produced by slight deviations from exact chemical equivalence. It thus was necessary to have a control system with special response characteristics. Also, the large current levels placed severe demands on the cell, the electrode assembly, and the output current amplifier.

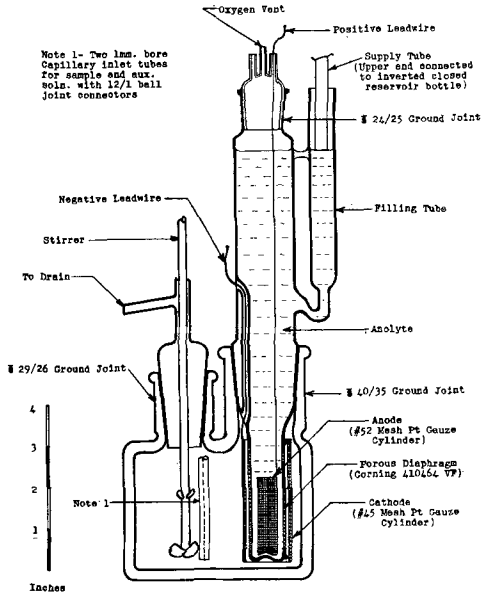

Fig. 2. Electrolysis cell

Equipment

Cell construction.—The cell chamber, shown in Fig. 2, was a short cylindrical vessel of 560-ml capacity and of all-glass construction to provide chemical inertness. A cell of this large a volume was needed for the more concentrated sample solutions. When the cell was in use the outward flow of discharge solution around the propeller shaft prevented the atmosphere from making contact with the interior solution and thus minimized possible loss of chlorine. The speed of stirring was kept as rapid as possible without allowing cavitation to occur.

The electrolyzing electrodes were part of a subassembly that could be removed from the cell as a unit. Sixteen louver-like openings were formed in the outer, titrating electrode to promote circulation of solution in the region between the electrode and the diaphragm. Provisions were made in the subassembly construction to prevent the two electrodes, one on either side of the diaphragm, from actually touching the diaphragm.

The interior of the subassembly was kept filled with a 20% sulfuric acid anolyte. The hydrostatic pressure inside resulted in a slow outward flow of about 20 ml/hr. This leakage of anolyte into the analytical reaction zone caused no harm. The inner solution level was maintained by a reservoir that operated on the chicken-feeder principle.

The detecting electrode system (not shown) consisted of a platinum oxidation-reduction electrode operating in conjunction with a saturated calomel reference electrode. The redox electrode comprised a 2-in. strip of flattened No. 22 platinum wire, wrapped in three turns around the lower, 6-mm diameter end of the calomel tube, and terminated in a loop placed at the bottom of the tube, adjacent to the liquid junction construction (4). This detecting system was placed in the upper region of the cell, not far from the outlet ground joint. False potentials from the field of the electrolysis current were minimized by the arrangement described.

Solution flow metering.—The chlorine sample solution was introduced into the cell by means of a positive displacement metering pump of piston type which had been developed for a previous application (2). The fluorocarbon plastic construction of the pump provided good chemical resistance, but in the present application the pulsating nature of the solution flow was objectionable, because of the large variations in signal voltage caused by influx surges of chlorine solution. The sample flow to the cell therefore was rendered relatively smooth by interposing a small chamber in the line to the cell, followed by a flow-restricting capillary tube. All solution lines were of glass or polyethylene plastic. Frequently the sample flow rate was checked precisely and during the course of the work remained at approximately 6 ml/min.

Auxiliary solution.—The auxiliary solution was a mixture of 17% sulfuric acid and 17% ferric sulfate in water. Because of the impure nature of commercially available ferric sulfate it was found desirable to prepare the solution from ferrous sulfate which salt is available commercially in suitably pure form. Potassium permanganate was preferred for the oxidation of ferrous to ferric sulfate. Two-gallon batches of solution were made using ingredients as follows: $FeSO_4 \cdot 7H_2O$, U.S.P. or C.P., 2.39 kg; H_2SO_4, assay 97%, S.G. 1.84, C.P., 1.35 l; $KMnO_4$, C.P., 0.271 kg; water (good grade), 4.92 l. With the aid of mechanical agitation, the ferrous sulfate was added to the water, and then the sulfuric acid, to the mixture. The potassium permanganate then was added until it was in very slight excess. At this stage the solution redox potential somewhat exceeded + 1.00v, referred to SCE. After the solution had stood for a half hour or so in the oxidizing condition it was passed through a fritted glass filter and then adjusted to equivalence potential of + 0.80v, referred to a SCE, by making appropriate additions of ferrous sulfate or potassium permanganate as saturated solution. If the auxiliary solution was to be used for making measurements on dilute chlorine solutions, moderate care was exercised in adjusting the potential to + 0.80v. If concentrated bleach solutions were to be measured, correspondingly less care was needed in adjusting the final solution potential. A properly prepared solution was stable with time and was not affected adversely by temperature changes.

The auxiliary solution was added to the cell through a separate section of the sample metering pump. The flow rate was adjusted to maintain the concentration of the ferric sulfate in the cell at about 0.1*N*, although this figure was not critical.

Cell resistance.—The cell resistance was obtained by measuring the voltage drop across the generating electrodes under typical operating conditions at several current levels. Figure 3 is a plot of the data. Assuming a constant electrode polarization voltage of 2.1v, the electrical resistance of the cell was calculated to be 0.13 ohm. A current of 7 amp in this magnitude of resistance produces only about 6.4w of heat. In actual operation the temperature of the cell solution never exceeded about 50°C.

Control system.—The automatic control system

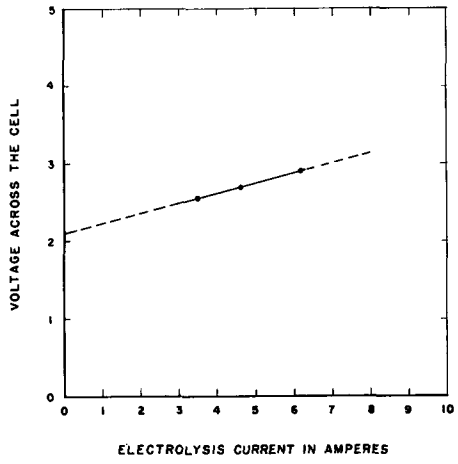

Fig. 3. Electrical characteristics of electrolysis cell

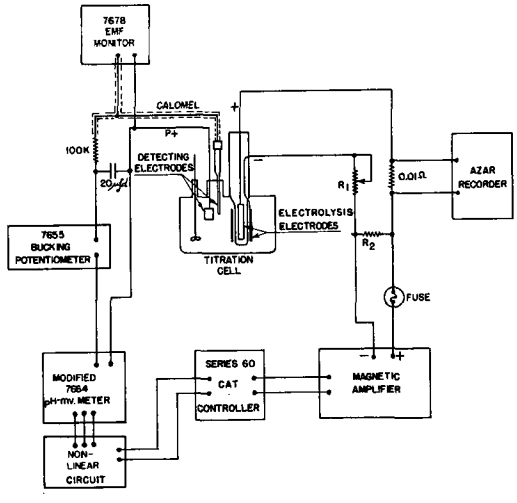

Fig. 4. Block diagram of control system

comprised a combination of essentially stock instruments as shown diagrammatically in Fig. 4. The L&N 7655 potentiometer was set at 800 mv, thereby establishing the intended equivalence potential of the cell solution. The L&N 7678 instrument (a *p*H meter) served only as a monitor to reveal the actual redox condition of the cell solution. The modified L&N 7664 *p*H meter and associated function-generating circuit introduced an important signal-transforming effect. The L&N series 60 current-adjusting controller was connected in a manner to produce full output response from small input voltage swings. The magnetic amplifier which produced the electrolysis current was obtained from Fidelity Instrument Corporation (model No. 1150) and had a maximum rated output of 12 amp d.c. at 25v.

All components requiring 115v a-c power were connected to the 60 cycle power line through a Raytheon voltage stabilizing transformer of 500w rating. This unit improved the stability and performance of the system. Additionally, the magnetic amplifier was powered through a 300 VA isolating transformer to eliminate possible interferences between the electrolysis and detection electrodes, as might otherwise have occurred through common connections to the power line.

The electrolysis current was measured by determining the voltage drop across a calibrated resistor

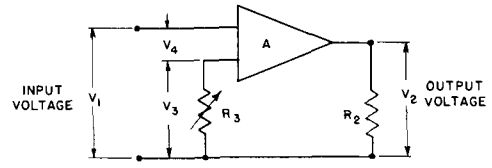

Fig. 5. Schematic representation of modified 7664 pH meter

in the circuit and was displayed on an L&N AZAR recorder.

Function-generating circuit.—The redox electrode produced a typical S-shaped titration curve. Ordinary process controllers, such as the one used in the present study, do not work well with such error signals, because they are designed to operate from a signal that varies linearly with respect to process deviations.

The modifications introduced in the 7664 instrument were intended to linearize the response signal. As schematically represented in Fig. 5, the modified circuit comprised a zero-stabilized d-c amplifier, A, provided with a feed-back loop including a resistor R_2 and a varistor R_3. The amplifier of high gain caused the *Ir*-drop voltage V_3 across the varistor virtually to equal the input voltage V_1. The varistor R_3 exhibited high resistance when the current through it was of small magnitude, but as the current increased its resistance decreased significantly. A situation of variable gain thus existed in the overall circuit. A small input voltage V_1 produced a small output voltage V_2, while a larger input voltage produced a proportionately much larger output voltage.

The actual modifications in the circuit are shown in Fig. 6. The variable resistance element in the feedback loop was composed of two rectifier-type varistors (International Resistance Co., type 28PA1-V) placed in opposing-conductance orientation and in parallel with each other. The potentiometer R_1 of relatively high resistance provided adjustment of the width of the "dead-band." By moving the setting towards 0, the dead band was widened. The magnitude of the output signal was made adjustable by using an adjustable resistor at R_2.

The characteristics of the modified 7664 instrument are shown in Fig. 7 which is a graphical plot of error signal *vs.* output voltage, at several arbitrary settings of R_1 and R_2. The response at the particular settings employed in the present work is shown as curve 4. The difference in the shape of these curves in the first and third quadrants was caused by the use of unmatched varistors in the network. This lack of symmetry was used advantageously to compensate for lack of symmetry in the titration curve. The modifications made in the 7664 instrument appreciably straightened out the S-shaped titration curve and significantly improved the automatic control action.

Testing Procedure

Samples.—The chlorine sample solutions were prepared by diluting ordinary Clorox bleach solution with water. A number of solutions were prepared to cover the wide concentration range of interest.

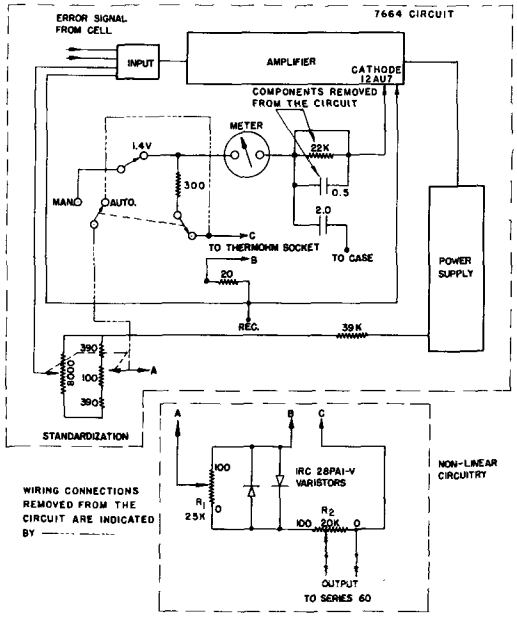

Fig. 6. Circuit diagram of modified 7664 pH meter

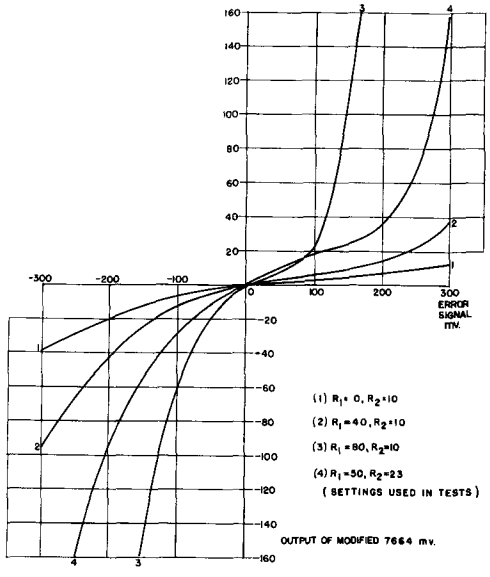

Fig. 7. Response characteristics of modified 7664 pH meter

Operating the Equipment.—At the beginning of the work the optimum settings of the various adjustments were determined by experimenting with the equipment. The proportional band setting of the series 60 unit was the principal sensitivity adjustment for the entire system. This unit also provided an appropriate amount of reset action. Rate action did not help the control action and accordingly was not used. Although the equipment was quite capable of automatically commencing operation, the time taken for start up was reduced by initially producing a condition of approximate equivalence in the cell. This was done by manually adjusting the current and sample addition. The system then was turned over to automatic operation.

The 7678 emf monitor was helpful in revealing the condition of the cell solution. Not only did this instrument serve in the start up procedure but also gave clear evidence of satisfactory operation when the equipment was running. Under operating

Table I. Control settings at various electrolysis current levels

Maximum current level, amp	Resistors of modified 7664 meter (circuit of Fig. 6) R_1, % of total	R_2, % of total	Series 60 controller Proportional band, %	Reset, repeats/min	Resistors of circuit of Fig. 4 R_1 (series), ohm	R_2 (Parallel), ohm
8	50	23	200	1.0	0.8	Open circuit
1.0	50	22	80	1.0	17	2
0.10	50	20	20	1.0	160	2

conditions the cell voltage stayed close to 800 mv. The slight swings on either side of this voltage indicated that the reaction was under control.

Response studies.—The response characteristics of the control system were studied in a number of runs in which the chlorine concentration was changed abruptly from one value to another. Adjustments were made in the control settings to obtain both a rapid response to concentration change, with a minimum of overshoot, and a narrow current trace under steady conditions. These objectives conflicted somewhat and compromises were necessary. The settings were somewhat dependent on the chlorine concentration level and once established were left alone for experimental work in a particular concentration range. The preferred control settings at various current levels are summarized in Table I.

The response to a slowly changing solution concentration also was determined. While the instrument was running, a chlorine solution was added slowly to and mixed with a more dilute solution contained in a vessel connected to the instrument inlet. The operation required about 3 hr, and the final concentration was almost double that at the start.

To test the long-term stability of the entire system, a 28-hr continuous run was made with the equipment left unattended. In addition, tests also were made to determine the upper limit of electrolysis current for this cell and control system.

Determining analytical accuracy.—The analytical accuracy of the continuous coulometric method was studied by comparing the coulometric results with independent results obtained by a standard chemical method (5). In that method iodide first was added to the sample to convert the chlorine to an equivalent amount of iodine, and the liberated iodine then was titrated with standardized thiosulfate solution. The coulometric concentration was computed from the measured values of current and solution flow rate, using Eq. [1]. In most cases the current trace had an appreciable width caused by hunting of the automatic control, and in such cases it was necessary to estimate the average current for the analytical calculation.

Results and Discussion

Response characteristics.—The performance of the system and its response to changes in concentration are shown in Fig. 8 and 9. These figures were constructed by tracing over the pen line of the original chart record. Although a sample in actual practice would probably never undergo abrupt step changes in concentration, as in Fig. 8, such changes nevertheless demonstrate the performance of the equipment under extreme conditions of reaction upset. As Fig. 8 and 9 show, the equipment quite satisfactorily followed abrupt and gradual concentration changes. In the case of the gradual change, the solution voltage stayed very close to 800 mv during the entire transition.

The 28-hr continuous run was accomplished quite satisfactorily without any difficulties occurring. Al-

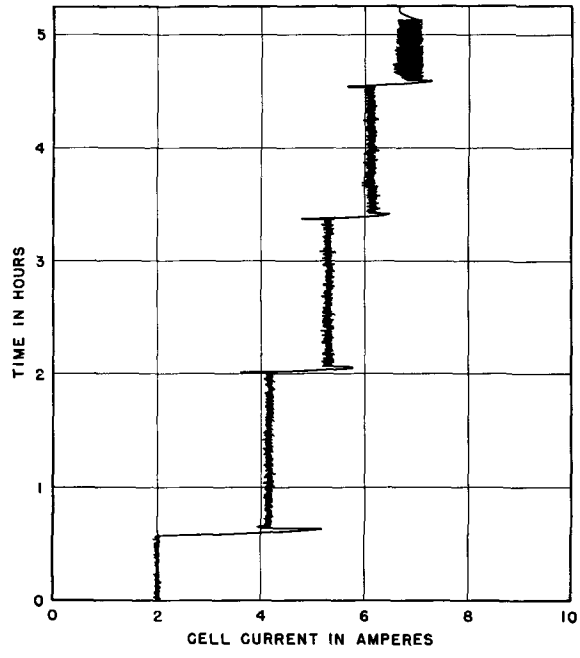

Fig. 8. Response of system at high current levels

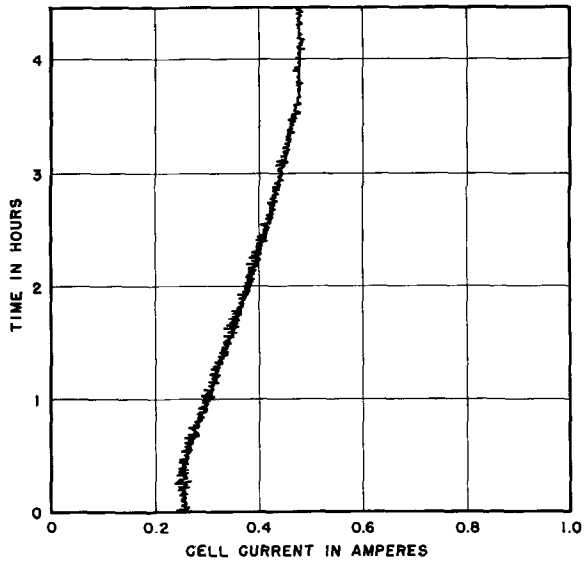

Fig. 9. Response of system to slowly changing solution concentration at intermediate current levels.

Table II. Comparison of electrical and chemical analyses of chlorine solutions

Current level, amp	Electrical normality	Chemical normality	Difference (Elec.-Chem.) × 100 / Chem. %
0.0295	0.00335	0.00337	−0.6
0.0704	0.00800	0.00812	−1.5
0.253	0.0286	0.0285	+0.4
0.460	0.0516	0.0516	0
0.812	0.0912	0.0922	−1.1
2.02	0.224	0.225	−0.5
2.15	0.252	0.254	−0.8
2.82	0.320	0.320	0
3.24	0.380	0.381	−0.3
3.32	0.382	0.385	−0.8
3.63	0.416	0.412	+1.0
4.18	0.462	0.468	−1.3
4.85	0.547	0.543	+0.7
5.30	0.588	0.590	−0.3
5.98	0.685	0.681	+0.6
6.12	0.679	0.683	−0.6
6.95	0.771	0.771	0
Average difference (disregarding sign)			0.6%
Average difference (taking sign into account)			−0.3%

though representing only meager experience, this run nevertheless suggests that the continuous coulometric technique is suitable for extended and unassisted measurement of concentrated chlorine solutions.

The maximum electrolysis current for practical operation with the present cell was found to be about 7 amp. At currents above about 8 amp hydrogen evolution was noted at the cathode, and the system gave poor analytical results. The evolution of hydrogen gas was obviously a sign of poor efficiency of the coulometric reaction. When this occurred, the cathode interestingly enough became ineffective and required an hour or so of operation at a considerably lower current level to recover its normal high efficiency.

Chlorine-measuring accuracy.—The effectiveness of the coulometric system in measuring chlorine is shown in Table II, which presents analyses by the electrical and chemical methods. A comparison of the two methods is given by the percentage difference figures.

These comparisons show that the cell system operated at very close to 100% efficiency throughout the entire range of concentration studied, up to a current level of almost 7 amp. The average of the electrical values was 0.3% lower than the average of the chemical values. While the cause of this minor difference was not ascertained, it might have resulted from a slight loss of chlorine accompanying the discharge of the cell solution.

The upper limit of measurable concentration attained in the present work (0.77*N* or approximately 3%) does not represent necessarily a maximum chlorine concentration that is analyzable by the continuous coulometric technique. To push this figure upward, the sample solution flow rate might have been reduced somewhat, or the critical components of the cell might have been made suitably larger to enable the cell to tolerate currents of greater magnitude.

In contrast with existing methods of measuring chlorine, the present technique would appear to offer a continuous, rapid, and automatic measurement of an accuracy that heretofore was attainable only by conventional titrimetric methods.

Manuscript received Aug. 28, 1961; revised manuscript received Jan. 26, 1962. This paper was prepared for delivery before the Indianapolis Meeting, April 30-May 3, 1961.

Any discussion of this paper will appear in a Discussion Section to be published in the December 1962 JOURNAL.

REFERENCES

1. E. L. Eckfeldt, W. E. Proctor, Jr., and G. A. Perley, Paper presented at The Electrochemical Society Meeting, Philadelphia, May 7, 1952.
2. E. L. Eckfeldt and J. U. Eynon, I.S.A. Paper No. 55-10-1, Presented at the Tenth Annual Instrument-Automation Conference, Instrument Society of America, Los Angeles, Sept. 12-16, 1955.
3. E. L. Eckfeldt, U. S. Pat. 2,758,079 (Aug. 7, 1956); U. S. Pat. 2,886,496 (May 12, 1959).
4. G. A. Perley, *Trans. Electrochem. Soc.*, **92**, 497 (1947).
5. *Solvay Tech. and Eng. Bull.* No. 12, p. 34, Solvay Process Div., Allied Chemical Corp., New York (1957).

Technical Notes

An Electrolytic Polish and Etch for Lead Telluride

Marriner K. Norr

United States Naval Ordnance Laboratory, White Oak, Silver Spring, Maryland

Chemical etches for detecting dislocations (1, 2) and an electrolytic polish (3) have been published for lead telluride. With two of these (2, 3) the crystals are sometimes cracked by thermal shock because the procedures must be carried out at temperatures near 100°C. The etch of ref. (1), however, is used at room temperature and therefore avoids this difficulty.

This note describes a method for electropolishing lead telluride at room temperature, where the danger of thermal cracking is avoided. Also, a closely related, room temperature electrolytic etch for detecting dislocations is described. When used under the conditions given below, it is simpler and faster than the procedure of ref. (1).

Procedure

The surface to be electropolished is ground on 600 grit silicon carbide paper lubricated with water, after which it is washed with water and thoroughly wiped with lens paper. The electrolyte is prepared by dissolving 20g of potassium hydroxide pellets in 45 ml of distilled water. To this are added, with stirring, 35 ml of glycerol and 20 ml of ethanol. The chemicals are reagent grade; the cell container is a 250 ml beaker. The cathode is a piece of platinum foil, 2-20 cm^2, and the anode is the lead telluride to be electropolished, with its ground surface oriented horizontally. The electrolyte is stirred with a magnetic stirrer at the rate of 75-200 rpm and the anode is slowly rotated around its vertical axis, at about 4 rpm, to prevent the formation of flow lines on its surface. The voltage drop across the cell during electropolishing is 6v, and the current density is about 0.2 amp/cm^2. (Since the surface area to be polished has generally varied with different samples, the cell voltage, rather than the current density, has proven to be the more convenient parameter to control.) The temperature of the electrolyte is about 25°C. The anode is electropolished until the surface is smooth and free from scratches (generally 5-15 min). It is then rinsed with water, immersed a few seconds in 1:10 nitric acid, rinsed with distilled water, and carefully dried on lens paper.

When lead telluride is to be etched, either a fresh cleavage or an electropolished surface may be used. In the latter case, a surface parallel to a cleavage plane is prepared and electropolished as described in the preceding paragraph. Then (without removing it from the cell) it is etched by reducing the cell voltage to 1v for 15 sec. Rinsing and drying are carried out in the manner previously described. If the surface to be etched is a freshly cleaved one, it is etched in the manner described above, except that the electropolishing step is omitted.

The pits can be erased by electropolishing for about 5 min.

Results and Discussions

The surface produced by the electropolishing procedure has proven satisfactory for reflectivity measurements used for the calculation of the carrier effective mass (4). The procedure was successful on both single-crystalline and polycrystalline p-type lead telluride. Under a magnification of 9X, a few tiny raised specks of lead telluride could be seen occasionally on the surface. With material that contained more than one phase, the surface was shiny but not smooth.

A graph of "current density *vs.* cell voltage" did not show the pronounced plateau frequently observed with successful electropolishing solutions. During electropolishing, a thin film was sometimes visible, but it disappeared when the cell was disconnected or when the anode was withdrawn from the solution. Consistent with the presence of the film were the facts that (i) the vertical and horizontal surfaces of the anode were polished equally well, (ii) the cell current did not vary significantly when the cathode area was increased from 2 to 20 cm^2, and (iii) the cell current did not vary significantly when the anode-cathode distance was increased by a factor of 7. A possible explanation of these observations is that an anode film, rather than the electrolyte, was the current-limiting unit within the cell during electropolishing.

The electroetching procedure produced pits on p-type lead telluride, but only on planes approximately parallel to the cleavage planes. The pits were generally square and pyramidal and were 3-13μ across. As the surfaces departed from the {100} planes, the pits became distorted and finally disappeared. The diagonals of the pits were parallel to the <110> directions. Pits occurred along small-

angle grain boundaries, traces of active slip planes, and at random points on the surface. Crystals deformed plastically and etched before and immediately after the deformation showed new pits which appeared to be due to dislocations introduced by the deformation.

Acknowledgment

The author wishes to express thanks to Dr. Bland B. Houston, Jr. for helpful advice and encouragement.

Manuscript received Dec. 28, 1961.

Any discussion of this paper will appear in a Discussion Section to be published in the December 1962 JOURNAL.

REFERENCES

1. D. G. Coates, R. R. E. Memorandum No. 1374 (1957) (reported by G. P. Tilly, *Brit. J. Appl. Phys.*, **12**, 524 (1961)).
2. B. B. Houston and M. K. Norr, *J. Appl. Phys.*, **31**, 615 (1960).
3. P. H. Schmidt, *This Journal*, **108**, 104 (1961).
4. J. R. Dixon, Private communication.

The Dissolution Reaction and Attack of Beryllium by HF, HCl, and H_2SO_4

M. E. Straumanis and D. L. Mathis

Department of Metallurgy, University of Missouri School of Mines and Metallurgy, Rolla, Missouri

The kinetics of dissolution of Be in various acids can be studied easily, if the rate of reaction is followed by measuring the volume of hydrogen evolved. However, there is a complete absence of quantitative data in this respect. Inorganic chemistry literature sources state that Be metal dissolves vigorously in dilute acids, except dilute HNO_3, where the reaction ceases soon in the cold (1-4). The stoichiometry of these reactions is not revealed.

Since Be exhibits a stable valency of two, it may be expected to react with the three acids as follows

$$Be + 2HF \rightarrow BeF_2 + H_2 \quad [1]$$

$$Be + 2HCl \rightarrow BeCl_2 + H_2 \quad [2]$$

and

$$Be + H_2SO_4 \rightarrow BeSO_4 + H_2 \quad [3]$$

The respective salts are soluble in water; no residue should appear therefore. By dissolving a weighed amount of the metal in the acids and measuring the volume of hydrogen evolved the reactions can be checked.

Experimental

The Be was obtained from the Brush Beryllium Company as premium grade vacuum cast metal lump and contained about 99.0% Be, the rest mainly oxygen. Iron, aluminum, silicon, magnesium, and carbon were present in still smaller amounts. As the other metals also develop hydrogen while dissolving in acids, it was calculated that the Be sample was approximately equivalent to a metal containing 99.5% Be.

The apparatus used for the dissolution of the Be samples and the collection of hydrogen consisted of a constant temperature reaction vessel sealed to a gas burette (5, 6). The reaction temperature was 36.0° ± 0.2°; the gas burette was at room temperature, but protected with an outer glass tube from sudden temperature changes.

Because of the low atomic weight of Be, the samples were weighed with an accuracy of ± 0.00001g on a gold balance. The concentration of the acids was so chosen that the dissolution of the samples was complete in about 30 min. The air in the reaction vessel was not replaced by an inert gas as no oxidation of the Be ions was expected.

Results

The results obtained with the Be samples are summarized in Table I.

Despite the not very accurate knowledge of the composition of the Be samples, the agreement, as shown by Table I, between the H_2 volume developed by the samples and the volume calculated from Eq. [1], [2], and [3] is sufficient to prove the correctness of these reactions. The H_2 volume evolved can therefore be used for the determination and monitoring of reaction rates of Be with H_2-developing acids. No residue was left after dissolution of the samples.

Although the quantitative reactions [1], [2], and [3] are quite similar, the attack of the metallic surface by HCl differed from that by the two other acids. A polished surface of Be, subjected to the action of HF or H_2SO_4 remained smooth, as if polished, even after a longer etching time. How-

Table I. Measured and calculated volume of H_2 evolved from complete dissolution of Be samples in 3 acids. Deviation Δ in % from calculated values

Acid, *N*	Be, g	Evolved H_2, STP, ml	Calc. H_2 (99.5% Be), ml	Δ, %
HF, 3*N*	0.02866	71.05	70.91	+0.20
	0.02725	67.51	67.43	+0.12
	0.03042	75.30	75.27	+0.04
	0.02843	70.45	70.35	+0.14
			Average	+0.13
HCl, 2*N*	0.02940	72.89	72.75	+0.19
	0.02740	67.68	67.80	−0.18
	0.02840	70.38	70.27	+0.16
	0.02818	69.57	69.73	−0.23
			Average	−0.02
H_2SO_4, 2*N*	0.02831	69.99	70.05	−0.09
	0.03105	76.84	76.83	+0.01
	0.02845	70.42	70.40	+0.03
				−0.01

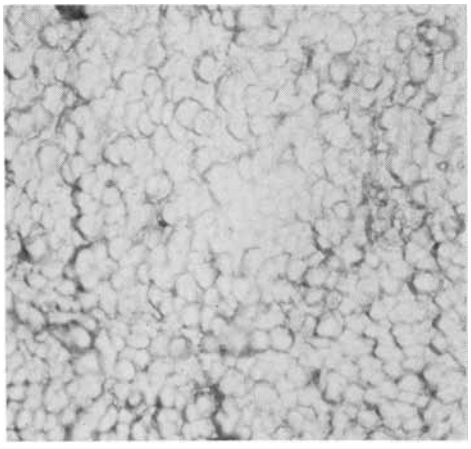

Fig. 1. Attack of a smooth Be plate by 0.5*N* H_2SO_4. Magnification 1300X.

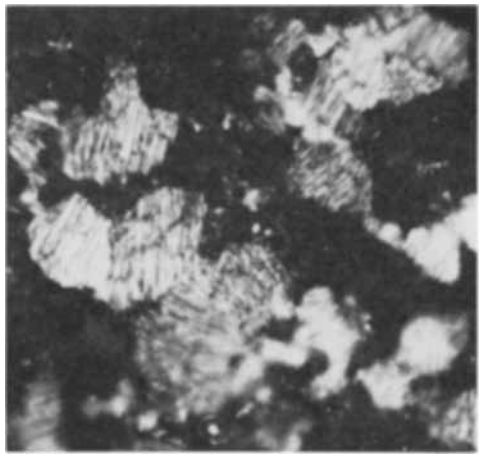

Fig. 2. Plate of Be (powder metallurgy) after etching it deeply with concentrated HCl. Magnification 300X.

ever, high magnifications revealed some structure (Fig. 1). Contrary to this, the reaction with HCl (about 0.5*N*) was strongly localized since the structure of the metal appeared clearly with striations across the grains (Fig. 2).

Another observation was made while Be dissolved in HCl at concentrations lower than 0.5*N*: a black deposit covered the metal which then separated from the latter and turned the whole solution black. It could be shown that the deposit consisted mainly of very fine Be needles which separated from the compact metal during the dissolution process (7). The formation of the needles on the edge of Be pieces is shown in Fig. 3 and 4.

The blackening of the Be surface while dissolving in HCl was previously observed by Bockris (8). Later the phenomenon also was described by Laughlin *et al.* (9) and by Heusler (10), who observed it while dissolving Be anodically in a NaCl solution. However, they did not recognize the blackening of the solution as a result of a partial disintegration of the anode, although such phenomena are known and are mentioned by Evans (11). Nevertheless, since the black deposit was found to consist of metallic Be, the mentioned authors (9) explained the formation of it by the following disproportionation reaction

$$2\,Be^{+} = Be^{2+} + Be \qquad [4]$$

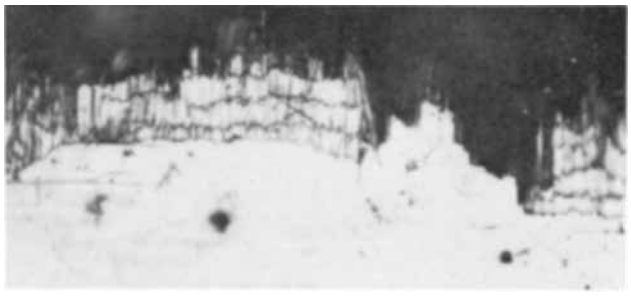

Fig. 3. Initial attack of vacuum cast Be by HCl. Magnification 750X.

Fig. 4. Crystal needles formed on vacuum cast Be corroding in HCl. Magnification 1300X.

Consequently it was assumed that Be was expelled by the anode in form of monovalent Be^{+} ions which then in a very short spread of time react with each other according to [4]. There are three main objections to this explanation:

1. It could be observed during the present investigation that Be needles (Fig. 3 and 4) and particles separated from the compact metal while dissolving in HCl; they also were formed anodically in neutral NaCl solutions.

2. Particles which are observable microscopically must grow, if reaction [4] is correct, from a nucleus; however, nobody could deposit metallic Be in a process of growth from aqueous solutions.

3. To form visible metallic Be particles according to [4] a great number of Be^{+} must travel against the forces of repulsion to collide with each other so that the second valence electron of one Be^{+} could leap to another Be^{+} to give metallic Be. This is quite impossible.

The deviation from Faraday's law therefore is not by formation of Be^{+}, but simply by partial disintegration of the Be anode as observed, while the current was flowing. This phenomenon also was investigated by Marsh and Schaschl (12). The Be disintegration is one of the possible explanations of the negative difference effect (13).

No formation of a black deposit was observed in concentrations higher than 0.5*N* HCl. This is one of the reasons why a stronger concentration of HCl was chosen for the measurements of Table I. No blackening of the acids could be observed in any concentration of HF and H_2SO_4.

However, formation of a black deposit and hence, disintegration of Be was observed in $HClO_4$. Quali-

tative experiments showed that chunk formation started while Be was dissolving in about 0.3*N* $HClO_4$. In stronger concentrations of the acid the amount of the deposit increased, but it dissolved after some time. The same phenomenon also was observed in HBr, only the concentration of the acid at which the black deposit started to appear was about 1*N*. In higher concentrations the formation of the deposit was abundant, but it dissolved soon afterward.

Acknowledgment

The authors are grateful to the U. S. Atomic Energy Commission (Contract AT(11-1)-1047) for the financial assistance received.

Manuscript received Oct. 16, 1961; revised manuscript received Jan. 29, 1962.

Any discussion of this paper will appear in a Discussion Section to be published in the December 1962 JOURNAL.

REFERENCES

1. G. E. Darwin and J. H. Buddery, "Beryllium," pp. 63, 78, Academy Press, Inc., New York (1960).
2. D. W. White, Jr. and J. E. Burke, "The Metal Beryllium," ASM, Cleveland, Ohio (1955).
3. N. V. Sidgwick, "The Chemical Elements and Their Compounds," Vol. 1, pp. 198-99, Oxford Press, London (1950).
4. H. Remy, "Treatise on Inorganic Chemistry," Vol. 1, p. 249, Elsevier, New York (1956).
5. M. E. Straumanis and J. T. Ballass, *Z. anorgan. Chem.*, **278**, 36 (1955).
6. M. E. Straumanis, C. H. Cheng, and A. W. Schlechten, *Analyt. Chem.*, **28**, 1883 (1956).
7. M. E. Straumanis and D. L. Mathis, *J. Less Common Met.*, **4** (1962).
8. J. O'M. Bockris, *Trans. Faraday Soc.*, **43**, 424 (1947).
9. B. D. Laughlin, J. Kleinberg, and A. W. Davidson, *J. Am. Chem. Soc.*, **78**, 559 (1956).
10. K. E. Heusler, *Z. Elektrochem.*, **65**, 192 (1961).
11. U. R. Evans, "The Corrosion and Oxidation of Metals: Scientific Principles and Practical Applications," p. 883, Edward Arnold Ltd., London (1960).
12. G. A. Marsh and E. Schaschl, *This Journal*, **107**, 960 (1960).
13. M. E. Straumanis, *ibid.*, **108**, 1087 (1961).

Electron Microscopic Investigations on the Structure and Topography of Electrodeposited Nickel

B. C. Banerjee and P. L. Walker, Jr.

Mineral Technology Division, The Pennsylvania State University, University Park, Pennsylvania

As a result of successful application of electron waves in revealing many structural details of electrodeposited metal surfaces (1-6), the mechanism of growth of cathodic deposits is becoming better understood. It has become evident that a detailed knowledge of surface conditions of the initial cathode surface (based on chemical, electrochemical, and metallurgical studies) is necessary before one can arrive at a valid conclusion as to the factors determining not only the cathodic growth processes but also many of the physical and mechanical properties of the electrodeposits (2, 3, 7, 8). Experimental evidences in favor of the dislocation theory of crystal growth processes are overwhelming, but very few attempts have been made, to the authors' knowledge, to explain many structural details that develop on the surfaces of electrodeposited metals on the basis of this theory. In our electron microscopic investigations of the topography of such surfaces, we have observed not only the formation of substructures but also striations or steps and dendritic type of growth during initial stages of deposition and microcavities resembling etch pits at an advanced stage of deposition. These finer structures formed on a growing cathode surface, stress the importance of the various structural imperfections and the thermal energies involved in the growth of electrodeposited metals (2, 7, 8).

Experimental

Our experiments mainly consist of an electron microscopic study of the structures and topography of Ni at various stages of electrodeposition on reagent grade Cu, Ag, Au, Ni, and Pt cathode surfaces. Results for Ni, electrodeposited on two types of Cu cathodes are presented in particular detail. Carbon replicas of surfaces preshadowed with Pt at angles varying from 15° to 25° generally were used for electron microscopic investigations. The Ni was electrodeposited at a current density of 10 ma/cm^2 and at a bath temperature of 25°C from a purified sulfate-chloride bath adjusted to different *p*H conditions (2.1, 3.2, 5.1). Deposition times generally ranged from about 1 min to about 120 min. The procedures involved in the preparation, purification, and *p*H adjustments of the reagent grade plating solutions have been given elsewhere (1, 2). The thickness of the Cu and Ag foils was adjusted to about one mil by etching them slowly in dilute acid solutions, followed by washing in distilled water. Slow etching generally helps in revealing grain boundaries in greater detail. The Au foils, originally of 0.4 mil thickness, were further thinned to reveal grain boundaries by slow etching in dilute aqua regia. Figure 1 is a typical electron micrograph revealing the small grained structures of the Ag foil. Foils of Au, Cu, Ni, and Pt possess similar structure. Details of the preparation of the carbon replicas and the method of their separation from the metal surfaces have been published previously (2). Two types of Cu surfaces were used as the cathodes for electrodeposition: (A) Two mil thick copper foils were etched in moderately dilute HNO_3 to adjust the ultimate thickness to about one mil followed by a dip in concentrated HCl and a rinse in distilled water (2). (B) This surface was prepared by electrodepositing Cu for 15 min on a type (A) surface of Cu

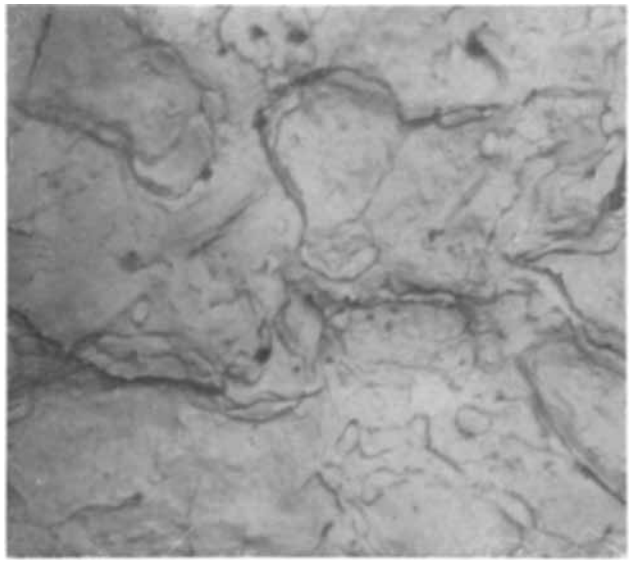

Fig. 1. Electron micrograph of the surface of the Ag cathode obtained by etching in moderately dilute HNO_3 · (5500X).

foil from a complex Cu-glycine bath of *p*H 2.5 maintained at 25°C and a current density of 10ma/cm². The deposits mostly consist of grains with well-developed boundaries and $(10\bar{1}0)$ + (211) preferred orientations (2).

Results and Discussion

Nickel was deposited on Cu surface (A) for 1 min from baths having a *p*H of either 2.1 or 5.1. An electron micrograph of this Ni surface (Fig. 2) shows that the Ni deposits reproduced the particle size and texture of the Cu substrate. Similar results also were found for Ni deposits formed from the same bath on substrates of Ag, Au, Ni, or Pt.

On the other hand, if electrodeposition of Ni is conducted for 1 min from a bath having a *p*H of 3.2, different results are obtained. When deposition occurs on Cu substrate (A), an elongated type of subgrain structure develops [Fig. 3a to 3c]. These sub-

Fig. 2. Electron micrograph of the surface of Ni obtained by electrodepositing Ni from a sulphate-chloride bath at 25°C and at a current density of 10ma/cm² on Cu cathode (A) for 1 min at a *p*H of either 2.1 or 5.1. (2400X).

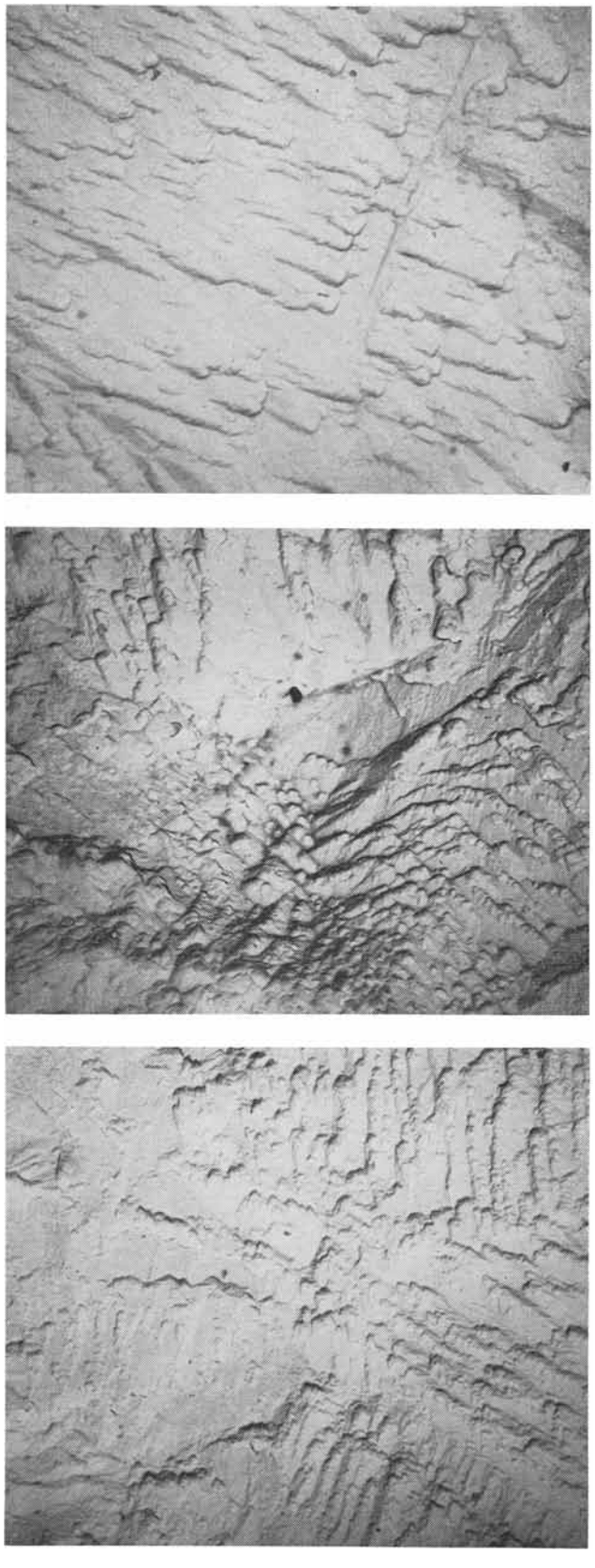

Fig. 3a-c. Electron micrographs of subgrain structures formed on Cu cathode (A) when Ni is electrodeposited from a sulphate-chloride bath of *p*H 3.2, at 25°C and at a current density of 10ma/cm² for a deposition time of 1 min. (2400X).

structures are oriented parallel to each other within a grain, but considerable difference in grain orientation is noted. When deposition occurs on the Ag or Au substrates, a similar type of substructure also is

observed. Analogous substructures were obtained by Deslisle (9) who heated a polycrystalline Cu foil near its melting point for more than 1 hr and then etched the surface of the annealed copper in a suitable reagent. When deposition occurs on Cu substrate (B), large (111) facets containing a dendritic type of structure (Fig. 4) and striations or steps (Fig. 5) are observed. Figure 4 is very similar to the photomicrograph of the surface dendrites obtained by Laukonis and Coleman (10) in the case of γ-phase Fe formed on Fe whisker surfaces that were annealed in H_2 for 2 hr at 1200°C.

No such substructures, dendritic type of growth, and striations or steps were found for Ni electrodeposited on the surface of Pt or Ni at any of the above *p*H conditions.

The development of subgrains on metal surfaces generally is thought to be a thermally activated process. Subgrains have been obtained by various workers (11-13) by annealing a slightly deformed high-purity metal near its melting point, followed by an etch in a suitable solution. Dislocations require sufficient mobility in order to arrange themselves in dislocation walls to produce this effect. There is evidence, such as that put forward by Lambot (14), that deformation itself is able to produce subgrains without the requirement of substantial thermal energy. In this connection, it has been found that electrodeposits develop large amounts of internal stresses (7, 8, 15) which vary in magnitude with deposition conditions.

Electrodeposited Ni generally develops (210), (100), and $(10\bar{1}0)$ + (211) preferred orientations at the deposition conditions used in these experiments at *p*H conditions of 2.1, 3.2, and 5.1, respectively (1, 2). Another interesting feature of our results, then, is the development of microcavities, which resemble etch pits, on parts of the (210) and (100) surfaces of Ni, when the deposit thickness exceeds

Fig. 4. Electron micrograph showing the tendency of Ni deposits to form a dendritic type of growth on a (111) facet of Ni when Ni is electrodeposited on Cu cathode (B) from a sulphate-chloride bath, of *p*H 3.2, at 25°C, and at a current density of 10ma/cm² for 1 min. (7100X).

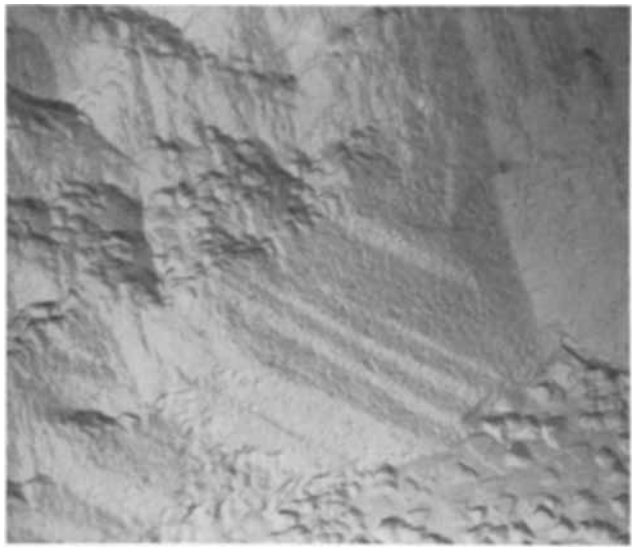

Fig. 5. Electron micrograph showing striations or steps formed on parts of the Ni surface under deposition conditions similar to those in Fig. 4. (7100X).

20μ. The development of these microcavities is found to be independent of the original cathode material used. They are often found to be either square or rectangular in cross section, the shape depending on the crystal symmetry of the surface on which they are formed. Figures 6 and 7 show microcavities formed on (210) and (100) Ni surfaces, respectively. No cavities were found on surfaces at thicknesses below 20μ. For example, Fig. 8 is an electron micrograph for either the (210) or (100) nickel surface at a deposit thickness of about 12μ.

Many structural features of our results at the advanced stages of deposition can probably be explained on the basis of a "Bunching Mechanism" of cathodic crystal growth, proposed recently by the Birmingham School (3, 4). They suggest that kinks or structural inhomogeneities present on the surface of the original cathode may become extended and

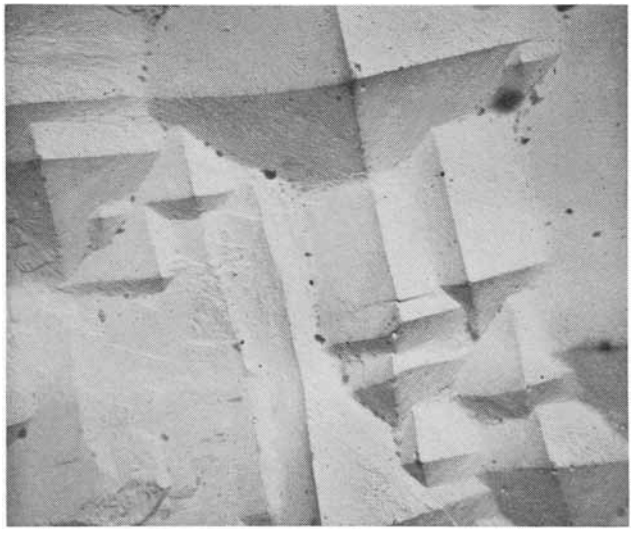

Fig. 6. Electron micrograph showing microcavities formed on the (210) surface of Ni electrodeposited for 120 min on cathode surfaces from the sulphate-chloride bath of *p*H 2.1, at 25°C, and at a current density of 10ma/cm². (2400X).

Fig. 7. Electron micrograph showing microcavities formed on the (100) surfaces of Ni at 25°C from the bath of pH 3.2, at a current density of 10ma/cm^2 when the deposit thickness is about 20μ. (2400X).

Fig. 8. Electron micrograph of (210) surface of Ni, obtained by electrodeposition of Ni from the bath of pH 2.1, at 25°C and at a current density of 10ma/cm^2 with a time deposition which favors a thickness of about 12μ. (1300X).

hence magnified on a macroscopic scale as the deposit grows thicker (3). But the development of substructures, the formation of dendritic-type of structures, and steps or striations during the early stages of deposition cannot be understood on the basis of any one of the existing mechanisms for the cathodic crystal growth processes. The importance of considering some of the parameters involved in the solid-state reactions operative in cathodic crystal growth processes at the various stages of deposition might be helpful in the understanding of this complex phenomena, rather than restricting our ideas wholly to classical mechanisms of crystal growth processes (5, 6). Consideration of the porosity of thinner electrodeposits, the properties of line imperfections in acting as scattering centers for conduction electrons (16), the exothermic nature of the electrodeposition processes (7, 8), and the large deformations of cathode surface layers during various stages of deposition resulting from high magnitudes of internal stresses (7, 8, 15) in the deposits might be particularly helpful in explaining many of the structural anomalies which are often encountered on the surface of a growing deposit during cathodic growth processes.

Acknowledgment

This work was supported by the Atomic Energy Commission, Contract No. AT (30-1)-1710.

Manuscript received April 13, 1961; revised manuscript received Jan. 12, 1962.

Any discussion of this paper will appear in a Discussion Section to be published in the December 1962 JOURNAL.

REFERENCES

1. B. C. Banerjee and A. Goswami, *This Journal*, **106**, 596 (1959).
2. B. C. Banerjee and P. L. Walker, Jr., *ibid.*, **108**, 449 (1961).
3. H. J. Pick, G. G. Storey, and T. B. Vaughan, *Electrochim. Acta*, **2**, 165 (1960).
4. G. G. Storey and S. C. Barnes, *Trans. Inst. Met. Finishing*, **37**, 11 (1960).
5. G. I. Finch, H. Wilman, and L. Yang, *Discussions Faraday Soc.*, **1**, 144 (1947).
6. W. K. Burton, N. Cabrera, and F. C. Frank, *Trans. Royal Soc. (London)*, **A243**, 299 (1951).
7. H. P. Murbach and H. Wilman, *Proc. Phys. Soc.* (London), **66B**, 905 (1953).
8. H. Wilman, *Proc. Phys. Soc.*, (London), **68B**, 476 (1955).
9. L. Deslisle, *J. Metals*, **5**, 660 (1953).
10. J. V. Laukonis and R. V. Coleman, *J. Appl. Phys.*, **32**, 242 (1961).
11. M. S. Hunter and D. L. Robinson, *J. Metals*, **5**, 717 (1953).
12. E. R. Parker and J. Washburn, "Creep and Recovery," p. 227, American Society of Metals (1956).
13. L. V. Azaroff, "Introduction to Solids," p. 115, McGraw-Hill Book Co., Inc., New York (1960).
14. H. T. Lambot, *J. Inst. Metals*, **84**, 473 (1956).
15. I. Laird Newell, *Metal Finishing*, p. 56, October 1960.
16. H. G. Van Bueren, "Imperfections in Crystals," pp. 294, 458, Interscience Publishers, Inc., New York (1960).

Controlled Electrode Potential Deposition of Nickel-Iron Films

F. H. Edelman

RCA Laboratories, Radio Corporation of America, Princeton, New Jersey

The relationship of the decrease in iron content of a nickel-iron film with increasing thickness when electrodeposited from a constant current source has been reported (1, 2). It is a fairly common practice in the field of analytical chemistry, since the introduction of the commercially available potentiostats, to use the controlled electrode potential (CEP) method to permit the deposition of one cation from a solution containing more than one species whose electrode potentials are close (3). The procedure used in this note was not to separate nickel from iron, but to deposit them in a fixed ratio by the CEP method.

The electroplating bath was a conventional sulfate-chloride type similar to those reported elsewhere (1, 4). The substrates were 1.8 cm square cover glasses that were made conducting by evaporating about 350Å of chromium followed by 2000Å of gold. The anode was a 1½ in. platinum gauze cylinder which encircled the cathode. The cathode was rotated at 200 rpm, and a calomel reference electrode was used. Similar data can be obtained without using a rotating cathode, or stirring, and by using other plating-cell geometries. The substrates were cleaned in a caustic-peroxide solution, followed by a distilled water rinse and activation by a stannous chloride dip. No separation of the anolyte and catholyte or a nitrogen flush of the solution were found necessary

A commercial potentiostat and current integrator were used (5). The potentiostat worked by continuously comparing an accurately known selected voltage to the potential difference between the controlled and reference electrode. The difference voltage was used to drive a motor which rapidly adjusted the voltage between the working electrode and the reference electrode until it became zero.

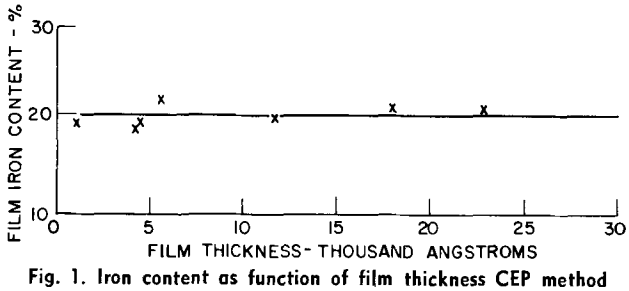

Fig. 1. Iron content as function of film thickness CEP method

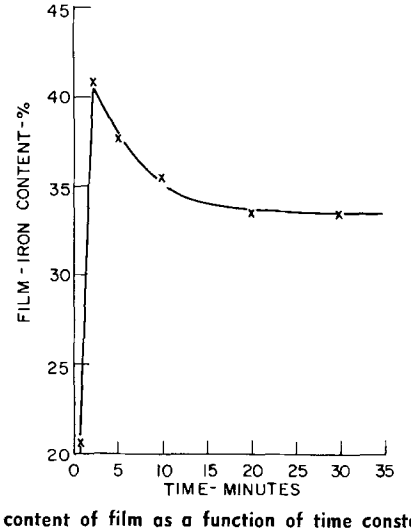

Fig. 2. Iron content of film as a function of time constant current

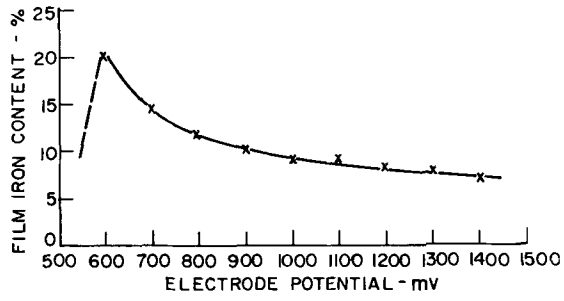

Fig. 3. Iron content as a function of electrode potential

The polarization curves were obtained by adjusting the potentiostat for a given potential and reading the current after stabilization. A separate metallized glass substrate was used for each run. The duration of the electrodeposition was controlled by the integrator. The film composition and thickness were measured by x-ray fluorescence (6). This procedure had an accuracy of ± 5%.

The relative invariance of the iron content of a permalloy film with thickness when prepared by the CEP method is shown in Fig. 1. For comparison Fig. 2 shows the variation in iron content with time of deposition of a film electrodeposited using a constant-current source. For reference purposes, the film composition as a function of electrode potential is presented in Fig. 3.

It may be therefore concluded that the CEP method can be used to prepare alloy films whose composition remains relatively constant with deposition time.

Acknowledgment

It is a pleasure to acknowledge the efforts of Thomas J. Ward in the preparation of the films. The x-ray fluorescent measurements were made by A. Month and J. Antelac.

Manuscript received Dec. 14, 1961.

Any discussion of this paper will appear in a Discussion Section to be published in the December 1962 JOURNAL.

REFERENCES

1. F. H. Edelman, PB 151,525, Nov. 1958, U. S. Government Research Report, **32**, 377 (1959).
2. G. H. Cockett and E. S. Spencer-Timms, *This Journal*, **108**, 906 (1961).
3. H. S. J. Sand, "Electrochemistry and Electrochemical Analysis," Blackie and Son, Ltd., London (1940).
4. I. W. Wolf and V. P. McConnell, "Nickel-Iron Alloy Electrodeposits for Magnetic Shielding," Tech. Proc. of the 43rd Annual Convention of the Amer. Electroplater's Society, 1956.
5. Analytical Instruments, Inc., RFD No. 2, Bristol, Conn.
6. M. J. Schindler, A. Month, and J. Antelac, X-ray Fluorescent Analysis of Thin Magnetic Films, to be published.

Thermodynamic Properties of the Tantalum and Tungsten Borides

James M. Leitnaker and Melvin G. Bowman

Los Alamos Scientific Laboratory, University of California, Los Alamos, New Mexico

and Paul W. Gilles

The Department of Chemistry, University of Kansas, Lawrence, Kansas

During the course of extensive experiments on the thermodynamic and vaporization properties of ZrB_2, information relating to the thermodynamic properties of the tantalum and tungsten borides has been obtained. The purpose of this paper is to present the results of these experiments.

Brewer and Haraldsen (1) have studied the thermodynamic properties of various refractory borides by studying three component systems. The three components were either two metals and boron, or a metal, boron and carbon, or a metal, boron and nitrogen. They have presented their results in phase diagrams and in limits on the heats of formation of the boride phases.

Some of our experiments also were of this type. The experiments involved high-vacuum heating of samples of the tantalum borides, or tantalum and ZrB_2, or tungsten and ZrB_2. The identification of the resulting phases by x-ray diffraction procedures served to indicate what chemical reactions occurred and what products can exist together at the test temperature. The results are used to obtain limiting values for the heats of formation of the various phases.

Experimental

Four types of experiments were performed in our previous work: (*A*) vaporization experiments with the tantalum borides, (*B*) phase diagram studies of the tantalum borides, (*C*) investigation of the ternary system Ta-Zr-B, and (*D*) investigation of the ternary system W-Zr-B.

(*A*) It was demonstrated in recent work on the phase diagram of the tantalum borides between tantalum and TaB (2) that tantalum metal appeared on the surfaces of tantalum boride samples that had been subjected to high-temperature vaporization. Thus, gaseous boron is lost preferentially from all the tantalum borides at high temperature.

(*B*) In the same work, it was shown by a large number of experiments that "Ta_2B" disproportionates at temperatures below 2040° ± 30°C into tantalum and "Ta_3B_2" and that "Ta_3B_2" disproportionates at temperatures above 2180° ±20°C into "Ta_2B" and TaB. This unusual behavior is fortunate for our purposes; it indicates the closeness of thermodynamic stability of these three phases. The work furthermore showed that Ta_2B has the chemical composition $Ta_{2.420.2}B$ and that the composition of Ta_3B_2 is really $Ta_{1.60\pm0.05}B$. Simple experiments revealed that boron reacts with TaB to produce TaB_2 and that TaB_2 reacts with tantalum to produce TaB.

(*C*) During the course of the work on the vaporization properties of ZrB_2 (3), tantalum metal was considered as a possible crucible material to use in effusion experiments. Samples of tantalum metal and ZrB_2 were heated together in high vacuum to temperatures of 1650° to 2200°C. The results indicated that tantalum liberates zirconium, forming Ta_2B, Ta_3B_2, or TaB depending on the temperature and the initial proportions of reactants. No reaction occurs, however, between TaB and ZrB_2.

(*D*) In the same investigation of the vaporization properties of ZrB_2 (3), possible reactions of the diboride with tungsten also were investigated. Samples of tungsten metal and ZrB_2 were heated together in high vacuum between 2075° and 2140°C for several days. The only result was the sharpening of x-ray lines of the two phases in the diffraction pattern of the quenched sample and the eliminating of faint impurity lines in the pattern. Hence, no reaction occurred.

Results

(*A*) Consider the two reactions by which Ta_2B might evaporate

$$Ta_{2.4}B(s) = 2.4\,Ta(g) + B(g) \qquad [1]$$

and

$$Ta_{2.4}B(s) = 2.4\,Ta(s) + B(g) \qquad [2]$$

Experimental observations showed that reaction [2] instead of reaction [1] occurred; hence the rate of loss of B(g) must be greater than 2.4 times the rate of loss of Ta(g) from Ta(s). The limiting standard free energy for reaction [2] can be computed by assuming the rate of loss of B(g) equals 2.4 times the rate of loss of Ta(g) from Ta(s). This assumption is equivalent to assuming the pressure of B(g) equals 1/9.82 times the pressure of Ta(g) over Ta(s). The limiting heat of formation for Ta_2B was computed from the free energy. The actual heat of formation of Ta_2B will be less negative than this.

For this calculation we selected a vapor pressure of tantalum of 8.69×10^{-14} atm at 2000°K from Stull and Sinke (4), Robson's (5) value of 135.0 kcal/mole for the heat of sublimation of boron, free energy functions for tantalum solid and boron gas from Stull and Sinke (4), and free energy functions for Ta_2B by summing free energy functions for the elements (4). The result is $\Delta H_{Ta_{2.4}B} > -64.9$ kcal/mole.

(*B*) The equilibria mentioned among Ta, Ta_2B, Ta_3B_2, and TaB lead to the conclusion that the heats

of formation of the three borides are nearly the same per boron. We have taken $\Delta S = 0$ for all reactions involving only crystalline phases. Thus

$$\Delta H_{Ta_{2.4}B} = \Delta H_{Ta_{1.6}B} = \Delta H_{TaB} > -64.9 \text{ kcal/mole} \quad [3]$$

(*C*) The results of the experiments involving ZrB_2 and Ta metal can be described in terms of the equation

$$ZrB_2(s) + 2Ta(s) = 2TaB(s) + Zr(s) \quad [4]$$

The failure of TaB to reduce ZrB_2 implies that the reaction

$$2TaB_2(s) + Zr(s) = 2TaB(s) + ZrB_2(s) \quad [5]$$

will take place as written. Since Huber, Head, and Holley (6) have given the ΔH of formation of ZrB_2 as -76.7 ± 1.5 kcal/mole, one can deduce that the ΔH of formation of TaB is more negative than -38.4 kcal/mole.

A lower limit for the ΔH of formation of TaB_2 can be imposed by considering the results of Brewer and Haraldsen (1) who have shown that the reaction

$$2TaC(s) + B_4C(s) = 2TaB_2(s) + 3C(s) \quad [6]$$

proceeds as written. The ΔH of formation of TaB_2 can be calculated to be more negative than -45.5 kcal/mole by using Kelley's data [quoted by ref. (1)] on TaC of -38.5 kcal/mole and the data of Smith, Dworkin, and Van Artsdalen (7) on B_4C of -13.8 kcal/mole.

Results for the tantalum borides are summarized in Table I.

(*D*) The stability of W_2B can be estimated in a fashion quite similar to that used for Ta_2B. Since the experimental evidence indicates that the reaction

$$ZrB_2(s) + 4W(s) = 2W_2B(s) + Zr(g) \quad [7]$$

does not proceed as written, one concludes that the partial pressure of boron in equilibrium with ZrB_2 is less than that in equilibrium with tungsten and W_2B. Taking the partial pressure of boron arising from the evaporation of ZrB_2 as 1.6×10^{-10} at 2000°K (3), the ΔH of formation of W_2B is computed to be less negative than -26.0 kcal/mole.

A lower limit of stability has been derived for W B by Brewer and Haraldsen (1) who have shown that the heat of formation is more negative than -20 kcal/mole. Hence, the limits of stability of W_2B are set as

$$-26.0 < \Delta H_{W_2B} < -20 \text{ kcal/mole} \quad [8]$$

Brewer and Haraldsen also have shown that the heat of formation of WB is less negative than that for W_2B by no more than 8 kcal/mole.

The ternary phase diagrams in Fig. 1 and 2 summarize the results of this work. The possible existence of ternary compounds and regions of homogeneity have been ignored since the purpose is to provide an easy-to-visualize thermodynamic relationship among the respective binary compounds of the system.

Table I. Limits on heats of formation
(Based on -76.7 for ZrB_2)

	kcal/mole
$Ta_{2.4}B$, $Ta_{1.6}B$, TaB	-64.9 to -38.4
$\frac{1}{2}TaB_2$	-51.7 to -22.7
W_2B	-26.0 to -20.

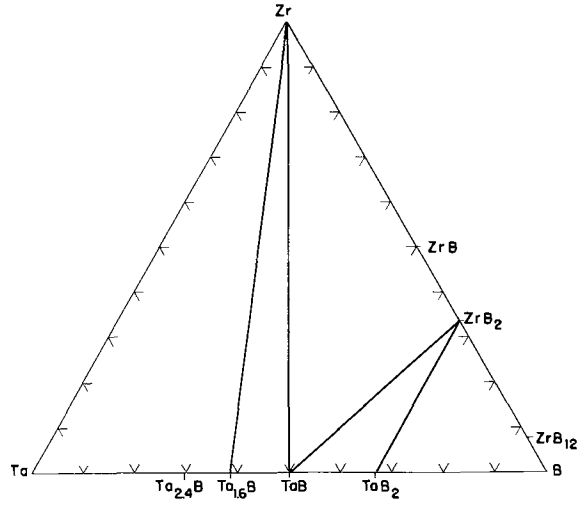

Fig. 1. Schematic phase diagram for the Ta-Zr-B system for a temperature of 1500°C.

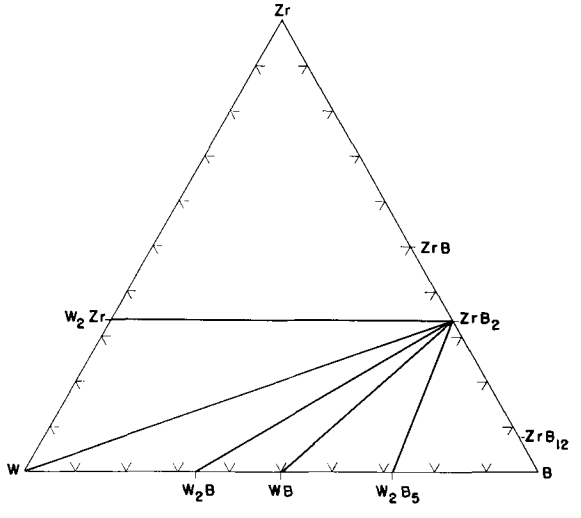

Fig. 2. Schematic phase diagram for the W-Zr-B system for a temperature of 1500°C.

Discussion

Results reported here reveal the kind of data and information that can be obtained from relatively simple experiments. Great accuracy is not claimed for the results, yet they are meaningful and worthwhile.

The results are not in disagreement with those of Brewer and Haraldsen, but they do indicate greater stability for the tantalum borides than were reported previously and, furthermore, have set bounding limits on the stability of lower borides of both tantalum and tungsten.

The solid solubility that is present in these systems has been ignored, but relatively little error results.

Manuscript received July 31, 1961; revised manuscript Jan. 26, 1962. This work was done under the auspices of the Atomic Energy Commission and abstracted in part from the doctoral thesis presented by James M. Leitnaker to the University of Kansas.

Any discussion of this paper will appear in a Discussion Section to be published in the December 1962 JOURNAL.

REFERENCES

1. Leo Brewer and Haakson Haraldsen, *This Journal*, **102**, 399 (1955).
2. J. M. Leitnaker, M. G. Bowman, and P. W. Gilles, *ibid.*, **108**, 568 (1961).
3. J. M. Leitnaker, M. G. Bowman, and P. W. Gilles, "The High Temperature Evaporation and Thermodynamic Properties of Zirconium Diboride," To be published in *J. Chem. Phys.*
4. D. R. Stull and G. C. Sinke, "Thermodynamic Properties of the Elements," Am. Chem. Soc., Washington, D. C., 1956.
5. H. E. Robson, Thesis, University of Kansas, 1958.
6. E. J. Huber, Jr., E. L. Head, and C. E. Holley, Jr., Unpublished work.
7. D. Smith, A. S. Dworkin, and E. R. Van Artsdalen, *J. Am. Chem. Soc.* **77**, 2654 (1955).

Experimental Study of the Anode Effect When Electrolyzing Mixtures of Fused Sodium Chloride and Zirconium Tetrafluoride

C. Decroly and R. Winand

Department of Metallurgy and Electrochemistry, University of Brussels, Brussels, Belgium

Work done in our laboratory (1, 2) on the electrolytic production of zirconium metal by electrolysis of fused mixtures of sodium chloride and zirconium tetrafluoride showed that under certain conditions it was possible to observe the apparition of the anode effect with all its setbacks. We thought it worthwhile to study the several factors which could have an influence on this phenomenon and to determine the best conditions of electrolysis to avoid its occurrence.

The anode effect is well known and was mentioned by Bunsen. It is particularly well known by the aluminum metallurgists, and it is specially for this case that researches have been conducted to elucidate this complex phenomenon. Work on the subject by Arndt and Probst (3), by von Wartenberg (4), and by Schischkin (5) may be cited. More recently, Drossbach (6) and his pupil Ostrowski (7), as well as Piontelli and coworkers (8), have published the results of their investigations on this problem.

Arndt and Probst appear to have been the first to have spoken of a critical anodic current density above which the anode effect is always observable. From the results of recent researches it can be said that the anode effect has several causes. Piontelli (8) and Drossbach (6) have shown that such factors as time, temperature, bath viscosity, and nature of the anodic gases can influence the anode processes. Taylor (9) has shown that addition of oxides to the melt also had an action on the anode effect. Since all of these factors can act together, it is rather difficult to determine separately the role of each of them. In the present work we have tried to find out what could be the importance of each of these causes on the anode effect in the special case of the electrolysis of zirconium tetrafluoride dissolved in molten sodium chloride. As is well known, in this case chlorine is evolved at the anode.

Experimental

Apparatus.—The main features of the apparatus used have been described elsewhere (1, 2, 10). However, in the present work the anode was the central electrode and was made of graphite. The crucible, also of graphite, was the cathode.

Experimental procedure.—All measurements were recorded photographically. Mirror galvanometers were used to measure the several electrical variables and the difference of potentials between silver wire electrodes and the anode. The reproducibility of the results is not perfect, but it is possible to observe a general trend of the phenomena as a function of the several variables which can be changed independently. The duration of the electrolysis must be taken into account and the "induction period," already observed by Piontelli, must be determined to fix the critical current density under which the anode effect is not observed.

The sequences of the experimental procedure were as follows.

(*A*) Measurements begin with a fresh anode, either new or not having been submitted to the anode effect for at least 15 min. Current is first set at a low value, then the cell voltage is progressively and continuously increased up to the moment the anode effect is observed. The value of the corresponding current is noted and immediately afterwards the cell is shut off. The related current density is called D_i.

(*B*) After 10 sec, the same voltage is applied to the cell. The induction time is observed, the cell is again shut off when the anode effect is observed. This procedure is repeated several times but with small increases of the voltage after each current interruption. After a certain number of these operations the anode effect is observed as soon as the voltage is applied to the cell. Such measurements allow plotting of the observed induction time against the anodic current density. Figure 1 shows the curve obtained, which has the shape of an hyperbola. The asymptote parallel to the ordinate axis gives the critical current density $D_{i_{crit}}$. In this particular case the value of $D_{i_{crit}}$ is 120 amp/dm^2.

(*C*) When the anode has been submitted several times to the anode effect, it behaves as if it has a certain memory, and it is no longer possible to avoid the anode effect even when shutting off or applying

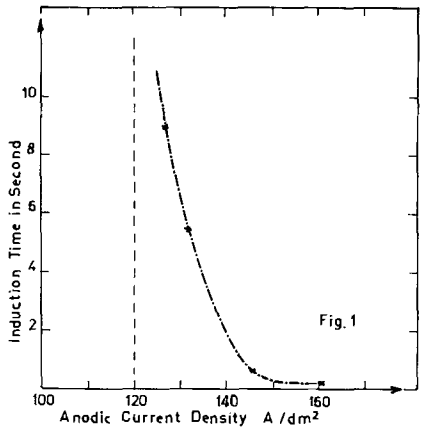

Fig. 1. Induction time vs. anodic current density. Composition of the bath: 25 w/o ZrF_4 and 75 w/o NaCl; temperature, 850°C. The position of the vertical asymptote to the curve gives the critical anodic current density.

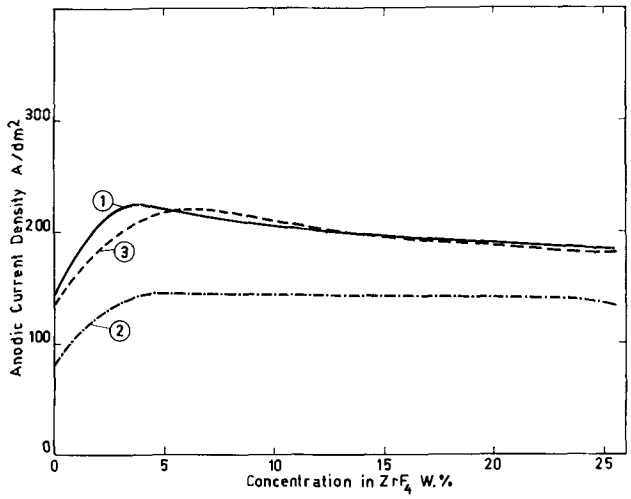

Fig. 2. Influence of the composition of the molten electrolyte on the critical current density; temperature, 850°C; anode diameter: curve 1: 16 mm, curve 2: 32 mm, curve 3: 64 mm.

the voltage to the cell. The surface of the anode is in a sort of excited state which gives it peculiar properties. It is possible to get the anode in this particular state by the following technique: one applies the voltage with such a value as to observe immediately the anode effect, and this state is maintained for 5 sec. Then the current is shut off for 10 sec. Afterwards the voltage is applied again for 5 sec and the current is shut off for 10 sec. These operations are repeated 20 times.

(*D*) After the last interruption of the current the procedure described in (*A*) and (*B*) is repeated, and it is possible to observe a new value of the anodic current density which produces the anode effect and a new value of the critical anodic current density. They are called respectively D_2 and D_{2crit}.

The four values of the anodic current density found when using the procedure described above are considered as defining the behavior of a given anode when all other factors are known.

Raw materials.—Commercial chemically pure sodium chloride was used. Zirconium tetrafluoride was prepared in our laboratory by a procedure described elsewhere (11). Before use it was purified by sublimation under vacuum and kept dry under argon atmosphere.

Experimental program.—Influence of the following factors has been studied: (*a*) electrolyte composition: concentrations of zirconium tetrafluoride in sodium chloride varied from 0 to 25 w/o. A bath obtained after electrolysis with 300 amp-hr of a mixture of 1800g sodium chloride and 600g zirconium fluoride was also studied. This bath is called "bath of end of electrolysis"; (*b*) diameter of the cylindrical central anode; (c) temperature; (*d*) rotation of the anode; and (*e*) addition of zirconium dioxide.

Results and Discussion

Influence of Bath Composition

Figure 2 shows how the critical current density is dependent on the bath composition for anode diameters of 16, 32, and 64 mm. Rather large discrepancies appear between the results of experiments made under similar conditions, and a mean curve has been drawn which shows the trend of the phenomena.

For pure sodium chloride the critical current density is rather small. When adding zirconium tetrafluoride it begins to increase, has a maximum for about 5 w/o of zirconium tetrafluoride, then decreases slowly with increasing concentration of zirconium tetrafluoride.

The shape of these curves might be explained when considering the influence of the interfacial tension. Although we did not make measurements of interfacial tension, we have been able to observe empirically that additions of zirconium tetrafluoride to molten sodium chloride could change the adherence of the mixture to the graphite crucible after solidification. When pure sodium chloride is molten in a graphite crucible and then allowed to solidify and cool off, it is very easy to get the solid salt out of the crucible. On the contrary, solidified mixtures of sodium chloride and zirconium tetrafluoride stick to the graphite crucible. This shows that the interfacial tension of the mixtures of salts is probably lower than that of pure sodium chloride and this might have an influence on the anode effect.

Measurements made with the "bath at end of electrolysis" have shown that the critical current density was of the same order of magnitude as that of the pure sodium chloride for the same electrode diameter. This mixture after solidification did not stick to the crucible.

An explanation of the decrease of the critical current density when the concentration of zirconium tetrafluoride is higher than 5 w/o might be that when the proportion of zirconium fluoride increases the vapor pressure of the salt increases also, a phenomenon which could have an influence on the anodic processes.

Influence of Anode Diameter

Some preliminary experiments had shown that, for a given current density, the area of the anode might have an influence on the anode effect. On the other hand our measurements of the critical current density gave results which were much lower

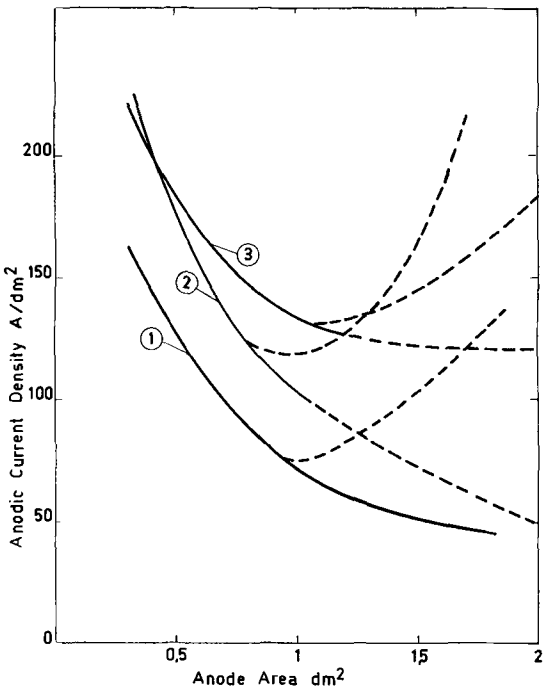

Fig. 3. Influence of the anode area on the critical current density; temperature; 850°C; electrolyte: curve 1: pure sodium chloride, curve 2: 7.7 w/o ZrF_4 + 92.3 w/o NaCl, curve 3: 25 w/o ZrF_4 + 75 w/o NaCl.

than those obtained by Piontelli and his coworkers when electrolyzing pure chlorides with a small hemispherical anode. As our electrolytic cell had a cylindrical symmetry and as the anode was always in the same position with regard to the level of the molten salt, we choose to define the geometrical characteristics of the anode with only one number: its diameter in mm. Five values of the diameter were chosen: 16, 22.6, 32, 45.2, and 64 mm. The ratio between each diameter is $\sqrt{2}$, so that the anode area increases by a factor of 2 when passing from one anode to the next and when using the same bath level.

Figure 3 shows the curves obtained when plotting the critical anode current density against the anode area for a given bath and a given temperature of 850°C. Curve 1 is obtained with pure sodium chloride; curves 2 and 3 are obtained with mixtures of sodium chloride and zirconium tetrafluoride containing, respectively, 7.7 and 25 w/o of this last salt.

The three curves show that, up to an anode area of about 1 dm^2, the critical current density decreases rather sharply, but for anode areas above 1 dm^2 the anode effect appears to obey two different laws. In some cases there is a minimum in the curve and the critical current density increases again; but in some other cases the critical current density becomes continually smaller when the anode area is increased. The minimum in the curves might be explained if it were supposed that, for areas above 1 dm^2, under certain conditions, there are parts of the anode which are working without anode effect, the remainder being submitted to this effect. Everything is going on as if the true anode area were smaller than the measured one. When the minimum does not appear in the curve it might be supposed that all of the anode area bears the anode effect. We have already said that Piontelli and his co-workers have found critical current densities higher than ours. This is probably due to the fact that Piontelli used much smaller anodes.

All these experimental facts show that anodic phenomena are rather intricate and it is not easy to give a theoretical explanation. Thermal considerations do not support the observed facts, namely, the high value of critical current density when anode diameter is small. At first sight, the local production of heat by joule effect and the small area of the electrode should not be in favor of a high critical current density. Other causes may prevail, and the hydrodynamics of the processes occurring at the anode surface should be studied to get a reasonable explanation.

Influence of Temperature

Between 780° and 950°C with a salt mixture containing 25 w/o of zirconium tetrafluoride no noticeable change of the critical current density could be observed. This shows that the thermal effect in our special case had not a predominant influence and that, as already mentioned, a simple thermal theory does not fit with the facts.

Influence of the Rotation of the Anode

Some experiments have been performed with a rotating anode. Between 0 and 100 rpm no significant change in the value of the critical anodic current density could be observed when using a bath containing 25 w/o zirconium tetrafluoride and with anode diameter of 32 mm. Further research should be carried out modifying the anode diameter and with greater speed of rotation to see if the hydrodynamic viewpoint has actually some importance.

Influence of Addition of Zirconium Dioxide

For a bath containing 25 w/o zirconium tetrafluoride as well as for baths of end of electrolysis, additions of zirconium dioxide up to saturation did not influence appreciably the critical current density. This may be due to the fact that additions of zirconium dioxide has no influence on the anodic reaction and that the wettability of the anode is not influenced either.

Conclusions

Factors which appear to play an important part in the processes involved in the anode effect are: (*a*) the wettability of the electrode by the bath, (*b*) nature of the gas evolved by the normal anodic reaction, and (c) the hydrodynamics of the gas evolution.

To get a clearer idea of the anode effect mechanism, it is necessary to carry out viscosity and interfacial tension measurements and to study the hydrodynamics of the gas evolution on a working anode.

From a practical viewpoint our work has shown that when electrolyzing baths containing sodium chloride and zirconium tetrafluoride it is possible to work with fairly high current densities, provided the anodes are of sufficiently great area.

Manuscript received Oct. 25, 1961. This paper was prepared for delivery before the Detroit Meeting, Oct. 1-5, 1961.

Any discussion of this paper will appear in a Discussion Section to be published in the December 1962 JOURNAL.

REFERENCES

1. R. Winand, *Mém. Scientif. Rev. Métallurgie*, **58**, 25 (1961).
2. R. Winand, Thesis, University of Brussels, June 1960.
3. K. Arndt and H. Probst, *Z. Elektrochem.*, **29**, 323 (1923).
4. H. von Wartenberg, *ibid.*, **32**, 330 (1926); **33**, 526 (1927).
5. I. V. Schischkin. *ibid.*, **33**, 83 (1927).
6. P. Drossbach, "Grundriss der allgemeinen technischen Elektrochemie," p. 216, Gebrüder Bornträger, Berlin (1952).
7. G. Ostrowski, quoted by Drossbach, *op. cit.* p. 226.
8. R. Piontelli, G. Sternheim, and F. Fumagalli, *Ricerca Sci.*, **28**, 160 (1958).
9. C. S. Taylor, *Trans. Am. Electrochem. Soc.*, **47**, 301 (1925).
10. R. Winand, To be published in Electrochemica Acta.
11. C. Decroly, D. Tytgat, and J. Gerard, *Energie Nucléaire*, **1**, 155 (1957).

Copper Corrosion

I. Thermodynamic Aspects

D. J. G. Ives
Department of Chemistry, Birkbeck College, London, England
and A. E. Rawson
Colne Valley Water Company, Watford, Hertfordshire, England

ABSTRACT

Thermodynamic data for reactions concerned in the corrosion of copper in waters containing dissolved oxygen and carbon dioxide are assembled and are used to demonstrate certain features of the corrosion processes. These include the extreme vulnerability of copper to attack, the critical effects of oxygen, and the inadequately protective properties of films of solid corrosion products. Confirmation and extension of these conclusions are obtained by experimental studies of systems derived from copper, cuprous oxide, cupric oxide, malachite, and azurite in water kept in equilibrium with gaseous atmospheres containing known partial pressures of oxygen and carbon dioxide. It is shown, *inter alia*, that cuprous oxide is highly susceptible to dissolution, both by disproportionation and oxidation, and that metallic copper dissolves in such media at a constant rate, despite the accompanying film growth, accumulation of cupric bicarbonate in solution, and rise of pH. The maximum rate of dissolution is attained at a molar ratio of $O_2/CO_2 = 7/3$ in the gas phase, when a substantial oxide film is formed on the metal.

The general (nonpitting) corrosion of copper by waters containing oxygen and carbon dioxide produces cupric bicarbonate in solution and an inadequately protective film of cuprous oxide on the metal. This action, which may be indefinitely prolonged, is an insidious industrial hazard, because the copper in solution may initiate acute corrosion elsewhere by setting up local cell action. Yet little effort has been made to study it systematically, even to discover whether the reactions producing soluble and insoluble corrosion products are functionally inter-related. There is thus a need for thermodynamic and kinetic studies of the Cu, H_2O, O_2, CO_2 system (both without and with saline additions), which the present series of papers is intended to initiate.

In attempting to correlate laboratory experiments with practical corrosion problems, a difficulty arises in the disparity of time scales; some adjustment of conditions must be made to hasten the experiments, with unavoidable introduction of an element of artificiality. In the present work, this adjustment has been confined to an increase above normal of the partial pressures of oxygen and of carbon dioxide with which the experimental systems have been kept in equilibrium. It is believed that this is a better compromise than some others which have been adopted.

Application of Thermodynamic Data

The thermodynamic data in Table I were derived from entries in the N.B.S. Circular 500 (1), except for the case of reactions involving the basic carbonates. For these substances, only heats of formation could be found (2), and an attempt to obtain the required Gibbs free energies of formation on the basis of entropy estimates [using approximate figures quoted by Latimer (3) for carbonate and hydroxide] was unsuccessful, giving results widely at variance with experiment. The entries in Table I for reactions involving malachite (5) and azurite (6) are therefore derived from our own experimental work and are of correspondingly limited accuracy.

Each reaction in Table I produces one mole of cupric bicarbonate in solution, so that subtraction of one equation from another (with the appropriate free energy changes) provides information about a third reaction in which cupric bicarbonate is not involved. The table thus summarizes data for 28 re-

Table I. Standard free energies, $\Delta G°$, and equilibrium ionic products, $K' = (Cu^{2+})(HCO_3^-)^2$, for copper corrosion reactions at 25°C

Reaction	$\Delta G°$, kcal	log K'
[1] $Cu + H_2O + 2CO_2 + \frac{1}{2}O_2 = Cu(HCO_3)_2$	−19.88	$14.57 + 2 \log P_{CO_2} + \frac{1}{2} \log P_{O_2}$
[2] $\frac{1}{2}Cu_2O + H_2O + 2CO_2 + \frac{1}{4}O_2 = Cu(HCO_3)_2$	−2.39	$1.75 + 2 \log P_{CO_2} + \frac{1}{4} \log P_{O_2}$
[3] $Cu(OH)_2 + 2CO_2 = Cu(HCO_3)_2$	8.73	$-6.40 + 2 \log P_{CO_2}$
[4] $CuO + H_2O + 2CO_2 = Cu(HCO_3)_2$	10.52	$-7.71 + 2 \log P_{CO_2}$
[5] $\frac{1}{2}[CuCO_3 \cdot Cu(OH)_2] + \frac{1}{2}H_2O + 1\frac{1}{2}CO_2 = Cu(HCO_3)_2$	11.9	$-8.69 + 1\frac{1}{2} \log P_{CO_2}$
[6] $1/3[2CuCO_3 \cdot Cu(OH)_2] + 2/3H_2O + 1\ 1/3CO_2 = Cu(HCO_3)_2$	12.1	$-8.84 + 1\ 1/3 \log P_{CO_2}$
[7] $Cu_2O - Cu + H_2O + 2CO_2 = Cu(HCO_3)_2$	15.10	$-11.07 + 2 \log P_{CO_2}$

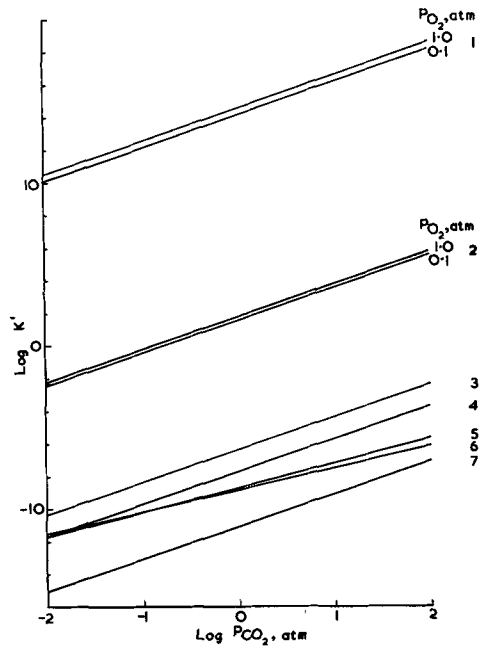

Fig. 1. Log K' = log $(Cu^{2+})(HCO_3^-)^2$ as function of log P_{CO_2} at 25°C for reactions [1] to [7] of Table 1. Plots relating to P_{O_2} = 1.0 atm and 0.1 atm are shown for reactions [1] and [2].

actions which may be concerned in the corrosion of copper in the Cu, H_2O, O_2, CO_2 system. The last column contains values of log K', where $K' = (Cu^{2+})(HCO_3^-)^2$, the ionic activity product, which would be attained in solution if each reaction proceeded to equilibrium. Figure 1 shows the dependence of the log K' values on appropriate gas pressures.

Certain inferences may be drawn from this thermodynamic survey.

Reaction [1] is accompanied by a free energy loss of nearly 20 kcal, indicating that copper has a considerable tendency to dissolve in water containing oxygen and carbon dioxide. Since it is this dissolution which constitutes the main problem, it is reasonable to regard this quantity as an over-all "corrosion potential" of copper in this connection. It is, however, unlikely to be fully effective because the system can decrease its free energy still further by undergoing any of the reactions [3] to [7] in reverse. All of these produce solid compounds, which are likely to deposit on the metal and exert some protective action.

The same inference may be drawn by inspection of Fig. 1. Thus, it can be seen that for $P_{O_2} = P_{CO_2} = 0.1$ atm, log K' for reaction [1] has a value of around 12. This corresponds with cupric bicarbonate in solution at molality ~6000 mole kg^{-1}. This striking result is absurd only because it expresses the corrosion potential of copper on an unsuitable scale. It correctly indicates that copper, far from being noble, is extremely vulnerable and is protected from rapid destruction only by the solid films which form on it. Thermodynamic information about these secondary film forming processes can be obtained from Fig. 1. Thus, a concentration of cupric bicarbonate defined by a point on this diagram will exceed the equilibrium concentration for a reaction represented by a line passing below the point. Such a concentration of cupric bicarbonate will therefore have a thermodynamic tendency to drive this reaction backwards. It is emphasized that these thermodynamic arguments are unlikely to be related to mechanisms of reaction and certainly carry no implication that all solid corrosion products arise from consecutive dissolution and deposition steps. Such arguments should, on the other hand, give the true sequence of stabilities of the solid corrosion products under defined P_{O_2} and P_{CO_2} conditions.

Reaction [7] is a disproportionation reaction occurring anaerobically. The data indicate that, by this reaction, cuprous oxide in presence of metallic copper can send appreciable concentrations of cupric ion into solution. Thus, for $P_{CO_2} = 1$ atm, the equilibrium concentration of cupric ion is 8 ppm,[1] indicating that cuprous oxide is unlikely to form a protective film of any permanence unless it is constantly regenerated; such regeneration, however, implies continued attack on the copper substrate.

The waters in which copper corrosion normally occurs contain oxygen as well as carbon dioxide; this greatly worsens the situation because reaction [2], which is much more favored thermodynamically, comes into play. Even if the effects of this should be largely nullified by deposition of hydroxide, oxide, or basic carbonate (reactions [3] to [6] in reverse), the damage is not entirely repaired, for all these substances provide far from negligible concentrations of cupric ions in solution. This provides an additional reason why it is unlikely that copper will, in course of time, provide its own adequately protective film.

The critical effects of oxygen are well illustrated by calculating equilibrium molalities of cupric bicarbonate in solution for reactions [1] and [2] over a complete range of oxygen-carbon dioxide mixtures at a total pressure of 1 atm. The results are shown in Fig. 2. The very steep rise of the curves as the oxygen partial pressure increases from zero is obvious; the tendency of copper to dissolve increases rapidly, and the protective action of a cuprous oxide film decreases even more rapidly.

Exploratory Experiments and Results

Although not all the equilibria of interest could be accessible, experiments were carried out to check the inferences made from the available thermodynamic data and to serve as a guide for further work. Pow-

[1] The convenient notation of parts per million (mg l^{-1}) is used for very low concentrations of solutes.

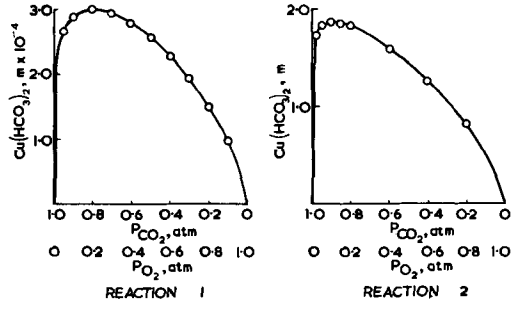

Fig. 2. Calculated molalities of $Cu(HCO_3)_2$ for reaction [1], $Cu + H_2O + 2CO_2 + \frac{1}{2}O_2 = Cu(HCO_3)_2$ and reaction [2], $\frac{1}{2}Cu_2O + H_2O + 2CO_2 + \frac{1}{4}O_2 = Cu(HCO_3)_2$ for systems in equilibrium with mixtures of O_2 and CO_2 at a total pressure of 1 atm.

dered (100 mesh) solid phases, carefully freed from electrolytic impurities, were maintained in contact with circulating water continuously equilibrated with known gas mixtures (O_2, CO_2, N_2) at a total pressure slightly greater than barometric. Samples of aqueous phase were periodically withdrawn for estimation of copper content, and records were kept of conductance and *p*H. Accuracy in these experiments, conducted in a thermostatically controlled room at 24° ±1°C, was not better than ±5%, but the following useful indications were obtained.

Dissolution of cupric compounds, or of cuprous oxide, or copper in oxygenated media, led to increase in *p*H and (sometimes after an initial decrease) conductance. In conjunction with copper analyses and P_{CO_2} values, such results were invariably consistent with the existence of copper in solution solely as fully dissociated cupric bicarbonate, and with *p*H determined by the bicarbonate/carbonic acid buffer ratio. To establish this, use was made of the electroneutrality requirement, of data for the solubility of carbon dioxide in water (4) and its dependence on partial pressure (5), of the ionic product of water (6), the dissociation constants of carbonic acid (6), and ion conductances of hydrogen (7), cupric (8) and bicarbonate (9) ions.

Cupric oxide, prepared from cuprous oxide (see below) by heating in oxygen at 400°C, was used in studies of equilibria in CuO, H_2O, N_2, CO_2 and CuO, H_2O, O_2, CO_2 systems. The results, shown in Fig. 3(a), agreed reasonably well with some earlier determinations (10) and with those calculated thermodynamically for reaction [4], from which the curve in Fig. 3(a) was constructed.

The thermodynamic data indicate, however, that cupric oxide is not the most stable solid phase except at very low partial pressures of carbon dioxide. This

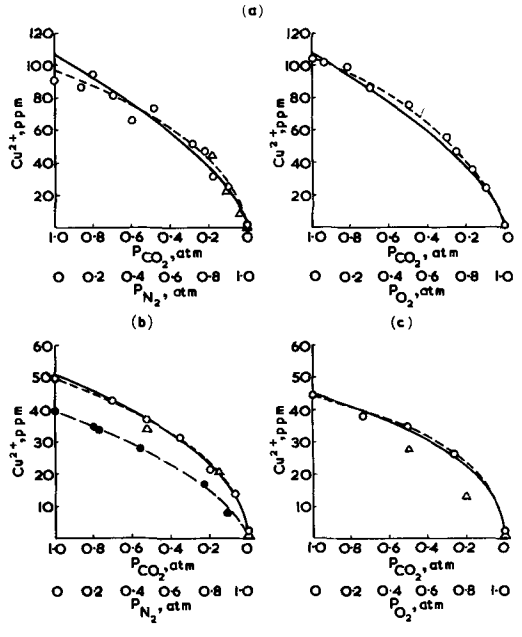

Fig. 3. Experimental concentrations of Cu^{2+}, ppm, for (a) CuO, (b) malachite, and (c) azurite equilibrated with water and with N_2 and CO_2 mixtures (left-hand diagrams) or with O_2 and CO_2 mixtures (right-hand diagrams) at a total pressure of 1 atm. ——— Thermodynamic curve; - - - ○ - - - experimental, present work; △ Tronstad and Veimo; —— ● —— free.

was confirmed by the occasional appearance of green-blue solids at $P_{CO_2} \sim 1$ atm. In two cases these were identified by x-rays as malachite, or a mixture of malachite and azurite.

Malachite (Burra Burra, Australia) and azurite (MacAlder Mine, Kenya), hand-picked, ground, and extracted with water to constant conductance of the aqueous phase, were used in similar equilibrium studies. The results are shown in Fig. 3(b) and 3(c), in which the curves represent the requirements of the data in Table I for reactions [5] and [6]; these data were, however, derived from these same experiments, so the agreement is not significant. Agreement with some earlier data (10, 11) is not good, but it is believed that the present results slightly improve an unsatisfactory situation, even though they are derived from rough, exploratory experiments quite inadequate for setting up new standards (thus, the experimental values, for reactions [4], [5], and [6], respectively, of $\partial \log K'/\partial \log P_{CO_2}$ were 1.84, 1.40, and 1.20).

There is some subsidiary evidence relating to the placing of the lines in Fig. 1. If, by some means (possibly reaction [1]), a concentration of cupric bicarbonate has been set up in solution, then, in the presence of metallic copper, reaction [7] in reverse is thermodynamically preferred, and there is no doubt that cuprous oxide is the first solid corrosion product to appear under these circumstances. In long-term experiments in which copper strips were allowed to corrode for many months in aerated solutions the second product was malachite. Azurite, cupric oxide, or hydroxide were not found. This is in agreement with expectations from Fig. 1. On the other hand, in experiments in which cuprous oxide has been subjected to prolonged treatment with water in equilibrium with $P_{CO_2} = 0.3$ atm, malachite, not azurite, has been identified by x-rays as the final product. This suggests that the malachite line in Fig. 1 should be slightly dropped relative to the azurite line. Such adjustments, however, must await the provision of more satisfactory data. It must also be remarked that purely thermodynamic arguments of this kind cannot be taken as an infallible guide to the sequence in which corrosion products may appear and can certainly not be taken as evidence on the mechanisms of their formation.

Cuprous oxide, prepared by glucose reduction of cupric acetate solution, was extracted with water in absence of air to constant conductance of the aqueous phase, dried, graded (100 mesh), and used in studies of Cu_2O, H_2O, N_2, CO_2 and Cu_2O, H_2O, O_2, CO_2 systems. The results for the first of these are shown in Fig. 4(a) and are seen to be erratic, corresponding with observations of instability and deposition of green-blue solid phases. Copper in solution was undoubtedly predominantly, if not exclusively, in the form of cupric bicarbonate (basic cupric carbonate was recovered on displacement of dissolved carbon dioxide by nitrogen), which must have been formed by the disproportionation reaction [7]. Yet at $P_{CO_2} =$ 1 atm, the concentration of cupric ion in solution, 83 ppm, was ten times that expected from the thermodynamic data. This result could not have been due to imperfect deoxygenation of the system (residual

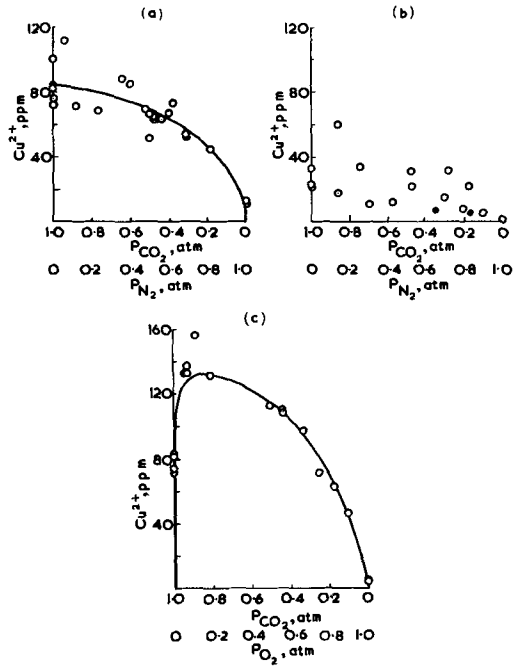

Fig. 4. Experimental studies of systems (a) Cu_2O, H_2O, N_2, CO_2, (b) Cu, Cu_2O, H_2O, N_2, CO_2, and (c) Cu_2O, H_2O, O_2, CO_2 for binary gaseous mixtures to a total pressure of 1 atm. ○ Present work; • Tronstad and Veimo.

oxygen 0.0 — 0.7 ppm) and must be attributed to nonstoichiometry of the oxide and to the absence of metallic copper, except for that produced in the reaction itself, from the system. Such copper could, perhaps, be accommodated in lattice defects and certainly fell short of attaining the standard state for the metal. This point was checked by carrying out a set of experiments in which copper powder was included with the cuprous oxide. The results, shown in Fig. 4(b), were even more erratic, but appreciably lower. Instability was very marked, and some of the copper in solution must have been in the cuprous valency state.

Although these results have no absolute, quantitative significance, they underline the extreme vulnerability of cuprous oxide to dissolution, both by disproportionation and oxidation, and indicate the necessity of giving separate consideration to Cu_2O and Cu, Cu_2O systems. In the latter case it seems that the copper may have some difficulty in controlling its somewhat thermodynamically undisciplined lower oxide. This general point seems to have escaped Tronstad and Veimo (10), who set out to determine the solubility of cuprite in water containing dissolved carbon dioxide. Their results (in presence of added copper) are included in Fig. 4(b) and fall within the scatter of the present determinations, but their conclusion that cuprous oxide is only 1/5 to 1/10 as "soluble" as cupric oxide in water containing carbon dioxide is untenable; their subsequent discussion of copper corrosion, hinging on this conclusion, consequently loses significance.

Inspection of Fig. 1 indicates that there could be no hope of realizing equilibria in the Cu_2O, H_2O, O_2, CO_2 system, for molalities of cupric bicarbonate up to nearly 2 mole kg^{-1} would have to be attained. In spite of this, an attempt was made to study this system. Instability was encountered, but the highest attainable concentrations of copper in solution were recorded and appear as functions of gas composition in Fig. 4(c). Surprisingly enough, a curve can be placed through the somewhat scattered results (orders of magnitude lower than those corresponding with equilibrium) identical in shape with the thermodynamic curve of Fig. 2. Coincidental though this may be, the extreme vulnerability of cuprous oxide in such systems, containing even traces of oxygen, is demonstrated.

Since the limit of thermodynamic studies had been reached, and since in practical problems kinetic and thermodynamic factors are often not easily disentangled, experiments were made in order to follow the course of all the solid phase dissolution reactions over an initial period of 3 hr. In general, the results served only to confirm conclusions already reached, with the following exceptions.

For the cupric compounds, a fast initial reaction decreased smoothly in rate, giving a copper concentration curve concave to the time axis, a form not unexpected and easily explained. In the case of cuprous oxide, however, these features were accentuated; thus for the conditions $P_{O_2} = 0.2$ atm and $P_{CO_2} = 0.8$ atm, the aqueous phase contained 15 ppm of dissolved copper within 5 min, but required 3 hr to attain 30 ppm. This behavior could be due to a change in that part of the solid phase accessible to the aqueous medium, impoverishment in oxygen, or enrichment in copper of nonstoichiometric surface layers. But perhaps the most important aspect is again the high reactivity of cuprous oxide, now demonstrated kinetically as well as thermodynamically, when not under the restraining control of metallic copper in its standard state. Again, remarkably, the extent of copper uptake after 1, 2, or 3 hr of dissolution reproduced approximately the shape of the thermodynamic curve.

Copper powder, formed by reduction in hydrogen at 200°C of the same cuprous oxide (in the hope of preserving some correspondence of specific surface areas), was used to study the Cu, H_2O, O_2, CO_2 system. Attention was necessarily confined in this case to kinetic aspects, which were later studied in more detail by modified methods, but the following preliminary results of some significance were obtained.

The dissolution of metallic copper, often delayed by an induction period, took place at a constant rate. This is illustrated in Fig. 5(a) and stands in marked contrast to the behavior found for the four copper compounds examined in this way. This remarkable constancy of rate, later shown to be preserved for prolonged periods, suggested some sort of automatic self-regulation, the nature of which was not clear at this stage.

The extent of dissolution in a fixed time, as a function of gas composition, did not reproduce the shape of the thermodynamic curve in Fig. 2. The maximum copper uptake was found in the range 20-30 mole % of carbon dioxide, 80-70 mole % of oxygen. For gas mixtures containing less than 20 mole % of oxygen, the copper retained its pristine pink color, but for mixtures richer in oxygen, it rapidly became brown or black. This may be related to the peak in the solu-

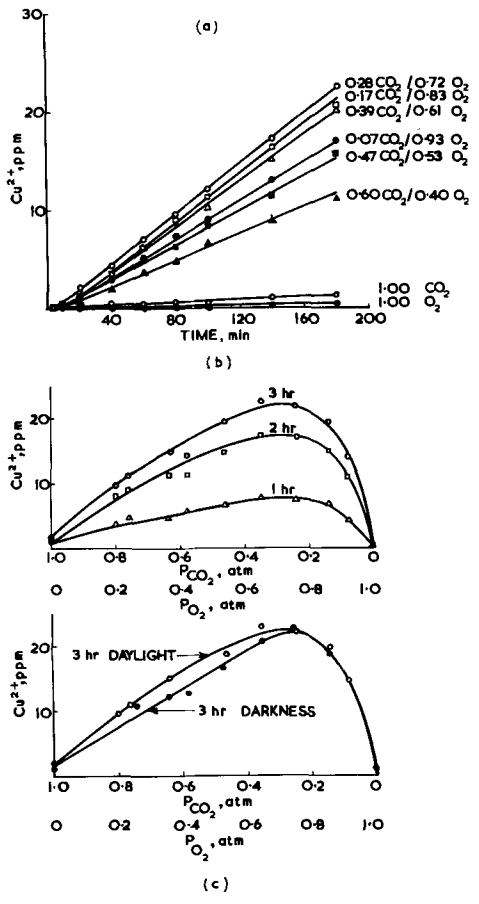

Fig. 5. Dissolution of Cu powder in water equilibrated with mixtures of O_2 and CO_2 to a total pressure of 1 atm (a) as a function of time for various gas mixtures, (b) as a function of gas composition for various times, and (c) as a function of gas composition for constant time, in daylight and in darkness.

bility of cuprous oxide at around 10 mole % of oxygen (Fig. 2 and 4(c)), which perhaps gives a film little chance to thicken. It was certainly the case that the maximum rate of dissolution was attained when the copper powder, as indicated by its color, was covered with a substantial oxide film. Although it was clear from the present and previous (12, 13) work that neither cuprous oxide nor cupric oxide can be very protective in an aqueous medium, this conclusion does not imply an accelerated rate of dissolution as a consequence of progressive oxide formation. The idea that a film, far from giving increased protection with increasing thickness, might be active in promoting dissolution was novel.

In these experiments, previous observations (12, 14-16) that light accelerates chemical attack on copper was confirmed; steps were subsequently taken to eliminate this photo effect. Features of these experiments are illustrated in Fig. 5(b) and 5(c) and confirm that neither carbon dioxide nor oxygen is particularly aggressive toward copper in the absence of the other.

Manuscript received Oct. 2, 1961; revised manuscript received Jan. 23, 1962. This paper was prepared for delivery before the Ottawa Meeting, Sept. 28-Oct. 2, 1958.

Any discussion of this paper will appear in a Discussion Section to be published in the December 1962 JOURNAL.

REFERENCES

1. Selected Values of Chemical Thermodynamic Properties, Nat. Bur. Stand. Circular 500 (1952).
2. W. A. Roth, *J. prakt. Chem.*, **158**, 117 (1941).
3. W. M. Latimer, "Oxidation Potentials," 2nd. ed., Prentice-Hall, Inc., New York (1952).
4. Landolt-Börnstein, "Tabellen," **1**, 768 (1923).
5. International Critical Tables, **3**, 260 (1928).
6. R. A. Robinson and R. H. Stokes, "Electrolytic Solutions," p. 496, Butterworths, London (1955).
7. B. B. Owen and F. H. Sweeton, *J. Am. Chem. Soc.*, **63**, 2811 (1941).
8. B. B. Owen and R. W. Gurry, *ibid.*, **60**, 3074 (1938).
9. T. Shedlovsky and D. A. MacInnes, *ibid.*, **70**, 3281 (1948).
10. L. Tronstad and R. Veimo, *J. Inst. Metals*, **66**, 17 (1940).
11. E. E. Free, *J. Am. Chem. Soc.*, **30**, 1366 (1908).
12. G. D. Bengough and O. F. Hudson, *J. Inst. Metals*, **21**, 37 (1919).
13. W. H. J. Vernon, *Trans. Faraday Soc.*, **27**, 255 (1931).
14. T. W. Case, *Trans. Am. Electrochem. Soc.*, **31**, 351 (1917).
15. R. Audubert, *Compt. rend.*, **177**, 818 (1923).
16. O. Gatty and E. C. R. Spooner, "Electrode Potential Behavior of Corroding Metals," p. 184, Oxford (1938).

Copper Corrosion

II. Kinetic Studies

D. J. G. Ives
Department of Chemistry, Birkbeck College, London, England

and A. E. Rawson
Colne Valley Water Company, Watford, Hertfordshire, England

ABSTRACT

Experimental methods are described for studying rates of formation of soluble and insoluble corrosion products of copper exposed to water containing dissolved oxygen and carbon dioxide. Coulometric reduction indicates that the films formed on copper under these conditions are predominantly of cuprous oxide. Generation of cupric bicarbonate in solution and film growth are constant in rate over long periods, and both are kinetically of first order with respect to dissolved oxygen. Dependence of these rates on the concentration of dissolved carbon dioxide follows no obvious kinetic law, but is such as to suggest that the initial pH of solution is a major factor. Experiments in which either solution or metallic phase is replaced during kinetic measurements demonstrate that a cuprous oxide film on copper may have either an activating or a passivating effect, depending on its mode of generation. The evidence indicates the existence of an electrochemical mechanism for general corrosion of copper by which dissolution and film growth are kinetically linked processes.

Preliminary work (Part I; preceding paper) indicated the need for concurrent measurements of rates of formation of soluble and insoluble corrosion products in the Cu, H_2O, O_2, CO_2 system. The technique developed for this purpose was designed to break a wide area of new ground, rather than to obtain precise kinetic data.

Experimental Methods

Corrosion Apparatus

Units of the kind illustrated in Fig. 1, which is largely self-explanatory, were used to circulate glass-distilled water (initial $\kappa \sim 3$ μmho cm^{-1}, free $NH_3 < 0.1$ ppm) at a constant rate of 4-5 l hr^{-1} through vessels containing copper electrodes, each of 15 cm^2 apparent surface area. The water was kept in equilibrium with gas mixtures of known composition (Orsat) by means of a diaphragm pump, which continuously circulated the gas through the main water reservoir. The apparatus, of silicone-treated Pyrex, was assembled with glass-to-glass junctions inside PVC sleeves, and neoprene stoppers were used for mounting electrodes and a dipping conductance cell. The electrodes were screened from light by shields round the electrode vessels.

Before use, the apparatus was repeatedly flushed out with batches of water to remove residual traces of copper and until the conductance of the water fell to about 3 μmho cm^{-1} (residual CO_2; glass-derived solutes). It was then charged with a standard volume (3.1 l) of water, which was brought into equilibrium with a prepared gas mixture; conductance and pH determinations were made and showed reasonably good correlation with the CO_2 contents of the mixtures concerned. The electrodes, prepared as described below, were then inserted and the run commenced.

The electrodes were made from electrolytic copper foil, 0.01 cm thick, initially degreased with acetone and polished to a mirror finish by use successively of "3/50 slow cutting Microid" alumina and "γ-Microid" alumina. The foil was then cut into strips 2 cm wide and annealed in hydrogen (~700°C). Shortly before use, these strips were cut to form electrodes, each provided with a tang which was gripped by a claw formed at the end of a heavy copper wire (1.6 mm diameter), sealed into a glass mounting tube with vacuum wax. Uncovered portions of the wire and tang were coated with beeswax, applied to leave only the desired area of foil exposed. The electrodes were stored in hydrogen and, immediately before use, were immersed for 1 min, with gentle agitation,

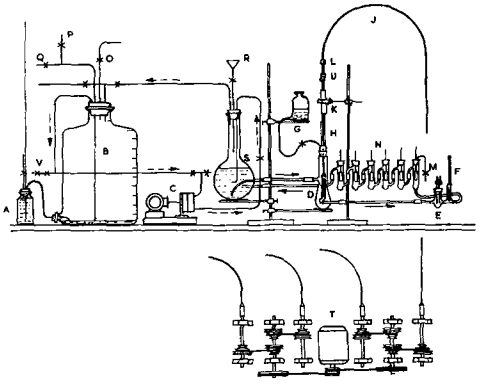

Fig. 1. Diagrammatic section of modified corrosion apparatus: A, gas seal and manometer; B, aspirator (22 l); C, gas circulating pump; D, solution circulating pump; E, conductance cell; F, thermometer; G, gas release; H, gas seal; J, flexible drive; K, bearing; L, drive connection; M, solution sampling point; N, electrodes and cells; O, gas sampling and filling point; P, water filling point; Q, water outlet; R, funnel for solution replacement; S, solution reservoir (2 l); T, 3-speed drive unit; U, worm drive; V, connection to second section.

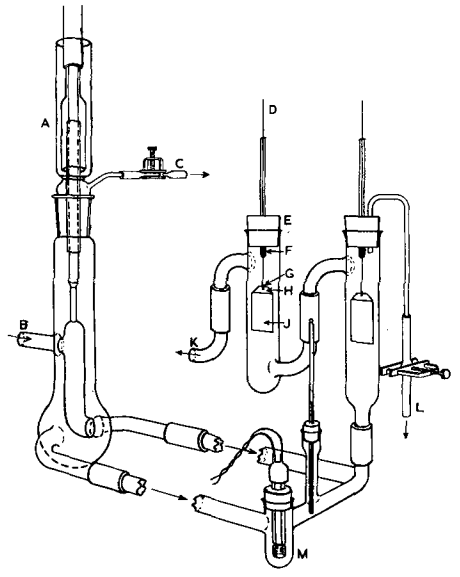

Fig. 2. Modified corrosion apparatus: solution circulating system: A, gas seal; B, from solution reservoir; C, gas release; D, 16 SWG hard copper wire; E, neoprene bung; F, picien wax seal; G, wire attached to foil; H, beeswax insulation; J, exposed copper foil; K, to solution reservoir; L, solution sampling point; M, conductance cell.

in 10% ammonium persulfate solution (1), washed rapidly in air-free water and inserted directly into the corrosion apparatus. This procedure removed any coulometrically measurable oxide film and gave a lightly etched surface hoped to be of reasonably reproducible properties. Details of electrode mounting and of part of the water-circulating system are shown in Fig. 2.

The progress of the kinetic runs, normally conducted for 100 hr at 21° ±2°C was followed by conductance measurements, determinations of dissolved copper, and coulometric analyses of solid films formed on the electrodes.

Solution Analysis

Copper in solution (as cupric bicarbonate; cf. Part I) was determined colorimetrically (Hilger "Spekker"), using sodium diethyldithiocarbamate, *bis*-cyclohexanone oxalyldihydrazone, or rubeanic acid (preferred), against reference standards prepared from "Specpure" copper. Sampling reduced the volume of water in the corrosion apparatus progressively to 2.9 l, but a mean volume of 3.0 l was assumed, without appreciable error.

Electrodes were removed at intervals for examination, and correction was applied to the observed rates of change of cupric ion concentration (and of conductance) for the step-wise reduction of total area of metal-solution interface; all the results reported relate to a total apparent surface area of exposed copper of 90 cm^2. At the conclusion of each run, *pH was redetermined. Checks on gas composition* by analysis indicated a maximum variation of about 0.01 atm in partial pressures.

Examination of Solid Films

Solid films on the electrodes were estimated coulometrically by galvanostatic cathodization in nitrogen-saturated, 0.2*N* ammonium chloride solution. The apparatus was designed to secure reasonable uniformity of current density over the whole surface of an electrode undergoing cathodic reduction and was provided with Luggin capillaries leading to a saturated calomel electrode. The ammonium chloride electrolyte was recommended by Miley (2), but, because of its appreciable film-stripping action under open-circuit conditions (3), it has been replaced in some later work of this kind (1, 3-5) by 0.1*N* or 1.0*N* potassium chloride solutions. We have found, however, that ammonium chloride is preferable because it tends to reduce electrode polarization (reduction potentials less negative) and gives more sharply defined arrests on the potential-time curves. No serious discrepancies were found in estimates of film thickness due to this variation in the electrolyte, and 1.0*N* or 0.1*N* potassium chloride solution was frequently employed in confirmatory or duplicated measurements.

Although this coulometric method is unique in its suitability for a long series of routine measurements, it is, unfortunately, limited in accuracy and unsatisfactory in its powers of discrimination between alternative reducible copper compounds. Observed reduction potentials are not related to reversible potentials calculated for various copper-copper compound couples and vary considerably according to the current density within a practicable range. They also vary quite widely according to the physical nature and distribution of a given film substance, *i.e.*, with the "topography" of the film (5). It is not surprising that films deposited in various ways, many of them conferring appreciable passivity, do not conform to the conditions required for electrode reversibility, nor that properties such as film conductance, permeability, and solubility should control irreversible reduction potentials, which are consequently thermodynamically unpredictable. In any case, no electrode carrying a composite deposit can be at equilibrium, and no reversible basic copper carbonate electrode exists.

The method therefore had to be used empirically, with calibration using films of known constitution. For this purpose, electrodes were subjected to the following treatments: (*a*) anodization for 15 min at 4.0 ma cm^{-2} in 4*N* NaOH solution. Halliday (6) has shown that this provides a composite film, in which he identified $Cu(OH)_2$, CuO, and Cu_2O by electron diffraction; (*b*) exposure to moist oxygen at room temperature for 22 hr to produce a film consisting mainly of Cu_2O; (*c*) ignition (~300°C) for 1 min in air, then for 1 min in oxygen, to ensure the presence of CuO; (*d*) long-term spontaneous corrosion in very dilute salt solutions [~200 ppm of NaCl, Na_2SO_4, $NaNO_3$, $Ca(HCO_3)_2$] in equilibrium with air, to produce basic salts. In all cases the films consisted of cuprous oxide overlaid with malachite, identified by x-rays.

Coulometric reduction curves of these electrodes are shown in Fig. 3. It is seen that cupric hydroxide and oxide, and cuprous oxide, are reduced at well-separated potentials, which differ from reversible potentials appropriate to the experimental conditions [$Cu(OH)_2 \rightarrow Cu_2O$, 0.268v; $CuO \rightarrow Cu_2O$, 0.190v; $Cu(OH)_2 \rightarrow Cu$, 0.130v; $CuO \rightarrow Cu$, 0.091v; $Cu_2O \rightarrow Cu$,

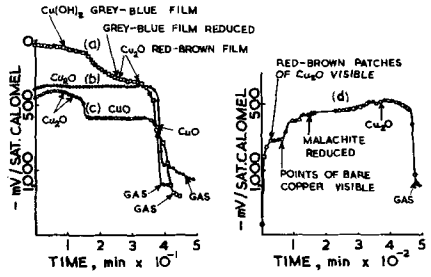

Fig. 3. Coulometric reduction of films on copper; control experiments, (a) to (d), details as in text [c.d.: (a) 0.2 ma/cm²; (b) 0.3 ma/cm²; (c) 0.5 ma/cm²; (d) 1.0 ma/cm²].

−0.008v).[1] Even the sequence of the reduction potentials is not the same, but is identical with that found by Halliday (6), although his cathodizations were performed in 4*N* NaOH solutions. The latter fact suggests that the irreversible reduction potentials are determined largely by the properties of the solid phases.

It is also seen that the malachite-bearing film initially was very resistant to cathodic reduction, and that no characteristic reduction potential could be identified. This was the case for all the electrodes of this kind. Fortunately malachite seems invariably to be a very long-term corrosion product which appears as an easily distinguishable, bright green phase. Neither malachite nor gray-blue cupric hydroxide has appeared in any of the kinetic corrosion experiments, so that attention may be confined to cuprous and cupric oxides.

The calibration experiments lead to typical reduction potentials for Cu_2O and CuO of −390 ±30 mv and −660 ±60 mv, in 0.2*N* NH_4Cl solution, with respect to the saturated calomel electrode. This agrees tolerably with Miley's (2) results of about −360 to −390 mv and −670 to −710 mv for these two oxides, and with −370 mv for Cu_2O obtained by Price and Thomas (7). Although Lambert and Trevoy (5) were unable to confirm that CuO is reduced at a potential some 300 mv more negative than is Cu_2O, this fact is now substantiated and is supported by Halliday's findings (6). In the present work, it was expedient to arrange for all the corrosion films to be cathodically reduced in a period not exceeding 40 min, and current densities were adjusted accordingly within the range 0.1-1.0 ma cm^{-2}. Under these conditions, the films were generally reduced at potentials between −350 and −450 mv with respect to the saturated calomel electrode. Occasionally it was necessary to use higher current densities, with a corresponding negative displacement of potential. It was concluded that all the films were composed of cuprous oxide, and mean film thicknesses were calculated throughout on this assumption. At first sight somewhat questionable, this conclusion is strongly supported by the fact that, apart from initial eccentricities assigned to elimination of tendencies to passivity, or gentle gradients attributed to variation in physical nature, all the potential-time curves at constant current showed but a single plateau. Since it is undoubted that in all cases cuprous oxide was a major film constituent, the inference may be drawn

[1] The Stockholm sign convention, 1953, is used throughout.

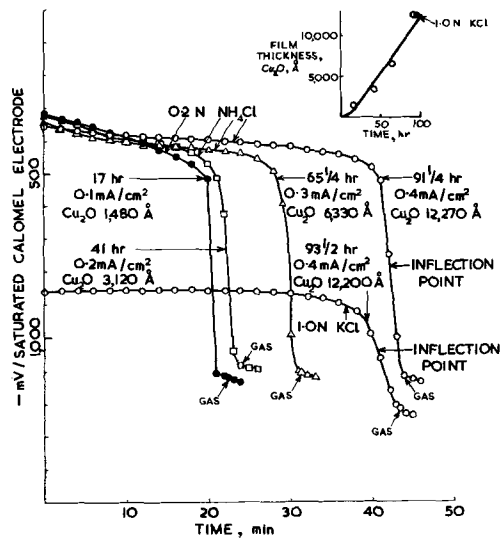

Fig. 4. Typical set of coulometric reduction curves used to follow growth of cuprous oxide film (inset).

that it was essentially the only constituent. It must be mentioned, however, that in a few isolated cases a second, ill-defined arrest occurred at −500 to −550 mv, the source of which was not identified. A typical set of coulometric reduction curves, illustrating the course of film growth on electrodes successively removed from the corrosion apparatus during a kinetic run, is shown in Fig. 4.

Results

Since a complete survey of the effects on corrosion rates of two independent variables (*i.e.* partial pressures of oxygen and of carbon dioxide) was impracticable, one of these pressures was fixed in turn at 0.30 atm while the effect of variation in the other was studied. This choice was made in the light of the results of the preliminary experiments with copper powder described in the preceding paper, and led to the following sets of results.

Experiments at constant pressure of carbon dioxide: $P_{CO_2} = 0.30$ atm; $P_{O_2} = 0.10 - 0.70$ atm.—In these experiments, rates of copper dissolution and of film growth were measured as a function of the partial pressure of oxygen, total gas pressure being maintained slightly in excess of atmospheric by the required addition of nitrogen.

Difficulty was experienced in obtaining reproducible results, only partly due to the occurrence of an induction period in the dissolution reaction. This trouble, which appears to be common in this field of work, is no doubt to be associated with difficulty in reproducing the surface states of polycrystalline metal specimens and was reflected in the uneven early stages of film growth, particularly at low P_{O_2} values. As corrosion proceeded, however, the films became more uniform and were light brown or red-brown in color, except that blue, green, or purple patches were sometimes formed. Even in these cases subsequent coulometric reduction gave rise only to the single plateau assumed to be characteristic of cuprous oxide.

Considerable scatter had therefore to be tolerated in the results, a typical selection of which is pre-

sented graphically in Fig. 5(a) and 5(b), and establish beyond reasonable doubt that there is a constant rate of copper dissolution for each value of P_{O_2}, confirming the results of the earlier experiments with copper powder. It is also shown, with somewhat less certainty, that there is a constant rate of film growth which is a function of P_{O_2}. It is noteworthy that a film of cuprous oxide about 25,000Å thick seems to confer no additional protection to the metal, for dissolution continues at the same constant rate when such a film has been formed.

The erraticity of these results has been countered to some extent by replication of experiments. In later studies of the effects of saline additions (Part IV), each experiment was accompanied by a control, identical in all respects except that no salt was added. Many such control experimental results were combined by interpolation and averaging and gave rise to the plots shown in Fig. 6(a) and 6(b). These give the average concentrations of dissolved copper and the average thicknesses of cuprous oxide films, attained at 20, 50, and 100 hr of corrosion time, as a function of P_{O_2} at constant P_{CO_2} (0.30 atm).

In these plots, the lines are those predicted by the equations $d[Cu^{2+}]/dt = 0.00645\ P_{O_2}$ ppm hr^{-1} for dissolution and $d(Å)/dt = 390\ P_{O_2}$ Å hr^{-1} for film growth. It is justifiable to conclude that, after an induction period, both of these processes follow first order kinetics with respect to oxygen; at least, first order kinetics fit the results better than any other. It is perhaps more important to observe that dissolution and film growth may be linked together kinetically, or both may be controlled by the same rate-limiting process. This seems all the more probable in the light of the fact that, in this set of experiments, the ratio of film thickness to cupric ion concentration in solution was constant to ±7% over the range of P_{O_2} = 0.25 to 0.70 atm for 60 determinations. It

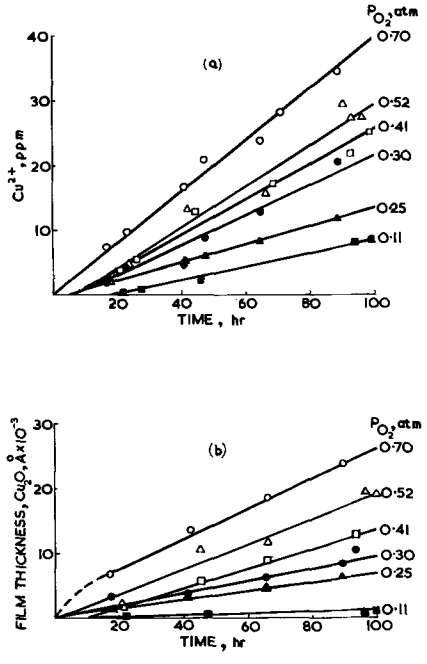

Fig. 5. Typical selection of corrosion experiments; P_{CO_2} = 0.30 atm (const.), P_{O_2} = 0.11 to 0.70 atm, P_{N_2} = (1.00 − P_{O_2} − P_{CO_2}) atm; (a) Cu^{2+}, ppm, as function of time, (b) Cu_2O, film thickness, Å x 10^{-5}, as function of time.

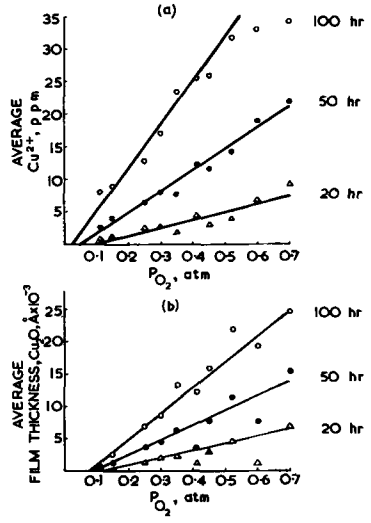

Fig. 6. Average results of corrosion experiments; P_{CO_2} = 0.30 atm (const.), P_{O_2} = 0.10 to 0.70 atm, P_{N_2} = (1.00 − P_{O_2} − P_{CO_2}) atm; (a) dissolution, (b) film growth, for periods of 20, 50, and 100 hr.

was shown that diffusion of oxygen in solution (P_{O_2} = 0.70 atm; C ~ 9 x 10^{-4} mole l^{-1}; D ~ 2 x 10^{-5} cm^2 sec^{-1}; δ ~ 0.05 cm) could cope with a dissolution rate more than tenfold that observed and could be excluded from rate control. Some confirmation of this point came from two corrosion runs (P_{O_2} = 0.20 and 0.40 atm) with 250 ppm of EDTA (sodium salt) added to the aqueous phase, with the idea of suppressing back reaction (disproportionation of Cu_2O in reverse). Dissolution rates were increased by factors of about 3 and 2, respectively, and were independent of P_{O_2}. Film growth was largely inhibited.

Experiments at constant pressure of oxygen: P_{O_2} = *0.30 atm*; P_{CO_2} = *0.10-0.70 atm*. Reproducibility was even less satisfactory, but was adequate, within each kinetic run, to establish that rates of dissolution and film growth were constant for periods up to 100 hr. Averaged results are displayed in Fig. 7(a) and 7(b), which are to be compared with Fig. 6(a) and 6(b). The dependence of the corrosion rates on P_{CO_2} at constant P_{O_2} is seen to be quite different from the dependence on P_{O_2} at constant P_{CO_2}. Nevertheless, although some imagination was required in drawing the representative curves, similarity of shape is retained between those relating to dissolution and those relating to film growth. This adds a little weight to the idea that these two processes may be functionally related.

The two sets of experiments differ in an important respect. In the first set (P_{CO_2} constant) the initial pH was the same for all the kinetic runs, but in the second (P_{CO_2} variable), this was not the case. Attention must therefore be given to the variation of pH with P_{CO_2}, and this is shown in Fig. 7(c), for the initial waters (calculated values) and for the solutions produced after 100 hr corrosion time (observed values). In the latter case, the expected flattening of the curve due to the accumulation of bicarbonate ion in solution is discernible. If the corrosion rates increase with falling pH, and it can hardly be otherwise, it therefore seems that the dependences of pH on P_{CO_2} and on concentration of

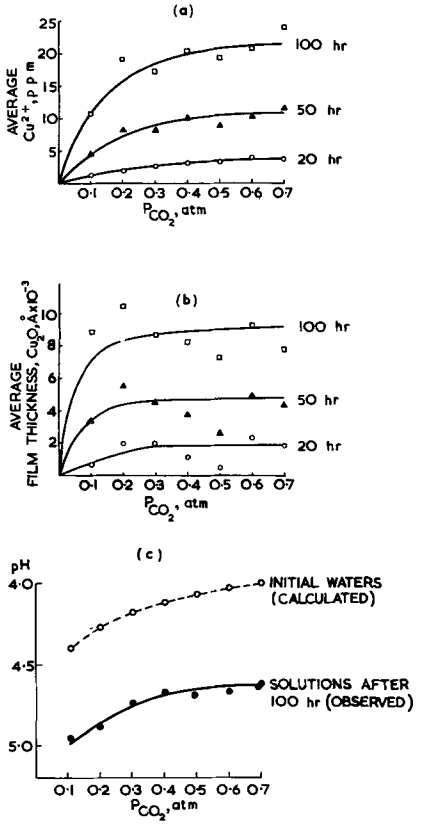

Fig. 7. Average results of corrosion experiments; $P_{O_2} = 0.30$ atm (const.), $P_{CO_2} = 0.10$ to 0.70 atm, $P_{N_2} = (1.00 - P_{O_2} - P_{CO_2})$ atm; (a) dissolution, (b) film growth, for periods of 20, 50, and 100 hr, and (c) pH values at 0 and 100 hr.

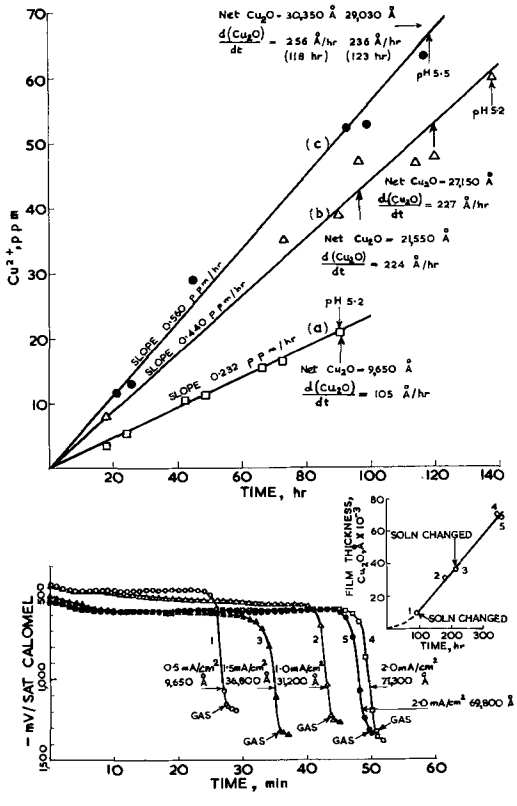

Fig. 8. Solution replacement experiments

cupric bicarbonate in solution might be the factors principally concerned in determining the shapes of the curves in Fig. 7(a) and 7(b). This assumption, however, leads to a paradox, for during a kinetic run pH continuously rises and this should cause the corrosion rates to fall, which they do not. On any grounds, the constancy of these rates is remarkable; there is no indication of a falling away by reason of an approach to an equilibrium state and no sign of the increasing incidence of a back reaction, which might favor the production of cuprous oxide at the expense of cupric ion in solution.

This paradox can be resolved by assuming that the thickening film of cuprous oxide progressively promotes both dissolution and its own continued growth, so compensating the increasing effects of factors adverse to these processes. It was recollected that, in the preliminary experiments (Part I), the maximum rate of dissolution of copper powder was attained when the latter was discolored by the presence of a substantial oxide film.

The possible functional properties of oxide films were investigated accordingly by means of two kinds of "replacement experiments," as follows.

Replacement Experiments

Solution replacement.—The course of an experiment of this kind is recorded in detail in Fig. 8. A normal kinetic run was carried out, with $P_{O_2} = P_{CO_2} = 0.30$ atm, for 92 hr; the increasing concentration of cupric ion in solution is shown in curve (a) of Fig. 8. One electrode was then removed for coulometric estimation of film thickness (these estimations are represented in the lower part of Fig. 8). The entire solution in the apparatus was then removed and replaced by a fresh charge of water, already equilibrated with the same gaseous mixture. A similar run was at once started with the remaining five electrodes, carrying the films deposited on them in the first run. It is seen from curve (b) of Fig. 8 that dissolution proceeded at about twice the original rate and continued constantly at this higher rate for a further 140 hr. This increase in dissolution rate did not occur at the expense of the existing oxide film on the copper, for tests on two of the electrodes showed that the rate of film growth had also been approximately doubled. A further replacement of the solution led to another increment in dissolution rate, curve (c) in Fig. 8, but not in rate of film growth.

Copper replacement.—Under the same standard conditions of $P_{O_2} = P_{CO_2} = 0.30$ atm, a kinetic run was followed for 110 hr. Dissolution and film growth are represented by the rectilinear curves (a) in Fig. 9. The remaining electrodes were discarded and six new ones, prepared by the standard method, were introduced. The kinetic run was then continued, with the solution unchanged. It is understandable that the dissolution reaction was temporarily reversed, and that a film grew rapidly upon the fresh copper surfaces, as shown by curves (b) in Fig. 9. But it can be seen that, after the initial spurt, film growth practically ceased and a normal rate of dissolution was reached only after a delay of 60-80 hr. A second replacement of the same kind produced even more marked effects on dissolution and film growth, curves (c) in Fig. 9.

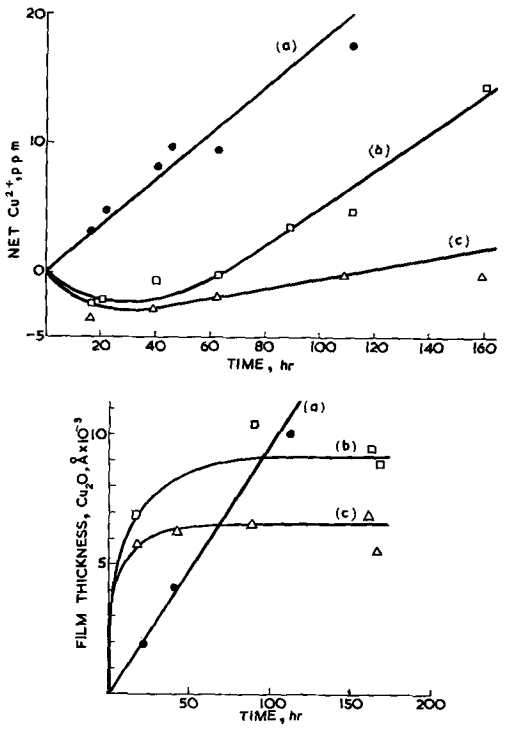

Fig. 9. Copper replacement experiments

Conclusions from Replacement Experiments

At first sight, the results of these experiments seem to be explicable in terms of a back reaction

$$Cu + Cu(HCO_3)_2 = Cu_2O + H_2O + 2CO_2$$

eliminated when the solution is changed, and facilitated when oxide coated copper is replaced by fresh metal. Although such a reaction must play its part in the latter case, it is inadequate to explain all the facts. This can be seen from the data collected in Table I, which shows the state of affairs toward the end of experiments lasting approximately two weeks, in each of which two replacements had been made.

If, for a given total rate of corrosion, the much lower concentration of cupric ion attained in solution were due to the back reaction, the deficit should appear as an excess of cuprous oxide. This is not the case, and it is obvious that the total corrosion rates are quite different after the two kinds of replacement. It is quite remarkable that in one case copper bearing a film about 73,000Å thick should be growing more film and dissolving (at a less favorable pH) enormously faster than in the other case, where the copper is carrying a film less than one tenth as thick. The conclusion is inescapable

Table I

	Replacement of Solution	Copper
Cu converted to Cu^{2+}, g	0.35	0.09
Cu converted to Cu_2O, g	0.13	0.12
Total Cu metal lost by corrosion, g	0.48	0.21
Total area of Cu exposed for corrosion, cm^2	90	270
Total area of Cu × period of exposure, cm^2 hr × 10^{-3}	21	39
Final concentration of Cu^{2+} in solution, ppm	60	21
attained in hr	117	440
Final rate of dissolution, ppm hr^{-1} (per 90 cm^2)	0.56	~0
Final film thickness, Å	73,000	6,500
attained in, hr	350	160
Final rate of film growth, Å hr^{-1}	236	~0
Final pH of solution	5.5	5.2

that the "naturally grown" film, generated in the course of corrosion, is catalytically active for dissolution and autocatalytic for film growth. On the other hand, the "unnaturally deposited" film is appreciably protective.

These results have some bearing on practical corrosion problems. The effects of the intermittent flow of water in copper pipes and over other types of copper surfaces are likely to be similar to those observed in the solution-replacement experiments. It is seen that these are adverse, and films with activating rather than passivating properties are likely to be formed. Perhaps the copper replacement experiments give a pointer to one method by which this undesirable effect could be countered. It is, however, clear that a rather complex electrochemical mechanism for the linked corrosion processes remains to be identified; one possible mechanism is presented in the following paper.

Manuscript received Oct. 2, 1961; revised manuscript received Jan. 23, 1962. This paper was prepared for delivery before the Ottawa Meeting, Sept. 28-Oct. 2, 1958.

Any discussion of this paper will appear in a Discussion Section to be published in the December 1962 JOURNAL.

REFERENCES

1. G. R. Hill, *This Journal*, **100**, 345 (1953).
2. H. A. Miley, *J. Am. Chem. Soc.*, **59**, 2626 (1937).
3. W. E. Campbell and U. B. Thomas, *Trans. Electrochem. Soc.*, **76**, 303 (1939).
4. J. A. Allen, *Trans. Faraday Soc.*, **48**, 273 (1952).
5. R. H. Lambert and D. J. Trevoy, *This Journal*, **105**, 18 (1958).
6. J. S. Halliday, *Trans. Faraday Soc.*, **50**, 171 (1954).
7. L. E. Price and G. J. Thomas, *Trans. Electrochem. Soc.*, **76**, 329 (1939).

Copper Corrosion

III. Electrochemical Theory of General Corrosion

D. J. G. Ives

Department of Chemistry, Birkbeck College, London, England

and A. E. Rawson

Colne Valley Water Company, Watford, Hertfordshire, England

ABSTRACT

The oxidative dissolution of copper in acidic, aqueous media is limited in rate by the presence at the metal-solution interface of a growing film of cuprous oxide. A brief survey of what is known about the nature and modes of growth of such films provides the basis for a "duplex film" model of the corroding copper system. This leads to an interpretation of some features of the observed kinetics of the corrosion reactions reported in the preceding paper, including the constancy of rates of dissolution and film growth following induction periods, the kinetic link between them, the absence of effects due to concentration polarization of dissolved oxygen, and the results of "replacement experiments." The interpretation is made in terms of the operation of a hypothetical double electrochemical cell, corresponding with the duplex film model, and leaves unresolved problems associated with possible special functions of carbon dioxide and the mechanism of oxygen reduction.

The oxidative dissolution of copper in an acidic, aqueous medium, $Cu + 2H^+ + \frac{1}{2}O_2 = Cu^{2+} + H_2O$, has a standard free energy change of −41.16 kcal, comparable with that of the reaction of sodium with water, but does not in practice occur as a vigorous, exothermic reaction because of the restraining influence of, *inter alia,* the cuprous oxide film which forms on the metal, at least at pH values greater than 3.5. In the absence of control by diffusion of hydrogen ions or dissolved oxygen, it is clear that this film, itself undergoing growth, must determine reaction rate, and this certainly seems to be the case for the corrosion experiments reported in the preceding paper. The kinetics of corrosion must therefore be intimately related to the nature and mode of growth of cuprous oxide films on copper, which accordingly require consideration.

Oxidation of Copper in Gaseous Media

Attention has hitherto been largely confined to the oxidation of copper in gaseous media, and the reaction has been discussed in terms of the properties of cuprous oxide as a metal-deficient, p-type semiconductor containing vacant cation sites and positive holes. At high temperatures, thick films of cuprous oxide grow at a rate inversely proportional to their thickness (1-4), following the so-called parabolic law first interpreted by Wagner (5) in terms of rate limitation by transport of ions across the film. Discussions of parabolic film growth by Hoar and Price (6) and, more recently, by Grimley (7) provide the following representation of reaction mechanism.

For the Cu, Cu_2O, O_2 system at equilibrium, with P_{O_2} equal to the oxygen dissociation pressure of the Cu, Cu_2O couple, vacant cation sites and positive holes are distributed uniformly throughout the oxide film. For greater oxygen pressures, however, a gradient of these defects is established in the film. They are generated at the oxide-oxygen interface, where reduction of oxygen and generation of cuprous oxide occur, and are destroyed at the copper-oxide interface, where oxidation of copper takes place, with provision of cuprous ions and electrons. The system is analogous to a nearly reversible, working galvanic cell in which the outer surface of the film is the cathode and the inner surface the anode. The film itself serves both as electrolyte, transporting cuprous ions by diffusion *via* vacant cation sites, and as "external" resistive circuit, conducting electrons. The rate of film growth can be expressed in terms of a current conforming to Ohm's law, a function of appropriate film resistivities and a potential difference calculable from the free energy of the net oxidation process.

This model serves as a satisfactory basis for the more comprehensive theory of Mott (8), which deals with lower temperature, thin film oxidations which follow different kinetic growth laws, such as cubic (9, 10) or logarithmic (11). It is envisaged that electrons can penetrate an oxide layer by thermionic emission from the metal into conduction levels of the oxide or, for thin films, by quantum mechanical tunnelling, and cooperate in dissociative adsorption of oxygen at the oxide-gas interface. There is evidence (12) that singly charged oxygen ions and oxygen atoms are formed in this process, but the essential result is the establishment of a layer of negative charge, which gives rise to an electrical field in the oxide layer. This field may be strong enough to enforce an outward movement of cations at temperatures too low for normal diffusional mobility to sustain an adequate supply of them. In the general case, various kinetic consequences follow the dependence of cationic drift velocity on field strength. On scales of decreasing temperature and film thickness, there is a change from zero, through linear, to exponential

dependence, and this sequence corresponds with observed growth laws.

At low temperatures, many metals show asymptotic film growth, leading to the formation of very thin, limiting films which increase in thickness as the temperature is raised to a critical value, when continuous growth supervenes. This behavior, possibly due to rate limitation by release of cations from the metal to the film (13), is familiar in the case of self-passivating metals such as aluminum and is also shown by copper (14, 15). Such protective films must clearly be coherent and adherent, and this is no doubt associated with the tendency of the first formed layers of the oxide film to adopt the lattice parameters of the parent metal on which they are growing. This can occur if the dimensions of the cation lattice in the oxide do not exceed 109-114% of those in the metal lattice (16); this condition is satisfied for cuprous oxide on copper. It is to be expected, and is found, that rates of growth and limiting thicknesses should vary widely from one crystallographic plane of the metal to another (14, 17) so that some irregularity of behavior must be anticipated for polycrystalline metal samples. Films formed in this way must become increasingly metastable as they thicken because of lateral compressional strains, which ultimately will lead to breaking up. Lattice distortion in very thin films and absence of preferred orientation in thicker films of cuprous oxide on copper have been observed (18), but it has also been reported that cuprous oxide formed on a polished surface of polycrystalline copper has a unique orientation (19), no doubt through operation of other factors.

The stages through which oxygen must pass as it is transformed into its final "lattice ion" state are interesting and complex. It seems that p-type semiconductors are able to chemisorb oxygen "externally to the lattice" and can provide electrons for the process $\frac{1}{2}O_2 + e^- \rightarrow O^-_{ads}$ at room temperature (20). The participation of the singly charged ion-radical O^- is supported by magnetic measurements (21) and has important implications, discussion of which is reserved. It has already been indicated that the initial uptake of oxygen by copper is extremely rapid, and the initial heat of reaction, 109 kcal mole^{-1}, is so great that hydrogen cannot completely reduce the surface oxide so formed (22). This super-normal stability of "elementary" cuprous oxide films, no doubt due to strong adhesive forces, is supported by electrochemical evidence (23). After the formation of 3-4 layers of oxide, however, heat of reaction has fallen to about 55 kcal mole^{-1} and remains sensibly constant for film thicknesses up to at least 170Å (22). Although the dissociation of oxygen molecules normally requires 117 kcal mole^{-1}, dissociative adsorption at a cuprous oxide surface proceeds by a first order reaction (24) to provide oxygen atoms in two situations (25). One of these atoms is incorporated into the cuprous oxide film, generating vacant cation sites and positive holes (associated with cupric ions), and the other remains in a mobile adsorbed state until trapped at a surface discontinuity. In this state, it retains an exceptional chemical reactivity (as in the oxidation of carbon monoxide at room temperature) which decays with time (21). Discussions of the oxidation of copper, however, are not always conducted in terms of a mechanism involving the O^- radical ion.

This introductory survey provides the minimum background for the theory of copper corrosion in aqueous media which follows.

Oxidation of Copper in Aqueous Media

It is assumed that copper, immersed in an oxygenated aqueous medium, almost instantaneously forms a very thin film of cuprous oxide with a compressed structure fitted to that of the metal. Adherent, self-healing, and complete, it cannot grow in thickness beyond perhaps 20Å before mechanical strains break up its outer regions, and this is thought to occur before an asymptotic stage of growth can be reached. The film therefore never becomes fully protective and oxidation continues, leading at quite an early stage to a porous film of disorganized structure, somewhat loosely adherent to the compact, underlying layer, which is imagined to be constantly regenerated. It is further assumed that film growth is based primarily on dissociative adsorption of dissolved oxygen and passage outward through the film of cuprous ions and electrons. Without any implications as to detailed mechanism, and purely for the sake of simplicity, this may be represented

$\frac{1}{4}O_2 + e^- = \frac{1}{2}O^{2-}$ occurring at the outer surface of the film

$Cu = Cu^+ + e^-$ at the inner surface, followed by outward migration of cuprous ions and electrons

$Cu^+ + \frac{1}{2}O_2^- = Cu_2O$ at the outer surface

Thermodynamic Treatment

Taking a thermodynamic view of the corroding system, it is seen that between the extremes of the fully reduced substrate, metallic copper, and the fully-oxidized, aggressive reactant, oxygen, there is the possibility of various redox systems, one or another of which may be close to equilibrium. The least oxidized of these is the Cu, Cu_2O couple, which, in aqueous solution free from dissolved copper, would confer on the metal phase a potential of

$$E_{Cu,Cu_2O,H^+} = 0.471 - 0.0592\ pH \quad \text{abs. V}$$

at 25°C. The most oxidized is the oxygen electrode equilibrium which, for a gaseous mixture typically used in the corrosion experiments described in the preceding paper (0.30, 0.30, and 0.40 atm, respectively, of O_2, CO_2, and N_2), has a potential of

$$E_{O_2(0.30\ atm),H^+} = 1.222 - 0.0592\ pH \quad \text{abs. V}$$

This is much more positive than any potential encountered in the Cu, H_2O, O_2 system within the relevant pH range, corresponding with the fact that completion of corrosion would oxidize all the copper to the cupric state. There must therefore be a considerable oxidation gradient within the corroding system, no doubt mainly, if not exclusively, confined to a number of oxidation jumps, at the biggest of which rate limitation is likely to occur.

Oxidation beyond the cuprous state probably begins in the film itself, in virtue of the capacity of cuprous oxide to take up excess of oxygen. This is

unlikely to proceed far, as long as electrical contact with the copper substrate is preserved and, because the conductance of the oxide increases with its departure from stoichiometry, there may be a kind of automatic regulation of the state of oxidation of the film; the more it becomes oxidized, the better able is the copper substrate to keep it reduced. But the electrical resistance of the film is bound to increase as it grows, particularly when it begins to break up. This may allow the potential of the copper to deviate somewhat toward that of the Cu, CuO couple, namely

$$E_{Cu,CuO,H^+} = 0.570 - 0.0592\ pH \qquad \text{abs. V}$$

Certainly, oxidation of the film is thermodynamically favored, since

$$\tfrac{1}{2}Cu_2O + \tfrac{1}{4}O_2 = CuO; \qquad \Delta G^\circ = -12.9 \text{ kcal}$$

and so is subsequent dissolution

$$CuO + 2H^+ = Cu^{2+} + H_2O; \qquad \Delta G^\circ = -10.8 \text{ kcal}$$

There is no reason why cupric oxide should be formed as an intermediate between these reactions occurring consecutively. Combined, they give

$$\tfrac{1}{2}Cu_2O + \tfrac{1}{4}O_2 + 2H^+ = Cu^{2+} + H_2O; \qquad \Delta G^\circ = -23.7 \text{ kcal}$$

This is regarded as the primary dissolution reaction, which could occur reversibly in the cell

$$Pt \mid Cu_2O, Cu^{2+}, H^+ \mid\mid H^+ \mid O_2$$

The potential of the left-hand electrode would be

$$E_{Cu_2O,Cu^{2+},H^+} = 0.203 + 0.0592\ pH + 0.0592 \log (Cu^{2+}) \qquad \text{abs. V}$$

For relevance to the Cu, H_2O, O_2, CO_2 system, the last two reactions should be combined with

$$2CO_2 + 2H_2O = 2H^+ + 2HCO_3^-; \qquad \Delta G^\circ = 21.3 \text{ kcal}$$

to give the corrosion reactions, with their much less negative standard free energy changes, previously discussed (Part I).

These electrochemical considerations may be applied to the model of the corroding system, illustrated in Fig. 1, arising out of the preceding discussion.

Duplex Film Corrosion Model

The copper substrate is covered by a compact, adherent film of cuprous oxide, in good electrical contact with it. Superimposed on this is a porous film, formed in the corrosion process by the disruption of the growing film underneath it. This disruption must be accompanied by a large increase in the resistance

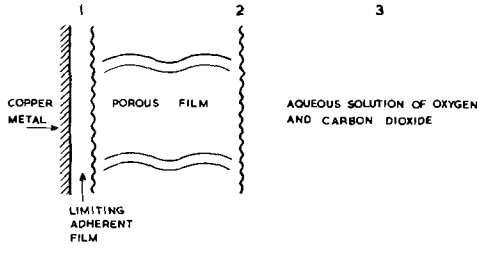

Fig. 1. "Duplex film" model of the copper corrosion system

of the electrical path between the metal and the partially broken away oxide. It is unlikely, however, that this resistance will become infinite, for any oxide which became insulated from the metal would either fall off, or dissolve quite rapidly, as free cuprous oxide has been shown to do (Part I). Thus, even the porous film remains to some extent under the influence of the copper substrate because of a significant electrical conductance of the film, over and above that of the aqueous phase which permeates it.

Attention is directed to the potentials at the three "zones," or locations, indicated in Fig. 1. The first of these is to be identified with that of the copper phase, acting as part of a copper-cuprous oxide couple. The second and third may be regarded as the potentials which would be recorded by hypothetical redox probes, appropriately situated. In so far as it is electronically conducting, the substance of the porous oxide film can assume a potential related to electrochemical reactions which may occur at its surface. The "probes" and the separation of zones 2 and 3 in space are devices introduced in the interests of clarity.

Ideally, these potentials would be

$$\left.\begin{aligned} E_1 &= 0.471 - 0.0592\ pH \text{ at zone 1} \\ E_2 &= 0.203 + 0.0592\ pH \\ &\quad + 0.0592 \log (Cu^{2+}) \text{ at zone 2} \\ E_3 &= 1.222 - 0.0592\ pH \text{ at zone 3} \end{aligned}\right\} \text{abs. V at } 25^\circ\text{C}$$

as previously enumerated. In the very early stages of corrosion when only the thin, compact film has been formed, zone 2 coincides with zone 1, and E_2 must be identical with E_1. Under these conditions, it can be shown that at $pH = 4$, the equilibrium concentration of cupric ions in solution is 21 ppm, but is diminished by a factor of two powers of ten for each unit rise of pH. This indicates that there will be little tendency for dissolution to occur, except at quite low pH values. The development of an appreciable rate of dissolution must wait upon the growth of sufficient resistance between the copper and the surface of the dissolving film. This provides an interpretation of the induction periods reported in both preceding papers, and the behavior of "new" electrodes placed in "old" solution in the second kind of replacement experiment described in Part II.

Consideration may next be given to the case in which extensive corrosion has proceeded, with formation of cupric ions in solution and establishment of the suggested "duplex film." If it is supposed, by way of example, that the solution is at $pH = 5$ and contains 20 ppm of cupric ions, the potentials at the three zones will be

$$E_1 = 0.175; \quad E_2 = 0.292; \quad E_3 = 0.926 \text{ abs V at } 25^\circ\text{C}$$

except that E_2 may be somewhat depressed toward E_1.

The primary dissolution process, which is imagined to occur at the hypothetical electrode at zone 2, is

$$\tfrac{1}{2}Cu_2O + H^+ = Cu^{2+} + \tfrac{1}{2}H_2O + e^-$$

while

$$\tfrac{1}{4}O_2 + H^+ + e^- = \tfrac{1}{2}H_2O$$

occurs at the imaginary oxygen electrode at zone 3.

These two, added together, give the complete dissolution reaction

$$\tfrac{1}{2}Cu_2O + \tfrac{1}{4}O_2 + 2H^+ = Cu^{2+} + H_2O$$

But zones 1 and 2 together constitute a cell which is, moreover, a working cell because the electronic conductance of the film is equivalent to an external, resistive connection between the electrodes. At 1 an anodic reaction proceeds

$$Cu + \tfrac{1}{2}H_2O = \tfrac{1}{2}Cu_2O + H^+ + e^-$$

which will supply electrons to 2 and bring about the reverse of the dissolution reaction, *i.e.*, the cathodic process

$$Cu^{2+} + \tfrac{1}{2}H_2O + e^- = \tfrac{1}{2}Cu_2O + H^+$$

The electrode process at zone 1 may be regarded as the normal, primary film growth mechanism as it occurs in an aqueous medium, for, added to the cathodic process at zone 3, it gives

$$Cu + \tfrac{1}{4}O_2 = \tfrac{1}{2}Cu_2O$$

It is, however, no longer directly depolarized by elementary oxygen, but by cupric ion acting as an intermediary. This is no doubt why no sign of concentration polarization of dissolved oxygen has been found in any of the corrosion experiments, even when thick, porous films have been formed.

The cathodic reaction at zone 2 has the effect merely of diminishing the net anodic dissolution which occurs there, for electrode 2 is the anode with respect to 3 as cathode. At the same time, however, it provides more cuprous oxide at the expense of cupric ion and thus ensures that dissolution and film growth reactions remain in step with each other. It may also be regarded as a secondary film forming reaction, which generates cuprous oxide elsewhere than at the outer boundary of the compact film. Such a process is required to explain why even the thickest films are essentially composed of nothing but cuprous oxide. It may also be important that the rise in pH which accompanies the net anodic dissolution at zone 2 will facilitate the generation of cuprous oxide at zone 1 in the close vicinity. This reaction scheme may be clarified by the formal illustration of the hypothetical double cell given in Fig. 2.

The rise in pH and cupric ion concentration, which accompanies corrosion, might be expected to cause a decrease in dissolution rate with time, but this is observed not to be the case. This is because film growth proceeds in step with dissolution, and film thickening allows the potential at zone 2 to become more positive, thus counteracting any tendency for the rate to fall away. When, however, the film becomes very thick, its worsening electrical conductance favors dissolution rather than film growth; this trend was observed in the first kind of "replacement experiment" described in the preceding paper. Ultimately, with a runaway dissolution reaction, the pH may rise so high close to the outer surface of a thick film that basic carbonate is formed. If the corroding medium is a natural water containing calcium bicarbonate in solution, calcium carbonate may be deposited. It is to be noted, however, that this is likely to occur only on a cuprous oxide film that is already thick, porous, and rather loosely attached to its substrate; a calcium carbonate film laid down on such a foundation is unlikely to have the adhesion and cohesion necessary to confer good protection. This may be associated with the fact that copper pipes, even when conveying such hard waters, often continue for years to send copper into solution; nevertheless calcium carbonate films, consolidated by traces of organic material, can afford a marked degree of protection, even if not complete protection.

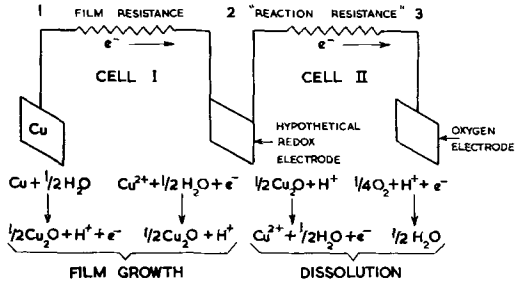

Fig. 2. Hypothetical double cell involved in copper corrosion

Rate Limitation of the Corrosion Reaction

The final contribution to this theory of copper corrosion is concerned with over-all rate limitation. It has already been shown that this does not reside in oxygen diffusion, even through the pores of a thick film. The suggestion is made that it is due to hindrance of the oxygen electrode reaction, which must occur at some solid-solution interface at a rate proportional to the exponential factor familiar in electrode kinetics, $\exp -(\omega - \alpha VF)/RT$, where ω is an activation energy, α is a transfer coefficient probably much less than 0.5, and V is a potential difference effective in promoting reaction. If V can be identified with the difference between the oxygen and copper-cuprous oxide potentials

$$E_{O_2,H^+} - E_{Cu,Cu_2O,H^+} = 0.759 + 0.0148 \log P_{O_2}$$

abs. V at 25°C

a possible basis is obtained for the observed first order kinetics with respect to oxygen, although this is likely to be a gross oversimplification.

Even if the theory of general corrosion of copper which has been proposed is along the right lines and uniquely explains some otherwise puzzling features, it cannot at present be extended without unwarrantable speculation, because it is obviously incomplete. Two outstanding defects may be mentioned.

Carbon dioxide has been treated merely as a component of a buffer system controlling pH, whereas it is quite strongly adsorbed from aqueous solution by cuprous oxide (cf. Part IV) and may play a far more intimate part. This is all the more likely in view of the observation (26) that cuprous oxide adsorbs carbon dioxide from the gas phase only if oxygen is simultaneously, or has been previously, adsorbed. This cooperative process leads to the formation of a reactive CO_3 complex.

It is highly probable that the reduction of oxygen proceeds *via* the formation of hydrogen peroxide or its derivatives, for this is almost invariably the case (27) and is a tolerable certainty if the radical

ion O^- is involved. Delahay (28) has shown that hydrogen peroxide is almost always formed when oxygen is cathodically reduced, even at copper electrodes; the yield is small in this case because of catalytic decomposition, but this might in itself indicate functional participation in oxidation mechanism. The Russell effect (29) has been re-investigated and has been shown to be due to the formation of hydrogen peroxide by the action of moist air on abraded metals (30, 31); it is attributed to the abnormal availability of electrons trapped in anion vacancies in freshly formed or disrupted oxide films (32). It is claimed that hydrogen peroxide has been detected in the vicinity of, *inter alia*, atmospherically corroding copper (33). The case for the formation and probable participation of hydrogen peroxide in the corrosion of copper is therefore quite strong, and there is also evidence (34) that it could cooperate with carbonic acid in a special way. The possible significance of this to corrosion problems has been noted (35).

Manuscript received Oct. 2, 1961; revised manuscript received Jan. 23, 1962. This paper was prepared for delivery before the Ottawa Meeting, Sept. 28-Oct. 2, 1958.

Any discussion of this paper will appear in a Discussion Section to be published in the December 1962 JOURNAL.

REFERENCES

1. G. Tammann, *Z. anorg. Chem.*, **111**, 78 (1920).
2. N. B. Pilling and R. E. Bedworth, *J. Inst. Metals*, **29**, 529 (1923).
3. H. Dünwald and C. Wagner, *Z. phys. Chem., B*, **22**, 212 (1933).
4. C. Wagner and K. Grünewald, *ibid.*, B, **40**, 455 (1938).
5. C. Wagner, *ibid., B*, **21**, 25 (1933); *B*, **32**, 447 (1936).
6. T. P. Hoar and L. E. Price, *Trans. Faraday Soc.*, **34**, 867 (1938).
7. T. B. Grimley, "Chemistry of the Solid State," W. E. Garner, Editor, p. 336, Butterworths, London (1955).
8. N. Cabrera and N. F. Mott, *Repts. Progr. Phys.*, **12**, 163 (1948-49).
9. N. Cabrera, *Phil. Mag.*, **40**, 175 (1949).
10. W. E. Campbell and U. B. Thomas, *Trans. Electrochem. Soc.*, **91**, 623 (1947).
11. A. L. Dighton and H. A. Miley, *ibid.*, **81**, 321 (1942).
12. T. J. Gray, "Chemistry of the Solid State," W. E. Garner, Editor, p. 140, Butterworths, London (1955).
13. N. F. Mott, *Trans. Faraday Soc.*, **43**, 429 (1947).
14. T. N. Rhodin, *J. Am. Chem. Soc.*, **72**, 5102 (1950).
15. J. A. Allen and J. W. Mitchell, *Discussions Faraday Soc.*, **8**, 309 (1950).
16. J. H. van der Merwe, *ibid.*, **5**, 201 (1949).
17. A. T. Gwathmey and F. W. Young, *Rev. mét.*, **48**, 434 (1951).
18. R. F. Mehl, E. L. McCandless, and F. N. Rhines, *Nature*, **134**, 1009 (1934).
19. G. D. Preston and L. L. Bircumshaw, *Phil. Mag.*, **20**, 706 (1935).
20. F. S. Stone, "Chemistry of the Solid State," W. E. Garner, Editor, pp. 396, 398, Butterworths, London (1955).
21. P. J. Fensham, "Magnetochemical Studies of Oxides of Copper and Nickel," Thesis, Bristol University (1955).
22. W. E. Garner, F. S. Stone, and P. F. Tiley, *Proc. Roy. Soc.*, **A211**, 472 (1952).
23. A. R. Tourky and S. E. S. El Wakkad, *J. Chem. Soc.*, **1948**, 740.
24. W. E. Garner, T. J. Gray, and F. S. Stone, *Discussions Faraday Soc.*, **8**, 246 (1950).
25. W. E. Garner and F. J. Veal, *J. Chem. Soc.*, **1935**, 1437.
26. F. S. Stone and P. F. Tiley, *Discussions Faraday Soc.*, **8**, 254 (1950).
27. D. J. G. Ives, "Reference Electrodes," Ives and Janz, Editors, p. 365, Academic Press, New York (1961).
28. P. Delahay, *This Journal*, **97**, 198 (1950).
29. W. J. Russell, *Proc. Roy. Soc.*, **61**, 424 (1897).
30. L. Grunberg and K. H. R. Wright, *Nature*, **170**, 456 (1952).
31. L. Grunberg, *Proc. Phys. Soc.*, **B66**, 153 (1953).
32. L. Grunberg, *Research*, **8**, 210, (1955); *Brit. J. Appl. Phys.*, **9**, 95 (1958).
33. I. L. Roykh, *Zhur. Fiz. Khim.*, **32**, 1136 (1958).
34. P. Van Rysselberghe, *et al., J. Phys. Coll. Chem.*, **54**, 754 (1950).
35. R. B. Hoxeng and C. F. Prutton, *Corrosion*, **5**, 330 (1949).

Copper Corrosion

IV. The Effects of Saline Additions

D. J. G. Ives

Department of Chemistry, Birkbeck College, London, England

and A. E. Rawson

Colne Valley Water Company, Watford, Hertfordshire, England

ABSTRACT

The effects on the corrosion of copper, under the influence of dissolved oxygen and carbon dioxide, of trace additions of salts have been studied. In the case of chloride ion, radical changes in the kinetics of dissolution and film growth processes have been observed and have been interpreted in terms of a transition from general to local action corrosion. The effects of sulfate, nitrate, and bicarbonate ions are also reported. The influence of calcium bicarbonate, under conditions which preclude the deposition of calcium carbonate, in retarding corrosion is particularly noteworthy.

A study has been made of the effects on corrosion reactions in the Cu, H_2O, O_2, CO_2 system of the ions Cl^-, SO_4^{2-}, NO_3^-, and HCO_3^- (as the sodium salts) and of HCO_3^- (as the calcium salt) at concentrations in which they may occur in natural waters. The "powder method" of Part I was first used to explore the influence of these ions on rates of dissolution of cuprous oxide and of copper. This was followed by

kinetic studies of concurrent dissolution and film growth reactions by the method of Part II. In all cases, experiments were accompanied by salt-free controls in which all other conditions were identical.

Results

Preliminary Powder Experiments

Dissolution was followed in each case for 3 hr in solutions (or water in the controls), at 24° ±2°C, kept in equilibrium with analyzed mixtures of oxygen and carbon dioxide at a total pressure slightly in excess of atmospheric.

Cuprous oxide dissolution.—For cuprous oxide, a qualitative report is adequate. Sodium chloride (100 ppm of Cl^-) produced a marked acceleration of dissolution; the rate was approximately doubled near the mid-point of the gas composition range. Even 50 ppm of chloride ion produced about 30% increase in rate under these conditions. That this remarkable effect was specific to chloride ion was shown by the complete lack of influence of 100 ppm of sulfate or nitrate ion on dissolution rate. Both sodium and calcium bicarbonates depressed the rate of dissolution markedly, but to an extent commensurate with the rise in pH which they produced. Although in no case was equilibrium approached, it may be recollected that the equilibrium concentration of cupric ion is decreased by two powers of ten for each unit rise of pH (cf. Part III). It may be noted that, for the case of calcium bicarbonate, the Langelier (1) saturation index varied between −1.6 and −2.0, which ostensibly precluded the deposition of calcium carbonate.

Metallic copper dissolution.—The results of the copper powder experiments are summarized in Fig. 1, in which each small-scale plot of the course of a dissolution run is disposed along a gas-composition axis to define the conditions under which it was carried out. The broken curves, which are all approximately rectilinear, represent the parallel control runs. Each curve was characterized by a minimum of seven analytical determinations of dissolved copper.

It is evident that these very low concentrations of salts (~0.001 — 0.002 g equiv l^{-1}) have surprisingly marked and variable effects on the dissolution of copper under the influence of dissolved oxygen and carbon dioxide. Perhaps the most outstanding effect is that of chloride ion in destroying constancy of dissolution rate; comparison with the appropriate controls indicates an initial acceleration of attack on the metal (particularly in darkness), followed by retardation, the latter making its appearance at an earlier stage in the more oxygenated systems. Conversely, the acceleration effect tends to be more prolonged, and perhaps more marked, in the least oxygenated systems. The other additions seem generally to depress dissolution rate (except that nitrate ion increases it at low P_{O_2} values) while usually maintaining its constancy. A very marked degree of passivation is attained in the presence of calcium bicarbonate in the least oxygenated solutions, but again a negative Langelier index suggests that this cannot be due to calcium carbonate deposition. The effects of illumination have not been systematically studied, but are in some cases seen to be considerable. It is suggested that the powder technique by which these results were assembled may be valuable for the rapid assessment of the corrosive or inhibitory properties of aqueous solutions on metals, for the indications obtained were generally confirmed subsequently. Nevertheless, significant color changes of the copper

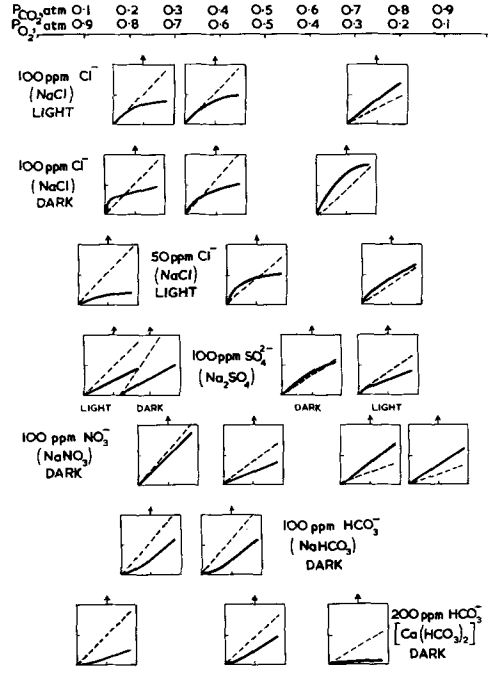

Fig. 1. Dissolution of Cu powder in water containing added salts, approximately at the concentration (ppm) indicated, equilibrated with mixtures of O_2 and CO_2 to a total pressure of 1 atm. Each plot is appropriately placed along the common gas composition axis, and has the same scales of abscissas (0-200 min) and ordinates (0-20 ppm of Cu^{2+}). Broken lines indicate salt-free control experiments.

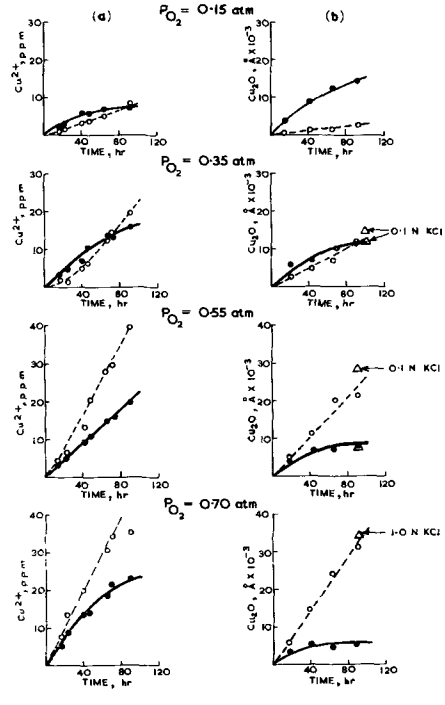

Fig. 2. Corrosion experiments showing influence of approximately 100 ppm Cl^- (NaCl); P_{CO_2} = 0.30 atm (const.), P_{O_2} = 0.15-0.70 atm, P_{N_2} = (1.00 — P_{O_2} — P_{CO_2}) atm, (a) dissolution, (b) film growth. Broken lines indicate salt-free control experiments.

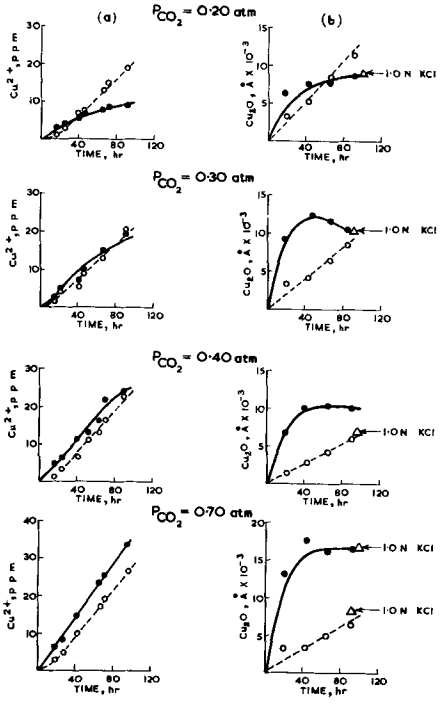

Fig. 3. Corrosion experiments showing influence of approximately 100 ppm Cl^- (NaCl); P_{O_2} = 0.30 atm (const.), P_{CO_2} = 0.20-0.70 atm, P_{N_2} = (1.00 — P_{O_2} — P_{CO_2}) atm, (a) dissolution, (b) film growth. Broken lines indicate salt-free control experiments.

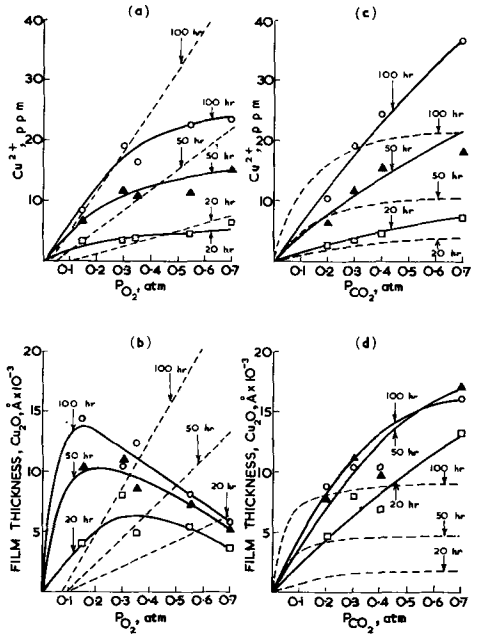

Fig. 4. Collected results of corrosion experiments involving the presence of approximately 100 ppm Cl^- (NaCl); (a) and (b) dissolution and film growth, respectively, for P_{CO_2} = 0.30 atm (const.); (c) and (d), the same for P_{O_2} = 0.30 atm (const.). Broken lines indicate salt-free control experiments.

powder during the course of dissolution indicated the need for film formation studies.

Rates of Dissolution and Film Growth

The same two sets of conditions were used as in the studies of salt-free systems described in Part II; P_{CO_2} then P_{O_2} were successively fixed at a value of 0.30 atm while the other was varied, the total pressure being made up to 1 atm with nitrogen when necessary. Each kinetic run was continued for 100 hr at 21° ±2°C.

Sodium chloride additions.—The results for systems containing 100 ppm of chloride ion as sodium chloride are shown in Fig. 2 and 3, the simultaneous controls being represented by broken lines. Three observations can be made immediately. Chloride ion does not always promote corrosion; on the contrary, it sometimes retards it. Rates of dissolution and film growth are no longer constant, but show a tendency to decrease with time, so that sometimes an initial activation of corrosion passes sooner or later to inhibition. There is obviously no longer a general relation between the kinetics of dissolution and film growth, except the tenuous one that the highest rate of dissolution was observed for the system in which the thickest film was developed. The main features of the results are summarized in Fig. 4, which contains plots of the copper concentrations in solution and the film thicknesses attained after 20, 50, and 100 hr of corrosion time, together with similar data for the controls, shown by broken lines. Although, even in these averaged data, the scatter is very large, it is clear that the almost dramatic effects of only 100 ppm of chloride ion are not obscured; the kinetics of the corrosion reactions are greatly changed, and the only regularity previously observed (first order kinetics with respect to P_{O_2}) has gone.

Comparison of Fig. 4(a) and 4(c) suggests a reversal of the kinetic roles of oxygen and carbon dioxide, *i.e.*, that in presence of 100 ppm of chloride ion, first order kinetics of dissolution with respect to oxygen has been replaced by first order kinetics with respect to carbon dioxide. A similar trend is less convincingly shown by comparison of Fig. 4(b) and 4(d) relating to film growth. It is not known if anything can be made of this, promising as it may appear in elucidating the role of carbon dioxide. The case for giving significance to this observation is weakened by the lack of relation between rates of dissolution and film growth, by the evidence which follows for a transition of corrosion mechanism, and by the great deterioration in reproducibility of physical conformation of the corroding system. It is felt that very careful and detailed studies would be needed to arrive at a decision on this point.

The main effects of chloride ion can perhaps best be seen by a formal tabulation, where acceleration or retardation of dissolution and film growth are indicated by + and — signs.

Acceleration (+) or retardation (—) of dissolution (D) and film growth (F) produced by 100 ppm of Cl^-

		D	F
P_{CO_2} const.	low P_{O_2}	+	+ +
	high P_{O_2}	—	— —
P_{O_2} const.	low P_{CO_2}	—	—
	high P_{CO_2}	+	+

Still more generally, increase of P_{O_2} has a relatively depressing effect on both dissolution and film formation; increase of P_{CO_2} has a relatively stim-

ulating effect. Perhaps the most significant observation of all is the complete breakdown of the kinetic relationship between dissolution and film growth.

Other diagnostic observations which were made may be enumerated.

The films, mainly red or red-brown in color, with sometimes greenish or purple areas, were less uniformly deposited. They were flocculent and loosely adherent, suggesting an enhanced degree of structural disorder. In some cases loss of film substance unavoidably occurred before coulombic estimation could be effected, and this is thought to be the reason for the apparent decrease in film thickness with time which was sometimes observed for the thickest films (cf. Fig. 3). This effect may be associated with the enhanced rate of dissolution of cuprous oxide in presence of chloride ion (already noted), with the effect of this ion upon a bed of cuprous oxide (reported below), and with the peptizing action reported by Gatty and Spooner (2) and the general facility of chloride ions in penetrating oxide films noted by Evans (3).

The coulometric film analysis method was insensitive to cuprous chloride in a film consisting essentially of cuprous oxide, but chemical analysis indicated the presence in the film substance of 0.7-1.5% of chloride. Although it has been shown (4) that atacamite may be present in films formed on copper in chloride solutions, it is unlikely that this was the case in films formed from solutions so dilute in chloride ion as ours. This basic cupric chloride would almost certainly have to appear as a discernible, separate phase, and the evidence is that when this does occur under our experimental conditions it is malachite which appears, not atacamite. These conditions were also outside the range of those required for stability of cuprous chloride as a solid phase (5), and it is therefore regarded as justified to regard the films as consisting of cuprous oxide, perhaps somewhat contaminated.

"Chromatographic" experiments with cuprous oxide columns, using solutions kept in equilibrium with standard pressures of oxygen and carbon dioxide ($P_{O_2} = P_{CO_2} = 0.30$ atm) indicated strong chloride ion adsorption, which also considerably reduced the adsorption of carbon dioxide, observed to take place from salt-free aqueous solution. Further, the chloride ion had a marked effect on the cuprous oxide column, causing a lightening of color, with a loosening and disruption of the bed, which led to channelling. In long-term experiments of this kind, the upper regions of the column were converted to malachite, identified by x-rays. Chloride ion caused this conversion to extend to a much lower level in the column.

Films formed on copper in chloride-containing solutions were punctured by tiny holes, revealing bright spots of apparently bare metal. This was not observed in any salt-free control experiment.

These results, taken as a whole, seem to justify the following tentative interpretation of the influence of chloride ion on copper corrosion.

It is suggested that chloride ion is incorporated to a limited extent into the growing cuprous oxide film. If Cl^- is substituted for O^{2-}, the deficiency of negative charge is likely to promote the formation of a vacant cation site. This may initially increase the ionic conductance of the film and accelerate the general corrosion reactions, both dissolution and film growth. It is also likely to lead to a more disrupted and porous film in which cracks and fissures may more readily develop, exposing the lower layers to easy access of the solution phase. This opening up process may have several consequences, as follows.

There may be a switch from general to local action corrosion and, perhaps, eventually to pitting corrosion. Local anodic dissolution, $Cu \rightarrow Cu^{2+} + 2e^-$ supervenes, at exposed bare sites, from the anodic process which previously could only occur at the metal-oxide interface. The existing film in the vicinity has a much higher electronic than ionic conductance (all the more if the cuprous oxide has acquired n-type characteristics), and assumes a predominately cathodic function, $\frac{1}{2}O_2 + H_2O + 2e^- \rightarrow 2\ OH^-$ occurring at its outer surface. This short-circuits the normal film growth mechanism, so that film growth practically stops. At the same time, the considerable increase in pH which now takes place at areas of film surrounding the anodic cavities, which are exuding cupric ions, favors the deposition of basic carbonate. This view is supported by the behavior of copper strips left corroding in very dilute, aerated salt solutions for many months. A uniform and often very beautiful red layer of cu-

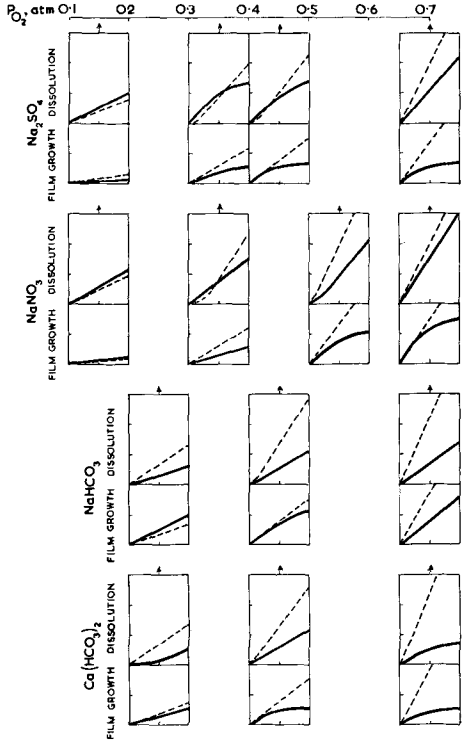

Fig. 5. Graphical summary of corrosion experiments involving the presence of approximately 100 ppm of SO_4^{2-}, NO_3^-, HCO_3^- as Na^+ salts and of approximately 200 ppm of HCO_3^- as Ca^{2+} salt, $P_{CO_2} = 0.30$ atm (const.), $P_{O_2} = 0.15$-0.70 atm, etc. The pairs of plots (upper, dissolution; lower, film growth) are appropriately placed along the common gas composition axis and have the same scales of abscissas (0-100 hr) and of ordinates (0-30 ppm of Cu^{2+} or 0-20Å x 10^{-3} thickness of Cu_2O film). Broken lines indicate salt-free control experiments.

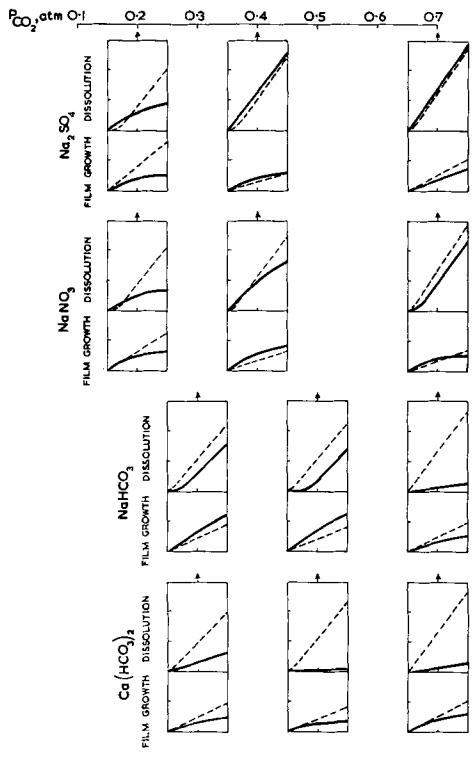

Fig. 6. As for Fig. 5 except that P_{O_2} = 0.30 atm (const.), P_{CO_2} = 0.20-0.70 atm, etc.

prite is overlaid by brilliant green islands of malachite. These have the appearance of having grown outward, over the cuprous oxide, from centers at which anodic pits may well have been located.

The effect of penetration of the aqueous phase into the porous film may be critically dependent on their respective conductances; if the solution is well-conducting, this will again have a short-circuiting effect and promote the switch to local action. On the other hand, if the solution is highly oxygenated, this may lead to a recrudescence of the primary film-forming process, with a corresponding tendency toward passivation by the sealing up of cracks and pores. Examples of the promotion of passivity by a sufficiently high concentration of dissolved oxygen are available (6). This is no doubt why a generally depressing effect of increasing oxygen partial pressure on corrosion is found in these particular systems.

In review, it is suggested that the main effects which have been observed are intelligible in terms of a rather delicate balance between general and local action corrosion, the latter taking over from the former sooner or later under the influence of added chloride with, however, a tendency to reversion in the more highly oxygenated systems.

Other saline solutions.—The effects of the addition of salts other than sodium chloride are summarized in Fig. 5 and 6, which are arranged similarly to Fig. 1. The information they contain may be supplemented by the observations that sulfate ion is strongly adsorbed from solution by cuprous oxide, but that nitrate and bicarbonate ions are not. Surprisingly, however, calcium bicarbonate shows strong adsorption. It may also be relevant to note that copper corrosion in the presence of 100 ppm of nitrate ion as sodium nitrate is accompanied by formation of traces of nitrite (Griess-Ilosvay reaction; 0.006-0.024 ppm).

Detailed interpretation of these results is not practicable at the present stage, and the main purpose must be to place them on record, for they demonstrate further the very large effects which trace concentrations of added salts may have on corrosion processes. The very remarkable passivating effect of calcium bicarbonate under certain conditions is worthy of special attention. Only partly due to a pH effect (largely shared by sodium bicarbonate), it cannot be due to deposition of calcium carbonate. Attention is also drawn to the possibility of establishing a criterion for the existence of general corrosion, as opposed to local action corrosion, of copper. It is the retention of constancy of rates of dissolution and of film growth.

Acknowledgments

Thanks are due to the Chairman and Directors of the Colne Valley Water Company for facilities and permission to publish. The authors also record their indebtedness to Professor J. D. Bernal, F.R.S., for x-ray analyses.

Manuscript received Oct. 2, 1961; revised manuscript received Jan. 23, 1962. This paper was prepared for delivery before the Ottawa Meeting, Sept. 28-Oct. 2, 1958.

Any discussion of this paper will appear in a Discussion Section to be published in the December 1962 JOURNAL.

REFERENCES

1. W. F. Langelier, *J. Am. Waterworks Assoc.*, **28**, 1500 (1936).
2. O. Gatty and E. C. R. Spooner, "The Electrode Potential Behaviour of Corroding Metals," p. 188, Oxford (1938).
3. U. R. Evans, "Metallic Corrosion, Passivity and Protection," pp. 21-23, Arnold (1948).
4. H. P. Rooksby and R. C. Chirnside, *J. Soc. Chem. Ind.*, **53**, 33T (1934).
5. M. J. N. Pourbaix, "Thermodynamics of Dilute Aqueous Solutions," p. 72, Arnold (1949).
6. U. R. Evans and D. E. Davies, *J. Chem. Soc.*, **1951**, 2607.

Electrochemical Dissolution of Single Crystalline Copper

Leslie H. Jenkins and James O. Stiegler

Solid State Division, Oak Ridge National Laboratory, Oak Ridge, Tennessee[1]

ABSTRACT

Galvanostatic studies of single crystal copper anodes in oxygen-free, 0.2M copper sulfate solutions revealed discontinuities in the curves resulting from a plot of electrode overpotentials *vs.* current density. Using observations of changes in electrode surface topography as supporting evidence, the discontinuities were explained on the basis of dissolution processes which were related to the defect structure of the electrode.

Since the early work of Glauner and Glocker (1) on the difference in chemical dissolution rates of the different crystallographic faces of copper crystals, similar effects have been noted for electrochemical dissolution. Early in his studies of anodic polishing of metals, Jacquet (2) established that, under certain conditions of current density and voltage, a difference in the reactivity of grain boundaries and other surfaces of copper polycrystals undergoing anodic dissolution in phosphoric acid could be demonstrated, and Bakish and Robertson (3) observed a potential difference between grains and grain boundaries in polycrystalline copper.

An orientation dependence of electrochemical dissolution of single crystalline copper in acidic copper sulfate was demonstrated by Leidheiser and Gwathmey (4), who also determined that the potential differences between different crystalline faces in their systems were changed by the presence of dissolved oxygen in the solution. The variation of equilibrium potential with crystallographic orientation of single crystalline copper in acidic copper sulfate was studied by Tragert and Robertson (5). They concluded that the (111) was the only truly stable surface in the system investigated. Faizullin and co-workers (6) observed a difference in the current density-potential relationships of anodes containing oriented and nonoriented copper deposits. More recently Piontelli's group has collected current-potential data for the low index faces of copper anodes (7) as well as hydrogen overvoltages on the same orientations (8).

The use of single crystals to study dissolution processes generally has two advantages: (i) the effect, if any, of crystallographic orientation of the reacting surface can be observed; (ii) if the defect structure of the metal affects the dissolution process, the effect is often more easily observed on single crystalline surfaces. It is generally assumed that anodic processes involving the dissolution of an ion from a metallic single crystal into a solution containing the metal ions of interest is most difficult at a theoretical, atomically smooth, close-packed surface. The most reactive site is assumed to be at a kink in a step on the surface, and the next most reactive site is at the straight step edge. Screw dislocations intersecting the surface may be considered sources of steps, but since it is very rare that a difference in reactivity between edge and screw dislocations can be observed on metal surfaces (9), it is reasonable to consider the points where all line defects intersect the surface as reaction sites which are less active than step edges but more active than the idealized flat surface. This paper demonstrates that under certain conditions these assumptions are reasonable for (100) oriented surfaces of copper single crystals undergoing galvanostatic dissolution in acidic solutions of copper sulfate.

[1] Oak Ridge National Laboratory is operated by Union Carbide Corporation for the United States Atomic Energy Commission.

Experimental

Materials.—Copper single crystals, 0.1 x 1 x 7 cm, of (100) orientation on the 7 x 1 cm area were grown from 99.999% metal, supplied by American Smelting and Refining Company, by seeding from the melt in graphite crucibles. From these crystals two samples, 0.1 x 1 x 3 cm, were carefully cut with a jeweler's saw and a 1/16 in. diameter hole drilled in one end of the crystal. The specimens were then chemically polished on a polishing wheel with a $CuCl_2$-HCl solution. Details of this operation have been discussed by Young and Wilson (10). Finally, the crystals were electropolished (usually ~ 40 min) to a smooth, bright finish in a phosphoric acid bath. Then in the manner recommended by Young and Gwathmey (11), they were rinsed in dilute H_3PO_4, washed in running distilled water, and dried in a jet of oxygen. Chemical polishing was necessary only to remove minor grown-in topographic irregularities (due to the graphite molds) in the surface of interest or to obtain a flatter surface over the entire crystal after the edges of the sample had become excessively rounded from repeated electropolishing. Usually, a crystal could be electropolished and used to obtain data about three times before another chemical polish was judged to be necessary.

With the one exception noted below, all the water used in these studies, both for preparation of solutions and for washing crystals, was prepared by distilling demineralized water through a tin-lined still. The storage reservoir for water was of seasoned polyethylene.

Hydrogen was purified by passing commercial tank gas over hot copper, then through magnesium perchlorate drying towers. Oxygen-free hydrogen saturated with water vapor was obtained by bypassing the drying towers and bubbling the gas through a series of three fritted glass disks in gas washing bottles.

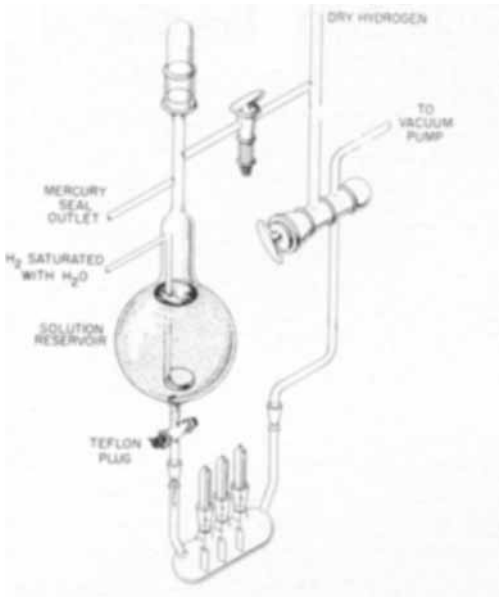

Fig. 1. Portion of filling rack with reaction cell

Two types of copper sulfate solutions were prepared. One was made from material obtained by dissolving a weighed sample of 99.999% copper in excess reagent grade nitric acid. The resulting mixture was then evaporated in excess reagent grade sulfuric acid until free of nitric acid. Water for these solutions was prepared by triply distilling water from the polyethylene reservoir in an all-quartz apparatus. One distillation was from alkaline permanganate solution. Other solutions were prepared from reagent grade $CuSO_4 \cdot 5H_2O$. All the solutions used in this study were 0.2M in $CuSO_4$ with *p*H adjusted to 1.0 with H_2SO_4. Approximately half the data presented here were obtained from solutions of the first type. However, identical results were obtained both for surface effects and current-potential relationships regardless of which solutions were used.

After introducing the solutions into the 2-liter storage reservoir shown in Fig. 1 they were freed of dissolved oxygen in the following manner: After about 20 ft^3 of water saturated hydrogen had been bubbled through a fritted disk in the solution, the reservoir cover cap was momentarily removed, and a polycrystalline bar of ASR copper which had been cleaned in nitric acid and washed for 2 min in running distilled water was quickly immersed in the solution. The cover cap was replaced and about 80 ft^3 of moist hydrogen was passed through the solution at a rate of 10 ft^3 day^{-1}. In this manner, not only was the resulting oxygen-free solution at equilibrium with a hydrogen atmosphere, but also the presence of metallic copper (surface area $\sim$ 15 cm^2) allowed the equilibrium requirements of the following reaction to be satisfied

$$Cu^{++} + Cu^{\circ} \leftrightharpoons 2Cu^{+} \qquad [1]$$

The previous precautions were taken to prevent changes in surface topography of the electrodes resulting from the oxidation and dissolution of the metal by oxygen and/or ions in solution.

Experimental procedure.—The reaction cell was attached to the filling rack as shown in Fig. 1. Three

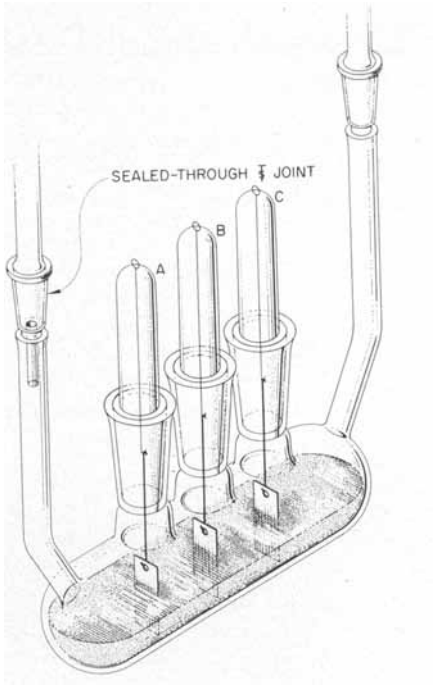

Fig. 2. Reaction cell with electrodes

polished samples of (100) orientation were then suspended from copper hooks which were fabricated from ASR metal. Prior to use, the hooks were cleaned in nitric acid, washed in running distilled water for 2 min, and then air dried. The hooks were attached to platinum wires sealed through the male standard taper joints which were then positioned in the cell as shown in Fig. 2. All joints on the cell were mechanically clamped to help guard against leaks in the system. The cell was alternately evacuated and filled with hydrogen for about 20 cycles, and then the samples were annealed in the dry hydrogen atmosphere overnight at 450°C. During annealing, jets of cooling air were blown over the sample port joints so that their outside temperature never exceeded 50°C. After the 16-20 hr anneal the furnace was removed and the system cooled to room temperature under positive hydrogen pressure. Solution from the rack reservoir was then admitted to the reaction cell until the copper crystals were immersed to a depth of 2 cm. The bottoms of the holes which had been drilled in the crystal were about 5 mm above the solution level. A portable constant temperature bath was then placed about the cell. This procedure permitted data to be gathered from oxide-free, electropolished metal surfaces in chemical equilibrium with oxygen-free, hydrogen-saturated solutions.

All the data reported here were gathered at 25° ±0.1°C under galvanostatic conditions using a 6v dry cell with in-line, fixed resistors as a source of constant current. One copper crystal served as the anode, another as the cathode, and the third as a reference electrode. Potential differences of the working electrodes were measured *vs.* that of the third crystal in the system with a "master-slave" matched pair of vibrating reed electrometers,[2] outputs of which were coupled to Brown recorders so that potential-

[2] The model 31-31 VMS electrometers manufactured by the Applied Physics Corporation of Monrovia, California, permits synchronous reed drive in the two units by the oscillator in the "master" unit.

time relationships were recorded. The small currents used were measured with Weston model 301 DC microammeters which were accurate within 2%. Currents were constant within the accuracy of the meters under all experimental conditions. Although both anodic and cathodic overpotentials were measured, only anodic data are discussed here.

All the tapered joints on the cell were greased with silicone vacuum stopcock grease. The male through joint attaching the solution arm of the filling rack to the cell, as well as the joint on the vacuum side, was lightly greased prior to attaching the cell to the rack. Also, the male joints serving as sample holders were greased near the top just before the samples and joints were inserted in the female entry ports. At the completion of an experiment the apparatus was cleaned of grease by repeated scrubbings with benzene, then acetone. Next the apparatus was scrubbed with alcoholic potassium hydroxide, rinsed with alcohol, and then water. Finally, after soaking in hot nitric acid it was thoroughly rinsed with distilled water. Frequently the alcoholic potassium hydroxide treatment was eliminated without observable effect on the ensuing determinations.

Experimental Results

Anodic current-potential relationships.—The sample ports of the reaction cell were approximately on 3 cm centers making it possible to vary the separation between working electrodes. Data were taken with the electrode surfaces parallel to each other, but at right angles to the long axis of the cell, and with the crystals at ports A and B (Fig. 2) serving as working electrodes. The polarity of the samples at each port was varied each time new assemblies were used. At other times the crystals at ports A and C, again at right angles to the long axis of the cell, served as working electrodes. In the latter series the reference electrode at port B was parallel to the long axis of the cell. Also, other cells of different design which allowed working electrode separations of 1 and 2 cm were used. These cells are discussed more fully below. No differences in potential-current (η *vs.* i) relationships or surface effects due to changes in cell geometry could be found.

At equilibrium, the potential differences of the three electrodes were almost always zero. Occasionally, immediately after exposure to the solution, a difference which never exceeded 0.1 mv and which rapidly decayed to zero was observed. To demonstrate that these systems were at chemical equilibrium and that, therefore, there were no changes in electrode surface topography due to reaction [1], and also to determine if there were similar effects resulting from the reasonably large exchange current densities reported for systems such as these (12), several different assemblies were allowed to stand for various periods up to 8 days. During these times, in which no current was passed through the system, no potential differences were observed, nor were any changes in surface topography such as faceting, etc., detected when the samples were removed from the solutions and surface replicas observed with the electron microscope. It was concluded that, from the standpoint of surface topography, the system was in a state of at least metastable equilibrium.

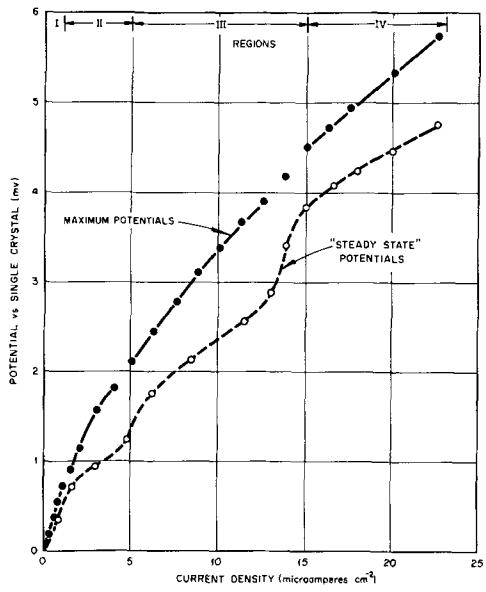

Fig. 3. Experimental current-potential data at 25°C in 0.2M $CuSO_4$, pH adjusted to 1.0 with H_2SO_4.

Anodic overvoltages, resulting from the passage of current through the system, were characterized by initial maxima, the build-up times of which were functions of the current densities applied. At the lower current densities studied, ~ 0.5 μa cm^{-2}, the build-up times were 2-3 min while at the relatively high current density of ~ 20 μa cm^{-2} the time was 6-8 sec. After the maxima were established, anodic potentials rapidly decayed to about 70-80% of the peak values. They then decreased very slowly with time as long as current was passed through the system. A typical plot of these quasi-steady-state, post-maxima potentials are shown as a function of applied current density in Fig. 3. The inflections in the curves always occurred at the same current densities, but the values of the corresponding potentials varied widely from one assembly to another.

In most assemblies the applied current was interrupted as soon as possible after the maxima had been established so as to minimize surface changes due to pitting and faceting. The anodic potentials then decayed slowly to the initial zero value. At current densities of approximately 7 μa cm^{-2} this usually required 15-20 min. At higher current densities, and correspondingly higher potentials, the decay, in addition to being slower, was characterized by a minimum value which was more negative than the reference crystal. The minima were never observed to be more than —0.7 mv and may have been present, although too small to be observed, at lower current densities. This behavior led to decay times of as much as 2 hr at the highest current densities studied before the anode regained equilibrium potential.

In any one assembly the maximum anodic potential values were reproducible within 3% if the current was quickly interrupted after the maxima were attained, and if true equilibrium had been es-

tablished before current was again applied. However, at a given current density, maximum potential values varied as much as 20% from system to system, but in all cases discontinuities in the η_{max} *vs.* i curves occurred at the same current densities. The maximum potentials shown in Fig. 3 as a function of anodic current density are experimental values obtained from one assembly. Coincidentally, they are near the average values obtained from determinations in more than thirty different assemblies. Smoother curves could have been drawn, but it was desired to emphasize the incoherent nature of the data. Inflections in the η_{max} *vs.* i curves ordinarily could be attributed to experimental error. However, the reproducibility of the shapes of the curves from one assembly to another as well as their obvious relationship to the post maxima potentials *vs.* current curves and the topographic changes of electrode surfaces, which are discussed later, suggest that the discontinuities were real and significant.

By normalizing the maximum potentials observed at 15 and 20 μa cm^{-2} to values arbitrarily selected as standard for these current densities, conversion factors were obtained which permitted all η_{max} *vs.* i curves to be fitted to each other very well indeed. This fact suggested that the discontinuities in the curves were a function of the apparent current densities rather than the anodic overvoltages.

Surface effects.—In the presentation of the data below and in the discussions which follow, it is assumed *ipse dixit* that dissolution occurs from monatomic steps on the metal surface. Since, in systems such as these, it is possible to observe only the net effect of many single atom processes, the arguments advanced can in a sense be regarded as speculative at best. However, the data presented are capable of explanation and understanding on the self-consistent atomistic basis adopted.

The inflected nature of the anodic η *vs.* i curves suggested that possibly four different dissolution phenomena, each associated with a definite range of current densities as shown in Fig. 3, were occurring on the metal surfaces. Galvanostatic studies in which currents were passed for long periods of time were, therefore, conducted. After attaining the initial maxima, anodic potentials rapidly fell to about 80% of the maximum values. Thereafter, they decreased monotonically with time, although at a very slow rate, as long as current was passed through the system. Since the topography and area of an anode surface changed with time and rate of dissolution, and since the post-maxima potentials were reproducible only to $\sim \pm$ 10-15%, their utility was limited. However, they were useful in determining which areas of current density should be investigated for electrode surface effects as well as lending credence to the much less pronounced inflections in the η_{max} *vs.* i curves. Although the times required to establish the potential maxima were longer than would be expected to be required to charge the double layer, the reproducibility of any one series of such potentials, as well as the coincidence of different η_{max} *vs.* i curves when normalized to an arbitrary standard, suggest that these potentials reflect a real property of the system. Their true significance is not clear at this time.

After interrupting the current, the anode was removed from the cell, washed in distilled water, and dried in a jet of oxygen. Crystal surfaces were then examined by optical and/or electron microscopy. Surface replicas for the electron microscope were platinum preshadowed carbon replicas which were chemically stripped from the metal (13). The results discussed below, obtained from observations on more than twenty anodic surfaces, strengthened the belief that different removal processes were operative at certain current densities. Changes in surface topography were the net result of both deposition and dissolution processes at the anode. To facilitate presentation, the surface effects are discussed solely in terms of the dissolution process. This problem is explored more completely in the discussion section.

Region I (0-1 μa cm^{-2}).—Figure 4 illustrates that, in this region of current density, removal of material from the anode apparently occurred at atomic steps[3] on the crystal surface. The movement of steps across the surface was restricted in some manner for with time, facets, which must have resulted from the coincidence of steps, were developed. The electron micrograph seen in Fig. 5 shows the facets in detail. Large areas which protruded above the remainder of the surface, and which were therefore less reactive than steps, were also seen (Fig. 4). These areas, which seemed to serve as obstacles to restrict step motion, produced surface patterns of the type usually associated with subgrain bound-

[3] In this presentation the term "step" is used in the monatomic sense. Steps higher than ~50A (approximately the limit of resolution of the carbon replica technique used) are arbitrarily termed facets. Step facet signifies a facet formed by growth of steps, as opposed to facets developed from pits.

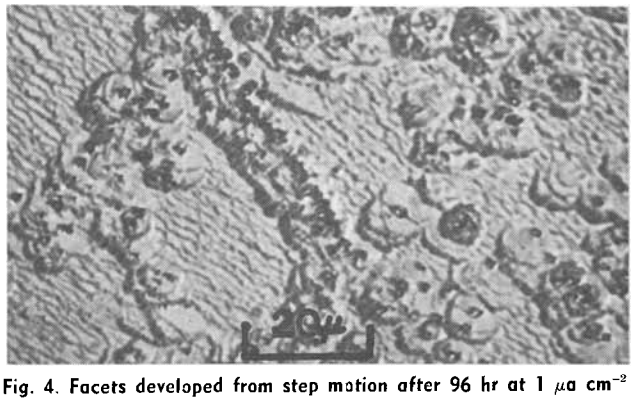

Fig. 4. Facets developed from step motion after 96 hr at 1 μa cm^{-2}

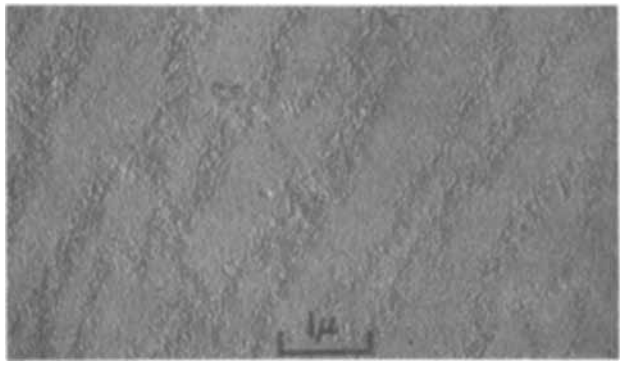

Fig. 5. Electron micrograph of facets on same surface seen in Fig. 4

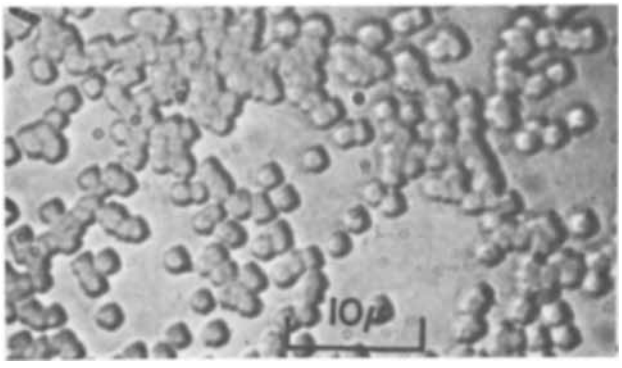

Fig. 6. Pits developed after 5 hr at 10 μa cm^{-2}

aries and points where line defects intersect crystal surfaces. It has previously been observed that crystals of (100) surface orientation undergoing chemical dissolution were less reactive at subgrain boundaries (14).

Region II (1-5 μa cm^{-2}).—The inactive areas of Region I became active in this region. At current densities $\sim$ 2 μa cm^{-2} some tendency to form step facets was still observed, but no large, protruding unreacted areas were seen. As the current density approached $\sim$ 5 μa cm^{-2} no tendency to facet was observed nor were any differences in reactivity observed at areas corresponding to subgrain boundaries. Rather, surface replicas revealed a smooth surface much like that of the unpitted area shown in Fig. 9 and only slightly more roughened than the original surface.

Region III (5-15 μa cm^{-2}).—A further increase in dissolution rates resulted in pit formation as shown in Fig. 6. In the lower portions of Region III the less stringent removal demands resulted in pits which were very shallow, broad, and difficult to detect. The pits grew into each other and, in one experiment conducted at 5 μa cm^{-2}, formed a surface completely covered with very shallow facets after four days of such treatment. As the current density increased the area:depth ratio of pits decreased, and the pits were more easily discerned. However, the increased rate of removal also increased the rate at which pits grew together and consequently shortened the time before pits disappeared as facets developed from them.

Figure 6 shows pits in the earlier stages of development. After prolonged reaction at the same current density, the pits grew into each other and started facet formation as shown in Fig. 7. Even

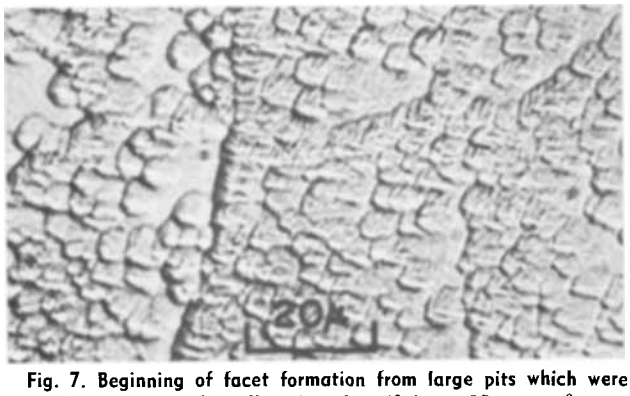

Fig. 7. Beginning of facet formation from large pits which were formed from union of smaller pits after 40 hr at 10 μa cm^{-2}.

Fig. 8. Surface just before pits obscured by facet development after 72 hr at 9 μa cm^{-2}.

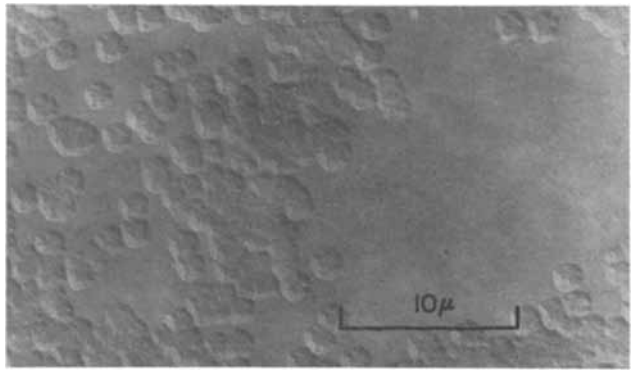

Fig. 9. Electron micrograph showing detail of pits developed after 5 hr at 10 μa cm^{-2}.

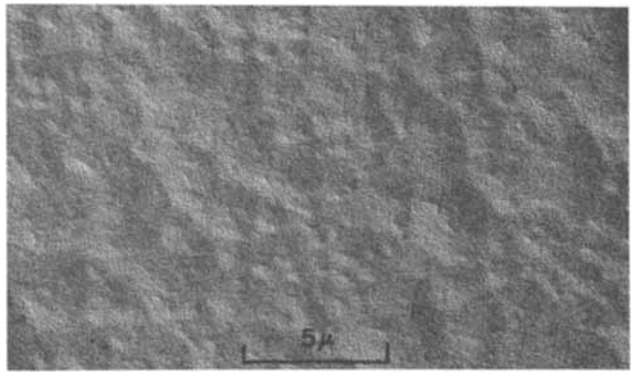

Fig. 10. Initial stages of facets developed from growth of pits after 40 hr at 10 μa cm^{-2}.

more material could be removed at slightly lower current densities, as is illustrated in Fig. 8, before the pits completely lost their identity. An electron micrograph of the same surface seen in Fig. 6 is shown in Fig. 9. The relative smoothness (lack of faceting) of the area between pits was typical of all surfaces in this region, as well as the nonpitted surfaces obtained at higher current densities in Region II. The electron micrograph of Fig. 10 illustrates the initial stages of facet development from pit growth. The faceted structure seen in Fig. 11 was initially developed by pit growth, for in the early stages of reaction this surface was pitted like that shown in Fig. 9. These facets are completely developed while the surface of Fig. 8 still shows distinguishable pits, even though approximately the same amount of material had been removed from each surface.

Region IV (15-20 μa cm^{-2}).—In this region the rates of dissolution were such that facet formation did

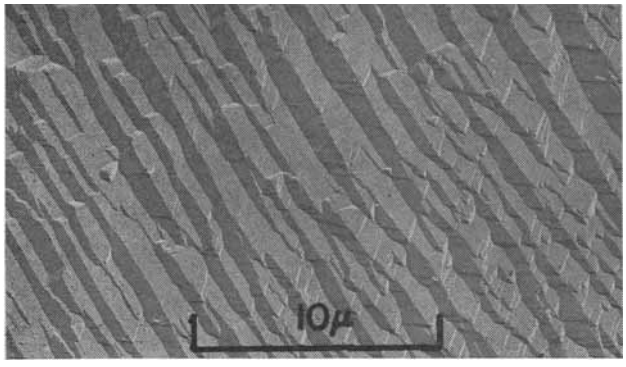

Fig. 11. Facets developed from pits after 47 hr at 14 μa cm^{-2}

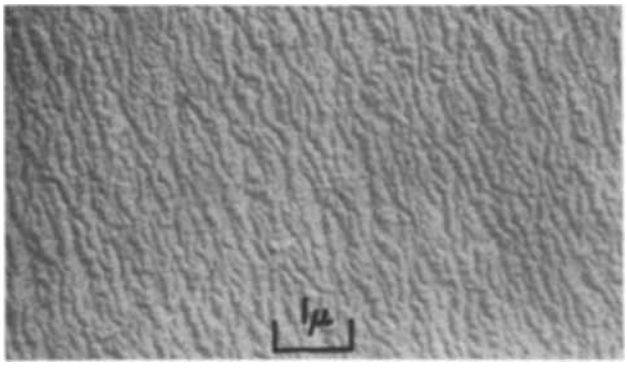

Fig. 12. Initial development of facets not resulting from pit growth after 2 hr at 20 μa cm^{-2}.

not result from the growth of pits, but rather small facets immediately developed as material was removed. Figure 12 shows a surface with facet development well started even though less material has been removed than from the pitted surface of Region III shown in Fig. 9. With time the small facets grew together to form a surface indistinguishable from the surface with pit-developed facets shown in Fig. 11.

The preceding data and comments do not refer to observations made at equivalent microcoulomb values, but rather to the values indicated on the relevant figures. The values were chosen to best represent the cumulative changes in surface topography occurring at typical current densities within the various regions.

Discussion

Experimental method.—Initially data were gathered using an adaptation of a previously described cell (14) designed for chemical dissolution studies. All stopcocks in this apparatus, which allowed anode-cathode separation of 1-2 cm, were of Teflon. Unfortunately, the mechanical pressure required to make the stopcocks vacuum tight resulted in a high rate of failure of the Teflon plugs, with the subsequent loss of samples and contamination of solutions in the reservoir by air. For this reason the cell design was changed to that shown in Fig. 2. Some weeks later the reservoir Teflon stopcock failed and was replaced with a glass stopcock lightly greased with silicone vacuum grease. Fortunately, no differences in η *vs.* i characteristics or surface effects resulted from these changes. It would, of course, have been ideal had no grease been used. However, the final experimental conditions seemed to be the best available choice between compromises involving vacuum requirements, annealing conditions, etc. Apparently the cleaning method used was effective, and the major source of contamination was probably from the stopcock at the solution reservoir.

Surface effects and current-potential data.—Additional experiments were conducted to test further the hypothesis that discontinuities in the current *vs.* potential curves were governed by applied current densities rather than the corresponding overvoltages exhibited by the anode. Since the sides and ends of the electrodes were not of the desired orientation they were obviously a source of error. Therefore, data were gathered from crystals 0.2 cm thick so that the misoriented area of the electrode was increased to about 20%. Also, 0.1 cm thick crystals were electropolished for long periods so that the edges of the area of desired orientation were rounded. In both cases the current-potential data produced curves with less pronounced discontinuities, but with wide variations in potential values. However, the entire surface of proper orientation of the thick crystals, as well as the center of the corresponding area of the thin, rounded-edge crystals, did pit and/or facet at the same current densities previously observed. These observations—when considered with the previously discussed variations of potentials in different assemblies at a given current density, as well as the reproducibility of the shape of the η *vs.* i curves from one assembly to another, and the fact that the observed potentials in any one assembly could be normalized to an arbitrary standard—certainly indicate that the hypothesis is not an untenable one. Furthermore, the surface effects observed on typical crystals, as well as those crystals with a higher percentage of misoriented areas, were almost certainly a function of current densities. It was not unusual to observe pit development on a crystal which exhibited, at a low Region III current density, both a maximum and a "steady-state" potential lower than the corresponding potentials developed by another nonpitting anode at a high Region II current density in another assembly. Therefore, it is reasonable to assume that changes in current densities, rather than overvoltage changes, were responsible not only for discontinuities in η *vs.* i. curves, but also for the different surface structures developed in the current density Regions defined by these discontinuities.

The following discussions of the different methods of facet formation in Regions I, III, and IV, as well as the lack of facet development in Region II and the development of pits in Region III, are based on the previous hypothesis.

Region I.—The development of step facets on anodic surfaces in Region I and the presence of less reactive areas which were compatible with a typical line defect structure suggested that material was removed by the motion of steps across the surface. Decreased reactivity at sites similar to subgrain boundaries and points where line defects intersect the surface could have been due to a "Cottrell atmosphere" of impurities at such imperfections. These sites could have served as pinning points to retard step motion and eventually would result in facets developed from the pile-ups of steps. The total number of steps present

on a surface before the passage of any current was surely not a reproducible number. Also, the pile-up of steps to form facets must have decreased the number of steps available. Therefore, it is not unreasonable to conclude that new steps were being nucleated, and that it was the maximum rate at which such steps could be nucleated which determined where this region ended. When the apparent current density reached 1 μa cm^{-2} this rate was apparently at a maximum. If the areas where line defects intersected the surface did not act as step sources, then crystal edges and point defects must have served as nucleation sites for steps.

Region II.—The faster rate of removal in Region II apparently required nucleation of reaction sites more numerous than could be supplied by the sources active in Region I. The tendency to produce only step facets in lower portions of the region and the lack of faceting or pitting observed near the top of the region indicate that removal of material was still proceeding *via* a step motion mechanism. The smooth surfaces obtained at the higher current densities in the Region suggest that both line and point defects were acting as sources for step formation, and that at these current densities, steps were being removed at a rate at least equal to the rate at which they were created. Furthermore, it would appear that just before the onset of pitting at current densities greater than 5 μa cm^{-2}, steps were being generated at the maximum rate possible. It seems that, as in Region I, it was the maximum rate at which steps could be nucleated which determined the end of this region.

Region III.—Having reached a maximum rate at which dissolution could proceed *via* step motion, pitting began to occur at current densities greater than 5 μa cm^{-2}. The pits shown in Fig. 6, 7, and 8 reveal patterns which are typically associated with the defect structure of crystals such as these. Also, it was determined that the number of pits (5×10^6 cm^{-2}) agreed with the measured number of dislocations in these crystals.[4] Pits then are believed to have formed at subgrain boundaries and at areas surrounding points where line defects intersected the surface of the crystals. It is probable that these areas were active as step sources in Region II, but the lower removal rates did not require more material than could be supplied by the immediate surface. When dissolution rates increased, the additional material was more easily removed at these defect areas.

Region IV.—If removal rates exceeded the maximum amounts of material which could be supplied both by steps nucleated at areas surrounding defects and by pitting, nucleation of reaction sites apparently occurred at random on the crystal surface. This change marked the boundary between Regions III and IV. It is a reasonable assumption that in Region IV removal was by step motion. If so, the large number of steps nucleated and their rapid interaction resulted in such rapid development of facets (Fig. 12) that the mechanism of their early formation and growth could not be determined.

Exchange current.—By evaluating the slope of the overvoltage *vs.* current density curve at the lowest current densities the exchange current density for the system was estimated to be $\sim 5 \times 10^{-5}$ amp cm^{-2}. This value agrees well enough with that anticipated from results on similar systems (12). Therefore, even the measurements obtained at the highest current densities studied represented relatively minor deviations from the equilibrium state. It is then reasonable to assume that deposition at the anode, as well as dissolution, contributed to changes in surface topography. However, it should be recalled that: (*A*) After eight days at equilibrium, surface replicas showed there had been no changes in electrode surface topography. (*B*) At higher current densities in Region II the anode surface remained relatively smooth after prolonged dissolution. (C) Even after pitting had been well developed in Region III the nonpitted area of the surface remained smooth.

Pitting in Region III obviously did not result directly from deposition, but it can be argued that the maintenance of smooth surfaces in non-pitted areas was aided by the simultaneous deposition reaction. The latter argument could also be applied to the upper portions of Region II. Thus it would be expected that as equilibrium was approached in the lower portions of Region II and in Region I, the deposition reaction became more important and contributed greatly to the development of facets. Finally, it should follow that at equilibrium, topographic changes, much like those seen in Region I, would be expected to occur. Such was not the case. Therefore, it is not unreasonable to conclude that the observed anodic topographic changes were due primarily to the dissolution reaction.

Structural aspects.—Assuming previously postulated processes of dissolution to be correct, some interesting calculations can be made. For the Region III surface illustrated in Fig. 9 only 5 μa cm^{-2} of the total of 10 μa cm^{-2} contributed to the formation of pits since half the material was being removed by the step mechanisms postulated for Region I and II. Using the measured dislocation density value of 5×10^6 cm^{-2} and the coulombs of material removed by 5 μa cm^{-2} after 5 hr, it was possible to calculate the average volume of material removed from each pit. Surface replicas showed the pits to be approximately 2×10^{-4} cm^3. To accommodate the volume of material calculated to have been removed at each pit, the pits should have been an order of magnitude wider than they were deep. This was approximately the value observed, and since there was some slope to the sides of the pits, the agreement between calculated and observed results was considered good.

The operation of two sources of dissolution in Region III is illustrated by the surfaces shown in Fig. 6 and 7. Although almost an order of magnitude more material had been removed from the latter surface, faceting was not well developed since half the total material removed was supplied by steps which had also been active in Region II. This point is augmented by the surfaces seen in Fig. 8 and 11. Although approximately the same amount of material had been removed from both surfaces, the latter was well faceted due to the growth of pits since about 65% of the total material removed had been supplied by pitted areas, the remainder of the metal

[4] Dislocation densities were determined by the persulfate etch method [see ref. (9) for details].

dissolving by step motion. Only 45% of all metal removed from the surface shown in Fig. 8 came from pits.

Just before the onset of pitting at 5 μa cm^{-2} it has been postulated that 1 μa cm^{-2} was removing material at sites which had been active in Region I and which were not related to line defects. The remaining 4 μa cm^{-2} were associated with a dislocation density of 5 x 10^{6} cm^{-2}. Therefore, assuming the maximum rate of step removal to be constant regardless of the origin of the step, there would have been ~10^{6} sites cm^{-2} in Region I which acted as sources for nucleation of steps. The maximum dissolution rate in both Region I and II would then be ~3 x 10^{6} atoms site^{-1} sec^{-1}. The maximum rate of removal at a pit would be about twice as great.

It should be pointed out that an alternative explanation exists for the mechanism of removal in Region I. The approximately 10^{6} cm^{-2} sources of step sites calculated above may have been associated with screw dislocations. Even if the presence of impurities prohibited dissolution near the core of the dislocation, a permanent step on the surface would emerge from the screw dislocation. The calculated number of step sources is probably of the proper magnitude for a correspondence to screw dislocations, and since all crystals were grown and handled in a similar manner, this number should have been reasonably constant from crystal to crystal. Therefore, if removal in Region I occurred at steps resulting from screw dislocations, it would be reasonable to expect the surface effects observed in this Region, as well as the reproducible ending of the Region, when removal rates exceeded those allowed at screw dislocation steps. However, it can be shown that for every ½° variation from the (100) orientation, ~5 x 10^{5} monatomic steps cm^{-1} result on a copper surface. It is difficult to believe that the electropolishing techniques used in this study produced exact (100) surfaces, or that the degree of variation from the desired orientation, and consequently the total number of steps resulting from orientation changes and screw dislocations, was reproduced on every crystal. Also, the results obtained with rounded-edge, thin crystals, which must have contained more steps per unit area than crystals with flatter surfaces, cannot be ignored. Therefore, the argument that the end of Region I was determined by the rate at which new steps could be nucleated, regardless of their origin, seems preferable to the authors.

Overpotential and kinetics.—In all assemblies an interesting relationship was observed between the potential maxima at current densities corresponding to discontinuities in the η *vs.* i curves. In any one system the ratio of the potential at the Region II—Region III boundary to that at Region I—Region II was always ~3, and that of the Region III—Region IV discontinuity to the Region I—Region II value was always ~5. These potential ratios were reasonably constant even though, as previously noted, the measured potential maxima varied as much as 20% from one assembly to another. Perhaps if ϵ was the energy required to nucleate steps at dislocations, then 3ϵ was required to remove material at points where dislocations with a "Cottrell atmosphere" of impurities intersected the surface, and 5ϵ was necessary for removal from smooth surfaces of (100) orientation.

Since different anodic sites were reactive at distinct current densities, a distribution of reaction rates must have occurred over the surface. It would be a difficult, and not a particularly rewarding, task to adapt electrode kinetics, as well as to approximate the time dependence of surface structure and η *vs.* i data, in order to interpret the observed data kinetically. In systems of the type studied it is possible that the simpler equations of electrode kinetics should apply only at current densities as large as, or greater than, those of Region IV where nucleation of reactive sites apparently occurred in a random manner; that is, the metal surface acted homogeneously. For these reasons, and also since their solutions were more concentrated in both copper sulfate and sulfuric acid, these results could not be compared with those of Piontelli *et al.* (7) whose lowest current densities correspond to those of Region IV reported here.

Conclusions

It should be emphasized that the discussions and interpretations of the data presented here were based on the reasonable assumption that dissolution occurred from monatomic steps on the anode surface. Obviously it is impossible to prove absolutely the validity of this assumption in a system of the type investigated. The following conclusions should be regarded solely as deductions arising from a self consistent explanation of experimental observations:

1. It is believed that galvanostatic dissolution from (100) oriented surfaces of copper single crystals occurred initially at steps on the surface. These steps were not nucleated at areas where line defects intersected the crystal surface. The rate at which new steps could be nucleated determined the rate at which material could be removed in this manner.

2. An increase in dissolution rates demanded the formation of additional reaction sites. These sites were supplied by the nucleation of additional steps at areas where line defects intersected the crystal surface. The subsequent motion of steps across the surface provided a means of removing the metal from the anode.

3. After the maximum rate of step formation was reached, further increases in the rate of dissolution resulted in pit formation at points where line defects intersected the surface and at subgrain boundaries. As dissolution continued the pits grew together to form facets.

4. When removal demands exceeded the rate at which material could be supplied by the previous sources, reaction sites were apparently nucleated at random on the metal surface. A faceted structure, which was not formed by the growth of pits, developed rapidly.

5. The nucleation of reaction sites was probably governed by the rate of anodic dissolution, *i.e.*, impressed current density, rather than by the overpotential exhibited by the electrode.

6. The relative energies required to nucleate steps at dislocations, remove material from points where line defects intersected the surface and from the

idealized flat surface were apparently in the ratios of 1:3:5.

7. The applicability of simple kinetic electrode theory to the system studied could not be demonstrated. This was thought to be due to the heterogeneous nature of the anodic surface.

Acknowledgment

Dr. F. A. Posey made many helpful suggestions both while the work was in progress and during the preparation of this manuscript. The authors also acknowledge helpful discussions with Drs. F. W. Young, Jr. and D. K. Holmes.

Manuscript received Aug. 24, 1961; revised manuscript received Jan. 30, 1962.

Any discussion of this paper will appear in a Discussion Section to be published in the December 1962 JOURNAL.

REFERENCES

1. R. Glauner and R. Glocker, *Z. Krist.*, **80**, 377 (1931).
2. P. A. Jacquet, *This Journal*, **69**, 629 (1936).
3. R. Bakish and W. D. Robertson, *ibid.*, **103**, 320 (1956).
4. H. Leidheiser, Jr., and A. T. Gwathmey, *ibid.*, **91**, 97 (1947).
5. W. Tragert and W. D. Robertson, *ibid.*, **102**, 86 (1955).
6. F. F. Faizullin *et al.*, *Uchen. Zap. Kazan. Univ.*, **115**, 123 (1955).
7. R. Piontelli *et al.*, *Inst. Lombardo Rend. Sci.*, **91**, 355 (1957).
8. R. Piontelli *et al.*, *ibid.*, **91**, 378 (1957).
9. F. W. Young, Jr., *J. Appl. Phys.*, **32**, 192 (1961).
10. F. W. Young, Jr. and T. Wilson, *Rev. Sci. Inst.*, **32**, 559 (1961).
11. F. W. Young, Jr. and A. T. Gwathmey, *Acta Met.*, **4**, 145 (1956).
12. B. E. Conway and J. O'M. Bockris, *Plating Mag.*, April (1959).
13. J. O. Stiegler and T. S. Noggle, *J. Appl. Phys.*, **31**, 1827 (1960).
14. L. H. Jenkins, *This Journal*, **107**, 371 (1960).

The Oxidation of Sputtered Tantalum Films

Harold Basseches

Bell Telephone Laboratories, Incorporated, Allentown, Pennsylvania

ABSTRACT

The oxidation of sputtered tantalum films has been studied over a temperature range of 100°-600°C in oxygen at a gas pressure of 7.6 cm of Hg. The results obtained by means of a vacuum microbalance are compared with data on bulk tantalum, and it is found the rate of oxidation and amount of oxidation is considerably smaller than the bulk. A logarithmic relation was found to represent the data best in the range 400°-600°C. The factors which may give rise to the differences found between the film and the bulk are discussed.

In the course of an investigation of the stability of the electrical resistance of thin sputtered tantalum films (1), the oxidation of these films has been studied as a function of temperature.

The oxidation of sputtered tantalum films was carried out using a vacuum microbalance to obtain weight gain over a range of temperatures from 100° to 600°C in pure oxygen at a pressure of 7.6 cm of Hg. A logarithmic relation of the form $y = a \ln (1 + bt)$ was found to give a slightly better fit of the data over the range of temperatures 400°-600°C than a parabolic one. y is the weight gain of tantalum in $\mu g/cm^2$, t is the time in minutes, a and b are constants at any given temperature and have the dimensions $\mu g/cm^2$ and min^{-1}, respectively. The results indicate that the amount and rate of oxidation of the film are considerably smaller (by about an order of magnitude) than that reported for bulk tantalum. Vermilyea's (2) results are in somewhat closer agreement.

Although quantitative correlations are not yet possible, the factors which may affect the weight gain measurements and may explain the differences in oxidation between film and bulk tantalum are discussed.

Experimental Procedure and Results

The details of the sputtering technique and the sample preparation have been described elsewhere (1). The samples consisted of tantalum films (600-2500Å in thickness) sputtered on quartz substrates ½ in. x 2 in. x 30 mils in thickness. The oxidation was performed in a vacuum microbalance (3-5) by Gulbransen. The oxidation was carried out over a range of temperatures from 100° to 600°C in a pure oxygen atmosphere at a pressure of 7.6 cm of mercury. The total oxidation time was 2 hr. The graphs of the results are shown in Fig. 1 and 2 in which the weight gain per unit area is plotted as a function of time. The sensitivity of the apparatus is between 0.1-0.2 $\mu g/cm^2$ and indicates that films of the order of 7-15Å of tantalum oxide could be detected (69 Å/$\mu g/cm^2$ based on Ta_2O_5) (6).

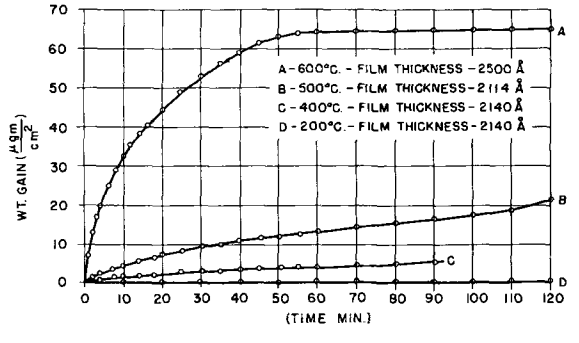

Fig. 1. Effect of temperature on oxidation of sputtered tantalum films (O_2 pressure, 7.6 cm of Hg).

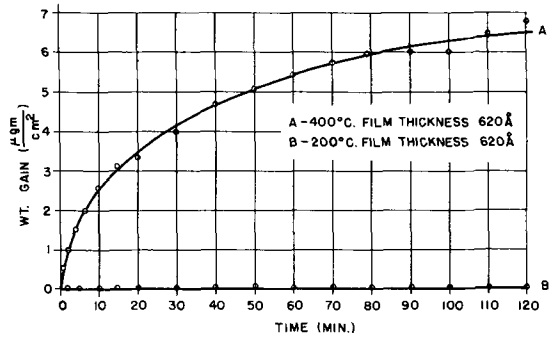

Fig. 2. Effect of temperature on oxidation of sputtered tantalum film (O_2 pressure 7.6 cm of Hg).

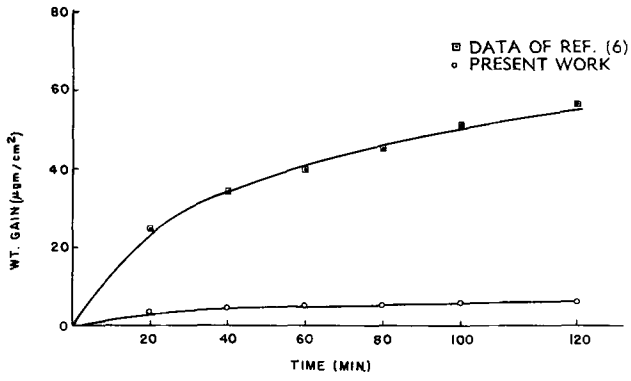

Fig. 3. Comparison of weight gain of sputtered tantalum film and bulk tantalum (400°C, O_2 pressure, 7.6 cm of Hg).

There are several points that can be noted on these curves. The flat portion of curve A on Fig. 2 after the 60-min mark may result from the consumption of all the tantalum. Oxidation at a temperature of 200°C produced no measurable change, nor was there a visible color change. This is confirmed on two samples of different thicknesses, namely, curve D of Fig. 1 and curve B of Fig. 2. There appears to be no thickness effect in the oxidation since the value at 90 min for the total weight gain of curve C, Fig. 1 and curve A, Fig. 2 agree quite well.

It should be noted that the same samples were used for the 400°C tests as in the 200°C tests. Electron diffraction studies were made on the oxidized deposits on the quartz by Gulbransen. The results of this work are reported in Table I. In only one case does there seem to be an indication of the tantalum oxide structure. The patterns in the other cases were very diffuse and difficult to interpret.

Comparison of Oxidation Data on Thin Tantalum Films with That of Bulk Tantalum

In Fig. 3 the data of the present work are compared to earlier work of Gulbransen and Andrew (6). The data for both bulk and sputtered tantalum were obtained in the same apparatus. The total amount of oxidation, as well as the rate of oxidation, is much less on the sputtered film than on the bulk material. Further comparisons are also available in Table II. The difference between Vermilyea's work and others may be related to differences in surface preparation; however, his

Table I. Oxidation of sputtered tantalum films, electron diffraction data

Sample thickness, A	Oxidation temp, °C	Oxidation time, min	Weight gain, μg/cm²	Color	Crystal structure	Physical characteristics
2140	400	90	5.17	Tarnished silver	Diffuse pattern	
620	400	120	6.76	Purple-orange	Diffuse pattern	
2500	600	120	65.0	—	Diffuse pattern	Film spalled off of quartz
2115	500	120	21.1	Green-blue	Probably Ta_2O_5	

Table II. Comparison of weight gain data in oxidation of tantalum in various investigation

	Temp, °C	Length of oxid. run, hr	Pressure of oxygen, cm	Weight gain (μg/cm²) at end of run	Reference and remarks
1.	400	2	7.6	6.5	Present work
2.	400	2	7.6	57.2	Gulbransen and Andrew (6)
3.	600	1	7.6	63	Present work
4.	450	1	7.6	85	Gulbransen and Andrew (6)
5.	200	2	7.6	~0.1	Present work
6.	250	2	7.6	3.25	Gulbransen and Andrew (6)
7.	250	2	air ~15.2	~0.362*	Vermilyea (2)
8.	300	2	air ~15.2	~0.58*	Vermilyea (2)
9.	300	2	7.6	10	Gulbransen and Andrew (6)
10.	220	913	air ~15.2	20.5	Waber *et al.* (13)
11.	250	1400	air ~15.2	66	Waber *et al.* (13)
12.	216	2	air ~15.2	~3	Waber (14); value extrapolated from data given
13.	320	913	air ~15.2	227	Waber (7)
14.	500	1½	76 cm	~130	Cathcart, Bakish, & Norton (23)
15.	500	1½ hr	7.6 cm	16	Present work

* Represent values obtained by conversion of Vermilyea's thickness data of 25 and 40A at the respective temperatures, utilizing a factor of 69Å/μg/cm² based on an oxide formula of Ta_2O_5 (6).

comes closest to agreeing with the data of the present work.

It will be helpful to get some idea of what kind of reproducibility one can expect in oxidation studies of the type reported by Gulbransen. Although data are not available on tantalum, Gulbransen has worked on two other materials, columbium and zirconium, at several different times. In the case of columbium (6, 7) and zirconium (6, 8, 9) differences of a factor of from 2 to 4 have been observed among samples studied at different times. The comparisons have been made at similar temperatures, but other conditions such as surface preparation and pressure of oxygen have not necessarily been the same. There is some risk in trying to compare sputtered films with bulk material since purity of samples, differences in surface treatment prior to oxidation, etc., could have strong influences on the result. It might have been expected that the conditions existent in films would tend to increase the rate over that of bulk rather than decrease it, as has been found.

It is also possible to make a comparison with bulk results and the present study as far as rate of oxide formation is concerned. From Gulbransen and Andrew's data (6) at 300°C for tantalum, an estimate can be made of the rate of oxide formation over the time interval of 1-2 hr to be of the order of 0.04 Å/sec. On the basis of Vermilyea's work (2), assuming that an oxide film of the order of 600Å has built up after oxidation of between 1 and 2 hr, one can estimate that at 300°C the rate of oxide formation would be of the order of 0.0001 Å/sec. This value is obtained from Fig. 4 which is a plot made from calculations of McLean (10) who used Vermilyea's data. However, this graph extends the calculations up to higher temperatures.

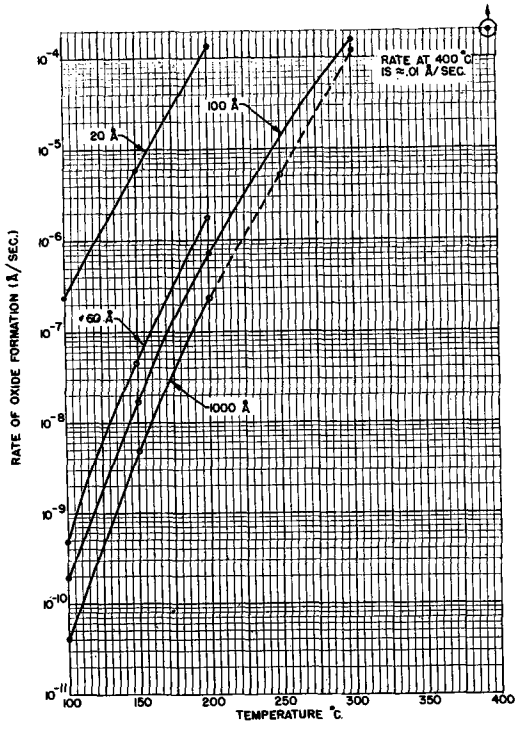

Fig. 4. Rate of oxidation of tantalum as a function of temperature and oxide thickness [data from Vermilyea (2)].

Table III. Constants for logarithmic rate law

Temp, °C	a	b
600	20.985	0.3820
500	7.029	0.0901
400 (2140Å)	2.399	0.0836
400 (620Å)	1.828	0.293

Unit of a is $\mu g/cm^2$; unit of b is min^{-1}.

In an effort to make some comparisons with the present work, Vermilyea's data (2) have been extrapolated to 400°. Assuming a thickness of oxide of somewhere between 100-1000Å, extrapolation gives an oxidation rate of 0.01 Å/sec. as noted in Fig. 4. The data in the present study which can be used to best advantage to make a comparison are that of Fig. 2 at 400°C. The tangent to the 2-hr point gives the rate of 0.015 Å/sec. The rate calculated from a logarithmic relation deduced from the present study, as given below, is $(dy/dt) = ab/(1 + bt)$. Utilizing the values of a and b derived at 400°C for the 620Å film (see Table III) the rate is 0.017 Å/sec. Although it is dangerous to carry out the extrapolation of Vermilyea's data, the agreement may be noted.

A number of different equations has been proposed to account for the observed oxidation behavior of metals (11, 12). In comparing parabolic with logarithmic behavior, on the basis of a least squares criterion, a logarithmic equation of the form $y = a \ln (1 + bt)$ was found to fit the data slightly better than a parabolic one in the temperature range 400°-600°C. The various values of a and b are listed in Table III for data in the range of 400°-600°C. The units for t are in minutes. No theoretical significance is attached to this logarithmic behavior at the present time.

It appears that the amount of oxidation of sputtered tantalum is less, by about an order of magnitude, than that of bulk tantalum. Variations obtained over periods of time using the same apparatus suggest factors of somewhere between two and four could arise. Therefore, the factor of nearly ten obtained as the difference between the bulk material and the present thin film material does indeed suggest it to be a significant difference. A consideration of those factors which could affect this variability all tend to substantiate that differences exist between the bulk material and the sputtered film.

Discussion

Previous studies of the oxidation of tantalum over various temperature and pressure ranges have characterized the behavior in various ways either as parabolic (6) logarithmic (2, 13), cubic (14), and linear (15, 16). In most of these studies the products of reaction were not completely identified so detailed discussion of the mechanism is not possible. In most cases the formation of tantalum pentoxide has been assumed. Recent studies of Kofstad *et al.* (17), however, give considerable detail on the products in the temperature range 500°-700°C.

X-ray diffraction and electron diffraction studies indicate that in the early stages, described as an incubation period, (for example, extending to 150-250 min at 500°C) oxygen dissolution occurs along with the formation of Ta_4O and a compound characterized by TaO_z. During the transition from the incubation period to the linear oxidation region, Ta_9O_5 is formed as traces on the surface, and in the linear region there is heavy formation of β-Ta_2O_5. The present electron diffraction studies have not characterized the products adequately. There was some suggestion that Ta_2O_5 formed. However, if it is assumed from curve A in Fig. 1 that all of the tantalum is consumed at the point where the curve flattens out, then from the weight gain data it is shown that 65 $\mu g/cm^2$ of oxygen react with 415 $\mu g/cm^2$ of tantalum. On an atom basis this corresponds to a compound $TaO_{1.76}$ which is one of the types of product indicated by Kofstad.

Although the evidence found in the present study indicates only a slight preference for a logarithmic over a parabolic behavior over the time periods studied, there seems to be no indication of linear behavior. This region may well correspond to the incubation period described by Kofstad (17). This incubation period, before the linear region, varied with the temperature and became shorter as the temperature and pressure increased. At 600°C and above it became too short to observe experimentally. The data of Albrecht *et al.* (16) still show an incubation period at 600°C. Kofstad (17) concluded that the oxidation during the incubation period was difficult to interpret in terms of any definite rate law although it was most closely approximated by a parabolic function.

Kofstad found oxygen dissolution to be an important step in the initial oxidation of tantalum. At 500°C the weight gain due to oxygen dissolution could amount to more than 75% of the weight gain found experimentally. Computations of the time necessary for oxygen to diffuse through a 2500Å thick tantalum film (18) using diffusion data of Gebhardt (19) were made. At 600°C this is 0.1 sec, at 400°C it is 10 sec, but at 300°C it is 6 min. It would appear therefore that in range of 400°-600°C oxygen dissolution is of minor importance in the rate measurements, although at lower temperatures it could become a major factor. Thus as far as measurements with thin films are concerned the relative importance of oxygen dissolution could change with temperature. The diffusion data used are those available for bulk tantalum, and it is conceivable that they are not strictly applicable to thin films.

The reasons for the difference between the behavior of the thin film and the bulk are not obvious. It may be due to differences in the oxides formed on the bulk as compared to that on the film. There is some evidence from studies on the anodization of sputtered tantalum films (20) made in connection with work on sputtered tantalum capacitors (21) that the oxide is different and does not crystallize as readily as on bulk tantalum. A strip of bulk tantalum was anodized in the same solution with a film of tantalum sputtered on a microscope slide. The solutions used were those reported to promote crystallization (22). The strips were pulled out after a given time and examined microscopically. The bulk piece showed crystals, the sputtered film did not. The sputtered film was reimmersed for a period ten times longer and removed and examined. There were still no signs of crystallization.

The electron diffraction obtained on the present study suggests an amorphous structure at the elevated temperature. Vermilyea (2) showed on bulk tantalum, however, that at 350°C oxide films began to crystallize. His other work on tantalum (22) has shown that where crystalline oxide exists the rate of oxidation is more rapid than where the oxide film is amorphous. This may be the basis for the differerences observed between the present study and bulk material.

The difference may arise because the surfaces of the films are in some way very different from most of the bulk samples studied. The oxidation data of Kofstad showed a profound effect of surface treatment on the oxidation behavior during the incubation period. Although no careful studies were made, chemical etching and high-vacuum annealing increased the incubation period. Albrecht's data at 600°C using vacuum annealed tantalum did indicate an incubation period (16). The structural results of Cathcart (23) on tantalum indicated a relationship between the state of perfection of the metal surface and its oxidation characteristics.

One perhaps may view the present work as giving a picture of what happens at the surface of the tantalum by greatly enhancing the surface to bulk relationship and hence the surface effects. Further kinetic and structural work using longer time periods, more intermediate temperatures, and a variety of thicknesses is necessary to get further understanding of the factors which appear to cause a difference between the oxidation results with thin film and bulk tantalum.

Acknowledgment

The author is indebted to Mr. E. A. Gulbransen of the Westinghouse Electric Corporation for carrying out the oxidation studies with his microbalance. Mr. S. S. Gupta and Miss Phyllis Groll contributed to the statistical analyses and data testing. He wishes to thank Mr. U. B. Thomas and Mr. N. Schwartz for helpful comments and discussion and Mr. P. Kofstad for detailed comments on the manuscript and the opportunity to discuss his work prior to publication.

Manuscript received May 8, 1961; revised manuscript received Jan. 30, 1962.

Any discussion of this paper will appear in a Discussion Section to be published in the December 1962 JOURNAL.

REFERENCES

1. H. Basseches, *IRE Trans. on Comp. Parts*, **CP-8**, 51 (1961).
2. D. A. Vermilyea, *Acta Met.*, **6**, 166 (1958).
3. E. A. Gulbransen, *Trans. Electrochem. Soc.*, **81**, 187 (1942).
4. E. A. Gulbransen, *Rev. Sci., Instr.*, **15**, 201 (1944).
5. E. A. Gulbransen and K. A. Andrew, *J. Phys. and Colloidal Chem.*, **53**, 690 (1949).

6. E. A. Gulbransen and K. A. Andrew, *J. Metals, Trans. AIME*, **188**, 586 (1950); *This Journal*, **96**, 364 (1949).
7. E. A. Gulbransen and K. A. Andrew, *This Journal*, **105**, 4 (1958).
8. E. A. Gulbransen and K. A. Andrew, *Trans. AIME*, **209**, 394 (1957).
9. R. G. Charles, S. Barnartt, and E. A. Gulbransen, *ibid.*, **212**, 101 (1958).
10. D. A. McLean, Private communication.
11. T. Mills, Corrosion Symposium held at University of Melbourne Nov. 28, 1955, p. 204, Wilke and Company Ltd., Melbourne, Australia (1955).
12. U. R. Evans, "The Corrosion and Oxidation of Metals," p. 819 ff, Edward Arnold, Ltd., London (1960).
13. J. T. Waber, G. E. Sturdy, E. M. Wise, and C. R. Topton, *Journal (and Trans.) Electrochem. Soc.*, **99**, 121 (1949).
14. J. T. Waber, *J. Chem. Phys.*, **20**, 734 (1952).
15. R. C. Petersen, W. M. Fassell, and M. E. Wadsworth, *J. Metals, Trans. AIME*, 1038 (1954).
16. W. M. Albrecht, W. D. Klopp, B. G. Koehl, and R. I. Jaffee, *ibid.*, **221**, 110 (1961).
17. P. Kofstad, Central Institute for Industrial Research, Oslo-Blindern, Norway, Technical Note #4, April 1961, for Contract #AF61 (052)-90, Air Research and Development Command, European Office, Brussels, Belgium.
18. L. S. Darken and R. W. Gurry, "Physical Chemistry of Metals," p. 446, McGraw Hill Book Co. Inc., New York, N. Y. (1953).
19. E. Gebhardt, H. D. Seghezzi, and A. Stegherr, *Z. Metallkunde*, **48**, 624 (1957).
20. R. W. Berry, Private communication.
21. R. W. Berry and D. J. Sloan, *Proc. IRE*, **47**, 1070 (1959).
22. D. A. Vermilyea, *This Journal*, **102**, 207 (1955); **104**, 542 (1957).
23. J. V. Cathcart, R. Bakish, and D. R. Norton, *ibid.*, **107**, 668 (1960).

The Influence of Residual Stress on the Magnetic Characteristics of Electrodeposited Nickel and Cobalt

Robert D. Fisher

Physical Research Department, The National Cash Register Company, Dayton, Ohio

ABSTRACT

Cobalt and nickel were electrodeposited from aqueous solutions at a current density of 16 ma/cm^2. The influence of the metal chloride salt and saccharin concentrations on the residual stress and microstructure of the cobalt and nickel electrodeposits was investigated in conjunction with measurements of their magnetic characteristics. In all cases the residual stress in the deposits as measured with a stressometer was found to be tensile in nature, *i.e.*, the deposits tend to contract. The coercive force of the cobalt and nickel deposits was determined as a function of the residual or internal stress at a thickness of approximately 7μ. This coercive force was compared with a theoretical coercive force obtained from the relation $Hc = \sigma\lambda/Is$ as proposed by Kersten where σ is the experimentally determined internal stress, λ is the magnetostriction value, and Is is the saturation magnetization. It is shown that the coercive force of nickel deposits is directly proportional to the internal stress. However, the coercive force of cobalt deposits appears to be dependent on the crystal structure as well as the internal stress. Heat treatment of the cobalt deposits for 2 hr at 440°C in nitrogen results in a decrease in the squareness and an increase in the coercive force while nickel deposits increased in squareness and decreased in coercive force. The former results are explained on a crystal structure basis while the latter results can be explained on a stress relief basis.

The magnetic characteristics of most ferromagnetic materials change with the application of stress. For example, the effect of a macroscopic unidirectional stress on the remanence and permeability of positive and negative magnetostrictive materials is well known (1). Electrolytic and vacuum deposited ferromagnetic materials possess an inherent residual or internal stress. Numerous investigators have determined this stress in both electro and vacuum deposited metals, but very little attention has been given to the effects of the internal stress on the magnetic characteristics of electrodeposits. In this investigation the internal stress and surface characteristics of electrodeposited cobalt and nickel were determined in conjunction with measurements of their magnetic properties at the same thickness. Deposits were prepared at a thickness of 7μ in order to: (*a*) minimize any effect of the substrate on the magnetic properties through epitaxial growth, and (*b*) obviate any changes in the coercive force of the deposit due to thickness. Cobalt and nickel were electrodeposited from aqueous solution containing primarily their metal salts. The influence of the metal salt concentration and small additions of saccharin to the solution was investigated as to their effects on the magnetic properties, internal stress, orientation, and surface characteristics of the deposited cobalt and/or nickel.

Experimental

Deposit preparation and stress measurements.— Deposits for magnetic studies and stress measurements were made using a stressometer developed by J. B. Kushner. Its use and operation are described in detail elsewhere (2) and consequently will not be

discussed in this paper. The cathodes used in the stressometer were brass disks, 9 cm in diameter and 0.052 cm in thickness. All cathodes were cleaned in an identical manner and cut from the same sheet. The cleaning procedure was as follows: (*a*) alkaline cathodic cleaning, (*b*) distilled water rinse, (*c*) acid dip in 6*N* hydrochloric acid, and (*d*) distilled water rinse. The cathodes were then dried, weighed, and placed directly into the stressometer. The anode used with the stressometer was a platinum disk with the same diameter and area as the cathode, but the thickness was 0.21 cm. The stressometer was then calibrated and placed in the metal salt solution. Reagent grade metal salts of nickel chloride and cobalt chloride hexahydrate were dissolved in distilled water, and the single metals were independently deposited on the cathode of the stressometer at a current density of 16 ma/cm². The total volume of solution in which the stressometer was immersed was approximately 7 liters. Agitation was not used in any of the solutions. Temperature of all solutions was 25°C, and the pH was adjusted with hydrochloric acid to a value of 2.0 ±0.1.

Magnetic measurements.—B-H loops of the deposits were obtained from a low frequency (60 cycle) hysteresis loop tracer. The drive field was supplied by a pair of Helmholtz coils in series consisting of 400 turns each which permitted drive fields up to 400 oersteds without overheating. A Type 53/54B Tektronix preamplifier was used on the horizontal drive oscilloscope input. The sensing circuit consisted of a 5000-turn sense coil, a corresponding canceling coil wound in opposition, an R-C integrator and a Type 53/54E Tektronix preamplifier on the vertical oscilloscope input. The oscilloscope was a Tektronix 536.

Thickness measurements.—The thickness of all the deposits was determined by weight-density calculations. The thickness was then checked utilizing an x-ray diffraction technique. The integrated intensity of a diffraction peak of the brass substrate and the integrated intensity of the same peak with the magnetic coating over the substrate were obtained and related to the thickness. Agreement between the two methods was ±5%.

Electron microscopy and x-ray diffraction.—Samples examined with the electron microscope were replicated by applying a collodion-platinum replica followed by shadowing with carbon. The magnification in all instances was 20,000 diameters. The x-ray diffraction patterns were obtained using a Norelco x-ray diffractometer. Copper Kα radiation and iron Kα radiation were used on the nickel and cobalt deposits, respectively.

Errors and reproducibility.—The standard deviation of the stress measurements for electrodeposited cobalt was calculated as 140 kg/cm². A value of 14 kg/cm² was determined for nickel electrodeposits. The average stress value of nickel deposits was 780 kg/cm², and for cobalt deposits the average value was 1,660 kg/cm². The stress measurements in each given system were reproducible within twice the standard deviation. Magnetic measurements were reproducible within the error of reading the oscilloscope which was ±3%.

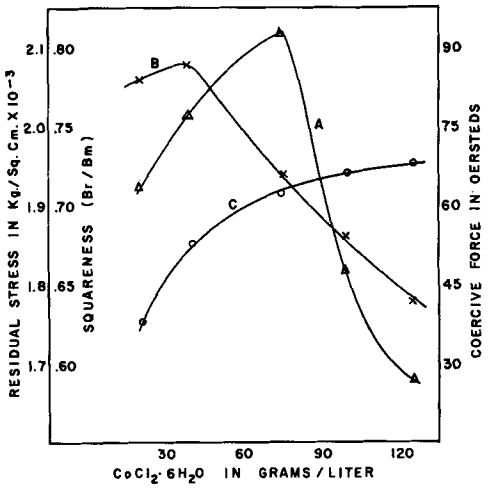

Fig. 1. Effect of cobalt chloride concentration on the residual stress and magnetic properties of electrodeposited cobalt; (A) residual stress; (B) squareness (Br/Bm); and (C) coercive force *vs.* $CoCl_2 \cdot 6H_2O$ concentration.

Experimental Results

Cobalt deposits.—The internal stress was determined in cobalt deposits from solutions containing 0.084M (20 g/l), 0.168M (40 g/l), 0.315M (75 g/l), 0.42M (100 g/l) and 0.525M (125 g/l) cobalt chloride hexahydrate. The current density was 16 ma/cm². The internal stress gradually increases as the cobalt chloride concentration increases up to 75 g/l. Further increase in the cobalt chloride concentration (100-125 g/l) decreases the residual stress. Thus a maximum stress occurs at 75 g/l cobalt chloride hexahydrate (see Fig. 1A).

The magnetic characteristics of the deposits were obtained by observation of the hysteresis loop of the deposits. The squareness (Br/Bm) of the cobalt deposits tends to decrease (0.78-0.64) with increasing salt concentration (Fig. 1B). The coercive force varies from 38 to 68 oersteds and increases as the salt concentration increases. The coercive force increases rapidly with a small increase in metal salt concentration, but further additions results in smaller changes of the coercive force (Fig. 1C). The coercive force as a function of the internal stress is shown in Fig. 2A. The coercive force appears to be directly

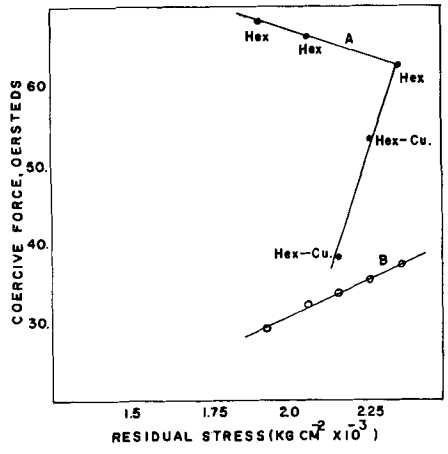

Fig. 2. Experimental and theoretical coercive force of cobalt as a function of the residual stress produced by varying salt concentration: (A) experimental coercive force vs. residual stress; (B) theoretical coercive force ($Hc = \sigma\lambda/Is$) vs. residual stress.

proportional to the internal stress up to 75 g/l cobalt chloride and then increases with a decrease in the internal stress. The increase in coercive force with a decrease in stress is similar to the results of Polukarov (3).

X-ray diffraction patterns of the deposits prepared from the low salt (20 and 40 g/l) concentrations have a hexagonal-cubic structure, but the other deposits at high salt concentrations have only a hexagonal structure with no discernible cubic peaks. Deposits which are hexagonal have the $(11\bar{2}0)$ plane parallel to the substrate while deposits with the mixtured structure have the $(11\bar{2}0)$ and in addition the (220) cubic plane parallel to the substrate. There appears to be more cubic phase in the 20 g/l deposit than in the 40 g/l deposit based on the relative diffraction peak areas.

Electron micrographs (20,000X) of the cobalt deposits obtained at 20, 75, and 125 g/l of cobalt chloride hexahydrate were examined to determine the surface characteristics. A series (12 areas) of micrographs was obtained to assure a representative picture of the surface of each deposit. The 20 g/l deposit is relatively smooth with a fine texture in the range of 50-100 mμ. Approximately 15-20% of the surface shows a grain or crystallite development in the size range of 0.3μ. The 75 g/l deposit displays the same fine texture as the 20 g/l deposit but the surface has become very rough (on the 1μ scale) with little evidence of a characteristic grain structure. The 125 g/l deposit is also extremely rough, but there is better evidence of the development of grains similar to those observed in the 20 g/l deposit.

Heat treatment of these deposits at 440°C in nitrogen for 2 hr resulted in a decrease in the squareness and an increase in the coercive force of the deposits (Table I). X-ray diffraction patterns indicate that the percentage cubic phase present in the deposits prepared at 20 and 40 g/l cobalt chloride hexahydrate has decreased, especially in the case of the 40 g/l deposit. Also the diffraction peak heights increase and are sharper in nature, indicating an increased particle size and/or stress relief. No cobalt oxide phase was discernible from the diffraction peaks prior to or after the heat treatment. The deposit prepared at 20 g/l cobalt chloride showed the least increase in the coercive force after heat treatment and the 40 g/l cobalt chloride deposit showed the greatest increase in the coercive force after heat treatment. The other deposits increased in coercive force by approximately the same amount after heat treatment.

The influence of saccharin (Na salt O-benzoic sulfimide) on the internal stress of cobalt deposits was

Table I. Cobalt deposits

g/l $CoCl_2$	Magnetic properties after heat treatment, 440°C: Coercive force	Squareness Br/Bm	Magnetic properties prior to heat treatment: Coercive force, oersteds	Squareness Br/Bm
20	46.5	0.54	38.0	0.78
40	76.5	0.68	53.0	0.79
75	80.5	0.64	62.5	0.72
100	84.5	0.64	66.0	0.68
125	80.5	0.66	68.0	0.64

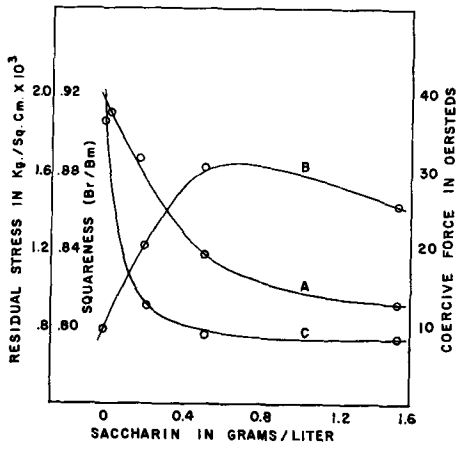

Fig. 3. Effect of saccharin on the residual stress and magnetic properties of electrodeposited cobalt: (A) residual stress; (B) squareness (Br/Bm); and (C) coercive force vs. saccharin concentration.

determined by depositing cobalt from a 20 g/l cobalt chloride hexahydrate solution containing 0.2 g/l (0.83×10^{-3}M), 0.5 g/l (2.07×10^{-3}M), and 1.5 g/l (6.22×10^{-3}M) of saccharin. The current density was 16 ma/cm². The internal stress decreases with increasing saccharin concentration. Initial concentrations of saccharin (0 g/l, 0.2 g/l, and 0.5 g/l) decrease the stress linearily, but the 1.5 g/l addition decreases the stress less rapidly, *i.e.*, it is less effective in reducing the stress (Fig. 3A)

The magnetic characteristics of the deposits were obtained as before by observation of the hysteresis loop of the deposits. The squareness of the deposits tends to increase slightly from approximately 0.8 Br/Bm to approximately 0.9 Br/Bm (Fig. 3B). Since the magnetostriction of the cobalt deposits is negative the increase in squareness may be partially attributed to a tensile stress relief. The coercive force of the deposits decreases with increasing saccharin concentration but not in a linear manner (Fig. 3C). Additions of small amounts of saccharin (0.2 and 0.5 g/l) decreases the coercive force from 38 oersteds to 8.5 oersteds at 0.5 g/l of saccharin. However, the coercive force remains constant with further additions of saccharin up to 1.5 g/l, although the internal stress continues to decrease. Deposits at high saccharin concentrations (0.5 and 1.5 g/l) have a coercive force which is the same as normal bulk deposits, namely, 8 oersteds (4). The coercive force of the deposits as a function of the internal stress is shown in Fig. 4A.

X-ray diffraction patterns of the deposits indicate a mixed hexagonal-cubic structure. Saccharin alters the orientation of the deposits from a hexagonal $(11\bar{2}0)$, cubic (220) planes parallel to the substrate to a hexagonal $(10\bar{1}0)$, cubic (111). In addition saccharin increases the amount of cubic phase in the deposit as based on the relative peak heights.

Electron micrographs of the surface characteristics of each deposit were obtained at a magnification of 20,000 diameters (Fig. 5A-D). The surface characteristics of the 0.5 and 1.5 g/l saccharin deposits are nearly identical as far as can be estimated from the electron micrographs (Fig. 5C and D). Both

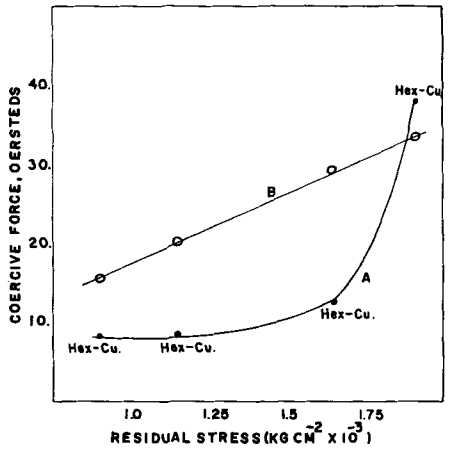

Fig. 4. Experimental and theoretical coercive force of cobalt as a function of the residual stress produced by additions of saccharin: (A) experimental coercive force *vs.* residual stress; (B) theoretical coercive force ($Hc = \sigma\lambda/Is$) vs. residual stress.

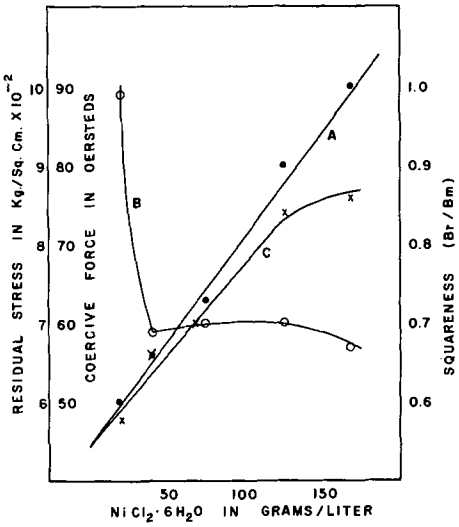

Fig. 6. Effect of nickel chloride concentration on the residual stress and magnetic properties of electrodeposited nickel; (A) residual stress; (B) squareness (Br/Bm); and (C) coercive force *vs.* $NiCl_2 \cdot 6H_2O$ concentration.

possess rounded surface projections which appear to be polycrystalline aggregates in the range of 3-5μ. The remainder of the surface (background) has an extremely fine texture in the range of 10-50 mμ. Similar projections or aggregates in the 0.2 g/l saccharin deposit have dimensions in the range of 0.3-1.0μ region. The background appears fine grained, but is more coarse than in the case of the 0.5 and 1.5 g/l saccharin deposits (Fig. 5B). The deposit without saccharin (20 g/l $CoCl_2 \cdot 6H_2O$) is relatively smooth with a fine texture in the range of 50-100 mμ (Fig. 5A). A few projections or grains in the size range of 0.3μ appear over approximately 15-20% of the surface but are not shown in Fig. 5A.

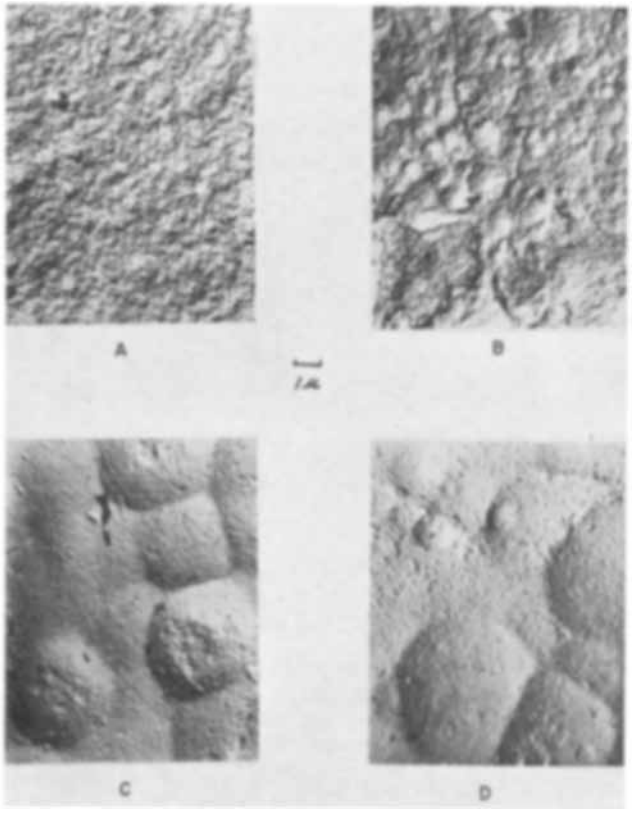

Fig. 5. Electron micrograph (magnification approximately 10,000 X) of the surface of cobalt deposits prepared in the presence of: (A) 0 g/l; (B) 0.2 g/l; (C) 0.5 g/l; and (D) 1.5 g/l of saccharin and 20 g/l of $CoCl_2 \cdot 6H_2O$.

Nickel deposits.—The internal stress was determined in nickel deposits from solutions containing the following amounts of nickel chloride hexahydrate: 0.084M (20 g/l), 0.168M (40 g/l), 0.294M (70 g/l), 0.526M (125 g/l), and 0.702M (167 g/l). The current density was 16 ma/cm^2. The internal stress increases as the nickel chloride concentration increases. In fact the increase is linear and is approximately 2.7 kg/cm^2/gram/liter addition of nickel chloride hexahydrate (Fig. 6A).

The magnetic characteristics of the deposits were obtained by observation of the hysteresis loop of the deposits. The squareness of the deposits decreases with increasing nickel chloride concentration from approximately 0.9 Br/Bm to 0.57 Br/Bm (Fig. 6B). Thus the remanent magnetization decreases with increasing metal salt concentration. The coercive force of the deposits increases from 48 oersteds at the lowest salt concentration to 76 oersteds at highest salt

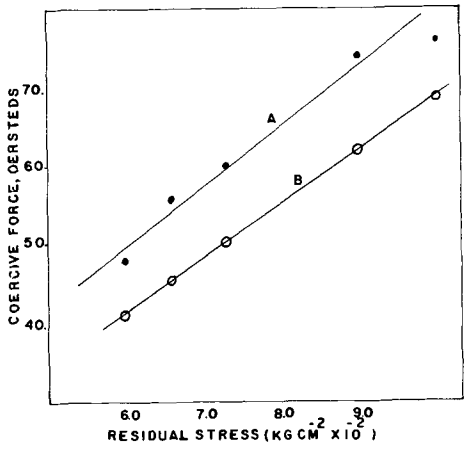

Fig. 7. Experimental and theoretical coercive force of nickel as a function of the residual stress: (A) experimental coercive force *vs.* stress; (B) theoretical coercive force ($Hc = \sigma\lambda/Is$) vs. residual stress.

concentration (Fig. 6C). Thus the coercive force increases with increasing internal stress. This has also been pointed out by Polukarov (5). The coercive force as a function of the internal stress is shown in Fig. 7A.

X-ray diffraction patterns of the deposits indicate a face-centered cubic structure typical of nickel with a decreasing (220) orientation of the deposit as the nickel chloride concentration increases from 20 to 125 g/l. The deposit at 167 g/l nickel chloride concentration appears to be random in orientation.

Electron micrographs of the deposits were obtained at a magnification of 20,000 diameters. The grain size distribution is very broad in the 20 and 40 g/l deposits making an estimate of the grain size difficult. The texture or background of the deposit is finely crystalline in nature and smooth. It would appear that the 20 g/l deposit has a larger grain size than the 40 g/l deposit. The 70 g/l deposit includes large continuous masses which are probably single crystals or grains with dimensions in the neighborhood of 10μ. These large flat crystals are connected by smaller crystals or grains in the neighborhood of 1μ (Fig. 8A). The 125 g/l deposit displays these large grain masses, but in much smaller proportions. These are occasionally joined to each other, but in most intances they are separated by areas containing crystals in the range of 1.0μ (Fig. 8B). The 167 g/l deposit does not contain any large crystal or grain masses, but consists of a relatively uniform crystallite size of 0.5-1.0μ (Fig. 8C).

Annealing of the deposits at 440°C in nitrogen for 2 hr results in a general increase in squareness and a decrease in the coercive force (Table II). This is in direct contrast with those results obtained with the cobalt deposits under a similar heat treatment (Table I). X-ray diffraction patterns of heat treated deposits indicate slight changes in the orientation of the deposits. The deposit which was initially random in orientation (167 g/l) showed the largest decrease in the coercive force. It should be pointed out that the results from the heat treatment could have been predicted qualitatively from the coercive force *vs.* internal stress curves if a stress relief should occur (Fig. 7A).

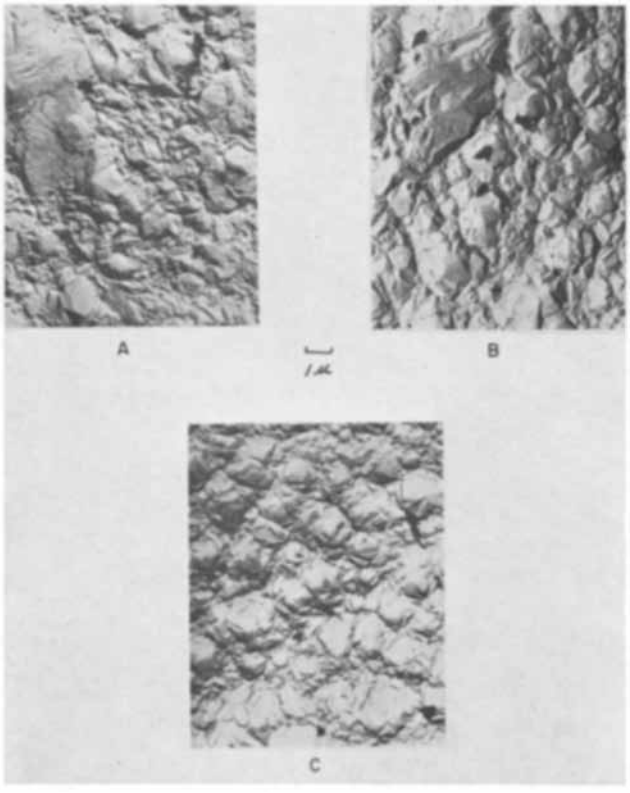

Fig. 8. Electron micrographs (magnification approximately 10,000 X) of the surface of nickel deposits prepared from a solution containing: (A) 70 g/l; (B) 125 g/l; and (C) 167 g/l $NiCl_2 \cdot 6H_2O$.

Table II. Nickel deposits

g/l $NiCl_2 \cdot 6H_2O$	Magnetic properties after heat treatment, 440°C Coercive force, oersteds	Squareness Br/Bm	Magnetic properties prior to heat treatment Coercive force, oersteds	Squareness Br/Bm
20	42.0	0.93	48.0	0.89
40	51.0	0.74	56.0	0.59
70	51.0	0.78	60.0	0.60
125	65.0	0.79	74.0	0.60
167	56.0	0.81	76.0	0.57

Discussion

A source of internal stress may be imperfections in the crystal structure of the electrodeposited material. A tensile stress can be attributed to the existence of a certain proportion of vacant sites in each lattice layer. A compressive stress occurs with an interstitial occupancy of a foreign material in the crystal structure. The measured stress may be determined by a preponderance of one type of imperfection over the other. The stressometer used in this investigation measures the average stress. Consequently, there could be highly localized stresses of both a tensile and compressive nature in the deposit which are not detected by simply measuring the average stress. However, it can be assumed that generally the average stress is a result of localized stress gradients in the deposit. The higher the stress gradients in the deposit, the higher will be the value of the average stress. This assumption is obviously invalid if the stress gradients in the deposit are highly nonuniform in nature. Under the conditions investigated, all of the deposits exhibited a tensile stress.

No extensive effort was made in this investigation to eliminate impurities other than the use of reagent grade chemicals, and therefore the effect of impurities cannot be disassociated from those of stress. Thus, even though in certain instances the stress can be correlated directly with the coercive force, it does not necessarily mean that the stress is the cause of the coercive force. However, it is likely that whatever influences the internal stress subsequently causes the same effect on the coercive force.

Heat treatment of the cobalt deposits at 440°C in nitrogen for 2 hr resulted in a decrease in squareness (Br/Bm) and an increase in the coercive force of all deposits. The increase in coercive force after heat treatment may be attributed to a decrease in the internal stress of the deposits prepared from solutions containing 75, 100, and 125 g/l cobalt chloride according to the coercive force *vs.* internal stress relation as shown in Fig. 2A. However deposits prepared from the low concentration of salt (20 and 40

g/l) cannot be explained on a stress relief basis since the coercive force should have decreased with a stress relief rather than increased (see Fig. 2A). This anomalous behavior may be explained by the decrease in the cubic crystal structure of these deposits on heat treatment as shown by x-ray diffraction. Consequently, the cubic structure of cobalt decreases the coercive force over that of the hexagonal cobalt structure, and as the cubic phase decreases due to heat treatment the coercive force increases. These data substantiate results shown in Fig. 2 which indicate that the cubic phase decreases the coercive force of hexagonal cobalt deposit under the same stress conditions.

Heat treatment of the nickel deposits at 440°C in nitrogen for 2 hr decreased the coercive force and increased the squareness (Br/Bm). The decrease in coercive force could have been predicted qualitatively from the coercive force *vs.* internal stress curve in Fig. 7A. The increase in squareness can be explained on a stress relief basis since it is well known that a tensile stress relief on a negative magnetostrictive material will increase the remanence (1). Thus the magnetic properties of nickel deposits before and after heat treatment can be explained on a stress relief basis rather than on a crystal structure-stress basis as in the case of the cobalt deposits.

The coercive force of nickel deposits is directly related to the internal stress. This suggests a model proposed by Kersten relating the coercive force to stress in the material. Kersten (6) (neglecting the energy associated with magnetic pole effects) relates the coercive force to the stress as follows: $Hc = \sigma\lambda/Is$, where λ is the magnetostriction, σ the internal stress, and Is the saturation magnetization. Thus the coercive force at a given composition and orientation (constant λ and Is) is directly proportional to the residual stress. Calculations of the coercive force of nickel deposits prepared at various salt concentrations by substituting the experimental value of the internal stress, a magnetostrictive value of 34×10^{-6}, and a saturation magnetization of 484 gauss results in coercive force values of 41-68 oersteds. A plot of the calculated and experimental coercive force *vs.* the internal stress is shown in Fig. 7A and B. The agreement between the calculated and experimental results is quite good.

Calculating the coercive force of cobalt deposits on the same basis at varying salt concentrations by substituting the experimental stress values, a saturation magnetization value of 1422 gauss, and a magnetostrictive value of 25×10^{-6} results in coercive force values of 29-37 oersteds. The internal stress *vs.* the calculated coercive force is shown in Fig. 2B. Experimentally the coercive force ranges from 38 to 68 oersteds. Agreement between the calculated and experimental coercive force *vs.* internal stress is obviously poor due to the fact that the experimental results are not linear with stress. In the case of cobalt deposits in the presence of various amounts of saccharin similar calculations of the coercive force range from 15 to 34 oersteds, and a plot of the coercive force *vs.* residual stress is shown in Fig. 4B. Again agreement with the calculated results is poor since the experimental coercive force *vs.* residual stress is not linear. Although the initial and final values of the calculated coercive force agrees well with the experimental values, intermediate values are generally too high. Thus the coercive force of cobalt deposits is dependent on other factors in addition to the residual stress, *e.g.*, Cu-Hex structure. In fact the coercive force of the hexagonal cobalt deposits (high salt concentration) is inversely proportional to the residual stress, *i.e.*, the coercive force increases with decreasing residual stress.

The surface characteristics of the deposited cobalt is dependent on the salt concentration and on the saccharin concentration. Increasing cobalt salt concentration increases the surface roughness of the deposited cobalt. Additions of saccharin result in a finer background texture of the cobalt deposit with the formation of large polycrystalline aggregates on the surface. Thus a stress relief can be associated with a grain refinement or a finer background texture. In the case of nickel deposits increasing salt concentration results in the formation of small crystallites at high salt concentration, but large flat crystals are formed at low salt concentrations. The internal stress increases with increasing salt concentration, and a decrease in stress can be associated with the formation of large flat crystals.

Summary

It has been shown that a mixed cubic-hexagonal structure of cobalt occurs at a low cobalt chloride concentration. The cubic phase results in a lower coercive force since at the same internal stress value the cubic-hexagonal structure has a lower coercive force than the hexagonal structure. The effect of the cubic phase may be attributable to a lowering of the high crystalline anisotropy of the deposit which results in lower coercive force values. It should also be noted that a stress relief of a hexagonal cobalt deposit increases the coercive force. Saccharin increases the cubic phase of the cobalt with respect to the hexagonal phase and reduces the coercive force. It also reduces the residual stress considerably, but the reduction of the coercive force is more likely due to an increase in the cubic phase rather than a stress relief. The residual stress *vs.* the coercive force of cobalt deposits is not linear, and it would appear that the coercive force is primarily determined by the crystalline anisotropy. In contrast to the cobalt deposits the magnetic properties of nickel deposits appear to be directly related to the residual stress. This is shown by the linear relation of the coercive force *vs.* stress curve. In addition the coercive force calculated as proposed by Kersten ($Hc = \sigma\lambda/Is$) agrees quite well with the experimental coercive force. A low stress appears to be associated with a grain refinement in the case of cobalt deposits and with the formation of large flat crystals in the case of nickel deposits.

Acknowledgment

The author would like to acknowledge the assistance of Patrick O'Bryan, of the University of Cincinnati and The National Cash Register Company, for his effort in obtaining many of the stress meas-

urements; Donald Koopman, of The National Cash Register Company, for performing x-ray diffraction studies; and Alfred F. Prebus, of Ohio State University, for obtaining electron micrographs of the deposits.

Manuscript received Nov. 22, 1961; revised manuscript received Feb. 14, 1962. This paper was prepared for delivery before the Detroit Meeting, Oct. 1-5, 1961.

Any discussion of this paper will appear in a Discussion Section to be published in the December 1962 JOURNAL.

REFERENCES

1. R. M. Bozorth, "Ferromagnetism," p. 595, D. Van Nostrand Co., New York.
2. J. B. Kushner, *Proc. Amer. Electroplaters' Soc.*, **41**, 188 (1954).
3. Y. M. Polukarov, *Zh. Fiz. Chim.*, **34**, 150 (1960).
4. R. M. Bozorth, "Ferromagnetism," p. 280, D. Van Nostrand Co., New York.
5. Y. M. Polukarov, *Zh. Fiz. Chim.*, **32**, 1008 (1958).
6. M. Kersten, Probleme Der Technischen Magnetisierungkurve, Springer, Berlin, 42-72. (Ref. 1, p. 824).

Preparation and Magnetic Characteristics of Chemically Deposited Cobalt for High-Density Storage

R. D. Fisher and W. H. Chilton

Physical Research Department, The National Cash Register Company, Dayton, Ohio

ABSTRACT

Chemically reduced cobalt coatings on a nonconductive substrate (Mylar) have been prepared which are suitable for high-density data storage applications. The influence of deposition parameters such as temperature, total solution concentration of cobalt plus hypophosphite ion, and *p*H on the hysteresis properties and surface characteristics of chemically reduced cobalt was investigated. The deposits are isotropic in nature so that no preferred direction of magnetization exists in the plane of the film. The coercive force of the deposits is an inverse function of the thickness, and the squareness (Br/Bm) is primarily dependent on the thickness. The saturation magnetization may vary from 8,000 to 14,000 gauss depending on the impurity content of the deposit. A typical deposit has a coercive force of 360 oersteds at a thickness of 13,000Å. The deposits are crystalline as evidenced by x-ray diffraction patterns and electron microscopy in contrast to chemically reduced nickel deposits which are reported to be amorphous. Recording characteristics of the deposits are similar to those of commercial oxide recording tapes.

Electrodeposited cobalt-nickel films and iron oxide (Fe_2O_3) coatings have been used as high-density data storage materials on drums, disks, and tapes. Requirements for high-density data storage are well known and have been discussed by many investigators (1). In general, the requirements are: (*a*) a magnetic coating with a nearly rectangular B-H loop, (b) a high coercive force generally greater than 200 oersteds, and (c) a relatively low ratio of remanent magnetization to coercive force. The work reported here was undertaken to ascertain whether chemically reduced films of cobalt could be obtained with suitable magnetic properties for high-density storage applications. Subsequently, the hysteresis properties of chemically reduced cobalt were evaluated with respect to thickness, deposition parameters, and microstructure. Chemical reduction is essentially a controlled autocatalytic reduction of cobalt and/or nickel on an active metal (Pd, Al, Ni, Co, and Fe) in the presence of hypophosphite ion. The method is attributed to Brenner (2).

Experimental Procedure

Film preparation.—In this investigation Mylar was used as a substrate material. The Mylar film (7.16 cm x 10^{-3} cm thick) was cleaned by: (*a*) dipping into a solution of 3*N* NaOH, (*b*) rinsing in distilled water, (*c*) dipping into a solution of 3N HCl, and (*d*) rinsing in distilled water followed by rinsing in acetone. Direct deposition of cobalt onto the Mylar resulted in a deposit which did not adhere. To enhance the adhesion an intermediate organic coating (an adhesive) was placed between the Mylar and the cobalt deposit. The adhesive was applied by immersing the Mylar into a 1:3 mixture of adhesive[1] with methyl ethyl ketone and withdrawing at a rate of 0.84 cm/sec. The adhesive coated Mylar was then air dried for 30 min and cured for 10 hr at 80°C. To activate the Mylar-adhesive surface, stannous chloride and palladium chloride were used. The stannous chloride solution (sensitizing solution) contained 20 g/l of stannous chloride, 10 ml of concentrated HCl acid/liter, and 0.0166 g/l of sodium lauryl sulfate. The solution will not wet the Mylar-adhesive surface satisfactorily unless 2-3 hr has elapsed before immersion of the sample. The solution is used in a precipitated condition, *i.e.*, a yellow coloration due to the formation of stannous oxychloride. The palladium chloride solution (activating solution) contained 0.5 g/l of palladium chloride and 5 ml of concentrated HCl acid/liter. The temperature of the sensitizing and activating

[1] Adhesive No. 200 TF supplied by the Shipley Company, Wellesley, Massachusetts.

solutions was 25°C. A standard cobalt-hypophosphite solution was prepared and contained the following unless otherwise specified: 7.5 g/l (0.031M) cobalt chloride hexahydrate, 3.52 g/l (0.033M) sodium hypophosphite monohydrate, 12.5 g/l (0.23M) ammonium chloride, 17.9 g/l (0.093M) citric acid, 0.0145 g/l sodium lauryl sulfate, and sufficient sodium hydroxide to adjust the *p*H to 8.2. The temperature of the cobalt-hypophosphite solution was 80°C and was controlled to ±0.5°C by means of a heating mantle. The total volume of the solution was 27.6 liters. All solutions were prepared by dissolving reagent grade chemicals in distilled water and were used without further treatment or purification.

Magnetic measurements.—B-H loop measurements were made with a low-frequency (60 cycle) hysteresis loop tracer similar to that described by Howling (3). The maximum drive field without overheating was 1,030 oersteds. A Tektronix 536 oscilloscope was used with a type 53/54E preamplifier on the vertical input (B) and a 53/54B preamplifier on the horizontal input (H). The maximum vertical sensitivity was 0.29 maxwells/cm deflection.

Electron microscopy and x-ray diffraction.—Samples examined with the electron microscope were replicated by applying a collodion-platinum replica followed by shadowing with carbon. The magnification in all instances was 20,000 diameters. The x-ray diffraction patterns were obtained using a Norelco x-ray diffractometer. Chromium K α radiation was used on the cobalt deposits.

Errors and reproducibility.—Coating thicknesses were calculated from the coating weight and the theoretical density of cobalt corrected for the phosphorous content (approximately 4%). The phosphorous content was determined using a standard colorimetric procedure (4). Any appreciable porosity of the coating will result in thickness values that are smaller than the actual thickness. However, microscopic examination of the coatings indicated that the porosity error was small since the volume of the pores was approximately 1-4% of the total volume of the deposit.

For fixed preparation conditions the values of the coercive force of the deposits are reproducible within ±10% and the flux density values (Br and Bm) within ±5%. The calculated flux densities are not necessarily absolute as the applied field was only two to three times the coercive force of the deposited cobalt.

Experimental Results

Total concentration of cobalt plus hypophosphite.—Initially, cobalt solutions were prepared according to Brenner (2). These solutions produced deposits with a coercive force of 20-50 oersteds depending on the experimental conditions. The deposits were unsatisfactory since the coercive force was much too low for high-density data storage applications. It was determined early in this investigation that a high concentration of cobalt and hypophosphite ions (typical of solutions described by Brenner) generally produced deposits with a low coercive force. After considerable investigation a standard solution was formulated which produced deposits with values of coercive force greater than 200 oersteds at thicknesses less than 2μ. The solution constituents are similar to those described by Brenner, the essential difference being that the solution was very dilute (see Experimental).

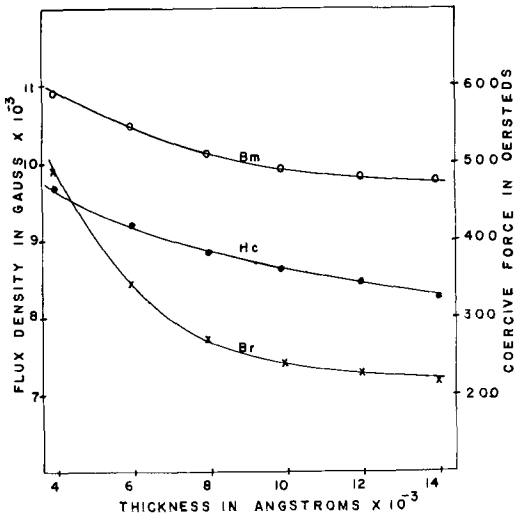

Fig. 1. Coercive force, remanent and maximum flux densities of cobalt deposits as a function of thickness.

The magnetic properties of cobalt deposits prepared from the standard solution are a function of the thickness. The coercive force, remanent (Br) and maximum (Bm) flux density of deposits as a function of thickness are shown in Fig. 1. Both the remanent and maximum flux density appear to decrease with increasing thickness from 4,000 to 13,000Å.[2] The squareness (Br/Bm) of the deposits decreases with increasing thickness from 90% at approximately 4,000Å to 74% at approximately 10,000Å. The average (4,000-14,000Å) flux density of cobalt deposits was 10,500 gauss in comparison to 18,000 gauss for pure cobalt. Analysis of the deposits indicates an average phosphorous content of 4% with a trace quantity (less than 0.5%) of copper and nickel. The phosphorous content undoubtedly is primarily responsible for the loss in maximum flux density of the deposited cobalt in comparison to pure cobalt. The coercive force decreases with increasing thickness from 470 oersteds at 4,000Å to 360 oersteds at 10,000Å. In extremely thin films (<2,500Å) the coercive force may be greater than 650 oersteds (Table I). Under the conditions investigated the coercive force was determined to be an inverse function of the thickness to the one third power. By plotting the logarithm of the coercive force *vs.* the logarithm of the thickness a

[2] In the case of Bm the decrease in flux density may be fortuitous since any error in thickness will result in relatively large errors of Bm in the thin film region. However, $\phi r/\phi m$ as well as Br/Bm definitely decreases as evidenced by hysteresis loops.

Table I. Grain size and coercive force of thin films of chemically reduced cobalt

Thickness, Å	Grain size, μ	Coercive force, oersteds
700	0.1	>650
1,200	0.2	>600
2,300	0.45	500

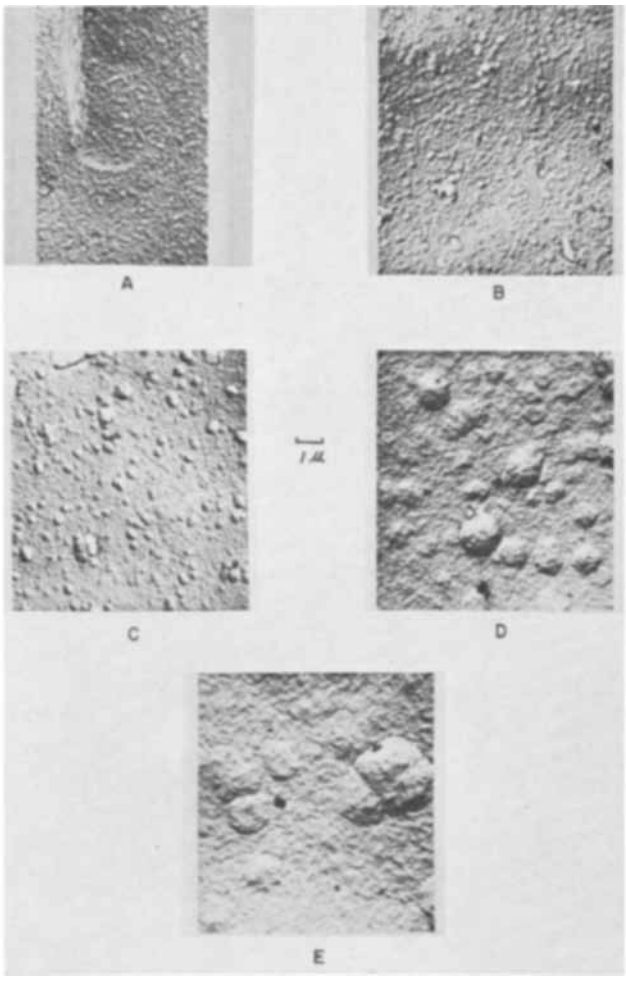

Fig. 2. Electron micrographs (magnification approximately 10,000X) of cobalt deposits at thicknesses of (A) 700Å, (B) 1200Å, (C) 2,300Å, (D) 7,000Å and (E) 14,000Å.

linear plot was obtained whose slope is one third. Thus the coercive force may be expressed as $Hc = KT^{-1/3}$.

Electron micrographs (20,000X) of the surface of deposits prepared at 700Å (3 min), 1,200Å (5 min), 2,300Å (10 min), 7,000Å (30 min) and at 14,000Å (60 min) were obtained to study the effect of thickness on the surface characteristics. The electron micrographs are shown in Fig. 2 A,B,C,D, and E. Examination of the micrographs indicated that initially (Fig. 2A) the deposit consists entirely of crystallites in the size range of 0.08-0.15μ projecting above the surface; as the deposit becomes thicker these crystallites become larger (colonies, aggregates, or single crystals) but fewer in number. For example, at 10 min these crystallites have a size of approximately 0.40-0.50μ (Fig. 2C) and at 60 min (Fig. 2E) the size (diameter) increased to 1.5μ to 2.0μ. The height of these crystallites above the surface (estimated from shadow) apppears to decrease slightly with increasing thickness, but the number per unit area decreases rapidly. Therefore, the average smoothness increases as the deposit becomes thicker, but locally the surface may be quite rough. The surface texture or background of the deposit becomes apparent at a thickness of approximately 2,300Å (Fig. 2C). The background growth becomes more well-defined as the thickness increases, *i.e.*, edges and facets are apparent in the thicker deposits (Fig. 2E).

X-ray diffraction data indicate that the deposits are crystalline, finely grained, and have a hexagonal structure typical of cobalt. The crystallinity is in contrast to chemically deposited nickel which is reported to be amorphous (5). The diffraction patterns indicate a $(10\bar{1}0)$ preferred orientation parallel to the substrate. The relative peak broadening increases as the thickness decreases indicating a finer grain size and/or increasing stress with a decrease in thickness.

The deposition rate increases directly with an increase in solution concentration of cobalt plus hypophosphite ion. Therefore, to determine the effect of total concentration on the magnetic properties, deposits were compared at equal thicknesses. Solutions were prepared at 1.8, 4.0 (standard solution), 7.3, and 14.5 g/l of cobalt plus hypophosphite concentration at a fixed cobalt to hypophosphite ratio of 0.86. The magnetic properties as a function of thickness were determined at each concentration of cobalt plus hypophosphite ion. The coercive force vs. thickness for deposits prepared at 1.8, 4.0, and 7.3 g/l concentration is shown in Fig. 3 while the results for 14.5 g/l are shown in Fig. 4. Increasing the total concentration of cobalt and hypophosphite ion at a fixed ratio of cobalt to hypophosphite (0.86) increases the coercive force from 315 oersteds (10,000Å) to 390 oersteds (10,000Å) at a concentration of 1.8-7.3, but at 14.5 g/l the coercive force decreases to 47 oersteds (10,000Å). Thus a high concentration of cobalt plus hypophosphite ion, *i.e.*, between 7.3 and 14.5 g/l at a cobalt to hypophosphite ratio of 0.86, produces deposits with a low coercive force. The remanent flux density decreases as the thickness increases in all cases (1.8, 4.0, 7.3, and 14.5 g/l Co^{++} plus $H_2PO_2^-$). The desposits prepared at the low concentration (1.8) have the highest

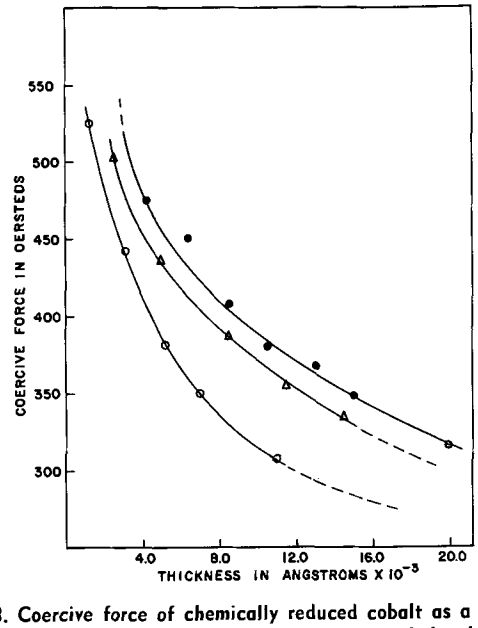

Fig. 3. Coercive force of chemically reduced cobalt as a function of thickness at various total concentrations of cobalt plus hypophosphite ion: • Co^{++} plus $H_2PO_2^-$ = 7.3 g/l; △ Co^{++} plus $H_2PO_2^-$ = 4.0 g/l; ○ Co^{++} plus $H_2PO_2^-$ = 1.8 g/l; cobalt ion to hypophosphite ion ratio = 0.86.

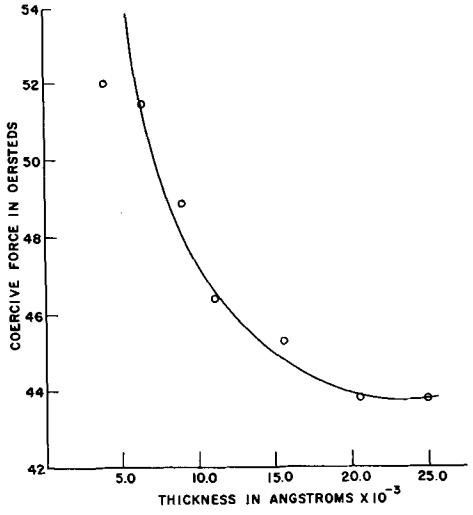

Fig. 4. Coercive force of chemically reduced cobalt as a function of thickness from a solution containing 14.5 g/l of Co^{++} plus $H_2PO_2^-$ ion; ratio of cobalt ion to hypophosphite ion = 0.86.

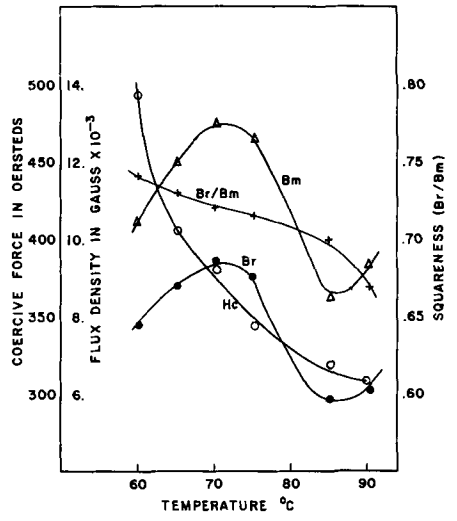

Fig. 5. Magnetic properties of chemically deposited cobalt at various temperatures but at constant time (60 min). • Remanent flux density; △ maximum flux density; ○ coercive force; and X squareness (Br/Bm).

remanent and maximum flux densities. The squareness (Br/Bm) of the deposits generally decreases with increasing thickness, but deposits from the dilute solutions tend to have a slightly higher squareness in comparison with deposits prepared at the higher (14.5 g/l) concentration of cobalt plus hypophosphite ion.

Influence of pH.—The influence of pH on the coercive force of chemically deposited cobalt was determined at pH values from 7.0 to 9.0 at intervals of 0.2 pH unit. The coercive force as a function of thickness was determined at each individual pH value. The coercive force decreases with increasing thickness at all pH values. The magnitude of the coercive force at a given thickness is nearly constant at pH values between 7.4 and 8.2. However, an increase in coercive force at a given thickness occurs at pH values from 8.2 to 8.6, *e.g.*, 389 oersteds (8.2) to 406 oersteds (8.6). Between a pH of 8.6 to 9.0 a drastic decrease in coercive force occurs from 406 oersteds (8.6) to 50 oersteds. This drastic decrease in coercive force with pH is similar to that which occurs with an increase in cobalt plus hypophosphite ion concentration. Below a pH of 7.4 cobalt will not deposit readily, and at a pH of 7.0 deposition ceases.

Volume to area ratio.—A few experiments were performed to determine if the magnetic properties of the deposits from the standard solution were dependent on the ratio of volume of plating solution to sample surface area. The volume to area ratio was varied by a factor of 100 by varying the sample area (cm^2) and solution volume (ml). The coercive force, remanent, and saturation flux densities were then determined as a function of thickness (time) at volume to area ratios of 8.0, 55.0 and 800. The coercive force does not appear to be appreciably dependent on the volume to area ratio. However, the lowest maximum flux density occurs at the highest volume to area ratio. The rate of deposition increases slightly with increasing volume to area ratio, *e.g.*, approximately 330 Å/min at a volume/area ratio of 800 and approximately 240 Å/min at a volume/area ratio of 8.0. The decrease in flux density may be associated with greater occlusion of impurities with increasing rate of deposition. However, the squareness of the deposits does not appear to be significantly different at various volume to area ratios. Consequently, all the magnetic properties remain similar with volume/area changes with the exception of the maximum flux density.

Influence of temperature.—The effect of temperature on cobalt deposits prepared from the standard solution was investigated by depositing for a constant time (60 min) at solution temperatures varying from 60° to 90°C at intervals of 5°C. The effect of solution temperature on the magnetic properties of the deposits is shown in Fig. 5. The coercive force decreases with increasing temperature. The saturation and remanent flux densities increase to a maximum at approximately 75°C and then decrease with further increases in temperature. The thickness (or deposition rate) increases directly with solution temperature for the 60-min deposition time. The squareness of the deposits decreases with increasing temperature. Thus the decrease in coercive force and squareness can be attributed primarily to an increase in the thickness. However, the variation of flux density with temperature cannot be explained by the change in thickness since the flux density decreases from the standard solution (80°C) without going through a maximum.

Electron micrographs (20,000X) of the surface of these deposits were examined. It can be seen from these micrographs that the deposits contain a fine textured background crystal growth with relatively large aggregates or colonies of crystallites growing perpendicular to the background. These aggregates or colonies increase in size as the solution temperature increases (increasing thickness), but the number per unit area decreases with increasing temperature. The surface roughness of the deposit is determined primarily by the height of these projections above the surface. The micrographs appear similar to those shown in Fig. 2 depending on

Table II. Recording Characteristics

Tape	Thickness, mils	Coercive force, oersteds	Pulse width, mils	Packing density, bits/in.	Signal amplitude, Mv	Saturation current, ma
Cobalt	0.03	400	1.0	800	700	60
Cobalt	0.055	330	1.5	550	925	70
3M #189	>0.3	278	1.3	665	1,200	80
3M #198	>0.3	282	1.2	770	1,100	80
Ampex 832	>0.3	278	1.2	770	1,100	65

the temperature and indicate that the primary effect of temperature on the magnetic properties is to vary the thickness. For further verification some measurements of the effect of solution temperature were made at (various deposition times) constant thickness. The coercive force was nearly constant as the temperature increased from 65° to 90°C.

Heat treatment.—A cobalt deposit from the standard solution was heat treated at low temperature (40°-175°C) for 24 hr in air to determine the effect of a stress relief on the magnetic properties of the cobalt deposit. Increasing temperature increases the coercive force of the deposit from 320 oersteds at 40°C to 354 oersteds at 175°C. The squareness (Br/Bm) remains nearly constant although a slight decrease is noted from 0.80 to 0.78 Br/Bm prior to and after heat treatment. Therefore a stress relief results in an increase in the coercive force of chemically reduced cobalt since at such a low-temperature grain growth, diffusion or orientation changes can hardly occur. This result is in agreement with previous results (6) showing that a stress relief of hexagonal cobalt electrodeposits results in an increase in coercive force.

Recording characteristics.—Preliminary recording tests of chemically deposited cobalt samples were made to determine their recording characteristics such as pulse width, packing density, signal amplitude, and saturation current. Nonreturn to zero saturation recording was used. The tests were made on a conventional closed-loop tape transport mechanism utilizing an Ampex head for recording and reading. The tape speed was 100 ips. The saturation current was determined at 20 kc as the value beyond which output and/or uniformity no longer increased. The maximum packing density in bits/in. was determined by the pulse interval at the value of recording frequency which reduced the output signal by 20%. The recording characteristics of several cobalt deposits were compared with three commercial oxide recording tapes, namely, Minnesota Mining and Manufacturing Tapes #189 and #198 and Ampex Tape #832. The tests were made under identical conditions of recording and reading. Results are shown in Table II. It is obvious that the cobalt deposits may have a slightly higher or equivalent packing density to that of oxide tapes. In addition the pulse width may be slightly higher or less than that of the tapes. However, the signal amplitudes were generally less. The saturation current is lower despite the higher coercive force of the cobalt deposits since the coating is much thinner than the oxide coatings.

Discussion

It is apparent from the experimental data that, in order to define the magnetic properties of chemically deposited cobalt, the concentration of cobalt plus hypophosphite ion, the pH, the solution volume to sample area ratio and temperature must be specified. The effect of these parameters on the magnetic properties can be explained by their subsequent effect on the thickness, crystal growth, and impurity content of the deposit. However, there does not appear to be any single factor which determines the magnetic properties.

The coercive force of the deposits is a function of the thickness. It would appear that the grain size in thin films (Fig. 2A) is approximately the same size as the background texture in thick films (Fig. 2E), *i.e.*, if one assumes that no subdivisions of the background texture or grains in the thin films occur. Also the grains would appear to be more isolated in the thin films. In addition, thick films contain aggregates, colonies, or large crystals. These large crystals, colonies, or aggregates may be responsible for the lowering of the coercive force as the deposit becomes thicker.

Generally, a high coercive force (Hc>300 oersteds) may be attributed to a rotational mechanism either coherent or some mode (fanning, curling) of incoherent rotation of the magnetization against the anisotropy (magnetocrystalline, magnetoelastic, magnetostatic) (7). In such cases the particle size determines the coercive force, and the coercive force is independent of the thickness. In the case of these deposits, the coercive force is dependent on the thickness, but it is not entirely clear from the electron micrographs whether the grain size is dependent on the thickness. Thus it cannot be determined whether a rotational model is applicable.

It is interesting to note that Neel (8) has proposed a relationship between grain size of a multidomain grain and the coercive force as $Hc = \gamma_o^{2/3} K^{1/6} Is^{-2/3} D^{-2/3}$ where γ_o is the wall energy, K is the anisotropy constant, Is the saturation magnetization, and D is the grain size of the film. Substituting the following values of $\gamma_o = 1$ erg/cm^2, $K = 4.0 \times 10^6$ ergs/cm^3, $Is =$ 1422 gauss for cobalt, and $D = 0.2\mu$, the average background grain size in thick films estimated from the electron micrographs (neglecting the clumps or aggregates), a coercive force of 350 oersteds is obtained. This agrees with the experimental coercive force of 360 oersteds at a thickness of 13,000Å. However, this model fails to explain the high coercivity in thin films which appear to have approximately the same grain size as thick films.

Thus, the source of the relatively high coercive force and the mechanism of reversal such as wall motion or rotation is unknown.

Manuscript received Dec. 8, 1961; revised manuscript Feb. 20, 1962. This paper was prepared for delivery before the Detroit Meeting, Oct. 1-5, 1961.

Any discussion of this paper will appear in a Discussion Section to be published in the December 1962 JOURNAL.

REFERENCES

1. J. J. Miyata and R. R. Hartel, *IRE Trans.* on Electronic Computers, **EC-8** [2] (June 1959).
2. A. Brenner and G. Riddell, *Proc. Amer. Electroplaters Society*, **34**, 156 (1947).
3. D. H. Howling, *Rev. Sci. Instr.*, **27**, 952 (1956).
4. Snell and Snell, "Methods of Colorimetric Analysis," D. Van Nostrand and Co., New York (1949).
5. A. W. Goldenstein, W. Rostoker, F. Schossberger, and G. Gutzeit, *This Journal*, **104**, 104 (1957).
6. R. D. Fisher, *ibid.*, **109**, 479 (1962).
7. C. Kittel, *Revs. Modern Physics*, **21**, 541 (1949).
8. L. Neel, *J. phys. Radium*, **17**, 250 (1956).

Effect of Binary Alloy Plating on Delayed Brittle Failure of Ultrahigh Strength Steel

Walter Beck and E. J. Jankowsky

Aeronautical Materials Laboratory, Naval Air Material Center, Philadelphia, Pennsylvania

ABSTRACT

In a number of applications, involving high strength steel, tin-cadmium alloy plating has been substituted for cadmium plating. In this study, notched specimens of high strength steel were plated with tin-cadmium alloys, produced by codeposition of the components from a fluoborate bath. The steel was also plated separately with tin from the stannate bath and cadmium from the cyanide bath and the two layer system subjected to a thermal treatment. The marked differences in delayed cracking of specimens plated from baths with different compositions were discussed in the light of the coverage of the steel surface with adsorbed atomic hydrogen in conjunction with a recently advanced theory of the kinetics of crack propagation in delayed failure.

Some years ago the corrosion protection afforded a steel substrate by cadmium, zinc-cadmium, and tin-cadmium alloy coatings was evaluated at the Naval Air Material Center (1, 2). The protection offered by tin-cadmium systems was found to be most promising, and they have been used extensively on aircraft engine components since that time.

Recently, failures of tin-cadmium plated, carburized, and nitrided engine parts were reported, and hydrogen embrittlement was considered to be a possible cause. No information was available regarding embrittlement characteristics of the process, and inasmuch as hydrogen embrittlement could seriously curtail its use and extension to other high strength steel parts, it was deemed necessary to investigate the problem thoroughly.

Binary alloy coatings are formed by direct plating from an alloy bath and also may be formed by thermal treatment of separately plated layers of the constituent metals.

In either case, the embrittlement problem is probably more complex than it is for single metal deposition, as may be expected, particularly for the two-layer system. A study of this problem, therefore, appears of general interest.

The baths used in this investigation for tin and cadmium plating in producing the two layer system were different from each other and from that employed for plating the alloy directly, because they were patterned after industrial and governmental practice now extensively used for plating internal steel components of aircraft engines. The same is true for the coating thicknesses and alloy compositions selected for this study.

The principal objective of this study was the determination of the differences in embrittlement resulting from the plating of tin-cadmium coatings on a high strength steel by two different processes, and if differences resulted, to determine to what extent the component parts of each process contributed to the total embrittlement.

A secondary objective was to apply an existing theory of the kinetics of delayed brittle failure to the results and to interrelate hydrogen coverage with this theory.

The embrittlement was determined by sustained loading delayed failure measurements on notched specimens of ultrahigh strength AISI SAE 4340 steel. Some delayed fracture studies were also conducted on a type H-11 hot work die steel plated with cyanide cadmium and a diffused, heat resistant nickel-cadmium alloy, respectively.

Experimental Procedures and Results

Specimens and testing.—Most of the work was done with specimens fabricated from 4340 steel heat treated to a strength level of 260-280 (R_c 51-52) ksi. Some studies were made on a type H-11 hot work die steel heat treated to the same strength level as the 4340 steel. Cylindrical, notched tension specimens were selected for the experiments because they are known to be very sensitive to hydrogen embrittlement. Notches were ground after heat treatment, to the dimensions shown in Fig. 1. Notches were lightly polished, gauge sections highly polished. Static tension tests were performed in a universal testing machine, at a constant cross head speed of 0.05 in./min. Times to fracture under sustained loading were determined in constant load lever arm stress rupture machines at room temperature. The loading devices used were designed to insure concentricity of load application.

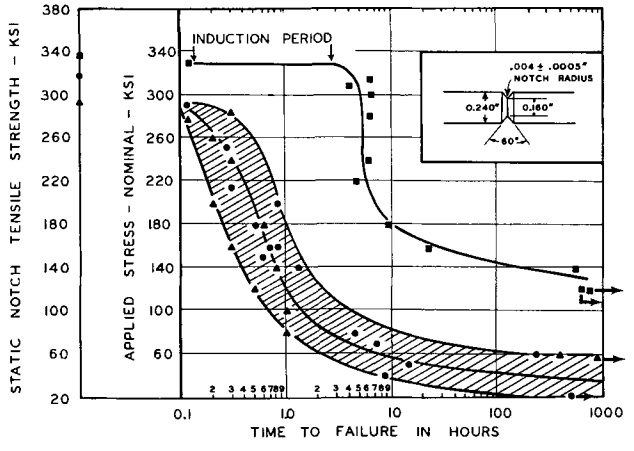

Fig. 1. Hydrogen embrittlement by plating of 4340 steel with tin, cadmium, and tin followed by cadmium and a thermal treatment. ■, Cyanide cadmium plating; ▲, stannate tin plating; ●, stannate tin, followed by cyanide-cadmium plating. All plated specimens treated for 30 min at 340°F. The tin-cadmium double coating consisted of approximately 50% tin and remainder cadmium. UTS unplated steel 260-280 ksi; NTS unplated steel 360-380 ksi; $K_T = 4.2$.

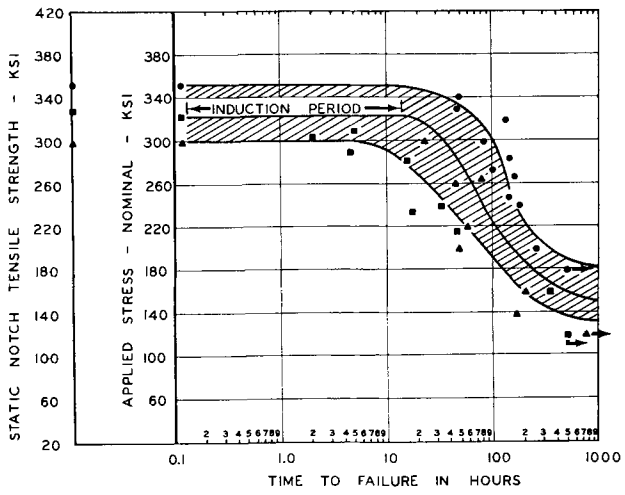

Fig. 2. Hydrogen embrittlement by plating of 4340 steel with tin-cadmium alloy and its components. ■, Fluoborate cadmium plating; ▲, fluoborate tin plating; ●, tin-cadmium alloy formed by codeposition of the metals from fluoborate bath; approximate composition of alloy 30% tin, remainder cadmium.

When no thermal treatment was to be applied, specimens were stressed 5 min after plating. Thermally treated specimens were stressed immediately after cooling down to room temperature. Threads were carefully masked before immersion in the plating bath to avoid thread breaks during load application.

Two-layer tin-cadmium plating followed by a thermal treatment.—Prior to plating, the specimens were anodically cleaned in a hot alkaline solution and dipped in 50% HCl solution for 50 sec at room temperature. This pretreatment insured good adhesion of the plating without affecting the notch dimensions. The acid dipped specimens, stressed immediately after dipping to 95% of the notch tensile strength of the untreated steel (4340 steel average 370 ksi, type H-11 steel average 385 ksi), did not fail when kept underload for the maximum time of 1000 hr.

Tin was plated from a stannate bath to an approximate thickness of 0.00008 in. measured on the gauge section. Immediately following tin plating and rinsing, cadmium was plated to the same thickness from a cyanide bath.

To alloy the tin with the cadmium, a recommended thermal treatment (1) at 340°F, for a period of 30 min, was used. Nominal composition of the alloy was 50% tin, 50% cadmium.

Specimens were also plated singly with tin or cadmium under the same conditions as those used for plating each of the two layers, and the same thermal treatment was applied.

Delayed failure curves are presented in Fig. 1 for tin, cadmium, and tin-cadmium plated specimens. Failure times determined for tin-cadmium plated steel and for those plated only with tin were close enough to be covered by a scatter band, typical of delayed brittle failure measurements under sustained loading.

Tin-cadmium alloy formation by codeposition of its components.—After alkaline cleaning and acid dipping, the alloy was directly plated from a complex fluoborate bath (1, 3, 4) recommended in the literature. The approximate thickness of the plating, measured on the gauge section, was 0.0005 in. and its composition, as determined by chemical analysis, was approximately 30% tin, remainder cadmium. Tin and cadmium were also plated separately from fluoborate baths to thicknesses of approximately 0.00015 in. and 0.00035 in., respectively, corresponding to their ratio in the alloy.

Figure 2 is a plot of the failure curves recorded with specimens plated from fluoborate baths. Again, the values for the failure times are randomly distributed in the field of a comparatively wide scatter band.

Plating of nickel followed by cadmium and a diffusion heat treatment.—The nickel-cadmium coating system was applied on hot work die steel specimens pretreated in the same manner as the 4340 specimens. Nickel was plated to an approximate thickness of 0.0002 in. from a Watt-type bath without brightener, and cadmium to an approximate thickness of 0.0001 in. from a cyanide bath, according to ref. (5). The coating system, with a nominal composition of 65% nickel, remainder cadmium, was diffusion heat treated in a circulating air furnace at 630°F for 40 min (5).

The comparatively high diffusion temperature did not have a detrimental effect on the strength of the substrate which was an air hardening steel tempered at a temperature of 1050°F. This type of steel is used at elevated temperatures and, therefore, not plated with tin-cadmium but heat and oxidation resistant nickel-cadmium alloy. The delayed failure behavior of this steel, coated with diffused nickel cadmium or plated with 0.0005 in. cyanide cadmium[1] is depicted in Fig. 3. Cyanide cadmium was plated on this steel to allow comparison with 4340 steel.

Metallographic and electrochemical evaluation.—The work on tin-cadmium alloy plating was considered incomplete without some information about the metallurgical structure of the system obtained by thermal treatment of the separately plated layers.

The opinions concerning the question of whether or not alloy formation takes place under the thermal

[1] Fed. Spec. QQ-P-416a (1956).

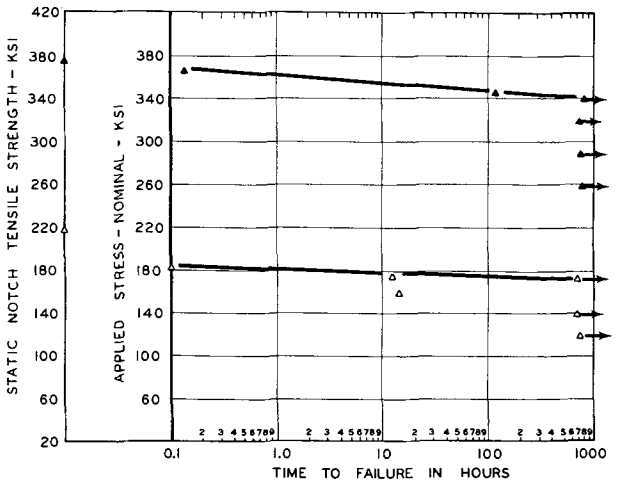

Fig. 3. Hydrogen embrittlement by plating of a hot work die steel with nickel followed by cadmium and a diffusion heat treatment, and by cyanide cadmium plating. Inverted solid triangle, Watts-type nickel plating followed by cyanide cadmium plating, diffusion heat treated for 40 min at 630°F; inverted open triangle, cyanide cadmium plating; the nickel cadmium system consisted of approximately 65% nickel and remainder cadmium; UTS unplated steel 260-280 ksi, NTS unplated steel 380-390 ksi, $K_T = 4.2$.

treatment conditions used in this investigation are divided. According to Britton and de Verre Stacpoole (6), the coating remains in layers; however, Scott and Gray show evidence that tin diffuses through the cadmium matrix (7).

In the studies made at this laboratory, steel panels were plated first with 0.002 in. of tin, and then with 0.002 in. of cadmium. After plating, the panels were thermally treated at 340°F for 1, 2, and 24 hr, respectively. The specimens were then sectioned at a low angle, mounted in cold hardening epoxy, rough polished with emery paper of increasingly finer grades up to 000, final polished with diamond dust of 3 and 0.5μ, and etched for 2 min in 30% aqueous NaOH solution at room temperature.

According to the phase diagram, at 340°F, under conditions near or approaching equilibrium, the only phases that can be present are α, ranging in composition from pure tin to 1% cadmium in solid solution, in contact with β, with from 4.0 to 5.5% cadmium in solid solution, and γ, ranging from pure cadmium to 0.25% tin in solid solution, in contact with β. The α solid solution can be in equilibrium only with the β (4.0% tin); likewise, γ may only be in equilibrium with β (5.5% tin). Since no evidence of a eutectoid structure resulting from the decomposition of a β phase was observed metallographically, even after 24 hr at 340° ± 3°F, it must be concluded that little or no diffusion of either tin or cadmium in other than the terminal solid solutions took place.

The metallographic findings were in excellent agreement with the electrochemical behavior of the coatings. Average steady-state potentials of two layer, thermally treated coating systems containing from 10 to 75% cadmium, measured in 0.1*N* NaCl solution at room temperature, were found to be —800 mv on the saturated calomel scale. Similar values were obtained on steel panels plated only with cyanide cadmium. The average potential of tin plated panels was —500 mv.

These results are in good agreement with the statements by Britton and de Verre Stacpoole (6), but do not concur with the results obtained by Scott and Gray (7). There are indications that the diffusion of tin into cadmium, demonstrated microscopically by the latter investigators, may be due to overheating, because the alloy appears homogeneous from the edge to the base, even though the time of thermal treatment (30 min at 350°F) appears much too short to ensure complete diffusion.

Because alloy formation could not be detected, the tin-cadmium system will now be designated a two-layer plating.

With respect to alloy formation by codeposition of the tin and cadmium components, attention is directed to a very recent paper by Smart *et al.* (8) who studied alloys formed by codeposition of the two metals from a complex sodium stannate-cyanide cadmium bath. According to these investigators, the plated tin-cadmium alloy is a simple eutectic system which consists of a mixture of the two high-purity components.

No metallographic investigations were made of the nickel-cadmium system. Therefore, diffusion of cadmium into nickel was only assumed to take place because it was implied in the aeronautical specification (5).

Discussion of Results

The discussion of the curves presented in Fig. 1-3 will be based partially on a recently advanced theory of the kinetics of crack initiation and propagation in delayed failure (9, 10). According to this theory, delayed brittle cracking can be aptly described by various parameters such as the incubation period, failure time, and the static fatigue limit.

The incubation time is the period required for initiation of the first crack, and the failure time is a measure of the crack propagation rate subsequent to crack initiation. The stress below which delayed failure cannot take place for an indefinite period and above which it must occur is called the static fatigue limit.

The incubation period represents the time which is needed for the hydrogen atoms to accumulate in the region of maximal triaxial stress state until a critical concentration, required for crack initiation, has been attained. Following crack initiation, there is a period of crack propagation, and finally, failure takes place. The parameter called "induction period" in the following discussion, includes both the incubation period and the crack propagation period at the highest stress at which delayed failure occurs (see Fig. 1).

It has been shown that immediately after cadmium plating (9) or cathodic charging (10) the hydrogen atoms remain concentrated in a thin layer underneath the steel surface, and from there, they diffuse into the interior of the specimen. With decreasing surface concentration of hydrogen, incubation, fracture time, and static fatigue limit increase, progressively.

Based on the work of Troiano and his co-workers (11, 12), it is inferred that a long induction time results, at least in part, from a long incubation period.

Induction time.—To simplify the analysis of the results of determinations of the induction times, they

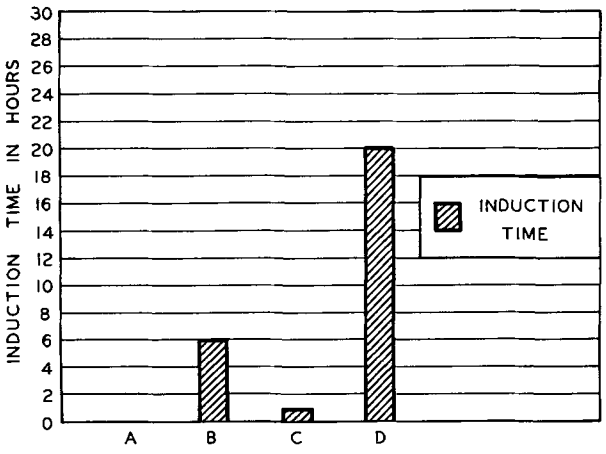

Fig. 4. Effect of plating on induction time of various steels. A, plating of stannate tin (sodium stannate bath operated at 160°F) followed by thermal treatment, plating of stannate tin followed by cyanide cadmium and a thermal treatment; B, plating of cyanide cadmium layer to approximately 0.00008 in. followed by a thermal treatment; C, plating of cyanide cadmium layer to approximately 0.0005 in.; D, platings from the fluoborate baths. A-D — 4340 steel.

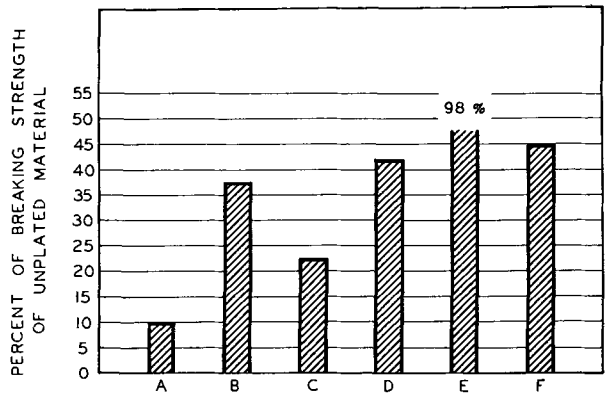

Fig. 5. Effect of plating on breaking strength of various steels, A,B,C,D as in Fig. 4. E, Plating of nickel followed by cadmium and a diffusion heat treatment; F, plating of cyanide cadmium to approximately 0.0005 in; E-F, hot work die steel.

are presented as bars in Fig. 4. Two interesting features of the results obtained with plated 4340 steel specimens are revealed in this figure: 1. The induction time is increased about twentyfold by plating the steel from the fluoborate bath (bar D) instead of the cyanide bath (bar C). 2. On specimens thermally treated after plating, that is, stannate tin plated specimens, and specimens plated with stannate tin and cyanide cadmium, respectively, the induction time is zero (bar A), and in the case of cyanide cadmium plated specimens, it was observed that the induction time was comparatively short (bar B).

In accordance with the theory discussed above and the results summarized under 1, it is concluded that the rate of crack initiation and propagation in specimens plated from the cyanide bath exceeds that in fluoborate plated specimens very appreciably. It is more difficult to explain the nonexistence of an induction period for the stannate tin or the stannate tin-cyanide cadmium plated specimens subjected to the same thermal treatment. It may be the result of homogenization (11) of the hydrogen distribution in the steel produced by the thermal treatment. It may also be speculated that the tin coating is a better hydrogen diffusion barrier than the thin cadmium coating (13) and that it therefore more effectively prevents outgassing of the embrittling hydrogen during thermal treatment, which would explain the short but finite induction time of the cyanide cadmium plated specimens. In any case, it is difficult to make predictions, based on induction time, about crack propagation in specimens coated with different metals and subjected to a thermal treatment.

Static fatigue limit.—The static fatigue limit should provide a more direct and more easily interpreted measure of embrittlement damage than the induction period. Figure 5 is a bar diagram of the static fatigue limits expressed in terms of percent of the breaking strength of the untreated notched specimens.

The differences in the static fatigue limits determined for fluoborate and cyanide cadmium plated specimens without thermal treatment, respectively, (bars D and C), confirm qualitatively the conclusions drawn from the induction times.

The low relative breaking strength (bar A) indicates that despite a comparatively short plating time (3.5 min for stannate tin, 2 min for cyanide cadmium) and the subsequent thermal treatment, the susceptibility of the steel to brittle cracking is very high as a result of stannate tin plating.

Hydrogen surface coverage.—The foregoing discussion clearly illustrates the usefulness of the theory of the kinetics of crack initiation and propagation, and particularly of the static fatigue limit, in accessing hydrogen embrittlement damage. However, the theory does not suggest a mechanism which determines the accumulation of hydrogen atoms in the metal surface.

For a number of years, extensive efforts have been made in the Aeronautical Materials Laboratory to obtain more information about this mechanism during cathodic polarization or plating. These efforts have been based on electrochemical and radioactive tracer studies on ultrahigh strength 4340 steel charged cathodically in sodium hydroxide solutions with and without sodium cyanide added, as well as electrochemical studies on steel plated with cadmium from cyanide and fluoborate baths. A comprehensive report of the results will be presented in a forthcoming paper (14). A few that relate to this paper are summarized below.

By radioactive measurements on steel surfaces after cathodic polarization in a 0.1M NaOH solution containing $NaC^{14}N$ in low concentrations, cyanide compounds were detected which tenaciously adhered to the metal. A positive heat of adsorption, in conjunction with increasing concentration of these cyanide compounds with temperature of radioactive charging solution, clearly indicated the mechanism of layer formation to be controlled by chemisorption. Hydrogen overvoltage measurements on steel electrodes with chemisorbed cyanide indicated a retardation of the hydrogen recombination reaction and hence a rise in the coverage of the surface with hydrogen. By means of the hydrogen permeation current method of Bockris and Devanathan (15) important information has been secured about this hydrogen coverage.

Addition of 0.02M sodium cyanide to a 0.1M sodium hydroxide solution raised the steady-state coverage of the steel surface with adsorbed atomic hydrogen during cathodic hydrogen evolution about 4.5 times above that in the pure sodium hydroxide solution.

In the case of cadmium plating from the cyanide bath, the coverage was only 3 times greater than that in the pure sodium hydroxide solution. It dropped further when cadmium was plated from the fluoborate bath, which was ascribed to the absence of a highly capillary active anion such as cyanide.

The extraordinarily high susceptibility of the stannate tin plated specimens to delayed failure is believed to be related to chemisorption accelerated by the comparatively high temperature of the plating bath. The rate of diffusion of the hydrogen atoms into the steel depends on the coverage of the surface with hydrogen (16). A high coverage will ensure that the hydrogen atoms diffusing from the thin layer underneath the specimen surface into its interior will be replenished at a high rate.

It is suggested that the differences in delayed brittle failure behavior of the specimens plated with tin followed by cadmium and those plated directly from an alloy bath be explained by combining the concept of hydrogen surface coverage with the theory of the kinetics of crack propagation.

In the case of the tin-cadmium coating applied by plating the constituent metals separately, the short stress rupture life is intimately related to a high hydrogen surface coverage, and it follows that the lower embrittlement imparted to the alloy plated specimens is the result of a comparatively low surface coverage with adsorbed hydrogen atoms, surface coverage being determined by the electrochemical action of the different bath anions.

Finally, the effect of plating on delayed failure of the hot work die steel will be discussed briefly.

As shown in Fig. 3, the embrittlement response of this type of steel is somewhat different from that of the 4340 steel. As can be seen from the diagram, the static notch tensile strength of the nickel-cadmium plated steel and its static fatigue limit are very close to the notch tensile strength (380 to 390 ksi) of the untreated specimen. The cyanide cadmium plated specimens again showed severe embrittlement (bar F in Fig. 5) but they were not as badly embrittled as the 4340 specimens (bar C in Fig. 5).

The almost complete absence of embrittling hydrogen in the steel (bar E in Fig. 5) may be the result of the high-temperature diffusion treatment or the proven effectiveness (17) of the low embrittling Watts nickel plating as a hydrogen diffusion barrier.

It is hoped that the studies now being conducted in this laboratory will give more information about the response to delayed brittle fracturing of H-11 and similar high strength hot die steels.

Summary

Delayed brittle cracking of ultrahigh strength 4340 steel, plated with stannate tin, followed by cyanide cadmium and a thermal treatment, is controlled by the tin phase of the plating process.

Embrittlement induced by plating the metals in two separate layers from the above baths appreciably exceeds that by codeposition of tin and cadmium from a complex fluoborate bath.

Delayed brittle failure in an ultrahigh strength hot work die steel plated with nickel from Watts type bath, followed by cyanide cadmium and a thermal treatment at a comparatively high temperature, was only of a negligible order.

The relative breaking strength derived from the static fatigue limit is representative of the embrittlement damage imparted to the steel. The marked differences in the stress rupture behavior of the plated specimens were related to differences in the surface coverage with adsorbed atomic hydrogen and discussed in the light of a recently advanced theory of the kinetics of crack propagation in delayed failure.

Acknowledgment

The authors are much indebted to Mr. F. S. Williams, Superintendent of the Metallurgical Division and Mr. Samuel Goldberg, Special Materials Section of the Bureau of Naval Weapons for the great interest taken in this study, to Mr. Manuel Raefsky for his assistance with the metallographic evaluations, and to Mr. Peter Sabatini, who performed much of the experimental work.

Manuscript received Oct. 30, 1961; revised manuscript received Feb. 8, 1962. This paper was prepared for delivery before the Detroit Meeting, Oct. 1-5, 1961. The opinions or assertions expressed in this paper are the private ones of the writers and are not to be construed as official or reflecting the view of the Department of the Navy or the Naval service at large.

Any discussion of this paper will appear in a Discussion Section to be published in the December 1962 JOURNAL.

REFERENCES

1. Aeronautical Materials Laboratory NAM AE 41, 1027, Pt. I and II issued April 28, 1948 and May 12, 1950, by J. H. James and C. M. Dougherty.
2. N. E. Promisel and G. S. Mustin, *Corrosion*, **7**, 379 (1951).
3. Bennie Cohen, *Plating*, **44**, [9], 965 (1957).
4. E. S. Hedges, et al., "Tin and Its Alloys," p. 104-106, E. Arnold Ltd., London (1960).
5. Aeronaut. Materials Specifications AMS 2416A issued by SAE (1956).
6. S. C. Britton and R. W. de Vere Stacpoole, *Trans. Inst. Met. Finishing*, **32**, 237 (1955).
7. B. E. Scott and R. D. Gray, Jr., *Iron Age*, **167** (Jan. 18), 60 (1951).
8. R. F. Smart, R. M. Angles, and D. A. Robins, *J. Inst. Metals*, **89** [9] 351 (1961).
9. H. H. Johnson, J. G. Morlet, and A. R. Troiano, *Trans. Met. Soc. AIME*, **212**, 528 (1958).
10. Taiji Toh and W. M. Baldwin, Jr., "Stress Corrosion Cracking and Embrittlement," p. 185, John Wiley & Sons, Inc., New York (1956).
11. A. R. Troiano, *Trans. ASM*, **52**, 61 (1960).
12. E. A. Steigerwald, F. W. Schaller, and A. R. Troiano, *Trans. Met. Soc. AIME*, **218** [5], 832 (1960).
13. H. H. Johnson, E. Schneider, and A. R. Troiano, *Iron Age*, **182** (July 31), 47 (1958).
14. W. Beck, Al Glass, and Ed Taylor, to be submitted to *This Journal*.
15. J. O'M. Bockris and M. A. V. Devanathan, University of Pennsylvania, Tech. Report No. 4 to ONR Contract Nonr 551 (22) N.R. 036-028 28 Feb. 1961.
16. L. I. Freiman and V. A. Titov, *Russian J. Phys. Chem.*, **34**, [1], 11 (1960).
17. W. Beck and E. J. Jankowsky, *Proc. Am. Electroplaters Soc.*, **47**, 152 (1960).

Rotating Disk Electrode Techniques for the Study of Addition Agents

I. Preliminary Studies with Cupric Sulfate Solutions

Seward E. Beacom and Robert N. Hollyer, Jr.

Research Laboratories, General Motors Corporation, Warren, Michigan

ABSTRACT

The rotating disk electrode is being used as a tool to study the influence of organic addition agents on the electrodeposition of metals; the initial phases of the study are reported in this paper. Rotating disk electrode theory has been verified for deposition of copper from cupric sulfate solutions in the presence of certain ratios of inert electrolyte ions. The experimental conditions required to proceed with a study of the role of organic additives have been established. It is found that current density is distributed uniformly across the surface of the disk electrode.

Many details of the influence of organic addition agents on the electrodeposition of metals are still unresolved. To attack certain phases of this problem, it is desirable to study the electrodeposition process under the most elementary conditions, *i.e.*, with the number of uncontrolled variables at a minimum. Because of its simplicity, an electrode system consisting of a stationary anode and a rotating disk cathode was chosen for the present investigation. This system has been successfully employed by a number of investigators to study redox reactions (1-7), but its use for the examination of the electrodeposition of a metal ion is relatively recent; the few reports in the literature indicate only limited success (4, 8, 9).

The rotating disk cathode is attractive because of the large volume of readily available literature concerning its flow pattern and the related mathematical analyses (1, 2, 5, 10-14). Examination of the equations shows that deposition must be carried out at the limiting current plateau and that migration due to electrical fields must be made negligible; the latter is accomplished by the use of a large excess of indifferent electrolyte.

The primary aim of the experimental program is to establish the conditions for which the mathematical description can be applied to the deposition of copper from an aqueous cupric sulfate solution. This is a necessary step in a program to employ the rotating disk electrode for examination of the influence of organic addition agents on the electrodeposition of metals.

Experimental

Description of apparatus.—Figure 1 is a block diagram of the apparatus which permits the rotation of a disk electrode at accurately controlled angular velocities. The shaft is driven by a variable speed motor. The frequency of rotation, recorded as revolutions per minute, is counted electronically by a scaler. Electrical contact to the shaft is made through a torroidal mercury cup. The glass vessel which holds the electrolyte is equipped with a side arm to permit the introduction of the 5 x 5 cm copper anode without disturbing the solution flow symmetry. The vessel, 12.7 cm in diameter, is sufficiently large to prevent the walls from interfering with the solution flow about the disk. A tight-fitting Lucite cover permits the maintenance of a nitrogen atmosphere above the electrolyte.

The potential, which is supplied by 1.5v dry cells and varied by means of a potentiometer, is measured with a vacuum tube voltmeter while current is measured with a milliammeter.

Electrodes.—The cathodes are stainless steel or solid copper disks, 6 mm thick and 1.27, 1.91, and 2.54 cm in diameter, respectively, mounted normal to the drive shaft. The sides and backs of the disks, as well as the drive shaft, are insulated from contact with the electrolyte. Very careful polishing and cleaning procedures are required. When the stainless steel disks are used they must be flash plated, first with a Wood's nickel strike, and then with cyanide copper. Experience has shown that the disks must be polished between runs and, if any roughness or staining develops, the complete plating preparation must be repeated. Because trouble was experienced with porosity in the cyanide copper deposit, the more recent work has been done with electrodes machined from high-purity copper.

Composition of electrolytes.—The electrolyte used in the majority of the work done thus far is an aqueous solution of cupric sulfate containing potassium sulfate as inert electrolyte. The cupric sulfate concentrations range from 0.001 to 0.020M and the po-

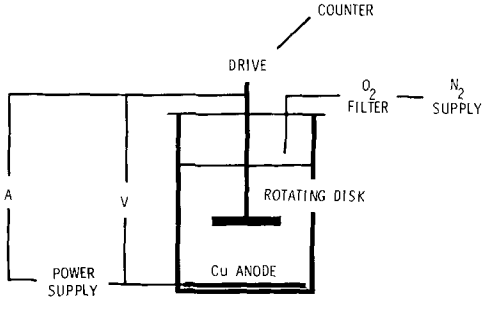

Fig. 1. Schematic diagram of apparatus

Table I. Composition of solutions used

Solution No.	$CuSO_4$ concentration (molar)	K_2SO_4 concentration (molar)
1A	0.001	0.1
4A	0.004	0.1
6A	0.006	0.1
1B	0.001	0.2
4B	0.004	0.2
6B	0.006	0.2
12B	0.012	0.2
20B	0.020	0.2
1C	0.001	0.3
4C	0.004	0.3
6C	0.006	0.3
4D	0.004	0.05

tassium sulfate concentrations from 0.05 to 0.3M. The pH of all solutions was adjusted to 3.0 by the addition of sulfuric acid. The composition of the solutions is recorded in Table I.

Removal of oxygen.—To provide an oxygen-free environment, the nitrogen used for gassing is purified by passage through a solution containing vanadyl sulfate over amalgamated zinc as recommended by Meites (15). Gassing is carried out for 30 min before the start of each experiment, and a nitrogen atmosphere is maintained above the electrolyte during the run.

Procedure and Results

The plateau voltage, that is, the cell voltage required for the deposition of cupric ions at the limiting current, is determined from the current-potential curve obtained at a constant frequency of rotation. The plateau for the $CuSO_4$ solutions extends over a range of 0.35-0.45v; the value 0.4v was used for all experiments. The same general shape of the curve and the same plateau voltage is obtained regardless of disk size or of the frequency of rotation. As expected, the magnitude of the current varies with disk size and the frequency of rotation used.

Under the experimental conditions being employed, the mathematical description predicts that a plot of current density *vs.* the square root of the frequency of rotation will yield a straight line passing through the origin. A further consequence of the theory, which holds that the distribution of current will be uniform across the surface of the disks irrespective of size, was checked by using three disks of different diameters. As shown in Fig. 2, both of these requirements are met. The fact that the average current density is the same for all three disk sizes can be assumed to indicate that the local current density is everywhere the same. An additional check of this point was made by measuring the thickness of copper deposits along the radii of the 1.91- and 2.54-cm disks using the interference microscope. Within the limit of experimental error (±5%) the deposit thicknesses are uniform over the disk surfaces.

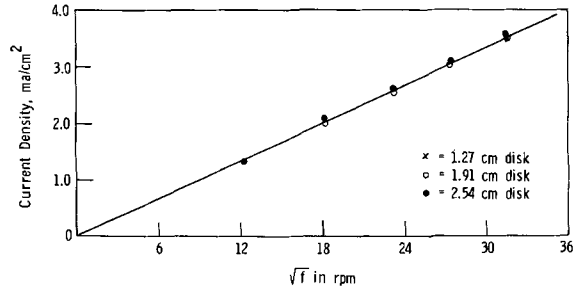

Fig. 2. Current density *vs.* root frequency for various sized disks

Since the general objective of this investigation is to use the controllable deposition conditions at the rotating disk electrode to examine the role of addition agents in the electrodeposition of metals, it is important to determine a range of cupric ion and potassium sulfate concentrations over which the requirements of the rotating disk theory may be met. When this range is once established, it then becomes possible to investigate the influence of organic addition agents.

Using the electrolytes listed in Table I, the current density *vs.* root frequency relationship is determined over a range of solution compositions. A plot, typical of the results obtained, is given in Fig. 3. It will be noticed that the plots, which are straight lines passing through the origin, meet the predictions of rotating disk theory. A plot of the slope $i/\sqrt{f}$, *vs.* the cupric sulfate concentration should be a straight line intersecting the origin. Figure 4 is a plot of this expression for the A, B, and C solutions. The agreement with theory is apparent.

Inspection of Fig. 5 shows that the plots of solutions 12B and 20B deviate from a straight line. The

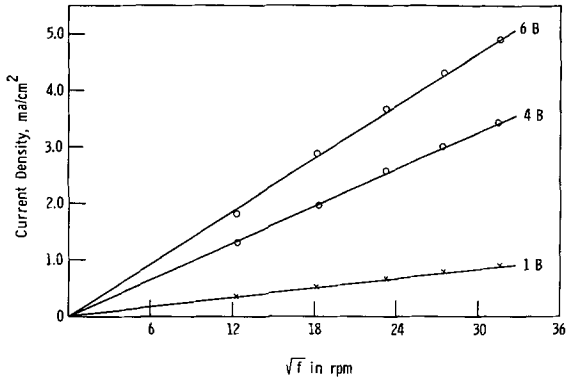

Fig. 3. Current density *vs.* root frequency for a series typical of electrolytes used.

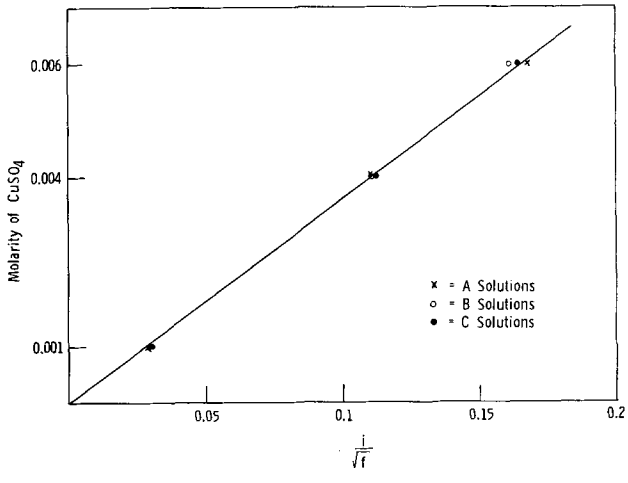

Fig. 4. Plot of slope, $i/\sqrt{f}$, *vs.* molarity of cupric sulfate solutions

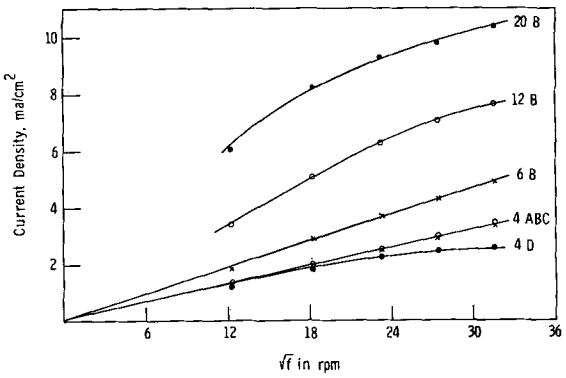

Fig. 5. Current density vs. root frequency for some extreme values of electrolyte composition.

plot for solution 6B is included for comparison. A similar deviation is observed for the plot of solution 4D which is compared with solutions 4A, B, and C. Apparently the compositions of solutions 12B, 20B, and 4D do not provide the electrolyte characteristics required to meet the predictions of rotating disk electrode theory.

Discussion

It is apparent that the predictions of rotating disk electrode theory may be met under certain very carefully controlled conditions. Analysis of the results shows that plots of current density *vs.* root frequency are straight lines passing through the origin when the ionic ratio of potassium ions to cupric ions is fifty or larger. Solutions with a ratio of fifty and up show straight lines; solutions 12B, 20B, and 4D, having ionic ratios of 33.3, 20, and 25, respectively, deviate from a straight line. Apparently an electrical transport factor is introduced, and transfer of metal ions to the electrode is no longer diffusion and convection controlled. It appears safe to assume that ionic ratios above fifty provide electrolyte conditions which are suitable for investigating the influence of organic additives on the electrodeposition of copper.

Manuscript received Dec. 21, 1961; revised manuscript received Feb. 19, 1962. This paper was prepared for delivery before the Detroit Meeting, Oct. 1-5, 1961.

Any discussion of this paper will appear in a Discussion Section to be published in the December 1962 JOURNAL.

REFERENCES

1. V. G. Levich, *Acta Physicochim., URSS*, **17**, 257 (1942).
2. V. G. Levich, *Discussions Faraday Soc.*, **1**, 37 (1947).
3. Yu. G. Siver and B. N. Kabanov, *Zhur. Fiz. Khim.*, **22**, 53 (1948).
4. E. A. Hogge and M. B. Kraichman, *J. Am. Chem. Soc.*, **76**, 1431 (1954).
5. D. P. Gregory and A. C. Riddiford, *J. Chem. Soc.*, **1956**, 3756.
6. J. D. Newson and A. C. Riddiford, *This Journal*, **108**, 695 (1961).
7. *Ibid.*, **108**, 699 (1961).
8. Yu. Yu. Matulis and M. A. Mitskus, *Trudy Akad. Nauk Litvoskii, SSSR*, Ser. B, **1958**, [1], 39.
9. E. Baydevskii and S. Toskev, *Doklady Akad. Nauk. SSSR*, **130**, 1047 (1960).
10. T. von Karman, *Z. angew. Math. Mech.*, **1**, 244 (1921).
11. W. G. Cochran, *Proc. Camb. Phil. Soc.*, **30**, 365 (1934).
12. C. Wagner, *J. Appl. Phys.*, **19**, 837 (1948).
13. K. Millsaps and K. Polhausen, *J. Aeron. Sci.*, **19**, 120 (1953).
14. N. Gregory, J. T. Stuart, and W. S. Walker, *Phil. Trans. Royal Soc.*, **248**, 155 (1955).
15. L. Meites and T. Meites, *Anal Chem.*, **20**, 984 (1948).

A Flow Synthesis of Gallium Phosphide and Some Properties of Gallium Phosphide Powder Layers

Lewis J. Bodi[1]

General Telephone & Electronics Laboratories, Incorporated, Bayside, New York

ABSTRACT

A simplified synthesis of gallium phosphide powder in an open flow-system is described. Phosphorus vapor is carried over gallium(III) oxide by a stream of hydrogen. The oxide undergoes complete conversion to phosphide at about 1000°C. A thermal treatment enhances average particle size, and electroded GaP powder layers are fabricated. Electrical properties and electroluminescence characteristics of these layers are reported.

The projected utilizations of the unique properties of gallium phosphide have effectively dictated approaches to its synthesis which are directed at yields of single crystals. The simplest synthesis from a chemical standpoint is the most complicated in terms of implementation. Gallium is generally induction heated in a graphite container which is part of a two or three thermal-zone, sealed-quartz system. A phosphorus atmosphere is maintained by one of the heated zones which acts as a phosphorous reservoir. The attainment of sound polycrystalline ingots in such a system requires the maintenance of the equilibrium phosphorous pressure (~ 20 atm) at the melting point of the stoichiometric material (~1500°C) to facilitate zone refining. These conditions of pressure and temperature are stringent impositions on such systems, and the system of Frosch and Derick (1) aptly illustrates the degree of sophistication necessary to idealize the experi-

[1] On leave from Department of Chemistry, Brooklyn College, Brooklyn, New York.

mental conditions. Other syntheses have been published, however, in which the synthesis' reaction is not a direct combination of elements. Notable among these are the efforts of Antell and Effer (2, 3) which, in addition to providing a variety of approaches utilizing sealed systems, also include an open-flow-system procedure. Recently, Gershenzon and Mikulyak (4) described a preparation in which a mixture of gallium and gallium (III) oxide reacted to form the suboxide which in turn reacted with phosphorus vapor in a sealed two-thermal-zone system. An interesting variety of single crystal morphologies resulted, but the reaction failed to go to completion.

Among the properties of gallium phosphide which suggest device application the electroluminescent character is of particular interest in these Laboratories. The possibility of employing this material in the preparation of a broad area light source is especially intriguing because of its fast ($\sim 10^{-8}$ sec) response to stimulating fields (5). One broad area electroluminescent source of simple conception but of considerably more challenging execution is the single crystal containing a p-n junction which has been effected by impurity in-diffusion. The difficulty of attaining this end begins with the aforementioned, nontrivial problem of producing uniform-cross section, single-crystal ingots of GaP. It is evident that a broad area light source consisting of gallium phosphide powder should have the double advantages of simplified fabrication of the light producing layer and of an easing of the stringent pressure-temperature conditions attending synthesis. It was this interest in a powder technology of gallium phosphide, promoted to some extent by occasional calamitous experiences with sealed system syntheses of GaP, which provoked a search for a chemically reliable powder preparation which presents no explosion hazard.

Synthesis

Previous to the development of an open-flow synthesis of gallium phosphide, sealed tube syntheses were successfully carried out which established the method which would eventually be employed. Phosphorus and gallium (III) oxide were sealed into a quartz ampoule. The ampoule was sufficiently long to permit heating in a two-zone furnace. The vapor pressure controlling end was heated to about 400°C, the reaction end containing the oxide to about 1000°C. A brownish granular product resulted which gave a clean, GaP x-ray diffraction pattern. All of the oxide underwent conversion. The reaction is presumed to be the reduction of the oxide to the phosphide accompanied by the formation of oxides of phosphorus.

The GaP produced consisted of powder, of about the fine state of subdivision of the starting oxide, and a surface mat of needles. It would seem that the latter is a recrystallization of the initially formed powder by a vapor phase transport mechanism.

Although the approach described was successful chemically, it did not provide the stability guarantees which were desired; several such tubes achieved self-destruction while undergoing post-reaction cooling. Examination of the tube fragments in those cases revealed the existence of an inner surface layer of a gallium silicate (indicated by x-ray diffraction analysis) suggesting that the synthesis runs were terminated by differential thermal contraction between the quartz envelope and the adhering silicate. Although surface silicate formation could have been prevented by appropriate modification of the oxide position within the tube, it was decided to attempt the same synthesis in an open system. An inert carrier gas was to be used to transport phosphorus vapor over the gallium oxide. To that end, the following system was set up employing argon as the carrier

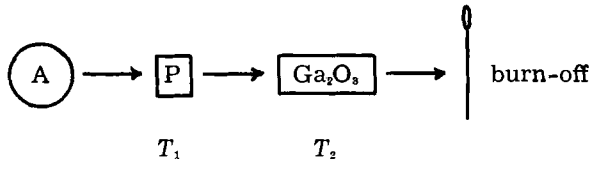

$T_1 \sim 400°C$ $T_2 \sim 1000°C$ $t \sim 1$ hr

The product was an orange-pink material which, under the microscope, was seen to consist of a mixture of separate orange and white granules. X-ray diffraction analysis indicated the presence of GaP and $GaPO_4$ as major phases. The incompleteness of the reaction (or re-oxidation of product) was attributed to the presence of oxygen and/or moisture in the system. To reduce these the system was modified to include a copper trap for oxygen which was maintained at 500°C and a dry-ice, acetone moisture trap. The product which resulted from the modified system was not an improvement over the initial flow-system material. The copper turnings exhibited no darkening indicating the low oxygen content of the argon. The acetone-dry ice trap did, however, pick up observable moisture. At this point it seemed evident that an additional source of oxidizing impurity must be the phosphorus itself (Fisher P. 99). It is known that this grade of phosphorus contains moisture, phosphoric acid, oxides of phosphorus, and water soluble salts. Because of the oxidizing nature of the impurities a reducing carrier was utilized to resolve the difficulty. (Although purer phosphorus was available the necessity for break seals for such phosphorus detracted from the over-all objective of operating simplicity.) A consequent system modification resulted in:

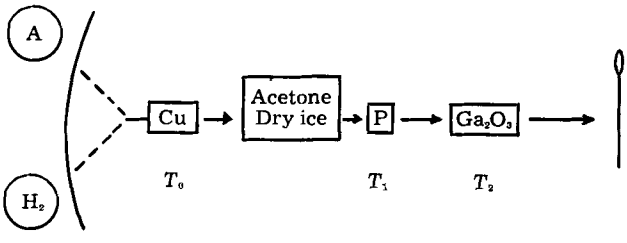

Conditions of time and temperature were those of the preceding synthesis attempt. Argon was used to flush the system prior to and following the hydrogen flow which was maintained during heating of the gallium oxide. The effect of the reducing atmosphere was decisive. The product was a granular orange-brown material covered with a mat of needles (Fig. 1 and 2). A well-defined x-ray diffraction pattern verified the presence of a single

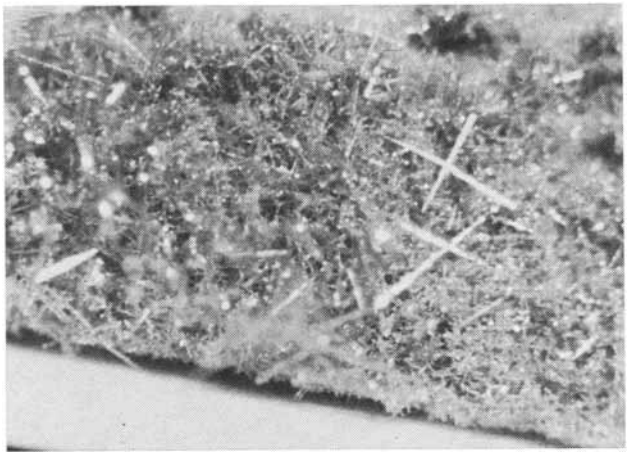

Fig. 1. Mat of GaP needles covering crucible resulting from reaction of phosphorus with gallium (III) oxide. Magnification about 30X.

Fig. 2. Fine grained GaP underlying the surface mat of GaP needles. Magnification about 30X.

cubic phase consisting of gallium phosphide. Spectroscopic examination of the starting Ga_2O_3 (prepared in our laboratories by high-temperature oxidation of 9[5] gallium in a vitreosil vessel) revealed the presence of traces of Al, Cu, Fe, and Mg as well as Si at higher levels ($\sim$ 200 ppm). The resulting GaP contained the preceding plus additional traces of Ni, Mn, and Cr which had evidently been introduced when the Ga_2O_3 was milled. The red phosphorus seems not to have been a source of additional impurities.

Recrystallization and Layer Preparation

The product obtained in the described synthesis was of approximately the same grain size as the parent gallium oxide, namely submicron to micron. In the applications for which the powder was intended, particle size is important and growth from the micron range was necessary. Because of the relatively high volatility of gallium phosphide, the appreciation of particle size posed no real difficulty. That vapor transport is the probable grain growth mechanism is indicated by our experiments in which appreciable crystal growth was observed on the upper walls of crucibles in which GaP powder was heated at as low as 900°C. The small grained gallium phosphide was sealed into an evacuated quartz ampoule which was rotated in a furnace

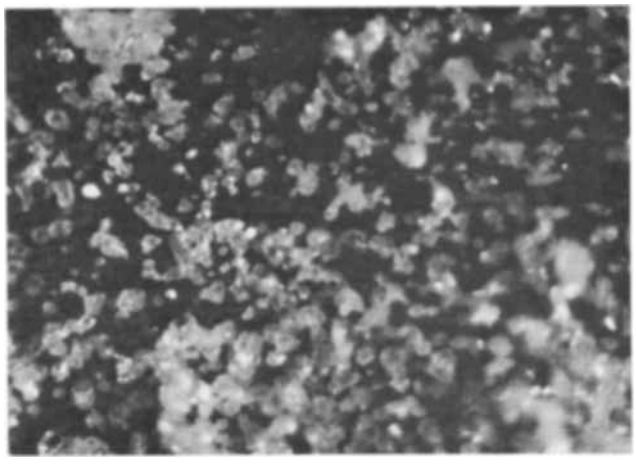

Fig. 3. Material of Fig. 2 after recrystallization. Magnification about 30X.

at 1050°C for several hours. The appreciation in particle size can be readily observed by reference to Fig. 2 and 3. Although it would have been possible to conduct experiments which would relate time and temperature of heating to particle growth, granules in the desired size range were obtained by conventional milling and sieving of the recrystallized material. The usual techniques of layer preparation were utilized. The properties of such layers do, not unexpectedly, exhibit some dependence on the mode of construction. In these laboratories powder layers of gallium phosphide have been prepared by spraying, settling, and blade spreading. Each method involves the use of a binder. Various organics and low-melting inorganics have fulfilled that function. Phosphor particle size is limited to a narrow range to eliminate the problems attending layer preparation when an undiscriminated milling mix is employed. The foremost of these problems is that of obtaining a continuous evaporated aluminum electrode on the exposed side of the powder layer. The other and transparent electrode is tin oxide coated glass.

Current-Voltage Characteristics of GaP Powder Layers

The presence of p-n junctions in gallium phosphide is indicated by the light emission observed in excited crystallites at intergranular boundaries (6). In addition there seem to be point-like regions in the crystalline material with p-n junction character judging by the roles of these sites as well-defined light sources in electric field (7-9). That preferred junction sequences seem to exist in crystallites of GaP is indicated by the rectifying properties they exhibit when identical electrodes are used as anode and cathode. Because of the randomness of grain orientation in a powder layer it would not be expected that the layer exhibit rectification except as the possible result of differences between the contacts, in this case SnO_x to GaP and Al to GaP. Such differences are mitigated in the present consideration by the intervening binder. It cannot be stated with certainty, however, that all of the grains are completely encapsulated. A voltage-current plot for a gallium phosphide powder layer with a plastic binder is represented in Fig. 4. It can

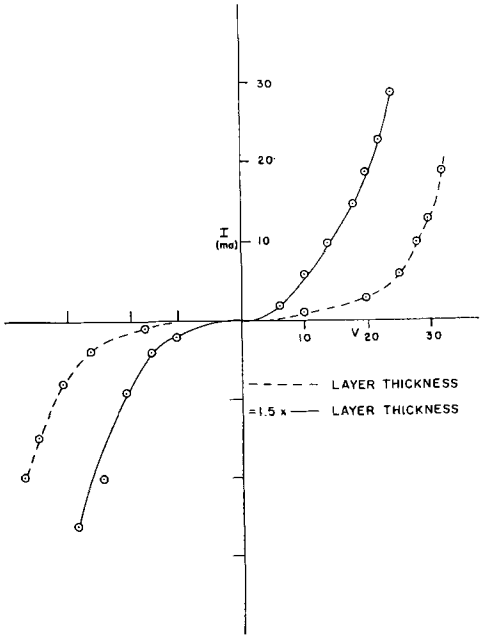

Fig. 4. Current-voltage plot for a gallium phosphide powder layer with a plastic binder. The contacts are SnO_x and evaporated aluminum.

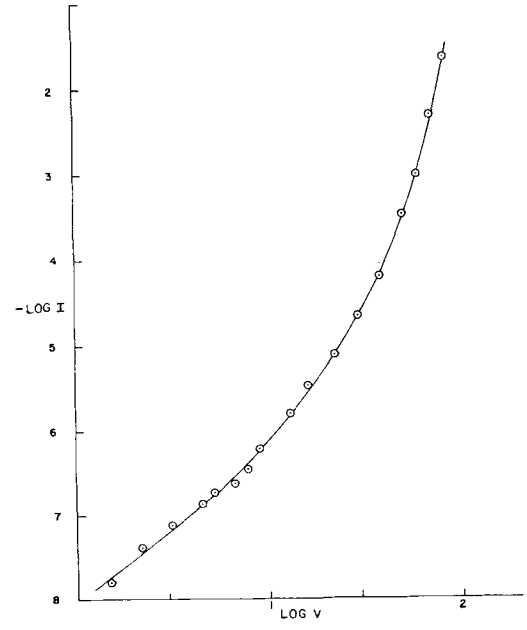

Fig. 5. General current-voltage relationship for a layer as in Fig. 4 on a log-log plot.

be readily appreciated that significant rectification does not take place. (However, below the milliampere level there is frequently an order of magnitude or so difference between the conductivities corresponding to the two polarities). Figure 5 depicts a log-log plot of current *vs.* voltage. No simple relationship of the type $I = KV^n$ fits the data. The nonlinear character of current as a function of voltage is reflected in the slopes of the plot. At low voltages, the current increases as roughly the square of the voltage, whereas at high voltages for some layers an extrapolated n value of 13 has been observed. Plotting the log of I *vs.* V yields connected linear segments. Each segment obeys the diode equation: $I = I' \exp(V/V' - 1)$, Fig. 6. The discontinuities represent abrupt changes of the parameters I' and V' as a function of the applied voltage. Individual crystallites exhibit a similar I-V relationship.

Electroluminescent Characteristics

Figure 7 shows a gallium phosphide powder layer as it appears under d.c. excitation and viewed through the transparent contact. Brightness measurements were made as functions of voltage and current. The photo measurements were made employing a Wratten No. 106 eye response compensated filter and a 1P21 photomultiplier feeding a Photovolt Model 520-M photometer. Brightness measurements were limited in voltage range by the sensitivity of the measuring system on the low voltage side and by excessive heating of the cell on the high voltage side.

A plot of brightness *vs.* power is presented in Fig. 8. The linearity observed for powder layers has also been observed for the emission from sintered pressed-pellets of gallium phosphide powder. A plot of the log of the brightness against $V^{-1/2}$ also yields a linear plot. The functional relationship between brightness and voltage for the two cases is vastly different and the simultaneous linearities must be

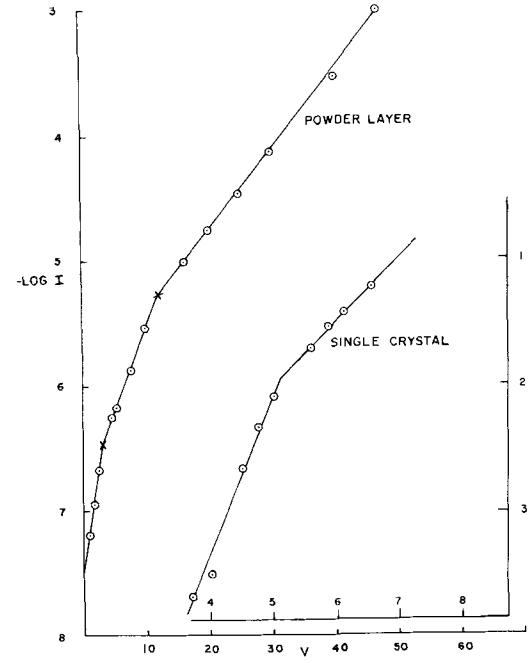

Fig. 6. Log I *vs.* V plot for a GaP powder layer and for a small single crystal illustrating adherence to the diode equation.

an accident of the narrowness of the voltage range encountered in these measurements. Wolff, Hebert, and Broder (10) have previously reported the linear character of a log B *vs.* $V^{-1/2}$ plot over a range of voltages somewhat broader than those of the author's measurements.

Microscopically the layer looks identical for reversed polarities. Light is seen to originate in point-like regions within the granules (not all of the granules by any means). The light emitted at these sites appears to be of considerably different spectral distribution than that which seems to characterize the layer as a whole. The latter is somewhat orange while the former is yellow-green. The difference between the two is due to optical filtering by the

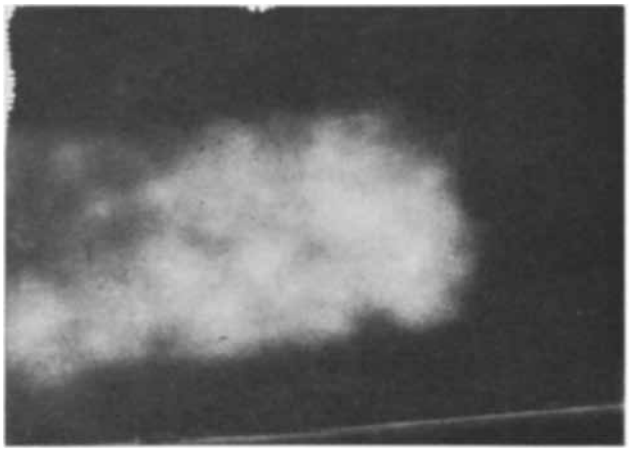

Fig. 7. GaP powder layer photographed under its own emission while d.c. excited.

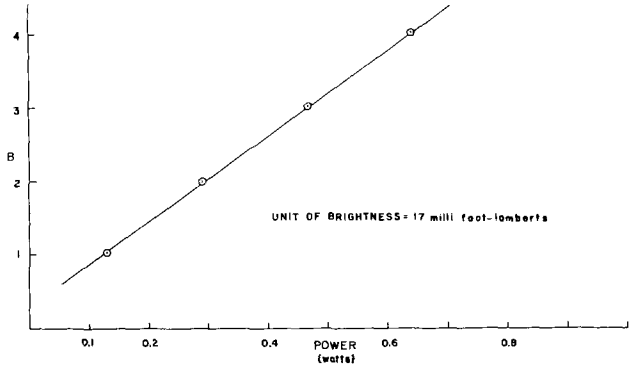

Fig. 8. Brightness *vs.* power for a gallium phosphide powder layer

granules. The efficiency of the powder layer as a light source has been calculated to be of the order of 10^{-4} lumens per watt. After the eye response character of the measured brightnesses has been taken into account, as well as internal absorption, the efficiency is of the order of 10^{-7} photons per electron.

Summary

Gallium phosphide can be synthesized by flowing phosphorus vapor in a hydrogen carrier gas over gallium (III) oxide. The oxide should be maintained at about 1000°C; the phosphorous reservoir at about 400°C. Moisture and oxygen traps in the flow train reduce the oxidant content of the carrier gases. The product can undergo a subsequent heating in a sealed-evacuated ampoule to effect particle size appreciation. The recrystallized material, after mechanical sizing has been carried out, may be used to make powder layers of gallium phosphide. Such layers have been fabricated and exhibit minimal rectification. Light emission from the layers is simultaneously linear in I x V and in exp $(aV^{-1/2})$. This seems to be a consequence of the limited range in V over which brightness measurements were made. As light sources, the layers have efficiencies of approximately 10^{-4} lumens per watt which correspond to about 10^{-7} photons per electron.

Acknowledgments

The technical assistance provided by Mr. James Yee, Jr. and Mr. Robert Fuller was of great value in the course of this investigation. Also contributing significantly to this research effort was Dr. Rubin Summergrad who initiated the powder layer studies. Special thanks are the due of Dr. Albert K. Levine for the encouragement which led to the author's researches in semiconductors. Dr. Paul Goldberg and Dr. Donald Baird made helpful suggestions pertaining to the manuscript.

Manuscript received Jan. 4, 1962; revised manuscript received Feb. 26, 1962.

Any discussion of this paper will appear in a Discussion Section to be published in the December 1962 JOURNAL.

REFERENCES

1. C. J. Frosch and L. Derick, *This Journal*, **108**, 251 (1961).
2. G. R. Antell and D. Effer, *ibid.*, **106**, 509 (1959).
3. D. Effer and G. R. Antell, *ibid.*, **107**, 252 (1960).
4. M. Gershenzon and R. M. Mikulyak, *ibid.*, **108**, 548 (1961).
5. J. W. Allen, Tech. Rpt. No. 119, Services Electronics Research Lab., July 1961.
6. G. F. Alfrey and C. S. Wiggins, International Congress on the Physics of Solid State, Brussels, 1958, vol. 2, part 2, p. 747, Academic Press, Inc., New York (1960).
7. M. Kikuchi and I. Iizuka, *J. Phys. Soc. Japan*, **15**, 935 (1960).
8. J. W. Allen and P. E. Gibbons, *J. Electronics and Control*, **7**, 518 (1959).
9. M. Gershenzon and R. M. Mikulyak, *J. Appl. Phys.*, **32**, 1338 (1961).
10. G. A. Wolff, R. A. Hebert, and J. D. Broder, *Phys. Rev.*, **100**, 1144 (1955); Proceedings of the International Colloqium on Semiconductors and Phosphors in Garmisch, Interscience Publishers Inc., New York (1958).

Preparation and Properties of ZnO Phosphors

Arnold Pfahnl

Bell Telephone Laboratories, Incorporated, Murray Hill, New Jersey

ABSTRACT

ZnO phosphors were prepared at a variety of firing temperatures according to the reaction $2ZnO + ZnS \rightarrow 3Zn$ (excess) $+ SO_2$. The absolute values of the cathodoluminescent intensity, I, and the decay time, τ, were determined for the green emission band of these phosphors at 5 ma/cm² and 10 kv excitation. The temperature dependence of I and τ, the form of the decay, the dependence of τ on exciting current density, the aging characteristics, and the spectral distribution were also measured.

It was found that, at liquid nitrogen temperature, I and τ are nearly constant for all samples regardless of the firing temperature used during the phosphor preparation. As the sample temperature is raised above that of liquid nitrogen, I and τ both become temperature dependent, which is attributed to nonradiative quenching processes that compete with the luminescent transitions. At room temperature a nearly linear relationship exists between I and τ. This behavior is independent of sample preparation methods or commercial source of the phosphor. It was also observed that the decay was nonexponential and that τ is dependent on the exciting current density, which shows that the green luminescence is the result of a second-order recombination process. The influence of the firing temperature on the structure of the luminescent center is also evident from the increased aging rate of those samples which were prepared at higher temperatures.

Many different conditions and methods of preparation are reported in the literature for luminescent ZnO (Table I). The present work describes some of the properties of phosphors obtained according to the reaction $2ZnO + ZnS \rightarrow 3Zn$ (excess) $+ SO_2$.

Emphasis in this study has been placed on the relationship between emission intensity and decay time of the green emission, and no attempt was made to investigate the relationship between the green and the u.v. emission. High emission intensities and decay times $\leqq$250 nanosec were desired, in view of the intended use of a phosphor of this type in a special purpose flying-spot scanner cathode-ray tube (1,41).

Results also were sought which may contribute to a better understanding of the basic processes involved in the green luminescence of ZnO.

Table I. Preparation conditions for ZnO phosphors as indicated in the literature

Emission	Preparation	Reference
Blue	Zn in O	(2-5)
	Zn in N_2	(6)
Green	Zn in O, incomplete	(7)
	ZnS in O or air	(4, 6-10)
	ZnO in CO	(3)
	ZnO in H_2	(3, 6, 8, 10-13)
	$Zn(OH)_2$ in H_2	(7, 14)
	$ZnCO_3$ in H_2	(6, 8, 10, 15)
	ZnO in vacuum	(16)
	ZnO + ZnS in N	(6, 13)
	ZnO + S in N	(17, 18, 26)
	ZnS + Pb in O	(17)
	ZnO + Bi in H_2	(11, 18, 19, 27)
	ZnO + MgO + $LiSO_4$	(20, 28)
	ZnO + NH_4Cl	(16)
	Zn + S	(25)
Orange	ZnO in O	(7, 12, 21)
	ZnO in O + Ga, Al, Gd, Cl, Br	(22)

Experimental

For the preparation of the phosphors, 5 or 10g of ZnO (r.p.) + X weight % ZnS (X = 0,1,5,10,15) were fired for 1 hr at various temperatures in covered quartz crucibles and in an atmosphere of nitrogen. The samples were cooled rapidly after firing.

All samples used in the present experiments were prepared from the same batches of ZnO and ZnS, as some variations in the emission intensity were found among batches from different producers. It was necessary that the luminescent pure (l.p.) grade of ZnS be used, since the use of reagent pure (r.p.) grade resulted in a considerable reduction of the emission intensity (Table II).

For the cathode-ray tube screen preparation, the phosphor was suspended in a solution of potassium silicate using ultrasonic agitation and was then settled on microscope slides with barium nitrate as the coagulant. A series of tests on several selected samples showed that the ultrasonic treatment did not change the intensity or the decay time. For each phosphor sample, the optimum screen weight was determined by measuring the emission intensity as a function of the screen weight.

Table II. Emission Intensity of ZnO + 5% ZnS Samples prepared with combinations of base materials from various producers

Firing time: 1 hr; firing temperature: 850°C; excitation: mercury lamp with blue glass filter

ZnO batches (all r.p.)	ZnS batches (all l.p. except c)	Intensity
A	a	29
A	b	30
B	a	30
B	b	31
A	c (r.p.)	10

The particle size of the phosphors increases with the firing temperature and reaches an average of about 30-40μ for the samples fired at the highest temperatures. This is well within the limits of the particle size of commercial samples. On the other hand it was found that it is possible to change the particle size distribution considerably without reducing the maximum intensity if careful mechanical treatment (grinding) is applied. The grain of the screens obtained with the present powders is comparable to that of screens prepared with commercial samples of ZnO (Zn).

A demountable cathode-ray tube was used to measure the emission intensity and decay time. All data (except aging data) were taken under identical excitation conditions (anode voltage 10 kv; current density 5 ma/cm^2; pulse length 5 μsec; repetition frequency 1000 pulses/sec). These are the operation conditions under which the cathode-ray tube would be finally used (1), but they are milder than those of other flying-spot scanner operations where the product of excitation time for a screen element and the current density may be increased by a factor of ten.

The green emission from the side opposite from that of excitation was detected by a photomultiplier with S11 response. The u.v. emission band was filtered out (Corning filter CS3-72, 2.9 mm thick). The photocurrent was displayed on an oscilloscope. The time constant of the circuit was small enough to permit measurement of decay times down to 50 nanosec.

The aging data, needed in practical phosphor applications for the determination of the useful screen life, were obtained with sealed-off cathode-ray tubes having aluminized screens (seal-off pressure 10^{-7} mm Hg). Clean vacuum conditions were required during aging measurements, since burn from positive ions or contamination from back-streaming pump fluid vapors might otherwise have introduced major errors (29). To reduce the aging time, a stationary beam was used with the beam focused to a power density of 0.5 w/cm^2 at the phosphor screen. This is low enough to avoid thermal damage.

The spectral distribution of the fluorescent emission was determined with a Bausch and Lomb "Model 250 mm" monochromator and a photomultiplier tube. An absolute calibration of the ensemble was made.

Results

Emission intensity and decay time.—At and above room temperature, the emission intensity and the decay time (measured at the 1/e point) depend strongly on the firing temperature (Fig. 1). The intensity increases with the firing temperature up to about 1100°C and then decreases monotonically. The decay time goes through a similar maximum, which is about 100°C lower than that of the intensity. Samples fired at higher temperatures have, consequently, shorter decay times for equal emission intensities. Similar curves are obtained for preparation with 1%, 10%, and 15% ZnS content.

The data for the 20°C curve of Fig. 1 are replotted in Fig. 2 showing the decay time τ as a function of

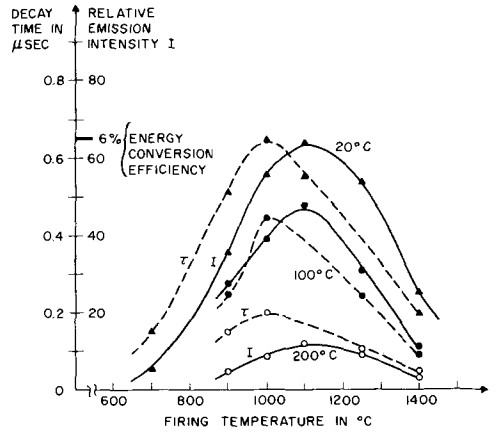

Fig. 1. Relative emission intensity *I* and decay time τ of ZnO(Zn) phosphors as a function of the firing temperature. Base material: ZnO + 5% ZnS; atmosphere: nitrogen; firing time: 1 hr. Phosphor temperature varied from 20° to 200°C.

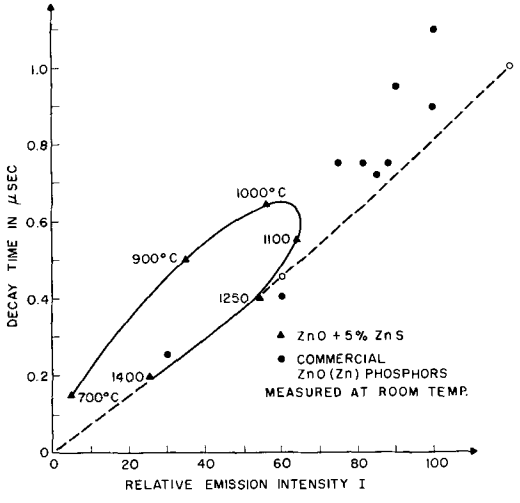

Fig. 2. Decay time τ vs. emission intensity *I* for ZnO(Zn) phosphors prepared at various firing temperatures, as well as for several industrial samples.

the emission intensity *I*. This is a convenient method of determining the quality of a phosphor sample when the shortest decay time at a given intensity is sought. The lower part of this curve, corresponding to the higher firing temperatures, can be continued through the points representing the best ZnO phosphor samples obtained from various industrial sources. This shows that, at the present state of the art, most of the industrially produced ZnO phosphors possess nearly the optimum combination of decay time and intensity, but it does not mean that this curve necessarily represents a physical limit. Improvements in the quality (purity) of the base materials may lead to improved quality of the phosphors (see Table II).

A comparison between the commerical samples and those prepared in the present experiments shows that most of the former have higher intensities than the latter (Fig. 2). The method used for the preparation has certainly a strong influence on the maximum intensity as can be seen in Fig. 3 where the results of various preparation methods and commercial samples are compared. The highest intensity in the present experiments was obtained by the oxidation of luminescent pure ZnS, but this

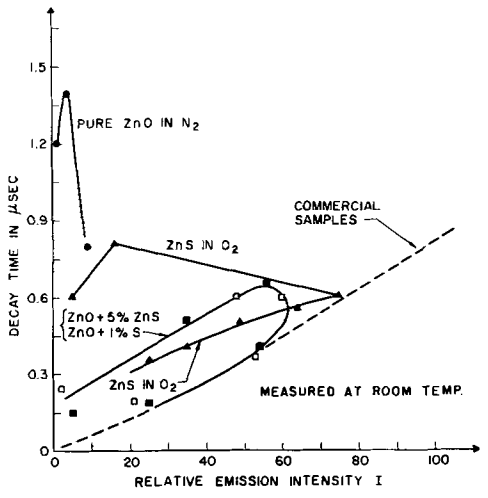

Fig. 3. Relative emission intensity *I* vs. decay time τ for ZnO(Zn) phosphors prepared by various methods.

is still about 20% below the maximum found for commercial samples. Another possible method to achieve higher intensities would be doping [ref. (17), Table I]. Further investigation would be necessary to elucidate this point.

It is interesting to note that ZnO phosphors prepared according to various other methods have quite similar properties. This is shown in Fig. 3, where the emission intensities and the decay times of ZnO + 5% ZnS are compared with the values measured on ZnS oxidized in pure O_2 for 20 min, ZnO + 1% S fired in N_2, and reagent-pure ZnO fired in N_2. ZnS oxidized at a temperature greater than 1000°C rapidly loses its green luminescence and acquires properties similar to calcined pure ZnO.

Data for a fixed firing temperature of 1000°C and varying ZnS concentrations are given in Fig. 4. ZnO without a special addition of ZnS exhibits very low intensities but long decay times of the order of 1 μsec when fired at 1000°C. Addition of 1% ZnS causes an increase of the intensity and a decrease of the decay time. Greater concentrations of ZnS have relatively little effect.

The presence of larger quantities of sulfur in the samples fired below 1000°C (see section on Analysis of samples) indicated that, at these firing temperatures, a firing time of 1 hr may not suffice to complete the reaction. A few experiments with various

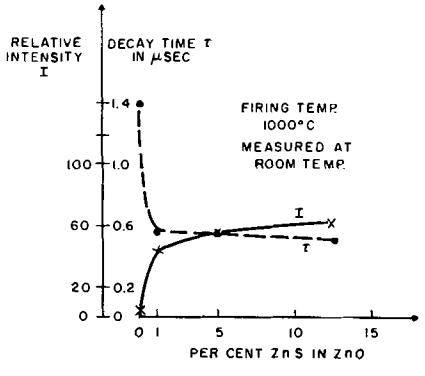

Fig. 4. Emission intensity *I* and decay time τ as a function of increasing ZnS content in the ZnO + ZnS preparation. Firing time, 1 hr.

firing times, up to 6 hr, at a firing temperature of 850°C showed a continuous increase of *I* with firing time, in which *I* was proportional to the logarithm of the firing time. To reach the full intensity of 65 rel. units measured at room temperature, a firing time of over 12 hr would be necessary as shown by an extrapolation. At 910°C, the intensity reaches 90% of its saturation value after 1 hr. At 1100°C, less than 7 min are necessary. For the purpose of practical ZnO phosphor preparation, firing temperatures at or above 1000°C therefore seem advisable.

If the temperature of the sample is lowered, the intensity, *I*, increases monotonically, the rate of increase being a function of the firing temperature. If the temperature is lowered from 20 to −180°C the intensity increases 1.8 times if the sample was fired at or below 1000°C, 2.0 times for a firing temperature of 1250°C, and 4.3 times for a firing temperature of 1400°C. In the vicinity of −180°C the slopes level off, and a common value of the intensity is reached for all samples except those fired below 1000°C for which the firing time of 1 hr was not long enough to give the maximum possible intensity (Fig. 5). The decay times measured at the 37 and 5% points are also practically constant and independent of the firing temperature if measured at −180°C (Fig. 5).

Figure 6 shows the decay time, τ, as a function of the sample temperature. For the samples fired up

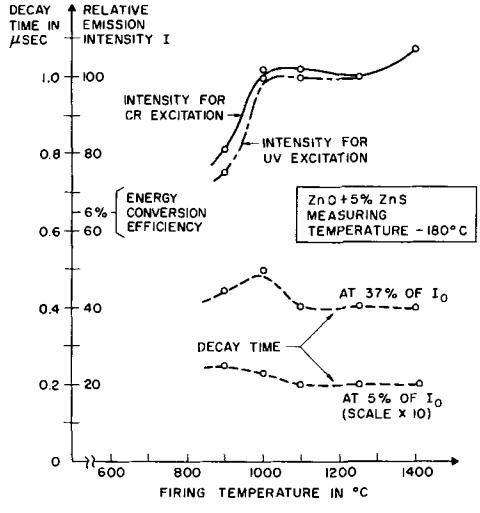

Fig. 5. Emission intensity *I* and decay time τ of ZnO(Zn) phosphors prepared from ZnO + 5% ZnS as a function of the firing temperature (measured at −180°C). Firing time, 1 hr.

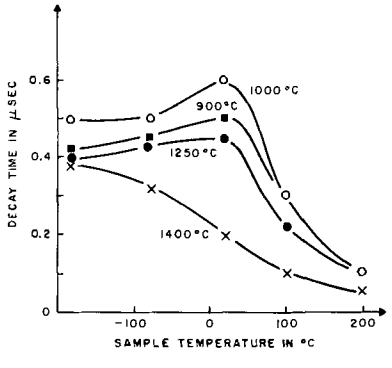

Fig. 6. Variation of the decay time as a function of temperatures. ZnO + 5% ZnS. Firing time, 1 hr.

to 1250°C there is a slight increase of τ up to room temperature and then a rather sharp decrease. The sample fired at 1400°C exhibits a steady decrease of τ with increasing temperature.

The absolute value of the energy conversion efficiency, which depends on the experimental conditions, was determined by comparison with optical measurement standards developed at this laboratory (30). It was found that the value of 65 rel. units of the intensity scale as used in Fig. 1-5 corresponds to an energy conversion efficiency of 6% for the excitation conditions mentioned in the experimental section above. This is in good agreement with other published data (31) taken at 1-10 μa/cm^2 at 6-8 kv, which indicate an efficiency of 7.5% for a ZnO (Zn) phosphor having approximately 1 μsec decay time.

Other parameters.—The form of the decay is nonexponential regardless of the firing temperature of the samples (Fig. 7) or the temperature at which the measurement is taken (Fig. 8).

The decay time is also a function of the current density, as shown in Fig. 9. It decreases by approximately 30% if the current density is increased by a factor 10. This has been found to hold over a range of 1 μa/cm^2 to 50 ma/cm^2, with either pulse or raster excitation.

Figure 10 shows the relative aging characteristics of four ZnO phosphors fired at different temperatures. The decrease in intensity due to electron bombardment has been observed to be most sensitive to the accumulated charge per unit area deposited by the beam and is relatively independent of accelerating voltage; hence coulombs/cm^2 is used as the abscissa of the aging curve. The samples fired at a higher temperature (1400°C) age slightly more rapidly at the beginning than those fired at a lower temperature (1000°C). This is in agreement with observations of the sensitivity of the luminescence to mechanical damage (*e.g.*, grinding) recorded by other authors (32). The curves coincide after a deposited charge of about 100 coulombs/cm^2 has been reached. Some aging data obtained under raster excitation were also available but only for a total deposited charge up to 10 coulombs/cm^2. No difference in the results was found.

The green emission spectrum of six representative samples fired between 900° and 1400°C was determined at various temperatures ranging from −180° or + 130°C. The spectra were found to be identical, each having its maximum at 500 mμ regardless of the firing temperature, the measurement temperature, or the amount of ZnS in the base material before firing. This is in good agreement with data published in the literature (40).

Analysis of samples.—A mass-spectrometric analysis of the gases liberated from three representative fired samples by reheating at 650°C under high vacuum showed that sulfur is still present in quantities up to about 0.01% of the initial content (Table III). The quantities of SO and SO_2 liberated decrease exponentially for a linear increase of the firing temperature. The remaining sulfur is present in the form of ZnS which was shown by the

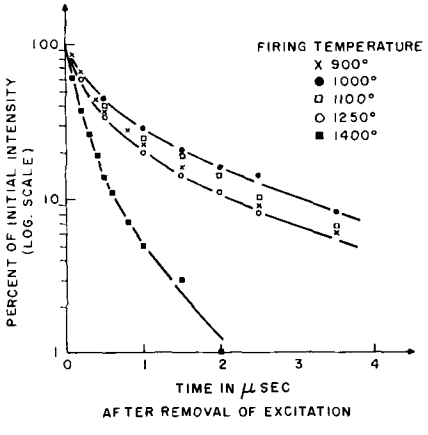

Fig. 7. Form of the decay of ZnO(Zn) phosphors prepared at various firing temperatures. Preparation conditions as in Fig. 6.

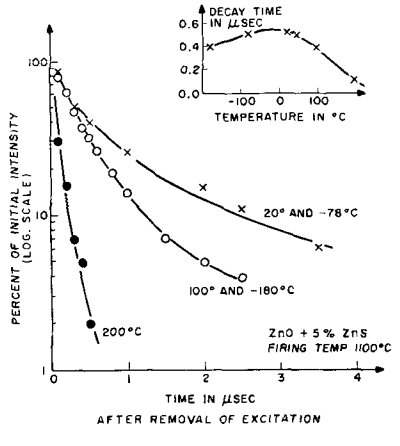

Fig. 8. Form of the decay and decay time τ as a function of the temperature for a ZnO(Zn) sample fired at 1100°C.

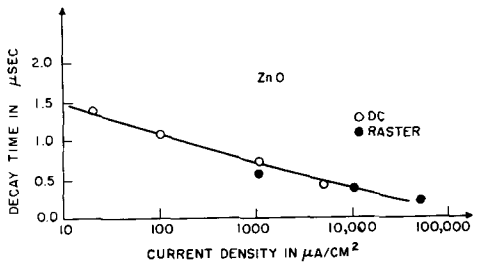

Fig. 9. Decay time of a representative ZnO(Zn) phosphor as a function of the exciting current density.

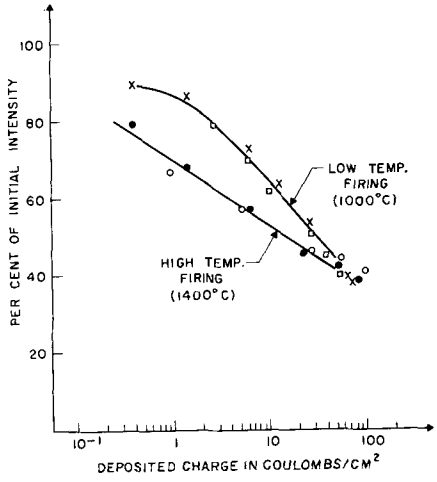

Fig. 10. Relative aging characteristics of ZnO(Zn) phosphors fired at high and low temperature.

Table III. Gas quantities (in $cm^3 \cdot mm$) liberated from 1g samples of ZnO phosphors heated under vacuum at 650°C, as determined by mass-spectrometric analysis

Sample composition before firing: ZnO + 5% ZnS

Firing temp, °C	H_2	CO	H_2O	CO_2	SO	SO_2	CH_4
700	91.2	90.3	243.4	82.3	20.4	26.3	—
1100	22.9	93.5	51.1	55.2	5.2	1.9	—
1400	8.2	12.6	0.6	13.2	0.1	1.4	—
Commercial sample	57.0	11.5	14.0	68.0	—	—	0.63

detection (by means of x-ray diffraction) of α-ZnS crystals in the green luminescent samples fired at 1000° and 1400°C. At 1400°C the crystallites have grown large enough to give a relatively strong diffraction pattern. The analysis of an industrial sample with similar luminescent properties revealed no sulfur.

Discussion

ZnO is typically an n-type semiconductor, with donor levels at 0.04 to 0.05 ev. They result from an interstitial excess of Zn in concentrations ranging from 10^{15} to 10^{18} atoms/cm^3, depending on the mode of preparation of the material (33). Green luminescence appears if ZnO is prepared under reducing conditions (see Table I), which produces a further excess of Zn. The oxygen vacancies corresponding to the deviation from stoichiometry must be produced during the formation of the crystal and cannot be obtained by a reducing agent acting solely on the surface (7).

Based on these and other considerations, it has been proposed by various authors that the green luminescence corresponds to a transition from $Zn^{\cdot}$ to $Zn^{\cdot\cdot}$ in the excess Zn ions (23) or to a transition in an oxygen vacancy (7, 42b).

As an alternative explanation, it has been advanced that the green band could be the result of a small amount of ZnS (0.1% or less) present in solid solution in the ZnO (26).

On the basis of the experiments previously reported, it is not possible to decide between these two interpretations, even though the mass spectrometric analysis of the green luminescent industrial sample did not reveal any sulfur content (see the Experimental section above). Therefore high-purity Zn 99.9998% was oxidized, and it was found, in agreement with other authors (22), that a green luminescent ZnO was formed. The reducing agent (ZnS, S, etc.,) consequently would serve only to create oxygen vacancies in the ZnO lattice. Considering the high sensitivity of the luminescent materials to small amounts of impurities further investigations would be necessary to ascertain the absence of sulfur in these experiments.

At a given firing temperature certainly only a limited number of excess Zn ions and oxygen vacancies can be incorporated in the crystal. This explains the leveling-off of the intensity even when increasing quantities of reducing agent are added to the base material (Fig. 4). (The form of the curves is similar for firing temperatures up to 1400°C where the reaction is completed before one hour of firing time.)

At low concentrations of the reducing agent (*e.g.*, in the r.p. ZnO containing less than 0.001% S used in the present sample preparation) only a few luminescent centers are formed and the intensity is low. It is also possible in this case that a small amount of oxygen leaves the lattice without requiring the action of a reducer. This also agrees with the observation of the appearance of a new band of dipolar Debye absorption above 1000°C, corresponding to an activation energy of 0.25 ev (35).

From the data shown in Fig. 5 and from the experiments relating the intensity to the firing time it can be concluded that, for the present preparation method, the number of luminescent centers produced in the crystal is independent of the firing temperature. For firing temperatures below 1000°C longer firing times than 1 hr are necessary to incorporate the maximum possible number of luminescent centers, but an increase of the firing temperature from 1000° to 1400°C increases only the number of quenching processes which may be associated with some lattice defects.

The number of these quenching processes is strongly temperature dependent and seems to disappear completely below —180°C. Other limitations on the maximum attainable efficiency must nevertheless still be present, due probably to the basic absorption processes of cathode rays in the phosphor, as the best efficiency at —180°C is only 10% (Fig. 5).

The form of the I *vs.* T curves can be represented by the equation: $\eta = L/(L+N)$ where η is the luminescent efficiency, L the number of radiative, and N the number of radiationless transitions. It is generally assumed, that L is nearly independent of T and that N increases rapidly with the ambient temperature of the phosphor. Further measurements extending the range to liquid helium temperature would here be valuable.

The nonexponential decay (Fig. 7, 8) indicates a second-order recombination process between holes and electrons. As green luminescent ZnO has a high dark conductivity (23, 42) there should not be a great change of the electron concentration in the conduction band during the excitation. It could therefore be assumed that the rate-determining process is the trapping of holes in the center. The green emission then takes place immediately after the hole has been trapped. This would be in agreement with the different temperature dependence of decay time as compared to that of intensity, the latter being determined by the action of the quenching process on the luminescent transition, the former by the thermal action on the hole-capture process.

The increase of the decay time at low excess Zn concentrations (Fig. 4) could be explained by the sensitivity of the lifetime of the holes to lattice imperfections (43), which probably increase with increasing amounts of excess Zn. Possibly no impurity conduction band has yet been formed, and the luminescent centers are independent of one another.

At high excitation densities and low center concentration, two effects should consequently be observed: (*a*) a relative increase of the intensity of the u.v. emission as a consequence of the reduced possibility for recombination via activator centers, and (*b*) an exponential form of the decay of the green band due to the fact that the number of holes is much greater than the number of centers (at least at the beginning of the decay). Unfortunately the decay form of these samples could not be measured, but an increase in u.v. emission was observed in the present experiments. The hypothesis could also explain that exponential decay forms have repeatedly been indicated in the literature (8, 42).

The decrease of the luminescent efficiency with electron bombardment may result from damage to the luminescent centers (37) or from an increase in the number of radiationless transitions by formation of lattice defects (38). If the luminescent process takes place in a center formed by one or several ions and the electron does not leave this center during the excitation, destruction of a center decreases only the intensity and the decay time remains practically constant. This is the case, for example, with $CaWO_4$ (29). Measurements on several samples of ZnO showed (29) that the decay time decreases about 30% after a bombardment with 100 coulombs/cm^3. This would indicate an increase of the possibility for radiationless transitions. The different aging behavior of crystals prepared at various temperatures indicates also that the aging process is sensitive to structural differences in the lattice.

Acknowledgments

This project was under the general direction of R. W. Sears, whose encouragement throughout the study has been most valuable. Mr. R. S. Ehle performed many of the measurements, and his help is greatly appreciated. Mrs. M. H. Read did the x-ray analysis, and E. J. Becker provided the mass spectrometric data.

Manuscript received Nov. 6, 1961; revised manuscript received Feb. 20, 1962. This paper was prepared for delivery before the Indianapolis Meeting, April 30-May 3, 1961.

Any discussion of this paper will appear in a Discussion Section to be published in the December 1962 JOURNAL.

REFERENCES

1. C. W. Hoover, G. Haugh, and D. R. Herriot, *Bell System Tech. J.*, **38**, 365 (1959).
2. H. W. Leverenz, "Luminescence of Solids," chap. 3, p. 74, J. Wiley & Sons, New York (1950).
3. R. E. Shrader and H. W. Leverenz, *J. Opt. Soc. Am.*, **37**, 939 (1947).
4. E. Mollwo, *Z. Physik*, **138**, 478 (1944).
5. Gmelin's, "Handbuch d. Anorganischen Chemie," Vol. Zn, p. 125 (1924); pp. 805, 788 (1956).
6. G. Heiland, E. Mollwo, and F. Stockmann, "Solid State Physics," vol. 8, p. 228, Academic Press, New York (1959).
7. N. Riehl and H. Ortmann, *Z. Elektrochem.*, **60**, 149 (1956).
8. H. Gobrecht, D. Hahn, and K. Scheffler, *Z. Physik*, **139**, 365 (1954).
9. Telefunken, Swedish Pat. 97059, 1938/1939.
10. G. Brauer, "Handbuch d. Präperativen Anorg. Chemie," p. 1332, F. Enke, Stuttgart (1951).
11. C. A. Nickle, Fluorescent ZnO, U. S. Pat. 2,408,475, (1951).
12. Keiji Maeda, *Bull. Chem. Soc. Japan.*, **33**, 456 (1960).
13. F. A. Kröger and J. A. M. Dickhoff, *Physica*, **16**, 297 (1957).
14. J. Klikora, J. Horak, and A. Celikovsky, *Chem. lis*, **52**, 2226 (1958).
15. E. Beutel and A. Kutzelnigg, *Monatsh. Chem.*, **70**, 297 (1957).
16. I. K. Versechagin and V. S. Teslyuk, *Izvest. Vysshikh Ucheb. Zavedenii*, Fig. 6, 114 (1958).
17. H. W. Leverenz, *R. C. A. Rev.*, **7**, 199 (1946).
18. British Thomson-Houston Co., British Pat. 558, 213, 1943.
19. E. G. Pettsol'd, *Izvest, Akad. Nauk. S.S.S.R.*, Ser. Fiz., **24**, 104 (1960).
20. L. J. Reimert and E. A. Futzinger, U. S. Pat. 2,481,-344, 1947/49.
21. V. V. Osiko, *Optika i Spektrosk.*, **7**, 770 (1959).
22. F. A. Kröger and H. J. Vink, *J. Chem. Phys.*, **22**, 250 (1954).
23. F. I. Vergunas and G. A. Konivalov, *J. Exp. H. Theoret. Phys. (U.S.S.R.)*, **23**, 712 (1952).
24. S. R. Morrison, "Advances in Catalysis," vol. 7, p. 262, Academic Press, New York (1955).
25. K. Kamm, German Pat. 859, 782, 1952.
26. S. M. Thomsen, *J. Chem. Phys.*, **18**, 770, 1950; U. S. Pat. 2,573,817, 1949.
27. A. H. Joung, U. S. Pat. 2,734,872, 1956.
28. P. R. Celmer, U. S. Pat. 2,683,293, 1954.
29. A. Pfahnl, "Advances in Electron Tube Techniques," p. 204, Pergamon Press, New York (1961).
30. C. W. Hoover and H. Raag, "Solid State Physics in Electronics and Telecomm., vol., 4, p. 688, Academic Press, New York (1960).
31. A. Bril and H. A. Klasens, *Philips Res. Repts.*, **7**, 401 (1952).
32. A. Kutzelnigg, *Sitzber. Wiener Akad Wiss.*, **142**, 715 (1933).
33. A. R. Hutson, *Bull. Am. Phys. Soc.*, **2**, 56 (1957).
34. F. A. Kröger, "Some Aspects of the Luminescence of Solids," pp. 205 ff, Elsevier, New York (1947).
35. M. L. Blanchard, *Compt. rend.*, **244**, 757 (1957).
36. G. F. J. Garlik and M. F. H. Wilkin, *Proc. Roy. Soc.*, **A184**, 408 (1945).
37. Bandow, "Luminescence," pp. 166-170, Wiss. Verlagsges., Stuttgart (1950).
38. I. Broser and W. Reichardt, *Naturforsch.*, **6a**, 466 (1951); *Z. Physik*, **134**, 222 (1953).
39. J. A. Amik, *R. C. A. Rev.*, **20**, 753 (1959).
40. F. H. Nicoll, *J. Opt. Soc. Am.*, **38**, 817 (1948).
41. H. G. Cooper, *Bell System Tech. J.*, **39**, 1161 (1961).
42. (a) A. Pfahnl, to be published; (b) also: E. Mollwo, *Z. Physik*, **162**, 557 (1961).
43. See for example, C. Kittel, "Solid State Physics," p. 369, J. Wiley & Sons, New York (1956).

Dissolution of Germanium in Aqueous Hydrogen Peroxide Solution

N. Cerniglia and P. Wang

Semiconductor Division, Sylvania Electric Products Inc., Woburn, Massachusetts

ABSTRACT

The dissolution of germanium in aqueous hydrogen peroxide of from 3 to 90% H_2O_2 and *p*H from 1 to 9 has been studied at temperatures varying from 25° to 90°C. It has been found that dissolution rate remains constant in solutions of 3-30% by weight of H_2O_2 at low *p*H, then decreases with increasing H_2O_2 content. The reaction is highly *p*H dependent above *p*H 4, and this *p*H dependence varies as a function of H_2O_2 concentration. This indicates that the rate-controlling step in low and high H_2O_2 concentration solutions at *p*H 5 and above may be different. Reaction mechanism to explain this situation is proposed.

The use of hydrogen peroxide solution as a final clean-up etch for germanium is an established practice in the semiconductor industry. The use of dilute aqueous hydrogen peroxide solutions as an etch for germanium was first suggested by Camp (1). Miller (2) determined the dissolution rate of germanium at various temperatures in 3.4% by volume hydrogen peroxide solutions of *p*H 5. The present study has been carried out in order to obtain a better understanding of the mechanism of the dissolution reaction and to determine its dependence on the hydrogen peroxide concentration, temperature, and *p*H of solution. The effects of the resistivity, resistivity type, and crystalline perfection of the germanium on the dissolution rate also have been studied.

Experimental

The samples used were 1 x 1.5 x 0.010 in. single crystal n- and p-type germanium of 2 to 6 ohm-cm resistivity.[1] Samples were oriented with the major surfaces in the <111> plane within one degree and were prepared with an aluminum oxide lapped finish. Random area measurements on the slices showed less than 2% variation in apparent surface area. Resistivity measurements on individual samples showed variations less than 5%. Prior to etching, each sample was degreased in trichloroethylene, chloroform, and methanol, dried, cleaned in hydrofluoric acid, and rinsed in distilled, deionized water of better than 15 megohm resistivity. After drying, samples were weighed to the nearest hundredth of a milligram and thickness was measured with a dial micrometer to the nearest tenth of a mil.

Samples were placed in small passivated stainless steel wire baskets and were etched individually in separate beakers containing 150 ml of solution, each maintained within ±1°C of temperature. No agitation of the etchant was used. The heat of reaction was low and quickly dissipated through the beaker so that the reaction was effectively carried out at constant temperature in all cases. At the end of each etch period, the germanium samples were quickly removed and quenched in a large volume of deionized water. After rinsing and drying, the samples were measured and weighed again.

Samples were etched a number of times in the same solution in order to establish a constant etch rate. The assumption was made that the constant etch rate reached after the work damaged layer had been removed was close to the true etch rate. Since the decrease in thickness per etch period was below the sensitivity of the dial micrometer for the slow etching in very high concentration hydrogen peroxide, the majority of data for etch rate is presented in units of milligrams per square centimeter-hour, in order to be consistent from low to high hydrogen peroxide concentrations.

The etching solutions were prepared by diluting Becco reagent grade 90% hydrogen peroxide (in some cases, electronic grade 30% hydrogen peroxide from Solvay was used to prepare the solutions). Dilutions were volumetrically measured from a burette to the nearest 0.1 ml. Control of the composition for any etch run was established by analyzing for hydrogen peroxide composition using potassium permanganate titration. For dilute solutions in the neutral and alkaline *p*H regions, the peroxide solutions were neutralized with 10% reagent grade NH_4OH. Stability of high *p*H solutions at elevated temperatures was accomplished by addition of a small amount of hydrated sodium stannate. The higher *p*H samples taken for analysis were acidified with dilute sulfuric acid immediately after quenching in order to minimize hydrogen peroxide decomposition. Precautions to maintain hydrogen peroxide stability during etching made it possible to control the H_2O_2 composition to ±0.5%. This variation in hydrogen peroxide concentration was less at lower *p*H and temperatures. During the etching period *p*H measurements were taken periodically and adjustment was made whenever necessary to control variations within ±0.1 *p*H unit.

Results

Dependence of germanium dissolution rate on H_2O_2 concentration.—A plot of dissolution rate of nondegenerate germanium with respect to H_2O_2 con-

[1] Specific experiments were carried out with germanium specimens of other resistivity ranges.

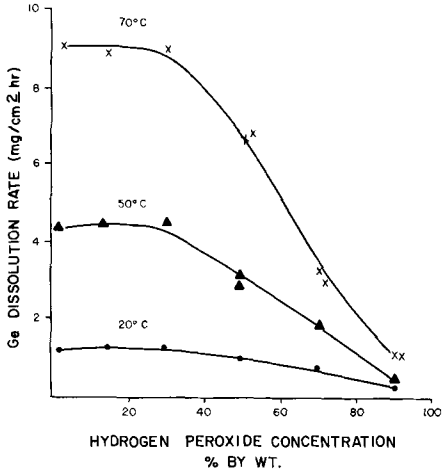

Fig. 1. Germanium dissolution rate as a function of H_2O_2 concentration.

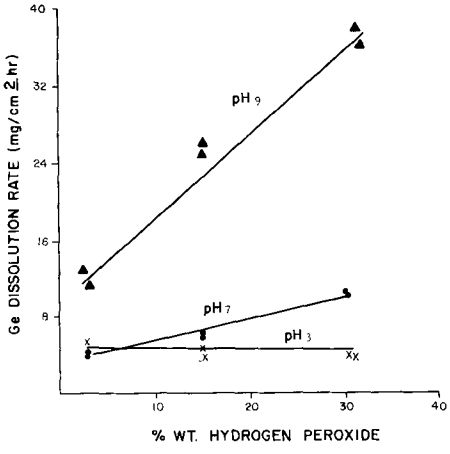

Fig. 2. Dependence of etch rate on H_2O_2 concentration, pH 3, 7, 9

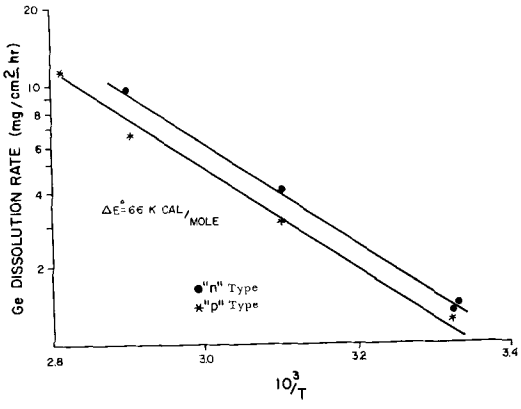

Fig. 3. Dissolution vs. temperature for n and p type germanium in 30% H_2O_2 aqueous solutions pH 4.

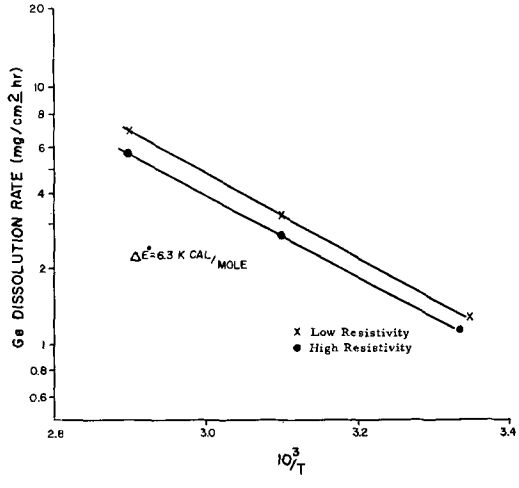

Fig. 4. Dissolution rate vs. temperature for high and low resistivity n type germanium in 30% H_2O_2 aqueous solutions at pH 4.

centration is given in Fig. 1. In H_2O_2 solutions of 3-30% H_2O_2 by weight, the dissolution rates at each temperature are essentially constant. Above 30% concentration, they decrease linearly with increasing H_2O_2 concentration. All the solutions were prepared by diluting 90% H_2O_2 with water, and no attempt was made to control the pH.

In Fig. 2, germanium dissolution rate is plotted as a function of H_2O_2 concentration at three pH values. At pH 3 the rate is independent of H_2O_2 concentration in the range 3-30%. At pH values of 7 and 9, there is a linear relationship between dissolution rate and H_2O_2 concentration.

Dependence of dissolution rate on solution temperature.—The relation between germanium dissolution rate and solution temperature was studied for n-type and p-type nondegenerate germanium and for degenerate n-type germanium. Etching experiments were performed at several H_2O_2 concentrations ranging from 15 to 90% H_2O_2 by weight, at several pH values ranging from 1.0 to 9.0, and at four temperatures, 25°, 50°, 70°, and 90°C. In general a 50% increase in dissolution rate is obtained with each 10°C temperature rise. Figure 3 is a plot of dissolution rate as a function of $1/T \times 10^3$ for n- and p-type germanium of 10^{15} atom/cm³ impurity level etched in 30% H_2O_2 solution at pH 4.0. The activation energy $\mathring{E}$ is estimated at 6.6 kcal/mole by application of the Arrhenius equation.

Figure 4 plots dissolution rate as a function of temperature for n-type germanium samples of 10^{15} and 10^{19} atom/cm³ impurity levels in 30% H_2O_2 solutions at pH 4.0. The activation energy is estimated at 6.3 kcal/mole.

Table I gives values of estimated activation energy for the dissolution of n-type germanium in aqueous H_2O_2 solutions determined by these investigations at various solution pH and % composition by weight. Values determined for p-type germanium are quite similar. From these data it is seen that at pH 5 and above the activation energy is about 10.5 kcal/mole and at pH 4 and below the value

Table I. Activation energy for various H_2O_2 etching compositions using n-type germanium (2-6) ohm-cm

Composition, % by weight H_2O_2	pH	Activation energy, kcal/mole
90	1.0	6.4
70	2.1	6.8
50	3.0	7.9
30	4.0	6.6
30	5.1	11.0
30	7.1	11.0
15	4.9	10.0
15	7.0	10.5
15	9.1	10.3

is approximately 6.5 kcal/mole. The activation energy is the same for germanium of both n-type and p-type conductivity and for low and high impurity levels up to 10^{19} atom/cm^3.

Dependence of dissolution rate on pH of solution.—In Fig. 5, germanium dissolution rates are plotted against *pH* of solution for etching experiments carried out with n-type nondegenerate germanium in 15, 30, and 50% H_2O_2 solutions at 50°C. At each H_2O_2 concentration the dissolution rate stays relatively constant until a critical *pH* is reached and increases rapidly thereafter. The critical *pH* is a function of H_2O_2 concentration. At 50% H_2O_2 it is 4.5, at 30% H_2O_2 it is 5.5, and at 15% H_2O_2 it is 6.0. In Fig. 6 and 7, similar plots are given for dissolution rates in 15 and 30% H_2O_2 solutions at 25°, 50°, and 70°C. The dependence of dissolution rate on *pH* increases at higher temperatures.

Effect of impurity concentration and crystal perfection on germanium dissolution rate.—Etching experiments were carried out using n-type germanium specimens with resistivities from about 30 down to 0.007 ohm-cm, corresponding to an impurity concentration range from 10^{13} to 10^{19} atom/cm^3. The high impurity germanium has a dissolution rate about 30% higher than near intrinsic germanium. Typical results are given in Table II.

Dislocation density variation in the 1 x 10^3 to 1 x 10^4/cm^2 range does not change the dissolution rate appreciably, although macroscopic crystal imperfections such as lineage appear to increase the dissolution rate.

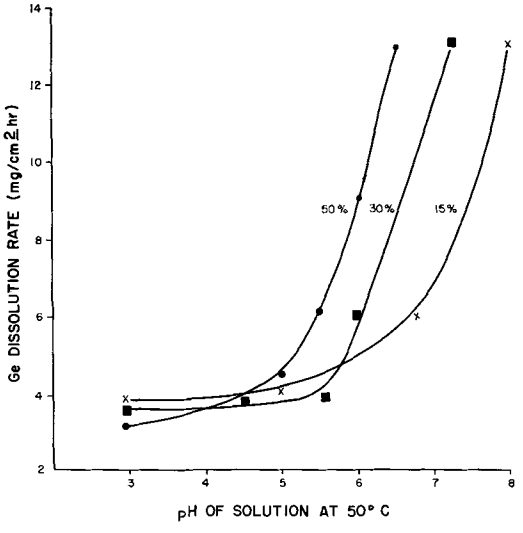

Fig. 5. Dependence of germanium dissolution rate on *pH* of solution for three H_2O_2 concentrations.

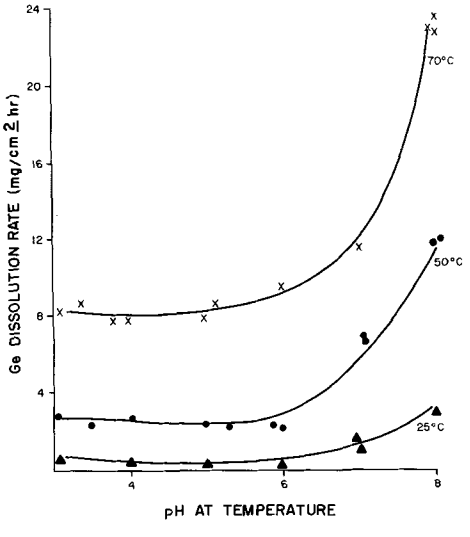

Fig. 6. Variation in dissolution rate as function of *pH* in 30% H_2O_2.

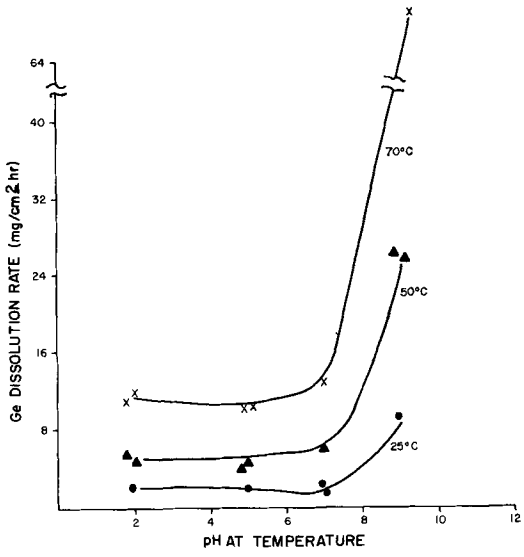

Fig. 7. Dependence of dissolution rate on *pH* in 15% H_2O_2 aqueous solution.

Discussion

From the experimental results it is clear that: (*a*) the germanium dissolution rate remains essentially constant in aqueous H_2O_2 solutions of from 3 to 30% by weight H_2O_2 in the *pH* 1 to 5 range, even at elevated temperatures; (*b*) in the concentration range above 30% H_2O_2 and at low *pH* the rate decreases linearly with increasing H_2O_2 content; (*c*) in *pH* range above 5, there is a certain critical *pH* value above which the rate increases linearly with increasing *pH* as seen in Fig. 2. This critical *pH* varies with H_2O_2 concentration, as seen in Fig. 5 and 6; (*d*) in solutions of *pH* 4 and below the activation energy of the reaction is approximately 6.5 kcal/mole and at *pH* 5 and above it is approximately 10.5 kcal/mole. Activation energy given by Miller

Table II. Dissolution rate vs. impurity concentration for n-type germanium at 70°±1°C

Impurity level, atom/cm^3	H_2O_2 weight percentage	*pH* at 70°C	Dissolution rate, mg/cm^2-hr
10^{13}	30	4.0 ± 0.1	6.60
10^{15}	30	4.0 ± 0.1	7.38
10^{19}	30	4.0 ± 0.1	8.64
10^{13}	32-33	3.9 ± 0.1	7.50
10^{19}	32-33	3.9 ± 0.1	8.82
10^{16}*	32-33	3.9 ± 0.1	10.68
10^{19}**	32-33	3.9 ± 0.1	10.14
10^{13}	33-35	7.0 ± 0.1	25.2
10^{15}	33-35	7.0 ± 0.1	25.8
10^{19}	33-35	7.0 ± 0.1	27.6

* Heavy lineage.
** Lineage.

(2) is 11 kcal/mole in a solution of 3% H_2O_2 of *p*H 5; (*e*) p-type germanium etches at a slightly faster rate than n-type germanium; (*f*) germanium with gross imperfections and high impurity concentration has a higher dissolution rate than nondegenerate germanium of better crystalline perfection.

On the basis of the above experimental results, the following two-step mechanism for germanium dissolution in H_2O_2 is proposed.

In aqueous solutions of H_2O_2, as suggested by Schumb *et al.* (3), the dissociation of H_2O_2 occurs as in reaction Eq. [1]

$$2H_2O_2 \longrightarrow H_3O_2^+ + O_2H^- \qquad [1]$$

When the O_2H^- ions diffuse to the germanium surface, they attach instantly to surface germanium atoms forming surface complex $> Ge(OH)_2$, or $Ge(OH)_2^{++}$, by reaction shown in Eq. [2]

$$Ge + O_2H^- + H_2O + 2e^+ \longrightarrow \underset{\text{surface}}{Ge(OH)_2^{++}} + OH^- \qquad [2]$$

The chemical bonds between the surface germanium atom and underlying atoms remain unbroken. The rate of this reaction is determined by the supply of O_2H^- ions and supply of holes, and the number of available surface germanium atoms. If the supply of holes is more abundant than O_2H^- ions at the interface, the reaction rate will be limited by the diffusion of O_2H^- ions to the interface. In this aqueous system it is proposed that holes are supplied by the reaction between H^+ ions and H_2O_2, as shown in Eq. [3]

$$H_2O_2 + 2H^+ \longrightarrow 2H_2O + 2e^+ \qquad [3]$$

The supply of holes is abundant and not rate determining. In p-type Ge, the availability of holes in the germanium bulk may aid this supply, resulting in slightly faster dissolution rates in p-type Ge under similar experimental conditions.

The formation of the final dissolution products, metagermanate ions or metagermanic acid, can proceed by one of the following two reactions, Eq. [4] and [5]

$$\underset{\text{surface}}{Ge(OH)_2^{++}} + H_2O \longrightarrow H_2GeO_3(aq) + 2H^+ \qquad [4]$$

$$\underset{\text{surface}}{Ge(OH)_2^{++}} + 2OH^- \longrightarrow H_2GeO_3(aq) + H_2O \qquad [5]$$

Either reaction will occur instantly as soon as the reactants are brought together. In solutions of low *p*H, the final dissolution reaction is believed to proceed primarily according to Eq. [4]. In the *p*H range of 1 to 5 where the dissolution rate remains essentially constant, the O_2H^- ion availability at the interface is probably quite constant. This occurs because the variation in H_2O_2 concentration and *p*H does not change the (O_2H^-) gradient in the diffusion layer and the layer thickness. At higher temperatures, the availability of O_2H^- ion will improve and give faster dissolution rates.

In Fig. 1 it is seen that at 30% hydrogen peroxide the dissolution rate begins to decrease linearly with increasing H_2O_2 concentration or decreasing H_2O concentration. The formation of metagermanic acid involves a $Ge(OH)_2^{++}$ ion and a H_2O molecule as evidenced by the linear relation indicating that under these conditions reaction [4] becomes rate limiting. The rate for a certain $Ge(OH)_2^{++}$ surface concentration is limited primarily by the availability of H_2O molecules at the interface, *i.e.*, a diffusion mechanism. The activation energy for all these cases is approximately 6.5 kcal/mole.

According to Greischer (4) germanium reacts preferentially with hydroxyl ions in aqueous solutions. When OH^- ions are consumed as fast as they reach the surface by Eq. [5], dissolution takes place with H_2O molecules as shown in Eq. [4]. With increasing *p*H, the reaction with OH ions becomes more important. Since OH^- ions react much faster than H_2O molecules in the formation of H_2GeO_3, the dissolution steps become very fast in neutral and basic solutions where reaction [5] predominates. In a basic solution, the situation is further complicated by another mechanism in forming the $Ge(OH)_2^{++}$ surface complex, as shown in Eq. [6]

$$Ge + 2\,OH^- + 4e^+ \longrightarrow Ge(OH)_2^{++} \qquad [6]$$

This reaction may become competitive with Eq. [2], involving a different activation energy. The experimental value here is 10.5 kcal/mole. Since each germanium surface atom requires two OH^- ions to form the surface complex $Ge(OH)_2^{++}$ and requires two additional OH^- ions for the final dissolution product, the dependence of the rate on OH^- ion concentration is very strong. Because the reaction can proceed by Eq. [2] and [4] just as well, there is no simple relationship established between rate and *p*H. It is interesting to note in Fig. 5 that after reaching the critical *p*H, the germanium dissolution rates in 50, 30, and 15% H_2O_2 solutions increase in the same fashion with increasing *p*H, indicating the same mechanism where OH^- ion availability plays an important role. Since reactions [2] and [6] proceed simultaneously in the more concentrated H_2O_2 solutions the effect of increasing OH^- ion concentration becomes more noticeable at lower *p*H.

For very impure germanium (*i.e.*, 10^{19} atoms/cm^3) and germanium with macroscopic imperfections such as gross lineage, the dissolution rates are higher. This may be due to the electric field built-in with these imperfections or by postulating that the chemical bond between Ge surface atoms and the bulk can be broken more readily by H_2O_2 when the presence of these defects weakens the bond. At the present time we have no quantitative explanation of the dependence of the dissolution rate on the degree of crystal perfection in germanium.

This proposed mechanism can only explain the experimental facts qualitatively. Experimental difficulties limit the conditions where controlled dissolution can be obtained. For instance, experiments in a 30% H_2O_2 solution of *p*H greater than 9 at high temperatures or in a 90% H_2O_2 concentration solution of *p*H greater than 9 cannot be carried out. Extreme instability of the H_2O_2 solution makes it impossible to maintain constant temperature and com-

position. However, it is feasible to carry out experiments at temperatures below 25°C. For more quantitative results, further experimental work at lower temperature is required.

Acknowledgment

The authors wish to thank Mrs. A. R. Waters for her assistance in the experimental work, and to Mr. S. Crytzer and Mrs. B. Zaffina for their help in the chemical analyses of the hydrogen peroxide solutions. They would also like to acknowledge the assistance of Mr. F. Bower in preparation of the manuscript.

Manuscript received Oct. 16, 1961; revised manuscript received Feb. 14, 1962. This paper was prepared for delivery before the Houston Meeting, Oct. 9-13, 1960.

Any discussion of this paper will appear in a Discussion Section to be published in the December 1962 JOURNAL.

REFERENCES

1. P. R. Camp, *This Journal*, **102**, 586 (1955).
2. K. J. Miller, *ibid.*, **108**, 296 (1961).
3. W. C. Schumb, C. N. Satterfield, and R. L. Wentworth, "Hydrogen Peroxide," p. 370, Reinhold Publishing Co., New York (1955).
4. Greischer, "The Surface Chemistry of Metals and Semiconductors," H. C. Gatos, editor, p. 183, John Wiley and Sons, Inc., New York (1960).

Batch Evaporation or Crystallization at Constant Composition by a Two-Container Method

W. G. Pfann, J. R. Patel, and H. C. Theuerer

Bell Telephone Laboratories, Incorporated, Murray Hill, New Jersey

ABSTRACT

A two-container method is described for producing a vapor or pulling a crystal of constant composition from a binary or multicomponent liquid solution. As the liquid level falls in the first container due to evaporation or crystal growth, liquid enters from the second container. The cross section and liquid composition of the second container are selected in a manner such that the composition in the first container remains constant.

In a companion paper (1) a method is described for evaporating essentially all of a batch of liquid solution at constant vapor composition. In this paper we describe a different method of achieving the same result, which is also applicable to crystallization. Our method is less generally useful, as it requires a knowledge of the volatilities of the components of solution and vapor and is less flexible in other respects. Nevertheless, it appears to be a useful alternative.

The basis of the method is as follows. Because the vapor differs in composition from the liquid, continued evaporation changes the composition of the remaining liquid. This change is automatically nullified by introducing feed liquid of appropriate composition.

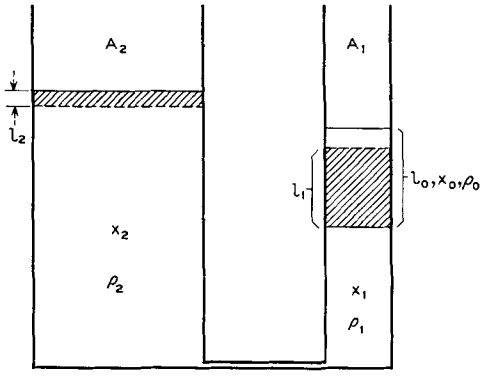

Fig. 1. Schematic illustrating quantities involved in the two-container method.

The apparatus consists essentially of two columns or reservoirs of liquid connected by a one-way passage that permits flow only from the second to the first, as shown in Fig. 1. The liquid heads are the same in the two columns, both being maintained at the same atmospheric pressure. As liquid is removed from column 1 by evaporation (either by heating it or by a hydrogen bubbler, for example), the level falls and liquid flows into column 1 from column 2 so as to equalize the heads.

If the cross-sectional area, A_2, of column 2 is chosen correctly with respect to the area, A_1, of column 1, the vapor leaving 1 will be of constant composition. (We assume rapid mixing in 1, which a bubbler would provide.)

The required area ratio, (A_1/A_2) is given by:

$$\frac{A_1}{A_2} = \frac{M_0(1 - x_2/x_1)}{M_2(1 - x_0/x_1)} - 1 \qquad [1]$$

where subscripts 0, 1, and 2 refer to the product vapor, the liquid in 1, and in 2, respectively, M denotes average molecular weight of the solution, and x denotes mole-fraction of heavy (less volatile) component. Equation [1] is derived in the Appendix. The ratio (x_0/x_1) may be called a distribution coefficient, k.

In terms of M_H and M_L, the molecular weights of heavy and light components, respectively, [1] may be written:

$$\frac{A_1}{A_2} = \frac{[x_0 M_H + (1 - x_0)M_L](1 - x_2/x_1)}{[x_2 M_H + (1 - x_2)M_L](1 - k)} - 1 \qquad [2]$$

In general, it will be preferable to have pure light component in column 2, *i.e.*, $x_2 = 0$, in which case 2 reduces to

$$\frac{A_1}{A_2} = \frac{k + x_0\left(\frac{M_H}{M_L} - 1\right)}{1 - k} \qquad [3]$$

If the liquids in 1 and 2 differ in density, they will be at different levels. But if they do not (as when x_0 is very small), they will be at the same level. Equation [3] shows that the ratio (A_1/A_2) depends only on k at small x_0, but on x_0 as well, at larger x_0, because of the density difference which large x_0 introduces.

The apparatus can be adapted for solutions of different k-values by designing for small k (that is, A_1/A_2 small), and either providing inert glass rods to reduce A_2 to the proper value, or adjusting the composition of column 2 as described in the next section.

Extension to Ternary or Higher Order Solutions

The method can be generalized to accommodate a higher-order system having solutes, a, b, c . . . $(n-1)$, and "solvent," n. It is merely necessary to choose the proper mole fraction, x_{2a}, x_{2b}, etc., of these solutes in column 2. This is done by selecting (A_1/A_2) to match the solute of lowest k (call it solute "a"), with $x_{2a} = 0$. It is then possible to choose values of x_{2b}, x_{2c}, etc., for which this same area ratio will be correct.

Let R designate (x_2/x_1), then, in accord with Eq. [1], and since M_2 and M_0 pertain to the solutions as a whole, we may write

$$\left(1 + \frac{A_1}{A_2}\right)\left(\frac{M_2}{M_0}\right) = \frac{1 - R_a}{1 - k_a} = \frac{1 - R_b}{1 - k_b} = \cdots\cdots \frac{1 - R_{n-1}}{1 - k_{n-1}} \qquad [4]$$

It is evident from [4] that as k increases (from component to component), R must also increase.

The generalized expression for M_0 is

$$M_0 = x_{0a}M_a + x_{0b}M_b + x_{0c}M_c \ldots + x_{0(n-1)}M_{n-1} + (1 - x_{0a} - x_{0b} - x_{0c} \ldots - x_{0(n-1)})M_n \qquad [5]$$

An analogous expression holds for M_2.

The value of (A_1/A_2) for $R_a = 0$ is

$$\frac{A_1}{A_2} = \frac{M_0}{M_2} \cdot \frac{1}{1 - k_a} - 1 \qquad [6]$$

The value of x_{2b}, for $R_a = 0$, is

$$x_{2b} = x_{0b} \cdot \frac{1 - k_a/k_b}{1 - k_a} \qquad [7]$$

The value of x_{1b} is

$$x_{1b} = x_{0b}/k_b \qquad [8]$$

Equations analogous to [7] and [8] hold for each of the other solutes.

Relationship to Crystallization

These considerations apply to the withdrawal of a solid, rather than a vapor, from column 1, as by crystal pulling. In fact, Patel and Mullen (2) have described the application of the two-container technique to the pulling of germanium crystals lightly doped with gallium. The equations derived in the present paper represent a generalization which accounts for density differences and for the presence of two or more solutes.

There is a zone leveling technique (3) which accomplishes for solids the same result described here. This is the method in which a zone containing solute advances into a charge of pure solid solvent, and in which the zone-length, l, decreases linearly with distance, s, at a rate, dl/ds, given by

$$\frac{dl}{ds} = -k \qquad [9]$$

where k now refers to the solid rather than the vapor. The zone length falls to zero at $s = l_0/k$, where l_0 is the initial length. As described, the method was restricted to values of k less than unity. By analogy with the two-container technique, it can be seen that this zone leveling technique can be extended to k's greater than unity by having a uniform concentration x_2 in the charge, in which case the required rate of change of zone length is:

$$\frac{dl}{dx} = -k \cdot \frac{1 - x_2/x_0}{1 - k} \qquad [10]$$

For k's > 1, Eq. [10] permits operation at increasing zone length (for $x_2/x_0 > k$). However, this leaves one at the end of the operation with a large zone of concentration x_0/k.

Manuscript received Jan. 4, 1962.

Any discussion of this paper will appear in a Discussion Section to be published in the December 1962 JOURNAL.

REFERENCES

1. H. C. Theuerer, Being reviewed for *This Journal.*
2. J. R. Patel and J. Mullen, *This Journal,* **105**, 253C (1958); Abstract of paper presented at Ottawa Meeting, Sept. 29, 1958.
3. W. G. Pfann, *Trans. AIME,* **194**, 747 (1952).

APPENDIX

Derivation of Eq. [1]

Assume the liquid heads in columns 1 and 2 of Fig. 1 to be initially equal. Imagine a length l_0 of the liquid in 1 to be made to have composition $x_0 < x_1$ (where x denotes mole fraction of heavy component) by a segregation process occurring within column 1, where x_0 is the desired vapor composition. Remove length l_0 of this liquid whose composition is x_0 and density is ρ_0.

Then allow the pressure heads to equalize by flow of volume l_2A_2 of liquid from 2 into 1. The net changes in head as a result of these two operations must be equal. Therefore:

$$-l_2\rho_2 = -l_0\rho_0 + l_1\rho_2 = -l_0\rho_0 + l_2\left(\frac{A_2}{A_1}\right)\rho_2 \qquad [A\text{-}1]$$

From which:

$$\frac{l_2}{l_0} = \frac{\rho_0}{\rho_2} \cdot \frac{A_1}{A_1 + A_2} \qquad [A\text{-}2]$$

If the composition of the liquid in column 1 is to be unchanged by these operations (and we assume complete mixing in 1), then the composition of the net material leaving 1 must equal x_1. We therefore obtain an expression for the mole fraction of heavy component, H, leaving 1, using the relation:

$$\text{mole } H = \text{mole fraction } H \times \frac{\text{total moles}}{\text{unit volume}} \times \text{volume} \qquad [A\text{-}3]$$

Let B denote total moles per unit volume of solution. Then:

Moles H leaving in vapor $= x_0 B_0 l_0 A_1$
Moles L leaving in vapor $= (1 - x_0)\ B_0 l_0 A_1$
Moles H entering from 2 $= x_2 B_2 l_2 A_2$
Moles L entering from 2 $= (1 - x_2)\ B_2 l_2 A_2$

$$x_1 = \frac{x_0 B_0 l_0 A_1 - x_2 B_2 l_2 A_2}{x_0 B_0 l_0 A_1 - x_2 B_2 l_2 A_2 + (1-x_0) B_0 l_0 A_1 - (1-x_2) B_2 l_2 A_2} \quad [A\text{-}4]$$

which reduces to

$$\frac{A_1}{A_2} = \frac{l_2 B_2 (x_1 - x_2)}{l_0 B_0 (x_1 - x_0)} \quad [A\text{-}5]$$

Substituting for (l_2/l_0) from [A-2], we obtain

$$1 + \frac{A_1}{A_2} = \frac{B_2 \rho_0 (x_1 - x_2)}{B_0 \rho_2 (x_1 - x_0)} \quad [A\text{-}6]$$

which can be used to solve for area ratio (A_1/A_2). However, a more useful form of [A-6] can be obtained using the relation

$$B = \rho/M \quad [A\text{-}7]$$

where M denotes average molecular weight of the solution, and for solutions 2 and 0 is given by

$$M_2 = x_2 M_H + (1 - x_2)\ M_L$$
$$M_0 = x_0 M_H + (1 - x_0)\ M_L \quad [A\text{-}8]$$

where subscripts H and L refer to heavy and light components. Equation [A-6] then reduces to

$$1 + \frac{A_1}{A_2} = \frac{M_0 (x_1 - x_2)}{M_2 (x_1 - x_0)}$$
$$1 + \frac{A_1}{A_2} = \frac{M_0 (1 - x_2/x_1)}{M_2 (1 - k)} \quad [A\text{-}9]$$

Epitaxial Deposition of Silicon in a Hot-Tube Furnace

Bruce E. Deal

Raytheon Company, Mountain View, California

ABSTRACT

A method has been developed for depositing single crystal silicon epitaxially in a conventional hot-tube furnace. Silicon is deposited on a silicon substrate by the reduction of a silicon halide at temperatures in excess of 1200°C. A modification of the gas inlet system prevents decomposition of the silicon halide before contacting the silicon substrate. Several silicon slices can be treated simultaneously with good reproducibility of deposit thicknesses and resistivities.

The announcement of the successful fabrication of an epitaxial transistor was made a little over a year ago (1). There has been much interest in the subject since then, as is demonstrated by the large number of papers concerning epitaxial deposition presented at technical societies and in the literature (2-8). There appear to be many possibilities for improved semiconductor devices using epitaxial material. At the same time, many problems exist regarding the actual deposition of an epitaxial layer suitable for a particular device. Reported here are the results of a particular program in which it was demonstrated that single crystal silicon can be successfully deposited using a conventional diffusion furnace. The program was undertaken to determine if the more expensive, less common types of apparatus using resistance heated or induction heated substrates are necessary for silicon epitaxial deposition. These methods involve the use of a relatively cool reaction tube or chamber, as contrasted to a diffusion apparatus where the tube is as hot as the specimen being treated.

Apparatus and Materials

The furnace used in our experiments was a Hevi-Duty Globar furnace, 26 in. long, with three heat zones. All three zones were controlled to ±1°C with a L&N Speedomax H recorder with C.A.T. controller. Reaction tubes, 45 mm ID, constructed of either Mullite or quartz were used in the experiments. The silicon used for the substrate material was single crystal, (111) oriented, n-type, antimony-doped with resistivities ranging from 0.01 to 0.05 ohm-cm. The slices were prepared similarly to those used for conventional transistors. After being sliced and coarse-lapped to 9-mils thickness, they were polished with Linde A on one side to 8 mils. They were given a hot acetone rinse, two rinses in hot trichloroethylene, one rinse in warm isopropyl alcohol (with the appropriate deionized water rinses), and dried. They were then oxidized 1 hr in steam at 1250°C and the oxide removed by a standard oxide etch solution. The purpose of the oxidation procedure was to remove any lapping damage as well as to provide a cleaner surface.

The method of silicon deposition chosen for this program was that of hydrogen reduction of silicon tetrachloride

$$SiCl_4 + 2H_2 \leftrightharpoons Si + 4HCl$$

Various sources of silicon tetrachloride were used in this program, including some prepared in our own laboratory. For most of the experiments described here, however, ultrapure $SiCl_4$ was obtained from Matheson Coleman and Bell Co. with boron specified as being less than 10 ppb and phosphorus less than 50 ppb.

Experimental—Single Slice Deposition

Initially, hydrogen gas was passed through a bubbler of $SiCl_4$ maintained at −25°C and directly into the reaction tube as in a diffusion process. The silicon substrate was placed flat on a quartz slab at about 1200°C. Some slices were first subjected to a hydrogen treatment, others were not. However, results were all unsatisfactory. Reduction of the silicon tetrachloride was occurring well ahead of the silicon substrate or at too low a temperature. Numerous

reaction products were being carried to the substrate, tube wall, and elsewhere. No suitable deposits were obtained.

These results suggested that reduction of the silicon tetrachloride should be prevented until it reached the substrate. This would have to be accomplished by cooling the reacting gas mixture of hydrogen and silicon tetrachloride as it flowed into the furnace. Therefore, the system shown in Fig. 1 was designed and constructed. A 4 mm ID quartz insert tube, surrounded by a cooling jacket, extended into the furnace tube. Nitrogen gas was found to be the most efficient coolant. The optimum rate of nitrogen flow, determined experimentally, was 25 liters/min. The furnace temperature profile with and without a flow of cooling gas is shown in Fig. 2. It is evident from this profile that the reacting gases are maintained below 1000°C until contacting the silicon substrate. The use of a cooled insert tube resulted in smooth silicon deposits, later shown to be single crystal. As is shown in Fig. 1, the reaction gases were directed vertically and perpendicular to the substrate through a nozzle. The latter had an opening diameter of approximately 15 mm. The silicon substrate was about 10 mm beneath the nozzle opening. By varying the flow rate and the deposition time, optimum process conditions were determined for uniform deposit formation. A silicon deposit about 10-20μ thick could be produced in from 5 to 15 min. Flow rates of between 1 and 2 liters/min were found to be the most satisfactory. Resistivities were in the neighborhood of 2 ohm-cm, n-type. The deposits appeared uniform across the surface except for a slight

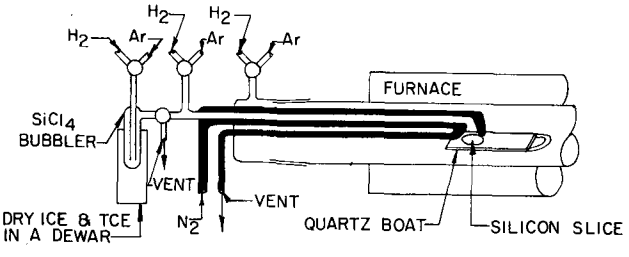

Fig. 1. Apparatus for epitaxial deposition of silicon in a hot-tube furnace.

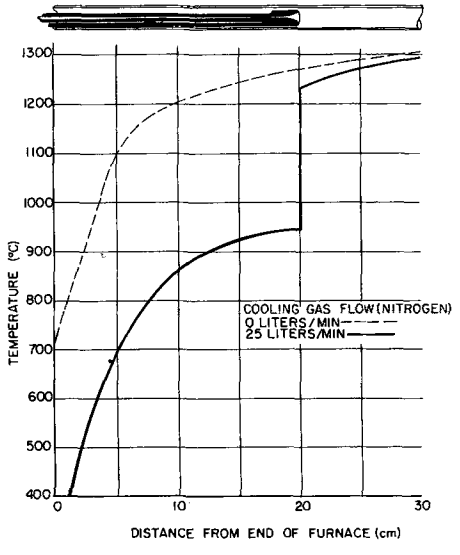

Fig. 2. Temperature profile of epitaxial reaction chamber

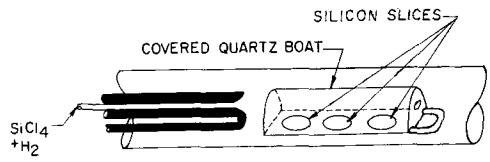

Fig. 3. Modified apparatus for epitaxial deposition on more than one silicon slice.

tapering at the edges. No deposit was observed on the underside of the substrate.

For a typical run, silicon tetrachloride was maintained at −25°C, providing a mole fraction of about 0.025 in hydrogen. The system was first purged with argon. The substrate was placed in position on a flat quartz boat and was exposed to hydrogen for 15 min at 1250°C. Deposition was then carried out under conditions necessary to obtain a desired deposit thickness. For instance, if the flow rate was 1.5 liters/min, a deposit thickness of about 18μ could be obtained in 6 min. After purging again with argon, the slice was removed from the furnace and evaluated. The total time that the slice remained in the furnace was about 30 min.

It was demonstrated that the process is extremely sensitive to any water vapor or air admitted to the system through leaks in the apparatus. Thus a very tight system is required.

Deposition of Several Slices

After successful deposition on a single slice, three slices were treated simultaneously using the modification of the system shown in Fig. 3. As can be observed, the stream of reacting gases was directed straight out from the insert tube into a covered quartz boat. The latter was referred to as a "covered wagon." It was approximately 10 cm long, 2.8 cm high, and 2.5 cm wide at the bottom. The distance between the covered boat and the nozzle opening was about 5 cm. The nozzle opening was 10 mm in diameter. The covered boat was used originally to prevent reaction products from dropping from the top of the furnace tube onto the substrates. In addition, deposited silicon could be removed from the sides of the boat between runs. But it was soon found that by selecting the correct size of hole in the end of the boat and the correct flow rate, the covered boat would permit better control of the reacting gas mixture. A hole diameter of 10 mm and flow rates of 2-4 liters/min provided satisfactory results. As was the case for the single slice system, the mole fraction of $SiCl_4$ in hydrogen was 0.025, and the substrate temperature was maintained in the range of 1230°-1270°C. The 15-min hydrogen pretreatment was also used for the multislice depositions. Deposition times were longer than for the single slice depositions, about 10-15 min.

By using this system, uniform deposits could be produced on several slices. Deposit thicknesses were equal among the slices and from run to run for a given set of operating conditions. Resistivities were also reproducible among runs, provided the same source of $SiCl_4$ was used. No tapering at the edges of the deposits was observed as was the case in the previous one-slice system. This was undoubtedly due to the more uniform gas concentration above the substrates in the covered boat system.

Table I. Thickness and resistivity profile of silicon epitaxial deposits produced in hot-tube furnace

Slice No.	Position	Deposit thickness, μ	Resistivity, ohm-cm
58R	1	21.6	1.4
	2	27.8	1.6, 1.3
	3	22.5	1.2, 1.3
	4	23.0	1.4
Average		23.5	1.4
Standard deviation		2.4	0.1
70R	1	23.0	—
	2	27.1	—
	3	28.6, 26.1	—
	4	25.8	—
Average		26.1	
Standard deviation		1.8	

To better understand the deposition process, a smoke chamber was assembled which duplicated the geometry of the multislice system. Nitrogen flowing through hydrochloric acid and ammonium hydroxide represented the hydrogen-silicon tetrachloride flow pattern. By observing these patterns, process variables could be optimized for uniform deposition on several slices. The smoke chamber experiments also indicated where certain beneficial changes in the geometry of the system could be made. One proposed modification was the formation of a grid of quartz fibers across the opening of the covered boat, thus providing better dispersion of the gas mixture. The smoke chamber also permitted the evaluation of other sizes and shapes of boats, including some with more than one shelf.

During continuing deposition experiments, it was found the quartz insert tube would last several weeks if used under proper conditions. If the outlet of the tube became plugged or broken, the entire insert assembly was removed from the furnace and the tube end replaced by the glassblower. Thus, the main portion of the insert assembly had a relatively long life.

Evaluation of Deposits

Deposits were evaluated in the following manner. All slices were weighed before and after deposition. In addition, deposit thickness values were obtained by angle lapping and staining. As mentioned above, deposit thicknesses across a sample prepared in the multislice system were quite uniform. Profiles of thicknesses for two typical, deposited slices are listed in Table I. These values were obtained at various locations on the slice. It was soon found that a definite relationship existed between deposit weight per unit area and thickness, approximating the density of silicon. A plot of weight-thickness data is presented in Fig. 4. Weights are expressed as weight gain per total slice, the slices being 20.6 mm in diameter and 0.2 mm thick. We were able, therefore, to estimate the thickness values to ±10% from the weight measurements. This would not have been possible if deposition occurred to any extent on the underside of the substrate.

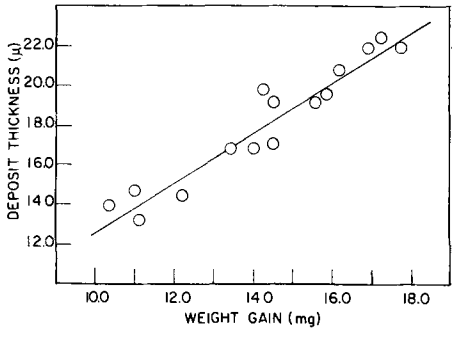

Fig. 4. Relationship of weight gain to deposit thickness for hot-tube, epitaxial deposition of silicon.

Resistivities were determined from capacitance-voltage measurements (9) and were generally found to be quite uniform across the deposit and through the deposit. An example of a resistivity profile is given in Table I. Early in our experiments it was obvious that the resistivity of the deposits was dependent on the specific supply of silicon tetrachloride. Later, it was observed that the hydrogen source is also a factor. For a given source of these reactants, we could obtain good reproducibility of resistivities. Special experiments were conducted in which boron tribromide was added to the silicon tetrachloride. Predicted increases in deposit n-type resistivities were obtained initially. However, if the doped silicon tetrachloride was allowed to stand for 24 hr, resistivities dropped back down to close to the original value. It was concluded, therefore, that boron tribromide was probably unstable in silicon tetrachloride and that doping should be carried out at the time of deposition.

A series of runs was made using the single slice system. The same supply of silicon tetrachloride was used for all runs of this series. Deposition conditions were as follows: $SiCl_4$ was maintained at −24°C, substrate temperature was 1200°C, flow rate was 1.5 liters/min, and deposition time was 6 min. Deposit weight and resistivity results as well as calculated thickness values are tabulated in Table II. All deposits were n-type. These results indicate reasonable reproducibility of deposit characteristics.

Similar data are listed in Tables III and IV for the multislice system. The reproducibility among

Table II. Results of a series of silicon vapor depositions in a hot-tube furnace using the single slice system

Slice No.	Weight gain, mg	Deposit thickness, μ*	Resistivity, ohm-cm
B-9B	14.0	17.5	2.2
B-10B	13.5	17.0	2.6
B-11B	13.2	16.5	1.8
B-12B	14.5	18.2	2.7
B-13B	14.1	17.6	3.6
B-14B	18.3	22.8	2.3
B-15B	15.8	19.8	3.0
B-16B	11.5	14.5	2.3
B-17B	18.7	23.0	2.6
B-19B	12.0	15.0	2.5
B-20B	12.4	15.5	2.3
Average	14.4	17.9	2.5
Standard deviation	2.3	2.7	0.4

* Deposit thicknesses were calculated from weight measurements.

Table III. Reproducibility of deposit properties among slices in individual runs using multislice system

Run No.	Deposition conditions	Weight gain, mg	Deposit thickness, μ*	Resistivity, ohm-cm
88	Deposition time: 10 min	10.9	13.6	—
	Flow rate: 3 l/min	11.8	14.7	—
	$SiCl_4$ temp: —24°C	10.5	13.1	—
	Si temp: 1255°C			
91	Deposition time: 15 min	17.7	22.2	0.5
	Flow rate: 3 l/min	19.1	23.9	1.0
	$SiCl_4$ temp: —22°C	14.5	18.1	0.9
	Si temp: 1255°C			
89	Deposition time: 12 min	15.7	19.7	1.4
	Flow rate: 3.5 l/min	14.1	17.6	1.4
	$SiCl_4$ temp: —24°C	13.5	16.9	1.1
	Si temp: 1255°C			
97	Deposition time: 15 min	16.7	20.9	—
	Flow rate: 3.5 l/min	17.5	21.9	—
	$SiCl_4$ temp: —25°C	14.4	18.0	—
	Si temp: 1255°C			

* Deposit thicknesses were calculated from weight measurements.

Table IV. Results of a series of silicon vapor depositions in a hot-tube furnace using the multislice system

Run No.*	Weight gain, mg	Deposit thickness, μ		Resistivity, ohm-cm
138	17.0	23.6		2.0
	17.2	24.0		1.9
139	15.8	19.5		3.3
	16.2	20.7		1.3
140	11.0	14.6		2.6
	11.5	9.1		1.3
141	17.2	22.4		1.3
	18.4	18.4		1.5
			Average =	1.9
			Std. deviation =	0.7
142	17.2	18.4		0.2
	17.5	19.1		1.3
144	17.7	21.9		0.8
	15.9	15.7		0.8
145	16.6	17.4		0.8
	16.9	21.9		1.5
			Average =	0.9
			Std. deviation =	0.4
Average	16.2	19.1		
Standard deviation	2.1	3.8		

* Runs 138-141 used $SiCl_4$ Batch A.
Runs 142-145 used $SiCl_4$ Batch B.

slices in each of four runs is indicated in Table III. Runs 88 and 91 are both for depositions using a flow rate of 3 liters/min but for different times. A slightly higher flow rate was used for runs 89 and 97. The deposit weights are reasonably reproducible among the three slices of each run, as are resistivities.

Table IV demonstrates reproducibility of deposit weights, thicknesses, and resistivities for a series of runs in the multislice system. Only two slices were deposited per run. Substrate temperature was 1270°C, flow rate was 4 liters/min, deposition time was 12 min, and $SiCl_4$ was maintained at —25°C for this series of runs. It should be noted that the silicon tetrachloride was changed between runs 141 and 142. This change affected the resistivity values, as is indicated in the table. With one or two exceptions, all values are fairly consistent.

Various deposited slices were turned over to our development pilot line for fabrication of transistors. A number of mesa switching transistors were completed and tested for electrical properties. As expected, collector-emitter saturation voltages as well as storage times were considerably lower than those of similar nonepitaxial transistors.

Conclusions

The results of this program have demonstrated that silicon can be deposited epitaxially on a silicon substrate in a conventional hot-tube diffusion furnace. Several slices can be treated simultaneously. Deposits produced are uniform in thickness and resistivity and have very few surface irregularities. For a given source of silicon tetrachloride and hydrogen, results are reproducible from run to run. As is the case with any silicon vapor deposition process, the process is highly sensitive to the presence of water vapor or air. Resistivities of deposit can be controlled by doping the reacting materials at the time of deposition. It is probable that this system can be used for the vapor deposition of other materials, both elements and compounds, required in the various phases of electronic device fabrications.

Acknowledgments

The author wishes to thank W. Peterson for his help in the experimental portion of this program. Also, W. R. Lamb and E. A. Swanson of these laboratories provided valuable assistance in evaluating the deposits.

Manuscript received Oct. 19, 1961; revised manuscript received Jan. 15, 1962. This paper was prepared for delivery before the Detroit Meeting, Oct. 1-5, 1961.

Any discussion of this paper will appear in a Discussion Section to be published in the December 1962 JOURNAL.

REFERENCES

1. H. C. Theuerer, J. J. Kleimack, H. H. Loar, and H. Christensen, *Proc. IRE*, **48**, 1642 (1960).
2. J. E. Allegretti, D. J. Shombert, E. Schaarschmidt, and J. Waldman, "Metallurgy of Elemental and Compound Semiconductors," Vol. 12, p. 255, R. O. Grubel, Editor, Interscience Publishers, New York (1961).
3. R. Glang and B. W. Kippenhan, *IBM J. Rsch. Dev.*, **4**, 299 (1960).
4. J. C. Marinace, *ibid.*, **4**, 248 (1960).
5. A. Mark, *This Journal*, **108**, 880 (1961).
6. W. G. Spitzer and M. Tanenbaum, *J. Appl. Phys.*, **32**, 744 (1961).
7. H. C. Theuerer, *This Journal*, **108**, 649 (1961).
8. E. S. Wajda, B. W. Kippenhan, and W. H. White, *IBM J. Rsch. Dev.*, **4**, 288 (1960).
9. J. S. Saby and W. C. Dunlap, *Phys. Rev.*, **90**, 630 (1953).

Polarography of Mercaptoalkyl Compounds and Their Disulfides

Walter Stricks, J. K. Frischmann, and R. G. Mueller

Department of Chemistry, Marquette University, Milwaukee, Wisconsin

ABSTRACT

The polarography of 2-mercaptoethylguanidine (RSH), 2-mercaptopropylguanidine (R_ISH), 2-mercaptoethylamine ($R_{II}SH$), and 2-mercaptoethanol ($R_{III}SH$) and their disulfides (RSSR, R_ISSR_I, $R_{II}SSR_{II}$ and $R_{III}SSR_{III}$) has been studied. The mercaptans behave in the same way as other mercaptans described previously in the literature. RSSR gives well-defined reduction waves. The characteristics of the RSSR waves in the absence and presence of RSH are the same as those of oxidized glutathione and can be accounted for by the sequence of the two reactions: $RSSR + e + H^+ \rightleftarrows RS^\cdot + RSH$, $RS^\cdot + e + H^+ \rightarrow RSH$ in which the first reaction is the rate and potential determining step. R_ISSR_I, $R_{II}SSR_{II}$, and $R_{III}SSR_{III}$ are reduced irreversibly at the dropping mercury electrode.

In recent years a large number of mercaptoalkyl compounds have been studied with regard to their properties as radiation protective drugs for animals. In the course of systematic investigations of reactions of these compounds with metal ions and proteins it appeared to be useful to study the polarographic behavior of a few typical mercaptoalkyl compounds under various experimental conditions.

This paper deals with a polarographic study of 2-mercaptoethylguanidine (denoted as RSH), 2-mercaptopropylguanidine (R_ISH), 2-mercaptoethylamine ($R_{II}SH$), and 2-mercaptoethanol ($R_{III}SH$) and their disulfides which for the sake of brevity will be referred to as RSSR, R_ISSR_I, $R_{II}SSR_{II}$, and $R_{III}SSR_{III}$, respectively. The results obtained for these compounds are compared with each other and with those obtained for other mercaptans and disulfides described in the literature (1-3).

Experimental

Materials.—Solutions of mercaptoalkyl guanidine were prepared from S,2-aminoalkylisothiouronium bromide hydrobromide which undergoes rearrangement in neutral solution to form mercaptoalkylguanidine (4). Stock solutions of 10^{-2}M mercaptan were prepared by weighing an appropriate amount of the isothiouronium compound in a glass cap which together with the compound was introduced into a bottle provided with metal screw cap into which a few holes were bored. In order to obtain an airtight seal the cap was fitted with a self sealing Buna N rubber gasket. Now a given volume of air free sodium hydroxide solution containing an amount of sodium hydroxide exactly equimolar to the isothiouronium salt was added in order to neutralize the liberated hydrobromic acid. The bottle was sealed immediately and after dissolution of the sample the solution was purged thoroughly with nitrogen introduced by means of a hypodermic needle which pierced the cap of the bottle. Samples were withdrawn from the bottle by means of a 2 ml calibrated syringe. When not in use the solution was stored in a refrigerator. The mercaptan solutions were found to be stable for a week. Stock solutions of mercaptoethylamine and mercaptoethanol were prepared in the same way as described for RSH and R_ISH except that no sodium hydroxide was added to the solution.

The isothiouronium compounds were obtained from Dr. D. G. Doherty of the Biology Division, Oak Ridge National Laboratory. The mercaptoethylamine hydrochloride was obtained from the Walter Reed Army Medical Center, and the mercaptoethanol was an Eastman Kodak white label product. The mercaptan solutions were analyzed by amperometric titration with ethylmercury chloride at the rotated dropping mercury indicator electrode (5).

The disulfide solutions were obtained by air oxidation of the mercaptans. A slow stream of carbon dioxide and dust free air was passed through 50 ml of 0.01M mercaptan solution. The progress of the oxidation was followed polarographically. The air bubbling was continued until the anodic wave of the mercaptan had disappeared. The oxidation of RSH and R_ISH was performed in neutral medium and found to be complete after 15-20 hr. The oxidation of $R_{II}SH$ and $R_{III}SH$ was sluggish in neutral medium and faster in alkaline solutions. The solutions of these compounds were therefore made 0.1M in ammonia which was driven out from the solution with air toward the end of the reaction. The oxidation of $R_{III}SH$ was slow even in alkaline medium and a trace of copper (10^{-5}M) was added as a catalyst in order to accelerate the oxidation. The resulting stock solutions were 5×10^{-3}M in disulfide.

All the other chemicals used were commercial C.P. reagent grade products.

Methods.—Current-voltage curves were obtained at 25.0° ± 0.1° with a Fisher Electropode, Model 65, the manual apparatus and circuit described by Lingane and Kolthoff (6) and with a self-recording Sargent Polarograph, Model XXI. All potentials were measured against the saturated calomel electrode (S.C.E.). Oxygen was removed from the solution with a stream of nitrogen (Linde nitrogen, 99.996% pure). During an experiment an atmosphere of nitrogen was maintained over the solution. Corrections were made for the residual current.

Two capillaries were used: capillary I: $m = 1.76$ mg sec^{-1}; $t = 4.4$ sec (in 0.10N KCl, open circuit); $h = 75.5$ cm; capillary II: $m = 1.98$ mg sec^{-1}; $t = 4.1$ sec (open circuit); $h = 67.4$ cm.

The pH of the solutions was measured with a Beckman zeromatic pH meter. A Beckman "General Purpose" glass electrode was used.

The ionic strength of the supporting electrolyte was adjusted by the addition of appropriate quantities of potassium chloride or sodium nitrate.

Results and Discussion

Mercaptans

Some 100 polarograms were taken with solutions of various concentrations in mercaptan in buffers at pH 1-12.1. The polarographic behavior of the mercaptans is similar to those of other mercaptans such as cysteine (1), glutathione (3), and thioglycolic acid (7) described previously in the literature and the equations for the electrode reactions are therefore not derived in this paper. In contrast to cysteine the mercaptans investigated in this work give a well defined anodic wave, the shape and the height of the wave being somewhat affected by the pH of the solution. RSH gives steep waves at pH higher than 4.6 (curve B of Fig. 1) while at pH equal to or smaller than 4.6 the wave becomes drawn out (curve A, Fig. 1). The diffusion current is markedly smaller at the lower pH. $R_{II}SH$ and $R_{III}SH$ give drawn out waves in solutions of pH smaller than 2. In contrast with glutathione no specific buffer effect was observed with the mercaptans investigated and reversible waves were obtained in acetate, phosphate, and ammonia buffers and in dilute sodium hydroxide.

Surface active substances like gelatin (0.01%) or polyacrylamide (0.01%) have no effect on the shape of the anodic wave. The mercaptans markedly reduce the surface tension of mercury as is evident from the electrocapillary curves which are similar in shape to those obtained with glutathione (3).

The waves obtained with solutions at pH 5.4-11.6 at ionic strength one and 0.1 were analyzed as described previously (3) and found to correspond to the reversible formation of mercurous mercaptide (RSHg).

The half-wave potential can be expressed by

$$E_{1/2} = E' + 0.059 \log \{[H^+] + K\} \qquad [1]$$

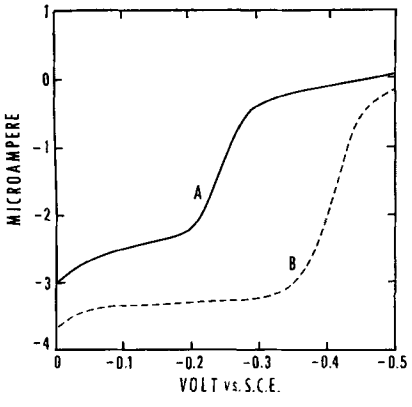

Fig. 1. Polarograms of 10^{-3}M RSH in various buffers ($\mu = 1$). A, acetate, pH 4.67; B, phosphate, pH 7.4.

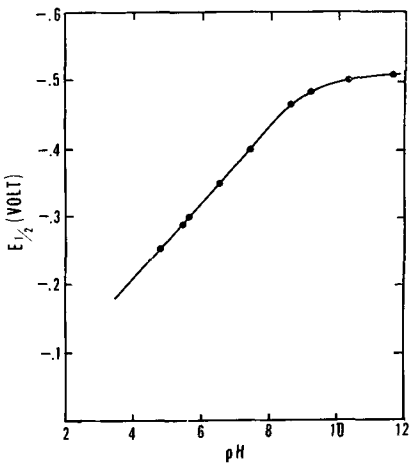

Fig. 2. Half-wave potential of RSH vs. pH ($\mu = 1$).

where the constant E' is $E^\circ + 0.059 \log k_1/k_2$ at 25°C, K is the dissociation constant of the sulfhydryl group, k_1 and k_2 are constants which are proportional to the square roots of the diffusion coefficients of RSH and RSHg, respectively, and E° is the standard potential of the electrode reaction.

The half-wave potentials of RSH which were taken from the plots log $(i_d - i)/i$ *vs.* the potential are plotted in Fig. 2. By extrapolation of the curve of Fig. 2 the value of E' which corresponds to the half-wave potential at a pH of zero is obtained. Values of E', the half-wave potentials at pH 11.5 corresponding to the horizontal portion of the $E_{1/2}$ — pH plot, and the apparent dissociation constants of the sulfhydryl group of the mercaptans are listed in Table I. The apparent dissociation constants K of the sulfhydryl group were obtained from titrations of the mercaptans with sodium hydroxide, using a glass electrode. With the exception of cysteine which forms a film at the electrode (1) the half-wave potentials in acid medium are approximately of the same order of magnitude, while the

Table I. Polarographic data of mercaptans and disulfides. pK of the sulfhydryl groups of mercaptans

Compound	$E' \times 100$, volt *vs.* S.C.E.	$E_{1/2}$ at pH 11.5 volt *vs.* S.C.E.	pK	$D \times 10^6$, $cm^2\ sec^{-1}$
RSH	1.4	—0.508	8.8	7.1 (G)
R_ISH	4.1	—0.534	9.4	4.4 (G)
$R_{II}SH$	6.0	—0.560	10.75	8.9 (G)
$R_{III}SH$	3.0	—0.537	9.6	13.0 (G)
Thioglycolic acid (8)	0.62	—0.580	10.68	8.6 (A)
Cysteine (1)	10.6	—0.580	10.28	7.0 (B)
Glutathione (3)	3.0	—0.480	9.12	4.7 (C)
RSSR				8.8 (G)
R_ISSR_I				6.7 (D)
$R_{II}SSR_{II}$				11.0 (G)
$R_{III}SSR_{III}$				37.0 (D)
Dithiodiglycolic acid (7)				6.0 (E)
Cystine (2)				5.3 (F)
Oxidized glutathione (3)				4.5 (G)

(A) pH not given in literature; (B) in 0.1M $HClO_4$; (C) at pH 10.82; (D) at pH 9.2; (E) at pH 3.0; (F) in 0.1M HCl; (G) at pH 10.3.

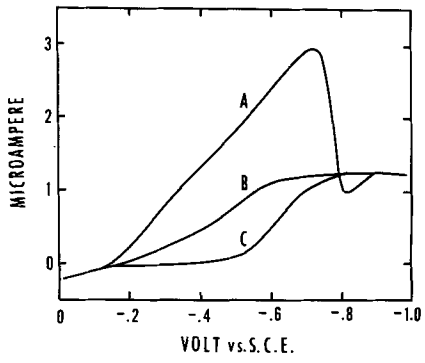

Fig. 3. Reduction waves of 2.5 x 10^{-4}M RSSR in (A) acetate buffer (pH 2.8), (B) same as (A) with 5 x 10^{-3}% gelatin, (C) borax buffer (pH 9.2).

half-wave potentials in the alkaline pH region vary according to the variation of the pK values of the sulfhydryl group as required by Eq. [1].

Diffusion currents of the anodic wave of the mercaptans were measured in the concentration range between 2.6 x 10^{-4} to 1.4 x 10^{-3}M. The diffusion current is independent of the pH in the pH region from 5 to 12. At pH smaller than 5 the diffusion current decreases. Thus the diffusion current of a 10^{-3}M RSH solution was found to be 3.30 and 2.36 μa at pH 11.6 and 4.7, respectively. Polarographic diffusion coefficients of the various mercaptans and disulfides are compared in Table I.

Disulfides

Guanidinoethyldisulfide (RSSR) gives a single reduction wave over the entire pH range investigated. In 2.5 x 10^{-4}M RSSR solutions a pronounced maximum occurs at pH 2.8 (curve A of Fig. 3). As the pH of the solution is increased the maximum becomes considerably flatter. At pH equal to or higher than 7 the maximum disappears (curve C of Fig. 3). Gelatin at concentrations of 0.001-0.003% suppresses the maximum at low pH and has hardly any effect on the half-wave potential and on the diffusion current. Increasing amounts of gelatin give rise to waves which are drawn out, the effect becoming more pronounced with decreasing pH (curve B, Fig. 3).

Electrocapillary curves taken with RSSR solutions have exactly the same shape as those obtained with RSH.

Analysis of current voltage curves obtained with RSSR solutions of various concentrations (1 to 3.8 x 10^{-4}M) at pH 11.6 to 5.82 at ionic strength 1 and 0.1 in the absence and presence of 1.23 to 6.17 x 10^{-4}M RSH revealed that the characteristics of the wave is exactly the same as that of oxidized glutathione (3). The equation of the wave at 25°C is therefore given by

$$E = E' + 0.059 \log \{[H^+] + K\} + 0.059 \log (i_d - i)/i^2 \quad [2]$$

where E' is a constant. The reaction mechanism suggested for the reduction of oxidized glutathione also explains the experimental results obtained with RSSR (RSSR + e + $H^+ \rightleftharpoons$ RS· + RSH, RS· + e + $H^+ \rightarrow$ RSH, the first reaction being the rate and potential determining step).

The diffusion current of RSSR hardly changes with pH in solutions at pH lower than 10 (i_d/c=6.0) but is higher at pH above 10 (i_d/c=6.8). At a concentration range between 6.7 x 10^{-5} to 3.2 x 10^{-4}M the diffusion current was found to be proportional to the concentration.

The experiments performed with guanidino propyldisulfide (R_ISSR_I), aminoethyldisulfide ($R_{II}SSR_{II}$), and hydroxyethyldisulfide ($R_{III}SSR_{III}$) were essentially of the same kind as those mentioned for RSSR.

The current voltage curves of R_ISSR_I and $R_{II}SSR_{II}$ have the appearance of reversible waves. However, the analysis of the R_ISSR_I-wave gave a plot log $(i_d-i)/i^2$ *vs.* potential which was a curved line. In the presence of an excess of R_ISH (2.5 x 10^{-4}M R_ISSR_I, 5 x 10^{-4} to 4 x 10^{-2}M R_ISH) the plots log $(i_d-i)/i$ gave straight lines of slopes 0.052 to 0.062 as required by Eq. 2. The plot log C_{RSH} (C_{RSH} is molar concentration of RSH) *vs.* $E_{1/2}$ gave a straight line of slope 0.071 instead of the theoretical value of 0.059. The wave of $R_{II}SSR_{II}$ analyzed to give a plot log $(i_d-i)/i^2$ *vs.* E which was a straight line of the theoretical slope of 0.059. The plot log $i_d/2$ *vs.* $E_{1/2}$ was a straight line of slope 0.076 instead of the theoretical value of 0.059. Mixtures of 2.5 x 10^{-4}M $R_{II}SSR_{II}$ with varying concentrations of $R_{II}SH$ (2.5 x 10^{-4} to 1.2 x 10^{-3}M) gave plots log $(i_d-i)/i$ *vs.* E which were straight lines of theoretical slopes of about 0.060 similar to the waves obtained with R_ISSR_I. The plot log $C_{R_{II}SH}$ *vs.* $E_{1/2}$ was found to be a curved line and therefore does not conform to the requirements of Eq. 2.

The observations with R_ISSR_I and $R_{II}SSR_{II}$ indicate that the reduction of these two compounds at the dropping mercury electrode is not reversible since the experimental results do neither satisfy the conditions for a two electron reduction nor do they agree with the conditions for a free radical mechanism (Eq. [2]).

Polarograms of $R_{III}SSR_{III}$ were taken with solutions at various pH (12 to 4) in the absence and presence of gelatin. All waves obtained with $R_{III}SSR_{III}$ were distorted and drawn out, indicating an irreversible electrode process. Therefore an analysis of these waves was not attempted.

It is of interest to note that, while the polarographic behavior of all mercaptans reported in the literature is essentially the same, the disulfides differ rather markedly as far as their polarography is concerned. The difference between RSSR on one hand and R_ISSR_I, $R_{II}SSR_{II}$, and $R_{III}SSR_{III}$ on the other hand is remarkable, considering that all these compounds are of a similar structure. In contrast to this it is noteworthy that compounds as different as oxidized glutathione and RSSR show the same polarographic behavior.

Acknowledgment

This investigation was supported by the U.S. Army Medical Research and Development Command, Department of the Army, under Research Contract No. DA-49-193-MD-2146. Part of this work is based on the M.S. Thesis of one of the authors (J.K.F.).

Manuscript received Sept. 18, 1961; revised manuscript received Jan. 26, 1962.

Any discussion of this paper will appear in a Discussion Section to be published in the December 1962 JOURNAL.

REFERENCES

1. I. M. Kolthoff and C. Barnum, *J. Am. Chem. Soc.*, **62**, 3061 (1940).
2. I. M. Kolthoff and C. Barnum, *ibid.*, **63**, 520 (1941).
3. W. Stricks and I. M. Kolthoff, *ibid.*, **74**, 4646 (1952).
4. D. G. Doherty, R. Shapira, and W. T. Burnett, Jr., *ibid.*, **79**, 5667 (1957).
5. W. Stricks and S. K. Chakravarti, *Anal. Chem.*, **33**, 194 (1961).
6. J. J. Lingane and I. M. Kolthoff, *J. Am. Chem. Soc.*, **61**, 825 (1939).
7. D. L. Leussing and I. M. Kolthoff, *This Journal*, **100**, 334 (1953).
8. A. Liberti and E. Cerone, *Ann. Chim. Rome*, **41**, 95 (1951).

Equilibrium Studies in the Reduction of Thorium Oxide by Aluminum

Douglas O. Raleigh

Atomics International, Canoga Park, California

ABSTRACT

When metallothermic reductions are carried out with an excess of the reducing metal, formation of an intermetallic compound between the reactant and product metals can make reduction energetically more favorable. Thorium oxide can be reduced by an excess of aluminum despite unfavorable standard-state energetics. The intermetallic compound involved is shown to be $ThAl_3$. From equilibrium experiments, its standard free energy of formation is estimated to be —36 kcal.

Recent interest in our laboratory in alloys of thorium and their preparation led us to experimental work on the reduction of thorium oxide by metals less reactive than calcium. The reduction of thorium oxide by aluminum as a process for preparing thorium-aluminum alloys was achieved; studies on the optimum conditions for reduction are reported elsewhere (1). The occurrence of the reduction despite nominally unfavorable energetics was of interest to us. The standard-state reaction

$$ThO_2(s) + \frac{4}{3}Al(l) \rightarrow \frac{2}{3}Al_2O_3(s) + Th(s) \quad [1]$$

is associated with a positive free energy of reaction at all temperatures of interest. At 1050°C, the temperature chosen for our work, $\Delta F = +38$ kcal from the reported (2) standard free energies of formation of $ThO_2(s)$ and $Al_2O_3(s)$. In the process developed by us, however, the thoria is suspended or dissolved in a molten fluoride mix in contact with liquid aluminum and, since the product thorium is dissolved in the aluminum, the actual reaction is

$$ThO_2(\text{sol. fluoride}) + \frac{4}{3}Al(\text{sol. Al-Th}) \rightarrow \frac{2}{3}Al_2O_3(\text{sol. fluoride}) + Th(\text{sol. Al-Th}) \quad [2]$$

It was suspected that the required chemical potential for the reaction was derived primarily from the formation of one or more intermetallic Th-Al compounds and their solution in the metallic melt. The possibility, however, of strong solute-solvent interaction between the alumina and the fluoride melt could not be eliminated. To clarify the situation, the series of experiments reported here was carried out. Thorium-aluminum melts were equilibrated with a molten fluoride salt that was saturated with thoria and alumina and contained a solid excess of both. Under these conditions, the dissolved and solid oxides are in equilibrium, so that the reaction occurring may be written

$$ThO_2(s) + \frac{4}{3}Al(\text{sol. Al-Th}) \rightleftharpoons \frac{2}{3}Al_2O_3(s) + Th(\text{sol. Al-Th}) \quad [3]$$

By determining the equilibrium concentration of thorium in aluminum in this system and carrying out the necessary supplemental work, it was shown that the primary driving force for the reaction is the free energy of formation of $ThAl_3$, and an estimate of its value was made. The results indicate that intermetallic compound formation may play a useful role in promoting metallothermic reductions in a number of systems.

Experimental

Apparatus.—The experimental work required a high-temperature inert atmosphere furnace system with provision for outgassing, stirring, and withdrawing samples from the reaction mix. The apparatus is shown in Fig. 1. The chemical systems of interest were heated in cylindrical graphite crucibles set inside a Vycor tube vacuum furnace as shown. Heating was provided by an induction coil connected to a 2½ kv-amp Lepel induction unit. Temperature was measured with a nickel-sheathed chromel-alumel thermocouple set into the crucible as shown and connected, through sealed copper leads, to a type 8662 L & N Millivolt Indicator. The thermocouple sheath was carefully grounded to

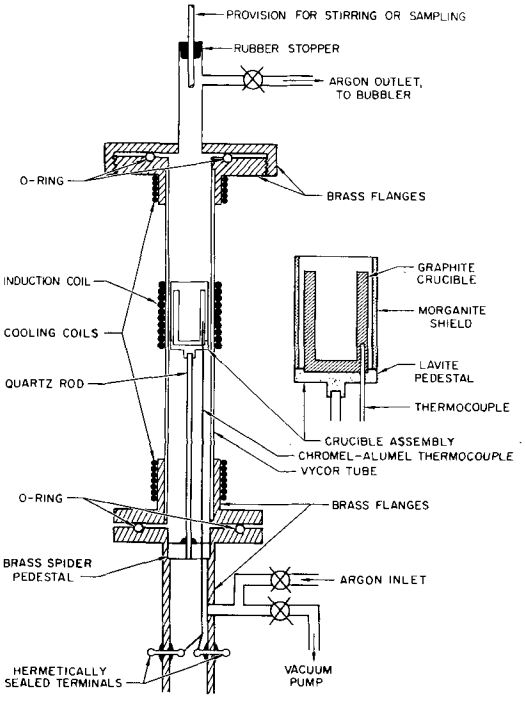

Fig. 1. Apparatus

insulate the thermocouple from induction currents. The temperature measured with this arrangement checked that of a test quantity of molten aluminum in the crucible as measured with a calibrated optical pyrometer to within several degrees at 1050°C. The temperature was controlled to ±5°C by a Wheelco Capacitrol controller.

Vacuum and argon lines allowed outgassing and provision of the required inert atmosphere. The argon used was purified by passing it over uranium turnings at 500°C. The vacuum line was connected to a Kinney KC-5 vacuum pump and the vacuum pressure measured with a standard thermocouple gauge. By use of a greased rubber stopper, the furnace top was equipped for gastight operation of either a motor-driven stirring rod or a sampling tube.

The metals used in this work were reactor grade thorium and 99.99% ingot aluminum. The chemicals employed were reagent grade lithium fluoride, aluminum oxide, and thorium oxide. No further purifications were carried out.

Selection of salt phase.—To carry out the equilibration studies between Al-Th alloy and the oxides of aluminum and thorium with favorable kinetics, a suitable molten salt flux was required. Since the salt mix was to be saturated with both oxides, the oxide solubilities in the mix needed to be moderate, but not high, to achieve saturation conveniently and avoid unfavorable increases in the viscosity of the melt. Further, no reaction or compound formation is allowable between the salt melt and either the oxides or the molten metal phase. Fluoride salts were favored because of their solubilities for metallic oxides, but cryolite mixes were found to be unsuitable because of reaction with the aluminum[1] and excessive alumina solubility. The following experiments showed lithium fluoride to be inert toward aluminum under the planned equilibration conditions.

Identical mixtures of lithium fluoride and aluminum were heated for 1 and 2 hr, respectively, at 1050°C under 1 atm of argon in the described apparatus. Analysis of both metal phases by flame photometry showed less than 0.03 w/o (weight per cent) Li present. The aluminum content in the molten LiF was found to be 2.28 w/o in both runs as determined by EDTA titration, but the absence of the corresponding amount of Li in the metal phase and the constancy of the Al content indicated that this represented the solubility of aluminum in molten LiF at 1050°C.

That no solute-solvent reactions occurred between the oxides and LiF was shown later, in the equilibrium reduction runs, where x-ray diffraction analyses on the salt phase showed patterns only for ThO_2, Al_2O_3, and LiF.

As will be seen later, solution of the thorium in aluminum reduces its activity sufficiently that it could not be expected to react with the LiF.

Solubilities of oxides.—To obtain useful background information for the equilibration studies, the solubilities of Al_2O_3 and ThO_2 in molten LiF at 1050°C were determined separately and in common solution. In several preliminary runs, limits of solubility and relative supernatant and precipitate volumes were determined by heating LiF-ThO_2 and LiF-Al_2O_3 mixtures for ½ hr at 1050°C in our apparatus and examining the frozen melts. In each case, sharp separation into precipitate and supernatant regions was evident.

To determine the solubilities, two experimental procedures were used. In the first, a mixture of 0.4g of Al_2O_3 and 7.1g LiF was placed in the furnace setup, outgassed, and heated at 1050°C under argon. After heating for ½ hr at this temperature, a quartz tube in the apparatus was lowered into the crucible to just above the melt surface. After several minutes to allow the tube end to come to the melt temperature, the tube was lowered into the supernatant zone and a melt sample withdrawn by means of a suction gun. The tube was then removed from the furnace, the sample recovered, and the tube replaced. Acceleration of the argon flow during tube removal minimized entry of air into the system. Following replacement of the tube, the crucible temperature was raised to 1100°C, held at this temperature for ½ hr to hasten saturation, lowered to 1050°C, held at 1050°C for ½ hr, and the next sample taken. This procedure was then repeated twice more for a total of four samplings. Samples were analyzed for Al by EDTA titration. The procedure was repeated in a second run with a mixture of ThO_2, Al_2O_3, and LiF to determine the solubilities of the oxides in common solution.

In the second procedure, used as a partial check, the apparatus was equipped with a motor-driven, graphite-tipped stirring rod. A ThO_2-LiF mixture was outgassed, heated to 1050°C, and held at this temperature. Three cycles were then carried out in which the mixture was stirred for 3 min, allowed to settle for 25 min, and sampled as before. The furnace was then shut down, a portion of Al_2O_3 added atop the cooled mix, the crucible reheated to 1050°C, and

[1] $Na_3AlF_6 + Al \rightarrow 3Na\uparrow + 2AlF_3$.

Table I. Solubilities of Al_2O_3 and ThO_2 in LiF at 1050°C

Run	Procedure	Solute	w/o Solute in sample 1	2	3	4	Assumed solubility
1	1st	Al_2O_3	0.26	0.26	0.28	0.32	0.30 (?)
2	1st	Al_2O_3	0.28	0.32	0.38	0.38	0.38
		ThO_2	0.05	0.05	0.08	0.06	0.06
3	2nd	ThO_2	<0.04	<0.03	<0.04	—	<0.04
4	2nd	Al_2O_3	0.41	0.43	0.38	—	0.41
		ThO_2	0.05	0.09	0.06	—	0.07

three more cycles of stirring, settling, and sampling carried out.

The results of all solubility determinations appear in Table I. Accuracies of individual sample analyses were about 0.01 w/o for the ThO_2 contents and 0.02 w/o for the Al_2O_3 analyses. Of primary interest in our work were the solubilities of the oxides in common solution, which agree well in the two procedures, despite the nearness to the limits of analysis for the thoria content. In interpreting sample analyses from the runs carried out by the temperature cycling (first) procedure, constant solute contents in the last few samples are taken to indicate saturation. Thus, the choice of 0.38 w/o as the alumina solubility in run 2 seems reasonable, and the absence of any significant progression in the ThO_2 content in this run allows us to take a simple average. Results, however, are not as clear-cut in run 1. One believes that the runs with stirring (second procedure) are more reliable in that the constancy of alumina contents in the samples indicate a rapid attainment of saturation. The thoria solubility in run 3 is seen to be below the limit of analysis, but the general picture indicates somewhat of an increase of the solubilities of both ThO_2 and Al_2O_3 when present in common solution in LiF.

Equilibration experiments.—Several preliminary runs, in which LiF-ThO_2-Al_2O_3 mixes were heated in contact with Th-Al alloy melts for several hours at 1050°C, indicated that great care was needed to achieve equilibrium. Continuous stirring was required, so the motor-driven graphite-tipped stirring rod was installed in the apparatus. The arrangement, however, led to poor phase separation and extensive aluminum carbide formation from the metallic aluminum, so the graphite crucible was fitted with a liner of recrystallized alumina and a stirring rod tip of the same material was used. Partial solution or disintegration of the stirring rod tip occurred during runs, despite the presence of more than the saturation limit of Al_2O_3 in the initial salt mix. However, since the runs were to be carried out at any rate with the salt flux saturated with both oxides, this constituted no problem.

The series of equilibration runs was carried out as follows. Preliminary runs showed an achievable thorium build-up of at least 10 w/o in the metal phase, so a quantity of Al 10 w/o Th alloy was prepared by heating the alloy components for several hours at 1050°C in an argon atmosphere. A mixture of LiF and enough ThO_2 and Al_2O_3 to well exceed their solubility limits was then outgassed and heated for 15 min at 1050°C under argon to provide a suitable salt phase. The metal and salt phases were then heated together to 1050°C under argon, the motor-driven stirring rod gradually lowered into the melt, and the mixture heated for 2 hr, with continuous stirring, at 1050°C. The stirrer was then withdrawn, the mix cooled quickly, and the metal phase from the run recovered and analyzed *in toto*. The analysis showed a considerable increase in the metal phase thorium content, so a metal phase of the approximate new alloy composition was prepared and another run carried out with a salt phase of the same composition. This was repeated until the metal phase showed only a small further increase in thorium content, whereupon a metal phase with a much higher thorium content was prepared and a similar run carried out. This run showed a decrease in thorium content of the metal phase, so the procedure was repeated with initial metal phases of successively smaller thorium content.

The results of the experiments are shown in Table II. It is seen that the procedure resulted in a near-approach to equilibrium. The assumed equilibrium concentration of Th in the metal phase is 28.1 ± 0.2 w/o thorium.

Metal phase studies.—As seen later, the above equilibrium concentration can be used with the known free energy of reaction of Eq. [1] to estimate the standard free energy of formation of the intermetallic compound involved in Eq. [3]. To do this, however, requires knowing the exact identity of this compound and the solubility of thorium in aluminum at the temperature of interest. In both cases, reported work is in some disagreement. For our work, the intermetallic compound of interest was the one which is in equilibrium with a saturated solution of thorium in aluminum at 1050°C. Aluminum-thorium phase diagrams by different workers (3-5) however, variously indicate this compound to be ThAl, $ThAl_2$, and $ThAl_3$. Work by Leber (3) indicated the solubility of Th in Al at 1050°C to be 55 w/o, but other work (4) was in disagreement.

The solubility of thorium in liquid aluminum at 1050°C was determined by the first procedure used for oxide solubilities. A mixture of 10g aluminum and 26.5g thorium, the latter in small pieces, was heated to 1050°C in argon, under 0.5g LiF to serve

Table II. Weight per cent Th in equilibration run metal phases

Run	Initial	Final
1	10.0	20.3
2	18.9	26.2
3	25.0	27.9
4	40.0	35.2
5	35.0	28.3

as a flux. The mixture was heated at 1050°C for ½ hr and a sample of the melt withdrawn. Then, as in previous runs, the melt was heated at 1100°C for ½ hr, cooled and held at 1050°C for ½ hr, and the second sample taken. The process was repeated to obtain a third sample, using, as before, a quartz tube and suction gun. The thorium analyses on the three samples were 52.4, 54.6, and 54.6 w/o, respectively. Since the previous solubility data of Leber were obtained by cooling curve analysis, it was felt that an adequate check was obtained and that 55 w/o is the correct solubility of thorium in aluminum at 1050°C.

The identity of the intermetallic compound in equilibrium with a saturated solution of thorium in aluminum at 1050°C was established as follows. A mixture of Th and Al corresponding to a 55 w/o thorium alloy was heated at 1060°C for 2 hr to dissolve all of the thorium. The melt was then cooled to 925°C over a period of ½ hr, and the temperature held at 925°C for another half-hour. The bulk of the melt liquid was then removed from the crucible at 925°C by means of a quartz tube and suction gun. The material remaining in the crucible was a mat of well-defined needlelike crystals. The crucible was quickly cooled to room temperature and the crystals separated from an adhering residue of solidified melt liquid by dissolving away the latter with 10% aqueous NaOH. Chemical analysis and x-ray diffraction identified the crystals as $ThAl_3$. Since none of the phase diagrams reported showed any phase changes or thermal arrests between 1060° and 925°C, and since melt liquid was not available for reactions below 925°C, it was assumed that the crystals recovered are those of the stable aluminide at 1050°C. The result is in agreement with the work of Murray (5), which is the most recent work on this portion of the Th-Al phase diagram.

Discussion

The results of the preceding experimental work can be used to estimate the standard free energy of formation of $ThAl_3$. The reduction of thorium oxide to produce thorium-aluminum alloy can be considered in terms of the virtual formation of $ThAl_3$ and its solution in a sufficient excess of aluminum to result in the metal phase of equilibrium composition. Accordingly, Eq. [3], for the reaction at 1050°C, can be written in terms of the equivalent series

$$ThO_2(s) + \frac{4}{3}Al(l) \rightarrow \frac{2}{3}Al_2O_3(s) + Th(s) \qquad \Delta F_1 = +38 \text{ kcal}$$

$$Th(s) + 3Al(l) \rightarrow ThAl_3(s) \qquad \Delta F_2 = \Delta F_f^\circ\ (ThAl)_3$$

$$ThAl_3(s) \rightarrow Th(\text{liquidus sol.}) + 3Al(\text{liquidus sol.}) \qquad \Delta F_3 = 0$$

$$Th(\text{liquidus sol.}) \rightarrow Th(\text{sol. Al-Th}) \qquad \Delta F_4 = -RT \ln \frac{a^{sl}{}_{Th}}{a_{Th}}$$

$$3Al\ (\text{liquidus sol.}) \rightarrow 3Al(l) \qquad \Delta F_5 = -RT \ln (a^{sl}{}_{Al})^3$$

$$\frac{4}{3}Al(\text{sol. Al-Th}) \rightarrow \frac{4}{3}Al(l) \qquad \Delta F_6 = -RT \ln (a_{Al})^{4/3}$$

where $\Delta F_f^\circ\ (ThAl_3)$ is the standard free energy of formation of $ThAl_3$, a^{sl} refers to activities in the liquidus Th-Al melt (*i.e.*, saturated solution of Th in Al), and a_{Al} and a_{Th} to activities in the melt of equilibrium composition. Since the over-all reaction is an equilibrium reaction, $\Sigma \Delta F = 0$, and thus

$$-\Delta F_f^\circ\ (ThAl_3) = 38 - RT \ln (a^{sl}{}_{Al})^3 (a_{Al})^{4/3} \left(\frac{a^{sl}{}_{Th}}{a_{Th}} \right)$$

We recall that the concentrations of thorium in the equilibrium and liquidus melts at 1050°C were 28 w/o and 55 w/o, respectively. In terms of mole fractions, however, the solutions are considerably more dilute, the mole fractions being 0.043 and 0.125. Thus, there is some basis for evaluating the above activities by the use of Raoult's and Henry's laws. While the concentrations involved are admittedly marginal for this approach, no specific data on activity coefficients exist. Further, it will be seen that the activity factor term in the above expression provides only a small contribution to the calculated free energy of formation, so that even large inaccuracies in evaluating the term will have a small effect on the final result. The assumption of Raoult's and Henry's laws, then, allow the following substitutions: $a_{Al} = N_{Al}$ and $a^{sl}{}_{Th}/a_{Th} = N^{sl}{}_{Th}/N_{Th}$, and accordingly,

$$-\Delta F_f^\circ\ (ThAl_3) = 38 - RT \ln (N^{sl}{}_{Al})^3\ (N_{Al})^{4/3}\ (\frac{N^{sl}{}_{Th}}{N_{Th}})$$

Using the stated values for the indicated mole fractions, one obtains, for the standard free energy of formation of $ThAl_3$ at 1050°C, an estimate of 36 kcal.

It is seen that the predominant driving force for the nominally unfavored reduction of thorium oxide by aluminum is the free energy of formation of the intermetallic compound $ThAl_3$; associated dilution effects play an energetically small role. Even large errors in the activities, which may be involved in assuming the applicability of Raoult's and Henry's laws, will not significantly affect the calculated free energy of formation. What is more important in this respect, however, is the accuracy to which the relative free energies of formation of thoria and alumina at 1050°C are known. Estimated limits of error from Kubaschewski (2) and various original reports of these measurements indicate that the 38 kcal figure may be in error by as much as 5 kcal. Accordingly, until more accurate data become available, the −36 kcal free energy of formation of $ThAl_3$ at 1050°C must be regarded as subject to the same uncertainty. It is felt, however, that this value at least gives some indication of the stability of such compounds. It would be of interest if this quantity could be determined experimentally by an independent method.

Acknowledgments

The author wishes to thank Mr. W. D. Turner for considerable assistance in the experimental work reported. The support of the United States Atomic Energy Commission is gratefully acknowledged.

Manuscript received Sept. 25, 1961; revised manuscript received Feb. 16, 1962.

Any discussion of this paper will appear in a Discussion Section to be published in the December 1962 JOURNAL.

REFERENCES

1. D. O. Raleigh, *Ind. Eng. Chem.*, **53**, 445 (1961).
2. O. Kubaschewski and E. L. Evans, "Metallurgical Thermochemistry," John Wiley & Sons, Inc., New York (1956).
3. A. Leber, Z. *anorg. u. allgem. Chem.*, **166**, 16 (1927).
4. F. A. Rough and A. A. Bauer, U. S. Atomic Energy Commission Report BMI-1300 (1958).
5. J. R. Murray, *J. Inst. Metals*, **87**, 349 (1959).

Diagrammatic Representation of the Thermodynamics of Metal-Fused Chloride Systems

R. Littlewood[1]

Tube Investments Research Laboratories, Hinxton Hall, Saffron Walden, Essex, England

ABSTRACT

Previously, diagrammatic methods of presentation have been used to study the thermodynamics of metallic corrosion in fused chlorides, and the method has now been extended to metal-winning reactions. Diagrams in which the equilibrium potential E (relative to the standard chlorine electrode) in the system is plotted against the activity of oxide ion in the chloride melt (expressed as its negative logarithm, pO^{2-}) are presented for the metals Mg, Ni, Zr, and Ti in contact with one or more of the chlorides LiCl, KCl, NaCl, and $MgCl_2$ at 800°C. As an example of the use of E-pO^{2-} diagrams, it is shown how they can be applied to metal extraction processes involving chlorides. The main advance here is that the method offers an approach to the prediction of impurity levels and is applicable equally well to electrowinning from fused chlorides and to reduction of chlorides by base metals. Levels of impurity, particularly of oxygen, in the metal product are obtainable directly from the diagrams.

The thermodynamics of metal-fused chloride systems is more complicated than appears at first sight especially when reactions involving impurities, particularly anions, are taken into consideration. The success of graphical methods of presenting thermodynamic data for aqueous systems led us to develop similar ways of presentation for fused salt systems, and we have already applied some of these to study the thermodynamics of metallic corrosion in fused chlorides (1, 2).

The presentation of thermodynamic data in a diagram has certain advantages which have not always been fully appreciated. When considering a system of a number of components, one method involves conversion of the data into linear equations linking free energy with logarithmic functions of composition. There is one such equation for each possible reaction of all the various constituents present. The relations are plotted graphically, and the resulting diagram summarizes the thermodynamic properties of the system at a given temperature. This simplicity of presentation is to be compared with the application of a similar series of equations to each particular set of conditions, from which the behavior of the system under that particular set of conditions is inferred. In this case, if the properties of the system under several different conditions are required, the whole procedure usually has to be repeated. Where a general appreciation of the effect on the system of a variety of different conditions is required, presentation of the properties of the system in a diagram has obvious advantages.

The thermodynamic diagrams of Pourbaix (3) have been particularly useful in understanding the behavior of metals in contact with aqueous solutions. Pourbaix plots equilibrium potential against pH, and the diagrams divide themselves into regions of stability of different solid phases (compounds of the metal in question).

In the fused salts also, free energies can be expressed as equilibrium potentials, and there are a number of functions of composition which might be used as the other variable. In the present paper, the composition variable chosen is the activity of oxide ion in the melt, expressed in terms of its negative logarithm, pO^{2-}. The resulting E-pO^{2-} diagrams are particularly useful when considering systems involving oxides, or oxygen, in contact with fused chlorides, and in practice this covers all conditions under which fused chlorides are normally used. As an example, the paper shows in particular how E-pO^{2-} diagrams are applicable to metal extraction processes involving chlorides.

Conventions.—In aqueous systems, the conventions used in a thermodynamic treatment are well established. With reactions in fused salts, the conventions adopted in a particular treatment need to be defined at the outset. The conventions chosen for the present paper are identical with those used previously by the author (1, 2). Free energies are converted to an emf scale using the expression

$$E^\circ = -\Delta G^\circ/n\mathbf{F} \qquad [1]$$

and the potential *zero* is taken as the potential of a chlorine electrode (1 atm pressure) in contact with a chloride melt at unit chloride activity. Activities in condensed phases are based on the pure component as the standard state, or in the case of gases, the gas at unit fugacity, approximately 1 atm pressure.

[1] Present address: The British Iron and Steel Research Association, London, England.

Principles

A fused chloride melt is stable over a range of potential, which at one atmosphere pressure extends from *zero* on the chlorine electrode scale, where the melt will be in equilibrium with chlorine at 1 atm pressure, to a negative value of potential equal to the decomposition potential of the melt. The latter is related to the free energy of formation of the chloride by Eq. [1], and the decomposition potential will be more negative the more stable the chloride. Between these two potentials, the chloride will always be partially dissociated and the activities of metal and chlorine in the melt will vary with potential, while conforming to the equilibrium constant (parentheses denote activities).

$$K = \frac{(Cl_2)^{1/2}\,(M)}{(MCl)} \qquad [2]$$

of the reaction

$$MCl = M + \tfrac{1}{2}Cl_2 \qquad [3]$$

This equilibrium constant is obtainable from the expression

$$\log K = -\Delta G^\circ_{MCl}/2.303\,RT \qquad [4]$$

where ΔG°_{MCl} is the free energy of dissociation of the chloride MCl. The activity of free metal and of free chlorine present in the melt at any given potential E can be calculated from the Nernst equations for the two half-reactions.

$$\tfrac{1}{2}Cl_2 + e^- = Cl^- \qquad [5]$$

$$M^+ + e^- = M \qquad [6]$$

Thus, when MCl is present at unit activity,

$$E = E^\circ_{Cl} + (2.303\,RT/\mathbf{F})\,\log\,(Cl_2)^{1/2} \qquad [7]$$

for half-reaction [5], and

$$E = E'_M - (2.303\,RT/\mathbf{F})\,\log\,(M) \qquad [8]$$

for half-reaction [6], where E°_M can be calculated from relation [1].

The two expressions for E (Eq. [7] and [8]) are identities, since the equilibrium potential in the system has a unique value, and in fact Eq. [7] and [8] are interrelated by Eq. [2].

To deal with a system containing oxygen and oxides, it is necessary to define a standard state for the oxide ion, and in accordance with the conventions adopted, we have chosen the pure oxide of the cation of the chloride melt under consideration as unit activity of oxide ion. For example, in the case of a KCl melt the standard state for oxide ion would be pure K_2O and the standard free energy of formation of O^{2-} ion would be calculated as follows:

$$K^+ + e^- = K;\ \mu^\circ_K = +\,78.83\text{kcal} \qquad [9]$$

$$2K + \frac{1}{2}O_2 = 2K^+ + O^{2-};\ \mu^\circ_{K_2O} = -\,53.71\ \text{kcal} \qquad [10]$$

therefore

$$2e + \frac{1}{2}O_2 = O^{2-};\ \mu^\circ_{O^{2-}} = +\,103.95\ \text{kcal} \qquad [11]$$

A standard free energy of formation of the oxide ion defined in this way will differ in value according to the particular melt chosen. In mixed chlorides, the activity of O^{2-} will be expressed in terms of one particular oxide, but provided a single definition is adhered to throughout the treatment, the final results will be the same whichever oxide is chosen, although oxides of cations other than the standard one might have either extremely large or extremely small activity coefficients.

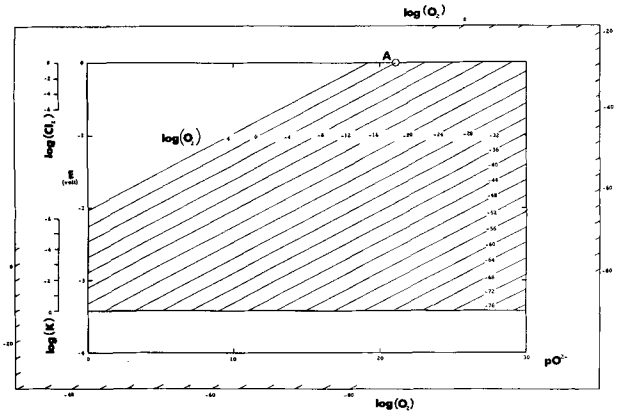

Fig. 1. Relationship between oxygen pressure, oxide activity, and potential for KCl at 800°C. E is electrode potential relative to the standard chlorine electrode. For point A, see text.

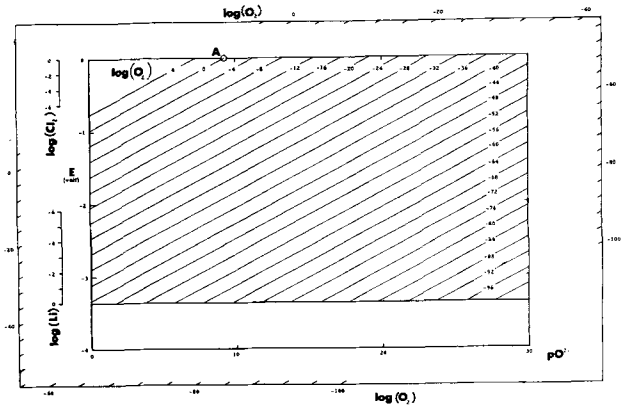

Fig. 2. Relationship between oxygen pressure, oxide activity, and potential for LiCl at 800°C.

The standard free energy of formation for the oxide ion can now be used to express the relationship between potential, oxygen pressure, and oxide activity

$$E = E^\circ_{O^{2-}} + (2.303RT/2\mathbf{F}\,\log\,[(O_2)^{1/2}/(O^{2-})] \qquad [12]$$

This relationship is shown graphically for KCl at 800°C in Fig. 1 and for LiCl at 800° in Fig. 2. For a given oxygen pressure, Eq. [12] gives rise to a straight line dependence of E on pO^{2-} and in the figures, oxygen pressures at intervals of 10^4 apart are shown, giving a grid of parallel lines. The position of these lines corresponds with the two oxygen pressure scales external to the diagrams (the line for a given oxygen pressure is found by laying a ruler on the diagram joining the appropriate points on the two scales). The upper and lower limits to the diagrams are set by the potentials at which the melt is oxidized to chlorine or reduced to metal, respectively. The other two external scales on the left-hand side give the activity of chlorine or metal present at a given potential, according to Eq. [7] and [8].

Figures 1 and 2 illustrate the marked differences in properties between melts of LiCl and KCl, which will be discussed in more detail later. Note, however, that the oxide activities in melts of LiCl and KCl prepared under atmospheres of identical composition will be very different. For example, the equilibrium conditions in melts prepared under an atmosphere of equal parts of oxygen and chlorine at a total pressure of 2 atm would be represented by the points marked A in Fig. 1 and 2. These correspond to oxide activities of $10^{-9.3}$ in LiCl and $10^{-21.1}$ in KCl, illustrating the effect of the higher affinity for oxygen of Li relative to K.

There is provision in the diagram for oxygen pressures down to extremely low values. These pressures are still meaningful and are particularly important when dealing with systems under reducing conditions, such as in the presence of metals which are strong oxygen getters, or in hydrogen atmospheres. For example, hydrogen gas at 1 atm pressure containing 1 volume per million of water vapor would be in equilibrium with an oxygen partial pressure of about 10^{-40} atm, and these conditions could therefore in principle be represented on the E--pO^{2-} diagram by the line corresponding to an oxygen pressure of 10^{-40} atm.

The solubility product of any oxide in a given chloride MCl can also be calculated, relative to the oxide M_2O. For example, the solubility product of nickel oxide in a KCl melt at 800°C is obtained as follows. When the melt is saturated with NiO, excess solid oxide will be present at unit activity, and since the system is at equilibrium, the free energy change for the dissolution reaction

$$NiO = Ni^{2+} + O^{2-} \qquad [13]$$

will be zero, so that

$$\log S = \log (Ni^{2+})\ (O^{2-}) =$$

$$(\mu^{\circ}_{NiO} - \mu^{\circ}_{Ni^{2+}} - \mu^{\circ}_{O^{2-}})/2.303RT \qquad [14]$$

Table I gives the values of activity solubility products of some oxides in melts of LiCl and in KCl calculated in this way. These illustrate the greater solubility of oxides in LiCl than in KCl, as observed experimentally (4). In addition, the relative magnitudes of solubility product of the oxides in either chloride are in the order

$$CaO > NiO \sim ZnO > MgO > ZrO_2$$

which corresponds well with experimental observations of oxide solubilities in LiCl (4), KCl (4), and LiCl-KCl eutectic (5).

Experimental data on oxide solubilities in fused chlorides are very scanty, and no attempts to determine solubility products appear to have been made. Solubility products cannot, of course, be obtained directly from simple solubility measurements of the oxide in the chloride alone, but this point will be commented on later. It will only be possible to assess fully the significance of the calculated values when experimental values of activity solubility products become available, but it appears justifiable at the moment to accept solubility products calculated in this way.

Table I. Calculated solubility products of oxides in fused chlorides at 800°C

Oxide	log S in LiCl	log S in KCl
NiO	−7.8	−19.7
CaO	−3.8	−15.8
ZnO	−8.2	−20.0
MgO	−9.9	−21.8
ZrO_2	−26.8	−50.6

The grid showing equilibria in the system KCl $-$ O_2 $-$ O^{2-} (Fig. 1) can now be used as a reference frame on which to superimpose domains of thermodynamic stability of compounds formed between components of this system and another metal, such as in Fig. 3, which is for the Mg—KCl system. For clarity, the reference grid of oxygen pressure lines has been omitted, but any line may be found simply by laying a ruler on the diagram joining the appropriate points on the two external oxygen pressure scales. Scales showing the activity of chlorine and of potassium in the melt are also given on the left as before. KCl is stable at 800°C down to a potential of −3.42v. The region of stability of KCl divides up into three domains (as shown by the heavy lines in Fig. 3) in each of which one and only one compound of Mg can be present at unit activity. In the domain marked MgO, MgO (solid, unit activity) is in equilibrium with a melt of KCl containing $MgCl_2$ and O^{2-} ions. The activity of Mg^{2+} in the melt can be found from the vertical isoactivity lines connecting with the log (Mg^{2+}) scale directly above the diagram. It can be seen that as the activity of O^{2+} ion in the melt falls, the activity of Mg^{2+} rises until at a value of pO^{2-} of 21.83 (and provided E is above −2.47v), solid MgO at unit activity can coexist with $MgCl_2$ at unit activity. At values of pO^{2-} greater than 21.83, MgO can only exist at an activity less than unity (*i.e.*, in solution) and we pass into the domain marked $MgCl_2$. At values of pO^{2-} greater than 21.83, Eq. [19], in which the activity of MgO is taken to be unity, tells us that (Mg^{2+}) must be greater than unity. This is physically meaningless, since activities can never exceed unity using the present conventions. Hence the activity of MgO must be less than unity.

In the domain $MgCl_2$, the melt may contain Mg^{2+}, O^{2-}, and Mg in solution in KCl, but the only compound of Mg which can be present at unit activity is $MgCl_2$. Its activity is not necessarily unity, and it can have any value between unity and values approaching zero. This is because the value of E defines only the value of the ratio $(Mg^{2+})/(Mg)$ and not the absolute values of (Mg^{2+}) or (Mg) which accordingly can vary over a wide range while keeping the ratio of their activities constant. The same components Mg^{2+}, O^{2-}, and Mg are present in the melt in the domain marked Mg metal, which is divided from the $MgCl_2$ domain by a horizontal line at a value of E of −2.47v, but in this domain, it is possible for Mg metal to be present at unit activity. The potential of −2.47v is simply that potential at which Mg metal at unit activity can coexist with unit activity of $MgCl_2$. The horizontal isoactivity lines, which connect with the log (Mg^{2+}) scale to the

right of the diagram, can be used to find the activity of Mg^{2+} in the melt which would be in equilibrium with Mg metal at any given potential. The boundary between the Mg metal and MgO domains is a line representing the conditions under which Mg metal and MgO can coexist, each at unit activity, and corresponds to a value of log (O_2) of −47.72, the dissociation pressure of MgO.

Figure 3 shows that solubility of an oxide in a fused chloride at a given temperature depends on several factors, an understanding of which is needed to obtain values of solubility products from solubility measurements. The solubility of MgO in KCl would be estimated by measuring the concentration of Mg^{2+} ions in the KCl melt, but this will depend on the value of pO^{2-} in the melt as in the case of an oxide in contact with an aqueous solution. For example, at a value of pO^{2-} of 21.83, the Mg^{2+} activity in the melt would be unity; at a value of pO^{2-} of 15.83, it would be 10^{-6} (Fig. 3). The results of solubility measurements will therefore depend very markedly on the value of pO^{2-} in the melt and this will need to be closely controlled. Solubility experiments described in the literature (4, 5) have not been deliberately controlled in this way, although contact with a glass or ceramic container would fix pO^{2-} at a value dependent on the nature of the oxides present in the container material (1, 6, 7) (contact with an air atmosphere would not fix the value of pO^{2-}, Fig. 1 and 2). The experimental solubilities obtained in a particular case, can in fact, be used to estimate the conditions in the melt during the experiment. Voskresenskaya and Kashcheev (4) obtained a value for the solubility of MgO in KCl at 900°C of about 0.002%: for the purpose of this example at 800°C, let us say a mole fraction of Mg^{2+} in the melt, of 10^{-5}. The measurements were made in an air atmosphere (oxygen at 0.2 atm pressure), so that writing mole fraction of Mg^{2+} as activity of Mg^{2+}, after Temkin (8), we can plot a point representing this result on Fig. 3 (point A). The conditions in the melt during these experiments must therefore have been as follows

potential −0.5v, pO^{2-} 16.83

Diagrams similar to Fig. 3 can be constructed for any metal and those for nickel in KCl and in LiCl at 800°C are shown in Fig. 4 and 5. For metals having more than one stable chloride (Figs. 6, 7, 9, 10), the situation is more complex because there is more than one way of presenting the data. For example, a set of isoactivity lines corresponding to the equilibrium of each chloride could be plotted, and at some potential the sum of the activities would become equal to unity. At potentials above this value, the only significance of the scales would be to indicate the ratios of the ion activities to that of the metal in the melt, and since the latter would be undefined, this would be a somewhat indefinite way of presenting the data. It is more convenient not to attempt to show separately the activity of every possible metal ion, but instead to express melt compositions in terms of other variables. In the diagrams presented here, the variables chosen were the sum of the activities of all ions of the metal, $(M^+) + (M^{2+}) + (M^{3+})$ + etc., and the ratios of the activities of ions with a valency difference of one, $(M^{2+})/(M^{3+})$, etc. The latter are plotted as scales external to the diagram in Fig. 6 and 7, while the sum of the metal ion activities is plotted as isoactivity lines on the diagram. Changes in redox equilibria in the melt cause these lines to curve, but nevertheless, this type of diagram is much simpler than one showing separately the activities of all possible chlorides. A diagram for Zr in contact with a KCl melt at 800°C is shown in Fig. 6. The domains are exactly analogous to the magnesium case, but are distorted in shape at potentials where changes in redox equilibria occur. The two scales at the right-hand side of the diagram indicate the position of redox equilibria of zirconium ions in the melt. These, in con-

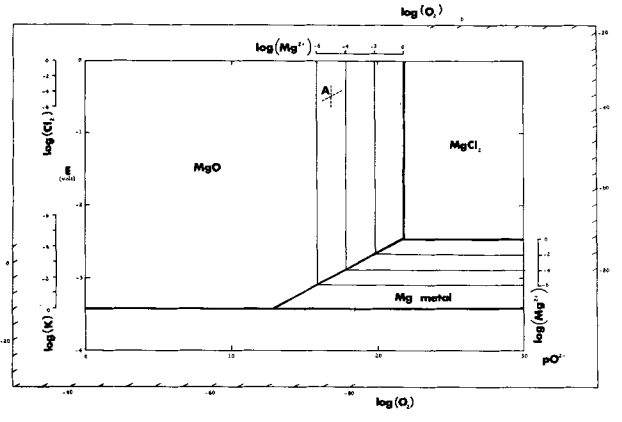

Fig. 3. E-pO^{2-} diagram for the system Mg-KCl at 800°C. For point A, see text.

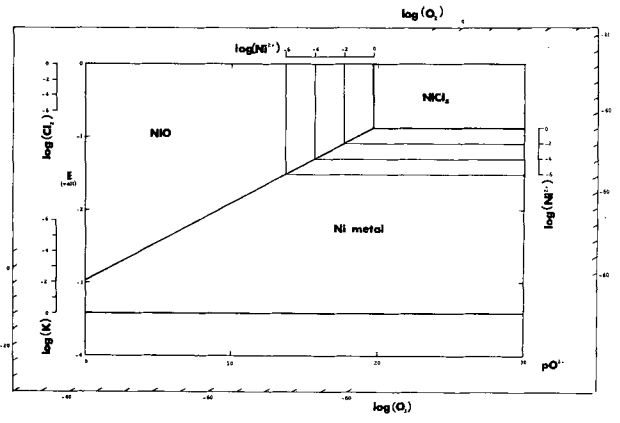

Fig. 4. E-pO^{2-} diagram for the system Ni-KCl at 800°C

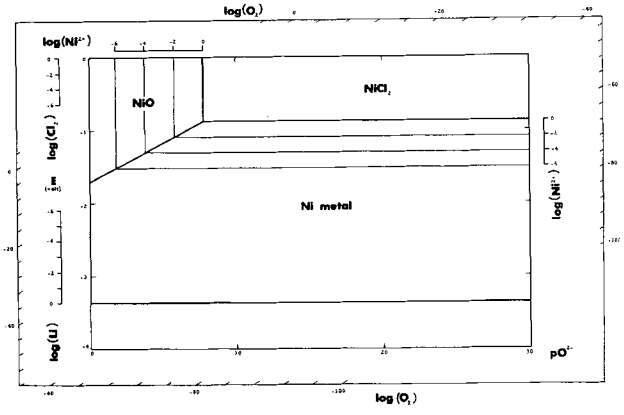

Fig. 5. E-pO^{2-} diagram for the system Ni-LiCl at 800°C

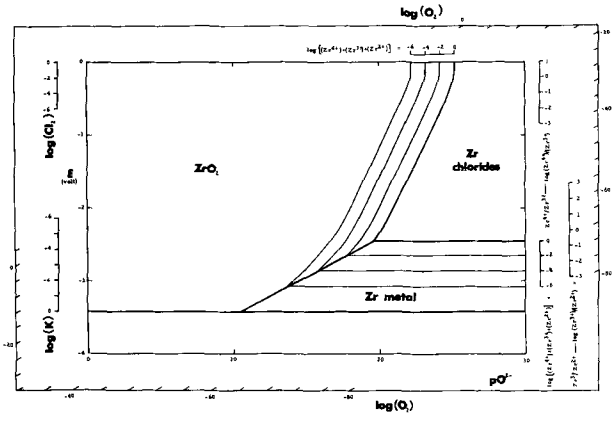

Fig. 6. E-pO^{2-} diagram for the system Zr-KCl at 800°C

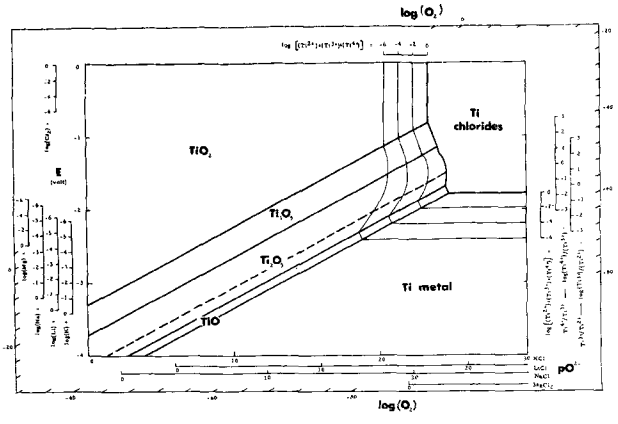

Fig. 7. E-pO^{2-} combined diagram for the systems Ti-$MgCl_2$, Ti-NaCl, Ti-LiCl, and Ti-KCl at 800°C.

junction with the isoactivity lines on the diagram showing the sum of the activities of Zr ions, allow the exact composition of the melt in terms of KCl, $ZrCl_4$, $ZrCl_3$, and $ZrCl_2$ to be found.

For metals with more than one oxide, there are further domains, one for each stable oxide, as in the case of titanium (Fig. 7). In addition to domains showing the conditions under which each of the oxides is thermodynamically stable, domains can also be delineated in which one of two solid substances is stable with respect to the other. For example, the dotted line shows where TiO_2 becomes stable with respect to Ti metal. (The corresponding lines for the other oxides are not shown, as they would increase the complexity of the diagram without materially increasing its usefulness). It should be clearly understood that TiO_2 is stable only in the region within the TiO_2 domain, but in view of the sluggishness of solid-state transformations, it might be kinetically favored over a wider range of conditions than indicated by the stability region of the diagram. The position of the dotted line gives an indication of this extension of the range of conditions under which TiO_2 might exist, for reactions involving metallic titanium.

In Fig. 7, a further modification has been introduced which makes the diagram applicable to titanium in LiCl, NaCl, or $MgCl_2$ as well as in KCl. The scales to the left of the diagram show the limits of stability of these melts, and the parts of the diagram extending below these limits in each particular case have, of course, no physical significance. pO^{2-} scales for each chloride are given on the lower edge of the diagram and again, parts of the diagram to the left of the zero value of pO^{2-} for each particular chloride have no meaning. The O_2 pressure scales and isoactivity lines referring to titanium ions are common to all the four chlorides, LiCl, NaCl, KCl, and $MgCl_2$.

Details of the construction of these diagrams are given in the appendix.

Applications of the Diagrams

The present diagrams have much in common with E-pH diagrams for aqueous systems, which have become well-known largely through the work of Pourbaix and his collaborators (3). It is expected that E-pO^{2-} diagrams for fused salts will prove at least as useful as these and if anything, they should be more directly applicable because at the higher temperatures common in salt melts, reactions have a greater chance of reaching equilibrium than in aqueous solutions at room temperature. In other words, predictions made about metal-fused salt systems from E-pO^{2-} diagrams are likely to be as exact as the thermodynamic data on which they are based, since most reactions in melts at high temperatures are reversible.

The condition of any system is represented on the diagrams by a point, and the equilibrium positions of all the reactions which the constituents can undergo is determined by projecting this point on to the appropriate scales, or by noting its position relative to appropriate isoactivity lines. The position of the system-point can be found if any two independent variables in the system are known. For example, if besides potential, we know either the activity of oxide ion in the melt or the partial pressure of oxygen at equilibrium, the position of the system-point is defined.

Some general conclusions regarding the possible applications of E-pO^{2-} diagrams in fused chlorides can be reached without recourse to detailed practical examples, and it is felt that the following are some of the main fields in which they might be used. The list is not considered to be exhaustive and simple cases are chosen to make the principles clear.

Aggressiveness of melts.—Consideration of the factors affecting corrosion of metals in fused chlorides has shown (1,2) that the stability of the chloride is of primary importance. Since the decomposition potentials of LiCl and KCl have similar values, it might be expected that their aggressiveness would be similar under comparable conditions. It is well known, however, that this is not so and under the same conditions of temperature, atmosphere composition, drying procedure etc. LiCl is the more aggressive towards metals. This is often loosely ascribed to the greater ease of hydrolysis of LiCl during drying or melting which leads to a greater amount of oxide or oxychloride in the LiCl melts, but it is felt that this idea is incomplete and inexact. While there will no doubt be different amounts of oxide in LiCl and KCl melts prepared by identical procedures, the greater the amount of oxide in the melt, the lower will be the redox potential of the melt at any given oxygen pressure (Fig. 1) and therefore the lower

its initial aggressiveness should be. This is the reverse of what is found in practice, and hence this effect must in practice be offset in the opposite direction by some other essential difference between melts of LiCl and KCl. Comparison of Fig. 1 and 2 shows that at any given oxygen pressure and value of pO^{2-} the redox potential of a LiCl melt is about 1.2v higher than that of a KCl melt. In other words, even if the two melts have the same oxide activity and are under atmospheres of identical composition, a LiCl melt will still be more oxidizing than a KCl melt and will thus be more aggressive. This intrinsic difference in redox potential is due to differences between the free energies of formation for oxides and chlorides of lithium and potassium and is likely to have a far-reaching effect on many chemical reactions in melts besides corrosion reactions.

It should be pointed out that the effect of water on the reactivity of chloride melts may be more complicated, since hydrolysis leads to the formation of H^+ ions as well as O^{2-} ions and the water will also dissociate to H_2 and O_2. These effects have been discussed at length elsewhere (1, 2), and the effects of water on redox potential of chloride melts are still incompletely understood experimentally (6). However, when comparing redox potential behavior in melts so different in properties as KCl and LiCl, such complications will probably be secondary to the differences due to relative oxide stability described above.

General application to corrosion in fused chlorides.—As already pointed out, the properties of E-pO^{2-} diagrams are similar in many respects to those of E-pH diagrams for aqueous solutions. For aqueous systems, Pourbaix (3) has defined domains in which the corrosion of metals is thermodynamically possible or impossible by assuming that a metal will only corrode when the substance forming its surface has a solubility in excess of an arbitrary value of 10^{-6}M. He distinguishes between two types of "domains of noncorrosion," one where the surface is actually bare metal (immunity domain) and the other where the metal is covered with a deposit of oxide or salt (passivity domain), and in the latter case, only if the substance covering the metal forms a completely perfect and nonporous screen will corrosion be prevented.

The E-pO^{2-} diagrams for fused chlorides may be divided into analogous domains, but effective passivity is less likely to occur in fused chlorides than in aqueous solution and any conclusions made from such diagrams regarding "passive" behavior should be treated with reserve. It appears safer to designate simply as "oxide-covered" the region equivalent to the passive domain, as in Fig. 8. These regions represent the conditions under which the corrosion product is insoluble in the melt, and whether these conditions do in fact lead to passivity will depend on details such as the morphology of the oxide and its tenacity to the metal surface. Figure 8 shows the nickel-KCl diagram divided into domains of corrosion and noncorrosion on the assumption that no corrosion occurs if the solubility of the metal in the melt (as ions) is less than 10^{-6} activity. Such diagrams predict whether the corrosion products of a given metal in a given fused chloride medium will be soluble metal ions or solid oxide, which may be an important consideration in some types of operation using fused chlorides.

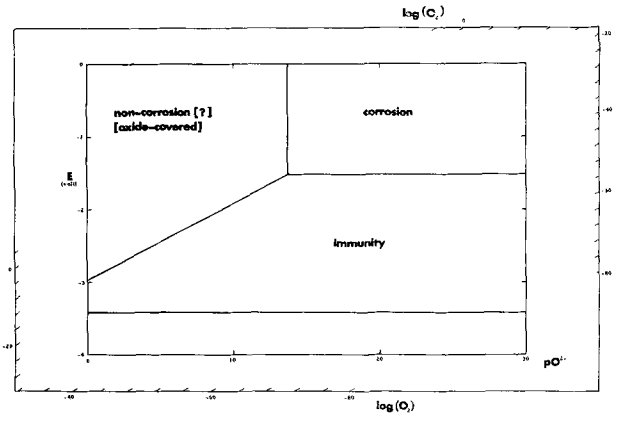

Fig. 8. Application of E-pO^{2-} diagram to corrosion of nickel in KCl melt at 800°C.

It is not proposed to consider here in detail the application of E-pO^{2-} diagrams to corrosion in fused salts, as a generalized treatment is available elsewhere (1, 2).

Electrowinning of metals from fused salts.—One of the most promising applications of E-pO^{2-} diagrams appears to be to electrowinning of metals from fused chlorides where in particular the diagrams give some guidance on the effect of variables on product purity.

Let us consider as an example the extraction of nickel by electrolysis of a bath of molten KCl containing 10^{-2} activity of Ni^{2+} ions. This is not at present a commercial process and is used only to illustrate the principles involved. Figure 4 shows that, provided the value of pO^{2-} exceeded 17.7, the Ni^{2+} ions would remain in solution as $NiCl_2$, but if the value of pO^{2-} was less than 17.7, a proportion of the Ni^{2+} ions would be precipitated as NiO. The activity of Ni^{2+} remaining in solution in the chloride melt at any pO^{2-} value less than 17.7 could be found by reference to the vertical isoactivity lines or to the scale of Ni^{2+} activities along the top of the diagram. An alternative point of view is that if the oxygen activity (partial pressure) in the system exceeded the dissociation pressure of NiO (about $10^{-13.5}$ atm), NiO would be precipitated, but if the partial pressure of oxygen were less than $10^{-13.5}$ atm, the Ni^{2+} ions would stay in solution (Fig. 4).

Deposition of nickel metal from a KCl melt containing a Ni^{2+} activity of 10^{-2}, according to Fig. 4, would not begin to occur until the potential of the cathode had fallen below −1.09v. [The potential is given by the log (Ni^{2+}) scale to the right of the diagram.] As regards the impurities in the product, the potassium content of the nickel electrodeposited at any given potential can be found from the log (K) scale on the left hand side of the diagram (extrapolation would be necessary in this particular example), and the chlorine content can be found in a similar manner. The oxygen content of the product electrodeposited at a given potential from a melt of given O^{2-} ion activity can be estimated by finding

from the external oxygen scales the value of oxygen pressure (activity) corresponding to the position of the system-point. The oxygen content of the metal product will be less, the lower the oxide ion activity in the melt and the lower the potential at which the product is deposited, but low potentials lead also to excessive contamination by potassium metal.

Besides giving quantitative guidance to the extent of product contamination in a given process under various operating conditions, E-pO^{2-} diagrams can be used as a guide to possible ways of improving product purity by altering the process itself. One possible way of obtaining a product with a lower oxygen content would be to use a solvent with a higher affinity for oxygen, *i.e.*, with a more stable oxide. For example, LiCl might be substituted for KCl. Figures 4 and 5 show that electrolysis of a melt of given $NiCl_2$ content under identical conditions of potential and pO^{2-} will lead to a product containing less oxygen if LiCl is used as solvent rather than KCl. For example, nickel metal with an oxygen activity of 10^{-10} would be obtained by electrolysis of a KCl melt with a pO^{2-} value of 20 at a potential of −1.0v, whereas the product from an LiCl melt under the same conditions would contain an oxygen activity of only 10^{-40}. In practice, of course, the preparation of a melt with a low oxide content might be more difficult for LiCl than for KCl, but these difficulties could in any case be overcome by use of an oxide "getter," which will be discussed now.

The purpose of adding a getter to the melt is to raise the pO^{2-} value and/or lower the oxygen activity in the system. For example, magnesium metal or magnesium chloride might be added to the bath to precipitate oxygen as MgO, and the values of pO^{2-} and O_2 activity obtainable in this way in KCl could be obtained from Fig. 3. For example, if Mg were gradually added so that MgO was precipitated at a constant Mg^{2+} activity of 10^{-2}, the potential of the system would fall along the vertical isoactivity line for 10^{-2} (Mg^{2+}) until a potential of −2.68v was reached, after which further additions of Mg would produce no further gettering. The addition of Mg might also lead to reduction of the $NiCl_2$ in the melt at a potential higher than −2.68v, leading to precipitation of metallic nickel, and the potentials at which precipitation would begin to occur at a given activity of $NiCl_2$ could be obtained from Fig. 4. If electrolytic separation of nickel was the requirement, the gettering process would, of course, be halted at a potential higher than that at which precipitation of metallic Ni began to occur in the body of the melt.

These simple principles are equally applicable to more complicated cases such as the winning of Ti or Zr from chloride melts, where the metal has more than one oxide or chloride. In such cases, the isoactivity lines are not always straight, and interpolation or extrapolation of activity values is sometimes less straightforward than in the simple case.

Reduction of chlorides by reactive metals.—Part of the previous section was concerned with the application of E-pO^{2-} diagrams to chloride reduction by reactive metals in the presence of a chloride solvent taking no direct part in the reaction. Many technologically important metals such as Ti or Zr are produced on a commercial scale by chloride reduction, but usually there is no "inert" chloride melt present in these processes and in its initial state the system base metal/chloride is highly reactive. However, when reduction is complete, the final products will be at, or near, equilibrium at a potential which determines the composition of all the phases then present. E-pO^{2-} diagrams can therefore be used to describe the final state of the system, the base metal chloride by-product filling the role of the "inert" chloride in previous examples, and this is particularly useful because the purity especially the oxygen content, of the product is often an important factor in determining its metallurgical properties.

As an example, the E-pO^{2-} diagram for Ni in KCl (Fig. 4) could be applied to the reduction of $NiCl_2$ to nickel by potassium metal, and to predict impurity levels in the product. If excess potassium were used, the final equilibrium potential in the system would be −3.42v and the nickel metal product would be contaminated with potassium (the extent of contamination would be determined by the solubility of K metal in Ni metal at 800°C). If less potassium were used, the equilibrium potential in the system could be measured either directly or by analysis of the KCl slag for $NiCl_2$ [which is connected with the equilibrium potential by the log (Ni^{2+}) scale to the right of the diagram]. Measurement of the oxide content of the slag would give the value of pO^{2-}. From these data, the content of oxygen and other impurities in the metallic product could be estimated as already described.

Reasoning based on these principles can give considerable guidance when a choice of process is to be made, and for example, comparison of Fig. 4 and 5 leads to the conclusion that, provided the two systems can be operated at the same levels of oxide contamination, reduction of $NiCl_2$ by Li metal is likely to lead to a metal product containing less oxygen than reduction by K metal. The extent of contamination by alkali metal would probably be roughly the same in the two cases.

As another example, let us consider the production of titanium by the reduction of $TiCl_4$. Both Mg and Na have been used as reducing agents on an industrial scale, and from Fig. 7 the relative purities of product from the two processes can be estimated for reductions at 800°C. For clarity, simplified, approximate diagrams for Ti in NaCl and Ti in $MgCl_2$ have been redrawn in Fig. 9 and 10. Comparison of these two diagrams shows immediately that for a given value of pO^{2-} the oxygen activity in the Ti metal product would be much lower for magnesium reduction than for sodium reduction. For example, let us suppose that the oxide contamination present in the two cases has been sufficient to produce a pO^{2-} value of 20 in the slag, and that in both cases excess of reductant has been used. The equilibrium potentials after reaction has gone to completion will be −3.20v in the case of sodium and −2.47v in the case of magnesium. Figure 9 shows that under these conditions, the oxygen activity in the titanium metal produced by sodium reduction would be about 10^{-62},

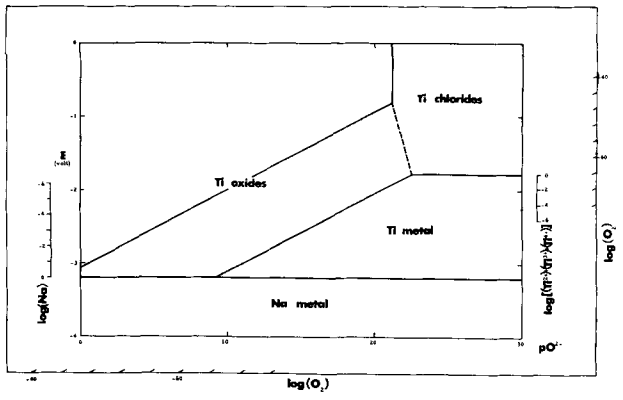

Fig. 9. E-pO^{2-} diagram for Ti-NaCl system at 800°C (approximate)

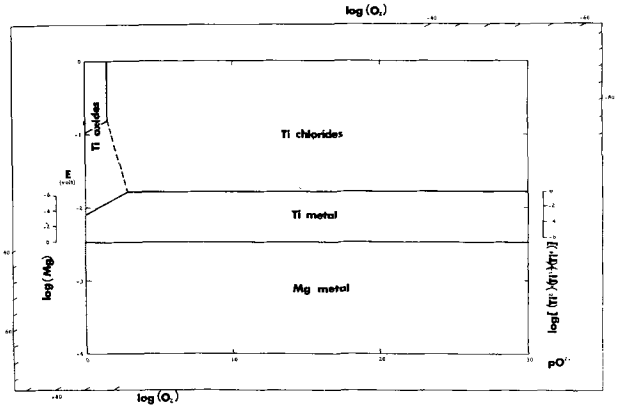

Fig. 10. E-pO^{2-} diagram for Ti-$MgCl_2$ system at 800°C (approximate).

while that in titanium produced by magnesium reduction would be about 10^{-93}. The amount of contamination by Mg or Na would depend on their solubility in titanium at 800°C, which would need to be determined experimentally. Any attempt to reduce Na or Mg contamination by carrying out reduction under conditions of a deficiency of reductant would produce titanium with a higher oxygen content, besides increasing the amount of unreacted titanium chlorides left in the $MgCl^2$ melt. The interplay of the three factors, titanium chloride content of $MgCl_2$ melt, Mg or Na content, and oxygen content of product, can be readily investigated by detailed comparison of Fig. 9 and 10. The more detailed Ti diagram (Fig. 7) would also give the actual composition of the melt in terms of $TiCl_2$, $TiCl_3$, and $TiCl_4$ if this were required.

In exactly the same way, factors affecting the purity of other metals produced by chloride reduction can be investigated, and similar trends are apparent.

Discussion

No attempt has been made to discuss in detail all possible applications of the present method, but it can be seen from the examples given that E-pO^{2-} diagrams are applicable to a wide variety of physicochemical processes in metal-fused chloride systems. The ideas presented are still at the development stage, and the approach a tentative one, but the present treatment makes an important contribution to thought in at least one major technology, the winning of metals from fused salts. The main advance here is that the method offers an approach to the prediction of impurity levels in the products of such processes. Impurity levels are calculated as activities of the impurity under equilibrium conditions and thus represent the highest product purity that could be obtained from the process under ideal conditions. Oxygen is one of the most important impurities encountered in refractory metals such as Ti or Zr, and the treatment is especially suited to deal with this impurity. It has also been shown how the levels of contamination by other metals involved in fused-salt reductions can be estimated and the treatment could easily be extended to include any impurity present in feed materials either as chloride or as metal. The treatment is applicable to electrolytic reduction processes in fused chlorides and to chloride reduction by base metals, but it obviously cannot take account of additional impurities introduced during subsequent operations, such as leaching-out of the product. In many cases, oxide contamination during leaching far exceeds the oxygen originally present in the metal product, but as nonaqueous methods become available for extracting the metal product, the purity of the original product will become more important. Unfortunately at the present time the purity of the original product cannot be maintained through the subsequent recovery operations.

Besides giving general guidance on the relative impurity levels to be expected in products from different types of processes or from a single process operated in different ways, the data may be applied to predict impurity levels in specific practical cases, when any deviation in the expected purity could be taken to indicate departure from ideal processing conditions. To make purity predictions from the E-pO^{2-} diagrams, values of only two independent variables need be known at the completion of reduction, which then fix the position of the system-point on the diagrams. It is relatively easy to measure the redox potential of a chloride melt, either directly (6, 7), or by chemical analysis for the components of any suitable redox system present. Oxide activity could also be measured by a suitable electrode, or alternatively the oxygen pressure in the system could be measured either directly or in some cases calculated from the pressures of two other suitable constituents of the atmosphere (H_2 and H_2O, for example). The measurement of redox potential and pO^{2-} in fused salts may ultimately become as routine as potential and pH measurement in aqueous systems.

Impurity levels in the products are given by the diagrams as activities and these could be translated into, say, percentages where oxygen solubilities in the product metal are available or in the case of a metallic impurity, where activity data in the appropriate alloy are available.

Besides making this contribution to an understanding of metal-winning processes, the present treatment seems also applicable to a wider field of fused-salt chemistry, and some examples involving reaction of fused chlorides with metals—the reverse of electrowinning processes—have been given. The calculation of solubility products will probably be

of particular importance. The treatment can be extended to other halides where sufficient thermodynamic data are available; the most urgent extension now is probably to fluorides because of current interest in metal winning from fluorides. It is suggested that the general features of the present method may prove of value over a wider field than fused halides; in fact, attempts have already been made to understand certain metallurgical problems by plotting thermodynamic data in a somewhat similar manner (9).

The treatment described in this paper is thermodynamic and has the limitations common to all thermodynamic treatments. The advantage of a diagrammatic method over simple consideration in terms of equations is that it allows the relative importance of all the possible reactions of the constituents of the system to be assessed at a glance.

Acknowledgment

The author wishes to thank Dr. C. Edeleanu for many stimulating discussions during the development of the ideas presented in this paper, which is published by permission of the Chairman of Tube Investments Ltd.

Manuscript received Sept. *18, 1961; revised manuscript* received Feb. 12, 1962. This paper was prepared for delivery before the 18th International Congress of Pure and Applied Chemistry, Montreal, Aug. 6-12, 1961.

Any discussion of this paper will appear in a Discussion Section to be published in the December 1962 JOURNAL.

REFERENCES

1. C. Edeleanu and R. Littlewood, *Electrochimica Acta*, **3**, 195 (1960).
2. R. Littlewood and C. Edeleanu, *Silicates Industriels*, **26**, 447 (1961).
3. M. Pourbaix, "Thermodynamics of Dilute Aqueous Solutions," Arnold, London (1949).
4. M. K. Voskresenskaya and G. N. Kashcheev, *Isvest. Sektora. Fiz. Khim. Anal.*, **27**, 255 (1956).
5. G. Delarue, *Recueil*, **79**, 510 (1960).
6. R. Littlewood and E. J. Argent, *Electrochimica Acta*, **4**, 114 (1961).
7. R. Littlewood and E. J. Argent, *ibid.*, **4**, 155 (1961).
8. M. Temkin, *Acta Physicochemica U.R.S.S.*, **20**, 411 (1945).
9. L. S. Darken and R. W. Gurry, "Physical Chemistry of Metals," McGraw-Hill Book Co., London (1953).
10. O. Kubaschewski and E. L. Evans, "Metallurgical Thermochemistry," Pergamon Press, London (1958).
11. W. J. Hamer, M. S. Malmberg, and B. Rubin, *This Journal*, **103**, 8 (1956).
12. A. Glassner, ANL-5107, Argonne National Laboratory (1953). (This is now superseded by ANL-5750).

APPENDIX

Sources of thermodynamic data.—In equilibrium calculations, it is essential to use a self-consistent set of basic data. Standard free energies of formation were calculated from the equations given by Kubaschewski and Evans (10) where possible. Where no data was available in reference (10), the chloride data of Hamer *et al.* (11) and the oxide data of Glassner (12) were used. Where data from more than one reference was available for a particular compound, these invariably agreed with each other to within a few kilocalories. In a few cases (*e.g.*, $ZrCl_3$, $ZrCl_2$), extrapolation of data to 800°C was necessary.

Table II. Standard free energies of formation at 800°C

Compounds	cal/mole	Reference
LiCl	−77,580	(12)
Li_2O	−109,660	(12)
KCl	−78,830	(10)
K_2O	−53,710	(10)
NaCl	−73,680	(10)
Na_2O	−65,350	(10)
$MgCl_2$	−113,940	(10)
MgO	−117,210	(10)
$NiCl_2$	−40,350	(11)
NiO	−33,180	(10)
$ZrCl_2$	−112,300	(11) *
$ZrCl_3$	−165,300	(11) *
$ZrCl_4$	−170,000	(11) *
ZrO_2	−210,590	(10)
$TiCl_2$	−81,560	(11) *
$TiCl_3$	−120,300	(11) *
$TiCl_4$	−152,370	(10)
TiO	−99,440	(10)
Ti_2O_3	−292,590	(10)
Ti_3O_5	−472,560	(10)
TiO_2	−173,630	(10)

* Extrapolated value.

The standard free energies used in all the calculations are given in Table II. The standard free energies of formation of oxide ion in LiCl, KCl, NaCl, and $MgCl_2$ at 800°C, calculated as in relations [9], [10], and [11], were as follows

in LiCl	:	+ 45,500 cal/mole
in KCl	:	+ 103,950 cal/mole
in NaCl	:	+ 82,010 cal/mole
in $MgCl_2$	:	− 3,270 cal/mole

Construction of the diagrams.—The condition for equilibrium of the electrochemical reaction

$$\Sigma\nu M + ne^- = 0 \qquad [15]$$

is given by (3)

$$-\Sigma\nu\mu + 23{,}060nE = 0 \qquad [16]$$

where the constituents M have free energies of formation of μ (cal/mole) and E is expressed in volts. Relation [16] enables equilibrium relations to be set up in terms of the two variables of interest, E and pO^{2-}. The basic equations used in constructing the diagrams are given below; Fig. 5, 8, 9, and 10 were constructed graphically from the other diagrams.

Figure 1

$\frac{1}{2}O_2 + 2e^- - O^{2-} = 0$ (in KCl)

$$E = -2.255 + 0.1065 \log (O_2)^{1/2} + 0.1065\, pO^{2-} \qquad [17]$$

Figure 2

$\frac{1}{2}O_2 + 2e^- - O^{2} = 0$ (in LiCl)

$$E = -0.9865 + 0.1065 \log (O_2)^{1/2} + 0.1065\, pO^{2-} \qquad [18]$$

Figure 3

$MgO - Mg^{2+} - O^{2-} = 0$

$$\log (Mg^{2+}) = -21.83 + pO^{2-} \qquad [19]$$

$Mg^{2+} - Mg + 2e^- = 0$

$$E = -2.469 + 0.1065 \log (Mg^{2+}) \qquad [20]$$

$MgO - Mg - O^{2-} + 2e^- = 0$

$$E = -4.796 + 0.1065\, pO^{2-} \qquad [21]$$

Figure 4

$NiO - Ni^{2+} - O^{2-} = 0$

$$\log (Ni^{2+}) = -19.71 + pO^{2-} \qquad [22]$$

$Ni^{2+} - Ni + 2e^- = 0$

$$E = -0.875 + 0.1065 \log (Ni^{2+}) \qquad [23]$$

$NiO - Ni - O^{2-} + 2e^- = 0$

$$E = -2.973 + 0.1065\, pO^{2-} \qquad [24]$$

Figure 6

$Zr^{4+} - Zr^{3+} + e^- = 0$

$$E = -0.204 + 0.213 \log (Zr^{4+})/(Zr^{3+}) \qquad [25]$$

$Zr^{3+} - Zr^{2+} + e^- = 0$

$$E = -2.299 + 0.213 \log (Zr^{3+})/(Zr^{2+}) \qquad [26]$$

$ZrO_2 - Zr^{4+} - 2\,O^{2-} = 0$
$\log (Zr^{4+}) = -50.6 + 2\,pO^{2-}$ [27]

$Zr^{2+} - Zr + 2e^- = 0$
$E = -2.436 + 0.1065 \log (Zr^{2+})$ [28]

$Zr^{3+} - Zr + 3e^- = 0$
$E = -2.390 + 0.071 \log (Zr^{3+})$ [29]

$Zr^{4+} - Zr + 4e^- = 0$
$E = -1.843 + 0.05325 \log (Zr^{4+})$ [30]

$ZrO_2 - Zr^{2+} - 2\,O^{2-} + 2e^- = 0$
$E = -6.639 - 0.1065 \log (Zr^{2+}) + 0.213\,pO^{2-}$ [31]

$ZrO_2 - Zr^{3+} - 2\,O^{2-} + e^- = 0$
$E = -10.98 - 0.213 \log (Zr^{3+}) + 0.426\,pO^{2-}$ [32]

$ZrO_2 - Zr - 2\,O^{2-} + 4e^- = 0$
$E = -4.537 + 0.1065\,pO^{2-}$ [33]

Figure 7

$Ti^{4+} - Ti^{3+} + e^- = 0$
$E = -1.391 + 0.213 \log (Ti^{4+})/(Ti^{3+})$ [34]

$Ti^{3+} - Ti^{2+} + e^- = 0$
$E = -1.681 + 0.213 \log (Ti^{3+})/(Ti^{2+})$ [35]

$TiO_2 - Ti^{4+} - 2\,O^{2-} = 0$
$\log (Ti^{4+}) = -46.67 + 2\,pO^{2-}$ [36]

$Ti_2O_3 - 2Ti^{3+} - 3\,O^{2-} = 0$
$\log (Ti^{3+}) = -37.04 + 3/2\,pO^{2-}$ [37]

$TiO - Ti^{2+} - O^{2-} = 0$
$\log (Ti^{2+}) = -24.79 + pO^{2-}$ [38]

$Ti^{2+} - Ti + 2e^- = 0$
$E = -1.769 + 0.1065 \log (Ti^{2+})$ [39]

$Ti^{3+} - Ti + 3e^- = 0$
$E = -1.740 + 0.071 \log (Ti^{3+})$ [40]

$Ti^{4+} - Ti + 4e^- = 0$
$E = -1.652 + 0.053 \log (Ti^{4+})$ [41]

$TiO_2 - Ti^{3+} - 2\,O^{2-} + e^- = 0$
$E = -11.32 - 0.213 \log (Ti^{3+}) + 0.426\,pO^{2-}$ [42]

$TiO_2 - Ti^{2+} - 2\,O^{2-} + 2e^- = 0$
$E = -6.504 - 0.1065 \log (Ti^{2+}) + 0.213\,pO^{2-}$ [43]

$Ti_3O_5 - 3Ti^{3+} - 5\,O^{2-} + e^- = 0$
$E = -27.38 - 0.639 \log (Ti^{3+}) + 1.065\,pO^{2-}$ [44]

$Ti_3O_5 - 3Ti^{2+} - 5\,O^{2-} + 4e^- = 0$
$E = -16.21 - 0.160 \log (Ti^{2+}) + 0.266\,pO^{2-}$ [45]

$Ti_2O_3 - 2Ti^{2+} - 3\,O^{2-} + 2e^- = 0$
$E = -9.568 - 0.213 \log (Ti^{2+}) + 0.3195\,pO^{2-}$ [46]

$Ti_3O_5 - 3Ti^{4+} - 5\,O^{2-} - 2e^- = 0$
$E = 11.61 + 0.320 \log (Ti^{4+}) - 0.532\,pO^{2-}$ [47]

$Ti_2O_3 - 2Ti^{4+} - 3\,O^{2-} - 2e^- = 0$
$E = 6.498 + 0.213 \log (Ti^{4+}) - 0.3195\,pO^{2-}$ [48]

$TiO - Ti^{3+} - O^{2-} - e^- = 0$
$E = 3.604 + 0.213 \log (Ti^{3+}) - 0.213\,pO^{2-}$ [49]

$TiO - Ti^{4+} - O^{2-} - 2e^- = 0$
$E = 1.106 + 0.1065 \log (Ti^{4+}) - 0.1065\,pO^{2-}$ [50]

$TiO_2 - Ti - 2\,O^{2-} + 4e^- = 0$
$E = -4.127 + 0.1065\,pO^{2-}$ [51]

$Ti_3O_5 - 3Ti - 5\,O^{2-} + 10e^- = 0$
$E = -4.303 + 0.1065\,pO^{2-}$ [52]

$Ti_2O_3 - 2Ti - 3\,O^{2-} + 6e^- = 0$
$E = -4.366 + 0.1065\,pO^{2-}$ [53]

$TiO - Ti - O^{2-} + 2e^- = 0$
$E = -4.410 + 0.1065\,pO^{2-}$ [54]

$Ti_2O_3 - 2TiO - O^{2-} + 2e^- = 0$
$E = -4.287 + 0.1065\,pO^{2-}$ [55]

$2Ti_3O_5 - 3Ti_2O_3 - O^{2-} + 2e^- = 0$
$E = -3.714 + 0.1065\,pO^{2-}$ [56]

$2TiO_2 - Ti_3O_5 - O^{2-} + 2e^- = 0$
$E = -3.301 + 0.1065\,pO^{2-}$ [57]

Technical Notes

A Pulse Measurement of the Semiconductor-Electrolyte Space Charge Capacity

Paul T. Wrotenbery

The University of Texas and Texas Research Associates, Austin, Texas

A. W. Nolle

The University of Texas, Austin, Texas

Measurements of the space charge capacity of a semiconductor surface in contact with an electrolytic environment have been made recently by Bohnenkamp and Engell (1), Hurd and Wrotenbery (2), Efimov and Erusalimchik (3), and Zviagin and Liutovich (4). All of these measurements were made using standard bridge techniques. In these previously reported measurements the magnitude of the measured capacity at 1-10 kc measuring frequency has been at least an order of magnitude higher than values expected on the basis of theoretical space charge calculations. This deviation has been assumed to be at least partially due to the presence of surface states with time constants small relative to the period of the measuring frequency used in these bridge measurements. Hurd and Wrotenbery have utilized a radio-frequency bridge system and extended the range of measuring frequency to a megacycle in an attempt to eliminate the discrepancy between theory and experiment; however, due to the low value of the reactive component of the measured impedance, significant results could be obtained only up to about 200 kc (2). It was with this problem of obtaining a measurement of the capacity of the space charge independent of surface states that the writers conceived the idea of utilizing a current pulse method. Pulse techniques have been used previously in metal-

electrolyte capacity measurements by Hackerman and co-workers (5). In this paper the initial results of application of this method to silicon and germanium in basic environments are reported and compared to similar results obtained previously by the bridge method (2).

The method used consists of applying a constant current pulse with rise time of less than 0.2 μsec to the silicon surface through a platinum electrode in the electrolyte. The platinum electrode is also utilized to apply a controlled polarizing potential to the surface so that the space charge distribution can be altered. Changes in the electrode potential are measured relative to a saturated calomel half cell. Initially, the constant current pulse was obtained by use of a mercury switch and a constant current source. However, the results reported here were obtained by use of the pulse generator described by Riney, Schmid, and Hackerman (5). The voltage-time relationship between the platinum electrode and the bulk of the semiconductor is recorded photographically by means of an oscilloscope which is triggered as the current pulse is applied. From this recorded response, the capacity, C, of the surface at the time the pulse is applied, *i.e.*, at $t \cong 0$, can be computed. The calculation is valid even though C may be time dependent.[1] The presence of surface states would, after some finite time of the order of the response time of the state, tend to cause a deviation of the observed response from that expected without surface states. The detection of this deviation is interpreted as evidence for the presence of surface states. The experimental system used in this work is shown in Fig. 1. The inductor, L, in the d-c bias circuit is used to prevent shorting of the current pulse through the bias supply. It can be replaced by a large resistor; however, this makes necessary a much larger bias supply voltage source. In the Riney apparatus used to obtain all results reported in this paper with the exception of the results shown in Fig. 3, a resistance is used in place of L. The Riney pulse generator contains internally the bias supply and the rectification represented by the diode, D, which is necessary to prevent the pulse generator from shorting the bias supply on application of the pulse. The resistor, R_k, was used to allow measurement of the amplitude of the current pulse. Prior to electrochemical measurements, the system was checked by use of standard components of appropriate magnitude which were inserted in place of the cell. The pulse rise time was checked by use of a resistor in place of the cell. The normally assumed semiconductor surface equivalent circuit, ignoring for the moment any possible surface states, is enclosed in dotted lines. If surface states exist, additional components must be introduced into the equivalent circuit so as to make C_p effectively a time varying capacitance. In Fig. 1, C_p represents the true space charge capacity and R_p represents an effective shunting resistance, necessary since d-c current flow occurs across the interface. The resistance, R_s, is the equivalent series resistance of the semiconductor crystal, electrolyte, and contact. If the response of this circuit to a constant current pulse of magnitude, I_o, is analyzed, it is found that the capacity, C_p, is given by

$$C_p\Big|_{t=0} = I_o\left(\frac{dE}{dt}\Big|_{t=0}\right)^{-1} \qquad [1]$$

In the absence of surface states, E would be an exponential function of time, and the voltage reponse would be linear over a time $<< R_pC_p$; and under these conditions, the slope is easily and quite accurately obtained and the capacity at $t \cong 0$ consequently determined. The only effect of R_p in determination of the initial slope is in the length of time over which the response is linear. It is not necessary for C_p to be time independent (and thus the response exponential) for this equation to hold. If surface states or other possible charge transfer sites exist, the measured capacity will in effect be frequency dependent, since it will depend on the surface-state distribution. However, in a pulse measurement this frequency dependence will be observed as a time dependence. For example, if one assumes that the frequency dependence is brought about because of a set of surface states of some response time, say, 1 μsec, then the measured capacity will be frequency dependent in the vicinity of a megacycle. At frequencies with periods small compared to a microsecond, these surface states are incapable of equilibrating, while at frequencies with periods of the order of a microsecond or greater, these states will equilibrate and thus contribute to the capacity. When the constant current pulse is applied, the surface states will accept appreciable charge after a time of the order of a microsecond has elapsed; thus, the capacity, as measured by the slope of the recorded response, will initially represent the true space charge capacity and will change with the presence of new charge transfer sites. Assuming that this change occurs at $t << R_pC_p$, *i.e.*, over the linear region, the voltage response as a function of time can thus be utilized to detect the presence of surface states by observing the change of slope of the recorded response from that at times less than the time constant of the surface state to that at times greater than the time constant of the state. If it is assumed that the capacity changes from some value C_p to some value $C_p + C_{ss}$, then the second slope would allow computation of $C_p + C_{ss}$. On the basis of this simplified model, some very interesting and informative results have been obtained.

[1] Where we find that dE/dt decreases with time for $t << R_pC_p$, we shall arbitrarily describe the system as having a time varying effective capacitance.

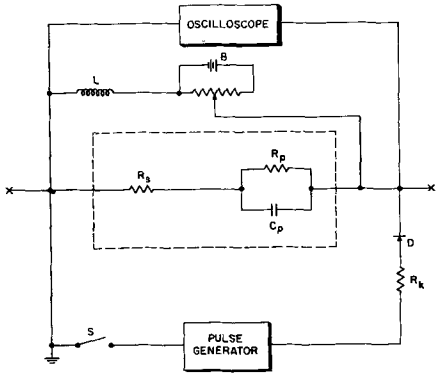

Fig. 1. Circuit diagram for pulse measurements, including semiconductor surface equivalent circuit.

The basis for estimating the effective value of R_p was the Bridge result of Bohnenkamp and Engell on germanium and Hurd and Wrotenbery on silicon (1, 2). In the vicinity of the capacity minimum, where the measurements being reported were made, and at the highest measuring frequency of 160 kc, R_p for germanium in 1*N* KOH (1) is in the range of 200-1000 ohm/cm^2. As the frequency is decreased, R_p approaches 10,000 ohm/cm^2 at 1 kc. In transforming to the time domain necessary in time dependent measurements, the approximate corresponding time dependence of R_p would be obtained by considering the R_p values associated with the reciprocal of the frequency, thus yielding from the above stated values a value of R_p at 5 μsec of 200-1000 ohm/cm^2 and increasingly larger values at greater times. The exact time dependence would have to be obtained from the Fourier Transform of the power spectrum of R_p. The results on silicon are essentially identical, with slightly higher values throughout the frequency range of 1-200 kc (2). As previously pointed out, the only effect of R_p in the linear response region is in the determination of the length of time over which the response is linear. Based on these values of R_p and theoretically computed values of C_p, the corresponding values of R_pC_p at times of the order of a microsecond and at the potentials used in this work are greater than 50 μsec in the vicinity of the minimum where good agreement with theory was obtained. At the most negative potential used in the case of germanium, *e.g.*, —0.925v relative SCE, the value of R_pC_p is in the vicinity of 20-30 μsec. For this smallest value of R_pC_p the nonlinearity at 2 μsec would be only a few per cent, and for the majority of the measurements reported, R_pC_p is sufficiently great that negligible nonlinearity would occur at 1-10 μsec.

Evidence of fast surface states with response times of the order of a few microseconds have been observed in germanium; however, in the case of silicon, no similar states were indicated. This implies that in the case of silicon, fast states, if existent, have time constants of less than a microsecond, whereas in germanium, at least some of the fast surface states have time constants greater than a microsecond. It is pointed out that the pulse rise time of 0.2 μsec sets the lower limit on observation of the voltage response.

Typical traces recorded for 10 ohm-cm n-type silicon and for 10 ohm-cm n-type germanium in 1*N* KOH are shown in Fig. 2a and 2b, respectively. The change in slope noted, in the case of germanium, during the first 2 or 3 μsec is assumed to be the result of fast surface states with time constants of the order of this time. It was found that this slope change occurs primarily on the 2-4 μsec range and that a second rather well-defined linear region follows. This rather distinct change in slope would be expected if the surface states responsible for it were of a distinct time constant of the order of 2-4 μsec. The response on silicon is linear to less than a microsecond, thus, leading to the tentative conclusion that fast states on silicon, if existent, have time constants of less than a microsecond. It is evident from the values of R_pC_p discussed previously

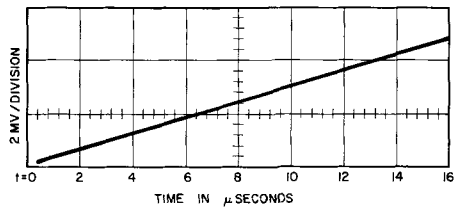

Fig. 2a. Typical voltage-time response for 10 ohm-cm n-type Si

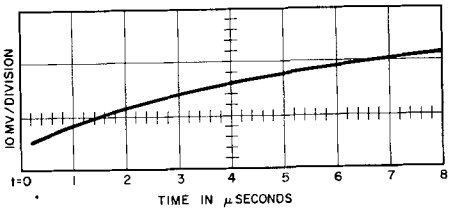

Fig. 2b. Typical voltage-time response for 10 ohm-cm n-type Ge

for germanium that this relatively large change in slope is not associated with the R_pC_p time constant.

In Fig. 3 and 4 are shown some results of capacity measurements made by this method on silicon and germanium in 1*N* KOH. In Fig. 3, a capacity measurement on silicon made by Hurd and Wrotenbery (2) by the bridge method is included for comparison. The bridge measurements were made at 10 kc, and the slope obtained from the pulse method was taken after an elapsed time of 10 μsec. It is noted that the measured capacity on silicon by the pulse method corresponds closely to the values obtained by the bridge technique at 10 kc, which would include the effect of fast surface states. The deviation between the two curves is probably due to slightly different premeasurement conditions, since the two measurements were not made on the same sample, and difference in true surface area alone can contribute significantly to this deviation. In the case of germanium (see Fig. 4), the values of capacity computed for the two slopes observed in Fig. 2b show the reduction in capacity which would be expected as the effect of equilibrating states is eliminated. It is emphasized that the difference in capacity values between the two curves in Fig. 4 is independent of direction of the current pulse, *i.e.*, whether or not it is anodic or cathodic, and also that the values are obtained

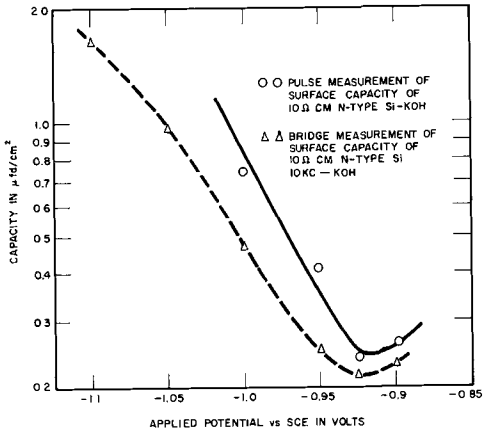

Fig. 3. Comparison of capacity of 10 ohm-cm n-type silicon measured by pulse method and by bridge method.

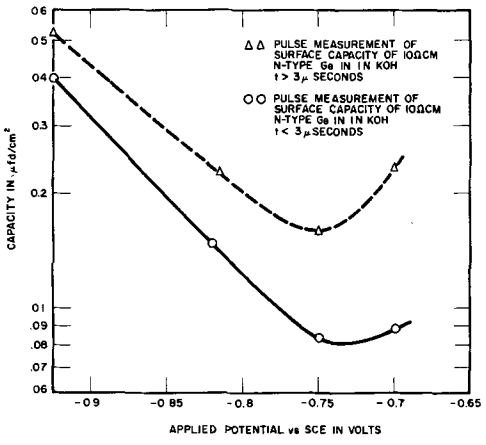

Fig. 4. Capacity of 10 ohm-cm n-type Ge, measured by pulse method showing decrease in slope obtained for times less than 3 μsec.

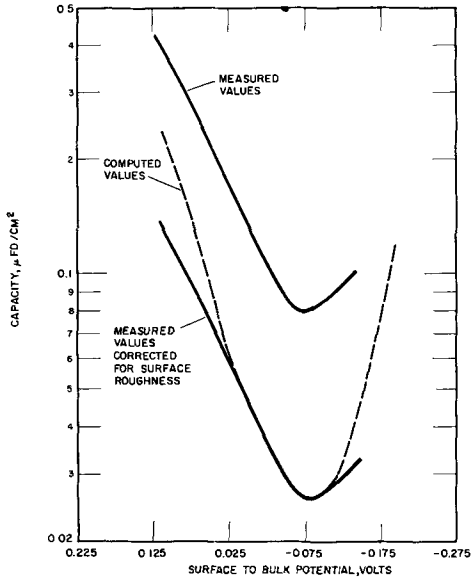

Fig. 5. Comparison of results of pulse measurement on 10 ohm-cm n-type Ge with computed values.

simultaneously in time on the same surface. The measured values on germanium at the minimum is 0.08 $\mu f/cm^2$, whereas the theoretically predicted value for the space charge of this sample is 0.027 $\mu f/cm^2$. The measured capacity of the germanium surface obtained by the above described technique is only a factor of about three greater than values predicted on the basis of previous space charge calculations (1, 2). Deviations between the true and projected surface areas could reasonably account for some or all of this difference. In Fig. 5, the measured capacity for 10 ohm-cm n-type germanium for times less than 3 μsec is compared with values theoretically calculated from the well-known Poisson-Boltzman approach.[2] The upper curve in Fig. 5 gives the measured values while the lower dotted curve gives the measured value corrected for a surface roughness factor of 3. The good agreement in the vicinity of the minimum is noted. This agreement on 10 ohm-cm germanium is somewhat better than that obtained by Bohnenkamp and Engell (1) at 160 kc bridge measurement on intrinsic germanium.

The interpretation of larger deviations from the theoretical values, obtained in all previous measurements (1-4), as being at least partially due to the fast surface states, is supported by these results. Closer agreement to theoretical space charge capacities are obtained than have previously been reported. Further application of this technique to semiconductor electrolyte systems appears a promising approach to the solution of many of the unresolved problems in these systems.

Acknowledgment

This work was supported in part by Texas Instruments, Inc., Dallas, Texas.

Manuscript received Oct. 23, 1961; revised manuscript received Feb. 11, 1962.

Any discussion of this paper will appear in a Discussion Section to be published in the December 1962 JOURNAL.

REFERENCES

1. K. Bohnenkamp and H. J. Engell, *Z. Elektrochem.*, **61**, 1184 (1957).
2. R. M. Hurd and P. T. Wrotenbery, Paper, Electrochemical Soc. Meeting, Houston, 1960; Indianapolis, 1961.
3. E. A. Efimov and I. G. Erusalimchik, *Doklady Akad. Nauk S.S.S.R.*, **124**, 609 (1959).
4. V. I. Zviagin and A. S. Liutovich, *Izvest. Akad. Nauk Uzbek S.S.S.R., Physics—Math. series No. 1*, 25 (1959).
5. J. S. Riney, G. M. Schmid, and Norman Hackerman, *Rev. Sci. Instr.*, **32**, 588 (1961).

[2] See, for example, ref. (1).

Electrolytic Etching of Germanium in Water

W. Rindner and R. C. Ellis, Jr.

Research Division, Raytheon Company, Waltham, Massachusetts

Chemical etching with water (1) has several advantages were it not for the impractically slow rate at which water attacks Ge. It is the purpose of this paper to discuss electrolytic etching with water which has been found to attack Ge at a useful rate. In addition to Ge the III-V semiconducting compounds GaAs and GaP have been etched by the same method.

Most of the work reported was done with Ge slices about 15 mils thick. These slices were held horizontally either by clip leads or metallic bases on which they were mounted by gold bonding. A positive potential was applied to the slice in actual contact with or in close proximity to a thin wire used as the negative electrode. Etching was performed by placing on the substrate a drop of water

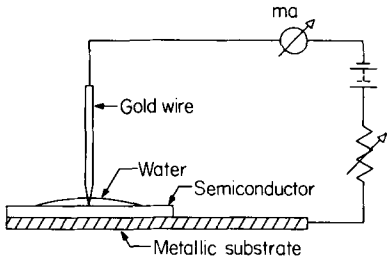

Fig. 1. Experimental arrangement for electrolytic etching in water

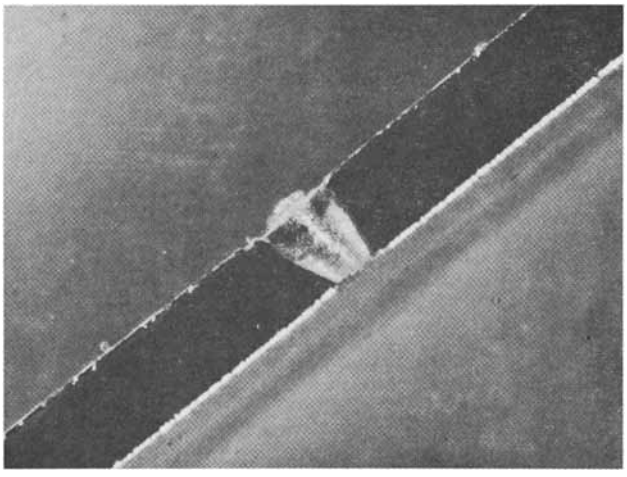

Fig. 2. Etching of a hole in Ge with a thin Au cathode. Magnification approx. 40X.

around the wire and passing currents of a few milliamperes through the system. Tap water and distilled gave the same results. Figure 1 shows the experimental arrangement and Fig. 2 a cross section of a slice etched through in the manner described.

Various materials such as Au, W, Cu, steel, and Ge were used as cathodes without very significant differences being observed among them. Similarly, Ge substrates covering the resistivity range from degenerate to near-intrinsic, both n- and p-type, were found to be equally attacked within experimental error. For good resolution the cathode had to be very close to the substrate. With high resistivity semiconductors and a sharply pointed cathode the resolution could be improved by actually making light contact between the substrate and the cathode. As the pressure was increased the resolution deteriorated and the etching rate eventually decreased by about two orders of magnitude. In the case of low resistivity material actual contact had to be avoided to allow etching to take place.

Usually current densities at the cathode were of the order of 100 amp/cm^2. With a 2 mil diameter cathode, about 5 x 10^{-7} cm^3 Ge was removed per hour. To improve resolution the current path was confined as nearly as possible to the direction of the cathode axis by immersing only the very tip in water. Alternatively, good results were obtained using a wire insulated everywhere except on the part facing the substrate.

Surrounding the point facing the cathode a concentric structure of the surface was observed as shown in Fig. 3. Around the strongly etched region

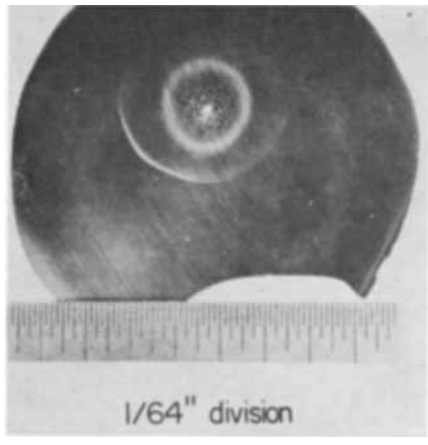

Fig. 3. Appearance of the Ge surface around the area facing the cathode.

(central white spot) there is a flat, shallow, dish-shaped depression about 3/16 in. in diameter. The entire area under the drop of water is slightly stained and is bordered by a circular white deposit. The latter was identified as hexagonal germanium oxide by its electron diffraction pattern. Removal of the oxide ring with tartaric acid solution revealed that some contact etching had taken place underneath. The dish-shaped depression is surrounded by a halo-shaped stained or etched region which corresponds in size to the extent of great turbulence during etching. The striations visible around the central spot were brought out by the etching and are due to disturbances introduced in the process of slicing the semiconductor. Etching leaves undamaged material with a smooth surface.

One experiment was performed in the following manner. A germanium slice was cut in half. The two halves were connected to a d-c power supply and brought in contact with their edges at right angles, and immersed in water. In this way the effect of current polarity on etching rate was determined under otherwise equal conditions. It was found that etching took place on both slices, but at different rates. The volume removed from the slice under positive potential was about five times larger than that removed from the other slice.

When no current was passed through the system but contact was established between cathode and substrate in the presence of water, preferential etching at the point of contact was observed after about 12 hr. This appears to be the previously described effect of contact etching (2) with water as the etchant.

Etching of GaAs and GaP was performed in a manner similar to that described for Ge.

The two conditions required for etching are met in this process: the impetus for oxidation is supplied by the potential between anode and cathode and the removal of oxidized germanium is accomplished by the slight solubility of germanium oxide in water. Excess oxide precipitates and collects in those volumes of the solution with the least turbulence.

Definition is obtained by the greatest current density being supported through the shortest distance. The greater etching rate of this region is

abetted by local heating and a subsequent increase in the solubility of GeO_2. The increased solubility facilitates the germanium removal and results in a greater conductance in the solution.

The reason for the improved resolution obtained with high resistivity substrates and light contact between the cathode and the semiconductor is probably due to the confinement of current flow being more effective than the current flow lost due to direct passage from cathode to substrate.

Hydrogen gas is formed at the cathode as expected, while little observed gas is given off at the anode. Germanium is therefore probably being oxidized to Ge^{+4} directly, unlike the case of silicon where hydrogen is found escaping from both anode and cathode in a slightly conducting solution. It has been postulated that this is due to the silicon being oxidized to Si^{+2} electrolytically with a subsequent decomposition of water by this active species (3).

Superimposed on the germanium etching is the straight electrolysis of water which in addition introduces oxygen into the water. This oxygenation by electrolysis and air solubility can account for the various contact etching phenomena observed on germanium.

Acknowledgment

The authors wish to express their appreciation of the efficient assistance in the experimental work by J. Gould and R. Flagg.

Manuscript received Aug. 14, 1961; revised manuscript received Feb. 14, 1962. This paper was prepared for presentation before the Detroit Meeting, Oct. 1-5, 1961.

Any discussion of this paper will appear in a Discussion Section to be published in the December 1962 JOURNAL.

REFERENCES

1. W. Harvey and H. Gatos, *This Journal*, **105**, 659 (1958).
2. W. Rindner and J. Lavine, Contact-Etching of Semiconductors, Solid-State Electronics, **2**, 190 (1961).
3. W. Erikson and A. Baker, Reactions of Silicon with Aqueous Solutions of HF and Various Oxidizing Agents, Electrochem. Society Meeting, Ottawa, 1958.

Discussion Section

This Discussion Section includes discussion of papers appearing in the JOURNAL of The Electrochemical Society, Vol. 108, No. 5-11 (January-November 1961). Discussion not available for this issue will appear in the Discussion Section of the December 1962 JOURNAL.

Photoluminescent Effects in Contact Electroluminescence

B. Morosin and F. A. Haak (pp. 477-478, Vol. 108, No. 5)

W. Lehmann[1]: The emission of visible radiation from a mechanical mixture of an ordinarily non-electroluminescent phosphor powder and a metal (or well-conducting semiconductor) powder, suspended in castor oil and subjected to an alternating electric field, was described by Lehmann in 1957.[2] The effect was qualitatively explained as electroluminescence of the phosphor particles in the extremely high electric field strength near sharp edges of the metal particles and, because of the necessary close contact between the phosphor and the metal, was termed "Contact Electroluminescence." These experiments recently were repeated by Morosin and Haak. They explain the light emission as due to the glow of local discharges which partly can be seen directly by eye (violet in air) or which may excite adjacent phosphor particles to photoluminescent emission, which is characteristic of the particular phosphor. They supported their view by the observation that emission could even be obtained with cells containing metal powder but no phosphor.

Morosin and Haak's explanation is identical to that presented by Herwelly[3] who tried to understand the Destriau Effect, *i.e.*, the "intrinsic" electroluminescence of ZnS-type phosphors, as photoluminescence excited by the ultraviolet generated in glow discharges near the phosphor particles. It has been shown fairly convincingly by Destriau[4] that this explanation does not hold in the case of "intrinsic" electroluminescence, and it will be shown here that it does not hold either in the case of contact electroluminescence. The arguments to be used are almost identical to those used by Destriau to oppose Herwelly's view.

A glow discharge can, indeed, be observed in many cases under improper operating conditions. It may occur in air bubbles accidentally present in the cell or in bubbles caused by gaseous decomposition products of the oil and, in either case, is favored by the presence of metal or other conducting particles. Such glow can also visibly photoexcite adjacent phosphor particles. However, it is fairly easy to distinguish this photoluminescence from real electro- or contact-electroluminescence. The following facts may be mentioned.

1. Many, but not all, phosphors respond with different emission colors to photo- and electroluminescence.[5] The color of contact electroluminescence also may vary with variation of the frequency of the exciting field in the same fashion as for intrinsic electroluminescence (*e.g.*, blue at high and green at low frequencies). The color of photoluminescence is independent of the exciting frequency of the glow discharge.

2. If contact electroluminescence were actually photoluminescence, then all efficient photoluminescent phosphors should respond about equally well. This is by far not the case. As an example, green-emitting zinc silicate activated by manganese responds very well to an alternating electric field if mixed with a metal powder while red-emitting magnesium fluorogermanate, also activated by manganese, does not respond at all. One may even mix equal parts of these two phosphors with a metal powder. The germanate can well be excited by ultraviolet of wave length 2537Å or 3650Å, the silicate practically only by 2537Å. Hence, the photoluminescent emission spectrum consists of the green band of the silicate and of the red of the germanate simultaneously if excited by 2537Å, and practically only of the red germanate emission if excited by 3650Å. However, if subjected to contact electroluminescence, the spectrum of the blend shows only the green emission of the silicate phosphor while the germanate remains completely dead.

3. Morosin and Haak explain the color differences between contact electroluminescence and photoluminescence, which can sometimes be observed, by a superposition of the violet color of the glow with the emission of the phosphor excited by this glow. If so, then the color shift should be observed with all phosphors, not only with a few as actually is the case. Further, Morosin and Haak obviously do not realize that a superposition of the color of photoluminescence with the violet of the glow discharge in air does not always agree with the observed color of contact electroluminescence. As an example, the yellow photoemission of the (Zn,Cd)S:Ag phosphor mentioned in the table in Footnote 2 superimposed to the violet of a glow in air should result in a pink to reddish purple color, while yellow-green actually

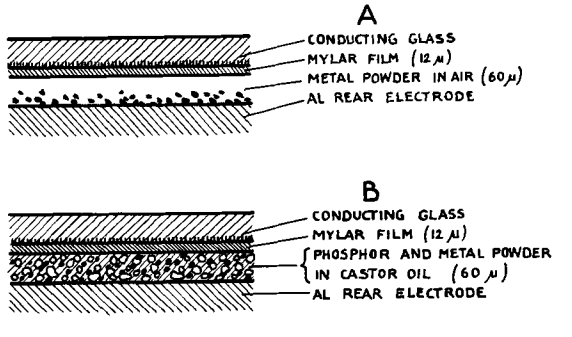

Fig. 1. The experimental arrangement used. A—Metal (or semiconductor) powder in air producing glow discharge. B—Phosphor and metal (or semiconductor) powder in castor oil producing contact electroluminescence.

[1] Research Dept., Westinghouse Electric Corp., Bloomfield, N. J.
[2] W. Lehmann, *This Journal*, 104, 45 (1957).
[3] A. Herwelly, *Acta Physica Austriaca*, 5, 30 (1951).
[4] G. Destriau, *J. phys. radium*, 14, 307 (1953).
[5] The table in Footnote 2 lists six examples instead of only one as stated by Morosin and Haak.

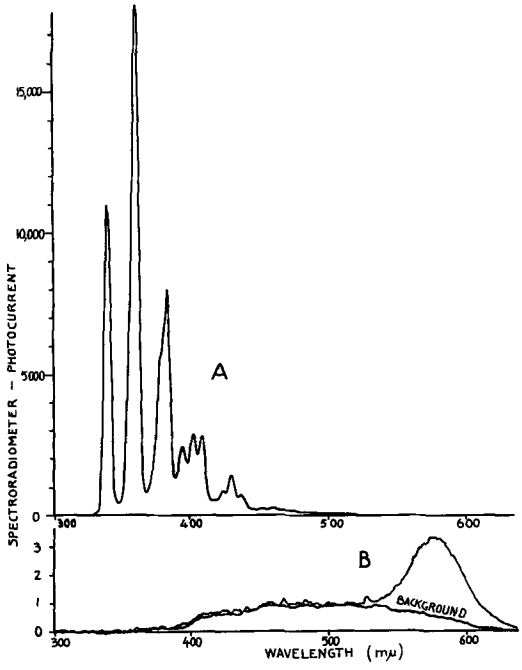

Fig. 2. A—Spectrum of a glow discharge in air (arrangement of Fig. 1A). B—Spectrum of contact electroluminescence of a ZnS:Mn phosphor and aluminum powder in castor oil (arrangement of Fig. 1B). Both spectra are uncorrected, as recorded. The background in spectrum B is due to stray light from room illumination.

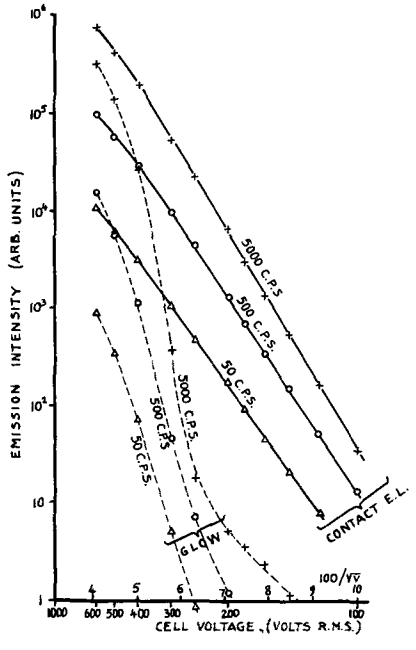

Fig. 3. Brightness-voltage dependences of a glow discharge (aluminum powder in air, arrangement of Fig. 1A) and of contact electroluminescence (green ZnS:Cu,Cl phosphor in contact with Cu_2S, arrangement of Fig. 1B.

was observed. Finally, the characteristic line spectrum of a glow discharge should be easily detectable in the spectrum of contact electroluminescence if it were present. The examples of Fig. 2 of this discussion (using the experimental arrangement of Fig. 1) show that this is not the case and that the emission of contact electroluminescence under proper conditions consists only of the spectrum emitted by the phosphor.

4. The emission of contact electroluminescence normally is confined to many small "spots" scattered over the area of the cell. If such spots were due to photoexcitation, the exciting glow discharge would also have to be concentrated in very small spots and, hence, to be very intense within each spot (otherwise, the intense but very localized emission of the phosphor could not be understood). However, microscopic examination of contact electroluminescence reveals no visible glow discharge in the vicinity of emitting spots. On the other hand, glow discharges require dimensions of many times the mean free path of the gas molecules, which in air at atmospheric pressure is about 10^{-5} cm, *i.e.*, just slightly below the limit of resolution of a good microscope (2 to 3 x 10^{-5} cm). Hence, an intense glow discharge in submicroscopically small dimensions is most unlikely.

5. The time-average of the light emittted by a phosphor excited by contact electroluminescence is fairly stable. Its dependence on the exciting voltage can well be described by the same equations which hold in the case of intrinsic electroluminescence, *e.g.*, by $L = L_o \exp [-(V_o/V)^{1/2}]$, where L_o and V_o are constants. An example of a green ZnS:Cu,Cl phosphor (originally nonelectroluminescent) in contact with Cu_2S (arrangement of Fig. 1B) is shown in Fig. 3. The emission created by a glow discharge in air (arrangement of Fig. 1A) ordinarily is much less stable and tends to strong fluctuations in intensity. The time average of its emission does not approach straight lines in Fig. 3 and, hence, cannot be described by the above equation.

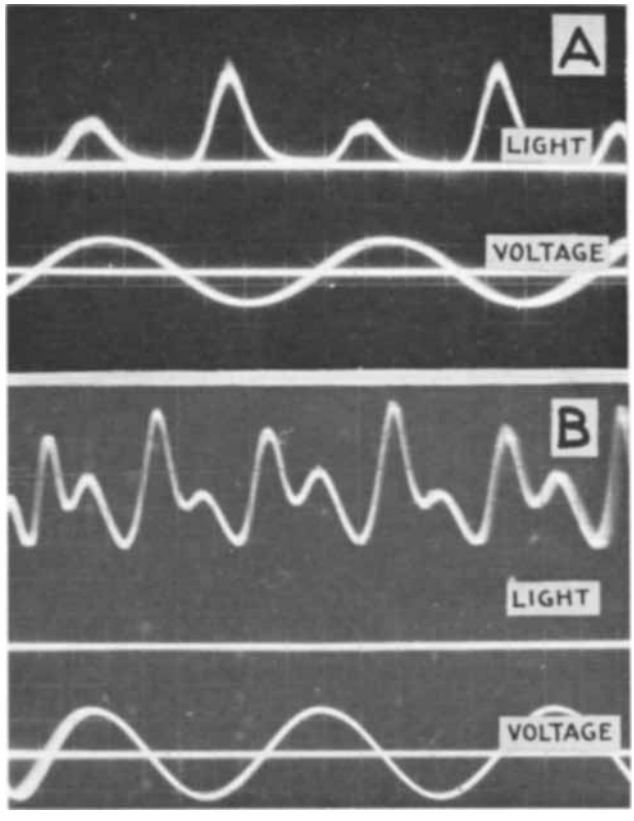

Fig. 4. Light waves of a glow discharge in air (A—arrangement of Fig. 1A, aluminum powder) and of contact electroluminescence (B—arrangement of Fig. 1B, blue-green ZnS:Cu,Cl phosphor in contact with Cu_2S), both excited by a sinusoidal voltage of 100 cps.

6. The brightness waves of contact electroluminescence excited by a sinusoidal voltage resemble those observed in "intrinsic" electroluminescence and frequently show, as do the latter, a main and a secondary peak for each half cycle of the exciting voltage. An example is shown in Fig. 4B. The brightness waves of a glow discharge in air are quite different (Fig. 4A) and never show secondary peaks.

These effects prove that contact electroluminescence can very easily be distinguished from photoluminescence excited by local glow discharges and that its mechanism in all likelihood is identical to that of intrinsic electroluminescence. In all cases, a well-conducting second phase must be present and in intimate contact with the phosphor. This may be metal particles, *etc.*, in case of contact electroluminescence, or thin coats of copper sulfide or metallic copper on the surfaces,[6] or inclusions of Cu_2S inside of the phosphor particles.[7] Inclusions of Cu_2S segregate predominantly in lattice faults, *e.g.*, in stacking faults, rather than in the otherwise undisturbed ZnS lattice. A correlation between the occurrence of electroluminescence and of stacking faults thus can readily be understood.

B. Morosin[8] and F. A. Haak[9]: Our Technical Note gave experimental evidence of the generation of ultraviolet light in these so-called contact EL cells. To state that cells in which this u.v. light is observed are operating under "improper operating conditions" is justified only if one defines what the "proper" conditions are. The occasional apparent absence of u.v. emission from certain cells may well be due to the high efficiency of absorption of short wave-length radiation by the phosphor and by the experimental cell, and is determined by the thickness and packing density of the cell. Also: the presence of only a small amount of u.v. with respect to visible light in the output of such cells does not mean that only a small amount of u.v. is internally produced. Probably it should be pointed out that we observed the u.v. bands only on photographs of several hours' exposure. Let us keep in mind the well-known wave-length dependence of intensity as far as our eye is concerned in the evaluation of comments by Lehmann regarding the addition of colors.

Conclusion: We have shown that u.v. light is generated in contact EL cells which, to the best of our knowledge, are operating properly. We obviously were aware of Herwelly's paper (our reference 3) and Destriau's response to it (Lehmann's Footnote 4); however, in our note we did not question the existence of "intrinsic" electroluminescence. The only pertinent criticism of our paper would be to show unambiguously that in certain cases no u.v. radiation is generated internally (which is not the same as emitted from the cell). Interested scientific investigators may easily quench their intellectual curiosities by performing a few simple experiments which will elucidate for them the so-called phenomenon of "contact" electroluminescence.

[6] P. Zalm, G. Diemer, and H. A. Klasens, *Philips Research Repts.*, 9, 81 (1954).
[7] W. Lehmann, *This Journal*, 107, 657 (1960).
[8] Kassel-Harleshausen, Niederfeldstr. 38 E/O, Western Germany.
[9] K. Heldmaier, "Leitfähigkeitsmessungen und Verlustfaktormessungen an Isolieröl, abhängig von Spannung, Temperatur und relativer Feuchtigkeit," Diploma paper, Institute for High Tension Techniques, Technical University Fridericiana, Karlsruhe (1959/1960).

The Conductivity of Undehydrated Insulating Liquids

R. Guizonnier (pp. 519-522, Vol. 108, No. 6)

E. Baumann[8]: Professor Guizonnier has shown that the conductivity of insulating liquids and waxes must be due to the moisture content in these materials. We measured[9,10] the conductivity of paraffin oil with a moisture content of less than 50%. Thus we found the activation energies and the gram molecules produced per unit of volume and time of dissociated light and heavy water, respectively. The transformer insulating oil examined contained 13.3% aromatic bond parts, 22.3% naphthenic, and 64.4% paraffinic bond parts. Its mean molecular weight was 267. At 20°C the oil water-saturation content was 50 ppm[11] H_2O. The results described in this paper were obtained at a water content of 12 ppm. Consequently, at 20°C our oil had a relative humidity of 24%. The relative humidity decreases at steady water content with increasing temperature. So the measurements were carried out far from the saturation point of water solubility and there could be no disturbing minimum of the conductivity (*see* Fig. 5 of the discussed paper).

Measuring set.—First, the examined oil was moistened with distilled light water (H_2O) and then with heavy water (D_2O) having a purity of 96.7 mole %. We measured the conduction current in three oil samples of light and heavy water, respectively, at temperatures from 20° to 70°C with the applied voltage increasing and decreasing. Out of these six measuring points, the average was calculated. The voltage of the power supply was highly stable having an alternating current ripple of less than 0.01%.

Between 150v and 800v, the voltage could be adjusted to a certain value with an accuracy of ±0.25%. The average field strength during measurements could be varied from 400 v/cm to 2300 v/cm at a gap distance of 0.376 cm ±0.5% between the cylindrical measuring electrodes. We measured the current with the sensibility of 10^{-12}Å and an accuracy of about ±3% in a measuring range up to $7 \cdot 10^{-11}$Å. The testing cell had shielding electrodes and was airtight.

Measuring procedure.—As soon as the temperature balance was reached a 50-cycle a-c voltage was applied up to 9 kv and the loss factors were measured. Then we applied a continuous voltage of 400v for 6 min. The desired test d-c voltage was fixed and we waited 1.5 to 2 min until we read the current, such that it had been stable for 30 sec. Then we measured the current as a function of the voltage at different temperatures between 20° and 70°C. In all the cases, the current density first increased linearly with the applied field strength reaching a saturation point near a field strength E_s (*see* Fig. 1 of this discussion).

Evaluation of the results.—As we can see from Fig. 1, there are two components of the current density j_1 and j_3 which are proportional to the test field strength. In the case of j_1, this is only true for $E < E_s$. If the field strength is higher ($E > E_s$) j_1 turns into

[10] My thanks are due to Professor H. Lau, director of the Institute of High Tension Techniques, Technical University of Karlsruhe; under his guidance, the tests (Footnote 9) could be completed successfully
[11] ppm = parts per million and means a weight ratio.

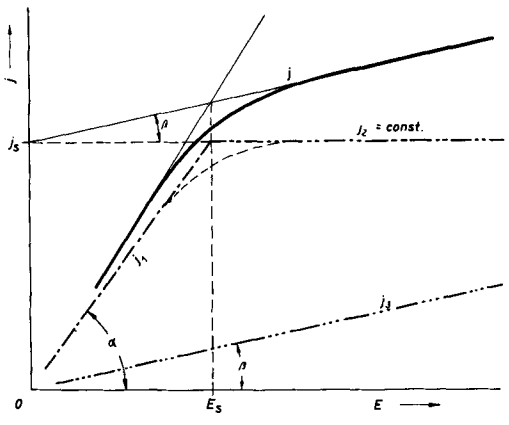

Fig. 1

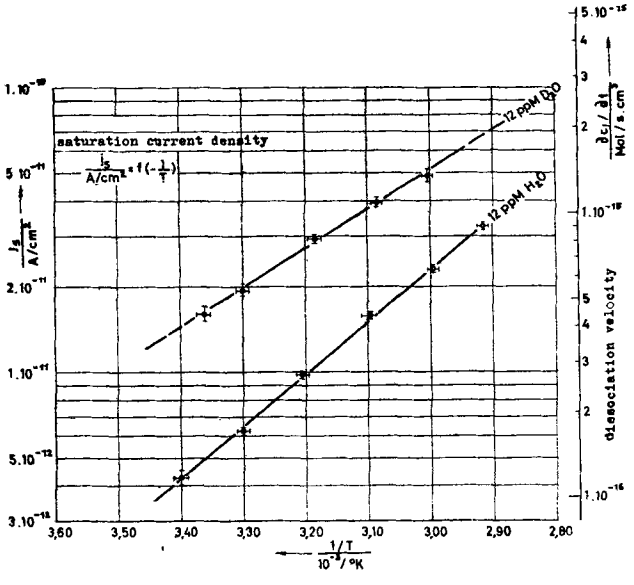

Fig. 2

the saturation current density j_2 which does not depend on the electric field.

Here we are going to treat exclusively the temperature dependence of this field-independent saturation current density $j_2 = j_s$. In our paraffin oil, we measured the saturation current and the so-called saturation field strength E_s at a humidity content of 12 ppm heavy and 12 ppm light water, respectively. While the values for E_s are very nearly independent from the temperature, the saturation current density j_s increases exponentially with the negative reciprocal value of the absolute temperature (in degrees Kelvin). Fig. 2 of this discussion shows how the saturation currents depend on the reciprocal value of the absolute temperature at a humidity content of 12 ppm H_2O and 12 ppm D_2O, respectively.

From the rise of the line

$$\ln j_s/j_o = w/k \cdot T \qquad (see\ Fig.\ 2)$$

we can calculate an activation energy w (k = Boltzmann constant, T = absolute temperature in degrees Kelvin). Above the saturation field strength E_s, we found that the viscosity variation of the oil with temperature did not influence the motion of the charge carriers.

Therefore, w represents an activation energy required to produce disintegration. The saturation field strength E_s is the same at all temperatures between 20° and 70°C. For light water (H_2O), E_s is 0.8 kv/cm, and, for heavy water (D_2O), E_s is 1.1 kv/cm.

From the field independent components of the saturation current which were measured at field strength $E > E_s$, we calculated the energies required to produce disintegration for the essentially current contributing components of light and heavy water in the insulating oil.

From Fig. 2 (12 ppm H_2O in oil) follows:

$$w_{H_2O} = 0.4\ eV \pm 3\%$$

and for 12 ppm D_2O in the paraffin oil:

$$w_{D_2O} = 0.27\ eV \pm 9\%$$

The activation energy w is approximately 1.4 times greater in oil with light water than in oil with heavy water. Thereby it is proved true that the protons and deuterons, respectively, influence the conductivity in moistened oil decisively. Our former opinions about the water influence on the dielectric qualities of insulating oils[12, 13] are herewith well confirmed.

Conclusion.—By means of many measurements, Professor Guizonnier has shown that the conductivity in insulating oils and waxes must be due to their water content. We measured and examined the saturation current of paraffin oil which was moistened with light and heavy water, respectively. We found that the activation energy is 1.4 times greater in light water than in heavy water. This pronounced isotope effect means that protons and deuterons, respectively, influence the conductivity in paraffin oil decisively.

From the characteristic of the saturation current dependent on the absolute temperature [in degrees Kelvin (*see* Fig. 2)], we see that the thermal motion of the particles causes conductivity when the field strength is smaller than 3 kv/cm. According to Eigen and De Maeyer,[14] it is possible to calculate a dissociation velocity from the field independent saturation current, at a given water concentration. The dissociation velocity is shown in the right scale of Fig. 2. At the same water concentration, more dissociation processes take place per unit of time and volume with heavy water in the oil than with light water in it.

In this thermal process, the formation of free ions may take place in several phases successively. The phase which determines the speed of the whole process needs most activation energy, and it is this energy which we measured. From the very clear isotope effect, we see that it can only be a proton transition.

The absolute values of the activation energies alone are not sufficient to design the correct model of the reaction as to where the proton transition takes place. It is necessary to examine also further test results concerning the dependence of the current on the water concentration and on the field strength. Supplementary measurements, also in other oil samples, must be made in order to investigate more ex-

[12] E. Baumann, "Measurements of the Breakdown in Insulating Oils," Paper No. 12, Symposium on Liquid Dielectrics of The Electrochemical Society, May 5, 1959, Philadelphia, Pa.

[13] E. Baumann, "Messung der Durchschlagsspannung in Isolierölen," *Bull. schweiz. elektrotech. Ver.*, 51, No. 6, 254 (1960).

[14] M. Eigen and L. De Maeyer, "Ein stationäres Feldverfahren zur Untersuchung von Dissoziationsprozessen in Flüssigkeiten und Festkörpern," *Z. Elektrochem.*, reports of the Bunsen Society for Physical Chemistry, 60, H. 9/10, 1037 (1956).

actly the proton transition we found in moistened paraffin oil.

R. Guizonnier: In conditions slightly different from ours, Dr. Baumann found the relation between current and temperature that we already mentioned.

While, though approximately, we sought the initial current i_o after the application of the tension, Dr. Baumann applies, first of all, an alternating current of 50 Hertz, then 400v during 6 min, and, at last, the continuous tension V in experiment during 1.5 to 2 min, the current being read as soon as it seems to be stable for 30 sec.

Instead of considering the value thus measured, he draws the curb $i = f(V)$ and the size he thinks of is what we must call the current of saturation i_s. When the liquid is dry enough—and that is the case—the difference between i_o, that we measured, and i_s, considered by Dr. Baumann, is not very important.

Under such conditions, the value $W = 0.4$ ev that we found, is reached when the field is superior to E_s. We made evident recently[15] that, when the applied field is very low (some volts/cm), the exponential form of the relation between i_o and T is preserved, but then $W = 0.27$ ev.

It is interesting to see that this value is found by Dr. Baumann, when heavy water is added to oil. As we pointed out, that is the value obtained when using deionized water with low fields, or only distilled water.

Desensitization of Zirconium Powder, Especially Zirconium Powder Used in Primers

Peter Karlowicz, George Norwitz, and Joseph Cohen (pp. 659-663, Vol. 108, No. 7)

D. R. Zaremski[16]: This article, which appears in the July 1961 JOURNAL, has been reviewed with great interest in view of its close relationship to work performed by our laboratory in the year 1956. Specifically, the objectives of our experimental work at that time were to investigate the pyrophoric properties of potentially hazardous scrap materials, such as titanium and zirconium grindings, and to determine ways and means for our production plants to dispose of these materials safely. As an approach to the latter objective, treatment in acid solutions was one of the methods evaluated with the thought in mind that, if proven successful, it would readily lend itself to mill operations where spent nitric-hydrofluoric pickle liquors, available in large quantity, could be used as the treating medium.

Briefly, the results of our work indicated that disposition through acid treating was highly satisfactory although the type of acid medium used appeared to be an important factor. Greatest success was met in using solutions containing ½% to 1% hydrofluoric acid. Good results also were obtained in nitric-hydrofluoric acid solutions and aqua regia (3 HCl:1 HNO_3). Sulfuric acid solutions, on the other hand, were not too effective.

[15] R. Guizonnier, *Comptes rendus Académie des Sciences*, July 24, 1961.
[16] Research & Development Labs., Allegheny Ludlum Steel Corp., Brackenridge, Pa.

Our methods for evaluating the effects of a given acid treatment were not too involved and consisted simply of dispersing treated and untreated grindings over a open flame and observing the relative tendencies for the materials to ignite. In following this procedure, untreated zirconium samples and those treated in sulfuric acid solutions were found to emit a radiant white spark. In contrast, samples treated in aqua regia and in solutions containing hydrofluoric acid were found inert, exhibiting no ignition tendencies. Spent pickle liquors, as discovered in subsequent studies, also produced the desired effect provided the solutions contained at least ½% hydrofluoric acid.

In concluding this discussion, we would like to emphasize the fact that the treatments described above and used by Allegheny Ludlum were for the sole purpose of desensitizing material which was to be disposed of. In no instance were our intentions related to reclaiming material or preparing it for another application.

Anodic Polarization of Stainless Steel in Chloride Solutions

G. M. Schmid and Norman Hackerman (pp. 741-744, Vol. 108, No. 8)

U. R. Evans[17]: The authors kindly quote a very early paper by myself. This, however, concerned unalloyed iron, not stainless steel. Some later papers from my laboratory describe work on stainless steel and seem to provide evidence of the existence of a film. For instance, a detailed study carried out by Berwick[18] aimed expressly at deciding whether the resistance of stainless steel to dilute sulfuric acid should be related to adsorbed oxygen or to an oxide film; Berwick's measurements were capable of being explained on the assumption of a film thickening by the logarithmic law, but appeared incapable of explanation by assuming adsorbed oxygen. Still later, Stern,[19] using a different method, reached the conclusion that there was a film growing by the logarithmic law; as he appears to have been unaware of Berwick's work, this probably can be regarded as entirely independent evidence.

It is thought that a satisfactory theory should explain not only the new experimental data put forward in the paper propounding the theory, but also the measurements of others—providing that those measurements are regarded as experimentally accurate. It would be interesting to know how the authors of the paper under discussion are inclined to interpret the results of Stern and of Berwick.

G. M. Schmid and Norman Hackerman: We thank Dr. Evans for his remarks and the interest he has shown in this work.

We agree that the work cited by Dr. Evans provides experimental evidence for the growth of an oxide film according to a logarithmic law. We also agree that passivity of iron and stainless steel is not caused by physically adsorbed oxygen.

[17] Cambridge University, Grange Rd., Cambridge, England.
[18] I. D. G. Berwick and U. R. Evans, *J. Appl. Chem.*, 2, 576 (1952).
[19] M. Stern, *This Journal*, 106, 376 (1959).

It has to be pointed out, however, that the first step in the formation of, as well as the last step in the reduction of, an oxide film must involve a chemisorbed layer of oxygen or some oxygen-containing species. Our contention is that this layer of chemisorbed oxygen causes the rapid electrochemical changes associated with passivity, permanent passivity being effected by subsequent growth of an oxide film, the structure of which depends on the nature of the earlier step.[20] In this laboratory, stripping experiments on iron have shown that coverages of much less than one monolayer are sufficient to cause the metal to show passive characteristics.[21] Both the work of Berwick and Evans and that of Stern is entirely compatible with this point of view.

Porosity Measurements on Gold Plated Copper

M. S. Frant (pp. 774-778, Vol. 108, No. 8)

Wm. H. Fischer[22]: The use of the ammonia-ammonium persulfate solution as a test for porosity in gold plates on copper is quite interesting. About five years ago, a somewhat similar method was employed to evaluate the porosity of Inconel-clad copper.

The test solution consisted of 400g of ammonium persulfate per liter of distilled water plus 2 liters of concentrated ammonium hydroxide, thus being somewhat stronger than that used by Frant.

The test was performed by immersing a constant surface area of the Inconel-clad copper in a fixed volume of test solution in a test tube at room temperature without agitation. At ¼, ½, 1 hr, and each succeeding hour, up to 8 hours, a cuvetteful of solution was removed and its copper content determined with a Fisher Electrophotometer using a 650Å red filter, against a distilled water blank. Comparison tests employing a Beckman DK-2 Ratio Recording Spectrophotometer were in good agreement with the filter photometer tests. The solution was returned to the test tube after each reading. The data were plotted as ppm copper *vs.* time as shown in Fig. 1 of this discussion which portrays the four main types of curves obtained.

Type 1 curves are obtained from samples having large holes in the cladding. The blue color appears almost immediately upon immersion of the sample and rapidly increases in density. The test solution may get hot and evolve gas so vigorously as to appear to be boiling.

Type 2 curves are obtained from samples having one or both of two types of defects in the cladding: 1—copper on the surface or 2—small holes or thin spots in the cladding. The test solution may enlarge the small holes or perforate the thin spots. Hole enlargement may be due to gas evolution rather than to direct attack on the Inconel, although the test solution does attack Inconel slowly. Independent experiments have shown that etching accompanied by preferential removal of nickel from the alloy occurs. However, when solid Inconel is immersed in the test solution for periods up to 8 hr, a reading equivalent to less than 5 ppm copper is obtained. Emission spectrography of used solution indicated no significant amounts of any of the three main constituents of Inconel: nickel, chromium, or iron. Rough calculations showed that nickel is about 60 times less sensitive in this test than is copper. This means that if 60 ppm nickel were removed from the alloy by the test solution, it would be read as 1 ppm copper.

Type 3 curves are obtained from samples whose Inconel surface is contaminated by copper but which has no holes or thin spots.

Type 4 curves are given by cladded specimens free of all defects. The color developed is yellow in hue, not blue. It is due mainly to reagent deterioration.

Occasionally, an anomalous green color is developed. This is not due to nickel or very small amounts of copper. Its cause remains unknown. However, it does not interfere with interpretation of the results.

This test was designed as an incoming inspection method for cladded material to weed out unsuitable material. An unexpected bonus was that the shapes of the curves obtained allowed the identification of the causes of the rejections, thus aiding in preventing their reoccurrence. Thus, by using not only the amount of copper removed but also its rate of removal, additional useful information was gained.

M. S. Frant: Fischer's experience with the use of the ammonia-ammonium persulfate solution as a porosity test for Inconel-clad copper is most enlightening, particularly his comments on being able to use the test despite a very slight attack of nickel by the reagent, and his use of the test to distinguish different causes of failure.

About four years ago, we used the same reagent as a means of quantitatively measuring corrosion rates for nickel-plated copper in salt spray. The basic concept is that the observed "porosity" will measure the discontinuities produced in the plating as corrosion proceeds. The test is regarded as destructive, and the corroded samples are discarded after the porosity test. The test was run by exposing identical pieces from a sulfamate bath[23] (prepared in a single barrel load—average thickness 15μ) to varying lengths of time in salt spray, and then measuring the amount of copper dissolved by the reagent under standard conditions (the same as those described on page 775 of the discussed paper). When the log of the

[20] Norman Hackerman, *Z. Elektrochem.*, 62, 632 (1958); K. Schwabe, *Electrochim. Acta*, 3, 186 (1960).
[21] W. H. Wade and Norman Hackerman, *Trans. Faraday Soc.*, 53, 420 (1957).
[22] General Engineering Lab., General Electric Co., Schenectady, N. Y.

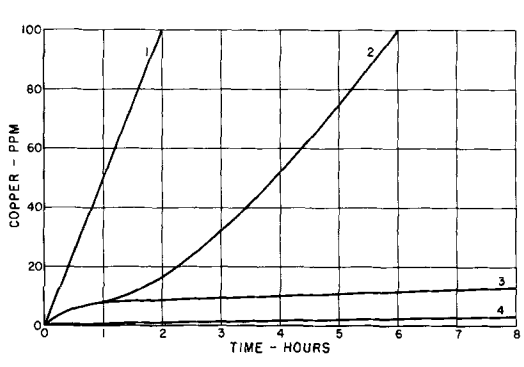

Fig. 1. Typical absorbance *vs.* time curves obtained in persulfate test for copper.

[23] R. C. Barrett, *Tech. Proc. Am. Electroplaters' Soc.*, 41, 169 (1954).

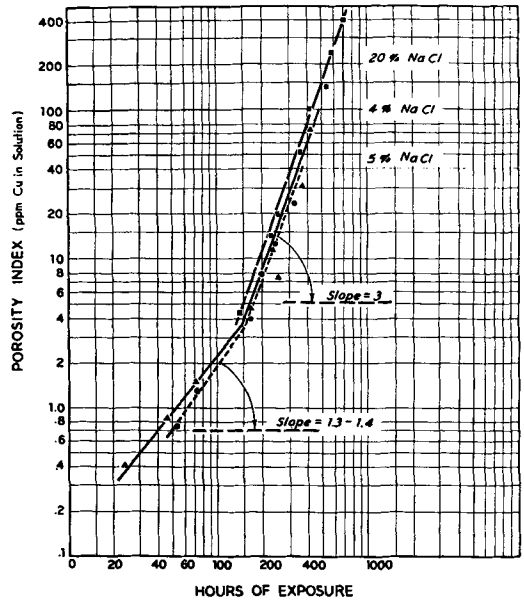

Fig. 1. Salt spray corrosion rates for sulfamate nickel, porosity index vs. time of exposure. Log-lot plot: 4% NaCl solution, solid triangles; 5% NaCl solution, solid circles; 20% NaCl solution, solid squares.

amount of copper dissolved is plotted against the log of the time of salt spray exposure, an initial period is observed with a slope of *1.3* to *1.4* (*See* Fig. 1 published here.) After about 150 hr the slope becomes almost exactly proportional to the *cube* of the time of exposure. As can be seen from the graph, it is independent of the salt spray concentration.

Similar experiments on two sets of nickel samples from the Watts bath gave the following slopes: 5% NaCl—*1.85, 2.10;* 20% NaCl—*2.45, 1.99.* For Watts nickel, the amount of copper dissolved by the reagent is approximately proportional to the *square* of the exposure time.

A portion of the sulfamate nickel samples used above were chrome plated and the test repeated. Three distinct slopes were observed: a zero slope (at 0.6 ppm copper) for the first 60 hr; from 60 to 150 hr the slope was about 0.7; thereafter the slope was 2.0.

In our previous work in which this same reagent was used to follow the corrosion rate of tin-plated copper in salt spray,[24] the amount of copper dissolved was found to vary as the *square* of the time of exposure. Results from the persulfate reagent technique agree with the corrosion rate for tin measured by following the corrosion of thin tin films by light transmission.[25] The square rate was attributed to a radial (or 2-dimensional) growth of pits; while it can be visualized in terms of a single pit, the average of many pits would have the same rate of change of area.

If this line of reasoning holds for nickel and chrome plate, then a slope of *2* is believed to indicate that it is the Watts nickel or chrome which is attacked even after basis metal is exposed. The slope of *3* obtained with sulfamate nickel after a variable initial slope would indicate that, once the corrosion

[24] M. S. Frant, *Plating*, 45, 157 (1958).
[25] M. S. Frant, *Science*, 127, 288 (1958).

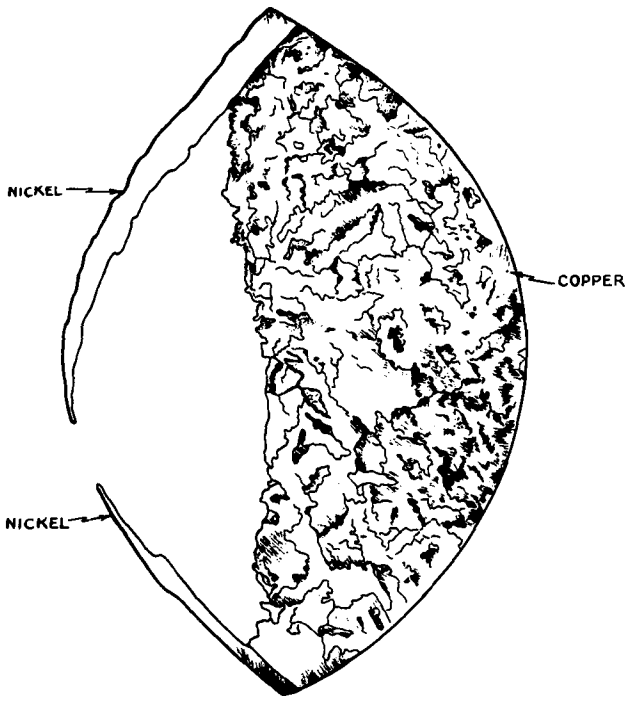

Fig. 2. Cross sectional view of a pit in sulfamate-plated nickel as seen under the microscope. Magnification of original photograph: 280X.

process has proceeded to the exposure of copper, the copper is preferentially attacked. If attack is visualized as the growth of the segment of the sphere out from an exposed point in the nickel coating, a cubic term would be expected.

Microscopic cross sections of the corroded samples have confirmed this hypothesis. For the Watts nickel samples, no attack of the copper was observed. Fig. 2 published here shows a drawing made from a microsection of a corroded sulfamate nickel specimen which was not exposed to the persulfate reagent.

Fischer's results, like ours, indicate the range of information on coating condition and behavior which can be achieved through interpretation of results from a generally neglected technique.

Some Observations of Copper Deposits on Single Crystals of Copper

Isaac Giron and Fielding Ogburn (pp. 842-846, Vol. 108, No. 9)

S. C. Barnes[26]: I was particularly interested to note that the work reported by Giron and Ogburn completely confirmed that of the Birmingham University team. That similar structures have been obtained in two independent studies is of particular importance in view of the known susceptibility of the acid copper sulfate bath to trace impurities. It seems fairly certain that the crystallographic features formed on single crystal electrodes develop by a bunching mechansim and, in this respect, the work of Poli and Bicelli[27] is also of relevance.

It still remains to be decided, however, whether the particular growth forms evident on crystals of a par-

[26] Joseph Lucas Ltd., Group Research Centre, Marston Green, Birmingham 33, England.
[27] G. Poli and L. P. Bicelli, *Metallurgia Ital.*, 51, 548 (1959).

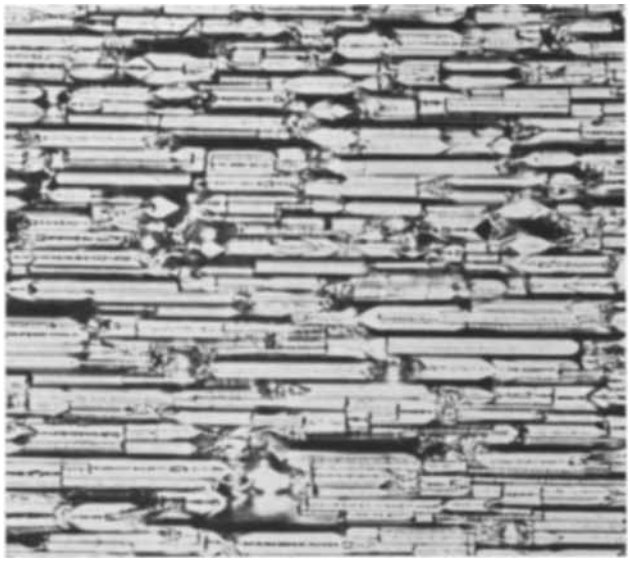

Fig. 1. Surface structure of copper deposit formed on a (110) copper single crystal cathode after plating for 20 min at 30 mA/cm² from an $N.H_2SO_4$ + N. $CuSO_4$ bath at 35°C. Magnification 575X. [110] direction parallel to long edge.

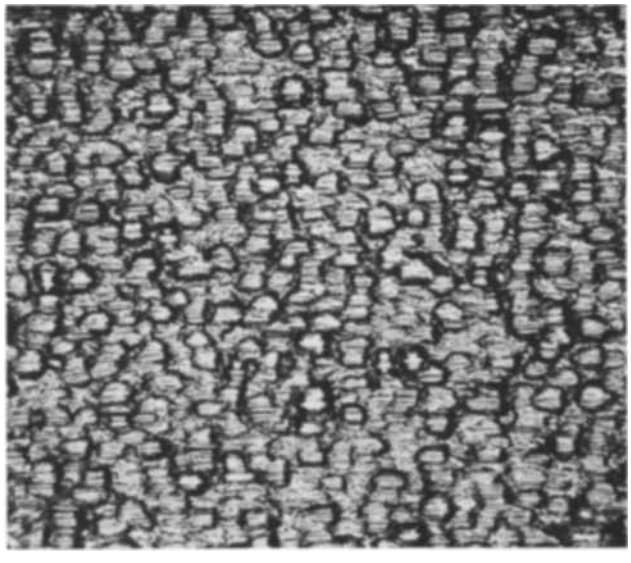

Fig. 2. Deposit obtained under the same conditions in the presence of 10^{-5} M/l thioacetamide. Magnification 575X. [100] direction parallel to long edge.

ticular orientation are rate or potential dependent. Although the information in the paper by Giron and Ogburn does not shed any light on this topic by itself, it does when considered in conjunction with observations on the effects of addition agents on the growth habit of copper deposits.

Giron and Ogburn report that at low c.d.'s the deposit surface on (110) crystals is composed of ridges aligned at right angles to a close packed [110] direction (*i.e.*, parallel to a [100] direction). At higher c.d.'s, the ridges extend parallel to the [110] direction. Previously unpublished results obtained by myself during an investigation into the effects of thio compounds on the structure of copper electrodeposits indicate that additions of thioacetamide (at a concentration of the order 10^{-5} M/l) cause the deposit form on (110) crystals to change from ridges parallel to a [110] direction to ridges at right angles to this direction (Fig. 1 and 2 of this discussion). This change is also accompanied by a large reduction in cathodic overvoltage.

It would appear, therefore, that since the habit change can be produced by either a reduction in c.d., or by the use of an addition agent which lowers polarization, the structure of the deposit is controlled by the electrode potential rather than by the applied c.d. Further work on the exact relationships between deposit structure and electrode kinetics seems warranted, and perhaps the recently developed relaxation techniques will be of use in this connection.

Cathodic Behavior of Iron Single Crystals and the Oxides Fe_3O_4, Gamma-Fe_2O_3, and Alpha-Fe_2O_3

C. D. Stockbridge, P. B. Sewell, and M. Cohen
(pp. 928-933, Vol. 108, No. 10)

An Electrometric and Electron Diffraction Study of Air-Formed Oxide Films on Iron

P. B. Sewell, C. D. Stockbridge, and M. Cohen
(pp. 933-941, Vol. 108, No. 10)

U. R. Evans[28]: The second paper ends with the words, "Stripping the film for identification, as was done by Davies and Evans, would give an erroneous result because exposure of the underlying thin magnetite layer to air would oxidize it to γ-Fe_2O_3."

These words may leave the reader with the idea that all our work is held to be invalid. It is, therefore, important to point out that, even if the three authors are right in condemning results based on film-stripping, our main conclusions remain unaffected, since the quantitative data in our two papers rest on methods independent of film-stripping. In our first paper,[29] the curves showing logarithmic growth at low temperatures, and parabolic at high temperatures (in general confirmation of Vernon and his colleagues[30]), were obtained by quite different techniques. In our second paper,[31] stripped films certainly were studied in two out of the three sections; the method was not felt to be ideal, and any attempt to fix exactly the composition of the film would have been unjustified; the conclusions, however, only claimed to show approximate values—*e.g.*, that cubic oxide contained more or less than 80% Fe_2O_3.

Despite the authors' statement at the end of their second paper, that the oxidation of magnetite is so rapid as to render measurements based on stripped films inaccurate, their own measurements recorded in Tables II and III of the first paper suggest that the oxidation is quite a slow process. This certainly accords with our experience. We generally have found that magnetite films, in absence of liquid water, are fairly stable. If it were a fact that magnetite was oxidized too rapidly for the use of the stripped-film techniques, then any film rapidly stripped, or trans-

[28] Cambridge University, Grange Rd., Cambridge, England.
[29] D. E. Davies, U. R. Evans, and J. N. Agar, *Proc. Roy. Soc.*, A225, 443 (1954).
[30] W. H. J. Vernon, E. A. Calnan, C. J. B. Clews, and T. J. Nurse, *Proc. Roy. Soc.*, A216, 375 (1953).
[31] D. E. Davies and U. R. Evans, *J. Chem. Soc.*, 1956, 4373.

ferred to glass, should be found to be wholly ferric oxide on testing. Throughout our work, however, we have found ferrous iron in the stripped or transferred film in cases where there was reason to think that it had been present in the film before stripping or transfer. In particular, we would recall an optical difference between duplex films (α-ferric oxide over magnetite) and simplex films (ferric oxide only) after transfer to glass; the simplex films showed the same color by transmitted light, whether the glass or the oxide was nearest to the eye, whereas the duplex film showed two different colors. If the magnetite layer oxidized so quickly as to invalidate methods based on stripping, the duplex specimen would surely acquire the optical properties of a simplex film on storage in air; this was not found to be the case. No doubt, methods based on film-stripping are less satisfactory than the more direct study of the films attached to the metal, but they need not be ruled out for all purposes.

The authors should be congratulated on much careful work. It is satisfactory that the thicknesses obtained by them agree fairly well with those of other authors but, as they point out, such estimates "do not serve to identify the film." Fresh information regarding composition is, therefore, particularly welcome, but their conclusions are somewhat contradictory. On page 940 it is stated that, "The two phase nature of the thin oxide film is clearly established," but lower down we read, "it seems unlikely that two discrete structures exist." Which represents the authors' final opinion?

M. Cohen: I would like to thank Dr. Evans for his discussion. As he points out, the thicknesses of oxide reported agree quite well with those reported by himself and others at comparable temperatures. The main disagreements between Dr. Evans' papers[32, 33] and those published from this laboratory[34–37] concern the composition of the films and the stability of Fe_3O_4 in the presence of air.

Although Dr. Evans did not observe Fe_3O_4 at any temperature below 250°C on Swedish iron and observed Fe_3O_4 at higher temperatures only after some time of oxidation, we observed Fe_3O_4 at all temperatures and from the beginning. This lack of identification of magnetite is rather surprising in view of the results obtained by annealing in vacuum by both Dr. Evans (Footnote 32, p. 454) and ourselves which show that the underlying iron reduces Fe_2O_3 to Fe_3O_4 very rapidly (<2 hr) even at 200°C. This would indicate that nucleation of Fe_3O_4 is not a problem.

I believe that the reason for the above difference lies in the methods of cathodic reduction. In a previous study from this laboratory,[38] it was shown that cathodic reduction in the ammonium chloride solution used in Reference 32 gave highly variable results such that it was not possible to correlate coulometric weight loss and iron analysis measurements. It was for this reason that the buffer solution was developed. Use of the deaerated buffer solutions allows both identification and measurement of the quantities of oxides involved. It also makes quite clear the presence of magnetite in all the cases studied. The large difference between both the immersion and reduction potentials of γ-Fe_2O_3 and Fe_3O_4 is evident in both papers.[34, 35] It should be noted that Dr. Evans observed Fe_3O_4 from the beginning with pure iron (Reference 32, pp. 455-456).

Regarding the remarks pertaining to the color of duplex films, the low temperature oxidation of magnetite to γ-Fe_2O_3 would still leave a duplex film of γ-Fe_2O_3 and α-Fe_2O_3. γ-Fe_2O_3 is a good electronic conductor in comparison to α-Fe_2O_3 and probably has quite different optical properties.

The oxidation of magnetite to γ-Fe_2O_3 by air at room temperature presents a real problem. With thick compact films, the percentage change in composition on exposure to air for short times can be quite small. However a film of Fe_3O_4, 40Å thick, exposed to air on both sides would oxidize completely to γ-Fe_2O_3 in about 30 hr and would convert over half its thickness to γ-Fe_2O_3 within 2 hr. A stripped air-formed film 25Å thick would oxidize to γ-Fe_2O_3 within ½ hr on exposure to oxygen. Although this is not rapid oxidation in the ordinary sense, it is sufficiently rapid to cause errors in analyses for ferrous-ferric ion ratios and to change electron diffraction patterns.

The points brought up in the last paragraph relate to the word thin and the two quotations refer to an 80Å film formed at 200°C and a 25Å film formed at room temperature on a (112) single crystal pure iron. In both cases, all the oxides are cubic and the cathodic reduction curves show evidence of a duplex film. With the 80Å film there is an appreciable amount of both Fe_3O_4 and γ-Fe_2O_3. At these thicknesses, it is probably permissible to write in terms of two distinct phases. With the thinner air-formed film, although the outer part of the film is γ-Fe_2O_3 and the inner part of the film is Fe_3O_4, the phase boundary probably occupies such a large portion of the thickness that it may not be permissible to insist on two discrete structures in the total thickness of 25Å. One should keep in mind that the structures of γ-Fe_2O_3 and Fe_3O_4 are very similar so that one might expect a thick phase boundary between them.

D. Gilroy and J. E. O. Mayne[39]**:** In the second paper, the authors claim that it is possible to differentiate between Fe_3O_4 and γ-Fe_2O_3 owing to different efficiencies of cathodic reduction at constant current density. In view of the similarity in structure of these two oxides, it seems very remarkable that there should be such a sharp change in reductive efficiency as suggested by the authors in their interpretation of Curve 1, Fig. 4. The air-formed film is very thin and it may not behave on reduction in a similar way to the much thicker duplex film formed at higher temperatures.

Hancock[40] examined the cathodic reduction of the air-formed film in 0.2N potassium chloride and 0.1N

[32] D. E. Davies, U. R. Evans, and J. N. Agar, *Proc. Roy. Soc.*, **A225**, 443 (1954).
[33] D. E. Davies and U. R. Evans, *J. Chem. Soc.*, 1956, 4373.
[34] C. D. Stockbridge, P. B. Sewell, and M. Cohen, *This Journal*, **108**, 928 (1961).
[35] P. B. Sewell, C. D. Stockbridge, and M. Cohen, *This Journal*, **108**, 933 (1961).
[36] E. J. Caule, K. H. Buob, and M. Cohen, *This Journal*, **108**, 829 (1961).
[37] E. J. Caule and M. Cohen, *This Journal*, **108**, 834 (1961).
[38] H. G. Oswin and M. Cohen, *This Journal*, **104**, 9 (1957).

[39] Dept. of Metallurgy, University of Cambridge, Cambridge, England.
[40] Hancock, *J. Chem. Soc.*, 1958, 4167.

sodium hydroxide. Virtually no iron passed into solution and the coulombs passed at the points of inflexion were identical. These experiments have been repeated with neutral 0.1*N* sodium sulfate and benzoate; again, virtually no iron passed into solution. However, with the borate/chloride buffer, used by the authors, ferrous ions passed into solution, but not in sufficient quantity to account for the entire film. It appears that in neutral unbuffered or alkaline solutions the cathodic process is the reduction of oxide to iron; whereas, in buffered solutions, this is accompanied by the reduction of ferric to ferrous ions, which pass into solution. A probable explanation is that upon cathodic reduction the liquid in contact with the surface of the specimen becomes alkaline; in the presence of a buffer the rise in pH will be delayed, but not indefinitely. It is suggested that in Curve 1, Fig. 4, on Section $E_{A'}$-E_B the process is essentially a one-electron reduction, whereas on Section E_B-E_C a three-electron process is involved.

If these suggestions are accepted, then it follows that the values given for the film thickness in the Tables should be recalculated, and higher values will be obtained; furthermore, the difference in the efficiency of reduction of the two oxides is not a characteristic of the oxides, but arises owing to the buffering action of the solution.

Hancock's value of 26 ± 3Å for the thickness of the air-formed film on iron, reduced in hydrogen, has been criticized because he assumed that the film was composed of γ-Fe_2O_3. Had he assumed that it was composed entirely of Fe_3O_4, the value would be greater by less than 9%. It is generally agreed that the film is of intermediate composition; the corrected value would, therefore, be within the limits of his measurements.

M. Cohen: With regard to the remarks of D. Gilroy and J. E. O. Mayne, the work in the two papers differentiates between γ-Fe_2O_3 and Fe_3O_4 by immersion potential and reduction potential as well as current efficiency of reduction. In some thousands of cathodic reduction runs made in either the borate/chloride buffer or a borate/boric acid buffer at a pH of 8.4, we always have found that the outer layer reduces to form ferrous ion in solution with high current efficiency. That the buffer appears to be quite effective for long periods of time is shown in Curves 1 and 2, Fig. 11, where the time to reach the magnetite potential obviously is dependent on the thickness of the outer γ-Fe_2O_3 layer.

I agree that with the thin films some of the magnetite is reduced to iron. This assumption was made to obtain the thicknesses shown in Table IX. As can be seen in this table, the thickness and composition of a film on polycrystalline iron will depend on the distribution of orientations of the individual grains, and probably on the oxidation characteristics of grain boundaries as well. We also have some evidence of the formation of iron from reduced magnetite by electron diffraction. From the point of view of identification and measurement of the thin films on iron, the difference in behavior of γ-Fe_2O_3 and Fe_3O_4 on cathodic treatment in the buffered solution is very useful.

The Application of an X-Y Pulsed Measuring System to Polarization Studies, I. The Hydrogen Reaction on Platinum

C. H. Presbrey, Jr., and Sigmund Schuldiner (pp. 985-995, Vol. 108, No. 10)

M. W. Breiter[41]: Presbrey and Schuldiner report experimental results which are in agreement with the results on hydrogen evolution published by the late Professor Knorr, by me, or our co-workers in recent years. However, the interpretation of the measurements by the two schools differs greatly. The results of Presbrey and Schuldiner can be explained satisfactorily by the interpretation of hydrogen overvoltage phenomena on activated platinum metals which has been given by us without drastic changes in the years since 1954:

(*A*) Mass-transport processes are rate determining for stationary current potential curves over a wide potential range.

(*B*) The exchange current densities of the two discharge reactions

$$\text{(i)} \quad H^+ + e^- \overset{i_{01}}{\rightleftharpoons} H_{ad}$$

$$\text{(ii)} \quad H^+ + H_{ad} + e^- \overset{i_{02}}{\rightleftharpoons} H_2$$

are large at $\eta = 0$ ($i_{01} \approx i_{02} \approx 0.3$ Å/cm²).

(*C*) The equilibrium of the recombination reaction

$$\text{(iii)} \quad H_{ad} + H_{ad} \overset{i_{03}}{\rightleftharpoons} H_2$$

is established for $\eta < +0.08$v. It does not exist for $\eta > +0.08$v.

The experiments which lead to the above conclusions were discussed and summarized by me recently.[42] Our interpretation is in qualitative agreement with the important contributions to the understanding of hydrogen overvoltage by Frumkin's school.

Schuldiner's interpretation ($i_{01} >> i_{03} >> i_{02}$) is based to a large extent on the occurrence of cathodic Tafel lines with $b \approx 30$ mv. These curves are measured at a high flow rate of the stirring gas. A further increase of the flow rate does not influence the current potential curves any more. So Schuldiner concludes that reaction (iii) is rate determining. However, his observation does not necessarily imply that diffusion is eliminated. It means that the thickness of the diffusion layer does not change to a measurable extent any more if the flow rate is increased above a certain value. An anodic limiting current density i_{0d} of diffusion (and convection) of molecular hydrogen of 15 ma/cm² is required to reduce the influence of the transport processes to 10% if i_{03} is 1.5 ma/cm². Such a high i_{0d}-value has not been reported in literature even under the most extreme stirring conditions (flow of electrolyte or rotating disk) at $p_{H_2} = 1$ atm.

It is felt that the Tafel relations in Fig. 7 and Fig. 8 of Schuldiner's present paper and in many of his former publications are valid for a very small range of current densities only. The range is too small to

[41] Research Lab., General Electric Co., Schenectady, N. Y.
[42] M. Breiter in "Transactions of the Symposium on Electrode Processes," Edited by E. Yeager, pp. 307-324, John Wiley & Sons, Inc., New York (1961).

draw reliable conclusions. The asumption of a slow combination step requires that the concentration of atomic hydrogen which is involved in the reaction is very small at $\eta \approx +0.06$v. Therefore it cannot be large at $\eta = 0$ either. This forces Schuldiner to postulate the formation of a second monolayer of hydrogen atoms which is completed at negative potentials. However, the a-c impedance measurements at cathodic overvoltages in $8N$ H_2SO_4 show conclusively that a second monolayer of hydrogen atoms is not formed up to cathodic current densities of 0.3 Å/cm^2. The high capacity of the platinum electrode during the cathodic pulse is due to the accumulation of molecular hydrogen in the diffusion layer, not to the formation of a second monolayer. The anodic charging curves in Fig. 10, like our charging curves, do not give evidence for a third "plateau" due to the anodic removal of a second monolayer. A better picture of the anodic oxidation of hydrogen atoms is obtained by the potentiostatic application of a sawtooth.[43, 44] The so-called plateaus of the charging curves are not well enough distinguishable to determine their length. Only part of the hydrogen associated with the surface at equilibrium is ionized near the equilibrium potential because the adsorption isotherm is very flat in the vicinity of $\eta = 0$.

The "reversible" hydrogen adsorption on platinum in the gaseous phase occurs at pressure $p_{H_2} < 1$ atm. As hydrogen adsorption in electrolytes without specifically adsorbable ions starts at about the same low pressure as in the gaseous phase, the "reversible" hydrogen adsorption was attributed by me[45] to the region of the left peak[43, 44] of the potentiostatic i-U-curves.

S. Schuldiner: Unfortunately, Dr. Breiter has misconstrued several important points in our paper. His statement that we are "forced to postulate the formation of a second monolayer of hydrogen atoms which is completed at negative potentials," is not correct. What we do postulate is that, since a double atomic layer is unfeasible, a quantity of H atoms, which coulometrically may amount to a second layer, forms Pt-H alloy on the surface layer of platinum.

Concerning the diffusion *vs.* slow combination rate-controlling mechanisms, I shall not reiterate here detailed arguments in favor of the combination mechanism since this type of redundancy is an unnecessary rehashing of the literature. A comparison of a steady-state hydrogen overvoltage curve[46] (Fig. 2) with the transient overvoltage curves shown in Fig. 8 of the paper under discussion shows a convergence at increasing current densities. If mass transport were rate controlling, then the steady-state overvoltage should diverge from the transient overvoltage curve as the current density increases.

In addition, in Fig. 2,[46] Tafel curves which extend over two and one half orders of magnitude of current density are shown. Fig. 8[46] of the same reference shows Hammett relations for three orders of magnitude of current density. These are long enough ranges of current density to be highly significant.

[43] F. G. Will and C. A. Knorr, *Z. Elektrochem.*, **64**, 258, 270 (1960).
[44] W. Böld and M. Breiter, *Z. Elektrochem.*, **64**, 897 (1960).
[45] M. Breiter, *Electrochimica Acta*, In press.
[46] S. Schuldiner, *This Journal*, **106**, 891 (1959).

Since both the X-Y and sawtooth methods use measuring instruments of essentially the same precision and resolution (commercial oscilloscopes, *etc.*), neither has an advantage over the other in this respect. The disadvantage of the sawtooth method is that at fast sweep rates a displacement current, which cannot be corrected for, is included in the oscilloscope trace. The X-Y method avoids this difficulty.

Rhenium-Tungsten-Carbon Interactions

R. F. Havell and Y. Baskin (pp. 1068-1069, Vol. 108, No. 11)

Charles P. Kempter[47]: The authors state that "Interactions between rhenium and carbon are limited to absorption of about 1% carbon in the rhenium lattice producing slight changes in the lattice constants and a reduction of the c/a ratio from 1.615 to 1.600," quoting only the early work of Trzebiatowski.[48] They did not quote the recent articles by Hughes[49] ("A Survey of the Rhenium-Carbon System") or Nadler and Kempter[50] ("Some Solidus Temperatures in Several Metal-Carbon Systems"). Hughes reviewed work on the Re-C system prior to that of Trzebiatowski, and published the Re-C phase diagram above 1500°C from 0 to ~30 atomic per cent (a/o) carbon. He reported a simple eutectic system at 16.9 a/o carbon and 2480 ±50°C, with the solid solubility of carbon in rhenium varying from 11.7 a/o at the eutectic temperature to 4.2 a/o at 1800°C. In an alloy of 20 a/o carbon, the "a" parameter increased from 2.760Å to 2.792Å and the "c" parameter increased from 4.458Å to 4.471Å—thus the axial ratio decreased from 1.615 to 1.601. In agreement with Hughes, Nadler and Kempter reported the minimum solidus temperature in the rhenium-carbon system to be 2486 ±18°C. In addition, although Havell and Baskin quoted a recent reference[51] for the Re-W phase diagram, they quoted no references pertaining to the W-C system, but did state a 2600°C melting point for WC and a 2475°-2730°C range for melting points of tungsten carbides and/or eutectics in the W-C system. Nadler and Kempter[50] have reviewed work on the W-W_2C eutectic and the WC melting point, and have determined values of 2732 ±22°C and 2720 ±20°C for these, respectively. (A final pertinent reference, which appeared after the submission of the Havell and Baskin note, is a paper by Sara[52] entitled "Phase Equilibria in the System Tungsten-Carbon." Sara found the minimum solidus temperature in the W-C system to be the W-W_2C eutectic temperature and agreed well with the above N. and K. value.)

The Miller indices tabulated for the "rhenium-WC solid solution" in Table III are consistent with space group D^4_{6h}-$P6_3/mmc$, which occurs for Re (Strukturbericht type A3) and W_2C (type L'_3). Both types[53]

[47] Los Alamos Scientific Lab., University of California, Los Alamos, N. Mex.
[48] W. Trzebiatowski, *Z. anorg. Chem.*, 233, 376 (1937).
[49] J. E. Hughes, *J. Less-Comm. Met.*, 1, 377 (1959).
[50] M. R. Nadler and C. P. Kempter, *J. Phys. Chem.*, 64, 1468 (1960).
[51] J. M. Dickinson and L. S. Richardson, *Trans. Am. Soc. Metals*, 51, 758 (1959).
[52] R. V. Sara, 14th Regional Meeting, American Ceramic Society, Oct. 26, 1961, San Francisco, Calif.
[53] W. B. Pearson, "A Handbook of Lattice Spacings and Structures of Metals and Alloys," Pergamon Press, New York (1958).

have two metal atoms per unit cell in set (c) at 1/3, 2/3, 1/4, and 2/3, 1/3, 3/4, and W_2C also has a carbon atom in an octahedral hole. Thus, it seems reasonable that Re would form solid solutions with W_2C, and, therefore, the use of "(Re, WC)ss" in Table I and in reference to Table III might be misleading. Although WC has a hexagonal lattice, the space group[54] is D^1_{3h}-$P\bar{6}m2$ and the assignment of Miller indices is different from the case of Re or W_2C. Even though the *initial* tungsten to carbon molar ratio was unity, this does not preclude the existence of W-C structures other than WC in the observed solid solution. Until further characterization of the solid solution is carried out, it seems appropriate to refer to it as the Re-W-C solid solution as Havell and Baskin did in Table II.

R. F. Havell and Y. Baskin: We are thankful to Mr. Kempter for citing the recent work on the binary systems Re-C and W-C which bear directly on our study. We agree that the expression (Re, WC)ss is somewhat misleading, as it implies that the structure WC exists in the solid solution. We prefer either (Re-W-C)ss or Re-W_x-C_x solid solutions. The Re-W_x-C_x solid solution is structurally similar to that of W_2C despite the fact that the W/C mole ratio is a unity. As discussed in the article, rhenium and tungsten powders with a W/C mole ratio of 2 were not reacted, since contact of these samples with the graphite plate at 2300°C would have resulted in carbon absorption, thus shifting the ratio toward unity.

We feel that Mr. Kempter's implication that the W/C mole ratio of our powders changed on firing is not justified. Accurate weighings showed negligible weight change and, consequently, no shift in this ratio. Actually, it is not necessary to alter the W/C mole ratio from unity to obtain solid solutions having a close-packed hexagonal structure. The solid solution composition (Re_2, W, C) possesses this structure and, except for a different metal constitution, has the same metal to carbon ratio as the composition (Re, W_2, C), which would be intermediate between Re and W_2C. Moreover, the lattice constants of (Re_2, W, C) (a = 2.877, c = 4.561, c/a = 1.585) are very close to those calculated for Re, W_2C on the basis of Vegard's Law (a = 2.88, c = 4.59, c/a = 1.59). The small difference in atomic radius between rhenium and tungsten might account for some of the above difference.

On the Electrodeposition of Arsenic and Its Role in Corrosion Prevention

Gösta Wranglén (pp. 1069-1070, Vol. 108, No. 11)

R. Piontelli and G. Poli[55]: According to Dr. Wranglén's opinion, the insulating properties of the amorphous arsenic layers, obtainable by plating or displacement, involve the following consequences:

(*A*) The intervening of an ohmic drop contribution in the overvoltages, concerning both arsenic and hydrogen reduction as given by the direct method,

[54] J. Leciejewicz, *Acta Cryst.*, 14, 200 (1961).
[55] Lab. of Electrochemistry, Physical Chemistry, Metallurgy, Polytechnic of Milan, Milan, Italy.

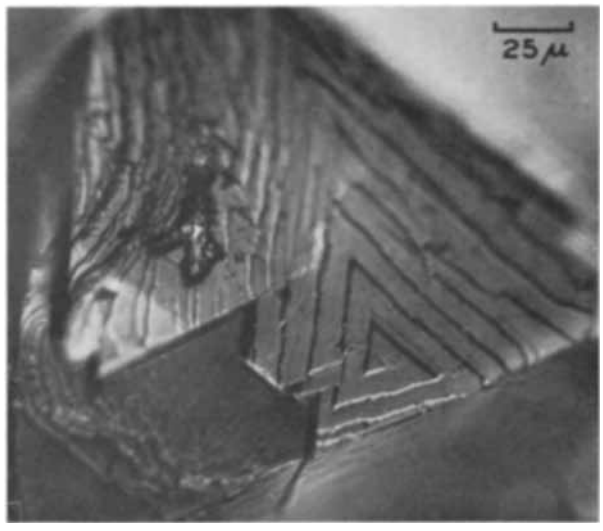

Fig. 1. Arsenic deposited in crystalline form (chloride bath); example of growth spiral. Magnification 400X.

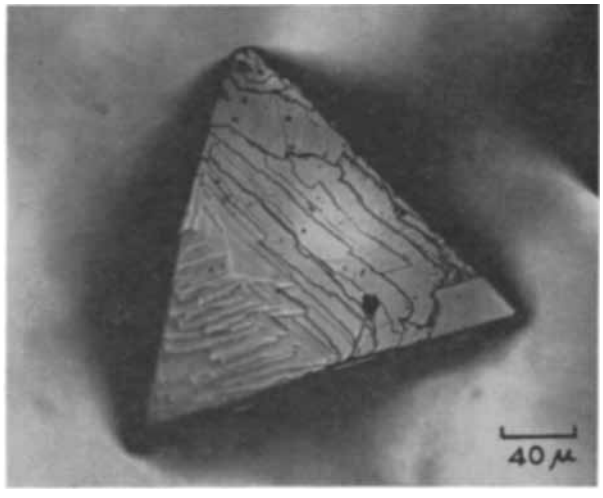

Fig. 2. Arsenic deposited in crystalline form (chloride bath). Magnification 270X.

so as to render meaningless the results thus obtainable;

(*B*) High voltages and a very poor current efficiency in the arsenic electrowinning;

(*C*) A very efficient inhibitive influence of arsenic with respect to the corrosion of iron materials, formerly explained[56] by considering the hydrogen overvoltages.

1. We agree on the point that the "cumulative overvoltages" given by the direct methods in a quasi-steady condition, although representing the item to be considered in the cell voltage-balance, are affected in this case by a quite significant ohmic contribution, which may become largely predominating for thick arsenic layers.

2. The "true overvoltages" (that is, corrected from any ohmic contribution), in the arsenic separation on arsenic layers, are definitely high (in the order of several tenths of a volt), however, also at low c.d.[57]

3. Arsenic may be plated, at least partially, also in crystalline form (*see* Fig. 1 and 2 of this discussion),

[56] O. P. Watts, *Trans. Am. Electrochem. Soc.*, 21, 339 (1912).
[57] In the succession, Bi, Sb, As, a strong increase of these "true overvoltages" corresponds to the increase of the metalloidic character (*see* R. Piontelli, *Z. Elektrochem.*, 55, 128 (1951)).

the corresponding "true overvoltage" again being quite high.[58]

4. In any case, the low and decreasing current efficiency encountered by Wranglén could not be accounted for on the basis of the assumed insulating power of the arsenic layer, which would influence both of the concurrent cathodic processes. The current efficiency in the As deposition is low, due to the high true overvoltage involved by this process, while its decrease in time, in Wranglén's experiments, is due perhaps: (*a*) to composition changes in the bath; (*b*) to the structure changes of the cathodes. As a matter of fact, we found evidence that these last, although not involving any appreciable decrease in the (true) overvoltage in the As deposition, may appreciably decrease the hydrogen overvoltage.

5. The conclusion that the strong inhibition that As may exert on the corrosion of Fe cannot be explained solely on the basis of the hydrogen overvoltage has been largely substantiated by previous experiments from this laboratory.[59]

In our opinion, however, this very efficient protection is due largely to the structure and, in particular, to the very peculiar perfection of the separated layers (which eliminate any potentially anodic area), in spite of their origin by a displacement reaction, and thanks to the very high throwing power which characterizes, under favorable conditions, arsenic deposition on some foreign metals.

The opinion that this protective influence cannot merely be attributed to the insulating power of the As layer, as Wranglén seems to consider, may be directly confirmed as follows. An iron specimen, after adequate treatment in an inhibiting arsenical solution, does not displace hydrogen from strong acids, nor copper from copper sulfate.

Let us eliminate the arsenic layer from the contour or from some other localized area, by scraping.

The specimen will now displace hydrogen, or respectively copper, but the cathodic process will then occur not only on the newly exposed area but, moreover, on a rather large fraction of the still covered one.

The very presence of the arsenic layer would be unable, therefore, to prevent the occurrence of cathodic processes complementary to the anodic ones when these last are made possible by the availability of anodic areas.

G. Wranglén: The discussion by Professors Piontelli and Poli, complementing their previous extensive work in this field, is most welcome. They have correctly interpreted and summarized the conclusions of the present writer. It seems necessary to emphasize, however, that the nonconductivity of the arsenic electrodeposited by the author was not "assumed" but experimentally established.

It is now very interesting to learn that arsenic can be deposited, "at least partially," also in crystalline form, as the micrographs 1 and 2 show. It also would have been of great interest to learn the conditions of deposition, however, since it would seem as if crystalline electrodeposits of arsenic are exceptional at low temperatures and normally to be expected only in fused salt electrolysis. Amorphous deposits (according to x-ray diffraction analysis) were obtained not only by the present writer but also by Stillwell and Audrieth[60] from solutions of $AsCl_3$ in glacial acetic acid, and by Finch, Quarrel, and Wilman[61] from aqueous cyanide baths. Deposits from the $AsCl_3$-HAc bath were used by Salzberg and Goldschmidt[62] in their studies of hydrogen overvoltage on arsenic. It is also known that arsenic precipitated chemically from aqueous solutions by reducing agents is obtained in various amorphous forms.[63] These are considered to be transition forms between the nonmetallic yellow, cubic, and the metallic gray, rhombohedral modification of elementary arsenic. They are transformed to the metallic modification on heating. According to origin, the transformation temperature varies from 100° to 377°C.[64] Their nonconductivity seems to be a direct consequence of their amorphous structure. This connection often seems to have been overlooked, however, particularly in electrochemical studies.

Piontelli and Poli maintain that the insulating properties of electrodeposited arsenic would affect the two concurrent cathodic processes equally and thus not influence the current efficiency of arsenic deposition. It must be observed, however, that the arsenic is deposited in a noncoherent condition (porous from the acid chloride bath, flaky from the alkaline arsenite bath) leaving small areas of the basis metal uncovered. On these the current density will be very high, much higher than the limiting c.d. for arsenic deposition. This is particularly true for arsenite solutions where the AsO^-_2-ions migrate away from the cathode, resulting in a low limiting c.d. Hence, copious hydrogen evolution from water will take place resulting in a low current efficiency of arsenic deposition. It seems natural that this effect is accentuated during the course of an electrolysis experiment.

The high throwing power in the electrodeposition of arsenic, referred to by Piontelli and Poli, is also a natural consequence of the low conductivity of the deposit, transferring the electrodeposition reaction to still uncovered areas. In this respect, the electrodeposition of arsenic resembles certain anodic processes, such as anodizing of aluminum.

The corrosion experiment described by Piontelli and Poli and involving the local removal of the nonconducting arsenic film very much resembles localized corrosion, such as pitting, on metals passivated by an oxide film, *e.g.*, aluminum and stainless steel. There the cathode reaction also occurs all over the passivating film or on active parts of it.

[58] For further details, *see* R. Piontelli and G. Poli, In print.

[59] *See* for this purpose the following papers (concerning the inhibition by As, Sb of the corrosion of Fe, Ni, Co, and similar phenomena): R. Piontelli, *et al.*, *Chimica Industria*, 24, 122 (1942); *ibid.*, 25, 203 (1943); *Gazz. chim. ital.*, 77, 45 (1947); *ibid.*, 79, 279, 293, 297, 533, 722 (1949).

[60] C. W. Stillwell and L. F. Audrieth, *J. Am. Chem. Soc.*, 54, 472 (1932).

[61] G. E. Finch, H. G. Quarrel, and H. Wilman, *Trans. Faraday Soc.*, 31, 1051 (1935).

[62] H. W. Salzberg and B. Goldschmidt, *This Journal*, 107, 348 (1960).

[63] "Gmelins Handbuch der Anorganischen Chemie, 8:te Aufl.," Verlag Chemie, GmbH., Weinheim/Bergstr. (1952).

[64] Work cited in Footnote 63, p. 121.

Raney Type Transition Metals as Fuel Electrode Catalysts

H. Krupp, H. Rabenhorst, G. Sandstede, and G. Walter
Battelle-Institut e.V., Frankfurt (Main), Germany

and R. McJones
Cummins Engine Company, Inc., Columbus, Indiana

ABSTRACT

Porous metal electrodes incorporating Raney catalysts are prepared by powder techniques from transition metals of the first and eighth groups. Half-cell and fuel cell measurements are taken in various aqueous electrolytes at temperatures from 20° to 100°C. At 80°C in either 5*N* KOH or 5*N* H_2SO_4 electrolyte, both hydrogen and methanol yield current densities beyond 300 ma/cm². In 5*N* K_2CO_3 electrolyte, there are limiting current densities of the order of 10 ma/cm². Neither hexane nor methylcyclohexane display appreciable electrochemical oxidation under the conditions of this report. The methanol reaction appears to approach complete oxidation; this conclusion applies in both acid (CO_2-formation) and alkaline (carbonate formation) electrolyte as well as for both half-cell and fuel cell operation.

There is so far no satisfactory low-temperature hydrocarbon fuel electrode. On the other hand, electrochemical conversion at an appreciable rate of partially oxidized hydrocarbons such as methanol and glycol seems to be possible, but only in the case of methanol was complete oxidation reported (1). At least some of the reactions involved in the stepwise oxidation at the anode must be accelerated catalytically in order to achieve a sufficient reaction rate at low temperatures (below 200°C). The electrode must, therefore, contain catalysts accelerating, above all, the acceptance of electrons from the fuel by the anode.

The activity of a catalyst seems to be related to the number of crystallographically disoriented surface atoms. Defect structures are attained by several processes which are not discussed here. In the present investigations it was decided to use Raney catalysts because, on the one hand, they can be produced at room temperature so that recrystallization enhanced by elevated temperatures is avoided, and because, on the other hand, a relatively simple method of Raney electrode preparation was described by Justi (2-4). Raney catalysts are made by alloying the catalyst material with a base metal, for instance aluminum, which is subsequently dissolved from this alloy leaving the catalyst metal in a highly active state.

Justi has used Raney nickel electrodes, especially as hydrogen electrodes, with outstanding success. He also mentioned work with Raney electrodes based on copper, tungsten, molybdenum (for carbon monoxide oxidation), and palladium (as a *p*H electrode), but he did not discuss his results with these metals in detail. The present work must be regarded as an application, and possibly an extension, of Justi's technique.

The preparation of fuel electrodes from Raney copper, cobalt, nickel, rhodium, palladium, and platinum is described in the following along with the results obtained from tests with hydrogen, methanol, and hydrocarbon fuels.

Experimental Procedure

All electrode specimens were prepared in the form of porous disks by compressing a mixture of skeleton metal powder with powdered Raney alloy and subsequent dissolution of the base metal of the Raney alloy. In all cases the skeleton material and the catalytic substance of the Raney alloy were identical. The diameter of the disks was 1.2 cm. They were glued around the circumference into an electrode support ring made of Plexiglas. The projected surface area of the active part of the disk was 0.65 cm².

The Raney alloys were prepared by alloying the catalyst metal with aluminum. In order to achieve a high alloying rate without melting the components beforehand, the two metals were mixed in the form of powders and compressed into disks. The disks contained in individual crucibles were heated in an electric furnace until the alloying reaction started with conflagration at about 700°C. Owing to the heat of reaction, the temperature increased, causing the mixture to melt and to form a homogeneous alloy. Immediately after this reaction was completed, the alloy solidified; it was then removed from the furnace. It would not be possible, at least under mild conditions, to eliminate the aluminum from, in particular, the XAl compound where the catalyst metal X is compounded with aluminum at an atomic ratio of 1:1. The percentage of the catalytically active metal in the alloy, therefore, must be lower than the stoichiometric ratio of 1:1. It must, however, be above, say, 20 at. % because the alloy becomes too ductile for powdering below this limit.

For the preparation of the electrode disks, one part by volume of a pure metal powder, the skeleton material, was mixed with one part by volume of powdered Raney alloy. The mixture was subsequently compacted by pressing it into disks. Justi's

technique to achieve homoporosity by fractionation of the powders was not applied at this research stage.

The copper, cobalt, and nickel electrodes were prepared by compacting the powders at a pressure of 3,000 kg/cm^2, and sintering them at 400°C (Cu) and 600°C (Co, Ni). The platinum, palladium, and rhodium electrodes were left unsintered in order to prevent the formation of the stable compound XAl from the Raney alloy and the skeleton metal during the heat treatment. The unsintered electrodes were compacted at a pressure of 10,000 kg/cm^2, and at the same time two platinum screens were included with a view to increase the mechanical stability.

After cementation of the disks into a Plexiglas ring, the aluminum of the Raney alloy was dissolved by treating the electrode first with a dilute and then with a concentrated KOH solution, finally at a temperature of 80°C. The aluminum is not completely eliminated by this process. Further aluminum was dissolved anodically. A KOH solution was employed irrespective of whether the disks were used in alkaline or acid electrolytes because the dissolution rate of aluminum in acids is too large.

The electrodes were tested by taking current-potential plots using the half-cell system depicted in Fig. 1.

The test electrodes (porous disk cemented into a Plexiglas ring) were fixed in a Plexiglas holder providing a gas inlet. The electrical contact with the disk was established by two spring-type platinum wires to insure good contact. A platinum wire served as counter electrode. The electrode potential was measured against a calomel electrode using a Luggin capillary placed at a distance of 5 mm from the electrode surface, which gave a maximum measuring error of 50 mv. The ohmic polarization due to the ohmic resistances in the electrode and the electrolyte was not measured and consequently is still included in the potential values as reported. The measured potentials were not corrected for the diffusion potential between the electrolyte contained in the liquid junction (5*N*) and that at the reference electrode (0.1*N*); the involved error would not exceed 30 mv. The current was adjusted by means of a galvanostat. The measured amperages were converted into current densities by taking the projected surface area of the electrode to be 0.65 cm^2.

All electrodes were tested with gaseous hydrogen and methanol and some, in addition, with methylcyclohexane and hexane. The latter three fuels were admitted to the electrodes using nitrogen as a carrier gas. The electrode gas excess pressures totalled 0.5-1 atm. Reference runs were made using pure nitrogen.

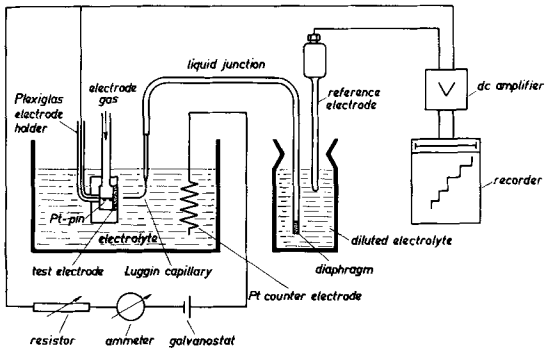

Fig. 1. Diagram of test stand for measuring current-potential plots.

In addition to the gaseous fuels, the tests included formaldehyde, formic acid, and methanol, dissolved in the electrolyte.

Alkaline, acid, and carbonate electrolytes have been employed as 5*N* solutions in water. The majority of the tests performed to date have been run at 80°C.

After the described chemical dissolution of aluminum, further aluminum was dissolved in the half-cell anodically. To this end the electrode was used as a hydrogen electrode. The electrode potential was increased stepwise to about 200 mv below the reversible oxygen potential. Although mainly hydrogen is oxidized during this process, part of the current is due to dissolving aluminum.

In the case of nickel, the electrode activity was much greater when electrochemical activation was used. For example a Raney nickel electrode using hydrogen in a half cell at −650 mv yielded current densities of 12 and 80 ma/cm^2, respectively, when the electrode was activated chemically in 5*N* KOH at 40°C for 24 hr or activated electrochemically for ½ hr in 5*N* KOH at 40°C with an electrode potential of +150 mv. Electrochemical activation was not necessary with the other metals of the eighth group tested.

The amount of hydrogen dissolved in the electrode was reduced substantially prior to tests with methanol or hexane by passing a nitrogen stream through the electrode. To accelerate this process, a potential was applied which was about 200 mv below the standard reversible oxidation potential of the corresponding electrode metal:

Current Density-Potential Plots

Most of the results are plotted in the form of current density-potential characteristics.

All reported potential values were obtained within a few minutes after adjustment of the current and remained constant during the measuring period up to several hours. Figure 2 depicts the results with hydrogen in KOH solution.

With all electrodes the open-circuit potential reached the reversible hydrogen potential. Deviations within ±30 mv are due to variations of the potential of the calomel reference electrode. The nickel electrode shows a distinct limiting current density beyond which the polarization as a function of the current deviates strongly from linearity. As the diagram shows, the platinum electrode has

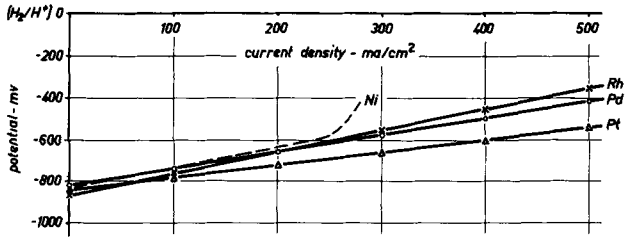

Fig. 2. Current density-potential plots of Raney electrodes with H_2 in 5*N* KOH at 80°C.

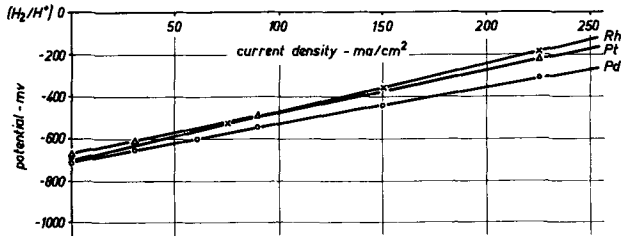

Fig. 3. Current density-potential plots of Raney electrodes with CH_3OH in 5*N* KOH at 80°C.

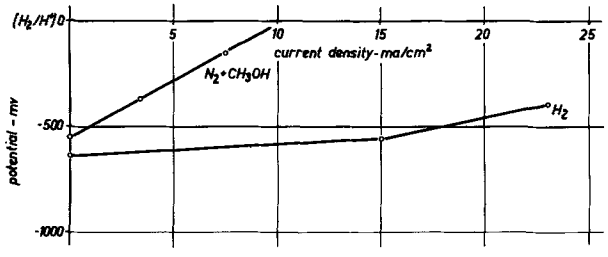

Fig. 4. Current density-potential plots of Raney palladium electrode with H_2 and CH_3OH in 5*N* K_2CO_3 at 80°C.

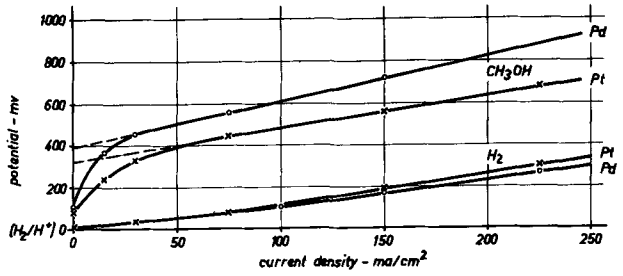

Fig. 5. Current density-potential plots of Raney electrodes in 5*N* H_2SO_4 at 100°C.

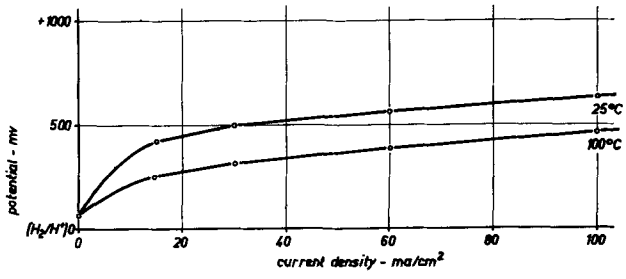

Fig. 6. Current density-potential plots of a Raney platinum electrode with CH_3OH in 5*N* H_2SO_4 as a function of temperature.

the smallest polarization. With palladium, platinum, and rhodium as hydrogen and methanol electrodes, the tests were not extended beyond current densities of about 500 ma/cm² and 300 ma/cm², respectively, so that the respective limiting current densities were not ascertained.

The results obtained with the sintered nickel electrode, using hydrogen as fuel were inferior to those reported by Justi, presumably because of the much smaller number of active pores. It is thus assumed that all electrodes investigated may be improved by employment of better techniques of powder metallurgy.

Figure 3 shows the results with methanol fuel in KOH solution.

Again the polarization increased linearly with the current. The open-circuit potential was about 100-150 mv smaller than that with hydrogen. Here palladium furnished the best results.

If the KOH electrolyte is replaced by K_2CO_3, very large polarizations are obtained both with hydrogen and methanol as fuels (see Fig. 4).

Large current densities were obtained not only in KOH solution but also in H_2SO_4 solution with hydrogen and methanol as fuel (see Fig. 5 and 6).

With methanol, the polarization shows a peculiar nonlinearity at small current densities. With methanol in an acid solution, platinum proves to be superior to palladium as a catalyst. The open-circuit potential exceeds that of hydrogen by about 100 mv.

Figure 6 shows the temperature dependence of methanol oxidation as a function of the temperature between 25° and 100°C.

The above results are summarized in Table I together with results not illustrated so far. "Specific polarization" is defined as the slope of the curve potential *vs.* current density. For methanol in acid electrolyte, the slope is taken from the linear portion of the curve at large currents; in these cases the value of the open-circuit potential is complemented by the interception of the extrapolated linear part of the polarization curve with the ordinate. Copper and cobalt turned out to be unsatisfactory catalysts for methanol or hydrogen electrodes.

Table I. Open-circuit potential, specific polarization, and limiting current density with hydrogen and methanol, respectively, at 80°C

		H_2			CH_3OH		
Catalyst	Electrolyte	Open-circ. pot., mv	Spec. polar., ohm·cm²	Limit. curr. den., ma/cm²	Open-circ. pot., mv	Spec. polar., ohm·cm²	Limit. curr. den., ma/cm²
Cu	KOH	−780	3	10	—	—	zero
Cu	H_2SO_4	+20	24	10		not tested	
Co	KOH	−850	4	50	—	—	zero
Ni	KOH	−820	0.9	240	—	—	small
Pd	KOH	−820	0.8	>500	−710	1.8	>300
Pd	K_2CO_3	−640	5	15	−550	55	10
Pd	H_2SO_4	+10	1.1	>300	+100 (+380) *	2.3	>300
Rh	KOH	−860	1.0	>500	−700	2.3	>300
Pt	KOH	−840	0.6	>500	−670	2.0	>300
Pt	H_2SO_4	+10	1.2	>300	+80 (+320) *	1.5	>300

* Basis for calculation of the specific polarization.

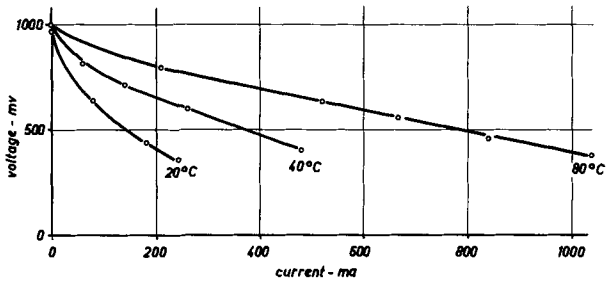

Fig. 7. Current-voltage plots of a fuel cell in 5*N* KOH as a function of temperature with methanol fuel (electrode area 12 cm²).

In addition, the following remarks may be made: (*A*) There was no appreciable electrochemical oxidation of hexane or methylcyclohexane with the described types of electrodes and under the described conditions. (*B*) Sintering of the noble metal electrodes destroys their activity with methanol and seriously affects their activity with hydrogen. (*C*) The current-potential plots with methanol are independent of whether the fuel is admitted as a vapor or dissolved in the electrolyte in excess concentrations. (*D*) In both KOH and H_2SO_4 solutions, formaldehyde and formic acid, dissolved in the electrolyte, are converted with current densities similar to those achieved with methanol.

Experiments with a Laboratory-Stage Alkaline Methanol Fuel Cell

A laboratory-stage methanol fuel cell was set up, using a palladium fuel electrode and a silver oxygen electrode of a projected surface area of 12 cm² each. The electrodes were spaced at 1 cm in an aqueous 5*N* KOH electrolyte to which methanol was added in amounts of 1 mole/l as a liquid admixture.

The current-voltage characteristic of the cell was plotted at 20°, 40°, and 80°C (Fig. 7).

It is apparent that, at the same voltage, the cell output rises about fourfold on increasing the temperature from 20° to 80°C. The characteristic does not change even after continuous operation for several weeks; the electrolyte had to be replaced several times during this period owing to the KOH consumption. The cell was used to examine the degree of conversion of, alternatively, methanol, formaldehyde, and formic acid.

Tests were run which showed that there was negligible activity of the methanol at the oxygen electrode.

A known amount of methanol was added to a cell, and the cell was operated until completely discharged. The total amount of current withdrawn was measured and compared to the calculated total current for complete oxidation to carbonate. The measured current corresponded to about 95% of the calculated current.

Methanol Oxidation Reactions

Various experimenters (1, 5-9) have found different reaction end products in methanol fuel cells. During the present program, several avenues have been followed in an attempt to investigate the course and the completeness of the methanol conversion.

In order to test their electrochemical activity, the supposed intermediates of the methanol oxidation were anodically oxidized in a half-cell arrangement. With formaldehyde as well as with formic acid large current densities were obtained at polarizations comparable to those observed with methanol. This holds for both an alkaline and an acid medium.

Another approach to the problem of the degree of oxidation is the chemical analysis of the electrolyte after extended operation. Therefore, the amounts of formaldehyde and formic acid were determined that were formed after a cell had been operated for 2 hr at, alternatively, 20° and 80°C from methanol owing to incomplete oxidation. The applied analytical procedure was based on the formation of an intensely colored complex of formaldehyde and chromotropic acid which was determined colorimetrically. Formic acid is reduced to formaldehyde by magnesium and sulfuric acid before its determination. Such a procedure was carried out for half-cells after 5000 coulombs had been withdrawn. In the case of alkaline electrolyte with a palladium electrode, the amounts of formaldehyde and formic acid totalled 5% of the converted electricity. With a rhodium electrode, they were about 10% thereof. In the case of an acid electrolyte, using a platinum electrode, the amount of formaldehyde was about 1%, and that of formic acid smaller than 0.1% of the converted electricity. There was no appreciable temperature effect.

The same analyses were conducted for the alkaline methanol fuel cell with a palladium electrode after 8000 coulombs had been withdrawn. The amounts of formaldehyde and formic acid corresponded to 1 and 3%, respectively, of the converted electricity.

Finally, at 20°C the laboratory stage alkaline fuel cell was operated on defined amounts of formaldehyde and formic acid in separate runs. Total current withdrawal was measured for each fuel and was found to be about 95% of the calculated current for complete oxidation in each case. This was in agreement with the tests run to determine fuel activity with methanol as the fuel.

These various findings lead to the conclusion that even at room temperatures methanol oxidation proceeds almost completely to carbonate or carbon dioxide on the Raney electrodes of the present study. This result appears to be independent of the electrolyte and of the half-cell *vs.* fuel cell operation.

Acknowledgments

The authors wish to acknowledge the valuable assistance of A. Köhling and K. Richter, members of Battelle-Institut, Frankfurt, and are particularly grateful to Cummins Engine Company for the active support of the research.

Manuscript received Nov. 30, 1961; final revised manuscript received March 23, 1962. This paper was prepared for delivery before the Detroit Meeting, Oct. 1-5, 1961.

Any discussion of this paper will appear in a Discussion Section to be published in the June 1963 JOURNAL.

REFERENCES

1. O. Block, M. Prigent, and J. C. Balaceanu, Paper presented at the Indianapolis Meeting, Electrochemical Society 1961.
2. E. Justi *et al.*, "High Drain H_2—Diffusion Electrodes," Franz Steiner Verlag, Wiesbaden (1960).
3. E. Justi and A. Winsel, paper presented at the Indianapolis Meeting, Electrochemical Society, 1961.
4. M. Dittman, E. Justi, and A. Winsel, paper presented at the Chicago Meeting, Am. Chem. Soc., 1961 (on oxygen electrodes made of silver).
5. M. J. Schlatter, *ibid.*
6. J. F. Yeager, paper presented at the Indianapolis Meeting, Electrochemical Society, 1961.
7. W. Vielstich, *ibid.*
8. L. R. Griffith, 15th Annual Power Sources Conference, 1961.
9. J. E. Wynn, 14th Annual Power Sources Conference, 1960.

Determination of the Internal Resistance of Leclanche Cells by Square-Wave Method

Aladar Tvarusko

The Carl F. Norberg Research Center, The Electric Storage Battery Company, Yardley, Pennsylvania

ABSTRACT

The internal resistance of Leclanché dry cells was studied on shelf and during discharge by means of a square-wave technique. A constant-current square-wave signal was passed through the cell on test, and the potential variation across the cell displayed on a high-sensitivity oscilloscope with differential input. The instantaneous voltage drop in the oscilloscope pattern, caused by the leading edge of the constant current square wave, indicated the internal resistance of the Leclanché cells. The internal resistance is independent of the amplitude and frequency of the applied square-wave current and of the momentary d-c current. The type of manganese dioxide used in the cathode mix and the composition of the electrolyte influenced the internal resistance of D-size Leclanché cells, both undischarged and during 4-ohm continuous discharge.

In the past, both steady-state and transient measuring methods using either alternating or direct current were investigated for determining the internal resistance of dry cells. Results obtained by these methods were inconsistent. One of the simplest and least accurate methods is the d-c steady-state method in which the resistance is calculated from the potential drop at a certain current drain (1-4). Several d-c transient methods were developed (5-8). Generally, the a-c steady-state methods use various types of impedance bridges to separate the resistive (real) and reactive (imaginary) part of the impedance. Various arrangements were used by the several authors (9-18). The a-c transient method is represented by Brodd's (19) current pulse method.

Impedance of an electrical circuit consists of two parts: resistive and reactive. The resistive part is frequency independent while the reactive part varies with the frequency. The reactive part can include inductance or capacitance or both. In the case of Leclanché cells with relatively short leads, the inductance is negligible, and only the capacitive reactance and the pure resistive component have a role in the impedance.

In general, the separation of the resistive and reactive components of the impedance by the a-c bridge methods is a fairly lengthy operation or complicated instrumentation is involved, *e.g.*, the use of double-servo-controlled a-c bridge (20). During the changes taking place in the discharge and storage of cells, not only the resistive part can change but also the reactive part. Brodd's pulse method (19) yielded only the resistive part of the impedance, whereas the square-wave current method gives information concerning the reactive part of the impedance as well as the resistive part. Very recently however, a pulse method was described (21) to measure parameters of the electrical double layer, namely, the reactive part of the impedance. Various square-wave techniques have been utilized previously for electrochemical studies (22-25).

In this modification of the method developed at this laboratory (25), a constant-current square-wave signal was passed through the test cell and the potential variation across the cell displayed on an oscilloscope. The instantaneous voltage drop in the oscilloscope pattern, caused by the leading edge of the constant-current square wave, represents the internal resistance of the Leclanché cell. Results concerning the reactive part of the impedance will be described in a later article.

Experimental

The block diagram of the circuit used to measure the internal resistance of Leclanché cells is shown in Fig. 1. The Leclanché cell A, was connected in series with a noninductive resistor B. This converted the constant-voltage output of the square-wave generator C, to constant current, since the value of resistor B is much larger than the sum of the impedances in the constant-current circuit loop (C-A-G-F). The voltage response of the square-wave current across the Leclanché cell was measured through oscilloscope probes (5X)D, with a high-

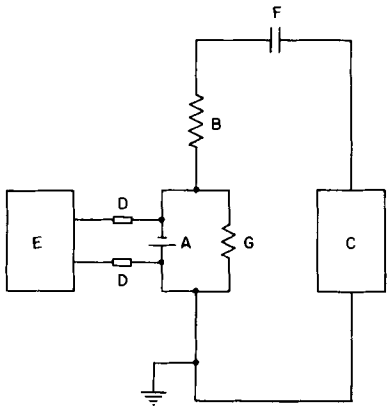

Fig. 1. Block diagram of the circuit: A, Leclanché cell; B, resistor; C, square-wave generator; D, oscilloscope probe (5X); E, oscilloscope; F, blocking capacitor; G, discharging resistor.

sensitivity differential input oscilloscope E, equipped with a Robot recorder camera. A capacitor F was used in series with the dry cell to prevent the discharge of the dry cell through the square-wave generator. Resistor G, in parallel with the cell, was used for discharging the Leclanché cell.

The use of matched oscilloscope probes and shielded cables together with the differential input of the oscilloscope minimized stray pick-up and noise. Ground loops were avoided by grounding the measuring circuitry only at one point. The shielding of the oscilloscope probes was grounded through the oscilloscope.

A Hickok Model 710 sine-square-wave generator was used with a rise time of less than 0.1 μsec for a range of 20 cycles to 1 Mc frequency. The square-wave current limiting resistor was 4200 ohm except for the study of internal resistance as a function of the square-wave current. The voltage used was 42.0v peak-to-peak. The blocking capacitor was 16 μF. The oscilloscope was a Tektronix Model 502 with a passband of d.c. to 100 kc at the most frequently used sensitivities and a rise time of 3.5 μsec.

Square waves of a certain base frequency can be represented by the Fourier series of sine waves of its fundamental and odd numbered harmonics. The leading edge of the square wave represents the high-frequency harmonics. If the inductance of the sample and leads is negligible, the instantaneous voltage drop of the signal corresponds to the resistive part of the impedance only. Knowing the square-wave current amplitude and the measured instantaneous voltage drop (times oscilloscope probes' attenuator factor 5X) the R is simply calculated from Ohm's law. When discharging the Leclanché cell, the resistor G is in parallel with the cell, and R is calculated with the help of Kirchoff's law.

All the Leclanché cells investigated were pasted-type D-size dry cells. In order to study the effect of the type of MnO_2 on the course of the internal resistance curves, MnO_2 of different origins was used. African ore (Ghana) represented the naturally occurring manganese dioxide. The African ore was also blended with a synthetic hydrous MnO_2 (4% alkali and 10% water content). The x-ray diffraction pattern of this synthetic MnO_2 had weak intensity γ-MnO_2 and very weak pyrolusite and cryptomelane peaks. The two electrolytic MnO_2 samples (sources A and B) were γ-MnO_2. The MnO_2: carbon black ratio was 8:1 for all cells. The electrolyte in the core was the same for all compositions with the exception of the African ore, synthetic MnO_2 mix which contained 20% less $ZnCl_2$ and 10% less NH_4Cl than the others. The same paste composition was used for all Leclanché cells except for the electrolytic MnO_2 from source B. The paste for this cell contained 120% more $ZnCl_2$ and 25% more NH_4Cl than the other one.

Results and Discussion

The internal resistance of the Leclanché cells was measured by a constant square-wave current. It was of interest to investigate the internal resistance as a function of the applied square-wave current amplitude. The current was varied from 1 to 20 ma peak-to-peak, and no change was observed in the internal resistance of the cell. The internal resistance is thus independent of the square-wave current amplitude, *i.e.*, it obeys Ohm's law. A current of 10 ma was subsequently chosen to obtain a convenient voltage drop.

The frequency dependence of the internal resistance was investigated in the frequency range of 20-10,000 cps. The internal resistance of Leclanché cells, R_i was thus found to be independent of the frequency as shown in Fig. 2. This frequency independence of the R_i was found for all the Leclanché cell compositions investigated.

The very slight deviation at low frequencies is due to the difficult readability of the voltage drop (where large vertical deflection factors are needed), while at high frequencies it is due to the distortion of the leading edge. The internal resistance of D-size Leclanché cells is in the range 0.1-0.4 ohm, according to the composition. These low values necessitated the use of the most sensitive range of the oscilloscope's vertical amplifier (200 μv/cm). At this range the passband of the amplifier is d.c. to 100 kc. The fifth odd harmonic component of the 10 kc square-wave signal is cut out by the amplifier, whereas the forty-ninth odd harmonic component of the 1 kc square-wave signal is carried over. The readability of the instantaneous voltage drop is good at 1 kc also. All the measurements were done at 1 kc.

Dry cells are made as uniformly as is practically possible. A certain deviation in the composition, as-

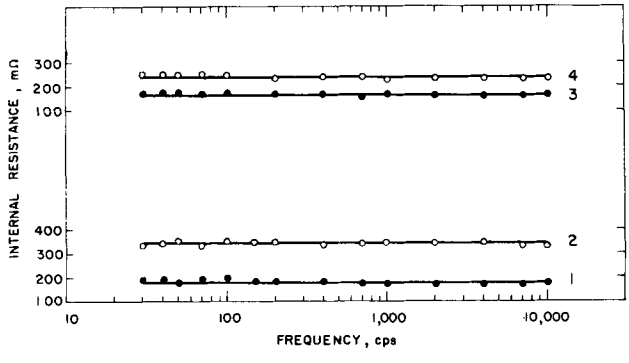

Fig. 2. Internal resistance of Leclanché cells as a function of frequency. Curve 1, African ore; curve 2, African ore, synthetic MnO_2; curve 3, electrolytic MnO_2, source B; curve 4, electrolytic MnO_2, source A.

Table I. Internal resistance of undischarged Leclanché cells (D-size) and its deviation

Type of MnO_2	Number of cells	R_{Mean}, ohm	Δ_{Max}, ohm	
African ore	15	0.18	+0.03	−0.01
Electrolytic MnO_2, source A	12	0.21	+0.06	−0.04
Electrolytic MnO_2, source B	12	0.16	+0.02	−0.01

sembly, etc., is unavoidable. This naturally shows up in the internal resistance values also. The arithmetical mean of at least 12 undischarged D-size Leclanché cells per lot, and the maximum deviation from it can be seen in Table I. The reproducibility of the internal resistance values for individual cells is good (±0.01 ohm).

On replacing part of the African ore in the core with a synthetic hydrous MnO_2, the internal resistance of the undischarged Leclanché cell was markedly increased (curve 2 *vs.* curve 1, Fig. 2). The slightly lower salt concentration in the mix electrolyte cannot be responsible alone for this marked resistance increase. Therefore, it is safe to assume that the synthetic MnO_2 in the core contributed largely to the internal resistance increase. Leclanché cells made with electrolytic MnO_2, source B, had a paste of significantly higher salt concentration which was mainly responsible for the internal resistance decrease of these cells (curve 3).

The internal resistance of Leclanché cells of various compositions was investigated also during discharge. Three cells or more were discharged for each composition to insure proper validity of results. Momentary current drains did not affect the internal resistance of cells except at very high current drains where it increased due to changes taking place which cannot be ascertained at this time. This confirms the results of Brodd (19), Fukuda *et al.* (14), and Panzer *et al.* (8) and is contrary to the studies reporting the dependence of the "internal resistance" of Leclanché cells on current drain (1, 4, 6, 14, 15). In the latter cases, the "internal resistance" includes not only the pure resistance, R_i, of Leclanché cells but also other types of polarization.

The internal resistance of Leclanché cells changes during discharge due to the current producing and secondary reactions. The internal resistance change for Leclanché cells containing African ore during 4 ohm continuous discharge can be seen in Fig. 3. The internal resistance of the cells having African ore only increased constantly, and the curve (No. 1) can be separated into two parts having slightly different slopes. Cells with synthetic hydrous MnO_2 and African ore produced a curve of an entirely different character. This curve was duplicated several times. The rapid internal resistance increase in the very beginning of the discharge and the nearly horizontal portion of the curve can be attributed to the presence of the synthetic MnO_2. In the second half of the discharge the synthetic MnO_2 had lost its influence, and the curve resembles that of cells with natural ore mixes. The voltage values on the individual

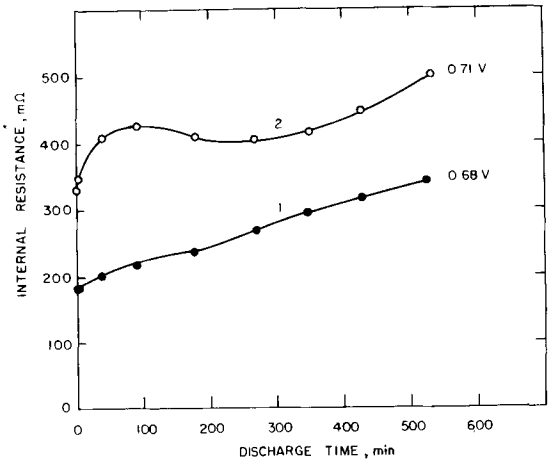

Fig. 3. Internal resistance of Leclanché cells containing natural ores discharged continuously through 4 ohm. Curve 1, African ore; curve 2, African ore, synthetic hydrous MnO_2.

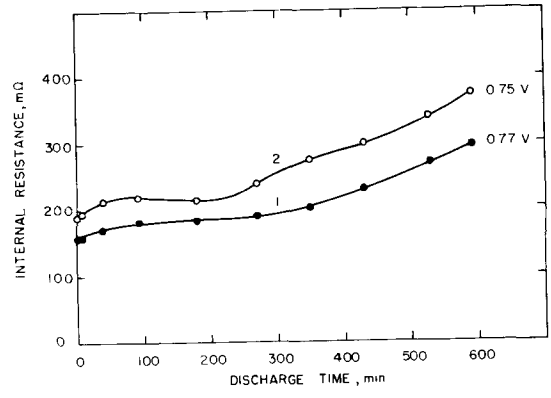

Fig. 4. Internal resistance of Leclanché cells having electrolytic MnO_2 discharged continuously through 4 ohm. Curve 1, electrolytic MnO_2, source B; curve 2, electrolytic MnO_2, source A.

curves represent the closed-circuit voltages at the cut-off time.

In the manganese dioxides of the above cells the amount of γ-MnO_2 was much less than in electrolytic MnO_2, as judged by the intensity of the γ-MnO_2 peaks in the x-ray diffraction patterns. The amount of γ-MnO_2 seems to influence the first portion of the internal resistance curve. African ore has a fair amount of γ-MnO_2, and its internal resistance curve for cells can be characterized by two slightly deviating slopes. The internal resistance curves of electrolytic MnO_2 (dominantly γ-MnO_2) can be separated into two parts with distinctly different slopes (Fig. 4). This is more evident in Leclanché cells (MnO_2, source B, curve 1) with a paste of much higher zinc chloride content (lower *p*H).

The two distinct slopes and the initial portion of the curves for the latter and other Leclanché cells represent various reactions taking place in the cells. With a paste of higher *p*H, the course of the internal resistance curve (No. 2) deviates from that previously described (No. 1) mainly in the 250-450 min range.

The previously described square-wave current method to determine the internal resistance naturally is not limited to Leclanché cells but can be applied to other electrochemical systems and their half-cells.

Acknowledgment

The author is indebted to Mr. B. Romvári for helpful discussions, and to the Ray-O-Vac Company, Madison, Wisconsin, for supplying the special Leclanché cells.

Manuscript received Oct. 18, 1961; revised manuscript received Feb. 1, 1962. This paper was prepared for delivery before the Detroit Meeting, October 1-5, 1961.

Any discussion of this paper will appear in a Discussion Section to be published in the June 1963 JOURNAL.

REFERENCES

1. C. Drotschmann, "Moderne Primärbatterien," pp. 68-72, Nikolaus Branz, Berlin-Schoeneberg (1951).
2. D. L. Ordway, *Trans. Electrochem. Soc.*, **17**, 341 (1910).
3. G. W. Vinal, "Primary Batteries," pp. 133-4, John Wiley & Sons, Inc., New York (1950).
4. N. K. Chaney, *Trans. Electrochem. Soc.*, **29**, 183 (1916).
5. H. Steinwehr, *Elektrotechnik*, **2**, 91 (1948).
6. R. Glicksman and C. K. Morehouse, *This Journal*, **102**, 273 (1955).
7. K. Kordesch and A. Marko, *ibid.*, **107**, 480 (1960).
8. R. E. Panzer, W. S. Harris, and W. C. Spindler, Paper presented at the Detroit Meeting of The Electrochemical Society, 1961.
9. H. D. Holler, *This Journal*, **97**, 271 (1950).
10. H. E. Lawson and F. J. Kirkman, *Trans. Electrochem. Soc.*, **70**, 441 (1936).
11. N. C. Cahoon, *ibid.*, **92**, 159 (1947).
12. C. Drotschmann, "Elektrochemie und Elektrotechnik im Batteriebau," V. Teil, pp. 77-88, Nikolaus Branz, Berlin (1953).
13. J. J. Coleman, *Trans. Electrochem. Soc.*, **90**, 545 (1946).
14. M. Fukuda, T. Hirai, and H. Manabe, *J. Electrochem. Soc., Japan*, **27**, 247 (1959); Overseas Edition, **27**, E 108 (1959).
15. J. Euler, *Z. Elektrochem.*, **60**, 1056 (1956).
16. C. Drotschmann, ref. (1), pp. 72-79.
17. J. Euler and K. Dehmelt, *Z. Elektrochem.*, **61**, 1200 (1957).
18. R. J. Brodd and H. J. DeWane, Paper presented at the Columbus Meeting of the Electrochemical Society, 1959.
19. R. J. Brodd, *This Journal*, **106**, 471 (1959).
20. C. O. Anderson, F. Möhl, and E. Stenhagen, *Acta Chem. Scand.*, **12**, 415 (1958).
21. J. S. Riney, G. M. Schmid, and N. Hackerman, *Rev. Sci. Instr.*, **32**, 588 (1961).
22. U. Bertocci, G. Bianchi, and C. Guerci, *Ann. Chim. (Rome)*, **44**, 44 (1954).
23. R. J. Brodd and N. Hackerman, *This Journal*, **104**, 704 (1957).
24. J. J. McMullen and N. Hackerman, *ibid.*, **106**, 341 (1959).
25. B. D. Cahan and P. Rüetschi, *ibid.*, **106**, 543 (1959).

Oxidation Studies on 304 Stainless Steel

E. A. Gulbransen and K. F. Andrew

Research Laboratories, Westinghouse Electric Corporation, Pittsburgh, Pennsylvania

ABSTRACT

The kinetics of oxidation of 304 stainless steel are studied between 500° and 1150°C at 0.1 atm for reaction times up to 6 hr. At 500°C about 2.3 $\mu g/cm^2$ of oxide are formed in a time period of 6 hr. The rate of increase after 6 hr is 0.1 $\mu g/cm^2/hr$. At 800°C a transition is observed in the rate of oxidation with the kinetics changing from the parabolic rate law to the linear rate law. This transition occurred for a weight gain of 9 $\mu g/cm^2$. At 900°C and for weight gains above 90 $\mu g/cm^2$ the parabolic rate law again was found to hold. A second transition is found in the kinetics of oxidation at 1150°C. This transition we relate to the vapor pressure of iron and chromium which acts to speed up the transfer of metal atoms through the oxide scale. A comparison of the kinetics of oxidation is made with the heat-resistant Kanthal alloys and with pure chromium.

This paper presents a systematic study of the kinetics of oxidation of 304 stainless steel between 500° and 1150°C at 0.1 atm and for reaction times up to 6 hr. Since 304 stainless steel is being used as a high-temperature material, one of the objectives of this work is to study the conditions under which the alloy fails in oxidation. Failure occurs when a rapid oxidation reaction develops in which diffusion processes are no longer rate controlling. For some metals and alloys failure is due to poor adhesion of the oxide. With other metals the oxide may volatilize. For those metals which form nonvolatile and adherent oxide films, failure may result from vaporization of the metal through the oxide film. This type of failure has been observed in the oxidation of chromium (1) and several heat resistant alloys (2-3).

From a thermodynamic point of view oxidation and corrosion are functions of the chemical potentials of the components in the environment and the chemical potentials of the metallic components in the alloy. The chemical potential of an alloying component is a function of the activity of the metal in the alloy. From a kinetic point of view the rate of oxidation or corrosion depends in part on the nature and properties of the oxide or corrosion film formed on the alloy.

Since both gaseous oxidation and corrosion in high-temperature water atmospheres depends on the same metallurgical factors in the alloy, a study of the kinetics of oxidation may help our interpretation of corrosion in water atmospheres.

Since the chemical activity of metal atoms in an alloy and the characteristics of the oxide film can be controlled by alloying additions (4), it is possible to

predict the oxidation and corrosion behavior of alloys.

Experimental

Apparatus.—The vacuum microbalance reaction system was used (5-6) for all of the measurements. The sensitivity of the microbalance was 0.83 μg per 0.001 cm. Weight changes of 0.3 μg could be estimated.

A mullite furnace tube was used to surround the specimen. This tube was sealed directly to the all-Pyrex glass vacuum system. After introducing the specimen into the reaction system and closing off, the system was evacuated for 16 hr at a pressure of 10^{-6} mm Hg or less. To avoid evaporation of metal at 1000°C and higher, the specimen and reaction tube were heated rapidly to the reaction temperature. After thermal equilibrium was established, purified oxygen was added to 0.1 atm pressure.

For the same surface treatment the reproducibility of the oxidation experiments was about 10-20%.

The furnace temperature was maintained constant to ±1.5°C by the use of a calibrated high-sensitivity recorder-controller and a calibrated Pt-Pt 10% Rh thermocouple.

Samples.—The 304, stainless steel analyzed 17.7 Cr, 8.34 Ni, 1.11 Mn, 0.02 P, 0.16 N, 0.11 C, and balance iron. Strips of 5 mil sheet were abraded through 4/0 polishing paper under purified kerosene. They were carefully cleaned before using (7). Depending on the amount of reaction, four specimen sizes and weights were used. The largest was 11.25 cm² in area and weighed 0.6831g while the smallest was 1.36 cm² in area and weighed 0.0820g.

Results

The results are presented in weight gain *vs.* time graphs. The weight gain is in micrograms per square centimeter and the time is in minutes. Although the oxide film is a mixture of oxides (8), we can estimate the thickness of the oxide by assuming the oxide to be Cr_2O_3 and by assuming a surface roughness ratio of unity. A factor of 60 is calculated to relate the weight gain to thickness in angstroms. An oxygen pressure of 0.1 atm is used for all of the experiments.

Both annealed and unannealed specimens were used. The annealed specimens were prepared by heating in a high vacuum system at a pressure of 9 x 10^{-6} mm Hg at 843°C for 2 hr and quenching. This treatment precipitates carbides and nitrides which could occur during normal oxidation at this temperature.

Oxidation at 500° and 600°C—unannealed specimens.—Figures 1 and 2 show the time courses of the experiments at 500° and 600°C. The oxide thicknesses and colors are given in Table I. No spalling of the oxide occurred on cooling the oxidized alloy to room temperature. After 6 hr of oxidation at 500°C, about 2.3 μg/cm² of oxide were formed. Since the room temperature oxide was not removed, the total oxide must include an additional 0.3-0.5 μg/cm². The reaction rate after 6 hr of reaction was of the order of 0.1 μg/cm² of oxide per hour at 500°C.

A plot of the weight gain squared against time shows a straight line between 2 and 6 hr of reaction time. A value of 1.67 x 10^{-16} $(g/cm^2)^2$/sec is calculated. No evidence was found for a transition in the kinetics of the reaction. We conclude that the reaction of 304 stainless steel with oxygen at 500°C is a slow reaction.

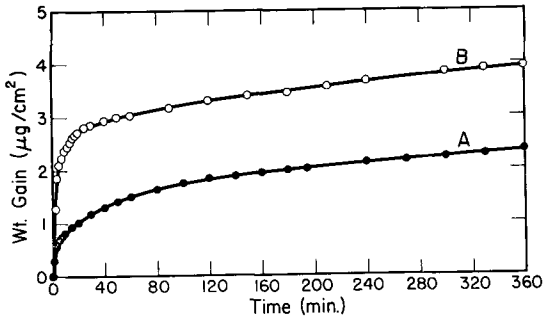

Fig. 1. Effect of temperature on oxidation of unannealed 304 stainless steel, abraded through 4/0, 7.6 cm of Hg of O_2; curve A, 500°C; curve B, 600°C.

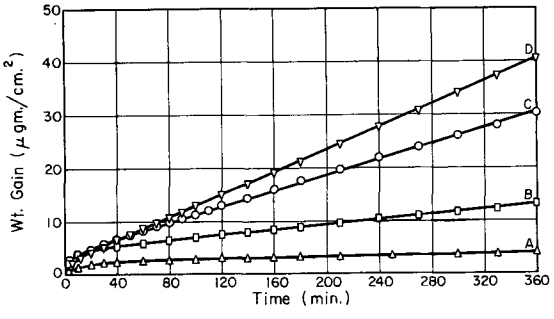

Fig. 2. Effect of temperature on oxidation of annealed stainless 304, abraded through 4/0, 7.6 cm of Hg of O_2; curve A, 700°C; curve B, 800°C; curve C, 850°C; curve D, 900°C.

Electron microscope observations on the edges of the specimens showed no evidence for oxide whiskers or platelets.

Oxidation at 700° and 1150°C.—Figures 2 and 3 show the time courses for the oxidation experiments over the temperature range of 700°-1100°C. Oxide thicknesses and colors are shown in Table I. None of the oxide films or scales spalled away from the metal on cooling to room temperature.

In this study we are particularly interested in transitions in the rate of oxidation and "breakaway" type of oxidation reactions. For this purpose we use

Table I. Thickness and color of oxide films on 304 stainless steels

Temp, °C	Unannealed Thickness,* μg/cm²	Color	Annealed Thickness,* μg/cm²	Color
500	2.33	Straw		
600	3.91	Purple		
700	8.01	Blue	3.95	Blue
750	12.33	Straw-pink		
800	24.6	Blue-green	13.1	Light purple
850	39.3	Gray	30.2	Gray-green
900	46.6	Gray	40.5	Gray-pink
950	90.0	Gray	56.8	Gray
1000			136.0	Gray
1050			254.0	Gray
1100			490.0	Gray
1150			905.0‡	Gray

* 6-hr experiments.
‡ 7-hr experiment.

the parabolic rate law to interpret the rate data. This law states that the weight gain, W, depends on the time, t, by the equation $W^2 = At + C$. Here A is the parabolic rate law constant and C is a constant. The parabolic rate law based on the principles of formation and diffusion of ions or lattice defects has been the most successful rate law for explaining oxidation. Parabolic rate law plots are used to test for changes in the mechanism of reaction. Figures 4-8 show parabolic rate law plots of the 800°, 850°, 950°, 1050°, and 1150°C experiments. The first evidence for a transition in the rate of oxidation was found in the 800°C parabolic plot shown in Fig. 4. After the initial period of reaction, a good fit was obtained with the parabolic rate law for the thickness range of 5-9 $\mu g/cm^2$. An increase in slope was observed in the parabolic rate law plot above this thickness. A value of 5.83×10^{-15} $(g/cm^2)^2/sec$ was calculated for the pretransition thickness range parabolic rate law constant.

Deviations from the parabolic rate law are also observed in the 850°C plot as shown in Fig. 5. This deviation occurs after 70 min of reaction or at an oxide thickness of 9 $\mu g/cm^2$. A similar transition

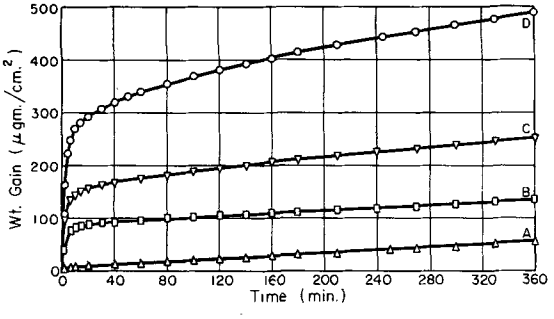

Fig. 3. Effect of temperature on oxidation of annealed stainless 304, abraded through 4/0, 7.6 cm of Hg of O_2; curve A, 950°C; curve B, 1000°C; curve C, 1050°C; curve D, 1100°C.

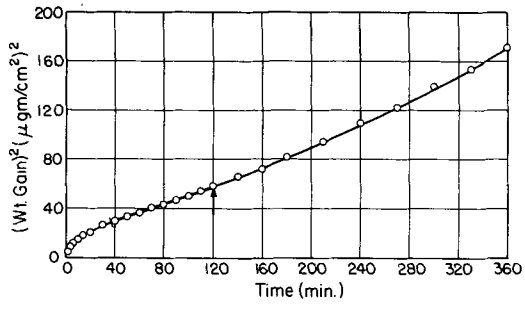

Fig. 4. Oxidation of stainless steel, 800°C, 7.6 cm of Hg of O_2; parabolic plot, abraded through 4/0; A = 5.83×10^{-15} $(g/cm^2)^2/sec$.

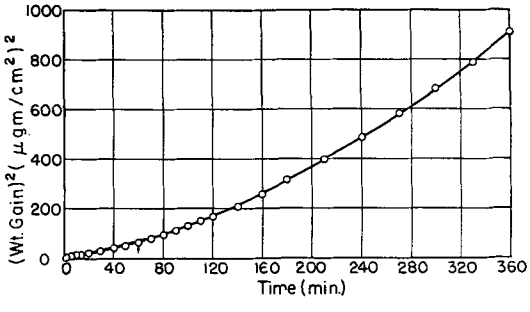

Fig. 5. Oxidation of stainless steel, 850°C, 7.6 cm of Hg of O_2; parabolic plot, abraded through 4/0; A = 1.79×10^{-14} $(g/cm^2)^2/sec$.

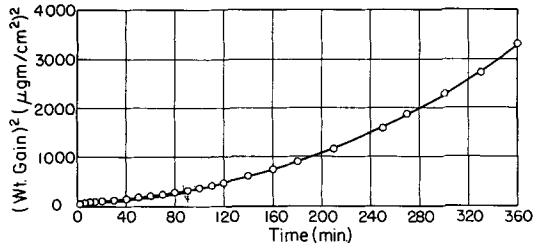

Fig. 6. Oxidation of stainless steel, 950°C, 7.6 cm of Hg of O_2; parabolic plot, abraded through 4/0; A = 2.78×10^{-13} $(g/cm^2)^2/sec$.

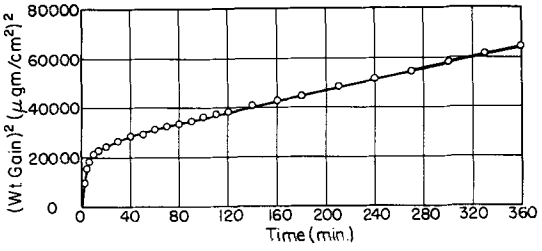

Fig. 7. Oxidation of stainless steel, 1050°C, 7.6 cm of Hg of O_2; parabolic plot, abraded through 4/0; A = 1.72×10^{-12} $(g/cm^2)^2/sec$.

thickness is found for the 900°C experiment. We conclude a transition occurs in the kinetics of the reaction for an oxide thickness of about 9 $\mu g/cm^2$. This transition thickness is the lowest we have observed for any metal or alloy. For the oxidation of chromium the first transition occurred at a thickness of 80 $\mu g/cm^2$.

Above 900°C it is not possible to observe the pretransition period of oxidation. The parabolic rate law plot of the 950°C experiment in Fig. 6 shows a continuously increasing slope. The initial value for the rate law constant is given in Fig. 6 and Table II. We interpret the changing value for the parabolic rate law constant as due to a change in oxide composition. The parabolic rate law of oxidation does not apply for the oxide composition range of 9-90 $\mu g/cm^2$. Instead the rate of oxidation follows the linear rate law.

Figure 7 shows a parabolic rate law plot for the 1050°C experiment. A straight line is found after the first hour of reaction.

A second transition is found to occur in the 1150°C parabolic rate law plot shown in Fig. 8. The rate law is observed to hold for the intermediate section of the plot. After 330 min of oxidation the rate law con-

Table II. Summary of parabolic rate law constants

Temp, °C	A. Unannealed $(g/cm^2)^2/sec$ Pretransition	A. Unannealed $(g/cm^2)^2/sec$ Posttransition	B. Annealed $(g/cm^2)^2/sec$ Pretransition	B. Annealed $(g/cm^2)^2/sec$ Posttransition
500	1.67×10^{-16}			
600	3.33×10^{-16}			
700	1.08×10^{-15}		3.61×10^{-16}	
750	2.64×10^{-15}	8.34×10^{-15}		
800	9.16×10^{-15}	3.92×10^{-14}	5.83×10^{-15}	8.89×10^{-15}
850	1.11×10^{-14}	1.055×10^{-13}	1.79×10^{-14}	6.34×10^{-14}
900	2.36×10^{-14}	1.583×10^{-13}	2.38×10^{-14}	1.33×10^{-13}
950	1.193×10^{-13}	5.69×10^{-13}	7.22×10^{-14}	2.78×10^{-13}
1000			5.0×10^{-13}	5.91×10^{-13}
1050				1.728×10^{-12}
1100				6.11×10^{-12}
1150				1.67×10^{-11}

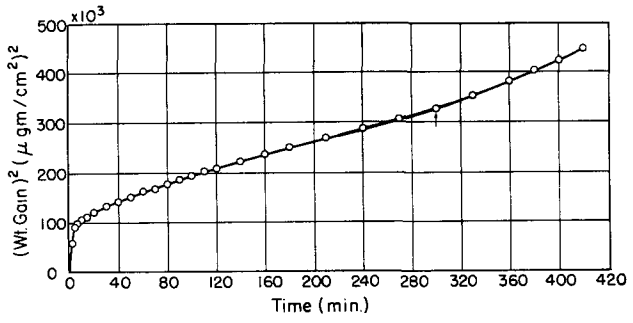

Fig. 8. Oxidation of stainless steel, 1150°C, 7.6 cm of Hg of O_2; parabolic plot, abraded through 4/0; A = 1.67 x 10^{-11} $(g/cm^2)^2$/sec.

stants increase. This increase is probably due to a vapor pressure effect which is discussed in a later section.

Temperature dependence.—To interpret the temperature dependence of the parabolic rate law constants A we use the simple form of the Arrhenius expression

$$A = Be^{-\Delta H/RT}$$

Here ΔH is the heat of activation of the rate-controlling mechanism, B is a constant, and R is the gas constant. ΔH is determined from the slope of a log A *vs.* $1/T$ plot. More elaborate equations may be used if the entropy terms are evaluated (9).

Table II shows a summary of the parabolic rate law constants for the annealed and unannealed samples. Pre- and posttransition values are given where possible. Figure 9 shows a log A *vs.* $1/T$ plot of the data.

Three straight lines are observed in Fig. 9. Curve DE gives the constants for the pretransition region. A value of 33,200 cal/mole for ΔH is calculated. The posttransition values are given by the line ABC. Line BC has about the same value for ΔH as line DE.

Point B shows a major change in the mechanism of oxidation. A heat of activation of 88,000 cal/mole is calculated.

We interpret the change in rate between line DE and line BC as due to a crystal structure transformation in the oxide system. Electron diffraction studies on a similar alloy by Hickman and Gulbransen (8) shows a crystal structure transformation occurring for this temperature range of oxidation.

Vapor pressure effect.—Figure 9 shows a drastic change occurs in the mechanism of oxidation at point B. We suggest that this change is due to the vapor pressure of the metals in the 304 stainless steel. We explained a similar change in the rate oxidation of chromium (1) at 900°C as due to the vapor pressure of chromium. At some temperature for all metals the rate of evaporation of metal into and through the oxide film acts to aid normal ion formation and transfer processes. Since all sides of the oxide crystals may be exposed in part to the metal vapor, a short circuit of the normal diffusion process is possible. However, if the oxide film is impervious to metal vapor, the metal transfer process may be limited. This occurs for oxide films on aluminum-iron alloys (4). Much smaller effects were observed for oxide films on simple chromium-iron alloys (4).

To test for the vapor pressure effect on 304 stainless steel we compare the rate of evaporation of metal from a clean surface of a 21.9 Cr-Fe alloy with the rate of oxidation calculated on the basis of chromium reacting. Due to the possibility of side reactions, such as decarburization, effecting the vapor pressure measurements, special alloys must be used. We have studied recently the vapor pressure of a clean 21.9 Cr-Fe alloy (4) both in the oxide-free condition and in the presence of an oxide film. Although this alloy differs in composition from the 8 Ni-18 Cr-74 Fe alloy, we feel that the two alloys do not differ appreciably in their vapor pressure curves since chromium is the metal vaporizing in each alloy.

Figure 10 shows a comparison of the rate of evaporation from an oxide-free surface of the 21.9 Cr-Fe alloy with the rate of oxidation of the 304 stainless steel. Below 1000°C the rate of oxidation is higher than the rate of evaporation. The two rates become equal at 1000°C, and above 1000°C the rate of oxidation is less than the rate of evaporation.

Since the oxide film is thick, the transition is not sharp. The effect of oxide films on the vapor pressure would act to lower curve A slightly.

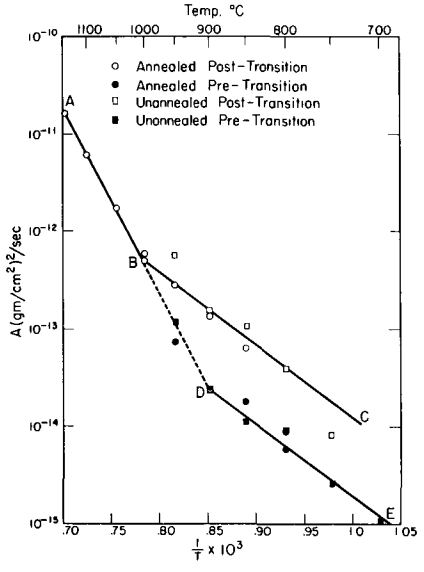

Fig. 9. Oxidation of 304 stainless steel. Log A *vs.* $1/T$. Curves A,B,C, posttransition; curves D,E, pretransition. ΔH_{AB} = 88,000 cal/mole.

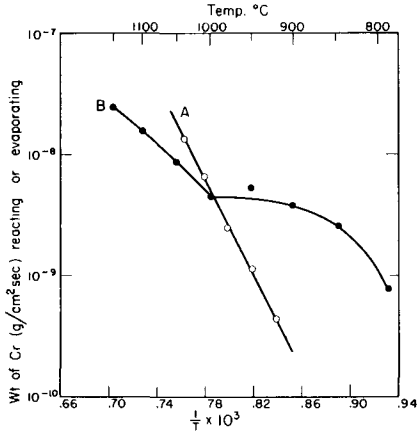

Fig. 10. Comparison rate of evaporation from clean 21.9 Cr-Fe alloy (curve A) with rate of oxidation of 304 stainless steel (curve B), log rate *vs.* $1/T$.

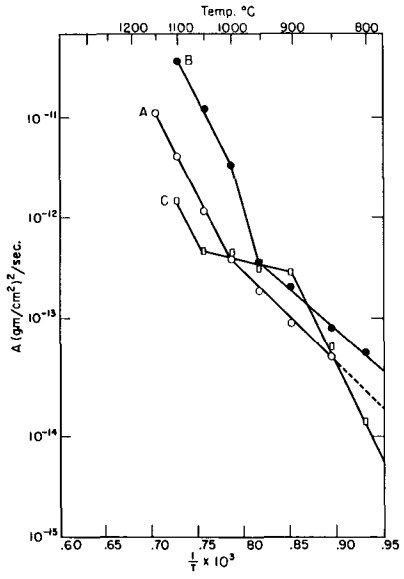

Fig. 11. Oxidation of stainless steel (A), chromium (B), Kanthal A_1 (C). Log *A* vs. 1/*T*.

Comparison with Kanthal Alloy.—Figure 11 shows a comparison of the parabolic rate law constants for Kanthal A_1 and chromium with the posttransition values for 304 stainless steel. Kanthal A_1 shows a transition in the rate of oxidation at 1050°C, 304 stainless steel at 1000°C, and chromium at 950°C. We have related all of these transitions to vapor pressure effects.

Since the aluminum oxide film is nearly impervious to the metal atoms the transition temperature is higher for Kanthal A_1. The effect of the Al_2O_3 film is shown by the nearly constant values for the parabolic rate law constants between 900° and 1050°C.

Aluminum has another favorable influence on the oxidation process. Aluminum in combination with iron and chromium forms oxides which are closely matched to the metal lattice. Thus, γ-Al_2O_3 and $FeAl_2O_4$ are both spinels which match closely the iron-iron spacings in the metal lattice.

Discussion

The effect of aluminum and nickel in chromium iron alloys can be considered from the electron configuration point of view. Aluminum can contribute one 3p electron to the unfilled 3d bands of iron and chromium with the result that aluminum is strongly bonded in the alloy. This is confirmed experimentally by the lowered chemical potential of iron and chromium in the alloy (4). Since nickel has a fraction of a 3d level unfilled, the bonding between nickel and iron and chromium is not as strong as when aluminum is added. Nickel is not expected to lower the chemical activity of iron and chromium to the same extent as aluminum.

Nickel forms a less stable oxide than aluminum. Therefore, solid phase reactions can occur in the oxide (10) which can lower the protective character of the oxide film. Although the initial rates of oxidation of stainless steel are low it would be expected that the oxide composition changes with time. Nickel oxide is also much more readily attacked by chlorides or acid vapors than aluminum oxide.

We conclude that both nickel and aluminum are good alloying elements to add in the chromium-iron series of alloys from a protection and corrosion point of view. The low permeability of the aluminum oxide film to iron and chromium atoms gives an alloy of high heat resistance. Nickel, on the other hand, gives an austenitic alloy of high strength with moderate oxidation resistance.

Manuscript received Oct. 27, 1961; revised manuscript received Feb. 26, 1962. This paper was prepared for delivery before the Los Angeles Meeting, May 6-10, 1962.

Any discussion of this paper will appear in a Discussion Section to be published in the June 1963 JOURNAL.

REFERENCES

1. E. A. Gulbransen and K. F. Andrew, *This Journal*, **104**, 334 (1957).
2. E. A. Gulbransen and K. F. Andrew, *ibid.*, **106**, 294 (1959).
3. E. A. Gulbransen and K. F. Andrew, Westinghouse Research Laboratories Scientific Paper 6-94602-1-P14, Nov. 20, 1957.
4. E. A. Gulbransen and K. F. Andrew, Westinghouse Research Laboratories Scientific Paper 6-94602-1-P20, June, 1958.
5. E. A. Gulbransen, *Trans. Electrochem. Soc.*, **81**, 187 (1942).
6. E. A. Gulbransen, "Advances in Catalysis," Vol. V, pp. 119-175, Academic Press, Inc., New York (1953).
7. E. A. Gulbransen and K. F. Andrew, *This Journal*, **99**, 402 (1952).
8. J. W. Hickman and E. A. Gulbransen, *Trans. Electrochem. Soc.*, **91**, 605 (1947).
9. E. A. Gulbransen, *Anals. N. Y. Acad. Sciences*, **58**, 830 (1954).
10. E. A. Gulbransen and W. R. McMillan, *Industrial and Engineering Chem.*, **45**, 1734 (1953).

Growth of Halide Layers on Copper Single Crystals

A. Goswami

National Chemical Laboratory, Poona, India

ABSTRACT

Structures and orientations of cuprous halides formed on copper (111), (110), and (100) faces by reaction with halogen vapors at room temperature have been studied and the crystal growth process discussed.

Previous electron diffraction studies (1-3) on the growth of oxide or sulfide films on copper single crystals in air or sulfur vapor at various temperatures showed that these films were crystalline and had two-degree orientation with respect to substrate if the substrate temperature was high enough, but were amorphous when formed at room temperature. During the initial stage of their growth, the films consisted of cuprous compounds alone. If the growth continued for a sufficiently long time and the temperature was favorable, the top layers consisted entirely of cupric compounds either with two-degree orientation or in polycrystalline state with or without a preferred orientation. Similar reactions, however, at room temperature with halogen vapors or by anodic treatment in halide solutions, produced, on the other hand, crystalline cuprous halides even when the time of reactions was sufficiently prolonged (4-6). Since there has been little work on the growth of cuprous halide films or on their epitaxial relationship to the substrate a study has been made on single crystals of copper and the results compared with those obtained by anodic treatments.

Experimental

Samples of copper with (111), (110), and (100) faces were prepared by cutting pieces from a single crystal rod, grinding, surfacing with different grades of emery, etching in nitric acid, and finally electropolishing in phosphoric acid in a manner already described in previous papers (1, 7). The diffraction patterns (not shown) from these faces revealed that they were extremely smooth and nearly parallel to (111), (110), and (100) planes of the copper lattice. The samples were then exposed to vapors of iodine or bromine for a few seconds and immediately transferred to an electron diffraction camera (cold cathode type, 60 kv) and examined by the reflection method, in more than one azimuth. The crystals were again treated in halogen vapor and re-examined. Similar studies were also made on polycrystalline copper (spec. pure) disks.

For comparison, these crystals after etching and reelectropolishing were treated anodically (4-6) in KI or KBr solution in the presence of H_2SO_4 for a few seconds to half a minute and the surface layers examined by the diffraction technique in a similar way.

Results

Halide layers formed on copper crystals by progressive reactions with halogen vapors showed various interference colors, *viz.*, brownish orange, pink, golden yellow, etc., depending on the thickness of the layers; they finally became pale yellow accompanied by considerable roughening of the surface.

The diffraction patterns from the halide films generally consisted of spots and faint rings passing through these spots. With the rotation of the copper crystals around an axis normal to the electron beam direction, the spot patterns changed, thus indicating that the halide crystals grew epitaxially on the substrates. In other words, they developed two-degree orientations such that certain planes and axial directions of the halide crystals were parallel, respectively, to the substrate face and to an important direction lying in that face. The ring patterns were due to the formation of polycrystalline material. Arc patterns, which did not change even with the rotation of copper crystals, showed the presence of one-degree orientated halide crystallites which had a common axis parallel to one another or had a common plane, but otherwise were randomly disposed in space. Clarity or sharpness of patterns depended to a large extent on the crystal size. Hence with increase in crystal size the clarity was better. It was also noticed that sometimes with progressive reaction the spot pattern changed and ultimately became confused by the appearance of many new spots, no doubt due to the formation of new crsytals with different orientations.

Measurements of d_{hkl} values from rings as well as spots and also of their relative intensities agree with those of γ-forms of halides alone.

On Cu*(111) face.*—Cuprous iodide formed on this face yielded diffraction patterns (Fig. 1 and 2) consisting of spots and faint rings, when the electron beam was grazing along the <110> and <112> axes of the crystal, respectively. The appearance of 111

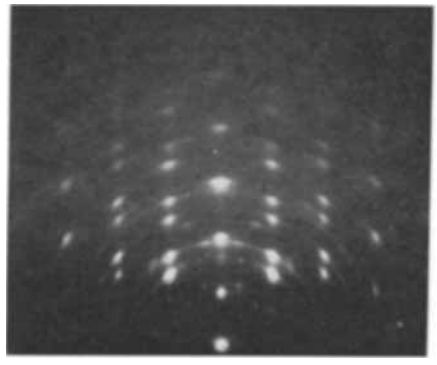

Fig. 1. 2-d {111} orientation of CuI; beam along <110>

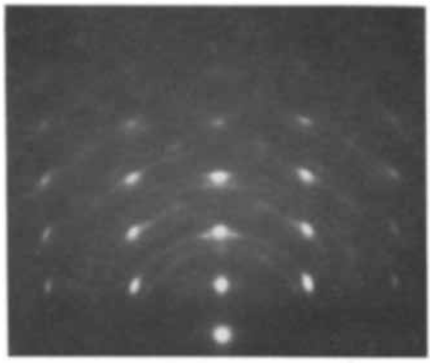

Fig. 2. 2-d {111} orientation of CuI; beam along <211>

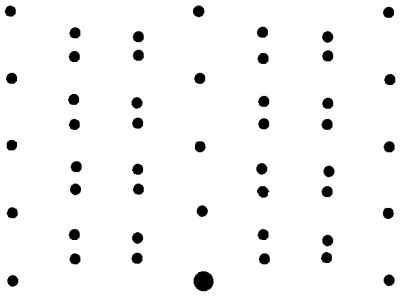

Fig. 3. Theoretical pattern for parallel and antiparallel {111} orientation of CuI; beam along <110> direction.

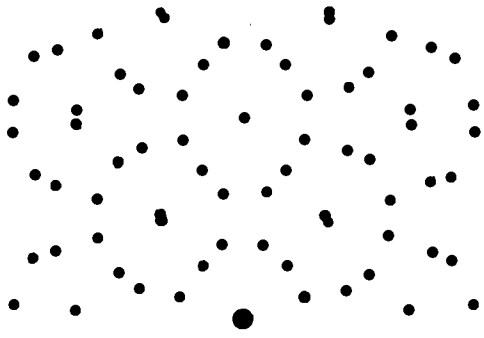

Fig. 4. Theoretical pattern for {115} orientation of CuI; beam along <110> direction.

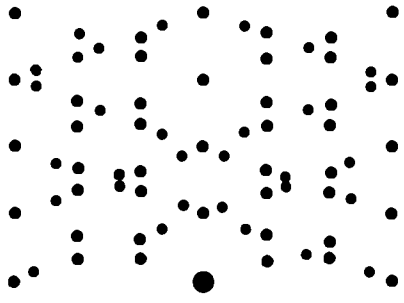

Fig. 5. Fig. 3 and 4 together

reflection and its higher orders in the plane of incidence for all azimuthal rotation of the crystal with respect to the beam, together with the fact that the spot patterns changed with the rotation of the crystal but repeated themselves after every rotation of 60°, clearly showed that the halide crystals grew epitaxially with a {111} orientation. The disposition of spots was such that <112> of cuprous iodide was parallel to <110> of Cu(111). Normally electron diffraction patterns from two-degree {111} oriented crystals would be symmetrical with the beam along <112> axis, and asymmetrical along <110>. The symmetrical nature of the diffraction patterns (Fig. 1 and 2) in both of the azimuths suggested that the deposit crystals consisted of parallel and antiparallel {111} orientations such that the electron beam was grazing along $[1\bar{1}0]$ and $[\bar{1}10]$ directions of the crystals, giving rise to symmetrical patterns. Figure 3 shows the patterns expected from such orientations.

A detailed consideration of the position of spots (Fig. 1), however, shows that a number of reflections (spots), *viz.*, 111 appearing approximately at 40°, 200 at 15°, 220 at 75°, 311 at 10° and 40°, and 422 at 52° from the plane of incidence, cannot be accounted for from Fig. 3. If, on the other hand, the halide crystals developed a two-degree {115} orientation, the positions of the spots are well explained, and also 115 spots would coincide with 333 reflection (spots) in the plane of incidence with the electron beam along <110> of the crystals (Fig. 4). Thus all these spots are well accounted for by the formation of crystals having both {111} and {115} orientations (Fig. 5).

It would seem unlikely, as pointed out before (8), that crystals would grow with an odd plane such as {115} parallel to a simple face such as (111). This orientation, however, could result from a single or multiple twinning process (8-10). Thus if an (111) orientated crystal twinned on its $(11\bar{1})$ plane, it would bring the $(\bar{1}\bar{1}\bar{5})$ plane of twinned crystals parallel to the initial (111) plane. In a similar way other orientation would result by multi-twinning process. This also explains the simultaneous presence of {111} and {115} orientated crystals. The faint spots at 1/3 or 2/3 of unit distance along a <111> direction are due to double diffraction as observed in many other cases (1, 10, 11).

Generally {111} oriented halide crystals had their <112> direction parallel to <110> of Cu(111), but sometimes they were azimuthally rotated by 30°, *i.e.*, the crystals grew with parallel orientations such that CuI <110>//Cu <110>.

Cuprous bromide also grew epitaxially in the same way as iodide, but the rate of reaction was much more rapid. The reaction with moist bromine vapor was similar to that for iodine or bromine.

On Cu(110) face.—On a Cu(110) face, dry iodine and bromine vapors formed halides which again developed a two-degree {111} orientation, but with their <110> axes parallel to <100> of Cu(110). Diffraction patterns were similar to Fig. 1 and 2.

In the presence of moist bromine vapor, however, halide crystals developed two-degree mixed {100} + {211} orientations such that $[0\bar{1}1]$ and $[01\bar{1}]$ of each were parallel to $[1\bar{1}0]$ of copper (similar to Fig. 6).

On Cu(100) face.—On a Cu(100) face, surface layers formed by reacting with iodine vapor yielded patterns consisting of spots and rings which became more distinct with increased time of reaction. The centered $\sqrt{2}$ type of rectangular patterns (Fig. 6) with 200 and higher orders of reflection in the plane of incidence, obtained when the electron beam was along the cube axis of the copper crystal, showed that the halide crystals grew epitaxially with {100}

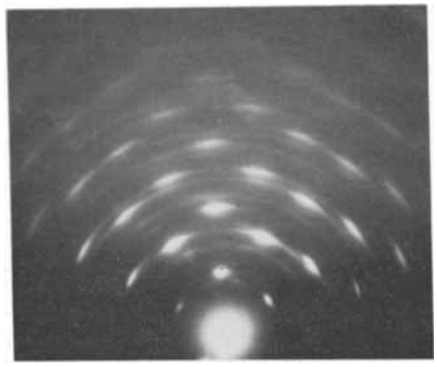

Fig. 6. 2-d {100} orientation of CuI; beam along <110> direction

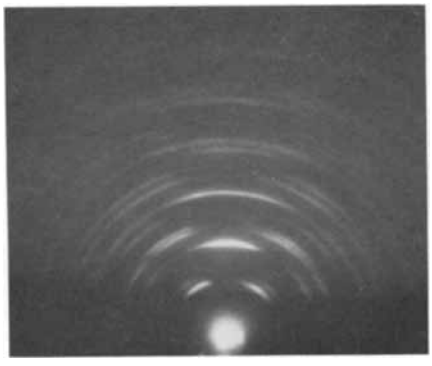

Fig. 7. 1-d {110} orientation of CuI

orientation, but with their axes azimuthally rotated by 45° with respect to the substrate crystal. The slight arcing of spots indicated that the crystals deviated from their mean position by a few degrees. There are indications that crystals had also developed a {111} twinned structure. Exposure to both dry and moist bromine vapors produced similar crystal orientations.

On polycrystalline copper.—The reaction products on polycrystalline copper were polycrystalline in nature, but they sometimes exhibited a strong one-degree {110} orientation (Fig. 7) depending on the time of reaction. The formation of polycrystalline films, even on single crystals, was facilitated with longer time of reaction, and ultimately they developed again a one-degree {110} orientation.

The texture of these crystals was also studied by the electron microscope. The technique used was to expose copper grids (≅400 mesh) to iodine vapor (very low concentration) for 10-16 hr after which time most of these grids were covered with iodide crystals. The growth was heavy and often all the holes in the grids were filled. Under a strong electron beam, the crystals melted quickly, and hence it was often difficult to photograph them in their original shape. The crystals appeared to be flaky, although sometimes needles were also observed (Fig. 8 and 9). By breaking the crystals in a Mickel microshaker it was possible to obtain good micrographs (Fig. 10).

Anodic treatment.—Copper samples treated anodically in bromide or iodide solution also formed cuprous halide crystals with similar orientations, although sometimes the halide crystals were mixed with Cu_2O crystals as reported earlier (5).

The crystal orientations obtained on different faces of copper together with the percentage lattice misfit are shown in Table I.

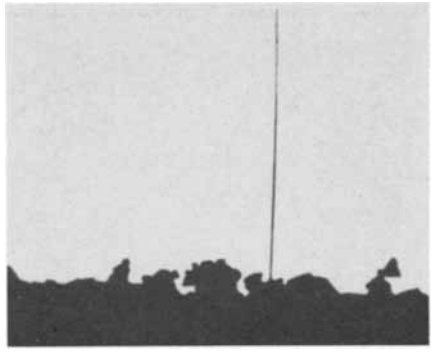

Fig. 8. Needles and flaky nature of CuI. Magnification 3500X

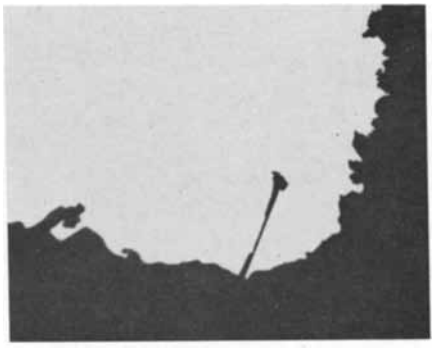

Fig. 9. Needles and flaky nature of CuI. Magnification 3500X

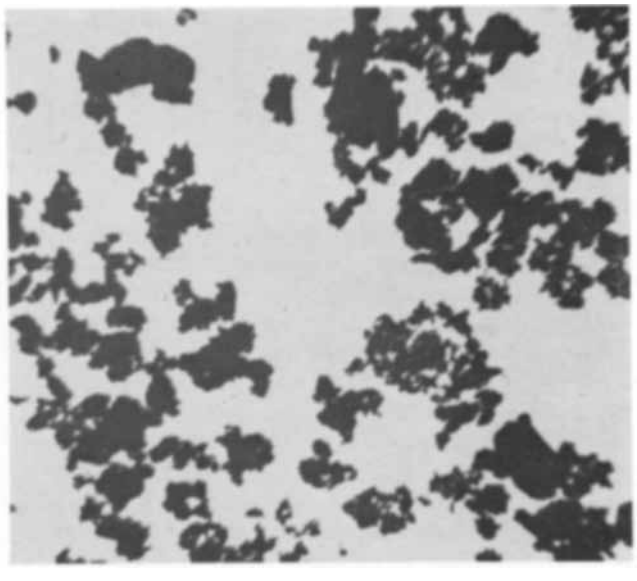

Fig. 10. Flakes of CuI. Magnification 7600X

Discussion

The halide layers formed were always cuprous in type, and no trace of cupric halide was observed. The intensities of all reflections, spot or otherwise, were consistent with the zinc blende type of structures (T^2_d).

It is, however, known that cuprous iodide and bromide exhibit polymorphism (12). The normal γ-forms (cubic $a_o = 6.051$Å and 5.6905Å, respectively, for CuI and CuBr) change to β varieties (h.c.p. $a_o = 4.31$Å, $c_o = 7.09$Å, $c_o/a_o = 1.646$ for CuI at 369°C, and 4.06Å, 6.66Å, 1.625 for CuBr at 430°C) and finally to α modifications ($a_o = 6.15$Å f.c.c. at 407°C for CuI and 4.56Å b.c.c. at 480°C for CuBr). In the present experiments only γ phases were de-

Table I. Orientations of halide films on copper single crystals

Copper substrate Plane	Axis	Orientations of cuprous halides Type	Plane	Axis	% Misfits on copper CuI	CuBr
(111)	<110>	1	(111)	<211>	+3	+9
		2	(111)	<110>	+68 (effective-16)	+57 (effective-21)
(110)	<100>	1	(111)	<110>	+19	+11
(110)	<110>	2	(115)	<110>		
		3	(100)	<100>	+19	+11
(100)	100		(100)	<110>	+19	+11
(111), (110), (100) and Polycrystalline copper			1-d	{110}*		

* 1-d = one-degree orientation.

tected in the top surface layers, although their formation lower down could not be ruled out.

It is thus seen that at room temperature the halides formed on single crystals of copper were crystalline even in very thin layers, whereas cuprous oxide and sulfide were not in that state (1-3). This difference appears to be related to the high mobility of halides which facilitates the epitaxial growth even at room temperature compared to oxide or sulfide (m.p. of CuI, CuBr, Cu_2O, and Cu_2S are 605°, 500°, 1232°, and 1100°C, respectively), since mobility at a particular temperature below the melting point is greater, the lower the melting point (13).

Epitaxially grown halides often developed more than one azimuthal orientation on the same face of a copper crystal (Table I), and hence the tolerable lattice mismatch varied. It is seen that the lattice misfit, which may be defined by $100(b-a)/a$, where a and b are the corresponding lattice spacings in the substrate and deposit, respectively, could be as high as +68% without affecting the epitaxial growth. It has often been suggested in the literature that a good fit is an *a priori* condition for epitaxial growth of crystals. Our work and also that of other (14) clearly shows that crystals can grow epitaxially on the substrate even when there is a considerable misfit and even in cases where the distribution of atoms in the contact planes is very dissimilar, *viz.*, in the development of two-degree {103} and {203} orientations of Cd or {205} and {101} of Zn on Cu(110) and (100) faces (4) and {100}, {203}, etc., of Zn on (100) of NaCl (15). It may only be said that the lower the lattice misfit, the greater is the probability that the deposit will grow thicker while remaining epitaxial. It may be pointed out here that when the lattice misfit is more than 50%, the effective mismatch is much less since the spacing between 2 or 3 atoms of one is often nearly equal to that of 3 and 4 of the other. Thus a misfit of +68% of CuI on Cu(111) is nearly equal to −16% (effective) (Table I).

The change of crystals from a two-degree orientation type to polycrystalline but random, and finally to a one-degree orientated type showed that the orientation of the surface layers was gradually changing with the reaction time. This appears to be related to the migration of copper ions from inside in an outward direction to react with halogen ions (atomic radius of $Cu^{1+} = 0.96Å$, $Br^{1-} = 1.96Å$), as in the case of the growth of Cu_2O and CuO layers (1). An alternate suggestion that the halides grow by the diffusion of halogen ions inward to the copper surface may not be ruled out completely, although their ionic sizes are unfavorable. Preferential grain boundary diffusion may however facilitate a process of this kind.

Acknowledgment

The author is thankful to Dr. M. K. Gharpurey for taking the electron micrographs.

Manuscript received June 19, 1961; revised manuscript received March 26, 1962. This is Communication No. 456 from the National Chemical Laboratory, Poona, India.

Any discussion of this paper will appear in a Discussion Section to be published in the June 1963 JOURNAL.

REFERENCES

1. A. Goswami and Y. N. Trehan, *Trans. Faraday Soc.*, **52**, 358 (1956); **54**, 1703 (1958).
2. K. Leu, Ph.D. Thesis, London University (1951).
3. Y. N. Trehan and A. Goswami, *Trans. Faraday Soc.*, **55**, 2162 (1959).
4. A. Goswami, Ph.D. Thesis, London University (1950).
5. A. Goswami, *Proc. Phys. Soc.*, **69B**, 583 (1956).
6. I. H. Usmani, *Phil. Mag.*, **32**, 89 (1941).
7. D. M. Evans, *et al.*, *Proc. Roy. Soc.*, **205A**, 17 (1951).
8. A. Goswami, *J. sci. & ind. Res.*, **13B**, 677 (1954); **15B**, 322 (1956).
9. Y. N. Trehan and A. Goswami, *Proc. Nat. Inst. Sci. (Ind)*, **25A**, 210 (1959).
10. A. Goswami, *Trans. Faraday Soc.*, **54**, 821 (1958).
11. A. Goswami, *J. Sci. indust. Res.*, **17B**, 133 (1958).
12. A.S.T.M. Card No. 6-0246, 0685, 0623, 0292, 0700, 0310.
13. D. M. Evans and H. Wilman, *Acta Cryst.*, **5**, 731 (1954).
14. D. W. Pashley, *Phil. Mag. Suppl.*, **5**, 173 (1956).
15. D. M. Evans, Ph.D. Thesis, London University (1950).

Manganese-Activated Cadmium Pyrophosphate Phosphors

R. C. Ropp

Chemical and Metallurgical Division, Sylvania Electric Products Inc., Towanda, Pennsylvania

ABSTRACT

The effects of preparation on absorption and excitation properties have demonstrated that $Cd_2P_2O_7$:Mn is a host-sensitized phosphor whose efficiency to 2537Å becomes appreciable only when a step involving refiring in a reducing atmosphere is employed. The experimental data allow an insight into the nature of the luminescent center in $Cd_2P_2O_7$:Mn.

The combination of manganese with cadmium phosphates to form luminescent systems is by no means new, and many authors have reported on such phosphors. $Cd_2P_2O_7$:Mn was described by Williams (1) as an efficient cathode-ray excitable phosphor. Fonda (2) described tribasic cadmium orthophosphate phosphors activated by manganese. Other investigators have described various modifications of the cadmium phosphate phosphors including fluorophosphate doubly activated by Pb and Mn (3, 4). Smith and Power (5), as well as Zelinskii *et al.* (6), described tribasic cadmium and zinc orthophosphates. The references to cadmium chlorophosphate phosphors are too numerous to mention. However, none of these authors recognized the effect of reduction on excitation properties, particularly for $Cd_2P_2O_7$:Mn.

The present work will describe a phenomenon whereby reduction of the matrix produces host-sensitization in $Cd_2P_2O_7$:Mn. A model will be postulated to show the nature of the luminescent center and the absorption properties as a function of preparation.

Method of Preparation and Measurement

The phosphors were easily prepared according to the following reactions:

1. $2CdNH_4PO_4 \cdot H_2O + 0.04\ MnNH_4PO_4 \cdot H_2O \xrightarrow{\Delta} Cd_2(P_2O_7)_{1.02}:Mn_{0.04} + 2.04NH_3 + 3.06\ H_2O$
2. $2CdNH_4PO_4 \cdot H_2O + CdO_2 + 0.04\ MnNH_4PO_4 \cdot H_2O \xrightarrow{\Delta} Cd_3(PO_4)_{2.04}:Mn_{0.04} + 2.04\ NH_3 + 3.06\ H_2O + 0.49\ O_2$

One could prepare $Cd_2P_2O_7$:Mn and $Cd_3(PO_4)_2$:Mn and refire with a volatile chloride to form cadmium chloroapatite:

3. $3Cd_3(PO_4)_2:Mn + CdCl_2 \xrightarrow{\Delta} 2\ Cd_5Cl(PO_4)_3:Mn$
4. $3Cd_2P_2O_7:Mn + xCdCl_2 \xrightarrow{\Delta} 2Cd_{3+0.5x}Cl(PO_4)_3:Mn + (X-1)Cl_2$

The use of HCl gas as a firing atmosphere enabled a further clarification of the gross reactions:

5. $Cd_3(PO_4)_2:Mn + 2HCl \xrightarrow{\Delta} Cd_2P_2O_7:Mn + CdCl_2 + H_2O$
6. $Cd_2P_2O_7:Mn + HCl \xrightarrow{\Delta}$ no change
7. $3CdNH_4PO_4 \cdot H_2O + 2CdO_2 + HCl \xrightarrow{\Delta} Cd_5Cl(PO_4)_3 + 3NH_3 + O_2 + 5H_2O$

Thus, $Cd_2P_2O_7$ was the stable structure once the matrix was formed in the absence of halogen. The apatite was stable otherwise.

Considerable effort was made to obtain $CdNH_4PO_4 \cdot H_2O$ and not $Cd_5H_2(PO_4)_4(H_2O)_4$ (7). The former gave a nearly stoichiometric $Cd_2P_2O_7$, whereas the latter gave $Cd_3(PO_4)_2 \cdot Cd_2P_2O_7$, a product containing 1.25 Cd atoms per 1.00 P atom. The similarity in x-ray diffraction patterns may lead to mistaken identity, particularly for mixtures containing small amounts of $Cd_5H_2(PO_4)_4(H_2O)_4$.

Manganese may be added to the phosphor mix in several forms, but was best added as $MnNH_4PO_4 \cdot H_2O$. CdO_2 (8) was preferred because of the ease in obtaining a purified material of high reactivity which gave a product of specific composition (CdO) when heated.

Measurements followed those described in a previous paper (9).

Experimental Results

Phosphors efficient to 2537Å irradiation were produced by prefiring in air to form the matrix and refiring in a reducing atmosphere. These results are shown in Table I. Note that refiring in a reducing atmosphere markedly improved the plaque response, but that refiring in air or N_2 did not. Thus, the effect could not be attributed to refiring alone, but to the combination. Prefiring in N_2-H_2 (40%) gave a black inert mass. The effect of firing atmosphere was pronounced, particularly for the pyrophosphate. If $Cd_2P_2O_7$:Mn was refired in HCl, bright phosphors were obtained, but in the case of $Cd_3(PO_4)_2$:Mn, HCl converted it to $Cd_2P_2O_7$:Mn according to reaction 5.

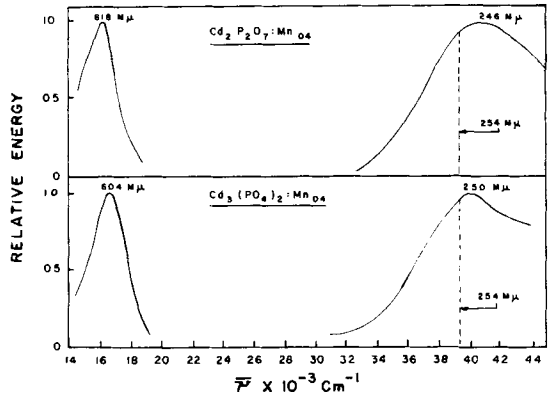

Fig. 1. Spectral properties of some cadmium phosphate phosphors

Table I. Effect of refiring

Nominal phosphor composition	Atmosphere: Prefiring	Atmosphere: Refiring	X-ray structure	Lum. color (2537Å excit.)	% Red plaque (*vs.* Cd borate std.)
$Cd_3(PO_4)_{2.10}$: $Mn_{0.04}$	Air	—	$Cd_3(PO_4)_2$	Dull pink	10
	N_2	—	$Cd_3(PO_4)_2$	Dull pink	19
	Air	Air	$Cd_3(PO_4)_2$	Dull pink	18
	HCl	—	Apatite	Bright orange	83
	Air	N_2	$Cd_3(PO_4)_2$	Dull pink	15
	Air	HCl	$Cd_2P_2O_7$	Bright red	67
	Air	N_2-H_2 (40%)	$Cd_3(PO_4)_2$	Dull pink	35
$Cd_2(P_2O_7)_{1.02}$: $Mn_{0.04}$	Air	—	$Cd_2P_2O_7$	Dull pink	15
	N_2	—	$Cd_2P_2O_7$	Dull pink	9
	HCl	—	Apatite	Orange	70
	Air	Air	$Cd_2P_2O_7$	Dull pink	20
	Air	HCl	$Cd_2P_2O_7$	Bright red	52
	Air	N_2	$Cd_2P_2O_7$	Dull pink	22
	Air	N_2-H_2 (40%)	$Cd_2P_2O_7$	Bright red	51

The emission properties of these phosphors were identical to those presented by previous authors (1, 4) for cathode-ray excitation (see Fig. 1). It was in the excitation and absorption spectra that differences were observed. Since $Cd_2P_2O_7$:Mn was by far the more efficient, the present discussion will be limited to this phosphor.

Effect of firing atmosphere.—Measurement of the excitation bands as a function of preparation is given in Fig. 2 for the $Cd_2P_2O_7$:Mn phosphors shown in Table I. (The discontinuity in the curves is the result of increasing the instrument gain at 34.0 x 10^3 cm^{-1} before proceeding to the lower energy absorption peaks.) When prefired under oxidizing or neutral conditions (air or N_2), the excitation band peaked at 2370Å and was relatively narrow, whereas on refiring under reducing conditions (N_2-20% H_2), the peak wavelength shifted to 2460Å and the 2537Å response increased markedly. The effect was not due to refiring alone since the phosphor refired in N_2 only did not change in its excitation spectrum. All spectra, and particularly the reduced phosphor spectrum, showed evidence of low level excitation spectra composed of several narrow bands in the near-ultraviolet and visible regions in addition to the broad excitation band in the higher energy region. The former have been termed edge-absorption bands (10), due to Mn^{+2}.

Figure 3 shows the spectral properties of $Ca_2P_2O_7$:Mn and $Sr_2P_2O_7$:Mn. Although these phosphors were previously said to be excited only by cathode rays (11), further reduction produced some excitation bands in the near-ultraviolet. $Zn_2P_2O_7$, $Mg_2P_2O_7$, and $Ba_2P_2O_7$, by contrast, were not found to form ultraviolet excitable phosphors even when the matrix was refired repeatedly in a reducing atmosphere. The excitation bands in $Ca_2P_2O_7$:Mn and $Sr_2P_2O_7$:Mn phosphors are due directly to energy absorption in the Mn^{+2} activator center and may be compared to the Mn^{+2} absorption bands in known phosphors such as Zn_2SiO_4:Mn^{+2} (10).

Effect of manganese.—Variation of manganese changed the relative response to 2537Å radiation, but did not shift the emission peak wavelength of $Cd_2P_2O_7$:Mn from 6180Å.

The relative plaque brightness as a function of Mn content and firing is given in Fig. 4. Note the large change in response on reduction of the preformed matrix. The plaque response to 2537Å irradiation increases to 8 mole % Mn, remains essentially constant to 20 mole % Mn and decreases beyond that

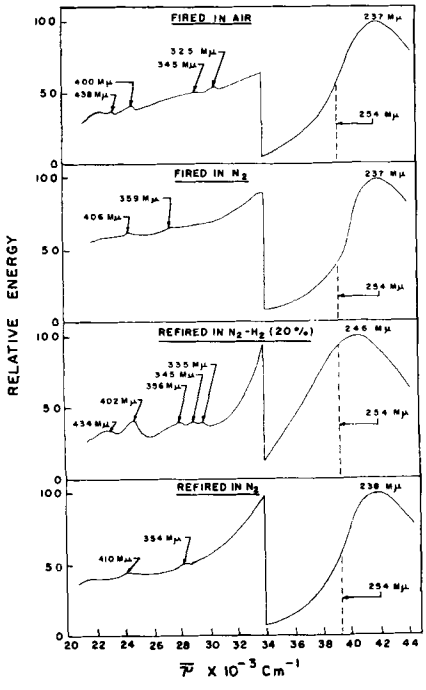

Fig. 2. Effect of firing atmosphere on excitation spectra of $Cd_2P_2O_7$:Mn_{04} phosphor.

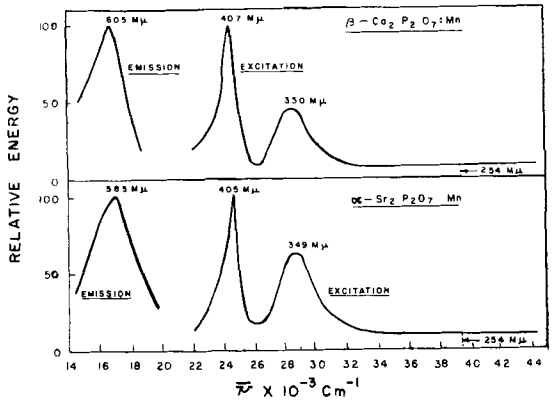

Fig. 3. Spectral properties of manganese-activated alkaline-earth pyrophosphates.

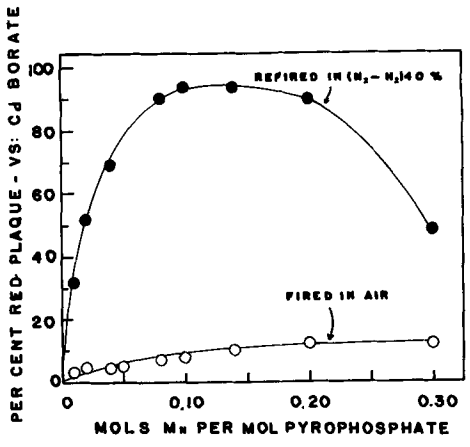

Fig. 4. Effect of manganese concentration on efficiency of $Cd_2P_2O_7$:Mn phosphor.

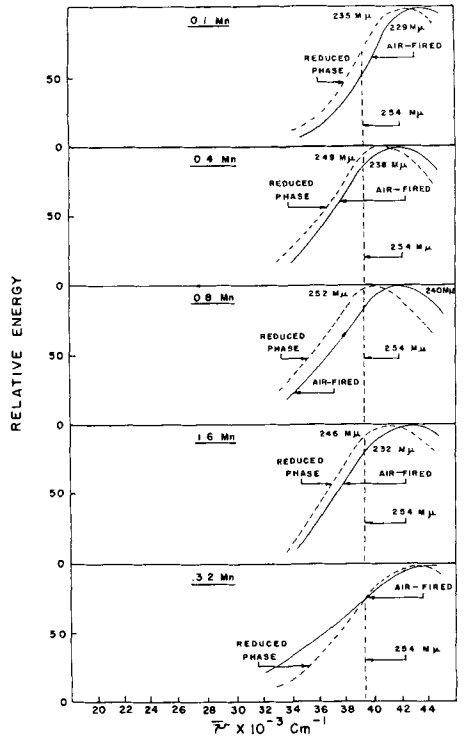

Fig. 5. Excitation spectra as a function of preparation conditions

concentration. It was further instructive to determine the effect of preparation atmosphere as a function of manganese on excitation spectra (see Fig. 5). In all cases, the excitation peaks are shifted toward lower energy by the reduction step and, in addition, these peaks shift with Mn content. However, when a concentration of 0.32 mole Mn is reached, a decided decrease in brightness was noted as reflected in the change in excitation spectra. The shift of peak wave number due to reduction was approximately constant irrespective of Mn content.

In order to establish that Mn was the primary activator, an analysis was made of the components and phosphor (see Table II). No other elements were present.

Reversibility.—The effect of reduction on response to 2537Å was reversible, and a phosphor which was efficiently excited lost brightness when reheated in air. This effect was a function of Mn content. One could heat and reheat the phosphor $Cd_2P_2O_7$:Mn alternately in an oxidizing or reducing atmosphere and change the response to 2537Å radiation providing the sintering point was not reached with consequent degradation of the structure.

Table II. Spectrographic analysis of components

	Mn	Impurities in ppm (Spec. Qual.) Ca	Mg	Cu	Fe	Ni	Sn	Sr	Al	Si
$Cd_2P_2O_7$:Mn	29,600	500	—	0.5	5	5	50	50	—	—*
$CdNH_4PO_4 \cdot H_2O$	0.5	500	50	0.5	5	—	—	—	5	5
$Cd_2P_2O_7$	0.5	500	50	0.5	5	—	—	—	5	50*

* Fired in a silica crucible.

Unactivated $Cd_2P_2O_7$.—If $Cd_2P_2O_7$ was formed from $CdNH_4PO_4 \cdot H_2O$ by prefiring at 1800°F in air and then subjected to refiring in a 40% H_2-60% N_2 atmosphere, a phosphor was produced as shown in Fig. 6. Although the brightness was low under 2537Å excitation, the phosphor responded to the higher energy wavelengths. Chemical analysis of the Mn present in this phosphor gave a value of <0.0001% or 1 ppm. Note that the absorption band is similar to the excitation band.

The matrix, $Cd_2P_2O_7$, exclusive of Mn^{+2}, possessed a high-energy excitation band. This is the fundamental absorption band for the matrix. The incorporation of Mn^{+2} into $Cd_2P_2O_7$ to form $Cd_2P_2O_7$:Mn did not change the fundamental absorption band, as shown in Fig. 7. The absorption or excitation band shifted with reduction, when Mn was present, to a greater

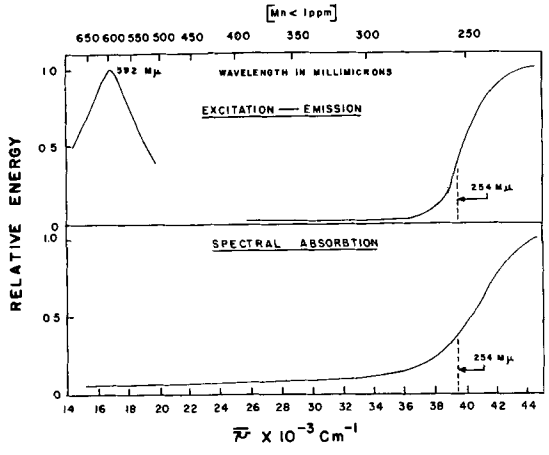

Fig. 6. Spectral properties of unactivated $Cd_2P_2O_7$

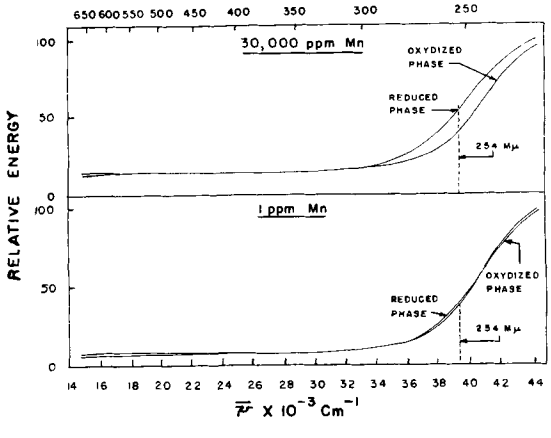

Fig. 7. Spectral absorption of $Cd_2P_2O_7$:Mn phosphor

extent than in its absence. The position of the excitation band also changed as a function of the Mn content and the shift was accentuated by reduction of the matrix (see Fig. 5). Reduction of the matrix increased the 2537Å absorption markedly in the phosphor containing 30,000 ppm Mn, but little in that containing 1 ppm Mn. In contrast, the matrices, $Ca_2P_2O_7$ and $Sr_2P_2O_7$, did not possess the broad excitation band (Fig. 3) at the higher energies (~2250Å), and therefore incorporation of Mn^{+2} did not produce 2537Å excitable phosphors.

Mn^{+2} as a luminescent center.—The spectroscopic functions of Mn^{+2} are well known. The ground state is $^6S_{5/2}$ and the four excited states are $^4G_{5/2}$, $^4D_{5/2}$, $^4P_{5/2}$, $^4F_{5/2}$, in order of ascending energy, for the free ion. In the presence of a crystal field, a d^5 ion such as Mn^{+2} has the symmetry $^6A_{1g}$ in a weak octahedral field. The configuration d^5 is exceptional in that no spin-allowed transitions are to be expected, since the ^6S ground state is not split significantly by the field (12), whereas the excited states are split, depending on the strength of the field. Weak absorptions are expected corresponding to the sextet-quartet transitions. It is generally accepted that yellow to red emission is indicative of Mn^{+2} in an octahedral site, whereas green emission is associated with Mn^{+2} in a tetrahedral site. However, in the absence of specific structure data for $Cd_2P_2O_7$, such an assumption would be illusory since the determination of the effect of crystalline field on the luminescent processes of Mn^{+2} presupposes a knowledge of site symmetry.

A long decay is characteristic of Mn^{+2} emission and probably arises from the spectroscopically forbidden transition, $^4G \rightarrow {}^6S$. Since $Cd_2P_2O_7$:Mn also possesses a long decay, it is logical to assume that the energy transition is identical since the emission is typical of Mn^{+2} as an activator. Coupled with the marked similarity in diffraction pattern between $Mn_2P_2O_7$ and $Cd_2P_2O_7$ (of which there is but one structure each), the data indicate that the luminescent center is composed of Mn^{+2} in a cationic site.

Discussion

The specific effect of reduction is difficult to assess since there are several end-results which could be attributed to reduction. Before discussing these, it would be well to summarize the observations made:

1. The matrix $Cd_2P_2O_7$, exclusive of Mn^{+2}, possessed a high-energy, stimulable excitation band. This is the fundamental absorption band for the matrix. The incorporation of Mn^{+2} into $Cd_2P_2O_7$ to form $Cd_2P_2O_7$:Mn did not change the fundamental absorption band, although a shift was observed with Mn content.

2. The equivalence between the absorption-excitation band of $Cd_2P_2O_7$ and the high-energy excitation band of $Cd_2P_2O_7$:Mn leads to the conclusion that $Cd_2P_2O_7$:Mn is a host-sensitized phosphor in which matrix absorption of radiant energy precedes fluorescence.

3. $Ca_2P_2O_7$:Mn and $Sr_2P_2O_7$:Mn are not host-sensitized. The excitation peaks are due to transitions in the Mn^{+2} activator.

4. Reduction of the matrix following formation shifts the excitation peak wave number to lower energy. Absorption bands due to Mn^{+2} are also observed.

5. The shift in peak wave number due to reduction is obtained only in the presence of manganese and is constant at each Mn^{+2} content.

6. The position of the excitation band is dependent both on Mn^{+2} content and reduction.

The logical conclusion to be drawn is that reduction simply increases the manganous ion concentration which causes a shift of the host lattice absorption edge. This explanation was first demonstrated for willemite by Kroeger (10). The data in Fig. 4 and Fig. 5 and observations 5 and 6 are thus explained. A relevant extension of this conclusion would include the role of the matrix, particularly since the host-lattice absorption edge is involved and since the experimental data indicate that host sensitization takes place. It is unlikely that the broad absorption band can be attributed to the manganese center alone.

If the effect were due entirely to the presence and number of Mn^{+2} activator centers, then one would expect the broad absorption band to be due to (*a*) the manganese center, or (*b*) the manganese center as affected by the lattice, that is, a manganese-lattice interaction. However, the broad absorption band cannot be due to transitions in the Mn^{+2} atom itself because of the edge absorption bands observed in the same spectra (Fig. 2), which are comparable to those of Mn^{+2} in $Ca_2P_2O_7$:Mn and $Sr_2P_2O_7$:Mn. Therefore, the possibility remained that the effect could be caused by an increase in the number of Mn^{+2} centers as well as an increase in the host-lattice coupling. This would give rise to a band whose width would increase or decrease with temperature.

One would then expect in the case of the comparable $Ca_2P_2O_7$:Mn and $Sr_2P_2O_7$:Mn phosphors that reduction should cause the appearance of a broad high-energy excitable band denoting that the effect of reduction was to increase the lattice-coupling of the Mn^{+2} center with its lattice surrounding. Although the position of this broad absorption peak would not be expected to be exactly at the same energy in $Ca_2P_2O_7$ or $Sr_2P_2O_7$, it should be close if the broad absorption band did arise only from the Mn^{+2} center, and not from the matrix, as in $Cd_2P_2O_7$:Mn.

Since it has been demonstrated that reduction does not result in broad absorption bands in these other phosphors, but only narrow bands directly attributable to Mn^{+2}, one can conclude that absorption is a function of both Mn content and reduction, but only in the presence of cadmium. Thus, it is probable that absorption by the matrix is involved rather than absorption in the manganese centers alone, and that host-sensitization occurs (observations 1 and 2).

One is then left with the conclusion that reduction affects both the matrix and the activator, Mn^{+2}. The effect cannot be chemical in nature since only changes in optical spectra are observed and no chemical changes were noted in the materials so treated, as determined by x-ray and infrared analysis.

Since reduction has an effect on the lattice as determined by absorption measurements, it is, perhaps, more logical to assume that the effect is electronic in

Table III. Spectroscopic levels for various ions

Atomic species	No. of Electrons	Transition	State Ground	State Excited
Mn III	23	$3d^5 \leftrightarrow 3d^4 3d^*$	$^6S_{5/2}$	$\leftrightarrow {}^4G_{5/2}$
Cd III	46	$4d^{10} \leftrightarrow 4d^9 4d^*$	$^1S_0$	$\leftrightarrow {}^3D_1$
Cd II	47	$4d^{10} \leftrightarrow 4d^{10} 5p^*$	$^2S_{1/2}$	$\leftrightarrow {}^2P_{3/2}$
Sb IV	48	$4d^{10}5s^2 \leftrightarrow 4d^{10}5s5p^*$	$^1S_0$	$\leftrightarrow {}^3P_1$
Sn III	48	$4d^{10}5s^2 \leftrightarrow 4d^{10}5s5p^*$	$^1S_0$	$\leftrightarrow {}^3P_1$
Pb III	80	$5d^{10}6s^2 \leftrightarrow 5d^{10}6s6p^*$	$^1S_0$	$\leftrightarrow {}^3P_1$
Tl II	80	$5d^{10}6s^2 \leftrightarrow 5d^{10}6s6p^*$	$^1S_0$	$\leftrightarrow {}^3P_1$

* Excited state.

nature. Since host-sensitization requires transport of energy by other than movement of charge, a study of energy transport processes within the crystal is applicable.

The theory of impurity-sensitized luminescence as developed by Dexter (13), and independently by Botden (14), is applicable to the present case. Impurity-sensitized luminescence refers to the luminescence mechanism whereby energy is absorbed in one type of center (the sensitizer) and emission occurs in a different type of center (the activator). The mechanisms involved in the transport and transfer of excitation energy from the absorbing to the emitting center are of particular concern.

For the $Cd_2P_2O_7$:Mn system, it is interesting to compare the electronic spectroscopic transitions which may be involved. These data are given in Table III, taken from ref. (15).

The last four species in Table III represent mercury-like ions which are known sensitizers as shown by Williams (16) and Seitz (17). In regard to the Cd III species, note that the transition to the excited state is a spin forbidden transition much like that of the activator center (Mn III). The electronic $d^{10}s$ configuration of the cadmium II species is similar to that of known sensitizers and involves a spectroscopically allowed transition. Thus, the effect of reduction could be assigned to the localization of an electron in the vicinity of a Cd^{+2} atom to form the spectroscopic species, Cd II:

$$Cd^{+2} + e^- \rightarrow (Cd)^+$$

This equation is meant to imply that an electronic defect exists which utilizes the modified energy levels of the ion. Thus, the presence of Cd^+ could lead to sensitization as proposed in Table IV. The resonance-exchange mechanism is applicable for the Cd^+ (II) species, but exchange would not be expected to occur between Cd^{+2} sites, since it is recognized that the strength of an electric quadrupole (qq) transition is weaker by a factor of 10^{-7} than that of an electric dipole (dd) transition (12). Thus, for the propagation of energy in both the oxidized and reduced phosphors, the following mechanism is possible as shown in Table IV. (The double-headed arrows denote the resonance exchange mechanism.)

Theoretically, one would expect, for Cd^{+2}, a very weak interaction only at nearest-neighbor sites between cadmium and manganese atoms, and the corresponding luminescent efficiency should be very low as is observed experimentally. In the reduced form, Cd^+(II), the transitions are allowed (S → P), and therefore the response to excitation should be much higher.

The formation of such a species is not entirely without basis since it is well known that x-ray irradiation of alkali halide crystals containing Ca^{++}, Sr^{++}, or Ba^{++} distributed in the cationic sites will form so-called Z centers, which, according to Seitz (18), involve electrons trapped by the alkaline-earth ions at the cationic sites. The spectral characteristics of these centers are comparable to the free Ca^+, Sr^+, or Ba^+ ions. Furthermore, Lushchik and Lushchik (19) have studied the absorption excitation and emission spectra of various homologous ions in alkali halides which included Cd^+.

The shift in absorption peak due to reduction is attributed to formation of the Cd^+(II) species, and the dependence of peak absorption energy on manganese content is attributed to formation of Cd^+(II)-Mn^{+2} pairs. It is unfortunate that specific structure data are not available so that a more quantitative estimate could be obtained of the luminescent center.

It is apparent that reduction has an effect on the energy gap of $Cd_2P_2O_7$, and a possible explanation would be the injection of carriers in the valence band with consequent effects on resistivities as well as excitation energies. Perhaps photoconductive or Hall-coefficient measurements might clarify this matter.

Acknowledgment

The author is indebted to Dr. C. W. W. Hoffman for x-ray measurements, to H. D. Layman and J. E. Webster for some of the preparations, and to Dr. J. S. Smith for valuable discussions.

Manuscript received May 26, 1961; final revised manuscript received March 16, 1962. This paper was prepared for delivery before the Chicago Meeting, May 1-5, 1960.

Any discussion of this paper will appear in a Discussion Section to be published in the June 1963 JOURNAL.

REFERENCES

1. F. E. Williams, U.S.Pat. 2,463,449 (1949).
2. G. R. Fonda, U.S. Pat. 2,605,227 (1952).
3. R. W. Wollentin, U.S. Pat. 2,865,863 (1958).
4. N. A. Gorbacheva, *Zhur. Eksptl. Teoret. Fiz.*, **21**, 305 (1951).

Table IV. Mechanism of energy transfer in $Cd_2P_2O_7$:Mn phosphor

Oxidized form

(a) $E_1 + Cd^{+2} \rightarrow (Cd^{+2})^* \xleftarrow[(10^{-7})]{(qq)}$

Reduced form

(b) $E_1 + Cd^+ \rightarrow (Cd^+)^* \xleftrightarrow[(10^4)]{(dd)} (Cd^+)^* \xrightarrow[(1.0)]{(dq)}$

$$Mn^{+2} \rightarrow (Mn^{+2})^* \rightarrow Mn^{+2} + E_2$$

5. A. L. Smith and A. D. Power, *This Journal*, **101**, 244 (1954).
6. V. V. Zelenskii, F. M. Pekerman, T. V. Timofeeva, and B. I. Vainberg, *Zhur. Eksptl. Teoret. Fiz.*, **20**, 395 (1950).
7. R. C. Ropp and R. W. Mooney, *J. Am. Chem. Soc.*, **82**, 4848 (1960).
8. C. W. W. Hoffman and R. C. Ropp, *ibid.*, **81**, 3830 (1959).
9. R. C. Ropp and R. W. Mooney, *This Journal*, **107**, 15 (1960).
10. F. A. Kroeger, "Some Aspects of the Luminescence of Solids," Elsevier Publishing Co., New York (1948).
11. E. Nakano and K. Takagi, *Nippon Kagaku Zasshi*, **78**, 1146 (1957).
12. L. E. Orgel, *J. Chem. Phys.*, **23**, 1004 (1955).
13. D. L. Dexter, *ibid.*, **21**, 836 (1953).
14. T. P. J. Botden, *Philips Research Repts.*, **7**, 197 (1952).
15. Circular 467, "Atomic Energy Levels," National Bureau of Stds., U.S. Dept. Commerce, U.S. Gov't Printing Office, Washington, D. C. (1958).
16. F. E. Williams, *J. Chem. Phys.*, **19**, 457 (1952).
17. F. Seitz, *ibid.*, **6**, 150 (1938).
18. F. Seitz, *Phys. Rev.*, **83**, 134 (1951).
19. N. E. Lushchik and Ch. B. Lushchik, *Optika i Spektroskopiya*, **8**, 839 (1960).

The Interface between Germanium and a Purified Neutral Electrolyte

W. H. Brattain and P. J. Boddy

Bell Telephone Laboratories, Murray Hill, New Jersey

ABSTRACT

Measurement of the differential capacity of the interface between germanium (100) and M/10 K_2SO_4, phosphate buffered to pH 7.4, yields data indicating that only the capacity of the semiconductor space charge region is observed. Analysis of the data yields the simple relationship for distribution of potential

$$\psi_s - \frac{kT}{e} \ln \lambda = V_E + K$$

where K is a constant for a given condition at the interface. Surface recombination velocity is found to be close to zero. This, coupled with the absence of capacity additional to the space charge region, indicates the absence of fast surface states under these conditions. Measurement of the surface conductivity of germanium as a function of surface potential does not agree with theory but is reproducible.

Measurements of the electrical properties of germanium surfaces in gaseous ambients have shown a marked dependence of these properties on the immediate history of the sample and the nature of the ambient. It is inferred that the variations are due either to trace impurities deposited on the surface during etching (1) or other cleaning and handling procedures, interaction with the ambient (2), or to physical defects in the surface (*e.g.*, emerging dislocations, steps, etc.) developed in different ways by different chemical environments. The variation in the observations precludes the interpretation that the properties are entirely those of the surface of a single crystal of germanium *per se*.

The object of the present work was to seek relationships between the chemical and electrical properties of such surfaces.

Recent investigations of the semiconductor solution interface have yielded detailed information on the electrical properties of both zinc oxide (3) and silicon (4). To the present time, with the exception of the work of Bohnenkamp and Engell (5), the potentially fruitful area of the germanium-electrolyte interface has been little studied from this point of view, although the basic electrochemistry of germanium is fairly well understood (6).

This paper describes some initial experiments on the electrical properties of germanium surfaces in contact with aqueous solutions. It has been found that in a properly purified solution of K_2SO_4 a germanium surface can be obtained free of fast surface states, *i.e.*, having no additional capacity over that of the space charge layer and no measurable decay of added carriers over and above body recombination.

Experimental

General.—The experiments were conducted in a Pyrex glass cell (shown schematically in Fig. 1) consisting of two compartments separated by a salt bridge containing a porous plug. The larger compartment contained the germanium electrode, which was connected to ground, and two large area plati-

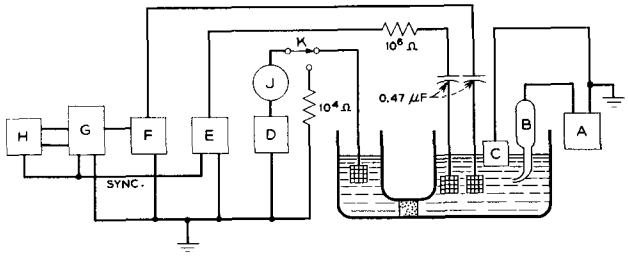

Fig. 1. Experimental arrangement: A, high impedance millivoltmeter; B, calomel electrode; C, germanium electrode; D, high impedance current source; E, pulsed voltage source; F, preamplifier; G, oscilloscope; H, exponential generator; J, ammeter; K, switch.

num gauze electrodes connected to external circuits through 0.47 μfd capacitors. A calomel electrode was connected through a second salt bridge and the germanium electrode potential measured on a high impedance (2 x 10^9 ohm) millivoltmeter. Stirring was achieved either by rotating the germanium electrode, or by means of a magnetically operated, Teflon enclosed stirring bar in the solution. The other compartment contained a third large area platinum gauze electrode connected directly through a high-impedance current source to ground. The atmosphere above the solution was purified nitrogen or helium. Provision was made for illuminating the germanium electrodes through windows set into the bottom and side of the cell, but unless otherwise stated the experiments were carried out in the dark. The temperature throughout was close to 25°C.

Electrodes.—Germanium electrodes were of two types. The simpler ones were either square (1-2.5 cm on a side) or circular (1 cm diameter) in cross section and 1-2 cm thick. Electrical contact was made either by rhodium plating one face and holding the electrode by vacuum onto a stainless steel chuck or by attaching a platinum wire with a solder containing indium. In the latter case the platinum wire was pulled through a glass tube until the back of the electrode was firmly against the end of the tube, which was then filled with paraffin wax which had been boiled for several days in 1M H_2SO_4, 1M KOH, and finally several changes of distilled water. The electrodes were not masked. To ensure a constant superficial area exposed to the solution for a given electrode in different experiments the following procedure was used. The adjustable electrode holder was lowered into the solution until contact was made, and by visual inspection the lower surface of the electrode was aligned with the solution surface. The electrode was then lowered an arbitrary 0.19 cm further into the solution.

The second type of electrode was more complex and requires special description. It takes the form

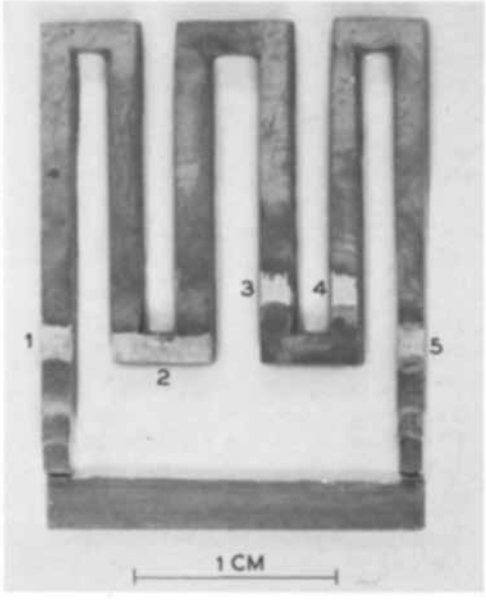

Fig. 2a. Germanium bridge. The scale is in centimeters

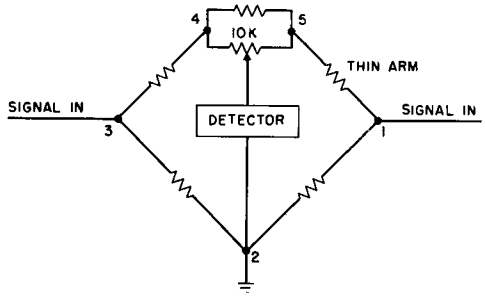

Fig. 2b. Electrical schematic of germanium bridge

of a bridge cut from a slice of single crystal germanium and is illustrated in Fig. 2a and shown schematically in Fig. 2b. The bridge had five contacts, the active arm being between 1 and 5. The other arms, which were much thicker, were not etched, their surfaces being left in a lapped or sandblasted condition making them insensitive to ambient changes. Contact to the bridge was by means of soldered platinum wires. During an experiment the thin portion of arm 1-5 was completely immersed, contacts 1 and 5, however, being kept out of the solution. The major advantage of the bridge is that it is internally temperature compensated provided there are no temperature differences in the bridge itself.

The arms were designed so that if either d-c or a-c power was applied between 1 and 3 a detector would read null between 2 and some point (x) between 4 and 5. This point was determined by adjustment of a calibrated 10,000 ohm Helipot connected between 4 and 5.

The condition for balance is

$$R_{12}R_{23}^{-1} = R_{1x}R_{x3}^{-1} = \beta \qquad [1]$$

where R_{12} is the resistance between contacts 1 and 2, etc. The added surface conductivity, $\overline{\Delta G}$, in the thin arm as defined by Brattain and Garrett (14) is

$$\overline{\Delta G} = (1 + \beta)wt(X_m - X)R_{45}(2e\mu_p\rho\mathcal{L}n_i(w + t)R_{15})^{-1} \qquad [2]$$

where X_m is the fractional helipot reading for minimum conductivity, X is the fractional reading at a point where $\overline{\Delta G}$ is to be evaluated, μ_p is hole mobility, ρ specific resistance, e electronic charge, $\mathcal{L}$ the Debye length, n_i the concentration of holes and electrons in intrinsic germanium, w and t the width and thickness of the thin part of arm 15. Due correction was made for those parts of 15 out of the solution. Appropriate measurements gave two independent estimates of the values of the resistances of each of the five arms, exclusive of contact resistance, which could also be evaluated. Since the dimensions of the arms were known, the specific resistance and its uniformity throughout the bridge could be determined. Once the bridge had been measured, any changes in the dimensions of arm 15 due to etching could be simply determined from the change in balance point at the conductivity minimum.

In the experiments contact 2 was at ground and so placed that R_{12} was equal to $R_{23} + R_{34} + R_{45}$, so that

the midpoint of arm 15 had equal resistance to ground either way around the bridge. When capacity measurements were made on this arm, contacts 1 and 5 were grounded to eliminate the potential drop to ground through the other arms.

Materials and purification.—The solutions were M/10 K_2SO_4 buffered to appropriate *p*H values. All solutions were gettered by stirring with finely crushed germanium for several hours before use. This was produced *in situ* by rapidly stirring a solution containing a few small pieces of high-purity germanium with a magnetically operated, Teflon enclosed stirring bar. Over the course of several hours collisions between the pieces produced a dense cloud of fine particles. In some cases the solutions were also pre-electrolyzed at a germanium cathode for up to 72 hr, but the data were identical in solutions which had been simply gettered. Generally, the germanium powder was left in the solution throughout the experiment. The solutions were made up either with de-ionized water or de-ionized water that had been distilled from permanganate solution. In both cases the data were identical, from which it may be concluded that the gettering process effectively removes any trace impurities originally present in the electrolyte or the D.I. water active with respect to a germanium surface. Analytical grade K_2SO_4 was used. In some experiments not described here, K_2SO_4 was recrystallized three times from distilled water and the buffer omitted. The data were exactly similar in both sets of experiments.

Nitrogen was passed over hot copper gauze. Helium was passed through anhydrite, Hopcalite, soda-lime, active copper on kieselguhr at 200°C (8), charcoal at −196°K and through a fitted disk into distilled water, the gas train being all glass. Identical results were obtained with either gas. The electrodes which were all oriented to the (100) face were etched in CP4 and rinsed in distilled water (or gettered D.I. water) before each experiment. In a few cases they were etched in M/10 potassium ferricyanide solution after the CP4. Anodic currents of 100-200 $\mu a/cm^2$ (n-type electrodes illuminated) were applied for around 5 min before data were taken. Ferricyanide appeared to produce a surface similar to that obtained after anodic etching whereas the CP4 surface (before anodic etching) was more variable with respect to the initial value of the surface potential and the behavior of the capacity.

Measurements.—The capacity of the germanium electrode solution interface was measured by means of a current pulse technique. Short duration square current pulses (up to a maximum value of 100 μa and of 1 μsec to 50 μsec duration, but most frequently 5 μsec) were applied from a pulsed constant voltage source, through a 10^6 ohm resistance and 0.47 μfd capacity in series, to one of the platinum electrodes in the larger compartment. The change of potential between the bulk of the germanium electrode and the solution was detected at the other platinum electrode in this compartment, amplified, and presented on an oscilloscope.

The form of the response, which was independent of the sign of the current pulse, is shown in Fig. 3.

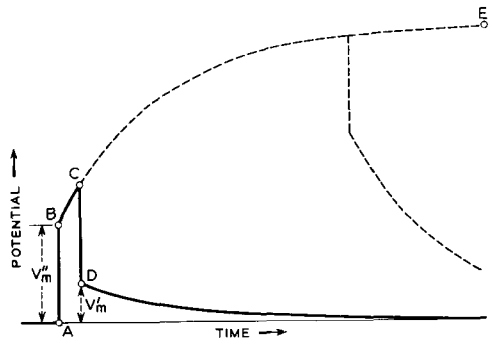

Fig. 3. Response of the interface to a short duration square current pulse.

When the pulse was turned on there was an initial potential change V''_M(A to B) which was generally vertical at the highest trace speed of our oscilloscope (0.1 $\mu sec\ cm^{-1}$). The potential increased with time from B to C where the pulse was turned off resulting in an instantaneous decrease (C to D) equal to V''_M. The residual potential V'_M at D decayed to the original potential in an exponential manner. In a typical experiment V'_M, V''_M and the time constant (τ) for decay of V'_M were measured, although in some cases only V'_M was measured. Care was taken to keep the differential pulse sufficiently small that the response was less than 25 mv. During an experiment the differential pulse was applied repetitively through the interface about 20 times per second, and the voltage response was continuously displayed.

The photovoltaic response of the electrodes was measured with a 40 cps square wave tungsten filament light source, the potential with respect to a platinum electrode in the solution being presented on an oscilloscope. The major point of interest here was to determine, as a function of doping, the electrode potential at which the "fast" response changed sign.

Both the interfacial capacity and the photovoltaic response were measured as a function of electrode potential, the bias being applied through the platinum electrode in the smaller compartment by means of a direct current source (D in Fig. 1). Two methods of varying the electrode potential were used. The first (method I) was simply to set a certain current through the electrode, wait for the electrode potential (V_E) to come to a steady value and then measure it and the quantities V''_M, V'_M and τ. Alternatively (method IIa) by manipulation of switch S the desired current could be set through the 10K ohm auxiliary resistor and then switched into the system for a brief period of time (approximately 1 sec) during which instantaneous values of V_E and V'_M were measured. The currents were such as to make the germanium anodic and were sufficiently small not to upset significantly the hole electron equilibrium in the electrodes. In an extension of the second method (method IIb) an additional current source, in parallel with D, was used to provide a continuous current (germanium anodic) superimposed on which was the manually pulsed current from D which could now be of either sign, but not sufficiently great in the negative sense to reverse the sign of the net current.

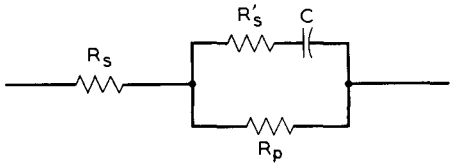

Fig. 4. Equivalent circuit of the interface

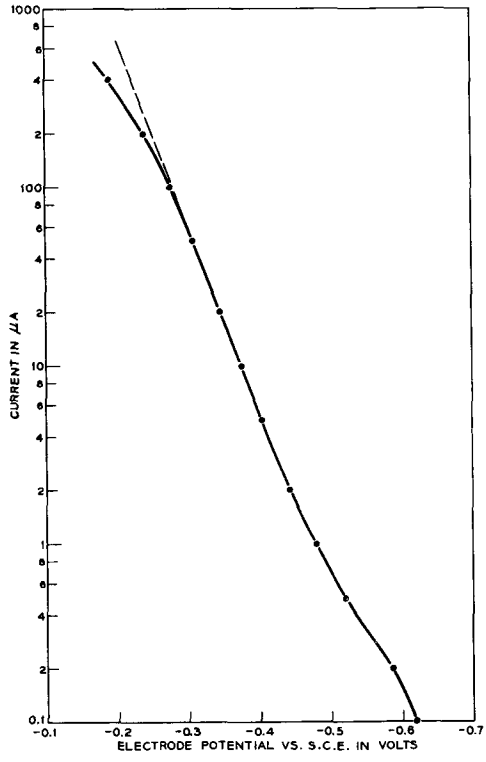

Fig. 5. Tafel curve for 1.1 cm² germanium electrode in $\frac{M}{10}$ K_2SO_4, phosphate buffered to pH 7.4.

Experimental Results

The response shown in Fig. 3 does not uniquely determine an equivalent circuit. It does, however, suggest a simple combination of resistance and capacity such as shown in Fig. 4, which is basically similar to a previously proposed model (5) with the addition of R'_s. Assuming any model, one can, from pulse data, calculate a differential resistance. If the method and analysis are valid, this differential resistance should agree with the differential resistance determined from the current-voltage curve taken at

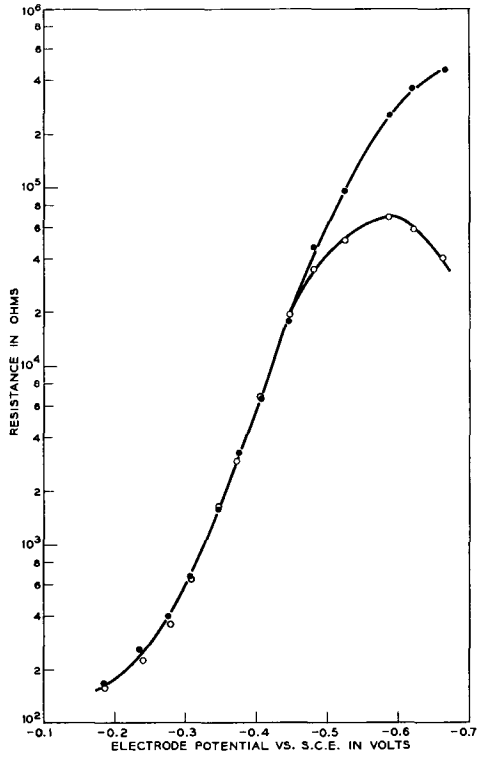

Fig. 6. Differential resistance vs. electrode potential, derived from Fig. 5 (●) and from pulse data (○).

zero frequency. The d-c data are shown in Fig. 5, and in Fig. 6 is shown the comparison of differential resistance determined graphically from Fig. 5 and from the pulse data in Table I. The agreement is excellent except at the more negative potentials. This deviation is due to the fact that in order to measure the differential resistance correctly here by the pulse method the low-frequency response of our measuring system should be good down to 0.2 sec or better, whereas it actually falls off at about 0.05 sec. The agreement is independent of the equivalent circuit chosen provided only that the circuit is consistent with the response shown in Fig. 3 and that it has a continuous resistive path from one terminal to the other.

It has been found in this case and in previous work (7) that at moderate current densities in the anodic direction the Tafel relation between d-c current and voltage is obeyed, subject to correction for a constant series resistance R_s (due to the germanium,

Table I. Analysis of a 25.5 ohm-cm p-type germanium electrode in terms of the equivalent circuit of Fig. 4

I, ma	V_E volts vs. S.C.E.	V''_M, mv	V'_M, mv	τ, μsec	R'_s/R_p	R_s, ohms	R_p, ohms	$R_p + R_s$, ohms	$\Delta V_E/\Delta I$, ohms	C 10^{-8}, farads	R^*_s, ohms	R^*_p, ohms	C^* 10^{-8}, farads
0.400	—0.189	12.5	1.18	15	1.27	103	81	161	167	11.5	125	36	42
0.200	—0.238	12.5	2.8	18	0.446	65	146	226	285	8.3	125	100	18
0.100	—0.277	13.7	4.8	22	0.27	76	281	361	440	6.5	137	224	10.4
0.050	—0.307	15.0	7.1	35	0.14	80	570	650	670	5.4	150	500	7.1
0.020	—0.345	17.3	10.7	69	0.063	98	1,560	1,640	1,600	4.2	173	1,570	4.6
0.010	—0.375	18.2	12.7	107	0.037	104	2,820	2,900	3,600	3.65	182	2,720	3.9
0.005	—0.403	17.7	14.1	231	0.015	99	6,580	6,660	6,700	3.45	177	6,520	3.5
0.002	—0.444	16.8	15.0	660		98	19,000	19,000	18,000	3.3	168	18,800	3.3
0.001	—0.480	16.8	13.6	1,360		98	37,000	37,000	46,000	3.7	168	37,000	3.7
0.0005	—0.521	15.0	10.2	2,700		80	55,000	55,000	97,000	4.9	150	55,000	4.9
0.0002	—0.586	11.4	5.0	7,200		44	72,000	72,000	260,000	10.0	114	72,000	10.0
0.0001	—0.619	9.8	3.45	8,500		28	59,000	59,000	360,000	14.5	98	59,000	14.5
0	—0.665	8.0	1.78	11,500		10	41,000	41,000	440,000	20.0	80	41,000	20.0

electrolyte, and leads) and provided the data are taken under conditions where the electron or hole concentration does not depart essentially from the equilibrium value. The departure of the current voltage curve in this region (as shown in Fig. 5) serves to determine R_s. This series resistance is found to be about one-half of the resistance necessary to explain the initial rise in V''_M in Fig. 3. This is the reason for including the resistance R'_s in Fig. 4. It should be emphasized that over most of the range of interest R_s and R'_s are small compared with R_p, and the exact values used from R_s equal to zero to R'_s equal to zero (their sum being known from V''_M) have very little effect on the calculated values of C and R_p. Assuming the circuit in Fig. 4, the following relations may be obtained

$$V''_M = i[R_s + R'_s(1 + R_s/R_p)^{-1}] \quad [3]$$

$$V'_M = C^{-1} i\, t(1 + R'_s/R_p)^{-2} \quad [4]$$

and

$$\tau = R_p(1 + R'_s/R_p)^{-1} i\, t(V'_M)^{-1} \quad [5]$$

whence

$$R'_s/R_p = t(V''_M - R_s i)(V'_M \tau)^{-1} \quad [6]$$

where i is the magnitude of the current pulse, t is the pulse duration, and τ is the decay constant for the voltage after the pulse is turned off. In these equations it has been assumed that t/τ is very small so that $\exp(-t/\tau)$ is equal to $(1 - t/\tau)$. For cases where this is not so, the appropriate correction has been made.

Typical data taken on a p-type electrode are shown in Table I. The magnitude of the current pulse was 0.1 ma and its duration was 5 μsec. R_s was taken as 80 ohms from Fig. 5. The starred values R_s*, R_p*, and C_p* are the results one would obtain if one assumed R'_s to be equal to zero, assuming V''_M and not Fig. 5 gives the correct value for R_s. The correct circuit is between these limits with the one for $R_s = 80$ ohms being the more likely. It is to be noted that for V_E more anodic than —0.300v the capacity values are considerably different in the two cases. In methods IIa and IIb, where we did not have time to take all the data shown in this table, we could not correct V'_M for t/τ being too large, and we could only calculate C on the basis of $R'_s = 0$. These two errors for very anodic potentials tend to compensate each other. For less anodic potentials it matters little which equivalent circuit one chooses.

Charge may be distributed over three distinct regions of the interface, the space charge layer in the germanium and its associated surface states ($C_{SC} + C_{SS}$), the Helmholtz region encompassing the geometrical interface, and the space charge (Gouy layer) in the solution. At the electrolyte concentrations used in this work the Gouy layer was essentially nonexistent, and all excess charge on the solution side of the interface can be considered to be in the Helmholtz layer. Typical values for the capacity of the Helmholtz layer (C_H) at a metal electrode (ca. 20 μfd/cm^2) are two to three orders of magnitude greater than calculated values for the minimum space charge capacitance in the semiconductor, so that since these capacities are in series the observed capacity at the interface is $(C_{SC} + C_{SS})C_H (C_{SC} + C_{SS} + C_H)^{-1}$ and since $C_H > 100\, C_{SC}$ the observed capacity should be C_{SC} to within about 1% in the absence of fast surface states. R'_s and R_p are the resistances to the flow of capacitative or faradaic current, respectively, from the bulk of the electrode to the bulk of the solution.

Figure 7 shows a typical curve of capacity *vs.* steady-state electrode potential at *p*H 7.4 measured on a simple electrode. An investigation of these curves as a function of *p*H indicated that over the range *p*H 5-12 they were similar in shape, but displaced along the electrode potential axis by an amount depending on the change in *p*H. Beyond *p*H 5 and 12, the curves changed shape and the minimum value increased by about a factor of 2. These data will be dealt with in detail at a later date. All the data contained in this paper were obtained at *p*H 7.4.

Figure 7 is in general agreement with Bohnenkamp and Engell (5) that a considerable part of the potential change occurs across the space charge region. Their data were taken at *p*H 0 and 14 and the minimum capacities were about a factor of 2 larger than we find at *p*H 7.4, but in agreement with our values at extremes of *p*H. It is of particular interest that our minimum capacity agrees closely with the theoretical value if the experimentally measured roughness factor of 1.3 is assumed (9).

Similar data taken instantaneously on the application of a current through the interface, method IIa as described previously, are shown in Fig. 8. Further data taken by method IIb are also shown in Fig. 8.

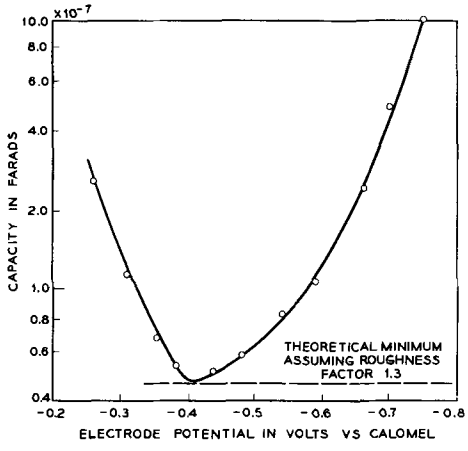

Fig. 7. Capacity *vs.* electrode potential (method I) for a 42.2 ohm-cm n-type germanium electrode.

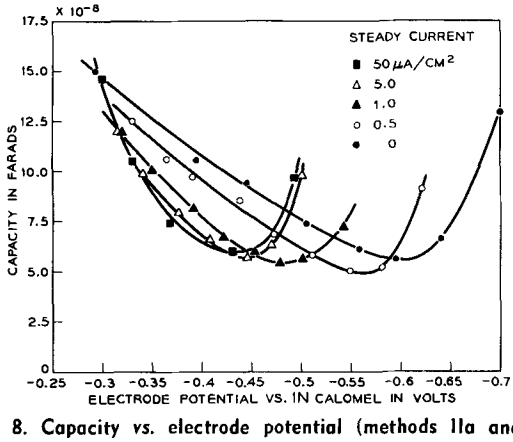

Fig. 8. Capacity *vs.* electrode potential (methods IIa and IIb) for a 25.5 ohm-cm p-type germanium electrode.

Additional experiments were conducted with the bridge electrodes. The capacity of the interface was measured exactly as for the simple electrodes, and good agreement was found for similarly doped material. The apparent variation in conductivity of the thin arm of the bridge was measured (Eq. [2]) as a function of electrode potential varied by method IIa.

The decay of photoconductivity in the thin arm was determined in two ways. The decay was compared directly with the signal from an exponential generator while the electrode potential was changed by method I. Method II does not allow sufficient time to adjust the exponential generator to an accurate reading so the procedure adopted in this case was to measure the increase in conductivity due to the 40 cps square light pulse, directed onto the thin arm only, the duration of which was long compared with the photoconductivity lifetime. Once the conductivity increase (observed as a square voltage response on the oscilloscope) was calibrated against the photoconductivity lifetime at one point (conveniently zero current density across the interface), the latter could be derived from the former by simple proportionality, the longer the lifetime the larger the photoconductive response. The results by either method yield the same result, namely, that over the accessible range of electrode potential the lifetime was essentially constant and equal to the body lifetime of the electrode material, *e.g.*, for the p-type bridge 640 ± 40 μsec.

Discussion

Dewald (6) has discussed the distribution of potential and charge at the semiconductor-aqueous solution interface and has pointed out that when the solution is sufficiently concentrated the Gouy layer is suppressed, and in the absence of a considerable number of surface states near the semiconductor Fermi level or changes in surface dipole almost all of any potential change at the interface occurs across the space charge region in the semiconductor. Hence, in the absence of these effects, or of concentration polarization in the solution, changes in electrode potential should correspond to changes in the germanium surface potential.

It is anticipated that the observed capacity is due to the space charge layer plus surface states sufficiently fast to respond to the differential current pulse (3). If the assumption is made that the measured capacity is solely that of the space charge layer, then the surface potential (ψ_s) may be deduced by comparing the experimental capacity values (divided by the roughness factor) with the theoretical curve calculated from (10)

$$C_{sc} = dQ_{sc}/d\psi_s = A(dF/dY)dY/d\psi_s \qquad [7]$$

where Q_{sc} is the charge in the space charge layer, A is the electrode-solution interfacial area, and

$$F = \pm[\lambda(e^{-Y} - 1) + \lambda^{-1}(e^{Y} - 1) + (\lambda - \lambda^{-1})Y]^{1/2} \qquad [8]$$

where $\lambda = p/n_i$, p is hole concentration, and $Y = e\psi_s/kT$, ψ_s being the electrostatic potential (in volts) across the space charge region. The assumption is made in the above form of F that the carrier density does not depart appreciably from equilibrium under the conditions of our experiments.

Theory indicates that for the same steady-state conditions in identical solutions, the surface potential will vary with the doping of the electrode by an amount kT/e ln λ compared with intrinsic (6, 11). If the capacity we observe is that of the space charge layer and there are no potential changes in the system except across the space charge layer, then for all electrodes the plots of $\psi_s - kT/e$ ln λ *vs.* electrode potential should coincide and should be straight lines with a slope of unity. The data for variously doped electrodes is shown in Fig. 9. It is seen that only the first requirement is satisfied. There are two possible explanations for this behavior. Either the capacity values and, hence, the values of ψ_s are incorrect due to the existence of a sufficient number of fast surface states within the experimental range of $\psi_s - kT/e$ ln λ or there is a potential change in some other region of the interface.

In taking the above data it was observed that the behavior of the electrode potential, particularly at low current densities, was dependent on the immediately previous condition of the electrode, *i.e.*, was a particular current density established from a higher or lower value, the data in Fig. 9 being the final steady-state values. An analysis of the data taken by method IIa, in which the long time effects are disregarded, is shown in Fig. 10. In this case, over a range of potential, the electrodes behave in an ideal fashion and obey the simple relation

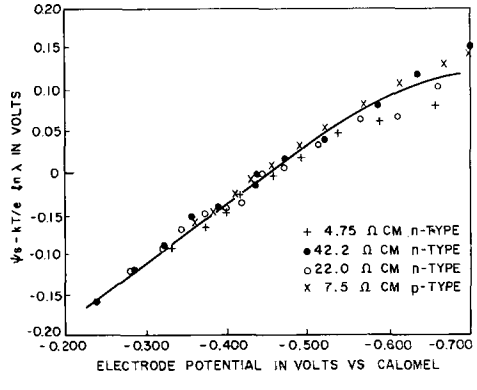

Fig. 9. ($\psi_s - \frac{kT}{e}$ ln λ) *vs.* **electrode potential (method I) for various electrodes.**

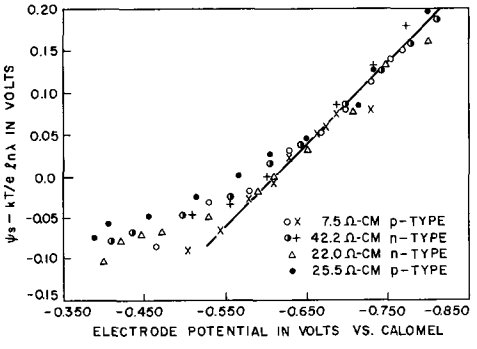

Fig. 10. ($\psi_s - \frac{kT}{e}$ ln λ) **vs. electrode potential (method IIa) for various electrodes.**

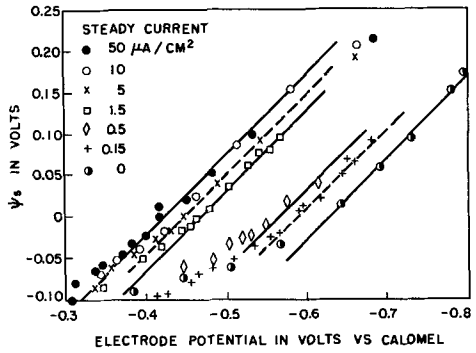

Fig. 11. ψ_s vs. electrode potential (method IIb) for a 22 ohm-cm n-type germanium electrode.

$$\psi_s = \frac{kT}{e} \ln \lambda = V_E + \text{constant} \qquad [9]$$

which has been predicted (6, 11). In Fig. 10 the points at the most negative potentials represent zero net current, while less negative potentials represent increasingly anodic polarization. Data taken by method IIb throw light on the reason for the departure from Eq. [9] at higher anodic current densities. It can be clearly observed from Fig. 11 that the constant in Eq. [9] varies with current density up to about 10 μa/cm^2, but at a sufficiently slow rate that for not too large changes in current it remains essentially constant during the time that the electrode potential and V'_M, *i.e.*, capacity, are read. The disposition of these lines is independent of the stirring rate, indicating that the potential shift is not due to concentration polarization in the solution. Concentration polarization may, however, be observed in unbuffered solutions of the same *p*H as shown in Fig. 12, where the capacity-electrode potential curves exhibit a similar shift over the range of current density from zero to approximately 10 μa/cm^2 and then, unlike the situation in Fig. 8, undergo a further shift at higher current densities.

The only remaining region where the potential shift may occur in buffered solutions is the Helmholtz layer. The potential may change appreciably in this region due either to a change in the adsorbed dipoles or to a change in the occupation of slow surface states. (The surface states must necessarily be slow since they do not respond to the capacity measurements.) The present data are not sufficient to distinguish between these two possibilities. Figure 13 shows an analysis of some data taken by method I at low current densities. The surface potentials have been computed from the capacity and hence, knowing the surface potential, it is possible to deduce how changes in the electrode potential due to small anodic current are distributed between the space charge and Helmholtz layers. The space charge potential is known absolutely, while only changes in Helmholtz potential from the zero current value are obtained. The curves for n- and p-type electrodes show a sharp step in the Helmholtz potential over a fairly narrow range of surface potential. The value of $(\psi_s - kT/e \ln \lambda)$ at which this potential change occurs is approximately the same for both n- and p-type electrodes which would be expected for a surface state localized in energy. Unfortunately, equal values of $(\psi_s - kT/e \ln \lambda)$ represent also equal current densities across the interface, and the results do not clearly distinguish between a purely electrical effect dependent on surface potential and a chemical effect dependent on current density. Slow surface states, however, are usually considered to be associated with thick oxide films and disappear when such films are reduced in thickness (12). Under the conditions of our experiments, thick films are unlikely to be present (13). For this reason, it would seem more likely that we are observing a change in surface dipole due to adsorbed molecules or ions oriented at the surface. The structure of the adsorbed layer could be strongly affected by anodic current since this actually removes the surface atoms of the electrode. The various lines in Fig. 11 might then represent a steady state attained between the formation of an oriented adsorbed layer, probably of water molecules, and its disruption by anodic etching.

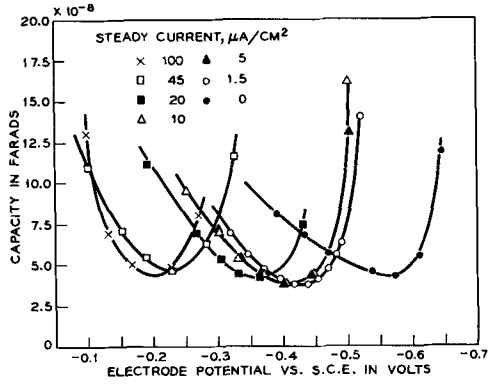

Fig. 12. Capacity vs. electrode potential (method IIa) for a 25.5 ohm-cm p-type germanium electrode in unbuffered $\frac{M}{10}$ K_2SO_4.

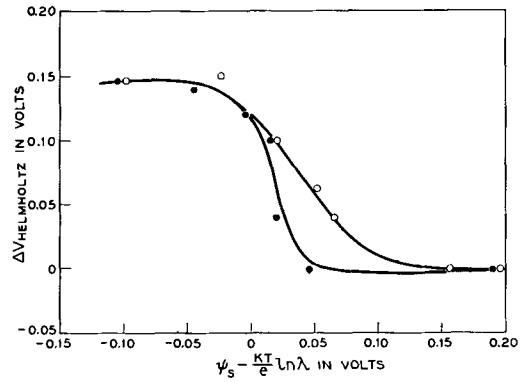

Fig. 13. $(\psi_s - \frac{kT}{e} \ln \lambda)$ vs. $\Delta V_{\text{Helmholtz}}$ for a 25.5 ohm-cm p-type electrode (○) and a 42.2 ohm-cm n-type electrode (●).

The constancy of the decay lifetime for excess carriers deduced from the bridge electrode and its close correspondence with the body lifetime indicates the absence of surface recombination centers over the investigated range of surface potential (approximately 0.2v on each side of the center of the gap).

Additional information is provided by fast photovoltaic response. In the absence of fast surface states,

this quantity should change sign at flat band (10), *i.e.*, $\psi_s = 0$. Experimentally, the range is +0.03 to −0.02v for the variously doped electrodes.

It may be concluded on the above evidence of the distribution of charge and potential and kinetic recombination effects that a germanium surface which has been recently anodically etched in nearly neutral solution is free from measurable densities of fast surface states. It should be emphasized here that this conclusion only applies to the case of the purified electrolyte. A similar conclusion with regard to the absence of fast states has recently been reached in the case of the zinc oxide electrode (3).

An attempt was made to calculate ψ_s from the bridge conductivity data. Here two questions arise. First, do the values of ψ_s calculated from the capacity changes in the thin arm of the bridge agree with results for the simple electrodes. These results are compared in Fig. 14. The agreement is reasonably good, considering that in the case of the bridge there is necessarily a distribution of potential along the thin arm and both the potential V_E and the capacity are some kind of average over this arm. The second question, how do the values of ψ_s calculated from conductivity agree with the capacity data, is illustrated in Fig. 15. Over a range of potential the agreement is fairly good, but at higher anodic potentials the two methods do not agree. The lack of success encountered in this attempt may be ascribed to two potential sources of error. There is a possibility of conduction through the solution by virtue of the fact that a potential difference must be applied across the electrode to measure the conductivity. In most cases this potential was quite small, about 10 mv between the ends of an arm 2 cm long, and the frequency of the applied signal kept low (17 cps) to reduce capacitative coupling through the solution. It is felt, however, that the major discrepancy arises from another source which is the fact that, due to the geometry of the bridge, at any interfacial current there will be a distribution of potential along the thin arm because of current flow along its length. Calculations indicate that at our maximum overvoltage of about 0.450v there is a potential difference between the ends and center of the thin arm of some 0.045v, becoming rapidly less at lower current densities. In this event there will be a fairly complicated averaging of surface conductivity along the length of the arm which could give deviations in the direction observed.

Although the conductivity experiment does not exhibit ideal behavior, the observed conductivities are a constant function of potential. This may be inferred from Fig. 16, where the bridge balance reading, being proportional to conductivity (see Eq. [2]), is plotted as a function of the electrode potential. These experiments were carried out over an extended period of time in solutions of *p*H 7.4, and include a correction for the reduction in thickness of the active arm each time it is etched, deduced from the balance reading for minimum conductivity. Insofar as capacity measurements carried out at the same time indicate a constant relationship between V_E and $(\psi_s - kT/e \ln \lambda)$, the V_E axis could be replaced by suitably normalized values of $(\psi_s - kT/e$

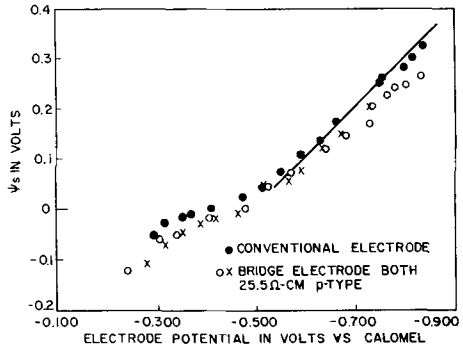

Fig. 14. ψ_s vs. electrode potential (method IIa) for a simple electrode (•), and a bridge (o,x) both 25.5 ohm-cm p-type.

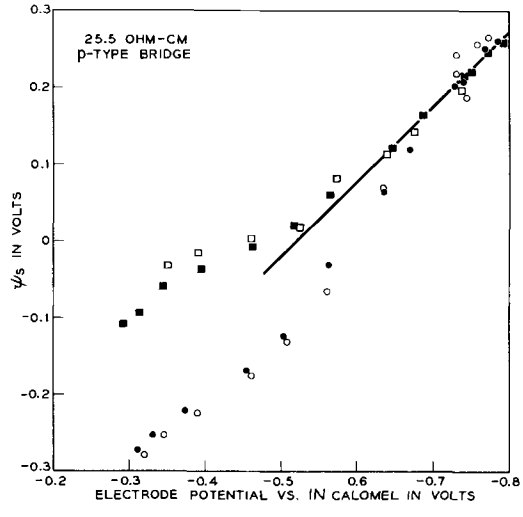

Fig. 15. ψ_s calculated from capacity (□,■) and from conductivity change (o,•) vs. electrode potential (method IIa) for a 25.5 ohm-cm p-type bridge.

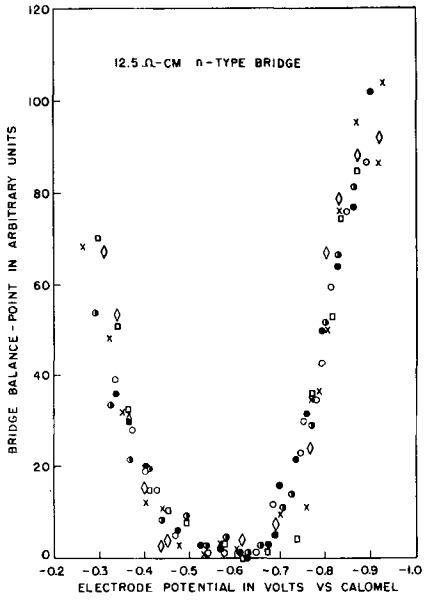

Fig. 16. Balance point (arbitrary units) of 12.5 ohm-cm n-type bridge vs. electrode potential (method IIa). The various symbols represent experiments carried out at different times. The thickness of the active arm is different in each case due to etching.

$\ln \lambda$), and conductivity measurements could be used to deduce this quantity from Fig. 16.

Conclusion

The capacity of the interface between a germanium single crystal electrode and an aqueous solution of K_2SO_4 buffered to pH 7.4 when measured by a high-frequency pulse method is explicable solely in terms of the space charge capacity in the electrode and reveals no fast surface states (less than ca. $10^{0.5}$ cm^{-2}) within ± 8 kT/e measured from mid-gap. The conclusion of no fast surface states is supported by the absence of significant surface recombination phenomena. The distribution of potential across the interface in response to anodic bias is expressed by

$$\psi_s - \frac{kT}{e} \ln \lambda = V_E + K$$

where the quantity K is arbitrary and depends on steady-state current density up to 10 μa cm^{-2}, but otherwise at a given pH and for a given reference electrode is a constant.

Surface conductivity data yield incorrect values of the surface potential except at small polarizing currents, but are quite reproducible and could be used to predict surface potential if properly calibrated in terms of the capacity. It is the authors' conviction that values of surface potential deduced from the capacity are most likely the correct ones.

In other words, it is possible under these conditions to obtain an almost "perfect" germanium surface, *i.e.*, no fast states.

Acknowledgments

The authors are indebted to J. F. Dewald, U. B. Thomas, Jr., and D. R. Turner for helpful discussion, and to W. J. Sundburg for technical assistance.

Manuscript received Jan. 5, 1962; revised manuscript received March 19, 1962. This paper was prepared for delivery before the Detroit Meeting, Oct. 1-5, 1961.

Any discussion of this paper will appear in a Discussion Section to be published in the June 1963 JOURNAL.

REFERENCES

1. E. Harnick and Y. Margoninski, *J. Phys. Chem. Solids*, **8**, 96 (1959).
2. W. H. Brattain and J. Bardeen, *Bell System Tech. J.*, **32**, 1 (1953).
3. J. F. Dewald, *ibid.*, **39**, 615 (1960).
4. H. U. Harten, *Z. Naturforsch.*, **16a**, 459 (1961).
5. K. Bohnenkamp and H. J. Engell, *Z. Elektrochem.*, **61**, 1184 (1957).
6. J. F. Dewald in "Semiconductors," N. B. Hannay, Editor, Reinhold Publishing Co., New York (1959).
7. W. H. Brattain and C. G. B. Garrett, *Bell System Tech. J.*, **34**, 129 (1955).
8. F. R. Meyer and G. Ronge, *Z. angew. Chem.*, **52**, 637 (1939).
9. J. T. Law, *J. Phys. Chem.*, **59**, 543 (1955).
10. C. G. B. Garrett and W. H. Brattain, *Phys. Rev.*, **99**, 376 (1955).
11. W. H. Brattain in "The Surface Chemistry of Metals and Semiconductors," H. C. Gatos, Editor, John Wiley & Sons, Inc., New York (1960).
12. M. Lasser, C. Wysocki and B. Bernstein in " Semiconductor Surface Physics," R. H. Kingston, Editor, University of Pennsylvania Press (1957).
13. D. R. Turner, *This Journal*, **103**, 252 (1956).
14. W. H. Brattain and C. G. B. Garrett, *Bell System Tech. J.*, **35**, 1019 (1956).

Investigation of Some Uncommon Surface Treatments on Germanium

W. A. Albers, Jr.* and A. M. Rickel

Research Laboratories Division, The Bendix Corporation, Southfield (Detroit), Michigan

ABSTRACT

Several surface treatments have been applied to germanium and characterized with respect to the surface energy level configuration and the sensitivity to variations in ambient atmosphere. The characterization was accomplished by making simultaneous measurements of the a-c field-effect conductivity change and the surface recombination velocity, both as functions of surface potential. Experimental results suggest certain relationships between etched germanium surface properties and those properties resulting from a subsequent surface treatment, which may be exploited to yield a surface condition that is relatively passive to ambient atmosphere variations.

Attempts to stabilize and/or passivate semiconductor surfaces for the purpose of improving manufactured semiconductor device uniformity and reliability often involve a sequence of several distinct operations. It is well known that each step of such a sequence can contribute to the ultimate electrical properties of the resultant surface. It is not generally understood, however, just how these steps contribute, in a quantitative sense, to the resultant surface properties. The purpose of this paper is to report some preliminary studies of the effect of two successive surface operations on the electrical properties of the semiconductor surface. The two steps chosen for investigation are (i) an etching operation and (ii) a surface treatment applied to the etched surface. The surface treatments investigated are "uncommon" in the sense that they have not been reported extensively in the literature.

* Present address: General Motors Research Laboratories, Warren, Michigan.

The results of the measurements to be reported suggest a method of characterization of a given surface condition that affords a first-order approach to the "engineering" of surfaces into devices. The experimental data also yield some information about the interaction of the two operations on the surface that suggests possible approaches for obtaining relatively high degrees of surface passivation. Both of these aspects of the experimental results are discussed in some detail.

Experimental Approach

Rectangular sample with their large-area surfaces oriented in either the (100) or the (111) crystallographic planes were cut from 35 ohm-cm n-type single crystals of germanium. The rectangles were subsequently lapped to a thickness of 10.5 to 11.5 mils and then etched to a final thickness of 5.0 ± 0.1 mils in either CP4A or a 1:1:1 ratio of H_2O_2, HF, and H_2O.[1] A specific sample was then subjected to one of several surface treatments, the nature of which will be detailed later. Finally leads were attached,[2] and the sample was placed in the experimental apparatus.

The method employed for the characterization of a given surface treatment was to observe, simultaneously, the large-signal a-c field effect and the surface recombination velocity (s.r.v.) as a function of surface potential in various ambient atmospheres. The data were then analyzed in the manner employed by Many *et al.* (1) to obtain surface trap densities and energies. In addition, the sensitivity of the electrical properties of the experimental sample to changes in the ambient atmosphere was also monitored. The surface treatment data were then compared to similar data obtained on the etched, untreated surfaces previously described, which were employed as controls.

The apparatus for mounting the samples in order to accommodate the simultaneous measurement of the field-effect conductivity and the s.r.v. is drawn schematically in Fig. 1. The experimental technique is similar to those employed by Wang and Wallis (2), Bath and Cutler (3), and Rzhanov *et al.* (4), with some modification. The above authors all performed simultaneous measurements of the field-effect conductivity and the conductivity change on illumination. The photoconductivity was then related to the s.r.v. through suitable theoretical expresssions [see, for example, ref. (3)]. These workers used, for the most part, nonpenetrating illumination and, in some cases, field-effect electrodes were coupled to only one of the two large area surfaces of their experimental samples. The apparatus in Fig. 1 employs a germanium filter D which is thick compared to the sample thickness. The radiation that reaches the sample C is thus penetrating. If the filter is sufficiently thicker than the sample, the generated carrier density due to illumination is nearly constant throughout the volume of the illuminated portion of the sample. The germanium filter also serves as one of the two field-effect electrodes, the other being an ordinary brass plate A. The experimental specimen is sandwiched between these two electrodes and insulated from them by the mica spacers B. The germanium filter thus serves both as a field-effect probe and as a means of obtaining a low-level,[3] uniform generation of carriers in the specimen.

The circuitry for the field-effect observations was patterned after that of Low (5). A 200-v peak, 70 cps, alternating voltage was applied to the field effect probes, and the resulting change of sample conductivity *vs.* induced surface charge was displayed on an oscilloscope. An ordinary tungsten filament projector lamp was used as a source of illumination. The light was chopped at a rate of 120 cps so that, upon illumination, the photoconductivity pulse appeared superimposed on the ordinary field-effect curve. Since the chopping rate was out of sync with the field-effect voltage, the photoconductivity pulse ran back and forth on the field-effect pattern on the oscilloscope. By employing a high persistency phosphor, a double field-effect trace is obtained, the vertical separation being proportional to the photoconductivity voltage.[4] The necessity of calibrating the intensity of illumination is eliminated by obtaining a value of the s.r.v. by the photoconductivity decay method at the equilibrium surface potential (the value of the surface potential for zero induced surface charge). This value of the s.r.v. serves to calibrate the photoconductivity voltages obtained with the field effect.

The type of data that results from the methods of observation described above is presented in Fig. 2 and 3 for some typical surface treatments[5] (the surface treatments will be referred to only by abbreviated names in the text; the physical and chemical details are presented in an Appendix). In Fig. 2 is plotted the charge in "fast" surface states, Q_{ss}, as a

[1] The CP4A etch consists of a 5:3:3 ratio of nitric, hydrofluoric, and glacial acetic acids. The chemicals employed were all reagent grade or better, the HNO_3 was 70% by weight, the HF 48% by weight, and the H_2O_2 (unstabilized) 30% by weight. The H_2O was distilled and deionized.

[2] In order to avoid contaminating the previously prepared surface, the samples were made much longer than the active surface region under investigation; the attachment of leads was thus accomplished at a distance somewhat removed from the surface area of interest.

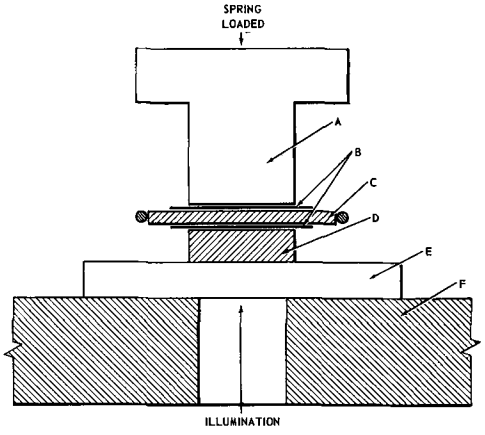

Fig. 1. Detail of sample mounting for field effect and photoconductivity measurements: A, brass field effect electrode; B, mica spacers; C, germanium sample; D, germanium filter and field effect electrode; E, quartz microscope slide mount for germanium filter; F, wall of enclosing box.

[3] The low generation level is a necessary condition for the applicability of the expressions relating s.r.v. and photoconductance (3).

[4] Photographs of oscilloscope traces like those discussed have been published by Rzhanov (4).

[5] For the purposes of this paper, a "surface treatment" is defined as an operation on the surface which does not involve the removal of germanium material, as opposed to an "etch," which does involve the removal of material.

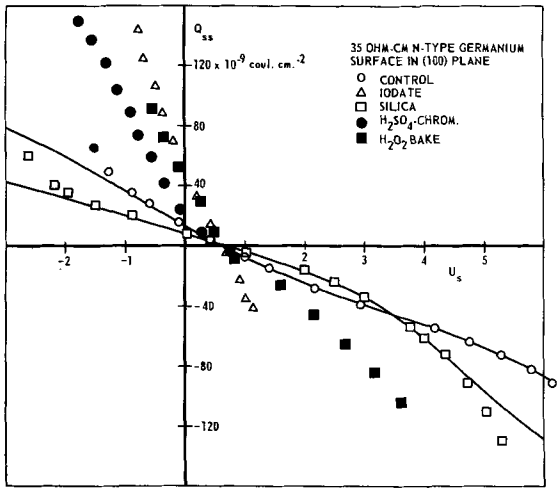

Fig. 2. Charge in fast surface states, Q_{ss}, as a function of surface potential, u_s, in units of kT/q for several surface treatments on an H_2O_2:HF:H_2O etched surface. Solid curves represent best theoretical fit for the control surface and the silica treatment.

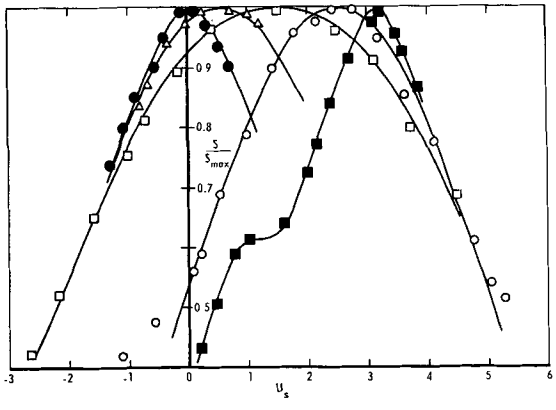

Fig. 3. Normalized surface recombination velocity, s/s_{max}, as a function of surface potential, u_s, in units of kT/q for the same samples as Fig. 2. Solid curves represent the best theoretical fit to the experimental points.

function of surface potential, u_s, in units of kT/q.[6] The corresponding curves of the normalized s.r.v., s/s_{max} *vs.* u_s are plotted in Fig. 3. The points represent data obtained experimentally while the solid curves are the theoretical curves which are the best fit with the experimental points. The result is that the densities and energies of the fast surface states can be deduced, thus partially characterizing each surface treatment.

The data of Fig. 2 and 3 were all obtained in a dry O_2 ambient atmosphere, after sufficient time was allowed for the sample surface to come to equilibrium with this atmosphere. The reason for choosing a reference atmosphere is due to the fact that the fast surface state configuration changes with varying ambient atmosphere. This effect is illustrated in Fig. 4. The data presented here are the result of varying the ambient atmosphere about a typical H_2O_2:HF:H_2O-etched surface.

It will be noted that there is an appreciable variation in some of the recombination trap parameters.

[6] The quantity u_s is defined as

$$u_s = \frac{q\phi_s}{kT}$$

where ϕ_s is the surface potential. The symbols employed for all other quantities throughout this paper follow those of ref. (1).

	u_o	$\frac{E_t - E_i}{kT}$	$\frac{C_p}{C_n}$	$N_t \times 10^{-11}$	S_{max}
○	1.8	5.5	36.5	2.3	320
△	1.0	4.3	7.4	0.7	370
■	2.0	5.0	54.4	--	370

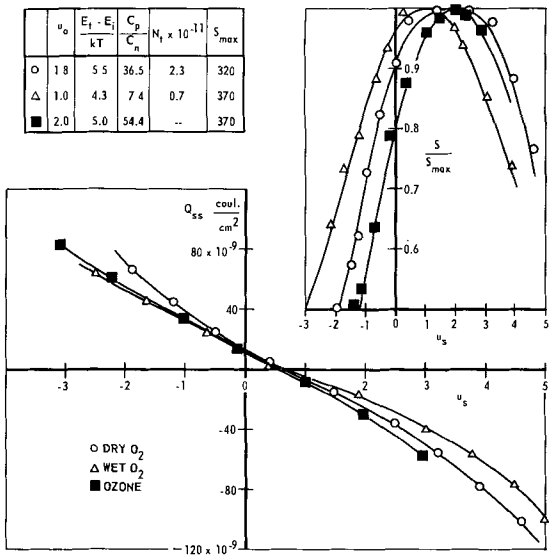

Fig. 4. Effect of varying ambient atmosphere on the surface state parameters. H_2O_2:HF:H_2O etched surface in a (100) plane of 35 ohm-cm n-type germanium.

The values of c_p/c_n, the ratio of hole-to-electron capture probabilities (which is proportional to $l\,n\,(u_o)$, u_o being the value of u_s about which the s.r.v. curves are symmetrical), and the state density, N_t, appear to vary considerably. On the other hand, the energy of the state (as measured from the center of the energy gap E_i) and the maximum value of the s.r.v., do not exhibit such drastic changes. This behavior is typical of most of the surfaces that we have investigated. It was found that a dry oxygen atmosphere yielded the most reproducible results, and thus, this atmosphere was chosen for the standard.

It follows that the variation of the surface properties with ambient atmosphere changes should be an essential part of characterizing any surface condition. We chose to do this by noting the value of the equilibrium surface potential in the field effect for two ambients, namely dry O_2 and wet O_2.[7] The difference in surface potential, Δu_s, and the mid-point of the range of Δu_s were thus obtained for these two ambients, the values of which are indicative of the sensitivity of the surface to ambient atmosphere changes. These data, along with data concerning surface state densities and energies are taken as a characterization of a given surface treatment. The data obtained on a total of 43 samples are summarized in the following section.

Results and Discussion

Some representative results, on (100) surfaces, are summarized in Table I. All of the data were obtained in a dry oxygen atmosphere at 295°K. Similar data were obtained on (111) surfaces, and, within experimental error, the data were substantially the same as those presented in Table I for the (100) surface. Although a total of 43 samples were investi-

[7] Dry O_2, in our case, was obtained by passing ordinary low dew-point compressed cylinder oxygen through a Drierite column. Wet O_2 was obtained by bubbling dry O_2 through distilled, deionized water and filtering through Pyrex wool. The sample conductivity would stabilize, typically, about 3 min after admission of wet O_2. Although there was a slow, long term drift evident for several hours in either ambient atmosphere the measurements were performed in a time interval sufficiently small that this drift was insignificant.

Table I. Summary of experimentally determined surface energy level parameters and sensitivity to ambient atmosphere variations for several surface treatments

Dry O_2 atmosphere — Surfaces in (100) plane — T = 295°K

(a) H_2O_2:HF:H_2O etch

Surface treatment	Recombination levels								Trapping levels											
	U_o	$\frac{C_{p1}}{C_{n1}}$	$\frac{E_{t1}-E_i}{KT}$	$N_{t1}\times 10^{-11}$	S_{max}	$C_{p1}\times 10^8$	$C_{n1}\times 10^8$	U_o	$\frac{C_{p2}}{C_{n2}}$	$\frac{E_{t2}-E_i}{kT}$	$N_{t2}\times 10^{-11}$	S_{max}	$C_{p2}\times 10^8$	$C_{n2}\times 10^8$	$\frac{E_t'-E_i}{KT}$	$N_t'\times 10^{-11}$	$\frac{E_t''-E_i}{KT}$	$N_t''\times 10^{-11}$	$\frac{E_t'''-E_i}{kT}$	$N_t'''\times 10^{-11}$	Δu_s
Control	2.50	148	4.8	4.4	290	2.43	0.016	—	—	—	—	—	—	—	−1.0	3.0	—	—	<−5.0	>N_{t1}	(1.8) 5.5
Iodate	0.55	3.0	2.8	>10	420	~0.21	~0.07	—	—	—	—	—	—	—	—	—	—	—	—	—	(−0.4) 2.1
H_2O_2-bake	3.20	600	3.3	3.5	260	1.82	0.003	0.50	2.7	~1.0	6.0	104	0.030	0.011	—	—	—	—	—	—	(1.6) 4.5
Thermal oxide	4.00	~3000	~4.0	~10	210	~1.0	~10^{-4}	~1.0	~7.5	~1.5	~3.0	120	~1.0	~0.1	~−1.0	~3.0	—	—	—	—	(3.1) 1.8
Silica	1.50	20	5.0	6.0	315	2.07	0.103	—	—	—	—	—	—	—	−1.0	3.5	>7.0	>N_{t1}	<−6.0	>N_{t1}	(2.0) 5.0
H_2SO_4-chromate	0.05	1.1	1.0	>10	450	~0.59	~0.54	—	—	—	—	—	—	—	−1.5	~15	—	—	—	—	(−0.15) 2.0

(b) CP4A etch

Control	2.30	190	4.5	4.0	146	1.01	0.01	—	—	—	—	—	—	—	−1.1	2.5	>7.0	>N_{t1}	<−6.0	>N_{t1}	(2.2) 5.0
Iodate	0.50	2.7	3.3	>10	200	~0.25	~0.09	—	—	—	—	—	—	—	—	—	—	—	—	—	(−0.3) 2.0
H_2O_2-bake	3.00	400	3.2	5.0	130	0.53	0.001	0.6	3.3	~1.0	3.0	50	0.32	0.002	—	—	—	—	—	—	(1.8) 4.0
Thermal oxide	2.40	122	4.7	4.1	115	0.93	0.01	—	—	—	—	—	—	—	−1.5	1.3	>7.0	>N_{t1}	—	—	(1.8) 3.2
Bromine	3.00	400	6.2	~10	100	~1.34	~0.003	—	—	—	—	—	—	—	−1.3	2.2	>7.0	>N_{t1}	—	—	(1.0) 3.6

gated, the data for each surface condition in Table I represent results typical of, at most, three samples per surface treatment. In several cases, only two samples per surface treatment were prepared. Consequently, the results may be interpreted only in terms of trends, since the statistical sample sizes for each surface treatment were too small to establish any degree of confidence.

The data in Table I are organized into three primary groups. The first of these includes the parameters associated with energy levels which are active in recombination. The second group lists parameters of energy levels which are not active in recombination, referred to as trapping levels. The third group of data constitutes a measure of the sensitivity of a given surface condition to a variation of the ambient atmosphere. This appears in the column headed "Δu_s" in Table I. The quantity Δu_s, the total swing in surface potential, in units of kT/q, in going from a dry O_2 to a wet O_2 atmosphere, is listed along with the value of u_s at the midpoint of this swing. The midpoint values are the quantities in parentheses.

The data for each set of levels are broken up into several columns according to the following parameters: the value of the surface potential u_o about which the s.r.v. curves are symmetrical, the ratio of the capture cross sections for holes and electrons c_p/c_n, the energy of the level $E_t - E_i$ in units of kT, the density of the level N_t, the maximum surface recombination velocity s_{max}, the capture cross section for holes c_p, and the capture cross section for electrons c_n. The subscript numerals refer to two separate recombination levels while the superscript primes represent different trapping levels. In many cases, only estimates of some of these parameters are available due to the fact that the applied electric field could not induce sufficiently large swings in surface potential. Where such estimates were made are evident in Table I as represented by appropriate symbols.

The main results suggested by the data are the following:

(*A*) The only significant difference between the two etched surfaces (controls in Table I) appears in the values of s_{max} and c_p. The energy and density of the recombination levels are comparable.

(*B*) The surface energy levels can be grouped as follows: (*a*) a recombination level between about 3.0 and 6.0 units of kT above the center of the gap; (*b*) a recombination level between about 1.0 and 1.5 units of kT above the gap center; (c) a trapping level about 1.0 to 1.5 units of kT below the center; (*d*) a trapping level at an energy somewhat greater than 7.0 units of kT above the gap center; (*e*) a trapping level at an energy somewhat greater than 6.0 units of kT below the gap center.

These are all consistent with the levels reported by several authors in the literature (2, 6-9).

(*C*) The iodate and H_2O_2-bake surface treatments yielded remarkably similar results on either of the etched surfaces.

In analogy, one could expect that thermal oxidation should also be similar for the two etched surfaces. Although the H_2O_2:HF:H_2O surface was successfully oxidized thermally, similar oxidation on a CP4A surface was not achieved. This is evident from the data of Table I, but additional support of this observation appeared in the form of oxide films on the samples. The thermal oxidation treatment on CP4A surfaces did not exhibit any interference colors or patterns characteristic of thick oxide layers. The thermally oxidized H_2O_2:HF:H_2O surface, however, exhibited uniform interference colors that suggested oxide film thicknesses of the order of 1000Å.

(*D*) It will be noted in Table I that, with the exception of the H_2SO_4-chromate treatment, a surface treatment on either control surface generally preserves the energy of the first recombination level. It appears to be characteristic of treatments that are known to be oxidizing (H_2O_2-bake and thermal oxidation), that a second recombination level is introduced. The H_2SO_4-chromate surface, however, does not preserve the first recombination level, but rather introduces a second recombination level in the $1.0 < (E_t - E_i/kT) < 1.5$ range. It is to be noted further that at least an order of magnitude reduction in the electron capture cross section for the first recombination level is associated with a heavily oxidized surface.

(*E*) The Δu_s column of Table I indicates that three of the surface treatments investigated (iodate, thermal oxidation, and H_2SO_4-chromate) are relatively

insensitive to ambient atmosphere variations, suggesting that such surface treatments could possibly be employed to passivate partially a semiconductor device surface. This aspect of the data will be developed more fully in a following section.

(*F*) Although not explicitly mentioned previously, weight loss measurements were taken for all of the surface treatments listed in Table I. The iodate, H_2SO_4-chromate, and bromine treatments exhibited weight losses after processing; the other treatments did not suffer a loss of weight within experimental error. The iodate and H_2SO_4-chromate weight losses were relatively small, *e.g.*, of the order of 2-4%. The weight loss for the bromine treatment, however, was of the order of 50-75%. We conclude that each of these treatments actually etches to some degree. The bromine treatment is definitely an etch and is thus improperly placed in the category of a surface treatment. The significant point to make is that it is just these surface treatments that alter most drastically the characteristics of the control surface. Those surface treatments which do not exhibit any evidence of etching seem to preserve the characteristics of the control surfaces to some extent.

(*G*) The most widely fluctuating trap parameter for recombination levels is the capture cross section for electrons, c_n. The capture cross section for holes, c_p, varies only approximately an order of magnitude in the range of surface conditions investigated. The value of c_n, however, experiences variations over a range of three orders of magnitude. Of particular interest is the reduction of c_n consistently observed for those surface treatments which are known to oxidize heavily (H_2O_2-bake and thermal oxidation).

The data as a whole clearly indicate the existence of at least two recombination levels and three trapping levels which are always present. Whether or not these levels can be observed experimentally depends on (i) the total range of u_s covered, (ii) the relative densities of the levels, and (iii) the capture cross sections for holes and electrons for each level. Evidently, the capture cross sections are relatively small for the trapping levels, rendering them inactive as recombination centers.

Result (*D*) above suggests a possible explanation of the origin of the two different recombination centers. It can be assumed that the levels in the range $3.0 < (E_t - E_i)/kT < 6.0$ are associated with a Ge-O bond of some form, while the levels in the $1.0 < (E_t - E_i)/kT < 1.5$ are associated with lack of stoichiometry and other imperfections in the Ge-to-GeO_x transition region. If it is further assumed that the heavy oxidation mechanism is one that requires the transfer of Ge atoms from the germanium-oxide interface to the outer surface of the oxide, then the origin of the two recombination levels could be as follows: the thin, equilibrium layer of oxide which results from etches gives rise to a relatively uniform and nearly perfect transition from germanium to the oxide. Thus, the first type of recombination level dominates. On heavy oxidation, however, the Ge atoms that are transferred to the outer surface of the oxide leave the transition region disturbed and farther removed from perfection. Thus, the second type of recombination level becomes more prominent, but not at the expense of the first type. The decrease in the capture cross sections for electrons that accompanies heavy oxidation may possibly be explained through an interaction between the two types of levels.

Employing the same assumptions of the previous paragraph, one could then explain the results observed for the H_2SO_4-chromate treatment as the domination of the second type of level while the first type is rendered insignificant. This would be possible if the H_2SO_4-chromate treatment is really etching moderately, yielding a resulting germanium-to-oxide transition region which is grossly disordered. Evidence that this explanation is reasonable comes from visual observation of the H_2SO_4-chromate treated surface. The resulting surface appears slightly textured, as compared to the original H_2O_2:HF:H_2O control surface, suggestive of a large number of nucleation sites for a surface layer decidedly different from the control surface.

Now, an extension of the arguments presented for the oxide surface layer can be employed to discuss some aspects of surface passivation. It will be noted that the smaller values of Δu_s (corresponding to surfaces relatively insensitive to ambient atmosphere variations) are correlated with large surface state densities. This is expected, since large quantities of trapped charge in surface states offer a more effective shield from the influence of a variation of surface charge. Let it be further noted that the thermal oxidation on an H_2O_2:HF:H_2O surface affords the smallest value of Δu_s. Based on our assumptions regarding the origin of the recombination states, it might then be possible to reduce the value of Δu_s by another large factor by thermally oxidizing one of the other surface treatments rather than the unstable control surfaces. What we really wish to emphasize is that the data suggest a very significant relationship between the etched surface characteristics and those characteristics which result from a subsequent surface treatment. It is concluded that a fruitful approach to the problem of passivating a semiconductor surface can be found in studying, in more detail, just what these relations are and how they can be exploited.

Application to Devices

The data of Table I can be employed to anticipate the effect of the listed surface treatments as applied to a semiconductor device. Most semiconductor rectifiers and transistors require that both the surface conductivity and the surface recombination velocity simultaneously assume their lowest practical values. It is further desirable that neither of these quantities vary with varying ambient atmosphere (passivated surface) and with time (stabilized surface). Information about all but the time variations is implicit in Table I.

Consider the plot of the change in conductivity $\Delta\sigma$ *vs.* surface potential, u_s, in units of kT/q in Fig. 5. A similar plot for any resistivity and type can be reproduced from the calculations of Kingston and Neustadter (10). Now this curve is independent of the surface treatment since it depends only on the

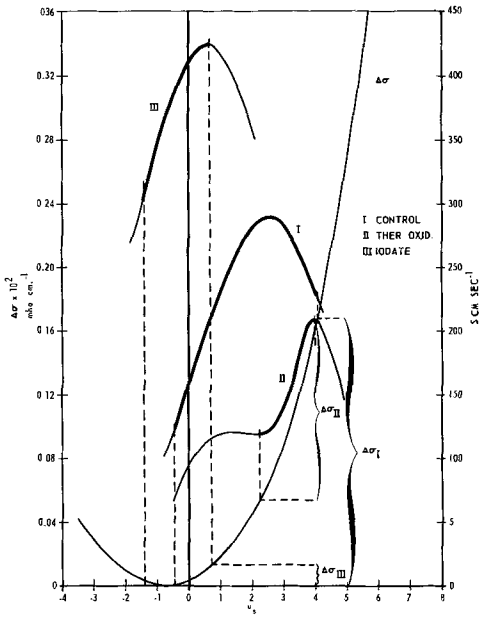

Fig. 5. Surface recombination velocity, s, and change in conductivity, $\Delta\sigma$, as functions of the surface potential, u_s, in units of kT/q for determining the range of s and $\Delta\sigma$ corresponding to a variation of the ambient atmosphere from dry to wet oxygen.

bulk potential and the surface potential regardless of how the value of surface potential is achieved. However, the surface recombination velocity as a function of surface potential does vary considerably with surface treatment (see Fig. 3). Thus, in order to establish both the value of the conductivity and the surface recombination velocity (s.r.v.) simultaneously for a given value of surface potential, it is necessary to superimpose the s.r.v. *vs.* u_s curve for each surface treatment. This has been done in Fig. 5 for three representative surface treatments (control, iodate, thermal oxidation) on an H_2O_2:HF:H_2O etched surface. The s.r.v. *vs.* u_s curves can be constructed from the data of Table I by putting the appropriate values of the listed surface recombination level parameters into the theoretical expression for the surface recombination velocity (2).

It is then possible, by employing the Δu_s column of Table I, to evaluate the ranges of conductivity and s.r.v. to be expected with a variation of ambient atmosphere from dry to wet oxygen as defined previously. Consider the s.r.v. curve I of Fig. 5, along with the $\Delta\sigma$ *vs.* u_s curve, appropriate for an H_2O_2:HF:H_2O etched surface on 35 ohm-cm n-type germanium. The Δu_s for this surface condition is 5.5 units of kT/q while the midpoint of this range is 1.8. Bracketing this range on the horizontal scale, it is found that the corresponding changes in the s.r.v. (portion of the curve that is heavy line) and the conductivity are from 125 through the maximum of 290 and back to 230 and $\Delta\sigma = 0.16$, respectively. Similar consideration of the iodate and thermal oxidation treatments yields corresponding ranges of s and $\Delta\sigma$, as indicated in Fig. 5. The significance of characterizing a surface treatment by including the Δu_s data is now apparent. It will be noted that, although the Δu_s of the thermal oxidation treatment is slightly smaller than the same quantity for the iodate treatment, the changes in both $\Delta\sigma$ and s.r.v., percentagewise, are smaller for the latter treatment. The reason for this result is that the midpoint of the Δu_s range is near the conductivity minimum (—0.4) for the iodate case, where the conductivity is varying relatively slowly as a function of u_s. The thermal oxidation case, however, exhibits a midpoint of Δu_s (3.1) which is on the portion of the conductivity *vs* u_s curve which is rapidly varying. The importance of stating not only the range of u_s but also the midpoint (or some such arbitrary reference) is thus evident.

It is conceivable, then, that extensive tabulation of data after the manner of Table I for the wide range of resistivities encountered in device technology could afford a device engineer a first-order approach to the engineering of surfaces into devices. Employing such tabulations, it should be possible to delineate the range of values of important parameters to be expected from a given surface treatment after a fashion similar to that discussed in connection with Fig. 5.[8]

There remains at least one major obstacle to device surface engineering. This has to do with the question of how the existence of a junction at the surface affects the important parameters associated with a given surface treatment. It is well known that many etches and/or surface treatments can be employed to delineate junctions in semiconductors. This, by definition, is evidence that a specific operation on a surface will yield characteristics in the vicinity of the junction that could be significantly different from the characteristics on the surface of homogeneous material. Thus, work such as that described above must be complemented with studies on materials containing junctions that come out to the surface.

Summary

An attempt has been made to define a method of characterizing a semiconductor surface condition which would be conducive to an engineering approach to the surface problem. This method consists of listing not only the surface parameters associated with surface traps, but including also the range and location, in values of surface potential, that are introduced by a specific surface condition. The methods discussed in this paper are not intended to be all-inclusive or final, but rather suggest an approach which could possibly allow for the eventual engineering of surfaces into semiconductor devices.

Features of the experimental data of particular interest are (*a*) the relatively constant capture cross sections for holes for the variety of surface conditions investigated, (*b*) the wide variation of capture cross sections for electrons, (*c*) the appearance of a second recombination level which is apparently associated with heavy oxidation, and (*d*) the reduction in sensitivity of the surface conductivity to variations of ambient atmosphere due to a relatively large concentration of charge in fast surface states which effectively "shield" the semiconductor from the influences of the atmosphere.

[8] It must be recalled that the approach considered in connection with Fig. 5 tacitly assumes that, in the range Δu_s, the surface parameters of Table I do not change. The fact that they do change is demonstrated in Fig. 4. The assumption has been made that the s.r.v. curves are not significantly different for a dry and a wet oxygen atmosphere. The ranges of s and $\Delta\sigma$ obtained are thus accurate only within the limits implied by such an assumption.

Acknowledgments

It is a pleasure to acknowledge the assistance of Mr. R. F. Voigts in the design and construction of the experimental apparatus and the procurement of experimental data.

Manuscript received Dec. 18, 1961; revised manuscript received March 9, 1962. This paper was presented in part before the Detroit Meeting, Oct. 1-5, 1961.

Any discussion of this paper will appear in a Discussion Section to be published in the June 1963 JOURNAL.

REFERENCES

1. A. Many, E. Harnik, and Y. Margoninski, "Semiconductor Surface Physics," R. H. Kingston, Editor, p. 85, University of Pennsylvania Press, Philadelphia (1957).
2. S. Wang, and G. Wallis, *Phys. Rev.*, **105**, 1459 (1957); *This Journal*, **106**, 231 (1959).
3. H. M. Bath and M. Cutler, *J. Phys. Chem. Solids*, **5**, 171 (1958).
4. A. V. Rzhanov, *Fizika Tverdogo Tela*, **2**, 2431 (1960). English Translation: *Soviet Physics-Solid-State*, **2**, 2166 (1960).
5. G. G. E. Low, *Proc. Phys. Soc. London*, **B68**, 10 (1955).
6. E. Harnik and Y. Margoninski, *J. Phys. Chem. Solids*, **8**, 96 (1959).
7. Y. Margoninski, *J. Chem. Phys.*, **32**, 1791 (1960).
8. Y. Margoninski and H. E. Farnsworth, *Phys. Rev.*, **123**, 135 (1961).
9. W. L. Brown, W. H. Brattain, C. G. B. Garrett, and H. C. Montgomery, "Semiconductor Surface Physics," R. H. Kingston, Editor, p. 111, University of Pennsylvania Press, Philadelphia (1957).
10. R. H. Kingston and S. F. Neustadter, *J. Appl. Phys.*, **26**, 718 (1955).

APPENDIX

Descriptions of Surface Treatments

H_2O_2 *bake.*—The sample is placed in contact with glass, flooded with a small amount of stabilized 30% H_2O_2, and baked in room atmosphere for 1 hr at 100°C.

Thermal oxidation.—The sample is placed in a flow of approximately 1 c.f.h. of dry oxygen for 72 hr at 500° ±10°C. (The sample is stored in methanol between the preparatory etch and the thermal oxidation surface treatment.)

Iodate.—The sample is treated for 1 hr at room temperature in an agitated solution containing HF, H_2SO_4, M/5 KIO_3, and H_2O in the proportions 4:1:1:2. The sample is rinsed in the sequence: H_2O, acetone, and H_2O, and is then stabilized by baking for several hours in room atmosphere at approximately 150°C.

Bromine.—The sample is placed in 4.0M KOH without agitation, warmed to 55°-60°C, held there for 20 min, and cooled to 35°C. The sample is then flooded free of KOH with a solution containing Br_2 and 4.00M KBr in the proportions 3:250, and is allowed to stand in this solution without agitation for 15 min. The KOH-bromine solution sequence outlined above is repeated as often as necessary, always flooding away one solution with the other, until visual inspection shows a uniform attack at the end of the 15-min exposure to the bromine solution. When this condition is satisfied, the sample is left in the bromine solution for 6 hr, without agitation, and is then rinsed in H_2O.

Silica.—The sample is placed in agitated HF for 1½ hr, and then silicic acid powder is added to the agitated solution until a 20% excess has been reached in 5 min according to the reaction

$$SiO_2 + 4HF \rightarrow SiF_4 + 2H_2O$$

The agitated solution is allowed to cool for ½ hr and then is flooded away with H_2O.

H_2SO_4-*chromate.*—The sample is warmed in agitated, M/20 $Na_2Cr_2O_7 \cdot 2H_2O$ solution in H_2SO_4 to 140°-145°C and is held at this temperature for 1 hr. The solution is then cooled to 35°C, and the sample is removed and rinsed in H_2O.

Descriptions of Chemicals Used

Bromine, analytical reagent.
Oxygen, "Airco" U.S.P.
Hydrofluoric acid, 49% electronic grade.
Silicic acid powder, 78% SiO_2, reagent grade.
Sulfuric acid, 97%, electronic grade.
Potassium hydroxide, reagent grade.
Potassium bromide, reagent grade.
Potassium iodate, analytical reagent.
Sodium dichromate, dihydrate, reagent grade.
Hydrogen peroxide, 30%, stabilized, electronic grade.
Acetone, electronic grade.
Methanol, absolute, electronic grade.
Water, distilled and deionized, used for all rinsing and preparation of solutions.

Selection of Germanium Transistor Parameters by Control of Moisture at Low Levels within the Device Encapsulation

Robert J. Gnaedinger, Jr., Steward S. Flaschen, Marie A. Hall, and Edward J. Richez

Semiconductor Products Division, Motorola Inc., Phoenix, Arizona

ABSTRACT

Experiments have been carried out which indicate that moisture in air at levels below 1% relative humidity (200 ppm H_2O) has a strong influence on the surface recombination velocity of germanium and on the parameters of transistor devices derived from it. By controlling the moisture partial pressure at any of various given levels within hermetically sealed transistors, it has been found possible to preselect different ranges of several, stabilized, device parameters, such as h_{fe}, I_{CO}, and I_{EO} without changing the device fabrication procedure. A method for controlling the moisture partial pressure using pairs of inorganic compounds is presented together with data obtained from its application to large-scale manufacture. In addition to showing the practical value of these controlled moisture materials, these results emphasize the need for a more precise knowledge of the moisture level present in the "dry" gaseous ambients commonly used in studies of semiconductor surface properties.

It is well-known that the chemical composition of the gas phase adjacent to a semiconductor surface plays an important role in determining the electrical properties of that surface (1-3). Water vapor is perhaps the most striking example of this fact. High relative humidities produce severe and erratic current leakage paths across the surface of silicon and germanium crystals; changes in the humidity at moderate levels produce pronounced changes in the surface conductivity and surface recombination velocity. In the manufacture of semiconductor devices it was this high sensitivity to changes in the moisture level which caused the introduction of hermetic sealing of devices. Yet, although this hermetic sealing generally removed the erratic behaviors associated with gross moisture, there remained day-to-day, seasonal, and aging variations in the parameters of production devices. In order to reduce these variations, it was found necessary to insert moisture adsorbing materials into the hermetically sealed device encapsulations. This technique yielded a more reproducible product, but it frequently accomplished this at the expense of large shifts in the levels of some of the device parameters.

It is the purpose of this paper to present the results of new experimental studies of the effects of moisture on the parameters of germanium transistors. These results indicate that the presence of moisture vapor at very low levels continues to exert a strong influence on semiconductor surface properties, a conclusion suggested by previous work (4-7), but not experimentally verified. In addition, these results show that the rather disruptive role commonly associated with moisture in the manufacture of semiconductor devices can be converted into a constructive one by selection and control of the moisture level. Lastly, these results emphasize the necessity of being able to make a quantitative, rather than qualitative, statement of the dryness level in the adjacent gaseous ambient in experimental studies of semiconductor surfaces and semiconductor devices.

Experimental Method

The experimental method consisted of establishing, in principle, a constant moisture partial pressure within an hermetically sealed semiconductor device. This controlled moisture pressure was achieved through the utilization of the thermodynamic equilibrium that exists between two chemical phases in different, but adjacent, degrees of hydration. This is illustrated by Eq. [1] where the

$$2CaSO_4 \cdot \tfrac{1}{2}H_2O(\text{Solid}) \rightleftarrows 2CaSO_4(\text{Solid}) + H_2O(\text{Vapor Phase}) \quad [1]$$

half-hydrate of calcium sulfate is shown in equilibrium with anhydrous calcium sulfate and water vapor. The equilibrium constant for this reaction is the water partial pressure (Eq. [2]). As long as specific, crystalline

$$K_{eq} = p_{H_2O} \quad [2]$$

phases of both solids are present in a closed system, and as long as sufficient time for equilibration has been allowed at a given temperature, the moisture partial pressure in the adjacent gas phase will remain constant, independent of the total amount of moisture enclosed in the system.

The equilibrium pressure of water will be temperature dependent, varying in accordance with an Arrhenius expression, as long as no phase changes occur in the two solids. In Eq. [3] $\Delta H°$ is the standard heat of reaction. ($\Delta H°$ can be

$$K_{eq} = A \exp -\Delta H°/RT \quad [3]$$

expected to have some temperature dependence. In addition, the water partial pressure will show a small dependence on total pressure if an inert gas is present in the system; this dependence is deter-

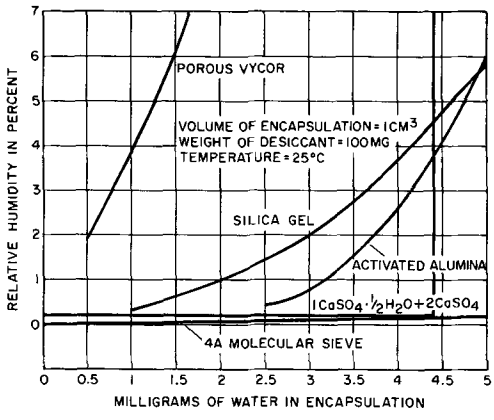

Fig. 1. Comparison of reactive and adsorptive moisture getters. Relative humidity *vs.* total encapsulated moisture.

mined by the volume change occurring in the reaction.)[1]

This type of behavior is distinctly different from the commonly used, adsorptive desiccants, *e.g.*, silica gel, activated alumina, etc., where the moisture partial pressure is strongly dependent on the total amount of moisture that is enclosed in the system. In Fig. 1[2] there is shown a comparison of the reactive type of moisture getter *vs.* the adsorptive types. This figure has been constructed for the following hypothetical situation. Consider that in a 1 cm^3 volume is 100 mg of getter. One then asks: What is the relative humidity in that volume at equilibrium at 25°C for various amounts of encapsulated water within that volume? The answer for the adsorptive getters is that there is a wide variation in the relative humidity with the amount of encapsulated moisture. In the example shown here, the molecular sieve shows variation, but at a very low level of relative humidity in comparison with the porous vycor, silica gel, and activated alumina. These curves show behaviors characteristic of true surface adsorption.[3] In contrast, the mixture of anhydrous and hemihydrated calcium sulfate shows a constant relative humidity up to the point where the anhydrous phase completely disappears. After this has occurred, the addition of further moisture causes an abrupt increase in the relative humidity.

If other chemical species are used in place of the calcium sulfate, different but similarly controlled moisture partial pressures can be achieved. In Table I are shown several systems of inorganic compounds together with calculated values of their equilibrium moisture partial pressures. All of the values shown have been computed from thermodynamic data in the literature (11), using the relation[4] given by Eq. [4]. Some have been qualitatively

$$\Delta F^\circ = -RT \ln K_{eq} \qquad [4]$$

[1] For further discussion of the subject of heterogenous equilibrium, see, for example, the treatise on the phase rule by Ricci (8).

[2] The data for this figure were obtained from Corning Glass (9) and Linde Company (10) and from thermodynamic data tabulated by the NBS (11). It was necessary to extrapolate the data to show the low relative humidity behavior of the adsorptive getters. The curves shown should be considered purely qualitative.

[3] See, for example, the treatise on surface films by Harkins (12).

[4] No value is listed for ΔF° of formation of $Ba(OH)_2$. Since it was observed that the ΔS° for the reaction $Ca(OH)_2 \rightleftarrows CaO + H_2O$, was identical to that for the $Mg(OH)_2$ reaction, this same value was assumed for $Ba(OH)_2$ in order to calculate the ΔF°. Note also that fugacity = pressure at these low pressures (13).

Table I. Equilibrium moisture partial pressures above several inorganic compound systems as calculated from thermodynamic data

System	Partial pressure at 25°C in mm of Hg
$BaO:Ba(OH)_2$	2×10^{-15} (approx)
$CaO:Ca(OH)_2$	5×10^{-9}
$MgO:Mg(OH)_2$	5×10^{-4}
$B_2O_3:HBO_2$	3×10^{-2}*
$CaSO_4:CaSO_4 \cdot \frac{1}{2}H_2O$	3×10^{-2}**
$HBO_2:H_3BO_3$	1×10^{-1}
$CaSO_4 \cdot \frac{1}{2}H_2O:CaSO_4 \cdot 2H_2O$	5†
Liquid water	23.76

* Calculated for a glassy B_2O_3 phase.
** Calculated for the β-hemihydrate and the β-anhydrous phases.
† Calculated for the β-hemihydrate phase.

checked by the Knudsen Method of measuring the rate of effusion through a pin hole.[5]

The materials listed above have been found experimentally to satisfy the criteria of chemical and electrical inertness with respect to germanium device surfaces, as shall be seen subsequently, apparently exerting influence on the devices primarily through their control of the moisture partial pressure.

Experimental Results

The following results were obtained by encapsulating, within hermetically sealed transistors, the specified "controlled ambient" materials in amounts sufficient to maintain the required, two solid phase system. The germanium pnp power transistors were processed normally through electrolytic etch in basic solution, rinse, and dry. The specified materials were then added and the encapsulation sealed immediately in room air. The materials were added with no attempt to prevent their contacting the germanium surface.

The high-frequency, germanium pnp transistors were processed normally through electrolytic etch, rinse, dry, and vacuum bake. The controlled ambient materials were then added and the encapsulation sealed immediately. In this case physical contact between the materials and the germanium was prevented for mechanical reasons.

Figure 2 shows the effect of different moisture controlling materials on the power gain of germanium power transistors. Each chart is a histogram showing the distribution of devices in the various power gain ranges for the given controlled ambient mixture. (The power gain range to the right of 41 db contains devices with P.G. $\geqq$ 41 db.) The ordered dependence of power gain on the calculated moisture partial pressure (Table I) at these very low levels is strikingly apparent. Increasing the moisture pressure increases the power gain.

Parameter measurements were made following a 96 hr thermal treatment at 125°C and a subsequent recovery at room temperature for a minimum time of 12 hr.

[5] Our measured values on reagent grade hemihydrate of calcium sulfate were approximately 0.06 mm of Hg at 25°C. Several phase modifications of anhydrous and hemihydrated calcium sulfate are reported in the literature. The value shown in Table I was calculated for the β-phase of each.

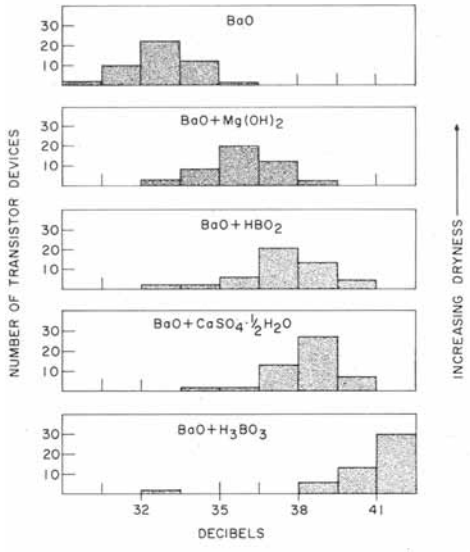

Fig. 2. Effect of moisture level on power gain of germanium pnp power transistors.

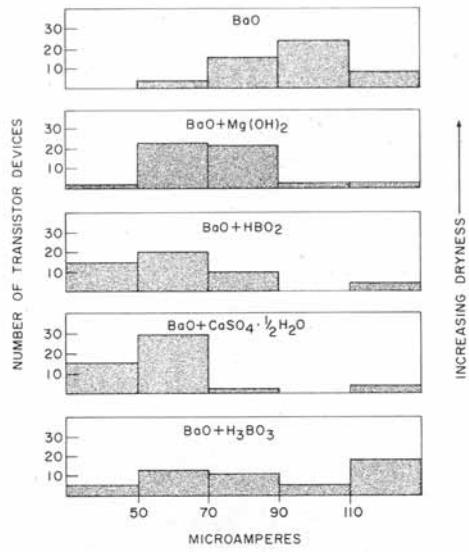

Fig. 3. Effect of moisture level on low voltage saturation current of germanium pnp power transistors.

The designed function of the BaO in these mixtures is to dehydrate a portion of the hydrated phase in order to establish the two phase equilibrium. The BaO becomes completely converted to $Ba(OH)_2$ by this process and does not apparently affect the equilibrium in any other manner. That this is, in fact, the real function of the BaO is borne out by the behavior of the data; in addition, it was verified experimentally by varying the ratio of BaO to $CaSO_4 \cdot \frac{1}{2}H_2O$ and by using mixtures of $CaSO_4 \cdot \frac{1}{2}H_2O$ and $CaSO_4$ without BaO, both of which produced results that were statistically indistinguishable from the $BaO + CaSO_4 \cdot \frac{1}{2}H_2O$ results shown in Fig. 2.

Each of the histograms in Fig. 2 was prepared from 50 devices which were randomly selected from one week's production run. Statistical analysis of the data used for Fig. 2 indicates that the difference between the mean of each mixture and that of the BaO lies in the interval shown in Table II, with 95% confidence. From this it can be seen that by reducing the moisture level from a calculated 50 ppm ($BaO + CaSO_4 \cdot \frac{1}{2}H_2O$) in air to an extremely dry condition (BaO), the power gain can be lowered by about 6 db. [It might be noted that "vacuum bake-out" plus molecular sieve getter gives power gains that are similar to the $BaO + Mg(OH)_2$ system.]

Table II. Comparison of mean power gains of pnp germanium power transistors for different controlled ambient materials

Mixture	No. of devices	Mean P.G. after thermal treatment	P.G.—P.G. (BaO) ± 95% confidence limits
BaO	240	32.9	—
$BaO + Mg(OH)_2$	46	35.8	2.9 ± 0.8
$BaO + HBO_2$	45	37.6	4.7 ± 0.8
$BaO + CaSO_4 \cdot \frac{1}{2}H_2O$	49	38.5	5.6 ± 0.7
$BaO + H_3BO_3$	48	42.6	9.7 ± 1.1

BaO represents 5 day, 48 devices per day. Remainder represent single days. Comparison is with 5 day BaO average, this being the control group. A histogram for one of these BaO groups is given in Fig. 2.

These represent good devices in the sense that both emitter and collector diodes showed reasonable reverse breakdown voltages and collector to emitter punch-through voltages were reasonably high.

The behavior of the common emitter current gain was measured and was as expected from the power gain measurements, *i.e.*, P.G. (db) $\propto \log h_{fe}$ for the same emitter current.

Figure 3 shows histograms of the low voltage saturation current for the same devices used in Fig. 2. (The cell to the right of 110 μa contains devices with $I_{CBO} \geqq 110$ μa.) The temperature of measurement was 26° ± 1°C. As can be seen, there is again an ordered dependence of I_{CBO} on the calculated moisture pressure. Increasing the moisture level decreases the I_{CBO} of these devices, except for the orthoboric acid group which shows a bimodal distribution. After further recovery at room temperature, this distribution becomes unimodal, like the other groups, with a strong peak in the cell with the lowest current. Since the power gain in this group recovers more rapidly from the 125°C heating than does the I_{CBO}, it appears that in this case those chemical processes, which affect the surface recombination velocity, stabilize within 12 hr; on the other hand, there appears to be an additional factor affecting the I_{CBO}, which factor requires a longer time for recovery than does the surface recombination velocity.

Figure 4 shows that the effect of ambient moisture control persists up to 100°C. Here each histogram includes 100 devices. The low voltage saturation currents of devices containing the metaboric acid mixtures are clearly well below those of the dryer devices which were given a "vacuum bake-out" and which contain molecular sieve.

Other device parameters were also followed in these experiments. The low voltage I_{EBO} showed a behavior that was very similar to that of I_{CBO}. The breakdown voltages of the collector junctions were approximately the same for all of the "controlled ambient" materials except for the boric acid groups which caused breakdown at lower voltages.[6] The emitter breakdown voltages behaved in a manner similar to those for the collectors.

[6] The orthoboric acid appeared to lower the breakdown voltage slightly. The metaboric acid lowered it by an average of about 20v. Thus, it appears that the boric acids may be acting in some capacity in addition to providing moisture.

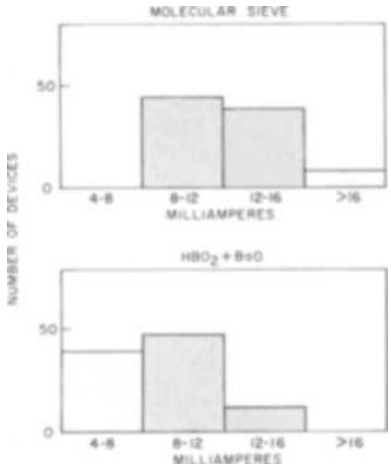

Fig. 4. Effect of controlled ambient material on low voltage saturation current of germanium pnp power transistors at 100°C.

Cold tests showed no diode looping associated with condensed water, a result consistent with the low relative humidities within these devices. Strenuous shake tests produced no changes in most parameters and only slight changes (within specifications) in others.

The effects of 1000 hr of 125°C shelf aging on the power gain and the low voltage I_{CBO} are presented in Tables III and IV.[7] These data indicate that accelerated aging at 125°C of these devices containing controlled ambient materials produces changes that are comparable to current production practice.

[7] The device groups in Tables III and IV are not the same as those in Table I. The small differences in the means for the same controlled ambient material can be ascribed to differences in group sizes and to variations in production runs.

Table III. Thermal aging of pnp germanium power transistors at 125°C for 1000 hr, effect on power gain

Mixture	No. of devices	Mean P.G. after thermal treatment	Mean P.G. after 1000 hr at 125°C	Change in mean with 95% confidence limits
BaO	19	32.4	33.0	0.6 ± 0.2
Molecular sieve	239	35.2	34.9	−0.3 ± 0.1
$BaO:Mg(OH)_2$	20	36.1	35.1	−1.0 ± 0.3
$BaO:HBO_2$	237	38.8	37.2	−1.6 ± 0.1
*$BaO:CaSO_4 \cdot \frac{1}{2}H_2O$	113	39.5	38.2	−1.3 ± 0.2

* This group received 1300 hr at 125°C.

Table IV. Thermal aging of pnp germanium power transistors at 125°C for 1000 hr, effect on low voltage I_{CBO}

Mixture	No. of devices	Median** after thermal treatment, μa	Median** after 1000 hr at 125°C, μa	Per cent change in median with 95% confidence limits
BaO	19	75.9	80.8	6.4 (2.8–10.0)
Molecular sieve	239	68.7	81.0	18.1 (16.5–19.8)
$BaO:Mg(OH)_2$	20	58.1	68.0	17.1 (4.5–31.1)
$BaO:HBO_2$	237	50.3	71.6	40.5 (37.6–43.5)
*$BaO:CaSO_4 \cdot \frac{1}{2}H_2O$	113	62.1	57.9	−4.0 (−7.4–−0.5)

* This group received 1300 hr at 125°C.
** Median computed from the formula:

Median = $10^{\overline{\log I}}$, where $\overline{\log I}$ is the mean value of log I_{CBO}.

Comparisons were made of the rate of stabilization of h_{fe}, after canning, at room temperature *vs.* that at 125°C, all measurements being made at room temperature. In the case of BaO, greater than 95% of the total drop in h_{fe} after 1000 hr at 125°C had occurred within the first day. On the other hand, the room temperature stabilization showed a continuously dropping h_{fe} out to 1000 hr, with a constantly decreasing rate. At 1000 hr the h_{fe} level was still considerably higher than in the devices that were heated at 125°C. It is not clear from these data whether or not the h_{fe} level during 25°C stabilization is asymptotically approaching the level rapidly attained at 125°C (although this is the best surmise). Likewise it is not clear that the stabilization process at 25°C is kinetically controlled by the oxidation of the germanium surface, or by the dehydration of the surface oxide, or by the desorption of moisture from the device interior, or by the uptake of water by the BaO.

The effect of power aging ($T_j = 90$°C and $V_{CE} = 40$v) is shown in Table V. Tabulated there are the power gains of eight devices of each group: BaO, molecular sieve, and $BaO + CaSO_4 \cdot \frac{1}{2}H_2O$. Measurements were made after 125°C thermal treatment at 500 hr and at 1000 hr. There appears to be little difference in power aging behavior with these different controlled ambient materials and the molecular sieve. Statistical analysis corroborates this observation for the above groups and also for $BaO + HBO_2$ and $BaO + Mg(OH)_2$, on both power gain and low voltage I_{CBO} parameters.

Table V. Power aging of pnp germanium power transistors with $T_j = 90$°C and $V_{CE} = 40$v, effect on power gain

Initial	500 hr	1000 hr
Eight devices containing BaO		
32.3	32.0	32.1
33.2	33.0	32.7
32.5	32.7	32.7
33.0	33.2	33.2
34.9	34.9	35.2
34.0	34.3	34.5
34.6	34.7	35.0
34.5	34.7	35.0
Eight devices containing molecular sieve		
41.7	38.0	38.4
36.4	36.5	36.3
36.8	35.8	35.5
37.8	37.6	37.8
40.2	40.4	40.9
39.4	40.3	40.7
41.4	41.5	41.8
40.4	40.6	40.8
Eight devices containing $BaO + CaSO_4 \cdot \frac{1}{2}H_2O$		
39.4	39.4	39.5
38.2	38.3	38.2
34.0	34.0	34.2
35.2	35.3	35.3
39.0	39.1	39.4
40.1	40.7	41.0
39.2	39.1	39.6
38.2	38.6	36.4

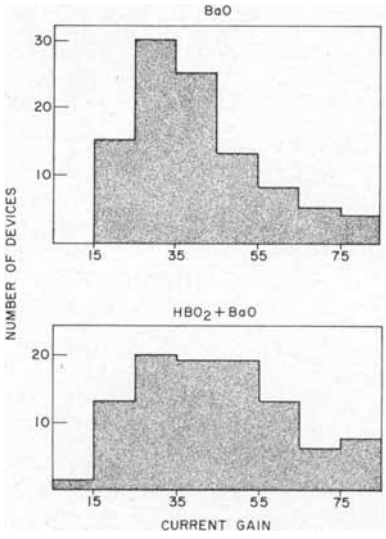

Fig. 5. Effect of moisture level on current gain of germanium pnp high-frequency transistors.

Controlled ambient materials were applied to another device, a high-frequency pnp germanium transistor. Figure 5 shows the effect of moisture control on the current gain of this diffused junction device. These histograms were each prepared from 100 devices, representing 20 random samples from the production on each of five days. The enhancement of gain achieved by controlling the moisture at a finite level over that obtained in the very dry condition is most evident in the high gain portion of the distributions. Parameters were measured on these devices after a thermal treatment of 144 hr at 125°C. The histogram was prepared from these data. The median β's in these two groups were: BaO, 35.9; BaO + HBO_2, 39.6. The median value of β has been calculated on the basis of a log normal distribution.

Figure 6 shows the effect of 125°C shelf aging on β. The initial aging pattern is distinctly better with metaboric acid than with the very dry system containing BaO. At longer times the two curves appear to age downward at about the same rate with the controlled moisture system maintaining its enhanced current gain relative to the very dry system.

Discussion

The data presented above indicate that certain parameters of germanium transistors depend very sensitively and reproducibly on moisture partial pressures at levels from about 80 ppm to below 1 ppm in air. The parameters thus affected are those which are strongly influenced by surface recombination velocity (or surface generation rate). The simplest interpretation to be made of these observations is that even at these very low partial pressures, sufficient water is adsorbed onto the germanium (or germanium oxide) surface to affect the surface properties appreciably. According to the work of Law (14), monolayer adsorption of water onto a germanium surface does not become complete until a relative humidity of about 10% is reached (this relative humidity in air at 1 atm pressure at 25°C corresponds to about 2000 ppm of H_2O). Consequently, the present results suggest that water plays perhaps its dominant role in affecting surface recombination velocity in the region below one monolayer, a conclusion that is consistent with the work of Law and Meigs (4).

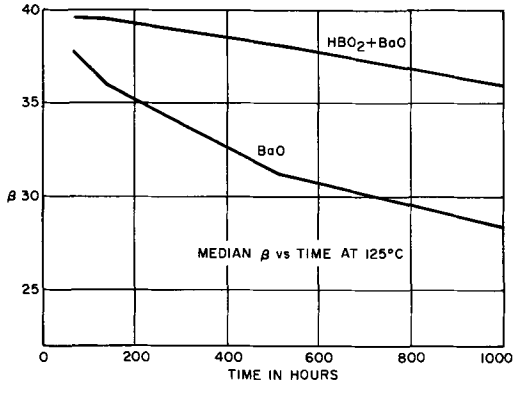

Fig. 6. Effect of ambient moisture control on elevated temperature shelf aging of β. High-frequency germanium transistors.

The detailed mechanism of how adsorbed water achieves this effect is not clear. However, since water is known to induce n-type channels (15) on p-type germanium, it has been postulated that adsorbed water molecules behave like slow, hole-trapping states. This same postulate has been used to explain observations of the effect of Brattain-Bardeen ambient cycling on the surface recombination velocity of germanium (16).[8] On the other hand, more recent work by Margoninski and Farnsworth (18), and others, has suggested that adsorbed water modifies the fast state energies and densities as well as slow state densities. (It should be borne in mind, however, that these latter studies used very moist ambients, resulting in multiple layers of adsorbed water in a region where the adsorption isotherm is rising very rapidly with increasing relative humidity. Thus, not only are films of water present, with attendant effects associated with ion drift and other electrolytic phenomena, but also the film thickness is in questionable control; severe complications in reproducibility and interpretation of measurements are present. It might be hoped that ambient cycling between a truly dry ambient and one that produces less than monolayer adsorption would give results that can be reproduced.) No structure has yet been proposed for either the slow or fast states, although it has been suggested that they are associated somehow with the formation of hydroxy groups in the surface oxide (1, 7) during a slow hydration reaction. [At higher moisture partial pressures, Hutson (19) ascribes the effect of water on surface potential to a dielectric polarization of the multilayer water film about unspecified surface donor ions; the first monolayer was specifically excluded from his analysis.]

However, the slow hole-trapping state model can be used to give a qualitative explanation of the results presented here. Figure 7 consists of a conventional energy band diagram for an n-type semiconductor as it terminates at a surface. Adsorbed water molecules are shown symbolically as H_2O $\oplus$ after

[8] Brattain and Bardeen (1), Stevenson and Keyes (16), and Many, Harnik, and Margoninski (17) consider the theory of surface recombination velocity.

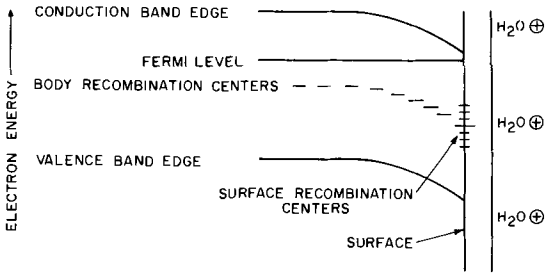

Fig. 7. Simple model of the effect on the surface recombination velocity of water adsorbed on an n-type semiconductor.

electronic equilibration with the crystal, in accordance with the slow state model. If it is assumed that the water molecules are neutral when first adsorbed, they must then give up electrons to the semiconductor during the equilibration process. These electrons may be trapped predominantly in fast surface states, if the latter are sufficiently numerous, resulting in a negligible effect on the surface conductivity and the surface potential. This was the result found in the original field-effect transistor experiments (20). However, if the fast surface states are relatively few in number, the electrostatic field associated with the ionized slow states will penetrate into the semiconductor, resulting in a strong effect on the surface conductivity and the surface potential, as shown in the Fig. 7.

This simplified model is sufficient to explain the present data as can be seen as follows: Although the electron population in the surface traps is increased by moisture, the electric field in the surface space charge region opposes the diffusion of holes toward the surface. This latter accounts for the reduction of injected carrier loss and the consequent increase in alpha with higher moisture levels. At the same time the higher electron population in the fast surface traps reduces the likelihood of thermal generation of holes at the surface since vacant electron traps are necessary. This accounts for the reduction of the surface generated component of the low voltage, reverse diode current with increasing moisture.

In order to obtain estimates of the surface recombination velocity at the different moisture levels, $h_{fe} - I_E$ plots were fitted to the Webster equation (21), which relates h_{fe} to doping, geometry, and surface recombination velocity. Figure 8 shows typical $h_{fe} - I_E$ plots for power transistors from several groups of controlled ambient encapsulants. The dominating influence of surface recombination velocity at low I_E is clear. The power gain distributions previously presented corresponded to $I_E = 0.5$ amp, where the effects of surface recombination velocity are being partially masked by strongly reduced emitter injection efficiencies due to conductivity modulation in the base.

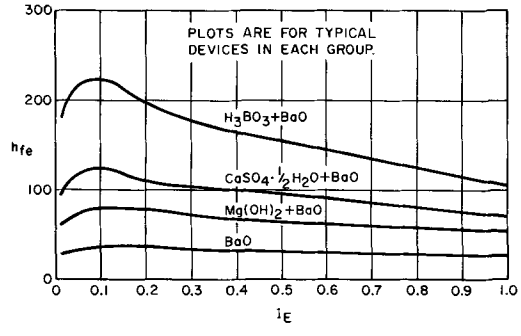

Fig. 8. h_{fe} vs. I_E for germanium pnp power transistors encapsulated with different controlled ambient mixtures.

Table VI. Surface recombination velocities for different controlled ambient mixtures as approximated using Webster's formula for germanium pnp alloy transistors

Moisture control mixture	Surface recombination velocity (approx), cm/sec
BaO	4000
$Mg(OH)_2$ + BaO	2000
HBO_2 + BaO	1000
$CaSO_4 \cdot \frac{1}{2}H_2O$ + BaO	1000
H_3BO_3 + BaO	500

Only very approximate fits to Webster's equation were made. The results are shown in Table VI. Qualitatively, they suggest that in going down from a relative humidity of approximately 0.4% (H_3BO_3 system) to very low moisture levels, one can change the surface recombination velocity by a factor of about ten.

It should be noted that the effect of adsorbed moisture (as slow states) on device parameters will depend on the distribution of fast states and other slow states already present at the surface; the effects will also depend on the conductivity type of the body region. This is clearly demonstrated in the experiments of Buck and McKim (22) on silicon.

Experiments have also been carried out with silicon devices containing controlled ambient materials. The parameters of some of these devices have been affected in a similar pronounced manner; the behavior pattern seems to be consistent with that found with germanium devices, as described above.

Conclusion

1. These experiments have indicated that moisture vapor in air within the sealed, device encapsulations has a pronounced effect on the surface recombination velocity of germanium transistors at extremely low relative humidities, relative humidities as low as 10^{-3}% (0.2 ppm).

2. These experiments indicate the necessity of carrying out studies of semiconductor surface properties with a quantitative knowledge of the moisture level present in the gaseous ambient adjacent to the surface.

3. These experiments suggest that the use of ambient control materials for the stabilization of moisture partial pressures can be an asset in semiconductor device production. These materials allow the selection and control of certain device parameter levels over wide ranges without the requirement of modifying the body construction of the device.

Acknowledgment

This study was initiated with the active and willing assistance of David A. Kallander, Camille M. Lutfy, and Dale R. Lowe. It has proceeded only because of the complete cooperation we have received from individuals in the production and quality control

departments of Motorola's Semiconductor Products Division, in particular, Valmore E. Turcotte, John R. Welty, and Leo E. Dwork. It prospered under the protective wing of our statistical guardian angel, Dr. Irwin Miller of Arizona State University. And lastly, it is our pleasure to acknowledge manuscript suggestions by Dr. Trevor E. Law, Dr. Raymond M. Warner, Jr., and the reviewers of this paper.

Manuscript received Nov. 1, 1961; revised manuscript received Feb. 23, 1962. This paper was prepared for delivery before the Indianapolis Meeting, April 30-May 3, 1961.

Any discussion of this paper will appear in a Discussion Section to be published in the June 1963 JOURNAL.

REFERENCES

1. W. H. Brattain and John Bardeen, *Bell System Tech. J.*, **32**, 1 (1953).
2. R. H. Kingston, *J. Appl. Phys.*, **27**, 101 (1956).
3. N. B. Hannay, Editor, "Semiconductors," Chap. 16, "Semiconductor Surfaces," by J. T. Law, Reinhold Publishing Corp., New York (1959).
4. J. T. Law and P. S. Meigs, *J. Appl. Phys.*, **26**, 1265 (1955).
5. A. J. Wahl and J. J. Kleimack, *Proc. Inst. Radio Engrs.*, **44**, 494 (1956).
6. J. J. A. Ploos van Amstel, *Philips Tech. Rev.*, **22**, 181 (1961).
7. J. T. Wallmark and R. R. Johnson, *RCA Rev.*, **18**, 512 (1957).
8. J. E. Ricci, "The Phase Rule," p. 140, D. Van Nostrand Co., Inc., New York (1951).
9. "Vycor Brand Porous Glass, Code 7930—A Unique Drying Agent," T. H. Elmer and M. E. Nordberg, Research and Development Laboratory, Corning Glass Works.
10. "General Information on Linde Molecular Sieves," Linde Company.
11. "Selected Values of Chemical Thermodynamic Properties," Circular of the National Bureau of Standards 500, issued Feb. 1, 1952.
12. W. D. Harkins, "The Physical Chemistry of Surface Films," Chap. 3, Reinhold Publishing Corp., New York (1952).
13. G. N. Lewis and W. Randall, "Thermodynamics," Chap. 17 and 24. McGraw-Hill Book Co., Inc., New York (1923).
14. J. T. Law, *J. Phys. Chem.*, **59**, 67 (1955).
15. W. L. Brown, *Phys. Rev.*, **91**, 518 (1953).
16. D. T. Stevenson and R. J. Keyes, *Physica*, **20**, 1041 (1954).
17. R. H. Kingston, Editor, "Semiconductor Surface Physics," p. 85, "Surface Recombination Processes," A. Many, E. Harnik, and Y. Margoninski, University of Pennsylvania Press, Philadelphia (1957).
18. Y. Margoninski and H. E. Farnsworth, *Phys. Rev.*, **123**, 135 (1961).
19. A. R. Hutson, *ibid.*, **102**, 381 (1956).
20. W. Shockley, "Electrons and Holes in Semiconductors," Section 2.1b, D. Van Nostrand Co., Inc., Princeton (1950).
21. W. M. Webster, *Proc. Inst. Radio Engrs.*, **42**, 914 (1954).
22. T. M. Buck and F. S. McKim, *This Journal*, **105**, 709 (1958).

The Role of Selenium Vapor Pressure in the Formation of Silver Doped Manganese Selenide

W. D. Johnston

Research Laboratories, Westinghouse Electric Corporation, Pittsburgh, Pennsylvania

ABSTRACT

The effect of selenium vapor pressure on MnSe containing small additions of Ag_2Se has been studied by both weighing and electrical measurements. Three distinct regions have been noted. At low selenium pressures selenium is taken up by the mixture to form the mixed valence compound $Ag_xMn_{(1-x)}Se\oplus_x$. The value of $\oplus$, the hole concentrations, increases as a function of the selenium pressure until all Ag_2Se is used up and the sample becomes a single phase. At this equivalence point the pressure then increases rapidly with little change in composition. Finally, the pressure becomes sufficiently high that manganese vacancies are produced. These regions are described in terms of mass action expressions which link the vapor pressure with vacancies and electrical charge carrier concentrations.

The substitution of monovalent lithium for divalent manganese in MnSe has been shown to be possible up to 11 atomic %, *i.e.*, $Li_{0.11}Mn_{0.89}Se$ (1). Throughout this composition range the rock salt symmetry of MnSe is maintained. The products of such substitutions have been found to be electrical conductors with the conductivity increasing with lithium content. An electrically balanced formula for the composition $Li_xMn_{(1-x)}Se$ may be given as $Li^+_xMn^{+3}_xMn^{+2}_{(1-2x)}Se^=$ or alternatively $Li^+_x\oplus_xMn^{+2}_{(1-x)}Se^=$. The formulas are written for convenience in ionic form. In the latter formula $\oplus$ refers to holes and emphasizes that the holes are not localized on any particular manganese at normal temperatures (2).

A survey was made to determine what other doping additives could be used in order to induce p-type semiconductivity in MnSe. To this end Na, Cu, Ag, Au, Tl, and Cu were substituted for Mn. Selenium was replaced by As, P, and Si. The only successful doping agents proved to be Na and Ag as indicated by room temperature electrical measurements. The silver seemed to be soluble to only about 2 atomic % on the basis of a discontinuity in the thermoelectric power *vs.* resistivity curve as shown in Fig. 1. In this preliminary survey the reactants were fired iso-

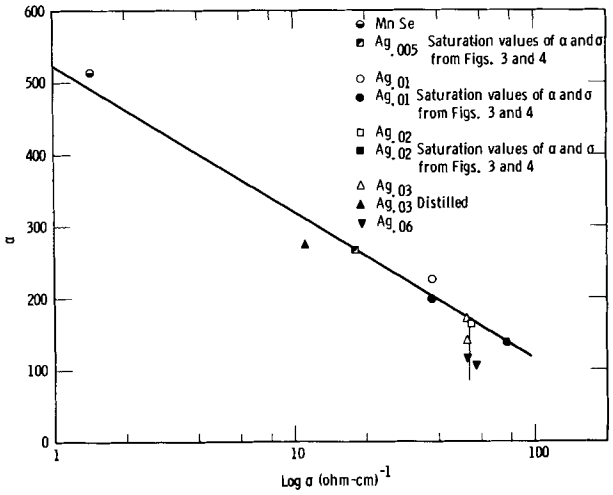

Fig. 1. α vs. log σ for $Ag_xMn_{(1-x)}Se$

thermally at 800°C in small sealed Vycor tubes. Additional qualitative experiments with silver substituted MnSe showed that the doping level decreased as selenium was removed by volatilization at elevated temperatures. The study described in this paper was undertaken in order to understand this relationship more fully. In brief the experiment performed was designed to give the stoichiometry or charge carrier concentration at various pressures of selenium vapor.

Experimental

The stoichiometry of the MnSe used in this work was critical to the success of the experiments. MnSe was prepared from −60 mesh vacuum distilled manganese and −60 mesh 99.99% selenium supplied by the American Smelting and Refining Company. The reactants, including a 10% excess of selenium, were either placed in a graphite crucible and sealed in Vycor or alternatively they were sealed in a Vycor tube which had been carbon coated by the pyrolysis of acetone. The material was heated up slowly to avoid any sudden evolution of heat to a final temperature of 700° and held for 24 hr. The product was crushed to 160 mesh and reheated for another 24 hr at which point the excess selenium was distilled off at 800°C. The recrushing was necessary to react all the manganese, and the 800° distillation quantitatively removed the excess selenium.

Products of the type $x/2\ Ag_2Se + (1-x)$ MnSe were prepared from a mixture of a −100 mesh powder composed of weighed amounts of the stock MnSe and silver and selenium powders. The powders were pressed at 15,000 lb in a 3/8 in. diameter carbide die. The pellet was sealed in a graphite crucible and Vycor tube which had been previously outgassed. The mixture was heated isothermally at 800°C for 20 hr, then one end of the tube was placed at room temperature and volatile material, if any (none was ever observed), was allowed to distill to the room temperature end. The pellets obtained in this manner were clearly composed of two phases consisting of a small amount of shiny material distributed in the black pellet.

For the vapor pressure studies a 6g pellet of $x/2Ag_2Se + (1-x)$ MnSe as prepared above was weighed and placed in a graphite boat which was sealed in a 12 in. long 19 mm diameter Vycor tube. In one end of the tube was a ½ in. long chamber which contained selenium. The pellet was held at the other end. The tube was placed in a two zone furnace such that the pellet was maintained at 800°, and the temperature of the selenium reservoir was at some lower temperature which could be chosen at will. The selenium reservoir temperature was arranged to be the coldest temperature of the tube, and thus the selenium vapor pressure was controlled by this temperature. In this manner the reaction

$$\frac{x}{4}\ Se_2\ \text{vapor} + x/2Ag_2Se + (1-x)\ MnSe \rightleftarrows Ag_xMn_{(1-x)}Se$$

may be studied. By quenching the sample tube at the end of the experiment and weighing the pellet, the uptake of selenium may be determined. Since selenium requires two electrons to be donated from the lattice to form the selenide ion ($Se^=$), creating two holes, the weight uptake of selenium may be expressed in terms of the hole concentration of the MnSe phase. It should also be noted that for each selenium added from the vapor two silvers are also added to the MnSe lattice and thus are equal to the hole content. It was found that equilibrium was achieved in less than 16 hr at all selenium pressures since an additional 16 hr or more did not result in a substantial additional weight change (generally less than ½ mg). Data were taken at random temperatures of the selenium reservoir which results in both adding and removing selenium from the sample in a random manner.

The first run however was an exception to this and was always at 600° reservoir temperature since, as will be seen later, the selenium pressure generated at 600° generally is sufficient to drive the formation reaction to completion. This first experiment thus acts as a check on the stoichiometry of the starting material. Apparently manganese and silver are not lost in any measurable amount from the pellets, nor does handling result in any appreciable weight loss since, on removal of the selenium added during a series of experiments by distilling this selenium to a room temperature reservoir, the starting weight is reproduced to within ± 1 mg.

As mentioned previously, repeat measurements are reproducible in pellet weight to ~ ½ mg. The weight changes recorded in this work range from 2-3 mg obtained at the lowest selenium additions to 30 mg at the highest selenium additions. The effect of this error is clearly visible in the wide scatter of the data at the low pressure-low selenium addition region of Fig. 2.

One must inquire as to the uptake of selenium vapor by MnSe and Ag_2Se individually in order to evaluate properly the uptake of the mixture. The MnSe case has been studied in detail, and the results are shown in Fig. 2. The change in weight of Ag_2Se maintained at 800° has been examined after equilibration with both a 600° selenium reservoir and a room temperature reservoir. In the case of the distillation to room temperature a weight loss

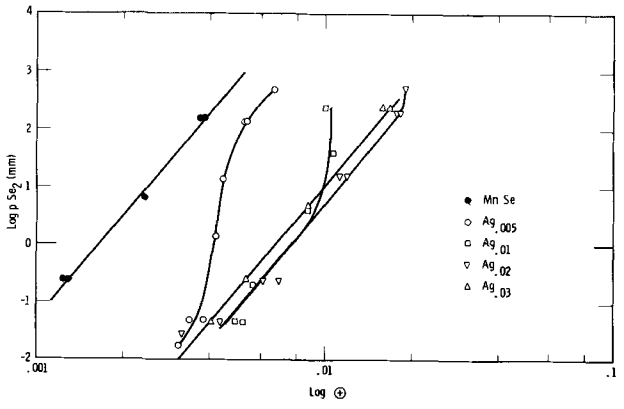

Fig. 2. Log p Se_2 vs. log $\oplus$ for $Ag_xMn_{(1-x)}Se$

of 0.24% was observed. In the case of the 600° Se reservoir experiment the sample gained a total ~ 1.1% by weight of selenium and was a liquid at 800°[mp reported (3) 897°] which liberated selenium on cooling. This weight change is negligible when one considers that only small amounts of Ag_2Se are used in the experiments combined with MnSe.

The selenium vapor pressure used is that reported by Brooks (4). It is taken as being purely dimeric Se_2. This approximation is not strictly correct since at 800°C and a pressure of Se_2 of 1 atm the pressure of the hexamer, Se_6, would be 0.02 atm (5). However, the relative pressure of the hexamer decreases rapidly with decreasing pressure of the dimer, and therefore, the 2% contribution is the worst possible case. The use of a lower sample temperature than 800°C would rapidly lead to an increased hexamer content, so 800° must be considered a minimum operating temperature to avoid this additional complication in the calculations.

After each experiment electrical measurements were made. Resistivities were measured by the standard four terminal technique and the thermoelectric power was measured as described elsewhere (6).

Samples of $Ag_xMn_{1-x}Se$ where x = 0.01, 0.02, 0.03, and 0.06 were made for the preliminary studies by firing all reactants in small isothermal sealed tubes at 800°C. In this way the samples would decompose until their equilibrium vapor pressures were reached. The samples where x = 0.03 and 0.06 were examined by x-ray and metallography. The x-ray patterns of both samples showed NaCl cubic MnSe and weak lines of β-Ag_2Se. By metallography the small amounts of a second phase appears in the grain boundaries and may have been liquid at one time.

Results

The results of the vapor pressure experiments are summarized in Fig. 2. This figure gives the appearance of a group of titration curves which in fact it is. The figure gives a plot of log vapor pressure *vs.* log of the electron hole concentration as determined by the weight of the sample pellet, assuming each selenium added permits the formation of two holes. The data can be described in terms of three distinct regions. There is the doping region in which selenium vapor is taken up while a corresponding amount of Ag_2Se is reacted. This continues until the total amount of Ag_2Se present has been reacted. At the conclusion of this region $Ag_xMn_{(1-x)}Se$ is completely formed. The next region is the equivalence point region or the controlled valence region. Finally, there is the vacancy region. The figure shows that in the doping region the curves coincide within the rather large experimental error. This region is shown on the graph as a straight line with slope = 6. As the equivalence point for each sample is reached, the curve rapidly becomes vertical. It would be expected that the vertical region would occur exactly where there is selenium uptake equal to Ag_2Se added. Any departure from this is assumed to reflect experimental error. In the sample $Ag_{0.005}Mn_{0.995}Se$, the only one where measurements could be made substantially beyond the equivalence point, the curve again assumes a slope similar to that of the doping region. Further, this region is approaching the data for MnSe containing no silver additions which also has a slope =6. This additional uptake beyond the silver equivalence point represents the creation of manganese vacancies in the lattice.

From Fig. 2 it is clear why the phase boundary suggested in Fig. 1 comes about. The data plotted in Fig. 2 are terminated at nearly 1 atm of Se_2. This occurs near the equivalence point for $Ag_{0.02}Mn_{0.98}Se$. Insufficient Se has been added for the formation of $Ag_{0.03}Mn_{0.97}Se$. In fact, this composition is impossible at a sample temperature of 800° under any circumstances. If the Se_2 reservoir temperature were increased to 800°C (the sample temperature), Fig. 2 indicates that the selenium uptake would only be sufficient for the formation of $Ag_{0.027}Mn_{0.973}Se$. The selenium pressure would be 3.5 atm at these conditions on the basis of an extrapolation of the data of Brooks (4).

The electrical conductivity data corresponding to the sample compositions in Fig. 2 are plotted in Fig. 3. The correspondence between Fig. 2 and Fig. 3 is quite apparent. The doping region is again of slope 6. The equivalence points for x = 0.005, 0.01, and 0.02 are at conductivities 19, 37, and 76 ohm^{-1} cm^{-1}. Thus the conductivities at the equivalence point es-

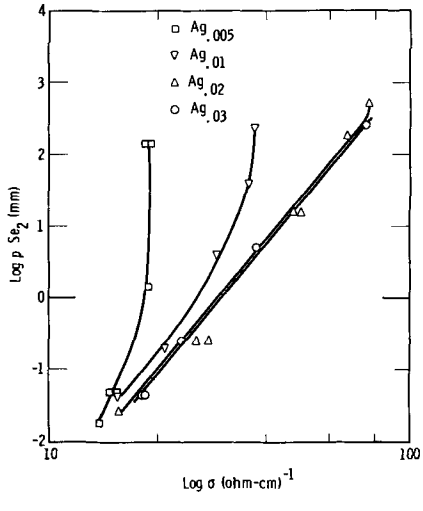

Fig. 3. Log p Se_2 vs. log σ for $Ag_xMn_{(1-x)}Se$

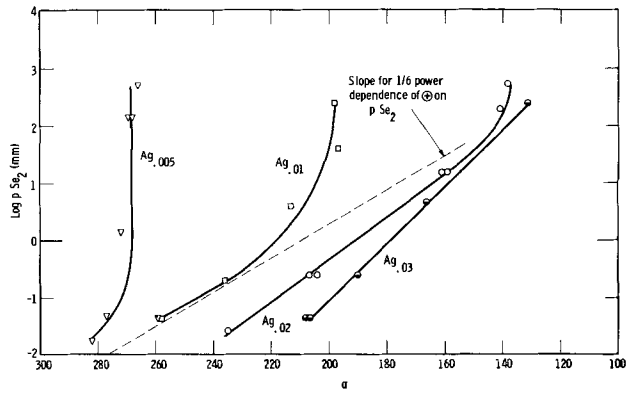

Fig. 4. Thermoelectric power of $Ag_xMn_{(1-x)}Se$ as a function of log p Se_2.

sentially double with each doubling of x, as would be expected. The data on this graph are actually probably more accurate than that of Fig. 2 since the data in Fig. 2 involves a very large weighing error at low selenium additions.

Thermoelectric power data corresponding to the compositions of Fig. 2 and Fig. 3 are plotted in Fig. 4. At the equivalence point the thermoelectric power, α, changes from +137 to +197 to +268 μv/°C for $x = 0.02$, 0.01, and 0.005. Theoretically a decrease of ~60 μv/°C for each doubling of $\oplus$ would be expected since $\alpha \sim -k/e \ln \oplus + C$ so there is agreement at this point (6). In the doping region however, the curves might be expected to coincide on the basis of Fig. 2 and 3. Actually at a given selenium pressure the higher the value of Ag in this region the lower value of α. This is due to the presence of the second phase of n-type Ag_2Se in the product which will give rise to internal circulating currents between the p- and n-phases. [Ag_2Se normally (7) has the electrical properties $\alpha = -150$ μv/°C and $\sigma = 10^3$ ohm^{-1} cm^{-1}.] As indicated earlier in Fig. 1, this has a large effect on α, but little effect on σ. In Fig. 4 a slope corresponding to that of Fig. 2 and 3 is indicated by a dotted line showing that where the silver content is low there is good agreement with this slope but, as the silver content increases, the deviation becomes marked showing the effect of increased amounts of the Ag_2Se second phase.

No data for MnSe are given in Fig. 3 and 4 in spite of the fact that considerable nonstoichiometry was indicated in Fig. 2. It was found that all MnSe samples had nearly constant values of α and σ of ~ +500 μv/°C and 1 ohm^{-1} cm^{-1}, respectively. Actually, values of α as low as ~ +280 and values of σ are high as ~15 would be expected from the figures, and further the values would be expected to vary systematically with composition. Evidently the vacancy structure of MnSe is not stable at room temperature, and the vacancies are eliminated rapidly on quenching with the probable formation of $MnSe_2$. This experience indicates the risk associated with inferring high-temperature data from room temperature electrical measurements as is frequently done. Such inferences from weight data are much more sound since weight data are not structure sensitive and processes involving changes in weight are much slower than just an atomic or electronic rearrangement. This comparison also bears out the hypothesis that has been held for some time that doped semiconductors are thermally much more stable than those relying only on nonstoichiometry for the control of charge carriers.

Discussion

A number of cases involving the relationship between the electrical conductivity and the vapor pressure of a gaseous component have been reported in the literature. These are generally cases of simple nonstoichiometry. The approach is usually through the use of mass action. The groundwork was laid in 1930 by Wagner and Schottky (8). It has been pursued experimentally by Wagner (9), Hauffe (10), and others. A graphical method of approximating these interactions has been introduced by the Phillips workers, notably Kroger and Vink (11). A similar approach using semiconductor terminology has recently been discussed by Brebrick (12). A simple mass action approach will be used in the discussion to follow.

The simplest case to be treated is that of nonstoichiometric MnSe. The chemical equation may be written

$$MnSe + \frac{x}{2} Se_2 \rightarrow MnSe_{1+x} \boxed{Mn^\circ}_x \oplus_{2x}$$

where $\boxed{Mn^\circ}$ is assumed to be a neutral (or doubly ionized) manganese vacancy, and $\oplus$ is a hole. With respect to the manganese lattice, the manganese vacancy as written has a net charge of −2 and is therefore a potential trap for holes. The mass action expression for this equation may be written

$$K_1 = \frac{\boxed{Mn^\circ}^2 \oplus^4}{p\,Se_2}$$

but since $2 \cdot \boxed{Mn^\circ} = \oplus$

$$K_1 = \frac{\oplus^6}{4\,p\,Se_2}$$

Thus it can be seen that the slope of the log p Se_2 *vs.* log $\oplus$ plot should have a slope of 6 as is indeed observed. The agreement indicates that the manganese vacancies are not trapping electron at the temperature of the experiments, in accord with the starting equation.

This same approach may be used beyond the equivalence point in the silver doped samples

$$Ag_xMn_{(1-x)}Se \oplus_x + \frac{y}{2} Se_2 \rightarrow Ag_xMn_{(1-x)}Se_{1+y} \boxed{Mn^\circ}_y \oplus_{x+2y}$$

Here the expression for the equilibrium constant turns out to be the same as before, but now $\oplus = Ag + 2\boxed{Mn^\circ}$

so

$$K_1 = \frac{(\oplus - Ag)^2 \oplus^4}{4\,p\,Se_2}$$

This is clearly not a simple exponential. A series of curves were calculated using K_1 derived from the MnSe data and the silver concentrations of the experiments and are shown in Fig. 5. The derived

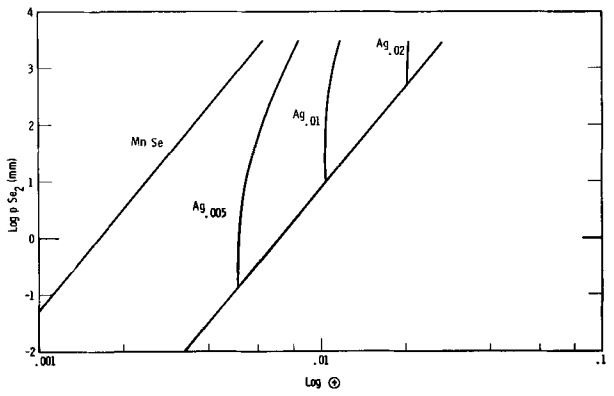

Fig. 5. Derived log p Se_2 vs. log $\oplus$ calculated using log $K_1 = -16.1$.

curves give the very slow change in composition with changing selenium pressure near equivalence points and then a less steep approach to the MnSe curve. The MnSe and $Ag_xMn_{(1-x)}Se$ curves will become indistinguishable when $\oplus >> Ag$. At that point the $Ag_xMn_{(1-x)}Se$ curve will have a slope of 6. Thus both the equivalence region and the vacancy region are described by one equation.

The region in which doping occurs has not been successfully evaluated in these terms. The over-all formation reaction may be written

$$\frac{x}{2} Ag_2Se + \frac{x}{4} Se_2 + 1 - x\, MnSe \rightarrow Ag_x \oplus_x Mn_{(1-x)}\, Se$$

If Ag_2Se is assumed to be at a fixed activity, a slope of 8 would be derived for the plot of Fig. 2. The observed slope is 6, however. The lack of agreement is believed to be due to the changing activity of Ag_2Se with selenium pressure that has been demonstrated earlier and which has also been described in the work of Wagner (13), Miyatani (14), and Rahlfs (15).

The presence of a phase containing selenium vacancies as a result of the silver addition, *i.e.*, $Ag_xMn_{(1-x)}Se_{1-x/2}\boxed{Se}_{x/2}$, instead of a two phase mixture of $x/2$ $Ag_2Se + (1-x)MnSe$ can be ruled out since it would lead to a variation in vapor pressure with the silver content at the start of the selenium addition which is far beyond the experimental error involved. Instead the data are completely independent of the silver content in this region. Moreover insolubility of Ag_2Se in MnSe has been demonstrated, at least at room temperature, by visual observation and thermoelectric power measurements. Therefore, in terms of the ternary phase diagram, the process of selenium addition can be described in terms of cutting across the tie lines of the Ag_2Se-MnSe binary field.

Finally one might consider the behavior of $Li_xMn_{(1-x)}Se$ within this framework. A rather serious attack of Vycor by lithium precludes any accurate experimental work since a continuous undoping will arise from this attack. Electrical data indicate, however, that at least in the case of $Li_{0.03}Mn_{0.97}Se$ the material probably is completely within the controlled valence range throughout the range of selenium pressures used in this work. It is also reasonable to suppose that when $x = 0.11$ in $Li_xMn_{(1-x)}Se$, which is the previously reported phase boundary composition (1), the selenium equilibrium vapor pressure has increased to the vicinity of 1 atm. This in itself would require a large extension of the range of controlled valence by the mechanism of lowering the doping curve for $Li_xMn_{(1-x)}Se$ away from the vacancy curve which is common to both systems.

Acknowledgments

The author wishes to thank Drs. R. L. Longini, A. J. Panson, Y. L. Sandler, and J. Weissbart for many useful discussions and critical review of this manuscript. Technical assistance was rendered by Mr. D. E. Sestrich. This work was done in connection with U. S. Navy Buships Contract No. NOBS-78365 WGO No. WG 79150 CE.

Manuscript received Dec. 8, 1961; revised manuscript received March 2, 1962.

Any discussion of this paper will appear in a Discussion Section to be published in the June 1963 JOURNAL.

REFERENCES

1. W. D. Johnston and R. R. Heikes, *J. Am. Chem. Soc.*, **80**, 5904 (1958).
2. R. R. Heikes, R. McGuire, and R. J. Happel, *Phys. Rev.*, **121**, 703 (1961).
3. M. Hansen, "Constitution of Binary Alloys," McGraw-Hill Book Co., New York (1958).
4. L. S. Brooks, *J. Am. Chem. Soc.*, **74**, 227 (1952).
5. D. R. Stull and G. C. Sinke, "Thermodynamic Properties of the Elements," American Chemical Society, Washington (1956).
6. R. R. Heikes and R. W. Ure, "Thermoelectricity," Interscience Publishers, New York (1961).
7. J. B. Conn and R. C. Taylor, *This Journal*, **107**, 977 (1960).
8. C. Wagner and W. Schottky, *Z. Physik, Chem.*, **B11**, 163 (1930).
9. C. Wagner, *ibid.*, **B22**, 181 (1933); H. H. Baumback and C. Wagner, *ibid.*, **B22**, 199 (1933); H. H. Baumback and C. Wagner, *ibid.*, **B24**, 59, (1934); C. Wagner and E. Koch, *ibid.*, **B32**, 439 (1936).
10. K. Hauffe and A. L. Vierk, *ibid.*, **196**, 160 (1950); K. Hauffe and J. Block, *ibid.*, **196**, 438 (1951); K. Hauffe and H. Greenwald, *ibid.*, **198**, 248 (1951.)
11. F. A. Kroger and H. J. Vink, *J. Phys. Chem. Solids*, **5**, 208 (1958); F. A. Kroger and H. J. Vink, "Solid State Physics," Academic Press Inc., New York (1956); J. Bloem, *Philips Research Rept*, **11**, 273 (1956). F. A. Kroger, H. J. Vink, and J. van der Boomgaard, *Z. Physik, Chem.*, **203**, 1 (1954).
12. R. F. Brebrick, *J. Phys. Chem. Solids*, **4**, 190 (1958).
13. C. Wagner, *J. Chem. Phys.*, **21**, 1819 (1953).
14. S. Miyatani, *J. Phys. Soc., Japan*, **13**, 317 and 341 (1958).
15. P. Rahlfs, *Z. Physik. Chem.*, **B31**, 157 (1936).

Electrical Conductivity of Nonstoichiometric a-Nb_2O_5

E. H. Greener and W. M. Hirthe

College of Engineering, Marquette University, Milwaukee, Wisconsin

ABSTRACT

The electrical conductivity of reduced α-Nb_2O_5 was measured after prior reduction in 10^{-6} atm of air from 350°-1150°K for both single crystals and sintered specimens. The conductivity of single crystals was found to be exponentially dependent on temperature with an activation energy of 0.9 ev in the range from 1150°-650°K and 0.2 ev in the range from 650°-350°K. The electrical conductivity of sintered specimens was also found to be exponentially dependent on temperature, but only a single activation energy was obtained over the entire temperature range. This activation energy was dependent on defect concentration and varied from 1.0 ev for the smallest degree of reduction to almost zero at the highest degree of reduction where the behavior was essentially that of a degenerate semiconductor. An explanation based on overlapping orbitals of trapped electrons is offered to explain both the dependence of activation energy on defect concentration and the absence of a low-temperature activation energy in sintered material. Finally, two mechanisms are discussed to explain the observed conductivity of reduced α-Nb_2O_5. Comparison of conductivity data and thermoluminescence data tends to favor a model in which two trapped electrons are excited from an oxygen vacancy to the "d" band of the niobium cations.

A discussion of the past work on the electrical properties of Nb_2O_5 has been presented in an earlier paper (1). In this work α-Nb_2O_5 has been shown to be a metal-excess n-type semiconductor. The defect producing this structure is most probably an oxygen ion vacancy which has trapped two electrons. A possible energy band model for the defect oxide semiconductor appears in Fig. 1.

In near-stoichiometric α-Nb_2O_5, between 600°-900°C, the conduction band carrier concentration[1] $[\ominus]$ has been shown to obey a law of the form

$$[\ominus] = \sqrt{K_{o1}K_{o2}}\, P_{O_2}^{-1/4} \exp -(W_D + E_1)/2kT \quad [1]$$

where K_{o1} and K_{o2} are, respectively, the temperature independent terms of the equilibrium constants for the creation of the defect (Eq. [2]) and the excitation of the first electron from the oxygen vacancy trap (Eq. [3]). W_D is the energy required to create the defect, and E_1 is the energy necessary to excite the first electron from the defect into the conduction band. Experimentally, the quantity $-(W_D + E_1)/2$ was found to be 1.65 ev (Fig. 2).

These reactions may be summarized as

$$O_i'' \rightleftharpoons \frac{1}{2} O_2 + O_v^x \qquad -W_D \quad [2]$$

$$O_v^x \rightleftharpoons O_v^{\cdot} + \ominus \qquad -E_1 \quad [3]$$

[1] The temperature dependence of conduction band carrier mobility in near-stoichiometric α-Nb_2O_5 is assumed to be negligible when compared to the change in conduction band carrier concentration over the temperature range 600°-900°C. A discussion of this is included in the earlier paper (1).

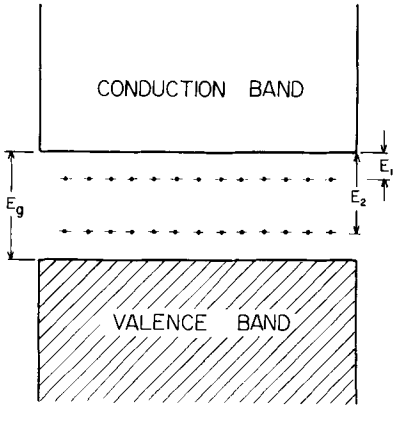

Fig. 1. Band model for a metal-excess oxide semiconductor with an oxygen ion vacancy trapping two electrons.

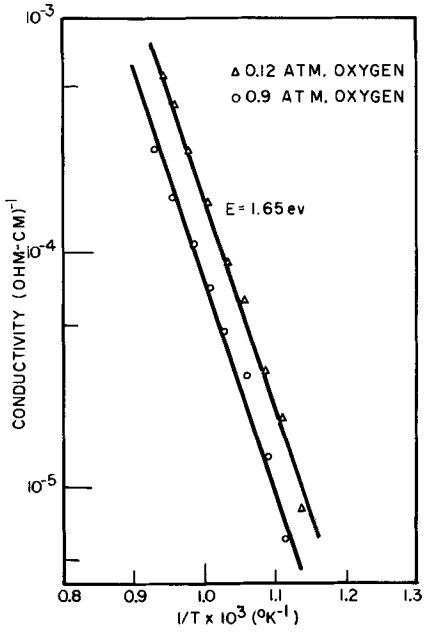

Fig. 2. Logarithm of the conductivity of sintered near-stoichiometric α-Nb_2O_5 as a function of $1/T$ for two oxygen pressures. The value of 1.65 ev calculated from the slopes of these curves represents $(W_D + E_1)/2$.

where O_i^{2-} is an oxygen ion in a normal lattice position, O_v^x is an oxygen vacancy which has trapped two electrons in its field, $O_v^{\cdot}$ is an oxygen vacancy from which an electron has been excited, and $\ominus$ is an electron in the conduction band.

It is further possible to write an analogous expression for the excitation of the second electron

$$O_v^{\cdot} \rightleftharpoons O_v^{\cdot\cdot} + \ominus \qquad -E_2 \quad [4]$$

where $O_v^{\cdot\cdot}$ is an oxygen ion vacancy from which both electrons have been excited, and E_2 is the energy necessary to excite the second electron from the vacancy trap into the conduction band.[2]

Thus, the conductivity of near-stoichiometric α-Nb_2O_5 is seen to depend on both temperature and oxygen partial pressure.

In the case of materials of near-stoichiometric composition, Eq. [2], [3], and [4] control the change in conduction band carrier concentration with temperature and pressure. Consequently, E_1 and E_2 cannot be separated from W_D. On the other hand, if the concentration of defects were increased so that the change in conduction band carrier concentration would be controlled by Eq. [3] and [4] it should be possible to determine E_1 and E_2 experimentally.

Experimental Details

Small single crystals of α-Nb_2O_5 approximately 2 mm in diameter were kindly furnished by Linde Air Products Company. Flat surfaces were ground and polished with 420 grit carborundum on the crystals for electrical contact. No chemical analysis of the Linde crystals or knowledge of their perfection was available. Since the dimensions of the Linde crystals were very irregular the data for these specimens are reported as conductance rather than as conductivity.

High-purity Nb_2O_5 powder furnished by the Fansteel Metallurgical Corporation was a mixture of α and β modifications. It was cold-pressed without a binder at a pressure of 40,000 psi and sintered at temperatures between 1300° and 1350°C for 2 hr. After this treatment, the Nb_2O_5 existed entirely as the α modification. The apparent densities of the sintered compacts were measured pycnometrically and were found to be within 80-90% of the theoretical density of 4.55 g/cm³ reported by Holtzberg *et al.* (2). Rectangular parallelepipeds approximately ½ x ¼ x 0.05 in. were cut from the sintered compacts and used for conductivity specimens, the surfaces being polished with 420 grit carborundum.

The equipment for measurement of resistance as a function of temperature in the range 300°-1000°K and oxygen partial pressure has been described previously (1, 3). Two types of apparatus were used: the first system consisted of a furnace in a vacuum bell jar, and in the second, a Vycor tube connected to a vacuum system separated the specimen from the furnace. The single crystals were investigated in the bell jar whereas the sintered specimens were investigated in the Vycor tube. Because of the size limitations, the two-probe technique was used for single crystals whereas four-probe techniques were used for sintered specimens. Compositional changes were measured by weight loss, the entire weight change being attributed to the loss of oxygen.

[2] Another possible explanation for the occurrence of a second activation energy is mentioned at the end of the paper.

Experimental Results and Discussion

In an attempt to freeze in a constant defect concentration the reduction was carried out directly in the vacuum apparatus. Specimens were held at 10^{-6} atm O_2 for from 1 to 8 hr at temperatures from 700° to 900°C. The specimens were cooled quickly (5°-10°C/min for the sintered specimens, faster for the single crystals) *in vacuo,* and resistance readings were taken on cooling. It is felt that in the case of the data reported in this paper this treatment was successful in maintaining the defect concentration produced by the high-temperature reduction. Slower cooling or holding at the higher temperatures produced discontinuities in the log σ *vs.* $1/T$ curve due to further reduction. No such discontinuities were found in the data reported in this investigation.

A typical run on a single crystal of Nb_2O_5 in a vacuum of 10^{-6} atm of air in the temperature range from 300° to 1000°K is given in Fig. 3. Essentially the same log σ *vs.* $1/T$ curve was obtained for six different specimens initially reduced at 800°-850°C for from 2 to 4 hr. The observed data can be rationalized with the normal semiconductor equation

$$\sigma = \sigma_o \exp\,(-E_D/2kT) \qquad [5]$$

where E_D is the energy of the donor level, k is Boltzmann's constant, and T is the absolute temperature. The activation energy calculated from the high-temperature slope is about 0.9 ev (E_2) and from the low-temperature slope about 0.2 ev (E_1). The break in the log σ *vs.* $1/T$ curve occurs at $1/T$ x 10^3 equal

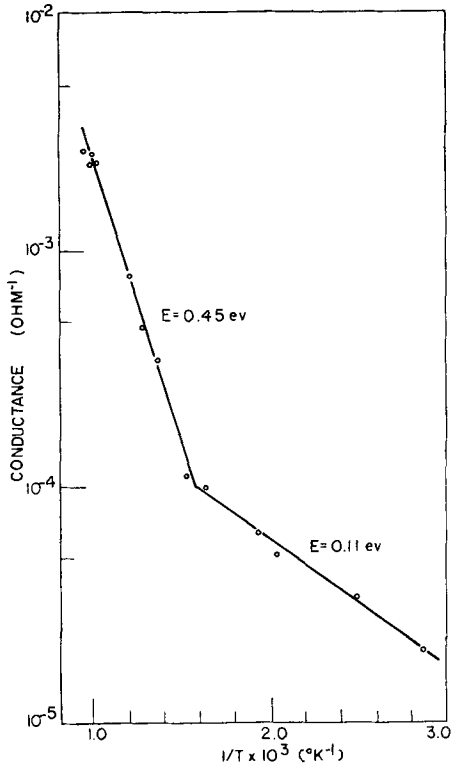

Fig. 3. Logarithm of the conductance of single crystal α-Nb_2O_5 as a function of $1/T$ after reduction at 800°C for 4 hr in a vacuum of 10^{-6} atm of air. The values of 0.45 ev and 0.11 ev calculated from the slopes of the curve represent $E_2/2$ and $E_1/2$, respectively.

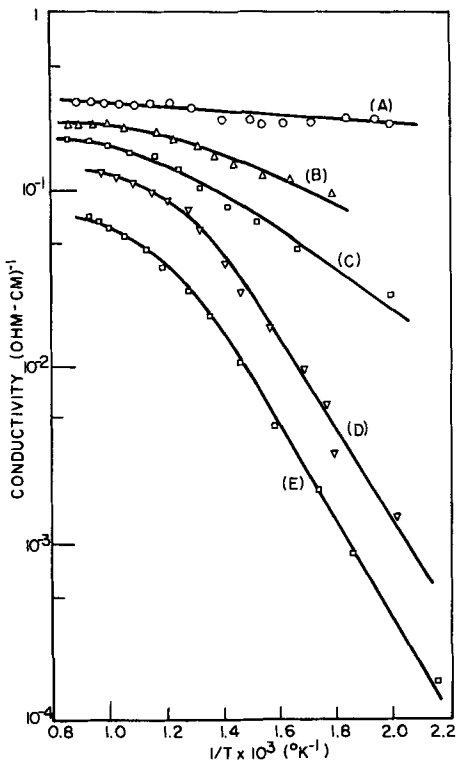

Fig. 4. Logarithm of the conductivity of sintered α-Nb_2O_5 in 10^{-6} atm of air as a function of $1/T$ for the following reduction treatments in a vacuum of 10^{-6} atm of air: (A) 8 hr at 875°C; (B) 8 hr at 860°C; (C) ½ hr at 860°C; (D) 8 hr at 750°C; (E) ½ hr at 800°C.

to 1.5 or 650°K which corresponds to a thermal energy of about 0.06 ev. The change in slope of the curve is due to the exhaustion of electrons trapped at E_1 because the thermal energy at 650°K is within $4kT$ of E_1.

Typical curves of log σ *vs.* $1/T$ for reduced sintered specimens shown in Fig. 4 can be characterized by two distinct regions. In the low-temperature region the conductivity changes exponentially with temperature and can be represented by a straight line, the slope of which will yield the activation energy from the donor level according to Eq. [5]. In the high-temperature region the conductivity is essentially independent of temperature and can be explained on the basis of an exhaustion process in which the thermal energy is large enough to excite all trapped electrons from available donor centers, but is too small for any intrinsic excitation to occur. The thermal energy for exhaustion is compared with the energy level of the donor state in Table I for all curves in Fig. 4 and can be seen to be within approximately $4kT$ of the donor level E_2. For the smallest degree of reduction attempted, the observed activation energy is (according to Eq. [5]) 1.0 ev. This is in good agreement with 0.9 ev obtained from the high-temperature slope of the single crystal curve.[3] As the degree of reduction and consequently the concentration of defect levels and trapped electrons increases, the conductivity also increases. In addition, there is a decrease in the activation energy due to the fact that the electrons trapped in donor levels can no longer be considered as isolated defects because their orbitals begin to overlap. As treated by Pearson and Bardeen (4), increasing the concentration of donor levels to the point where overlapping occurs moves the Fermi level up toward the conduction band. This will lower the activation energy necessary for electronic excitation and the beginning of the exhaustion region will occur at successively lower temperatures as is seen in Fig. 4.

[3] Since good agreement was obtained between the high-temperature activation energies of the single crystal (two-probe method) and sintered specimens (four-probe method), contact resistance was not deemed to be a problem in the case of the single crystal studies. Certainly if any problem were to exist it would have appeared in the high-temperature range of measurement where specimen resistance is lower than in the low-temperature range. Since the high-temperature activation energies agreed, it is reasonable to assume that contact resistance is not a problem in the low-temperature range of measurement.

Table I. Comparison of thermal energy for exhaustion with energy level of the donor state

Curve	Thermal energy for exhaustion from Fig. 4	Activation energy from Fig. 4
A	Degenerate	
B	0.08	0.15
C	0.09	0.23
D	0.09	0.45
E	0.10	0.50

This may be the reason why only a single activation energy is obtained with sintered materials over the same temperature range where two activation energies are found in single crystals. For obvious reasons, the kinetics of reduction of the sintered materials can be considered to be faster than that for single crystals. Consequently, even at the smallest degree of reduction in sintered specimens, the concentration of oxygen vacancies and trapped electrons would be higher than for single crystals receiving the identical reduction treatment. The electrons trapped at E_1 will be more loosely bound than those traped at E_2 (Eq. [3] and [4]) and can be thought of as having a larger orbit. Therefore a concentration of defects sufficient to cause overlapping of the E_1 levels may be insufficient to cause overlapping of the E_2 levels. In this case the E_1 level would shift toward the conduction band in a manner analogous to the shifting of the E_2 level in Fig. 4. Since from the single crystal data the E_1 level is about 0.2 ev, the smallest reduction attained in this investigation may provide a sufficient number of defects to shift the E_1 level within $4kT$ (at room temperature $4kT = 0.1$ ev) of the conduction band. If this occurs, the first level would be exhausted at all temperatures utilized in this research, and the conductivity of sintered specimens would change only through excitation of electrons from the second level into the conduction band.

At the highest degree of reduction (curve A, Fig. 4) the conductivity is essentially independent of temperature over the entire temperature range investigated, and thus the material in this region may be classified as a degenerate semiconductor, *i.e.*, both E_1 and E_2 levels are exhausted. Since in a degenerate semiconductor the Fermi level may be considered to be in the conduction band, the exponential term for the dependence of the conductivity may be replaced by unity, and the conductivity σ may be expressed as

$$\sigma = \sigma_0 Nev \qquad [6]$$

where N is the number of carriers in the conduction band, e is the electronic charge, and v is the electronic mobility. Thus, if it is possible to estimate the number of carriers and measure the conductivity, a calculation of the electron mobility could be made. From x-ray data of Holtzberg and co-workers (2), it is possible to estimate the total number of molecules in Nb_2O_5/cc as 1.2×10^{20}. This means that there would be 6×10^{20} normally occupied oxygen anion lattice sites. From measurement of weight changes, however, it was found that the compositional change from insulator to degenerate semiconductor amounted to the change Nb_2O_5-$Nb_2O_{4.95}$, with the composition $Nb_2O_{4.95}$ corresponding to about 1% vacancies per cubic centimeter. Since an oxygen vacancy can trap two electrons, N can be approximated as 1.2×10^{19}/cc. From Fig. 4 the conductivity for the degenerate case can be approximated as 10^{-1} ohm-cm. Therefore, the electron mobility is of the order of 10^{-1} cm^2/volt-sec. This value of mobility is close to that found by Breckenridge and Hosler (5) for the case of heavily reduced TiO_2 and was related by them to a conduction process in the narrow "d" band of Ti ions. Thus, by analogy to the TiO_2 case, it would be possible for the narrow "d" band of the Nb cation to act as the conduction band.

Conclusion

On the basis of the conductivity studies presented, two alternative mechanisms may be offered.

1. Excess electrons produced as a result of reduction are locally trapped at Nb^{4+} ions. Since an oxygen vacancy may be considered to have a virtual charge of +2, these Nb^{4+} ions would be found near a vacancy. Conduction might take place via excitation of an electron from an Nb^{4+} ion into the conduction band (high-temperature activation energy) or by "hopping" of an electron from an Nb^{4+} site to an Nb^{5+} site (low-temperature activation energy). The activation energies are summarized in Table IIa. Mitoff (6) has recently treated the case for hopping in NiO. He reports an activation energy of about 0.2 ev over the same low-temperature range used in this investigation. A standard diffusion analysis can treat this problem quite adequately; *i.e.*, the conductivity σ may be expressed as

$$\sigma = nev = nev_0 \exp(-E/kT) \qquad [7]$$

where n is the number of carriers trapped in defect levels, e is the electronic charge, and the term $v_0 \exp(-E/kT)$ expresses the temperature dependence of the mobility.

2. Excitation of two electrons from an oxygen vacancy trap into the "d" band of the Nb^{5+} ions according to Eq. [3] and [4]. The observed activation energies substituted into the standard semiconductor equation (Eq. [5]) yield the energies necessary to excite these electrons from a vacancy trap into the conduction band, Table IIb. Recent thermoluminescence studies by Greener, Fehr, and Angino (7) tend to substantiate this model. In this investigation specimens of powdered near-stoichiometric α-Nb_2O_5 were subjected to Co^{60} and u.v. irradiation after which they exhibited two thermoluminescence peaks. The activation energies calculated from these peaks closely correspond to those calculated from single crystal conductance data based on activation to a band from two discrete levels (Tables IIb and IIc). This suggests that the trapping mechanisms in both experiments were the same.

Table II. Summary of activation energies

	(a) Mechanism 1 (Activation energies from Fig. 3)	(b) Mechanism 2 (Activation energies from Fig. 3)	(c) Thermoluminescence
E_1	0.1	0.2	0.4
E_2	0.9	0.9	0.9

Further, two activation energies were obtained in powdered material. In the case of thermoluminescence experiments one may expect an extremely small concentration of electrons trapped at vacancies. For example, irradiation produces no color change, while reduction does. Thus no overlapping of electrons trapped at E_1 occurs, and a second activation energy is seen which is in good agreement with the single crystal conductance data. The hopping mechanism discussed earlier (mechanism 1) could not give rise to a thermoluminescence peak. It is also of interest to note that a Bohr He model for the traps predicts that the energy to excite the second electron from the vacancy is about four times the energy to excite the first. Such a relationship is evident in Table II.

Although at present the model which best explains all experimental data seems to be the excitation of two trapped electrons into the "d" band of the niobium cations, the final decision as to which mechanism occurs must depend on an experiment which can differentiate between the temperature dependence of carrier concentration and carrier mobility. In the case of excitation into a band it is the carrier concentration which is exponentially dependent on temperature whereas in the case of a hopping process the mobility is exponentially dependent on temperature. Clearly in order to distinguish between the two possible mechanisms, Hall Effect data would be most valuable.

Acknowledgment

The authors wish to acknowledge the Office of Naval Research for their support of the portion of this work done at Northwestern University.

Manuscript received Dec. 18, 1961; revised manuscript received March 1, 1962. This paper was prepared for delivery before the Indianapolis Meeting, April 30-May 3, 1961.

Any discussion of this paper will appear in a Discussion Section to be published in the June 1963 JOURNAL.

REFERENCES

1. E. Greener, D. Whitmore, and M. Fine, *J. Chem. Phys.*, **34**, 1017 (1961).
2. F. Holtzberg, A. Reisman, M. Berry, and M. Berkenblit, *J. Am. Chem. Soc.*, **79**, 2039 (1957).
3. E. Greener, Ph.D. Thesis, Northwestern University (1960).
4. G. Pearson and J. Bardeen, *Phys. Rev.*, **75**, 86 (1949).
5. R. Breckenridge and W. Hosler, *ibid.*, **91**, 793 (1953).
6. S. Mitoff, *J. Chem. Phys.*, **35**, 882 (1961).
7. E. Greener, G. Fehr, and E. Angino, *J. Am. Ceram. Soc.*, **45**, 93 (1962).

Cross Sections and Ohmic Resistance of Diffusion Pipes in Silicon

A. Goetzberger and C. Stephens

Shockley Transistor, Unit of Clevite Transistor, Palo Alto, California

ABSTRACT

Diffusion pipes were deliberately produced by contamination with phosphorus as described previously by Goetzberger and their cross sections measured as a function of depth from the surface by removing thin layers of silicon by anodic oxidation. The results are in qualitative agreement with theory as derived from a simple diffusion model. In particular some pipes were found having diameters that increase with depth, and others were found having decreasing diameters. "Submerged pipes" were also detected experimentally for the first time. Deviations from the predicted theoretical behavior were relatively unimportant and seem to be caused by enhanced diffusion close to the surface by the finite size of the n-type source and by the influence of background doping. The proposed theoretical model was further confirmed by measurement of the ohmic resistance of pipes which was in agreement with predictions based on spreading resistance from the concentration end of the pipe.

This paper reports new investigations on diffusion pipes in silicon. In an earlier paper (1) it had been shown that pipe-like regions of high donor concentration through diffused p-layers in silicon can originate from localized sources of n-type impurity on the surface.

It had further been shown that this n-type impurity was phosphorus in the majority of cases and that pipes are formed by diffusion from the localized sources. The results reported in (1) were recently confirmed by Flint (2) who was able to detect a high concentration of phosphorus in pipes with an electron probe x-ray analyzer. According to the diffusion theory given in (1), pipes should have different profiles dependent on diffusion conditions (Table I and Fig. 1). Of particular interest are the so-called "submerged" pipes (case IV). This type of pipe cannot be detected on the surface because it does not contain a junction intersecting the surface.

In this publication evidence that all the predicted shapes exist is reported. This evidence, obtained with a sectioning technique employing anodic oxidation, is discussed below.

The results of the profile measurements were checked by measuring the ohmic resistance of a number of pipes. Since pipes result from diffusion from the surface, the resistivity along a pipe increases from the surface according to a diffusion distribution. The most important contribution to the resistance, therefore, arises from the spreading resistance in the bulk material lying beyond the end of the pipe. The area of the conducting channel through the diffused layer can thus be estimated from resistivity measurements and is found in a later section to compare with optical measurements of the pipe shape.

Table I. Pipe shapes for different diffusion conditions

Case	Condition	Shape
I	$C_{o2} > C_{o1}$, $D_1t_1 > D_2t_2$	Ellipsoid
II	$C_{o2} > C_{o1}$, $D_1t_1 < D_2t_2$	Hyperbola of rotation
III	$C_{o2} > C_{o1}$, $D_1t_1 = D_2t_2$	Cylinder
IV	$C_{o2} < C_{o1}$, $D_1t_1 < D_2t_2$	Hyperbola of rotation (submerged pipe)

Definition of symbols: C_o is surface concentration; D, diffusion coefficient; t, diffusion time; subscript 1 refers to the plane diffusion; subscript 2 refers to the spherical pipe diffusion.

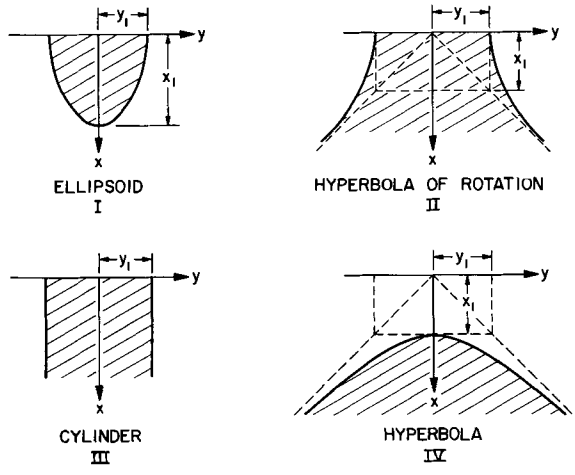

Fig. 1. Four different pipe shapes according to mathematical model.

Cross Section Measurements

Experimental procedure.—Diode preparation and observation of pipe diameter at the surface were identical to the procedures described in (1). Pipes were introduced into boron diffused p^+n planar diodes by exposure to P_2O_5 aerosol before boron predeposit and were optically observed by light emission from microplasmas at the surface.

Afterwards the thickness of the silicon slices containing diodes with pipes was reduced in small in-

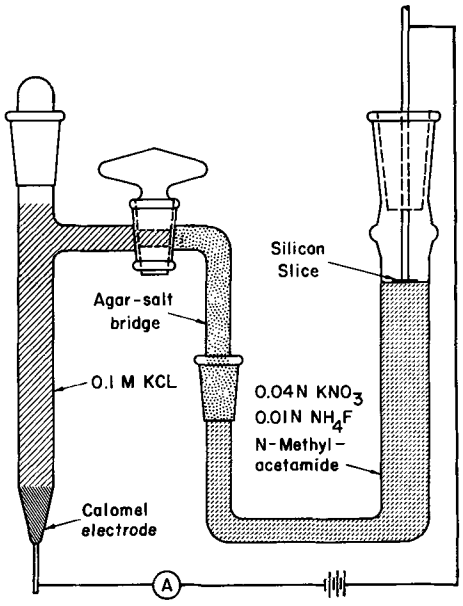

Fig. 2. Anodic oxidation apparatus

crements by anodic oxidation, and the variation of the pipe shapes studied. The technique of anodic oxidation of silicon has been described by Schmidt (3), and Tannenbaum (4). The procedure followed in this investigation had been worked out by McDonald and Collins (5). One anodization step in the apparatus shown in Fig. 2 removes approximately 0.05μ. After each anodization the oxide was removed in HF, and after every five oxidation steps the thickness of the removed layer and the diameter of the pipe were measured. Thickness was determined by weighing with a microbalance with an accuracy of $\pm$ 4 μg, corresponding to a depth accuracy of 0.016μ for a slice of 1 cm^2 area. This accuracy, however, is only applicable for slices of uniform doping over the whole surface because it has been observed during this investigation that the etching rate is different for n- and p-type and for different resistivities. Therefore the depth measurements represent only an average over the whole slice and may not apply accurately to the pipes themselves. The error is thought to be less than 10%.

The dimensions of the pipes were determined by taking photomicrographs of the diodes under reverse bias, utilizing avalanche radiation to delineate the intersection of the pipes with the surface. Some of the pipes deviated from a circular geometry. In these cases the diameter was always measured in the same direction.

An alternative to the avalanche method is the chemical staining technique (6). The avalanche method was chosen because of its greater reproducibility.

Results.—When phosphorus was introduced as an aerosol before boron predeposition, in general a greater percentage of pipes were found to have diameters which decreased with depth corresponding to the ellipsoidal type. The remainder of the pipes showed a widening with increasing depth; this type of pipes is believed to be due to unintentional contamination during or before the oxidation step with

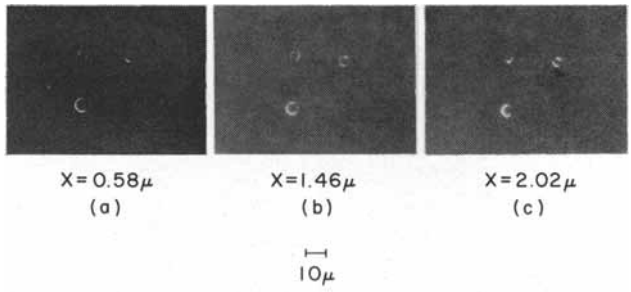

Fig. 3. Group of pipes showing constriction. Light emission photographs are taken at increasing depths. X is depth of cross section.

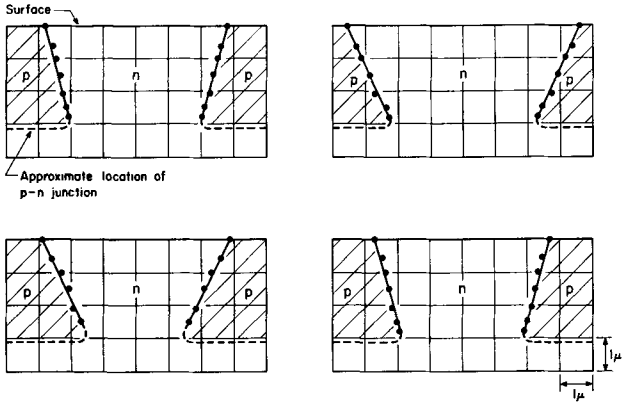

Fig. 4. Cross sections for four different pipes showing constriction

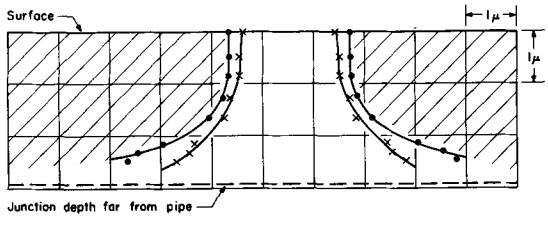

Fig. 5. Cross section of a pipe showing widening of diameter with depth.

consequently larger values of Dt for the phosphorus than for the boron.

Figure 3 a-c shows light emission from the same group of pipes as it appeared at different depths. The cross sections of two of these pipes and of some others found in the same sample are given in Fig. 4.

Figure 5 shows the cross section of a pipe with increasing diameter, the two outlines corresponding to two perpendicular directions across the pipe which was not exactly circular.

In Fig. 6 the detection of a submerged pipe during sectioning is shown. In Fig. 6a a small light spot can be seen to the left of a well-developed pipe. At greater depths this light spot developed into a ring of light characteristic for a pipe. It can be assumed that the light emission that emerges before the pipe itself is sectioned is caused by avalanche breakdown at the top of the n-region where the impurity gradient is increased.

In Fig. 7a the cross section of this pipe is given. The two traces again apply to two perpendicular directions. Figure 7b shows a similar structure found in another diode.

Discussion.—The observed pipe cross sections are in qualitative agreement with the theory given in

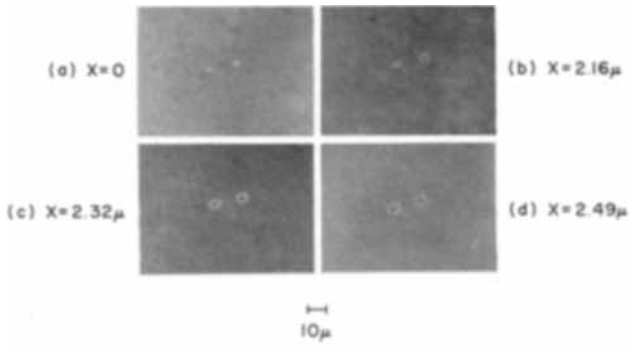

Fig. 6. Light emission photographs showing detection of a submerged pipe. X is depth of cross section.

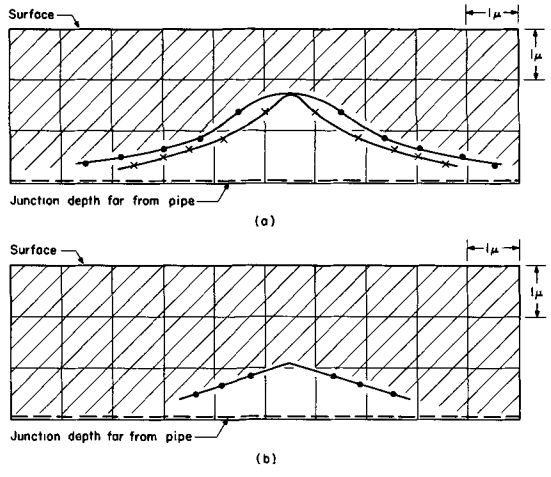

Fig. 7. Cross sections of two submerged pipes

(1). The following deviations from the expected behavior can be noticed: (*A*) Pipes which show a decrease in diameter in depth (Fig. 4) are wider at the surface than the expected ellipsoid. (*B*) Pipes showing an increase in diameter with increasing depth, including the submerged types, do not follow a hyperbolic outline exactly, but show more curvature at the bottom end.

Effect (*A*) might be caused by enhanced diffusion close to the surface as has been reported by different observers (4, 5, 7). Little is known about diffusion along surfaces, but in general it is assumed to be much faster than bulk diffusion. Because the observed effect can be explained adequately by a small modification of the bulk diffusion coefficient, it is believed to be due to enhanced bulk diffusion and probably not to surface diffusion.

Effect (*B*) can be accounted for by (i) finite extension of the source initially over the surface and (ii) influence of the doping of the crystal from which the slice was prepared; this constant concentration term was not taken into consideration in the simple mathematical model.

For several pipes an evaluation of phosphorus content was carried out using the known data of the plane diffusion and a diffusion time for the pipes corresponding to the time elapsed after introduction of phosphorus. The number of phosphorus atoms per pipe was estimated as between 10^8 and 10^9, in good agreement with earlier estimates (1) based on measurements of the growth rate of pipes.

Submerged pipes had an impurity content in the lower range, as anticipated.

It should be noted here that the lower limit for the phosphorus content which will make a pipe observable is determined by the surface concentration of the plane boron diffusion. If the surface concentration of the plane diffusion is lowered, then the number of impurity atoms required to form comparable types of pipes will be lowered by the same factor.

One of the results of the present investigation is a proof of existence of the submerged pipes (Fig. 7). This type is characterized by relatively small amounts of impurities which started diffusing a considerable time before diffusion of the p-type layer is frequently found in planar devices. The long high-temperature oxidation necessary to produce the initial oxide layer provides a chance for submerged pipes to be introduced. It appears to be very difficult to avoid contamination with phosphorus during this step. In the opinion of the authors this problem will have to be solved before large area planar devices become technically feasible in silicon.[1]

Pipe Resistance

Technique of measurement and results.—The main problem in measuring the resistance through a pipe is the small size of the pipe areas. James and Flint (8) attempted to measure the ohmic resistance by placing a fine probe in the center of a pipe. They obtained only a rough estimate of the resistance.

In this investigation a different contacting method was chosen. Contact to the pipe was made by means of a shallow diffused n^+-layer of a lateral extension smaller than the planar p-type junction containing the pipe (Fig. 8). Application of this technique is possible because, owing to the high doping level at the surface, the top part of the pipe does not contribute appreciably to its resistance. Before diffusion of the contacting emitter layer certain diodes containing pipes were photographed to obtain the pipe diameter. The n^+-layer was then produced by conventional oxide masking and photoresist techniques. Only those devices which contained a single pipe were selected for measurement. In order to be sure that no submerged pipes were also contacted by the n^+-layer, after the resistance had been measured the specimens were anodically sectioned and examined again for the presence of submerged pipes.

The arrangement for resistance measurement is shown in Fig. 8. Separate probes were used for

[1] For example, in device production submerged pipes can produce emitter-collector shorts in structures which, prior to the emitter diffusion, exhibit perfectly satisfactory collector base junctions.

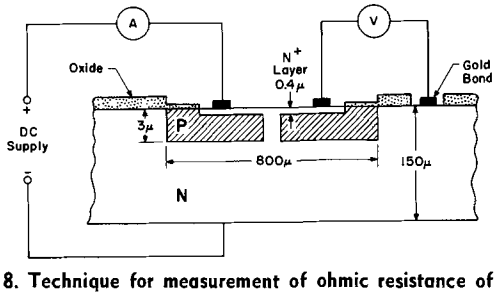

Fig. 8. Technique for measurement of ohmic resistance of pipe

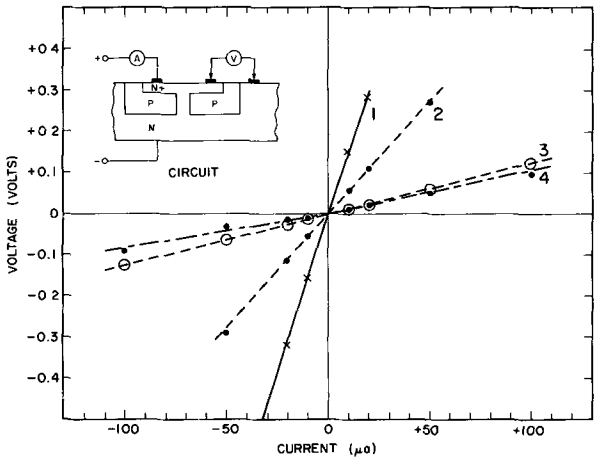

Fig. 9. V-I curves for four different pipes, which were used to determine ohmic resistance.

voltage and current readings so that the influence of contact resistances could be eliminated. All the resistances measured were ohmic in the range between −0.5 and +0.5v. At higher voltage the measurements were disturbed by injection effects within the npn structure. Voltage *vs.* current values for four different pipes are given in Fig. 9.

Discussion.—In Table II the results of the resistance measurement are presented. The first column gives the number of the pipe, the second the measured resistance. In the third column the observed diameters of the pipes at the surface are listed. These diameters had been measured before the contacting n^+-layer was diffused. For comparison the diameter of the pipe was calculated from the spreading resistance on the basis of two different models (9). The first model assumes that current spreads from a disk of negligible resistance of diameter d into the bulk silicon of resistivity ρ. Resistance in this case is given by

$$R = \frac{\rho}{2\,d}$$

In the second model resistance is thought to arise by spreading of current into the bulk from a hemisphere with negligible resistance, and diameter d

$$R = \frac{\rho}{\pi\,d}$$

(A rigorous treatment would require calculation of the spreading resistance of a hemispherical diffusion distribution whose top part is cut off by the junction.) For both cases d was calculated for $\rho = 3$ ohm-cm from the measured R values. These d-values are given in the third and fourth column of Table II.

The pipes in Table II can be separated into two groups. One group (No. 1 and 2) consists of pipes with a small diameter. For these we calculate a diameter which is too small with either model. The other group which consists of bigger pipes (No. 3 and 4) can best be approximated by the spherical model.

Table II. Results of pipe resistance measurements

No.	R measured, K ohms	d measured, μ	d_{calc}, disk model, μ	d_{calc}, spher. model, μ
1	11.0	5	1.35	0.87
2	5.5	6.2	2.7	1.75
3	1.2	8	12.5	8.0
4	1.1	10	13.6	8.7

In order to explain the disagreement for the first group, we have to assume that the diameters at the junction are smaller than at the surface. Indications for such a constriction of these pipes were indeed found when the sample containing the slice was sectioned anodically. Occurrence of surface contamination, however, prevented accurate measurements of pipe diameters close to the junction. We conclude, however, that in general the agreement with the model is satisfactorily within the limits set by experimental errors.

Conclusions

Pipes through diffused layers that were found in a preceding paper to be caused by diffusion of n-type impurity from localized specks of contamination were studied in detail in this investigation. Cross sections of pipes that were obtained by anodic oxidation were found to be in qualitative agreement with theory. Three types of pipes were found corresponding to the theoretically postulated type shapes: ellipsoid (I), hyperbola of rotation (II), and submerged hyperbola of rotation (IV). The existence of the latter type, which had only been postulated theoretically, was thus confirmed.

Deviations from the calculated shapes can be explained by enhanced diffusion close to the surface.

Measurement of the ohmic resistance of a number of pipes gave satisfactory agreement between optically and electrically determined pipe diameters.

Acknowledgments

The authors wish to thank W. Shockley for many helpful suggestions. They also are indebted to B. McDonald and R. Julien for the preparation of samples. This research was supported by Air Force Cambridge Laboratories under Contract AF 19(604)8060.

Manuscript received Jan. 15, 1962.

Any discussion of this paper will appear in a Discussion Section to be published in the June 1963 JOURNAL.

REFERENCES

1. A. Goetzberger, To be published in *Solid State Electronics;* also *IRE Trans. E. D.*, **8**, 429 (1961), and Interim Scientific Report No. 1, Contract AF 19(604) 8060.
2. P. S. Flint, Paper given at the Detroit Meeting, Electrochemical Society, October 1961.
3. P. F. Schmidt in "Semiconductors and Phosphorus," p. 570, Interscience Publishers, New York (1958).
4. E. Tannenbaum, *Solid State Electronics*, **2**, 123 (1961).
5. B. McDonald and F. C. Collins, *Bull. Am. Phys. Soc.*, **6**, 106 (1961).
6. C. S. Fuller and J. A. Ditzenberger, *J. Appl. Phys.*, **27**, 544 (1956).
7. A. Goetzberger and W. Shockley, *Bull. Am. Phys. Soc.*, **4**, 455 (1959).
8. B. D. James and P. S. Flint, Paper given at the Chicago Meeting, Electrochemical Society, April-May 1960.
9. W. Shockley, "Electrons and Holes in Semiconductors," p. 99, D. Van Nostrand Co., Inc., Princeton, N. J.

Hysteresis in the Large-Signal Field Effect in Semiconductor Surfaces

D. R. Frankl

General Telephone & Electronics Laboratories Inc., Bayside, New York

ABSTRACT

The finite generation and recombination rates of excess minority carriers can lead to large hysteresis effects even at frequencies $<<(2\pi\tau)^{-1}$ in large-signal field effect measurements. The hysteresis loop occurs on the inversion-layer side of the conductance *vs.* field curve and widens with increasing frequency and with increasing minority carrier lifetime in the sample. Experimental results on germanium and a simple theoretical treatment are presented.

Owing to the existence (usually) of a large concentration of slow surface states in semiconductors, any changes in sample properties induced by constant transverse electric fields tend to decay to zero. In other words, equilibrium field effects usually vanish. However, since at least in most germanium and silicon surfaces there is a large separation in the time constants of the slow and fast states, it is often possible to achieve a "quasi-equilibrium" condition, with the carriers in the bands and the fast states virtually in equilibrium, but with the carriers in the slow states virtually unaffected. The usual analysis (1) of field-induced conductance changes, to obtain information about the fast states, entails the implicit assumption that this condition exists.

The experimental requirement is that the time variations of the applied field be too rapid to be followed by the slow states, yet slow enough to be followed by all other processes affecting the carrier concentrations. These include drift and diffusion of free carriers, trapping in and release from fast states, and generation and recombination of minority carriers.

The latter processes are of principal concern in this paper. As is well known (2), under small-signal a-c conditions their finite rates lead to a relaxation in the field-effect mobility, centered at a frequency $f = (2\pi\tau)^{-1}$ (τ = sample lifetime), which for ordinary samples lies in the neighborhood of 10 kcps. Under large signal conditions, this effect can lead to appreciable departures from quasi-equilibrium even at much lower frequencies, and these give rise to hysteresis in the curve of conductance *vs.* applied field. The purpose of this paper is to illustrate this hysteresis effect, and to present a simple theoretical treatment to account for the order of magnitude of the observed deviations.

Theory

We consider, for definiteness, a p-type sample, and let P, N, and N_t be, respectively, the numbers per unit area of free holes, free electrons, and electrons trapped in fast surface states, all measured relative to some arbitrary reference level such as the flat-band condition. Also let P^0, N^0, and N_t^0 be the corresponding quasi-equilibrium values of these quantities. Then the induced surface charge density at any instant is

$$CV = -e(\Delta P - \Delta N - \Delta N_t) \qquad [1]$$

where C is the capacitance per unit area between field plate and sample, V the applied voltage, Δ denotes change from zero-voltage value. The excess surface conductance is, neglecting the surface mobility correction (3) which is usually small

$$\Delta\sigma = e(\mu_n\Delta N + \mu_p\Delta P)$$
$$= e[\mu_n\Delta N + \mu_p(\Delta N + \Delta N_t - CV/e)] \qquad [2]$$

where μ_n and μ_p are the electron and hole mobilities, respectively, Hence, the departure from the quasi-equilibrium conductance is

$$\delta\sigma = e[(\mu_n + \mu_p)\,\delta N + \mu_p\delta N_t] \qquad [3]$$

where $\delta N \equiv N - N^0$, etc.

It remains to compute δN and δN_t from the rate equations governing the approach to quasi-equilibrium. These are, in general, quite complicated (4), and an exact treatment was not attempted. Instead, we introduce the following simplifying assumptions:

1. The carriers in each band are separately in equilibrium among each other. This requires that the field period be >> the time constant for redistribution, by diffusion, of localized excess carrier concentrations. From the diffusion equation, this time constant may be estimated to be $\leq B^2/D$ (D is the diffusion constant, $2B$ the sample thickness) which is, for germanium at room temperature, about 10^{-5} sec. Hence, the assumption should be reasonably valid for the low frequencies of interest here. Since the assumed distribution is essentially the same as the fundamental decay mode distribution (6) for small surface recombination velocity, this assumption permits us to write the rate equations in terms of the ordinary lifetime, as measured, for example, in photoconductive decay.

2. The transitions between the traps and at least one of the bands are so rapid (2) that the trapped carriers are always in equilibrium with this band. Then two limiting cases may be distinguished, depending on which band this is.

Case A, Traps in equilibrium with conduction band.—In this case, as the applied field is increasing electrons are generated and some of these fall into the traps. Hence

$$\frac{dN}{dt} = \frac{N^0 - N}{\tau} - \frac{dN_t}{dt} \qquad [4]$$

Note that this equation gives an underestimate for dN/dt since, in actuality, some fraction of the rate dN_t/dt comes from transitions to the valence band. This must be so because at least some of the surface states are the generation-recombination centers. In discussing this case, therefore, we are assuming that these centers comprise a negligible fraction of all the fast states. Since the latter are in equilibrium with the conduction band, we may take

$$\frac{dN_t}{dt} = \beta \frac{dN}{dt} \qquad [5]$$

where

$$\beta = \frac{dN_t}{dN} \cong \frac{dN_t^0}{dN^0} \qquad [6]$$

Then [4] becomes, in terms of the phase angle $\phi = \omega\tau$

$$\frac{d\,\delta N}{d\phi} + \frac{\delta N}{(1+\beta)\omega\tau} = -\frac{dN^0}{d\phi} \qquad [7]$$

The solution that vanishes at the accumulation-layer extreme of the voltage cycle (taken as $\phi = 0$) is

$$\delta N(\phi) = -\int_0^{\phi} d\phi' \frac{dN^0}{d\phi'} \exp\left[-\int_{\phi'}^{\phi} \frac{d\phi''}{(1+\beta)\omega\tau}\right] \qquad [8]$$

If ω is not too large, the exponential factor is very small except when $\phi' \cong \phi$, so that we may approximate [8] by

$$\delta N(\phi) \cong -\int_0^{\phi} d\phi' \frac{dN^0}{d\phi'} \exp\left[\frac{\phi' - \phi}{[1+\beta(\phi)]\omega\tau(\phi)}\right]$$

$$\cong -(1+\beta)\omega\tau \frac{dN^0}{d\phi}\left[1 - \exp\frac{-\phi}{(1+\beta)\omega\tau}\right]$$

$$\cong -(1+\beta)\omega\tau\, dN^0/d\phi \qquad [9]$$

This result states that N lags behind N^0 by the amount that the sum of $N^0 + N_t^0$ changes in one lifetime. Physically, the reason for this is that $N + N_t$ together form an equilibrium population that is generated at a rate proportional to the deficit in N only.

From [5] we have

$$\delta N_t = \beta\, \delta N \qquad [10]$$

and Eq. [9] and [10] provide the values to be inserted in [3]. The computation will be illustrated in the next section.

Case B, Traps in equilibrium with valence band.—In this case, the rapid communication with the majority-carrier band keeps δN_t always essentially equal to zero. The sole rate equation is then simply

$$\frac{dN}{dt} = \frac{N^0 - N}{\tau} \qquad [11]$$

giving, in the same approximation as was used in [9],

$$\delta N(\phi) = -\omega\tau(\phi) \frac{dN^0}{d\phi} \qquad [12]$$

Experimental Results and Discussion

The experimental method used in this work has been described in detail elsewhere (7). In brief, a small constant current is passed through the sample (a thin plate) and the voltage drop between two probes is displayed on the Y axis of an oscilloscope while the field voltage is displayed on the X axis. Thus, with suitable scale factors and with proper precautions to balance out spurious signals due to the displacement current, the oscillogram gives directly $\Delta\sigma$ *vs* V. With the addition of chopped light, τ can also be measured from the instantaneous photoconductance.

Typical dark curves for a p-type sample are shown in Fig. 1. The hysteresis occurs in the n-type surface conductivity branch of the curve and increases with increasing frequency. With n-type samples the hysteresis occurs in the other branch. And with either type of sample the width of the loop at a given frequency may vary widely depending on the surface treatment; with high-lifetime surfaces the loop is wide and *vice versa*.

The computation of the quantities entering Eq. [9], [10], and [12] is illustrated in Fig. 2, 3, and 4. Values of u_s are obtained by the usual analysis (1) of the lowest-frequency curve, and N^0 is then calculated as $N^0 = n_i L_D G(u_s, u_B)$, where n_i is the intrinsic concentration, L_D the Debye length, and G is the function tabulated by Kingston and Neustadter (8) and others (9); finally, $dN^0/d\phi$ is obtained by graphical differentiation. These quantities are shown in

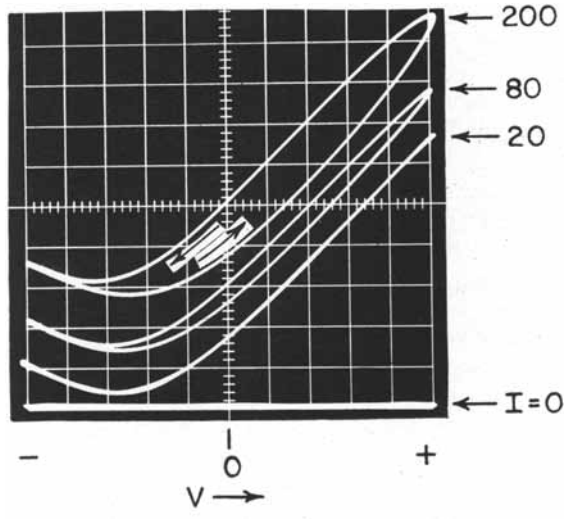

Fig. 1. Oscillograms of conductance vs. voltage on field plate at frequencies of 20, 80, and 200 cps for a p-type Ge sample. The field amplitude was about 10^5 v/cm. The line marked $I = 0$, obtained with no current through the sample, illustrates the cancellation of spurious signals.

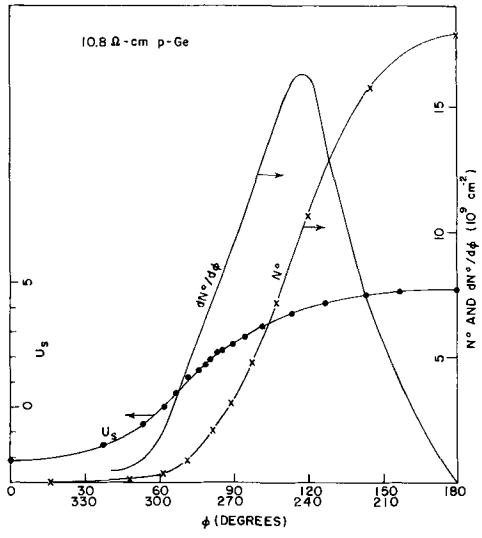

Fig. 2. Values of u_S, N°, and $dN^\circ/d\phi$, as functions of the phase angle ϕ.

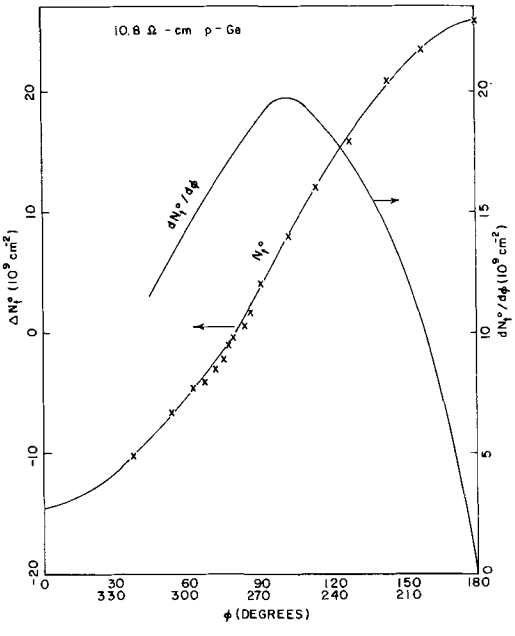

Fig. 3. Values of N_t° and $dN_t^\circ/d\phi$ as functions of the phase angle ϕ.

Fig. 2. N_t° and $dN_t^\circ/d\phi$, computed similarly, are shown in Fig. 3. Finally β, the ratio of the two derivatives, and τ, measured separately, are shown in Fig. 4.

The hysteresis data obtained on the same surface at higher frequencies are illustrated in Fig. 5. Here the total vertical separation $2|\delta\sigma|$ between the branches of the loop is plotted as function of the applied voltage. (Note that $V = -V_a \cos\phi$ as we have defined ϕ). Calculated curves for the two limiting cases discussed above are also shown. It is seen that the curve for Case A fits the data quite well at the right-hand end, but deviates markedly at the left. This deviation occurs because at these low values of u_S, the assumption of no communication between traps and valence band is untenable. At the extreme left-hand end of the loop, the curve for Case B gives an approximate fit to the data, but it is clear that over an appreciable range of surface potentials the true situation is intermediate between the two limiting cases. We shall not attempt to analyze this in detail.

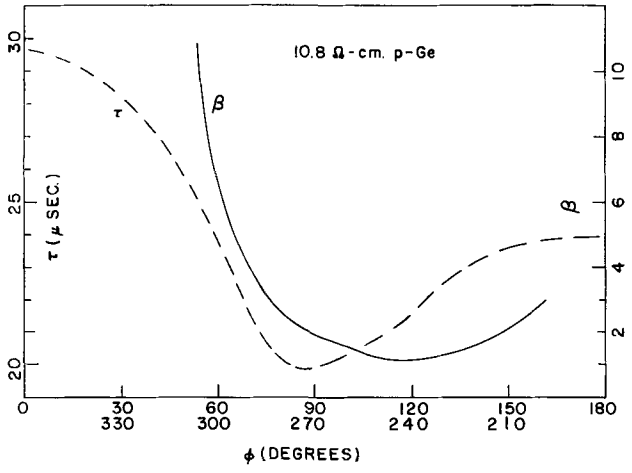

Fig. 4. Values of β and τ as functions of the phase angle ϕ

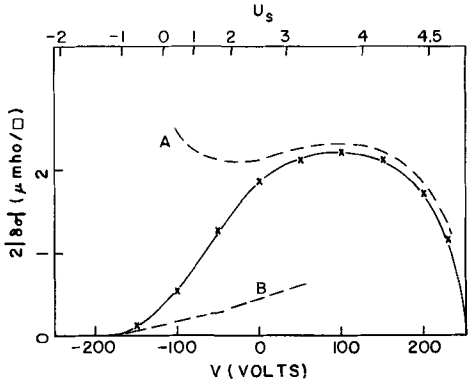

Fig. 5. Total vertical separation $2|\delta\sigma|$ between branches of hysteresis loop at 200 cps. Solid line is experimental; broken lines are theoretical for the two limiting cases discussed in the text.

The loop width at constant ϕ is found experimentally to be quite closely proportional to the frequency, as predicted by Eq. [9], [10], and [12], over the range from about 100 to 500 cps. However, below about 100 cps, the widths deviate from proportionality toward smaller values. The reason is the onset of another hysteresis mechanism, the exchange of charge with the slow surface states, which produces a loop that extends over the entire curve and widens with decreasing frequency. It is usually, although not always, possible to find a frequency at which the over-all hysteresis is negligible.

At frequencies above about 500 cps (in the present samples) still another effect was observed to set in: the mean of the two branches of the hysteresis loop sags below the equilibrium curve. This corresponds to the beginning of the field-effect mobility relaxation found by Montgomery (2). In samples with very high lifetime, this effect would set in at lower frequencies and might cause appreciable errors in field-effect measurements. This is particularly true when point-by-point methods (10) are used, since the hysteresis might easily be overlooked. It is one of the advantages of the oscilloscope method used here that any appreciable hysteresis present is clearly evident and serves as a warning that caution must be exercised in interpreting the results.

Acknowledgments

It is a pleasure to thank A. E. Feuersanger for assistance in the experiments and helpful discussions. Especial thanks are due also to H. C. Montgomery for pointing out some deficiencies in an earlier formulation of the theory.

Manuscript received Oct. 18, 1961; revised manuscript received Jan. 18, 1962. This paper was prepared for delivery before the Detroit Meeting, Oct. 1-5, 1961.

Any discussion of this paper will appear in a Discussion Section to be published in the June 1963 JOURNAL.

REFERENCES

1. H. C. Montgomery and W. L. Brown, *Phys. Rev.*, **103**, 865 (1956).
2. H. C. Montgomery, *ibid.*, **106**, 441 (1956).
3. J. R. Schrieffer, *ibid.*, **97**, 641 (1955); R. F. Greene, D. R. Frankl, and J. Zemel, *ibid.*, **118**, 967 (1960).
4. For treatments of the small-signal case, cf. C. G. B. Garrett, *ibid.*, **107**, 478 (1957) and F. Berz, *J. Electronics and Control*, **6**, 97 (1959).
5. A. Many and R. Bray, article in "Progress in Semiconductors," A. F. Gibson, Editor, **3**, 117, John Wiley & Sons, Inc., New York (1958).
6. W. Shockley, "Electrons and Holes in Semiconductors," p. 318 ff, D. Van Nostrand Co., Inc., New York (1950).
7. D. R. Frankl, *This Journal*, **109**, 238 (1962).
8. R. H. Kingston and S. F. Neustadter, *J. Appl. Phys.*, **26**, 718 (1955).
9. D. R. Frankl, *ibid.*, **31**, 1752 (1960); C. E. Young, *ibid.*, **32**, 329 (1961).
10. A. Many and D. Gerlich, *Phys. Rev.*, **107**, 404 (1957).

Thermodynamic Functions for the Tantalum-Hydrogen System

M. W. Mallett and B. G. Koehl

Battelle Memorial Institute, Columbus, Ohio

ABSTRACT

Equilibria in the tantalum-hydrogen system were determined in the range 300°-700°C, at hydrogen pressures of 10-1000 mm of Hg, and atomic fractions, N_H, 0.05-0.333. A single-phase solid solution of hydrogen in tantalum was produced throughout the experimental ranges. Obedience to Sieverts' law is approached at 500°C and higher for compositions below $N_H = 0.20$. The data were used to calculate the relative partial molar and total enthalpies, entropies, and free energies for formation of the solid solutions.

In order to evaluate properly the effects of interstitial elements on the mechanical properties of a metal, it is useful and, in some cases, necessary to know their kinetics of sorption by and diffusion in the metal. The literature is lacking in this type of information for the behavior of hydrogen and tantalum. At the temperatures of interest, above 300°C, the tantalum-hydrogen system shows a continuous solid solution up to compositions corresponding to $TaH_{0.5}$ and higher. It has been demonstrated (1, 2) that kinetic data for such a system are more readily rationalized when kinetic experiments are designed to produce a reaction product of constant composition. Therefore, it was necessary to know the equilibria of the tantalum-hydrogen system before starting the kinetic experiments. A number of earlier observations on the solubility of hydrogen in tantalum have been made (3). However, all of the data, with exception of those of Sieverts and Bergner and Sieverts and Brüning, appear to suffer from the impurity of the tantalum. The results show gross effects presumably of dissolved or surface oxide inhibiting reaction and quantitatively affecting the solution. Sieverts' equilibria were too limited for our purpose since they are largely for a pressure of 760 mm of Hg.

A recent paper (4) by Kofstad, Wallace, and Hyvönen gave good equilibrium data for a number of compositions of interest and for temperatures up to 400°C. Because our study was to cover temperatures up to 700°C, it was necessary to determine equilibria for the temperature range of 400°-700°C not covered by the literature. In addition, data were taken at 300°-400°C for comparison with the work of Kofstad *et al.*

Also, some thermodynamic functions readily obtainable from the equilibrium factors were calculated.

Material

The tantalum used in this work was obtained from the Wah Chang Corporation of Albany, Oregon. It had been electron-beam melted to an ingot, 3½ in. in diameter, and cold forged and swaged to a 7/16-in. diameter. Final fabrication was carried out at Battelle and consisted of cold swaging to rod, ¼ and ⅛ in. in diameter, and vacuum annealing for 1 hr at 1200°C. A length of the ⅛-in. rod was cold rolled to 0.0146-in. sheet for equilibrium experiments. The analysis of the tantalum before final fabrication is given in Table I.

Pure hydrogen was obtained from the thermal decomposition of uranium hydride prepared from dry tank hydrogen and degreased uranium chips.

Equilibrium Studies

Experimental procedure.—The method to obtain equilibrium data has been described (5). Briefly, the data were obtained as follows: A measured quantity of hydrogen was added to the calibrated reaction tube containing approximately 4g of sheet tantalum. At the desired temperature, the system was allowed to come to constant (equilibrium) pressure as measured on a mercury manometer. The equilibrium composition was calculated from the equilibrium

Table I. Analysis of tantalum

Element	PPM by weight
Al	<20
B	<1
C	42
Cd	<1
Cr	<20
Cu	<40
Fe	<100
Mg	<20
Mn	<20
Mo	<20
Nb	700
Ni	<20
Pb	<20
Si	<100
Sn	<20
Ti	<150
V	<20
W	<300
Zn	<20
H_2	<2*
O_2	<20*
N_2	3

Average BHN 80.1
* Vacuum-fusion analysis after final fabrication.

pressure, specimen weight, volume of gas addition, and gas capacity of the reaction system at the experimental room and furnace temperatures.

Results

The pressure-temperature-composition equilibria of the tantalum-hydrogen system were determined in the range 300°-700°C, 10-1000 mm Hg pressure, and atomic ratios, H/Ta, of about 0.05-0.50. These atomic ratios correspond to atomic fractions N_H for hydrogen of about 0.05-0.333. Equilibrium pressures were measured for at least three different temperatures for each composition. Figure 1 is a logarithmic plot of the equilibrium pressure against the H/Ta ratio. The plot shows that the isotherms are linear at temperatures of 500°C and higher; at lower temperatures, the isotherms show curvature which becomes increasingly marked with decrease in temperature. This curvature suggests a trend toward the formation of two phases at lower temperatures. However, since none of the isotherms shows an invariant pressure, no two-phase region was indicated in our experimental range. It seems that such a region would appear only at some temperature below 100°C.

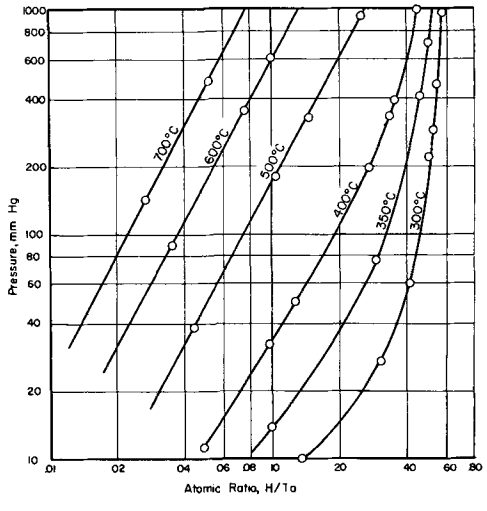

Fig. 1. Logarithmic plot of isotherms in the Ta-H system. Additional points at 300°C: 5.3 mm at H/Ta = 0.05, 7.4 mm at H/Ta = 0.10.

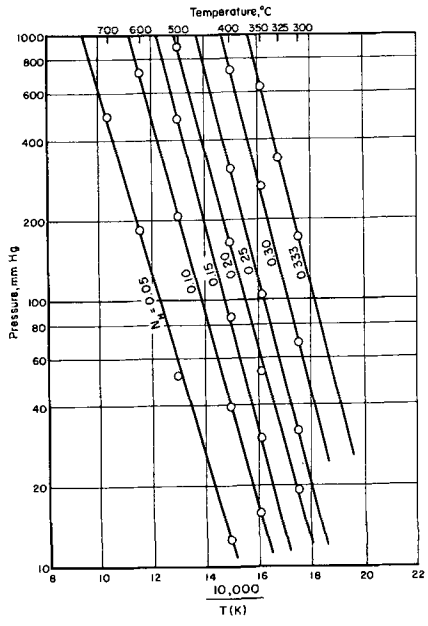

Fig. 2. Representative isopleths for the Ta-H system

After completion of this paper, a thesis by Veleckis (6) came to the authors' attention. He calculated the critical temperature to be −58.5°C at the H/Ta ratio of 0.205.

The equilibria were interpreted in terms of the conditions needed to form various products (solid solutions) having definite H/Ta and N_H ratios. This placed the data in the most convenient form for use in subsequent kinetic experiments. Several representative constant composition lines or isopleths are shown in Fig. 2. The equilibria for a given composition in these plots of logarithm of equilibrium pressure against reciprocal temperature can be expressed as

$$\log_{10} P_{mm} = -[A/T\ (K)] + B \qquad [1]$$

Values for the constants A and B determined by the method of least squares are given in Table II.

Since it may be desirable to relate thermodynamic and kinetic properties rather directly, the compositions are listed primarily according to round N_H values or atomic fractions of H.

Table II. Equations for equilibrium pressures

N_H*	Atom ratio, H/Ta	Constants in** $\log_{10} P_{mm} = -A/T + B$	
		A	B
0.05	0.0526	3480 ± 50	6.26 ± 0.06
0.10	0.1111	3620 ± 30	7.00 ± 0.05
0.15	0.1765	3860 ± 10	7.69 ± 0.02
0.20	0.2500	3740 ± 80	7.78 ± 0.13
0.25	0.3333	3800 ± 60	8.14 ± 0.09
0.30	0.4286	3960 ± 110	8.77 ± 0.17
0.333	0.5000	4020 ± 5	9.26 ± 0.01

* N_H = atomic fraction of H.
** ± values in this table are the probable errors for A and B.

Table III. Equilibrium pressure isotherms for Ta-H solid solutions

$\text{Log}\ \frac{\sqrt{P}}{N_H}$ mm

N_H	300°	304°*	325°	324°*	350°	349.5°*	400°	402°*	500°	600°	700°
0.05	1.391	1.305		1.420	1.635	1.579	1.842	1.819	2.177	2.435	2.640
0.10	1.343	1.305		1.420	1.596	1.579	1.811	1.819	2.163	2.427	
0.15	1.294	1.305		1.420	1.564	1.579	1.795	1.819	2.167		
0.20	1.327	1.307		1.423	1.590	1.581	1.812	1.822	2.171		
0.25	1.355	1.351		1.470	1.621	1.637	1.848	1.882			
0.30	1.450	1.487		1.613	1.728	1.757	1.964	(2.011)**			
0.333	1.599	1.649	1.746	1.777	1.880	(1.909)**	2.124	(2.158)**			

* Data from ref. (4). All temperatures in °C.
** Values extrapolated from low-temperature isotherms.

A comparison of the equilibrium pressure isotherms of the present study and those of Kofstad *et al.* is given in Table III. The agreement between the two sets of data is reasonable. A point worthy of note is that the pressures for the higher concentrations are consistently lower for the present study. This may indicate that our tantalum contained less interstitial contamination, particularly oxygen, than the metal of Kofstad. As will be seen later, the lower pressures also are reflected in lower relative partial molar free energy values at 350°C.

Also, it appears from the collective data that the Sieverts law is obeyed approximately for the N_H composition range 0.05-0.20. This is evidenced by the (relative) invariance of the value of $\log \sqrt{P}/N_H$ for different compositions at a given temperature. Large deviations from the Sieverts law are seen for higher compositions. That these deviations are related to entropy effects rather than enthalpy changes will be shown later. Deviations were also found by Kofstad at compositions lower than those of this study.

Thermodynamic Functions

When the dissolution of hydrogen in tantalum is expressed as

$$\tfrac{1}{2}\,H_2\ (\text{gas}) \rightleftharpoons H_i\ (\text{dissolved in Ta}) \qquad [2]$$

the relative partial molar free energy of hydrogen in a given Ta-H solution (i) is

$$\bar{F}_{H_i} - \tfrac{1}{2}F^\circ_{H_2} = RT \ln (P_{H_2})^{1/2} \qquad [3]$$

P_{H_2} is the pressure of hydrogen gas in equilibrium with the solution at temperature T and R is the gas constant.

The values for the relative partial molar enthalpies, $\bar{H}_H - H^\circ_{H_2}/2$, and entropies, $\bar{S}_H - S^\circ_{H_2}/2$, were calculated by the method of least squares from plots of $\log \sqrt{P}$ against reciprocal temperature. This treatment also yielded the probable errors for these values. The free energy values were then calculated according to

$$\Delta F = \Delta H - T\Delta S \qquad [4]$$

which applies to both the integral and partial molar quantities. The calculated relative partial molar thermodynamic functions for hydrogen in solution in tantalum are given in Table IV.

The relative partial molar enthalpy (the negative of the heat of dissociation) decreases systematically with increasing hydrogen content, if the value for

Table IV. Relative partial molar thermodynamic functions* for hydrogen in Ta-H solid solutions

	N_H:	0.05	0.10	0.15	0.20	0.25	0.30	0.333
				This Study				
Temperature range, °C		400°-700°	350°-600°	300°-500°	300°-500°	300°-400°	300°-400°	300°-350°
$\bar{F}_H - \frac{F^\circ_{H_2}}{2}$	cal/g-atom	−3149	−2406	−1987	−1566	−1202	−673	−104
$\bar{S}_H - \frac{S^\circ_{H_2}}{2}$	eu/g-atom	−7.73 ± 0.14‡	−9.42 ± 0.10	−11.00 ± 0.04	−11.21 ± 0.29	−12.02 ± 0.21	−13.47 ± 0.40	−14.60 ± 0.03
$\bar{H}_H - \frac{H^\circ_{H_2}}{2}$	cal/g-atom	−7965 ± 115‡	−8275 ± 75	−8840 ± 25	−8550 ± 190	−8690 ± 130	−9065 ± 245	−9200 ± 15
				From ref. (4) for 350°C				
$\bar{F}_H - \frac{F^\circ_{H_2}}{2}$	cal/g-atom	−3310	−2510	−2010	−1600	−1210	−520	−1
$\bar{S}_H - \frac{S^\circ_{H_2}}{2}$	eu/g-atom	−9.9	−11.1	−12.1	−12.7	−13.6	−14.8	−14.9
$\bar{H}_H - \frac{H^\circ_{H_2}}{2}$	cal/g-atom	−9500	−9400	−9500	−9500	−9700	−9700	−9300

* The relative partial molar free energies, enthalpies, and entropies are for 1 g-atom of hydrogen.
† These free-energy values are for 350°C only.
‡ The ± values in this table are probable error.

N_H 0.15 is omitted. This indicates an increase in hydrogen binding in the Ta-H lattice over the N_H range 0.05-0.333. This agrees with the conclusions of Kofstad who reported an increase in partial heat of dissociation.

The relative partial molar entropy also decreases rapidly with increasing hydrogen contents. This may be caused by the decreasing availability of interstitial sites as more hydrogen is added to the metal. Thus, the enthalpy and entropy changes in the tantalum-hydrogen system make for opposite deviations in behavior from Sieverts' law. However, abnormal increases in pressure are observed with increasing hydrogen concentration indicating that the entropy effect is the stronger. This, of course, is a demonstration of a rise in relative partial molar free energy, $\bar{F} - F^{\circ}_{H_2}/2$, such as shown by calculated values for 350°C given in Table IV.

The relative partial molar enthalpies and entropies of the tantalum-hydrogen system show the same trends and are of the same general magnitude as those of the niobium-hydrogen system (7). However, for a given temperature and composition, the tantalum-hydrogen system shows the higher dissociation pressure of hydrogen, *i.e.*, the relative partial molar free energy for the dissolution reaction is higher.

An equation for calculating the partial molar free energy for tantalum in a given solution and the total free energy of formation of the solution was obtained by modification of the Duhem-Margules equation (8)

$$N_{Ta}\, d\bar{F}_{Ta} + N_H\, d\bar{F}_H = 0 \qquad [5]$$

where N is the mole or atom fraction. Since $N_{Ta} + N_H = 1$

$$N_{Ta}\, d \ln N_{Ta} + N_H\, d \ln N_H = 0 \qquad [6]$$

From Eq. [3]

$$d\bar{F}_H = RT\, d \ln P^{1/2}_{H_2} \qquad [7]$$

at constant temperature. Transposing one term of Eq. 5, dividing by N_{Ta}, and then substituting the equivalent of $d\bar{F}_H$ from Eq. [7]

$$d\bar{F}_{Ta} = -\frac{N_H}{N_{Ta}}\, d\bar{F}_H = -RT\frac{N_H}{N_{Ta}}\, d \ln P^{1/2}_{H_2} \qquad [8]$$

Also, from Eq. [6] by multiplying by RT and dividing by N_{Ta}

$$RT\, d \ln N_{Ta} + RT\frac{N_H}{N_{Ta}} \ln N_H = 0 \qquad [9]$$

Subtracting Eq. [9] from [8]

$$d\bar{F}_{Ta} = RT\, d \ln N_{Ta} - RT\frac{N_H}{N_{Ta}}\, d \ln \frac{P^{1/2}_{H_2}}{N_H} \qquad [10]$$

Integrating, we obtain

$$\bar{F}_{Ta_i} - F^{\circ}_{Ta} = RT\left[\ln N_{Ta_i} - \int_{N_H=0}^{N_{H_i}} \frac{N_H}{N_{Ta}}\, d \ln \frac{P^{1/2}_{H_2}}{N_H}\right] \qquad [11]$$

which is the equation for the relative partial molar free energy for tantalum in solution. The standard reference states at any temperature are 1 atm pressure for hydrogen and the pure hydrogen-free condition for tantalum.

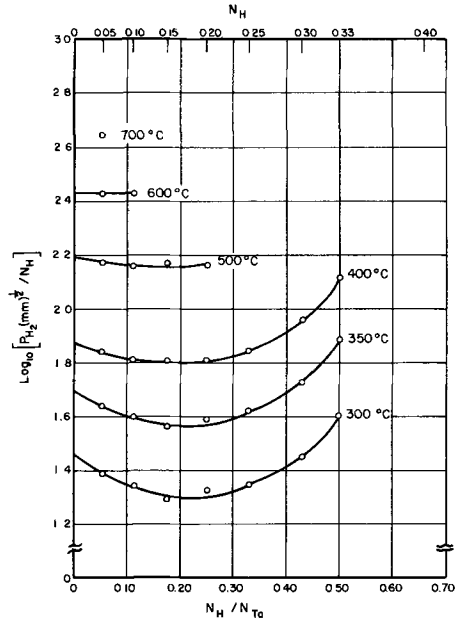

Fig. 3. Equilibrium isotherms for the tantalum-hydrogen system

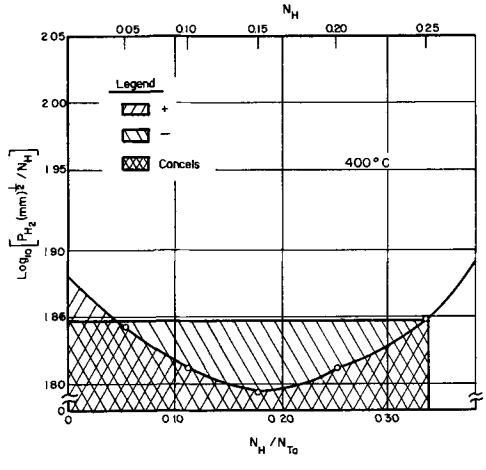

Fig. 4. Integration for $N_H = 0.25$ at 400°C

The negative integral in Eq. [11] is the natural logarithm of the activity coefficient of tantalum in a solution (i). To solve the equation it is necessary to integrate the last term graphically. To help visualize the areas to be integrated it is useful to consider the case of integration by parts where the negative integral becomes

$$-N_{H_i}/N_{Ta_i} \ln \frac{P^{1/2}_{H_2}}{N_{H_i}} + \int_{N_H=0}^{N_{H_i}} \ln \frac{P^{1/2}_{H_2}}{N_H}\, d\, N_{H_i}/N_{Ta_i}$$

Figure 3 shows several equilibrium isotherms plotted for integration. The 500° and 600°C curves approach the horizontal position which would indicate obedience to Sieverts' law. Figure 4 is a plot of a typical curve expanded for graphical integration. The negative and positive areas involved for the composition, $N_H = 0.25$ are indicated. The regions of overlap where the terms cancel each other are shown in cross-hatch. The computed relative partial

Table V. Relative partial molar free energies for tantalum in tantalum-hydrogen solutions

	$\bar{F}_{Ta_i} - F°_{Ta}$ (cal/mole of alloy)					
	Temperature, °C					
N_{Ta}	300°	350°	400°	500°	600°	700°
0.95	—54.0	—56.8	—62.8	—77.0	—87.4	—99.2
0.90	—105	—113	—128	—156	—179	
0.85	—159	—175	—198	—246		
0.80	—222	—257	—286	—341		
0.75	—329	—374	—408			
0.70	—527	—576	—640			
0.666	—754	—839	—935			

molar free energies for tantalum are listed in Table V.

The equation for the total free energy of formation for a given solution (i) is a combination of Eq. [3] and [6].

$$\Delta F_{f_i} = N_{H_i}\left(\bar{F}_{H_i} - \frac{1}{2}F°_{H_2}\right) + N_{Ta_i}(\bar{F}_{Ta_i} - F°_{Ta}) \quad [12]$$

Values for ΔF_{f_i} are given in Table VI. Equations of the same basic form as Eq. [11] and [12] were used by Katz and Gulbransen (7) for calculating the thermodynamic functions for the columbium-hydrogen system.

Both the relative partial molar free energy values (for tantalum) *vs.* temperature plots and the total free energy *vs.* temperature plots for each composition were linear. Therefore, the respective enthalpy and entropy functions and their probable errors could be calculated by a least squares treatment of the data for a given composition. It follows that both functions were invariant over the experimental temperature range. The relative partial molar enthalpies and entropies of tantalum in several hydrogen-in-tantalum solutions are given in Table VII. Corresponding total enthalpies and entropies for these solutions ranging in compositions from $N_H = 0.05$ to 0.333 are given in Table VIII.

Data of Kofstad *et al.* (4) are listed for comparison in Tables VI and VIII. Although their total enthalpies ranged from 96 to 307 cal/mole higher than those of our study their total free energies were higher by only 7 to 27 cal/mole.

The uncertainties in the values of $\bar{H}_{Ta_i} - H°_{Ta}$ and $\bar{S}_{Ta_i} - S°_{Ta}$ in the present study are from 9 to 30% and 2 to 5%, respectively. Since the investigations of similar systems have either omitted presenting uncertainties in values for these functions or even the values themselves, no comparison can be made. However, because of the indirect means of deriving these values the uncertainties appear quite reasonable. It is seen that the uncertainties in the values for relative partial molar energy functions for tantalum have an insignificant effect on the total energy functions. This is evidenced by the probable errors for ΔH_f and ΔS_f which are of the order of only 1%.

Table VI. Total free energies of formation in the tantalum-hydrogen system

	ΔF_f (cal/mole of alloy)						
	Temperature, °C						
N_H	300°	350°	350°*	400°	500°	600°	700°
0.05	—228	—211	(—230)	—198	—173	—144	—116
0.10	—382	—343	(—370)	—308	—240	—166	
0.15	—516	—447	(—470)	—348	—260		
0.20	—603	—518	(—540)	—430	—250		
0.25	—697	—581	(—600)	—457			
0.30	—773	—605	(—620)	—448			
0.333	—780	—593	(—600)	—414			

* Data from ref. (4).

Table VII. Relative partial molar enthalpies* and entropies† of tantalum in tantalum-hydrogen solutions

N_{Ta}	$\bar{H}_{Ta_i} - H°_{Ta}$	Probable error	$\bar{S}_{Ta_i} - S°_{Ta}$	Probable error
0.95	14.8	±2.1	0.117	±0.003
0.90	42.9	±4.1	0.255	±0.006
0.85	100	±11	0.445	±0.017
0.80	115	±10	0.593	±0.015
0.75	127	±27	0.798	±0.043
0.70	119	±37	1.12	±0.06
0.666	286	±26	1.81	±0.04

* Cal/mole of alloy.
† Cal/deg-mole of alloy.

Acknowledgments

The authors wish to express their appreciation for the sponsorship of this research by Materials Central, Directorate of Advanced Systems Technology, Wright Air Development Division, Wright-Patterson Air Force Base, Ohio, and for permission to publish this paper. The work was performed under Contract No. AF-33(616)-7604. They also wish to thank Dr. John W. Droege of Battelle Memorial Institute for his helpful discussions.

Manuscript received Dec. 15, 1961; revised manuscript received March 7, 1962. This paper was prepared for delivery before the Los Angeles Meeting, May 6-10, 1962.

Any discussion of this paper will appear in a Discussion Section to be published in the June 1963 JOURNAL.

REFERENCES

1. W. M. Albrecht and M. W. Mallett, *This Journal*, **105**, 610 (1958).
2. W. M. Albrecht, W. D. Goode, Jr., and M. W. Mallett, *ibid.*, **106**, 981 (1959).

Table VIII. Total enthalpies* and entropies† of formation in the tantalum-hydrogen system

N_H	ΔH_f	Probable error	ΔS_f	Probable error	Kofstad's data ΔH_f	Kofstad's data ΔS_f
0.05	—384	±2	—0.275	±0.003	—480	—0.40
0.10	—789	±4	—0.713	±0.005	—940	—0.92
0.15	—1242	±10	—1.27	±0.01	—1410	—1.5
0.20	—1618	±8	—1.76	±0.01	—1860	—2.1
0.25	—2077	±20	—2.41	±0.03	—2370	—2.8
0.30	—2636	±27	—3.25	±0.04	—2860	—3.6
0.333	—2873	±17	—3.66	±0.03	—3180	—4.08

* Cal/mole of alloy.
† Cal/deg-mole of alloy.

3. G. L. Miller, "Tantalum and Niobium," pp. 445-447, Academic Press, Inc., New York, (1959).
4. P. Kofstad, W. E. Wallace, and L. J. Hyvönen, *J. Am. Chem. Soc.*, **81**, 5015 (1959).
5. W. M. Albrecht, M. W. Mallett, and W. D. Goode, Jr., *This Journal*, **105**, 216 (1958).
6. E. Veleckis, "Thermodynamic Properties of the System Nb-H, V-H, and Ta-H," AFOSR-1107.
7. O. M. Katz and E. A. Gulbransen, "Thermodynamic Functions for the Columbium-Hydrogen System," Scientific Paper 11-0807-11-P3, May 20, 1960, Westinghouse Research Lab. Presented at Columbium Metallurgy Symposium, Lake George, N. Y., June 6, 1960.
8. L. S. Darken and R. W. Gurry, "Physical Chemistry of Metals," p. 259, McGraw-Hill Book Co., Inc. (1953).

New Experiments on Thermoosmosis

Charles W. Carr and Karl Sollner

Department of Physiological Chemistry, University of Minnesota, and Laboratory of Physical Biology, National Institute of Arthritis and Metabolic Diseases, National Institutes of Health, Bethesda, Maryland

ABSTRACT

Thermoosmosis, the transport of liquid across a membrane which separates two solutions of identical composition but different temperature, was studied by means of a specially constructed apparatus. No thermoosmosis was observed with water or aqueous solutions of nonelectrolytes. With aqueous solutions of electrolytes thermoosmosis occurs across electrically charged membranes but not across uncharged membranes. While thermoosmotic effects are small their reproducibility is good. The rate of thermoosmosis is proportional to the temperature difference across the membrane. The direction of the thermoosmotic movement depends on the sign of charge of the membrane and the nature and concentration of the electrolyte in the solution. The results confirm those of Lippmann and Aubert (1907, 1912) and prove their tentative conclusion that thermoosmosis with electrolytic solutions is an electrochemical phenomenon and related to electroosmosis. The present results show in addition that the direction and rate of thermoosmosis depend in a strikingly similar manner on those factors which determine the direction and rate of anomalous osmosis, namely, the charge of the membrane and the nature and concentration of the electrolyte. This similarity is strongly suggestive evidence of a fundamental, close relationship between the two phenomena.

The study of the fundamental aspects of membrane phenomena has almost always been carried out in isothermal systems. Very little attention has been paid to the possible effects which might arise when the temperature of a liquid on one side of a membrane is different from that on the other. This is not surprising in view of the fact that the study of nonisothermal phenomena in liquid systems, such as the Ludwig-Soret effect (that is the uneven distribution of solute due to a thermal gradient in a solution) and thermopotentials in electrolytic systems, was for a long time a neglected field of research, not only because of the inherent complexity of nonisothermal systems in general, but also because they seemed to be somewhat outside the conventional scope of physical chemistry.

In the last two decades, however, novel and to a large extent successful attempts have been made to treat nonisothermal phenomena from a theoretical point of view (1, 2). Thus experimental information on nonisothermal membrane phenomena has assumed a renewed physicochemical interest. In addition nonisothermal phenomena deserve some interest because very few processes in nature occur under completely isothermal conditions. Temperature gradients of varying magnitude certainly exist across numerous types of living membranes and could conceivably influence the transfer of solvent and solutes across such membranes.

Thermoosmosis

Only a limited number of well-controlled experiments to determine the possible magnitude of nonisothermal membrane effects are reported in the literature. Lippmann (3) and Aubert (4) (in Lippmann's laboratory) were the first to describe the phenomena which occur when a membrane separates a cold from a hot solution. A transfer of liquid across the membrane, which they called "thermoosmosis," was observed in numerous instances with solutions of electrolytes; with nonelectrolytes the effect was doubtful or nonexistent. With some membranes (parchment paper and regenerated cellulose) an osmotic flow was observed from the side of the warmer to the side of the cooler liquid. With other membranes (pig's bladder, gelatin, and animal parchment) the osmotic flow was in the opposite direction. The phenomenon also seemed to be dependent on the presence of some foreign material that could be leached from the membrane. In addition, membranes which in use had become inactive could be restored to a state of activity by traces of suitable electrolytes, and similarly, certain membranes which were naturally inactive became active in the presence of some electrolytes. On the basis of their experiments, Lippmann and Aubert concluded that the thermoosmosis which they observed was linked closely to electroosmosis. This view was shared by Freundlich who, more specifically, surmised a funda-

mental similarity between thermoosmosis and anomalous osmosis (see below) (5).

The work of Ernst, and Ernst and Koczkás (6) on thermoosmosis was criticized by Ursprung (7) and need not be considered further here. Derjaguin and Sidorenkov (8) reported that appreciable quantities of water and other liquids are transported through sintered glass filters by thermoosmosis. Hutchison, Nixon, and Denbigh (9) have repeated and expanded these experiments and conclude that the results of the former investigators are due almost entirely, if not entirely, to the thermal expansion of the liquid. They agree with Lippmann and Aubert that there is no observable thermoosmosis of pure liquids across an inert barrier such as sintered glass or porous clay. Hutchison, Nixon, and Denbigh are of the opinion that those instances where thermoosmosis definitely occurs are most likely due to some electrokinetic mechanism; they also point out that probably not a single case of thermoosmosis has been found which can be explained on the basis of classical thermodynamics.

Riehl (10) in a paper on a rapid method of determining Ludwig-Soret coefficients by the use of a membrane separating a hot from a cold solution observed the transport of moderate quantities of liquid across membranes, but did not study this phenomenon further.

Winterkorn (11) finds a very close correlation between the mass movement of water in soils under a thermal gradient and the electrokinetic properties of these systems and believes that the thermal osmotic effects in soils may be an instance of thermoosmosis.

Haase (12) expressed the feeling of those familiar with the literature when he stated recently that only a few, and in part questionable, observations on thermoosmosis in liquid systems are extant (while analogous processes in gaseous systems were proven beyond doubt and are amenable to theoretical treatment). Haase has presented theoretical considerations concerning thermoosmosis with pure liquids and with solutions of nonelectrolytes and carried out experiments to test his conclusions; he did not consider thermoosmosis in systems with electrolytic solutions.

Thermoosmosis, a Problem in the Electrochemistry of Membranes

A review of the quoted and the other available literature indicates that thermoosmosis in systems free of electrolytes, if it occurs at all, is in all instances much less pronounced than in many systems with electrolytic solutions. The published data suggest that the essential mechanism of thermoosmosis in electrolytic systems is electrochemical in nature, most likely related in some manner to electroosmosis. Thus, it seemed promising to attack the problem of thermoosmosis from an electrochemical point of view and apply to it some of the current basic information on the electrochemistry of membranes as exemplified by the classical work on the electrochemistry of membranes by Loeb (13), by Michaelis (14), the fixed charge theory of electrochemical membrane behavior of Teorell (15) and Meyer and Sievers (16), and the work on "activated" membranes carried out in our laboratories (17-24).

The degree of the electrochemical activity of ionic membranes, for instance their electromotive action, their electroosmotic efficacy, or their ability to give rise to anomalous osmosis are more pronounced the greater the density of ionic groups at the walls of the pore system which constitutes the membrane (17-24). These ionic groups may be an inherent part of the matrix material from which the membranes are prepared or they may be introduced by intentional "activation" such as a chemical reaction, *e.g.*, oxidation which creates ionic groups, adsorption of ionic materials such as polyelectrolytes or proteins on formed membranes, and mixing of polyelectrolytes with the matrix material before the membranes are cast (17-24). It is evident that the methods of activating membranes should be very helpful in determining whether thermoosmosis is really an electrochemical effect. If this is the case, activated membranes with solutions of electrolytes should show greatly enhanced thermoosmotic effects as compared with nonactivated ones.

Experimental

An apparatus similar to that used by Aubert (4), was constructed for measuring thermoosmosis; it is shown in Fig. 1 and 2.

Essentially the apparatus consists of two very narrow circular chambers separated by a membrane, the two chambers being arranged for heating and cooling, respectively (see Fig. 1a and 1b.) Two round

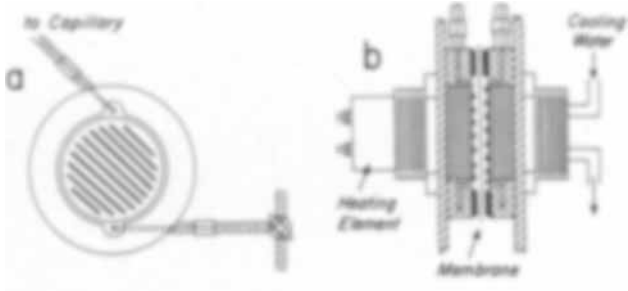

Fig. 1. Cell for the study of thermoosmosis across membranes (slightly schematic): (a) side view of a solution compartment; (b) cross-sectional view of main parts of thermoosmosis cell.

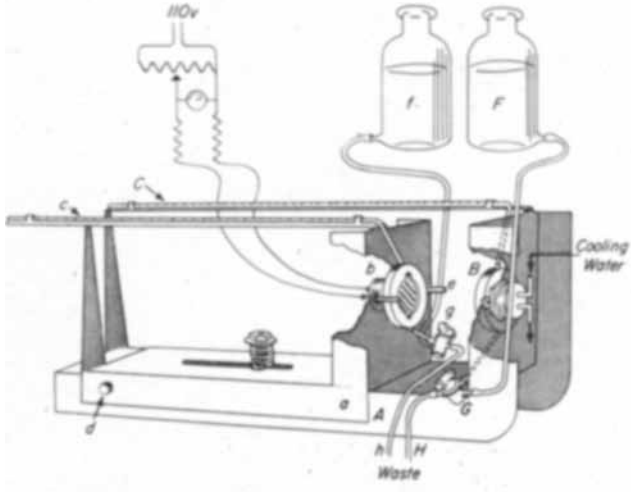

Fig. 2. Complete thermoosmosis apparatus with thermoosmosis cell and auxiliary equipment.

copper blocks of 50.7 mm diameter are set in hard rubber rings of 90 mm outer diameter. One of the blocks was heated by a 100-w (nominal at 110v) electric heater whose temperature was adjusted by a variable voltage control, routinely set at 60v (corresponding to about 30w) unless otherwise stated; the other copper block was cooled by water circulating through it, the temperature of which was maintained at 25°C. The surfaces of both copper blocks were painted with an inert and electrically insulating lacquer thus excluding corrosion and any possibility of an outside electrical connection between the solutions in the two compartments. Rubber gaskets 1 mm in thickness with an internal opening of 56 mm in diameter (and small cut outs for the inlet and outlet for the solution) were cemented to the hard rubber rings surrounding the copper blocks. To keep the membrane in an exactly defined, unchanging position, several narrow strips of the gasket material (about 1 mm in width) were cemented parallel, in opposite diagonal positions onto each of the copper blocks. When a membrane was clamped between these two parts, two cylindrical chambers were formed, each 55 mm in diameter and 1 mm in depth. The free membrane area, not blocked by the rubber strips, was about 20 cm^2. Each chamber was connected with a horizontal glass capillary. In the assembled apparatus (see below) the two capillaries were on the same level to prevent the development of any difference in hydrostatic pressure in the chambers while an experiment is in progress. A scale graduated in millimeters was attached under each capillary so that the rate of movement of the meniscus could be observed.

These essential parts of the thermoosmotic cell were mounted in the apparatus shown in Fig. 2 consisting of an L-shaped stand *A* and an L-shaped sledge *a* which can be moved back and forth along the longer limb of the stand *A*. The two assemblies (Fig. 1b) which form the thermoosmosis cell proper, *B* and *b*, connected to the measuring capillaries *C* and *c* (inner diameter about 0.9 mm) are mounted in the upright parts of *A* and *a* as shown in Fig. 2. To put the apparatus together for an experiment, it is first turned 90° into the vertical position with the sledge *a* raised and held by the catch bolt *d*. The membrane to be used is then placed over the lower copper block and rubber gasket, *B*, mounted on *A*; it should be large enough to cover all of the gasket. The assembly with the upper copper block, *b*, mounted on the sledge *a*, is then lowered onto the membrane. The two parts are then clamped tightly together with two large screws *e*. The apparatus is then returned to the horizontal position. Figure 2 shows in addition the arrangement for filling and flushing the two cell compartments by means of two solution reservoirs *F* and *f*, the three-way stopcocks *G* and *g*, and the attached waste lines *H* and *h*.

For an experiment the chambers were filled by gravity feed with the same solution from the two reservoirs. The positions of the menisci in the capillaries *C* and *c* are regulated by the three-way stopcocks, *G* and *g*. With both chambers at the same temperature, the apparatus is allowed to stand for 30 min, the position of the meniscus in each tube being observed every 5 min to ascertain that there are no leaks. When it has been established that the system is watertight, the heater for the one chamber is turned on, and the cooling water is circulated through the copper block of the other chamber. When the assembly has warmed up, a steady state is reached in which the rate of movement of the menisci in the two capillaries becomes constant; this usually requires 15-30 min after the start of the experiment. Thereafter readings of the positions of the menisci are taken every 10 or 15 min for about 1 hr, confirming thereby that the observed rate of water movement is constant at least during this period.[1] This rate is take as a measure of the magnitude of the thermoosmosis.[2]

The solutions must be carefully degassed by boiling (and replacement of the water lost by equally carefully degassed water); 15-20 min vigorous boiling were adequate. With not properly degassed solutions, gas bubbles form, particularly in the compartment of the hot solution and give rise to spurious volume readings.

The possibility of a disturbing thermometric effect must also be considered. As will be shown later, with distilled water in the apparatus no thermoosmosis is observed, *i.e.*, there is no continuous unidirectional movement of the meniscus. There is also no detectable fluctuation in the position of the meniscus after the steady state has been attained. Thus a significant contribution of the thermometric effect to the observed volume changes during the experimental period is ruled out.

All membranes used were of the porosity of conventional dialyzing membranes. They included membranes prepared from electrochemically rather inactive collodion of high purity which were used without further treatment; collodion membranes that had been made strongly electronegative by oxidation with NaOH (20);[3] and collodion membranes that had been made electropositive by the adsorption of protamine (23).[4] The preparation and properties of these types of membranes have been described previously (17-24).[5] In addition, some

[1] In the limited number of experiments which were carried out over 3-4 hr, a gradual but significant decrease in the rate of liquid movement occurred, an effect reported already by Aubert (4).

[2] The described apparatus and the technique used are obviously not suitable to determine minor thermoosmotic effects which might occur during the warming up period. Our experimental procedure, like that of Aubert, is designed to study processes which extend over periods substantially longer than the warming up period. A thermoosmotic process which comes to a stop during the warming up period and is not of the magnitude of at least a sizable fraction of the total thermometric (thermal expansion) effect occurring during this period, would not be detected. Any negative result obtained by our experimental method should be considered in this light.

[3] Collodion in contact with alkaline solution is not hydrolyzed in a straightforward manner to cellulose and nitric acid; rather, it undergoes a gradual decomposition of a complicated nature. Nitrite is formed in large quantities and the nitrocellulose is gradually oxidized. The oxidation of collodion membranes by means of alkaline solutions tends to produce membranes of higher electrochemical activity than conventional oxidizing agents.

[4] Protamines are simple strongly basic proteins, ordinarily derived from salmon sperm, with molecular weights of about 4000 in the hydroxyl form. They are of somewhat varying composition, most probably consisting of 19 molecules of arginine, a dibasic amino acid with a pK of 12.5, and six or seven monobasic amino acids. The ionizable groups in the protamine molecule, which are not blocked by the formation of peptide linkages, are: one carboxyl group, one imino group, and 19 guanidino groups.

[5] It should be noted that the activation of the wide pored membranes of the dialyzing type by oxidation (to render them acidic) or the adsorption of protamine (to make them basic in character) does not change to an extent which is significant in the present connections either their water permeability or their osmotic behavior with solutions of nonelectrolytes, while electroosmosis or anomalous osmosis across them are increased manyfold.

experiments were carried out with cellophane and animal parchment.

A shortcoming of our thermoosmosis apparatus is the lack of provisions for the measurement of the temperature difference between the two sides of the membrane.[6] For the purpose at hand, however, this shortcoming is more apparent than real, since our aim here is the comparison of the behavior of different membranes and different solutions under otherwise constant, standardized conditions. The temperature difference across membranes must vary to some extent according to their different thicknesses and water contents. However, the difference in temperature can be assumed to be virtually the same across generically related membranes of the same thickness and water content. The nonactivated, the oxidized, and the protamine collodion matrix membranes with which the bulk of the experiments were carried out fall into this category.

In the experimental results presented later, a flow of liquid from the hot side to the cold side is arbitrarily assigned a positive sign, a flow in the opposite direction a negative sign. This convention was chosen to avoid confusion in the discussion, when the flow of liquid in thermoosmosis will be compared to the flow of liquid in anomalous osmosis. The results obtained from the rates of movement of the menisci in the capillaries are expressed in $mm^3/100\ cm^2$ of membrane area per minute. It is estimated that the reproducibility of a given measurement is about $\pm$ 1 $mm^3/100\ cm^2$-min.

Results and Discussions

Our initial survey experiments were concerned with the influence of the nature of the membrane, and of the nature and the concentration of various solutes. A summary of representative data is given in Table I. The results were clear cut: In systems with pure water, thoroughly freed of all solutes, thermoosmosis does not occur to an extent detectable with our equipment, that is less than 0.3 $mm^3/100\ cm^2$-min. The same holds true with solutions of sucrose in agreement with the observation of Aubert who did not observe any thermoosmosis with solutions of various nonelectrolytes. With solutions of electrolytes, however, thermoosmosis may occur depending on the electrical charge of the membrane. The effect is not measurable in our system with cellophane membranes or membranes prepared from pure collodion, which are known to be rather inactive electrochemically, having only a few stray fixed ionic wall groups in their pores (18-20). "Activated" or inherently active membranes such as oxidized collodion membranes or protamine collodion matrix membranes or membranes of animal parchment are thermoosmotically active, corresponding to the fact that they are electrically charged, carrying numerous fixed ionic groups in their pore structure.

The direction of the thermoosmotic flow in the majority of simple systems is from the hot to the cold compartment–"positive" in our terminology.

It may be useful to add here that the thermoosmotic effect, as stated already by Aubert, becomes larger with an increase of the temperature difference between the solutions in the hot and cold compartment. It would require a special, rather elaborate arrangement to determine accurately the magnitude of the driving force, that is the temperature drop across the membrane itself.[6] We confined ourselves to the simple expedient of correlating the extent of thermoosmosis to the voltage applied to the heating element of the hot side of our apparatus. While water of 25°C flowed at a constant rate through the copper block of the cold side, a stepwise increased voltage, 30, 40, 50, 60, and 65v, was applied to the heater. The corresponding rates of thermoosmosis with an oxidized collodion membrane and 0.01*M* K_2SO_4 solution were: 1.3, 2.2, 6.3, 10.8, and 11.4 $mm^3/100\ cm^2$-min. When these values are plotted against the square of the voltage applied to the heater, they are found to lie on a straight line within the limits of the accuracy of the data and to be proportional to the square of the voltage, that is proportional to the quantity of heat which flowed across the thermoosmosis cell. The temperature drop across the membrane proper must be assumed to be proportional to the flux of heat across the cell. Therefore it can be concluded that the rate of thermoosmosis is proportional to the driving force, the temperature difference between the two membrane-solution interfaces, a not unexpected result.

The results of Table I, and of other experiments omitted here, fully confirm those of Aubert. There is excellent agreement with respect to the most important points, namely, the influence of the nature of the solute, the direction of the thermoosmosis as dependent on the nature of the membrane, and the order of magnitude of the observed effects. Our observation that the electrochemical "activation" of membranes increases thermoosmosis many-fold

[6] In the narrow solution compartments of our apparatus, which are indicated by other considerations, stirring of the liquid is due only to natural convection, and therefore rather ineffective. In addition, adjacent to the membrane, there are unstirred (Nernst) layers of solution which are of the same order of magnitude in thickness as the membrane itself. Thus, a large fraction of the temperature difference between the two bulk solutions is not operative across the membrane. In further work it will be advisable to use membranes of greater thickness, 1 mm or more, than that of the membranes used here (30-50μ), combined with effective mechanical stirring.

Table I. Thermoosmosis with different solutions across various membranes†

Membrane	Solution	Rate of thermoosmosis in $mm^3/100\ cm^2$-min*
Nonoxidized collodion	H_2O	0.0
	0.02*M* K_2SO_4	0.0
Oxidized collodion	H_2O	0.0
	0.02*M* KCl	+6.4
	0.02*M* K_2SO_4	+18.0
	Sucrose	0.0
Protamine-collodion	H_2O	0.0
	0.02*M* KCl	+5.4
	0.02*M* $MgCl_2$	+13.2
Cellophane	H_2O	0.0
	0.02*M* K_2SO_4	0.0
Animal parchment	0.02*M* NaOH	−11.3

† The voltage applied to the heater was 60v in all instances.
* A positive sign represents flow of solution from the hot side to the cold side, a negative sign the reverse.

strongly supports the hypothesis of Lippmann and Aubert that thermoosmosis is of an electrochemical nature and probably closely linked to electroosmosis.

As stated before, Freundlich had surmised that thermoosmosis might be closely related to anomalous osmosis (5). In the course of our experiments two regularities of importance in this connection have been noted consistently. First, thermoosmosis across acidic membranes, such as oxidized collodion membranes, is always stronger with uni-bivalent electrolytes such as K_2SO_4 than uni-univalent salts; with basic, electropositive membranes, such as protamine collodion matrix membranes, the effect is stronger if the electrolyte has a bivalent cation. Second, without exception the thermoosmotic effect was strongest with solutions in a medium concentration range (with most systems about 0.01-0.03*M*) and considerably smaller at lower and higher concentrations. These regularities are also very characteristic for the phenomenon that is known in the literature as "anomalous osmosis." Thus, it seems indicated to compare the influence of concentration on the transport effects arising in thermoosmosis and in anomalous osmosis.

The term anomalous osmosis is commonly used to denote those osmotic phenomena arising with solutions of electrolytes which seem to be contrary to the common experience that the flow of liquid across a membrane which separates a solution from pure solvent (or a more dilute solution) occurs ordinarily toward the side of the more concentrated solution, and at a rate roughly proportional to the concentration difference. In the very common instance of "anomalous positive osmosis" the rate of movement of liquid toward the side of the solution depends on the concentration of the solution used, the rates of flow in a medium range of concentrations being much higher than with more concentrated or more dilute solution. In the relatively rare instances of "anomalous negative osmosis" a flow of liquid occurs toward the side of the pure solvent (or the more dilute solution).

Investigators in this field agree unanimously that anomalous osmosis through porous membranes is an electrochemical phenomenon (25). Its magnitude is closely correlated with the product of the electrokinetic charge of the membrane and the dynamic membrane potential which results from the diffusion of electrolyte across the membrane as stressed particularly by Bartell (26, 27) and Loeb (13). The details of the mechanism of anomalous osmosis across porous membranes are still controversial and the subject of continuing investigation (25, 28-31). One of us proposed some time ago that anomalous osmosis arises from the interaction of pores which yield different potentials (for instance, due to their different width), when the electrolytic solute diffuses across the membrane (25, 28). Local electric circuits arise, superficially similar to the local circuits assumed generally in corrosion. One set of pores acts as the source of the driving electromotive force, another set of pores plays the role of an electroosmotic diaphragm through which the current is driven passively, thereby producing electroosmosis according to the electrokinetic charge of the pores. Schlögl, in a most ingenious manner, has developed the idea that anomalous osmosis arises in the individual pores, without interaction of different pores (29). According to Schlögl, the potential which arises at each pore due to the diffusion of the electrolyte across it, acts as a moving force on the pore water according to the electrokinetic charge of the latter. Whichever of these and similar concepts may ultimately be proven correct, the electrochemical character of anomalous osmosis seems beyond doubt.

Most experiments on anomalous osmosis have been performed with systems in which a membrane separates pure water from a solution of an electrolyte, and the pressure rise in an osmometric capillary is read after an arbitrarily chosen time (20 min in the experiments presented below). The observed effect consists of two components, the true anomalous osmosis and the normal osmotic effect as it arises also with nonelectrolytes. To avoid this uncertainty and to determine the magnitude of true anomalous osmosis Grim and Sollner had recourse to the easily demonstrated fact that anomalous osmosis does not occur with electroneutral membranes (22). Accordingly, with membranes which can be charged and discharged reversibly (without significant changes in geometrical structure), such as many proteinized membranes, the osmotic effects caused by an electrolyte can be measured both when only normal osmosis arises (with the membrane in the electroneutral state) and when normal as well as anomalous osmosis occurs (with the membrane in a charged state). The difference between these two effects is considered as the true anomalous osmosis. Using this procedure Grim and Sollner have measured the true anomalous osmotic effects arising in systems in which the concentration ratio of the two solutions separated by the membrane was 2:1. Such systems are, of course, more similar to those used in the thermoosmosis studies, where the membrane separates solutions of equal concentration, than to the conventional solution-water system.

Figure 3 presents data on the extent of thermoosmosis across an oxidized, electronegative, collodion membrane with K_2SO_4 as electrolyte (heater set at 60v), and two sets of data on anomalous positive osmosis with the same electrolyte; the one set was obtained with an oxidized collodion membrane by the pressure rise method (18), the other one by the volume method with an oxyhemoglobin collodion matrix membrane in the negative state (at pH 10.0) (22).

Figure 4 gives analogous data on thermoosmosis with $MgCl_2$ across an electropositive protamine collodion matrix membrane (heater set at 60v), and data on anomalous positive osmosis by the pressure rise method across a similar protamine collodion membrane,[7] and by the volume method across the same oxyhemoglobin membrane referred to in Fig.

[7] The data shown in Fig. 4 for the pressure rise methods were actually obtained by Abrams and Sollner (23) with $CaCl_2$ as the electrolyte. The work of Loeb (13) and experience in our own laboratories show that there is no reason to believe that the curve would be any different in its form if $MgCl_2$ had been used instead of $CaCl_2$.

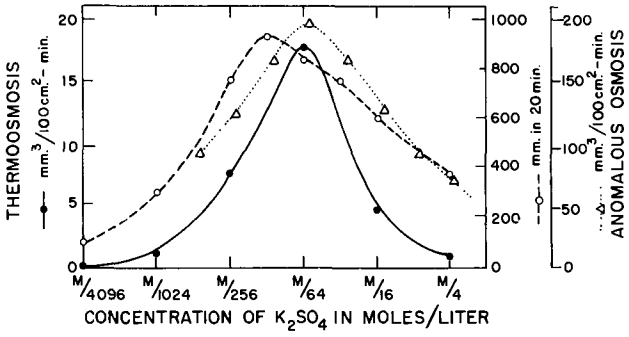

Fig. 3. Comparison of thermoosmosis and anomalous osmosis across negatively charged, acidic membranes; ——●—— thermoosmosis; — — ○ — — anomalous osmosis by the pressure rise method; . . . . △ . . . . anomalous osmosis by the volume transport method.

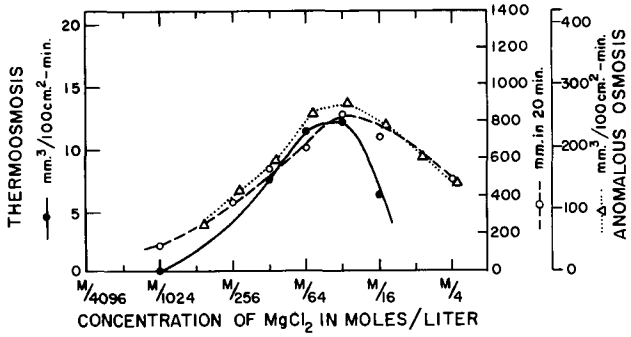

Fig. 4. Comparison of thermoosmosis and anomalous osmosis across positively charged, basic membranes; ——●—— thermoosmosis; — — ○ — — anomalous osmosis by the pressure rise method; . . . . △ . . . . anomalous osmosis by the volume transport method.

3, but now in the positively charged state (at *p*H 4.0) (22).

Figures 3 and 4 show the great similarity of the concentration dependence of thermoosmosis and of anomalous positive osmosis; the maximum effects of thermoosmosis and of anomalous osmosis occur in the same concentration range, with a fairly sharp decline both at higher and lower concentrations. In view of this correlation the next, obvious step was to test whether or not thermoosmosis occurs in the opposite direction (from the cold to the hot compartment) in systems the analogues of which are known to give anomalous negative osmosis.

Anomalous negative osmosis has been shown to arise in systems which satisfy these requirements: (i) the electrolyte must be such that its faster diffusing ion has the same sign as the charge of the membrane, and (ii) the porosity and charge density of the membrane and the concentration of the electrolyte must be adjusted so that the membrane potential is in the direction which gives the more dilute solution the same charge as that of the membrane (28).

In those instances where anomalous negative osmosis has been observed, the concentration of electrolyte necessary to produce maximal effects is considerably higher than that to produce maximal anomalous positive osmosis with the same membranes (and different electrolytes). For example, with positive membranes, acids, particularly di- and tri-basic acids, are especially effective in the concentration range of 0.5-1.0*M*; similarly, with negative membranes LiCl and strong bases will produce anomalous negative osmosis in this concentration range.

We have carried out a limited number of test experiments on thermoosmosis, simulating the above-described conditions which produce anomalous negative osmosis. In all instances the movement of liquid was from the cold to the hot compartment, that is the direction opposite to that in the experiments shown in Fig. 3 and 4. For example, with a protamine collodion matrix membrane, 0.5*M* H_3PO_4, and the same temperature gradient as used before, the rate of flow was —7.4 mm³/100 cm²-min. Similarly, with 0.02*M* NaOH[8] and oxidized collodion membranes, the rate of flow was —8.4 mm³/100 cm²-min.

These results confirm our anticipation based on the previous results which showed a strong correlation of thermoosmosis and anomalous positive osmosis. That the correlation of thermoosmosis and anomalous negative osmosis in appropriate systems is equally strong lends further strength to the hypothesis that mechanisms of thermoosmosis and anomalous osmosis are intimately related. However, we are not prepared at this time to propose a detailed mechanism for thermoosmosis. Before this can be done, it will be necessary to have measurements of the thermopotentials which arise under the conditions of the experiments. If one considers that the rate of anomalous osmosis in 2:1 concentration systems is at least 10 times larger than that of thermoosmosis under our experimental conditions (compare Fig. 3 and 4), and that the membrane potentials which arise in the former systems are of the order of 10 mv, it can be seen that the thermopotential required to produce the observed thermoosmosis may be only of the magnitude of 1 mv or less. Further, one should try to correlate the thermoosmotic mass movement with the Ludwig-Soret distribution of electrolytes across membranes. With such further information available, it will be of considerable interest to discuss possible mechanisms of thermoosmosis in the light of current theories of anomalous osmosis.

[8] This is not the optimum concentration for NaOH, but higher concentrations could not be used because the membranes are rapidly destroyed when such solutions are heated.

Acknowledgment

The authors wish to express their gratitude to the National Foundation for Infantile Paralysis under whose auspices this study was started in 1945, and to the Josiah Macy, Jr. Foundation which during the year 1946 supported the bulk of the experimental work presented in this paper.

Manuscript received Aug. 16, 1961; revised manuscript received Feb. 1, 1962. This paper was presented before the Colloid Division of the American Chemical Society at the Chicago Fall Meeting, 1946.

Any discussion of this paper will appear in a Discussion Section to be published in the June 1963 JOURNAL.

REFERENCES

1. S. R. DeGroot, "L'Effet Soret, Diffusion thermique dans les phases condensées," N. V. Noord-Hollandsche Uitgevers Maatschappij, Amsterdam (1945).

2. K. G. Denbigh, "The Thermodynamics of the Steady State," Methuen and Co. Ltd., London (1951).
3. G. Lippmann, *Compt. rend.*, **145**, 104 (1907).
4. M. Aubert, *Ann. chim. phys.*, [8], **26**, 145, 551 (1912).
5. H. Freundich, "Kapillarchemie," 2nd ed., p. 371, Akademische Verlagsgesellschaft, Leipzig (1922); 3rd ed., Vol. 1, *ibid.*, 386 (1930).
6. E. Ernst, *Nature*, **141**, 80 (1938); E. Ernst and J. Koczkás, *Z. Physik.*, **109**, 625 (1938); E. Ernst, *Kolloid Z.*, **87**, 276 (1939).
7. A. Ursprung, *Protoplasma*, **33**, 200 (1939).
8. B. Derjaguin and G. Sidorenkov, *Compt. rend. (Doklady) Acad. Sci. USSR.*, **32**, 622 (1941).
9. H. P. Hutchinson, I. S. Nixon, and K. G. Denbigh, *Discussions Faraday Soc.*, **3**, 86 (1948).
10. N. Riehl, *Z. Elektrochem.*, **49**, 306 (1943).
11. H. F. Winterkorn, Proc. 27th Ann. Meeting Highway Research Board, 443 (1947).
12. R. Haase, *Z. phys. Chem., (N.F.)*, **21**, 244, 270 (1959).
13. J. Loeb, *J. Gen. Physiol.*, **1**, 717 (1918-19); **2**, 173, 255, 387, 563, 577, 659, 673 (1919-20); and many more papers in the succeeding volumes of the same journal.
14. L. Michaelis and collaborators, *Biochem. Z.*, **158**, 28 (1925); **161**, 47 (1925); **162**, 258 (1925); **164**, 23 (1925); **173**, 411 (1926); *J. Gen. Physiol.*, **10**, 575, 671, 685 (1926-27); L. Michaelis, *Bull. Natl. Research Council*, **69**, 119 (1929); *Kolloid Z.*, **62**, 2 (1933); etc.
15. T. Teorell, *Proc. Soc. Exptl. Biol. Med.*, **33**, 282 (1935); *Proc. Natl. Acad. Sci. U.S.*, **21**, 152 (1935); *Z. Elektrochem.*, **55**, 460 (1951); *Progr. Biophys. Biophys. Chem.*, **3**, 305 (1953); *Discussions Faraday Soc.*, **21**, 9 (1956).
16. K. H. Meyer and J.-F. Sievers, *Helv. Chim. Acta*, **19**, 649, 665, 987 (1936); K. H. Meyer, *Trans. Faraday Soc.*, **33**, 1073 (1937).
17. K. Sollner, *J. Phys. Chem.*, **49**, 47, 171, 265 (1945); *This Journal*, **97**, 139C (1950); *Ann. N. Y. Acad. Sci.*, **57**, 177 (1953); K. Sollner, S. Dray, E. Grim, and R. Neihof, "Ion Transport Across Membranes," H. T. Clarke and D. Nachmansohn, Editors, p. 144, Academic Press Inc., New York (1954); "Electrochemistry in Biology and Medicine," T. Shedlovsky, Editor, p. 65, John Wiley & Sons, Inc., New York (1955); K. Sollner, *ibid.*, p. 33.
18. K. Sollner and I. Abrams, *J. Gen. Physiol.*, **24**, 1 (1940).
19. K. Sollner, I. Abrams, and C. W. Carr, *ibid.*, **24**, 467 (1941); **25**, 411 (1942); K. Sollner and J. Anderman, *ibid.*, **27**, 433 (1943); K. Sollner and C. W. Carr, *ibid.*, **28**, 1 (1944); H. P. Gregor and K. Sollner, *J. Phys. Chem.*, **50**, 53 (1946); etc.
20. K. Sollner, I. Abrams, and C. W. Carr, *J. Gen. Physiol.*, **25**, 7 (1941).
21. K. Sollner and R. Neihof, *Arch. Biochem. Biophys.*, **33**, 166 (1951); R. Neihof, *J. Phys. Chem.*, **58**, 916 (1954).
22. E. Grim and K. Sollner, *J. Gen. Physiol.*, **40**, 887 (1957).
23. I. Abrams and K. Sollner, *J. Gen. Physiol.*, **26**, 369 (1943); C. W. Carr, H. P. Gregor, and K. Sollner, *ibid.*, **28**, 179 (1945); H. P. Gregor and K. Sollner, *J. Phys. Chem.*, **50**, 88 (1946); M. Lewis and K. Sollner, *This Journal*, **106**, 347 (1959); etc.
24. M. H. Gottlieb, R. Neihof, and K. Sollner, *J. Phys. Chem.*, **61**, 154 (1957).
25. K. Sollner, *Z. Elektrochem.*, **36**, 36 (1930).
26. F. E. Bartell and C. D. Hocker, *J. Am. Chem. Soc.*, **38**, 1029, 1036 (1916); F. E. Bartell and O. E. Madison, *J. Phys. Chem.*, **24**, 444, 593 (1920).
27. F. E. Bartell, Colloid Symposium Monograph, **1**, 120 (1923).
28. K. Sollner, *Z. Elektrochem.*, **36**, 234 (1930); A. Grollman and K. Sollner, *Trans. Electrochem. Soc.*, **61**, 477, 487 (1932); K. Sollner and A. Grollman, *Z. Elektrochem.*, **38**, 274 (1932).
29. R. Schlögl, *Z. phys. Chem. (N.F.)*, **3**, 73 (1955).
30. Y. Kobatake, *J. Chem. Phys.*, **28**, 146, 442 (1958); *Progr. Theoret. Phys. (Kyoto)*, Supplement No. *10*, 226 (1959).
31. O. Kedem and A. Katchalsky. *J. Gen. Physiol.*, **45**, 143 (1961); A. Katchalsky, "Membrane Transport and Metabolism," A. Kleinzeller and A. Kotyk, Editors, pp. 69-86, Academic Press, New York and London (1961).

Anodic Oxidation of Methanol on Platinum

I. Adsorption of Methanol, Oxygen, and Hydrogen on Platinum in Acidic Solution

M. W. Breiter and S. Gilman

Research Laboratory, General Electric Company, Schenectady, New York

ABSTRACT

The coverage of bright platinum electrodes with methanol, oxygen, and hydrogen was determined as a function of potential and bulk concentration of methanol in perchloric acid. Two different techniques which lead to the same results for the coverage with the respective species are described. The methanol coverage was obtained for equilibrium conditions at open circuit and under the conditions of a quasistationary current-potential curve. The methanol coverage is potential independent between +0.1 and +0.6v and decreases rapidly with potential above +0.6v during the anodic sweep of the current-potential curve. The oxygen coverage differs only slightly in 1*N* $HClO_4$ and 1*N* $HClO_4$ + 1M CH_3OH. Hydrogen adsorption is decreased by 75% if the saturation coverage of methanol is present on the surface.

The mechanism of the anodic oxidation of lower alcohols on solid electrodes, particularly platinum, is of great importance in connection with fuel cell technology. An intensive study of one particular system, acid methanol, was carried out since it was felt that the results would advance the understanding of similar systems. Results on the mechanism of the anodic methanol oxidation will be reported in a series of papers. The first paper deals with the adsorptive properties of platinum with respect to

methanol, oxygen, and hydrogen in 1N $HClO_4$, containing different amounts of methanol.

Current-potential curves and analytic determination of the reaction products in different solutions have been mainly used to come to conclusions on the reaction mechanism (1-7). It is assumed in the existing theories of the oxidation mechanism that adsorption of methanol plays an important role. However, little is known about the adsorption of methanol in the so-called double layer region, about a possible simultaneous adsorption of hydrogen and methanol in the hydrogen region, and of methanol and oxygen in the oxygen region. A detailed description of the three well-known potential regions can be found in a paper (8) on the adsorption of amyl alcohol at platinum in which similar problems were discussed.

Pavela (3) was the first to establish direct experimental evidence for the adsorption of methanol on platinized platinum. He kept the electrode at open circuit in solutions of water and methanol for 15 min and then briefly immersed it in distilled water. The electrode was then immersed in 1*N* NaOH and an anodic charging curve measured. An arrest is observed which Pavela attributes to the quantitative oxidation of methanol to formic acid. The adsorbed amount is computed from the transition time of the arrest and the current. Pavela found a saturation coverage for methanol concentrations $C_M > 0.5M$. The experimental adsorption isotherm is in fairly good agreement with Langmuir's isotherm.

Pavela's procedure is based on two conditions: (*A*) Methanol is desorbed only to a negligible amount during the rinsing while only an adherent liquid layer of methanol is removed. (*B*) All the adsorbed methanol is oxidized before the anodic formation of a chemisorbed oxygen layer starts. As the fulfillment of the conditions was not verified, Pavela's results may include a considerable error. Therefore other techniques were developed and used to obtain the equilibrium coverage with methanol at open circuit and the coverage under the conditions of a potentiostatic current-potential curve. A comparison of the methanol coverage under the two conditions shows that equilibrium coverage is attained in the double layer region during the anodic sweep of current-potential curves. The oxygen coverage was measured as a function of potential in the base electrolyte solution and in solutions containing methanol. The information on methanol adsorption and oxygen coverage under different conditions has not been available in the literature. The results of this paper will be used to discuss the potentiostatic current-potential curve in a second paper of the series.

Experimental

Two techniques were used for the determination of the coverage with methanol, hydrogen, and oxygen. The first method is the potentiostatic application of voltage pulses to the electrode by means of a Wenking potentiostat. The second method consists in the chronopotentiometric (galvanostatic) application of current pulses. The form of the pulses was chosen such as to meet the experimental requirements for the determination of the adsorbed amount of one of the three species.

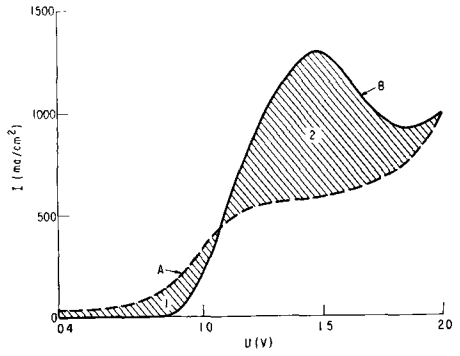

Fig. 1. Potentiostatic i-U-curves with v = 800 v/sec in *1N* $HClO_4$ + 1M CH_3OH (curve B) and in *1N* $HClO_4$ (curve A) starting from the open-circuit potential.

Potentiostatic technique.—A single triangular potential sweep of very short duration was applied to study methanol adsorption. The anodic sweep started at a desired potential and extended to 2.0v. It could also be started when the electrode potential changed linearly and periodically as under the conditions of a potentiostatic current-potential curve. The current was registered as a function of potential (or time) by means of an oscilloscope during the fast potential sweep. The nonstationary anodic current-potential curves (i-U-curves) were measured in the electrolyte (1*N* $HClO_4$) and in 1*N* $HClO_4$ with different amounts of methanol. Curve B in Fig. 1 was obtained in 1*N* $HClO_4$ + 1M CH_3OH and curve A in 1*N* $HClO_4$. The sweep started at the open-circuit potential of the platinum electrode in the respective solutions. All the potentials in this paper are referred to a hydrogen electrode in the same solution. The voltage speed of the sweep was 800 v/sec. The methanol was Spectro-quality Reagent (Matheson Coleman & Bell), the perchloric acid Analytical Reagent (Mallinckrodt), the water was double distilled with a specific resistivity of $8 \cdot 10^6$ ohm-cm at 25°C. Methanol concentrations up to 1M were used. The solutions were intensively stirred with argon before the measurements. The measurements were made in a Pyrex glass vessel with three compartments. The vessel was thermostated at 30°C. The prehistory of the electrode influences the i-U-curves markedly and is always given. The electrode pretreatment for the curves in Fig. 1 is described in the next section on the equilibrium coverage with methanol.

Shaded area 2 minus shaded area 1 (see Fig. 1) yields the charge, Q_M(coul/cm²) required for the removal of the adsorbed methanol by anodic oxidation, or

$$Q_M = \int_0^t i_B dt - \int_0^t i_A dt \qquad [1]$$

The applicability of the potentiostatic technique is based on four conditions: (*A*) The number of coul/cm² which are used for the anodic formation of an oxygen layer and for oxygen evolution during the sweep is the same in the electrolyte and in the solution containing methanol. (*B*) The same number of electrons per molecule is involved in the oxidation, independent of the adsorbed amount of meth-

anol. (*C*) The nonfaradaic currents which change the charge of the double layer are the same in the electrolyte and in the solution containing methanol. (*D*) The anodic sweep is sufficiently rapid that oxidation of methanol which diffuses to the electrode during the sweep is negligible.

The precision of the determination of $\ominus_M$ by the potentiostatic method is estimated at ± 0.1. The i-U-curves (see Fig. 1) coincide at high potentials. This shows that the electrode surface is oxidized to the same extent in the electrolyte and in the solution with methanol. Condition (*A*) is approximately fulfilled. This conclusion is supported by the result that the oxygen coverage of the electrode under the conditions of a potentiostatic current-potential curve is nearly the same at any potential independent of the methanol concentration as described in the section on the oxygen coverage. The coincidence of the i-U-curves is evidence that all the adsorbed methanol is removed during the anodic sweep. The i-U-curves have the same shape independent of the adsorbed amount of methanol. This suggests the fulfillment of condition (*B*). It was estimated that condition (*C*) might introduce an error of up to 7%. The nonfaradaic currents are relatively large due to the high voltage speed. They will differ to some extent as the double layer capacity is likely to be smaller during the sweep in the solution with methanol than in the electrolyte solution. Simultaneous adsorption of amyl alcohol and oxygen on platinum resulted in a lowering of the double layer capacity in the oxygen region (8). The same effect can be expected for methanol. To verify the fulfillment of condition (*D*), i-U-curves were measured at different voltage speed in 1*N* $HClO_4$ + 1M CH_3OH. Figure 2 represents the result. Q_M is plotted *vs.* log *v*. A limiting value for Q_M is obtained for $v > 200$ v/sec. Therefore the determination of Q_M was carried out with $v = 800$ v/sec. As condition (*D*) is fulfilled for 1M CH_3OH, it is valid for $C_M < 1M$ also.

The oxygen coverage at potentials in the oxygen region was obtained by interrupting the circuit at the desired potential and applying a potential of + 0.4v very rapidly. This was done with the Western Electric 275 C Relay. The oxygen layer is completely reduced at + 0.4v. The area under the current-time curve gives the amount Q_o in coul/cm² of adsorbed oxygen. The reduction occurs very fast

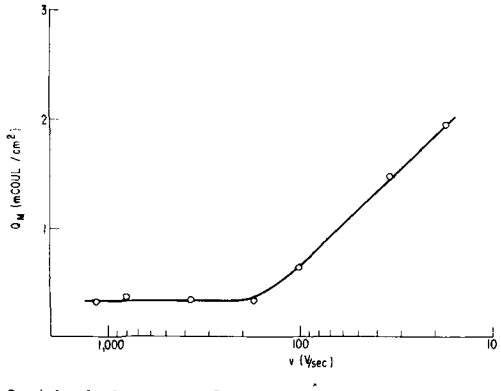

Fig. 2. Adsorbed amount Q_M of methanol in 1*N* $HClO_4$ + 1M CH_3OH as a function of the voltage speed *v* of the potentiostatic sweep.

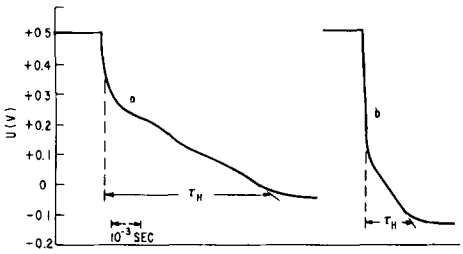

Fig. 3. Cathodic charging curves from 0.5v with 0.06 amp/cm² in 1*N* $HClO_4$ (curve a) and in 1*N* $HClO_4$ + 1M CH_3OH (curve b). The determination of the transition time τ_H for the hydrogen branch is shown.

(in about 5.10^{-3} sec). Therefore the influence of a simultaneous oxidation of methanol which diffuses to the surface is negligible.

Galvanostatic technique.—The second method consists in taking cathodic charging curves from different initial potentials. Q_o is determined as a function of potential in the oxygen region from the transition time of the oxygen branch of the charging curve and the current density (9). The length of the hydrogen branch yields the number Q_H of coul/cm² to fill the sites available for hydrogen adsorption. If the charging curve starts at a potential where methanol is adsorbed, the number N_M of hydrogen adsorption sites which are occupied by adsorbed methanol can be computed from the decrease in Q_H. Curve a in Fig. 3 is a charging curve with 0.06 amp/cm² from + 0.5v in 1*N* $HClO_4$, curve b from + 0.5v in 1*N* $HClO_4$ + 1M CH_3OH. Both curves were taken during the anodic sweep of potentiostatic current-potential curves with $v = 30$ mv/sec by switching from the potentiostatic to the galvanostatic circuit when the potential reached + 0.5v. Curve b shows a marked decrease in the length of the hydrogen branch. If ${}_sQ_H$ designates the number of coul/cm² for the cathodic formation of a completely covered surface in the electrolyte and Q_H is the value in the presence of methanol, then for potentials $U \geqq + 0.3v$

$$N_M = ({}_sQ_H - Q_H) \cdot L/\mathbf{F} \qquad [2]$$

F is the faraday and *L* is Avogadro's number. It was found from charging curves starting between + 0.8 and + 1.5v that ${}_sQ_H$ was approximately the same (0.34 mcoul/cm²) in all solutions. The above concept was used by Oikawa and Mukaibo (10) to study the adsorption of acetic acid on platinum, and by Franklin and Sothern (11) for the adsorption of nitrides on platinum. These authors took the quantity

$$\theta' = \frac{{}_sQ_H - Q_H}{{}_sQ_H} \qquad [3]$$

as a measure for the coverage with organic substance. This implies the validity of the relation

$$\theta = \frac{Q_M}{{}_sQ_M} = \theta' \qquad [4]$$

for the whole range of θ' values. The validity of relation [4] has already been questioned by one of the authors (8). The objection is based on the possibility that hydrogen atoms could be adsorbed on

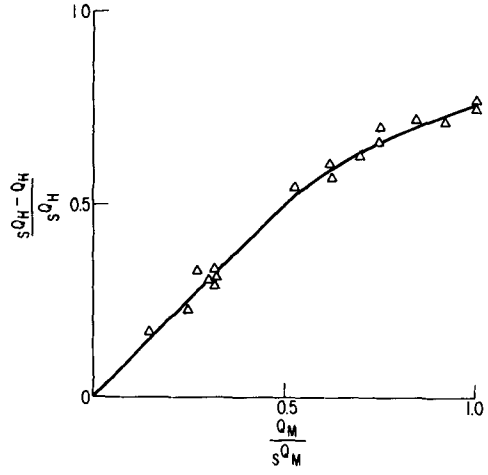

Fig. 4. Apparent coverage $\frac{{}_sQ_H - Q_H}{{}_sQ_H}$, as determined from the decrease of the hydrogen arrest of the cathodic charging curve, as a function of the coverage $\frac{Q_M}{{}_sQ_M}$, determined with the anodic potential sweep.

sites which are not accessible to methanol adsorption for geometric reasons. θ and θ' were determined for various concentrations of methanol in 1*N* $HClO_4$ under the conditions of a quasi-stationary potential sweep. The values reported for θ were obtained potentiostatically and those for θ' were obtained galvanostatically. Figure 4 gives the experimental results. Equation [4] is fulfilled for $\theta' \leqq 0.5$. Above $\theta' = 0.5$ the $\theta' - \theta$ curve bends and tends toward $\theta' = 0.75$ for $\theta = 1$. Only 75% of the sites which are accessible to the adsorption of hydrogen atoms are available for methanol adsorption. The calibration curve in Fig. 4 permits interconversion of θ and θ'. Since the galvanostatic method is simpler than the potentiostatic one, it was used in many cases. Adsorption isotherms of organic substances which were determined solely from the decrease of the amount of adsorbed hydrogen are in error for $\theta' > 0.5$. The latter statement holds for any method of determining Q_H. The fair agreement between θ and θ' for $\theta' < 0.5$ confirms the reliability of the potentiostatic and the galvanostatic method. The accuracy for θ' is estimated at $\pm$ 0.1. Precision for θ by the potentiostatic method is better than 0.03.

Results and Discussion

Adsorption Isotherm for Methanol

It is well known from reported polarization curves that methanol is oxidizable at relatively low potentials. Therefore the isotherm for equilibrium conditions can only be determined with certainty if the adsorption occurs at open circuit. The following pretreatment led to reproducible results. The electrode was polarized at 1.8v for 15 sec and at 1.55v for 30 sec while stirring with bubbled argon. Under these conditions the electrode surface is completely stripped of organic materials and is completely covered with an adsorbed oxygen layer. Desorbed organic materials are swept into the bulk solution and highly diluted. Then the stirring was interrupted and the potential held at 1.55v for 1½ additional minutes. The potential was then stepped instantaneously to + 0.4v and held there for 0.015 sec. This time is sufficient for the reduction of the chemisorbed oxygen layer. After 0.015 sec the circuit was opened. After a specified period at open circuit, Q_M was determined by the potentiostatic method. Two minutes were sufficient for establishment of adsorption equilibrium at all bulk concentrations of methanol. The described procedure was carried out in all solutions with the potentiostat and suitable circuits of Western Electric C275 Relays. The pretreatment described above not only provides a reproducible surface state for methanol adsorption, but largely excludes the possibility that oxidation products formed during the measurements or during the removal of the oxygen layer are adsorbed.

The potential shifts toward less positive values than +0.4v at open circuit in solutions with methanol. The potential which is reached after 2 min depends on the bulk concentration of methanol. Potential shifts of the described nature which start from a surface free of adsorbed oxygen and hydrogen were reported by Shlygin and co-workers (4, 5) as evidence for an electron-radical oxidation mechanism for CH_2O, HCOOH, CH_3OH, and other oxidizable substances. However, Vielstich (12) has stated that the measured open-circuit potentials are likely to be mixed potentials. Two interpretations for the potential shift, between which a distinction cannot yet be made, are more probable than Shlygin's interpretation. A small amount of hydrogen atoms is formed cathodically during the potential shift. The cathodic current is equal to an anodic current of methanol oxidation at the same electrode. As the rate of methanol oxidation becomes smaller with decreasing potential, a final open-circuit potential is approached. The amount of hydrogen formed in 2 min is still immeasurable. On the other hand the adsorbed methanol molecules may dissociate into radicals and hydrogen atoms to a small extent (1, 2). The adsorbed hydrogen atoms produce the potential shift. Traces of adsorbed hydrogen are detectable by anodic charging curves if the electrode rests for 20 min at open circuit in 1*N* $HClO_4$ + 1M CH_3OH.

Figure 5 represents isotherms of methanol adsorption at different times after opening the circuit (15

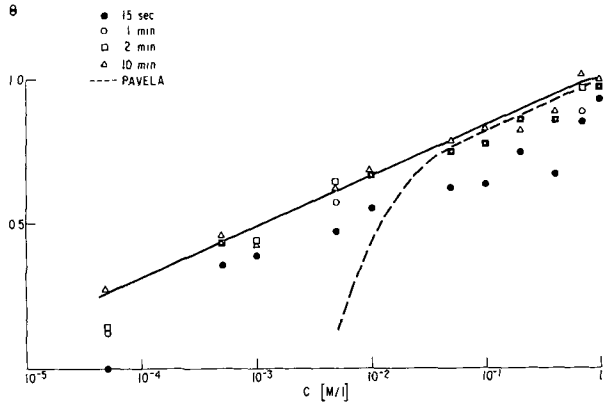

Fig. 5. Methanol coverage after different times at open circuit. The solid line represents the isotherm, the dashed line Pavela's results.

sec, 1 min, 2 min, and 10 min). Equilibrium coverage is practically achieved after 2 min. $\theta = Q_M/{}_sQ_M$ is plotted against log C_M. A semilogarithmic representation is chosen since a relatively large coverage is already found at small C_M-values. The saturation value ${}_sQ_M$ was reached for $C_M > 0.4M$ and is approximately equal to ${}_sQ_H$. It was 0.3 mcoul/cm^2 for the measurements in Fig. 5. If 0.75 ${}_sQ_H$ is taken as representing the number of platinum atoms available for methanol adsorption and if six electrons are involved in the oxidation of the adsorbed methanol, one methanol molecule occupies 4.5 platinum atoms. If the oxidation goes only to formic acid (4 electrons) the number of occupied platinum atoms is three. Both numbers appear acceptable as the cross section of the methanol molecule is about 25Å^2 (13), and the distance between platinum atoms in the (111)-plane is about 3Å.

Pavela's tabulated Q_M-values for platinized platinum were used to compute an isotherm. This isotherm is plotted as a dashed line in Fig. 5 while our results correspond to the solid line. Agreement exists at high concentrations while Pavela's values are too low at low concentrations. Obviously conditions (*A*) and (*B*) of Pavela's procedure discussed in the introduction are not fulfilled.

The adsorption isotherm in Fig. 5 is linear in a large concentration range. Temkin's isotherm describes the results to a first approximation. Such behavior is characteristic of a heterogeneous surface. Although an indication of steps is given by the experimental points, the experimental precision does not allow a decision as to whether or not these steps are a real phenomenon. The attainment of saturation coverage does not appear as pronounced on the semilogarithmic plot as on a linear plot.

Methanol-Coverage under the Conditions of a Potentiostatic Current-Potential Curve

Potentiostatic current-potential curves of fuel oxidation have peaks (1, 2, 5, 7, 12, 14) characteristic of every fuel. The method devised by Will and Knorr (15) was used here. A periodic triangular voltage sweep from +0.1 to 1.5v was applied to the electrode by means of the electronic potentiostat. The voltage speed was 30 mv/sec. After a certain potential was reached the potentiostatic circuit was interrupted manually by means of a Western 275C Relay. A cathodic charging curve was taken immediately after the interruption. The coverage was determined in the way described in the previous section. The current-potential curves became independent of time in unstirred solutions after a few cycles had been impressed.

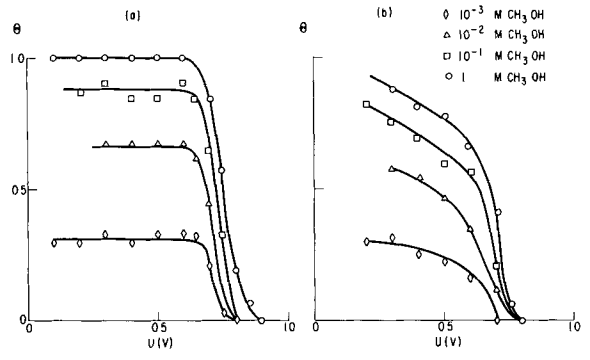

Fig. 6. Methanol adsorption at different potentials during the anodic sweep (Fig. 6a) and the cathodic sweep (Fig. 6b) of potentiostatic current potential curves in different solutions.

Figure 6a represents the coverage as a function of potential and of the bulk concentration of methanol during the anodic potential sweep, Fig. 6b during the cathodic sweep. The θ-values at +0.2 and +0.1v were determined by the potentiostatic method. The coverage is independent of potential between 0.1 and 0.6v at all concentrations during the anodic sweep. Then it decreases rapidly with potential. The θ-U-curves have a similarity with corresponding curves for the adsorption of organic substances on mercury (16) although the cause for desorption differs greatly. In this case it is due to the oxidation of methanol on platinum in the potential range of desorption. This effect will be discussed in the second paper. The methanol adsorption between 0.9 and 1.5v is very small and plotted as equal to zero in Fig. 6a and 6b where the abscissa is not extended beyond +1.0v. However, this statement may be slightly in error as the reproducibility of ${}_sQ_H$ is about ±10%.

A comparison between the θ values of Fig. 5 and the potential-independent values in Fig. 6a suggests that equilibrium is practically established under the conditions of a quasistationary potentiostatic current-potential curve. The rate of oxidation is not yet sufficient to lead to a decrease in coverage.

The coverage increases during the cathodic sweep at all concentrations and does not reach the constant value of the anodic sweep before 0.1v. The θ-U-curves show that the coverage is formed rapidly in the beginning while the attainment of a final value above 0.5 is slow. No adsorption takes place above 0.8v. The electrode remains covered with a chemisorbed oxygen layer between 1.0 and 1.5v during the cathodic sweep (see next section). Methanol adsorption starts after about 75% of the oxygen coverage is reduced.

So far it has been assumed that the coverage under the conditions of a potentiostatic current-potential curve is due to methanol adsorption. This need not necessarily be true as an oxidation peak is observed between 0.8 and 0.6v during the cathodic sweep (1, 2, 7, 12). It is conceivable that intermediates are formed then which are more strongly adsorbed than methanol and remain on the surface during the following part of the sweep. At the higher methanol concentrations the intermediates might produce as much as 50% of the measured θ-value (see Fig. 6b). However, a comparison of the potential-independent θ-value during the anodic sweep with the θ-value of the adsorption isotherm at the same concentration shows fair agreement between the two coverages. The agreement suggests that the coverage during the sweep is due mainly to methanol adsorption. The influence of intermediates is probably within the error of the θ-determination ($\leqq$10%). An accidental agreement is felt to be unlikely for all concentrations.

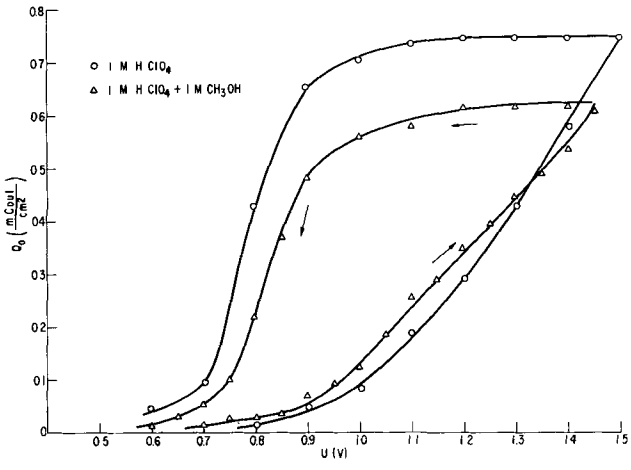

Fig. 7. Oxygen adsorption at different potentials during the anodic and cathodic sweep of potentiostatic current potential curves in 1N $HClO_4$ and in 1N $HClO_4$ + 1M CH_3OH.

Oxygen Coverage

It is well known that the anodic formation of a chemisorbed oxygen layer starts on platinum in acidic solutions at about +0.8v *vs.* a hydrogen electrode in the same solution. The coverage increases with potential. Approximately a monolayer is attained at +1.5v (9). The influence of the oxygen layer on the form of the potentiostatic current potential curves was already recognized and correctly interpreted in the early work on fuel oxidation (1, 2). However, a quantitative determination of the oxygen coverage under the conditions of a potentiostatic current-potential curve is not yet reported in literature. The oxygen coverage was determined by the potentiostatic method and the galvanostatic method at different potentials in the oxygen region during a potentiostatic current potential curve with 30 mv/sec in 1N $HClO_4$ and in 1N $HClO_4$ + 1M CH_3OH. The results obtained by the two methods agree fairly well.

The adsorbed amount Q_o obtained galvanostatically is plotted in Fig. 7 as a function of potential for the two solutions. A correction for the double layer charging during the oxygen branch of the cathodic charging curve was not made as the change of the double layer capacity with potential during the charging curve is not known. This leads to an error in the Q_o-values estimated to be less than 10%. The Q_o-U-curves are nearly the same in both solutions. This follows from the Q_o-U-curves during the anodic sweep. The potential of reversal differed by 50 mv in the two solutions. Therefore, the Q_o-U-curves are shifted against each other during the cathodic sweep. However, the same shape of the Q_o-U-curves is observed. There is an indication that the oxygen coverage is a bit larger at the same potential in 1N $HClO_4$ + 1M CH_3OH than in 1N $HClO_4$ up to +1.3v during the anodic sweep. Q_o increases more rapidly with potential above 1.3v in 1N $HClO_4$ than in 1N $HClO_4$ + 1M CH_3OH. The influence of methanol on the Q_o-U-curve is small. Therefore the Q_o-U-curve in 1N $HClO_4$ can be taken as a good approximation for the Q_o-U-curve in the presence of methanol up to $C_M = 1M$.

Manuscript received Dec. 6, 1961; revised manuscript received March 12, 1962. This paper was prepared for delivery before the Los Angeles Meeting, May 6-10, 1962.

Any discussion of this paper will appear in a Discussion Section to be published in the June 1963 JOURNAL.

REFERENCES

1. E. Müller and A. R. Miro, *Z. Elektrochem.*, **27**, 54 (1921).
2. S. Tanaka, *ibid.*, **35**, 38 (1929).
3. T. O. Pavela, *Ann. Acad. Sci.* Fennicae, Series A, II. Chemica, **59** (1954).
4. G. A. Martinyuk and A. I. Shlygin, *Zhur. fir Khim.*, **164**, 32 (1958).
5. A. I. Shlygin and G. A. Bogdanovsky, *Proc.* 4th Conference on Electrochemistry, Moscow 1956, pp. 282-286, Academy of Sciences, Moscow (1959).
6. See Extended Abstracts of Papers Presented at the Sessions of the Battery Division and at Joint Symposia on Fuel Cells with the Corrosion, Industrial, Electrolytic, and Theoretical Divisions of The Electrochemical Society, October 1961, Abstract No. 109, p. 138, No. 113, p. 149, No. 116, p. 159, No. 17, p. 38, No. 8, p. 42, No. 19, p. 45.
7. L. R. Griffith, R. P. Buck, *et al.* Proceedings 15th Annual Power Sources Conference, p. 16.
8. M. Breiter, *This Journal*, **109**, 425 (1962).
9. See M. Becker and M. Breiter, *Z. Elektrochem.*, **60**, 1080 (1956).
10. M. Oikawa and T. Mukaibo, *J. Electrochem. Soc. Japan*, **20**, 568 (1952).
11. T. C. Franklin and R. D. Sothern, *J. Phys. Chem.*, **58**, 951 (1954).
12. W. Vielstich, Paper presented at the Joint Symposia on Fuel Cells of The Electrochemical Society, May 1961.
13. W. D. Harkins, *Chem. Rev.*, **29**, 385 (1941).
14. Ye. M. Skobets and N. N. Atamenko, Kiev. Forestry Institute, Report VII, Zavodskaja Lab. Vol. 15, pp. 1291-1299.
15. F. C. Will and C. A. Knorr, *Z. Elektrochem.*, **64**, 258 (1960).
16. See M. Breiter and P. Delahay, *J. Am. Chem. Soc.*, **81**, 2938 (1959).

Studies on Alternating Current Electrolysis

IV. Mathematical Treatment of Reversible Electron Transfer with Alternating Voltage Control and Distorted Current

A. Edward Remick and R. A. Marcus[1]

Departments of Chemistry, Wayne State University, Detroit, Michigan and Polytechnic Institute of Brooklyn, Brooklyn, New York, respectively

ABSTRACT

A mathematical treatment is developed which yields equations relating faradaic current, voltage, and time when an alternating voltage is applied to an electrolytic cell composed of a plane and auxiliary electrodes immersed in a solution containing initially supporting electrolyte and only reversibly oxidizable or reducible species. Both oxidant and reductant are taken to be soluble, and specific adsorption is assumed to be absent. The voltage across that branch of the equivalent circuit through which only faradaic current flows is assumed to be periodic with fixed amplitude and with or without an additional direct applied voltage component; the resultant current is distorted. Diffusion controlled kinetics is postulated, and it is assumed that equilibrium is essentially established at the electrode surface. The equations developed show that a "steady state" (*i.e.*, a periodic state) is quickly attained, yield diagnostic tests of use in establishing the reversible mechanism, make it possible to determine the standard potential, and finally yield for the periodic state a relation between faradaic current and time. These results are then generalized so as to include systems in which the reversible electrochemical step is followed by a sufficiently slow secondary reaction step. One diagnostic result of interest in the latter connection is that the mean faradaic current vanishes in the periodic state, regardless of the amplitude or of the shape of the applied periodic potential, when the follow-up reaction occurs to a negligible extent.

The problem of developing a mathematical description of the chemical effects of alternating current on reversible redox systems has been attacked with varying degrees of success by several investigators (1-12) subject to the following restrictions: (*a*) undistorted voltage and current waves, and/or (*b*) both components of the redox system must either be present in the solution initially or present at the electrode's surface as the result of superimposed direct current. Berzins and Delahay (8) assumed what in the classification of Delahay, Senda, and Weis (17) may be called alternating voltage (A.V.) control [*i.e.*, controlled sinusoidal potential difference across that branch of the equivalent circuit for one electrode through which only faradaic (*f*) current is flowing]. They derived an equation for the instantaneous value of the (distorted) faradaic current as a function of time. This equation contained transient terms and a "steady-state" (or, better, a "periodic-state") term. Plane electrodes were involved.

Recently Matsuda and Delahay (13) extended the A.V. control problem to derive an equation for the transient current produced by faradaic rectification after the periodic component had reached a steady state. Their equation was restricted to small values of the A.V. and to solutions initially containing both oxidant and reductant.

Koutecky (14), assuming A.V. control, derived an equation for the instantaneous value of the faradaic current as a function of time for the general case of a periodic voltage of optional wave shape and applied it to the special cases of sine waves, square waves, and triangular waves. His equations were largely, although not entirely, concerned with the conditions characteristic of polarography (*i.e.*, dropping electrode), but his work and an initial portion of the present work are related. We shall be concerned with stationary electrodes, with a treatment for (in some ways) slightly more general systems, with a detailed treatment of the statement of the periodic state, and with devising a method of determining the standard potential and other properties (*m* and *n* below) of a reversible electrochemical step in an otherwise irreversible process.

In the present paper we shall discuss a system undergoing A.V. electrolysis with or without superimposed direct applied voltage for the case employing voltage control when the initial concentration of either oxidant or reductant is zero. Clearly, large A.V. amplitudes may be necessary to bring concentrations at the electrode surface into the poised region where reasonable accuracy in potential-concentration relationships may be achieved.[2]

This case is of only limited practical interest for

[1] Alfred P. Sloan Fellow; N.S.F. Senior Post Doctoral Fellow at Institute of Mathematical Sciences, New York University (1960-61).

[2] A certain experimental difficulty which, it has been suggested [p. 313 of ref. (17)], could complicate interpretation of the more usual (low amplitude) A. V. control systems, is absent here because of the different method used to interpret the results.

potentiometrically reversible redox reactions but should be important in the study of oxidations or reductions involving "follow-up" mechanisms, *e.g.*

$$\text{Red} \rightleftharpoons \text{ne} + \text{Ox} \text{ (fast)}$$

$$\text{Ox} \rightleftharpoons \text{products (slow)}$$

especially when the half-life period of the unstable (or highly reactive) intermediate substance is short compared to the polarographic drop time but long compared to the period of the A.V. in a usable frequency range.

General Assumptions

In the theoretical treatment along the lines indicated, the following restrictions and assumptions will be made.

(i) A plane electrode is used and conditions for the semi-infinite linear diffusion are achieved.

(ii) A. V. control is employed (A. V. alone or with a superimposed direct voltage component).

(iii) The only depolarizer initially present is the reductant. (This is an unessential restriction, as noted later, and is made only to emphasize the case that is of practical interest here.)

(iv) A supporting electrolyte eliminates migration of the depolarizer and also keeps the *p*H constant through buffer action. Convection is assumed absent.

(v) "Spontaneous depolarization" (15) occurs only by diffusion, *i.e.*, the depolarizer concentration at the electrode changes only by diffusion or electron transfer to the electrode and not by secondary chemical reaction or by convection.

(vi) Specific adsorption is absent.

(vii) Electrochemical equilibrium exists between the electrode and the concentrations of the electrochemically active species just outside the region effectively occupied by the electrical double layer.

(viii) In view of the transient nature of faradaic rectification, it will be ignored as a possible source of disturbance of over-all concentration after a steady state (*i.e.*, a periodic state) is achieved.

In principle, the above assumptions are all that are needed. In practice, however, it is desirable that the electrolytic resistance is rendered negligible by the high concentration of supporting electrolyte, and that the working electrodes of the electrolytic cell are a measuring electrode and an unpolarizable auxiliary electrode. A negligible resistance ensures an undistorted voltage wave across the faradaic branch, a very desirable restriction, as discussed later. It should also be noted that when a second faradaic process of the above type occurs, it can be treated as a parallel branch in the equivalent circuit.

Assumption (vii) that chemical equilibrium is achieved with alternating voltage does not imply that the charge transfer resistance (Grahame's θ) is zero, but it does mean that the θ is negligible in comparison with the mass transfer resistance (diffusion) for the experimental conditions, *i.e.*, that the frequency used is low enough to enable close approach to equilibrium in a small fraction of a cycle. The validity of this assumption in the case of a poised ferrocyanide-ferricyanide solution was demonstrated by Remick and McCormick (16) who showed that the introduction of the Nernst equation into Grahame's equations for the faradaic admittance (6) adequately predicted the experimentally observed relation of depolarizer concentration to polarization resistance and capacitance up to the highest frequency used, *viz.*, 5000 cps. Less reactive systems would be expected to behave reversibly only up to lower frequencies.

The assumption that electrochemical equilibrium exists between the electrode and species just outside the double layer implies that the salt concentration is high, so that the width of the double layer is appropriately small. Were this condition not fulfilled, one would have to include in the diffusion equation of the i^{th} electrochemically active species the usual migration term $(D_i e_i/RT)(\partial\phi/\partial x)C_i$, ϕ being the potential at point x, and D_i, e_i, and C_i being the diffusion coefficient, charge and concentration (at x) of species i.[3]

The system as a whole will also be undergoing a periodic buildup and disappearance of the electrical double layer at the electrode. The total current at any time is the sum of this nonfaradaic current and the faradaic current i_f calculated below. That is, as discussed by Grahame (6), the additional process of charging and discharging the double layer can be regarded as corresponding to a condenser (of capacity depending on instantaneous voltage) in parallel with the faradaic branch of the equivalent circuit. We consider first the behavior of the faradaic branch.

Boundary Value Problem

The reversible electrode reaction

$$\text{Red} \rightleftarrows m\,\text{Ox} + ne \qquad [1]$$

involves the soluble species Red and Ox whose charge types are not specified. In Eq. [1] m and n are rational numbers. The molar concentrations of these species, respectively, will be symbolized by C_R and C_{ox} and the bulk concentration of Red by C°_R. C_R and C_{ox} are functions of the time, t, and the distance, x, from a plane parallel to the electrode surface but just outside the electrical double layer region. To express diffusion control, Fick's second law will be employed as usual, expressed in terms of concentration rather than activities:

$$\partial C_{ox}(x,t)/\partial t = D_{ox}[\partial^2 C_{ox}(x,t)/\partial x^2] \qquad [2]$$

$$\partial C_R(x,t)/\partial t = D_R[\partial^2 C_R(x,t)/\partial x^2] \qquad [3]$$

where D_R and D_{ox} are diffusion coefficients. Equations [2] and [3] will be solved subject to the initial and

[3] This assumption concerning the width of the double layer will often be satisfied even when the assumption would be inaccurate for systems for which a kinetic boundary condition is appropriate (*i.e.*, a boundary condition such as $-D\partial C/\partial x = kC_{ox} - k'C_R$ at the electrode surface). In this kinetic case, Bockris (26) believed that the "zeta potential" is largely suppressed at concentrations above ca. 1*N*. This conclusion, however, was not substantiated by Breiter, Kleinerman, and Delahay (27) whose calculations (based on a theoretical equation which was found to be in accord with experimental data obtained in the polarographic reduction of iodate ions) indicated that the zeta potential might well be ca. 0.05v even in 1M solution. Since electron transfer proceeds from positions immediately adjacent to the electrode, we see that for double layer effects to be negligible in the kinetic case, the double layer should be narrower than a few Angstroms. In the electrochemical equilibrium case (assumption vii), however, to satisfy our assumption, it merely suffices that diffusion be rapid across the double layer so that concentration ratios inside it are given by a local Nernst (i.e., Boltzmann) relation. Accordingly, our assumption will often be valid when it is not valid to neglect double layer effects on rate constants for electron transfer to the electrode.

boundary conditions (and to the assumption of a bounded solution):

$$C_R(x, 0) = C^\circ_R \quad [4]$$

$$C_{ox}(x, 0) = 0 \quad [5]$$

$$D_{ox}\,\partial C_{ox}(x, t)/\partial x + m\,D_R\,\partial C_R(x, t)/\partial x = 0 \quad \text{at } x = 0 \quad [6]$$

plus a condition on $C_{ox}(0, t)$.

If one considers instead of [5] the alternative condition that $C_{ox}(x, 0)$ equals a nonzero quantity C°_{ox}, Eq. [7], [13], and [15] remain valid, if $C_{ox}(x, t)$ in [7] is replaced by $C_{ox}(x, t) - C^\circ_{ox}$, and f in [13] and [15] by $f - C^\circ_{ox}$. Equation [8] remains intact, but in Eq. [9] and [14] the second C_{ox} and f should be replaced by $C_{ox} - C^\circ_{ox}$ and $f - C^\circ_{ox}$, respectively.

In Appendix I, Eq. [2] to [6] are solved by[4] the Laplace transform method. The solution is given by

$$i_f = -nFA\,(D_{ox}/\pi)^{1/2}\frac{\partial}{\partial t}\int_0^t C_{ox}(0, t-\tau)\,\tau^{-1/2}\,d\tau \quad [7]$$

As the boundary condition at $x = 0$, we employ the Nernst relation between $C_{ox}(0, t)$ and $C_R(0, t)$ for $t > 0$:[5]

$$\tilde{E}_f p(\omega t) = E'_o + (RT/nF)\ln\{C_{ox}(0,t)^m/C_R(0,t)\} \quad [8]$$

where $\tilde{E}_f$ is the amplitude of the applied alternating voltage, $p(\omega t)$ is any continuous periodic function of ωt, of period 2π and of unit amplitude, and E'_o is a quantity defined later.

From Eq. [8] and Eq. [24] of Appendix I, it follows that for $t > 0$, $C_{ox}(0, t)$ in Eq. [7] satisfies the relation:

$$[C_{ox}(0, t)]^m = [C^\circ_R - (D_{ox}/D_R)^{1/2}\,C_{ox}(0, t)/m]\exp[(nF/RT)(\tilde{E}_f p(\omega t) - E'_o)] \quad [9]$$

The quantity E'_o is defined through the following argument: Since the electrolytic resistance is assumed negligible, the potential difference across the cell is the sum of the two half-cell potentials, $E_a + E_c$, where E_c is the half-cell potential across the auxiliary unpolarizable electrode. If E_d is the direct component of the applied potential, we thus have

$$E_a = E_d + \tilde{E}_f p(\omega t) - E_c \quad [10]$$

Writing E_a in terms of its standard potential E_o of the reversible step of the half-cell, we have

$$E_a = E_o + (RT/nF)\ln\{C_{ox}(0, t)^m/C_R(0, t)\} \quad [11]$$

From Eq. [10] and [11], Eq. [8] is obtained with E'_o given by

$$E'_o = E_o + E_c - E_d \quad [12]$$

Delahay, Senda, and Weis (17) have emphasized the desirability that, in specifying the type of control used, both the alternating and mean components of the current or voltage control should be designated. The argument of the preceding paragraph shows that we are here dealing with the case of A.V. control, with $\overline{E}_{cell} = E_d$ (when the mean value of $p(\omega t)$ is zero), *i.e.*, with $\overline{E}_a = \overline{E}_c - E_d$.

It sometimes happens that $\tilde{E}_f p(\omega t)$ is treated as a piecewise continuous function,[6] for example, when it is treated as a square wave applied potential. Strictly speaking, it is continuous, but is approximated by this discontinuous function. To adapt Eq. [13] to this case, one uses the fact that the derivative of a step function is a Dirac δ-function (19).[7]

Applications of Equations [7] and [9]

Silverman and Remick (18) observed oscillographically that a periodic state was achieved very rapidly using $\tilde{I}_{cell}$-control, [*i.e.*, A.C. control (17)], plane electrodes, and solutions initially containing only one component of a reversible redox system. We know of no comparable experimental demonstration involving A.V. control; however, Eq. [7] and [9] can be shown to predict the attainment of a periodic state. Moreover, this periodic state is a convenient one for application of the equations to experimental data. Accordingly, we first show how these equations lead to the periodic state.

For this purpose, it is very convenient to introduce a function $f(\omega\theta)$ which agrees with $C(0, \theta)$ for $\theta > 0$, but which is the periodic continuation of $C(0, \theta)$ for $\theta \leq 0$.

In Appendix II it is then shown that Eq. [7] can be rearranged to give

$$i_f = nFA\,(\omega D_{ox}/\pi)^{1/2}\left\{\int_0^\infty \frac{\partial}{\partial y}[f(\omega t - y)]\,y^{-1/2}\,dy - \tfrac{1}{2}\int_{\omega t}^\infty f(\omega t - y)\,y^{-3/2}\,dy\right\} \quad [13]$$

where $f(\omega t - y)$ satisfies Eq. [14] for all t. Equation [14] is obtained from Eq. [9] by replacing $C_{ox}(0, t)$ by $f(\omega t - y)$.

$$[f(\omega t - y)]^m = [C^\circ_R - (f(\omega t - y)/m)\,(D_{ox}/D_R)^{1/2}]\exp\{(nF/RT)[\tilde{E}_f p(\omega t - y) - E'_o]\} \quad [14]$$

In Appendix II, it is shown that $f(\omega t - y)$ is bounded by some quantity, M say, so the second integral in [13] tends to zero as ωt tends to infinity

[4] Equation [7] can also be obtained, after a somewhat involved series of substitutions, from the first half of Eq. [21] of ref. (14). However, the derivation given in Appendix I of this paper has certain advantages for our purposes and is referred to later.

[5] The apparent discontinuity between the limit which this $C_{ox}(0, t)$ approaches as $t \to 0$ and that which Eq. [5] approaches as $x \to 0$ causes no difficulty. It is indeed a standard type of discontinuity (22) in diffusion and heat conduction problems.

[6] It may be recalled that a piecewise continuous function is one which has in any finite interval at most a finite number of discontinuities.

[7] In the case of piecewise continuous $p(\omega t)$, one may utilize Eq. [22] and [9] as follows. Piecewise continuous $p(\omega t)$ implies piecewise continuity of the function $C_{ox}(0, t)$ defined by Eq. [9], and even (Appendix II) its finiteness for the $p(\omega t)$ of interest. Its Laplace transform $\overline{C}_{ox}(0, s)$ therefore exists and has "nice properties." Consider now the contour integral expression obtained for $C_{ox}(x, t)$ by applying the usual Inversion Theorem (23) to Eq. [22], where $\overline{C}_{ox}(0, s)$ has just been described. This expression has the desirable convergence behavior outlined in ref. (23) (uniform convergence in x and in t) and one may proceed to test as discussed in ref. (23) whether it and the corresponding contour integral for $u(0, t)$ (u is defined in Appendix II) satisfy the differential equations and boundary conditions. $\partial C_{ox}(x, t)/\partial x$ and thereby i_f may be obtained then by differentiating under the integral sign. Indeed, some of the proofs in Appendices II and III might well have been shortened through use of the contour integral.

Equations [13] and [15] do not apply at those times t for which $f(\omega t)$ is discontinuous since Eq. [24] of Appendix I (and hence Eq. [9]) does not.

since its majorant, $M\int_t^x y^{-3/2}\,dy$, behaves in this way. Hence, this integral is a transient term. The first integral in [13] is periodic in ωt, because $f(\omega t - y)$ is periodic in ωt (as shown in Appendix III), its derivative, therefore, being periodic also, and because its limits are not functions of t. This integral, therefore, describes the periodic state.

An equivalent form of Eq. [13], derived in Appendix II, is given by Eq. [15], the first integral being the periodic term and the second being the same transient term as in Eq. [13].

$$i_f = -\tfrac{1}{2}\, nFA(\omega D_{ox}/\pi)^{1/2}\{\int_0^x [f(\omega t) - f(\omega t - y)]y^{-3/2}\,dy + \int_{\omega t}^{\infty} f(\omega t - y)y^{-3/2}\,dy\} \quad [15]$$

Using these equations, it is shown, incidentally, in Appendix III that the mean value of the periodic state integral in Eq. [13] or [15] is zero, for arbitrary periodic functions $p(\omega t)$ and for arbitrarily large amplitudes. This theorem generalizes earlier discussions by other investigators for small amplitudes. It should have diagnostic value since it would obviously be false if the irreversible follow-up reaction occurred appreciably.

To examine a possible way for determining E'_os and other properties, it is convenient to convert the integral for the periodic state into a "reduced" form. That is, we proceed to deduce an "equation of corresponding states" for the faradaic current and for its dependence on applied potential.

We see from Eq. [14] that at any given temperature $f(\omega t - y)$ depends on nE'_o, m, C°_R and on the value of the function nE_f at the time $\omega t - y$ (taking $\sqrt{D_{ox}/D_R} \cong 1$). Therefore, we may write (for given T), $f(\omega t - y)$ as a function of C°_R, of nE'_o, of m, of the value of nE_f at time ωt, and of y.[8] Similar remarks apply to the y-derivative of $f(\omega t - y)$. Accordingly, the periodic state term in either [13] or [15] satisfies the formal relation:

$$i_f = nFA(\omega D_{ox}/\pi)^{1/2}\int_0^\infty h(y, nE'_o, m\, nE_f, C^\circ_R)\,dy \quad [16]$$

where the function h can be written in the two equivalent forms (forms which differ only by a quantity whose integral from 0 to ∞ vanishes):

$$\left.\begin{aligned} h &\equiv y^{-1/2}\,\partial f(\omega t - y)/\partial y \\ h &\equiv \frac{1}{2}\, y^{-3/2}\,[f(\omega t - y) - f(\omega t)] \end{aligned}\right\} \quad [17]$$

Equation [16] is a convenient one for our purposes, for we see from Eq. [13] that at a given temperature, C°_R and electrode area A, a plot of nE_f *vs.* $i_f/n\,(\omega D_{ox})^{1/2}$ depends only on nE'_o and m. Therefore, by adjusting the direct voltage E_d and (in multiples of some preassigned amplitude) $\tilde{E}_f$, the E_f *vs.* i_f plot could be made to conform to a standard shape, a shape which, for any preassigned nE'_o, $n\tilde{E}_f$, C°_R and T, depends only on m. From the value of E_d needed to attain this specified nE'_o, E_o could be calculated from Eq. [12], n could be determined from the $\tilde{E}_f$ needed to attain the standard shape, and m could be determined from the C°_R-dependence of the data. (For example, for $m = 1$ Eq. [14] shows that $f(\omega t - y)$ is directly proportional to C°_R, so h and hence i_f in [16] are directly proportional to C°_R, for any given E_f.) Again, Eq. [16] provides other diagnostic tests. A plot of $i_f/\omega^{1/2}$ *vs.* E_f should be independent of ω and of $\tilde{E}_f$.[9]

Instead of plotting E_f *vs.* i_f, i_f can be plotted *vs.* ωt, after first writing Eq. [16] for the periodic state in the appropriate reduced form. Since $E_f = \tilde{E}_f p(\omega t)$, the integrand in [16] can be written as a function of ωt and of $n\tilde{E}_f$ as well as of y, nE'_o, m, and C°_R. Once again, for any given C°_R, T and electrode area, the adjusting of E_d and, in multiples of some amplitude, of $\tilde{E}_f$, would lead to a standard shape which depends on m. The values of E_o and n could then be determined as before, and m could be determined from the C°_R dependence of the plot. Again, as before, diagnostic tests could be devised: The plot of $i_f/\omega^{1/2}$ *vs.* ωt should be independent of ω and, if $m = 1$, should be proportional to C°_R.

In actual fact, one measures total current rather than only the faradaic branch. The nonfaradaic component is independent of C°_R, so that a plot of i *vs.* E_f or *vs.* t would now be a linear function of C°_R when $m = 1$. On the other hand, no standard shape of a plot of i *vs.* E_f or t can be attained simply by adjusting E_d and $\tilde{E}_f$.[10]

Accordingly, in this situation, recognizing that under the assumptions listed earlier, the total current is the sum of the faradaic and nonfaradaic branches and that the nonfaradaic component is independent of C°_R, the value of i_f corresponding to any particular phase angle of E_f can be obtained by subtracting from the measured, instantaneous current the value of that current when $C^\circ_R = 0$. Examples where this type of subtraction has been made in potentiometric work may be found in ref. (25) and (16). If the condition mentioned earlier that the iR be negligible had not been imposed, no such subtraction process would be permissible for obtaining i_f, for the iR drop at any given t would cause the instantaneous potential drop across the electrode to depend on C°_R, contrary to assumption. Furthermore, since the cell is a nonlinear circuit element, the iR drop through the bulk of the solution would contain harmonics which would invalidate the assumption of a sinusoidal E_f.

Information about the characteristic behavior of the integral in Eq. [16], and hence about the faradaic current, can be deduced either from numerical integration or from investigation of the properties of known reversible systems. However, some prelimi-

[8] The value of E_f at $(\omega t - y)$ is determined if one knows for all t its value at ωt and if one knows y, i.e., $E_f(\omega t - y)$ is a function of the function $E_f(\omega t)$ and of y.

[9] To be sure, at small values of $\tilde{E}_f$, points on this plot corresponding to large values of i_f will not be attained. Note that although i_f and E_f depend on $\tilde{E}_f$, the plot does not.

[10] For, if nE'_o and $n\tilde{E}_f$ were each made to conform to their preassigned values by such adjustments, the nonfaradaic current *vs.* E_f plot would then differ from system to system: Any two systems normally differ in E_o and hence, for a preassigned nE'_o, in E_d (cf. Eq. [12]). But for a given E_d, a plot of nonfaradaic current *vs.* E_f would be a standard one only for a preassigned E_d and $\tilde{E}_f$.

nary insight into its behavior as far as the dependence of i_f on E_f in Eq. [16] can be obtained as follows. We shall consider, by way of a concrete example, the important case in which $m = 1$, $D_{ox} = D_R$, and $p(\omega t)$ is sin ωt. The integral for the periodic state in Eq. [16] becomes (using it in the form of Eq. [13], after introducing Eq. [14] and performing the differentiation:

$$i_f = -\frac{nFA\,C^\circ_R\,nF\,\tilde{E}_f}{(\pi/\omega D_{ox})^{1/2}\,RT}\int_0^\infty \frac{\exp\left[nF(\tilde{E}_f \sin(\omega t - y) - E'_o)/RT\right]\cos(\omega t - y)\,y^{-1/2}\,dy}{\{1 + (D_{ox}/D_R)^{1/2}\exp\left[nF(\tilde{E}_f \sin(\omega t - y) - E'_o)/RT\right]\}^2} \quad [18]$$

When $|nF\,E'_o/RT| >> 1$ and $\tilde{E}_f << |E'_o|$, the coefficient of $y^{-1/2}\cos(\omega t - y)$ in the integrand, is very small at all times, *i.e.*, for all $|E_f| \leq \tilde{E}_f$.[11] Accordingly, i_f is then small for all such E_f, a result expected on physical grounds. In the very special instance that $\tilde{E}_f$ is sufficiently small, the integral in Eq. [18] becomes[12]

$$\pi^{1/2}\cos\left(\omega t - \frac{\pi}{4}\right)\exp(-nFE'_o/RT)/[1 + (D_{ox}/D_R)^{1/2}\exp(-nFE'_o/RT)]^2 \quad [19]$$

When $\tilde{E}_f$ becomes comparable in magnitude with E'_o, however, the current will become large at the appropriate times and, because of the sensitivity of the exponential terms to $\tilde{E}_f$, this effect should presumably occur fairly suddenly as $\tilde{E}_f$ is increased. Indeed a plot of faradaic current *vs.* $\tilde{E}_f$ may ultimately provide a convenient way for the determination of E'_o.

Up to this point, we have restricted our attention to reversible systems. If in addition, the reversible electrochemical step [1] is followed by an irreversible decomposition of the product of [1] to yield an electrochemically inactive substance, Eq. [3] to [6] remain unchanged, as does Eq. [8]. Only Eq. [2] is modified, namely, through the addition of the reaction rate term. If the irreversible step is very slow, this additional term represents only a minor perturbation of Eq. [2]. Physical considerations indicate that the solution for i_f should depend continuously on the value of the reaction rate constant in this perturbation term. When this constant is sufficiently small, therefore, the results will approach those previously obtained. That is, our final equations are still applicable, provided the irreversible step is sufficiently slow. As mentioned earlier, it is this situation where the present equations are likely to be of the most interest.

[11] For $E'_o > 0$, the numerator is then very small and the denominator is about unity. For $E'_o < 0$, the denominator is very large compared with unity, so that the first factor in the integrand approximately equals $(D_R/D_{ox})\exp\{nF[E'_o - \tilde{E}_f \sin(\omega t - y)]/RT\}$ which is very small.

[12] Upon expanding $\cos(\omega t - y)$ and recalling that

$$\int_0^\infty y^{-1/2}\cos y\,dy = \int_0^\infty y^{-1/2}\sin y\,dy = (\pi/2)^{1/2}$$

and noting that $\cos\omega t + \sin\omega t = \sqrt{2}\cos(\omega t - \frac{\pi}{4})$, Eq. [19] is obtained.

Manuscript received May 29, 1961; revised manuscript received April 10, 1962.

Any discussion of this paper will appear in a Discussion Section to be published in the June 1963 JOURNAL.

REFERENCES

1. J. E. B. Randles, *Discussions Faraday Soc.*, **1**, 11 (1947).
2. B. Breyer and F. Gutman, *ibid.*, **1**, 19 (1947); B. Breyer, F. Gutman, and S. Hacobian, *Australian J. Sci. Research*, **A3**, 558, 567 (1950); **A4**, 595 (1951); B. Breyer and S. Hacobian, *ibid.*, **A4**, 604, 610 (1951); *Australian J. Chem.*, **7**, 225 (1954).
3. B. Ershler, *Zhur. Fiz. Khim.*, **22**, 683 (1948); K. Rozental and B. Ershler, *ibid.*, **22**, 1344 (1948).
4. H. Gerisher, *Z. physik. Chem.*, **198**, 286 (1951); *ibid.*, (*N.F.*) **1**, 278 (1954).
5. M. Fournier, *Compt. rend.*, **232**, 1673 (1951).
6. D. C. Grahame, *This Journal*, **99**, 370C (1952).
7. P. Delahay and T. J. Adams, *J. Am. Chem. Soc.*, **74**, 5740 (1952).
8. T. Berzins and P. Delahay, *Z. Elektrochem.*, **59**, 792 (1955).
9. I. Tachi and T. Kambara, *Bull. Chem. Soc. Japan*, **28**, 25 (1955).
10. M. Senda and I. Tachi, *ibid.*, **28**, 632 (1955).
11. T. Kambara, *Z. physik. Chem. (N.F.)*, **5**, 52 (1955).
12. H. Matsuda, *Z. Elektrochem.*, **62**, 977 (1958).
13. H. Matsuda and P. Delahay, *J. Am. Chem. Soc.*, **82**, 1547 (1960).
14. J. Koutecky, *Collect. Czech. Chem. Communs*, **21**, 443 (1956).
15. M. Wien, *Ann. Physik. u. Chem.*, **58**, 37 (1896).
16. A. E. Remick and H. W. McCormick, *This Journal*, **102**, 534 (1955).
17. P. Delahay, M. Senda, and C. H. Weis, *J. Am. Chem. Soc.*, **83**, 312 (1961).
18. J. Silverman and A. E. Remick, *This Journal*, **97**, 335 (1950).
19. *cf* B. Friedman, "Principles and Techniques of Applied Mathematics," p. 440, John Wiley and Sons, Inc., New York (1956).
20. *cf* A. E. Taylor, "Advanced Calculus," p. 599, Ginn and Co., New York (1955).
21. Ref. (20), p. 529.
22. H. S. Carslaw and J. C. Jaeger, "Conduction of Heat in Solids," 2nd ed., pp. 304-5, 27 or 30, etc., Oxford University Press, London (1959).
23. Ref. (22), pp. 479-480.
24. Ref. (22), p. 301.
25. J. E. B. Randles, *Discussions Faraday Soc.*, **1**, 11 (1947).
26. J. O'M. Bockris, "Modern Aspects of Electrochemistry," p. 219, Academic Press Inc., New York (1954).
27. M. Breiter, M. Kleinerman, and P. Delahay, *J. Am. Chem. Soc.*, **80**, 5111 (1958).

APPENDIX I
Derivation of Eq. [7]

We let $u(x,t)$ denote the quantity

$$u(x,t) = C^\circ_R - C_R(x,t) \quad [20]$$

Seeking a bounded solution of Eq. [2] to [6], we introduce boundary conditions [4] and [5] into the Laplace transforms of Eq. [2] and [3], respectively, and obtain two differential equations in the domain $x > 0$ which can easily be solved to give equations for the transforms, $\bar{u}$ and $\bar{C}_{ox}$:

$$\bar{u}(x,s) = \bar{u}(0,s)\,\exp(-s^{1/2}x/D_R^{1/2}) \quad [21]$$

$$\bar{C}_{ox}(x,s) = \bar{C}_{ox}(0,s)\,\exp(-s^{1/2}x/D_{ox}^{1/2}) \quad [22]$$

where s is the Laplace variable.

Differentiation of these equations with respect to x followed by evaluation at $x = 0$ and combination with the transform of Eq. [6] yields

$$\bar{C}_{ox}(0,s) = \bar{u}(0,s)m(D_R/D_{ox})^{1/2} \quad [23]$$

Taking the inverse transform of Eq. [23] gives

$$m\,u(0,t) = C_{ox}(0,t)\,(D_{ox}/D_R)^{1/2} \quad [24]$$

except at points of discontinuity, using a uniqueness theorem (24).

The instantaneous anodic current, i_f, is related to the flux according to Eq. [25]

$$i_f = nFAD_{ox}[\partial C_{ox}(x,t)/\partial x]_{x=0} \quad [25]$$

wherein we use the convention that an anodic current is negative, and where A denotes the electrode area. The term $[\partial C_{ox}(x,t)/\partial x]$, may be calculated from the preceding equations as follows. Differentiating Eq. [22] with respect to x and setting $x = 0$, one finds

$$[\partial \bar{C}_{ox}(x,s)/\partial x]_{x=0}$$

$$= -\bar{C}_{ox}(0,s)\,(s/D_{ox})^{1/2} = -s\bar{C}_{ox}(0,s)\,(D_{ox}s)^{-1/2}$$

$$= [-s/(\pi D_{ox})^{1/2}] \int_0^\infty e^{-st}\, C_{ox}(0,t)\,dt \int_0^\infty e^{-\epsilon t}\, t^{-1/2}\,dt \quad [26a]$$

$$= [-s/(\pi D_{ox})^{1/2}] \int_0^\infty e^{-st}\, [\int_0^t C_{ox}(0,t-\tau)\tau^{-1/2}\,d\tau]dt \quad [26b]$$

$$= -(\pi D_{ox})^{-1/2} \int_0^\infty e^{-st} \left[\frac{\partial}{\partial t}\int_0^t C_{ox}(0,t-\tau)\tau^{-1/2}\,d\tau\right]dt \quad [26c]$$

where we have introduced into (a) the fact that $s^{-1/2}$ is simply the Laplace transform of $(\pi t)^{-1/2}$. In obtaining (b) we have employed the convolution theorem for Laplace transforms, and in obtaining (c) we have used the standard relation between the Laplace transform of a function (here of $\int_0^t C_{ox}(0,t-\tau)\tau^{-1/2}\,d\tau$) and of its derivative.

It is now immediately apparent from [26c] that

$$[\partial C_{ox}(x,t)/\partial x]_{x=0} = -(\pi D_{ox})^{-1/2}\frac{\partial}{\partial t}\int_0^t C_{ox}(0,t-\tau)\tau^{-1/2}\,d\tau \quad [27]$$

Equation [7] of the text is then obtained from [25] and [27].

APPENDIX II

Derivation of Eq. [13] and [15] from [7]

We shall consider the behavior of Eq. [7] for times greater than 0, and we may therefore replace $C_{ox}(0,t-\tau)$ in that equation by the function $f(\omega t - \omega\tau)$, which satisfies Eq. [14] for all values of the argument of f, positive or negative. The time derivative in Eq. [7] can then be written as in Eq. [28], after first performing the differentiation and making use of the identity

$$\partial f(\omega t - \omega\tau)/\partial t = -\partial f(\omega t - \omega\tau)/d\tau$$

$$\frac{\partial}{\partial t}\int_0^t f(\omega t - \omega\tau)\tau^{-1/2}\,d\tau$$

$$= f(0)t^{-1/2} - \omega\int_0^t\left[\frac{\partial}{\partial(\omega\tau)}f(\omega t - \omega\tau)\right]\tau^{-1/2}\,d\tau \quad [28]$$

where f(0) is to be obtained from Eq. [14] by setting $\omega t - y$ equal to zero there.

Introducing into Eq. [28] a change of variable, $y = \omega\tau$, the right-hand side of the equation becomes:

$$f(0)t^{-1/2} - \omega^{1/2}\int_0^\infty\left[\frac{\partial}{\partial y}f(\omega t - y)\right]y^{-1/2}\,dy$$

$$+ \omega^{1/2}\int_{\omega t}^\infty\left[\frac{\partial}{\partial y}f(\omega t - y)\right]y^{-1/2}\,dy \quad [29]$$

It is evident from Eq. [14] that $f(\omega t - y)$ is a bounded function[13] of $\omega t - y$, so that upon integrating the third term of [29] by parts we get in place of [29]

[13] For any value of $\omega t - y$, $f(\omega t - y)$ is the positive root of an algebraic equation, all of whose coefficients are finite. The roots of such equations always lie in a finite region of the complex plane.

$$-\omega^{1/2}\int_0^\infty\frac{\partial}{\partial y}f(\omega t - y)\,y^{-1/2}\,dy + \frac{\omega^{1/2}}{2}\int_{\omega t}^\infty f(\omega t - y)\,y^{-3/2}\,dy \quad [30]$$

From Eq. [7], [28], and [30], Eq. [13] then follows.

The first integral in Eq. [13] can also be written in the alternative form

$$\lim_{\epsilon\to 0^+}\int_\epsilon^\infty\frac{\partial f}{\partial y}(\omega t - y)\,y^{-1/2}\,dy \quad [31]$$

Upon integrating by parts, this term becomes

$$-\lim_{\epsilon\to 0^+}\left[f(\omega t - \epsilon)\,\epsilon^{-1/2} - \frac{1}{2}\int_\epsilon^\infty f(\omega t - y)\,y^{-3/2}\,dy\right]$$

$$= -\frac{1}{2}\lim_{\epsilon\to 0^+}\left[\int_\epsilon^\infty f(\omega t - \epsilon)\,y^{-3/2}\,dy - \int_\epsilon^\infty f(\omega t - y)\,y^{-3/2}\,dy\right] \quad [32]$$

where we have introduced the identity

$$\epsilon^{-1/2} = \frac{1}{2}\int_\epsilon^\infty y^{-3/2}\,dy$$

Rewriting the integrals in [32] as:

$$[f(\omega t - \epsilon) - f(\omega t)]\int_\epsilon^\infty y^{-3/2}\,dy + \int_\epsilon^\infty [f(\omega t) - f(\omega t - y)]y^{-3/2}\,dy \quad [33]$$

and proceeding to the limit $\epsilon = 0$, the first expression in [33] varies as (constant) (ϵ) $(\epsilon^{-1/2})$ using the conditions on f specified in footnote[14] and so vanishes. Introducing the second integral of [33] into [31], Eq. [15] is obtained.

APPENDIX III

Proof that the Mean Value of i_f Equals Zero in the Periodic State

In this section we consider the behavior at positive times, and it follows therefore that $t >> t_o$. Thus, we may replace C_{ox} by f.

It is first noted that physical arguments show that there can be only one positive solution of Eq. [14] for $f(\omega t - y)$, even when this equation has more than one solution (*i.e.*, when $m \neq 1$). All other solutions must either be negative or partly imaginary. We further note that since $p(\omega t) = p(\omega t + 2\pi)$, $f(\omega t - y)$ and $f(\omega t - y + 2\pi)$ satisfy the same Eq. [14]. Because of the uniqueness of the physically real $f(\omega t - y)$ just mentioned, it then follows that for our positive f's, $f(\omega t - y + 2\pi) = f(\omega t - y)$, *i.e.*, $f(\omega t - y)$ is also a periodic function of ωt with the same period as $p(\omega t)$.

We next observe that the mean value of the integral describing the periodic state is obtained by averaging it with respect to ωt over a period of 2π. Using Eq. [15], the integral which occurs in this average can be written in the equivalent form

$$-\frac{1}{4\pi}\int_\theta^{\theta+2\pi}\left[\lim_{\epsilon\to 0^+}\int_{y=\epsilon}^\infty [f(\omega t) - f(\omega t - y)]y^{-3/2}\,dy\right]d(\omega t) \quad [34]$$

where θ is any large value of ωt. It can easily be shown[14] that the convergence of the y-integral as $\epsilon \to 0^+$ is uniform in ωt and, hence, lim and $\int$ can be interchanged, using a standard theorem [20]. Thus we obtain

$$-\frac{1}{4\pi}\lim_{\epsilon\to 0^+}\int_{\omega t=\theta}^{\theta+2\pi}\left[\int_{y=\epsilon}^\infty [f(\omega t) - f(\omega t - y)]y^{-3/2}\,dy\right]d(\omega t) \quad [35]$$

[14] For ϵ small and y lying in the interval $(0, \epsilon)$, $|f(\omega t) - f(\omega t - y)| \cong |\frac{\partial}{\partial \omega t}f(\omega t)| \cdot y$, whence $|\int_0^\epsilon [f(\omega t) - f(\omega t - y)]y^{-3/2}\,dy| \leq N\int_0^\epsilon y^{-1/2}\,dy = 2N\epsilon^{1/2}$, where N, an upper bound to the derivative, is independent of ωt. Actually the differentiability of $f(\omega t)$ needn't have been used. The milder Hölder condition, $|f(\omega t) - f(\omega t - y)| \leq$ constant $\cdot\, y^\alpha$ but where $\alpha > \frac{1}{2}$, would have sufficed.

Because of the readily proven convergence of the y-integral with respect to the upper limit (∞), uniform in ωt, [35] may be written as

$$-\frac{1}{4\pi}\lim_{\epsilon\to 0^+}\lim_{L\to\infty}\int_{\omega t=\theta}^{\theta+2\pi}\left[\int_{y=\epsilon}^{L}[f(\omega t) - f(\omega t - y)]y^{-3/2}\,dy\right]d(\omega t) \quad [36]$$

The integrals $\int_{\epsilon}^{L}[f(\omega t) - f(\omega t - y)]y^{-3/2}\,dy$ and $y^{-3/2}\int_{\theta}^{\theta+2\pi}[f(\omega t) - f(\omega t - y)]d(\omega t)$ exist for any $\epsilon > 0$ and L, and the double integral also exists not only for continuous $f(\omega t)$ but also for piecewise continuous $f(\omega t)$. It then follows from a standard theorem [21] that the order of integration can be interchanged. We obtain

$$-\frac{1}{4\pi}\lim_{\epsilon\to 0^+}\lim_{L\to\infty}\int_{y=\epsilon}^{L}y^{-3/2}\left[\int_{\theta}^{\theta+2\pi}[f(\omega t) - f(\omega t - y)]d(\omega t)\right]dy \quad [37]$$

But, since $f(\omega t)$ was seen earlier to be a periodic function of ωt, it is true that

$$\int_{\theta}^{\theta+2\pi}f(\omega t)\,d(\omega t) = \int_{\theta}^{\theta+2\pi}f(\omega t - y)\,d(\omega t) \quad [39]$$

since it is easily shown that the value of a periodic function averaged over its period is independent of the initial value of the phase angle.

We see, therefore, that the ωt integral in Eq. [37] must vanish which proves the desired result.

This result of Appendix III can be proven under milder restrictions, such as piecewise continuity of $f(\omega t)$. As pointed out in the text, Eq. [15] for i_f is valid for piecewise continuous $f(\omega t)$, except at the isolated points of discontinuity of the latter. The derivation of Eq. [35] from [34] proceeds as before, when points ωt of discontinuity of f are excluded. The derivation of [37] from [35] and the use of [38] remain valid. Thus, if one defines i_f arbitrarily but finite at the isolated points of discontinuity of $f(\omega t)$, the mean value of i_f is zero in the periodic state for piecewise continuous functions $f(\omega t)$.

SYMBOLS

A, area of electrode's surface, cm^2.
C_{ox}, concentration of oxidant, mole l^{-1}.
C_R, concentration of reductant, mole l^{-1}.
C^o_R, concentration of reductant in bulk of solution, mole l^{-1}.
D_{ox}, diffusion coefficient of oxidant, cm^2 sec^{-1}.
D_R, diffusion coefficient of reductant, cm^2 sec^{-1}.
E_a, half-cell potential difference of measuring electrode, v.
E_c, half-cell potential difference of auxiliary, nonpolarizable electrode, v.
E_f, half-cell potential difference between electrode and the solution just outside of electrical double layer, in Ox-Red system under investigation, v.
E_d, direct component of applied cell potential, v.
$\tilde{E}_f$, amplitude of the periodic E_f wave, v. $E_f = E_f p(\omega t)$.
E_o, standard potential of the Ox-Red system, v.
E'_o, $E_o + E_c - E_a$.
$\overline{E}_{cell}$, mean cell potential, v.
f, function of, (a particular function).
f, (as a subscript) faradaic.
F, faraday (96514 abs.-coulombs g-equiv.$^{-1}$).
h, function of, (a particular function).
i_f, instantaneous faradaic current, amp.
m, number of oxidant molecules produced from oxidation of 1 mole of reductant.
n, number of electrons involved in oxidation of 1 mole of reductant.
R, gas constant (8.3166 x 10^7 erg deg^{-1} mole^{-1}).
t, time, sec.
T, absolute temperature.
u, $C^o_R - C_R$.
x, perpendicular distance from a plane which is parallel to the planar electrode of Ox-Red system, but which is just outside the electrical double layer region.
ω, angular frequency of alternating voltage, sec^{-1}.

Technical Notes

The Discharge Properties of α-PbO_2 in Dilute H_2SO_4 Electrolyte

Harry B. Mark, Jr.

Department of Chemistry, University of North Carolina, Chapel Hill, North Carolina

The discharge properties and discharge mechanism of β-PbO_2 in H_2SO_4 electrolyte have been studied in considerable detail (1-3). There is disagreement as to the mechanism (1-3), but the experimental characteristics of the discharge, such as reduction overpotentials, shape of the potential-time discharge curves, etc., are well known (1, 3). Although some of the electrochemical properties (electrodeposition conditions and self-discharge) of α-PbO_2 have been the subject of considerable study (4-8), there is little information in the literature concerning the properties of pure α-PbO_2 under an applied discharge current (3, 4, 9). Almost no work has been reported on the properties of pure α-PbO_2 in dilute H_2SO_4 electrolyte, although a previous paper (3) showed that the discharge properties of β-PbO_2 change considerably and in an unexpected way as the acid strength of the electrolyte decreases. The discharge capacities of lead storage batteries, which have positive plates containing a mixture of α-PbO_2 and β-PbO_2, have been studied (10), and there is a brief description of the discharge curve obtained in 4.4M H_2SO_4 for an anodized Pb electrode (6). Microphotographs of the cross section of this electrode and x-ray and electron diffraction patterns seemed to indicate that there is a layer of a mixture of the two modifications of PbO_2 between the lead metal and the β-PbO_2 film which was in contact with the electrolyte (4). The discharge of an electrode, which consists of a layer of α-PbO_2 between a layer of β-PbO_2 and a Pt support, in a 4.4M H_2SO_4 electrolyte has been reported (9).

In this investigation the discharge in dilute (0.1M) H_2SO_4 of α-PbO_2 and β-PbO_2 have been studied, as

also electrodes consisting of a layer of α-PbO_2 on top of a layer of β-PbO_2 and *vise versa*. The effect of variation of discharge current and theoretical discharge capacity were also studied. A comparison of the experimental results obtained by this study indicate that the discharge mechanism of the two forms in dilute H_2SO_4 are quite different. These property differences were not very apparent in the experimental results reported in the work which used a more concentrated acid electrolyte, which may mask the effects arising from the two different mechanisms or may result in yet a third discharge mechanism. Both forms might discharge by this third or combination mechanism in the concentrated acid electrolyte.

Experimental Procedure

Preparation of electrodes.—The PbO_2 was electrodeposited on Pt cylinders sealed in glass as described in previous work (3). The electrodes had an apparent surface area of 8 cm^2. The β-PbO_2 was deposited from a solution of 0.020M $Pb(NO_3)_2$ and 0.3M HNO_3 with a current density of 10 ma/electrode (1.25 ma/cm^2) at room temperature for 4 to 40 min. The α-PbO_2 was deposited from a solution of 1.5M NH_4OH and 6.5M $NH_4C_2H_3O_2$ saturated with $Pb(C_2H_3O_2)_2$ (3,5) with a current density of 10 ma/electrode for 3 to 40 min at room temperature.

Discharge apparatus.—The discharge cell used was described previously (3). A saturated calomel electrode (SCE), which was used as the reference electrode, made contact with the solution in the cell through an agar-agar KCl bridge. A stream of nitrogen was used to stir the electrolyte, and a cylindrical sheet of lead metal was used as the anode.

Currents for discharge were furnished by an electronic constant-current source (11). The electromotive force of the cell was applied to a high input impedence (about 10^{11} ohms) follower amplifier of gain of −1. The output of the follower amplifier was fed first to a voltage inversion amplifier (gain of −1) and then to a voltage divider to attenuate the signal. The signal was then recorded by a Sargent model SR recorder. The follower and inversion amplifiers were constructed from plug-in analog computer amplifiers using circuits designed by DeFord (12).

When the electrodes had come to open-circuit equilibrium, as shown by constancy of potential for 15 min, a current, either continuous or interrupted (3), was introduced into the circuit. Previous work (3) has shown that under the conditions used no corrections are necessary for iR drop, electrolyte concentration polarization, and self-discharge.

Results

Examples of the discharge curves for α- and β-PbO_2 in 0.10M H_2SO_4 saturated with $PbSO_4$ and with excess solid phase are shown in Fig. 1. Curve 1 is for α-PbO_2 when an interrupted discharge current of 3 ma/electrode was passed. The α-PbO_2 electrode does not reach a steady-state closed-circuit potential in the time allowed, and the electrode recovers, when the current is interrupted, to a lower equilibrium open-circuit potential than it had before discharge. Thus, reliable and reproducible overpotentials could not be obtained for α-PbO_2 electrodes (3). Curve 2 is a typical continuous discharge of α-PbO_2 (a current density of 5 ma/electrode was passed in this example). The electrode does not reach a steady-state closed-circuit potential even under prolonged continuous discharge. Toward the end of discharge the potential decreases more and more rapidly. The actual discharge capacity of this electrode was only 40 ma-min, although the theoretical capacity was 250 ma-min. The actual capacity of all α-PbO_2 electrodes tested in H_2SO_4 electrolyte was considerably less than the theoretical and was independent of the theoretical capacity. When an α-PbO_2 electrode had reached the state of discharge indicated by point e of curve 2, it was removed from the cell and placed in a solution of KI and $HC_2H_3O_2$. The formation of considerable I_3^- indicated that appreciable PbO_2 remained undischarged. The surface of an α-PbO_2 electrode, that was initially very smooth and shiny black, was observed at point e to be covered with a white and strongly adhering uniform film of $PbSO_4$ (4). If this film was removed by a solution of $NH_4C_2H_3O_2$ (6) and the electrode returned to the cell, the initial open-circuit potential was reattained and the electrode rejuvenated. Further discharges could then be made. The surface of the α-PbO_2 after removal of the $PbSO_4$ was black but no longer smooth and shiny. By washing the electrode with $NH_4C_2H_3O_2$ each time the potential broke down sharply and then continuing the discharge, 80-90% of the theoretical discharge capacity can be obtained. Much larger current densities could be passed through α-PbO_2 than could be passed through β-PbO_2 (3) without destruction of the electrode. No potential minimum was found on the second discharge of α-PbO_2 as was reported by other investigators (9) using a 4.4M H_2SO_4 electrolyte.

The above experiments suggest that the $PbSO_4$ film may be the only cause of the poor discharge

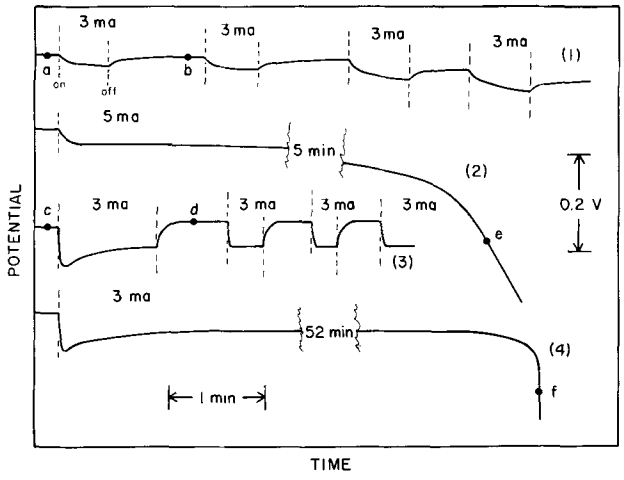

Fig. 1. Potential-time curves of α- and β-PbO_2 electrodes discharging under constant current. The electrolyte was 0.1M H_2SO_4 (sat. with $PbSO_4$): curve 1, α-PbO_2 under successive short constant current discharges of 3ma/electrode; curve 2, α-PbO_2 under continuous constant current discharge of 5 ma/electrode; curve 3, β-PbO_2 under successive short constant current discharges of 3 ma/electrode; curve 4, β-PbO_2 under continuous constant current discharge of 3 ma/electrode.

capacity of α-PbO_2. To check this, two discharges were made in 1.0M $HClO_4$ electrolyte which gave 93 and 94% of the theoretical capacity (based on 100% current efficiency on electrodeposition). The Pt electrodes were entirely bare at the end of discharge.

The curves for the interrupted discharge of β-PbO_2 (curve 3 of Fig. 1) were quite different from those of α-PbO_2 (curve 1) under similar conditions. The potential of the first discharge went through a pronounced minimum before reaching a steady-state closed-circuit potential and, on subsequent discharges, passed through very slight minima which were barely detectable. The β-PbO_2 electrode recovers to a more positive open-circuit equilibrium potential after the first discharge than it had initially, and recovers to this new emf after each subsequent discharge until the electrode breaks down (3). Discharge overpotentials for single β-PbO_2 electrodes are quite reproducible (3). On continuous discharge β-PbO_2 electrodes go through a potential minimum, reach a steady closed-circuit potential which remains constant for a long time, and finally the potential drops very rapidly, as shown by curve 4 of Fig. 1. Removal of the electrode at point f in the discharge shows that most of the PbO_2 (70-95%) has been reduced. Some I_3^- is formed on placing the electrode in acidic KI, but bare Pt is seen over much of the surface. For the particular electrode used as the example in curve 4, a test showed that about 75% of the PbO_2 had discharged electrolytically. All attempts to rejuvenate β-PbO_2 electrodes at this point by washing with $NH_4C_2H_3O_2$ were unsuccessful. Although there were some crystals of white $PbSO_4$ (before washing) widely scattered on the PbO_2 surface, there was no white film as observed for α-PbO_2.

Partially discharged α-PbO_2 electrodes which were allowed to recover to open-circuit equilibrium were washed with 40% $NH_4C_2H_3O_2$ solution to strip off the $PbSO_4$ on the surface and the wash solution analyzed for Pb^{++} by a dithizone method (13). This test indicated that practically all of the $PbSO_4$ produced on discharge of α-PbO_2 remained on the surface of the electrode, as shown in Table I. Blank tests showed that the correction for the reduction of PbO_2 by the 40% $NH_4C_2H_3O_2$ was negligible. A similar test on partially reduced β-PbO_2 electrodes showed that only part (16-50%) of the $PbSO_4$ produced on discharge remained on the surface after recovery, as shown in Table II.

Table I. Per cent $PbSO_4$ on the surface of α-PbO_2 electrodes at open-circuit equilibrium following discharge in an electrolyte of 0.1M H_2SO_4 saturated with $PbSO_4$

Discharge conditions			% $PbSO_4$ produced by discharge remaining on electrode surface
Current, ma/electrode	Time, min	$i - t$ ma-min	
1.5	10	15	105
3.0	5	15	98
3.0	4	12	96
4.0	4	16	96
5.0	3	15	95
5.0	2	10	90

Table II. Per cent $PbSO_4$ on the surface of β-PbO_2 electrodes at open-circuit equilibrium following discharge in an electrolyte of 0.1M H_2SO_4 saturated with $PbSO_4$

Discharge conditions			% $PbSO_4$ produced by discharge remaining on electrode surface
Current, ma/electrode	Time, min	$i - t$ ma-min	
2.0	21	42	16
1.0	35	35	37
1.5	40	60	19
2.3	15	34.5	50
1.2	15	18	42

The overpotentials obtained for interrupted discharges of α-PbO_2 were considerably less than those for β-PbO_2, and the rates of growth and decay of polarization were greater for β-PbO_2 than α-PbO_2, as shown by comparing curves 1 and 3 of Fig. 1. The initial open-circuit potential of α-PbO_2 was somewhat higher than that of β-PbO_2, in agreement with other work (6, 7). The larger overpotentials of β-PbO_2 may be a result of smaller true surface areas of β-PbO_2 electrodes which would increase the double layer capacity of the electrodes. However, the much rougher appearance of the β-PbO_2 surface indicates that it has the larger surface area.

Rüetschi and Cahan (6) studied the discharge of a film produced by anodizing Pb and Pb alloys (film consists of a layer of a mixture of the two modifications of PbO_2 between an external layer of pure β-PbO_2 and the metal). They found that the discharge curve went through an initial potential minimum before reaching a closed-circuit plateau. As the discharge continued, the potential went through a second minimum and came to a second, still lower, steady-state potential. The potential then dropped sharply as the film of PbO_2 was completely discharged. They suggested that the two potential plateaus represented the discharge of α- and β-PbO_2, respectively, and the difference between the plateaus represented the differences in the overpotential for the two modifications. Because the present investigation showed that the shapes of the discharge curves of the two pure modifications are quite different, these characteristics could be used in studies of the discharge properties of electrodes consisting of layers of the two modifications.

Electrodes were made consisting of a thin layer of α-PbO_2 (theoretical discharge capacities varying from 30 to 70 ma-min) on the Pt and a thin exterior layer of β-PbO_2 (capacities varying from 30 to 150 ma-min). The β:α ratios varied from 0.6 to 3. These electrodes were discharged by passing constant currents of 3-12 ma/electrode, and the discharge potentials were recorded. All the discharge curves had the characteristic shape of curve 2 of Fig. 2. In no case were two plateaus and two minima observed. Initially the discharge curves resembled that of pure, undischarged β-PbO_2 electrodes. As the capacity of the β-PbO_2 layer was nearing exhaustion, about point h of curve 2, the potential started to drift downward, and the electrode from there to the end of the discharge resembles that of an α-PbO_2 electrode which was partially discharged. If the current was interrupted at a point along the line

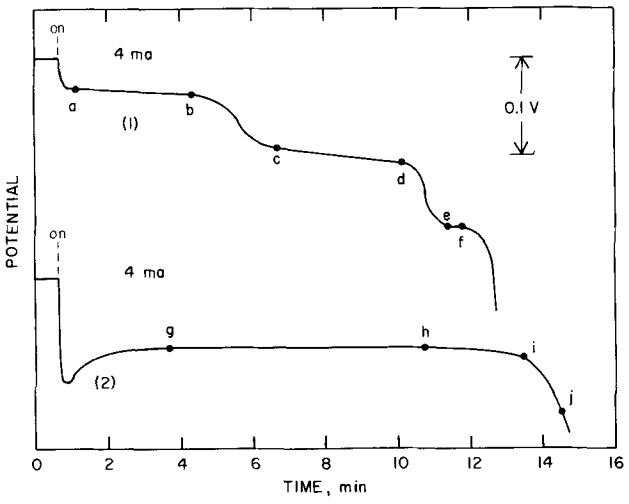

Fig. 2. Potential-time curves. The electrolyte was 0.1M H_2SO_4 (sat. with $PbSO_4$): curve 1, electrode consisting of a layer of β-PbO_2 (discharge capacity of 40 ma-min) on Pt support and layer of α-PbO_2 (capacity of 70 ma-min) on the β-PbO_2 surface, under a continuous discharge of 4 ma/electrode; curve 2, electrode consisting of a layer of α-PbO_2 (capacity of 40 ma-min) on Pt and a layer of β-PbO_2 (capacity of 60 ma-min) on the α-PbO_2 surface, under a continuous discharge current of 4 ma/electrode.

hi and the electrode allowed to recover before resuming discharge, the resulting curves for the growth and decay of polarization show rates and shapes characteristic of α-PbO_2 and not of β-PbO_2. If the electrode at point j was washed with 40% $NH_4C_2H_3O_2$, the electrode was rejuvenated and on subsequent discharge behaved like pure α-PbO_2. The potential minimum was least pronounced for the electrode having the smallest β-PbO_2 layer (30 ma-min capacity).

Electrodes consisting of a thin layer of β-PbO_2 (theoretical capacities varying from 40 to 70 ma-min) on Pt and a thin layer of α-PbO_2 (capacities varying from 30 to 120 ma-min) on the β-PbO_2 surface were also made. The α:β ratios varied from 0.75 to 2. These electrodes were discharged by currents varying from 2 to 5 ma/electrode. The discharge curves, for the most part, had characteristic shapes as shown by curve 1 of Fig. 2. Three distinct plateaus were observed. Initially (to point b) the discharge curves resembled that of pure α-PbO_2. Interrupting the current along line ab, allowing the electrode to recover, and then resuming discharge, resulted in decay and growth of polarization curves having the characteristics of pure α-PbO_2. Interruption, recovery, and resumption of discharge along the second plateau (line cd) resulted in curves that had characteristics between those of α- and β-PbO_2 (rate of growth and decay of polarization greater than for α-PbO_2 but less than for β-PbO_2). These rates increased from point c to d. The same treatment along the third plateau (line ef), yielded curves which had the characteristics of pure β-PbO_2 (no minimum was detected, but this might not be expected at the recorded sensitivity used).

One electrode gave a discharge curve differing from that of curve 1 of Fig. 2. For the electrode having the largest capacity of the external α-PbO_2 layer (120 ma-min), the curve had only one plateau and was no different from that of a pure α-PbO_2 electrode (see curve 2 of Fig. 1).

It had been suggested (3) that an expansion of the crystal lattice of β-PbO_2 early in discharge caused the minimum and the rise in the open-circuit potential, and that the lattice of α-PbO_2 did not undergo this expansion. Powder x-ray diffraction patterns of the oxide films were made for β-PbO_2 before and after the first discharge (point c and d in curve 3 of Fig. 1). Patterns were also before and after the first discharge of α-PbO_2. The β-PbO_2 patterns failed to reveal any appreciable shift in the lines which would indicate an expansion of the lattice. If the expansion does occur, it is too small to detect by this method.

Discussion

The studied discharge characteristics of the two modifications of PbO_2 in 0.1M H_2SO_4 show that the $PbSO_4$ produced on the discharge of α-PbO_2 remains as a tightly adhering film on the surface of the remaining undischarged α-PbO_2, and that produced on discharge of β-PbO_2 remains only in part on the surface and not as a film but as widely dispersed crystalline nuclei. This suggests that the discharge mechanism of the two forms may be quite different. The adherent $PbSO_4$ film on the α-PbO_2 electrode suggests that the Pb(II) reduction product reacts without leaving the electrode surface to form $PbSO_4$. The corresponding product in the reduction of β-PbO_2 passes into solution and then deposits on existing $PbSO_4$ crystals, only part of which are on the surface. Experiments in 4.4M H_2SO_4 electrolyte (9) seem to indicate that an adherent $PbSO_4$ film forms of both modifications on discharge. Although the discharge properties of PbO_2 electrodes in the more concentrated acid electrolytes and the conclusions drawn from these properties (9) were, for the most part, very different from those of this study in 0.1M H_2SO_4, these differences are not too surprising. A previous study of the discharge properties of β-PbO_2 as a function of H_2SO_4 concentration in the electrolyte (3) also revealed unexpected results at the higher acid concentrations. The magnitude of the overpotentials was at a minimum at about 0.1M H_2SO_4, and the rates of growth and decay of polarization were at a maximum at this value. No satisfactory explanation of this behavior has yet been found.

The discharge characteristics of the electrodes consisting of a thin layer of α-PbO_2 between the Pt surface and the β-PbO_2 layer indicate that the outer β-PbO_2 layer reacts first, and not until this layer has been nearly exhausted does the α-PbO_2 layer begin to react. This is in agreement with the conclusions drawn by Ikari, Yoshizawa, and Okada (9) for the discharge of a similar electrode in 4.4M H_2SO_4. These authors found, however, two distinct plateaus in the discharge curve, while only one plateau was observed under the conditions of this paper. They, also, found one minimum which preceded the first plateau. Rüetschi and Cahan (6) found two plateaus and two minima in the discharge curves of their two layer electrodes, which consisted of a layer of an α-PbO_2-β-PbO_2 mixture (4) between a

Pb or Pb alloy surface and a pure β-PbO_2 layer. They suggested that the α-PbO_2 probably discharged first. Although it is possible to argue that the modification having the higher electrode potential might discharge first at low current densities, that is not probable with the relatively large apparent current densities (0.1-1.0 ma/cm^2) used in all these investigations. Under these conditions the species, β-PbO_2, which is in more immediate contact with the electrolyte, will discharge first.

The discharge curves of the electrodes consisting of a thin layer of β-PbO_2 between the Pt surface and the thin outer layer of α-PbO_2 indicate that the α-PbO_2 alone starts to reduce first (initial plateau), followed by a "mixed" reduction of both forms (second plateau), and finally a reduction of the β-PbO_2 only (third plateau).

Acknowledgment

The author wishes to thank Dr. Warren C. Vosburgh, Department of Chemistry, Duke University, for his interest and suggestions concerning this research and preparation of this manuscript. He also wishes to thank Dr. J. C. Morrow, Department of Chemistry, University of North Carolina, who made the x-ray diffraction patterns.

This manuscript received Jan. 17, 1962; revised manuscript received March 14, 1962.

Any discussion of this paper will appear in a Discussion Section to be published in the June 1963 JOURNAL.

REFERENCES

1. W. H. Beck, R. Lind, and W. F. K. Wynne-Jones, *Trans. Faraday Soc.*, **50**, 147 (1950).
2. W. H. Beck, P. Jones, nd W. F. K. Wynne-Jones, *ibid.*, **50**, 1249 (1950).
3. H. B. Mark, Jr., and W. C. Vosburgh, *This Journal*, **108**, 615 (1961).
4. J. Burbank, *ibid.*, **104**, 693 (1957).
5. P. Rüetschi and B. D. Cahan, *ibid.*, **104**, 406 (1957).
6. P. Rüetschi and B. D. Cahan, *ibid.*, **105**, 369 (1958).
7. P. Rüetschi, R. T. Angstadt, and B. D. Cahan, *ibid.*, **106**, 547 (1959).
8. I. G. Kiselava and B. N. Kabanov, *Doklady Akad. Nauk SSSR*, **122**, 1042 (1958). *C. A.* **54**, 24014c (1960).
9. S. Ikari, S. Yoshizawa, and S. Okada, *J. Electrochem. Soc. Japan*, Overseas Ed., **27**, E223 (1959).
10. V. H. Dodson, *This Journal*, **108**, 406 (1961).
11. C. N. Reilley and W. G. Scribner, *Anal. Chem.*, **27**, 1210 (1955).
12. D. D. DeFord, Div. of Analytical Chemistry, 133rd Meeting, ACS, San Francisco, 1958.
13. G. L. Guettel, *Ind. Eng. Chem.*, Anal. Ed., **11**, 639 (1939).

Electrolytic Polarization Resulting from Longitudinal Current in Electrodes

Walter W. Harvey

Lincoln Laboratory,[1] Massachusetts Institute of Technology, Lexington, Massachusetts

Longitudinal current in a metal wire contacting an electrolyte leads to polarization of the interphase. If the variation in potential within the metal along the contact with the electrolyte is not negligibly small, *i.e.*, if the resistance or longitudinal current is sufficiently large, some portion of the current will be conducted through the electrolyte. That this must be so can be seen from the following argument. With no current flowing in the wire or in the electrolyte, the magnitude of the potential difference (p.d.) between the interior of the electrolyte and the interior of the wire will be the same over the entire length of the wire; measured with respect to a reference half-cell, this difference in potential is the "rest potential" of the given metal-electrolyte half-cell. If now a p.d. is impressed across the ends, causing current to flow through the wire, the result is that different parts of the wire will be at different potentials, so that the metal-electrolyte p.d. can equal the rest potential at only one position along the contact. It follows that electrolysis will take place, the current densities normally being greatest at the ends of the metal-electrolyte contact, where the anodic and cathodic overpotentials have their maximum values.[2] Similar considerations have been expressed before, particularly with reference to palladium wires containing hydrogen (1, 2); however, to the author's knowledge, the problem has not previously been analyzed quantitatively.

For the reasons indicated, the apportionment of current between wire and electrolyte will not be determined by the ratio of their resistances, as for a parallel arrangement of resistors, but (for a given wire) by the current density-overpotential characteristic of the given electrode material in the given electrolyte. Owing to polarization, the instantaneous current across the contact can be considerably greater than the steady value, so that the apparent resistance of an immersed wire from a-c measurements would be expected to decrease with increasing frequency (3). It goes without saying that the significant current density-overpotential characteristic is that pertaining to the conditions of the resistance measurement, *e.g.*, instantaneous or steady-state current densities for the d-c characteristic. It is equally clear that the desired characteristic would not be obtained using a fine wire electrode because of the anticipated nonuniform current density distribution.

Although we shall not be concerned here with mapping the paths of current flow in the electrolyte, it is reasonable to conclude that they extend to some small distance from the interface. Thus, in the immediate vicinity of the wire, the electric field in the electrolyte has a longitudinal component. If it is

[1] Operated with support from the U.S. Army, Navy, and Air Force.

[2] This statement requires modification if passivation effects are encountered.

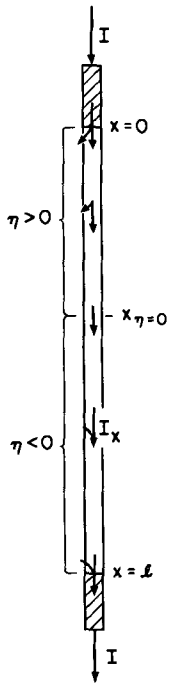

Fig. 1. Distribution of longitudinal current in a wire contacting an electrolyte.

true that the establishment of a potential gradient in a wire leads to current flow in the surrounding electrolyte, the converse must also be true. Accordingly, if a second wire is placed close to the wire carrying current, some current will flow in the second wire in addition to that flowing in the electrolyte. Apart from magnetic effects, therefore, an arrangement of closely situated parallel wires immersed in an electrolyte would be expected to exhibit coupling in a-c impedance measurements (4).

Derivation of the Potential Distribution

We treat the case of a uniform wire, a portion of whose surface contacts an electrolyte. The x-direction is taken parallel to the wire, and I_x denotes the longitudinal current in the wire. I_x varies with position along the wire-electrolyte contact, having a minimum value at the position of zero overpotential (see Fig. 1); in the pre-contact regions, $x < 0$ and $x > l$, I_x has the value I.

At points in the electrolyte sufficiently removed from the wire, the potential will be unaffected by longitudinal current in the wire. Thus, the p.d. between interior of the electrolyte and interior of the wire will vary as the potential $V(x)$ in the wire. That is,

$$\frac{d}{dx}(\phi_{\text{metal}} - \phi_{\text{electrolyte}}) = \frac{dV}{dx} \qquad [1]$$

The total metal-electrolyte p.d. appropriate to Eq. [1] is made up of a potential drop across the interphase plus any additional potential drop in the body of the electrolyte:

$$\phi_{\text{metal}} - \phi_{\text{electrolyte}} = \Delta\phi_{\text{interphase}} + \Delta\phi_{\text{electrolyte}} \qquad [2]$$

The electrolytic overpotential $\eta(x)$ is determined by the potential drop across the interphase; more particularly,

$$\frac{d}{dx}(\Delta\phi_{\text{interphase}}) = \frac{d\eta}{dx} \qquad [3]$$

Therefore, to the extent that $\Delta\phi_{\text{electrolyte}}$ is small in comparison to $\Delta\phi_{\text{interphase}}$, the gradients of potential and overpotential will be equal.

The potential gradient along the wire is

$$\frac{dV}{dx} = -\frac{\rho}{\pi r^2} I_x \qquad [4]$$

where ρ is the resistivity, and r the radius of the wire. We write the complete electrolytic current density-overpotential characteristic as $j = j(\eta)$, assigning positive values to j and η for anodic polarization. Then the integrated electrolytic current at position x is given by

$$i = 2\pi r \int_0^x j(\eta)\,dx \qquad [5]$$

whereupon I_x may be formulated as

$$I_x = I - 2\pi r \int_0^x j(\eta)\,dx \qquad [6]$$

and the potential gradient as

$$\frac{dV}{dx} = -\frac{\rho}{\pi r^2} I + \frac{2\rho}{r}\int_0^x j(\eta)\,dx \qquad [7]$$

According to our basic postulate, dV/dx may be set equal to $d\eta/dx$, so that on taking derivatives Eq. [7] becomes

$$\frac{d^2\eta}{dx^2} = \frac{2\rho}{r}\frac{d}{dx}\int_0^x j(\eta)\,dx \qquad [8]$$

from which we wish to obtain $\eta = \eta(x)$. Substituting $f(x)$ for j (η), the derivative of the integral is simply $f(x)$, leading to

$$\frac{d^2\eta}{dx^2} - \frac{2\rho}{r} j(\eta) = 0 \qquad [9]$$

subject to the boundary conditions

$$\left.\frac{d\eta}{dx}\right)_{x=0} = \left.\frac{d\eta}{dx}\right)_{x=l} = -\frac{\rho I}{\pi r^2} \qquad [10]$$

A possible distribution of potential along the wire in accordance with Eq. [9] and conditions [10] is shown in Fig. 2. Identical considerations apply to a metal strip; the potential distribution for a thin strip is given by Eq. [9], with the radius r of the wire replaced by the thickness δ of the strip.

Unless $j(\eta)$ has a particularly simple form, it will not be possible to obtain an analytical solution to Eq. [9]. We illustrate the procedure for a linear characteristic $j(\eta) = b\eta$, such as often pertains at potentials not too far removed from the rest potential. It is evident that for a linear characteristic, η will be zero at $x = l/2$. The equation

$$\frac{d^2\eta}{dx^2} - \frac{2\rho}{r} b\eta = 0 \qquad [11]$$

obtained by substituting $j(\eta) = b\eta$ into Eq. [9] has the general solution

$$\eta = c_1 e^{\alpha x} + c_2 e^{-\alpha x} \qquad [12]$$

where

$$\alpha = (2\rho b/r)^{1/2} \qquad [13]$$

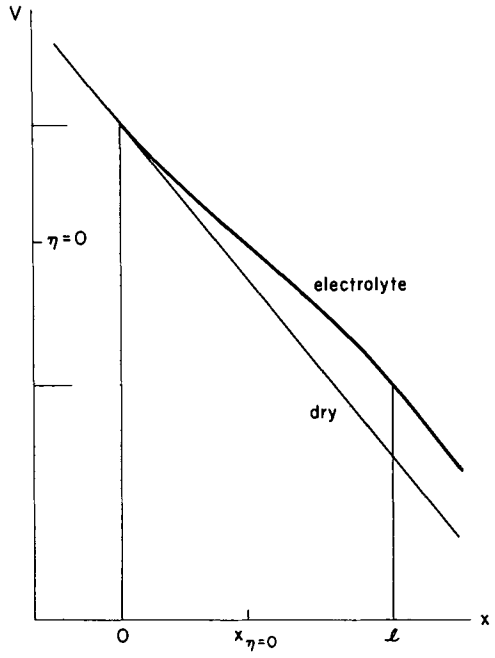

Fig. 2. Distribution of potential in a wire contacting an electrolyte

The constants c_1 and c_2 are evaluated from the boundary conditions [10] leading to the following analytical solution

$$\eta = \frac{\alpha I/b}{4\pi r \sinh \alpha l}\left[(e^{-\alpha l}-1)e^{\alpha x} + (e^{\alpha l}-1)e^{-\alpha x}\right] \quad [14]$$

Using this result, the current carried by the electrolyte is evaluable either as the total anodic current

$$i_+ = 2\pi r \int_0^{l/2} b\eta\, dx = I\left(1 - \operatorname{sech}\frac{\alpha l}{2}\right) \quad [15]$$

or the total cathodic current

$$i_- = 2\pi r \int_{l/2}^{l} b\eta\, dx \quad [16]$$

with, of course,

$$i_+ + i_- = 0 \quad [17]$$

For the general characteristic $j(\eta)$, the total electrolysis current is obtained from

$$i_+ = 2\pi r \int_0^{x_{\eta=0}} j(\eta)\, dx \quad [18]$$

Remarks

The distributions of potential and longitudinal current in an immersed metal wire through whose ends a current I is passed are seen to be determined by the radius and resistivity of the wire, the length of the contact with the electrolyte, and the current density-overpotential characteristic $j(\eta)$. The resistivity of the electrolyte does not enter explicitly since its influence is indirect, being confined to polarization effects which are included in the measured $j(\eta)$. The analysis on which the foregoing statements

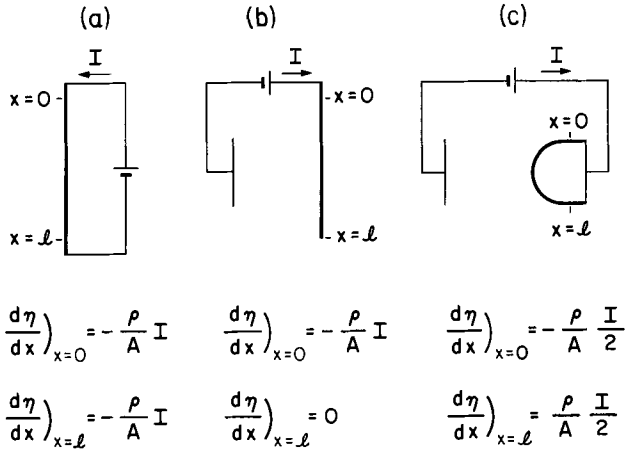

Fig. 3. Boundary conditions for (*a*) longitudinal current in an immersed wire, (*b*) a wire electrode with metallic contact at one end, (*c*) a wire electrode with metallic contacts at both ends. $A = \pi r^2$.

are based presupposes the condition $\Delta\phi_{\text{interphase}} >> \Delta\phi_{\text{electrolyte}}$. If this condition does not pertain in a practical case, details of the current flow in the electrolyte must be worked out. Even so, the method of treatment developed above should provide a useful approximation to the actual distributions of potential and current in the wire.

In most instances, the fraction of current conducted through the electrolyte will be small. For example, for a 10-cm length of 10-mil platinum wire and for a linear characteristic with $b = 100$ ma/v, i_+/I would be 0.002 according to Eq. [15], increasing roughly proportionally with b. However, for a very thin metal strip or film, or for a semiconductor, the fraction can be appreciable. For a 10-cm length of 0.00005-in. gold sheet and for the same $j(\eta)$ as in the previous example, the electrolytic current would be 5% of the total.

The basic Eq. [9] can be applied to other situations of interest including that of a wire electrode of the usual sort, with metallic contact at one end, or a wire electrode, possibly in the form of a wide loop, with metallic contacts at both ends. The three configurations which have been considered are compared in Fig. 3, where the appropriate boundary conditions are also to be found.

Manuscript received Nov. 30, 1961.

Any discussion of this paper will appear in a Discussion Section to be published in the June 1963 JOURNAL.

REFERENCES

1. C. A. Knorr and E. Schwartz, *Z. Elektrochem.*, **39**, 281 (1933).
2. See J. C. Barton and F. A. Lewis, *Trans. Faraday Soc.*, **58**, 103 (1962) for an account of recent work and references to the early literature.
3. G. M. Schmid and N. Hackerman, *This Journal*, **107**, 647 (1960).
4. G. M. Schmid and N. Hackerman, *ibid.*, **107**, 142 (1960).

The Anodic Dissolution of Nickel in Acetonitrile

Thomas C. Franklin and Charles R. Parsons[1]

Chemistry Department, Baylor University, Waco, Texas

Nickel normally occurs in solution as nickel(II). However, there are a number of complex compounds containing nickel(I) (1). Ni(I) has also been postulated as an intermediate in the electrodeposition of nickel (2) and anodic dissolution in aqueous systems (3). It has also been indicated that nickel dissolves anodically in acetonitrile to produce a mixture of nickel(I) and (II) (3). This is a report of a further investigation of the anodic dissolution of nickel in dimethylformamide and acetonitrile.

Experimental Method

Determination of oxidation number by weight loss of nickel.—The electrolysis cell was a 400 ml beaker containing a 100 ml porous porcelain cup as the anode compartment. The constant current was supplied by a regulated 500v d-c power supply and a series resistor. Most of the runs were for 1000 to 5000 sec with a current of approximately 0.1 amp and a current density of approximately 0.0004 amp/cm^2. The current was maintained constant by frequent manual adjustment. The cathode and anode were coils of 14 gauge nickel wire.

Fisher certified Reagent Grade acetonitrile and dimethylformamide were used as solvents. Tetramethylammonium chloride was used as an electrolyte in both the anode and cathode compartments.

Determination of nickel(II) concentration in solution.—In order to check on the possibility of nickel entering solution by a secondary process a colorimetric comparison was made between the amount of nickel(II) in solution and the amount of nickel(II) that would be expected in solution if the nickel had dissolved as nickel(II).

The standard curve for nickel(II) was prepared by dissolving 23 mg of dried reagent grade nickel chloride in 100 ml of acetonitrile. This was then diluted to form a series of standards and measured on a Klett Summerson colorimeter.

The anodic dissolution curves were obtained using an apparatus and procedure similar to that of Franklin and Roth (4) in which the anode compartment, the cell of a Klett Summerson colorimeter, was connected by an acetonitrile tetramethylammonium chloride bridge to the cathode compartment. A constant current of 0.0020 amp was passed (approximately 0.0002 amp/cm^2), and the colorimeter readings were taken at regular intervals. The cell was open to the atmosphere, but it was bubbled with nitrogen prior to and during the anodic dissolution.

Coulometric titration of nickel(I).—In order to determine if nickel(I) were actually present in solution, the solution was titrated coulometrically with iodine. It was very difficult to detect visually the iodine color in the solution already colored with nickel; therefore, the Klett-Summerson colorimeter was again used. Following an anodic dissolution run, potassium iodide was added to the solution. The colorimeter filter was changed from the red one used with nickel dissolution to a green one, and the colorimeter zero adjustment was changed to coincide with the reading before the filter change. The nickel anode was replaced with platinum wire and a current of 2.0 ma was passed. The colorimetric readings were recorded as a function of time.

Results and Analysis of Results

The experiments on the loss in weight of the nickel anode showed that in all experiments in acetonitrile

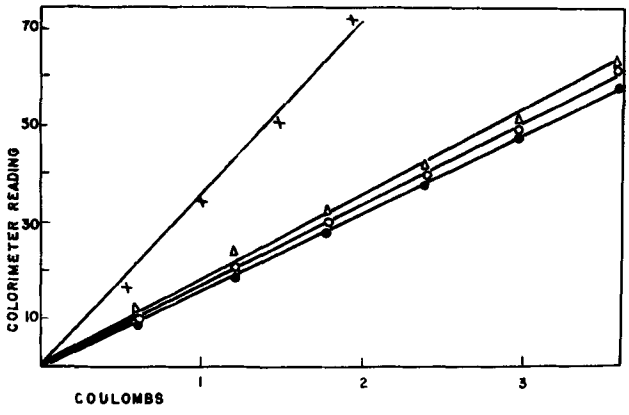

Fig. 1. Anodic dissolution of nickel in acetonitrile using a colorimetric coulometer: X, standardization curve of nickel (II) prepared from nickel (II) chloride; △, ○, •, runs 1, 2, and 3 for the anodic dissolution of nickel in acetonitrile.

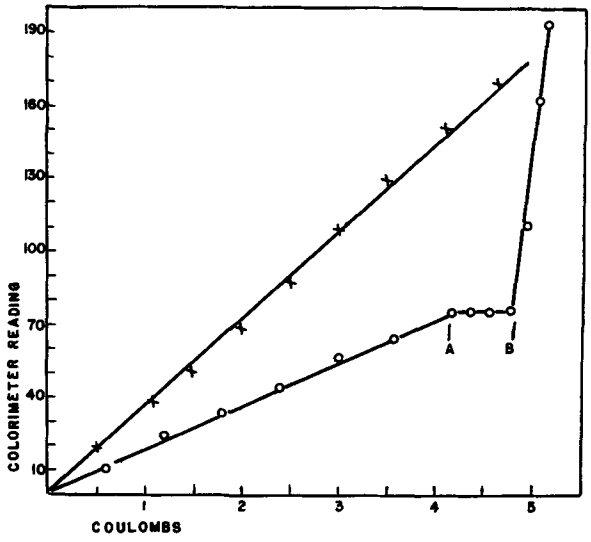

Fig. 2. Anodic dissolution of nickel in acetonitrile and coulometric titration of nickel (I) in a colorimetric coulometer: x, standardization curve of nickel (II) prepared from nickel (II) chloride; ○, anodic dissolution and titration curve for the titration of nickel (I).

[1] A student at La Vega Junior High School, Waco, Texas, at the time this work was done. He is now a student at Douglas MacArthur High School, San Antonio, Texas.

and dimethylformamide nickel dissolved with an oxidation number less than two. In dimethylformamide the average oxidation number for 5 runs was 1.66±0.12. For acetonitrile experiments the average oxidation number for twelve runs was 1.39±0.17.

Figure 1 shows typical data on the comparison of the nickel(II) concentration in solution as determined colorimetrically with that that would be in solution if the nickel had dissolved as nickel(II). As can be seen in all cases, there was less nickel(II) in solution than would be expected if nickel(II) were the only anodic product.

Figure 2 shows a typical run in which the nickel was anodically dissolved up to point A. Potassium iodide was then added, and the nickel anode was replaced with a platinum anode. As can be seen, the nickel(I) is titratable with the iodine generated, and the sudden break at B is the end point for this titration. The displacement of the anodic dissolution curve indicates that 2.0 coulombs of nickel dissolved as nickel(I). The titration indicates that 0.7 coulombs of nickel was present in solution as nickel(I). In all experiments the amount titrated was less than the colorimetric data indicated it should have been, probably because of air oxidation since the system was open to the air.

In summary, it has been shown that nickel dissolves anodically in acetonitrile and dimethylformamide containing tetramethylammonium chloride as a mixture of nickel(I) and nickel(II). The nickel(I) was shown to be stable enough in acetonitrile to be titrated with iodine.

Manuscript received Dec. 18, 1961; revised manuscript received Feb. 21, 1962.

Any discussion of this paper will appear in a Discussion Section to be published in the June 1963 JOURNAL.

REFERENCES

1. N. V. Sidgwick, "The Chemical Elements and Their Compounds," Vol. II, pp. 1429, 30, 52, Oxford at the Clarendon Press, (1950).
2. R. H. Sanborn and E. F. Orlemann, *J. Am. Chem. Soc.*, **78**, 4852 (1956).
3. T. C. Franklin and Jack Goodwyn, *This Journal*, **106**, 269 (1959).
4. T. C. Franklin and C. C. Roth, *Anal. Chem.*, **27**, 1197 (1955).

On the Crystallinity of GaAs Grown Horizontally in Quartz Boats

L. R. Weisberg, J. Blanc, and E. J. Stofko

RCA Laboratories, Radio Corporation of America, Princeton, New Jersey

While transparent fused quartz boats have been previously found to provide the highest purity GaAs grown by the horizontal Bridgman technique (1), the crystallinity of the GaAs has frequently been unsatisfactory. Therefore, a study has been carried out of factors affecting the crystalline quality of GaAs, such as boat treatment, arsenic pressure, furnace gradient, growth speed, melt temperature, impurities, and seeding. Over 50 crystals have been prepared, each roughly 9 cm long, and weighing 20g. Subsequent to growth, the crystals were examined for surface markings before and after "sand" blasting, and samples were removed for emission spectrographic analysis and Hall measurements. Several ingots that were essentially single crystals were x-ray analyzed for their axial orientation. Prior to growth, the transparent fused quartz boats were given either of two cleansing treatments: boats were either etched in HF acid for 10 min, or alternatively, sand blasted. In either case, the final treatment was an etch in 1:1 $HCl:HNO_3$ acid followed by extensive rinsing.

Two factors were observed to have a major effect on the crystallinity, namely, the boat treatment and the arsenic pressure. Concerning the former, crystals grown in HF treated boats generally had a poor crystal structure, with many small angle grain boundaries running through the crystal. However, crystals grown in sand blasted boats at growth speeds of 1.9 cm/hr were consistently of good quality. Visual observation of the ingot cross section showed that, without exception, ingots with good crystallinity wet the boat either not at all or to only a small degree. However, the absence of wetting proved to be only a necessary condition for good crystallinity and not a sufficient one, since many polycrystalline ingots were produced in HF treated boats when no wetting occurred. Furthermore, nucleation of new grains could not be correlated directly with places where wetting of the boat occurred. These results suggest that the crystallinity can be affected in part by a growth poison (2) which is introduced by the HF etching of the quartz boat. The effect of sand blasting the boat is both to prepare a more passive surface and also to reduce the contact area between the melt and the boat.

The second major growth factor was the arsenic pressure over the melt. A series of 22 GaAs crystals were grown with arsenic reservoir temperatures between 585° and 660°C, using growth speeds of either 1.3 or 1.9 cm/hr. When a reservoir temperature below 600°C was employed, the melt had a strong tendency to supercool, and the ingots were polycrystalline. As higher arsenic temperatures were used, the crystallinity continually improved; however, porosity began to occur, due to the escape of excess arsenic at the freezing interface. Porosity was encountered at 640°C using a growth speed of 1.3 cm/hr., and at 630°C using a growth speed of 1.9 cm/hr. However, the porosity does not destroy the crystallinity, since nearly single crystals of

GaAs have been prepared with an arsenic temperature of 640°C with a growth speed of 1.9 cm/hr. In general, an arsenic temperature of 625°-630°C is desirable for good crystallinity.

Only minor and inconsistent effects on the crystallinity were produced by most other growth factors such as variations in growth speed between 0.4 and 2 cm/hr, furnace temperature gradients between 5° and 24°C per cm across the freezing interface, and melt temperatures between 1250° and 1275°C. With respect to seeding experiments, it was observed first that there was no marked preferred growth direction for GaAs. Of ten unseeded single crystals, none had orientations close to the three principal crystallographic directions <001>, <011>, and <111>, and only four had orientations at all close to each other, clustering about the <013>. Twenty-one GaAs crystals were grown using seeds with either a <013>, <112>, or <011> orientation, but the seeding did not produce a significant improvement in the crystallinity.

No correlation could be observed between the crystallinity and the presence of any spectrographically detectable impurity in the as-grown ingots, which contained silicon, magnesium, copper, aluminum, and iron in quantities varying from 0.1 to 50 ppm in different crystals. Next, a series of crystals were grown, doped separately with either silicon, oxygen, carbon monoxide, water vapor, hydrogen, or copper. No noticeable effect on the crystallinity occurred for additions of up to 0.04 mg of oxygen, 0.8 mg of carbon monoxide, 0.03 mg of hydrogen, and 1 mg of copper. In two attempts, additions of 1 mg of silicon caused the melt to wet the boat appreciably, and the crystallinity was poor, indicating that the silicon acted differently when added in elemental form than when introduced due to reaction with the boat in an as-grown ingot where oxygen may be simultaneously introduced. Water vapor had the most pronounced effect. Two ingots, one doped with 56 mg and the other with 0.5 mg of water, adhered very badly to the boat resulting in very polycrystalline porous ingots containing cracks. In addition, the water vapor caused several grams of the GaAs ingot to be transported to the cooler end of the tube. This result implies that trace quantities of water vapor, perhaps due to the outgassing of the quartz ampoule, can be deleterious to the crystallinity of GaAs.

Acknowledgments

The authors are grateful to Mr. H. H. Whitaker for the spectrographic analyses, to Mr. G. Neighbor for the x-ray analyses, and to Mr. P. G. Herkart for important cooperation in some growth experiments. This research has been sponsored by the Electronics Research Directorate, Air Force Cambridge Research Laboratories, Office of Aerospace Research under Contract No. AF19(604)-6152.

Manuscript received Feb. 6, 1962; revised manuscript received March 23, 1962.

Any discussion of this paper will appear in a Discussion Section to be published in the June 1963 JOURNAL.

REFERENCES

1. L. R. Weisberg, F. D. Rosi, and P. G. Herkart, "Properties of Elemental and Compound Semiconductors," Metallurgical Society Conferences, Vol. 5, Interscience Publishers, Inc., New York (1960).
2. See, for example, G. W. Sears, *J. Chem. Phys.*, **29**, 979 (1958).

Epitaxial Silicon Thin Films

K. J. Miller, R. C. Manz, and M. J. Grieco

Bell Telephone Laboratories, Incorporated, Murray Hill, New Jersey

Study of silicon epitaxial film growth by the hydrogen reduction of silicon tetrachloride (1) has shown that constant deposition temperature affords a high degree of run-to-run thickness reproducibility. The process has been found to have a versatility especially useful for fabrication of grown junctions.

Hydrogen was bubbled through thermostated $SiCl_4$ and carried over an R. F. heated (111) oriented silicon sample in a quartz reaction chamber. If the reaction

$$SiCl_4(g) + 2H_2(g) \rightleftarrows Si(s) + 4HCl(g)$$

is assumed to be the idealized deposition reaction and reactants and products are in their standard states, calculations based on data in the literature (2) show that this reaction proceeds with the absorption of heat according to the equation

$$\Delta H_T^\circ(\text{cal.}) = 60.2\text{x}10^3 - 6.51T + 1.23\text{x}10^{-3}T^2 - 2.67\text{x}10^5T^{-1} \quad (298\text{-}1000^\circ\text{K})$$

The standard Gibbs free energy change, ΔG°, is favorable above about 1225°C. The curve obtained from the equation

$$\Delta G_T^\circ(\text{cal.}) = 60.2\text{x}10^3 + 15.0T\log T - 1.23\text{x}10^{-3}T^2 - 1.33\text{x}10^5T^{-1} - 85.9T \quad (289\text{-}1000^\circ\text{K})$$

was extrapolated beyond 1000°K. The flow conditions during epitaxial growth favor the reaction proceeding spontaneously at a lower temperature, however, because of the actual product and reactant activities, a, which are related to the free energy change, ΔG, by the equation

$$\Delta G = \Delta G^\circ + RT \ln \frac{a^4_{HCl}}{a_{SiCl_4}\, a_{H_2}{}^2}$$

Figure 1 shows the deposition reaction chamber. A Pt-10% Rh-Pt thermocouple sensing element provided a control voltage and was located in a well drilled in the susceptor on which samples were placed. The control temperature obtained from the thermocouple was held constant to $< \pm 1^\circ$C. The temperature control apparatus was similar to that conventionally used for growing semiconductor single crystals from the melt and included a recorder-controller (Leeds and Northrup Co., Model S AZAR recorder and C.A.T. Control Unit) used with a 10 kw, 4 M.C., R. F. generator. Sample surface temperature was measured by an optical pyrometer through a right angle prism and a quartz optical

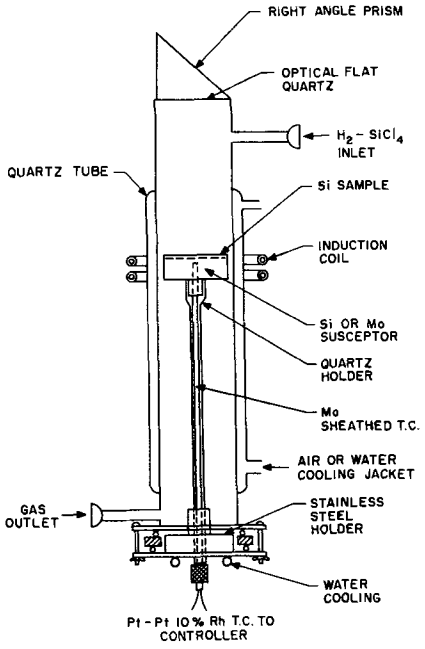

Fig. 1. Epitaxial silicon deposition reaction chamber

flat sealed to the top of the reaction chamber as seen in Fig. 1. Sample temperatures could be measured optically with a precision of ±3°C.

Films have been deposited with $SiCl_4$ concentrations of 1-2 mole % and with 1-3 l/min total hydrogen flows. Reaction chambers used have had inside diameters from 1 to 2 in. depending on sample size. Films up to 1¼ in. in diameter have been deposited in this apparatus using both silicon and molybdenum susceptors. When high resistivity silicon susceptors were used, infrared lamps were used initially to heat the silicon to increase R. F. coupling.

With ½ in. diameter substrates, a run-to-run control of film thickness as a function of time of deposition of approximately ±3% was obtained as compared with a ±15% reproducibility usually obtained for manual temperature control. For a sample temperature of 1200°C and a 2 l/min hydrogen flow through a 1 in. ID reaction chamber and with 1.3 mole % $SiCl_4$, the rate of deposition was 1.7 μ/min. At 1300°C the rate was found to be 2.1 μ/min. These deposition rates give $\Delta(\text{rate})/\Delta(\text{temp °C}) \cong 0.2\%/$°C. As an example, for a 5 min deposition at 1250°C, with a 1°C temperature difference from the control temperature, the film thickness difference should be 0.02μ from a 9.5μ predicted thickness.

Thicknesses measured interferometrically by angle-lapping-staining have been found to be uniform within measurement error across ½ in. diameter substrates. However, film smoothness has been found to vary across samples in proportion to the smoothness of the substrate material. For ½ in. diameter samples no center to edge temperature gradient was observed during epitaxial deposition. For 1¼ in. diameter samples heated on silicon susceptors, a 20°-25°C temperature gradient has usually been observed, which should contribute approximately 0.5μ to a film thickness variation for 10μ thick films. By angle-lapping-staining across 1¼ in. diameter samples, interference measurements have shown maximum deviations of ±0.5μ from 5-6μ mean thicknesses. When 1¼ in. diameter samples were heated on molybdenum susceptors, this temperature gradient was observed to be approximately 5°-10°C.

Higher temperature has been found to favor increased orientation of depositing silicon atoms. Epitaxial growth of silicon films with a high degree of crystalline perfection has been found to require a 1200°-1275°C temperature of deposition. Using the conditions outlined, films grown below 1050°C often are polycrystalline, while those films grown between 1050° and 1200°C generally have growth defects.

Water-free as well as oxygen-free hydrogen has been necessary to prevent the formation of oxide films on sample surfaces. The Deoxo Puridryer (obtained from Engelhard Industries, Inc.) and liquid nitrogen cold traps used have proven adequate to maintain the moisture level below 1 ppm. However, air as well as dust particles are introduced when samples are placed in the deposition apparatus. Sample surface defects sometimes observed are believed to be primarily caused by such contamination.

Doping of films to obtain desired resistivities has been accomplished by addition of PCl_3 to the $SiCl_4$. Film resistivity has been measured with a 4-point probe using films of the opposite conductivity type from the substrate and by capacitance^{-2} *vs.* reverse bias plots obtained from alloyed aluminum dot diodes fabricated on the films. Percentage variation of film resistivity across a sample has been found to be proportional to the nonuniformity of film thickness and to the magnitude of the film resistivity.

Reverse diode characteristics of some epitaxial film-substrate junctions have been studied. An example of an epitaxial film-substrate junction can be seen in Fig. 2a. The reverse I-V characteristics measured on 9 x 10 mil mesa etched diodes are shown in Fig. 2b. The n-type, 2 ohm-cm, film was 6μ thick and was deposited on a 1 ohm-cm, p-type silicon substrate. Measurements of capacitance^{-2} as a function of reverse voltage showed a linear relation for diodes and indicated that the interface was a step junction. The substrate in Fig. 2 was prepared for deposition by chemical polishing. The reverse current just before breakdown was less than 0.1 μa and the breakdown voltages of the diodes were found to agree with those usually obtained for step junction

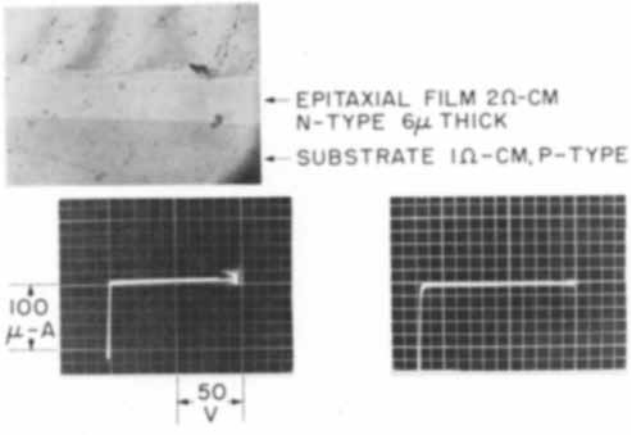

Fig. 2. a (top) Epitaxial film to substrate junction; Magnification, approximately 80X; b (bottom) reverse diode characteristics obtained for junction shown in a.

avalanche breakdown voltage as a function of resistivity.

Manuscript received Jan. 19, 1962. This paper was prepared for delivery before the Detroit Meeting, Oct. 1-6, 1961.

Any discussion of this paper will appear in a Discussion Section to be published in the June 1963 JOURNAL.

REFERENCES

1. H. C. Theuerer, *This Journal*, **108**, 649 (1961).
2. F. D. Rossini, D. D. Wagman, W. H. Evans, S. Levine, and I. Jaffe, U. S. Natl. Bur. Standard Circ. 500 (1952); K. K. Kelley, U. S. Bur. Mines Bull. 584 (1960); K. K. Kelley and E. G. King, *ibid.*, 592 (1961); D. R. Stull and G. C. Sinke, "Thermodynamic Properties of the Elements," Am. Chem. Soc., Washington, D. C. (1956).

Extent of Solid Solution in the GaSb-InSb System from Crystal Pulling Experiments

F. A. Trumbore, P. E. Freeland, and A. D. Mills

Bell Telephone Laboratories, Incorporated, Murray Hill, New Jersey

The literature contains a number of conflicting reports on the extent of solid solution in the GaSb-InSb pseudo-binary system. Reports of limited solid solubility (1-3) have been discredited by various workers (4-8) who showed that the system contains a complete series of homogeneous solid solutions. The latter workers used experimental techniques such as long term annealing of powders, slow directional freezing, and zone equalization. The purpose of the present paper is to report successful attempts to grow these solid solutions by the crystal pulling technique together with the results of x-ray measurements which are interpreted in terms of the phase diagram.

Experimental

Conventional rf induction heated crystal pulling machines (9) were used to pull ten GaSb-InSb samples under a hydrogen atmosphere at pull rates of 3-5 mm/hr and rotation rates of 140-144 rpm from alloy melts containing between 9 and 92 mole % InSb. Seed crystals of randomly oriented GaSb were used. In one case a crystal of GaSb-InSb solid solution grown in a previous run was used as a seed. Single crystals were often obtained, even when pulled from melts containing as much as 60 mole % InSb. The other samples usually contained large grains, and the x-ray powder patterns were quite sharp except for slight fuzziness in the case of crystals grown from melts containing about 70-80 mole % InSb. A number of the melts were doped with zinc or germanium, both of which acted as acceptors in the solid solutions. However, the concentrations of these dopants were negligible insofar as their effect on the x-ray results are concerned. X-ray powder patterns were taken with Straumanis-type Norelco cameras (114.6 mm diameter) using CuKα radiation. For five of the crystals the melt compositions were determined from weight loss measurements and were corrected for the composition of the grown material as calculated from the x-ray data. Weight losses, presumably due to evaporation of antimony, were only on the order of 0.1% or less. For the other five crystals, grown prior to the decision to study this system more extensively, the melt compositions were assumed to be weighed-in compositions. The uncertainty introduced by this assumption was small because the samples for x-ray analysis were taken from as near the seed as possible, and the size of the crystals was small compared to the total melt volume.

Results and Discussion

The results of the x-ray measurements are summarized in Table I together with the mole fraction of InSb in the melt, x^{L}_{InSb}. With the exception of three samples, as noted in Table I, the x-ray lines were essentially as sharp for the GaSb-InSb solid solutions as for the pure GaSb and InSb samples.

In order to obtain the compositions of the solid solutions from the measured lattice parameters it was first assumed that Vegard's law is valid for the GaSb-InSb system as indicated by Woolley and Smith (7). However, more recent work (10) indicates the presence of small deviations from Vegard's law. Accordingly, we have recalculated the alloy compositions by using the experimental x-ray data supplied by Woolley (10). While the calculated compositions of the InSb-rich solid solutions do not differ appreciably from the Vegard's law results there is a significant difference for the GaSb-rich alloys, at least in terms of x^{S}_{InSb}, the mole fraction of InSb in the solid solution. This is shown in Fig. 1 which is a plot of log k_{InSb} *vs.* x^{L}_{InSb} where k_{InSb} is the distribution coefficient defined by $k_{InSb} = x^{S}_{InSb}/$

Table I. Lattice constants of pulled GaSb-InSb solid solutions

Sample No.	x^{L}_{InSb}	Lattice constant, Å
GaSb (pure)	—	6.095 ± 0.003*
5EP	0.088	6.100 ± 0.003
7EP	0.125	6.101 ± 0.003
15PF	0.248†	6.108 ± 0.003
16PF	0.422†	6.121 ± 0.003
10EP	0.605	6.138 ± 0.003
9PF	0.647	6.155 ± 0.003
12PF	0.717	6.167 ± 0.005**
17PF	0.814†	6.220 ± 0.005**
24PF	0.827†	6.245 ± 0.005**
27PF	0.918†	6.343 ± 0.003
InSb (pure)	—	6.479 ± 0.003*

* These values compare with the figures 6.095 and 6.478Å obtained for GaSb and InSb by Swanson *et al.* [NBS Circular 539, 6, 30 (1956); *ibid.*, 4, 73 (1955)].
** Slightly fuzzy lines.
† Melt compositions determined from weight loss measurements. Should be most reliable points.

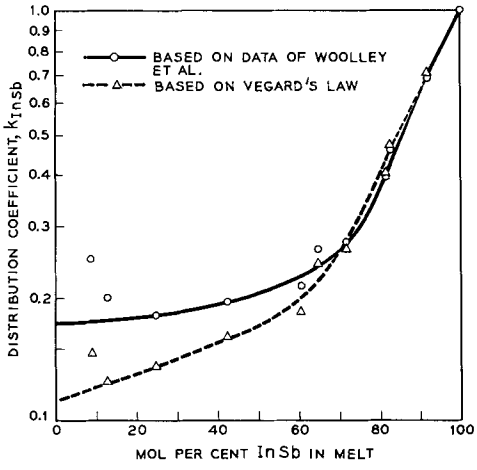

Fig. 1. Plot of log k_{InSb} as a function of x^{L}_{InSb} from the crystal pulling data. The dashed curve corresponds to the results if Vegard's law is used to calculate the alloy compositions from the x-ray data in Table I. The solid curve is derived from the x-ray data in Table I and Woolley and Smith's work on the variation of the lattice parameter with composition showing deviations from Vegard's law. In extrapolating k_{InSb} to $x^{L}_{InSb} = 0$ the points corresponding to samples No. 5EP and No. 7EP (Table I) were essentially neglected since the uncertainties in x^{S}_{InSb} were relatively large due to the small changes in lattice parameter compared to pure GaSb. The curves have also been drawn to favor those points obtained from the runs where weight loss measurements were made.

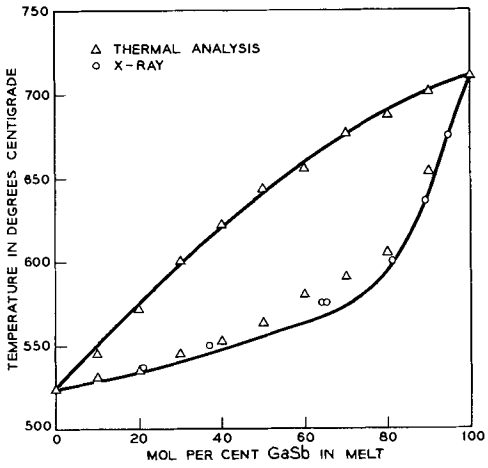

Fig. 2. GaSb-InSb phase diagram. The experimental points are those of Woolley and Smith. The liquidus curve has been drawn by the authors through these points. The solidus curve was calculated from the liquidus curve and distribution coefficient data obtained from the solid curve in Fig. 1.

x^{L}_{InSb}. The scatter in the points at the GaSb-rich end of the curve reflects the sensitivity of the calculation of x^{S}_{InSb} to slight errors in the lattice parameters and to the way we have drawn a curve to fit Woolley *et al.*'s x-ray data.

If the distribution coefficient data in Fig. 1 are equilibrium values, a knowledge of the GaSb-InSb liquidus curve would be sufficient to construct the equilibrium solidus curve for this system. Phase diagrams have been determined by Woolley and Smith (7) and Gorshkov and Goryunova (5). Although both diagrams indicate a complete series of homogeneous solid solutions, there are quantitative differences in the positions of the liquidus and solidus curves. (Some of the differences are due to the use of two different melting points for pure GaSb.) It appears that the work of Woolley and Smith is the more extensive and more reliable of the two sets of data, and we have plotted their experimental points, determined from x-ray data and from thermal analysis, in Fig. 2. The liquidus curve drawn through these points is our estimate of a reasonable curve considering the scatter of the data. The solidus curve in Fig. 2 was then calculated from the liquidus curve and the k_{InSb} data (Fig. 1), taking into account the reported departures from Vegard's law.

It is seen in Fig. 2 that the agreement between the calculated solidus curve and the experimental data of Woolley and Smith, especially the x-ray data, is relatively good. If one considers the latitude available in drawing the liquidus curve, the shallow solidus curve in the InSb-rich region where the importance of a slight error in temperature is magnified and the other possible sources of error in the present work and in that of Woolley *et al.* the agreement is probably within experimental error. Hence, it appears that the crystal pulling technique is capable of yielding equilibrium solid solubility data in systems of this type.

Conclusion

To the best of our knowledge this study represents the first application of the crystal pulling technique to the relatively complete coverage of a homogeneous alloy system of this type. The relative ease of growth and the short period of time involved (hours instead of days or months for some methods) indicates that more extensive application of the pulling technique to the study of phase diagrams would be profitable. Although a liquidus curve is necessary to obtain the complete phase diagram from crystal pulling data, a preliminary survey of a given system with the pulling method would serve to minimize confusion such as that caused by the erroneous reports of a miscibility gap in the GaSb-InSb system.

Acknowledgments

The authors gratefully acknowledge the assistance of E. M. Porbansky who grew the first GaSb-InSb crystals for this study and stimulating discussions with C. A. Burrus whose interest in these alloys led to the present work.

Manuscript received Feb. 5, 1962. This paper was prepared for delivery before the Los Angeles Meeting, May 6-10, 1962.

Any discussion of this paper will appear in a Discussion Section to be published in the June 1963 JOURNAL.

REFERENCES

1. W. Koster and B. Thoma, *Z. Metallkunde*, **46**, 293 (1955).
2. J. S. Blakemore, *Can. J. Phys.*, **35**, 91 (1957).
3. C. Kolm, S. A. Kulin, and B. L. Averbach, *Phys. Rev.*, **108**, 965 (1957).
4. N. A. Goryunova and N. N. Fedorova, *J. Tech. Phys. (USSR)*, **25**, 1339 (1955).
5. I. E. Gorshkov and N. A. Goryunova, *Zhur. neorg. khim.*, **3**, 668 (1958).
6. J. C. Woolley, B. A. Smith, and D. G. Lees, *Proc. Phys. Soc. London*, **69B**, 1339 (1956).

7. J. C. Woolley and B. A. Smith, *ibid.*, **72**, 214 (1958).
8. V. I. Ivanov-Omskii and B. T. Kolomiets, *Soviet Physics Solid State*, **1**, 834 (1959); *ibid.*, **2**, 363 (1960).
9. See M. Tanenbaum, in "Semiconductors," N. B. Hannay, Editor, Chap 3, Fig. 3.15 and 3.16. Reinhold Publishing Corp., New York (1959).
10. J. C. Woolley and C. M. Gillett, *J. Phys. Chem. Solids*, **17**, 34 (1960); also J. C. Woolley, Private communication.

Preparation of Small Samples of Ductile Titanium and Zirconium from the Isotopic Oxides by Iodide Refining

N. D. Veigel and J. M. Blocher, Jr.

Battelle Memorial Institute, Columbus, Ohio

To provide material for thin-foil work at the Argonne National Laboratory, 1-2g samples each of ductile titanium-46, -47, -48, -49, -50, and zirconium-90, -91, -92, and -94 in the form of 1-in. long rods were prepared by calcium reduction of the isotopic oxides[1] followed by two-step iodide refining. Iodide refining of titanium and zirconium is described by van Arkel (1). Information on calcium reduction of the oxides is given by Kubaschewski and Dench for TiO_2 (2) and by Lilliendahl, Gregory, and Wroughton for ZrO_2 (3).

The oxide was placed in a shallow molybdenum boat which straddled a bed of calcium chips in a horizontal cylindrical molybdenum tube provided with a tight-fitting cover. The oxide was reduced by exposure to calcium vapor overnight at 1000°C. After the resulting calcium oxide was leached out by water continuously neutralized with HCl, the crude metal powder was dried and treated again with calcium vapor for 5 hr at 1000°C. The resulting zirconium powder was heated to 900°C in vacuum to insure complete removal of excess calcium. In the case of titanium prepared similarly, it was necessary to heat the crude metal at 1300°C for 1 hr in vacuum to remove the excess calcium. Removal of the calcium is essential to prevent "tie up" of iodine as nonvolatile stable CaI_2 in subsequent iodide processing.

A small Pyrex glass van Arkel-de Boer bulb containing 0.5g of iodine and provided with two 1-in.-long 0.005-in. diameter tungsten filaments was used to refine the crude metal which was contained in the original molybdenum boat placed about 1 in. below the filaments. One filament was energized for transfer of the metal from the crude. When transfer to the first was complete (in about 4 hr), the second filament was energized and the first allowed to cool for the final transfer. A bulb (condensed TiI_4) temperature of about 135°C, a feed temperature of about 250°C, and a filament temperature of 1200°-1300°C were used for the titanium deposition. A bulb temperature of about 230°C, a feed temperature of about 300°C, and a filament temperature of 1200°-1300°C were used for zirconium deposition.

[1] Obtained from the Oak Ridge National Laboratory.

The effectiveness of the two-step refining is evident from the fact that the final products could be cold rolled directly to foil less than 0.025 mm thick while the products of the one-step process cracked in attempts to reach this thickness. The improved fabricability is consistent with the fact that hardness of the two-step products ranged from 71 to 150 KHN (50-g load), as compared with that of a previous single-step product which ranged from 250 to 350 KHN. To conserve the isotopic product it was desirable to measure hardness on the curved as-deposited surface of the crystal bar. Hence, the reported hardnesses are considered to be only indicative of the relative purity and are not directly comparable with hardness measured on flat surfaces. Hardness measurements taken on the as-deposited surface of a natural iodide titanium sample were 38% higher than those obtained on a sectioned and polished sample of the same material. The extent to which crystal orientation is a factor was not determined.

The relatively high contamination in the single-step process is attributed to a lower ratio of product weight to processing equipment surface than is normally encountered in iodide processing. The two-step process is believed to have resulted in intermediate gettering of the residual gaseous impurities in the processing bulb.

The ductility of the final product indicates low contamination by interstitial elements. The following Table compares spectrographic analyses of the one sample of titanium oxide and single-step refined titanium product for which analyses were obtained. The accuracy of the spectrographic procedure is reported to be ±50% at an impurity level

Table I. Spectrographic analysis (w/o) of titanium oxide and titanium prepared by calcium reduction and single-step iodide refining

	Si	Mg	W	Al	Cu	Ca	Zr	Fe	Mo	Sn	Ni
TiO_2	>0.1	0.03	N.D.	>0.1	0.001	0.05	0.03	0.01	0.005	0.003	<0.001
Deposited Ti as TiO_2	0.02	0.005	>0.1 (Core wire)	<0.03	0.001	0.01	<0.01	0.01	<0.001	0.003	0.002

of 0.0X w/o and ±100% at a level of 0.00X w/o.

Over-all recoveries of 70-90% of the isotopic zirconium and titanium were obtained.

Acknowledgment

The authors wish to thank Dr. Jan Yntema of Argonne National Laboratory for initiating this interesting work which was done under AEC Contract W-7405-eng-92.

Manuscript received Feb. 19, 1962.

Any discussion of this paper will appear in a Discussion Section to be published in the June 1963 JOURNAL.

REFERENCES

1. A. E. van Arkel "Reine Metalle," Julius Springer, Berlin (1939).
2. O. Kubaschewski and W. A. Dench, *J. Inst. Metals*, **82**, 87 (1953).
3. W. C. Lilliendahl, E. D. Gregory, and D. M. Wroughton, *This Journal*, **99**, 187, (1952).

A Transistorized 60 cps Sine Wave Commutator for Resistance and Potential Measurements

G. F. Pollnow[1] and Robert M. Kay

Research Division, Allis-Chalmers Manufacturing Company, Milwaukee, Wisconsin

The use of half-cell potentials in studying the nature of electrode processes is well known, and for processes at very low current densities there is usually no great experimental difficulty in making accurate measurements. However, at high current densities an error in the potential measurement is introduced by the large internal *IR* drop between the working electrodes. The *IR* drop between the reference electrode and the electrode of interest can be minimized by means of a Luggin capillary. In some systems the geometry of the cell precludes the use of a Luggin capillary; hence, a device to measure the potential of the electrode in its polarized state, but independent of the purely ohmic resistance, is desirable. A number of such mechanical and electronic current interrupters have been described in the literature (1-5), most of them operating on square waves and having the problems associated with generating such distortion-free, high-amplitude, and high-frequeincy wave forms. The present apparatus was designed primarily to obtain reliable, resistance-free terminal and half-cell potentials in connection with fuel cell research and development. In addition, the direct measurement of the ohmic voltage drop provides a convenient method of determining the resistance and the specific resistivity of the electrolyte in its working environment.

[1] Present address: Department of Chemistry, Wisconsin State College, Oshkosh, Wisconsin.

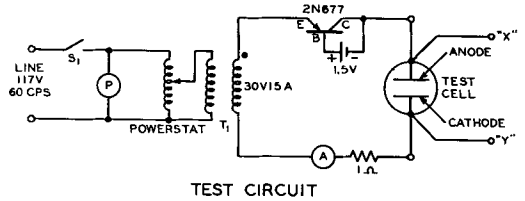

TEST CIRCUIT

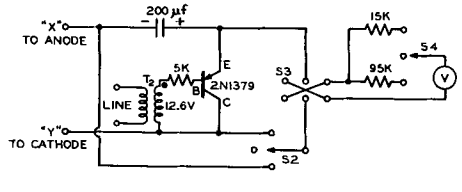

MEASURING CIRCUIT

Fig. 1. Commutator circuit

Theory

The instrument described herein is a transistorized modification of a device reported by Kordesch and Marko (3) and is based on the same half-wave rectified 60 cps sine wave principle. The circuit shown in Fig. 1, however, possesses several advantages over the one previously mentioned. In particular, use of a power transistor with inverse bias in place of the diode rectifier reduces the external current at zero applied voltage from 60 ma to 25 μa when a 1.5v source of emf is under test. Second, the stability of the voltage measuring clamping circuit allows the direct measurement of the difference voltage, corresponding to the *IR* drop, to better than ± 1 mv. The bridge circuit employed by Kordesch and Marko requires zeroing before each measurement because of the aging of the bridge diodes employed and is not stable enough to measure the *IR* drop with the required precision.

Loading of the test cell is accomplished by means of the Powerstat controlled input to the transformer, T_1, whose output is rectified by the 2N677 power transistor. The bias supplied to the power transistor by the 1.5v dry cell keeps the current at zero in the load circuit until the input voltage from the transformer exceeds this voltage. Since no current is drained from the dry cell in operation, its life expectancy is sufficiently long to render uneconomic its replacement with an a-c rectifier. With the 2N677 power transistor mounted on a 3 x 4 x 1/16 in. copper heat sink, currents of 9-10 amp can be safely obtained. Greater currents can be obtained by decreasing the 1 ohm current limiting resistor and providing for the increased heat dissipation of the transistor.

Figure 2 shows the waveform of the current, I, through the cell, the voltage across the cell, V_b, the voltage across the capacitor, V_c, and the voltage across the clamping transistor, V_t, as a function of time.

As the current, I, is passed through the cell, the terminal voltage, V_b, decreases because of its inter-

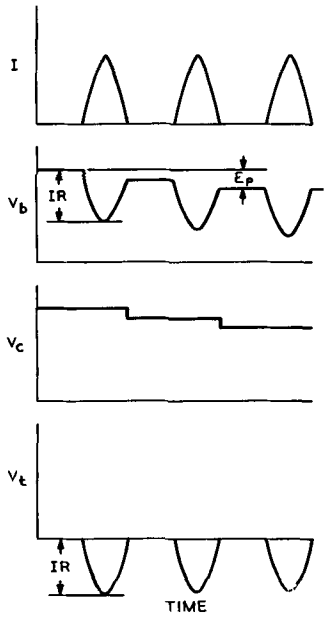

Fig. 2. Waveforms in the commutator circuit

nal ohmic resistance, R, and polarization voltage, E_p, as shown in Eq. [1]

$$V_b = E - IR - E_p \qquad [1]$$

The small filament transformer, T_2, supplies an alternating voltage to the base of the clamping transistor. When the base is negative, the emitter to collector path becomes a very low impedance. With a positive base voltage this path becomes essentially an open circuit. The voltage from T_2 is in phase with the voltage from T_1 so that the clamping transistor is conducting when the current through the test cell is zero. V_t then is zero, and the ohmic-free potential of the test cell in its polarized state is given by Eq. [2]

$$V_c = E - E_p \qquad [2]$$

On the other half cycle, current flows through the test cell and the clamping transistor becomes a very high impedance. V_c cannot change during this half cycle and so

$$V_t = E - E_p - IR - V_c = -IR \qquad [3]$$

This operation can be seen from the waveforms of Fig. 2. The open-circuit voltage E is obtained prior to loading of the cell.

In order to use the apparatus only for half-cell measurements with a calomel reference electrode, the capacitor should be reduced in size to 1-10 μf, and a high impedance voltmeter substituted for the built in meter. Half-cell measurements *vs.* a fiber type calomel electrode, with a microammeter in series, showed that even with the 200 μf capacitor the transient charging current did not exceed 20 μa and persisted for only a few seconds during the initial closing of the circuit. No permanent polarization of the calomel electrode was apparent, and once the capacitor was charged the current through the calomel electrode did not exceed 1 μa during further loading. A single pole, function selector switch, S_2, connects the internal voltmeter, V, across the capacitor, across the transistor, or permits opening the circuit to allow for an external high impedance voltmeter which for half-cell measurements is connected across the capacitor. In all cases, the four terminal method of voltage measurement is used to eliminate the IR drop due to the resistance of contacts and current carrying leads. The double-pole, double-throw switch, S_3, reverses the polarity of the 20,000 ohms/v voltmeter as required when the cell under test is changed from a source of emf to a pure resistive load. Connection of the clamping circuit leads to the test cell must be such that the correct polarity is maintained at all times on the electrolytic capacitor.

For cells having a small internal resistance a three-way range switch, S_4, to the voltmeter is provided, having positions of 0-1.0v, 0-5.0v, and one for an open circuit.

Experimental Results

A set of precision resistors were used to calibrate the commutator over the full range of the instrument. From the set of calibration curves shown in Fig. 3, it is apparent that the commutator is direct reading, well within the ±3% accuracy of the meters used to measure the current and the IR drop.

In order to demonstrate the equivalence of the commutator and the Luggin capillary when making half-cell measurements, a solution of 1M H_2SO_4: 2M CH_3OH, at 25 C° was subjected to the pulsed discharge of the commutator applied to two parallel, 1 in. by 1 in., electrodes placed 1 cm apart. Results are

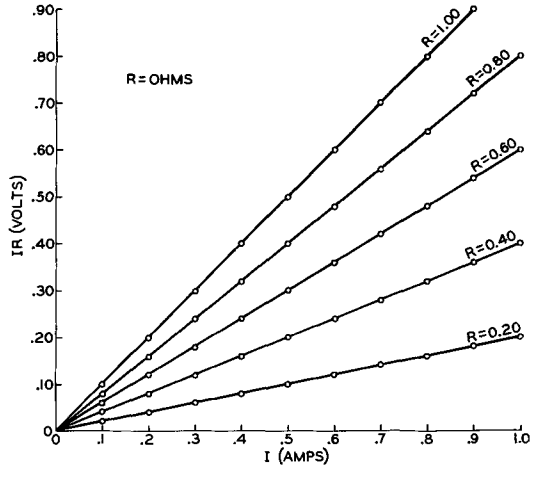

Fig. 3. Calibration of the commutator with a precision resistance box.

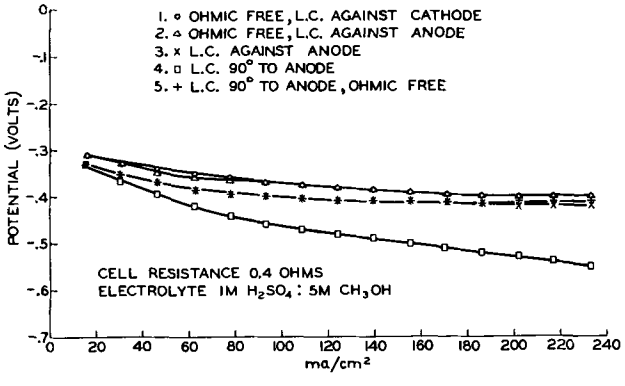

Fig. 4. Terminal and ohmic-free anode potentials vs. the saturated calomel electrode.

shown in Fig. 4. For curve 1, a Luggin capillary was first placed against the back side of the cathode while half-cell measurements, V_c, *vs.* a saturated calomel electrode were made with the VTVM across the capacitor as the current density was varied from 0 to 240 ma/cm^2. Next, the Luggin capillary was placed against the rear side of the anode and the foregoing procedure repeated to yield the data shown in curve 2.

The coincidence of curves 1 and 2 demonstrate that the half-cell potential measurements are, indeed, free of any ohmic component; however, their absolute accuracy is of course dependent on the rapidity with which the activation polarization decays.

Curves 3 and 5 demonstrate the equivalence of the Luggin capillary and the commutator with the capillary in the latter case turned through 90° away from the anode. With the Luggin capillary in this position, and the VTVM connected directly to the calomel electrode and the anode, curve 4 was obtained. It is interesting to note that the large *IR* drop shown here occurred even with the reference electrode behind the anode and clear of the field between the working electrodes. The small displacement of curves 3 and 5 from 1 and 2 is due to the change in geometry of the cell which occurred when the anode and cathode were interchanged with respect to the Luggin capillary; hence, curve 4 is to be compared to curves 3 and 5.

Conclusions

A 60 cps sine wave transistorized commutator has been constructed which measures directly, and displays on a meter, the internal ohmic *IR* drop and the ohmic-free terminal or half-cell voltage. Calibration of the instrument shows it to be direct reading within the ±3% accuracy of the meters employed. It has also been demonstrated that this device virtually eliminates the need for a Luggin capillary when making half-cell measurements on load, providing the decay time of the activation polarization is substantially less than 1/120 of a second.

Manuscript received Aug. 24, 1961; revised manuscript received Jan. 15, 1962.

Any discussion of this paper will appear in a Discussion Section to be published in the June 1963 JOURNAL.

REFERENCES

1. R. Glicksman and C. K. Morehouse, *This Journal*, **102**, 273 (1955).
2. R. A. Hickling, *Trans. Faraday Soc.*, **33**, 1540 (1937).
3. K. Kordesch and A. Marko, *This Journal*, **107**, 480 (1960).
4. W. Richeson and M. Eisenberg, *ibid.*, **107**, 642 (1960).
5. D. Staicopalous, E. Yeager, and J. Hovarka, *ibid.*, **98**, 68 (1951).

Brief Communication

Directional Thermal Expansion Coefficients of β-MnO_2

R. C. Bradt and J. S. Wiley

Research Division, Fansteel Metallurgical Corporation, North Chicago, Illinois

Directional thermal expansion coefficients of β-MnO_2 were determined over the range 25° to 500°C using high-temperature x-ray methods. This was accomplished by employing relationships between lattice constants and the angular shift of Bragg reflections (1). Thermal expansion coefficients obtained using x-ray techniques have been demonstrated to compare very favorably with those obtained by the more familiar dilatometric methods (2).

Samples were prepared by the thermal decomposition of manganous nitrate solution (J. T. Baker Reagent Grade) a well-established method of producing β-MnO_2 (3). Chemical analysis by total manganese and available oxygen determinations showed the sample to have the formula $MnO_{2.00}$ (0.04-0.09 H_2O). The samples were ground to pass a 200 mesh screen and the powder used to make an ether slurry which was painted on a platinum high-temperature sample holder for x-ray observation.

Using a G. E. Model XRD-5 diffractometer, and Fe-$K_{\alpha 1}$ radiation, observations were made in air from room temperature to 500°C, where decomposition to

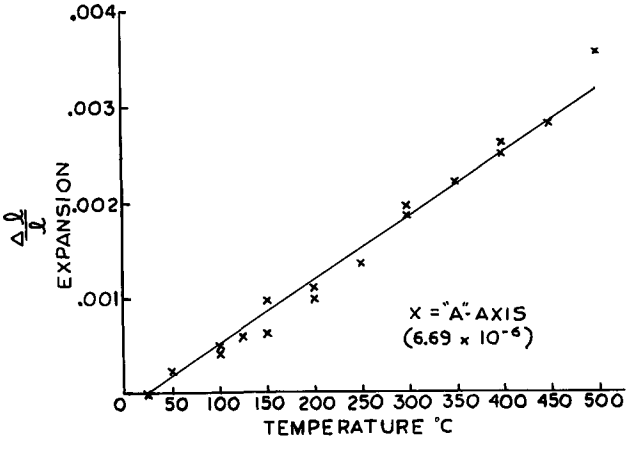

Fig. 1. Thermal expansion of MnO_2

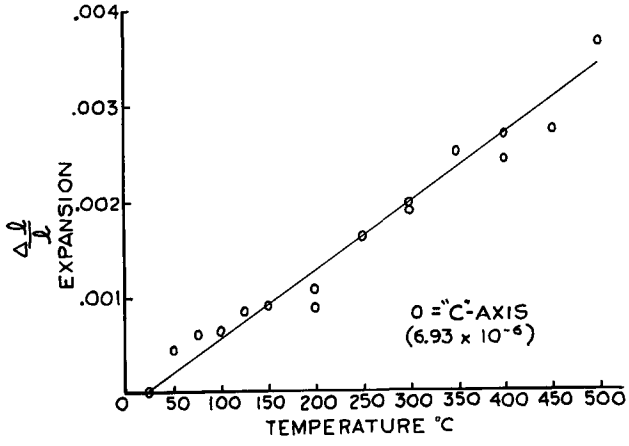

Fig. 2. Thermal expansion of MnO_2

Mn_2O_3 prevented further data accumulation. Except for the initial observation, where total decomposition occurred, the heating and cooling observations agreed quite favorably. Data were treated using the least squares method. Figures 1 and 2 show the results.

The measurements showed that the tetragonal unit cell of β-MnO_2 has a thermal expansion coefficient of 6.69 x 10^{-6} cm/cm-°C along the "a"-axis and 6.93 x 10^{-6} cm/cm-°C along the "c"-axis over the temperature range of 25°-500°C.

Manuscript received Feb. 19, 1962.

Any discussion of this paper will appear in a Discussion Section to be published in the June 1963 JOURNAL.

REFERENCES

1. Gunji Shinoda, *Mem. Coll. Sci. Kyoto Imp. Univ.*, Series A, **16**, 193 (1933).
2. William J. Campbell, Stephan Stecura, and Clark Grain, *Report of Investigation 5738*, U. S. Dept. of the Int., Bureau of Mines (1961).
3. T. E. Moore, M. Ellis, P. W. Selwood, *J. Am. Chem. Soc.*, **72**, 856 (1950).

The Sodium|Tin Liquid-Metal Cell

Robert D. Weaver, Stanley W. Smith, and Norman L. Willmann

Delco-Remy Division, General Motors Corporation, Anderson, Indiana

ABSTRACT

Preliminary studies of the liquid-metal cell have shown it to possess promising characteristics for application to the conversion of thermal energy. Polarization effects commonly associated with electrochemical cells are essentially absent; charge-discharge curves are straight lines passing through the open-circuit intercept. The conductivity of the fused electrolyte, 2.3 mhos, provides for low internal losses. Nongalvanic losses occur causing an apparent loss of reactants to the extent of 0.018 amp/cm^2. It is shown that a cell constructed of the materials and electrolyte employed in the study should allow operation at 0.7 amp/cm^2 at maximum power and that the coulombic efficiency would be 95% when continuously operated at this current density during balanced charge and discharge periods.

The thermally regenerative liquid-metal cell, which has elsewhere been conceived and described (1-3), effects the transformation of thermal power to electrical power by the thermal decomposition of the products of electrochemical reaction. The reactants are liquid metals which combine to form alloys and to produce electrical energy. It is this liquid alloy which is then thermally decomposed, at a higher temperature, to the original liquid-metal reactants. The transducing system is, therefore, limited to Carnot efficiencies.

The liquid-metal cell, employing Na and Sn as examples of reactants, may be represented as $Na|Na^+$ electrolyte$|Na\cdot Sn$, in which oxidation occurs at the Na electrode. The potential of this cell is greater than that of a simple concentration cell due to the decrease in Na activity at the Sn cathode due to the formation of compounds represented by $Na_x\cdot Sn_y$. Since high potentials are desirable, the concentration of Na in the cathode will be maintained at levels usually less than 10 weight per cent (w/o). The electrochemical reaction involves the transfer of Na^+ formed at the anode, through the electrolyte, to the cathode. Thus, it is desirable to employ electrolytes which are chemically stable to Na metal and in which the only cation present is that of Na. Such electrolytes are provided by fused Na salts. The use of a fused-salt electrolyte will further provide high electrical conductivity.

The use of electrochemical cells to acquire thermodynamic data of liquid-metal alloys is well established (4, 5). Solid electrolytes have usually been employed in such cells, and none have been capable of producing power at high current densities. One other electrochemical transducer has been described which involves thermal decomposition of the electrochemical product, in this case LiH, (6-8).

This paper presents a study of the electrochemical cell associated with the liquid-metal system. Because of the novelty of this cell system and the problems attendant to the use of reactive liquid metals in a cell which is operated at high temperatures, this paper is devoted to a description of the experimental techniques involved, the materials employed, and the preliminary results obtained.

Experimental Procedures

The use of Na at high temperatures in a cell requires that a containing material be employed which is an electrical insulator, is inert to Na, is nonporous (*i.e.*, impervious), and is capable of withstanding high temperatures. Aluminum oxide has been found to be such a material. To study cell behavior, cells were constructed, as shown in Fig. 1, consisting of an alumina crucible[1] whose composition is given as 99 + % Al_2O_3. It has been found that low silica-content alumina is necessary for this work. The cell must be sealed in order to prevent long-time loss of Na through vaporization, and this has been accomplished by use of a ground tapered joint between the cell and a solid alumina cap. The angle of the joint is 5°, and the grinding is accomplished by use of diamond grinding techniques.

[1] Norton Company, Crucible No. MD 70319 B.

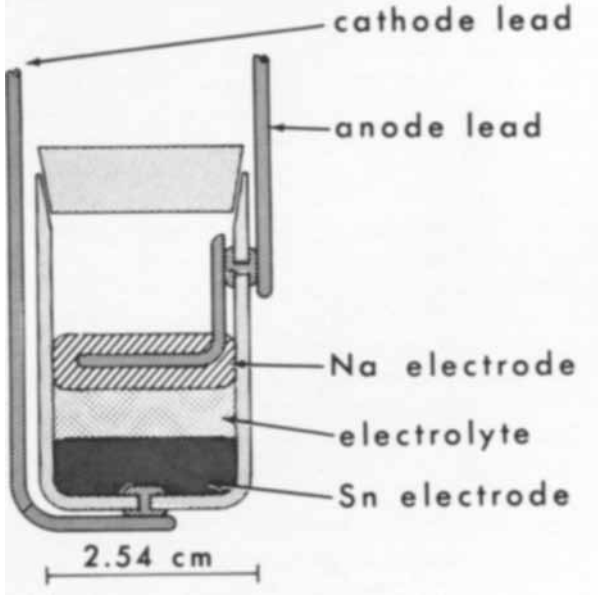

Fig. 1. Static Na|Sn cell

Electrical leads are necessary through the cell walls and necessitate a metal-to-alumina seal which is vapor tight. Such seals are made by grinding a 0.03 cm oversize hole in the cell wall and inserting a steel rivet. The rivet is seated by use of a spot welder which allows the rivet to be heated to a cherry-red heat and which supplies pressure to flatten the rivet end. Electrode wires may then be spot-welded to either end of the rivet as necessary. Such seals are quite satisfactory, but require some experience to effect a tight seal which will not crack the alumina as the rivet contracts.

The densities of the metals and the electrolytes are such that the layers are stable as shown in Fig. 1. The projected area of the metal electrodes is 3.87 cm^2. A cell such as this allows the static performance (*i.e.*, the liquid metals are not flowing) of the system to be evaluated. The cell must be operated in an inert atmosphere of N_2 or A as a safety precaution, for cracks and leaks may occur. This is accomplished by placing the entire cell in a bottomed glass tube, wires and inert gas being introduced through a rubber stopper. The lower half of the tube, containing the cell, is then placed in a vertical tube furnace.

Both cell resistance and cell voltage are functions of temperature, and it is therefore necessary to provide for a constant temperature environment for the cell. During short duration runs it is possible to control furnace temperature by means of manually operated adjustable autotransformers. Line voltage variations overnight were found to cause temperature excursions of as much as 50°C. To achieve satisfactory temperature regulation, an inexpensive thermocouple-controlled galvanometer relay[2] was employed to control furnace temperature.

The galvanometer relay was set up to short-circuit a resistor in series with the furnace heater. Temperature level was established by means of an autotransformer, and the value of the series resistor was chosen to accommodate the effects of daily line-voltage variations. The temperature of the cell was controlled for a one-month interval with variations of less than 2°C by this technique.

The use of aluminum oxide in this work is, as stated, necessary, but entails some difficulties. Thus, a cell of more than simple geometry is difficult to fabricate from a single solid block while, on the other hand, further seals are required if the cell is fabricated from parts. It has been found possible to effect a liquid-metal tight seal between pieces of alumina tubing by use of the tapered joint already described, and by use of a tapered joint which has been sealed by formation of a spinel of $MgO-Al_2O_3$ between the alumina surfaces.[3] It is also possible to effect a seal between flat surfaces of alumina and steel by use of a pressure seal. The surfaces of such a seal must be ground flat and polished to a near gauge-block finish. Electrical leads may be incorporated by use of the rivets as described, or if in a metal surface, successful performance has been

[2] Simplytrol P. R. Controller, Assembly Products, Inc., Chesterland, Ohio.

[3] Further particulars of this technique may be obtained from the Technical Development Department, Refractories Division, Norton Company, Worcester, Mass.

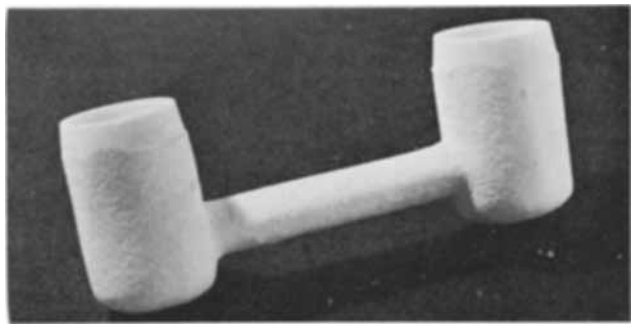

Fig. 2. Flame-sprayed alumina "H" cell

achieved by use of brazed nickel-to-alumina feed-through terminals[4] which may then be welded to the metal surface. The machining of solid alumina in intricate shapes has been found to be readily performed employing high-frequency abrasive cutting techniques.

In the search for methods by which sufficient cell complexity might be achieved to allow half-cell voltage measurements to be taken,[5] an approach to a cell fabrication was made employing flame-spraying techniques. The "H" cell of Fig. 2 was prepared by flame-spraying[6] a wood mandrel, shaped to the desired inside dimensions of the "H" cell with Al_2O_3. The thickness of the flame-sprayed layer was about 3 mm. The wood mandrel was then removed by charring in a furnace at temperatures increasing from room temperature to 260°C over an 8-hr period. The charred wood residue was then removed, and the hollow cell leached with dilute HCl, dilute HNO_3, and H_2O and finally fired to 1090°C. The porous flame-sprayed cell was then reduced to near zero porosity by high-temperature firing.[7] This procedure resulted in a liquid-tight cell. Further attempts at this technique are expected to provide vacuum-tight apparatus of sufficient strength and of proper design to allow half-cell measurements to be performed.

For cells which are to be operated in an environment of vibration or with the liquid metal electrodes in a vertical position, it is necessary to separate the two liquid metals to prevent internal short circuits. Attempts to effect such separations are being made by use of an electrolyte-impregnated matrix of a porous, nonconducting substance. Various forms and compositions of alumina and MgO have been tested, the 99+% Al_2O_3 matrix having thus far been found to be best for this application. A commercially available filter disk[8] of 99% Al_2O_3, a nominal porosity of 36%, and a permeability of 20-30% has most frequently been employed as a matrix in these studies.

A liquid-metal cell, operated as a fuel cell, will be operated with a closed-ended anode, *i.e.*, the Na stream will terminate in the cell. At the cathode,

[4] Alite Terminals, 99% Al_2O_3 (Special) Alite Division, The U. S. Stoneware Co., Orrville, Ohio.

[5] An excellent reference source to the study of electrochemistry in fused salts has recently been published: "Reference Electrodes," David V. G. Ives and George J. Janz, Academic Press, N. Y. (1961) especially ch. 12.

[6] Cincinnati Metal-Blast Company, Cincinnati, Ohio.

[7] See Footnote 6 for further particulars, also ref. (9).

[8] Norton Alundum Lab Ware Filter Disk, Mixture RA 139, Norton Company, Worcester, Mass.

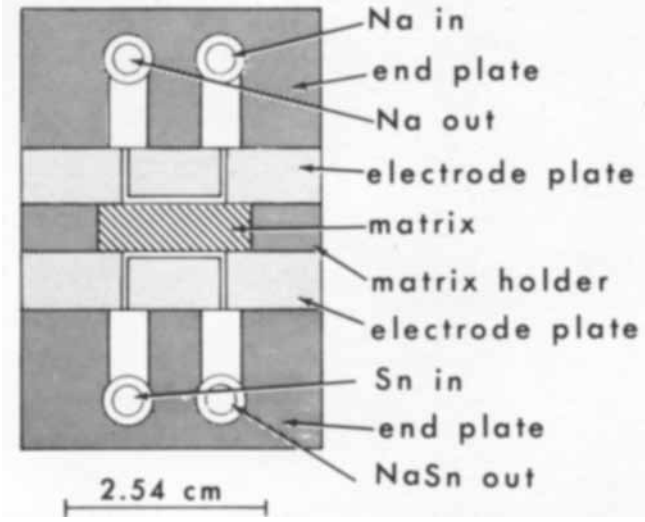

Fig. 3. Flowing-metal cell diagram

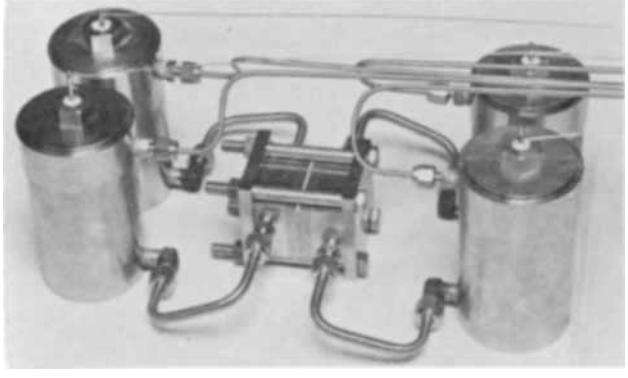

Fig. 4. Flowing-metal cell assembly

the Sn stream, low in Na content, will enter the cell, pass by the electrolyte, and exit from the cell enriched in Na content. The fact that the Sn cathode is moving past the electrolyte will tend to reduce any concentration polarization in the Sn cathode. To allow a determination of the influence of Sn velocity upon concentration polarization, the cell of Fig. 3 and 4 was constructed. Each cell-half consisted of an end plate, through which fittings allowed the reactant to be introduced and removed, and an electrode plate which allowed the liquid metal to assume a known geometry. The channel for the liquid metals in the electrode plate was a rectangle of 2.540 cm length, 1.270 cm width, and a depth of 0.0508 cm. The flow streams are therefore believed to be of uniform velocity past the electrolyte and of a known area. The assembled cell was made leak tight by use of the pressure seals already mentioned and with pressure supplied by the vice shown. The bolts employed were 5/16-18 and were tightened to a torque of 1.4 to 2 kg-m. The porous matrix was contained with a zero-clearance fit in a frame of impervious alumina.

All potential measurements were made employing potentiometers or strip-chart potentiometric recorders. Reagent grade chemicals were employed. The N_2 or A was passed over Cu turnings at a temperature of 450°C, and H_2O was removed with $CaSO_4$ drying towers. Temperatures were measured with

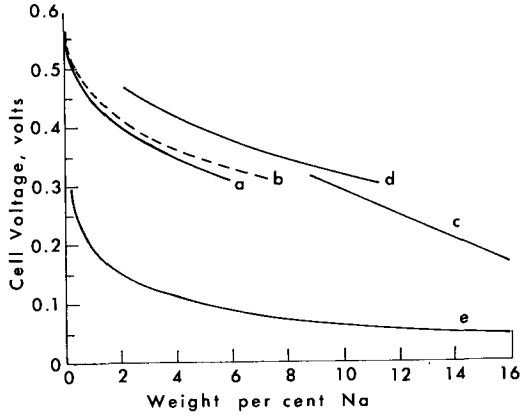

Fig. 5. Variation for Na|Sn cell voltage with Na concentration

chromel-alumel single-junction thermocouples. Electrolyte mixtures were prepared from stock reagents, in correct weight proportions, then fused to further remove traces of water.

Results

A search for a suitable electrolyte was made of the salts of Na. Anions found to be chemically compatible were: the halogens, CN^-, $CO_3^=$ and $S^=$. The electrolyte employed in these studies was an eutectic of 62.5 mole % NaI, 37.5 mole % NaCl, mp = 562°C. Cell data presented were obtained employing this electrolyte in cells which were maintained at 625°C. A low melting composition of 20.3 mole % Na_2CO_3, 47.3 mole % NaI, 32.4 mole % NaCl, mp = 520°C, has also been found. In addition a low melting mixture, mp = 512°C, for the NaI-NaCN system, of an approximate composition of 35 w/o NaCN has also been found.

Static-Cell Studies

Cell voltage *vs.* Na concentration data are presented in Fig. 5. Data for curve (a) were obtained employing the static cell loaded with Sn, the electrolyte, and Na, and raised to operating temperature. Known quantities of coulombs were then withdrawn from the cell, the open-circuit potential measured, and the weight per cent of Na in the Sn calculated. The open-circuit voltage of the cell continuously decreases during the period in which the electrolyte is molten. This nongalvanic voltage loss is presumably due to the solubility of Na in the melt or to chemical or physical decomposition of the electrolyte (I_2 coloration may be seen in the fused, evacuated melt). For this reason, the Na concentration calculated by coulomb measurement is a minimum value. Employing the results of the life-test to be described, the results presented in curve (a) have been corrected to an approximate true concentration, and these corrected data are presented in curve (b). Curve (c) was obtained from the data of ref. (4), p. 23, for a Na|Sn cell operated at 480°C and curve (d) obtained from ref. (10) for the cell operated at 500°C. Curve (e) was obtained by calculating the potential of the cell assuming behavior due to a simple concentration cell.

Charge-discharge data were obtained by employing the static cell. Such data were collected at dif-

ferent levels of Na concentration in the Sn layer. Experience with these measurements resulted in the design of the cell of Fig. 1. The data accumulated with this cell were corrected for the resistance of the leads which provided electrical contact from the top of the inert-gas enclosure to the cell rivets. The precise and repeatable measurement of the resistance of these leads, which were subject to a temperature gradient of 600°C, was found to be difficult. For this reason, the cell of Fig. 1 was modified by the addition of two rivets which served to allow the potential between the Na and Sn electrodes to be measured while passing current through the other two leads. In all cases, a plot of cell voltage against current density resulted in a straight line passing through the open-circuit intercept. The measurements were repeatedly taken to current densities of 0.775 amp/cm². From these data the conductivity of this electrolyte was calculated. The results of three identical experiments provided a value of the conductivity of 2.5 ± 0.1 mho at 625°C. Measurements of the conductivity using conventional techniques with glass conductivity cells whose constants were above 100, provided a value of 2.3 mho. This value was unaltered by the use of Ag, Pt, or 3 w/o Na in Sn electrodes. This difference in conductivity value is attributable to the assumption that the liquid-metal electrodes were flat, *i.e.*, meniscus free, which is not the case. The value of 2.3 mhos is believed to be valid.

Life-Test Studies

Most of the experiments performed with the static cell were run for not more than five days, and during these times most data were manually collected. In order to study the long-time behavior of the cell, an automated life test was established. By means of a relay which was driven by a synchronous motor, a cyclic sequence of cell operations was established, and the information obtained during each phase of the cycle was recorded with a single potentiometer strip-chart recorder. The sequence of events and the fraction of the cycle devoted to each phase were: open-circuit voltage, 10%; charging current, 40%; open-circuit voltage, 5%; cell temperature, 5%; discharge current, 40%. Each cycle was of 20-min duration, and the length of time devoted to either charging or discharging the cell was thus 8 min. Since the cell was on open-circuit during the measurement of cell temperature, the total time per cycle that the cell was on open-circuit was 4 min.

The results of this life test are presented in Fig. 6. The charge and discharge currents were adjusted during the early part of the run in an attempt to keep the voltage after charge and discharge at a constant level. The degree to which these adjustments were successful is presented in Fig. 6, curve (A) showing the variation in open-circuit voltage of the cell after the charge and discharge cycles. The cell may be considered to have operated in a stable manner during most of the 31 day period. The ratio of equivalents of Na consumed during a discharge cycle to those recharged during the charge cycle are presented in Fig. 6C. The coulombic efficiencies of the cell approached a maximum of 70% during the

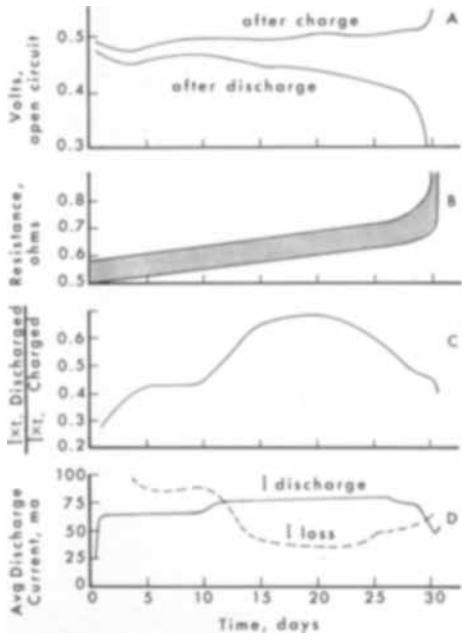

Fig. 6. Na|Sn cell life-test results

run. The average coulombic efficiency was 50.6% and 1.97 equivalents of Na were discharged during the run. Since the cell contained 0.116 equivalents at the start of the run, the quantity of electricity withdrawn from the cell was 16 times that represented by the original quantity of Na placed in the cell. The discharge current during the run is shown in Fig. 6D. The average discharge current for the entire cycle was 71.0 ma corresponding to 18.3 ma/cm². This value corresponds to an average discharge current of 45.9 ma/cm² during the 40% portion of the cycle. The difference between charge and discharge current averaged over the complete cycle, I_{loss}, is plotted as the dashed line of Fig. 6, curve (D). Measurements of cell resistance during charge and discharge were taken periodically during the run. These values were obtained by measuring the change in cell voltage due to a known current flow, both charging and discharging. The results were variable and are presented as the range of resistance shown in Fig. 6B. Based on the average coulombic efficiency and the average discharge current, the loss in current due to nongalvanic processes in calculated to be 17.9 ma/cm². This value has been applied as a correction to the data of Fig. 5, curve (b).

Inspection of the cell after the conclusion of the life test showed that cell failure was caused by loss of Na from the cell due to an imperfect seating between the cell and the cell cap. The alumina and the rivets showed no sign of attack, other than a surface blackening of the alumina, presumably due to the reduction of traces of SiO_2. The porous matrix employed showed no major attack, but after washing with water, the disk exhibited a loss of mechanical strength.

The studies performed with the static cells demonstrated that the concentration polarization was not of a magnitude to observe with the techniques employed. It was difficult to decide between concentration polarization and pen-lag effects even though the cell voltage during the life test was re-

corded employing the 12.5 mv span of a recorder whose pen-response speed was 1 sec for full-scale deflection of 25 cm. Such a low extent of concentration polarization is not significant to the operation of cells in which the greatest voltage loss is due to resistivity, and it was thus unnecessary to study this polarization further. Nevertheless, the cell of Fig. 4 was assembled and run to study the behavior of the seals and the matrix. It was found that the pressure sealing techniques were quite satisfactory and were capable of preventing liquid-metal leaks at absolute pressures as high as 2.3 atm. It was discovered, however, that the matrix employed allowed the pores to be flooded with Na metal, causing almost immediate cell failure. This short-circuiting was presumably due to the use of too large a pore size.

The high conductivity of the electrolyte, the excellence of kinetic behavior as indicated by the linear charge-discharge curves, and the low extent of nongalvanic processes have thus been demonstrated. On the basis of these results, a cell constructed of a 3 mm thick, 40% permeable matrix of the type used in these studies, employing the NaI-NaCl eutectic, should allow operation at 0.767 amp/cm^2 at 0.25v, the maximum power capability of a cell of 0.5v open-circuit potential. Such a cell would exhibit 95% coulombic efficiency when continuously operated at this current density during balanced charge and discharge periods.

Acknowledgments

The authors wish to express their gratitude to the management and personnel of development laboratories of the Norton, Alite, and Cincinnati Metal-Blast Companies. The assistance provided by these groups made possible the construction of the experimental apparatus necessary to this study.

Manuscript received Nov. 10, 1961; revised manuscript received March 15, 1962. This paper was prepared for delivery before the Detroit Meeting, Oct. 1-5, 1961.

Any discussion of this paper will appear in a Discussion Section to be published in the June 1963 JOURNAL.

REFERENCES

1. B. Agruss, Paper presented at the Detroit Meeting of The Electrochemical Society, October, 1961.
2. E. L. Shriver, "Design of a Liquid Metal Regenerative Electrochemical Cell System," Allison Division, G. M. C., 1960, Internal publication.
3. S. W. Smith and R. D. Weaver, "A Comparison of the System Weight of the Na|Sn Liquid-Metal Cell for Various Applications," Electrochemical Research Dept., Report No. 4337-E, Delco-Remy Div., G. M. C., Internal publication.
4. O. Kubaschewski and V. A. Catterall, "Thermochemical Data of Alloys," Pergamon Press, New York (1956).
5. Max. Hansen, "Constitution of Binary Alloys," McGraw-Hill Book Co., New York (1958).
6. R. E. Shearer, J. W. Mausteller, J. A. Ciarlariello, and R. C. Werner, *Proc. 14th Annual Power Sources Conference*, p. 76-7 (1960). Published by PSC Publications Committee, P. O. Box 891, Red Bank, N. J.
7. C. B. Jackson, *Proc. 12th Annual Battery Research and Development Conference*, p. 107 (1958). Published by the Battery Conference Committee, Power Sources Division, U.S.A.R.D.L., Fort Monmouth, N. J.
8. R. C. Werner, R. E. Shearer, and J. A. Ciarlariello, *Proc. 13th Annual Power Sources Conference*, p. 122-4 (1959). Published by the Power Sources Conference Committee, Power Sources Division, U.S.A.S.R.D.L., Fort Monmouth, N. J.
9. Niel N. Ault and L. H. Milligan, *Am. Ceramic Soc. Bull.*, **38** [11], 661 (1959).
10. "Selected Values for the Thermodynamic Properties of Metals and Alloys," Minerals Research Laboratory, Institute of Engineering Research, University of California, Berkeley, Calif., Sept. 1959, Na, Sn Section, p. 3-4.

Formation of Porous Metal Plates by Electrolytic Reduction

I. Electrolytic Reduction of Metal Compounds under Controlled Physical Pressure

C. M. Shepherd and H. C. Langelan

United States Naval Research Laboratory, Washington, D. C.

ABSTRACT

Porous metal plates having high surface areas and considerable mechanical strength were produced by the reduction of pasted metal compounds under controlled physical pressures in an electrolytic cell. The porosity of the metal plate is a function of the pressure applied during electrolysis and the metal content of the compound being reduced. Successful reduction depends upon using the proper combination of metal compound and electrolyte. Porous metals formed successfully by this technique included Ag, Fe, Bi, Sn, Sb, Zn, Cu, Cd, Pb, and the following mixtures, Sn-Pb, Zn-Hg, Cd-Zn, Ag-Cu, and Cu-Zn. Porosities as low as 42% and as high as 89% were obtained. A small variation in the porosity of such a metal electrode may have a serious effect on its capacity as a battery anode.

A large number of metal compounds can be mixed with a suitable liquid, pasted on a metal screen, and reduced to the corresponding metal when made the cathode in an electrolytic cell. If such an electrode is suspended openly in the electrolyte, the pasted compound may be shed from the screen before it has a chance to be reduced. If a metal deposit is obtained in this manner, it is apt to be

crumbly, slightly adherent, and have little strength. Zinc oxide gives such a deposit in a potassium hydroxide electrolyte. However, when a cell assembly consisting of pasted zinc oxide cathodes, silver anodes, and separators is packed into a tight fitting cell case and charged in a potassium hydroxide electrolyte, the zinc oxide is reduced to a compact, adherent, porous zinc plate which has considerable physical strength. It seemed probable that the tight packing of this cell assembly placed a pressure on the pasted zinc oxide which was responsible for the reduced zinc being in a compact form. Special equipment was designed for reducing pasted electrodes in an electrolytic cell under controlled physical pressure.

Metal plates formed in this manner are highly porous, resistant to crumbling in most cases, and have a large surface area that is readily contacted by liquids upon immersion. They are particularly excellent for use as battery anodes that are to be discharged at high rates.

The purpose of this study was to determine some of the factors that are involved in the formation of porous metal plates by the electrolytic reduction of pasted metal compounds under pressure.

Experimental

A paste of the proper composition was made from the particular compound and electrolyte, and it was applied evenly to both sides of a 3.8 cm^2 fine-mesh, wire screen. Enough material was used to give metal plates approximately 0.2 cm thick. The pasted screen was pressed in a die to remove any slight excess of liquid present, to remove air bubbles, to give better adherence to the wire screen grid, to distribute the paste evenly over the grid, and to give the flat, parallel surfaces that were necessary in the subsequent cell assembly. The paste extended well above the surface of the wire screen in which respect it was different from the average commercial battery plate where the paste is inside the pockets of the grid. The problems involved in pasting are so serious that they have been made the subject of a separate study (1).

The order of assembly of the charging equipment is shown in Fig. 1. The pressed electrode was placed between two flat-sheet, inert anodes, generally nickel, each of which was wrapped in a single layer of unsealed cellophane. The electrode assembly was then put in a cell case which consisted of a snug-fitting, flexible bag made of 3-mil polyethylene. The cell assembly was put in a rigidly secured container and placed solidly against one end. A thick polystyrene pressure plate was placed against the other side of the cell assembly. The rounded tip of the lever arm was placed in the rounded indentation in the center of the pressure plate. The upper extension of the lever arm was kept level as weights were added to the hook to give the desired pressure on the pasted electrode. The applied pressure is a linear function of the weight used and was determined theoretically and checked by calibration. After the pressure was applied to the cell assembly, the current was turned on and sufficient electrolyte was added to cover the electrodes. The cells were charged at a rate that gave complete reduction in about 18-24 hr. In general, the charging conditions did not appear to be critical.

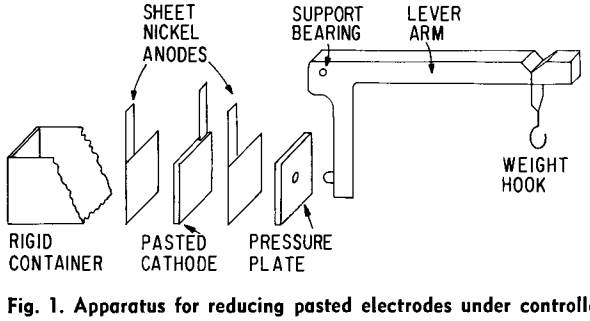

Fig. 1. Apparatus for reducing pasted electrodes under controlled pressure.

At the end of the charge, the porous metal electrode was removed from the cell, thoroughly washed, dried in a vacuum and stored in an inert atmosphere. The porosity, P, which is defined as that fraction of the total volume of the plate that is occupied by pores or void spaces, was determined by liquid absorption. The results were reproducible to ± 0.0007.

Results

Sixty grids were pasted with a mixture of 5.0g ZnO and electrolyte and then reduced in 32.6% KOH to form porous zinc plates approximately 2 mm thick and containing 4.0g of zinc. The average porosity obtained at various pressures is plotted in Fig. 2 and was found to decrease from 0.81 to 0.71 as the pressure was increased. The rate of decrease was fastest at the lowest pressure where the porosity was highest and the physical structure was weakest. When the initial pressure on the cell assembly was greater than 0.2 kg/cm^2, the paste generally flowed to a certain extent and formed a bulge around the edge of the electrode which reduced to give a crumbly metal. This undesirable condition was avoided by holding the pressure during the first 20 min or so of charging at 0.2 kg/cm^2. The paste was then stiffened by the presence of reduced metal, and the pressure could be increased to as much as 0.8 kg/cm^2. At the end of approximately another 20 min the pressure could be increased to as much as 1.6

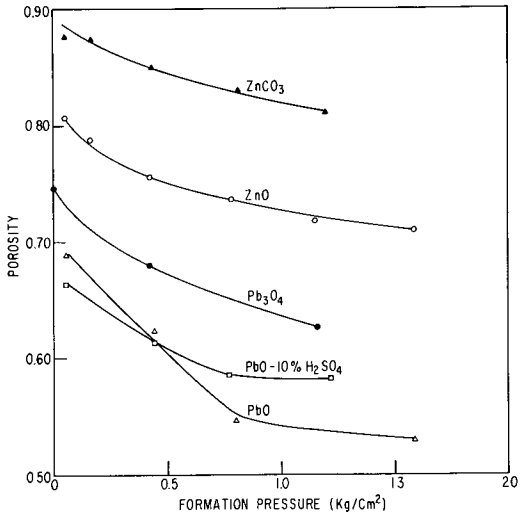

Fig. 2. Effect of formation pressure on porosity

kg/cm². An increase in the length of these initial forming periods at low pressures was accompanied by an increase in the porosity. The optimum length of the initial low-pressure formation periods varied somewhat with the material being reduced and the conditions of reduction.

Porous zinc electrodes were also produced by the reduction of $ZnCO_3$ in 32.6% KOH. Results are shown in Fig. 2.

A number of these zinc electrodes were discharged individually in an alkaline cell between two AgO cathodes at 20°C and 10 amp using 10 cc of 40% KOH electrolyte. Under these conditions, the zinc electrode was the limiting factor on cell capacity. In Fig. 3, the capacity in minutes is plotted against per cent porosity. A peak is reached at a porosity of 82%. At higher porosities, the physical structure is weakened and the zinc crumbles during discharge, and at lower porosities the electrode is stronger physically, but the total surface area is less; therefore, the current density is higher and the capacity is lower. The curves in Fig. 2 and 3 show that the capacity was seriously affected by the porosity and consequently was also affected by the pressure used during the electrolytic reduction. The maximum capacity was obtained only under a fairly narrow range of porosities. Careful control of these conditions is essential if one is interested in specialized characteristics such as high current density discharge rates or minimization of battery weight.

The porosity-pressure curves for lead plates formed by the reduction of Pb_3O_4 and PbO are shown in Fig. 2. Pb_3O_4 can be reduced at zero pressure to give a solid physical structure. Many materials that reduce satisfactorily in an electrolytic cell under pressure, either fail to reduce at all if no pressure is applied or reduce incompletely or reduce to give a nonadherent, spongy metal deposit. All of the reductions discussed here were made with a 32.6% KOH electrolyte unless otherwise indicated on the porosity-pressure curves. PbO was reduced in a 32.6% KOH and also in a 10% H_2SO_4 solution. The difference between the two pressure-porosity curves for PbO is not nearly as large as the difference between the PbO and Pb_3O_4 curves. In the case of a particular metal, changing the compound to be reduced probably has more effect on the porosity than changing the electrolyte that is being used with a given compound.

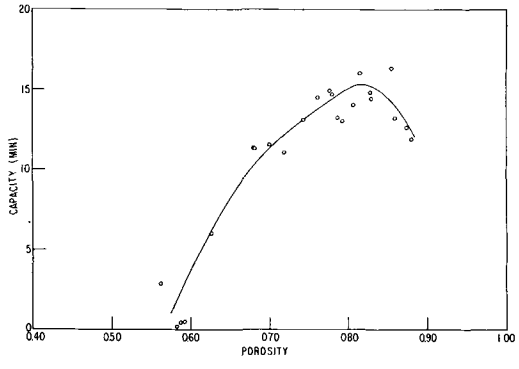

Fig. 3. Effect of porosity on cell capacity

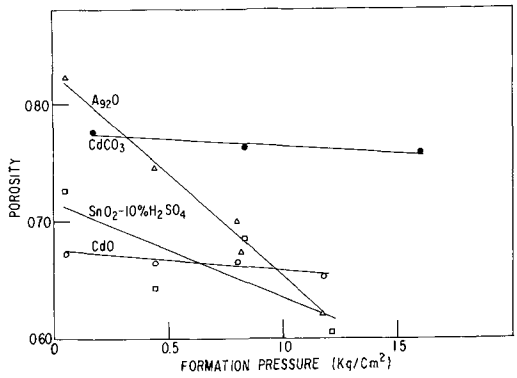

Fig. 4. Effect of formation pressure on porosity

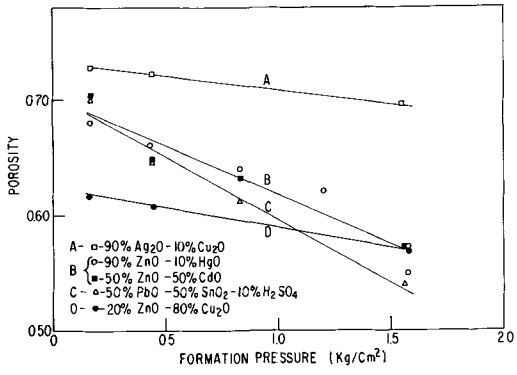

Fig. 5. Effect of formation pressure on porosity

Porosity-pressure curves for the formation of porous plates of cadmium, tin, and silver are shown in Fig. 4. Results obtained from the reduction of various mixtures are shown in Fig. 5. Satisfactory porous plates were not obtained whenever a mixture of compounds was tried that contained an appreciable amount of a compound that would not reduce by itself. Porosity curves for copper and antimony are given in Fig. 6. By using three different compounds, it was possible to prepare copper plates covering most of the range between 0.40 and 0.90 porosity.

In addition to the compounds shown in Fig. 2, 4, 5, and 6 successful reductions to satisfactory porous metal plates were also obtained using FeS, AgO, $Bi_2O_2CO_3$, and PbO_2 in KOH electrolyte. The reduc-

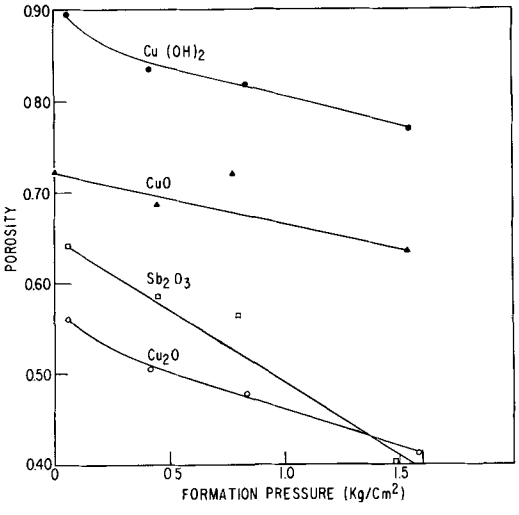

Fig. 6. Effect of formation pressure on porosity

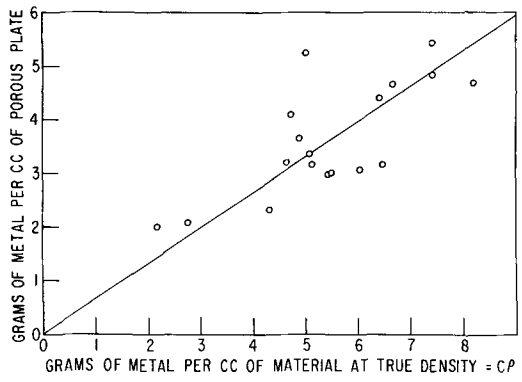

Fig. 7. Estimation of porosity from the amount of metal in the original material. Pressure = 1.5 kg/cm².

tion of HIO_3 in a saturated solution of KIO_3 gave a porous plate of iodine that was adherent and had some physical strength. This was the only porous plate of a nonmetallic substance that was formed by electrolytic reduction.

A wide range of porosities was obtained from the various compounds that were successfully reduced. In the case of a particular metal such as zinc, lead, cadmium, or copper, the compound that contained the lowest percentage of that metal gave a porous plate having the highest porosity when reduction was made at constant pressure. This is illustrated in Fig. 2, 4, and 6. In Fig. 7 the grams of metal per cubic centimeter of porous plate have been plotted against the grams of metal per cubic centimeter of compound at its true density for a formation pressure of 1.5 kg/cm². Similar curves were obtained at other formation pressures, and in all cases a straight line through the origin gave a reasonable fit and was statistically significant.

An approximate prediction of the porosity may be made from the empirical equation

$$P = 1 - (0.472 + 0.127p)C\frac{\rho}{\rho_m} \qquad [1]$$

where P is the porosity expressed as a fraction, ρ_m is the density of the metal, p is the formation pressure, C is the per cent of metal in the compound being reduced, and ρ is the true density of the compound. Porosities were calculated by means of Eq. [1] on all available data and found to have an average deviation of 0.056 from the measured values.

The shape and slope of the porosity curve may be a function of the particular metal involved. In Fig. 2, it can be seen that the $ZnCO_3$ porosity-pressure curve is roughly equidistant from the ZnO curve, and the curve for Pb_3O_4 is roughly equidistant from the two PbO curves. In Fig. 4 the straight lines for $CdCO_3$ and CdO are nearly equidistant and the same is true for the CuO, Cu_2O, and Cu $(OH)_2$ porosity-pressure curves in Fig. 6. Although these data are too limited to be conclusive, they do indicate that the porosity-pressure curves for various compounds of a given metal may be approximately equidistant.

Discussion

Not all metals can be formed into porous plates by electrolytic reduction using the techniques described here. All but one of the metals that were reduced in this manner were observed to have 18 electrons in their penultimate electron shell.

On the basis of their behavior in electrode systems and various other properties, Piontelli (2) divided metals into three classes, namely normal, inert, and intermediate. Lyons (3) has discussed Piontelli's classification of metals on the basis of their electrodeposition from aqueous solutions. These divisions are shown in Table I which omits some of the metals that cannot be electrodeposited readily. All but one of the metals that formed porous plates by reduction was in the normal group. One success was obtained in the inert group.

The normal metals have considerable variation in their properties, particularly in regard to their electrodeposition from aqueous solutions. A study of these anomalies shows that they can be reconciled by dividing the normal metals into two sub groups, the normal-electropositive, which contains the normal metals having a low electronegativity and the normal-electronegative which contains the normal metals having a high electronegativity. The normal-electronegative metals can be electrodeposited readily from aqueous solutions, and most of them are plated commercially at efficiencies of approximately 100%. The amount of ionic character in a bond involving a metal of this group is considerably less than for the corresponding compound involving a metal of the normal electropositive group.

All of the porous metals that were formed by the technique described here belong to this normal-electronegative group with the exception of iron and of antimony which is on the border line and possibly should be reclassified. No failures were obtained within this group. However, no experiments

Table I. Electrolytic classification of metals

Normal (normal-electropositive)			Inert							Normal (normal-electronegative)					Intermediate
Li															
Na															
K	Ca	Sc	Ti	V	Cr	Mn	Fe	Co	Ni	Cu	Zn	Ga	Ge	As	
Rb	Sr	Y	Zr	Nb	Mo	Tc	Ru	Rh	Pd	Ag	Cd	In	Sn	Sb	Te
Cs	Ba	La*	Hf	Ta	W	Re	Os	Ir	Pt	Au	Hg	Tl	Pb	Bi	Po
Fr	Ra	Ac**													

* Lanthanides.

** Actinides.

were conducted using gold, gallium, indium, and thallium. Attempts to reduce porous plates from arsenic, selenium, and tellurium compounds were unsuccessful, even though some reduction could be obtained. Most of the 15 inert metals lying to the right of vanadium in Fig. 1 can be electrodeposited successfully from the proper aqueous solution with current efficiencies that vary from quite low on up to 100% in a few cases. However, all attempts to produce pure porous plates of these metals were failures. A considerable number of unsuccessful attempts were made using various electrolytes and a good many different compounds of nickel, cobalt, iron, manganese, chromium, molybdenum, and tungsten. All attempts were unsuccessful that used mixtures of these compounds and other compounds that reduced readily such as HgO. However, FeS containing 20% graphite reduced readily in a 15% KOH solution. When success is obtained with any of these metals, it probably will be under conditions that are much more restricted than those observed in the normal-electronegative group.

Given a metal that can be formed by reduction using these techniques, it is necessary to find the proper combination of metal compound and electrolyte that will make this reduction possible. Whenever a compound of a metal in the normal-electronegative group that was slightly soluble in the electrolyte was tried, successful reduction to a porous metal plate was always achieved. A slight solubility is not a necessary condition and probably not a sufficient one. If the compound was highly soluble in the electrolyte, failure resulted due to the paste dissolving off the grid. In the case of moderately soluble compounds, the reduction is generally more apt to be successful if the electrolyte is saturated with the compound to be reduced. The solubility of the material indicated that electrodeposition from the metal ion could be the major factor in the reduction mechanism.

A number of compounds were found that could be reduced to a porous metal plate even though they were very insoluble in the electrolyte. Most of these could be checked in the literature and were found to be relatively good conductors of electricity. This suggests the possibility that the compound is reduced to metal in the solid state without first going into solution.

Some compounds might be reduced by atomic hydrogen evolved at the cathode. Sancelme (4) has proposed this mechanism for the reduction of certain oxides. His compounds were placed loosely on top of a platinum cathode, and consequently their reduction might also be explained on the basis of other mechanisms.

Manuscript received Oct. 20, 1961; revised manuscript received April 11, 1962. This paper was prepared for delivery before the Houston Meeting, Oct. 9-13, 1960.

Any discussion of this paper will appear in a Discussion Section to be published in the June 1963 JOURNAL.

REFERENCES

1. C. M. Shepherd and H. C. Langelan, *This Journal*, **109**, 661 (1962).
2. R. Piontelli, *J. Chim. Phys.*, **45**, 115 (1948).
3. E. H. Lyons, *This Journal*, **101**, 363 (1954).
4. A. Sancelme, *J. Chim. Phys.*, **49**, C117 (1952).

Formation of Porous Metal Plates by Electrolytic Reduction

II. Electrode Pasting

C. M. Shepherd and H. C. Langelan

United States Naval Research Laboratory, Washington, D. C.

ABSTRACT

The successful formation of a porous metal plate from a pasted electrode under pressure in an electrolytic cell depends on the use of an ideal paste wherein the individual particles of the pasted material are compacted closely together. Just enough liquid is present to fill the interstices between the particles and to take care of what is adsorbed on the surface and in the pores of the particles.

Ideal pastes were prepared from 29 water-insoluble, inorganic metal compounds, and it was found that the ease of pasting and the quality of the paste improves markedly with decrease in particle size of the material being pasted. The best pasting conditions are obtained with materials whose particle size distribution has a geometric mean diameter of less than 0.7μ. The best estimate of pasting quality can be obtained from R, the ratio of the true density of a material to its tap density. When R is greater than 3.8 for a material, it has good pasting qualities.

In using the techniques of Shepherd and Langelan (1) to prepare a porous metal plate by electrolytic reduction of a pasted compound under controlled pressure, successful results depend on several essential factors, one of which is the pasting properties of the compound or mixture that is being used. There is an optimum range of pasting conditions which must be maintained in order to obtain a good porous metal plate. For some materials, this range is very narrow and difficult to maintain. For other materials the range is somewhat wider; satisfactory pasting is comparatively easier to achieve, and the quality of the reduced metal plate is better. The problem is aggravated by the fact that the com-

pound is spread as a stiff paste on top of a wire screen which has a minimum of support to hold it in place and then is immersed in an electrolyte which may tend to cause shedding. A much simpler problem exists in the pasting of commercial battery plates, where the paste is held in pockets and can vary in consistency from very stiff to soft and mushy.

A brief study was made here of each of a large number of compounds in an attempt to find some of the general principles involved in pasting. Although the substances surveyed were limited to metal compounds that were insoluble in water, it is highly probable that the results of this study will apply to many other types of materials. The metal compounds tested included many that could not be reduced to porous metal plates.

Experimental

Five to ten grams of powdered material plus a suitable amount of liquid were made into a paste and applied evenly to both sides of a 3.8 cm^2 wire screen. The pasted screen was wrapped in a single layer of facial tissue to prevent sticking, then put between two Teflon sheets, placed in a close fitting metal die the size of the screen, and pressed in a Carver press at enough pressure to give a final, flat, smooth homogeneous pasted electrode. The plunger was made slightly smaller than the cavity of the die, thus avoiding a waterproof seal and making it possible to press excess liquid out of the pasted plate. An ideal paste was completely retained under these conditions. When the first increment of the pressure was applied to a properly prepared paste, the paste flowed some and was accompanied by a flow of liquid out of the paste. Consequently, the pressure dropped. Further increments of pressure were applied fairly rapidly until a pressure was reached that held steady for several seconds before it started to drop. This pressure was called the minimum pasting pressure. At this point the pasted grid was finished and ready to remove from the die. Large variations of the pasting pressure had no detectable effect on the porosity of the final metal plate as long as the minimum pasting pressure was achieved.

If the compound was to be reduced to metal, the plate was removed from the die and placed quickly without drying or curing into a special cell where it was reduced electrolytically under a controlled physical pressure.

Experimental Results and Discussion

It was found that a porous metal plate having optimum properties in regard to such characteristics as strength and resistance to crumbling could be produced whenever the individual particles in the pressed paste were compacted closely together and had just enough liquid present to fill the interstices. Pastes of this type, prepared from various compounds, were found to have a number of physical properties in common and are defined here as ideal pastes. The ideal paste has a dry appearance, is slightly flexible, and yet is not crumbly. The percentage of liquid present in a particular powder-liquid combination is fixed within fairly narrow limits. An excess of liquid tends to separate from the ideal paste, particularly when it is subjected to pressure. A deficiency of liquid causes the paste to be dry and crumbly. In this condition it readily absorbs liquid. This description of an ideal paste is not limited to pastes that can be reduced electrolytically to a porous metal plate. This study was made using a large number of various water-insoluble, reducible, and irreducible metal compounds pasted with water or aqueous electrolytes and undoubtedly can be extended to pastes made from many other types of compounds and liquids. If the compound was to be reduced electrochemically to the metal, the liquid medium used to prepare the paste was some of the electrolyte in which the reduction was to take place. If the material being pasted was slightly soluble, then a saturated solution of the material in the electrolyte was used in most cases as the pasting liquid. All of the numerical data presented here were obtained from pastes made with a liquid binder of pure water.

The amount of liquid used is the main factor that has to be controlled in making a satisfactory paste. The best results are obtained by using a very slight excess of liquid in forming the paste. This excess is pressed out and can be detected when the pasted grid is removed from the die. Under ideal conditions the excess liquid is accompanied by no more than a very slight trace of the material being pasted. The reading of the minimum pasting pressure is clear on a paste containing the proper amount of liquid. If the paste is too dry, it does not flow well under pressure and forms low spots in the electrode where the amount of paste is less than average. A dry paste does not wet the grid properly and will not be adherent. It is grainy, crumbly, and tends to shed, particularly on edges and corners, whenever it is handled and when the electrolyte is added. When this dry paste is charged, reduction may be incomplete in the low spots, and any metal formed there may be crumbly and nonadherent. The pressure present in the electrolytic cell is light and is applied mainly to the high spots where the paste is thickest and these areas reduce satisfactorily.

If the paste is too wet, it is sticky and tends to pull off the screen when removed from the die. If the paste is excessively wet it flows off the screen like water when pressure is applied in the die.

There is a considerable variation in the pasting properties of various compounds. It was possible to divide all of the compounds tested into five arbitrary groups depending on their ease of pasting and quality of the paste. These groups were labeled "very poor," "poor," "fair," "good," and "very good." Since these divisions were based on the judgment of the operator, they were not sharp and there was a certain amount of overlapping. It was very difficult to maintain proper pasting conditions with compounds in the very poor group. The poor group was somewhat better. Compounds in the good group pasted satisfactorily by using a little care. Compounds in the very good group were pasted successfully over a fairly wide range of conditions, and the pasted grids were subjected to considerable handling and other abuse without showing any appreciable deteriora-

tion. The liquid content in the paste had a wider range of acceptable limits for a very good material than it had for a very poor material. Compounds in the good and very good groups were the only ones that came close to forming "ideal" pastes. The fair to very poor groups deviated to some extent from the above description. Thus, the ideal paste can be looked on as a limit that is approached as one moves from a very poor to the very good material. Very poor compounds when pasted and reduced electrolytically under pressure generally gave porous metal plates that were grainy and crumbly whereas the good and very good compounds gave porous metal plates that had good physical properties and were not crumbly. The fair and poor compounds also produced good porous metal plates, if they were properly pasted.

At this point the concept of an ideal paste and the outline of pasting conditions as given here are qualitative descriptions based on the qualitative observations and personal opinion and evaluation of the authors. A more scientific evaluation of pasting is needed. It is desirable to have some quick reproducible test or measurement that will predict the pasting properties of a powdered material, thus simplifying industrial control and also making it possible to evaluate the relationship of pasting properties to other variables. The liquid content and minimum pasting pressure give a fairly good estimate of the paste group, but can be determined only after the material has been successfully pasted and consequently the pasting properties are already known.

It was found that good predictions of pasting properties could be made from the quantity R_1, which is defined as the ratio of the true density to the apparent density. The apparent density is defined as the grams per cubic centimeter of unpacked material, which is free from pockets or unfilled cavities. In this condition, adjacent particles are as close together as they will get without being subjected to some compacting, mechanical force such as tapping. In Fig. 1 the pasting properties of the various materials under study are plotted against values of the dimensionless quantity R_1. The compounds and mixtures are listed from top to bottom in the order of their ease of pasting. The paste groups are also indicated. These materials cover a wide range of water-insoluble metal compounds. There are a few materials of this type that would not fit into this analysis such as MoS_2 which does not wet and $CaSO_4$, which hardens.

The data in this report are subject to considerable variation because the relationships are not exact and because the assignment of paste groups is an arbitrary factor. By the use of statistical procedures all of the relationships presented in this paper were shown to be highly significant. The Spearman rank coefficient of correlation, r_s, for the data in Fig. 1 is 0.914. Values of r_s for other relationships are given in Table I.

An excellent prediction of the paste groups can be made from

$$R = \frac{\rho}{\gamma}$$

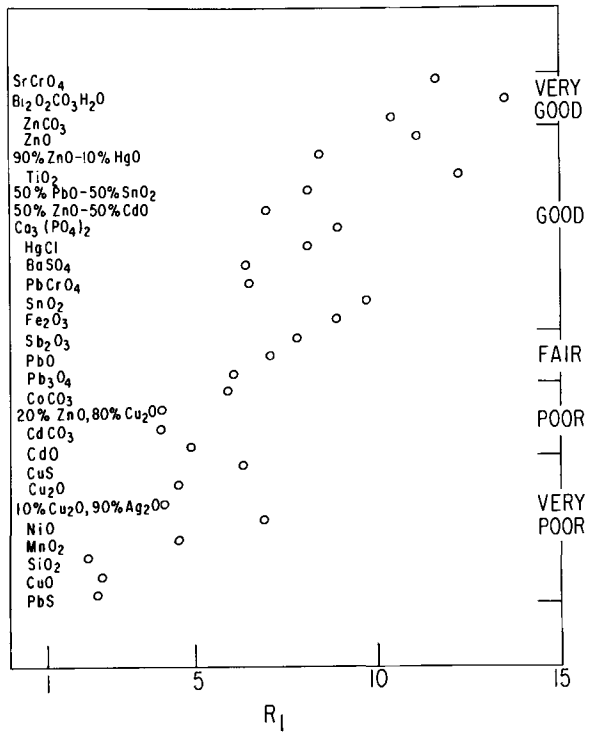

Fig. 1. Relationship between the ease of pasting and R_1, the ratio of the true density to the apparent density.

where ρ is the true density of the material and γ is its tap density. The tap density which has also been called packed density, bulkiness, and bulk density is the density in grams per cubic centimeter obtained by placing the powder in a cylinder and tapping to a constant volume. There are a large number of factors in the determination of the tap density that may cause variations as high as 7% in the results (2-5). All of the measurements used here were made with a glass cylinder which weighed 22g and had an internal diameter of 1.15 cm. The height of powder at the end of the tapping was approximately 6 cm and the tapping rate was 30 times per minute. The cylinder was inclined 10° from the vertical and dropped in a free fall of 2 in. on a hardwood base. If a loose layer formed on the top of the powder, it was either poured off or compacted by rapid vibration. Tapping was continued until no change in volume was observed for eighty taps. Under these fixed conditions the results were reproducible in most cases to within 2% if ordinary care were taken.

Average values of R for the various paste groups are shown in Table I. R can be determined in a few

Table I. Properties of the paste groups

Paste group	Average value of $R = \frac{\rho}{\gamma}$	Average value of particle size, d_g μ	Average value of the minimum pasting pressure kg/cm²	Average H_2O content vol-%
Very good	5.48	0.303	4.16	59.7
Good	4.61	0.536	59.7	54.2
Fair	3.22	0.780	156	42.8
Poor	2.53	0.971	194	36.5
Very poor	2.12	1.240	245	32.1
Spearman rank coefficient of correlation, r_s	0.918	0.794	0.834	0.821

minutes and gives an excellent estimate of the pasting properties. All of the materials in the good and very good paste groups had values of R greater than 3.8. All of the materials that were more difficult to paste were in the very poor, poor, and fair paste groups and had values of R less than 3.8.

Roller (2) and Shapiro and Kolthoff (6) have shown that the bulkiness of various powders increases rapidly as the particle size decreases below a critical value. As a consequence, R should increase with decrease in particle size, and the particle size should decrease in going from the very poor to the very good paste group. The particle size distribution was determined microscopically on the materials listed in Fig. 1. The geometric mean diameter, d_g, was chosen as the typical particle size. It is defined by the formula

$$\ln d_g = \sum f \left(\frac{\ln d}{n} \right)$$

where n is the number of particles and f is the frequency of occurrence for particles having a particular measured diameter, d. The average values of d_g for each of the paste groups are shown in Table I. From a practical viewpoint most materials that had a value of d_g less than 0.7 microns fell in the good or very good paste groups and could be pasted easily. This was not a particularly sharp division and did not give as good a separation of the paste groups as R. Moreover, it was much more difficult to determine. However, it seems likely that the particle size distribution is the most important factor in determining the paste group of a given material. Consequently, a poor pasting material can be converted in most cases into a good pasting material by preparing it in a finer size.

The average values of the minimum pasting pressures for each of the paste groups are shown in Table I. The very poor paste group had an average minimum pasting pressure that was more than 50 times as large as the average for the very good group.

The average water content of the different paste groups is shown in Table I. Humidity changes affect the pasting of a very poor compound since the volume of liquid used is quite small and must be held within very narow limits. For a very good material the volume of pasting liquid can be varied over much wider limits and still give satisfactory pasting conditions over a moderate range of humidities. If a satisfactorily pasted screen is allowed to dry, it cracks and becomes crumbly. The time of storage in open air before this deterioration occurs depends on the humidity and was about 2 min for a very poor paste and about 20 min for a very good paste. Longer storage periods can be achieved by the use of controlled humidity chambers.

The pasting properties of a particular compound depend to a certain extent on the liquid used in making the paste. A better, more homogeneous paste is obtained in most cases if the compound is slightly soluble in the liquid or reacts chemically with it to a limited extent. An excessive reaction or a high solubility is generally undesirable. Water is a comparatively poor liquid for pasting water insoluble compounds. Ten per cent H_2SO_4 is much better. The best liquid tested was 32.6% KOH, and this was used for pasting most of the compounds that were reduced electrolytically. Tests on a number of compounds using these three liquids show that, if the compounds are labeled by rank according to ease of pasting with a particular liquid, there is a good correlation with the results obtained by using another pasting liquid. Thus, the compounds that paste best with water paste best with 32.6% KOH and the ones that paste poorest with water are poorest with KOH even though water gives poorer over-all results. The difference in the pasting properties of liquids showed up mainly in the fair, poor, and very poor groups. All of the numerical data presented in this report were obtained by using pure water as the liquid medium.

In preparing a porous metal electrode of controlled porosity by electrolytic reduction of a pasted metal compound a number of difficulties are encountered due to the fact that the paste rests on top of the grid and is subjected to physical pressure. These difficulties are minimized by preparing an ideal paste of controlled composition and physical properties from a material having a fine particle size distribution.

Manuscript received Oct. 20, 1961; revised manuscript received April 11, 1962. This paper was prepared for delivery before the Houston Meeting, Oct. 9-13, 1960.

Any discussion of this paper will appear in a Discussion Section to be published in the June 1963 JOURNAL.

REFERENCES

1. C. M. Shepherd and H. C. Langelan, *This Journal*, **109**, 657 (1962).
2. P. S. Roller, *Ind. Eng. Chem.*, **22**, 1206 (1930).
3. D. M. Peppard, *Anal. Chem.*, **24**, 1869 (1952).
4. T. T. Cocking, *Pharm. J.*, **107**, 226 (1921).
5. J. C. Macrae, P. D. Finlayson, and W. A. Gray, *Nature*, **179**, 1365 (1957).
6. I. Shapiro and I. M. Kolthoff, *J. Physical and Colloid Chem.*, **52**, 1020 (1948).

Multiple Rate Transitions in the Aqueous Corrosion of Zircaloy

B. Griggs, H. P. Maffei, and D. W. Shannon

Hanford Atomic Products Operation, General Electric Company, Richland, Washington

ABSTRACT

The weight gain of Zircaloy-2, -3, and low nickel Zircaloy-2 during water and steam corrosion is shown to go through two or more repetitive cycles. The evidence indicates these weight gain curves truly represnt the corrosion kinetics. Several corrosion mechanisms are considered in the light of these kinetics. While no definite mechanism can be established, a supposition that stresses in the film periodically cause it to crack at or near the oxide-metal interface appears consistent with the data. Preliminary micrographic evidence supporting the existence of a cyclic corrosion process also is shown.

The rate of corrosion of Zircaloy-2 in high-temperature water has usually been represented (1, 2) as an initial cubic relation of weight gain to time, followed by a linear relation. The "transition point" between these two modes of corrosion is sometimes accompanied by a change in the appearance of the oxide film (2, 3) from black to gray or white. Most of the previous data have indicated only one transition point in the corrosion process. More recently, there has appeared (4, 5) some evidence that the cubic portion of the curve is followed by two linear curves, the first a short steep curve and the second a flatter curve for the balance of the test.

The "weight gain *vs.* time" data for several Zircaloys presented were obtained over several years at the Hanford Atomic Products Operation. These weight gain curves demonstrate a cyclic corrosion process with several rate transitions. The two-step transition (4, 5) would be interpreted as the second cycle of this repetitive process.

Experimental Details

Zircaloy coupons were exposed in refreshed autoclaves at 360° and 400°C. Deionized water (4 ppm O_2 from air) was pumped through the preheater, through the AISI 316 stainless steel autoclave, and out through a cooler and relief valve. The 5-gal, 360°C autoclave was operated at a flow of about 8 l/hr. The 1-liter, 400°C autoclave was operated at a flow of 0.4 l/hr. The coupons were suspended on AISI 347 stainless steel wire racks.

The coupons were rolled sheet material of Zircaloy-2, -3, and low nickel Zircaloy-2 (Table I), prepared by chemical etching 2 mils of each surface in 33 w/o HNO_3-1.85 w/o HF, and thorough rinsing. The etched coupons were weighed, autoclaved, dried at 110°C for 1 hr, reweighed, and returned to the autoclave for further exposure.

Coupons were weighed to ±0.02 mg and measured to ±0.002 dm^2. The samples in Fig. 4, however, were weighed to only ±0.2 mg and measured to

Table I. Alloys used in studies

Alloy No.	Alloy	Description
1021	Zircaloy-2	Rolled sheet (30 mils) produced from ingot 5Y-HO-9. Analysis below.
ZH	Zircaloy-2	Rolled sheet (62 mils) produced from ingot SA-11857. Analysis below.
L or H	Low nickel Zircaloy-2	Rolled sheet (25 mils) produced from ingot 28260-4-6V. Analysis below.
KE-46	Low nickel Zircaloy-2	Rolled sheet (30 mils) produced from ingot KE-46. Analysis below.

Analyses

	Per cent					ppm					
Alloy	Sn	Cr	Fe	Ni	N_2	O_2	Al	Cd	B	Cu	Pb
1021	1.34	0.16	0.13	0.05	0.004	—	40	<0.5	<0.5	16	60
ZH	1.31	0.14	0.18	0.05	0.003	1083	32	<0.5	0.4	23	33
L	1.50	0.097	0.14	<0.003	0.003	—	<30	<0.5	<0.5	<20	<15
KE-46	1.39	0.09	0.14	<0.002	0.005	—	26	<0.5	0.4	<20	<20

	ppm								
Alloy	Mg	Mn	Si	Ti	V	Mo	Co	Zn	C
1021	<20	<10	30	10	<10	<10	<5	—	42
ZH	13	57	27	25	<20	<10	<5	<50	—
L	<15	<10	43	20	<20	<20	<5	<10	176
KE-46	<20	<20	49	<20	<20	<20	<20	—	<100

± 0.002 dm^2. Coupons were about 7 to 13 cm^2 of surface area. Corrections for edges and holes were included in the areas. Weight gains were not corrected for hydrogen pickup. Errors in weight of ± 0.02 mg could give rise to a maximum deviation of ± 0.3 mg/cm^2 and ± 0.2 mg/cm^2 for samples of 7 cm^2 or 13 cm^2, respectively.

Discussion

The corrosion of Zircaloy-2 in high-temperature water and steam produces adherent layers of zirconium oxide on the surface of the metal. Inert marker experiments indicate that the corrosion takes place by the diffusion of oxygen ions through the oxide film to form new film near the metal surface (1, 2). This oxide is quite inert and has not been removed quantitatively without damage to the metal. Therefore, corrosion measurements on Zircaloy are determined by weight gain until it becomes apparent the oxide is sloughing. Using weight gain as a true measure of corrosion involves several assumptions. These assumptions are:

1. The ZrO_2 corrosion product is not lost from the sample. During the period prior to the first transition, the black oxide adheres tightly and there is no evidence of spalling. After the first transition, some alloys spall severely and thereby make weight gain measurements useless. However, Zircaloy-2 is noted for its adherent oxide and even after extensive corrosion, weight gains are thought to indicate the corrosion process, although some errors result. Zirconium oxide is very insoluble in water and losses from this source are insignificant.

2. Substances other than oxygen are not picked up from the system. Since all the corrosion experiments were done with high-quality demineralized water, there is no possibility for salt deposition nor were any foreign deposits observed. The weight gains of samples in different stages of the corrosion process, all of which were exposed in the same autoclave at the same time, differ considerably. Presumably any deposition would be more or less uniform on all samples. Thus there is no apparent deposition on the samples. From 5-50% of the corrosion hydrogen is absorbed by the metal. However, even at 100% absorption, the hydrogen weight gain cannot exceed 13% of the oxygen weight gain. Usually, the hydrogen analysis is destructive, and thus hydrogen cannot be corrected for until testing is complete. For normal Zircaloy-2, the hydrogen weight is negligible except for very long exposures.

3. The composition of the corrosion product is known and constant. X-ray analysis of the film before and after transition shows the film to be ZrO_2 and indicates no gross change in its composition. The oxide is said to absorb some water (6), but no hydrates are known, and the film is assumed to have constant water content after drying at 110°C.

These assumptions have been considered correct in most previous studies of zirconium corrosion. If so, the weight gain and the corrosion process go through a series of repetitive patterns, finally approaching a linear relation with time. This repetitive pattern was common to all alloys tested.

The weight gain data and the corrosion rates of Zircaloy coupons is seriously affected by minor surface or metal impurities (1, 11). Graphs of different runs using different coupon stock, different autoclaves, different surface preparation, and different autoclaving conditions show the generality of this repetitive process (12). Figures 1 and 2 are characteristic of good Zircaloy in 360°C water or 400°C steam, respectively. Figure 3 shows the corrosion curve for a poor alloy.

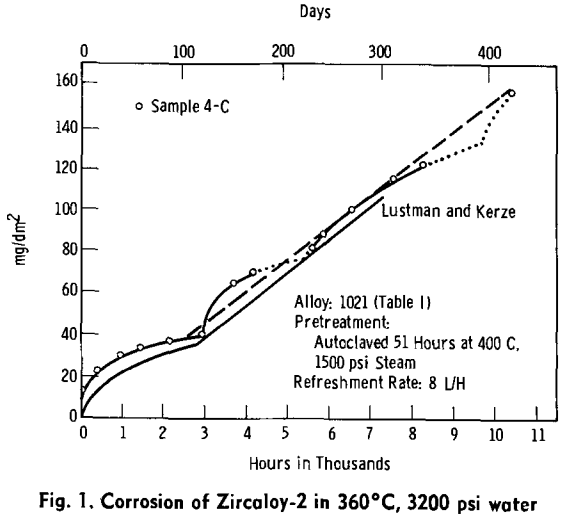

Fig. 1. Corrosion of Zircaloy-2 in 360°C, 3200 psi water

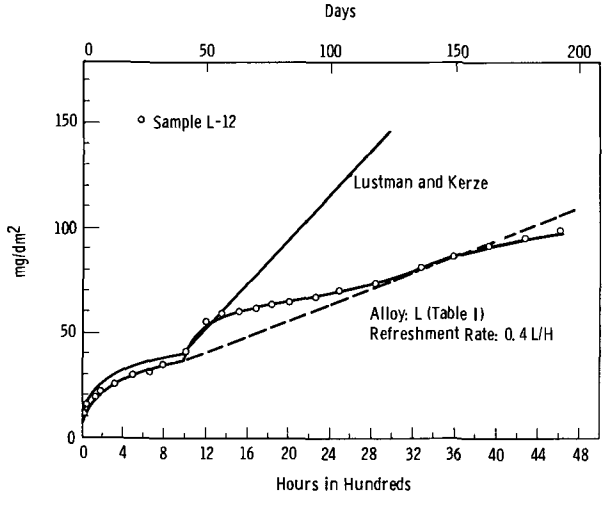

Fig. 2. Corrosion of low nickel Zircaloy-2 in 400°C, 1500 psi steam.

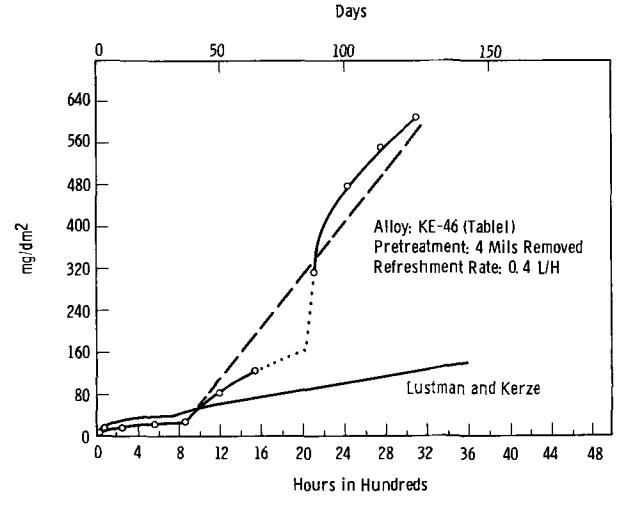

Fig. 3. Corrosion of low nickel Zircaloy-2 in 400°C, 1500 psi steam.

The weight gain of a sample *vs.* time appears in the form of at least two, and as many as four, more or less repetitive curves which resemble the initial cubic curve. Since the weight gain is more accurate than the deviations from linearity, the cycles cannot be explained by experimental error. The successive cycles of the weight gain curve are similar, but not identical. In general, the weight increase during the second cycle is somewhat lower than during the first cycle. The slope at the end of the cycle increases slightly with each cycle, finally approaching a straight line drawn from the transition point. The repetitive effect can also be observed in data from other laboratories (4, 5, 7).

Although all cycles on all coupons have nearly the same period, there is enough difference in their periods to make the use of average weight gains for several coupons misleading. There is also a difference in corrosion from one grain to the next (8), making the weight gain of a single coupon an average for many grains. Therefore, as the number of cycles increases, the coincidence of their periods could decrease and the resultant curves appear as a linear relation with time. The average corrosion of a large number of samples should cause the corrosion curve to appear as a linear function much sooner than would that of the individual samples. An example of this is shown by Fig. 4. These data show an almost linear relation with time. However, this curve was not constructed from repetitive measurements on the same sample, but from samples removed from test for each point. The cyclic behavior is lost due to variation from sample to sample.

It is not possible to define the corrosion mechanism with the available data. However, a mechanism based on mechanical stresses in the film which periodically causes the film to break away from the metal appears consistent with the data. In this model, the ZrO_2 film grows until the stresses, continually set up in the oxide, are relieved by a series of microcracks parallel to the corroding surface. This crack layer is connected to the surface by a network of larger transverse cracks, illustrated in Fig. 6, thus making the bulk of the oxide porous and not protective. After these cracks form, the diffusion path to the metal through any remaining adherent oxide is much shorter; hence, the corrosion rate increases and initiates a second cycle. This alternating process of growth and cracking continues until differences in cycle period from grain to grain become sufficiently out-of-phase to make the average weight gain of the sample appear linear with time.

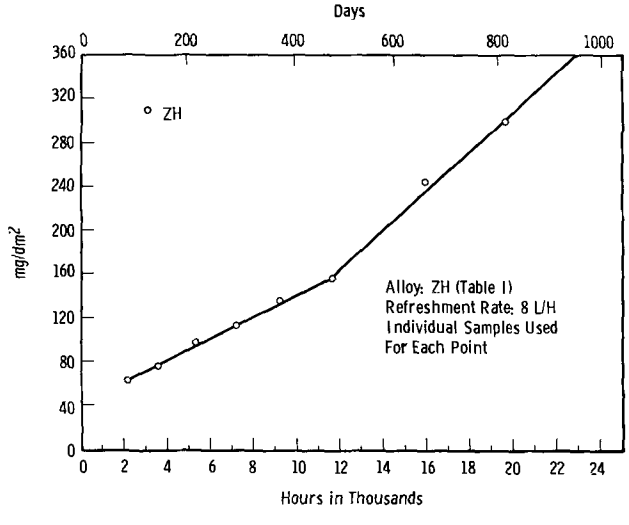

Fig. 4. Corrosion of Zircaloy-2 in 360°C, 3200 psi water

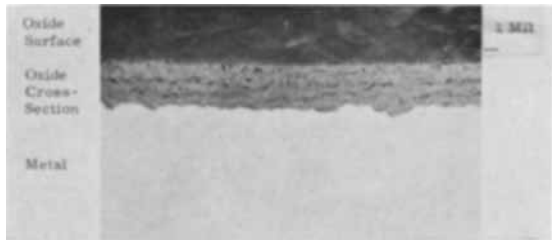

Fig. 5. Cross section of oxide on Zircaloy-2 coupon exposed 10,414 hr in 360°C water. Polishing angle: approximately 20° to oxide surface; etch: vacuum cathodic etch; magnification, 250X, bright field.

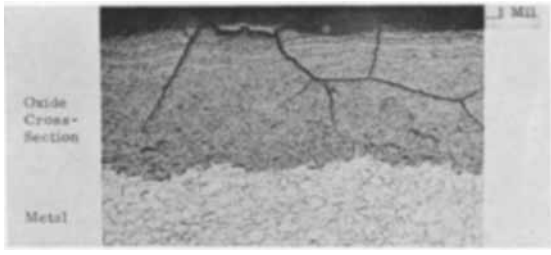

Fig. 6. Cross section of oxide on low nickel Zircaloy-2 coupon exposed 3100 hr in 400°C, 1500 psi steam. Polishing angle: approximately 20° to oxide surface; etch: vacuum cathodic etch; magnification, 75X, bright field.

Several mechanisms of Zircaloy corrosion after the "transition point" have been proposed, but none have gained universal acceptance (1, 2). These include phase transformation of the oxide film at the transition point (1) and cracking of the film at a critical thickness (1, 9). A mechanism similar to the above cracking has been described for titanium in oxygen (10).

A metallurgical section of a Zircaloy-2 coupon exposed to 360°C water for 10,414 hr is shown in Fig. 5. (The corrosion curve is in Fig. 1.) A low nickel Zircaloy-2 exposed in 400°C steam for 3100 hr is shown in Fig. 6. (The corrosion curve is in Fig. 3.) These coupons show a layered structure with the number of layers corresponding to the number of apparent cycles on the weight gain curve. This agreement tends to confirm the conclusion that the corrosion process is cyclic.

The corrosion rate curves presented by Lustman and Kerze in their Fig. 11.38 (1) are plotted to show agreement or disagreement of our data with theirs. The 360°C data agree fairly well. The 400°C data do not agree (Fig. 2 and 3). The KE-46 low nickel Zircaloy-2 is higher than the Lustman and Kerze curve. For reasons not as yet known, the other alloys corrode at a rate lower than the Lustman and Kerze data. Superior corrosion resistance in more recent lots of material may be part of the answer.

It is not possible to tell whether the Lustman and Kerze data show the cyclic process. First, their data do not cover a sufficient time span. Second, only the averages are probably represented and thus any

cyclic behavior is masked. On the other hand, their data are not inconsistent with a cyclic process.

In summary, the weight gain data of several zirconium alloys of various pretreatments all show periodic changes in corrosion rate. Layers observed in the corrosion product oxide further substantiate the cyclic character of the corrosion past the transition point.

Acknowledgments

The assistance of R. A. Thiede, W. C. Craven, S. D. Deusser, D. B. Mackey, and G. W. Mettler in autoclaving samples and processing data is gratefully acknowledged. For the cathodic vacuum etching and the electron microscopy, the authors are indebted to R. L. Hales. All are members of Hanford Laboratories.

Manuscript received Sept. 11, 1961; revised manuscript received March 26, 1962.

Any discussion of this paper will appear in a Discussion Section to be published in the June 1963 JOURNAL.

REFERENCES

1. B. Lustman and F. Kerze, Jr., "Metallurgy of Zirconium," pp. 635-640, McGraw-Hill Book Co., New York (1955).
2. G. E. Zima, HW-60908, p. 10 (1959).
3. B. Cox, AERE-R-2931 (1959); *This Journal*, **108** (1961).
4. H. Coriou *et al.*, CEA-1387 (1959); *Mem. Sec. Rev. Met.*, **57**, 511 (1960).
5. S. H. Bush, R. S. Kemper, and D. L. Gray, HW-69681 (1961).
6. A. B. Riedinger, KAPL-2000-3, p. 57 (1958).
7. A. B. Riedinger, M. S. Thesis, Union College (1958).
8. J. P. Pemsler, NMI-1177 (1957).
9. U. R. Evans, "The Corrosion and Oxidation of Metals: Scientific Principles and Practical Applications," pp. 45-6, Edward Arnold Ltd., London (1960).
10. J. Stringer, *Acta. Met.*, **8**, 758 (1960).
11. D. W. Shannon and B. Griggs, HW-60433 (1959).
12. B. Griggs, H. P. Maffei, and D. W. Shannon, HW-67818 REV (1960).

The Growth of Electrodeposits

J. M. Keen and J. P. G. Farr

Department of Industrial Metallurgy, The University, Birmingham, England

ABSTRACT

The crystal habit of copper electroplate has recently been explained in terms of the aggregation of growth layers. Experiments are described to test the applicability of this, the concept of "bunching," to the development of other electrodeposits. Zinc has been electroplated from acid sulfate solutions on zinc polycrystalline and single crystalline cathodes and on copper single crystal surfaces. The surface features observed are explained and related to those of copper electrodeposits, in terms of the supposed atomic structure of the substrate surface, of the bulk crystal structure of the deposited metal, and of the growth process. Exploratory work on the deposition of lead, cadmium, and iron on the same metals, respectively, indicates that, although the idea of "bunching" may be of wide application, caution is required in explaining growth features where chemical or electrochemical processes may be structure determining.

Recent work by Storey and Barnes (1) has indicated that the conclusions drawn from a study of the electrolytic growth habit of single crystals of copper (2-4) can be applied to the growth of polycrystalline copper substrates. Electropolished and electroetched surfaces behaved similarly. Briefly, Pick and his colleagues found, for copper, that epitaxial growth occurred with coarse crystallographic facets developing on the surface of the electroplate, up to 50 ma/cm^2. The structure could be related to the atomic configuration of the original substrate surface and to the conditions at the interface between the metal and the electrolyte. In particular the structures were consistent with the supposition that growth occurs by a bunching mechanism (5).

In normal laboratory solutions, as in practical plating solutions where additives are absent, there is an abundance of surface active material, impurity that will compete with depositing atoms for available growth sites on the substrate. Thus, if growth occurs by the spreading of atomic layers, these will tend to coalesce because of the continuous deactivation of growth sites; the coarsening will eventually be observable under the microscope, and ultimately non-epitaxial nucleation will be required if growth is to be maintained at a given rate. "Break-away" then occurs.

While the idea of "bunching" gives a satisfactory qualitative explanation of growth and it may lead to useful experiments on both the plating process and on the metallurgy of the metal produced, it is clearly not without inadequacies. It is not quantitative, even as applied to electrodeposition under laboratory conditions, but explains the growth process as being to a large extent controlled by adsorption of adventitious substances of unknown chemical nature, specific effect, or concentration. However, the concept is a general one and should apply not only to the deposition of copper; an important test of the idea is to compare the electrolytic growth of other metals. For this reason a metallographic and crystallographic study has been made of the growth of zinc electrodeposits from acid zinc sulfate solutions under conditions which were thought to be

comparable with those under which the study of copper had been made. Zinc has been plated onto single crystalline and polycrystalline substrates and onto single crystal copper surfaces. The electrolytic growth of lead, cadmium, and iron have also been examined.

Experimental Part

Preparation of the cathodes.—(In general the anodes were of similarly prepared metal.)

Copper.—Single crystal substrates were prepared as by Pick et al. (2). After electropolishing, the mounted specimens were washed with dilute phosphoric acid (6) and with water immediately before plating.

Zinc.—Large-grained polycrystalline cathodes were prepared by the critical strain-anneal method; single crystals were grown by a modified Bridgman technique. Crystals were cut and mounted in cold-setting resin. Such specimens had a heavily deformed surface layer which had recrystallized to a depth of some 900μ. After mounting they were polished carefully metallographically, the deformed layer remaining after diamond polishing being removed by electropolishing. The best surfaces were produced in a 50% by volume orthophosphoric acid-ethyl alcohol solution using a stainless steel cathode with the anode held horizontally. Optimum polishing conditions were found to exist between 1.6 and 2.0v with the solution at room temperature. All traces of deformation were removed by polishing for 4 to 6 hr.

Immediately before plating the specimens were given a further electropolish for 5 min, washed with methanol, aqueous sodium hydroxide and briefly (2-3 sec) with concentrated nitric acid. They were then washed thoroughly with water and transferred to the plating bath.

In experiments on cleavage surfaces, these were produced by cleaving a suitable crystal at liquid nitrogen temperature. A number of such faces were plated without further preparation, the remainder were mounted and etched as has been described.

Cadmium.—This metal is exceptionally soft so mechanical polishing was avoided in the later stages of electrode preparation. Coarse-grained 99.995% cadmium cathodes were prepared by the strain-anneal method. Immediately before plating they were electropolished in an aqueous phosphoric acid bath, etched lightly in dilute nitric acid, and washed with water.

Lead.—Large-grained cathodes were obtained by annealing at 150°C in vacuum. These were masked, electropolished in perchloric acid-aqueous ethanol and immediately before plating lightly etched in dilute nitric acid followed by washing with water.

Iron.—Large-grained electrodes were prepared from 99.985% N.P.L. iron by the strain-anneal method. Before plating they were electropolished in perchloric acid-acetic acid, lightly etched in dilute nitric acid, and washed.

Where "stopping-off" was required, "Lacomit" (supplied by W. Canning & Company Limited, Great Hampton Street, Birmingham) was used.

The plating solution.—Zinc.—"Analar" zinc sulfate, "M.A.R." sulfuric acid, and double-distilled water were used. The following solutions were examined: 0.5M zinc sulfate containing 0.5M, 0.1M, 0.05M, 0.025M, and 0.005M sulfuric acid, respectively. As hydrogen was evolved at the cathode, the efficiency of plating was not 100%, but the evolution was not sufficient to necessitate an increase in concentration of the zinc ions in order to maintain the comparison with copper.

Cadmium.—The electrolyte was a solution of 180 g/l "Analar" cadmium sulfate and 27.1 m/l "M.A.R." sulfuric acid in double distilled water.

Lead.—The electrolyte was prepared by saturating a dilute aqueous solution of perchloric acid containing 118.2 ml of "Analar" grade perchloric acid (S. G. 1.70), with "Analar" lead monoxide and filtering. To this was added a further 118.2 ml of "Analar" perchloric acid and the volume made up to two liters with double distilled water, giving 0.5M lead perchlorate in 0.5M perchloric acid.

Iron.—"Analar" grade ferrous sulfate and "M.A.R." sulfuric acid were used. The following three electrolytes were tried: (i) 0.5M ferrous sulfate, 0.5M sulfuric acid; (ii) 0.5M ferrous sulfate, 0.025M sulfuric acid; (iii) 0.5M ferrous sulfate, 0.025M sulfuric acid, 0.01M hydrazine sulfate.

The plating cell.—The electrolyte was contained in a 2 liter beaker suspended in a constant temperature bath normally maintained at 25°C ± ¼°. The relative positions of anode and cathode were fixed by means of a perspex jig, out of contact with the electrolyte. The current used was supplied from a 12v battery through variable series resistances.

The plating technique.—This was so designed that the cathode could be transferred to the cell and brought up to full current density with the least possible delay. After plating the current was switched off, the specimen removed from the cell and immersed in water. It was washed with methanol and stored in a vacuum dessicator over phosphorous pentoxide.

Examination of the deposits.—The cathodes were examined before and after plating by a selection of the following techniques.

Optical microscopy.—The structures were examined using direct and oblique illumination and line profile techniques. A number of plated specimens were sectioned to reveal surface contour and the metallurgical nature of the deposit.

Optical goniometry.—The Miller indices of the growth facets on deposits grown on single crystal substrates were deduced from their inclination to the cathode surface as was determined using a two-circle goniometer.

X-ray diffraction.—The complete orientation of single-crystal cathodes was determined before and after plating by the back reflection Laue method. Strain or distortion in the surface or deposit could also be detected. The interpretation of the diffraction pattern, as is fully described by Greninger (7) and by Barrett (8), was simplified by the low symmetry of zinc. It was found that, using white copper radiation produced at 18 ma and 40 kv with an ex-

posure time of 25 min, zinc deposits were penetrated to a depth of 35.8μ by the x-rays. This is a thickness twice that corresponding to the passage of 36 coulombs in a standard deposition experiment. However, although complications arose occasionally, in general the reflection from the base through the deposit was weak compared with reflection from the deposit, and any misorientation between the two was immediately obvious.

Reproducibility.—It is probably true that all workers who have investigated the surface topography of electrodeposits have found difficulty in obtaining reproducibility. The experiments described did not prove exceptional, and it was regarded as essential to apply a criterion to test that solutions gave reproducible structures in the deposition of zinc. During work by Pick *et al.* (2) on copper a satisfactory criterion was developed which fulfilled the requirements of structure sensitivity and convenience. This was based on the sensitivity of the structures obtained on a copper (100) surface to solution impurity. The structure accepted as typical of a satisfactory solution is shown in Fig. 9; all the structures described by Pick and his co-workers were obtained from solutions tested to give this structure on a copper (100) substrate. It was decided to use a similar criterion for zinc; a zinc single crystal surface, with an (0001) orientation, was plated at 10 ma/cm^2 for 60 min in a solution of 0.5M zinc sulfate, 0.5M H_2SO_4 maintained at 25°C. Figure 1a shows the deposit structure considered typical from such a solution. From solutions of different acidity the structures were not identical and secondary standards were necessary. These are also illustrated in Fig. 1.

Results

As far as possible the results of this investigation are given pictorially and in comparison with the growth of copper deposits.

The first point of note is that, in general, zinc deposits give less variety of structure than do copper. Figure 2 shows the variations in crystal habit produced in plating zinc onto zinc cathodes of orientations shown in Fig. 3; these structures may be compared with those observed in copper deposition (4). The crystallographic indices of facets developing as determined by goniometry are given in Table I.

The second point is that, unlike in copper deposition, hydrogen is evolved and also zinc is an amphoteric metal. It may be thought that the effect of hydrogen evolution is trivial; however, the volume of gas evolved is sufficient to lead to a marked disturbance of the layers of electrolyte in the immediate vicinity of the cathode. Figure 4 gives some indication of the relative effects of acid concentration and current density. There are more inclusions at low acidity and low current density; under these conditions it is thought that the pH may rise locally allowing basic salts to form (9).

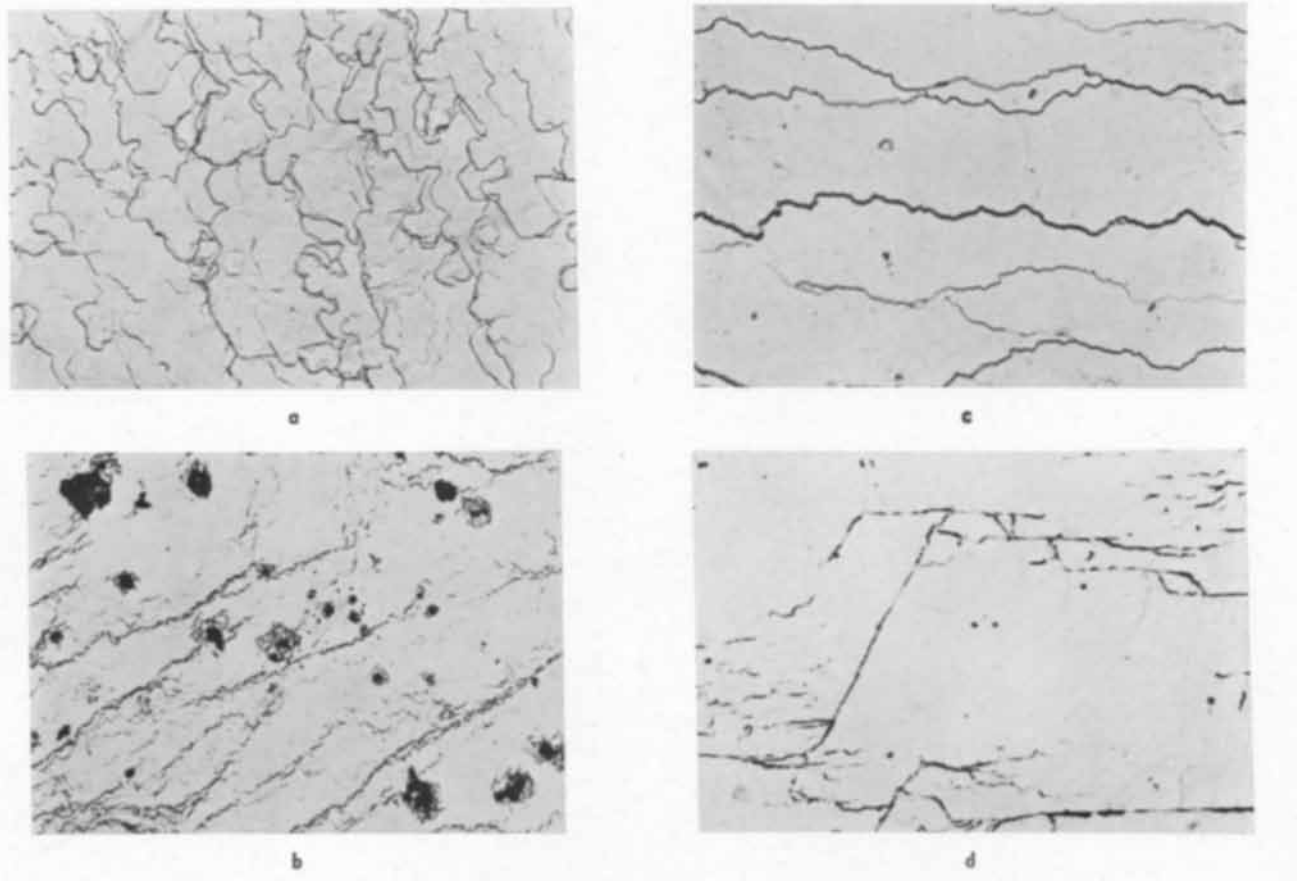

Fig. 1a. Reproducibility test, standard structure; deposit produced at 10 ma/cm^2 for 60 min at 25°C in 0.5M $ZnSO_4$, 0.5M H_2SO_4 electrolyte on a (0001) electropolished face; magnification 900X. Fig. 1b 270X; Fig. 1c 270X; Fig. 1d 86X. (Fig. 1b, c, d. Secondary standards; reproducible structures.) Fig. 1b 30 ma/cm^2, 20 min, 25°C, 0.5M $ZnSO_4$, 0.1M H_2SO_4 electrolyte; Fig. 1c 30 ma/cm^2, 20 min, 25°C, 0.5M $ZnSO_4$, 0.5M H_2SO_4 electrolyte; Fig. 1d 30 ma/cm^2, 20 min, 25°C, 0.5M $ZnSO_4$, 0.005M H_2SO_4 electrolyte. Deposits on (0001) faces.

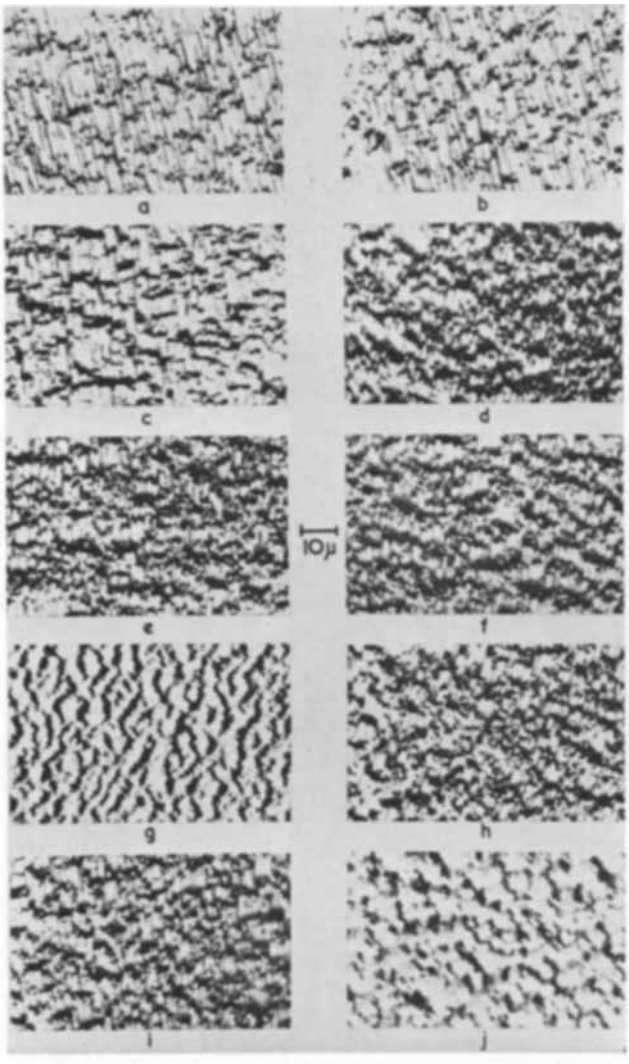

Fig. 2. Structure of deposits formed on single crystal substrates of orientation given in Fig. 3.

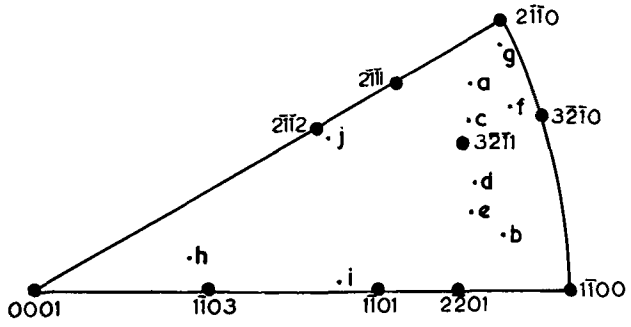

Fig. 3. Orientations produced in plating zinc on zinc cathodes

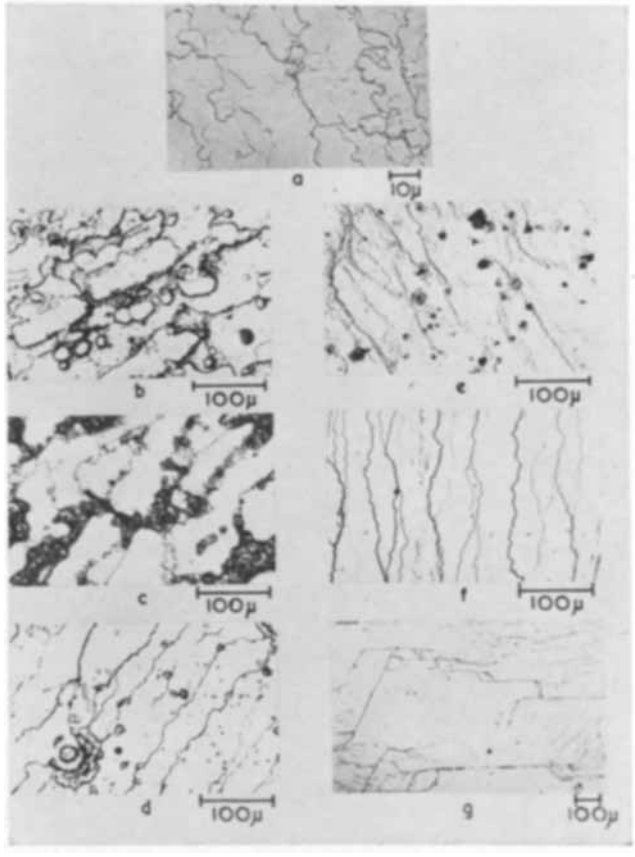

Fig. 4. Effect of acid concentration and current density on the structure of deposits formed on single crystal bases with an orientation within 4° of (0001). (a) 5 ma/cm² 0.5M H_2SO_4; (b) 5 ma/cm² 0.1M H_2SO_4; (c) 5 ma/cm² 0.05M H_2SO_4; (d) 5 ma/cm² 0.005M H_2SO_4; (e) 30 ma/cm² 0.1M H_2SO_4; (f) 30 ma/cm² 0.05M H_2SO_4; (g) 30 ma/cm² 0.005M H_2SO_4. Deposition was for 36 coulombs/cm² and the concentration of zinc sulfate was 0.5M in each case.

The third notable feature is that deposit structures developed with time in a way directly comparable with the growth of copper; see, for example, Fig. 5. Some analysis of the coarsening exhibited was possible.

The effect of temperature was complex; it is shown in Fig. 6, but no explanation for the variation in structure is offered at this stage.

Table I. Indices of reflecting facets from deposits on single crystal bases with orientations as shown in Fig. 3

Specimen	Indices of reflecting facets									
a	(0001) vs	{1$\bar{1}$01} s	{10$\bar{1}$1} m	{01$\bar{1}$1} w						
b	(0001) vs	{1$\bar{1}$01} s	{10$\bar{1}$1} w	{01$\bar{1}$1} vw	(2$\bar{1}\bar{1}$0) w			(1$\bar{2}$12) w	(2$\bar{1}\bar{1}$4) vw	
c	(0001) vs	{10$\bar{1}$1} s	{1$\bar{1}$01} s	{01$\bar{1}$1} w	(2$\bar{1}\bar{1}$4) vw					
d	(0001) vs	{1$\bar{1}$01} s	{10$\bar{1}$1} m	{01$\bar{1}$1} w						
e	(0001) vs	{1$\bar{1}$01} s	{10$\bar{1}$1} m	{01$\bar{1}$1} mw						
f	(0001) vs	{1$\bar{1}$01} s	{10$\bar{1}$1} s	{01$\bar{1}$1} vw	(2$\bar{1}\bar{1}$2) w			(3$\bar{2}$10) vw		
g	(0001) vs	{1$\bar{1}$01} s	{10$\bar{1}$1} s	{01$\bar{1}$1} vw	(2$\bar{1}\bar{1}$2) vw					
h	(0001) vs	{1$\bar{1}$01} s	{10$\bar{1}$1} m	{01$\bar{1}$1} vw						
i	(0001) vs	{1$\bar{1}$01} s	{10$\bar{1}$1} m	{01$\bar{1}$1} w						
j	(0001) vs	{1$\bar{1}$01} s	{10$\bar{1}$1} s	{01$\bar{1}$1} w	(2$\bar{1}\bar{1}$2) w	(2$\bar{1}\bar{1}$1) w		(2$\bar{1}\bar{1}$0) vw	(2$\bar{1}\bar{1}$4) vw	

vs, very strong; s, strong; m, medium; mw medium weak; w, weak; vw, very weak (just detectable).

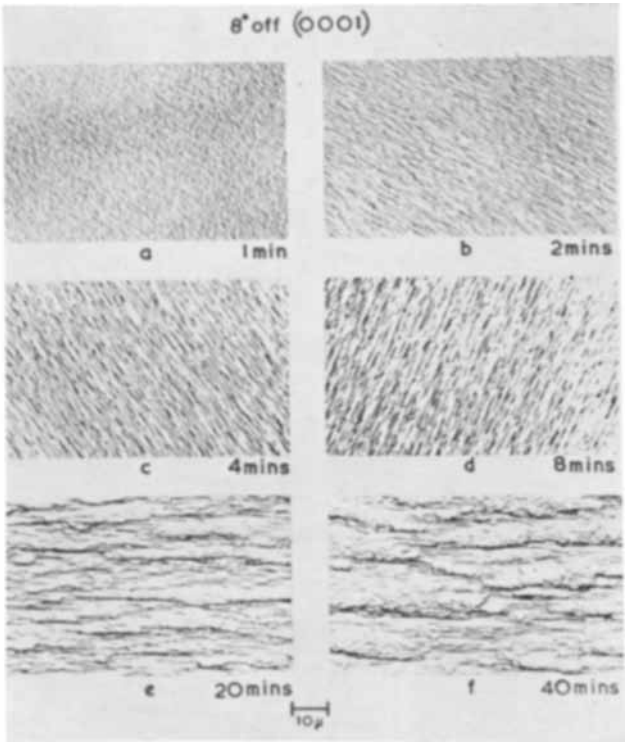

Fig. 5. Time series. The cathode was plated at 30 ma/cm² in an electrolyte of 0.1M H_2SO_4 and 0.5M $ZnSO_4$ at 25°C.

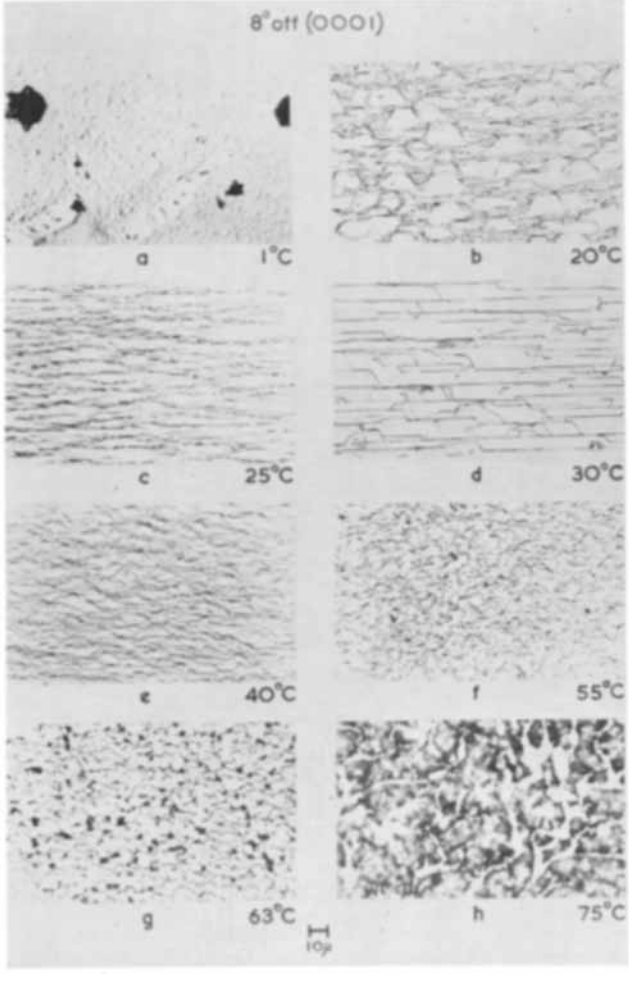

Fig. 6. Temperature series. These deposit structures were observed on a zinc single crystal cathode after deposition for 20 min at a current density of 30 ma/cm² in 0.5M $ZnSO_4$, 0.1M H_2SO_4 electrolyte.

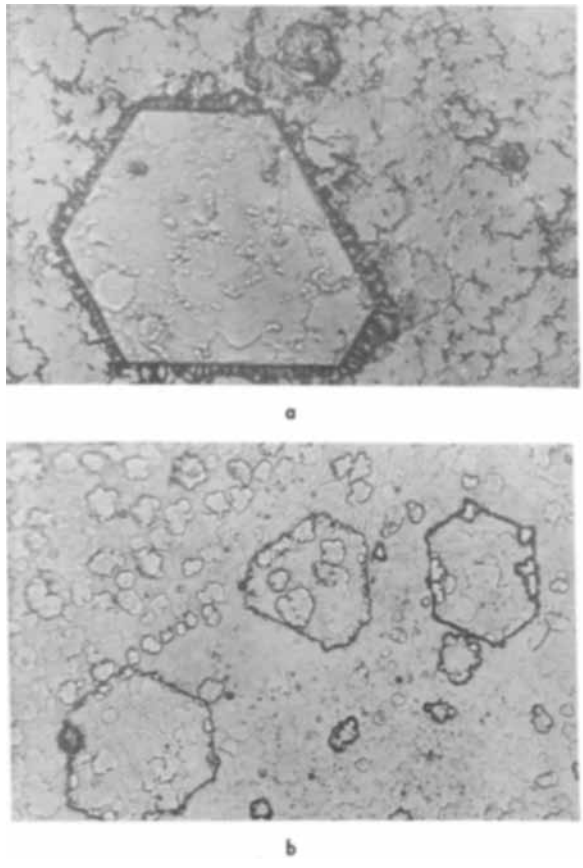

Fig. 7a and b. Epitaxial deposits on cleavage surfaces. Magnifications, a (top) 1200X, b (bottom) 900X.

Influence of the Substrate

The influence of the nominal orientation of the etched zinc single crystal cathode has been shown in Fig. 2. Deposits on unetched cleavage surfaces were very different from those shown in this figure. In general such deposits were not epitaxial and were

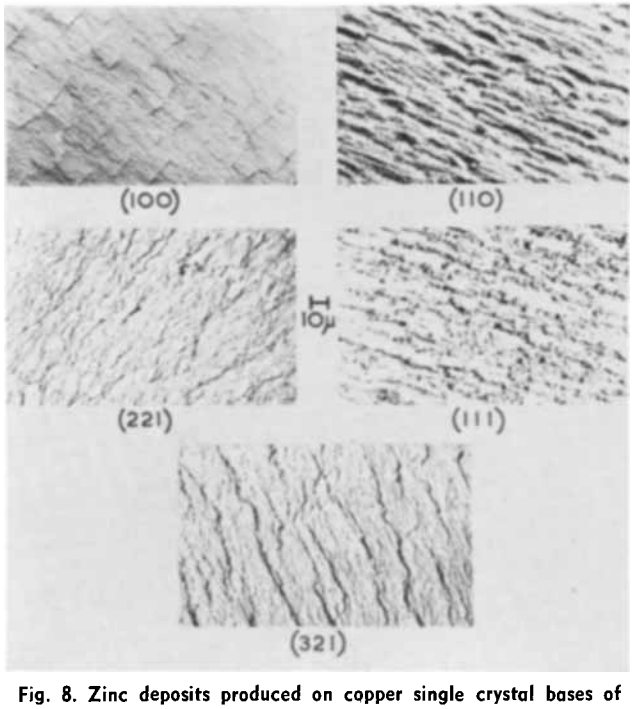

Fig. 8. Zinc deposits produced on copper single crystal bases of various orientations by plating at 10 ma/cm² for 60 min in a 0.5M $ZnSO_4$, 0.5M H_2SO_4 electrolyte at 25°C. Magnification 575X.

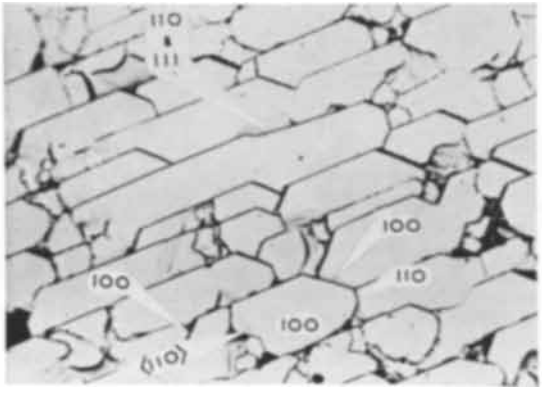

(100)

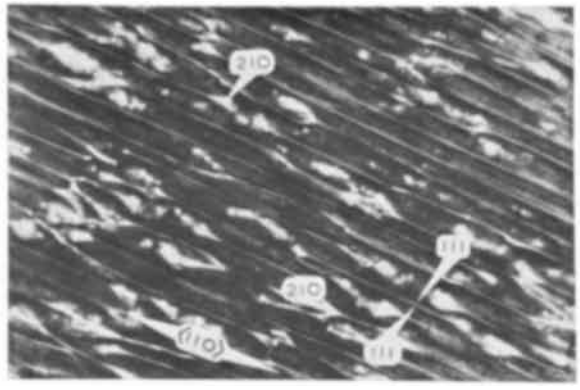

(110)

(331)
(Resembles 221)

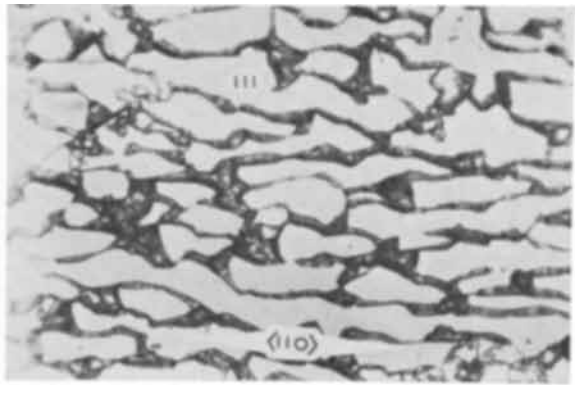

(111)

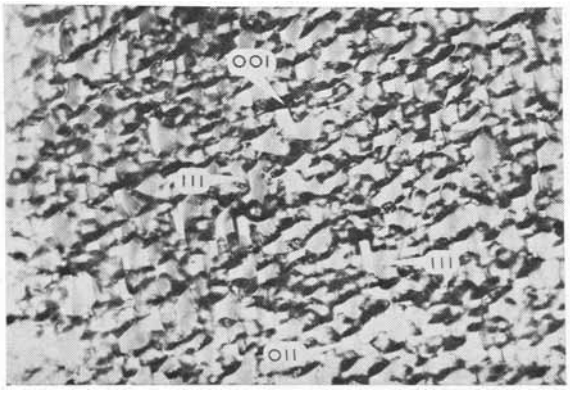

(321)

Fig. 9. Copper deposits produced on copper single crystal bases of the same orientation as in Fig. 8, by plating at 10 ma/cm² for 60 min in a 0.5M $CuSO_4$, 0.5M H_2SO_4 electrolyte at 25°C (2). Magnification 460X.

fine but nonuniform [cf. Cavallero and Bolognesi (10)]. Hexagonal growth features and spirals were sometimes visible. The deposits on etched cleavage surfaces were quite different from those obtained on electropolished surfaces near (0001); compare Fig. 7 and 4. Certain areas of the cleaved surfaces were heavily twinned; the deposit structure on the twin was typical of that on orientations away from (0001), but around the twin growth was typical of the cleavage plane. Cleavage steps only influenced the deposit locally.

More interest attaches to the deposition of zinc on prepared copper surfaces. The deposits coarsened with time, an effect that might be expected if conventional bunching occurs, but the deposits showed a marked difference from the development of copper on the same substrates; compare, *e.g.*, Fig. 8 and 9. In Table II the results of a goniometric examination are given.

Figure 10a shows the structure of a grain of a polycrystalline zinc cathode after the passage of 36 coulombs during electrodeposition. Figure 10b shows the same area after removing part of the electrodeposit by mechanical and electropolishing, and etching the surface so produced. Clearly the development of the crystal habit is continuous, and the distribution of etch pits indicates that the regions where neighboring growth features impinge are disordered and probably contaminated.

Finally, in Fig. 11 and 12, examples are shown of the growth of cadmium and lead polycrystals. The comparison of the structures observed with the habit of copper electrodeposits [*e.g.*, Fig. 9, also ref. (4)] is discussed below. No iron was deposited on iron or copper electrodes from electrolytes (i) and (ii) described above. Iron was deposited with very slight evolution of hydrogen from solutions containing hydrazine sulfate. X-ray diffraction photographs taken of the deposit on individual grains showed them to be polycrystalline. Iron deposits on copper single crystals were discontinuous. The growth of iron under our conditions clearly could not be compared with the growth of the other metals considered and will not be discussed further.

Discussion

Deposit Topography

At first sight, the considerable differences between the crystal habits of electrodeposited copper

Table II. Crystallographic relationships between the zinc deposit and the various copper bases

Base orientation (Copper)	Orientation of deposit w.r.t. base Zinc parallel to	Copper	
(111)	(0001)	(111)	plane
	$3 \times [\bar{1}\bar{1}20]$	[110]	directions
	$\{10\bar{1}\bar{1}\}$	{111}	zones
(100)	(0001)	(100)	plane
	$1 \times [\bar{1}\bar{1}20]$	[110]	directions
	$1 \times [\bar{1}100]$	$[\bar{1}10]$	
	$\{10\bar{1}\bar{1}\}$	{111}	zones
(110)	(0001)	(111)	plane
	$3 \times [\bar{1}\bar{1}20]$	[110]	direction
	$\{10\bar{1}\bar{1}\}$	{111}	zones
(117)	(0001)	(113)	plane
	$1 \times [\bar{1}\bar{1}20]$	[110]	direction
	{1011}	{111}	zones
(321)	(0001) $4\frac{1}{2}°$ off	(100)	plane
	$1 \times [11\bar{2}0]$	[110]	directions
	$1 \times [1\bar{1}00]$	$[1\bar{1}0]$	
	$\{10\bar{1}\bar{1}\}$	{111}	zones
(221)	(0001)	(111)	plane
	$3 \times [11\bar{2}0]$	[110]	direction
	$1 \times \{10\bar{1}\bar{1}\}$	{111}	zones

and zinc are disconcerting, but some understanding can be obtained from a consideration of the crystallography of the two metals. Pick, Storey, and Vaughan (2) have explained the structure forms on copper in terms of the arrangement of atoms in the substrate surfaces; the surface atoms of zinc substrates are arranged very differently due to the difference in crystal structures. The close-packed planes are normally present in the final form, to the exclusion of planes of higher indices, and so the number and symmetry of these has a direct bearing on the deposit topography. Copper, having a greater symmetry has many more close-packed planes than zinc and so one would expect to find different structures on zinc electrodeposits if growth occurs by a bunching mechanism. However, the arrangement of the surface atoms in the copper (111) and zinc (0001) planes are identical; correspondingly very similar deposit structures have been obtained by the deposition of (*a*) zinc onto a zinc (0001) plane; (*b*) zinc onto a copper (111) plane; (*c*) copper onto a copper (111) plane (Fig. 13).

The apparently complex structures observed on the various zinc substrates orientations shown in Fig. 2 can be interpreted in terms of one basic model. Ball models of facets of the zinc crystal show clearly that apart from the (0001) basal plane the faces of the $\{10\bar{1}\bar{1}\}$ zones are far more important than the remainder, and these faces do not vary very much in importance one from the other. For any base orientation away from the (0001) plane there are no planes suitably orientated, sufficiently close packed and isolated to predominate over the remainder. Thus a simple platelet, block, or ridge

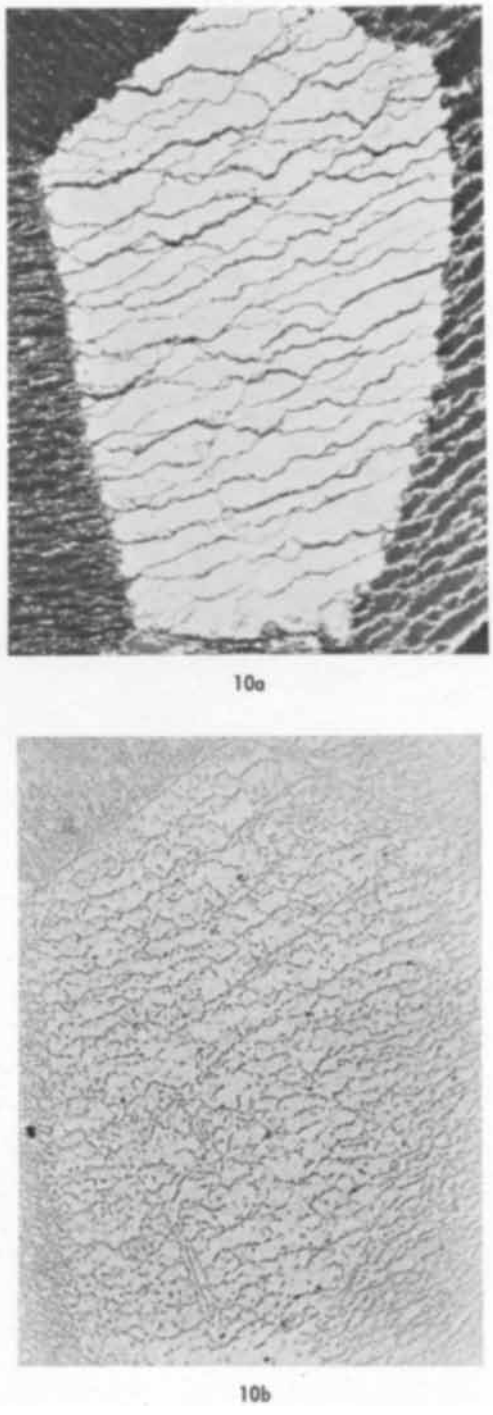

Fig. 10a (top). Deposit on a single grain of a zinc polycrystalline cathode after passing 36 coulombs/cm^2; Fig. 10b (bottom) Etched horizontal section through the same deposit. Magnification 320X.

structure is not formed. One has, instead, complete zones of faces developing. This is illustrated in Fig. 14b which is an idealized structure for an orientation near a $(1\bar{1}00)$ plane. As can be seen from the stereographic projection illustrating the facets developed on this orientation in practice (Fig. 14a) there is some complication of the idealized structure by a few minor facets which develop between two adjacent $\{10\bar{1}\bar{1}\}$ zones. Figure 14b shows only one step edge whereas a real surface will be covered by many such steps; the density and closeness of packing of these will be determined by the base orientation.

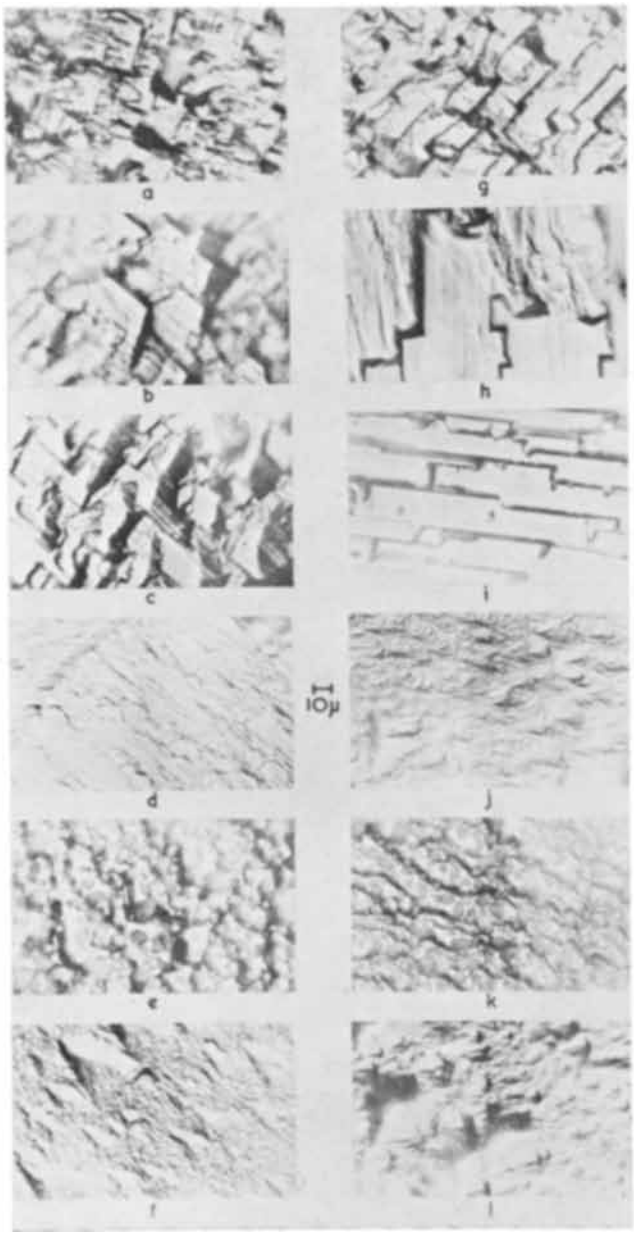

Fig. 11. Structure of cadmium deposits on cadmium polycrystals, produced by plating in 1.4*N* $CdSO_4$, *N* H_2SO_4 electrolyte at 25°C. (a) to (f) current density 10 ma/cm²; (g) to (l) current density 30 ma/cm².

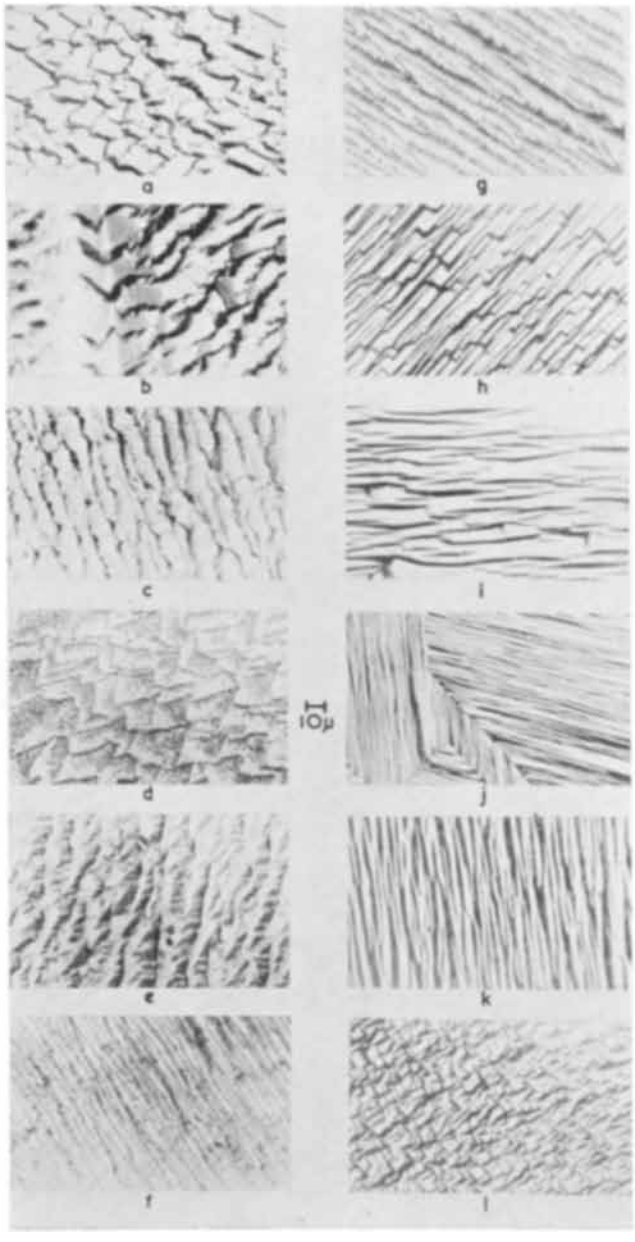

Fig. 12. Structure of lead deposits on lead polycrystals, produced by plating in 0.5M lead perchlorate, 0.5M perchloric acid electrolyte at 25°C; (a) to (f) current density 10 ma/cm²; (g) to (l) current density 20 ma/cm².

The structure on any substrate orientation is made up of "unit blocks" which can be obtained from the one in Fig. 14b by rotating that structure with respect to the plane of the paper until the desired substrate orientation is obtained. Thus for base orientations near a $\{1\bar{1}01\}$ zone there is one zone of $(1\bar{1}01)$ faces with their close-packed direction parallel to the surface and a second zone at approximately 60° to the surface. Hence the deposit structure consists of long lands of the former zone of planes terminated by facets of the second zone, *i.e.*, a pencil-like type of structure (Fig. 2 a, b, g).

As the substrate orientation approaches the (0001) plane the (0001) face becomes increasingly dominant, and at the same time the angles which the zones subtend at the surface decrease, the differences between these angles decrease, and so the zones became more equivalent to each other. Thus in the limiting case–the (0001) basal orientation–each of the three $\{10\bar{1}1\}$ zones are of equal importance and an hexagonal structure results (Fig. 1). Just off this orientation a platelet structure will be formed.

From Fig. 14c it can be seen that on base orientations on a $\{2\bar{1}\bar{1}1\}$ zone, two zones of $(10\bar{1}1)$ faces will develop to an equal extent, and on orientations between this and a $\{10\bar{1}1\}$ zone or the (0001) plane there will be a gradual transition in structure similar to that already described. It is worth noting that at a $(2\bar{1}\bar{1}2)$ orientation the (0001) $(10\bar{1}0)$ and $(1\bar{1}00)$ planes lie symmetrically in the surface. With the development of the two $\{10\bar{1}1\}$ zones and the basal plane a pyramidal structure results as is shown in Fig. 2j. Figure 15 shows the development of this type of structure.

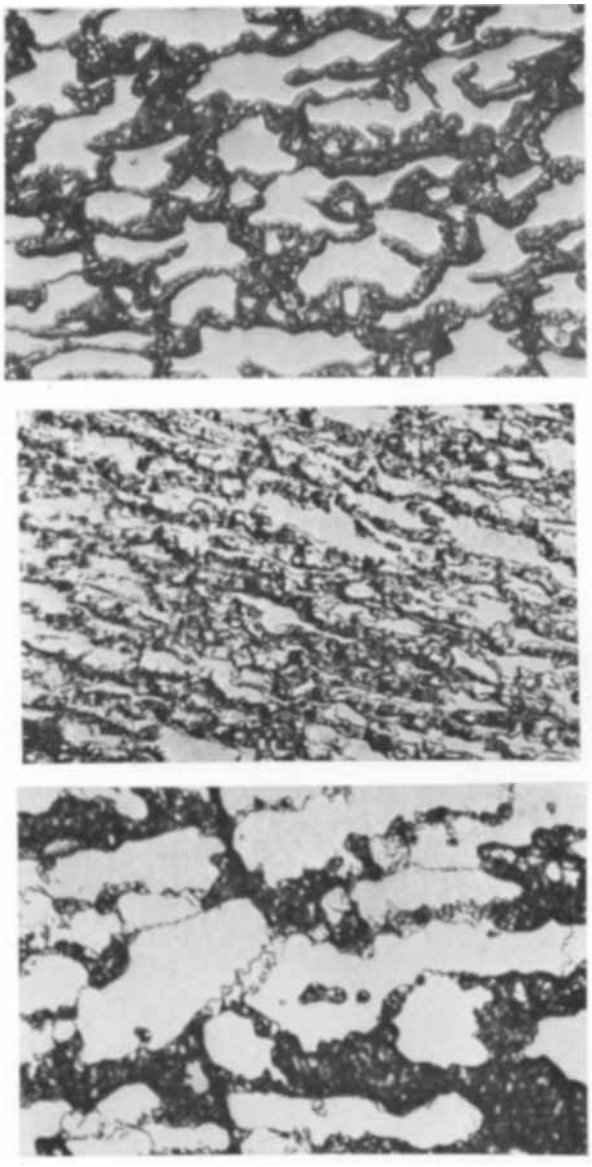

Fig. 13. Comparison between the structure obtained by Pick, Storey, and Vaughan (2) on a (111) face of a copper single crystal and structures obtained during the present investigation by plating zinc on a copper (111) face and zinc on a zinc (0001) face. (a) (top) Deposit structure on a copper single crystal orientation 3½° off (111) formed by plating at 10 ma/cm² in a 0.5M $CuSO_4$, 0.5M H_2SO_4 electrolyte (2); copper anode. Magnification 610X. (b) (center) Deposit structure on a copper single crystal orientation 3° off (111), formed by plating at 10 ma/cm² in a 0.5M $ZnSO_4$, 0.5M H_2SO_4 electrolyte; zinc anode. Magnification 610X. (c) (bottom) Deposit structure on a zinc single crystal, orientation 3½° off (0001) formed by plating at 5 ma/cm² in a 0.5M $ZnSO_4$, 0.5M H_2SO_4 electrolyte; zinc anode. Magnification 168X.

Deposits of Zinc on Copper Single Crystals

The final structure of the zinc deposits is influenced by the copper substrate in the very early stages of deposition. During this time the crystallographic orientation of the deposit will be fixed. Once the copper substrate is covered, the electrochemical conditions are those where zinc is plated on a zinc substrate; the deposits are influenced by variations in current density and electrolyte composition in exactly the same way as deposits on zinc cathodes, and for the same reasons.

The deposits obtained were epitaxial, usually with the basal plane parallel with the closest packed copper plane in the surface, and with the close-packed directions of the two lattices parallel.

The lattice parameters for the zinc and copper structures are widely different, as are the crystal symmetries. However, the spacings along the [11$\bar{2}$0] and [110] directions (*i.e.*, the close-packed directions) are 2.644Å and 2.556Å, respectively, a misfit of only 4.22%. The degree of misfit between the deposit and the base will depend on the orientations of one with respect to the other. The orientation of the deposit will be determined by the energies involved which will be minimized by having the close-packed directions parallel and the basal plane parallel to the low index plane, thereby minimizing the misfit. Due to the high symmetry of copper, this results in a platelet structure on all orientations (Fig. 8). The angle of the platelets to the surface is determined in the first instance by the angle of the nearest (111) or (100) plane to the surface. In the case of a (110) orientation (Fig. 8) this is at 35° to the surface giving platelets a ridgelike appearance. These ridges are not identical with those obtained in copper deposits on this orientation (Fig. 9). The basal plane is not always parallel to a low index plane because a smaller degree of misfit can sometimes be obtained by having the close-packed and densely packed zones parallel.

Deposits on Cleavage Surfaces

Zinc deposits on lightly etched zinc cleavage surfaces were markedly different from structures on lightly etched electropolished faces of the same nominal orientation. Electropolished surfaces are known to be undulating, providing an abundance of growth sites and steps for growth by bunching. Zinc cleavage surfaces are not perfect [see, *e.g.*, Bassett, Menter, and Pashley (11)]; they contain cleavage steps, twins, and a certain rumpling due to basal plane bending and kinking. In the vicinity of imperfections the deposit structures were similar to those on electropolished surface. It is presumed that, on the remainder of the surface, there are insufficient step sites for the number of atoms arriving and growth proceeds by way of epitaxial nucleation. This is indicated by the circular layers on the upper surfaces of the large hexagonal growth features (Fig. 7), remote from the edges. The structure of the deposit away from the hexagons was very similar to the substructures on the hexagon, which suggests that the whole of the deposit, except possibly the initially formed hexagons, grew by a nucleation process, bunching following during the growth process. On unetched cleavage surfaces deposit structures were anomalous, possible indicating that under the present conditions the freshly prepared surface rapidly became contaminated.

Development of Zinc Deposit Structures with Plating Time

The principles of the "bunching" process have been mentioned earlier, and the results shown in Fig. 5 support the hypothesis. Howes (16), in particular, has shown that the average step height of a copper deposit increases with time, and that steps

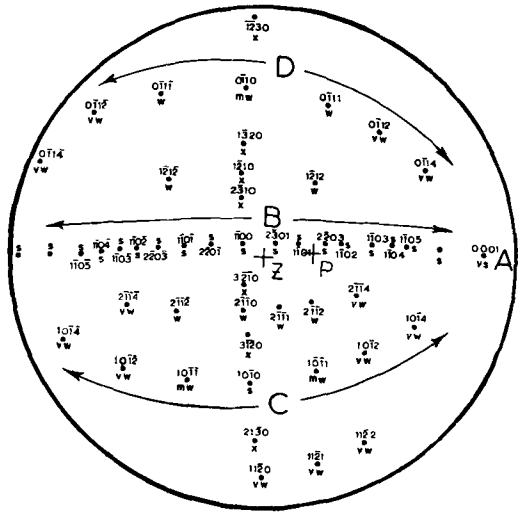

a

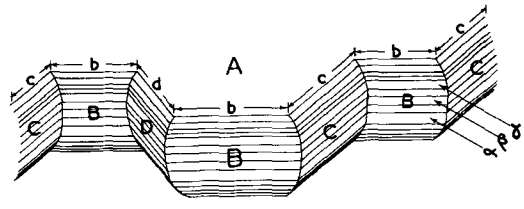

b

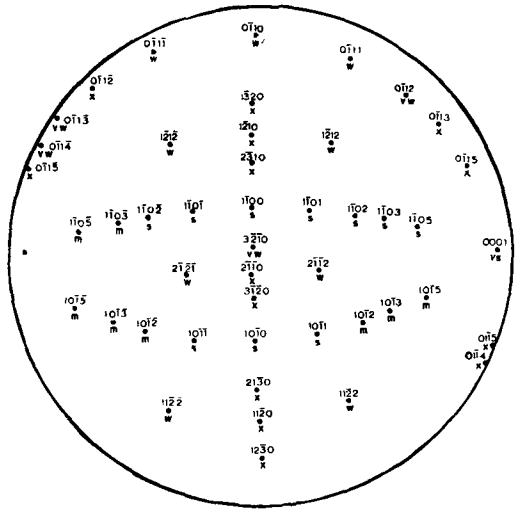

c

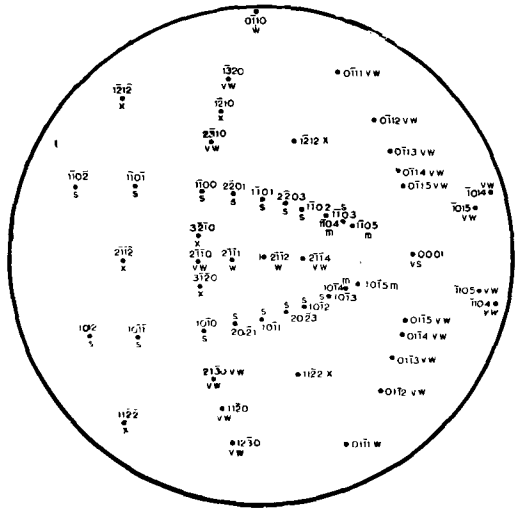

d

Fig. 14. Surface topography of zinc electrodeposits. (a) Stereographic projection of the facets developed (as indexed by optical goniometry) on a substrate of orientation Z, near $(1\bar{1}00)$ (actually orientation b, Fig. 3). The strength of reflection is indicated. Zones of planes B, C, D occurred, together with basal plane A. (b) Idealized structure corresponding to the reflections indicated in Fig. 14(a). The plane of the paper corresponds to the point P in the stereographic projection. The lettering corresponds to the zones. In reality, because the basal plane A lies at an angle to the plane of the paper in the idealized drawing, A intersects zones B, C, D so that re-entrant facets probably do not occur at the step edges. α, β, γ correspond to the $(1\bar{1}00)$ $(1\bar{1}01)$ and $(1\bar{1}02)$ faces, respectively. (c) Stereographic projection of facets developing on a substrate oriented on a $\{1\bar{1}21\}$ type zone, *i.e.*, at orientation f, Fig. 3. (d) Stereographic projection of facets developing on a substrate oriented at $(2\bar{1}12)$, *i.e.*, Fig. 3j.

of small height are gradually eliminated. During the present investigation, it was found that the number of platelets per square centimeter varied exponentially with plating time. The rate of bunching corresponded roughly to a first order process.

Deposits of Lead and Cadmium
Electrochemical Effects

It should be emphasized that this discussion has concerned the accommodation of flux of atoms in the growing crystal lattice. Of course the electrochemistry of deposition cannot be ignored; Frumkin (12) recently reviewed the effect of the structure of the electrolytic double layer on the kinetics of electrode processes. It is not possible to study these effects in a conventional electroplating experiment because of the overwhelming interference of transport effects. Even the extent to which the idea of "bunching" may be applied is limited by the electrochemistry of the deposition process. Figures 11 and 12 show cadmium and lead deposits. Clearly the structures observed in these exploratory experiments indicate a growth process that may resemble that of copper and zinc. The lead deposits show ridge and platelet structures similar, but not identical, to those on copper. Lead has the same crystal structure as copper but with a larger lattice spacing ($a = 4.9495$Å for lead, 3.6153Å for copper), and it would appear that the crystallographic influences of the base are similar. However, the deposit structures obtained on cadmium were dissimilar to those obtained on zinc, although crystallographically the two metals are very similar. They are both close-packed hexagonal with axial ratios greater than ideal, and their equilibrium crystal forms, as calculated by Stranski (13) are identical. Work is needed on large-grained or single crystalline cathodes to clarify the relation between substrate orientation and the growth forms, but it is likely that the exchange current for cadmium is much greater than that for zinc from sulfate solutions, hydrogen is not evolved, and the conditions for the adsorption of surface active material are widely different. It would be of interest to know whether the electrodeposition of cadmium occurs predominantly directly at growth sites, or if an appreciable surface diffusion of adatoms is involved [c.f., Conway and Brockris (14)].

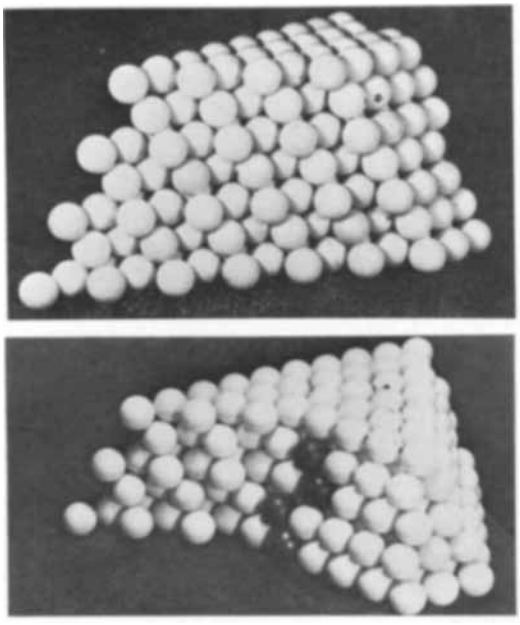

Fig. 15a. (top) Model of the (11$\bar{2}$1) plane in zinc; Fig. 15b. model showing the development of a (11$\bar{2}$1) face into a ($\bar{1}$101) face by bunching.

Conclusions

It is concluded from this examination of zinc electrodeposited on zinc and copper substrates that the concept of "bunching" may be applicable to a range of electroplating systems.

Limitations in the application of the bunching hypothesis result from the many chemical and physical processes involved in a single electrodeposition. Most of these factors are uncontrollable except under special laboratory conditions. The idea may only apply where deposition involves a surface concentration of adatoms rather than deposition directly onto active sites.

Acknowledgments

The authors wish to thank Messrs. Joseph Lucas Ltd., Birmingham, England, for their generous financial support, and Professor E. C. Rollason for providing laboratory facilities.

Manuscript received Aug. 4, 1961; revised manuscript received March 16, 1962. This paper was prepared for delivery before the Detroit Meeting, Oct. 1-5, 1961.

Any discussion of this paper will appear in a Discussion Section to be published in the June 1963 JOURNAL.

REFERENCES

1. G. G. Storey and S. C. Barnes, *Trans. Inst. of Metal Finishing*, **37**, 11 (1960).
2. H. J. Pick, G. G. Storey, and T. B. Vaughan, *Electrochim. Acta*, **2**, 165 (1960).
3. T. B. Vaughan and H. J. Pick, *ibid.*, **2**, 179 (1960).
4. S. C. Barnes, G. G. Storey, and H. J. Pick, *ibid.*, **2**, 195 (1960).
5. F. C. Frank, "Growth and Perfection of Crystals," John Wiley & Sons, Inc., New York (1958).
6. E. C. Williams and M. A. Barrett, *This Journal*, **103**, 363 (1956).
7. A. B. Greninger, *Trans. A.I.M.E.*, **117**, 61 (1935).
8. C. S. Barrett, "Structure of Metals," 2nd, ed., McGraw Hill Book Co., p. 185 (1952).
9. R. Sato, *This Journal*, **106**, 206 (1959).
10. L. Cavallaro and G. O. Bolgnesi, *Rev. Met.*, **52**, 706 (1955).
11. G. A. Bassett, J. W. Menter, and D. W. Pashley, *Discussions Faraday Soc.*, **28**, 1 (1959).
12. A. N. Frumkin, *This Journal*, **107**, 461 (1960).
13. I. N. Stranski, *Discussions Faraday Soc.*, **5**, 13 (1949).
14. B. E. Conway and J. O'M. Bockris, *Proc. Roy. Soc.*, **A248**, 394 (1958).
15. V. A. Roitar, V. Juza, and S. Poluyan, *Acta Physicochim.*, **10**, 389 (1939).
16. V. R. Howes, *Proc. Phys. Soc.*, **74**, 616 (1959).

Decay of Cathodoluminescence and Nonradiative Processes in Manganese Activated Phosphors

G. F. J. Garlick
Physics Department, The University, Hull, Yorkshire, United Kingdom

and M. Sayer
Physics Department, University of British Columbia, Vancouver, British Columbia, Canada

ABSTRACT

Cathodoluminescence emission spectra and decay processes have been investigated as a function of primary electron energy and density for single crystals, evaporated layers, and powder layers of manganese activated calcium fluoride and zinc silicate. The emission spectra were found to be unchanged by the conditions of excitation. The value of the decay constant for powder layers was also unchanged, but that for single crystals and evaporated layers increased as the primary energy was decreased. This behavior is explained in terms of an Auger recombination leading to an interaction between the luminescence centers and the high density of electrons in the conduction band at low primary voltages. It is shown that for such an effect to occur the rate of nonradiative recombination of electrons in the conduction band of the host lattice must be small. This criterion is satisfied in the case of single crystals and evaporated layers, but not in microcrystalline powder layers.

Cathodoluminescence represents the final stage of a series of processes beginning with the absorption of an electron beam in a crystal and ending with the emission of radiation. Information regarding the intermediate stages in the process can only be inferred from the characteristics of the final emission. In many phosphors, the nature of the final radiative transition is uncertain and deductions about the pre-

ceding stages may be ambiguous. The inclusion of manganese as an activator ion in several crystal lattices is known to give rise to an emission resulting from a spin-flip transition within the 3d shell of the manganese ion itself. Under ultraviolet excitation, such a phosphor is characterized by an exponential growth and decay of emission with a time constant independent of the intensity of excitation. Such a phosphor should be of use in experiments designed to investigate the intermediate stages in the cathodoluminescence process.

Many investigations of cathodoluminescence emission spectra and growth and decay time constants have been reported in the literature. Almost without exception, the measurements have been made on phosphors in the form of microcrystalline powders. It is possible that the properties of a phosphor in this form differ from that of the same material in the form of a single crystal. In the present work, the cathodoluminescence of zinc silicate and calcium fluoride with controlled concentrations of manganese has been investigated with special reference to the effect of primary electron energy and density on the emission spectra and decay constant. The phosphors were studied in three different forms, single crystals, evaporated layers, and microcrystalline power layers.

Experimental

Single crystal specimens of calcium fluoride approximately 1 mm in thickness were obtained from large single crystals containing different amounts of manganese. These crystals were grown from the melt by the Stockbarger technique (1) at the Department of Natural Philosophy of the University of Aberdeen. The plates were either cleaved directly from the bulk or cut with a wire saw and polished, using diamond paste. The results reported in this paper were obtained for specimens cut from a crystal containing 0.9% manganese. Powder layers were formed by grinding the single crystal and settling the powder from an aqueous suspension. Evaporated layers were produced by vacuum evaporation of a calcium fluoride-2% manganese fluoride powder mixture with subsequent heat treatment of the evaporated layer (2). Evaporated and powder layers of zinc silicate were prepared in a similar manner with an activator concentration of between 1 and 2% manganese. No large single crystals of zinc silicate were available, but measurements were made on a sintered layer formed by fusing the powder at a temperature close to the melting point. After cooling, the face of the sintered layer was ground smooth with carborundum and polished using diamond paste.

The phosphors were examined in a demountable cathode-ray tube for primary electron potentials of 1-15 kv, and for a steady and uniform excitation of 1-10 $\mu a/cm^2$ over a selected phosphor area. Emission spectra were measured by means of a double monochromator and photomultiplier system, while decay measurements were obtained by measuring the fall of emission after cut-off of steady excitation using a photomultiplier and cathode-ray oscilloscope. The specimen temperature could be varied from room temperature up to a few hundred degrees centigrade. With the system used secondary electron emission characteristics could not be measured, and in order to reduce spurious effects from this source most specimens were aluminized by vacuum evaporation, the coating being connected to the final anode of the cathode-ray tube. Several measurements using unaluminized specimens were also performed to check that the results obtained were independent of the aluminum coating.

Results

Emission spectra.—No significant change in the emission band due to manganese was found as the electron potential or beam current density were varied over a wide range. Small shifts in the spectrum to longer wavelengths were found as the manganese concentration was increased in the case of calcium fluoride. The shift occurred for concentrations at which spin-spin interaction was beginning to be evident in electron resonance spectra of the same specimens. From these results it is evident that the high concentration of electrons at low primary energies has little effect in any direct way on the 3d shell energy levels.

Decay of the emission.—In contrast to spectral measurements, the measurements of decay constant showed variations with form of specimen and with primary electron energy. The results for calcium fluoride and zinc silicate are shown in Fig. 1 and 2, respectively. In all cases powder layers showed

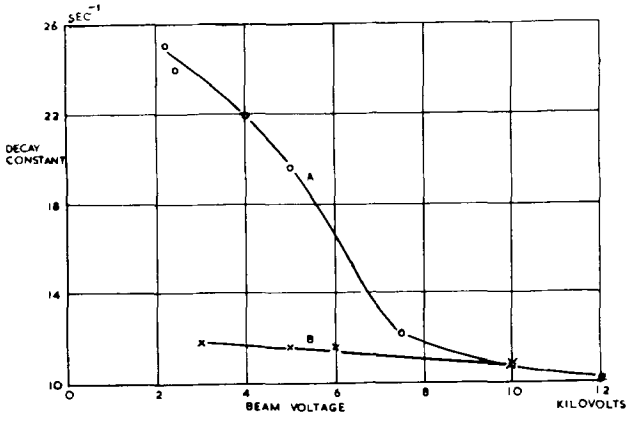

Fig. 1. Decay constant vs. primary electron energy for manganese activated calcium fluoride: (A) single crystal; (B) powder layer.

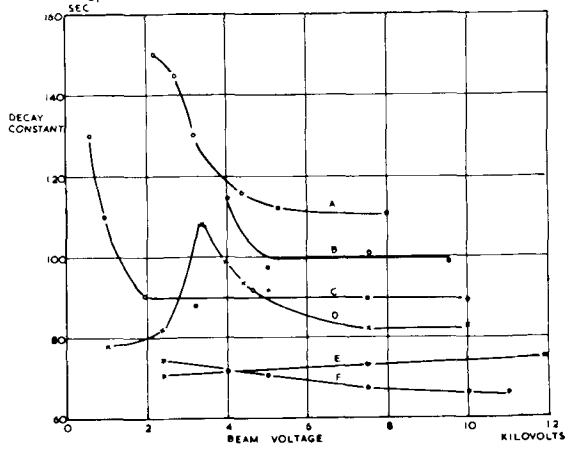

Fig. 2. Decay constant vs. primary energy for manganese activated zinc silicate: (A), (B), (C), evaporated layer; (D), sintered layer; (E), (F), powder layer.

little change in decay constant with electron energy, the value being identical with that measured using ultraviolet excitation, and characteristic of the Mn^{2+} center in the particular host lattice. This is in agreement with the results of other workers (3). The behavior of single crystals and evaporated layers was more complex. For single crystals, the decay constant was high at low primary energies and decreased as the electron energy was increased until the value approached that for powder layers. The variation with primary electron energy was relatively independent of whether the crystal surface facing the electron beam was polished, freshly cleaved, or coated with aluminum. This result is shown more effectively by the logarithmic plot of the change in decay constant $\delta - \delta_\infty$, where δ_∞ is the decay constant at large primary energies, *vs.* primary energy shown in Fig. 3 and 4 for calcium fluoride and zinc silicate, respectively. Except at low primary energy, these plots are linear with approximately the same slope. This suggests that the decay constant may be represented by a relation

$$\delta - \delta_\infty = CV^{-p} \qquad [1]$$

where C and p are constants. The average value of p obtained from the graphs is 3.0 ± 1.0 for calcium fluoride and 3.6 ± 0.2 for zinc silicate. The existence of an aluminum coating on the surface was not critical, the principal effect being an over-all shift of the curve to higher voltages. Further changes along the voltage axis could be tentatively attributed to the method of surface preparation, *e.g.*, the curve for a cleaved crystal appeared at a lower voltage than that for the polished specimen. A similar dependence on electron energy was observed for evaporated layers, although the over-all decay constants were usually higher than those for either powders or single crystals. This over-all increase was attributed to an increase in the transition probabilities of the luminescence centers due to perturbations introduced by the imperfect host lattice. In a few cases, the most notable being the sintered zinc silicate layer, the decay constant showed a maximum at an intermediate primary energy. This behavior is a guide to the interpretation of the results and will be discussed later.

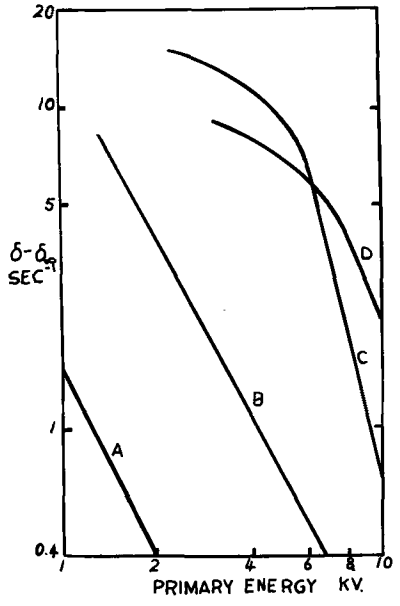

Fig. 3. Change in decay constant $\delta - \delta_\infty$ *vs.* primary energy for single crystal specimens of calcium fluoride: (A) cleaved unaluminized; (B) cleaved, aluminized; (C), (D) polished, aluminized.

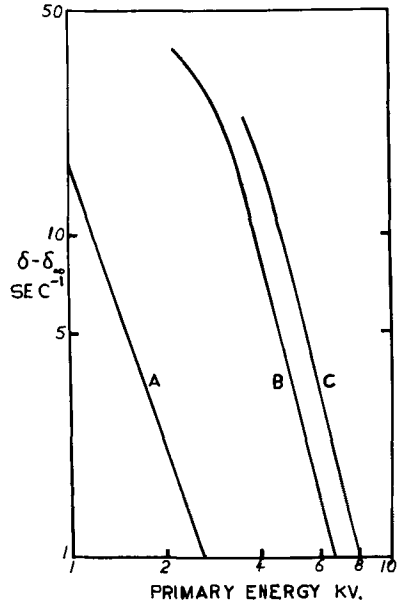

Fig. 4. Change in decay constant $\delta - \delta_\infty$ *vs.* primary energy for zinc silicate: (A) *evaporated layer unaluminized;* (B) *evaporated layer,* aluminized; (C) sintered layer, aluminized.

Variation of the beam current density produced a change in the decay constant at low primary energy, but was less effective at higher primary energies. This behavior in a crystal of calcium fluoride is shown in Fig. 5.

Effect of phosphor temperature.—The change in decay constant with temperature was relatively independent of the primary beam energy and density and agrees with that for photoexcitation. This is shown in Fig. 6 for a single crystal of calcium fluoride. The effect of nonradiative transitions within the emission centers was only noticeable at temperatures between 100° and 200°. The absolute luminescence efficiency at ordinary temperatures was only a few per cent.

Discussion of Results

The important effect shown in the above experiments is the change of decay constant with primary energy for single crystals and evaporated layers,

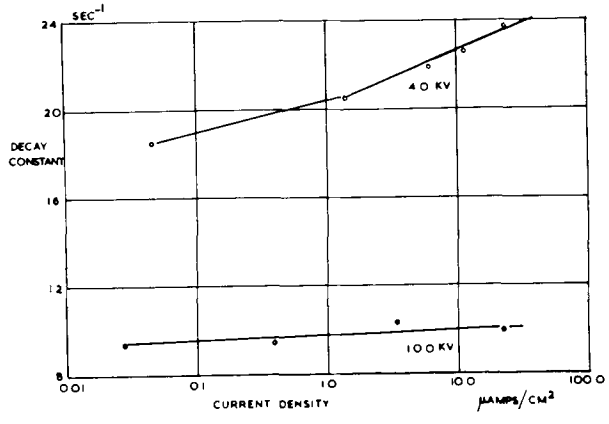

Fig. 5. Decay constant *vs.* beam current density for a single crystal of calcium fluoride: Mn: (A) 4 kv; (B) 10 kv.

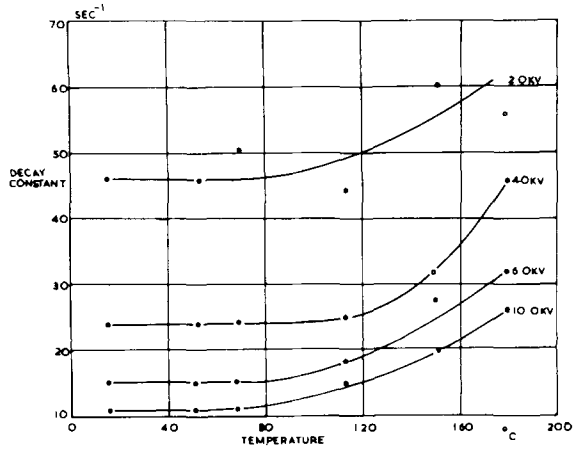

Fig. 6. Decay constant vs. temperature at different primary energies for a single crystal of calcium fluoride: Mn.

which is in contrast with the negligible effect for powder layers. The energy of the primary electrons is a measure of the penetration of the beam into the crystal, the most generally accepted relation being of the form $R = AV^n$, where R is the penetration depth, V is the primary voltage, and A and n are constants characteristic of the material (4, 5). The most obvious interpretation of the results is that the change in decay constant is due to either (*a*) a 'dead' surface layer or (*b*) thermal effects arising from the increased density of power dissipation at low primary voltages. If (*a*) is the case, the effect should be enhanced in powder layers in which the surface area is greatest. This disagrees with experiment. If macroscopic thermal effects are involved, a crystal temperature of the order of 200°C would be required to give the observed decay constants at low beam voltages. Calculations involving the thermal conductivity of the crystals indicate that under the given experimental conditions the crystal temperature rises by a maximum of 1°-2°C. A third possibility is in the increase of electron density within the crystal at low primary energies, due to the power-law dependence of the penetration depth on the primary energy. This may be considered in conjunction with the model for the cathodoluminescence process shown in Fig. 7.

Electron transitions may occur either in the lattice or in the luminescence centers. Due to the small number of activator ions, the bulk of the excitation is assumed to take place in the lattice, with subsequent transfer of energy to the luminescence centers. The emission spectrum is unchanged for optical and electron excitation; hence it may be assumed that the emission arises from a self-contained, monomolecular transition within a luminescence center with radiative and nonradiative transition probabilities δ and ϕ, respectively. The lattice excitation arises from the production of secondary electrons in the conduction band and positive holes in the valence band. As an approximation, if recombination is neglected, it may be assumed that the primary beam excites

$$n_1 = \mathrm{I} = [i_0 V/\Delta E \cdot AV^n] \qquad [2]$$

secondary electrons, where ΔE is the energy required to produce a hole-electron pair, and i_0 is the beam current density. Under these conditions, bimolecular recombination kinetics are to be expected in the lattice with a nonradiative recombination probability β (this includes both band-to-band and impurity transitions) and a probability for energy transfer to a luminescence center γN, where N is the total number of centers. The detailed kinetics of such a model have been treated elsewhere (6). It is found that the maximum value of decay constant is determined by the sum of the transition probabilities for the center $(\delta + \phi)$ sec^{-1}. This would be the value obtained in a measurement using ultraviolet radiation for direct excitation of the center. If the excitation takes place via the lattice a value of $(\delta + \phi)$ sec^{-1} is obtained if recombination processes in the lattice are completed in a time short compared to the lifetime of the radiative decay. Any process which increases the rate of lattice recombination is therefore ineffective to explain decay constants greater than $(\delta + \phi)$ sec^{-1}. A marked change can occur if the lifetime of a free lattice electron is comparable with that of an excited center, but this is again ineffective since the analysis shows that the decay constant is decreased under these circumstances. This is also the case if the effect of saturation of luminescence centers is included. Thus an increase in decay constant cannot be attributed to a change in any lattice process, but can only be a property of the luminescence center itself.

If any form of interaction between the electron density in the conduction band and the luminescence centers is to be reflected in the magnitude of the decay constant, two criteria must be satisfied: (*a*) the electron density must be large, (*b*) the lifetime of electrons in the conduction band must be comparable with that of the luminescence centers. Both criteria are principally determined by the parameter β, since it can be shown that (6)

$$n_1 = I/(\beta + \gamma N)^{1/2} \qquad [3]$$

and the lattice time constant

$$b = (I/(\beta + \gamma N)^{1/2} \qquad [4]$$

In a region of heavy recombination, *e.g.*, the surface regions of a crystal, β is large, and therefore n_1 is small and also decays in a time short compared to the lifetime of an excited center. Thus interaction between the electron density and the centers occurs for a very small fraction of a center lifetime. In the relatively perfect lattice of a crystal, recombination will be reduced, β is small, n_1 is large and remains

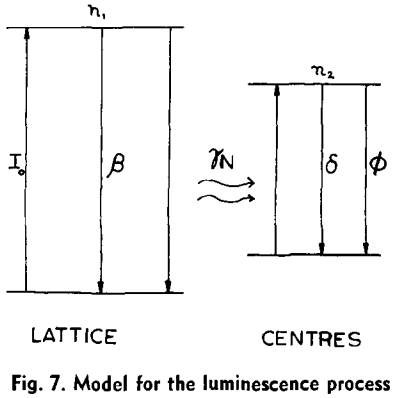

Fig. 7. Model for the luminescence process

appreciable throughout a large portion of the center lifetime. In this case a perturbation of the centers may be observed. Note that the effect of the surface will be enhanced in microcrystalline powders in that the average penetration depth is less than that for a single crystal due to the random orientation of the individual crystallites to the primary beam. A maximum in the value of decay constant is to be expected if the disordered surface region extends for a considerable depth into the crystal.

This behavior is observed in the sintered layer of zinc silicate (Fig. 2, curve D) and may also explain the nonlinearity at lower voltages of curves C and D of Fig. 3 for the polished specimens of calcium fluoride. The presence of such a region would also give rise to a shift of the curves along the voltage axis in the direction of higher voltages. Further comment may be made for the case of the evaporated layers. It has been shown that increased lattice recombination cannot increase the luminescence decay constant beyond that defined by the center transition probabilities $(\delta + \phi)$ sec^{-1}. Thus the over-all increase in decay constant in the evaporated layers must be due to an increase in the center probability $(\delta + \phi)$ sec^{-1} caused by perturbations in the imperfect crystal field surrounding the activator atoms. However, interaction with the excited lattice electron density can still occur as in the single crystal since the localized electron density is still predominantly determined by lattice recombination processes independent of the centers.

The specific nature of the interaction between the secondary electron density n_1 and the luminescence centers requires interpretation. A purely electrostatic interaction between the electron-hole plasma in the lattice and the luminescence centers is difficult to formulate. However, it has been well established in semiconductors such as germanium and silicon that at large majority carrier densities a recombination process proportional to the square of the carrier density is observed (7, 8). This is termed Auger recombination and involves three carriers—an electron and hole which recombine, transferring energy to a third electron. It is suggested that this process is observed in the present experiments. Two forms of interaction may be possible: (*a*) Auger recombination between a free hole, a free electron, and an excited luminescence center; the energy transferred to the center could raise its effective temperature for a short time with a resulting increase in nonradiative transition probability; (*b*) Auger recombination involving two free electrons and a bound hole in the vicinity of an excited center, the energy imparted to the second electron being dissipated by phonon generation in the vicinity of the center. This again results in an increase of nonradiative transition probability. Both processes may be termed a form of microscopic thermal quenching.

A quantitative estimate of the decay constant-beam voltage may be made on this basis since

$$\delta = (\delta + \phi)_\infty + Bn_1^2 \qquad [5]$$

where B is a constant.

If the approximation is made that n_1 is constant for a time comparable to the center lifetime, substituting for n_1 from [2]

$$\delta - (\delta + \phi)_\infty = B\left\{\frac{1}{\Delta E}\frac{i_o V}{AV^n}\right\}^2 = D\left\{\frac{i_o}{V^{n-1}}\right\}^2 \qquad [6]$$

Using the reported values of n (4), the decay constant should show a power law dependence on V with exponents 3.8 and 4.0 for calcium fluoride and zinc silicate, respectively. Considering the many approximations involved in the calculations, these values are compatible with the experimental values of 3.0 ± 1.0 and 3.6 ± 0.2, respectively. Note that the relation also indicates that the variation of decay constant with current density is greater at low rather than high primary voltages. This is also in agreement with experiment.

Conclusion

It has been shown that a rise in decay constant at low primary electron energies may occur in phosphors in which the rate of lattice recombination is relatively small. The suggestion that the rise is due to an interaction between the conduction electrons and the excited luminescence centers by means of Auger recombination in the lattice is borne out by the quantitative agreement between experiment and theory.

Acknowledgments

This work was submitted as part of a Ph.D. thesis to the University of Hull. One of the authors (M. S.) wishes to thank the University of Hull and the Department of Scientific and Industrial Research for Research Studentships.

Manuscript received Jan. 15, 1962. This paper was prepared for delivery before the Indianapolis Meeting, April 30-May 3, 1961.

Any discussion of this paper will appear in a Discussion Section to be published in the June 1963 JOURNAL.

REFERENCES

1. D. C. Stockbarger, *J. Opt. Soc. Amer.*, **39**, 731 (1949).
2. C. Feldman and M. O'Hara, *ibid.*, **48**, 816 (1958).
3. J. W. Strange and S. T. Henderson, *Proc. Phys. Soc.*, **58**, 368 (1946).
4. C. Feldman, *Phys. Rev.*, **117**, 455 (1960).
5. A. F. Makov, *Sov. Phys. Solid State*, **2**, 1934 (1961).
6. M. Sayer, *Proc. Phys. Soc.*, **B78**, 1017 (1961).
7. A. P. der Carvalho, *Compt Rend.*, **241**, 461 (1957).
8. J. R. Haynes and J. A. Hornbeck, *Phys. Rev.*, **100**, 606 (1955).

Transient Effects in Cadmium Sulfide-Cadmium Selenide Type Photoconductors

Ronald D. Weiss[1]

Clairex Corporation, New York, New York

ABSTRACT

Cadmium sulfide and cadmium selenide sintered polycrystalline layers have been investigated with respect to the transient effects in their photoconductive rise and decay curves. Under suitable conditions both types of layers exhibit a maximum in the rise curve and a minimum in the decay curve. The specific results are strongly dependent on the excitation history of the layer. The relationship of these effects to trapping processes is discussed, and some comparisons with earlier experimental works are made. The dependence of photosensitivity on these effects is emphasized.

A transient effect was previously found to be associated with single crystal photoconductors of both CdS (1) and CdSe (2). The experiments of Bube and others have shown that, because of their excitation history, the photoconductive response curves of CdS and CdSe single crystal photoconductors exhibit both a maximum in the rise curve and a minimum in the decay curve. The present paper will show that the effect is more strongly evidenced with CdS and CdSe polycrystalline sintered layers at room temperature.

Figure 1, curve a, is representative of most room temperature photoconductive response curves reported by others. In the same figure, curve b represents the general shape of the photoconductive response curve, which was obtained for these sintered layers under similar conditions. It is interesting to note that at the onset of the excitation the latter curve goes through a maximum before approaching its long time equilibrium or steady-state photocurrent value. The area between the long time equilibrium value and the maximum of curve b is the principal subject of this work, *i.e.*, the additional amount of photocurrent above the long time equilibrium value [overshoot (2)]. A result similar to the forementioned may be obtained by replacing the initial dark or quenching[2] history, required prior to the onset of the excitation, by a relatively high light intensity or excitation history. In this instance the photoconductive response curve must be taken from the high light intensity to the lower light intensity (the level at which the long time equilibrium value had been previously established). This second curve will be of the same shape as curve b, except for its inverted nature, *i.e.*, the photocurrent will now pass through a minimum below the long time equilibrium value before approaching this value [undershoot (2)].

[1] Present address: Applied Research Laboratory, General Instrument Corporation, Newark, New Jersey.

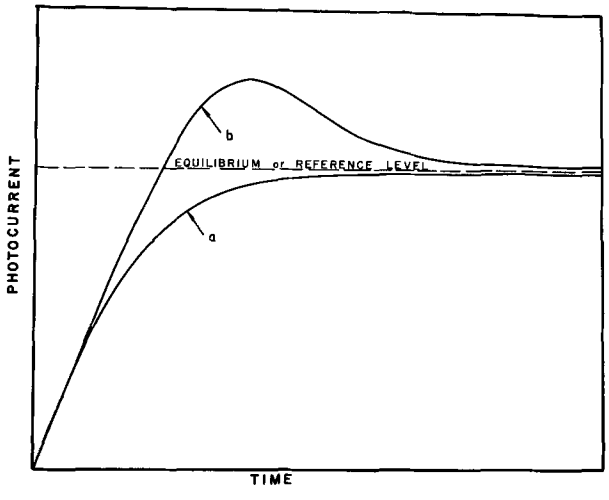

Fig. 1. Comparison of the general nature of the photoconductivity curves (until the equilibrium condition is established) of the works being discussed.

Experimental Apparatus and Procedure

Since the transient effect evidences itself in the growth of the photoconductivity a special procedure was devised to measure the true effect. The experimental procedure consists of three basic operations. The first operation is to determine the long time equilibrium value of the sintered polycrystalline layer at the reference light level of the experiment. This long time equilibrium value is defined by the steady-state photocurrent of the layer after it has been subjected to the reference light level for a considerable length of time. The time required for the steady-state photocurrent condition is primarily dependent on several factors, *i.e.*, the type of photoconductor, the intensity of the light, and the previous history of the layer. To ensure attainment of the steady-state photocurrent in all the layers of a particular group, the group was subjected to the necessary conditions for a period not less than ten days. This time had proved more than sufficient for all the layers in question. The second operation is to expose the layer to either an intense light, semidark, or dark environment for fixed amounts of time. This second operation will determine the type of transient obtained in the photoconductive response curve. The intense light environment will produce a minimum (with respect to the equilibrium value), whereas

[2] The term "quenching" is generally associated with the emptying of filled traps. In most photoconductors this quenched condition is obtained by either storage in a dark environment, heating of the photoconductor, or excitation with infrared. The net result of these methods is a de-excited photoconductor, a condition which can be reproduced.

the dark or semidark environment will produce a maximum. The third and final operation involves the measurement of these layers, at fixed intervals, at the reference light level established in the first operation.

The measuring circuit used was a series circuit consisting of a 1.34v Mallory Mercury battery (RM 42R), a Hewlett Packard ammeter (Model 412a), and the photocell. Provisions for taking these measurements requires an accurate light source which is stable and reproducible over long periods of time. This requirement is necessary in order to determine accurately photocurrent variations from the equilibrium value. It is for these reasons that the photometer used has been operated by means of the circuitry recommended by the National Bureau of Standards (3). The photometer bulbs used are of the GE No. 1763 series. They have been aged or seasoned prior to this application to avoid drift during the long periods of their use. The GE No. 1763 bulb is a secondary standard (operating color temperature 2870°K) which is checked periodically against a set of primary standards (4). In this manner, all available light levels have been maintained to within 1 or 2% over indefinite periods of time. In very low light level applications a series of Bausch and Lomb neutral density filters, which were found to be linear in the visible spectrum, were used. It should also be noted that the photoconductive layers were in the form of hermetically enclosed units. The hermetic enclosure gives some assurance that the measurements will not be affected by daily changes in atmospheric conditions. Since the results of one photoconductive layer could be misleading, measurements have been made with several layers of the same type. The statistical averages of these groups were used for all the data contained herein.

Experimental Results

Transient Maxima

Most of the data presented at this time deal specifically with transient maxima (overshoot) rather than minima (undershoot). The present data on transient maxima seem to indicate that at very high light levels there exists a saturation point at which no maximum or overshoot will be observed; however, to date this saturation point has not been determined accurately. It is quite reasonable to assume that this saturation point is related to a situation where the saturation of photocurrent (5), by means of light intensity, can occur.

Both transient maxima and minima have been shown to be functions of several factors aside from temperature (1, 2).[3] Recent experimentation has confirmed that these transients are strongly dependent on reference levels, time of exposure to the excitation, and type of photoconductive material used. This section will attempt to discuss these factors in greater detail. At this time a short explanation of the notation used throughout the paper will be helpful. The changes due to the transient effect have been designated as $\Delta I/I_o$, where ΔI is the change in photocurrent from the equilibrium value (I_o). I_m is the current value associated with the maximum height of the transient obtainable for a given set of conditions. In most curves presented 100 $\Delta I/I_o$ ($\Delta I/I_o\%$) is plotted as a function of time or time intervals. The ΔI is the maximum change in photocurrent, observed at the onset of the excitation, above the equilibrium value (I_o).

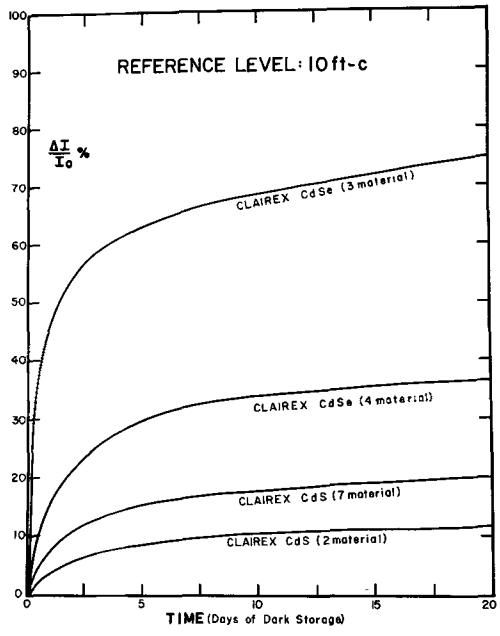

Fig. 2. Transient maxima or overshoot of several CdS and CdSe photoconductive layers obtained for a reference level of 10 ft-c.

Maxima or overshoot experiments, as described above, were performed on several polycrystalline cadmium sulfide and cadmium selenide photoconductive layers. The results of these experiments are shown for a particular reference level, in Fig. 2, for layers coming from a dark history. It can be seen from this set of curves that under the same conditions the cadmium selenide materials exhibit greater transient maxima than do the sulfides. This characteristic of cadmium selenide has been found to be true at all the reference levels thus far tested. It should also be noted that the maxima curves are all of an exponential nature, indicating that there is an upper limit for maxima ($\Delta I/I_o$), at each reference level, for a particular material. Figure 3 is a comparison of transient maxima of several commercially available photoconductors (all of the polycrystalline sintered layer type). These curves were taken at a reference level of 2 ft-c. Although the RCA prepared photoconductive layers show more of a transient maxima effect than the Clairex ones, it does illustrate that the effect is inherent in sintered polycrystalline materials at room temperature. As previously indicated experimentally it would normally be expected that CdSe layers would exhibit greater transient maxima than would CdS layers, but our data indicate that the RCA prepared CdS layers exhibit greater transient maxima than even the Clairex CdSe layers. This anomaly as well as other evidence suggested that this transient effect may be either a function of the layer thickness and/or the activation of the layer. These two possibilities were investi-

[3] It is known that heating effects will often cause similar overshoots. However the circuit used in the experimental set up is so designed that any joule heating (I^2R) within the layer is negligible.

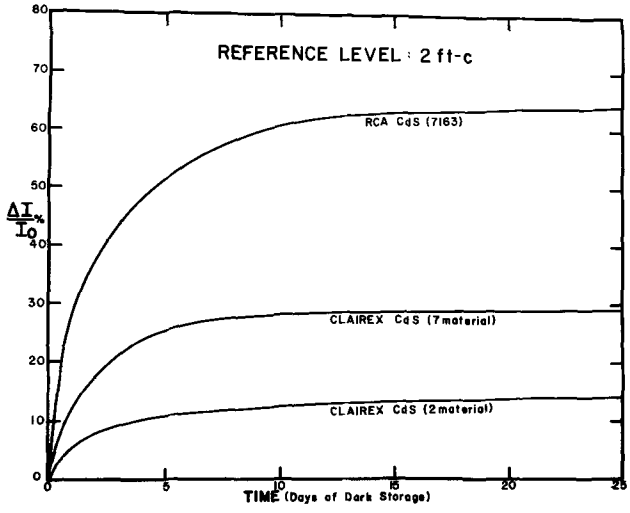

Fig. 3. Transient maxima or overshoot of several commercially available CdS photoconductive layers obtained for a reference level of 2 ft-c.

gated and yielded the results shown in Fig. 4 and Fig. 5. The data in Fig. 4 represent transient maxima, obtained at one reference level, for a particular CdS material which was varied in layer thickness. The thickness of layer (b) was 2-3μ, 4-6μ for (a), and 8-10μ for (c). It is evident from this phase of the data that the transient effect is not a function of the layer thickness. The second part of this investigation, however, yielded more interesting results. In this instance, variation of the copper activator concentration was made for a particular group of CdS layers, all having the same thickness. Thus, for a reference level of 10 ft-c we obtained the data in Fig. 5. These data illustrate that the transient effect, among other parameters, is directly dependent on the concentration of activator within the photoconductive layer. This experiment was repeated using several of the known photoconductor activators, and similar results were obtained as those already reported here for copper. Figure 5 shows the increase in the transient effect as a function of activator concentration. In addition these data show that the transient effect as a function of activator concentration also reaches an ultimate value.

In order to verify some of the room temperature transient data previously reported for single crystals of CdSe (2) and to gain additional information on room temperature transient data in CdS, if any, some

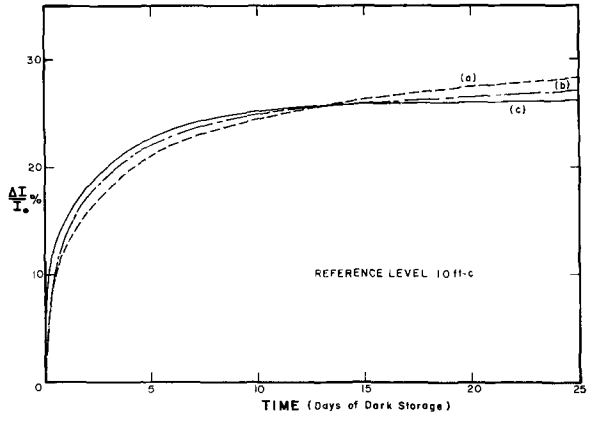

Fig. 4. Comparing transient maxima or overshoot of the same type CdS layers for which the layer thickness is the variable.

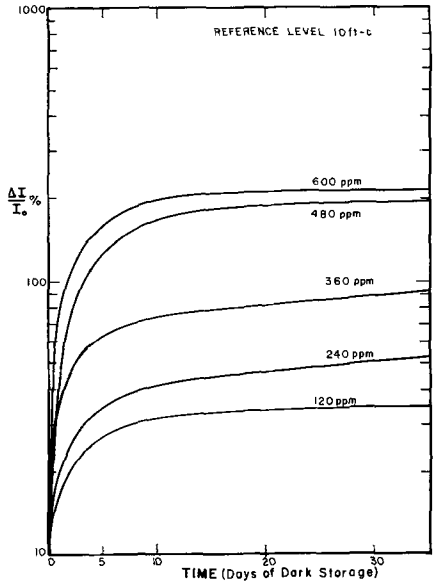

Fig. 5. Comparing transient maxima or overshoot of the same type CdS layers for which the activator concentration is the variable.

single crystals of these types were mounted and hermetically sealed in glass enclosures. They underwent the previously described experimental procedures, and transient maxima were observed in both types of crystals at room temperature. We believe that this is the first time that transient maxima have been reported for CdS single crystals at room temperature. It should be noted that single crystal transient maxima obtained for similar conditions were not as uniform, from crystal to crystal, as are the polycrystalline layers from layer to layer. This nonuniform result had been anticipated with single crystals because of the individuality of these crystals. This individuality is not as predominant with polycrystalline layers because of the statistical distribution that one gets with the many small fused single crystals. Because of this individuality of single crystals no direct comparison with the available data can be made at this time.

The reference level for which the long time equilibrium values are established is an extremely important factor in relation to the transient effect. Figure 6 is a comparison of transient maxima curves

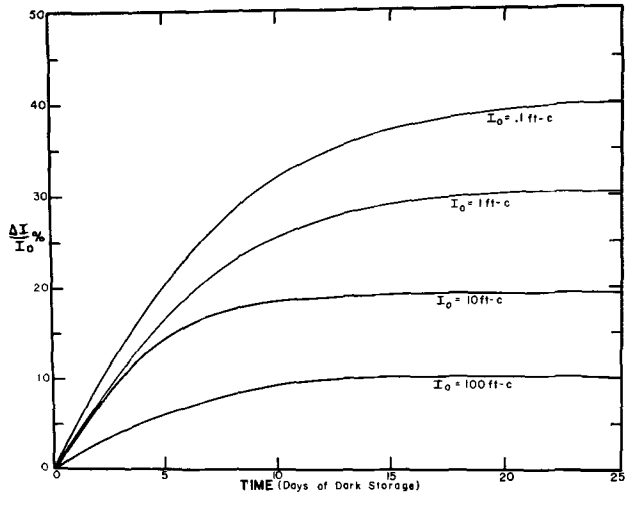

Fig. 6. Comparison of transient maxima or overshoot of the same type CdS photoconductive layers for which the reference level is the variable.

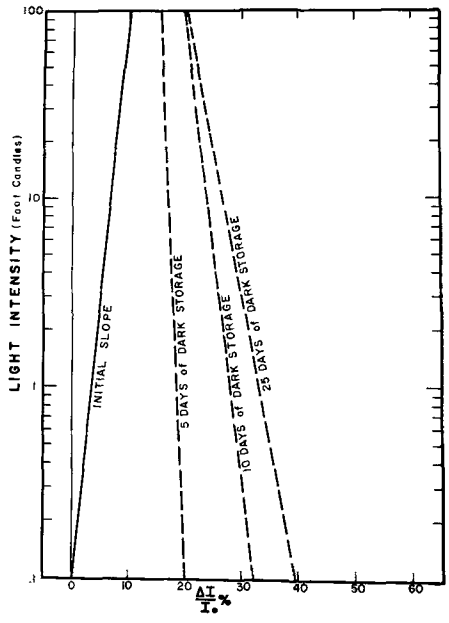

Fig. 7. The "initial slope" is based on some arbitrary photocurrent at 0.1 and 100 ft-c after the equilibrium condition has been established. The change of slope with time of dark storage is due to the fact that transient maxima or overshoots at high light levels are considerably smaller than those associated with the low light levels.

for the same CdS layer at several different reference levels (ranging from 0.1 to 100 ft-c in various steps). These data establish the fact that the transient maxima effect is more pronounced at low reference levels than at high reference levels. When considering this aspect it is easy to conceive that the slope of the photocurrent *vs.* light intensity curve will be strongly dependent on the excitation history of the layer prior to the taking of measurements. Figure 7 is a plot of the slopes for a group of CdS layers corresponding to various days of dark storage. These slopes are based on the data presented in Fig. 6. It is from these data that one may also envisage that at some high light level no transient maximum will be observed.

Decay of the Transients

The transient effect, as its name implies, is not a permanent effect, and photoconductors evidencing this effect have the ability, with light irradiation and time, to return to their long time equilibrium condition. The experimental results obtained for the recovery of sintered polycrystalline photoconductive layers to such an equilibrium condition, is presented herein.

A large group of these sintered layer photoconductors was subjected to an absolute dark environment for several months. The photoconductors were individually taken out of the dark and subjected to various light intensities for approximately 20 hr of continuous exposure. The initial photocurrent readings (I_m) of transient maxima from the dark were taken for the purpose of this experiment as the 100% value. The percentage decrease in photocurrent with time of light exposure is represented by $\Delta I/I_m\%$; this will be the expression used for this decaying effect. The data for the curves of Fig. 8 were taken with a Multi-Ranger Rustrak recorder (Model No. 111-A) which directly recorded the current readings of the

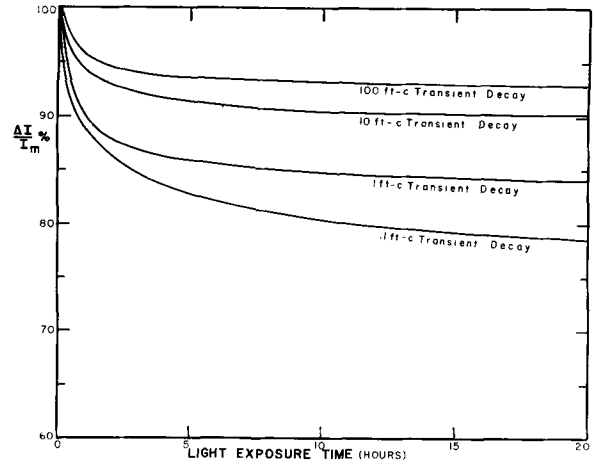

Fig. 8. Transient maxima or overshoot decay for a period of 20 hr for CdS type layers at various constant light intensity levels.

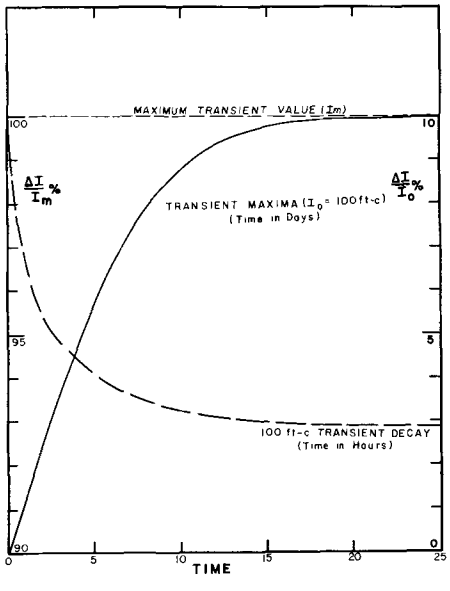

Fig. 9. Comparison of the growth of the transient maximum with the decay of that maximum for a reference level of 100 ft-c.

Hewlett Packard ammeter in the series circuit previously described. It should be noted, percentagewise, that there is less decay, with exposure time, from maxima at high light levels than from maxima at low light levels. This is apparent since there is correspondingly less overshoot associated with the higher light levels than the lower ones. Again attention should be called to the exponential nature of these transient decay curves.

In Fig. 9 the transient decay curve of Fig. 8 (for the 100 ft-c reference) has been superimposed upon the maximum curve of Fig. 4 (also for the 100 ft-c reference). We have equated the 100 ft-c maximum with I_m at 100 ft-c (the 100% level of the decay experiment). The superimposed curves show that in 20 hr of light exposure, at least for the case of the 100 ft-c reference, most of the transient maximum associated with this reference level has been erased or disposed of. These data also suggest that at low light levels the existence of these transient maxima will be of long time duration.

Rise Times

These experiments, as well as previously reported data (6-8), have evidenced the fact that photocon-

ductors coming from long time dark histories had much longer rise times than the same photoconductors which had a long time light history. The difference between these two conditions is approximately 37% for the case of the CdS layer under discussion, with a 10 ft-c reference. Specifically, those photoconductive layers taken from the dark had an average rise time of 31.5 msec, whereas the same layer with a long time 10 ft-c light history had an average rise time of 19.8 msec. Here again the excitation history of the layer plays a decisive role in their respective rise and decay times.

Discussion

When considering the data already presented in this paper, it is plausible to associate the transient effect with some trapping mechanism. It is at this time that a comparison of these data with some related data (2, 6, 9) and corresponding photoconductivity models is made.

The major difference between most previously reported works and this work is the manner in which the respective samples reach their true equilibrium condition. In Fig. 1 this difference has been shown by superimposing the general shapes of photoconductivity curves obtained from the aforementioned works with those obtained here (curve a is that curve which was reported by others (7-9) and curve b for the work reported herein). The general assumption of the band model necessitates an attempt to explain the transient effect in terms of what has already been recognized. Bube (2) has taken this first step by analyzing the transient effect as follows. He has asserted, in terms of the dual trap theory (8, 10), that the slow rise of the photocurrent from a quenched state is due to both the simultaneous increase of the concentration of holes in recombination or type I centers (*i.e.*, centers which have a greater probability for recombination than for thermal freeing) and a decrease in the concentration of holes in compensated acceptor or type II centers (*i.e.*, centers which have larger capture cross sections for holes than electrons). This theory implies that most holes are located in class II centers initially. Considering this aspect and the conditions set forth for transient minima (undershoot) it may be postulated that for transient maxima (overshoot) the density of free plus shallow trapped electrons must be greater than the density of holes in the Class II centers. Now, on excitation, the rate of ejection is greater than the rate of recombination, and simultaneously during this process both the free and shallow trapped electrons are being drained off rapidly. Thus the free electron density will eventually decrease until equilibrium is reached. A set of equations similar to those presented for undershoot (2) can be presented for overshoot by considering the rate of change of the density of free electrons (dn/dt) in the presence of excitation. By equating this term to zero, n_{max} can also be calculated, whence for the case of overshoot n_{max} must be greater than n_{equil}.

It has been stated that the prerequisite condition of this theory is that most holes must initially be located in centers of type II in order for the transient effect to be observed. For the case of CdS, elevated temperatures (above 100°C) were believed necessary to reproduce this situation (2). Nevertheless the existence of this transient effect at room temperature has been found for all CdS photoconductors reported here. In light of these results there now appears to be some correlation between the transient effect at high temperature with lightly activated materials and that at room temperature with highly activated materials. More specifically the degree of activation will strongly effect the temperature at which CdS will exhibit these transients.

The decreasing amount of overshoot observed with higher light intensities is obviously related to the previously obtained results on undershoot. Bube has reported (2) that if sudden changes in light intensity are made, whereby the lower light intensity of the change lies above the supralinear range,[4] no undershoot can be observed. Thus, it can now be said that above the supralinear range no undershoot nor overshoot can be observed in CdS or CdSe-type photoconductors.

If one assumes the transient effect is common to all photoconductive type materials, some clarification of conflicting rise time data can be made. Earlier papers (6-8) on CdS-type photoconductors convey the idea that the equilibrium value can be immediately reached by the first excitation of a quenched photoconductor (Fig. 1, curve a). Although the photoconductors prepared for this study follow curve b of Fig. 1 , it is still possible, under certain conditions, to reproduce most experimental variations in rise times that have been previously associated with photoconductors that follow curve a. The earlier papers have shown that previously quenched photoconductors will exhibit a decrease in their response times (to the equilibrium value) when subjected to a short quenching history and re-excited a second time. This decrease in response time, under similar conditions, has also been observed (see section on Rise Times) with photoconductors characteristic of curve b, Fig. 1. However there exists one major difference, *i.e.*, the decrease is observed only if the response time is taken with respect to the transient maximum and not the equilibrium value. In another work (11) the authors have shown that previously excited photoconductors exhibit an increase in their response time (to the equilibrium values) when also subjected to a short quenching history and re-excited again. Duplication of this result can be obtained only if the photoconductors under discussion have also had an initial excitation history. However, in both these cases the response time is obviously taken with respect to the true equilibrium value and not the transient maximum. The experimental data show that one can observe entirely different results by mistaking the equilibrium value for the transient maximum. The importance of recognizing this difference for the proper evaluation of photoconductive rise times is also emphasized.

[4] It is known that the photocurrent *vs.* light intensity curve is usually divided into three distinct ranges, *i.e.*, at low light intensities, a range where the photocurrent varies as the square root of light intensity; at intermediate light intensities, a range where the photocurrent is proportional to the light intensity; and at high light intensities, a range where the photocurrent rises supralinearly with the light intensity.

Acknowledgment

The author wishes to extend his gratitude to the members of the Clairex Corporation for making this paper possible. It is also his pleasure to acknowledge the many helpful discussions with Dr. Bernard Kramer of New York University.

Manuscript received Dec. 27, 1961; revised manuscript received March 20, 1962.

Any discussion of this paper will appear in a Discussion Section to be published in the June 1963 JOURNAL.

REFERENCES

1. K. W. Boer, *Physica*, **20**, 1103 (1954).
2. R. H. Bube, *J. Phys. Chem. Solids*, **1**, 234 (1957).
3. "Instructions for Using the Radiation Standards, (revised Dec. 27, 1951)." A reprint furnished by the National Bureau of Standard with their Standard Lamps.
4. National Bureau of Standards Report of Calibration for Color Temperature and Luminous Intensity of two 100 watt Inside frosted Lamps. NBS 5632, 5633. Test #2.1/163319.
5. R. H. Bube, *J. Appl. Phys.*, **31**, 1301 (1960).
6. H. Kallmann and B. Kramer, *Phys. Rev.*, **87**, 91 (1952)
7. R. H. Bube, "Photoconductivity of Solids," p. 290, John Wiley & Sons, Inc., New York (1960).
8. A. Rose, "Performance of Photoconductors," in Photoconductivity Conference, p. 3, John Wiley & Sons Inc., New York (1956).
9. H. Kallmann and P. Mark, *Phys. Rev.*, **105**, 1445 (1957).
10. R. H. Bube, article in Photoconductivity Conference, *op. cit.* p. 575.

The Dember Effect in ZnS-Type Materials

F. F. Morehead and A. B. Fowler

Thomas J. Watson Research Center, International Business Machines Corporation, Yorktown Heights, New York

ABSTRACT

A convenient system is described for measuring the diffusion current pulse produced by the sudden incidence of strongly absorbed radiation (Dember effect) on powder materials of the ZnS type. A model adequately representing the physics of the effect is given. It is shown that it is desirable to eliminate d-c contact effects in order to obtain reliable and reproducible results. The sign of the Dember current pulse indicates the sign of the more mobile carrier when the incident radiation is in the strongly absorbed, fundamental region. Reversals in the sign of the pulse are often encountered for weakly absorbed, longer wavelengths and are attributed to the effect of fast surface states. The excitation spectra for the Dember effect, photoluminescence, and electrophotoluminescence in a ZnS phosphor are given and correlated.

The relaxation processes involved in the Dember effect have kinetics determined by many factors: the variable dark times between light pulses, temperature, irradiation with long wavelength light during "dark" times, etc. These effects are described. It is found, for example, that the spectral dependence of the relaxation effected by long wavelength radiation correlates with the photoluminescence quenching spectrum of phosphor materials. Some of the potentialities of the Dember effect in studying these materials are pointed out.

One of the many photoeffects discovered before 1935 is the Dember effect, a diffusion dependent photovoltage. Strongly absorbed radiation incident on only one face of a crystal produces a diffusion current of the more mobile carrier away from the illuminated surface. The sign of the current is determined by the sign of the mobile carrier. The effect was first reported by Dember in Cu_2O (1) but except for a few papers by Russian workers, notably Zhuze and Ryvkin (2), and Bukke (3), and recent reports on AgCl (4) and GaAs (11), little use of the Dember effect has been reported in the evaluation of photoconductors and phosphors.

The technique employed in the present work and described in detail in a later section is essentially the transient condenser method (2) in which the possibility of spurious effects from illuminated contacts between the electrodes and the phosphor is eliminated. Several approximate quantitative treatments of the basic equations governing the effect are in the literature (5, 6), but even for the simplest, steady-state cases the results are too complex to be of much value in interpreting experimental results. A simple, phenomenological treatment, based on experiments, will be pursued in describing the physics involved in the measurements.

The purpose of this paper is simply to show that the Dember effect is an easily made measurement which gives information concerning the sign of the more mobile, or majority, carrier in materials for which Hall effect or thermoelectric power measurements are extremely difficult. Dember measurements can detect the approximate position of the absorption edge, its shift with temperature, the existence of significant impurity absorption and of fast surface states. The results of these measurements usually show useful correlation with the photoconductive, photoluminescent, electroluminescent, and electrophotoluminescent properties of these ZnS-type materials.

Experimental Technique

The experimental arrangement for observing this effect in polycrystalline material is shown in Fig. 1. A suitable mixture of the powder and an insulating

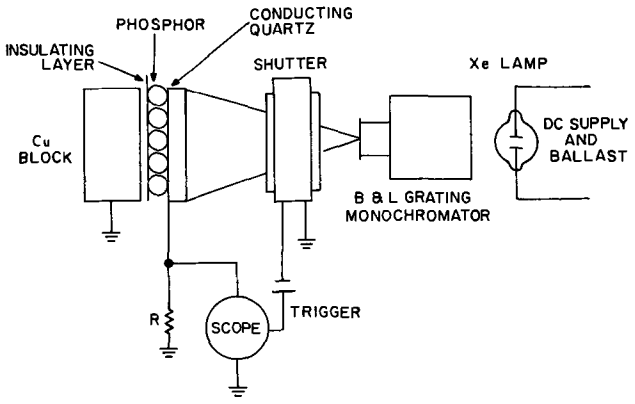

Fig. 1. Schematic arrangement of Dember pulse apparatus

binder (which is sometimes omitted) is compressed between the two plates of what is essentially an electroluminescent cell. One or more layers of ¼ mil Mylar are usually included to eliminate the possibility of electrode effects. None of the latter has ever been observed, however, with the Mylar omitted, and so in most measurements the layer between the powder and the silica disk which bears a conducting coat of SnO_2 is omitted. This latter arrangement permits transmission of intense u.v. down to below 300 mμ. When strongly absorbed light is flashed onto the transparent electrode, a current pulse is observed in the external circuit, a typical oscillogram of which is shown in Fig. 2a. The diffusion of the more mobile carrier away from the illuminated electrode leaves this electrode charged oppositely to that of the diffusing carrier, so that the positive current pulse shown in Fig. 2a identifies these carriers as electrons. A return pulse of lower peak value and opposite sign results when the shutter is closed, as shown in Fig. 2b.

A high pressure Xenon lamp is used as a source. The 250 mm Bausch and Lomb grating monochromator emits equal photon intensities (about 4 x 10^{14} photons/cm^2/sec) for appropriate slit width settings determined at each wavelength with a thermocouple. The Graflex 1000 shutter flashes the full intensity onto the cell in less than a millisecond. For studies of the temperature dependence of the effect, both the insulating layer and the binder are omitted. The latter omission causes considerable loss in signal, but it is important to eliminate effects which might be caused by the temperature dependence of the dielectric constant of the binder. The cell chamber can be evacuated to a pressure below 1μ Hg and the Cu block electrode cooled to liquid nitrogen temperature or heated to above 200°C.

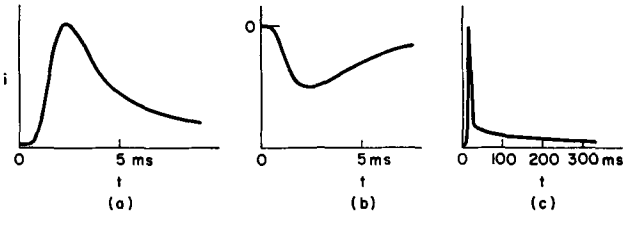

Fig. 2. (a) Typical electron diffusion current pulse; (b) return pulse (electrons); (c) contact current tail of (a).

Experimental Results and Discussion

The physics of the effect.—A brief description of the phenomenological physics of the "condenser method" for measuring the Dember effect in powdered materials may prove helpful in the subsequent examination of results. It will be shown that in addition to the fast displacement current there exists a slow interparticle contact current. This latter current can be observed either as a steady-state short circuit d-c current in the absence of an insulating layer or as the long tail on the displacement current pulse when the insulator is present. It will also be shown that the fast, displacement current is the more reliable and reproducible indication of the type and quantity of the more mobile carrier and that the effects of the contact current should be minimized. The rise time of the Dember current pulse (cf. Fig. 2a) is the same order as the shutter opening time t_s (about 1 msec) and is never significantly slower. The fall time from the current maximum can be related roughly to an exponential decay time, RC. The peak current i_m is given by

$$i_m = (i_m)_0 \frac{RC}{t_s}(1 - e^{-t_s/RC})^1 \qquad [1]$$

where $(i_m)_0$ is the maximum peak current that would occur for t_s/RC equal to zero. This equation relates only the effect of shutter speed for a given material in a given set of experimental conditions. This relationship has been found to hold experimentally by varying the shutter speed. A fast shutter is therefore advantageous.

A long tail with a much slower time constant (cf. Fig. 2c) is considered to be due to the direct flow of current between particles, although the detailed mechanism is unknown. This latter current flow must depend on the effect of internally scattered radiation in changing the contact emf between particles and evidently requires a much longer time to establish than the photodiffusion emf responsible for the fast displacement current pulse. Since the contact photovoltages must involve accumulation or depletion of space charge, it is reasonable that they should require a longer time to reach a peak value. This slow current will be discussed further later.

The fast current pulse is due to the charge which moves in the external circuit corresponding to the diffusion of the more mobile carriers away from the

[1] A "curtain" shutter, moving with velocity v, exposes fresh areas of the cell with maximum current I_m amp/cm^2 at the instant of exposure which subsequently decays exponentially with a time constant RC. For a square cell of width w and length l, along which latter the shutter moves, the shutter opening time $t_s = v$. For $t \leq t_s$, the measured current at time t from the start of the shutter movement

$$i(t) = I_m w \int_0^x e^{-\frac{x}{vRC}} dx$$

$$= (I_m wl) \frac{RC}{t_s}[1 - e^{-t/RC}]$$

where $x = vt$. For $t \geq t_s$

$$i(t) = i_m w \int_0^l e^{-\frac{t-x/v}{RC}} dx$$

$$= (I_m wl) \frac{RC}{t_s}[e^{t_s/RC} - 1]\, e^{-t/RC}$$

The maximum value of $i(t)$ occurs at $t = t_s$

$$i_m = (I_m wl) \frac{RC}{t_s}(1 - e^{-t_s/RC})$$

which, for $(i_m)_0 = I_m wl$ is Eq. [1].

illuminated surface of the top layer of particles. It is independent of interparticle contacts and the more reliable and reproducible indication of the quantity and type of mobile carriers in the material. One therefore should choose those experimental parameters (intensity of incident light, cell thickness, volume fraction of material in the phosphor-liquid dielectric mixture, etc.) which enhance the fast pulse and minimize the slow interparticle current.

The RC decay time of the fast displacement current pulse arises from a capacitance C which is experimentally equal to the cell capacitance and an R which apparently arises from isolated photoconducting areas on the particle surfaces parallel to the direction of the measured current. Incident light (which is not absorbed by the imbedding medium) can be scattered into the interior of the cell and illuminate these parallel particle surfaces. Hence the equivalent circuit can be characterized as a series resistance R and capacitance C. R can be estimated from the reduction in current pulse height caused by the insertion of a large resistor in series with the cell. R varies directly with cell thickness in the range of 50-500μ; it decreases with increasing light intensity as shown in Fig. 3. C can be estimated from the value of R and the exponential decay time of the pulse. This value of C agrees well with the capacitance of the cell computed from the current produced by applying a high frequency a-c field. C is very nearly independent of light intensity (cf. Fig. 3). As long as the oscilloscope input resistance used to measure the Dember current is small compared to R, the decay time of the current (the fast part) is independent of the cell thickness, since R varies directly and C inversely with thickness.

The charge Q moves a diffusion length d from the surface of the top layer of particles. The fraction of this charge which contributes to the pulse current observed in the external circuit is d/l, where l is the thickness of the cell. Since the exponential decay time RC is independent of l, the peak external current

$$i_m = \frac{Q(d/l)}{RC} \qquad [2]$$

varies inversely with the cell thickness l. Typically $(i_m)_0$ varies with the intensity of the incident light as shown in Fig. 3 for a ZnS:Cu, Cl phosphor for 320 mμ excitation.

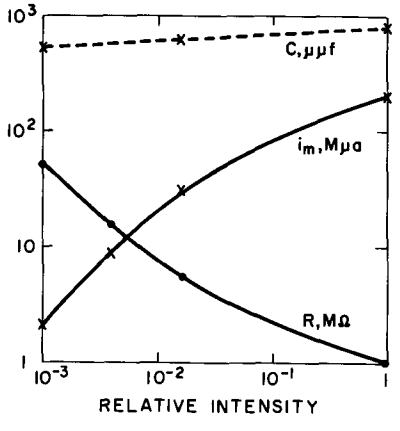

Fig. 3. Variation with incident intensity of 320 mμ light of: i_m, the peak pulse current; R, the effective resistance; and C, the capacitance. See text.

One can estimate a lower limit for the diffusion distance d from the peak current, $(i_m)_0$, produced by a known photon flux $W_{h\nu}$ falling on a cell of known thickness l. Because of the insulated contact each photon striking the surface of the cell can produce at most one mobile carrier to diffuse away from that surface an average distance d and contribute to $(i_m)_0$ in the ratio d/l. Since

$$(i_m)_0/e < W_{h\nu}\frac{d}{l} \qquad [3]$$

we have

$$d > l[(i_m)_0/e\, W_{h\nu}] \qquad [4]$$

The maximum estimate of the lower limit of d is obtained at that incident intensity for which the current is varying most strongly with intensity. Experimentally this variation is at most linear and occurs in Fig. 3 for a value of the intensity 2 x 10^{-8} times the maximum photon flux used, which is 2 x 10^{15} photons/sec. For this case $W_{h\nu}$ is 4 x 10^{12} photons/sec, l is 55μ, and i_m is 5 x 10^{-9} amp. Substitution of these values in Eq. [4] shows that d must be at least 0.4μ. This distance represents an appreciable penetration into the particle bulk and at least indicates that more than the surface is involved in these measurements.

The effect of variation of the volume fraction of the active material in the imbedding medium on $(i_m)_0$ can be summarized as follows: For thin cells (less than 100 microns) $(i_m)_0$ increases first linearly with increasing volume fraction of the phosphor, but appears to saturate above 40%. For thicker cells the saturation occurs at lower values of the volume concentration. The value of the volume concentration of the active material used in most measurements was 30%.

In the absence of an insulating layer a direct photocurrent is produced by the incident, strongly absorbed radiation. It is probably due to the photovoltaic effects at the interparticle contacts. One can measure an open-circuit voltage and a short-circuit current with an electrometer and from these values compute an effective d-c resistance, assuming ohmic character. With the insulating Mylar present, this interparticle current and the fast displacement current build up a charge on the Mylar which is measurable as an open-circuit voltage on the electrometer. This voltage increases with cell thickness, indicating that most of the charge accumulating on the insulating layer is carried by the interparticle contact current since the fast displacement current pulse decreases linearly with increasing cell thickness, as described above. The open-circuit voltage of a cell without the Mylar layer increases with increasing cell thickness. This result is as one might expect since the photovoltages of a larger number of contacts add to give a larger value for a thick cell than for a thin cell.

The decay of the slow, interparticle contact current, which forms the tail of the Dember pulse as shown in Fig. 2c, can also be characterized as the exponential decay of a series RC circuit. The capacitance is that of the ¼ mil Mylar layer and the

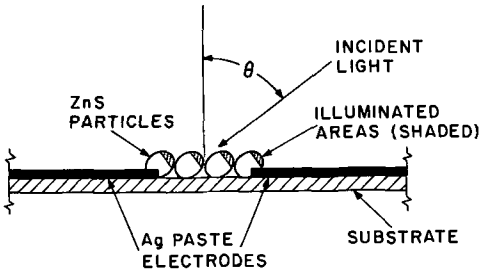

Fig. 4. Experimental arrangement used to measure the angular dependence of a d-c Dember voltage. See text.

resistance is the effective d-c photoresistance of the cell without the insulating layer, calculated from the open-circuit voltage and the short-circuit current of the latter cell. This agreement of the decay time of the Dember pulse tail with the product of the capacitance of the Mylar and the computed resistance of the d-c cell substantially identifies the two effects. That is, the direct photocurrent and the slow Dember pulse tail have the same origin, probably interparticle contact photovoltages.

This interparticle contact current depends on a gradient in the incident flux, as the following experiment demonstrates. A mixture of ZnS and binder was laid on two silver paste electrodes as shown in Fig. 4. A measurable open-circuit direct photovoltage (or a short-circuit current) is produced which is a function of the angle θ between the direction of the field between the two electrodes and the direction of the incident light. For θ different from zero there will be a component of the incident light in the same direction as that of the electrodes; this parallel component is proportional to sin θ. Since the measured photovoltage varies as the ¼ power of the intensity over two orders of magnitude in intensity, while the intensity of the light incident on the sample varies as cos θ, the expected variation in the open-circuit photovoltage is

$$V_{oc} = (\overline{V_{oc}})_m \cos^{1/4}\theta \sin\theta \qquad [5]$$

Equation [5] fits the experimental values of V_{oc} quite well for $(\overline{V_{oc}})_m = 1.8$v, correctly predicting a maximum of 1.3v at $\theta = 63° 25'$.

Experimentally it has been found that the value of the peak pulse displacement current is far more reproducible than the d-c contact photovoltage, both for measurements made at different times on the same sample and for different samples prepared in the same way from the same starting material. The uncertainty concerning the exact mechanism of the d-c effect makes it a less reliable indication of the sign of the more mobile carrier than the displacement current pulse. However, for fundamental radiation, the two effects do have the same sign for all samples examined thus far.

In summary the experimental conditions that have been found to favor the displacement pulse and to minimize the interparticle contact current tail are the following: (i) high intensity of incident light, (ii) as thin a cell as feasible, (iii) not too high a volume concentration, to minimize interparticle contacts, and (iv) the fastest available shutter speed.

Effects observed in ZnS *phosphors–general remarks.*—A large difference in depth between the electron trapping states and hole trapping states is the usual situation in ZnS. This fact, plus the higher microscopic mobility of electrons, leads to the possibility that not only completely compensated but also a significant range of p-type samples will yield electronic Dember currents. (An experimental technique for distinguishing the two types when both give electronic Dember currents will be described later.) At room temperature the absorption of fundamental radiation by compensated or n-type ZnS results in a concentration gradient in both holes and electrons. The holes are quickly trapped at the compensated and hence ionized acceptor levels which usually lie around 1 e. v. up from the valence band edge. The electrons are not strongly trapped at the shallow (~ 0.25 e. v.) ionized donor levels (in both compensated and n-type material) and therefore readily diffuse in the concentration gradient established by the strongly absorbed incident light. An electronic Dember current results.

Despite the rather large energy difference between acceptor levels and the valence band in ZnS, which allows almost no dark conductivity for even strongly p-type materials at room temperature, a p-type Dember current from fundamental radiation has been observed in such samples. Band gap radiation at the surface produces, as always, both electrons and holes in a strong gradient. In strongly p-type material, electrons will first be captured in the uncompensated and therefore unionized acceptors before the diffusion current of the holes is impeded by the resulting ionized acceptors, which are hole traps. More holes than electrons can move in the concentration gradient and a net hole current is observed. It should also be remarked that a given number of uncompensated acceptors per unit volume can produce a hole current only if the number of compensated acceptors (hole traps) is small. If this latter number is large, an electron Dember current results.

Excitation spectrum of the Dember effect, photoluminescence, and electrophotoluminescence.—Figure 5 shows the spectral distribution of the size and

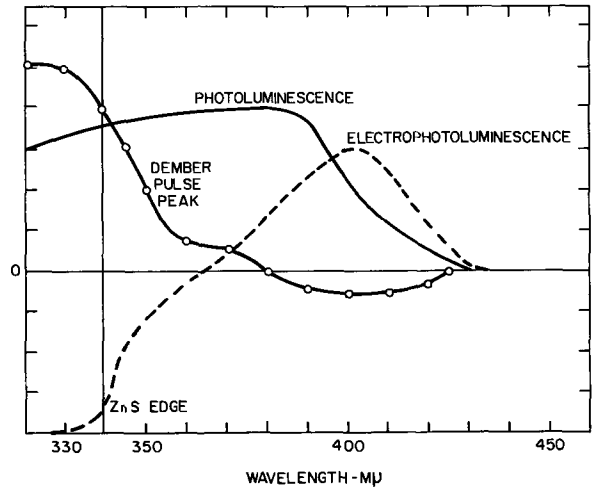

Fig. 5. Excitation spectra of photoluminescence, Dember pulse, and electrophotoluminescence for a ZnS:Cu,Cl phosphor. See text.

sign of the peak Dember pulse current for a ZnS phosphor containing 4 x 10^{-3} (mole fraction) Cu and 3 x 10^{-3} Cl. Significant absorption by impurities is shown by the finite positive current (indicating electron diffusion) extending up to 380 mμ. Unactivated ZnS yields a significant Dember pulse below 350 mμ at room temperature, indicating an absorption edge at around 340 mμ. The weaker absorption of wavelengths above 380 mμ by the Cu, Cl activated phosphor results in a reversal of the direction of the Dember pulse. This reversal is ascribed to the effect of fast surface states whose rapid capture of electrons produces a net flow of these carriers toward the illuminated surface and hence a negative pulse [cf. ref. (4)]. The weakly absorbed long wavelength light produces too moderate a concentration gradient in the mobile carriers to overcome their rapid depletion by the surface states. An attempt to change the occupation and hence the effect of the surface states with various ambient gases was unsuccessful. The close-packed and necessarily enclosed structure of the cell may have been responsible for this failure.

The excitation spectrum of the green photoluminescence of this ZnS:Cu, Cl phosphor is also shown in Fig. 5. No luminescence is excited by wavelengths greater than the Dember pulse cut-off around 450 mμ.

The electrophotoluminescence excitation spectrum in Fig. 5 shows the effect of a pulsed electric field applied to the cell on the luminescence excited at each wavelength. In the long wavelength region the usual Godden-Pohl (7) effect appears. A pulsed enhancement of the photoluminescence occurs for both the application and the reversal of the electric field. This behavior is depicted in Fig. 6a for 400 mμ. The field (of either polarity) served to empty filled traps, either by direct field ionization or by the impact of field-accelerated electrons, and a temporary increase in emission results. It is interesting to note that the applied fields required to produce this effect are only of the order 5 x 10^3 v/cm for electroluminescent ZnS:Cu, Cl phosphors, but over 5 x 10^4 v/cm are necessary for nonelectroluminescent ZnS:Cu, Cl phosphors. This observation corroborates the postulated existence of regions of much higher than average fields in the electroluminescent material (8).

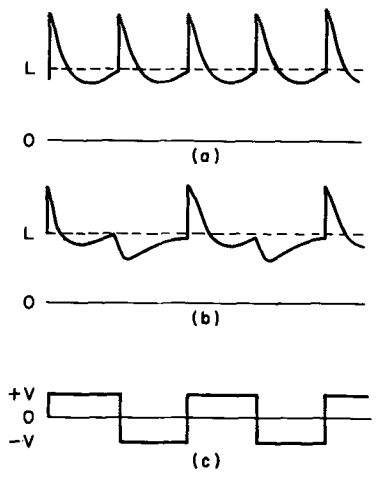

Fig. 6. Field modulation of photoluminescence in a ZnS:Cu,Cl phosphor (electrophotoluminescence): The effect of pulsed electric field (c) on the luminescence excited by 400 mμ (a) and 320 mμ (b). The dashed line is the unmodulated photoluminescence.

For short wavelengths a different type of modulation of the luminescence by the field occurs, which has been described by Halsted (9). Here the field apparently moves the mobile carriers into or out of the narrow excitation region determined by the absorption constant of the material for the incident light. If electrons are the more mobile carriers and if the radiative recombination is that of a free electron and a trapped hole, then making the illuminated surface positive will increase the luminescence by pulling more electrons into the excitation region. Application of a negative voltage to the surface produces a temporary diminution in the emission. This type of electrophotoluminescence is illustrated in Fig. 6b for which the exciting wavelength is 330 mμ. The electrophotoluminescence excitation spectrum in Fig. 5 shows the peak relative change (arbitrary units) in the photoluminescence produced by applying a negative field of 3 x 10^4 v/cm. At 365mμ there is a change in sign of this electrophotoluminescence, denoting a transition from one effect to another. Above 365 mμ the field has the effect of emptying electron traps while below this point the field moves the free carriers in and out of the excitation region. For the field of opposite polarity (positive) the sign of the electrophotoluminescence is opposite to that shown in Fig. 5 below 365 mμ and the same as shown above that wavelength. The results of the electrophotoluminescence and Dember measurements are consistent with mobile electrons and the radiative recombination of free electrons and trapped holes.

Relaxation and temperature effects.—In most instances the size and in some cases the direction and shape of the Dember pulse is a sensitive function of the time the cell has remained in the dark since last exposed to the exciting light. When the wavelength of the incident radiation is in the fundamental region, longer dark relaxation times give larger peak Dember currents. The more time that is available for the relaxation of the polarization field produced by a previous exposure to the strongly absorbed radiation, the greater the diffusion current which can flow when the excitation is again applied to the sample. In many cases the maximum current flows following a definite dark time. Both longer and shorter dark times can result in a smaller pulse peak. There are at least two possible explanations for the occurrence of this maximum. One possibility is the increase in the effective mobility of the carriers caused by filling some of the traps in the excitation region. The degree to which these traps are filled is greatest for short dark intervals.

One other possible explanation invokes the undoubted heterogeneity of the powder samples. A distribution of p-type and n-type (or compensated) particles is assumed. The electronic displacement in the n-type particles relaxes after only small dark intervals; the polarization of the p-type particles relaxes much more slowly since the holes are

trapped in much deeper levels than are the electrons (~1.0 e. v. for holes, ~0.25 e. v. for electrons). At the dark time for which the maximum electron Dember current is produced nearly all of the electrons in the n-type particles and only a few of the holes in the p-type particles have returned to the region from which they were excited near the surface. Longer dark times allow the return of an appreciable number of holes, so that the net electron Dember current pulse is reduced.

In some instances the sign of the Dember current pulse for sufficiently long periods of dark relaxation is opposite (p-type) in sign to that measured for short periods in the dark (n-type). A relatively short exposure (1 min) to intense long wavelength radiation (over 600 mμ) produces the same reversal (or reduction in value) in the Dember pulse (at 320 mμ) as the extended dark period (overnight). The effect of the long wavelength light will be discussed in more detail in the section on optical relaxation effects.

One can conclude from the above model that a Dember signal that monotonically increases with increasing dark time characterizes n-type or completely compensated material. A maximum pulse at a particular dark time indicates an appreciable amount of p-type material. A more convenient experimental criterion is the following: the Dember pulse is measured after 1 min in the dark (Pulse A) and after 1 min exposure to intense IR (Pulse B). Figure 7 schematically illustrates the four experimental possibilities and lists the nature of the material deduced from the experiment. If Pulse B is equal to or greater than a positive Pulse A, then there is no detectable p-type material. For Pulse A positive and greater than Pulse B (positive or negative), the absolute value of B − A is taken as a measure of the degree of p-type uncompensation in the sample. If Pulse A as well as Pulse B is negative, the value of Pulse B alone measures the degree of p-typeness, since there is apparently no measurable electron current. The deduced Pulse C is, in each instance, a measure of the p-typeness of the material.

Since the interparticle contact photocurrent does not, in general, reverse its direction at the same wavelength as the Dember pulse (cf. Fig. 5), quite complicated pulse shapes are possible in this re-

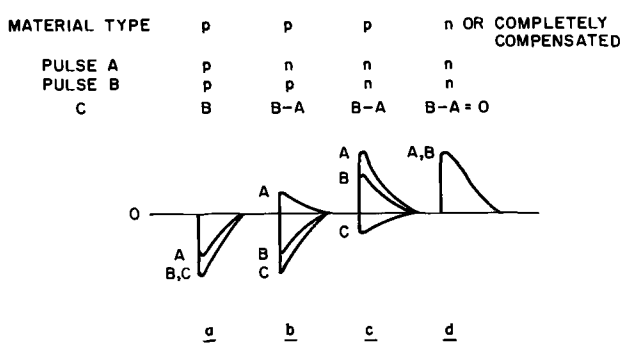

Fig. 7. Four possible Dember pulse combinations obtained from ZnS materials: Pulse A, after 1 min dark relaxation; Pulse B, after 1 min infrared exposure; Pulse C, deduced p-type current in Pulse B. See text.

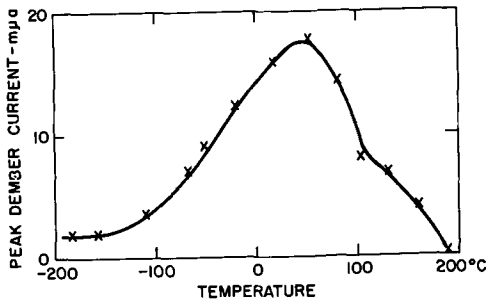

Fig. 8. Temperature dependence of the Dember pulse peak (30 sec dark interval) for a ZnS:Cu,Cl phosphor.

versal region. At least two extrema are observed when the reversal is present. The relative size and position of these extrema depend on the dark relaxation time, the wavelength, and the intensity of the exciting light. Some materials have given as many as four extrema in this reversal region.

A typical dependence of the height of the Dember pulse on temperature is shown in Fig. 8, for a ZnS:Cu, Cl 4 x 10^{-3} phosphor. The exciting wavelength was 320 mμ and a dark interval of 30 sec was used at each point. The Dember pulse is smaller at high temperatures for n-type or compensated specimens for either of two reasons. One is that both electrons and holes can diffuse in the concentration gradient, yielding a lower net electron current; the other is that the electron mobility could decrease at high temperatures. At low temperatures the electrons are frozen at shallow (~ 0.25 e. v.) traps. In the region of maximum response only the holes are immobilized at deep (~ 1 e. v.) hole traps, resulting in a large electron diffusion current. Shorter (< 30 sec) dark times tend to shift the temperature of maximum response to higher temperatures.

For a specimen of unactivated ZnS fired at 1200°C in a sealed vacuum and presumed (because of the higher volatility of S_2 compared to Zn) to contain excess Zn and therefore some uncompensated donors (sulfur vacancies) an interesting behavior was observed. At room temperature only a small peak Dember current (<10^{-8} amp) appeared for reasonable dark times of the order of minutes. This current could be increased to around 1.0 x 10^{-7} amp by very long periods of relaxation in the dark or by heating to above 150°C and returning to room temperature before flashing with the 320 mμ. After cooling the sample to nitrogen temperature from room temperature and subsequent exposure to the 320 mμ light, the measured current was 1.5 x 10^{-7} amp. If the sample was first heated to 150°C before cooling to −180°C, a peak Dember pulse of 2 x 10^{-7} amp was measured. The second pulse at −180°C is in every case negligibly small, less than 10^{-9} amp. The high value of the first pulse at this temperature may be due to the freezing of the dark electrons on the uncompensated donors, with a consequent decrease in the scattering due to charged, ionized donors present at room temperature. Thus a higher Dember current pulse results than for even the completely relaxed sample at room temperature (2 x 10^{-7} *vs.* 1 x 10^{-7} amp). ZnS materials expected to be completely compensated do not exhibit this behavior.

Optical relaxation effects.—The continuous exposure of the test cell to a beam of radiation other than that which is flashed onto it to produce a pulse of diffusion current usually results in lower peak value. This reduction of the pulse height is most prominent when the two beams of radiation are the same wavelength. An exception to this behavior is the case in which the continuous exposure is to wavelengths in the fundamental and the pulsed beam is in the reversed region at longer wavelengths. (cf. Fig. 5). The extrinsic carriers ionized by the weakly absorbed long wavelength radiation move in the polarization field maintained by the strongly absorbed fundamental radiation. The result is an increase in the reversed pulse normally observed in this wavelength region. In fact, to obtain this increase, simultaneous exposure is not necessary in some cases, so that a previous exposure to fundamental radiation suffices to enhance the reversed current in the long wavelength region. Hence, in order to obtain unambiguous results from long wavelength excitation, one should proceed from long to short wavelengths in measuring the spectral dependence of the Dember effect, using a sample kept in the dark for a prolonged period.

In some cases ZnS materials which yield positive (electron current) Dember pulses for short dark time intervals not only give reduced positive signals for long relaxation periods, but for sufficiently long dark times produce a negative (hole current) Dember pulse. This reversal in sign (for fundamental excitation) can also be effected by exposure to long wavelength radiation. Figure 9a shows the size of the Dember pulse peak obtained at 320 mμ for a ZnS sample after relaxing for 30 sec while exposed to the radiation whose wavelength is indicated on the abscissa. The unactivated ZnS was fired for 24 hr at 900°C in a sealed quartz tube in a sulfur pressure of

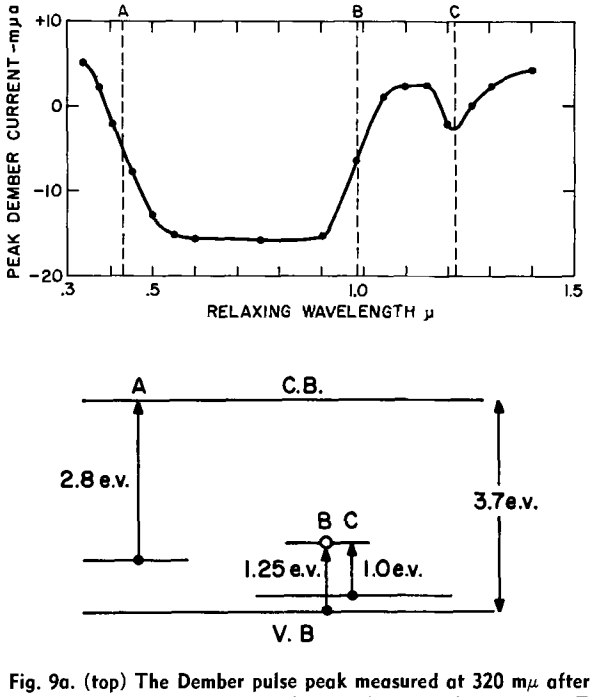

Fig. 9a. (top) The Dember pulse peak measured at 320 mμ after 1 min exposure to the plotted wavelengths for an undoped p-type ZnS sample. Fig. 9b (bottom) The energy levels deduced from (a). The transitions A, B, and C are described in the text.

6 atm. There is no luminescence. Figure 9b shows an energy level scheme consistent with the data of Fig. 9a. Wavelengths between 450 mμ (A) and 1.0μ (B) raise electrons from the valence band to the ground state of an unionized acceptor, freeing a hole in the valence band to return to the excitation region and relaxing the sample (transition B). Radiation of 1.2μ (C) lifts an electron from an excited hole state of the unionized acceptor (which is in thermal contact with the valence band) to the ground state of the unionized acceptor (transition C). The hole, which is now situated at the excited hole state of the acceptor, can now be thermally released into the valence band. Wavelengths below 450 mμ (A) are more effective in ionizing electrons from a filled center (transition A) than holes from an empty center, increasing the probability of a positive (electron current) Dember pulse. The proposed energy level structure of the acceptor is remarkably close to that deduced by Apple and Prener (10) from the infrared fluorescence and diffuse reflectance of ZnS into which Cu had been fired under sulfur pressure to produce uncompensated acceptors. Whether the acceptor in the present material is due to impurities such as Cu which were present in the "pure" (RCA luminescent grade) unactivated material or simply arise from a singly ionized zinc vacancy is uncertain.

A ZnS:1.5 x 10^{-3} Cu, 1.0 x 10^{-3} Cl blue-green emitting phosphor also exhibited this reversal of a positive (electron current) pulse at 320 mμ after relaxing with long wavelength radiation. A relaxation spectrum similar to Fig. 9a was obtained. The Dember pulse in the 350 to 420 mμ region, which is negative for short dark times, becomes positive after long wavelength relaxation. The complete Dember current spectrum (cf. Fig. 5) is reversed in this instance in going from short dark times to long wavelength relaxation between pulses. One possible explanation of the positive (electron current) pulses obtained in p-type samples such as those described above for short dark times is that of holes going toward the surface, from which they could escape (depolarize) more readily than from the bulk where they might be trapped more deeply. Since going to longer exciting wavelengths could hardly reverse this process, as it does in the present instance, this explanation must be discounted.

For the above phosphor (ZnS:1.5 x 10^{-3} Cu, 1.0 x 10^{-3} Cl) the blue-green photoluminescence produced by 365 mμ ultraviolet is strongly quenched when infrared radiation is also shone on the sample. The spectral dependence of the quenching effect is in close agreement with the relaxation spectrum. This result confirms the hypothesis that the release of holes into the valence band from the empty activator level (transitions B and C in Fig. 9b) is the first step in both the quenching of luminescence and the optical relaxation of the Dember polarization.

Measurements on other materials.—Some measurements have been performed on other compounds than ZnS in powder form, including CdSe, ZnSe, ZnTe, and mixed crystals of ZnS and ZnSe. The results are of the same form as for ZnS, yielding information on the type of carrier which is either more mobile or a true majority carrier. The shift in band

edge of ZnS, ZnSe alloys as a function of composition, as well as its shift with temperature, is easily measured, for example. Shifts in stoichiometry produced by various thermal treatments have been followed in at least a semiquantitative sense with CdSe as well as ZnS.

Similar measurements are possible with thin films deposited on a conducting substrate. A piece of conducting quartz separated from the film by a quarter mil Mylar layer forms the second electrode of the Dember cell. Films of p-type CdTe and both p- and n-type CdSe have been prepared (by G. Somorjai) and measured in this manner.

Summary and Conclusions

The pulsed Dember effect measured as described above is a useful tool for indicating the type of mobile carrier and to a degree the extent of activation of powder and thin film materials of the ZnS type. The displacement current pulse is probably a more reliable and certainly a more reproducible measurement than a direct current measurement relying on interparticle contacts. Careful control of such experimental parameters as cell thickness, volume concentration of the material, and radiation intensity are necessary for good reproducibility.

The change in size and direction of the Dember pulse can be used to follow shifts in stoichiometry and impurity content resulting from various treatments. For example, unactivated ZnS fired in sealed quartz tubes under various sulfur pressures shows a shift from n- to p-type pulses with increasing sulfur pressure. The algebraic value of the peak current is linear with $\sqrt{p_{S_2}}$. Uncontrolled impurities in the starting material have lead to ambiguous results in many cases, however. Experiments of this type are still being pursued.

In luminescent materials, measurements of the Dember effect and of the electrophotoluminescent response can unambiguously determine the nature of the radiative recombination under certain conditions. Often a relaxation spectrum such as that shown in Fig. 9a can be obtained. Information on the existence and nature of such levels as shown in Fig. 9b can thus be obtained and correlated with, for example, the photoluminescence excitation and quenching spectrum of the same material. Such levels can even be demonstrated to exist in materials that are otherwise uncommunicative, that is nonluminescent.

Acknowledgments

The writers wish to thank Drs. S. P. Keller, R. S. Title, F. Jona, G. Mandel, L. Suchow, and G. Somorjai for much helpful discussion and many suggestions. The services of Mr. J. A. Kucza for many preparations and Mr. W. N. Hammer for assistance in making many of the measurements is gratefully acknowledged.

Manuscript received Jan. 15, 1962.

Any discussion of this paper will appear in a Discussion Section to be published in the June 1963 JOURNAL.

REFERENCES

1. H. Dember, *Physik. Z.*, **32**, 554, 856 (1931); **33**, 207 (1932).
2. V. P. Zhuze and S. M. Ryvkin, *Doklady Akad. Nauk. SSSR*, **62**, 55 (1948).
3. E. E. Bukke, *Optika I. Spektroskopiya*, **3**, 334 (1957).
4. A. M. Goodman and G. Warfield, *Phys. Rev.*, **120**, 1142 (1960).
5. R. H. Bube, "Photoconductivity of Solids," p. 384, John Wiley & Sons, New York (1960).
6. J. S. Moss, L. Pincherle, and A. M. Woodward, *Proc. Phys. Soc.*, **66B**, 743 (1953).
7. B. Gudden and R. Pohl, *Z. Physik.*, **2**, 192 (1920).
8. W. W. Piper and F. E. Williams, "Solid State Physics," Vol. 6, Academic Press, New York (1958).
9. R. E. Halsted, *Phys. Rev.*, **99**, 1897 (1955).
10. E. F. Apple and J. S. Prener, *J. Phys. Chem. Solids*, **13**, 81 (1959).
11. C. M. Hurd, *Proc. Phys. Soc. London*, **79**, 42 (1962).

The Effect of the Phosphor-Embedding Medium on the Performance of Electroluminescent Cells

Gabriel P. Katona[1]

Corning Glass Works, Corning, New York

ABSTRACT

The higher the dielectric constant of the phosphor-embedding medium, the higher is the field on the embedded phosphor. When working with ZnS-type phosphors, not much is to be gained from embedding media having dielectric constants higher than 50. In the case of embedding media having a low dielectric constant the emission can be increased by making the embedding medium of greater loss materials. This move will not necessarily lower the efficiency, but at points it will even improve it. It is shown that maximum efficiency can be obtained when the dielectric constant of the embedding medium and the phosphor are identical.

The primary goals of research for better electroluminescent lamps and devices are to develop materials and structures that will result in higher brightness and better luminous efficiency. Much has been reported in the literature of the work to achieve these aims through improved phosphors. In this paper the effect of the dielectrics on the brightness and efficiency of electroluminescent cells is discussed.

[1] Present address: Nolte and Nolte, New York, N. Y.

Dielectrics perform two basic roles in electroluminescent structures: (*a*) they act as embedding media, (*b*) they are used as breakdown protecting layers. The second function will be discussed in a later article.

The properties of the embedding medium have a multifold effect on the performance of an electroluminescent lamp. Such effects can be due to dielectric properties of the materials, physicochemical interaction between the phosphor and dielectric, viscosity of the dielectric allowing movement of the embedded phosphor, moisture penetrability of the dielectric affecting maintenance, etc. This paper investigates the effect of the dielectric properties.

The availability of embedding materials embracing a wide range of dielectric properties is rather limited. Therefore, the considerations to be presented may aid in the selection of the materials that are most suitable for a required purpose.

The same green emitting ZnS:Cu, Cl electroluminescent phosphor was used throughout the investigation; thus the considerations presented can be assumed to be valid in case of other phosphors only when the voltage response of the other phosphor is similar to that of the phosphor used here. Definitions of the symbols used are listed at the end of the paper.

Effect of the Dielectric Constant

Roberts (1) and Kerner (2) have shown that the internal field, directly acting on the embedded phosphor, is related to the applied field by

$$E_o = E_2 \frac{3K_1}{2K_1 + K_2 - N(K_2 - K_1)} \qquad [1]$$

The value of $K_2 = 10$ was used for the dielectric constant of the phosphor in the subsequent calculations. This is an approximate average of the various values reported in the literature for ZnS-type electroluminescent phosphors.

The internal field was calculated as a function of the dielectric constant of the embedding medium, by means of Eq. [1]. The results are shown in Fig. 1. The arbitrary value of 23% by volume of phosphor was used. The applied field was 100 v/cm.

As Fig. 1 and Eq. [1] indicate, by choosing embedding media having a dielectric constant higher than the dielectric constant of the phosphor, the internal field acting on the phosphor becomes greater than the field applied across the cell proper.

Using the above example of 23% by volume phosphor and 100v applied across a thickness of 1 cm, it is possible to obtain internal field values which are higher than the applied electric field. When the dielectric constant (permittivity) of the embedding medium is infinite, it allows unimpeded passage of the applied field, which then appears across a continuous phosphor layer that is in effect 0.23 cm thick. The resultant field across the phosphor then is 100/0.23 = 435 v/cm.

The results obtained by using Eq. [1] were used to plot the effect of the dielectric constant of the embedding medium on the emission intensity. A cell was prepared by embedding a commercial EL phosphor in glass[2] and the brightness values, measured as a function of voltage on this cell, were used for the calculations. The phosphor concentration was 23% by volume, and the frequency was 1000 cps. The dielectric constant of the embedding glass was about 5.

[2] Corning Code 1970, a glass specially developed for electroluminescent phosphor-embedding purposes.

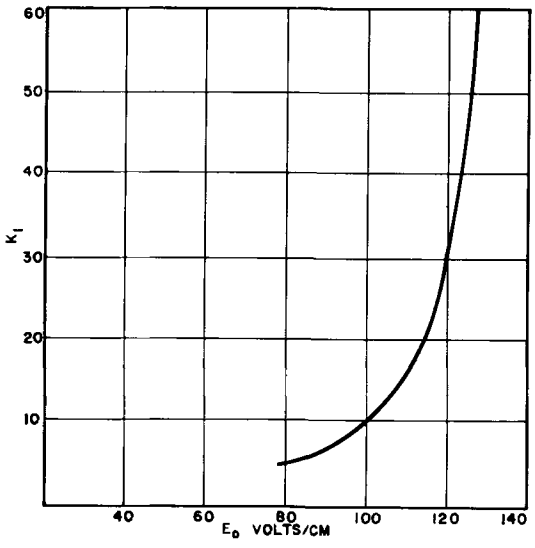

Fig. 1. Effect of the dielectric constant of the phosphor embedding medium on the internal field.

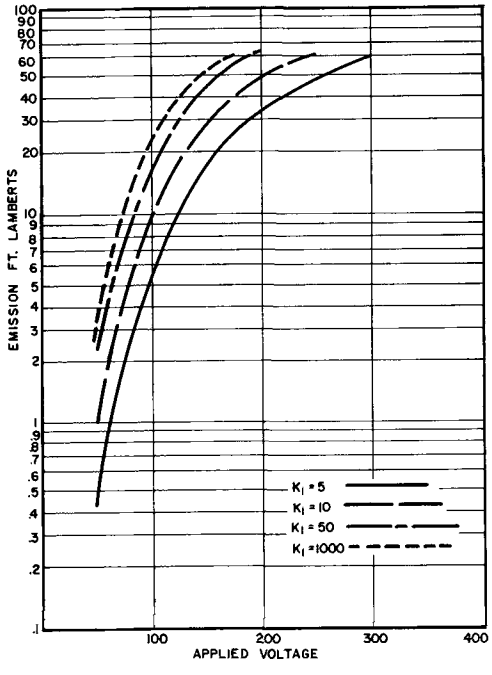

Fig. 2. Effect of the dielectric constant of the phosphor embedding medium on the emission intensity.

As Fig. 2 shows, by raising the dielectric constant of the embedding material from 5 to 10, a brightness gain of about 100% can be predicted. By further raising the dielectric constant from 10 to 50 a further brightness gain of nearly 100% can be predicted. By raising the dielectric constant from 50 to 1000, a brightness gain of only about 30% could be realized theoretically within the validity of Eq. [1]. These data indicate that, when striving to raise the dielectric constant of the presently available embedding media by intensified materials development efforts, a practical limit of 50 would be adequate.

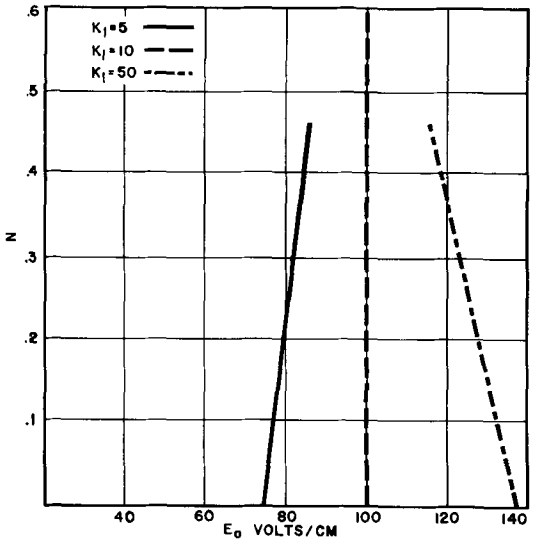

Fig. 3. Effect of the phosphor volume ratio on the internal field

Effect of Phosphor Concentration

Equation [1] can also be used to calculate the effect of phosphor concentration on the field distribution within the electroluminescent layer. Figure 3 shows the internal field as a function of the volume fraction of the embedded phosphor. As above, the dielectric constant of the phosphor was assumed to be 10, and the applied field, 100 v/cm.

Effect of the Loss Tangent

The complex dielectric constant of the form

$$K^* = K' - jK'' \qquad [2]$$

was substituted into Eq. [1] for the dielectric constants of the embedding medium (K_1) and the phosphor (K_2). Thus one obtains

$$E_o = E_2 \frac{3(K'_1 - jK''_1)}{(K'_1 - jK''_1)(2+N) + (K'_2 - jK''_2)(1-N)} \qquad [3]$$

By using the loss characteristics of the phosphor that was used throughout this work (3) it was found that the phosphor can be represented only by its dielectric constant and that neglecting the phosphor loss has only a very small effect on E_o in case of phosphor concentrations in the 20% by volume range.[3] Consequently Eq. 3 was modified to read:

$$E_o = E_2 \frac{3(K'_1 - jK''_1)}{(K'_1 - jK''_1)(2+N) + K_2(1-N)} \qquad [4]$$

By substituting $K''_1 = K'_1 \tan\delta$ one obtains for the absolute value of the internal field:

$$E_o = 3E_2 \sqrt{\left\{\frac{K'_1K_2(1-N) + K'^2_1(2+N)(1+\tan^2\delta)}{[K_2(1-N) + K'_1(2+N)]^2 + [(2+N)(K'_1\tan\delta)]^2}\right\}^2 + \left\{\frac{(1-N)(K'_1K_2\tan\delta)}{[K_2(1-N) + K'_1(2+N)]^2 + [(2+N)(K'_1\tan\delta)]^2}\right\}^2} \qquad [5]$$

The values of E_o *vs.* tan δ are shown in Fig. 4 for different values of K'_1. The phosphor concentration was chosen to be 20% by volume and the applied field was 27.39 kv/cm (69.57 v/mil). The calculations were executed by a Royal McBee LGP-30 digital computer. The corresponding tan δ *vs.* emission curves are plotted in Fig. 5 and were obtained by utilizing the E_o *vs.* emission values of the same phosphor. This curve was calculated from an experimental E_2 *vs.* emission curve, using Eq. [1].

The curves indicate that, in the case of embedding media having a relatively low dielectric constant, the emission can be considerably enhanced by choosing a lossy material. Only small effects can be achieved by progressing from a low loss value to about tan δ = 0.5. There is no reason to believe that Eq. [5] should not be valid for higher values of tan δ, because (except for the assumption of spherical phosphor particles) the equation was derived by rigorous mathematical treatment from Eq. [1].

By using the values plotted in Fig. 5, one can observe that, when an embedding medium with a dielectric constant of 2.5 (approximately the permittivity of polystyrene) is used, the emission of the electroluminescent cell theoretically can be increased by a factor of 6, by theoretically increasing the loss tangent to 1 (45°). When an embedding medium having a dielectric constant of 5 (approximately Corning Code 1970) is used, the emission theoretically can be doubled by increasing the loss tangent from a low value to 1.

It is evident that it would be more advantageous to select embedding media with a high dielectric constant, if one wishes to increase the output of the lamp. If such a material is not available, the same effect can be obtained by using a higher loss material, although possibly at the cost of lower efficiency and heating of the lamp.

An attempt was made to check Eq. [5] and Fig. 5 experimentally. The dielectric constants and loss tangents of various liquids were measured on a General Radio 650A impedance bridge at 1 kc, using a GE three terminal, liquid sample holder (G. E. Co., Cat.

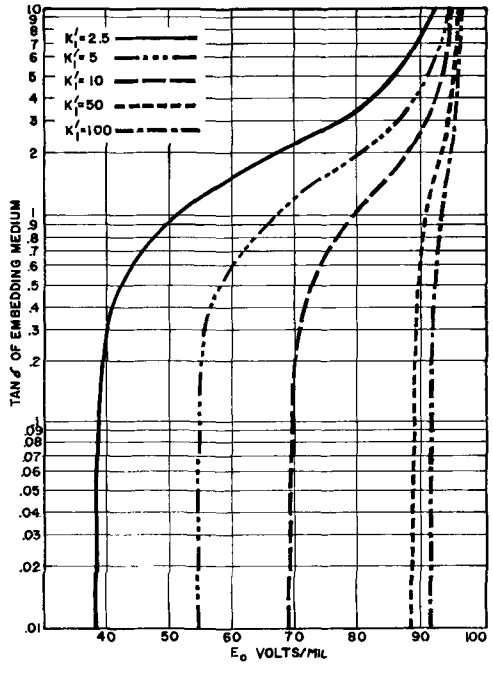

Fig. 4. Internal field as a function of the loss tangent of the phosphor embedding medium.

[3] This is not necessarily applicable to all electroluminescent phosphors and phosphor-embedding medium combinations. For detailed discussion on the subject see: A. N. Ince and C. W. Oatley, *Phil. Mag.*, 46, 1081 (1955); W. Lehmann, *This Journal*, 103, 24 (1956).

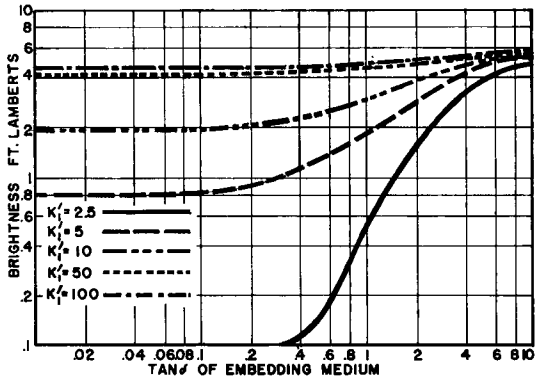

Fig. 5. Emission intensity as a function of the loss tangent of the phosphor embedding medium.

5100774). The measurements were made with the phosphor and the liquid being in a sample holder with a 0.00584 cm (2.3 mil) gap. An audio oscillator and a high powered amplifier were used as power source. The emission measurements were made with a VISCOR visibility correcting filter-equipped Weston 856 type photocell and a L&N Type E galvanometer. In instances where tan δ was very high, a resistance had to be used in a series with the cell, to limit the current.

Table I contains the measured dielectric properties and the results of the electroluminescent evaluation, together with the calculated values. The phosphor was the identical phosphor used in the earlier parts of the study where it was used in a glass embedding medium. 20% by volume was used, the emission was measured at 1 kc, and the applied field was 27.39 kv/cm. To obtain the values in the "calculated" column of Table I, the value of E_o was calculated and the corresponding brightness value was obtained from the E_o *vs.* brightness curve of the phosphor.

The fact that all experimental data are lower than the calculated ones led to a reexamination of Eq. [5]. Small discrepancies in the values of K_2 and N cannot account for the difference. Only two significant figures were obtained in the measurement of the dielectric constant and loss tangent because the balance of the bridge was rather broad, due to the relatively high loss values. The K'_1 and loss tangent values of most of these liquids are extremely frequency-sensitive. For example, in case of acetone at 10 kc, values were measured of $K'_1 = 23$ and tan $\delta = 0.7$; therefore an inaccurate frequency adjustment may have been a large source of error. The effect of orientation of the phosphor in the liquid medium under the applied field was not considered. In the light of the above considerations, the agreement between the measured and calculated values can be considered good.

Table I. Calculated and measured emission intensities of an electroluminescent phosphor in various phosphor embedding media

Liquid	K'_1	Tan δ	Brightness/ft-L	
			Calculated	Measured
Acetone	1300	25	5.1	4.8
Benzene	2.3	0.01	(<0.4)	(<0.4)
Castor oil	4.7	0.082	0.7	0.6
Glycerol	90	3.7	5.0	3.9

Power Requirement and Efficiency

The calculation of power input and efficiency from the available data can be made with the aid of the following equation:

$$P = 2\,\epsilon_o\, f\, V^2 K'' \frac{A}{D} \qquad [6]$$

A similar formula has been quoted by von Hippel (4).

The results of the power and efficiency calculations are shown in Fig. 6 and 7. It is interesting to note that in case of a dielectric constant of 2.5 there are three different solutions for the same efficiency. This means that a brightness increase by a factor of 25 can be obtained at no loss of efficiency by increasing the tan δ of the embedding medium. With higher dielectric constants that effect rapidly diminishes.

Figures 6 and 7 indicate that the maximum obtainable efficiency, regardless of the brightness, can be obtained with embedding media having a dielectric constant somewhere between 5 and 50. The efficiencies were calculated for a series of dielectric constant values in order to determine the maximum. Figure 8 shows the results of these calculations for a value of tan δ of 0.01 in each case. The curve shows the maximum efficiency is obtained at a point where K'_1 is near 10. At this point the assumed dielectric constant of the phosphor and the dielectric constant of the embedding medium are identical.

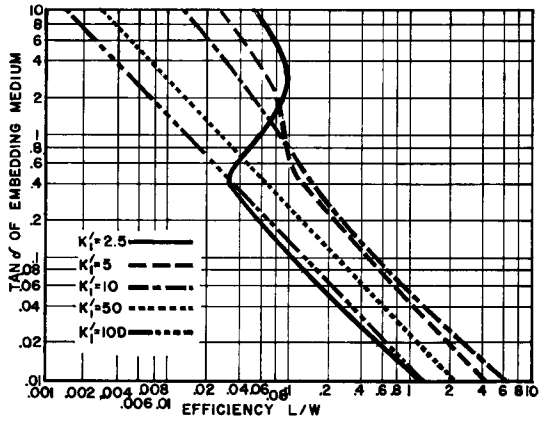

Fig. 6. Effect of the loss tangent of the phosphor embedding medium on the efficiency.

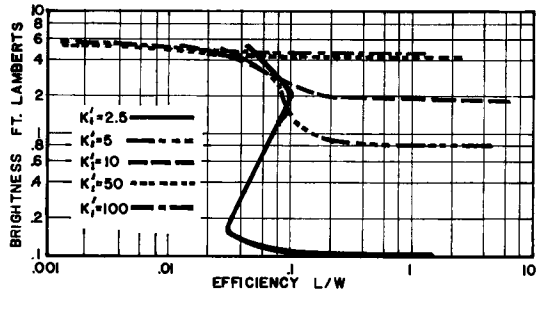

Fig. 7. Efficiency as a function of the emission intensity and the dielectric constant of the embedding medium.

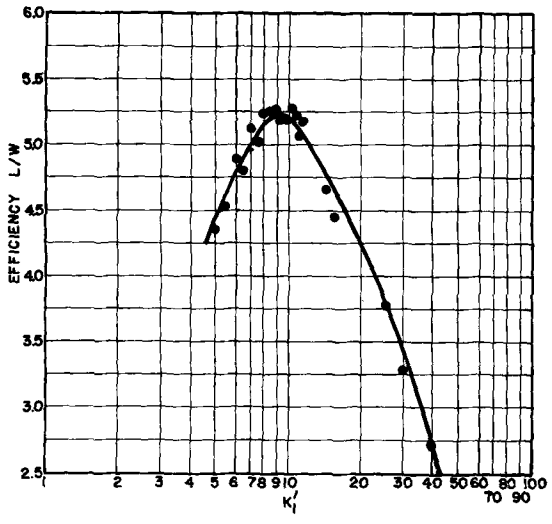

Fig. 8. Maximum efficiency of an electroluminescent cell as a function of the dielectric constant of the phosphor embedding medium.

The incidence of maximum efficiency when the dielectric constants of the phosphor and the embedding medium are identical can be considered only indicative at the most, because the voltage value substituted into Eq. [6] was not the voltage at which peak efficiency (5) can be obtained, but was the same arbitrary voltage used in earlier parts of the study.

Summary

The effect of the dielectric properties of electroluminescent phosphor-embedding media on brightness and efficiency have been examined. Using a formula by Roberts (1), it was established that an increase in the dielectric constant of the embedding medium above a value of 50 does not result in an appreciable gain in emission.

By expanding Roberts' formula to include the loss factor, the effect of the loss tangent of the embedding material was investigated. The results show that from a low loss tangent value of 0.01 to about 0.5, very little change in light emission can be obtained, but above 0.5 a rapid increase in brightness occurs. At successively higher dielectric constant values this increase diminishes. The theoretical calculations were in good agreement with experimental measurements.

In case of a lower dielectric constant embedding media, three different emission values can be obtained at the same efficiency if the loss tangent is varied. Consequently, in such a case the brightness can be increased substantially at no cost in efficiency. Indications are that maximum efficiency can be obtained when the dielectric constant of the phosphor and the embedding medium are identical. In this case the applied field equals the internal field.

Acknowledgments

The valuable suggestions made by Drs. R. V. Harrington and V. D. Mochel and Mr. W. H. Barney are greatly appreciated. Mr. K. R. Kiehl programmed the computer. Miss M. T. Splann has made the dielectric and Mr. J. C. Pinkston the electroluminescent measurements.

Manuscript received March 27, 1961; final revised manuscript received March 16, 1962.

Any discussion of this paper will appear in a Discussion Section to be published in the June 1963 JOURNAL.

REFERENCES

1. S. Roberts, *J. Opt. Soc. Amer.*, **42**, 850 (1952).
2. E. H. Kerner, *Proc. Phys. Soc.*, **69B**, 802 (1956).
3. W. Lehmann, Private communication.
4. A. von Hippel, "Dielectrics and Waves," p. 26, John Wiley & Sons, New York (1959).
5. W. Lehmann, *Illum. Engrg.*, **51**, 684 (1956).

DEFINITION OF SYMBOLS

E_o, Internal electric field, acting on suspended phosphor particles.
E_2, Applied, external electric field.
K_1, Dielectric constant of embedding medium.
K_2, Dielectric constant of phosphor.
N, Volume fraction of embedded phosphor.
K^*, Complex dielectric constant.
K'_1, Real dielectric constant of embedding medium.
$K''_1 = K'_1 \tan \delta$, Loss factor of embedding medium.
$\tan \delta$, Loss tangent (of embedding medium).
V, Voltage, rms.
f, Frequency, cps.
A, Area, cm^2.
D, Thickness, cm.
ϵ_o, Permittivity of free space $= 8.85 \times 10^{-14}$, Farads/cm.
P, power, watts.
Eff., Efficiency, lpw.

Neutron-Activation Study of Gallium Arsenide Contamination by Quartz

Werner Kern

Semiconductor and Materials Division, Radio Corporation of America, Somerville, New Jersey

ABSTRACT

Gallium arsenide crystals were synthesized by the horizontal Bridgman method in neutron-activated boats of natural and synthetic fused quartz. Instrumental radiochemical techniques were applied to determine the silicon concentrations from Si^{31} radioactivity measurements and to identify other trace elements transferred to the gallium arsenide during the process. All crystals were found completely enveloped in an impurity-enriched surface layer containing silicon concentrations up to 1500 ppm. Bulk concentrations of silicon ranged from 1×10^{17} to 3×10^{18} atoms/cm^3 GaAs, and varied in different sections of the crystals within a factor of 1.7. Evidence of several types of transfer mechanisms was obtained. Other impurities that originated from natural fused quartz and were detected in the form of their radioactive isotopes in the crystals include copper, gallium, antimony, and gold at concentrations below 10^{16} atoms/cm^3; the concentrations of these contaminants were effectively decreased by use of high-purity synthetic quartz.

The majority of gallium arsenide crystals made for use in semiconductor devices have been synthesized by the horizontal Bridgman technique (1) using reaction vessels of fused quartz. Experience has indicated that gallium arsenide becomes contaminated by silicon from the quartz during the processes of preparation. In fact, silicon has been detected consistently in gallium arsenide crystals as one of the major impurities and has been recognized as the main electron donor in this semiconductor compound (1). Because the degree of purity is one of the most important quality parameters in semiconductor-grade gallium arsenide, the present investigation was undertaken to provide more knowledge concerning the role of contamination by quartz.

A radiochemical method of analysis appeared to be most promising because of its inherent sensitivity and specificity for trace quantities. Gallium arsenide was synthesized in a neutron-activated quartz boat, and the crystal samples were then analyzed by radiocounting and gamma-ray spectrometry. The experiments were designed primarily to provide information on the extent of silicon contamination. Other impurities originating from the quartz and encountered in the course of this work were identified as a secondary objective.

Bombardment of pure quartz with neutrons in a nuclear reactor leads to several known nuclear transformations (2, 3). Considerations of the relative quantities and half-lives of the product nuclides and the prevailing experimental conditions show that the only reaction of importance in this work is the Si^{30} (n, γ) Si^{31} transformation which takes place between the Si^{30} isotope present in natural silicon and the thermal neutrons from the re-

Table I. Impurity concentrations in fused quartz (ppm, weight/weight)

Impurity element	G.E. Quartz* Found	(4)	(5)	Vitreosil** Found	(5)	(6)	Spectrosil*** Found	(6)
Al		42	20-30		10-100	50-60		<0.02
Ca		16			10	0.4		<0.1
Na	2-6	7		1		4	<0.04	0.04
Fe		4	1		<1-10			<0.1
K		2.5					<0.02	<0.005
Ti		2						
Li		2						
B		0.94				0.5		<0.01
Mg			0.1-1		3-10			
Cu	<0.5		<1-1	<0.2	<1-1	0.01	<0.02	<0.0002
Sb	0.7			<1		0.23	<0.02	<0.0001
Ga							<0.01	<0.004
Mn						0.026		<0.001
P						0.01		<0.001
As								<0.0002

* Clear fused quartz (99.97 to 99.98% SiO_2) from naturally occurring quartz crystals; General Electric Company.
** Ordinary quality transparent fused quartz (99.98% SiO_2) from naturally occurring quartz; Thermal American Fused Quartz Company.
*** Synthetic fused quartz (>99.9999% SiO_2); Thermal American Fused Quartz Company.
(4, 5, 6)—References to literature data.

actor. The Si^{31} decays with a half-life of 2.62 hr to stable P^{31} by emitting one 1.471 Mev negatron per disintegration. In addition, one gamma photon of 1.26 Mev energy is emitted in 0.07% of the disintegrations. Part of the accumulating P^{31} is in turn activated during the bombardment to P^{32}, which transmutes by 1.707 Mev negatron emission with a 14.3-day half-life to stable S^{32}. However, the presence of P^{32} does not conflict in the analysis because of its long half-life with respect to that of Si^{31}.

Possible interference from neutron-activated impurities in fused quartz manufactured from natural sources can be anticipated. Impurity concentrations in three types of quartz from various sources (4-6) are summarized in Table I; also included are some neutron-activation analysis data obtained during this work. A multitude of radionuclides can be expected to arise when these elements are bombarded with nuclear reactor neutrons of thermal and high energies. In the early stages of the radioactivity analysis, the beta activity in the quartz from any of these impurities is relatively small in comparison to the Si^{31} activity. The situation in the gallium arsenide, however, cannot be predicted. One impurity nuclide which could seriously interfere with the radiochemical silicon analysis is Mn^{56}, if it were present in the gallium arsenide crystals. This nuclide has a 2.58-hr half-life and emits beta and gamma rays; it is produced by the thermal-neutron reaction $Mn^{55}(n,\gamma)Mn^{56}$ and by the fast-neutron reaction $Fe^{56}(n,p)Mn^{56}$. The other predictable thermal-neutron activation products have half-lives of either less than 0.5 hr or more than 12 hr and can be resolved from the Si^{31} radioactivity by decay counting.

Experimental

The quartz boats were cleaned before and after activation by submersion in concentrated nitric acid for 20-60 min, followed by extensive rinsings with deionized and doubly quartz-distilled water. The boats were then placed in quartz tubes and irradiated in the water-cooled nuclear reactor of the Industrial Reactor Laboratories, Inc., at Plainsboro, New Jersey. The fluxes employed for the five experiments varied depending on the reactor core position available and ranged between 2×10^{13} and 9×10^{13} thermal neutrons cm^{-2} sec^{-1}, as determined by separate measurements with flux monitor foils and nuclear counters. An irradiation period of 8 hr was chosen to obtain an 88% saturation activity yield of Si^{31}, and to minimize the activation of impurity elements yielding longer-lived nuclides. The activated boats were extracted from the reactor, allowed to "cool off" for 1 hr to decrease the high radiation levels from short-lived nuclides, and were then transferred into the "hot cell" for remote manipulations.

The gallium arsenide synthesis and crystal growth were maintained as close to the normal standard techniques as possible, except that smaller ingots (7g) were prepared and shorter growth periods were employed than usual to minimize radioactivity losses of the rapidly decaying Si^{31}. A weighed quantity of >99.9999% pure gallium as obtained from the manufacturer was placed in the activated quartz boat and introduced in the reaction tube of natural fused quartz. A stoichiometric quantity of >99.999% pure arsenic, plus an excess sufficient to produce an operating pressure of 1 atm, was placed in a second quartz boat, which was not activated, and was positioned in the reaction tube. The tube containing the two boats was first evacuated to 10^{-6} mm Hg and outgassed for purification purposes for 1 hr at temperatures of 200°C for the As and 600°C for the Ga zone. The tube was tipped off in vacuum and introduced into the preheated resistance furnace. A temperature of 1240°C was maintained around the boat zone in which the gallium arsenide crystal was growing during a period of either 3 or 5 hr, while the arsenic reservoir temperature was kept at 600°C. Gallium arsenide crystals were grown at speeds of up to 2 in./hr. The temperature was then reduced to 900°C, the tube was pulled out of the furnace, cooled, and opened on a cutting machine. The vicinity of the radioactive boat was kept closely shielded at all times to minimize radiation hazards. The gallium arsenide crystal was then removed for radioscanning, surface treatments, sectioning, powdering, and radioactivity measurements. Radioactive silicon standards were prepared by crushing and powdering the activated quartz boat and intimately mixing portions weighed on an analytical balance with inactive gallium arsenide powder as diluent; the radiation emitted from the quartz was thereby modified in a similar manner to the radiation from the gallium arsenide samples.

Gas-flow counting was selected as the primary method for beta radioactivity measurements to provide a high sensitivity for the Si^{31} beta radiation and to minimize interfering gamma radiation from activated impurities. The counting rates were normalized and corrected according to radiochemical standard techniques and expressed as relative specific activities, cpm/g GaAs or SiO_2. Survey radiocounting was made with Geiger-Mueller end-window and probe counters connected to a count-rate meter. Integral gamma counting was performed with a scintillation counting unit. Gamma-ray spectrometry was carried out with a heavily shielded 3 x 3 in. thallium-activated sodium iodide crystal as a detector; pulses were transmitted to the linear amplifier of either a 100- or a 200-channel differential pulse-height analyzer. Spectral-data presentation by an automatic programmed printer and an automatic plotter provided scanning curves of differential counting rates *vs.* pulse heights. Energy calibration and counting efficiency of the spectrometers were made with gamma-rays from suitable radionuclide reference sources. Spectra chosen for complete evaluation were plotted in terms of net counting rate per channel as a function of channel number and gamma-ray energy.

The silicon concentrations in gallium arsenide samples were determined from beta radiation counting data which was plotted semilogarithmically as a function of the time. Graphical resolution of the decay curves into the components made it possible to obtain the 2.62-hr Si^{31} activity. The quantity

Table II. Si concentrations in GaAs crystals

Crystal No.	Quartz type of boat	Crystal growth, hr	Surface treatment prior to analysis	Part of crystal analyzed	Si concentration ppm (weight/weight)	Si concentration atoms/cm³
1	G.E. natural fused quartz	3	A	Bottom section	8 ± 4	9.4×10^{17}
2	G.E. natural fused quartz	5	B	Bottom half	20 ± 10	2.3×10^{18}
3	G.E. natural fused quartz	3	C	Surface layer, bottom side	$1{,}500 \pm 150$	1.7×10^{20}
			C	Surface layer, top side	<168	$<2.0 \times 10^{19}$
			C and D	Bulk crystal	<28	$<3.3 \times 10^{18}$
4	Vitreosil natural fused quartz	3	C	Surface layer, bottom side	395 ± 40	4.6×10^{19}
			C	Surface layer, top side	<55	$<6.4 \times 10^{18}$
			C and D	Bulk crystal	1 ± 1	1.2×10^{17}
5	Spectrosil synthetic fused quartz	3	D	Front and rear sections	13 ± 2	1.6×10^{18}
			D	Center section	10 ± 2	1.2×10^{18}

A = lapping; B = sandblasting; C = carborundum paper abrasing; D = chemical etching in H_2O_2-NaOH solution.

of silicon was calculated on the basis of the specific net beta Si^{31} activities in the gallium arsenide samples and the corresponding quartz standards of known silicon contents, analyzed under similar conditions. Determination of the decay half-lives and the maximum beta energies of the resolved components aided in the identification of beta-radiation-emitting nuclides.

Gamma-ray emitters were identified by gamma scintillation spectrometry on the basis of their characteristic energy spectra and decay constants, using standard spectra (7) as comparison. Absolute disintegration rates were calculated by integrating the areas under the characteristic photopeaks resulting from the successive graphical resolution (8) of the spectra into the components. Typical spectra from gallium arsenide and the corresponding quartz standard are shown in Fig. 1 and 2. Concentrations of the detected elements were determined from the total number of disintegrations and the method of absolute neutron-activation calculation (9).

Results

Successive removal of thin surface layers by lapping showed that each of the five gallium arsenide crystals grown in activated quartz boats was completely enveloped in an impurity-enriched surface skin less than 0.02 mm thick. Silicon concentrations in these layers ranged up to 1500 ppm (Table II) for gallium arsenide crystal surfaces that had been in direct contact with the quartz during the preparation. The radioactive impurities in various sections and layers below the surface skin were rather homogeneously distributed, showing variations within a factor of only 1.7. Because of the fast crystal-growth rates necessary, no systematic gradient freeze segregation was expected, and none was detected. The concentrations of silicon inside the five crystals varied from 1 to 28 ppm by weight, as shown in Table II. In some experiments the radioactivity decay measurements of gallium arsenide and quartz standard samples were continued for 30 days following the neutron bombardment of the quartz boat. Resolution of the decay curves obtained identified component activities with half-life and beta-radiation-energy values corresponding closely to those of Si^{31}, Cu^{64}, Na^{24}, Sb^{122}, and P^{32}.

Depending on the time of analysis, different radionuclides were observed by gamma spectrometry. For instance, 30 hr after the quartz boat activation the nuclides indicated in Fig. 1 and 2 dominated the spectra. The maximum at 0.511 Mev in the Cu^{64} spectrum is caused by the annihilation radiation from the positrons associated with the Cu^{64} disintegrations. The unidentified peak at the 1.05 Mev energy position in Fig. 1 had a half-life of 14 hr. Numerous spectra were taken several days and weeks later when the radioactivity of the 15.0 hr-Na^{24}, 12.8 hr-Cu^{64}, and 14.2 hr-Ga^{72} had decreased below the detection limit. The major gamma component in gallium arsenide crystals grown in natural fused quartz boats had a gamma energy peak and a half-life corresponding to Au^{198} (0.412 Mev, 2.69 days). Energy and half-life measurements of other

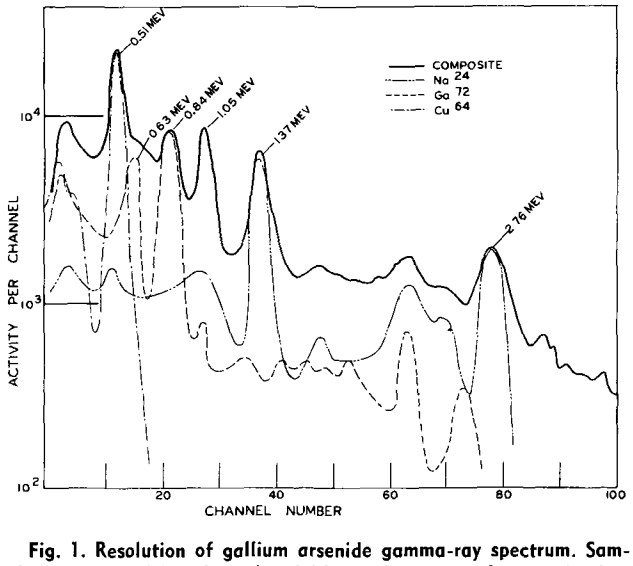

Fig. 1. Resolution of gallium arsenide gamma-ray spectrum. Sample from crystal No. 3 analyzed 30 hr after quartz boat activation. Solid line shows experimental composite spectrum. Normalized standard spectra as defined. Major energy maxima are indicated in Mev.

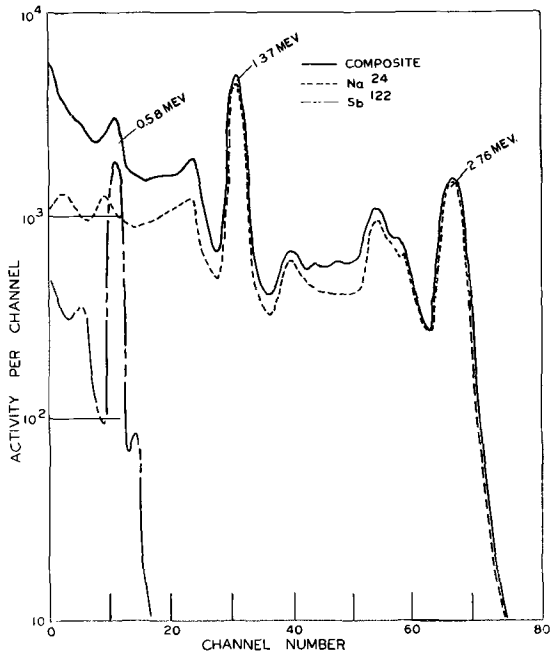

Fig. 2. Resolution of gamma-ray spectrum from quartz. Standard sample from quartz boat No. 3 analyzed 30 hr after neutron activation. Solid line shows experimental composite spectrum. Normalized standard spectra as defined. Major energy maxima are indicated in Mev.

components in these gamma spectra revealed the presence of Sb^{122} (0.564 Mev, 2.75 days), Sb^{124} (0.605 Mev, 60 days), and possibly Cr^{51} (0.323 Mev, 27.8 days). Corresponding gamma spectra from the natural fused quartz were dominated by the full energy photopeaks associated with the disintegration of the Sb^{122} and the Sb^{124} nuclides. The energy peak of the Sb^{124} isotope became observable after the shorter-lived activity from Sb^{122} with a similar energy maximum had disappeared from the spectra. Both radioisotopes were formed by the (n, γ) reaction from natural antimony (57.25% Sb^{121}, 42.75% Sb^{123}) contained in the quartz.

Although the gamma spectra of various gallium arsenide crystals from the natural fused quartz boats were similar in composition, the crystal grown in synthetic fused quartz had considerably more complex spectra which were difficult to resolve by instrumental analysis. Na^{24} and Ga^{72} were positively identified, while the identity of Zn^{65m}, K^{43}, Cu^{64}, Sb^{122}, W^{187}, La^{140}, and Au^{198} was not conclusively established. Concentration levels calculated on the basis of (n, γ) reactions are summarized in Table III. Synthetic fused quartz also has gamma spectra which are different from those of natural fused quartz brands and are characterized by impurity concentrations orders of magnitude lower (Table I).

Discussion

The radioactivity measurements of the gallium arsenide samples could not be started until at least 12 hr after the neutron bombardment of the quartz boats had been terminated because of the necessary manipulations, preparations, and crystal growing. This time delay is the severest of the difficulties in the analysis because of the diminishing sensitivity and accuracy of the Si^{31} radioactivity measurements and cannot be substantially reduced unless the synthesis conditions are altered unrealistically.

Furthermore, an unfavorable change of the radioactivity composition in the gallium arsenide samples takes place. The beta-radioactivity decay curve of natural fused quartz showed that the Si^{31} concentrations during the early stages of radiocounting are about two orders of magnitude greater than the longer-lived background radiation levels; in gallium arsenide samples, however, the relative Si^{31} activity is sharply reduced. These differences in the radioactive impurity concentrations in quartz and gallium arsenide indicate that the contamination process proceeds selectively with respect to different impurities. The transfer is not simply a dissolution process of quartz, but involves diffusion of trace impurities to various degrees. Gamma-ray spectrometry supported these findings and extended them to additional impurity elements. For instance, Au^{198} represented the major radioactive constituent in a "one-week-old" gallium arsenide sample, but could not be detected in the corresponding spectra of the quartz tube from which the boat had been made. In contrast, Sb^{122} and Sb^{124} were taken up by the gallium arsenide to a limited extent only, but represented the major residual radioactivity in the quartz

Table III. Radiochemically detected elements in GaAs transferred from activated quartz boats

Impurity, atoms/cm³	Crystal No. 1 from G.E. natural fused quartz	Crystal No. 2 from G.E. natural fused quartz	Crystal No. 3 from G.E. natural fused quartz	Crystal No. 4 from Vitreosil natural fused quartz	Crystal No. 5 from Spectrosil synthetic fused quartz
Si	9×10^{17}	2×10^{18}	$<3 \times 10^{18}$	1×10^{17}	1×10^{18}
Zn	—	—	—	—	$<2 \times 10^{15}$*
Na	—	$\sim 4 \times 10^{15}$	$\sim 5 \times 10^{14}$	$\sim 5 \times 10^{14}$	$<5 \times 10^{13}$
K	—	—	—	—	$<8 \times 10^{14}$*
Cu	—	—	$<5 \times 10^{14}$	$<5 \times 10^{14}$	$<2 \times 10^{13}$*
Ga	—	—	$\sim 1 \times 10^{14}$	$\sim 2 \times 10^{14}$	$<1 \times 10^{13}$
P	—	$<2 \times 10^{13}$	—	—	—
Sb	—	$\sim 2 \times 10^{12}$	—	—	$<5 \times 10^{12}$*
Cr	—	$<5 \times 10^{12}$*	—	—	—
W	—	—	—	—	$<7 \times 10^{12}$*
La	—	—	—	—	$<5 \times 10^{12}$*
Au	—	$\sim 3 \times 10^{11}$	$<5 \times 10^{11}$	$<3 \times 10^{11}$	$<3 \times 10^{10}$*

— No determination made; * identity not definitely established.

after decay of the shorter-lived nuclides. Controlled etching experiments with activated fused quartz excluded the possibility that the impurities originated from the quartz surface, indicating that they must have diffused from the bulk toward the inner surface of the quartz boat.

The possible sources of error in the analysis were carefully examined. The homogeneity of the neutron flux within the sample area was demonstrated by measuring the induced radioactivity in samples from various positions of the quartz boats. Flux hardening and self-shielding effects (10) by strong absorption of thermal neutrons are considered negligible at the quartz thickness of only a few millimeters. Surface contamination of the quartz boats was minimized by acid cleaning before and after the work at the nuclear reactor facility.

The estimation of impurity elements other than silicon should be considered as semiquantitative because it was not possible to include standards during the neutron activation. Consequently, it was necessary to use theoretical calculation methods which are based on several assumptions. The neutron flux was known with an accuracy of not better than $\pm$ 25%. Nuclear reactions with fast neutrons may contribute to the formation of a particular radioactive nuclide. For instance, besides the main reaction Na^{23} (n, γ) Na^{24}, radiosodium is also formed by the reactions Al^{27} (n, α) Na^{24} and Mg^{24} (n, p) Na^{24}. However, calculations showed that the errors introduced were less than the uncertainties in the neutron flux.

The possibility of changes in the properties of the irradiated quartz used as boat material and their effect on the results were evaluated in the light of present literature (11-13), but seemed to impose no critical complications under the activation conditions used. While all samples of activated natural quartz were typically purple colored from the ionization of impurity-atoms, synthetic fused quartz remained colorless, which is consistent with the extremely low impurity concentrations in this material. Although the formation of color is the most immediately apparent radiation effect, it is easily reversed by annealing at elevated temperature.

Systematic errors in the radioactivity measurements were avoided by use of the usual corrections, calibrations, and statistical treatments of the data. The determination of the silicon concentration in the gallium arsenide was based on a direct comparison with the induced Si^{31} activity in the quartz boat used, so that error factors associated with the activation and the radiocounting were essentially eliminated. The accuracy of the silicon analysis was curtailed by large proportions of extraneous radioactivity from which the Si^{31} had to be resolved. The specificity of the Si^{31} analysis was ascertained by demonstrating the absence of interfering radioactivity levels from other nuclides with half-lives similar to Si^{31}. Mn^{56}, the most critical potential impurity in gallium arsenide, was looked for by both beta-radiation transmission measurements designed to detect the energetic 2.86 Mev beta rays and by gamma-ray spectrometry to discover the characteristic 0.845 Mev major gamma photons emitted by this nuclide. Chemical separation of the silicon from the gallium arsenide was considered, but was avoided after exploratory experiments showed that more work was needed to develop a rapid method.

The radiochemically determined silicon concentrations in the five surface-treated gallium arsenide crystals ranging from 1 x 10^{17} to 3 x 10^{18} Si atoms/cm^3 (Table II) checked with the emission spectrographic analyses for total silicon, but are higher than those presently obtained with more refined crystal growing techniques. Additional reasons might be the polycrystallinity of these ingots, their small size which introduced a larger quartz surface area per unit weight of gallium arsenide than in normally grown crystals, and the rapid pulling rate which prevented gradient freeze segregation. For comparison, typical published (1) silicon concentrations compiled from 100 gallium arsenide crystals ranged from 5 x 10^{15} to 5 x 10^{18} Si atoms/cm^3, with the majority of data falling between 5 x 10^{16} and 5 x 10^{17}.

As shown in Table III, the concentrations of other radiochemically detected impurity elements in the gallium arsenide were in nearly all cases less than 10^{16} atoms/cm^3. Emission spectrographic analysis also showed the usual concentrations of impurities at or below the detection limits, including copper, iron, and magnesium.

The transfer of impurities from the quartz to the gallium arsenide appears to be possible by several routes: (i) adhesion of quartz particles to the crystal, (ii) dissolution of quartz in the melt, (iii) gas phase transport of volatile impurities, and (iv) diffusion of impurities through the quartz and the gallium arsenide.

Adhesion of quartz particles to the ingot was observed with synthetic quartz. Irregular areas of high radioactivity were located by microprobe counting on the bottom side of the crystal prior to surface treatments. A high degree of wetting of the gallium to the boat was observed during the bake-out, and the gallium arsenide crystal adhered to the surface after removal from the furnace. Although this condition cannot be considered typical, it has been observed irregularly in production with Spectrosil boats and may be caused by the high water-vapor content of this quartz, which lowers its softening point (5).

The electrical properties of silicon at concentrations normally encountered in gallium arsenide suggest that this impurity is present in the elemental state. Experimental evidence indicates that silicon is formed by a chemical reaction of gallium with quartz. Silicon dioxide can be reduced by gallium at high temperature to free silicon and volatile gallium suboxide (14). Some of the silicon formed dissolves in the gallium or the gallium arsenide melt. Furthermore, free silicon gives rise to volatile silicon monoxide by reacting with quartz and may subsequently deposit on the exposed gallium arsenide surfaces.

It is clear from the data presented that the exclusive application of synthetic fused quartz for

the preparation of gallium arsenide offers distinct advantages in minimizing the impurity transfer. It is important, however, that the entire surface of the crystals be completely removed before further processing. This removal is best accomplished by abrasive blasting, followed by chemical etching. Other factors which are beneficial include effective surface treatments of the quartz by nitric acid cleaning, water rinsing, and vacuum baking; reduction of the reaction temperature and time as far as permissible; and reduction of the gallium arsenide-quartz contact area by growth of large-diameter crystals.

Acknowledgments

The author wishes to thank L. J. Vieland for his suggestion of neutron activation of quartz boats for investigating crystal contamination; D. A. Ross and R. F. Bailey for their cooperation and contributions in the activation phase, T. H. Baker and W. Oshinsky in the synthesis phase, and H. M. Hyman and G. Hornberger for the emission spectrographic analyses; G. M. Loiacono for his conscientious technical assistance in the project; and A. Mayer for critically reviewing the manuscript.

Manuscript received Jan. 15, 1962; revised manuscript received March 23, 1962. This paper was prepared for delivery before the Detroit Meeting, Oct. 1-5, 1961. The work described in this paper was sponsored by the Electronic Technology Laboratory, Aeronautics Systems Division, Air Force Systems Command, United States Air Force.

Any discussion of this paper will appear in a Discussion Section to be published in the June 1963 JOURNAL.

REFERENCES

1. L. R. Weisberg, F. D. Rosi, and P. G. Herkart, "Properties of Elemental and Compound Semiconductors," Vol. 5, p. 25, Interscience Publishers, New York (1960).
2. D. J. Hughes and R. B. Schwartz, "Neutron Cross Sections," BNL 325 and Supplement No. 1, U.S. AEC, (1958, 1960).
3. G. Friedlander and J. W. Kennedy, "Nuclear and Radiochemistry," John Wiley & Sons, Inc., New York (1957).
4. "Fused Quartz Catalog Q7A," p. 10, General Electric Company, Willoughby Quartz Plant, Willoughby, Ohio (1959).
5. L. R. Weisberg, Private communications.
6. M. H. Robinson, Private communications on data originally reported by C. A. Parker, Admirality Materials Laboratory, England.
7. R. L. Heath, "Scintillation Spectrometry Gamma-Ray Spectrum Catalogue," OTS IDP-16408 TID-4500 (1957).
8. R. E. Connaly, *Anal. Chem.*, **28**, 1847 (1956).
9. T. I. Taylor and W. W. Havens, Jr., "Physical Methods in Chemical Analysis," Vol. III, pp. 447-621, W. G. Berl, Editor, Academic Press, New York (1956).
10. R. C. Plumb and J. E. Lewis, *Nucleonics*, **13** [8], 43 (1955).
11. G. J. Dienes, *J. Phys. Chem. Solids*, **13**, 272 (1960).
12. W. Primak, *J. Phys. Chem. Solids*, **13**, 279 (1960).
13. I. Simon, *J. Am. Ceramic Soc.*, **40**, 150 (1957).
14. L. M. Foster and R. A. Kramer, *This Journal*, **107** [8], 189C (1960).
15. R. T. Sanderson, "Chemical Periodicity," p. 123, Reinhold Publishing Corp., New York (1960).

Evaluation of Germanium Epitaxial Films

J. R. Biard and Stacy B. Watelski

Texas Instruments Incorporated, Dallas, Texas

ABSTRACT

A method has been developed for rapid and accurate determination of the resistivity of p-type epitaxial germanium films deposited on p^+ germanium substrates. Determination of the resistivity is not dependent on a knowledge of film thickness. Data are presented for films with resistivities of 0.05-7.0 ohm-cm deposited on 0.002 ohm-cm substrates; film thicknesses range from 0.15 to 0.6 mil.

Several methods have been proposed and used to determine the resistivity of a p-type epitaxial germanium film deposited on a p^+ germanium substrate. Most of these methods relate breakdown, diffusion depth, or junction capacitance to resistivity and require a lengthy fabrication cycle employing exactly repetitive diffusion runs. The most serious objections to these methods of resistivity determination are the requirements for an optimum surface treatment and a precise junction delineation. In specific instances the resistivity and thickness of the films may also become serious objections. The simultaneous epitaxial deposition on an n-type pilot slice along with the normal p^+ substrate suffers from partial or complete thermal conversion of the pilot slice and yields erroneous results.

The purpose of this investigation was to develop a rapid and accurate technique for measuring the resistivity of p-type epitaxial germanium films deposited on p^+ germanium substrates. This technique, which has been developed, is called the elevated temperature technique and is based on the characteristic variation of resistivity with temperature exhibited by most semiconductors. The use of temperature as a parameter makes it possible to determine the resistivity of an epitaxial film without requiring a knowledge of the film thickness.

The characteristic variation of resistivity with temperature for noncompensated p-type germanium is theoretically calculated using the Brooks-Herring mobility theory. Only lattice and impurity scattering are considered in these calculations; other scat-

tering phenomena such as coulomb, neutral, and dislocation scattering are considered to have no first order effects on the mobilities. The calculated resistivity *vs.* temperature characteristics are compared with those empirically measured using homogeneous p-type germanium and found to be in good agreement. Results of the empirical tests form a standard of comparison for measuring any p-type germanium epitaxial film deposited on a p^+ germanium substrate with an accuracy of ± 20% (95% confidence limits) between 0.1 and 4.0 ohm-cm.

Discussion

The resistance of a semiconductor sample is determined by the size and shape of the sample and its resistivity. Due to the low value of the coefficient of expansion of germanium, variations in the resistance of a semiconductor sample with temperature are almost entirely due to the temperature dependence of resistivity. The equations used for calculating variation of resistivity with temperature are given in the Appendix. As indicated by Eq. [1] of the Appendix, resistivity is controlled by the number of free carriers and their mobilities; a discussion of the theoretical temperature variation of mobility and carrier concentration follows.

Only impurity scattering and lattice scattering mobilities will be considered of prime importance for this discussion. The impurity scattering mobility, Eq. [7], may be simplified for analysis as

$$\mu_I = K_1 T^{3/2} \left[\frac{1}{\ln(1 + K_2 T^2) - \dfrac{K_2 T^2}{1 + K_2 T^2}} \right]$$

At increasing temperatures above 100°K the bracketed expression remains relatively constant and the resulting mobility curve follows the $T^{3/2}$ slope. For temperatures below 20°K the bracketed term is dominant and, in conjunction with the $K_1 T^{3/2}$ term, yields a mobility curve with a $T^{-5/2}$ slope. The lattice scattering mobility Eq. [6], Fig. 1, yields a slope of $T^{-2.33}$. When these two mobilities are combined as in the Brooks-Herring equation (1), Eq. [7] of the Appendix, the resultant mobility curve μ_{LI} is as shown in Fig. 1.

Referring to Eq. [3], as temperatures increase into the intermediate (extrinsic) range, $P_I \rightarrow N_e$. That is, the number of free holes caused by ionization of the impurity atoms approaches the magnitude of the net impurity concentration and remains constant. Since for normal doping ranges $p_i << N_e$, p (the total number of free holes) also approaches N_e and $n << p$. At high temperature (in the intrinsic region) the number of free holes caused by intrinsic ionization, p_i, increases due to the dominant exponential term as does the number of free electrons, n_i, $(n \approx p)$. Thus, the total number of free holes, p, is determined by P_I at intermediate temperatures and p_i at high temperatures while the number of minority carrier electrons is negligible at intermediate temperatures and determined by n_i at high temperatures. The curve representing the magnitude of p *vs.* temperature is shown in Fig. 1.

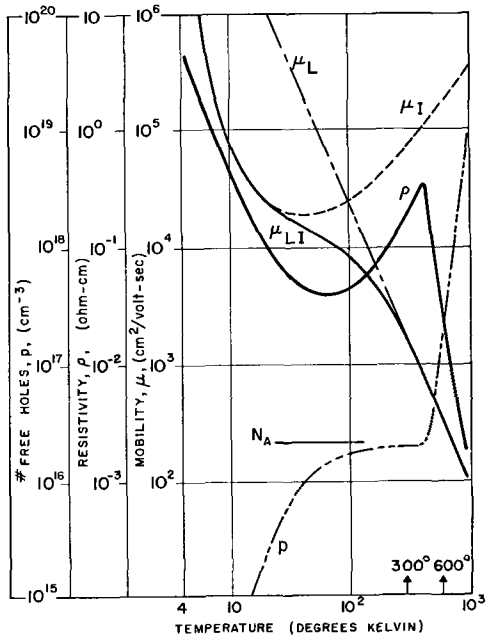

Fig. 1. Calculated mobility, resistivity, and free hole concentration *vs.* temperature, p-type germanium, $N_A = 2 \times 10^{16}$ atoms/cm³.

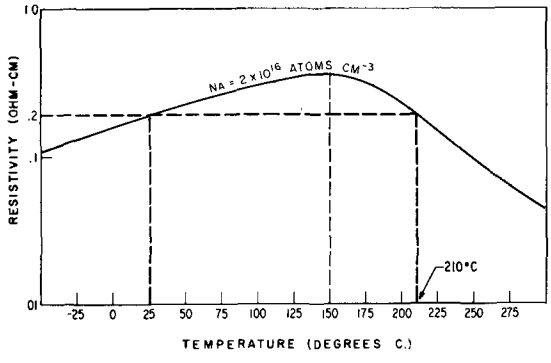

Fig. 2. Resistivity *vs.* temperature, p-type germanium

The variation of resistivity with temperature may be calculated by combining the characteristic curves of p, μ_{LI}, n, and μ_{LN} as dictated by Eq. [1].[1] One such curve of ρ *vs.* T for a wide range of temperature is shown in Fig. 1.

Note that the point at which the total number of free holes, p, begins to increase sharply (≈400°K) corresponds to that point at which the resistivity, ρ, reaches its inflection point, *i.e.*, beginning of intrinsic conduction.

The two arrows at the bottom of Fig. 1 indicate the range of temperature (300°-600°K) with which this report is mainly concerned.

Figure 2 shows the calculated resistivity *vs.* temperature characteristics of 0.2 ohm-cm p-type germanium. A resistor made from this material exhibits the same value of resistance at 25°C (extrinsic

[1] The contribution of the minority carrier electrons is negligible except in the intrinsic range where lattice scattering dominates. Therefore only the lattice scattering mobility, μ_{LN}, is used for electrons in Eq. [1].

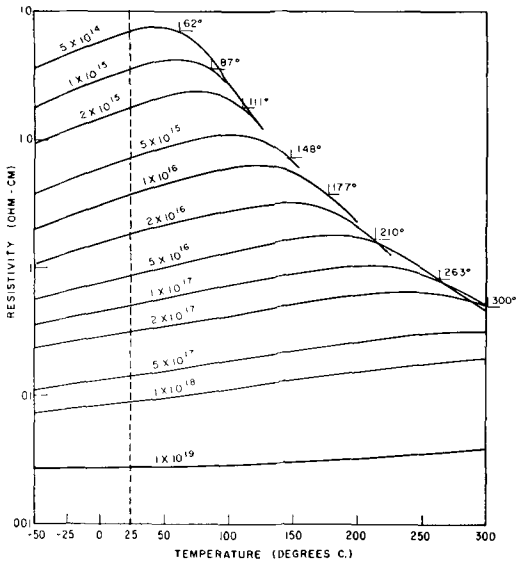

Fig. 3. Resistivity *vs.* temperature, p-type germanium

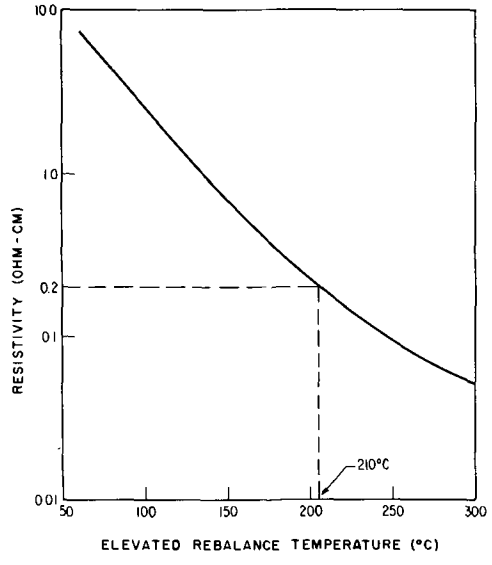

Fig. 4. Calculated resistivity *vs.* elevated rebalance temperature

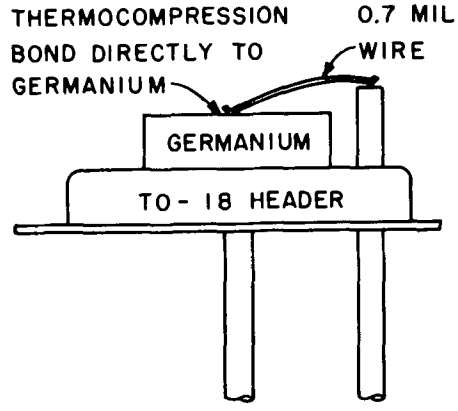

Fig. 5. Ohmic device. Resistance, $R = \frac{\rho}{2d}$, where ρ is the resistivity in ohm-cm and d the diameter of contact in cm; d remains constant throughout temperature range. $\therefore R \propto \rho$.

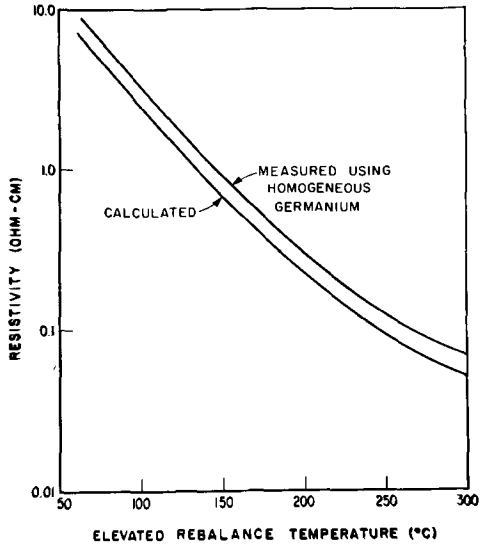

Fig. 6. Calculated and measured resistivity *vs.* elevated rebalance temperature.

range) and 210°C (intrinsic range). From Fig. 3 it is seen that the elevated temperature at which the resistivity is equal to the room temperature value is uniquely related to the resistivity. Thus, a resistivity measurement may be made by balancing a germanium resistive element in a low-frequency a-c bridge at room temperature and determining the elevated temperature of the resistive element at which the bridge returns to the balanced conditions.

Note in Fig. 3 the relatively constant resistivity corresponding to a doping level $N_A = 1 \times 10^{19}$ atoms cm^{-3}. This doping level is representative of p^+-type substrate material used in epitaxial depositions.

A calculated curve of resistivity *vs.* elevated rebalance temperature is presented in Fig. 4.

Figure 5 illustrates the construction of the homogeneous germanium resistors used for calibration purposes. The resistance of these ohmic devices is pure spreading resistance, $R = \rho/2d$, where d is the diameter of the contact (2). The resistance of the device is directly proportional to the resistivity as a result of the constancy of the contact diameter throughout the temperature range. Figure 6 compares the measured and calculated curves of resistivity *vs.* elevated rebalance temperature as determined from homogeneous resistive elements of known resistivity. Note that in the experimental case a unique relationship exists between resistivity and elevated rebalance temperature. Thus it is possible to generate an experimental calibration curve for a given test set using known homogeneous samples.

The construction details for epitaxial resistive devices are shown in Fig. 7; this type of mounting is used in determining the resistivity of the epitaxial layer. In order for the elevated temperature technique to give accurate results on epitaxial samples, it is necessary to construct the ohmic devices such that the temperature sensitive part of the total resistance is contributed by the epitaxial layer. Such a construction is possible due to:

(*a*) the use of small contact diameter (≈1.5 mil) to take advantage of spreading resistance in the substrate (substrate resistance is usually less than 2% of the total except for heavily doped thin epitaxial layers where it may approach 15%); (*b*) the fact that the resistivity of the heavily doped sub-

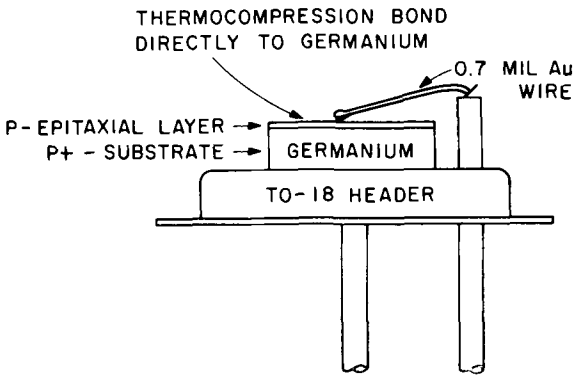

Fig. 7. Ohmic device. Epitaxial layer resistance, $R_E = \frac{\rho t}{A}$; substrate resistance, $R_S = \frac{\rho}{2d}$, where ρ is the resistivity in ohm-cm, t the thickness of epitaxial layer in cm; A the area of contact in cm^2; and d the diameter of contact in cm. t and d remain constant throughout temperature range. $\therefore R \propto \rho$.

strate material (≈0.002 ohm-cm) is nearly independent of temperature (corrections for the substrate may be applied where necessary).

The test set is composed of a temperature chamber, an a-c resistance bridge, and a phase-sensitive detector.

Results

Based on a statistical analysis of resistivity data the accuracy of the test set is ± 20% (95% confidence limits) between 0.1 and 4.0 ohm-cm, with reduced accuracy outside this range. These limits are based on resistive elements constructed from homogeneous material of known resistivity. By exercising extreme care in construction of the temperature chamber and the individual resistive elements it may be possible for an accuracy of ± 10% to be achieved.

It should be pointed out that the elevated temperature resistivity measurement is a destructive test; however, the volume of material required for the resistive element is small. If this technique is to be used as a measure of carrier concentration it is subject, like the 4-point probe, to errors due to compensation and inhomogeneous material.

The indicated rebalance temperature for an inhomogeneous film yields an "average" value for the film resistivity which is a function of the impurity profile within the film. From Fig. 3 it may be seen that the portion of the film having a resistivity higher than the indicated "average" is at a temperature greater than its rebalance temperature, while the lower resistivity portion is at a temperature less than its rebalance temperature. The profile of the film resistivity may be incrementally derived from elevated rebalance temperature vertical profile data. These data may be conveniently obtained by bevel lapping and staggered bonding.

An experiment was performed to determine the quantitative effect of the interfacial diffusion gradient on this measurement technique. A high resistivity (>8 ohm-cm) p-type epitaxial film was deposited on a highly doped p-type substrate; film thickness was 0.25 mil with a diffused gradient width of 0.06 mil as determined by chemical delineation. Consistent rebalance temperature readings were obtained throughout the film thickness, except for those within the interfacial diffused region.

Conclusions

The elevated temperature technique for resistivity measurement is a powerful tool for evaluating p-type germanium epitaxial films deposited on p$^+$ germanium substrates. Aside from routine evaluation of epitaxial film resistivity the technique has also been used to determine resistivity profiles at 5.0 mil increments across the face of epitaxial deposits. Used in conjunction with bevel lapping and staggered bonding, epitaxial deposits may be profiled for resistivity through the thickness of the layer in 0.05 mil increments.

Acknowledgments

The calculated resistivity *vs.* temperature data were supplied by Henry Riser and the statistical analysis of experimental data was performed by Vic Paulos. The test set was built and operated by Jack Leezer. Special fabrication techniques were supplied by Nadene Bedford and O. J. Lewis.

Manuscript received Feb. 12, 1962; revised manuscript received April 4, 1962. This paper was prepared for delivery before the Detroit Meeting, Oct. 1-5, 1961.

Any discussion of this paper will appear in a Discussion Section to be published in the June 1963 JOURNAL.

REFERENCES

1. P. P. Debye and E. M. Conwell, *Phys. Rev.*, **93**, 693 (1954).
2. H. C. Torrey and C. A. Whitmer, "Crystal Rectifiers," MIT Rad Lab Series, Vol. 15, McGraw-Hill Book Co. Inc., New York, Appendix C (1948).

APPENDIX

Equations for calculating resistivity of p-type germanium.

$$\rho = \frac{1}{e(n\mu_{LN} + p\mu_{LI})} \qquad [1]$$

$$e = 1.6 \times 10^{-19} \text{ coulomb}$$

$$n = \sqrt{\frac{P_I^2}{4} + p_i^2} - \frac{P_I}{2}$$

$$p = \sqrt{\frac{P_I^2}{4} + p_i^2} + \frac{P_I}{2} \qquad [2]$$

$$P_I = -\frac{B}{2}\left(1 - \sqrt{1 + \frac{4N_e}{B}}\right) \qquad [3]$$

$$B = 2.4147 \times 10^{15}\left(\frac{m_p}{m}\right)^{3/2} T^{3/2}\, e^{-1.1605 \times 10^4 E_D/T};$$

$$\left(\frac{m_p}{m}\right) = 0.2;$$

T = absolute temperature in °K;

$E_D = 0.0104\ (N_A < 2 \times 10^{17})$;

$= 0\ (N_A = 2 \times 10^{17})$; $= -\infty\ (N_A > 2 \times 10^{17})$

$$N_e = (N_A - N_D)$$

$$P_i = 1.76 \times 10^{16}\, T^{3/2}\, e^{-4560/T} \qquad [4]$$

$$\mu_{LN} = \frac{4.9 \times 10^7}{T^{1.66}}$$

$$\mu_{LI} = \frac{\mu_I\left(1 + 0.556\frac{\mu_I}{\mu_{LP}}\right)}{1 + 2.99\frac{\mu_I}{\mu_{LP}} + 0.556\left(\frac{\mu_I}{\mu_{LP}}\right)^2} \quad [5]$$

$$\mu_{LP} = \frac{1.05 \times 10^9}{T^{2.33}} \quad [6]$$

$$\mu_I = \frac{3.29 \times 10^{15}\, k^2\, T^{3/2}}{\left(\frac{m_p}{m}\right)^{1/2}(P_I + 2N_D)} \cdot \frac{1}{\ln(1+b) - \frac{b}{1+b}}$$

(Brooks-Herring equation) [7]

$$K = 16$$

$$b = \frac{1.29 \times 10^{14}\, K\left(\frac{m_p}{m}\right)T^2}{P_I + \left(1 - \frac{P_I + N_D}{N_A}\right)(P_I + N_D)}$$

EXPLANATION OF SYMBOLS

ρ, Resistivity in ohm-cm
e, Electronic charge in coulombs
n, Number of free electrons
p, Number of free holes
P_I, Number of free holes caused by ionization of impurity atoms
$\left(\frac{m_p}{m}\right)$, Effective mass of hole
E_D, Activation energy in electron volts for Boron dopant
N_e, Net impurity concentration in atoms cm^{-3}
N_A, Majority carrier concentration in atoms cm^{-3}
N_D, Minority carrier concentration in atoms cm^{-3}
p_i, Number of free holes caused by intrinsic ionization if impurity ionization were not present in cm^{-3}
n_i, Number of free electrons caused by intrinsic ionization if impurity ionization were not present in cm^{-3}
μ_{LN}, Lattice scattering (drift) mobility for electrons in cm^2/volt-sec
μ_{LP}, Lattice scattering mobility for holes in cm^2/volt-sec
μ_{LI}, Combined lattice and impurity scattering for holes in cm^2/volt-sec
μ_I, Scattering caused by ionized impurity atoms
K, Dielectric constant for germanium
T, Absolute temperature in °K

Thickness Measurement of Epitaxial Films by the Infrared Interference Method

M. P. Albert and J. F. Combs

Monsanto Chemical Company, St. Louis, Missouri

ABSTRACT

The infrared interference measurement has proved to be an accurate and nondestructive means for evaluating the thickness of epitaxially grown films on silicon. The measuring technique is discussed and the necessary relationships are presented. A fringe wavelength *vs.* film thickness chart is constructed, which enables rapid thickness determination without calculation. The chart is derived for use with silicon films of relatively low carrier concentration deposited on silicon substrates of high carrier concentration (0.007 ohm-cm-N-type). The chart is most useful for low order interference fringes including 12th order. Similar charts are applicable for other semiconductor materials.

Of the various methods examined for making thickness measurements on epitaxial films, the infrared interference method described by Spitzer and Tanenbaum (1) has proved to be best suited for most measuring applications. This method has the advantages of being accurate, quick, nondestructive, and well adapted for routine measurements. Interference fringes are observed only if there is a difference between the optical properties of epitaxially grown film and those of the substrate. This relationship between film thickness and the optical wavelengths of interference fringe maxima is given by a chart which is useful for rapid and accurate data reduction without calculation.

The Beckman spectrophotometers IR-4 and IR-5A equipped with NaCl optics and the Beckman specular reflectance attachment were used for this work. Additional measurements have also been made with KBr and CsBr optics.

Optical Properties of Epitaxial Films on Silicon

The primary requirement for production of interference fringes by reflection from a film is that the optical constants of the film differ from those of the substrate material. The optical constants of a silicon epitaxial film and substrate do not differ significantly unless the free carrier concentration at one side of the interface is very high, approaching degeneracy.

The reflectance at the interface between a nonabsorbing medium (n_1) and an absorbing substrate (n_2,k_o) at normal incidence is

$$R = \frac{(n_1 - n_2)^2 + k_o^2}{(n_1 + n_2)^2 + k_o^2} \quad [1]$$

where R is the reflectance, n is the refractive index, and k_o is the extinction coefficient of the substrate.

$$k_o = \frac{\alpha\lambda}{4\pi} \quad [2]$$

where α is the absorption coefficient and λ is the wavelength.

The influence of the very large free carrier concentration on the electrical susceptibility is such that as the optical wavelength is increased the refractive index decreases, and at still longer wavelengths the absorption effect predominates (2).

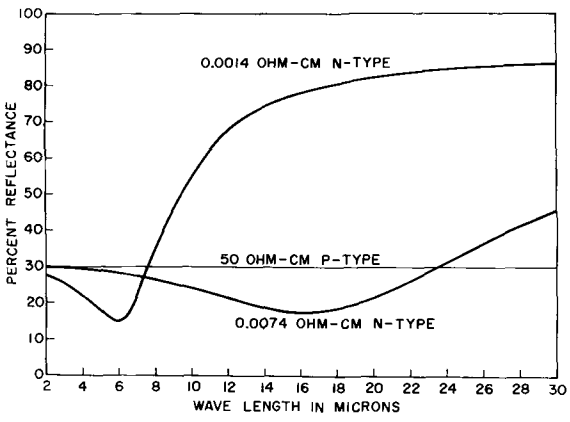

Fig. 1. Reflectance spectra of silicon samples showing the effects of carrier concentration on the optical constants. Decreasing reflectance, below 30%, indicates decreasing refractive index and large increasing reflectance indicates large increasing extinction coefficient.

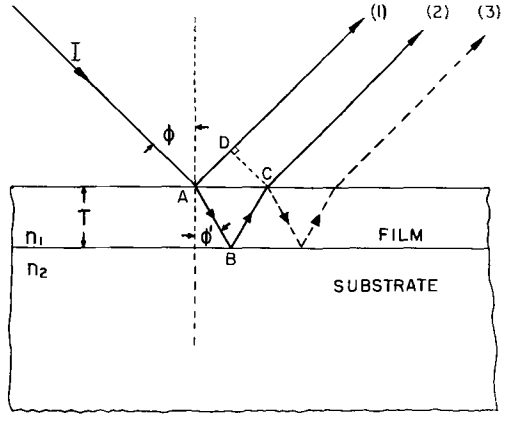

Fig. 2. Ray diagram for reflection from a film deposited on a thick substrate. The amplitudes of rays 1, 2, 3, etc., add vectorially resulting in maxima and minima in the reflectance spectrum.

The reflectance curves of Fig. 1 were obtained from silicon wafers prior to film deposition. The dip and subsequent rise in the reflectance curves for 0.0074 ohm-cm and 0.0014 ohm-cm N-type silicon, similar to reflectance curves shown in a paper by Spitzer and Fan (3), identify the decreasing refractive index and high absorption portions of the spectrum. Contrasted to the very low resistivity samples is the 50 ohm-cm sample which exhibits a nearly constant reflectance indicating a relatively constant refractive index.

Production of Interference Fringes

Figure 2, a ray diagram showing reflection from an epitaxial film at oblique incidence, is used to calculate the optical path difference between the first and second surface reflections. Interference fringes are observed when the first and second surface reflected rays interfere locally as the wavelength is varied.

The optical path difference is

$$\delta = n_1(AB + BC) - AD \qquad [3]$$

The refractive index, n_1, multiplies the apparent optical path in the film, (AB + AC), converting it to an equivalent air path.

Using Snell's law ($\sin \phi = n_1 \sin \phi'$) and Eq. [3] it can be shown that

$$\delta = 2Tn_1 \cos \phi' \qquad [4]$$

where T is the film thickness, ϕ is the angle of incidence, and ϕ' is the angle of refraction.

At point A, in Fig. 2, the reflected ray undergoes a phase change of π or $\lambda/2$ while the transmitted ray remains in phase with the incident ray. These phase relationships apply to reflection from an optically more dense (greater refractive index) dielectric.

At point B the reflected ray undergoes a phase change which may vary from 0 to π depending on the optical constants at the reflecting interface. However, if we limit this discussion to the spectral region where the reflecting substrate is known to have a lower refractive index than the film and also a negligibly small extinction coefficient, k_0, the phase change at point B can be taken as zero.

At point C, both the transmitted and reflected rays are in phase with the incident ray, BC.

For some wavelength, λ_0, the optical path difference will be

$$\delta = \lambda_0/2$$

At this wavelength ray 1 is advanced by $\lambda_0/2$ and ray 2 retarded by $\lambda_0/2$ giving a net difference of λ_0. It is assumed that maxima will occur at wavelengths where ray 2 is in phase with ray 1. The first (zero order) fringe will occur at λ_0, the next fringe (first order) will occur at λ_1, where

$$\delta = \lambda_1 + \frac{\lambda_1}{2} \qquad [5]$$

and the mth order fringe maxima will occur at λ_m where

$$\delta = \left(m + \frac{1}{2}\right)\lambda_m \qquad [6]$$

Minima occur at intermediate wavelengths where $\delta = m\lambda$, (m, an integer).

The additional reflections which occur within the film interfere with the resultant of rays 1 and 2. Each succeeding ray is delayed an additional amount δ relative to the preceding ray. At a fringe maximum these additional reflections alternately aid and oppose with a net result of decreasing the fringe maxima by a small amount. The additional reflections also reduce the values of the fringe minima. The fringes grow in intensity as the difference in refractive index between film and substrate increases. Fringe intensity is observed to increase with both wavelength and doping level of the substrate. These effects are predictable from the influence of wavelength and carrier concentration on the susceptability (1, 3).

Deviations from parallelism within the film and low gradient interfaces are common causes for fringe cancellation when it would appear that there is a sufficient difference of optical constants for fringes to occur.

As the extinction coefficient increases with increasing wavelength it predominates in determining the interface reflectance, Eq. [1]. Relatively high

interface reflectance is characteristic of this spectral region yielding large intensity fringes. The transition between low refractive index and high extinction coefficient is accompanied by a varying phase change upon reflection from the interface. The phase change is nearly zero if k_0 is small enough to be neglected in Eq. [1], and it increases approaching π for long wavelengths and large k_0 (5).

The transitional region should be avoided when making thickness measurements because of the varying phase change which introduces thickness measuring errors. Successive fringe pairs yield different thickness values in this region.

Thickness Computation

A convenient thickness relationship can be obtained from [4] and [6] utilizing two wavelengths corresponding to fringe maxima, λ_m and λ_{m+x}.

$$T = \frac{x(\lambda_m \lambda_{m+x})}{2n_1 \cos \phi' (\lambda_m - \lambda_{m+x})} \qquad [7]$$

where x is an integer representing the number of fringes occurring from λ_m to λ_{m+x}. An equivalent expression applies to linear wavenumber spectra where the fringe period is uniform.

Equation [7] can be applied to fringe minima as well as maxima and it is also independent of the phase change which may occur at the interface, provided the phase change is constant in the interval λ_m to λ_{m+x}.

The value for the refractive index of the film given by Salzberg and Villa (4) for optical grade silicon at 10μ is 3.4179, which is rounded to 3.42 and assumed constant over the 6-16μ range. The reflectance data also verifies this value.

The angle of incidence, ϕ, for the Beckman specular reflectance attachment is 30°, which corresponds to an angle of refraction of 8.4° and $\cos \phi' = 0.99$. The rays within the film are nearly normal to the surface, which makes the measurement relatively insensitive to ϕ.

The constant, $2n_1 \cos \phi' = 6.77$, when used with Eq. [7] gives film thickness in the same units as those used for wavelength.

The conditions imposed for the development of Eq. [7] were:

1. Fringe maxima occur at wavelengths where the first and second surface reflections are in phase (the phase difference is $2\pi m$, m an integer).

2. The phase change at the interface is zero or constant from λ_m to λ_{m+x}.

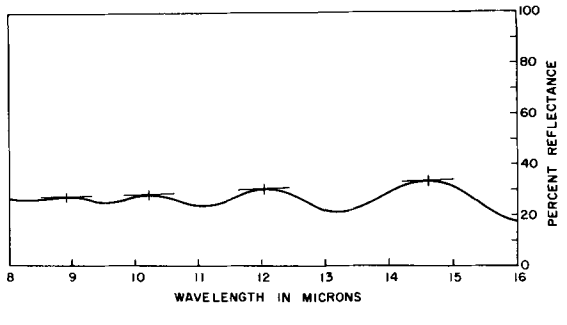

Fig. 3. Reflectance spectrum of a silicon epitaxial film showing the evaluation of fringe maxima.

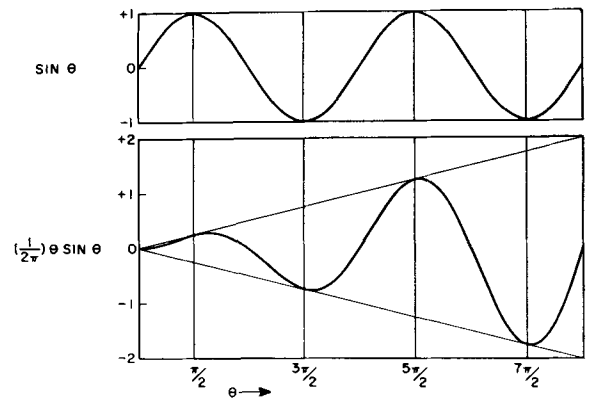

Fig. 4. Fringe model demonstrating the error which can arise by evaluating simple maxima. The desired phase relationship is satisfied at the points of tangency to the fringe envelope.

Evaluation of Fringe Maxima

In the preceding section the interference relationships given were based on wavelength values for which fringe maxima occur, as stated in condition 1. Condition 1 is correct only for equal intensity fringes, and it is incorrect for epitaxial films where the fringes grow in intensity with increasing wavelength. Figure 3 shows a typical reflectance spectrum, obtained from an epitaxial film as described in this paper, illustrating the growing intensity of the fringes.

A simplified model which illustrates the error made in condition 1 is given in Fig. 4. Interference fringes produced by two beams of constant intensity (independent of wavelength) would be of uniform intensity also. However, the second surface reflection from an epitaxial film varies with wavelength, and thus the fringes vary in intensity also. For this condition the simple maxima of the fringe no longer corresponds to the wavelength of $2\pi m$ relative phase shift. The $2\pi m$ relative phase shift can be shown, by differentiation, to correspond to the wavelength for which the fringe curve is tangent to the envelope of the fringes.

The wavelength values needed for the calculation of film thickness utilizing Eq. [7] are obtained by a method of tangents. For each point a tangent line is drawn approximating the slope of the envelope function. The resulting point of tangency is the desired value and will be termed the adjusted maximum. Large intensity fringes can be evaluated at the simple maxima with small error.

Fringe Chart

By using Eq. [4] and [6], it is possible to express film thickness in terms of the fringe order and wavelength of the fringe maxima

$$T = \frac{\left(m + \frac{1}{2}\right) \lambda_m}{2n_1 \cos \phi'} \qquad [8]$$

Equation [8] includes a phase change of π at the first surface but no phase change at the interface, which is the situation for silicon films on 0.007 ohm cm N^+ substrate in the 6 to 16μ range. Plotting Eq. [8], Fig. 5, with thickness as a function of wavelength for

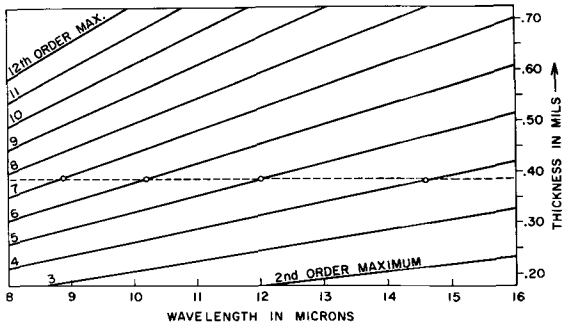

Fig. 5. Fringe chart for silicon epitaxial films, giving the wavelengths of fringe maxima as a function of film thickness. Thickness is determined by fitting fringe maxima data on this chart as shown by the dashed line.

integer values of m, results in a family of straight lines of constant fringe order. A horizontal line, T = constant, intersects the fringe order lines at wavelength values corresponding to the fringe maxima for that thickness.

Use of the Fringe Chart

For low order fringes, through 10th or 12th order, the chart can be used to simplify conversion of fringe wavelength data into accurate film thickness values. An important step is determining the correct fringe wavelength values by the tangent method. This wavelength evaluation method is also important when Eq. [7] is used. Errors up to 5% can occur if simple maximum values are used instead of the adjusted values, especially if only 2 or 3 fringes are available.

The chart will give reliable thickness values with three well-defined fringes. Improved accuracy achieved by use of the chart is due to the fact that all fringe maxima are used, showing up faulty data points.

Once the adjusted maximum values have been determined, a straight edge is positioned horizontally on the fringe chart lining up the wavelength of one of the fringe maxima and a fringe order line for a trial fit of the remaining fringes. Fringe maxima should fall at the intersections of the horizontal line with successive fringe order lines (see Fig. 5). If a good fit of the data is not possible at that thickness, a second trial should be made by moving the initial point up or down to the next fringe order and checking once more to see if the other fringes fit on a horizontal line. When a good fit is obtained, the horizontal line is extended to the right margin to read film thickness.

To aid in using the chart the wavelengths of adjusted maxima can be marked on a calibrated straight edge as they are read from the spectrum. The straight edge is then moved vertically across the chart, maintaining a horizontal position and wavelength reference until a thickness value is found where the marks are located on consecutive fringe order lines. Adjacent solutions should be tried, thicker and thinner, until the best solution is obtained.

Good accuracy will result if four or more fringes are located on the chart. Three fringes will give dependable results through 9th or 10th order. Equation [7] should be used in preference to the chart for fringes of 10th order and higher.

Very thin films are difficult to measure because only one or two fringes are observed. Additional data points can be obtained from the fringe minima which can also be included on the fringe chart. Equations [7] and [8] are converted to equivalent minima expressions by subtracting ½ from the integer values. When using Eq. [7] the interval between a maximum and the next minimum is ½ fringe. The method of tangents also applies to the evaluation of minima.

Experimental Check

An experimental check by an independent thickness measuring method was performed to verify the accuracy of the interference method. The cleavage method was chosen as the most desirable alternate measuring method. The cleaved wafer is etched for 10 to 15 sec in an HF, HNO_3 acetic acid (1-3-10 volume parts) etch and then measured directly with a microscope. The etch delineates the NN^+ interface very well, and the measurement is reasonably easy to make. The major disadvantage of the cleavage method is that it is destructive. This method can be utilized as a periodic check on the interference method and for films which are not sufficiently parallel to produce fringes.

Five different samples were measured by both cleavage and interference methods. The results of these measurements are tabulated.

Sample No.	1	2	3	4	5
T in mils, interference	0.24	0.26	0.33	0.83	0.43
T in mils, cleavage	0.26	0.28	0.32	0.82	0.42
Percentage difference	8%	7%	3%	1.2%	2%

Sample 4 was evaluated by Eq. [7], and the other samples were measured using the chart.

The agreement between the two methods is very good. The cleavage method has been reported to be accurate to ±10%. It is felt that interference methods as described are within a ±5% accuracy range.

Other Materials

Interference methods are applicable to epitaxial films of other semiconductors (1). A similar fringe chart can be constructed for use with materials other than silicon. Equation [8] used to construct the chart includes the refractive index of the film and the angle of refraction. These values must be evaluated for each particular material and reflectance apparatus. Should the refractive index of the film vary over the spectral range, where the fringes are observed, the chart can be constructed to include this variation. The chart would then be a set of curved lines. Should the film have a lower refractive index than the substrate, the chart equation should be rewritten to include the π phase shift at the interface. However, this situation will be very complex due to the attendant high absorption of the film and varying refractive index.

Manuscript received Oct. 5, 1961; revised manuscript received March 16, 1962. This paper was prepared for delivery at the Detroit Meeting, Oct. 1-5, 1961.

Any discussion of this paper will appear in a Discussion Section to be published in the June 1963 JOURNAL.

REFERENCES

1. W. G. Spitzer and M. Tanenbaum, *J. Appl. Phys.*, **32**, 744 (1961).
2. F. A. Jenkins and H. E. White, "Fundamentals of Optics," 3rd ed., pp. 261-264, McGraw Hill, New York (1957).
3. W. G. Spitzer and H. Y. Fan, *Phys. Rev.*, **106**, 882 (1957).
4. C. D. Salzberg and J. J. Villa, *J. Optical Soc. Am.*, **47**, 244 (1957).
5. O. S. Heavens, "Optical Properties of Thin Solid Films," pp. 46-62, Butterworths, London (1955).

Ultrafine Tungsten and Molybdenum Powders

H. Lamprey and R. L. Ripley

Technology Department, Union Carbide Metals Company, Division of Union Carbide Corporation, Niagara Falls, New York

ABSTRACT

A process is described for producing tungsten and molybdenum metal powder of 0.01-0.1μ average particle diameter by hydrogen reduction of the metal chlorides. Some of the physical and chemical properties of this material are discussed, together with data pointing to metallurgical uses of the product. Safety precautions to be observed in handling these fine powders are also described.

There is considerable evidence to indicate that metal compacts made by sintering ultrafine metal powders have improved engineering properties. The pronounced effect of grain size on the mechanical properties of iron and steel (1-5), copper (6), zinc (7), and other metals (8), is clearly shown in the literature. In general, a reduction in grain size is accompanied by an increase in hardness, yield strength, and fracture strength, and by a decrease in the ductile-brittle transition temperature. Ultrafine grain structure is also said to be the key to improving the properties of dispersion-strengthened metal and alloy systems (9,10).

In order to extend our knowledge of such effects to the refractory metals, it was decided to produce tungsten and molybdenum powders for metallurgical evaluation. Theory predicts that the maximum mechanical benefits should be found in sintered products having grain diameters smaller than 0.1μ, and so our efforts were directed toward producing the powders in the 0.01-0.1μ range. This paper will be restricted to describing production by a chemical process, namely, hydrogen reduction of tungsten and molybdenum chlorides in the vapor state.

There are two keys to the production of ultrafine metal powder by chloride reduction processes: one is to carry out the reduction in the vapor phase, whereby, through control of dilution, only a minimum number of atoms or molecules of the reacting species can get together to form agglomerates; the other is to carry out the reaction in free space, away from solid walls on which a continuous metal plating can deposit.

Thermodynamic data compiled by Glassner (11) indicate that the by-product HCl is more stable than any of the tungsten and molybdenum chlorides by 10-20 kcal/g atom of chlorine over the temperature range from 25° to 900°C. Thus, the reaction should proceed readily at elevated temperature, and no back reaction is to be expected as the product is cooled.

The apparatus used for carrying out the reaction is sketched in Fig. 1. Purified hydrogen and tungsten or molybdenum chloride vapors, carried in a stream of argon if desired, are preheated to the chosen temperature and brought together in a large reaction space; the gases react immediately on contact to form submicron metal powder and hydrogen chloride vapor.

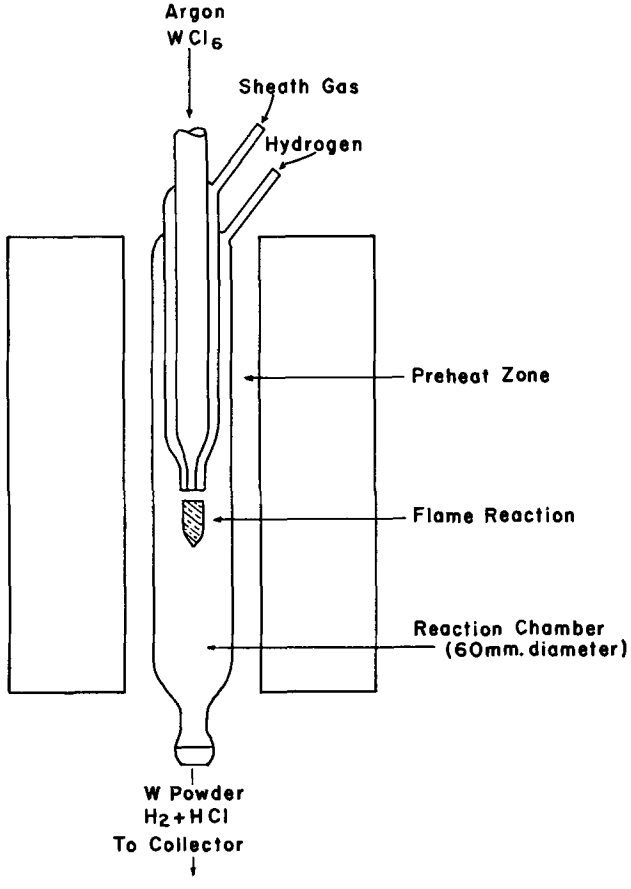

Fig. 1. Quartz apparatus for producing ultrafine tungsten and molybdenum by a flame reaction.

One purpose of flowing argon or chlorine through the sheath gas nozzle in Fig. 1 is to prevent formation of metal at the metal chloride orifice tip, with consequent plugging of the apparatus. Chlorine is somewhat more effective than argon for this purpose. The gases issuing from the concentric tubes react as a flame and the sheath gas serves to position the metal chloride-hydrogen flame at some distance from the orifice.

The metal may be collected by gravity settling with or without the use of an electrostatic precipitator; or the reaction gases may be filtered through a large diameter column of steel wool, the trapped powder shaken free of the wool and separated from small steel fragments by magnetic means. When using electrostatic precipitation, it is necessary to prevent bridging the gap between the electrodes with a conducting film of tungsten powder. When this bridging occurs, the alternating high potential field (20,000-50,000v) is no longer positioned between the collecting electrodes but between the inside and outside walls of the glass sheath over the "hot" electrode. While this over-all process works well for producing submicron powder down to 0.01μ particle size, various chemical and mechanical refinements are necessary to the process in order to control particle sizes within narrow ranges, to operate with high materials efficiency, and to produce powder of high purity.

The quality of the powder produced depends on a number of factors; one of them is the reactant preheat temperature just prior to mixing. As this temperature increases, the powder product becomes somewhat finer (Table I), and the amount of chlorine impurity is reduced.

Runs 1 through 5 were all carried out in the apparatus shown in Fig. 1. The mole ratio of hydrogen to chlorine in the system was maintained at 3 and the inert gas flow was held constant. Ultrafine molybdenum powder was also prepared in the same apparatus at a preheat and reaction chamber temperature of 800°C. This powder contained 0.15% oxygen, 0.35% chlorine, 0.01% silicon, 0.1% carbon, and had a surface area of 11.1 m^2/g corresponding to an average particle size of 0.05μ.

In most of the tests run thus far, the powdered product has analyzed approximately 99.5% metal, the balance being largely chlorine, oxygen, and carbon, with very small amounts, on the order of 0.01% or less, of nitrogen, silicon, and hydrogen. Tungsten and molybdenum chlorides commonly contain oxychlorides, and some of this oxygen finds its way into the powder. The carbon impurity gets into the system during a prior purification of chlorine by passing it over hot carbon to remove oxygenated compounds. This carbon impurity could be reduced or eliminated if necessary.

Table I. Production of ultrafine tungsten powder by the hydrogen reduction of tungsten hexachloride at various temperatures

Run No.	Preheat and reaction chamber temp, °C	% Chlorine in product	Product diam, μ
1	430	1.82	0.029
2	620	0.24	0.025
3	695	0.10	0.031
4	800	0.27	0.026
5	905	0.13	0.021

Oxygen and chlorine impurities in the metal powder products are present as lower valent compounds and as chemisorbed gases.[1] X-ray diffraction patterns show the presence of W_3O in the tungsten powder. Part of the oxygen and chlorine can be removed by post-treatments of various kinds. Vacuum pumping, alone, is relatively ineffective. A product analyzing 0.39% oxygen and 0.24% chlorine with a surface area of 12 m^2/g was heated to 800°C for 24 hr under a flow of dry hydrogen. The oxygen content was reduced to 0.21% and the chlorine content to 0.04%. Simultaneously, the surface area decreased to 6.49 m^2/g as a result of this treatment. Obviously, a tungsten powder product low in oxygen and carbon content is more easily obtained by a careful distillation of the tungsten hexachloride. This distillation removes the oxychlorides and chlorinated hydrocarbons which commonly contaminate tungsten hexachloride made from commercial chlorine.

Powder Properties

The particle sizes of the tungsten powders were determined by surface area measurements (12) and confirmed by electron micrography. Figure 2 shows a typical photomicrograph obtained at a magnification of 50,000 diameters. The particles approach spheres in shape. There is considerable aggregation of particles in this photomicrograph.

The bulk density of the powder as collected was approximately 0.2 g/cc. This is remarkably low for tungsten with a density of 19.3.

The chemical properties of the ultrafine powder are greatly modified by the presence of the chemi-

[1] All oxygen analyses in this study were determined by a vacuum fusion analysis in which the encapsulated sample is dropped into an iron-carbon melt at 1800°C, and the resulting carbon monoxide is measured.

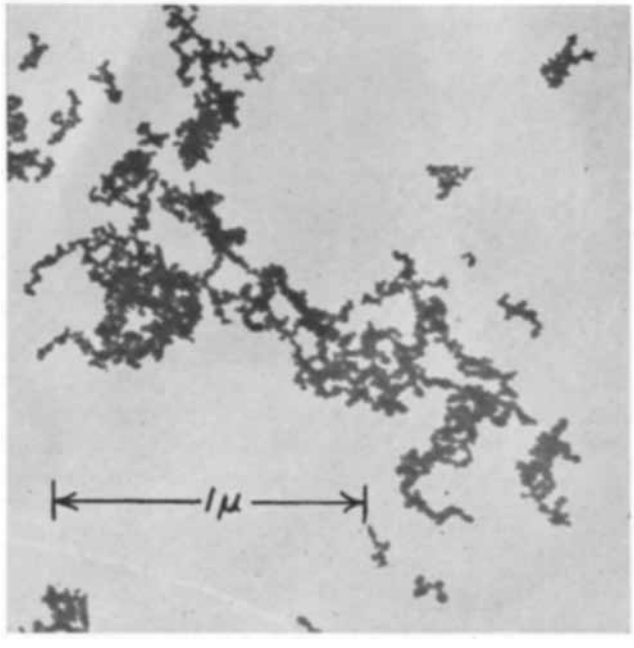

Fig. 2. Photomicrograph of ultrafine tungsten powder. Magnification 40,625X.

sorbed gas films. Powder which is relatively free of chlorine and oxygen appears to be much more reactive than powder made as described above. Finely divided metal powder is sometimes pyrophoric. Great variability in the reactivity of tungsten powder toward air and water has been encountered. Some samples oxidize rapidly on exposure to air. For example, when a sample containing 1.5% of adsorbed chlorine was exposed to air at room temperature, thermocouples embedded in the powder showed temperature rises of 10-20°C due to air reaction, but no ignition occurred. When a red-hot wire was placed in the powder, the material in the vicinity of the wire reacted, turning yellow-green, the color of WO_3, but the remainder of the powder was not affected. Other samples exposed to air have become red hot on the surface within a few seconds' time. Factors such as the rate of heat loss from the powder and the degree of packing of the sample also affect the possibility of ignition.

More usually, however, the tungsten powder is completely inert. For example, a sample of powder analyzing 0.10% oxygen, 0.09% chlorine, 0.01% carbon, and 0.01% silicon, and having an average particle diameter of 0.02μ, was heated in air on a thermogravimetric balance of 1 mg sensitivity, *i.e.*, 0.1% of the weight of the sample. No measurable weight gain occurred until the temperature reached 140°C, when the powder converted rapidly and completely to tungstic oxide. The same result was obtained when oxygen was substituted for air, or when the tungsten powder was pretreated with hydrogen at 800°C, or when it was treated with chlorine until 1% by weight was adsorbed; the ignition temperature in air or oxygen was, in all cases, 130-140°C on the thermogravimetric balance. Powder of the same particle size, from another batch, containing 0.20% chlorine, 0.24% oxygen, 0.16% carbon, and 0.16% silicon, behaved identically.

The submicron tungsten powder physically adsorbs water reversibly at 25°C and does not react appreciably with water up to 1200°C. This powder chemisorbed several per cent of chlorine when exposed to a 20:80 chlorine-argon mixture at room temperature; the chlorine, unlike water vapor, was not driven off by dry argon at room temperature, but was removed, together with a little tungsten chloride, by argon heated to above 350°C.

These tests indicate that the fine tungsten powder can be handled safely if a few simple precautions are taken. However, any finely divided metal powder, mixed with air or other oxidizing agent, is a potential source of uncontrollable reactions. For example, when an operator inadvertently let a small amount of the fluffy tungsten powder come in contact with hot chlorine gas in a large glass receiver, a violent reaction shattered the equipment and could have injured the operators if they had not been wearing safety clothing and goggles. There is a limit to how casually any ultrafine powder can be handled. Currently this problem is being studied further to try to determine the cause of the variability in pyrophoricity of different lots of powder.

Uses

A few tests have been made to determine whether pressed compacts of ultrafine tungsten powder would have improved mechanical properties, as theory predicts. Specimens of rather impure powder (0.6% oxygen and 0.3% chlorine) were pressed at 40 tons/in.^{2}, giving compacts of only about 40% theoretical density, probably because of incomplete removal of entrapped air. The green strength was, however, very good. These specimens sintered poorly at 1750°C, giving compacts of 80% theoretical density. However, grain growth was excessive at these temperatures, *i.e.*, to about 30μ, and it was immediately apparent that low-temperature sintering would have to be possible if the desired fine structure is to be retained. Later, similar green compacts were sintered at 1550°C for 30 min in hydrogen atmospheres to give products of 94% theoretical density.

These results point up a rather remarkable property of ultrafine tungsten powder: that it can be sintered effectively at temperatures nearly a thousand degrees lower than conventional tungsten powder. This seems to be a general phenomenon, not restricted to tungsten. Lowering of the sintering temperature with other ultrafine metal powders has been observed in the same way.

Metallurgical data are currently being collected on these fine powders, including pressing, rolling, extruding, slip casting, dispersion strengthening, and so on. Some of these results should be available soon for publication. The powders, because of their unusual sizes and surface characteristics, may have unique applications as catalysts, fillers, fuels, nucleation agents in alloy production, and other diverse applications.

Acknowledgment

The authors wish to thank Dr. H. V. Seklemian and Mr. R. L. Reddy, who carried out some of the work described in this report.

Manuscript received Oct. 30, 1961. This paper was prepared for delivery before the Indianapolis Meeting, April 30-May 3, 1961.

Any discussion of this paper will appear in a Discussion Section to be published in the June 1963 JOURNAL.

REFERENCES

1. N. J. Petch, *J. Iron Steel Inst.*, **174**, 25 (1953).
2. A. Cracknell and N. J. Petch, *Acta Met.*, **3**, 186 (1955).
3. R. L. Smith, G. Spangler, and R. M. Brick, *Trans. A.S.M.*, **46**, 973 (1954).
4. C. A. Edwards, H. N. Jones, and B. Walters, *J. Iron Steel Inst.*, **139**, 341 (1939).
5. L. D. Jaffe, F. L. Carr, and D. C. Buffum, *Trans. A.I.M.E.*, **197**, 1147 (1953).
6. R. P. Carreker and W. R. Hibbard, *Acta Met.*, **1**, 654 (1953).
7. G. W. Greenwood and A. G. Quarrel, *J. Inst. Met.*, **82**, 551 (1954).
8. L. M. T. Hopkin, *ibid.*, **84**, 102 (1956).
9. N. J. Grant and O. Preston, *Trans. A.I.M.E.*, **209**, 349 (1957).
10. F. V. Lenel, A. B. Backenstro, Jr., and N. V. Rose, *ibid.*, **209**, 124 (1957).
11. A. Glassner, The Thermodynamic Properties of the Oxides, Fluorides, and Chlorides to 2500°K., Argonne National Lab. Report ANL-5750, Supt. of

Documents, U.S. Printing Office, Washington, D. C.
12. P. A. Faeth and C. B. Willingham, Technical Bulletin on the Assembly, Calibration and Operation of a Gas Adsorption Apparatus for the Measurement of Surface Area and Density of Finely Divided Solids, Mellon Institute of Industrial Research, Sept. 1955.

Effect of Adsorbed Anions on Reduction Processes on Passive Stainless Steel

F. A. Posey and R. F. Sympson[1]

Chemistry Division, Oak Ridge National Laboratory,
Operated by Union Carbide Corporation for the U. S. Atomic Energy Commission, Oak Ridge, Tennessee

ABSTRACT

The effects of sulfate, thiocyanate, chloride, and hydroxide ions on the reduction of cupric ion on passive stainless steel have been studied by use of potentiostatic techniques. Specific adsorption of the anions catalyzes the rate of the reduction reaction, and analysis shows that the adsorption follows a potential-dependent Langmuir isotherm. A simple model is proposed, based on electrochemical kinetic theory, which yields isotherms having properties in good agreement with experimental observations.

Studies on the kinetics of electrode processes have shown that anions exert specific effects in many systems. Among numerous contributions to the literature on this subject are papers concerned with the effect of anions on the exchange current of redox systems (1), on the corrosion of metals (2, 3), and on electrode reactions at a mercury surface (4). Frumkin (5, 6) and Piontelli (7) have reviewed anion effects in electrocapillarity and electrode kinetics, and the influence of anions in polarography was the subject of a review by Brdicka (8). Electrode processes occurring on passive metals are also affected by anions, and the sensitivity of the electrode potential of iron passivated in $CrO_4^=$, TcO_4^-, $MoO_4^=$, or $WO_4^=$ to additions of Cl^- or SCN^- was noted by Sympson and Cartledge (9). In a previous paper (10), the reduction of cupric ion on passive stainless steel in sulfate solution was studied by use of potentiostatic, galvanostatic, and tracer techniques. This reaction is catalyzed by the addition to solution of certain anions (11, 12), and the purpose of the present paper is to present results of electrochemical measurements on the effects of Cl^-, $SO_4^=$, OH^-, and SCN^- ions on the kinetics of reduction of Cu^{++} on passive stainless steel.

In order to obtain detailed information on the nature of the anion effects, a series of potentiostatic experiments was performed. The effect of SCN^- on the reduction of Cu^{++} on passive stainless steel was determined in various H_2SO_4-Na_2SO_4 solutions. These results suggested that both sulfate ion concentration and acidity are important variables in the kinetics of the reduction reaction. Hence further experiments were performed in aqueous perchlorate media in order to minimize any effect of complexing of cupric ions by anions in solution. Experiments in perchlorate solutions included the effects of Cl^-, $SO_4^=$, and, in particular, OH^- (acidity) on the kinetics of Cu^{++} reduction as a function of electrode potential and temperature. Since it was desirable to distinguish between complexing and adsorption aspects of the anion effects, accurate values of association quotients were determined spectrophotometrically for the association of Cu^{++} with the anions studied under conditions prevailing in the potentiostatic experiments. The results of the electrochemical measurements are presented below and analyzed on the basis of electrochemical kinetic theory.

Experimental

The experimental cell was a five-necked, spherical reaction flask of 500 ml capacity, fitted with a water-cooled condenser for use with heated solutions. Standard taper ports provided space for a thermometer, the entry and egress of gas, a platinum polarizing electrode, the stainless steel electrode assembly, and for additions of aliquots of stock solutions. Temperature was controlled by means of a Glascol heating mantle operated from a Variac supplied with regulated voltage. The constancy of the ambient temperature ensured control of the solution temperature to approximately $\pm 0.5°C$ over long periods of time. Purified helium or nitrogen effused into the solution at a constant rate through a sintered glass disk; the flow was sufficient to ensure vigorous stirring. Residual oxygen was removed from the gas by use of a tube furnace containing heated copper turnings, and columns of Drierite and Ascarite provided further purification.

Electrode potential measurements were made using a L&N *p*H Indicator (No. 7664) as a potentiometer coupled with a Brown recorder. Potentials were measured and recorded with time by the direct method, using a Luggin capillary bridged to a saturated calomel reference electrode maintained at room temperature. The concentration of the electrolyte was such that no significant ohmic potential drop occurred in solution between the electrode and the tip of the reference electrode capillary over the entire range of polarizing currents employed.

[1] Present address: Department of Chemistry, Ohio University, Athens, Ohio.

Galvanostatic circuitry consisted of high-capacity batteries furnishing 135v output, together with large load resistors in series with the cell. The concentration of cupric ion in solution was always such that comparatively small currents (usually no greater than 10 μa/cm^2) were sufficient to allow observations over the entire usable potential range of passive stainless steel in the chosen environments. Currents were measured by recording voltage drop across precision resistors in the circuit. The potentiostat used in these studies was developed in this laboratory for the special purpose of providing an all-electronic instrument suitable for precise control of electrode potentials in polarizable systems over extended periods of time. The potentiostat, a single-amplifier type, was constructed using a Reeves Instrument Corporation A-400 Dual D. C. Amplifier (REAC); this is a chopper-stabilized operational amplifier of high gain. Maximum output voltage was ±100v and output current could attain ±20 ma. Electrode potentials were constant to within ±0.1 mv at all times when the potentiostat was controlling, as could be ascertained oscilloscopically. Because of the chopper stabilization, response time was slow compared to potentiostats of the straight-amplifier type, but this was a negligible disadvantage for the present purposes considering the gain in long-term stability and precision afforded by the design adopted.

Electrodes were machined from type 347 stainless steel[2] in cylindrical form with a diameter of 1 cm and a height of 2 cm, thus permitting an exposed geometrical area of 7 cm^2 when mounted on the electrode holder. A Teflon cylinder abutted one end of the steel electrode and was followed by a conical Teflon piece machined to fit the standard taper joint of the cell. The entire assembly was tightened by use of a stainless steel rod which penetrated cylindrical and conical pieces axially and threaded into the steel electrode. A solution-tight seal was easily made, and no further attention was necessary during the life of the electrode. The surface of the stainless steel electrodes was electropolished in a solution of 60% by volume of 85% H_3PO_4 + 20% of 95% H_2SO_4 + 20% of H_2O at 65°C for 3-5 min at a current density of 0.5 amp/cm^2. This procedure produced a mirror-like surface of reproducible polarization characteristics in the solutions studied. Electrodes were stored between measurements in triple-distilled water.

All solutions were prepared using triple-distilled water, obtained by redistilling tap distilled water from the laboratory supply in a two-stage quartz still manufactured by Heraeus-Quarzschmelze. All reagents used were analytical grade. Recrystallization of crystalline reagents was found to be without appreciable effect on the results, and most experiments were performed using analytical grade chemicals without further purification.

In potentiostatic experiments, stainless steel electrodes were allowed to attain steady states at a preselected value of electrode potential. This procedure was time-consuming, as long-term transients are observed on passive stainless steel, especially in perchlorate solutions.[3] After attainment of steady states, aliquots of concentrated stock solutions were added to the experimental solution by micropipettes and the applied current necessary to maintain the chosen potential constant was recorded with time. Most experiments were performed in 0.3f $NaClO_4$ acidified with $HClO_4$. Stock solutions of 1f Na_2SO_4 and 5f NaCl in 0.3f $NaClO_4$ were used in experiments on the effects of $SO_4^=$ and Cl^-, respectively. In experiments on the effect of SCN^-, which were performed in dilute H_2SO_4-Na_2SO_4 solutions, freshly prepared stock solutions of 0.25f KSCN dissolved in the experimental solutions were used. Experiments on the effect of acidity were performed in $10^{-5}f$ $HClO_4$ + 0.3f $NaClO_4$ by adding aliquots of stock solutions of 1f $HClO_4$ + 0.3f $NaClO_4$ or concentrated $HClO_4$.

Results

Data from a series of potentiostatic experiments on the effect of SCN^- on the reduction of Cu^{++} on passive stainless steel in dilute sulfate solution are shown in Fig. 1. Cupric ion concentration was 2.5 or 5.0 x $10^{-6}f$ in this series; the over-all formal rate constant, $\bar{k}$, was calculated by dividing the current density in amp/cm^2 by the cupric ion concentration in moles/liter. The sigmoid curves observed in Fig. 1 are typical of all the data obtained in experiments on the SCN^- effect. Evidently the rate of reduction of Cu^{++} approaches a limiting value at high [SCN^-]. Solid lines drawn through the experimental data of

[2] Commercial type 347 stainless steel, although by no means a simple alloy, was chosen as a working material because its electrochemical behavior is typical of that of a large number of steels of similar composition. In addition, our experience has shown that the kinetics of reduction reactions are relatively insensitive to the type of stainless steel used, provided a standardized method of surface preparation is employed.

[3] The half-times of transients were found to depend greatly on the acidity of the solution, being least (approximately 5 min or less) in solutions of high pH (approaching neutrality), and increasing to values of the order of half an hour at low pH. The necessity of waiting for true steady states in these passive systems cannot be overemphasized. Whatever the nature of the transients, whether they be due to readjustment of charge distribution in the passive oxide film, to change in the film thickness, or to slow processes akin to a reaction capacity at the oxide-solution interface (or a combination of all of these), considerable charge is required to establish a new steady state. Premature judgment of the existence of steady states or arbitrary selection of times for changing parameters such as added ion concentration, electrode potential, or applied current result in confusion of the desired properties of the Faradaic processes in the system with properties of the non-Faradaic processes occurring during the transients.

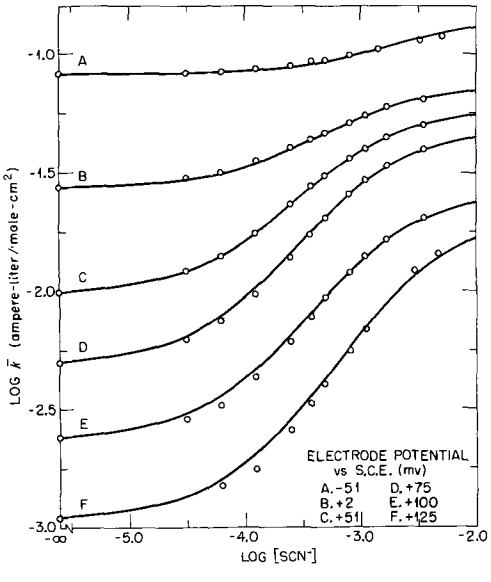

Fig. 1. Effect of SCN^- on the reduction of Cu^{++} on passive stainless steel in 1 x $10^{-3}f$ H_2SO_4 plus 9 x $10^{-2}f$ Na_2SO_4; 65°C, nitrogen atmosphere. Potential vs. S.C.E. at room temperature.

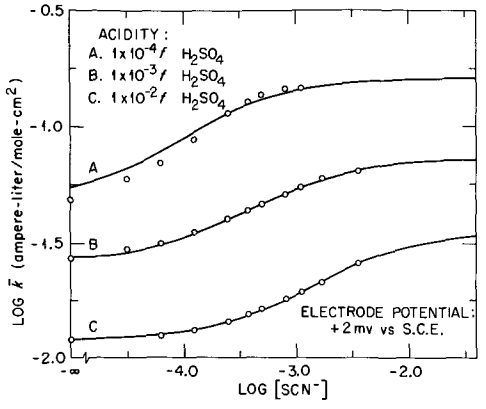

Fig. 2. Effect of acidity and SCN^- on the reduction of Cu^{++} on passive stainless steel in 9 x $10^{-2}f$ Na_2SO_4; 65°C, nitrogen atmosphere. Potential vs. S.C.E. at room temperature.

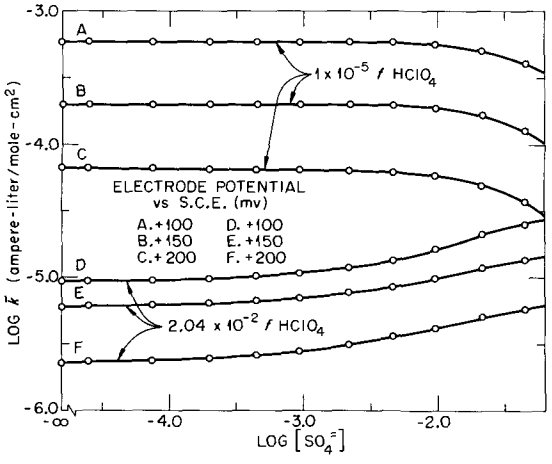

Fig. 3. Effect of $SO_4^=$ on the reduction of Cu^{++} on passive stainless steel in 3 x $10^{-1}f$ $NaClO_4$; 85°C, helium atmosphere. Potential vs. S.C.E. at room temperature.

Fig. 1 are least-squares fits of the data with an expression of the form of Eq. [1].

$$k = (\alpha + \beta\gamma[X])/(1 + \gamma[X]) \qquad [1]$$

In Eq. [1], the formal electrochemical rate constant, $\bar{k}$, is a function of added anion concentration, [X], and of the three constants, α, β, and λ. The constant α is the rate constant for the reduction reaction in the absence of added anions, β is the limiting rate constant for large [X], and γ may be regarded as an equilibrium quotient for the interaction between anions and system reactants. The meaning of the constants of Eq. [1] is considered further below.

Experiments on the SCN^- effect were run at several acidities and at several over-all concentrations of sulfate ions. The effect of total sulfate ion concentration was found to be slight over the range 10^{-4} to $10^{-2}f$ Na_2SO_4. At constant $[H^+]$, little difference exists between rate constants at $10^{-4}f$ and at $10^{-3}f$ Na_2SO_4; some change of rate constant occurs at $10^{-2}f$ Na_2SO_4, but even here the difference is small. On the other hand, the effect of SCN^- on the reduction of Cu^{++} depends greatly on the acidity of the solution, as shown in Fig. 2. Changing the acidity of the solution not only affects the rate constants but also shifts the curve parallel to the log $[SCN^-]$ axis.

Data on the effect of $SO_4^=$ on the reduction of Cu^{++} on passive stainless steel in perchlorate solutions are shown in Fig. 3. Exploratory experiments had proven that NO_3^- and ClO_4^- ions have no effect on the kinetics of the reduction reaction, so that $0.3f$ $NaClO_4$ was chosen as inert electrolyte for experiments on the effects of $SO_4^=$, OH^-, and Cl^-, and crystalline $Cu(NO_3)_2 \cdot 3H_2O$ was used as the source of cupric ions. Even at $10^{-2}f$ $SO_4^=$, there is little change in the reduction rate of Cu^{++}, especially at lower acidity. These data are not extensive enough to show definitely whether or not a limiting value of rate constant is attained at high $[SO_4^=]$, but the aspect of the curves suggests not only the possibility of a limiting value but also the possibility of a common value independent of acidity.

The effect of acidity on cupric ion reduction is shown in Fig. 4 as a function of electrode potential. In addition to studies at 25°C, potentiostatic experiments were run at 45°, 67°, and 85°C. Figure 5, showing data on the effect of temperature at constant electrode potential, demonstrates that sigmoid curves are also obtained at the higher temperatures. Solid lines in Figs. 4 and 5 are least-squares fits of Eq. [1] to the experimental data. A limiting rate constant is attained at lower acidities in analogy to observations on the SCN^- effect; this effect is more pronounced at higher temperatures as may be seen in Fig. 5. In addition, a limiting rate is observed at the higher acidities (up to $10^{-1}f$ $HClO_4$).

Results of potentiostatic experiments on the effect of Cl^- on the reduction of Cu^{++} are shown in Fig. 6 as a function of electrode potential and acidity. Solid lines through data obtained in $10^{-5}f$ $HClO_4$ are least-squares fits; lines through data referring to $10^{-2}f$ $HClO_4$ are visual fits. The results at low acidity are similar to those shown in Fig. 1 for the effect of SCN^-. However, the experiments at higher acidity revealed a more complex behavior. Curve E of Fig. 6 shows the existence of a minimum in the $\bar{k}$ *vs.* $[Cl^-]$ relationship at ±0 mv *vs.* S.C.E. The influence of the phenomenon responsible for the minimum in curve

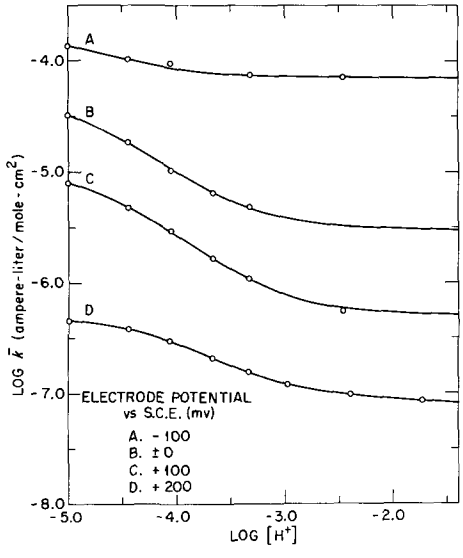

Fig. 4. Effect of acidity on the reduction of Cu^{++} on passive stainless steel in 3 x $10^{-1}f$ $NaClO_4$; 25°C, helium atmosphere.

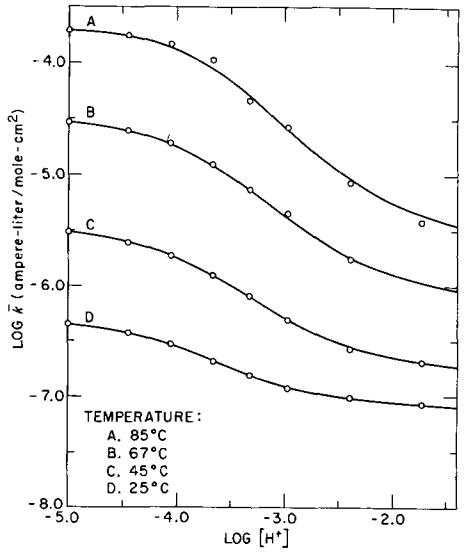

Fig. 5. Effect of temperature on the reduction of Cu^{++} on passive stainless steel in 3 x $10^{-1}f$ $NaClO_4$; helium atmosphere. Electrode potential: +200 mv vs. S.C.E. at room temperature.

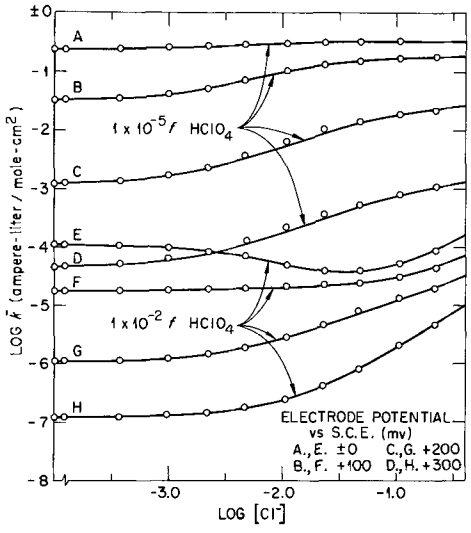

Fig. 6. Effect of Cl^- on the reduction of Cu^{++} on passive stainless steel in 1 x $10^{-5}f$ $HClO_4$ or 1 x $10^{-2}f$ $HClO_4$ plus 3 x $10^{-1}f$ $NaClO_4$; 85°C, helium atmosphere. Potential vs. S.C.E. at room temperature.

E seems to extend also to curve F, the behavior of which is more closely akin to the usual sigmoid relation obtained at lower acidity. Since meaningful data could not be obtained at chloride ion concentrations much larger than those shown in Fig. 6 without drastic changes in the ionic strength of the solution, evidence is insufficient on the question of whether or not rate constants are independent of acidity at high [Cl^-].

Discussion

Attempts to interpret the previous observations quantitatively on the basis of a complexing explanation encountered difficulties. Assuming that cupric ion and the anions studied react to form 1:1 complexes in solution and that rate constants differ for reduction of aquo ion and complex, one may derive an equation for the over-all rate constant which has the form of Eq. [1]. In this instance, the constant γ of Eq. [1] becomes the association quotient for the 1:1 association reaction. Values of γ were calculated from experimental data[4] for comparison with values of the 1:1 association quotients obtained from independent measurements. Examination of the literature showed that measurements of the 1:1 association quotients of Cu^{++} with the anions $SO_4^=$ and SCN^- were not reported for the experimental conditions of this study. Therefore, these quotients were measured spectrophotometrically as a function of temperature at ionic strengths of interest. Comparison of calculated values of γ with measured values of the 1:1 association quotients revealed sharp disagreement between the orders of magnitude. Furthermore, it was found that values of γ vary systematically with electrode potential. These observations forced abandonment of a complexing explanation as the predominant factor in the effect of anions on the reduction of Cu^{++} in the present system.

[4] If log $\bar{k}$ is plotted against log [X], the coordinates of the inflection point of a curve obeying Eq. [1] are given by the following equations; $\bar{k}$(infl.) = $\sqrt{\alpha\beta}$; [X](infl.) = $(1/\gamma)\sqrt{\alpha/\beta}$. These equations are useful for estimating γ from graphical data. However, the alternative procedure of calculating γ from a least-squares fit of Eq. [1] to experimental data was used here.

The previous data are better understood if it is assumed that the role of the anions lies in their affinity for the surface of passive stainless steel. The anions may be specifically adsorbed at the surface, thereby affecting the kinetics of rate processes occurring at the oxide-solution interface. An expression of the form of Eq. [1] may be derived by assuming that the number of adsorbed anions is related to anion concentration in solution by a Langmuir isotherm. The Langmuir isotherm is derived from considerations of coverage, without regard to lateral interaction effects or change of adsorption energetics with number of adsorbed particles (13). It can be expected to hold best for localized monolayer adsorption where adsorbed particles are relatively nonmobile and the adsorption bond is relatively nonlabile. At constant electrode potential the data of Fig. 1, 2, 4, 5, and 6 are represented by Eq. [1] to a good approximation, and this suggests that adsorption of anions on passive stainless steel involves strong specific interactions with the substrate. As shown below, combination of Langmuir adsorption model with the formalism of electrochemical kinetics leads to equations which adequately describe the results obtained in this study.

It has been shown previously (10) from analysis of polarization curves that the reduction of Cu^{++} on passive stainless steel proceeds by a two-stage mechanism involving a cuprous intermediate. In order to derive an expression for the effect of anions on the overall reduction rate, we assume for simplicity that three types of surface are available as reaction sites for the reduction of Cu^{++}: (i) the surface present at high acidity, which probably consists of adsorbed H_2O molecules and may be called the "aquo" surface; (ii) the surface present at low acidity because of adsorption of OH^- ions (or because of desorption of H^+ from the aquo surface), which may be called the "hydroxy" surface; and (iii) the surface resulting from specific adsorption of anions, which may be called the "anionic" surface. Equations [2], [3], and [4] show the reaction schemes at aquo, hydroxy, and anionic

surfaces, respectively, together with appropriate formal electrochemical rate constants for the individual charge transfer steps.

$$Cu^{++} \underset{\bar{k}_2}{\overset{\bar{k}_1}{\rightleftharpoons}} Cu^{+} \xrightarrow{\bar{k}_3} \text{products} \quad \text{(aquo surface)} \qquad [2]$$

$$Cu^{++} \underset{\bar{k}_5}{\overset{\bar{k}_4}{\rightleftharpoons}} Cu^{+} \xrightarrow{\bar{k}_6} \text{products} \quad \text{(hydroxy surface)} \qquad [3]$$

$$Cu^{++} \underset{\bar{k}_8}{\overset{\bar{k}_7}{\rightleftharpoons}} Cu^{+} \xrightarrow{\bar{k}_9} \text{products} \quad \text{(anionic surface)} \qquad [4]$$

If the fraction of the total electrode surface existing as hydroxy surface is designated by θ, the fraction as anionic surface by η, and the fraction as aquo surface by $(1-\theta-\eta)$, the total current density for reduction of cupric ion is given by Eq. [5].

$$j/\mathbf{F} = K_1(1-\theta-\eta) + K_2\theta + K_3\eta \qquad [5]$$

K_1, K_2, and K_3 are the rates of reduction on aquo, hydroxy, and anionic surfaces, respectively, in units of equivalents/cm²-sec, $\mathbf{F}$ is the Faraday, and j is current density in amp/cm². K_1, K_2, and K_3 are given by Eq. [6], [7], and [8], respectively.

$$K_1 = \bar{k}_1 C_0(a) + (\bar{k}_3 - \bar{k}_2) C_R(a) \qquad [6]$$

$$K_2 = \bar{k}_4 C_0(\theta) + (\bar{k}_6 - \bar{k}_5) C_R(\theta) \qquad [7]$$

$$K_3 = \bar{k}_7 C_0(\eta) + (\bar{k}_9 - \bar{k}_8) C_R(\eta) \qquad [8]$$

$C_0(a)$ and $C_R(a)$ refer to concentrations of cupric and cuprous ions, respectively, at the interface of the aquo surface, with analogous definitions for $C_0(\theta)$, $C_R(\theta)$, $C_0(\eta)$, and $C_R(\eta)$.

The flux of each of the six species in Eq. [6], [7], and [8] may be related to the bulk concentration of cupric ions in solution by using the Nernst diffusion layer approximation to Fick's first law. When this is done, the results may be substituted into Eq. [6], [7], and [8] to give explicit expressions for rates of reduction on the several types of surface; these are given in Eq. [9], [10], and [11].

$$K_1 = C^\circ \frac{\bar{k}_1(D_0/\delta_0)(2\bar{k}_3 + D_R/\delta_R)}{\bar{k}_1(\bar{k}_3 + D_R/\delta_R) + (D_0/\delta_0)(\bar{k}_2 + \bar{k}_3 + D_R/\delta_R)} \qquad [9]$$

$$K_2 = C^\circ \frac{\bar{k}_4(D_0/\delta_0)(2\bar{k}_6 + D_R/\delta_R)}{\bar{k}_4(\bar{k}_6 + D_R/\delta_R) + (D_0/\delta_0)(\bar{k}_5 + \bar{k}_6 + D_R/\delta_R)} \qquad [10]$$

$$K_3 = C^\circ \frac{\bar{k}_7(D_0/\delta_0)(2\bar{k}_9 + D_R/\delta_R)}{\bar{k}_7(\bar{k}_9 + D_R/\delta_R) + (D_0/\delta_0)(\bar{k}_8 + \bar{k}_9 + D_R/\delta_R)} \qquad [11]$$

In these equations, C° is the concentration of cupric ions in the bulk of the solution, and D_0/δ_0 and D_R/δ_R are ratios of diffusion coefficient to thickness of Nernst diffusion layer for cupric ions and cuprous ion intermediates, respectively.

The pertinent adsorption equilibria are given by Eq. [12], [13], and [14].

$$OH^- + \text{aquo surface} \underset{\bar{k}_\beta}{\overset{\bar{k}_\alpha}{\rightleftharpoons}} \text{hydroxy surface} \qquad [12]$$

$$X + \text{aquo surface} \underset{\bar{k}_\delta}{\overset{\bar{k}_\gamma}{\rightleftharpoons}} \text{anionic surface} \qquad [13]$$

$$X + \text{hydroxy surface} \underset{\bar{k}_\alpha'}{\overset{\bar{k}_\gamma'}{\rightleftharpoons}} OH^- + \text{anionic surface} \qquad [14]$$

Since charge is transferred during adsorption or desorption of anions, it is necessary to use formal electrochemical rate constants to allow for the potential dependences of the several processes. Equation [14] represents an anion exchange process which is possible when more than one kind of anion is available for adsorption on the surface. In the cases of $X = SCN^-$ or Cl^-, this process probably is only slightly potential dependent since no net charge transfer is involved.

Equations relating the rate of change of hydroxy and anionic surface fractions to adsorption process rate constants and concentrations of OH^- and X in solution may be solved for θ, η, and $(1-\theta-\eta)$ at equilibrium. These are given by Eq. [15], [16], and [17].

$$\theta = (1/\Delta)\left\{(\bar{k}_\alpha/\bar{k}_\beta)[OH^-] + \bar{k}_\alpha'/\bar{k}_\delta[OH^-]\cdot\left[(\bar{k}_\alpha/\bar{k}_\beta)[OH^-] + (\bar{k}_\gamma/\bar{k}_\beta)[X]\right]\right\} \qquad [15]$$

$$\eta = (1/\Delta)\left\{(\bar{k}_\gamma/\bar{k}_\delta)[X] + (\bar{k}_\gamma'/\bar{k}_\beta)[X]\cdot\left[(\bar{k}_\alpha/\bar{k}_\delta)[OH^-] + (\bar{k}_\gamma/\bar{k}_\delta)[X]\right]\right\} \qquad [16]$$

$$1-\theta-\eta = (1/\Delta)\left\{1 + (\bar{k}_\alpha'/\bar{k}_\delta)[OH^-] + (\bar{k}_\gamma'/\bar{k}_\beta)[X]\right\} \qquad [17]$$

The denominator Δ which is common to all three equations is given explicitly by Eq. [18].

$$\Delta = 1 + (\bar{k}_\alpha/\bar{k}_\beta)[OH^-] + (\bar{k}_\gamma/\bar{k}_\delta)[X] + (\bar{k}_\alpha'/\bar{k}_\delta)[OH^-]\left[1 + (\bar{k}_\alpha/\bar{k}_\beta)[OH^-]\right] + (\bar{k}_\gamma'/\bar{k}_\beta)[X]\left[1 + (\bar{k}_\gamma/\bar{k}_\delta)[X]\right] + \left[(\bar{k}_\alpha\bar{k}_\gamma' + \bar{k}_\alpha'\bar{k}_\gamma)/\bar{k}_\beta\bar{k}_\delta\right][OH^-][X] \qquad [18]$$

Finally the equation for the over-all rate constant is obtained by combining Eq. [5], [9], [10], [11], [15], [16], [17], and [18] and dividing through by C° to give $\bar{k} \equiv j/\mathbf{F}C^\circ$.

The quantity Δ occurring in the denominators of Eq. [15], [16], and [17] is also the denominator of the general equation for $\bar{k}$. When the theoretical expression for $\bar{k}$ is put into the form of Eq. [1], we find that the equilibrium quotient γ takes the form of Eq. [19], provided [X] of Eq. [1] is taken to be the same as the added ion concentration [X] of Eq. [18], etc.[5]

$$\gamma = \frac{\frac{\bar{k}_\alpha[OH^-]}{\bar{k}_\beta[X]}\left(1 + \frac{\bar{k}_\alpha'}{\bar{k}_\delta}[OH^-]\right) + \frac{\bar{k}_\gamma}{\bar{k}_\delta} + \frac{\bar{k}_\gamma'}{\bar{k}_\beta}\left(1 + \frac{\bar{k}_\gamma}{\bar{k}_\delta}[X]\right) + \left(\frac{\bar{k}_\alpha\bar{k}_\gamma' + \bar{k}_\alpha'\bar{k}_\gamma}{\bar{k}_\beta\bar{k}_\delta}\right)[OH^-]}{1 + \frac{\bar{k}_\alpha'}{\bar{k}_\delta}[OH^-]} \qquad [19]$$

[5] [X] in Eq. [1] may be $[Cl^-]$, $[SO_4^=]$, $[SCN^-]$, or $[OH^-]$, while [X] of Eq. [18], etc., may be $[Cl^-]$, $[SO_4^=]$, or $[SCN^-]$.

For certain special cases, γ becomes much simpler. If no anions other than OH^- are present, the equation for the over-all rate constant as a function of $[OH^-]$ possesses the form of Eq. [20].

$$\bar{k} = \frac{K_1 + K_2\bar{k}_\alpha[OH^-]/\bar{k}_\beta}{C^\circ(1 + \bar{k}_\alpha[OH^-]/\bar{k}_\beta)} \qquad [20]$$

γ for this special case is simply the ratio $\bar{k}_\alpha/\bar{k}_\beta$, the equilibrium quotient for the adsorption reaction of Eq. [12]. On the other hand, the theoretical form of $\bar{k}$ for experiments performed in strong acid solution on the effect of X is given by Eq. [21].

$$\bar{k} = \frac{K_1 + K_3\bar{k}_\gamma[X]/\bar{k}_\delta}{C^\circ(1 + \bar{k}_\gamma[X]/\bar{k}_\delta)} \qquad [21]$$

Under these conditions γ is the simple ratio $\bar{k}_\gamma/\bar{k}_\delta$, which is the equilibrium quotient for the adsorption reaction of Eq. [13]. Evidently the complications of Eq. [19] arise when the exchange reaction of Eq. [14] is important.

Values of a quantity proportional to the equilibrium quotient for adsorption of OH^- on passive stainless steel are shown in Fig. 7 plotted against electrode potential. The quantity γ of Fig. 7 is related to $\bar{k}_\alpha/\bar{k}_\beta$, the true adsorption quotient (cf. Eq. [20] and [12]), by Eq. [22].

$$\gamma = (\bar{k}_\alpha/\bar{k}_\beta)K_w^c \qquad [22]$$

K_w^c of Eq. [22] is the ion product of water ($K_w^c = [H^+]\,[OH^-]$) expressed in concentration units. Use of Eq. [22] is convenient since values of γ were determined by least-squares fits of Eq. [1] to experimental data with $[X] \equiv 1/[H^+]$.

The potential dependence of the equilibrium quotient $\bar{k}_\alpha/\bar{k}_\beta$ is assumed to be given explicitly by Eq. [23], where $\Delta\phi_{ads}$ is the inner potential difference between the layer of specifically adsorbed hydroxide ions and the solution and λ is the absolute value of the charge on the adsorbed ions ($\lambda = 1$ for OH^- adsorption).

$$\bar{k}_\alpha/\bar{k}_\beta = (k_\alpha/k_\beta)\exp(+\lambda\mathbf{F}\Delta\phi_{ads}/RT) \qquad [23]$$

$\Delta\phi_{ads}$ may be assumed to vary with changes in the over-all inner potential difference between metal and solution, $\Delta\phi_T$, the latter being composed additively of the potential difference between metal and oxide layer, the potential drop across the passive film, the potential between the oxide layer and the position of the adsorbed ions, and the potential difference $\Delta\phi_{ads}$. Changes of the equilibrium quotient, $\bar{k}_\alpha/\bar{k}_\beta$, with the over-all potential $\Delta\phi_T$ depend on the variation of the specific rate constants for adsorption and desorption steps of the reaction of Eq. [12] with $\Delta\phi_{ads}$, the latter being some fraction of $\Delta\phi_T$. Combination of Eq. [22] and [23] and differentiation with respect to $\Delta\phi_T$ leads to Eq. [24].

$$\frac{d\ln\gamma}{d\Delta\phi_T} = \frac{\lambda\mathbf{F}}{RT}\left(\frac{d\Delta\phi_{ads}}{d\Delta\phi_T}\right) \qquad [24]$$

The slope of the line in Fig. 7 is $+6.75 \times 10^{-3}$ (mv^{-1}) and $2.303\,RT/\mathbf{F} = 71$ mv at 85°C, so that $(d\Delta\phi_{ads}/d\Delta\phi_T) = 0.48$. On the basis of the stated assumptions, this result suggests that a change in $\Delta\phi_{ads}$, which affects adsorption processes, accounts for only approximately half of the total change in those components of the over-all interfacial potential difference ($\Delta\phi_T$) which change their values appreciably during polarization.

The temperature dependence of $\bar{k}_\alpha/\bar{k}_\beta$, the equilibrium quotient for adsorption of OH^-, is shown in the Arrhenius-type plot of Fig. 8. Values of $\bar{k}_\alpha/\bar{k}_\beta$ were computed from Eq. [22] using values of K_w^c calculated according to the method given by Harned and Owen (14). The solid lines of Fig. 8 are least-squares fits of the data; in spite of scatter, which is expected because of the approximate nature of the model used, the slopes of the lines are roughly the same. Evaluation of the ratio k_α/k_β of Eq. [23] in terms of thermodynamic quantities leads to Eq. [25],

$$k_\alpha/k_\beta = \exp(+\Delta S^\circ_{ads}/R)\exp(-\Delta H^\circ_{ads}/RT) \qquad [25]$$

where ΔS°_{ads} and ΔH°_{ads} are standard entropy and enthalpy of adsorption, respectively. Combination of

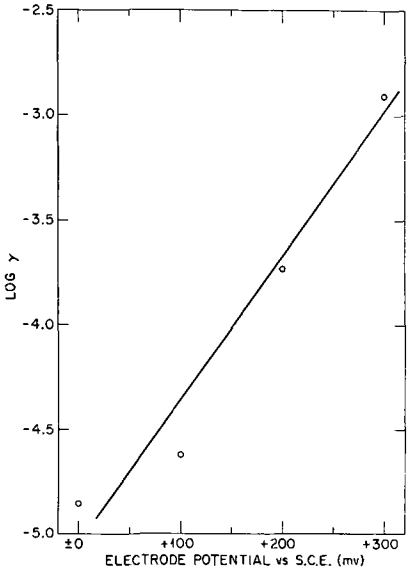

Fig. 7. Potential dependence of equilibrium quotient for adsorption of OH^- on passive stainless steel in 3 x $10^{-1}f$ $NaClO_4$ at 85°C. Potential vs. S.C.E. at room temperature.

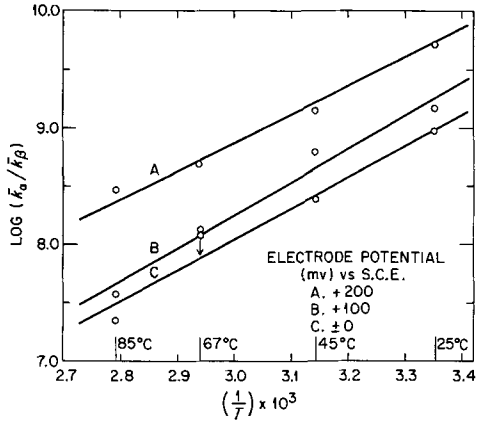

Fig. 8. Temperature dependence of equilibrium quotient for adsorption of OH^- on passive stainless steel in 3 x $10^{-1}f$ $NaClO_4$. Potential vs. S.C.E. at room temperature.

Eq. [23] and [25], followed by differentiation, leads to Eq. [26] relating the slope of the lines in Fig. 8 to the apparent standard enthalpy of the adsorption reaction (ΔH°_{app}).

$$\Delta H^\circ_{app} \equiv \Delta H^\circ_{ads} - \lambda \mathbf{F} \Delta\phi_{ads} - (\lambda \mathbf{F}/T)[d\Delta\phi_{ads}/d(1/T)]_{\Delta\phi_T} = -R[d \ln (\bar{k}_a/\bar{k}_\beta)/d(1/T)]_{\Delta\phi_T} \quad [26]$$

Use of Eq. [26] with the data of Fig. 8 leads to $\Delta H^\circ_{app} = -11.3$, -13.0, and -12.3 kcal/mole for curves A, B, and C, respectively. Therefore the adsorption reaction is exothermic. Using an average value of $\Delta H^\circ_{app} = -12.2$ (± 0.6) kcal/mole and neglecting the potential dependence of the apparent enthalpy of adsorption (cf. Eq. [26]), calculation of the standard entropy of the adsorption reaction from the data in Fig. 8 leads to $\Delta S^\circ_{ads} = +1.7$ (± 1.4) e.u. Instead of adsorption of OH^- onto an aquo surface as in Eq. [12], an alternative and electrochemically equivalent reaction scheme is given in Eq. [12′].

$$\text{aquo surface} + H_2O \rightleftharpoons \text{hydroxy surface} + H_3O^+ \quad [12']$$

The low value of standard entropy of adsorption calculated from these data is consistent with the mechanism of Eq. [12′], since proton transfer from an aquated surface probably involves less configurational entropy change than a process involving adsorption of hydroxide ion.

Results shown in Fig. 2 on the SCN^- effect receive qualitative explanation on the basis of Eq. [19]. For most choices of rate constants, the numerator of Eq. [19] essentially determines the effect of acidity, and γ increases with $[OH^-]$ as observed. Evidently SCN^- displaces adsorbed OH^- more readily than adsorbed H_2O, although information is needed on the relative magnitudes of the ratios $\bar{k}_\gamma/\bar{k}_\delta$ and $\bar{k}_\gamma'/\bar{k}_a'$, the equilibrium quotients of the reactions in Eq. [13] and [14], before definite conclusions can be made. As seen in Fig. 3, the opposite situation appears to hold with $SO_4^=$ higher $[SO_4]$ being required to produce a significant change in rate constant at low acidity than at high acidity.

Under certain conditions, the over-all rate constant $\bar{k}$ varies with added ion concentration [X] in the manner shown in curve E of Fig. 6. Analysis of the theoretical model shows that this behavior is possible provided the association quotients of Eq. [12], [13], and [14] have appropriate values. Specifically, these quotients must satisfy the inequality of Eq. [27].

$$\left(\frac{\bar{k}_\gamma}{k_\delta} - \frac{\bar{k}_a}{k_\beta} \cdot \frac{\bar{k}_\gamma'}{k_a'}\right) << 0 \quad [27]$$

The left-hand side of Eq. [27] must be sufficiently negative to compensate for positive terms appearing in the equation for the slope of a plot of over-all rate constant against added ion concentration. Mechanistically, the ratio of aquo to hydroxy surface increases to a maximum at low added ion concentrations before decreasing at higher [X] because of the peculiarities of the mixed isotherm when the mechanism of Eq. [14] is important. Since $K_1 << K_2 < K_3$ in the present system ($[X] = [Cl^-]$), the over-all rate constant goes through a minimum with increasing [X]. Analysis further shows that no minimum should be observed at very high or very low acidity, and this is in accord with experimental observation.

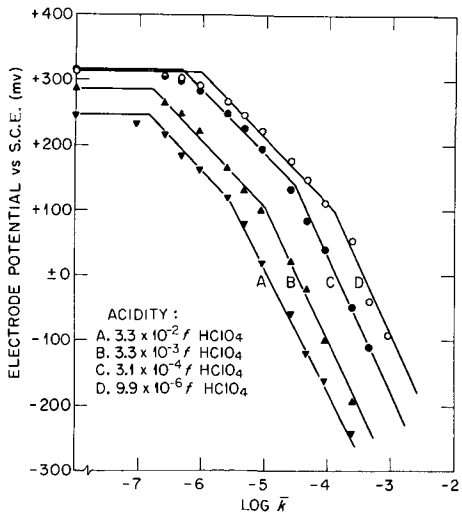

Fig. 9. Effect of acidity on polarization curves for reduction of Cu^{++} on passive stainless steel in 3 x 10^{-1} f $NaClO_4$; 67°C, helium atmosphere. Potential vs. S.C.E. at room temperature.

Polarization curves for the reduction of Cu^{++} on stainless steel in perchlorate medium are similar to those observed previously (10) in dilute sulfuric acid solution. A typical set of curves is shown in Fig. 9; closely analogous results were obtained from galvanostatic measurements at other temperatures. The change of slope of the polarization curves results from a change with potential of the rate-determining step in the mechanisms of Eq. [2] and [3]. Examination of Eq. [9] shows that, neglecting diffusion ($D_0/\delta_0 >> \bar{k}_1$ and $D_R/\delta_R << \bar{k}_2 + \bar{k}_3$), the rate of reduction of Cu^{++} on the aquo surface reduces to the form of Eq. [28].

$$K_1 = C^\circ 2\bar{k}_1\bar{k}_3/(\bar{k}_2 + \bar{k}_3) \quad [28]$$

At low potentials $\bar{k}_3 >> \bar{k}_2$ and K_1 is proportional to $\bar{k}_1$, the rate constant for the reduction of Cu^{++} to the cuprous intermediate. At high potentials, $\bar{k}_2 >> \bar{k}_3$ and K_1 becomes proportional to $\bar{k}_1\bar{k}_3/\bar{k}_2$, implying that in this potential region there is virtual equilibrium between cupric and cuprous species and that reduction of the cuprous intermediate is rate determining. Rate control by diffusion (plus convection in stirred solution) becomes important at potentials more negative than those shown in Fig. 9. The results of Fig. 9 show that the transition between high and low potential regions of the polarization curve is essentially independent of acidity. Since the transition occurs when $\bar{k}_2 = \bar{k}_3$, this observation supports the assumption implicit in the derivation of the isotherm that the rate constants of the charge transfer steps in the mechanisms of Eq. [2], [3], and [4] are independent of acidity. When plotted as a function of temperature at constant acidity, polarization curves show that the potential of the transition region increases with temperature, implying different ener-

getics for the alternative modes of decomposition of the cuprous intermediate.

Values of differential capacity for the present system were estimated by analysis of recordings of the initial potential-time transients observed during the establishment of new steady states in galvanostatic measurements. Although this manual procedure is inexact, reasonably reproducible numbers were obtained. In units of microfarads/cm^2, the capacity of the interface was 35 to 40 at +300 mv *vs* SCE., 40 to 50 at +200 mv, 60 to 80 at +100 mv, 90 to 120 at ±0 mv, and 110 to 160 at −100 mv. Slight increases of capacity with temperature were observed, the range of values in the above listing corresponding to measurements at 25° and 85°C. Values of capacity were found to be independent of the current density of the Cu^{++} reduction reaction at the oxide-solution interface. A slight acidity effect was detected; values of capacity increased with acidity at constant potential, but in no case did the capacity change by more than a factor of two over the acidity range, 10^{-5} to 10^{-2} *f* $HClO_4$. Capacities were also essentially independent of added anion concentration, so that measurements of capacity in the present system did not appear to include a contribution from the reaction capacity of the adsorption processes. The foregoing observations allow the speculation that the capacity of the interface is determined largely by the properties of the passive oxide; *i.e.*, the smallest capacity in the interfacial system depends on the thickness and the charge distribution within and on each side of the oxide layer.

We conclude from the evidence presented that the rates of reduction reactions on passive stainless steel are sensitive to specific adsorption of anions from solution. To a good approximation this specific adsorption follows a potential-dependent Langmuir isotherm. Analysis of data on the adsorption of hydroxide ion yields results in good agreement with theory, thus permitting calculation of the energetics of the adsorption reaction. Adsorption of anions other than hydroxide follows a similar, although much more complex isotherm, the properties of which allow qualitative interpretation of salient observations. Similar anion effects undoubtedly occur for other reduction reactions and in other passive systems, for which the foregoing analysis may also prove to be useful.

Acknowledgment

The authors wish to express appreciation to their colleagues, Dr. G. H. Cartledge and Dr. R. E. Meyer, for stimulation and encouragement during the course of this work.

Manuscript received Dec. 6, 1961; revised manuscript received March 5, 1962. This paper was prepared for presentation at the Los Angeles Meeting, May 6-10, 1962.

Any discussion of this paper will appear in a Discussion Section to be published in the June 1963 JOURNAL.

REFERENCES

1. H. Gerischer, *Z. Elektrochem.*, **54**, 366 (1950).
2. J. M. Kolotrykin, *This Journal*, **108**, 209 (1961).
3. K. E. Heusler and G. H. Cartledge, *ibid.*, **108**, 732 (1961).
4. J. Heyrovsky, *Discussions Faraday Soc.*, **1**, 212 (1947).
5. A. N. Frumkin, *Uspekhi Khim.*, **24**, 933 (1955).
6. A. N. Frumkin, *Trudy 4-go Soveshchaniya Po Elektrokhimii, Moscow, 1956*; trans. Consultants Bureau, N. Y., 1961, p. 39.
7. R. Piontelli, *Compt. rend. C.I.T.C.E.*, **2**, 185 (1950).
8. R. Brdicka, *Chem. Listy*, **38**, 252 (1944).
9. R. F. Sympson and G. H. Cartledge, *J. Phys. Chem.*, **60**, 1037 (1956).
10. F. A. Posey, G. H. Cartledge, and R. P. Yaffe, *This Journal*, **106**, 582 (1959).
11. R. F. Sympson and F. A. Posey, "Chem. Div. Ann. Prog. Rept. June 20, 1959," ORNL-2782, p. 57.
12. R. F. Sympson and F. A. Posey, "Chem. Div. Ann. Prog. Rept. June 20, 1960," ORNL-2983, p. 54.
13. R. H. Fowler and E. A. Guggenheim, "Statistical Thermodynamics," p. 426, Cambridge (1952).
14. H. S. Harned and B. B. Owen, "The Physical Chemistry of Electrolytic Solutions," p. 643, Reinhold Publishing Co., New York (1958).

A Solid Electrolyte Fuel Cell

J. Weissbart and R. Ruka

Chemistry Department, Research Laboratories, Westinghouse Electric Corporation, Pittsburgh, Pennsylvania

ABSTRACT

A high-temperature oxide electrolyte galvanic cell of the type H_2/H_2O, Pt || $(ZrO_2)_{0.85}(CaO)_{0.15}$ || Pt, O_2 is described. Experimental data for reaction of oxygen with hydrogen-water and methane-water mixtures are given. Open-circuit voltages for the hydrogen-oxygen reaction are close to theoretical, and current-voltage curves show that the output of the cell is limited essentially by the resistance of the electrolyte. The data suggest that solid oxide electrolyte cells of this general type may offer attractive possibilities as fuel cells for utilizing hydrocarbons as fuel and oxygen or air as oxidant.

High-temperature galvanic cells with solid oxygen ion conducting electrolytes have features which may make them attractive as fuel cells. Catalytic problems are reduced at high temperatures, and a mechanically stable electrode-electrolyte interface is possible with an all-solid construction.

Schottky (1) discussed the problem of solid electrolytes from the theoretical point of view in 1935 and two years later Baur and Preis (2) constructed the first solid oxide-electrolyte fuel cell. The electrolyte was in the form of a ceramic tube of $(ZrO_2)_{0.85}(Y_2O_3)_{0.15}$, a material which Nernst had previously

shown to possess a relatively high ionic conductivity. The tube was filled with coke to form the anode and surrounded with iron oxide in an air atmosphere to form the cathode. An output of less than 1 ma/cm^2 of electrolyte area at 1050°C and 0.65v was obtained and it was concluded that sufficient cation conductivity[1] was occurring to damage the cell.

A number of researches have contributed information on the physical and chemical properties of ceramics with high oxygen ion mobility. Nernst (3) observed qualitatively the electrolytic evolution of oxygen from a rod of $(ZrO_2)_{0.85}$ $(Y_2O_3)_{0.15}$ (Nernst glower). More recently Weininger and Zemany (4) made a quantitative measurement of the electrolytic evolution of oxygen from a Nernst glower of similar composition and found that 7-80% of the current could be accounted for by ionic conduction, depending on temperature, current flow, and previous history of the material.

Wagner (5) proposed in 1943 that oxide solid solutions such as $(ZrO_2)_{1-x}$ $(CaO)_x$ or $(ZrO_2)_{1-x}$ $(Y_2O_3)_x$ contain vacant oxygen ion sites, one vacancy occurring for each Ca^{+2} or two Y^{+3} ions that substitute for Zr^{+4} ions in the fluorite-type crystal structure. He assumed that this would lead to high oxygen ion conductivity. Hund (6) determined the density of these oxides by x-ray and pycnometric methods. The data are consistent with the oxygen ion vacancy model.

Kingery (7) and co-workers calculated the oxygen ion mobility in $(ZrO_2)_{0.85}$ $(CaO)_{0.15}$ from the Nernst-Einstein relation[2] and the diffusion coefficient obtained from measurements of the rate of exchange of oxygen in the oxide with O^{18}. Comparing this data with measurements of electrical conductivity of the oxide they concluded that the conductivity is wholly ionic and that the transference number is near unity for the oxygen ion.

Kiukkola and Wagner (8) and several other authors have obtained high temperature thermodynamic data using galvanic cells with electrolytes of zirconia of thoria containing CaO, Y_2O_3, La_2O_3, and other oxides.

Weissbart and Ruka (9, 10) have constructed vacuum tight cells of the type

$$O_2\ (p_1), Pt \mid\mid (ZrO_2)_{0.85}(CaO)_{0.15} \mid\mid Pt, O_2(p_2)$$

in which the electrode reactions at temperatures above 600°C were shown to correspond closely to the reversible reaction

$$O_2 + 4e^- \rightleftharpoons 2\,O^= \qquad [1]$$

The voltages obtained are in good agreement with the theoretical emf E calculated from the thermodynamic relationship for reversible transfer of oxygen from cathode to anode at the given pressures.

$$E = \frac{RT}{4F} \ln \frac{P_{O_2}\ (\text{cathode})}{P_{O_2}\ (\text{anode})} \qquad [2]$$

This shows that the cells act as oxygen concentration cells.

[1] Cation conductivity is undesirable since it results in transfer of electrolyte from anode to cathode of the galvanic cell. This would damage the electrode-electrolyte interfaces.

[2] $D_i = B_i kT$ where D_i is the self-diffusion coefficient and B_i is the absolute mobility of the i-th species.

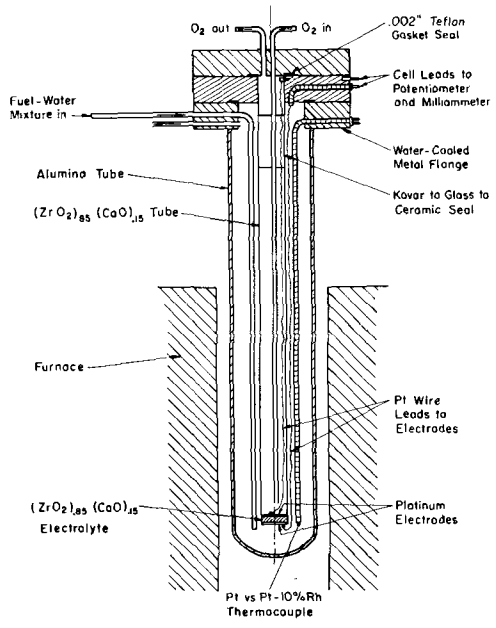

Fig. 1. Schematic diagram of galvanic cell with solid oxide electrolyte.

Faraday's laws were found to be obeyed closely for current flow through a cell of this type as determined by microweighing of the oxygen transferred. The electronic contribution to the total conductivity was found to be less than 0.5% near 1000°C in an oxygen atmosphere.

Experimental

The construction of the galvanic cell is illustrated schematically in Fig. 1. It is similar to that previously described (9) except that it is arranged to flow gases past both electrodes.

The essential elements of the cell are the flat bottom portion of the $(ZrO_2)_{0.85}(CaO)_{0.15}$ tube, which acts as the electrolyte, and two porous platinum electrodes (9) of less than 0.001 in. thickness. Cell dimensions were of the order of 2.5 cm^2 area and 0.15 cm thickness. For these cells contact resistances of the order of 1-2 ohms were encountered depending on the thickness of the porous platinum films.

For all experiments pure oxygen at atmospheric pressure flowed slowly past the cathode, and the various water-hydrogen or water-methane mixtures flowed at a faster rate through the anode chamber. The experimental arrangement of the cell is designed for current-voltage measurements rather than for optimum conversion of fuel. An appreciable fraction of the total gas flowing through the anode chamber does not come in contact with the electrode. Consequently a high flow rate of gas was used to minimize concentration polarization and thermal diffusion effects. The volume of preheated gas flowing per minute into the anode chamber was about 3.7 times the volume of the chamber. For a decrease in flow rate to one-third of this value the temperature of a thermocouple placed near the anode changed less than 1°C.

The hydrogen or methane was first passed through water bubblers and the effluent gas from the anode chamber was analyzed for H_2, H_2O, CO, CO_2, and

CH_4. Calculations of the theoretical emf for the experiments are based on these analyses.

Results and Discussion

When current is drawn from a galvanic cell the voltage may be lower than the open-circuit value due to (*a*) activation polarization, (*b*) concentration polarization, (*c*) ohmic resistance of the cell. The voltage drop due to each of these is a function of the current density. (*a*) depends on the particular rate-determining chemical and electrochemical reactions at the electrodes, (*b*) involves mass transfer of reactants and products, and (*c*) ordinarily depends largely on electrolyte resistance.

Activation polarization is frequently encountered in low temperature cells, and significant reaction of hydrocarbons at the fuel electrode is particularly difficult to attain. In addition, the oxygen electrode reaction proceeds by a peroxide mechanism which even in the presence of peroxide decomposing catalysts results, according to Kordesch (11), in a lower voltage than the ideal oxygen electrode value.

At higher temperatures the mechanism at the oxygen electrode is different. Thus the peroxide reaction is not detected in a fused carbonate cell which has been shown to act as an oxygen-carbon dioxide concentration cell by Chambers and Tantram (12).

The present solid oxide cell involves even less complicated electrode reactions since it acts as a simple oxygen concentration cell (9). If hydrogen is present at the anode, we write the cell diagrammatically as

$$H_2/H_2O, Pt \;||\; (ZrO_2)_{0.85}(CaO)_{0.15} \;||\; Pt, O_2$$

The emf E is given by the standard thermodynamic relation

$$E = E^\circ + \frac{RT}{4\mathbf{F}} \ln P_{O_2}\,(\text{cathode}) + \frac{RT}{2\mathbf{F}} \ln \frac{P_{H_2}}{P_{H_2O}}\,(\text{anode}) \qquad [3]$$

Figure 2 shows a comparison of experimental and theoretical open-circuit voltage values *vs.* the $H_2/(H_2 + H_2O)$ ratio for a constant oxygen pressure at the cathode. The theoretical curve is calculated from Eq. [3]. The experimental points are based on the measured emf and the analytically determined $H_2/(H_2 + H_2O)$ mole ratio. Agreement is within 5 mv of the theoretical value. This is within the error of the H_2 and H_2O analyses.

Figure 3 shows current-voltage curves for the hydrogen-oxygen reaction in the cell at four temperatures at approximately constant $H_2/(H_2 + H_2O)$ ratios and oxygen pressure. The curves are all straight lines with slopes $\Delta E/\Delta I$ agreeing within 5% of the values of resistance determined directly by 1000 cycle a-c resistance measurements. Figure 4 shows further current-voltage curves at two temperatures for two different water-hydrogen ratios. The two sets of parallel lines indicate that the d-c resistance was the same at the same temperature. Although the internal resistance of a cell stayed nearly constant during measurements of individual current-voltage curves, variations in either direction were found over longer periods of time, even

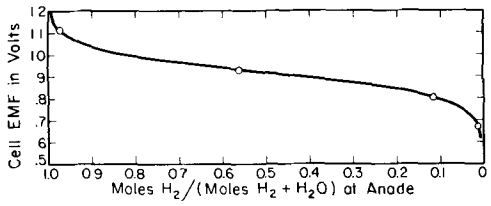

Fig. 2. Comparison of measured voltage with theoretical emf of cell,

O_2, Pt||$(ZrO)_{0.85}$ $(CaO)_{0.15}$||Pt, H_2/H_2O

------ Theoretical line; ○ experimental point; temperature 1015°C, O_2 pressure at cathode 731.2 mm.

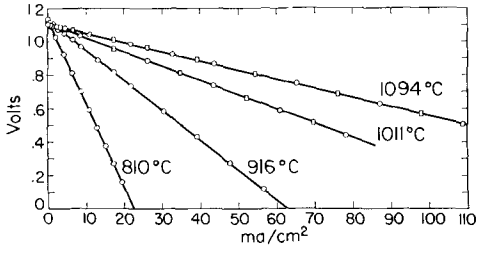

Fig. 3. Current-voltage behavior of cell,

O_2, Pt||$(ZrO_2)_{0.85}$ $(CaO)_{0.15}$||Pt, H_2/H_2O

at O_2 pressure ≅ 730 mm and $H_2/(H_2+H_2O)$ ≅ 0.973 for four temperatures. ○ Increasing current; □ decreasing current.

on open circuit. Open-circuit voltages were reproducible to about 1 mv in duplicate runs, independent of this effect, while the slopes of the current-voltage curves changed in accordance with the measured resistance changes. According to Dietzel and Tober (13) the lower temperature limit for existence of the fluorite phase in the zirconium-calcium mixed oxide lies in the neighborhood of 850°C, but phase boundaries are very uncertain since equilibrium was not attained over a wide temperature range. This suggests that resistance changes under open-circuit conditions encountered in the present work could possibly be associated with slow phase changes occurring as a function of temperature, composition and homogeneity of the mixed oxide.

Figure 5 shows the current-voltage curve obtained for a mixture of 3.8% methane, 2.1% water and 94.1% N_2 as fuel. The rate of fuel flow was sufficiently rapid that chemical equilibrium was not attained for the reforming reaction and 80% of the methane remained undecomposed by passage through the cell. The open-circuit voltage of 0.945v

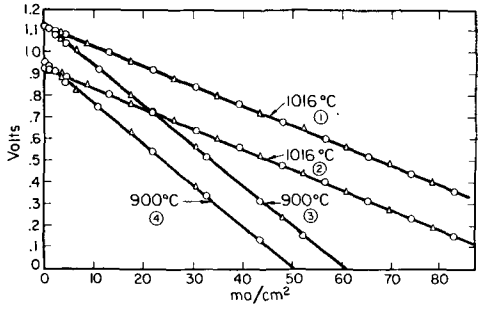

Fig. 4. Current-voltage behavior of the cell,

O_2, Pt||$(ZrO_2)_{0.85}$ $(CaO)_{0.15}$||Pt, H_2/H_2O

at two temperatures for two H_2/H_2O ratios. ○ Increasing current; △ decreasing current; O_2 pressure ≅ 731 mm. $H_2/(H_2+H_2O)$ ≅ 0.97 for curves 1 and 3; $H_2/(H_2 + H_2O)$ ≅ 0.54 for curves 2 and 4.

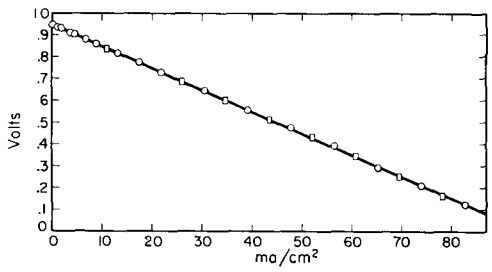

Fig. 5. Current-voltage behavior of the cell, O_2, Pt‖$(ZrO_2)_{0.85}$ $(CaO)_{0.15}$‖Pt, CH_4/H_2O
Composition of inlet fuel gas: CH_4 3.8%, H_2O 2.1%, N_2 94.1%; temperature 1015°C. ○ Increasing current; □ decreasing current; O_2 pressure 731 mm.

is within 5 mv of the value calculated for the simple hydrogen-oxide reaction and approximately 50 mv lower than the value for the carbon monoxide-oxygen reaction. The calculations are based on the H_2/H_2O and CO/CO_2 ratios in the effluent gas from the anode chamber and the known oxygen pressure at the cathode. At slower flow rates a higher percentage of methane was converted, probably largely by the reforming reaction $CH_4 + H_2O \rightarrow CO + 3H_2$. This results in higher H_2/H_2O and CO/CO_2 ratios and thus higher open-circuit voltages. The data indicate that the major electrochemical reactions probably involve the reformed gases, H_2 and CO rather than CH_4. The moles of CH_4 and H_2O decomposed is consistent with the CO, CO_2, and H_2 formed as determined from the analysis of the exit gases. This shows that carbon formation did not occur within the cell. However, analysis of exit gases indicated that carbon formation did occur in some other experiments at similar low H_2O/CH_4 ratios.

The ultimate life expectancy of the cell under optimum conditions has not been determined, although an individual cell of this type using a 30 to 1 H_2/H_2O mixture as fuel has been operated continuously at 10 ma/cm² of electrolyte area for two months at temperatures between 1000° and 1200°C. Some platinum loss from electrodes by evaporation, possibly as an oxide, occurs at these temperatures.

The current-voltage data indicate that the cell has an output for the hydrogen-oxygen reaction which is essentially resistance limited and thus should be capable of higher output by simply decreasing the thickness of the electrolyte, provided contact resistances are low.

The studies necessary to improve the cell include investigations of the cation conductivity and phase stability of the electrolyte, the electrode structure, properties of thin films of the electrolyte and substitution of other electrodes and electrolytes.

Acknowledgment

The authors wish to thank W. Hickam and coworkers for the mass spectrometric analyses of the gas samples. Helpful discussions were held with Y.L. Sandler and S. Barnartt.

Manuscript received Nov. 6, 1961. This paper was prepared for delivery before the Los Angeles Meeting, Oct. 6-10, 1962.

Any discussion of this paper will appear in a Discussion Section to be published in the June 1963 JOURNAL.

REFERENCES

1 W. Schottky, Wiss. *Veröffentl. Siemens-Werken,* **14**, 1 (1935).
2. E. Baur and H. Preis, *Z. Elektrochem.*, **43**, 727 (1937).
3. W. Nernst, *ibid.*, **6**, 41 (1900).
4. J. L. Weininger and P. D. Zemany, *J. Chem. Phys.* **22**, 1469 (1954).
5. C. Wagner, *Naturwissenschaften,* **31**, 265 (1943).
6. F. Hund, *Z. physik. Chem.*, **199**, 142 (1952).
7. W. D. Kingery, J. Pappis, M. E. Doty, and D. C. Hill, *J. Am. Chem. Soc.*, **42**, 394 (1959).
8. K. Kiukkola and C. Wagner, *This Journal,* **104**, 379 (1957).
9. J. Weissbart and R. Ruka, *Rev. Sci. Instr.*, **32**, 593 (1961).
10. J. Weissbart and R. Ruka, Paper presented at the Electrochemical Society Fall Meeting, Detroit, Mich. (Oct. 2-5, 1961) (Extended Abstract No. 44, Battery Division).
11. K. Kordesch, *Ind. Eng. Chem.*, **52**, 296 (1960).
12. H. H. Chambers and A. D. S. Tantram, *ibid.*, **52**, 295 (1960).
13. A. Dietzel and H. Tober, *Ber. deut. keram. Ges.*, **30**, 47 (1953).

Studies of the Electrochemical Kinetics of Indium

I. Kinetics of Deposition and Dissolution in the Indium + Indium Sulfate System

B. Lovrecek and V. Markovac

Institute of Electrochemistry and Electrochemical Technology, Faculty of Technology, University of Zagreb, Zagreb, Yugoslavia

ABSTRACT

The kinetics of the deposition and dissolution of indium (from indium amalgam) in indium sulfate solutions at pH 2.5 have been studied by observing variations of overpotential during individual constant current pulses. The electrode was in the form of a hanging drop of the amalgam, which was renewed for each pulse. The steady-state activation overpotential was reached approximately 1 msec after application of the pulse, which corresponds to a mean value of double layer capacity of 25.4 μF/cm^2. Plots of the activation overpotential *vs.* log current density show good Tafel relations in both the cathodic and anodic regions. Analysis of these data shows the mechanism to consist of three consecutive electron transfer steps

$$In^{3+} \underset{e^-_0}{\overset{+e^-_0}{\rightleftarrows}} In^{2+} \underset{e^-_0}{\overset{+e^-_0}{\rightleftarrows}} In^{1+} \underset{e^-_0}{\overset{+e^-_0}{\rightleftarrows}} In^0$$

The rate-determining step for both anodic and cathodic polarization is

$$In^{3+} \underset{e^-_0}{\overset{+e^-_0}{\rightleftarrows}} In^{2+}$$

for which the transfer coefficient α was determined to be approximately 0.83.

The mechanism of electrochemical deposition and dissolution of metals, because of its great theoretical and practical importance, has been the subject of numerous studies and discussions. This paper deals with the mechanism of deposition and dissolution of indium, in which studies methods similar to those used by Gerischer (1), Berzins and Delahay (2), and Mattsson and Bockris (3) have been applied. Kangro and Weingärtner (4), and Duić, Kovac, and Lovrecek (5) have already established that the deposition of indium(III)-ion and the dissolution of metallic indium, respectively, follow in a "many step" electrode process over an ion of lower valency, but have not determined either the electrochemical step in question or the rate-determining step. The kinetics of the system have been studied[1] on basis of theoretical expressions for the kinetics of "many step" electrode reactions (6), with due consideration to possible reaction steps in the electrochemical deposition and dissolution of indium.

Experimental

Apparatus.—The apparatus (Fig. 1) comprised an electrolytical cell with nitrogen purification unit and electrical device.

The electrolytic cell resembles those used earlier (1, 2) and comprises a main compartment and a reference electrode compartment. The main compartment is shaped like a vessel with a cap through which a carrier for measuring electrode, a capillary with an amalgam reservoir on the top, a spoon for catching of the amalgam drops, and a bubbler are fixed. The carrier is a glass tube with a thin platinum wire sealed into the top. After sealing the wire was cut level with the glass and electrolytically gold-plated. The measuring electrode is a hanging drop of amalgam, of determined surface area, on which the polarization takes place. The carrier for the measuring electrode passes through the center of the cap into the cell following its vertical axis. The capillary resembles those used in polarography. The capillary with reservoir is connected to the mercury pressure system by means of a tygon tube. The pressure system regulates the pressure in the reservoir and thus regulates the rate of dropping through the capillary. The spoon for catching drops

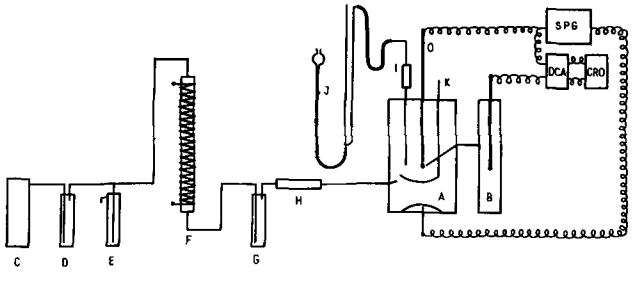

Fig. 1. Schematic diagram of apparatus: A, main compartment of electrolytic cell; B, reference electrode compartment; C, nitrogen tank; D, washing bottle; E, mercury security valve; F, electric furnace with active copper; G, washing bottle; H, drop collector containing glass wool; I, capillary with amalgam reservoir; J, pressure system; K, glass spoon; SPG, square pulse generator; DCA, direct current amplifier; CRO, cathode-ray oscilloscope; O, hanging drop electrode; P, reference electrode (S.C.E.).

[1] Further experiments with this system and description of details of the apparatus and procedure will be found in the Ph.D. thesis of V. Markovac.

is fastened by its handle to the cap by a cylindrical ground glass joint and revolves freely in the direction and around its vertical axis. It catches the drop of amalgam from under the capillary and hangs it on the tip of the carrier.

The main compartment of the cell has in its side a tube for the introduction of nitrogen, which is introduced before the electrolysis so as to remove the dissolved oxygen from the electrolyte, and immediately proceeding each measurement, to level the concentration. In the opposite side of the main compartment of the cell an electrolytical bridge is built in, connecting this compartment with the reference electrode compartment. The electrolytical bridge is executed so that one end enters the main compartment of the cell approximating the form of a capillary to the hanging drop of the measuring electrode (distance of 3 mm). At the bottom of the cell there is a quantity of amalgam of the same composition as the hanging drop, *i.e.*, the measuring electrode. This quantity of amalgam is continually increased by the drops discharged from the carrier of measuring electrode. In the reference electrode compartment there is a standard saturated calomel electrode in the electrolyte of the same composition as that in the main compartment of the cell. During the pre-electrolysis, a platinum electrode is put into this compartment to serve as an anode instead of the calomel electrode.

Before the electrolysis and immediately proceeding each measurement, purified nitrogen is forced through the cell and the electrolyte. The ordinary tank nitrogen is purified (oxygen removed) in the manner introduced by Meyer and Ronge (7), by forcing the gas through a column filled with active copper, spread on the infusorial earth. The column is heated to 200°C by an electric heater in the sheath around the column. The electrolytic cell and purification units are made of Pyrex glass. All joint and stopcocks are made in the ground glass technique and sealed with distilled water.

The electrical device (Fig. 2) has three main components: a square-wave pulse generator SPG, a direct current amplifier DCA, and a cathode-ray oscilloscope CRO.

A relay RE built into the generator synchronizes the beginning of the square-wave pulse and the time

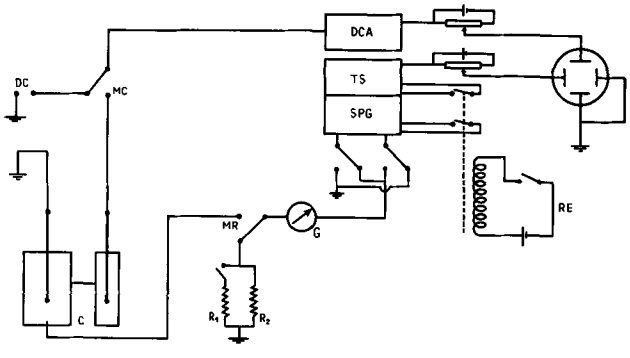

Fig. 2. Schematic diagram of electrical arrangement: RE, relay; SPG, square pulse generator; TS, time sweep; DCA, direct current amplifier; CRO, cathode-ray oscilloscope; AC, switch anodic-cathodic polarization; G, galvanometer; MR, switch measurement regulation; R_1 and R_2, resistors (5.6 KΩ and 56Ω); MC, switch measurement-calibration; DC, calibration device; C, electrolytical cell.

sweep TS, so that the time sweep begins a little earlier, for safety's sake. The time sweep, built into the generator, regulates the recording time in a 0.3 msec to 3 sec range. The square-wave pulse is electronically stabilized by means of a penthode, so that changes in the resistance of the cell do not influence the constant current of a pulse. Pulses obtained cover the range of 2.0×10^{-6}-8.0×10^{-2} amp. The switch AC serves to change the direction of the pulse current. Before the measurement the selected current is read on the galvanometer G by passing the current through a combination of resistors R_1 and R_2, instead of through the cell. The rise time of a pulse is less than 10 μsec.

The direct current amplifier DCA is constructed to let pass a 10 MHz span of frequencies, which makes possible the observation of pulses with rise time up to 1 μsec. The factor of amplification is up to 1.700. The switch MC and a device DC serve for the calibration of the amplifier.

Procedure.—Before the experiments the glass apparatus was washed in chrom-sulfuric acid (16 hr), washed out in running water, and then washed in distilled water (16 hr).

The composition of the electrolyte used was $0.116N$ $In_2(SO_4)_3$ in $0.5N$ K_2SO_4, $pH = 2.5$ solution. The electrolyte was prepared by the dissolution of a wire of very pure indium[2] in the calculated amount of H_2SO_4 with regard to indium sulfate and potassium sulfate. Once the dissolution was completed the corresponding amount of KOH solution was added successively until a certain pH value was reached. Chemicals used were of the analytical reagent grade.

As the measuring electrode a hanging drop of 0.3% by weight In-amalgam was used. In-amalgam in such concentrations has the physical properties of liquids (8). It is prepared in the reservoir of the capillary, covered by electrolyte in the stream of nitrogen. The rate of dropping is regulated by the change of pressure of nitrogen in the pressure system. The presence of nitrogen eliminates the possibility of oxidation of In-amalgam (9). The size of the drop in the electrolyte depends on the diameter of the capillary. It was determined by weighing a number of drops, and from the weight the surface of a drop was set at 2.78×10^{-2} cm².

The electrolyte is in the main compartment of the cell and in the reference electrode compartment. Before the experiments purified nitrogen is forced through the cell (12 hr). Pre-electrolysis with the current of 0.32 ma is undertaken as a last purification step (10 hr). The mass of amalgam on the bottom of the main compartment of the cell serves as a cathode. A platinum electrode in the reference electrode compartment serves as an anode.

Single d-c square-wave pulses of selected intensity pass through the hanging drop as the measuring electrode and the amalgam mass as the counter electrode. Resulting overpotential changes are recorded in relation to the reference electrode (S.C.E.) over the d-c amplifier, on the screen of the

[2] For the preparation of electrolyte and In-amalgam a wire with the guaranteed minimum purity of 99.95% of indium was used (Dr. E. Durrwächter, DODUGO K.G. Pforzheim, West Germany).

cathode-ray oscilloscope as the overpotential-time ($\eta_t - t$) curves. The duration of pulses and the degree of amplification is suited to the intensity of current so that the overpotential can reach a constant value before the concentration polarization sets in. Measurements were made from low current densities to higher ones. For each pulse a new drop of amalgam was used. All the cathodic transients were taken first and then the anodic ones, covering the current density range of 8.1 x 10^{-5} to 2.1 x 10^{-1} amp/cm^2.

The overpotential-time curves on the screen of the cathode-ray oscilloscope were photographed on Ilford-HPS 6 x 9 cm film with a Rolleicord camera.

Results

Overpotential-time relationship.—An example of experimentally obtained $\eta_t - t$ curve for anodic polarization is shown in Fig. 3. The ohmic overpotential η_Ω is represented by the gap at the initial part of the curve, as has already been done by other authors (3, 10). In cathodic curves the part of the ohmic overpotential is very small in relation to the total overpotential η_t, which is not the case in anodic $\eta_t - t$ curves, so it is very difficult to obtain exact and precise values by experimentation. To obtain the values, the sensitivity of the measuring device was increased and only the initial part of the $\eta_t - t$ curve was recorded, regardless of the fact

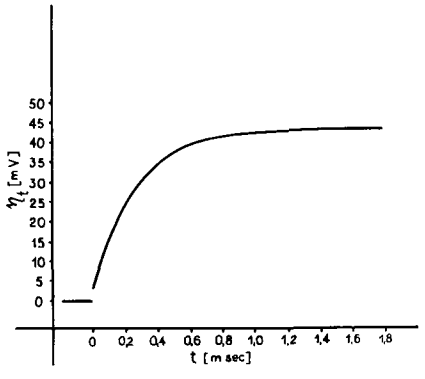

Fig. 3. Curve η_t — t for anodic current density 3.6 x 10^{-3} amp/cm^2.

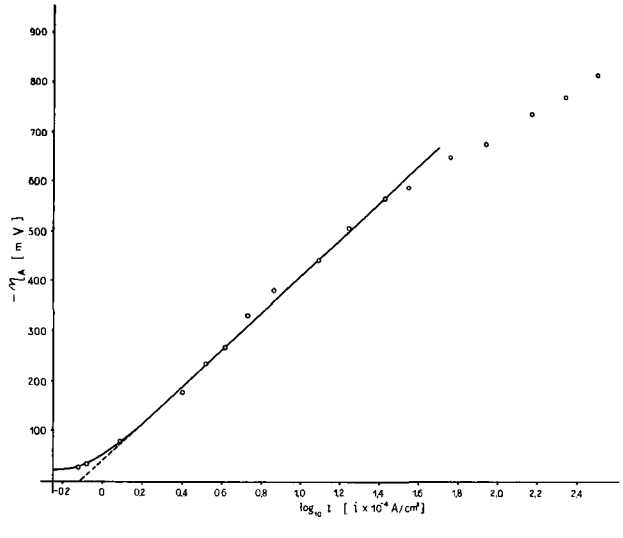

Fig. 4. Tafel line for cathodic polarization, $\alpha = 0.844$

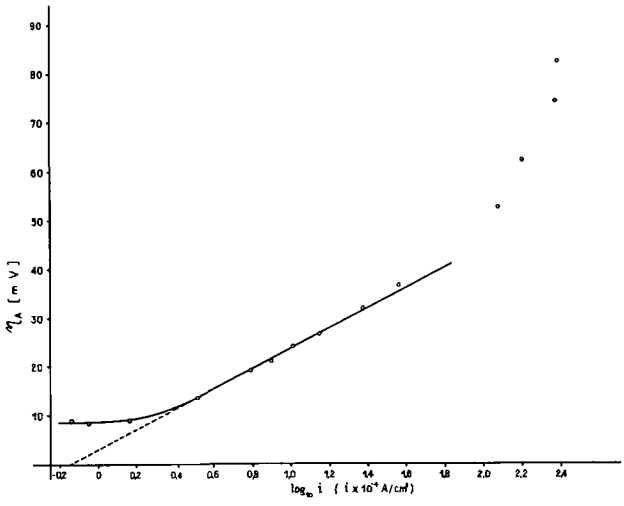

Fig. 5. Tafel line for anodic polarization, $\alpha = 0.800$

that overpotential did not build up to its steady-state value.

The change of potential, minus the ohmic overpotential, until the building up to the steady-state value, represents activation overpotential η_A.

The linear part of the curve $\eta_t - t$ (Fig. 3) corresponds to the charging of double layer, and from the slope of this part of the curve the double-layer capacity can be calculated (11).

$$C = i\left(\frac{dt}{d\eta}\right)_{t \to 0} \qquad [1]$$

The mean value, obtained from the experimental data, is 25.4 μF/cm^2.

Activation overpotential-current density relationship.—When the experimental values of activation overpotential η_A were plotted against the logarithm of c.d. $\log_{10} i$, curves obtained of cathodic and anodic polarization (Fig. 4, 5) show in one region Tafel's linear relation.

Further, experimental Tafel lines were treated with an earlier developed method (6) using expression for the slowest reaction step, *i.e.*, rate-determining step.

$$\frac{\partial \log i_-}{\partial V} = -\frac{\mathbf{F}}{2{,}303\,RT}(n_c^* - \alpha) \qquad [2]$$

$$\frac{\partial \log i_+}{\partial V} = \frac{\mathbf{F}}{2{,}303\,RT}(n_a^* - 1 + \alpha) \qquad [3]$$

i_- and i_+ being parts of the total cathodic and anodic c.d. used in the slowest reaction step, ∂V the change of potential, n_c^* and n_a^* the ordinal numbers of the slowest reaction step for the cathodic and anodic polarization (small integer), α the transfer coefficient ($0 < \alpha < 1$), **F** the Faraday, R the gas constant, and T the absolute temperature.

As mentioned earlier (6) the left sides of the Eq. [2] and [3] represent the slopes of the experimental Tafel lines, so out of the experimental data it was possible to obtain α, n_c^*, and n_a^*.

The calculations indicate that the slowest reaction step for the cathodic polarization is the first, and for the anodic the third; for results see Table I.

Table I. Parameters for the deposition and dissolution of indium in 0.116*N* $In_2(SO_4)_3$ + 0.5*N* K_2SO_4, pH 2.5

Experiment	$\frac{\partial \log i}{\partial V}$ cathodic	$\frac{\partial \log i}{\partial V}$ anodic	α transfer coefficient cathodic	α transfer coefficient anodic
1	3.00	49.7	0.826	0.880
2	2.69	47.8	0.844	0.775
3	2.92	49.2	0.831	0.855
4	2.69	48.3	0.844	0.800
5	2.54	47.8	0.853	0.773
Mean of experiments 1-5.	2.77	48.6	0.840	0.817

Discussion

Overpotential-time curves.—Ohmic overpotential η_Ω plotted against the current for individual measurements shows, as was expected, a linear relation (Fig. 6). The corresponding resistance R represents the slope of the line and has the mean value of 33.04 ohms. The general expression for the calculation of resistance between the Haber-Luggin capillary and the electrode, given by Mattsson and Bockris (3), is

$$R = \frac{1}{4 \cdot \pi \cdot \kappa} \left(\frac{1}{r} - \frac{1}{x} \right) \qquad [4]$$

where κ is the specific conductance of the solution, r the radius of the electrode, and x the distance between the tip of the Haber-Luggin capillary and the center of the electrode. Using in our case the κ-value (for 0.116*N* $In_2(SO_4)_3$ + 0.5*N* K_2SO_4, pH = 2.5) 4.45 x 10^{-2} mhos/cm, the radius of the amalgam drop r = 4.7 x 10^{-2} cm, x = 3 mm, the value of R = 32.1 ohms, in agreement with the experimental values.

The double-layer capacitance is calculated from the slope of the initial linear part of the curve η_i —t. The experimentally obtained value of 25.4 μF/cm^2 is within the limits of expected values for similar systems.

The slope of the curve η_i — t gradually levels off, and after some time, t_A, the potential value becomes almost constant. This value diminished by ohmic overpotential represents the activation overpotential η_A. The state of the "constant" potential, in relation to the duration of the pulse, is defined as $t_A < \tau$, τ^{12} being the transition time (for flat surfaces)

$$\tau^{1/2} = \frac{\pi^{1/2} \cdot n \cdot \mathbf{F} \cdot C \cdot D^{1/2}}{2\, i} \qquad [5]$$

n being the number of electrons involved, **F** the Faraday, C the concentration of In^{3+} in mole/cm^3, D the diffusion coefficient of In^{3+} with the value set at 0.5 x 10^{-5} cm^2/sec, and i the c.d. in amp/cm^2.

Only after a time t_c, t_c being $t_c > \tau$, more marked concentration polarization occurs, which manifests itself in the rise of the potential. Considering the short duration of the current pulse (Fig. 3) there is hardly any concentration polarization, consequently it can be considered that the buildup to the constant values of the potential indeed does represent the activation overpotential.

Activation overpotential-logarithms of current density curves.—When the experimental values of activation overpotential η_A were plotted against the logarithms of c.d. $\log_{10} i$ the curves (Fig. 4, 5) of the cathodic and anodic polarization were obtained. Both curves show in the c.d. range 2.5 x 10^{-4}-2.5 x 10^{-3} amp/cm^2 a marked Tafel linear relation.

Considering Eq. [2] and [3] and the theoretical discussion (6) it is clear that the slope of the Tafel line is directly indicative of the determination of the parameters of the electrode kinetics of electrochemical processes with several reaction steps.

The slope of the linear part of the curve of the cathodic polarization (Fig. 4) is some 20 times more steep than the slope of the anodic curve (Fig. 5), and it can be shown easily that small experimental errors, while having a negligible influence on the slope of cathodic curves, can seriously influence the slope of anodic curves. Besides, the Tafel line of anodic polarization forms itself in a narrow region of the activation overpotential (η_A = 10 — 40 mv) and in the expression

$$i = i_a - |i_c| \qquad [6]$$

the corresponding cathodic part of c.d. i_c must not be neglected. From expression [6] it follows that

$$i_a = i + |i_c| \qquad [7]$$

which means that to get the correct anodic c.d. under these conditions the measured value i ought to be corrected by the corresponding cathodic c.d. i_c. The cathodic c.d. which would correspond to individual measuring points of the anodic polarization can be obtained graphically if the Tafel line of the cathodic polarization is extrapolated to corresponding anodic overpotentials. The execution of this procedure has shown, as is expected, that the correction values i_c for the measuring points of low anodic overpotentials are such that correction is justified, while for the higher values of the anodic overpotential the corrective i_c are so small, that correction is of no essential importance, *i.e.*, that the second element on the right side of Eq. [6] can be ignored. Such corrections of the measuring points of the low overpotentials of the anodic polarization prove the correctness of the extrapolation of the Tafel line, because the corrected measuring points fall just into

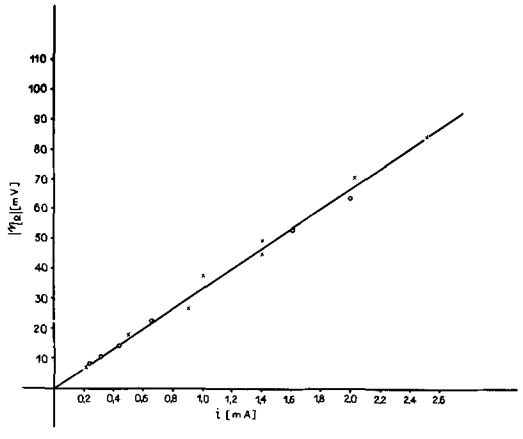

Fig. 6. Curve η_Ω — i. Slope — R = 33.04 ohms
x — cathodic data; o — anodic data

the extrapolated line. This of course enables a more accurate determination of the linear part of the Tafel line, especially if it is formed in the narrow area of low overpotentials.

Considering the fact that in our case the experimental errors influence the anodic curves more, the use of values obtained by extrapolation from the cathodic curves is justified, while the reverse is not the case.

For the electrochemical process of deposition and dissolution of indium in an aqueous solution the following reactions are assumed

$$In^{3+} \xrightarrow{+e^-_o} In^{2+} \xrightarrow{+e^-_o} In^{1+} \xrightarrow{+e^-_o} In^{o} \qquad [8]$$

$$In^{o} \xrightarrow{-e^-_o} In^{1+} \xrightarrow{-e^-_o} In^{2+} \xrightarrow{-e^-_o} In^{3+} \qquad [9]$$

On grounds of expressions [2], [3], [8], and [9] and the experimentally obtained slope of the linear part of Tafel line for the cathodic and anodic polarization, calculations indicate that the slowest reaction step for the cathodic polarization is the first, and for the anodic the third.

Consequently

$$In^{3+} + e^-_o \xrightarrow{\text{slow}} In^{2+} \qquad [10]$$

and

$$In^{2+} - e^-_o \xrightarrow{\text{slow}} In^{3+} \qquad [11]$$

From this it follows that the reaction step

$$In^{3+} \underset{-e^-_o}{\overset{+e^-_o}{\rightleftharpoons}} In^{2+} \qquad [12]$$

is the rate-determining step for the over-all electrochemical process of deposition and dissolution of indium.

Experiments have shown that when c.d. is increased above 2.5 x 10^{-3} amp/cm^2 the measuring points do not follow Tafel line, but show reproducible deviations. There are indications that in this current region there may be some other processes which interfere in the processes described above. The phenomena will be treated in detail in further investigations.

Manuscript received Aug. 25, 1961; revised manuscript received March 1, 1962.

Any discussion of this paper will appear in a Discussion Section to be published in the June 1963 JOURNAL.

REFERENCES

1. H. Gerischer, *Z. physik. Chem.*, **202**, 302 (1953).
2. T. Berzins and P. Delahay, *J. Am. Chem. Soc.*, **77**, 6448 (1955).
3. E. Mattsson and J. O'M. Bockris, *Trans. Faraday Soc.*, **55**, 1586 (1959).
4. W. Kangro and Fr. Weingärtner, *Z. Elektrochem.*, **58**, 505 (1954).
5. LJ. Duić, Z. Kovac, and B. Lovrecek, *Croat. Chem. Acta*, **32**, 213 (1960).
6. B. Lovrecek, *J. Phys. Chem.*, **63**, 1795 (1959).
7. F. R. Meyer and G. Ronge, *Z. angew. Chem.*, **52**, 637 (1939).
8. N. Sunden, *Z. Elektrochem.*, **57**, 100 (1953).
9. M. v. Stackelberg and V. Toome, *Z. Elektrochem.*, **58**, 226 (1954).
10. A. R. Despić and J. O'M. Bockris, *J. Chem. Phys.*, **32**, 389 (1960).
11. G. Kortüm, "Lehrbuch der Elektrochemie," (2 Aufl.) S.354. Verlag Chemie GmbH, Weinheim/Bergstr. (1957).
12. P. Delahay, "New Instrumental Methods in Electrochemistry," p. 184. Interscience Publishers, Inc., New York (1954).

Technical Notes

A Continuous Flow Cell for Electrochemical Synthesis

M. J. Allen

Chemical Research Department, Electro-Optical Systems, Inc., Pasadena, California

One of the more important aspects of organic electrochemistry which has received little attention in the literature, is the design, construction, and performance of electrolytic cells. Two cells have been described which utilize porous carbon electrodes (1) and a third designed for use with a mercury cathode (2). Unfortunately neither of the designs can be used with solid or amalgam type electrodes. Therefore a cell was developed (Fig. 1) which was not only suitable for the type of electrodes mentioned, but also had in common with the previously reported cells the advantages of continuous flow operation for extended periods.

This cell consists of 22 compartments constructed of "annealed" polystyrene, ½ in. thick x 5 in. wide x 6 in. high. A center section is removed leaving a chamber 2 in. wide x 4½ in. high. A ¼ in. hole is drilled on one side so that it is flush with the bottom of the center section, and on the other side so that the hole is 2⅜ in. to center from the top. Approximately ½ in. of the outside portion of each of these holes is bored out (approximately 13/32 in.) so as

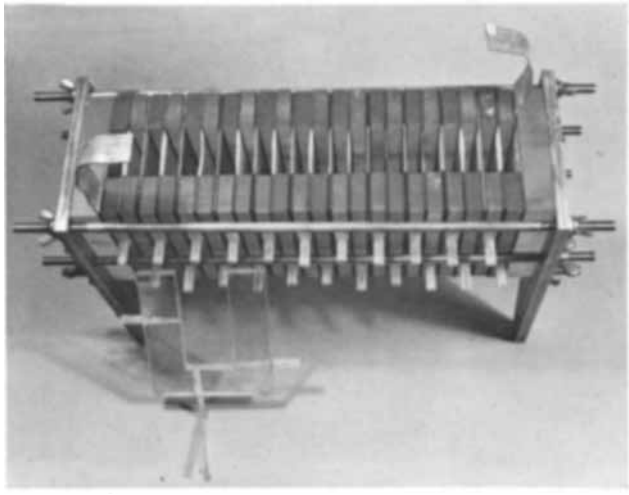

Fig. 1. Cell for continuous flow operation

to loosely accept a 1½ in. length of ¼ in. ID polystyrene tubing. These are cemented in place by dropping methylene chloride with a hypodermic syringe and fine needle in the space between the polystyrene tubing and the plate. The bond is quite solid and leak-free within an hour. A bottom outlet for drainage of each compartment is fabricated in the same manner.

The end plates consist of ½ in. stock steel through which seven holes have been drilled to accommodate 21 in. lengths of ⅜ in. rod, threaded on each end. Next to the inner face of these end plates is placed a 1 in. thick x 5 in. wide x 6 in. high polystyrene sheet, followed by an electrode (approximately 1/16 in. thick) with a connector flap, a neoprene gasket (1/16 in. thick), a polystyrene compartment, an ion-exchange type membrane between 2 neoprene gaskets, another compartment, a floating electrode between 2 neoprene gaskets, another compartment, etc. Each compartment contains approximately 54.5 ml. The active electrode area was 32.26 cm².

In practice the opposing electrolyte, *e.g.*, catholyte and anolyte, are pumped through alternate tygon tube connected compartments, utilizing a Sigmamotor pump. The rate of flow is so adjusted that when the electrolyte containing the depolarizer comes from the last compartment, the reaction is complete. If cooling is found necessary in the process, it is possible to place glass cooling coils within each compartment. It is, of course, obvious that the surface of the first floating electrode facing the cathode, for example, will be positive, its reverse surface negative, and so on to the power connected anode.

Experimental

In order to study the operational characteristics of this cell, the reduction of p-hydroxybenzaldehyde to its corresponding hydrobenzoin was investigated at a tin cathode. For comparison purposes, batch-type experiments were performed under controlled potential, as well as constant current density conditions. In each batch-type experiment the catholyte consisted of 12g (0.098 mole) p-hydroxybenzaldehyde dissolved in 100 ml 2*N* NaOH. The anolyte consisting of 2*N* NaOH was separated from the catholyte by an "Alundum"[1] membrane. The tin electrode area was 93.3 cm². A platinum anode was used in these experiments and the temperature maintained between 24°-26°. The reference potential used in the controlled potential experiments was similar to that previously reported in the literature (3). At a potential of −1.8v *vs.* SCE the initial current density was 0.064 amp/cm². The current plateaued at 0.0048 amp/cm², and during the course of the reaction 1.14 times the theoretical current (10,850 coulombs) was passed, yield 9.8g (81.3%), mp 214°-215° (3), current efficiency 71%. Utilizing constant current density conditions (0.064 amp/cm²) for 1.14 times theory in order to duplicate the 10,850 coulombs passed in the previous typical controlled potential experiment gave a yield of 7.9g (65.6%), current efficiency 57.3%. The lower efficiency of the constant current density experiments was due to the partial use of the current toward the latter part of the experiment for hydrogen production. This was indicated by gas evolution at the cathode during this period. An experiment was performed at the lower current density of 0.0048 amp/cm². After the passage of 10,850 coulombs the catholyte was examined and found not to contain any detectable amount of the desired hydrobenzoin.

The catholyte for a typical continuous flow cell experiment consisted of 244g (2.0 mole) p-hydroxybenzaldehyde dissolved in 2000 ml 2*N* NaOH. The anolyte was a solution of 2*N* NaOH. The 11 cathode compartments were filled with approximately 600 ml of the catholyte from the reservoir; the anode compartments were filled with the 2*N* NaOH. A current density of 0.064 amp/cm² (2.1 amp/electrode) was used. The probe, a saturated calomel electrode placed at the surface of the first and last cathode, initially indicated a reference potential of −1.8v. The catholyte was recirculated through the cathode compartments at the rate of 25 ml/min until the reference potential at the last cathode reached a potential of −2.0v, at which time the reacted catholyte was delivered to a receiver and fresh unreacted catholyte permitted to enter the cell. The rate of flow was then so adjusted that the potential and the last cathode did not go above −2.0v *vs.* SCE. The flow rate for the catholyte was 12.5 ml/min and for the anolyte 5 ml/min. The applied voltage varied from 30-36v. After 162 min a total of 224,000 coulombs (1.16X theory) has been passed. Yield 184.7g (75.7%), mp 214°-215°, current efficiency 65%.

Discussion

From the results obtained a continuous flow cell appears to be more efficient than a batch type cell operating under the same constant current density conditions. This increased efficiency can be attributed to the fact that, in a flow cell operation of the type described, the potential at the electrode surface does not reach destructive heights which might result in undesirable side reactions; the depolarizer is being replenished at the electrode surface at such a rate as to enable maximum use of the electric

[1] Norton Company, Worcester, Mass.

current for the reduction process; we are dealing essentially with a flowing film in which the path the depolarizer must travel to reach the electrode is shorter than in a stirred solution.

Manuscript received Oct. 13, 1961; revised manuscript received Feb. 8, 1962. This paper was prepared for delivery before the Detroit Meeting, Oct. 1-5, 1961.

Any discussion of this paper will appear in a Discussion Section to be published in the June 1963 JOURNAL.

REFERENCES

1. G. W. Heise and N. M. Winslow, *Trans. Electrochem. Soc.*, **75**, 164 (1939); D. R. Allen and A. S. Allen, *Res. and Dev.*, **12**, 91 (1961).
2. P. C. Condit, *Ind. Eng. Chem.*, **48**, 1252 (1956).
3. M. J. Allen, *J. Am. Chem. Soc.*, **72**, 3797 (1950).

Thermal Oxidation of GaAs

Henry T. Minden[1]

General Electric Company, Syracuse, New York

Oxide masking (1) is the key technique in the fabrication of modern silicon semiconductor devices. If a silicon single crystal wafer is exposed to oxygen under controlled conditions an amorphous layer of silica will form (2). This layer is impervious to the diffusion of doping impurities into the wafer. By etching holes in the silica, diffusion can be localized for the purposes of device preparation, and the oxide protects the p-n junctions from attack by ambients.

To determine whether this technology can be carried over to gallium arsenide, a brief study of the thermal oxidation of this material was undertaken. Wafers were placed in a simple tube furnace through which gas flowed in the conventional manner. Best results in terms of the evenness of the oxide were obtained with pure oxygen, and a flow rate of about 1.3 l/min was used in the runs reported here. Temperatures between 600° and 900°C were used. Below 600° the oxidation was negligible, while above 900° the sample tended to burn up. In general, increasing the temperature merely increased the rate of oxidation, while the character of comparable films was the same.

Films of intermediate thickness (1000Å to ~6000Å) showed typical interference colors. Films which were either too thin or too thick to show interference colors were gold or brown. Even thicker films were transparent and glassy in appearance. The thickest films which were formed at 900°C were white, obviously crystalline, and somewhat waxy in texture. In some experiments water vapor was introduced into the oxygen stream. This had no discernable effect at temperatures below about 800°. Above 800° white, hard crystalline spots formed; these spots grew to cover almost the whole surface. This oxide could easily be flaked off the wafer, whereas the thinner layers were quite adherent.

Oxidation on the (110) surface of gallium arsenide was slower and more uniform than on either (111) surface. Fine white pits tended to form under the oxide on the latter surfaces, whereas even, gold films could readily be produced on the (110) surface by oxidation at 700° for ½ hr. Thicker films tended to have extensively pitted and irregular surfaces under the oxide layer. The extent of oxidation on polycrystalline surfaces varied markedly from grain to grain. No difference was noted between the oxidation of n and p material.

Electron diffraction pictures consisted of sharp rings which had spots characteristic of partial orientation of the crystallites in the film. Indexing of the rings showed unequivocably that the film consisted of β Ga_2O_3, the commonest form of gallium oxide. This was the only phase found in all the films investigated, regardless of the thickness of the film and the temperature of oxidation. In none of the samples investigated were there any electron diffraction rings which could be attributed to an arsenic containing phase. The white oxide formed in the presence of water vapor was flaked off and examined by powder x-ray diffraction. This too revealed the presence of only β Ga_2O_3.

Several samples of n GaAs were oxidized on the (110) face at 700° for ½ hr to form an attractive, uniform gold film. Part of the surface was covered with black wax, and the oxide on the exposed surface was dissolved in warm concentrated hydrochloric acid. The wax was removed, and the sample was sealed in an evacuated tube with a trace of zinc metal. The zinc was diffused into the wafer at 800° for ½ hr. After diffusion the remaining oxide was removed with warm hydrochloric acid and the surface probed with a hot point. The surface was p at both the masked and unmasked areas. The penetration of the zinc through the oxide could not be correlated with any macroscopic imperfection in the film. It is presumed that the microcrystalline nature of the oxide film allowed extensive grain boundary diffusion to the surface of the gallium arsenide. Finally an oxidized and an unoxidized wafer were simultaneously heated to 950° in an argon atmosphere overnight; both samples were reduced to a droplet of gallium. It is felt that the oxide does not prevent the outdiffusion of arsenic from gallium arsenide.

From these discouraging but fairly clear results, it does not appear that thermal oxide masking is readily applicable to gallium arsenide.

Acknowledgment

The author wishes to thank Mr. C . V. Bielan who did the electron diffraction and x-ray diffraction studies.

Manuscript received March 7, 1962; revised manuscript received April 25, 1962.

Any discussion of this paper will appear in a Discussion Section to be published in the June 1963 JOURNAL.

REFERENCES

1. C. J. Frosch and L. Derick, *This Journal*, **104**, 547 (1957).
2. M. M. Atalla, E. Tannenbaum, and E. J. Scheibner, *Bell Syst. Tech. J.*, **38**, 749 (1959).

[1] Present address: Sperry Rand Research Center, Sudbury, Massachusetts.

Solid Solubilities of Antimony, Arsenic, and Bismuth in Germanium from a Saturation Diffusion Experiment

F. A. Trumbore, W. G. Spitzer, R. A. Logan, and C. L. Luke

Bell Telephone Laboratories, Incorporated, Murray Hill, New Jersey

In the course of growing arsenic-doped germanium crystals for Esaki diodes, it was noted (1) that anomalously low carrier concentrations were obtained in crystals grown from the more heavily doped melts. Minden (2) and Cardona and Sommers (3) also have reported that only a fraction of the arsenic present in heavily doped material is electrically active. Furthermore, it has been shown (4) that appropriate heat treatment and quenching procedures can lead to significant increases in carrier concentrations, thus indicating a precipitation effect. Even after quenching, however, there remained a discrepancy of about a factor of two between the carrier concentrations and the arsenic concentrations expected from available solidus curve data (5). As pointed out previously (5), the evaporation technique used to determine this solidus curve was quite conducive to the formation of occlusions containing arsenic and hence could lead to high results.

In order to obtain an unambiguous check on the solidus curve a long term saturation diffusion experiment has been carried out at a temperature where a solid solubility of arsenic in germanium in excess of 1×10^{20} atoms/cc would be expected from the solidus curve. By using a diffusion technique the presence of germanium arsenide occlusions, formed in grown crystals by trapping of the melt during growth, should be eliminated. In addition to arsenic, antimony and bismuth were also diffused into germanium in the same experiment. The purpose of the present paper is to present the results of chemical, optical, and electrical measurements on the resulting samples.

Experimental

Available diffusion coefficient data (6) indicated that at a temperature of about 865°C one might obtain essentially complete saturation of germanium samples of a reasonable thickness in a reasonable length of time. Accordingly, the samples were diffused for 97 days at a temperature of 865° ± 5°C.

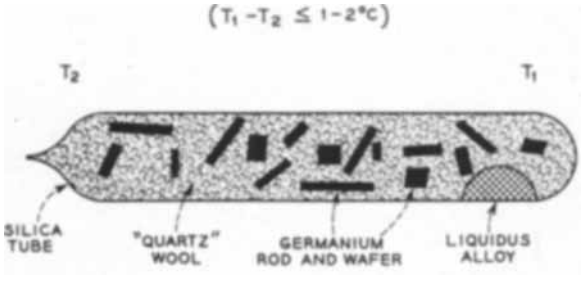

Fig. 1. Schematic diagram of the experimental arrangement during the diffusion run.

Square wafers and rods of single crystal undoped germanium were sealed, together with high-purity (> 99.9999%) arsenic, antimony, or bismuth, in evacuated ($\sim 10^{-6}$ mm Hg) vitreous silica tubes. The wafers [150 x 150 x (10-25) mils] and rods [500 x (15-25) x (15-25) mils] were of various thicknesses to permit a check for saturation at the end of the experiment. As shown in Fig. 1 "quartz" wool (99.9% pure) was used to separate the various samples to permit free access of the impurity vapor. To prevent random melting of the germanium samples the tubes were placed in a slight thermal gradient (only $\lesssim$ 1-2° over the length of the sample tube). The amounts of the group V impurity elements contained in the tubes were sufficient to form and maintain a liquidus alloy with some of the germanium in the hotter ends of the tubes during the course of the experiment. Since the partial pressure of arsenic (and, in this temperature range, probably that of antimony) over the liquidus alloys decreases with increasing temperature (4) no melting of the germanium should occur in the cooler portions of the tube. In the case of bismuth where the predominant vapor species is the monomer, instead of the tetramer or dimer, as in the case of the other two impurities, it is doubtful whether the bismuth partial pressure behaves in the same way. In fact, there was evidence of random melting in the tubes containing bismuth.

One striking feature of this experiment was the presence of a considerable amount of transport of germanium through the vapor phase, especially in the tube containing arsenic. This is illustrated in Fig. 2 which shows two examples of deposition of germanium on the germanium wafers. The presence of this vapor transport caused some difficulty since the rods became tapered and were unsuitable for Hall effect or resistivity measurements. The mechanism responsible for this transport is not known. One interpretation of the present results is that transport in the slight thermal gradient via a volatile Ge-As species was a factor since the amount of transported material was so much greater in the tubes containing arsenic. However, the presence of oxygen and transport via GeO(g) is a distinct possibility and perhaps either or both mechanisms were operative. Holonyak, Jillson, and Bevacqua (7) have observed a similar transport of silicon with group V impurities and do not believe that oxygen is responsible.

The arsenic- and antimony-doped germanium samples were analyzed chemically for the impurity concentration by using spectrophotometric methods. (The concentration of bismuth was too low for

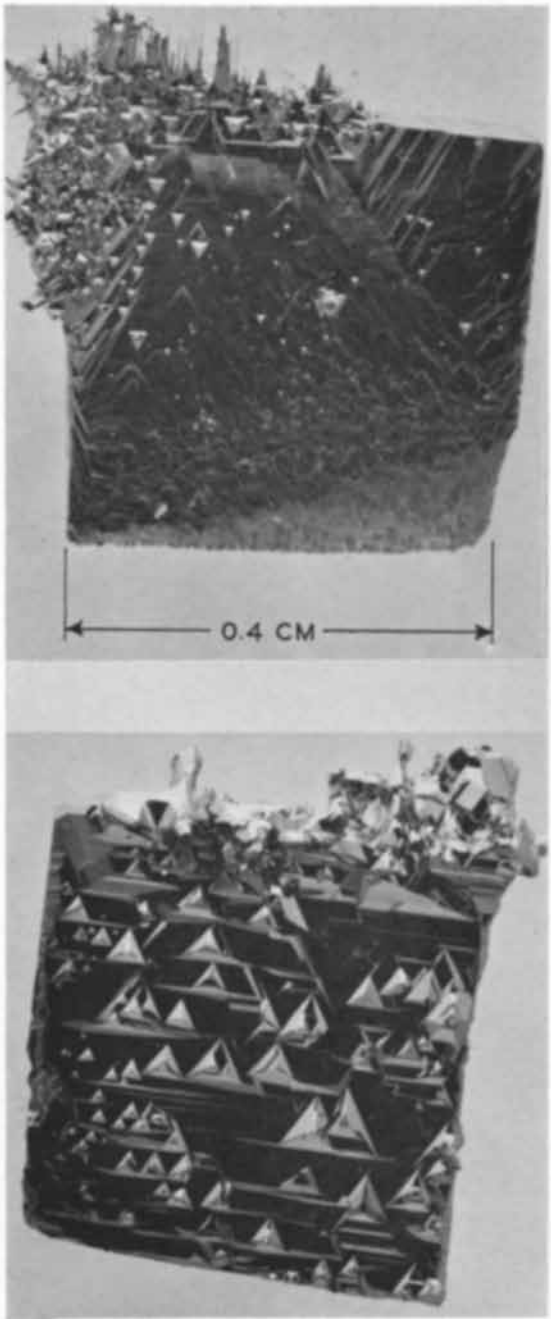

Fig. 2. Two examples of vapor transported germanium deposited on the Ge wafers. The major faces of the wafers are {111} surfaces.

analysis by these techniques.) In both cases the germanium was removed by distillation as the chloride. The antimony and arsenic contents were then determined by the iodoantimonite and heteropoly molybdenum blue methods (8, 9), respectively. In order to insure that only diffused material was analyzed, the wafers were lapped to eliminate any trace of vapor deposited germanium (Fig. 2). The samples were then etched to remove any contaminants introduced in the lapping process and analyzed. In the case of arsenic one of thickest and one of the thinnest wafers were analyzed to determine whether sufficient time had elapsed for saturation of the germanium by arsenic.

Optical reflectivity measurements were made on the arsenic- and antimony-doped samples by using the same techniques described previously (4). The carrier concentrations were determined from the known variation of the reflectivity minimum with carrier concentration in heavily doped materials (4). (The optical method is not applicable to the bismuth-doped samples because of the low concentration of bismuth.) To test for saturation in the antimony-doped samples one wafer was measured near the surface and then lapped down for a measurement near the middle of the sample. One arsenic sample was heated to 850° ± 5°C for 30 min and quenched in a jet of nitrogen as described previously (4), following which the reflectivity was measured.

By using van der Pauw's method (10) room temperature Hall effect and resistivity measurements were made on disks cut from the wafers. The carrier concentration, n, was calculated from the Hall coefficient assuming a Hall to drift mobility ratio of unity. As a check on the resistivity measurements, two-point probe measurements were made on some rods cut from the wafers. The results agreed to within 3% or better with the data obtained by the disk method.

Results and Discussion

The most important results of the various measurements are summarized in Table I which gives n and C_I^s, the concentration of the impurity. A more detailed discussion of the individual systems is given below.

Antimony.—Saturation of the germanium by the antimony was achieved as evidenced by the fact that within experimental error the positions of the reflectivity minima at the surface (14.2-14.5μ) and near the middle (14.3-15.1μ) of a 23 mil thick wafer were identical. (The attenuation distance for the optical measurement is $\lesssim$ 1 mil for these samples.) The chemical analyses, performed on two sets of four wafers each, yielded identical results of 0.036 w/o antimony, believed to be accurate to better than ±5% of the antimony content. The agreement among the impurity and carrier concentrations summarized in Table I is well within experimental error. The most likely value of the equilibrium solid solubility is believed to be (1.00 ± 0.05) x 10^{19} atoms/cc.

The available solid solubility data (4, 5, 11-13) are presented in Fig. 3 in the form of a log k *vs.* $1/T$ plot, where k is the distribution coefficient, based on the liquidus data of Thurmond and Kowalchik (14). Included in this plot is a point obtained from resistivity measurements on a polycrystalline sample grown at ~ 708°C by the sealed tube ther-

Table I. Summary of chemical, optical, and electrical data

Impurity	n (cm^{-3}) (reflectivity)	n (cm^{-3}) (Hall effect)	C_I^s (atoms/cc) (chemical)
Antimony	$1.08 \pm 0.07 \times 10^{19}$	1.02×10^{19}	9.5×10^{18}
Bismuth	—	3.5×10^{16}	—
Arsenic	5.0×10^{19}	4.8×10^{19}	7.3×10^{19}
Arsenic*	7.5×10^{19}*	7.4×10^{19}*	—

* Heat treated at 870°C and quenched.

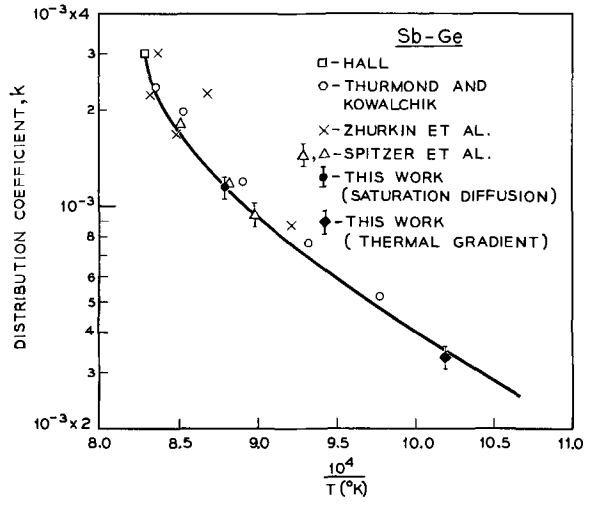

Fig. 3. Plot of log k as a function of $1/T$ for antimony in germanium.

mal gradient technique described previously (15).[1] With the exception of a few of the points due to Zhurkin *et al.* (13), there is good agreement among the various sets of data which were obtained by crystal pulling (12, 13) radiotracer diffusion profile (11), solvent evaporation and cooling (4), thermal gradient, and saturation diffusion methods. Since the saturation diffusion technique should yield an unambiguous equilibrium solid solubility and since the agreement with an adjacent solvent evaporation-cooling data point is very good, the curve has been revised from that given in ref. (4) to favor the lower values of k obtained from these experiments and from the thermal gradient experiment.[2] This results in a relatively slight modification of the previous solidus curve (5). The revised solidus curve, shown in Fig. 4, is based on the log k *vs.* $1/T$ plot in Fig. 3 and on the liquidus curve (14).

Arsenic.—Chemical analyses on two wafers of different thicknesses (10-15 and 20-25 mils) gave identical values of the amount of arsenic (0.17 w/o) indicating saturation had been achieved. (The chemical analysis is believed to be accurate to better than ±10% of the arsenic content.) This fact and the excellent agreement between the value of n in the quenched sample and the arsenic concentration indicate that a reliable value of the equilibrium solid solubility has been obtained.[3] The saturation diffusion value obtained here is about a factor of two lower than expected from the solidus curve reported previously. Hence, the latter is in error, probably due to failure to eliminate arsenide occlusions.[4] A revised solidus curve is plotted in Fig. 4 based on available liquidus data (14) and on the log k *vs.* $1/T$ plot shown in Fig. 5 which includes the crystal pulling data of Jillson and Scheckler (18) and the radiotracer diffusion profile data of Thurmond and Kowalchik (19).[5]

These experiments also indicate that the presence of micro-occlusions of germanium arsenide is not necessary for nucleation of the precipitation of arsenic as postulated earlier (4). The probability is that dislocations serve as nucleation sites. In the present samples the dislocation density of the original wafers was the order of 10^3-10^4 cm^{-2}. However, even if one should start with dislocation free germanium, Prussin (20) has shown that dislocations may be introduced in the process of diffusion.

Bismuth.—Since no chemical analyses were made, the identification of n in Table I with the bismuth

[1] This sample contained small amounts of occluded antimony which could not be separated chemically from the antimony-doped germanium so that no reliable chemical analyses could be run. However, two rods were cut from sections which appeared to contain no significant number of occlusions. The resistivities of these two rods were 1.25 × 10^{-3} and 1.42 × 10^{-3} ohm-cm corresponding to a carrier concentration of (8.8 ± 0.5) × 10^{18} cm^{-3}.

[2] The agreement between the saturation diffusion point and the adjacent solvent evaporation-cooling point of Spitzer *et al.* in Fig. 3 indicates that equilibrium data were also obtained from the latter experiments and also supports the earlier conclusion that no significant "facet" effect (16, 17) was present in the crystal growth work (4).

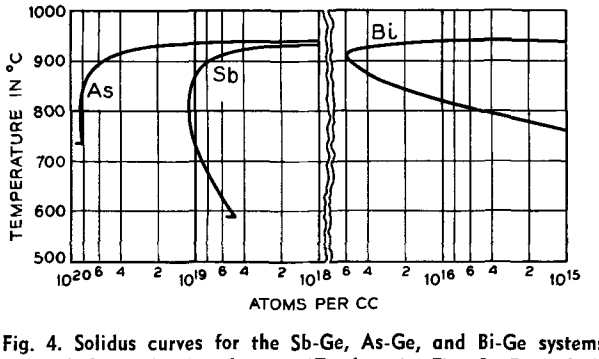

Fig. 4. Solidus curves for the Sb-Ge, As-Ge, and Bi-Ge systems calculated from the log k *vs.* $1/T$ plots in Fig. 3, 5, and 6, respectively.

[3] The fact that the Hall effect and resistivity measurements on the arsenic- and antimony-doped samples are consistent with our earlier resistivity *vs.* n curves (4) demonstrates conclusively that the difference in mobility between antimony- and arsenic-doped material is an inherent property and is not due to the presence of occluded material such as germanium arsenide.

[4] One further observation remains to be explained, namely, the apparent attainment of a very small amount of 0.0003-0.0004 ohm-cm material in a thermal gradient crystal (4). From the present work it would seem that this was just a spurious result. However, it is possible that this small region grew on a {111} facet and by the facet effect trapped in a nonequilibrium amount of arsenic. A facet effect of about a factor of two has been reported for arsenic in germanium (17).

[5] The curvature in the log k *vs.* $1/T$ plot derives from the results of the quenching experiments on As-doped samples prepared by thermal gradient crystallization reported earlier (4). The present quenching experiments indicate that the total arsenic in solid solution can be quenched in the electrically active state. Therefore, it was assumed that the maximum figure for the quenched-in carriers, 8.1 × 10^{19} cm^{-3}, represented the arsenic concentration corresponding to a melt composition between 25 and 40 mole % arsenic [see Table I, ref. (4)]. The points joined by the dashed tie line in Fig. 5 represent the values of k and $1/T$ corresponding to the melt compositions of 25 and 40 mole % arsenic, the true value lying somewhere along the tie line. If the 8.1 × 10^{19} cm^{-3} figure was not the total arsenic concentration, then a minimum value should lie somewhere on the tie line.

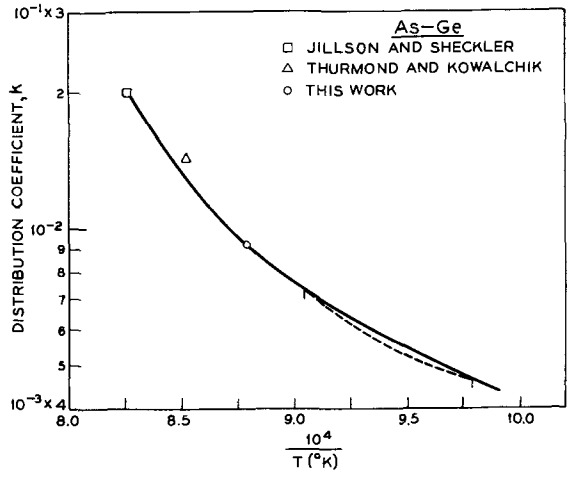

Fig. 5. Plot of log k *vs.* $1/T$ for arsenic in germanium. The dashed curve is a tie line on which one point is located (see footnote 5).

concentration is obviously not as certain as in the arsenic and antimony experiments due to the possibility of impurity contamination. However, the likelihood of significant contamination is slight in view of (*a*) the relatively low concentrations of the more soluble impurities in the silica and bismuth, (*b*) the low diffusion coefficient of these impurities (*e.g.*, Al and B) and (*c*) perhaps most important, the "gettering" action of the liquid Bi-Ge phase. Thus, we believe the value of n may be taken as equal to the bismuth concentration. Except for a value of the distribution coefficient at the melting point of germanium, no other solid solubility data have been reported for bismuth.

Utilizing these two data points, an approximate estimate of the temperature dependence of the distribution coefficient, k, may be obtained as shown in Fig. 6. This estimate is based on considerations of the departures from ideality in the liquid and solid phases as discussed previously for the Al-Ge and Ga-Ge systems (15). Specifically, the distribution coefficient is given by $k = \gamma^L/\gamma_n{}^S F_n$ where γ^L is the activity coefficient of the impurity in the liquidus alloy, $\gamma_n{}^S$ is the activity coefficient of the neutral impurity species in the solid (both referred to the same standard state), and F_n is the fraction of the impurity atoms which remain neutral in the solidus alloy. It is reasonable to assume that log $\gamma_n{}^S$ is a linear function of $1/T$. Thus, by plotting log k'' *vs.* $1/T$, where $k'' \equiv kF_n/\gamma^L = 1/\gamma_n{}^S$, for the two available data points and extrapolating one can obtain k'' and hence k at a lower temperature if one knows F_n and γ^L. The values of F_n were obtained from the treatment of Blakemore (21) while γ^L was approximated from the data of Thurmond and Kowalchik (14). In the temperature range covered only a small departure from linearity is predicted as shown in Fig. 6. An estimate of the solidus curve based on this approximation is plotted in Fig. 4. It should be stressed that there are several possible sources of error in this approximation which is carried out here in lieu of other experimental data.

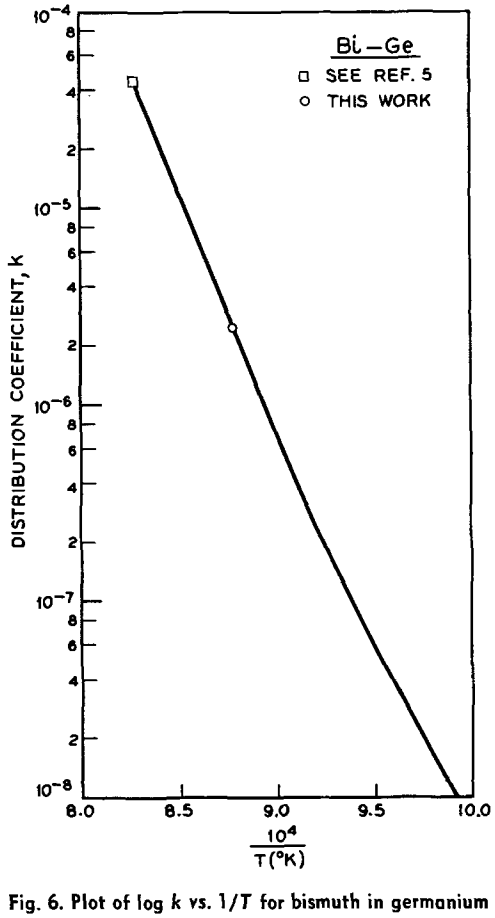

Fig. 6. Plot of log k vs. $1/T$ for bismuth in germanium

Summary

The present work has yielded unambiguous determinations of the equilibrium solid solubilities of arsenic and antimony at one temperature. It is believed that these data represent the most definitive equilibrium solid solubility measurements to date for any impurity in germanium or silicon except perhaps for fast diffusers such as copper, lithium, etc., where saturation is readily achieved. While the antimony result agrees well with previous measurements, the arsenic value indicates the previous solidus data are in error by about a factor of two. An estimate of the Bi-Ge solidus curve has been made based on a solid solubility measurement which was not quite as conclusive as the arsenic and antimony results.

Acknowledgments

The authors are indebted to J. F. Gilbert for the Hall effect measurements and for performing the quenching experiment, to L. Howarth for some of the reflectivity measurements, to M. Kowalchik for assistance in carrying out the diffusion experiment, to Miss A. Mills for some of the resistivity measurements, and to A. A. Tartaglia for the photographs.

Manuscript received Feb. 12, 1962; revised manuscript received April 12, 1962. This paper was prepared for delivery before the Detroit Meeting, Oct. 1-5, 1961.

Any discussion of this paper will appear in a Discussion Section to be published in the June 1963 JOURNAL.

REFERENCES

1. F. A. Trumbore in "Metallurgy of Elemental and Compound Semiconductors," R. Grubel, Editor, p. 15, Interscience Publishers, New York—London (1961).
2. H. T. Minden, *ibid.*, p. 35.
3. M. Cardona and H. S. Sommers, Jr., *Phys. Rev.*, **122**, 1382 (1961).
4. W. G. Spitzer, F. A. Trumbore, and R. A. Logan, *J. Appl. Phys.*, **32**, 1822 (1961).
5. F. A. Trumbore, *Bell System Tech. J.*, **39**, 205 (1960).
6. H. Reiss and C. S. Fuller in "Semiconductors," N. B. Hannay, Editor, p. 244, Reinhold Publishing Corp., New York (1959).
7. N. Holonyak, Jr., D. C. Jillson, and S. F. Bevacqua in "Metallurgy of Elemental and Compound Semiconductors," R. Grubel, Editor, p. 81, Interscience Publishers, New York-London (1961).
8. ASTM Methods of Chemical Analysis of Metals, p. 419, Am. Soc. Testing Materials, Philadelphia (1960).
9. C. L. Luke and M. E. Campbell, *Anal. Chem.*, **25**, 1590 (1953).
10. L. J. van der Pauw, *Philips Res. Repts.*, **13**, 1 (1958).
11. C. D. Thurmond and M. Kowalchik, see ref. (5).
12. R. N. Hall, *Fortschritte der Hochfrequenztechnik*, **4**, 129 (1958).
13. B. G. Zhurkin, V. S. Zemskow, D. A. Petrov, and

A. D. Suchkova, *Izvestia Akad, Nauk SSSR*, OTN, MiT, No. 5, 86 (1959).
14. C. D. Thurmond and M. Kowalchik, *Bell System Tech. J.*, **39**, 169 (1960).
15. F. A. Trumbore, E. M. Porbansky, and A. A. Tartaglia, *J. Phys. Chem. Solids*, **11**, 239 (1959).
16. K. F. Hulme and J. B. Mullin, *Phil. Mag.*, **4**, 1286 (1959).
17. J. A. M. Dikhoff, *Solid State Electronics*, **1**, 202 (1960).
18. D. C. Jillson and A. C. Sheckler, *Phys. Rev.*, **98**, 229 (1955).
19. C. D. Thurmond and M. Kowalchik, Private communication.
20. S. Prussin, *J. Appl. Phys.*, **32**, 1876 (1961).
21. J. S. Blakemore, *Proc. Phys. Soc.*, **71**, 692 (1958).

A Simple Technique for Seeding and Growing Oriented, Relatively Unstrained, Single Crystal Antimony, Square-Sectioned Rods

Seymour Epstein[1]

U. S. Army Signal Research and Development Laboratory, Fort Monmouth, New Jersey

Systematically preparing oriented, square-sectioned, long, single crystal rods of antimony and its dilute alloys with tin, having uniform and reproducible electrical properties and dimensions, presents many difficulties. For example, mechanical cutting, in addition to cold working the crystal, usually introduces fissures; these frequently cause large changes in the resistivity or break the specimen, according as the principal plane is parallel or not parallel to the rod's longest dimension. Acid cutting, on the other hand, is characterized by nonuniform rod faces. These difficulties can be avoided by growing oriented crystals in the desired shape, a technique first used by Kapitza (1) for bismuth and soon after by others (2) for bismuth and higher melting point materials. In principle, any one of these modified apparatuses are directly applicable to antimony, and Rausch (3), using Hasler's modification, has grown circular-sectioned antimony rods in the two principal orientations. However, our experience with these modifications and the conditions implied or specified (slow rates) is that we were able to seed and grow only rods in which the c-plane is parallel to the rod axis. The same result was obtained with our own modified apparatus only until both a fast rate of crystallization, not less than 2 cm/min, and a crucible material of low thermal conductivity relative to antimony were used. Under these conditions seeding and growing single crystal antimony rods, whose axes are at either 0°, 45°, and 90° with the <111> direction, becomes almost a routine operation. The rods are 6 cm or more long and have nearly square, 3 mm × 3 mm, cross sections.

Our modified apparatus also allows for easy control of the binary axis orientation, and the growth of rods seeded in arbitrary orientations appears possible. The fast rate of growth also minimizes the segregation of added impurities and does not appear to strain the rods.

In these experiments the undoped antimony is nominally 99.997% pure and is used as supplied by the Bradley Mining Company, San Francisco, California.

[1] Most of this material is included in a Dissertation on the "Galvanomagnetic Effects and Band Structure of Pure and Tin-Doped Antimony Single Crystals," submitted in partial fulfillment of the requirements for the Doctor of Philosophy (in Physics) degree at the Polytechnic Institute of Brooklyn (1961), to be submitted for publication.

Description of Apparatus and Procedure

The technique combines many of the desirable features of the earlier ones (1, 2). It consists of seeding and recrystallizing precast rods in a partly enclosed crucible mold. The motion of the temperature gradient through the rod is obtained by cutting off the heater power; both furnace and crucible are stationary. The latter can be taken apart, permitting strain free removal of the recrystallized rod. The furnace, crucible mold, seed orienting jigs and procedure, and seeding and growing procedure are next described.

Furnace.—By not insulating the furnace from its ambient room temperature, rapid heat dissipation and cooling rates are made possible. Simple in design and construction, it consists of two concentric, clear Vycor tubes, 1 and 3 in. in diameter, with a continuous nichrome heater element uniformly wound on the outside of the inner tube. The spacing between adjacent turns is about ⅜ in. so that the furnace charge can be seen. Two temperature zones, one 40° above the other, are used; a slight gradient exists within each. The two zones and their gradients are obtained by stretching the heater element, initially, a close wire-wound helix. For a wire diameter of 0.062 in. and a total zone length of 5 in. the heater resistance is 12 ohms; about 600 watts are sufficient to melt antimony. The gradient, the furnace and rod axes, and the growth direction are parallel.

Crucible mold.—Square cross sections are obtained in the manner prescribed by Hasler (2). Square precast rods are recrystallized in a crucible chamber of the same shape and dimensions as the rod. This technique also serves to minimize straining of the single crystal rod due to antimony's expansion upon solidification. Straining while removing the rod from the mold is avoided by designing the mold so that it can be taken apart.

The basic crucible, Fig. 1, is made up of two thin slats for side walls, a thin bottom slat, a top cover (not shown), and two channeled holding blocks. It is taken apart by axially sliding the hold-

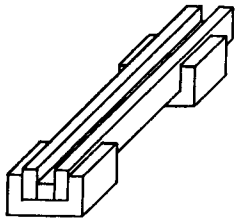

Fig. 1. Basic crystal growing crucible. The crucible is held together by the two channelled blocks. After the rod is recrystallized it is separated from the crucible by taking the latter apart.

ing blocks away from the slats, which, if they do not adhere to the rod, simply fall away. The slats are 1/16 in. thick; their remaining dimensions are determined by the size of the rod. The top cover is about ¼ in. thick for added weight.

Many crucible materials exist which neither adhere to nor react with antimony at temperatures below 700°C in the argon atmosphere used. In addition, a suitable material must have a low heat conductivity relative to the substance being crystallized (4). One such material is the mineral pyrophyllite.[2] Its advantage over most other materials is that it can be easily machined before it is fired, and it was chosen because of this additional property. (With carbon crucibles, we were able to obtain only the 90°-oriented rods, where the growth direction is the preferred one, and at lower yield.)

Seed orienting jigs and procedure.—Three orienting jigs, schematically shown in Fig. 2, have been conveniently used, although with truly perpendicular rod faces only one is required. A holding block is part of each jig and positions it accurately in relation to the rod chamber. The remaining parts of the jigs are, of course, used to orient the principal and binary crystallographic axes. The jig of Fig. 2(a) provides a flat horizontal surface which is parallel to and at the same level as the bottom of the crucible chamber; that of Fig. 2(b) provides an inclined plane at 45°; the third jig, Fig. 2(c), aligns a screw, on which a 90°-vee is grooved, along the crucible axis.

The initial seed is a single crystal chip cleaved in the principal plane. The binary directions are known from the directions of three lines in the principal plane which make acute angles of 60° with one another. To seed a 90°-oriented rod, the cleaved plane is placed in contact with the flat of jig 2(a) and the binary axis direction at the desired angle with the crucible axis. Because the resulting 90° rod's vertical faces may not be precisely at right angles to the bottom surface, jig 2(b) is used for generating seeds in the 45°- and 0°-orientations. The bottom surfaces of the 90° rod and, in turn, of the 45° rod it seeds, are placed on the incline. Alignment of the seed rod and crucible axes is assured if a part of each seed rod is inserted into the mold chamber. To change the binary axis orientation of the 0°-oriented rods, jig 2(c) is used. The seed is placed in the groove and the screw turned through an appropriate angle.

Once a set of accurately oriented square-sectioned seed rods is obtained, each orientation is reproduced by innoculating other rods. No special jig is required. Each seed rod is simply placed in the crucible chamber with its bottom face referenced against the bottom of the mold.

Seeding and growing procedure.—Successful seeding is not difficult. It is neither necessary to fuse the seed to the precast rod with a reducing flame prior to melting in the crucible nor to use freshly cleaved or etched surfaces, as some of the earlier researchers found necessary for bismuth (2). Satisfactory contact is obtained simply by pushing one against the other. The rod and seed are joined by melting the former back to the latter at the time the single crystal is to be grown. As a general rule, a minimum of the seed is melted; usually 3 mm or less is satisfactory. However, the amount appears not to be critical because seeding was successful when lengths up to 15 mm were inadvertently used. For a given heater power the position of the seed junction in the furnace determines the amount of the seed melted. This position also appears to be a factor which influences the frequency of successful seeding. The optimum location is the region of the steep gradient between the zones.

In order not to stress the junction and to watch the wetting process, about 2 mm of the precast rod and the seed are not covered. Because of this, surface tension may act to form a blob at the junction. If the blob extends too far above the crucible walls, the seed orientation frequently does not survive.

The procedure for melting and resolidifying the precast rod is simple, once the optimum position and the corresponding heater power are determined. With the seed junction properly placed the system is flushed with argon; a positive pressure is maintained and the heater circuit is closed. Melting begins in nearly 10 min and is completed in about 2 min. A few seconds after the seed is wetted, the heater circuit is opened. Although the growth rate could not be determined accurately, it is not less than the 2 cm/min rate mentioned nor greater than 10 cm/min; more than likely, it is about 6 cm/min. The resulting rods are either thermally etched or etched in dilute aqua regia to bring out any gross grain structure.

[2] Spectroscopic analysis of the recrystallized rods does not show contamination.

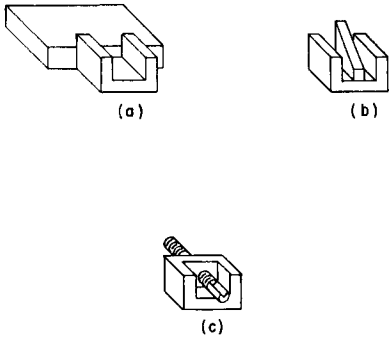

Fig. 2. Schematic representation of orienting jigs. Jig (a) can be used to obtain arbitrary orientations, jig (b) to obtain the 45° and 0° orientations, or multiples of the inclination angle, from 90°-oriented rods; jig (c) to adjust secondary axis orientation of 0° rods. Each jig is attached and referenced to the crucible by the channelled holding block which is an integral part of each jig.

Evaluation of Crystals

A measure of the quality of the rods is obtained by describing some of their physical properties and, where possible and meaningful, by comparing these with those of both slow-grown cast single crystal antimony rods and other single crystal specimens cut from large slow-grown ingots. The properties examined are their room temperature mechanical behavior, their ability to recrystallize in the solid, their room temperature galvanomagnetic coefficients, the segregation of added impurity due to normal freezing, their fine structure, the variation of one of the two principal resistivity coefficients with temperature, and the liquid helium-room temperature resistivity ratio. Our characterization is for the most part qualitative.

Allowing for anisotropy in mechanical behavior, the unworked undoped antimony rods are invariably more plastic than correspondingly oriented machined specimens. Unworked rods of the 45° and 90° orientation can be bent and twisted easily; the 0° rods are brittle. For orientations where it is not parallel to the rod axis, the c-plane is the one along which the rods break when dropped or otherwise stressed. Where the principal plane is very close to being parallel, the rods almost invariably break along secondary cleavage planes whose traces on the c-plane are the lines giving the binary axes directions. The cleavages and breaks are sharp and well-defined as shown in Fig. 3. Alloy rods are in general less plastic than their undoped antimony counterparts and appear to become brittle as tin is added.

Before breaking, not all rods of a given orientation deform to the same extent. This nonuniformity may be due to the fact that the one rate of growth used, or some unspecified factor(s), unknowingly and uncontrollably varied slightly. An exceptionally plastic rod, which we have not been able to reproduce, has been bent through nearly 95° and twisted. The rod is a single crystal in the region of deformation whose <111> axis is neither parallel to the lateral faces nor makes an angle of 0°, 45°, or 90° with the rod axis. Another interesting difference between our cast and cut single crystal rods is that many of the latter recrystallize in the solid at temperatures just below the melting point and none of the former do.

The nonuniformity also extends to the room temperature electrical properties in the form of spurious fluctuations about an average value for a given alloy. An example of this is the spread in ρ_{11}, the resistivity in the c-planes, and ρ_{33}, the resistivity across the c-planes. Values for these are, respectively, 43-46 x 10^{-6} ohm-cm and 32-36 x 10^{-6} ohm-cm for pure antimony and 38-39 x 10^{-6} ohm-cm and 42-45 x 10^{-6} ohm-cm for nominally 0.8% tin-doped specimens. These numbers show the percentage fluctuation to be orientation dependent, and, indeed, the spread in resistivity for 45° oriented rods of a given alloy is almost midway between the spreads for the 0° and 90° rods. On this basis it can be concluded that the nonuniform qualities of the rods are caused by minor flaws and inhomogeneities associated with the principal planes, probably the same ones which determine the planes of highest stress, or the weakest ones, at which a rod will break. The numbers, together with the spread in resistivities for our 0.2% alloys, also show the fluctuations to decrease on the addition of tin in amounts up to 0.8%.

Compared to independently obtained published values measured on specimens cut from Bridgman grown ingots of the same nominal and probably lower purity stock (5), our average values for ρ_{11} and ρ_{33} at room temperature agree to within 3% but our Hall coefficients and most of the magnetoresistance coefficients are lower by 10% and 20%, respectively. This agreement for the ρ's and the disagreement for the Hall and magnetoresistance coefficients, the latter larger than the former, cannot be accounted for by differences in purity and are compatible with different states of strain in the unworked and cut rods. A positive assignment is not possible from our data. Theory, however, does point to strain dependent coefficients (6).

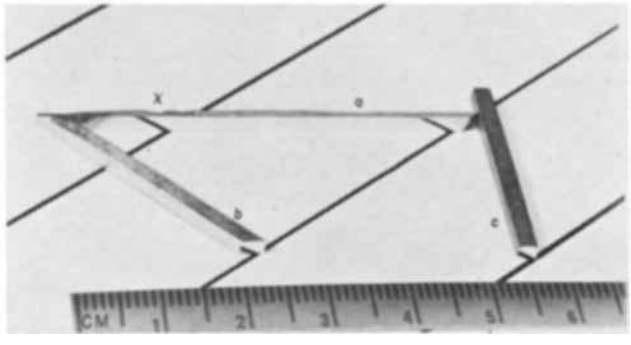

Fig. 3. Oriented single crystal antimony rods cleaved in the principal plane. The cleaved surfaces are unpolished and mirror the black stripes. Rod a has been grown in the 0° orientation; rods b and c in the 45° and 90° orientations, respectively. The region marked x is the seeding junction. The 45° and 90° specimens are cleaved by placing the tip of a thin blade on the edge of the rod and, with the blade parallel to the cleavage plane, pressing the blade into the rod; rod a is split by inserting the blade into a small crack obtained in the way just described and then sliding the blade, which is parallel to the cleavage plane, along the rod. A secondary cleavage plane on which fracture takes place bounds the right end of rod a.

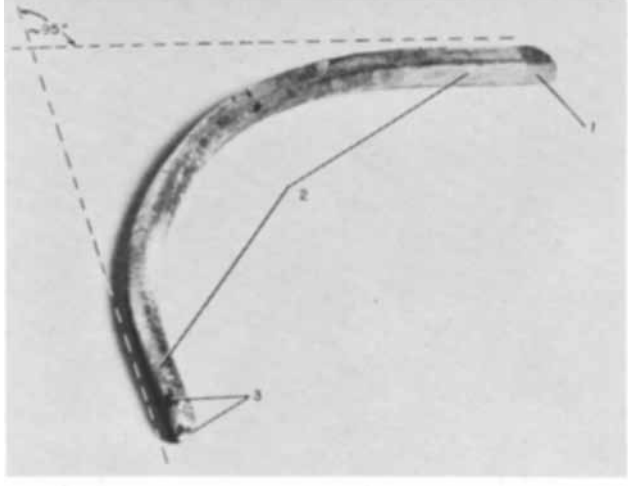

Fig. 4. An exceptionally plastic antimony rod. In response to a slight torque, the rod has simultaneously bent and twisted in the large single crystal region shown by the number 2. The traces of slip planes can be seen at the bend. Differently oriented grains at the ends of the rod, marked by 1 and 3, are clearly visible.

The segregation of tin due to normal freezing in the rods was checked by measuring ρ_{11} or ρ_{33} and spectroscopic sampling along the rod. On some long specimens where the resistivities did vary with length, the end-to-end change is less than 1% and orientation independent. Spectroscopic sampling shows some local fluctuations in doping, but these can be minimized by using zone-levelled starting stock.

As to fine structure, the dislocation density on a (111) plane appears to be about the $10^4/cm^2$ value recently reported by Wernick and co-workers for zone-refined, 99.999% pure, slowly grown, antimony crystals (7). We also find, in agreement with their observations, low-angle grain boundaries on some principal plane surfaces. Because our etching techniques are rather crude and not reproducible, our agreement and disagreement may not be significant.

Consistent with low-angle grain boundaries but not necessarily directly related to them are slightly split back reflection Laue spots. The amount of splitting is less than that obtained from specimens grown by Bridgman and horizontal techniques at slow rates and slightly more than that obtained from one carefully selected slow-grown Czochralski specimen. The slight degree of misorientation does not prevent the rods, as we have stated before, from being sharply cleaved at room temperature, nor does it distort the image mirrored in the principal cleavage plane, Fig. 3.

A complete evaluation should include extensive data on their electronic properties at low temperatures. In this connection our remarks are limited to the general features of the temperature variation of resistivity between room temperature and 77°K and to a brief discussion of known values for $\rho_{11}(4.2°K)/\rho_{11}(\sim 295°K)$. Our undoped and 0.2% tin-doped crystals respectively reproduce Lane and Dodd's (8) curves for cast, 3 mm diameter (9), undoped and 0.25% tin-doped, slow-grown, single crystal rods, and our 0.8% alloy data fall on their 0.5% alloy curve. Also in good agreement with the cast undoped antimony curve are a few of our undoped specimens cut from large slow-grown ingots. The remainder, however, have the same temperature coefficient of resistivity but prescribe curves which are shifted upward by constant arbitrary amounts. Although a detailed definitive explanation of these observations is not warranted because the possible variables involved were not systematically controlled, it would appear that the amount of defects in the cast slow- and fast-grown rods, and in selected specimens cut from large slow-grown ingots, is about the same. We would also expect to reproduce Browne and Lane's (9) value of 0.0012 for $\rho_{11}(4.2°K)/\rho_{11}(297°K)$ even though their nominal purity is 99.94%, for Steele (5), on cut specimens of about 0.5 mm x 2 mm, obtained a value of 0.014 on what appears to be the same antimony stock as ours but zone-refined to 99.999%. With higher purity materials a value of 0.0017 (10) has been reported for roughly 2 mm thick specimens (11). Using ultrapure antimony, less than 1 part in 10^7, Datars (11), who, incidentally, gives 0.0017 as the upper limit for cyclotron resonance in antimony, reports a value of 0.0005. This marked dependence of the 4.2°K resistivity on low-level impurity content plus our tentative conviction about the internal condition of our cast rods suggest that the technique described can yield low resistivity ratio crystals.

Conclusion

From the observed properties, the unworked single crystal antimony rods grown at a fast rate appear to be relatively unstrained compared to rods prepared by most other techniques. Their properties are reproducible within specifiable limits, and, although some properties differ from those of cut rods, the differences appear to reflect favorably on the technique. The rods are adequate for measuring the room temperature galvanomagnetic coefficients of pure and tin-doped antimony, the purpose for which this technique was developed, and ought to be satisfactory for cyclotron resonance and anomalous skin effect experiments where a long mean free path is necessary provided sufficiently pure starting material is used. The technique is applicable to the bismuth-antimony alloy system, and antimony-rich alloy rods have been grown in the nonpreferred, 0° orientation with the conditions optimum for pure antimony.

Acknowledgments

The author wishes to thank J. W. Mellichamp of the Institute for Exploratory Research at this Laboratory, for the spectroscopic analyses, and H. Jacobs, Deputy Director of the Laboratory's Solid State and Frequency Control Division, and H. J. Juretschke, of the Polytechnic Institute of Brooklyn, for their encouragement.

Manuscript received Jan. 25, 1962; revised manuscript received April 12, 1962. This paper was prepared for delivery before the Detroit Meeting, Oct. 1-5, 1961.

Any discussion of this paper will appear in a Discussion Section to be published in the June 1963 JOURNAL.

REFERENCES

1. P. Kapitza, *Proc. Roy. Soc.*, **A119**, 358 (1928).
2. Some of these are: L. Schubnikow, *K. Acad. Amst. Proc.*, **33**, 327 (1930); A. Goetz, *Phys. Rev.*, **35**, 193 (1930); E. Donat and O. Stierstadt, *Ann. Physik* (Leipzig), **17**, 897 (1933); M. F. Hasler, *Rev. Sci. Instr.*, **4**, 656 (1933).
3. K. Rausch, *Ann. Physik*, **1**, 190 (1947).
4. B. Chalmers, *Can. J. Phys.*, **31**, 132 (1953). This reference qualitatively presents the factors to be controlled in growing, seeding, and orienting metallic single crystals in horizontal containers.
5. P. W. Bridgman, *Proc. Am. Acad. Arts Sci.*, **60**, 305 (1924); M. C. Steele, *Phys. Rev.*, **99**, 1751 (1955); S. J. Freedman and H. J. Juretschke, *ibid.*, **124**, 1379 (1961).
6. R. W. Keyes, "Solid State Physics," Vol. 11, F. Seitz and D. Turnbull, Editors, Academic Press, Inc., New York (1960).
7. J. H. Wernick, J. N. Hobstetter, L. C. Lovell, and D. Dorsi, *J. Appl. Phys.*, **29**, 1013 (1958).
8. C. T. Lane and W. A. Dodd, *Phys. Rev.*, **61**, 183 (1942).
9. S. H. Browne and C. T. Lane, *ibid.*, **60**, 895 (1941).
10. W. R. Datars and R. N. Dexter, *ibid.*, **124**, 75 (1961).
11. W. R. Datars, Private communication.

Steady-State Evaporation Method for Composition Control of Thin Films Prepared by Halide Reduction

H. C. Theuerer

Bell Telephone Laboratories, Incorporated, Murray Hill, New Jersey

A widely used method for the preparation of thin films of elemental and compound semiconductors or metals is the hydrogen reduction of the appropriate halides. The inherent flexibility of this method makes it possible to prepare films with a large variety of compositions by appropriate adjustments of the vapor phase introduced to the reduction vessel. However, the precise composition control required for research and device purposes has, heretofore, made it necessary to meter accurately the very small amounts of halide vapors required in the reduction process. Metering of components is eliminated with the steady-state evaporation method, herein discussed. In essence, this is a simple and efficient method for maintaining a fixed vapor phase composition during the evaporation of binary or multicomponent solutions, the composition obtained being that of the starting liquid used.

The objective in steady-state evaporation is to promote evaporation from the surface of a liquid column using a carrier gas such as hydrogen with thermal and mechanical agitation of the liquid eliminated. Under these conditions, the surface layers of the liquid become enriched in the constituents with lower vapor pressures. Diffusion in the liquid results in an exponential concentration gradient in the region near the surface. Steady state is reached when the composition at the liquid surface is such that the gas phase in equilibrium with this liquid is that of the bulk liquid. For an ideal binary system, steady state is realized when the liquid surface has the composition $N_a p_b^\circ / N_b p_a^\circ$ where N_a/N_b is the mole ratio of the constituents initially, with p_a° and p_b° being the vapor pressures of the pure constituents.

Using this evaporation method, once steady state has been established, the gas phase composition will remain invariant so long as the gas flow rate, temperature, and the composition gradient near the liquid surface are not changed significantly. Conventional means of maintaining temperature and gas flow are adequate, and control of the liquid concentration gradient can be realized by containing the liquid in a porous medium such as a glass frit filter. The fine capillaries in such filters effectively block thermal and mechanical agitation. Moreover since the quantity of liquid held in the frit is small and the rate of liquid transport through the capillaries is high the diffusion gradient is restricted to a small region near the frit surface. In consequence, this evaporator design is insensitive to minor fluctuations in temperature and gas flow rate. A major change in either temperature or flow rate will result in a large transient change in composition of the evaporating liquid. It should be noted that as soon as the new steady state is established the evaporating liquid will revert to its original composition. Since the same steady state is achieved for any temperature at which the solution remains liquid and for any maintainable evaporation rate, control of these variables makes it possible to vary the quantity of vapors introduced to the reaction vessel over a wide range.

The apparatus for steady-state evaporation and halide reduction is shown in Fig. 1. With this apparatus it is possible to carry out all operations required to obtain steady state by proper manipulation of the stop cocks. Initially, the halide mixture is forced above the glass frit by applying hydrogen pressure to the reservoir. The pressure within the reservoir and evaporation chamber is then equalized which allows the liquid to drain back into the reservoir. Due to capillarity, the liquid column will remain in contact with the frit, and the upper surface of the frit will be uniformly wet. The liquid level in the reservoir should be below the frit, but other control of this height is not required since capillarity and the cohesive strength of the liquid will support the column in contact with the frit against an appreciable gravity head. After these preliminary operations, the desired hydrogen flow is maintained for a period of 10 min which is adequate to establish steady-state conditions. Following this, the gaseous mixture can be introduced to the reduction chamber for film deposition.

While this evaporator has been designed primarily to maintain a uniform vapor phase composition for the preparation of films with uniform composition, it is possible when desired to produce temporarily sharp concentration gradients by perturbing the evaporation rate. With an increase in

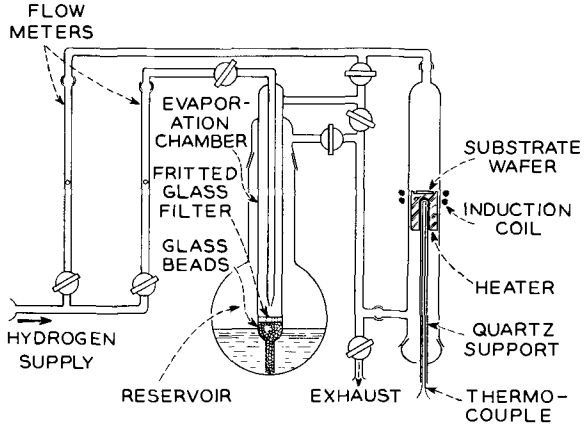

Fig. 1. Apparatus for steady-state evaporation and halide reduction.

evaporation rate, solutes with lower vapor pressure than the solvent will increase in concentration, the effect being greater the larger the difference between the solute and solvent vapor pressures. Solutes with higher vapor pressures than the solvent similarly decrease in concentration for an increase in evaporation rate. A decrease in evaporation rate from the initial steady-state rate results in solute concentration changes the opposite of those stated above. Since the composition of the vapor differs from that of the liquid only during the transient period while steady state is being reestablished, it is possible to produce sharp gradients in the deposited films. In the case of semiconductors, with the proper balance of donor and acceptor halides, in for example $SiCl_4$, it should be possible to produce p-n junctions. The mechanism here is analogous to that for rate grown junctions from the melt. The mathematics for solute distribution during solidification has been developed by Smith, Teller, and Rutter (1) and this may be used as a guide in utilizing the perturbed steady-state evaporator.

Acknowledgment

The author gratefully acknowledges the fruitful discussions and assistance of his colleagues J. J. Hauser, J. E. Kunzler, W. G. Pfann, and D. D. Bacon.

Manuscript received March 2, 1962. This paper was prepared for delivery before the Los Angeles Meeting, May 6-10, 1962.

Any discussion of this paper will appear in a Discussion Section to be published in the June 1963 JOURNAL.

REFERENCE

1. V. G. Smith, W. A. Tiller, and J. W. Rutter, *Can. J. Phys.*, **33**, 723 (1955).

Nature of the Damaged Layer on Abraded Silicon Specimens

R. Stickler and G. R. Booker

Research and Development Center, Westinghouse Electric Corporation, Pittsburgh, Pennsylvania

The damaged layer associated with semiconductor surfaces after abrasive treatments has been investigated extensively during the last few years; for a review see ref. (1). However, most of the work was directed toward determining the depth of the layer rather than the nature of the layer. Several investigators (2-5) hold the view that the damaged layer consists of a narrow outer region of cracked material together with a wide inner region of high dislocation density material. On the other hand, Pugh and Samuels (6) recently concluded that the entire layer consists of cracked material, and that dislocations are not present. However, both groups of investigators(6, 7) found that dislocations were formed if abraded specimens were subsequently annealed. We have investigated the damaged layer associated with abraded Si specimens by chemically thinning the specimens and examining them by transmission electron microscopy. Some preliminary results are described.

Procedure and Results

Silicon slices were cut, chemically polished with CP4 to remove the surface damage arising from the cutting, and abraded unidirectionally for a few minutes on one side using a No. 400 SiC paper with water as a lubricant. The slices were then chemically polished from the unabraded side using an HNO_3/HF solution (8) until portions of the slices were only a few 1000Å thick. These specimens were then mounted on a tilting specimen stage, and the thin portions were examined in transmission in the electron microscope.

The micrographs show areas corresponding to regions below the Vs of grooves gouged out of the surface by the abrasive particles. Directly beneath the Vs, two types of structure were observed. The less common type (Fig. 1) consisted of numerous single, and sometimes superposed, electron interference fringe systems. The fringes were in general curved and were not oriented along crystallographic directions. These fringes are of the kind which would result if small blocks of material located directly above one another were slightly misaligned, as in cracking.

The second more common type of structure (Fig. 2) consisted of an irregular network running along the length of the grooves. The structure comprised intersecting lines oriented along crystallographic directions and appears to be a severely strained dislocation network.

The regions directly adjacent to these two types of structure mainly exhibited only a surface texture structure. The appearance of this structure sug-

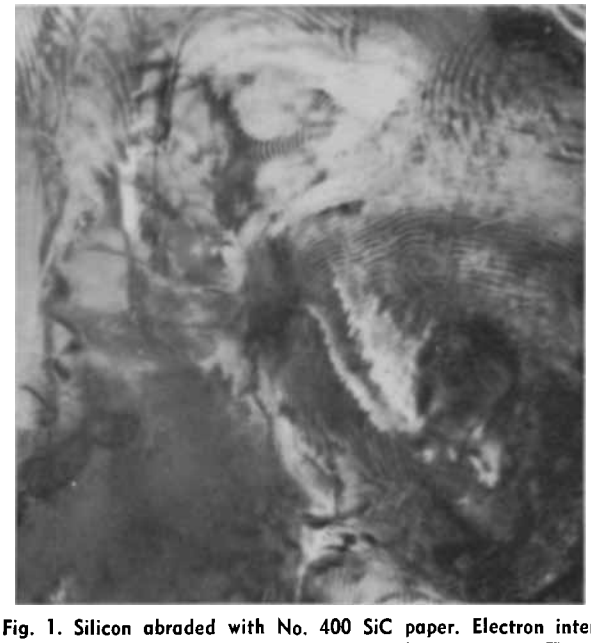

Fig. 1. Silicon abraded with No. 400 SiC paper. Electron interference fringes arising from cracked material are present. Transmission electron micrograph 50,000X.

Fig. 2. Silicon abraded with No. 400 SiC paper. Severely strained dislocation network is present. Transmission electron micrograph 100,000X.

gested that it arose during the abrasion process by small pieces of material being chipped away from the surface.

If the type of structure shown in Fig. 2 does consist of strained dislocation networks, then one would expect the dislocations to rearrange themselves during an annealing treatment and to assume a more equilibrium form, ideally a hexagonal network. Accordingly, Si slices were abraded with No. 400 SiC paper, annealed at 850°C for 1 hr in a hydrogen atmosphere and then prepared for transmission electron microscope examination as previously described.

The annealing treatment had two effects. First, a rearrangement of the dislocations in the networks occurred (Fig. 3), many areas adopting an approximately hexagonal form. Second, single dislocation lines ran outward from the edges of the networks (Fig. 3) into the surrounding, previously dislocation-free, regions. It is presumably this latter type of dislocation which was revealed by Faust (7) and Pugh and Samuels (6).

Summary and Conclusions

When silicon specimens were abraded with No. 400 SiC paper, the regions directly beneath the grooves gouged out by the abrasive particles were heavily damaged. The damage consisted of severely strained dislocation networks and cracks. Annealing of the abraded specimens at 850°C caused the dislocations within the networks to rearrange themselves into an approximately hexagonal form, and

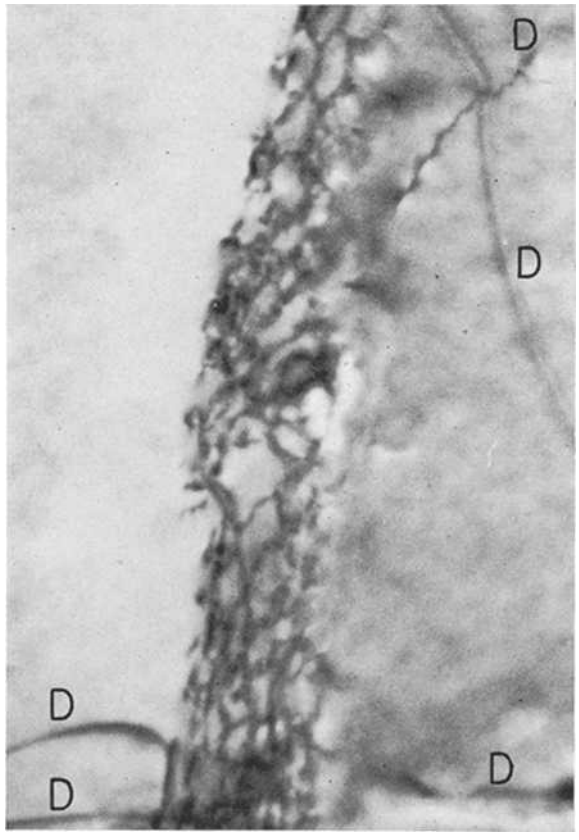

Fig. 3. Silicon abraded with No. 400 SiC paper and annealed at 850°C for 1 hr. Dislocations within the network have rearranged themselves into an approximately hexagonal form, and single dislocations (D) have propagated from the network into the surrounding regions. Transmission electron micrograph 50,000X.

single dislocation lines to propagate outward from both networks and cracks into the surrounding regions.

Conventional metallographic techniques would in most instances not reveal the individual dislocations of such networks because of the small distance between the dislocations (<1000Å). Moreover, such networks would etch as grooves, and hence would not be distinguishable from cracks. However, the single dislocations formed during annealing are relatively widely spaced, and are readily revealed.

Manuscript received April 12, 1962.

Any discussion of this paper will appear in a Discussion Section to be published in the June 1963 JOURNAL.

REFERENCES

1. T. M. Buck in "The Surface Chemistry of Metals and Semiconductors," H. C. Gatos, Editor, p. 107, John Wiley & Sons, Inc., New York (1960).
2. J. W. Faust, Jr., Paper presented before the Buffalo Meeting, October 1957.
3. R. L. Hopkins, *Phys. Rev.*, **98**, 1567 (1955).
4. D. Baker and H. Yemm, *Brit. J. Appl. Phys.*, **8**, 302 (1957).
5. J. W. Allen, *Phil. Mag.*, **4**, 1046 (1959).
6. E. N. Pugh and L. E. Samuels, *This Journal*, **108**, 1043 (1961).
7. J. W. Faust, ASTM Symposium on Cleaning of Electronic Device Components and Materials, Special Tech. Publ. No. 246.
8. G. R. Booker and R. Stickler, To be published.

Silver-Silver Chloride Electrodes Using Optical Silver Chloride Crystals

J. Greyson

Thomas J. Watson Research Center, International Business Machines Corporation, Yorktown Heights, New York

For a current investigation of membrane potentials, we require silver-silver chloride electrodes which can maintain stability for long time periods even when subjected to frequent moves from one dilute (less than 1M) aqueous chloride solution to another. A very simple preparation which requires only routine laboratory precautions and yields electrodes with excellent stability is described in this note.

Electrode Preparation

Silver chloride optical crystal sheet,[1] 1 mm thick, is cut into small sections about 0.5 cm on an edge. A piece of 0.030-in. silver wire[2] is heated over a bunsen flame until the end melts to a small sphere and while hot is pressed into an edge of one of the sections. The wire must be hot enough to melt the crystal around itself to secure an adequate electrical and mechanical connection. A piece of glass tubing, somewhat shorter than the silver wire, and previously filled with Apiezon W is warmed to soften the filling. The wire is pushed through the tube drawing the crystal as close to the end as possible. After the assembly has cooled, the crystal is rinsed several times successively and briefly in reagent grade concentrated nitric acid, water, and concentrated ammonium hydroxide, and is finally washed for several minutes in distilled water. Using the crystal as the cathode and platinum wire or foil as the anode, a deposit of metallic silver is developed on the crystal surface by immersing it in a 0.05-0.1*N* redistilled hydrochloric acid solution and then slowly withdrawing it while passing about 10 ma of current. The silver deposit forms at the contact of the crystal and the wire and grows down the surface in a thin jagged line. After obtaining the initial deposits, a group of electrodes are cathodized in the same solution for 30-40 min at a current of 2-3 ma per electrode. During this period the initial deposits broaden and become more diffuse. The current is reversed on completion of cathodizing and the electrodes are anodized at 0.2-0.3 ma/electrode for 2-3 min. They are then washed for a few minutes in distilled water and can be used.

Electrode Performance

Taniguchi and Janz (1) have defined "bias potential" as the difference in potential between a pair of identical electrodes immersed in a uniform solution. The term is used throughout the following to characterize electrode performance.

Bias potentials of all electrode pairs were measured, initially and for one week thereafter, in 0.1*N* HCl. After the first week, the medium was changed periodically. No attempt was made to stir the solutions or free them of oxygen. Potential measurements were made with negligible current flowing by using a microvoltmeter with a 6 megohm input impedance or a Rubicon Portable Potentiometer in conjunction with a Keithley 151R Null Detector with an input impedance of 100,000 ohms.

Three groups of electrodes were prepared at different times, the second group four hours after the first and the third, four days later. Of the first group of four, two were removed and used for measurements of cell potentials. All possible pairs in the second two groups, each composed of six electrodes, and the remaining two of the first group were compared at regular time intervals. The two in use for cell potential measurements were periodically returned to the bias potential cell and compared with all the rest.

Within any of the groups of electrodes which were prepared simultaneously, the bias potentials never exceeded ± 0.1 mv (and frequently were less than ± 0.05 mv) within 30 min after completion of anodizing. The average of the absolute values of the bias potentials for electrode pairs within a simultaneously prepared group was about 0.07 mv initially. After 100 hr in hydrochloric acid this average value decreased to about 0.05 mv. Changes in media (*i.e.*, 0.01*N* lithium chloride, 0.1*N* sodium chloride) caused an initial rise in bias potentials, but within 30 min the average of the absolute values reduced to that in the hydrochloric acid. The electrodes which were periodically returned to the bias cell always compared to those of the same group within 0.1 mv within 30 min.

A newly prepared electrode was usually about 1 mv negative with respect to an old one. This value increased to -0.15 mv in about 100 hr with a half time of about 15 hr. Changes in the nature of the surrounding solutions did not affect the magnitude of the potentials between new and old electrodes. It is interesting to note that in using standard preparative techniques, new electrodes are positive with respect to older ones. Janz (2) has discussed this effect and has pointed out that it may arise from a depletion of solute in the electrode pores during long anodizing periods. In the present technique the ratio of cathodization to anodization is high, and solute may concentrate in the electrode pores giving rise to a reversal in polarity.

We have examined several other characteristics of these electrodes. The electrical resistance of a pair is approximately 500 ohms. In dilute ethanol-HCl solutions, bias potentials were larger by an

[1] Harshaw Chemical Company, Cleveland, Ohio.

[2] Spectroscopically analyzed grade, Jarrell-Ash Co., Newtonville, Mass.

order of magnitude (> 1.0 mv) than in aqueous solutions. Over the temperature range 5°-100°C, bias potentials remained less than 0.1 mv. After passing 10 μa for 1 min, the bias potential reduced to the prepolarizing value in under 60 min with a half time of about 1 min.

These electrodes are used as probes to measure membrane potentials between chloride solutions. Within 15 min after cell assembly the potential reaches a value (P_1) which remains steady within 20 μv for 30 min or more. The electrodes are interchanged, and a potential P_2 is determined in the same way. The cell potential is taken as $\frac{1}{2}(P_1 + P_2)$ while $\frac{1}{2}(P_1 - P_2)$ may be compared with the bias potential B for the same electrodes in a mixture of the solutions in the two cell compartments. We find $\frac{1}{2}(P_1 - P_2) - B$ is at most 40 μv. A slow variation in bias potential has been noted in moving the probes through a succession of solutions of varying composition and concentration but the absolute magnitude has never exceeded 0.15 mv even after several weeks of use.

Acknowledgment

The author wishes to thank P. R. Mackey for his assistance and H. P. Charbnau for contributing the silver chloride crystals.

Manuscript received Dec. 11, 1961; revised manuscript received April 24, 1962.

Any discussion of this paper will appear in a Discussion Section to be published in the June 1963 JOURNAL

REFERENCES

1. H. Taniguchi and G. J. Janz, *This Journal*, **104**, 123 (1957).
2. J. G. Ives and G. J. Janz, Editors, "Reference Electrodes," Academic Press, New York (1961).

Ionic Conductivity of Zirconium Phosphate

R. P. Hamlen

General Engineering Laboratory, General Electric Company, Schenectady, New York

Ion exchange membrane hydrogen-oxygen fuel cells employing proton or hydroxyl ion conducting membranes as the electrolyte and gas barrier are under development at present (1-4). The organic ion exchange membranes employed in these cells have high conductivities (5), so that the internal resistances of these cells are relatively low. However, it would be desirable in some cases to employ solid electrolytes with greater thermal stability, oxidation resistance, and resistance to ionizing radiation. The operation of a cell employing such an electrolyte, zirconium phosphate, has been reported by Dravnieks and Bregman (6).

Since ionic solids in general are noted for being relatively poor ionic conductors at low temperatures when compared with aqueous electrolyte solutions, it is pertinent to mention the desired conductivity, and the order of magnitude of the conductivity observed for some types of ionic conduction in solids. Broers (7) has estimated that the specific resistance should be no higher than 10 ohm-cm in order that the ohmic voltage drop in the electrolyte will not be too great. Ionic conduction by lattice vacancy migration usually yields room temperature specific resistances of the order of 10^5 to 10^{11} ohm-cm. It is possible to increase the number of vacancies, and also the conduction, by doping with the proper impurity, but in general the maximum conductivity observed at room temperature is of the order of 10^{-5} $ohm^{-1}cm^{-1}$. Doped oxides of Zr, W, etc., have been employed in fuel cells (7) as oxide ion conductors, but in order to increase the conductivity to a reasonable value the temperature must be maintained at or above 1000°C.

In a few isolated cases the conductivities encountered in interstitial ion migration are very high. AgI undergoes a phase transition at 146°C wherein the silver ions become almost completely mobile in a fixed lattice of iodide ions (8), and batteries have been designed around this property (9). However, measurement of the proton conductivity in solid hydrated acetylene dicarboxylic acid, which has a high density of acid groups (although a weak acid), yields a specific resistance of 3 x 10^5 ohm-cm at 50°C (10). Ice has been doped with HF to increase the proton density, thereby producing a mode of conduction somewhat analogous to that of aqueous solutions, but in so doing the specific resistance was decreased to only about 10^5 ohm-cm (11).

The specific resistances of hydrated organic ion exchange membranes can run as low as 10 ohm-cm. Because of the large difference between this value and the values mentioned above, reasonable conductivities might be attained only in a material which conducts by a similar aqueous mechanism, such as in zirconium phosphate (6). The amorphous aluminosilicates and the zeolites also show cation exchange properties (12), but they are relatively unstable in acids, so that they are not readily hydrogen-exchanged to form proton-conducting solid electrolytes.

Recent investigations of inorganic ion exchangers for use in nuclear reactor water purification have dealt with the phosphates, arsenates, tungstates, and molybdates of zirconium, thorium, and titanium (13). Amphlett (14) has made an extensive study of the properties of zirconium phosphate, which appears to be one of the more stable hydrogen exchangers. He reports that it can be refluxed in water for several weeks without appreciable breakdown. It is an amorphous solid formed by the precipitation of a soluble zirconyl salt with phosphoric acid, consisting essentially of an O-Zr-O-Zr chain with $-O-PO(OH)_2$ groups attached to each Zr atom. Naturally the number of phosphate groups per Zr atom is going to depend on the conditions under

which it is made, and the cross linkage between adjacent phosphate groups by dehydration is going to depend on the thermal treatment of the product. Zirconium phosphate prepared using an excess of phosphoric acid and not subjected to high temperature has a high density of replaceable protons and is relatively insoluble.

Experimental

Preparation of zirconium phosphate.—The zirconium phosphate employed in these conductivity measurements was prepared as follows: 20g of $ZrO(NO_3)_2 \cdot 2H_2O$ were dissolved in 500 cm^3 of water. To this a solution of 50 cm^3 of 86.3% phosphoric acid in 250 cm^3 of water was added rapidly. The solution was stirred rapidly during the addition of the reagents, and the stirring was continued for about 5 min. Water was added so that the total volume was increased to 3.5 liters, and the solids were allowed to settle. The solids were washed by decantation several times, and were finally filtered and dried overnight at 60°C. More water was added to the solid product, and the gel particles broke apart with audible crackling to a final product having a particle size in the range 0.1-0.5 mm.

During the preparation the ratio of phosphorus to zirconium in the starting solutions was high, approximately 10, so that the solid product would be the normal phosphate $ZrO(H_2PO_4)_2$, which has the maximum hydrogen content.

Preparation of powder compacts for conductivity measurements.—Since there were no particles of the product large enough for use in conductivity measurements, it was necessary to employ powder compacts. These were 17.0 mm in diameter and about 3 mm thick. The densities of the compacts fell in the range 2.0-2.2 g/cm^3. On soaking in water, the pellets were observed to undergo a 20-30% increase in volume, although the pellets retained their shape and appeared to suffer no degradation of mechanical properties. Because of this expansion conventional electrodes, such as those made from conducting paints, could not be employed. In order to overcome this difficulty, 100 mg of finely divided zirconium phosphate and 50 mg of platinum black were mixed, and one half of this mixture was spread over each face of the compact after it had been formed at a pressure of 13,000 psi. After a final pressing at 33,000 psi the electrode layers showed no tendency to peel off when the pellets were soaked in water. The electrodes so formed showed a resistance of only a few ohms from one point to another on each face.

Conductivity measurements.—For measurements of conductivity *vs.* temperature the apparatus shown in Fig. 1 was placed in an oven. Platinum disks were pressed against each face of the compact, and silicone rubber gaskets prevented the escape of water vapor from the apparatus. Therefore, the measurements were conducted under conditions of constant water content. A General Radio Company type 1650A Impedance Bridge was used for the measurements, with a variable capacitor across one leg of the bridge to balance out capacitive effects in the sample.

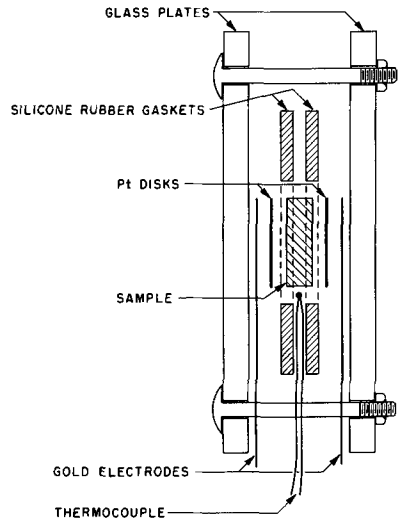

Fig. 1. Conductivity apparatus

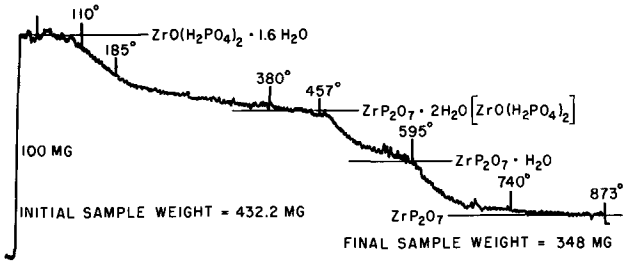

Fig. 2. Thermogram for zirconium phosphate

The frequency dependence of the conductivity was low, as is seen in Table I, an indication that electrode polarization effects were absent (15).

Results and Discussion

Thermogravimetric analysis.—In order to obtain a rough idea as to the thermal stability of the zirconium phosphate a thermogravimetric analysis was conducted on the material as dried at 60°C at a heating rate of 5°C/min. This is shown in Fig. 2. When prepared in the manner described previously it should have a composition near $ZrO(H_2PO_4)_2 \cdot XH_2O$. If one assumes that the final product has the empirical formula ZrP_2O_7, as is done in the standard phosphate analysis for zirconium, the two breaks in the curve correspond closely to the loss of one water molecule at 470°C and another at 600°C by the condensation of adjacent phosphate groups. The water lost at lower temperatures is water originally retained in the gel structure, and the initial composition is then approximately $ZrO(H_2PO_4)_2 \cdot 1.6H_2O$.

On soaking in water the volume of the compact used for the conductivity measurements increased

Table I. Frequency dependence of conductivity

Frequency, cps	Resistance, ohms × 10^{-4}
2000	3.98
1000	4.00
500	4.00
200	4.02
100	4.02
50	4.02
25	4.02

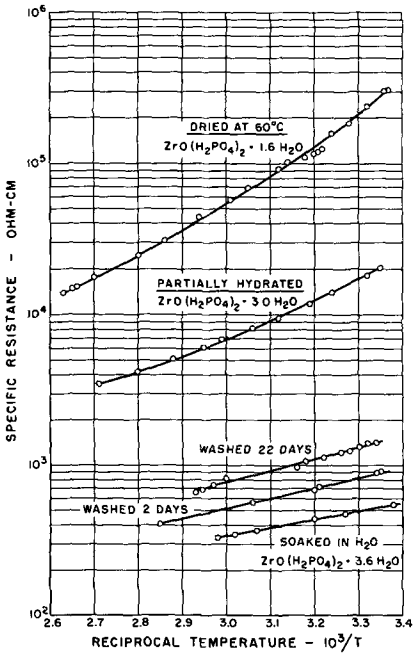

Fig. 3. Specific resistance of zirconium phosphate *vs.* $1/T$

by 22%. Assuming the increase in volume was due to the addition of water with a density of 1.0, and since the density of the compact initially was 2.0, the composition of the soaked compact should be approximately $ZrO(H_2PO_4)_2 \cdot 3.6H_2O$.

Conductivity measurements.—Measurements of conductivity *vs.* temperature were carried out on a pellet immediately after pressing from zirconium phosphate dried at 60°C, and on the same pellet after partial and complete hydration. The temperature dependence of resistivity ρ can usually be expressed over narrow ranges by an equation of the form $\rho = \rho_0 e^{E/RT}$, where E is an activation energy for the conduction process. Therefore, E can be obtained from the slope of a plot of log ρ *vs.* $1/T$. Figure 3 contains plots of log ρ *vs.* $1/T$ for the samples in each of the three states of hydration. It is seen that the activation energy decreases from 9.8 kcal/mole to 2.6 kcal/mole as the sample becomes more hydrated. The activation energy for the soaked pellet falls in the range normally found for conduction in aqueous solutions (5). If the assumption is made that there is a solution of $2H_3PO_4$ units for every $3.6H_2O$ molecules, a rough calculation of the expected conductivity can be made using the second ionization constant of phosphoric acid. The above ratio of H_3PO_4/H_2O corresponds to a 75% solution of phosphoric acid, which would have a density of 1.58 g/cm^3. K_2 for phosphoric acid at 25°C is 6.2 x 10^{-8} (16), and this would result in a proton concentration of about 9 x 10^{-4}g equivalent/liter. Since each cubic centimeter of solid would contain about 0.80 cm^3 of the above solution, and since the equivalent ionic conductance of protons is about 350 ohm^{-1}-cm^2, the conductance would be of the order of 3 x 10^{-4}ohm^{-1}. This would correspond to a specific resistance for the solid of about 3000 ohm-cm. This is about a factor of 5 greater than the specific resistance of 550 ohm-cm observed on this material at 25°C. Considering the assumptions involved, especially the assumption that K_2 for the phosphoric acid is not affected by reaction with the hydrated zirconium oxide, the agreement is within reason. It has already been observed by Amphlett that a titration curve of zirconium phosphate *vs.* NaOH does not give two inflection points characteristic of K_2 and K_3 for phosphoric acid, but gives a relatively smooth curve.

Activation energies were calculated from the slopes of the three curves at the low end of the temperature range. They are 9.8, 6.4, and 2.6 kcal/mole for increasing degrees of hydration. The last value corresponds to the temperature variation observed in aqueous solutions as a result of the decrease in viscosity with increasing temperature.

Effect of continuous washing on the conductivity.—Because of the nature of the zirconium phosphate, it would be expected that continuous washing would hydrolyze the solid, releasing phosphoric acid and eventually converting the zirconium phosphate to zirconium hydroxide (hydrous zirconium oxide). The compact employed in the measurements above was washed continuously, and the conductivity was measured after 2 and 22 days. These results are also shown in Fig. 3. The figure shows that the conductivity decreased, although the slope of the plot remained relatively constant. This would indicate that the mode of conduction remained the same, namely, transport of H^+ ions in an aqueous system, but that the number of current carriers (H^+ ions) decreased as a result of the hydrolysis mentioned above.

Fuel cell using a zirconium phosphate membrane.—A cell similar to that of Dravnieks and Bregman was prepared by pressing a 1 mm thick disk from 90% zirconium phosphate and 10% powdered Teflon at a pressure of 35,000 psi. This was soaked in water, each face was sprinkled with Pt black, and a Pt screen was placed against this in a simple hydrogen-oxygen fuel cell configuration. The polarization curve for this cell is shown in Fig. 4. The resistance of the membrane as calculated from the slope of the polarization curve was 110 ohms, which agrees roughly with the measured value of 150 ohms. This value of 110 ohms corresponds to a specific resistance of about 6000 ohm-cm, showing that the Teflon binder in this case decreased the conductivity sub-

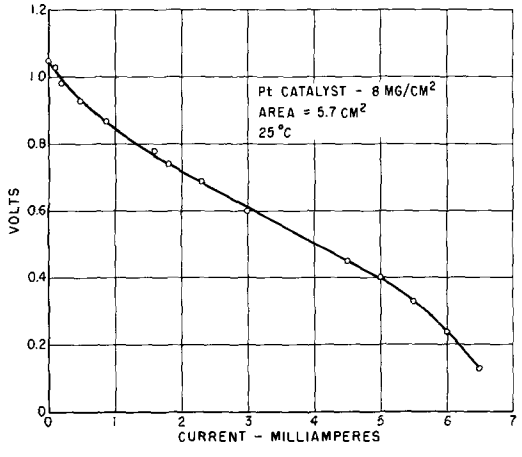

Fig. 4. Polarization curve for H_2-O_2 fuel cell with zirconium phosphate membrane.

stantially. Obviously, it is desirable to increase the conductivity by better membrane construction and by the use of higher temperatures. Because of the aqueous mechanism of ion transport pressurization would be required above 100°C.

It is evident that such a membrane has two major drawbacks from the standpoint of fuel cell applications: (*A*) Low conductivity. This might be partially overcome if sufficiently thin membranes could be fabricated. (*B*) Changes due to hydrolysis.

Manuscript received Nov. 13, 1961; revised manuscript received March 16, 1962.

Any discussion of this paper will appear in a Discussion Section to be published in the June 1963 JOURNAL.

REFERENCES

1. W. T. Grubb and L. W. Niedrach, *This Journal*, **107**, 131 (1960).
2. E. Joachim and W. Vielstich, *Electrochim. Acta*, **3**, 244 (1960).
3. H. F. Hunger, *Proc.* 14th Annual Power Sources Conference, Atlantic City, May 17, 1960.
4. R. M. Lurie, C. Berger, and R. J. Shuman, American Chemical Society Symposium on Recent Advances in Fuel Cells, Chicago, September 3, 1961.
5. W. T. Grubb, *J. Phys. Chem.*, **63**, 55 (1959).
6. A. Dravnieks and J. I. Bregman, Fuel Cell Symposium of the Electrochemical Society, Detroit, Oct. 1, 1961. (See also *Chem. and Eng. News*, Oct. 16, 1961, p. 40.)
7. G. H. J. Broers, "High Temperature Fuel Cells," Dissertation, University of Amsterdam (1958).
8. R. C. Evans, "An Introduction to Crystal Chemistry," Cambridge University Press (1948).
9. J. L. Weininger, *This Journal*, **106**, 475 (1959).
10. J. M. Pollack and A. R. Ubbelohde, *Trans. Faraday Soc.*, **52**, 1112 (1956).
11. H. Granicher, C. Jaccard, P. Scherrer, and A. Steinemann, *Discussions Faraday Soc.*, **23**, 50 (1957).
12. R. Kunin, "Ion Exchange Resins," 2nd ed., John Wiley & Sons, Inc., New York (1958).
13. H. F. Walton, *Ann. Rev. Phys. Chem.*, **10**, 123 (1959).
14. C. B. Amphlett, L. A. McDonald, and M. J. Redman, *J. Inorg. and Nuclear Chem.*, **6**, 220 (1958).
15. G. Kortum and J. O'M. Bockris, "Textbook of Electrochemistry," Elsevier, New York (1951).
16. C. D. Hodgman, Handbook of Chemistry and Physics, 42nd ed., Chemical Rubber Publishing Co., Cleveland.

Brief Communications

The Chemical Polishing of Rare Earth Tellurides

P. Bro

Research and Advanced Development Division, Avco Corporation, Wilmington, Massachusetts

There is a growing interest in the semiconducting compounds of the rare earth metals, and several compounds have been reported (1) with interesting thermoelectric properties. One of the problems associated with the electrical measurements on these compounds is the preparation of reproducible surfaces. Mechanical polishing can be employed, but it generates a strained surface which gives rise to anomalies in the surface properties of the samples. A chemical or electrochemical method generally is preferred in the preparation of semiconductor surfaces for electrical and optical measurements.

We have investigated a variety of chemical etches for the rare earth tellurides and the main problem was that of finding a reactive medium that could dissolve the metal and the tellurium at comparable rates under conditions which would produce a polished surface. A satisfactory chemical polish was found for the sesqui- and higher tellurides, and it consisted of 10 ml glacial acetic acid and 1 ml bromine. It gave an etch rate on La_2Te_3 at room temperature of 0.84 g/sec m^2 when freshly prepared. An etching period of 20-60 sec appeared satisfactory. The etch rate could be increased by the addition of ethyl alcohol, and an etch rate of 1.63 g/sec m^2 was obtained with 5 ml HAc, 5 ml EtOH, and 1 ml Br. The gradual heating of the latter etch due to the exothermic Br/EtOH reaction also increased the etch rate. An inferior polish was obtained in the presence of excess amounts of alcohol or when the etch was not strictly fresh.

An interesting observation was obtained with La_2Te_3 in etches composed of HBr, H_2O, and Br, *e.g.*, 10 ml fuming HBr, 30 ml H_2O, 1 ml Br. Initially, the sample acquired a high apparent polish, but a continued exposure to the etch under quiescent conditions led to the formation of long, twisted tellurium whiskers which grew profusely and very rapidly from the surface of the sample. The initial polish was found to be due to the formation of a tellurium phase on the surface which could be removed quite readily. The growth of the tellurium whiskers appeared to depend on the formation of highly mobile tellurium atoms in the crystal lattice by the preferential dissolution of the rare earth metal, and it is a phenomenon which lends itself to experimentation in the interesting field of crystal growth mechanisms.

Acknowledgments

The synthesis of the rare earth tellurides was carried out by W. Mularz and his assistance is gratefully acknowledged.

Manuscript received March 15, 1962.

Any discussion of this paper will appear in a Discussion Section to be published in the June 1963 JOURNAL.

REFERENCE

1. J. F. Miller, F. J. Reid, and R. C. Himes, *This Journal*, **106**, 1043 (1959).

Gallium Phosphide Crystal Growth by Vapor Phase Iodide Transport

A. S. Roy[1]

Bell Telephone Laboratories, Incorporated, Murray Hill, New Jersey

The growth of small GaP crystals from the vapor phase has been reported by Antell and Effer by mixing GaI and phosphorus and slowly cooling from 1050°C in a quartz tube (1). Gershenzon and Mikulyak (2) allowed Ga_2O to react with phosphorus at about 1000°C in a sealed quartz tube and obtained thin whiskers and filaments of GaP up to 0.2 mm in width. Epitaxial films of GaP have been grown by Frosch and Foy (3) and by Moest and Shupp (4). Holonyak reported growth of massive polycrystals of GaP using halides as transport agents (5).

[1] Present address: Israel Atomic Energy Commission, Rehovoth, Israel.

The experiments reported here describe the growth of GaP single crystals whose sizes were up to 2 mm in each dimension. Growth was from the vapor phase at temperatures between 780° and 935°C and about atmospheric pressure in a sealed quartz tube containing a polycrystalline GaP source (about 0.5g), H_2, and I_2, with initial mole ratios of 8:7:1. The tube was 18 cm long and of 2 cm inside diameter. A temperature gradient provided the potential for the net reaction of transferring GaP from the source to a lower tempera-

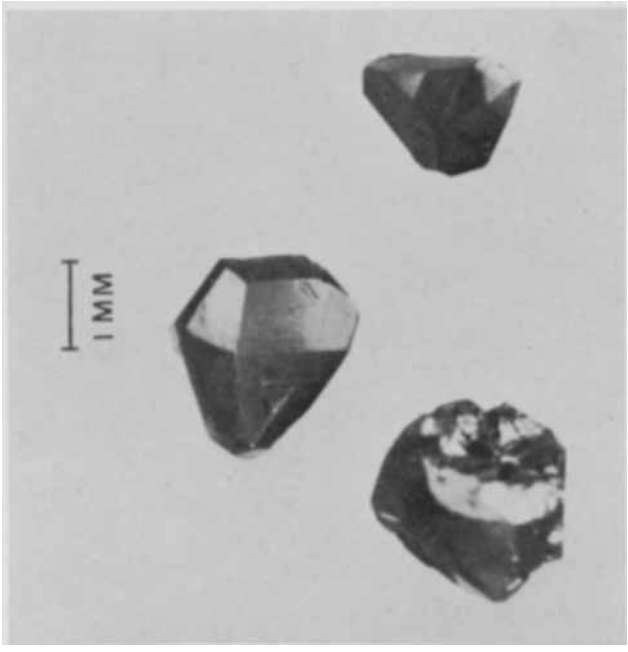

Fig. 1. GaP single crystals grown at 946°C at a point of 5°C below source temperature.

ture. Larger crystals were obtained when the gradient along the tube was small. The largest crystals were, in general, found at the middle of the tube rather than at the coolest end. Figure 1 shows several crystals over 2 mm in size grown at 946°C at a point 5°C below the temperature of the source material. Smaller crystals were obtained with larger gradients. When the cold end was reduced to 780°C with the source at 950°C, aggregates of crystallites approximately 0.02 mm in size deposited at the cold end. In one case, a similar gradient produced GaP needles with typical dimensions of 0.1x0.4x2 mm. The transport rate increased with the source temperature. For a temperature difference of 50°C between the source and the colder end of the tube and with the source at 850° and 950°C, the transport rates were 25 and 75 mg/hr, respectively.

The crystals adhered strongly to the quartz. The contact area was observed by reversing the temperature gradient and transferring the GaP to a cooler region of the tube. Gallium phosphate and α-quartz crystals ~0.1 mm in size were side reaction products. These were identified by x-ray diffraction measurements. Typical GaP crystals were analyzed spectrographically after removing the regions adhering to the quartz by etching. The concentrations of detectable impurities, Ca, Mg, Al, Si, Fe, and Ni, were less than 50 ppm. The crystals were always n-type, suggesting that Si was the dominant electrically active impurity.

The results of these preliminary experiments indicate the feasibility of relatively rapid growth of large GaP crystals at comparatively low temperature and pressure.

Manuscript received March 22, 1962.

Any discussion of this paper will appear in a Discussion Section to be published in the June 1963 JOURNAL.

REFERENCES

1. G. P. Antell and D. Effer, *This Journal*, **106**, 509 (1961).
2. M. Gershenzon and R. M. Mikulyak, *ibid.*, **108**, 548 (1961).
3. C. J. Frosch and P. W. Foy, Electrochem. Soc. Meeting Abstract No. 142, Detroit, October 1961, *This Journal*, **108**, 177C (1961).
4. R. Moest and B. R. Shupp, *ibid.*, Abstract No. 143, **108**, 178C (1961).
5. N. Holonyak, Jr., Scientific Report No. 2b (GE Company, Syracuse, New York) AF 19 (604)-6623, October 1960.

Polarization Studies on High-Temperature Fuel Cells

M. L. Kronenberg

Research Laboratory, Union Carbide Consumer Products Company, Division of Union Carbide Corporation, Parma, Ohio

ABSTRACT

Immobilized-electrolyte, high-temperature fuel cells of nonconventional design were operated successfully on a wide variety of fuel gases. This design permits the incorporation of a reference electrode and avoids gasketing problems for low-pressure operation. The performance of these cells was compared with preliminary results on free electrolyte and solid electrolyte cells. Oscilloscopic observations of polarization decay indicated that ohmic rather than concentration or activation polarization limits the performance of matrix cells in most instances.

It is well known that gaseous fuel cell reactions take place within a relatively restricted reaction zone since the fuel must make simultaneous contact with the electrode and electrolyte. There are three general approaches that have been used in the development of high-temperature fuel cells which in principle fulfill this requirement. These are matrix cells, solid electrolyte cells, and cells using gas diffusion electrodes in free electrolyte. Most of the results presented here are concerned with matrix cells, although some preliminary results on gas diffusion and solid electrolyte cells are also presented as a comparison.

The advantage of a solid electrolyte in achieving a three-phase reaction zone without the difficulties of wetting was recognized by Schottky (1). However, it was Baur and co-workers (2-4) who conducted extensive experiments on solid electrolyte cells. No practical solid electrolytes were found despite the many systems that were studied. In his well-known thesis on high-temperature fuel cells, Broers (5) concluded that a good solid electrolyte might never be found and that a salt which transports oxygen-containing ions such as a carbonate salt would be second best to an ideal solid electrolyte. The cell he developed with these thoughts in mind essentially consists of a carbonate-impregnated disk covered with metal catalyst powders and current collectors and with anode and cathode compartments built up by gaskets and spacers.

This disk-type construction served as a starting point for our research on high-temperature cells. Fuel cells of this design were run on a wide variety of fuel gases. The performance data obtained were about the same as reported by Broers (5), *i.e.*, a current density of 50 ma/cm^2 at approximately 0.7v on hydrogen with slightly lower operating levels on carbon monoxide and hydrocarbon fuels. However, because of the high operating temperatures and corrosive nature of the carbonate melt under these conditions, it was difficult to obtain a well-gasketed system with this design.

A tubular cell design was decided to be a better laboratory approach to the matrix cell since gasketing problems would be eliminated. A cell of this type is shown in Fig. 1. The porous ceramic tube is impregnated by immersion at 700°C with a ternary eutectic alkali carbonate which has a melting point slightly under 400°C (6). The inside of the tube is catalyzed as an anode or fuel electrode and the outside as a cathode. Catalysts were normally applied as slurry powders to the surface and baked at 500°C prior to fixing the perforated foil collector in place. Air and carbon dioxide are the cathode gases normally used.

This construction readily permits the incorporation of a reference electrode as shown. The reference electrode in this case should be reversible to O_2 and CO_2 which are the active cathode gases. Broers (5) suggested that silver was a good CO_2, O_2 electrode, but did not report the use of a reference electrode in his studies. The reversibility of the silver electrode was checked in a concentration cell of the type represented in the following equations

$$1/2\ O_2 + CO_2 + 2e \underset{\text{anodic}}{\overset{\text{cathodic}}{\rightleftharpoons}} CO_3^{=} \qquad [1]$$

$$Ag, CO_2(P^c), O_2(P^c)/CO_3^{=}/O_2(P^a), CO_2(P^a), Ag \qquad [2]$$

$$E = \frac{2.3\,RT}{2F} \log \frac{(P^a_{O_2})^{1/2}\ P^a_{CO_2}}{(P^c_{O_2})^{1/2}\ P^c_{CO_2}} \qquad [3]$$

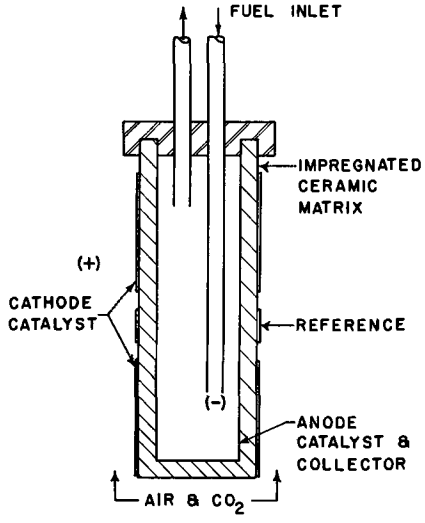

Fig. 1. Tubular fuel cell

Equation [1] represents the reversible reaction; Eq. [2] is a representation of the concentration cell, and Eq. [3] is an expression for the Nernst potential one would calculate at low and moderate pressures for a reversible electrode.

By holding three partial pressures constant and varying the fourth, Nernst dependence of potential was observed on variation of either CO_2 or O_2 partial pressures. This is shown for CO_2 variation in Fig. 2. The solid line was obtained from experimental results and the lower curve from potentials calculated using the Nernst equation. The 2-mv displacement that is observed is attributed principally to errors in flow-meter adjustments. The Nernst slope consistently observed in these experiments demonstrated the reversibility of the powdered silver electrode as a CO_2, O_2 electrode. Nernst dependence was observed down to 400°C.

Figure 3 shows one of the ways tubular cells can be simply built into batteries by joining tapered sections. The series connections can then be made internally and common gas feeds used. Several tubular multicell batteries have been made, and no special difficulties were encountered in their operation.

In Figure 4 are shown typical anode-reference, resistance-free[1] polarization curves for several gases. The reference electrode in all cases is carbon dioxide and oxygen on powdered silver. There is very little polarization outside of resistive effects for these gases above 600°C. One cannot be sure if the hydrogen-containing gases are actually galvanically utilized or whether they are running on thermally produced hydrogen. The carbon monoxide was carefully dried to contain less than several ppm water vapor, so that a direct galvanic utilization appears to be the case. However, one cannot overlook the possibility that any of the fuels may act as a reducing agent to keep the oxygen partial pressure low, resulting in a concentration cell based on the reaction given in Eq. [1], which has been shown to be reversible on silver. The cell potential would correspond to the partial pressure difference of oxygen across the cell caused by chemical utilization at the anode by the fuel. Identical products are normally obtained whether the fuel reacts chemically first or whether it is galvanically utilized directly. So, the question of whether or not the fuel is galvanically utilized in a high-temperature cell cannot be decided on the basis of product analysis.

In Figure 5 are shown the operating cell voltages as a function of current density for several fuels. The potentials are much lower than for the anode-reference (resistance-free) polarization curves of the previous figure. The dotted line represents the resistance-free cell potential drawn in as a comparison. So, while resistance-free potentials at prac-

[1] The resistance-free polarization data were obtained using a Kordesch-Marko pulse-current interrupter (7). The instrumentation used to distinguish between ohmic and activation polarization was similar to the electronic commutator described in the literature by Staicopoulous and co-workers (8).

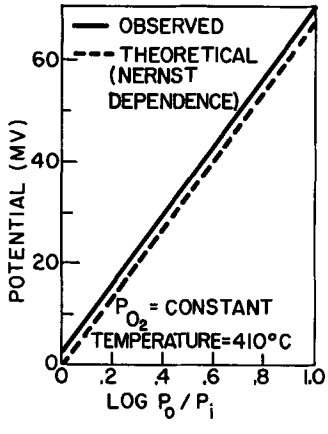

Fig. 2. Potential dependence on partial pressure of CO_2

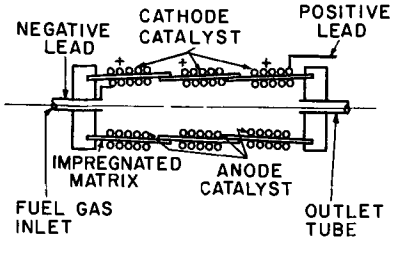

Fig. 3. Three cell battery

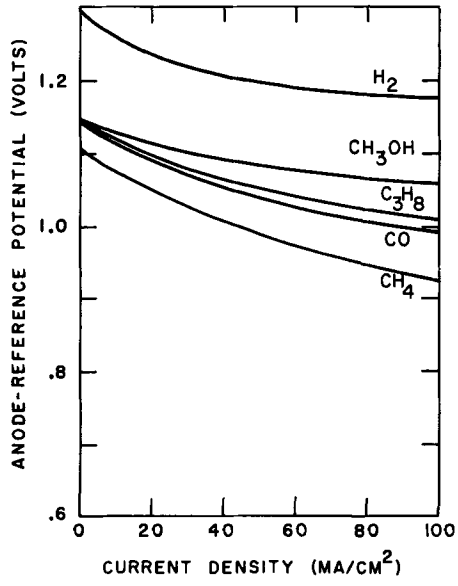

Fig. 4. Resistance-free polarization curves for various fuel gases at 610°C.

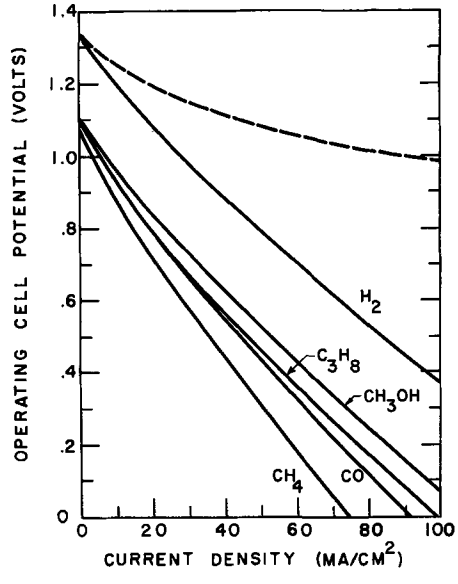

Fig. 5. Operating voltages for various fuels at 610°C

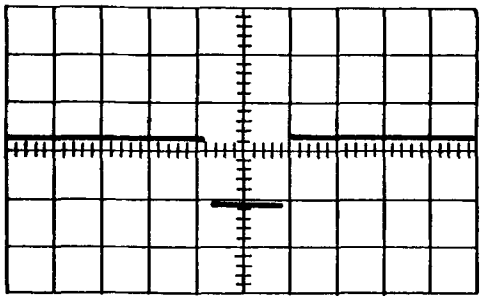

Fig. 6. Oscilloscope trace of anode-reference potential for methane at 500°C and 25 ma/cm².

tical current densities look quite promising, the high cell resistance drastically reduces the cell output.

Oscilloscopic observations of polarization decay indicate that above 500°C there is virtually no activation polarization associated with any fuel, even methane at moderate current densities. Figure 6 shows an oscilloscope trace of the anode-reference potential for methane at 500°C and 25 ma/cm². The long line represents the anode-reference potential during the current-on period. The current-off period is approximately 80 μsec. There is no evidence of activation polarization here since this would show up as a sloped line or curve on this time scale. The virtually instantaneous potential change is attributed to ohmic polarization and corresponds to approximately 90 mv. There also appears to be about 150 mv of concentration polarization since the open-circuit potential is that much below the current-off portion of the trace. This latter difference from open-circuit voltage may also be partially attributed to voltage drops within the pores of the porous electrodes, but this is not believed to be a significant contribution since this difference is only several millivolts when hydrogen is used as fuel.

The high concentration polarization, in this case, suggests that hydrogen resulting from the thermal decomposition of methane is the galvanically active species under these conditions. This possibility was discussed above. With increasing temperatures, concentration polarization decreases to approximately 80 mv at 600°C. At temperatures above 800°C, there was no appreciable concentration polarization difference between hydrogen and methane. This question could not be resolved since methane polarization curves at several temperatures could not be reproduced with a dilute mixture of hydrogen in inert gas with our fuel cell system.

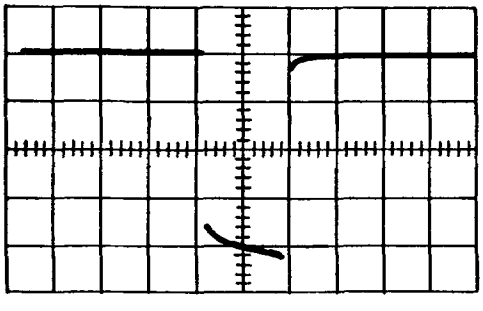

Fig. 7. Oscilloscope trace of anode-reference potential for propane on a poorly catalyzed electrode.

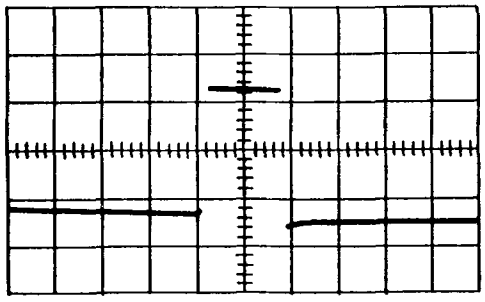

Fig. 8. Oscilloscope trace of anode-cathode potential for methane at 600°C and 25 ma/cm².

Evidence of activation polarization on a poorly catalyzed electrode is shown in Fig. 7. This was for propane fuel at 25 ma/cm² at 600°C. The differential capacitance obtained from the initial slope of the activation polarization was approximately 6 μF/cm² on this electrode. This indicates that the effective surface area is probably less than the geometrical surface area. In Fig. 8 is shown the anode-cathode potential at the same current density which shows the 200 mv of ohmic polarization associated with the whole cell at 25 ma/cm² and 600°C. Methane was the fuel gas used. This shows also that there is no evidence of activation polarization at the cathode under these conditions.

As evidenced by the performance data presented, the main limitation on the performance of matrix cells is the high cell resistance. The resistivity of the melt is increased because of its dilution in the ceramic matrix and the contact resistance is high because it results from a series of point contacts rather than a continuous contact area. A continuous contact area cannot be used because of the 3-phase requirements of gas electrodes and the required nonelectronic conducting properties of the matrix. The minimum dilution effect on potential can be estimated from the following considerations assuming a minimum current density of 100 ma/cm² is required for practical operation.

$$E = IR = I\frac{\rho}{D}\frac{l}{A}$$

$$= 0.1 \text{ amp} \times \frac{1.0}{0.3} \text{ ohm cm } \frac{0.4 \text{ cm}}{1 \text{ cm}^2} = 0.133\text{v} \quad [4]$$

where E is the potential loss, I the current (0.1 amp), ρ the resistivity of melt (1 ohm-cm), R the cell resistance ($\rho l/A$), D the dilution effect of 30% porous matrix, and l the thickness of matrix (0.4 cm).

Contact resistances for 1 cm² were determined experimentally. For porous impregnated matrices, 0.4 cm in thickness, the contact resistance/cm² at each face was approximately equal to the resistance/cm² of the impregnated matrix. Therefore, the over-all loss in cell voltage due to ohmic effects above for a matrix cell using a 30% porous matrix is 0.133 + 2(0.133), or approximately 0.4v. This reduces working voltages at 100 ma/cm² to at least 0.8v without considering forms of polarization and is in accord with working voltages observed experimentally.

The longest period a tubular matrix cell has been run was for 10 weeks of intermittent operation. The

cell was turned off at night and heated up again the next morning and consequently went through approximately 50 heating and cooling cycles. In order to maintain operation for even this length of time, it was necessary to provide for periodic addition of carbonate to the matrix. This was accomplished by using a reservoir cap, containing ternary alkali carbonate, which was directed into the tube wall through carefully machined tube channels. The procedure was only partially successful. It prolonged the life of the cell, but resulted in the accumulation of excess electrolyte at the base of the cell. Failure was attributed principally to cracks and deterioration of the MgO matrix and to loss of electrolyte.

Because of the inherent limitation on performance attributed to the high cell resistance of matrix cells, controlled porosity metal electrodes used directly in the melt have been investigated in ours and other laboratories (9, 10). Here the important 3-phase reaction sites are provided within the pores of an electronic conductor, and the electrolyte is not diluted so that cell resistance is much lower than with matrix cells. However, the free carbonate electrolyte represents a highly corrosive environment under these conditions. Some preliminary results that have been obtained with diffusion cells are summarized in Fig. 9. The "a" curves represent resistance-free potentials for matrix, 1, and free electrolyte, 2, cells. Although resistance-free potentials are significantly higher for matrix cells than for the porous metal electrodes used thus far, the working cell potentials ("b" curves) are much higher at moderate and high current densities for free electrolyte cells due to their low cell resistance.

Polarization measurements have been made on solid electrolyte cells using the calcia-stabilized zirconia electrolyte investigated by Kingery (11), Wagner (12), and others (13), and which has been ap-

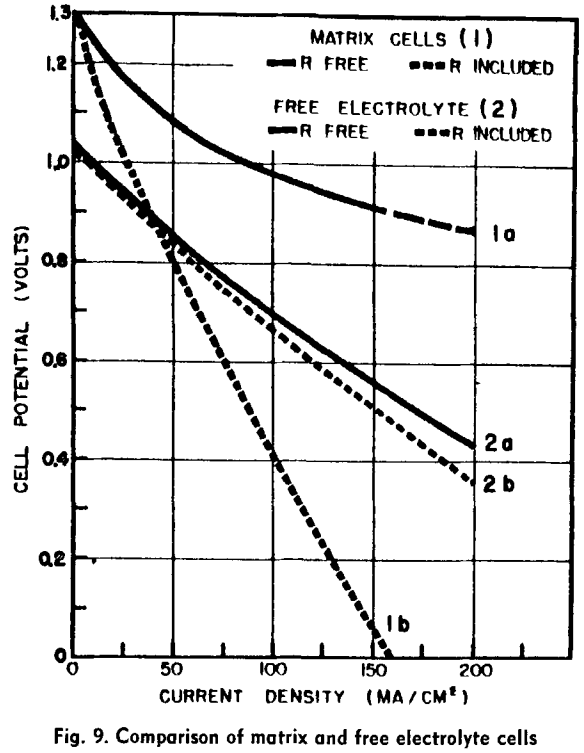

Fig. 9. Comparison of matrix and free electrolyte cells

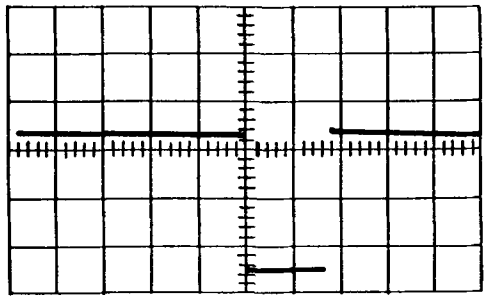

Fig. 10. Oscilloscope trace of anode-reference potential for hydrogen at 900°C and 10 ma/cm².

plied to high-temperature fuel cell technology by groups at Westinghouse (14, 15) and the Institute of Gas Technology (16). Figure 10 shows an oscilloscope trace of the decay pattern for this type of cell. The fuel gas was hydrogen, oxygen was the cathode gas, and the operating temperature was 900°C. No carbon dioxide need be added to the cathode gas since the cathode reaction is believed to be as given in Eq. [5].

$$1/2\ O_2 + 2e = O^= \qquad [5]$$

Oxide ion transport from cathode to anode occurs via oxide ion vacancies introduced in the cubic zirconia lattice by substitution of calcium (+2) cations for zirconium (+4) cations.

No activation polarization was observed at the anode at these temperatures and a current density of 10 ma/cm², although there is considerable ohmic polarization due to the high resistivity of the solid electrolyte. The electrolyte thickness was 1.5 mm, and the effective resistivity for the electrolyte and catalyst used was approximately 1000 ohm-cm.

The current density at practical operating voltages was only a few ma/cm². The high resistivity of the solid electrolyte is principally responsible for the relatively low operating level. Practical cells, therefore, would require the use of thin, impervious, solid electrolyte films.

In conclusion then, on the basis of work on matrix cells and preliminary work with gas diffusion and solid electrolyte systems, it appears that, although formidable problems remain to be solved with each approach before dependable high-temperature fuel batteries will be produced, most of these problems are of a practical nature. The output of matrix cells and solid electrolyte cells was limited principally by high cell resistance rather than other forms of polarization. The life of matrix and especially gas diffusion cells was limited mainly by the lack of inexpensive, stable materials which were able to withstand the combination of high temperature and corrosive environment.

The solid electrolyte cell because of its simplicity, apparent stability, less corrosive nature could become a practical high-temperature fuel cell system if operating levels are improved. At any rate, it appears attractive compared to the highly corrosive molten carbonate systems.

Acknowledgment

The author would like to acknowledge the helpful suggestions of Dr. K. V. Kordesch in the course of

this work and the assistance of G. R. Tucholski who carried out many of the experimental measurements.

Manuscript received Feb. 6, 1962; revised manuscript received April 2, 1962. This paper was prepared for delivery before the Detroit Meeting, Oct. 1-5, 1961.

Any discussion of this paper will appear in a Discussion Section to be published in the June 1963 JOURNAL.

REFERENCES

1. W. Schottky, *Wiss. Veröffentl. Siemens-Werken*, **14** (1935).
2. E. Baur and R. Brunner, *Z. Elektrochem.*, **43**, 725 (1937).
3. E. Baur and H. Preis, *ibid.*, **43**, 727 (1937).
4. E. Baur and H. Preis, *ibid.*, **44**, 695 (1938).
5. G. H. J. Broers, "High Temperature Galvanic Cells," Thesis, University of Amsterdam, 1958.
6. G. J. Janz and M. R. Lorenz, Tech. Report No. 2, ONR Cont. Nonr. 591-10, October 1958.
7. K. Kordesch and A. Marko, *This Journal*, **107**, 480 (1960).
8. D. Staicopoulos, E. Yeager, and F. Hovorka, *ibid.*, **98**, 68 (1951).
9. H. H. Chambers and A. D. S. Tantram, in "Fuel Cells," G. J. Young, Editor, pp. 94-108, Reinhold Publishing Co., New York (1960).
10. D. L. Douglas, *ibid.*, pp. 129-149.
11. W. Kingery *et al.*, *J. Am. Ceram. Soc.*, **42**, 393 (1959).
12. K. Kinkkola and C. Wagner, *This Journal*, **104**, 379 (1957).
13. F. Hund, *Z. physik Chem.*, **199**, 142 (1952).
14. J. Weissbart and R. J. Ruka, *Rev. Sci. Instr.*, **32**, 593 (1961).
15. J. Weissbart and R. J. Ruka, Symposium on Fused Salt Corrosion and High Temperature Fuel Cell, presented at the Electrochemical Society Meeting, Detroit, Oct. 1-5, 1961.
16. E. B. Shultz *et al*, Symposium on Fuel Cells, presented at American Chemical Society Meeting, Chicago, Sept. 3-8, 1961.

The Lithium Hydride Electrode

Maurice E. Indig and Richard N. Snyder

Delco-Remy Division, General Motors Corporation, Anderson, Indiana

ABSTRACT

The anodic character of a soluble lithium hydride electrode was studied electrochemically in the lithium chloride-potassium chloride eutectic for possible consideration as a high-energy, low-weight electrode material. The results show that current densities as high as 1.55 amp/cm^2 (10 amp/in.^{2}) can be maintained on the lithium hydride anode without appreciable polarization. Variation of coulombic efficiency and gassing studies led to the postulation of a one and two electron oxidation of lithium hydride. The oxidation was found to be quite dependent on current density and the physical nature of the grid.

Lithium hydride, molecular weight 7.95, is one of the saline hydrides with a well-known reducing character. While undergoing chemical or electrochemical reactions, the negative hydride ion can be oxidized to the H° or the H^+ state. Certainly free energy considerations allow for the one-electron oxidation. A calculation found in Latimer (1) based on the solid hydride and the metal ion gives an E° for the reaction $LiH \rightarrow Li^+ + \frac{1}{2}H_2 + 1e$ as 2.32v. In the electrolysis of molten lithium hydride by Moers (2) and later by Peters (3), it was noted that hydrogen was liberated solely at the anode, which indicated the one-electron oxidation of the negative hydride ion. However, a study by Gianatasio (4) of solid-solid reactions of lithium hydride with lithium chloride and beryllium chloride indicated the two-electron oxidation can occur. In the latter work both lithium chloride and beryllium chloride were reduced to the metals by lithium hydride with hydrogen chloride evolved as one of the products.

Although lithium hydride reacts spontaneously with water, it has been found to dissolve without decomposition in the 60-40 mole % lithium chloride-potassium chloride eutectic (5). The use of LiH in a fused salt-type battery appeared attractive due to its low molecular weight and even lower equivalent weight, based on the two-electron oxidation.

Experimental

Cell studies.—In the initial experimental work small pellet cells, which consisted of a lithium hydride anode, a LiCl-KCl eutectic electrolyte, and a $CaCrO_4$ cathode, were compacted in a dry argon atmosphere. The compaction was accomplished with a jackscrew press under 2100 kg/cm^2 (15 tons/in.^{2}) and resulted in pellets that were 0.95 cm (0.375 in.) long with an exposed electrode area of 0.97 cm^2 (0.150 in.^{2}).

The pellet cells were encased in silver cups which served as containers and electrode connectors. Activation heat was supplied externally. The pellet cells were discharged through an external variable resistor which held the cells at a constant voltage. In all the experimental work reagent grade LiH, as supplied by the Lithium Corporation of America, was used.

Single electrode studies.—In order to characterize the properties of the LiH electrode, a series of single electrode studies was conducted. Powdered LiH and dry eutectic electrolyte, 0.35 and 35g, respectively, were loaded into a 347 stainless steel crucible, which contained a nickel screen electrode of 50 mesh with an exposed electrode area of 6.45 cm^2 (1 in.^{2}) and a nickel wire reference electrode. The stainless steel crucible also served as the counter electrode. Details

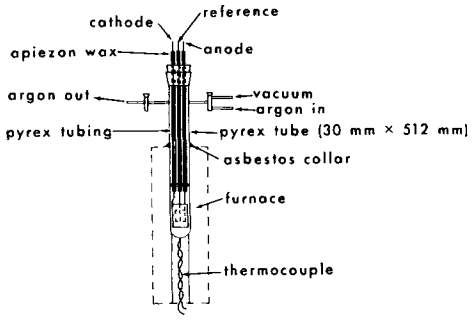

Fig. 1. Discharge cell assembly

of the cell assembly are shown in Fig. 1. The stainless steel crucible was loaded into a Pyrex furnace tube and resistively heated to 300°C under continuous vacuum. At this temperature a stream of dry argon was introduced, and the heating was continued until fusion occurred. At 380°C the LiH was anodically discharged by means of a d-c power supply. Single electrode measurements were obtained between the nickel working electrode and nickel reference electrode with a potentiometer. The potential determining species on the nickel working and nickel reference electrodes were lithium hydride and its oxidation products.

In separate runs the current was varied from 0.0775 to 1.55 amp/cm² (0.5-10 amp/in.²). In the higher current discharges from 0.775 to 1.55 amp/cm² (5-10 amp/in.²), the LiH concentration was increased to 3.3% in the electrolyte in order to increase the run time. In these discharges the argon flow was cut off, and the gas evolved during the oxidation of the LiH was collected in a 1000 ml gas buret. At open-circuit conditions, just prior to any discharge and just after termination of a discharge, the voltage between the reference and the working electrode was zero.

In addition to the nickel screen electrodes of 50 mesh size, nickel screen electrodes of 100 mesh size and nickel battery plaques of 80% porosity were used as discharge electrodes.

The coulombic efficiency was determined by considerations of the weight of a lithium hydride sample and the total coulombs passed during discharge, as compared to the theoretical coulombic capacity, based on the two-electron oxidation.

Concentration potential studies.—The effect of concentration on the potential of the LiH electrode was studied in a cell shown in Fig. 2. Nickel screen electrodes of 100 mesh size were suspended in each compartment of the cell, which contained different amounts of LiH dissolved in the KCl-LiCl eutectic. The furnace apparatus and methods of preparation were similar to those described in the constant-current discharges. Potential measurements were obtained under open-circuit conditions between 385° and 575°C.

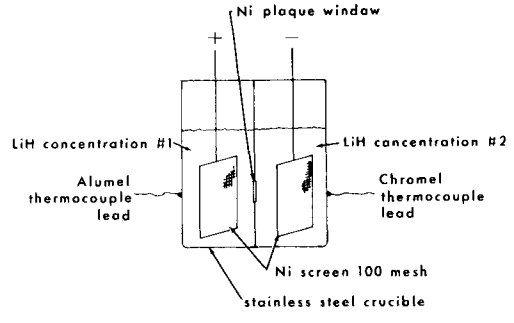

Fig. 2. Concentration cell

Results and Discussion

The Ag-LiH/KCl-LiCl/$CaCrO_4$-Ag pellet cells gave an open-circuit voltage of 2.15v. Flash currents of 3.1 amp/cm² (20 amp/in.²) could be obtained. During a typical discharge the cell voltage was held constant at 1v and in a 4-min period the current density gradually decreased from 0.775 to 0.31 amp/cm² (5-2 amp/in.²). When the cell voltage dropped below 1v, the discharges were terminated. These pellet cell discharges indicated that LiH could serve as an effective anodic depolarizer.

The effect of the different electrode materials in the constant current discharges is shown in Fig. 3, 4 and 5. In Fig. 3 it is observed that the polarization voltage, including the ohmic contribution, was higher for the 50 mesh nickel screen electrodes than for the plaque electrodes, although the effective discharge times for the screen electrodes were longer than for the plaque electrodes. In Fig. 4 the current-voltage plots indicate the polarization of the plaque electrodes was 50 mv lower than the screen electrodes throughout the discharges. The 100 mesh nickel screen electrodes had extrapolated polarization values that were in close agreement with the plaque electrodes. The slope of the current-voltage plots was 0.108 ohms. This is in excellent agreement with the 0.105 calculated resistance of the internal discharge circuit. Thus, the plateau polarization values, excluding IR drop, were constant in all the

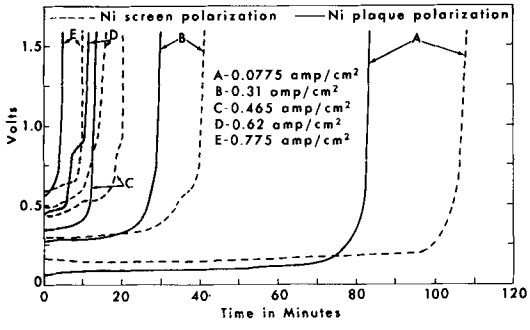

Fig. 3. Discharge curves for 1% LiH solutions at various rates

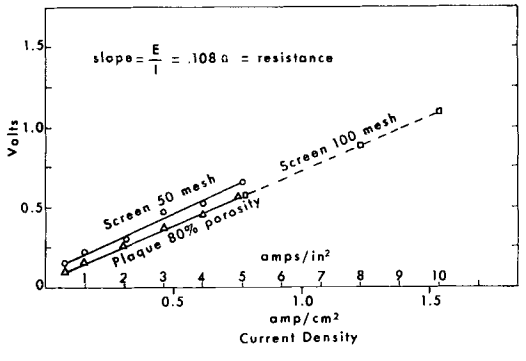

Fig. 4. Polarization voltage including ohmic contribution vs. current density.

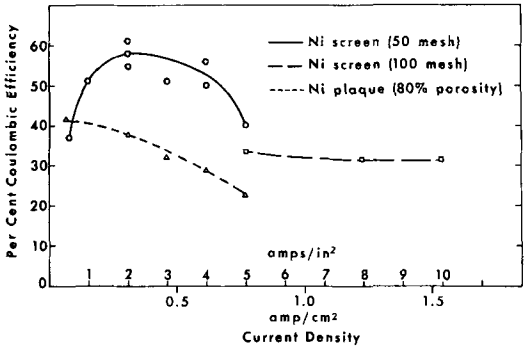

Fig. 5. Coulombic efficiency *vs.* current density

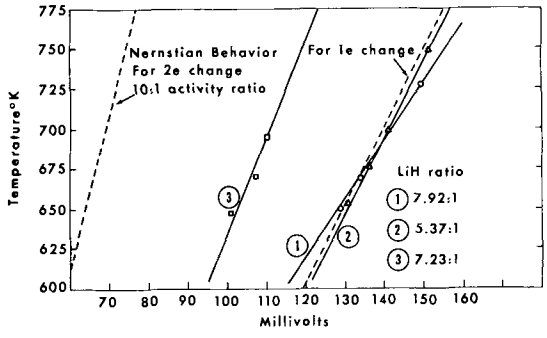

Fig. 7. Temperature *vs.* voltage for concentration cell

measured cases and had values of 50 mv for the plaque and 100 mesh nickel screen electrodes and 100 mv for the 50 mesh nickel screen electrode.

The screen electrodes gave consistently higher coulombic efficiency than the plaque electrodes as shown in Fig. 5. Based on the proposed two-electron oxidation, a coulombic efficiency of 71% was calculated for a particular discharge. The variations of the coulombic efficiency and the large amount of hydrogen gas produced during discharge suggested that two competing reactions were occurring. These may be given as:

$$LiH \rightarrow Li^+ + H^+ + 2e \qquad [1]$$

$$LiH \rightarrow Li^+ + \tfrac{1}{2}H_2 + 1e \qquad [2]$$

It is evident that reaction [1] would result in twice the coulombic efficiency of reaction [2]. In order to verify the proposed reactions, a V-tube stainless steel apparatus, shown in Fig. 6, was built to measure hydrogen evolution at the anode or cathode under various loads. If hydrogen was detected at the anode, reaction [2] had occurred. If hydrogen was detected at the cathode, reaction [1] had occurred followed by a reduction of the hydrogen ion. It can be said that hydrogen was produced at both the cathode and anode compartments. However, the gassing at the cathode compartment was slight at low current densities and reached a maximum at 0.31 to 0.465 amp/cm² (2-3 amp/in.²), which corresponds to the maximum in Fig. 5, the coulombic efficiency curve for the 50 mesh nickel screen.

The effect of concentration on potential can be seen in Fig. 7. In this case, if a one-electron process is assumed, the slope of the lines is 2.30 R/F, and if concentrations are substituted for activities, the behavior is essentially Nernstian. The dashed lines represent Nernstian behavior for the one- and two-electron processes assuming a 10 to 1 activity ratio. It can be noted that the behavior under open-circuit conditions closely approaches the one-electron process.

One of the most interesting and puzzling facts to emerge from the data is the difference in coulombic efficiency between the LiH electrodes of 50 mesh nickel screen and the plaque electrodes. Apparently the one-electron oxidation of LiH takes place on the plaque electrodes, and a mixed anodic oxidation occurs on the 50 mesh screen, the two-electron process occurring most readily at a current density between 0.31 to 0.465 amp/cm² (2-3 amp/in.²).

The lower polarization values on the plaque and 100 mesh screen are explained by their larger effective surface area. However, the increased polarization on the 50 mesh screen electrodes could drive the oxidation of LiH toward the two-electron process and thus account for the higher coulombic efficiency.

A calculation of $i \cdot t^{1/2}$, where i is current in amp/cm² and t is time in seconds, at the knees of the discharge curves for the 50 mesh Ni screen, led to a constant average value of 10.2. This suggested that the oxidation is a diffusion-limited situation and, when the hydride concentration in the bulk electrolyte decreases below a certain value, polarization becomes appreciable. At current densities below 0.155 amp/cm² (1 amp/in.²) this model breaks down. This is not unexpected as, at low current densities, diffusion limitations would become negligible.

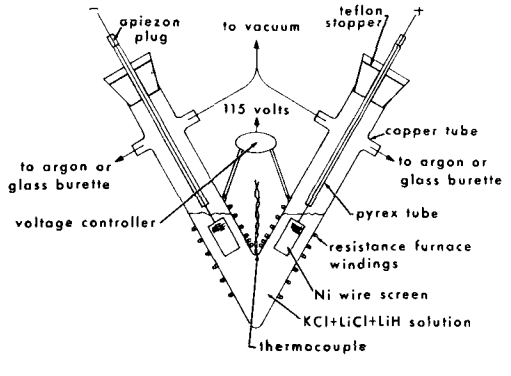

Fig. 6. V-tube cell assembly

Acknowledgment

The authors wish to thank Dr. J. J. Lander for suggesting the problem and for helpful advice during the investigation.

Manuscript received March 8, 1962; revised manuscript received May 4, 1962. This paper was prepared for delivery before the Detroit Meeting, Oct. 1-5, 1961.

Any discussion of this paper will appear in a Discussion Section to be published in the June 1963 JOURNAL.

REFERENCES

1. W. M. Latimer, "Oxidation Potentials," 2nd ed. p. 35, Prentice-Hall, Englewood, N. J. (1956).
2. K. Moers, *Z. anorg. u. Allgem. Chem.*, **113**, 179 (1920).
3. K. Peters, *ibid.*, **131**, 140 (1923).
4. M. Gianatasio, Thesis, Polytechnic Institute of Brooklyn, June 1936.
5. D. W. Pearce, R. E. Burns and E. St. Clair Gantz, *Proc. Indiana Acad. Sci.*, **58**, 99 (1949).

Crystallogenesis in the Forming of Plates for the Lead-Acid Storage Battery

A. C. Simon and E. L. Jones[1]

United States Naval Research Laboratory, Washington, D. C.

ABSTRACT

Changes in microstructure have been observed during the forming of the positive and negative plates which provide clues as to the optimum conditions for formation. The microstructure produced was found to be dependent on the conditions under which forming took place. The conversion to lead dioxide in the positive plate was found to be initiated on the surface of a definite type of crystal, as yet not identified. The quantity, size, and shape of this crystal varied with the temperature and specific gravity of the electrolyte and with the current density employed. The indications were that a basic sulfate crystal was being converted directly to lead dioxide, without change in external form, through some solid-state reaction. The conversion to lead in the negative plate was definitely by solution of the lead sulfate and deposition of reduced lead. The form and size of the lead crystals in the negative could also be varied with method of forming, but not to the extent of those in the positive plate. While there was indication that subsequent life of the positive plate might depend on the microstructure developed during forming, there was no such correlation found for the negative plate.

Plates for lead-acid storage batteries of the type used for automotive purposes usually have as a support a lead alloy grid into which is spread a pastelike material consisting of a mixture of lead oxides to which sufficient dilute sulfuric acid has been added to produce a workable paste. Reaction of the oxides with the sulfuric acid produces a mixture of lead sulfate and basic lead sulfates that sets the paste into a cementlike mass. Electrolysis in dilute sulfuric acid then produces an oxidation to lead dioxide at the positive plate and reduction to a spongelike mass of lead crystals at the negative. The chemistry of this process has been very thoroughly investigated, but the physical changes that accompany these reactions have been largely ignored, and little or no attempt has been made to determine the crystallogenesis in the process.

Using the methods that have been described previously (1) an attempt was made to study the changes in microstructure that accompany the so-called forming, or conversion of the lower oxides of lead to lead dioxide and sponge lead. The experimental methods were extremely simple, and hindsight has shown that the microscopical observations should have been supplemented with data concerning single electrode and cell potentials during operation, the capacities developed by the various treatments, etc. These derelictions will be remedied in future investigations, but at the time this experiment was begun it was intended only to investigate the suitability of the method. The wealth of information obtained from the study of the few samples prepared was far beyond expectations and produced more questions than could be answered with the limited data that had been recorded concerning the experimental conditions. Experimentation is continuing under conditions conducive to the attainment of more complete data, and the results will be reported. Meanwhile, in view of recently published work by other investigators it appears advisable to report on this phase of the investigation and to point out its possible correlation with their data.

As will be shown in the description of the experimental results and subsequent discussion, the following observations, among others, were made which are considered of prime importance in influencing the course of future investigation.

1. There were observed to be two or more distinct species of crystal present in the positive plate. These could be formed either during mixing and drying or at a very early stage of formation. These separate crystal species could be readily distinguished by microscopic examination because of radically different crystal habit and chemical reactivity. They have not, as yet, been separated and identified with a definite chemical composition, but are assumed to be among the forms of sulfate which have been found in unformed battery paste by various workers. These forms are: normal lead sulfate, $PbSO_4$; monobasic lead sulfate, $PbSO_4 \cdot PbO$; the monohydrate of lead tribasic sulfate, $PbSO_4 \cdot 3PbO \cdot H_2O$; and tetrabasic lead sulfate, $PbSO_4 \cdot 4PbO$.

2. One of these crystal forms, in the unformed positive plate, consisted of needlelike or rectangular crystals, usually with much greater length than breadth. The conversion to lead dioxide was always observed to initiate on the surface of crystals of this type, which were in contact with the metal grid, and to spread from one crystal to another of this type at points of contact. The crystals were thus converted into lead dioxide without change of form. Crystals of this type will be referred to as type A in the subsequent discussion. From evidence accumulated by

[1] Died March 1, 1962.

others it is concluded that the large type A crystals must consist of either the monohydrate of tribasic lead sulfate, $PbSO_4 \cdot 3PbO \cdot H_2O$, or the tetrabasic lead sulfate, $PbSO_4 \cdot 4PbO$. After crystals of this type had been converted to lead dioxide there was a slower but continuous conversion of another type of crystal also found in the unformed paste.

3. This second form of crystal in the unformed positive plate always consisted of very small, regular polyhedrons of nearly equal size which were not changed in size, shape, or quantity by any method of forming used in the experimental series. This crystal form, subsequently referred to as type B, appeared to convert to lead dioxide with greater difficulty than did the type A crystals, and was converted only after a long time and after the prior oxidation of the type A. It is believed that this type of crystal represented either monobasic lead sulfate, $PbSO_4 \cdot PbO$, or normal lead sulfate, $PbSO_4$.

4. It was noted that the lead dioxide that formed on the surface of the large crystals of rectangular or needlelike form (type A) was always harder and more dense than that which formed on the small regular polyhedrons (type B). Evidence accumulated by others supports the assumption that α-PbO_2 is formed on the type A crystals while β-PbO_2 is formed on the type B crystals.

5. The large rectangular or needlelike crystals (type A) were sensitive to the forming conditions, and the size, shape, and quantity of these crystals could be altered considerably by changes in temperature, specific gravity of electrolyte, or current density. Under certain conditions the size and shape of these crystals became such that, on formation, the α-PbO_2 that formed on their surfaces created a hard, dense network or cellular structure throughout the active material.

6. Examination of cycled and floated plates obtained from commerical sources indicated that this network remained unchanged by service conditions which suggested that the creation of such a cellular structure would aid materially in positive plate active material retention, and it has been found by examination of a limited number of commercial plates that active material retention is indeed better in the presence of such a structure.

It should be realized that the experimental data from a microscopic examination of this sort consist of numerous photomicrographs which are best examined simultaneously or in various definite combinations to detect crystallographic changes. The limitations imposed by publication require a condensed written description that is admittedly confusing and lacking in conviction. For those sufficiently interested, more complete reports with additional illustrations are available (1) which cover various phases of this work.

The reminder should also be included that this series of experiments, dealing with the mechanism of forming, was performed on automotive type plates of one composition and manufacture only. Preliminary examination of other types of plate indicate that, in general, their crystallogenesis is somewhat different, but forming behavior is similar to that outlined for this plate. Exceptions have been found, however, even in such a preliminary examination so that it would be unwise to regard this behavior as universal.

Experimental Procedure

The microscopical method was based on the impregnation of samples, obtained at various stages in the forming process and under various controlled conditions of forming, with an epoxy resin and the subsequent examination at both low and high magnification of the microstructure revealed by sectioning and polishing the specimens. For convenience the experiment was divided into two parts. The first dealt with an examination of the changes in structure that occurred as the forming process proceeded, the second with the changes that could be induced by altering the forming conditions from those commonly employed by industry.

For the first part of the experiment a series of cells were constructed each consisting of one positive and one negative plate separated by a distance of approximately 1.3 cm. These plates were obtained in an unformed but dried condition from a manufacturer of storage batteries. The electrolyte consisted of sulfuric acid diluted with water to a specific gravity of 1.05. No effort was made to control the temperature of this experiment, but it remained fairly constant at about 27°C.

Following the information given by Vinal (2), the current density used was 0.25 amp/dm^2 (approximately 2.5 amp/ft^2). The cells were connected in series so that the same current passed through all. A cell was removed at ½-hr intervals during the first 8 hr, at 1-hr intervals for the next 4 hr, and finally at 2-hr intervals until no further change could be detected. The plates were thoroughly washed immediately after removal and after drying were impregnated with an epoxy resin, using vacuum. The plates were then cut in such a manner that sections could be obtained across the grid thickness both horizontally and vertically and also parallel to the plate surface but at varied depths beneath the surface. In this manner and after suitable polishing a rather complete picture of what had happened could be obtained.

To produce the second series of samples individual cells were prepared as in the previous case. The cells were arranged in groups with each group having acid of a different specific gravity, ranging from 1.05 for the lowest to 1.45 for the highest. One cell from each acid group was then placed in a constant temperature bath, and these cells when connected in series were all operated at the same current density. This was repeated at current densities of 0.023, 0.23, and 2.3 amp/dm^2. The water bath was then raised to a higher temperature and the process repeated with a new set of samples taken from each acid group as before. Temperatures employed varied from 4° to 80°C. The time that current flowed was so adjusted that regardless of current density each cell received the same total quantity of electricity. An automatic leveling device added water to maintain the electrolyte at constant level. In this and also the previously described series the unformed plates were allowed to

stand for 30 min at room temperature in electrolyte of the same concentration as employed in the experiment to insure that the plates were thoroughly wet with electrolyte and that gas evolution, apparently from carbonates which had formed in the dried plate, was finished so that electrolyte could enter the pores of the plate. As mentioned above all cells received the same total quantity of electricity, an amount selected so that no cell would have plates so completely formed as to make observation and comparison difficult and which would result in approximately one-third the amount required for theoretically complete formation.

As before, the samples were prepared for microscopical examination immediately on removal from the electrolyte. The samples were compared for similarities and differences at various magnifications ranging from a low of 13 diameters to a high of 1000 diameters to avoid the possibility of overlooking any feature because of its magnitude.

Observations

The progress of the forming process, the accompanying changes in color, and the variation in the relative amount of lead dioxide and lead produced under different conditions of forming were readily visible to the unaided eye on examination of the polished sections, but the details of the process were not revealed until microscopic examination was made of each specimen. Initially the unformed positive plate was a light yellow color while the unformed negative appeared gray. Under the microscope, using polarized light, both the positive and negative plates appeared to be yellow, although the negative was of a much lighter hue. The initial soaking caused considerable increase in the amount of sulfate which was made evident to the unaided eye by a fading of the yellow color in the positive plate, but which did not become evident in the negative until examination under considerable magnification. Under the microscope the resulting white or light yellow background caused the formations of the reddish-brown lead dioxide or metallic lead to stand out clearly.

The Mechanism of Formation—Positive Plate

In both the positive and negative plate the conversion to lead dioxide and lead, respectively, invariably began at the grid member. At low magnification the positive plate reaction was observed to proceed outward from the grid as a fairly uniform cylinder of lead dioxide with the exception that reaction appeared to slow down as the surface of the plate was reached, so that the cylinder became ovoid with its greater diameter parallel to the plate surface. There was a thin surface layer in which conversion to lead dioxide did not take place until quite late in the process so that the last portions of the plate to form were at the surface and at points midway between grid members. The material within the cylindrical area of reaction was not uniformly converted to lead dioxide, but in cross section presented a fernlike appearance as if the reaction were proceeding by the formation of branched filaments of lead dioxide. These features are illustrated in Fig. 1.

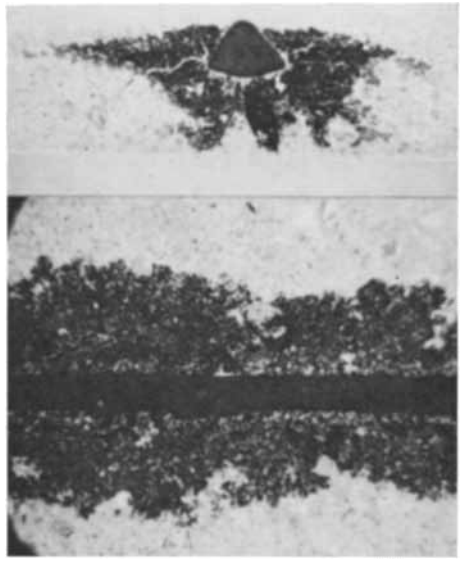

Fig. 1. Upper photograph: Cross section through the positive plate. The light areas represent unformed positive paste, the dark areas result from conversion of paste to reddish-brown PbO_2. Dark triangular area at top center is cross section of small lead alloy horizontal grid member as is also the dark line bisecting the lower photograph horizontally. Lower photograph: Section of same plate parallel to surface. Formation took place at room temperature, in 1.05 sp gr electrolyte, at 0.25 amp/dm^2 current density. Total time of formation was 6 hr. Note that cross section gives less misleading view of total area of formation than does plane section since latter gives widely varying areas at different depths. Magnification approximately 8X.

Examination at higher magnification revealed that the formed portions of the positive plate were made up of at least two varieties of crystal. Most numerous were the polyhedral crystals of nearly equal size, herein designated as type B. These were interspersed with larger crystals of a different configuration, herein designated as type A.

The small, polyhedral crystals, type B, were usually quite regular in form, but so small (2 or 3μ) that the general impression was of a rough sphere. These polyhedral crystals predominated under all of the conditions where formation to lead dioxide had occurred. Crystals identical in size and shape to these but consisting of sulfate were found in the unformed portions of the same plate and in the original dried paste of the plates as received from the manufacturer. These crystals did not vary significantly in size, shape, or number under any of the forming conditions used. It appeared that the polyhedral crystals of sulfate were being converted directly into lead dioxide without external change of form. It was found moreover that this conversion occurred subsequent to and with greater apparent difficulty than that which took place on a second form of sulfate present in the paste.

This second form of crystal (type A) appeared usually in the formed areas of the plate as long needlelike or rectangular crystals of lead dioxide. [The excellent electron micrographs of Buskirk, Boyd, and Smith (3) show thin plates of rectangular form at the surface of formed positive plates. There is a possibility that the crystals herein described may be of a similar form and appear needlelike only as a consequence of having been sectioned edgewise.

While the term needlelike will appear frequently in the subsequent discussion as a description of the actual appearance of the crystal in the section, the above possibility should be retained in mind.] This type A crystal varied in size, shape, uniformity, and quantity depending on the conditions under which forming took place, as will be discussed in a later section. The size of these type A crystals varied with the conditions from a maximum of about 150μ in length when long and needlelike to a minimum of about 10μ when short and rectangular. Crystals similar in size, shape, and frequency of occurrence were always found in the unformed portions of the same plate, indicating that these crystals were being converted directly from a sulfate to type A lead dioxide crystals without change in external form.

In the dried unformed plates as received from the manufacturer, the small, polyhedral crystals of type B predominated. Only a few of the type A crystals were formed and these were all long, slender needles with no hint of the rectangular structure seen in some of the plates after forming under certain conditions. Examination of unformed plates from several manufacturers, however, disclosed that in some of these the rectangular crystals of large size (type A) predominated. Thus it appears that the presence of the type A crystals can be induced either by certain conditions associated with paste composition, temperature, time of drying, specific gravity of the acid, etc., during pasting, or by the control of similar conditions in the forming process. In the present experiment it was certain that crystal structure of the crystals of type A was modified (and, in some instances, the number of crystals was changed) either during the soaking prior to passage of current or in that period at the beginning of current flow when no conversion to lead dioxide could be detected.

Fig. 2. Large needlelike crystals of what is presumed to be a basic sulfate overlaid with hard PbO_2. Each needlelike crystal is surrounded by a slightly less dark area of soft PbO_2 that formed on crystals of a much smaller type and at a later time than the overlay on the needlelike crystals. The white or very light areas represent unformed paste. Compare with Fig. 3. Formed at 4°C, in 1.25 sp gr electrolyte and 0.25 amp/dm^2 current density. Photographed by polarized light. Magnification approximately 650X.

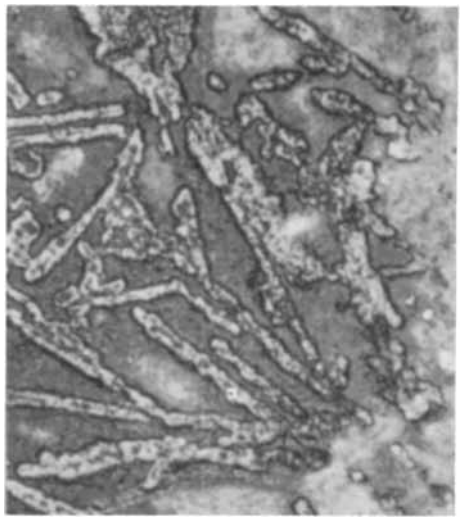

Fig. 3. More detailed view, of crystals similar to those shown in Fig. 2, obtained by relief polishing. The hard dense PbO_2 stands in relief, outlining the original crystal of basic sulfate, and because of its hardness is brightly reflecting. The softer PbO_2 surrounding these needles is featureless and dark in color while some as yet unformed paste may be seen as a featured, light colored material at upper and lower right margin. Photograph represents the type of crystal obtained when positive plate was formed at 30°C, in 1.05 sp gr electrolyte and 0.25 amp/dm^2 current density. Magnification approximately 650X.

It was also found that the initial oxidation always began on the surface of the larger crystals of type A, forming a hard dense layer of lead dioxide that caused these crystals to appear much darker than the small polyhedrons when illuminated by polarized light and to stand outlined in relief when subjected to relief polishing and oblique illumination with unpolarized light, Fig. 2 and 3. The reaction spread promptly and rapidly from one to another of this type A crystal wherever there were points of contact either with the grid or other crystals on which this lead dioxide layer had already formed. At a later stage in the forming reaction, and much more slowly, the small polyhedral sulfate crystals (type B) were converted to a softer, lighter hued lead dioxide. The fernlike appearance of the conversion boundary observed at lower magnification was a result of the initial stage of the reaction rapidly spreading through a thinly dispersed mass of the large crystals to cover a fairly large area while some of the small polyhedral grains in the spaces between these larger crystals remained unchanged at this stage. As a consequence an area of small polyhedrons adjacent to each large crystal was converted to lead dioxide which was sufficient in extent both to mask the outline of the original large crystal and to make the area visible at low magnification, but insufficient to completely fill the area between the points of primary reaction. (Since the conversion of both the large needlelike, and the small polyhedral crystals of lead sulfate to lead dioxide appeared to take place without change in external form of the crystal, the terms type A and type B will be used to identify the corresponding crystal shape in both its sulfate and dioxide form.)

It was also established that the presence of the large type A crystals was not absolutely essential for the conversion of the small polyhedral sulfate crys-

tals to lead dioxide crystals of type B. However, in the absence of the former, the process was extremely slow and required a much greater total quantity of electricity to convert a given area of plate than when they were present. For reasons that will be outlined later in the paper it is assumed that the initial formation process that resulted in the production of hard, dense lead dioxide on the surface of the large crystals produced the rhombic form of lead dioxide, α-PbO_2, whereas the later conversion of the small polyhedral crystals to a softer, lighter colored lead dioxide produced the tetragonal form, β-PbO_2.

Effect of Changing the Forming Conditions— Positive Plate

As to the second part of the experiment, that of studying the effect of changes in forming conditions, very definite and significant changes were noted, especially in the positive plate. In the first place, although all of the samples received the same total quantity of electricity, there was a decided difference in the amount of lead dioxide formed. It would be better, perhaps, to say that the area of lead dioxide in comparable sections varied rather than the amount since some doubt remains whether those plates that exhibited the greatest apparent coverage by lead dioxide would have indeed had the greatest capacity. This is because unformed material remained in all reacted areas, and in some cases reacted areas of small extent had also a noticeably lesser amount of unreacted material within this area or, in other words, a much higher density of reacted particles per unit area. Nevertheless, the size of the area converted to lead dioxide appears to be a good means of judging the efficiency of the process for several reasons. In order to reach the plate interior where reaction begins the electrolyte must diffuse through a relatively nonporous paste, consisting largely of lead sulfate which is a very poor conductor of electricity as well. Those particles that are converted to lead dioxide immediately become a much better conductor, and because the lead dioxide has a lesser specific volume than the lead sulfate the plate becomes more porous to the flow of electrolyte. The greater the area of formation for a given total current, the more easily should the balance of the unformed material be converted to lead dioxide because of the more extended circuit paths and greater porosity under these conditions. A careful study at higher magnification indicated that even with more reacted particles per unit area those plates with a small total area of reaction could not be as completely formed as those with a larger area of reaction.

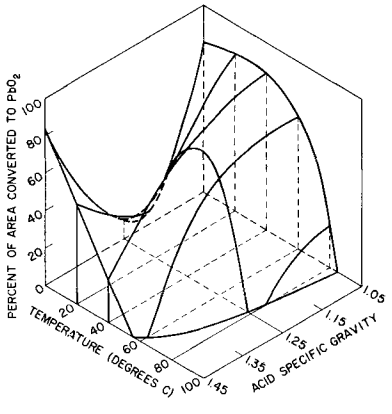

Fig. 4. This graph shows how the area of formed material in the positive plate varied as the specific gravity and temperature were changed although all samples received the same total quantity of electricity, using a current density of 0.025 amp/dm².

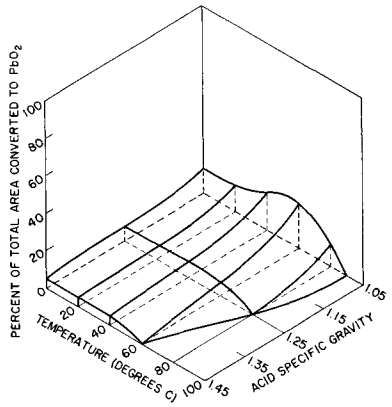

Fig. 5. As for Fig. 4, this graph shows variation of area of formed material in the positive plate with variation of temperature and specific gravity, but at a higher current density. The total quantity of electricity that these samples received was the same as in Fig. 4, but the much lower average area of formation was apparently caused by the use of the higher current density of 0.25 amp/dm².

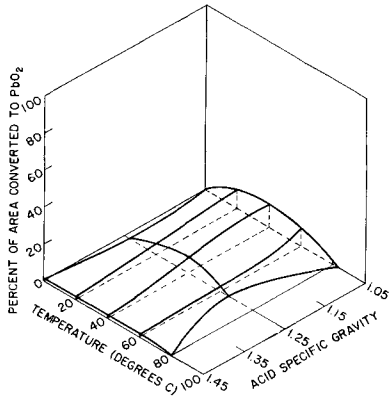

Fig. 6. Graph similar to Fig. 4 and 5 but showing the lowered area of forming in the positive plate when a current density of 2.5 amp/dm² was used. Comparison of Fig. 4, 5, and 6 indicates a maximum in area of formation at temperatures in the region of 40°-60°C, at the lowest specific gravity of 1.05 and at the lowest current density used, 0.025 amp/dm².

For the purpose of evaluating results, therefore, an estimate was made of the area of the plates involved in the forming reaction, ignoring the actual density of formed particles within this area. From these estimates, based on an averaged value of the plate surface, the sections parallel to the surface and cross sections, the graphs shown in Fig. 4, 5, and 6 were prepared. Each graph represents the variation in the total area of formed material with changes in acid specific gravity and temperature when the current density and total current are maintained constant. The successive graphs show the change in area, at a given acid specific gravity and temperature, with change in current density. The results indicate that the area of formation continuously increased with decreasing specific gravity of electrolyte and with

decreasing current density. In general the maximum area of formed lead dioxide, for a given specific gravity and current density, appeared between 40° and 60°C.

The microstructure of the positive plate was also found to vary with the conditions used in forming. This was not true of the small polyhedral crystals previously referred to as type B which apparently retained the same size and shape regardless of conditions, but applied to the larger crystals of type A on which the forming process appeared to initiate and which changed shape, size, and frequency of occurrence with changes in conditions. The subsequent description of the changes in crystal form is incomplete. There were not only variations in form that are not included, but variations in size and frequency of occurrence for a given type that would be superfluous to describe. The main point to be made is that change from one form to another of the type A crystal was reproducibly obtained and that definite correlation could be drawn between experimental conditions and the obtained microstructure. It might be wise to reiterate that the subsequent description refers only to the changes that occurred in the larger crystals of type A that produce the initial and harder form of lead dioxide, and not to the small polyhedral crystals that produced the subsequent softer form of lead dioxide, and which apparently were not influenced by the forming conditions.

The large crystals of lead dioxide fell into several main categories, and as has been mentioned, varied in size from 10 to 150μ. At the lowest current density, temperature, and specific gravity, Fig. 4, the area of formed lead dioxide was near the maximum. Yet under these conditions the lead dioxide so formed did not seem to be much harder than the original lead sulfate, because relief polishing produced only a uniformly smooth section in which the unformed areas could not be distinguished from those where formation to lead dioxide had occurred. (Relief polishing, done on a very soft lap with light pressure, tends to preferentially remove the softer material, leaving the harder exposed in relief on the surface. Any such irregularity in surface can be easily detected by using oblique illumination for the microscope.) It was found, however, that this apparently soft material contained large numbers of extremely long and thin needlelike crystals of lead dioxide, Fig. 7. These only became visible when the section was examined by polarized light. It is believed that these long crystals consisted of the hard, dense modification of lead dioxide, but that because of their thinness they could not be resolved in the relief polishing process. It is significant that in the as yet unformed portions of the same plate there were found sulfate crystals of similar shape and size.

When samples were compared in which the temperature and current density used in the forming had been the same, but in which the specific gravities of electrolyte had differed, the area of formation was found to decrease with each increase in specific gravity. At the same time the crystals of type A in the microstructure were found to become increasingly shorter, thicker, and more rectangular in outline as the specific gravity increased to about 1.25. As the crystals became shorter and more rectangular in shape they also increased in thickness, and it was found that a harder layer of lead dioxide had formed on the surface of the crystal than on the interior and that this hard material outlined the boundaries of the original crystal, Fig. 8. Thus, each increase in specific gravity of electrolyte produced structures that were more clearly outlined and had a more definite demarcation between the outer coating and the interior. Above a specific gravity of 1.25 this demarcation became increasingly less distinct, and at the highest value of specific gravity the formed area was small

Fig. 7. Illustrating the very long and thin needlelike crystals produced at low specific gravity of electrolyte, 1.05, and low temperature, 4°C. Such crystals were visible only by polarized light. These were produced at a current density of 2.5 amp/dm^2. At lower current densities they are even longer, but more difficult to see. Dark line at left is a portion of the grid. Compare these crystals with those of Fig. 2. Magnification approximately 650X.

Fig. 8. Illustrating the more rectangular type of crystal obtained with increasing specific gravity of electrolyte. Compare this figure where forming was at a specific gravity of 1.25 with Fig. 3, where the specific gravity was 1.05. Current density and temperature were as in Fig. 3. A portion of the grid metal alloy with segregated light-colored particles of antimony appears as a dark material at the left side of the photograph. Magnification approximately 650X.

and appeared to be uniformly soft. In this case no large crystals could be found with either relief polishing or polarized light, and it must be concluded that conditions were unfavorable to their formation. Under these conditions only the small polyhedrons were detected in either the formed or unformed portions of the plate.

It was found that for a given specific gravity of electrolyte and current density that the area of formation was at a maximum between 40°-60°C and decreased at both higher and lower temperatures. Temperature also influenced the microstructure. Thus, if at the lowest temperature there were present only the long needlelike crystals similar to those shown in Fig. 7, these were replaced at a higher temperature by the shorter, harder, more rectangular forms shown in Fig. 8, but usually of larger size. This latter form was almost invariably found at those temperatures where the area of formation was at a maximum. At still higher temperatures the open rectangular forms were replaced by large rough, irregularly shaped particles that had a uniform hardness throughout their cross section, Fig. 9, but which were not very numerous. In general, the effect of a temperature increase was to produce shorter, thicker crystals, with a more irregular outline than those formed under otherwise equivalent conditions but at a lower temperature.

Comparison of Fig. 4, 5, and 6 shows that with a given temperature and specific gravity there was an increasingly large area of formation as the current density was decreased. The microcrystals formed at the three current densities employed had roughly the same shape when compared at equivalent temperature and specific gravity of electrolyte except that the individual crystals were much smaller and more numerous for each increase in current density.

Mechanism of Formation—Negative Plate

The process of formation in the negative plate followed a quite different course from that in the positive. Initially reduction took place at the negative grid just as oxidation also originated at the grid of the positive plate. But whereas the lead dioxide formed a more or less uniform cylinder of reaction around the grid the negative plate reaction proceeded at once to the surface by the most direct route. This route was usually along both sides of any cracks that opened to the surface. Wherever the reaction reached the surface it spread rapidly to cover it, so that the two surfaces of the plate were quickly converted to crystals of lead although the interior of the plate remained unformed until long afterward, Fig. 10. This was quite the opposite to what occurred in the positive plate, and erroneous conclusions would have been obtained if the plate had not been sectioned.

In the original dried, unformed, negative plates used for these experiments only the small polyhedral lead sulfate crystals were found. In the formed or partially formed plates this also appeared to be the case. During the forming these crystals were observed to become translucent and finally to dissolve in the immediate vicinity of lead crystals already formed or at the grid. Under the conditions used for the first part of the experiment, where a study was made of sections removed at various stages of the forming process, the lead crystals that formed at the grid or on other lead crystals in contact with the grid were observed to have long needlelike structure and to be so densely intermingled as to make difficult individual examination, Fig. 11.

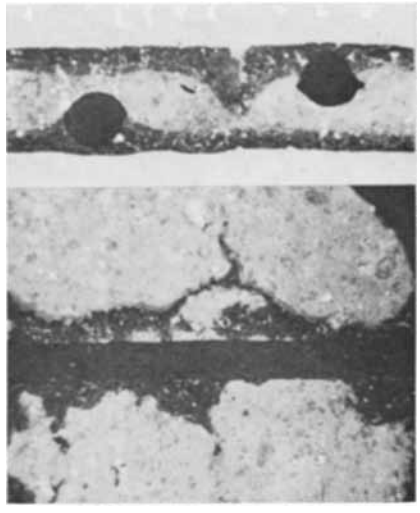

Fig. 9. The large irregular crystals that appear at high temperature. Note that these are hard and dense throughout and are surrounded by an area of the softer lead dioxide, which is shown as the dark featureless material surrounding the large grains. Do not confuse this with the dark appearing grid at the left of the picture. Unformed paste also appears at the right. Formed at 80°C, specific gravity and current density were as in Fig. 8. Magnification approximately 650X.

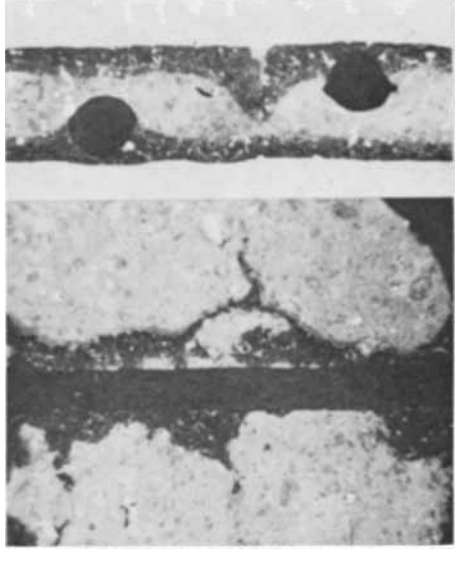

Fig. 10. Upper photograph: Cross section through negative plate after 6 hr forming time, showing how surface is formed prior to the interior. The two oval dark areas are cross sections through grid members as is the dark line that bisects the lower photograph horizontally. Lower photograph: Plane section of negative plate with 2 hr forming time. Note that formation does not proceed uniformly from the grid, but preferentially along the sides of cracks that allow entrance of electrolyte. Conditions of formation the same as for Fig. 1. Magnification approximately 8X.

Effect of Changing the Forming Conditions—Negative Plate

In the negative plate it was found that the greatest area of formed material was at a specific gravity of electrolyte of about 1.25, between 30° and 60°C and

Fig. 11. Appearance of lead crystals in the negative plate. Such crystals are scattered fairly uniformly throughout the area where formotion has occurred. The area containing such crystals increased with the time of forming rather than the number of crystals per unit area. As a result the material in the area between crystals, as shown here, would not be converted until quite late in the process. Toward the end of the forming period, however, the number of crystals of lead would enormously increase and would no longer be individually distinguishable. Magnification approximately 200X.

that current density did not have very much effect when the temperature and specific gravity was as stated above, Fig. 12, 13, and 14. As can be seen from Fig. 12 the lowest current density did cause an increase of the area of formed material when forming took place in low specific gravity electrolyte, but the amount does not appear to be significant. The combination of high temperature and high acid gravity not only produced no forming but caused actual shedding of plate material.

When the negative plates were examined at high magnification it was found that considerable change occurred in the structure of the lead crystals when the conditions of forming were varied. Since the lead crystals were definitely formed by deposition from solution after the dissolution of the necessary amount of lead sulfate their structure did not depend on the presence of any particular kind of crystal but only on the availability of lead ion.

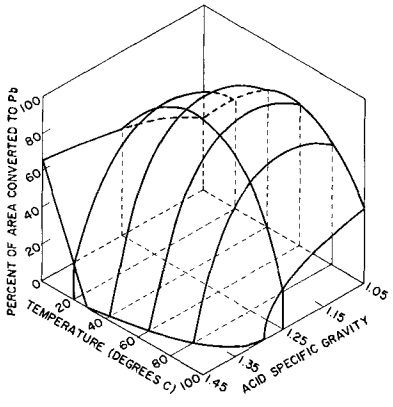

Fig. 12. Graph showing that a maximum occurred in the area of formed material of the negative plate when the electrolyte had a specific gravity of between 1.15 and 1.25 and was used at about 40°C. The same total quantity of electricity was employed for all samples and the current density was 0.025 amp/dm².

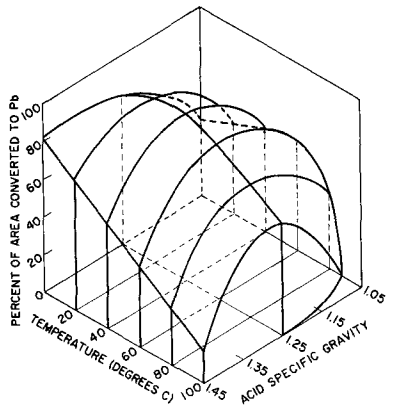

Fig. 13. Graph showing a very slight increase in area of formed material over the previous figure, but here the current density was increased to 0.25 amp/dm².

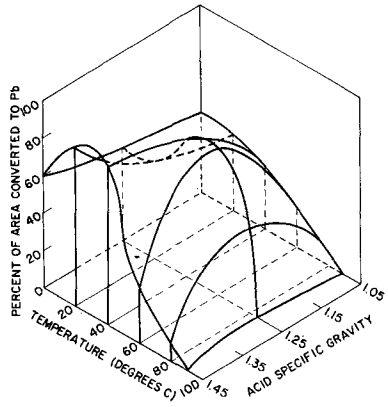

Fig. 14. Graph showing the somewhat lower area of formed material obtained when the current density was further increased to 2.5 amp/dm². Comparison of Fig. 12, 13, and 14 with Fig. 4, 5, and 6 indicates that current density had a more pronounced effect on positive plate formation than on that of the negative plate.

Two main types of structure were observed. Depending on the conditions employed the lead crystals were either long and needlelike or roughly spherical. It was suspected that the needlelike crystals at times had a branched structure, but they were usually so closely intermingled that it was difficult to determine this, Fig. 15. For the same reason there was a possibility that the so-called spherical crystal, since it showed no clearly defined faces, might in reality be a mass of needlelike filaments radiating from a common nucleus but with each needle so fine as to be below the limit of optical microscope resolution thus giving the impression of a solid spherical object, Fig. 16.

The major change in crystal appearance produced by varying the forming conditions was to alter the size of these crystals and to convert one type into the other. The largest crystals of the needlelike appearance were produced when temperature, specific gravity, and current density were all at the minimum of the series. The crystals did not appear very sensitive to changes in temperature within the range investigated. There was a slight tendency, however, for the average crystal size to become smaller as the temperature was increased. Change in the specific gravity of electrolyte had the most effect on crystal appearance. When the specific gravity was increased

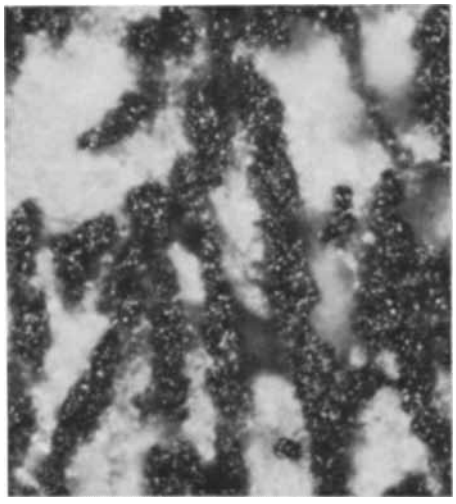

Fig. 15. View of the unusually large dendritic type crystals of lead formed in the negative plate at 4°C, an electrolyte specific gravity of 1.05 and at a current density of 0.025 amp/dm^2. The long lead filaments appear to have an irregular and porous surface that may possibly consist of much smaller secondary filaments. Magnification approximately 650X.

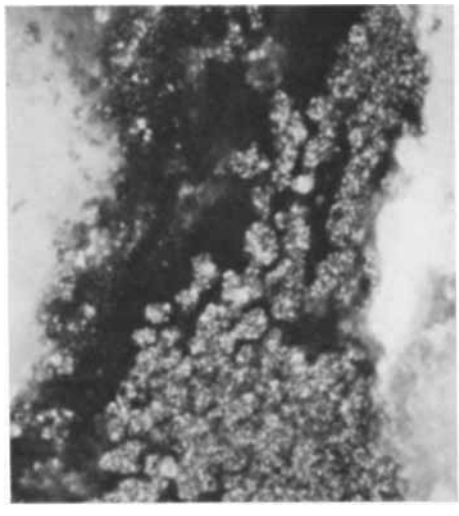

Fig. 16. View of the spherical type of lead crystals formed in the negative plate when the specific gravity of electrolyte was 1.45, the temperature 4°C, and the current density 2.5 amp/dm^2. Magnification approximately 650X.

the crystals were found to become coarser, that is, the needlelike forms became short and thick and appeared in dense groups. At the higher specific gravities these groups appeared to be replaced by the spherical particles of lead which, as has been said, might possibly be composed of many extremely small needlelike forms.

At a constant temperature and specific gravity, forming at an increased current density produced smaller crystals in the same manner as that caused by increasing the temperature when specific gravity and current density were held constant.

The most extensive area of formation occurred in the samples with the needlelike crystals and the minimum area of formation in those plates containing the spherical particles of lead. The area of formation was more extensive when the needlelike crystals were of small size than when they were large.

Discussion

The data obtained are insufficient to arrive at any definite conclusions, but some very interesting suppositions can be made, particularly in the case of the positive plate. There was definite evidence that a particular large type of crystal was the first to undergo reaction to form the lead dioxide. At the same time it was found that forming could take place in the absence of this type of crystal but apparently at a much slower rate.

It therefore appears obvious that this type of crystal which produces a crystal structure and affinity for oxygen so different from that of the far more numerous small regular polyhedrons must represent a different chemical compound. While determination of the identity of these compounds was not attempted in the present experiment it is possible to make a tentative identification based on previously published work.

Lander (4) established the composition of three compounds obtained by boiling water suspensions of lead monoxide, PbO, and lead sulfate, $PbSO_4$, in the proper ratios. Two of these compounds were found to be basic sulfates: tetrabasic lead sulfate, $PbSO_4 \cdot 4PbO$ and monobasic lead sulfate, $PbSO_4$ PbO. The third compound appeared to be a hydrate and was tentatively identified as the monohydrate of tribasic lead sulfate, $PbSO_4 \cdot 3PbO \cdot H_2O$. Ikari (5) studied the preparation of the monohydrate of tribasic lead sulfate and concluded that its formation was modified by the particle size of the PbO used and by whether the red or yellow modification was employed. The method of drying and the amount of CO_2 in the drying atmosphere also influenced the yield. Takagaki (6-8) and Ikari, Yoshizawa and Okada (9, 10) studied the basic oxides that were found in pasted plates made from various ratios of PbO and $PbSO_4$. They found variations in the amount of basic oxides and the points of maxima depending on whether they used the red or yellow form of PbO and on the size of the lead monoxide particles. They agreed on the additional significant observation that the tetrabasic lead sulfate was entirely absent from those pastes that were dried at temperatures below 60°C and was found in pastes that were dried above 80°C or steam dried, apparently formed at the higher temperature by the decomposition of the hydrated tribasic salt into the tetrabasic and monobasic forms.

The theoretical points of maxima in the PbO, $PbSO_4$ mixtures should occur at approximately 25 weight percent of the lead sulfate for the formation of tetrabasic lead sulfate, $PbSO_4 \cdot 4PbO$; at approximately 31% of lead sulfate for the formation of the monohydrate of tribasic lead sulfate, $PbSO_4 \cdot 3PbO \cdot H_2O$; and at approximately 58% of lead sulfate for the formation of monobasic lead sulfate, $PbSO_4 \cdot PbO$. None of the authors cited above reported agreement with the theoretical percentages under all of the conditions investigated, but Ikari, Yoshizawa, and Okada (9) appeared to attain agreement with these values when using steam dried pastes made from either modification of the lead monoxide with mean particle size of 0.9μ or

less. Takagaki (6) apparently reached agreement only when using the yellow modification and steam drying, but particle size was not specified.

In summarizing the work of these various authors it would appear that in mixtures containing from 0 to 25% $PbSO_4$ the unreacted PbO will diminish to insignificant amounts and the $PbSO_4 \cdot 3PbO \cdot H_2O$ will increase to a maximum at 25% $PbSO_4$. Provided the temperature of mixing has been maintained below 60°C no crystals of $PbSO_4 \cdot 4PbO$ would be expected. If the temperature has exceeded this value the amount of $PbSO_4 \cdot 3PbO \cdot H_2O$ found in this region will decrease greatly and be replaced by increasingly large amounts of $PbSO_4 \cdot 4H_2O$ as the amount of $PbSO_4$ in the original mixture increases toward 25%. Paste mixtures with from 25 to 60% will contain increasingly large amounts of $PbSO_4 \cdot PbO$ while $PbSO_4 \cdot 3PbO \cdot H_2O$ in significant amounts will disappear at about 45-50% and $PbSO_4 \cdot 4PbO$ will likewise become insignificant at about 31%. Paste mixtures above 60% $PbSO_4$ will contain increasing amounts of unreacted lead sulfate and decreasing amounts of $PbSO_4 \cdot PbO$ as the $PbSO_4$ content in the original mixture increases toward 100%.

Ikari, Yoshizawa, and Okada (9) and Dodson (11) found that the amount of α-PbO_2 found in a formed pasted plate increased as the specific gravity of the electrolyte used in forming decreased and as the density of the original paste used in forming increased. They also found that the amount of α-PbO_2 increased as the temperature used in formation was increased, but the temperatures used in their experiments apparently did not exceed 60°C. The Japanese authors also showed that an incubation period, after electroformation began, was required before PbO_2 could be detected in the paste. Both Dodson and the Japanese workers reported that α-PbO_2 was formed first, followed at a later stage in the electroforming by increasing amounts of β-PbO_2. Comparing these observations with those in the present paper that the first conversion to PbO_2 is at the surface of a particular species of crystal, that these crystals increase in number, length and regular habit with decreasing electrolyte specific gravity, current density, and temperature, and that these crystals apparently form as a first step in electrolysis, develops a strong suspicion that the hard dense surface layer on these crystals must be the α-PbO_2 observed by the earlier workers employing x-ray analysis. Further data from the cited papers indicate that maximum formation of α-PbO_2 occurred under conditions that would cause maximum formation of $PbSO_4 \cdot 3PbO \cdot H_2O$. This indicates that the observed crystals on which the PbO_2 formation first occurred were probably the monohydrate of the tribasic lead sulfate. Doubt is cast on this conclusion by Takagaki's photomicrographs (7) which show crystals similar in size and shape to those reported in the present paper but which he identified as the tetrabasic lead sulfate, $PbSO_4 \cdot 4PbO$. However, since the formation of α-PbO_2 is generally observed as a surface layer on the underlying crystal it is probable that in this layer of the crystal there has occurred some change prior to PbO_2 formation. This might be caused by the transformation of $PbSO_4 \cdot 3PbO \cdot H_2O$ into $PbSO_4 \cdot 4PbO$ and $PbSO_4 \cdot PbO$, as reported by Lander (4) or the formation of some as yet unidentified, relatively unstable, intermediate compound on the crystal surface. It is evident that further investigation will be required to settle this.

On the basis of the foregoing some very interesting speculation is in order concerning the ever present problem of increasing the efficiency and longevity of battery plates. For if a continuous film of hard dense lead dioxide is being formed on the surface of a particular crystal, the presence of a sufficient number of such crystals of the proper size and shape should ensure a continuous network of such hard structure throughout the plate and the separation of the softer material into small cells held together by the hard film, somewhat as shown in Fig. 17. This hard lead dioxide film should have a greater density than the surrounding softer material and therefore greater electrical conductivity. If it does consist of α-PbO_2 then this would assuredly be true because of the greater oxygen deficiency. Less electrical resistance would therefore be encountered between the grid and the more distant portions of the active material and the electron flow would be expedited.

Perhaps an even more important point would be the possibility of prolonging plate life by the retention of active material. Ikari, Yoshizawa, and Okada (13, 14) and Dodson (12) showed that the discharge capacity of the α-PbO_2 was not as great as that of the β-PbO_2. In experiments with solid electrodes of the two forms of lead dioxide (13) the Japanese workers showed that the dischargeable thickness when the porosity of the material was zero was between 0.3 and 0.4μ on α-PbO_2 and about 1μ on β-PbO_2. Provided a sufficiently thick film of

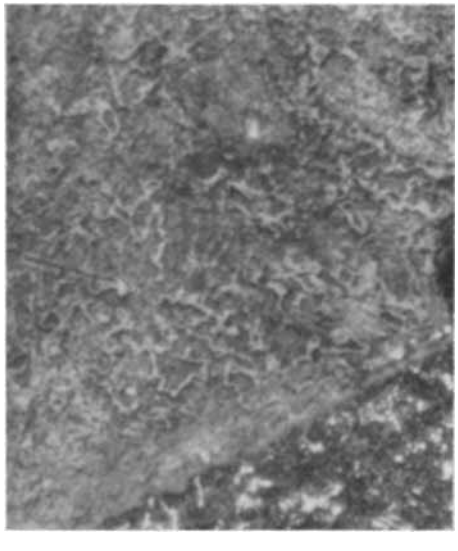

Fig. 17. Photomicrograph illustrating a type of structure that might assist in active-material retention and electrical conductance for the positive plate. Here the original crystals have been overlaid by a hard, dense surface layer of what is presumably α-PbO_2. These crystals are sufficiently interlaced so that this surface layer of PbO_2 when envisioned in three dimensions could act as a cellular network throughout the paste. Crystals were formed at 40°C, 0.23 amp/dm^2 current density, and 1.05 sp gr of electrolyte. Magnification approximately 650X.

α-PbO_2 was present initially on the appropriate crystal forms, it can be seen that the surface layer of lead sulfate formed by the initial discharge would be converted to β-PbO_2 on the next charge cycle and that subsequent charge-discharge cycles would tend to take place in this surface layer and that penetration into the underlying α-PbO_2 would occur very slowly or not at all. It has been reported by Ikari, Yoshizawa, and Okada (13) that when layers of α-PbO_2 were present under the β-PbO_2 that discharge of the β-PbO_2 occurred first, followed by the discharge of the α-PbO_2. These experimenters have also reported the interior of plates to be strongly alkaline even after long immersion in acid, and it is likely that the interior of a two-layer coating such as has been proposed would remain permanently in a state of low hydrogen ion concentration. The present authors in the light of the foregoing reports see no real obstacle to the formation of a network of α-PbO_2 throughout the mass of active material that would serve simultaneously as a continuous current path and a binder to retain and support the balance of the paste made up of small polyhedrons of β-PbO_2. By the mechanism previously outlined this network, provided it had sufficient thickness, would be covered by an outer layer of β-PbO_2 which would protect the underlying structure and alternate from PbO_2 to $PbSO_4$ with each cycle of charge and discharge. The underlying α-PbO_2 would not cycle at all or conversion would be at such a slow rate that many cycles would be required to destroy it.

In an attempt to confirm this line of reasoning an examination was made of a limited number of plates that were available with known performance data. It was found that in all cases of successful performance a type of structure such as has been anticipated and described above was present and still visible, for example, in plates that had been on open circuit for four years, or on float for nine. For the cases of unsuccessful operation it was found that a hard network was completely lacking although hard isolated particles were occasionally present. It was reported by Burbank (15), who studied the x-ray diffraction pattern of some of these plates, that those plates having the type of structure described above also gave evidence of large amounts of α-PbO_2 whereas those in which it was absent did not. The absence of the above described network of hard material and the simultaneous absence of α-PbO_2 in plates with unsatisfactory performance appears significant.

Further confirmation is supplied by the work of Dodson (12) in which he reported that on SAE Overcharge Life Tests the batteries containing α-PbO_2 outlasted production batteries, and the same appeared to be true of SAE Cycle Life Tests although the test results were not as conclusive as in the former case.

Since the reports of Dodson and of the various Japanese workers previously cited indicate the steps necessary to produce a paste with these characteristics it should prove to be a relatively simple matter to produce a positive paste of good retention and long life should these suppositions prove to be correct.

In the case of the negative plate the basic cause of failure is not loss of active material, but appears to be through the formation of large sulfate crystals that block the pores of the plate and through a gradual conversion of the needlelike lead crystals to polyhedral forms with much less reactive surface. There was no indication from the foregoing experiment that any solution to this problem could be found in the method used for the forming process. Here the mechanics of the process require the solution and reprecipitation of the crystals alternately either as lead or as lead sulfate according to whether the cell is charging or discharging. It does not appear likely that the form of crystal produced by the forming process could exist long enough to have any prolonged effect on performance.

Manuscript received Jan. 16, 1962; revised manuscript received May 18, 1962.

Any discussion of this paper will appear in a Discussion Section to be published in the June 1963 JOURNAL.

REFERENCES

1. A. C. Simon and E. L. Jones, *This Journal*, **102**, 279 (1955); U. S. Naval Research Lab. Reports No. 5149, June 25, 1959; No. 5679, Oct. 2, 1961; No. 5733, Feb. 1, 1962.
2. G. W. Vinal, "Storage Batteries," p. 35, John Wiley & Sons, Inc., New York (1940).
3. J. E. Buskirk, P. D. Boyd, and V. V. Smith, Paper presented at The Electrochemical Society Meeting, Houston, October 1960.
4. J. J. Lander, *This Journal*, **95**, 174 (1949). U. S. Naval Research Lab. Report No. C-3262, March 22, 1948.
5. S. Ikari, *J. Electrochem. Soc. Japan*, **27**, 385 (1959); overseas ed., **27**, E150 (1959).
6. T. Takagaki, *ibid.*, **26**, 278 (1958); overseas ed., **26**, E87 (1958).
7. T. Takagaki, *ibid.*, **26**, 320 (1958); overseas ed., **26**, E103 (1958).
8. T. Takagaki, *ibid.*, **26**, 354 (1958); overseas ed., **26**, E118 (1958).
9. S. Ikari, S. Yoshizawa, and S. Okada, *ibid.*, **27**, 426 (1959); overseas ed., **27**, E167 (1959).
10. S. Ikari, S. Yoshizawa, and S. Okada, *ibid.*, **27**, 487 (1959); overseas ed., **27**, E186 (1959).
11. V. A. Dodson, *This Journal*, **108**, 401 (1961).
12. V. A. Dodson, *ibid.*, **108**, 406 (1961).
13. S. Ikari, S. Yoshizawa, and S. Okada, *J. Electrochem. Soc. Japan*, **27**, 552 (1959); overseas ed., **27**, E223 (1959).
14. S. Ikari and S. Yoshizawa, *ibid.*, **27**, 613 (1959); overseas ed., **27**, E247 (1959).
15. Jeanne Burbank, Private communication.

The Behavior of the Metal-Oxide Interface During the Early Stages of the High-Temperature Corrosion of Aluminum

J. H. Greenblatt and J. T. N. Atkinson

Department of National Defense, Defense Research Board, Naval Research Establishment, Dartmouth, Nova Scotia, Canada

ABSTRACT

The oxide-metal interface of samples of two iron- and nickel-containing aluminum alloys and commercial aluminum was examined by optical microscopy after short exposures to high-temperature pure water. The initial attack proceeds faster on the second phase particles in the aluminum than on the surrounding matrix, but with time a reversal in relative corrosion rates occurs. The time at which this reversal occurs varies with temperature, and after it occurs the aluminum matrix surface recedes past the second phase particles leaving them isolated and not further corroded. The method of preparing the sample for examination is described briefly.

Draley *et al.* (1-3) have shown that aluminum can be made very much more resistant to corrosion in high-temperature water by alloying with cathodic metals, such as iron and nickel. Krenz and Biefer (4, 5) have reported considerable testing of two such alloys (alloy 10155 and alloy 10157) developed at Atomic Energy of Canada Ltd., and have correlated the enhanced properties of these alloys with presence of second phase particles in the metal and their size and distribution. This requirement for a uniform fine distribution of second phase particles had also been put forward by Draley and Ruther (6), Coriou *et al.* (7), and Brown *et al.* (8). Carlsen (9) has made observations on the behavior of second phase material when segregated in grain boundaries of cast alloys and showed that attack occurred more rapidly in these regions. However, in the previous work no specific information was obtained as to how the second phase particles themselves behaved.

The program of investigation at the Naval Research Establishment has concentrated on the initial period of film formation, and films from specimens exposed for periods varying from 1 min to 7 hr have been examined by electron and optical microscopy. Some of the results of this work, as reported previously (10-12), had revealed the behavior of second phase particles at the metal-oxide interface after 7 hr of exposure and the relation between these particles and topological features of the innermost and outermost surface of the oxide film. More recently, complete sets of exposures were completed on commercial aluminum and two special iron- and nickel-containing alloys over the time range 1 min to 7 hr at 5 different temperatures. Each metal-oxide interface was examined in detail on cross-sectioned samples using specially developed metallographic techniques (13-15). By following the condition of the oxide-metal interface during the initial stages of corrosion, this work has yielded new information on the behavior of second phase particles.

Experimental

The techniques and apparatus used in obtaining corroded samples are standard and have been used by the authors already cited as well as numerous others. As the focus in this work was on short exposure times, slight modifications were made in the more usual apparatus and these have been described previously in detail (10). In brief, a tandem autoclave system was used so that heated water at the proper temperature could be brought in contact with an annealed metal specimen, held at test temperature in argon, by turning a valve connecting both autoclaves. The exposure period was terminated by opening an exit valve and allowing the water to escape as steam.

The nominal composition of the alloys used is shown in Table I. This material was originally supplied by Atomic Energy of Canada Ltd. as ½ in. extruded rod and later material was obtained from the Aluminum Company of Canada as cast 100-lb ingots which were subsequently given the same physical treatment as the earlier material and finally extruded as ½ in. diameter rod. In the cast material the second phase particles were segregated in grain boundaries, but in the extruded rod the second phase material was dispersed. In alloy 10155 the second phase particles were larger and more irregularly distributed than in 10157. Such observations had also been made earlier by Biefer (4) in his work with these alloys.

Specimens 3/8 in. in diameter and 5/16 in. long were cut and machined from the extruded 1/2 in. rod, and then one end was polished metallographically to 0.25μ diamond in batches of 14 in a special jig. Following this the samples were degreased in refluxed trichlorethylene for 2 hr. The specimens were mounted on stainless steel racks

Table I. Nominal composition of alloys

Alloy	% Ni	% Fe	% Si
10155	0.5	0.5	0.2
10157	2.0	0.5	0.2
2S			

(Commercial) Fe + Si 0.4% total for typical material.

while in the autoclave and subsequently annealed for 2 hr in argon at 344°C in the dry autoclave. After this procedure, the samples were then brought to the test temperature while in argon, and water at the proper temperature admitted to the autoclave. Samples were exposed at 5 temperatures over the range 150°-350°C and for 8 times varying from 1 min to 7 hr.

After exposure, the samples were examined in cross section. To reveal greater detail at the oxide-metal interface the following technique was used. The specimens were coated with a thin film of aluminum by vacuum evaporation, mounted in diallyl phthalate plastic, and cross-sectioned by grinding on the sample preparation wheel. This procedure has been described in detail previously (13-15) and leads to mounted specimens, with excellent edge preservation, clearly revealing the detail at the interface.

After mounting and cross sectioning, the specimens were polished down to 0.25μ diamond on waxed Pellon[1] disks given a final polish to 0.1μ using Gamal.[2] Following polishing, specimens were etched for approximately 3 sec in dilute HF (10 drops of 28% HF in 100 ml water). The etching time was governed by the thickness of the evaporated aluminum film, and when this was thin, the samples were given a lighter etch. The specimens were then washed in water and alcohol, hot air dried, and examined. All grinding and polishing down to 0.25μ was done with kerosene as a lubricant, while polishing with Gamal was done in water. The specimens were photographed at a magnification of 800 using 35 mm film to record the data. The polishing technique is currently undergoing further refinement and will be described in detail elsewhere when fully developed. For each exposure condition at least one representative photograph was taken, and for thicker corrosion films at longer exposure times and higher temperatures more than one photograph was taken.

Results

In general the results for very short exposures, *i.e.*, 1-30 min, revealed considerable difference from the behavior at the interface previously observed for the 7-hr samples. The difference was a reversal in the electrochemical behavior of the second phase particles. Whereas in the previously described 7-hr work, the second phase particles of the alloys were observed to be uncorroded and standing proud of the surface, at 1 min they were more rapidly corroded than the surrounding aluminum, and pitting initiated in the second phase particles. Blanks that had gone through the cleaning and annealing cycle, but had not been exposed to high-temperature water showed no attack of the second phase particles. With 10155 the second phase particles were larger than with 10157, and the pits in them were correspondingly larger.

Examples of conditions at the metal-oxide interface for these alloys are shown in Fig. 1-4. Figure 1 shows the metal-oxide interface of 10155 after 1 min of exposure at 150°C, and the more rapid attack on the second phase particles is clearly seen. Such behavior also occurred at the highest temperature of exposure as can be seen in Fig. 2 at 350°C. By 10 min of exposure at this higher temperature the reversal in relative rates had occurred and the aluminum matrix was receding faster. Figure 3,

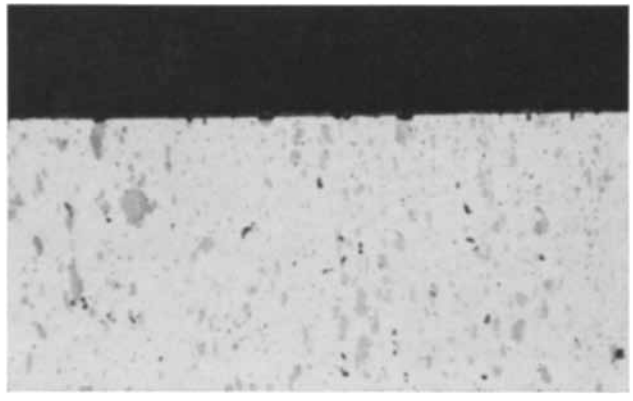

Fig. 1. Cross section of 10155 alloy at 1000X after exposure to water at 150°C for 1 min.

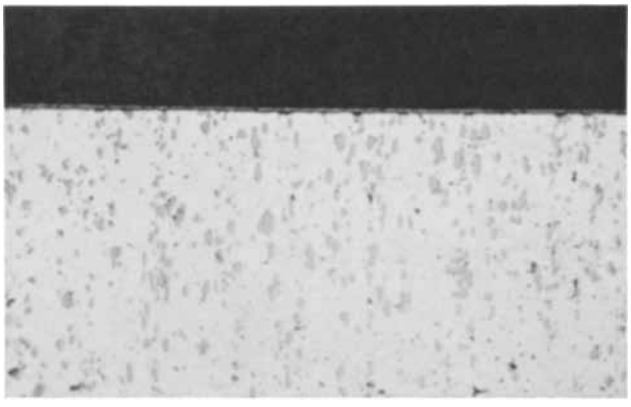

Fig. 2. Cross section of 10155 alloy at 1000X after exposure to water at 350°C for 1 min.

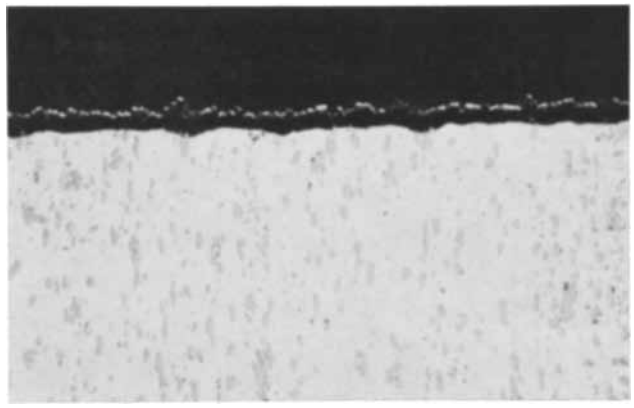

Fig. 3. Cross section of 10155 alloy at 1000X after exposure to water at 350°C for 2 hr.

[1] Geoscience Instruments Corporation.

[2] Fisher Scientific Co. Gamma Alumina.

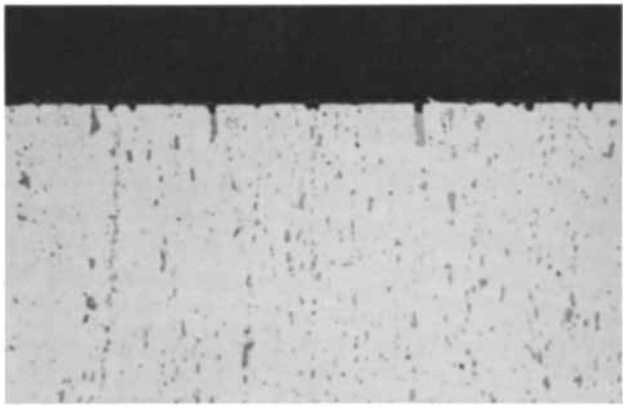

Fig. 4. Cross section of 10157 alloy at 1000X after exposure to water at 250°C for 1 min.

taken after 2 hr exposure at 350°C, shows small second phase particles just isolated within the oxide and in the process of being isolated at the oxide-metal interface, as the aluminum matrix recedes past them. In Fig. 4 the interface of 10157 after 1 min exposure at 250°C is shown. Again with this alloy it is seen that the initial corrosion attack proceeds rapidly on the second phase particles. The empty pits in the aluminum are presumably the sites of small second phase particles that have been completely corroded. A summary of the behavior of the particles at the corroding interface is given in Table II.

The behavior of 2S, although analogous, does not follow such clearly defined trends. With this material, several types of behavior can be distinguished in the second phase particles. The very small ones that always appeared blue under the microscope were invariably uncorroded and remained so and were usually eventually isolated from the surrounding aluminum matrix. The larger particles were initially more rapidly corroded; some appeared to maintain the more rapid corrosion over the entire range of times and temperatures investigated, while others appeared to change, since with time the aluminum around them corroded faster than the particles. The latter tendency results in an evening out of the surface over some sections and the partial or complete isolation of the remnants of the second phase particles in the oxide. The particles that did not change continued to corrode faster than the surrounding aluminum, leading to deep irregular pits. Grain boundary attack leading in from the surface was observed at higher temperatures and appeared consistently at 350°C. With 2S at longer exposure times there were also a few examples of slower corroding second phase particles protruding through the metal-oxide interface, and the corrosion of the aluminum for regions immediately sur-

Table II. Summary of interfacial corrosion behavior

Time of exposure, min	Aluminum alloy	More rapidly corroding phase at: 150°C	200°C	250°C	300°C	350°C
1	10155	2nd phase particles	2nd phase particles	2nd phase particles	2nd phase particles	2nd phase particles
5	10155	2nd phase particles	2nd phase particles	2nd phase particles	2nd phase particles	2nd phase particles
10	10155	2nd phase particles	2nd phase particles	Matrix beginning to corrode faster	Matrix beginning to corrode faster	Matrix
15	10155	2nd phase particles	2nd phase particles	Matrix	Matrix	Matrix
30	10155	Matrix beginning to corrode faster	Matrix beginning to recede faster	Matrix	Matrix	Matrix
60	10155	Matrix	Matrix	Matrix	Matrix	Matrix
120	10155	Matrix	Matrix	Matrix	Matrix	Matrix
420	10155	Matrix	Matrix	Matrix	Matrix	Matrix
1	10157	2nd phase particles	2nd phase particles	2nd phase particles	2nd phase particles at some areas, matrix at others	2nd phase particles, matrix beginning to corrode faster
5	10157	2nd phase particles	2nd phase particles	Matrix beginning to corrode faster	2nd phase particles at some areas, matrix at others	2nd phase particles at some areas, matrix at others
10	10157	2nd phase particles	2nd phase particles	Matrix	Matrix	Matrix
15	10157	2nd phase particles	2nd phase particles	Matrix	Matrix	Matrix
30	10157	Matrix beginning to corrode faster	Matrix beginning to corrode faster	Matrix	Matrix	Matrix
60	10157	Matrix	Matrix	Matrix	Matrix	Matrix
120	10157	Matrix	Matrix	Matrix	Matrix	Matrix
420	10157	Matrix	Matrix	Matrix	Matrix	Matrix
1	2S	2nd phase particles except for some spherical ones	2nd phase particles except for some spherical ones	2nd phase particles in some areas, matrix in others	2nd phase particles intergranular corrosion	Matrix, intergranular plus attack on second phase
5	2S	2nd phase particles except for some spherical ones	2nd phase particles except for some spherical ones	Matrix	2nd phase particles intergranular corrosion	Matrix and intergranular corrosion
10	2S	Same as above, but matrix showed signs of faster corrosion in some areas	2nd phase particles in some areas, matrix in others	Matrix	Matrix. Some large 2nd phase particles corroded faster. Intergranular corrosion	Matrix and intergranular corrosion
15	2S	Matrix in some areas. 2nd phase particles in others	2nd phase particles in some areas, matrix in others	Matrix	Matrix. Some large 2nd phase particles corroded faster. Intergranular corrosion	Matrix and intergranular corrosion
30	2S	Matrix	Matrix	Matrix	Matrix. Some large 2nd phase particles corroded faster. Intergranular corrosion	Matrix and intergranular corrosion
60	2S	Matrix	Matrix	Matrix	Matrix. Some large 2nd phase particles corroded faster. Intergranular corrosion	Matrix and intergranular corrosion
120	2S	Matrix	Matrix	Matrix	Matrix. Some large 2nd phase particles corroded faster. Intergranular corrosion	Matrix and intergranular corrosion
420	2S	Matrix	Matrix	Matrix	Matrix. Some large 2nd phase particles corroded faster. Intergranular corrosion	Matrix and intergranular corrosion

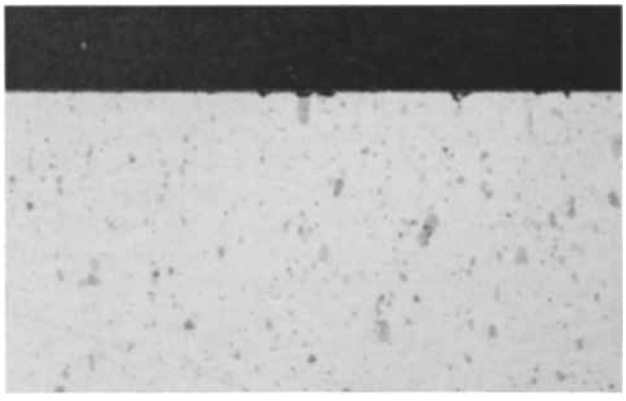

Fig. 5. Cross section of 2S alloy at 1000X after exposure to water at 150°C for 1 min.

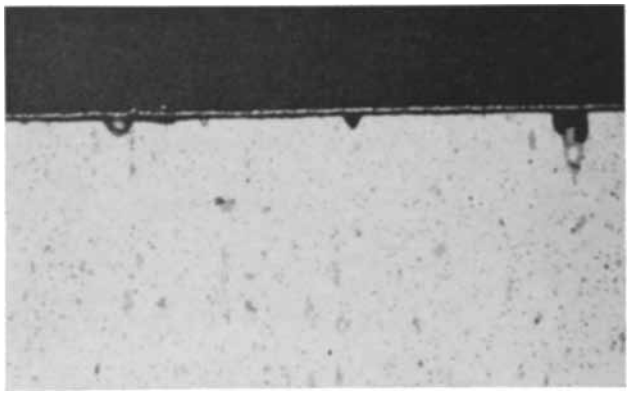

Fig. 6. Cross section of 2S at 1000X after exposure to water at 250°C for 2 hr.

rounding these particles resembled that of the special alloys.

Typical behavior for 2S is shown in Fig. 5 and 6. In Fig. 5 after 1 min of corrosion at 150°C it can be seen that a large second phase particle has corroded faster than the matrix. In Fig. 6 the interface after 2 hr exposure at 250°C is seen. At the extreme left of the figure is an oxide filled cavity with pieces of second phase particles isolated in the oxide. To the right of this can be seen one of the small blue second phase particles that were always observed to be slower corroding than the surrounding aluminum, and on the extreme right a large second phase particle becoming isolated in a pit formed in the now more rapidly corroding surrounding aluminum.

The vacuum evaporated film of aluminum on all samples varied in thickness, and when thin, a limitation was imposed on the time a specimen could be etched to bring up microstructure, lest this aluminum boundary be etched off. For this reason the contrast of the photographs presented varies to some extent, with the microstructure etched up more clearly in the case of thick aluminum covering films than thin ones. This difference can be seen by comparing Fig. 4 and 7.

Observations on the whole of the sample interface rather than on the fields of view selected for photography show that the conclusions as to the behavior of second phase particles are generally correct and that the summary in Table II is a valid one for their behavior.

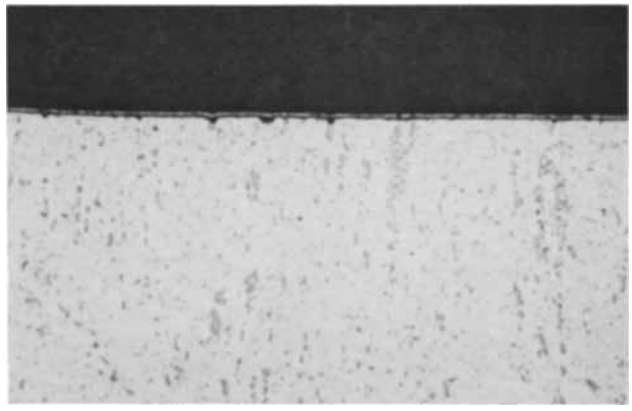

Fig. 7. Cross section of 10157 at 1000X after exposure to water at 150°C for 10 min.

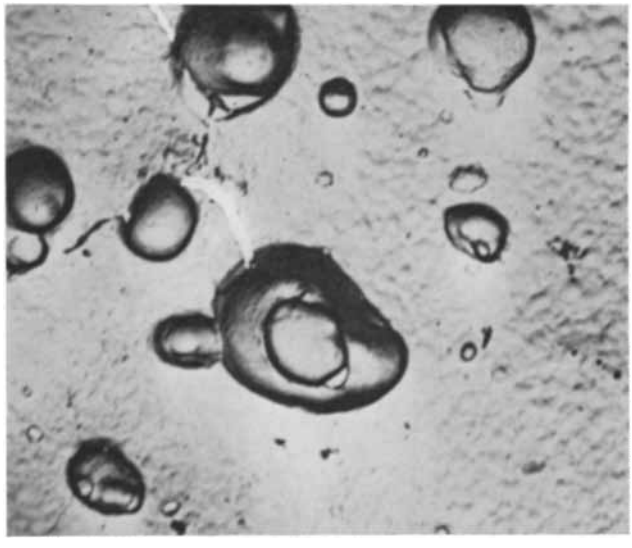

Fig. 8. Electron micrograph of the inner surface corrosion film on 10155 alloy at 6000X after exposure to water at 300°C for 1 min.

Electron micrographs of the surface of the oxide film give corroborating evidence of the pitting of the second phase particles. Electron micrographs of the oxide-metal interface of 1 and 5 min samples, which were previously reported (10, 12), showed that the film protrudes into cavities in the metal. In the earlier reports, it was presumed that these mounds on the underside of the film were due to excessive corrosion of aluminum around the second phase particles, and the depressions observed in the mounds corresponded to the already isolated second phase particles. The cross sections of samples exposed 1 min show that this is not the case, but that the pitting to which the mounds correspond is in the second phase particles themselves. Figure 8 shows an electron micrograph of the inner surface (oxide-metal interface) of the oxide film on 10155 alloy at 6000X after 1 min exposure to water at 300°C showing typical mounds.

Discussion and Results

The results of the present study show that, in the early stages of corrosion, the second phase particles in the alloys tested, with the exceptions noted for 2S, corrode faster initially than the surrounding aluminum, but subsequently a reversal of behavior

occurs. Stimulation of a preferential attack, by cathodic current densities of the order of 0.1 ma/cm^2 at 100°C, has been observed by Carlsen (9, 16) in the eutectic precipitated in the grain boundaries of cast iron and nickel containing aluminum alloys. One possible explanation of our observations of more rapid initial corrosion of second phase particles could be based on Carlsen's concept of cathodic stimulation. However, other work done by us on the effects of cathodic polarization on the corrosion of the alloys described in this paper has shown no effect of current densities of up to 0.1 ma/cm^2 and greater over a 24 hr period at 300°C. Thus Carlsen's observations may not be extrapolated unequivocally to our operating conditions. Figure 2 shows that the preferential attack is still occurring at the much higher temperatures. An alternate explanation is that the second phase particles are initially anodic, but that once a film forms over the specimen the rate of attack on the particles slows down while that on the aluminum continues. The information on hand at present does not allow an unequivocal choice of either alternate, but the authors prefer the latter.

Regardless of which possible explanation is correct the initial, more rapid attack on the second phase particles must produce an oxide film enriched in dissolved iron and nickel which may affect the subsequent corrosion behavior of the alloys. Thus Draley *et al.* (6) have found marked influence of such variables as start up time on the corrosion resistance of aluminum alloys, the nickel- and iron-containing alloys showing better resistance to steam with a slow start up than with a fast one. Our data indicate more corrosion of the second phase particles at low temperature than at high, and thus a slow start up would yield an initial film more enriched in iron and nickel than those with fast start up. In addition, polarization measurements made *in situ* in autoclaves have indicated that the resistance of the films on iron and nickel containing alloys is considerably less than that of 2S. Current-voltage curves obtained on specimens with preformed films indicate that the films on the alloys have many different properties than those on 2S, *e.g.*, they do not show the same rectifying properties and they require less energy to promote additional conducting electrons from the valence bands of the oxide. Such properties must be related to the dissolved iron and nickel ions in the aluminum oxide.

With the passage of time, the noncorroding second phase particles protrude and eventually become isolated in the oxide where they can act to decrease further its resistance by providing a metallic path through an otherwise insulating medium. The effects of decreased oxide resistance by this mechanism, in causing the hydrogen discharge to occur at the oxide water interface, have been discussed by Brown (8) as one alternate explanation to Draley's original hypothesis that the iron and nickel alloying elements function as cathodes for the discharge of hydrogen (1-3).

The data presented in this paper show that the role of the second phase particles is not as simple as originally conceived and that ideas on what actually occurs must be modified in the light of the information presented.

Acknowledgment

The work described formed part of Defense Research Board of Canada Project D-12-75-10-35, and the authors acknowledge the Board's permission to publish. The authors also acknowledge the work of the laboratory staff generally and in particular that of Mr. C. A. Godden who obtained the optical micrographs and Mr. T. P. Copps who obtained the electron micrographs.

Manuscript received Dec. 5, 1961; revised manuscript received March 12, 1962. This paper was prepared for delivery before the Detroit Meeting, Oct. 1-5, 1961.

Any discussion of this paper will appear in a Discussion Section to be published in the June 1963 JOURNAL.

REFERENCES

1. J. E. Draley and W. E. Ruther, Argonne National Lab. Report No. ANL-5001.
2. J. E. Draley and W. E. Ruther, Argonne National Lab., Report No. ANL-5430.
3. J. E. Draley and W. E. Ruther, *Corrosion*, **12**, 481 (1956).
4. G. J. Biefer, Atomic Energy of Canada Report No. CRMet 796, Chalk River.
5. F. H. Krenz, *Corrosion*, **13**, 575 (1957).
6. J. E. Draley and W. E. Ruther, Argonne National Lab. Report Nos. ANL-5658, April 1957 and ANL-6207, April 1961.
7. H. Coriou *et al.*, *Proc.* Second United Nations International Conference on the Peaceful Uses of Atomic Energy, Geneva, **5**, 128 (1959).
8. M. H. Brown *et al.*, Publication 60-13, p. 82-96, NACE High Purity Water Corrosion of Metals (1960). L. C. Catalogue Card, 60-16899.
9. K. M. Carlsen, *Corrosion*, **14**, 54t (1958).
10. D. F. MacLennan, *ibid.*, **17**, 181 (1961).
11. D. F. MacLennan, *ibid.*, **17**, 239 (1961).
12. J. H. Greenblatt, D. F. MacLennan, and A. F. McMillan, *Proc.* First International Conference on Corrosion, London, April 1961.
13. C. A. Godden, *Metal Progr.*, **79**, 121 (1961)
14. C. A. Godden and J. T. N. Atkinson, *Metallurgia*, **63**, 151 (1961).
15. C. A. Godden and J. T. N. Atkinson, Presented at March 1961 Meeting, Canadian Institute of Mining and Metallurgy and submitted for publication in their bulletin.
16. K. M. Carlsen, *This Journal*, **104**, 147 (1957).

On The Defect Structure of Ta_2O_5

Per Kofstad

Central Institute for Industrial Research, Blindern, Oslo, Norway

ABSTRACT

The defect structure of Ta_2O_5 has been studied by measurements of the electrical conductivity and the weight change of Ta_2O_5 as a function of the partial pressure of oxygen. Ta_2O_5 exhibits p-type conductivity at pressures close to 1 atm oxygen and n-type conductivity at lower oxygen pressures. The defect structure is interpreted in terms of interstitial oxygen ions (p-type) and oxygen vacancies (n-type). Ta_2O_5 has been found to have a small homogeneity range. The heat of formation of oxygen vacancies is $\Delta H_v \geqq 150$ kcal/mole.

Tantalum is receiving considerable attention as a material for high-temperature applications. A major shortcoming of tantalum under such conditions is, however, its great reactivity with oxygen and other gases.

Above 800°C and during initial stages tantalum shows a parabolic oxidation behavior (1). This is interpreted in terms of a rate-determining transport of oxygen ions through a growing oxide scale consisting of Ta_2O_5. For a better understanding of the oxidation mechanism it was desirable to study the defect structure of Ta_2O_5. For this purpose the electrical conductivity of Ta_2O_5 has been studied as a function of oxygen pressure at high temperatures. In addition, attempts have been made to study the weight change of Ta_2O_5 under corresponding conditions. The work also constitutes part of a more general study of defect structures and diffusion in metal oxides (2-5).

According to Lagergren and Magneli (6) and Wasilewski (7) Ta_2O_5 exists in two modifications with a transition temperature of 1320° ± 20°C. The low-temperature modification, β-Ta_2O_5, is isostructural with the low-temperature modification of Nb_2O_5, γ-Nb_2O_5 (8-10). In disagreement with the above results Schönberg (11) found no high-temperature modification of Ta_2O_5. The melting point of Ta_2O_5 is approximately 1470°C.

Attempts to reduce Ta_2O_5 with tantalum metal have mostly proved unsuccessful (6, 7, 12). However, Lapitsky, Simanov, and Artamonova (13) report having produced TaO by reduction of Ta_2O_5 with tantalum metal, magnesium, carbon monoxide, or carbon.

There does not appear to have been any previous investigations of the defect structure of Ta_2O_5.

Material and Methods

The studies on Ta_2O_5 were carried out in conjunction with investigations of the oxidation behavior of tantalum. The oxide was therefore prepared by oxidizing tantalum metal powder in air. The tantalum powder was supplied by National Research Corporation. The amount of impurities in the metal powder was as follows: Fe, Cr, Ni, and Nb, each 0.01%; Si and Al, each <0.025%; Mg, Ti, Zr, Cu, and Co, each <0.005%. Specimens were prepared by sintering cold-pressed oxide powder in air at 1400°C. After this treatment the specimens had a density of approximately 65% of theoretical density (8.73 g/cm³).

The thermogravimetric measurements were carried out with a quartz helix-type apparatus. Measurements were carried out in 1 atm O_2 and in mixtures of CO + CO_2 with a total gas pressure of 1 atm. Detailed descriptions of both the apparatus and the procedure used have been given elsewhere (2).

In the measurements of electrical conductivity the specimen had a cylindrical shape with a diameter of 1.4 cm and a length of 1.3 cm. Two Pt-10% Rh plates served as electrodes. In the measurements of thermoelectric force a small platinum wound furnace was placed in contact with one of the electrodes. The temperature of the specimens was measured with two Pt-Pt 10% Rh thermocouples melted to the electrodes. The resistance of the specimen was measured with a Wheatstone bridge.

Measurements were carried out in pure oxygen and in mixtures of CO + CO_2. During measurements at low oxygen pressures, oxygen was continuously pumped through the system. Measurements were taken at both increasing and decreasing partial pressures of oxygen. A more detailed description of the apparatus and the procedure has been given elsewhere (4).

Results and Discussion

Thermogravimetric studies.—By comparing with thermogravimetric studies on α-Nb_2O_5 (2) it was expected that the defect structure of Ta_2O_5 could be studied by the same technique. Several attempts were therefore made to study the weight change of Ta_2O_5 specimens as a function of oxygen pressure at temperatures of 1200°-1400°C. However, in these studies only very small weight changes were observed when equilibrating the specimens successively in 1 atm O_2, in mixtures of CO + CO_2, and in pure CO. If the formula of the oxide is written as Ta_2O_{5-x}, the maximum weight loss observed in going from 1 atm O_2 to 1 atm CO ($p_{O_2} \sim 10^{-15} - 10^{-16}$ atm) correspond to a change in the value of x of about 0.005-0.006 at the indicated temperatures. Furthermore, because of the small magnitude of the weight

changes it was not possible to evaluate their oxygen pressure dependence.

The small weight changes may of course be due to slow kinetics. However, specimens were held in CO atmospheres for periods up to 2-3 hr without any further weight loss. Furthermore, in the electrical conductivity studies at the same temperatures equilibrium was established as fast as the oxygen pressure could be changed from one value to another. Thus it appears that the small weight losses are not due to slow kinetics; rather, it is concluded that this reflects a very small homogeneity range for Ta_2O_5 and a correspondingly large free energy and heat of formation of defects. As discussed below this conclusion was also confirmed by the electrical conductivity measurements.

From the above values ($x=0.005$ at 10^{-15} atm) a rough estimate may be made of the partial molar free energy of dissociation. This is given by $\Delta\bar{G}_{O_2} = -RT \ln p_{O_2}$, and at $x = 0.005$ and $T = 1500°K$ the value of $\Delta\bar{G}_{O_2}$ is about 100 kcal/mole.

Studies of electrical conductivity.—The results of the studies of electrical conductivity as a function of oxygen pressure are shown in Fig. 1, in which the logarithm of the resistance of the specimen has been plotted as a function of the logarithm of the partial pressure of oxygen at temperatures ranging from 877°-1380°C. The results at 1380°C suggest an anomalous behavior. This may be due to the fact that one is dealing with the high-temperature modification of Ta_2O_5 under these conditions.

From Fig. 1 it is seen that the oxygen pressure dependence is a function of the partial pressure of oxygen. Expressing the resistance as

$$R = \text{const. } p_{O_2}^{\ n} \qquad [1]$$

it is found that the exponent n has a value of 1/6 at the lower oxygen pressures. With increasing partial pressure of oxygen n increases to 1/5-1/4, after which the value of n again decreases and the resistance goes through a maximum. At oxygen pressures higher than that of the maxima n takes on small negative values. The maxima in the resistance become more pronounced and are found to be displaced toward lower oxygen pressures with decreasing temperature.

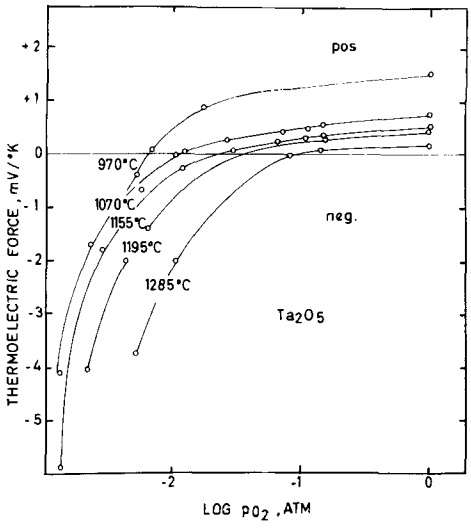

Fig. 2. Thermoelectric force of Ta_2O_5 specimen as a function of the logarithm of the partial pressure of oxygen.

A positive value of n indicates n-type conductivity in the oxide, while a negative value suggests p-type conductivity. The maxima in the resistance *vs.* p_{O_2} curves thus suggest a transition from an n-type to a p-type conductivity.

To study this, measurements of thermoelectric force were carried out. Results are given in Fig. 2. A positive thermoelectric force was found at oxygen pressures higher than those of the maxima, while at lower oxygen pressures a negative thermoelectric force was observed. On this basis it is concluded that the maxima do represent transitions for n- to p-type conductivity.

The p-n transition takes place at lower oxygen pressures with decreasing temperature. This relationship is illustrated in Fig. 3 where the logarithm of the oxygen pressure at the p-n transitions is plotted as a function of the reciprocal absolute temperature.

For an n-conducting oxide with a defect structure involving oxygen vacancies, the defect structure

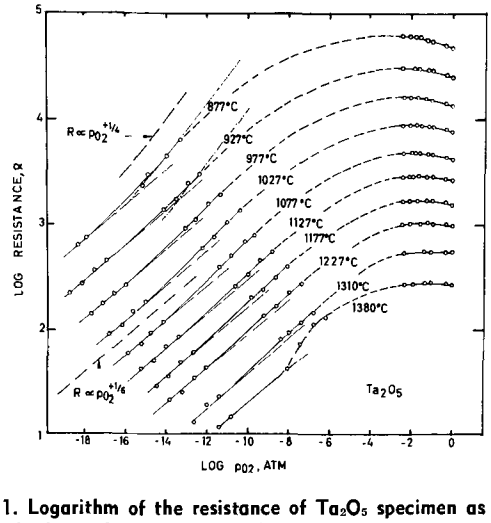

Fig. 1. Logarithm of the resistance of Ta_2O_5 specimen as a function of the logarithm of the partial pressure of oxygen.

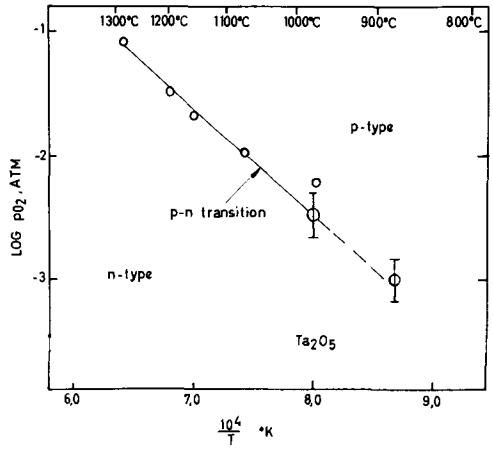

Fig. 3. Logarithm of the oxygen pressure at p-n transitions as a function of the reciprocal absolute temperature. Open circles taken from Fig. 2, values at 877° and 977°C from maxima in Fig. 1.

may be described by the following equations (2, 4)

$$O_i^{=} = Ov + 1/2\ O_2^{(g)} \quad ; \text{Equil. const.} = K_a \quad [2]$$

$$Ov = Ov^{\cdot} + e^{-} \quad ; \text{Equil. const.} = K_b \quad [3]$$

$$Ov^{\cdot} = Ov^{\cdot\cdot} + e^{-} \quad ; \text{Equil. const.} = K_c \quad [4]$$

$$Nil = e^{+} + e^{-} \quad ; \text{Equil. const.} = K_d \quad [5]$$

Ov denotes an oxygen vacancy with two trapped electrons, $Ov^{\cdot}$ and $Ov^{\cdot\cdot}$ represent singly and doubly ionized oxygen vacancies, respectively, e^{+} denotes an electron hole and e^{-} an electron in the conduction band. Equation [5] describes intrinsic ionization.

By applying the condition of electroneutrality and the law of mass action the concentration of electrons, $[e^{-}]$, is given by

$$[e^{-}]^3 = K_a K_b p_{O_2}^{-1/2} (2K_c + [e^{-}]) + K_d [e^{-}] \quad [6]$$

The following limiting conditions may be considered:

i. if intrinsic ionization (Eq. [5]) predominates

$$[e^{-}] = K_d^{1/2} \quad [7]$$

ii. if intrinsic ionization is negligible and if

$$(a)\ 2[Ov^{\cdot}] >> [Ov^{\cdot\cdot}] \ (i.e., [e^{-}] >> 2K_c)$$

$$[e^{-}] = (K_a K_b)^{1/2} p_{O_2}^{-1/4} \quad [8]$$

$$(b)\ 2[Ov^{\cdot}] << [Ov^{\cdot\cdot}] \ (i.e., [e^{-}] << 2K_c)$$

$$[e^{-}] = (2K_a K_b K_c)^{1/3} p_{O_2}^{-1/6} \quad [9]$$

Thus for an oxide with oxygen vacancies the value of the exponent n (Eq. [1]) may vary from $n = 1/4$ to $n = 0$ depending on the relative values of K_a, K_b, K_c, and K_d.

The temperature dependence of the equilibrium constants may be expressed as

$$K = K_o\, e^{-E/RT} \quad [10]$$

where E is equal to ΔH_a (Eq. [2]), E_b (Eq. [3]), E_c (Eq. [4]), and $Ed_{/2}$ (Eq. [5]). ΔH_a represents the heat of formation of an oxygen vacancy with two trapped electrons, E_b and E_c denote the ionization energies of the first and second trapped electrons, respectively, and E_d represents the intrinsic energy gap.

A p-type conductivity in oxides may be ascribed either to cation vacancies or to interstitial oxygen ions. Marker studies in connection with initial parabolic oxidation of tantalum at 1 atm O_2 at temperatures above 800°C suggest that oxygen ions are the most mobile species in Ta_2O_5 (1). It thus seems reasonable to assume that the p-type conductivity in Ta_2O_5 at the higher oxygen pressures may be ascribed to interstitial oxygen.

Defect structures involving interstitial oxygen has been considered unlikely on the grounds of an unfavorable size factor of the O^{-2}-ion (14). However, interstitial oxygen should not be excluded on the basis of size considerations alone; factors such as polarizability of the oxygen ions and the correspondingly better accommodation should also be taken into account. Furthermore, interstitial oxygen may also be present as singly ionized ions, which are more favorable from a size standpoint.

Interstitial oxygen may be described by the equation

$$1/2\ O_2 = O_i^{-2} + 2e^{+}; \text{Equil. const.} = K_e \quad [11]$$

where O_i^{-2} represents an interstitial oxygen ion.

Applying the law of mass action and combining Eq. [5] and [11] the concentration of charge carriers is given by

$$[e^{+}]^3 = 2K_e p_{O_2}^{1/2} + K_d [e^{+}] \quad [12]$$

Equation [11] could of course be considered in more detail, similarly to Eq. [3], [4], [5], and [6].

The present results are interpreted in terms of the above considerations. At the maxima in the resistance *vs.* p_{O_2} curves (Fig. 1), where the conductivity is independent of oxygen pressure, it is concluded that the conductivity is essentially determined by the intrinsic ionization (Eq. [7]). At oxygen pressures higher than those of the maxima the defect structure predominantly involves interstitial oxygen ions (Eq. [12]) and at the lower oxygen pressures predominantly oxygen vacancies (Eq. [6]). At the maxima it is also believed that the oxide has an approximately stoichiometric composition with some anti-Frenkel defect structure (involving both oxygen vacancies and oxygen interstitial ions) of the oxygen lattice. The formula of Ta_2O_5 is consequently considered to be Ta_2O_{5+y-x}, where y represents the fractional amount of interstitial oxygen and x oxygen vacancies.

A plot of the resistance at the maxima as a function of the reciprocal absolute temperature gives a value for the activation energy of the intrinsic conductivity. This is shown in Fig. 4. An approximately straight line relation is obtained with an activation energy of 41.2 kcal/mole or 1.79 ev. This indicates that the intrinsic energy gap in Ta_2O_5 is equal to 3.58 ev. As a comparison it has been found that the intrinsic energy gap in rutile (TiO_2) has a value of 3.04 to 3.12 ev (15-17). It should be emphasized that for Ta_2O_5 the evaluation neglects both the effect of

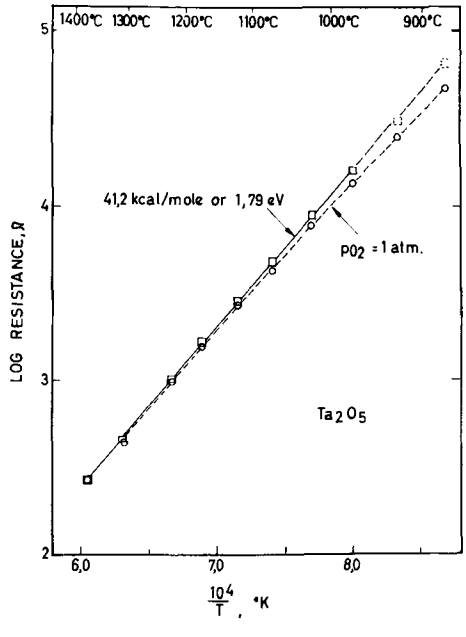

Fig. 4. Logarithm of the resistance of Ta_2O_5 specimen at the maxima in log R *vs.* log p_{O_2} curves (Fig. 1) as a function of the reciprocal absolute temperature.

mobility of the charge carriers which has a negative temperature coefficient (17) and the effect of the proposed anti-Frenkel disorder of the oxygen lattice under these conditions.

At oxygen pressures smaller than those of the maxima the intrinsic ionization becomes of less relative importance. With decreasing oxygen pressure and depending on the temperature the value of n (Eq. [1]) reaches values of 1/4 to 1/5. At the very lowest oxygen pressure n is equal to 1/6.

The latter value of n is concluded to reflect a defect structure predominantly involving doubly ionized oxygen vacancies (Eq. [9]). Correspondingly a value of $n = 1/4$ is concluded to reflect a defect structure in terms of singly ionized oxygen vacancies (Eq. [8]).

In order to explain the change in oxygen pressure dependence from $n = 1/4$ to $n = 1/6$ (*e.g.*, at 877°C) it is necessary to assume that the ionization energies of trapped electrons, *i.e.*, E_b and E_c, decrease with increasing defect concentrations. The same interpretation has been given of changes in the oxygen pressure dependence of the electrical conductivity in α-Nb_2O_5 (4) and of similar changes in thermogravimetric studies on rutile (5). In the latter cases it has been proposed that the ionization energies may be expressed as

$$E_i = E_o - aN^{1/3} \qquad [13]$$

where E_i represents the ionization energy, E_o is the ionization energy for an isolated donor, and N is the number of donors. Equation [13] was originally proposed by Pearson and Bardeen (18) for electron holes in silicon. As discussed by Cronemeyer in connection with studies of infrared absorption of reduced rutile a similar behavior is expected for oxide semiconductors (15).

According to Eq. [13], E_i changes rapidly when degeneracy ($E_i = 0$) is approached. This may in turn explain qualitatively the relatively rapid change in oxygen pressure dependence in going from a value of $n = 1/4$ to $1/6$ (*e.g.*, at 877°C in Fig. 1).

When $n = 1/6$ the temperature dependence of the carrier concentration is given by

$$[e^-] = (2K_{Oa}K_{Ob}K_{Oc})^{1/3}\, p_{O_2}^{-1/6} \exp\left(-\frac{\Delta H_a + E_b + E_c}{3RT}\right) \qquad [14]$$

K_{Oa}, K_{Ob}, and K_{Oc} represent pre-exponential factors according to Eq. [10].

A plot of the logarithm of resistance as a function of the reciprocal absolute temperature when $n = 1/6$ (*e.g.*, at $p_{O_2} = 10^{-12}$ atm) is given in Fig. 5, and as seen the activation energy equals 50 kcal/mole. This experimentally observed activation energy also includes the effect of carrier mobility which has a negative temperature coefficient. Thus depending on the relative importance of the mobility, it may be concluded that 1/3 $(\Delta H_a + E_b + E_c) \geqq 50$ kcal/mole or $(\Delta H_a + E_b + E_c) \geqq 150$ kcal/mole. In terms of the theory of decreasing ionization energy with increasing defect concentrations, E_b and E_c may be considered negligibly small when $n = 1/6$, and thus $(\Delta H_a + E_b + E_c) \approx \Delta H_a$.

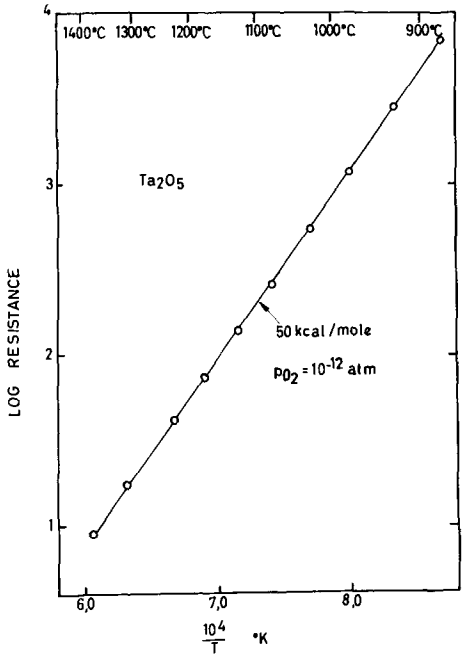

Fig. 5. Logarithm of the resistance of Ta_2O_5 specimen at $p_{O_2} = 10^{-12}$ atm as a function of the reciprocal absolute temperature.

According to Eq. [8] the temperature dependence of the charge carrier concentration when $n = 1/4$ should equal

$$[e^-] = (K_{Oa}K_{Ob})^{1/2}\, p_{O_2}^{-1/4} \exp\left(-\frac{\Delta H_a + E_b}{2RT}\right) \qquad [15]$$

If E_b is assumed small under these conditions the activation energy for the charge carrier concentration should be about $\frac{150}{2} = 75$ kcal/mole.

From the present results it is difficult to evaluate the temperature dependence of the resistance (or conductivity) under these conditions. For the results at 877° and 927°C it has, however, been attempted to draw the curves with values of $n = 1/4$. This is indicated by the stippled lines in Fig. 1. These two curves suggest an activation energy of about 70-75 kcal/mole for the conductivity when $n = 1/4$. Although no great accuracy can be claimed for such evaluation from but two temperatures, the results indicate satisfactory agreement with the above interpretation.

A corresponding treatment for the p-type conductivity does not appear possible because of the lack of knowledge of the exact oxygen pressure dependence under these conditions. From the results it is difficult to resolve the contribution from intrinsic conductivity and that of the p-type conductivity resulting from interstitial oxygen. However, the fact that the maxima become more pronounced at decreasing temperatures suggests that the p-type conductivity has a smaller activation energy than the intrinsic conductivity. This also explains that the maxima are displaced towards lower oxygen pressures at the lower temperatures.

The transition from the low-temperature to high-temperature modification of Ta_2O_5 has been reported to take place at about 1320°C (6, 7). This transition may be expected to influence the electrical conduc-

tivity in Ta_2O_5. The results at 1380°C also show anomalies which may be traced to such effects.

From Fig. 5 it is seen that at $p_{O_2} = 10^{-12}$ atm there is no change in the activation energy at the transition temperature. This may indicate that the transition temperature is a function of the oxygen pressure, and that the *low*-temperature modification is stable even at 1380°C at oxygen pressures smaller than about 10^{-8} atm. An alternative interpretation may also be that the heat of formation of oxygen vacancies are not appreciably different in the two modifications of Ta_2O_5.

Similarly from Fig. 4 it is also seen that no change in the activation energy is observed at the transition temperature. This thus indicates that the intrinsic energy gap is not appreciably different for the two Ta_2O_5 modifications.

As shown above the value of the heat of formation of oxygen vacancies in β-Ta_2O_5 was found to be $(\Delta H_a + E_b + E_c) \geqq 150$ kcal/mole. The corresponding value for α-Nb_2O_5 has been found from thermogravimetric studies to be 103 kcal/mole (2). Thus the heat of formation of oxygen vacancies is 1.5 times larger for β-Ta_2O_5 than for α-Nb_2O_5. For α-Nb_2O_5 the value of x was found to be about 0.01 at 1227°C and at an oxygen pressure of 10^{-14} atm. On the basis of the differences in heat of formation of oxygen vacancies in α-Nb_2O_5 and in β-Ta_2O_5 and assuming the same entropy change for the defect equilibrium in the two oxides, it may be estimated that the value of x in Ta_2O_{5-x} under the same conditions should be about $x \approx 10^{-9}$. This thus explains the very small weight changes observed in the thermogravimetric studies on Ta_2O_5. Considering the experimental errors involved in weight measurements, it also appears impossible on this basis to study the defect structure of Ta_2O_5 by thermogravimetric techniques.

Below about 700°-800°C the defect reactions apparently become sluggish, and several hours (and at lower temperatures even days) were needed to establish an apparent equilibrium. Therefore the oxygen pressure dependence of the conductivity was not studied in detail under these conditions. However, the temperature dependence at 1 atm O_2 was measured down to 450°C. In these measurements equilibration periods of 1 day were used. The results are shown in Fig. 6, which gives the logarithm of the electrical resistance of the specimen as a function of the reciprocal absolute temperature. A change in the activation energy is observed in the temperature range 600°-800°C, and at the lower temperatures the activation energy amounts to about 14 kcal/mole or 0.61 ev. This may reflect conduction due to impurities in the oxide.

In the above discussion of the defect structure of Ta_2O_5 effects of impurities have not been considered. Impurities may of course greatly affect the defect structure and the associated electrical conductivity. In the present work it is not possible to evaluate eventual effects of impurities present in the oxide. When considering impurities it is likely that these have larger effect close to stoichiometry where the defect reactions such as Eq. [2], [3], and [4] are of minor relative importance. In future studies in this

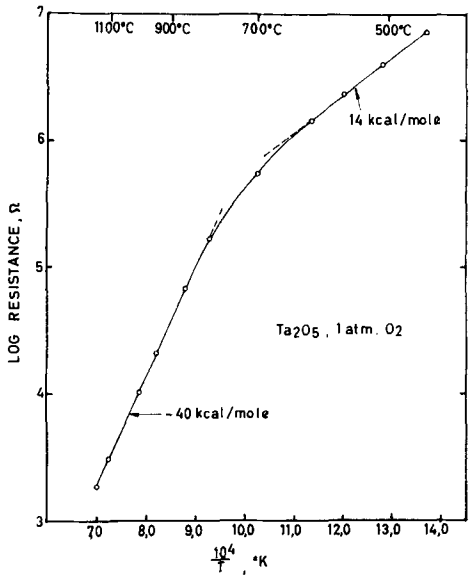

Fig. 6. Logarithm of the resistance of Ta_2O_5 specimen at 1 atm O_2 as a function of the reciprocal absolute temperature.

institute the effect of known amounts of impurities on the defect structure of Ta_2O_5 will be studied.

In this connection it is of interest to note that rutile doped with small amounts of Fe^{+3} (0.02 and 0.2 mole %) exhibits similar transitions from n- to p-type conductivity as observed in the present work (16). The transitions take place at lower oxygen pressures for the more heavily doped sample. Undoped rutile only shows n-type conductivity below 1 atm O_2. This may indicate that an n-type to p-type transition takes place at a higher oxygen pressure than 1 atm for the undoped oxide.

At high temperatures n-conducting rutile has a defect structure involving oxygen vacancies (5). As for Ta_2O_5 it may be proposed that p-conducting rutile at high temperatures also involves interstitial oxygen. In these terms it may be concluded that trivalent iron in rutile has different relative effects on the defect reactions involving interstitial oxygen and oxygen vacancies (Eq. [11] and Eq. [2], [3], and [4]) so as to cause a displacement of the transition of n- to p-type conductivity to lower oxygen pressures. The exact mechanism involved is difficult to elucidate at present and will have to await further studies on this system.

The present work on Ta_2O_5 is of importance for the understanding of the oxidation mechanism of tantalum at high temperatures. A detailed discussion of the effect of the transition from n- to p-type conductivity on the oxidation behavior will, however, be given elsewhere (1).

Acknowledgment

The work has been sponsored by the Aeronautical Systems Division, AFSC, through the European Office, Office of Aerospace Research, United States Air Force.

The author is indebted to Mrs. M.-K. Melsom for carrying out most of the experimental work. Thanks are also due to Mr. P. B. Anderson, Mr. Ö. Kalvenes and other members of the Central Institute for In-

dustrial Research for their assistance and helpful discussions.

Manuscript received March 12, 1962.

Any discussion of this paper will appear in a Discussion Section to be published in the June 1963 JOURNAL.

REFERENCES

1. P. Kofstad, To be published.
2. P. Kofstad and P. B. Anderson, *Inst. J. Phys. Chem. Sol.*, **21**, 280 (1962).
3. P. Kofstad, Ö. Kalvenes, P. B. Anderson, and G. Lunde, TN No. 3, AF 61(052)-460, Central Institute for Industrial Research, Oslo, Norway.
4. P. Kofstad, In press, *Inst. J. Phys. Chem. Sol.*
5. P. Kofstad, *ibid.*
6. S. Lagergren and A. Magnéli, *Acta Chem. Scand.*, **6**, 444 (1952).
7. R. J. Wasilewski, *J. Am. Chem. Soc.*, **75**, 1001 (1953).
8. H. J. Goldschmidt, *J. Inst. Metals*, **87**, 253 (1959).
9. F. Holzberg, A. Reisman, M. Berry, and M. Berkenblit, *J. Am. Chem. Soc.*, **79**, 2039 (1957).
10. A. Magnéli and S. Lagergren, A.S.T.M. Index Card 5-0379.
11. N. Schönberg, *Acta Chem. Scand.*, **8**, 240 (1954).
12. N. Norman, P. Kofstad, and O. J. Krudtaa, *Less Common Metals*, **4**, 124 (1962).
13. A. U. Lapitsky, Yu. P. Simanov, and E. P. Artamonov, *Nucl. Sci. Abstr.*, **12**, 64083 (1958).
14. K. Hauffe, "Reaktionen in und an Festen Stoffen," Springer Verlag Berlin (1955).
15. D. C. Cronemeyer, *Phys. Rev.*, **87**, 876 (1952); **113**, 1222 (1959).
16. J. Rudolph, *Z. Naturforschung*, **14a**, 727 (1959).
17. F. A. Grant, *Revs. Mod. Phys.*, **31**, 646 (1959).
18. G. L. Pearson and J. Bardeen, *Phys. Rev.*, **75**, 865 (1949).

The Anodic Oxidation of Iron in a Neutral Solution

I. The Nature and Composition of the Passive Film

Masa-ichi Nagayama[1] and Morris Cohen

Division of Applied Chemistry, National Research Council, Ottawa, Ontario, Canada

ABSTRACT

Iron was anodically oxidized in a borate-boric acid buffer solution of pH 8.4 in the potential range extending from the active region to oxygen evolution. In the active region there appeared to be some Fe_3O_4 on the surface. In the passive region the iron was covered with an oxide film 10-30Å thick, depending on the potential. The structure of the film was studied by its cathodic behavior and electron diffraction and was found to consist of an inner "Fe_3O_4" and an outer "γ-Fe_2O_3" layer. The outermost part of the film had a defect structure of the general formula $Fe_x^{6+} \cdot Fe_{2-2x}^{3+} \cdot \square_x \cdot O_3$. The thicknesses of the layers and the number of defects were found to be functions of the anodic potential. The chemical reactions involved in the anodic passivation and the subsequent cathodic reduction processes are discussed.

The phenomenon of "passivity" of iron was first noted over one hundred years ago by Faraday and Schönbein, and since that time the factors controlling the establishment and maintenance of this state have been investigated by many workers (1-5). There is as yet no commonly accepted view of the nature of the passive film or the role that it plays in passivity. In this investigation the electrochemical quantities involved in the anodic formation and subsequent cathodic reduction of passive films on iron in a neutral borate-boric acid buffer solution were measured and compared. From the results information has been obtained regarding the chemical reactions in the passivation and reduction processes and on the thickness, chemical composition, and structure of the passive film.

Experimental

Materials.—Ferrovac iron sheets of 5 x 1 cm with small handles were used as test specimens.[2] After polishing with 4/0 emery paper, the specimens were electropolished in a mixture of glacial acetic and 70% perchloric acids (20:1) at a c.d. of 0.45 amp/cm^2 (6). Temperature of the bath was kept between 15° and 17°, and polishing was done in 10-sec bursts to avoid overheating. A total thickness of more than 20μ was dissolved so as to remove the deformed layer due to abrasion. The specimen was withdrawn from the bath and immediately washed with a jet stream of anhydrous methyl alcohol, then dried quickly by absorbing the methanol with Fisher lens paper. Electron microscopic observation (Fig. 10(a)) indicated a very smooth surface; the surface roughness factor would be very close to unity (6, 7). This procedure was followed by annealing in a hydrogen atmosphere for about 2 hr at 700°C. The specimens were electropolished again for a short period just before measurement.

A deaerated equivolume mixture of 0.15N sodium borate and 0.15N boric acid solutions was used for both the anodic passivation and the cathodic reduction experiments. The pH of this solution is 8.41. The solution was kept in a storage vessel under a stream of nitrogen which was purified by bubbling through Fieser's solution and then passing through

[1] N.R.C. Postdoctorate Research Fellow. Present address: Faculty of Science, Hokkaido University, Sapporo, Japan.

[2] The composition of the iron was: C 0.007 (%), N 0.0002, O 0.013, P 0.0002, S 0.0017, Si 0.0095, Al 0.001-0.003, Cu 0.001-0.003, Mn 0.002-0.004, Pb none detected <0.01, Sn none detected <0.004.

a column of finely dispersed copper on Kieselguhr, heated to 220°C. The oxygen content of the solution was checked by an electrochemical method with a Pt cathode, and it was found that the concentration was less than 1 x 10^{-7} m/l. The corresponding limiting diffusion current of oxygen, 0.04 μa/cm^2, would not have affected the results of the experiments.

Cell.—The electrolytic cell used was similar to that described by Oswin and Cohen (8). It had a capacity of about 80 ml and was usually filled with 30 ml of the solution. Solution could be transferred from the storage vessel to the cell or removed from the cell for analysis under a nitrogen atmosphere through a three-way solution-lubricated glass stopcock at the bottom. For the purpose of polarizing the specimen two auxiliary Pt electrodes were provided. The one employed for the cathodic reduction of the specimen consisted of a set of two Pt wires sealed at the top of glass side arms. The other was a cylindrical Pt sheet having a large geometrical surface area (80 cm^2) fixed in position so as to surround the specimen, being used only for the anodic passivation experiment. The specimen was suspended on a heavy tungsten wire sealed into the ball-joint on the top of the cell, and the potential of the specimen was measured against a saturated calomel electrode via a salt bridge filled with the electrolytic solution.

Electrical circuit.—A schematic diagram of the electrical circuit used is shown in Fig. 1. The right-hand side is a potentiostatic polarization circuit employed to apply a constant anodic potential to the specimen. The design of the potentiostat is basically that of Gerischer and Staubach (9). It consists of a differential amplifier having an amplification factor of 600 and a band width of about 5 kc/sec. Zero point drift was found to be less than 5 mv/day. The change of current with time after applying a constant potential was followed by recording the ohmic drop across a standard resistance of 100 ohms inserted in the polarizing circuit in the usual way. A recorder of the direct writing oscillograph type (range 0-200 mv) was used for the initial current of several milliamperes, and it was then switched over to a strip chart recorder of higher sensitivity (range 0-10 mv) when the current went down to about 100 μa. The response times of these recorders were about 1/100 sec and 1 sec for the full scale shift of the needle, and chart speeds were 25 mm/sec and 8 mm/min, respectively. As has been pointed out recently by Will (10) and others (11), the time required to attain a constant potential is a function of the total impedance in the polarizing circuit, so that an effort was made to keep the resistance of the cell and of the recorder low so as to obtain a constant potential within 5 sec. The left-hand side of the figure is a galvanostatic polarization circuit consisting of a transistor rectifier of 30v output voltage and variable large resistance. It was used mainly to apply a constant cathodic current to the specimen. The change of potential with time during cathodic reduction was recorded with a Speed-o-Max recorder (range 0-100 mv) through an electron-tube potentiometer having an input impedance of about 10^8 ohms. The direction of polarization could be changed rapidly by means of a multiple switch. All the experiments were conducted at room temperature, which ranged from 24° to 25.5°C, and potential data given here are always referred to the saturated calomel electrode.

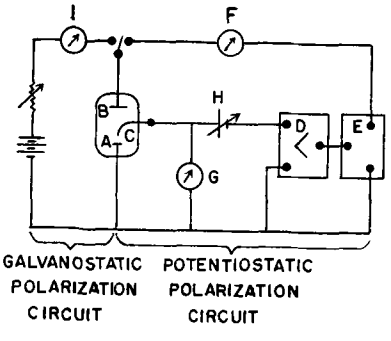

Fig. 1. Schematic representation of circuit. A, specimen; B, auxiliary Pt electrode; C, saturated calomel electrode; D, differential amplifier; E, output tube of the amplifier; F, current-recorder; G, vacuum tube voltmeter with recorder; H, signal voltage; I, microammeter.

Analysis.—Colorimetric analysis of the solution for iron by the orthophenanthroline method could be carried out after any desired period of time of cathodic or anodic polarization by removing the specimen quickly from the solution while the polarization was going on and dumping the solution from the cell. The technique of analysis can be briefly described as follows: The analytical reagent was made up from 200 ml of 0.25% o-phenanthroline, 300 ml of 3% hydroxylamine-hydrochloride and 500 ml of 10% acetic acid, and it was stored in a refrigerator. Ten milliliters of the mixed reagent was transferred to a 50 ml volumetric flask, being followed by the addition of the solution and washings to the mark. The amount of acetic acid in the reagent had been chosen so as to make the *p*H of the final mixture about 4. Measurement of optical density in a 50 mm silica cell was carried out 30 min after mixing with a Beckman Model B spectrophotometer at 508 mμ. Experimental error of the analysis is claimed to be less than ± 1.0%. The limiting sensitivity of this method is 0.05 μg Fe^{++} in the total solution.

Results

Anodic polarization curve.—The nearly stationary anodic polarization curve obtained by means of the potentiostat is shown in Fig. 2. Before the measurement of each point, the specimen was pretreated at a cathodic current of 10 μa/cm^2 until the air-formed or passive oxide film was completely removed. This could be checked by the cathodic potential measurements which will be described later. The solution was changed after the cathodic treatment. The transition from the active and the passive states takes place in the potential region from —650 mv to —550 mv (E_a^1). In the passive potential region from —550 to +850 mv, the magnitude of the current falls to less than 0.01 μa/cm^2 after 10 hr of polarization, and even then it was still tending to decrease with time. Beyond a potential of about +850 mv (E_a^3), the current again begins to increase steeply with potential presumably because of the onset of oxygen evolution.

Potentiostatic measurement of the amount of film.—Each experiment was started from the completely reduced surface condition. The change in the anodic

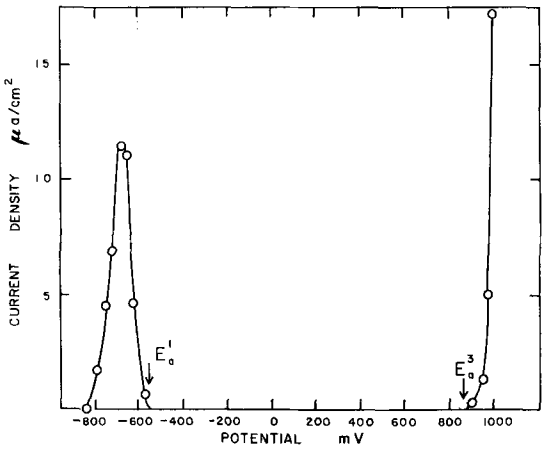

Fig. 2. Anodic polarization curve

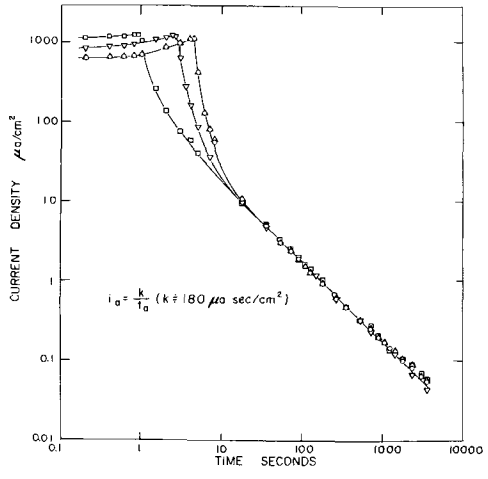

Fig. 3. Change of current with time after applying anodic polarization. Dotted circle, E_a = +600 mv, 20 min additional cathodic treatment after completing the reduction; dotted triangle, E_a = +600 mv, just after completing the reduction; inverted dotted triangle, E_a = +200 mv, just after completing the reduction; dotted square, E_a = —300 mv, just after completing the reduction.

current i_a with time t_a was followed immediately after applying a constant passive potential. Log-log plots of the $i_a - t_a$ relationship obtained at three passive potentials are shown in Fig. 3. The relatively large current of the order of 1 ma/cm² flowing in the initial period of time decreases rapidly, but the change then becomes much slower. While the shape of the initial part of the curve is markedly dependent on the impedance of the polarizing circuit, the succeeding part of the curve is a straight line of slope approximately 45° independent for both applied potentials and practical values of the circuit element; the point of transition between these two parts of the curve is quite dependent on the impedance. The linear relation was ascertained to continue for at least 15 hr. This relationship has been reported by many workers for the passivation of iron and other metals (12). The charge passed can be calculated by graphic integration of the curve. For different values of impedance, and consequently for different shapes and heights of the initial part of the curve, it is still an experimental fact that the total charge passed up to the transition point is a constant for a constant applied potential. Thus, the amount of charge passed during 1 hr of polarization was calculated, and the results obtained for the various anodic potentials E_a ranging over the passive region are shown in Fig. 4. The amount of charge Q_a accumulated in the film was then obtained by subtracting the equivalent coulombs for the amount of iron found in the solution from the total charge passed. The dissolution of iron occurs as ferrous ion below —200 mv, the amount being increased as the potential is lowered. In the potential range between 0 to +850m, the relation between Q_a and E_a is essentially a straight line having a slope of 0.34 mC/cm²/100 mv. This slope is similar to that roughly estimated by Weil (13) for passive iron in phthalate buffer solution at pH 6. A slight negative deviation from the linear relationship is observed in the potential region below about 0 mv (E_a^2). The fact that Q_a commences to increase steeply with potential beyond +850 mv would be explained as being due to the oxygen evolution reaction. Hence, the amount of the oxide film above +850 mv cannot be determined by this method.

The effect of time of polarization t_a on the Q_a — E_a curve is roughly estimated as shown in Fig. 5,

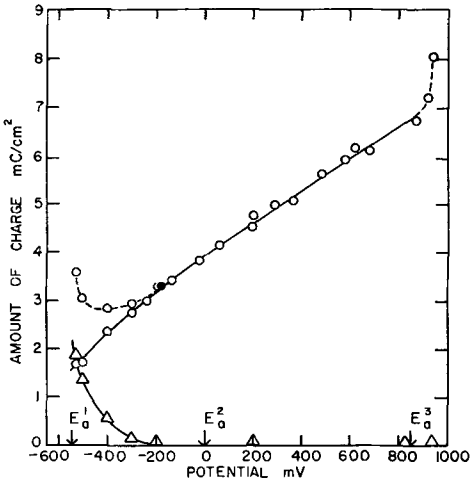

Fig. 4. Effect of potential on the amount of charge passed during 1 hr anodic polarization . . . . ○ . . . , Total amount of charge passed; ——△——, amount of charge corresponding to the Fe^{++} dissolution; ——○——, amount of charge for the formation of passive film; ●, amount of charge for a [112] single crystal specimen.

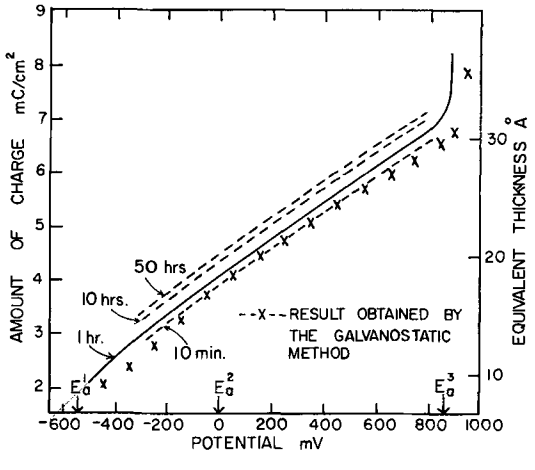

Fig. 5. Effect of time of polarization on the amount of passive film.

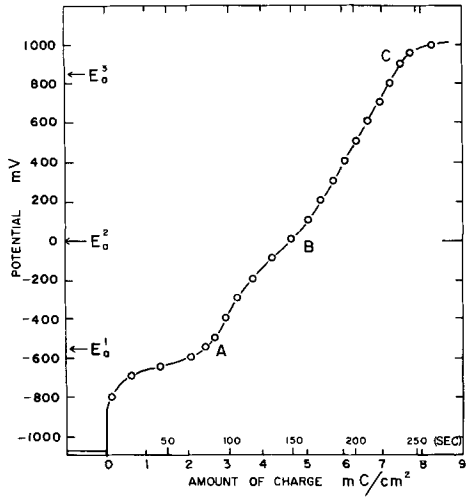

Fig. 6. Change of potential with time during galvanostatic anodic polarization (c.d. = 31.4 μa/cm², amount of corrosion = 0.28 μg Fe^{++}/cm² = 0.97 mC/cm²).

assuming that the linear relation between log i_a and log t_a does not depend on the applied potential and that it will also hold for up to 50 hr. It can be seen that the curves do not change very much from the one obtained for one hour's experiment even if the polarization is continued for 50 hr.

Galvanostatic measurement for the amount of film.—The amount of charge required to passivate a specimen, which had been pretreated by cathodic polarization, was estimated by the galvanostatic method for comparison with the result obtained by the potentiostatic method. A current higher than the maximum current which is observed in the active potential region of the polarization curve (Fig. 2) was applied, and the resulting change of potential with time t or charge passed was followed. The result is shown in Fig. 6. Two waves are observed in the initial and middle parts of the curve. The first transition point, A, is in the potential region of E_a^1 where the transition from the active to the passive state takes place in the potentiostatic experiments. The second transition, B, at about 0 mv corresponds to the point E_a^2 on the potentiostatic polarization curve where a negative deviation in the $Q_a - E_a$ curve was observed. Point C corresponds to the oxygen evolution potential E_a^3. A similar type of curve was reported by Heusler and Weil (14) for iron in an amino-acetic acid buffer solution of pH 9.3. The quantity of charge accumulated in the film Q_a was obtained by subtracting the equivalent coulombs for the amount of iron found in solution from the total charge passed, assuming that the corrosion had occurred as $Fe \rightarrow Fe^{++} + 2e$ before the point A was reached. The result is shown in Fig. 5 as crosses. The $Q_a - E_a$ curve obtained by this method is quite similar to that obtained by the potentiostatic method for a very short period of polarization such as several minutes. This method, however, seems to have disadvantages for the purpose of obtaining a reproducible passive condition or for controlling the film thickness of the specimen at a certain passive potential.

Cathodic reduction curve.—The anodic passivation experiments were immediately followed by

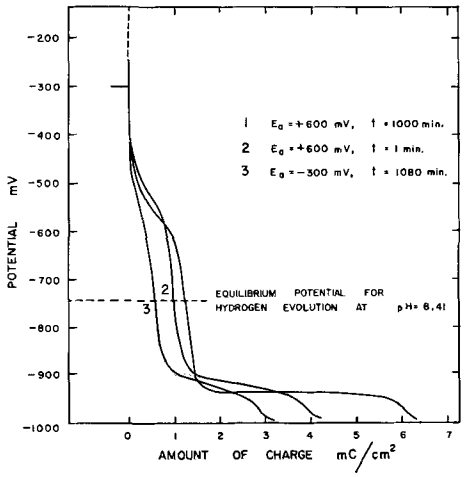

Fig. 7. Effect of anodic polarization and time of polarization on the cathodic reduction curve.

measurement of the cathodic reduction curve; the change of cathodic potential E_c with time or amount of charge Q_c was traced at a constant c.d. of about 10 μa/cm². Typical cathodic reduction curves obtained for various passivating conditions are shown in Fig. 7. Three arrests or two waves can be seen in the curves, and the points of inflection corresponding to these arrests appear around −550 mv, −920 mv, and −1000 mv, respectively. The potential for the first arrest is in the same potential region where the active-passive transition occurs (E_a^1). In general, the change from the first to the second wave becomes much more clearly defined and more charge seems to be associated with both waves, the more positive the anodic potential and the longer the time it is applied. Thus, the amount of charge Q_c^1 and Q_c^2 associated with these two waves is measured as a function of passive potential, and the time of polarization, and the results are shown in Fig. 8 and Fig. 9.[3] It might be interesting to point out here that the slope of the $Q_c^1 - E_a$ curve (Fig. 8) changes at

[3] The intersection of the extrapolated lines of the descending part of the first wave and the second arrest, and the point of inflection between the second arrest and the third plateau are used for calculation of coulombs passed.

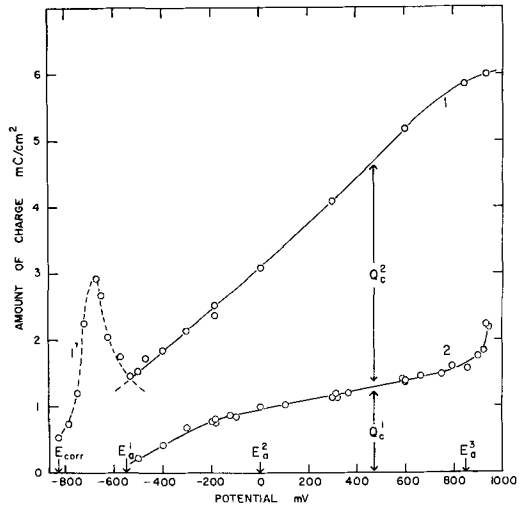

Fig. 8. Effect of anodic polarization on the first and second waves of the cathodic reduction curve (t_a = 1 hr). 1,1', Total amount of charge for the complete cathodic reduction; 2, amount of charge for the first wave of cathodic reduction.

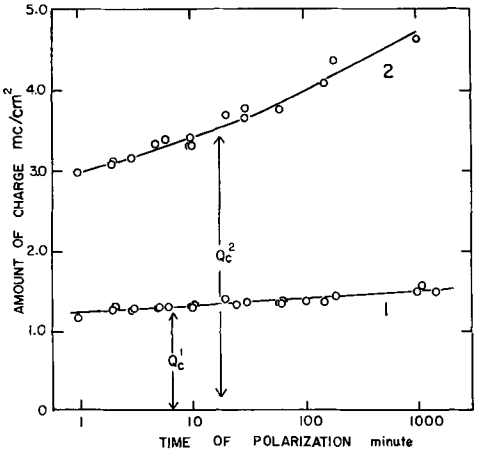

Fig. 9. Effect of time of anodic polarization on the amount of charge for the first and the second waves of the cathodic reduction curve (E_a = +600 mv). 1, amount of charge for the first wave; 2, amount of charge for the second wave.

the same characteristic potentials of E_a^2 and E_a^3 as is shown in Fig. 4, and that Q_c^1 approaches zero at the transition potential between the active and the passive states E_a^1.

Cohen and his co-workers (8, 15) have recently obtained the cathodic reduction curve for oxidized iron in a neutral borate-HCl buffer solution at a c.d. similar to ours, and have found by means of electron-diffraction that the composition of the oxide when the first wave appears around −850 mv is α-Fe_2O_3 and unreducible magnetite remains on the second plateau of about −930 mv. Stockbridge, Sewell, and Cohen (16) have further studied the cathodic reduction of thin air-formed oxide films on iron and have ascertained that when the first wave appeared at a much higher potential (−500 mv *vs.* S.C.E. at *p*H 7.6) than that for α-Fe_2O_3, it was mainly due to the existence of γ-Fe_2O_3 as the outer layer of the film. Hence, by referring to these results, the first and the second waves and the third plateau observed here in the cathodic reduction curve are probably related to a structure of a surface of γ-Fe_2O_3, magnetite, and the bare metal, respectively. The magnetite layer seems to be completely reducible in this case. This reducibility of the magnetite is confirmed by the fact that if cathodic reduction is used as the pretreatment for an anodic passivation and if the reduction has been carried on until the third plateau or the bare surface condition is attained, then the $i_a - t_a$ curve or the amount of charge Q_a accumulated during the anodic passivation becomes reproducible and independent of the previous treatment of the specimen (cf. Fig. 3). An electron diffraction examination by reflection was made for the passive film of about 15Å produced at −190 mv on a [112] single crystal specimen (cf. Fig. 4). The pattern shown in Fig. 10 indicates a cubic structure of the film having an average lattice parameter of a = 8.37 ± 0.04Å. This could also be explained by the concept that the outer and the inner layers of passive film are mainly composed of γ-Fe_2O_3 and Fe_3O_4 (17). An attempt to obtain a reflection diffraction pattern for the film of about 30Å obtained at higher passive potential

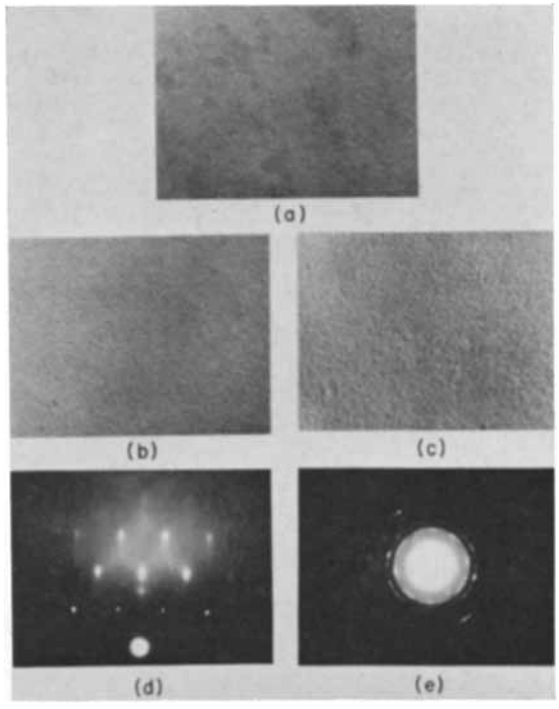

Fig. 10. Electronmicrograph of surface and electron diffraction of passive film. Series treatment of surface, Pt-C replicas, co-evaporated at 45°, magnification 100,000X. (a) Electropolished; (b) anodically passivated for 1 hr at +600 mv; (c) cathodically reduced at 10 μa/cm²; (d) reflection electron diffraction of anodically passivated 112 single crystal, 112 surface from $1\bar{1}1$ azimuth. Specimen was passivated at +190 mv for 1 hr, film thickness ca. 15Å. $d_{(100)}$ = 8.37 ± 0.04Å; (e) transmission electron diffraction of passive film stripped from polycrystalline specimens passivated at +850 mv for 1 hr. $d_{(100)}$ = 8.40 ± 0.04Å.

was also made, but no clear information was obtained. A transmission pattern showing the structure of cubic iron oxide was obtained for a film of similar thickness stripped from a polycrystalline specimen by the iodine-methanol method (Fig. 10).

As a matter of interest, cathodic reduction curves were obtained for specimens which were anodically polarized at nearly steady states in the active potential region. Only the second wave of the curve, which could not be clearly defined, was observed. This would indicate that in the active region no ferric oxide is formed, but that there may be some magnetite present on the surface. The $Q_c - E_a$ curve in Fig. 8 shows a maximum amount of charge of about 3 mC/cm² at E_a = −660 mv which agrees with the potential where maximum anodic current is observed.

Ferrous ion dissolution during cathodic reduction. —The amount of the ferrous iron dissolution $W_{Fe^{++}}$ at various stages of the cathodic reduction was measured for a specimen which was polarized anodically at +600 mv for 1 hr. The results obtained are shown together with the cathodic reduction curve in Fig. 11. The broken line OA indicates the relationship between $W_{Fe^{++}}$ and Q_c which would be expected if the cathodic reduction from ferric oxide to ferrous ion followed the reaction

$$Fe_2O_3 + 6H^+ + 2e \rightarrow 2Fe^{++} + 3H_2O$$

with a current efficiency of 100%. As can be noted, there is a distinct negative deviation from the theo-

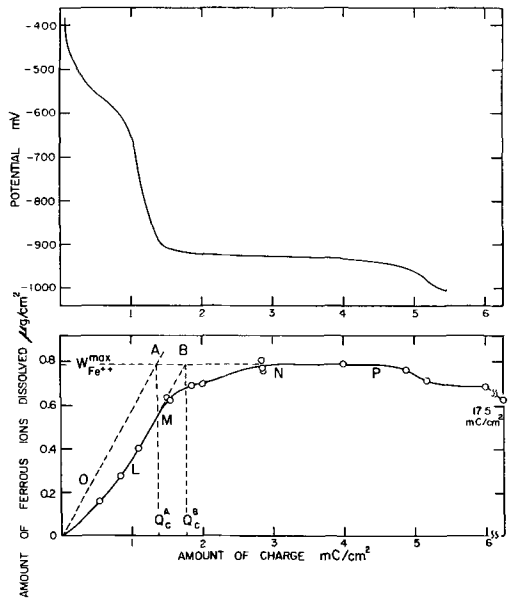

Fig. 11. Amount of ferrous ion found in the solution during cathodic polarization (E_a = +600 mv, t_a = 1 hr).

retical line OA in the early part of the reduction process, followed by a section LM in which cathodic reduction is essentially 100% efficient. The reduction efficiency then begins to drop sharply from the point M onward. This point corresponds to the point of inflection at the second wave of the reduction curve, and the reduction efficiency finally becomes nearly zero at point N. No change in the Fe^{++} ion concentration is observed until the point P that corresponds to the end of the magnetite wave is reached. A drop in Fe^{++} concentration is observed after completing the reduction of the oxide film.

Similar curves for films formed at other potentials are shown in Fig. 12. In all cases these show the negative deviation from 100% current efficiency at low values of Q_c. In every case 100% current efficiency (corresponding to point L in Fig. 11) is reached at a cathodic reduction potential of −700 mv. If we assume that the cathodic processes between M and N on Fig. 11 consist of 100% current

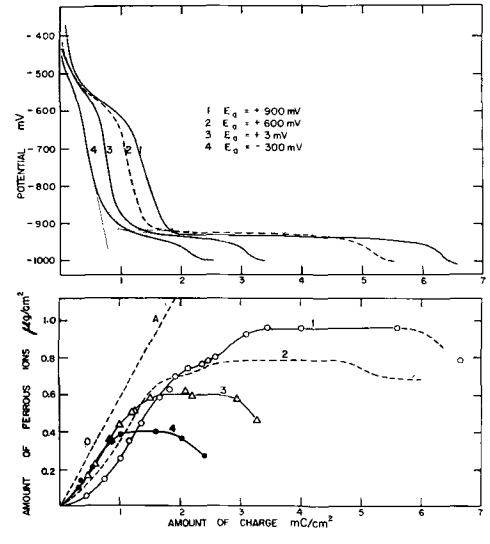

Fig. 12. Effect of anodic polarization for $W_{Fe^{++}}$ — Q_c curve (t_a = 1 hr).

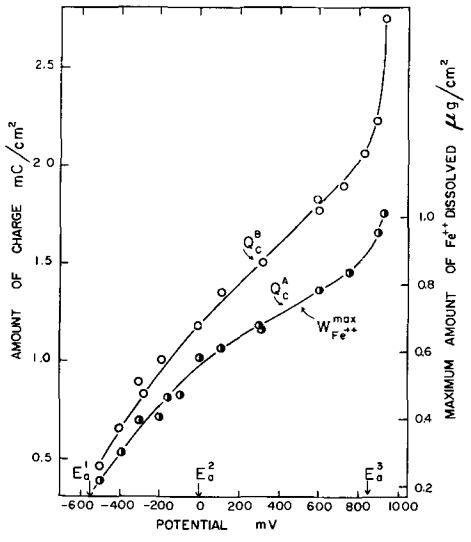

Fig. 13. Effect of anodic polarization on Q_c^A, $W_{Fe^{++}}^{max}$ and Q_c^B (t_a = 1 hr).

efficiency of reduction of γ-Fe_2O_3 to dissolved Fe^{++} ion and low current efficiency reduction of Fe_3O_4 to the metal, then extrapolation of LM to the line at which the maximum amount of dissolved ferrous ion is observed gives the actual amount of charge Q_c^B required to reduce the outer layer.

A series of experiments were then made to determine the number of coulombs required to reach −700 mv and the accompanying amount of iron in solution for specimens which had been anodically treated for 1 hr at various potentials.[4] The maximum amount of dissolved iron $W_{Fe^{++}}^{max}$ which could be produced was also measured by analyzing the solution when cathodic reduction had been carried on to about the middle part of the second wave of the reduction curves. The theoretical number of coulombs for the reduction of stoichiometric ferric oxide Q_c^A was calculated from the experimental value of $W_{Fe^{++}}^{max}$. Q_c^B was obtained as described above. The results are shown in Fig. 13. As can be seen the deviation (Q_c^B — Q_c^A) becomes larger as the applied anodic potential E_a is raised. Inflection points on the curves appear around 0 mv and +850 mv, *i.e.*, in the same potential regions E_a^2 and E_a^3 where the characteristic inflection appears in the Q_a — E_a curve shown in Fig. 4.

Discussion

Anodic Reactions

In the active region the reactions are probably

$$Fe \rightarrow Fe^{++} + 2e \qquad [1]$$

$$3Fe + 4H_2O \rightarrow Fe_3O_4 + 8H^+ + 8e \qquad [2]$$

At this stage there always appears to be some magnetite on the surface, as judged from the cathodic reduction potentials.

When the anodic potential is made more positive, *i.e.*, electrochemical conditions are more oxidizing,

[4] Since changing the solution immediately following anodic polarization had been found not to affect the behavior on cathodic reduction, the solution was changed twice just before cathodic reduction for the case where anodic polarization had been at potentials < -200 mv or $> +850$ mv in order to remove ferrous ions or oxygen which had been produced during anodic polarization.

the outer part of the Fe_3O_4 is converted to γ-Fe_2O_3 by reactions such as

$$2Fe + 3H_2O \rightarrow \gamma\text{-}Fe_2O_3 + 6H^+ + 6e \quad [3]$$

$$2Fe_3O_4 + H_2O \rightarrow 3\gamma\text{-}Fe_2O_3 + 2H^+ + 2e \quad [4]$$

It is probable that the oxidation takes place through reaction [4]. The oxidation of magnetite to γ-Fe_2O_3 by air or oxygen at room temperatures has been observed previously (16), and the anodic oxidation was discussed in a previous paper (18). Under the more strongly oxidizing conditions of higher potentials during anodic polarization the outer layer of the γ-Fe_2O_3 may be oxidized even more to form a cation vacancy structure which is still in the cubic system by the reaction

$$(2-x)\gamma - Fe_2O_3 + 3xH_2O \rightarrow$$

$$2Fe_x^{6+} \cdot Fe_{2-2x}^{3+} \square_x \cdot O_3 + 6xH^+ + 6xe \quad [5]$$

Some electron diffraction evidence for this type of vacancy structure leading to a lowered lattice parameter of the cubic oxide has been reported elsewhere for films formed by electropolishing (19).

In essence the above discussion treats the anodic passivation system in a manner similar to the treatment given for air oxidation of iron where the oxide is formed by a re-arrangement of oxygen and iron ions to form a lattice in which the oxygens form a face-centered cubic lattice with iron atoms fitted into octahedral and tetrahedral sites. The oxidation of magnetite to γ-Fe_2O_3 and of γ-Fe_2O_3 to the vacancy structure oxide take place by diffusion of iron ions out of the lattice accompanied by oxidation to a higher valency state.

On the basis of the above considerations the film formed by anodic polarization would have the composition shown in Fig. 14. Because of the close crystallographic resemblance of the oxides and the thinness of the film phase boundaries are probably not sharp. However, in general the phase next to the metal most closely resembles Fe_3O_4 and that next to the solution a cation vacancy cubic oxide containing iron of a valency greater than three, with γ-Fe_2O_3 between them.

Cathodic Reactions

The cathodic reduction curve has three plateaus corresponding to three electrochemical reactions. These can be considered to be

$$Fe_x^{6+} Fe_{2-2x}^{3+} \square_x \cdot O_3 + 3H_2O +$$

$$(2+2x)e \rightarrow (2-x)Fe^{++} + 6\,OH^- \quad [6]$$

$$Fe_3O_4 + 4H_2O + 8e \rightarrow 3Fe + 8\,OH^- \quad [7]$$

$$2H_2O + 2e \rightarrow H_2 + 2\,OH^- \quad [8]$$

In contrast to the results of Hancock and Mayne (20) which indicated that γ-Fe_2O_3 was reduced to metallic iron, the data obtained here show that the reduction product is always Fe^{++} ion in solution. In the middle part of the first wave of the reduction curve (from −700 mv to −900 mv) where γ-Fe_2O_3 is being reduced to ferrous ion with almost 100% current efficiency, any other side reactions such as

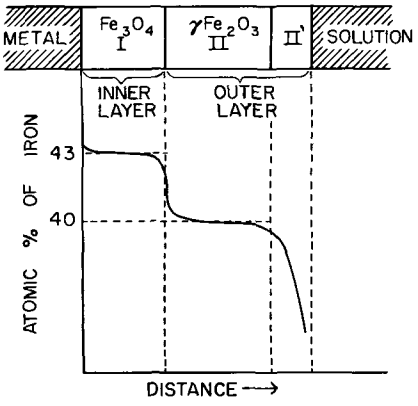

Fig. 14. Postulated change of film composition with the distance outward from metal/oxide interface.

hydrogen evolution or the conversion of γ-Fe_2O_3 to Fe_3O_4 (13, 14) are not likely to occur. Hydrogen evolution, even without polarization, cannot be expected above −750 mv at the *p*H of solution used. The lower current efficiency of reduction observed during the early period (above −700 mv) must therefore be due to a cation vacant (high iron valence) oxide.[5] In Eq. [6] showing the reduction of the outer γ-ferric oxide layer with the cation vacant structure in the outermost part, the value of x may vary from some finite value to zero consistent with stability of the structure and the applied anodic potential. The change of polarization potential E_c with Q_c in the first wave could be interpreted as being due to the gradual decrease of defect concentration at the oxide surface and to the increase of Fe^{++} ion concentration in the solution with the time of cathodic reduction.

In the second wave of the reduction curve except for the initial period of reduction, Fe_3O_4 is the only oxide present, and no ferrous ion is produced in solution. The Fe_3O_4 is reduced directly to iron with a low current efficiency, as is shown in Eq. [7], the accompanying reaction probably being hydrogen evolution on the surface of oxide, which will be further discussed below. After completing the reduction of Fe_3O_4, a potential which is characteristic of hydrogen evolution on iron (the third plateau) is reached. At this stage there appears to be some redeposition of iron from the ferrous ion in the solution. The concept of the complete reduction of the magnetite layer is supported by the fact that the number of coulombs used during anodic oxidation after complete cathodic reduction is independent of the time of cathodic reduction or of the thickness of the previous oxide before cathodic reduction (cf. Fig. 3). If the magnetite layer was not completely reduced, a very marked change was observed in the number of coulombs used during subsequent anodic passivation.

The ferrous ion dissolution observed in the initial period of the second wave (or in the final period of

[5] An interpretation of the low current efficiency of reduction could also be made by assuming either an oxygen rich type of oxide or an absorption of oxygen atoms on the surface of a stoichiometric oxide layer. However, the first idea is discarded because too much energy is needed to insert oxygen ions in the interstitial positions of the crystal lattice. The second possibility did not fit the experimental results on the decay of the passive potential which will be described in a following publication.

the first wave) is probably to be interpreted as due to the reduction of γ-ferric oxide still remaining as isolated areas on the surface of the underlying magnetite layer. This would be expected at the cathodic current density used for the reduction of such thin films. The relatively high c.d. was required in order to avoid self-corrosion or autoreduction of films. Thus in this stage the reduction of γ-Fe_2O_3 to Fe^{++} ion, the reduction of Fe_3O_4 to metallic iron and the evolution of hydrogen on the oxide are all taking place simultaneously. The lack of sharp definition in the transition between the first and the second waves of the cathodic reduction curve is related to the above situation.

Composition of the Film

The thickness and composition of the films formed during anodic passivation have been calculated from the number of coulombs used for anodic treatment and a study of the cathodic reduction data.

In order to calculate the exact number of coulombs associated with the anodic formation of passive film it is necessary to consider the amount of charge for the possible side reactions. Thus, the amount of charge equivalent to the ferrous ion dissolution which was found only in the potential region below −200 mv was subtracted from the total charge passed during the passivation experiment. The second possibility is the oxygen evolution reaction. Although the equilibrium potential for oxygen evolution in this solution is about +480 mv there is no change in the polarization curve until about +900 mv which indicates a high overvoltage for oxygen evolution. The fact that there is no discontinuity in the polarization curve and also in the $Q_a - E$ curve at +480 mv would indicate that oxygen formation plays no part in the passivation process. However, due to oxygen evolution above +900 mv, thicknesses could not be calculated above that potential.[6] The third possible reaction is the oxidation of hydrogen produced during the cathodic pretreatment to hydrogen ions at the early stage of passivation. The possibility of this reaction is discounted for two reasons. First, the number of coulombs required for anodic passivation was independent of the time of cathodic treatment after the magnetite was reduced. Second, any correction for hydrogen oxidation at the low passivation potentials would reduce the amount of magnetite only, and even a small correction would eliminate it. This is contrary to the observation that the potential wave for magnetite is always observed during cathodic reduction. On this basis, the rough estimation of film thickness is first made assuming a roughness factor of 1.2, a density of oxide of 5, and an average film composition of Fe_2O_3. The result is shown in Fig. 5. However, corrections to the thickness are required because of a change of film composition with the distance outward from the metal/oxide interface as described below.

Cathodic reduction of the outer layer of the oxide produces ferrous ion in solution. In that the reduction is done at constant current the time during reduction is a measure of charge passed. Iron in solution may also be formed by autoreduction. To check this point, cathodic reduction was carried out at three different current densities with a negligible effect on the number of coulombs Q_c^1 for the first wave. This is shown in Table I and indicates that there is no autoreduction during the cathodic reduction. An autoreduction reaction would reduce the number of coulombs required for cathodic reduction.

Table I. Effect of current density on the cathodic reduction curve

	$E_a = -182$ mv, $t_a = 1$ hr		$E_a = +850$ mv, $t_a = 1$ hr	
i_c, μa/cm²	Q_c^1, mC/cm²	Δ, %	Q_c^1, mC/cm²	Δ, %
5	0.796	+3.9	1.572	+0.9
10	0.766	—	1.558	—
20	0.762	−0.5	1.548	−0.6

A comparison was therefore made between the coulombs passed during cathodic reduction and the theoretical coulombs required for the production of Fe^{++} from Fe_2O_3 at various points on the cathodic reduction curve (Fig. 13). The excess of experimental to theoretical charge ($Q_c^B - Q_c^A$) before magnetite was uncovered was attributed to the presence of Fe^{6+} ion in the outer layer of the oxide.

If we assume that the vacancy structure is associated with the presence of Fe^{6+} in the outer layer of the film, the number of electrons required to reduce the film will be greater than the number based on a stoichiometric film of γ-Fe_2O_3. The proportion of Fe^{6+} (or vacancies) can be calculated as follows. The charge passed in reducing a ferric oxide film containing Fe^{6+} to ferrous iron in solution is

$$Q_c^B = (W_{Fe^{++}}^{max} - W_{Fe^{6+}}^{(S)})/A + (4W_{Fe^{6+}}^{(S)})/A \quad [9]$$

where $W_{Fe^{++}}^{max}$ [μg/cm²] is the maximum amount of ferrous ion dissolution during the cathodic reduction, $W_{Fe^{6+}}^{(S)}$ [μg/cm²] is the amount of hexavalent iron ion or the amount of vacancy in the outer layer of the film, and A [0.5787 μg/mC] is the electrochemical equivalent of iron for the one-electron reaction $Fe^{3+} + e \rightarrow Fe^{2+}$. Accordingly, the expression for the amount of hexavalent and trivalent ion in the film is

$$W_{Fe^{6+}}^{(S)} = \frac{1}{3}(Q_c^B \cdot A - W_{Fe^{++}}^{max}) \quad [10]$$

and

$$W_{Fe^{3+}}^{(S)} = W_{Fe^{++}}^{max} - W_{Fe^{6+}}^{(S)} = \frac{1}{3}(4W_{Fe^{++}}^{max} - Q_c^B \cdot A) \quad [11]$$

The amount of charge $Q_a^{(O)}$ [mC/cm²] used for the anodic formation of the outer oxide layer from metallic iron is then calculated by referring to Eq. [10] and [11] as

$$Q_a^{(O)} = 6W_{Fe^{6+}}^{(S)}/A + 3W_{Fe^{3+}}^{(S)}/A = 2W_{Fe^{++}}^{max}/A + Q_c^B \quad [12]$$

The difference between this and the total charge Q_a [mC/cm²] passed during anodic passivation would

[6] Estimation of the thickness of the outer ferric oxide layer by means of the cathodic reduction technique is possible even for the specimen prepolarized above +900 mv as will be seen below, if the solution is changed just before the reduction so as to eliminate oxygen produced during the anodic polarization.

Table II. Results of calculation

E_a, mv	$W_{Fe^{++}}^{max}$, $\mu g/cm^2$	Q_c^B, mC/cm^2	$W_{Fe^{6+}}^{(S)}$, $\mu g/cm^2$	$W_{Fe^{3+}}^{(S)}$, $\mu g/cm^2$	x —	Q_a, mC/cm^2	$Q_a^{(O)}$, mC/cm^2	$Q_a^{(M)}$, mC/cm^2	$W_{Fe}^{(M)}$, $\mu g/cm^2$	Q_c, mC/cm^2	$Q_c - Q_c^B$, mC/cm^2	$\eta_c^{(M)}$, %	$\Sigma W_{Fe}^{(S)}$, $\mu g/cm^2$
−500	0.22_3	0.46_5	0.01_5	0.20_8	0.12_9	1.82	1.23_6	0.58_5	0.12_7	1.52	1.09	53.7	0.35_0
−400	0.30_0	0.63_5	0.02_8	0.27_8	0.13_9	2.34	1.67_1	0.66_9	0.14_5	1.84	1.20	55.8	0.44_6
−300	0.37_5	0.79_1	0.02_8	0.34_7	0.13_7	2.79	2.08_7	0.71_3	0.15_5	2.13	1.34	53.2	0.53_0
−200	0.44_2	0.93_6	0.03_3	0.40_9	0.14_0	3.19	2.46_3	0.72_7	0.15_8	2.46	1.52	47.8	0.60_0
−100	0.50_8	1.07_0	0.03_7	0.47_1	0.13_6	3.57	2.82_5	0.74_5	0.16_2	2.76	1.69	44.1	0.67_0
0	0.56_6	1.19_2	0.04_1	0.52_5	0.13_5	3.93	3.14_7	0.78_3	0.17_0	3.08	1.89	41.4	0.73_6
100	0.60_7	1.29_4	0.04_7	0.56_0	0.14_4	4.27	3.39_2	0.87_8	0.19_1	3.41	2.12	41.4	0.79_8
200	0.64_3	1.39_3	0.05_4	0.58_9	0.15_6	4.61	3.61_6	0.99_4	0.20_6	3.76	2.37	41.9	0.84_9
300	0.67_8	1.49_2	0.06_2	0.61_6	0.16_7	4.94	3.83_8	1.10_7	0.24_0	4.09	2.60	42.6	0.91_8
400	0.71_3	1.59_1	0.06_9	0.64_4	0.17_7	5.27	4.05_5	1.21_5	0.26_4	4.42	2.83	42.9	0.97_7
500	0.74_7	1.69_0	0.07_7	0.67_0	0.18_7	5.60	4.27_2	1.32_8	0.28_8	4.78	3.09	42.9	1.03_5
600	0.78_4	1.78_9	0.08_4	0.70_0	0.19_3	5.94	4.49_6	1.44_4	0.31_4	5.16	3.37	42.7	1.09_7
700	0.81_7	1.88_8	0.09_2	0.72_5	0.20_2	6.27	4.70_9	1.56_1	0.33_8	5.51	3.62	43.1	1.15_5
800	0.86_0	2.01_3	0.10_2	0.75_8	0.21_1	6.60	4.98_1	1.68_9	0.36_6	5.77	3.76	44.9	1.22_5
850	0.89_0	2.09_5	0.10_8	0.78_3	0.21_5	6.77	5.17_0	1.60_0	0.34_8	5.85	3.75	42.7	1.23_8
900	0.94_5	2.24_5	0.11_8	0.82_7	0.22_2	7.03	5.51_0	1.52_0	0.33_0	5.94	3.70	41.1	1.27_5
920	0.98_9	2.37_0	0.12_8	0.86_1	0.20_5	7.22	5.78_8	1.43_2	0.31_0	5.97	3.60	39.7	1.29_8
937	1.07_0	2.84_2	0.19_2	0.87_8	0.30_4	7.85	6.53_6	1.31_4	0.28_6	5.99	3.15	41.6	1.35_5

give the amount of charge required to form the inner magnetite layer $Q_a^{(M)}$. Thus,

$$Q_a^{(M)} = Q_a - Q_a^{(O)} \qquad [13]$$

The amount of iron in the magnetite $W_{Fe}^{(M)}$ [$\mu g/cm^2$] is

$$W_{Fe}^{(M)} = \frac{3}{8} A \times Q_a^M \qquad [14]$$

so that the total amount of iron in the passive film is

$$W_{Fe}^{(S)} = W_{Fe^{6+}}^{(S)} + W_{Fe^{3+}}^{(S)} + W_{Fe}^{(M)} \qquad [15]$$

Comparison between $Q_a^{(M)}$ and the amount of charge for the second wave of the cathodic reduction curve, which is reasonably expressed as the difference between the total amount of charge for the cathodic reduction Q_c and Q_c^B, would give the average current efficiency of the reduction reaction of magnetite $\eta_c^{(M)}$.

$$\eta_c^{(M)} = \frac{Q_a^{(M)}}{Q_c - Q_c^B} \times 100\ (\%) \qquad [16]$$

The possible side reaction which occurs simultaneously with magnetite reduction would be hydrogen evolution on both the magnetite and bare metal surface. The value of the subscript x in the formula of nonstoichiometric oxide which expresses the average defect concentration in the outer layer is obtained as

$$x = \frac{2W_{Fe^{6+}}^{(S)}}{W_{Fe^{3+}}^{(S)} + 2W_{Fe^{6+}}^{(S)}} = \frac{2(Q_c^B \cdot A - W_{Fe^{++}}^{max})}{2W_{Fe^{++}}^{max} + Q_c^B \cdot A} \qquad [17]$$

By using the equations described above, the composition of the film for various passive potentials was calculated. The experimental data for Q_a, Q_c, $W_{Fe^{++}}^{max}$ and Q_c^B which are shown respectively in Fig. 4, 8, and 13 were used, the results obtained being summarized in Table II and also in Fig. 15 and 16. In these results, the characteristic potentials E_a^1 (−550 mv), E_a^2 (0 mv) and E_a^3 (+850 mv) are again recognized. E_a^1 is related to the transition potential between the passive and the active states observed in the measurement of the anodic polarization curve and also to the first arrest of the cathodic reduction curve. It is clearly seen that "γ-Fe_2O_3" which is the characteristic material for the passive state commences to be produced and reduced above and below this potential. Accordingly, E_a^1 appears

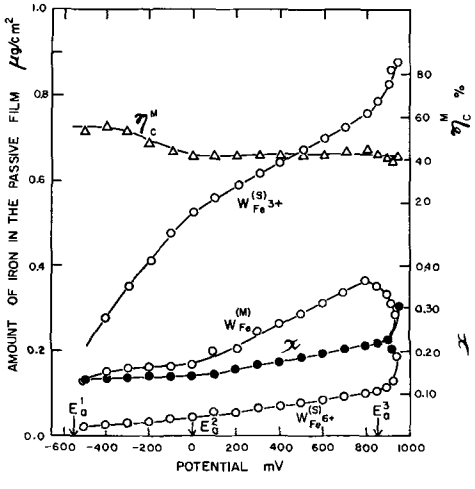

Fig. 15. Change of the composition of passive film with anodic potential (t = 1 hr).

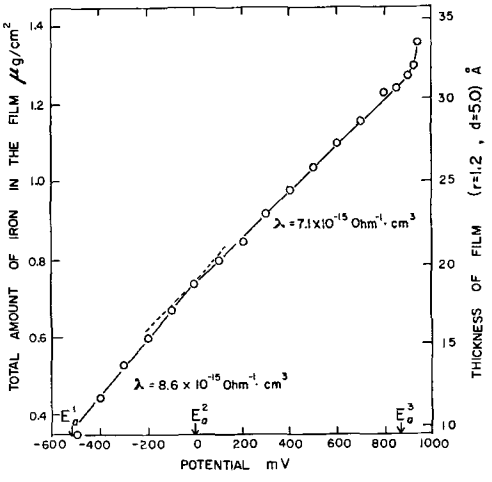

Fig. 16. Effect of anodic polarization on the film thickness

to be the threshhold potential above which γ-Fe_2O_3 is stable. At the characteristic potential E_a^2, a decrease in the slope of $W_{Fe^{3+}}^{(S)} - E_a$ curve and an increase in the slope of both $W_{Fe^{6+}}^{(S)} - E_a$ and $W_{Fe}^{(M)} - E_a$ curve were observed. The average current efficiency of the reduction of Fe_3O_4 ($\eta_c^{(M)}$) decreases with potential up to E_a^2 and stays constant at about 42% above E_a^2. This would suggest that a change in the nature of the Fe_3O_4 layer occurs below this potential. At the oxygen evolution potential E_a^3, a steep increase in both $W_{Fe^{3+}}^{(S)}$ and $W_{Fe^{6+}}^{(S)}$ is observed, while $W_{Fe}^{(M)}$ begins to decrease steeply with potential.[7]

The relation between total film thickness and potential shown in Fig. 16 was estimated according to Eq. [15] by assuming that the average density of both layers is 5 and the roughness factor of the surface is 1.2. A film thickness of about 10Å at the passivation potential E_a^1 corresponds to the order of one unit cell length of an iron oxide of spinel structure. It is not surprising that the individual thickness of γ-Fe_2O_3 or Fe_3O_4 layer at E_1^a is less than the unit cell length, because some continuous change in structure with the distance should be considered for such a thin oxide film, as is emphasized above. The total film thickness ranges from 10 to 30Å over the passive potential region. The apparent field strength in the film was estimated from the results shown in Fig. 5 by dividing the increase in potential by the increase in film thickness for a number of consecutive points on the curve and was found to be 5.8×10^6 v/cm and 7.0×10^6 v/cm below and above E_a^2 so that the apparent specific conductance of the film is 8.6×10^{-15} and 7.1×10^{-15} mho cm^2 for an anodic current density of 0.05 μa/cm^2. These values would be considered to correspond to cationic conductivity of the film which apparently controls the rate of growth of the film in the nonsteady condition of passivity. The significance of the characteristic potential E_a^2 and the role of defects in the mechanism of passivity will be discussed in a following publication.

Relationship between Composition and Anodic Potential

In the active region, that is at potentials below —500 mv, there appears to be a film, not necessarily continuous, of Fe_3O_4 on the metal. Above this potential both Fe_3O_4 and γ-Fe_2O_3 are formed. The major part of the passive film is formed within the first 10 sec of polarization (cf. Fig. 5). However, the composition of the film is very dependent on the potential of formation. Up to +850 mv there is an increase in thickness of the Fe_3O_4, Fe_2O_3 and the per cent vacancies. This is as one would expect if the outer layer of film is formed by anodic oxidation of magnetite and if the thickness of the total film required to decrease the migration rate below 0.01 μa/cm^2 is directly dependent on the potential drop across the film. In that a more positive anodic potential is the equivalent of a more strongly oxidizing environment, the increase in vacancies with increased anodic potential is also reasonable.

[7] The value of $W_{Fe}^{(M)}$ obtained above the oxygen evolution potential is probably not correct because a certain number of coulombs used for oxygen evolution would be included in the total amount of charge Q_a passed during the anodic polarization. However, if a correction were made for the partial amount of charge for oxygen production, the decrease of $W_{Fe}^{(M)}$ with potential would be much steeper.

Acknowledgment

The authors are indebted to Mr. L. Bradley for his help in constructing the electrical apparatus and to Mr. E. Brewer for the electron optical examination.

Manuscript received Dec. 27 1961.

Any discussion of this paper will appear in a Discussion Section to be published in the June 1963 JOURNAL.

REFERENCES

1. U. R. Evans, "The Corrosion and Oxidation of Metals," Edward Arnold Publishers Ltd., London (1960).
2. K. J. Vetter, "Passivierende Filme und Diecksichten," p. 72, Springer-Verlag, Berlin (1956).
3. T. P. Hoar, "Modern Aspects of Electrochemistry," No. 2, chap. 4, p. 262, Butterworths Scientific Publications (1959).
4. U. F. Franck, *Werkstoff und Korrosion*, **9**, 504 (1958).
5. *Z. Elektrochem.*, **62**, Nr. 6/7 (1958), Symposium on Passivity.
6. P. B. Sewell, C. D. Stockbridge, and M. Cohen, *Can. J. Chem.*, **37**, 1813 (1959).
7. L. O'Connor and H. H. Uhlig, *J. Phys. Chem.*, **61**, 402 (1957)
8. H. G. Oswin and M. Cohen, *This Journal*, **104**, 9 (1957).
9. H. Gerischer and K. E. Staubach, *Z. physik. Chem. N. F.*, **6**, 118 (1956).
10. F. G. Will, *Z. Elektrochem.*, **63**, 689 (1959).
11. H. Gerischer and K. E. Staubach, *ibid.*, **61**, 789 (1957).
12. cf. K. Hauffe, "Oxydation von Metallen," p. 110, Springer-Verlag, Berlin (1956).
13. K. G. Weil and K. F. Bonhoeffer, *Z. physik. Chem. N. F.*, **4**, 175 (1955).
14. K. E. Heusler, K. G. Weil, and K. F. Bonhoeffer, *ibid.*, **15**, 149 (1958).
15. K. H. Buob, A. F. Beck, and M. Cohen, *This Journal* **105**, 74 (1958).
16. C. D. Stockbridge, P. B. Sewell, and M. Cohen, *ibid.*, **108**, 928 (1961).
17. A. F. Wells, "Structural Inorganic Chemistry," 2nd ed., p. 382, Oxford University Press (1952).
18. M. Cohen, *Can. J. Chem.*, **37**, 286 (1959).
19. P. B. Sewell, C. D. Stockbridge, and M. Cohen, *This Journal*, **108**, 933 (1961).
20. P. Hancock and J. E. O. Mayne, *J. Chem. Soc. (London)*, **1958**, 4167, 4172.

On the Fundamentals of Etching High-Purity Aluminum Foil for Capacitor Use

R. Bakish

Electronics and Alloys Incorporated, Ridgefield, New Jersey

and E. Z. Borders and R. Kornhaas

Republic Foil Corporation, Danbury, Connecticut

ABSTRACT

Studies on the factors underlying the morphology of etched structures are presented. The importance of coulomb input and current density are evaluated for their contribution to the morphological effects observed. Experimental results on studies conducted both with single crystals and polycrystals are presented.

The fundamental parameters underlying the etching of aluminum foil for capacitor applications are complex. The establishing of the processing variable affecting the morphology and its correlation with electrical properties of etched foils are of great interest.

A number of studies on the etching behavior of aluminum have been reported in the literature (1-5). These studies, however, are only related but not truly pertinent to the work discussed here inasmuch as they deal with chemical and not electrochemical etching processes.

In the work to be reported the authors attempt to establish the role of processing variables in the electrochemical etching process. The morphological parameters revealed as functions of these etching variables are evaluated, in order to establish their correlation to electrical properties of interest. The relative significance of the different variables is discussed.

Experimental Conditions

These studies were conducted on annealed high-purity 0.0035 in. foil meeting the specifications for 99.99% Al and on single crystals of selected orientations. All etching experiments were conducted in a simple cell maintaining a 2 in. cathode-anode spacing throughout the studies; 64.5 cm^2 specimens were used in all etching experiments. The 10% NaCl etching electrolyte used in this study was prepared from deionized water with resistivity better than 10^6 ohm-cm and 99.99% NaCl. All etching was performed under stationary conditions.

Weight loss, capacitance at 6, 75, and 550v, and morphological changes in the etched material were used as indices for the variables investigated.

Capacitance measurements were conducted in accordance with procedure given in Table I for 6v data, Table II for 75v data, and Table III for 550v data; 12.9 cm^2 specimens were used in all electrical tests. A current density range of 0.00698-0.489 amp/cm^2

Table I. Procedure for 6v data

Formation electrolyte	Measuring electrolyte	Forming procedure	Measuring procedure
Ammonium pentaborate 80 g/l. Solution resistivity 30 ohm-cm. Temperature 65°C.	Ammonium pentaborate 80 g/l. Solution resistivity 30 ohm-cm. Temperature 65°C.	1. Apply 23.3 ma/cm^2 until 6v is reached. 2. Hold at 6v for 30 min. 3. Record leakage current.	Record capacity into $\mu F/cm^2$. Record % dissipation factor.

Table II. Procedure for 75v data

Formation electrolyte	Measuring electrolyte	Forming procedure	Measuring procedure
Ammonium dihydrogen phosphate 1 g/l. Demineralized water 10^6 ohm-cm or better. Solution resistivity 400 ohm-cm at 90°C.	Boric acid 27.5g and ammonium pentaborate 20g/final liter of solution. Demineralized water 10^6 ohm-cm or better. Solution resistivity 190 ohm-cm at 25°C.	1. Apply 15.5 ma/cm^2 until 75v is reached and maintain voltage for 30 min. 2. Record leakage current.	Record capacity in $\mu F/cm^2$. Record % dissipation factor.

Table III. Procedure for 550v data

Forming electrolyte	Measuring electrolyte	Forming procedure	Measuring procedure
100g boric acid per final liter of solution.	27.5 g/boric acid 20g of ammonium pentaborate per final liter of solution.	1. Hydrate sample in boiling demineralized water for 5 min.	Measure capacity and record in $\mu F/cm^2$.
Demineralized water 10^6 ohm-cm or better.	Demineralized water 10^{-6} ohm-cm or better. Solution resistivity 190 ohm-cm at 25°C.	2. Apply 38.7 ma/cm² until 400v is reached.	
Solution resistivity 3000 ohm-cm at 90°C.	Temperature 25°C.	3. Decrease current to 25.7 ma/cm² and hold until voltage reaches 550v. Hold voltage at 550v for 30 min.	
Temperature 90°C.		4. Record leakage current.	

was investigated at 38.7, 72.9, and 108.5 coulombs/cm². These values were selected arbitrarily for this study. The single crystal current densities are calculated on basis of square centimeters of projected area.

All capacitance measurements were made with a General Radio 1611-A capacitance bridge with an accuracy of ± 1%. Polarizing current was not utilized in the measurements. Measurements were made at a frequency of 60 cps. The bridge circuit is so arranged that a maximum of 1 v-amp of reactive power is delivered to the sample.

Leakage current and dissipation factors were also measured and fell into a range considered to be good by the capacitor industry. It is hoped that these factors will be the subject of future study in connection with different anodizing electrolytes. All photomicrographs, unless otherwise specified, are at 750X.

Low index planes (100), (110), (111) of single crystals of aluminum grown from the melt of 99.99% Al were also used in these studies. The orientations were determined in accordance with classic Laue back reflection method, and all measurements are accurate within 2°. Current density and amount of charge with which all these single crystal planes were processed were selected on the basis of the polycrystalline etching experiments. After careful cutting, the crystal faces selected for these studies were wet ground through 0, 00, 000, and 0000 corrundum papers prior to final wet diamond abrasive polish on rotating wheel. Surface areas of these faces needed for calculations of current densities were measured by a planimeter. All surfaces, other than the one of interest, were masked with Hysol epoxy resin after making suitable electrical connections.

Experimental Results

Electrical measurements.—Capacitance and weight loss data obtained in the course of these studies for specimens etched at 38.7, 72.9, and 108.5 coulombs/cm² are plotted in Fig. 1. These data give the current density dependence of processing as function of amount of charge passed, weight loss, and capacitance for 6, 75, and 550v. Each point represents the arithmetic average of measurements conducted on 3 independently processed specimens. Capacitance of annealed foil, before etching or cleaning, was measured and gave results of 0.23 μF/6.45 cm² at 550v, 0.91 μF/6.45 cm² at 75v, and 17 μF/6.45 cm² at 6v. Etch ratios can be established from these data. The capacitance appears to vary in a similar fashion as a function of the current density at the different coulomb levels. Some differences in this mode of variation are observed as, for example, the apparent reaching of a plateau value at the high current density for the 72.9 coulomb/cm² measurements, with indications of continual increase, but at a lower rate,

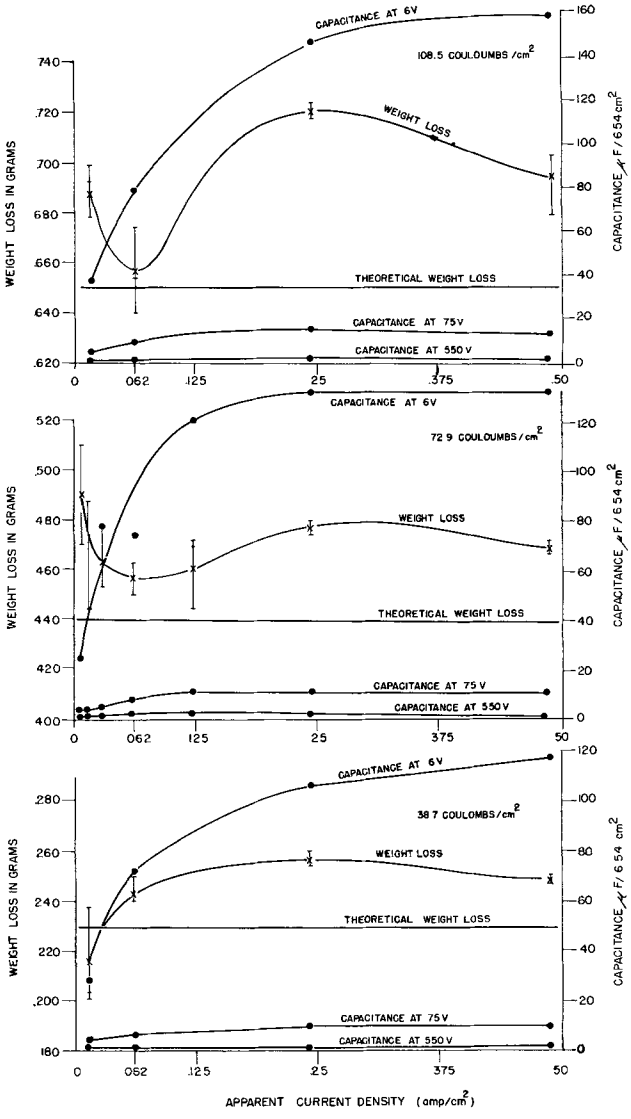

Fig. 1. Data for 99.99% Al processed at 38.7, 72.9, and 108.5 coulombs/cm².

with increase of current density for both the 38.7 and 108.5 coulomb/cm² measurements, this being true for the 6v formation. These trends are interesting, but it is felt that much additional data are needed before quantitative functional relations can be derived. At the present these curves will be considered only as indicative of significant trends.

The weight loss dependence on the current density appears to be different with the different amounts of charge passed. There is some similarity between the 72.9 and 108.5 coulomb/cm² weight loss curves, but this is only as a first order approximation. The curves themselves are extremely interesting because of possible processing significance, but to these authors they are difficult to interpret fully. Weight loss is plotted against current density calculated on the basis of the initial surface area of the samples, ignoring the fact that the real surface area was continually changing and at each measuring level was substantially different from the initial surface area.

The weight loss is basically a function of the amounts of charge passed, the efficiency of the process, and the initial configuration of the surface. The exact nature of this function is not known. The weight loss values obtained in this study are above the (calculated) theoretical weight loss data which are plotted as a straight line in the same figures. It appears that the most likely reason for this discrepancy is the high percentage of edge area relative to the sample size which must contribute to nonuniform current density distributions. In addition the possibility of chemical attack superimposed on the anodic dissolution exists. Loss of grains from the foils is also likely as a consequence of preferential grain boundary attack. It would be desirable to study further the weight loss dependence and to establish the real significance of this factor in the etching process.

Morphology.—Figure 2 shows the structures of foils etched at current densities of 0.489, 0.243, 0.118, 0.061, 0.030, 0.015, and 0.007 amp/cm² with 72.9 coulombs/cm². A clearly manifested systematic increase in the dimension of structural detail within the etched structure is observed as the current density decreased. Fine surface details leading to high capacities of formed foils result from etching with high densities while rather coarse structures are observed in the low range of current densities studied with corresponding decrease of capacities for the formed foils. In passing from the region of extreme fineness of detail to the relatively coarse structures shown there appears to be a range of current density where structure-sensitive details in the foil are revealed.

Fig. 2. Etched structures produced at current densities of 0.489, 0.243, 0.118, 0.061, 0.030, 0.015, and 0.007 amp/cm² and 72.9 coulombs/cm². Magnification 350X.

Fig. 3. Etched configuration associated with poligonized grain boundaries.

Fig. 4. Etched configuration associated with slip elements

Configuration of these indicates the possibility of these being dislocation arrays associated with poligonized sub-boundaries and slip lines. This appears to be true in the middle range of the current densities investigated and in particular at about 0.118 and 0.061 amp/cm². Figure 3 shows configuration believed associated with a poligonized grain boundary while Fig. 4 shows configuration associated with the 3 slip elements of this lattice.

To get additional details on the structures a set of specimens were etched at 38.7 coulomb/cm² and current densities of 0.015, 0.061, 0.243, and 0.489 amp/cm² and examined also by electron microscopy. Figure 5 shows both optical and electron optical detail on these structures. This set of microphotographs as well as morphological details observed with experi-

Table IV. Single crystal processing data

Crystal identification	Surface area/cm²	Etching current, amp	Etching current density, amp/cm²	Etching time, min	Coulombs/cm²	Orientation	Structure manifestation
NO1	5.54	0.378	0.0693	10.66	43.6	(110)	Delineate <100>
NOR	4.84	0.608	0.125	5.33	40.2	(110)	Delineate <100>
NO5	4.77	0.288	0.0817	10.66	38.7	(100)	Delineate <100>
NO3	5.68	0.343	0.0686	10.66	38.7	(111)	3-directional pitting
110An	6.26	0.378	0.0623	10.66	38.7	(110)	Delineate <100>
NO2	5.48	0.332	0.0712	10.66	38.7	(100) approx.	Delineate <100>
Coarse grained	22.19	1.35	0.00176	10.66	38.7	(110) (100) (110)	Delineate <100>
Cube geometry	6.45	3.90	0.605	10.66	38.7	(110) (111) and approx. 100 face	Delineate <100> Grossly overetched. No visible structural detail.
100_2 AN	6.26	0.125	0.0199	30	35.9	(110)	Delineate <100>
NO32	5.68	0.114	0.0148	30	36.7	(111)	Delineate <100>

ments at 108.5 coulomb/cm² level show, quite conclusively, the importance of current density in producing a given structure, with the amount of charge passed having apparently only secondary importance. This is particularly observable when Fig. 2 and 5 are compared. The discussion hereto only considered the size of the structural detail without consideration of the crystallographic parameters involved.

After discussing the experiments conducted with single crystals the authors will come back to the crystallographic parameters involved both in the single and polycrystalline material.

Single crystal experiments.—As already stated, a number of low index planes were cut and polished from single crystals, and Table IV gives the experimental variables under which these crystals were processed as well as a brief indication of results observed. In essence, it is indicated that the 100 directions within each of these planes were delineated. Etching is a result of dissolution along <100> directions both within the plane and normal to it; these manifest themselves as rectilinear grooves (Fig. 6) in addition to much deeper etched structures in which the 90° symmetry elements can also be seen. Etching on the (110) is typified by a series of parallel grooves or only ½ of the symmetry elements shown in the <100>, demonstrating as in the x-ray Laue back reflection photographs, 4-fold and 2-fold symmetry, respectively. Figure 7 shows structure produced by etching at 0.061 and 0.020 amp/cm², respectively. This figure also asserts the trend toward coarser structures as observed with the polycrystalline samples as a consequence of etching at lower current density. Figure 8 shows the appearance of a (111) face after etching under conditions, given in Table IV for crystal NO32. The 3 <100> directions within the (111) plane are delineated, and this type of micro detail leads to the observed etching and gross material removal.

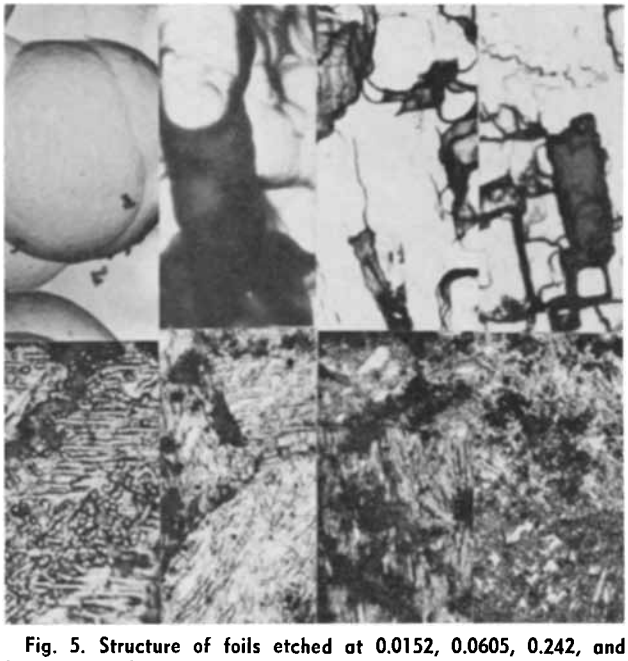

Fig. 5. Structure of foils etched at 0.0152, 0.0605, 0.242, and 0.48 amp/cm² at 38.7 coulombs/cm². Note the conversion from angular to bulbous structural detail with corresponding increase of detail size.

Discussion of Results and Conclusions

Considering the data presented the significant role of current density in the etching process is clearly

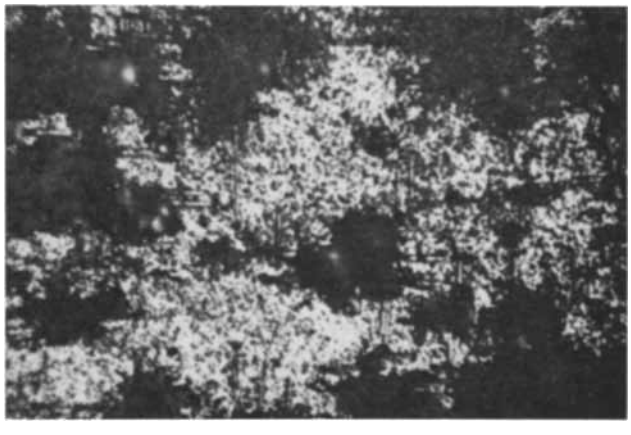

Fig. 6. Characteristic etch on a (100) crystal face processed with 0.0605 amp/cm² and 38.7 coulombs/cm².

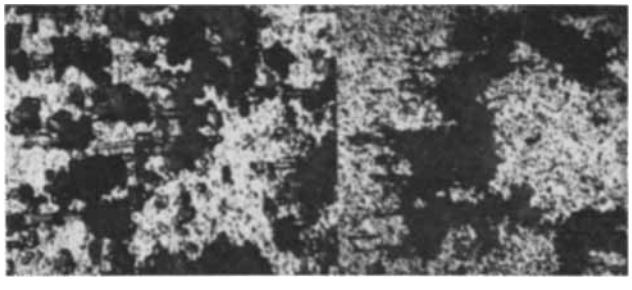

Fig. 7. Characteristic etch on a (110) crystal face processed with 0.0605 amp/cm² and 0.0202 amp/cm² at 38.7 coulombs/cm².

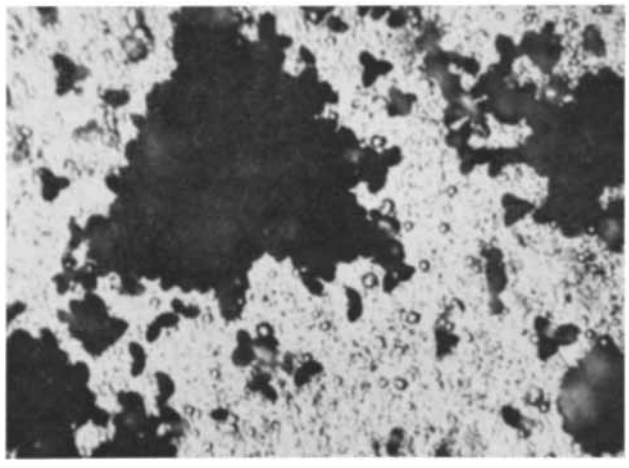

Fig. 8. Characteristic etch on a (111) crystal face processed with 0.0605 amp/cm^2 and 38.7 coulombs/cm^2.

demonstrated. The electrolyte composition and temperature can play an important role, but in this study they have not been investigated. As one increases current density at a given amount of charge passed the etched structure becomes finer, and an increase in the surface area is observed by the increased capacitance of the foil. Within the current density ranges studied it also appears that one tends to reach a limiting value above which capacitance cannot be greatly improved even by significant increase in the amount of charge passed. This capacitance behavior, namely, the increase of capacitance with increase of current density, can well be interpreted by the analysis of the morphology of the etched structures conducted in this study.

The significant crystallographic factors remain constant and are not subject to variation by either coulomb or current density variation. On the basis of observations made on the single crystals it can be stated that the <100> directions appear to play a most important role in the etching process under the experimental conditions of this study. Chemical etching processes with different electrolytes tend to change this behavior (1). A number of grains which are apparently of substantially higher index do not appear to exhibit the 100 crystallographic features, but instead tend to show essentially noncrystallographic, almost spherical, structural details. The mechanism and exact reasons leading to these different morphological manifestations are not fully understood. It is hoped that continuation of the work initiated and reported here with single crystals will lead to the eventual understanding of these observations. The ability to control variation of structural detail through control of current density appears to be a step in the right direction in the quest of manufacturing good custom property etched foil. The full understanding of the phenomenon and the true relationships involved are yet to be established.

Acknowledgments

The authors wish to acknowledge the permission of Republic Foil, Inc. to publish this work. They are also thankful for Mr. W. Hooper's enthusiastic support and participation in discussions in the course of this work. Also acknowledged is the assistance of Mr. M. Richman in the electron microscopy work.

Manuscript received Nov. 28, 1961; revised manuscript received April 15, 1962. This paper was prepared for presentation before the Detroit Meeting, Oct. 1-5, 1961.

Any discussion of this paper will appear in a Discussion Section to be published in the June 1963 JOURNAL.

REFERENCES

1. T. H. Orem, *J. Nat. Bur. Standards*, **58**, 157 (1957).
2. A. Politycki and H. Fischer, *Z. Elektrochem.*, **57**, 393 (1953).
3. A. Politycki and H. Fischer, *ibid.*, **57**, 326 (1952).
4. H. Kostron, H. Hoffler, and W. Sauter, *Z. Metallkunde*, **44**, 17 (1953).
5. E. J. Burger and V. F. G. Tull, *Nature*, October 1953.

Polarization and Inhibition of Steel in the NH_4NO_3-NH_3-H_2O System

J. D. Goodrich[1] and Norman Hackerman

Department of Chemistry, The University of Texas, Austin, Texas

ABSTRACT

Anodic and cathodic polarization for the system steel-NH_4NO_3-NH_3-H_2O were measured with and without added inhibitor. Phenomena typical of passivation were obtained on anodic polarization. Steel deliberately covered with thin oxide showed similar effects and provides the basis for a discussion of the possibilities of bulk oxide as the cause of passivity. Although this is shown to be feasible, it is by no means conclusive since charge needed for active-passive transition is very much less than that equivalent to bulk oxide iron transition. Inhibition by SCN^- operates by replacement of the reduction reaction NO_3^- to NO_2^- by H_2O to H_2.

Dissolution rates have been reported for this system (1) as high as 29,000 mdd at 30°C. The primary cathodic reaction involves reduction of NO_3^- to NO_2^-. Formation of an iron-ammonia complex was offered as the primary effect responsible for the high dissolution rates.[2] The oxidation product was reported

[1] Present address: Department of Chemistry, Louisiana State University at Alexandria, Alexandria, Louisiana.

[2] The possibility of a more stable product such as "ammonium hexanitritoferrate (II)" is being considered at this time.

as being a hydrated or ammoniated form of ferrous hydroxide.

Several interesting facts arose from earlier work (2) on this system. The open-circuit dissolution potential was found to change about 0.2v in an anodic direction when the inhibitor SCN^- was added. Also, an inactive to active transition was observed when the system was subjected to stress. For example, rates changed from near 0 to 29,000 mdd in some cases when small stresses were applied. This investigation attempts to explain these and other phenomena exhibited by this system.

Experimental

Polarization data were taken both potentiostatically and galvanostatically, but unless stated the data were obtained by the former procedure. An electronic "Wenking" potentiostat, modified for use with U.S. tubes, was used in conjunction with a L&N student-type potentiometer. All currents were time dependent as usual. The values given here were constant for at least 5 min. All points on the curves are averages of two or more measurements, and the data were all within ± 3% of the averages. The solution composition in all experiments was as follows: NH_4NO_3, 66.4; NH_3, 14.3; H_2O, 19.3 w/o. The NH_4NO_3 was reagent grade and gave a negative test for nitrite ion. Distilled water and anhydrous NH_3 were used with no further purification. The solutions were held at 25° ± 1°C and were not stirred. An H-type cell was used with the arm containing the steel test electrode having a 50 ml capacity. A reference saturated calomel electrode made contact with the test solution via a KNO_3 salt bridge. No junction potential corrections were applied. The test electrode of type MICO steel (should be designated as D269B) was mounted in paraffin, while the polarizing electrode consisted of a coiled platinum wire 4 cm long. This steel was obtained from the U. S. Steel Company with the composition in w/o given as 0.048 C, 0.32 Mn, 0.006 Si, and 0.028 S.

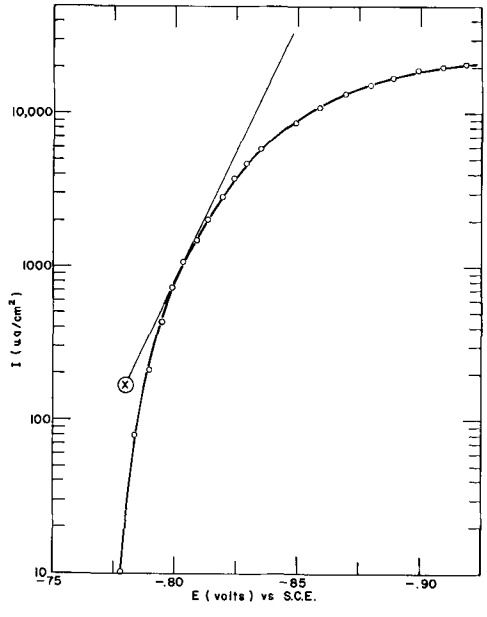

Fig. 1. Cathodic polarization curve (potentiostatically), steel D269B, 25° ± 1°C, *E* vs. Log *i*.

Results

Upon cathodic polarization a curve was obtained (Fig. 1) which exhibited no readily discernible "Tafel" region. Gas was not evolved below 10 ma/cm², but above this hydrogen was produced as shown by gas chromatography. The absence of gas evolution below 10 ma/cm² substantiates the proposition that the reduction reaction was NO_3^- to NO_2^-. Assuming a two-electron change in the over-all reaction, point X (Fig. 1) is obtained from the intercept of the measured steady-state dissolution potential and from the dissolution rates via Faraday's law. If the rate could have been determined in this system from a polarization curve which exhibited a distinct Tafel line, point X should lie on this line. From the slope of the line through this point and tangent to the curve a value of 0.03 ± 0.01v was obtained for the Tafel b. Of course, the method is subject to error if concentration polarization is controlling to any appreciable degree.

Figure 2 gives a typical anodic polarization curve for this system. It is characteristic of passivation of iron or steel in other solutions. There is no distinctly linear portion in the region of active iron dissolution, *i.e.*, −0.6 to −0.8v but again a line was constructed by using point B. It has a slope of 0.07 ± 0.01v, about the same as for iron dissolution generally. Gas evolution occurring in the region of +0.8v was shown to be oxygen by flame tests.

Galvanostatic anodic polarization gave Fig. 3, again typical of such curves for Fe in other solutions. It is similar to Fig. 2 between the open-circuit potential and an apparently critical current density, but discontinuous from there to oxygen evolution. Decreasing the current density once oxygen evolution occurs gives a curve which is similar to all of the curve of Fig. 2. If the applied current is turned off after the oxygen evolution region is reached, the electrode maintains a potential within the region −0.4 to +0.7v unless disturbed. In summary, this is typical passivity behavior.

Effect of inhibitors.—The inhibitor efficiency of SCN^- is quite high as shown by the weight-loss data of Table I for different NH_4SCN concentrations.

The open-circuit potential changed 170-200 mv in the anodic direction when this inhibitor was added.

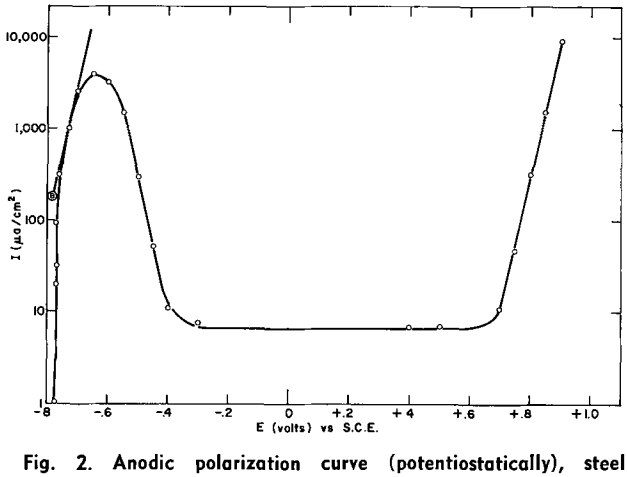

Fig. 2. Anodic polarization curve (potentiostatically), steel D269B, 25° ± 1°C, *E* vs. Log *i*.

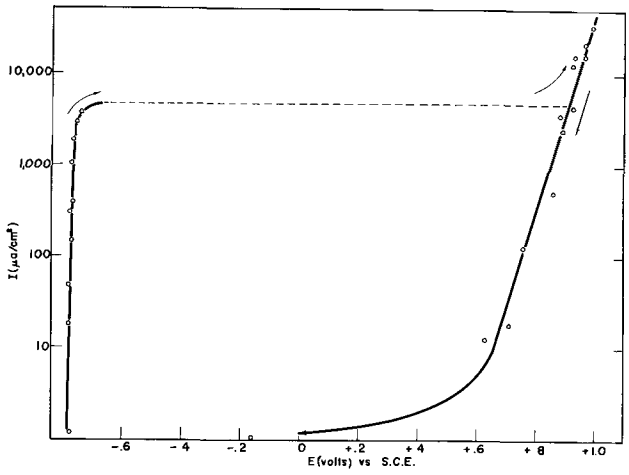

Fig. 3. Anodic polarization curve (galvanostatically), steel D269B, 25° ± 1°C, *E* vs. Log *i*.

Anodic and cathodic polarization curves, such as those in Fig. 4, were obtained for steel inhibited with 0.013M NH_4SCN. Linear plots extending over several log cycles were obtained. The slope of the cathodic curve is 0.11 ± 0.005v and that of the anodic curve is 0.05 ± 0.005v. The effects shown in Fig. 4 are for the steel in the active state. Polarizing anodically to current densities higher than shown on Fig. 4 gives a discontinuous curve (similar to Fig. 3) with galvanostatic measurements while potentiostatic measurements yield a curve similar to Fig. 2. Thus the inhibition has not induced passivity.

In this case, hydrogen evolution occurred immediately upon cathodic polarization. Anodic polarization to positive enough potentials give curves like those of Fig. 2 or 3, depending on the procedure used.

The open-circuit potential of steel in NH_4OH solutions is very near that of the steel in the solutions in this study inhibited with SCN^-, *e.g.*, —0.95v. The dissolution rates are also similar, near 30 mdd at 30°C.

Inhibition by other sulfur-containing compounds, such as thiourea, 2, 3-quinoxalinedithiol, mercaptoacetic acid, and sodium sulfide, was as complete as with SCN^-. In each case, the potential shifted 170-200 mv in the anodic direction.

The dissolution rate of inhibited steel (SCN^-) increased slightly when oxygen was bubbled over its surface.

Active-inactive transitions.—Steels with potentials of the order of —0.78v were always active, and those with potentials more positive than —0.3v were always inactive. Sample activation was accompanied by an increase in rate by as much as 1000 times and a shift of potential of 400-500 mv in an anodic direction. Activation was obtained by application of small stresses, by acid pickling, by pre-exposure to hot dry H_2, among other methods.

Table I. Effect of NH_4SCN on dissolution rate

M × 10^2 NH_4SCN	Rate, mdd, 30°C
0	22,200
0.086	13,500
0.22	11,000
0.46	150
0.65	50
1.3	50
2.4	25
3.3	30

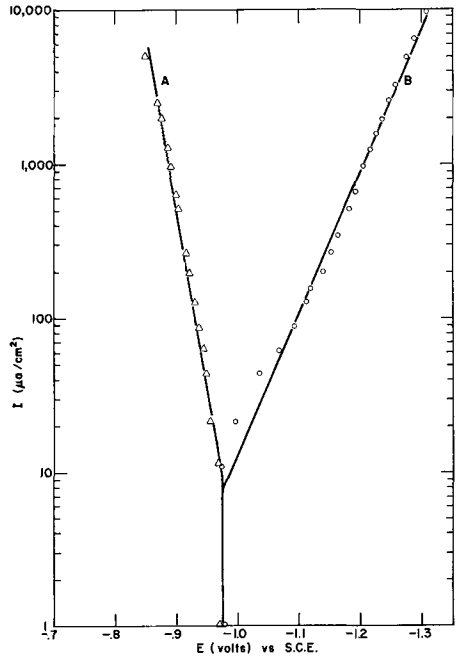

Fig. 4. Anodic (A) and cathodic (B) polarization (potentiostatically), steel D269B, 25° ± 1°C, 0.013M NH_4SCN, *E* vs. Log *i*.

A series of experiments were performed in which the steel samples used throughout this work were heated at 750°C in a stream of dry H_2 for 1 hr and then placed in the NH_4NO_3-NH_3-H_2O solution without coming into contact with air. This was done by closing the heated tube, reducing the pressure, and placing one end in the solution. All samples showed high dissolution rates in the NH_4NO_3-NH_3-H_2O system after being subjected to the high-temperature H_2 treatment. A set of steel samples with preformed thin (blue) oxide on them was kindly provided by John Griess of Oak Ridge National Laboratory. These lay inactive for months in this solution, but were activated by the high temperature H_2 treatment. Oxide covered steel always exhibited open-circuit potentials in the region —0.4 to +0.7v.

Conclusions

Certainly the changes shown in Fig. 2 and 3 indicate that the steel is being passivated. The fact that the anodically treated steels and the oxide covered steel exhibit similar potentials, —0.4 to +0.7v, and equally low rates suggest that an oxide film is involved in both cases. The insolubility of Fe_2O_3 in NH_4NO_3-NH_3 solutions as reported by Leonard (3) would justify this viewpoint. Also, the inactive-active transition resulting in potential changes of 400-500 mv in a cathodic direction when small stresses are applied could be caused by oxide cracking. Certainly it is difficult to explain it on the basis of stress effect alone. Yet the argument is not conclusive because in the anodic polarization the total number of coulombs passed between active dissolution (therefore clean steel surface) and *E* of about —0.4 in Fig. 2 is manifold less than that equivalent to the blue oxide of the deliberately coated samples.

Thus, one is left with the conclusion that the metal uniformly covered by thin film simply lends itself very readily to self-passivation, given that a small amount of dissolution occurred.

Of interest is the fact that oxygen is not needed in this system; and of considerable significance is the fact that the iron appeared to be in the dipositive oxidation state in the solution.

The small differences between the slopes of the inhibited and uninhibited anodic curves, *e.g.*, 0.05 and 0.07v, shows that the anodic reaction is being affected to only a small extent by SCN^-, although they might be affected importantly. However, the slope of the cathodic curves changed considerably (0.03-0.11) even when taking into account the large experimental error in the slope of Fig. 1. This indicates a change of reaction. The formation of hydrogen gas on cathodic polarization of the inhibited system (Fig. 4) confirms the replacement of $NO_3^- \rightarrow NO_2^-$ by $H_2O \rightarrow H_2$. The observed increase of rate by a hydrogen depolarizer such as oxygen further substantiates this. Cessation of the NO_3^- reduction reaction by inhibition results in a system which is essentially $Fe\text{-}NH_3\text{-}H_2O$, and it is a fact that iron in $NH_3\text{-}NH_4NO_3\text{-}H_2O\text{-}NH_4SCN$ exhibits the same potential. —0.95v, and rate as does iron in NH_4OH. Thus, the effect is largely one of alteration of the cathodic reaction.

Although sulfur appears to be the element responsible for inhibition in these experiments, no attempt is made to explain its function at this time.

Acknowledgment

The authors are pleased to acknowledge the financial support of this work by the Robert A. Welch Foundation of Houston and by the Office of Naval Research under Contract NONR 375(02). They also wish to take this opportunity to thank the U. S. Steel Company for some of the steel samples used in this study and J. Griess for the oxide covered steel which he kindly provided to them for this work.

Manuscript received Feb. 7, 1962; revised manuscript received May 15, 1962.

Any discussion of this paper will appear in a Discussion Section to be published in the June 1963 JOURNAL.

REFERENCES

1. N. Hackerman and J. Goodrich, *This Journal*, **108**, 1092 (1961).
2. N. Hackerman, R. M. Hurd, and E. Snavely, *Corrosion*, **14**, 203t (1958).
3. G. W. Leonard, Jr., and D. E. Sellers, *This Journal*, **102**, 95 (1955).

The Effect of Some Addition Agents on the Kinetics of Copper Electrodeposition from a Sulfate Solution

I. Cathode Potential-Current Density Relation

D. R. Turner and G. R. Johnson[1]

Bell Telephone Laboratories, Incorporated, Murray Hill, New Jersey

ABSTRACT

The mechanism whereby certain organic addition agents modify the crystal growth of copper electrodeposits was studied with the aid of cathode polarization measurements and microscopic examination of the deposit. Thiourea and l(-) cystine refine grain size and brighten the deposit. The effect is attributed to a degradation of the additive at the cathode surface with the formation of sulfide ions and precipitation of CuS. The normal crystal growth habit is modified by the incorporation of copper sulfide into the deposit. Gelatin, a grain refiner and hardener, modifies crystal growth of copper electrodeposits by being adsorbed on growth sites thereby interfering with normal growth. Glycine, a "leveling" agent, affects cathode polarization only between about 0.1 and 1 ma/cm^2. Additions of up to 0.1 g/l dextrin have no effect on the cathode polarization curve for copper plating.

The purpose of this work was to study the mechanism of addition agents in electroplating. An addition agent is defined as any material which is added to an electroplating bath for the specific purpose of modifying the physical properties of the deposit.

Relatively small amounts of addition agents have large effects on physical properties of deposits such as brightness, smoothness, hardness, and ductility. Most addition agents are organic compounds, but occasionally inorganic materials are employed. Organic addition agents are used in concentrations from 10^{-6} to 10^{-1}M, while inorganic materials (usually codepositing metals) may range from 10^{-6}M up to concentrations which give deposits better described as alloys.

Practically all commercial electroplating baths contain one or more addition agents. In spite of this extensive use, however, little is known about how addition agents function. The art of electroplating is still far ahead of the science. This is not because of a lack of effort, but rather it is an indication of the degree of difficulty encountered in conducting significant experiments or in carrying out rigorous theo-

[1] Present address: Sprague Electric Company, North Adams, Mass.

retical analyses of electroplating processes. The difficulty lies in the fact that the process of electroplating contains a large number of variables, and some are not easily controlled. Attempts to control as many variables as possible often lead the experimenter to a large cumbersome piece of apparatus which only gives up data at a painfully slow rate. The theoretician must make a great many assumptions to make any headway, and these often destroy the value of the effort. Addition agents appear to work by somehow interfering with the normal crystal growth of electrodeposits. This interference should modify the kinetics of electrodeposition. One method of studying the kinetics of electrode processes is by means of analyzing electrode potential-current density data (polarization curves). This technique was applied in the work to be described in this paper.

As many of the known variables as possible were controlled without markedly interfering with the process of obtaining data. The simplest plating system is one which deposits metal from uncomplexed ions in solution and where there is only one electron transferred for each metal atom deposited. Strange as it may seem, there is no plating system in practical use which meets the two requirements. As a compromise, we chose to work with copper plated from an acid sulfate solution. This is a simple salt solution, but a two electron transfer is involved.

General theory of electrodeposition.—In order to understand how addition agents work, it is desirable first to have some concept of how metal ions are discharged and built into a crystal lattice in the absence of addition agents. In the discussion to follow, the process of metal ion desolvation or stripping of complex ion ligands prior to metal deposition will not be considered although it certainly is part of the overall mechanism. It has been suggested that metal electrodeposition occurs in three steps: (i) charge transfer to give adatoms (or adions); (ii) surface diffusion of adatoms; and (iii) adatom deposition into kink sites on the cathode. Adatoms may carry some positive charge which is discharged when the adatoms are incorporated into the crystal lattice. The rate of metal deposition is generally considered to be determined by either the initial charge transfer process or the surface diffusion of adatoms (1-4). In copper plating from acid solutions, Mattsson and Bockris (3) have shown that the rate-determining step at low current densities ($< i_o \cong 3$ ma/cm^2) is surface diffusion of adatoms while at high current densities the charge transfer process is controlling. Barnes (5) found a correlation between crystal growth habit and the overpotential above 3 ma/cm^2 which was explained in terms of adion mobility over the crystal surface and supersaturation.

The theoretical rate equation for the charge transfer process is

$$i = i_c + i_a = i_o \left[\exp\left(\frac{-\alpha_c F \eta_A}{RT}\right) - \exp\left(\frac{\alpha_a F \eta_A}{RT}\right) \right] \quad [1]$$

where i is the net plating current density, i_c is the total plating c.d. (cathodic currents taken as +), i_a is the deplating c.d., α_c is the cathodic transfer coefficient (that portion of the activation overpotential, η_A, which lowers the energy barrier for plating); i_o is the exchange c.d., α_a is the anodic transfer coefficient; R, T, and F have their usual meaning. The discharge of cupric ions is a two electron transfer process per ion, thus $\alpha_c + \alpha_a = 2$. If the activation overpotential is more negative than about 50 mv, the second term in the brackets of Eq. [1] can be neglected, *i.e.*, the anodic or deplating current, i_a, is negligible as compared to i_c and

$$i = i_o \left[\exp\left(\frac{-\alpha_c F \eta_A}{RT}\right) \right] \quad [2]$$

On rearranging:

$$\eta_A = \frac{RT}{\alpha_c F} \ln i_o - \frac{RT}{\alpha_c F} \ln i \quad [3]$$

Let

$$a = -\frac{RT}{\alpha_c F} \ln i_o$$

and

$$b = \frac{2.3RT}{\alpha_c F}$$

and we have the Tafel equation

$$-\eta_A = a + b \log i \quad [4]$$

The kinetic parameters α_c and i_o are easily determined from experimental data by plotting η_A against log i. Above ~50 mv, the η_A-log i curve is linear. The slope b is equal to $0.059/\alpha_c$ at 25°C while a straight line extrapolation to the current density axis at $\eta_A = 0$ gives i_o (see Eq. [3]).

Experimental and Apparatus Procedure

Careful consideration was given to the design of the electrolytic cell in order to achieve uniform current distribution over the cathode surface while permitting, at the same time, an accurate measurement of the cathode potential. A cross-section view of the arrangement used is shown in Fig. 1. It is a modified form of a cell devised by Barnartt (6) for anodic studies.

The cathode is OFHC[2] copper machined to a sphere with a cylindrical post for support and electrical contact. A glass sleeve masks the cylindrical portion so only the spherical surface is exposed. The end of the glass sleeve is beveled, as shown in

[2] Oxygen-free high conductivity.

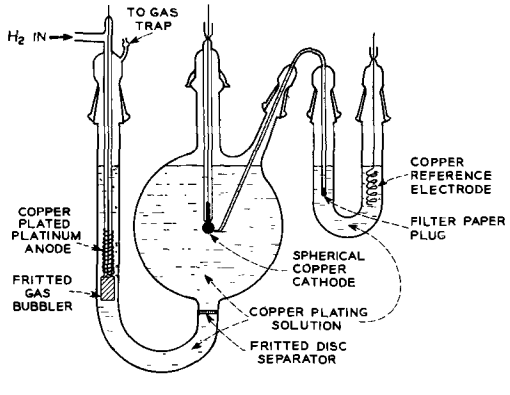

Fig. 1. Cross-section view of electrolytic cell

Fig. 1, to avoid a current masking effect by the sleeve around that portion of the sphere (6). A small hole is drilled into the top of the cylinder to take the OFHC copper wire which conducts current to the cathode. The top of the cylinder is squeezed in a vise to fasten the copper wire without resorting to a contaminating solder. Prior to use, the copper spheres are electropolished in 50% (by volume) orthophosphoric acid and rinsed in 10% (by volume) sulfuric acid. The cathode assembly is mounted to the cell by means of a ball and socket ground glass joint so the electrode can be positioned close to but not touching the capillary tip leading to the reference electrode.

The cell is constructed from a 500 ml round bottom flask which serves as the cathode compartment. It is separated from the side arm anode chamber by a medium porosity sintered glass disk. In addition to the opening for the cathode at the top of the flask, there are three other ports. Only the one to the reference electrode is shown in Fig. 1, to simplify the drawing. The other two are at right angles to the one shown, one projects outward and the other inward from the illustration. Standard taper ground glass joints were used throughout. The joints were protected from freezing by using tapered polyethylene sleeves. One of the ports not shown in Fig. 1 is for a gas bubbler so that oxygen and other gases can be displaced from the plating solution by hydrogen gas. Bubbling hydrogen over the cathode also provided a convenient means of stirring the solution to minimize concentration polarization. The other port not shown was used to add or withdraw material from the cathode chamber.

Initial experiments were carried out using a saturated KCl calomel reference electrode, but it proved to be unsatisfactory since chloride ions diffused into the cathode chamber and gave anomalous results. A copper plated copper reference electrode in the copper plating solution worked very well. The copper reference electrode had an added advantage in that the cathode potentials measured were polarization values. Connecting the reference electrode to the cathode was done with a syphon as shown in Fig. 1. The glass is drawn to a fine capillary tip at one end (~0.4 mm OD) and plugged with rolled-up filter paper at the other end. The IR drop included in the electrode potential measurement was computed to be negligible, < ~1 mv, in the highly conducting plating solution.

The anode for the plating experiments was a copper plated platinum wire wound on a gas bubbling plug. The copper was plated from a purified solution. Hydrogen gas was bubbled over the anode continuously to avoid concentration gradients in the solution and to sweep out any oxygen produced. The hydrogen bubbled through both the anode and cathode chambers was vented through gas traps.

The entire cell up to the solution level was immersed in a water thermostat set at 25.0° ± 0.01°C.

The electrolyte used in this study consisted of 1M $CuSO_4$+1M H_2SO_4. In order to determine the true effect of the addition agents to be studied, the plating solution must be purified of all important impurities, inorganic as well as organic. Our first concern was to determine if it was necessary to purify reagent grade chemicals of trace inorganic impurities. Copper sulfate was recrystallized 3 times using freshly deionized water filtered free of bacteria. Sulfuric acid was purified by distillation and only the middle portion of the distillate was collected. The cathode potential-current density curves obtained in the highly purified solution were not significantly different from the results obtained without improving reagent purity. It was important to remove all surface-active material from the plating solution, however. This was done by passing the plating solution through a carefully prepared "Chromatograph type" column containing about 12 lb of Baker activated alumina and about ½ lb of Darco Red Label activated carbon. A IM H_2SO_4 solution was used to wash the column beforehand and also as the displacing liquid to extract the desired amount of plating solution. It was customary to make up and treat five liters of plating solution at a time. Of this, four liters were collected and stored in a glass-stoppered Pyrex bottle. The material in the purifying column was used to treat only one batch of plating solution.

Thiourea, 1(-)cystine, glycine, gelatin, and dextrin were used as addition agents. Most of these materials are used in the commercial plating of copper from acid sulfate solutions. Thiourea refines the grain size and brightens the deposit. 1(-) Cystine is not commonly used in acid copper plating. However, its chemical structure is similar to thiourea so one would expect a similar behavior as an addition agent. Glycine affects the microdistribution of copper plating and is called a "leveling" agent. Gelatin is a colloidal material which reduces grain size and hardens the deposit. Dextrin is generally used with thiourea and enhances brightening. The structural formulas of the additives are given in Fig. 2 for the purpose of noting the parts of structure they have in common. All contain amine groups except dextrin. The sulfur in thiourea and 1(-) cys-

THIOUREA

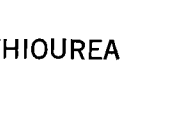

1(—) CYSTINE

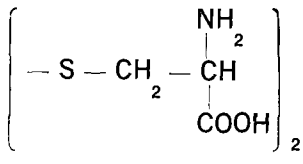

GLYCINE

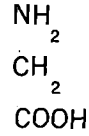

GELATINE (PURIFIED CALF SKIN—PROTEINS)

DEXTRIN (POLYSACCHARIDE) $(C_6H_{10}O_5)_x$

Fig. 2. Structural form of addition agents

tine is an active group since the corresponding oxygen substituted compounds such as urea are not effective as addition agents.

The addition agents were dissolved in a sample of plating solution and then added to the bath. The speed of addition agent dissolution in the sample solution was increased markedly by dipping the beaker into an ultrasonic cleaner tank.

Since many polarization measurements were to be made, it was considered worthwhile to develop an apparatus which would automatically plot electrode polarization-log current density curves. A block diagram of the apparatus is given in Fig. 3. The control unit in the center of the diagram is the heart of the arrangement. A 21 contact-6 section step by step relay is actuated at 1-min intervals using a synchronous motor-cam-microswitch pulsing device. Each time the stepping relay is actuated, the current from the power supply to the cell is changed. This is done by changing the resistance in the circuit of a Teletronics Model PS-110 constant current power supply. As the cell current changes with each relay step, another electrical circuit provides a voltage which deflects the pen along the X-axis of a L&N X-Y recorder in proportion to the logarithm of the cathode current density. The voltage between the copper sphere and copper reference electrode is passed through a cathode follower-type amplifier to the recorder to avoid drawing an excessive current from either electrode. Just before the plating current is changed, the X-Y recorder pen makes a dot on the paper as shown in Fig. 3. A direct plot of polarization-log current density speeds data analysis since the apparent exchange current and Tafel slope can be read off immediately.

Results and Discussion

Purified solutions.—Initial experiments were carried out in 1M copper sulfate + 1M sulfuric acid solution free of addition agents. Anodic as well as cathodic polarization curves were obtained and a summary of the results are given in Fig. 4. The rest potential of a copper electrode in the plating solution at 25°C is +0.31v *vs.* H_2 electrode. A Tafel slope of 100 ± 3 mv/current decade was observed when cathodic (copper plating) and 43 ± 3 mv/current decade when anodic (deplating copper). These values were obtained from six cathodic and 5 anodic polarization curves. The corresponding transfer coefficients from $b = 0.059/\alpha$ are $\alpha_c = 0.59 \pm 0.02$ and $\alpha_a = 1.38 \pm 0.10$. The sum of α_c and α_a is 1.97 ± 0.12, close to the theoretical value of 2.

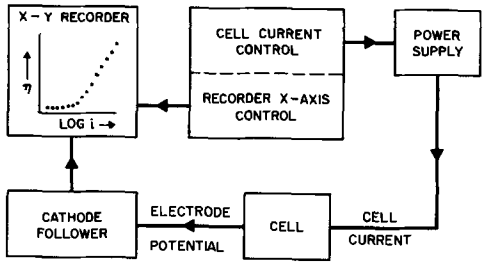

Fig. 3. Block diagram of apparatus for automatically recording electrode potential-log current density curves.

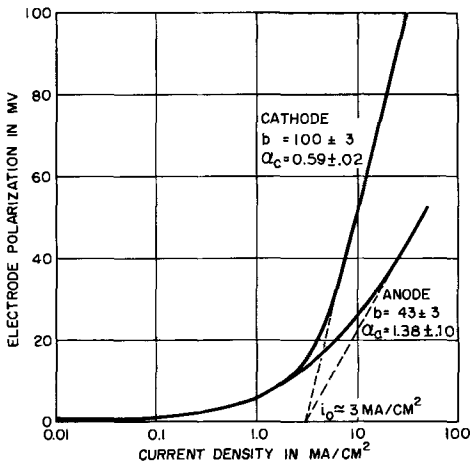

Fig. 4. Anodic and cathodic polarization curves for a copper electrode in purified IM $CuSO_4$ + IM H_2SO_4.

Both the anodic and cathodic Tafel slopes extrapolate to an exchange current density of about 3 ma/cm².

The transfer coefficients and exchange current density obtained in this study agree closely with results obtained by Mattsson and Bockris (3) who used a constant current pulsed plating-deplating technique. They concluded that the rate-determining reaction at high current densities (> 50 mv) for plating and deplating copper in acid sulfate solutions is

$$Cu^{++} + e^- \underset{\longleftarrow}{\overset{\text{SLOW}}{\longrightarrow}} Cu^+ \qquad [5a]$$

while

$$Cu^+ + e^- \underset{\longleftarrow}{\overset{\text{RAPID}}{\longrightarrow}} Cu \qquad [5b]$$

exists in reversible equilibrium with Cu at the electrode surface.

Plating on single crystal copper.—The results of electroplating copper from additive-free solutions on single crystal copper will be mentioned here as background material for the discussion to follow on the effect of gelatin in acid copper plating. Copper was electroplated on the (100) face first at 1 ma/cm² current density and later at 10 ma/cm². Photomicrographs were taken of the same area after a sequence of anodic etching and plating operations. These are given in Fig. 5. The etch pits in Fig. 5A are square shaped as expected for the (100) face. Outlines of the etch pits are barely visible after 1 hr plating at 1 ma/cm² (B); however, a four sided pyramidal crystal has started growing out of the surface. After 2 hr plating at 1 ma/cm² (C), the pyramid has grown and no new ones appeared in the area viewed. Next, the surface was anodically etched in the plating solution for 10 min at 1 ma/cm², Fig. 5D. Square etch pits were again evident which indicated that copper had deposited as a single crystal with the same orientation as the base layer. Large steps appeared on the pyramid faces. When copper plating was resumed at ten times the original current density, 10 ma/cm², the plating time was reduced by a factor of ten in order

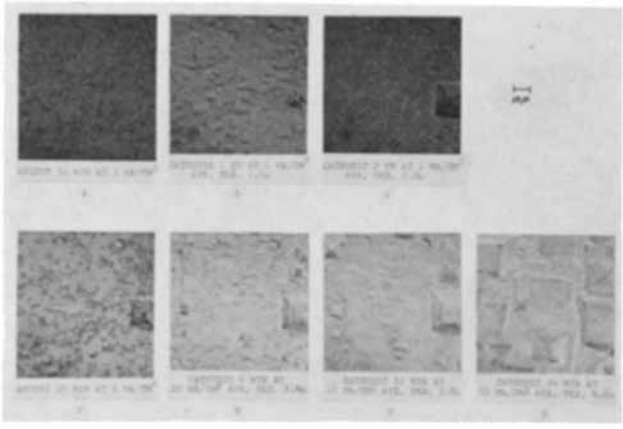

Fig. 5. Photomicrographs of the same area on a single crystal of copper (100) after anodic etching and copper plating at 1 and 10 ma/cm². 750X before reduction.

to compare deposits of the same thickness. In Fig. 5E, two things are immediately evident: (i) the number of pyramids growing has increased markedly, and (ii) the original pyramid appears truncated. All the pyramids growing at 10 ma/cm² plating c.d. eventually become truncated. Previous workers (7, 8), reporting on the crystal growth form in copper plating, have stated that an abrupt transition occurs from pyramidal growth to cubic layer growth at a critical current density (~2 ma/cm²). Our results show that even above the critical c.d., copper crystals begin to grow as pyramids and later develop flat tops and convert to cubic layer growth.

Effect of addition agents.—The effect of thiourea, l(-) cystine, glycine, gelatin, and dextrin in the copper sulfate bath on the cathode potential-current density relation was determined at various addition agent concentrations. Additions of up to 0.1 g/l dextrin had no effect on the η-log i curve for copper plating. All the other additives did influence the polarization curve and each one behaved differently. The reproducibility of the polarization curves varied with the addition agent and experimental conditions. Thus it is possible to give only a qualitative evaluation of the results.

Thiourea in acid copper sulfate solutions displaces the rest potential of a copper electrode in the positive direction. At low thiourea concentrations, 10^{-6}M, the electrode potential requires several hours to reach a steady value. The potential change increases with thiourea concentration and reaches a limiting value of about +15 mv, with respect to a copper reference in additive-free solution, at about 10^{-4}M, thiourea.

The potential of a copper electrode in the acid copper plating solution containing thiourea is a mixed potential between the equilibrium reduction potential of thiourea and the dissolution potential of copper. In effect, thiourea causes copper to corrode in acid copper plating solutions.

When a copper electrode is made cathodic in 1M $CuSO_4$+1M H_2SO_4 with thiourea at low current densities, the electrode potential remains near the rest potential up to about 0.1 ma/cm² where an abrupt change occurs. This is shown in Fig. 6 where cathode potential-current density curves are given for various thiourea concentrations. The current density at the step in potential appears independent of thiourea concentration, but the step height increases with thiourea concentration. The curves for 4 x 10^{-6} and 4 x 10^{-5}M thiourea, show that there is a region between about 5 and 50 ma/cm² plating c.d. where the electrode potential is lower with addition agent than without it. All the curves reach the lower end of the Tafel line at about 20 ma/cm². The transfer coefficient for copper plating, α_c, derived from the Tafel slope, decreases with increasing thiourea concentration and reaches a limiting value of about 0.2 at about 10^{-4}M thiourea. The corresponding exchange current density, i_o, obtained by extrapolating the Tafel line to zero polarization, increased abruptly at low thiourea concentrations to about 10 ma/cm², and then it gradually decreased with increasing thiourea back to the original value of 3 ma/cm² at about 4 x 10^{-4}M thiourea.

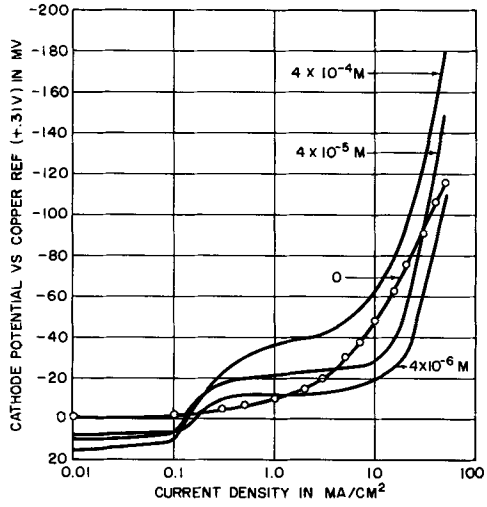

Fig. 6. Effect of thiourea concentration on the cathode potential-current density relation in copper plating.

An interpretation of the effect of thiourea on copper plating from acid sulfate solutions and the polarization curves in Fig. 6 is aided by measurements of the cathodic plating efficiency with and without thiourea over a range of current densities, Fig. 7. These experiments were carried out with cylindrical copper cathodes (5.0 cm² surface area) in unstirred solutions. Cathode efficiencies were determined from the weight gain after plating to a theoretical deposit thickness of 0.005 in. assuming 100% efficiency. Below about 1 ma/cm² current density, the cathode efficiency for copper plating decreases. With the additive-free solution, the de-

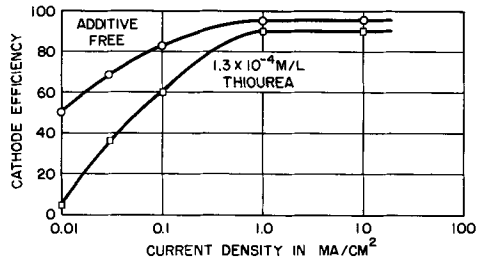

Fig. 7. Effect of current density on the copper plating efficiency with and without thiourea.

crease can be attributed either to the reduction of dissolved oxygen or to the incomplete reduction of some cupric ions. The effect is much greater with thiourea which suggests that either thiourea is reduced at the cathode or it complexes cuprous ions as they form so that a great portion of cupric ions are not completely reduced to copper. Llopis and co-workers (9), using radioactive tracers, found sulfur but not carbon in the copper deposit when the plating bath contained thiourea. This indicates that the thiourea molecule comes apart in the course of electroplating. There are two possibilities: (i) thiourea hydrolyzes to urea and H_2S, or (ii) thiourea is reduced forming perhaps NH_4CN and H_2S. The latter mechanism appears to be the most likely one of the two although there is no proof to offer at this time. The solubility product of CuS in aqueous solutions is very low, 8.5×10^{-45} $(M/L)^2$ in water. Thus, CuS will precipitate at the cathode surface at a relatively low sulfide ion concentration. The potential step in Fig. 6 at 0.1 ma/cm^2 may be the point at which CuS begins to precipitate and interfere with normal crystal growth. Below the exchange current density (~3 ma/cm^2), the rate of crystal growth without addition agent is controlled by surface diffusion of copper adatoms. Therefore CuS may interfere with crystal growth by inhibiting the surface diffusion of copper adatoms to growth sites. Copper sulfide may even block a growth site and force renucleation. The increase in step height with higher thiourea concentrations may be interpreted to mean that the cathode surface reaches the mass transfer limiting condition.

The depolarizing effect of relatively small amounts of thiourea in the plating solution at about 10 ma/cm^2 has also been observed by others (10, 11). Since the Tafel slope increases with thiourea concentration, the apparent "Tafel" exchange current density at 4×10^{-6} and 4×10^{-6}M thiourea is larger with the additive than without it. We have no satisfactory explanation for this anomaly. The result suggests that, as the current increases, thiourea delays the transition of the rate-determining step in copper plating from surface diffusion of adatoms to charge transfer according to Eq. [5a].

As stated earlier, dextrin by itself does not affect the η-log i curve for copper plating. Dextrin does appear to enhance the effect of thiourea. However, the results were erratic, not reproducible, and will not be discussed further.

The effect of the other "active" addition agents at a concentration of about 10^{-4}M on the η-log i relation in acid sulfate copper plating is shown in Fig. 8. The curves obtained with no additive and 4×10^{-4}M thiourea are included for comparison. l(-) Cystine and thiourea have a similar effect on the η-log i curve except that l(-) cystine does not shift the rest potential and a hystersis loop was observed between increasing and decreasing current curves. The same inhibiting effect of precipitated CuS is proposed for the effect of l(-) cystine on copper plating. Sulfide ions are formed by hydrolysis or cathodic reduction of l(-) cystine. l(-) Cysteine may be an intermediate.

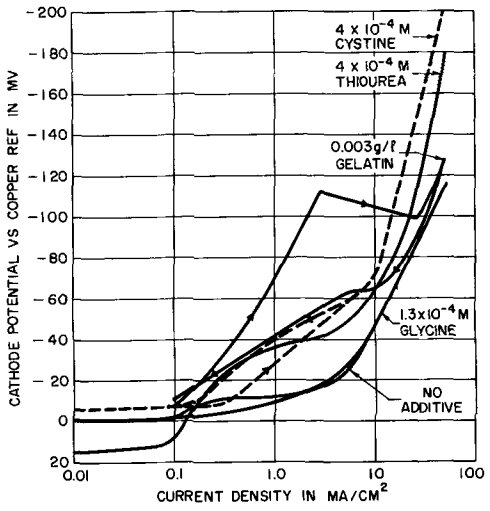

Fig. 8. Cathode potential-current density curves for copper plating with and without the various addition agents.

Glycine affects the η-log i curve only between about 0.1 and 1 ma/cm^2. The remainder of the curve is essentially the same as the no-additive curve. Glycine is noted as a leveling agent in acid-copper plating. The mechanism whereby metal distribution is affected by glycine does not involve an appreciable change in the kinetics of copper electrodeposition.

The largest polarization effect at low current densities was obtained with gelatin as shown in Fig. 8. The η-log i curve with increasing current has the same general form as the no-additive curve except that is is displaced about one order of magnitude lower in current density. At a critical current density of about 3 ma/cm^2, a sharp break occurs in the curve, and the cathode potential decreases up to about 30 ma/cm^2 where it again increases. On decreasing the current from 50 ma/cm^2, the η-log i curve traced is different from the increasing current curve. The sharp break in the η-log i curve for copper plating from acid solutions containing gelatin has been observed before. Lyzlov and co-workers (12) proposed that, below the critical current density, a small portion of the surface is active and gelatin accumulates on these isolated active sites. They suggest that all the cathode surface becomes active when the current density exceeds the critical value.

A significant factor in interpreting the results obtained with gelatin is that the break in the η-log i curve occurs at about the transition current density at which pyramidal crystal growth changes to cubic layer growth in copper plating (7, 8). We propose that below the critical c.d. gelatin molecules inhibit pyramidal growth by adsorbing on the screw dislocations that generate the pyramids as illustrated in Fig. 9. A gelatin molecule adsorbed on one of the steps can be buried by advancing steps whereas a molecule on the initial growth site at the top of the pyramid cannot. The net result is that gelatin blocks pyramidal growth, and cubic layer growth predominates even below 3 ma/cm^2. This is demonstrated in Fig. 10. Copper was plated on the (100) face of a copper single crystal for 1 hr at 1 ma/cm^2

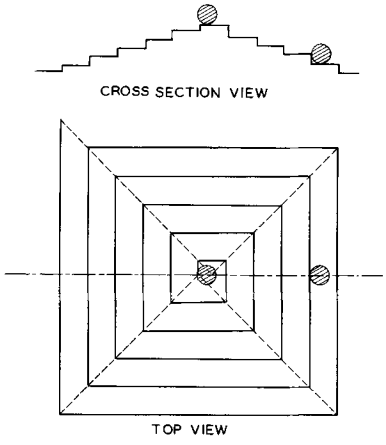

Fig. 9. Mechanism for inhibiting pyramidal crystal growth of copper with gelatin molecules.

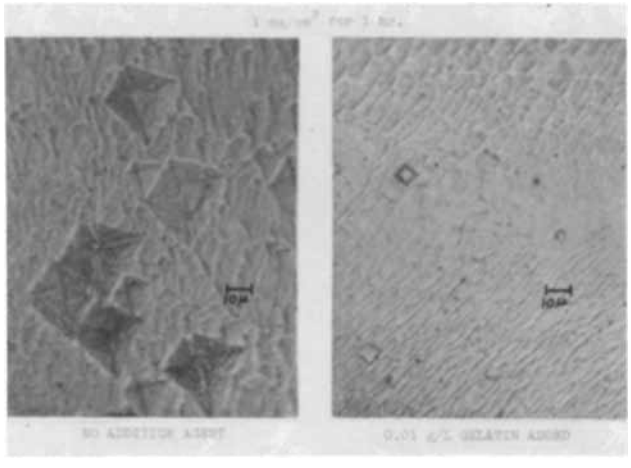

Fig. 10. Copper plating on (100) face of single crystal copper with and without gelatin at 1 ma/cm^2.

first without addition agent and then with 0.01 g/l gelatin. The results are apparent from the photomicrographs (750X). The cubic layer growth predominates throughout when gelatin is added.

At the transition current density, the adatoms or adions reach supersaturation (8), and the natural crystal growth habit becomes cubic layer growth without gelatin. In order to maintain the polarization effect above 3 ma/cm^2, the gelatin would need to inhibit cubic layer growth. The concentration of gelatin available, however, is insufficient, and the cathode potential decreases with increasing current density until the polarization due to charge transfer again increases the cathode potential above 30 ma/cm^2.

The hysteresis effect observed on decreasing the current from 50 ma/cm^2 with gelatin and l(-) cystine was not observed with rotating disk electrodes (13). Both ascending and descending η-log i curves were identical in form with the ascending curve for gelatin shown in Fig. 8. This suggests that the hysteresis effect in these studies, using spherical electrodes, is the result of inefficient stirring.

Conclusions

Thiourea and l(-) cystine have similar behavior as addition agents in acid copper plating. Both addition agents contain sulfur groups, and it is proposed that they are either hydrolyzed or electrochemically reduced during plating to form sulfide ions which precipitate copper as CuS at the cathode surface. The depolarization effect of relatively low thiourea concentrations in the vicinity of 10 ma/cm^2 suggests that the kinetics of copper electrodeposition is limited by surface diffusion of adatoms up to a higher current density with small amounts of thiourea than without it. Higher thiourea concentrations inhibit the surface diffusion of adatoms as expected.

Glycine has only a small effect on the cathode potential-current density relation. Therefore, while glycine has a profound effect on the distribution of copper plating on a microscale, it does not influence the kinetics of copper deposition.

Gelatin appears to affect the crystal growth of copper electrodeposits by a mechanism involving the adsorption of gelatin at growth sites. Relatively few gelatin molecules are needed to inhibit pyramidal crystal growth as compared to cubic layer growth.

Dextrin by itself has no effect on the kinetics of copper electrodeposition. It does appear to enhance the effect of thiourea, but these results are not conclusive.

Manuscript received Feb. 7, 1962; revised manuscript received April 2, 1962. This paper was prepared for delivery before the Detroit Meeting, Oct. 1-5, 1961.

Any discussion of this paper will appear in a Discussion Section to be published in the June 1963 JOURNAL.

REFERENCES

1. W. Mehl and J. O'M. Bockris, *J. Chem. Phys.*, **27**, 818 (1957); *Can. J. Chem.*, **37**, 190 (1959).
2. H. Gerischer, *Z. Elektrochem.*, **62**, 256 (1958); *Electrochem. Acta*, 2 (1960).
3. E. Mattsson and J. O'M. Bockris, *Trans. Faraday Soc.*, **55**, 1580 (1959).
4. N. F. Mott and R. J. Watts-Tobin, *Electrochem. Acta*, **4**, 79 (1961).
5. S. C. Barnes, *ibid.*, **5**, 79 (1961).
6. S. Barnartt, *This Journal*, **106**, 722 (1959).
7. R. Sroka and H. Fischer, *Z. Elektrochem.*, **60**, 109 (1956).
8. H. Seiter and H. Fischer, *ibid.*, **63**, 249 (1959).
9. J. Llopis, J. M. Gamboa, and L. Arizmendi, C.I.T.C.E. Meeting Paris (1951), p. 448, Butterworths (1959).
10. L. I. Shreir and J. W. Smith, *Trans. Faraday Soc.*, **50**, 393 (1954).
11. S. C. Barnes, Private communication.
12. Yu. V. Lyzlov, A. G. Samartsev, and T. A. Mechkovskaya, *Zhur. fiz. Khim.*, **31**, 2720 (1957).
13. G. R. Johnson and D. R. Turner, Unpublished results.

Carrier Injection Electroluminescence in GaP

F. G. Ullman

The National Cash Register Company, Dayton, Ohio

ABSTRACT

Two types of carrier injection electroluminescence can occur in GaP. The luminescence resulting from minority carrier injection at a p-n junction (p-n luminescence) reported here and previously by others peaks near 5650 and 7000Å in Zn-doped GaP. A much lower efficiency luminescence results from majority carrier excitation at electrode barriers in apparently junction-free crystals and does not seem to result from an avalanche breakdown process. The emission spectrum for this form of excitation peaks at 5800 and 6500Å and is the same for n- and p-type material (with the addition of the 7000Å "Zn" emission from Zn-doped, p-type material). The 5800Å emission is attributed to recombination across the band gap, the 6500Å emission to recombination at deep donor levels, and the 7000Å emission to recombination at deep-lying Zn acceptor levels. The 77°K photoluminescence peaking at 6300Å, reported previously by others, is also attributed to recombination at the donor levels. The shift in the peak for the band gap emission to 5800Å, rather than 5650Å as in the corresponding p-n luminescence band, is suggested to be caused by the high field at the electrode barrier. Photoluminescence and photoconduction excitation spectra were also obtained and are consistent with these hypotheses.

Until recently, little information was available on the luminescent properties of GaP. The observed electroluminescence has been attributed to minority carrier injection at p-n junctions (1-3) and to avalanche breakdown at metal contacts or at reverse biased p-n junctions (1, 3). Emission bands peaking at energies less than the band gap were observed and described as resulting from impact excitation of luminescent centers (3), indirect recombination of free electrons with free holes (4), recombination at Cu or Zn impurity centers (1, 3), or recombination at levels resulting from Ga and P vacancies (5). Recently, two detailed studies of electroluminescence at p-n junctions in GaP have been published (6, 7); these also differ on several points of both observation and interpretation.

The luminescence resulting from minority carrier injection at a p-n junction differs significantly from the luminescence resulting from majority carrier excitation at electrode barriers in apparently junction-free crystals. If junctions are present, both processes may occur simultaneously; this could account for some of the disagreement among the observations of others.

The results reported here suggest that there are three major radiative recombination processes active in our crystals, indirect electron-hole recombination across the band gap, recombination of a free hole with an electron in a donor level of unknown origin, and in Zn-doped crystals recombination of free electrons with deep-lying Zn acceptor levels. The observed luminescence depends on which are dominant, and this in turn depends on the excitation process and the conductivity type of the recombination region. Some of the disagreement among earlier observations can be resolved if allowance is made for the type of excitation and the relative probabilities of the various recombination mechanisms possible.

Description of Crystals

All of the crystals studied were prepared by the solution growth method of Wolff, Keck, and Broder (8) in sealed, evacuated, silica tubes. Solutions of the order of 10 at. % of phosphorus in gallium were heated to 1300°C, maintained at this temperature for at least 2 hr, and then cooled to room temperature in 24 hr following a programmed parabolic cooling curve. (Increasing the cooling time to 72 hr had no significant effects on the crystal growth.) The quartz tubes often expanded, indicating that the dissociation pressures were greater than 10 atm at these growth temperatures. Dopants (*e.g.*, Zn metal) were mixed with the gallium prior to evacuation. Starting materials of at least 99.999% purity were used in all cases.

The crystals selected for study are of two types, (i) platelets with (111) major faces, that are 1 mm or less in thickness and range from a few millimeters to a centimeter in the other dimensions, and (ii) <111> axis needles a centimeter or more in length and of triangular cross section with sides of the order of a tenth of a millimeter or less. The needles are found at the opposite end of the growth vessel from the solution and are often intermingled with deposits of mixed oxides of gallium. The vapor phase growth and properties of similar needles have been described by Gershenzon and Mikulyak (9). Some results of x-ray diffraction indicate that the plate-like crystals may not be single but may contain one or more 180° twin planes. The needles, however, are single crystals.

Spectrographic analyses indicate that the only major impurity in the crystals is Si, in the concentration range of 10-100 ppm. The source of the Si impurity is unknown; it is believed to result from a high-temperature reaction between Ga and silica (14). In addition, 1 ppm or less of Fe and Mg are

found in undoped GaP crystals and in the initial phosphorus. Cu and Ag, in about the same concentrations as the Fe and Mg, are found in Zn-doped crystals and in the initial Zn.

The crystals were separated mechanically from the Ga solvent and then boiled in about a 1:1 mixture of concentrated HCl and water. In most cases, this treatment was sufficient to remove all the surface Ga. The samples studied were carefully selected; crystals with occluded gallium or obvious grain boundaries were not used. Electrodes of various metals in the form of point and area contacts were tried. The luminescent properties did not depend on the electrode metal; hence silver paste or ultrasonically applied In were used in most cases.

Hall effect measurements have shown that undoped crystals are n-type with room temperature carrier concentrations in the range of 10^{15}-10^{16} electrons/cc and a donor ionization energy of 0.07 ev. The Zn-doped crystals discussed in this article are p-type with about 2×10^{17} holes/cc at room temperature and an acceptor ionization energy of 0.03 ev; spectrographic analysis indicates 10-100 ppm of Zn in these crystals. Room temperature mobilities for both electrons and holes are in the 50-100 cm^2/v sec range.

Apparatus

Electroluminescence emission spectra were measured with d-c excitation. The sample was mounted at the entrance slit of a Bausch and Lomb grating monochromator (Model 33-86-45). A Photovolt photometer with a 1P21 photomultiplier served as the detector, and its output was recorded on a Moseley X-Y recorder whose X-axis was suitably coupled to the wavelength drive of the monochromator. Photoluminescence emission and excitation spectra were similarly obtained except that a light pipe was used to channel the emitted light to the monochromator or the exciting light to the sample so that the sample could be immersed in liquid nitrogen. The photoluminescence is only observable at low temperature because of temperature quenching (5, 7). The photomultiplier was calibrated against a thermocouple, and all spectra were corrected for the constant incident energy response of the photomultiplier. The spectral range covered was limited to wavelengths shorter than 8000Å by the over-all sensitivity of the system.

The photoconductivity excitation spectrum was obtained with a Perkin-Elmer Model 99 double-pass monochromator. The resulting 13 cps photocurrent was amplified by a 13 cps twin-tee amplifier. The incident energy was measured with a Perkin-Elmer thermocouple and associated Model 107 13 cps amplifier. An isophotonic correction was applied to this spectrum.

Electroluminescence at a p-n Junction

An initial objective of this work was to study the red emission that had been reported to result from doping GaP with Zn (3). Zn-doped crystals were prepared, the "Zn" red emission was observed, and the emission spectrum, which peaks at 7000Å, was determined (10). Light emission was observed only at the negative electrode (3, 10). In some samples with identically prepared electrodes the red emission occurred at only one electrode. Negative bias on the other electrode produced only an emission of much lower intensity and yellow in color. (Its spectrum had a shoulder at about 5900Å and then increased out to 6500Å, the detection limit for that particular measurement.) The similarity to the p-n luminescence reported by others (6, 7) suggests that this asymmetry results from the presence of junctions in the crystal. Crystals containing both p and n regions have been found and discussed (5, 7). Zn-doped crystals prepared with higher purity starting materials and improved growth conditions did not exhibit this anomalous behavior, indicating the absence of junctions.

One Zn-doped crystal was found, however, that had a junction located near the crystal surface. It was characterized by an asymmetrical current-voltage characteristic with a rectification ratio of the order of 100. Emission from the junction, not in contact with the electrode, could be seen clearly as a bright spot. The room temperature emission spectrum for forward bias is shown in Fig. 1; it consists of a narrow band (0.1 ev at half maximum), peaking in the green near 5650Å as reported by others (4, 6, 7) and the previously reported "Zn" band (7, 10) peaking near 7000Å.[1] The effect on the spectrum of absorption by the crystal was determined by measuring only the light escaping through the back side of the crystal; light emitted at the junction had to pass through at least 1 mm of crystal before entering the monochromator. This result is also shown in Fig. 1. It can be seen that the shape of the 7000Å band is unaffected by absorption whereas the 5650Å band is attenuated with the attenuation becoming more severe at shorter wavelengths. There is, however, no shift in the peak.

Since similar results have been presented in detail by others, as indicated above, this discussion has been included only for comparison with the results described in the following sections.

[1] Errors in the correction for the photomultiplier spectral response and in the wavelength measurements prevent the determination of the peak wavelengths to better than ±50Å. Although the peaks in Fig. 1 are at about 5550 and 6900Å, the results of several measurements indicate that 5650 and 7000Å are reasonable choices for the peak wavelengths. Since other workers have reported these to be the peak wavelengths, we have used the same designation throughout this article.

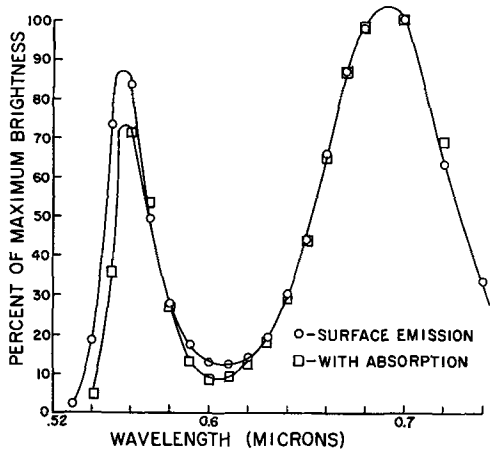

Fig. 1. Emission spectrum of forward biased p-n junction

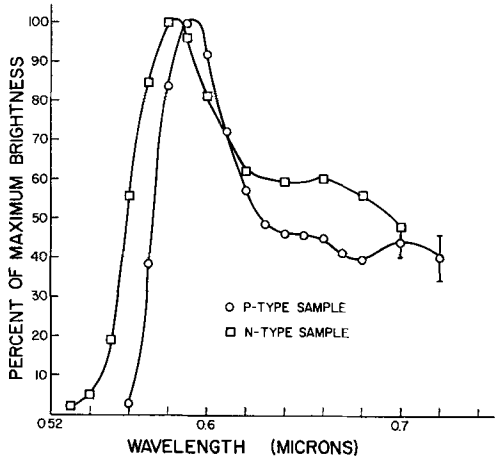

Fig. 2. Emission spectra from metal-crystal contact to n-type crystal and p-type crystal.

Electroluminescence at a Metal-Crystal Contact

There is general agreement that electroluminescence is never observed at ohmic contacts to GaP. Ordinary metal contacts, *e.g.*, Ag paint, ultrasonically applied In, pressure contacts, however, do not make ohmic contact to GaP without special treatment to penetrate the surface oxide (13). Samples with symmetrical contacts behave like two rectifiers opposed in series; breakdown potentials[2] are usually between 1 and 5v. The current-voltage characteristics are often asymmetrical, as shown by Wolff *et al.* (3). Kinks in the characteristics as reported by Gorton *et al.* (11) have also been observed, but are not usual.

The electroluminescence at a metal-crystal contact is at least one or two orders of magnitude lower in efficiency than the p-n luminescence. Since GaP has a high index of refraction, 3.4 (12), the crystals appear to glow uniformly. However, microscopic examination indicates that the emission is actually localized close to one electrode. The emission has been reported to occur only at the negative electrode (3, 10). However, observations of apparently junction-free crystals[3] have shown that the emission is at the negative electrode for n-type crystals but at the positive electrode for p-type crystals, indicating that this process is governed by majority carriers.

The emission spectrum obtained with majority carrier excitation consists of two bands with half widths of about 0.2 ev and peaking at about 5800 and 6500Å; in the crystals made p-type by Zn-doping the peak at 7000Å is also observed. In Fig. 2, two typical spectra are shown, one for an n-type crystal and one for a p-type crystal. In this figure it can also be observed that (i) there is no detectable emission at wavelengths shorter than the absorption edge, (ii) the 5800Å band is shifted to longer wavelengths in the p-type crystal, and (iii) the 6500Å band of the p-type crystal has a smaller relative amplitude than it has in the n-type crystal.

The first observation is general; we have never detected emission wavelengths shorter than the absorption edge for any of our crystals. The second and third effects do not result from the difference in conductivity type, but rather from heating of the sample. For the measurements shown in Fig. 2, the power dissipation in the p-type crystal was 0.37w; in the n-type crystal it was only about 0.05w. Power dissipations greater than 1.5w (as great as 3.0w in some cases) will produce incandescence in crystals of the same size and mounted in the same way. The energy shift of the 5800Å band computed from the peak positions in Fig. 2 is close to 0.05 ev; this is roughly consistent with the thermal shift of the band gap, 5.5×10^{-4} ev/°K (12), for the p-type crystal at about 120°C.

Grimmeiss *et al.* (5, 7) have suggested that both gallium and phosphorus vacancies play an important role in the observed luminescence. This conclusion suggests that the emission spectra of crystals prepared in different environments would differ. Since the vapor phase environment in which the needles are grown would tend to be much less rich in Ga than the solution in which Ga is present in large excess, the emission spectra of needle crystals were determined for comparison with the spectra found for solution-grown crystals. The electroluminescence of the needle crystals is identical to that found for n-type solution-grown crystals, as shown in Fig. 3. These needles have at least an order of magnitude higher resistance than the solution-grown crystals (6) and therefore require higher voltages for observable electroluminescence. The two curves shown in Fig. 3 were taken at about 100v-10 ma and 20v-2 ma, respectively (about 40 ma at 7 or 8v is usual for comparable light emission from solution-grown crystals). The shift of the 5800Å band (to 6000Å) and the quenching of the 6500Å band, for the higher power dissipation, are similar to that for solution-grown crystals. The shift to 6000Å, assuming a band gap transition, indicates a crystal temperature of the order of 200°C for the higher power dissipation.

Photoluminescence and Photoconductivity

At liquid nitrogen temperature, most of the solution-grown GaP exhibits a red fluorescence which is quenched on heating. The emission spectrum for 3650Å excitation peaks at about 6300Å and is almost identical with the photoluminescence spectrum re-

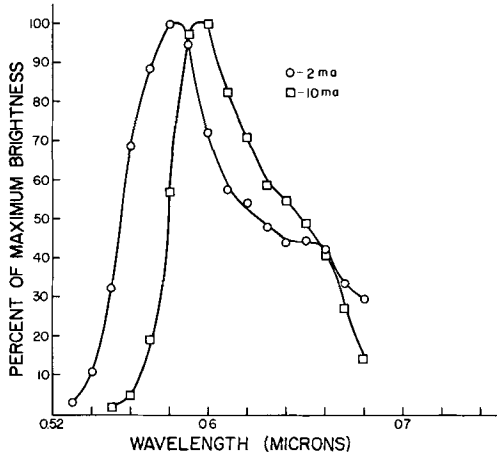

Fig. 3. Emission spectra from metal contact to n-type needle crystal for two currents.

[2] The rectification characteristic is "soft." The applied voltage at which the knee occurs in the current-voltage characteristic is taken to be the breakdown potential.

[3] The basis for this description is given in the Discussion section.

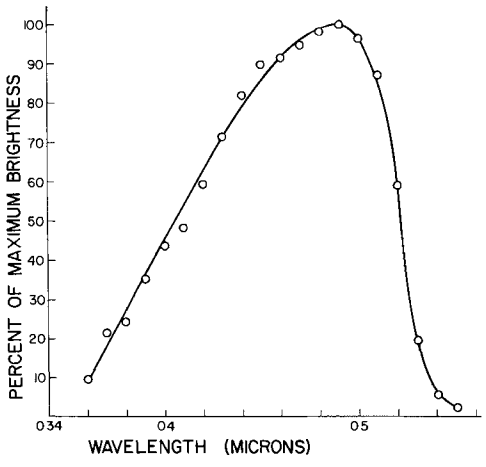

Fig. 4. Excitation spectrum of 77°K fluorescence

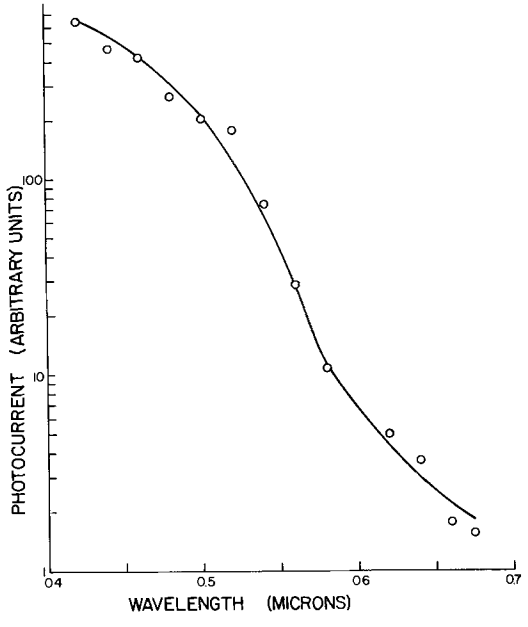

Fig. 5. Excitation spectrum of photocurrent in n-type needle crystal.

ported by Grimmeiss and Koelmans (5). Zn-doped samples gave the same spectrum and appeared to have additional emission near 7000Å, but the difference between the emission at 7000Å and the background of scattered light was not outside of experimental error. The 7000Å "Zn" photoluminescence has, however, been observed by Grimmeiss *et al.* (7). The excitation spectrum (relative photoluminescent brightness *vs.* incident wavelength for constant incident energy) follows the fundamental absorption as shown for powdered, undoped material in Fig. 4. The decrease at short wavelengths is probably caused by the increased absorption and scattering of the exciting light in the powder sample, although a difference in surface *vs.* bulk efficiency may also be involved. No excitation was observable with wavelengths longer than 5500Å.

Photoconductivity can be observed in many of these crystals. It is difficult to measure in the relatively low resistance, solution-grown crystals because of the large dark-current noise. In the high resistance needles, however, photocurrents are easily observed. Since no short circuit photovoltaic effects could be observed, these are believed to be bulk photocurrents rather than barrier layer photoeffects. The photocurrent excitation spectrum for a needle crystal with In electrodes is shown in Fig. 5. The applied voltage was of the order of 45v which was well above the breakdown voltage of these contacts. This spectrum follows the optical absorption, but extends to wavelengths as long as 6800Å. However, no long wavelength maxima were observed. The photocurrent varied linearly with light intensity over the range of light levels used for this measurement.

Discussion of Results

A complete explanation of the observed luminescence of GaP requires an understanding of the mechanisms of both excitation and recombination. In GaP, electroluminescence is excited by injection of either minority or majority carriers. However, the possibilities for their recombination and therefore the possible emission spectra are numerous. Reasonable arguments, supported by experiment, have been given for (i) indirect recombination of free electrons and free holes across the band gap (2, 6), (ii) recombination at levels resulting from both P and Ga vacancies, (iii) recombination at deep-lying Zn acceptor levels (7), (iv) recombination at deep donor levels of unknown origin (6), and (v) recombination at impact-ionized centers associated with excess Ga or Zn (3). If the recombination processes that are operative are competitive, both the conductivity type of the recombination region and the excitation mechanism can be expected to influence the relative magnitudes of the various possible emission bands. A discussion of the excitation and recombination mechanisms indicated by our results and their relation to previous work, follows.

Excitation by majority carrier injection.—It has been pointed out (3, 6) that a contact barrier or p-n junction must be present for electroluminescence to occur in GaP; no luminescence is observed with ohmic contacts. GaP forms a protective oxide layer on its surface (13) which accounts for its stability, in contrast to its cousins, AlP and AlAs, which decompose continuously in moist air (3). This oxide serves as an insulating layer between metal contacts and the GaP bulk unless special means are employed to make ohmic contact by penetration or elimination of the intervening oxide. The rectifying contacts thus obtained break down and luminesce for applied potentials of only a few volts (except for the high resistance needles). This luminescence is excited by majority carrier injection, occurring at the positive contact to p-type material and the negative contact to n-type material.

If p-n junctions are present, however, they could dominate both the electrical characteristics and the light emission. This may account for the observations of essentially only the forward bias p-n luminescence in Zn-doped GaP (3, 5, 7, 10) with nonohmic contacts. The presence of junctions may result from an inhomogeneous distribution of the Zn acceptors in the normally n-type solution-grown GaP, similar to that found in InSb (16).

Gershenzon and Mikulyak (6) have proposed three excitation mechanisms for light emission from reverse biased p-n junctions: an avalanche process for diffused junctions, tunneling through the narrower alloyed junctions, and thermal generation of carriers in the depletion layer for prebreakdown emission. For all three mechanisms the emission spectrum was a broad, essentially structureless band with a significant portion at wavelengths shorter than the absorption edge, similar to the emission spectrum at breakdown of junctions in silicon (17). This indicates that the pair production threshold was exceeded in all three cases. Such reverse bias p-n luminescence cannot account for our observations of the metal-crystal contact luminescence because of the absence of emission at wavelengths shorter than the absorption edge, because of the structure of the emission spectrum, and because only a linear dependence of photocurrent on light intensity was found in samples biased above breakdown.

It is possible that the electrode barrier is lowered sufficiently by the applied electric field for the most energetic carriers to surmount it; their energies, however, are below the pair production threshold. The crystal will still have a higher resistance than with ohmic contacts since only the most energetic carriers contribute to the current; a reduction in resistance by about two orders of magnitude was found when ohmic contacts were made. The resistance should show some dependence on the work function of the metal contact. No systematic variation with electrode metal was found, but low work function metals such as In have been reported to make a low resistance contact to GaP (18, 19).

Recombination processes for p-n luminescence.— Gershenzon and Mikulyak (6) found the room temperature emission spectrum with forward bias to consist of a narrow band (~3kT band width) peaking at 5650Å, and a red band peaking at about 6700Å. No emission bands characteristic of the diffused impurities were found. Both bands were observed to shift to shorter wavelengths on cooling by approximately the band gap shift of 5.5×10^{-4} ev/°K (12). They attributed the 5650Å emission to indirect recombination across the band gap and the 6700Å emission to recombination of an injected hole with the electron in a deep (0.3 ev) donor level known to be present in all their material.

Grimmeiss *et al.* (7) also found the 5650Å band, but observed no shift in emission peak with temperature. They found a second band at 7000Å in both electroluminescence and photoluminescence from Zn-doped samples which also showed little wavelength shift with temperature. They attributed the 5650Å band to recombination of a free hole with the electron in a shallow (0.07 ev) donor level and attributed the donor levels to phosphorus vacancies. The 7000Å band was attributed to recombination at a deep (0.4 ev) Zn acceptor level. A 6200Å emission band was found in undoped n-type material only, although a corresponding photoluminescence emission band was found for both n-and p-type material.

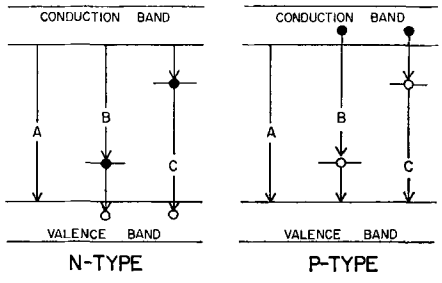

Fig. 6. Simplified energy band model illustrating major radiative recombination mechanisms in GaP; ●—electron, ○—hole.

The p-n luminescence emission spectrum reported here for Zn-doped samples resembles that of Grimmeiss *et al.* rather than that reported by Gershenzon and Mikulyak. However, a plausible explanation can be given for the differences in emission spectra found by different observers if consideration is given to the conductivity type of the recombination region. This is illustrated by the model shown in Fig. 6. Only three recombination processes are considered in this model, (*A*) electron-hole recombination across the band gap, (*B*) recombination of a free electron with the hole in a deep (0.4 ev) Zn acceptor level,[4] and (C) recombination of a free hole with the electron in a deep (0.3 ev) donor level of unknown origin. The shallow donor and acceptor levels responsible for the conductivity are not included. The donor concentration is assumed the same in both n- and p-type material since no donors were deliberately introduced and the undoped material is n-type. The acceptor concentration, however, will vary from greater than the donor concentration in the p-region to less than the donor concentration in the n-region. Free holes injected into the n-region can recombine with either the donor (largely occupied because of its depth) or acceptor electron; these levels will then recapture electrons from the majority carrier population. However, the donor concentration exceeds the acceptor concentration in the n-region and process *C* will dominate the emission. Since Gershenzon and Mikulyak (6) have shown that recombination occurred in the n-region in their diodes, this argument accounts for their inability to observe emission bands characteristic of the Zn and Cd acceptors they introduced.

Let us now consider the recombination of electrons injected into the p-region. The deep acceptor levels are largely un-ionized because of their depth, and the acceptor concentration now exceeds the donor concentration. For this case, process *B* will dominate the emission.

Process *A* will occur in both regions with a probability dependent on its cross-section relative to the probabilities for *B* and *C*. These, in turn, depend on both their cross sections and the relative concentrations of donors and acceptors.

We conclude that the emission spectrum for n-region recombination should consist principally of the 5650Å band and the 6500Å band as observed by

[4] It has been shown previously (7, 10) that the 7000Å band results from Zn-doping. Since the activation energy for Zn acceptors is 0.03 ev (Hall effect), Zn must be at least a double acceptor in GaP similar to Cu in GaAs (15).

Gershenzon and Mikulyak (6). For p-region recombination the spectrum will consist principally of the 5650Å band and an emission characteristic of the acceptor if it gives rise to deep levels (the 7000Å band with Zn-doping) as reported by Grimmeiss *et al.* (7) and here.

In the model, the transition producing the 5650Å band is shown as the suggested band gap recombination (4, 6) rather than the free hole capture at a shallow donor level suggested by Grimmeiss *et al.* (7). Our results for the p-n luminescence are insufficient to make a choice between these two hypotheses, but the arguments just presented deal only with the impurity recombination and are valid in either case. However, the results with majority carrier excitation, discussed below, do indicate a band gap transition.

Recombination with Majority Carrier Excitation. —The model discussed in the previous section must also be consistent with the results found with majority carrier excitation, namely, the emission of the 6500Å band from both n- and p-type material, the emission peak at 5800Å in contrast to the 5650Å peak in the p-n luminescence, and the low radiative efficiency relative to the p-n luminescence.

These spectra are distinctly different from those found for both forward and reverse biased p-n junctions. It is this fact, as well as the different character of the current-voltage characteristics for the metal-crystal contact, on which the designation of these crystals as apparently junction-free is based. In crystals believed to contain junctions, the more efficient p-n luminescence dominates, and the emission resulting from majority carrier excitation appears as a low level background (10).

The recombination level for the 6500Å emission should be situated about 0.3 ev from one of the band edges. If it were near the valence band, effects due to an impurity absorption at about 2.0 ev should be expected in the excitation spectrum of photoluminescence. (The 6350Å photoluminescence and 6500Å electroluminescence may be assumed to result from recombination at the same level.) Since such effects are not observed, we conclude that the low-temperature photoluminescence and 6500Å electroluminescence result from recombination of a free hole with the electron in a 0.3 ev deep donor level as indicated in the energy band model. This could be the same donor level postulated by Gershenzon and Mikulyak.

With majority carrier excitation, the 6500Å emission, attributed to n-type recombination with p-n luminescence, is observed from both n- and p-type crystals. This lack of dependence of emission spectrum on conductivity type, the low efficiency of the majority carrier excitation relative to the p-n luminescence, and the absence of any superlinear dependence of brightness on current as found for p-n luminescence (6, 7), all suggest that the recombination kinetics for majority carrier excitation are controlled by a small free carrier population rather than the recombination center concentrations. Since the results indicate a band gap transition, minority carriers must, somehow, be involved. Approximate calculations indicate that minority carrier densities less than 10^{10}/cc can account for the observed intensities. However, the room temperature np product for GaP is of the order of unity, so there are no minority carriers. We can only suggest that minority carriers are produced in the barrier region by some mechanism such as electric field or impact ionization of impurities. The 6500Å band will then be produced by hole capture at the occupied donor levels in n-type crystals; in p-type crystals the donor is ionized and must first capture a minority electron. As long as the minority carrier density is very much smaller than the donor concentration the 6500Å emission will be observed from crystals of both conductivity types. For larger minority carrier densities, as in p-n luminescence, the 6500Å emission from p-type crystals is obscured by the other, much more efficient emission bands.

We turn now to the 5800Å band. The shift of emission peak with temperature (high current effect) and the sharp cut-off at short wavelengths suggest that this emission is produced by band gap recombination. The fact that the emission peaks at 5800Å rather than 5650Å as in the p-n luminescence could result from the effect of the high field at the electrode barrier on the absorption edge or the band gap. Field-induced strains or possibly the Franz-Keldysch (20, 21) effect could produce such a shift in the emission band edge. Consideration was given to the possibility that the 5800Å emission might be the 5650Å emission shifted by absorption, which might occur if it originated deep in the crystal. The measurements shown in Fig. 1, however, eliminate absorption as a possible explanation.

Grimmeiss *et al.* have attributed some of the luminescent centers to levels resulting from Ga and P vacancies. Since our vapor-grown crystals showed the same luminescence as solution-grown crystals although their growth environments were different, and since the 0.07 ev donor identified as a phosphorus vacancy by Grimmeiss *et al.* is found in crystals prepared in different laboratories and in widely different environments, impurities such as silicon and oxygen [possibly from a high-temperature reaction of gallium with silica (14)] seem more likely suspects than lattice vacancies.

Summary of Results

The emission spectra produced by majority carrier injection from a metal-crystal contact consist of two emission bands peaking at 5800 and 6500Å and additional emission at 7000Å in crystals made p-type by Zn-doping. The 6500Å band and the low-temperature photoluminescence are attributed to recombination at a donor level situated about 0.3 ev below the conduction band. The 5800Å band is suggested to be band gap recombination in the high field region of the electrode barrier where the emission band edge has been shifted to longer wavelengths as a consequence of the high electric field at the electrode barrier. The majority carrier injection is suggested to occur by thermal excitation over the electrode barrier which is lowered by the applied field. The charge carrier energies, however, are less than required for pair production since the emission spectra and dependence of photocurrent on light intensity are not

characteristic of avalanche breakdown processes. The low efficiency for this form of excitation is suggested to be a consequence of a relatively small concentration of minority carriers produced by electric field or impact ionization of impurities, which control the recombination kinetics.

Consideration of competitive recombination processes in a simplified energy band model has been used to demonstrate that the emission spectrum for p-n luminescence will be as reported here and elsewhere (7) for p-region recombination. For n-region recombination, however, the 6500Å band will be dominant, as found by Gershenzon and Mikulyak (6). This is not the case with majority carrier excitation where the relative concentrations of recombination centers do not enter significantly into the recombination kinetics; the emission is controlled by the small minority carrier population produced in the barrier region.

Acknowledgments

The author is indebted to M. S. Hall and S. H. Liebson for critical reading of this manuscript, to W. M. Becker for his contributions to the early part of this work, to E. L. Peirson for preparation of the crystals, and to C. V. Osterday for technical assistance. The author would also like to thank M. Gershenzon for making his results available prior to publication.

Manuscript received Jan. 8, 1962; revised manuscript received April 23, 1962.

Any discussion of this paper will appear in a Discussion Section to be published in the June 1963 JOURNAL.

REFERENCES

1. E. E. Loebner and E. W. Poor, *Bull Am. Phys. Soc.*, Ser. II, **4**, 45 (1959).
2. D. B. Holt, G. F. Alfrey, and C. S. Wiggins, *Nature*, **181**, 109 (1958); G. F. Alfrey and C. S. Wiggins, "Solid State Physics in Electronics and Telecommunications," Vol. 2, p. 747, Academic Press, New York (1960).
3. G. A. Wolff, R. A. Hebert, and J. D. Broder, *Phys. Rev.*, **100**, 1144 (1955); "Semiconductors and Phosphors," p. 547 Interscience Publishers, Inc., New York (1958).
4. E. E. Loebner and E. W. Poor, *Phys. Rev. Letters*, **3**, 23 (1959).
5. H. G. Grimmeiss and H. Koelmans, *Philips Research Rpts.*, **15**, 290 (1960).
6. M. Gershenzon and R. M. Mikulyak, *J. Appl. Phys.*, **32**, 1338 (1961).
7. H. G. Grimmeiss and H. Koelmans, *Phys. Rev.*, **123**, 1939 (1961); H. G. Grimmeiss, A. Rabenau, and H. Koelmans, *J. Appl. Phys.*, suppl., **32**, 2123 (1961).
8. G. A. Wolff, P. H. Keck, and J. D. Broder, *Phys. Rev.*, **94**, 753 (1954).
9. M. Gershenzon and R. M. Mikulyak, *This Journal*, **108**, 548 (1961).
10. F. G. Ullman, *Nature*, **190**, 161 (1961).
11. H. C. Gorton, J. M. Swartz, and C. S. Peet, *ibid.*, **188**, 303 (1960).
12. O. G. Folberth and F. Oswald, *Z. Naturforsch.*, **9A**, 1050 (1954).
13. C. J. Frosch, M. Gershenzon, and D. F. Gibbs, Symposium on "Preparation of Single Crystals of the III-V Compounds," Battelle Memorial Institute, Columbus, Ohio (1959).
14. L. M. Foster, Symposium on "Impurities in III-V Elements and Compounds," Battelle Memorial Institute, Columbus, Ohio (1960).
15. J. Blanc, R. H. Bube, and H. E. MacDonald, *J. Appl. Phys.*, **32**, 1666 (1961).
16. W. P. Allred and R. K. Willardson, The Electrochemical Society Electronics Division Abstracts, **9**, 178 (1960).
17. A. G. Chynoweth and K. G. McKay, *Phys. Rev.*, **102**, 369 (1956).
18. J. Mandelkorn, *Proc. IRE*, **47**, 2012 (1959).
19. J. W. Allen and P. E. Gibbons, *J. Electronics and Control*, **7**, 518 (1959).
20. R. L. Williams, *Phys. Rev.*, **117**, 1487 (1960).
21. K. W. Böer, H. J. Hänsch, and U. Kümmel, *Z. Physik*, **155**, 170 (1959).

Effect of Cupric Ion on the Electrical Properties of the Germanium-Aqueous Electrolyte Interface

P. J. Boddy and W. H. Brattain

Bell Telephone Laboratories, Murray Hill, New Jersey

ABSTRACT

The capacity of the germanium-aqueous electrolyte interface measured at high frequency after interaction with cupric ion in concentrations of the order of 10^{-7}M cannot be interpreted as simply that of the semiconductor space charge. Since the deviation is in the direction of larger observed capacity the data can be understood in terms of a capacity in parallel with the semiconductor space charge, *i.e.*, fast surface states in the vicinity of the Fermi level. Conductance measurements allow the extra capacity to be determined as a function of surface potential. From the form of this relationship the data are shown to be consistent with two charge traps, the parameters of which are $\nu = +1.9\ kT/e$, $N_t \sim 1 \times 10^{11}$ cm^{-2} and $\nu' = -1.2\ kT/e$, $N'_t \sim 1.9 \times 10^{10}$ cm^{-2}. Surface recombination, which is not present at a significant level on the freshly anodized surface in the absence of cupric ion, appears as a result of the interaction. These data identify the recombination center as that with $\nu' = -1.2\ kT/e$, the capture cross section for holes being 400 times greater than that for electrons. The phenomena are similar to those on the dry etched surface, and a common origin for the states is indicated.

The electrical properties of germanium surfaces after anodic etching in carefully purified solutions have been discussed in a previous communication (1). The major conclusion to be drawn from these experiments is the absence of a significant density of fast surface states over a range of about 200 mv each side of the middle of the energy gap. It has been reported that etched germanium surfaces in gaseous ambients are generally n-type, but that the presence of traces of certain impurities, including cupric ion, in the final rinse water results in the surface becoming p-type (2). We have observed a similar phenomenon on a germanium surface in contact with an aqueous solution containing cupric ion and have determined some of the electrical changes occurring at the surface as a result of this interaction.

Experimental Method

The measurement of the differential capacity of the germanium-solution interface by a current pulse method and the bridge electrodes used in these experiments have been previously described (1). The two electrodes were 12.5 ohm-cm n-type and 25.5 ohm-cm p-type with the thin arm oriented to the (100) plane.

The solution was M/10 K_2SO_4, phosphate buffered to *p*H 7.4. Purification was effected by gettering with crushed germanium produced *in situ* by the collision of small pieces agitated by rapid stirring. Solution was introduced into the cell through filter paper that had previously been washed with several portions of purified solution. Nitrogen, which had been passed over hot copper gauze, displaced the air in the cell.

Dilute solutions of cupric nitrate or sulfate were made of sufficient concentration that when a few milliliters were added to the purified solution in the cell (ca. 250 ml) a final concentration of 10^{-8}-10^{-6} M was achieved.

The thin arm of the electrode was etched initially, and between each addition of cupric ion to the solution, in CP-4. Before the CP-4 etch the electrode was dipped for about 10 sec in hydrofluoric acid containing 5% nitric acid, producing a gold-colored stain. The advantage of this procedure was that the "gold film" was instantaneously attacked by CP-4 and even after dissolution of the film (ca. 5 sec) the etching continued uniformly over the whole surface. Without the gold film, CP-4 was initially active only on certain areas of the thin arm, although etching would become uniform after 15-20 sec. However, it was desired to keep the material removed by etching down to a minimum, consistent with a uniformly etched surface, and the gold film technique seemed to afford a method of doing this. After rinsing in germanium-gettered deionized water, the electrodes were put into the cell and anodically etched at about 200 μa cm^{-2} for 5 min (n-type electrodes illuminated). Before each series of experiments the changes of capacity and conductivity with applied bias in solution free from cupric ion were checked for consistency with previous data (1) in purified solutions. All other experimental details and the experimental arrangement were as previously reported (1).

After addition of cupric nitrate to the cell, the electrode potential was followed with time until approximately constant (about 30 min). Measurements of capacity, change in conductivity, and filament lifetime as a function of electrode potential were then made on the thin arm of the bridge. The electrode potential was varied by switching a preset current through the interface for about 1 sec or less. The instantaneous values of electrode potential

and either change in potential at the interface due to the differential current pulse, balance point of the bridge, or decay of photoconductivity were measured, each of the latter three quantities being determined in separate experiments on the identical system. The potential response to the square 5 μsec current pulse is similar to that obtained for the clean surface; the change in potential at the interface being linear with time over 5 μsec. The same equivalent circuit applies and the capacity may be calculated as before (1).

Results

The electrode potential as a function of time for various cupric ion concentrations is shown in Fig. 1. When the potential had reached a steady value the capacity was measured as a function of electrode potential. In Fig. 2 the capacity for a simple block electrode before and after adding cupric ion is shown. When the cupric ion is added, additional capacity appears peaked about a given value of V_E. The immediate inference is that this capacity is due to fast surface states that were not present before the cupric ion was added to the electrolyte. Since it was desirable to determine this added capacity as a function of the surface potential ψ_s (the electrostatic potential across the semiconductor space-charge region) and also to make surface recombination velocity measurements, the subsequent data were taken on a germanium bridge with the thin arm in the electrolyte.

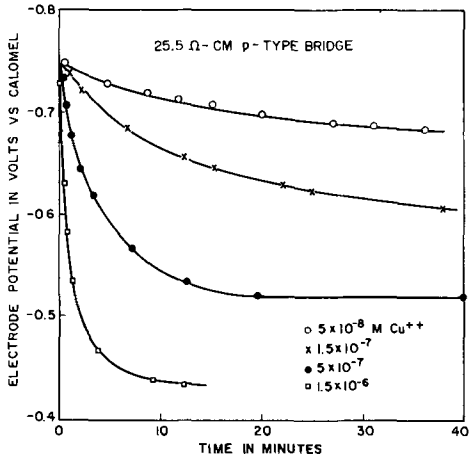

Fig. 1. Electrode potential *vs.* time immediately after CP-4 etching and anodizing.

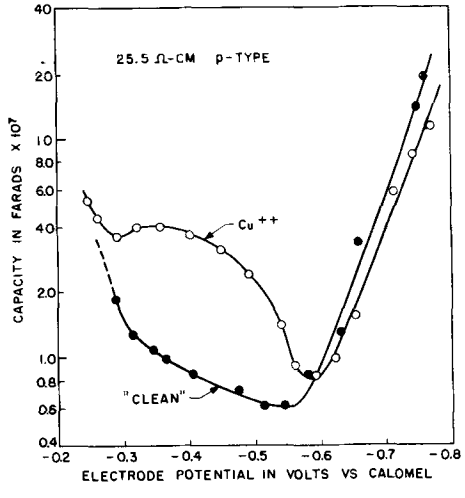

Fig. 2. Interfacial capacity *vs.* electrode potential before and after addition of Cu^{++}.

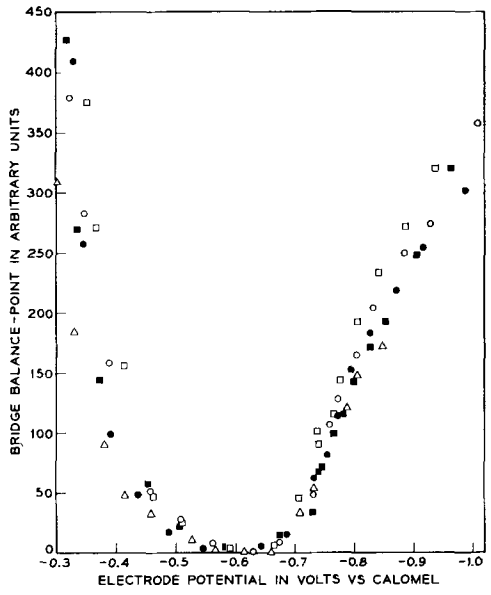

Fig. 3. Bridge balance (normalized to the conductivity minimum and corrected for changes in thickness due to etching) *vs.* electrode potential.

It has been shown previously (1) that analysis of the apparent change in conductivity of a thin slice of germanium in contact with electrolyte gives values of surface potential that do not agree with those derived from capacity and that the values from the capacity are probably correct. However, it was shown that the discrepancy in the conductivity is reproducible, so that in a purified solution of given pH a plot of bridge balance (normalized to the conductivity minimum and corrected for decrease in thickness of the active arm due to etching) *vs.* electrode potential is a constant curve for a given electrode. Figure 3 shows the normalized bridge balance *vs.* electrode potential for the p-type bridge. Further, since from capacity measurements on the uncontaminated surface the surface potential may be deduced as a function of electrode potential, an empirical correlation between surface potential and bridge balance may be derived. Use is made of this relationship to determine surface potential in the present experiments, where the interaction with cupric ion results in additional capacity, and consequently the surface potential cannot be deduced directly from the capacity. It should be noted that surface potential derived from capacity measurements involves no mobility correction. Experimentally, the surface potential-electrode potential relationship in the presence of up to 10^{-6}M cupric ion is similar in form to that derived in purified solutions (*i.e.*, essentially a one-to-one relationship over a range of potential), but with a shift in the curve toward more positive values of electrode potential, the magnitude of the shift depending mainly on the Cu^{++} concentration.

Capacity was determined as a function of surface potential (Fig. 4 and 5), each of these quantities

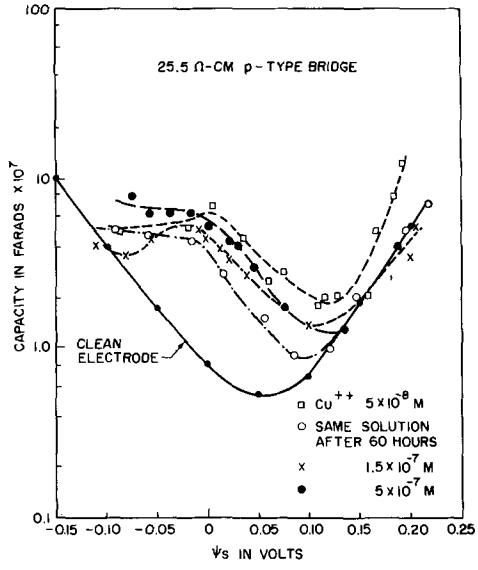

Fig. 4. Measured capacity vs. ψ_s for a 25.5 ohm-cm p-type electrode. The curve marked "clean electrode" is the theoretical curve normalized to fit the experimental minimum (roughness factor ca. 1.3).

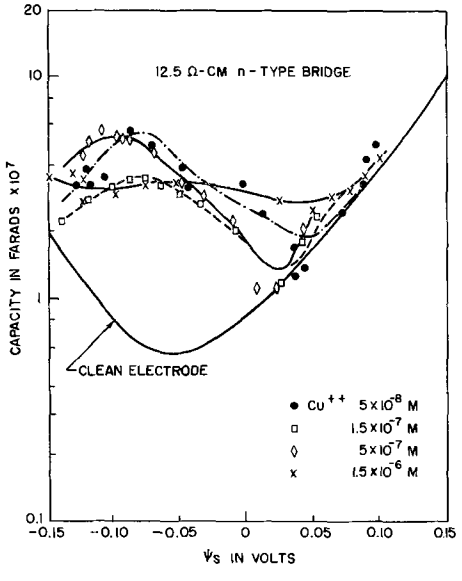

Fig. 5. Measured capacity vs. ψ_s for a 12.5 ohm-cm n-type electrode. The curve marked "clean electrode" is the theoretical curve normalized to fit the experimental minimum (roughness factor ca. 1.3).

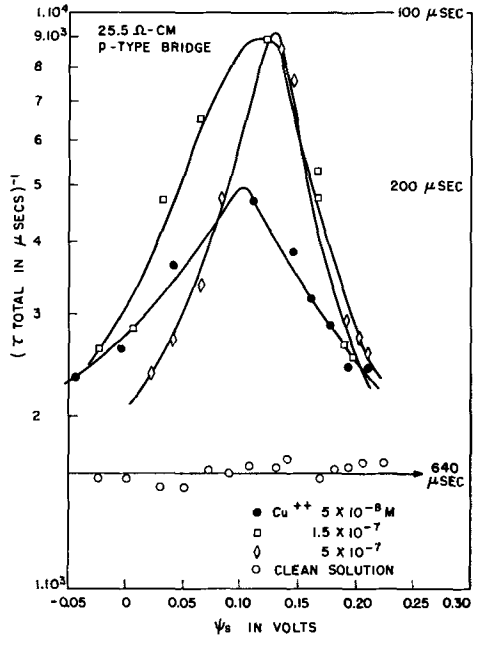

Fig. 6. Reciprocal filament lifetime vs. ψ_s for a 25.5 ohm-cm p-type electrode. Note the constant value vs. ψ_s for the uncontaminated surface.

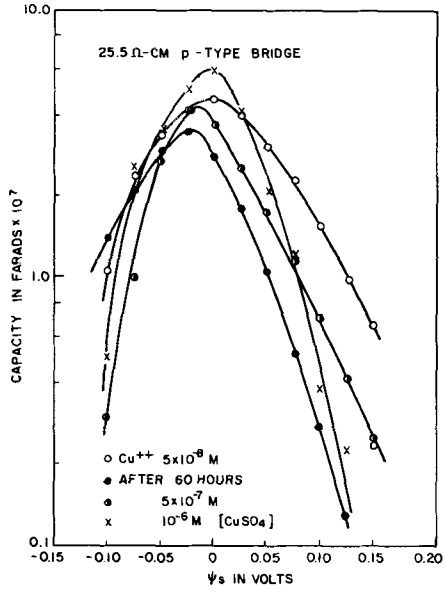

Fig. 7. Additional capacity after interaction with cupric ion vs. ψ_s for the p-type electrode.

being determined separately as a function of electrode potential. In addition, the filament lifetime was measured indirectly by first calibrating the photoconductivity due to a 40 cps square light pulse with a measured decay lifetime, then measuring the photoconductivity and deducing the lifetime by simple proportionality. Some typical data for the p-type bridge are shown in Fig. 6. The experiments were repeated at a variety of cupric ion concentrations. Identical data were obtained with both cupric nitrate and cupric sulfate.

Discussion

The additional capacity observed in the presence of cupric ion is determined by subtracting the space-charge capacity from the total observed capacity at each value of ψ_s. The results are shown in Fig. 7 and 8 for n- and p-type electrodes. The implicit assumption here is that the real surface area of the electrode is the same in both cases. The justification for this lies in the fit of the capacity data (in most instances) to the theoretical curve at extreme positive and negative values of ψ_s. The additional capacity can be explained only in terms of fast surface states, distributed in some manner in the energy gap.

For a surface state at a given energy the resulting capacity is

$$C_{ss} = dQ_{ss}/d\psi_s = eAN_t df_t/d\psi_s \qquad [1]$$

where e is electronic charge, A electrode area, N_t number of surface states in cm^{-2}, and f_t the fraction of the states occupied (3). The states are assumed

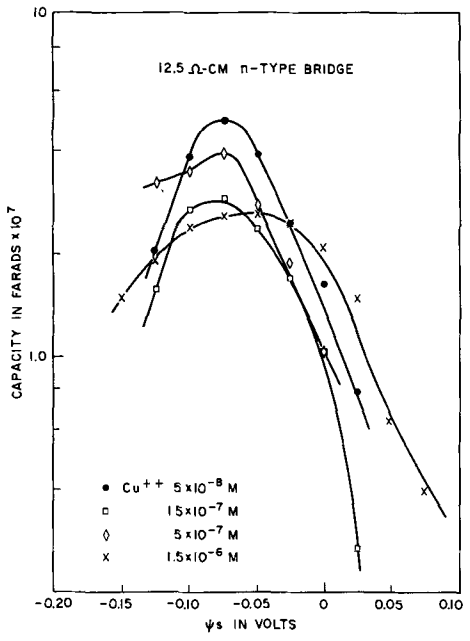

Fig. 8. Additional capacity after interaction with cupric ion vs. ψ_s for the n-type electrode.

to reach equilibrium with the semiconductor in times that are short compared with the duration of the measuring pulse. This may be rewritten

$$C_{ss} = e^2 A N_t k^{-1} T^{-1} (2 \cosh 1/2(Y + \nu - \ln \lambda))^{-2} \quad [2]$$

where $Y = e\psi_s/kT$, ν is the energy of the state in units of kT/e measured positive downwards, *i.e.*, toward the valence band, from the center of the gap, λ is p/n_i, where p is the hole concentration in the sample and n_i is the intrinsic hole or electron concentration in germanium.

The data in Fig. 7 and 8 can be satisfactorily accounted for by assuming surface states at two discrete energies. The nature of the fit that may be obtained is shown in Fig. 9 and 10 for p- and n-type electrodes in one instance. The remaining data have been similarly fitted with two states, a small latitude being allowed in positioning the states on the potential scale in order to obtain average values. In eight sets of data, four for each electrode, the maximum variation in position of either state is less than 10 mv from the arithmetic mean for that state and the particular electrode. The state of higher density, at more negative potentials, has its position and density fixed by the maximum in the additional capacity. The second state accounts for the remaining capacity at more positive potentials. Reference to Fig. 4 and 5 shows that this is the region of minimum space-charge capacity and, hence, of maximum sensitivity for our measurements. These potentials are also close to the steady-state open-circuit value and are accessible with a minimum of polarization of the interface. No attempt has been made to account for extra capacity at more positive potentials, since this is a region of poorer sensitivity due to the relatively large space-charge capacity and high polarization from the open-circuit state.

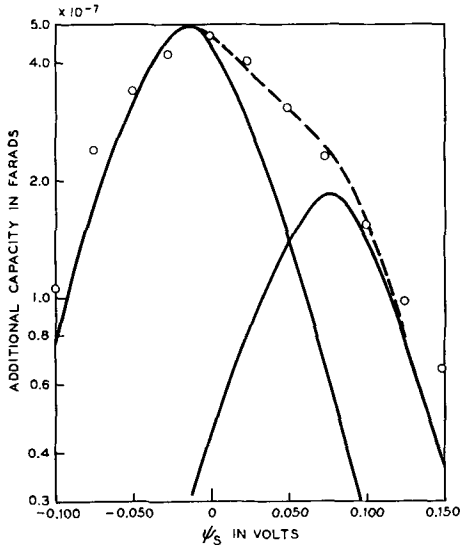

Fig. 9. Theoretical fit of additional capacity for the p-type electrode. Parameters of the states are $N_t = 1.26 \times 10^{11}$ cm^{-2}, $\nu = 2.2$ kT/e and $N_t = 4.4 \times 10^{10}$ cm^{-2}, $\nu = -1.3$ kT/e.

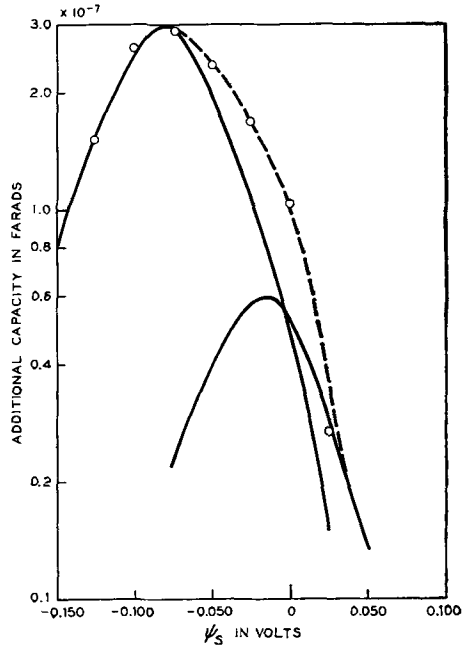

Fig. 10. Theoretical fit of the additional capacity for the n-type electrode. Parameters of the states are $N_t = 0.71 \times 10^{11}$ cm^{-2} $\nu = 1.5$ kT/e and $N_t = 1.47 \times 10^{10}$ cm^{-2}, $\nu = -1.2$ kT/e.

Since, from Eq. [2], at the potential of the maximum in capacity for each state $Y - \ln \lambda + \nu$ must equal zero, the energies of the two states may each be determined, and N_t may be calculated from the magnitudes of the maxima.

From the filament lifetime and dimensions of the thin arm, surface recombination velocity (s) may be calculated by means of the expression

$$\tau^{-1}_{\text{Total}} = \tau^{-1}_{\text{Body}} + (2s/t)(1 + t/w) \quad [3]$$

where w and t are the width and thickness of the thin arm. This equation is valid up to $s = 2D/t$, where D is the diffusion constant for the minority carrier. Surface recombination velocity, normalized to the maximum value, is plotted *vs.* $Y - \ln \lambda - \ln \chi$ for the p-type electrode in Fig. 11. The theo-

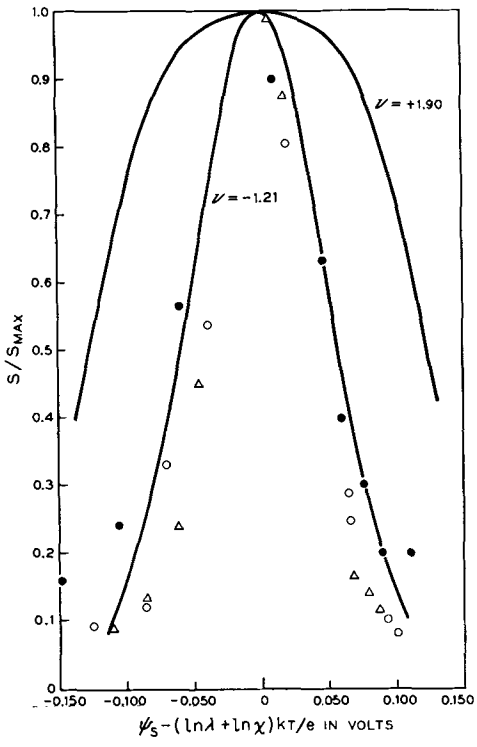

Fig. 11. Surface recombination velocity, normalized to the maximum value, *vs.* ψ_s—(ln λ+ln χ)kT/e for the p-type electrode. The curves are constructed using the experimental values ln χ = 3.0, ln λ = 1.72 and ν' = —1.2 or +1.9kT/e. The various points represent different initial Cu^{++} concentrations.

retical expression for surface recombination velocity at a surface potential Y, due to surface states at an energy ν', is (3)

$$s = (\lambda + \lambda^{-1})(C_n C_p)^{1/2}\{2\cosh(\nu' + \ln\chi) + 2\cosh(Y - \ln\lambda - \ln\lambda)\}^{-1} \quad [4]$$

where C_n and C_p as defined by Shockley and Read (4) are

$$C_p = N_t v_{T,p}\,\sigma_p \quad [5]$$

and

$$C_n = N_t v_{T,n}\,\sigma_n \quad [6]$$

where $v_{T,p}$ and $v_{T,n}$ are the thermal velocities of holes and electrons, σ_p and σ_n the capture cross sections for holes and electrons, and

$$\chi = (C_p/C_n)^{1/2} \quad [7]$$

Equation [4] indicates that at the maximum in surface recombination Y — ln λ — ln χ equals zero, since only this term in the denominator depends on Y, whence ln χ is known and ($C_n \cdot C_p$) may be calculated from Eq. [4].

In experiments on the dry germanium surface it is customary to analyze the surface recombination data by fitting it to a curve, the shape of which is determined essentially by the magnitude of the quantity cosh (ν' + ln χ) and hence, knowing ln χ from the position of the recombination maximum, obtain a value for ν' which is used as a basis for analyzing the field effect data. Since we measure the differential with respect to surface potential of the trapped charge, our field effect data are more sensitive than that on the dry surface and, as has been shown, we are able to fit that data to discrete surface states without recourse to the recombination. As is evident from Fig. 11, our recombination data are not of a high order of reproducibility and are not wholly suitable for a detailed analysis. They are sufficiently good, however, to distinguish which, if either, of the states that we observe by added capacity is effective in recombination. The two curves in Fig. 11 are constructed using the known energies of these states. Clearly, the state at ν' = — 1.2 kT/e is the one involved. A point of interest here lies in the fact that when fitting the hyperbolic cosine to the recombination data two solutions, equal in magnitude but opposite in sign, are obtained. For ln $\chi \neq 0$ this leads to two possible values of ν'. Many and Gerlich (5) in a typical case obtain ln χ = 1.1 and (ν' + ln χ) = ± 3.0, giving values for ν' of +1.9 or —4.1. On the basis of the variation of s/s_{max} with temperature they chose — 4.1 as the proper value, *i.e.*, the negative solution. We obtain, on the other hand, ln χ = 3.0 and are able to show that the state at ν' = —1.2 fits the recombination data, *i.e.*, the positive solution applies. If we were to take the negative solution (ν' + ln χ) = —1.8, then we would obtain ν' = —4.8, in much closer agreement with Many and Gerlich. Wang and Wallis (7) have taken both solutions and interpret their data in terms of a pair of states of equal density.

In our data, in the region of ψ_s corresponding to ν' = —4.8, we lack precision due to the larger value of the space-charge capacity (relative to that at ψ_s corresponding to ν' = —1.2) and also to the fact that at the former potential the space-charge capacity is changing rapidly with surface potential. Hence, we cannot unequivocally state that there is no state located at this energy nor that both signs of the solution do not correspond to recombination centers, only that the evidence is that the positive solution is a proper one.

The data are summarized in Table 1. The state not effective in recombination is designated I, the other II. The analysis indicates a charge trap 1.9 kT/e below and a recombination center 1.2 kT/e above the intrinsic level. In Table II are shown the results of four experiments on the p-type sample illustrating how the values in Table I were obtained. The values of the cross sections were calculated from C_p and C_n by assuming a thermal ve-

Table I. Analysis of data for 12.5 ohm-cm n-type and 25.5 ohm-cm p-type electrodes

	n-type	p-type	Average
State I			
ν	+1.5	+2.3	+1.9
N_t	0.9×10^{11}	1.2×10^{11}	1.0×10^{11}
State II			
ν	—1.2	—1.2	—1.2
N_t	1.6×10^{10}	2.1×10^{10}	1.9×10^{10}
ln χ	3.2	2.8	3.0
$(C_pC_n)^{1/2}$	540	450	485
C_p	1.1×10^{4}	0.9×10^{4}	1.0×10^{4}
C_n	2.8×10	2.3×10	2.5×10
σ_p	7.2×10^{-14}	4.7×10^{-14}	6.0×10^{-14}
σ_n	1.8×10^{-16}	1.2×10^{-16}	1.5×10^{-16}

Table II. Breakdown of some data from Table I for 25.5 ohm-cm p-type electrode; effective area 2.4 cm²

Maximum surface recombination velocity, cm sec⁻¹	$(C_pC_n)^{1/2}$, cm sec⁻¹	$(C_p/C_n)^{1/2}$	C_p, cm sec⁻¹	N_t, cm⁻²	σ_p, cm²
600	860	20	1.7×10^4	4.4×10^{10}	3.9×10^{-14}
300	430	20	0.86	2.3	3.7
200	290	20	0.58	0.87	6.7
150	215	20	0.43	0.99	4.4
Averages	450		0.90	2.1	4.7

Table III. Comparison of surface states at the germanium electrolyte interface with those on the dry surface

	Present data	Many *et al.* (10)
State I		
ν	+1.9	+1.0
N_t	1×10^{11}	0.1 to 1×10^{11}
State II		
ν	−1.2*	−3.0 to −6.0
N_t	1.9×10^{10}	1 to 4×10^{11}
$\ln \chi$	3.0	0.14 to 1.7
σ_p	6.0×10^{-14}	6 to 15×10^{-15}

* This value would be −4.8 taking the negative sign for the argument of the cosh.

locity 1×10^7 cm/sec. The density of state I varied from 0.94 to 1.6×10^{11}, somewhat less than the variation for state II. It will be noted that variation in σ_p is much less, as it should be. The various data in Table II refer to different cupric ion concentrations over the range 5×10^{-8} to 10^{-6}M. There was no obvious correspondence between these concentrations and the parameters N_t and s_{max}.

Data on the dry germanium surface have been obtained by several workers (5-9). In Table III the averages of our data for n- and p-type electrodes are compared with some data summarized by Many (10), which are typical for the dry surface. There is a reasonable similarity between the two sets of data. They agree in that there is a charge trap just below and a recombination center just above the intrinsic level. The densities of states are also quite similar. The only markedly dissimilar feature is the ratio of hole to electron capture cross sections and the shapes of the surface recombination velocity curves.

It is pertinent to compare the magnitudes of surface recombination obtained by various observers. One notes from Eq. [4] that in any recombination mechanism (due to a state or distribution of states of fixed parameters such as density, energy, and trapping cross section) the quantity $s_{max}/(\lambda + \lambda^{-1})$ should be a constant, independent of doping. The various values obtained for this quantity range from about 20 cm sec⁻¹ on a (110) oriented surface (7) to 1000 cm sec⁻¹ on surfaces heat treated in vacuum (8) with considerable evidence that an etched (100) surface in air (5, 9, 11) has values between 100 and 200 cm sec⁻¹. These are to be compared with the values we find on a (100) surface in aqueous solution of 30-100 cm sec⁻¹, depending on the density of state II.

The general agreement between the states observed on the dry surface and those produced by the interaction of cupric ion with the germanium surface in an aqueous electrolyte suggests that they have a common origin. However, it is not possible to state unequivocally that the phenomena we observe are due directly to the presence of copper species *per se;* we may be certain only that the states arise as a consequence of the interaction of cupric ion with the surface. Since copper is a more noble element than germanium, cupric ion will tend to be displaced from solution by an appropriate ion containing germanium in an oxidized state with the production of a lower oxidation state of copper. It has recently been shown that metallic copper may be deposited by the oxidation of germanium monoxide to the dioxide with cupric ion (12). Germanium monoxide may be present on the surface of a germanium electrode under steady-state conditions in aqueous solutions of intermediate pH (13, 14). In our experiments, however, the electrode has been CP-4 etched and subjected to anodic current, and it would seem unlikely that under these highly oxidizing conditions significant amounts of monoxide remain unconverted to the soluble dioxide.

It is more probable that cupric ions interact directly with surface atoms, discharging to metallic copper and either injecting holes (*i.e.*, consuming valence electrons) or consuming conduction electrons

$$Cu^{++} \rightarrow Cu + 2e_o^+$$

or

$$Cu^{++} + 2e_o^- \rightarrow Cu$$

and correspondingly to maintain charge balance

$$Ge + me_o^+ \rightarrow Ge^{+n} + (n-m)e_o^-$$

where n is 2 or 4. If n is 2, then a further oxidation by cupric ion to Ge^{+4} may occur.

It would appear that copper may be present at the surface either as copper atoms deposited directly on germanium atoms or bound in the ionic state in a surface complex. In either case it is not at all apparent why the density of surface states should be essentially independent of cupric ion concentration and should be such a small number relative to the density of surface atoms, since approximately monolayer coverage of copper atoms (or ions) has been demonstrated for germanium in contact with solutions of cupric ion of the order of those used here (12). Taking our data alone, there would seem to be good arguments in favor of a surface state due to neutral or negatively charged copper atoms. (This would permit the state to be negatively charged when occupied by an electron, as indicated by the relatively large capture cross section for holes.) The low density of states could be rationalized by postulating that only those copper atoms in certain select sites (*e.g.*, along dislocations at the surface) are effective.

Copper is electrically active in the bulk of germanium, giving rise to at least three levels (17), the species and approximate energies being Cu^{-} ($+14\ kT/e$), Cu^{--} ($+2.5\ kT/e$), and Cu^{---} ($-5.0\ kT/e$). Our state I is not in serious disagreement with the Cu^{--} state, while the Cu^{---} energy agrees well with the alternative value for state II, although our data indicates that we should strongly prefer the value $\nu' = -1.2\ kT/e$ for state II. On this picture, since state II has the higher negative charge, it would have a relatively higher hole capture cross section and could dominate in the recombination process, as observed.

The close similarity between the parameters we observe and those commonly observed on the dry surface, which are by and large almost independent of the way the dry surface was etched, tend to weaken, although not disprove, the specific relationship between surface states and the presence of cupric ion in solution. It should be recalled in this regard that unless rigorous precautions are taken most etched germanium surfaces are contaminated to some degree with copper. This constitutes the "deathnium" or "thermium" that was observed some years ago to cause most samples of germanium to become p-type if heated to a sufficiently high temperature for diffusion of the surface contamination to occur (15).

The present data are not sufficient to distinguish the chemical nature of the surface state other than to say that since it appears as a consequence of the interaction of cupric ion with the surface, it must be due to some copper containing species or to an oxidation product deposited on the surface as a consequence of the spontaneous reduction of cupric ion. More recent data on surface states produced by ions of silver and gold (14) indicate a similar, although not identical, effect. Experiments on the dry surface pretreated with dilute cupric nitrate solutions (16) indicate that there is a relationship between the parameters of fast surface states and such pretreatment, albeit not a simple one, in that case also. More recently a definite level ($+6\ kT/e$) and value of C_p/C_n (~ 200) have been ascribed to copper on the dry surface (18).

Conclusions

The interaction of cupric ions with the germanium-aqueous electrolyte interface results in capacity and surface recombination which may be interpreted in terms of two surface states, one a charge trap $1.9\ kT/e$ below the intrinsic Fermi level with a density $1 \times 10^{11}\ cm^{-2}$, the second a recombination center $1.2\ kT/e$ above the intrinsic level with a density of $1.9 \times 10^{10}\ cm^{-2}$.

Acknowledgment

The authors are indebted to W. J. Sundburg for technical assistance.

Manuscript received March 28, 1962. This paper was prepared for delivery before the Detroit Meeting, Oct. 1-5, 1961.

Any discussion of this paper will appear in a Discussion Section to be published in the June 1963 JOURNAL.

REFERENCES

1. W. H. Brattain and P. J. Boddy, Electrochemical Society Meeting, Detroit, 1961; *This Journal*, **109**, 574 (1962).
2. S. R. Morrison in "Semiconductor Surfaces," J. N. Zemel, Editor, Pergamon Press, Ltd. (1960).
3. C. G. B. Garrett and W. H. Brattain, *Bell System Tech. J.*, **35**, 1041 (1956).
4. W. Shockley and W. T. Read, Jr., *Phys. Rev.*, **87**, 835 (1952).
5. A. Many and D. Gerlich, *ibid.*, **107**, 404 (1957).
6. S. Wang and G. Wallis, *This Journal*, **106**, 231 (1959).
7. S. Wang and G. Wallis, *Phys. Rev.*, **105**, 1459 (1957).
8. A. V. Rzhanov e.a. in "Proceedings of the International Conference on Semiconductor Physics Prague 1960," Czechoslovak Academy of Sciences, Prague (1961).
9. W. H. Brattain and C. G. B. Garrett, *Bell System Tech J.*, **35**, 1019 (1956).
10. A. Many, *J. Phys. Chem. Solids*, **8**, 87 (1959).
11. Y. Margoninski, *J. Chem. Phys.*, **32**, 1791 (1960).
12. V. S. Sotnikov and A. S. Belanovskii, *Zhur. Fiz. Khim.*, **35**, 509 (1961).
13. B. Lovrecek and J. O'M. Bockris, *J. Phys. Chem.*, **63**, 1368 (1959).
14. W. H. Brattain and P. J. Boddy, To be published.
15. C. S. Fuller and J. D. Struthers, *Phys. Rev.*, **87**, 526 (1952).
16. D. R. Frankl, *This Journal*, **109**, 238 (1962).
17. H. H. Woodbury and W. W. Tyler, *Phys. Rev.*, **102**, 647 (1956); *ibid.*, **105**, 84 (1957).
18. D. R. Frankl, *Bull. Am. Phys. Soc.*, **7**, 179 (1962).

Electrical Properties of Mg_2Sn Crystals Grown from Nonstoichiometric Melts

Barry D. Lichter

Metals and Ceramics Division, Oak Ridge National Laboratory, Oak Ridge, Tennessee[1]

ABSTRACT

Resistivity and Hall measurements were carried out on Mg_2Sn crystals in the temperature range 300°-60°K. Single crystals were grown by a modified Bridgman technique from stoichiometric melts and from melts containing 1, 2, 10, and 18 at. % excess Sn and 3 at. % excess Mg. In the mixed conduction and extrinsic ranges, it was found possible to describe the calculated temperature dependence of the conduction mobility on the basis of a combination of lattice vibration (acoustic mode) and ionized impurity scattering. A stoichiometry effect is observed. The Mg_2Sn crystals appear to dissolve the excess constituent producing n-type crystals (excess Sn) and p-type crystals (excess Mg). The observed effect corresponds to a solubility of 10^{-5}-10^{-6} atom fraction excess constituent. This result is briefly discussed in terms of bonding in Mg_2Sn.

The intermediate phase Mg_2Sn has been the subject of a number of investigations of electrical properties (1-5) as have been the other "II-IV compounds" Mg_2Si, (2, 6) Mg_2Ge, (2, 7), and Mg_2Pb (1, 2). These investigations have established that Mg_2Si, Mg_2Ge, and Mg_2Sn are semiconductors while Mg_2Pb is metallic.

The width of the forbidden energy gap in Mg_2Sn is reported as 0.33 ev at 0°K with a value of approximately -4×10^{-4} ev °K^{-1} for the temperature dependence (4). The mobility ratio is close to unity, $b = 1.5$ according to Busch and Winkler (2), and $b = 1.23$ according to Blunt *et al.* (4). Theoretical calculations (3) indicate that the intrinsic carrier concentration $n_i = 2.76 \pm 0.51 \times 10^{17}$ cm^{-3} at room temperature and that b remains nearly constant with temperature. The Mg_2Sn crystallizes in the fluorite (CaF_2) structure, magnesium occupying F^- sites, and tin occupying Ca^{++} sites. At present no measurements as to the form of the band structure are available.

It has been noted by previous investigators (4, 6, 7) that crystals of Mg_2Si, Mg_2Ge, and Mg_2Sn are predominantly n-type when grown and can be made p-type by addition of Cu, Ag, or Au to the melt. Since evaporation of Mg from the melt can be considerable, one may inquire whether or not the conductivity type is influenced by stoichiometry. Recently it has been shown that the carrier concentration is markedly changed after annealing in magnesium vapor (5). The present investigation offers evidence tending to confirm the stoichiometric effect in crystals grown from melts whose compositions were controlled during the course of solidification. In addition, some information on carrier mobilities in the mixed conduction range is presented.

[1] Operated for the U. S. Atomic Energy Commission by the Union Carbide Corporation.

Experimental

Growth of Single Crystals

Single crystals of Mg_2Sn were grown under 2 atm pressure of purified argon by a modified Bridgman procedure from high-purity, zone-refined Sn ingots (Varlacoid Company, New York City) and high-purity Mg rods (Varlacoid Company and Johnson, Matthey and Company). Typical results of emission spectroscopic analysis for impurities in Mg, Sn, and Mg_2Sn are given in Table I. In addition, 14 other elements were sought for and not detected. Values in parentheses in Table I were obtained by neutron-activation analysis. Copper, silver, and gold are known acceptors in Mg_2Sn (4, 5), and Sb is a known donor (8).

The furnace was a water-cooled, cylindrical, vacuum chamber used conventionally to pull Ge and Si crystals and modified to operate under 2 atm pressure of argon. A cylindrical, graphite, re-

Table I. Spectrochemical analysis of impurities in Mg, Sn, and Mg_2Sn (ppm)

	Mg	Sn	Mg_2Sn
Ag	1	1	ND[a]
Al	5	0.1	5
As	ND[a]	10	5
Bi	ND[a]	0.01	ND[a]
Cr	<1	0.3	<1
Cu	1	2	5 (0.05)[b]
Fe	3	0.05	5 (0.6)[b]
Mn	2	0.05	<0.1 (<1)[b]
Ni	ND[a]	4	<0.1
Pb	ND[a]	8	0.5
Sb	ND[a]	2	ND[a]
Si	10	0.5	10
V	ND[a]	<0.5	<0.1

[a] Not detected.
[b] Neutron-activation analysis.

sistance heater was employed, and the temperature was controlled with a chromel-alumel couple to ± 1°C using a high-speed controller and motor-driven variac.

Cylindrical crucibles (8 × 1.2 cm OD) were machined from high-purity graphite (National Carbon Company, grade CCH). Premachined and etched Sn and Mg rods were inserted into a graphite liner which fit tightly in the crucible. The inside diameter of the top 2-4 cm length of the liner was 0.6 cm, and the remaining section diameter was 1 cm. The crucible was closed with a graphite cap which was threaded to the end of a stainless steel pulling rod. Small holes were drilled through the cap to allow initial evacuation before melting and subsequent access of argon to the melt. In this manner, and by means of partial encapsulation of the crucible in fused silica and stainless steel outer liners, vaporization of magnesium was minimized.

After evacuation and flushing with argon, the furnace was heated to 200°C above the liquidus temperature (650°-778°C) corresponding to the melt composition, and a pressure of 2 atm was established. The furnace was adjusted to obtain a maximum gradient (50°C cm^{-1}) at the liquidus temperature, which coincided roughly with the top of the heater. Directional solidification was effected starting from the top of the crucible. Stoichiometric Mg_2Sn undergoes a 2% volume expansion on solidification, according to the data of Sauerwald (17). The associated strain was presumably taken up either by expansion into the small volume of dead space above the crystal or by compression of the graphite liner and crucible. The pulling rod was rotated at 1 rps. For melt compositions close to stoichiometric (N_{Sn} = 0.33) pulling speeds of 5 mm hr^{-1} or less yielded single crystals. For melts containing excess Sn or Mg, pulling speeds as low as 0.5 mm hr^{-1} were required to obtain single crystals.

Figure 1 shows the orientation of resulting Mg_2Sn crystals with respect to the growth axis. A decided preference for {211} orientation is observed. It is interesting to note that the three orientations obtained constitute three adjacent planes of the five low index planes in the <210> zone. Rotation

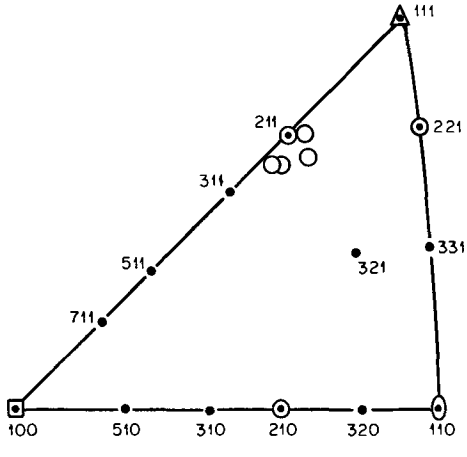

Fig. 1. Orientation of Mg_2Sn crystals

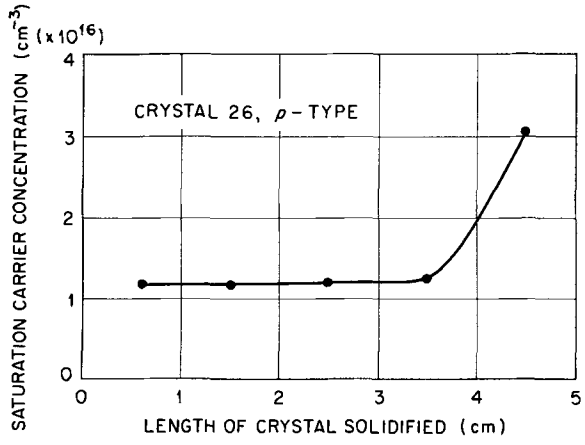

Fig. 2. Variation in saturation carrier concentration for p-type crystal grown from nearly stoichiometric melt.

about a [$\bar{1}$02] zone axis yields in sequence the low index planes (201), (211), (221), (231), and (010).

In order to minimize the effect of concentration changes in the melt during directional solidification, only the first 1.5-cm length of crystal was used for electrical measurements. Since the distribution coefficients for Mg and Sn are very small, the approximate variation in melt compositions can be calculated. The inside dimensions of the graphite liner were adjusted so that the maximum variation in melt composition that occurred after 1.5 cm of solidification was less than 1% of the initial composition in all cases. In Fig. 2, the variation in the direction of solidification of saturation carrier concentration is shown for a nearly stoichiometric melt. For p-type crystals, excess Mg was observed in the final fraction solidified, whereas, for the n-type crystals, a Mg_2Sn-Sn eutectic was observed. Melt compositions are listed in Table II.

Electrical Measurements

Samples were prepared from the top 1.5-cm length of each crystal. The usual sample dimensions were 0.5 × 0.1 cm^2 cross section and from 1.0 to 1.5 cm long. Sample surfaces were sandblasted with 600-grit SiC abrasive, cleaned in a stream of compressed argon, and rinsed in acetone. As noted by previous investigators, it was not possible to employ suitable chemical etchants or electropolishing techniques in the preparation of sample surfaces (1, 4).

Hall and resistivity measurements were carried out over the temperature range 60°-300°K using

Table II. Melt composition, carrier concentration, and mobilities for p- and n-type Mg_2Sn crystals

Crystal		N_{Sn}, liquid	N_D or N_A, cm^{-3}	$b = \mu_n/\mu_p$	μ_p (300°K), $cm^2\ v^{-1}\ sec^{-1}$	μ_p (77°K), $cm^2\ v^{-1}\ sec^{-1}$
15	↑	0.30	3.4×10^{16}	1.21	300	3000
26	p ↓	0.33	1.5	1.21	290	2500
19	↑	0.33	4.6×10^{16}	—	310	2300
30		0.33	6.2	—	285	1875
25		0.34	3.3	—	270	1675
28	n	0.35	8.3	—	265	1450
24		0.43	4.4	—	330	1580
29	↓	0.51	3.2	—	—	470

conventional d-c techniques. A permanent magnet with 3-in. diameter pole pieces was used to establish a field of 1000 gauss at approximately a 4-in. gap. Tungsten probes ground to conical points were spring-loaded to form pressure contacts. The probes were arranged in a "diamond" pattern (9), and resistivity and Hall voltages were measured with a type K-3 potentiometer. The sample holder was a boron nitride block, advantage being taken of the relatively high thermal conductivity of this insulator.

The sample holder was contained in an evacuated Dewar flask surrounded by a second Dewar flask filled with liquid nitrogen. Relatively slow heat transfer from the inner to the outer flask (approximately 2° min^{-1} initial cooling rate) allowed continuous measurements to be made during cooling. For measurements below 150°K, liquid nitrogen was added directly to the inner flask, and the sample was cooled at 60°K by evacuation of the space over the liquid nitrogen. Measurements were made as the sample temperature increased slowly.

Results

The resistivity (ρ) and Hall coefficient (R) are plotted *vs.* the reciprocal of the absolute temperature in Fig. 3-6 for *n*- and p-type samples. The temperature dependence of the Hall mobility, $\mu_H = R/\rho$, is given in Fig. 7 and 8. For comparison, the high-temperature data of Busch and Winkler (2) and the low-temperature data of Blunt *et al.* (4) are shown in Fig. 7 and 8. The conduction mobility ratio for electrons and holes, $b = \mu_n/\mu_p = 1.21$, was determined from the Hall coefficients of p-type samples according to Breckenridge *et al.* (10) and was assumed to be constant with temperature in the calculation of conduction mobilities presented below.

The equations relating the Hall coefficient and resistivity to the conduction mobility and carrier concentrations may be written

$$R/R_s = (\alpha b^2 - 1)(\alpha - 1)/(\alpha b + 1)^2 \quad [1]$$

$$\mu_H/\mu_p = b\mu_H/\mu_n = -G(\alpha b^2 - 1)/(\alpha b + 1) \quad [2]$$

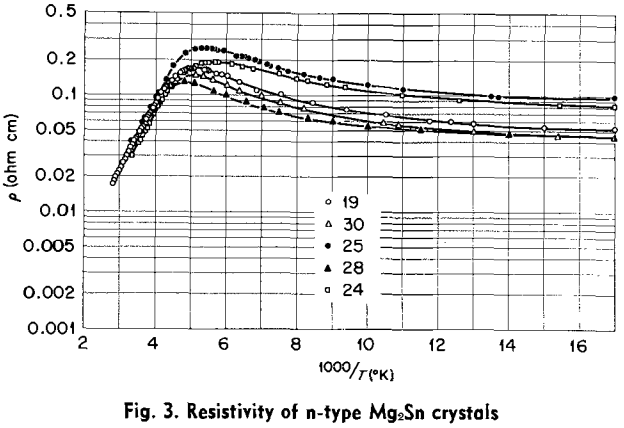

Fig. 3. Resistivity of n-type Mg_2Sn crystals

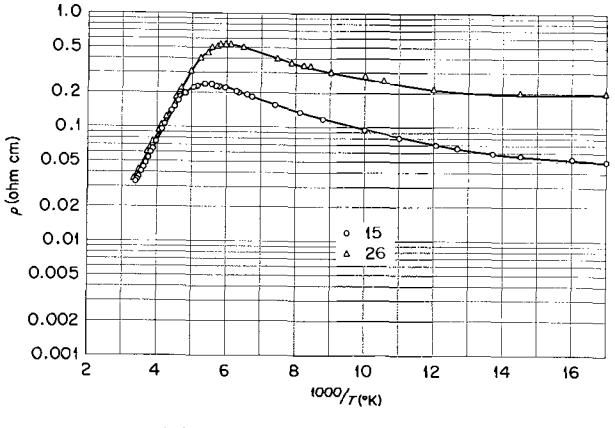

Fig. 4. Resistivity of p-type Mg_2Sn crystals

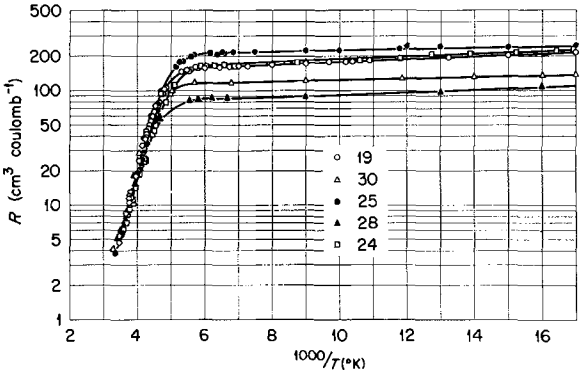

Fig. 5. Hall coefficient of n-type Mg_2Sn crystals

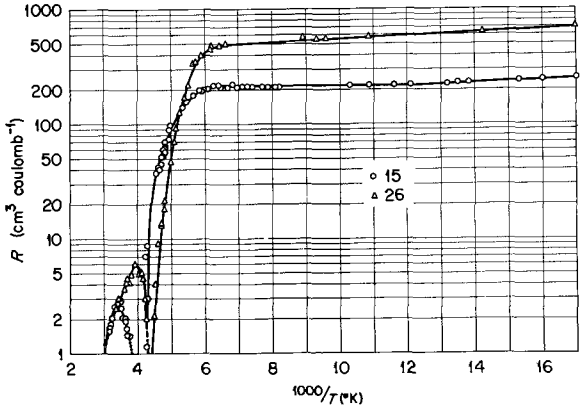

Fig. 6. Hall coefficient of p-type Mg_2Sn crystals

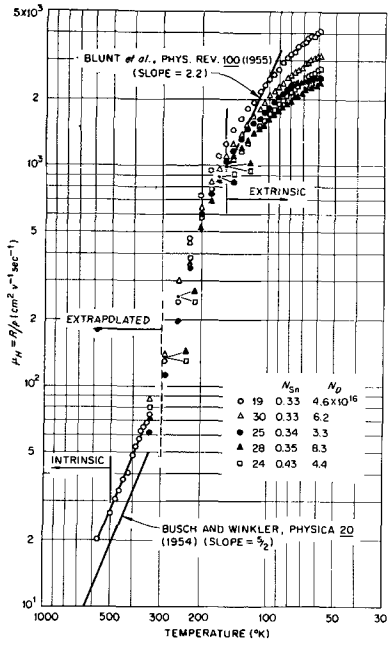

Fig. 7. Hall mobility of n-type crystals

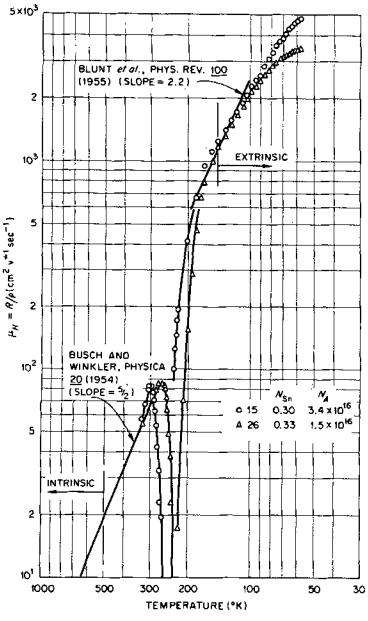

Fig. 8. Hall mobility of p-type crystals

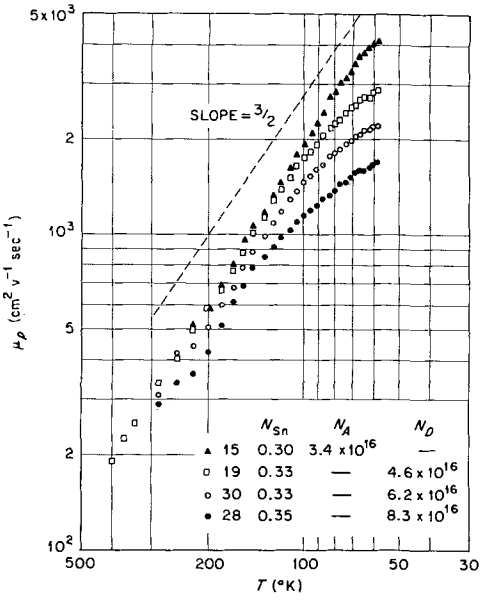

Fig. 9. Hole conduction mobility of n- and p-type crystals

where R_s is the saturation value of the Hall coefficient estimated from Fig. 5 and 6, $\alpha = n/p$ is the carrier concentration ratio for electrons and holes, and $G = 3\pi/8$. Equations [1] and [2] are essentially in the form given by Dunlap (11) except that Eq. [1] assumes complete ionization of uncompensated donors or acceptors. Equations [1] and [2] are therefore especially useful in the mixed conduction range. In the extrinsic range, Eq. [2] becomes

$$\mu_p = -\mu_H/Gb; \ (\alpha \text{ very large, n-type}), \quad [3a]$$

$$\mu_p = \mu_H/G; \ (\alpha \text{ very small, p-type}). \quad [3b]$$

The temperature dependence of μ_p calculated using Eq. [1], [2], and [3] is given in Fig. 9. Values of μ_p at 300°K and 77°K are given in Table II.

Uncompensated donor or acceptor concentrations (N_D or N_A) were determined from the Hall coefficients according to the relation

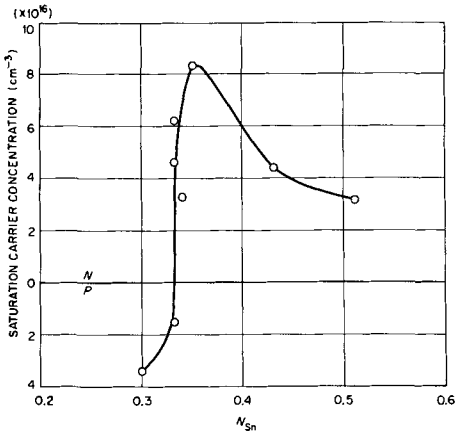

Fig. 10. Saturation carrier concentration vs. melt comopsition

$$N_D \text{ or } N_A = G/e|R_s| = 7.4 \times 10^{18}/|R_s| \quad [4]$$

As shown in Table II, values of 1.5-8.3 x 10^{16} cm^{-3} were obtained for N_D or N_A. These values are plotted in Fig. 10 *vs.* the corresponding melt composition, N_{Sn}. When Sn was added to the melt in excess of the stoichiometric composition ($N_{Sn} = 0.33$) n-type crystals were always obtained, whereas, a p-type crystal was obtained from a melt containing excess Mg.

These results are consistent with results of Guenoc (5) who earlier had observed that Mg acts as a p-type impurity in Mg_2Sn: the carrier concentration of a p-type crystal annealed in Mg vapor was observed to increase from 7 x 10^{16} to 1.5 x 10^{19}. However, similar annealing experiments performed during the present investigation were less conclusive. The carrier concentration of an n-type crystal increased from 7.4 x 10^{16} cm^{-3} to 1.2 x 10^{17} after annealing for 4 hr at 650°C in an argon atmosphere. No change in carrier concentration was observed after annealing for 20 hr at 650°C in the presence of a Mg-Sn melt containing excess Mg($N_{Sn} = 0.24$).

If the observed carrier concentrations are attributed entirely to the presence of the excess constituent, one obtains a solubility of 10^{-5}-10^{-6} atom fraction of excess Sn or Mg in Mg_2Sn.

Discussion

Mobility of Charge Carriers

The sigmoidal shape of the log-log plots of the Hall mobility in Fig. 7 is not present in the corresponding plots of the calculated conduction mobility shown in Fig. 9. Throughout the mixed conduction region, the slopes of log-log plots of μ_p *vs.* $1/T$ are constant, the values lying between 1.4 and 1.7. At lower temperatures, the slopes of curves decrease to lower values. If both lattice scattering and impurity scattering are present, tentatively it may be assumed that the individual cross sections for scattering are additive. Hence,

$$1/\mu = 1/\mu_L + 1/\mu_I \quad [5]$$

where

$$\mu_L \approx A/T^m \quad [6]$$

$$\mu_I \approx BT^{1.5} \quad [7]$$

Combining Eq. [5], [6], and [7], one obtains

$$T^{1.5}/\mu = T^{1.5+m}/A + 1/B \quad [8]$$

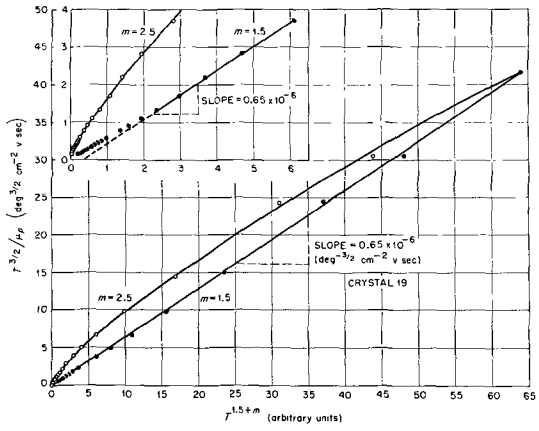

Fig. 11. ($T^{1.5}/\mu_p$) vs. $T^{1.5+m}$ for sample 19

A value of $m = 1.5$ corresponds to lattice scattering according to simple theory. A value of $m = 2.5$ corresponds to the observed high-temperature dependence of the mobility in the intrinsic range according to Busch and Winkler (2). In Fig. 11, the quantity ($T^{1.5}/\mu_p$) is plotted *vs.* $T^{1.5+m}$ for sample 19. A straight line with slight deviations below 125°K is obtained for $m = 1.5$, whereas large deviations from a straight line are obtained for $m = 2.5$. Actually, a straight line is best approximated over the entire temperature range (60°-400°K) for $m = 1.6$, the slope of the log-log plot of μ_p *vs.* $1/T$ in the mixed conduction region for sample 19. Similar results are obtained for other samples.

It is therefore possible to describe the mobility in the mixed conduction and extrinsic regions as a combination of lattice (acoustic mode) and ionized impurity scattering. Such a simplified view, however, neglects the fact that at higher temperature a $1/T^{2.5}$ dependence is observed, and therefore scattering mechanisms associated with optical mode lattice vibrations may be involved. Attempts to explain observed mobilities of Mg_2Ge and Mg_2Si (6, 7) in terms of optical mode scattering mechanisms, while successful in part, involved a large degree of arbitrariness in the selection of critical parameters. Similarly, an explanation of observed mobility behavior in PbS, PbTe, and PbSe in terms of optical mode scattering has not been successful at higher temperatures where approximately a $1/T^{2.5}$ dependence has been observed (12). At present no complete theory exists either involving optical mode scattering or explaining a $1/T^{2.5}$ dependence.

Other scattering mechanisms such as scattering by neutral impurities, dislocations, or atom clusters apparently cannot be neglected in view of the fact that the low-temperature mobilities are not completely consistent with extrinsic carrier concentrations as seen in Fig. 7 and 8. Also, sample 29, which suffered a large decrease in mobility as shown in Table II, is thought to have contained occluded or precipitated Sn as a second phase.

Stoichiometry and Conductivity Type

The effect of departures from the ideal stoichiometric composition on the electrical properties of compound semiconductors depends on the nature of "bonding" in the crystal. Wagner (13) has generalized the situation in predominantly ionic crystals, for which case, interstitials, vacancies, quasi-free electrons, and electron holes are considered. A composition corresponding to a cation/anion atom ratio slightly greater than stoichiometric leads to the creation of donor levels (*e.g.*, Zn interstitials in ZnO), whereas a cation/anion atom ratio slightly less than stoichiometric leads to the creation of acceptor levels (*e.g.*, Cu vacancies in Cu_2O). These effects may occur independent of the nature of the defect responsible for the stoichiometric departure (*i.e.*, interstitials or vacancies on either cation or anion sublattice) and arise chiefly from the requirement of maintaining electrical neutrality. Thus, if $Mg_2^{+2}Sn^{-4}$ (corresponding to transfer of electrons from the less electronegative Mg to the more electronegative Sn) represented the configuration of the crystal, the effects of stoichiometric departures on conductivity type would be opposite to that actually observed.

For predominantly valence crystals, involving only small electronegativity differences between constituent atoms, the normal electron affinities may be reversed in view of the greater stability of possible covalent bond structures (14), *e.g.*, transfer of an electron from Sb to In leading to sp^3 hybridization in InSb (15). Alternatively, no charge transfer takes place, but electrons are shared between bonds by means of "pivoting resonance" (16). In this case, stoichiometric departures may arise from disordering in the constituent sublattices. Replacement of a *B* atom in the *B* sublattice by an excess *A* atom, where *A* has fewer valence electrons than *B*, results in acceptor states and *vice-versa*. The effects of antistructure disorder are analogous to the effects of substitutional impurities in Ge and Si.

The observed results are therefore consistent with antistructure disorder in Mg_2Sn. The following facts suggest that bonding in Mg_2Sn is predominantly covalent: (*A*) Mg_2Sn undergoes a volume contraction on melting (17) similar to the observed behavior in Ge and Si and corresponding to a change from covalent to metallic bonding. (*B*) The electronegativity difference ($\Delta x = 0.6$) between Mg and Sn is relatively small (compare InSb, $\Delta x = 0.2$; SiC, $\Delta x = 0.7$; PbS, $\Delta x = 0.9$; NaCl, $\Delta x = 2.1$). (C) The hard sphere approximation to the fluorite structure, *i.e.*, $r_{Ca^{++}}/r_{F^-} = \sqrt{3} - 1$; $a_o/r_{F^-} = 4$, is most nearly realized by assuming the single bond covalent radius for Sn ($r_{Ca^{++}}^{Sn} = 1.40$Å) and the metallic radius for Mg ($r_{F^-}^{Mg} = 1.62$Å) for the observed lattice parameter ($a_o = 6.76$Å).

Conclusions

1. In the mixed conduction range, the temperature dependence of the electron and hole conduction mobilities may be approximated by a combination of lattice and ionized impurity scattering.

2. Crystals of Mg_2Sn grown from melts containing either constituent in excess of the ideal stoichiometric ratio appear to dissolve the excess constituent producing n-type crystals (excess Sn) and p-type crystals (excess Mg). This result is consistent with antistructure disorder and predominantly covalent bonding in Mg_2Sn.

3. If the observed carrier concentrations are attributed entirely to the presence of the excess constituent, one obtains a solubility of 10^{-5}-10^{-6} atom fraction of excess Sn or Mg in Mg_2Sn.

Acknowledgments

The work described in this paper was carried out at the Air Force Cambridge Research Laboratories, Bedford, Massachusetts. The author would like to thank S. Wall for assistance during the experimental work. The author is grateful for discussions with H. Lipson, Air Force Cambridge Research Laboratories; Dr. H. Schweinler, Oak Ridge National Laboratory, Solid State Division; and Dr. A. Strauss, M.I.T. Lincoln Laboratories.

Manuscript received March 2, 1962; revised manuscript received April 27, 1962. This paper was prepared for delivery before the Boston Meeting, Sept. 16-20, 1962.

Any discussion of this paper will appear in a Discussion Section to be published in the June 1963 JOURNAL.

REFERENCES

1. W. O. Robertson and H. H. Uhlig, *Trans. Met. Soc. AIME*, **180**, 345 (1949).
2. G. Busch and U. Winkler, *Physica*, **20**, 1067 (1954); U. Winkler, *Helv. Phys. Acta*, **28**, 633 (1955).
3. W. D. Lawson *et al.*, *J. Electron.*, **1**, 203 (1955-56).
4. R. F. Blunt, H. P. R. Frederikse, and W. R. Hosler, *Phys. Rev.*, **100**, 663 (1955).
5. H. Guenoc, "A Preparation and Study of Compounds of the II-IV Type and Mixtures Thereof," Quar. Tech. Status Rep. No. 7, U. S. Air Force Contract AF 61(052)243 (December, 1960).
6. R. G. Morris, R. D. Redin, and G. C. Danielson, *Phys. Rev.*, **109**, 1909 (1958).
7. R. D. Redin, R. G. Morris, and G. C. Danielson, *ibid.*, **109**, 1916 (1958).
8. H. P. R. Frederikse, W. R. Hosler, and D. E. Roberts, *ibid.*, **103**, 67 (1956).
9. The author is indebted to Dr. Allan Strauss of the M.I.T. Lincoln Laboratories for advice in performing the electrical measurements. Preliminary measurements at room temperature and at liquid nitrogen temperature were made in Dr. Strauss' laboratory.
10. R. G. Breckenridge *et al.*, *Phys. Rev.*, **96**, 571 (1954).
11. W. Crawford Dunlap, "An Introduction to Semiconductors," pp. 122-24, John Wiley & Sons, Inc., New York (1957).
12. W. W. Scanlon, "Polar Semiconductors," in "Solid State Physics," Vol. 9, pp. 125-31, Academic Press, New York (1959).
13. H. H. von Baumbach and C. Wagner, *Z. physik. Chem.*, **B22**, 199 (1933); **B24**, 59 (1934).
14. L. Pauling, *Proc. Natl. Acad. Sci.*, **36**, 333 (1950).
15. E. Mooser and W. B. Pearson, *J. Electron.*, **1**, 629 (1955-56).
16. L. Pauling, *Proc. Roy. Soc. (London)*, **196A**, 533 (1949).
17. F. Sauerwald, *Z. Metallforschung*, **2**, 188 (1947).

Molten Metal Etches for the Orientation of Semiconductors by Optical Techniques

J. W. Faust, Jr., A. Sagar, and H. F. John

Research Laboratories, Westinghouse Electric Corporation, Pittsburgh, Pennsylvania

ABSTRACT

Under controlled conditions the dissolution and redeposition of semiconductors in molten metals proceed along the same definite crystallographic planes. It has been found that these planes are {111} for Ge and Si and {111} and {100} for the III-V intermetallic compounds. Conditions are given for producing pits whose facets give good light reflection for accurate orientation by optical techniques.

Several types of semiconductor devices and many fundamental investigations on semiconductors require a specific surface orientation. In some cases the surface need only be oriented to within one degree of a crystallographic plane, while in others accuracies of a few minutes of arc are necessary. Various x-ray techniques are widely used to determine orientation. Since x-rays penetrate the crystal and are reflected from planes of atoms within the crystal, all that is required of an etch in preparing the surface is that it remove the damaged layer caused by abrasive processes. A carefully constructed optical goniometer used on a suitably etched surface can, however, give accuracies comparable to those obtained with x-rays, *i.e.*, within 1-2 min of arc. Optical goniometry (1) is attractive because of the simplicity of the equipment and the fact that intensive training is not necessary for an operator. Since light has a much longer wavelength than x-rays, it is reflected from the surface of the crystal; thus the etch must be capable of producing etch pits whose facets are definite crystallographic planes, preferably of low Miller indices. The accuracy of the orientation determination depends on the accuracy of the goniometric instrument, the size of the revealed planes on the faceted surface, and the flatness of these planes.

Chemical etches have been used exclusively for producing such pits; Faust (2) has tabulated chemical etchants that produce such surfaces for numerous materials. Studies on chemical etches for the III-V intermetallic compounds have produced some useful results (3) although, in general, the results leave much to be desired. Etching silicon with NaOH (2, 4) produces excellent pits that allow orientation to within a few minutes of arc; however, the chemical etches for germanium (2) are not as good, often giving accuracies no better than 10 min (5).

The preferential nature of the dissolution and recrystallization of germanium and silicon from molten metals is well known to those who have

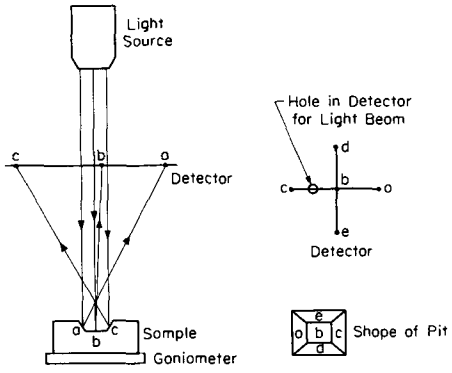

Fig. 1. Essentials of an apparatus for optical goniometry, and details of reflection from a pit.

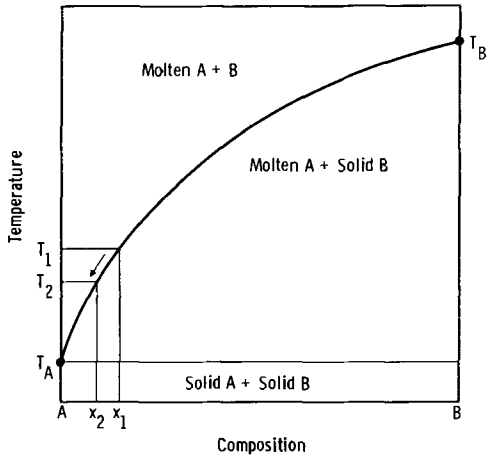

Fig. 2. Phase diagram illustrating molten metal etching

studied the alloy-fusion technique for preparing p-n junctions. This has been discussed by Mueller and Ditrick (6), Pankove (7), John (8), and in an incidental way by others. It was found that the reflected light pattern from pits produced by alloying In onto Ge (8) consisted of very bright sharp points which are necessary for accuracy in orienting surfaces. This paper reports on studies on "alloy etching," *i.e.*, molten metal dissolution and recrystallization, for preparing surfaces of germanium and the III-V intermetallic compounds for accurate orientation by optical methods.

Experimental Procedures

Since the purpose of this paper is to describe a technique for producing good facets for orientation rather than the operation of particular goniometers, the reader is referred to Barrett (1), Hancock and Edelman (9), and Wolff (5) for the detailed operation of goniometers. However, it seems appropriate to sketch the essentials of an optical goniometer apparatus, Fig. 1. The small parallel or slightly convergent beam of light is reflected from facets of the etched specimen back onto the detector, as shown in Fig. 1 for a nearly {100} surface etched to reveal {100} and {111} planes. If the specimen surface is only slightly different from the basal facet, b, the orientation of the specimen can be calculated very accurately from the specimen-detector distance and the displacement of the spot, b, from the light beam. Because of the large angles between the side facets and the basal facet, their angular relationship must be determined from a calibrated goniometer head.

Ingots of the semiconductor were oriented by x-rays or by optical methods using chemical etches to produce the proper surface. Wafers were cut whose large faces were parallel to the {111}, {001}, and {110} planes; in some cases wafers with surfaces parallel to other planes were also used. The surfaces were lapped to remove saw marks and to leave a less deeply damaged surface. The surfaces, or parts of the surfaces, were etched by placing a metal foil or pellet in contact with the wafer and heating to the desired temperature in a quartz tube under vacuum. A particularly convenient technique was to coat the metal "etchant" onto the surface with an ultrasonic soldering iron before heating. This procedure insured more uniform wetting over the entire surface. After the alloying operation, the metal was removed by a suitable reagent, *i.e.*, one that dissolved the metal but did not attack the semiconductor. The planes revealed by the etching were identified by measuring angles between various facets with an optical goniometer and by calculating angles from microscopic measurements.

The molten metal etching process may be understood by referring to Fig. 2. When a metal A is placed on another metal or semiconductor B of higher melting point and the system is heated to temperature T_1, metal A melts and dissolves enough of metal B to give the molten solution its equilibrium concentration X_1. Upon cooling, the dissolved metal B separates out to keep the molten solution at its equilibrium concentration. The concentration follows the arrow on the liquidus curve; for example, at T_2 the molten solution will have a concentration of X_2. Metal B can separate in one or both of the following ways: (i) It will redeposit epitaxially onto the solid along the solid-liquid interface. (ii) Crystallites will nucleate and grow in the molten solution. If the molten solution is caused to cool more slowly than the base, most or all of metal B will separate by (i): thus the observed facets will be those of redeposited material. Metal B can be prevented from redepositing onto the substrate if (*a*) metal B is caused to cool more slowly than the molten solution, particularly if a strong reverse thermal gradient is imposed, (*b*) the molten solution is decanted from the base, or (*c*) metal B is removed so far away from the interface that it cannot diffuse back. In these cases the facets will be those formed by the dissolution process.

Although (*a*) above can be accomplished by the use of large carbon blocks with cooling coils in them, it was found easier to obtain dissolution pits by (c) as follows. A large sphere of alloying metal was placed on the surface of the material to be etched in such a way that there was only a small area of contact. If the system is brought up to temperature rapidly and the heating cycle kept short, the equilibrium concentration in the molten metal will not be attained. Metal B can diffuse easily throughout the volume of metal A. The large area

ratio of melt-gas to melt-solid will discourage redeposition at the melt-solid interface.

Experimental Results

Germanium.—Indium, aluminum, gallium, gold, lead, and tin were studied as alloy "etchants" for germanium, being listed in order of decreasing usefulness. The actual amount of alloying element was not found to be critical; more element merely resulted in a more deeply etched area. For the technique that yields redeposition facets, the time of etching is not too important since the alloying element dissolves only its equilibrium amount of germanium in a few minutes. Leaving the molten metal in contact with a wafer for many hours, however, can result in alloying through a wafer by a thermal gradient transport process if the temperature is not controlled better than ±0.5°C (8). Although the cooling rate did not appear to be too critical, it was found that cooling rates slower than 25°C/min produced more nearly perfect facets. The facets produced at various temperatures were examined under the microscope for size and flatness; the light reflections on the optical goniometer were also checked. It was found that the best facets were produced over the temperature range of 400°-600°C. Higher temperatures tended to produce large but uneven facets, and lower temperatures tended to produce fewer and poorly defined facets.

Faceted pits produced by dissolution were examined as well as the faceted figures produced by redeposition. The results were identical. Microscopic examination of the pits and regrowth figures produced on {111}, {110}, {100}, and {221} surfaces by In, Au, and Al showed their shapes to be truncated triangular pyramidal figures or truncated hexagonal pyramidal pits (only three of whose side facets were visible), "roof"-type figures, four-sided pyramidal figures, and tilted truncated triangular pyramidal figures, respectively. Drawings of the pits and regrowth figures for {111}, {100}, and {110} surfaces are given in Fig. 3. From measurements made on many facets, angles were calculated. Only {111} planes were found. The angles between all facets were also measured with an optical goniometer; these measurements also showed that only {111} planes were revealed. Pits and regrowth figures on {411} and {211} surfaces were also examined and found to give the predicted pattern for {111} facets only. Gallium seems to reveal at least one additional set of planes which were not identified, while tin and lead did not produce satisfactory results. Small dissolution pits with very perfect {111} facets can be obtained on Ge by technique (*c*) described above. Such pits are probably capable of giving somewhat greater accuracy than the regrowth figures obtained by redeposition from molten metals. The latter, however, were found to be more convenient for goniometric measurements because of the larger areas available. Accuracies of 1 min of arc can be obtained; this is much better than that obtainable from chemical etching techniques. Although the molten metal etching techniques are applicable to silicon as shown in Table I, the quality of the facets produced by the NaOH chemical etch are adequate for almost all orientation requirements.

III-V Intermetallic compounds.—Antimony, arsenic, and phosphorus form intermetallic compounds with many metals; some of these compounds are more stable than the III-V intermetallic compounds. If a metal that formed one of the more stable compounds with the group V component were used as the etchant for a III-V intermetallic compound, the dissolution and redeposition processes may proceed along different crystallographic planes or the redeposition may not be epitaxial. To avoid such difficulties, only the group III component of the intermetallic compound was used as the etchant.

In these materials, as in germanium, the amount of metal etchant was not found to be critical. From the examination of the pits produced at various temperatures, the temperature range for producing the best facets was determined. The temperatures chosen for use are summarized in Table I along with the reagent used to remove the metal etchant. Facets formed by dissolution and by redeposition were examined and found to be the same.

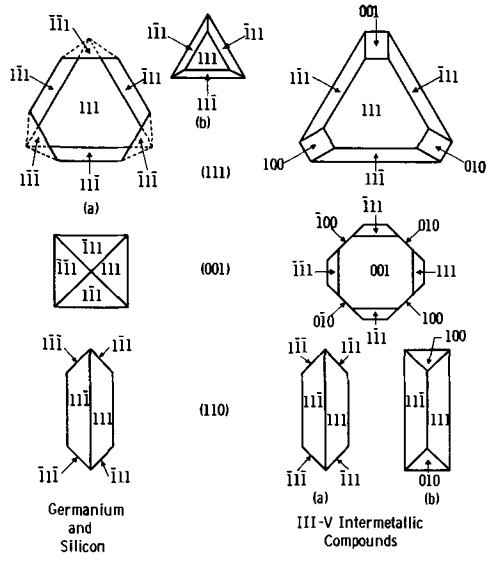

Fig. 3. Drawings of figures obtained by etching germanium and the III-V intermetallic compounds with molten metals.

Table I. Experimental conditions for molten metal etching

Material	Metal used as etchant	Temperature of etching, °C	Equilibrium concentration in at. %	Reagent for removing metal	References
InSb	In	350	10	HCl	
GaSb	Ga	500	5	HCl	
InAs	In	600	6	H_2SO_4	
GaAs	Ga	800	7.5	HCl	
AlSb	Al	800	5	NaOH	
Ge	In	450	10	HCl	
Ge	Ga	137	1	HCl	(14)
Ge	Sb	600-700	15-30		(14)
Si	Sn	1000	7.5	HCl	(5)
Si	Ga	500	1	HCl	(14)
Si	Bi	1150	11		(14)
Si	In	600	1	HCl	(5)
Si	Al	700	20*	HCl	

* Only 9 at. % of the Si recrystallizes, the remainder being tied up in the eutectic.

Microscopic examination of the regrowth figures showed the redeposition process was the same for all of the III-V intermetallic compounds, but different than germanium. Drawings of the regrowth figures are given in Fig. 3 for comparison with the germanium figures. One can see that the {111} surfaces gave truncated hexagonal pyramidal figures; however, all side facets were visible, as can be seen in Fig. 4. Figure 5 shows the flats obtained on a large area. The {001} surfaces gave square and rectangular figures with one or more corners cut off as shown in Fig. 6 while Fig. 7 shows a figure with some visible side facets. The {110} gave "roof"-type figures, Fig. 8, similar to those found on germanium; however, figures with the shape shown in (*b*) of Fig. 3 were also observed. (These are indicated by arrows in Fig. 8).

The regrowth figures produced on the various surfaces of GaSb and InSb were carefully measured by microscopic and by optical goniometric techniques. The measurements show that not only are {111} planes revealed but also {100}. The identification of the planes that form the facets on the various surfaces are given in Fig. 3. For the {111} and {110} surfaces, the reflected light spot on the viewing plate of the goniometer was strong and sharp from the {111} facets: the reflections from the {100} facets were weaker. From the intensity and small

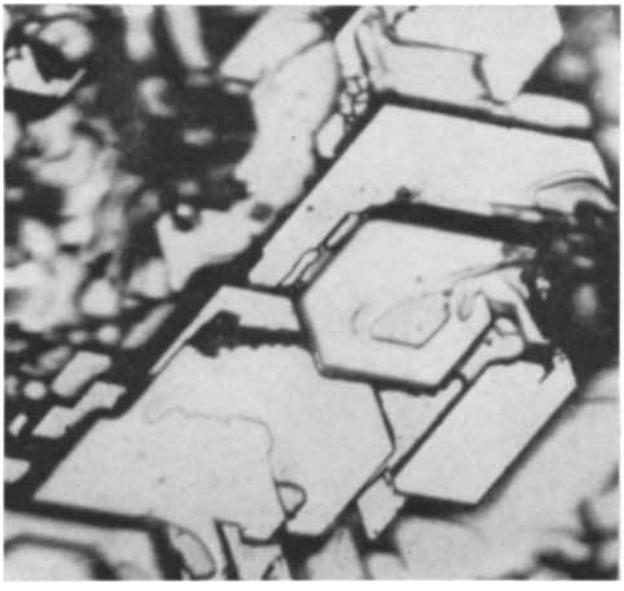

Fig. 4. {111} surface of InSb etched by molten In. Magnification approximately 150X.

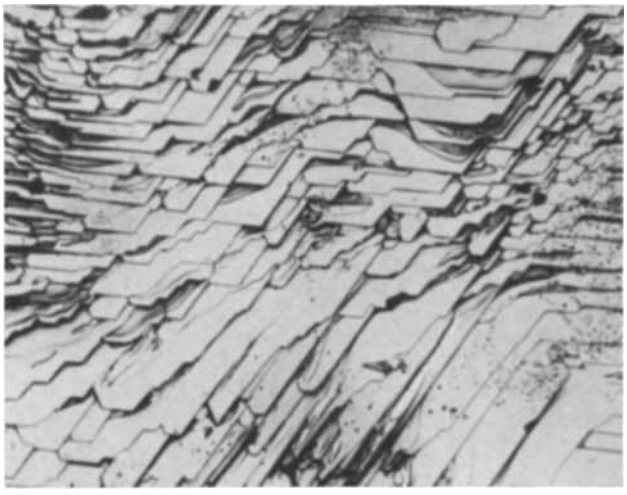

Fig. 5. {111} surface of GaSb etched by molten Ga. Magnification 75X.

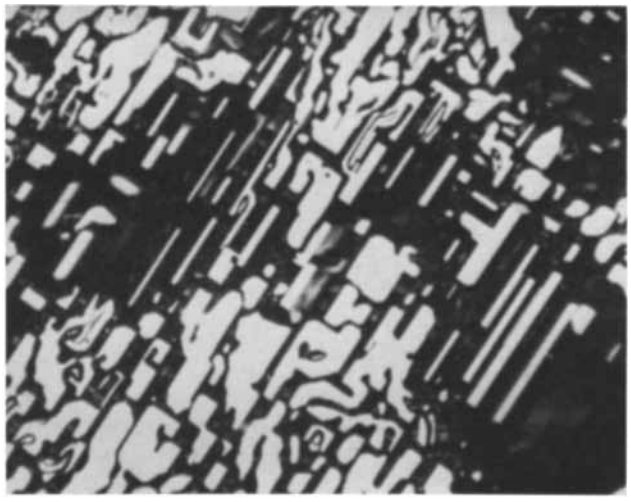

Fig. 6. {100} surface of GaSb etched by molten Ga. Magnification approximately 75X.

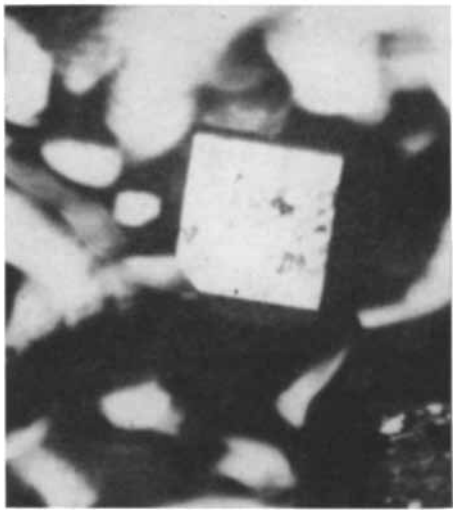

Fig. 7. Details of figure produced on {100} surface of GaSb by molten Ga. Magnification approximately 150X.

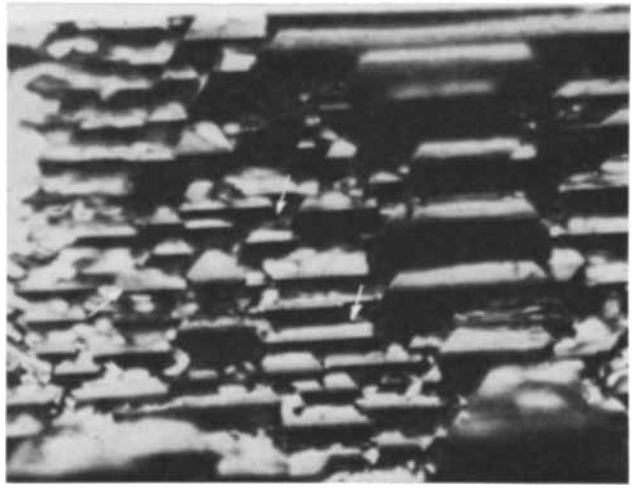

Fig. 8. {110} surface of GaSb etched by molten Ga. Arrow shows b type figures. Magnification approximately 150X.

area of the reflected light spot, it is estimated that accuracies of better than 1 min of arc can be obtained from these surfaces. Figures of the shape b on the {110} surface were not as frequent as those of shape a. No reflections from the four {100} side facets of the figures found on the {001} surface were obtained which is understandable since these planes are perpendicular to the surface. The {111} plane and the $\{\bar{1}\bar{1}\bar{1}\}$ plane gave the same type of pits as did the {001} and the $\{00\bar{1}\}$, indicating that the polarization which is found to give a difference in the attack of chemical etches on these planes (3, 10) does not affect the alloying process. The stability of {100} facets is apparently related to molecular association in the liquid, as discussed elsewhere (11).

Examination of the figures produced on GaAs and InAs gave the same results as those reported above for GaSb and InSb. Only partial results were obtained for AlSb because of difficulties in obtaining complete wetting of the surface by the aluminum; however, the results indicated that the same planes were revealed.

Discussion

The difficulty in devising chemical or electrolytic etchants for revealing low index planes should, by now, be appreciated. Alloy etching, however, affords a convenient method for revealing low index planes. The principle on which it is based is completely general; thus the technique can be used on any material provided the material can meet certain requirements. Certain metal-metal systems have suitable phase diagrams. Bailey and Watkins (12) show photomicrographs of Cu deposited onto Cu from Cu-saturated Pb which indicate the applicability of Pb as an alloy etchant for Cu.

There are two techniques which may be used for this method of etching, namely, the foil method used here and the decanting technique (5). Temperatures and reagents for the foil method are given in Table I along with pertinent data from other work. The success of this method depends on finding a suitable metal etchant and a reagent that will dissolve the metal etchant but not the material being etched. Existing phase diagrams (13) are helpful in deciding on the metal etchant and also in choosing the temperature. Since some of the dissolved material will recrystallize on the surface, it is necessary to choose a metal-material system that does not form intermetallic compounds since such compounds may be of a different crystal system or might not grow epitaxially on the substrate.

The generally greater accuracy obtainable from molten metal etches is the result of the fact that larger and more nearly perfect facets are produced by this technique than by chemical etches. Optimum conditions to produce large and perfect facets often represent a compromise between quantity of alloying material, alloying temperature, and cooling rate.

In Table I we have included the equilibrium concentration of the material in the metals at the alloying temperatures which were chosen for the various materials. One can see that these values fall between 1 and 15 at.%. Concentrations above this value often produce less satisfactory facets; thus in choosing a temperature for a new system the temperature should be chosen so that the equilibrium concentration falls within these limits. Although the planes revealed are generally of low Miller indices, Wolff (5) has reported that certain metals on silicon, for example gold and zinc, reveal other planes in addition to the {111}; thus it is necessary to determine experimentally the planes revealed in a new system.

Perhaps the most stringent requirement for the success of this method lies in finding a suitable reagent for removing the alloying metal; this is particularly troublesome for metal-metal systems. Decanting techniques can, to a certain extent, overcome such difficulties. Broder (14) used a bath of molten metal and dipped the material to be etched in it and then rapidly removed it from the bath (a decanting technique). In this method, however, one may be troubled by the alloying metal adhering to the edges of the pits (12). The time of etching also becomes important since there is a large quantity of alloying metal present. In spite of these difficulties, decanting techniques are attractive for systems that present insurmountable obstacles to the technique used here.

Manuscript received Feb. 26, 1962; revised manuscript received April 20, 1962.

Any discussion of this paper will appear in a Discussion Section to be published in the June 1963 JOURNAL.

REFERENCES

1. C. S. Barrett, "The Structure of Metals," McGraw-Hill Book Co., Inc., New York (1943).
2. J. W. Faust, Jr., "Surface Preparation" in "Methods in Experimental Physics," Vol. 6, K. Lark-Horovitz and V. Johnson, Editors, Academic Press, Inc., New York (1959).
3. J. W. Faust, Jr. and A. Sagar, *J. Appl. Phys.*, **31**, 331 (1960).
4. J. W. Faust, Jr., paper presented at Electrochem. Soc. Meeting, San Francisco, May 1956.
5. G. A. Wolff, J. M. Wilbur, Jr., and J. C. Clark, *Z. Elektrochem.*, **61**, 101 (1957).
6. C. W. Mueller and N. H. Ditrick, *RCA Review*, **17**, 46 (1956).
7. J. Pankove, *J. Appl. Phys.*, **28**, 1054 (1957).
8. H. F. John, paper presented at I.R.E.-A.I.E.E. Devices Conference, Philadelphia, June 1955 (unpublished).
9. R. D. Hancock and S. Edelman, *Rev. Sci. Instr.*, **27**, 1082 (1956).
10. H. C. Gatos and M. C. Lavine, *This Journal*, **107**, 433 (1960).
11. J. W. Faust, Jr. and H. F. John, To appear in *J. Phys. and Chem. of Solids.*
12. G. L. J. Bailey and H. C. Watkins, *J. Inst. Metals*, **80**, 57 (1952).
13. M. Hansen and K. Anderko, "Constitution of Binary Alloys," 2nd ed., McGraw-Hill Book Co., Inc., New York (1958).
14. J. D. Broder and G. A. Wolff, paper presented at Electrochem. Soc. Meeting, Cleveland, October 1956.

Distribution of Sulfur in InSb Single Crystals

Mario D. Banus and Harry C. Gatos

Lincoln Laboratory,[1] Massachusetts Institute of Technology, Lexington, Massachusetts

ABSTRACT

The distribution of sulfur impurity in single crystals of InSb pulled from the melt in the <111> direction was studied by high resolution autoradiography, electrical measurements, and analytical techniques. Autoradiography was found to be more suitable for the microdistribution of sulfur than the other techniques employed. A (111) facet present at the solid-melt interface led to the formation of a longitudinal core with a higher sulfur concentration than the rest of the crystal. The ratio of the on-core to off-core concentration of sulfur was greater with rotation than without rotation. It also varied with sulfur concentration in the melt (C_L) going through a broad maximum for values of C_L between 1.5×10^{18} and 4×10^{18} sulfur atoms/cc. The effective distribution coefficient (k_{eff}) of sulfur was found to vary with sulfur concentration in the melt and with orientation. For $C_L = 10^{18}$ sulfur atoms/cc the following values were obtained: on-core $k_{eff} = 0.4$, off-core $k_{eff} = 0.16$. The results are explained on the basis of specific adsorption of sulfur at the solid-melt interface and on the dependence of adsorption on crystallographic orientation.

The distribution of electrically active impurities continues to be of basic interest in semiconductor materials. Although incorporation of impurities in solids under equilibrium solidification conditions is in many respects a straightforward problem, commonly employed crystal growth conditions lead to impurity distributions of a rather complex nature.

In growing semiconductor single crystals from the melt by Czochralski-type techniques heterogeneous distribution of impurities is quite frequently encountered. Thus, it has been found (1) that in germanium single crystals, antimony and other impurities are periodically distributed along the growth axis (striations). In addition, it has been observed (1) by autoradiographic techniques that along the axis of growth a distinct impurity core is formed containing an increased concentration of the impurity elements.

Hall (2) has found that, during growth of germanium single crystals from the melt, the distribution of impurities is a function of the growth rate and orientation. He developed an expression for the variation of the impurity segregation as a function of the growth rate, assuming that the impurity atoms are preferentially adsorbed at the surface of the crystal. Similar observations on germanium (3) and other semiconductors (4) have been reported by many investigators, who have shown that the formation of the core is associated with the presence of an (111) facet on the crystal at the growth interface.

The present study was aimed at the detailed distribution of sulfur in single crystals of InSb. Sulfur was chosen because it is a soft beta-ray emitter (0.167 mev) and lends itself to high resolution autoradiography.

Experimental Techniques

Crystal growth.—InSb single crystals were grown by conventional Czochralski techniques in a purified hydrogen atmosphere. In view of the high vapor pressure of sulfur at the melting point of InSb (523°C), the sulfur impurity was first incorporated into InSb ingots in evacuated and sealed quartz ampules as follows. The radioactive sulfur (2-5 millicuries S^{35}) together with the desired amount of inert sulfur was dissolved in benzene, and the solution was introduced in the quartz ampule whereupon it was evaporated to dryness on a low-temperature airbath. Subsequently, the pure InSb was placed in the ampule which was then evacuated and sealed off. To prepare ingots containing only inert sulfur, elementary sulfur was placed directly in the quartz ampule. On melting, the ampule was manipulated so that the melt was displaced from one end of the ampule to the other to insure an effective incorporation of the sulfur into the melt.

The sulfur-containing ingots prepared as above were etched in CP4 to remove any surface slag formed during preparation. It was found by chemical analysis that about 50% of the sulfur originally employed was incorporated in the polycrystalline ingots. In one instance where detailed mass balance was performed after single crystal growth, it was found that, within experimental error, all of the sulfur present in the ingot was retained in the grown crystal and the residual melt.

Each crystal was grown under a constant pulling rate in the range of 0.3-0.6 in./hr. The principal rotation rate was 8 rpm, but on occasions rotation rates of 0, 4, and 100 rpm were employed.

The single crystals were 20-25 mm in diameter, and growth was continued until each crystal touched the bottom of the crucible. At this point the crystal was suddenly removed from the crucible. Actual growth rate (length per unit time) of the main portion of the crystal was carefully determined and was found to be 1.5 to 1.8 times the pull rate (the diameter of the crystals was rela-

[1] Operated with support of the U.S. Army, Navy, and Air Force.

tively large in comparison with the diameter of the crucible).

After growth, the crystals were sectioned in two halves (excluding the seed portion) along the growth axis. The two longitudinal sections were polished with 1600 grit abrasive and then submitted to electrical measurements, autoradiography, and preferential etching.

Autoradiography.—Because of pronounced self-absorption, autoradiographs obtained with soft β-ray emitters (such as S^{35} with a β-ray of 0.167 mev) essentially reflect the concentration of the radiotracer at the surface of the solid sample. In such instances intimate contact between the sample and the photographic emulsion is most important in obtaining the highest attainable resolution. For this reason stripping films with an emulsion 0.005-0.010 in. thick were employed. These films have a potential resolution of about 1μ. Two types of films were tested: The Kodak Autoradiographic Stripping Film "Experimental" exhibited excellent sensitivity but it presented difficulties in handling. The Kodak AR10 Stripping Film gave very satisfactory results with a minimum of handling difficulties, although its sensitivity is approximately one-fifth of the "Experimental" film. The AR10 film was employed predominately in the present study.

The emulsion bearing layer of the film was stripped from the backing, floated in cold water, and then brought in contact with the sample. The emulsion bearing layer could thus follow even minute irregularities of the sample surface. After suitable exposure, the emulsion was developed while in contact with the sample; then it was removed from the sample and mounted on a glass slide. A resolution of 5-20μ was attained by employing a scanning microdensitometer.

Direct calibration of the stripping films was not attempted since standard S^{35} sources could not be immersed in water. However, duplicate autoradiographs were obtained on plates (Kodak Autoradiographic Plate Type A) which were calibrated with standard S^{35} sources. These plates were employed in determining the concentration ratios of sulfur. Photographic enlargements (approximately 15X) of the autoradiograms on the AR10 film made convenient the visual examination of the impurity distribution over the whole longitudinal section of the crystal.

Determination of sulfur concentration.—A calibration curve was established relating the concentration of sulfur to the room temperature electrical resistivity of sulfur-doped InSb single crystals. The sulfur concentration was determined from Hall measurements at liquid nitrogen temperature. The electrical resistivity was measured with a four-point probe having a spacing of 0.008 in. between points. The calibration curve is shown in Fig. 1. Electrical resistivity measurements were taken only with single crystals.

Radiotracer analysis was employed for determining the sulfur concentration in the starting polycrystalline ingots and the residual melts. It was

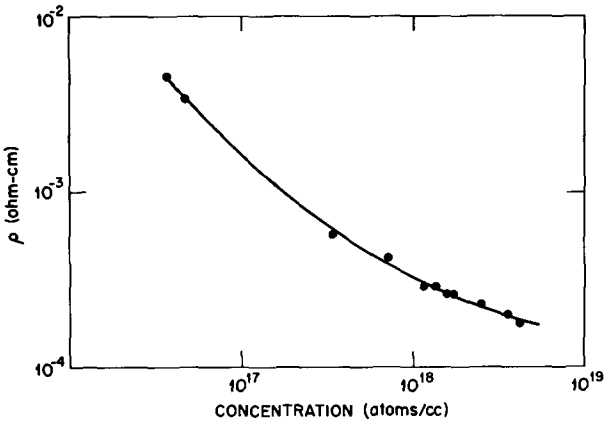

Fig. 1. Correlation between the room temperature resistivity of InSb and the concentration of sulfur impurity as determined from Hall measurements at 78°K.

first established (calibration tests) that the counting rate of InSb powder intimately mixed with elementary sulfur of known specific activity was proportional to the amount of sulfur present. In these calibration tests the sulfur (tagged with S^{35}) was mechanically incorporated in the powder from standardized benzene solutions. The powdered samples were placed on specially designed planchets which fitted into a flow counter. The samples to be analyzed (ingots, single crystals, or residual melts) were ground to a powder, and then their counting rate was determined.

The sulfur concentration was also determined by combustion techniques adopted for InSb by D. Guernsey of the Metallurgy Department, Massachusetts Institute of Technology. Concentrations in the vicinity of 20 ppm represented the lower limit for reasonably accurate determinations. Results obtained by radiotracer analysis and combustion techniques on identical samples, were in good agreement (within 6-20%).

Results

Impurity core and impurity striations.—A distinct core containing an increased amount of sulfur impurity was observed along the length of the InSb crystals grown in the <111> direction as found in germanium (3) and InSb (5) crystals grown with other impurities. The formation of the core was found to take place on the onset of crystal growth on the seed crystal and regardless of growth conditions or size of the seed.

An autoradiograph of the longitudinal section of an InSb crystal is shown in Fig. 2, together with a photograph of the other half of the same crystal which was chemically etched. It is seen that a markedly better definition is obtained by autoradiography than by etching. This result is to be expected since preferential etching initiated by impurities, imperfections, or orientation effects does not in general remain localized with time.

The autoradiograph of Fig. 3 shows the presence of the (111) facet at the bottom of the crystal and illustrates clearly that the size of the core corresponds precisely to the size of the facet. Figures 2 and 3 further show that appreciable changes in the

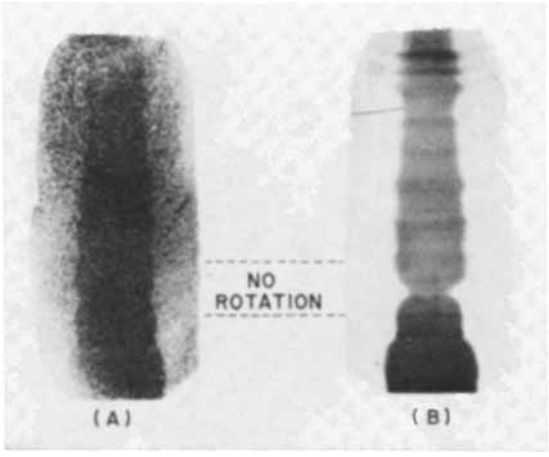

Fig. 2. Distribution of sulfur impurity (tagged with S^{35}) in an InSb single crystal. A, one half of the crystal (longitudinal section) etched with 0.2*N* Fe^{+++} in 6*N* HCl; B, autoradiograph of the other half of the crystal using Kodak Type A plate.

Fig. 3. Autoradiograph (Kodak Type A plate) of a longitudinal section of an InSb single crystal containing S^{35}.

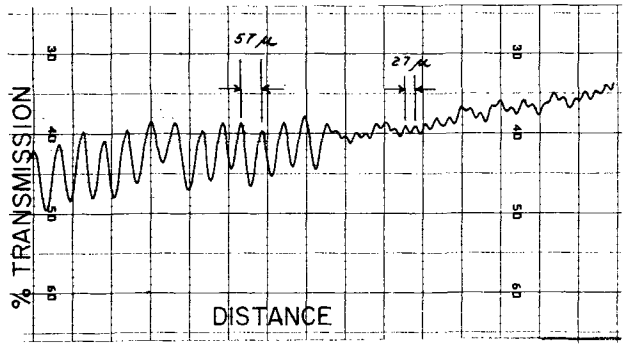

Fig. 4. Microdensitometer tracing of autoradiograph of crystal shown in Fig. 2. A Kodak AR10 Stripping Film was used. Change of rotation from 4 to 8 rpm is clearly reflected in the period of striations. The microdensitometer slit employed was 5μ wide and 0.5 mm high.

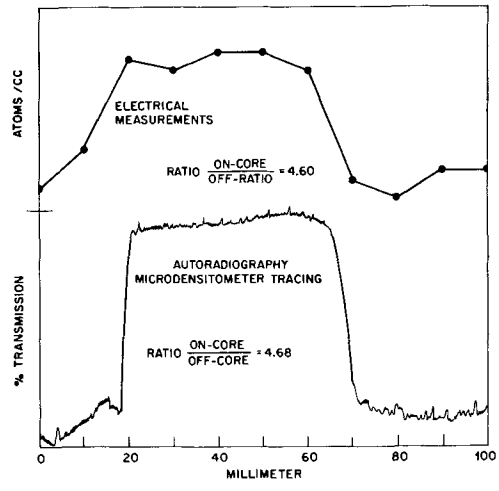

Fig. 5. Sulfur concentration profile normal to direction of growth obtained from resistivity measurements and from autoradiography. By employing S^{35} calibration standards it was found that the film density is linearly related to the sulfur concentration.

size of the core, resulting of course from corresponding changes in the size of the facet, occur during growth, whereas relatively small changes occur in the over-all morphology of the crystal. These changes must be related to temperature variations at the solid-melt interface (shape of the growth isotherm). Consequently, the size of the facet is more sensitive to temperature changes than the over-all size of the crystal. Thus, during growth by the Czochralski method, abrupt changes occur in the shape of the isotherm unless elaborate precautions are taken. If the growth interface (isotherm) is flat, the (111) facet extends the full width of the crystal, as was found in a crystal rotated at 100 rpm during growth.

Periodic variations in impurity concentration (striations) along the growth axis were found in all crystals rotated during growth. The spacing of striations was found to be inversely proportional to the rotation rate (5) as shown in the microdensitometer tracing of Fig. 4. Variations in impurity concentration of approximately 30% were detected. However, the difference between the maximum and minimum impurity concentration in the striations was not found constant in the various crystals even for the same rotation rate.

In the unrotated portions of the crystal striations were not unambiguously present, although in Se-doped InSb crystals, grown without rotation, striations were clearly observed (5). Possible reasons for the absence of striations are discussed below.

On-core to off-core impurity ratio.—The concentration profile of sulfur impurity obtained by electrical measurements and autoradiography along the diameter of the same cross section of an InSb crystal is shown in Fig. 5. A good agreement of the two methods is apparent. The microdensitometer tracing of the autoradiogram, however, represents more precisely the corresponding impurity distribution. In Fig. 5 the on-core to off-core ratio as determined by electrical measurements is in excellent agreement with the value obtained by autoradiography. Such good agreement was not always found, apparently because a much greater thickness of material contributes to the four-point probe measurement than to the autoradiogram. A comparison of the ratios obtained by electrical measurements and autoradiography at various cross sections of this crystal is shown in Table I. Best correlation between the two techniques was obtained when the long axis of the four-point probe was traversed along the traversing path of the slit.

Effect of rotation rate.—It is seen in Table I that there is a distinct increase in the on-core to off-core ratio in going from 8 to 0 rpm and a decrease in

Table I. Ratios of on-core to off-core concentrations of sulfur at various cross sections of an InSb single crystal (as determined by electrical measurements and autoradiography)

Distance from seed, mm	Rotation rate, rpm	Ratio	
		Electrical measurements	Autoradiography*
26	8	4.1	3.18
34	0	4.6	4.68
40	0	4.6	4.97
48	0	6.2	5.46
54	8	5.7	4.36
59	8	6.9	—

* Microdensitometer slit size: 1.5μ × 2.0 mm.

Table II. Effect of change of rotation rate on the on-core and off-core concentration of sulfur in InSb single crystals

Crystal No.	Rotation rate, rpm	Concentration, atoms/cm³		Ratio
		On-core	Off-core	
8	8	20.0	5.9	3.39
8	0	22.0	5.7	3.86
9	8	1.7	0.49	3.5
9	0	3.4	0.47	7.2
10	8	10.3	2.5	4.1
10	0	10.7	2.3	4.6

the ratio in going from 0 to 8 rpm. The same effect can also be seen in Table II. The observed change in ratio without changing the rotation rate in Table I is discussed below. As shown in Table II, the increase in the concentration ratio associated with the decrease in rotation rate results from a decrease in the off-core concentration and an increase in the on-core concentration. These changes in concentration can often escape detection by electrical resistivity but are always unambiguously observed by autoradiography as shown typically in Fig. 6 (see also Fig. 2).

The above observations are readily understood in terms of changes in the melt concentration at the interface brought about by changes in rotation rate. Stirring of the crystal under the present experimental conditions apparently causes a flow of the melt near the axis of the crystal (facet area) toward the perimeter of the crystal as illustrated

Fig. 6. Effect of stopping rotation on the concentration of sulfur on and off the core (autoradiograph). Note decrease in the off-facet concentration and increase in the on-facet concentration upon stopping rotation. Shifting of the core results from the eccentric position of the crystal in the apparatus.

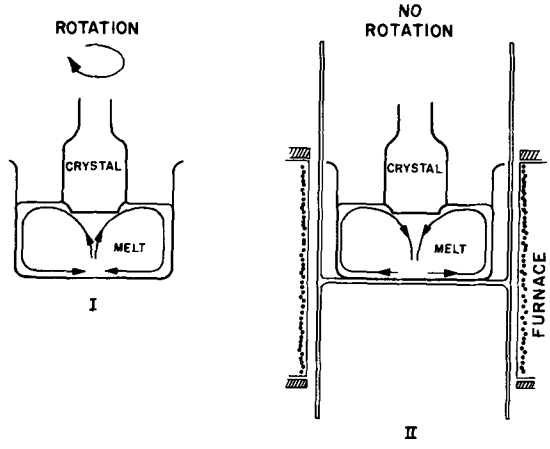

Fig. 7. Schematic representation of flow currents in melt under growth conditions.

schematically in Fig. 7(I). This type of flow was experimentally demonstrated by simulating the growth conditions employing a viscous liquid and a rotating crystal. The direction of flow was observed by employing a dye injected at the interface near the axis of the crystal. As a result of this flow, melt from the facet interface enriched in impurity by rejection from the solid is brought to the off-facet area. It is thus apparent that during rotation the melt at the off-facet interface is more enriched in impurity by rejection from the solid than the facet interface. In the absence of rotation, and owing to the existing thermal gradients, the convection currents are expected to flow in a direction opposite to the direction of flow caused by rotation, as illustrated in Fig. 7(II). Thus, in going from 8 to 0 rpm, the impurity concentration in the melt at the facet interface increases whenever the impurity concentration in the melt at the off-facet interface decreases. Similar effects have been discussed by Goss and Adlington (6).

It is of interest to note that the stirring pattern does not appear to be altered significantly in going from 8 to 100 rpm since, within experimental error, no corresponding change in ratio was observed as shown in Table III. Furthermore, the individual on-core and off-core concentrations decrease only to a small extent in going from 8 to 100 rpm suggesting that under the present experimental conditions rotating at 100 rpm is not appreciably more effective in eliminating the enriched layer than rotating at 8 rpm.

Effect of impurity concentration in the melt.—It has been already pointed out (Table I) that the on-core to off-core ratio of sulfur concentration does

Table III. Effect of the change of rotation rate on the on-core and off-core concentration of sulfur in a single crystal of InSb

Distance from seed, mm	Rotation rate, rmp	Concentration, atoms/cm³		Ratio
		On-core	Off-core	
31	8	8.5	3.2	2.7
34	8	9.4	3.3	2.9
36	100	8.8	3.0	2.9
41	100	8.8	3.0	2.9
46	8	8.8	3.2	2.8

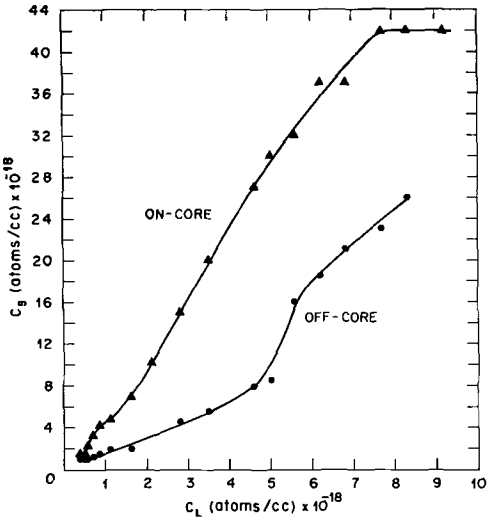

Fig. 8. Concentration of sulfur in InSb single crystals, on and off the core (C_S) as a function of melt concentration (C_L). The results were obtained from three crystals grown by rotating at 8 rpm.

not remain constant during crystal growth even under constant rotation rate. For an impurity with a distribution coefficient less than one, it is, of course, expected that the impurity concentration in the melt will increase, and consequently the on-core and off-core concentrations will increase as crystal growth proceeds. The dependence of the concentration in the crystal on the impurity concentration in the melt is shown in Fig. 8. The sulfur concentration in the solid (C_S) was determined by resistivity measurements and in the residual melt (C_L) by chemical and radiotracer analysis. C_L in the melt during growth was back-calculated by a detailed mass balance of the impurity concentration in the residual melt and in various parts of the crystal.

The on-core to off-core ratio as a function of the impurity concentration in the melt for the three crystals of Fig. 8 is shown in Fig. 9. It is seen that in the crystal grown from the melt with the lowest impurity concentration the ratio increases as crystal growth proceeds; the ratio remains essentially constant in the crystal of intermediate concentration and decreases as crystal growth proceeds in the crystal grown from the melt with the highest impurity concentration.

Effective distribution coefficient of sulfur in InSb.—The effective distribution coefficient of sulfur ($k_{eff} = C_S/C_L$) in InSb as a function of impurity concentration in the melt is shown in Fig. 10. It is seen that k_{eff} on-core increases with increasing C_L until C_L reaches a value of approximately 6×10^{18} sulfur atoms/cc; k_{eff} for the off-core portion of the crystal remains approximately constant at first and then increases with increasing C_L.

The k_{eff} was also determined for several crystals grown in the <100> direction. For $C_L \simeq 2 \times 10^{18}$ sulfur atoms/cc, k_{eff} in the <100> crystals was found to be 0.14 which is in good agreement with the corresponding off-core $k_{eff} = 0.16$. These results are in reasonable agreements with the preliminary data obtained by Harman (7).

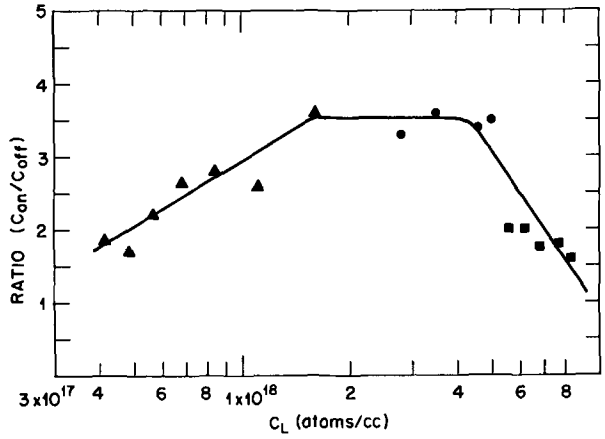

Fig. 9. Ratio of C_S on-core to C_S off-core as a function of C_L. Data calculated from same three crystals (indicated by three different symbols) as in Fig. 8.

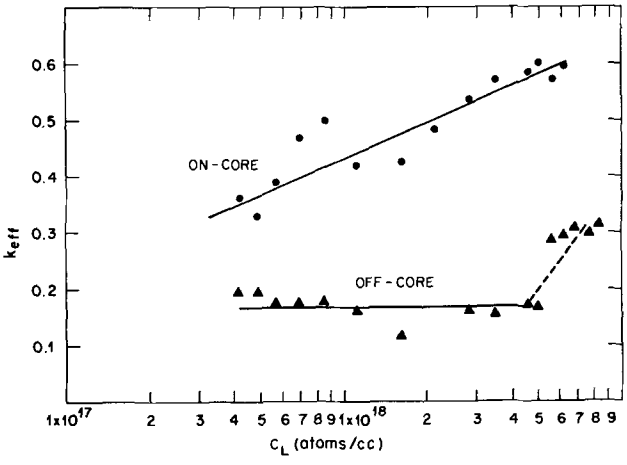

Fig. 10. Effective distribution coefficient, k_{eff} as a function of C_L.

Discussion

General observations.—Autoradiography techniques as employed in this study show unambiguously that along the <111> growth axis of sulfur-doped InSb single crystals (pulled from the melt) a core is formed containing more sulfur impurity than the rest of the crystal. A core is present over the whole range of conditions commonly encountered in Czochralski-type techniques. The size of the core was found to vary appreciably more than the over-all morphology of the crystal. Although no effort was made to study the factors affecting the size of the core (size of the (111) facet), it appears that the shape of the isotherm at the interface is changing during growth. It also appears that the degree of supercooling necessary for solidification changes during growth since such supercooling depends on many factors, such as impurity concentration and stirring.

The increased concentration of impurity in the core of the crystals has been considered to be associated with the detailed mechanism of the (111) facet formation (8, 9). Adsorption phenomena alone, however, can account for the observed dependence of impurity concentration on orientation as discussed below. Consequently, the factors responsible for the formation of the facet will not be considered here.

Variations in the distribution coefficient of impurities with crystallographic orientation have been observed and discussed in detail by Hall (2) for germanium single crystals pulled from the melt. He concluded that the incorporation of impurities in the crystal depends on specific adsorption of the liquid solid interface. The transport theory of Burton and others (1) does not account for Hall's observations. This theory is not applicable either to the results described here, since drastic changes in the stirring conditions did not alter the core formation significantly.

Adsorption model.—The results of the present study can be readily understood assuming a difference in the adsorption characteristics of the various crystallographic planes and, in particular, that preferential adsorption is exhibited by the {111} planes. Thus, the impurity adsorption isotherm for the {111} surfaces is significantly different from the adsorption isotherm of the other crystallographic planes. The amount of impurity incorporated into the solid depends directly on the amount of impurity adsorbed. In turn, the amount adsorbed depends on the impurity concentration in the melt at the interface, but this latter dependence is a strong function of orientation. An adsorption model requires, of course, that the concentration of the solute atoms on the solid surface is greater than the concentration near the interface. It requires further that the incorporation of adsorbed solute atoms into the solid takes place faster than the establishment of adsorption equilibrium. Such conditions can be readily realized, particularly if a portion of the adsorbed atoms is rejected, in which case the transport of solute atoms from the interface layer to the solid surface is not exclusively rate determining. Figure 11 illustrates schematically two adsorption isotherms, one for the {111} planes and one for the other crystallographic planes. The assumption that the crystallographic planes, other than the {111}, exhibit similar adsorption isotherms is consistent with the experimental results reported above, whereby the off-facet k_{eff} is, within experimental error, the same as the k_{eff} found for crystals grown in the <100> direction.

The results presented in Fig. 9 are entirely consistent with the two-adsorption isotherm model. It

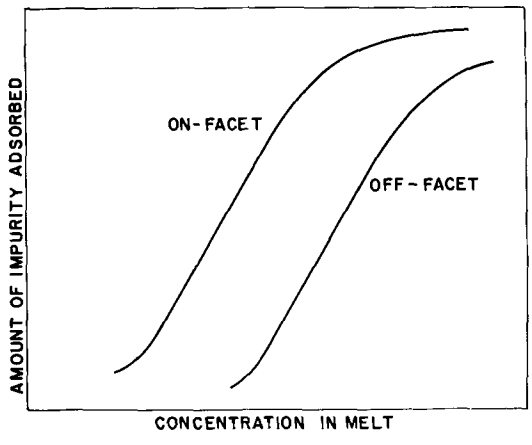

Fig. 11. Schematic representation of two sulfur adsorption isotherms, on and off the {111} facet.

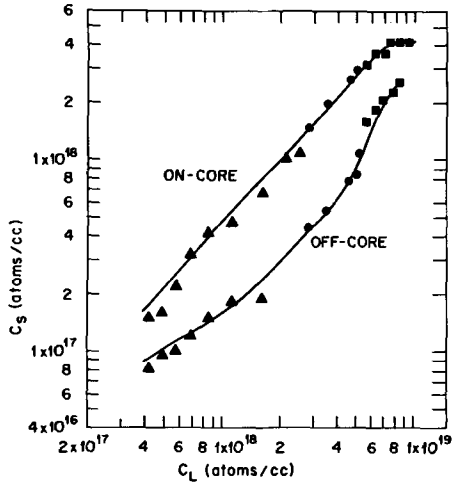

Fig. 12. Logarithmic plot of sulfur concentration in InSb as a function of C_L. The three types of symbols correspond to three different crystals.

is seen that the on-facet/off-facet ratio first increases, then stays constant, and finally decreases with increasing impurity concentration in the melt. In fact, the experimental results as plotted in Fig. 12 reflect two adsorption isotherms.

To the extent that the amount adsorbed is a function of the solute concentration in the melt, the amount of impurity incorporated into the solid depends on the concentration of the impurity in the melt under nonequilibrium conditions of growth. The maximum amount of impurity incorporated into the solid is related to the amount adsorbed at the leveling off point of the isotherms. The leveling off of the on-facet isotherm accounts rather uniquely for the small values of the on-facet/off-facet ratio at high impurity concentrations.

Consistent with an adsorption model are the results reported by Hall (2) and Dikhoff (3) for germanium single crystals. They found that nonmetallic elements (donors) exhibited more pronounced orientation affects than metallic elements (acceptors). It is quite reasonable to expect that nonmetallics exhibit a greater tendency for preferential adsorption than metallic impurities.

Of particular interest is the case of gallium impurities which are more readily incorporated in the off-core than in the on-core region of germanium crystals (3). Adsorption of gallium atoms on the {111} planes must be less pronounced than on the other crystallographic planes. This unusual behavior of gallium impurity is probably associated with the rather complex crystalline structure of gallium. Another relevant aspect of the complex structure of gallium is its low tendency to serve as a nucleation catalyst in solidification processes involving more common crystalline structures (10).

Impurity striations.—The adsorbed impurities undoubtedly influence the nucleation of the solidification process and consequently must affect the degree of supercooling necessary for crystal growth. For given conditions of crystal growth the period of the pulsating growth during no rotation (5) must then depend strongly on the nature of impurities present in the melt. In the present case,

sulfur apparently is more effective in decreasing the degree of supercooling so that it does not allow a pronounced striated growth during no rotation, as does selenium impurity (5).

Acknowledgment

The authors wish to thank W. J. LaFleur, Miss S. Nye, J. A. Kafalas, and Dr. A. J. Strauss for their assistance and profitable discussions during the course of this study.

Manuscript received April 4, 1962. This paper was prepared for delivery before the Detroit Meeting, Oct. 1-5, 1961.

Any discussion of this paper will appear in a Discussion Section to be published in the June 1963 JOURNAL.

REFERENCES

1. W. P. Slichter and J. A. Burton in "Transistor Technology," Vol. 1, p. 119, Bell Telephone Laboratories, Inc. and Western Electric Co. (1952).
2. R. N. Hall, *J. Phys. Chem.*, **S7**, 836 (1953).
3. J. A. M. Dikhoff, *Solid State Electron.*, **1**, 202 (1960).
4. K. F. Hulme and J. B. Mullin, *Phil. Mag.*, **4**, 1286 (1959).
5. H. C. Gatos, A. J. Strauss, M. C. Lavine, and T. C. Harman, *J.Appl. Phys.*, **32**, 2057 (1961).
6. A. J. Goss and R. E. Adlington, "Solid State Physics," M. Désirant and J. L. Michiels Editors, p. 28, Academic Press, New York (1960).
7. T. C. Harman, *This Journal* **103**, 128 (1956).
8. J. B. Mullin and K. F. Hulme, *J. Phys. Chem. Solids*, **17**, 1 (1960).
9. W. P. Allred and R. T. Bate, *This Journal*, **108**, 258 (1961).
10. D. Turnbull, *J. Appl. Phys.*, **20**, 817 (1950).

Thermodynamic Properties of VC at High Temperatures

S. Fujishiro

Fuji Iron and Steel Company, Tokyo, Japan

and N. A. Gokcen

Aerospace Corporation, El Segundo, California

ABSTRACT

Equilibrium pressure P_V of V(g) over VC(c) + C(graph.) has been determined in the range of 2346°-2545°K by means of graphite Knudsen cells. The results may be expressed by $\log P_V \text{ (atm)} = \frac{-30{,}700}{T} + 7.63$ in the range of 2400° ± 200°K. Further, $\Delta H°_{298.15} = 145.4 \pm 3$ kcal for VC(c) = V(g) + C(graph.) and $\Delta H°f_{298.15}$ (VC) = −22.7 ± 5 kcal for the standard heat of formation of VC, have been obtained by combining the data with appropriate free energy functions and the heat of sublimation of pure vanadium.

The transition metal carbides of Group IVB, VB, and VIB in the periodic chart have such useful properties as high melting points, great hardness, and chemical stability. Published data on their thermodynamic properties, however, are inadequate as shown in a number of systematic reviews (1-4). The heat of formation of VC(c) has been estimated (3, 4), but not determined experimentally, and its heat capacity has been determined by Shomate and Kelley (5) from 52° to 297°K and by King (6) from 298° to 1611°K. The results, together with the related thermodynamic properties are summarized by Kelley (7, 8). Slade and Higson (9) investigated the equilibrium in VO(c) + VC(c) = 2V(c) + CO(g) by measuring the pressure of CO at a single temperature, but in view of the fact that the stoichiometry of condensed phases is questionable (10, 11), their data cannot be used for reliable thermodynamic calculations.

The purpose of this investigation was to measure the equilibrium pressure of gaseous vanadium over VC(c) by using graphite Knudsen cells, *i.e.*, to investigate equilibrium in the following reaction

$$\text{VC(c)} = \text{C (graph.)} + \text{V(g)} \qquad [1]$$

From the equilibrium constant $K = P_V$ for this reaction, the related thermodynamic properties of VC(c) have been obtained.

Experimental Method

The experimental method has been described elsewhere in detail (12-14); a brief description here is therefore adequate. The apparatus is shown in Fig. 1. A transparent quartz tube A contains a graphite

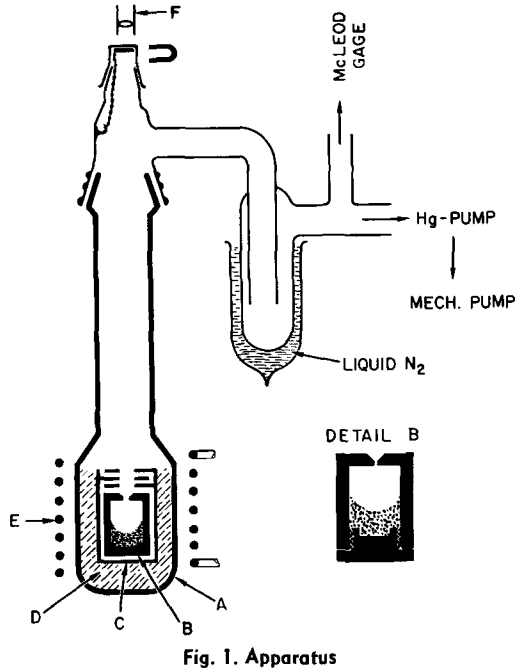

Fig. 1. Apparatus

Knudsen cell B, 25 mm diameter, 40 mm high. The densest, commercially available graphite was used in making the cell in order to minimize the amount of metal diffused through the pores. The cell orifice was drilled and its area was determined with a microscope. A graphite susceptor C with baffles is packed into A with −35+48 mesh insulating graphite powder D. The susceptor was heated by an induction coil E connected to a 20-kc mercury-gap type converter. Temperature measurements were made with a disappearing-filament optical pyrometer F sighted through a window protected with a magnetically closed shutter. The transmissivity corrections for the glass window were made under the prevailing experimental conditions. The accuracy of temperature measurements was better than ± 10°C. The system was kept under a vacuum of better than 5×10^{-6} mm Hg.

Vanadium carbide was prepared by heating the metal of 99.9% purity, from Electro Metallurgical Company, in a graphite crucible and maintaining it at 2400°C for about 10 hr. The combined carbon content of the resulting carbide was 18.89%, free carbon 0.1%, and Fe 0.04%. The lattice parameter of the carbide was found to be 4.160 ± 0.002Å.

Powdered VC was placed in the cell and the bottom plug was screwed on tightly. The cell was placed in the apparatus, degassed for 3-4 hr at 2200°C, and then cooled prior to breaking the vacuum by admitting pure argon. The cell was removed, weighed accurately, and again placed in the apparatus. The cell was quickly heated to the desired temperature and maintained there within ± 5°C for a period of 6-10 hr. The weight loss during this period was determined by reweighing after the termination of experiment. The result represents the weight loss (i) through the orifice and (ii) by vaporization of graphite and diffusion of V through the pores in the cell. The latter loss was determined by making a run by using a cell without orifice and containing VC. Subtraction of weight loss (ii) from (i) yields the loss m due to the effusion of V(g) through the orifice. Substitution of m in the following equation yields the vapor pressure P'_v of V(g) over VC(c) and C(graph.)

$$P' = \frac{m}{W_o a t}\left(\frac{2\pi RT}{M}\right)^{1/2} \qquad [2]$$

Where P' is in dynes per cm², W_o the clausing factor (15) defined by $1/W_o = 1 + 0.5\ h/r$, h and r being the thickness and the radius of orifice, respectively; T is in °K, a the orifice area in cm², t time in seconds, and M the molecular weight of V(g). Experimental runs with empty cells (without a carbide) reported earlier by the authors (12) show that vanadium diffuses out of the cell wall and that a considerably large fraction of weight loss is due to the vaporization of graphite, but this is not essential in the calculation of vapor pressure.

The absence of a gaseous carbide of vanadium, simultaneously effusing with V(g), was ascertained as follows: 155.3 mg of VC, containing 126.0 mg V, was placed in a cell with a large orifice and held at 2400°K for 16 hr. The total loss of weight minus that of graphite was found to be 59.2 mg. The weight of vanadium which remained in the cell was 66.1 mg as determined by chemical analysis of the crushed cell. The total amount of V accounted for in this manner was therefore 125.3 mg of initial V, showing conclusively that the carbide species in the gas phase were absent.

Results

Experimental results are listed in Tables I and II. Table I shows the loss of weight for cells without orifice, from which the loss for temperatures in Table II have been computed by interpolation or short extrapolation. The loss of weight through the orifice was obtained by subtracting this from the total weight loss in the fourth column of Table II.

The effect of orifice area on the observed vapor pressure was investigated by varying a in Eq. [2] from 0.0075 to 0.0212 cm² at two temperatures (Cf. runs 32, 24, 40, 21, 23, 41). The observed preessure, P_{obs} varies with a according to the following equation derived by Motzfeldt (16)

$$\frac{1}{P_{obs}} = \frac{1}{P_{eq}} + \frac{W_o a}{\alpha A P_{eq}} \qquad [3]$$

In this equation P_{eq} is the equilibrium pressure, α the accommodation coefficient; A the surface area of VC,

Table I. Results for cells without orifice and containing VC

Run No.	Temp, °K	Time, hr	Wt loss, mg/hr
26	2429	7.00	1.41
27	2461	10.00	2.45
28	2497	10.00	3.51
29	2408	10.00	0.96
30	2534	7.00	3.40
31	2377	10.00	0.24

Table II. Results for cells with orifice and containing VC

Run No.	Temp, °K	Time, sec	Total wt loss, mg	Wt loss from orifice, mg	P (atm) × 10^5
Orifice area a = 0.0071 cm², W_o = 0.75					
8	2482	16200	23.4	9.81	1.79
9	2534	10800	26.1	11.53	3.19
10	2377	18000	4.3	3.10	0.50
11	2492	19800	31.9	13.20	1.97
12	2398	21600	8.1	4.26	0.57
13	2419	16200	10.1	5.06	0.91
14	2440	21600	21.7	11.50	1.56
15	2461	18700	24.3	11.56	1.82
16	2398	14400	5.8	3.24	0.65
17	2503	18000	29.4	10.75	1.77
18	2524	14400	30.6	12.64	2.62
19	2545	9000	21.8	8.80	2.93
20	2408	19800	9.9	4.62	0.68
21	2513	14400	27.3	10.82	2.24
22	2346	28800	5.2	3.60	0.36
32	2429	32400	25.3	12.61	1.14
33	2450	28800	29.7	13.70	1.30
Orifice area a = 0.0147 cm², W_o = 0.75					
23	2513	14400	38.0	21.52	2.15
24	2429	28800	33.3	22.02	1.08
Orifice area a = 0.0212 cm², W_o = 0.75					
40	2429	28800	42.10	30.81	1.05
41	2513	28800	93.60	60.65	2.10

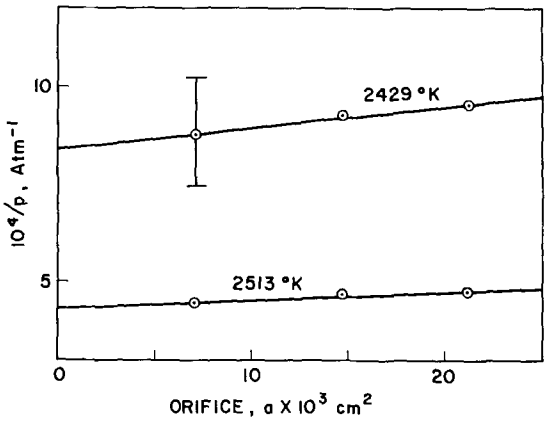

Fig. 2. Effect of orifice size on observed pressure of V(g). Limits shown by ⊖ is obtained from Standard Deviation in $\Delta H°$ for reaction [1].

W_0 and a are the same quantities as before. When the orifice area is plotted *vs.* $1/P_{obs}$ as in Fig. 2, extrapolation to $a = 0$ yields $1/P_{eq}$. The slope is very small and well within experimental errors showing that virtual equilibrium prevailed in all the cells.

Thermodynamic calculations are summarized in Table III. The third column is calculated from P_v in Table II substituted in $\Delta F° = -RT \ln P_v$. The fourth column is obtained by the interpolation of the change in free energy function for reaction [1], $-\Delta[(F° - H°_{298.15})/T]$, whose values are 37.013, 36.931, 36.843, and 36.762 at 2300°, 2400°, 2500°, and 2600°K, respectively. These values are obtained by using $-(F° - H°_{298.15})/T$ for graphite from JANAF Interim Thermochemical Tables (17), for V(g) from Stull and Sinke (18), and for VC(c) computed from

$$\frac{F° - H°_{298.15}}{T} = \frac{H° - H°_{298.15}}{T} - S°_{298.15} - \int_{298.15}^{T} \frac{C_p}{T}\,dT$$

by using $S°_{298.15}$ from Kelley (19) and his recommended equations (20) for $H° - H°_{298.15}$ and C_p and representing King's data (21) within 0.4% in the range of 300-1700°K. The results in the third column are related to those in the fourth by the identity

$$\Delta\left(\frac{F° - H°_{298.15}}{T}\right) \equiv \frac{\Delta F°}{T} - \frac{\Delta H°_{298.15}}{T}$$

from which the last column, the heat of reaction at 25°C, is calculated. The average value of $\Delta H°_{298}$ for reaction [1] is therefore 145,442 cal with a standard deviation of 778 and a maximum deviation of 1746 cal. The probable error in $\Delta H°_{298.15}$ is obtained in the following manner. An unlikely error of 10% in weighing, *i.e.*, nearly 1 mg in most cases, would cause an error of ± 0.5 kcal in $\Delta H°_{298.15}$, but an error of ± 10°K in temperature measurements would cause about ± 2.1 kcal of error. Assuming that the free energy functions contribute an additional error of ± 0.4 kcal, leads to $\Delta H°_{298.15} = 145.4 \pm 3.0$ kcal for reaction [1] or $\Delta H°_0 = 145.0 \pm 3.0$ kcal. Combination of $\Delta H_{298.15}$ with $\Delta H°_{298.15} = 122.72$ cal for the heat of sublimation of pure vanadium, obtained by Edwards, Johnston, and Blackburn (22) yields $\Delta Hf°_{298.15} = -22.7 \pm 5.0$ kcal for the standard heat of formation of vanadium carbide, or $\Delta H°_0 = -22.5 \pm 5.0$ kcal. This value is obtained by subtracting two large values and may be subject to larger unexpected cumulative errors than that indicated arbitrarily as 5 kcal; hence, additional data on $\Delta H°f_{298.15}$ by other methods would be desirable. It may be noted, however, that this is the only value for the heat of formation of VC which is based on experimental data. Estimates from the periodic law correlating $\Delta H°F_{298.15}$ with the atomic numbers of metals agree well with the foregoing result. Thus, if it is assumed that $\Delta H°_{f298.15}$ for TiO_2, VO_2, and CrO_2 follows the same pattern as TiC, VC, and CrC, $\Delta H°_{f298.15}$ for VC is found to be −23.6 kcal, whereas, if the values of $\Delta H°_{f298.15}$ for TiN and VN are assumed to be related to each other in the same way as those for TiC and VC, $\Delta H°f$ for VC becomes −22.2 kcal in agreement with the authors' result. Other such estimates are 15 kcal (4) and 20 kcal (3).

Table III. Thermodynamic calculations

Run No.	T, °K	$\frac{\Delta F_T°*}{T}$	$\Delta fef_{298.15}$†	$\Delta H°_{298.15}$
8	2482	21.725	−36.859	145,405 cal.
9	2534	20.576	−36.815	145,429
10	2377	24.265	−36.950	145,508
11	2492	21.528	−36.850	145,478
12	2398	23.987	−36.933	145,870
13	2419	23.065	−36.914	145,089
14	2440	21.996	−36.896	143,696
15	2461	21.691	−36.877	144,136
16	2398	23.724	−36.933	145,455
17	2503	21.742	−36.841	146,633
18	2524	20.969	−36.824	145,870
19	2545	20.746	−36.807	146,472
20	2408	23.648	−36.924	145,857
21	2513	21.282	−36.832	146,405
22	2346	24.916	−36.975	145,196
23	2513	21.362	−36.832	146,242
24	2429	22.727	−36.905	144,846
32	2429	22.623	−36.905	144,594
33	2450	22.216	−36.887	144,802
40	2429	22.787	−36.887	144,948
41	2513	21.407	−36.832	146,355
			Average:	145,442
			Standard dev:	778

* Computed from the last column in Table II.
† Δfef: change in free energy function.

The experimental data may be represented by

$$\log P_v\,(\text{atm}) = -\frac{30{,}700}{T} + 7.63$$

in the range of 2400° ± 200°K where it is assumed that $\Delta H°$ and $\Delta S°$ are independent of temperature and equal to $\Delta H°_{2400}$ and $\Delta S°_{2400}$.

Acknowledgments

This paper is based on a thesis submitted by Shiro Fujishiro to the Faculty of Sciences of Kyoto University in partial fulfillment of the requirements for the degree of Doctor of Philosophy. The experimental work was completed at the University of Pennsylvania in Philadelphia under the auspices of the U. S. Atomic Energy Commission, Contract AT (30-1) 1976. The manuscript was prepared at Aerospace Corporation, El Segundo, Calif. where the calculations were checked by Eileen A. Mathias.

Manuscript received Jan. 15, 1962. This paper was prepared for delivery before the Los Angeles Meeting, May 6-10, 1962.

Any discussion of this paper will appear in a Discussion Section to be published in the June 1963 JOURNAL.

REFERENCES

1. L. Brewer, L. A. Bromley, P. W. Gilles, and N. L. Lofgren, "Thermodynamic and Physical Properties of Nitrides, Carbides, Sulfides, Silicides and Phosphides" in "Chemistry and Metallurgy of Miscellaneous Materials," L. L. Quill, Editor, McGraw-Hill Book Co., Inc., New York, (1950).
2. L. Brewer and A. W. Searcy, *Ann. Rev. Phys. Chem.*, **7**, 259 (1956).
3. J. F. Elliott and M. Gleiser, "Thermochemistry for Steelmaking," Vol. 1, Addison Wesley Publishing Co., Inc., Boston, Mass. (1960).
4. O. H. Krikorian, Univ. of California Radiation Lab. No. 2888 (1955).
5. C. H. Shomate and K. K. Kelley, *J. Am. Chem. Soc.*, **71**, 314 (1949).
6. E. G. King, *ibid.*, p. 316.
7. K. K. Kelley "Contributions to the Data on Theoretical Metallurgy" U. S. Bureau of Mines Bull. 584 (1960).
8. K. K. Kelley, *ibid.*, Bull. 592 (1961).
9. R. E. Slade and G. I. Higson, *J. Chem. Soc.*, **115**, 205 (1919).
10. M. Hansen and K. Anderko "Constitution of Binary Alloys," McGraw-Hill Book Co., Inc., New York (1958).
11. H. Krainer and K. Konopicky, *Berg u hüttenmänn. Monatsh. Montan. Hochschule Leoben*, **92**, 166 (1947).
12. S. Fujishiro and N. A. Gokcen, *Trans. Am. Inst. Min. Met. Engrs.*, **221**, 275 (1961); see also S. Fujishiro and N. A. Gokcen, *J. Phys. Chem.*, **65**, 161 (1961).
13. M. Knudsen, "Kinetic Theory of Gases," Methuen, Ltd. (1934).
14. J. L. Margrave, chap. 10 in "Physico-chemical Measurements at High Temperatures," Edited by J. O. Bockris, J. L. White, and J. D. Mackenzie, Butterworth Scientific Publications (1959).
15. C. I. Whitman, *J. Chem. Phys.*, **20**, 161 (1952).
16. K. Motzfeldt, *J. Phys. Chem.*, **20**, 161 (1955).
17. "JANAF Interim Thermochemical Tables," The Dow Chemical Co., Midland, Mich. (1961).
18. D. R. Stull and G. C. Sinke, "Thermodynamic Properties of the Elements." Advances in Chem. Series No. 18, Am. Chem. Soc. Washington, D. C. (1956).
19. K. K. Kelley, U. S. Bureau of Mines, Bull., 592 U. S. Govt. Printing Office, Washington, D. C. (1961).
20. K. K. Kelley, *ibid.*, Bull. 584 (1960).
21. E. G. King, *J. Am. Chem. Soc.*, **71**, 316 (1949).
22. J. W. Edwards, H. L. Johnston, and P. E. Blackburn, *ibid.*, **73**, 4727 (1951).

Pressure-Temperature-Composition Relationships of the Yttrium-Hydrogen System

C. E. Lundin and J. P. Blackledge

Denver Research Institute, University of Denver, Denver, Colorado

ABSTRACT

Pressure-temperature-composition studies of the yttrium-hydrogen system were made in the temperature range 900°-1350°C and the pressure range 1-760 mm Hg. The existence of a yttrium-solid-solution phase and a yttrium-hydride phase, which approaches YH_2 in composition, was established. These phases occur over a range of composition and are separated by a two-phase region at intermediate hydrogen compositions. The calculated heat of reaction of the dihydride phase from the saturated solid solution is $\Delta H = -44.42 \pm 0.40$ kcal/mole H_2, and the entropy of reaction is $\Delta S = -27.07 \pm 0.30$ cal/mole $H_2 \cdot$ degree. Partial molal heats and entropies of solution of hydrogen in the single phases are also presented. The nature of the solubility relationships in the yttrium-hydrogen system below 900°C was studied at atmospheric pressure. The existence of a stable trihydride phase was established below approximately 300°C and 1 atm pressure. The solubility relationships of the yttrium-hydrogen system were developed from the pressure-temperature-composition relationships and from x-ray diffraction analysis and metallographic examination. X-ray diffraction structural analysis of yttrium metal, the dihydride and trihydride phases gave the following structures and x-ray densities:

Yttrium metal	YH_2	YH_3
Hexagonal close-packed	Face-centered cubic	Hexagonal
$a_o = 5.750 \pm 0.001$Å	$a_o = 5.201 \pm 0.001$Å	$a_o = 3.674 \pm 0.001$
$c_o = 3.654 \pm 0.001$Å	$\rho = 4.293$ g/cc	$c_o = 6.599 \pm 0.001$Å
$\rho = 4.440$ g/cc		$\rho = 3.958$ g/cc

Yttrium metal is a transition metal in subgroup III-A included with scandium, lanthanum, the lanthanides, and actinium. Because of similar properties and occurrence in nature, yttrium is generally associated with the rare-earth metals. In general, the metals in this subgroup as well as some actinide metals for which hydriding data are available (1-5) form both di- and tri-hydride compositions. Therefore, one would surmise that yttrium forms a similar type of hydride system. Being practically nonexistent in form and purity until recently, very little was known of the various properties of yttrium metal. Therefore, the literature does not provide any information concerning the hydriding characteristics of yttrium metal. The objective of the research program described in this paper is to determine fully the high-temperature phase equilibria presented by the yttrium-hydro-

gen system and to establish some of the associated thermodynamic data of solutions of hydrogen in yttrium.

Experimental Procedure

The apparatus used for the hydriding work is a modified Sieverts' apparatus. Essentially it consists of a source of pure hydrogen, a precision gas-measuring buret, a heated reaction unit, and a mercury manometer for pressure measurement. Pure hydrogen is obtained from the thermal decomposition of uranium hydride. A 100-ml precision gas buret graduated to 0.1 ml divisions is used to measure and admit to the reaction chamber the quantity of hydrogen gas desired to react with the metal sample. The reaction unit consists of a Globar tube furnace surrounding two concentric mullite reaction tubes. The Globar furnace is controlled with a L&N Speedomax G temperature recorder-controller in conjunction with a Claud S. Gordon X-actline. The sample temperature is measured independently with a L&N precision potentiometer and a Pt/Pt-Rh (13%) thermocouple. The temperature was controlled within ± 2°C. The inner reaction chamber contains the specimen to be reacted. The outer chamber is isolated from the inner chamber, but maintained at the same partial pressure of hydrogen to prevent hydrogen loss or air contamination due to permeation through the mullite. A mercury manometer is used to measure the partial pressure of gas in equilibrium with the specimen. Pressures were measured to approximately ± 0.5 mm Hg.

The technique used to study the equilibrium pressure-temperature-composition relationships of the yttrium-hydrogen system was to develop experimentally a family of isothermal curves of composition *vs.* pressure. The range of pressure through which each isotherm was developed was from 1 mm to atmospheric pressure. Isotherms were established at each 50°C interval in the temperature range from 900° to 1350°C.

The yttrium specimens used were from ½ to 1g in weight, cut into rectangular shapes from arc-melted buttons. Analysis of impurities of the yttrium metal showed that zirconium and oxygen were the principal impurities at 0.57% and 0.32%, respectively. The surface of each specimen was prepared by filing with a clean, mill file. The chamber was flushed with hydrogen and evacuated several times prior to each run. The temperature of the initially evacuated chamber was then attained and held constant. Measured quantities of hydrogen gas were repetitively admitted to the chamber. After each admission, time was allowed for equilibrium. Equilibrium was considered complete after the pressure became constant. Calculation of the quantity of gas absorbed in the metal after each admission of gas was done by knowing the system volume which determined the amount of hydrogen in the gas phase. Subtracting this quantity from the total gas admitted gave the quantity of gas in the metal. The individual equilibrium pressures were recorded *vs.* the calculated amount of gas absorbed for each respective pressure. The isotherm was traced until atmospheric pressure was reached. A total of 244 data points was obtained using this procedure.

Additional data on the yttrium-hydrogen system were obtained below 900° down to 100°C. However, these data were not obtained as isotherms of equilibrium partial pressures *vs.* composition. The equilibrium partial pressures below 900°C for compositions less than the ultimate hydrides were less than 1 mm of Hg; therefore measurements could not be made with the manometer (the YH_2-YH_3 region being excepted). The data were obtained in the form of the ultimate equilibrium compositions attained at atmospheric pressure of hydrogen at each of the desired temperature levels: 800°, 700°, 600°. 500°. 400°, 300°, and 200°C.

The x-ray diffraction data were obtained with a Norelco unit in conjunction with a wide-angle diffractometer. All samples for x-ray analysis were prepared in the modified Sieverts' apparatus, allowing the specimen to absorb the quantity of gas required to bring it to the required composition. Samples immediately below YH_2 in composition were easily crushed without causing cold work. Samples between YH_2 and YH_3 were powder as hydrided, and needed no further preparation. The samples in the yttrium-rich region were not amenable to crushing. Therefore, massive fine-grained samples of yttrium metal were used for hydriding to the required composition prior to x-ray diffraction analysis.

Representative structures of metal-gas samples were examined metallographically to verify the solubility relationships determined from the isotherms. Standard metallographic techniques were used with one exception. Cold-mounting plastic was used to mount the specimens to prevent loss of hydrogen. The etchant used was 42 ml H_3PO_4, 47 ml glycerine, and 11 ml 2-ethoxyethanol.

Results and Discussion

The hydriding characteristics of yttrium are similar to the heavy rare earths. In general, a dihydride and trihydride phase are formed, the trihydride phase being stable only at lower temperatures. The dihydride structure is face-centered cubic, and the trihydride is hexagonal close-packed, exhibiting

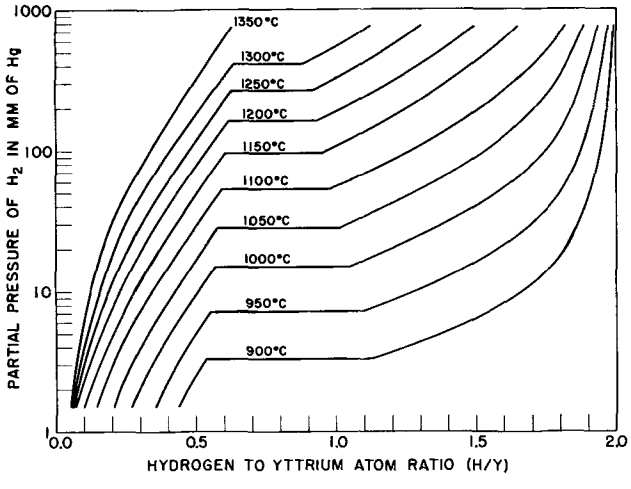

Fig. 1. Isothermal curves of equilibrium partial pressure vs. composition for the yttrium-hydrogen system.

isomorphism with the comparable structures in the heavy rare-earth series.

The region of temperatures from 900° to 1350°C in the yttrium-hydrogen system was of primary concern in this study. To determine the thermal-stability characteristics in this temperature region and at partial pressures up to 1 atm of hydrogen, the pressure-temperature-composition relationships were determined. The data were developed as a series of isotherms at 50°C intervals. The family of isotherms is presented in Fig. 1.

By applying phase rule theory to the series of curves, three distinct regions of partial pressure and hydrogen composition delineate the solubility relationships in the complete range of hydrided yttrium. In the first region, as hydrogen is added to the unreacted metal, the partial pressure and composition both increase up to a certain value. The extent of this rise indicates the limit of solid solubility of interstitial hydrogen in yttrium. Thus, a single homogeneous phase exists in conformity with the phase rule which predicts that only one phase can exist for bivariant conditions.

In the dilute region of hydrogen composition of the yttrium solid solution, a log-log plot of each isotherm yielded straight lines with a slope of essentially 2. This value indicates that Sievert's law is followed, which states that the solubility of hydrogen in yttrium is proportional to the square root of molecular hydrogen pressure. The isotherm slopes were constant up to 0.3 H/Y atom ratio at which point they began to deviate upward.

The second region consists of a series of plateaus of equilibrium partial pressure. Here, the system is reduced to a univariant system with pressure constant. Thus, a two-phase field exists where increasing amounts of the second phase form as the hydrogen content increases.

The third region is similar to the first wherein the pressure and composition rise rather rapidly from each plateau. This end of the plateau represents the metal rich solubility limit for the second phase. Again, bivariant conditions predict a single, homogeneous phase region which exists over a range of composition. In this case the phase is the hydride phase. In the higher temperature regions this phase is comprised of a hydrogen-deficient YH_2 lattice. The ultimate composition approached at 1 atm pressure as the temperature decreases toward 900°C is approximately the stoichiometric ratio, YH_2.

Table I. Solubility boundaries for yttrium solid solution and the yttrium-hydride phase

Isotherm temp, °C	Solubility of H_2 in Y (H/Y)	Solubility of Y in YH_{2-x} (H/Y)
1300	0.63	0.91
1250	0.62	0.93
1200	0.61	0.96
1150	0.60	0.97
1100	0.59	0.98
1050	0.58	1.00
1000	0.57	1.03
950	0.56	1.07
900	0.55	1.09

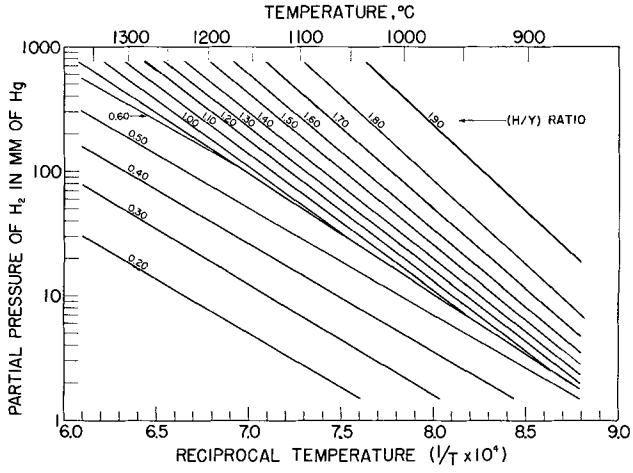

Fig. 2. Family of isopleths of the yttrium-hydrogen system as a function of equilibrium partial pressure and reciprocal temperature.

Table I presents the composition of the solubility boundaries *vs.* temperature between the two single phases and the two-phase region separating them.

From the experimental data, another plot of the logarithm of equilibrium partial pressure *vs.* reciprocal temperature was prepared for a family of isopleths (constant composition). The points of each isopleth fell on a straight line as expressed by the equation,

$$\log_{10} p \text{ (mm Hg)} = -A/T + B$$

Figure 2 presents the family of isopleths. The compositions are presented as the hydrogen-to-yttrium atom ratio, varying in 0.10 increments. The single-phase yttrium solid solution is represented by the isopleths from 0.20 to about 0.60 H/Y atom ratio. The partial pressure plateaus are represented by a series of isopleths which superimpose on one another as one line in the plane of the page wherein the composition ranges from about 0.60 to 1.00 H/Y atom ratio. The hydride phase is represented by the isopleths from about 1.00 to 1.90 H/Y atom ratio. The constants A and B for each isopleth composition level were determined by a least-squares treatment of the data. The standard deviations were also calculated. Table II presents the equilibrium dissociation pres-

Table II. Equilibrium dissociation pressure equations for the yttrium-hydrogen system*

Atomic ratio (H/Y)	Constants in $\log_{10} p = -A/T + B$	
	A	B
0.20	8,285 ± 240	6.50 ± 0.17
0.30	8,676 ± 150	7.10 ± 0.10
0.40	8,684 ± 139	7.50 ± 0.10
0.50	8,615 ± 134	7.74 ± 0.10
0.60	8,250 ± 122	7.77 ± 0.08
0.70-0.90	9,709 ± 43	8.80 ± 0.03
1.00	10,690 ± 100	9.53 ± 0.07
1.10	10,870 ± 78	9.76 ± 0.06
1.20	11,190 ± 104	10.09 ± 0.07
1.30	11,450 ± 96	10.39 ± 0.07
1.40	11,710 ± 139	10.69 ± 0.10
1.50	12,050 ± 122	11.07 ± 0.09
1.60	12,460 ± 161	11.53 ± 0.10
1.70	12,600 ± 113	11.79 ± 0.09
1.80	12,910 ± 296	12.28 ± 0.23
1.90	14,190 ± 122	13.78 ± 0.10

* In the temperature range 900°-1350°C.

Table III. Thermodynamic data for a series of yttrium-hydrogen compositions*

Composition (H/Y)	$-\Delta\bar{H}$, kcal/mole H_2	$-\Delta\bar{S}$, cal/mole H_2·degree
0.20	37.90 ± 1.11	16.56 ± 0.75
0.30	39.69 ± 0.70	19.64 ± 0.46
0.40	39.73 ± 0.64	21.15 ± 0.46
0.50	39.41 ± 0.62	22.24 ± 0.44
0.60	37.74 ± 0.56	22.38 ± 0.38
0.70-0.90	44.42 ± 0.40	27.07 ± 0.30
1.00	48.91 ± 0.46	30.42 ± 0.32
1.10	49.74 ± 0.36	31.46 ± 0.26
1.20	51.21 ± 0.48	32.99 ± 0.34
1.30	52.38 ± 0.44	34.34 ± 0.32
1.40	53.56 ± 0.64	35.71 ± 0.48
1.50	55.13 ± 0.56	36.46 ± 0.42
1.60	57.01 ± 0.74	39.58 ± 0.58
1.70	57.63 ± 0.52	40.77 ± 0.40
1.80	59.08 ± 1.35	42.98 ± 1.05
1.90	64.94 ± 0.46	49.87 ± 0.46

* In the temperature range 900°-1350°C.

sure equations for the yttrium-hydrogen system. From these equations the partial molal entropies can be calculated for each of the isopleths in either single-phase region by employing the Gibbs-Helmholtz and van't Hoff equations. These thermodynamic data are presented in Table III. The values at the plateau of equilibrium partial pressure may be considered the heat of reaction, −44.42 ± 0.40 kcal/mole H_2, and the entropy of reaction, −27.07 ± 0.30 cal/mole H_2 · degree, of the hydride phase from the saturated yttrium solid solution.

Inasmuch as the high-temperature studies indicated the existence of only a dihydride phase, it was felt necessary to survey the low-temperature region for a possible trihydride phase. The approach to the study in the lower temperature region was different from that of the high-temperature region. The study was conducted at atmospheric pressure of hydrogen. Specimens were hydrided to their limiting equilibrium compositions. The formation of the trihydride phase was found to occur between room temperature and slightly above 300°C. When the trihydride is formed from the massive dihydride, the specimen is reduced to a very fine powder. The rate of formation and decomposition of trihydride as the temperature is cycled above and below the critical temperature is rapid.

The range of solubility of the individual dihydride and trihydride phases near room temperature appears to be rather restricted. X-ray diffraction analysis of structures immediately below and above the YH_2 composition were made. Single-phase structures were seen at $YH_{1.95}$ and $YH_{2.00}$. Two-phase structures were seen at $YH_{1.90}$ and $YH_{2.10}$. A two-phase structure was seen at $YH_{2.80}$ with strong lines of YH_2 phase still evident. A single-phase structure was obtained at $YH_{3.00}$.

X-ray diffraction analysis of the line patterns of the yttrium metal, the YH_2 phase, the YH_3 phase, and specimens with intervening compositions confirm the solubility relationships deduced from the thermodynamic data. The x-ray diffraction data are summarized in Table IV.

Table IV. Summary of x-ray diffraction data

Sample	Structure	Lattice parameters	X-ray density, g/cc
Y	Hexagonal-close packed	$a_o = 3.654$Å $c_o = 5.7501$Å	4.440
$YH_{0.63}$	HCP + FCC		
$YH_{1.80}$	HCP + FCC		
$YH_{1.90}$	HCP + FCC		
$YH_{1.95}$	FCC		
$YH_{2.00}$	Face-centered cubic	$a_o = 5.201$Å	4.293
$YH_{2.10}$	FCC + H		
$YH_{2.20}$	FCC + H		
$YH_{2.40}$	FCC + H		
$YH_{2.60}$	FCC + H		
$YH_{2.80}$	FCC + H		
$YH_{3.00}$	Hexagonal	$a_o = 3.674$Å $c_o = 6.599$Å	3.958

Metallographic examinations of structures of representative compositions were made in the yttrium-hydrogen system except in the case of compositions above YH_2, where the material became powdered.

The structures of these samples confirmed the solubility relationships as deduced from the pressure-temperature-composition relationships.

Summary

The yttrium-hydrogen system was studied by determining the pressure-temperature-composition relationships and the resulting solubility relationships. In the high-temperature region of the system, a series of isothermal curves were developed at 50°C intervals between 900° and 1350°C. The ultimate dihydride, YH_2, was approached in composition as the temperature of hydriding decreased toward 900°C.

Thermodynamic data concerning the two single-phase regions and the two-phase region were calculated from the experimental data. In the low-temperature region of the system, the dihydride was stable down to approximately 300°C and 1 atm pressure. At approximately 300°C and below, a stable trihydride phase was found to exist at 1 atm of hydrogen pressure. Metallographic and x-ray diffraction analysis data are also presented to confirm the existence of the solubility relationships as deduced from the thermodynamic data. The x-ray diffraction data of the single phase structures are presented below:

Yttrium metal	YH_2	YH_3
Hexagonal close-packed	Face-centered cubic	Hexagonal
$a_o = 5.750$Å	$a_o = 5.201$Å	$a_o = 3.674$Å
$c_o = 3.654$Å	$\rho = 4.293$ g/cc	$c_o = 6.599$Å
$\rho = 4.440$ g/cc		$\rho = 3.958$ g/cc

Acknowledgment

The authors are grateful to the management of the General Electric Company, Aircraft Nuclear Propulsion Division for granting permission to publish this paper. The authors also wish to thank Dr. V. Calkins, J. McGurty, and E. Funston for their assistance and support in carrying through the research work. The work was conducted under Subcontract

AT-33. Special thanks are due to C. R. Hoggatt for the Sievert's work, R. A. McCune for the x-ray data, R. L. Clark and R. J. McManis for the metallographic work, and to D. Sutton for the arc-melting of the alloys.

Manuscript received Nov. 29, 1961.

Any discussion of this paper will appear in a Discussion Section to be published in the June 1963 JOURNAL.

REFERENCES

1. R. N. R. Mulford and C. E. Holley, Jr., *J. Phys. Chem.*, **59**, 1222 (1955).
2. C. E. Holley, Jr., R. N. R. Mulford, F. H. Ellinger, W. C. Koehler, and W. H. Zachariasen, *ibid.*, **59**, 1226 (1955).
3. G. E. Sturdy and R. N. R. Mulford, *J. Am. Chem. Soc.*, **78**, 1083 (1956).
4. R. N. R. Mulford, AECU-3813.
5. W. L. Korst and J. C. Warf, *Acta Cryst.*, **9**, 452 (1956).

Mercuric Halides as Molten Electrolytes: Physical Properties, Vibrational Spectra, Constitution, and Electrical Conductance

George J. Janz and James D. E. McIntyre

Department of Chemistry, Rensselaer Polytechnic Institute, Troy, New York

ABSTRACT

Densities, viscosities, electrical conductances, and Raman spectra for the mercuric halides, $HgCl_2$, $HgBr_2$, and HgI_2, are reported from the melting points to the boiling points. In contrast to ionic fused salts, the energies of activation for electrical conductance are greater than those for viscous flow. Evidence for autocomplex formation is discussed. A model for these molten electrolytes is advanced in which the primary constituents are simple molecules together with the complex ionic species HgX^+ and HgX_3^-. The entropy of fusion is shown to arise, in large part, from an increase of rotational freedom rather than positional randomization, and the cohesive intermolecular forces are of the dispersion and multipole type rather than coulombic as in highly ionic melts. The mechanisms of transport processes for the solid and liquid states of these salts are discussed in the light of concepts current for molten electrolytes.

Current surveys (1-3) show that, whereas very accurate values for the physicochemical properties and electrical conductances are known for the halides of the Group I and Group IIA elements, very little information has been reported for the Group IIB metal halides. The problems of the structure of the molten mercuric halides have been discussed elsewhere (4) in detail. More recently the electrical conductances have been reported with a limited interpretation of the constitution of this class of molten salts (5). The present communication reports the results of investigations on the densities, viscosities, electrical conductances, and Raman spectra for the mercuric halides in the molten state. This broad cross section of properties is discussed to develop the structure and interactions in this class of molten salts.

Experimental

The three mercuric halides, $HgCl_2$ (mp. 277°C), $HgBr_2$ (mp. 238°C), and HgI_2 (mp. 259°C), reagent grade chemicals, were dried under vacuum at 120° and twice sublimed through a Pyrex fritted disk under reduced pressure, using dry argon as a carrier gas, prior to use. Because of the relatively low melting points and relatively small liquid state range (27°, 81°, and 95°C, respectively, for the chloride, bromide, and iodide) the complete range from the melting point to the boiling point could be investigated, and the design of the various apparati was simplified since Pyrex glass could be used throughout. However the high sublimation and vapor pressures dictated the use of experimental assemblies for electrical conductance, density, and viscosity, hermetically sealed under vacuum. The furnace had viewing ports for observation of the melts during measurements; at 300°C a 12 in. flat hot zone (± 0.15°) was gained using a bank of auxiliary shunts and resistors in the heating circuit. Temperatures were monitored with a calibrated Pt-Pt, 10% Rh thermocouple and an electronic recording differential potentiometric circuit (6). There follows a brief description of the salient features of the apparatus and techniques used for the property measurements on these highly volatile salts in the molten state.

Density.—The design of the dilatometer and loading tube assembly is shown in Fig. 1(a); the volumes of the dilatometer were calibrated with mercury at room temperature. Measuring pipettes (0.2 ml capacity) having a 1.6 mm capillary bore were used for the stems; the bulbs were of 3 ml capacity. A suitable quantity of the mercuric halide was weighed into the loading tube containing a fritted disk. This tube was then closed at the top, A, with a torch and sealed to the dilatometer, taking care to avoid moisture condensation at all steps. Residual traces of water vapor were removed by vacuum pumping before the assembly was hermetically sealed at B under vacuum. The unit was heated in an auxiliary furnace until the salt was molten. The vapor pressure of the salt in A served to force the melt through the Pyrex filter disk to

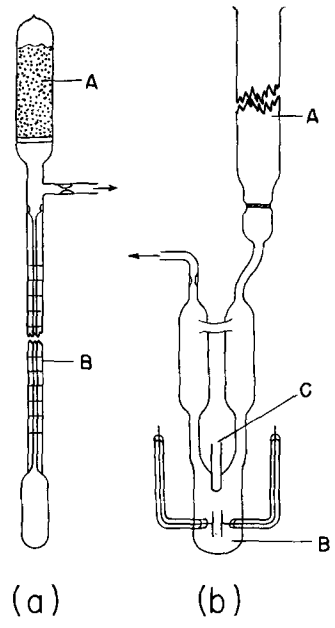

Fig. 1. Details of dilatometer and conductance cell and loading tubes for volatile molten salts. (a) Dilatometer assembly; A, sealed loading tube with salt over fritted disk; B, graduated stem (total vol. 3 ml); (b) conductance cell assembly; A, loading tube and fritted disk; B, platinum disk electrodes below reservoir compartments; C, thermocouple well.

fill the dilatometer; the loading tube was removed after this operation by sealing at C. The dilatometer bulb was seated in a metal block and placed in the furnace with the stem carefully aligned vertically. The menisci were observed through the furnace ports with a cathetometer. On completion of the measurements, the weight of the salt in the dilatometer was determined by direct weighing.

Conductance.—The design of the conductance cell used for molten $HgCl_2$ and $HgBr_2$ is illustrated in Fig. 1(b), the platinum electrodes (1.5 cm diameter) being spaced to give a cell constant of 0.17 cm^{-1}. For the more highly conducting iodide, the cell constant was increased to 17.6 cm^{-1} by use of a U-tube to increase the electrode separation. The procedure for cell filling was similar to that just described for the density measurements. The reservoir chambers provided for thermal expansion of the melt, and after an experiment the cell was inverted to transfer the molten salts from the electrode chamber to the reservoirs before solidification. A high precision conductance bridge of a new design (7) was used for these measurements, test frequencies of 1, 2, 5, and 20 kc being used to gain the value of the polarization-free values for the conductances by extrapolation to infinite frequency.

Measurements of the solid-state electrical conductance were made in a U-tube type cell using a vacuum-tube voltmeter with an 11-megohm impedance. The change of this property during the process of fusion was also studied in this manner.

Viscosity.—The oscillation method (8, 9) is readily adapted for very volatile liquids. For this purpose a Pyrex sphere, 4.6 cm diameter, having a 10-cm tubular stem, was filled with the appropriate mercuric halide using the same technique as for filling the dilatometers; the top of the stem was finally sealed under vacuum. The bulb was chuck-mounted on a stainless steel rod which extended from the furnace to take the inertia bar and the torsion head suspension. The viscosities were determined from the observed logarithmic decrement in the damping of the torsional oscillations of the Pyrex spheres filled with the molten halides. Angular deflections over a range of 0.27-0.068 radians were observed by a telescope-scale-mirror assembly, each determination involving 100 swings of 8-12 sec periods. Corrections for air-damping were made. Typical values for the logarithmic decrements are 0.00848 and 0.05275 for the air-damping and the total damping effects, respectively (HgI_2, 314°). Details for the calculation of absolute viscosities from such data may be found in the work of Andrade and Chiong (9). The absolute value for the internal radius of the sphere was determined by direct weighing with water. The experimental assembly and technique were evaluated using water as the fluid in the sphere at room temperature. The viscosity thus found deviated less than 3% from the accepted value.

Raman spectra.—The spectra for molten $HgCl_2$ and $HgBr_2$ were measured in the high-temperature cell assembly and excitation source for the Hilger Type E612 spectrometer in this laboratory and are described elsewhere in detail (10). The Hg 4358Å and 5461Å lines were used for excitation of the spectra for the colorless $HgCl_2$ and straw-colored $HgBr_2$ melts, respectively. The study of melts such as HgI_2 (red-black) awaits the development of Raman sources for the near infrared region.

Results

Density.—The densities for the three molten mercuric halides were calculated after making corrections for the thermal expansion of the dilatometers (*ca.* 0.026%) and air buoyancy, menisci shapes, and weight of salt vapor above the melt (negligibly small). The complete liquid-state ranges for the three halides ($HgCl_2$, 27°; $HgBr_2$, 81°; HgI_2, 95°C) were investigated in 20-30 uniformly spaced incremental steps. The average deviation from the best straight line of the empirical points was one part in four thousand. The least squares equations for the densities thus found are:

$HgCl_2$: $d_t = 5.1577 - 2.8624 \times 10^{-3}t$ (277°-304°C)

$HgBr_2$: $d_t = 5.8889 - 3.2331 \times 10^{-3}t$ (238°-319°C)

HgI_2: $d_t = 6.0603 - 3.2351 \times 10^{-3}t$ (259°-354°C)

The present values for $HgCl_2$ are 1%-1.5% higher than the values reported by Prideaux (11) in 1910, whereas the results for $HgBr_2$ and HgI_2 are in remarkably close agreement, the average deviation being less than 0.1%. The more recent data for HgI_2 reported by Polyakov (12) (by the Archimedean principle) appear about 1% too high by comparison. The precision attained in the present work is higher than in the studies of Prideaux (11) and Polyakov (12).

Electrical conductance.—The molar conductances for the three mercuric halides are summarized in

Table I. Molar electrical conductance of the molten mercuric halides

(a) $HgCl_2$ t, °C	$\mu \times 10^3$, ohm^{-1} cm^2 mole^{-1}	(c) HgI_2 t, °C	$\mu \times 10^3$, ohm^{-1} cm^2 mole^{-1}
281.3	4.268	260.4	2,638
289.5	4.490	260.7	2,633
295.8	4.679	273.3	2,476
301.9	4.839	282.5	2,394
		286.3	2,358
(b) $HgBr_2$		293.2	2,283
	$\mu \times 10^3$, ohm^{-1} cm^2	299.8	2,244
t, °C	mole^{-1}	303.0	2,207
240.2	10.00	310.3	2,159
247.1	10.86	318.2	2,096
255.0	11.90	320.3	2,078
257.8	12.20	329.0	2,042
259.6	12.41	334.5	1,970
265.1	13.23	343.8	1,896
276.7	14.91	351.1	1,843
289.8	16.83	364.2	1,747
305.3	19.14		
315.4	20.60		

Table I. The much higher conductivity and the negative temperature coefficient of conductance for HgI_2 are in marked contrast to $HgCl_2$ and $HgBr_2$. Comparison with the earlier and limited results by Jander and Broderson (13) and Belyaev and Mironov (14) shows that the earlier values are in good agreement for the bromide near the freezing point, but that the conductivities of the chloride are greater by a factor of 10. Recalculation of the values of electrical conductance for the three mercuric halides reported most recently by Bockris, Crook, Bloom, and Richards (5) to the present density results shows that these are in close agreement (better than 1%) for the bromide and iodide. The conductance values for the chloride thus found are about 10% lower than the results observed at present, most probably due to the use of a more refined sample (triply sublimed) by Bockris, Crook, Bloom, and Richards. The temperature dependence of the solid-state resistance in the process of melting is illustrated in Fig. 2, showing a characteris-

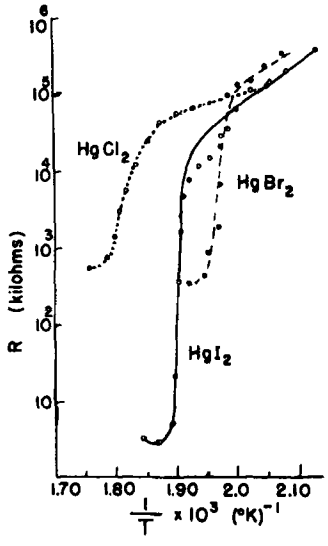

Fig. 2. Resistance change on fusion of the mercuric halides. O . . . O . . . , $HgCl_2$; —●— —●— $HgBr_2$; —●—●—, HgI_2.

Table II. (a) Activation energy for electrical conductance

kcal mole^{-1}	$HgCl_2$	$HgBr_2$		HgI_2
$\Delta E_{\kappa(solid)}$	13.0	22.5		25.7
$\Delta E_{\kappa(liquid)}$	6.15*	6.2	4.6	—3.00
$\Delta E_{\Lambda(liquid)}$	6.49*	6.5	4.9	—2.48

(b) Activation energy for viscosity and vaporization energy

kcal mole^{-1}	$HgCl_2$	$HgBr_2$	HgI_2
ΔE_η	3.4_5	3.5_5	4.5_8
$\Delta E_{vap(T_b)}$‡	12.9_4	12.7_8	13.0_2
$\Delta E_\eta / \Delta E_{vap}$	3.7_6	3.5_9	2.8_4

* Values calculated from conductance data for triply sublimed $HgCl_2$ (6) after correction to present density results.
‡ Values calculated from the latent heats of vaporization (15).

tically large increase in electrical conductance for the three mercuric halides at this point of phase change. The electrical conductances for the liquid state could be expressed by the Arrhenius-type exponential rate equation:

$$(\kappa, \Lambda) = A_{(\kappa, \Lambda)} e^{-\Delta E}(\kappa, \Lambda)/RT$$

within the precision of the results; for $HgBr_2$, ΔE showed a marked temperature dependence. The values thus found for the energies of activation are summarized in Table II(a); two values are listed for $HgBr_2$ at the lower and upper extremes for the liquid state of this salt. The unusual negative temperature coefficient of conductance for HgI_2 is reflected in the negative values for ΔE.

Viscosity.—In Table III are listed the viscosities for $HgCl_2$ and HgI_2 from this work and the results for $HgBr_2$ of Jander and Broderson (13) for consistency. The results fitted a simple Arrhenius-type rate expression well within the precision of the measurements. The activation energies thus found for viscous flow are given in Table II(b), together with the energies of vaporization which were calculated from the heat of vaporization data reported elsewhere (15).

Vibrational spectra.—The Raman shifts found in the present study were:

$HgCl_2$: 313 cm^{-1} (vs) ($\rho = 0.7$);
382 cm^{-1} (w) ($\rho = 0.6$)

$HgBr_2$: 206 cm^{-1} (vs) ; 271 cm^{-1} (w)

where the intensities are indicated as very strong (vs) and weak (w) and the depolarization ratio for the chloride (ρ) was also gained. Polarization

Table III. Viscosity of the molten mercuric halides

(a) $HgCl_2$ t, °C	η, poise	(b) $HgBr_2$ t, °C	η, poise	(c) HgI_2 t, °C	η, poise
280.8	0.01768	255	0.02155	268.4	0.02669
287.0	0.01738	265	0.02052	292.4	0.02244
292.1	0.01694	275	0.01913	314.0	0.01995
298.9	0.01600			334.2	0.01715
306.1	0.01543			358.1	0.01458

Table IV. Vibrational spectra and frequency assignments for the mercuric halides

	ν_1, cm^{-1}		ν_2, cm^{-1}			ν_3, cm^{-1}
(i) $HgCl_2$						
Gas	(16) 310	(17) 355 (R)	(18) 70 (calc'd) (uv)			(19) 413 (ir)
Solution (H_2O)	(17) 320 (R)					
Solution (CH_3OH)	(17) 320	(20) 319 (R)				
Solution (C_2H_5OH)	(17) 331 (R)					
Solution (ethyl acetate)	332 (R)					
Liquid (molten)	(16, 17) 314	* 313 (R)	(16) ($2\nu_2$) 377	(17) 376	* 382 (R)	—
Solid (crystal)	(16) 314	(20, 21) 312 (R)	(16) ($2\nu_2$) 378	(20, 21) 381	(22) 377 (R)	
(ii) $HgBr_2$						
Gas	—			—		(18) 293 (ir)
Liquid (molten)	(17) 195	* 206 (R)	* ($2\nu_2$) 271			
(iii) HgI_2						
Gas	(17) 155 (R)			—		(19) 237 (ir)
Solution (C_2H_5OH)	(17) 150 (R)			—		

* Present investigation.

measurements were not possible for $HgBr_2$ owing to the much weaker intensity of the 5461 cm^{-1} Hg excitation line. The Raman, infrared, ultraviolet spectra (16-22) and vibrational assignments are summarized in Table IV. Based on a molecular linear triatomic model, it is apparent that of the three fundamental vibrational modes, only ν_1 is Raman active, the remaining two, ν_2 and ν_3, being infrared active. The evidence for a linear triatomic species in the gas phase and solid phase, reviewed elsewhere in detail (4), leaves little doubt that the configuration of the mercuric halides is linear. The assignment of the Raman-active mode, ν_1, for the gas, molten, and solid states (Table IV) leaves nothing to be desired. The two values reported for the gas phase, 310 (16) and 355 cm^{-1} (17), are not in close agreement, and there is need for additional work to resolve this. For nonpolar substances of relatively simple structure it is known that the Raman shifts are relatively insensitive to the change of the state of aggregation, a maximum deviation of 3% having been recently reported by Stammreich and Forneris (23) for gaseous and liquid Br_2. The value of ν_1 for the gaseous state based on the earlier study (17) appears high by this criterion. The weak Raman frequencies, at 377-381 cm^{-1} for the chloride and at 271 cm^{-1} for the bromide, which have been noted by various investigators as well as in the present study, are assigned as an overtone of the Raman forbidden fundamental, ν_2, in the condensed state, although an alternate assignment to the forbidden fundamental, ν_3, assuming a breakdown in the selection rules, has also been advanced (22). In HgClBr, ν_2 is no longer Raman forbidden; this fundamental has been recently observed (24) at 139 cm^{-1} in this molecule in the condensed state. This is strong support for the present assignment of the above weak Raman line in the chloride and bromide as $2\nu_2$. The calculated value for ν_2 based on ultraviolet spectral data in the gas phase seems improbably low. Additional measurements for the gaseous spectra of these inorganic salts are required to resolve the uncertainties in the assignments for the vapor phase spectra of the mercuric halides.

While no visible and ultraviolet absorption spectra have been reported for the molten mercuric halides, some information on the nature of the bonding can be gained (25, 26) from the color changes observed qualitatively. The samples of mercuric chloride remain a clear and colorless liquid when heated in the sealed cells from 279°C (melting point) to 535°C (normal bp 304°C). Mercuric bromide changes from colorless to pale yellow on fusion, and as the temperature is increased, the color intensifies until it is an orange liquid in the sealed cell at 385°C (normal bp 320°C). Mercuric iodide changes from an orange-colored solid to a clear deep red liquid at the melting point and, as the normal boiling point (354°C) is approached, becomes nearly black. All these color changes were reproducible and reversible. The coloration of the solid and liquid mercuric halides undoubtedly relates to the perturbation of the partial covalent bonds, Hg ← X, by nearest neighbors in the condensed states. A quantitative study of the absorption spectra for the molten mercuric halides would contribute to the determination of the mechanism of the exciton transitions and the identity of the perturbed species; the preceding observations nevertheless give additional support to the "molecular" nature of the molten mercuric halides.

Discussion

It is of interest to examine the structure and interactions of the mercuric halides in the molten state in light of the preceding physicochemical properties. It is apparent that the vibrational spectra for these molten salts are understood on a model for the molten salts in which the primary constituents are linear-symmetrical triatomic molecules; no spectral lines corresponding to anionic species such as HgX_3^- and HgX_4^{-2} were found; nevertheless the finite, if but small, electrical conductivities of

these salts indicate that ionic species due to self-ionization in the molten state cannot be ruled out.

The thermal expansion coefficients for the molten mercuric halides $HgCl_2$, $HgBr_2$, and HgI_2 at corresponding temperatures $T(T = 1.10\,Tm)$ are 6.81, 6.52, and 6.40 deg^{-1}, respectively. These values are two to three times greater than those for the ionic halides of the Group IA and Group IIA metal cations, but are less than those for typical nonpolar liquids, *e.g.*, A, O_2, CH_4. The cohesive forces in mercuric halide melts are thus weaker than the coulombic forces in simple ionic melts, but are greater in strength than the London dispersion forces operative in purely nonpolar liquids. Some polar character is thus apparent in the HgX_2 species in the molten state for these salts, and the physical properties would be governed largely by dispersion and multipole forces rather than the coulombic interactions of ionic melts, *viz.*, molten KCl.

Some insight of the constitution of the liquid state can be gained from the entropy of fusion. Ubbelohde (27) has classified the principal mechanisms responsible for the increase of randomization on melting as follows: (i) increase in vibrational entropy due to looser packing and a consequent decrease of characteristic frequencies in the melt; (ii) increase of orientational randomization due to the marked reduction of repulsion barriers accompanying the expansion in volume on melting; (iii) increase in positional disorder, giving rise to the communal entropy term; (iv) randomization of the internal configuration of molecules or ions containing flexible groups; and (v) changes of association or chemical bonding on melting. The entropy of fusion for the mercuric halides, assuming linear triatomic molecules as the predominant species, may be calculated following the statistical thermodynamic treatment of Hirschfelder, Stevenson, and Eyring (28) for the fusion of linear molecules assuming that the molecules can only librate in the solid and that the onset of free rotation occurs at the melting point. It can be readily shown in this treatment that the contribution of the librational motion to the entropy in the solid state is given by

$$\Delta S_{11b} = 2R \left| \ln \left(\frac{kT}{h\nu} + 1 \right) \right|$$

and that of the free molecular rotational term in the molten state by the expression:

$$\Delta S_{rot} = R \left| \ln \frac{8\pi^2 IkT}{\sigma h^2} \right| + 1$$

where the symbols R, I, k, and h have their conventional significance, ν is the librational frequency, and the symmetry number, σ, is introduced to account for the identical molecular configurations. The results of this calculation are summarized in Table V. The lattice oscillations for the mercuric halides have not been determined, but the librational frequencies would be predicted to be somewhat less than the value, 50 cm^{-1}, for Cl_2, Br_2, and I_2 used by Hirschfelder, Stevenson, and Eyring (28) because of the greater coupling interactions among the mercuric halide molecules; an average frequency of 40 cm^{-1} was assumed for the present calculations. Comparison with the observed entropies of fusion (4), also listed in Table V, shows that there is qualitatively good agreement with the theoretically predicted results; it follows that for the mercuric halides the principal contribution to the entropy of fusion thus arises from "rotational melting." If significance may be attached to the fact that $\Delta S_{f_{theor}} > \Delta S_{f_{obs}}$ for each of the three mercuric halides (Table V), it is apparent that a modified form of the rotational partition function, to allow for the fact that, at the melting point, not all molecules are able to rotate simultaneously in the melt, but that groups of molecules undergo a form of hindered rotation in the liquid, should be introduced in this treatment. In the absence of knowledge of the exact values of the librational frequencies, it is not possible to introduce this refinement at present.

Table V. Entropies of fusion of the mercuric halides

Salt	$\frac{h\nu}{kT}$	ΔS_{11b}, e.u.	$I \times 10^{38}$, g cm²	ΔS_{rot}, e.u.	ΔS_{comm}, e.u.	ΔS_f (calc.) e.u.	ΔS_f (obs.) e.u.
$HgCl_2$	0.1039	13.0	6.20	18.6	2.0	7.6	7.5
$HgBr_2$	0.1126	12.6	15.39	20.3	2.0	9.7	8.4
HgI_2	0.1086	12.8	28.3	21.5	2.0	10.7	8.6

Transport properties.—The ratios $n = \Delta E_{vap}/\Delta E_\eta$ [Table II(b)] for the mercuric halides are near 3.5. Ewell and Eyring (29) have noted that there is a relatively sharp separation into two classes of molecular-type liquids with $n = 3$ and $n = 4$. The liquids for which $n = 3$ have approximately spherical fields of force (*e.g.*, A, CH_4, CCl_4, N_2, CO . . .) the other group of liquids with $n = 4$ (*e.g.*, C_6H_6, C_2H_5I, CS_2, C_2H_4 . . .) are not of spherical symmetry and most of them are "polar." For polar or elongated molecules, preferred orientations are possible and a smaller fraction of the energy of vaporization (*i.e.*, the energy required to form a hole of molecular size) is apparently sufficient for the flow process to occur.

The low values of ΔE_η (Table II(b)) are understood if these liquids are not associated or "network" liquids; the units of viscous flow are kinetically free molecular species.

The low electrical conductivities of the molten mercuric halides would indicate that these salts are slightly dissociated to ionic species; the order of decreasing conductance, iodide > bromide > chloride, undoubtedly reflects the relative degrees of dissociation. An estimate of the degree of dissociation, α, of electrolytes which obey Walden's rule ($\Lambda\eta$ = constant) is possible using Greenwood and Martin's (30) equation:

$$\alpha = \frac{\mu\eta}{100}$$

where μ is the molar conductivity and η the viscosity.[1]

[1] For covalent melts, which are only slightly dissociated and for which the viscosity is primarily determined by undissociated molecular species, the simple form of the Walden product should be used even though $\Delta E_\eta/\Delta E_\Lambda \neq 1$; for ionic melts, $\mu \cdot \eta^{1/m}$ as proposed by Greenwood and Martin (30) elsewhere should be used in estimates of α.

Table VI. Degree of dissociation of some molten inorganic salts

Salt	t, °C	ΔE_Λ, kcal mole^{-1}	ΔE_η, kcal mole^{-1}	m†	μ, ohm^{-1} cm^2 mole^{-1}	η, cp	α
$HgCl_2$	279 (mp)	6.2	3.4	0.55	1.95×10^{-3}	1.79	3.5×10^{-5}
	304 (bp)	6.2	3.4	0.55	2.56×10^{-3}	1.57	4.0×10^{-5}
$HgBr_2$	238 (mp)	6.5	3.6	0.55	0.979×10^{-2}	2.38	2.3×10^{-4}
	319 (bp)	4.9	3.6	0.73	2.11×10^{-2}	1.55	3.3×10^{-4}
HgI_2	256 (mp)	−2.5	4.6	−1.8	2.63	2.96	7.8×10^{-2}
	354 (bp)	−2.5	4.6	−1.8	1.35	1.51	2.0×10^{-2}
KBr	836*	3.4	7.9	2.3	109	1.29	1.22‡
$CdCl_2$	652*	2.1	4.0	1.9	117	2.03	1.71‡
$AgNO_3$	259*	3.1	3.1	1.0	38.2	3.56	1.36‡

* $T = 1.10\ T_f$.
† $m = \Delta E_\eta / \Delta E_\Lambda$.

‡ Highly ionized molten salts, *i.e.*, the values for these salts indicate that the estimates are more qualitative than quantitative in significance since for a *completely* ionized salt α has a maximum value of of 1.0.

In covalent melts which are only slightly dissociated, viscosity is determined primarily by undissociated molecules rather than by ionic species. The molecules may be considered as constituting a solvent medium in which the ions are dissolved and with which they are in dynamic equilibrium with respect to the process of ionization. These melts may therefore be considered as dilute electrolytic solutions and may be expected to obey Walden's rule to the extent to which the conditions for Stokes' law are applicable. Table VI lists values of α calculated from the Greenwood-Martin equation for the molten mercuric halides at their freezing and boiling points. The value $\alpha = 2 \times 10^{-4}$ for $HgBr_2$ is in good qualitative agreement with the value from emf measurements, $\alpha = 1 \times 10^{-5}$, reported elsewhere (13). The ionic concentrations in the pure molten mercuric halides at the temperatures of their melting points are: 5.5×10^{-4}, 3.3×10^{-3}, and 0.90 g ion l^{-1} for the chloride, bromide, and iodide, respectively. Estimates of α are included as well for some typical ionic salts at corresponding temperatures T ($T = 1.10\ T_m$), where T is in °K.

An interesting feature in the relative values of ΔE_η and ΔE_Λ is that, in direct contrast to ionic fused salts, $\Delta E_\eta < \Delta E_\Lambda$ for the molten mercuric halide melts. An explanation for this apparent "anomaly" is seen on critical examination of the temperature dependence of the degree of ionization, α.

In the absence of excess halide ions, X^-, the most probable entities in these melts are HgX_2 with HgX^+ and HgX_3^- ions at low concentration. The corresponding dissociation scheme is thus

$$2\ HgX_2 \overset{K_i}{\rightleftarrows} HgX^+ + HgX_3^-$$

The temperature dependence of this dissociation is of the form

$$\alpha = K_i^{1/2} = \exp(-\Delta F_i/2RT) = \exp(\Delta S_i/2R)\exp(-\Delta H_i/2RT)$$

If ΔH_i remains constant, α varies exponentially with temperature, and no deviation from linearity of the log Λ *vs.* $1/T$ plot is produced by the changing ionic concentration. The empirical activation energy for conductance, ΔE_Λ, is now seen as a composite quantity

$$\Delta E_\Lambda = \Delta H_i/2 + \Delta H_\Lambda^\ddagger = \Delta H_i/2 + \Delta H_h + \Delta H_j$$

where ΔH_i is the heat of ionization, $\Delta H_\Lambda^\ddagger$ is the enthalpy of activation for the migration process, ΔH_h is the heat of hole formation, and ΔH_j is the energy required to jump over the potential barrier into the adjacent hole. When ΔH_i is very small, ionization is virtually complete, and α is insensitive to temperature change. For salts such as the alkali halides, $\Delta H_i = 0$ since the salts are completely ionic in the crystalline state. A heat of ionization term is thus not observed in the empirical activation energy for conductance for most molten salts of the ionic type. For slightly dissociated molecular melts such as the mercuric halides, however, ΔH_i is appreciable. It can be readily shown that molten salts that are essentially covalent or molecular would be expected to obey the simple Walden rule. It follows that for the mercuric halides $\Delta H_\Lambda^\ddagger \approx H_\eta^\ddagger \equiv \Delta E_\eta$. The difference of the experimental activation energies thus gives an estimate for the heat of ionization, *i.e.*

$$\frac{1}{2}\Delta H_i = (\Delta E_\Lambda - \Delta E_\eta)$$

The measured values of Λ and ΔE_Λ for the poorly conducting $HgCl_2$ are extremely sensitive to trace amounts of ionic impurities, *i.e.*, quite similar to solvents such as water.

The tendency for complex formation in the systems

$$HgX_2 \text{-} MX\ (X = Cl, Br, I;\ M = Na, K, NH_4)$$

in the molten state and the stability of complexes formed have been observed to increase in the order I, Br, Cl (31). This order is the reverse of that found in aqueous solutions. The most characteristic compounds in the halide mixtures were $2MX \cdot HgX_2$ and $MX \cdot HgX_2$, corresponding to the complex anions $HgX_4^=$ and HgX_3^- in the melts.

Values of ΔE_Λ obtained in the present investigation lend support to the existence of autocomplexes in the pure melts. If, as proposed elsewhere (5), the dissociation scheme of the mercuric halides is $HgX_2 \rightarrow HgX^+ + X^-$, a large heat of ionization, ΔH_i, comparable to the energy of an Hg—X bond, should be included in ΔE_Λ. In Table VII are listed values of: the bond dissociation energy, D(X—HgX) (32); the bond energy, E (33); the gas phase dissociation constant, K_p (33); and the heat of ionization, ΔH_i; for

Table VII. Dissociation and ionization parameters for the mercuric halides at their boiling points

Salt	D, kcal mole^{-1}	E, kcal mole^{-1}	ΔH_i, kcal mole^{-1}	K_p, mole
$HgCl_2$	81	54	2.8	2.76×10^{-13}
$HgBr_2$	72	44	1.4	5.50×10^{-11}
HgI_2	60	35	−7.1	3.47×10^{-6}

the mercuric halides at their respective boiling points. Lack of knowledge of ionization potentials, electron affinities, and solvation energies precludes an accurate evaluation of ΔH_i from the Born-Haber cycle. It is evident, however, that ΔH_i is very much less than D and E. This strongly suggests that ionization in the melt occurs with the formation of complex anions, *e.g.*

$$2HgX_2(1.) \rightarrow HgX^+(1.) + HgX_3^-(1.)$$

or

$$3HgX_2(1.) \rightarrow 2HgX^+(1.) + HgX_4^=(1.)$$

Since no net Hg-X bonds are broken in such a process, the heat of complex anion formation should largely cancel the large heat of ionization required to produce free HgX^+ and X^- ions.

The temperature dependence of ΔE_A found in molten $HgBr_2$ and the negative temperature coefficient of electrical conductance for HgI_2 are additional features for consideration. The temperature dependence of ΔE_A ($HgBr_2$) may be attributed, in large part, to a variation of ΔH_i with temperature [cf. H_2O and acetic acid (34)], and to the thermal instability of the autocomplex ionic species. That the effect is due to the decrease in ΔH_j (the part of activation energy associated with the "jump" displacement in the migration process) as has been suggested elsewhere in ionic melts (35) seems much less probable in the molten mercuric halides since intermolecular force fields are much weaker than the interionic force fields of highly ionized molten electrolytes.

The changes of resistance on fusion of the three salts are illustrated in Fig. 2. At their melting points the specific conductivities are strikingly similar for the solids, *ca.* 10^{-6} ohm^{-1} cm^{-1}. These salts, after fusion, have increases in specific electrical conductivity of 10^2-10^4 ohm^{-1} cm^{-1}. Electronic conductors exhibit a decrease in conductivity on fusion owing to the increased lattice scattering of electrons in the conduction band. The molten salts may be regarded as ionic conductors. The marked curvature in the log R — $1/T$ graph which sets in *ca.* 25° below the melting point in HgI_2 is evidence of homophase premelting by onset of ionic conductance. Similar behavior was noted in the dilatometric measurements of the change in volume on fusion of HgI_2. Additional support for this view is found in the value for ΔE obtained near the melting point. The value, 1.11 ev mole^{-1} (25.7 kcal mole^{-1}), well within the limits of experimental error (± 5%), is almost identically one-half the band gap, 2.13 ev, from Bube's optoelectric measurements (36) on solid HgI_2. Ionic conductance in the solid state is thus negligibly small until the melting point is approached. The value of ΔE for solid $HgBr_2$ (0.95 ev) is similar to that of HgI_2, but the value for solid $HgCl_2$ (0.56 ev) is notably less. The former two salts form layer lattices of the same type; the chloride has a somewhat different packing in the solid state.

Both the chloride and bromide have positive temperature coefficients, and in accord with the criterion, it is apparent that ion conductance prevails in these melts. It was observed in the present work that visible amounts of iodine appeared at the anode in an electrolysis of molten HgI_2 at 80 ma for several hours. Belyaev and Mironov (14) have reported, in contrast to aqueous solutions, the iodomercurates are the least stable of the complex anions, HgX_3^- and $HgX_4^=$. The decrease in electrical conductance may thus arise from a retrogression of ionization with increase in temperature. A possible ionization scheme for the iodide is as follows

$$HgI_2 \rightleftarrows HgI^+ + I^- \qquad \Delta H_1$$

and

$$I^- + HgI_2 \rightleftarrows HgI_3^- \qquad \Delta H_2$$

or:

$$2HgI_2 \rightleftarrows HgI^+ + HgI_3^- \qquad \Delta H_3$$

The thermal instability of the species HgI_3^- would repress the primary ionization with increasing temperature. From the temperature dependence of the ionization constant, K_i, *i.e.*, $(\ln K_i/T)_p = \Delta H_3/RT^2$, it is seen that, if ΔH_3 is negative, the electrical conductance would decrease with an increase in temperature. A recent study (37) of the electrical conductance of the interhalogen compound, BrF_3, has shown a negative temperature coefficient. This has been attributed to a repression of the primary ionization due to the thermal instability of the species, BrF_2 and BrF_4, much as advanced for molten mercuric iodide above. Thus while the possibility of some partial electronic conductance is not ruled out for molten HgI_2, there is chemical evidence in strong support for the view that the conductance is predominantly ionic in this molten electrolyte, as in molten $HgCl_2$ and $HgBr_2$.

Acknowledgments

Dr. Y. Mikawa and Dr. D. W. James, of this laboratory, are thanked for helpful discussions and experimental aid in the Raman studies of the molten mercuric halides. This work was made possible in large part by support received from the National Science Foundation, Washington, D. C., (Raman Spectroscopy of Molten Salts) and the U. S. Air Force, Office of Scientific Research, Washington, D. C., (Properties and Constitution of Molten Salts).

Manuscript received Feb. 6, 1962. Abstracted in part from a thesis by one of the authors (J. D. E. McI.) in partial fulfillment of the requirements for the Ph.D. degree, R. P. I., January 1961.

Any discussion of this paper will appear in a Discussion Section to be published in the June 1963 JOURNAL.

REFERENCES

1. G. J. Janz, C. Solomons, and H. J. Gardner, *Chem. Revs.*, **58**, 461 (1958).
2. H. Bloom and J. O'M. Bockris, "Modern Aspects of Electrochemistry," Vol. 2, Academic Press Inc., New York (1959).
3. H. Bloom, *Rev. Pure Appl. Chem.*, **9**, 139 (1959).
4. G. J. Janz and J. D. E. McIntyre, *Ann. N. Y. Acad. Sci.*, **79**, 790 (1960).

5. J. O'M. Bockris, E. H. Crook, H. Bloom, and N. E. Richards, *Proc. Roy. Soc.*, **A255**, 558 (1960).
6. C. Solomons and G. J. Janz, *Anal. Chem.*, **31**, 623 (1959).
7. G. J. Janz and J. D. E. McIntyre, *This Journal*, **108**, 272 (1961).
8. J. O'M. Bockris, J. L. White, and J. D. MacKenzie, "Physico-Chemical Measurements at High Temperature," Chap. 15, p. 323, Academic Press Inc., New York (1959).
9. E. N. da C. Andrade and Y. S. Chiong, *Proc. Phys. Soc.*, **48**, 247 (1936).
10. G. J. Janz, Y. Mikawa, and D. W. James, *J. Appl. Spectroscopy*, **15**, 47 (1961).
11. E. B. R. Prideaux, *J. Chem. Soc.*, **97**, 2032 (1910).
12. V. D. Polyakov, *Akad. Nauk S.S.S.R.*, **26**, 191 (1955).
13. G. Jander and K. Broderson, *Angew. Chem.*, **62**, 264 (1950); *Z. anorg. Chem.*, **264**, 57, 76, 92 (1951).
14. I. Belyaev and K. E. Mironov, *Zhur. Obschei Khim.*, **21**, 1484 (1952); **22**, 1529, 1734 (1952).
15. "Selected Values of Chemical Thermodynamic Properties," Natl. Bur. Standards Circ. 500, Washington, D. C. (1952).
16. K. V. K. Rao, *Proc. Indian Acad. Sci.*, **14A**, 521 (1941).
17. H. Braune and G. Engelbrecht, *Z. physik. Chem.*, **B19**, 303 (1932).
18. W. Klemperer and L. Lindeman, *J. Chem. Phys.*, **25**, 397 (1956).
19. W. Klemperer, *ibid.*, **25**, 1066 (1956).
20. W. Bues, *Z. anorg. u. allgem. Chem.*, **279**, 104 (1955).
21. P. Krishnamurti, *Indian J. Phys.*, **5**, 113 (1931); **6**, 7 (1931); *Nature*, **125**, 892 (1931).
22. E. K. Plyler, reported by J. Duchesne and L. Burnell, *J. Chem. Phys.*, **19**, 1191 (1951).
23. H. Stammreich and J. Forneris, *ibid.*, **22**, 1624 (1954).
24. M. L. Delwaulle, *Compt. rend.*, **206**, 1965 (1938).
25. F. R. Bichowsky, *J. Am. Chem. Soc.*, **40**, 500 (1918).
26. K. S. Pitzer and J. H. Hildebrand, *ibid.*, **63**, 2472 (1941).
27. A. R. Ubbelohde, *Quart. Revs. (London)*, **4**, 356 (1950); *Proc. Chem. Soc. (London)*, **1960**, 332.
28. J. Hirschfelder, D. Stevenson, and H. Eyring, *J. Chem. Phys.*, **5**, 896 (1937).
29. R. H. Ewell and H. Eyring, *ibid.*, **5**, 726 (1937).
30. N. N. Greenwood and R. L. Martin, *J. Chem. Soc.*, **1953**, 1427.
31. S. Ahrland, *Acta Chem. Scand.*, **10**, 723 (1956).
32. M. Wehrli, *Helv. Phys. Acta*, **10**, 258 (1937); **13**, 153 (1940).
33. H. Braune and S. Knoke, *Z. physik. Chem.*, **A152**, 409 (1931).
34. H. S. Harned and B. B. Owen, "Physical Chemistry of Electrolytic Solutions," 3rd ed., Reinhold Publishing Corp., New York (1957).
35. I. S. Yaffe and E. R. Van Artsdalen, *J. Phys. Chem.*, **60**, 1125 (1956).
36. R. H. Bube, *Phys. Rev.*, **106**, 702 (1957).
37. A. A. Banks, H. J. Emeléus, and A. A. Woolf, *J. Chem. Soc.*, **1949**, 2861.

Rates of Electrode Processes by the Rotating Disk Method

D. Jahn and W. Vielstich

Institut für Physikalische Chemie der Universität Bonn, Germany

ABSTRACT

A rotating disk electrode has been applied to the measurement of the kinetics of fast electrode reactions. Standard exchange current densities up to about 10 amp/cm²/mole/liter have been obtained for reversible redox systems by extrapolating the measured current to infinite speed of rotation in order to eliminate diffusion polarization.

In recent years increasing use has been made of the rotating disk electrode in diffusion and kinetic investigations, mainly for determining diffusion coefficients. This electrode has the advantage that there exists a precise theory of convective diffusion at a rotating disk. According to Levich (1) the diffusion layer has the same thickness over the entire area of a rotating disk provided edge effects can be neglected. For laminar flow the diffusion layer thickness is given by the following function

$$\delta = a\, D^{1/3}\, \nu^{1/6}\, \omega^{-1/2} \qquad [1]$$

where D is the diffusion coefficient of the solute species ($cm^2\ sec^{-1}$), ν is the kinematic viscosity of the solution ($cm^2\ sec^{-1}$), ω is the angular velocity of the disk (sec^{-1}), and a is a factor which equals 1.62 according to Levich. A closer approximation (2) yields $a = 1.805\ [0.8934 + 0.316\ (D/\nu)^{0.36}]$.

A diffusion controlled limiting current density is given by

$$j_{lim} = nF\, D\, c/\delta \qquad [2]$$

nF being the number of coulombs per mole transfered at the electrode, c being the bulk concentration of the reacting species. From measurements of limiting diffusion currents thus the quantity $D \times c$ can be obtained with better precision as compared to values obtained with the dropping mercury electrode.

The application of the rotating disk method to the study of chemical kinetics has been proposed by Koutecky and Levich (3). They have derived a formula containing both diffusion and kinetic parameters. Thus, under certain conditions, by measuring currents limited by diffusion and chemical kinetics as a function of the revolution number of the disk and by extrapolating to $\omega \to \infty$, one can determine rates of chemical reactions preceding the electron transfer. This has been demonstrated by the evaluation of the dissociation rates of weak acids (4).

Electrode Kinetics and Mass Transfer

The combined effects of mass transfer and electrode kinetics at a convection electrode which have already been studied by Frumkin and Tedoradse (6) for the chlorine electrode will be described here for the reaction

$$Ox + n\,e^- \underset{k_b}{\overset{k_f}{\rightleftharpoons}} R$$

with the assumption that no preceding chemical reaction occurs. The general expression for the current density is

$$j = nF\,(k_f\, c_{Ox}^{x=0} - k_b\, c_R^{x=0}) \qquad [3]$$

where k_f and k_b are the formal rate constants (5) for the forward and backward electrode reaction, and x is the distance from the electrode surface. The mass transfer through the diffusion layer for the two reacting species is

$$j = nF\, D_{Ox} \frac{c_{Ox}^{x=\infty} - c_{Ox}^{x=0}}{\delta_{Ox}}$$

and

$$j = -nF\, D_R \frac{c_R^{x=\infty} - c_R^{x=0}}{\delta_R} \qquad [4]$$

δ_{Ox} and δ_R being the diffusion layer thickness for the species Ox and R, respectively.

In the case of a rotating disk electrode using Levich's equation (1) δ can be written in the form

$$\delta = A/\sqrt{\omega}$$

where $A = a\, D^{1/3}\, \nu^{1/6}$ Calculating the concentrations at the electrode surface from the bulk concentrations one gets using the Eq. [4]

$$c_{Ox}^{x=0} = c_{Ox}^{x=\infty} - j \frac{A_{Ox}}{nF\, D_{Ox}} \cdot 1/\sqrt{\omega}$$

$$c_R^{x=0} = c_R^{x=\infty} + j \frac{A_R}{nF\, D_R} \cdot 1/\sqrt{\omega} \qquad [5]$$

Introducing the relations [5] into Eq. [3] one readily obtains

$$j = \frac{nF\,(k_f\, c_{Ox}^{x=\infty} - k_b\, c_R^{x=\infty})}{1 + \dfrac{k_f\, A_{Ox}}{D_{Ox}\sqrt{\omega}} + \dfrac{k_b\, A_R}{D_R\sqrt{\omega}}} \quad \text{or}$$

$$1/j = \frac{1}{nF\,(k_f\, c_{Ox}^{x=\infty} - k_b\, c_R^{x=\infty})}\left[1 + \left(\frac{k_f\, A_{Ox}}{D_{Ox}} + \frac{k_b\, A_R}{D_R}\right)\frac{1}{\sqrt{\omega}}\right] \qquad [6]$$

This equation can be applied to the evaluation of kinetic data (standard exchange current density j_o, transition coefficient α) as follows: Plotting $1/j$ against $1/\sqrt{\omega}$ for constant values of the overvoltage (6) one deduces from the slope and the ordinate at $\omega = \infty$ two equations for k_f and k_b.

From the two rate constants at a given electrode overvoltage one can calculate both j_o and α in the usual way

$$nF\, k_f = j_o \exp\left(-\alpha \frac{nF}{RT}\eta\right)$$

$$nF\, k_b = j_o \exp\left((1-\alpha)\frac{nF}{RT}\eta\right) \qquad [7]$$

We have used Eq. [6] for the determination of kinetic data of several very fast redox systems. We found that in our arrangement standard exchange current densities up to nearly 10 amp/cm²/mole/liter could be measured. This limit is caused by the fact that an evaluation is no longer possible if the ratio of the slope to the ordinate intercept becomes too high. The accuracy of the method can be increased by using a higher speed of rotation. Varying the overvoltage η or the concentrations of the reacting species, however, only yields a small effect.

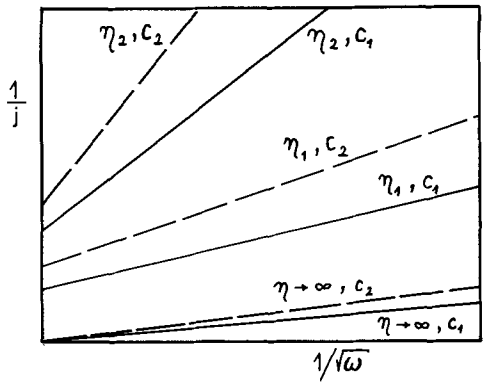

Fig. 1. Schematic $1/j - 1/\sqrt{\omega}$ plot with $c^{x=\infty}$ and η as parameters; $c_1 > c_2$; $\eta_1 > \eta_2$.

The influence of the experimental parameters c and η on the $1/j - 1/\sqrt{\omega}$ diagram can be understood by transforming Eq. [6]

$$1/j = \frac{1}{nF\,(k_f\, c_{Ox}^{x=\infty} - k_b\, c_R^{x=\infty})} + \frac{1}{nF\,(k_f\, c_{Ox}^{x=\infty} - k_b\, c_R^{x=\infty})}\left(\frac{k_f\, A_{Ox}}{D_{Ox}} + \frac{k_b\, A_R}{D_R}\right)\cdot 1/\sqrt{\omega}$$

By lowering the bulk concentrations $c^{x=\infty}$ both the slope $1/j - 1/\sqrt{\omega}$ and the intercept for $\omega = \infty$ increase (see Fig. 1). Therefore the accuracy of the evaluation is not noticeably improved by a change in concentration.

A change of the overvoltage η has a similar effect. In the region $\eta \leq RT/nF$ an increase of η results in a decrease at both the slope and the intercept (Fig. 1, 4, and 5), while for $\eta >> RT/nF$ the slope reaches constant values as is to be expected for purely diffusion controlled polarization (Fig. 1).

Experimental

A platinum wire (diameter 0.1 cm) which was sealed into a glass tube (Fig. 2) served as the disk electrode. The electrode was centered to within 0.002 cm, and the face was mechanically polished using Cr_2O_3 polishing powder. The rod was driven by a synchronous motor which was powered by an audiofrequency generator with an a-c amplifier. This arrangement allowed us to alter very simply the revolution number of the disk electrode in the range from 10 to about 120 cps without the necessity of any control. As we used a very small disk electrode there was no danger of turbulence at the surface of the electrode. At 120 cps a Reynold's number of about 200 is reached, the critical Reynold's number being $> 10^4$. At very low revolution numbers an influence of spherical diffusion at the edge between platinum and glass can become noticeable. The contribution of spherical diffusion can be neg-

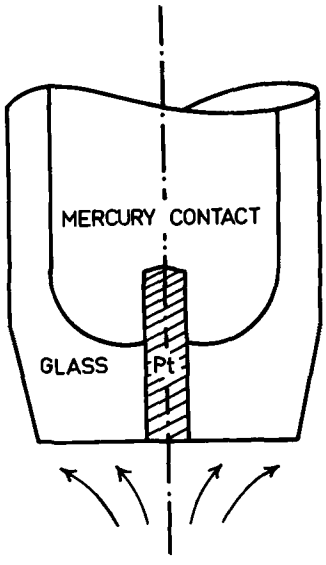

Fig. 2. Platinum wire disk electrode

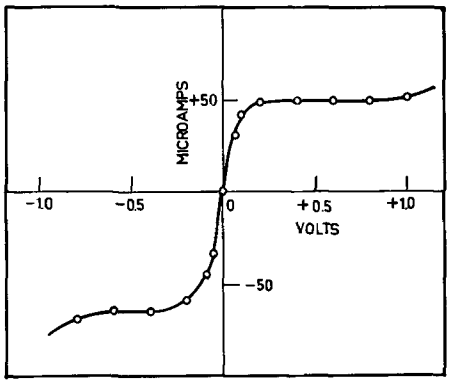

Fig. 3. Current vs. overvoltage at $\omega = 2\pi \times 48.2$ sec^{-1}; 0.5M K_2SO_4, 10^{-2}M $Fe(CN)_6^{3-}$, 10^{-2}M $Fe(CN)_6^{4-}$.

lected, if the condition $r/\delta \geqq 20$ is fulfilled. The radius of our electrode being $r = 0.05$ cm, a frequency of $f \geqq 10$ cps is required.

The experimental cell was thermostated and contained the rotating disk electrode, a platinum counter-electrode, and a second sheet of platinized platinum as a reference electrode. Pure nitrogen was bubbled through the electrolyte. Overvoltages were measured currentless, the currents by means of a microammeter.

The solutions were prepared from reagent grade chemicals. The concentration of each redox component was 10^{-2}M. A large excess of supporting electrolyte was added. The solutions were freed from oxygen by CO_2, and the access of light was excluded when the solutions were stored.

Before the measurements the carefully polished disk electrode was pretreated by alternating cathodic and anodic polarization up to the region of the beginning H_2- and O_2-evolution. Thus a high electrode activity and a relatively good repeatability could be reached.

Results

The method was tested on several reversible redox systems which had already been measured by Randles and Somerton (7) with the a-c method. Prior to the kinetic measurements diffusion coefficients of the reacting species have been determined from the anodic and cathodic limiting currents at a given speed of rotation (Fig. 3). The calculated diffusion coefficients at 25°C for the three systems investigated are listed in Table I.

Table I. Diffusion coefficients and kinetic data at 25°C

Redox system	Supporting electrolyte	$D \cdot 10^6$ R	$D \cdot 10^6$ Ox	α	j_0	j_0 (7)
Fe^{2+}/Fe^{3+}	1M $HClO_4$	5.7	6.5	0.63	0.23	0.5
$Fe(CN)_6^{4-}/Fe(CN)_6^{3-}$	1M KCl	5	7	0.61	5	9
$Fe(CN)_6^{4-}/Fe(CN)_6^{3-}$	0.5M K_2SO_4	4.9	7.2	0.56	7	13

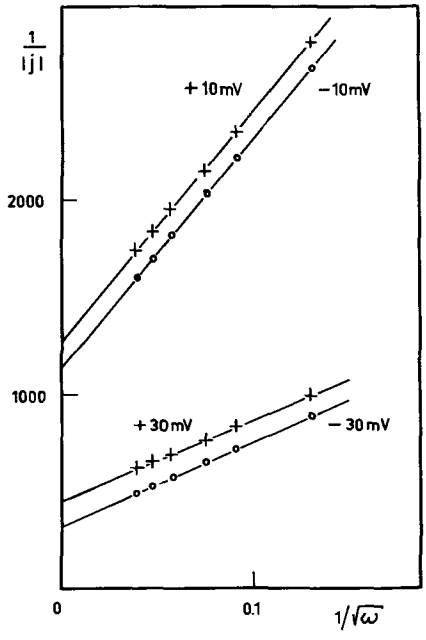

Fig. 4. $1/j - 1/\sqrt{\omega}$ plot for the system 1M $HClO_4$, 10^{-2}M Fe^{2+}, 10^{-2}M Fe^{3+}.

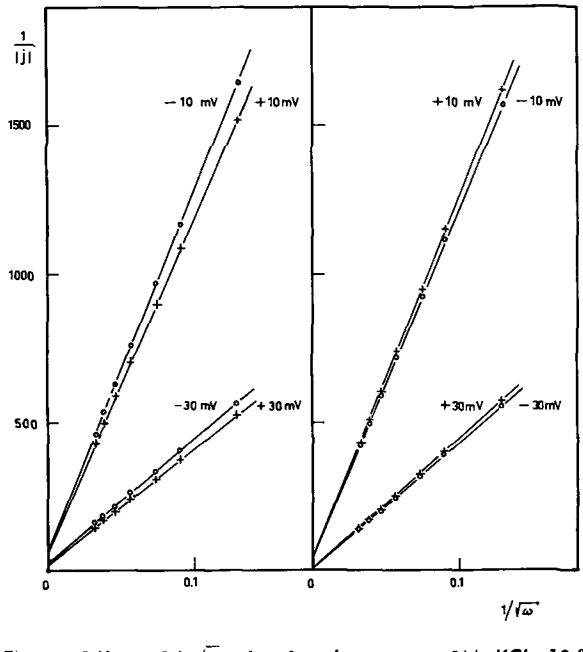

Fig. 5. $1/j - 1/\sqrt{\omega}$ plot for the systems 1M KCl, 10^{-2}M $Fe(CN)_6^{4-}$, 10^{-2}M $Fe(CN)_6^{3-}$ (left) 0.5M K_2SO_4, 10^{-2}M $Fe(CN)_6^{4-}$, 10^{-2}M $Fe(CN)_6^{3-}$ (right).

While in the regions of limiting currents there is no influence of the discharge reaction on the current, the shape of the curve at low overvoltages is determined by both mass transfer and discharge kinetics. Therefore the $j - \omega$ relation has to be studied at constant overvoltages in the ascending part of the current-voltage curve (Fig. 3). In Fig. 4 and 5 values of $1/j$ are plotted vs. $1/\sqrt{\omega}$ for the three systems. The observed dependence can be remarkably well represented by a straight line. The extrapolated kinetic data (for $\omega \to \infty$) are shown in Table I.

Comparing our j_o-values with those obtained by Randles and Somerton one can see that the latter are greater almost by a factor of 2. This may be due to the fact that applying an a-c current induces a continuous activation of the electrode surface. A disagreement of this order is not unusual with measurements on solid electrodes.

The results prove once more the suitability of this method for the investigation of fast electrode processes. With the different relaxation methods the elimination of the influence of the double layer causes considerable difficulties for the experimental procedure as well as for the evaluation and interpretation of the results. The rotating disk method as a steady-state method avoids these obstacles by yielding relationships which are easily explainable in terms of a well founded theory.

Manuscript received Dec. 27, 1961. This paper was prepared for delivery before the Indianapolis Meeting, April 30-May 3, 1961.

Any discussion of this paper will appear in a Discussion Section to be published in the June 1963 JOURNAL.

REFERENCES

1. V. G. Levich, "Physico-Chemical Hydrodynamics," Academy of Sciences of the USSR Press (1959).
2. D. P. Gregory and A. C. Riddiford, *J. Chem. Soc.*, **1956**, 3756.
3. J. Koutecky and V. G. Levich, *J. Phys. Chem. USSR*, **32**, 1565 (1958).
4. W. Vielstich and D. Jahn, Proc. 2nd Int. Congr. Polarography Cambridge p. 281, (1959).
5. J. Jordan, *Anal. Chem.*, **27**, 1708 (1955).
6. A. N. Frumkin and G. Tedoradse, *Z. Elektrochem.*, **62**, 251 (1958); E. Budewski and S. Toschev, *Doklady Akad. Nauk SSSR*, **130**, 1047 (1960); *Proc. Bulg. Acad. Sci.*, **1961**, 183.
7. J. E. B. Randles and K. W. Somerton, *Trans. Faraday Soc.*, **48**, 951 (1952).

Effects of Electrostatic Fields on the Surface Tension of Salt Solutions

G. M. Schmid, R. M. Hurd, and E. S. Snavely, Jr.

Texas Research Associates, Austin, Texas

ABSTRACT

The surface tension of air/NaCl solution interfaces with applied electrostatic fields of up to 6700 v/cm was measured using a surface energy balance. The NaCl concentration was 0-3.5%. It was found that fields of either polarity lower the surface tension of all investigated solutions. Maghitude of the surface tension changes and dependence on direction of the field lead to the conclusion that the potential drop at air/water interfaces is smaller than previously thought, that the water dipole orientation is only slight, and that the hydrogen in the oriented water molecule is facing the air. The experiments point out that the effect of the field is predominantly on the sodium ion. It is shown that the difference in the energy for adsorption at the interface between cations and anions cannot be neglected. Calculations on the basis of a modified Gibbs equation on the assumption of a diffuse double layer at the interface leads to unreasonably high surface deficiencies. Neglecting the diffuse double layer and reckoning on the basis of an inner double layer only leads to values of the same order of magnitude as those calculated from the Gibbs equation alone.

For uncharged particles, changes in surface concentration are related to surface tension through the Gibbs adsorption equation (1). For charged particles, this equation has to be modified to take into account the specific properties connected with their strong electrostatic fields. Attempts have been made in this direction by Lewis (2). A more direct approach has been used by Wagner (3) and was further developed by Onsager and Samaras (4) and by Falkenhagen and Schmutzer (5). No direct measurements of surface concentrations are available to check the validity of these theories.

According to Kamienski (6), the potential drop across the air/water interface leads to a field of the order of 10^7 v/cm. If this is true, then it is very unlikely that it would be possible to change the surface concentration of charged particles by externally applying an electrostatic field of, say, 10^4 v/cm. On the other hand, Barnett (7) and Guastalla (8) were able to show that this is not necessarily so. These experiments, however, still did not allow quantitative treatment.

The object of this investigation was to determine the effects of applied electrostatic fields on the surface tension of salt solutions and to try to correlate these to surface concentration changes.

Experimental

Apparatus.—The surface energy balance used in this work is essentially the same as that of Allan and

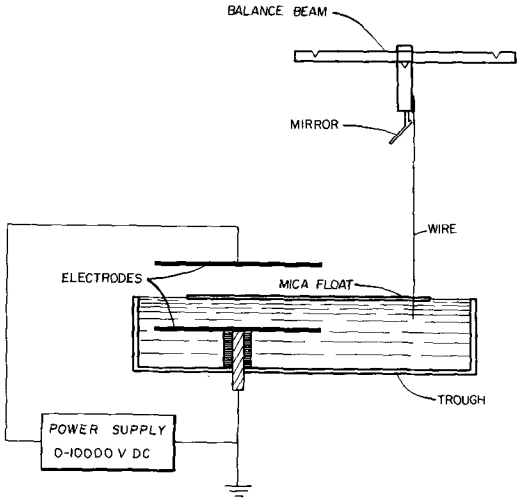

Fig. 1. Schematic of surface energy balance

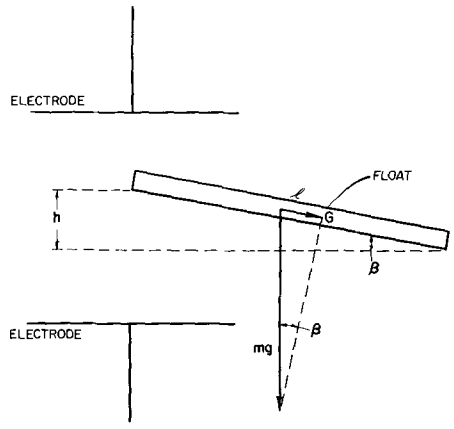

Fig. 2. Schematic of hydrostatic force on float; β, angle of tilt; h, hydrostatic overhead due to the field; mg, force of gravity; l, length of float; force on float.

Alexander (9), slightly modified so that a potential can be applied across the air/solution interface. A rigid, heavy brass frame, resting on three leveling screws, served as support for both a 25 x 15 x 4.5 cm Pyrex glass trough and an aluminum balance beam (Fig. 1). The electrodes, 11 x 9 x 0.1 cm, are made of plate Monel, to resist the corrosive action of the salt water. A hole is drilled into the bottom of the glass trough and the frame to allow mounting of the "water electrode." A water-tight seal is obtained with a Teflon gasket. The "air electrode" is mounted on an insulating Lucite plate directly above the water electrode. The air gap between the solution surface and air electrode was 1.2 cm.

The balance beam is supported 20 cm above water level by two diamond points which pivot on two microscope slides resting on the frame. The slides are replaced frequently to avoid formation of grooves by the cutting action of the diamonds. The beam has two notches to allow calibration of the balance. A rigid wire with a Pt wire prong reaches down into the solution. A small mirror attached to the beam projects a light beam onto a scale, 230 cm away, thus allowing accurate observation of balance deflections.

A thin sheet of mica, generally 7.3 x 12.8 cm, floating on the solution serves as indicator. It has two holes on one end, large enough for the Pt wire prong of the balance body to move in and out freely. The other end of the mica float projects 4.5 cm into the space between the electrodes. Thus a change in surface tension between the electrodes as compared to the area outside the electrodes results in a force on the mica float which is indicated by a deflection of the balance beam.

The voltage applied across the interface was taken from a 0-10,000v d-c power supply. Water electrode, frame, and balance beam were grounded at all times. The balance arrangement had a sensitivity of 0.052 dynes cm^{-1} per cm of deflection, as determined by calibration with small weights (pieces of Pt wire) placed directly on the balance beam.

Application of an electric field leads to an attractive force between the air electrode and balance beam. This force was blocked by separating the two with a mica sheet, perpendicular to the air/solution interface, reaching into the solution to obtain effective grounding and placed as close to the electrodes as possible without arcing. A slot was cut into the shield so as to allow free movement of the mica float.

In measurements of this kind, contamination of the air/solution interface with dust and other foreign substances must be eliminated. This was done by keeping the whole experimental setup covered with a Lucite hood. Float and balance beams were removed frequently and the solution surface cleaned by sweeping with mica barriers several times over the whole surface, including the edges of the trough.

Procedure.—At least two forces other than surface tension changes are indicated by the balance and have to be corrected for to obtain the desired effect of the field on surface tension.

First, application of an electric field across the air/solution interface raises the solution underneath the air electrode. The resultant forces on the mica float are represented schematically in Fig. 2. The mica float, the edge of which lies between the two plates, becomes tilted. This results in a force, G, on the balance body, in addition to the force due to a change in surface tension. G can be calculated to a first approximation as the force of gravity, mg, projected onto the float, *i.e.*,

$$G = mg \sin \beta \qquad [1]$$

with

$$\sin \beta = h/l \qquad [2]$$

where β is the angle of tilt, l the length of float, and h the hydrostatic overhead due to the field. The force, G, can be accounted for by keeping h and l constant (constant field strength, constant length of float) and varying m.

Second, it was observed that the balance deflection caused by a mica sheet, floating on a salt solution with an electric field impressed across the air/solution interface, is dependent on the position of the "working edge" of the float in the field. This is due to electrostatic attraction of the mica float, which must be proportional to the area of the part of the float in the field. Again, this area is proportional to the mass of the float in the field.

The experimental procedure used to make both corrections is based on the following. Consider a rec-

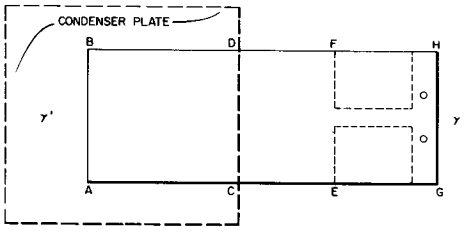

Fig. 3. Geometrical view of float; γ, γ', surface tensions

tangular float of fixed dimensions (Fig. 3) floating on a salt solution with area ABDC inside a perpendicular and constant electric field. There are four forces acting on the float. A surface tension γ' is effective on the "working edge" $\overline{AB}$ and a surface tension γ on the "balance edge" $\overline{GH}$ of the float ($\overline{AB} = \overline{GH}$). The force to be determined is $\gamma' - \gamma = \Delta\gamma$. Due to the hydrostatic head developed in applying the electric field, there is a force of gravity which is proportional to the area of the float between the electrodes. Since the float is of constant thickness, this area is proportional to the mass of that part of the float.

The float is now cut as indicated by the dotted line shown in Fig. 3, leaving a small bridge between the front part of the float, ABFE, and the rear part at GH. We assume that the width of the bridge is small, as compared to the balance edge $\overline{GH}$. The effects of the surface tension difference, $\Delta\gamma$, and the electrostatic force are not changed by this procedure, provided that area ABDC < ABFE. We do, however, change the mass of the float. Making ABFE successively smaller, keeping ABDC < ABFE, and plotting balance deflection *vs.* mass of float shows the dependence of the force due to effects of the hydrostatic head on the mass of the float.

As $\overline{AE}$ is made successively smaller by this process, we finally arrive at $\overline{AE} < \overline{AC}$. Provided that the constant electric field is homogeneous up to $\overline{CD}$, and the width of the bridge is negligible compared to $\overline{AB}$, then the net surface tension forces on the float should disappear at $\overline{AE} < \overline{AC}$. Since now the electrostatic attraction of the float is proportional to the area ABFE and thus also to the mass of the float, we still plot deflection *vs.* mass of float for ABFE < ABDC. This plot shows the electrostatic effect plus the gravity effect due to the remaining mass of the float, but without the surface tension effect.

Thus, we will have two plots of balance deflection *vs.* mass of float (Fig. 4), one of which, for $\overline{AC} < \overline{AE}$, gives the influence of gravity plus a constant electrostatic attraction and surface tension effect; the other, for $\overline{AC} > \overline{AE}$, gives the influence of electrostatic attraction plus the effect of gravity for the remaining mass of the float with no surface tension effect. Extrapolation of the two plots toward each other to a point to the left of which the surface tension effect is zero and to the right of which the surface tension effect as a definite value gives a difference in ordinate which corresponds to the surface tension effect only.

It is seen from Fig. 4 that the slopes of the upper part of the curves become larger with increasing field strength, which is expected for increasing hydrostatic head. The deflection exhibited a slight maximum at the greatest masses, which may be due to forces involved in "lifting" water outside the field by surface tension effects on the rigid float.

Extrapolation of the lower parts of the curves to $m = 0$ should intercept the origin. The small deviations from zero intercept in Fig. 4 occur because the bridge between front and rear part of the float cannot be made infinitely small, and also because a finite rear part is necessary to operate the balance.

The point to the left of which the surface tension effect is zero and to the right of which the surface tension effect has a finite value cannot be determined precisely. The point lies, however, between the abscissae of the highest point of the lower curve and the lowest point of the higher curve (between a and b in Fig. 4). Taking the difference in ordinates at these two points gives a lower and upper limit for the surface tension effects.

The method was checked by using floats having different working edges, different masses, and different areas in the field. The results for a 3.5% NaCl solution at positive air electrode are shown in Fig. 5 and are in satisfactory agreement. Each point in Fig. 5 is the mean of a maximum and minimum value obtained from a plot of mass of float *vs.* balance de-

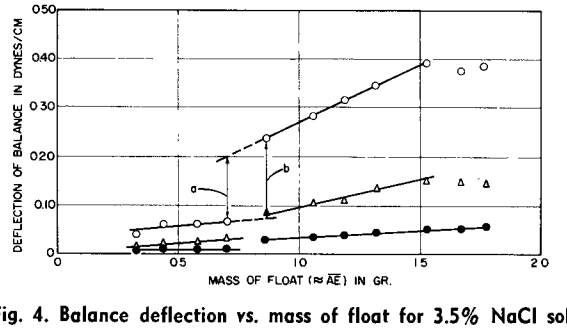

Fig. 4. Balance deflection *vs.* mass of float for 3.5% NaCl solutions, air electrode positive: ○, 6700 v/cm; a, lower limit; △, 4200 v/cm, b, upper limit; ●, 2500 v/cm.

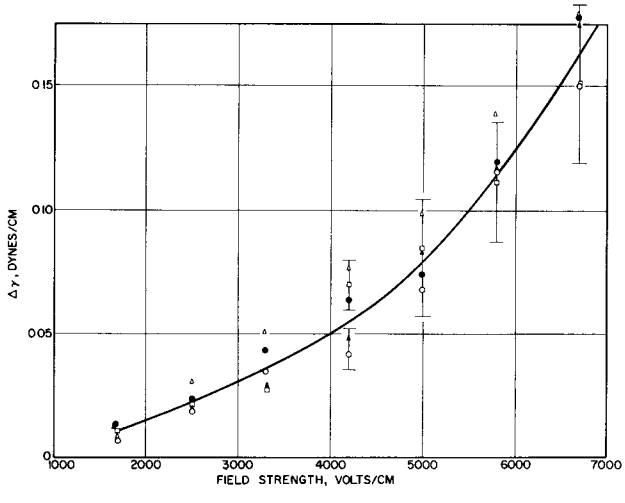

Fig. 5. Changes in surface tension of 3.5% NaCl solutions induced by electrostatic fields, air electrode positive: ○, float 1.774g, 4.5 cm between electrodes 7.3 cm working edge; △, float 2.747g, 4.5 cm between electrodes, 7.3 cm working edge; □, float 3.045g, 7.0 cm between electrodes, 7.3 cm working edge; ●, float 1.351g, 4.5 cm between electrodes, 7.3 cm working edge; ▲, float 1.055g, 4.5 cm between electrodes, 5.0 cm working edge.

flection. The curve is the average of the surface tension change thus obtained. Maximum and minimum values are indicated. Positive values of $\Delta\gamma$ correspond to a lowering of surface tension due to the electric field.

It has been pointed out to us (10) that the balance deflections observed on application of the field may be caused by Cl^- adsorption at the float/solution boundary, due to the differences in dielectric constants and induced by the applied field. This adsorption should depend strongly on dielectric constant and material of the float. A run was therefore made with a mica float carefully coated with paraffin. The results did not differ from the ones obtained with plain mica floats, proving that Cl^- adsorption at the float/solution boundary is either absent or does not influence the measurements.

Solutions of 0-3.5% NaCl content have been used for the experiments described here with the air electrode both positive and negative, using fields up to 7000 v/cm.

Results

The $\Delta\gamma$ values measured in the experiments just described were converted into absolute γ's using published data (11). Figures 6 and 7 give a plot of surface tension *vs.* NaCl concentration with field strength as parameter for positive and negative air electrodes, respectively. The surface deficiencies, Γ, have been calculated using the Gibbs adsorption equation and are presented in Fig. 8 and 9.

It is seen from Fig. 6 and 7 that both a positive and a negative air electrode lowers the surface tension of pure water, a negative air electrode more so than a positive one. The surface concentration of NaCl solutions is increased by a negative air electrode (Fig. 8),

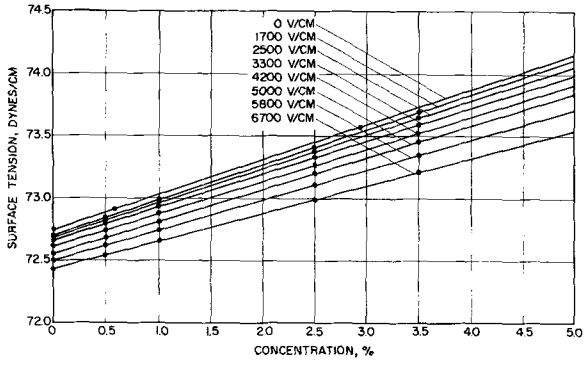

Fig. 6. Surface tension of NaCl solutions, air electrode negative

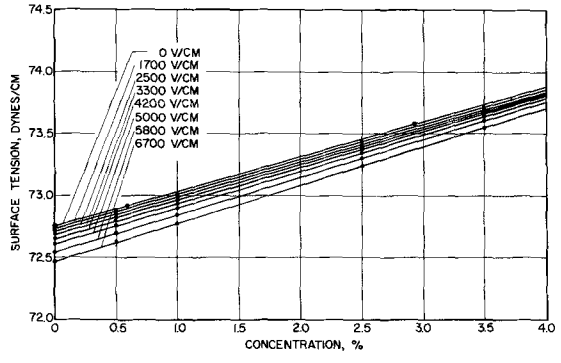

Fig. 7. Surface tension of NaCl solutions, air electrode positive

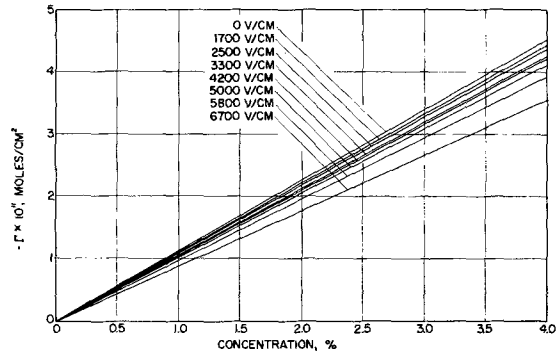

Fig. 8. Surface concentration of NaCl solutions, air electrode negative.

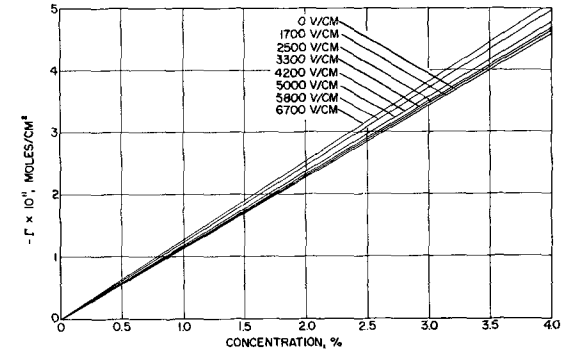

Fig. 9. Surface concentration of NaCl solutions, air electrode positive.

as compared to the surface concentration without a field. A positive air electrode leads, on the contrary, to a lower surface concentration (Fig. 9). The field strength necessary to lower the surface concentration by a given amount at a given bulk concentration is, however, considerably larger than the field strength necessary to raise the surface concentration by a like amount.

Discussion

Dipole orientation.—The potential drop at an air/water interface is, according to Kamienski (6), about 1v, and according to Frumkin (12), 0.1-0.2v. Assuming 10Å for the thickness of the oriented layer of water dipoles at the interface, one obtains a field strength of 10^7-10^8 v/cm. It is unlikely that with such a high field strength already present, application of less than 10^4 v/cm would produce a measurable change in surface tension. Since a measurable change is observed, it appears that either the potential drop across the interface is much smaller than previously thought, or that the thickness of the oriented layer of water dipoles is larger by one to two orders of magnitude.

Both a positive and a negative air electrode lowers the surface tension of pure water. It can be reasonably assumed that this lowering is caused by increased orientation of water dipoles. Equally oriented dipoles repel each other, thus leading to a decrease in surface energy. This leads to the conclusion that the orientation is very slight to start with, since both field directions enhance the orientation, *i.e.*, the surface potential is very close to zero. Pronounced orientation of water dipoles in one direction would

lead, on application of a field, to a lowering of surface tension with one polarity and a raising of surface tension with the other, which may be followed by a lowering in case the field is strong enough to reverse the dipoles. This has not been observed. The fact that a negative air electrode lowers the surface tension more than a positive electrode points to a slight orientation with the hydrogen atoms facing the air.

Surface concentration of NaCl.—The surface deficiency of solutions of strong electrolytes has been shown by Wagner (3) to be due principally to image forces. In his treatment, the concentration $c(x)$ is given as a function of the distance from the surface, x, by the usual Boltzmann expression

$$c(x) = c \exp(-W(x)/kT) \quad [3]$$

where the adsorption potential $W(x)$ is the work required to bring a charged ion from the solution bulk to a point x cm below the surface. For binary electrolytes, Wagner took $W(x)$ as equal for cations and anions, treated them as point charges, and from electrostatic theory obtained

$$W(x) = \frac{D-1}{D+1}\frac{e^2}{4Dx} \quad [4]$$

where D is the dielectric constant of water, and e is the charge on the ion. It is easily seen that integration of Eq. [3] with $W(x)$ as expressed by Eq. [4] would lead to an infinite amount of adsorbed solute. Ions, however, are not point charges, and in ionic solutions, the screening effect of the ion atmosphere limits the effective range of the electrostatic forces to a distance $1/\kappa$, where κ is defined by

$$\kappa^2 = \frac{4\pi}{DkT}\sum_i c_i z_i^2 \quad [5]$$

(13, 14), where c_1, c_2, . . . is the concentration (number of ions/cm^3) of ions with charges z_1, z_2, ... Introducing the mean distance of approach, a, from Debye-Hückel theory, and neglecting variation of κ with x, Eq. [4] is modified to

$$W(x) = \frac{e^{\kappa a}}{1+\kappa a}\frac{e^2}{4Dx}e^{-2\kappa x} \quad [6]$$

This expression, when introduced into Eq. [3], leads to a reasonable solution of c as a function of x. Onsager and Samaras (4) used this treatment to solve for a theoretical value of the surface excess, Γ:

$$\Gamma = -c_{bulk}\int_0^\infty [\exp(-W(x)/kT) - 1]\,dx \quad [7]$$

Values of Γ obtained from this integration were shown to agree satisfactorily with values of Γ obtained from the usual form of the Gibbs equation and surface tension measurements.

Application of an external field across the interface changes the value of the adsorption potential, $W(x)$, through a change in κ (assuming constant a and D) which in turn is a function only of the ionic strength (Eq. [5] and [6]). The changes in Γ with applied field, as indicated by our experiments, are a direct measure of these changes in ionic strength and could theoretically be used to calculate back to the change in adsorption potential induced by the field. This would, however, be a rather tedious procedure, and the uncertainties involved in many of the assumptions made by Wagner and by Onsager and Samaras are probably of greater magnitude than the influence of the field on this potential.

One conclusion which seems to be clear from the experiments, however, is that the difference in $W(x)$ between cations and anions must be taken into account in any refined treatment of the theory. No dependence of Γ on the direction of the applied field would be expected from the derivations above, yet a negative air electrode increases the surface concentration while a positive electrode decreases it, and the magnitude of the effects is different, being greater for the negative electrode (Fig. 8 and 9). From this dependence of Γ of the field direction, it appears that the main influence is centered on the sodium ion, although the reason for this behavior is not immediately clear. The explanation may lie in the difference in the screening effect $1/\kappa$ of the cations and anions as influenced by the electric field, which may be explained by the smaller radius (and resultant higher charge density) of the cation.

An alternative treatment of the concentration gradient at the surface of solutions of strong electrolytes has been given by Lewis (2). This treatment assumes an electrical double layer, made up of positive and negative ions, at the surface, and leads very simply to a modified form of the Gibbs equation

$$\Gamma = -\frac{a}{RT}\left(\frac{\partial\gamma}{\partial a}\right) - (\epsilon_1 + \epsilon_2)\frac{\partial\gamma}{\partial\psi} \quad [8]$$

where ϵ_1, ϵ_2 is the electrochemical equivalent of cations and anions, respectively, and ψ is the potential drop across the double layer.

The dependence of ψ on the externally applied potential, E, is not known. We assume, as a first approximation, a linear dependence of the interface potential on the applied potential, *i.e.*,

$$\Delta\psi = \beta\Delta E \quad [9]$$

where β is a dimensionless factor.

The charge, σ, for a diffuse double layer is given by the Gouy Chapman theory (13, 15) as

$$\sigma = \sqrt{\frac{DRTc}{2\pi}}\,(e^{F\psi/2RT} - e^{-F\psi/2RT}) \quad [10]$$

with c is the concentration of the electrolyte. On the other hand, σ is given by

$$\sigma = EC \quad [11]$$

where C is the capacity of the condenser formed between air-electrode and air/solution interface, per unit area,

$$C = \frac{D'}{4\pi d} \quad [12]$$

where D' is the dielectric constant of air and d the distance between air-electrode and air/solution interface. Combination of Eq. [10] and [11] gives

$$CE = \sqrt{\frac{DRTc}{2\pi}}\,(e^{F\psi/2RT} - e^{-F\psi/2RT}) \qquad [13]$$

and one can obtain

$$\frac{d\psi}{dE} = \beta = \frac{2RTC}{F}\sqrt{\frac{2\pi}{DRTc}}\,(e^{F\psi/2RT} + e^{-F\psi/2RT})^{-1} \qquad [14]$$

Using hyperbolic functions one obtains β as a function of E from Eq. [13] and [14]

$$\beta = \frac{2RTC}{F}\sqrt{\frac{\pi}{2DRTc + \pi E^2C^2}} \qquad [15]$$

For all practical purposes, $2DRTc >> \pi E^2C^2$ and one gets

$$\beta = \sqrt{\frac{2\pi RTC^2}{F^2Dc}}$$

$$= k\sqrt{\frac{1}{c}} \qquad [16]$$

with $k = \dfrac{2\pi RTC^2}{F^2D}$, and C as given by Eq. [12].

With D, the dielectric constant of the electric double layer, assumed to be about 4, and $C = 0.1$ e.s.u./cm^2, we obtain $k = 6.5 \times 10^{-11}$ (mole/cm^3)$^{1/2}$. For $c = 0.5$ mole/l and $\Delta\gamma/\Delta E = 10^{-4}$ dynes/v cm, one calculates (Eq. [8], [9], and [16])

$$(\epsilon_1 + \epsilon_2)\,\frac{1}{k}\sqrt{c}\,\frac{\Delta\gamma}{\Delta E} \approx 10^{-9}\ \text{moles/cm}^2$$

a number which seems unreasonably high.

In the preceding calculations, we have assumed the electrical double layer at the air-solution interface to be of a diffuse nature. This assumption was prompted by the experimental results showing that the effect of the field is mainly on cations, which are usually not thought of as being adsorbed in the inner double layer.

Grahame (16) found that the potential drop ψ_u across the inner double layer is a linear function of the adsorbed charge, σ. Using Grahame's equation for ψ_u

$$\psi_u = 2\pi\sigma\delta/D \qquad [17]$$

where σ is given by Eq. [11], δ is the radius of the hydrated ions; one obtains from Eq. [9], with ψ_u instead of ψ

$$\Delta\psi_u = \frac{2\pi\delta C}{D}\,\Delta E \qquad [18]$$

$$\beta' = \frac{2\pi\delta C}{D} \qquad [19]$$

Now, with $\delta = 10^{-7}$ cm, $C = 0.1$ e.s.u./cm^2, $D = 4$ e.s.u./cm, one obtains $\beta' \approx 10^{-5}$. This leads to a value of $\approx 10^{-11}$ moles/cm^2 for the correction term in the modified Gibbs equation (8), comparable to the order of magnitude given by the standard form of the equation and in good agreement with values of Γ obtained in our experiments with the field. There are too many assumptions involved, however, to warrant systematic calculations of Γ using Eq. [8].

Summary

Electrostatic fields of up to 6700 v/cm, positive and negative, have been applied to air/NaCl-solution interfaces and the surface tension changes measured with a surface energy balance. The NaCl solution concentration ranged from 0 to 3.5%.

It was found that either field direction lowers the surface tension of all investigated solutions. A positive air electrode lowers the surface tension of pure water less than a negative air electrode. This is taken as evidence that the field at the air-water interface is considerably smaller than the 10^7 v/cm previously assumed, that the orientation of the water dipoles at the interface is only slight, and that the predominant small orientation present is with the hydrogen facing the air.

The Gibbs equation has been used to calculate the surface deficiency of NaCl solutions under applied electric fields. The data show that a positive air electrode increases the surface deficiency and a negative air electrode decreases it. This behavior can be explained by assuming the electric field to be either exclusively or predominantly effective on the Na^+ ions alone, due to their smaller diameter. The conclusion is drawn that the difference in the adsorption energy, $W(x)$, of the Onsager-Samaras treatment for cations and anions cannot be neglected.

It is shown that the assumption of a diffuse double layer in the Lewis equation leads to a surface deficiency which is about two orders of magnitude too high. One obtains the right order of magnitude, however, by neglecting the diffuse layer and making the calculations on the basis of an inner double layer only. Most of the experience, which has led to the conclusion that cations are not usually adsorbed in the inner layer, has been obtained from studies of solid/solution interfaces. It is shown that this conclusion does not necessarily hold for air/solution interfaces.

Acknowledgment

This work was performed as part of Contract No. 14-01-001-200 with the Office of Saline Water/Department of the Interior. The authors wish to thank Dr. Norman Hackerman for many helpful discussions.

Manuscript received Jan. 25, 1962. This paper was prepared for delivery before the Indianapolis Meeting, April 30-May 3, 1960.

Any discussion of this paper will appear in a Discussion Section to be published in the June 1963 JOURNAL.

REFERENCES

1. J. W. Gibbs, *Scientific Papers*, **1**, 219.
2. F. C. Champion and N. Davy, "Properties of Matter," p. 189 ff, Blackie and Son Ltd., London (1959).
3. C. Wagner, *Physik. Z.*, **25**, 474 (1924).
4. L. Onsager and N. N. T. Samaras, *J. Chem. Phys.*, 2. 528 (1934).
5. H. Falkenhagen and E. Schmutzer, *Naturwiss.*, **40**, 92 (1955).
6. B. Kamienski, *Electrochim. Acta*, **3**, 208 (1960).
7. S. J. Barnett, *Phys. Rev.*, **6**, 257 (1898).

8. J. Guastalla, *J. Chim. Phys.*, **53**, 470 (1956).
9. A. J. G. Allan and A. E. Alexander, *Trans. Faraday Soc.*, **50**, 836 (1954).
10. A. Dravnieks, Discussion Remarks, Indianapolis Meeting, May 1960.
11. Lange's "Handbook of Chemistry," 9th ed., 1652 (1956).
12. A. N. Frumkin, *Electrochim. Acta*, **2**, 351 (1960).
13. J. Gouy, *J. Physique*, (4), **9**, 457 (1910).
14. P. Debye and E. Hückel, *Physik. Z.*, **24**, 185 (1923).
15. D. L. Chapman, *Phil. Mag.*, **25**, 475 (1913).
16. D. C. Grahame, Technical Report No. 1 (Second Series) to the Office of Naval Research, June 13, 1957.

Rest Potentials in the Platinum-Oxygen-Acid System

James P. Hoare

Research Laboratories, General Motors Corporation, Warren, Michigan

ABSTRACT

The rest potential of a platinum bead electrode in oxygen-stirred acid solution was investigated as a function of the pH, the partial pressure of oxygen, and the history of electrode preparation. It is believed that the theoretical equilibrium oxygen potential, +1.229v *vs.* N.H.E., cannot be obtained in any known system because all known electronic conductors interact with oxygen. One observes, then, a mixed potential. Such systems are not at equilibrium but in a steady-state condition. Evidence for the understanding of the nature of the potential-determining reactions in this system are presented.

Although a considerable amount of work has been done on the oxidation and reduction of oxygen on a platinum electrode, certain areas still require close examination. Some investigators (1-3) have detected the presence of peroxide intermediates in this system while others have not (4). From the work of Bockris and Huq (2) it appears that the presence of impurities may alter the behavior of this system. It is interesting to note that a platinum oxide electrode prepared by an anodizing process differs in electrochemical properties from one made in air (4-6).

A sizable barrier in the determination of the metal-metal oxide equilibrium potentials is the difficulty with which these relatively unstable oxides can be prepared (7). The dry oxides have different compositions than the hydrated ones (8). If one prepared a given platinum oxide, mounted it on a platinum gauze, and immersed it in an acid solution, the final state would most likely be quite different from the initial. As a result, the recorded potentials are quite uncertain (9-11).

It is the purpose of this work to study the rest potential of a platinum electrode immersed in an oxygen-saturated sulfuric acid solution as a function of the partial pressure of oxygen, pH, and previous history of the electrode preparation in order to present evidence for the understanding of the nature of the potential-determining reactions in this system.

Experimental

The test electrodes were small beads (0.1-0.2 cm in diameter) of platinum (99.9+% pure) melted on the end of the metal wire in an oxygen torch. Platinum wire leads were spot-welded to the test electrode.

The test cell, shown in Fig. 1, was made of Teflon and is composed of two compartments connected through a fritted disk and held together with a clamp made of Lucite. Leakage of solution around the frit is prevented by the use of a polyethylene gasket. In physical appearance this cell is similar to one described before (12). The right-side compartment, in which the test electrodes are placed, contains a large platinum gauze counterelectrode held in place against the cell wall with a Teflon ring. In the left-side compartment, in which the reference electrode is placed, a large platinum gauze, which may be used as a counterelectrode, and a small platinum gauze, which may be used as a hydrogen reference electrode, are held against the cell wall by a Teflon ring. Through the tops of both sides of the cell pass gas-inlet and -outlet tubes made of Teflon. Also, Teflon tubes passing through each top are available through which the test and reference electrodes may be inserted into the cell. At the

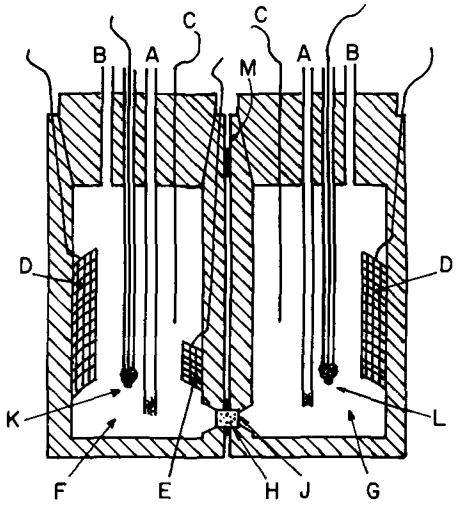

Fig. 1. Teflon dual cell. AA, gas inlet tubes; BB, gas outlet tubes; CC, pre-electrolysis electrodes, DD, large Pt-gauze counterelectrodes, E, small Pt-gauze electrode; F, left-side compartment; G, right-side compartment; H, polyethylene gasket; J, glass frit; K, α-palladium reference electrode; L, test electrode; M, spacer.

bottom of each inlet tube is placed a ball of platinum gauze to break the gas stream into fine bubbles. Finally, a small hole, through which a thin platinum wire may be inserted as a pre-electrolysis electrode, is made in each top.

The choice of a reference electrode system is a very important step in this investigation. The α-palladium-hydrogen (13, 14) reference electrode was chosen for the following reasons. Unfortunately, platinum-oxygen electrodes are neither reversible nor reproducible so that a Pt/O_2 electrode cannot be used in a manner similar to the Pt/H_2 electrode in the hydrogen overvoltage studies. Reference electrode systems such as the calomel and mercurous sulfate electrodes are undesirable because of the possibility of introducing chloride or mercury ions into the system. Another disadvantage with the calomel system is the presence of a junction potential. Finally, a platinum-hydrogen reference electrode is unsuitable because the dissolved hydrogen can pass through the frit and depolarize the oxygen electrode in the right-side compartment. The α-palladium reference electrode avoids these problems since it is reversible to hydrogen ions but independent of the partial pressure of hydrogen gas (14). Therefore, hydrogen gas need not be bubbled in the left-side compartment.

To make an α-palladium reference electrode, one proceeds as follows. A small bead (0.1-0.2 cm in diameter) is melted on the end of a palladium wire and a platinum lead wire is spot-welded to it. The bead is cleaned by heating it red-hot in a burning hydrogen jet and plunging the hot bead into concentrated nitric acid. This procedure is repeated about twenty times. Then the lead-wire and the bead are imbedded in virgin polyethylene so that the weld area is covered and only a hemisphere of the bead is exposed. After inserting the electrode through the Teflon tube in the cell top, it is sealed to the tube with molten polyethylene. The cell and the electrode are soaked in triply distilled water for 48 hr with frequent changes of water. After the test solution is added and after pre-electrolyzing against the auxiliary electrode for about 24 hr, purified hydrogen is bubbled through the solution until the potential of the bead has remained steady for 30 min at 50 mv against a Pt/H_2 electrode in the same solution. Then the hydrogen flow is stopped and the cell is sealed off to the atmosphere. In the absence of oxidizing agents, it has been shown that such an electrode will exhibit +50 mv *vs.* Pt/H_2 in the same solution for a week in a hydrogen atmosphere (15) and indefinitely in a helium atmosphere (16). It is very important that all three-phase contact between palladium, platinum, and solution be avoided, otherwise a local cell will be set up and a steady potential of 50 mv will not be observed (17).

All solutions were made from reagent grade chemicals and from triply distilled water obtained from an all-quartz still. The gases, H_2, N_2, and O_2, were purified in a standard multistage purification train containing heated copper turnings or copper oxide, silica gel, ascarite, heated palladium-on-asbestos, liquid nitrogen trap, and rotameter to monitor the gas flow. The partial pressure of oxygen was varied by diluting with nitrogen since the molecular weights are similar and the mixing of the gases would be facilitated thereby. The mixing was accomplished by connecting the outlets of the nitrogen and the oxygen trains by a "Y" tube and passing the gas through a coil of about 30 ft of tubing before entering the cell. The partial pressure was determined from the rotameter readings according to

$$(O_2 \text{ reading})/(O_2 + N_2 \text{ readings}) = P_{O_2}$$

Although this procedure involves a certain amount of error, consistent results have been obtained.

All electrodes were cleaned in the same manner as that just described for the palladium bead. The Teflon cell and the fritted disks were cleaned by soaking for 24 hr in concentrated HNO_3 and then rinsing in triply distilled water. After the cell had been assembled with the test electrodes mounted in the right side and the palladium bead in the left side, the cell was soaked in triply distilled water with frequent changes of water for at least 48 hr. Then the cell was filled half full (about 25 cc, total) with the test solution and the cell tops sealed in place with molten polyethylene. All the electrodes were tied together and pre-electrolyzed for at least 24 hr against the auxiliary platinum wire pre-electrolysis cathodes. Pre-electrolysis was stopped by removing the platinum wire cathodes and thus breaking the electrical circuit. Hydrogen gas was bubbled into the left side until the palladium bead showed a potential of +50 mv against a Pt/H_2 electrode in the same solution for at least 30 min. Then this side was sealed off to the atmosphere, and potential measurements on the oxygen electrode in the right side were made against the α-palladium electrode in the left side. It was found that the reference potential was invariant frequently for 48 hr and always so up to 24 hr. The reference potential decayed due to the diffusion of dissolved oxygen from the right side to the left side which depolarized the α-palladium electrode.

The pH of the solutions was varied by diluting the 2*N* H_2SO_4 solution with 2*N* Na_2SO_4 solution. At the end of an experiment, a saturated calomel electrode (S.C.E.) was placed in the cell, and the potential against at Pt/H_2 electrode in the same solution was determined. This value was compared to that for the stock solution which had been determined by a separate experiment, and the values agreed within 5 mv. By this measurement, the potentials can be recorded on the normal hydrogen scale (N.H.E.). *All potentials will be referred to N.H.E. unless otherwise noted.*

The temperature of all these experiments was 24° ± 1°C. Samples of solution can be removed from the cell by inserting the 4-in. needle of a hypodermic syringe into the gas exit tube. The potential was measured with a General Radio Electrometer, model number 1230-A, having a variable input impedance from 10^{14} to 10^{4} ohms.

Results and Discussion

Dependence of rest potential on presence of peroxide.—The potential of a platinum bead that was being anodized at about + 1.9v (*vs.* N.H.E.) in O_2-saturated 2*N* H_2SO_4 solution fell rapidly to about 1.5v after the circuit had been broken. Then the potential fell more or less slowly and regularly through a potential of 1.23v to a minimum value of about 850 mv in less than an hour, after which the potential became more noble again. Within three or four hours, the potential became steady at a value between +920 and +970 mv. A sample of the solution in the cell gave a positive test for peroxide with the $TiSO_4$ reagent (18).

Next, hydrogen gas was bubbled over the platinum bead for about 30 min so that the solution would become saturated with hydrogen. The potential fell to the hydrogen potential (—50 mv with respect to α-palladium). Then the H_2-stirring was replaced with O_2-stirring, and the potential rose rapidly to about +700 mv and more slowly afterwards. Within about 2 hr the potential had reached 1000 mv, and after about 20 hr the potential had become steady at a value between 1050 and 1080 mv. This potential remained steady for at least 24 more hours (further observation could not be made because the α-palladium potential began to decay due to O_2-diffusion into the left-side compartment). When the solution was tested with $TiSO_4$ reagent a negative test for peroxide was obtained.

With a hypodermic syringe, H_2O_2 solution was added to the cell until the sulfuric acid solution was about 4×10^{-6}M in H_2O_2. The potential dropped quickly to a steady value of about 825 mv.

These experiments indicate that the anodization of platinum in O_2-saturated solutions builds up the concentration of hydrogen peroxide which depresses the potential of the system as noted by Berl (19). If, however, the peroxide is removed by reaction with dissolved H_2, the potential can more nearly approach the reversible oxygen potential of 1.229v (11).

Dependence of rest potential on partial pressure of O_2.—In another set of experiments, the partial pressure of oxygen was varied in a system containing a platinum bead in oxygen-stirred acid solution which did not contain a detectable amount of peroxide. The data at three different mixed potentials corresponding to different stages of surface development are presented in Table IA in the sequence with which the experiments were performed. Each reading had been time independent for a duration of 10-20 min before being recorded. The data in rows 9, 10, and 11 show that the potential is independent of stirring which indicates that a potential-determining reaction free from diffusion control has been established. Since the potential is the same for various rotameter settings giving the same partial pressure of oxygen, *e.g.*, rows 2, 4, and 7, it seems that the method gives fairly consistent results.

Consider a general over-all apparent, potential-determining reaction involving oxygen, such as

$$O_2 + xX + ne^- = yYO \qquad [1]$$

where X is a substance such as H^+, n is the number of electrons transferred in the over-all reaction, YO is a substance such as H_2O, and x and y are stoichiometric coefficients. The Nernst relationship for this reaction is

$$E = E_o' + (RT/n\mathbf{F}) \ln [a_X^x P_{O_2}/a_{YO}^y] \qquad [2]$$

If only P_{O_2} is varied, then the activity terms may be combined with E_o' to give an expression for E as a function of P_{O_2}

$$E = E_o + (0.059/n) \log P_{O_2} \text{ (at 25°C)} \qquad [3]$$

E_o is the value of E when $P_{O_2} = 1$ so that n may be estimated from the data in Table I and is given in the last column of Table I. From the data in Table

Table I. Dependence of the rest potential of a platinum bead electrode on the partial pressure of oxygen gas in 2*N* sulfuric acid

$n = 0.059 \log P_{O_2}/(E - E_o)$

A—no detectable peroxide
B—peroxide from electrode anodization detectable
C—4×10^{-6}M hydrogen peroxide

Rotameter reading* O_2	Rotameter reading* N_2	Potential *vs.* α-Pd refer., mv	P_{O_2}	$E - E_o$, mv	n
		A			
5.4	0	855	1	0	—
5.3	6.7	851	0.44	—4	5.3
5.3	11.5	848	0.31	—7	4.3
10.5	11.5	851	0.48	—4	4.7
3.5	15.3	845	0.19	—10	4.1
5.1	0	855	1	0	—
4.9	5.9	851	0.45	—4	5.1
10.9	0	855	1	0	—
4.6	0	872	1	0	—
11.3	0	872	1	0	—
0	0	872	1	0	—
4.0	5.1	868	0.44	—4	5.3
3.9	9.3	866	0.29	—6	5.3
3.9	3.6	868	0.52	—4	4.2
5.4	0	872	1	0	—
12.0	0	998	1	0	—
4.2	0	998	1	0	—
4.2	6.5	993	0.39	—5	4.7
4.2	9.8	990	0.30	—8	3.9
4.2	14.0	989	0.23	—9	4.2
7.2	0	998	1	0	—
		B			
5.0	0	815	1	0	—
3.3	7.2	810	0.47	—5	3.8
4.1	12.9	805	0.24	—10	3.6
4.2	0	815	0	0	—
4.2	4.7	810	0.42	—5	4.4
3.3	6.7	808	0.3	—7	4.4
12.0	0	815	1	0	—
		C			
5.3	0	772	1	0	—
5.6	6.6	765	0.46	—7	2.8
5.5	10.0	760	0.35	—12	2.3
10.5	9.7	765	0.48	—7	2.6
5.3	15.0	757	0.26	—15	2.3
5.7	0	772	1	0	—

* The rotameter calibration curves are fairly linear from a reading of 3.0 corresponding to 95 cc/min to a reading of 13.0 corresponding to 600 cc/min.

IA, it seems that the apparent potential-determining reaction is one involving the transfer of 4 electrons. Because the values of n average about 16% higher, it would indicate that the method is more precise than accurate due to the errors in determining P_{O_2} and the inability to read the potential to better than one part in a thousand. Furthermore an uncertainty of $\pm$ 1 mv in $E - E_o$ indicates an uncertainty of 25%-10% in n. However, these data certainly favor the suggestion that the potential-determining reaction is one such as

$$O_2 + 4H^+ + 4e^- = 2H_2O \qquad [4]$$

In Table IB are recorded the potential-oxygen pressure data obtained on the system in which a detectable amount of H_2O_2 had accumulated in the electrolyte due to the anodization of the electrodes. By treating these data as before the estimated value for n is much lower than that in Table IA. The data in Table IC were found for the system in which the electrolyte was made 4×10^{-6}M in H_2O_2. Here the value for n is very close to 2 and leads to the suggestion that, as the H_2O_2 concentration increases the rest potential becomes increasingly determined by a 2-electron reaction such as

$$O_2 + 2H^+ + 2e^- = H_2O_2 \qquad [5]$$

It is to be noted that the potential falls as the H_2O_2 concentration increases towards the E_o value for Eq. [5] of + 682 mv (referred to N.H.E.).

The platinum-platinum oxide couples.—Another series of experiments was carried out in which purified nitrogen was used to stir the system after the potential had become steady in oxygen-stirred 2N sulfuric acid at 1045 mv. After about 2 hr of N_2-stirring, the potential became quite constant at 875 mv. As soon as O_2-stirring replaced the N_2 the potential returned to 1027 mv in about 2 hr. This procedure was repeated many times on different samples of platinum; the potential always came to a steady value between 870 and 890 mv with N_2-stirring.

El Wakkad (20) reports that the potential of a Pt/PtO couple is about 0.88v in acid solution. This corresponds to the point on the potential-time curves where oxide-formation first appears when a previously cathodized platinum electrode is anodized in acid solution (21-23). However, Latimer (11) and others (24) report a value of 0.98v for a $Pt/Pt(OH)_2$ couple in acid solution which is based on thermochemical data obtained from a chemically prepared compound. Since the chemically prepared $Pt(OH)_2$ may very likely be different from the hydrated PtO on the platinum electrode surface, the value of 0.98v for the Pt/PtO couple may be questionable. Coulometric determinations (4, 21, 22) of the quantity of oxygen existing on a platinum electrode anodized to the point of oxygen evolution in acid solution show that the platinum surface is covered with an oxide monolayer corresponding to PtO (23). Since this oxide layer is an electronic conductor (22), additional layers can be formed only under extreme conditions (25).

It is suggested, then, that the potential-determining reaction established at the platinum electrode in N_2-stirred 2N H_2SO_4 solution is most likely

$$PtO^* + 2H^+ + 2e^- = Pt + H_2O \qquad [6]$$

where the symbols PtO* and H^+ refer to the hydrated oxide on the platinum surface and to the hydrated proton in solution, respectively. In view of the data presented here, a potential value of 0.88v is favored for the equilibrium potential of Eq. [6]. It is believed that PtO* is not a formal oxide but is more akin to an adsorbed layer of oxygen, Pt-O. Platinum atoms do not seem to be pulled out of the lattice since the anodized Pt-bead is still bright and smooth. It may be, then, that there is really only one true oxide of platinum, PtO_2.

It has been reported (4) that the oxide film on anodized platinum electrodes contains a high percentage of PtO_2 and that the equilibrium potential for a $PtO_2/Pt(OH)_2$ is about 1.1v (11). When a platinum electrode is anodized, peroxide is accumulated in the electrolyte which interferes with the potential measurements, and, when the solution is stirred with hydrogen to remove the peroxide, the oxides on the platinum surfaces are removed as well.

To investigate the influence of PtO_2 on the potential the following experiment was devised. Two identical Teflon cells were used. In the first cell only the 2N H_2SO_4 solution was pre-electrolyzed, and in the second the test electrodes were pre-electrolyzed in the same solution. After the pre-electrolysis procedure was finished, hydrogen was bubbled into the first cell for 30 min to destroy any peroxide present. Afterward, the hydrogen was replaced with oxygen. When the electrolyte was saturated with O_2 (after 30 min), the electrodes were transferred from the second cell to the first. Potential measurements were taken. The potential fell from an initial value of about 1500 mv to about 935 mv in about 15 min and then became more noble again. Finally, it came to a value of 987 mv which remained steady for an observed 3-hr period. When the O_2-stirring was replaced by H_2 for 15 min and then resumed, the potential rose rapidly from the hydrogen potential (—50 mv *vs.* α-palladium) to + 1016 mv in about 45 min. These data indicate that the presence of PtO_2 causes a significant depression of the rest potential of a platinum bead in O_2-stirred acid solution.

The reason why a potential of 1.229v cannot be reached in the platinum-oxygen-acid system is the fact that the 4-electron reaction, Eq. [4], does not take place on a pure platinum surface but on a PtO surface. One can visualize the 4-electron process occurring at certain sites on the oxide covered platinum surface while at other sites the Pt/PtO couple, Eq. [6], occurs. Since the surface is an electronic conductor and therefore is an equipotential surface, these processes will proceed at the same mixed potential (26) due to the flow of the local cell current. The value of the mixed potential will be between about 0.88 and 1.23v; its exact position will depend on the relative polarization of the two

reactions. The flow of the local-cell current would be such that Eq. [4] would be cathodized and Eq. [6] would be anodized. From the experimental data, it appears that the 4-electron reaction proceeds on oxygen covered sites at a much faster rate than on bare sites, probably due to the relative strengths of the platinum-oxygen and platinum oxide-oxygen bonds. This may be seen from the following analysis.

Initially, after a platinum bead had been treated with hydrogen and then the H_2-stirring replaced by O_2-stirring, the surface had relatively few sites covered with oxygen. In this case, for a given local cell current, the current density for the 4-electron reaction occurring at covered sites is much higher than that for the Pt/PtO reaction occurring at uncovered sites and so the 4-electron reaction will be polarized to a greater extent. As a result, the mixed potential will have a value closer to 0.88v, as shown in Fig. 2(a). Because the local cell reaction is such that the Pt/PtO reaction is anodized, PtO will accumulate on the surface, providing more sites on which the 4-electron reaction can occur. Then the current density and, consequently, the polarization for this reaction decreases while the current density and polarization will increase for the Pt/PtO reaction. The mixed potential becomes more noble as shown in Fig. 2(b). If this process continued, eventually the surface would be completely covered with PtO and now only the 4-electron reaction would occur. A potential of 1.23v would be observed since the PtO layer is an electronic conductor and inert to oxygen.

The fact that the 1.23-v potential is not observed suggests that the cathodic reaction of Eq. [6] continuously provides a supply of bare platinum sites. The system then comes to a steady state involving the anodic and cathodic reactions of Eq. [4] and [6] to a point where the relative steady-state current densities produce a steady-state mixed potential value between 1.05 and 1.08v as shown in Fig. 2(c).

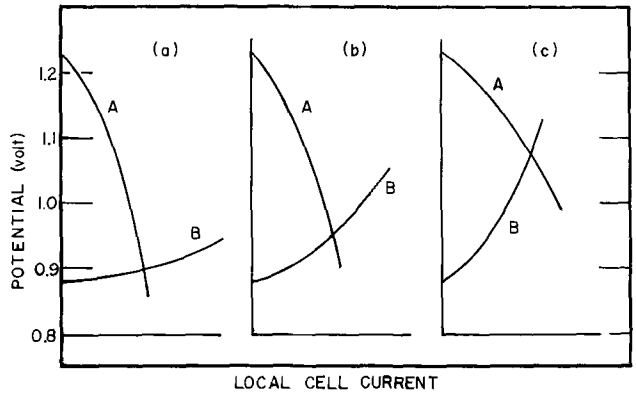

Fig. 2. Sketch of the polarization curves for the two component reactions of a local cell. The potential at the point where the curves cross is the mixed potential, and the current at that point is the total local cell current. Curve A is the polarization curve for the cathodic reaction, $O_2 + 4H^+ + 4e^- = 2H_2O$; curve B, that for the anodic reaction $Pt + H_2O = PtO + 2H^+ + 2e$. Vetter and Berndt (21) have estimated the local action current to be about 0.2×10^{-5} amp/cm^2 except that they attributed this current entirely to impurities. See text for (*a*), (*b*), and (*c*). Potential *vs.* N. H. E.

This means that under open-circuit conditions a certain number of platinum sites that are not covered with oxygen are always present.

The results of the following experiment support the suggestions presented in Fig. 2. Two platinum beads whose exposed geometric areas were nearly the same (0.019 and 0.022 cm^2) were placed side by side in oxygen-stirred acid solution after having been anodized previously. By chance the potentials were different, the one being 1066 mv and the other 911 mv. Then the system was stirred with hydrogen (240 cc/min) and by means of a Honeywell-Brown recorder the time required to reach the hydrogen potential (−50 mv *vs.* α-palladium) was determined for each bead simultaneously. The platinum bead, registering 1066 mv initially, required 450 sec while that registering 911 mv required 200 sec. This indicates that the more nearly the surface is covered with oxygen the more closely will the potential approach the equilibrium value of 1.229v.

A platinum wire was cleaned in a hydrogen flame, allowed to cool in air for 5 min, and then plunged into O_2-stirred acid solution with peroxide absent. The potential was initially 996 mv, but came to a steady value of 1060 mv within 15 min. This shows that the same type of oxide film is formed on platinum in air as by the adsorption of oxygen from acid solution. Also, the film must be nearly a complete monolayer thick because it required only 15 min to set up the steady state. This rapid establishment of a steady rest potential is to be compared with the slow rates observed in solution.

It seems strange that the mixed potential should become less noble when PtO_2 is present if the PtO_2/$Pt(OH)_2$ potential is 1.1v. Again one is justified in mistrusting a potential value derived from the data for chemically prepared $Pt(OH)_2$. In fact, it has been suggested (25) that the equilibrium potential of the PtO_2 electrode is closer to 0.8v. The experimental data seem to support this contention.

Attainment of the theoretical equilibrium-oxygen potential.—It seems, then, that the procedure including anodic pre-electrolysis followed by saturation of the electrolyte with hydrogen will produce a fairly reproducible platinum-oxygen electrode with a rest potential of 1.06 ± 0.01v. It appears, also, that the 1.23-v potential can never be observed because there are not any electronic conductors known that are inert to oxygen and, consequently, a mixed potential is always observed for practical oxygen systems.

Bockris and Huq (2) have reported that a rest potential with a value of 1.24v was established at a platinum electrode in oxygen-saturated acid solution after carrying out a careful purification procedure. However, they report further that this potential remained steady at the 1.24-v value for only 1 hr, after which the potential decayed rapidly to less noble values. It is interesting to note that the potential returned to a value of 1.24v for an additional hour after the purification procedure had been repeated. On consideration of these findings and in view of the work presented in this report,

it seems possible that the Bockris and Huq experimental procedure may have introduced a peroxide, a persulfate, or some other transitory substance that set up a fortuitous steady-state potential value close to the 1.229-v value.

Although the procedure of extrapolating the anodic and cathodic Tafel plots of oxygen overvoltage which have different slopes over such a long distance to the point of their crossing is dangerous, the value of 1.229v obtained (2, 27) at the crossing where the anodic and cathodic current densities are the same may not be as fortuitous as one may think. First of all, under pre-anodic polarization the surface is covered by a conducting monolayer of oxygen (22), and it seems that the over-all 4-electron reaction can proceed on this surface. It is noted that the Tafel lines were obtained at very low current densities, so that even on cathodic polarization the oxide layer would still be intact and any effect of Eq. [6] would not be present. Second, different Tafel slopes may mean that different steps of the same over-all reaction are rate-determining and not necessarily that different over-all reactions are operative. Therefore, by extrapolating the Tafel lines to their crossing point, it is possible to simulate a situation not possible to attain in practice, *i.e.*, the 4-electron reaction proceeding on a platinum electrode whose surface is covered by a stable, complete monolayer of oxygen. As mentioned above, this system should exhibit a potential of 1.229v because such a surface would be an electronic conductor inert to oxygen.

Dependence of rest potential on pH.—In a series of experiments in which a platinum bead was prepared as described above by using hydrogen stirring prior to oxygen stirring, the potential was determined as a function of pH. The data from three typical runs are presented in Table II. The composition of the solutions is given in the first column. The pH values recorded in Table II were obtained from tables in Lange's Handbook for Pt/H_2 *vs.* S.C.E. The potential values against both the α-palladium and N.H.E. for the case of O_2-stirring and for the case of N_2-stirring are presented. Since for all these reactions one electron is transferred for every H^+ ion involved, there should not be any difference in the potential with respect to α-palladium with changes in pH. As shown in Table II this was observed. However, the potentials *vs.* the N.H.E. should show a change of 59 mv per pH unit according to the Nernst relationship. In the last column of Table II for the N_2-stirred case, the ratio of the change in potential from that found in 2*N* H_2SO_4 to the corresponding change in pH is recorded. The agreement is quite good. Similar values are obtained in O_2-stirred solutions.

Table II. Dependence of the potential of a platinum bead electrode on pH

Solution composition	Potential of Pt/H_2 *vs.* S.C.E., mv	pH	Potential, mv O_2-stirred *vs.* α-Pd	O_2-stirred *vs.* N.H.E.	N_2-stirred *vs.* α-Pd	N_2-stirred *vs.* N.H.E.	ΔE/ΔpH
2*N* H_2SO_4	−246	0	1000	1046	830	876	—
0.1*N* H_2SO_4 + 2*N* Na_2SO_4	−345	1.7	1010	957	840	787	52
0.1*N* H_2SO_4 + 2*N* N_2SO_4	−408	2.7	1005	889	830	714	60

Polarization at low current densities.—By using the variable input impedance control on the General Radio electrometer, minute currents could be passed between the α-palladium reference electrode and the test electrode. Since the α-palladium electrode is quite reversible (13), since the electrolytes are highly conducting, and since the stirring-gas flow was between 200 and 300 cc/min, it is safe to assume that the measured polarization is due to that on the test electrode. The test electrode was cathodized in this setup. From the measured potential, the given input impedance, and the measured, exposed geometric area of the bead electrode, an apparent current density was estimated. These data are plotted in Fig. 3 with the difference between the open-circuit potential and the polarized potential, $E_{oc} - E$, as ordinate and the logarithm of the apparent current density as abscissa. Curve A shows the polarization of a platinum bead in O_2-stirred 2*N* H_2SO_4 solution in the absence of a detectable amount of peroxide; curve B, that in the presence of a detectable amount of peroxide; curve D, that for an anodized bead in O_2-stirred solution in the absence of peroxide; and curve C, that for the platinum bead in N_2-stirred solution in the absence of peroxide. The arrows on the curves show that these points could be reproduced within 2 mv going either up or down in current density. Curve C could not be reproduced in either direction due to an extremely large hysteresis, indicating that Eq. [6] proceeds with great difficulty. If this reaction is the main contributor to the formation of the surface film of PtO under open-circuit conditions rather than direct adsorption of dissolved O_2 molecules, it could explain the very great lengths of time (~10 or 12 hr) required to set up the steady state in O_2-stirred acid solutions.

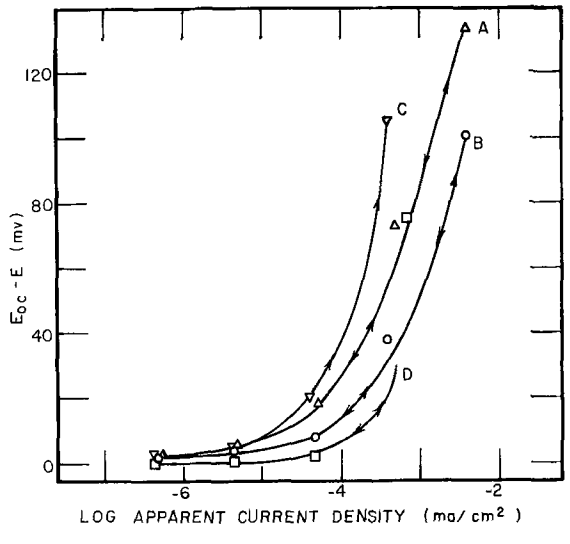

Fig. 3. Cathodic polarization data for Pt-O_2 system in absence of H_2O_2 (A), in presence of H_2O_2 (B), in N_2-stirring (C), and in presence of PtO_2 (D).

It will be noted that the polarization when peroxide is present is much less than when it is absent which agrees with the observations of Berl (19) that a good reversible oxygen electrode can be set up in peroxide solutions. This suggests that the O-O bond must be a very stable bond, so much so that if enough peroxide is present the 2-electron reaction, Eq. [5], becomes potential-determining as shown by the data in Table IC. In fact, this bond appears to be so strong that in the anodic process a certain concentration of peroxide must be built before oxygen can be evolved efficiently, since peroxide is always detected (1, 2, 23) in these cases. This may provide some justification for suggesting that direct adsorption of dissolved oxygen from solution under open-circuit conditions plays a minor role in forming the PtO film. It may be that the O-O bond is so strong that only adsorption at special high energy sites (the nature of which will not be defined) can provide energy enough to break it. The number of such sites would, of course, be few, indeed.

Apparently, from curve D, the presence of PtO_2 in the oxide film decreases the polarization. This may explain why some workers (4-6) find that a platinum electrode that has been anodized provides a more stable electrode in electroanalytical systems than one which has not. Besides, a certain amount of peroxide is formed under these conditions, and this will produce a much more reversible system also.

Effect of poisoning.—In order to test the effect of poisons on the platinum-oxygen-acid system, the following series of experiments was performed. In each case, a clean platinum bead in O_2-stirred 2*N* H_2SO_4 solution was the initial state. The cleanliness of the system was checked by observing the high pseudocapacitance (28) exhibited by a clean hydrogen electrode (29, 30) when H_2-stirring was used. This was done by cathodically polarizing the test electrode with an electronic current interrupter before the H_2-stirring was replaced by O_2-stirring. After the potential had come to a fairly steady value of 980 mv with O_2-stirring, it was polarized with a cathodic current density of about 0.5 μa/cm^2 by setting the input impedance of the electrometer at 10^8 ohms. This depressed the potential by 33 mv to 947 mv. Next, the platinum bead was removed from the cell, and only the bead was dipped in a weak solution of sodium arsenate. When it was replaced in the cell, it exhibited the same potential of 980 mv as before, even after about 45 min. Then the platinum bead was cathodized at 0.5 μa/cm^2 for about 15 min which caused a potential drop of 75 mv. After the polarizing circuit was broken, the potential returned directly to the original value of 980 mv. In a similar experiment, the platinum bead was poisoned by dipping it in a solution of carbon disulfide. In this case, the open-circuit potential dropped from the clean value of 985 mv to 855 mv. When this poisoned electrode was cathodized at 0.5 μa/cm^2, the potential was depressed 120 mv to 735 mv, but the potential returned to 853 mv when the circuit was broken. In a third experiment the bead was poisoned by touching the platinum bead with a finger. Here, the open-circuit potential rose to 1085 mv, and cathodic polarization at 0.5 μa/cm^2 dropped the potential by 202 mv. After opening the circuit the potential returned to 1085 mv. At the end of these experiments H_2-stirring was used, and the pseudocapacitance was observed again with the current interrupter. The pseudocapacitance, of course, was very low now in each case (29, 30).

As pointed out by Bockris and Huq (2) and as shown here, the presence of impurities can affect profoundly the kinetics and potentials in the platinum-oxygen-acid system. In the case of arsenic poisoning, it appears that the open-circuit potential is not significantly altered because arsenic is an electronic conductor. However, the kinetics are affected because As-O sites are poorer catalysts for the oxygen reaction than Pt-O sites. With carbon disulfide poisoning, apparently another electrochemical reaction is set up, and both rest potential and kinetics are affected. As for poisoning with grease, the system is completely changed, and coherent results are not obtained.

Summary and Conclusions

A platinum oxygen electrode in sulfuric acid with a reproducible potential of 1060 ± 15 mv *vs.* N.H.E. may be obtained by rigorous removal of impurities from the system and by anodic pre-electrolysis followed by saturation of the system with bubbling H_2 before the system is stirred with O_2. This procedure removed peroxides and higher oxides of platinum which depress the potential of the system. This final rest potential is reached very slowly (~10 to 12 hr) because atoms must be transferred across the double layer, *i.e.*, adsorption processes are involved. For these reasons this system is quite irreversible.

It is suggested that this rest potential is a mixed potential arising from the local cell composed of the reactions [4] and [6]. It is for this reason that the rest potential may never reach the theoretical equilibrium value of 1.229v for the 4-electron oxygen reaction. It seems that a value of 0.88v is a more realistic one than 0.98v for the potential of the Pt/PtO couple.

It appears that the O-O bond is so strong that the evolution of oxygen on anodic polarization of the platinum-oxygen-acid system is accompanied by an accumulation of H_2O_2 in the electrolyte. If enough peroxide is present the 2-electron oxygen reaction [5] becomes the potential-determining reaction. This system makes a good reversible oxygen electrode.

It is also suggested that the poor reproducibility of the rest potentials in the platinum-oxygen-acid system, noted in the literature, is due to the presence of uncontrolled amounts of H_2O_2, higher oxides of platinum, and organic and inorganic impurities. It may be the case that pre-anodized Pt/O_2 electrodes are more suitable in electroanalytical systems than those that are not pre-anodized because H_2O_2 and higher oxides of platinum are present.

When these substances are present the system becomes more reversible.

Acknowledgments

The author is indebted to Mr. C. F. Nixon, Head of the Electrochemistry Department, for his many helpful comments and for his continued interest in this work. He is also grateful to Dr. Paul Delahay, Dr. Raymond Thacker, and Dr. John L. Griffin for many interesting and fruitful discussions. The author is indebted to Mr. Sigmund Schuldiner of the Naval Research Laboratory, Washington, D. C., for his helpful suggestions in the preparation of the final manuscript.

Manuscript received Jan. 8, 1962; revised manuscript received May 14, 1962. This paper was prepared for delivery before the Los Angeles Meeting, May 6-10, 1962.

Any discussion of this paper will appear in a Discussion Section to be published in the June 1963 JOURNAL.

REFERENCES

1. S. Glasstone and A. Hickling, *Chem. Revs.*, **25**, 407 (1939).
2. J. O'M. Bockris and A. K. M. S. Huq, *Proc. Roy. Soc. London*, **A237**, 277 (1956).
3. A. V. Akopyan, *Zhur. Fiz. Khim.*, **33**, 82 (1959).
4. J. J. Lingane, *J. Electroanal. Chem.*, **2**, 296 (1961).
5. D. T. Sawyer and L. V. Interrante, *ibid.*, **2**, 310 (1961).
6. D. G. Davis, *Talanta*, **3**, 335 (1960).
7. N. V. Sidgwick, "Chemical Elements and Their Composition," Vol. II, p. 1581, Oxford Press (1950).
8. N. V. Sidgwick, *loc. cit.*, p. 1613.
9. G. Grube, *Z. Elektrochem.*, **16**, 621 (1910).
10. R. Lorentz and P. E. Spielman, *ibid.*, **15**, 293 (1909).
11. W. H. Latimer, "Oxidation Potentials," Prentice-Hall, New York (1952).
12. S. Schuldiner and J. P. Hoare, *This Journal*, **103**, 178 (1956).
13. J. P. Hoare and S. Schuldiner, *ibid.*, **104**, 564 (1957).
14. S. Schuldiner, G. W. Castellan, and J. P. Hoare, *J. Chem. Phys.*, **28**, 16 (1958).
15. J. P. Hoare, *This Journal*, **106**, 640 (1959).
16. J. P. Hoare, *ibid.*, **107**, 635 (1960).
17. J. P. Hoare, *J. Phys. Chem.*, **64**, 1780 (1960).
18. F. D. Snell and C. T. Snell, "Colorimetric Methods of Analysis," Vol. II, 3rd ed. (1949).
19. W. G. Berl, *Trans. Faraday Soc.*, **83**, 253 (1943).
20. S. E. S. El Wakkad and S. H. Emara, *J. Chem. Soc.*, **1952**, 461.
21. K. J. Vetter and D. Berndt, *Z. Elektrochem.*, **62**, 378 (1958).
22. H. A. Laitinen and C. G. Enke, *This Journal*, **107**, 773 (1960).
23. W. Böld and M. Breiter, *Electrochim. Acta*, **5**, 145 (1961).
24. K. Nagel and H. Dietz, *ibid.*, **4**, 141 (1961).
25. K. Nagel and H. Dietz, *ibid.*, **4**, 1 (1961).
26. C. Wagner and W. Traud, *Z. Elektrochem.*, **44**, 391 (1938).
27. T. P. Hoar, *Proc. Roy Soc. London*, **A142**, 628 (1933).
28. D. C. Grahame, *Chem. Revs.*, **41**, 441 (1947).
29. S. Schuldiner, *This Journal*, **99**, 488 (1952).
30. S. Schuldiner and J. P. Hoare, *J. Chem. Phys.*, **26**, 1771 (1957).

Electrochemical Evidence for Diatomicity of Tellurium

S. A. Awad

Chemistry Department, University College of Cairo, Ain-Shams University, Heliopolis, Cairo, Egypt

ABSTRACT

Overpotential on tellurium cathodes was studied at 25°C in 0.005-0.5*N* $Ba(OH)_2$ and in 0.5*N* NH_4OH solutions. Results were explained on the basis of tellurium dissolution, giving Te_2^{--} ions. In 0.5*N* NH_4OH and in 0.005-0.01*N* $Ba(OH)_2$ solutions the discharge of cations governs the rate of dissolution. At higher concentrations of $Ba(OH)_2$, the electrochemical reaction, with two slopes in the linear logarithmic section, becomes rate determining. Unexpected values for the electron number, amounting to 2 and 4 for the discharge and electrochemical mechanisms, respectively, were obtained. A modified mechanism, based on the assumption that tellurium exists as diatomic molecules, Te_2, was proposed. The mechanism accounted satisfactorily for both Tafel slopes and the electron number values.

The overpotential phenomena on tellurium cathodes in HCl solutions (1) indicated that the reaction taking place at the cathode is hydrogen evolution. On the other hand, work in NaOH solutions (2) showed that tellurium dissolves cathodically giving telluride ions, Te_2^{--}. The results obtained in concentrated solutions indicated that the dissolution is controlled by a rate-determining simple electrochemical mechanism, with two Tafel slopes in the linear-logarithmic section. In dilute solutions the discharge reaction becomes rate determining, and Tafel lines with only one slope were obtained. From the *p*H effect on overpotential, it was found that the discharge reaction involves sodium ions.

The aim of the present investigation was to study the overpotential characteristics for tellurium in $Ba(OH)_2$ and NH_4OH solutions and compare the results with those obtained in NaOH solutions.

Experimental

The experimental technique was essentially the same as that of Bockris and co-workers (3). The electrolytic cell was constructed of arsenic-free glass and was similar to that used by Ammar and Awad (1). In order to minimize the diffusion of gaseous anodic products toward the cathode, a sin-

tered glass disk was inserted between the cathode compartment and the compartment used for electrolytic purification of solutions. Water-sealed taps and ground glass joints were used to retard the diffusion of atmospheric oxygen into the cell. Before each run the cell was cleaned with a mixture of A.R. nitric acid and A.R. sulfuric acid. This was followed by thorough washing with conductance water.

The electrode was prepared from tellurium rods[1] (7 mm diameter) containing no impurities as shown by a spectroscopic analysis. A thin tungsten wire was wrapped around one end of the rod. This end was squeezed inside a clean glass tube, and the glass was sealed over the tungsten wire. The electrode was then washed with conductance water and fitted in its position in the cell. Although the physical appearance of the electrode does not change during the course of the experiment, each electrode was used to trace one Tafel line only.

Barium and ammonium hydroxide solutions were prepared from A.R. grade chemicals. The solution was pre-electrolyzed at 10^{-3} — 10^{-2} amp/cm^2 for 24 hr on a platinum electrode. With these precautions, reproducible results (within ±5 mv) were obtained in all the solutions studied.

Cylinder hydrogen was purified from oxygen, carbon monoxide, and other impurities by passing it over hot copper (450°C), then over a mixture of MnO_2 and CuO (technically known as "Hopcalite") to oxidize CO to CO_2. CO_2 was removed by soda lime.

A saturated calomel electrode with a saturated KCl bridge was used as a reference electrode. The potential of the hydrogen electrode, in the same solution and at the same temperature as the test cathode, was measured against the calomel electrode making use of a salt bridge.

Both a direct method of measurement and the rapid technique described by Bockris (3) were used. The current density was calculated from the apparent surface areas. The current was measured with a multirange micromilliammeter and the potential by a valve potentiometer. The temperature was kept constant with the aid of an air thermostat controlled to ± 0.5°C.

Results

All results included in this investigation are the mean of six individual results which are reproducible among themselves to within ± 5 mv.

Figures 1 and 2 show the mean Tafel lines at 25°C, in 0.005, 0.01, 0.05, 0.1, and 0.5*N* aqueous barium hydroxide solutions and in 0.5*N* ammonium hydroxide solution. It is clear from these figures that in the ammonium hydroxide solution as well as in 0.005 and 0.01N barium hydroxide solutions Tafel lines with only one slope are obtained. In higher concentrations of barium hydroxide the Tafel lines indicate two slopes in the linear-logarithmic section. At comparatively low current densities, a region of stationary potential is observed in all solutions. It is to be observed that the overpotential values in these figures are referred to the reversible hydrogen electrode in order to exclude the possibility of a hydrogen evolution reaction (see below).

[1] Prepared by Johnson and Matthey, Ltd., London, England.

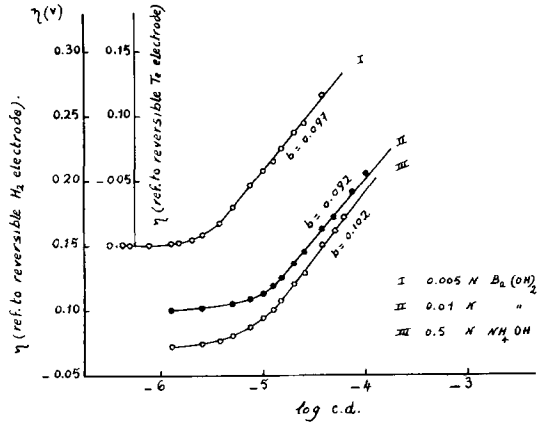

Fig. 1. Tafel lines for tellurium in 0.005 and 0.01*N* $Ba(OH)_2$ and 0.5*N* NH_4OH solutions.

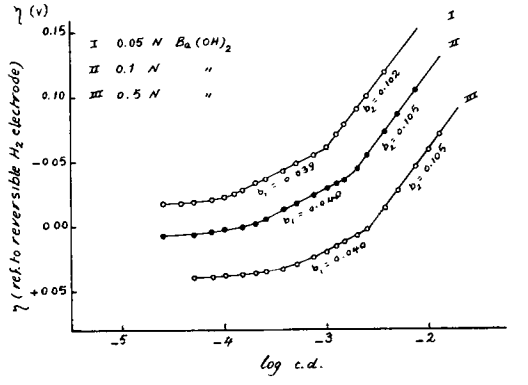

Fig. 2. Tafel lines for tellurium in 0.05, 0.1, and 0.5*N* $Ba(OH)_2$ solutions.

Table I contains the mean values of the slopes b_1 (at the low current density range) and b_2 (at the high current density range). The values of the stationary potentials, referred to the normal hydrogen electrode, for the various solutions studied are also included.

The values of the stationary potentials in the various solutions are considered as the reversible tellurium electrode potentials. To clarify this idea, an additional axis for overpotential in 0.005*N* $Ba(OH)_2$ is drawn in Fig. 1. The zero of this axis corresponds to the stationary potential in that solution. Treating similarly the other Tafel lines, overpotentials referred to the reversible tellurium electrode were calculated at 3.2 x 10^{-5}, 10^{-3}, and 3.2 x 10^{-3} amp/cm^2, and the values are given in Table II. This table contains also the values of $(\partial\eta/\partial\,\mathrm{pH})_i$, calculated for various solutions.

Table I. Slopes (b_1 and b_2) of the linear-logarithmic regions during cathodic polarization of tellurium

Solution	b_1	b_2	Stationary potential v *vs.* N.H.E.
0.005*N* $Ba(OH)_2$	—	97	—0.819
0.01*N* $Ba(OH)_2$	—	92	—0.800
0.05*N* $Ba(OH)_2$	39	102	—0.764
0.1*N* $Ba(OH)_2$	40	105	—0.748
0.5*N* $Ba(OH)_2$	40	105	—0.752
0.5*N* NH_4OH	—	102	—0.737

Table II. Overpotentials on tellurium electrodes and variation with solution pH

Solution	pH	Overpotential, mv *vs.* tellurium electrode at current densities: 3.2×10^{-5} amp/cm²	10^{-3} amp/cm²	3.2×10^{-3} amp/cm²	$(\partial\eta/\partial pH)_i$
0.005*N* $Ba(OH)_2$	11.38	110			
0.01*N* $Ba(OH)_2$	11.82	52	190*		132
0.05*N* $Ba(OH)_2$	12.68		46		167
0.1*N* $Ba(OH)_2$	12.78			68	
0.5*N* $Ba(OH)_2$	13.42			47	33

* This value was obtained by extrapolation.

The electron number λ, defined as the number of electrons necessary to complete one act of the rate-determining step, is calculated using

$$\lambda = -\frac{RT}{i_o F}\left(\partial i/\partial \eta\right)_{\eta \to 0} \qquad [1]$$

where i_o is the exchange current. For comparison, the calculation was extended to the results obtained previously in NaOH solutions (2). Figure 3 shows the relations between η and the current density at very low cathodic polarizations in 0.01 and 0.5*N* $Ba(OH)_2$, as well as in 0.5*N* NH_4OH solutions. The corresponding relations for 0.01 and 0.5*N* NaOH are shown in Fig. 4. The slopes of these linear relations, the exchange currents, and the values of λ in NH_4OH and $Ba(OH)_2$ solutions are given in Table III, whereas those for NaOH solutions are given in Table IV.

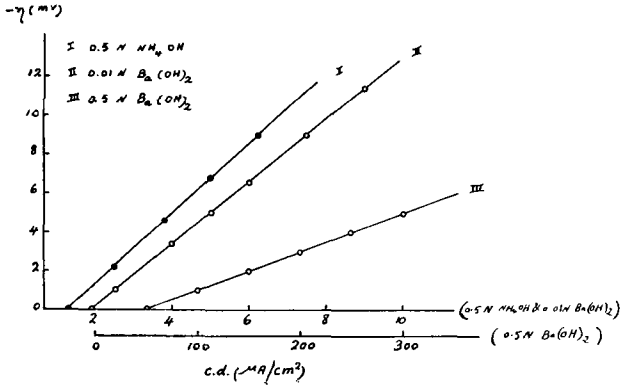

Fig. 3. Relation between overpotential and current density at low cathodic polarization in $Ba(OH)_2$ and NH_4OH solutions.

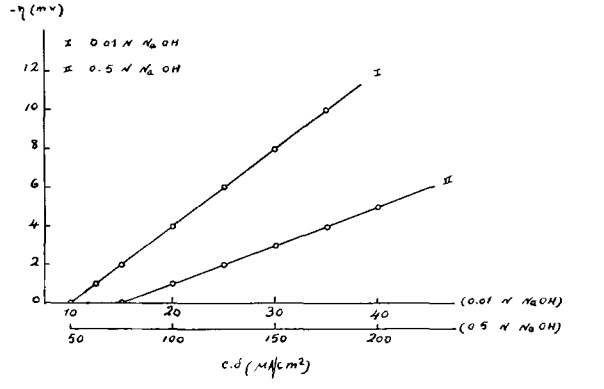

Fig. 4. Relation between overpotential and current density at low cathodic polarization in NaOH solutions.

Table III. Electrochemical parameters for cathodic polarization of tellurium in NH_4OH and $Ba(OH)_2$ solutions

Solution	i_o, amp/cm²	$-(\partial\eta/\partial i)_{\eta \to 0}$, v/amp/cm²	λ*
0.5*N* NH_4OH	6.8×10^{-6}	18×10^2	2.1
0.005*N* $Ba(OH)_2$	2.90×10^{-6}	40×10^2	2.2
0.01*N* $Ba(OH)_2$	7.94×10^{-6}	1.6×10^2	2.0
0.05*N* $Ba(OH)_2$	7.94×10^{-5}	0.8×10^2	4.0
0.1*N* $Ba(OH)_2$	1.19×10^{-4}	0.56×10^2	3.9
0.5*N* $Ba(OH)_2$	3.16×10^{-4}	0.2×10^2	4.1

Table IV. Electrochemical parameters for cathodic polarization of tellurium in NaOH solutions

Concentration of NaOH	i_o, amp/cm²	$-(\partial\eta/\partial i)_{\eta \to 0}$, v/amp/cm²	λ*
0.005*N*	2.65×10^{-6}	44×10^2	2.2
0.01*N*	3.60×10^{-5}	4×10^2	1.8
0.05*N*	3.98×10^{-5}	1.6×10^2	4.0
0.1*N*	7.94×10^{-5}	0.8×10^2	4.0
0.5*N*	1.52×10^{-4}	0.4×10^2	4.2
1*N*	2.00×10^{-4}	0.32×10^2	4.0
3*N*	2.52×10^{-4}	0.24×10^2	4.2
5*N*	3.10×10^{-4}	0.2×10^2	4.2

* Values of λ are given to the nearest first decimal figure.

Discussion[2]

The overpotential results on tellurium in barium hydroxide solutions are similar to those obtained in the corresponding solutions of sodium hydroxide (2). Thus, in 0.005-0.01*N* solutions, the Tafel lines exhibit one slope in a linear-logarithmic section covering a range of about 100 mv. In concentrations above 0.01*N*, the Tafel lines show two slopes, and they are shifted toward the reversible hydrogen electrode potential. The results in the ammonium hydroxide solution show only one slope covering about 100 mv, although the solution was 0.5*N*. This is because NH_4OH solution contains but a slight amount of NH_4^+ ions (4), with the result that this solution has a pH value (11.3) comparable with that of the 0.005*N* $Ba(OH)_2$, with a pH of 11.38. Similar to the behavior in NaOH solutions (2), Tafel lines lying in the opposite side with respect to the reversible hydrogen electrode were observed (cf. Fig. 2). This phenomenon indicates that the cathode reaction is not hydrogen evolution, and actual evolution of hydrogen has not been observed even at the higher current densities. The cathodic reaction is, therefore, considered to be the dissolution of the electrode material.

The dissolution of tellurium in $Ba(OH)_2$ and NH_4OH solutions takes place according to

$$2Te + 2e \longrightarrow Te_2^{--} \qquad [2]$$

This suggestion is based on the following evidences: (i) The standard potential of the above reaction is −0.84v, while the values for the other possible reactions

$$2Te + 2e \longrightarrow Te^{--} \qquad [3]$$

and

$$Te + 2H_2O + 2e \longrightarrow H_2Te + 2\,OH^- \qquad [4]$$

[2] The European convention of sign of potential is used.

are −1.14 and −1.57, respectively (5). It is, therefore, easier for tellurium to dissolve as Te_2^{--}, since this reaction takes place at the least negative potential. (ii) The stationary potentials at which the Tafel lines become parallel to the log c.d. axis are within the range −0.737 to −0.819v (cf. Table I). These values represent the reversible potentials for the tellurium electrode and are within the order of magnitude of the Te/Te_2^{--} potential. (iii) The solutions of $Ba(OH)_2$ and NH_4OH turn red during polarization. This color is not due to simple telluride Te^{--} ions, but to polytellurides (6), the simplest of which is Te_2^{--}.

The overpotential results in $Ba(OH)_2$ and NH_4OH solutions cannot be attributed to a direct charge reaction as represented by Eq. [2], since the relation between current and potential ($\Delta\phi$) would be

$$i = 2FV = 2Fk \exp\left(-\frac{F\Delta\phi}{RT}\right) \qquad [5]$$

The Tafel line slope according to the above equation is 0.06v at 30°C, a value which was not observed in the present investigation. The cathodic dissolution of tellurium may, therefore, involve the discharge of the cations or water molecules with the result that intermediate tellurides are formed. According to the entities discharged, the following mechanisms are formulated

(*A*) $$Ba^{++} + Te + e \rightarrow BaTe^{+} \qquad [6]$$

$$BaTe^{+} + Te + e \rightarrow Te_2^{--} + Ba^{++} \qquad [7]$$

In case of NH_4OH the reaction is represented by

$$NH_4^{+} + Te + e \rightarrow HTe + NH_3 \qquad [8]$$

$$HTe + Te + e \rightarrow Te_2^{--} + H^{+} \qquad [9]$$

Concerning the case of $Ba(OH)_2$, the mechanism requires the permanent persistence of the positively charged intermediate telluride, $BaTe^{+}$. It may be improbable that this compound remains without discharge, whereas other Ba^{++} ions are being discharged. Therefore, the following modification is suggested

(*B*) $$Ba^{++} + Te + 2e \rightarrow BaTe \qquad [10]$$

$$BaTe + 3Te + 2e \rightarrow 2Te^{--} + Ba^{++} \qquad [11]$$

(*C*) If water molecules are involved in the discharge reaction, the mechanism is represented by

$$Te + H_2O + e \rightarrow HTe + HO^{-} \qquad [12]$$

$$HTe + Te + e \rightarrow Te_2^{--} + H^{+} \qquad [13]$$

The Tafel slope and the *p*H effect associated with a rate-determining discharge step or a rate-determining electrochemical reaction are calculated for the different mechanisms. The values obtained, together with the corresponding electron numbers, are given in Table V. In case of the electrochemical reaction the *pH* effect corresponds to the higher slope.

It is clear that the Tafel slopes associated with modification (*B*) are half the values obtained experimentally, and accordingly, this mechanism is excluded. Table II shows that in concentrated solutions

Table V. Parameters for proposed mechanisms of cathodic dissolution of tellurium

	Mechanism	Slope, mv	Electron No.	*p*H effect, mv
(*A*)	discharge	120	1	120
	electrochemical	40 & 120	2	0
(*B*)	discharge	60	2	60
	electrochemical	20 & 60	4	0
(*C*)	discharge	120	1	0
	electrochemical	40 & 120	2	0

of $Ba(OH)_2$ the overpotential increases but slightly with *p*H, perhaps due to slight variations in ξ with concentration. Below 0.05*N*, η increases appreciably with *p*H. These findings are consistent with mechanism (*A*) involving the discharge of Ba^{++} ions. From the Tafel slopes given in Table I, it is clear that the rate of dissolution of tellurium in 0.5-0.05*N* $Ba(OH)_2$ is governed by the rate of the electrochemical reaction. Below 0.05*N* $Ba(OH)_2$, as well as in the 0.5*N* NH_4OH solution, the discharge reaction becomes rate-determining.

Calculation of the electron number λ, with the hope of providing support for the above-accepted mechanism, was carried out from the relation between current and overpotential at low cathodic polarization. It was expected that a value of λ equal to unity would be obtained in dilute $Ba(OH)_2$ solutions, whereas the value "two," required by the electrochemical mechanism, would be obtained in concentrated solutions. However, Table III shows that λ is equal to 2 in 0.005-0.01*N* $Ba(OH)_2$, and in higher concentrations it is equal to 4. These values satisfy mechanism (*B*), which is refused since it requires lower Tafel slopes. Such contradiction between Tafel slopes and the electron number values made it necessary to calculate λ from the results in NaOH solutions (2). Table IV shows that, even when the cations are monovalent, similar values for λ are obtained in the corresponding concentration ranges; consequently the simple mechanism (as mechanism *A*) suggested for NaOH solutions is also not valid. It is obvious, therefore, that tellurium dissolves according to a certain general mechanism, independent of the nature of the alkaline solution, and involving 2 electrons in the discharge reaction and 2 more in the electrochemical step.

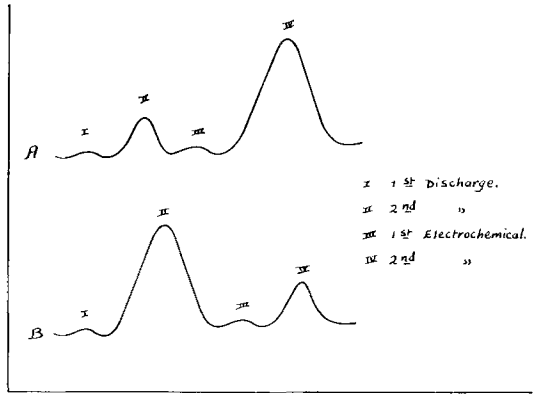

Fig. 5A. Energy barriers for the electrochemical mechanism; B, energy barriers for the discharge mechanism.

The observation that two electrons are involved in the discharge reaction, although the cations discharged are monovalent, necessitates the existence of tellurium in diatomic molecules, Te_2. Since the Tafel slope corresponds to one electron only, one has to assume that the discharge process takes place in two successive steps, the first of which is nearly potential independent and relatively faster than the second. This latter step governs, therefore, the rate of the over-all discharge reaction. Argument of the same type can be applied to the electrochemical reaction. The rate of dissolution of tellurium is, thus, controlled by either the second discharge step or the second electrochemical one. Figure 5 represents diagrammatically the energy barriers for the two mechanisms. Very low energy barriers are assigned to the first discharge and first electrochemical steps to indicate the assumption that these processes are not activation limited. In NaOH and NH_4OH solutions the new mechanism is represented by

Discharge reaction
$$M^+ + Te_2 + e \rightarrow M\,Te_2 \quad [14]$$
$$M^+ + M\,Te_2 + e \rightarrow M_2\,Te_2 \quad [15]$$

Ionization reaction
$$M_2\,Te_2 \rightarrow M\,Te_2 + M^+ + e \quad [16]$$
$$M\,Te_2 \rightarrow Te_2 + M^+ + e \quad [17]$$

Electrochemical reaction
$$M_2\,Te_2 + Te_2 + e \rightarrow M_2\,Te_4^- \quad [18]$$
$$M_2\,Te_4^- + e \rightarrow 2M^+ + 2Te_2^{--} \quad [19]$$

Another fundamental assumption is made that reactions [14] and [18] are reversible, with the result that the areas covered with $M\,Te_2$ and $M_2\,Te_4^-$ always remain small. Accordingly, the surface coverage x is due essentially to the persistence of $M_2\,Te_2$ formed according to Eq. [15].

The velocity of reaction [15] is given by

$$V_1 = k_1\,(a_{MTe_2})(a_{M^+})_{d.l.}\exp\left(-\frac{F\Delta\phi}{2RT}\right) \quad [20]$$

where (a_{MTe_2}) is the activity of $M\,Te_2$. Since the rate of formation of this compound is proportional to $(a_{M^+})_{d.l.}\,(1-x)$, then

$$V_1 = k_1'\,(1-x)\,(a_{M^+})^2_{d.l.}\exp\left(-\frac{F\Delta\phi}{2RT}\right) = a_1\,(1-x) \quad [21]$$

The ionization reaction rate, according to Eq. [16], is

$$V_2 = k_2'\,x_{10^{-9}}\exp\left(\frac{F\Delta\phi}{2RT}\right) = a_2\,x \quad [22]$$

The rate of the electrochemical reaction [19] is

$$V_3 = k_3\,(a_{M_2Te_4^-})\exp\left(-\frac{F\Delta\phi}{2RT}\right) \quad [23]$$

where $(a_{M_2Te_4^-})$ is the activity of $M_2Te_4^-$. Since the rate of formation of the latter intermediate is proportional to x, the electrochemical reaction rate is given the value

$$V_3 = k_3'\,x\,10^{-9}\exp\left(-\frac{F\Delta\phi}{2RT}\right) = a_3\,x \quad [24]$$

At the steady state corresponding to a constant coverage, current, and potential

$$V_1 - V_2 - V_3 = 0 \quad [25]$$

If the second electrochemical reaction is the slowest step, (cf. Fig. 5A), then it governs the dissolution of tellurium under the condition (7)

$$(a_1 + a_2) > 10\,a_3 \quad [26]$$

From Eq. [21], [22], [24], [25], and [26], the surface coverage becomes

$$x = \frac{a_1}{a_1 + a_2} \quad [27]$$

At low current densities a_1 is much smaller than a_2 and so x equals a_1/a_2. The net cathodic current is given by

$$i = 4FV_3 = 4F\frac{k_3'\,k_1'}{k_2'}\,(a_{M^+})^2_{d.l.}\exp\left(\frac{3F\Delta\phi}{2RT}\right) \quad [28]$$

With increase of cathodic polarization, x approaches unity since a_2 becomes much smaller than a_1, and accordingly the net cathodic current is given the value

$$i = 4FV_3 = 4Fk_3'\,10^{-9}\exp\left(-\frac{F\Delta\phi}{2RT}\right) \quad [29]$$

The Tafel line slopes at 30°C are, therefore, 0.04 and 0.12v at the low- and high-current density ranges, respectively.

When the dissolution is governed by the second discharge reaction (cf. Fig. 5B), x is equal to a_1/a_3, and the current is represented by:

$$i = 4FV_3 = 4Fa_1 = 4Fk_1'\,(a_{M^+})^2_{d.l.}\exp\left(-\frac{F\Delta\phi}{2RT}\right) \quad [30]$$

indicating that the Tafel line slope is 0.12v at 30°C.

The above discussion shows that this complex mechanism is in good agreement with the experimental Tafel slopes as well as the electron number values. The contradiction between these two parameters is eliminated by assuming that the first discharge and the first electrochemical steps (cf. Eq. [14] and [18]) are potential independent; and so the potential dependent steps involve one electron each.

In case of polyvalent cations, the mechanism is represented by

$$M^{z+} + Te_2 + e \rightarrow MTe_2^{(z-1)+} \quad [31]$$
$$MTe_2^{(z-1)+} + e \rightarrow MTe_2^{(z-2)+} \quad [32]$$
$$MTe_2^{(z-2)+} + Te_2 + e \rightarrow MTe_4^{(z-3)+} \quad [33]$$
$$MTe_4^{(z-3)+} + e \rightarrow M^{z+} + 2Te_2^{--} \quad [34]$$

It is to be mentioned that, instead of Eq. [2], the cathodic dissolution of tellurium can be represented by

$$2Te_2 + 4e \rightarrow 2Te_2^{--} \quad [35]$$

The latter equation satisfies the molecular nature of tellurium concluded from its electrochemical behavior in alkaline solutions.

Manuscript received April 3, 1961; revised manuscript received March 29, 1962.

Any discussion of this paper will appear in a Discussion Section to be published in the June 1963 JOURNAL.

REFERENCES

1. I. Ammar and S. A. Awad, *This Journal*, **103**, 182 (1956).

2. S. A. Awad, *ibid.*, **108**, 468 (1961).
3. A. Azzam, J. O'M. Bockris, B. Conway, and H. Rosenberg, *Trans. Faraday Soc.*, **46**, 918 (1950).
4. Fritz Ephraim, "Inorganic Chemistry," 5th English ed., p. 631, Gurney and Jackson (1949).
5. Wendell Latimer, "Oxidation Potentials," p. 85, Prentice Hall, New York (1952).
6. Ref. 4, p. 537.
7. J. O'M. Bockris, and E. C. Potter, *This Journal*, **99**, 169 (1952).

Technical Notes

Electroluminescence Emission Spectra of ZnS Single Crystals

E. Alexander and I. T. Steinberger

Department of Physics, The Hebrew University of Jerusalem, Israel

According to the Schön-Klasens model (1, 2) for the luminescence centers in Cu-activated zinc sulfide, the "blue" and "green" emission bands are due to recombination at two different hole-traps, the "blue" and "green" centers. Electroluminescence (EL) excitation is usually interpreted in the framework of this model by impact-ionization of the luminescence centers with accelerated conduction-band electrons (3).

In recent papers objections were raised both to the Schön-Klasens model and to the impact-ionization theory of EL excitation (4-6). As a contribution to this discussion, experiments on the voltage dependence of the EL emission spectra of ZnS are reported here.

It is possible to draw conclusions from the voltage dependence of the emission on the possible mechanism of EL excitation only if the voltage dependence of the light intensity is determined mainly by the rate of ionization of luminescence centers and not if it is masked by other voltage-dependent processes (*e.g.*, the sweeping out of liberated electrons by the field, or the supply of free electrons for the recombination process itself). Experimental evidence (7, 8) indicates that for single crystals and high audio frequencies this condition is satisfied. It seems reasonable to assume the same for powders, but an experimental proof is difficult to obtain. For this reason, single crystals were used in this study.

Crystals No. 1 and 2 were obtained through the courtesy of Dr. A. Kremheller (then at Sylvania Laboratories) and they contained 0.04% by weight of Cu and about 0.001% Al. The Mn, Cr, Ni, Fe, and Ag contents, if any, were less than 1 ppm. The other crystals were grown in our laboratory using commercial ZnS powder ("High purity ZnS," obtained from the New Jersey Zinc Company) as a starting material. Crystal No. 3 was grown in an atmosphere of 10 cm Cl_2 in a sealed-off silica tube for 70 hr. The temperature in the region of the charge was kept at 1240°C. The crystals appeared in a region where the temperature was about 1150°C. A similar method was used for the growing of crystal No. 4 with the following differences: 0.1% by weight of $ZnCl_2$ was added to the starting material; the tube was evacuated and sealed; it was kept for 90 hr at a constant temperature (1240°C at the charge and about 1150°C at the region of condensation). Cooling down to room temperature took about 8 hr in both cases.

Crystals No. 3 and 4 were activated by embedding them in electroluminescent powder contained in a quartz tube which was subsequently evacuated, sealed off, and heated to 800°C. The tube with its contents was kept at this temperature for 1 hr. The electroluminescent ZnS powder used had been prepared according to the description of Zalm (9); it contained 0.1-1% copper and 0.01-0.1% aluminum. The activated crystals contained 0.01-0.1% copper, and their aluminum content was about 0.001%. Again, the Mn, Cr, Ni, Fe, and Ag contents, if any, were less than 1 ppm. These impurity contents were determined by semiquantitative spectroscopic analysis.

The crystals were plate-shaped, their thickness ranging from 0.4 to 0.8 mm. The other dimensions of the crystals were of the order of millimeters. Under the polarizing microscope faintly colored high-order birefringent bands were observed. X-ray investigation showed that the crystals were cubic, but contained stacking defects. The (111) cubic axis was parallel to the faces of the platelets. The applied electric field was perpendicular to the face of the platelets. Electrical contacts were established by the application of indium amalgam. Experiments were performed at room temperature.

A Bausch and Lomb grating monochromator type 33-86-40 served as a spectrometer, in conjunction with a photomultiplier (generally E.M.I. type 9502S, but for crystal No. 1 a 1P21 tube was used). The spectral response of the 9502S tube was determined by using the monochromator, a tungsten ribbon lamp, and a calibrated BMV 31 photocell.

The determination of the spectral distribution was least reliable at the long-wavelength tail of the green band, where the sensitivity of the 9502S tube is only about 20% of its maximum. A synchronous motor driving the monochromator drum, a d-c amplifier, and a recorder completed the apparatus. Under alternating voltages, time averages of EL brightness were measured.

The EL emission of each crystal was determined for at least two audio frequencies and a series of voltages for each frequency. When an appreciable d-c EL was found (crystal No. 3), the d-c EL spectrum was also investigated as a function of applied voltage. For a given crystal and frequency the spectral distributions at different voltages were very similar, the main change being a slight displacement of the whole spectrum toward shorter wavelengths with increasing voltage. This displacement was of the order of 10^{-2} mμ/v.

For the quantitative evaluation of the voltage dependence, the following procedure was adopted. The spectra obtained from the photomultiplier-amplifier-recorder combination were corrected for the spectral response of the photomultiplier. Subsequently, $P(\tilde{\nu})$ *vs.* $\tilde{\nu}$ was plotted, where $P(\tilde{\nu})$ represents the radiant flux per unit wave number. In case of crystals No. 1 and 2 the spectral distribution could be represented unambiguously by the sum of two Gaussian bands

$$P(\tilde{\nu}) = P_1 \exp\left[-\frac{(\tilde{\nu}-\tilde{\nu}_1)^2}{1.44\,h_1^2}\right] + P_2 \exp\left[-\frac{(\tilde{\nu}-\tilde{\nu}_2)^2}{1.44\,h_2^2}\right]$$

Here P_1, P_2, h_1, and h_2 are constants and $\tilde{\nu}_1$, $\tilde{\nu}_2$ are the wave numbers of the blue and green band centers, respectively. For a given crystal, $\tilde{\nu}_1$ and $\tilde{\nu}_2$ were found to be almost independent of voltage and frequency. Figure 1 represents log $D(\lambda_1)$ and $D(\lambda_2)$ as a function of $V^{-1/2}$ for crystal No. 1 at 500 cps. (Here $\lambda_1 = \frac{1}{\tilde{\nu}_1}$ $\lambda_2 = \frac{1}{\tilde{\nu}_2}$, and D represents the deflection on the original records.) The graphs are parallel straight lines except at the region of the highest voltages applied, where the blue peak increases somewhat more steeply than the green one.

The EL emission spectra of crystals No. 3 and 4 could not be resolved into two Gaussian bands unambiguously. The corrected spectral distribution $P(\tilde{\nu})$ had a single peak in the blue region; the green band manifested itself by a strong asymmetry of $P(\tilde{\nu})$. $P(\tilde{\nu})$ fitted well a Gaussian for the large wave-number side of the peak. The center $\tilde{\nu}_1$ of this Gaussian was very near to $1/\lambda_1$, where λ_1 is the position of the single peak observed on the original records ($D(\lambda)$ *vs.* λ). On the other hand, the function

$$P^*(\tilde{\nu}) = P(\tilde{\nu}) - P_1 \exp\left[-\frac{(\tilde{\nu}-\tilde{\nu}_1)^2}{1.44\,h_1^2}\right]$$

was not another Gaussian. The voltage dependence of the spectral distribution was therefore evaluated as follows: $\tilde{\nu}_1$ was determined from the Gaussian plot for the blue band; $\tilde{\nu}_2$ was defined as the wave number corresponding to the peak $P^*(\tilde{\nu})$. Since it is not clear whether the value of $\tilde{\nu}_2$ thus chosen does represent the center of a single band, two wavelengths λ' and λ'' were defined as follows: $|\lambda'' - \lambda'| = 20$ mμ, $|\lambda'' - \lambda_2| \approx |\lambda_2 - \lambda'|$; here $\lambda_2 = 1/\tilde{\nu}_2$. For all voltages $\lambda_1 - \lambda'$ was kept constant even if λ_1 and λ_2 seemed to shift somewhat. Log $D(\lambda_1)$, log $D(\lambda')$, and log(λ'') were represented as functions of $V^{-1/2}$ (Fig. 2 for crystal No. 4 at 3 kc). It is seen that the lines are straight and parallel. In fact, the method of least squares yielded in this case the values $B_{\lambda_1} = 97.1$, $B_{\lambda'} = 97.1$, and $B_{\lambda''} = 95.5$v, calculated from $B = c \times \ln 10$, where c is the slope of the lines.

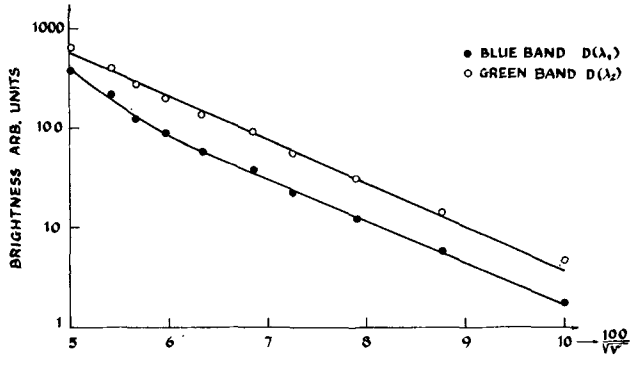

Fig. 1. Dependence of brightness at the band centers ($\lambda_1 = 458$ mμ $\lambda_2 = 521$ mμ) on voltage. Crystal No. 1, 5 kc.

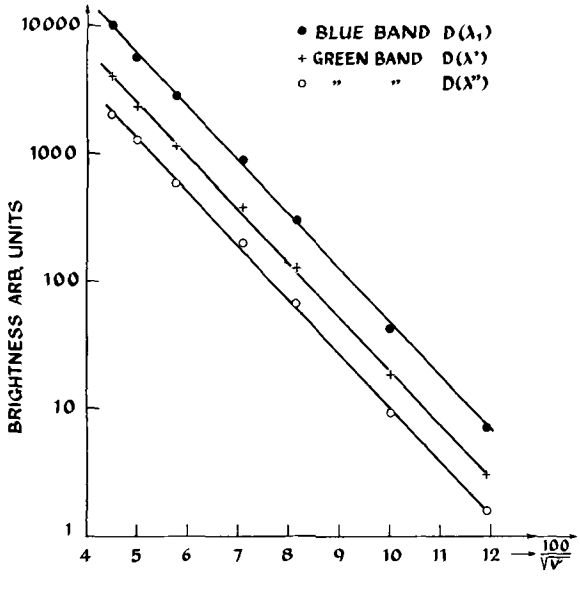

Fig. 2. Dependence of brightness at the center of the blue band ($\lambda_1 = 468$ mμ) and near the center of the green band (λ', λ'') on voltage. Crystal No. 4, 3 kc.

For all the crystals investigated, the spectral distribution was independent of voltage except for the small shift of the whole spectrum mentioned above. The same result was obtained by Mattler and Ceva (10) on electroluminescent ZnS:Cu phosphor powders. These facts have to be taken into account in any theory on EL excitation as they imply that the Schön-Klasens model of luminescence centers, and the theory of direct impact-ionization of the centers by accelerated electrons cannot be correct simultaneously. On these assumptions, the intensity of the blue emission should increase more steeply with voltage than that of the green one. Therefore, on the basis of the Schön-Klasens model one has either to discard impact-ionization altogether, or to assume that the impacts liberate valence-band electrons and not those in the different centers. If, however, future experiments and theory should further substantiate the direct impact-ionization theory, the Schön-Klasens model will have to be modified. Such a modification, which takes into account the results of Mattler and Ceva (10), was proposed by Curie (4).

Acknowledgment

The authors wish to thank Mrs. H. Jaffe, of the Weizmann Institute, Rehovoth, for performing the spectrochemical investigation of the crystals.

Manuscript received Sept. 25, 1961.

Any discussion of this paper will appear in a Discussion Section to be published in the June 1963 JOURNAL.

REFERENCES

1. H. A. Klasens, *Nature*, **158**, 306 (1946).
2. M. Schön, *Z. Naturforsch.*, **6a**, 287 (1951).
3. W. W. Piper and F. E. Williams, *Phys. Rev.*, **87**, 151 (1952).
4. P. F. Browne, *J. Electronics*, **2**, 1, 95, 154 (1956-57).
5. D. Curie in "Color Centers and Crystal Luminescence," edited by G. Bonfiglioli, Editor, p. 199, Torino (1960).
6. W. A. Thornton, *This Journal*, **108**, 636 (1961).
7. G. F. Alfrey, I. Cooke, and K. N. Taylor in "Solid-State Physics," F. Seitz and D. Turnbull, Editors, Vol. 2, p. 816, Academic Press, New York (1960).
8. I. T. Steinberger, V. Bar, and E. Alexander, *Phys. Rev.*, **121**, 118 (1961).
9. P. Zalm, *Philips Research Repts.*, **11**, 323 (1956).
10. J. Mattler and T. Ceva, Abstracts—International Conference on Luminescence, p. 33, New York 1961.

Two Unusual Effects in H_2-fired CaO:Mn,Li Phosphors

P. M. Jaffe

Research Department, Westinghouse Electric Corporation, Bloomfield, New Jersey

The stimulating and quenching action of infrared radiation on the luminescence of certain sulfide phosphors is well known (1, 2). Less well known are the stimulating and quenching effects due to higher-energy radiation, *i.e.*, x-rays, gamma rays, cathode rays, and ultraviolet (3-7). The phosphors that show these effects are "normal" phosphors in that no further treatment is necessary after phosphor preparation. That is, it is not necessary for them to be ground, crushed, surface-treated, etc. Kats (8) and Ewles and co-workers (9-11) have reported on luminescence effects in alkali-halide and alkaline-earth oxides due to grinding. The present work reports on two rather unusual effects with H_2-fired CaO:Mn, Li phosphors. The first effect is the production of a new blue emission due to the application of pressure (grinding, etc.). The second effect is a transient stimulation of the Mn emission by 3650Å only after previous excitation by 2537Å. The stimulation apparently only occurs in the phosphor which had previously been subjected to pressure. These two effects will be referred to as the pressure and stimulation effects, respectively. Stimulation is also obtained if ionizing radiation, *i.e.*, x-rays, is used in place of the 2537Å ultraviolet.

The experimental work to be described was obtained with CaO:Mn, Li phosphors, but similar effects were noted if the Li was replaced by Na or K.

Phosphors were prepared from Mallinckrodt's S.L. $CaCO_3$ and A.R. $MnCO_3$. Li, Na, and K were added as the respective carbonates and Al as the hydrated oxide. The Mn concentration was 0.1 atom % and that of Li, Na, K, or Al, 5 atom %. The samples were mixed as a slurry, dried at 110°C, and fired at 1050°C in Pt crucibles in a H_2 or N_2 atmosphere; samples fired in O_2 were similar to those fired in N_2. After firing the samples were well sintered.

The body color of the H_2-fired Mn-containing samples was white while the N_2-fired samples were light tan. This indicates that the valence state of Mn is probably +2 in the former samples and +3 or +4 in the latter.

The luminescent characteristics of the CaO:Mn, Li samples varied depending on the firing atmosphere. After H_2-firing, the samples as removed from the furnace, *i.e.*, no application of pressure (grinding, scratching or rubbing), showed an orange fluorescence and phosphorescence under 2537Å excitation and were dead under 3650Å irradiation. The results were the same regardless of the sequence of excitation. The application of pressure resulted in a new blue emission under 2537Å excitation. Now excitation by 2537Å resulted in a blue-white fluorescence (blue + orange). If, after 2537Å excitation, the sample was exposed to 3650Å radiation, there was a transitory orange emission. The N_2-fired samples, as removed from the furnace, were dead under both 2537Å and 3650Å. The application of pressure resulted only in the blue emission under 2537Å excitation and no stimulation.

In order to ascertain the relationship between the two effects and the presence of Li and/or Mn, samples of CaO:Mn and CaO:Li were prepared by firing in H_2 or N_2. The H_2-fired CaO:Mn samples had a white body color and were dead under 2537Å or 3650Å excitation. No pressure or stimulation effects

Table I. Characteristics of CaO phosphors containing Mn and/or Li

Additions	Firing atmosphere	Body color	Emission characteristics			
			2537Å		3650Å	
			Emission	Pressure effect	Emission	Stimulation effect
Mn	H_2	white	none	none	none	none
Mn, Li	H_2	white	orange	blue	none	orange
Mn	N_2	cream	orange	none	none	none
Mn, Li	N_2	cream	orange	blue	none	none
Li	H_2	white	none	blue	none	orange
Li	N_2	slightly off-white	orange	blue	none	none

were found. The N_2-fired samples had a weak orange fluorescence under 2537Å excitation and were dead under 3650Å. There were no pressure or stimulation effects. H_2-fired CaO:Li was dead under 2537Å or 3650Å excitation; weak pressure and stimulation effects were observed. N_2-fired CaO:Li had a weak orange fluorescence under 2537Å, but was dead under 3650Å. Only the pressure effect was observed. These data are summarized in Table I.

The emission spectra of the orange fluorescence from CaO:Mn with or without Li are the same and are independent of the firing atmosphere. The spectrum of the stimulated emission is the same as that for the fluorescence. The spectra of the blue fluorescence from CaO:Li are also the same independent of the presence or absence of Mn and the firing atmosphere. The orange and blue emission spectra are shown in Fig. 1. The excitation spectra of the two emissions are different as shown in Fig. 2. Figure 3 shows the temperature dependence of both emissions. The temperature breakpoint of the red emission is at 300°-320°C and at or below 20°C for the blue.

Samples similar to those reported in Table I were prepared using Na, K, or Al in place of Li. The results for Na and K were similar to those obtained with Li additions and are reported in Table II. Samples with Al showed only the pressure effect.

The luminescence of SrO phosphors containing Li and Mn were also examined. After O_2 firing the samples had a deep brown body color. Under 2537Å excitation there was a weak white emission and under 3650Å excitation a deep red emission. There was no stimulation effect, but there may have been a weak pressure effect. After H_2-firing the body color was slightly off-white. Excitation by 2537Å or 3650Å resulted in yellow-green fluorescence and phosphorescence. The pressure and stimulation effects were present, but the stimulated emission was yellow-green.

Examination of the data in Tables I and II shows that the 2537Å excited orange emission is due to the presence of Mn. The blue emission induced by the application of pressure is apparently due to the presence of a monovalent or trivalent cation. Spectroscopic analysis of the CaO samples containing only added Li but having the stimulation effect shows the presence of 10-20 ppm Mn so that apparently the stimulation effect requires the presence of both Li and Mn. Further, all the Mn must be in a reduced state (+ 2?) as evidenced by the fact that only H_2-fired CaO:Mn, Li samples show the stimulation effect. From the data listed in Table I and the measurements mentioned above, the orange and blue emissions are apparently unrelated. However, there appears to be some energy transfer from blue to orange centers as shown by the 3650Å stimulated emission only occurring with samples also having the blue emission.

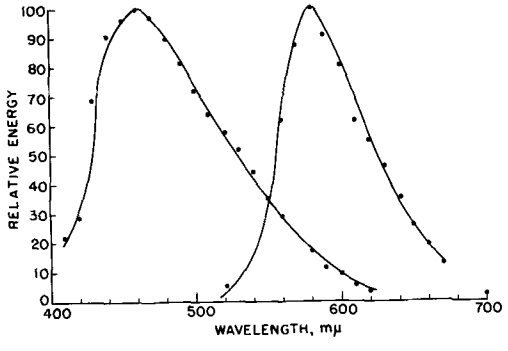

Fig. 1. Spectral distributions of the orange and blue emissions

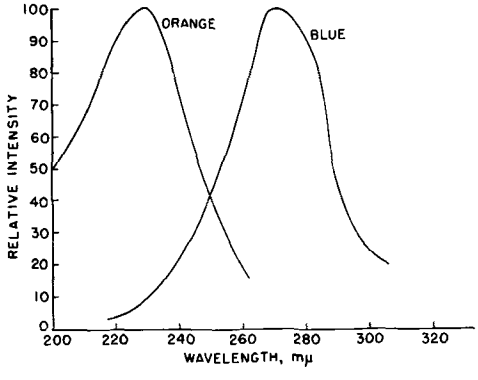

Fig. 2. Excitation spectra of the orange and blue fluorescence

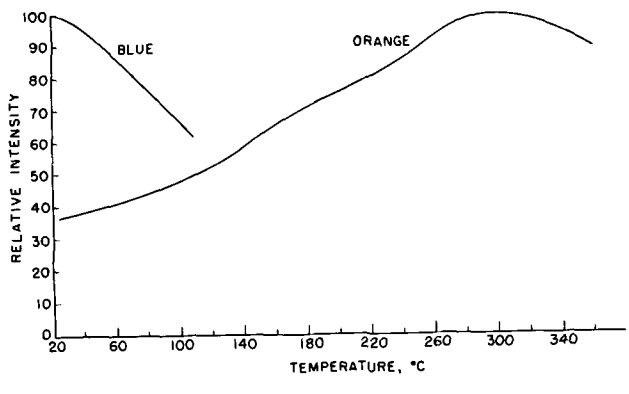

Fig. 3. Temperature dependence of the orange and blue fluorescence.

Table II. Characteristics of CaO phosphors containing Mn and Na, K, or Al

Additions	Firing atmosphere	Body color	Emission characteristics: 2537Å Emission	2537Å Pressure effect	3650Å Emission	3650Å Stimulation effect
Na	H_2	white	orange	blue	none	none
Mn, Na	H_2	white	orange	blue	none	orange
Na	N_2	white	orange	blue	none	none
Mn, Na	N_2	off-white	orange	blue	none	orange
K	H_2	white	none	blue	none	none
Mn, K	H_2	white	orange	blue	none	orange
K	N_2	white	orange	blue	none	orange
Mn, K	N_2	gr. yel.	orange	blue	none	orange
Al	H_2	white	none	blue	none	none
Mn, Al	H_2	white	none	?	none	none
Al	N_2	white	none	none	none	none
Mn, Al	N_2	white	none	none	none	none

A more detailed study of the two effects described here should be made in order to elucidate the nature of the energy levels and transitions responsible for the pressure and stimulation effects. Such a study might shed some light on the reason(s) for the decrease in light output in most phosphors on grinding.

Manuscript received Oct. 24, 1961; revised manuscript received April 17, 1962. This paper was prepared for delivery before the Philadelphia Meeting, May 3-7, 1959.

Any discussion of this paper will appear in a Discussion Section to be published in the June 1963 JOURNAL.

REFERENCES

1. R. Ward, Final Report for Contract NObsr-39045, June 30, 1949.
2. H. W. Leverenz, "Luminescence of Solids," p. 299, John Wiley & Sons, Inc., New York (1950).
3. J. Schulman, R. Ginther, C. Klick, R. Alger, and R. Levy, *J. Appl. Phys.*, **22**, 1479 (1951).
4. M. Furst and H. Kallmann, *Phys. Rev.*, **82**, 964 (1951); **83**, 674 (1951).
5. C. Hill, *Brit. J. Appl. Phys.*, Supp. No. 4, p. S6 (1955).
6. P. Ranby and S. Henderson, *Proc. Phys. Soc. (London)*, **67B**, 496 (1954).
7. J. Strange, *Brit. J. Appl. Phys.*, Supp. No. 4, p. S5 (1955).
8. M. Kats, *J. Exptl. Theoret. Phys., USSR*, **20**, 166 (1950).
9. J. Ewles and N. Lee, *This Journal*, **100**, 392 (1953).
10. J. Ewles and J. Stead, *Proc. Phys. Soc. (London)*, **69B**, 392 (1956).
11. J. Ewles, S. Jain, and R. Joshi, *Proc. Phys. Soc. (London)*, **71**, 852 (1958).

Diffusion Doping of Phosphorus in the Base of Silicon Tunnel Diodes

C. L. Gravel and A. D. Kurtz

Kulite Semiconductor Products, Inc., Ridgefield, New Jersey

and I. Berman

Air Force Cambridge Research Laboratories, Bedford, Massachusetts

One of the problems raised in the process technology of silicon tunnel diodes is the limit of impurity doping obtainable in the crystal as grown, which for phosphorus is approximately $10^{20}/cm^3$. The doping levels attainable using solid-state diffusion techniques to form an n-type layer on the base material are higher, and variation of the thickness of the diffused layer affords a measure of design control over the electrical characteristics of the tunnel diode. This note presents the results of a study of the effect of phosphorus diffused layers into phosphorus doped silicon base material on the tunnel diode peak to valley current ratios and the magnitude of the peak currents obtained under various alloying conditions.

Experimental

To investigate the effect of diffused layers on tunnel diode characteristics, phosphorus doped silicon of resistivity, 0.001 ohm-cm was selected for the base material. Additional diffusion doping was obtained using an open-tube, two-zone furnace with phosphorus pentoxide as the impurity source, and diffusing at 1200°C for times of 4, 16, and 64 hr. Impurity concentration at the surface of the diffused layers was determined as $4 \times 10^{20}/cm^3$ using sheet resistivity measurements and the data of Backenstoss (1). Rectangular bars of length 0.150 in. and width 0.030 in. were cut from the diffused material and also the 0.001 ohm-cm nondiffused base silicon to be fabricated into tunnel diodes. The p-type region was formed by alloying a 0.005 in. aluminum wire containing 1.0% boron into the silicon bars, with a gold wire subsequently being bonded to the bar for an ohmic contact. The alloying range investigated was from 700° to 1000°C and to obtain the steep impurity gradients necessary between degen-

erate n- and degenerate p-materials a short alloying cycle of 2 min at temperature followed by a quench in air was used.

The electrical parameters studied as a function of the two variables, depth of diffused layer and temperature of alloying, were the maximum peak currents obtained and the maximum peak to valley current ratios obtained with progressive etching. To obtain the maximum peak to valley current ratio, each diode was etched for 2-sec intervals in a composition of equal parts hydrofluoric, nitric, and acetic acids until the maximum ratio was passed. Normally, 4-6 such etching intervals were required.

Results

Figure 1 is a plot of the average maximum peak to valley current ratio as a function of alloying temperature with the diffusion time as a running parameter. Each point is the average of data taken on approximately twelve tunnel diodes. The curves exhibit the general tendency of a diffused layer to depress the peak to valley current ratio with increasing depth of the layer. For simplicity the data for the 4-hr diffused layer is not plotted. However, the results fall between the no-diffusion and 16-hr diffusion curves as expected. The effect of the alloying temperature on the peak to valley current ratio indicates that optimum current ratios are obtained in the range 825°-925°C, a range of relative flatness common to all the curves. There is also a tendency for the curves to cross in the vicinity of 1000°C as the material with diffused layers enable the fabrication of tunnel diodes at higher temperatures. The appearance of a negative resistance region persists at higher alloying temperatures the deeper the diffused layer. At an alloying temperature of approximately 1050°C only reverse or backward diodes are obtained.

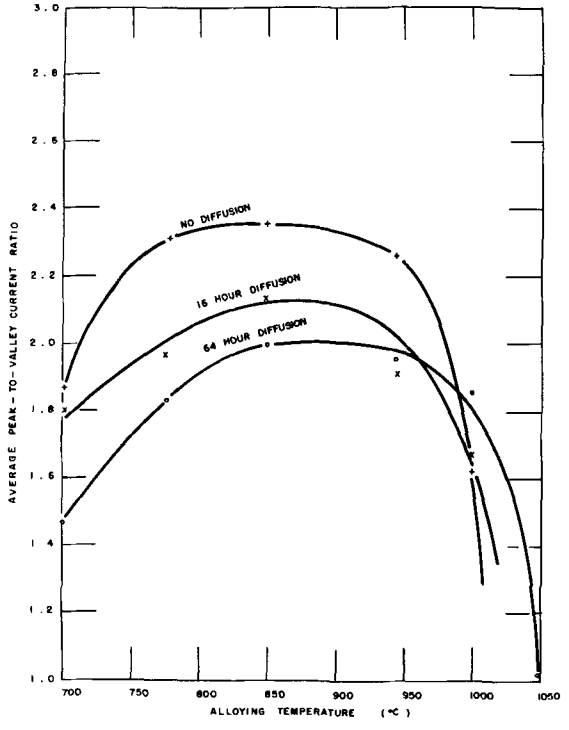

Fig. 1. Average maximum peak to valley current ratio as a function of alloying temperature.

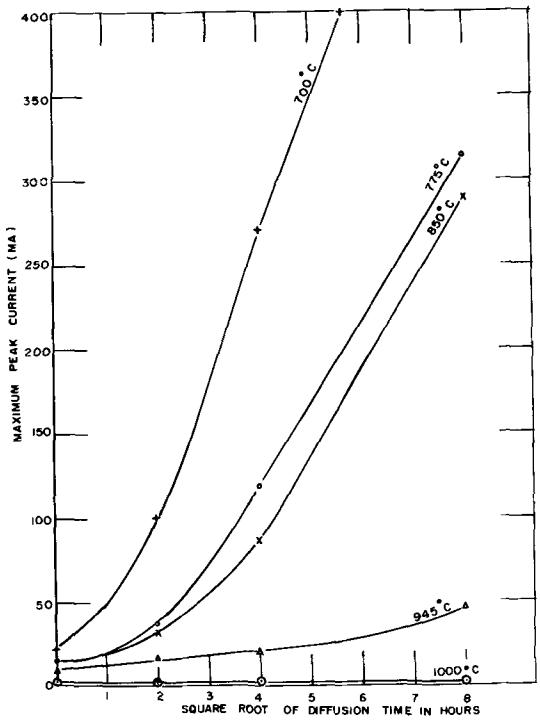

Fig. 2. Average maximum peak current vs. square root of the diffusion time.

Figure 2 is a plot of the average maximum peak current obtained against the square root of the time of diffusion, with the temperature of alloying as a running parameter. Since the increased peak currents resulting from diffused layers are presumed to come from a peripheral region around the alloyed junction, the total current should be proportional to the product of the diffused depth and the peripheral junction area. If it is assumed that the peripheral area remains essentially constant and the diffused depth, characterized by the complementary error function distribution, varies as the square root of the diffusion time, a plot of peak current *vs.* the square root of the diffusion time should be a straight line. The curves of Fig. 2 are reasonably straight lines with curvature appearing near the origin because of the 0.001 ohm-cm n-base material which is degenerate enough itself for tunneling current without having a diffused layer. As can also be seen from this plot the maximum peak current obtained is inversely proportional to the temperature of alloying.

Figure 3 is a plot of the average maximum peak current obtained against the temperature of alloying with the time of diffusion as a running parameter. The curves exhibit the general tendency to drop rapidly at the lower alloying temperatures, level out in the central range of 775°-875° where, incidentally, the maximum peak to valley current ratios are obtained, and then fall rapidly at the higher alloying temperatures. This behavior might be anticipated by considering two of the mechanisms which contribute to the tunneling current, the degree of degeneracy on the p-type side of the junction and the change in barrier width with alloying temperature. Tunneling theory indicates that the current through the barrier is given by the equation

$$I = A \int_{E_c}^{E_v} \{f_c(E) - f_v(E)\}\, Z\, P_c(E)\, P_v(E)\, dE$$

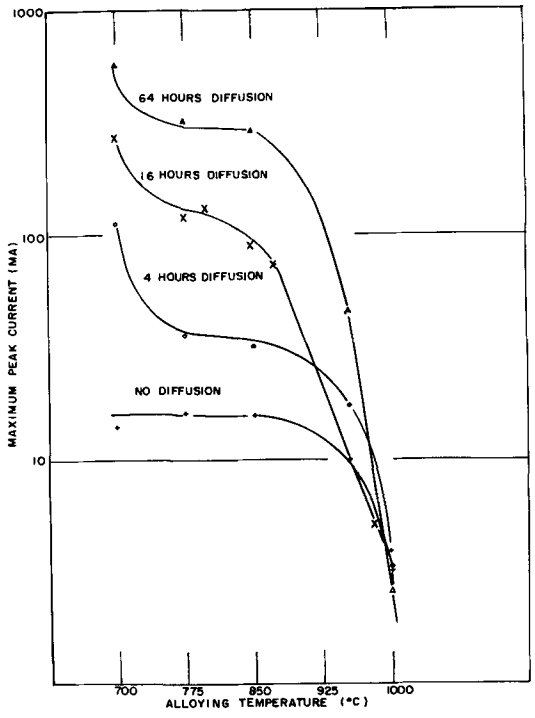

Fig. 3. Average maximum peak current vs. alloying temperature

where, $f_c(E)$ and $f_v(E)$ are the Fermi-Dirac distribution functions, $P_c(E)$ and $P_v(E)$ are the energy level densities in the conduction and valence bands, and Z is the probability of penetrating the barrier. The tunneling probability, Z, decreases exponentially with the width of the junction

$$Z \alpha \exp\{(-\beta m^{*1/2} Eg^{3/2})/F\}$$

where β is a constant, Eg is the energy gap, m^* is an effective mass, and F is the electric field in the junction. The maximum electric field for a step junction is

$$Fm = 2V/w$$

where V is the barrier voltage and w is the width of the junction. The junction width will increase with alloying temperature because of the increased diffusion of the doping impurities going from the liquid phase into the solid. Thus at higher alloying temperatures, 900°-1050°C, the increasing barrier width rapidly reduces the probability of tunneling, and the curves fall steeply to low current levels. At the lower alloying temperatures, 700°-775°C, the barrier width is small enough to permit the large peak currents observed, although the solubility of boron in silicon is smaller at these alloying temperatures. As the alloying temperature is increased to the intermediate range of 775°-900°C, a region of relative flatness in the curves of Fig. 3, the greater boron solubility in silicon increases the degeneracy on the p-type side of the junction. The higher p-type degeneracy increases the energy levels available for tunneling of electrons across the barrier and also decreases the extension of the junction into the p-type side of the junction as this extension is inversely proportional to the square root of the doping level. These two contributions toward an increased tunneling current counteract the reducing effect on the tunneling probability of the barrier width widening with alloying temperature.

Considerable care was taken to obtain reproducibility in the fabrication of the diodes; nevertheless, inhomogeneities in the aluminum-boron wire and the inherent difficulties of reproducibility in an alloying process and the subsequent measurement of structure-sensitive properties introduce scatter in the data. The mean deviation of the data is indicated for each point of Fig. 3.

Summary

Phosphorus diffused layers into phosphorus doped bulk silicon of resistivity 0.001 ohm-cm tend to increase the peak current of alloyed tunnel diodes by as much as an order of magnitude. At a given alloying temperature the maximum peak tunneling current is reasonably proportional to the depth of the diffused layer and decreases inversely with temperature of alloying.

Some negative resistance is observable throughout an alloying temperature range of 675°-1050°C, with the optimum peak to valley current ratios obtained between 825° and 925°C. The optimum temperature range shifts slightly higher with increasing depth of the diffused layer.

The presence of a diffused layer tends to depress the peak to valley current ratios by upwards of 20% when compared with diodes made with the identical nondiffused base material.

Acknowledgment

This work was sponsored in part by the Electronics Research Directorate, Air Force Cambridge Research Laboratories under Contract AF19(604)-7328.

Manuscript received Feb. 27, 1962.

Any discussion of this paper will appear in a Discussion Section to be published in the June 1963 JOURNAL.

REFERENCE

1. G. Backenstoss, *Bell System Tech. J.*, **37**, 699 (1958).

Undamaged Germanium Surfaces of High Optical Quality

T. M. Donovan and B. O. Seraphin

Michelson Laboratory, China Lake, California

By established mechanical polishing methods, germanium mirrors of suitable optical quality can be prepared. However, the mechanical action of the abrasive is known to introduce surface damage which affects the electrical properties of the semiconductor (1). Whenever this damage cannot be tolerated, as in most device applications, it is removed by etching. The etching operation removes the disturbed material and restores the electrical properties of the surface. Unfortunately, however, the etching operation degrades the optical finish of the surface at the same time (2).

With the development of epitaxial and other advanced semiconductor devices there is a need for flat and smooth substrate surfaces with unimpaired electrical properties. Sullivan (3, 4) developed an electrochemical technique which yields undamaged surfaces of 2.5 μ/in. flatness and an average roughness of 25Å. Related values for fused quartz optical flats are approximately 0.05 μ/in. and 10Å.

The present paper reports on a modification of Sullivan's technique which yields surfaces of about 0.1 μ/in. flatness and a rms roughness of only 10-13Å, approaching the finish of the best fused quartz optical flats. At the same time it shows by means of electron diffraction, surface recombination velocity, and field-effect measurements that these surfaces approach structurally and electrically surfaces that had been etched in CP-4.

Polishing Procedure

The material used for this study was 30 ohm-cm n- and p-type single crystal germanium. Two faces of the sample were lapped plane parallel, and electrical contact was made to one face using electroless nickel (5). The opposite face was polished[1], diamond paste with an average particle diameter of ¼μ being used for the final stage. The surface obtained at this stage will be referred to as the mechanically polished surface. It appeared scratch free at 30X magnification.

Two types of samples were used. Thick samples (25 x 9 x 9 mm) were mounted in a micarta cage. Thin samples (16 x 9 x 0.25 mm) were fixed to a nylon pressure plate. In both cases provisions were made to bring electrical contact from the samples to the top of the pressure plate. The sample was then made the anode in an electrolytic cell with a cloth covered polishing wheel as rotating cathode. A dilute solution of KOH made by dissolving KOH in polishing fluid was used as electrolyte and was made to flow drop-wise onto the polishing cloth at rates up to 25 ml/min.

[1] The following polishing materials were obtained from Buehler, Ltd., 2120 Greenwood St., Evanston, Ill.: Microcloth, Cat. No. 1576; Metadi Fluid, Cat. No. 1542-2SS; Polishing Compound, Cat. No. 1544-AB.

During the course of the electropolishing experiments it was found that a fresh polishing cloth would not give a scratch-free surface. By dissolving the KOH in polishing fluid so the samples would "ride" on a laminar layer of sufficient viscosity, and by using a cloth that had been broken in during a previous mechanical polishing stage it was possible to obtain a scratch-free surface. It was determined in etching rate experiments that there was no measurable sample weight loss, as determined with an analytical balance, following the above procedure without current flow.

Current densities up to 10 ma/in.^{2} have been used effectively with both n- and p-type germanium. At this current density an etching rate of 0.03 μ/min was obtained. This unusually small current density and the related low etching rate, which are about 50 times smaller than ordinarily used in electropolishing techniques for germanium and silicon, might partially account for the low roughness figure. Current density values up 10 ma/in.^{2} represent the range in the anode potential-current density diagram in which the characteristics for n- and p-type material are still identical (6). Since the removal of only 0.5-1μ of material was necessary to remove the damaged layer (1), an operating time of 20-30 min did not seem unreasonable.

Optical Measurements

The over-all flatness of the samples was checked by a standard interferometric technique using an optical flat and the yellow lines of a sodium lamp. The flatness for the thick samples was found to be better than 0.1 μ/in. The flatness of the thin samples was somewhat less due to the warping of the germanium when it was no longer backed by the pressure plate. No difference in flatness was observed between the last stage mechanical abrasive polish and the electrochemical treatment.

The roughness of the samples was measured according to an interferometric method developed by Koehler and White (7). The test surface is made one plate of a Fabry-Perot interferometer, with a fused quartz optical flat of known roughness as the other plate of the configuration. Using white light, a set of interference fringes of equal chromatic order is displayed behind a spectrograph. By choosing a low order of interference which increases the width of the fringe, and enlargement of the picture, the fine structure of the fringe can be measured, giving a fairly accurate replica of the surface. The precision of the method is given by the authors as 20%. The method is superior to mechanical probing by diamond stylus or brushes, especially in the range below a few microns where the mechanical

probe cannot bottom into the troughs and a value too favorable is usually read.

Figure 1a shows fringes of equal chromatic order from an interferometer consisting of two fused quartz optical flats of 8-10Å rms roughness. The picture represents a sample area of about 0.5 by 0.003 mm. Magnification before reduction for publication was 19. Analyzing the wiggles of the fringes the value for the surface roughness is obtained. Figure 1b shows fringes from an interferometer consisting of an electrochemically polished germanium sample and one of the above quartz flats. The measured rms roughness of the germanium is 10-13Å. Figure 1c shows fringes displayed from a mechanically polished sample and one of the quartz flats. The measured rms roughness is 25-30Å. Figure 1d shows the sample from Fig. 1c again after a 15-sec immersion in CP-4, the minimum time to remove the damaged surface layer of approximately ½ μ thickness. The rough surface obtained with CP-4 was typical of surfaces obtained with a number of chemical etchants, including most of the ones which are recommended for chemical polishing of germanium.

Electron Diffraction Measurements

Electron diffraction studies of the surfaces indicated that the mechanically disturbed layer that existed after the final mechanical polish was removed by the electrochemical treatment. Figure 2a shows the diffraction pattern obtained with the mechanically polished surface. The spot pattern indicates a randomly oriented mosaic structure in the surface. Figure 2b shows the diffraction pattern obtained from the electrochemically polished surface. The spot pattern and the sharp Kikuchi pattern are indicative of a high degree of surface orientation (8). Furthermore, this pattern compares with the pattern obtained by etching a mechanically polished surface in CP-4. This latter pattern is shown in Fig. 2c.

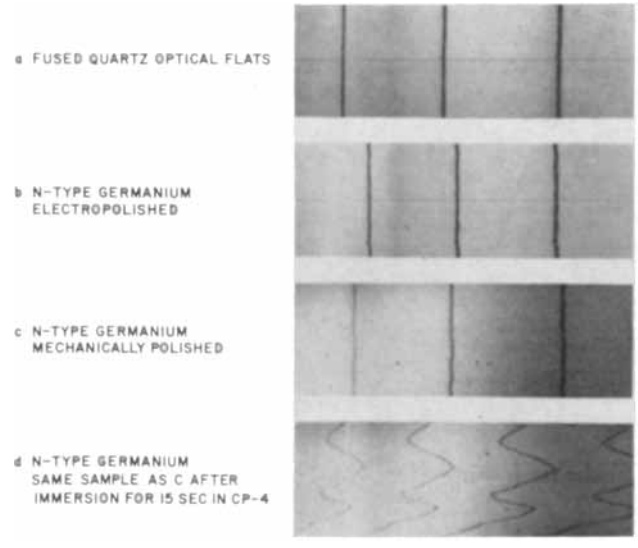

Fig. 1. Fringes of equal chromatic order corresponding to an interferometer made up of (a) two optical flats; (b) an optical flat and an electropolished germanium sample; (c) an optical flat and a mechanically polished germanium sample; and (d) an optical flat and a germanium sample that had been etched in CP-4 for 15 sec.

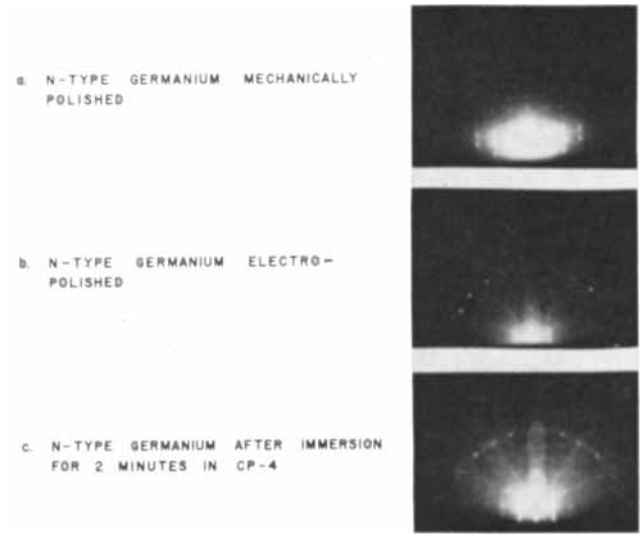

Fig. 2. Electron diffraction patterns corresponding to (111) germanium surfaces with (a) a mechanically polished surface; (b) an electropolished surface; and (c) a CP-4 etched surface.

Electrical Measurements

The surface recombination velocity was determined by measuring the filament lifetime by the photoconductivity decay method. This method which is sensitive to low values of the surface recombination velocity s, gave for mechanically polished samples s-values in excess of 5000 cm/sec. Electropolishing the surfaces of the sample brought this value down to 120 cm/sec. If, on the other hand, mechanically polished samples were immersed in CP-4 for 15 sec, s-values around 100 cm/sec were obtained.

Finally, sets of three thin samples were measured with respect to their field-induced change of the conductivity. The mechanically polished samples did not show any change due to the surface damage which gives rise to a fast state structure of very high density (9). On electrochemically polished surfaces, however, any mechanical damage is removed to the extent where it ceases to dominate the recombination process in the surface. Under otherwise identical conditions these samples showed a field effect which approached (50-75%) the one obtained for samples that had been etched in CP-4.

Acknowledgments

The authors wish to express their appreciation to Dr. Jean M. Bennett for assistance with the optical portion of the paper and to Mr. L. G. LaMarca for making the electrical measurements. Also, the Crystal Physics Branch of this Laboratory should be thanked for the electron diffraction photographs.

Manuscript received March 22, 1962. This paper was prepared for delivery before the Los Angeles Meeting, May 6-10, 1962.

Any discussion of this paper will appear in a Discussion Section to be published in the June 1963 JOURNAL.

REFERENCES

1. T. M. Buck, "The Surface Chemistry of Metals and Semiconductors," H. C. Gatos, Editor, pp. 107-128, John Wiley & Sons, New York (1959).
2. R. J. Archer, *Phys. Rev.*, **110**, 354 (1958).

3. M. V. Sullivan and R. M. Finne, "A New Technique for the Preparation of Flat Germanium Surfaces," presented at the Houston Meeting, The Electrochemical Society, Oct. 11, 1960.
4. D. L. Klein, G. A. Kolb, L. A. Pompliano, and M. V. Sullivan, "Electropolishing of N-Type Germanium and P- and N-Type Silicon," presented at the Indianapolis Meeting, The Electrochemical Society, April 30, 1961.
5. M. V. Sullivan and J. H. Eigler, *This Journal*, **104**, 226 (1957).
6. D. R. Turner, *ibid.*, **103**, 252 (1956).
7. W. F. Koehler and W. C. White, *J. Opt. Soc. Am.*, **45**, 1011 (1955).
8. P. S. Holmes and R. C. Newman, *Proc. Int. Elect. Engrs.*, **106**, Part B Supplement, 287 (1959).
9. E. Harnick and Y. Margoninski, *J. Phys. Chem. Solids*, **8**, 96 (1959).

Chemical Polish for Lead Telluride

P. H. Schmidt

Bell Telephone Laboratories, Murray Hill, New Jersey

The purpose of this note is to describe a chemical polish which will produce flat, mirror-like, ripple-free and strain-free surfaces on samples of lead telluride. At present there exist only two satisfactory methods for polishing lead telluride (1, 2). Both methods are electrochemical and produce surfaces which are smooth and strain-free but somewhat convex. However, some inherent disadvantages are associated with electropolishing. Some of these are the difficulty of producing flat, ripple-free surfaces, the complex equipment needed, and optimum conditions are sometimes difficult to control. Attempts to polish lead telluride chemically have thus far been unsuccessful (1). Most chemical methods produce an etched surface or an etched surface with an associated film which is difficult or impossible to remove.

Method

Samples are prepared by first abrading surfaces flat with water-lubricated No. 400 grit aluminum oxide paper, removing 0.002-0.004 in. of material with every few strokes on the abrasive paper. Coarse abrasion is then followed by finer abrasion on water-lubricated No. 600 grit silicon carbide paper and finally by abrasion on dry 4/0 grit French emery paper. Care must be exercised during all abrading stages to prevent the specimen from fracturing or cleaving (100 cleavage), and it is therefore recommended that a jig be used for mounting the sample. Quartz type sticky wax[1] (mp 68°C) has been found very satisfactory for mounting samples to metal inserts of jigs. Care must also be exercised not to load the abrasive paper, this being especially true of the No. 600 grit and 4/0 grit papers. Samples must be thoroughly cleaned between all abrading stages.

Using a figure eight 1-2 in. stroke, the sample is rubbed on twill jean cotton cloth that has been stretched over a flat glass plate and saturated with a solution of 50% C. P. hydrogen peroxide (H_2O_2 30%) and 50% glacial acetic acid and Linde A abrasive. Lapping is continued for 2-3 min. Material is removed at a rate of about 0.0002 in./min. The sample surface should appear cloudy-bright with fine scratches.

Finally the sample is twill jean polished (3) for another 2-3 min using the acid mixture without the Linde A abrasive. Material removal rate is about 0.0001 in./3 min. A warm water rinse should immediately follow polishing with a final flush in acetone or ethyl alcohol. The sample surface should appear highly reflective and with no fine grain ripple.

Back-reflection Laue photographs, using tungsten radiation and a film-to-specimen distance of 5 cm, of surfaces polished using the method described above indicate that they are free of strain.

Undesirable films that have formed on polished samples can be removed by immersion of the sample in a solution of equal parts of glacial acetic acid and 30% hydrogen peroxide for 3-4 min followed by swabbing with water. However, it is recommended that the twill jean polish (3) procedure be repeated as it will produce far superior surfaces.

The method described herein is simple and rapid, requiring little or no equipment or setup time. The surfaces so produced appear to be as strain-free as those obtained by electropolishing techniques and are visibly smoother and flatter.

[1] Manufactured by Corning Rubber Company, Inc., 578 Gates Avenue, Brooklyn 21, New York.

Acknowledgments

The author would like to thank W. M. Walsh, Jr., for encouragement to pursue this project. The majority of samples used in the course of this work were provided through the courtesy of Dr. Bland B. Houston of the Naval Ordnance Laboratory, White Oak, Silver Spring, Maryland.

Manuscript received April 27, 1962.

Any discussion of this paper will appear in a Discussion Section to be published in the June 1963 JOURNAL.

REFERENCES

1. P. H. Schmidt, *This Journal*, **108**, 104 (1961).
2. B. B. Houston, Private communication.
3. D. F. Gibbons and V. Chirba, Private communication.

Brief Communication

A Polishing Etchant for III-V Semiconductors

C. S. Fuller and H. W. Allison

Bell Telephone Laboratories, Incorporated, Murray Hill, New Jersey

The purpose of this communication is to report a new class of etchant which is capable of producing highly polished surfaces on GaAs and GaP crystals. A more detailed evaluation of this etchant for device purposes is described by Sullivan and Kolb (1). It is applicable to other III-V compounds, but is not as good as other etchants for Ge and Si. The etchant has definite application in removing thin diffusion layers since it is subject to very precise control. It also allows new types of resists to be used as masking materials, *e.g.*, water soluble polymers, and appears to be subject to less undercutting than the usual aqueous etches. Finally, the etchant is useful in the incremental removal of layers of material in order to obtain thin base layers for devices.

The etchant consists basically of an organic liquid in which a halogen, generally Cl_2 or Br_2, is dissolved. The best organic liquids so far found are methyl alcohol or glacial acetic acid. These materials have been "dry" but not intensively dried. Adding water slows the etching reaction. Obviously, organic liquids which react rapidly with halogens cannot be used. The use of perchloro compounds, such as CCl_4, results generally in very slow etching. However, mixtures of CCl_4 with methyl alcohol are quite satisfactory, *e.g.*, 1:1 by volume. Benzene or toluene with methyl alcohol are also useful.

It is well known that the chemical etchants suitable for producing polished surfaces on Ge and Si are not very effective on the III-V compound semiconductors. Mixtures of HF and HNO_3 in various proportions and concentrations can be used (2). However, poor surfaces generally result when used with GaAs even on the smoother etching (111) face. HNO_3 alone results in oxidized surfaces which are unsuitable. Aqua regia is a useful etchant, but does not provide the polish desired. It also attacks and lifts many of the resists employed as masking materials. The situation with GaP is even worse in that aqua regia is about the only etchant which attacks the material. The difficulties of masking are even more severe.

For GaAs the best solution for room temperature use is bromine[1] in methyl alcohol. A wide variety of concentrations may be employed depending on the application. For a high polish 5-20% of bromine by volume is used. For a light etch 0.1-1% by volume is best. Etch rates varied from a few tenths to 4 mils/min on a crystal pulled about 8° off of [111]. The etchant is conveniently removed by mean of methyl alcohol rinses.

[1] Care should be used in handling liquid bromine to avoid burns and breathing fumes.

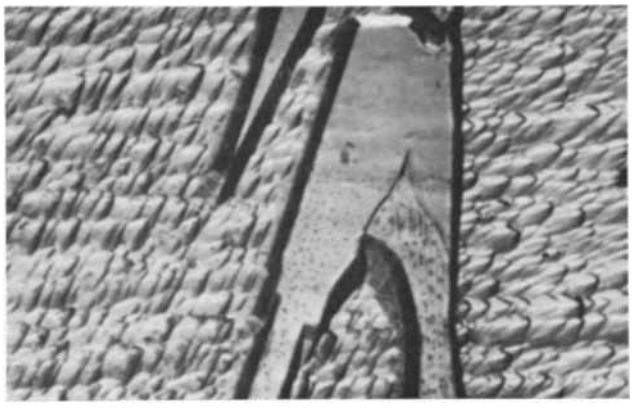

Fig. 1. GaP polycrystal etched for 3 min at 25°C in chlorine-methyl alcohol. Both smoothly etching surfaces and surfaces exhibiting etch pits are shown. Magnification 40X.

For GaP the bromine etch is too slow for most purposes. In this case, the best procedure is to bubble Cl_2 gas slowly through methyl alcohol with the specimen immersed.[2] The solution turns yellow indicating saturation with the gas, and the etching proceeds at a moderate rate at room temperature. Highly polished surfaces are obtained in from 5 to 20 min. Warming slightly will increase the rate. Etch rate is about 0.5 mil/min at 25°C.

Other III-V semiconductors have been etched in the manner described. Iodine in methyl alcohol, for example, has been found useful for etching InSb.

Finally the etchant has application in developing etch pits. The accompanying figure shows a polycrystal of floating-zone GaP. Both smoothly etching faces and faces exhibiting etch pits are shown.

Acknowledgment

The authors are indebted to A. A. Tartaglia for the photograph in Fig. 1.

Manuscript received June 13, 1962.

Any discussion of this paper will appear in a Discussion Section to be published in the June 1963 JOURNAL.

REFERENCES

1. M. V. Sullivan and G. A. Kolb, To be published.
2. "Properties of Elemental and Compound Semiconductors," H. C. Gatos, Editor, Interscience Publishers, New York (1959).

[2] Considerable caution should be used when Cl_2 gas and organic solvents are intermixed since violent reactions can occur. Methyl alcohol in vapor form *ignites spontaneously* in chlorine. To avoid this, use capillary tubing (1 mm bore) to lead the gas into the alcohol and use uncovered beakers.

The Transient Impedance of Leclanche Cells

Aladar Tvarusko

The Carl F. Norberg Research Center, The Electric Storage Battery Company, Yardley, Pennsylvania

ABSTRACT

The transient impedance of Leclanché cells was studied on open circuit and during discharge. The transient impedance is defined as the ratio of the Laplace transforms of voltage and current. An equivalent circuit was assumed for the Leclanché cell, and the values of the circuit elements were calculated with the help of the time constant for various electrolytes and manganese dioxides. The influence of the anode, cathode, and discharge on the transient impedance are discussed.

The modern use of Leclanché cells in electronic equipment usually requires cells of low impedance. The present study was undertaken to elucidate the nature of impedance and the parameters influencing it.

The Leclanché cell consists of a zinc anode, MnO_2-C cathode mix, and electrolyte absorbed in a separator and the cathode mix. It is a well-known fact that zinc in contact with an electrolyte forms an electrical double layer at the electrode-solution interface. This double layer together with the bulk of the metal and electrolyte can be represented by an equivalent circuit having a certain impedance.

The phase boundary of semiconducting metal oxides and carbon with electrolyte has been investigated by numerous authors. The cathode mix is composed of MnO_2 and carbon particles surrounded by the electrolyte. Euler (1) described the ionic and electronic resistance, the electrical double layer, and the reaction impedance of an MnO_2 particle by an equivalent circuit. The various MnO_2 and carbon particles are in contact with each other forming a porous electrode. This necessitates the interconnection of the individual equivalent circuits resulting in a 3-dimensional network. The individual equivalent circuits of this network are either in series or in parallel configuration to each other and can be reduced to a simplified equivalent circuit, for instance that of Euler (2). The total impedance will be the sum of the individual impedances or admittances, respectively, be it a-c steady state or a-c transient.

The electrolyte in the separator electrically connects the anode and cathode. Naturally this electrical path (electrolyte, anode, and cathode) is represented by a certain pure resistance. This resistance is the internal resistance of Leclanché cells as reported earlier (3).

Experimental and Discussion

The steady-state form of a time-varying quantity is the same as that of its drive. Thus, a sine voltage produces an a. c. of the same wave-form and frequency. The transient form, in contrast, is independent of the drive and depends only on the circuit investigated. Such a transient response can be achieved by using a unit impulse drive function (delta function). In the case of a square wave drive function the response contains both the transient and steady-state forms.

One can conceive of the transient impedance $Z(p)$ as a generalized impedance concept relating the Laplace transforms of voltage and current in the same manner as the steady-state a-c impedance relates the corresponding phasors (4),

$$\mathcal{L}v(t) = \mathcal{L}I(t) \cdot Z(p) \qquad [1]$$

Assuming the inductance of the leads and Leclanché cell to be negligible, only the pure resistive component and the capacitive reactance have a role in the impedance. The transient impedance will correspond to that of an RC network, *i.e.*, single-energy electrical system because the energy of the circuit is stored in one form only. The "single-energy electrical system" is used here in the sense of the network analysis. When an external voltage step is applied to an RC network, it must all appear across the series resistance (not paralleled by capacitance), since the voltage across a capacitance cannot change instantaneously. This series resistance is the internal resistance, R_i of Leclanché cells as determined by the square wave method (3) or pulse method (5).

Either a series or parallel equivalent circuit can be used to describe the Leclanché cell. The parallel arrangement is preferred here. The simplest possible parallel equivalent circuit is a resistance (R_i) in series with a resistance (R_1) and the capacitance (C_1) in parallel

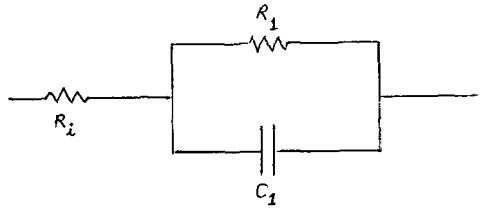

where R_i is always linear. For an equilibrium condition, R_1 and C_1 are linear; for a nonequilibrium condition, however, they may be nonlinear. A certain nonequilibrium condition within an infinitesimal time interval can be regarded as an equilibrium condition and can be represented by the same equivalent circuit but of differing values for the circuit elements. The capacitance, representing the electrical double layer, is parallel to a resistance and a second capacitance in parallel, representing the faradaic impedance (6). The two parallel capacitances can be added, resulting in C_1. A parallel re-

sistance and capacitance arrangement was considered for Leclanché cells by Euler and Dehmelt (7).

Let us consider the transient voltage response $v(t)$ of the aforesaid equivalent circuit when a constant current step function is applied. The differential equation of this and all single-energy systems is of the first order. Assuming that the circuit (Leclanché cell) is in steady state, the voltage response in one cycle is of the same form as the response in the next cycle. Furthermore, let us assume that the impressed current is $i(t) = Iu_{-1}(t)$, where $u_{-1}(t)$ denotes the unit step source current. The solution for $v(t)$ can be obtained by the classical method of solving differential equations, employing Heaviside operational calculus (8) or Laplace transformation:

$$v(t) = IR_i + IR_1\left(1 - \exp - \frac{1}{R_1C_1}t\right) \quad [2]$$

and the transient impedance, Z_{tr}

$$Z_{tr} = \frac{v(t)}{I} = R_i + R_1\left(1 - \exp - \frac{1}{R_1C_1}t\right) \quad [3]$$

where for

$$t = 0+ \qquad Z(0+) = \frac{v(0+)}{I} = R_i \quad [4]$$

for

$$t = \infty \qquad Z(\infty) = \frac{v(\infty)}{I} = R_i + R_1 \quad [5]$$

In the case of a square wave or pulse signal, the $t = 0+$ condition is practically represented by the leading edge of the signal and the instantaneous voltage drop is due to the internal resistance, R_i of the Leclanché cell. The other extreme ($t = \infty$) corresponds to the steady-state condition, and the parallel resistance can be calculated easily.

All single-energy transients of a d-c nature (square wave or pulse) start at one value and end at another value. In the case of an RC network there is an exp $- t/RC$ term multiplying the magnitude of the change, which describes the course of the voltage response between the two limit values. The exponent's denominator is the product of the values of the parallel resistance and capacitance. This product is called the time constant, τ, and is equal to the time required for a voltage in this circuit and all RC single-energy systems to rise to 63.2% of its steady final value ($t = R_1C_1$). The magnitude of the steady state does not depend on the magnitude of capacitance, since the term containing capacitance is eliminated from the Eq. [5]. Increasing or decreasing the time constant increases or decreases, respectively, the time required to reach the steady state. The time constant is increased or decreased by increasing or decreasing, respectively, either R_1 or C_1, or both.

The time constant can be determined by one of the following three methods: the 63.2% method, the initial-slope method, and the log-plot method. Here, the 63.2% method will be used. Figure 1 shows the oscilloscope traces of a pasted D-size Leclanché cell containing electrolytic MnO_2 of source B and conventional $ZnCl_2$-NH_4Cl electrolyte. The experimental arrangement used for this study is the same

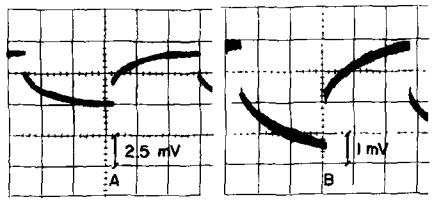

Fig. 1. Oscilloscope traces of the transient voltage responses of undischarged Leclanché cells containing electrolytic MnO_2 of source B and conventional $ZnCl_2$-NH_4Cl electrolyte. A, at 400 cps square wave; B, at 1000 cps square wave.

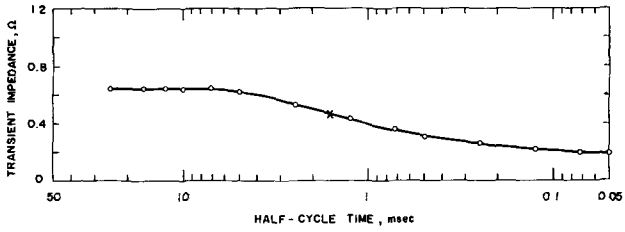

Fig. 2. Transient impedance of an undischarged Leclanché cell (same as Fig. 1) as a function of half-cycle time.

as described previously (3). The 5X attenuation factor is included in the voltage values shown in the figures of oscilloscope traces. Figure 1A shows the oscilloscope trace of $v(t)$ of the undischarged cell at 400 cps square wave. The steady state is already reached and the time constant, τ, can be determined by the 63.2% method. The value of the time constant, however, cannot be determined very accurately, not even on an enlarged picture of the trace.

The time constant, however, can be determined more accurately from the transient impedance-frequency curve since the frequency, by definition, is the number of cycles per second. The oscilloscope trace in Fig. 1B is that of the transient voltage response for the same undischarged Leclanché cell as above, at 1000 cps square wave. Figure 2 is obtained by plotting the $v(T/2)/I$ ratios, *i.e.*, the ratios of the magnitudes of the transient voltage responses at the end of the half-cycles and the magnitude of the constant current square wave, which is the transient impedance (Z_{tr}), as a function of the half-cycle time, $T/2$ (through varying the frequency of the square wave). The curve starts at one value, that of the internal resistance of the Leclanché cell, and increases to the steady-state value. Knowing the internal resistance (0.17 ohm) and the steady-state impedance (0.65 ohm), the parallel resistance is easily obtained and $R_1 = 0.48$ ohm. Taking 63.2% of the difference of the steady-state impedance and internal resistance, and adding it to the internal resistance, the time constant is found where it intersects the curve. In this case, $\tau = 1.59$ msec. Knowing the value of the parallel resistance, R_1 (0.48 ohm) and the time constant, τ(1.59 msec), the parallel capacitance is calculated. It is thus 3310 μF for the aforementioned cell. This value is in excellent agreement with Brodd's results (10) as calculated from his Table II. It is slightly larger than the 2140 μF reported by Euler and Dehmelt (7) for a D-size cell with African (Gold Coast) MnO_2 ore, and is 5 orders of magnitude larger than the 0.43 μF value of Drotschmann (9) for a smaller cell.

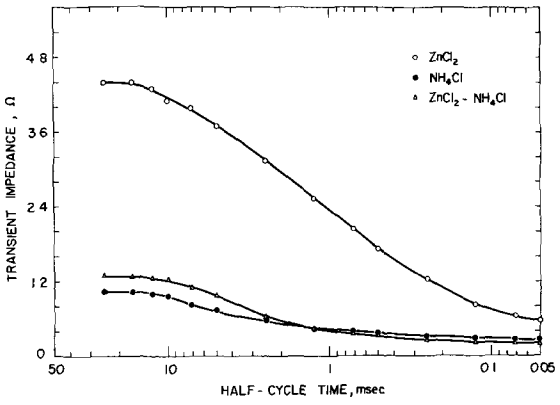

Fig. 3. Transient impedance of undischarged Leclanché cells with African ore and various electrolytes as a function of half-cycle time.

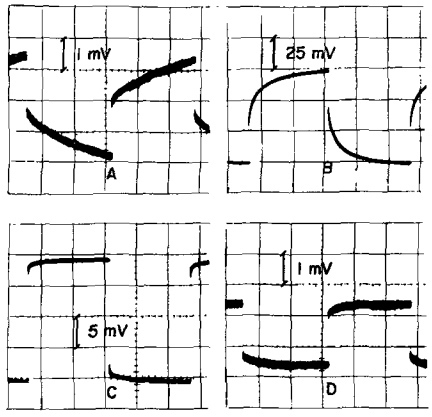

Fig. 4. Oscilloscope traces of transient voltage responses. A, Leclanché cell with African ore and conventional $ZnCl_2$-NH_4Cl electrolyte, 1000 cps square wave; B, two zinc anode portions of the above cell, 100 cps square wave; C, two cores of the above cell, 1000 cps square wave; D, Leclanché cell as above in the beginning of 4-ohm discharge, 1000 cps square wave.

Figure 3 shows the transient impedance of undischarged D-size Leclanché cells containing African ore and $ZnCl_2$, NH_4Cl, and $ZnCl_2$-NH_4Cl electrolytes of constant Cl^- content (225g Cl^-/1000 ml solution), as a function of the half-cycle time, $T/2$. The transient impedance curve of the undischarged cell with $ZnCl_2$ electrolyte is markedly different from the other two. Establishing the R_i and R_1, the time constant is determined by the 63.2% method. These data and the calculated parallel capacitances, C_1, are tabulated in Table I. The NH_4Cl electrolyte yielded a small parallel resistance, R_1, and a large parallel capacitance, C_1. On the other hand, the $ZnCl_2$ electrolyte resulted in a large R_1 and small C_1. The R_1 and C_1 values of a cell with an electrolyte containing both salts were between the values found for each constituent. The same relationship was also found for other natural ores.

The oscilloscope traces of D-size Leclanché cells having African ore and conventional $ZnCl_2$-NH_4Cl electrolyte can be seen in Fig. 4. Figure 4A shows the transient voltage response of an undischarged cell at 1000 cps square wave. It was of interest to see the influence of the zinc anode and MnO_2-C cathode on the transient voltage response. Therefore, four undischarged cells were carefully disassembled so that the paste remained intact on the zinc anodes from two cells and on the mix cores of the other two. Small portions of the zinc anodes were cut out, leads soldered to them, and with the pastes facing each other, pressed together. The trace of this at 100 cps is shown in Fig. 4B. The transient voltage response at 1000 cps of two cores with the original pastes pressed against each other is shown in Fig. 4C. For these two traces the d-c blocking capacitor was not included in the experimental circuit (3). The parallel resistance, R_1, is comparatively large for the zinc anode whereas it is small for the MnO_2-C core, which is in agreement with the findings of Euler and Dehmelt (7) and Brodd (10). The values of the R_1, τ, and C_1 will be calculated from experiments to be performed with more defined geometrical surface areas.

When a cell is being discharged, the magnitude of the transient voltage response (and hence the transient impedance) decreases. The rate of the decrease is a function of the magnitude of the current drain. The larger the current drain, the faster the decrease, and the shorter the time needed for Z_{tr} to reach the steady-state value. This will be reported in detail later in connection with the experiments obtained by a simple indicating instrument using 100 cps constant current square wave.

The oscilloscope trace at 1000 cps square wave of the transient voltage response of the aforementioned cell in the beginning of the discharge through 4 ohms is shown in Fig. 4D. It is evident that the decrease of $v(t)$ is due to the destruction of the interface equilibrium condition at the zinc anode alone and the trace resembles that of the two cores (Fig. 4C). In the measuring circuit (3), the 4-ohm discharging resistor is in parallel with the cell, and the R_i and R_1 is calculated with the help of Kirchoff's law. The value of R_1 is small and remains nearly constant as shown in Fig. 5. This shows the internal resistance R_i and the transient impedance Z_{tr} in ohms at 1000 cps square wave of the aforementioned Leclanché

Table I. Equivalent circuit parameters of undischarged Leclanché cells containing African ore and various electrolytes

Electrolyte	R_i, ohm	R_1, ohm	τ, μsec	C_1, μF
NH_4Cl	0.26	0.79	5430	6870
$ZnCl_2$	0.33	4.07	1950	480
$ZnCl_2 + NH_4Cl$	0.19	1.09	4160	3820

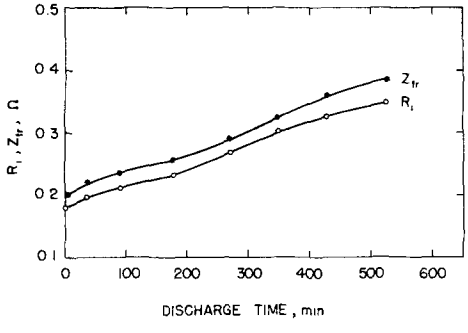

Fig. 5. Internal resistance, R_i and transient impedance, Z_{tr} of Leclanché cells (same as Fig. 4) discharged continuously through 4-ohms as a function of discharge time.

cells during 4-ohm continuous discharge as a function of discharge time.

Conclusions

The Leclanché cell can be approximated by an equivalent circuit where the internal resistance is in series with a resistance and capacitance in parallel arrangement. The transient impedance is given by the ratio of the Laplace transforms of voltage and current. From the steady-state value of the transient impedance one can calculate the parallel resistance and through the time constant, the parallel capacitance. A Leclanché cell with NH_4Cl electrolyte yielded a small resistance and large capacitance in parallel, whereas a large resistance and small capacitance in parallel was found for the Leclanché cell containing $ZnCl_2$ electrolyte. The values of the parallel components for a Leclanché cell containing both salts in the electrolyte are between the two limit values. When a cell is being discharged, the magnitude of the transient impedance decreases and the rate of the decrease is a function of the current drain. For high current drains the difference between the transient impedance and internal resistance is small and remains nearly constant during the continuous discharge of the Leclanché cell.

Acknowledgment

The author is indebted to the Ray-O-Vac Company, Madison, Wisconsin, for supplying the special Leclanché cells.

Mauscript received Jan. 5, 1962; revised manuscript received May 19, 1962.

Any discussion of this paper will appear in a Discussion Section to be published in the June 1963 JOURNAL.

REFERENCES

1. J. Euler, *Electrochim. Acta*, **4**, 27 (1961).
2. J. Euler, *ibid.*, **3**, 134 (1960).
3. A. Tvarusko, *This Journal*, **109**, 557 (1962).
4. E. Weber, "Linear Transient Analysis," Vol. 1, p. 175, John Wiley & Sons, Inc., New York (1954).
5. R. J. Brodd, *This Journal*, **106**, 471 (1959).
6. G. Falk and E. Lange, *Z. Elektrochem.*, **54**, 132 (1950).
7. J. Euler and K. Dehmelt, *ibid.*, **61**, 1200 (1957).
8. U. Bertocci, G. Bianchi, and C. Guerci, *Ann. Chim. (Rome)*, **44**, 44 (1954).
9. C. Drotschmann, *Batterien*, **14**, 116 (1961).
10. R. J. Brodd, *J. Research Natl. Bur. Standards*, **65A**, 275 (1961).

Oxygen Transport and Reaction Rates at an Air-Depolarized Copper Cathode

H. C. Weber, H. P. Meissner, and D. A. Sama[1]

Research Laboratory of Electronics, Massachusetts Institute of Technology, Cambridge, Massachusetts

ABSTRACT

Air-depolarized partially submerged electrodes were studied to determine the location of the zones of reaction and the rate-controlling steps in their operation. Reaction was found to occur primarily on that part of the surface of the electrodes covered by the electrolyte meniscus. The rate-controlling step was the diffusion of oxygen through the liquid meniscus to the electrode surface. The mass transport of oxygen as a rate-controlling step was eliminated in a specially constructed wiped, rotating, partially submerged copper electrode. This electrode was used to measure the oxidation rate of copper at room temperature for various partial pressures of oxygen. Oxidation rates were found to be great enough to support far larger current densities than are generally attainable in normal oxygen-electrode operation. The oxidation of copper was found to follow the logarithmic equation

$$w = k_1 \text{ Log } (k_2 t + 1)$$

where k_1 was independent of oxygen partial pressure, and k_2 was proportional to the square root of the oxygen partial pressure.

For a gas diffusion type of electrode to attain a given current output, two requirements must be met: (i) the necessary amount of reacting gas needed to sustain the current must reach the active zone of the electrode surface by transport through the surrounding gas and liquid, and (ii) the electrode surface must be active enough to allow the gas to react at this rate. The purpose here is to indicate which part of the electrode surface actually participates in the electrochemical reaction, and to present evidence on whether mass transport or chemical reaction kinetics is rate limiting. Discussion is limited to the oxygen electrode.

To achieve high current densities per unit of projected surface area, most oxygen or air electrodes are constructed of porous materials. In consequence, their total surface area per unit of cross-sectional area is quite high. However, the area and geometry of the active portions of such porous electrodes cannot be determined accurately, rendering analysis of operating results uncertain. Some clarification be-

[1] Present address: Lowell Technological Institute, Lowell, Massachusetts.

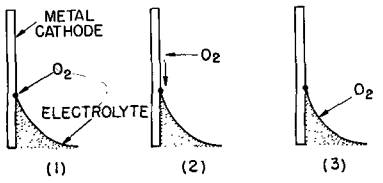

Fig. 1. Possible oxygen transport mechanisms

comes possible, however, if these porous electrodes are considered to be made up of a large number of cylindrical pores, with each pore in turn being made up of partially submerged flat plates. For a flat plate with a lyophilic surface, such as a metal, the electrolyte forms a concave meniscus against the electrode. In order for oxygen to react at such an electrode it must be transported to that part of the electrode area which is active and which is in contact with electrolyte. Three possible mechanisms are shown in Fig. 1. In the first of these, it is assumed that only the oxygen molecules which strike in the immediate vicinity of the boundary line at the intersection of the three phases enter into the electrochemical reaction. In the second, oxygen is first adsorbed on the dry electrode surface projecting above the electrolyte and then migrates along the surface until it enters the electrolyte. In the third, oxygen is first dissolved in the electrolyte and then carried to the submerged electrode surface by diffusion and convection.

The foregoing three alternatives can be tested experimentally. If alternative 1 is correct, then currents obtained would be proportional only to the length of the boundary line between the three phases and independent of the electrode's area above and below the electrolyte surface. If alternative 2 is predominant, then the currents obtained would be a function of the unwetted electrode area and also of the length of the line at the 3-phase intersection. For alternative 3, the current would be some function of the submerged area of the electrode and would be unaffected by the existence of either a 3-phase boundary line or of unwetted electrode area.

These alternative mechanisms were tested in the apparatus shown in Fig. 2. A 2.54 x 1.27 cm (1 x ½ in.) copper plate, about 0.04 cm (1/64 in.) thick, was placed in one leg of a U-tube. A steel wool anode of much larger area was placed in the other leg of the U-tube. The electrolyte was 20% KOH, and the degree of submergence of the copper cathode was varied by removing electrolyte from the anode side of the U-tube. The steel wool anode was so placed that it was completely submerged under all conditions of operation. The over-all reactions during the operation of the cell are:

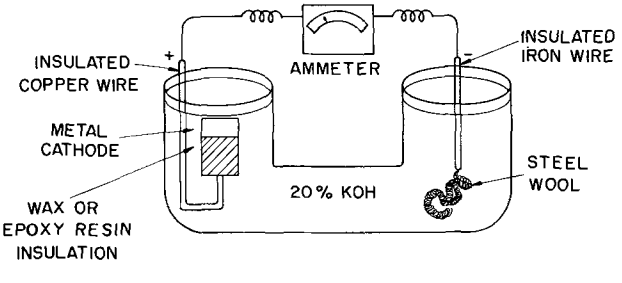

Fig. 2. Cell with air-depolarized electrode

$$\text{Cathode} \quad \tfrac{1}{2}\,O_2 + H_2O \rightarrow 2\,OH^- - 2e \qquad [1]$$

$$\text{Anode} \quad Fe + 2\,OH^- \rightarrow FeO + H_2O + 2e \qquad [2]$$

$$\tfrac{1}{2}\,O_2 + Fe \rightarrow FeO \qquad [3]$$

The experimental procedure was to start with the copper cathode completely submerged. The copper-steel wool couple was short circuited.[2] Under these conditions of large anode area relative to the cathode and of low electrical resistance, the cell current is limited by the operation of the cathode. The electrolyte level was varied, and the current generated was measured as a function of the height to which the electrode projected above the level of the electrolyte. Three separate areas are recognizable on a partly submerged electrode such as shown in Fig. 3, namely, the dry area above the meniscus (height u), the area under the meniscus itself (height m), and the area submerged below the bulk electrolyte. The dry area could be directly observed with copper electrodes, since it became discolored and black by oxidation, whereas the submerged areas retained their brightness during operation.

The following findings were made (see Table I):

1. When the electrode is completely submerged and well below the surface of the electrolyte, as at time zero, the current due to oxygen depolarization is essentially zero. Thus, the oxygen-depolarization current is independent of the area of the electrode which is submerged well below the surface of the electrolyte.

2. When the top of the electrode extends slightly above the level of the bulk electrolyte, and while a

[2] On open circuit, a noticeable blue color due to the solution of copper oxide developed in the electrolyte. No such coloration occurred, regardless of time of operation, when the cell was kept short circuited. This indicates that during short-circuit operation all the oxygen reacting at the active portion of the electrode is either directly or indirectly electrochemically reduced.

Table I. Air-depolarized, partially submerged copper cathode 2.54 x 1.27 x 0.0397 cm (1 x 1/2 x 1/64 in.). Steel wool anode and 20% KOH electrolyte

H, height above electrolyte surface	m, meniscus height	u, height above meniscus	Current, ma	Time, min
0	0	0	0.010	0
Edge at electrolyte surface	—	0	0.067	5
0.04 ~ 0.08 cm (1/64 ~ 1/32")	same as H	0	0.255	9
0.16 cm (1/16")	same as H	0	0.590	15
0.24 cm (3/32")	same as H	0	0.875	20
0.32 cm (1/8")	same as H	0	0.98	26
0.48 cm* (3/16")	same as H	**	1.02	31
0.64 cm (1/4")	~0.32 cm ~(1/8")	~0.32 cm ~(1/8")	0.75	105

* At this value of H, the projecting electrode plate was no longer completely covered by the electrolyte (see Fig. 3). Instead, a thin strip of uncovered area developed along the top of the electrode. This strip became visible as it discolored due to copper oxide formation.

** As the electrode is raised further, resulting in larger values of both H and u, no further changes occur either in the meniscus height m or in the current flowing.

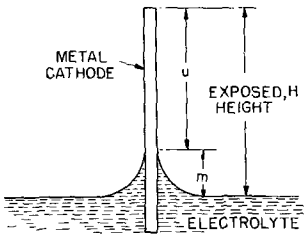

Fig. 3. Measurement of exposed height H and meniscus height m

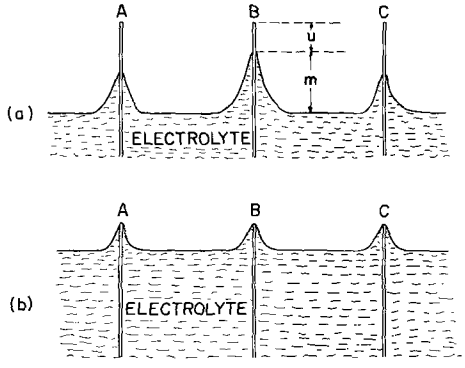

Fig. 4. Electrolyte menisci at different metals

thin electrolyte meniscus still covers the entire electrode as shown in Fig. 4b, a current due to depolarization of oxygen is generated. This is illustrated by the points in Table I up through 26 min.

3. The current increases as the height m is increased, and reaches a maximum when m is at its maximum. At this maximum, a three-phase boundary line between gas, electrolyte, and electrode forms. In the system described here the height m was found to be about 0.32-0.48 cm (1/8-3/16 in.).

4. As the plate is further withdrawn, m remains at its maximum value while u, the height of the unwetted portion of the electrode, increases. The current is found to be independent of u, as is shown by the points in Table I observed after 26 min of operation.

5. A decrease in current and a small contraction of the electrolyte meniscus tend to occur after an hour's time, as is shown by comparing the points at 31 and 105 min. This meniscus contraction may be the result of a change in the contact angle due to further oxide formation, or the slow return of the meniscus to its equilibrium position after being stretched when the electrolyte was lowered.

Rate-Determining Step

The foregoing evidence indicates that the bulk of the electrochemical reaction takes place on the electrode's area under the meniscus (see Fig. 3). This suggests that mass transfer of oxygen through the liquid within the meniscus "controls" the magnitude of the current flowing. Such control by oxygen transfer is compatible with the fact that oxygen diffusivity in the electrolyte is very small, and that the amount of oxygen transported through a unit area per unit time varies inversely with path length (see Eq. [4]). Calculations presented below indicate that significant current densities can be attained only in the electrode area lying under the upper end of the meniscus, where distances from the electrolyte surface to the electrode surface are small. The electrode areas in the lower part of the meniscus, and those electrode areas more deeply submerged, contribute very little to the total current because oxygen diffusion rates are very small for path lengths in excess of a fraction of a centimeter.

The actual quantity of oxygen transported through a liquid by diffusion can be calculated from the familiar equation (1)

$$N_A = \frac{D_L(C_i - C_o)}{z} \qquad [4]$$

where N_A is gram moles oxygen/(sec)(cm^2), D_L is the diffusivity[3] with a value of ~1 x 10^{-6} cm^2/sec, C_i and C_o are oxygen concentrations in the electrolyte at the gas-electrolyte interface and the electrolyte-electrode interface, respectively, and z is the diffusion path length in centimeters. Taking C_o as zero and C_i as 2.77 x 10^{-8} g mole/cm^3, corresponding to saturation with air, then N_A is 2.77 x 10^{-11} g mole/(sec)(cm^2) when z is only 0.001 cm. This corresponds to a current density of only about 0.01 ma/cm^2. When z is 1 cm, then N_A will be only 2.77 x 10^{-14}. It follows that even within the meniscus, current densities must vary, in that more oxygen reaches the electrode area under the top of the meniscus, where the film is thinnest, and less reaches the lower regions of the meniscus, where the film thickens.

Confirming evidence that mass transfer of oxygen to the electrode surface, rather than chemical reaction rate, controls the magnitude of the current generated was obtained by changing the temperature of cell operations. It was found that increasing the temperature resulted in a decrease in the current. This is attributable to lowered oxygen transport rate, which is a result of lowered oxygen solubility, or of changes in the meniscus geometry, or of both. If chemical kinetics had controlled, then a temperature rise would presumably have sharply increased the current flowing.

Further evidence on the nature of the controlling step was obtained from duplicate experiments with electrodes made of copper, nickel, and silver. With meniscus heights less than the maximum wetted height for any of the metals, the meniscus geometries are identical as shown in Fig. 4b. Under these conditions, for any given meniscus height, the current generated was the same for all metals. This again indicates that mass transfer controls, for if kinetics had controlled, then the oxidation rates and the currents obtained therefrom would not have been equal. Due to differences in contact angles, the meniscus shapes and surface areas were no longer the same after raising the electrodes sufficiently so that dry area developed, as shown in Fig. 4a. In consequence, the currents generated were different when the exposed heights were greater than the meniscus heights.

Finally, it is important to note that resistance of the liquid phase to oxygen travel, rather than resistance of the gas phase, will generally be the rate-

[3] This value is for diffusivity of dissolved oxygen in 20% NaOH (2). The diffusivity in 20% KOH was not available in the literature, but should not be appreciably different.

determining step in the operation of gas diffusion type electrodes. It is easily shown that, because of oxygen's very low solubility in strong electrolytes, for a given difference in partial pressure (and concentration) driving forces, a gas layer of given thickness will allow diffusion of 10^7 to 10^8 times as much oxygen as a liquid layer of equal thickness.[4] Thus even relatively long pores in an electrode when filled with gas, generally present less of an obstacle to oxygen diffusion than the liquid film through which this oxygen must travel to reach the electrode surface.

Kinetic Studies

The findings just described indicate that mass transfer limits the rate of operation of these oxygen electrodes. However, these studies yield no information on the kinetics of the reactions occurring at the electrode itself. These reactions involve an oxidation, in which oxygen somehow adsorbs or reacts with the surface, followed by the electrochemical removal of this oxygen. It appeared desirable to obtain information on the oxidation rate in order to determine what current densities might be attainable upon elimination of the liquid phase resistance.

To study kinetics of reactions at the electrode surface, it is first necessary to decrease to a negligible value the oxygen transport resistance through the liquid phase, which normally controls the current developed. This was accomplished by use of the partly submerged rotating electrode described below. The unsubmerged portion of this electrode was wiped free of electrolyte, giving oxygen from the surrounding gas atmosphere direct access to the electrode surface. The consequent oxide layer formation rate was obviously determined by oxidation kinetics, rather than by mass transfer through a liquid film. By suitable adjustment of conditions, this oxide layer was then removed electrochemically upon submergence in the electrolyte. The time and conditions required both to form and remove the oxide layer could be controlled and measured, and the apparent thickness of this layer could be calculated.

Rotating Electrode

The apparatus used, shown in Fig. 5, consisted of a Lucite disk in which a copper ring was embedded so that only the outer surface of this ring came into contact with the electrolyte. This disk assembly served as the oxygen electrode and was partly submerged in the electrolyte, which was 20% KOH. The anode was a zinc wire spiral whose surface area was at least 100 times that of the cathode, thus making the cathode the controlling electrode. The entire assembly was housed in a Lucite box with provisions whereby the oxygen partial pressure in the gas phase could be varied. The partial pressure of water in this gas was kept at equilibrium with the electrolyte at all times to prevent any local changes in electrolyte concentration and the possible consequent development of concentration cell effects. The current was measured under steady-state conditions, and its dependence on the rotational speed and on the partial pressure of oxygen was established. The surface of the copper ring emerging from the electrolyte was of course covered by a thin film of electrolyte, which if not removed acted as a large diffusional resistance to oxygen transport. This liquid film was therefore removed as extensively as possible by use of a rubber wiper, thus giving oxygen free access to the electrode surface. The oxide layer which formed on the electrode surface was then removed by electrochemical reduction when submerged. Thus the copper electrode is not consumed during operation, but instead undergoes alternate oxidation and reduction. In this apparatus, therefore, two things are accomplished: (i) the large liquid phase resistance to oxygen transport encountered in normal oxygen electrodes is reduced to a negligible level, and (ii) the oxidation step is separated from the electrochemical reduction step so that it can be studied separately. By this alternate oxidation and reduction of the rotating electrode, oxygen is removed from the gas phase and transferred as hydroxyl ions into the electrolyte. The resulting cathode reaction is

$$2e + \tfrac{1}{2}\,O_2 + H_2O \rightarrow 2\,OH^- \qquad [5]$$

with the copper alternating between the oxide and the metallic state. The zinc is oxidized to zinc oxide at the anode, which then dissolves in the electrolyte, exposing fresh surface, as follows

$$Zn + 2\,OH^- \rightarrow ZnO + H_2O + 2e \qquad [6]$$

$$ZnO + 2\,OH^- \rightarrow ZnO_2^= + H_2O \qquad [7]$$

making the over-all reaction

$$\tfrac{1}{2}\,O_2 + Zn + 2\,OH^- \rightarrow ZnO_2^= + H_2O \qquad [8]$$

When the rotating electrode is left unwiped, then the resultant liquid film of electrolyte covering the electrode reduces oxygen transport to a very small quantity. This is evident from the low current obtained from the rotating electrode when unwiped, as shown by the lower curve of Fig. 6. The current obtained here is at least partly attributable to the Cu-Zn couple. Removal of the liquid layer from the electrode by wiping results in a large increase in the current, as is evident from the upper curve of Fig. 6. The large resistance of even thin layers of electrolyte to oxygen transport is again evident from these findings.

[4] This assumes bulk diffusion of oxygen in the gas phase. In pores whose diameter is of the order of magnitude of the mean free path of oxygen molecules or less (6×10^{-6} cm, 0.06μ), oxygen transport occurs by Knudsen diffusion and can be considerably less than with bulk diffusion. Thus, in extremely small pores it is possible that oxygen transport through the gas phase may be limiting.

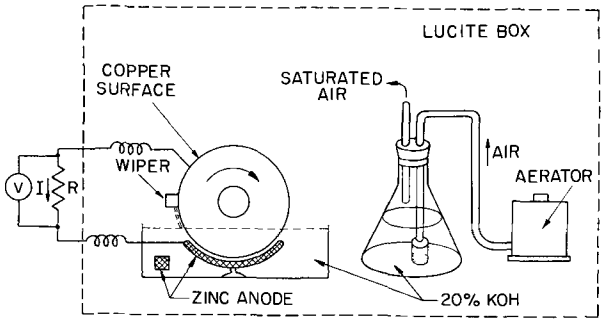

Fig. 5. Apparatus for oxidation studies

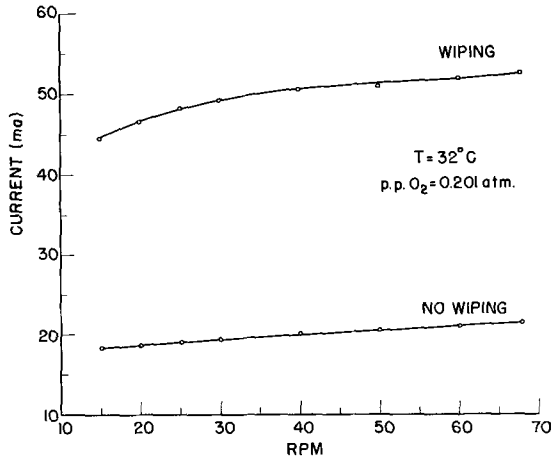

Fig. 6. Effect of wiping on current of rotating copper electrode

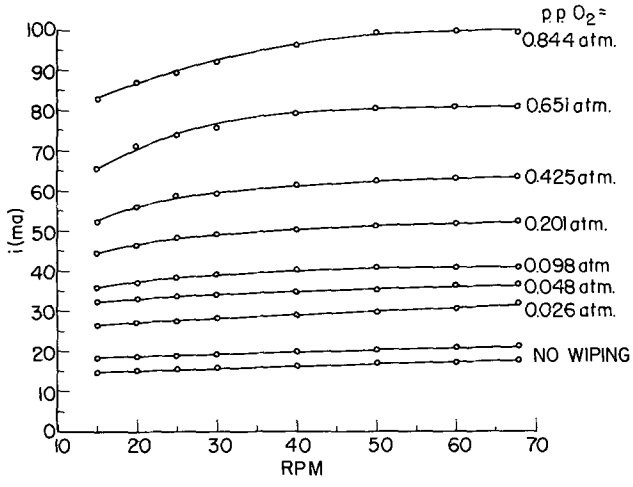

Fig. 8. Data from rotating copper electrode

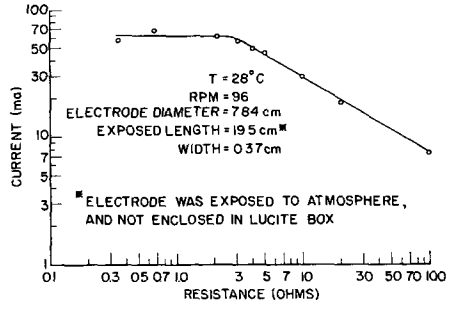

Fig. 7. Effect of resistance on current of rotating copper electrode

Figure 7 is a typical plot showing how the current produced by a cell using a wiped copper electrode rotating at a constant rpm varies with external resistance. Inspection indicates that the current increases with decreasing resistance until the external resistance has been reduced to about 3 ohms, after which the current remains constant. Doubling the zinc anode area does not change the results obtained, indicating that these findings are attributable to the behavior of the cathode. Similarly, decreasing the area of the cathode exposed to the gas phase decreases the magnitude of the maximum obtainable current, indicating that the controlling reaction is the oxidation of the wiped exposed electrode surface, not the electrochemical reduction at the submerged surface. The maximum current obtainable is evidently determined by the amount of oxygen present in the oxide film, which is completely removed upon submergence. The thickness of the film, which varies inversely with rotational speed, can therefore be calculated directly from this maximum current, the rotational speed, and the area of the copper ring on the cathode. At an oxygen partial pressure of 0.844 atm and 32°C, the wiped rotating copper electrode produced a current density of 26 ma/cm^2 of area exposed to the gas phase. It follows that if effective use could be made of the internal area of an air-depolarized porous electrode without being limited by mass transfer problems, then high current densities should be attainable.

The oxide film formed on this rotating electrode is probably thicker and otherwise not the same as that formed in an oxygen electrode operating partially submerged in the usual way. In consequence, the rates measured on the rotating electrode are probably lower than for normal electrodes. It is therefore significant that, even under these conditions, the reaction rates are found to be high. These findings serve to emphasize again the importance of adequate mass transport in gas depolarized electrodes.

Oxidation Studies

The primary purpose of the rotating electrode was to provide information about the relative magnitudes of the mass transport rate and the chemical reaction rate at an air-depolarized copper electrode; it can also be used to investigate the mechanism of metal oxidation.

The current obtained from the wiped, rotating copper electrode was measured as a function of rpm at a number of oxygen partial pressures. The data are presented in part in Fig. 8 and were found to follow the familiar logarithmic relation which often holds for the low-temperature oxidation of metals.[5]

$$w = k_1 \log(k_2 t + 1) \qquad [9]$$

where w is the weight of oxide, t is time, and k_1 and k_2 are constants. For these data k_1 is found to be independent of oxygen partial pressure, while k_2 is proportional to the square root of the oxygen partial pressure. The logarithmic equation has been derived by various workers who proposed a number of different models (4, 5). The finding that k_1 is constant while k_2 is a function of the oxygen partial pressure is consistent with a model proposed by Evans (4) in which it is assumed that the rate-limiting step is the transport of oxygen through the oxide film. The proportionality of k_2 to the square root of the oxygen partial pressure suggests, for the Evans model, that a monatomic form of oxygen is the species transported through the oxide film.

Manuscript received Dec. 27, 1961; revised manuscript received June 4, 1962. This paper was prepared for delivery before the Detroit Meeting, Oct. 1-5, 1961. This work was supported in part by the U. S. Army Signal Corps, the Air Force Office of Scientific Research, the Office of Naval Research; in part by the Air Force Aeronautical Systems Division; and in part by the Standard Oil of Indiana Foundation.

[5] Details of this development are presented in ref. (3).

Any discussion of this paper will appear in a Discussion Section to be published in the June 1963 JOURNAL.

REFERENCES

1. T. K. Sherwood and R. L. Pigford, "Absorption and Extraction," p. 21, McGraw-Hill Book Company, Inc., New York (1952).
2. T. Ipat'ev and A. Drushima, *Z. anorg. u. allgem. Chem.*, **216**, 66 (1933).
3. D. A. Sama, Sc.D. Thesis in Chemical Engineering, Massachusetts Institute of Technology, 1960.
4. U. R. Evans, *Oxidation of Metals, Review of Pure and Applied Chemistry*, **5**, 1 (1955).
5. H. H. Uhlig, *Acta Met.*, **4** [5], 541 (1956).

Surface Behavior of Silver Single Crystals in Fused Sodium Chloride

Jerome Kruger and Kurt H. Stern

National Bureau of Standards, Washington, D. C.

ABSTRACT

The effect of immersion in fused NaCl on a silver single crystal has been studied at 900°C. In the presence of a temperature gradient both dissolution and deposition of silver occurred. No effect of crystallographic orientation was noted. Mass-transfer, resulting from dissolution and deposition, occurs from the hot to the cold end of the crystal and is accounted for by shifts of the equilibria $2Ag + \frac{1}{2} O_2 = 2Ag^+ + O^=$ and $Ag + Na^+ = Ag^+ + Na$ to the right with increasing temperature. In the absence of a temperature gradient some effects due to orientation occurred. In the presence of oxygen, subgrain boundaries became delineated by the formation of ridges containing metal impurities, such as iron, whose oxides are insoluble in NaCl.

Recent work (1) on the oxidation of polycrystalline silver in fused NaCl has shown that silver ions appear in the melt by two mechanisms:

$$Ag^\circ + Na^+ = Ag^+ + Na^\circ \quad [1]$$

$$2Ag^\circ + \frac{1}{2} O_2 = 2Ag^+ + O^= \quad [2]$$

The relative contribution of the two reactions to the total silver ion concentration depends on conditions, [2] being most important when the rate of transport of oxygen to the NaCl-Ag interface is high. Metallic sodium formed by [1] may partly vaporize under some conditions; some of it diffuses from the Ag surface, where it is formed, into the metal, forming an Ag-Na alloy.

The microscopic examination of metal surfaces oxidized in fused salts is a neglected area of research. Single crystal surfaces are well suited for such studies since they permit the study of the effect of differences in atomic arrangement on reaction rate. That such differences occur in aqueous media (2) and in the case of thermal etching (3) is well known, but no corresponding study in a fused salt has, to our knowledge, been carried out.

In the present work we have selected a metal whose surface and oxidation behavior in air at high temperature has already been investigated (3) and whose chemical behavior in fused NaCl is known. This investigation is a qualitative study of what happens to a silver surface exposed to a fused salt.

Experimental

Materials.—Reagent grade sodium chloride was dried by heating at 500° under vacuum (~10^{-4} mm Hg) for several days. Most experiments were carried out in alumina crucibles. In a separate experiment the solubility of this container in NaCl was determined to be approximately 0.001%. Some experiments were carried out in Vycor test tubes, others in silver crucibles described elsewhere (1).

Single crystals of silver[1] in the form of spheres ¾ in. in diameter were used. These crystals were grown in a graphite mold of the proper shape by the Bridgman technique at the rate of 1 in./hr in a vacuum of 10^{-4} mm Hg. Flat surfaces parallel to {100}, {110}, and {111} crystallographic planes were ground at the appropriate sites on the sphere. After extensive etching, mechanical polishing, and electropolishing, the back-reflection Laue method of x-ray diffraction showed the flats to be free of cold work and within ±2° of the desired orientation. Four different crystals were used in the experiments. One of these, in addition to the 3 faces described, had one cut randomly. Its orientation was within 2° of the {211} plane. Each crystal was then mounted in a silver holder for convenience of handling.

The temperature in the 12-in. tubular furnace used in most experiments was regulated by a Marshall controller. Under the conditions obtaining in most experiments a temperature gradient undoubtedly existed along the crystal and its silver holder, the hottest region being at the bottom and at the walls of the container.

Runs in an oxygen-poor environment were carried out in an argon-filled drybox (partial pressure of $O_2 = 10^{-4} - 10^{-5}$ atm).

One experiment, to test for differences due to absence of temperature gradients, was carried out in a large muffle furnace.

Procedure.—Prior to an experiment, the flats on the crystals were mechanically polished using a diamond abrasive on canvas, then the same abrasive

[1] 99 98% pure with Cu, Fe, Ca, Al, and Mg as the major impurities.

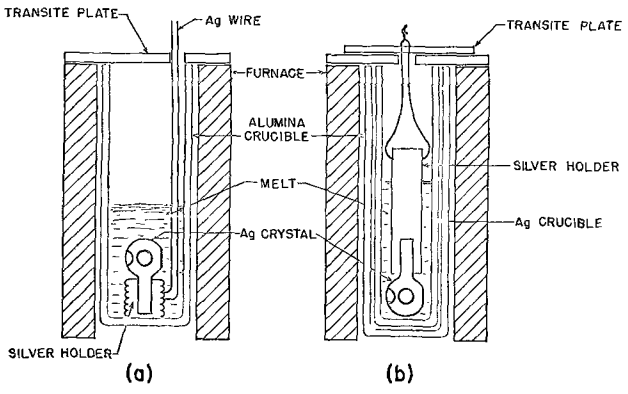

Fig. 1. Experimental arrangements used to immerse silver single crystals in molten sodium chloride.

on velvet. The whole crystal was finally electropolished in the cyanide bath described by Tegart (4). After washing in distilled water, spectroscopically pure methyl alcohol, and drying in a stream of warm air, the crystal was placed into the salt in one of the experimental arrangements shown in Fig. 1. In some experiments the crystal and solid salt were heated together from room temperature. There was no difference in results due to this change in procedure. The crystal was positioned as far away from the container walls as possible, although in some cases this amounted to only a few millimeters.

After removal from the melt the crystal was allowed to cool with a thin layer of solid salt on it. This was removed by quick rinsing in distilled H_2O. The silver surfaces were then examined by optical and electron microscopy, and with an electron probe microanalyzer.

Results

Two surface processes were observed when silver was immersed in molten NaCl at 900°C: (*a*) etching or dissolution as silver ions, and (*b*) deposition of silver onto the single crystal surfaces.

Etching Phenomena

Most of the experiments were carried out in either alumina or silver crucibles in the presence of air. Etching was identical in both kinds of crucibles, indicating that the alumina was essentially inert with respect to its influence on the behavior of silver in molten sodium chloride. Figure 2 shows the main features of etching at 900°C for 2 days in the presence of air. There are no marked differences in etching between the crystallographic orientations

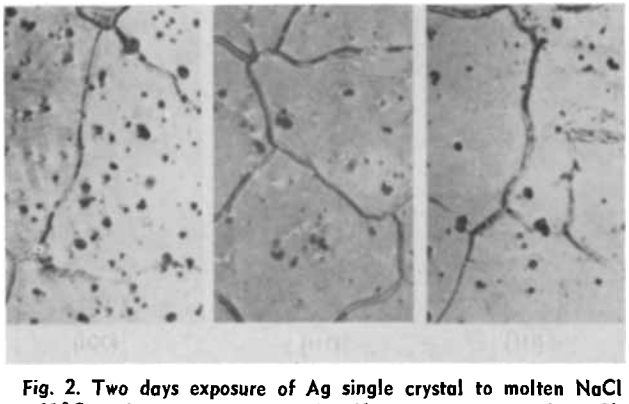

Fig. 2. Two days exposure of Ag single crystal to molten NaCl at 900°C in the presence of air. Magnification approximately 250X.

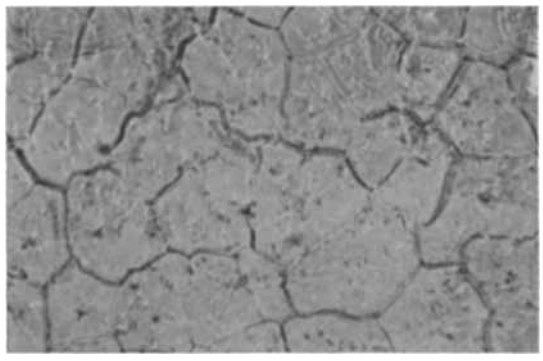

Fig. 3. Five days exposure of Ag single crystal to molten NaCl at 900°C in the presence of air. {111} surface. Magnification 200X.

studied. The most notable feature was the delineation of a cell-like network of material. The boundaries delineating these cells broadened with immersion time. In some instances this substructure exhibited a subgrain boundary appearance (Fig. 3), which was somewhat similar to the structures observed by Rutter and Chalmers (5). The boundaries studied by these authors were formed by segregation of impurities during the solidification of metals, including silver.

An electron probe microanalyzer was used to determine whether impurities were indeed segregated in the boundaries. This instrument, described elsewhere (6), allows one to determine the amount of a selected element in a circular area of 4μ diameter. Two common impurities of silver were studied, iron and copper. The boundaries had an iron content of approximately 0.6 mole % after etching, while the cell interiors contained almost no detectable iron. There was no detectable difference, however, between the copper content in the boundaries and in the cell interiors.

In order to see whether these boundaries were ridges or trenches, negative Parlodion replicas were made of the etched surfaces for study by the electron microscope. Prior to shadowing of the replicas they were sprayed with a suspension of polystyrene spheres. By looking at the positions of the shadows of the spheres one could tell that the boundary areas had a higher elevation than the rest of the etched surfaces. Figure 4 shows that the shadow cast by the boundary is exactly opposite to that cast by the sphere. Thus, since the Parlodion replicas were negative, the boundaries must project from the surface.

Only very short immersion times (as little as 2 min) were necessary to reveal these boundaries. After 10 min they are readily discernible. Thus, this characteristic feature of the etching of silver (of the purity described) in molten NaCl can be observed almost from the very beginning of the process. It is important to note that when other etching treatments were tried on the specimens used they did not bring out this substructure. Beside etching in conventional aqueous etchants, such as dilute HNO_3 or dilute NH_4OH, thermal etching in air at 900°C was also tried. This latter treatment produced grooves similar to those described by Moore (3) and others but with no substructure delineation as Fig. 5 shows. However, if such air etched surfaces were

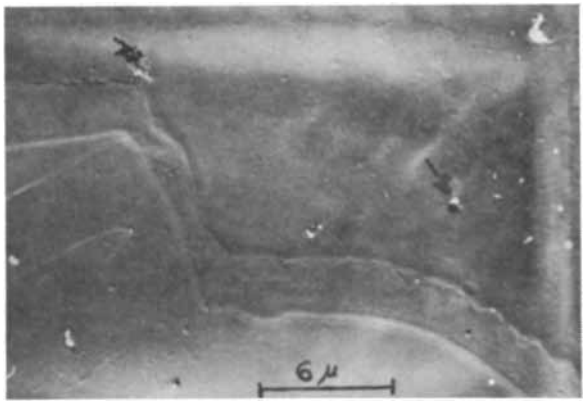

Fig. 4. Negative Parlodion replica (backed with carbon and shadowed by palladium) of raised sub boundary area. Arrow points to shadowed polystyrene sphere whose shadow is opposite to that of the boundary.

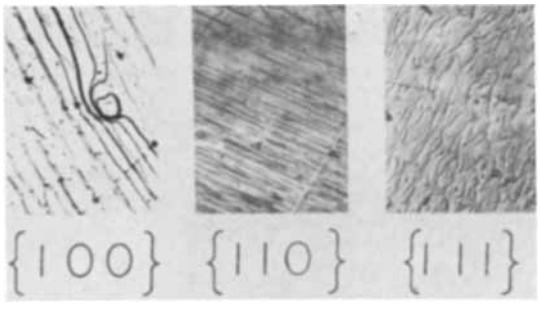

Fig. 5. Thermal etching of Ag single crystal in air at 900°C for 2 days. Magnification 200X.

then placed in molten salt, the grooves were erased and the structures shown in Fig. 2 and 3 were observed.

These structures also were not observed when a Vycor crucible was used or when reaction was carried out in a dry box in an inert atmosphere. Reactions in Vycor were rather irreproducible. Silica introduced by attack of the melt on the crucible has a profound influence on the reaction. A recent investigation by Littlewood and Argent (7) also points out this effect of silica in molten salt reactions.

Beside the delineation of a substructure, Fig. 2 and 3 show many spots which look like either pits or small hillocks sticking up from the surface. The electron microscope technique described above revealed that these spots are hillocks rather than pits. It was at first thought, on the basis of a large number of experiments carried out using one experimental arrangement, that the number of these small hillocks, or nuclei, per unit area depended on the crystallographic orientation of the underlying surface. However, when the geometry of the experimental arrangement (*i.e.*, the position of a given face with respect to the thermal gradient existing between the crucible wall and the specimen) was changed the number of such spots per unit area changed drastically. Figure 6 shows this effect.

In fact, no readily discernible differences in etching behavior or rate could be noticed with respect to crystallographic orientation. If differences in rate of attack did exist, they would produce symmetrical etch patterns on the spherical portion of the specimens used. Such patterns are found on single crystal

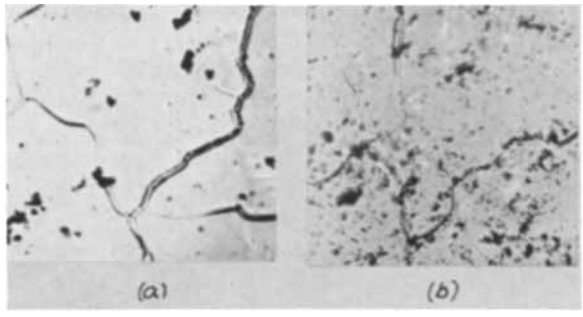

Fig. 6. Effect of position in thermal gradient. {111} surface exposed to molten NaCl at 900°C for 4 days; (a) was closer to the hot end of the thermal gradient than (b). Magnification approximately 250X.

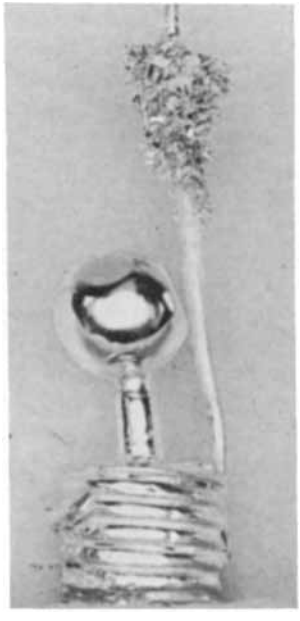

Fig. 7. View of whole crystal and silver wire (experimental arrangement (a)) for handling after 4 days exposure to molten NaCl at 900°C. Some dendritic crystals can be seen growing on the wire at the cold end of the thermal gradient, the molten salt-air interface.

spheres for other etching treatments (8). As Fig. 7 shows, the spherical portion remains quite smooth during the reaction with no evidence of differential attack at the different poles where different crystallographic orientations exist.

Besides the absence of any influence of crystallographic orientation crystal imperfections also do not influence the etching process when a temperature gradient is present. A single crystal disk was bent to a 2 cm radius and then etched in the molten salt for 3 days. At 900°C in this time polygonization probably would have occurred, and if nuclei formed at dislocations, rows of these related to the direction of bending would have been observed. For example, such effects were observed by Henderson and Machlin (9) for silver etched in dilute oxygen. No such effect was found for etching in molten NaCl.

All of the experiments described thus far were carried out under conditions where there existed a thermal gradient. When a silver crucible was used, the gradient was between the crucible wall and the crystal; for an alumina crucible it was between the crystal at the bottom of the crucible and the silver wire near the cooler air-salt interface.

The optical microscope showed no difference in etching when the thermal gradient was eliminated by placing the whole crystal-crucible assembly in a large closed muffle furnace. However, when the surface of silver etched in the absence of a thermal gradient was studied at higher magnifications, pitting and the formation of steps became evident. The formation of square pits and a spiral on the {100} surface, Fig. 8, also indicates that, when there is no thermal gradient, dislocations and crystallographic orientation may effect the etching behavior. These square pits in the interior of subgrains have a concentration of somewhat less than $10^6/cm^2$. This is a reasonable concentration if these pits occur at dislocations (9). An etchant recently described by Robinson and Levinstein (10) as forming pits at dislocations on {100} silver surfaces also gave a pit concentration of $10^6/cm^2$ when tried on the specimens used in this study. Figure 9 shows another area on the surface shown in Fig. 8 where hillocks may be seen occurring along with a pit and some steps. Some pits and steps or terraces were also found on the {111} surface etched in the absence of a thermal gradient, but not on the {110} and {211} surfaces.

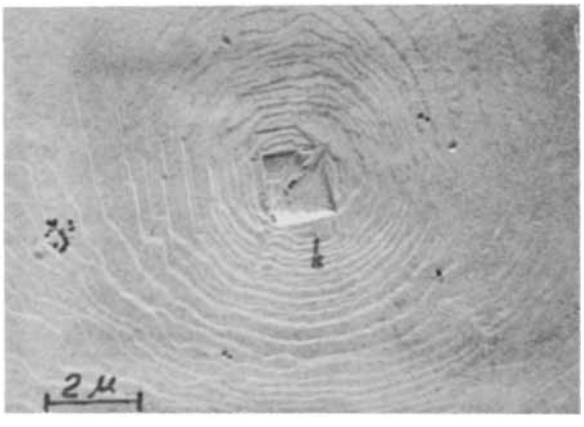

Fig. 8. Spiral and pit observed on {100} Ag surface exposed for 24 hr to molten NaCl at 900°C in the absence of a thermal gradient. Negative Parlodion replica backed with carbon and shadowed with palladium.

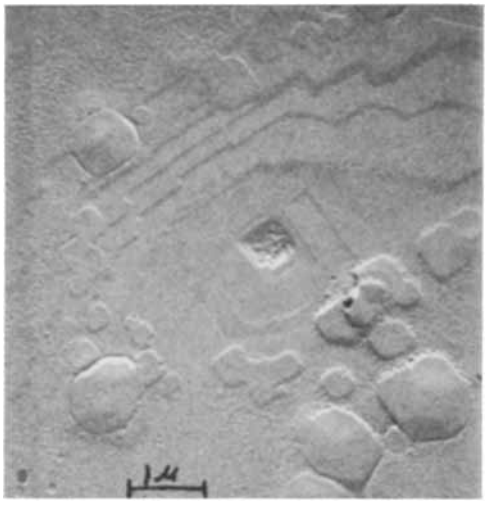

Fig. 9. Pit and hillocks occurring together on {100} Ag surface exposed for 24 hr to molten NaCl at 900°C in the absence of a thermal gradient. Negative Parlodion replica backed with carbon and shadowed with palladium.

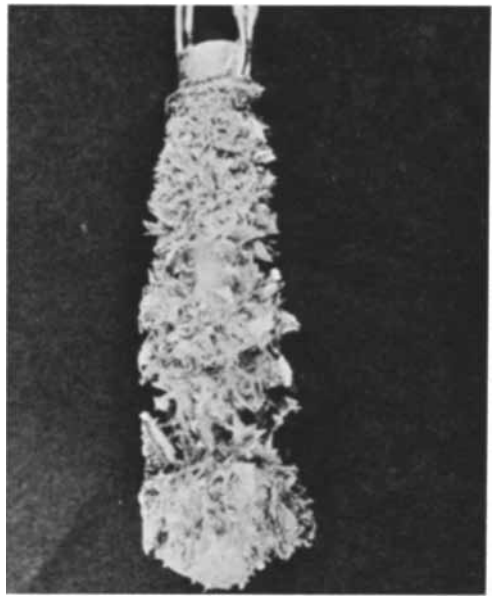

Fig. 10. Deposition on Ag crystal exposed to molten NaCl in silver crucible at 900°C for 15 hr in the presence of a thermal gradient. Experimental arrangement (b). Magnification 1X.

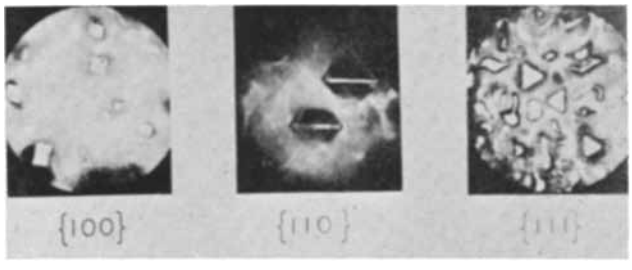

Fig. 11. Silver crystallites deposited on silver single crystal surfaces exposed to molten NaCl in silver crucible at 900°C for 15 hr in the presence of a thermal gradient. Experimental arrangement (b). Magnification approximately 115X.

Deposition Phenomena

Deposition by mass transfer of silver in the molten salt created no problem in the study of the etching phenomena when the experimental arrangement was that shown in Fig. 1a. As can be seen in Fig. 7, deposition occurred at the top of the melt near the air interface. In this case dendritic crystal deposits were formed at the coolest part of the system. When a silver crucible was used, however, (Fig. 1b) and a run was carried out for times greater than 1 hr, deposition occurred over the entire crystal and holder as shown in Fig. 10. In this experimental arrangement the entire crystal and its silver holder was at a lower temperature than the silver crucible wall with no metallic connection between crucible and crystal. The deposits were of two types, dendritic and small faceted crystals. The dendrites grew all over the specimen and holder. The faceted crystals were observed on the crystal itself. Since the crystal was near the bottom of the crucible, it was somewhat warmer than the holder where more dendritic growth was observed. These faceted crystals seemed to bear some epitaxial relationship to the crystallographic planes upon which they grew, as judged by the symmetry of their morphology (Fig. 11).

If the thermal gradient between the crystal and the crucible wall was eliminated by placing the

whole arrangement in a muffle furnace, no growth at all was observed for times as long as 24 hr.

Summary of Results

For the purposes of the discussion that is to follow the more important results obtained are summarized:

1. No faceting nor rate differences due to the crystallographic orientation of the surface are observed in the presence of a temperature gradient.
2. The etching of silver in molten NaCl in the presence of air reveals a cell-like substructure. Small scattered hillocks are also formed on the surface. Iron was found to segregate in the ridges between the cells.
3. This substructure is not revealed by thermal or aqueous etching.
4. In an inert atmosphere this substructure is not delineated.
5. When the crystal is in a thermal gradient no pitting is observed at the hot end. When the gradient is absent pits are observed on {100} and {111} surfaces and some of these seem to be related to dislocations.
6. Dendritic crystals are deposited at the cold end of the thermal gradient by mass transfer of silver. Along with these dendritic growths some faceted growths occur; the orientation of the latter is dependent on the orientation of the surfaces on which they grow.
7. In the absence of a thermal gradient no mass transfer of silver occurs.

Discussion

Etching Phenomena

In the presence of a thermal gradient one of the most notable observations is the absence, in comparison with thermal etching and aqueous etching, of any effect of crystallographic orientation on the production of faceting. This implies that the differences in metal free surface energy used by Moore (3) to explain atomic rearrangement into simple and complex planes at 900° in air must be quite unimportant in the salt. In air etching these planes must develop because of atomic or ionic migration on the surface from planes of high to those of low energies. Moore's observation, that the growth patterns form only in the presence of oxygen but not in an inert atmosphere, suggests that migration occurs because Ag^+ ions formed by reaction [2] are mobile and can thus migrate along the surface, whereas silver atoms are not. In the salt any ions formed are removed from the surface into a very undersaturated melt. When a high temperature gradient exists, the difference in the chemical potential, $\Delta\mu$, between a silver atom, on the one hand, and an electron in the lattice and a silver ion in the melt, on the other, is greater than under isothermal conditions. The high driving force which this implies would swamp out any small differences in surface energies that may exist under equilibrium conditions at high temperatures. Not only was the temperature gradient responsible for the elimination of etching differences between crystallographic orientations, but also for the absence of differences in etching rate between imperfect (dislocations and/or impurities) and perfect sites on the same crystallographic plane. According to Cabrera (11) differences between the rate of removal of an atom at a dislocation and an atom not at a dislocation become insignificant when $\Delta\mu$ is large. Although his treatment is concerned almost exclusively with evaporation of a neutral atom from the metal into the surrounding medium, it can still give some qualitative insight into the case of the dissolution of ions from the metal lattice. Indeed, when $\Delta\mu$ was decreased by the elimination of the thermal gradient some indications of differences in surface free energies, such as the formation of pits with spirals, became evident. Thus, if his theory is applicable to this system, when the thermal gradient was eliminated, $\Delta\mu$ was lowered to a value where the rate of introduction of ions into solution from dislocations, R_d, was greater than that at nondislocation sites, R_p. $\Delta\mu$ was, however, still high enough so that R_d was large enough to produce observable pits.

There remains to be explained why, although an effect of crystallographic orientation on etching is observed in aqueous solution where a reaction similar to [2] operates, no such effect seems to occur in the fused salt. Two possible explanations are as follows: (*A*) Perhaps the most important reason is related to the temperature gradients in the unstirred melt, which are virtually absent in aqueous solutions. (*B*) The differences in surface energy are greater at room temperature than near the melting point (which seems reasonable since at the melting point these differences must disappear) and thus become less important for the oxidation at high temperatures. In the oxidation of copper, for example, Talbot and Benard (12) found that differences in the rate of oxidation disappeared at high temperatures.

Beside the results on the effect of crystallographic orientation, the other most evident feature observed when silver is etched in molten NaCl in the presence of air is the delineation of subgrain boundaries. The results obtained with the electron probe microanalyzer point to an explanation for this. When sufficient oxygen is present, iron in the subgrain boundaries is oxidized to Fe_2O_3, the oxide stable at 900°. This oxide is nearly insoluble in the fused salt (13) and would thus remain in the crystal while the silver between the boundaries dissolved. This interpretation is also consistent with the observation that no such delineation occurs under very low O_2 partial pressures since in this case the oxide will not form. On the other hand, copper, whose oxide (CuO) is relatively soluble in NaCl-0.7 mole percent (13), did not remain in the boundaries since it would presumably dissolve in the melt.

Deposition Phenomena

The presence of a thermal gradient has even greater bearing on deposition than on etching. When deposition occurs mass transfer must be involved. This transfer, *i.e.*, removal of metal from the hottest sites and deposition at the coldest, must occur, not by the differential solubility of atomic silver in the

melt (1), but because equilibria [1] and [2] lie further to the right at higher temperatures. For reaction [2] in NaCl the equilibrium constant $K_2 = [Ag^+]^2 [O^=]/P_{O_2}^{1/2}$ can be calculated (here for $P_{O_2} = 1$) from thermodynamic data.

The activity product of Ag_2O in NaCl can be calculated using free energies of formation compiled by Glassner (13) in

$$\log a^2_{Ag^+} a_{O^=} = \frac{\Delta F^\circ_{Ag_2O} - 2\Delta F_{Ag^+} + -\Delta F_{O^=}}{2.303\,RT}$$

an equation derived by applying the method of Edeleanu and Littlewood (15) for calculating the solubility of metal oxides in fused salts. The dilute solutions are nearly ideal and activities in this equation can be replaced by mole fractions. On the basis of these calculations, assuming a gradient of 50°, K_2 increases from 3.2×10^{-8} to 1×10^{-7} from 850° to 900°, leading to a corresponding Ag^+ ion increase (if [2] is the only reaction occurring) from 4.0×10^{-4} to 5.8×10^{-3}. Such a driving force is quite sufficient to account for mass transfer, *i.e.*, silver dissolves at the higher temperature and precipitates at the lower temperature where such a high Ag^+ concentration cannot be maintained. Corresponding calculations on reaction [1] lead to similar results. For example, K_1 increases from 2×10^{-11} to 1×10^{-10} from 850° to 900°.

At the lower temperature end of the gradient profuse dendritic growth occurs after relatively brief periods of time. In general, such growth usually commences in regions of supersaturation and extends into the concentration gradient (16). This is just what was observed (Fig. 10) when a temperature gradient existed between the silver crucible (high temperature) and the silver crystal (low temperature). Edeleanu and Gibson (17) have reported that mass transfer in fused chloride melts for silver occurs only when there is a metallic connection between the hot and cold ends of the gradient. They suggest a thermocell mechanism for mass transfer. The fact that there was no such metallic connection when the experimental arrangement shown in Fig. 1b was used indicates that mass transfer occurs by the mechanism given by Eq. [1] and [2] rather than by a thermocell mechanism. Faceted growth occurred along with dendritic growth on the crystal near the bottom of the silver crucible because here, since the temperature gradient was minimized, the driving force for dendritic growth was much lower and conditions for such growth became less favorable.

This faceted growth occurring in a small thermal gradient may also be looked at with reference to reactions [1] and [2]. Whenever silver atoms are oxidized, presumably by electron transfer to adsorbed oxygen atoms, (or molecules) and sodium ions, the concentration of Ag^+ and $O^=$ ions and Na° atoms near the surface can be lowered only by diffusion away from reaction sites, a relatively slow process. Thus, even though the bulk concentration of these species in the melt may be low, their concentrations at sites near the surface may exceed those permitted by K_1 and K_2, leading to reversal of reactions [1] and [2], *i.e.*, deposition. Chemical studies (1) of reaction rates in this system also support this mechanism.

When the thermal gradient was completely eliminated, neither dendritic nor faceted growth was observed in a comparable time because the localized supersaturation no longer existed.

Acknowledgments

The authors are greatly indebted to Joan P. Calvert for taking some of the photographs and carrying out some of the replication; to D. Ballard for the electron microscopy; to H. Yakowitz for the electron probe microanalyzer measurements; to Mrs. Martha M. Darr for carrying out the spectrochemical analysis of the silver. We are also grateful to R. L. Parker and A. W. Ruff, Jr., for helpful discussions.

Manuscript received April 18, 1962. This paper was prepared for delivery before the Detroit Meeting, Oct. 1-5, 1961.

Any discussion of this paper will appear in a Discussion Section to be published in the June 1963 JOURNAL.

REFERENCES

1. K. H. Stern, *J. Phys. Chem.*, **66**, 1311 (1962).
2. M. Yamamoto and J. Watanabe, *Nippon-Kinzoku-Gakkai-Shi*, **17**, 424 (1953).
3. A. J. W. Moore, *Acta Met.*, **6**, 293 (1958).
4. W. J. McG. Tegart, "The Electrolytic and Chemical Polishing of Metals," 2nd ed., p. 68, Pergamon Press, New York (1957).
5. J. W. Rutter and B. Chalmers, *Can. J. Phys.*, **31**, 15 (1953).
6. J. R. Cuthill, L. L. Wyman, and H. Yakowitz, *J. Research Natl. Bur. Standards*, Sec. A, In press.
7. R. Littlewood and E. J. Argent, *Electrochim. Acta*, **4**, 155 (1961).
8. A. T. Gwathmey and A. F. Benton, *Trans. Electrochem. Soc.*, **77**, 210 (1940).
9. A. A. Henderson and E. S. Machlin, *Acta. Met.*, **3**, 64 (1955).
10. W. H. Robinson and H. J. Levinstein, "Direct Observations of Imperfections in Crystals," J. B. Newkirk and J. H. Wernick, Editors, p. 566, Interscience Publishers, New York (1962).
11. N. Cabrera, "Semiconductor Surface Physics," R. H. Kingston, Editor, p. 327, Univ. of Pennsylvania Press, Philadelphia (1957).
12. J. Benard and J. Talbot, *Rev. Met.*, **45**, 78 (1948).
13. K. H. Stern, work presented at the XVIIIth International Congress of Pure and Applied Chemistry, Montreal, August 1961.
14. A. Glassner, "The Thermochemical Properties of Oxides, Fluorides, and Chlorides to 2500°K," ANL-5750.
15. C. Edeleanu and R. Littlewood, *Electrochim. Acta*, **3**, 195 (1960).
16. J. W. Rutter in "Liquid Metals and Solidification," pp. 251-253, American Society for Metals, Cleveland (1958).
17. C. Edeleanu and J. G. Gibson, *J. Inst. Metals*, **88**, 321 (1960).

Electron Diffraction Study of the Removal and Formation in Vacuo of Oxide Films on Uranium and Plutonium

James T. Waber, Clayton Olsen, and Dawn D. Whyte[1]

University of California, Los Alamos Scientific Laboratory, Los Alamos, New Mexico

ABSTRACT

Experiments and the development of apparatus relating to the removal of oxide film and the attempts to prepare an oxide-free surface on uranium are described. Polishing the metal in vacua of the order of 10^{-7} torr appears to be the most successful method. UH_3 and UO_2 were observed to form rapidly on the metal in such vacua. PuO_2 was found to form on plutonium in vacua at pressures of less than 1×10^{-8} torr. The possibility that plutonium hydride also formed could not be investigated, because of the similarity in crystal structure and lattice parameter between PuO_2 and PuH_2.

The oxide film that commonly occurs on uranium when it is exposed to aqueous or gaseous media has been identified as UO_2 in electron diffraction studies by Hickman (1), by Hart (2), and by Flint, Polling, and Charlesby (3). The presence of UO_2 in films that are too thin to give rise to interference colors can also be established by standard x-ray technique. Although the detection of thin films by x-ray diffraction is not possible for many metals, it is successful for uranium, because of the high scattering power of the uranium atom.

Hart (2) and Flint *et al.* (3) list additional lines which do not correspond to the diffraction pattern of uranium dioxide. Hart (2) interprets them as due to a mixture of U_2O_5 and U_3O_8. In our work, no evidence for these lines was obtained. Wilman (4) suggested that the lines observed by Flint *et al.* should be attributed to diaspore, which had been embedded in the metal surface during polishing. This explanation, however, is not applicable to Hart's work, because he employed diamond dust as an abrasive.

In the investigations (1-3) cited above, as well as in a number of the experiments described herein, the metal was polished in air before being admitted to the specimen chamber of the electron diffraction unit. Some of the experiments described below show that it is difficult to eliminate traces of UO_2 from the surface. A completely oxide-free surface on uranium (with which to study the formation of the oxide film without the influence of previously existing oxide) was not achieved; our efforts were directed toward improving the ultimate vacuum in which the polishing is conducted, so that the oxide-free portions of the surface would persist long enough to be studied.

Lattice Constants of Some Actinide Oxides and Hydrides

The structure and lattice parameters of most of the known oxides of uranium are cited by Hart (2). The so-called monoxide, UO, has the cubic, NaCl lattice with a parameter of 4.95Å. The dioxide has the face-centered cubic, CaF_2 lattice. The pure compound has a parameter of 5.4706 ± 0.0003Å. Hering and Perio (5) have found that the lattice parameter increases with decreasing oxygen content and shrinks with an increasing oxygen content to a value of 5.4380Å at the boundary of the β phase, where the composition is U_4O_9. Recent data on these and higher oxides of the uranium-oxygen system are reviewed by Gronvold (6).

Mulford, Ellinger, and Zachariasen (7) report that the low-temperature form of UH_3 has a simple cubic unit cell, containing two molecules, with $a_o = 4.160$Å; and the β (or common) form of UH_3 has eight uranium atoms per unit cell with $a_o = 6.63$Å.

Plutonium, like uranium, forms a fluorite-type dioxide, PuO_2, during exposure to air. Also, the oxides Pu_2O_3 and Pu_4O_7, which contain anion vacancies, have been prepared under special conditions. A monoxide similar in properties to UO has also been observed. The available information on the plutonium-oxygen system has been reviewed by Holley, Mulford, and Ellinger (8). The lattice parameter of stoichiometric PuO_2 is 5.396Å.

The two hydrides of plutonium have been investigated by Mulford, Sturdy, and Ellinger (9) and found to have extensive ranges of solid solubility. The compound PuH_x, where x lies between 2.0 and 2.7, has the fluorite structure. The lattice parameter decreases from 5.359 to 5.34 over the range of compounds from $x = 2.0$ to 2.5. The hexagonal hydride PuH_{3-y} is less stable.

Experimental Procedure

All specimens were mechanically polished to free them of the major portion of their overlying oxide films. The final metallographic paper used was 600-grit silicon carbide paper, and petroleum ether was used as a lubricant to reduce the specimen surface temperature during the later stages of polishing. Any SiC particles imbedded in the surface were removed by briefly polishing the specimen on clean

[1] Present address: Commercial Atomic Power Division, Westinghouse Electric Corporation, Forest Hills, Pennsylvania.

billiard cloth that had been moistened with petroleum ether.

In the experiments discussed below, the smooth metal surface was substantially freed of any residual oxide film by polishing *in vacuo*. Ceramic polishing wheels and metallographic polishing papers were both mounted on a shaft, and were used with about equal success for this purpose. ED (electron diffraction) patterns were obtained for the several abrasives used, so that any extra diffraction lines due to abrasive particles imbedded in the metal surface could be identified. The occurrence of such ED lines in individual experiments is not mentioned below; only the patterns of products and the metal are cited.

Apparatus employed.—An electron diffraction unit, available commercially from the General Electric Co., was modified to permit the attainment of vacua of the order of 10^{-7} torr. While such a "hard" vacuum is not required for the operation of the unit, preliminary oxidation experiments demonstrated that it was essential to the preservation of an oxide-free surface on uranium for even a few minutes.

Figure 1 illustrates the mechanical parts of the modified ED apparatus. Two roughing pumps were installed, one for the specimen chamber, F, and the other for the film chamber, J, to increase the pumping speed. By installing the large quarter-swing valve, G, the film and specimen chambers could be separately isolated and the air admitted to one without influencing the vacuum in the other. Fresh film plates could then be inserted without exposing the specimen surface to air. The quarter-swing valve was made of nonmagnetic metals and was mounted with its axis of rotation below the line of flight of the undeflected electrons.

A carefully machined collimator, consisting of two Armco iron disks containing carefully centered 25-mil diameter holes, was inserted between the magnetic lens, D, and the specimen chamber, F. To increase pumping speed, a separate line was added to connect the brass case of the electron gun to the large diameter vacuum line. This vacuum connection increased the beam stability of the electron gun.

In a preliminary modification an abrasive disk was mounted on the front door of the specimen

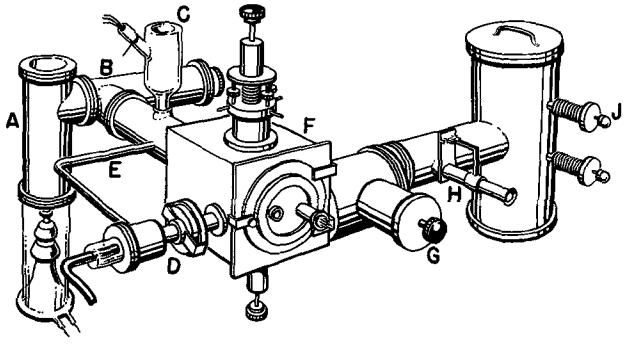

Fig. 1. Perspective sketch of the pumps and evacuated sections of the modified electron diffraction unit: A, diffusion pump and cold trap; B, vacuum valve; C, ion gauge and cold trap; D, electron gun and magnetic lens; E, electron gun vacuum connection; F, specimen chamber and manipulators; G, quarter swing vacuum valve; H, telescope; J, film chamber and film manipulators.

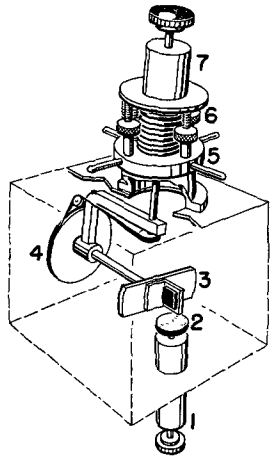

Fig. 2. Perspective sketch of the specimen manipulator used in polishing the specimen and aligning it for grazing incidence: 1, rotary vacuum manipulator; 2, abrasive disk; 3, specimen holder; 4, specimen rotating drive; 5, specimen height adjustment; 6, specimen tilting adjustment; 7, sealed rotating shaft.

chamber and could be rotated in a vertical plane. In the later design, shown in Fig. 2, any electrical charging of the abrasive disk had little influence on the electron beam, because the specimen was electrically shielded by the metal specimen holder when in the normal horizontal position for diffraction.

The specimen was polished by rotating it until its surface became parallel to the surface of the abrasive disk and then turning the shaft of manipulator 1 either by hand or by a motor.

The entire vacuum assembly with the exception of the glass liquid-air traps and the electron gun were wrapped with electrical heating tapes. By this means, the metallic surfaces of the ED unit were baked out for about a week at 100°C. It was observed that the ED unit could be evacuated more rapidly following each insertion of photographic plates, polishing disks, or specimens if dried helium (or argon) was admitted to the system before opening it to the atmosphere.

With the modifications of design and procedure indicated above and with careful attention to various details such as obtaining carefully soldered joints, pressures of 7×10^{-8} torr (or lower) have been obtained repeatedly. If, however, gas was released, due to high local temperatures, from various materials, such as the binder used in the manufacture of polishing wheels, the effective vacuum at the metal surface could be substantially poorer than recorded. The small quantities of gas that may be observed to enter through Wilson seals when their shafts are moved were largely eliminated by using a vacuum tight, nutating rotary shaft[2] sealed with a syphon bellows.

The instrument was frequently calibrated by using transmission patterns from freshly prepared magnesium oxide smoke.

Type of experiments conducted.—This experimental study was divided into two parts. The first was concerned with the examination of uranium and plutonium after exposure to various oxidizing conditions. The second was concerned with preparing an oxide-free surface on uranium.

[2] Marketed by National Research Corporation.

Several uranium oxides were observed during the first part of the work. It is surprising that in the second part one or both of the hydrides were found after almost all of the dioxide film had been removed by polishing. Details of the individual experiments are given below.

Also, experiments were made in which hydrogen was admitted to the specimen chamber. The uranium hydride that was formed on the metal surface was decomposed *in situ* by heating and evacuating the chamber. In connection with these experiments, dried air was subsequently admitted to the ED unit to study the formation of oxide on the hydride. Both gases were used without purification other than the removal of moisture. For these experiments, a simple wire-wound "furnace" was mounted on the specimen holder shaft of the ED unit. The metal specimen was bolted onto the front surface of the heater.

Experiments on Uranium and Plutonium

Uranium polished in air.—Uranium specimens that had been hand-polished in air through 400-grit silicon carbide paper were examined, and only uranium dioxide was observed. In a similar experiment with a uranium alloy containing 6 w/o niobium, uranium dioxide was observed. However, U_3O_8 was detected on the alloy (but not on the pure metal) after it had been polished in air with 240-grit silicon carbide paper attached to a rapidly rotating abrasive wheel.

When uranium is heated in air below 185°C, uranium dioxide is the major product. Above this temperature, the tetragonal U_3O_7 and the orthorhombic U_3O_8 are occasionally observed by x-ray diffraction. This observation suggests that the surface temperature of the 6 w/o niobium alloy rose to at least 185°C during polishing.

Vacuum annealed uranium.—It was observed by Rundle, Baenziger, and Wilson (10), who used x-ray diffraction, that uranium monoxide forms on a uranium surface when powder samples are heat-treated in evacuated silica capillary tubes. These monoxide films are thick enough to be studied readily by x-ray diffraction methods. Hoekstra and Siegel (11) doubt the existence of monoxide and point out that no supporting chemical analyses were made to demonstrate that the diffraction patterns were not due to monocarbide or mononitride films. The latter compounds have crystal structures identical with, and lattice parameters similar to, that of monoxide.

Williams and Westmacott (12) have reported the unusual sequence of products on uranium-monoxide/dioxide/metal and offer x-ray and substantial metallographic evidence to support their conclusion. However, no confirmatory analyses were made. They found that the products occurring in this sequence were thicker when partially oxidized uranium was heated in vacuum. They report, however, that, in initial experiments, dioxide was found by electron diffraction after mechanically polished specimens were heated in a vacuum of 2×10^{-5} torr to temperatures in the range 800°-1100°C. They present an extensive argument concerning the thermodynamic conditions that are necessary to permit the occurrence of this sequence of products. In an additional experiment in which a polished sample was heated in a vacuum at 9×10^{-3} torr they obtained the sequence of layers: dioxide/monoxide/dioxide/metal. Other of their experiments indicate that monoxide can be oxidized on cooling in a poor vacuum.

What appear to be monoxide films, on the basis of x-ray diffraction alone, have been prepared in this Laboratory by heating large specimens at 600°C in vacua of 10^{-6} torr and at 800°C, or higher, in vacua of 6×10^{-5} torr. As far as the x-ray evidence is concerned these films always contain a small amount of UO_2 associated with the monoxide. The electron diffraction method was employed to ascertain whether or not UO_2 was present on the exterior surface of these oxides.

Before discussing the ED results, it seems desirable to review the x-ray evidence obtained on the same specimens. Specimen 1802 was heated in a fused-silica furnace tube for 19 hr at 1000°C in a vacuum of 10^{-5} torr. The x-ray diffraction pattern of 1802 corresponded to α-uranium plus uranium monoxide plus a small amount of strongly oriented uranium dioxide [the (200) line was abnormally strong]. Orientation and pole figure studies reported elsewhere (13) indicate that this cubic orientation texture having the (100) planes of the dioxide lattice parallel to the metal surface is obtained on vacuum heat-treated samples.

Specimen 1804 was heated in a similar furnace tube for 15 hr at 800°C under a vacuum of 10^{-5} torr. Again, uranium metal, monoxide and dioxide were observed by x-ray diffraction.

For comparison purposes, the approximate intensity of the monoxide (111) line was 210 and dioxide (111) line was 36 on specimen 1802. The two (111) line intensities were 720 and 3, respectively, on the lower temperature specimen, 1804. The relative intensities of the metal lines indicated that the film was thicker on 1804 than on 1802. The percentages of UO and UO_2 are not directly related to these relative intensities because the monoxide has a different orientation than the dioxide, and orientation can cause large changes in the relative intensities of two lines of the same pattern.

The electron diffraction study of specimen 1802 gave only a pattern of uranium dioxide. Very broad lines, which made positive identification of the outermost film difficult, were obtained in a similar examination of specimen 1804. These line positions were intermediate between those of the monoxide and dioxide lattices. One cannot conclude from these experiments that the sequence observed by Williams and Westmacott (12) was present in these two tests.

A 5 a/o molybdenum alloy specimen was mounted on the furnace of the electron diffraction unit. The electropolished sample gave only Beilby lines at room temperature. At 100°C in a vacuum of 4×10^{-4} torr, very weak dioxide lines could be seen, and strong dioxide lines were obtained when the alloy specimen reached 400°C. At 600°C, however, in the same vacuum, the dioxide was partially reduced during a few hours, and weak lines corresponding to

Table I. Summary of the x-ray diffraction data and electron diffraction results relating to the oxidation of plutonium

Diffraction plane	X-ray values		Just after polishing in vacuum	30 min at 0.4μ	65 min at 0.4μ	1500 min at 1.0μ
	d in Å	Rel. int.*				
PuO_2 (111)	3.112	(100)		3.09m	3.16mw	
αPu (20$\bar{1}$)	3.076	~2	3.07w			
αPu (112) (20$\bar{2}$)	2.919	6				
αPu (013)	2.877	15				
αPu (201) (113)	2.782	33				
PuO_2 (200)	2.698	(30)				
αPu (004)	2.688	23				
αPu (20$\bar{3}$)	2.590	33	2.55s	2.56m	2.61m	2.57w
αPu (21$\bar{2}$)	2.489	3				
αPu (113)	2.450	3				
αPu (020)	2.415	69	2.41vs**	2.41m	2.44m	2.46w
αPu (211)	2.405	78				
αPu (014)	2.348	28				
αPu (11$\bar{4}$)	2.336	10				
αPu (21$\bar{3}$) (104)	2.282	10				
αPu (20$\bar{4}$)	2.252	2				
αPu (10$\bar{5}$) (212)	2.172	6				
αPu (30$\bar{1}$) (114)	2.065	2	2.10vw			
αPu (30$\bar{2}$)	2.034	8				
αPu 5 lines	1.95-1.89	10B	1.90vw			
PuO_2 (220)	1.907	(58)	1.90vw	1.87m	1.91m	1.91m
αPu (024)	1.796	12				
αPu (22$\bar{3}$)	1.765	20				
PuO_2 (311)	1.626	(60)	1.68w	1.65w	1.70w	
PuO_2 (222)	1.557	(8)	1.60w	1.58vw		1.60w
αPu (32$\bar{2}$)	1.555	6				
αPu 4 lines	~1.45	10B	1.48s	1.47s	1.49m	1.50m
αPu (31$\bar{6}$)	1.433	9				
αPu (231)	1.391	10				
PuO_2 (400)	1.348	(8)	1.35vw	1.38vw	1.36vw	1.31wB
PuO_2 (331)	1.237	(26)	1.28vw	1.26vw	1.29w	
PuO_2 (420)	1.206	(15)				
αPu (040) (234)	1.206	5				
αPu —	1.139	4				
PuO_2 (422)	1.102	(20)	1.10vvw			
αPu —	1.097	6				
αPu —	1.046	5				
PuO_2 (333)	1.036	(15)	1.02vw			

* Approximate relative intensities from an x-ray spectrometer trace. Data listed for PuO_2 are estimated from UO_2 and ThO_2 traces taken with powdered samples; the parentheses signify that the values are only indications of the relative intensities to be expected with a random sample.

** Probably this line corresponds to the unresolved doublet from (020) and (211) plutonium planes.

uranium monoxide were observed. This is consistent with the experience of Williams and Westmacott (12), who heated a 20 a/o molybdenum alloy specimen for 115 hr at 650°C while maintaining a vacuum of 2 x 10^{-5} torr. Their x-ray and ED patterns were identical and corresponded to monoxide having a lattice parameter of 4.953Å.

Oxide formation of plutonium.—Experiments concerning the vacuum polishing of plutonium were conducted before the vacuum system and specimen chamber were modified. As observed with uranium, some dioxide forms on the metal soon after polishing, and there is evidence that orientation occurs in the PuO_2. With both uranium and plutonium, there is growth in a preferred direction which results in the formation of the dodecahedral or (110) texture in the oxide. Lattice spacings and intensities observed for α-Pu and PuO_2 following polishing and storage in vacuum at a pressure of 1μ or less are presented in Table I. Because of preferred orientation in the metal, line intensities of the α-Pu sheet sample differed from those tabulated, which relate to randomly oriented plutonium powder specimens. Thus, weak diffraction lines occur, but a number of medium ones do not.

Because of the similarity in structure and lattice parameter between PuH_x and PuO_2, it is impossible to ascertain that the hydride is formed *in vacuo*, as has been observed with uranium.

Oxide Removal from A Uranium Surface

Two methods of oxide removal, mechanical and chemical polishing, were studied. In the latter method, an attempt was made to remove the dioxide by first hydriding, brushing, and then decomposing any residual hydride *in vacuo*. However, the mechanical method of polishing was more successful.

Oxide removal by hydriding.—Although UH_3 is known to ignite readily when exposed to air, in many instances it has been found to be reasonably

Table II. Products observed by electron diffraction during a sequence of cleaning operations

Surface preparation	Diffraction lines found
Uranium polished at room temperature through 3/0 paper in air.	UO_2
Heated to 150°C in vacuum, H_2 admitted to a pressure of 116 torr for 10 min, then evacuated.	Strong α-UH_3 + medium β-UH_3 + very weak α-U metal
Sample then polished in vacuum at 150°C with 2/0 paper.	Medium α-metal + UO_2
Residual hydride decomposed by heating 3 hr at 300°C in vacuum of 10^{-5} torr.	Strong UO_2 + weak α-U
Surface then polished at 300°C with 2/0 paper. Vacuum of 10^{-5} torr maintained.	Weak UO_2 + medium α-metal
Rehydrided at 150°C and cooled to room temperature. Evacuated to 10^{-5} torr.	α-UH_3 + β-UH_3
Surface polished *in vacuo* at room temperature.	α-UH_3 + medium α-metal
Held in vacuum of 10^{-5} torr for 12 hr at room temperature.	Strong α- and β-hydrides plus weak metal
Heated to 150°C, 10 torr air pressure admitted.	Weak UO_2 plus medium α-metal
Oxidation continued to blue interference color.	Medium UO_2 plus very weak α-metal

stable at room temperature. In the only ED experiment conducted with the powdered hydride, a sample was prepared from the elements at 150°C and transferred from the vacuum system through air to the specimen chamber of the ED unit. The pattern corresponded to a mixture of α- and β-hydrides plus a slight amount of uranium dioxide. This experiment is cited to show that the hydride is not usually reactive in air at room temperature and to account for the persistence of lines due to the hydrides in many patterns of partially oxidized specimens. This inertness of UH_3 may result because of an overlying dioxide film.

Because of the volume increase attending formation of UH_3 when hydride forms beneath the oxide film on uranium, the adherence of the dioxide to the metal is destroyed. Both UO_2 and some UH_3 can be removed by brushing the surface of a hydrided specimen in vacuum. The residual hydride was decomposed by heating the specimen to about 300°C, holding it at that temperature for several hours, and pumping away the evolved gas. Katz and Rabinowitch (14) report that one hour at this temperature is sufficient to decompose the β-hydride.

The products that were identified by electron diffraction at various stages during one such experiment are listed in Table II. Since, in general, hydride lines were not detected following vacuum heating and the dioxide line intensities increased during the experiment, it is a reasonable conclusion that new dioxide was being formed by reaction between the newly formed uranium and the residual gas in the evacuated ED unit. Evidently the hydrogen released by decomposition is not effective in sweeping away any oxidizing gases.

Oxide removal by vacuum polishing.—As a result of the improvements to the ED unit, vacua of 5×10^{-7} torr could be obtained within 15 min after placing a specimen in the unit. Pressures of the order of 8×10^{-8} torr (equivalent nitrogen pressure) were obtained after a few hours of additional pumping. Almost negligible amounts of dioxide remained on the uranium surface immediately after polishing. The amounts increased rapidly, however, even in such good vacua. Also, appreciable amounts of α- and β-hydride have been detected on the surface, after the uranium was polished in vacua. These give way to oriented dioxide. The diffraction data for one series of experiments on uranium are presented in Table III.

The UO_2 was initially detected on the high-purity uranium sample as it was placed in the ED unit. Three minutes after it was polished with 400 grit emery paper in a vacuum of 5×10^{-7} torr, the pattern corresponded to strong α-metal plus β-hydride plus a very weak pattern of UO_2. After standing 10 min in this vacuum, the lines of UO_2 had increased, but those of β-hydride and α-uranium remained the same. After 120 hr at 5×10^{-7} torr, the pattern corresponded to oriented UO_2 plus one very weak line located in the middle of the triplet of lines corresponding to α metal. This specimen was lightly repolished without breaking the vacuum, and a strong pattern of oriented UO_2 plus a medium weak α-metal pattern was observed. In all of these observations the ratio of intensities indicated a dodecahedral fiber texture of the oxide (13) rather than random texture, and the diffraction patterns were consistent therewith. It is inferred that the texture did change in degree of perfection but not significantly in type as the film grew thicker.

In six separate experiments, at a pressure of 6×10^{-8} torr strong patterns of alpha hydride were found on the surface of vacuum polished uranium. These hydride patterns were stronger than the metal or the dioxide patterns and persisted for as long as 15 min. The slow strengthening of dioxide lines after polishing was noted in each experiment, and lines due to the metal were observed to nearly disappear.

Discussion

The most significant product formed by the oxidation of uranium surfaces is the dioxide. At elevated temperatures some U_3O_8 is formed by reaction with air; in vacuum, however, the partial reduction of the dioxide yields monoxide.

The oxidant in a good vacuum must in all probability be water since both hydride and oxide are eventually formed. It is interesting that water is apparently the major gas pumped by the diffusion pumps when the ED unit is operating at a vacuum of the order of 10^{-7} torr. In one experiment, the ED unit was "blanked-off" from the pumps, and a glass collection bulb was connected to it. The presence of a virtual leak was confirmed with a helium leak detector. When the pressure built up in the unit, the collection bulb was closed off and the gas therein analyzed by mass spectrometry. Water was the ma-

Table III. Correspondence between observed electron diffraction patterns and known lattice spacings

Diffraction plane	X-ray values Rel. int.*	d in A	Polished in air	Polished in vacuum	After 10 min at 5×10^{-7} torr	After 120 hr in vacuum	Repolished in vacuum
βUH_3 (200)	[37]	3.30		3.31vvw	3.37vw		
UO_2 (111)	200[z]	3.16	3.14s				3.17m
βUH_3 (210)	[110]	2.95		2.97vvw	3.00w		
αUH_3 (110)	(5)	2.94					
αU (020)	2	2.91					
UO_2 (200)	56[z]	2.74	2.72m				2.73vw
βUH_3 (211)	[100]	2.69					
αU (110)	108	2.54		2.55w	2.55m		
αU (021)	450	2.50		2.50ms	2.50w	2.52m, B	2.51w
αU (002)	70	2.46		2.46ms	2.46m		
αU (111)	155	2.26		2.25w, B	2.25w		2.26vw
αUH_3 (200)	(50)	2.08					2.10 trace
UO_2 (220)	106[z]	1.94	1.93s	1.95 trace	1.95w, B	1.93m	1.93vs
βUH_3 (222)	[20]	1.91					
αU (022)	5	1.88					
βUH_3 (320)	[40]	1.84		1.84w			
αU or βUH_3	—	1.77					1.79vw
αUH_3 (211)	(90)	1.70		1.72vw	1.73m		
βUH_3 (400)	[40]	1.66					
UO_2 (311)	85[z]	1.65	1.64s	1.65vw, B		1.64w	1.65s
UO_2 (222)	5[z]	1.58	1.57w				
αU (131)	4	1.53		1.55m	1.54s		1.53w
βUH_3 (420)	[25]	1.48					
αUH_3 (220)	(5)	1.47					
βUH_3 (421)	[40]	1.45			1.45vw		
αU (200)	1	1.42					1.43 trace
βUH_3 (332)	2	1.41					
αU (041)		1.40					
αU (113)		1.38					
UO_2 (400)	3[z]	1.37	1.36vw		1.36w		
αU (132)	2	1.35					
αUH_3 (310)	(50)	1.32					
αU (220)	2	1.28			1.28w		
αU (042)	4	1.26					
UO_2 (331)	11[z]	1.26	1.25s			1.25m	1.26w, B
αU (221), (202), (004)		1.24					
βUH_3 (432)	[32]	1.23					
UO_2 (420)		1.22					
βUH_3 (521)	[23]	1.21					
αUH_3 (222)	(60)	1.20					
βUH_3 (440)	[15]	1.17					
αU (133)	14	1.15			1.16w		1.14w
UO_2 (422)	17[z]	1.12	1.11ms			1.11m	
αU (114)	14	1.11					
αUH_3 (321)	(60)	1.11					
βUH_3 (442)	[12]	1.10					
βUH_3 (601)	[8]	1.09					
αU (043)	—	1.08					
βUH_3 (611)	[22]	1.07					

* Approximate relative line intensities taken from various different x-ray spectrometer traces. Those unmarked are for uranium sheet. Data in ( ) are from α-UH_3 and those in [ ] are from β-UH_3 patterns. Intensities for UO_2 are designated by the superscript [z]. Relative intensities are not comparable between different crystal phases.

jor component, amounting to approximately 75%. Small amounts of nitrogen, oxygen, hydrogen, and carbon monoxide were also present. On the basis of other experiments the contaminants may be spurious.

It appears that UH_3 and UO_2 do appear simultaneously in the products from many corrosion experiments involving water (15). It is not clear, however, whether the simultaneous formation represented by the equation

$$7U + 6H_2O \rightarrow 4UH_3 + 3UO_2 \qquad [1]$$

properly describes the reaction mechanism or whether the formation of UH_3 precedes the UO_2 formation. That is, our experiments have not established whether the hydride can form initially by the thermodynamically unlikely reaction

$$4U + 6H_2O \rightarrow 4UH_3 + 3\,O_2 \qquad [2]$$

or whether, as suggested by Draley (16), the UH_3 forms by reaction of the metal with the hydrogen released during the formation of UO_2 as in

$$U + 2H_2O \rightarrow UO_2 + 2H_2 \qquad [3]$$

It has been suggested that the observed hydride could be formed by the outward diffusion of hydrogen contained in the metal (17). It is also possible that the small amounts of hydrogen present in the

residual gas react directly to form UH_3. None of our experiments offered evidence of the nature of the actual reaction mechanism.

The fact that the intensities of the hydride lines decrease as those of the dioxide lines increase suggests that the oriented oxide results from the subsequent oxidation of the hydride by water, or possibly by the oxygen released during reaction [2]. As indicated by [1], 4/3 of a mole of UH_3 is produced per mole of UO_2, if all of the hydrogen yielded by reaction [3] is consumed. The more intense hydride lines could be accounted for if the hydride, after being formed, protrudes from the surface and consequently scatters the electrons of the beam more effectively than does the dioxide film.

A significant feature of this ED study is that the (220) line of UO_2 is stronger, in some cases, than other dioxide lines and is certainly stronger than is normal for a randomly oriented sample of UO_2. This observation is consistent with the preferred orientation observed for uranium oxidized at high temperature by low-pressure water vapor (13). X-ray diffraction studies of uranium following its exposure to moist hydrogen or water vapor have led to the conclusion that the (220) UO_2 planes form parallel to the metal surface with little or no relation to the orientation of the underlying metal.

Recently Sella and Trillat (18) conducted a very interesting electron diffraction study of uranium surfaces that had been prepared in a variety of manners and subsequently treated. They observed that, during bombardment by argon ions, dioxide films were formed by the traces of oxygen in the argon. The films exhibited a strong dodecahedral fiber texture. A similarly oriented film occurred in certain of their anodizing and electropolishing experiments. They concluded that this texture might be associated with slightly anisotropic diffusion in the cubic UO_2 lattice, *i.e.*, with the growth process. They expressed some doubt that the portion of the film next to the metal, which was epitaxially oriented, could be detected. We, however, do not believe that such a region necessarily exists.

Experimental conditions determine which preferred orientation will develop, and the following examples are cited. The observed (220) orientation is not the same as that observed on vacuum annealed uranium. For the vacuum annealed uranium, the (200) planes of UO_2 are oriented parallel to the surface of the metal substrate (13). In other ED experiments it has been shown that UO_2 deposited from the vapor onto glass was oriented with (111) planes parallel to the substrate; when deposited onto a tantalum foil the [111] pole of the oxide was inclined with respect to the substrate and apparently was pointed toward the source of the UO_2 vapor.

These observations indicate that the dodecahedral texture is intimately associated with diffusion and growth processes. The results of Sella and Trillat (18) are consistent with this interpretation. The presence of the dodecahedral fiber orientation (rather than some other orientation or a random texture) in the UO_2 formed at room temperature in the vacuum of the ED unit, as well as at high temperature after exposure to water vapor, suggests that the same or similar mechanism operates and lends support to the conclusion that, in the ED unit, uranium is oxidized by traces of residual moisture.

The relative line intensities observed with an x-ray spectrometer are presented in Tables I and III for a number of substances. The intensities for the different phases are not comparable and are presented only as indicators. For the most part the patterns were obtained with randomly oriented samples, and it is well recognized that when preferred orientation is present in the specimen the relationships between intensities are markedly altered. It is probable that the relative intensities observed by electron diffraction with unalloyed plutonium sheet, which are cited in Table I, suffer from this effect; the x-ray intensities were obtained with a carefully randomized sample. This undoubtedly accounts for the apparent absence of some of the moderately strong lines of the monoclinic cell. It is sometimes difficult even for the x-ray spectrometer to resolve the individual lines of a doublet such as (020) and (211). With the characteristically poor resolution and high background of the electron diffraction instrument, several proximate lines may appear to merge into one broad one. For this reason and also because of the effect of preferred orientation, lines with weak intensities at the low angle region may have been inadvertently overlooked.

A few comments concerning alternative methods of preparing uranium surfaces free of overlying oxide films, are in order. One may (i) deposit the metal from the vapor onto a substrate, (ii) remove the oxide from the metal surface chemically or mechanically, or (iii) create a new surface by cleavage or fracture. Preliminary x-ray diffraction work showed that a substantial amount of oxidation occurred during the deposition of uranium from the vapor. Therefore this method was abandoned. The experiments involving electropolished metal were also disappointing. The removal by undermining with UH_3 has been described above. No other method of chemical attack was tried. Oxide removal by ionic bombardment is only partially effective as shown by Sella and Trillat; even with a beam of hydrogen ions, minute traces of oxygen will result in oxide films. The possibility that ions will be driven into the metal and exist as neutral atoms cannot be excluded. For these reasons, therefore, this method was not investigated. Hayman (19) demonstrated the formation of curious ridges, which appeared to be unrelated to the underlying metal, following bombardment of uranium by argon ions. The development of UO_2 nuclei in patterns on the metal surface following cathodic bombardment (20), due to traces of oxygen and water in the gas, could lead to misinterpretation. Other recent studies on surfaces following this type of ionic attack are cited (21-26).

Without question the uranium surfaces following mechanical polishing are very rough. The metal asperities projecting above the general level of the metal surface are heavily cold worked. Only a relatively few of them are thin enough to be penetrated by the electron beam. It may well be argued that the

diffraction from the oxide, which may occur as patches in the "valleys," is obscured by the high background scattering arising from the very rough surface. Nevertheless most of the observed diffraction pattern apparently results from the diffraction by the asperities, and these appear to be essentially denuded of oxide. The growth of oxide films on these surfaces is then easily detected and followed, although the oxide may be in the "valleys." The growth of UO_2 is surprisingly rapid at such low gas pressures.

Despite their shortcomings, the methods of oxide removal employed seem to be as satisfactory as any available. Although traces of dioxide persisted on the surface after it was polished *in vacuo*, doubtless the dioxide was present as patches, and a substantial portion of the surface was free of oxide. It would seem, then, that the goal of studying oxidation on the denuded uranium surface was achieved in the present study, and there is no compelling evidence that oxide-free surfaces on uranium were obtained in any of the previous investigations. However, the possible influence of the remaining patches of oxide on the nucleation and growth of new oxide was not eliminated in the present study.

Summary

Dioxide films are left on polished uranium and plutonium in the sense that they form so rapidly, even in good vacuum, that a truly oxide-free surface cannot be preserved for more than a few minutes after polishing. Also, the evidence presented suggests that the formation of uranium hydride may precede that of the dioxide.

The bare metal and the hydride react readily in vacua of the order of 10^{-7} torr to form dioxide, and it is necessary to maintain vacua of this quality to observe the reactions of relatively oxide-free uranium.

Some ED work that deals with the sequence of oxide films when both monoxide and dioxide are present is reported. Only the dioxide has been observed by the ED technique although x-ray diffraction work shows that the films formed by vacuum annealing consist mainly of uranium monoxide. From our evidence the sequence of products appears to be dioxide/monoxide/uranium, which is in contradiction to the results of Williams and Westmacott (12).

Acknowledgments

The authors are deeply indebted to Professor Lawrence Brockway for his inspiration, guidance, and interest during the work. A number of members of this Laboratory have assisted the authors from time to time. They should like particularly to mention Miss Gladys Sturdy, Ulrich Merten, Robert Mulford, Virginia Shadden, and Edward Wright. Finally, they should like to thank Gaza Nagy and his group of machinists for their careful work in fabricating the modified system. The assistance of William Miner in revising and of Mrs. J. Zastrow in typing this manuscript is gratefully acknowledged.

Manuscript received Feb. 29, 1960; revised manuscript received May 10, 1962. The work on this paper was done under the auspices of the U.S.A.E.C.

Any discussion of this paper will appear in a Discussion Section to be published in the June 1963 JOURNAL.

REFERENCES

1. J. W. Hickman, *Trans. A.I.M.E.*, **180**, 547 (1949).
2. R. K. Hart, *Trans. Faraday Soc.*, **49**, 299 (1953).
3. O. Flint, J. J. Polling, and A. Charlesby, *Acta Met.*, **2**, 696 (1954).
4. I. S. Kerr and H. Wilman, *J. Inst. Metals*, **84**, 383 (1956).
5. H. Herring and P. Perio, *Bull soc. chim. France*, **1952**, 351.
6. F. Gronvold, *J. Inorg. & Nuclear Chem.*, **1**, 357 (1955).
7. R. N. R. Mulford, F. H. Ellinger, and W. H. Zachariasen, *J. Am. Chem. Soc.*, **76**, 297 (1954).
8. C. Holley, R. N. R. Mulford, E. J. Huber, Jr., E. L. Head, F. H. Ellinger, and C. W. Bjorklund, *Second Inter. Conf. Peaceful Uses of Atomic Energy*, Geneva, **6**, 215 (1958).
9. R. N. R. Mulford and G. E. Sturdy, *J. Am. Chem. Soc.*, **77**, 3449 (1955); also **78**, 3897 (1956).
10. R. E. Rundle, H. C. Baenziger, and A. S. Wilson, *ibid.*, **70**, 99 (1948).
11. H. R. Hoekstra and S. Siegel, Proc. Inter. Conf. Peaceful Uses Atomic Energy, Geneva, 1955, **7**, 394 (1956).
12. J. Williams and K. H. Westmacott, *Rev. Met.*, **53**, 189, 204 (1956).
13. J. T. Waber, J. A. O'Rourke, and R. Kleinberg, *This Journal*, **106**, 96 (1959).
14. J. J. Katz and E. Rabinowitch, "The Chemistry of Uranium," Nat. Nuclear Energy Ser., VIII-5, p. 199, McGraw-Hill Book Co., New York (1951).
15. J. T. Waber, U.S.A.E.C. Report LA 2035, 45 pp (1958).
16. J. E. Draley, *This Journal*, **104**, 329 (1957); see also "Physical Metallurgy of Uranium," AIME Symposium on Nuclear Metallurgy, p. 113, New York (1955).
17. C. S. Smith, Private communication.
18. C. Sella and J. J. Trillat, *Rev. Met.*, **56**, 105 (February 1959).
19. P. Hayman, *Compt. rend.*, **248**, 2472 (1959).
20. P. Hayman and C. Lecomte, *ibid.*, **250**, 530 (1960).
21. J. J. Trillat, C. Sella, and P. Conjeaud, *Compt. rend.*, **249**, 1987 (1957).
22. J. J. Trillat, R. L. Cunningham, P. Haymann, C. Lecomte, and W. J. Moore, *J. Appl. Phys.*, **31**, 839 (1960).
23. K. Mihama, *Congress Int. on Electron Microscopy, Berlin*, p. 414-7, Springer (1960).
24. P. Haymann, *Compt. rend.*, **251**, 85 (1960).
25. P. Haymann, *Proc. European Reg. Conf. on Electron Microscopy*," Delft, **1**, 507 (1960).
26. P. Haymann, Memoires Scientifiques, *Rev. Met.*, **58**, 73 (1961).

Theory and Design Principles of the Reversible Electroplating Light Modulator

Solomon Zaromb[1]

Research Division, Philco Corporation, Blue Bell, Pennsylvania

ABSTRACT

The potential uses and advantages of adjustable light shutters and reflectors based on reversible electroplating on transparent, chemically inert electrodes are indicated briefly. Over the entire visible light range, the highest ratio of optical density change δ to applied charge density q_d appears to be achievable with Ag, especially when formed in conjunction with I_2 or I_3^- ions. An aqueous plating solution containing 3-3.5M AgI and 7M NaI appears to be most suitable for achieving (*a*) a maximum δ/q_d ratio; (*b*) a satisfactorily uniform plating; (*c*) a maximum plating speed; and (*d*) a maximum rate of unplating. Of several electrode geometries and electrode arrangements capable of yielding essentially uniform plating, those utilizing adjacent subelements composed of parallel, closely spaced, flat, and narrow transparent electrode strips with line-symmetrically situated contacts is preferred, especially for large-area modulators. A series connection between the subelements is especially desirable.

With aqueous electrolyte solutions, the shortest practical plating time must exceed $\rho_e q_d^2/400$ sec, where ρ_e is the electrolyte resistivity in ohm-cm, and q_d is in coul/cm^2. Hence, to achieve both a maximal speed and a high δ, it is necessary to use several plating cells back-to-back. To maintain the desired opacity, a low, continuous plating current may be required, following the initial plating pulse. The time required to clear the cell may vary from less than a msec, in cases where a fast plating pulse is followed instantly by a rapid unplating pulse, to a maximum of $3a^2/\pi^2 D$ (where a is the electrode spacing, and D is the diffusion coefficient of the main oxidizing component, *e.g.*, I_3^-) in cases where the plating is to be maintained for a long period of time prior to the application of the clearing pulse.

In view of the virtual omnipresence of light and its important part in most activities, an electronic method of controlling its transmission and/or reflection should have numerous potential applications ranging from glare and lighting adjustors through flash-blindness preventing goggles and display or information storage devices. An electrochemical color filter based on changes in the transmission of indicator dyes with changes in pH or redox potential of an electrolyte solution is known (1, 2). The main intrinsic limitations of these "reversible dye" devices are that: (i) they do not modulate the reflection of light; (ii) they are limited by relatively low speeds of reaction in solution and of migration of reacting species to and from the electrodes; (iii) the required dyes and electrolyte solutions deteriorate on prolonged exposure to intense light or on passage of an excessively high charge (at voltages above 2v); and (iv) they usually operate only within relatively narrow wavelength regions.

These objections are eliminated or reduced in the reversible electroplating light modulator discussed in the present paper.

Theoretical Considerations

Required Charge Density vs. Desired Opacity (and Wavelength)

Figures of merit.—The absorption coefficient α, as defined by the Lambert equation

$$I_t = I_i e^{-\alpha\theta} \qquad [1]$$

where I_i is the intensity of the incident light, and I_t the intensity transmitted through a thickness θ of a given metal, is related to the wavelength λ, the absorption index κ, and the index of refraction n of the metal (3)

$$\alpha = 4\pi n\,\kappa/\lambda \qquad [2]$$

The thickness θ of electrodeposited metal for a plating charge density q_d (in coul/cm^2) depends on its atomic weight W, density d, oxidation state z of the platable ions, and plating current efficiency ϵ

$$\theta/q_d = \epsilon W/z\mathbf{F}d \qquad [3]$$

where **F** is a faraday. Hence, the optical density change due to plating, δ, as defined by the equation

$$I_t/I_i = 10^{-\delta} \qquad [4]$$

should be, according to Eq. [1] through [4]

$$\delta = \alpha\theta/2.303 = (4\pi/2.303)\,\epsilon\, q_d\, n\,\kappa\, W/(\mathbf{F}\lambda z d) \qquad [5]$$

$$= 5.65 \times 10^{-5}\,\epsilon\, q_d\, n\,\kappa\, W/(\lambda z d) \qquad [5']$$

i.e., for $\epsilon \simeq 100\%$, the expected change in optical density per plating charge density becomes

$$\delta/q_d \simeq 5.65 \times 10^{-5}\, n\,\kappa\, W/(\lambda z d) \qquad [5'']$$

The ratio $n\kappa W/(\lambda z d)$ thus gives a relative figure of merit for comparing the minimum charge density requirements, using various platable metals. As seen in Table I, the highest values of δ/q_d may be ex-

[1] Present address: Research and Advanced Technology Department, Electronic Systems and Products Division, The Martin-Marietta Corporation, Baltimore, Md.

Table I. Estimated optical density change per plating charge density for various elements and wavelengths*

Element	d, g/cc	z	W	λ, μ	n_K	δ/q_d
Cd	8.64	2	112.4	0.589	5.01	31.3
Cr	7.2	3	52.0	0.579	4.85	11.4
Co	8.9	2	58.9	0.500	3.72	14.0
Co				0.650	4.40	12.7
Cu	8.92	2	63.6	0.347	1.47	8.5
Cu				0.500	2.34	9.4
Cu				0.650	3.26	10.1
Cu				0.870	3.85	8.9
Au	19.3	1	197.0	0.441	1.85	24.2
Au				0.589	2.83	27.6
I	4.93	−1	126.9	0.589	0.57	14.1
Ir	22.4	4	193.1	0.579	4.87	10.2
Pb	11.3	2	207.2	0.589	3.48	30.6
Mn	7.20	2	54.9	0.579	3.89	14.5
Ni	8.90	2	58.7	0.420	2.53	11.2
Ni				0.589	3.33	10.5
Ni				0.750	4.36	10.8
Pt	21.5	2	195.2	0.441	3.16	18.4
Pt				0.589	3.54	15.4
Pt				0.668	3.66	14.1
Rh	12.4	3	102.9	0.579	4.67	12.6
Se	4.80	−2	79.0	0.400	6.79	79.0
Se				0.490	4.65	44.1
Se				0.589	1.32	10.4
Se				0.760	0.156	0.95
Ag	10.5	1	107.9	0.332	0.65	11.4
Ag				0.395	1.91	28.1
Ag				0.500	2.94	34.2
Ag				0.589	3.64	35.9
Ag				0.750	5.16	40.1
Sn	7.28	2	118.7	0.589	5.25	41.1
Zn	7.14	2	65.4	0.441	3.19	18.7
Zn				0.589	4.66	20.5
Zn				0.668	5.08	19.7

* Data obtained from ref. (4).

pected for Se with $\lambda < 0.490\mu$, for Sn with $\lambda = 0.589\mu$, for Ag with $\lambda > 0.395\mu$, and for Cd with $\lambda = 0.589\mu$. It is also apparent that red light will be transmitted by thin Se films and violet light by Ag films, which should yield at least a limited choice of adjustable color filters.

Variation of absorption coefficient of thin films with thickness.—The values of δ/q_d in Table I are based on the optical constants of thick metal sheets. For thin films of less than 200Å, the optical constants are known to vary with thickness (5-8). Furthermore, the experimental values obtained by several workers are not in sufficiently good agreement to be considered reliable, probably due to differences in the mode of film deposition (8). Hence, the only conclusion which can be drawn from previous thin-film studies is that any quantitative predictions based on Table I may be in error by as much as a factor of 2 or 3 for plated film thicknesses of less than 200Å.

Possible supplementary absorption by a colored oxidation product.—For certain light-shutter applications, the formation of a light-absorbing oxidation product at a transparent anode may complement the absorption by the metal plated on the cathode. Of particular interest is the I_3^- ion formed with plating solutions of AgI in concentrated NaI. The wavelength dependence of the extinction coefficient of

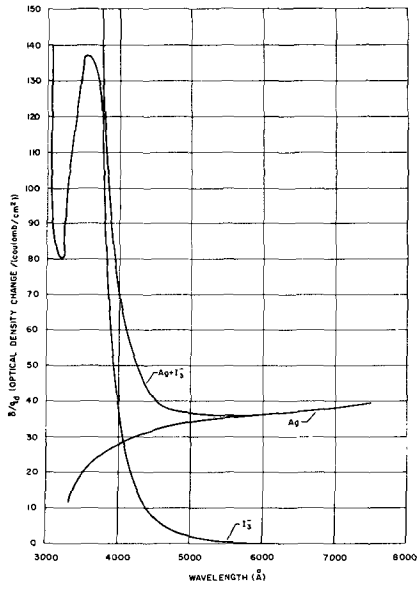

Fig. 1. Optical density change per plating charge density for AgI solutions.

I_3^- was estimated from the literature (9, 10) and the corresponding values of δ/q_d are plotted in Fig. 1 together with those for Ag and for the combined absorption by I_3^- and Ag. It can be seen that the I_3^- drastically reduces the transmission of blue and u.v. light ($\lambda < 4500$Å), and reduces the variation of transmission with wavelength for the remaining visible light region ($4500\text{Å} \leq \lambda \leq 7500\text{Å}$).

Estimated minimum charge requirements vs. desired optical density change.—According to Table I and Fig. 1, Ag gives the highest (or nearly highest) value of δ/q_d in the visible light range, especially in combination with I_3^-. Hence, any estimate of minimum charge requirements based on Fig. 1 should represent the lowest value achievable in practice with white light. Thus, for a desired optical density change of at least 3.0 for all visible wavelengths, the minimum required plating charge density is 0.08 coul/cm^2. Of course, much lower charge densities may be required for selected narrow wavelength regions.

Achievement of Uniform Plating over Large Areas

Effect of plating solution.—For 100% over-all plating current efficiency, the most serious deviations from the minimum charge requirements estimated in the previous section may arise from a nonuniform plating density. This is a common problem in electroplating, and most industrial plating solutions have the property of "smoothing out" the plating density even over somewhat irregularly-shaped substrates. Unfortunately, most industrial plating solutions contain unstable and/or highly toxic agents (*e.g.*, cyanides) which are unsuitable for common light-modulator applications.

The mechanism by which a plating solution tends to counteract the effect of geometric irregularities appears to be associated with an overpotential rapidly increasing with current density (11, 12). Negative complexing ions usually increase the overpotential by transforming readily platable cations into less readily platable anion complexes. Thus, Ag

plating solutions have been recommended based on fluoborate (13), rhodanide (14), thiosulfate (15), and iodide (16) complexes. The last appear especially suitable for reversible light modulators.

The mechanism by which Ag is plated from concentrated iodide solutions cannot occur via the steps:

$$AgI_2^- \rightarrow Ag^+ + 2I^- \qquad (I)$$

followed by

$$Ag^+ + e^- \rightarrow Ag \qquad (II)$$

because the concentration of free Ag^+ ions in 5-10M iodide solutions cannot appreciably exceed 10^{-17}M (the solubility product of AgI being 8.5 x 10^{-17}). Although the concentration of dissolved AgI molecules or AgI-H_2O molecular complexes should be more appreciable in view of the ease of precipitation of AgI from 1M iodide solutions, it still cannot exceed 10^{-6}M. Hence, the most likely mechanism must be of the form

$$AgI_p^{1-p} + e^- \rightarrow Ag + pI^- \qquad (III)$$

where p may be a value (17) between 2 and 4. The negatively charged AgI_p^{1-p} species approaching the cathode must proceed under the influence of a concentration gradient against the direction of the applied electric field. Hence, for continuous plating at high current densities, reaction (III) should be diffusion-controlled, and the current density i_c approaches an asymptotic limiting value i_L with increasing overvoltage η

$$i_c = i_L(1 - e^{zF\eta/RT}) \qquad [6]$$

where i_L depends mainly on the concentration of the platable complex and on the thickness of the stationary layer of electrolyte adjacent to the cathode (12, 18).

Reported polarization curves for a solution of 0.01M AgI_2^- in 1M KI (11) with different stirring rates actually show the asymptotic variation of i_c predicted by Eq. [6]. A similar asymptotic behavior or plateau in the i_c *vs.* η plot appears likely with more concentrated solutions (*e.g.*, 3M AgI in 7M NaI). However, the plateau could hardly extend over a range of more than a few tenths of a volt before the occurrence of H_2 evolution. Although the latter may not affect the uniformity of the plating, it would lower the current efficiency just the same. Thus, the use of a suitable plating solution and of an optimum plating rate may, at best, allow for geometric voltage drop irregularities amounting to no more than a few tenths of a volt.

Geometric considerations.—In view of the expected limited effectiveness of even the best possible plating compositions, special attention must be given to the geometric requirements for uniform plating densities, as discussed in detail in a concurrent paper (19). Of several possible cell geometries [cf. Figs. 1 and 4 of ref. (19)], those based on electrodes perpendicular to the cell walls are of primary interest because of the common availability of plate glass and the ease of aligning a large number of parallel subelement bands to form a large, flat area of any desired dimensions. Thus, if b is the max allowable subelement width, as established by Eq. (68)‡ or (92)‡ [ref. (19)],[2] then for a rectangular area A of width w and length L, *i.e.*

$$A = Lw \qquad [7]$$

the required number n_s of subelements of length L and width b is

$$n_s = w/b \qquad [8]$$

or

$$A = n_s bL \qquad [8']$$

These obvious relations will be used extensively in the following section.

Dependence of cell resistance and required plating charge on geometry and contact connections.—The resistance r_s of any subelement of width b and length L is by definition

$$r_s = (V_{c_1} - V_{c_2})/I_c \qquad [9]$$

where V_{c_1} and V_{c_2} are the potentials at the contacts C_1 and C_2, *i.e.*

$$V_{c_1} = V_{g'_1} \ (y_1 = b) \qquad [10]$$

for both the mirror-symmetric and line-symmetric electrode arrangement [Eq. (71')‡ and (88)‡, respectively],[2] whereas

$$V_{c_2} = V_{g'_2} \ (y_1 = 0) \qquad [11]$$

for the line-symmetric case [Eq. (72)‡ and (64)‡] or,

$$V_{c_2} = V_{g'_2} (y_1 = b) \qquad [12]$$

for mirror-symmetric contacts [Eq. (89)‡ and (85)‡]. Hence, Eq. [9] to [11], (71')‡, (72)‡, (64)‡, and (65)‡ yield

$$r_{s1} = \frac{\rho_{g'}}{L}\left[\frac{b}{2} + \frac{1}{\gamma}\coth(\gamma b/2)\right] \qquad [13]$$

for the line-symmetric case, which reduces to

$$r_{s1} \simeq \frac{\rho_{g'} b}{2L} + \frac{a\rho_e}{bL} \qquad [13']$$

for $\gamma b/2 << 1$, whereas Eq. [9]-[10], [12], (85)‡ and (65)‡ yield

$$r_{sm} = \frac{2\rho_{g'}}{L}\coth(\gamma b) \qquad [14]$$

for mirror symmetry, which reduces to

$$r_{sm} \simeq a\rho_e/bL \qquad [14']$$

for $\gamma b << 1$.

For a uniformity ratio u better than 0.65, a must be greater than $b^2/2k$ for the line-symmetric case [cf. Eq. (68)‡ and (82)‡], and $a \geqq 2b^2/k$ for mirror symmetry [Eq. (92)‡]. Hence, Eq. (82)‡ and [13'] yield

$$\frac{\rho_{g'} b}{2L} + \frac{2k\rho_e}{5bL} \geqq r_{s1} \geqq \frac{\rho_{g'} b}{L} \qquad [15]$$

whereas Eq. (92)‡ and [14'] lead to

$$r_{sm} \geqq 2\rho_{g'} b/L \qquad [16]$$

Thus, the minimum practical value of r_{s1} can be made half as small as that of r_{sm}, *i.e.*, line-symmetric contacts are preferable to mirror-symmetric ones where a minimum cell resistance is required (with fixed parameters b, L, and $\rho_{g'}$), whereas the mirror-

[2] The sign ‡ following an equation number denotes an equation from ref. (19).

symmetric arrangement may be more useful where a large electrode spacing $a > 2k/5$ is desired [cf. Eq. (82)‡].

For a cell made up of n_s subelements, the over-all resistance R_c and required plating charge Q will depend, of course, on whether these subelements are connected in parallel or in series. For parallel connection

$$R_p = r_s/n_s \qquad [17]$$

and

$$Q_p = n_s q_s \qquad [18]$$

where

$$q_s = A_s q_d \qquad [19]$$

is the required plating charge per subelement of area

$$A_s = bL \qquad [20]$$

i.e.,

$$Q_p = q_d n_s bL = q_d A \qquad [21]$$

For series connection,

$$R_s = n_s r_s \qquad [22]$$

and

$$Q_s = q_s = q_d\, bL = q_d A/n_s \qquad [23]$$

The eight possible multiple-contact arrangements are shown in Fig. 2. The parallel alternating connections, 2 and 5, and nonalternating subelements in series, 4 and 8, appear least practical, especially the last two, which require twice as many sets of contacts (one for each subelement) as the other arrangements. On the other hand, the arrangement most easily achievable by far is that of alternating subelements in series, 7, in which the adjacent contacts C_{1+}-C_{2-}, C_{2+}-C_{3-}, etc., are parts of the conducting glass-surface strips. The following calculations will, therefore, be concerned mainly with arrangement 7 (see also Fig. 3), and also, for purposes of comparison, with the parallel connections 6 of Fig. 2.

For both arrangements 6 and 7, the simplified approximate relation [13′] will be assumed to apply. Hence, Eq. [17] together with Eq. [13′], [15], and [8] yield

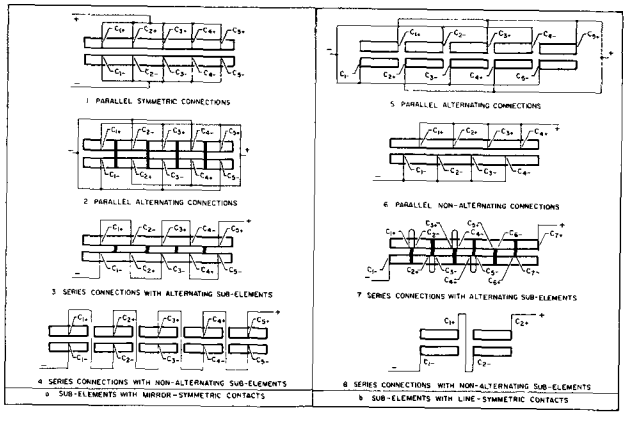

Fig. 2. Possible contact arrangements for a large-area light shutter. a, Subelements with mirror-symmetric contacts: 1, parallel symmetric connections; 2, parallel alternating connections; 3, series connections with alternating subelements; 4, series connections with nonalternating subelements. b, Subelements with line-symmetric contacts: 5, parallel alternating connections; 6, parallel nonalternating connections; 7, alternating subelements in series; 8, nonalternating subelements in series.

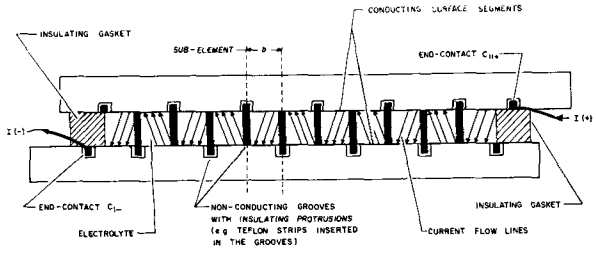

Fig. 3. Detailed drawing of arrangement 7 of Fig. 2

$$R_p = \frac{1}{n_s}\left[\frac{\rho_{g'}b}{2L} + \frac{a\rho_e}{bL}\right] \geqq \rho_{g'}b/(n_s L) \qquad [24]$$

or

$$R_p = [a\rho_e + 0.5\rho_{g'}b^2]/A \geqq \rho_{g'}b^2/A \qquad [24']$$

for arrangement 6, while Eq. [22] yields

$$R_s = n_s\left[\frac{\rho_{g'}b}{2L} + \frac{a\rho_e}{bL}\right] \geqq \rho_{g'}n_s b/L \qquad [25]$$

or

$$R_s = \frac{w}{L}\left[\frac{\rho_{g'}}{2} + \frac{a\rho_e}{b^2}\right] \geqq \rho_{g'}w/L \qquad [25']$$

for arrangement 7.

If the plating is to occur within a time τ_p at a constant value of the current I_c, then the resulting energy dissipation H is

$$H = \tau_p I_c^2 R_c = Q^2 R_c/\tau_p \qquad [26]$$

$$= [a\rho_e + 0.5b^2\rho_{g'}]q_d^2 A/\tau_p \qquad [26']$$

or

$$H \geqq b^2\rho_{g'}q_d^2 A/\tau_p \qquad [26'']$$

Equation [26′] can be derived either from Eq. [21] and [24] for the parallel arrangement 6, or from Eq. [23] and [25] for the series arrangement 7, which serves as a fair check of these relations.

Although no savings in H result from the use of either arrangement for fixed values of the parameters in Eq. [26], much smaller values of b can be achieved in practice with the series arrangement 7 than with 6, which, therefore, allows for lower over-all energy requirements. Besides greater ease of construction, the series arrangement 7 also reduces the over-all plating charge and current requirements (cf. Eq. [23] and [21]), and allows for a better uniformity of plating current distribution than the parallel connections 6.

All these advantages appear to counterbalance for most applications any possible objections to alternate light-reflecting and absorbing strips and to the higher voltages required by arrangement 7 (cf. Eqs. [17], and [21] through [23]).

Although the complete deterioration of a single subelement would render the series arrangement inoperative, such a failure appears much less likely than those tending to result from any imbalance among subelements connected in parallel.

Transient Effects

Plating speed limitations.—A major factor determining the usefulness of the electroplating light shutter for a given application is its maximum achievable speed of operation. One basic speed limitation which can be considered immediately is that

arising from thermal effects. The temperature rise ΔT in the electrolyte due to the passage of a high current pulse must be less than 100°C if boiling is to be avoided. Hence, the energy H rapidly dissipated in the electrolyte has an allowable maximum

$$H \leq v_e h_e \Delta T_{max} \simeq 100\, v_e \text{ (cal)} \simeq 400\, v_e \text{ (joul)} \quad [27]$$

where v_e and h_e are the volume and heat capacity per unit volume of the electrolyte. But, according to Eq. [26']

$$H \geq a\rho_e q_d^2 A/\tau_p = v_e \rho_e q_d^2/\tau_p \quad [28]$$

Eq. [27] and [28] yield

$$1/\tau_p \leq 400/(\rho_e q_d^2) \quad [29]$$

i.e., the maximum satisfactory operating speed is an inverse square function of the plating charge density or desired optical density change. Thus, for $\rho_e = 10$ ohm-cm and $q_d = 0.1$ coul/cm² (corresponding to an optical density change δ of 3 to 4), Eq. [29] yields a minimum τ_p of 250 μsec, whereas for $q_d = 0.02$ coul/cm² (corresponding to $\delta \simeq 2/3$) the minimum τ_p is 10 μsec. Hence, in order to achieve a high optical density change δ of say 3 to 4 in 10 μsec, it would be necessary to use 5 plating cells back-to-back, each yielding a low δ of only 2/3.

A more serious speed limitation, of a purely electrochemical nature, may be associated with the transition time (20)

$$\tau_{trans} = \pi \mathbf{F}^2 D c_p^2/4i^2 \quad [30]$$

corresponding to the time of depletion of platable ions at the electrode-electrolyte interface on application of a constant current density i (in amp/cm²). Setting $\mathbf{F} = 96{,}500$ coul, and assuming a value of $D \simeq 10^{-5}$ cm²/sec for the diffusion coefficient of the platable ions, one obtains

$$\tau_{trans} \simeq 2 \times 10^5\, c_p^2/i^2 \quad [30']$$

where c_p is the concentration of platable ions in moles/cc. On the other hand, for maximum plating speed,

$$i_{max}\, \tau_{trans} \simeq q_d \quad [31]$$

Hence,

$$i_{max} \simeq q_d/\tau_{trans} \simeq q_d\, i^2_{max}/(2 \times 10^5\, c_p^2) \simeq 2 \times 10^5\, c_p^2/q_d \quad [32]$$

and the minimum plating time τ_{min} becomes

$$\tau_{min} \simeq q_d/i_{max} \simeq 5 \times 10^{-6}\, q_d^2/c_p^2 \quad [33]$$

For $c_p = 0.01$ mole/cc (*i.e.*, a 10M solution of platable ions), Eq. [33] yields a τ_{min} of 500 μsec for $q_d = 0.1$ coul/cm², and $\tau_{min} \simeq 20$ μsec for $q_d = 0.02$ coul/cm², which is comparable with the thermal limitation given by Eq. [29]. However, the coefficient of q_d^2 in Eq. [33] may vary drastically with electrolyte composition. Thus, for $c_p = 0.004$ mole/cc, which is the limit of solubility of AgI in iodide solutions, τ_{min} as given in Eq. [33] becomes twelve times higher than that of Eq. [29]. However, the effective value of c_p need not necessarily be limited to that of the ultimately plated cations, but may include that of all the cation species. Thus, for a solution containing 4M AgI plus 8M NaI, the effective value of c_p may be 0.012 mole/cc. The actual plating mechanism would then involve a very rapid deposition of an Ag-Na alloy, followed by a somewhat less rapid displacement of the Na by Ag (and, what is less desirable, by H_2 if the H_3O^+ ion concentration of the solution or the rate of reduction of H_2O is sufficiently high).

It should also be noted that Eq. [30], [32], and [33] are based on the assumption of negligible electromigration of platable ions. In cases where most of the cationic species present are platable, the diffusion coefficient D of Eq. [30] should be replaced by an effective diffusion coefficient (18)

$$D' = D/(1 - t_+) \quad [34]$$

where t_+ is the transport number of the cations. Thus, for $t_+ \simeq 0.5$, the coefficient of Eq. [30] would be doubled, resulting in a reduction of τ_{min} by a factor of 2. Furthermore, at the plated electrode, t_+ should approach unity as the catholyte becomes depleted,[3] which should cause D' to approach ∞. All these considerations suggest that for maximum plating speeds:

i. the concentration c_p of platable ions should be as high as possible;

ii. the concentration of H_3O^+ ions should be kept as low as possible to avoid or minimize the formation of H_2; and

iii. if the solubility of the desired species to be plated is limited, as in the case of AgI in concentrated alkali-metal iodide solutions, the initial plating of alkali metal followed by its displacement by the metal to be plated (*e.g.*, Ag) may allow for increased plating speeds, provided that H_2 formation can be avoided. This last possibility may render Eq. [33] somewhat uncertain. Hence, the safest conclusion is that Eq. [29] imposes a definite limitation on the rate of darkening of a single-layer shutter, whereas, Eq. [30] through [33] may impose a further limitation for some electrolyte solutions. Here again it must be emphasized that these limitations apply only to single-layer shutters. With several shutters placed back-to-back, the limiting darkening speed will depend on the number of allowable layers, depending on required open-state transmission, maximum thickness, cost, etc.

Other transient effects.—Compared with the above-discussed speed limitations, most other effects are relatively unimportant. The "rise time" (or time required for charging the electrode double layer capacitance before plating can occur) is usually much shorter than the transition time, and may be further minimized, if need be, by peaking the applied voltage or current at the start of the plating pulse. The resistivity of the plated surface may decrease on deposition of a sufficiently heavy metal layer, but the resulting decrease in the over-all cell

[3] When all the cations are platable, charge neutrality requires that the depleted catholyte layer contain a low concentration of both cations and anions. The latter then diffuse toward the cathode, against the direction of the applied field. Hence, as the current becomes increasingly diffusion-controlled, it must be carried predominantly by cations, *i.e.*, t_+ must approach unity near the cathode.

resistance could not exceed 30% according to Eq. [13] through [15], and would probably be completely negligible (21) for the extremely thin layers (of 100Å or less) to be deposited in most applications.

Finally, some inductance may be associated with the parallel contact arrangement 6 of Fig. 2, but should be entirely negligible in the preferred series arrangement 7 which happens to be somewhat similar to the "transposed-conductor" configuration used to minimize mutual inductance between telephone lines.

Methods of Clearing (or Unplating)

The obvious method of removing a layer of plated metal from a transparent glass electrode, *i.e.*, that involving application of an unplating current pulse, may be satisfactory only in a limited number of cases, e.g., in modulated light reflectors in which transmissivity is not important, or in small-area shutters with specially shaped or hidden counter-electrodes. In large-area shutters, however, such as those involving arrangements 1 through 8 of Fig. 2, an unplating current pulse at one transparent glass electrode would ordinarily cause plating at the opposite glass electrode with no resulting improvement in transmission. It, therefore, becomes necessary to introduce an oxidizing component Ox in the electrolyte which can participate in the reversible reactions:

$$Ox + e^- \rightleftharpoons Red^- \qquad (IV)$$

and

$$Ox + M \rightarrow Red^- + M^+ \qquad (V)$$

where Red^- is the reduced form of Ox, and M is the plated metal. For example, for AgI-NaI solutions, the Ox component could be $\frac{1}{2}I_3$ (or IO_3 in basic solutions) so that reactions (IV) and (V) would take the form

$$\frac{1}{2}I_3^- + e^- \rightleftharpoons \frac{3}{2}I^- \qquad (IV')$$

and

$$\frac{1}{2}I_3^- + 2Ag\left(+ \frac{3}{2}I^- \right) \rightarrow (3\,I^- + Ag^+) \rightarrow AgI_3^= \qquad (V')$$

The Ox component (I_3^-) can, of course, be either added initially to the electrolyte or formed electrochemically via reaction (IV) or (IV') going from right to left. The following calculations will be concerned with the control of the concentrations $c_{ox}(x, t_p)$ and $c_{ox}(x, t_u)$ of the Ox component (in g-equivalents/cc) as a function of the distance x from the plated surface and of the respective times t_p and t_u after the start of a given plating and unplating operation.

The rate of reaction (V) or (V') may be limited by chemical kinetics or by the rate of flow

$$\vec{J}_{ox}(x \rightarrow 0, t)$$

of the Ox component towards $x = 0$ (the plated electrode).

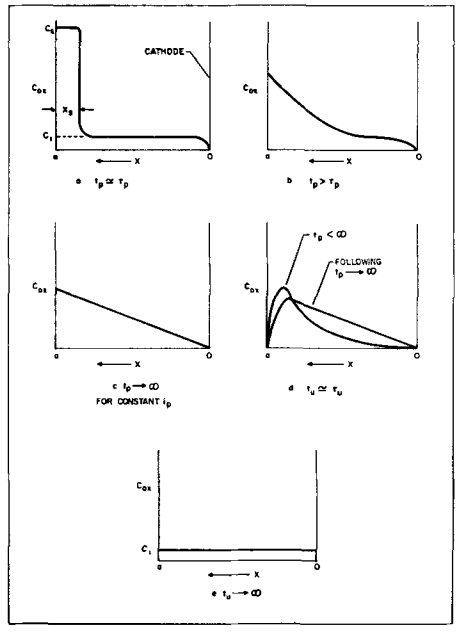

Fig. 4. Distribution of the Ox component at various stages of the plating-unplating cycle.

Now, by Fick's laws

$$\vec{J}_{ox} = -D(\partial c_{ox}/\partial x) \qquad [35]$$

and

$$\partial c_{ox}/\partial t = D\,\partial^2 c_{ox}/\partial x^2 \qquad [36]$$

For good initial plating efficiency and to maintain continued plating with minimal additional energy input, one should aim at minimal $c_{ox}(0, t_p)$ and minimal $\vec{J}_{ox}(0, t_p)$, whereas, for rapid clearing, high values of $c_{ox}(0, t_u)$ and $\vec{J}_{ox}(0, t_u)$ are desirable. The best way of achieving these aims appears to be by electrochemical formation of Ox when clearing is desired, *i.e.*, by application of an unplating current pulse. Plating at the opposite electrode ($x = a$) could then be minimized by the reaction with the Ox formed at $x = a$ during the preceding plating pulse, *i.e.*, by maintaining a high $c_{ox}(a, t_p)$ and a high $\vec{J}_{ox}(a, t_u)$. The full plating-unplating cycle is shown qualitatively in Fig. 4a through e. In Fig. 4a, a highly concentrated layer of Ox^+ is formed within a relatively short plating pulse period τ_p. If c_s is the solubility limit of Ox in the electrolyte, then the thickness of the initially formed layer x_s of Ox-saturated electrolyte is given by the materials balance

$$(c_s - c_i)x_s = q_d/\mathbf{F} \qquad [37]$$

or

$$x_s = q_d/[\mathbf{F}(c_s - c_i)] \qquad [37']$$

where

$$c_i = c_{ox}(x, 0) \qquad [38]$$

is the assumed (relatively low and) uniform initial Ox concentration. Hence, the initial boundary conditions are

$$c_{ox}(x, \tau_p) = c_i \text{ for } 0 < x \leq a - x \qquad [39]$$

$$c_{ox}(x, \tau_p) = c_s \text{ for } a - x_s \leq x \leq a \qquad [40]$$

and

$$c_{ox}(0, t_p) = 0 \text{ for } t_p \geq \tau_p \qquad [41]$$

the last condition [41] arising from an assumed rapid occurrence of reaction (V) at the plated layer $x = 0$.

Since $x_s << a$, the boundary conditions can be rewritten, as follows

$$c_{Ox}(x, \tau_p) = c_i \text{ for } 0 < x < a \qquad [39']$$

and

an amount $q_d/\mu\mathbf{F}$ injected at $x = a$ and $t_p = \tau_p$ [40']

The solution to Eq. [36], [41], [39'], and [40'] is:[4]

$$c_{Ox}(x, t_p') = \frac{2q_d}{z\mathbf{F}a}\sum_{n=0}^{\infty}(-1)^n e^{-(2n+1)^2\pi^2 D t_p'/4a^2}\sin\frac{(2n+1)\pi x}{2a} + \frac{4c_i}{\pi}\sum_{n=0}^{\infty} e^{-(2n+1)^2\pi^2 D t_p'/4a^2}\sin\frac{(2n+1)\pi x}{2a}$$

$$= \sum_{n=0}^{\infty}\left(\frac{2q_d(-1)^n}{\mathbf{F}a} + \frac{4c_i}{\pi}\right) e^{-(2n+1)^2\pi^2 D t_p'/4a^2}\sin\frac{(2n+1)\pi x}{2a} \qquad [42]$$

where

$$t_p' = t_p - \tau_p \qquad [43]$$

For

$$t_p' \geqq a^2/4D \qquad [44]$$

a simplified approximation of Eq. [42] is obtained

$$c_{Ox}(x, t_p' \geqq a^2/4D) \simeq \left[\frac{2q_d}{\mathbf{F}a} + \frac{4c_i}{\pi}\right] e^{-\pi^2 D t_p'/4a^2}\sin\frac{\pi x}{2a} \qquad [42']$$

as shown schematically in Fig. 4b. Equations [42'] and [35] give the rate of spontaneous unplating at $x = 0$

$$-\vec{J}_{Ox}(0, t_p' \geqq a^2/4D) \simeq D\left[\frac{\pi q_d}{\mathbf{F}a^2} + \frac{2c_i}{a}\right] e^{-\pi^2 D t_p'/4a^2} \qquad [45]$$

As seen from Eq. [45], the rate of unplating decreases rapidly with t_p' if the initial plating pulse is not followed by an additional plating current.

In order to maintain a desired opacity for an indefinitely long period ($t_p' \to \infty$), it is necessary to maintain a continuous plating current density i_p to counterbalance the effect of diffusion of Ox toward $x = 0$. The required value of i_p can be readily calculated for the steady-state condition ($t_p' \to \infty$) for which

$$c_{Ox}(x, \infty) = (\Delta c_{Ox}/\Delta x)x \qquad [46]$$

and

$$i_p = -\mathbf{F}\vec{J}_{Ox}(x, \infty) = \mathbf{F}D(\partial c_{Ox}/\partial x) = \mathbf{F}D(\Delta c_{Ox}/\Delta x) \qquad [47]$$

By a materials balance, one obtains

$$ac_i + \frac{q_d}{\mathbf{F}} = \int_0^a c_{Ox}dx = \int_0^a\left(\frac{\Delta c_{Ox}}{\Delta x}\right)x\,dx = \left(\frac{\Delta c_{Ox}}{\Delta x}\right)\frac{a^2}{2} \qquad [48]$$

[4] Cf. ref. (22) pp. 297-8 for our boundary conditions [41] and [40'] setting $x' = a/2$ in C and J's Eq. §132 (2), and p. 83 for boundary conditions [41] and [39'] setting $-c_i$ for V, a for l, and $a - x$ for x in C, and J's Eq. §36 (2), and adding $+ C_i$.

Hence

$$i_p = \frac{2D}{a^2}(q_d + \mathbf{F}\,a\,c_i) \qquad [49]$$

For example, for $D = 10^{-5}$ cm^2/sec, $a = 2 \times 10^{-3}$ cm, $q_d = 0.02$ coul/cm^2, and $c_i = 10^{-5}$ mole/cc, one obtains $i_p \simeq 0.12$ amp/cm^2. Under conditions where a constant current i_p (as given by Eq. [49]) is passed following the initial plating pulse, the boundary condition [40'] must be supplemented by the additional condition that:

a continuous injection of Ox occurs at $x = a$ and $t_p \geqq \tau_p$ at the rate $i_p/\mathbf{F}$

$$= \frac{2D}{a^2}\left(\frac{q_d}{\mathbf{F}} + ac_i\right) \qquad [49']$$

This, together with the conditions leading to Eq. [42], results in a solution of the form

$$c_{Ox}(x, t_p') = \sum_{n=0}^{\infty}\left[\left(\frac{2q_d(-1)^n}{\mathbf{F}a} + \frac{4c_i}{\pi}\right) e^{-(2n+1)^2\pi^2 D t_p'/4a^2}\sin\frac{(2n+1)\pi x}{2a}\right] + \frac{2}{a}\left(\frac{q_d}{\mathbf{F}} + a\,c_i\right)\left[\frac{x}{a} - \sum_{n=0}^{\infty}(-1)^n\frac{8e^{-(2n+1)^2\pi^2 D t_p'/4a^2}}{(2n+1)^2\pi^2}\sin\frac{(2n+1)\pi x}{2a}\right] \qquad [50]$$

which can be simplified under conditions [44] to

$$c_{Ox}(x, t_p') \simeq \left[\frac{2q_d}{\mathbf{F}a} + 2c_i\right]\frac{x}{a} + \left[\frac{2q_d}{\mathbf{F}a}\left(1 - \frac{8}{\pi^2}\right) + \frac{4c_i}{\pi}\left(1 - \frac{4}{\pi}\right)\right] e^{-\pi^2 D t_p'/4a^2}\sin\frac{\pi x}{2a} \qquad [50']$$

which finally reduces for $t_p' \to \infty$ to

$$c_{Ox}(x, \infty) = \frac{2}{a}\left(\frac{q_d}{\mathbf{F}a} + c_i\right)x \qquad [50'']$$

as expected from Eq. [46] through [48].

With the help of Eq. [50''], it becomes relatively easy to estimate the rate of clearing of the light shutter on application of a pulse of charge density $q_d' \leqq q_d$ in the reverse (unplating) direction. It is worth noting first of all that the rate of clearing is lowest if the unplating pulse is applied at $t_p' \simeq \infty$ at which time the average displacement of the Ox particles from $x = a$ is at its maximum (cf. Fig. 4b, c, and d). Hence, the minimum clearing rate can be obtained by solving Eq. [36] with the boundary conditions

$$c_{Ox}(x, 0) = \frac{2}{a}\left(\frac{q_d}{\mathbf{F}a} + c_i\right)x \text{ for } t_u = 0 \qquad [50''']$$

and

$$c_{Ox}(0, t_u) = c_{Ox}(a, t_u) = 0 \text{ for } t_u > 0 \qquad [51]$$

the latter condition presumably remaining valid as long as the plated metal is present at both electrodes

[5] Cf. ref. (22) p. 104 for our boundary conditions [41] and [49'] setting a for l, D for K, and $i_p/\mathbf{F}$ for Q in C and J's Eq. 43 (2).

($x = 0$ and $x = a$). The solution to Eq. [36], [50‴] and [51] is[6]

$$c_{ox}(x, t_u) = \frac{4}{\pi}\left(\frac{q_d}{Fa} + c_i\right)\sum_{n=1}^{\infty}\frac{(-1)^{n-1}}{n} e^{-n^2\pi^2 D t_u/a^2}\sin\frac{n\pi x}{a} \quad [52]$$

which simplifies for $t_u \geq a^2/(\pi^2 D)$ to

$$c_{ox}(x, t_u) \simeq \frac{4}{\pi}\left(\frac{q_d}{Fa} + c_i\right)e^{-\pi^2 D t_u/a^2}\sin\frac{\pi x}{a} \quad [52']$$

The net fraction of metal removed at a time t_u is (by materials balance)

$$f_r(t_u) = [a\,c_i + (q_d/F) - \int_0^a c_{ox}(x, t_u)\,dx]/(q_d/F) \quad [53]$$

Substituting Eq. [19] into [20] one obtains

$$f_r(t_u) = \left(1 + \frac{a\,c_i F}{q_d}\right)\left[1 - \sum_{m=0}^{\infty}\frac{8e^{-(2m+1)^2\pi^2 D t_u/a^2}}{(2m+1)^2\pi^2}\right] \quad [54]$$

which simplifies for $t_u \geq a^2/\pi^2 D$ to

$$f_r(t_u) \simeq [1 - (8/\pi^2)\,e^{-\pi^2 D t_u/a^2}](q_d + a\,c_i F)/q_d \quad [54']$$

For example, for $c_i \simeq 0$, the degree of unplating is approximately 70% for $t_u = a^2/(\pi^2 D)$, 91% for $t_u = 2a^2/(\pi^2 D)$, and 97.3% for $t_u = 3a^2/(\pi^2 D)$. Hence, if the initial plating pulse yielded an optical density change δ between 3 and 4, the reverse pulse should reduce δ by 97.3%, *i.e.*, to $\delta \simeq 0.1$ (corresponding to 90% of the original transmission) within a time $t_u \leq 3a^2/\pi^2 D$. Thus, for $D \simeq 10^{-5}$ cm^2/sec, nearly complete clearing should occur within 30 msec for $a = 0.001$ cm, within 0.5 sec for $a = 0.004$ cm, and within 3 sec for $a = 0.01$ cm.

Equations [52] through [54'] are based on the boundary conditions [51] which are satisfied only as long as plated metal is present at both electrodes. It is, therefore, necessary to calculate the value of the reverse charge density q_d' required to maintain this condition up to the time $t_u \simeq 3a^2/\pi^2 D$ when nearly complete clearing has been achieved. Following integration of the total fluxes of Ox toward $x = 0$ and $x = a$ within the time interval between $t_u' = 0$ and $t_u' = 3a^2/\pi^2 D$, one can make use of the following materials balance requirements at the electrodes $x = a$ and $x = 0$

$$q_d'/F \geq \int_0^{3a^2/\pi^2 D}\vec{J}_{ox}(a, t_u')\,dt_u' \quad [55]$$

and

$$(q_d - q_d')/F \geq -\int_0^{3a^2/\pi^2 D}\vec{J}_{ox}(0, t_u')\,dt_u' \quad [56]$$

Equations [55], [35], and [52] yield

$$q_d'/F \geq \frac{4}{\pi^2}\left(\frac{q_d}{F} + ac_i\right)\sum_{n=1}^{\infty}[(1 - e^{-3n^2})/n^2] \quad [57]$$

which simplifies to

$$q_d'/F \simeq \frac{4}{\pi^2}\left(\frac{q_d}{F} + ac_i\right)\sum_{n=1}^{\infty}(1/n^2)$$

$$= \frac{2}{3}\left(\frac{q_d}{F} + ac_i\right) \quad [57']$$

[7]

Similarly, Eq. [56], [35], and [52] yield

$$(q_d - q_d')/F \geq \frac{4}{\pi^2}\left(\frac{q_d}{F} + ac_i\right)\sum_{n=1}^{\infty}[(-1)^{n-1}(1 - e^{-3n^2})/n^2] \quad [58]$$

which simplifies to

$$(q_d - q_d')/F \simeq \frac{4}{\pi}\left(\frac{q_d}{F} + ac_i\right)\sum_{n=1}^{\infty}\frac{(-1)^{n-1}}{n^2} = \frac{1}{3}\left(\frac{q_d}{F} + ac_i\right) \quad [58']$$

[7]

Conditions [57'] and [58'] are satisfied for

$$c_i << q_d/aF \quad [59]$$

and

$$q_d' \simeq (2/3)\,q_d \quad [60]$$

It should be noted that requirement [60] is based on the boundary condition [50‴] which follows a steady-state opaque shutter condition $t_p' \simeq \infty$. For $t_p' << \infty$, most of the Ox component is located near the $x = a$ electrode, hence q_d' should preferably be higher than (2/3) q_d. For example, for $t_p' = 0$, a value of $q_d' = q_d$ would theoretically yield an instantaneous clearing [assuming no spurious mixing, $\tau_p \simeq 0 \cong \tau_u$, and an infinite rate constant for reaction (V)]. If, in lieu of condition [50‴], a simplified approximation of Eq. [50'] be satisfactory for $t_p' << \infty$

$$C_{ox}(x, 0) \cong \frac{2q_d}{zFa}\left[1 + \frac{1}{2}e^{-\pi^2 D t_p'/4a^2}\right]\frac{x}{a} \text{ for } t_u = 0 \quad [50'''']$$

then condition [60] could be replaced by

$$q_d'/q_d \simeq [2 + e^{-\pi^2 D t_p'/4a^2}]/3 \quad [60']$$

Equation [60'] results in optimum q_d'/q_d ratios of unity for $t_p' = 0$ and of 2/3 for $t_p' \to \infty$, and in nearly optimum ratios for intermediate values of t_p'.

In practice, condition [60'] can be readily met, *e.g.*, by supplying the charge q_d' from two capacitors, one having a permanent charge $Q' = 2Q/3$, and one having an initial charge $Q'' = Q/3$ at $t_p' = 0$, and a parallel leakage resistance R_l such that the leakage time constant is

$$\tau_l = C_l R_l = 4a^2/\pi^2 D \quad [61]$$

where C_l is the capacitance of the leaking condenser.

Summary and Conclusions

1. For a maximum darkening efficiency or ratio of δ/q_d over the entire visible wavelength region, the plating of Ag from AgI solutions appears most suitable.

2. For a maximum plating speed, the concentration of AgI in the electrolyte should be as high as possible (see Eq. [33]). The highest achievable AgI

[6] Cf. ref. (22) pp. 76-89, Eq. 34 (10).

[7] The summations $\sum_{n=1}^{\infty} 1/n^2$ and $\sum_{n=1}^{\infty}(-1)^{n-1}/n^2$ are $\pi^2/6$ and $\pi^2/12$, respectively [cf. ref. (23)].

concentration in aqueous solution appears to be that of 150g AgI to 180g NaI and 100g H_2O (24) corresponding to a volume concentration of approximately 3.7M AgI (based on an approximate specific gravity value of 2.47 g/cc, as measured by the author). To avoid any precipitation due to temperature fluctuations, a slightly undersaturated solution of 3.0-3.5M AgI in 6.9M NaI is recommended.

3. Acidified solutions may tend to evolve H_2 at high plating speeds, whereas alkaline solutions will convert the light-absorbing I_3^- ions into colorless IO_3^- ions. Hence neutral solutions appear to be preferable for best shutter performance.

4. To achieve uniform plating over a large area, the most practical geometry is that consisting of adjacent, narrow-band subelements disposed as in arrangement 6 or, preferably, 7 of Fig. 2, with the spacing a between the electrodes being greater than $b^2/2k$ [Eq. (82)‡] or the width b of each subelement being less than $(2\,ka)^{1/2}$. On the other hand, for fast clearing rates, the spacing a should be as low as feasible (depending largely on achievable electrode surface flatness).

5. The maximum operable plating speed is an inverse square function of the plating charge density q_d and cannot exceed $40/q_d^2$ sec^{-1} for an electrolyte resistivity of 10 ohm-cm (cf. Eq. [29]). Hence to achieve both maximum speed and a high optical density change it is necessary to use several plating cells back-to-back.

6. To maintain a large-area shutter in the opaque state for an indefinitely long period of time and yet be able to achieve rapid clearing when desired, it is necessary to maintain a continuous plating current density i_p as given by Eq. [49], and, when desired, to apply an unplating charge density q_d' as given by Eq. [60']. The time required to revert to 90% of the original transmission should then be less than $3a^2/(\pi^2 D)$.

Acknowledgments

Stimulating and informative discussions with Doctors J. O'M. Bockris and J. Y. Chang and constructive suggestions by Dr. J. Stuart Fordyce have contributed to a general improvement of this paper. This work was supported by the Aerospace Medical Laboratory, Aeronautical Systems Division, Wright-Patterson Air Force Base, under Contract No. AF 33(616)-7928.

Manuscript received Feb. 12, 1962.

Any discussion of this paper will appear in a Discussion Section to be published in the June 1963 JOURNAL.

REFERENCES

1. F. H. Smith, British Pat. No. 328, 017 (1930).
2. G. C. Sziklai, U. S. Pat. No. 2, 632, 045 (1953).
3. F. Seitz, "Modern Theory of Solids," pp. 630-632, McGraw-Hill Book Co., New York (1940).
4. C. D. Hodgman, R. C. Weast, and S. M. Selby, "Handbook of Physics and Chemistry," Chemical Rubber Publishing Co., Cleveland (1958).
5. A. Vasicek, "Optics of Thin Films," pp. 354-356, and references of p. 395, Interscience Publishers, Inc., New York (1960).
6. P. Rouard, *Ann. phys.*, **7**, 346 (1937).
7. P. Cotton and P. Rouard, *J. phys. radium*, **11**, 469 (1950).
8. O. S. Heavens, "Optical Properties of Thin Solid Films," pp. 167, and 192-4; Butterworth Scientific Publications, London (1955); also *Rept. Progr. Phys.*, **23**, 1 (1960).
9. A. D. Awtrey and R. E. Connick, *J. Am. Chem. Soc.*, **73**, 1842 (1951).
10. J. J. Custer and S. Natelson, *Anal. Chem.*, **21**, 1005 (1949).
11. A. Levin, *J. Phys. Chem. Moscow*, **18**, 53 (1944).
12. J. O'M. Bockris, "Modern Aspects of Electrochemistry," pp. 180-276, especially pp. 191 and 219, Academic Press, New York (1954).
13. E. B. Sarigar, *Trans. Electrochem. Soc.*, **59**, 307 (1931).
14. M. Schlotter, German Pat. No. 608268 (1932).
15. R. Weiner, *Z. Elektrochem.*, **45**, 757 (1939).
16. M. Schlotter, J. Korpiun, and W. Burmeister, *Z. Metallkunde*, **25**, 107 (1933).
17. K. H. Lieser, *Z. anorg. u. allgem. chem.*, **292**, 97 (1957).
18. G. Kortüm and J. O'M. Bockris, "Textbook of Electrochemistry," pp. 400-408, Elsevier Publishing Co., New York (1951).
19. S. Zaromb, *This Journal*, **109**, 912 (1962).
20. P. Delahay, "New Instrumental Methods in Electrochemistry," pp. 184-6, Interscience Publishers, Inc., New York (1954).
21. B. Pogany, *Ann. Physik*, **49**, 531 (1916).
22. H. S. Carslaw and J. C. Jaeger, "Conduction of Heat in Solids," pp. 76-80, 83, 104, and 297-8, Oxford University Press, London (1948).
23. W. Kaplan, "Advanced Calculus," p. 398, exercises 6(c) and (d), Addison-Wesley Publishing Co., Inc., Cambridge, Mass. (1953).
24. W. F. Linke and A. Seidell, "Solubilities," vol. I, p. 95, D. Van Nostrand & Co., Princeton (1958).

SYMBOLS

a	x-component of the distance between the origins O_1 and O_2
A	total area of light shutter
A_s	area of one-cell subelement in a multicell shutter
b	maximum value of y, y_1, or y_2
C_1, C_2, C_{1+}, C_{2-}, C_{2+}	current collecting contacts
C_l	capacitance of condenser having a parallel leakage resistance R_l
c_i	average value of c_{Ox} before the occurrence of plating
c_{Ox}	concentration of Ox component in g-equivalents/cc
c_p	concentration of platable ions in moles/cc
c_s	solubility limit of Ox in the electrolyte
d	density in g/cc
D	diffusion coefficient
D'	effective diffusion coefficient
$f_r(t_u)$	fraction of plated metal removed at time t_u
F	Faraday or 96,500 coul.
g', g_1', g_2'	flat transparent (glass) electrodes
H	energy dissipated upon passage of plating pulse
h_e	heat capacity of the electrolyte per unit volume
i	current density
i_c	continuous cathode current density
i_L	limiting continuous current density
i_{max}	maximum allowable current density
i_p	continuous plating current density required to maintain a desired opacity
I_c	current at the collecting contacts
I_i	intensity of incident light
I_t	intensity of transmitted light
$\vec{J}_{Ox}$	current density of Ox component
k	ρ_e/ρ_g'
L	length of cell in the direction perpendicular to Fig. 2 through 4.
M	plated metal
n	index of refraction
n_s	number of subelements in large-area shutter
Ox	oxidizing component in the electrolyte
p	number of anions in a complex ion
Q	over-all required plating charge
Q_p	value of Q for a cell with subelements con-

	nected in parallel
Q_s	value of Q for a cell with series-connected subelements
q_{pl}	plating charge density in coul/cm²
q_{pl}'	unplating charge density
q_s	plating charge per subelement
r_s	resistance of a single-cell subelement
r_{sm}	resistance of a mirror-symmetric subelement
r_{sl}	resistance of a line-symmetric subelement
R	gas constant
R_c	over-all cell resistance
R_i	resistance connected in parallel with a capacitance C_i
R_p	over-all resistance of cell having subelements connected in parallel
R_s	over-all resistance of cell with series-connected subelements
Red^-	reduced form of Ox
t_+	transport number of the cations
t_p	time after the start of a plating pulse
t_p'	$t_p - \tau_p$
t_u	time after the start of an unplating pulse
t_u'	$t_u - \tau_u$
T	absolute temperature
v_e	volume of electrolyte
V_{c1}, V_{c2}	potentials of contacts C_1, C_2
$V_{g'1}$, $V_{g'2}$	potential at electrode g'_1, g'_2, respectively
w	total width of large-area light shutter
W	atomic weight
x	distance along the direction parallel to the cell walls and the main current flow lines
x_s	thickness of Ox-saturated electrolyte layer
y_1	distance along the direction perpendicular to the cell walls and the x-direction [cf. ref. (19)]
z	oxidation state of platable ions
α	coefficient of light absorption
γ	constant defined by Eq. (59) of ref. (19)
δ	optical density change due to plating
Δc_{Ox}	increment in c_{Ox} corresponding to Δx
ΔT	rise in temperature due to high current pulse
ΔT_{max}	maximum allowable temperature rise
Δx	increment in x
ϵ	plating current efficiency
η	electrode overpotential
θ	thickness of an electrodeposited, light-absorbing metal layer
κ	light absorption index
λ	light wavelength
ρ_e	volume resistivity of the electrolyte solution
$\rho_{g'}$, $\rho_{g'1}$, $\rho_{g'2}$	respective surface resistivities of transparent conductors g', g'_1, g'_2
τ_{min}	minimum allowable plating time
τ_p	duration of plating pulse
τ_{trans}	transition time
τ_u	duration of unplating pulse

Geometric Requirements for Uniform Current Densities at Surface-Conductive Insulators or Resistive Electrodes

Solomon Zaromb[1]

Research Division, Philco Corporation, Blue Bell, Pennsylvania

ABSTRACT

The conditions for practically uniform current densities in the presence of ohmic potential drops along electrode surfaces are established for several configurations. Perfectly uniform current flow lines in the electrolyte can be obtained within limited ranges, with electrodes having cylindrical surfaces traced by Eq. [9], or be closely approximated with electrodes in the form of parabolic cylindrical or paraboloid segments traced by Eq. [11] or [20] or [22]. For practically uniform current densities at either curved or flat electrodes, the areas must be limited to narrow bands, rings, or small circles, as indicated in Fig. 2 or by Eq. [38], [49], [68], or [92]. For identical flat narrow-band electrodes perpendicular to the cell walls, a mirror-symmetric arrangement of external current-collecting contacts is shown to require a fourfold larger minimum electrode spacing than a line-symmetric arrangement.

In the Reversible Electroplating Light Modulator (RELM) (1-3), as well as in other devices or experiments involving reactions at semiconducting or even very thin metallic electrodes, the current density distribution may be seriously affected by ohmic potential drops along the electrode surfaces. The conditions for maintaining essentially uniform current densities in spite of nonuniform surface potentials are established in the following sections for several cell configurations.

Case 1. Perfectly Uniform Parallel Current Flow Lines in the Electrolyte

Let J_x be the current density in the electrolyte along the x-direction perpendicular to the surface of a rectangular (highly conducting) metal electrode M. The shape of a surface-conductive glass electrode g (Fig. 1a) required for J_x to be uniform will now be determined. Let x and y be the horizontal and vertical coordinates of any point P on the curve s_g defining the glass surface. The surface current I_g flowing along the glass surface toward the collector strip C (outside the cell) is then given by

$$I_g = L \int_0^y J_x \, dy \qquad [1]$$

where L is the length of the cell along the direction perpendicular to the plane of Fig. 1a. The difference in potential between points $P_1(x, y)$ and $P_2(x + dx, y + dy)$ on the curve s_g then becomes

$$-dV_g = (I_g/L)\rho_g \, ds_g \qquad [2]$$

$$= \rho_g \left(\int_0^y J_x \, dy\right) ds_g = \rho_g J_x \, y \, ds_g \qquad [2']$$

where ρ_g is the surface resistivity of the glass. On the other hand, assuming no change in overvoltage between the points P_1 and P_2 (*i.e.*, essentially uniform

[1] *Present address:* Research and Advanced Technology Department, Electronic Systems and Products Division, Martin-Marietta Corporation, Baltimore, Maryland.

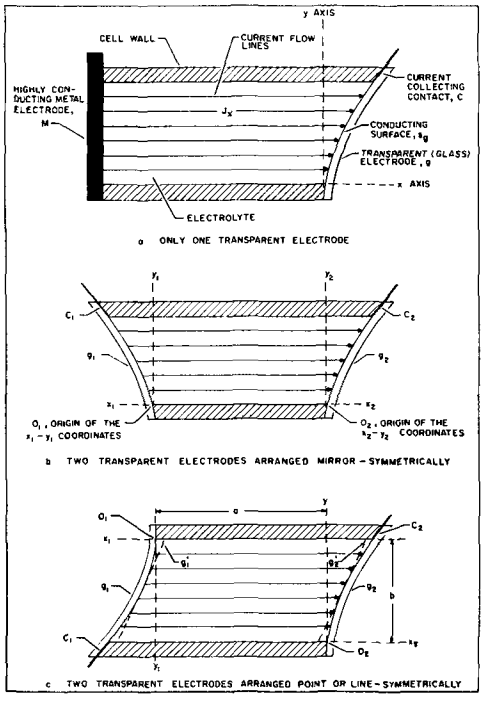

Fig. 1. Plating cells with parallel current flow lines in the electrolyte: (a) only one transparent electrode (b) two transparent electrodes arranged mirror-symmetrically (c) two transparent electrodes arranged point- or line-symmetrically.

current density), dV_g may be readily calculated by following a path through the electrolyte

$$-dV_g = J_x \rho_e dx \qquad [3]$$

where ρ_e is the resistivity of the electrolyte. Equations [2'] and [3] yield

$$ds_g/dx = \rho_e/(\rho_g y) \qquad [4]$$

but for any curve

$$ds_g/dx = [1 + (dy/dx)^2]^{1/2} \qquad [5]$$

Hence,

$$\frac{dy}{dx} = \frac{\rho_e}{\rho_g}\left[\frac{1}{y^2} - \frac{\rho_g^2}{\rho_e^2}\right]^{1/2} \qquad [6]$$

$$= (k^2 - y^2)^{1/2}/y \qquad [6']$$

where

$$k = \rho_e/\rho_g \qquad [7]$$

Rewriting [6']

$$dx = y\,dy/[k^2 - y^2]^{1/2} = -d[k^2 - y^2]^{1/2} \qquad [8]$$

one obtains

$$x = k\{1 - [1 - (y/k)^2]^{1/2}\} \qquad [9]$$

Equation [9] is plotted in Fig. 2. For

$$y << k \qquad [10]$$

one obtains by expansion

$$x \simeq y^2/2k \qquad [11]$$

and

$$x << y \qquad [12]$$

i.e., electrode g is almost parallel to M, and the actual current density on the glass surface

$$i_g = J_x\,dy/ds_g \qquad [13]$$

which, according to Eq [4] and [8], is

$$i_g = J_x[1 - (y/k)^2]^{1/2} \qquad [14]$$

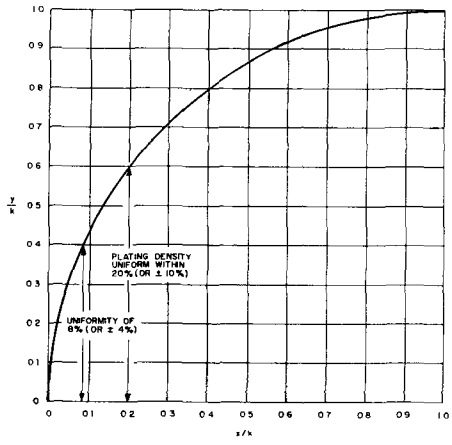

Fig. 2. Plot of Eq. [9]

becomes approximately uniform for condition [10]

$$i_g \simeq J_x \qquad [15]$$

As shown in Table I, Eq. [11] and [15] deviate from Eq. [9] and [14] by less than 10% for values of y/k up to 0.6 and 0.4, respectively.

The range for which J_x can be constant is, therefore, $0 \leq y/k \leq 1$ according to Eq. [9], while the range of fairly uniform electrode current density (Eq. [15]) is $0 \leq y/k \leq 0.4$ for a uniformity of 8% (*i.e.*, ±4%), and $0 < y/k < 0.6$ for a uniformity of 20% (or ±10%).

Similar calculations may be attempted for the cylindrical cell obtained by rotating Fig. 1a around the x-axis. For this case, Eq. [1] must be replaced by

$$I_g = \int J_x 2\pi y dy = 2\pi J_x \int y dy \qquad [16]$$

and Eq. [2] by

$$-dV_g = \frac{\rho_g I_g}{2\pi s_g} ds_g \qquad [17]$$

$$= \rho_g J_x (\int y dy)\, ds_g/s_g \qquad [17']$$

Combining Eq. [17'], [3], and [5], one obtains

$$\rho_e dx = \rho_g (\int y dy)\, ds_g/s_g \qquad [18]$$

$$= \rho_g (\int y dy)\, \frac{[1 + (dy/dx)^2]^{1/2} dx}{\int [1 + (dy/dx)^2]^{1/2} dx} \qquad [18']$$

Table I. Numerical comparisons of Eq. [9], [11], [14], and [15]

$\frac{y}{k}$	[14]/[15] $\sqrt{1-\frac{y^2}{k^2}}$	[9] $x/k = 1-\sqrt{\quad}$	[11] $y^2/2k^2$	$\frac{[9]-[11]}{[9]}$ $\frac{\frac{x}{k} - \frac{y^2}{2k^2}}{x/k}$
0.01		5×10^{-5}	5×10^{-5}	0
0.1	0.995	5×10^{-3}	5×10^{-3}	0
0.2	0.98	0.02	0.02	0
0.3	0.954	0.046	0.045	0.02
0.4	0.915	0.085	0.08	0.06
0.5	0.864	0.136	0.125	0.08
0.6	0.80	0.20	0.18	0.10
0.8	0.60	0.40	0.32	0.20
0.9	0.436	0.564	0.405	0.29
0.95	0.320	0.68	0.449	0.30
1.0		1.0	0.5	0.50

$$= \rho_s(\int y dy)\frac{[1 + (dx/dy)^2]^{1/2}dy}{\int[1 + (dx/dy)^2]^{1/2}dy} \quad [18'']$$

There does not appear to exist an analytical solution to Eq. [18]; however, the limiting case

$$(dy/dx) >> 1 \quad [19]$$

yields

$$(\rho_e/\rho_s)\,dx = k dx \simeq d(y^2)/4 \quad [20]$$

or

$$x \simeq y^2/4k \quad [20']$$

Equations [19] and [20'] are obviously equivalent to those obtained for the rectangular cell, Eq. [15] and [11].

Another approximate solution of Eq. [18] may be obtained for a cell comprising the annular space between two concentric cylinders of inner radius r_1 and outer radius r_2. Then, for the case

$$(dy/dx) << 1 \quad [21]$$

Eq. [18'] yields

$$x \simeq (y^2 - r_1^2)/2k \quad [22]$$

which is valid for

$$y/k >> 1 \quad [23]$$

The electrode current density then becomes

$$i_s \simeq J_x dy/dx \quad [24]$$

$$\simeq (k/y)J_x \quad [24']$$

which may be fairly uniform if the maximum radius r_2 is not much larger than r_1.

For either of the three configurations discussed above (rectangular, circular, and annular), the metal electrode M could be replaced by a second conducting glass electrode satisfying one of the appropriate Eq. [9], [11], [20'], or [22], as shown in Fig. 1b and 1c.

In Fig. 1b, the electrodes g_1 and g_2 and their current collectors C_1 and C_2 are arranged symmetrically with respect to a central plane so that the relations between their mirror-symmetric coordinates are

$$dy_1 = dy_2 \quad \text{and} \quad dx_1 = dx_2 \quad [25]$$

In Fig. 1c, the symmetry is with respect to a central point (or line perpendicular to the drawing in the rectangular cell) so that

$$dx_1 = -dx_2 \quad \text{and} \quad dy_1 = -dy_2 \quad [26]$$

Case 2. Flat Electrodes Causing a Minimal Nonuniformity in J_x

The line-symmetric arrangement is of special interest for cells utilizing parallel, flat, conducting glass electrodes, as indicated by the dotted straight lines g'_1 and g'_2 in Fig. 1c. The following calculations will now show under what conditions parallel, flat, glass electrodes can yield essentially uniform plating.

Considering first the rectangular cell, let the origins of x_1, y_1 and x_2, y_2 correspond to that of Eq. [19] or [11], and let the spacing between these origins be a and b along the x- and y-directions, respectively, as shown in Fig. 1c. Then

$$y_2 = b - y_1 \quad [27]$$

and the total spacing X between g_1 and g_2 for any value of y_1 is

$$X = a + x_1 + x_2 \quad [28]$$

Applying Eq. [9] to curves g_1 and g_2 and combining with Eq. [27] and [28], one obtains

$$X = a + k_1\{1 - [1 - (y_1/k_1)^2]^{1/2}\} + k_2\{1 - [1 - (y_2/k_2)^2]^{1/2}\} \quad [29]$$

$$= a + k_1 + k_2 - [k_1^2 - y_1^2]^{1/2} - [k_2^2 + 2by_1 - y_1^2 - b^2]^{1/2} \quad [29']$$

where k_1 and k_2 are the values of ρ_e/ρ_{s1} and ρ_e/ρ_{s2} corresponding to the surface resistivities ρ_{s1} and ρ_{s2} of electrodes g_1 and g_2. Where condition [10] is satisfied, Eq. [29] may be simplified to

$$X \simeq a + \frac{y_1^2}{2k_1} + \frac{y_1^2 - 2y_1b + b^2}{2k_2} \quad [30]$$

Furthermore, for

$$k_1 \simeq k_2 = k \quad [31]$$

one obtains

$$X \simeq a + (2y_1^2 - 2y_1b + b^2)/2k \quad [32]$$

The rate of change of X

$$dX/dy \simeq \frac{y_1}{k_1} + \frac{y_1 - b}{k_2} \quad [33]$$

will be zero for

$$(y_1)_{min} = \frac{bk_1}{k_1 + k_2} \quad [34]$$

resulting in a minimum spacing

$$X_{min} \simeq a + \frac{b^2}{2(k_1 + k_2)} \quad [35]$$

The maximum spacing, on the other hand, corresponds to either $y_1 = 0$ or $y_1 = b$, depending on the ratio of k_1 to k_2

$$X_{max} \simeq a + \frac{b^2}{2k_2} \quad \text{for } k_1 > k_2 \quad [36]$$

$$\simeq a + \frac{b^2}{2k_1} \quad \text{for } k_2 > k_1 \quad [36']$$

Hence, the maximum variation in spacing is

$$X_{max} - X_{min} \simeq \frac{b^2}{2k_2(\text{or } k_1)} - \frac{b^2}{2(k_1 + k_2)} \quad [37]$$

$$\simeq \frac{b^2}{4k} \text{ for } k_1 = k_2 \quad [37']$$

If the curved electrodes g_1 and g_2 in Fig. 1c are now replaced by the parallel, flat electrodes g'_1 and g'_2 separated by the distance a (equal to the actual spacing for all values of y_1), then the maximum resulting nonuniformity in J_x should be, in first approximation, (cf. Eq. [37])

$$u = (J_x)_{max}/(J_x)_{min} \simeq \frac{a + (b^2/8k)}{a - (b^2/8k)} \quad [38]$$

i.e., the plating current density should remain essentially uniform as long as $b^2/4ka << 1$, and should deviate from the average by a maximum of $\pm 25\%$ for $a \simeq b^2/2k$.

Equation [38] is based on the assumptions that (*a*) the potentials corresponding to any value of y are still approximately the same for the flat electrodes g'_1 and g'_2 as for the ideal electrodes g_1 and g_2; and (*b*) the current flow vectors J_x still remain essentially parallel and in the x-direction, *i.e.*, that the y components due to the deviation from the ideal geometry of Fig. 1c are negligible. Hence, any local variations in J_x would be dependent mainly on the deviation of the local resistance or length of path through the electrolyte along the x-direction from the value required by Eq. [32].

In order for assumption (*b*) to be nearly true, the slope $m = dx/dy$ of the parallel plates g'_1 and g'_2 should equal the average slope of the curves g_1 and g_2. Hence, according to Eq. [11], the optimum slope

$$m_{opt} = \frac{\int (dx/dy)\,dy}{\int dy} \simeq \frac{\int_0^b (y/k)\,dy}{b} \simeq \frac{b}{2k} \quad [39]$$

The same result can be obtained by setting

$$x' = my + e \quad [40]$$

as the equation of the line g', and

$$x = y^2/2k \quad [11]$$

as that of curve g, and minimizing the root-mean-square deviation:

$$\int_0^b (x - x')^2\,dy = \text{minimum} \quad [41]$$

Substituting Eq. [40] and [11], integrating the left-hand side, and setting the derivatives of the resulting integral with respect to m and to e equal to zero, one obtains

$$e = -b^2/12k \quad [42]$$

and

$$m_{opt} = b/2k \quad [43]$$

as in Eq. [39].

It may be noted that the optimum slope m_{opt} of Eq. [39] and [43] applies not only to the line-symmetric arrangement discussed in connection with Eq. [26] through [38], but also to cells with only one transparent and one solid metal electrode, or with two mirror-symmetrically arranged transparent conductors as in Fig. 1a and 1b, in which cells, however, the electrodes are not parallel. For cells with one solid metal electrode (Fig. 1a) the total spacing becomes

$$X = a + (y^2/2k) \quad [44]$$

Upon substitution of the curved electrode g by a flat electrode g' with the optimum slope of $b/2k$, the spacing X' becomes

$$X' = a + (by/2k) \quad [45]$$

The deviation

$$X' - X = (by - y^2)/2k \quad [46]$$

is maximum for

$$b - 2y_{max} = 0 \quad [47]$$

which yields

$$(X' - X)_{max} = b^2/8k \quad [48]$$

Since the minimum value of $X' - X$ is 0 for $y = 0$, the resulting nonuniformity ratio u using a similar reasoning as for Eq. [37] and [38] becomes

$$u \simeq \frac{a + (b^2/16k)}{a - (b^2/16k)} \quad [49]$$

Similarly, for a cell with mirror-symmetric flat electrodes of slope $b/2k$, it is easy to show that the nonuniformity ratio u is also given by Eq. [38].

Case 3. Parallel, Flat, Transparent Electrodes

A more general calculation can be made of the current-density distribution between two flat, transparent conductors having any slope m.

Let

$$\Delta V_{g'} = (V_{g'_1} - V_{g'_2})_{y_1} \quad [50]$$

and

$$\Delta I_{g'} = (I_{g'_1} - I_{g'_2})_{y_1} \quad [51]$$

be the difference between the surface potentials and currents at the flat electrodes g'_1 and g'_2 for a given value of y_1. Then by Eq. [1], and the above assumption (*b*) (current flow lines essentially parallel to J_x) one can write

$$dI_{g'_1}/dy_1 = LJ_x = -dI_{g'_2}/dy_1 \quad [52]$$

and

$$d\Delta I'_g/dy_1 = 2LJ_x \quad [53]$$

Also, by Ohm's law,

$$J_x = -\Delta V_{g'}/(a\rho_e) \quad [54]$$

and

$$d\Delta V_{g'}/dy_1 = (I_{g'_2}\rho_{g'_2} - I_{g'_1}\rho_{g'_1})(1 + m^2)^{1/2}/L \quad [55]$$

(cf. also Eq. [2] and [5], which become for identical electrodes ($\rho_{g'_1} = \rho_{g'_2} = \rho_{g'}$)

$$d\Delta V_{g'}/dy_1 = \rho_{g'}\Delta I_{g'}(1 + m^2)^{1/2}/L \quad [55']$$

Equations [53] and [54] yield

$$-d\Delta I_{g'}/dy_1 = 2L\Delta V_{g'}/(a\rho_e) \quad [56]$$

Differentiating Eq. [55'] and [56] and cross-substituting, one obtains

$$d^2\Delta V_{g'}/dy_1^2 = 2\Delta V_{g'}(1 + m^2)^{1/2}\rho_{g'}/a\rho_e = \gamma^2\Delta V_{g'} \quad [57]$$

and

$$d^2\Delta I_{g'}/dy_1^2 = \gamma^2\Delta I_{g'} \quad [58]$$

where

$$\gamma^2 = 2(1 + m^2)^{1/2}\rho'_g/(a\rho_e) = 2(1 + m^2)^{1/2}/(ak) \quad [59]$$

If I_c is the total current at the external line-symmetrically arranged contacts C_1 and C_2, then the boundary conditions are

$$\Delta I_{g'} = I_{g'_2} = -I_c \text{ for } y_1 = 0 \quad [60]$$

$$\Delta I_{g'} = I_{g'_1} = I_c \text{ for } y_1 = b \quad [61]$$

and finally, by symmetry

$$\Delta I_{g'} = 0 \text{ for } y_1 = b/2 \quad [62]$$

The solution to Eq. [55'] through [62] is

$$\Delta I_{g'} = I_c \sinh[\gamma(b/2 - y_1)]/\sinh(\gamma b/2) \quad [63]$$

and

$$\Delta V_{g'} = -K_o \cosh[\gamma(b/2 - y_1)]/\sinh(\gamma b/2) \quad [64]$$

where

$$K_o = \gamma a\rho_e I_c/2L = \rho_{g'} I_c(1 + m^2)^{1/2}/(\gamma L) \quad [65]$$

The minimum value of $|\Delta V_{g'}|$ corresponds to $y_1 = b/2$ (cf. Eq. [55'] and [62])

$$|\Delta V_{g'}|_{min} = -K_o/\sinh(\gamma b/2) \quad [66]$$

while the maximum value, corresponding to $y_1 = 0$ or $y_1 = b$, is

$$|\Delta V_{g'}|_{max} = -K_o \coth(\gamma b/2) \quad [67]$$

Hence, according to Eq. [54], [66], and [67]

$$u = (J_x)_{max}/(J_x)_{min} = \cosh(\gamma b/2) \quad [68]$$

For $m \simeq 0$, the uniformity ratio exceeds 0.98 for $\gamma b \leq 0.4$, or $b^2/4ka \leq 0.02$ (cf. Eq. [59]). Similarly, $u > 0.88$ for $\gamma b \leq 1.0$, and $u \geq 0.65$ for $\gamma b \leq 2.0$ or $a \geq b^2/2k$, which agrees with the results of Eq. [38].

The currents $I_{g'1}$ and $I_{g'2}$, and potentials $V_{g'1}$ and $V_{g'2}$ at the two electrodes can now be obtained. From Eq. [1], [54], and [63] through [65] one obtains

$$I_{g'1} = L\int_o^y J_x dy = \frac{-L}{a\rho_e}\int_o^y \Delta V'_g dy \quad [69]$$

$$= (I_c - \Delta I'_g)/2 \quad [69']$$

similarly,

$$I_{g'2} = (I_c + \Delta I'_g)/2 \quad [70]$$

Also, from Eq. [2], [5], [59], and [63] through [65]

$$V_{g'1} = \int dV_{g'1} = \frac{-\rho_g(1+m^2)^{1/2}}{L}\int I_{g'1}dy_1 \quad [71]$$

$$= [\Delta V_{g'} - \gamma K_o y_1 + 2V_o]/2 \quad [71']$$

where the constant V_o depends on the chosen reference potential. Similarly,

$$V_{g'2} = [-\Delta V_{g'} - \gamma K_o y_1 + 2V_o]/2 \quad [72]$$

The variation of $V_{g'1}/K_o$ and $V_{g'2}/K_o$ with γy_1 is shown in Fig. 3a for $\gamma b = 1.0$. The dotted line in Fig. 3a gives the potential in the midplane between the two electrodes, which is

$$(V_{g'1} + V_{g'2})/2 = -\gamma K_o y_1/2 \quad [73]$$

according to Eq. [71'] and [72].

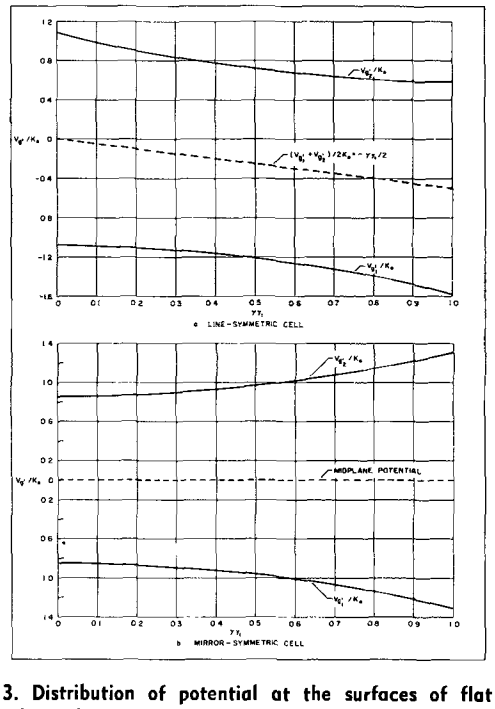

Fig. 3. Distribution of potential at the surfaces of flat transparent electrodes g'1 and g'2 (solid lines) and their midplane (dashed lines): (a) line-symmetric cell (b) mirror-symmetric cell.

Now, in order to have no flow in the electrolyte along the y_1-direction, the slope m of the electrodes g'_1 and g'_2 and their midplane should be such that

$$-\rho_e J_x dx = -\gamma K_o dy_1/2 \quad [74]$$

(cf. Eq. [3] and [73]) or

$$m_{opt} = \gamma K_o/(2\rho_e J_x) \quad [75]$$

But the average value of J_x is

$$(J_x)_{av} = I_c/bL \quad [76]$$

Hence,

$$m_{opt} = \gamma K_o bL/2\rho_e I_c \quad [77]$$

$$\simeq b/2k \quad [77']$$

(cf. Eq. [65] and [7] which confirms the above-derived Eq. [39], and also the approximate validity of the above assumption (b) under condition [77'].

Equation [73] also yields an estimate of the deviation from assumption (b) in cases where the slope m differs from that of Eq. [77]. Especially, for $m = 0$ (*i.e.*, electrodes perpendicular to the x-direction), the perpendicular component of the current flow J_y, in the central plane is by Ohm's law and Eq. [73]

$$J_y = \gamma K_o/(2\rho_e) \quad [78]$$

$$= I_c/(2kL) \text{ (cf. Eq. [7] and [65])} \quad [78']$$

and by Eq. [76] and [77]

$$J_y/(J_x)_{av} = b/2k \simeq m_{opt} \quad [79]$$

which means that the use of a slope differing from m_{opt} is equivalent to the introduction of spurious edge effects at $y_1 = 0$ and $y_1 = b$, resulting in distorted current flow lines, as shown in Fig. 4. To estimate the effect of these distortions on the current density distribution, one may calculate the respective spreading and compression of the flow lines at the lower and upper halves of electrode g'_1. From Eq. [79] one obtains

$$\Delta s/(a/2) = b/(2k) \quad [80]$$

Hence, the fractional spreading or compression of flow lines is of the order of

$$\Delta s/(b/2) \simeq a/(2k) \quad [81]$$

For the resulting nonuniformity to be below ±20%, it is necessary that $a \leq 2k/5$. But Eq. [68] requires that $a \geq b^2/2k$. **Hence,**

$$\text{for } m = 0,\ 2k/5 \geq a \geq b^2/2k \quad [82]$$

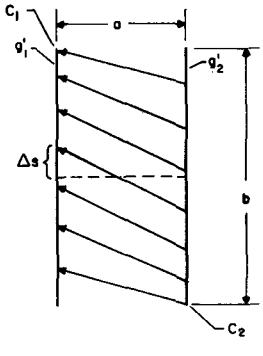

Fig. 4. Compression and spreading of current flow lines for m = 0

In cases where the a dimension may have to be larger than $2k/5$, the perpendicular flow component J_y may be eliminated by using a mirror-symmetric electrode and contact arrangement. The boundary conditions then become

$$\Delta I_{g'} = I_{g'_1} = I_{g'_2} = 0 \quad \text{for } y = 0 \qquad [83]$$

and

$$\Delta I_{g'} = 2I_c \quad \text{for } y = b \qquad [84]$$

Equations [55'] through [59], together with [83] and [84], yield

$$\Delta V_{g'} = 2K_o \cosh(\gamma y)/\sinh(\gamma b) \qquad [85]$$

$$\Delta I_{g'} = 2I_o \sinh(\gamma y)/\sinh(\gamma b) \qquad [86]$$

$$I_{g'_1} = I_{g'_2} = \Delta I_{g'}/2 \text{ (by symmetry)} \qquad [87]$$

$$V_{g'_1} = (\Delta V_{g'}/2) + V_o \qquad [88]$$

$$V_{g'_2} = -(\Delta V'_g/2) + V_o \qquad [89]$$

as shown in Fig. 3b. Finally,

$$|\Delta V_{g'}|_{max} = -2K_o \coth(\gamma b) \qquad [90]$$

$$|\Delta V_{g'}|_{min} = -2K_o \operatorname{csch}(\gamma b) \qquad [91]$$

and

$$u = |J_{mg'}|_{min}/|J_{mg'}|_{max} = |\Delta V_{g'}|_{min}/|\Delta V_{g'}|_{max} = \operatorname{sech}(\gamma b) \qquad [92]$$

For $m = 0$, $u \geq 0.89$ for $\gamma b \leq 0.5$ or $b^2/4ka \leq 0.03$ (cf. Eq. [59]), and $u \geq 0.65$ for $\gamma b \leq 1.0$ or $a \geq 2b^2/k$. Comparison of these results with those of Eq. [68] shows that the mirror-symmetric arrangement with flat electrodes perpendicular to the cell walls requires a minimum electrode spacing 4 times larger than the line-symmetric arrangement for the same electrode widths b.

Conclusions

The problem of current distribution may be extremely complex even for flat, parallel, metallic conductors (4, 5), and becomes further complicated by necessarily uneven voltage drops along the surface of poorly conducting electrodes, as shown in the preceding calculations. For the cell of Fig. 1a, the requirement for uniform, parallel current flow lines is that the conducting surface g be traced by the curve s defined by Eq. [9] or [11]. For $0 < y/k < 0.6$, the plating uniformity is then 20% (or ± 10%), as shown in Table I and Fig. 2.

The surface g may be either a cylindrical segment of length L perpendicular to the plane of Fig. 1a, or a surface of revolution obtained by revolving Fig. 1a around the x-axis. In the latter case, the curve s should approximate Eq [20']. Fair plating uniformity can also occur in an annular cell obtained by revolving the curve of Eq. [22] provided that $k << r_1 \leq r_2 \leq 1.5\, r_1$.

The above equations obviously remain unchanged when the highly conducting solid metal electrode M of Fig. 1a is replaced by a second surface-conductor arranged mirror-symmetrically as in Fig. 1b or center-or line-symmetrically as in Fig. 1c.

On replacing the curved electrodes g, g_1, g_2 of Fig. 1 by flat surface-conductors a minimal distortion in current flow lines will occur if the slope m of Eq. [40] satisfies Eq. [43]. The nonuniformity ratio u of maximum-to-minimum plating current density is then given approximately by Eq. [38] for the arrangements of Fig. 1b and 1c. Hence, for a plating uniformity better than ± 20%, it is necessary that $a \geq b^2/2k$. Similarly, for the arrangement of Fig. 1a, the same uniformity requires a minimum spacing $a \geq b^2/4k$ (cf. Eq. [49]).

A clearer and more complete analysis of the potential and current density distributions at the surfaces of flat, transparent conductors having any slope m is afforded by Fig. 3 (Eq. [50] through [92]). For $m = 0$ (electrodes perpendicular to the cell walls), the required minimum spacing is again shown to be $a \geq b^2/2k$ for the line-symmetric cells (Eq. [68]), but four times larger, $a \geq 2b^2/k$, for mirror-symmetric cells (Eq. [92]). On the other hand, with large electrode spacings, the line-symmetric cells may be subject to the distortions in current flow lines shown in Fig. 4. Hence, for satisfactory uniformity, the spacing in such cells must be in the range

$$b^2/2k \leq a \leq 2k/5 \qquad [82]$$

No such upper limit appears to exist for the spacing of mirror-symmetric electrodes, but a large spacing is usually not compatible with high efficiency and operating speed (1, 2).

Acknowledgments

Thanks are due to Doctors J. O'M. Bockris and J. Y. Chang for stimulating discussions and to the Aerospace Medical Laboratory, Aeronautical Systems Division, Wright-Patterson Air Force Base for support under Contract No. AF 33(616)-7928.

Manuscript received Feb. 12, 1962.

Any discussion of this paper will appear in a Discussion Section to be published in the June 1963 JOURNAL.

REFERENCES

1. S. Zaromb, *This Journal*, **109**, 903 (1962).
2. S. Zaromb and J. Y. Chang, *ibid.*, To be published.
3. J. Mantell and S. Zaromb, *ibid.*, **109**, 992 (1962).
4. C. Wagner, *ibid.*, **98**, 116 (1951), and references quoted therein.
5. R. H. Rousselot, *Metal Finishing*, **57**, 56 (1959), and quoted references.

SYMBOLS

a	x-component of the distance between the origins O_1 and O_2
b	maximum value of y, y_1, or y_2
C, C_1, C_2	current collecting contacts
e	intercept of planar electrode on the x-axis
g, g_1, g_2	surface-conductive glass electrodes with curved surfaces
g', g'_1, g'_2,	flat glass electrodes
I_c	current at the collecting contacts
$I_{g'}$, $I_{g'_1}$, $I_{g'_2}$	surface current along glass electrode g, g'_1, g'_2, respectively
J_x	current density in the electrolyte in the x-direction
J_y	current density in the electrolyte in the y-direction
k, k_1, k_2	respective ratios ρ_e/ρ_g, ρ_e/ρ_{g_1}, ρ_e/ρ_{g_2}
K_o	constant defined by Eq. [65]
L	length of cell in the direction perpendicular to the x- and y-axes
m	(inverse) slope of planar electrode as per Eq. [40]
m_{opt}	value of m yielding a minimum distortion in the current flow lines

M	highly conducting solid metal electrode
O_1 O_2	origins of the respective coordinate systems x_1-y_1 and x_2-y_2 in Fig. 1
P, P_1, P_2	points on electrode surface
r_1, r_2	radii of concentric cylinders confining annular plating cell
s, s_g	line and curve, respectively, defining the transparent conductor surfaces of Fig. 1
u	ratio of maximum to minimum current densities
V_g, $V_{g'_1}$, $V_{g'_2}$	potential at electrode g,g'$_1$,g'$_2$, respectively
X	x-spacing between electrodes g_1 and g_2
X'	x-spacing between electrodes g'$_1$ and g'$_2$
X_{min}	minimum value of X
X_{max}	maximum value of X
x	distance along the direction parallel to the cell walls and the main current flow lines
x_1, x_2	respective distances from the origins O_1 and O_2 of Fig. 1 along the x-direction
x'	x-coordinate for planar electrode g'
y	distance along the direction perpendicular to the cell walls and the x-direction
y_{max}	value of y corresponding to maximum $(X'$-$X)$
y_1, y_2	respective distances from the origins O_1 and O_2 along the y-direction
$(y_1)_{min}$	value of y_1 corresponding to X_{min}
γ	constant defined by Eq. [59]
$\Delta I_{g'}$	$(I_{g'_1} - I_{g'_2})_{y_1}$ (cf. Eq. [51])
Δs	y-distance between $y_1 = b/2$ and the mean current density line at an electrode (Fig. 4)
$\Delta V_{g'}$	$(V_{g'_1} - V_{g'_2})_{y_1}$ (Eq. [50])
ρ_e	volume resistivity of the electrolye solution
ρ_g, ρ_{g_1}, ρ_{g_2}, $\rho_{g'_1}$, $\rho_{g'_2}$	respective surface resistivities of glass electrodes g, g_1, g_2, g'$_1$, g'$_2$

The Effect of Some Addition Agents on the Kinetics of Copper Electrodeposition from a Sulfate Solution

II. Rotating Disk Electrode Experiments

G. R. Johnson[1] **and D. R. Turner**

Bell Telephone Laboratories, Incorporated, Murray Hill, New Jersey

ABSTRACT

The manner in which certain organic addition agents affect the crystal growth of copper electrodeposits was investigated with the aid of the rotating disk electrode technique. The results indicate that thiourea and l (-) cystine are cathodically reduced during copper plating. It is proposed that thiourea and l (-) cystine, or their reduction products, decompose to form sulfide ions which combine with cupric ions and precipitate as CuS on the cathode. Gelatin inhibits pyramidal crystal growth at low current densities by adsorbing on the apex of the pyramids. Above a transition current density, cubic layer crystal growth predominates, and much larger quantities of gelatin are required to inhibit crystal growth. Glycine and dextrin have little or no effect on the polarization curve for copper plating. Therefore, the rotating disk electrode technique was not useful in studying the mechanism whereby they act as addition agents.

The rotating disk electrode technique was employed in an effort to extend our understanding of the behavior of various addition agents used in the electroplating of copper from acid sulfate solutions. Stirring is one of the more difficult variables to control in studying electrode processes. The rotating disk electrode technique is one means of varying the rate of stirring at an electrode in a controlled and reproducible manner. The technique also enables one to separate the diffusion controlled current from the total current flowing during the course of metal electrodeposition.

Levich (1) has shown that the magnitude of a diffusion limited current at a rotated flat disk electrode is directly proportional to the square root of the angular rotational velocity of the disk. If there are two simultaneous electrode processes, one of which is diffusion controlled, the current due to the diffusion controlled process may be separated from the total current using a method described by Pleskov (2). The total current at a constant electrode potential is plotted against the square root of the disk angular rotational velocity and the straight line is extrapolated to zero angular velocity. The ordinate intercept yields the current at the constant potential due to the process which is not diffusion controlled. If this is done at a series of electrode potentials over the range of interest, current-potential data are obtained for the nondiffusion controlled process. The current-potential curve for the diffusion controlled process is found by difference.

The rotating disk electrode technique was used in this study to re-evaluate the effect of some organic addition agents on the kinetics of copper electrodeposition from a sulfate solution described in an earlier paper (3).

Experimental

The copper plating solution used in this study was 1M in copper sulfate and 1M in sulfuric acid. As reported in the earlier study (3), the solution was purified of surface-active material by treatment with Al_2O_3 followed by an activated carbon treatment.

A cross-section view of the cell used for these rotating disk studies is shown in Fig. 1. Water from a thermostat set at 25.0°C was circulated through a water jacket around the cell.

[1] Present address: Sprague Electric Company, North Adams, Mass.

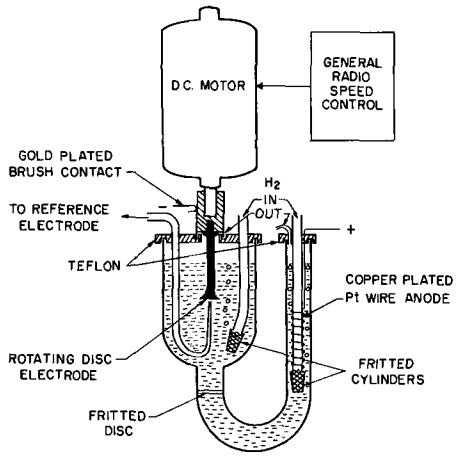

Fig. 1. Cross-section view of rotating disk electrode cell

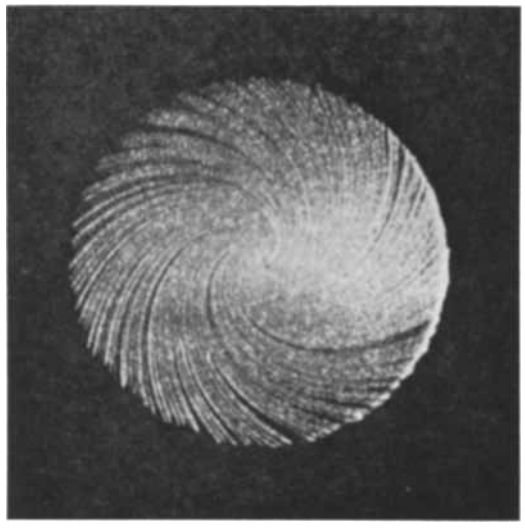

Fig. 2. Flow pattern on a rotating disk electrode

Disk electrodes with an exposed area of 1 cm^2 were machined from brass to the shape shown in Fig. 1. A 0.12 mm thick platinum foil disk was attached to the bottom of the brass mandrel with lead-tin solder. The platinum disk was in turn preplated with copper from the purified solution mentioned earlier. All but the bottom surface of the electrode was masked either with a neoprene coating prepared by "Gaco," or with "Apiexon" wax dissolved in toluene. Both materials were satisfactory insulators.

The simple disk electrode used in this work has the disadvantage in that the current distribution for copper plating is nonuniform even though current distribution for a simultaneous diffusion limited process is uniform (1). A guard ring around the disk electrode would improve metal plating current distribution.

The electrode was mounted close to the end of the motor shaft by means of a short gold-plated brass sleeve to minimize the eccentric motion of the rotating disk. A General Radio Variac speed control unit varied the speed of the d-c motor and a General Radio Strobotac measured the rotational speed in revolutions per minute (rpm). Rotational speeds of 100, 400, 900, and 1600 rpm were used in these studies since their square roots were 10, 20, 30, and 40, respectively. This simplified data plotting and provided uniformly spaced points.

Experiments were carried out at constant current densities using a regulated power supply. Cell currents were measured with a Sensitive Research multirange milliammeter. Electrical contact to the rotating disk was made by means of a gold-plated phosphor bronze spring pressing against the gold-plated sleeve.

The cathode potential was measured with a Millivac Type 17C vacuum tube voltmeter. Pure copper plated on a platinum wire coil dipped in the additive-free solution was used as the reference electrode. This reference electrode was connected to the main cell through a syphon filled with acid copper solution as shown in Fig. 1. The syphon had a long, fine capillary tip which projected up close to the center of the rotating disk electrode. This arrangement did not affect the solution flow pattern over the disk electrode significantly.

The flow pattern of solution over the surface of a rotating disk electrode is illustrated in Fig. 2. The spiral pattern was obtained by plating a heavy copper deposit on a rotating disk (~ 0.12 mm thick) from an acid sulfate bath containing 1 x 10^{-4} moles/l thiourea. Plating conditions and the addition agent produced a ridged deposit which outlined the flow of solution over the surface. The spiral is almost an Archimedes spiral, *i.e.*, displacement away from the center is almost proportional to the angular displacement. Another interesting feature is that the pattern does not change with rotational speeds.

All of these experiments were conducted using the 1M $CuSO_4$ + 1M H_2SO_4 solution described earlier. Oxygen-free hydrogen was bubbled through the electrolyte continuously. Measurements were made first in electrolyte free of addition agent and then with solutions containing one of the following additives: 1.3 x 10^{-4} moles/l thiourea, 4.2 x 10^{-5} moles/l l(−) cystine, 6.2 x 10^{-5} moles/l dextrin, 1.3 x 10^{-4} moles/l glycine, and 0.010 g/l gelatin.

Results and Discussion

Cathode potential-current density curves were obtained with and without the various addition agents in the copper plating solution at the several rotational speeds of the disk electrode. The results were similar to those reported in a previous paper (3), but they differ in some important respects.

In the purified solution without addition agent, disk rotational speeds from 100 to 1600 rpm had no effect on the cathode potential-current density relationship up to 50 ma/cm^2. The curve was the same as that obtained using a spherical cathode (3) and in good agreement with the results of other investigators (4-6).

Of the five addition agents studied, all but dextrin had an effect on the polarization curve, and the results were similar to those obtained in the earlier paper (3). Stirring, by means of the rotating disk electrode, gave some very interesting results which proved helpful in interpreting these and other data in terms of a mechanism whereby some addition agents modify crystal growth of electrodeposits.

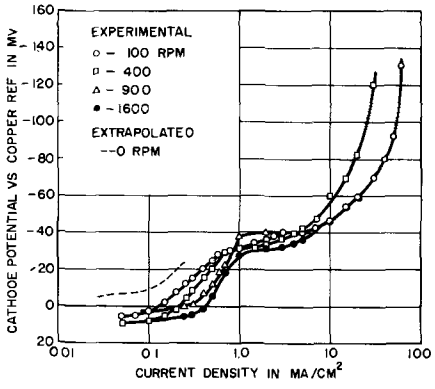

Fig. 3. Effect of disk rotation speed on the cathode potential-current density curve in 1M $CuSO_4$ + 1M H_2SO_4 solution containing 1.3 x 10^{-4} M/L thiourea.

The cathode potential-current density curves obtained with 1.3 x 10^{-4} M/L thiourea as the additive are shown in Fig. 3. When the disk rotation speed increases, the "step" in the curve is displaced toward higher current densities without being changed in form. The data for the $E - \log i$ curve at 400 rpm were obtained on a different day from the other curves. The higher polarization curve for 400 rpm above 10 ma/cm² was an anomaly and was not reproducible. This result illustrates the difficulties that are encountered occasionally in the study of addition agents. The cathode potential-current density relation at the "step," in the unstirred condition, was obtained by plotting i *vs.* $(\text{rpm})^{1/2}$ at various potentials in the "step" region and extrapolating to zero rpm. The results with thiourea will be discussed after the experiments with l(—) cystine are described.

l(—) Cystine is similar in chemical structure to both thiourea and glycine. It has an exposed sulfur group like thiourea, but the amine group is on the second carbon atom away from the sulfur group. A carboxyl group is attached also to the second carbon atom so that the molecule is similar to glycine (NH_2CH_2COOH). As an addition agent in copper plating from acid sulfate solutions, l(—) cystine behaves more like thiourea than glycine. The effect of disk rotational speed on the E-i curves in a copper plating solution containing 4.2 x 10^{-5} M/L l(—) cystine is shown in Fig. 4. There is the same shift in the potential step between 0.1 and 1 ma/

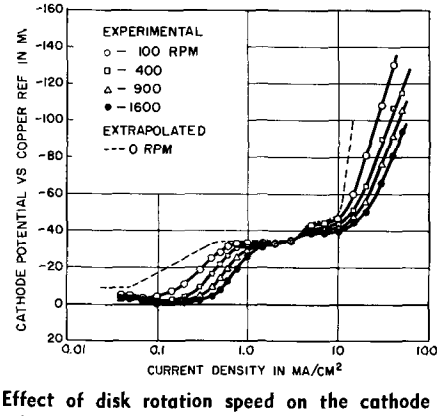

Fig. 4. Effect of disk rotation speed on the cathode potential-current density curve in 1M $CuSO_4$ + 1M H_2SO_4 solution containing 4.2 x 10^{-5} M/L l (—) cystine.

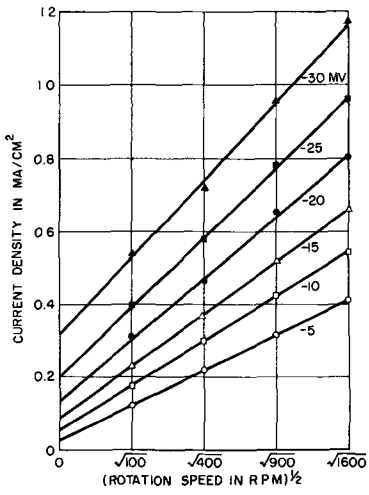

Fig. 5. Current density-(rotation speed)$^{1/2}$ relation between 5 and 30 mv cathode potential in 1M $CuSO_4$ + 1M H_2SO_4 solution containing 4.2 x 10^{-5} M/L l(—) cystine.

cm² toward higher current density as observed in Fig. 3. An additional effect was observed with l(—) cystine. After all the curves passed through a common point at 3 ma/cm², they again split into separate curves at higher current densities. The slope of the curve in the Tafel region (linear E — log i) decreases with increasing speed of disk rotation.

The unstirred (0 rpm) cathode potential-current density curve was obtained above and below 3 ma/cm² by plotting current density *vs.* $(\text{rpm})^{1/2}$ at a series of potentials and extrapolating to zero rpm. The intercept is the current density, at a given electrode potential, of cathodic processes which are not controlled by the mass transfer of a reacting species to the cathode surface. The method is illustrated in Fig. 5 for the low current density region. A similar plot and extrapolation was made for the high current density region.

If the rate of an electrochemical process is determined by the mass transfer of the reacting species,

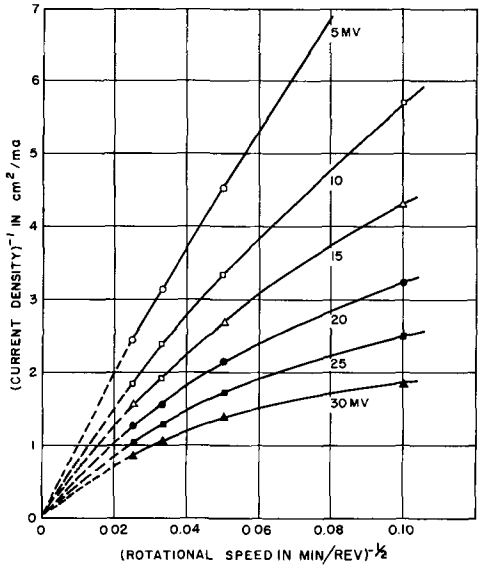

Fig. 6. Curves of (current density)$^{-1}$-(rotation speed)$^{1/2}$ at cathode potentials between 5 and 30 mv in 1M $CuSO_4$ + 1M H_2SO_4 containing 4.2 x 10^{-5} M/L l(—) cystine.

then the limiting current density should approach infinity as the stirring rate becomes infinitely large. When the inverse of the experimental points in Fig. 5 are plotted, that is, (current density)$^{-1}$ *vs.* (disk rotational speed)$^{-1/2}$, a series of curves is obtained as shown in Fig. 6. All the curves appear to extrapolate to, or close to, infinite current density at infinite rotational speed. This result confirms the earlier assumption that the rate of the electrode reaction is determined by the mass transfer of the reacting species. Since the potential step does not occur without addition agents, it must be concluded that the reacting species is some form of or involves the addition agent.

The polarization curves with thiourea or l(—) cystine as the addition agent, Fig. 3 and 4, may be considered to be the result of two effects. First, at the potential step between about 0 and 30 mv, the addition agent is electrolytically reduced, with the formation of H_2S; and second, cupric sulfide is precipitated at very low H_2S concentrations $\sim 1 \times 10^{-44}$ moles/l. The CuS interferes with normal crystal growth; thus the potential for copper deposition becomes more negative than normal (without addition agent). Increasing the disk rotational speed increases the supply of addition agent to the electrode and the current increases. An attempt to confirm this mechanism by measuring the copper plating efficiency at various disk rotational speeds was only partially successful. The trend was to lower plating efficiencies with increasing disk speeds as it should be, but a few of the results did not fall into the pattern.

Above about 30 mv cathode potential, the current density increases markedly with a slight potential rise. This is the potential region where it is believed control of the rate of copper deposition changes from a surface diffusion of adatoms to a charge transfer mechanism (4). The transition is also in the region where the crystal growth habit changes (3, 7). Whatever the mechanism, it is evident that the relative inhibiting effect of both thiourea and l(—) cystine decreases in the vicinity of 30 mv.

l(—) Cystine has an unusual effect on the polarization curves in the Tafel region as shown in Fig. 4. Increasing disk rotation speed has a depolarizing effect. The increase in current density is too great to be attributed entirely to reduction of the addition agent. One interpretation is that l(—) cystine changes the rate-determining step in the charge transfer process for copper deposition. Mattsson and Bockris (4) have presented evidence which tends to support the suggestion that copper deposition from purified acid sulfate solutions is a two step reaction

$$Cu^{++} + e^- \rightarrow Cu^+ \qquad [1]$$

and

$$Cu^+ + e^- \rightarrow Cu \qquad [2]$$

with reaction [1] being rate determining. If l(—) cystine causes reaction [2] to be the slow step, stirring by means of the rotating disk electrode will sweep away some cuprous ions before they can be cathodically reduced. The potential of the electrode is determined by the cuprous ion concentration at the electrode. Therefore, at a given current density, when stirring reduces the cuprous ion concentration at the electrode, the electrode potential becomes less negative.

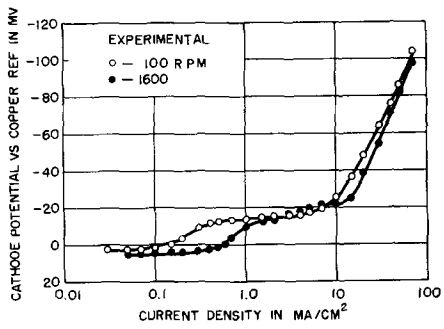

Fig. 7. Effect of disk rotation speed on the cathode potential-current density curve in 1M $CuSO_4$ + 1M H_2SO_4 solution containing 1.3×10^{-4} M/L glycine.

One of the reviewers of this paper has suggested that some study of the effects of temperature variation on E — log i curves might lead to a better understanding of the reaction processes, particularly with l(—) cystine, where a change in the charge transfer rate-determining reaction is proposed.

Glycine affects the polarization curve for copper plating only in the region between 0.1 to 1.0 ma/cm^2. The effect of disk rotational speed on the polarization curve is shown in Fig. 7. The potential step at low current densities is shifted toward higher current densities with increasing rotation speed as it is with thiourea and l(—) cystine. The results do not appear to contribute to our understanding of how glycine in an acid copper sulfate plating solution improves the microdistribution of plated copper.

In the previous paper (3), it was noted that gelatin produced a large polarization effect in copper plating in the low current density region, and that there was a sharp break in the E — log i curve at about 3 ma/cm^2. On decreasing the current, a hysteresis was always observed. These results were duplicated with a rotating disk electrode except for the hysteresis effect which was absent, *i.e.*, ascending and descending curves were identical. The rotational speed of the disk electrode affects the E — log i curve only beyond the break point as shown in Fig. 8; and the slope of the curve in this region decreases with increasing rotation speed. If the inverse of the slope, $(\Delta E/\Delta \log i)^{-1}$, is plotted against disk rotation speed and the data are extrapolated to 0 rpm, the slope appears to become infinite as illustrated in curve 1. The horizontal line, curve 2, for infinite rotation speed was obtained by extrapolating a plot of $\Delta E/\Delta \log i$ *vs.* (rpm)$^{-1}$. Zero rpm and infinite rpm correspond to the completely unstirred and infinitely stirred conditions, respectively. Both conditions are impossible to achieve experimentally but the information is important in understanding the behavior of gelatin as an addition agent.

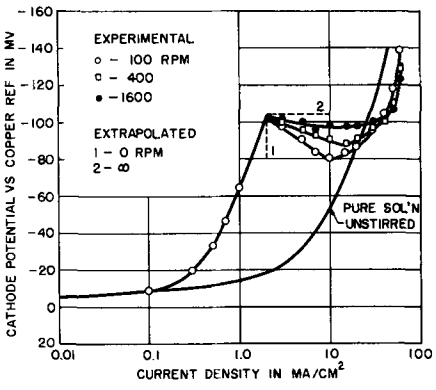

Fig. 8. Effect of disk rotation speed on the cathode potential-current density curve in 1M $CuSO_4$ + H_2SO_4 solution containing 0.010 g/l gelatin.

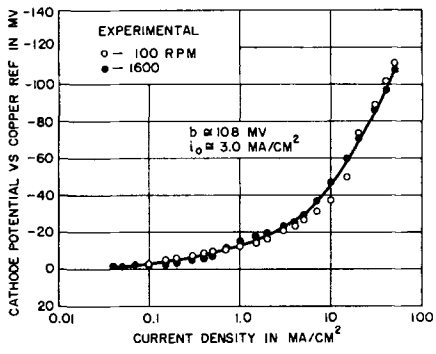

Fig. 9. Effect of disk rotation speed on the cathode potential-current density curve in 1M $CuSO_4$ + 1M H_2SO_4 solution containing 6.2 x 10^{-5} moles/l dextrin.

These results for gelatin using the rotating disk electrode support the mechanism proposed in the earlier paper (3). In the low current density region, the E — log i results clearly indicate a lack of dependence on the cathode angular rotational speed. This is interpreted to mean that even at the lowest stirring rate (rotational speed) employed, sufficient quantities of gelatin are provided to interfere with the normal crystal growth on the cathode. On a (100) oriented face, the crystal growth is pyramidal below the transition current density (~2 ma/cm²), and relatively small amounts of gelatin are needed to block crystal growth. Above the transition current density, it has been shown that cubic layer-type growth of the copper deposit predominates on the (100) face (3). With this growth pattern one would expect that a much greater amount of gelatin would be required to interfere with the lateral extensions of the steps generated from the original pyramid sides. The experimental results in Fig. 8 beyond the transition current density are in agreement with the previous suggestion. At zero rpm, the extrapolated E — log i curve drops almost vertically because the amount of gelatin available to inhibit crystal growth is very small as compared to the amount required for complete inhibition. Stirring by disk rotation mechanically conveys gelatin up to the cathode and the amount increases with rotation speed. Thus the negative slope of the polarization curve beyond the transition point decreases with increased disk rotation speed. The horizontal E — log i curve for infinite stirring may be interpreted to mean that the maximum inhibiting effect of gelatin in copper plating is never greater than that observed at the transition current density. The cathode potential increases again in Fig. 8 above 10 ma/cm² when the rate of copper plating becomes limited by the charge transfer process.

It was observed in the earlier study (3), that up to 0.1 g/l dextrin had no effect on the cathodic polarization curve for copper plating. This result was confirmed with the rotating disk electrode. It was also found that variable stirring rates did not change the result, as demonstrated in Fig. 9. The Tafel slope, b, and exchange current density, i_o, were identical to the values obtained in additive-free solutions.

Summary and Conclusions

Structurally, l(—) cystine is similar to both thiourea and glycine but, as an addition agent in acid sulfate copper plating solutions, it behaves more like thiourea than glycine. The polarization curves for copper plating with thiourea and l(—) cystine as addition agents are interpreted to mean that the additive is electrolytically reduced with the formation of H_2S and subsequent precipitation at the interface of CuS which is incorporated into the deposit. Copper sulfide markedly increases the copper electrodeposition potential at a given current density when crystal growth is pyramidal, but not when it becomes laminar. Stirring has a depolarizing effect above 3 ma/cm² with l(—) cystine. One interpretation is that l(—) cystine changes the rate-determining step in the charge transfer process for copper plating.

Gelatin inhibits pyramidal crystal growth during copper plating at low current densities by adsorbing on the apex of the pyramids. Above the transition current density, gelatin must be supplied in much larger quantities to interfere effectively with cubic layer type growth.

Glycine and dextrin in acid copper plating solutions have little or no effect on the polarization curve for copper plating. Therefore, the rotating disk electrode technique was not useful in studying the mechanism whereby they act as addition agents.

Acknowledgment

The authors are grateful to U. B. Thomas and P. C. Milner for their helpful discussions and valuable suggestions during the course of these studies.

Manuscript received April 16, 1962. This paper was prepared for delivery before the Detroit Meeting, Oct. 1-5, 1961.

Any discussion of this paper will appear in a Discussion Section to be published in the June 1963 JOURNAL.

REFERENCES

1. V. Levich, *Acta Physiochim, URSS*, **17**, 257 (1942).
2. Yu. A. Pleskov, *Zhur. Fiz. Khim.*, **34**, 523 (1960).
3. D. R. Turner and G. R. Johnson, *This Journal*, **109**, 798 (1962).
4. E. Mattsson and J. O'M. Bockris, *Trans. Faraday Soc.*, **441**, 1580 (1959).
5. E. Mattsson and R. Lindstrom, *Compt. rend*, 6th Reunion, C.I.T.C.E., 263 (1954).
6. R. Sroka and H. Fischer, *Elektrochem.*, **60**, 109 (1956).
7. H. Seiter and H. Fischer, *ibid.*, **63**, 249 (1959).

Electrophoretic Deposition: A Versatile Coating Method

Conrado P. Gutierrez, John R. Mosley, and Terry C. Wallace

University of California, Los Alamos Scientific Laboratory, Los Alamos, New Mexico

ABSTRACT

Electrophoretic deposition is shown to be a useful coating method for the deposition of metal, oxide, and carbide coats on metal or graphite. The time-current-voltage relationship on the rate of deposition is discussed, and factors important to preparation of suitable plating suspensions and to the formation of adherent deposits, with and without binders, are described. The method has been applied to the plating of coats of B, Dy, Zr, Au, Nb, Mo, W, Re, Nb_3Sn, ZrH_2, ThC, UC, NpC, PuC, (ZrU)C, UWC_2, UO_2, $UMoC_2$, Ta_2O_5, and both W-UO_2 and Mo-UO_2 composites.

The phenomenon of electrophoresis has been observed and investigated for at least 150 years, but only very limited use has been made of electrophoresis as a method of applying coatings to materials. Yet electrophoresis offers a very general and useful method of coating conducting materials such as metals and graphite with a wide variety of conductors and nonconductors.

The stability of a plating suspension has been explained in terms of an electrical layer (1-10). Various theories on the formation of an adherent deposit have been advanced (11-16); however, this feature of electrodeposition is the least understood and the most difficult to control.

This paper describes ways of preparing stable plating suspensions, and lists the important parameters for plating by electrophoretic deposition.

Experimental Procedure

Selection and purification of the suspension medium.—Polar organic liquids are most commonly used as suspension media for electrophoretic deposition since stable suspensions can be formed in these liquids, and the low electrical conductivity of these liquids minimizes electrolysis of the liquid and attendant gassing at the electrodes. The liquids used in this investigation were isopropyl alcohol (IPA) and nitromethane. These were selected on the basis of their proved utility as suspension media as shown by the important applications of electrophoretic deposition developed by Reichard *et al.* (17).

The IPA (Bakers Analyzed Reagent Grade) was untreated before use. The nitromethane (Eastman Kodak's No. 189) was dried by shaking for a few minutes with calcium sulfate (Drierite) and was then filtered through a "fine" fritted glass filter before use. The drying procedure also appeared to remove ionic impurities from the nitromethane.

Comminution of powders.—The suspensions used for electrophoretic deposition usually had a particle size ranging from 1-20μ. This range of particle size was chosen because colloidal size particles gave low plating rates, and particles coarser than 25μ led to uneven deposits. The optimum size was found to be about 6μ, and grinding times were selected to give a large fraction of the powder close to this size.

All powders were comminuted by jar milling in IPA. The niobium suspensions were prepared by milling −325 mesh Fansteel Metallurgical Corporation niobium for 8 to 12 hr with steel balls and jars. Suspensions of other materials were milled for 1 to 10 hr in Teflon or polyethylene containers with tungsten rods or tungsten carbide balls. The latter powders were separated by centrifugation, resuspended in IPA several times, then resuspended several times in dried nitromethane to remove the IPA. Finally, the desired particle size range was obtained by elutriation of the suspension in a vertical column of the solvent. A haemocytometer was used occasionally to confirm the particle size.

Use of additives.—Early in the investigation of Nb suspensions in IPA, it was observed that some suspensions gave adherent electrophoretic deposits, others gave only a partially adherent deposit, and many gave no deposit, all under the same plating conditions. The suspensions all had approximately the same sedimentation time and exhibited similar electrophoretic migration velocities as determined in a straight tube cell.

By the use of additives, suspensions could be made to form an adherent deposit. Of the additives investigated (ammonium and sodium hydroxides, hydrochloric, nitric and citric acids), a dilute solution of ammonium hydroxide was found to be the most effective. The ammonium hydroxide was added as a 0.15*M* solution prepared from concentrated aqueous ammonium hydroxide and IPA. The small amount of water added in this way was shown to be without effect. The amount of additive required is discussed later.

The use of zein, a corn protein, as an additive was first reported by Reichard *et al.* (17). It is an excellent binder, and deposits containing zein exhibit a "green strength" such that mechanical scraping is required to remove them from the substrate. However, it was not used in the Nb-IPA suspensions since it caused immediate flocculation. It was added to the nitromethane suspensions as a 60-40 vol % IPA-nitromethane solution containing 10 mg zein/cc. Although some suspensoids deposited

at the anode, all suspensoids, on the addition of zein, deposited at the cathode. The further addition of small amounts of benzoic acid, added as a saturated solution in nitromethane to these suspensions improved the smoothness of the deposit.

The zein could be removed from the deposit by heating the sample to 600°C *in vacuo*.

The electrophoretic deposition rate was much faster from nitromethane suspensions containing zein and benzoic acid than from IPA suspensions containing ammonium hydroxide.

Preparation of suspensions.—In the case of the Nb-IPA suspensions, samples of the jar-milled suspension were diluted with IPA to a concentration of 10 mg/cc or less and tested for plating characteristics using various concentrations of ammonium hydroxide additive and various voltages on the plating cell. A suspension that would plate to depletion in 10 sec or less, with formation of an adherent deposit, was considered a satisfactory plating suspension.

When nitromethane was the suspending medium, the ground powders were washed several times with IPA as described above. The number of washings in this step was often important in determining the plating characteristics of the suspension. After subsequent centrifuging and washing of the powder with nitromethane to remove the alcohol, the powder was ground again in nitromethane for a short period (10 min) to redisperse the powder. The suspension was then diluted to a dispersoid concentration of 10 mg/cc or less, and sufficient zein solution was added so that the weight of zein amounted to about 1% of the weight of dispersoid in the suspension. Often benzoic acid was added to improve the quality and adherence of the deposits. The amount of benzoic acid needed was determined in the same manner described above for ammonium hydroxide.

Plating cell.—The electrophoretic deposition experiments were performed by using the cell shown in Fig. 1. This design allowed: (i) the use of small samples of suspensions (6.4 ml), (ii) easy removal or substitution of small, easily weighable electrodes, and (iii) visibility of the suspension during plating. The glass portion of the cell was made from a 25 ml graduated cylinder. A micarta cap centered the electrode in the cell. The suspensions were magnetically stirred by means of a Teflon-covered bar.

Results

The Nb-IPA suspensions were particularly interesting due to their sensitivity to various experimental parameters. In particular, the rate of electrophoretic deposition of Nb on the anode was studied as a function of the following: (a) concentration of dispersoid, (b) plating time, (c) nature of cell electrodes, (d) cell voltage or current density, and (e) concentration of additive.

Dispersoid concentration.—The effect of the concentration of Nb on electrophoretic deposition rates in the Nb-IPA suspensions exhibited no unexpected features. For a given series of suspensions made by various dilutions of a concentrated stock suspension, the deposition rate at constant voltage was proportional to the Nb concentration.

Induction time and electrode studies.—One of the most surprising features of electrophoretic deposition from the Nb-IPA suspensions was the effect of time on the rate of deposition at a fixed voltage. Some of the suspensions exhibited an initial constant rate which then gradually decreased as the suspension became depleted. In contrast, the majority of suspensions, and all those that had been stirred in a Waring Blendor for 5 min, gave an initial "induction period" during which essentially no plating occurred. This was followed first by a gradually increasing rate of deposition and then by a decreasing rate, as before. A comparison of these two typical types of time dependence is shown in Fig. 2. The points of both curves were obtained from aliquots of each of the two types of suspensions which were electrolyzed at constant voltage with selected plating times. After the determination of each point, the cell was drained and cleaned, and a new graphite anode and a new portion of the 3.8 mg Nb/cc suspension were introduced for the next determination.

The induction time appeared to be unrelated to particle mobility since migration experiments indicated that particle mobilities were the same in suspensions with and without an induction period. Also, the anode did not appear to be involved in the induction periods. Figure 3 shows the experimental demonstration of the latter. The solid curve was obtained in the same way as the dotted curve in Fig. 2 (using "blendorized" suspensions), but

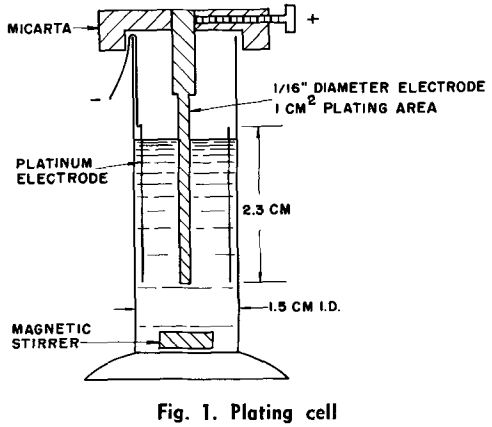

Fig. 1. Plating cell

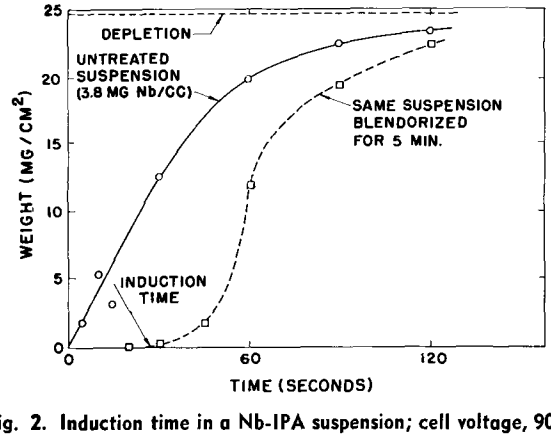

Fig. 2. Induction time in a Nb-IPA suspension; cell voltage, 900v.

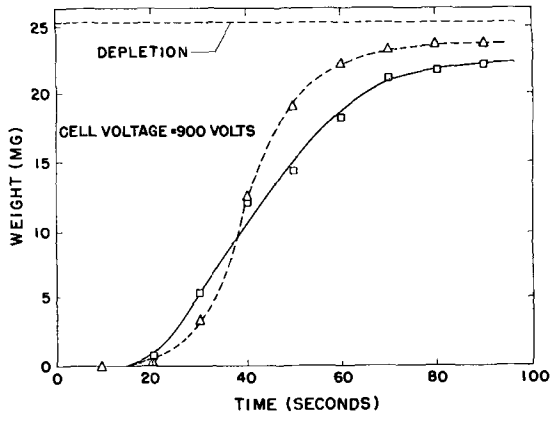

Fig. 3. Effect of the anode on induction time. □, weight obtained at indicated times in identical suspensions (4.0 mg Nb/cc); △, cumulative weight for successive coats on separate anodes in one suspension.

the dotted curve was obtained by the following procedure. Successive graphite anodes were coated at 900v for successive increments of time (10 sec) in the same portion of a blendorized Nb suspension, and the cumulative weight of the coats was plotted against the cumulative time. If an induction time were present with each new anode, no deposit, cumulative or otherwise, would have been obtained. However, the fact that the curves are so similar shows that the anode was not involved in the induction time. In this regard, it is interesting to note that several conductive anode materials were used in various phases of this investigation, and in no case did the anode influence electrophoretic deposition. Anodes of brass, Pt, graphite, Cu, and Mg were tested.

The results of a series of experiments with blendorized suspensions involving the cathode are shown in Fig. 4. When the Pt cathode was removed from the suspension after electrolysis at 900v for 15 sec, which was before the end of the induction period, then washed and dried before being placed back in the same portion of suspension with a new coating anode, the amount of deposit was negligible. The Pt cathode was replaced with successive Al cathodes, and the series was repeated both at 15 and 30 sec increments with essentially the same results: namley, unless the cathode, Al or Pt, was left in place for a plating time longer than

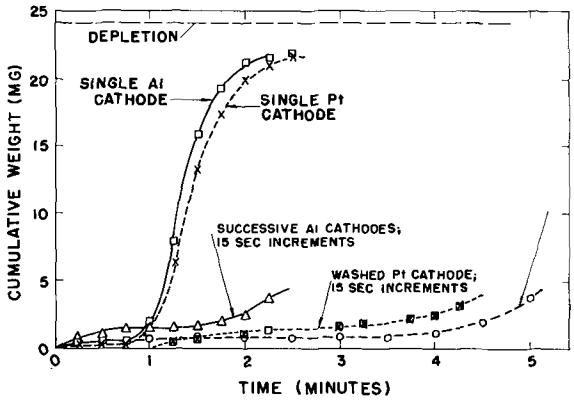

Fig. 4. Effect of the cathode on induction time; cell voltage, 900v, successive Al cathodes, 30 sec increments.

the induction time, no appreciable deposit was obtained. The cathode, therefore, was directly involved in the phenomenon causing the induction time. No plausible explanation of the nature of the cathode reaction which occurs during the induction period has been found. In general, suspensions that exhibited this phenomenon had rather high conductivities, and blendorized suspensions had conductivities two or three times as high as the untreated suspensions, probably due to the presence of impurity ions.

Current and voltage effects.—The initial deposition rate of Nb from straight Nb-IPA suspensions was also studied as a function of cell voltage and current density. The times selected for these studies were sufficiently short to cause only a third or less of the Nb to plate out. At low voltages (less than 1000v) and low current densities, the current density was proportional to the voltage during the short time intervals used. However, at high voltages (2000-4000v), the current quickly dropped (at constant voltage) to values that were sometimes one-half or one-third the initial current. This effect was probably caused by the depletion of impurity ions from the suspensions and led to a final conductance of the suspension that was constant but lower than the initial conductance. Since it was not possible to eliminate this effect, deposition rates were usually plotted as a function of voltage.

This drop in conductance has also been reported in the literature in the plating of nonconductors, and the authors (4, 12, 16) have explained this drop as a result of the resistance of the deposited layer. A different mechanism must account for the rapid drop in current when a conductive coating is being deposited. Since the conductance of the pure solvent, IPA, also falls quite rapidly when electrolyzed, it is probable that the decrease in conductance in the suspensions is caused by the depletion of ions and other current-carrying particles rather than by the electrical properties of the deposit.

The deposition rate increased with voltage at low voltages and decreased with voltage at high voltage. A typical deposition rate *vs.* voltage curve is shown in Fig. 5. The remarkable drop in deposition rate with voltage has not been explained, and only one paper in the literature on electrophoretic deposition (18) presented data which, when plotted, showed a similar decrease.

The initial increase in deposition rate is a result of the induction time of these suspensions since the induction time was found to decrease as the voltage

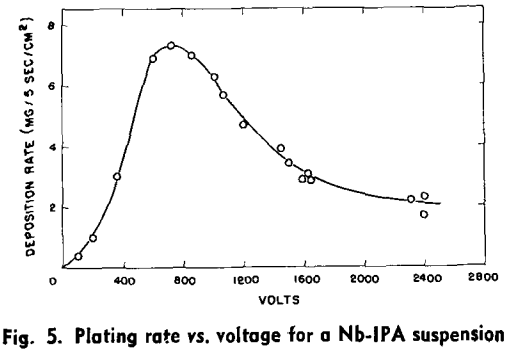

Fig. 5. Plating rate vs. voltage for a Nb-IPA suspension

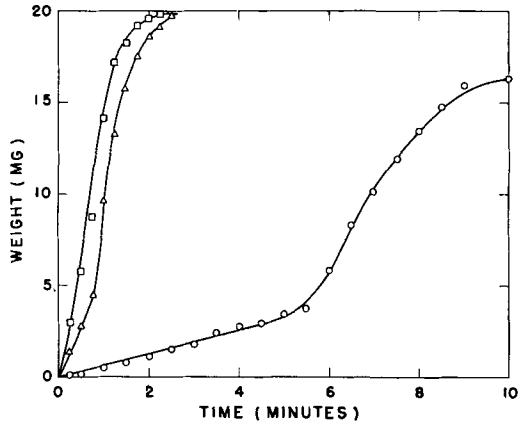

Fig. 6. Effect of voltage on induction time; ○, 100v; □, 250v; △, 450v.

was increased. This is shown in Fig. 6 for a series of experiments on blendorized Nb-IPA suspensions.

Additives.—One of the most important features in the use of electrophoretic deposition to obtain adherent deposits is the use of additives. In the case of Nb-IPA suspensions, ammonium hydroxide was found to be a useful additive that converted nonplating suspensions to ones that gave short induction times and adherent electrophoretic deposits. The effect of ammonium hydroxide as an additive or "activator" on the plating characteristics of a Nb suspension is shown in Fig. 7 which shows the weight of Nb deposited in unit times as a function of initial current density for the suspension as prepared, and for several concentrations of ammonium hydroxide. Such addition caused the peaks to shift to higher current densities with increasing concentration of additive. A similar plot against voltage, shown in Fig. 8, exhibited very little horizontal shift in the peak with concentration of additive. The results indicated that there is an optimum concentration of additive if only the deposition rate at the peak is considered.

Indeed, when the deposition rate at the peak was plotted against the initial conductance (in micromhos) of the suspension, a maximum rate of deposition was observed, as shown in Fig. 9. The

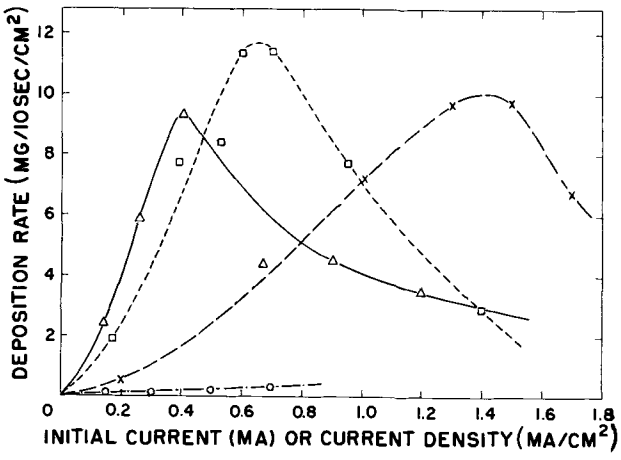

Fig. 7. Effect of additive on plating rate vs. current for a Nb-IPA suspension. Molarity of NH_4OH: ○, 0; △, 1.8×10^{-4}; □, 1.2×10^{-3}; x, 5.2×10^{-3}.

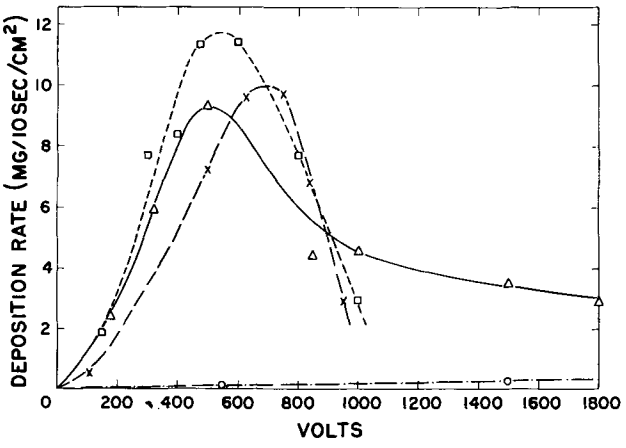

Fig. 8. Effect of additive on plating rate vs. voltage for a Nb-IPA suspension. Molarity of NH_4OH: ○, 0; △, 1.8×10^{-4}; □, 1.2×10^{-3}; x, 5.2×10^{-3}.

conductance at which this maximum occurred was shown in a separate experiment to correspond to a molarity of ammonia of about 1.3×10^{-3}M. The initial conductance of the suspension rather than the molarity was chosen as a variable because the conductance of the original suspension was lower than that of the starting IPA, showing that the powder adsorbs most of the foreign ions in the alcohol. Other experiments showed that the conductance of a suspension increases with further addition of ammonium hydroxide, although the relationship is not linear.

Applications.—The remarkable versatility of electrophoretic deposition has led to its use in a number of applications connected with other laboratory research problems. As discussed above, nitromethane suspensions containing zein and benzoic acid were used instead of IPA since codeposited zein gave strongly adherent deposits and since zein could not be used in the alcohol suspensions because of flocculation. Accordingly, results obtained in the Nb-IPA studies were applied qualitatively to the determination of plating conditions for various nitromethane suspensions. The technique was very effective, and adherent uniform deposits were obtained eventually with every material tested. Thus, although no systematic investigation was

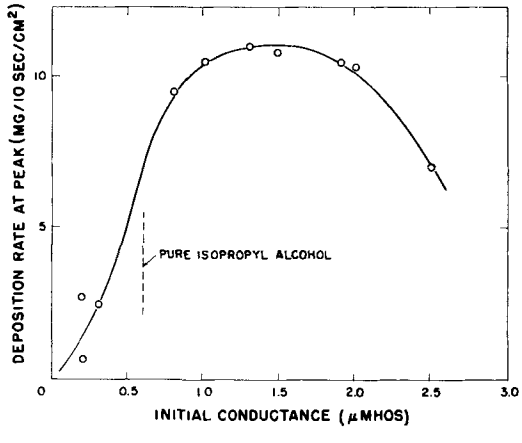

Fig. 9. Plating rate of Nb suspensions at the peak vs. initial conductance.

made of the general applicability of electrophoretic deposition to the coating of solids onto conductors in the nitromethane system, no limitation was found in those materials that were tried.

The following materials have been deposited as coatings by this method: B, Dy, Au, Nb, Mo, W, Re, Nb_3Sn, ZrH_2, ThC, UC, NpC, PuC, (ZrU)C, UWC_2, $UMoC_2$, UO_2, Ta_2O_5, and both W-UO_2 and Mo-UO_2 composites. Of particular interest were the simultaneous plating of W and UO_2 and of Mo and UO_2 powder mixtures of varying compositions. In both cases, the metal and oxide were uniformly distributed in the deposit in the same ratio as in the suspension.

Often, the coat was sintered in place by heating in vacuum to a temperature in the neighborhood of 2000°C. After such treatment, the coats were then used successfully in applications such as: (i) protective coatings to protect reactive materials from gaseous corrosion, (ii) bombardment targets for nuclear reaction studies, and (iii) samples for the determination of work functions.

Conclusions

The method can be adapted to coat any surface regardless of size or shape with surprisingly uniform deposits of preselected thickness. The latter can be accomplished by plating a suspension of known concentration to depletion.

Several factors have been found to be important in this type of plating. (i) The ability to obtain reproducible suspensions that will result in strong, adherent deposits depends, to a large extent, on the ionic impurities present in the suspending medium. (ii) Induction time and rate of deposition also appear to be related to the ionic impurities present. (iii) The effect of additives or "activators" is not clearly understood, but the amount needed for different materials can be determined by time-current-voltage experiments. (iv) These suspensions are sensitive to impurities; therefore grinding materials should be chosen to minimize the amount of impurities introduced. For instance, the use of steel balls and mills introduced as much as 1 w/o Fe in the Nb-IPA system. Also, when nitromethane was used for comminution in steel jars, the suspensions invariably flocculated.

Acknowledgments

The authors would like to thank Dr. R. D. Baker for suggesting this investigation initially, and Dr. M. G. Bowman, Dr. D. T. Vier, Dr. W. J. McCreary, and Dr. J. D. Farr, all of this laboratory, for their help during the course of this work.

Manuscript received March 6, 1961; revised manuscript received June 23, 1962. This paper was prepared for delivery before the Houston Meeting, Oct. 9-13, 1960. This work was performed under the auspices of the U.S.A.E.C.

Any discussion of this paper will appear in a Discussion Section to be published in the June 1963 JOURNAL.

REFERENCES

1. H. Helmholtz, *Ann. Phys.*, **7**, 337 (1879).
2. O. Stern, *Z. Elektrochem.*, **30**, 508 (1924).
3. G. Gouy, *J. phys. radium*, **9**, 457 (1910).
4. S. A. Troelstra, *Philips Tech. Rev.*, **12**, 293 (1951).
5. H. C. Hamaker, *Trans. Faraday Soc.*, **36**, 186 (1940).
6. E. J. W. Verwey, *Rev. trav. chim.*, **60**, 625 (1941).
7. E. J. W. Verwey, "The Role of the Double Layer in the Behavior of Lyophobic Colloids," pp. 47-66, in "Colloid Chemistry," Vol. VII, J. Alexander, Editor, Reinhold Publishing Corp., New York (1950).
8. J. Th. G. Overbeek, "Electrochemistry of the Double Layer," pp. 115-193, in "Colloid Science," Vol. I, H. R. Kruyt, Editor, Elsevier Publishing Co., Amsterdam (1952).
9. E. J. W. Verwey and J. Th. G. Overbeek, "Theory of the Stability of Lyophobic Colloids," Elsevier Publishing Co., Amsterdam (1948).
10. G. Kortum and J. O'M. Bockris, "Textbook on Electrochemistry," Elsevier Publishing Co., Amsterdam (1951).
11. H. C. Hamaker and E. J. W. Verwey, *Trans. Faraday Soc.*, **36**, 180 (1940).
12. H. C. Hamaker, *ibid.*, **36**, 279 (1940).
13. C. G. A. Hill, P. E. Lovering, and A. L. G. Rees, *ibid.*, **43**, 407 (1947).
14. H. Koelmans and J. Th. G. Overbeek, *Discussion Faraday Soc.*, **18**, 52 (1954).
15. C. L. Beal, *Ind. Eng. Chem.*, **25**, 609 (1933).
16. C. G. Sumner, *Trans. Faraday Soc.*, **36**, 272 (1940).
17. H. F. Reichard, H. G. Scheible, M. Kibrick, H. Katz, Report KLX-10029, Vitro Laboratories, West Orange, N. J., May, 1956.
18. K. A. Egerer and G. Landsberg, *Z. Elektrochem.*, **59** [3], 207 (1955).

The Dependence of Charge Transfer and Surface Diffusion Rates on the Structure and Stability of an Electrode Surface: Copper

J. O'M. Bockris and Hideaki Kita[1]

Electrochemistry Laboratory, University of Pennsylvania, Philadelphia, Pennsylvania

ABSTRACT

Experiments have been carried out to ascertain the effect on the parameters of the Cu deposition reaction of varying the surface configuration, of the substrate. Electrodeposited, He-quenched, H_2-quenched, dissolved, oxide film and chemically reduced surfaces were used. The observations were made by means of cathodic transients. An examination was also made of the change of activity of an electrode surface for times in the range 10^{-3} sec-10 min after production *in situ* of a fresh surface.

The charge transfer process per real sq. cm., is about ten times higher on electrodes prepared by quenching from the liquid than from those of other methods. The velocity of surface diffusion is about ten times lower on the quenched electrodes than on other electrodes. The concentration of adions on the quenched electrodes is much smaller than those on other substrates. The double layer capacity is approximately the same on He-quenched and electrodeposited electrode but much higher on oxide film and chemically reduced surfaces. There is a rapid fall of the velocity of surface diffusion on exposure of a fresh surface produced by anodic dissolution to a solution and no fall for oxide film electrodes. When the He-quenched electrodes were submitted to a successive series of cathodic pulses, such that Cu deposition was succeeded by H_2 evolution in each pulse, i_o, $C_{d\,l.}$ and τ all increased *linearly* with number of pulses. τ increased about ¼ the common rate of increase of i_o and $C_{d\,l}$.

The rate-determining step on electrodeposited, oxide film, dissolved and chemically reduced surfaces is shared at low current density by surface diffusion and transfer process: at high current density, it is predominantly by transfer process. On He- and H_2-quenched electrodes, surface diffusion control is predominant at low current density and transfer process at high current density. The change of rate constant for surface diffusion with time on exposure of a fresh surface to the solution is inconsistent with adsorption of impurities from solution and consistent with an equilibration of the adion concentration among the different planes on the surface. The dependence of i_o on substrate is probably a secondary effect of a larger concentration of adions on electrodeposited surfaces. Oxide film, chemically reduced, dissolved, and H_2-evolved electrodes all have similar surface configuration to that of the electrodeposited electrodes. The surface adion concentration arises from the dominance of 100 planes in the surfaces of these substrates. The remarkable effects of successive cathodic pulses arise from the increase in surface area attendant on the production of Cu in fine particle form by a secondary mechanism. The anomalous linear dependence of τ on the number of pulses is consistent with a horn-like shape of the pores.

Major attention during the recent development of electrode kinetics has been given to liquid-metal solution interfaces, *i.e.*, the charge transfer reaction has been the focus of attention. In advancing toward adequate models for the interpretation of the complex facts of the electrodeposition of solids, it is necessary to design experiments which manifest differences arising only from a change in the configuration of the metal surface.

Considerable differences have been reported in the rate constants for metal-solution exchange reactions depending on whether the metal is prepared by electrodeposition or by flash cooling of the liquid (1, 2). Consequently, systems involving Cu, prepared in various ways, have been subjected to electric pulses which modify the surface, and galvanostatic transient techniques have been applied to evaluate the effect of the modification of the surface on the rate constants.

Such work is intended to throw light not only on the mechanism of electrodeposition but also to indicate the molecular mechanisms which determine the empirical 'activity' of an electrically active catalyst.

Experimental

The apparatus, cell, and purification units were as reported earlier (1, 2). Solutions were purified by pre-electrolysis.

The electric device.—To apply a cathodic pulse at various times after switching off the anodic (or cathodic) polarizing current, an arrangement was devised analogous to that of Mehl, Devanathan, and Bockris (3) (Fig. 1). When switch S was closed, a

[1] On leave from the Research Institute for Catalysis, Hokkaido University, Sapporo, Japan.

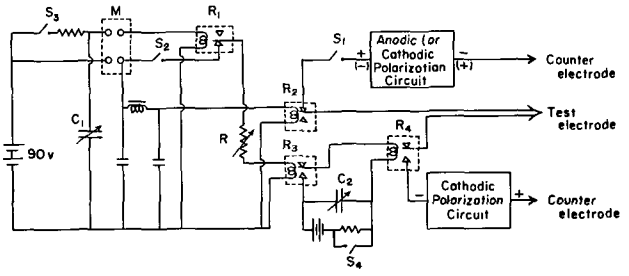

Fig. 1. Electrical arrangement: R_1, delay relay; R_2, anodic circuit relay; R_3, cathodic circuit relay; R_4, pulse relay; M, microswitch; C_1 and C_2, variable condenser; R, variable resistance; and S, switches.

constant anodic current began to pass through the test electrode. After the dissolution of a certain number (10^3-10^4) layers, a cathodic pulse was initiated by closing the microswitch M (S_2, S_3 in 'on' position and S_4 in 'off' position). This affects the circuit in Fig. 1 in such a way that the anodic current ceases and the cathodic current is switched on at a controlled time after the termination of the anodic current, *i.e.*, the fresh electrode surface is allowed to exist for a controlled (short) time in contact with the solution, before the kinetics of deposition on it are measured. The delay time between the two currents is controlled by C (Fig. 1). In this way, delay times between 9 msec and 1 sec were obtained. Delay times shorter than 9 msec could be obtained by controlling the variable resistance, R, when both terminals of the cathode circuit relay, R_3, were directly connected to the cathodic polarization circuit and to the test electrode (S_3 in 'off' position). The shortest time was a few μsec. The length of the cathodic pulse (msec-sec) was controlled by the variable condenser, C_2 (Fig. 1).

The electrodes.—The 'He-quenched' and 'electrodeposited' electrodes were prepared as reported earlier (1, 2). The 'H_2-quenched electrode' was prepared in a stream of prepurified hydrogen, and the 'oxide film electrode' was prepared by heating the He-quenched electrode in a stream of pre-purified oxygen at 600° ~ 650°C for 1 min. The oxidized electrode was sealed into a small glass bulb under an atmosphere of He, as were the other electrodes.

Concentrations of sulfuric acid and cupric sulfate were kept at 1.0 ± 0.03*N* and 0.05 ± 0.005M l^{-1}, respectively, except in specified cases.

Evaluation of Rate Constants

The most important parameters, the variation of which with surface state it was desired to determine, are: (i) the double layer capacity, $C_{d.l.}$ (and hence the roughness factor of the surface); (ii) the concentration of surface adions, c_o; (iii) the surface diffusion flux at the reversible potential, v_o; (iv) the exchange c.d. for the transfer process, i_o; (v) the transfer coefficients for anodic and cathodic reactions, α_a and α_c, respectively. These parameters were evaluated as follows.

Double layer capacity, $C_{d.l.}$.—This can be evaluated from $\left(\frac{d\eta}{dt}\right)_{t\to 0}$ by the equation

$$C_{d.l.} = i\left(\frac{d\eta}{dt}\right)^{-1}_{t\to 0} \qquad [1]$$

where η is the overpotential and i the current density. Equation [1] is valid (95% accuracy) under conditions (4)

$$\left.\begin{aligned} |\eta| &< 0.05\,\frac{RT}{(\alpha_c+\alpha_a)\mathbf{F}}\,\frac{i}{i_o} = 6.5\times 10^{-4}\,\frac{i}{i_o} \\ t &< \frac{C_{d.l.}}{0.95}\,0.05\cdot\frac{RT}{(\alpha_c+\alpha_a)\mathbf{F}} = 6.8\times 10^{-4}\,\frac{C_{d.l.}}{i_o} \end{aligned}\right\} \qquad [2]$$

where α_c and α_a are the Tafel constants for cathodic and anodic processes, i_o the exchange current density for the transfer process, and R, T, and $\mathbf{F}$ have their usual meaning. If conditions [2] are not satisfied, a contribution of the transfer reaction to the charging curve becomes appreciable and hence the validity of Eq. [1] decreases. Conditions [2] are only valid if charge transfer is rate controlling. Consequently, the c.d. for the measurement of $C_{d.l.}$ was always in a region such that this was so.

Surface concentration of adions, c_o, and the surface diffusion flux at the reversible potential, v_o.—These can be calculated using following equations (5) ($|\eta| < 10$ mv).

(*a*) c_o and v_o from the analysis of transient (at low current density) by

$$\ln(\eta_t - \eta_\infty) = \ln\frac{RT}{z\mathbf{F}}\,\frac{i}{z\mathbf{F}v_o} - \frac{v_o}{c_o}t \qquad [3]$$

where i is the Faradaic current density.

(*b*) v_o can be calculated from the steady-state value (at low current density) by

$$\eta_\infty = \frac{RTi}{z\mathbf{F}}\left(\frac{i}{i_o} + \frac{1}{z\mathbf{F}v_o}\right) \qquad [4]$$

utilizing i_o from the linear Tafel line.

The thus obtained v_o varies anomalously depending on the current density of measurement [cf. an interpretation discussed earlier (6)]. Hence, $(v_o)_{i=1\ ma\ cm^{-2}}$ will be quoted for the sake of comparison.

Equation [4] can be rewritten as

$$\eta_\infty = \eta_{\text{transfer}} + \eta_{\text{surface diff.}}$$

where $\eta_{\text{transfer}} = RTi/z\mathbf{F}i_o$ and $\eta_{\text{surface diff.}} = RTi/z^2\mathbf{F}^2v_o$, and hence

$$\frac{\eta_\infty}{\eta_{\text{transfer}}} = 1 + \frac{i_o}{z\mathbf{F}v_o}$$

which shows that when $\eta_\infty/\eta_{\text{transfer}}$ is close to unity (*e.g.*, < 1.3), estimation of v_o becomes inaccurate because i_o is known only to ±30%.

Exchange current density, i_o.—In systems in which the linear η — log i relations was observed, i_o was calculated in the usual way by extrapolation of log i to $\eta = 0$. In systems in which the effect of change of surface activity, *e.g.*, with time of contact of a fresh surface with the solution, was measured by means of a single transient at a given c.d., the i_o value was obtained assuming that the Tafel equation applied in the region concerned, if a Tafel time had been established for a similar state of the surface and similar overpotential range ($\eta_\infty = RT/\alpha\mathbf{F}\ln i_o/i$).

Transfer coefficients.—These were determined in the normal way.

Table I. Values of parameters for copper dissolution and deposition on various substrates

Electrodes	2.3RT/α_cF	2.3RT/α_aF	i_o ma cm^{-2} From Tafel line Cathodic	i_o ma cm^{-2} From Tafel line Anodic	i_o ma cm^{-2} From linear relation Cathodic	i_o ma cm^{-2} From linear relation Anodic	Capacity μF cm^{-2}	c_o mole cm^{-2}	zFv_o at i = 1 ma cm^{-2}
	118	44	4.6	4.0	1.9	4.2	50	5.8×10^{-9}	4.1
	116	44	10.0	6.0	3.5	3.5	58	4.7×10^{-9}	6.2
Electrodeposited	119	39	3.4	2.2	2.2	2.9	46	19×10^{-9}	7.0
	120	40	3.6	2.2	2.4	2.9	46	—	—
	128	42	4.7	5.0	2.9	3.7	—	—	6.6
	146	38	6.2	3.2	1.9	3.7	42	8×10^{-9}	5.8
	126	44	70	21	—	—	—	—	—
	110	50	25	16	—	—	—	6.5×10^{-10}	1.8
	106	47	22	12	—	—	—	3.6×10^{-10}	1.5
	112	35	56	32	—	—	—	7.9×10^{-10}	2.1
He-quenched	—	42	—	18	—	—	—	5.0×10^{-10}	1.6
	104	40	30	24	—	—	—	15×10^{-10}	3.9
	118	48	29	16	—	—	53	8.8×10^{-10}	2.8
	120	35	42	32	—	—	61	4.3×10^{-10}	1.3
	105	45	7	7	—	—	—	6.1×10^{-10}	1.6
Dissolved	125	40	30	17	—	—	61	9×10^{-9}	24
	115	44	24	5	—	—	51	10×10^{-9}	29
H_2-quenched	—	—	51	—	(0.75)	—	51	1.9×10^{-9}	4.0
	—	—	59	—	(0.87)	—	56	1.4×10^{-9}	3.2
	—	—	47	—	(0.71)	—	117		
H_2-evolved	—	—	23	—	(1.0)	—	89	Superpolarization	
	—	—	57	—	(0.54)	—	70		
	110	42	9	7	3.2	—	—	3.3×10^{-8}	13
	(166)	(63)	31	19	0.6	—	—	—	—
	—	53	—	14	4.5	—	—	1.3×10^{-8}	11
	122	43	15	11	6.0	—	90	—	—
Oxide film	—	—	40	—	9.4	—	137	1.7×10^{-8}	28
	—	—	—	—	0.7	—	183	—	—
	—	—	—	—	4.5	—	122	1.5×10^{-8}	14
	—	—	15	—	2.8	—	91	2.8×10^{-8}	20
	—	—	52	—	8.7	—	109	6.1×10^{-8}	32
	—	—	271	—	6.7	—	125	—	—

Transition time, τ.—When the current density exceeds the limiting current for diffusion of Cu^{++}, one finds a polarization curve with two steps. Thus, the first inflection point of the curve was taken as the transition time for $Cu^{2+} + 2e_o^- \rightarrow Cu$.

Results

Electrodeposited Electrode

(i) *Values of parameters.*—Values of α_c, α_a, i_o's, $C_{d.l.}$, c_o, and v_o on the electrodeposited electrode are shown in Table I.

The values of α_c, α_a, i_o, and $C_{d.l.}$ agree with those previously reported (1, 2). Values of c_o were analyzed as $\doteq 8.10^{-9}$ mole cm^{-2}. Values of i_o and zFv_o are approximately equal.

A typical Tafel line is shown in Fig. 2. Slight deviations from the ideal line at low current densities can be noticed.

(ii) *Change with time of the surface of the electrodeposited electrode after exposing to a solution, following anodic preparation of a fresh surface.*—In these experiments, the dependence on time of contact with solution of the rate constants for deposition at a surface prepared by anodic dissolution (16 ma cm^{-2}, $\sim 10^4$ layers) was studied. Results are shown in Fig. 3. $(\eta_\infty)_t$ changes roughly linearly with log t in the region observed. $\partial\eta_t/\partial \ln t \simeq 0.5$ mv (cf., the He-quenched electrode).

(iii) *Surface diffusion flux and exchange current density as a function of anodic current density by which a fresh surface is produced.*—The i_o and v_o for cathodic deposition were determined as a function of the anodic current density at which the 'fresh' copper surface had been formed, maintaining (al-

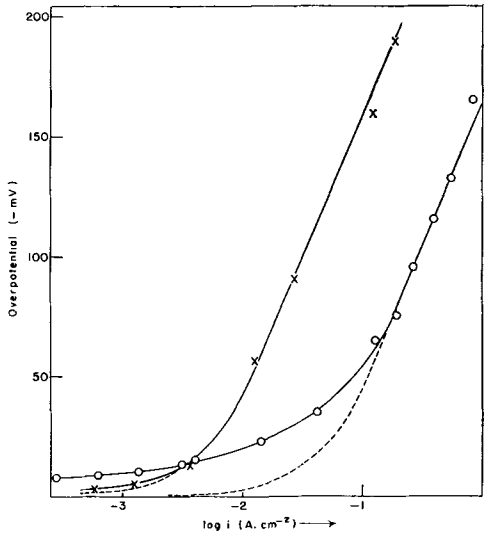

Fig. 2. Typical Tafel line for Cu deposition. x, Electrodeposited electrode; o, He-quenched electrode; - - - -, calculated line using i_o-value obtained by the extrapolation of linear line to $\eta = 0$.

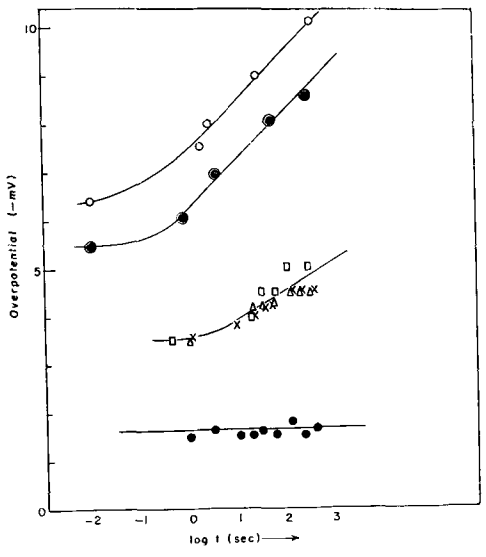

Fig. 3. Change of overpotential at $i = 8.7 \times 10^{-4}$ amp cm^{-2} with time of contact with solution after anodic dissolution. Open circle, circle with dot; He-quenched electrode square box; triangle, x, electrodeposited electrode; dark circle, oxide film electrode.

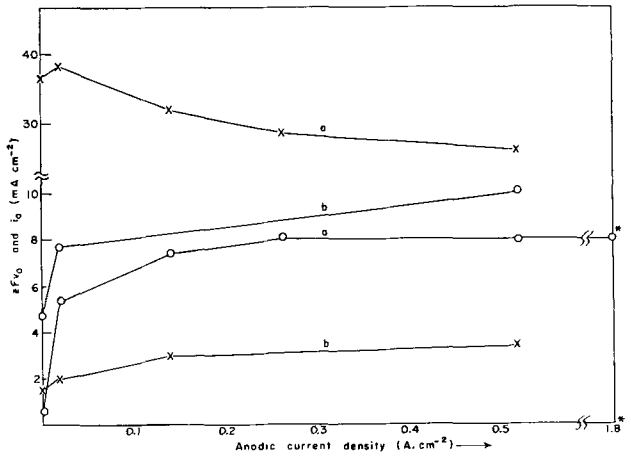

Fig. 4. Change of i_o and zFv_o as a function of anodic dissolution current by which a fresh surface was produced. x = i_o, o = zFv_o; curve a, He-quenched electrode; curve b, electrodeposited electrode. At the current density marked with *, O_2 evolution was observed during dissolution.

most) constant the time between the termination of dissolution and the commencement of deposition, *i.e.*, the age of the surface (20 sec). Measurements were carried out successively from low anodic current density to high ones, and the amount of dissolution was kept constant (10^4 layers) in each treatment.

Changes of i_o and v_o (obtained using Eq. [3] are shown in Fig. 4. They increase by approximately twice times and approach constant values.

(iv) *Surface diffusion flux and exchange current density as a function of cathodic current density by which a fresh surface is produced.*—(*a*) v_o: He-quenched electrodes were subjected to cathodic polarization with a current of $10^{-3} \sim 1$ amp cm^{-2} and a time sufficient for the deposition of 10^4 layers.

Results of v_o as a function of mode of preparation of the surface are shown in Table II. In the c.d. region 0.3 ~ 1 amp, after the transition time for the deposition of Cu is reached, v_o is increased by about 2 powers of 10 compared with that on He electrodes and becomes independent of the time of contact of

Table II. Effect on surface diffusion flux of formation of fresh surface by cathodic deposition

Method of preparation	zFv_o ma cm^{-2}	
He-quenched electrode	0.2 ~ 2.0	(cf. Table I)
Cathodic deposition of 10^4 layers:		
(*a*) Cu deposition.	2 ~ 10	(cf. Table I)
(*b*) Cu deposition + electrolytic H_2 evolution.	20 ~ 30	(from Eq. [4])

the surface with the solution, over a time of 9×10^{-3} sec to 1 hr. In the region of cathodic current density in which only copper deposits, v_o is increased by 5-10 times only.

(*b*) i_o: The effect of cathodic current density with which the equivalent of ~10^4 layers are deposited in the preparation of a new surface is shown in Fig. 5. (Each measurement was carried out on a fresh electrode.) It is seen that, for (i_o), the electrodeposited surface is a much less active one than is a He-quenched surface. However, after H_2 is codeposited, a considerable increase of i_o occurs.

After treatment at high cathodic polarization, where hydrogen codeposits 10^5 layers of copper was electrodeposited at various current densities. No decrease in i_o was observed (Fig. 6). This experimental result establishes that impurity adsorption from solution during electrodeposition of copper does not cause the decrease of surface activity which takes place on depositing Cu on He-prepared electrodes.

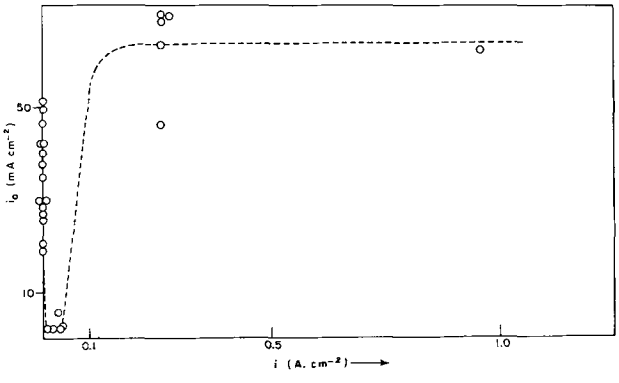

Fig. 5. Change of i_o as a function of cathodic deposition current by which a fresh surface was produced.

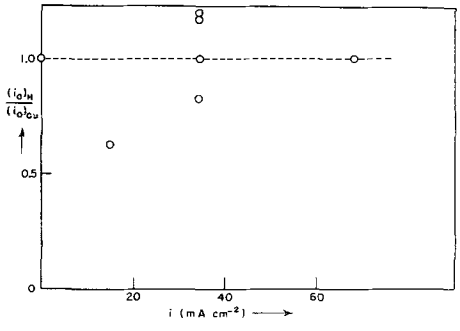

Fig. 6. Change of i_o with electrodeposition of Cu on the electrode which was previously subjected to the high cathodic polarization where hydrogen codeposited (2.6×10^{-1} amp cm^{-2}). $(i_o)_H$; i_o observed on the previously treated electrode with high cathodic polarization. $(i_o)_{Cu}$, after electrodeposition of Cu.

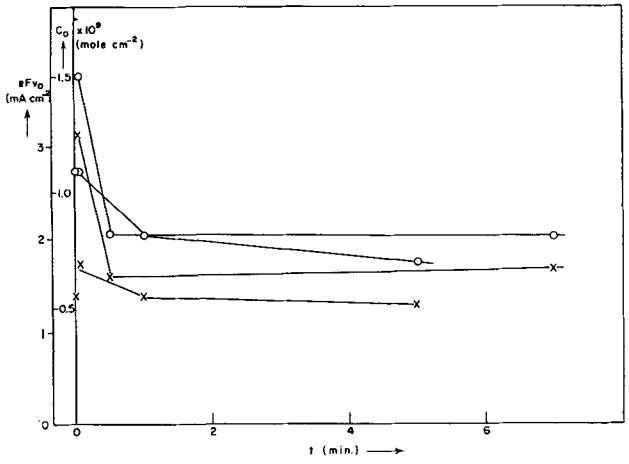

Fig. 7. Change of zFv_o and c_o with time of contact with solution after anodic dissolution. Calculated results from open circle, circle with dot in Fig. 3 using Eq. [3]. 0 = zFv_o, x = c_o.

He-*quenched Electrodes*

(i) *Values of parameters.*—Values of parameters on the He-quenched electrode are shown in Table I. Thus, (*a*) α_c and α_a are about the same as for electrodeposited electrodes; (*b*) the exchange c.d. is increased by about 10 times; (*c*) $C_{d.l.}$ is unchanged; (*d*) c_o is about 10 times less than on electrodeposited electrodes; (*e*) the parameter zFv_o is about five times less than on electrodeposited electrodes.

Comparison of i_o and zFv_o for the He-quenched electrodes indicates that the surface diffusion of adions is rate determining at low current densities.

A typical Tafel line is shown in Fig. 2. One sees a marked deviation at low current density from the expected line obtained assuming transfer to be rate controlling at all current densities.

Parameters were also evaluated after dissolution of the He-quenched electrode (Table I). Thus, c_o is nearly the same as that on an electrodeposited electrode (*i.e.*, it increases more than 10 times) and zFv_o increases more than 10 times. α_c, α_a, and $C_{d.l.}$ remain constant. The exchange current density becomes a little smaller (cf. Fig. 4).

(ii) *Change with time of the surface of the* He-*quenched electrode after exposing it to a solution, following anodic preparation of a fresh surface.*—The dependence of the rate constant for a surface prepared by anodic dissolution upon time of contact with the solution was studied. Results are shown in Fig. 3 for a current density of preparation of 8 ma cm^{-2} ~ 10^3 layers dissolved. In this c.d. region surface diffusion is rate controlling.

In Fig. 3 the section above 1 sec is linear. η_t, (or v_o) changes little during the first second. $\partial\eta_t/\partial \ln t \simeq 1$ mv. In Fig. 7, v_o and c_o calculated from Eq. [3] are shown as a function of time.

(iii) *Surface diffusion flux and exchange current density as a function of anodic current density by which a fresh surface was produced.*—(*a*) v_o increases considerably with the anodic current density and then becomes independent of it (Fig. 4). Contact of the surface with oxygen during dissolution does not effect the v_o value. (At the current densities marked with * in Fig. 4, oxygen evolution commenced.)

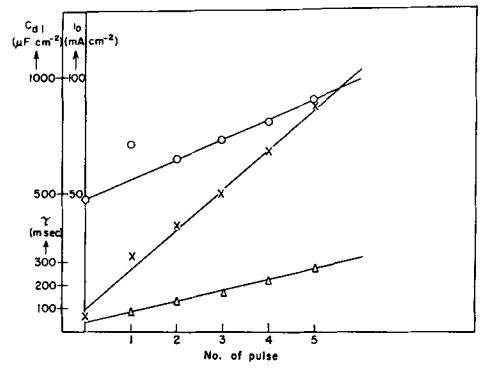

Fig. 8. Effects of the high cathodic polarization pulses (2.6 x 10^{-1} amp cm^{-2}, 20 sec) on i_o, $C_{d.l.}$, and τ (He-quenched electrode). Electrode was kept 30 min in solution after an application of each pulse and then measurements were carried out. ○, i_o; x, $C_{d.l.}$; and Δ, τ.

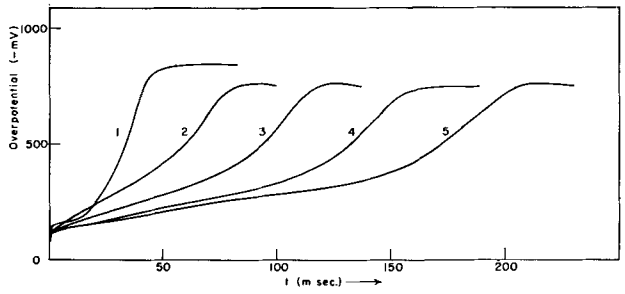

Fig. 9. Cathodic polarization curve at 2.6 x 10^{-1} amp cm^{-2}. Curve 1, on the He-quenched electrode, curves 2, 3, 4, and 5, after successive application of cathodic polarization pulse (2.6 x 10^{-1} amp cm^{-2} 20 sec).

(*b*) i_o: i_o decreases somewhat with increasing c.d. of dissolution (Fig. 4).

(iv) *Effects of repetitive application of high cathodic polarization pulses in which hydrogen co-deposits, on i_o, capacity, and transition time.*—He-quenched electrodes were subjected to a successive application of high cathodic pulse (2.6 x 10^{-1} amp cm^{-2}, 20 sec). Thus i_o, $C_{d.l.}$, and τ were observed, respectively, leaving the electrode 30 min in solution after the application of each pulse. Results are shown in Fig. 8. Changes of these quantities are linear with the number of pulse.

Figure 9 shows the change of the $\eta - t$ relation at constant current of 2.6 x 10^{-1} amp cm^{-2} after the application of successive cathodic pulses. When the current density of the pulses was kept sufficiently low (*e.g.*, if it was <2.6 x 10^{-2} amp cm^{-2}), the transition time did not increase with the number of pulses. Successive anodic dissolution similarly does not affect the transition time (Fig. 10). In Fig. 11, an increase of the transition time with the number of cathode polarization is shown under various conditions. The increase of transition time with the pulse depends sensitively on the concentration of cupric ions and not upon the concentration of protons. A powdery deposit of copper during the high cathodic polarization treatment was observed.

H_2-*treated Electrode*

(i) H_2-*quenched electrode.*—Values of parameters are shown in Table I. These values are almost the same with those of the He-quenched electrode.

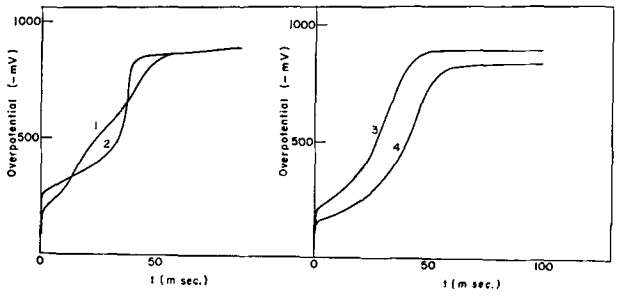

Fig. 10. Cathodic polarization curve at 2.6 x 10^{-1} amp cm^{-2}, as a function of surface state. Curves 1, 3; on the He-quenched electrode; curve 2, after electrodeposition of Cu (5 x 10^{-4} layers); curve 4, after dissolution of Cu (3 x 10^{4} layers).

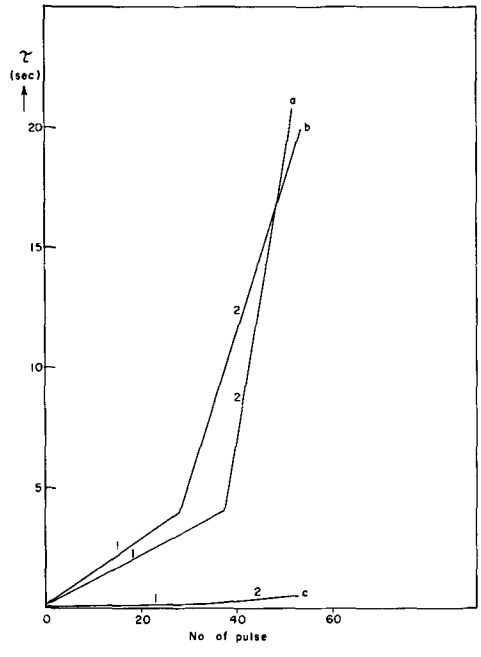

Fig. 11. Change of τ with number of successive high cathodic polarization pulses at various conditions. a, 0.055 mole l^{-1} $CuSO_4$, 1.1N H_2SO_4; b, 0.050 mole l^{-1} $CuSO_4$, 0.41N H_2SO_4; c, 0.013 mole l^{-1} $CuSO_4$, 1.1N H_2SO_4. Section 1; observed after 20 sec of the cathodic polarization pulse (2.6 x 10^{-1} amp cm^{-2} 20 sec); section 2, observed after 2 min of the cathodic polarization pulse (2.6 x 10^{-1} amp cm^{-2} 1 min).

Hence, the surface structure of He and H_2 quenched electrodes are the same.

(ii) H_2-*evolved electrode.*—A He-quenched electrode was polarized cathodically in 1N-H_2SO_4 solution for a certain time (~10^5 layers deposited). Thereafter, cupric sulfate solution was introduced and transient techniques were applied. Results are shown in Table I. No effect of the H_2-evolution treatment was observed. Consequently, there is no reducible surface complex (oxide) on the He-quenched electrode (cf. Section 4; oxide film electrode).

Oxide-film Electrode

(i) *Values of parameters.*—Values of parameters are shown in Table I. (*a*) α_c and α_a are essentially the same as on electrodeposited electrode. (*b*) i_o's are higher than those of the He-quenched electrodes. (*c*) $C_{d.l.}$ is larger (2 ~ 3 times) than on He-quenched electrodes. (*d*) c_o and $z\mathbf{F}v_o$ are slightly larger than those of the electrodeposited electrode.

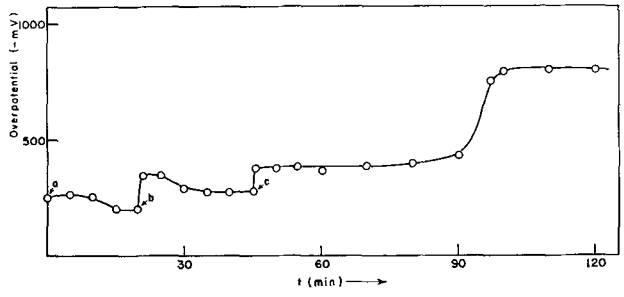

Fig. 12. 'Coulometry' on the oxide film electrode: a, i = 2.6 x 10^{-4} amp cm^{-2}; b, i = 8.7 x 10^{-4} amp cm^{-2}; i = 2.6 x 10^{-3} amp cm^{-2}; electrolyte, 0.2 mole l^{-1} N H_4Cl.

(ii) *Stability of the surface of the oxide film electrode after exposing the surface to the solution, following anodic dissolution.*—No change of the rate constant with time after dissolution of ~10^4 (15 ma cm^{-2}) layers was observed on the oxide film electrode. Results are shown in Fig. 3.

(iii) *Coulometry on the oxide film and He-quenched electrode.*—The thickness of the oxide film was measured by coulometry (4). Using aqueous NH_4Cl (0.2 M/L), a constant cathodic current was applied and the overpotential followed with time. Results on the oxide film electrode and the He-quenched electrode are shown in Fig. 12 and 13, respectively. The thickness of the oxide film electrode was determined as about 10^5Å according to the equation (7), $T = itA$, where T is the thickness in Å, i is the constant current in ma cm^{-2}, t is the time in seconds to the end point, and $A = 10^5 M/N\mathbf{F}\rho$, where M is the gram molecular weight of the compound composing the film, N is the number of Faradays required for the reduction of one-gram-molecular weight of film, $\mathbf{F}$ is Faraday's number, and ρ is the density of the film (for Cu_2O, taking $\rho = 6.0$, A = 12.4). It is seen from Fig. 14 that there is no oxide film on He-quenched electrode (Table III).

Discussion

Reaction Mechanisms

(i) *High current densities.*—The reaction mechanism on the electrodeposited electrode has been studied in detail and is concluded to be (1, 2)

$$Cu^{++} + e \rightarrow Cu^{+} \qquad [5]$$

$$Cu^{+} + e \rightleftharpoons Cu \qquad [6]$$

where reaction [5] is rate controlling. As can be seen from Fig. 2 and Table I, values of parameters, *i.e.*, α_c, α_a, and i_o, are reproduced on the electrodeposited

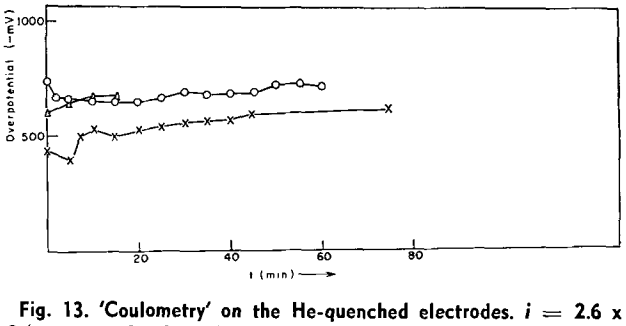

Fig. 13. 'Coulometry' on the He-quenched electrodes. i = 2.6 x 10^{-4} amp cm^{-2}; electrolyte; 0.2 mole l^{-1} N H_4Cl.

Table III. Relative effects of substrates on the kinetics of the copper deposition reaction

Quantity	Electrode: Quenched	Electrodeposited	Oxide film	Chemically deposited Cu
i_o	High	Low	Low	Very high increases with number of high cathodic pulses.
v_o	Low	High	High	Very high
c_o	Low	High	High	Very high
$C_{d.l.}$	Normal	Normal	High	Very high
$\eta_t\left(\alpha\frac{1}{v_o}\right)$	$\log t$ Rapidly decay	$\log t$ Slow decay	No decay	—

electrodes, and values of α_c and α_a on the other electrodes are also close to those of the electrodeposited electrodes. Hence, the reaction mechanism on the electrodes investigated, including He-quenched and oxide film electrodes, can be considered as [5]-[6] in the region where the linear Tafel line was observed.

(ii) *Low current densities.*—Were the mechanism [5]-[6] to be applicable, the η-i relationship at low current densities could be calculated from

$$i = i_o\left[e^{-\frac{\alpha_c F\eta}{RT}} - e^{\frac{\alpha_a F\eta}{RT}}\right] \qquad [7]$$

using i_o-values obtained by the extrapolation of the Tafel line in its linear region. From Fig. 2, it can be seen that the experimental results on the electrodeposited electrode at low current densities deviate only slightly from those calculated from [7], but on the He-quenched electrodes considerable deviations from the η-log i according to [7] occur. These deviations have been explained by assuming that the surface diffusion of adions is rate controlling at low current densities (1, 2, 6). As can be seen from the ratio of i_o to $z\mathbf{F}v_o$ in Table I, the rate constant of the transfer process is 15 ~ 17 times larger than that of the surface diffusion on the He- or H_2-quenched electrode, whereas on the other electrodes it is nearly unity.

On the H_2-evolved electrode, $z\mathbf{F}v_o$ and c_o could not be estimated because of superpolarization in the transient. However, η_∞ at low current densities was the same with that of the He-quenched electrode, *i.e.*, the surface diffusion is also rate controlling on this electrode surface. In Table IV, reaction mechanisms are summarized.

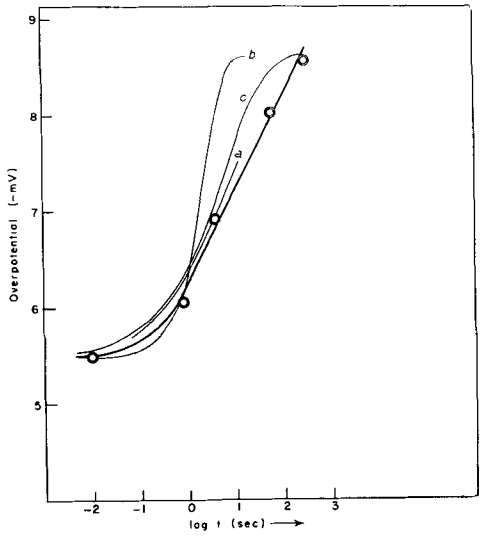

Fig. 14. Change of overpotential with time of contact with solution after dissolution. —circle with inner circle—; observed (circle with dot in Fig. 3); ———, calculated: a, from eq. [13] where D'/K^2 and $N_{t=\infty}'/N_o$ were taken as 1 and 0.7; b, from Eq. [16]; and c, from Eq. [19] where $c_{A,\,t=0}/c_B$, f_A, and zFD/x_o^2 were taken as 5, 0.2, and 10^6 (Table V).

Change of Parameters of Surface of He-Quenched Electrodes with Time after Cessation of Anodic Dissolution

The following models are considered.

(i) During anodic dissolution, spirals unwind, i at points of low radius of curvature being greater than that on the planes. Pits may develop. On cessation of the net dissolution current, dissolution or deposition occurs locally at peaks or pits, respectively, so that the surface tends to become smoother, *i.e.*, its real area less with increase of time. The rate constant per apparent square centimeter would then tend to decrease with time. However, such effects would be reflected in the capacitance measurements, and these show values independent of time after cessation of dissolution.

(ii) After cessation of the anodic current, impurities from the solution (*e.g.*, any dissolved from the electrode surface) may diffuse back to the surface and adsorb thereon, migrating to growth steps. Thus, assuming surface diffusion control and with a model in which the variation of adion concentration

Table IV. Reaction mechanisms as a function of type of electrode surface

Type of electrode surface	Low current density	High current density
Electrodeposited	Transfer and surface diffusion	Transfer control
He-quenched	Surface diffusion control	Transfer control
H_2-quenched	Surface diffusion control	Transfer control
Oxide film	Transfer and surface diffusion	Transfer control
Anodically dissolved	Transfer and surface diffusion	Transfer control
H_2-evolved	Surface diffusion control	Transfer control

between the growth steps is assumed linear with distance (5)

$$\frac{i}{z\mathbf{F}} = \frac{Dc_o}{x_o^2}\frac{c - c_o}{c_o} \qquad [8]$$

for steady state, where x_o is half distance between growth steps, D the diffusion constant, and c the concentration of adions at specified potentials (c_o at the reversible potential), respectively.

Or

$$\frac{i}{z\mathbf{F}} = \frac{Dc_o}{x_o^2}\left[e^{-\frac{z\mathbf{F}\eta}{RT}} - 1\right] \qquad [9]$$

x_o is related to the number of growth steps, N, arising from a pair of screw dislocations, by (6)

$$\frac{1}{(2x_o)^2} = 2N \qquad [9a]$$

Hence

$$\frac{i}{z\mathbf{F}} = 8Dc_oN_t\left[e^{-\frac{z\mathbf{F}\eta}{RT}} - 1\right] \qquad [10]$$

The number of growth steps at time t, N_t diminishes with time, after cessation of dissolution, as the impurities adsorb on them.

Now

$$N_t = N_o\left(1 - \frac{N_{t=\infty}'}{N_o}\frac{N_t'}{N_{t=\infty}'}\right) \qquad [11]$$

where N_t' is the number of 'poisoned' growth steps. But (8)

$$\frac{N_t'}{N_{t=\infty}'} = 1 - e^{\frac{D't}{K^2}}\operatorname{erfc}\left(\frac{D't}{K^2}\right)^{1/2\,2} \qquad [12]$$

if the rate of aggregation of impurities to growth steps is controlled by diffusion from solution (D' is the diffusion coefficient of the impurity in solution, and K is a constant characteristic of the corresponding adsorption isotherm).

From [11], substituted into [12] and [10], one obtains for $|\eta| << RT/z\mathbf{F}$

$$\eta_t = \eta_{t=0}\left[\left(1 - \frac{N_{t=\infty}'}{N_{t=0}}\right) + \frac{N_{t=\infty}'}{N_{t=0}}e^{\frac{D't}{K^2}}\operatorname{erfc}\left(\frac{D't}{K^2}\right)^{1/2}\right]^{-1} \qquad [13]$$

where $\eta_{t=0} = RT/8(z\mathbf{F})^2Dc_oN_o$, and c_o is constant with time.

This equation is consistent with experiment, as shown in Fig. 14. However, it is seen that the model involves c_o = constant, and in Fig. 7 it is seen that c_o decreases with time in a way parallel to v_o. The model is hence untenable.

(iii) During dissolution, crystal faces of various indices may be produced, some having higher bond strength to the adions than others. After the current is switched off, the planes on which the adions are present in the highest concentration may dissolve and metal ions deposit on those with a smaller adion concentration.

Assuming for simplicity an equal area of planes A and B, where $c_A >> c_B$, the change of c_A with time can be expressed by

$$-\frac{dc_{A,t}}{dt} = \frac{i_of_A}{z\mathbf{F}}\frac{c_{A,t} - c_{B,o}}{c_{B,o}} \qquad [14]$$

where f_A is the fraction of surface A/cm^2 of surfaces A and B.

Integration gives

$$c_{A,t} = c_{B,o} + (c_{A,t=0} - c_{B,o})\,e^{-\frac{i_of_A}{z\mathbf{F}c_{B,o}}t} \qquad [15]$$

From Eq. [9], [15], and the relationship $c_o = f_Ac_{A,t} + f_Bc_{B,t}$ one obtains

$$-\eta_t = \frac{RT}{z\mathbf{F}}\ln\left[1 + \frac{\left[1 + \left(\frac{c_{A,t=0}}{c_{B,o}} - 1\right)f_A\right]\left[e^{-\frac{z\mathbf{F}\eta_{t=0}}{RT}} - 1\right]}{1 + \left(\frac{c_{A,t=0}}{c_{B,o}} - 1\right)f_Ae^{-\frac{i_of_A}{z\mathbf{F}c_{B,o}}t}}\right] \qquad [16]$$

where

$$-\eta_{t=0} = \frac{RT}{z\mathbf{F}}\ln\left[1 + \frac{ix_o^2}{z\mathbf{F}D}\frac{1}{c_{B,o} + (c_{A,t=0} - c_{B,o}) + A}\right] \qquad [16a]$$

This model is compared with experiment in Fig. 14. It is qualitatively consistent with experiment, but the gradient of the η_t-log t relation is badly reproduced.

(iv) The same concept as that expressed in (iii), but the equilibration of adion concentration occurs by means of surface diffusion.

Hence

$$-\frac{dc_{A,t}}{dt} = \frac{f_A}{x_o}\sqrt{\frac{D}{\pi t}}(c_{A,t} - c_{B,o}) \qquad [17]$$

Integration gives

$$c_{A,t} = c_{B,o} + (c_{A,t=0} - c_{B,o})\,e^{-\frac{2f_A}{x_o}\sqrt{\frac{D}{\pi}}t^{1/2}} \qquad [18]$$

From Eq. [9], [18], and the relationship $c_o = f_Ac_A + f_Bc_B$

$$-\eta_t = \frac{RT}{z\mathbf{F}}\ln\left[1 + \frac{\left[1 + \left(\frac{c_{A,t=0}}{c_{B\,o}} - 1\right)f_A\right]\left[e^{-\frac{z\mathbf{F}\eta_{t=0}}{RT}} - 1\right]}{1 + \left(\frac{c_{A,t=0}}{c_{B,o}} - 1\right)f_Ae^{-\frac{2f_A}{x_o}\sqrt{\frac{D}{\pi}}t^{1/2}}}\right] \qquad [19]$$

The model agrees reasonably with experiment (Fig. 14). The slope of the η_t-log t relation may be

[3] It is assumed in the derivation of [12] that (a) $c' = c_o'$, $x \geq 0$ at $t = 0$; $c' = c_o'$, when $x \to \infty$ at $t \geq 0$; (b) $N_t' = Kc'$, where c' and c_o' are the concentrations of impurities at the Helmholtz double layer and in the bulk, and x is the distance from the electrode to the solution.

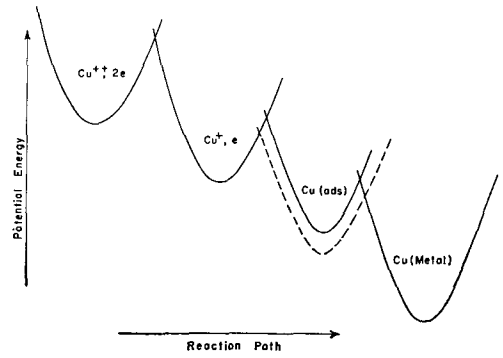

Fig. 15. Schematic expression of potential energy profile for Cu electrode reaction. Change of adsorption energy of Cu(ads) does not effect primarily reaction rate, since the rate determining step is $Cu^{++} + e \rightarrow Cu^{+}$.

qualitatively brought into better agreement with experiment if the formation of further adions from the growth steps on face A is taken into account, the effect being to slow down the equilibration of adion concentration among the crystal faces. It is not unplausible that the rearrangement occurs by surface diffusion, for the i_o value on electrode surfaces in which c_o is high, is small compared with the i_o values on He-prepared electrodes, *i.e.*, adions on the more populated surfaces go into solution less well than those on the less populated surfaces.

Dependence of Rate Constant of Transfer Reaction on Substrate of Metal Surface

For the transfer reaction, two factors may change when the surface of the metal is altered.

(i) The heat of adsorption of Cu adions is larger on the electrodeposited electrodes, as evidenced by the larger value of c_o on such electrodes than on He-quenched surfaces. Consideration of potential energy profile diagrams, however, indicates that the heat of activation for the transfer reaction [5] would not be effected by change of the bond strength between metal and adions (Fig. 15).

A secondary effect may, however, arise from the larger heat of adsorption on the electrodeposited electrode. When $\theta < 1$, where θ is the coverage of the surface with adions, and taking the rate constant for transfer for an electrodeposited and a quenched electrode as the same, the observed value of i_o on an electrodeposited electrode would be $i_o(1-\theta)$.

Thus, i_o can be defined as

$$i_o = \vec{k}_o\,[Cu^{++}]\,e^{-\frac{\beta F V_R}{RT}}\,e^{-\frac{\vec{\Delta H}^*}{RT}}\,(1-\theta) = \overleftarrow{k}_o\,[Cu^{+}]\,e^{\frac{(1-\beta) F V_R}{RT}}\,e^{-\frac{\overleftarrow{\Delta H}^*}{RT}}\,(1-\theta) \quad [20]$$

where $\vec{k}_o$, and $\overleftarrow{k}_o$ are rate constants, $[Cu^{++}]$ and $[Cu^{+}]$ the concentrations of the indicated ions in the Helmholtz layer, V_R the potential of the electrode at equilibrium, β the symmetry factor, and $\vec{\Delta H}^*$ and $\overleftarrow{\Delta H}^*$ are the activation energies of [5] in the forward and backward directions, respectively.

Then

$$\frac{(i_o)_{He}}{(i_o)_E} = \frac{e^{-\frac{\beta F V_{R,He}}{RT}}\,e^{-\frac{\vec{\Delta H}^*_{He}}{RT}}\,(1-\theta_{He})}{e^{-\frac{\beta F V_{R.E}}{RT}}\,e^{-\frac{\vec{\Delta H}^*_{E}}{RT}}\,(1-\theta_E)} = \frac{[Cu^{+}]_{He}\,e^{\frac{(1-\beta) F V_{R,He}}{RT}}\,e^{-\frac{\overleftarrow{\Delta H}^*_{He}}{RT}}\,(1-\theta_{He})}{[Cu^{+}]_{E}\,e^{\frac{(1-\beta) F V_{R.E}}{RT}}\,e^{-\frac{\overleftarrow{\Delta H}^*_{He}}{RT}}\,(1-\theta_E)} \quad [21]$$

Also

$$\vec{\Delta H}^* = H^* - H^{Cu^{++}} + e_o^- \quad [22a]$$

$$\overleftarrow{\Delta H}^* = H^* - H^{Cu^{+}} \quad [22b]$$

$$H_{He}{}^{Cu^{++}+e} = H_E{}^{Cu^{++}} + e \quad [22c]$$

Hence

$$H^*_{He} - H^*_E = \beta(H_{He}{}^{Cu^{+}} - H_E{}^{Cu^{+}}) \quad [22d]$$

where H^* and H's are the potential energies of the activated complex and the chemical species specified, respectively.

From Eq. [21] and [22], and the experimental result that $V_{R,He} = V_{R.E}$, and $(i_o)_{He}/(i_o)_E \simeq 10$

$$10 = e^{-\frac{\beta(H_{He}{}^{Cu^{+}} - H_E{}^{Cu^{+}})}{RT}}\,\frac{(1-\theta_{He})}{(1-\theta_E)} \quad [23]$$

It can be assumed that the potential energy of Cu^{+} will not change with change of surface configuration, and hence the difference in i_o between the two substrates can be attributed to a change of θ. Using $\theta_{He} \simeq 0.07$ (Table I), Eq. [23] gives 0.86 for θ_E which is in good agreement with the experimental result of $\theta_E \simeq 0.8$ (Table I).

However, the theory of the determination of θ involves the assumption that $\theta << 1$, so that the determined θ values cannot be numerically accurate for the electrodeposited electrodes. Thus, only qualitative significance attaches to the result that high adion coverage may cause the comparatively low i_o value of the electrodeposited surfaces (see Appendix).

(ii) The work function may change with the surface state, for electrodeposition determines the predominant crystal planes, which in turn influence the work function. Thus, the work function is less in the vicinity of defects (9). However, predominant transfer at local growth steps is not acceptable because of the observed surface diffusion control at low overpotential. Direct transfer to growth steps was concluded as an unlikely process for metal ions by Conway and Bockris (10) from consideration of potential energy profile diagrams.

On the oxide electrodes, the i_o values are higher than those on the electrodeposited electrodes (Table I), but if the values are divided by the ratio of $(C_{d.l.})$oxide/$(C_{d.l.})$electrodeposited, the values of i_o

for the oxide are of the same order as those on electrodeposited electrodes. This result is surprising. It could be consistent with two models of the surface.

(*a*) The oxide is relatively nonporous. On contact with an acid solution, the oxide film will be completely dissolved (the color of the surface is observed to change from black to dark brown), and a Cu surface is therefore exposed to the solution. The dissolution follows a certain preferred crystal plane in the oxide, and hence a roughening of the surface is caused, in consistence with the larger capacities observed for the (so-called) oxide electrodes.

(*b*) Alternatively, the oxide may be regarded as porous and the reaction to occur on the surface of the substrate. However, if this were so, the transition time should be greatly reduced because of the small fraction of available surface area (transition time is proportional to the square of area, Eq. [28]) and the ohmic overpotential is increased. However, the transition time and ohmic overpotential on the oxide electrodes are roughly equal to those of electrodeposited electrodes. Consequently, model (*a*) is valid and the rate of transfer, per true square centimeter, to the surface which arises from a freshly dissolved oxide is the same as that for electrodeposited electrodes (except for the greater area factor).

The equality of i_o would be explained if θ on the electrodeposited and oxide electrodes were about the same, *i.e.*, the attachment of the adions to the surface the same. On an electrodeposited electrode, a large number of kink sites will arise in the boundary of the growth spirals. At the same time, on oxide electrode, the surface will possess defects, arising from the removal of oxygen atoms in the surface, which will correspond to about half the number of sites. Thus, in both the reduced and electrodeposited electrodes, the number of kink sites is much greater than that on He-quenched electrodes and approaches a limitingly high value. This is consistent with the lower, and approximately equal, i_o value on electrodeposited and reduced electrodes.

The remarkable increases in i_o obtained by the repetition of high cathodic pulses of 20 sec, in which Cu is deposited followed by the evolution of hydrogen, is consistent with the concept that a chemical reduction of Cu^{++} in solution evolved H takes place. The change of standard free energy for $Cu^{++} \rightarrow Cu$ is −61.2 kcal (11), and the reversible potential of atomic hydrogen electrode is −1.98v (12) (hydrogen scale), so that the change of free energy of the reaction $Cu^{++} + 2H \rightarrow Cu + 2H^+$ is −107 kcal [cf. also ref. (13) and (14)].

The relation of i_o to the number of pulses is linear, and the increase per pulse is 8.6 ma. Since the increase of surface area per pulse in 3.6 cm^2, the activity of the surface produced is the same as that of the electrodeposited electrode (see Table I). It is noticed that the i_o value at the commencement of the pulsing increases compared with that on He-quenched electrodes. The i_o/cm^2 on the pulsed electrode is, however, that of an electrodeposited electrode. Hence, as the increase in surface area is only 3.6 times per pulse, an initial decrease of i_o would be expected. Its absence indicates that part of the original He-quenched surface remains active.

Table V. Values of $zFD\,x_o^2$ as a function of electrodes

Electrode	$zFD/x_o^2 (= zFv_o/c_o)$
Electrodeposited	0.7×10^6
He-quenched	2.8×10^6
H_2-quenched	2.2×10^6
Oxide film	0.7×10^6
Dissolved	2.8×10^6

Dependence of v_o and c_o on the Substrate of Metal Surface

Tables I and III show that, per cm^2, v_o and c_o are approximately parallel, *i.e.*, if the model considered is the first approximation model for surface diffusion on electrodes, with a linear concentration gradient, then, as, from this model (5), $v_o = Dc_o(x_o^2)$, the factor $D_{x_o}{}^2$ is roughly constant for quenched and electrodeposited electrodes. (The constancy is only to within about 2-3 times, but the possible variation of x_o are by several orders of magnitude, so that the result v_o/c_o is constant can be regarded as meaning that x_o is approximately constant, for D is unlikely to change for the same metal and adsorbed anion concentration). Results are shown in Table V.

Two models are possible in an interpretation of the variation of c_o with substrate: (*a*) the electrodeposited electrode contains more kink sites than does the quenched surface. Consequently, as $c_o = c_K \exp(-\Delta H/RT)$, where c_K is the concentration of kink sites, and ΔH the energy difference between the atoms at kink site and on the surface, the value of c_o would be greater on the electrodeposited (and oxide) surface than on the quenched electrode. (*b*) Alternatively, the increase of c_o observed on an electrodeposited electrode may arise from a greater bond strength for $M\text{-}M^+$ than on the quenched electrode.

The first model is the less likely, for, if the number of kink sites and hence, number of steps, is substantially larger on the electrodeposited electrode, x_o would be substantially smaller, in contradiction to the results.

The dependence of c_o (hence, v_o) on the surface, therefore, depends on the crystal plane developed in deposition. Let it be supposed, for illustration, that in the deposited surface, a 100 plane predominates (cf. Fig. 16). Then, the coordination number of an

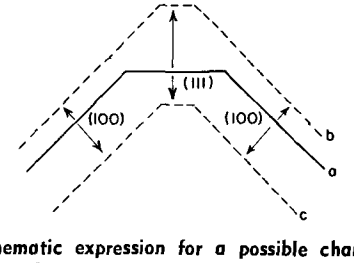

Fig. 16. Schematic expression for a possible change of surface structure during electrodeposition and dissolution. a, original surface; b, after deposition. The facet (111) will grow faster than facet (100) and hence fraction of (111) face in the surface will decrease with deposition. c, after dissolution. The facet (100) will dissolve faster than (111) face and hence fraction of (111) in the surface will decrease with dissolution.

atom in this plane is 8. Let it be correspondingly supposed that (111) planes predominate on the quenched electrode. Then, the coordination number is 9. Hence, the bond strength on the electrodeposited electrode for an adion is $\Delta H_{\text{sublimation}}/12$ greater than that on a quenched and thus 5 kcal mole^{-1} would be the order of increase in bond strength of an adion on an electrodeposited surface, compared with that on a quenched surface. Hence, the c_o value would be (for the same concentration of kink sites) about 60 times larger (experiment shows ten times) for electrodeposited than for He-quenched electrodes.

On oxide electrodes, the i_o and c_o are essentially the same as on electrodeposited electrodes. Thus, according to the model suggested, for these electrodes the metal-adion bond must be about the same as on electrodeposited electrode, *i.e.,* the predominant plane must be the same, and probably the 100 plane. The dominance of the 100 planes on the copper surface formed by reduction, as well as on that formed by deposition, is not surprising, if it is remembered that the atoms in the surface of a 100 plane have a coordination number of 8, compared with those in a 111 plane, where the coordination number is 9. The 100 plane will thus be more readily attacked in a chemical reaction, and in a polycrystalline surface will be preferentially consumed, thus undermining the 100 planes, and reducing the proportion of the other planes associated with the 100 planes in the surface. The 100 planes tend, thus, to be increased in their proportion on the surface (see Fig. 16). In the same consideration, deposition will occur more easily on 111 planes than on 100 planes because an electrodeposited atom can be incorporated into the lattice in a more stable form on a 111 plane than on a 100 plane (difference in coordination number). Hence 111 planes may grow faster than 100 planes as indicated in Fig. 16, and thus the 100 planes tend to be increased in their proportion on the surface.

Mechanism of Effects of Repetitive Application of Cathodic Pulses at High Applied Potential

Cathodic pulses of 20 sec, at a current density of 270 ma cm^{-2}, were applied to He-quenched electrodes for up to 50 consecutive pulses. Experimental results on i_o, $C_{d.l.}$, and τ (cf. Fig. 8 and 11) show that these all increase linearly with the number of pulses.

From Fig. 8, values of di_o/dp, $dC_{d.l.}/dp$, and $d\tau/dp$, where p is the number of pulse, are estimated as 8.6 ma, 180 μ**F** and 48 msec, respectively. Since $C_{d.l.}$ on the He-quenched and the electrodeposited electrode is about 50 **F** cm^{-2}, an increase of 180 μ**F** in $C_{d.l.}$ corresponds to an increase of 3.6 cm^2 in surface area. Dividing the increase of i_o per pulse by the increase of surface area, one obtains 2.4 ma cm^{-2} for i_o on the deposit. Hence, the surface activity of the deposit is the same as that of the electrodeposited electrode.

The suggestion that the extra area is produced, during pulsing, by a chemical reduction of Cu^{++} is supported by the constant increase of i_o and surface area with the number of pulses.

The average increase in thickness of a deposit was observed to be 2 x 10^{-3} cm per pulse. Assuming n layers of particles produced per pulse,

$$2 \cdot 10^{-3} = n \cdot 2r \qquad [24]$$

where r is the radius of the particles. The total number of particles, N, can be expressed as

$$N = \frac{4\pi}{4r^2}[(r_o + r)^2 + (r_o + 3r)^2 + (r_o + 5r)^2 + \ldots + (r_o + (2n-1)r)^2] \qquad [25]$$

However, assuming spherical particles of equal size,

$$4\pi r^2 \cdot N = \frac{dA}{dp} \qquad [26]$$

From Eq. [24], [25], and [26], $r \sim 10^{-4}$ cm, $N \sim 10^6$, and $n \sim 5$. Hence the rate of chemical reduction, i_c, is given by:

$$\frac{i_c \cdot 20 \cdot M}{z\mathbf{F}d} = N \cdot \frac{4}{3}\pi r^3 \qquad [27]$$

as $i_c \sim 10$ ma per apparent surface area.

The transition time, t, can be given by

$$t = \frac{[Cu^{++}]^2 z^2 \mathbf{F}^2 \pi D_{Cu^{++}}}{4i^2} f^2 = t^o f^2 \qquad [28]$$

where f is the effective roughness factor for diffusion (15) of cupric ions. Using numerical values of 7.2 x 10^{-6} cm^2 sec^{-1}, 5 x 10^{-5} mole cm^{-3}, and 2.6 x 10^{-1} amp cm^{-2} for $D_{Cu^{++}}$, $[Cu^{++}]$, and i, respectively, t^o is calculated as 8.4 msec. Figure 9, curve 1, and Figure 10, curves 1 and 3, indicate an observed transition time on the He-quenched, electrodeposited, and dissolved electrodes is about 35 msec. The discrepancy between the calculated and observed transition times may be attributed to f. The thus derived f is 2.0 which can be compared with 3.5, estimated from $C_{d.l.}$.

According to Eq. [28], when the surface area becomes larger, one can expect an increase of t proportional to the square of the surface area. However, the experimental results (Fig. 8 and 11) show a linear increase with the number of pulses, *i.e.,* a linear increase with the surface area, since $C_{d.l.}$ increases linearly with the number of pulses. This contradiction arises from the difference of the surface areas effective for the charging up of double layer and for diffusion. The deposit formed from chemically reduced Cu^{++} would be porous and co-deposited hydrogen escapes through pores in it. Let it be assumed that the hole shown in Fig. 17 is the relevant deposit shape. Thus, the linear relationships in Fig. 8 mean that some part of the original electrode surface is still active for the deposition of Cu,

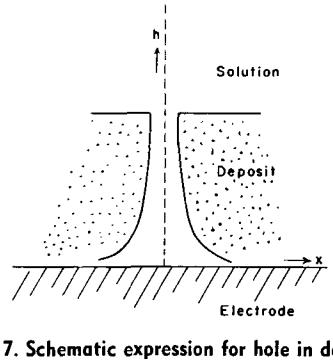

Fig. 17. Schematic expression for hole in deposit

after the application of many cathodic pulses. Similarly, such a shape may be regarded as expectedly arising from the pressure of H_2 evolved on the original substrate. As a rough approximation, let it be assumed that

$$h = \frac{a}{x^2} \qquad [29]$$

where h is the height of the hole, x the radius of the hole at h, and a is the constant, respectively. The total surface area of the holes can be given by

$$N_h \int_0^h 2\pi x \, dh = N_h 4\pi \sqrt{ah} \qquad [30]$$

where N_h is the number of holes.

Hence, t is given by Eq. [28] and [30] as

$$t = t^\circ f^2 \cdot (N_h 4\pi)^2 ah \qquad [31]$$

On the other hand

$$h = n \cdot 2r \cdot p \qquad [32]$$

when n is the number of layers per pulse and p the number of pulses. Hence, from Eq. [31] and [32]

$$t = t^\circ f^2 \cdot (N_h 4\pi)^2 a \cdot n \cdot 2r \cdot p \qquad [33]$$

Equation [33] indicates the linear increase of t with p which is observed experimentally. Taking 10^{-8} cm for x at $h = 10^{-1}$ cm and using $dt/dp = 40$ msec, one obtains N_h as $\sim 10^8$ holes per electrode, or $\sim 10^5/\text{cm}^2$, a plausible value.

Acknowledgments

The authors are indebted to the American Electroplaters' Society's Committee for their Project 16 for stimulating discussion, and to the Society for financial support. One of them (H. K.) wishes to thank Professor J. Horiuti for permission to take study leave.

Manuscript received March 26, 1962.

Any discussion of this paper will appear in a Discussion Section to be published in the June 1963 JOURNAL.

REFERENCES

1. E. Mattsson and J. O'M. Bockris, *Trans. Faraday Soc.*, **55**, 1586 (1959).
2. J. O'M. Bockris and M. Enyo, to be published.
3. W. Mehl, M. A. V. Devanathan, and J. O'M. Bockris, *Rev. Sci. Instr.*, **29**, 180 (1958).
4. M. Enyo, Dissertation, University of Pennsylvania, Philadelphia (1960).
5. W. Mehl and J. O'M. Bockris, *Can. J. Chem.*, **37**, 190 (1959).
6. H. Kita, M. Enyo, and J. O'M. Bockris, *ibid.*, **39**, 1670 (1961).
7. H. A. Miley, *J. Am. Chem. Soc.*, **59**, 2626 (1937); W. E. Campbell and U. B. Thomas, *Trans. Electrochem. Soc.*, **76**, 303 (1939).
8. P. Delahay and I. Trachtenberg, *J. Am. Chem. Soc.*, **79**, 2355 (1957).
9. C. Herring, "Metal Interfaces," p. 12. American Society for Metals, Metals Park, Ohio (1952).
10. B. E. Conway and J. O'M. Bockris, *Electrochim. Acta*, **3**, 340 (1961).
11. W. M. Latimer, "Oxidation Potentials," Prentice-Hall, Inc., New York (1952).
12. A. Hickling and F. W. Salt, *Trans. Faraday Soc.*, **38**, 474 (1942).
13. H. Fischer, "Elektrolytische Abscheidung und Elektrokristallisation von Metallen," p. 490, Springer-Verlag (1954).
14. D. Inman, G. J. Hills, L. Young, and J. O'M. Bockris, *Trans. Faraday Soc.*, **55**, 1904 (1959); *Ann. N. Y. Acad. Sci.*, **79**, 803 (1960).
15. J. M. Koltoff and J. J. Lingane, "Polarography," Interscience Publishers Inc., New York (1955).

APPENDIX

When $\theta < 1$, an effect of $(1 - 0)$ term in Eq. [20] on the Tafel slope at high current density is discussed below.

The reaction mechanism is:

$$Cu^{++} + e \rightarrow Cu^+ \qquad [5]$$

$$Cu^+ + e \rightleftharpoons Cu(ads) \qquad [6]$$

$$Cu(ads) \rightleftharpoons Cu \qquad [34]$$

where reaction [5] is rate-determining step.

For the steady state, the net rate, i is expressed for reactions [5], [6], and [34] as follows:

$$i = i_o \frac{1-\theta}{1-\theta_0}\left[e^{-\frac{\beta F\eta}{RT}} - \frac{[Cu^+]}{[Cu^+]_0} e^{\frac{(1-\beta)F\eta}{RT}}\right] \qquad [35]$$

where $[Cu^+]$ is the steady-state concentration of Cu^+ and $[Cu^+]_0$ is the equilibrium concentration of Cu^+.

$$i = i_o'\left[\frac{[Cu^+]}{[Cu^+]_0} e^{-\frac{\beta F\eta}{RT}} - \frac{\theta}{\theta_0} e^{\frac{\beta F\eta}{RT}}\right] \qquad [36]$$

$$i = zFv_o\left[\frac{\theta - \theta_0}{\theta_0}\right] \qquad [37]$$

where i_o' is the exchange current density for reaction [6]. Since reaction [5] is the rate-determining step, $i_o' >> i_o$. Hence, from Eq. [36]

$$\frac{[Cu^+]}{[Cu^+]_0} \simeq \frac{\theta}{\theta_0} e^{\frac{F\eta}{RT}} \qquad [38]$$

From Eq. [35] and [38], one obtains

$$i = i_o \frac{1-\theta}{1-\theta_0}\left[e^{-\frac{\beta F\eta}{RT}} - \frac{\theta}{\theta_0} e^{\frac{(1+\beta)F\eta}{RT}}\right] \qquad [39]$$

At high cathodic polarization:

$$i = i_o \frac{1-\theta}{1-\theta_0} e^{-\frac{\beta F\eta}{RT}} \qquad [40]$$

From Eq. [37], [40], and [8], one gets

$$i = i_o\left[1 - \frac{i}{zF\frac{GD}{x_o^2}(1-\theta_0)}\right] e^{-\frac{\beta F\eta}{RT}} \qquad [41]$$

where $G\theta_0 = c_o$. One can expect a deviation from the Tafel line at the condition

$$i > 0.1 \cdot zF\frac{GD}{x_o^2}(1-\theta_0)$$

Taking values for zFD/x_o^2 and D as 2×10^6 (Table V) and 10^{-7} cm^2 sec^{-1}, respectively, one gets: $i > 20\ (1-\theta_0)$ ma cm^{-2}. However, no deviation in the Tafel linearity was observed up to 800 ma cm^{-2} (Fig. 2). A possible explanation for this contradiction is that: (*a*) x_o decreases with i (2, 6); and (*b*) at high current density, another process, *e.g.*, nucleation, becomes predominant and displaces [37].

On the Emission of Electrons from Solids in Gas Discharges

I. Emission in the Vicinity of "Zero Field"

D. M. Speros and P. R. Buccilli

Lamp Research Laboratory, General Electric Company, Nela Park, Cleveland, Ohio

ABSTRACT

In the study of the electron emitting behavior of cathodes in practical gas discharge devices, a method for the determination and measurement of emission in the vicinity of zero field was found and is described.

The performance of cathodes is determined by their thermodynamic stability and their ability to emit electrons. Therefore, a general examination of materials intended for cathode use involves the study of both their thermochemical and electron emitting behavior. Factors involved in the thermochemistry of cathode components were examined previously (1). This paper begins the description of work concerned with their electron emitting behavior.

The conditions under which a cathode functions in a gas discharge may conveniently be classified as those involving an accelerating, a retarding, or a zero field in front of the cathode. When a condition of zero field prevails, in front of a uniform cathode, the discharge current equals the "discharge thermionic emission," J_θ, from the cathode.[1] Then the influence of an electron accelerating or retarding field on the cathode is removed and a measure, J_θ, of the thermionic capability of the cathode can be obtained. Methods for measuring the emission in the vicinity of zero field have been developed (2-8), but their use has been limited by the probes, auxiliary electrodes, or special structures that they involve. Because of the utilitarian need to perform measurements on normal standard production discharge devices such as phosphor coated fluorescent lamps, a new method was found and is described below. Since the first results of this investigation were reported (10), Forster-Brown and Cayless (11) and Waymouth (12) have published their work for measurements on normal lamps. Their procedures have assisted the task of interconnection between this work and the above probe techniques.

[1] As "distinguished" from the temperature-limited zero field thermionic emission in vacuum diodes determined by the Schottky and Richardson-Dushman plots. The interrelation between this and the thermionic emission J_θ above is not yet clarified (8, 9).

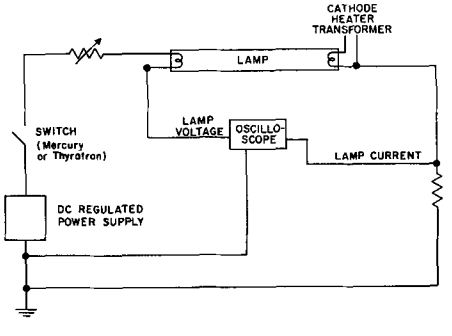

Fig. 1. Schematic diagram of apparatus

Preliminary Experiments

The determinants of cathode emission were sought in the starting or electrical breakdown behavior of the discharge. This behavior was investigated using the arrangement shown in Fig. 1. With the supply voltage set above the breakdown voltage of the discharge, closing of the switch produces oscilloscopic traces shown in Fig. 2 in their most general form. These are characterized by three plateaus termed, from left to right, A, B, and C. For purposes of subsequent reference, the quantities involved in the voltage *vs.* time trace are as follows: V_A is the height of plateau A in volts; this is the supply voltage; Δt_A is the length of plateau A in milliseconds; V_B is the height of plateau B in volts; Δt_B is the length of plateau B in milliseconds; and V_C is the height of plateau C in volts.

The corresponding quantities in the trace of current *vs.* time are in the same order, as follows: J_A, Δt_A, J_B, Δt_B, J_C.

During plateau B, the discharge has the appearance of a generalized glow engulfing the cathode. Immediately after the transition to plateau C, the glow is about as generalized, but has a different

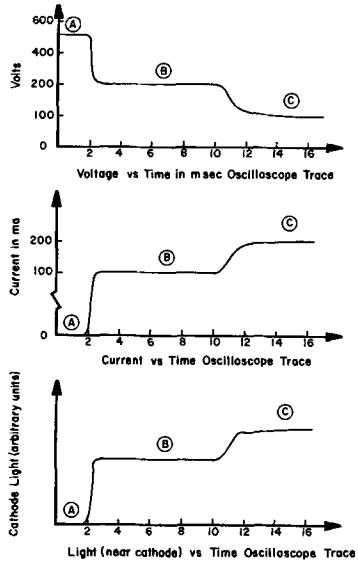

Fig. 2. Oscilloscopic traces of breakdown behavior: top, voltage *vs.* time; middle, current *vs.* time; bottom, light in cathode vicinity *vs.* time.

appearance with respect to both shape and color. After some time at this state, the discharge constricts to a "hot spot."

If a high tension spark of a few microseconds' duration is applied to the discharge during the interval Δt_A, the trace falls immediately to level V_B. If the spark is applied simultaneously with the application of the supply voltage, plateau A disappears while plateaus B and C remain unaffected. These facts and further evidence (13), indicate that plateau A corresponds to a type of formative time lag.

With respect to plateaus B and C, two stable and one transient states are recognized as follows:

(*A*) If the cathode is held at some high temperature before the application of the supply voltage, plateau B disappears, the trace falling directly from V_A, after a Δt_A, to level V_C. This level, V_C, is then the stable operating discharge voltage.

(*B*) If the cathode is at some low temperature, plateau C disappears, Δt_B becoming infinite. V_B under this condition is then the stable operating discharge voltage.

(*C*) If the discharge current is sufficiently high for the discharge to heat the cathode directly, then the temporal sequence seen in Fig. 2 is obtained as the state described in paragraph (*B*) above is made to revert to the state described in (*A*). The extent to which this can occur or, in other words, the height and the length of plateau B, depend on the relative magnitudes of discharge current and initial cathode temperature, as will be seen.

This general breakdown behavior is exhibited by all kinds of discharge devices tried thus far, including a number containing a few mm Hg of noble gas and having anode-cathode spacings of from 1 to 10 mm. As a result, this behavior does not seem attributable to some peculiarity of the positive column. Likewise, this behavior is discernible in some distorted shape if alternating current, square pulses or some sawtooth wave is used instead of direct current.

Correlation with Electron Emission Constants

Long gap discharges.—The bulk of this work was done using standard phosphor coated 40w fluorescent lamps, 48 in. in length and 1½ in. in diameter. In addition to a drop of mercury, they contained a mixture of 70% argon and 30% neon by volume at a pressure of 2.5 mm Hg. The cathodes consisted of a structure incorporating a coiled-coil filament originally coated, unless otherwise stated, with the standard production triple alkaline earth carbonates. The experimental procedure is illustrated by means of Fig. 3. At each setting of cathode heating current, the discharge current is read on the oscilloscope immediately after its rise from plateau A. Therefore, in order to obtain each experimental point, the lamp need be lighted for only a fraction of a second.

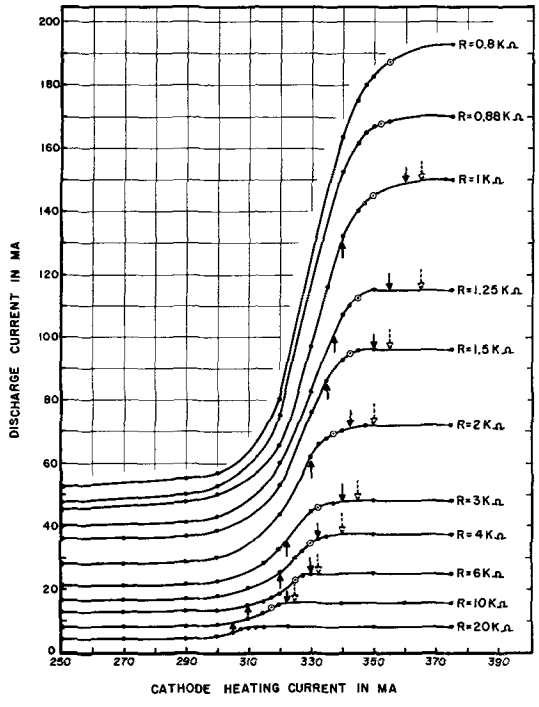

Fig. 3. Discharge current *vs.* cathode filament heating current for 40w standard fluorescent lamp. External resistance, *R*, values shown; supply voltage 300v. At circled points, $V_B = V_C$, $\Delta t_B = 0$. Full arrows show the limits for zero field identification according to Forster-Brown and Cayless (11); dotted arrows, the upper limit for zero field identification according to Waymouth (12).

At constant external resistance and supply voltage,[2] little change is observed in the discharge current as the cathode heating current is increased from zero up to a certain value. Beyond this value, the discharge current increases rapidly and reaches a new level within a narrow range of cathode heating current. Thereafter, the discharge current becomes quite constant again. At a new setting of external resistance, this general behavior is reproduced, and the family of curves shown in Fig. 3 is obtained.

At the low current branch of each curve, Δt_B can be of the order of several minutes, and the discharge has the appearance of a glow discharge. At low temperature and high external resistance values, the glow often covers the entire electrode structure, but as the cathode temperature is raised, the glow becomes localized on the coated portion of the filament.

In the cathode heating current ranges in which J_B increases rapidly, Δt_B decreases until, near the upper elbow of each curve, plateau B completely disappears, and the oscilloscope trace reverts directly from plateau A to plateau C.

In this range, first the appearance of the glow changes and then the discharge acquires the appearance of a "hot spot" mode of discharge. During a number of experiments in this and the subsequent series, the cathode heating current was changed from a.c. to a square wave. The behavior observed during the "off" (up to 8 msec) and "on"

[2] Usually 300v; it is often necessary to use a short duration ($\leq \Delta t_A$) high tension spark to light certain types of lamps at this voltage. V_B and Δt_B are not affected by the spark.

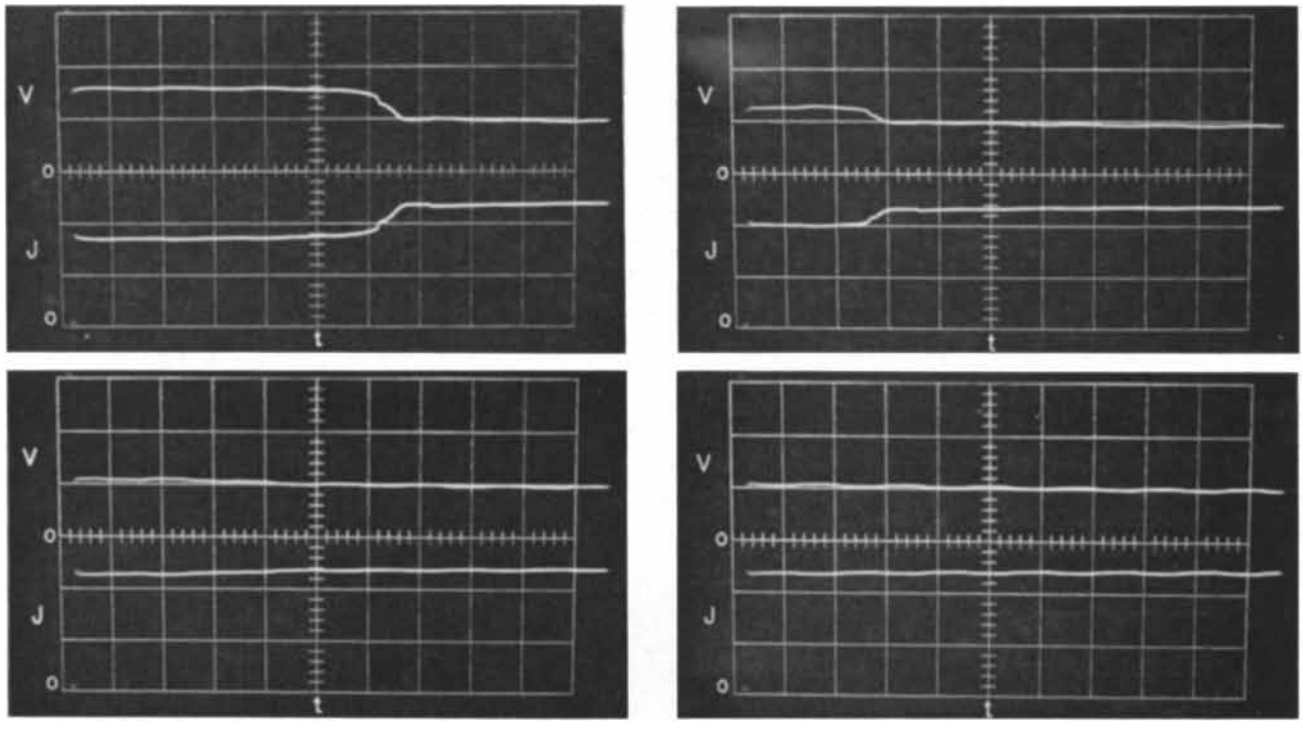

Fig. 4. Variation of V_B, upper trace, and J_B, lower trace, with cathode heating current. Supply voltage 500v; external resistance 3000 ohms. Cathode heating current progressively at 300, 320, 325 and 330 ma. Oscilloscope set at: ordinates, 167 v/cm, and 50 ma/cm; abscissa, 10 msec/cm.

periods indicated that the nature of the results described are not due to some interaction between the cathode heating and discharge circuits.

The possibility is considered that plateau B indicates that an accelerating field exists in front of the cathode. Consequently the cathode temperature at which plateau B disappears, that is, when

$$J_B = J_C;\ \Delta t_B = 0$$

is the lowest cathode temperature at which the state of zero field can possibly (but not necessarily) occur. This happens at the upper elbow of each curve as described above and shown on Fig. 3 by the circled points. Figure 4 shows the appearance of the oscilloscopic trace as the above condition is approached and attained with increasing cathode temperature. Often plateau B slopes smoothly into plateau C; then $\Delta t_B = 0$ is found by comparing the level of the tail end of the trace with the level of the trace immediately after the rise from plateau A. When these levels are first equal, $\Delta t_B = 0$. The level J_C rises slightly after this point is reached. For very high values of external resistance (bottom curve of Fig. 3) J_B rises very gradually and Δt_B is indefinite.

One of the prerequisites for the correctness of this assumption is that the cathode temperature and discharge currents as specified above should obey the Richardson-Dushman relation

$$J_\theta = AT^2 e^{-\frac{e\phi}{kT}}$$

A plot of $\ln J_\theta/T^2$ *vs.* $1/T$ in Fig. 5, line A, using the data (circled points) of Fig. 3 shows that this is the case.[3]

[3] The temperatures were computed from hot-to-cold resistance ratios; these were periodically checked with a micropyrometer. It is to be emphasized that J_θ is plotted in all cases as obtained without concern or correction for the amount of cathode area.

Further experimental evidence that the disappearance of plateau B is related to zero field emission can come from probe measurement methods such as that of Found (2, 13). Cayless and Waymouth also took pains to compare their respective methods to probe measurements. As a result their techniques are used to check this method.

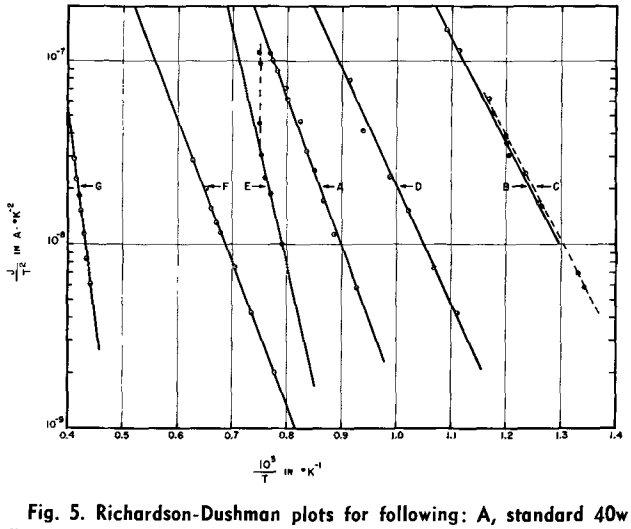

Fig. 5. Richardson-Dushman plots for following: A, standard 40w fluorescent lamp, data from Fig. 3, slope = 1.59 ev; B, standard triple oxide cathode; cathode-anode distance, 2 mm; Supply voltage 36v; data from Fig. 8; slope = 1.13 ev; C, same as B above but measured at 300v; discharge current *vs.* cathode heating current relationship qualitatively same as in Fig. 3; slope = 1.13 ev; D, average behavior for 40w fluorescent lamps; slope = 1.27 ev; E, 40w fluorescent lamp with cathode coated with LaB_6 (14), showing effect of attack on tungsten filament by boron at higher temperatures, initial slope = 2.54 ev; F, 40w fluorescent lamp with cathode coated with Ba_2ThO_3 (1), slope = 1.54 ev; G, 40w fluorescent lamp with uncoated tungsten filament as cathode, slope = 4.5 ev. The coated portion of the filament and coating uniformity in cases A-F vary greatly. J_θ is plotted without correction for the amount of cathode area.

Correlation with other methods.—The Forster-Brown and Cayless method (11) determines the zero field condition by the shrinking of the negative glow around the cathode filament and the sudden motion of the positive column away from the cathode as zero field is approached from retarding to accelerating field conditions. These phenomena are reversed when zero field is approached from accelerating to retarding field conditions.

For phosphor-coated fluorescent lamps, the details of the negative glow are not visible, and therefore the motion of the positive column and the resulting change in phosphor brightness near the cathode are used, according to (11), as the criterion for zero field. The solid arrows in Fig. 3 indicate the beginning and end of the motion of the positive column as visually observed. It is seen that the circled points are consistently within this range.

In order to obtain a definite correlation with the present work, a high speed photoelectric cell pick-up normally used for electronic flashtube work was employed. The 3 x 4 cm aperture of the instrument was placed against the wall of standard lamps, with its long dimension beginning at the cathode and extending in a direction parallel to that of the motion of the positive column at zero field, which amounted to about 3 cm. As a result, this motion was registered by the instrument, the output of which was fed to a dual trace oscilloscope. The second input of the oscilloscope was used for the simultaneous observation of J (see Fig. 2). A small "window" clear of phosphor on the side of the lamp wall away from the photocell allowed the observation of the negative glow.

Figure 6 gives an example of the results over a range of discharge current.

It is seen that the shrinking of the negative glow (or the disappearance of the cathode dark space) and the condition $J_B = J_C$, $\Delta t_B = 0$ bracket closely the beginning of the appearance and disappearance respectively of the Faraday dark space for this particular set of conditions at least. This connection of

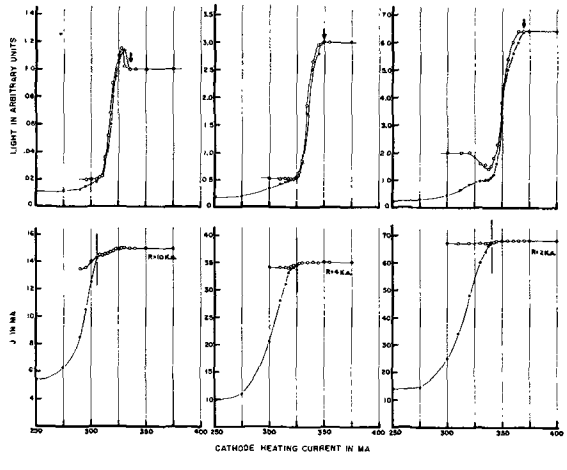

Fig. 6. Variation with cathode heating current of J_B (solid points) and J_C (circles), and corresponding light output in the vicinity of the cathode. Because of the experimental arrangement (see text) the light output increases as the head of the positive column advances toward the cathode. The arrows indicate the regions at which the cathode dark space first appears.

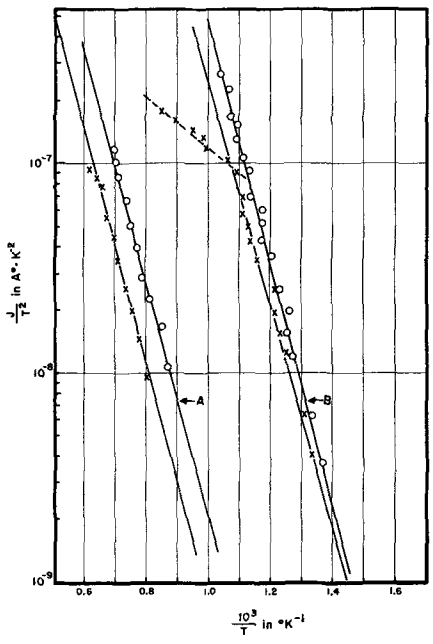

Fig. 7. A. Richardson-Dushman plot of data obtained as indicated in Fig. 6 and described in text, slope = 1.10 ev; B, Richardson-Dushman plot of data for short gap (2 mm) discharge; slopes = 1.05 ev; 1.13 ev. In both A and B circles are points obtained by this method, crosses are points obtained by method of ref. (11).

the disappearance of plateau B with the beginning of the rapid motion of the positive column toward the cathode was found valid for a variety of standard lamps with different cathode structures and tube diameters.

A Richardson-Dushman plot of data obtained as described above is given in Fig. 7A. It is seen that the apparent work functions correspond well within the experimental error of both methods and the intercepts are close enough as to make little practical difference.

The logical consequence of the above was experimentation involving discharges (3 mm Hg of argon plus a drop of mercury) with electrode gaps sufficiently small so as to avoid the formation of a positive column and therefore of a Faraday dark space. In order also to avoid possible electrode effects (see below) the arrangement used for this series involved a titanium anode in the shape of a semicylinder approximately 4 mm in diameter positioned with the cathode filament along its longitudinal axis. A supply voltage of 36v proved sufficiently high for this series. The cathode temperatures and discharge currents at which plateau B and the cathode sheath disappeared were measured, and Fig. 7B gives an example of the results. It is seen that the difference between the conditions at which these two phenomena occur is now smaller. The deviation from the straight line at higher discharge currents of the points determined by the shrinking of the negative glow reproduces the findings in references (8) and (11). This deviation begins to occur as the discharge current approaches 100 ma, also in agreement with reference (11).

The Waymouth method (12) detects the zero field condition by the onset of radio frequency noise as one proceeds from accelerating to retarding field

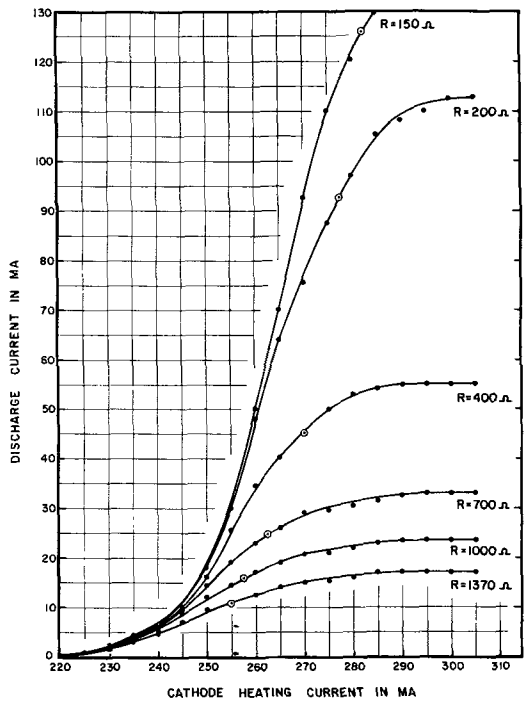

Fig. 8. Discharge current vs. cathode filament heating current for short gap (2 mm) discharge measured at supply voltage of 36v. Circled points indicate the $V_B = V_C = V_\theta$, $\Delta t_B = 0$ condition. The Richardson-Dushman plot using these data is shown in Fig. 5, line B.

conditions. Difficulty probably of instrumental nature, was experienced in obtaining consistent behavior utilizing this intriguing method. In a number of successful experiments, radio noise of the characteristics described in reference (12) was obtained during plateau C, while during Δt_B the noise was absent. The dashed arrows in Fig. 3 indicate the regions at which the radio frequency noise had become appreciable, but no sharp onset of noise was found in this particular instance.

Accelerating field phenomena.—Certain phenomena pertaining to the accelerating field mode appear relevant to the present subject.

It will be recalled that at lower cathode temperatures the cathode glow is not necessarily localized on the part of the cathode which is coated with the emission material. This happens regardless of electrode structure or cathode-anode spacing. In these cases the behavior obtained corresponds closely to that of Fig. 3 even for short gap (1-10 mm) discharges. However in the case of short gap discharges, by reducing the supply voltage from the 100 or more volts which is the "normal" range for fluorescent lamps to a few tens, the glow is made to envelop only the coated portion of the cathode filament even at room temperature. Then, the more anticipated behavior seen in Fig. 8 is obtained. The corresponding Richardson plot is seen in Fig. 5 line B. Line C in Fig. 5 shows the Richardson plot for the same lamp at 300v. It is seen that the two plots correspond quite well. Therefore the different behavior in the accelerating field region (*i.e.*, Fig. 3 *vs.* Fig. 8) does not affect the behavior in the vicinity of zero field, and the evaluation of a cathode either way is quite valid.

The above seem to apply to simple cathode structures as well as to structures incorporating parts variously of metallic and nonmetallic nature such as shields, ceramic supports, screens, wire structures, etc. It is also observed that the bulkier the electrode structure the more the Richardson plot result corresponds to that of Fig. 7A rather than that of Fig. 7B.

It is of pertinent interest to note that a Richardson plot of all the experimental points of Fig. 8 would give straight line portions for discharge current and cathode heating temperature conditions that are far into the accelerating field region (13). This can be readily seen from the exponential nature of the low-temperature portions of the curves of Fig. 8. This illustrates the fact that a straight line Richardson plot is a necessary but insufficient condition for the definition of zero field.

Substances other than triple oxides in standard lamps.—Figure 5, line E, gives an example of the results obtained with cathode filaments coated with LaB_6 (14).[4] At higher temperatures the interstitial attack by boron on the tungsten filament (14) proceeds at such a rate that the measurement of cathode temperature becomes uncertain. Figure 5, line F, gives the results from coatings of an interoxide, Ba_2ThO_4 (1). The above two coatings were not uniform with respect to thickness and filament coverage (see below).

Figures 9 and 5, line G, show the results obtained with uncoated tungsten filaments, the electrode structure being otherwise identical to the above. These filaments are ill-defined physicochemically but of interest because they are the cathode filaments used as base for all of the coatings of this work. It is noted that in this case even at 300v the

[4] Indebtedness is acknowledged to Dr. J. M. Lafferty for making this sample of LaB_6 available for this work.

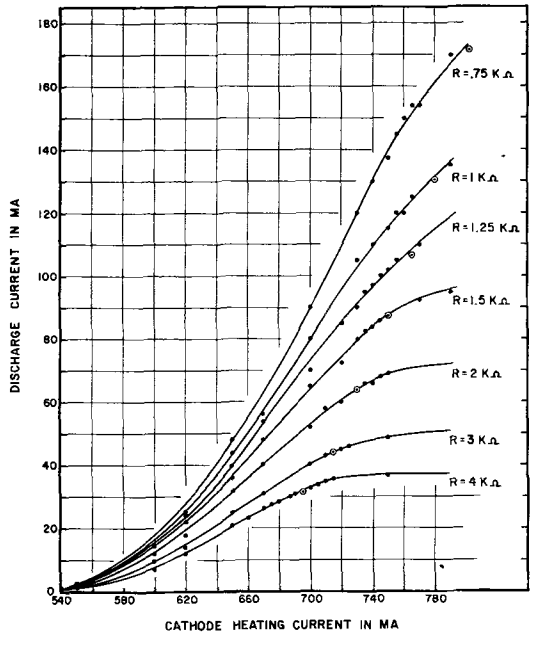

Fig. 9. Discharge current vs. cathode filament heating current for standard 40w fluorescent lamp with uncoated tungsten filament cathode; conditions of measurement same as for Fig. 3. The Richardson-Dushman plot using these data is shown in Fig. 5, line G.

behavior seen in Fig. 8 rather than that in Fig. 3 is obtained.

The above are compared with line D in Fig. 5 which appears thus far to be an average behavior for triple oxide cathodes.

Experimental Pitfalls

Measurements of cathodes in gas discharges are subject to all of the complicating factors of vacuum diode investigations plus some of their own. A number of these factors are pointed out below.

Progressive emission hysteresis.—Figure 10 shows curves of J_B *vs.* cathode heating current for a standard triple oxide cathode like those shown in Fig. 3. The arrows show the order in which the measurements were taken. The figure illustrates the effect of ionic bombardment at the lower level of J_B and the effect of heating at the upper level of discharge current. A reversal in the direction of the phenomenon is also observed. The insert in Fig. 10 gives an example of this. It should be recalled that the cathode operates for only a fraction of a second per experimental point.

To compensate, at least to some extent, for this rapid change in cathode characteristics, the experimental work was planned so that all points were obtained in consecutive ascending (or descending) order within each curve and from one curve to the next. The difference in the results obtained in an ascending or descending procedure involves small differences in the factors A and ϕ of Eq. [1], because this effect is more pronounced at higher than at lower discharge currents.

Temperature.—The cathode temperature is determined not only by the cathode heating current but also by the heating effect of the discharge. At high discharge currents, the latter can predominate to the extent that plateau B reverts to plateau C in a matter of milliseconds even if the cathode heating current is zero. This is the situation depicted in Fig. 2, where the discharge current is of the order of 200 ma. For lower discharge currents, the heating effect of the discharge manifests itself only near the zero field temperature ranges where a slight increase in heating rate, whether contributed by the cathode heating current or by the discharge, causes plateau B to disappear.

Because of these considerations, J_B is read immediately after the rise from plateau A when the heating action of the discharge has been in effect for only a few microseconds.

Temperature and coating uniformity.—Figure 11, from which the data for line F, Fig. 5 was obtained, shows an example of measurements identical to those of Fig. 3 but performed on nonuniformly coated filaments. As a result, these cathodes show rather severe temperature gradients along their length. This condition also affects the extent and uniformity of the activation of the cathode during manufacture.

It is seen that the rise of plateau B occurs over a wider range of cathode heating current as the various parts of the cathode tend to contribute to the total J_B to a different extent at each setting of cathode heating current.

In cases of this kind, the Cayless upper limits, indicated by the arrows in Fig. 11, tend to move further up the high current branch of the curves than in the case of uniformly coated cathodes. It was observed that at temperatures above those indicated by the arrows the brightness of the phosphor near the cathode and therefore the position of the head of the positive column were fairly constant with time. In the region between the arrows and

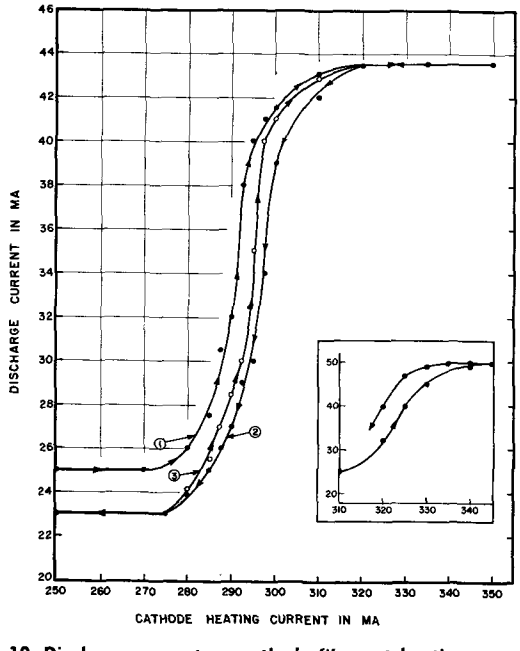

Fig. 10. Discharge current *vs.* cathode filament heating current for standard triple oxide cathode. Measurements followed the sequence shown by the numbers for each branch and the arrows within each branch, in order to illustrate the phenomenon of progressive emission hysteresis (see text). The reverse phenomenon is shown in the insert.

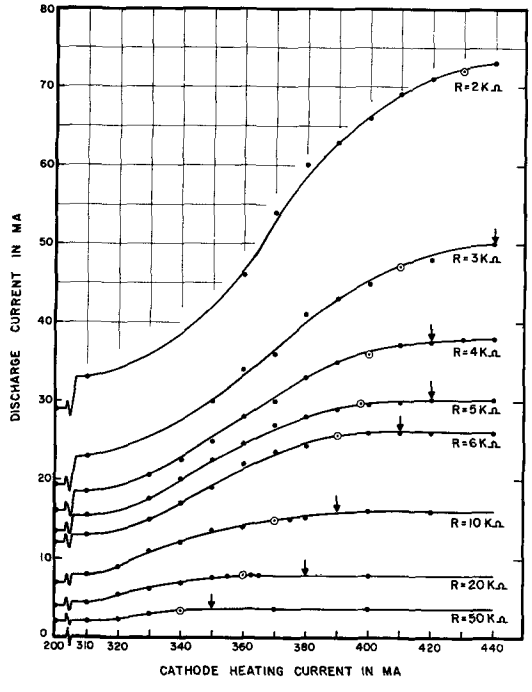

Fig. 11. Discharge current *vs.* filament heating current for standard 40w fluorescent lamp with cathode filament coated nonuniformly with Ba_2ThO_4. The Richardson-Dushman plot using these data is shown in Fig. 5, line F.

the $J_B = J_C$, $\Delta t_B = 0$ points however the position of the positive column was variable for nearly 1 min after the lamp was lighted. This indicated that the cathode activity was changing considerably because of the action of the discharge, causing a large difference between the "instantaneous" procedure described here and the "steady-state" procedure described in ref. (11). This difference is smaller in well activated, stable cathodes like that of Fig. 3 than in the nonuniform cathode of Fig. 11.

Impurities in discharge atmosphere.—The discharge in vessels of tubular shape interacts with the walls especially during Δt_A (13). The surface area of these walls can be large as in the case of a phosphor-coated fluorescent lamp. As a result, desorption or decomposition products can find their way from the walls into the gas atmosphere and to the cathode which in general is the most active getter available to them.

Species that become physically adsorbed on the cathode surface tend to give a sawtooth or "hashy" appearance to the J and V *vs.* time trace the first time the lamp is lighted after standing for some time.

The effect of species that combine with the cathode in a more intimate fashion is more pronounced and can be permanent. Usually those tend to change the cathode behavior from that of Fig. 3 to that shown in Fig. 11. Not infrequently this change can occur in the middle of a series of measurements and even reverse itself to the original behavior later on as the discharge cleans the cathode surface by sputtering or as these species diffuse into the bulk of the cathode.

Variable cathode composition.—A cathode involves a delicate balance between the processes producing the activating species such as "free" barium (1, 15) or lanthanum (14) and those that cause their loss from the cathode. Especially in a gas discharge, a precise balance is rarely if ever attainable. Therefore for each measurement the discharge is left operating for a fraction of a second, and an attempt is made to obtain each set of data uninterruptedly. This procedure can of course be altered to suit different purposes, as for instance the determination of an "equilibrium" state. Then the discharge is interrupted for the desired length of time.

The above factors tend to make the cathode an ever-changing system whether the discharge device is operating or not. However, if these factors are recognized and the experimental work planned accordingly, clear-cut results can be obtained.

Discussion and Conclusions

The purpose of the work described here was to obtain a measure of the thermionic capability of cathodes in gas discharges. The evidence is fairly convincing that there is little practical difference in the results obtained by the procedure described here and that described in ref. (8) and (11).[5] The "instantaneous" nature of the measurements described above offer advantages similar to these of pulsed, over d-c measurements in vacuum diodes. Especially in gas discharge cathode studies, this permits the resolution and hence the study of short duration effects such as the phenomenon of emission hysteresis described above. That this can also be done by a minor alteration of the method of ref. (11) has been demonstrated.

Fundamentally, there is little doubt that the condition $V_B = V_C$ and $\Delta t_B = 0$ occurs on the accelerating field side of the conditions at which the cathode dark space disappears. Evidence derived from spectroscopic[6] an probe (2) work[7] indicates that indeed plateau B disappears while an accelerating field still prevails (13). It is therefore of fundamental interest that the disappearance of the glow condition associated with plateau B is dependent on the behavior of the cathode at zero field and on the behavior of fundamental gas discharge phenomena such as of the Faraday dark space.

Acknowledgments

The writers are indebted to C. B. Collins, C. Kenty, J. S. Saby, and J. E. White for their active interest and discussions. For critical reading of the manuscript thanks are tendered to M. A. Cayless, G. Ecker, W. Elenbaas, J. M. Lafferty, and V. L. Stout.

Manuscript received April 18, 1962.

Any discussion of this paper will appear in a Discussion Section to be published in the June 1963 JOURNAL.

REFERENCES

1. D. M. Speros, *This Journal*, **106**, 791 (1959).
2. C. G. Found, *Phys. Rev.*, **45**, 519 (1934).
3. L. R. Koller, *Physics*, **7**, 225 (1936).
4. M. J. Druyvesteyn and N. Warmoltz, *Physica*, **4**, 41 (1937).
5. L. Malter E. O. Johnson, and W. M. Webster, *R. C. A. Rev.*, **12**, 415 (1951).
6. A. E. Pengelly and D. A. Wright, *Brit. J. Appl. Phys.*, **5**, 391 (1954).
7. E. O. Johnson and W. M. Webster, *R. C. A. Rev.*, **16**, 82 (1955).
8. M. A. Cayless, *Brit. J.. Appl. Phys.*, **8**, 331 (1957).
9. E. B. Hensley, *J. Appl. Phys.*, **32**, 301 (1961).
10. D. M. Speros, G. E. Report No. 10938 (1955).
11. A. D. Forster-Brown and M. A. Cayless, *Brit. J. Appl. Phys.*, **10**, 409 (1959).
12. J. F. Waymouth, *Sylvania Technologist*, **13**, 2 (1960).
13. Prepared for publication.
14. J. M. Lafferty, *J. Appl. Phys.*, **22**, 299 (1951).
15. E. S. Rittner, *Philips Research Repts.*, **8**, 184 (1953).

[5] It will be shown subsequently (13) that there should be and indeed there is a slight difference in the apparent work function determined by the two methods.

[6] In rare gas-Hg discharges, some of the rare gas spectral lines are still present in the negative glow after $\Delta t_B = 0$.

[7] Δt_B becomes zero above the zero field "point" of a plot of probe current *vs.* cathode temperature.

Minute Resistivity Variations in Germanium Crystals and Their Effect on Devices

Gurion Meltzer[1]

Semiconductor and Materials Division, Radio Corporation of America, Somerville, New Jersey

ABSTRACT

Minute variations of resistivity in germanium crystals were studied by the use of two methods of detection: selective copper plating and micropotential scanning. Results show that horizontal zone-leveled crystals have, in general, much larger minute resistivity variations than vertically grown crystals. Furthermore, n-type crystals have much larger resistivity variations than p-type crystals. These results, when applied to study of breakdown voltage in semiconductor devices, show that the range of breakdown voltage in p-n-p alloyed-junction transistors is much wider than the range in n-p-n devices.

Resistivity variations resulting from nonhomogeneous distribution of impurities have been observed in germanium crystals grown horizontally and by the Czochralski (1) technique. The nonuniform solute distribution appears to be caused by variations in growth conditions, such as rate of pulling, temperature gradients, furnace vibrations, and stirring (2). The variations of resistivity which result from these conditions can be categorized as follows: (*a*) resistivity difference between the seed and the base of the crystal (2); (*b*) nonuniformity across a wafer cut perpendicular to the direction of growth (3, 4); and (*c*) minute variations in the direction of growth (5).

The minute resistivity variations have often been referred to in the literature as resistivity striations (5).

The first type of variation mentioned above can be measured easily by conventional methods using four-point and two-point probes. The other types require methods of measurements providing much better resolution. One such method is the photovoltaic method (4), which is limited, however, to resistivity variations with periods which are long compared with the diffusion length of the minority carriers. Other methods employ radiographs (2) and copper plating (4). The use of radiographs to detect minute resistivity variations is very involved and is inherently restricted to general qualitative results only. The copper plating method, despite its simplicity, also yields only qualitative results.

Methods of measurement were sought because existing methods did not enable full qualitative and quantitative study of minute resistivity variations and their effect on devices. However employing two well-known methods and correlating the results of both provided satisfactory data.

This paper describes how two methods of measuring resistivity variations, copper plating and micropotential scanning, are correlated to give both qualitative and quantitative results with very good resolution. Results obtained by the use of these methods are discussed in terms of the effect of resistivity variations on the manufacturing yield of devices.

The experimental procedures outlined in this paper should act only as a guide to the performance of similar experiments in that the variables involved were not optimized unless so specified.

Experimental Procedures

Copper plating.—The detection of resistivity variations by the use of selective copper plating was suggested by Camp (5). In this method, the electrolytic cell consists of a copper sulfate solution as an electrolyte, a copper anode, and the sample to be plated as a cathode. An electrolyte which resulted in satisfactory selective plating in most cases consisted of 210g of copper sulfate pentahydrate and 52 cm^3 of concentrated sulfuric acid, diluted to a volume of 1000 cm^3 with water.

A pulsed voltage was applied to the electrodes by means of an automatic electromechanical switch. Very good selective plating was obtained with samples from 2 to 8 mm thick, which were covered on the back with solder and cast in an epoxy resin so that only the surface to be plated was exposed. The face to be plated was etched to obtain a clean smooth surface. Current densities ranged from as low as 1½ amp/cm^2 to approximately 30 amp/cm^2.

Both n- and p-type germanium in resistivity ranges of from 0.03 to 40 ohm-cm were satisfactorily plated. Although no exact rules for variations of parameters of the plating bath could be derived from the experiment, certain general rules can be given.

For p-type samples, the applied voltage ranged from 300 to 1700v, depending on the resistivity of the sample; *i.e.*, higher resistivities required higher voltages. The pulse rate was 3 cps. Selectivity of plating was improved in some cases by an increase in the conductivity and, therefore, the current density, of the solution through the addition of sulfuric acid. In other cases, an increase in the copper-ion concentration in the solution by the addition of copper sulfate resulted in better plating.

In plating n-type samples, especially those samples having higher resistivity, the best results were

[1] Present address: Ran Ltd., Tel Aviv, Israel.

Table I. Typical plating conditions for n- and p-type germanium sample

Type	Resistivity, ohm-cm	Plating, volts	Time of plating, sec.
p	0.3-0.4	360	30
p	2.0	630	30
p	9.0	810	21
p	15.0-18.0	810	30
p	25.0	1020	60
n	0.5	1020	17
n	2.0	1020	10
		1640	10
n	9.5-16.0		
		90	420
		1640	5
n	35.0		
		90	150

Pulse rate: about 3/sec.

obtained when high pulsed voltage (above 1500v) was applied for a few seconds, followed by relatively low voltage for a longer time. For some n-type samples, the selectivity was improved when the copper-ion concentration in the solution was reduced. Table I lists typical plating conditions for a few n- and p-type crystals. The plated surfaces of these samples were either in the direction of growth or perpendicular to the direction of growth as shown in Fig. 1.

Micropotential scanning.—Micropotential probing is essentially a two-point probe method except that the space between the probes is very small and the manipulation of the probes is mechanized. A pair of probes is arranged in a jig. One of the probes is coated with a 1-mil thickness of Teflon. The two probes are placed in a groove as wide as the sum of the diameters of the two probes, so that the probes are separated only by the Teflon film, *i.e.*, distance between the two probes is 1 mil. Various tests made with the aid of a high magnification microscope assure that the probe spacing does not change while the pair of probes is moving across the sample. This technique permits the measurement of relative resistivity as a function of distance. Although the conditions of the test make absolute resistivity very inaccurate, the main purpose of the tests is to investigate resistivity variations. Wires welded at right angles to the probes act as both an electrical contact and a pressure spring. After the jig is assembled, the probes are machined to chisel points. The jig is then mounted on a micromanipulator, which has the horizontal-movement control coupled to a very-slow-speed motor (a fraction of an rpm).

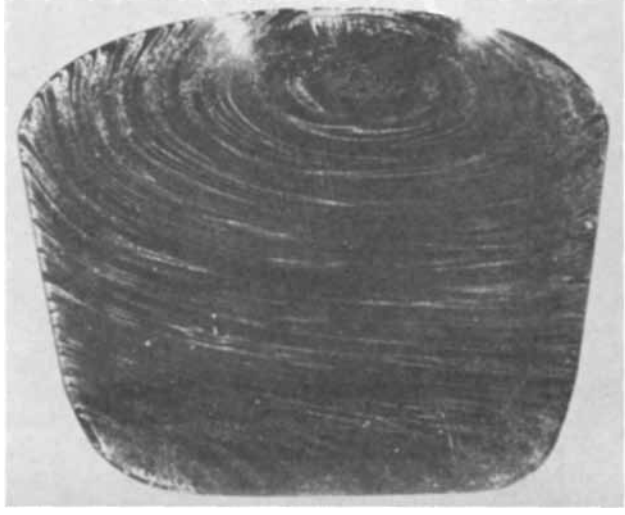

Fig. 1. Horizontal-zone-leveled p-type crystal 0.03 ohm-cm. Face shown is perpendicular to the direction of growth.

A d-c voltage is applied across the sample to be scanned. The voltage across the probes is either amplified or fed directly into a recorder, and the resistivity is plotted as a function of distance directly on the recorder chart. Adjustment of the chart and motor speeds permits the resistivity curve to be plotted to any degree of detail. The resolution of this method is obviously limited by the spacing between the two probes.

The sample to be scanned should be in the form of a bar having any desired length and a cross section of from 1 to 9 mm^2. The cross section of the bar should be chosen so that the current is sufficiently high to give a detectable voltage across the probes but low enough so that conductivity modulation does not affect the reading. The bar should be cut so that the long dimension, which is in the direction of scanning, is perpendicular to the direction of equiresistivity planes (planes represented by copper lines of selectivity plated samples).

Surface preparation is of extreme importance in the micropotential method. The surface to be scanned must be sufficiently smooth to prevent errors due to noise generated by the dragging probes. However, the surface must be sufficiently rough to reduce the metal-to-semiconductor contact resistance to a minimum (at least much smaller than the input impedance of the recorder amplifier). A surface which is lapped on a 600-grit emery paper with the lapping grooves in the direction of scanning provides a satisfactory balance between the two requirements.

Correlation of the methods.—Neither of the two methods outlined in this paper can independently give full information about resistivity variations of the crystal. For example, variations of voltage in the plating process can vary the selectivity of the plating and, consequently, the number of striations revealed; therefore, the exact period of striations cannot always be detected by the plating method alone. Furthermore, the copper-plating method does not yield any information about the magnitude of the variations. On the other hand, for a current which is uniform with respect to the cross section in a germanium bar, the resistivity variations must be perpendicular to the direction of the current; therefore, the bar must be cut accordingly.

It is important to detect the shape and general directions of the changes in resistivity and then cut the crystal so that the copper lines are perpendicular to the long dimension of the bar. A potential scan of the bar then indicates the magnitude and the exact periods of the variations. At this point it is important to emphasize that repeatability of shapes of curves was tested during the experiments; the method used was as follows:

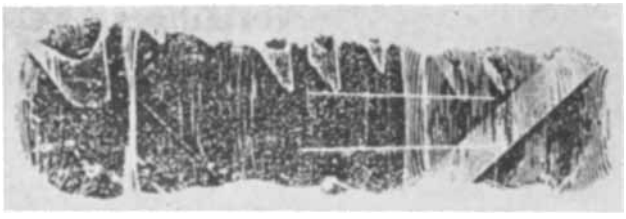

Fig. 2. Copper plating of a p-type crystal. Resistivity variations were purposely introduced in the top (striated) portion.

A specimen was copper-plated, a bar was cut according to the method mentioned above, the copper removed using nitric acid, and the surface of the sample prepared by lapping as explained. A resistivity scan was lapped again and another scan was taken once more. The two scans were to be identical for any conclusions to be drawn, and such was the case.

A comparison of the results obtained by the two methods was made on a crystal specially grown for the purpose of studying the nature of minute resistivity variations. The large resistivity variations were introduced by use of an off-on cycle which varied the pulling speed every 30 sec from 0 to 5 mm/min while the crystal rotated slowly at about 8 rpm. The more uniform section was pulled continuously at 1.5 mm/min and rotated at 70 rpm. Figure 2 shows the copper plating on a sample taken from the center of the crystal and Fig. 3 shows a magnified portion of Fig. 2. Lines were scribed on the sample for the purpose of indexing. Figure 4 shows the result of the micropotential scan parallel to and mid-way between the index line in Fig. 3. The comparison shows that there is complete agreement between measured results of the two methods. The five copper stripes inside the scribed rectangle correspond to the five low-resistivity regions indicated in Fig. 4. The region scanned was purposely chosen to be the one joining the striated and nonstriated region. Reproducibility was checked for both methods by means of plating and scanning a sample, lapping it further, and repeating the steps. Results showed very satisfactory reproducibility.

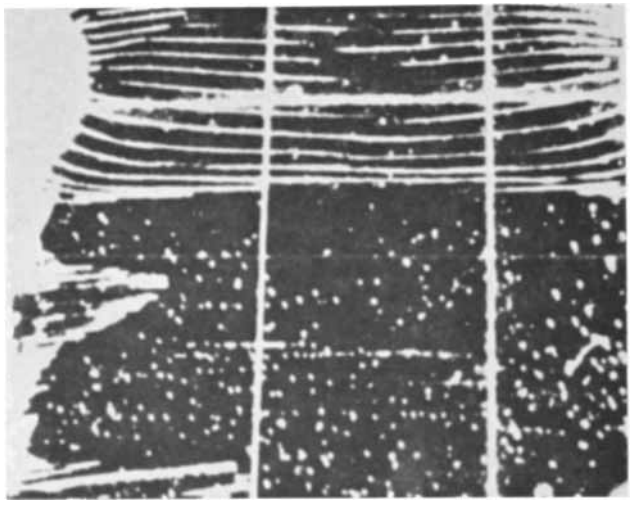

Fig. 3. A magnified portion of Fig. 2. Lines were scratched for indexing purposes.

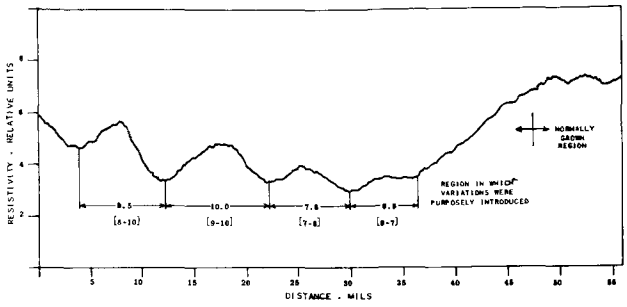

Fig. 4. A scan of the region shown in Fig. 3

Experimental Results

Vertically grown crystals vs. horizontally grown crystals.—In general, crystals which are grown by vertical pulling have smaller resistivity variations than crystals grown by the zone-leveling method. In the samples measured, horizontally grown crystals exhibited a 25-50% resistivity variation as compared with about 10% for vertically grown crystals. The degree of variation depends, of course, on the particular growth conditions and may itself vary widely, as shown by a comparison of the resistivity curves of Fig. 5. Figure 5A is a plot of a section from an n-type zone-leveled crystal having a resistivity of about 0.8 ohm-cm. Figure 5B is a typical plot of a vertically grown n-type crystal having a resistivity of about 8 ohm-cm. The resistivity of the horizontally grown crystal varies by about 25%; the variation in the vertically grown crystal is less than 10%. It was extremely difficult to plate the crystal from which the section of Fig. 5B was taken. In some vertically grown crystals the variations were so small that they could hardly be detected by the copper-plating method.

It was found that horizontally grown crystals also differ from vertically grown crystals with respect to striations in the cross-sectional direction. Although the equiresistivity surfaces in all the horizontally grown crystals tested had a concave shape, many of the vertically grown crystals had flat equiresistivity surfaces. The equiresistivity plane in the zone-leveled crystal is not perpendicular to the direction of the growth due to the nonuniformity of the temperature gradient in the direction perpendicular to the direction of growth. Figure 6 shows a copper-plated sample of a crystal in which resistivity variations were purposely introduced and the pattern of the equiresistivity

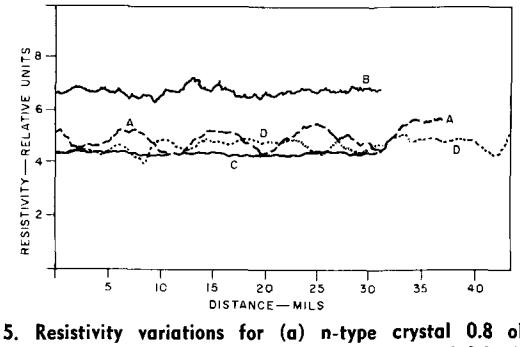

Fig. 5. Resistivity variations for (a) n-type crystal 0.8 ohm-cm horizontally grown, (b) vertically pulled n-type crystal 0.8 ohm-cm, (c) vertically pulled p-type crystal, (d) zone-leveled p-type crystal 2.0 ohm-cm.

plane was changed. At present, the temperature gradients are controlled more closely in the vertical furnace than in the zone-leveling furnaces.

It should be emphasized that no attempt was made during this work to suggest that vertical growing is superior to horizontal growing of crystals as far as minute variations of resistivity are concerned. However, it is to be stressed that, regarding methods used at present, vertical growing crystals do seem to have much smaller resistivity variations as explained above.

A further evidence of the relation between growth conditions and the resistivity variations is demonstrated by the potential scan made on a sample from the crystal of Fig. 6. Figure 7 shows that the distance between two adjacent peaks or valleys is constant and corresponds exactly to the length pulled during one revolution.

P-type crystals vs. n-type crystals.—Measurements made on crystals grown by the zone-leveling method show that variations from the average resistivity value are larger in n-type than in p-type germanium for crystals grown under similar conditions. This difference in resistivity variation can be explained as follows: such growth variables as pulling speed, mechanical vibrations, temperature variations, and variations in temperature gradients result in an effective change in growth rate (6). The segregation coefficient of the common n-type impurities varies very radically with any change in the rate of growth; however, most of the p-type impurities show much smaller changes (7, 8). For example, a comparison of Fig. 5A and 5D shows that the p-type crystals exhibit a 5-10% variation from average resistivity as compared to 30-50% for the n-type crystals. The variations between n- and p-type germanium are smaller in the vertically grown crystals, as shown by a comparison of Fig. 5B and 5C.

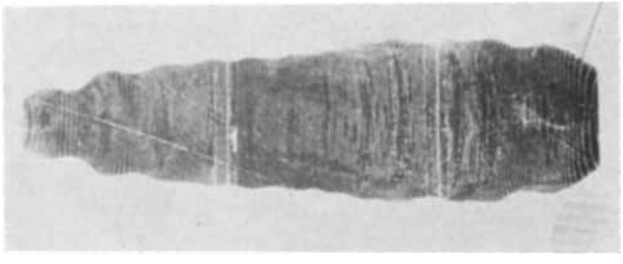

Fig. 6. Copper plating of a crystal in which resistivity variations were purposely introduced and equiresistivity plane was purposely changed.

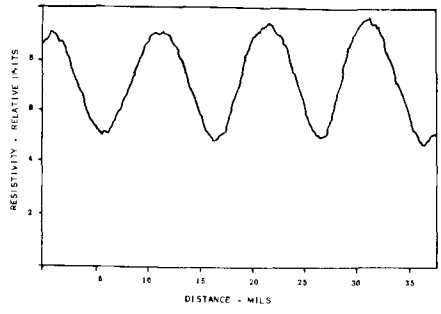

Fig. 7. A scan from a crystal in which resistivity was purposely varied (crystal of Fig. 6).

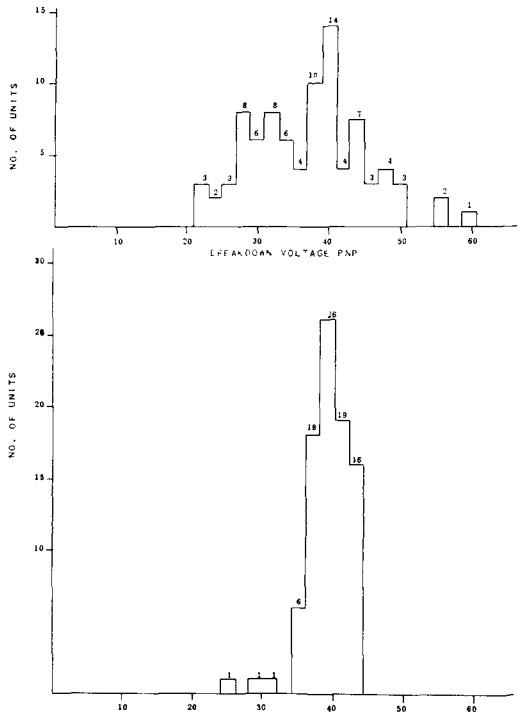

Fig. 8. Collector-to-base breakdown-voltage distribution of n-p-n and p-n-p transistors.

Comparison of breakdown voltage between n-p-n and p-n-p transistors.—Because breakdown voltage in p-n junctions depends mainly on the resistivity of the material at the depletion layer of the junction, large resistivity variations in a crystal result in a wide distribution of breakdown voltages in both alloyed and diffused junctions made from this material, provided production precautions are taken to assure that the breakdown is a bulk breakdown rather than a surface breakdown.

As mentioned previously, resistivity fluctuations are found, in general, to be larger in n-type than in p-type germanium. Thus, the collector-to-base and emitter-to-base breakdown voltages in normal production devices[2] have a much wider range in p-n-p alloyed-junction or diffused-junction transistors than in n-p-n transistors. Figure 8 shows the collector-to-base breakdown voltage distribution of two arbitrarily chosen lots of alloyed-junction. The base material used was with impurity concentration of about 1.8 x 10/15. The resistivity range of the material used was the same for all the lots, and both lots were manufactured by the same general processes. The final etch used was a peroxide etch because it was found to affect breakdown voltage of units much less than electrolytic etch.

A comparison of the two plots shows that the peaks of the distributions are at the same voltage, 40v. The width of the distribution range for the p-n-p transistors (n-type base material) was about 30v, which corresponds to a variation in resistivity of about 30-40% (8). The width of the distribution range for the n-p-n transistors was 10v, which corresponds to a variation in resistivity of about 10-

[2] Data provided by R. Pinto of the Computer Devices Group, RCA Semiconductor and Materials Division, Somerville, N. J.

15%. These values of resistivity variations agree in general with the values mentioned previously. It should be emphasized that the crystals from which the transistors were made did not have variations across the wafers (the so-called "top-to-bottom" variations) that could be detected by the four-point-probe method.

Effect of annealing.—Diffusion of impurities occurs when a crystal having resistivity variations is subjected to long annealing at high temperature. Because the impurities tend to diffuse in the region where an impurity gradient exists, the variations of impurities tend to be suppressed.

The effect of the annealing was determined by means of measurements of a section from an n-type 0.8-ohm-cm zone-leveled crystal which was divided into two parts. One of the portions was annealed for 130 hr at about 850°C; the other served as a control. Figure 5A shows typical resistivity variations in the nonannealed crystal of more than 25% with respect to the average resistivity as measured by the four-point-probe method. The period of the variations is about 9 mils. The annealed sample shows less than 10% variations with a very long period, the length of which is difficult to determine.

The breakdown voltages of alloyed-junction diodes made from the two parts of the crystal were also compared . The processes of the diode preparation were chosen to have as little effect as possible on breakdown voltage. The distribution range of the breakdown voltages of the units made of the annealed portion was narrower than that of the nonannealed portion.

Other processes occurred in addition to the smoothing out of the resistivity. An "out"-diffusion which apparently took place caused resistivity on the surface to increase from 8 to 27 ohm-cm. The resistivity of samples taken from the interior of the annealed portion were in the range of 1.4 to 1.8 ohm-cm. This behavior may possibly be attributed to an "in"-diffusion of impurities introduced into the systems either from the quartz container or by the acids and solvents used to etch and clean the crystals (18). The introduction of impurities from the acids and solvents used in crystal processing may also explain why the bulk lifetime of the material was reduced from about 60 μsec to a fraction of a microsecond as a result of the annealing process. Thus, it is unlikely that annealing can be used to remedy undesired resistivity variations.

Discussion

Explanation of selective copper plating

Camp (4) and Silverman and Benn (11) mention a possible explanation of the selective-plating mechanisms. These explanations, together with Uhlir's (12), and Brattain and Garrett's (13) discussions of the electrolyte-germanium interfaces, explain the initial phase of the plating, *i.e.*, why lower-resistivity sites plate preferentially. As to the subsequent plating phase, the following explanation is suggested. The sites which become copper plated first have a greater tendency to relinquish electrons to copper ions. Once the initial sites become activated and a small amount of copper is deposited on them, they become small copper cathodes in the copper sulfate bath. The measured activation voltage for copper deposition on germanium was found to be appreciable (several tenths of a volt), whereas copper deposition on a copper cathode requires no overvoltage (14). By use of a high-voltage pulse of short duration, the selectivity of copper deposition on copper is enhanced much more than on germanium because activation is time dependent as well as potential dependent (15). The thickness of the coating therefore does not indicate the magnitude of resistivity differences between the sites.

Effects of Variations on Devices

Breakdown voltage is only one of the parameters in a device which depends on the impurity concentration in the material used for the device. Others are, for example, saturation current in the p-n junction and current ratios in a tunnel diode. Impurity gradient in the base material may result in undesired built-in fields which can change the characteristics of a device.

Because uniformity of impurity concentration is a very desirable property for many devices, an effort should be made to provide proper growth conditions to minimize minute resistivity variations.

Acknowledgment

The author wishes to acknowledge the help of many associates. He is specially indebted to H. P. Kleinknecht for advice and fruitful discussions, to E. Jordan who worked on the initial phase of the experiments, to P. Lintz for growing special crystal material, and to A. Frey for assistance in the experimental work.

Manuscript received Feb. 16, 1961; revised manuscript received May 28, 1962. This paper was prepared for delivery before the Columbus Meeting, Oct. 18-22, 1959.

Any discussion of this paper will appear in a Discussion Section to be published in the June 1963 JOURNAL.

REFERENCES

1. C. K. Teal and J. B. Little, *Phys. Rev.*, **78**, 647 (1950).
2. H. E. Bridges, J. H. Scaff, and J. N. Shive, "Transistor Technology," Chap. 5, 6, D. Van Nostrand Co., New York (1958).
3. H. E. Bridges, *op. cit.*, p. 40.
4. J. Oroshnik and A. Many, *This Journal*, **106**, 360 (1959).
5. P. R. Camp, *J. Appl. Phys.*, **25**, 459 (1954).
6. H. E. Bridges, *op. cit.*, pp. 68 and 119.
7. R. N. Hall, *Phys. Rev.*, **88**, 139 (1952).
8. W. G. Pfann, "Zone Melting," John Wiley & Sons, New York (1958).
9. S. J. Miller, *Phys. Rev.*, **99**, 1234 (1955).
10. W. Bosenberg, **8**, 551 (1956).
11. S. J. Silvermann and D. R. Benn, *This Journal*, **105**, 170 (1958).
12. A. Uhlir, *Bell System Tech. J.*, **35**, 333 (1956).
13. W. H. Brattain and C. G. B. Garrett, *ibid.*, **34**, 129 (1955).
14. W. Blum and G. B. Hogaboom, "Principles of Electroplating and Electroforming," p. 52, McGraw-Hill Book Co., New York (1949).
15. S. Glasstone, "An Introduction to Electrochemistry," Chap. 8, D. Van Nostrand Co., Princeton (1942).

Epitaxial Growth of Silicon

C. H. Li[1]

General Instrument Corporation, Newark, New Jersey

ABSTRACT

An improved and reproducible method for epitaxial growth of silicon is described. The equipment is compact, simple, reproducible, and has an improved gas-mixing system. The process allows shorter time for preparing the first run and making each subsequent run. The layers produced are planar and uniform from center to edge. Under 500X magnification, they show no pits, oxides, pyramids, waviness, growth scales, or crystal structures. A description is given of the characteristics of diodes and transistors made from this material. Some results of statistically designed experiments on the growth parameters and their interactions are given.

An improved epitaxial process for silicon growth is presented here. The equipment, the process, and the products are discussed in some detail.

We shall first compare two vertical systems and show how some common problems are approached, such as temperature uniformity, gas flow, and gas mixing. Reproducibility of thickness and resistivity of grown layers are next considered. Finally visual defects and some device characteristics are examined.

The control of silicon epitaxial growth has generally been considered difficult. The growth parameters are known to interact in a complex manner. Systematic and reliable results on the significance of various parameters and their interactions are not frequently published.

This paper also gives some results of statistically designed and controlled experiments. The experimental errors or measuring precisions for layer thickness and resistivity were first determined, each from over 50 tests. The growth parameters then could be compared both qualitatively and quantitatively, as shown in the paper. Each conclusion for these comparisons was arrived at from the average of several controlled tests.

The method to be described is similar to the one originated at Bell Telephone Laboratories (1). Basically, the method consists of the reduction of silicon tetrachloride by purified hydrogen on heated silicon wafer substrates. More details of the process, and its modifications in our case, are described later in this paper.

The Two Systems

Figure 1 shows the comparison of two vertical systems. Figure 1a is an early model and is similar to the one described by Theuerer; Fig. 1b is the improved model.

With reference to Fig. 1a, the hydrogen enters at the left side through a flexible stainless steel tubing, passes through a Deoxo unit, a valve, and a first glass trap filled with molecular sieves and immersed in liquid nitrogen contained in a first Dewar flask. The purified hydrogen then bubbles through liquid silicon tetrachloride in a second glass trap kept at −30°C by a mixture of dry ice and alcohol in a second Dewar flask. The second trap has, on its top, a valve system consisting of a three-way valve and a two-way valve to allow switching the hydrogen gas either directly into the cylindrical reaction chamber or indirectly through the liquid silicon tetrachloride first and then into the reaction chamber. In the reaction chamber there is a silicon pedestal to be heated to 1150°C by an induction coil outside the reaction chamber. The heating is started by a molybdenum coil on the pedestal. The spent gases are exhausted from the reaction chamber through another liquid nitrogen trap to catch

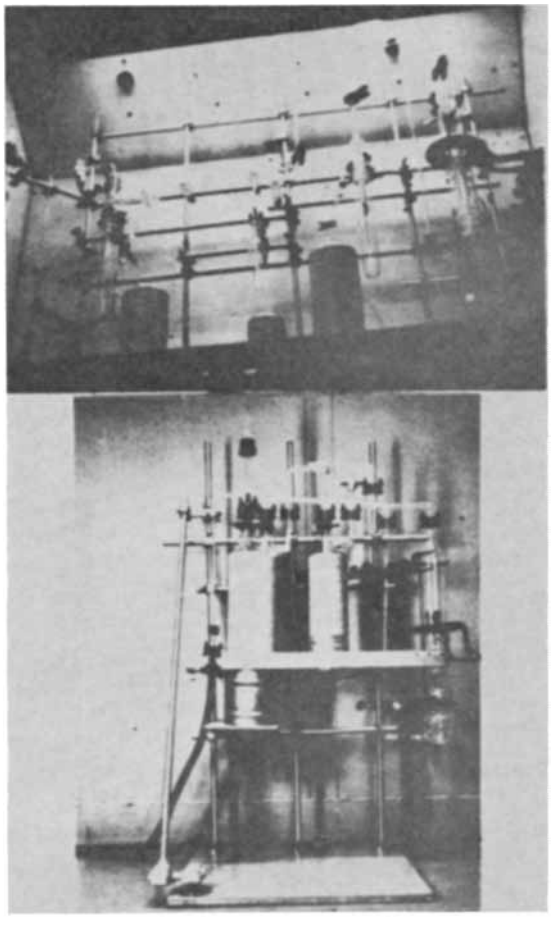

Fig. 1. The two small epitaxial systems: (a, top), an early model, (b, bottom), the improved model.

[1]Present address: Grumman Aircraft Engineering Corporation, Bethpage, N. Y.

any unused silicon tetrachloride. The remaining hydrogen then passes to an exit where it is burned off.

A normal run for transistor-grade wafers consists of a flushing period of 20 min, a deposition period of 10 min, and a cooling period of 20 min. The average thickness of the deposited layer is about 0.8 mils.

Figure 1b shows the later or improved model. It contains all the essential parts, but is more compact and rugged. The glass parts contain three interchangeable traps, a valve system, a flowmeter, five connecting tubes, and a reaction chamber. The total number of glass parts is 11, compared to 17 for the earlier model. Except for the quartz reaction chamber, all these parts are made of Pyrex glass. The total internal volume of the improved system is about 1450 cc compared with 1840 cc for the earlier model.

The smaller volume, internal area, number of parts, and number of ball and socket joints appreciably reduce the system contamination. This condition leads to more reproducible products.

All the parts of the improved system are mounted approximately in a single plane, with all the joints at convenient eye level for improved visibility. The whole system is mounted on an 18 x 18 in. board, occupying less than one third of the hood space required by the earlier system.

The improved system is unitized. To change a system, a single operator merely has to disconnect two clamps, one at the gas flowmeter and one at the reaction chamber. He can then lift the whole system out, replace a precleaned system, make the two clamp connections, and resume operation in a few minutes' time. The system downtime is therefore negligible.

The set-up and running time for the improved system is relatively short because of the small number of parts, compact arrangement, and reduced internal volume. An ice-water mixture is used rather than the alcohol-dry ice mixture, to control the temperature of liquid silicon tetrachloride. This ice-water mixture yields 0°C without adjustment.

Material Preparation

The substrate wafers for this work were normally N^+ type with resistivities ranging from 0.001 to 0.003 ohm-cm. They were prepared from 12-mil slices cut from ⅞ in. diameter, arsenic-doped Czochralski crystals, which were grown at the General Instrument Laboratory or bought from outside vendors, such as Merck or Texas Instrument. The cut slices had <111> orientations to within ½°, as determined by x-ray diffraction methods. The dislocation density of these slices were less than 1000 pits/cm^2, as revealed by a modified Dash etch.

Lapping of cut slices was carried out on a Lapmaster machine with silicon carbide particles. Mechanical polishing was finished on a Shuron polisher with Linde type 0.05B alumina, which has particle sizes of 0.05μ. The finished wafers, about eight mils thick, were visually inspected at 10X and 100X under vertical and inclined illumination. No scratches, pits, or other defects should be visible. Defective wafers may have to be repolished.

Chemical etching was not used to reduce wafer thickness or to remove damaged surface layers, except on some special test runs such as are described in connection with Table II. These wafers were chemically etched with a CP4 etching mixture. Instead of chemical etching, the mechanically polished wafers were steam-oxidized at 1200°C for 15 min with humidified oxygen gas. The oxidized wafers were stored in clean dishes until ready for use, when the oxide skin was removed by a brief HF etch. This oxidation step was designed to remove (or anneal) deformed silicon and other surface impurities of irregularities. This step also helped keep the wafer surface clean and uniform, and therefore give more reproducible results.

The silicon tetrachloride, from Anderson Chemical Company of Weston, Michigan, was used without purification. The volume of the liquid consumed for each filling of the Pyrex vacuum traps (38 mm diameter and 250 mm long) was either 16 ml (for no-bubbling type of gas mixing as described below) or 32 ml (for bubbling type of gas mixing).

Temperature Distribution

A uniform temperature across the substrate is desirable for uniform deposits. In general, a water-cooled reaction chamber gives steep temperature gradients. For this and other reasons, the reaction chambers are not water-cooled.

Even with an air-cooled reaction chamber, nonuniform temperatures still exist across the substrate wafer. The difference between the center and edge of the wafer has been variously reported to be between 10° and 35°C. It has been suggested that the use of metal supports would equalize the temperature. This problem has been approached from a different angle.

Tests were run to determine this temperature difference at various flow rates and induction coil positions. The silicon pedestal used here was about ⅞ in. in diameter and 2 in. long. The induction coil was of a pancake type placed either flush with the bottom or top surface, or in the middle, of the pedestal. Twelve temperature readings were taken at each combination of flow rate and coil position. Of these twelve readings, five were at the top pedestal surface, giving an average temperature difference, ΔT, or the temperature at center minus that at the edge on the top pedestal surface.

To optimize the temperature distribution, two criteria were used: (*a*) the temperature difference $\Delta T = Tc - Te$ should be nil, and; (*b*) the highest temperature should occur at the top pedestal surface.

In general, a higher gas flow rate reduced the temperature difference and the over-all temperature of the top pedestal surface. Coil position had, however, a much greater effect on temperature than gas flow rates. Average temperature differences at various coil positions are shown in Table I.

These averages suggested that if the pancake induction coil was put at the bottom plane of the

Table I. Temperature differences vs. coil position

Coil position	Temperature difference, $\Delta T = I_c - I_e$, °C
Bottom	+8.5
Middle	+2.1
Top	−17.5

pedestal, the top pedestal center was hotter than the edge, since in this case heat was generated at the bottom portion of the pedestal and there was appreciable cooling at the pedestal surface. If the induction coil was located at the top plane of the pedestal, the pedestal edge was overly heated by the RF energy; the center was therefore colder. A better coil position would be somewhere near the middle of the pedestal. To be more specific, by interpolation of the averages, it was found best to put the coil about ¾ in. below the top surface of the 2 in. pedestal, so that practically uniform temperature distribution across the top pedestal surface could be achieved. This coil position had the added advantage that the top portion of the pedestal was kept relatively hot, thereby reducing silicon deposition at unwanted areas.

Gas Flow

Some growth defects are found to relate to the gas flow. Therefore gas flow pattern was studied. The General Instrument Research Laboratory devised a method by which artificial fogs were produced in the reaction chamber. This was done by replacing the connecting tube between the silicon tetrachloride trap and the reaction chamber with another tube having an identical shape but also having a tiny water reservoir. The evaporating water then reacts with silicon tetrachloride to form a fog. Figure 2 shows the results of fog formation, taken over a time interval of 15 min. The build-up of fog could be watched progressively from the top left toward the bottom right.

Figure 3 is a sketch of the fog seen in detail. A cloud was observed to build up directly above the hot pedestal. This cloud was lens-shaped, being thicker at the center and thinner at the edge, possibly because of the gas flow in the annular space between the pedestal and reaction chamber. Further, this cloud was relatively stable in position and shape, but thickened with increasing gas flow rates. A moving eddy and isolated solid particles also were seen above this cloud. Both the eddy and the isolated particles settled down and disappeared in the same cloud. This gas dynamics approach aids in the study of the reaction mechanism and is the subject of a paper to be published elsewhere.

Layer Thickness

Next, thickness measurement and reproducibility are discussed. Layer thickness is measured simply be scribing and breaking the deposited wafer, staining with a mixture of nitric, acetic, and hydrofluoric acids (5:24:3 by volume), and measuring the thicknesses on the broken sections at 100X. This method of thickness measurement has been correlated with one using infrared interference methods.

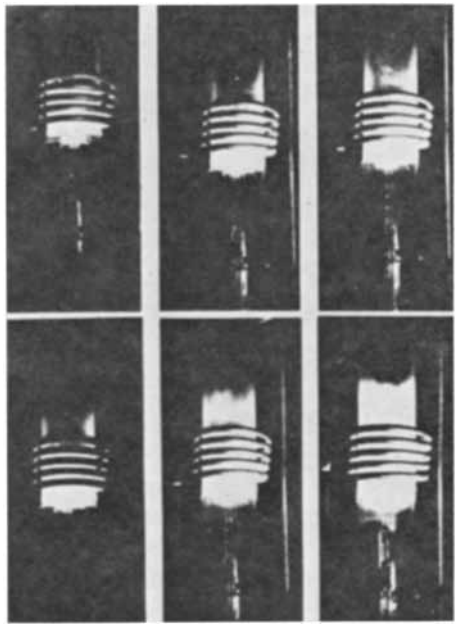

Fig. 2. Pictures of fog formation

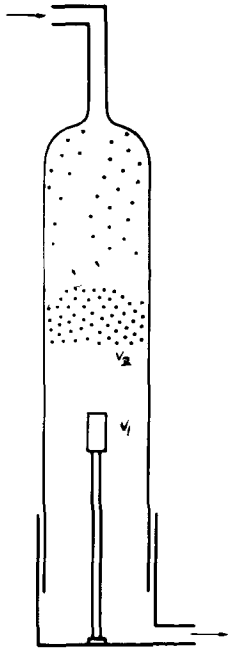

Fig. 3. Sketch of fog formation

To further check the precision of measurement, a number of deposited wafers were broken into quarters and thicknesses measured at ten fixed locations on each quarter, five on each of the two perpendicular edges. The two readings on the same location but different sides of the broken edge gave the desired precision, *i.e.*, 6.5%. Readings between different edges measured thickness reproducibility across the wafer. It was found that the wafers broke evenly except at the extreme outer edges, where complex fracture patterns unfavorably changed the precision to 10.4%. The practice was therefore not to read these edge thickness values. Any two readings on the broken section, except at the edges, checked within the reading error. Their

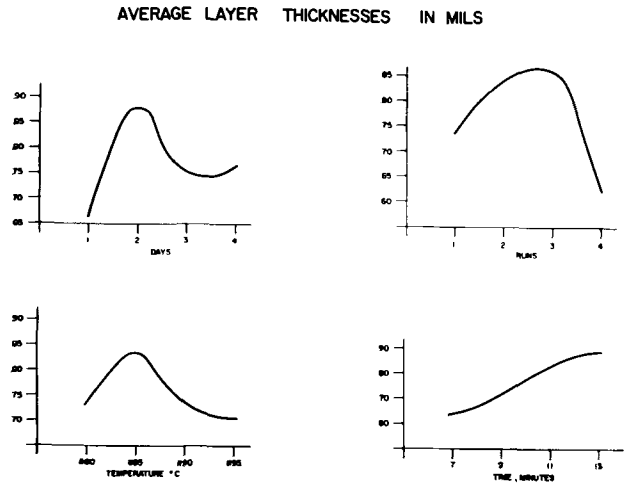

Fig. 4. Experiment on layer thickness

average thus gave an estimate of the layer thickness. Unless the two readings differed appreciably, no additional readings on layer thickness were taken.

Within the measuring precision, no significant thickness variation across the deposited wafer was detected. Temperature uniformity contributes to this desirable condition.

In an early experiment, four epitaxial wafers were made on each of four consecutive days at four different temperatures and times. The first run started with a thoroughly cleaned system on the first day, and with a cleaned reaction chamber and pedestal for the first run of each day. Figure 4 gives a summary of the results. Deposition time, among the four variables, appeared to have the greatest effect. The layer thickness increased nearly proportionately with the deposition time, with a slight leveling off of average rates at long deposition times. Deposition temperature (uncorrected) was next in importance, the deposition rate reaching its maximum at a medium temperature. Further, the layer thickness reached maximum on the second and third run of each day, and also on the second of the four days. This last conclusion seems to suggest that the system, the reaction chamber, and the silicon pedestal needed some decontamination period to operate at peak efficiency.

Table II shows the results of another experiment in which layer thickness was measured on the front side (facing gas) t_f, and at the edge of the back side (contacting pedestal), t_b. Each figure given represents the average of four (on specimen preparation and flow rate) or two (on temperature) readings. From these two thicknesses, the thickness ratios t_b/t_f were calculated. The specimen preparation, gas flow rates, and deposition temperatures were changed in this experiment. The (CP4) etched wafers had smaller layer thicknesses than lapped wafers, the difference being 24% in t_f and 16% in t_b. High flow rates increased the t_f by 61%, decreased the t_b/t_f ratio by 41%, but did not appreciably affect the t_b. The back side thickness also increased regularly with deposition temperature, while t_f reached a maximum, and the thickness ratio a minimum, at an intermediate temperature. These results, in view of the measuring precision of about 6.5%, suggest that the mechanisms of silicon deposition on the front and back side are different.

The data in Table II would also discourage the determination of layer thickness by weighing or the micrometer before and after the deposition, because the deposited thickness on the unwanted backside edge (which occupies large areas) may be close to four times the frontside thickness. The error of thickness measurement by weighing or the micrometer may, under unfavorable conditions, reach several hundred percent and become unsatisfactory.

Table II. Effect of specimen preparation, flow rate, and temperature on layer thickness

Variable	Condition	t_f, mils	t_b, mils	t_b/t_f
Specimen	Etched	0.58	1.35	2.31
Prep.	Lapped	0.76	1.61	2.28
Flow rate	380 cc/min	0.51	1.55	2.89
	720	0.84	1.41	1.70
Temp	1160°C	0.40	0.85	2.20
	1170	0.71	1.25	1.80
	1180	0.96	1.54	1.61
	1190	0.62	2.25	3.63

Gas Mixing

Two types of gas mixing or silicon tetrachloride pick-up methods have been used: the bubbling method, and the nonbubbling method. In the bubbling method, purified hydrogen is bubbled through the liquid silicon tetrachloride. In the nonbubbling method, the purified hydrogen is merely passed over the liquid surface. The same stock glass traps could be used in either method, depending on how much liquid was added to the trap.

Table III shows the results of calculations of the number of moles of silicon tetrachloride available per minute at different flow rates for the theoretical or equilibrium cases and the two actual cases with the bubbling and nonbubbling methods. The nonbubbling method gives a fairly constant number of moles of silicon tetrachloride per minute, whereas the bubbling method does not.

There are other advantages of the nonbubbling method over the bubbling method. In the nonbub-

Table III. Comparison of the bubbling and non-bubbling methods

Flow, cc/min	Calculated: Moles $SiCl_4$/min	Calculated: Moles H_2/min	Moles H_2 ÷ moles $SiCl_4$
950	0.00436	0.0386	8.8
1740	0.00798	0.0698	8.8
2450	0.0112	0.0982	8.8
	Experimental bubbling		
950	0.00274	0.0425	15.5
1740	0.00447	0.0779	17.4
2450	0.00669	0.109	16.3
	Experimental no bubbling		
950	0.000264	0.0424	161
1740	0.000274	0.0778	284
2450	0.000377	0.109	289

Table IV. Gas mixing and flow rates vs. layer thickness in mils

Flow rate, cc/min	Thickness deposited, mils Bubbling	Nonbubbling
950	0.95 ± 16%	0.42 ± 17%
1740	1.30 ± 7%	0.42 ± 7%
2450	1.11 ± 2%	0.41 ± 9%

bling method, the evaporating surface of the liquid tetrachloride is always flat and smooth and has a constant area and fairly constant surface temperature. In the bubbling method, the same surface is turbulent and bubbling and has no defined or stable surface area or evaporating temperature. There is always a large and unknown variable temperature gradient across the insulating bubbling layer. This condition makes the trap temperature almost meaningless. There is also an erratic bursting of bubbles giving rise to liquid droplets that are carried downstream to strike and re-evaporate at variable points along the walls at unpredictable temperatures. These droplets of liquid silicon tetrachloride are known sources of growth defects.

Table IV gives the summarized results on the effect of gas mixing and flow rates on layer thickness and thickness reproducibility. These results suggest that increasing gas flow increases thickness reproducibility. Also, in the nonbubbling method, the layer thickness is independent of the flow rate; whereas in the bubbling system, maximum deposition rate is reached at medium flow rates.

It has been suggested that in the bubbling method a system could be designed to trap all liquid droplets. Such a system would, according to our experience, suffer from some disadvantages such as:

1. It requires elaborate traps and filters.
2. It introduces contaminants through the extra filters, traps, joints, and internal surfaces.
3. The efficiency and operation of, and contamination from, these traps or filters are variable and strongly time-dependent.
4. Trapping wastes source liquid and requires more frequent filling of source containers and disturbing of the stable growth conditions.
5. It requires exact temperature controls on the source containers, traps, filters, and various connecting tubes. Still, the boundary layers near the walls of the containers or tubes may have temperatures, velocities, and concentrations entirely different from the inner layers, even at a given instant.
6. It complicates the systems, which are liable to be more variable from one to the other. The product reproducibility also suffers as a result.

Resistivity

Table V shows the typical resistivity variation within wafers. Here, the resistivity of each wafer is measured at six fixed positions, using the four-point probe method. From each set of six readings is obtained the average resistivity, the standard deviation, and the coefficient of variation (or the ratio of standard deviation to average resistivity). Within the wafer, these coefficients varied from 2 to 11%, with an average of 8%. These variations can be reduced by improved growth conditions, as shown below.

Table VI shows that the coefficient of variation in thickness and resistivity could be as high as 46% and 25% respectively on days when the gas valves or glass joints were leaking. Pedestal x was notably worse than the other three. Such variations were significantly greater than the average variations of 6.5 and 8%, respectively.

Designed experiments on resistivity (average 3.5 ohm-cm) have yielded the following lists of critical variables in order of decreasing importance:

To increase resistivity: 1. Increase flow rate; 2. nonbubbling method of gas mixing; 3. optimum deposition temperature; 4. clean substrate surface; 5. increased preheat time.

To decrease resistivity variation within wafers: 1. clean substrate surface; 2. nonbubbling method of gas mixing; 3. increased flow rate; 4. optimum deposition temperature.

Growth Defects

Figure 5 shows the magnified surface of a number of typical wafers after deposition. The wafer in Fig. 5a had a smooth surface. Figure 5b shows a wafer with triangular pits. A higher magnification of such pits is shown in Fig. 5d. These pits are caused by a dirty pedestal or reaction chamber.

Figure 5c shows a wafer having a polycrystalline growth of silicon, purposely deposited on an oxidized surface.

Figure 5e shows silicon deposition on a scratched surface. The gas flow in this case was directional, so that flow lines appeared only on the downstream side of the scratch.

Figure 5f shows the pyramidal silicon growth produced at relatively low deposition temperatures.

Another type of defect appears as a wavy surface

Table V. Resistivity variation within wafers

Wafer	Average	Standard deviation	Coefficient of variation, %
1	0.196	0.0159	8
2	0.958	0.0206	2
3	0.545	0.0617	11
4	1.950	0.1030	5
5	0.305	0.922	8
6	0.573	0.0063	11
7	0.371	0.0327	9
8	0.773	0.0688	9
Average	0.709	0.0503	7.75

Table VI. Reproducibility of t and ρ

Day	Pedestal	Runs	$\bar{t} \pm$ %	$\bar{\rho} \pm$ %	Notes
1	3	4	1.50 ± 14	0.78 ± 3	a
2	2	3	1.67 ± 19	0.42 ± 10	a
3	x	6	2.94 ± 46	0.63 ± 25	a
4	4	4	1.62 ± 5	—	b
5	4	6	0.86 ± 20	—	a
6	2	5	1.40 ± 12	—	b

Notes: (a) Helium leak during run. (b) No helium leak in valve. (c) No helium leak in system other than valve.

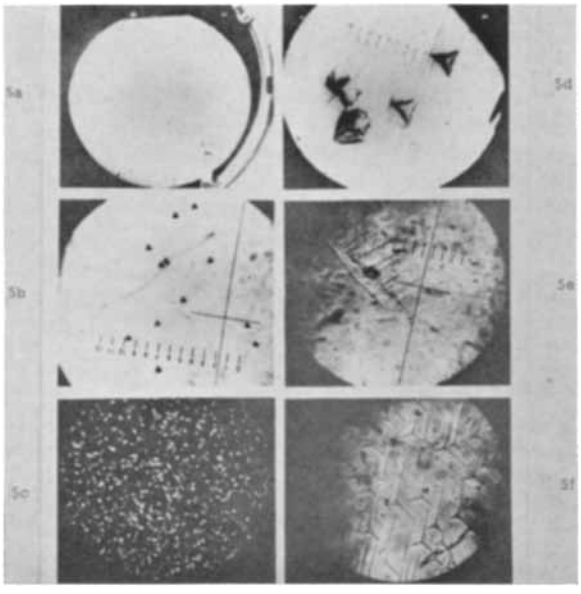

Fig. 5. Growth defects

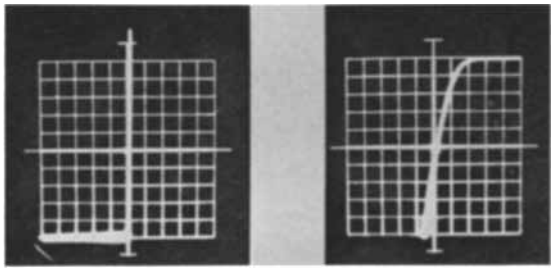

Fig. 6. Diode characteristics

on the wafer. This can be eliminated by proper substrate preparation and controlled gas flow rates.

Device Characteristics

On some of the wafers with n type layers deposited on n^+ substrates, 16 x 32 mil aluminum rectangles have been evaporated through metal masks. The aluminum was later alloyed in at 800°C for different periods of time to form alloyed diodes. The capacitance of these diodes has been measured at different reverse voltages. Within certain ranges, change of alloying time by even a factor of four did not appreciably change the capacitance. The slope of the capacitance *vs.* voltage plotted on a log-log scale had a typical value of −1/2.5, suggesting that these alloyed junctions have characteristics somewhere between step and graded junctions.

These epitaxially grown materials have been used to make small and large-area planar and mesa diodes and transistors. Both the forward and reverse characteristics of the devices are generally excellent. Figure 6 shows a typical planar epitaxial microdiode. This diode was a gold-diffused fast-switching type. It had a junction only 5 mils in diameter. The left side of the figure shows the forward characteristics. The scale is 100 ma per vertical division and 0.2v per horizontal division. The diode thus carries 60 ma at 1v of forward voltage.

The right side of Fig. 6 shows the reverse characteristics. The diode is shown to break down very sharply at 100v. Detailed measurements showed that under 60v reverse bias, the leakage current was only 5 x 10^{-10} amp. Further, this leakage current was maintained after the diode was subjected to thermal cycling and humidity tests. The switching time of the diode was less than two nanoseconds.

Acknowledgment

The author wishes to give credit to Messrs. D. Scaringella, K. Chen and R. Fairbanks, of General Instrument Research Laboratory for their helpful discussions and the numerous experiments carried out by them.

Manuscript received Feb. 21, 1962; revised manuscript received May 24, 1962. This paper was prepared for delivery before the Detroit Meeting, Oct. 1-5, 1961.

Any discussion of this paper will appear in a Discussion Section to be published in the June 1963 JOURNAL.

REFERENCE

1. H. C. Theuerer, *This Journal*, **108**, 649 (1961).

Epitaxial Growth of Silicon by Hydrogen Reduction of $SiHCl_3$ onto Silicon Substrates

J. M. Charig and B. A. Joyce

Caswell Research Laboratories, Plessey Company, Limited, Towcester, Northants, England

ABSTRACT

Epitaxial films of silicon have been grown on silicon substrates by hydrogen reduction of $SiHCl_3$. Reaction kinetics have been investigated and an over-all reaction mechanism suggested, assuming reduction to occur on the substrate surface. Electron micrographs and diffractograms of growing layers have been obtained in an attempt to determine the nature of the growth process. Preliminary results indicate that this occurs initially by the formation of individual nuclei rather than by continuous film formation, but the nucleation process is apparently not propagated continuously.

Experimental methods for the epitaxial growth of silicon by the hydrogen reduction of silicon halides have been described by several authors (1-3), and quantitative results have been presented by Theuerer (2) and Wajda and Glang (3) for $SiCl_4$ and $SiHCl_3$, respectively. The results of the two sets of authors show many differences, and only the former attempts to interpret them in terms of

a reaction mechanism which, he suggests, involves the adsorption of $SiCl_3$• onto the silicon substrate, followed by reduction and desorption of HCl, with an over-all activation energy of 37 kcal/mole.

The purpose of this paper is to present some kinetic data for the hydrogen reduction of $SiHCl_3$ on a silicon substrate, from which a reaction mechanism is postulated, and also some preliminary observations on experiments carried out to determine the growth mechanism. Electron micrographs and electron diffractograms of the grown layers have been obtained after various time intervals in the very early stages of growth and have revealed what are apparently individual nuclei distributed on the surface before complete coverage has occurred.

Experimental

The apparatus used was essentially similar to that employed by Sangster *et al.* (1). Hydrogen at a flow rate of 30 ml/min was passed over refluxing $SiHCl_3$ to ensure saturation, and the resulting gas mixture was stripped down to a known concentration in a thermostatted condenser, after which it was further diluted with hydrogen to give the required partial pressure of $SiHCl_3$ in the reactor, and a total flow rate of approximately 1.5 l/min. Partial pressure values calculated from vapor pressure and flow rate data were checked experimentally by determining the gas phase $SiHCl_3$ concentration and were found to be correct to within ± 5%. The hydrogen was purified by passing through a catalytic deoxygenating unit, and a 5A molecular sieve to remove water vapor and other condensable gases. The substrate was supported vertically from its ends with tantalum tapes and heated by a direct resistance method so that it was the hottest part of the system and silicon was not deposited preferentially on the walls (Fig. 1).

The substrates used were bars 2 mm x 7 mm x 4 cm long, and in all of the kinetic experiments the 7 mm face was the {110}, but both {100} and {111} faced substrates were also used in the growth mechanism work. Before growth the substrates were lapped on 15μ alumina and chemically polished to a mirror finish in an etch containing nominally 3 parts 40% HF, 6 parts 70% HNO_3, and 2 parts 60% acetic acid. Final oxide removal was carried out in the reactor by treating in hydrogen for 15 min at a temperature in excess of 1260°C.

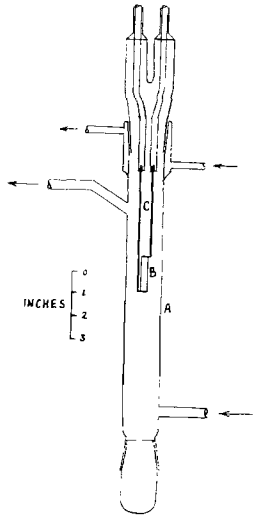

Fig. 1. $SiHCl_3$ reactor: A, quartz tube; B, silicon substrate; C, tantalum power leads.

Since it has been indicated (2) that boron compounds may influence the rate of this reaction, kinetic measurements were confined to n-type layers grown on n-type substrates. The substrate resistivity was 0.1 ohm-cm in each case, and the layers were all approximately 1 ohm-cm. In order to measure the layer thickness the specimen was cleaved or bevelled and the layer delineated by a pulse staining technique reported elsewhere (4).

The procedure for each run was as follows: the apparatus was evacuated and then flushed with hydrogen, the stream containing $SiHCl_3$ vapor initially bypassing the reactor. The substrate was heated for 15 min at a temperature in excess of 1260°C to ensure oxide removal, after which, with the stripping condenser set to the appropriate temperature, the $SiHCl_3$ stream was diverted into the reactor and at the same time the substrate temperature set to the required value as measured with an optical pyrometer calibrated at the melting point of silicon. The duration of the run was timed with a stopclock and terminated by again diverting the $SiHCl_3$ and allowing the substrate to cool in hydrogen.

Kinetic Measurements

The two factors which have been investigated are (*a*) influence of substrate temperature on growth rate of the epitaxial layer for a constant partial pressure of $SiHCl_3$ in the reactor and (*b*) the effect of varying the partial pressure of $SiHCl_3$ for a constant substrate temperature. In both cases the flow rates of hydrogen were held constant, and partial pressure was controlled by the temperature of the stripping condenser.

The rate of the reaction was measured as the growth rate of the epitaxial film, and in a system of this type reaction rates cannot of course be considered as absolute, but for a constant set of conditions experimental values were reproducible to within ± 10% and the general shapes of the curves were also reproducible. Errors in thickness measurement of the film and temperature control of the substrate probably accounted for most of the deviations found.

Wajda and Glang (4) report differences in growth rate along the length of the substrate depending on the geometry of the reactor. This was not observed in the system employed in the work reported here, but some small differences were observed on opposite (parallel) faces of the substrate when it was not positioned centrally in the reactor. Measurements were therefore made on both faces, and the mean thickness determined.

Deposition temperature.—The dependence of deposition rate on substrate temperature for a constant flow rate of hydrogen and partial pressure of $SiHCl_3$ is shown in Fig. 2. Over the temperature range 1110°-1220°C a normal Arrhenius plot is obtained, giving an over-all activation energy for the process of 22 kcal/mole, but above this, growth rate falls

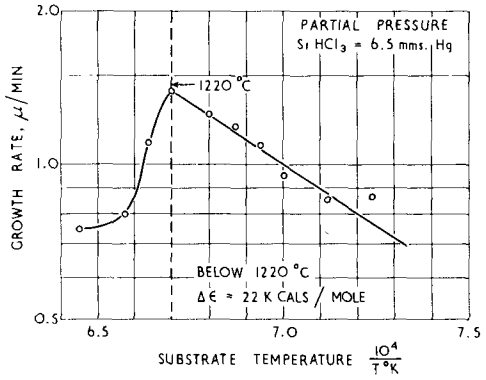

Fig. 2. Temperature dependence of layer growth rate

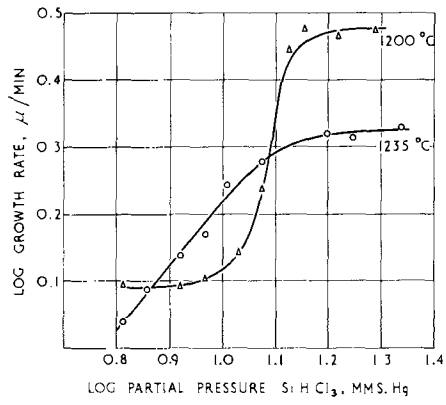

Fig. 3. Effect of $SiHCl_3$ partial pressure on layer growth rate

with increasing temperature. This is contrary to results obtained on $SiHCl_3$ by Wajda and on $SiCl_4$ by Theuerer. The latter followed a normal Arrhenius relationship over the whole temperature range considered (900°-1300°C) with an over-all activation energy of 37 kcal/mole, while the former showed little variation with temperature between 1100° and 1200°C, but this was attributed to the particular design of the substrate heater and gas flow pattern in the reactor.

Assuming the reduction reaction to occur by a heterogeneous mechanism on the substrate surface, then, of the steps which could be rate controlling, gaseous diffusion of the reactants or products is ruled out, since it is not an activated process. This leaves adsorption of the reactants, surface reaction followed by desorption of gaseous products, or in this case, the surface diffusion of silicon formed on the substrate as the possible slow steps in the over-all reaction. If it is assumed, however, that the equilibrium density of this self-adsorbed layer remains sensibly constant, surface diffusion cannot be the rate-determining step since under these conditions it is an equilibrium process. From the available data it is not possible to decide between adsorption and reaction with desorption as the slow step. A possible explanation of the maximum is that the total amount of chemisorption possible on the {110} surface decreases above a temperature of approximately 1220°C. This may be due either to a reduction in the length of time an adsorbed radical is retained on the surface before re-evaporation or reaction can occur, or to a reduction in the actual number of available surface sites.

$SiHCl_3$ *partial pressure.*—The influence of $SiHCl_3$ partial pressure on growth rate was investigated at substrate temperatures above and below the maximum in the growth rate-temperature curve. Results obtained are shown in Fig. 3, and it may be seen that in each case the growth rate reached a limiting value as the partial pressure of $SiHCl_3$ was increased. Since for the same flow conditions the process was found to be activated, it may be concluded that it was a reaction rate and not a mass flow effect which was measured. There are two main possibilities concerning the over-all nature of the reaction. (i) Reaction occurs between an absorbed $SiHCl_3$ molecule or radical and an adsorbed hydrogen molecule or atom (Langmuir-Hinshelwood mechanism), and (ii) reaction occurs between an adsorbed molecule and a molecule coming directly from the gas phase (Rideal mechanism). This gives rise to two alternatives depending on whether a $SiHCl_3$ radical is adsorbed and reaction occurs with a hydrogen molecule from the gas phase, or a hydrogen atom is adsorbed which reacts with a gaseous $SiHCl_3$ molecule.

If a Langmuir-Hinshelwood mechanism is followed, the rate will pass through a maximum as the pressure of either reactant is varied, while the rate will reach a limiting value if a Rideal mechanism applies. The results obtained therefore indicate one or other of the Rideal mechanisms to be the most probable over-all course of the reaction. At the start of the process, hydrogen alone is present over the substrate, and even during the course of growth it is present in considerable excess, but from the measured rate dependence on the partial pressure of $SiHCl_3$ it appears that, if the hydrogen is initially present as a chemisorbed layer on the surface, it is rapidly displaced as soon as a partial pressure of $SiHCl_3$ exists, particularly at the higher temperature (1235°C). At the lower temperature (1200°C) however, hydrogen chemisorption may be responsible for the small rate of change of reaction rate at low $SiHCl_3$ concentrations. Thus the rate curves indicate that essentially $SiHCl_3$ radicals are chemisorbed and react with gaseous hydrogen molecules.

Since it is not possible to measure reaction rates and reactant concentrations in terms of the same variable it is not possible to measure absolute orders of reaction (other than zero order). However Fig. 3 shows that at both temperatures the order becomes zero with respect to $SiHCl_3$ as its partial pressure increases and presumably a monolayer is formed. The relative variations of order with increasing initial concentrations of $SiHCl_3$ at the two temperatures are also evident, and over the linear portions the order at 1200°C is 2.8 times greater than at 1235°C. This difference presumably arises either because of the relative extent of hydrogen chemisorption, or because of the over-all amount of chemisorption possible at the two temperatures.

Influence of Kinetic Parameters on Layer Perfection

We have observed that at substrate temperatures above 1175°C film perfection is, macroscopically,

very high, irrespective of the partial pressure of $SiHCl_3$. As the temperature is reduced, however, imperfections of the type seen in Fig. 10 begin to appear. (This optical micrograph also shows the development of a {112} edge facet.) These imperfections eventually lead to regions of polycrystalline growth, but their onset and concentration with respect to temperature can be lowered by a reduction in trichlorosilane concentration. Below 1000°C it is very difficult to obtain even an imperfect single crystal layer, although the partial pressure of $SiHCl_3$ may be considerably less than 1 mm Hg. This of course suggests that it is the surface mobility of silicon atoms which is essentially responsible for single crystal layers, even when growth involves a chemical reaction.

Growth Phenomena

Epitaxial overgrowths of various metals and compounds evaporated onto an assortment of substrates such as other metals, the alkali halides, and mica have been studied for a number of years (5). Direct observations of the nucleation and growth have been made by evaporating and condensing thin layers actually in the electron diffraction camera and electron microscope (6).

Growth resulting from chemical reactions of mixed gases at solid substrate surfaces at high temperatures has received comparatively little attention.

Observations and Discussion

By using the resistive heating technique already described anomalous growth behavior can be observed at magnifications up to 100X by stereoscopic microscope using long working distance objectives focussed through the clear quartz walls of the reaction tube.

Platinum-carbon replicas (7) of substrate surfaces after chemical polishing and hydrogen etching have been compared with those from surfaces exposed to known growth conditions for different lengths of time (10 sec or more). Each surface so treated has been examined by glancing angle electron diffraction beam to assist in interpretation of the replica observations. The overgrowths prepared for electron microscopy (10 and 30 sec growth) were essentially featureless when examined in the optical microscope. They were grown at 1250°C under conditions equivalent to steady-state growth rates of 0.6-1.2μ/min. Preliminary treatment of the substrate was confined to exposure to dry hydrogen (2 liters/min) for 10 min at 1250°C.

All the layers cooled rapidly when the power supply to the specimen was switched off.

The smooth, featureless surface of a chemically polished {110} silicon substrate is shown in the electron micrograph, Fig. 4. Exposure of a similar substrate to dry hydrogen for 10 min at 1250° or 1300°C produced no detectable change in appearance. The diffraction pattern, Fig. 5 from the surface of the specimen illustrated in Fig. 4 consists of clearly defined Kikuchi lines only, indicating a high degree of crystal perfection and confirming the

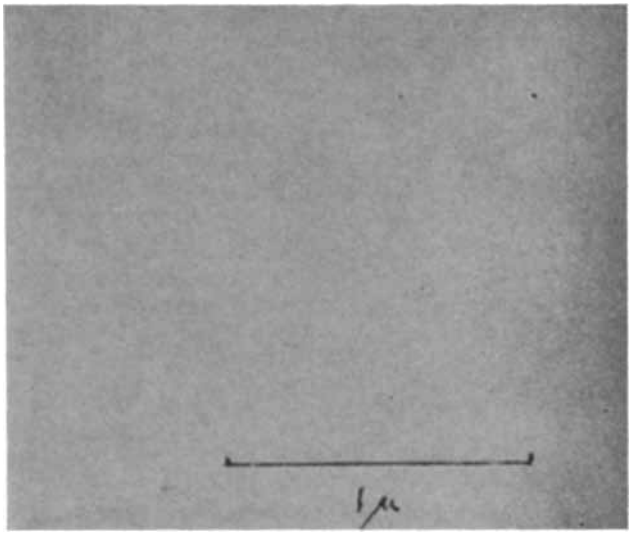

Fig. 4. Electron micrograph of Pt-C replica of chemically polished silicon substrate. {110} surfaces. Magnification 40,000X.

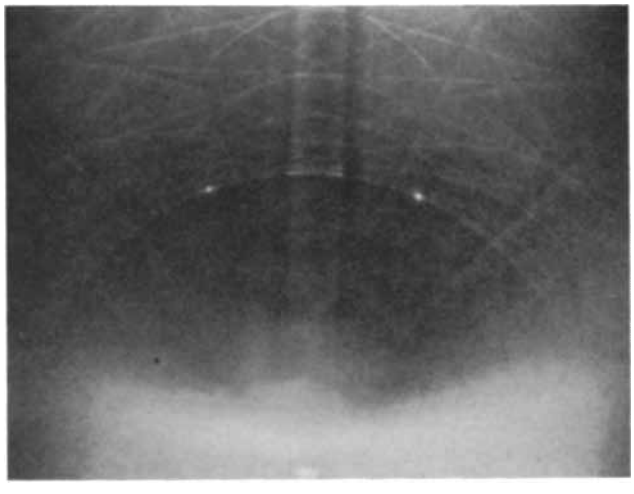

Fig. 5. Diffractogram corresponding to Fig. 4

essentially flat surface revealed in the electron micrograph.

Electron micrographs of replicas of the {110} surfaces of grown layers are shown in Fig. 6-8. After 10 sec growth (Fig. 6) the surface has become covered with a layer of discrete islands typically about 500Å across. After 30 sec, Fig. 7, the islands are still apparent but less clearly defined, the surface having a generally wavy appearance. Electron micrographs from the surfaces of thicker layers (>5μ) do not show the small islands but reveal very fine channels or ridges of a somewhat wavy nature (Fig. 8). Examination of {111} and {100} surfaces after 10 sec growth revealed islands similar to those on the {110} surfaces.

It would seem probable that growth commences by a nucleation process which leads to formation of the small islands observed. (Fig. 6). These islands gradually coalesce to form a relatively rough surface as illustrated in Fig. 8. The roughness of the surface is not, however, the only significant feature relevant to the growth morphology. A specimen with a 30μ deposit was removed from the reaction chamber and fractured. Half was then returned to the reactor for regrowth; 10 sec further growth

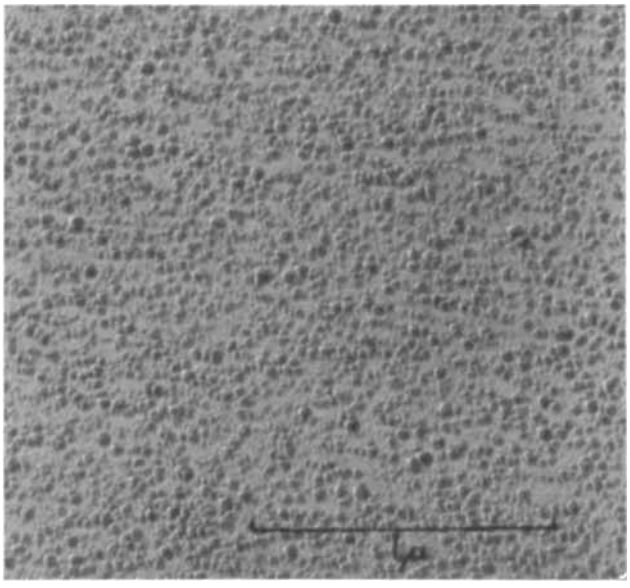

Fig. 6. Electron micrograph of Pt-C replica of epitaxial silicon layer on {110} surface after 10 sec growth at 1250°C. Magnification 40,000X.

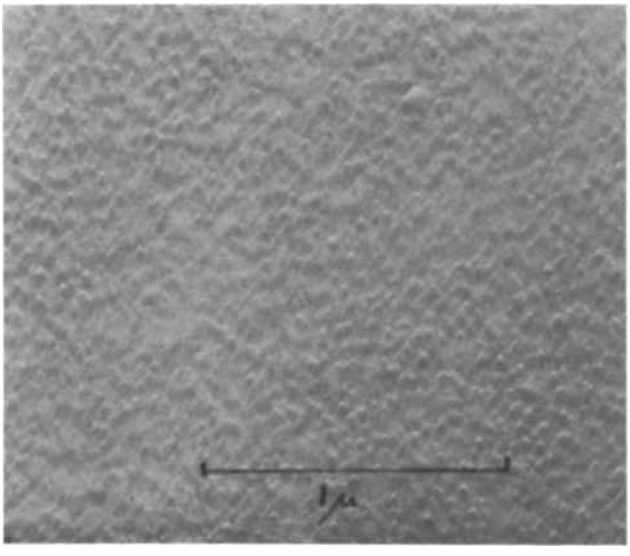

Fig. 7. As Fig. 6 but for 30 sec. Magnification 40,000X.

again resulted in the occurrence of the random islands. This suggests that the formation of individual nuclei when growth commences may be influenced by some residual surface contamination such as an incomplete oxide network. Any such contamination will be on a small scale, none having been detected by electron microscopy or diffraction.

Precise interpretation of the glancing angle electron diffraction patterns has not been attempted. The pattern shown in Fig. 9 is typical of that obtained from any of the grown surfaces in that it shows both Kikuchi lines and diffraction spots. There are, however, differences in the nature and configuration of the spot patterns which depend on the layer thickness.

The spot patterns from the short duration growths may be associated with the presence of the islands, but the occurrence of spot patterns from thick layers ($>5\mu$) indicates the possibility of alternative explanations. For example there is evidence for

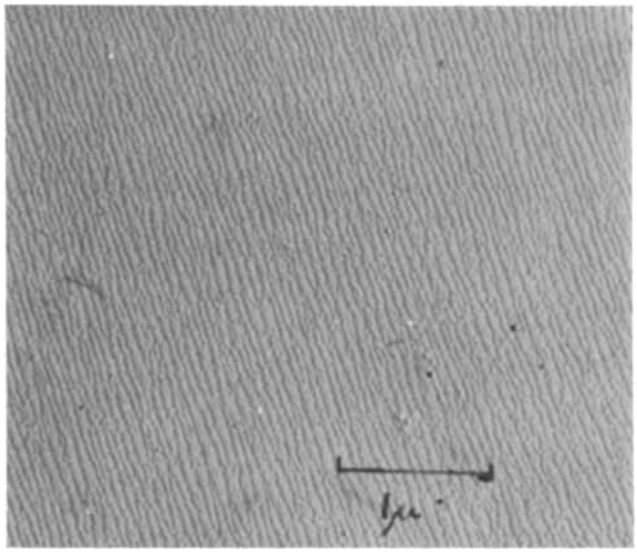

Fig. 8. Electron micrograph of Pt-C replica of 7μ epitaxial silicon layer on {110} surface. Magnification 20,000X.

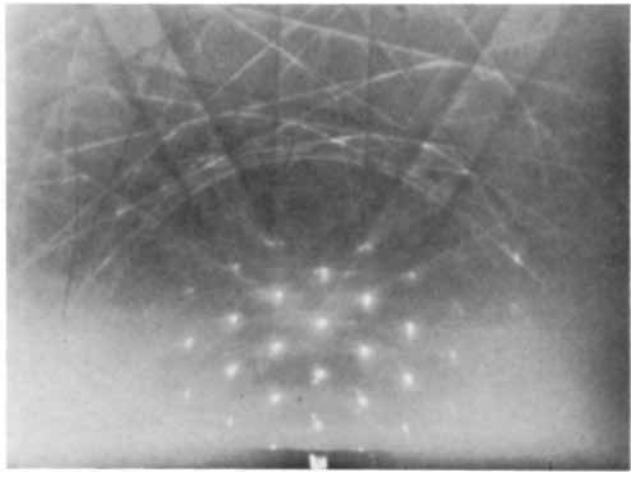

Fig. 9. Typical electron diffraction pattern from {110} growth surface.

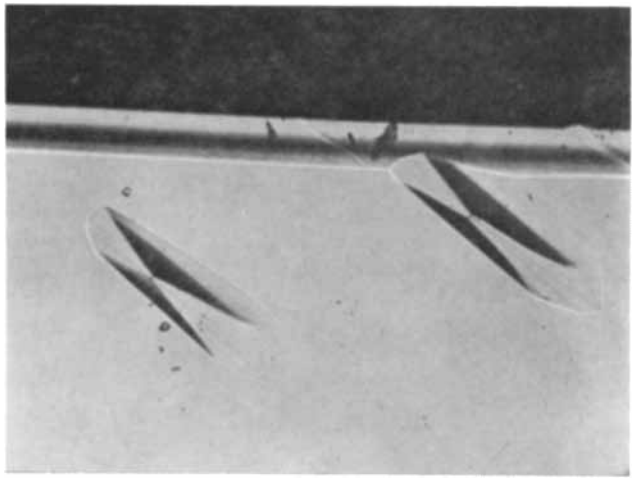

Fig. 10. Unetched surface of {110} epitaxial layer showing {112} facet and defects. Magnification approximately 90X.

the existence of twin bands or regions of stacking faults, the origins of which are currently under investigation. The electron micrographs, Fig. 11 and 12, show examples of such structural defects in the unetched and etched conditions, respectively. The

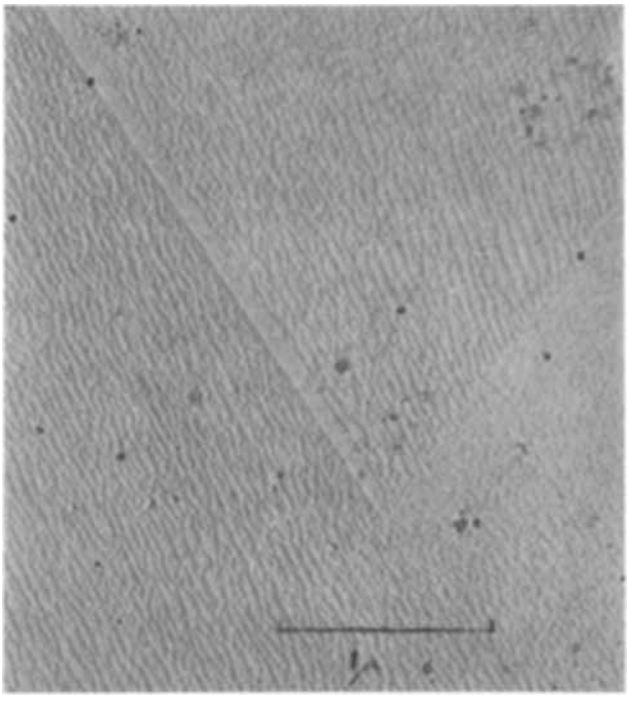

Fig. 11. Defect observed in epitaxial layer. Electron micrograph of Pt-C replica of unetched layer surface ({110}). Magnification approximately 29,000X.

results of this work will be published in the near future (8).

Summary and Conclusions

The results of the kinetic measurements indicate that the most probable over-all course of the reaction involves the chemisorption of a trichlorosilane radical on the substrate, which is reduced to silicon by a hydrogen molecule impinging directly from the vapor phase with subsequent desorption of HCl. A possible interpretation of the evidence from the electron micrographs and diffractograms is that initially the silicon produced on the substrate does not grow as a continuous monolayer, but rather by formation of individual nuclei which are considerably thicker than one atomic layer. Since chemisorption as such can only occur to monolayer depth, the nuclei must arise either by surface diffusion of silicon from unfavorable sites, or by preferential chemisorption. The former hypothesis seems much more probable, however, since layer perfection decreases with decreasing temperature, which would be expected to reduce surface mobility, not initiate nonpreferential chemisorption. The nucleation process does not appear to continue however, when a layer of the order of 1μ has been obtained.

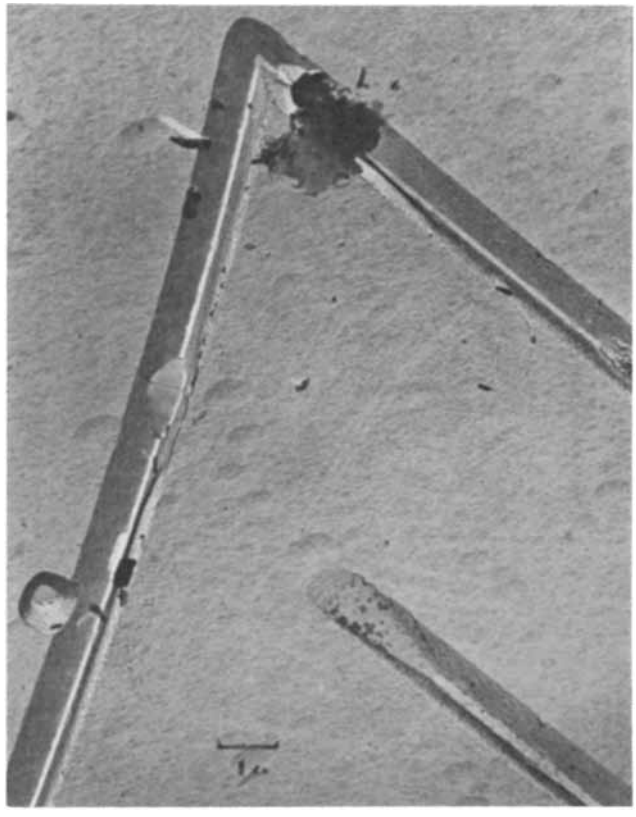

Fig. 12. Region of the layer shown in Fig. 11 but layer etched in the Dash dislocation etch for 20 min. Magnification approximately 8000X.

Acknowledgments

The authors are grateful to D. J. Stirland for the electron microscopy and R. Bicknell for the electron diffractograms and to them both, together with W. H. Shepherd for much valuable discussion. Thanks are due to the Plessey Company Limited, for permission to submit this paper.

Manuscript received Feb. 15, 1962.

Any discussion of this paper will appear in a Discussion Section to be published in the June 1963 JOURNAL.

REFERENCES

1. R. C. Sangster, E. F. Maverick, and M. L. Croutch, *This Journal*, **104**, 317 (1957).
2. H. C. Theuerer, *ibid.*, **108**, 649 (1961).
3. R. Glang and E. S. Wajda, A.I.M.M.E. Semiconductor Conference. Los Angeles, August, 1961.
4. B. A. Joyce, *Solid State Electronics*, **5**, 102 (1962).
5. D. W. Pashley, *Advances in Physics*, **5** (18), 173 (1956).
6. G. A. Bassett. European Regional conference on Electron Microscopy, 1960, p. 270, D. Nederlandse verenigining voor electronenmicoscope, Delft.
7. D. E. Bradley, *Brit. J. Appl. Phys.*, **11**, 506 (1960).
8. J. M. Charig, B. A. Joyce, D. J. Stirland, and R. Bicknell, *Phil. Mag.*, To be published.

Vapor Phase Equilibria for the Systems: GaAs-GaI_x-As_y and Ga-GaI_x

V. J. Silvestri and V. J. Lyons

Thomas J. Watson Research Center, International Business Machines Corporation, Yorktown Heights, New York

ABSTRACT

Analysis of pressure measurements has led to the determination of the vapor species resulting from the reaction of GaAs with I. The reaction determined from the analysis is $2GaAs(s) + GaI_3(v) \rightleftarrows 3GaI(v) + \frac{1}{2}As_4(v)$ in the range 560°-850°C. The equilibrium constant is given by the equation, $\log Kp = -23{,}650/T + 19.4$. The enthalpy calculated for the reaction is 54.1 kcal/mole of GaAs. A similar analysis for the system Ga-GaI_x resulted in the determination of the reaction $2Ga(l) + GaI_3(v) \leftarrow 3GaI(v)$ in the range 420°-650°C. The equilibrium constant for this reaction is given by $\log Kp = 11{,}000/T + 12.4$. The enthalpy for the reaction is 25.2 kcal/mole of Ga. By combining the two equilibria in the region of overlapping temperatures, the arsenic pressures in equilibrium with GaAs along the three-phase line are obtained. In the range 560°-640°C the predominant reaction is $GaAs(s) \rightleftarrows Ga(l) + \frac{1}{2}As_2(v)$. The enthalpy calculated for this reaction is 44.4 kcal/mole of GaAs. The dissociation pressures are in good agreement with extrapolations from two previous measurements made at higher temperatures.

The growth of crystals of binary compounds from a vapor phase composed of the species resulting from reactions of the compounds with a halogen element has become of significant importance in its application to the fabrication of solid-state device structures. In order to gain some insight into the nature of crystal growth by this method, it is first necessary to identify the reacting vapor species and determine equilibria between these species and the growing crystal. It was felt that this information could be obtained through analysis of pressure measurements.

Because of the current widespread interest in the semiconducting compound GaAs, and the demonstrated ability to grow crystals of the compound at low temperatures through reaction of the compound and certain halogens (1-3), pressure measurements were carried out to determine the equilibrium between solid GaAs and the vapor species resulting from reaction of the compound with iodine.

Of the possible iodide vapor species that might result from the reaction of iodine with GaAs, calculations based on published thermodynamic data (4) reasonably excluded all but GaI_3 and GaI. The excluded species were GaI_2 and the arsenic iodides. The calculations further indicated that GaI_3 would be more stable at lower temperatures and hence would be the predominant iodide species resulting from initial low-temperature reaction of iodine with GaAs. Preliminary experiments showed that iodine reacts completely with GaAs at temperatures below 200°C to form, at equilibrium, arsenic and a gallium iodide species presumed to be GaI_3. The presence of arsenic was verified by x-ray diffraction analysis of the condensed phases. GaI_3 was identified primarily by its melting point (5) and the color of the crystals. Positive identification by x-ray diffraction analysis was not obtained due to rapid hydrolysis of the compound and inadequate x-ray diffraction data for the gallium iodides. At higher temperatures, in the presence of excess GaAs, the vapor species GaI would become important according to Brewer (4).

From this information it was possible to postulate, as a model, a disproportionation reaction for the transport and crystal growth of GaAs from a vapor phase. The proposed reaction was

$$2GaAs(s) + GaI_3(v) \rightleftarrows 3GaI(v) + \tfrac{1}{2}As_4(v) \quad [1]$$

An additional equilibrium which must be considered is the dissociation of tetrameric arsenic according to the reaction

$$2As_2(v) \rightleftarrows As_4(v) \quad [2]$$

The system would be at least bivariant and therefore would require at least two sets of pressure measurements at different initial iodine concentrations in order to test the postulated model. The test of the model would be in a comparison of equilibrium constants calculated from each set of pressure measurements. Because of the invariance of the equilibrium constant, coincidence of the calculated Kp values would be considered a reasonable verification of the proposed equations. Variation of the initial iodine concentration would serve also to establish a possible univariant portion of the system, e.g., GaI_3 (condensed) $\rightleftarrows$ GaI_3 (vapor), and further corroborate the model.

In order to calculate values of the equilibrium constant it is necessary to calculate first the partial pressures of each vapor species. Since the model assumes four vapor species, four independent equations are needed for the determination of their partial pressures. The total pressure measurements need only to be carried out under conditions of known volume and known iodine concentration in order to provide the necessary information for solution of the four equations which are given below.

I. *Total pressure*

$$P_T = P_{GaI_3} + P_{GaI} + P_{As_4} + P_{As_2} \quad [I]$$

II. *Conservation of iodine*

n_I = moles of iodine added to each tube calculated as monatomic iodine

$$n_I = 3n_{GaI_3} + n_{GaI}$$

Multiplying both sides of the equation by RT/V, an equation in terms of pressure is obtained

$$\frac{n_I RT}{V} = 3P_{GaI_3} + P_{GaI} \qquad [II]$$

R is the gas constant; V the reaction tube volume.

III. *Conservation of* Ga *and* As.—For each GaI_x molecule resulting from the reaction of I with GaAs, an arsenic atom is present in the system. Therefore, in the vapor phase

$$n_{Ga} = n_{As}$$

$$\frac{n_{Ga}RT}{V} = P_{GaI} + P_{GaI_3}$$

$$\frac{n_{As}RT}{V} = 4P_{As_4} + 2P_{As_2}$$

hence

$$P_{GaI} + P_{GaI_3} = 4P_{As_4} + 2P_{As_2} \qquad [III]$$

IV. *Arsenic vapor equilibrium.*—$2As_2(v) \rightleftarrows As_4(v)$

$$P_{As_4} = Kp(P_{As_2})^2 \qquad [IV]$$

The values of Kp for Eq. [IV] are tabulated in Stull and Sinke (6). Since the values of n_I, P_T, R, and V would be known the partial pressures of the four vapor species could be calculated and hence Kp for reaction [1] may be calculated from

$$Kp(1) = \frac{(P_{GaI})^3 (P_{As_4})^{1/2}}{P_{GaI_3}}$$

In order to test the proposed model, three sets of pressure measurements were made each at a different initial iodine concentration. The measurements were carried out in sealed quartz tubes employing Bourdon gauges.

Pressure measurements also were carried out on the system resulting from the reaction of iodine with an excess of gallium. From the considerations cited above (4), the reaction proposed for this system was

$$2Ga(l) + GaI_3(v) \rightleftarrows 3GaI(v) \qquad [3]$$

$$Kp = \frac{(P_{GaI})^3}{P_{GaI_3}}$$

The two equations needed to calculate the gallium iodide partial pressures for this system are given below

$$P_T = P_{GaI_3} + P_{GaI}$$

$$\frac{n_I RT}{V} = 3P_{GaI_3} + P_{GaI}$$

The validity of the proposed reaction was tested through a comparison of values of the equilibrium constants calculated from the results of two sets of pressure measurements.

From the equilibria determined for the two systems, it was possible to derive the three-phase line dissociation pressures of GaAs in a temperature range wherein the arsenic pressures are below 1 x 10^{-7} mm. The arsenic pressures determined from this work are in good agreement with extrapolations of direct measurements made at higher temperatures and pressures.

Experimental Procedure

Iodine weighing procedure.—The iodine used in runs 1 and 2 was weighed in the following manner. An 8 mm OD quartz tube 5 in. long was fitted with a 10/30 male joint at one end and a break-off tip at the opposite end. The tube was cleaned with CH_3OH and CCl_4 to remove grease and then weighed on an analytical balance which had an accuracy of ± 0.2 mg. A quantity of 99.95% iodine (Gallard-Schlessinger) somewhat greater than that desired was then loaded into the tube. After evacuating the tube at a pressure of 0.1μ for 30 min, the tube was sealed by fusion of the quartz. The tube plus iodine was then reweighed to give the net weight of iodine. A correction was made for the air displaced from the iodine capsule. The iodine used in run 3 was weighed in the same manner but in Pyrex tubes. It was subsequently determined through control experiments that in the sealing process significant quantities of quartz and Pyrex were vaporized. The weighing results for the I-GaAs experiments are summarized in Table I.

Pressure measurements.—Figure 1 illustrates the apparatus used for the vapor pressure measurements and the loading procedure. For the system I-GaAs, high purity monocrystalline GaAs[1] was broken into 1-2 mm diameter pieces and loaded into the tube. The quantity of GaAs used in each run was approximately ten times greater than the quantity of iodine. This insured an excess of GaAs throughout each experiment thereby approximating the condition prevalent during vapor growth of the compound. The iodine capsule was contained in a separate tube connected to the reaction chamber. Both

[1] Provided by S. E. Blum of this laboratory.

Table I. Weighing results for I-GaAs experiments

	Tube vol., cc	Experimental weights (used for calculation of Kp values in Fig. 3) wt, mg	n_I, g-atom	Calculated weights (from best fit of Kp for all three runs; Fig. 4) wt, mg	n_I, g-atom	Δ weight found between experimental and calculated weights, mg	Expected error in weight due to sealing, mg
Run 1	59.4	100.5	7.92×10^{-4}	102.5	8.08×10^{-4}	+2.0	+1.5-4.0
Run 2	56.7	51.7	4.07×10^{-4}	54.1	4.26×10^{-4}	+2.4	+1.4-4.0
Run 3	58.2	22.9	1.80×10^{-4}	23.1	1.82×10^{-4}	+0.2	+0.2-0.5

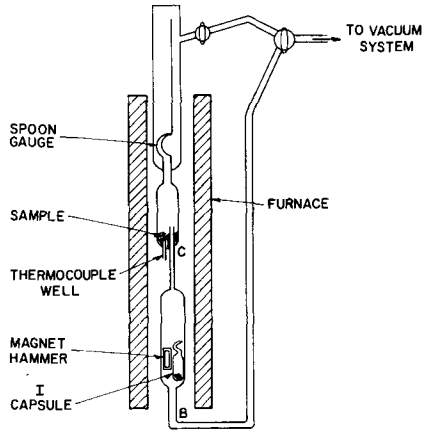

Fig. 1. Apparatus used for vapor pressure measurements showing additional connections used for iodine loading and vacuum bake-out procedure.

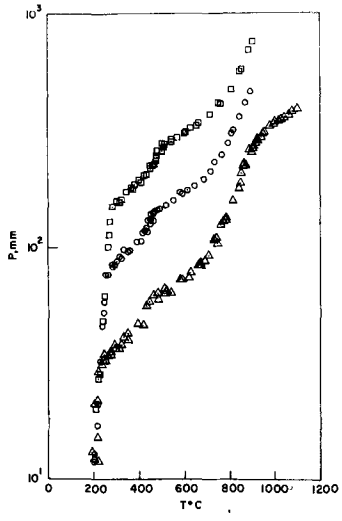

Fig. 2. Vapor pressures for three experimental runs on system GaAs-GaI_x-As_y. Square with dot, Run 1, $n_I = 7.92 \times 10^{-4}$ mole; circle with dot, run 2, $n_I = 4.07 \times 10^{-4}$ mole; triangle with dot, run 3, $n_I = 1.80 \times 10^{-4}$ mole.

sides of the spoon gauge were evacuated simultaneously to 1 x 10^{-6} mm Hg, and the apparatus was then heated for 6 hr at 190°-210°C to remove adsorbed water and other vapors. The tube was then sealed at point B. After breaking open the iodine capsule, the iodine was pumped into the reaction tube by cooling a region of the reaction tube with dry ice. The apparatus was then sealed at point C. A detailed description of the technique used in making the pressure measurements was given in an earlier publication (7). The furnace used in the measurements was found to have a 10°C temperature gradient over the length of the tube. The sample was situated at the lowest temperature in the reaction tube. The furnace was provided with a viewing slit so that visual observations could be made during the course of the measurements. Temperatures were measured with a Pt-Pt, 10% Rh thermocouple which was calibrated against a NBS standardized Pt-Pt, 10% Rh thermocouple. The thermocouple voltages were read with a Rubicon Potentiometer, Model 2732. Pressure measurements were made during both heating and cooling cycles. At each temperature where a measurement was taken, equilibrium times of 0.5 to 1 hr were allowed.

Reaction tube volumes were measured both before and after each run by filling the tubes with water from a buret. The volumes determined appear in Table I.

The procedure outlined above also was employed for measurements on the system I-Ga. The weight of Ga used in each run was approximately ten times the weight of iodine so that liquid Ga was present throughout the measurements. The gallium (99.999% pure) was obtained from Eagle-Picher. Reaction tube volumes for the two measurements were 33.6 cc for run 1 and 58.2 cc for run 2.

Several Bourdon gauges were used during the course of the experiments. In general, the gauges were insensitive to pressures below 4 mm.

Discussion

The reaction I-GaAs.—As the reaction tubes were heated iodine vapor was observed and the vapor pressure of the element was measured. At about 100°C, reaction of the iodine with GaAs was observed both as a color change in the vapor and as a rapid decrease in vapor pressure. After the initial reaction a condensed iodide phase was observed on the wall of the reaction tube. The vapor pressure at this point was below the limit of detectability of the gauges. After the initial reactions, the purple color of iodine vapor was not observed.

The pressure curves corresponding to the three different initial iodine concentrations are shown in Fig. 2. The initial rise in pressure for each set of data falls along a univariant curve which is coincident with that for the system $GaI_3(c) \rightleftarrows GaI_3(v)$ (5). The experimental curves break away from the univariant curve at different temperatures depending on the initial iodine concentration. In run 1 for example, the break-point occurs at approximately 285°C. At this temperature the liquid phase was observed to disappear thereby establishing a dew-point for that material. The number of moles of vapor at this temperature corresponds to one-third the number of moles of monatomic iodine added to the system. From this calculation and the coincidence of the curve with the vapor pressure of GaI_3 it was concluded that the predominant vapor species at this temperature was GaI_3.

The increase in pressure from 285°C to approximately 500°C (run 1) can be approximated by a perfect gas law expansion for the pressure of GaI_3 plus the equilibrium vapor pressure of elemental arsenic. Above approximately 500°C the curve again resumes a lower slope indicating that all of the solid arsenic resulting from the initial reaction was in the vapor phase. The analysis presented above relating to run 1 was also applied to runs 2 and 3. The GaI_3 and arsenic dew-points are consistent with values calculated from the initial iodine concentrations.

Above the arsenic dew-point temperatures it was observed that the only condensed phase remaining in the reaction tubes was GaAs. Since the objective of this work is to describe the equilibrium under conditions wherein the only known condensed phase

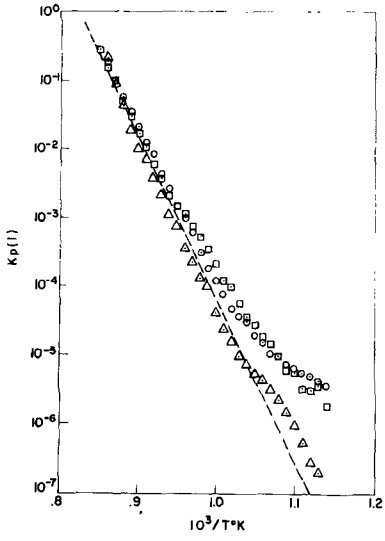

Fig. 3. Equilibrium constants for reaction [1]. Square with dot, Run 1; circle with dot, run 2; triangle with dot, run 3.

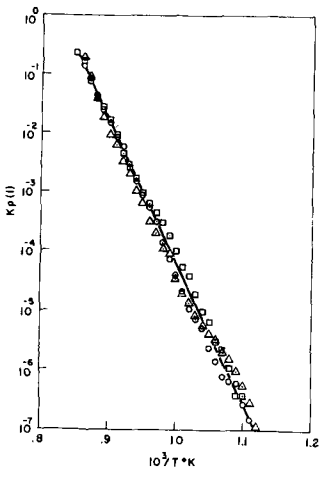

Fig. 4. Equilibrium constants for reaction [1] using corrected n_I values. Square with dot, Run 1; circle with dot, run 2; triangle with dot, run 3.

is GaAs, the data above 560°C are those which are pertinent to the model presented in the introduction. Reactions [1] and [2] were therefore assumed to represent the predominant equilibria in the temperature range 560°-890°C. The procedure outlined earlier was used to calculate values of the partial pressures of each species using the total pressure data from the three experimental runs. The equilibrium constant values for reaction [1] then were calculated in the following manner. A smooth curve was drawn between the vapor pressure points on each of the three experimental curves. Using n_I values calculated from the recorded iodine weights, the average values of P_T and Eq. [I-IV], values of the equilibrium constant were calculated using an IBM 7090 computer. A test of the assumed model was then to compare Kp values from run to run. The values are plotted as log Kp *vs.* reciprocal temperature in Fig. 3. (For convenience, the values were plotted only to $Kp = 1 \times 10^{-7}$). At higher temperatures the Kp values are in excellent agreement, and they describe a linear relationship between log Kp and reciprocal temperature. The deviations from the linear curve at lower temperatures were found to be well within experimental error. It was noted above that the iodine quantities used in runs 1 and 2 were weighed in quartz ampoules. Subsequent control experiments showed that during sealing of the ampoules, quantities of quartz were vaporized. The weight losses varied between 1.5 and 4.0 mg. These results indicated that weighing errors existed in runs 1 and 2; however the exact magnitude of the errors could not be determined experimentally. Further calculations of Kp were carried out using slightly higher values of n_I for both runs. At n_I values corresponding to iodine weights of 102.7 and 54.2 mg the calculated values of Kp formed a linear relationship of log Kp *vs.* $1000/T$ over the entire temperature range. The correction corresponded to an increase in iodine weight of 2.2 mg for run 1 and 2.5 mg for run 2. The increases agree quite well in magnitude with the expected error. The corrected data are plotted in Fig. 4. The slope is identical with that given for Fig. 3, since the correction shifted the higher temperature points only slightly. The large deviation in the calculated values of Kp at lower temperatures results from the value of P_{GaI} being smaller or comparable to the value of $(\Delta n_I RT)/V$ wherein Δn_I is representative of the iodine weighing error.

Similar control experiments were carried out to determine the loss in weight due to sealing a Pyrex ampoule similar to that used in run 3. The results showed an average weight loss of 0.2 mg. This correction was applied to the n_I value for run 3 and the results are also plotted in Fig. 4. This small correction obviously caused very little change in the Kp values. The values of n_I used for the determination of Kp are summarized in Table I. Thus, the good agreement, over the entire temperature range, of the Kp values calculated from the three sets of experimental data is considered a confirmation of the proposed model. The relationship between Kp and temperature for reaction [1] can be expressed as

$$\log Kp(1) = -\frac{23{,}650}{T°\mathrm{K}} + 19.4$$

From the slope of the curve of Fig. 4, the enthalpy calculated for reaction [1] is 54.1 kcal/mole of GaAs.

Above 930°C, the slope of curve 3 decreases gradually. In this region, the predominant vapor species are GaI, As_4, and As_2. Thus these data may be approximated by a perfect gas law expansion for the GaI pressure plus continued dissociation of As_4 to As_2.

Further evidence for the formation of GaI and arsenic vapors at high temperatures was gained from the results of two simple weight loss experiments. Weighed quantities of GaAs and I were reacted in sealed tubes of known volume. The initial iodine concentrations were approximately the same as used in run 3. The tubes were heated to 1050°C and then quenched. The original pieces of GaAs were then reweighed and the weight losses corresponded to the formation of GaI and arsenic vapor species. During the quenching, GaAs was crystal-

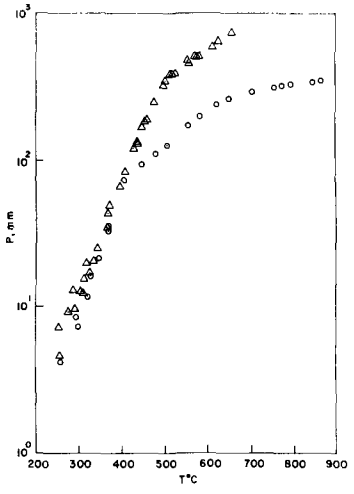

Fig. 5. Vapor pressures for two experimental runs on system Ga-GaI_2. Triangle with dot, Run 1, $n_I = 5.5 \times 10^{-4}$ mole; circle with dot, run 2, $n_I = 2.8 \times 10^{-4}$ mole.

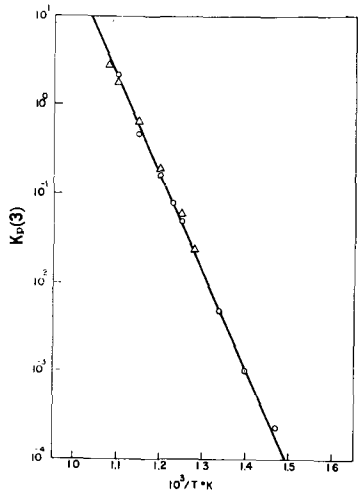

Fig. 6. Equilibrium constants for reaction [4]. Triangle with dot, Run 1; circle with dot, run 2.

lized from the vapor phase in the form of dendritic ribbons and whiskers.

The reaction I-Ga.—During the initial heating of the reaction tubes, iodine vapor was observed and the vapor pressure of iodine was measured. At approximately 80°C reaction of iodine with Ga occurred and the iodine vapor disappeared rapidly. An iodide condensed phase was observed at this point. The vapor pressure curves resulting from two experiments at different iodine concentrations are plotted in Fig. 5. There also appears to be a univariant curve for this system. Although the univariant curve is not coincident with the vapor pressure of GaI_3, calculations of the number of moles of vapor existing at the condensed phase dew-points indicate that the vapor species at the dew-points is GaI_3. The deviation of the univariant curve from the vapor pressure of GaI_3 is in the direction expected if gallium dissolved to an appreciable extent in liquid GaI_3 to form a liquid approximating the composition GaI_2. Since this paper is concerned primarily with vapor phase equilibria, a further investigation of the univariant part of the system was not carried out. In run 2, the slope of the pressure curve decreases above 650°C. Calculations show that the data above 650°C can be approximated by a perfect gas law expansion in pressure for the species GaI. This information, plus the dew-point calculations, experimentally support the assumed model (reaction [3]).

An analysis of the experimental data similar to that presented for the I-GaAs system was carried out for the temperature range 430°-650°C. Values of the equilibrium constant for each set of experimental pressures were calculated.

The values are plotted in Fig. 6. The agreement in slope and magnitude of the calculated *Kp* values shows the validity of the proposed model. The data can be represented by the equation

$$\log Kp\,(3) = -\frac{11{,}000}{T°K} + 12.4$$

The enthalpy for reaction [3] calculated from the slope is 25.2 kcal/mole of Ga.

Dissociation pressure of GaAs.—Through algebraic combination of reactions [1], [2], and [3], the following equilibria are obtained

$$GaAs(s) \rightleftarrows Ga(l) + \frac{1}{4}As_4(v) \qquad [4]$$

$$GaAs(s) \rightleftarrows Ga(l) + \frac{1}{2}As_2(v) \qquad [5]$$

The reactions describe the dissociation of solid GaAs along the three phase line. From the equilibrium constants for reactions [1], [2], and [3], the vapor pressures of the two arsenic species were calculated in the region 560°-636°C, the temperature range in which experimental results were obtained for both the I-GaAs reaction and the I-Ga reaction. The values of P_{As_4} and P_{As_2} are given in Table II. The dissociation pressure of GaAs from this calculation agrees reasonably well with extrapolations of two previous measurements made at higher temperatures (8, 9). Figure 7 is a plot of the dissociation pressure of GaAs showing the results

Table II. Values of P_{As4} and P_{As2}

T, °C	$\frac{1000}{T°K}$	$Kp\,(1)$	$\frac{Kp\,(1)}{\sqrt{Kp\,(2)}}$	$Kp\,(3)$	$\frac{Kp\,(1)}{Kp\,(3)}$	$\frac{Kp\,(1)}{Kp\,(3)\sqrt{Kp\,(2)}}$	P_{As_4}, mm	P_{As_2}, mm
636	1.100	2.5×10^{-7}	1.5×10^{-10}	2.05×10^{0}	1.24×10^{-7}	7.48×10^{-11}	1.17×10^{-11}	5.68×10^{-8}
616	1.125	6.8×10^{-8}	2.6×10^{-11}	1.1×10^{0}	6.18×10^{-8}	2.36×10^{-11}	2.90×10^{-12}	1.79×10^{-8}
596	1.150	1.7×10^{-8}	4.5×10^{-12}	5.9×10^{-1}	2.88×10^{-8}	7.63×10^{-12}	6.30×10^{-13}	5.80×10^{-9}
578	1.175	4.4×10^{-9}	7.5×10^{-13}	3.0×10^{-1}	1.47×10^{-8}	2.50×10^{-12}	1.64×10^{-13}	1.90×10^{-9}
560	1.200	1.1×10^{-9}	1.2×10^{-13}	1.61×10^{-1}	6.84×10^{-9}	7.46×10^{-13}	3.56×10^{-14}	5.67×10^{-10}

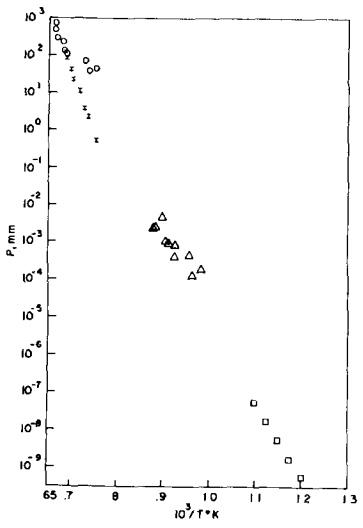

Fig. 7. Dissociation pressure of GaAs. Circles are from Boomgaard and Schol (10); vertical lines are from ref. (9); triangles are from ref. (8); squares are from this work.

of four investigations. The values given in the plot are total arsenic pressures. The calculated values from this work have extended the curve to a region wherein direct pressure measurements would be difficult to obtain.

The enthalpies calculated for Eq. [4] and [5] are given below

$$\Delta H = 28.9 \text{ kcal/mole of GaAs}$$
$$\Delta H = 44.4 \text{ kcal/mole of GaAs}$$

The value of the enthalpy for reaction [5] is slightly higher but in agreement with the value of 39.67 kcal reported earlier by Goldfinger and Drowart (8).

Acknowledgments

The authors wish to acknowledge the many helpful discussions of the work with Mr. R. F. Lever and Drs. A. Reisman and K. Weiser of this laboratory. We wish also to thank Miss Agnes Kuhlke for her assistance in programming the calculations on the IBM 7090 computer.

Manuscript received March 12, 1962. This paper was prepared for delivery before the Detroit Meeting, Oct. 1-5, 1961.

Any discussion of this paper will appear in a Discussion Section to be published in the June 1963 JOURNAL.

REFERENCES

1. G. Antell and D. Effer, *This Journal*, **106**, 509 (1959).
2. V. J. Lyons and V. J. Silvestri, *ibid.*, **108**, 177C (1961), Abstract 140.
3. R. L. Newman and N. Goldsmith, *ibid.*, **108**, 1127 (1961).
4. L. L. Quill, "The Chemistry and Metallurgy of Miscellaneous Materials, Thermodynamics," McGraw-Hill Book Co., New York (1950).
5. W. Fischer and O. Jubermann, *Z. anorg. u. allgem. Chem.*, **227**, 227 (1936).
6. D. R. Stull and G. C. Sinke, "Thermodynamic properties of the Elements," Advances in Chemistry Series, No. 8 (1956).
7. V. J. Lyons and V. J. Silvestri, *J. Phys. Chem.*, **64**, 266 (1960).
8. P. Goldfinger and J. von Drowart, *J. Chem. Phys.*, **55**, 721 (1958.)
9. V. J. Lyons and V. J. Silvestri, *J. Phys. Chem.*, **65**, 1275 (1961).
10. J. van der Boomgaard and K. Schol, *Phillips Research Rept.*, **12**, 127 (1957).

Kinetics of the Tantalum-Hydrogen Reaction

M. W. Mallett and B. G. Koehl

Battelle Memorial Institute, Columbus, Ohio

ABSTRACT

Kinetics of reaction of hydrogen with tantalum was studied for atom fraction compositions, N_H, 0.05 at 500° to 700°C and N_H, 0.10 at 450° to 600°C. The process was one of dissolution and diffusion of hydrogen. The diffusion coefficients obtained are expressed by the following equations:

$$D_{N_{H=0.05}} = 1560 \exp\left[(-32{,}230 \pm 3140)/RT\right] \text{ cm}^2/\text{sec}$$

$$D_{N_{H=0.10}} = 13{,}960 \exp\left[(-33{,}620 \pm 1370)/RT\right] \text{ cm}^2/\text{sec}$$

A single rate was obtained for $N_H = 0.25$ at 450°C. Regardless of composition, N_H 0.05 to N_H 0.33, samples at 300° to 400°C did not achieve surface saturation in the experimental time. The indicated activation energies are higher than the meager literature values for diffusion of hydrogen in most other metals.

The authors have previously reported the vapor pressure equilibria for the tantalum-hydrogen system and the thermodynamic functions derived therefrom (1). In the present study, the kinetics of sorption and diffusion of hydrogen in tantalum was investigated as part of an evaluation of the effects of interstitial elements on the mechanical properties of tantalum. The results of the only previous quantitative study of the kinetics of reaction of hydrogen with tantalum (2) are largely invalidated by inadvertent simultaneous oxidation of specimens.

Experiments were made to obtain kinetic data for the sorption of hydrogen by tantalum to produce compositions having atomic fractions, N_H, 0.05, 0.10, 0.25, and 0.33 in the temperature range of 300°-700°C. Experimental conditions of temperature and pressure were determined from the isopleth of the desired product as determined in the equilibrium studies. It has been shown (3, 4) that kinetic data for reactions producing solid solutions

(e.g., the tantalum-hydrogen reaction) are more readily rationalized when the experiments are designed to produce reaction products of constant composition.

Experimental

Samples were made from the same stock of electron-beam melted tantalum used for the equilibrium studies (1). They consisted of cylinders 0.6-0.7 cm in diameter and 2.5-3.5 cm long cut from rod cold-forged and swaged from the ingot. The cylinders were filed clean and finish dry-abraded through 240-, 400-, and 600-grit silicon carbide papers. Samples were spot welded to the bead of a platinum-platinum plus 10% rhodium thermocouple and suspended by the thermocouple in a Vycor reaction tube of a modified Sieverts apparatus (5). The system was evacuated to a pressure of less than 0.01μ of mercury. The sample was then activated by heating with a resistance-wound furnace at 900°C for 1 hr before adjusting the temperature to that of the run. This treatment served to remove dissolved hydrogen and dissolve invisible surface oxide films thus minimizing times for surface saturation of samples during reaction. Although 11 samples were used in the kinetic studies, 4 of them were reused 3 to 11 times without removal from the reaction tube. Reacted hydrogen was removed between runs by 900°C heating in vacuum. This treatment had no apparent effect on the physical properties of the metal. The sample used for 11 runs showed only moderate pickup of oxygen from a starting level of about 20 ppm to 37 ± 7 ppm after use.

The reaction was initiated by admitting hydrogen through the pressure regulator to the reaction tube. The hydrogen was obtained by thermal decomposition of uranium hydride. The buret was kept balanced at atmospheric pressure at all times. The regulator was set to maintain the pressure selected from a plot of isopleths (1), to correspond to the experimental temperature and composition. Readings of the buret were taken at convenient time intervals depending on the speed of the reaction. The amount of gas reacted with the sample was the difference between the volume added from the buret and the volume remaining in the gas phase in the calibrated dead space of the reaction tube.

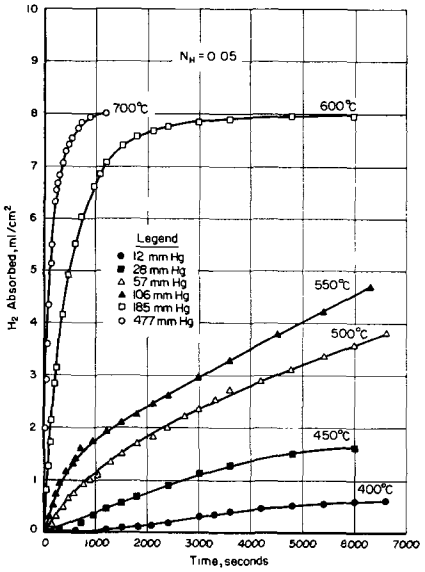

Fig. 1. Representative rate data for the reaction of hydrogen with tantalum (N_H = 0.05).

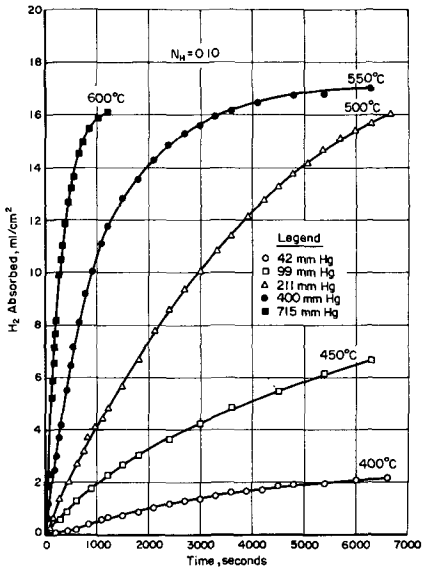

Fig. 2. Representative rate data for the reaction of hydrogen with tantalum (N_H = 0.10).

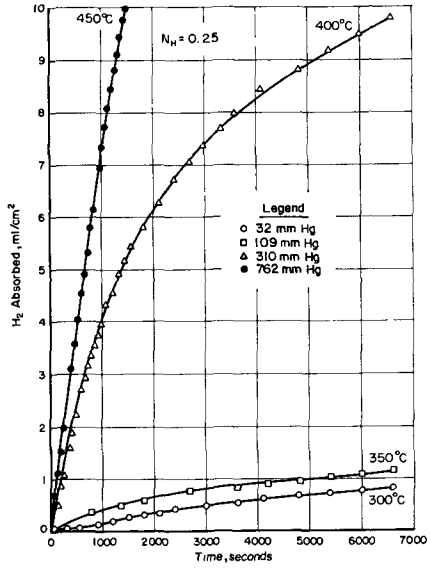

Fig. 3. Representative rate data for the reaction of hydrogen with tantalum (N_H = 0.25).

Results

Representative rate data are shown in Fig. 1-3. The initial parabolic character of the raw data for some of the reactions is apparent for reactions at and above 500°C but becomes obscure at lower temperatures. Since no compound was formed, the reaction was expected to be one of simple dissolution and diffusion of hydrogen in tantalum accompanied by possible secondary interface reactions. Accordingly interpretation of the data was attempted in terms of theoretical diffusion behavior.

Fick's second law for diffusion in a finite cylinder may be expressed as (4)

$$\frac{c}{c_o} = 1 - \frac{32}{\pi^2} \sum_{n=0}^{\infty} \sum_{m=1}^{\infty} \frac{1}{\beta_m^2 (2n+1)^2} \times \exp\left\{ -\frac{Dt}{a^2} \left[\frac{(2n+1)^2 \pi^2}{\left(\frac{l}{a}\right)^2} + \beta_m^2 \right] \right\} \quad [1]$$

where a is radius of sample; l, length of sample; D, diffusion coefficient; C, average hydrogen concentration; t, time; C_o, the final equilibrium concentration; β_m, the m^{th} root of the Bessel function $J_o(\beta)$ and the indices m and n range through integral values as desired.

Since the length to radius ratio, l/a, of the experimental cylindrical samples varied from about 5 to 12, theoretical curves were calculated from Eq. [1] to permit analysis of data for the sorption of gas by any cylinder. These curves are shown in Fig. 4 where C/C_o is plotted against $\sqrt{DT}/a$ for l/a ratios of 1, 2, 4, 8, 16, and infinity.

The fitting of the experimental data to the theoretical diffusion curves of Fig. 4 becomes quite difficult and impractical when the experimental reaction does not show ideal behavior. However, Demarez, Hock, and Meunier (6) offer a partial solution to this problem. They have shown that for values of t greater than some threshold time, t_o, the series such as appear in Eq. [1] degenerate to their first terms with adequate accuracy for interpretation of the experimental data. Then

$$\frac{C}{C_o} = 1 - \frac{32}{\pi^2 \beta_1^2} \exp\left\{ -\frac{Dt}{a^2} \left[\frac{\pi^2}{\left(\frac{l}{a}\right)^2} + \beta_1^2 \right] \right\} \quad [2]$$

Converting to logarithmic form one obtains

$$\log (1 - C/C_o) = \log \frac{32}{\pi^2 \beta_1^2} -$$

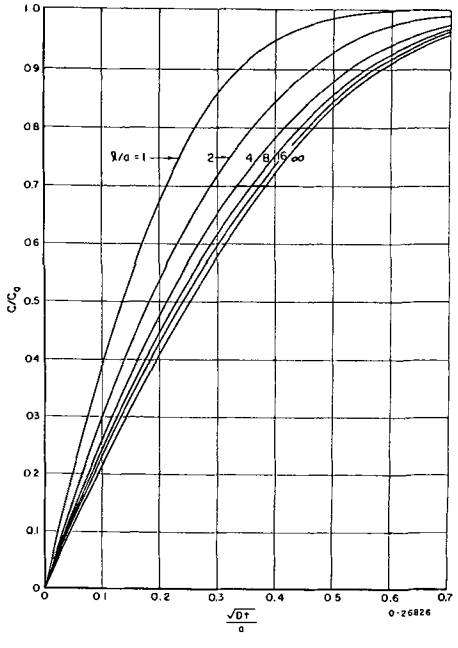

Fig. 4. Theoretical curves for sorption in cylinders

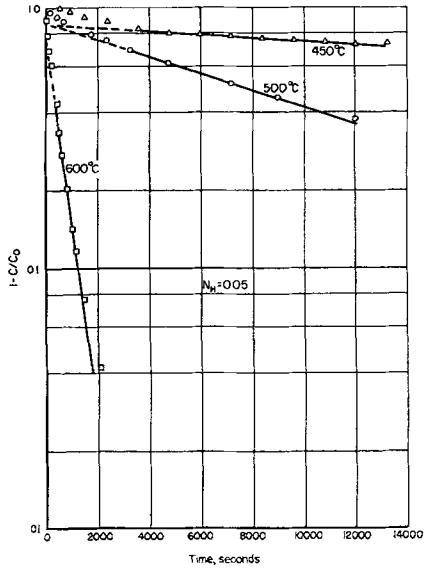

Fig. 5. Hydrogen absorption as a function of time ($N_H = 0.05$)

$$\frac{Dt}{2.303a^2} \left[\frac{\pi^2}{(l/a)^2} + \beta_1^2 \right] \quad [3]$$

Since β_1, l, and a are known, D can be determined from the slope of the straight line plot of log $(1 - C/C_o) = f(t)$. That is, slope $= -$ (const.) D/a^2. Re-examination of the values from the double series from which the curves of Fig. 4 were drawn revealed that they also could be plotted similarly as a function of t to yield lines which were adequately straight over reasonably large ranges. The intercepts of the lines differed from the calculated intercept and decreased with increasing values of l/a. The slopes differed only 2 or 3% from those calculated from Eq. [3]. The more refined values of slopes and intercepts calculated from the data in Fig. 4 were used in our treatment of the experimental data.

Figure 5 shows representative plots of log $1 - C/C_o$ *vs.* time. At 600°C the reaction was quite

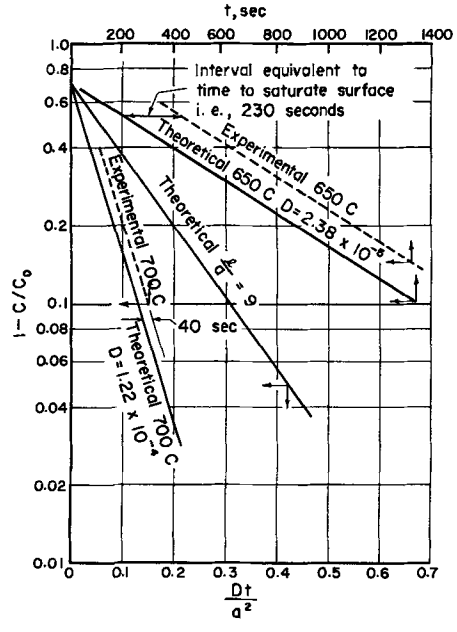

Fig. 6. Comparison of theoretical and experimental absorption rates

rapid and approached complete volume saturation in the experimental time. At 500°C the reaction was much slower and reached only 60% volume saturation in 3 hr. D values were calculated from these curves. In Fig. 6 the theoretical line for $l/a = 9$ is a replot according to the method of Demarez *et al.* (6), of a curve such as shown in Fig. 4. An experimental D value for 650°C was substituted in the Dt/a^2 values for the l/a line and the theoretical time behavior obtained. The theoretical time values were plotted against log $(1 - C/C_0)$ in Fig. 6 along with the experimental line. It is seen that these two lines are parallel and that the interval between them on the time ordinate is equivalent to the time lapse before the sample surface became saturated. This test of surface saturation eliminated use of data for $N_H = 0.05$ below 500°C, $N_H = 0.10$ below 450°C, and all the data for higher N_H values except one rate for $N_H = 0.25$ at 450°C. Except as noted, the lower temperature experiments did not produce surface saturation of the samples within the experimental times. The times for sample surface saturation of the good runs are listed in Table I. The times tend to increase with decreasing temperature from 40 sec at 700°C to about 3000 sec at 450°C for samples of essentially the same size.

Experimental diffusion coefficients for the tantalum-hydrogen systems at compositions of N_H 0.05, 0.10, and 0.25 over a temperature range of 450°-700°C also are given in Table I. Variation of diffusion coefficient as a function of temperature is shown for $N_H = 0.05$ in Fig. 7 and $N_H = 0.10$ in Fig. 8. A single point for $N_H = 0.25$ at 450°C also appears in Fig. 8. There is a trend toward faster diffusion rates at the higher pressures required to form the solutions with larger atom fractions of hydrogen.

The equations for the best straight lines in Fig. 7 and 8 were determined by the method of least squares. The equations are

$$D_{N_{H=0.05}} = 1560 \exp [(-32{,}230 \pm 3140)/RT] \text{cm}^2/\text{sec} \quad [4]$$

and

$$D_{N_{H=0.10}} = 13{,}960 \exp [(-33{,}260 \pm 1370)/RT] \text{cm}^2/\text{sec} \quad [5]$$

Table I. Diffusion coefficients for the tantalum-hydrogen system

Temperature, °C	Equilibrium pressure, mm Hg	Composition, N_H	Diffusion coefficient, $D \times 10^6$ cm²/sec	Time to saturate surface, sec
450	99	0.10	0.803	2600
	762	0.25	1.30	2400
500	57	0.05	1.42	2800
	211	0.10	5.77	1300
550	106	0.05	2.20	1700
	400	0.10	16.0	350
600	185	0.05	8.42	4100
	185	0.05	26.8	100
	185	0.05	30.4	350
	715	0.10	47.5	165
	715	0.10	55.4	125
650	306	0.05	23.8	400
	306	0.05	24.0	230
700	477	0.05	122	40
	477	0.05	85.6	40

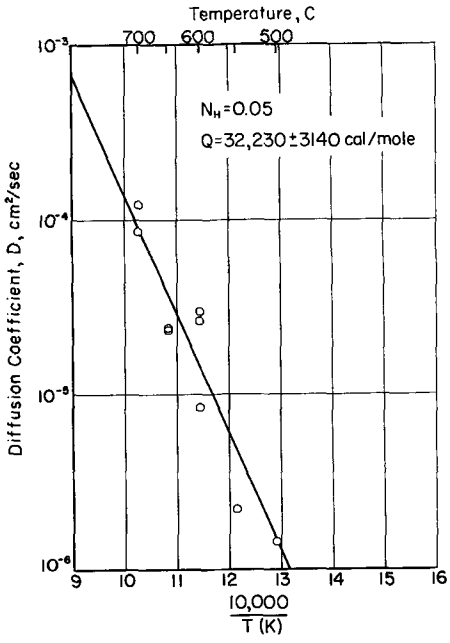

Fig. 7. Temperature dependence of the diffusion coefficient for hydrogen in tantalum ($\Delta_H = 0.05$).

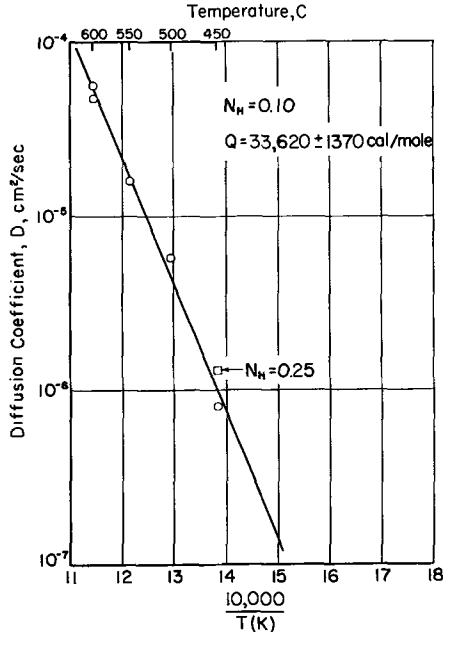

Fig. 8. Temperature dependence of the diffusion coefficient for hydrogen in tantalum ($N_H = 0.10$).

where the activation energy for hydrogen diffusion is 32,230 ± 3140 cal/mole for composition, $N_H = 0.05$, and 33,620 ± 1370 cal/mole for composition, $N_H = 0.10$. It is seen that these values of activation energy agree within the limits of experimental error.

Since Eq. [4] and [5] have the form $D = D_0 \exp(-E/RT)$ the entropy of diffusion can be calculated from D_0 and E by applying the theory of Wert and Zener (7, 8) for interstitial diffusion. For a body-centered-cubic lattice

$$D_0 = 1/6\, a_0^2 \nu \exp(\Delta S/R) \quad [6]$$

where a_0, the lattice constant, is 3.296Å for tanta-

lum. The vibration frequency, ν, of a solute atom in an interstitial position is given by the approximation

$$\nu = (E/2m\lambda^2)^{1/2} \quad [7]$$

where E is assumed approximately equal to the activation energy, m is the mass of the solute atom, and λ, the distance between interstitial positions, is assumed to be $a_o/2$. From Eq. [6] ΔS for diffusion of hydrogen in tantalum was calculated to be 24 cal/mole degree. Theory indicates that a positive ΔS is characteristic of interstitial diffusion and not diffusion through grain boundaries or other short circuiting paths.

Discussion

It was observed that the activation energies for diffusion of hydrogen in tantalum obtained in the present study are considerably higher than the few available literature values for diffusion of hydrogen in metals. Typical values in cal/mole are 12,380 for α-titanium (9), 6640 for β-titanium (9), 7060 for α-zirconium (10), and 9370 for niobium (4). Also the experimental value for D_o is several orders of magnitude higher than those reported for most other hydrogen metal systems. The high D_o value leads to a higher than usual value (24 cal/mole degree) of ΔS, the entropy of diffusion. However, Albrecht and Goode (11) report an equation for diffusion of hydrogen in β-zirconium, $D = 6.14 \times 10^4 \exp(-45{,}900/RT)$, in which all the factors and the calculated ΔS 30.7 cal/mole degree, are of the same magnitude as those of the tantalum study. This is of considerable interest since the diffusion coefficient for zirconium was obtained by a different method, that of permeation. Further data on the diffusion of hydrogen in metals is needed before a critical evaluation is possible. Diffusion in certain systems such as that of hydrogen and niobium requires study over a much wider temperature range.

Initial linear rates were reported for the reaction of hydrogen with niobium (4). Similar apparently linear reactions were noted for tantalum. However, after review of diffusion theory (6) it was concluded that such "linear" portions of the curves are fortuitous and not significant. One tantalum specimen (not activated) showed a linear reaction for 4 hr at 400°C. However, a duplicate run made with a specimen activated by heating in vacuum at 900°C for 1 hr gave the parabolic type curve seen in Fig. 3. It appears that the "linear" rates are the result of interface conditions which delay surface saturation of samples for long times.

Acknowledgments

The authors wish to express their appreciation for the sponsorship of this research by Materials Central, Directorate of Advanced Systems Technology, Wright Air Development Division, Wright-Patterson Air Force Base, Ohio, and for permission to publish this paper. The work was performed under Contract No. AF-33(616)-7604. They also wish to thank Dr. J. C. Bell of Battelle Memorial Institute for calculation of the data for the theoretical sorption curves.

Manuscript received Dec. 22, 1961. This paper was prepared for delivery before the Los Angeles Meeting, May 6-10, 1962.

Any discussion of this paper will appear in a Discussion Section to be published in the June 1963 JOURNAL.

REFERENCES

1. M. W. Mallett and B. G. Koehl, *This Journal*, **109**, 611 (1962).
2. E. A. Gulbransen and K. F. Andrew, *Trans. AIME*, **188**, 586 (1950).
3. W. M. Albrecht and M. W. Mallett, *This Journal*, **105**, 610 (1958).
4. W. M. Albrecht, W. D. Goode, Jr., and M. W. Mallett, *ibid.*, **106**, 981 (1959).
5. W. M. Albrecht and M. W. Mallett, *ibid.*, **103**, 404 (1956).
6. A. Demarez, A. J. Hock, and F. A. Meunier, *Acta Met.*, **2**, 214 (1954).
7. C. Wert and C. Zener, *Phys. Rev.*, **76**, 1169 (1949).
8. C. Zener, *J. Appl. Phys.*, **22**, 272 (1951).
9. R. J. Wasilewski and G. L. Kehl, *Metallurgia Manchr.*, **50**, 225 (1954).
10. M. W. Mallett and W. M. Albrecht, *This Journal*, **104**, 142 (1957).
11. W. M. Albrecht and W. D. Goode, Battelle Memorial Institute Report BMI-1373 (1959).

Chemical Vapor Deposition of Tungsten at Low Pressure

Arnold Miller and Gordon D. Barnett

Materials Sciences Section, Research and Development Division,

Autonetics, Division of North American Aviation, Downey, California

ABSTRACT

An experimental program utilizing low-pressure chemical vapor deposition techniques for applying thin tungsten films by the hydrogen reduction of tungsten hexafluoride for the ultimate formation of various electronic devices is described. The purpose of this work is to measure deposition rates at various reaction temperatures and pressures which might be accommodated to electron beam heating. Tungsten films formed by chemical vapor deposition are mirrorlike or grainy depending on deposition temperature, reactants, stoichiometry, and film thickness. Mirrorlike, polycrystalline, randomly oriented, alpha tungsten films of high purity with unit resistance values approaching that of single crystal tungsten have been formed in the 10^{-3} torr pressure range and 1000°C at deposition rates of about 3×10^{3} Å/hr. The unit resistance values of these films are considerably lower than those for sputtered tungsten films of comparable thickness. The adhesion between reaction deposited tungsten films and sapphire substrates is much better than that between sputtered tungsten films and Pyrex substrates. Application of tungsten films at 250°C and higher reaction pressures results in the formation of polycrystalline, randomly oriented, beta tungsten films which can be transformed to the alpha material by treatment at 900°C for an extended period.

Chemical vapor deposition processes can be described as the generation of deposits on suitably heated substrates by means of appropriate thermal reactions between volatile compounds directly on the surface to yield the desired product and gaseous by-products. Such processes have been in use for some time to produce massive quantities or thick coherent coatings of both metallic and nonmetallic materials. Their application to the generation of films of controlled structure and composition for electronic purposes has been limited. The work reported here is part of a continuing study of chemical vapor deposition techniques for the formation of thin films of controlled structure of metals, insulators, and semiconductors.

The purpose of this work is to measure deposition rates at various reaction temperatures and reaction pressures which might be accommodated to electron beam heating, and also to determine some of the resultant film properties such as composition, structure, and resistance. The specific model system selected for this study is the flow method for the hydrogen reduction of tungsten hexafluoride (1, 2) to apply a conductive tungsten film on an insulating aluminum oxide surface for several reasons: (i) Tungsten, the principle product, is a realistic refractory conductor for use in combined microelectronic circuits or in field emission devices on the basis of its physical and electrical properties; (ii) Relatively pure gaseous tungsten hexafluoride is commercially available at a reasonable cost; (iii) The reduction reaction occurs below 1500°C, temperatures which can be obtained with conventional resistance or induction heating methods.

Aluminum oxide was chosen as the substrate material because of its stability at the required tungsten deposition temperatures and because of its inertness to hydrogen fluoride, the reaction by-product. In addition, aluminum oxide itself can be formed by chemical vapor deposition from aluminum chloride, hydrogen, and carbon dioxide or by decomposition of the appropriate alkoxide.

Polycrystalline and single crystal tungsten, as well as epitaxially grown tungsten deposits, are of interest. Since an important requirement for epitaxial growth is that the lattice positions of the substrate and the deposit match within a small per cent, the degree of lattice mismatch between tungsten and sapphire for any crystal plane pair must be considered. Assuming the sapphire to be hexagonal in structure with lattice constants $a = 4.75$Å and $c = 12.97$Å and the tungsten to be body-centered cubic with a lattice constant of 3.15Å, it is possible to find sets of matching lattice parameters favorable to epitaxial growth. This compatibility as well as similar thermal coefficients of expansion properties also makes a study of the tungsten-alumina system appealing. In this program, however, the most readily available sapphire substrate surface, not the face providing the best lattice parameter match with tungsten, is used.

While the present program utilizes resistance heating methods or heating by high-frequency induction, the ultimate aim of the program is to determine reaction parameters adaptable to heating the substrates with an electron beam. Consequently, a low-pressure reaction system is suggested.

Experimental

The reaction system used for the deposition of tungsten on alumina, shown schematically in Fig. 1, is capable of an ultimate pressure of 5×10^{-7}. Pumps required by the vacuum system are pro-

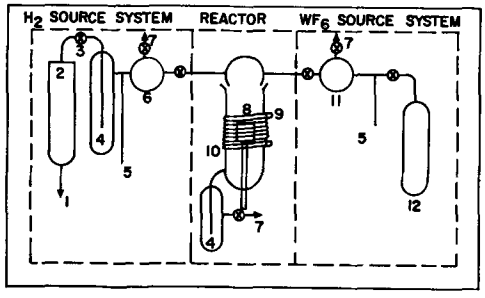

Fig. 1. Schematic representation of the chemical vapor deposition system: 1, to H_2 cylinder; 2, DEOXO H_2 purifier; 3, needle valve; 4, liquid N_2 trap; 5, thermocouple gauge; 6, H_2 ballast bulb; 7, to vacuum system; 8, carbon susceptor; 9, induction coil; 10 reactor, 11, WF_6 ballast bulb; 12, WF_6 cylinder.

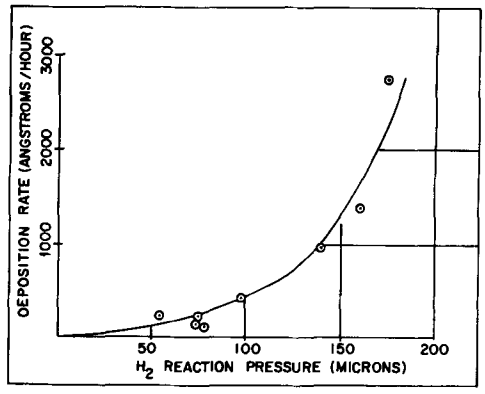

Fig. 2. Tungsten deposition rate as a function of hydrogen reaction pressure at 250°C. The reaction pressure ratio of hydrogen to tungsten hexafluoride is 3 to 1.

tected from reactant materials or reaction by-products with liquid nitrogen cold traps. Pressures in reactant storage bulbs are measured using calibrated thermocouple gauges. Reaction pressures, determined with an ionization gauge located in the reaction area and using typical hydrogen pressures in the storage bulb during a calibration run, are indicated to be a factor of 10 less than in the reactant bulb. Airco electrolytic hydrogen passed through a DEOXO catalytic purifier and a liquid nitrogen cold trap is used. The tungsten hexafluoride, used as received, is a General Chemical product described as 99.5% pure with the contaminant portion composed of oxygen, carbon, nitrogen, silicon, and nickel.

The sapphire substrates used in these experiments are 1 mm thick single crystals, with a metallographic polish on the deposit side, provided by the Crystal Products Department of the Linde Company; the crystals, produced by means of a flame fusion process, are furnished with the optical axis about 60° from the geometrical axis. The surface preparation includes a potassium dichromate-sulfuric acid etch, a distilled water rinse, a nitric acid-hydrochloric acid (3:1 by volume) etch, and a final double rinse in hot distilled water. In addition, after the substrate is positioned in the reactor, it is baked at a temperature greater than the actual deposition temperature in an atmosphere of hydrogen for about 30 min.

Reactant gas flow rates are established by means of a pressure drop across cylindical metering tubes of known conductance. A molecular conductance equation, applicable in this work where the mean free path of the molecules is of the same order of magnitude or greater than the tube diameters, is used to calculate the relative dimensions of the tubes.

Resistance or induction heating methods are used depending on the temperature range. For lower temperatures a resistively heated tungsten filament located under the substrate is used to elevate the substrate temperature. High-frequency induction methods are required in the higher temperature regions. Deposition temperatures are measured with an optical pyrometer where possible. In other cases, a chromel-alumel thermocouple placed in contact with the substrate is used. Where etching of the walls of the reaction tube occurred, it was very slow and became evident only after a series of runs. Since this usually occurred below the tungsten hexafluoride reduction zone, it did not interfere with the optical method for determining temperatures. Some tungsten deposited on the walls of the tube, and in some experiments it was necessary to view the substrate from above.

Interferometric techniques (3) are used to measure film thicknesses. Resistance values are determined following a method patterned after that of Judd (4). Spectrographic and x-ray diffraction methods are used to determine the composition and structure of the films.

Results and Discussion

Tungsten deposits were formed from the hydrogen reduction of tungsten hexafluoride at a substrate temperature of 250°C using hydrogen reaction pressures ranging from 55 to 175μ and a stoichiometric hydrogen-tungsten hexafluoride pressure ratio. A plot of film thickness versus hydrogen pressure for these experimental conditions is shown in Fig. 2. The plot indicates an increase of deposition rate as a function of pressure over the entire pressure range covered. Deposition rates under these conditions ranged from 100 to 2700 Å/hr. The maximum value in the pressure range examined is determined from the slope of the curve to be about 100 Å/hr/μ.

During the course of these experiments, a great deal of tungsten is deposited in the form of crystals and whiskers on tungsten filaments used as heat sources at temperatures of about 1000°C. Since this filament is located about 0.250 in. beneath the sapphire substrate and behind it in the gas flow stream, it is felt that the stream of reactant materials which reaches the substrate deposition surface is not robbed appreciably of tungsten source material. Probably more important than this is the efficiency of the process due to such factors as the design of the experimental system and the pattern of the gas flow which brings reactants into contact with the heated surface, the total pressure in the reaction zone as a result of incomplete reaction and formation of gaseous by-products, and so forth. No estimation of the effect of these factors on deposition rates has been prepared since it is probable that the same complicating effects exist regardless

of the heating method used, whether resistance heating or heating with high-frequency induction or the dissipated energy of a beam of electrons striking the surface of the substrate.

Films of less than 2000Å produced at 250°C are mirrorlike in appearance. Thicker films prepared at the same temperature appear to be more granular than thinner ones. Tungsten deposits thicker than 40,000Å have been produced.

A glancing angle x-ray diffraction pattern shows the film to be randomly oriented beta tungsten (5, 6), with particle size between 0.03 and 1μ. Because of the diffuseness and broadness of the diffraction lines the particle size is probably at the small end of the range. Treatment of this film for 48 hr at 900°C and 10^{-7} torr resulted in a glancing angle x-ray diffraction pattern typical of randomly oriented alpha tungsten with no evidence of the beta material. The crystallite size is estimated to be between 0.04 and 1.0μ.

Attempts to form thin mirrorlike deposits at 1000° and 1200°C under conditions similar to those used for the 250°C experiments resulted in extremely grainy deposits with infinite resistance. Such temperature effects are not unexpected. Literature information (7) in regard to various other systems shows that amorphous deposits of various materials can be produced at low temperatures, coarse-grained deposits at higher temperatures, and single crystal deposits on single crystal substrates at extemely high temperatures. No single crystal character nor epitaxial growth is in evidence in any of the films so far produced.

Because of the grainy appearance of the high-temperature deposits and because of the severe etching of the sapphire substrate probably as a result of high-temperature reaction of the substrate with the by-product hydrogen fluoride, the ratio of hydrogen to tungsten hexafluoride was increased to 6 to 1. Under these conditions it is possible to form mirrorlike deposits at 1000°C. At 1200°C, however, the deposits remain grainy and have infinite resistance. Tungsten deposition rates as a function of hydrogen pressures at H_2/WF_6 mole ratios of 6 to 1 were determined at these temperatures. Plots of these data are presented in Fig. 3 over a hydrogen pressure range extending from 2 to 14μ. The plots indicate that deposition rates increase with increasing temperature as well as with increasing pressures. At 1200°C and 2-μ hydrogen pressure, a tungsten deposition rate in excess of 400 Å/hr can be realized; at 1000°C and similar pressures, the tungsten deposition rate approaches 100 Å/hr. Maximum values, in angstroms per hour per micron, are determined by the slopes of the curves to be about 4×10^3 at 1200°C and 3×10^2 at 1000°C.

Glancing angle x-ray diffraction examination of a representative tungsten film laid down at 1000°C produces four smooth weak lines of alpha tungsten over a background of a Laue pattern of sapphire. No evidence of preferred orientation in the tungsten film is seen. The crystallite size is less than 1μ and more than 0.03μ.

Spectrographic analyses of selected mirrored films deposited at various temperatures indicate the film material to be very pure tungsten with only trace amounts of silicon and nickel present. This is consistent with the impurities of the tungsten hexafluoride listed by the manufacturer. No analysis of grainy deposits nor of deposits formed where etching of the alumina substrate is evident were performed since these deposits are not filmlike in nature and do not possess electrical properties of thin metallic films.

In general, adhesion between the sapphire and the tungsten film is extremely good with the mirrored deposits showing better adhesive properties than the granular ones. In most cases, it is not possible to remove the film by means of scotch tape. In fact, vigorous rubbing with an abrasive is required. However, instances of flaking have been observed in some early experiments where the surface treatment did not include the nitric acid-hydrochloric acid etch, but only the potassium dichromate-sulfuric acid etch and the distilled water rinse. The intermittent nature of such flaking tends to indicate a problem in surface preparation rather than in lattice mismatch or differences in the coefficient of thermal expansion between sapphire and tungsten. It should be noted here that tungsten films applied to Pyrex substrate surfaces using sputtering techniques are not as adherent as these reaction deposited tungsten films.

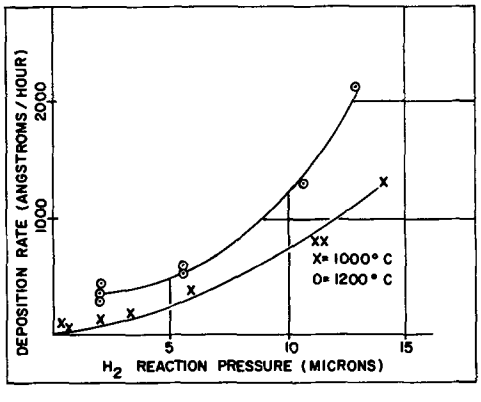

Fig. 3. Tungsten deposition rates at 1000° and 1200°C as a function of hydrogen reaction pressure. The hydrogen to tungsten hexafluoride reaction pressure ratio is 6 to 1.

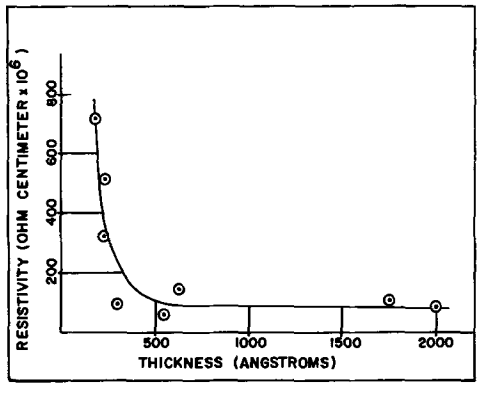

Fig. 4. Normalized resistivity of tungsten films as a function of thickness. These mirrorlike films are deposited at 1000°C with the $H_2 : WF_6$ reaction pressure ratio of 6:1.

Table I. Unit resistance values at various thicknesses for tungsten films applied using high- and low-temperature chemical vapor-deposition techniques and sputtering techniques normalized to the value of single crystal tungsten of 0.015 ohms per square

Reaction deposited* at 1000°C		Reaction deposited** at 250°C			
Thickness (Å)	unit resistance (ohms/square)	Thickness (Å)	unit resistance (ohms/square)	Thickness (Å)	unit resistance (ohms/square)
190	380	150	860	400	2700
300	33	150	860	600	2300
630	23	450	170	3000	100
1750	6.7				

* Mole ratio $H_2/WF_6 = 6$.
** Mole ratio $H_2/WF_6 = 3$.

A plot of resistivity *vs.* thickness for mirrorlike deposits formed at 1000°C is presented in Fig. 4. The data have been normalized to the value for bulk tungsten of 0.015 ohms per square, measured using the Judd method. This normalization process is necessary since the technique and equipment used have not been corrected for edge effects. A typical mirror deposit 190Å thick has a value of 380 ohms per square. For a 1750Å thick film, the unit resistance value is 6.7 ohms per square. Films less than 100Å thick have infinite resistance, while a heavy tungsten film, 5400Å thick, has a unit resistance value of 2.3 ohms per square.

Table I lists normalized unit resistance values for typical films applied using high- and low-temperature deposition methods as well as sputtering techniques. The table indicates that the high-temperature deposition techniques provide films with the best conductivity. Sputtered films have the highest values at comparable thicknesses.

Conclusions

1. Tungsten films resulting from the hydrogen reduction of tungsten hexafluoride deposit at rates in excess of 400 Å/hr/μ for reaction pressures in the 10^{-3} torr range.

2. The appearance of the tungsten deposits ranges from mirrorlike to grainy depending on deposition temperature, reactant pressure ratio, and film thickness.

3. Resistance values of the mirrorlike tungsten films produced by chemical vapor deposition compare favorably with those for sputtered films of comparable thickness. A heavy tungsten film, 5400Å thick, formed at 1000°C has a unit resistance value of 2.3 ohms per square normalized to the value for single crystal tungsten of 0.015 ohms per square. Sputtered tungsten films as thick as 3000Å have normalized unit resistance values as great as 100 ohms per square. The grainy-appearing reaction deposited films have extremely high unit resistance values.

4. Spectrographic analyses indicate that the mirrored deposits formed are high-purity tungsten with only trace impurities of silicon and nickel. X-ray diffraction studies show the low-temperature tungsten deposits to be randomly oriented crystallites with particle size between 0.03 and 1.0μ, probably at the small end of the range.

Treating the beta form over an extended period at 900°C produces the alpha material. X-ray diffraction patterns of mirrored tungsten films formed at the higher temperatures indicate the material to be randomly oriented alpha tungsten with particle size less than 1μ and more than 0.03μ.

5. Adhesion between the deposited tungsten and sapphire substrates is, in general, very good, considerably better than that between sputtered tungsten films and Pyrex substrate material.

Acknowledgment

The authors wish to express their appreciation to F. E. Fay, J. I. Medoff, G. R. Pulliam, K. H. Ryden, R. G. Warren, and R. M. Willard, for their contributions to this program.

Manuscript received July 18, 1961; revised manuscript received June 15, 1962.

Any discussion of this paper will appear in a Discussion Section to be published in the June 1963 JOURNAL.

REFERENCES

1. W. A. Reid and A. Brenner, *Natl. Bur. Standards (U.S.), Tech. News Bull.*, **44**, [2], 32 (February, 1960).
2. V. A. Neiberlein and H. Kenworthy, "High Purity Tungsten by Fluoride Reduction," Bureau of Mines Report of Investigation No. 5539 (1959).
3. S. Tolansky, "Multiple-Beam Interferometry," Clarendon Press, Oxford (1948).
4. N. C. W. Judd, BRAE Technical Note No. Chem. 1957 (November, 1959).
5. G. Hagg and N. Schonberg, *Acta Cryst.*, **7**, 351 (1954).
6. Von J. Neugebauer, A. J. Hegedus, and T. Millner, *Z. anorg. u. allgem. Chem.*, **293**, 241 (1958).
7. C. F. Powell, I. E. Campbell, and B. W. Gonser, *J. (and Trans.) Electrochem. Soc.*, **93**, 258 (1948).

Brief Communications

The JOURNAL accepts short technical reports having unusual importance or timely interest, where speed of publication is a consideration. The communication may summarize results of important research justifying announcement before such time as a more detailed manuscript can be published. Consideration also will be given to reports of significant unfinished research which the author cannot pursue further, but the results of which are of potential use to others. Comments on papers already published in the JOURNAL should be reserved for the Discussion Section published biannually.

Submit communications in triplicate, typewritten double-spaced, to the Editor, Journal of The Electrochemical Society, 30 East 42 St., New York 17, N. Y.

Hydrogen Overpotential on Nickel in Alkaline Solution

A. C. Makrides[1]

Metals Research Laboratory, Union Carbide Metals Company, Niagara Falls, New York

ABSTRACT

The exchange current, Tafel slope, stoichiometric number, and limiting anodic current of the hydrogen reaction on nickel in 0.1*N* NaOH depend on the pretreatment and the polarization history of the electrodes. The discharge step of the Volmer-Tafel mechanism is rate-determining on surfaces characterized by high fractional coverage with adsorbed hydrogen. Such surface states are metastable however and are transformed on anodic-cathodic cycling to states which adsorb hydrogen weakly. The exchange currents for the discharge and combination steps are then about equal.

The rate of the hydrogen reaction on nickel shows the familiar exponential dependence on potential; the Tafel slope b is about 0.1v and the exchange current i_o is in the range 10^{-7} to 10^{-5} amp/cm^2. The hydrogen overpotential on nickel is intermediate therefore between the large overpotentials on mercury and lead ($i_o \sim 10^{-13}$ amp/cm^2) and the relatively small overpotentials on metals of the platinum group ($i_o \sim 10^{-3}$ amp/cm^2).

Nickel dissolves slowly in acid and at a negligible rate in alkaline solutions. Side reactions can be neglected in the latter if the solution is free from reducible impurities, mainly oxygen. In spite of the relative simplicity of this electrochemical system the mechanism of the reaction is in doubt. A number of authors (1, 3, 4, 8) concluded from the magnitude of the Tafel slope and from the value of stoichiometric number that the discharge step, $H^+ + e^- \rightarrow H_{ads}$, controls the over-all rate. A simple slow-discharge mechanism does not explain however the frequently observed time-dependence of overpotential, nor does it give correctly the change of overpotential with solution composition.

Lukowzew, Lewina, and Frumkin (1) found that the potential of nickel cathodes which had been heated in H_2 at 400°-420°C and cooled in a water-saturated hydrogen atmosphere drifted for some hours after switching on the current. They attributed the drift of potential to reduction of a nickel oxide film formed during cooling.

Bockris and co-workers (3, 9) also found a potential drift in the first hour of cathodic polarization. Subsequent polarization curves did not follow the Tafel relation. Bockris and Potter (3) attributed the deviations from Tafel behavior to solution of hydrogen into nickel. They obtained satisfactory Tafel lines by making rapid measurements in the direction of increasing current density only and by using fresh electrodes for every run. Their procedure was opposite to that of Lukowzew, Lewina, and Frumkin (1) who carried out measurements after the potential had reached a steady value. Hoare and Schuldiner (10) found Tafel behavior (in acid solutions) with nickel electrodes "saturated" with hydrogen by cathodic polarization.

Ammar and Awad (4) found no time dependence using nickel electrodes electrodeposited from $(NH_4)_2SO_4$ + NH_4OH solutions; the overpotential at a fixed current density reached a constant value in less than a minute.

The reported dependence of overpotential on pH varies from about 0.010 to 0.060v per pH unit (1-4). If the discharge step is rate determining, the cathodic overpotential is given by [ref. (11)]

$$\eta = \psi_1 - 1/\alpha \ln i_c + 1/\alpha \ln a - \ln a_{H^+} + \text{const.} \qquad [1]$$

where η is the overpotential in units of $RT/\mathbf{F}$, ψ_1 is the potential (also in units of $RT/\mathbf{F}$) at a distance of one ionic radius from the electrode, a is the activity at this same distance of the entity discharged, and α is the transfer coefficient ($\alpha \sim 0.5$). Assuming that water is discharged in dilute alkaline solutions and taking its activity as constant, we have from Eq. [1]

$$(\partial\eta/\partial \text{pH})_{i_c} = 2.3 + \partial\psi_1/\partial \text{pH} \qquad [2]$$

In the absence of specific adsorption and in the presence of excess salt (or in concentrated alkaline solutions), $\theta\psi_1/d$ pH = 0 and $\theta\eta/d$ $pH = 0.060$v. In dilute alkaline solutions without salt, $\theta\psi_1/\theta$ pH = 0.060v and $\theta\eta/\theta$ pH = 0.120v. The observed dependence of η on pH (1-4) is generally not in agreement with these predictions. An attempt to remove this discrepancy by assuming that the activity of water molecules in the double layer depends on ψ_1 was not successful (3). In view of these anomalies, further experimental work on the kinetics of the reaction is worthwhile.

Experimental

Two types of cells were used. The solution was pre-electrolyzed in an auxiliary vessel in one series of experiments and then transferred under hydrogen to the cell containing the working electrode. Most runs were made however in the quartz cell shown in Fig. 1. Pre-electrolysis was carried out in the test cell. Nickel electrodes were mounted on the plungers of syringes; they could be immersed or

[1] Present address: Tyco Laboratories, Inc., Waltham, Massachusetts.

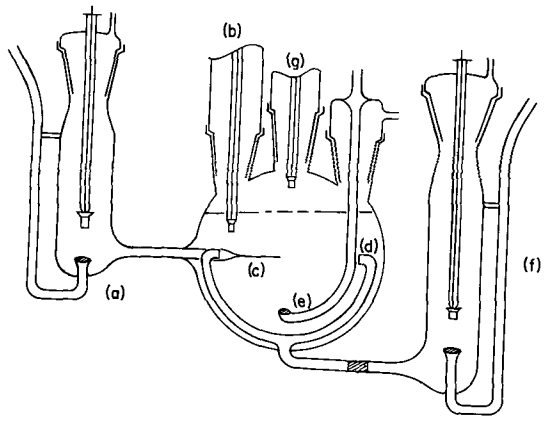

Fig. 1. Quartz cell: (a) reference electrode, (b) pre-electrolysis electrode, (c) Luggin-Haber capillary, (d) tubes leading to auxiliary compartment (two of four shown), (e) gas inlet, (f) auxiliary compartment, (g) working electrode. The pre-electrolysis and working electrodes (b and g) were mounted on the plungers of syringes. For details of mounting see ref. (5).

withdrawn from the solution without letting air into the cell. The solution was pre-electrolyzed using a nickel cathode. This electrode was then drawn up and the working electrode immersed. There was no difference in results between the two types of cells.

Electrodes were cylindrical and had a projected area of about 1 cm^2. Electrode assemblies were constructed as reported (5). Only quartz and Teflon, besides the electrode, came in contact with solution. To get a uniform current distribution on the working electrode it was placed in the center of a circle defined by the ends of four uniform tubes of equal length which connected the central section of the cell to the anode compartment. The tip of a Luggin capillary, 0.8 mm OD, through which potentials were measured, was placed 1.5 mm from the electrode. Screening effects were negligible (6). The iR correction (6) in any one solution was less than 5 mv at the maximum current density. Constant current was drawn from a 135v source through appropriate resistances ($R_{ext} >> R_{cell}$).

Laboratory distilled water was redistilled with a Pyrex still from dilute, alkaline, potassium permanganate into a two-stage quartz still and from there into quartz flasks. Solutions were prepared from freely boiling distillate. Sodium hydroxide solutions made by electrolysis gave the same results as solutions prepared from sodium hydroxide reagent. These last contained from 10^{-6} to 10^{-7} moles/l of carbonate ion. Solutions were routinely prepared from NaOH reagent.

Electrolytic hydrogen was purified by diffusion through a palladium tube heated to 450°C. Part of the hydrogen was bled off to prevent accumulation of impurities in the tube. Argon, used for sweeping the cell during pre-electrolysis, was passed first over copper at 500°C and then through a dry ice-acetone cold trap. Solutions were saturated with hydrogen for about 2 hr before a run. A stream of hydrogen swept the solution around the electrode during measurements. The resultant stirring minimized changes of hydroxyl concentration in the neighborhood of the electrode and also helped to detach hydrogen bubbles. Light tapping of the electrode assembly was necessary sometimes for removing bubbles formed at current densities higher than 10^{-3} amp/cm^2.

Electrodes were cut from nickel of "spectroscopic purity" (Johnson, Matthey, and Company). They were abraded with 2/0 emery paper and cleaned in chromic + sulfuric acid cleaning solution. They were washed in boiling conductivity water.

The cell was cleaned with chromic + sulfuric acid solution and washed several times in boiling water before each run. Ground joints (also of quartz) were of the mercury-cup type. They were moistened with conductivity water before they were sealed.

Solutions were pre-electrolyzed 18-24 hr at current densities ranging from 10 to 15 $\times$ 10^{-3} amp/cm^2. The sodium hydroxide concentration was determined by analysis at the end of each run.

Results

The rest-potential of nickel electrodes cleaned in chromic + sulfuric acid was + 0.2 to + 0.3v (referred to SHE) in 0.1N NaOH. Electrodes were activated by cathodic polarization. Results were independent of the current density and the number of coulombs in the activating step provided a minimum of the order of 10^{-4} coulombs/cm^2 was exceeded. A cathodic current of 2 $\times$ 10^{-3} amp/cm^2 for 5 min was used generally.

The rest potential after activation was 0 $\pm$ 0.002v *vs.* the hydrogen electrode. After a cathodic run, *i.e.*, after tracing a Tafel curve both in increasing and decreasing order of applied current, the electrode was polarized anodically to a potential greater than + 1.0v. Anodic current densities of 10-100 μa/cm^2 were used. The current was then switched off and the electrode left "passive" until the next cathodic run, whereupon it was activated again as described above. Measurements were taken in most cases over 2 to 4 days. Observations with about 30 different electrodes are reported.

Nickel electrodes gave distinctly different results when they had been polarized anodically once. However, no major change in the hydrogen evolution curve was found after the first cycle of anodic-cathodic polarization. Therefore, we differentiate in our discussion between "initial" Tafel lines and "steady state" Tafel lines measured after one or more anodic-cathodic cycles.

The overpotential with electrodes in the steady state reached its final value within the time needed to read the potentiometer after the current was set at a new value. It stayed constant for long periods. For example, in 0.1N NaOH the overpotential at 2 $\times$ 10^{-4} amp/cm^2 changed 0.4 mv in 30 min. Each current setting was held constant for at least 2 min in tracing polarization curves. A typical curve is shown in Fig. 2. It is obvious from the figure that there was no large change of the Tafel parameters in the 2 hr during which data were taken.

Initial Tafel curves (Fig. 3), *i.e.*, curves obtained with electrodes which had not been polarized anodically, had a definite time dependence. The

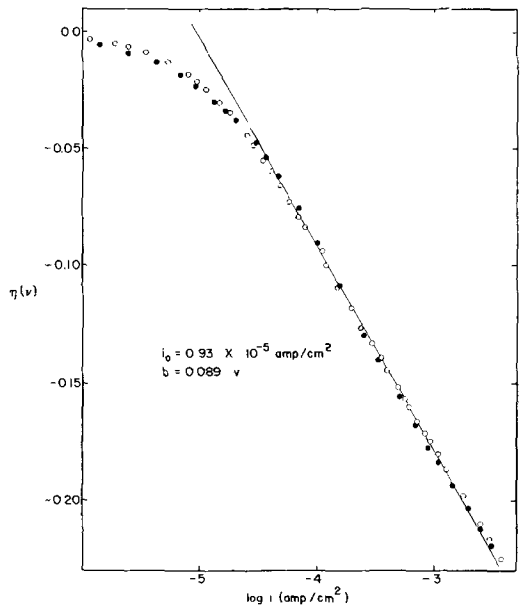

Fig. 2. Cathodic polarization curve with electrode in the steady state. Open circles are for increasing and full circles for decreasing current density. The curve was traced in about 2 hr. Overpotential in volts.

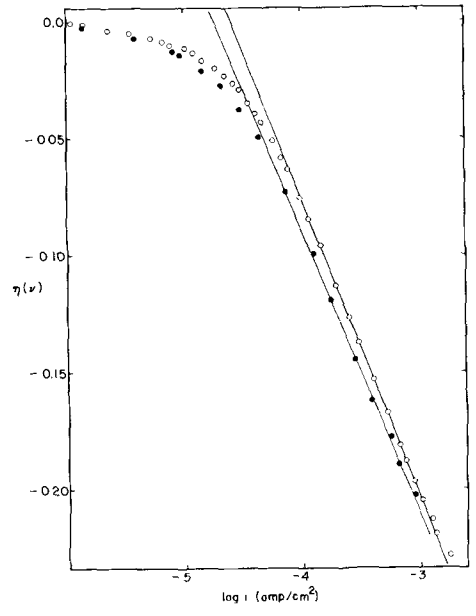

Fig. 3. Cathodic polarization curve with electrode in the "initial" state. Open circles are for increasing and full circles for decreasing current density. The Tafel constants for the open circles are b_c = 0.128v and $(i_o)_{extr}$ = 2.5 × 10^{-5} amp/cm^2; for the full circles overpotential in volts, b_c = 0.120 and $(i_o)_{extr}$ = 1.8 × 10^{-5} amp/cm^2.

drift of potential at a fixed current density was generally about 0.2 mv/min; in some cases it was as much as 0.5 mv/min. Tafel curves traced relatively rapidly (30 sec at each point) showed that both the slope and the exchange current decreased with time. The Tafel slope in a typical case changed from 0.128v to 0.120v and the exchange current decreased from 2.5 × 10^{-5} to 1.8 × 10^{-5} amp/cm^2 in about 30 min.

Table I shows the reproducibility of both initial and steady-state Tafel parameters with different electrodes. The variability of initial Tafel slopes is due, at least in part, to the time dependence noted above. Steady-state results with a given electrode

Table I. Hydrogen overpotential on nickel

0.1N NaOH at 30°C

Steady state			Initial		
b, v	i_o, amp/cm^2, × 10^{-5}	η, at 10^{-3} amp/cm^2	b, v	i_o, amp/cm^2, × 10^{-5}	η, at 10^{-3} amp/cm^2
0.092	0.7	0.198	0.110	1.6	0.198
0.092	1.2	0.176	0.120	1.8	0.210
0.093	1.0	0.186	0.135	1.8	0.235
0.090	1.0	0.180	0.125	2.5	0.200
0.090	0.95	0.182	0.130	2.5	0.208

Table II. Hydrogen overpotential on nickel electrodes in the steady state

0.1N NaOH at 30°C

Time, hr	b, v	i_o, amp/cm^2, × 10^{-5}	η, at 10^{-3} amp/cm^2
2.5	0.091	1.1	0.178
24.0	0.092	1.2	0.176
26.0	0.091	1.1	0.178
28.0	0.095	1.1	0.186
96.0	0.089	0.93	0.180

were reproducible for periods up to 100 hr (Table II).

Statistical treatment of results.—Bockris and coworkers (3, 7) and others after them [see, for example, ref. (4)] treat their results statistically by assuming a normal distribution for i_o and b. These statistical analyses are misleading in some respects. Experimental errors here are not connected with the measurement of either current or potential. For example, the potential is determined routinely with an accuracy of 0.1 mv, while the overpotential cannot be reproduced to better than ± 10 mv (1-4). Reproducibility of overpotential depends entirely on the state of the electrode surface. The mean value of a set of results gives essentially the probability of reproducing some surface condition and extent of surface contamination by some (unknown) impurity provided one follows a specified experimental procedure. It has no direct relation to the most probable value for a "clean" nickel surface. To illustrate, let us assume that a particular set of uniform surface states is produced by a chosen electrode preparation. Let us further assume that a substance Z is present and is adsorbed to an extent $\rho = \rho(C_z)$ where C_z is its concentration. The concentration of Z varies randomly from experiment to experiment. Thus ρ has values ρ_1, ρ_2, ρ_3 . . . in runs 1, 2, 3, ... In the simplest case substance Z decreases the exchange current by an amount proportional to ρ but does not alter the Tafel slope. The exchange current found in a particular run is then $i_o' = (1 - g\rho)i_o$ where g is a constant, probably not far from 1, and i_o is the exchange current for a clean surface ($\rho = 0$). With these assumptions the largest measured exchange current is closest to i_o. The best value therefore is not the average but the maximum observed exchange current.

If the surface is heterogeneous, the relation between i_o' and ρ is not linear. Further, impurities are expected to change both the exchange current

and the Tafel slope. A statistical analysis of a set of overpotential measurements is not justified therefore unless we know in detail the effect of impurities. We chose here to present our results in terms of typical experiments. Their reproducibility is illustrated in Tables I and II. We rejected about 15% of our observations because they appeared to be unreliable. The ground for rejection in most cases was excessive drift of potential.

Discussion

Mechanism of the Hydrogen Reaction on Nickel

There is general agreement (1, 3, 4, 8, 20) that the Volmer-Tafel mechanism is applicable to nickel cathodes. It is a matter of dispute (3, 20) whether discharge

$$H_2O + e^- \underset{v_2}{\overset{v_1}{\rightleftharpoons}} H_{ads} + OH^- \qquad [I]$$

or combination

$$H_{ads} + H_{ads} \underset{v_4}{\overset{v_3}{\rightleftharpoons}} H_2(g) \qquad [II]$$

are rate determining

The simplest kinetic equations for the Volmer-Tafel mechanism are (8, 14-18)

$$d[OH^-]/dt = v_1 = k_1 (1-\theta) = k_1^\circ e^{-a\eta} (1-\theta) \qquad [3a]$$

$$v_2 = k_2 \theta = k_2^\circ e^{\beta\eta} \theta \qquad [3b]$$

$$d[H_2]/dt = v_3 = k_3^\circ \theta^2 \qquad [4a]$$

$$v_4 = k_4^\circ (1-\theta)^2 \qquad [4b]$$

where the k's are rate constants in electrical units (amp/cm^2) and θ is the fractional degree of hydrogen adsorption. In writing Eq. [3] and [4] the electrode surface is assumed to be homogeneous. The ψ_1-potential effect is also neglected.

Equations [3] and [4] can be used to determine θ as a function of η (18). These equations also give the net cathodic current, $(i_c)_{appl}$, as

$$(i_c)_{appl} = k_1^\circ (1-\theta) e^{-a\eta} - k_2^\circ \theta e^{\beta\eta} \qquad [5]$$

At large negative η, Eq. [5] reduces to

$$(i_c)_{appl} = k_1^\circ (1-\theta) e^{-a\eta} = 2k_3^\circ \theta^2 \qquad [5a]$$

The net anodic current is obtained similarly. For large positive η

$$(i_a)_{appl} = 2k_4^\circ (1-\theta)^2 = k_2^\circ \theta e^{\beta\eta} \qquad [6]$$

It is convenient at this point to introduce the exchange currents for steps [I] and [II] which are defined by

$$i_{oI} = k_1^\circ (1-\theta^\circ) = k_2^\circ \theta^\circ \qquad [7a]$$

$$i_{oII} = 2k_3^\circ (\theta^\circ)^2 = 2k_4^\circ (1-\theta^\circ)^2 \qquad [7b]$$

where θ° is the value of θ at $\eta = 0$. The ratio γ of the exchange currents is (see ref. 18)

$$\gamma = \frac{i_{oI}}{i_{oII}} = \frac{k_2^\circ (k_1^\circ + k_2^\circ)}{2k_1^\circ k_3^\circ} \qquad [8]$$

The constant k_4° can be found from the anodic curve provided concentration polarization does not set in before i_a reaches its limiting value. Figure 4 gives typical anodic runs for electrodes in the "initial" and "steady" states. The limiting anodic current with electrodes in the initial state is sensitive to the rate of stirring by hydrogen; it appears therefore to be a diffusion current. However, with electrodes in the steady state and for the same hydrogen flow, the limiting anodic current is an order of magnitude less. Concentration polarization may be neglected in this case; the anodic overpotential is an activation overpotential and is given by Eq. [6]. The limiting anodic current is given by Eq. [6] when we set $\theta = 0$. It is

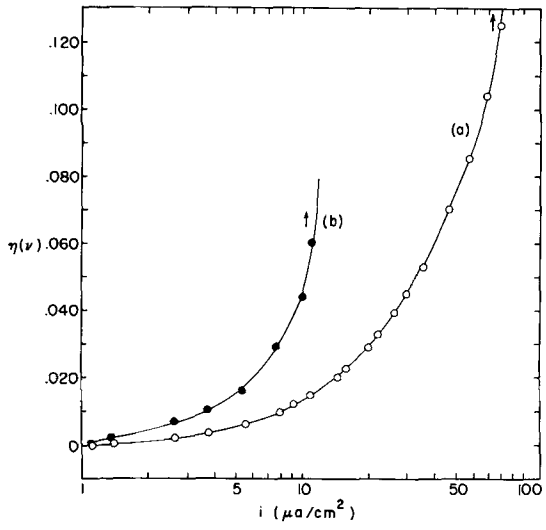

Fig. 4. Anodic polarization curves with electrodes in the initial state (a) and the steady state (b). The arrows indicate that the potential drifts to more positive values at the current densities shown. The limiting current with electrodes in the initial state is sensitive to stirring by hydrogen; it is a diffusion-limited current. The rate of gas flow was the same in (a) and (b). Overpotential in volts.

$$(i_a)_{lim} = 2k_4^\circ \qquad [9]$$

In the particular case shown in Fig. 5, $k_4^\circ = 7 \times 10^{-6}$ amp/cm^2. As shown below, k_4° is useful in determining γ.

Exchange Current

Exchange currents given in Tables I and II are 10 to 50 times those reported by others (1-4). This is attributed to the different electrode pretreatment used here. Electrodes produced by cathodically activating a surface formed under highly oxidizing conditions are less likely to be contaminated than electrodes treated in any of the conventional ways, *e.g.*, by heating in hydrogen at 400°-500°C (1, 3). The large exchange current found here is not caused by a high roughness factor as we have shown already (12).

A recent study of the hydrogen reaction on platinum corroborates our finding that electrode surfaces prepared in this way are to be preferred. The exchange current on platinum cleaned in chromic plus sulfuric acid is time independent and about 2.5 times that for "fresh" electrodes prepared in other ways (13). It should be noted also the Devanathan and Selvaratnam (8) working with nickel in 2*N* NaOH and using anodic-cathodic cycling, a procedure also used here, found an exchange current of 10^{-6} amp/cm^2 and a Tafel slope of 0.095v. These

parameters are in good agreement with our steady state results (Tables I, II).

The surface state of nickel in alkaline solution apparently varies considerably with electrode preparation and pretreatment. The present work shows that at least two states can be differentiated. In the "initial" state hydrogen is extensively adsorbed. Hydrogen is adsorbed to a much smaller extent in the steady state. These inferences are based mainly on anodic polarization studies which are presented and discussed below.

The fractional coverage of nickel cathodes by adsorbed hydrogen in 2N NaOH was determined recently by an anodic pulsing technique (8). The electrodes were subjected to anodic-cathodic cycling in the course of the measurements. These results refer therefore to our steady state polarization runs. According to this study (8) θ^2 is proportional to i_c and log $[i_c/(1-\theta)]$ to η as demanded by Eq. [5a] with $k_1 = 1.0 \times 10^{-5}$ and $k_2 = 3.2 \times 10^{-3}$ amp/cm^2. Using Eq. [7a] and [6] and the experimental value of $\theta^\circ = 0.04$ given in (8), it is found that $k_2^\circ = 2.4 \times 10^{-4}$ and $k_4^\circ = 5.5 \times 10^{-6}$ amp/cm^2. With these values of k's Eq. [3] and [4] give $\theta = \theta(\eta)$ in good agreement with experiment.

On the basis of the above results it was concluded in ref. (8) that discharge of water molecules was the slow step in the hydrogen reaction. This conclusion was based on a comparsion of the k constants and on their determination of a stoichiometric number of 2. However, the relevant quantities are i_{oI} and i_{oII} rather than the rate constants (18). Moreover, the usual way of determining stoichiometric numbers yields ambiguous quantities which are not necessarily diagnostic of the mechanism (18). The data given in ref. (8) actually show that $\gamma = i_{oI}/i_{oII} \simeq 1$, *i.e.*, that the rates of the discharge and combination reactions are the same at equilibrium.[2]

Devanathan and Selvaratnam's (8) Tafel lines are in good agreement with our steady-state results. Further, k_4° determined from the anodic polarization curve agrees well with the value calculated from θ° and k_2° given in ref. (8). Therefore, it may be assumed with some confidence that for electrodes in the steady state θ° is of the order found in (8), *i.e.*, $\theta^\circ \sim 0.05$. If $\theta^\circ << 1$, the exchange currents for steps I and II are

$$i_{oI} = k_1^\circ (1-\theta^\circ) \simeq k_1^\circ \qquad [10a]$$

and

$$i_{oII} = 2k_4^\circ (1-\theta^\circ)^2 \simeq 2k_4^\circ \qquad [10b]$$

The exchange current i_o for the over-all reaction (18) is then

$$i_o = \frac{i_{oI}\, i_{oII}}{i_{oI} + i_{oII}} = \frac{i_{oI}}{\gamma + 1} \simeq \frac{k_1^\circ}{\gamma + 1} \qquad [10c]$$

Stoichiometric Numbers

The two criteria used frequently for identifying the mechanism of the hydrogen reaction are the stoichiometric number ν and the Tafel slope. The stoichiometric number is given by

$$\nu = 2i_o/(\partial i_c/\partial\eta)_{\eta=0} \qquad [11]$$

wher i_o is the exchange current for the over-all reaction, *i.e.*, its total rate in the forward (or reverse) direction at $\eta = 0$. Commonly, i_o is obtained by extrapolating i_c from large $|\eta|$ to $\eta = 0$. An "exchange current" determined in this way may or may not coincide with i_o. To differentiate the two, we denote the extrapolated value by $(i_o)_{extr}$. The apparent stoichiometric number ν' may now be defined (14, 15, 18) by

$$\nu' = 2(i_o)_{extr}/(\partial i_c/\partial\eta)_{\eta=0} \qquad [12]$$

Consequently

$$\nu' = \nu\,(i_o)_{extr}/i_o \qquad [12a]$$

For the Volmer-Tafel mechanism, $\nu = (\gamma + 2)/(\gamma + 1)$ (18). Substituting for i_o from Eq. [10c] into [12a] we have

$$\nu' = (\gamma + 2)\,(i_o)_{extr}/i_{oI} \qquad [13]$$

It has been suggested that a value of 2 (or close to 2) for the stoichiometric number of the hydrogen reaction shows that the discharge step [I] is rate determining in the Volmer-Tafel mechanism (3, 17, 19). Since experimental values of the stoichiometric number are almost always apparent values, this conclusion is not valid frequently. The distinction between ν and ν' is particularly important when γ is of the order of 1.

The apparent stoichiometric number is arbitrary to a certain extent since it depends on the section of the total polarization curve chosen for extrapolation. The significant problem here is to find a γ consistent with the value of ν' and $(i_o)_{extr}$, rather than to use ν' as a criterion for determining the mechanism.

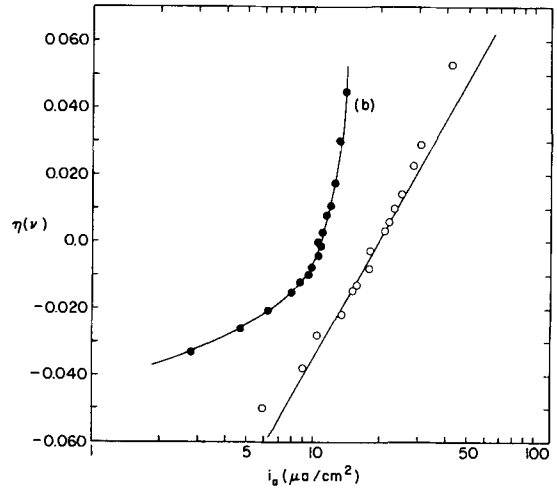

Fig. 5. Overpotential as a function of the total anodic current ($i_a = i_{appl} + i_c$) for electrodes in the initial state (a) and the steady state (b). The Tafel parameters for (a) are $b_a = 0.120$v and $i_o = 1.95 \times 10^{-5}$ amp/cm^2. Points for $\eta<0$ were calculated from the corresponding cathodic curve (Fig. 3) for which $b_c = 0.120$v and $i_o = 1.85 \times 10^{-5}$ amp/cm^2. The anodic curve for electrodes in the steady state (b) is not a Tafel line since θ varies rapidly in this region. The limiting anodic current for electrodes in the steady state is $(i_a)_{lim} = 2k_4^\circ = 1.4 \times 10^{-5}$ amp/cm^2. Overpotential in volts.

[2] The value $\gamma = 1$ is a lower limit. The value of γ depends on θ°. Devanathan and Selvaratnam obtained θ° by a short extrapolation from $\eta \simeq -10$ mv to $\eta = 0$. Any error in the extrapolation is in the direction of large i_{oII}.

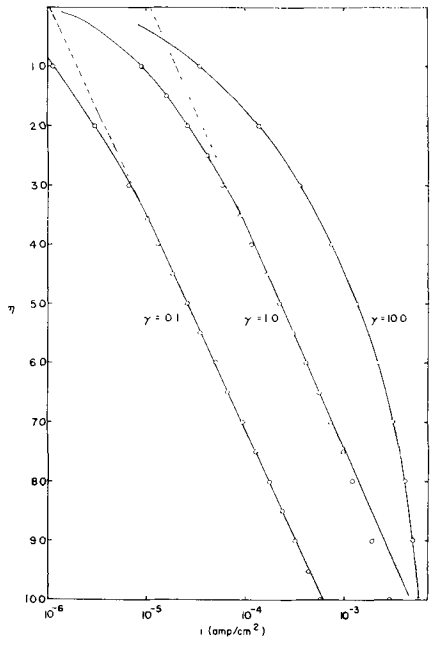

Fig. 6. Tafel plots for a Volmer-Tafel mechanism with $\gamma = 0.1$, 1.0, and 10.0. Surface coverage $\theta^\circ = 0.04$ at $\eta = 0$. The constants $k_3^\circ = 3.2 \times 10^{-3}$ amp/cm² and $k_4^\circ = 5.5 \times 10^{-6}$ amp/cm² are those given in ref. (8). The constant k_1° varies from 1.0×10^{-6} amp/cm² ($\gamma = 0.1$) to 1.0×10^{-4} ($\gamma = 10$) while k_2° varies from 2.4×10^{-5} amp/cm² ($\gamma = 0.1$) to 2.4×10^{-3} amp/cm² ($\gamma = 10$). The overpotential is in units of RT/F (26 mv at 30°C).

We consider first electrodes in the steady state. From Eq. [8] and [10]

$$i_{oI} = (2k_4^\circ)\,\gamma \qquad [14]$$

Substituting Eq. [14] into [13]

$$\nu' = (\gamma + 2)\,(i_o)_{extr}/2\gamma\,k_4^\circ \qquad [15]$$

In a typical case (Fig. 2 and 5), $(\partial i_c/\partial\eta)_{\eta=0}$ obtained from a linear plot of i_c *vs.* η ($|\eta| < 15$ mv), was 3.88×10^2 amp/cm²/v and $(i_o)_{extr}$ was 0.93×10^{-5} amp/cm². The corresponding apparent stoichiometric number was 1.85. From the anodic limiting current we have $2k_4^\circ = 1.4 \times 10^{-5}$ amp/cm². Substituting in Eq. [15] we find $\gamma = 1.1$.

Values of ν' for electrodes in the steady state ranged from 1.50 to 2.25, $i_{oII} = 2k_4^\circ$ ranged from 7×10^{-6} to 1×10^{-5}, amp/cm², and γ from 0.8 to 1.3.

The apparent stoichiometric number for electrodes in the initial state was between 1.8 and 3.0 The value of $2k_4^\circ$ is not known in this case since the anodic limiting current was a diffusion current. However, we can write

$$2k_4^\circ > (i_a)_d$$

where $(i_a)_d$ is the diffusion-limited anodic current density. In a typical case ν' was 2.10, $i_o = 1.85 \times 10^{-5}$ amp/cm², and $2k_4^\circ > 10^{-4}$ amp/cm² (Fig. 4). Using Eq. [15] we find $\gamma < 0.18$. The upper bound of γ calculated according to Eq. [15] for electrodes in the initial state was 0.2.

An extensive discussion of the stoichiometric number of the hydrogen reaction on nickel electrodes was given by Horiuti and Sugawara (20). The distinction made here between ν and ν' amplifies their argument and demonstrates that $\nu' \sim 2$ is consistent with a Volmer-Tafel mechanism for which $\gamma \sim 1$.

Table III. Kinetic parameters of the hydrogen reaction on nickel

O.1*N* NaOH at 30°C

	Initial state	Steady state
$(i_o)_{extr}$, amp/cm²	2.5×10^{-5}	1.0×10^{-5}
b, v	0.125	0.090
ν'	2.0 ± 0.23*	1.8 ± 0.15**
$(i_a)_{lim}$, amp/cm²	$(i_a)_d \sim 1 \times 10^{-4} < 2k_4^\circ$	$2k_4^\circ \sim 10^{-5}$
γ	<0.2	~1.1

* Average of 10 determinations.
** Average of 8 determinations.

Table III summarizes in terms of b, ν', and γ the distinction made previously between the initial and the steady state of nickel electrodes. Typical Tafel slopes and exchange currents are given rather than average values for the reasons discussed previously. However, mean values of ν' may be computed and these are given in Table III.

Tafel Slopes

It is apparent from Table III that the discharge step is rate determining for electrodes in the initial state while for electrodes in the steady state there is no rate-determining step, *i.e.*, the exchange currents for discharge and combination are about equal.

The cathodic polarization curve on electrodes in the initial state is given by Eq. [5a]. If $i_{oII} >> i_{oI}$, the change with η of the pre-exponential term is negligible with respect to $e^{-\alpha\eta}$. The polarization curve approaches

$$i_c \simeq k^1 e^{-\alpha\eta}$$

The Tafel slope gives directly the value of α. With electrodes in the initial state α was between 0.45 and 0.55.

The value of θ° for electrodes in the initial state is not known. If the specific rate of the combination reaction is the same as for electrodes in the steady state, *i.e.*, $k_3^\circ \sim 3 \times 10^{-3}$ amp/cm², then from

$$i_{oII} = 2k_3^\circ\,(\theta^\circ)^2 > 2 \times 10^{-4}\ \text{amp/cm}^2$$

we estimate $\theta^\circ > 0.2$. It is probable that k_3° is less for electrodes in the initial state since the (specific) rate of surface combination of hydrogen atoms is expected to decrease as the energy of adsorption increases. Consequently, the lower limit of θ° is probably considerably higher than 0.2.

The polarization curve for electrodes in the steady state is given also by Eq. [5a]. The variation of the pre-exponential term can be estimated in this case from the data given in ref. (8). We find over the range $2 < |\eta| < 8$

$$(1 - \theta) \sim (\text{const.}) \exp(+0.06\eta)$$

A plot of log i_c *vs.* η should be approximately linear over the range $\eta = -0.050$ to $\eta = -0.200$ mv (see also below) with a slope $-(\alpha - 0.06)$. The transfer coefficient calculated in this way for electrodes in the steady state (Tables I and II) is between 0.69 and 0.73. Devanathan and Selvarat-

nam (8) found $\alpha = 0.67$ (at 27°C) by plotting log $[i_c/(1-\theta)]$ *vs.* η.

Surface States

Since nickel adsorbs hydrogen extensively (21), we expect θ° to approach unity at 1 atm of H_2. The fractional coverage for electrodes in the initial state is at least 0.2 and may be considerably higher. However, θ° is only 0.05 in the steady state. The decrease in hydrogen adsorption implies that water, hydroxyl, or oxygen are adsorbed extensively upon cycling. It is doubtful that water adsorption would be increased significantly at positive potentials. It is also doubtful that water would produce, under any circumstances, a large change in hydrogen adsorption.

It is difficult to say which of the remaining two possibilities is more likely. Hydroxyl ion adsorption probably takes place. The rate and extent of its adsorption must be appreciably increased at positive potentials. However, hydroxyl ion should be desorbed at negative potentials with a return to the "initial" state. This is not observed. A resolution of this contradiction is possible if the free energy of adsorption of hydroxyl ion is larger than about 20 kcal/mole. Its desorption in the negative potential region traversed on cathodic polarization may be relatively small under these circumstances.

An oxide is probably formed during the anodic part of the cycle. Under normal circumstances, one expects this oxide to be reduced on cathodic polarization. The electrode capacity (8) is normal (20 μf/cm^2). Therefore, an oxide of the usual type is not present. However, a thin, conducting nickel oxide may be stable even on cathodic polarization. Its contribution to the total electrode capacity would be negligible if it were an electronic conductor.

In any case, the electrode surface is modified by the first anodic-cathodic cycle so that the energy of adsorption for hydrogen decreases. The increase of the transfer coefficient from about 0.5 to 0.7 is probably a result of the change in the hydrogen adsorption energy.

There are several theoretical interpretations of the coefficient α, none of which is entirely satisfactory (11). In the common representation of electrode reactions in terms of energy-reaction co-ordinate diagrams α is given by the slopes of the potential curves for the initial and final states at their point of intersection (22-24). Although an increase of α can be interpreted in a variety of ways with this theory (24, 25), the most probable interpretation is that the heat of adsorption of hydrogen decreases. For example, in the calculation cited above (25) for discharge of hydrogen ion on nickel, a decrease of the heat of adsorption by about 10 kcal would shift α from 0.5 to 0.7. The calculation (25) assumes that the curve for the final state is displaced vertically without changing its shape and that no displacement takes place along the reaction co-ordinate. Since both assumptions are doubtful, it can only be said that an increase of α is consistent with a decrease of the energy of adsorption of hydrogen.

It should be pointed out that the transition from "initial" to steady state is unrelated to the attainment of any possible equilibrium between adsorbed hydrogen and hydrogen dissolved in the metal. The transition is induced by anodic polarization. Positive potentials certainly do not promote dissolution of hydrogen into nickel.

High Current Densities and the Shape of the Overpotential Curves

The cathodic current is a simple exponential function of the overpotential in the Volmer-Tafel mechanism only if $\gamma >> 1$ or $\gamma << 1$. In both cases, θ is sensibly constant over several hundred millivolts and the Tafel plot is linear. If γ is between approximately 0.1 and 10, the relation between i_c and η is complicated by the term $(1-\theta)$ in Eq. [5a]. The Tafel plot is now linear at large $|\eta|$; it may be linear also at moderate $|\eta|$ (*i.e.*, −50 to −200 mv), but with a smaller slope, if the k's are such that Eq. [4] approximates a simple exponential relation between θ and η. The two linear parts are joined by a curved section.

To make the above remarks specific, let us consider the case $\gamma = 1$ using reported (8) rate constants. A plot of log θ, calculated from Eq. [3] and [4], against η is linear in the interval $\eta = 0$ to $\eta = -7$ (−180 mv); approximately, $\theta = \theta^\circ e^{-0.81\eta}$ in this range of η (18). We find from Eq. [5a] that $i_c = (i_o)_{extr} e^{-0.62\eta}$ which yields a linear Tafel plot with an apparent $\alpha = 0.62$. Deviations from linearity in the direction of larger $|\eta|$ for a given i_c appear at larger overpotentials. Calculated Tafel plots for $\gamma = 0.1$, 1, and 10 are shown in Fig. 6.

There are also experimental sources of deviation from linearity at high current densities which make it impossible frequently to observe the second linear section. The potential measured with the direct method includes a back emf produced by concentration changes in the solution next to the electrode. It includes also an iR potential drop in the solution between electrode and tip of the Luggin capillary. Both errors are in the direction of larger $|\eta|$ and both become appreciable at about 2×10^{-3} amp/cm^2 in 0.1*N* NaOH. Therefore, at high current densities we expect deviations from Tafel behavior in the direction of larger $|\eta|$ both because of the structure of Eq. [3-6] and because of concentration and ohmic overvoltages.

The deviations observed at current densities larger than 1×10^{-3} amp/cm^2 were actually in the opposite direction, *i.e.*, toward smaller $|\eta|$ for given i_c. For electrodes in the initial state, the deviations suggested a transition to another Tafel slope with smaller *b*. Deviations observed with electrodes in the steady state were similar but smaller and appeared at even higher current densities. Because of the experimental errors inherent in the direct method of measurement of η at high current densities, no attempt was made to study this potential region in detail. The results at high current densities suggest nevertheless that the kinetic equations for

hydrogen evolution on these electrodes are modified either by the emergence of an alternative path or by changes in the energy of hydrogen adsorption at high coverages.

Conclusions

The surface state of nickel electrodes in 0.1*N* NaOH depends on their pretreatment and polarization history; it determines the kinetics of the hydrogen reaction. If the fractional coverage with adsorbed (atomic) hydrogen at $\eta = 0$ is high, the discharge step is slow and rate determining. If the fractional coverage is small, the exchange rates for discharge and combination are about equal and there is no single rate-determining step.

Acknowledgment

The skillful assistance of Mr. R. E. Aikin in the experimental part of this work is gratefully acknowledged.

Manuscript received Nov. 27, 1961; revised manuscript received May 22, 1962.

Any discussion of this paper will appear in a Discussion Section to be published in the June 1963 JOURNAL.

REFERENCES

1. P. Lukowzew, S. Lewina, and A. Frumkin, *Acta Physiocochim.*, **11**, 21 (1939).
2. P. Lukowzew and S. Lewina, *Zhur. Fiz. Khim.*, **21**, 599 (1947).
3. J. O'M. Bockris and E. C. Potter, *J. Chem. Phys.*, **20**, 614 (1952).
4. I. A. Ammar and S. A. Awad, *This Journal*, **104**, 686 (1957).
5. M. Stern and A. C. Makrides, *ibid.*, **107**, 782 (1960).
6. S. Barnartt, *ibid.*, **99**, 549 (1952); *ibid.*, **106**, 722 (1959).
7. N. Pentland, J. O'M. Bockris, and E. Sheldon, *ibid.*, **104**, 182 (1957).
8. M. A. V. Devanathan and M. Selvaratnam, *Trans. Faraday Soc.*, **56**, 1820 (1960).
9. A. M. Azzam, J. O'M. Bockris, B. E. Conway, and H. Rosenberg, *ibid.*, **46**, 918 (1950).
10. J. P. Hoare and S. Schuldiner, *J. Phys. Chem.*, **62**, 229 (1958).
11. A. Frumkin, *Z. phys. chem.*, **164**, 121 (1933); *Acta Physicochim.*, **12**, 481 (1940); *ibid.*, **18**, 23 (1943).
12. A. C. Makrides and M. T. Coltharp, *This Journal*, **107**, 472 (1960).
13. R. Parsons, *Trans. Faraday Soc.*, **56**, 1340 (1960).
14. K. J. Vetter, *Z. Elektrochem.*, **59**, 435 (1955).
15. A. N. Frumkin, *Doklady Akad. Nauk SSSR*, **119**, 318 (1958).
16. J. O'M. Bockris, "Modern Aspects of Electrochemistry," J. O'M. Bockris, Editor, p. 201-205, Butterworths, London (1954).
17. J. O'M. Bockris and H. Mauser, *Can. J. Chem.*, **37**, 475 (1959).
18. A. C. Makrides, *This Journal*, **109**, 256 (1962).
19. R. Parsons, *Trans. Faraday Soc.*, **47**, 1332 (1951).
20. J. Horiuti and S. Sugawara, *J. Res. Inst. Catalysis*, **4**, 1 (1956).
21. O. Beeck, "Advances in Catalysis," p. 173-176 and p. 184-186, Acad. Press, Inc., New York (1950).
22. J. Horiuti and M. Polanyi, *Acta Physiocochim.*, **2**, 505 (1935).
23. J. Butler, *Proc. Roy. Soc.*, **157**, 423 (1936).
24. O. Essin and V. Kozheurov, *Acta Physiocochim.*, **16**, 169 (1942).
25. R. Parsons and J. O'M. Bockris, *Trans. Faraday Soc.*, **47**, 914 (1951).

Technical Notes

An All-Teflon Electrochemical Cell Assembly

J. L. Weininger and W. R. Grams

Research Laboratory, General Electric Company, Schenectady, New York

In electrochemical studies improved instrumentation and experimental techniques require a corresponding improvement in cell design. This note describes an all-Teflon cell in which the electrolyte saturated with an inert carrier gas is circulated past the electrodes.

It is now recognized that electrodes and electrolyte should only be exposed to each other and to inert container material. Such inert materials are Pyrex glass and fluorinated plastics, *e.g.*, Teflon. Each has distinct advantages. Pyrex glass can be blown easily, and cells made with it are assembled from interchangeable commercial parts. It is transparent and chemically inert to most solutions, concentrated alkali being an important exception. On the other hand, Teflon is readily machined from available stock and is quite inert. It has the disadvantage of flowing under mechanical pressure so that blocks of Teflon, particularly with machined threads, deform on being bolted together. It was found, however, that this could be avoided by using pipe threads instead of machine threads, and by the addition of a simple embossing on Teflon parts that are to be bolted. These two improvements have been incorporated in the construction of the following Teflon cell.

Figure 1 is a schematic of the assembly, which consists of the cell in the center, an impeller and its housing on the left, and a Teflon U-tube to the right. The electrolyte is circulated through this assembly in a counter-clockwise direction. In the drawing the cross-hatched parts are made of Teflon,

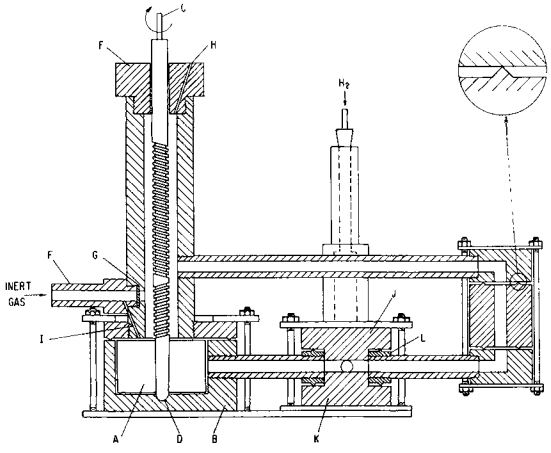

Fig. 1. Schematic of Teflon cell assembly

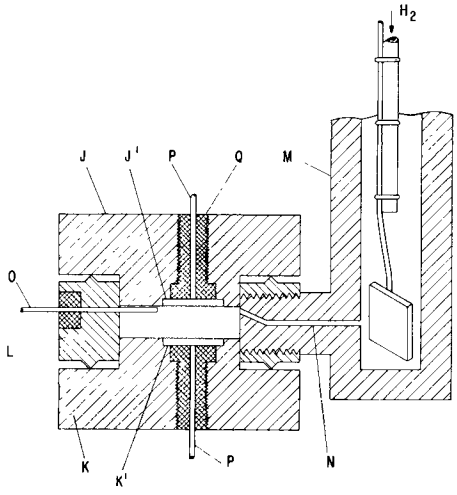

Fig. 2. Teflon cell with reference electrode

as is the rotating impeller, its shaft, and the hydrogen electrode in the background of the cell. The remaining parts are bolted brass plates. All liquid-sealing threads are pipe threads.

The impeller, A, is a flat paddle which rotates with reasonably close tolerance in its housing, B. The outlet tube is off diameter with respect to the impeller so that a pushing or swiping motion of the liquid into the tube leading to the cell is achieved. The impeller shaft is reinforced internally with a steel rod, C. The bottom end of the shaft is seated in the housing like a bearing, D, and in the cylinder at the top it is capped with a Teflon piece, E, thus providing self-lubrication. Opposing threads guide the gas which can be bubbled through the solution. The right-hand thread on the lower part of the shaft introduces fresh gas *e.g.*, inert argon, from tube F through the porous Teflon plug G, into the circulating electrolyte stream. At the end of a single pass gas bubbles are rejected by the left-hand thread of the upper part of the shaft through the hole, H, in the cylinder cap. The plug, G, can also be bypassed by the hole, I.

The U-bend on the right consists of three Teflon pieces bolted between brass plates. They are easily separated in order to make the cell itself readily accessible. The method of embossing these pieces, mentioned above, is shown in an inset. It it also used to make the impeller housing and the cell pressure-tight.

The cell, shown in detail in Fig. 2, also consists of three Teflon pieces, the test electrode J' in J, the counter-electrode K' in K, and the spacer L. The latter defines the cell volume (3.2 cm^3) by separating the electrodes and also provides access to the other electrodes. There is a housing M for a reference electrode connected to the cell by the Luggin capillary N. A hydrogen electrode is shown, but any other standard electrode can be used. Electrode O shows the possibility of introducing other electrodes. Specifically, O is a palladium wire used for capacity measurements. Test and counter electrodes, *e.g.*, a single crystal of nickel and a platinum foil later to be platinized, must be inserted into the Teflon pieces J and K without allowing the electrolyte to come in contact with the leads P. In this respect a simple pressure-fit is not completely satisfactory. Instead, a shoulder is machined into the Teflon piece with close lateral tolerance, and a hole is drilled and tapped through it. While the electrode material rests on this shoulder, the hole is filled with a thermosetting plastic (epoxide at room temperature) to impart rigidity to the electrode assembly. The epoxide Q is not threaded into the Teflon, but the threads are necessary to ensure good adhesion between Teflon and epoxide.

This construction resulted in an electrode-mount without creepage of electrolyte. This was prevented by the design of the shoulder (J' and K' in Fig. 2) as well as the epoxide protection of the lead wire. In an experiment with a nickel electrode under corrosive attack the lead wire did not come in contact with the electrolyte until the electrode was consumed.

The total volume of the assembly is distributed thus: 50 cm^3 in the impeller reservoir, 3.2 cm^3 in the cell itself, and 15 cm^3 in the tubing. The impeller is ordinarily rotated at 400 rpm, which propels the liquid at about 50 cm/sec, but higher speeds of rotation can be used.

In summary, the design of an electrochemical cell is shown which, in addition to the electrode materials, contains only Teflon. All Teflon parts are machined from simple stock and tubes. From the experimental point of view the cell has the advantage of a rapidly circulating electrolyte saturated with any desired gas. The stream of electrolyte is parallel to the electrode surfaces. Only a small volume of electrolyte, isolated from the surrounding, is used. The cell also provides for a symmetrical field between test electrode and counter electrode, and for close proximity to the Luggin capillary. We are using it for the study of electrode reactions at single crystal surfaces, as well as more conventional electrode materials.

Acknowledgment

The authors are indebted to Dr. R. W. Powers for his constructive suggestions.

Manuscript received May 31, 1962.

Any discussion of this paper will appear in a Discussion Section to be published in the June 1963 JOURNAL.

Use of a Precious Metal Anode in the Electrowinning of High-Purity Chromium from a Fluoride Bath

J. A. Whittaker

Fulmer Research Institute, Stoke Poges, Bucks, England

In connection with a research program on the ductility of chromium and its development as a high-temperature resistant material (1-3), a pilot plant (4) has been in operation for some years producing high-purity chromium at the rate of approximately 1 kg/day. Various modifications (4) have been made to the plant to improve the purity of the chromium, and this note refers specifically to the introduction of a palladium anode, designed to avoid tin contamination of the chromium, and its subsequent effects on the cathode current efficiency.

When the first palladium anode was received the experimental arrangement was briefly as follows; a high-density polyethylene plating tank (55 liters of solution), a Pb/7% Sn anode and a copper-tube cathode. This anode was first used in a bath which had been operated for some time with the Pb/7% Sn anode; the cathode current efficiencies obtained for a period before and immediately after its introduction are given in Table I.

When, however, the palladium anode was used in a freshly prepared bath, made necessary by the failure of the polyethylene tank, there was a serious decrease in the efficiency after only a few runs, as shown in Table II, the composition and conditions being exactly as described in Table I. Associated with this fall off in efficiency was a pronounced increase in the resistance of the bath and an increase also in its trivalent chromium content. This fall off in efficiency in the new bath may have been due to one or more of the following factors:

Table I. Cathode current efficiencies

Solution composition: 250 g/l CrO_3; 5 g/l HF

Conditions: 90°C; 460 amp/ft²; normal deposition time 24 hr; 55 liters of solution

	Cathode current efficiency, %
High-density polyethylene tank; Pb/7% Sn anode	36, 34, 26, 33, 36, 34, 36, 38, 37.
High-density polyethylene tank; Pd anode	33, 37, 31, 40, 30, 41, 41, 41, 34, 40, 37, 38, 38, 36, 39, 40.

Table II. Cathode current efficiency with Pd anode in freshly prepared bath

	Cathode current efficiency, %
New solution; H.D. polyethylene tank; Pd anode	30, 28, 25, 15, 14, 13

(*a*) the absence of lead salts in the new bath, (*b*) the absence of PbO_2 on the anode, and (*c*) the absence of tin salts.

The results of the investigation of factors (*a*) and (*b*) are given in Table III. These experiments were carried out in a 10-liter polytetrafluoroethylene (P.T.F.E.) beaker, 9 liters of solution, using a second palladium anode of identical construction.

The effect of tin was not investigated fully since one of the main reasons for introducing a palladium anode was to avoid tin contamination of the chromium, and tin salt additions would not have been a practical solution. However, 0.75 g/l of tin, as stannic chromate, was added to the solution in the P.T.F.E. beaker after run 13, and the efficiency of the next run was 29%, indicating no serious effect from tin in solution.

The results in Table III show that the presence of lead salts in the bath and PbO_2 on the anode are definitely associated with a maintained efficiency Despite the fact that the efficiencies in Table III are low compared with those in Table I, these modifications were introduced into the larger, 55 liters, bath, and the first six runs gave efficiencies of 34%, 38%, 37%, 37%, 36%, 38%. Laboratory scale work (5) has since indicated that a correlation exists between solution volume:cathode area ratio and the level of efficiency. The cathode area was here constant for both the 9 liter and 55 liter bath.

Table III. Factors contributing to decline of cathode current efficiency

Solution composition: 250 g/l CrO_3; 5 g/l HF

Run No.		Cathode c.d. amp/ft²	Duration of run, hr	Temp, °C	Cathode current efficiency, %
1	New bath; no additions	460	5.85	80	29
2		520	5.75	90	23
3		410	5.75	95	15
4	New bath; saturated	435	4.25	95	31
5	with $PbCrO_4$	435	6	95	32
6		435	5.5	95	27
7		460	6	95	22
8	New bath; saturated	460	6	95	26
9	with $PbCrO_4$; anode	460	5.75	95	30
10	coated with PbO_2 by	460	5	95	30
11	anodic treatment in	460	5.5	95	28
12	saturated PbF_2 solu-	460	5.75	95	29
13	tion	460	5.5	95	28

Spectrographic analysis has failed to detect either lead or palladium in the chromium.

Conclusions

The use of a palladium anode for the electrowinning of chromium from a fluoride bath, made necessary by tin contamination from a Pb/7% Sn anode, resulted in a serious fall off in efficiency of new baths. An increase in the bath resistance and also in the trivalent chromium content accompanied the fall in efficiency. It has been shown that these disadvantages can be overcome by saturating the bath with lead chromate and by preforming PbO_2 anodically on the surface of the anode.[1]

[1] British Patent applications have been filed for these results.

Acknowledgments

The author wishes to acknowledge the assistance of Mr. E. F. Crosswell in the experimental work.

Manuscript received March 12, 1962.

Any discussion of this paper will appear in a Discussion Section to be published in the June 1963 JOURNAL.

REFERENCES

1. A. H. Sully, E. A. Brandes, and A. G. Provan, *J. Inst. of Metals*, **81**, 569 (1952-3).
2. A. H. Sully, E. A. Brandes, and K. W. Mitchell, *ibid.*, **81**, 582 (1952-3).
3. E. A. Brandes and H. E. N. Stone, *ibid.*, **87**, 42 (1958-9).
4. E. A. Brandes and J. A. Whittaker, *Metallurgia*, **65**, 209 (1962).
5. Fulmer Research Institute, Unpublished work.

Electroless Ni-Co-P Films with Uniaxial Anisotropy

J. Bagrowski and M. Lauriente

Air Arm Division, Westinghouse Electric Corporation, Baltimore, Maryland

There has been considerable interest in the basic mechanism responsible for the phenomenon of uniaxial anisotropic energy in thin magnetic films as displayed by the rectangular hysteresis loop found in the easy direction and the closed loop in the transverse direction (1). In addition to satisfying the curiosity of the fundamentalist, such information is of engineering importance for solving the reproducibility problems posed by applications such as memories for computers.

In 1959, Heritage and Walker reported anisotropy for thin nickel-cobalt-phosphorous films made by electroless deposition in a magnetic field (2). In a check of this work, uniaxial anisotropy was also found when a magnetic field was not used, thus indicating that another source of anisotropy was present.

Experimental

Chemical deposition (also known as electroless deposition) requires a suitably activated surface to initiate the process. The oblique incidence effect which has been noted for films made by vacuum evaporation (3, 4) thus is impossible to study directly. The experiment was designed to ascertain if oblique incidence effects in a nonmagnetic substrate film would show up in the chemically deposited magnetic film.

The experiment consisted of evaporating one group of 1 x 3 in. glass slides with chromium-gold at oblique incidence and another group at normal incidence. These two groups were then each subdivided so that one group was plated in a magnetic field and the other without the field. The magnetic field was provided by a d-c magnet with a field strength of 200 oe. One set of slides was also mechanically polished in one direction.

Figure 1 indicates the general arrangement used for producing chrome-gold substrates for the oblique incidence study. Slides evaporated at normal incidence had the source distance increased to 16 in. Only two substrates, located directly above the source, were evaporated at any one time to further decrease the oblique incidence effect. The thickness was controlled by means of a resistance monitor. The chromium, used for purposes of adhesion only, was evaporated to 150,000 ohms per square while the gold was evaporated to 3 ohms per square.

The solution found to give the best results was a modification of the one given by Heritage and Walker (2). It consisted of nickel sulfate 7.5g, cobalt sulfate 5.0g, ammonium sulfate 21g, sodium citrate 42.0g, hypophosphorous acid 15.0 ml, and aqueous ammonium hydroxide in sufficient quantity to yield a solution *p*H of 8.5 in a volume of 500 ml. Deposition was at a rate of approximately 1000Å/min. The solution was used at 90° ± 1°C.

The thickness of the films averaged 5000Å as measured by the Tolansky multiple beam interferometry technique (5). This process yields a coercive force which is not too much higher than found for thin Permalloy films. This is very surprising in view of the coercivities of around 1000 oe reported by Sallo and Olsen (6) on films of similar composition which were electrodeposited. A check on the film composition using an electron probe microanalyzer compared favorably with the analysis reported by Heritage and Walker, which

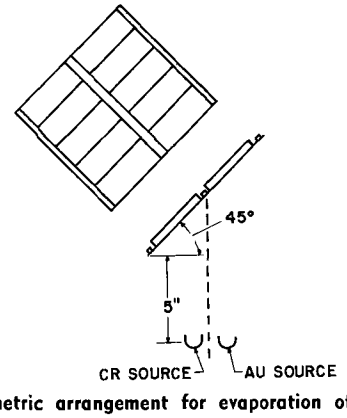

Fig. 1. Geometric arrangement for evaporation of substrates at oblique incidence.

Table I. Effect of oblique incidence

Spec.	Field	H_c (oe)	H_k (oe)	H_a (oe)
38.42	Yes	4.1	12.2	12
40.29	Yes	5.3	8.1	12
40.30	Yes	2.9	10.8	12
38.81	No	4.6	8	12
38.82	No	3.3	12	12
38.80	No	5.3	12.2	12

was of equal amounts of nickel and cobalt and 5% of phosphorous.

Measurements.—Magnetic parameters measured were, H_c the wall coercive force, and H_k, the anisotropy field. Measurements were made at 400 cps, using the familiar Crittenden (7) setup. The measurement of H_k is extrapolated from the initial transverse susceptibility to the saturation flux. H_A is the applied field.

Results

For all the films tested, $H_c < H_k$ indicating that the films were normal. The sensitivity of the films to oblique incidence in the substrate is shown in Table I by the consistency of the H_k values found independent of the magnetic field. This point is probably made more dramatically in Fig. 2, where the anisotropy is easier to perceive by the characteristic loop traces.

Now it will be interesting to test the corollary; *i.e.*, will the anisotropy be absent when there is no obliquity. Table II indicates by the absence of the H_k for specimens made without the field that this is the case. Figure 3 illustrates the same point.

Inducing uniaxial anisotropy by directional polishing has been reported (2) and verified experimentally by the authors. Directional polishing, since it offered no significant improvement in magnetic properties, was not pursued further. It did, however, confirm the significant contribution made by the substrate surface to uniaxial anisotropy.

Rotatable anisotropy similar to that reported for Permalloy by Prosen *et al.* (8) were found for some of the thicker films, *i.e.*, in excess of 10,000Å. In these films the easy direction of magnetization can be selected by application of a sufficiently large magnetic field. A closed loop can then be found 90° from this axis. Figure 4 shows typical loops for this phenomenon. This anisotropy could possibly be explained as an antiferromagnetic interaction between cobalt oxide and the cobalt-nickel layers, based on the Permalloy example.

Conclusion

The crystallites which form thin films made by oblique incidence evaporation are known to have a chain-like formation because of the self-shadowing effect. Assuming that the profiles thus exposed in the nonmagnetic film are replicated in detail by plating, the theory proposed by Smith (3) can then be applied. In a like manner, the anisotropy created by polishing scratches strengthens the theory that a shape anisotropy is taking place. This model provides a convenient linkage for relating anisotropy phenomena found for vacuum evaporated films to chemically deposited films.

Table II. Effect of normal incidence

Spec.	Field	H_c (oe)	H_k (oe)	H_a (oe)
38.89	Yes	8.6	20.3	35
38.90	Yes	5.6	16	30
40.47*B*	No	11.1	—	22.4
40.47*D*	No	14.4	—	22.4

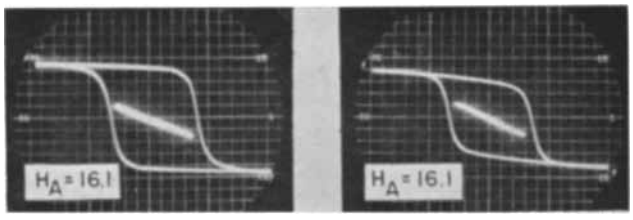

Fig. 2. 400 cps B-H loops for oblique incidence substrates: (left) plated in the field; (right) without the field. The transverse loop has been superimposed inside the easy direction loop. H_A is the applied field in the easy direction.

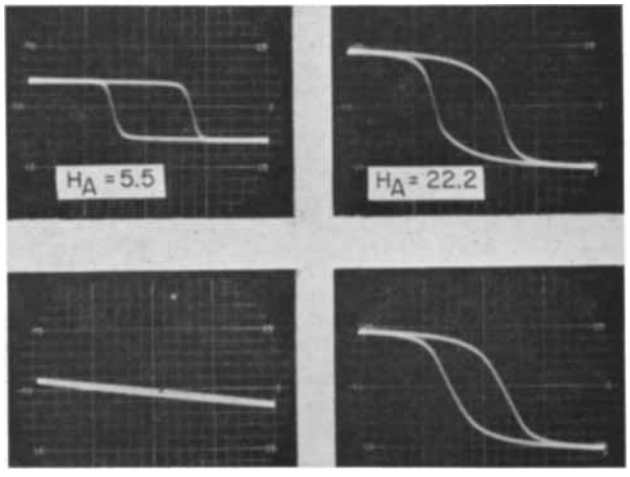

Fig. 3. 400 cps B-H loop for normal incidence substrates: (left) plated in the field; (right) without the field; (top) easy direction.

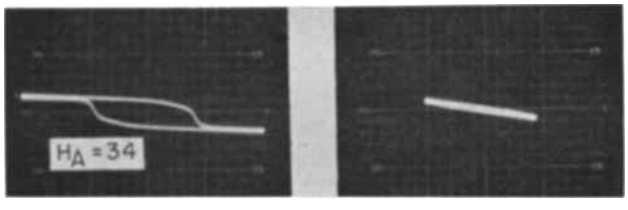

Fig. 4. 400 cps B-H loop of film with rotatable anisotropy: (left) easy direction; (right) transverse direction.

Manuscript received April 12, 1962. This paper was prepared for delivery before the Detroit Meeting, Oct. 1-5, 1961.

Any discussion of this paper will appear in a Discussion Section to be published in the June 1963 JOURNAL.

REFERENCES

1. J. B. Goodenough and D. O. Smith, "Magnetic Properties of Metal and Alloys," American Society for Metals, p. 332, Cleveland, Ohio (1959).
2. R. J. Heritage and M. T. Walker, *J. Elect. and Control*, **7** [6], 542 (1959).
3. D. O. Smith, *J. Appl. Phys.*, **32**, 70S (1961).
4. T. G. Knorr and R. W. Hoffman, *Phys. Rev.*, **113** [4], 1039 (1959).

5. *Ibid.*, ref. (1) p. 338.
6. J. S. Sallo and K. H. Olsen, *J. Appl. Phys.*, **32** [3], 2035 (1961).
7. *Ibid.* ref. (7), p. 332; E. C. Crittenden, Jr., A. A. Hudinoc, and R. I. Strough, *Rev. Sci. Inst.*, **22**, 872 (1951).
8. R. J. Prosen, J. O. Holmen, and B. E. Gran. *J. Appl. Phys.*, **32** [3], 915 (1961).

Electrodeposition of Thorium from Fused Salts into a Molten Zinc Cathode

Ralph E. Johnson

Atomics International, A Division of North American Aviation, Inc., Canoga Park, California

The nuclear industry has been interested in thorium chemistry since this metal constitutes the raw material in the breeding of U^{233}. A breeder reactor of this type may contain thorium in its core, as well as in the blanket. One step in the reprocessing of such a core or blanket could be the anodic solution of the impure thorium and the simultaneous deposition of pure thorium at the cathode. This is certainly not a new idea and has been applied with reasonable success in the past (1-7). Theoretically the electrolysis could take place in either an organic medium or a fused salt medium. The organic system has the advantage of room temperature operation and the disadvantage that complex organic reduction reactions compete with the deposition of the metal ion. The fused salt system operates at an elevated temperature, but the competition for electrons at the cathode is less severe.

Most workers in the field of thorium electrochemistry have selected the fused salt approach to the problem because of the relative simplicity of the electrochemistry (2). Thorium has been deposited from fused salts by a number of workers. Metallic thorium in the form of dendrites has been produced in this country by Gurklis and co-workers (3), and by Raynes and co-workers (4), in Russia by Evstyukhin (5), in Germany by Drossback and Neumayer (6), in Japan by Ogawa (7), and by others. The use of a molten metal cathode has been used previously in fused salt electrochemistry. Izbekov (8) used liquid tin and bismuth cathodes in fused salt electrolyses and Ogawa and his co-workers (9, 10) used a molten zinc cathode into which thorium was deposited. Murbach and Hansen (1) of this laboratory have also electrodeposited thorium into molten zinc. Thorium plated on a solid cathode yields a dendritic deposit which is loosely adherent and losses occur in the process of separation from the salt bath. A molten zinc cathode avoids this difficulty and it has been shown that zinc is easily removed from the thorium-zinc alloy (11).

In the work done to the present time on the electrodeposition of thorium from fused salt media, there has been little success in systematizing or improving the method. Smirov and Yushina (12, 13) have studied the cathode and anode process to some extent, but other works have been concerned only in trying to produce the metal. Gurklis (3) *et al.* report cathode current efficiencies ranging from 3-42%; Raynes (4) and his laboratory obtained 40-45%; and Evstyukhin (5) and co-workers found 75% entrained salt in the solid deposit. With the use of the molten zinc cathode, Ogawa (10) reports 30-60% cathode current efficiencies and Murbach and Hansen (1) were concerned with decontamination rather than efficiency.

In the present work, the technique of electrolytically depositing thorium into molten zinc from a fused salt has been perfected to the point that approximately 100% current efficiencies at the anode and cathode are obtained. The effect of the chlorination of the salt bath prior to electrolysis has been studied. The variation of current efficiency with thorium ion concentration and with current density has been established. In addition, a practical maximum concentration of thorium in zinc obtainable by this method has been established.

Experimental Method

Apparatus

The apparatus is shown in Fig. 1. The electrolysis cell was made from a tall, heavy-wall, Pyrex Dye beaker. The cathode electrical contact which entered from above was a ¼ in. tantalum rod which was threaded on the lower end. A mulite sleeve prevented contact between the salt and the tantalum, and a pin through the tantalum near the bottom retained the sleeve in position throughout the run. The thorium anode was suspended from a ⅛ in. tantalum rod. Care was taken to avoid getting the tantalum in the salt melt. Two short lengths of glass rod which fit into the holes of the stirring platform were fused to the bottom of electrolysis cell. The cell rested on the stainless steel stirring platform which was stirred from below.

The electrolysis cell was positioned in a vacuum furnace (Fig. 1). The main body of the furnace consisted of a 64-mm Vycor tube surrounded by a clamshell heater. The Vycor tube was sealed into water-cooled flanges with Apiezon W wax. The top flange had an exhaust valve leading to a bubbler and contained the rubber stopper through which the electrodes and thermocouple tube were lowered into the melt. The bottom flange was bolted to the vacuum system and sealed by a rubber O-ring. The system had facilities for placing it under vacuum or argon. The argon which was introduced is first passed over uranium chips at 500°C to remove oxygen.

Procedure

The electrolysis cell was prepared by cutting off the top of a 400 mel Dye Pyrex beaker and fusing short lengths of a 9 mm glass rod to the bottom of

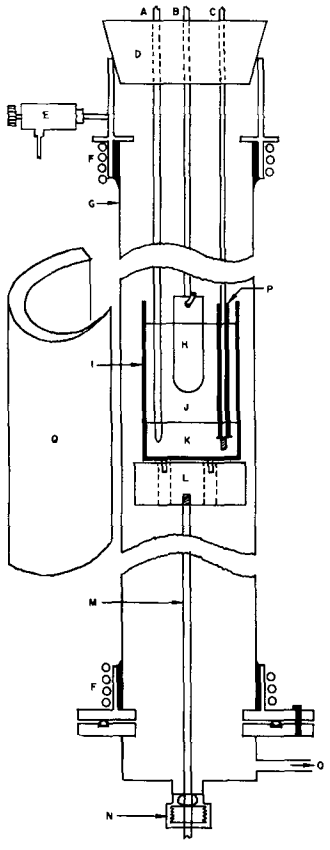

Fig. 1. Apparatus: A, alumina thermocouple well; B, tantalum anode hangar; C, tantalum cathode lead; D, rubber stopper; E, argon outlet valve; F, water-cooled flanges with Apiezon W seal; G, Vycor furnace tube; H, thorium anode; I, Pyrex beaker; J, fused salt; K, molten zinc cathode; L, steel platform; M, steel stirrer; N, O-ring seal for stirrer; P, ceramic insulator on cathode lead; Q, clam shell furnace around Vycor tube.

the beaker about 1½ in. apart. The anode was made by drilling a hole in a rectangular piece of pure thorium which was 6 x ½ x ⅛ in. in dimensions. The ⅛ in. tantalum was passed through the hole and made into a hook which was clamped against the thorium in the vise to insure contact. The cathode was prepared from a zinc ingot which weighed about 200g and the dimensions of which would permit lowering it into the beaker. A hole was drilled and tapped in the zinc to correspond to the threads on the end of the tantalum cathode contact.

The appropriate salt mixture was weighed into the cell. In all experiments, this was 150g LiCl, 150g KCl, and the desired amount of $ThCl_4$. The cell was then placed on the platform in the system, closed with a solid rubber stopper, and a vacuum was drawn overnight to remove most of the adsorbed water. The next morning argon was introduced into the system. The flow or argon was continued throughout the experiment. The uranium trap and the furnace were turned on. After the salt had melted, the solid rubber stopper was exchanged for one which held the electrodes and thermocouple tube. The thermocouple was introduced into the tube, and the zinc electrode was lowered into melt. After the zinc had melted, the tantalum contact was lowered to a point just above the bottom of the cell. This insured that the tantalum was under the surface of the zinc. The stirring motor was turned on so that the cell rotated about 40 rpm. When the temperature had reached 600°C, which was the temperature of all runs, the thorium was lowered into the melt to a depth of about ¾ in. and the current turned on. After a predetermined length of time, electrolysis was discontinued, the melt cooled, and the zinc-thorium ingot dissolved in acid and submitted for analysis.

Results

In the earlier experiments, many variations in apparatus and technique were used. Various crucible materials were used, several salt baths were employed, induction heating of the zinc as a means of heating and stirring the zinc was tried, and compound purification was attempted. High current efficiency was achieved only when a suitable stirring mechanism had been developed.

In a number of experiments, an effort was made to plate a relatively large amount of thorium into zinc. The solubility of thorium in zinc at 600°C is near 1 w/o (14). In this work, alloys with a much higher concentration of thorium were obtained with the highest having 16.2% thorium.

A series of experiments was run to determine the effect of concentration of $ThCl_4$ on the cathode current efficiency. Results are listed in Table I.

Another series was run to determine the effect of current density on the current efficiencies at the electrodes. The 15 w/o $ThCl_4$ salt mixture was chosen as being the optimum concentration based on the previous series of runs. The diameter of the cathode was 6 cm which gives 28.3 cm^2 area, and at the anode there was 1 $in.^2$ or 6.45 cm^2 area. These data are given in Table II. Experiment No. 94 was a blank to determine the weight loss at the anode in the absence of electricity. Each run was made for a duration of time necessary to deposit 19.5g of thorium according to the reaction

$$Th^{++} + 4e \rightarrow Th^{\circ}$$

For each run this was 32,400 coulombs.

The anode and cathode current efficiencies have been given without the correction for the blank run No. 94 since the effect is smaller than the inherent error.

As can be seen from Table I, the highest concentration of thorium in zinc attained was about 16%. It is possible to obtain this high a concentration even though the solubility is of the order of 1% because of the formation of Th_2Zn_{17} which precipitates. About 15% thorium represents a practical limit under the

Table I. Cathode current efficiency dependence on $ThCl_4$ concentration

Run No.	w/o $ThCl_4$	Current density, amp/cm^2	Current efficiency, %
61	2.5	0.11	81.6
59	5.0	0.11	80.0
60	10.0	0.11	55.2
57	11.1	0.11	92.4
62	15.0	0.11	106.6
63	20.0	0.11	80.5
64	25.0	0.11	81.6
65	30.0	0.11	69.3

Table II. Current efficiency as a function of current density

Run No.	Amp	Cathode C. D., amp/cm²	Anode C. D., amp/cm²	Theor. amt Th, g	G Th cathode	G Th anode	Cathode C. E.	Anode C. E.
94	0.0	0.0000	0.0000	0.0	0.022	0.7	—	—
91	0.5	0.02	0.08	19.5	17.7	19.8	91	101
82	1.0	0.04	0.15	19.5	18.0	19.0	92	97
90	1.5	0.05	0.23	19.5	21.0	20.2	107	103
89	2.0	0.07	0.31	19.5	18.7	20.1	96	103
87	2.5	0.09	0.39	19.5	18.4	19.1	94	98
86	3.0	0.11	0.42	19.5	19.5	19.9	100	102
85	3.5	0.12	0.54	19.5	18.4	19.8	94	101
84	4.0	0.14	0.62	19.5	20.2	19.9	103	102
83	4.5	0.16	0.70	16.2	17.3	16.2	106	100
81	5.0	0.18	0.76	19.5	20.1	19.8	103	101
92	10.0	0.35	1.5	19.5	19.5	20.8	100	106
93	15.0	0.53	2.3	19.5	20.4	20.9	104	107

conditions of this experiment even though the theoretical limit is 29.4% thorium with a cathode of pure Th_2Zn_{17}. At about 15% thorium, the alloy becomes paste-like, and further increases in the thorium concentration would stop the stirring action. Under these conditions of stirring, the zinc-thorium ingot has a smooth surface, and all of the thorium is under the surface. When stirring is omitted, thorium either is deposited as a layer on the zinc or dendritically grows out of the surface of the zinc.

The results of the experiments in which the $ThCl_4$ concentration was varied between 2.5 and 30%, indicate that the optimum concentration was 15 w/o $ThCl_4$ in a LiCl-KCl-$ThCl_4$ bath. It is felt that the 106% current efficiency figure is within the accuracy of the experiments. The difficulty encountered in maintaining a constant current over several hours is considerable. This lack of precision is also characteristic of the results of the series on current efficiency as a function of current density. In this case, the weight loss at the anode was determined simply by weighing before and after, while at the cathode, the solution was analyzed for thorium by first precipitating the thorium away from the zinc as a hydroxide and then reprecipitating the oxalate which was dried and weighed. Higher current densities were not possible with the power supply used in these experiments.

A technique has been established for the electrodeposition of thorium from a fused LiCl-KCl-$ThCl_4$ bath with a molten zinc cathode and thorium anode in which approximately 100% current efficiencies are obtained at both the cathode and anode. The most important condition in the process is the stirring of the zinc. The system developed here requires that the zinc surface be broken by the stirring action. It has been shown that 15% or so of thorium in zinc can be obtained readily by this technique. The concentration of $ThCl_4$ in the bath, which gave the highest current efficiencies, has been found to be 15% and current efficiencies at the electrodes are independent of current densities within the range studied. It was not necessary to purify chemicals or metals in this work in order to obtain maximum efficiencies.

Acknowledgment

The author wishes to acknowledge the efforts of W. D. Turner, who assisted in the laboratory work, and the work of the personnel of the Analytical Unit who performed the thorium analyses.

Manuscript received April 3, 1962

Any discussion of this paper will appear in a Discussion Section to be published in the June 1963 JOURNAL.

REFERENCES

1. E. W. Murbach and W. N. Hansen, *Ind. Eng. Chem.*, **51**, 177 (1959).
2. W. N. Hansen, North American Aviation-4885-Contract No. AT(11-1)-GEN-8 (June 15, 1960).
3. J. A. Gurklis *et al.*, Battelle Memorial Institute-781-Contract No. W-7405-eng-92 (Nov. 4, 1952).
4. B. C. Raynes *et al.*, *J. Metals*, **9**, 1373 (1957).
5. A. I. Evstyukhin *et al.*, *Met. i Metalloved Chistyheh Metal, Sbornick Nauch Rabot*, **1**, 7 (1959).
6. P. Drossbach and F. Neumayer, *Z. Elektrochem.*, **63**, 516 (1959).
7. Y. Ogawa *et al.*, *Nippon Kogyo Kaishi*, **73**, 109 (1957).
8. V. A. Izbekov, *Ukrain Khim Zhur.*, **20**, 14 (1954).
9. Y. Ogawa *et al.*, *Nippon Kogyo Kaishi*, **74**, 311 (1958).
10. Y. Ogawa *et al.*, *Trans. Natl. Research Inst. Metals (Tokyo)*, **2** [1], 37 (1960).
11. R. E. Johnson and J. D. Chilton, North American Aviation-5506-Contract No. AT(11-1)-GEN-8 (Dec. 1, 1960).
12. M. V. Smirnov and L. D. Yushina, *Fzvest, Akad Nauk, SSSR, Otdel Khim Nauk*, 1285-93, (1956).
13. L. D. Yushina and M. V. Smirnov, *Doklady Akad Nauk SSSR*, **115**, 949 (1957).
14. "Reactor Fuel Reprocessing," Vol. 3, No. 2, p. 28 (1960).

Inert Electrode Behavior of Tin Oxide-Coated Glass on Repeated Plating-Deplating Cycling in Concentrated NaI-AgI Solutions

J. Mantell and S. Zaromb[1]

Research Laboratory, Philco Corporation, Blue Bell, Pennsylvania

The theory and design principles of the Reversible Electroplating Light Modulator (RELM) are discussed at length in preceding papers (1, 2). The feasibility of RELM is, of course, contingent upon the existence of an electrochemically inert transparent conductor. Evaporated thin films of noble metals such as Pt or Au could not withstand more than a couple of deplating pulses exceeding 2v. Fortunately, however, conductive tin oxide coatings on glass proved much more resistant. The present experiments were performed with the simplest type of RELM, similar to (though not identical with) that shown in Fig. 2a of ref. (2). The actual cell design is shown in Fig. 1.

The electrolyte consisted of 1M AgI plus 1M NaOH in 5M NaI, the OH^- ions serving to convert any colored I_3^- ions into colorless IO_3^- ions. Because of complexing between the AgI and I^- ions, the electrolyte resistivity appeared higher ($\simeq$10 ohm-cm) than expected for 5M NaI solutions.

The cell resistance appeared to be in rough agreement with calculated values, *i.e.*, of the order of 15 ohms, as deduced from RC time constant curves recorded with a Type 545 Tektronix oscilloscope. With applied voltages of 4-22v, the resulting plating and deplating times τ were found to be of the order of 10 msec, in agreement with the calculated times

$$\tau \simeq Q/I = Q/(V/R) \qquad [1]$$

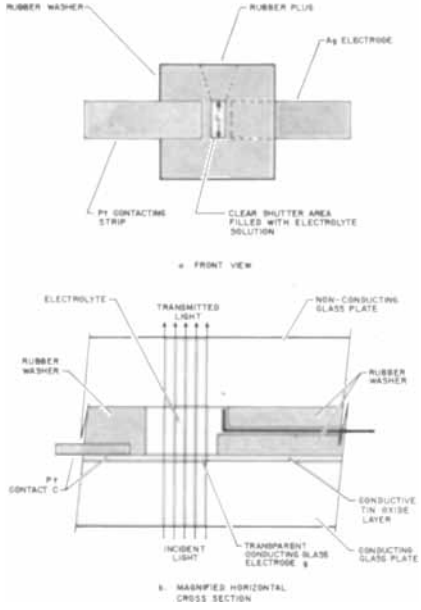

Fig. 1. Design of the reversible electroplating cell used in the present study.

[1] Present address: Research and Advanced Technology Department, Electronic Systems and Products Division, Martin-Marietta Corporation, Baltimore, Maryland

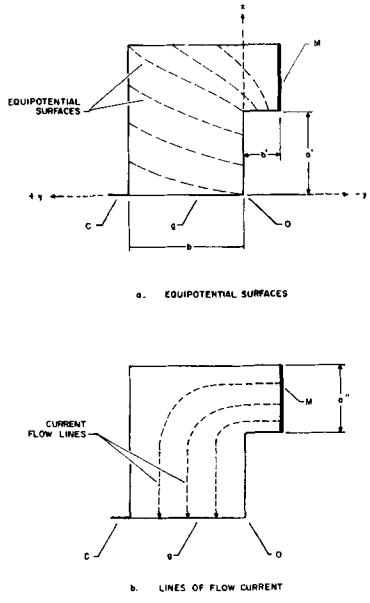

Fig. 2. Schematic representation of equipotential surfaces, current flow lines, and geometric design parameters of the electrode-electrolyte configuration used in Fig. 1b.

for square wave pulses or with the corresponding RC time constant values for condenser discharges. Both of these types of pulses were applied in both directions for a total of more than 1000 plating-deplating cycles without any sign of deterioration of the conductive tin oxide coating. A slow apparent deterioration of the cell was traced to the evaporation of the electrolyte and resulting solute precipitation of the saturated solution after more than 5 days of intermittent cycling.

Extrapolation of the results of ref. (2) shows that for fair plating uniformity, the dimensions of Fig. 2 should satisfy the conditions:

$$a' \geqq b^2/2k \qquad [2]$$

$$a'' \simeq b^2/2k \qquad [3]$$

and

$$b \leqq k \qquad [4]$$

where

$$k = \rho_e/\rho_g \qquad [5]$$

is the ratio of electrolyte resistivity ρ_e to glass surface resistivity ρ_g. The actual cell dimensions and resistivities were approximately $a' \simeq a'' \simeq 0.05$ cm, $b \simeq 0.3$ cm, $b' \leqq 0.1$ cm, $\rho_e \simeq 10$ ohm-cm, and $\rho_g \simeq 40$ ohms/square. These values fall just outside the limits set by Eq. [2] through [5]. Hence, the resulting plating uniformity could be expected to be poor or barely fair. The longer dimension L of the

Table I. Comparison of observed and calculated optical density changes*

Capacitance C, μfd	Condenser voltage, v	Plating charge 10^3Q, coulombs	No. of tests*	Optical density change: Average $\delta_{av.}$	Maximum $\delta_{max.}$	Calculated $\delta_{calc.}$
1000	6.1	6.1	3	0.27	0.32	0.9
1000	4.2	4.3	200	0.14	0.28	0.6
2000	4.3	8.6	66	0.39	0.80	1.2
2000	6.1	12.2	60	0.67	0.96	1.8

* Only those tests are listed here where the charge pulse Q was due to a condenser discharge. The square wave pulses used in most of these tests had serious uncertainties in the value of Q.

plated area was 0.7 cm. Hence, the plated area A was 0.2 cm^2.

According to Fig. 1 of ref. (1), the theoretical ratio of the optical density change δ to plating charge density q_d should be approximately

$$\delta/q_d \simeq 30 \text{ cm}^2/\text{coul} \quad [6]$$

for Ag plating solutions free of I_3^- ions. Hence, for $A \simeq 0.2$ cm^2, a total plating charge of Q coulombs should yield

$$\delta \simeq 150\,Q \quad [6']$$

As shown in Table I, the actual values of δ were usually between 25% and 50% of the theoretical ones. This is attributed partly to poor plating uniformity (related to excessive shutter width b) and partly also to the frequent presence of an appreciable concentration of oxidizing substance (IO_3^- ions formed by application of an excessive deplating charge) near the glass electrode.

In view of the latter factors, these preliminary results seem to be in fair agreement with theoretical expectations. The ability of the tin oxide coating to withstand the numerous relatively drastic plating-deplating pulses without any sign of deterioration renders the RELM promising for practical applications. Of course, the present experiments were performed in alkaline solutions in which the formation of nascent hydrogen (known to reduce the tin oxide) is least likely to occur. In neutral or acidic solutions greater care may have to be taken to operate under conditions of 100% plating current efficiency.

Manuscript received Feb. 12, 1962.

Any discussion of this paper will appear in a Discussion Section to be published in the June 1963 JOURNAL.

REFERENCE

1. S. Zaromb, *This Journal*, **109**, 903 (1962).
2. S. Zaromb, *ibid.*, **109**, 912 (1962).

Vapor Growth of Twinned Germanium Platelets

C. Pritchard[1]

Research Laboratories, Westinghouse Electric Corporation, Pittsburgh, Pennsylvania

Twinned germanium platelets have been formed from the vapor phase by a mechanism which appears similar to that governing the growth of dendrites from a supercooled melt. Regularly shaped and of {111} habit, the platelets are thin and flat with the twin planes extending parallel to the main faces. This is characteristic of dendrites of the diamond lattice materials, and both Wagner (1) and Hamilton and Seidensticker (2) have pointed out how the twins are essential to this type of growth. At least two closely spaced parallel twin planes are necessary. Together they form a set of self-perpetuating grooves where they reach the surface of the growing crystal. Nucleation takes place at these grooves more easily than elsewhere, and the crystal thus expands predominantly in their plane without appreciably thickening.

Within this preferred plane dendrites grown from the melt also exhibit preferred directions of growth (<211>) and propagate as long flat ribbons. This is partly a consequence of the thermal geometry which becomes set up in the system. Growth is rapid and becomes controlled by the diffusion of the liberated latent heat away from the growing interface. A more isotropic growth resulting in platelet formation has, however, been observed for germanium crystallizing from solution (3). Much slower than growth from the melt, it is governed less by the diffusion of heat from the crystal than by that of solute to it.

[1] Present address: English Electric, Leicester, England.

Platelet formation from the vapor is found to occur when germanium is heated in evacuated quartz capsules which have not been baked out prior to sealing off. The platelets nucleate at the quartz walls and grow there in great profusion, clinging by one edge and projecting into the capsule. They are flat, very thin, and regular in outline. Crystals up to a millimeter across have been obtained not more than 5μ in thickness. Both the main faces and the bounding edge facets are {111} planes and the edges consequently trace out <110> directions around the platelets. Thus, as illustrated by the examples in Fig. 1, their shape is either that of an equilateral triangle or some segment of a hexagon. In Fig. 1a two triangles are shown, one lying on the other. The smaller is tilted slightly and so appears dark under the normal illumination. Figure 1b is typical of the hexagonal type crystals. The longest edge, which is noncrystallographic in most cases, is that from which the growth takes place and by which the crystal is found attached to the quartz walls. Figure 1c is a crystal which points out directly the similarity between platelet and dendrite growth. From one apex of the triangle a tip is protruding in the <211> preferred growth direction much as that of a dendrite growing into a melt.

Twins have been revealed in these platelets by cross sectioning, polishing, and etching, and also by the fracturing technique of Faust and John (4). Etching is possible only on the thicker specimens,

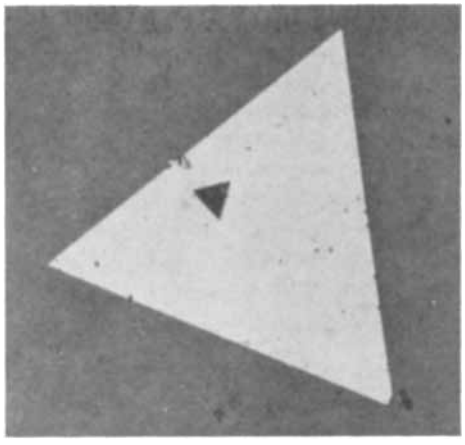

Fig. 1a. Vapor grown germanium. Two triangular platelets. Magnification 100X.

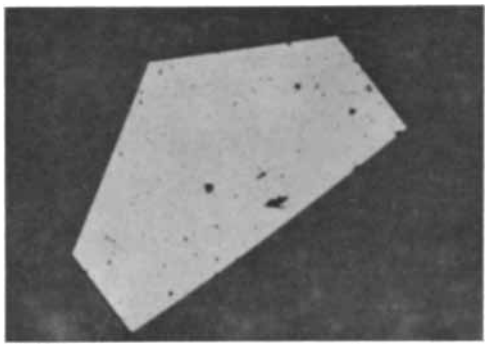

Fig. 1b. Hexagonal type platelet. Magnification 100X

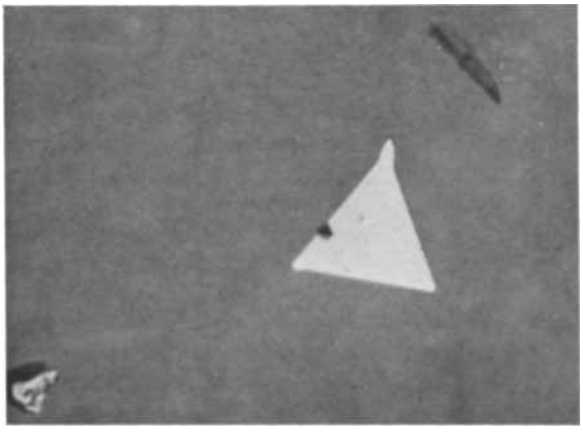

Fig. 1c. Triangular platelet with a "dendrite" growing from one apex. Magnification 200X.

and Fig. 2a shows the twin planes revealed in this way in a platelet about 20μ thick. A twin plane shown up by fracturing is illustrated in Fig. 2b. As revealed by either technique the twins in these crystals are always confined within a lamella which is at most 0.5μ thick. Individual twin planes cannot be resolved and, in particular, it has not been possible to tell from these observations whether there are more than one present or not. When fractured under a razor blade the material does tend to cleave along <110> directions, but the cleavage or fracture surface is invariably at right angles to the main face. This approximates the {211} cleavage discussed by Faust and John (4), and the {111} cleavage by which twins can most easily be resolved and counted was never obtained. However, it can be seen from in-

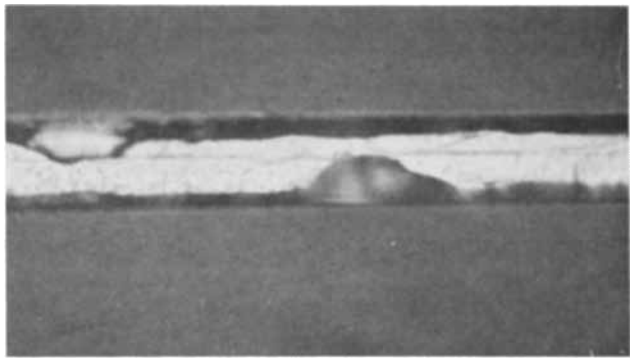

Fig. 2a. Twin planes revealed by etching a polished cross section. Magnification approximately 500X.

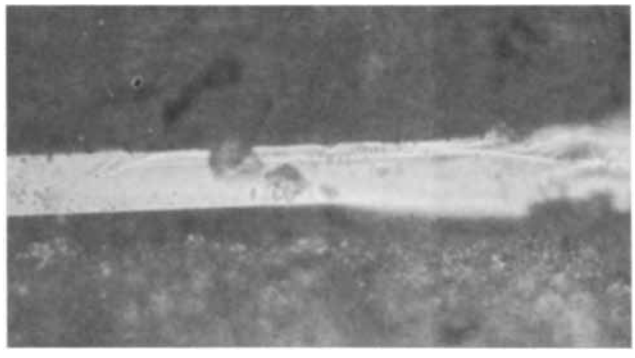

Fig. 2b. Twin planes revealed in a fractured cross section. Magnification approximately 500X.

spection of the edges of the platelets that in most cases there are an even number of twin planes in the crystals. As mentioned above the edges are themselves {111} planes and, were there an odd number of twins, they would be ridged and grooved according to the sense of the twinning operation. Some platelets are indeed ridged in this way, but the great majority have edges which are planar, sloping all in the same sense around the triangular crystals and alternately inwards and outwards around the edges of the hexagons. Thus, except for the few indeterminate examples, we can say that these platelets contain at least two twin planes and that the requirements of the twin plane growth mechanism are met.

About half of the platelets exhibit growth steps which indicate that new growth has nucleated on the main faces themselves at the edges of the fully formed crystal. The steps usually form at the outermost and growing edges and then sweep back toward the edge clinging to the quartz. Similar growth in germanium dendrites has been pointed out by Holmes (5). An early stage is illustrated in Fig. 3a where a rampart has formed round all three sides of a triangle. The rampart is about 1.5μ high, increasing the thickness of the platelet from 3.5 to 5μ. This particular triangle has grown to nearly 0.8 mm on a side before the edge growth has begun. Figure 3b illustrates the later stages typical of most of the overgrowth which has been observed. The growth steps have lost any crystallographic nature they might have had and have taken on the curved character as shown. The edge facets of the crystals retain their {111} orientations throughout and, presumably, nucleation at the twin planes is still going on.

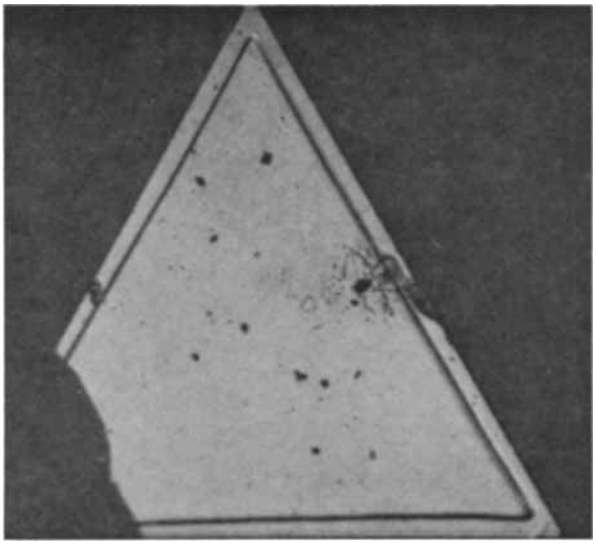

Fig. 3a. Triangular platelet with "rampart" type edge growth. Magnification 100X.

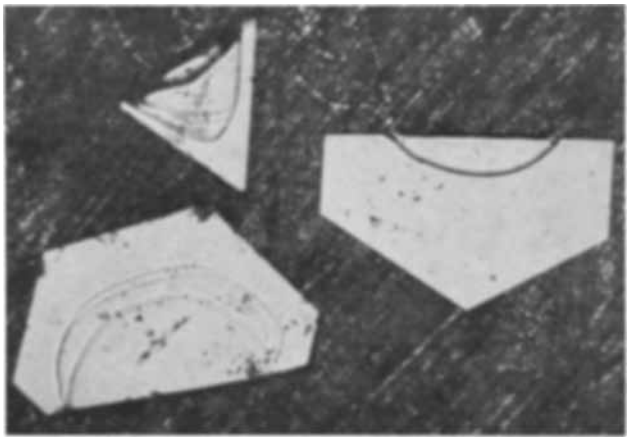

Fig. 3b. Platelets with growth steps arising from edge nucleation. Magnification approximately 100X.

The transport of the germanium to the walls of the capsule from the Czochralski slices sealed off inside must be by means of residual gases left in the system. Halides are known to transport germanium, and traces may remain from the aqua regia used to clean the quartz or from the CP4 used to etch the lapped Czochralski slices. No growth occurs if the system is first thoroughly degassed by baking out under vacuum. The capsules are about 10 cm long by 7 mm ID, and they are heated in a small tubular furnace. The temperatures used are 800° or 900°C, and the largest crystals have been formed in about 80 hr heating. Deposition of the platelets is more or less uniform over the whole length of the capsules except for rather more profuse growth at the two ends. These, in turn, face the ends of the furnace tube which are open to the cold surroundings, but apart from this there is no evidence of any controlling temperature gradient. Instead, it is considered that the transport is governed by the thermal cycling about the control temperature. Control is by an on-off device and the temperature cycle has an amplitude of about 4°C. Germanium which is dissolved into the transporting gas at the higher temperature is then deposited at the lower at any suitable nucleation site. Marinace (6) has discussed a disproportionation reaction between germanium and, in his case, iodine which has just this property of dissolving germanium at one temperature and depositing it at a lower.

Acknowledgments

The author wishes to thank Dr. H. F. John for helpful discussions. This work was done under Contract No. AF 33(600)39378 Wright Air Development Centre.

Manuscript received May 17, 1962.

Any discussion of this paper will appear in a Discussion Section to be published in the June 1963 JOURNAL.

REFERENCES

1. R. S. Wagner, *Acta Met.*, **8**, 57 (1960).
2. D. R. Hamilton and R. G. Seidensticker, *J. Appl. Phys.*, **31**, 1165 (1960).
3. J. W. Faust and H. F. John, Private communication.
4. J. W. Faust and H. F. John, *This Journal*, **107**, 562 (1960).
5. P. J. Holmes, "Metallurgy of Elemental and Compound Semiconductors," p. 161, Interscience (1961), Report on 1960 Boston Conference.
6. J. C. Marinace, *IBM J. R.&D.*, **4**, 248 (1960).

Open Tube Epitaxial Synthesis of GaAs and GaP

S. W. Ing, Jr., and H. T. Minden[1]

Electronics Components Division, General Electric Company, Syracuse, New York

In 1960 Antell and Effer (1) demonstrated the synthesis of III-V compound semiconductors by the reaction of metal halides in a sealed tube. Since then a great deal of work has been done on the halide transport, synthesis, and epitaxial deposition of these compounds (2-4). Much of this work has involved the use of the synthesized compounds as the source for the epitaxial deposition, and here there are certain disadvantages. The process of melt synthesis (to obtain the source) is fairly difficult, especially in the case of GaP. Moreover, high temperatures must be used to effect these synthesis, so that many impurities are introduced from the furnaces and the containers (5). It has been shown in this laboratory that these impurities will carry over to the deposit in unpredictable ways.

Holonyak *et al.* (4) deposited epitaxial GaP and GaAs from the elements; they used halogen trans-

[1] Present address; Sperry Rand Research Center, Sudbury, Massachusetts.

port in sealed tubes both for epitaxial deposition and for the synthesis of large GaP crystals. Blakeslee (6) has also used the sealed tube halogen transport technique to synthesize GaAs crystals. In this work an open tube system was used to effect the synthesis and epitaxial deposition; results were obtained much more quickly and easily with this system than by the earlier closed tube method.

The chemistry of the system deserves brief mention. HCl gas is passed in an H_2 stream over heated arsenic or phosphorous and over gallium at a higher temperature. An epitaxial deposit is obtained on a seed which is held at a lower temperature than the gallium. A subchloride of gallium is formed at the source

$$Ga + xHCl \rightarrow GaCl + (1/2)\, x\, H_2 \qquad [1]$$

The subchloride disproportionates at the seed

$$3GaCl_x \rightarrow (3 - x)\, Ga + xGaCl_3 \qquad [2]$$

These equations and processes are similar to those described by Williams (2). When the gallium deposits in the presence of arsenic or phosphorous vapor, the compound is formed in an atom for atom manner (4). Epitaxial deposition was obtained over a range of temperature, flow rate, etc., but no concerted effort was made to determine those values of the deposition parameters which would yield optimum growth rate, uniformity, etc. The work was undertaken to demonstrate the feasibility of the method and outline the effective region of operation.

The experimental arrangement is shown in Fig. 1. H_2 was metered through a flowmeter, 2, and passed through a Deoxo unit, 3, and a drying column filled with molecular sieve pellets, 4. HCl gas was metered through another flowmeter, 5, and dried in a trap, 6, which was immersed in dry ice. Teflon tubing and stainless steel fittings were used exclusively in the HCl line and wherever possible in the H_2 system. The argon gas was used as a purge. A 24 in. long two-zone furnace was used, and the temperature of each zone was controlled by a thermocouple (TCA and TCB) located next to the windings. A typical temperature profile is shown in Fig. 1. The reactions were carried out in a 1 in. ID quartz tube. A quartz boat, 7, containing the arsenic or phosphorous was located in the tube outside the upstream mouth of the furnace and was heated by wrapping heating tape, 10, around the exterior of the quartz tube. The quartz boat containing the gallium, 8, was located at the center of the hot zone, A. The seed, 9, was held on a small quartz plate which was sealed to the closed end of a quartz tube. This tube served both as a handle and as a shield for the seed temperature monitoring thermocouple, TCS. The seed holder was supported by a ring stand which could be moved back and forth to position the sample in the desired temperature region of the furnace.

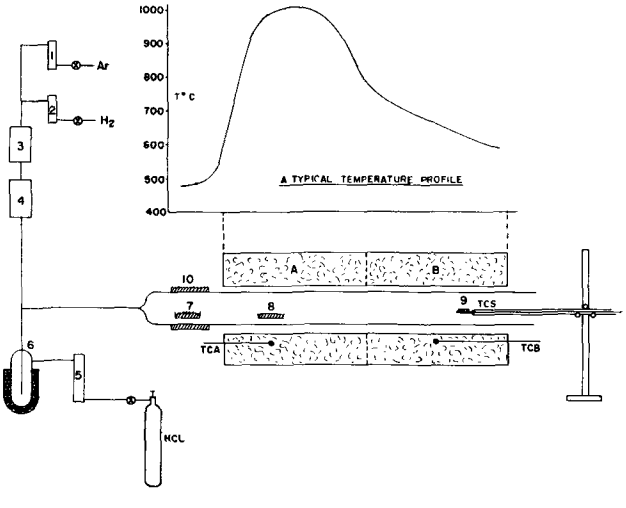

Fig. 1. Furnace and gas flow system for the epitaxial synthesis of GaAs and GaP.

The seed samples were lapped flat and washed in trichloroethylene, acetone and deionized water. The GaAs wafers were treated with a warm 1:1 H_2O_2-H_2SO_4 chemical polish, while the GaP was etched in a warm mixture of 1:1 HCl and HNO_3.

With the furnaces at temperature and Ar flowing, the seed was placed on the holder and introduced into the reaction tube. The H_2 was turned on and the Ar was shut off. The seed was allowed to come to temperature and positioned carefully so as to obtain the desired temperature. The HCl was turned on and the sample repositioned to maintain the required temperature. From time to time during the run the temperature was carefully monitored. At the end of the run the HCl was turned off, the Ar turned on, and the H_2 shut off. When the $GaCl_3$ fumes stopped coming from the mouth of the tube, the sample was moved progressively to cooler zones. The sample was held in the tube until the H_2 was purged. (Often the H_2 burned at the end of the tube during the run, and the dying of this flame was evidence of purge.) The sample was then removed.

In order to determine definitely whether deposition had taken place, the seed was weighed to 0.1 mg before and after the run. In addition, microscopic examination and x-ray measurements were made to determine the nature of the deposited layer. Epitaxial deposition usually gave rise to geometrical surface patterns which had the symmetry of the seed orientation. If the deposit was not epitaxial, *i.e.*, polycrystalline, crystallites were observed which had no symmetrical orientation with respect to each other.

The H_2 flow rate, the HCl flow rate, and the seed temperatures formed a related set of parameters which affected rate of deposition and the nature of the layer. GaAs deposited at a rate of about 0.5 μ/min on (110) oriented GaAs seeds which were held at 750°C; the H_2 flow rate was about 50 cc/min and the HCl flow rate was about 3 cc/min. The deposition rate increased when the HCl flow rate was increased. When the H_2 flow rate was increased to 500 cc/min, etching rather than deposition occurred if the seed temperature was above about 680°; this held true even when the HCl flow rate was increased to as much as 50 cc/min. Below this temperature deposition took place at rates from 0.1 to 1 μ/min.

At the high flow rates deposition occurred both on the seed and on the quartz on which the seed rested. It will be noted from Fig. 1 that there was a temperature gradient in the deposition region. The maximum temperature of deposition was delineated by an abrupt end of the deposit on the quartz sample holder in the high-temperature direction. It should be noted, however, that at the lower flow rates (*e.g.*, 50 cc/min for the H_2) deposition on the sample holder near the seed did not necessarily accompany deposition on the seed.

It will be noted that the effect of increasing the H_2 carrier flow rate was simply to decrease the efficiency of the process. Presumably since the gas mixture was in contact with the Ga source for a shorter length of time at the higher flow rates, the ratio of unreacted HCl to gallium subchloride arriving at the seed was higher. Hence the rate of deposition by disproportionation was lowered relative to the rate of etching the seed by the HCl.

The deposition rate of GaAs appeared to depend on crystallographic orientation of the substrate. When smooth polycrystalline seeds were used, some grains grew faster than others. No detailed study was made, however, on the effect of seed orientation on growth rate. For (110) and (112) oriented seeds the variation in thickness of the deposited layer across the face of the crystal was within ± 10%, while layers on the (111)B surface tended to be nonuniform in thickness at growth rates which exceeded 0.5 μ/min.

The source temperatures were not particularly critical. When the As was below 450°, no deposition of GaAs took place on the seed; when the Ga was below 900° there was no deposition and the seed was etched. Above these temperatures for both the As and the Ga the deposition rate was not observed to be dependent on the source temperature. During some of the runs the Ga melt was observed, and it was instructive to see that there was no skin of solid GaAs. On the other hand, such a skin was always present after the melt cooled; undoubtedly, some As was dissolved in the Ga melt during the run. The point is that for the deposition of GaAs by the disproportionation reaction a solid phase of the compound is not needed at the source.

Two factors affected the nature of the GaAs deposits. When the seed temperature was below about 660°, the deposit was nonepitaxial. Also when air was allowed to diffuse back (at low H_2 flow rates) from the tube exit to the seed, the deposition rate increased, but again the deposit was nonepitaxial.

The Van der Pauw (7) method was used to make Hall coefficient and resistivity measurements on some of the epitaxial layers. These layers were deposited on (111) oriented substrates which had a resistivity of 10^6 ohm-cm. The Hall coefficient was negative and $-1/Re$ ranged from 1×10^{17} to 4×10^{17} cm^{-3} while R/ρ was 2400-2800 cm^2/volt-sec.

For the deposition of GaP very similar results were obtained, although this material was not as extensively studied as GaAs. Here, as with GaAs at H_2 flow rates of about 500 cc/min the maximum seed temperature at which deposition took place was about 680°C. These facts, along with the absence of a solid phase at the gallium source strongly suggested to the authors the hypothesis that the basic deposition reaction involves only the Ga (see for example Eq. [2]). In general, deposition rates were somewhat lower for GaP than for GaAs, although they were of the same order of magnitude. Deposition rates varied from grain to grain on polycrystalline samples, but here again no quantitative study was made of the effect of orientation. The Ga source temperature was about the same as for GaAs, but the phosphorous source temperature was not measured.

GaP was also synthesized by using PCl_3 as the phosphorous source. H_2 was bubbled through the PCl_3 which was at room temperature, and the mixture was passed over Ga at 1000°. No HCl was used in these experiments. Fairly large bright orange needles and small crystallites were formed downstream from the Ga at 850°-890°. Further downstream from 850° to 600° the deposition took the form of fine orange and yellow hair. The formation of similar needles and crystallites were also observed to accompany the epitaxial deposition of GaAs.

Several heteroepitaxy experiments were performed. GaAs was deposited epitaxially on a (111) Ge seed. Both x-ray and electron diffraction measurements showed the deposited layer to be a (111) oriented single crystal. The epitaxial layer was found by chemical etching to have the A (Ga) face up. GaP was also epitaxially deposited on GaAs. In these experiments (110) seeds were used. Although the deposits often appeared gray by reflected light, sectioning revealed that the layers had the characteristic yellow color of GaP. Some of the deposited layers were red, however, even though all the GaP layers which were deposited on GaP were yellow. These results are in accord with those of Holonyak *et al.* (4) who obtained yellow and red deposits of GaP on GaAs in closed tube epitaxial experiments.

Manuscript received March 16, 1962; revised manuscript received June 8, 1962.

Any discussion of this paper will appear in a Discussion Section to be published in the June 1963 JOURNAL.

REFERENCES

1. G. Antell and D. Effer, *This Journal*, **107**, 252 (1960).
2. Much of the more recent and more definitive work was reported at The Electrochemical Soc. Electronics Div. Mtg. October 1961, Detroit. See: F. V. Williams and R. A. Ruehrwein, Abstract 141; V. J. Lyons and V. J. Silvestri, Abstract 140; R. R. Moest and B. R. Shupp, Abtract 143; C. J. Frosch and P. W. Foy, Abstract 142.
3. R. L. Newman and N. Goldsmith, *This Journal*, **108**, 252 (1961).
4. N. Holonyak, Jr., D. C. Jillson and S. F. Bevacqua. Trans. AIME Tech. Conf. on Semiconductor Mat'ls., Los Angeles, August 1961. (to be published, Interscience Press).
5. See for example, E. Arnold, J. Black, and S. Weisberger, The Electrochemical Soc. Mtg. Electronics Div. October 1959, Columbus, Ohio.
6. A. E. Blakeslee, Unpublished work.
7. Van der Pauw, *Phillips Research Rept.*, **13**, 1 (1958).

Brief Communications

The Effect of Electrolyte Composition on the Anodic Oxidation of Zirconium

N. J. M. Wilkins

Metallurgy Division, United Kingdom Atomic Energy Authority,

Atomic Energy Research Establishment, Harwell, Berkshire, England

In the course of current work on the growth of thin uniform oxide films on zirconium in high-temperature steam and oxygen, the color produced on individual crystals by optical interference is being measured by recording the wavelength of reflection minima at a fixed angle of incidence. To relate color to thickness or weight of thermal films, the color/weight gain relation of anodic films on zirconium has been determined.

Published data offered no reliable basis for this relation. The work of Young (1) showed the danger of attempting to use voltage/thickness and voltage/color data unless all conditions (procedure, current, temperature, electrolyte, concentration, etc.) were closely specified. The color/weight gain relation was therefore obtained by measuring the weight gain and reflection minima of large anodized specimens of annealed and chemically polished Van Arkel zirconium. Films of uniform color were obtained by anodizing at 10 ma/cm^2 and then allowing the current to decay to ~0.2 ma/cm^2 at the required voltage; prolonged oxidation at low current density resulted in the color varying from grain to grain. The films formed in three different electrolytes (0.2*N* H_2SO_4, saturated ammonium borate, 1% wt/v KOH) at room temperature fitted the same series of smooth curves when various orders of reflection minima were plotted against weight gain (Fig. 1). In contrast the voltage/color relation for the different electrolytes indicated a greater difference in the voltage/thickness relation than seems to have been reported previously (2). This is illustrated in Table I, in which the weight gain is derived from color using the relation in Fig. 1, with support from capacity measurements, the reciprocal capacity of a film being taken as a measure of its thickness. Weight/voltage and capacity/voltage relations vary with solution, but the capacity/weight relation is constant.

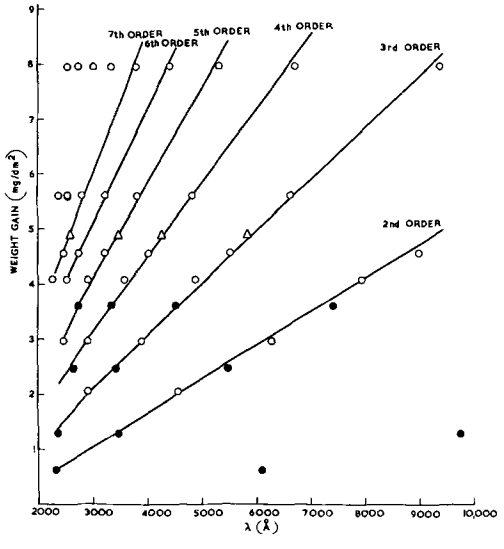

Fig. 1. Weight gain vs. reflection minima for anodized zirconium; ○, 1% KOH; ●, 0.2*N* H_2SO_4; △, saturated ammonium borate.

These results are most readily explained if only the voltage/thickness relation varies with electrolyte. If the density, refractive index, and dielectric constant of the film were to vary, they would have to do so in a most improbable compensating manner to fit the observed weight, optical, and capacity measurements. To determine whether this difference in the thickness/voltage relation resulted from changes within the film or at the film-electrolyte interface, experiments were performed in which specimens were transferred from one electrolyte to another. Results for transfers from 0.2*N* H_2SO_4 to 1% KOH

Table I. Measurements on films formed in two different electrolytes

Specimen No.	Electrolyte	Voltage, v	Weight* gain W, mg/dm²	Reciprocal capacity, 1/C, cm²/μF	W/V, mg/cm² V, X100	1/CV, cm²/μFV, X100	1/CW, cm⁴/μF, mg
1	0.2*N* H_2SO_4	65	1.63	5.71	2.51	8.79	350
2	0.2*N* H_2SO_4	100	2.5	8.73	2.50	8.73	350
3	1% KOH	65	2.5	8.70	3.85	13.4	348
4	1% KOH	100	4.0	14.0	4.0	14.0	350

* Computed from reflection minima.

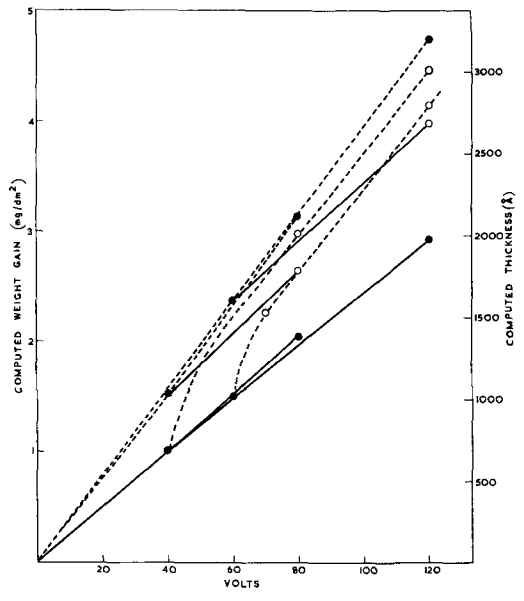

Fig. 2. Effect of changing electrolyte during anodizing of zirconium; •, anodized in 1 electrolyte; ○, behavior after changing electrolyte; ———, 0.2*N* H_2SO_4; — — —, 1% KOH.

solutions and *vice versa* are given in Fig. 2. In all transfers, further film growth always began exactly at the voltage at which the film had previously been formed. However, once new growth had started, the incremental voltage/thickness relation approached that of the new electrolyte, but the absolute thickness at a given voltage was not the same as that achieved if the whole film was grown in the second electrolyte. During the adjustment period after transfer from H_2SO_4 to KOH electrolyte, the thickness/voltage ratio was abnormally large, suggesting that once ionic movement occurred, changes were also taking place within the first-formed part of the film.

Assuming a density of 5.7 g/cm³ for the oxide film, a value of refractive index $n = 2.05$ at $\lambda = 5000$Å is obtained from the vertical separation of lines in Fig. 1. This is in good agreement with a value of $n \sim 2.1$ at $\lambda = 5000$Å measured on the stripped oxide by embedding in sulfur/selenium mixtures.

Acknowledgments

The author wishes to thank Mr. D. R. Silvester for the capacity measurements and Mr. J. N. Wanklyn for helpful discussion. Thanks are also due to Dr. J. H. O. Varley for his interest and encouragement.

Manuscript received May 15, 1962.

Any discussion of this paper will appear in a Discussion Section to be published in the June 1963 JOURNAL.

REFERENCES

1. L. Young, *Trans. Faraday Soc.*, **55**, 632 (1959).
2. A. Charlesby, *Acta Met.*, **1**, 340 (1953).

A Radiotracer Study of Anodic Oxidation

J. A. Davies, J. P. S. Pringle, R. L. Graham, and F. Brown

The Research Chemistry Branch, Atomic Energy of Canada Ltd., Chalk River, Ontario, Canada

The formation of anodic oxide films on metals, particularly aluminum and tantalum, has been extensively studied in recent years, and the results have been summarized by Young (1). While the gross features of the process are well established, some of the details are not; in particular, there is uncertainty as to which atomic species is mobile and carries the current through the oxide.

Attempts have been made in both aluminum (2) and tantalum (3) to tag the oxide film with radioactive $S^{35}O_4^{--}$ and find out whether, on continued anodizing, succeeding oxide layers are formed inside or outside the tagged layer. If the metal moves, fresh oxide will be laid down outside the marked layer; if the oxygen moves, then the new oxide will be formed between the existing tagged film and the metal surface. The experimental results, however, are inconclusive, partly because the mechanism of the oxide dissolution method used to determine the final position of the tagged layer is not established, and partly because the tagged layer itself has different properties from the rest of the oxide film (1). This difference in properties can probably be attributed to the presence of chemically significant amounts of sulfate ion in the tagged layer (4). Furthermore, it has yet to be established that an ionic marker such as SO_4^{--} does not itself move under the high potential gradient of the anodizing field. The present report describes some preliminary experiments in which these difficulties were overcome by injecting trace amounts of the radioactive inert gas, Xe^{135}, as a marker.

Previous investigations (5, 6) in this laboratory have been concerned with the range of accelerated atomic particles in metal targets. As a result of this work, it has been found that a beam of rare gas ions can be injected with a known distribution at various mean depths (15-500 atom layers) beneath the metal surface by using a suitable bombardment energy (1-200 kev), and that these injected atoms remain trapped when the metal lattice surrounding them is converted to oxide. In fact, Kelly and Brown (7) have found that there is no appreciable diffusion of the Xe atoms out of the anodic oxide, even on heating *in vacuo* to 500°C. The anodizing-stripping technique (8) employed to determine the distribution of embedded radioactive atoms in the metal cannot be used to determine the mean depth of the marker in the oxide; consequently, a more general method of determining the location of embedded atoms was sought. This has been found in the "atomic scale micrometer," whose development and calibration will be fully described elsewhere (9).

The principle of the method is as follows. Certain radioisotopes, of which Xe^{135} is one, have low energy γ transitions which are internally converted

with high efficiency; the most intense group of conversion electrons are ejected from the K shell and are essentially monoenergetic. If these electrons are released within a solid, they will lose energy in their passage to the surface, and so their energy spectrum will be modified. With suitable calibrations, these modifications can be related to the amount of matter traversed by the electrons, and hence to the mean depth of their sources, the Xe^{125} atoms, below the surface. Unfortunately, the energy lost by the electrons is not a simple function of the mass of material traversed, but also depends on its atomic number.

Accordingly, calibrations for Al and Ta were performed separately. For Al, a series of electron energy spectra were obtained from Xe^{125} embedded at various known depths within the metal and the spectra from the anodized samples compared. Since Al and O have almost the same atomic number, the presence of the oxygen should have little effect on the calibration (expressed in $\mu g\ cm^{-2}$). The same technique could not be used with Ta, because the Xe^{125} could not be given sufficient bombardment energy to inject it at depths comparable to those found in the anodic tantalum oxide. Instead, known thicknesses of gold were sublimed onto the surface of metal foils containing Xe^{125} at specified depths; the electron energy spectra were then recorded and used for calibrating the anodized specimens of Ta. Gold approximates to Ta in atomic number, but no correction can yet be made for the effect of the oxygen in Ta_2O_5. This calibration is therefore less accurate than that for Al.

Using the Chalk River $\pi\sqrt{2}$ β-spectrometer (10) depths can be estimated to as little as ± 3 atom layers (0.2 $\mu g/cm^2$ for Al) provided the Xe^{125} atoms are less than 3 $\mu g/cm^2$ beneath the surface; with increasing depth, the precision decreases considerably. The method is nondestructive and applicable to any solid; it has been used to measure the depth of the Xe^{125} markers in the growing oxide film.

For these preliminary experiments, aluminum and tantalum targets, each 5.0 x 1.0 x 0.1 cm, were bombarded on the flat face with a beam of 5 kev Xe^{125} ions in an electromagnetic isotope separator. The total integrated beam current striking each target was less than 10^{11} atoms/cm^2; since the number of metal atoms in one atom layer is approximately 2 x 10^{15}/cm^2, it is evident that chemical contamination of the target by the Xe^{125} is negligible. From other work (6) it is known that the mean penetration depth of 5 kev Xe^{125} ions in Al is 3.2 $\mu g/cm^2$, and in Ta 5.5 $\mu g/cm^2$.

After measuring the shape of the K-54.96 (21.79 kev) conversion electron peak, the targets were anodized at constant current, 0.1 ma/cm^2 for Al and 2 ma/cm^2 for Ta, using 3% aqueous ammonium citrate as electrolyte. At 10, 40, and 200v the anodizing was interrupted, and the shape of the conversion peak was measured again. The first step, 10v, converts the metal containing the Xe^{125} to oxide; subsequent steps show what happens to the Xe marker as the oxide film grows thicker. The conversion electron spectra observed are illustrated in Fig. 1

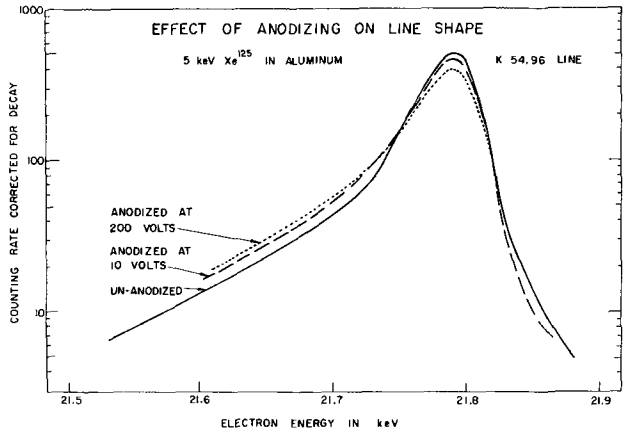

Fig. 1. Effect of anodizing on the shape of the K-54.96 (21.79 kev) conversion line; 5 kev Xe^{125} in aluminum.

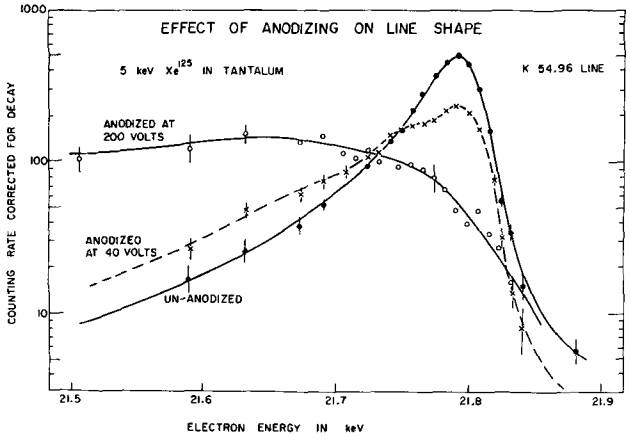

Fig. 2. Effect of anodizing on the shape of the K-54.96 (21.79 kev) conversion line; 5 kev Xe^{125} in tantalum.

and 2. The peak at 21.79 kev represents electrons which have not lost any energy; those electrons which have been scattered at least once before leaving the oxide appear in the low energy tail.

For Al, the line shape changes only slightly on anodizing to 200v, and at least half of the observed change occurs during the first 10-v step. Most of this initial change can be attributed to the conversion of the Al layer (3.0 $\mu g/cm^2$) above the Xe^{125} to a layer of Al_2O_3 (5.7 $\mu g/cm^2$). The results show that the Xe^{125} remains very close to the surface under these anodizing conditions, and therefore, that the fresh oxide layers are being formed under the existing ones. The alternative possibility, that Xe is diffusing toward the surface as fast as fresh oxide layers are laid down, seems very unlikely; Xe, due to its high ionization potential, is almost certainly present in the oxide as a neutral atom and so will not be influenced by the very large voltage gradient across the oxide. Furthermore, were such diffusion of the Xe^{125} occurring, there would probably be an appreciable loss of Xe^{125} to the electrolyte; in fact, the measured loss was less than 4%.

If fresh oxide layers are being formed underneath the old, oxygen must be the mobile species. However, it has been found (8) that, under conditions of constant voltage, about 20% of the aluminum consumed in the anodizing process appears dissolved in the electrolyte. The fraction dissolved

Table I. Burying of Xe^{135} during anodic oxidation

Target	Anodic voltage	Approximate thickness of oxide layer, $\mu g/cm^2$ [a]	Location of Xe^{135} beneath surface, $\mu g/cm^2$ [b]
Al	0	—	3.2
	10	5.5	5.0
	40	20	6.0
	200	95	7.5
Ta	0	—	5.5
	10	14	10
	40	56	22
	200	280	90

[a] Thickness of Al_2O_3 calculated from 0.475 $\mu g/cm^2/v$ (8); thickness of Ta_2O_5 calculated from 16 A/v (11).

[b] From change in K54.96 conversion-line shape. The estimated error in each Al determination is about 10% of the value quoted, and in each Ta determination about 30%.

under the constant current conditions used in this work has yet to be measured, but may well be considerable. Consequently, it seems probable that both metal and oxygen migrate, but that at 0.1 ma/cm^2 the film grows mainly by oxygen migration.

In Ta a drastic change in line shape is observed with increasing anodic voltage, as shown in Fig. 2. The Xe^{135} remains at about the middle of the oxide film (Table I), indicating that fresh oxide is being formed on both sides of it. Hence, once again, both metal and oxygen move. However, unlike Al, both types of migration are contributing to the oxide film growth.

These preliminary experiments show that by using Xe^{135} as an inert tracer unique and useful information about the mechanism of oxide film growth can be obtained. Further work is in progress to study the effect of various anodizing conditions, and to extend the technique to other metals.

Manuscript received May 31, 1962. Issued as A.E.C.L. No. 1600.

Any discussion of this paper will appear in a Discussion Section to be published in the June 1963 JOURNAL.

REFERENCES

1. L. Young, "Anodic Oxide Films," Academic Press, London and New York (1961).
2. J. E. Lewis and R. C. Plumb, *This Journal*, **105**, 496 (1958).
3. Ref. (1), p. 71.
4. R. B. Mason, *This Journal*, **102**, 671 (1955).
5. J. A. Davies and G. A. Sims, *Can. J. Chem.*, **39**, 601 (1961).
6. J. A. Davies, F. Brown, M. McCargo, and G. A. Sims, *Can. J. Phys.*, In press.
7. R. O. Kelly and F. Brown, *ibid.*, In press.
8. J. A. Davies, J. Friesen, and J. D. McIntyre, *Can. J. Chem.*, **38**, 1526 (1960).
9. R. L. Graham, J. A. Davies, and F. Brown, *Can. J. Phys.*, To be published.
10. R. L. Graham, G. T. Ewan, and J. S. Geiger, *Nuclear Instr. and Methods*, **9**, 245 (1960).
11. D. A. Vermilyea, *Acta Met.*, **1**, 282 (1953).

An Electrode Mount for Electrochemical Studies of Stressed Metal Specimens

N. D. Greene, S. J. Acello,[1] and A. J. Greif[2]

Corrosion Research Laboratory, Interdisciplinary Materials Research Center, Rensselaer Polytechnic Institute, Troy, New York

Electrochemical investigations of stressed metals have been hampered in the past by the lack of a suitable electrode mount. A satisfactory mount for stressed specimens should provide air and liquid tight seals, be noncontaminating, adaptable to varying environments and temperatures, and simple to clean and assemble. The design described here meets all of these requirements and, in addition, permits experimentation under conditions of either static or dynamic tension or torsion.

Figure 1 shows the lower end of the specimen holder in detail; the upper end is essentially the same. Only Teflon, Pyrex glass, and the electrode contact the solution. Wire specimens are used because they are easily stressed, and those not long enough to extend outside the flask are first inserted into a metal rod and held with a set screw. The lower end of the wire and the metal rod are shielded from the solution by a Teflon gasket through which the electrode extends into the solution. A compression seal is obtained by the pressure of a glass bushing on a Teflon gasket. Pressure is applied by screwing together the two halves of a Teflon compression joint.

Figure 2 shows the electrode holder mounted inside a standard polarization flask which has an addi-

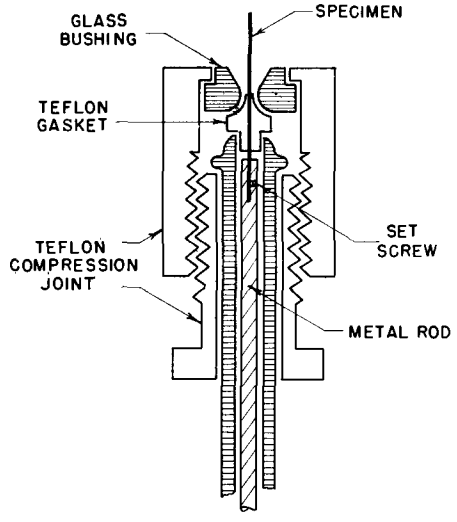

Fig. 1. Specimen holder

[1] Present address: Sprague Electric Company, North Adams, Massachusetts.

[2] Present address: Olin Mathieson Chemical Corporation, New Haven, Connecticut.

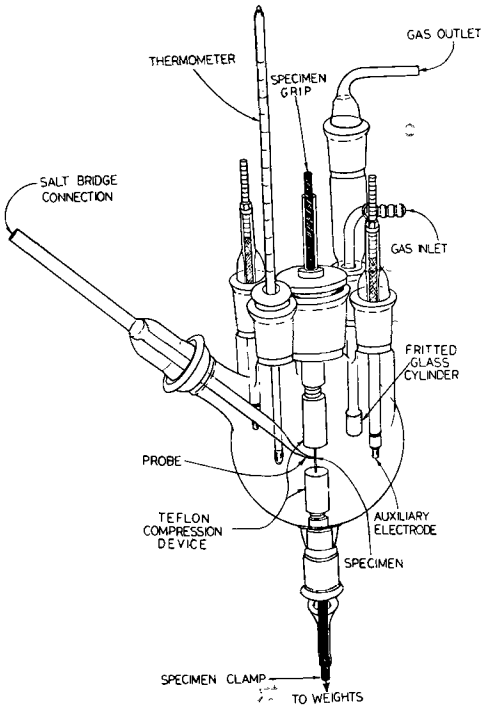

Fig. 2. Polarization cell

tional standard taper joint on the bottom. Vertical adjustment is supplied by passing the upper compression joint through a Teflon stopper. The polarization cell itself has been described in detail elsewhere (1-3).

Tensile or torsional stress can be applied to the electrodes before or after they are inserted into the cell. Tensile stress is applied after insertion by attaching suitable weights to the wire or metal rod. Small synchronous motors are used in a similar manner to apply torsional stress.

The electrode mount has performed satisfactorily in this Laboratory during numerous experiments at temperatures up to 130°C and in widely varying environments.

Acknowledgment

This work was supported by the U.S. Army Research Office (Durham).

REFERENCES

1. M. Stern, *This Journal*, **102**, 609 (1955).
2. R. A. Covert and H. H. Uhlig, *ibid.*, **104**, 537 (1957).
3. N. D. Greene, *Corrosion*, **15**, 369t (1959).

N^+N Delineation in Silicon

Irvin Berman

Air Force Cambridge Research Laboratories, Office of Aerospace Research, L. G. Hanscom Field, Bedford, Massachusetts

Recently many of the diffusion experiments in the Air Force Cambridge Research Laboratories have been oriented toward increasing the impurity levels in silicon for tunneling effects. Phosphorus pentoxide has been diffused into n-type silicon to give surface concentrations of 6×10^{19} or higher. Because the diffusant impurity is of the same type as the bulk, observation of the depth of penetration has been difficult.

The conventional methods of finding the depth of penetration by a resistivity profile, and by including a control of p-type silicon in the experiment, leave much to be desired. Until recently, this laboratory did not have anything similar to the Fuller Stain (1) for observing this penetration.

Silverman and Benn (2) have shown how excellent delineations of p-n junctions can be obtained through the use of Au chemiplating, good delineation on PP^+, but questionable results for NN^+ delineation. Although in the Air Force Cambridge Research Laboratories the original investigation was on diffused samples, it was extended to N^+ epitaxial layers on n-type bulk and to n-type alloys into n-type bulk material.

In all cases, good results are obtainable under proper control. There is staining by this technique, but also there is some etching. Through proper dilutions, good control of this etching has been established. This experiment was performed under ambient room temperature.

By way of difficulties, there are two conditions that should be mentioned in utilizing the procedure: (i) precaution is necessary in preserving the edges of the silicon, in order to have good reference points for measuring; (ii) the staining reagent should be stored under refrigeration for the maintenance of its potency.

The staining reagent consists of:

40 cc HF (49.2% 20 cc HNO_3 (70.2%)
100 cc H_2O 2g $AgNO_3$

The procedure consists of the following steps: (*a*) prepare sample by mounting in plastic, for angle lapping or for grooving (3); (*b*) lap first with 600 grit to expose desired area; (*c*) lap with successively smaller grits until the desired polish is obtained; (*d*) clean surface and dry; (*e*) use a wooden or plastic applicator to apply a drop of the stain reagent to the exposed silicon. At this point, silver will deposit on the entire surface, but the greatest deposit

Table I. Calculated diffusant depth vs. measured stain depth

Bulk material 5×10^{16} impurity atoms/cm^3

No.	Calculated depth, in.	Measured depth, in.
1	2.94×10^{-3}	2.38×10^{-3}
2	2.48×10^{-3}	2.48×10^{-3}
3	1.73×10^{-3}	1.54×10^{-3}
4	1.31×10^{-3}	1.4×10^{-3}
5	1.6×10^{-3}	1.42×10^{-3}

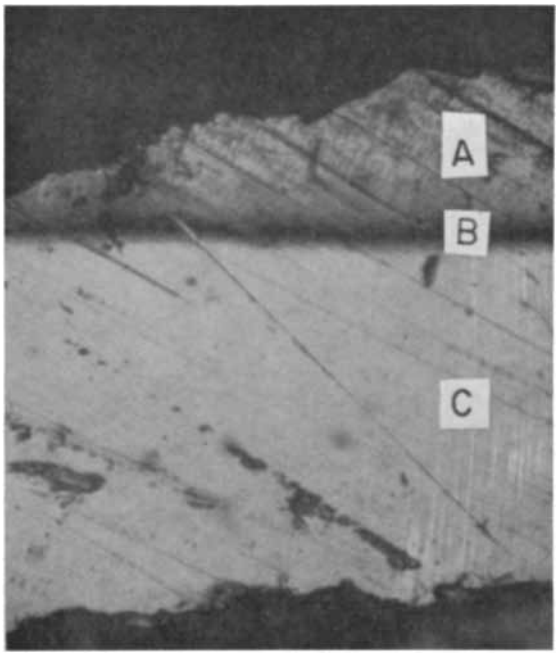

Fig. 1. Epitaxial n-type germanium layer: A, epitaxial layer; B, interface; C, substrate. Magnification 650X.

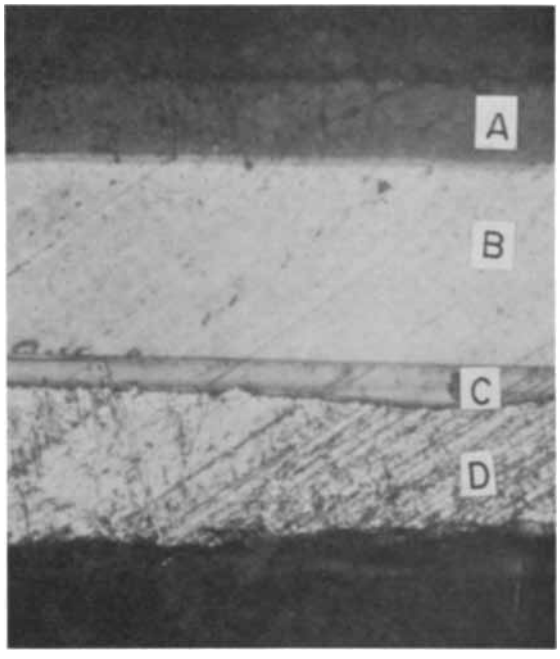

Fig. 2. Cross section of silicon die: A, diffused phosphorus; B, n-type silicon; C, N^+ regrowth; D, gold/antimony. Magnification 650X.

will be at the region of highest resistivity; (*f*) rinse off surface and dry; (*g*) Apply a drop of dilute nitric acid to the surface with a wooden or plastic applicator; (*h*) rinse off sample and dry.

The use of this technique establishes a good correlation between calculated diffusant depth and measured stain depths.

Some of the error can be attributed to the diffusion techniques. The greatest contribution to the error probably comes from the slight etching and subsequent rounding of the edge. This interferes with the point of reference for measuring. To minimize the etching, the solution was varied by diluting with water. As the bulk approaches the degenerate layer in impurity concentration, the delineation becomes more difficult to reproduce. A repetition of the addition of the stain reagent and the nitric acid steps will eventually bring out the delineation. The effect of light on the reaction was also investigated; it did not appear to contribute to the reaction.

The time required for the stain delineation to appear will depend on the impurity concentration and the dilutions of the reagent. By increasing the concentration of the reagent, the time will be reduced. However, the danger of etching will be increased.

Similar techniques employed with N^+N germanium delineation works fairly well, but in germanium the boundaries appear to lack sharpness. Figure 1, a 650X photograph, shows an epitaxial n-type Ge layer deposited by a closed cycle vapor growth process on an n-type Ge substrate. The epitaxial layer is designated as A. The interface labeled B appears so heavily oxidized that it loses its distinction in a photograph. The substrate is designated as C. Figure 2 is a photograph of a cross section (magnification 650X) of a silicon die stained by the techniques described here. Region A is a phosphorus diffusion (8×10^{19} atoms/cm^3) into n-type bulk silicon (region B), with 5×10^{16} impurity atoms/cm^3. On the opposite side, a disk of gold/antimony (1% Sb) has been alloyed. The delineation of the N^+ regrowth region labeled C is quite apparent. The area marked D is the alloy of gold/antimony.

Acknowledgment

The author wishes to thank Mr. Walter McLaughlin and Mr. John Hawley for their assistance in this investigation.

Manuscript received April 9, 1962.

Any discussion of this paper will appear in a Discussion Section to be published in the June 1963 JOURNAL.

REFERENCES

1. C. S. Fuller, Jr., *J. Appl. Phys.*, **27**, 553 (1956).
2. S. J. Silverman and D. R. Binn, *This Journal*, **105**, 170 (1958).

June 1963 Discussion Section

A Discussion Section, covering papers published in the July-December 1962 JOURNALS, is scheduled for publication in the June 1963 issue. Any discussion which did not reach the Editor in time for inclusion in the December 1962 Discussion Section will be included in the June 1963 issue.

Those who plan to contribute remarks for this Discussion Section should submit their comments or questions in triplicate to the Managing Editor of the JOURNAL, 30 East 42 St., New York 17, N. Y., *not later than March 1, 1963*. All discussion will be forwarded to the author(s) for reply before being printed in the JOURNAL.

Voltammetric and Chronopotentiometric Study of the Anodic Oxidation of Methanol, Formaldehyde, and Formic Acid

R. P. Buck[1] and L. R. Griffith

California Research Corporation, Richmond, California

ABSTRACT

The anodic oxidation of methanol, formaldehyde, and formic acid on platinized platinum electrodes was studied by the technique of voltammetry at linearly changing potential in 14 aqueous solutions ranging from 10M KOH to 9M H_2SO_4 and over a concentration range of 0.01 to 0.1M. The pH dependences of the current-voltage curves, peak currents, overpotentials, and kinetic parameters were investigated for each of the three compounds where possible. Mechanisms based on these results and the supporting chronopotentiometric and product studies are discussed.

A detailed knowledge of the mechanisms of methanol, formaldehyde, and formic acid oxidations on platinum electrodes is pertinent to consideration of these materials as fuel cell reactants. It may be a prerequisite for the understanding of anodic oxidation of hydrocarbons. Although the anodic oxidation of alcohols on platinum has been previously reported, the kinetics and mechanisms of these processes have not been well established. The work of Müller (1) led to the suggestion that methylate anion may be the oxidizable species in basic aqueous solutions. Tanaka (2) studied the anodic oxidation of methanol in base, but failed to observe formaldehyde as an intermediate. Pavela (3) made extensive use of constant current in his investigation of the oxidation of methanol in basic and acidic solutions. Other voltammetric studies of alcohols and aldehydes have been reported by MacNevin and Sweet (4), Bogdanovskii and Shlygin (5), and Vielstich (6).

In this paper we discuss our experiments designed to elucidate the reaction sequence and the rates of limiting processes in the anodic oxidation of methanol. We obtained electrochemical data from current-potential curves with linearly changing potential and potential-time curves at constant current (7). Comparative data are also given for formaldehyde, formic acid, and formate ion. In the case of voltammetry at linearly changing potential, quantitative descriptions for cases involving rate-determining adsorption processes or preelectrochemical solution reactions are not available. Qualitatively, the effects of preelectrochemical reactions are discussed using arguments similar to those of Koutecky and Brdicka (8). Earlier results of this program have been described (9-11).

Experimental

A versatile instrument, built around commercially available, chopper-stabilized computer amplifiers, was used. The equipment was built after designs by DeFord (12).

Most of the experiments, including all voltammetry in acidic solution, were done with a conventional H-cell using three electrodes. The electrolysis current flowed between a platinum sphere anode and a $Hg\text{-}Hg_2SO_4$, saturated K_2SO_4 auxiliary cathode, separated from the anode by a fritted glass disk and an agar plug saturated with K_2SO_4. Anode potentials were measured and controlled from a Beckman saturated calomel electrode separated from the anode compartment by a similar agar bridge. The anode was platinized from a 0.5 wt % platinic chloride solution to give a black platinum surface.

All solutions were prepared from commercially available C. P. grade chemicals, including: pH 10.0, approximately 0.2M in K_2CO_3 and $KHCO_3$; pH 2.12, approximately 0.1M in KH_2PO_4 and H_3PO_4.

Commercially pure methanol (99.8%), commercially pure sodium formate (100.0%), and Merck formaldehyde (37% in water stabilized with methanol) were used.

Microliter samples were pipetted into the anode compartment; anolyte volume was 50 ml. Samples were stirred into the solvent with a magnetic stirrer. The solvent was deaerated with nitrogen prior to adding the oxidizable sample, and a nitrogen atmosphere was maintained over the unstirred solutions during potential sweeps.

Potential sweeps were done from negative potentials in a positive direction to the beginning of oxygen evolution and then in reverse. Sweep rates were 4.00 and 8.00 mv/sec. Temperature was 23° ±0.5°C.

Early runs showed that electrode pretreatment was essential to the reproducibility of the current observed on successive potential sweeps. A few moments of rapid hydrogen evolution was sufficient to reduce the platinum oxide formed during previous sweeps. However, in solutions more acidic than pH 11.5, a platinized nickel anode had to be both oxi-

[1] Present address: Bell and Howell Research Center, Pasadena, California.

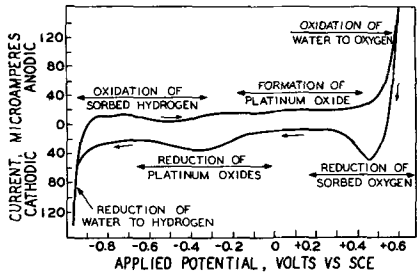

Fig. 1. Potential sweeps of sodium hydroxide solution. Platinized nickel ball; electrode, 2.6 mm diameter; arrows indicate sweep direction; 0.1M NaOH, sweep rate, 4 mv/sec.

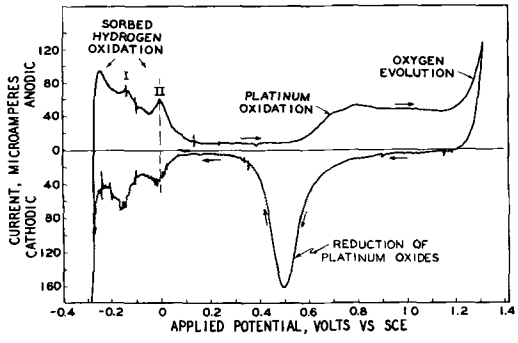

Fig. 2. Potential sweeps of sulfuric acid solution. Platinized platinum ball; electrode, 2.1 mm diameter; arrows indicate sweep direction; 1M H_2SO_4, sweep rate, 4 mv/sec.

dized and reduced, apparently to remove adsorbed materials. This procedure was not always successful.

Results and Discussion

Current-Potential Characteristics

A typical potential sweep of a basic solution containing no oxidizable sample is shown in Fig. 1. A sweep in 1M H_2SO_4 solution is shown in Fig. 2. Three peaks for the oxidation of sorbed hydrogen are clearly seen at the beginning of the latter sweep. Two of these, marked I and II, agree with those observed by Franklin and Cooke (13), who postulated the nature of three forms of sorbed hydrogen. Beyond +0.6v the oxidation of platinum to a platinum oxide layer begins (14). On the reverse sweep, the reduction of the oxide layer appears as a peak between +0.8 and +0.3v. The reduction of hydrogen ions to hydrogen shows two peaks at potentials more positive than hydrogen evolution. It appears that two kinds of sorbed hydrogen form before hydrogen evolution.

Typical cyclic voltammetric sweeps for methanol in four electrolytes are shown in Fig. 3. Data for other acidities are given in the original reports (11). In the basic region, *p*H 10-14, the first part of the ascending anodic current-potential curve obeys the Tafel equation. Toward more positive potentials, the anodic current reaches a maximum value and then decreases either because the surface concentration is depleted or because the surface becomes blocked by oxide formation or because of both. Aside from hydrogen oxidation, there are no other anodic peaks in basic solutions prior to oxygen evolution.

From *p*H 3.75 to low *p*H values, a second, broad peak appears after the main peak but prior to oxygen evolution. We interpret this to be a catalytic current due to regeneration of platinum oxides which are formed electrochemically in this potential region but are reduced chemically by methanol in acidic solutions. The locations of the main oxidation peaks of formaldehyde and formic acid as determined in separate experiments show that the second peak cannot be due to the oxidation of intermediates from the methanol oxidation. This catalytic pattern prevails only in acidic solutions for potentials between +1.0 to +1.3v, depending on the acidity. The height of the second peak for methanol is always about one half that of the first oxidation peak. On the reverse sweep, the second peak does not appear.

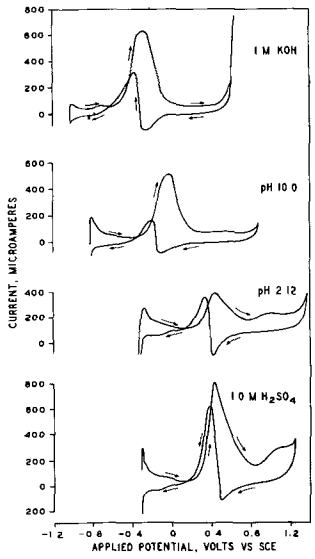

Fig. 3. Voltammetric behavior of methanol; 0.0247M (0.0124M for 1.0M H_2SO_4); sweep rate, 8 mv/sec. All sweeps begin at the most negative potentials; anodic current above zero, cathodic current below.

The direct anodic oxidation of methanol does not occur on platinum oxide in either acidic or basic media at rates comparable to the reaction on oxide-free platinum. This fact is clearly shown in base

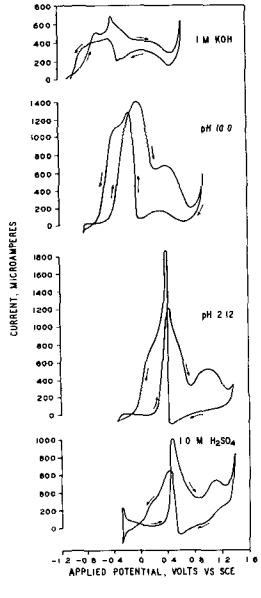

Fig. 4. Voltammetric behavior of formaldehyde; 0.026M (0.013M for 1.0M H_2SO_4); sweep rate, 8 mv/sec. All sweeps begin at the most negative potentials; anodic current above zero, cathodic current below.

where the methanol oxidation current is not observed during the reverse sweep until the oxide layer reduction peak is passed.

Cyclic voltammetric sweeps for formaldehyde in four electrolytes are shown in Fig. 4. In the region 10M KOH to 0.1M NaOH there are reproducible double peaks of remarkably similar fine structure. The peaks move together on decreasing basicity. The second peak, which is the smaller of the two at 10M KOH, becomes larger relative to the first (more negative) peak upon decreasing basicity until, at 0.1M NaOH, the first peak is almost a shoulder on the larger second peak.

The oxidation "peak" of formaldehyde retains a broad aspect in less basic solutions. Evidence of secondary processes giving rise to a shoulder on either the negative or the positive potential side remains until about *p*H 2. Only in solutions more acidic than *p*H 2 does the oxidation peak have a very sharp, spikelike shape. However, the prewave still persists as indicated by the presence of two Tafel slopes.

In all electrolytes, acidic or basic, in addition to the peak, peak and shoulder, or peaks at the negative potential side of the scan, there is a broad peak prior to oxygen evolution in the region where platinum oxide is known to form. In strong base, this third process appears as a mere drawn-out shoulder leading to oxygen evolution. In strong acid, this process appears as a peak of comparable size to, but never more than, the main peak. This third peak is very likely a catalytic current caused by the platinum oxide-catalyzed oxidation of formaldehyde as previously suggested for methanol.

In basic electrolytes, formaldehyde oxidizes on platinum oxide but at a slower rate than on the clean platinum. This reaction can be observed as a considerable anodic current during the reverse potential sweep after reduction of adsorbed oxygen but before platinum oxide is reduced. Greater formaldehyde concentrations produce greater anodic currents in this region. The platinum oxide reduction current subtracts from the anodic current and yields a net current which may be anodic or cathodic, depending on the formaldehyde concentration. When the potential is reached at which the platinum oxide is removed, the anodic current increases greatly. The same effects are observed in acidic solutions of formaldehyde. The region between +0.8 and +0.6v may be one where again both electrochemical oxidation of formaldehyde and electrochemical reduction of platinum oxide occur simultaneously.

Cyclic voltammetric sweeps of formate and formic acid show equally complex shapes. Typical curves are shown in Fig. 5. At all *p*H values, the oxidation peak shows two parts, although in strong base and strong acid it is difficult to tell because of the very small currents. Another peak close to oxygen evolution is observed in the potential sweeps in acidic solutions. This, again, may be a platinum oxide-catalyzed oxidation of formic acid.

Dependence of Peak Currents on Fuel Concentration

Plots of peak current *vs.* concentration of fuel were prepared for 14 aqueous electrolytes ranging from 10M KOH to 9M H_2SO_4. Two or more potential sweep rates were used for each fuel concentration in each electrolyte. These plots are not reproduced here, but are contained in the original progress reports (11).

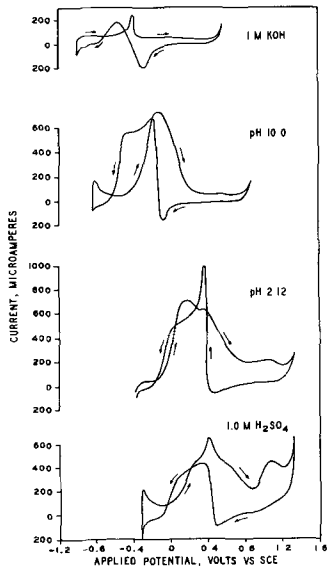

Fig. 5. Voltammetric behavior of formate and formic acid; 0.036M (0.0237M for 1.0M H_2SO_4); sweep rate, 8 mv/sec. All sweeps begin at the most negative potentials; anodic current above zero, cathodic current below.

Generally, peak currents vary linearly with fuel concentration as expected for reactions involving diffusion limitation up to about 0.05M; however, peak currents are much smaller than required for diffusion-limited processes. Two notable exceptions to the linear relationship are formate in basic solutions and methanol in all solutions more acidic than *p*H 11.5. The methanol curves are linear in the region of 0.001M to about 0.03M, but tend to level off at higher concentrations. Formaldehyde shows linearity over a wide concentration range and generally shows greater peak currents. The highest concentration investigated was 0.24M.

Deviations from linearity cannot be explained with the electron-transfer limiting model used by Delahay (15) since the peak currents should be linear in fuel concentration and should increase with the square root of the sweep rate. Methanol peak currents increase with sweep rate but in a proportion less than predicted by the square root relationship. This was also generally true for formaldehyde and formate ion. Only in the acidic range are the formaldehyde peak currents in the proper ratio for sweep rates 8.00 and 4.00 mv/sec.

These features of the variation of peak current with concentration and sweep rate cause us to conclude that the current peak is not diffusion limited. Factors not considered in the theory (15) are slow preelectrochemical solution reactions and dissociative adsorption on the electrode.

Dependence of Peak Current on pH

The slope of the peak current *vs.* fuel concentration curves represent the peak current per unit concentration or "reduced" peak current in microamperes per millimole per liter. These slopes depend on the *p*H of the electrolyte and the potential sweep

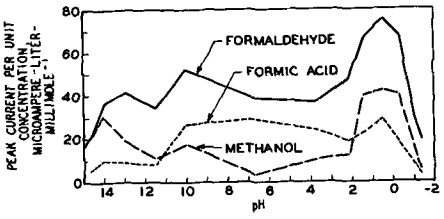

Fig. 6. Reduced peak currents vs. pH for methanol, formaldehyde, and formic acid; sweep rate, 8.0 mv/sec.

rate. When the curves were not linear, the slope chosen was the maximum value obtained at the lowest concentrations. The reduced peak currents are plotted *vs.* pH for methanol, formaldehyde, and formic acid in Fig. 6.

The optimum acidity for the oxidation of these materials is in the range pH 0-1. Decrease in peak currents for still higher acidities may be related to the increased bulk concentration of protonated methanol, formaldehyde, and formic acid (16). Increasing peak heights for methanol and formaldehyde with increasing basicity may be due to the greater concentrations of methylate ion and methylene glycolate ions, respectively. Ultimate decreasing of peak heights with increasing basicity may be due to increased adsorption of OH^- onto the anode.

Formate can be oxidized in base as shown by the small peak in the basic range in Fig. 6. However, it is not oxidized rapidly at the potential of rapid methanol and formaldehyde oxidation, and formate is, therefore, the principal product of the oxidation of methanol and formaldehyde at pH >11. This complication is not clear from Fig. 6, which merely shows the magnitude of the peak current wherever it happens to occur on the potential scale.

Formic acid gives larger reduced peak currents than methanol at intermediate pH values of 2-11. This suggests that formate anion (or formic acid) may not be the principal end product from methanol below pH 11 but merely an intermediate. Product analyses (9, 10) of methanol oxidation, which show buildup of formate in strong base but nearly complete conversion to CO_2 in strong acid, have not been performed for electrolytes in the range pH 2-11. The dropoff of reduced peak currents from pH 10 to about pH 12 for methanol and formaldehyde may reflect the change from six to four electrons for methanol and a change from four to two electrons for formaldehyde if it is true that formate becomes limiting only above pH 11.

At all pH values, formaldehyde gives greater peak currents than either methanol or formic acid. This result may seem puzzling since methanol is intrinsically capable of yielding six electrons while formaldehyde at best can yield only four. This result in basic solutions is consistent with a mechanism for methanol oxidation involving a slower preelectrochemical reaction for methanol than for formaldehyde, *e.g.*, a slow dissociative chemisorption step or a slow solution reaction to produce the electroactive species.

Position of Peak Current on the Potential Scale

The positions of peak current on the potential scale for methanol, formaldehyde, and formic acid or formate are shown in Fig. 7. The values are given as ranges incorporating data from both 4.00 and 8.00 mv/sec sweeps over a wide range of fuel concentrations. The spread in the potential range for each pH is smaller if the data for only one sweep rate are included.

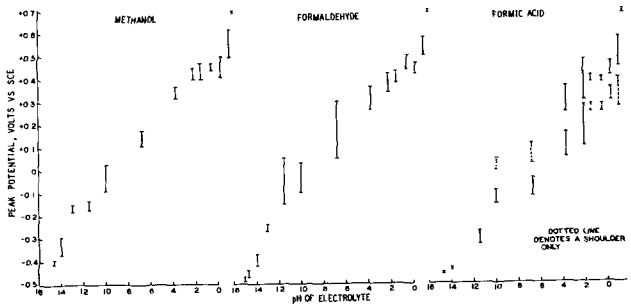

Fig. 7. Position of peak current for two sweep rates and various concentrations to 0.1M.

Rate Constants in Basic Solutions

In the low current region on the negative potential side of a current peak, the following equation is assumed to hold if the reaction rate is limited only by a slow electron transfer step and adsorption of the reactant is absent. The instantaneous current, at a given potential E, is given by the equation:

$$i = n\mathbf{F}C^\circ Ak_{s,h} \exp\left[\frac{(1-\alpha)n_a\mathbf{F}(E-E^\circ_c)}{RT}\right] \quad [1]$$

where n is the number of electrons in the over-all oxidation (n has the value 4 for methanol, 2 for formaldehyde, and 2 for formate in base), $\mathbf{F}$ the Faraday, C° the reactant concentration at the electrode surface and in the bulk, A the electrode area, $k_{s,h}$ the rate constant at a potential E°_c, the reversible potential for the rate-determining step, $(1-\alpha)$ the anodic transfer coefficient, and n_a the number of electrons in the rate-determining step. Applicability of Eq. [1] is restricted to high bulk reactant concentration and very low current drain so that the surface concentration is not depleted during the course of the experiment. If oxidation occurs from an adsorbed state, a constant value of $k_{s,h}$ is not expected with this calculation.

Methanol.—On a 2.6 mm platinized nickel ball anode using current densities in the range 1-500 $\mu a/cm^2$ and methanol of 0.0498M, our value for $b = 0.059/(1-\alpha)n_a$ is 0.21-0.28 at 25°C and b is independent of pH from pH 10 to 14.

Values of $Ak_{s,h}$, the product of electrode area and apparent heterogeneous rate constant for a possible rate-determining step

$$CH_3O^- + 2\,OH^- \rightarrow CH_2(OH)O^- + H_2O + 2e^- \quad [2]$$

were calculated from the following equations and are given in Table I.

$$i = 4\mathbf{F}Ak_{s,h}(CH_3O^-) \exp\left[\frac{(1-\alpha)n_a\mathbf{F}}{RT}(E-E^\circ_c)\right] \quad [3]$$

$$i = 4\mathbf{F}Ak_{s,h}\frac{K_A(OH^-)}{K_w}(CH_3OH) \exp\left[\frac{(1-\alpha)n_a\mathbf{F}}{RT}(E-E^\circ_c)\right] \quad [4]$$

and

Table I. Apparent heterogeneous rate constants for methanol at 25°C

pH	$Ak_{s,h}$, cm³/sec*	$E°_C$ vs. SCE	$Ak'_{s,h}$, cm³/sec**	$E°_C$ vs. SCE
~15 (10M KOH)		−0.972		
~14 (1M KOH)	1.6×10^{-6}	−0.913	8.9×10^{-8}	−0.834
~13 (0.1M NaOH)	5.6×10^{-6}	−0.854	3.3×10^{-8}	−0.775
12.21 (25% K_2CO_3)	5.0×10^{-5}	−0.807	5.0×10^{-8}	−0.728
11.50 ($PO_4^{\equiv}$, $HPO_4^{=}$)	7.9×10^{-5}	−0.765	1.4×10^{-8}	−0.686

* Based on methylate ion.
** Based on formal methanol.

$$i = 4\mathbf{F}Ak'_{s,h}(CH_3OH) \exp\left[\frac{(1-\alpha)n_a\mathbf{F}}{RT}(E - E°_C)\right] \quad [5]$$

$E°_C$ is the formal potential for molal concentrations of reactant and product in the rate-determining step stated by Eq. [2], and

$$E°_C(vs.\ SCE) = 0.913 - 0.059 \log (OH^-)$$

This value was obtained from $E°$ given by Latimer (17) by correcting for the acid dissociation constants of methanol, $pK_A = 15.54$ and methylene glycol, $pK_A \approx 12.8$ (17,19). Apparent formal rate constants based on total methanol concentration referred to $E°$ are given in Table I also.

Since a constant value of neither $k_{s,h}$ nor $k'_{s,h}$ is found, we conclude a preelectrochemical reaction occurs. This preelectrochemical reaction may be a reaction in solution to produce the electroactive species or it may be an adsorption process. Both processes may also occur.

Formaldehyde.—The results shown in Fig. 6, coupled with product analyses, show a two-electron oxidation (to formate) for pH 11.5 or higher and suggest a three- to four-electron oxidation from pH 7 to 10. In addition to this complication, formaldehyde exists in aqueous solution mainly as a hydrate, methylene glycol (19). The increase in peak current is not as extreme with increasing pH beyond pH 11.5 as would be necessary if methylene glycolate anion were the only oxidizable species and the rate of reaction [6] were slow.

$$CH_2(OH)_2 + OH^- \rightleftharpoons CH_2(OH)O^- + H_2O \quad [6]$$

For this reason, we postulate a fast preelectrochemical reaction, [6], is responsible for supplying the electrode with oxidizable methylene glycolate anion in addition to that which diffuses from the bulk. Because of the magnitude of the dissociation constant, methylene glycolate is a predominant species even in 0.1M NaOH.

In basic solutions, formaldehyde decomposes catalytically on the platinum anode to form sorbed hydrogen. The Tafel region is difficult to measure accurately because of the simultaneous oxidation of sorbed hydrogen. Best results have been obtained by sweeping applied potential from −1.0v in a positive direction to about −0.6v, depending on pH. In this region, bound surface hydrogen is removed. The potential is then swept negative to zero current. Upon the subsequent positive sweep, the low current formaldehyde oxidation can be observed without complication by sorbed hydrogen.

Plots of log i *vs.* E for formaldehyde in 0.1M NaOH between −0.8 and −0.5v give slopes corresponding to $(1-\alpha)n_a$ values between 0.3 and 0.4. Our best values for $(1-\alpha)n_a$ were obtained at the highest concentrations used, 0.078M and 0.13M formaldehyde; values of $(1-\alpha)n_a$ are approximately 0.35. A sweep rate of 4 mv/sec was used. The apparent heterogeneous rate constant at the reversible potential (−1.253 *vs.* SCE for 0.1M NaOH) multiplied by the surface area is approximately 10^{-9} cm³/sec.

Formate ion.—Very few observations suitable for quantitative description of formate oxidation in base have been obtained. The reversible potential for formate oxidation to carbonate follows the equation

$$E°_C = -1.252 - 0.059 \log (OH^-) \quad [7]$$

Qualitatively, the rate constant multiplied by the electrode area, at the reversible potential, will be smaller than that of formaldehyde by approximately a factor of 10.

Quantitative Behavior in Acidic Electrolytes

For methanol in 1 and 5M H_2SO_4, plots of log i *vs.* E are not so comparable from one run to another as had been observed for methanol oxidations in basic solutions. Rather than the normal positive deviations from the Tafel slope, due to the onset of concentration polarization at high current drain, methanol shows smaller than normal Tafel slopes at currents greater than 100 μa. This corresponds to the striking sharpness of the current-voltage peaks and is an indication of adsorption limitation.

For 0.0494M methanol in 1M sulfuric acid, $(1-\alpha)n_a$ values averaged 0.5 at currents less than 100 μa and reached 0.6 at higher currents. In 5M H_2SO_4, values for $(1-\alpha)n_a$ averaged 0.4 at the lower currents and increased to 0.7 at higher currents. Two sweep rates, 4.0 and 8.0 mv/sec, were used.

Analysis of formaldehyde data is complicated by the presence of shoulders or double peaks, indicating two electrode processes, one of which is probably adsorption limited. The $(1-\alpha)n_a$ values in 1M H_2SO_4 were 1.3-1.5 while in 5M H_2SO_4 the values ranged from 1.5 to 2.2 at two sweep rates and 0.05M formaldehyde. We have not attempted to analyze the formic acid peaks.

Consistency of Voltammetric Results with Product Studies

The apparent heterogeneous electron-transfer rate constants reported above for methanol, formaldehyde, and formate in base refer to the reversible potential for a given pH. This is, of course, different

for each species. From the point of view of fuel cell operation, it is more informative to compare formal rates at a specific potential. Formal rate constants at a potential E in the Tafel region can be computed from $k_{s,h}$ by correcting to the desired potential. At an arbitrary potential in the Tafel region of both methanol and formaldehyde in 1M hydroxide:

$$\frac{k_{f,h}(\text{Formaldehyde})}{k_{f,h}(\text{Methanol})} = \frac{10^{-9}}{10^{-7}} \times \frac{10^{6.06(E+1.312)}}{10^{4.67(E+0.834)}} \quad [8]$$

where $Ak_{s,h}$(formaldehyde) $= 10^{-9}$ cm³/sec, $Ak_{s,h}$ (methanol) $= 10^{-7}$ cm³/sec, and an average Tafel slope referred to base 10 of 0.16 for formaldehyde and 0.21 for methanol.

In fuel cell product studies by Schlatter (10) using 1.56M methanol in 4.5M NaOH, the cell was operated at constant current. However, because of the high concentration of methanol and the very low current drain, the cell potential remained approximately constant at −0.65v *vs.* SCE. Applying Eq. [8], it can be shown that the rate of oxidation of formaldehyde at −0.65v is much greater than the methanol oxidation rate. The over-all process yielding formate is analogous to a consecutive reaction of the type

$$A \xrightarrow{k_1} B \xrightarrow{k_2} C \quad [9]$$

where the concentration of methanol is (A), formaldehyde is (B), and formate is (C). Formaldehyde concentration should approach a steady state given by k_1/k_2 $(A°)$, where $(A°)$ is the initial concentration of methanol. At −0.65v, the ratio of formal rates given by

$$k_2/k_1 = \frac{k_{f,h}(\text{Formaldehyde})}{k_{f,h}(\text{Methanol})} = 1.4 \times 10^5 \quad [10]$$

Thus, we would predict a steady-state formaldehyde concentration of 11 x 10^{-4}M. Experimentally, the steady-state concentration reached by formaldehyde was 2.5 x 10^{-4}M after approximately 90 hr at 50 ma. Only order-of-magnitude values of the heterogeneous rate constants were used so that the prediction is in good agreement with the experimental value.

In acidic solutions, methanol and formaldehyde are irreversibly oxidized to yield peaks in nearly the same potential region. It is not surprising that formaldehyde steady-state concentration during methanol oxidations is much greater than in base as shown by Schlatter. Formic acid in acidic solutions is rapidly oxidized also, and product analyses show that formic acid is indeed an intermediate, and its steady-state concentration is comparable to that of formaldehyde.

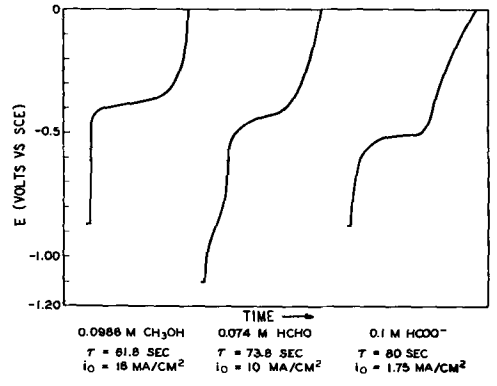

Fig. 8. Experimental potential-time curves for methanol formaldehyde, and formate ion in 1M KOH.

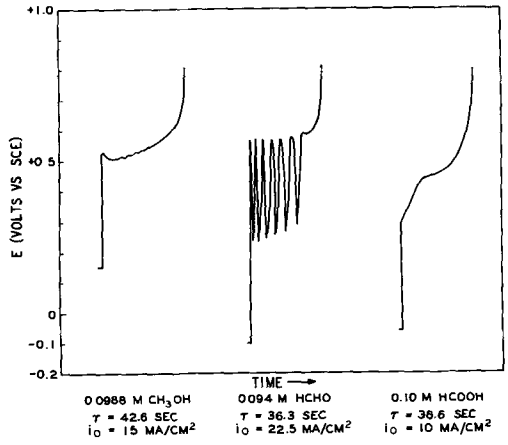

Fig. 9. Experimental potential-time curves for methanol, formaldehyde, and formic acid in 2.5M H_2SO_4.

Chronopotentiometry in Basic Solutions

We have obtained chronopotentiograms for the oxidation of methanol, formaldehyde, and formic acid in both basic and acidic solutions. Representative curves are shown in Fig. 8 and 9. Transition times were measured from recorder plots of anode potential *vs.* time. In general, these curves are not simple shapes associated with (i) reversible oxidations, (ii) irreversible oxidations, or (iii) irreversible oxidations with preelectrochemical solution reactions. The sole exception is methanol in base where the data can be fitted by equations for E *vs.* t for either case (ii) or (iii). Results from experiments using platinized platinum foil electrodes are given in Table II for comparison with voltammetric results.

In the potential sweep experiments at 8M NaOH and with 0.0988M methanol, the average value of $(1-\alpha)n_a$ for six experiments was 0.35 with a range of values between 0.31 and 0.41.

Values of the product $i_o\tau^{1/2}$ for the anodic oxidation of methanol in basic solution decrease with increasing current. For the reaction

$$CH_3OH + OH^- \underset{k_b}{\overset{k_f(OH^-)}{\rightleftharpoons}} CH_3O^- + H_2O \quad [11]$$

the relationship between $i_o\tau^{1/2}$ and i_o is given by:

$$i_o\tau^{1/2} = \frac{\pi^{1/2}nFC°D_o^{1/2}}{2} - \frac{\pi^{1/2}i_o}{2K[k_f(OH^-) + k_b]^{1/2}} \quad [12]$$

Table II. Electrochemical oxidation of methanol in 10M KOH on a platinized platinum electrode

$C°$, mole/liter	i_o, amp/cm²	$(1-\alpha)n_a$	$k°_{b,h}$, cm/sec	$k'_{s,h}$, cm/sec
0.0494	0.0075	0.30	1.6×10^{-2}	3.4×10^{-6}
0.0988	0.015	0.36	1.3×10^{-2}	5.9×10^{-7}

where

$$K = \frac{(CH_3O^-)}{(CH_3OH)} = \frac{k_f(OH^-)}{k_b}$$

and $k_f(OH^-)$ and k_b are the rate constants for the forward and reverse processes, respectively. From 10M KOH to pH 10, application of Eq. [12] gives $k_f \sim 10^3$ cm^3 mole^{-1} sec^{-1}. This value is much lower than is normal for a proton transfer of the type assumed; Luz, Gill, and Meiboom (20) reported a value of $k_f = 10^9$ cm^3 mole^{-1} sec^{-1} which they determined from NMR data. Since $i_o\tau^{1/2}$ varies with i_o when adsorption processes occur in the course of the reaction, we conclude that the rate-limiting process is not solely the formation of methylate ion, but also involves chemisorption of the methylate ion or methanol, itself.

Values of $i_o\tau^{1/2}$ for formaldehyde oxidation in base are not constant. The data were not treated because of the complexity of the chronopotentiograms caused, in part, by the formation of hydrogen on the electrode.

Values of $i_o\tau^{1/2}$ for formate oxidation in base are very nearly constant as shown in Table III. The usual plot of E *vs.* log $[1-(t/\tau)^{1/2}]$ is not a straight line in the region of small values of t. This fact and the shape of the chronopotentiogram indicate that the oxidation may be complicated by other reactions occurring on the electrode.

Chronopotentiometry in Acidic Solutions

In Fig. 9 chronopotentiograms for the oxidation of methanol, formaldehyde, and formic acid in 2.5M H_2SO_4 show variations from the form expected for totally irreversible processes with one rate-determining step. Similar variations are seen in 1M H_2SO_4. In extreme cases, potential oscillations occur in the oxidation of methanol and formaldehyde; however, in both of these cases, it is possible to oxidize the materials without potential oscillations. Although we did not observe oscillations in the case of formic acid, they have been reported by Pavela (3).

Methanol.—Potential oscillations are observed in the current density range of 10-15 ma/cm^2 with 0.0988M methanol in 1M H_2SO_4 at 25°C. At greater current densities where practically no oscillations occur, the measured transition times approach the calculated values neglecting corrections for surface roughness and kinetic complications due to preelectrode reactions.

Formaldehyde.—Typical chronopotentiograms for the oxidation of formaldehyde in acid solutions are shown in Fig. 9 and 10. The first 30-sec period from each of 8 chronopotentiograms at 8 current densities is shown in Fig. 10. The oscillations do not occur at current densities below 7.5 ma/cm^2. As current density is raised, the amplitude of the oscillation increases; the frequency does not change appreciably. We have also observed that the frequency increases with increasing acid concentration, the amplitude decreases with increasing acid concentrations, the frequency decreases with time, and the amplitude sometimes increases and sometimes decreases with time.

Table III. 0.1M formate in 1M KOH

i_o, amp/cm^2	$i_o\tau^{1/2}$, amp-sec$^{1/2}$
0.00175	0.0124
0.0020	0.0117
0.0025	0.011
0.0030	0.0115

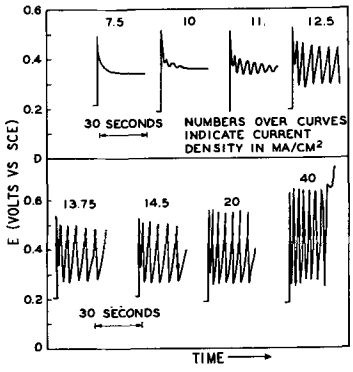

Fig. 10. Potential-time curves for the electrochemical oxidation of 0.1M formaldehyde in 1M H_2SO_4.

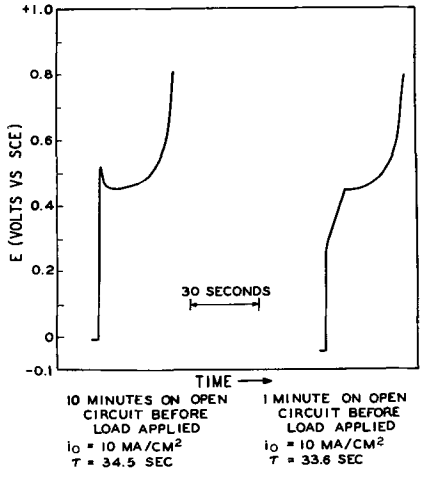

Fig. 11. Potential-time curves for the electrochemical oxidation of 0.1M formic acid in 2.5M H_2SO_4.

Formic acid.—Chronopotentiograms of 0.1M HCOOH in 2.5M H_2SO_4 have complicated shapes shown in Fig. 11. If the electrode remains in contact with the electrolyte for some time before current is drawn, the potential passes through a maximum after the load is applied. If the electrode is in contact with the solution for only a short time, this maximum is replaced by a shoulder. Transition times are not significantly different in the two cases.

Potential Oscillations

Oscillations during constant current anodic processes in acid solutions have been reported previously (3, 21-28). In the cases of methanol and formaldehyde, Pavela (3) believes that potential oscillations result from gas (CO_2) evolution at the electrode. Explanations invoking an alternation of processes, such as (i) the direct oxidation at the most negative potentials and (ii) oxidation via reaction with platinum oxide at the positive potential side of the oscillation, are difficult to defend. Whether or not the chemical reaction of the fuel with platinum oxide is slower than diffusion, the processes ought to seek a steady state at an intermediate potential.

A recent study by Sawyer and Seo (28) of the anodic oxidation of dissolved hydrogen suggests that potential oscillations arise from diffusion of absorbed hydrogen out to the electrode-solution interface from interior positions. Reduction of platinum oxides formed during the positive potential sweep brings the potential back to the negative extreme of the oscillation. In the meantime, the concentration of oxidizable material in solution at the interface has been replenished. This interpretation explains the sensitivity of the oscillations to time of exposure of the electrode to the solution before applying load.

Evidence for Surface Adsorption

All of our present evidence for a surface adsorption step in the mechanism for the oxidation of methanol and formaldehyde in base is indirect. It has been shown by Schlatter (10) that alcohols without an available hydrogen on the carbon containing the hydroxy group are not oxidizable on platinum anodes, *e.g.*, tertiary butanol is not oxidizable in aqueous base at room temperature. The only metals on which room temperature oxidations proceed are those commonly known as hydrogenation or dehydrogenation catalysts. The magnitude of the current peak heights for methanol may be smaller than those for formaldehyde because of a slow preelectrochemical adsorption step, and further, a slowing of the adsorption rate with current drain due to removal of methanol at the electrode surface may account, in part, for the small methanol peak currents. The presence of shoulders on the negative potential side of an oxidation current peak is analogous to the well-known adsorption prewaves in polarography.

These factors, plus the difficulty in reproducing voltammetric data depending on the time between the addition of the sample and the start of the potential sweep, suggest that adsorption plays a role in the mechanism. However, it is not clear that the adsorption rate is the slowest step or that it becomes entirely limiting during a potential sweep. Chronopotentiometric studies for the testing of adsorption rate limitation along lines suggested by Reinmuth (29) may elucidate the role played by adsorption.

Mechanisms and Conclusions

Our postulated mechanism for the oxidation of methanol, formaldehyde, and formate in base depends on extensive voltammetric studies and their analyses. No mechanism is proposed for the oxidation in neutral or acidic solutions. However, the over-all course of the reaction is clear in acidic media through the extensive product analyses of Schlatter (10). The suggestion that methylate, methylene glycolate, and formate anions are the electroactive species has already been suggested by Müller (1). Our mechanism is similar to one proposed by Pavela (3). The principal differences between his mechanism and ours are: (i) we consider that hydroxyl ion participates in a preelectrochemical step and not in the slow electron-transfer step, and (ii) we favor a dissociative chemisorption step which is of slower speed than the preelectrochemical reaction involving hydroxyl ion. Rate constants reported above are not corrected for fractional surface coverage by adsorbed species.

The mechanism for methanol oxidation in base appears to include

$$CH_3OH + OH^- \underset{k_b}{\overset{k_f}{\rightleftharpoons}} CH_3O^- + H_2O \qquad (A)$$

$$CH_3O^- \xrightarrow[\text{slow}]{\text{Pt}} CH_2O^-(\text{ad}) + H(\text{ad}) \qquad (B)$$

$$H(\text{ad}) + OH^- \xrightarrow{\text{fast}} H_2O + e^- \qquad (C)$$

$$CH_2O^-(\text{ad}) \xrightarrow[k_{s,h}]{\text{slow}} CH_2O + e^- \qquad (D)$$

$$CH_2O + H_2O \xrightarrow{\text{fast}} CH_2(OH)_2 \qquad (E)$$

$$CH_2(OH)_2 + 3\,OH^- \xrightarrow{\text{fast}} HCOO^- + 3H_2O + 2e^- \qquad (F)$$

$$HCOO^- + 3\,OH^- \xrightarrow{\text{slow}} CO_3^= + 2H_2O + 2e^- \qquad (G)$$

Details of the process represented by (*F*) are the same as those occurring when formaldehyde is the fuel

$$CH_2(OH)_2 + OH^- \underset{k_b}{\overset{k_f}{\rightleftharpoons}} CH_2(OH)O^- + H_2O \qquad (H)$$

$$CH_2(OH)O^- \xrightarrow[\text{moderate}]{\text{Pt}} CH(OH)O^-(\text{ad}) + H(\text{ad}) \qquad (I)$$

$$H(\text{ad}) + OH^- \xrightarrow{\text{fast}} H_2O + e^- \qquad (J)$$

$$CH(OH)O^-(\text{ad}) + OH^- \xrightarrow[k_{s,h}]{\text{slow}} HCOO^- + H_2O + e^- \qquad (K)$$

Process (*G*), the anodic oxidation of formate, may proceed by a mechanism analogous to those postulated above; however, we cannot rule out the possibility of a direct reaction of the formate without an adsorbed intermediate state. Also, we do not have evidence to exclude simultaneous direct reaction of methylate or methylene glycolate without an adsorbed intermediate state.

Acknowledgment

The authors gratefully acknowledge the support of the Army Ordnance Corps, Diamond Ordnance Fuze Laboratories, Washington. They wish to thank Drs. G. H. Denison, D. A. Hickson, D. R. Rhodes, M. J. Schlatter, and R. T. Macdonald for helpful discussions of this work and Mr. W. J. Doppe for assistance in data collection.

Manuscript received Dec. 15, 1961; revised manuscript received Aug. 1, 1962. This paper was prepared for delivery before the Detroit Meeting, Oct. 1-5, 1961.

Any discussion of this paper will appear in a Discussion Section to be published in the June 1963 JOURNAL.

REFERENCES

1. E. Müller, *Z. Elektrochem.*, **28**, 101 (1922).
2. S. Tanaka, *ibid.*, **35**, 38 (1929).
3. T. O. Pavela, *Ann. Acad. Sci. Fennicae* (Suo. Tied. Toim.), Series AII, Chem. No. **59**, 1 (1954).
4. W. M. MacNevin and T. R. Sweet, *Quart. J. Studies Alc.*, **12**, 46 (1951).

5. G. A. Bogdanovskii and A. I. Shlygin, *Russ. J. Phys. Chem.*, **33**, 151 (Eng. Trans.) (1959).
6. W. Vielstich, Extended Abstracts—Battery, Corrosion, Industrial Electrolytic, and Theoretical Divisions, The Electrochemical Society, Fall Meeting, Detroit, Oct. 1-5, 1961, Abstract No. 113.
7. P. Delahay, "New Instrumental Methods in Electrochemistry," Interscience Publishers, Inc., New York (1954).
8. J. Koutecky and R. Brdicka, *Collection Czechoslov. Chem. Commun.*, **12**, 337 (1947).
9. Mechanisms and Kinetics of the Fuel Cell Oxidation of Methanol, Formaldehyde, and Formic Acid," R. P. Buck, L. R. Griffith, R. T. Macdonald, and M. J. Schlatter, Fifteenth Annual Power Sources Conference, Atlantic City, May 9, 1961.
10. M. J. Schlatter, Reprint of the Division of Petroleum Chemistry, American Chemical Society, **6**, B-149 (1961).
11. Investigative Study Relating to Fuel Cells, Quarterly Reports 1 through 4 for the Diamond Ordnance Fuze Laboratories, Ordnance Corps, Department of the Army, Washington 25, D. C., Contract No. DA-49-186-ORD-929, No. 1, July 25, 1961; No. 2, December 30, 1960; No. 3, March 15, 1961; No. 4, June 26, 1961.
12. D. D. DeFord, Private communication, 133rd American Chemical Society Meeting, San Francisco, California, April 1958.
13. T. C. Franklin and S. L. Cooke, Jr., *This Journal*, **107**, 556 (1960).
14. H. A. Laitinen and C. G. Enke, *ibid.*, **107**, 773 (1960).
15. P. Delahay, "New Instrumental Methods in Electrochemistry," Chap. 6, Interscience Publishers, Inc., New York (1954).
16. a. L. S. Guss and I. M. Kolthoff, *J. Am. Chem. Soc.*, **62**, 1494 (1940); b. R. Bieber and G. Trumpler, *Helv. Chim. Acta*, **30**, 709 (1947).
17. P. Ballinger and F. A. Long, *J. Am. Chem. Soc.*, **82**, 795 (1960).
18. W. M. Latimer, "Oxidation Potentials," 2nd ed., p. 130, Prentice Hall, Inc., New York (1952).
19. R. J. L. Martin, *Australian J. Chem.*, **7**, 400 (1954).
20. E. Luz, D. Gill, and S. Meiboom, *J. Chem. Phys.*, **30**, 1540 (1959).
21. G. Armstrong and J. A. V. Butler, *Discussions Faraday Soc.*, **1**, 122 (1948).
22. C. D. Alley, Ph.D. Thesis, University of Tennessee, University Microfilms, Inc., Ann Arbor, Michigan, Mic. 59-6980 (1959).
23. J. A. V. Butler and G. Armstrong, *Nature*, **129**, 613 (1932).
24. M. Thalinger and M. Volmer, *Z. Physik. Chem.*, **150**, 401 (1930).
25. J. A. V. Butler, "Electrical Phenomena at Interfaces," p. 209, Macmillan Company, New York (1951).
26. M. J. Jonicich and N. Hackerman, *J. Phys. Chem.*, **57**, 674 (1953).
27. J. Osterwald and H. Feller, *This Journal*, **107**, 473 (1960).
28. D. T. Sawyer and E. T. Seo, *J. Electroanalytical Chem.*, In press.
29. W. H. Reinmuth, *Anal. Chem.*, **33**, 322 (1961).

The Effect of Acetylenic Molecules on Cathodic Overvoltage on Steel in Acid Solutions

E. J. Duwell

Minnesota Mining and Manufacturing Company, St. Paul, Minnesota

ABSTRACT

An apparatus was constructed for measuring changes in electrode potential at constant current density. Large increases in hydrogen overvoltage were noted when acetylenic molecules were adsorbed on a steel cathode, and cathodic reduction of dissolved oxygen was apparently inhibited. The effect on the anodic oxidation of steel was small. Thus, it can be concluded that these molecules slow down the oxidation of steel in acid solutions by inhibiting the cathodic reactions. The most effective adsorbates are characterized by steric availability of the acetylenic bond, non-ionic character, and large molecular size.

The adsorption of molecules from solution on a metal surface to prevent corrosion is a well-known process. Several techniques such as tagging the adsorbate with radioactive tracers, measurement of contact angles and surface potentials, and straightforward analysis of solution concentration before and after adsorption have been used to follow the adsorption process. The measurement of the change in potential of one electrode process as adsorption proceeds has been used to a much lesser extent to determine adsorption even though this technique has been used successfully by several investigators (1-3).

For an electrode process which is proceeding at a finite rate, the potential E is given by

$$E = E_R + \eta$$

where E_R is the reversible potential and η is the overvoltage. The overvoltage is related to current density i, by the well-known Tafel equation

$$\eta = a - b \log i$$

where a and b are constants. If the current is held constant, and the change in overvoltage is caused by adsorption, it may be assumed that

$$\Delta\eta = \eta' - \eta = b \log i/i'$$

where

$$i' = (1 - \theta)\, i$$

θ is the apparent fraction of the area covered by the absorbate. It then follows that

$$\theta = 1 - e^{-\Delta\theta/b}$$

The values of θ obtained by this method have been shown to be in reasonable agreement with values of θ obtained by double layer capacitance measurements for the adsorption of octanoic acid on silver

(3). It is assumed that the adsorbed layer is an inert blanket and does not change the reactions occurring at the electrode, and hence does not change the value of the constant b. This may not be entirely correct for the systems to be described in this paper, although some of the results support this assumption.

If η in the base solution is known, only a measurement of $\Delta\eta$ is needed for a comparison of adsorbates introduced to that solution. Since the purpose of this investigation was to compare the effect of various acetylenic chemicals on the electrode reactions which occur when steel is oxidized by acids, an apparatus was designed which gave a measurement of $\Delta\eta$.

It has been known for some time that some acetylenic chemicals will inhibit the oxidation of steel (4, 5). Our data support an earlier report that it is the cathodic process which is slowed down (5).

Apparatus

The essential features of the bridge circuit and cell are given in Fig. 1. The potential source consisted of two 6v lead storage cells in series. The loops in the left arms contain 1.5v batteries for a bias voltage, variable 300 ohm and 15 ohm resistors, and Texas Instrument 2N250 transistors. The current in the cell and reference arms were made equal by adjustment of resistors in the transistor circuit. These circuits then served to maintain a constant current even if the resistance of the cell changed. A Varian G-11A potentiometric recorder with variable ranges from 0-10 to 0-1000 mv was used to record the voltage difference between the cell and reference arms of the bridge. The reference "cell" consisted of a decade box which was adjusted to give a zero reading on the recorder. Thus, if the current in the cell is equal to that in the decade box, the resistance of the cell equals the resistance of the decade box when the experiment is begun. If an absorbate is now added to an electrode chamber and increases the overvoltage, the change, as a function of time, is noted on the potentiometric recorder.

The cell consisted of 500 ml cathode and anode chambers separated from a cylindrical center section by fritted glass disks. The fritted disks served as membranes to reduce the diffusion of molecules from the anode to the cathode chambers. The center section was also used to determine if a particular adsorbate changed the resistance of the solution by contributing to the ionic strength, or by changing the mobility of the ions in the base solution. Because the distance between the fritted glass disks was much larger than the distance from the electrodes to the disks, this type of change was magnified in comparison to what would be obtained in the anode or cathode chamber. Calibration could be accomplished by use of solutions of known resistance and measurement of the distances between the electrodes and the fritted glass disks. A buffered cell solution of 1M acetic acid-1M sodium acetate was used in all experiments reported in this paper.

The steel (S.A.E. 1010) cathode consisted of a flat plate with an exposed area of 8.25 cm^2. The back of the plate and the stem leading up out of the solution were coated with a high melting wax. Thus the entire exposed surface was at the same potential relative to the anode, and changes in the level of the liquid did not affect the size of the exposed area. Oxygen was evolved in the anode chamber on a rough platinum wire.

The cathode potential was measured relative to a saturated calomel half cell. The potentiometric circuit contained a Type 7552 L&N potentiometer and a Rubican multireflection galvanometer. A Luggin tubulus was used for electrical contact between the calomel cell and steel electrode. This technique for measuring electrode potentials in cells in which an appreciable current is flowing has been described in the literature (6).

Reagents

Butynediol was crystallized from 30% solutions obtained from General Aniline Company, and the crystals were washed with ethyl alcohol. Propargyl

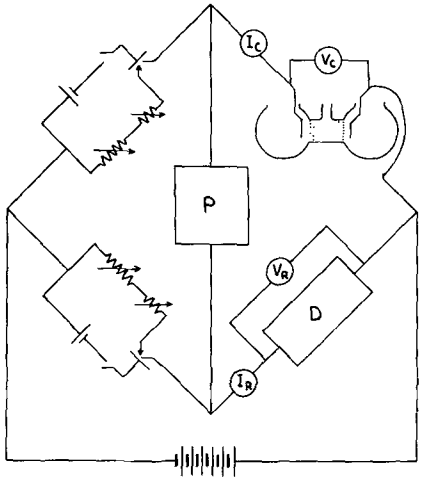

Fig. 1. Circuit diagram for the DPA apparatus. V and I are voltmeters and ammeters for measuring the current and voltage drop across the cell and reference arm of the circuit. A decade box (D) is used in the reference arm. P is a Varian G-11A potentiometric recorder.

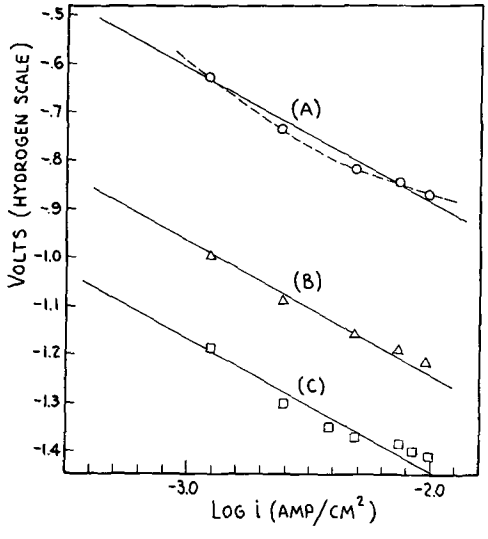

Fig. 2. Potential vs. current density for a mild steel cathode in: (A) 1M acetic acid-1M sodium acetate; (B) 1M acetic acid-1M sodium acetate-0.0116M propargyl alcohol; (C) 1M acetic acid-1M sodium acetate-0.0116 M 1-hexyne-3-ol. *i* is the current density on the steel cathode.

Table I. Changes in cathodic potential with additions of various acetylenic chemicals

Cell solution: 1M CH_3COOH—1M CH_3COONa; current: 30 ma; volume in cathode chamber: 500 cc; amount of acetylenic chemical ($R_1C \equiv C - R_2$) added to cathode chamber: 0.0116 mole.

	Additive ($R_1C \equiv CR_2$) R_1	R_2	
	Alcohols		
1.	$CH_2(OH)$	H	+370
2.	$CH_3CH(OH)$	H	+235
3.	$CH_2(OH)CH_2$	H	+108
4.	$CH_2(OH)$	CH_3	+105
5.	$CH_2(OH)$	CH_2OH	+110
6.	$CH_3C(CH_3)(OH)$	H	+295
7.	$CH_3CH_2CH(OH)$	H	+265
8.	$CH_3CH(OH)CH_2$	H	+127
9.	$CH_3CH_2C(CH_3)(OH)$	H	+325
10.	$CH_3CH_2CH_2CH(OH)$	H	+530
11.	$CH_2(OH)C \equiv C$	CH_2OH	+125
12.	$CH_3CH_2CH_2C(OH)(CH_3)$	H	+535
13.	$CH_3CH(CH_3)CH_2C(OH)(CH_3)$	H	+670
14.	$CH_3CH(CH_3)(OH)$	$C(CH_3)(OH)CH_3$	0
15.	$CH_3CH_2CH_2CH_2CH(CH_2CH_3)CH(OH)$	H	+690
16.	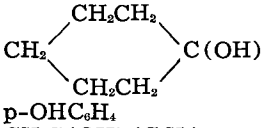	H	+540
17.	$p\text{-}OHC_6H_4$	$p\text{-}OHC_6H_4$	0
18.	$CH_3C(OH)(C_6H_5)$	H	+635
19.	$CH_3CH_2C(CH_3)(OH)$	$C(CH_3)(OH)CH_2CH_3$	+10
20.	$CH_3CH_2CH_2CH_2CH_2$	CH_2OH	+260
	Acetylenic hydrocarbons		
21.	$CH_3CH_2CH_2$	H	+650
22.	$CH_3CH_2CH_2CH_2$	H	+650
23.	$CH_3CH_2CH_2$	CH_3	+46
24.	CH_3CH_2	CH_3CH_2	+9
25.	$CH_3(CH_2)_4$	H	+800
26.	$CH \equiv C(CH_3)_3$	H	+720
27.	$CH_3(CH_2)_5$	H	+850
28.	$CH_3(CH_2)_4$	CH_3	+13
29.	$CH_3(CH_2)_6$	H	+810
30.	$CH_3(CH_2)_7$	H	+910
31.	C_6H_5	H	+610
	Acids and Esters		
32.	COOH	H	−35
33.	COOH	COOH	−33
34.	C_2H_5-O-CO	H	+162

alcohol and phenylacetylene were reagent grade from the Matheson Company. Reagents 6, 9, 13, 14, 15, 16, 17, and 19 (Table I) were commercial samples obtained from Air Reduction Company. The remaining reagents listed in Table I were reagent grade samples prepared by Farchan Research Laboratories.

Results

A determination was made of cathodic potential as a function of current density in the acetic acid-sodium acetate buffered solution (Fig. 2). Addition of propargyl alcohol or 1-hexyne-3-ol increased the voltage but did not appreciably change the shape of the curves within the limits of experimental error. This was found to be true in general for the acetylenic compounds which were investigated. With the exception of reagents 32 and 33 (Table I), none of the molecules investigated gave a change in cell potential when added to the center chamber.

Both the rate and total change in cathodic overvoltage depended on the concentration of the acetylenic compound. The maximum change, however, seemed to be reached at concentrations of about 0.01M for 2-butyne-1,4-diol, or 1-hexyne-3-ol (Fig. 3). The rate of change of overvoltage also depended on how vigorously the solution was stirred until some degree of agitation was reached, beyond which no increase in rate was obtained. The anode and cathode chambers were both rapidly stirred, so that neither an increase in agitation nor small decreases changed the rate at which the overvoltage increased.

0.0116 Moles of a number of acetylenic chemicals were added to the cathode chamber. If the compounds were soluble, this would result in 0.0232M solutions. Some of the molecules listed were not soluble to that extent, and the resulting solutions were therefore saturated. The solubilities are not in general known for the various compounds investigated.

Because the solutions were rapidly stirred and not protected from the atmosphere, it can be assumed that some oxygen was available for reduction at the cathode. Although a current of only 30 ma was used in all the experiments, the evolution of hydrogen gas was readily visible on the steel cathode surface. If no oxygen reduction had oc-

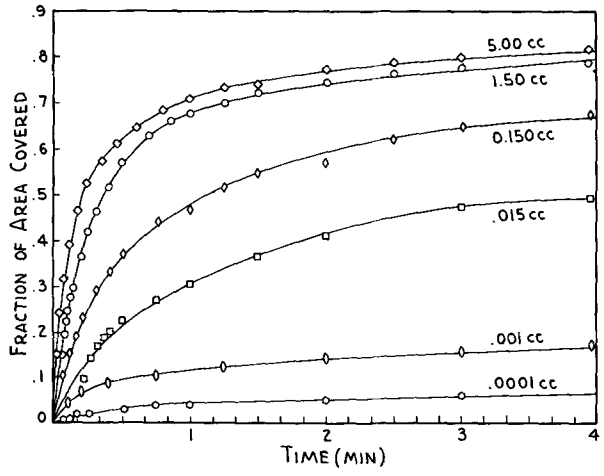

Fig. 3. Fraction of area covered on mild steel cathode as a function of time for additions of 1-hexyne-3-ol to 500 ml to 1M acetic acid-1M sodium acetate.

curred, the theoretical hydrogen production would have been 0.42 cc/min.

The bubbling of either hydrogen or nitrogen gas through the solution to remove oxygen resulted in a slow increase in cathode potential. If an acetylene compound such as 1-hexyne-3-ol was then added to the cathode chamber, the change in the cathode potential was decreased as compared to the changes noted in aerated acetic acid-sodium acetate buffer solutions (Fig. 4). The total increase in cathodic overvoltage resulting from oxygen removal and addition of 1-hexyne-3-ol to the deoxygenated solution was approximately equal to that obtained by addition of the 1-hexyne-3-ol to an aerated solution. Conversely, when oxygen was bubbled through a deaerated solution containing the acetylenic compound, there was a slow decrease in cathode potential. The magnitude of the decrease was less when the acetylenic compound was present.

The acetylenic compounds also increased the electrode potential for the anodic decomposition of iron.

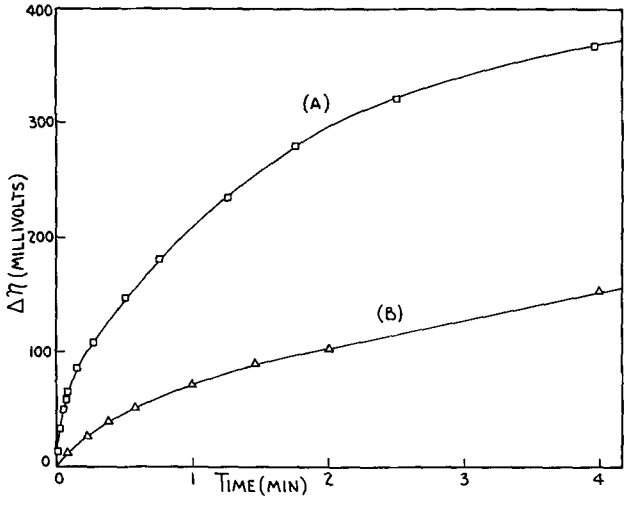

Fig. 4. Overvoltage as a function of time for the addition of 1-hexyne-3-ol (0.0116M) to an aerated 1M acetic acid-1M sodium acetate solution (A), and to the same solution except constantly deaerated with a hydrogen bubbler (B). The final change in $\Delta\eta$ was 530 mv for the aerated solution and about 200 mv less for the deaerated solution.

To measure this effect, the polarity of the cell was reversed. A slow but steady increase of the cell resistance was noted. Addition of one of the acetylenic compounds to the chamber containing the steel electrode gave an increase in electrode potential that was very small compared with the increase noted when the steel electrode was the cathode. 1-Hexynol, for example, gave an increase of 30 mv.

Discussion

Since there was no change in cell resistance when any of the acetylenic compounds were added to the center chamber, it can be concluded that the observed effects are due to changes on the electrode surface, and not to changes in the resistance of the solution. Therefore, the acetylenic molecules must in some way become adsorbed on the electrode surface.

The most apparent effect of the acetylenic chemicals is to raise the potential level of the Tafel plots (Fig. 2) rather than change their shape. The Tafel slopes as drawn have a value of about 250 mv, which is much higher than usually noted. However, a curved line of approximately the same slope would fit the experimental points better in each case (broken line). The slope of these curves at the higher current densities would be about 120 mv, which agrees more closely with the values usually reported. If the slope of the Tafel line is dependent on the reaction mechanism as has often been suggested, the data indicate that the reaction mechanism may change with current density. For this reason all of the acetylenic chemicals were compared at the same current density. The assumption that the addition of acetylenic chemicals does not change the reaction mechanism is of course very tentative in the absence of more complete analytical data.

The chemicals in Table I are listed approximately in order of increasing molecular size. It is apparent, all other things being equal, that there is an increase in overvoltage with increasing molecular size. Propargyl alcohol (reagent 1) is a notable exception. It gave a larger increase in overvoltage than some successively larger α-substituted acetylenic alcohols (reagents 2, 6, 7, and 9). The generalization is valid for all other α-hydroxy acetylene compounds listed. There are, however, other factors that greatly affect the change in overvoltage and lead to a partial understanding of how the acetylenic molecules become attached to the surface.

The position of the acetylenic bond in the carbon chain is the most important structural feature affecting cathodic overvoltage. If the acetylenic bond is not a terminal group, the effect on cathodic overvoltage is decreased or disappears as the size of the group on either end of the acetylenic bond is increased (reagents 4, 5, 14, 17, 19, 23, 24, and 28).

The acetylenic hydrocarbons are generally more effective than the acetylenic alcohols for increasing overvoltage. For example, 1-pentyne and 1-hexyne gave larger increases in overvoltage than any of the acetylenic alcohols with the same chain length. The hydrocarbons are much less soluble than the alcohols. Assuming that both the alcohols and hy-

drocarbons are held to the metal surface through the acetylene group, the alcohols would tend to be more easily solvated and desorbed as a result of hydrogen bonding of the alcohol group with water. The hydrocarbons are less rapidly adsorbed than the alcohols. This also is probably a result of their limited solubility.

The adsorbed layer of acetylenic molecules apparently behaves primarily as a barrier to diffusion, since both cathodic reduction of oxygen and reduction of hydronium ions are apparently inhibited. This would be effected by increasing the work necessary to bring oxygen and hydronium ions to the electrode surface. The larger the hydrocarbon tail on the molecule, the greater is the barrier to diffusion. The adsorbed layer appears to be loosely bound to the surface, however, since oxidation of the steel surface is not inhibited under ordinary atmospheric conditions. Also, the electrodes have a hydrophobic surface when withdrawn from the solution containing the acetylenic compound as evidenced by the high contact angle of water droplets on the surface. This hydrophobic surface is easily removed by rinsing in a stream of distilled water. Thus it appears that the acetylenic molecules are easily desorbed by either evaporation or dissolution.

Since the acetylenic molecules can be effective for increasing overvoltage even when the acetylenic group does not terminate the molecule, bonding to the surface probably occurs through the electron rich acetylenic group, rather than by displacement of the acetylenic hydrogen. The formation of acetylenic metal complexes of this type have been reported (7, 8, 9) and probably involve the filling of d band vacancies in the metal by π electrons of the acetylenic group. Though bonding both by this mechanism and by hydrogen displacement might occur, the former appears more likely since iron compounds formed by hydrogen displacement have been reported to be very unstable (9).

If the hydroxyl group is α to the acetylenic group, the increase in cathodic overvoltage is about twice that obtained for an isomer in which the hydroxyl group is β to the acetylenic group (reagents 2-3, 7-8). Since the hydroxyl group withdraws electrons from the acetylenic bond and makes the acetylenic hydrogen more acid, this observation does not appear to support the bonding hypothesis forwarded, but actually lends weight to the hypothesis that bonding may occur by displacement of the acetylenic hydrogen. However, since the acetylenic hydrocarbons give larger increases in overvoltage than the α-substituted alcohols, it is probable that there are other effects which may contribute or detract from a compound's ability to increase cathodic overvoltage.

Another factor which may contribute to increasing cathodic overvoltage is the insulating properties of the adsorbed layer. An adsorbed layer which is essentially a hydrocarbon can be expected to be a poor ionic conductor. Proprolic acid and acetylene dicarboxylic acid (reagents 32 and 33), which gave small decreases in cathodic overvoltage, may become adsorbed but serve as good conductors of hydronium ions to the surface because of their strongly acidic nature. These molecules gave decreases of only several millivolts in cell potential when added to the center chamber. Therefore, the change of over 30 mv resulting from their addition to the cathode chamber cannot be attributed to an increase in ionic strength.

Finally, the possibility that the acetylenic bond becomes hydrogenated must not be overlooked. Although such a reaction may change cathode potential and may occur to some extent, it is probably not a major factor contributing to the effect of the acetylenic chemicals on cathodic overvoltage. Qualitative observations support this conclusion. The evolution of hydrogen gas is readily visible and does not visibly diminish when the acetylenic chemical is added to the cathode chamber. Also, the increase in overvoltage continues far beyond the time at which the acetylenic additive would be consumed by hydrogenation. Finally, the effect of an olefin such as allyl alcohol on cathodic overvoltage is small (10 mv) compared to the effect of the acetylenic analog propargyl alcohol (370 mv).

Further work is in progress to elucidate the nature of the interaction of acetylenic molecules with metal surfaces. Initial efforts are being directed toward adsorption measurements.

Acknowledgment

The author wishes to thank Minnesota Mining and Manufacturing Company for their support of this work. He also wishes to thank Mr. Ivan Maw for his help in performing the experiments, and the members of the Physical Chemistry staff for many helpful and stimulating discussions.

Manuscript received Feb. 19, 1962; revised manuscript received June 15, 1962. This paper was prepared for delivery before the Boston Meeting, Sept. 16-19, 1962.

Any discussion of this paper will appear in a Discussion Section to be published in the June 1963 JOURNAL.

REFERENCES

1. Shih-Jen Ch'Iao and C. A. Mann, *Ind. Eng. Chem.*, **39**, 910 (1947).
2. J. O'M. Bockris and B. E. Conway, *J. Phys. Colloid Chem.*, **53**, 527 (1949).
3. R. S. Hansen and B. H. Clampitt, *J. Phys. Chem.*, **58**, 908 (1954).
4. J. W. Reppe, *Acetylene Chemistry*, P. B. Report 18852-S, Charles A. Meyer and Co., Inc., p. 101.
5. D. V. Sokol'skii and N. D. Azvorokhin, *Vestnik Akad. Nauk Kazakh. S.S.R.*, **13** [8], 59 (1957).
6. E. C. Potter, "Electrochemistry," p. 190, Macmillan Co., New York (1956).
7. H. W. Sternberg and I. Wender, International Conference on Coordination Chemistry, Special Pub., No. 13, The Chemical Soc., pp. 35-57 (1959).
8. E. O. Fischer, *ibid.*, pp. 73-93 (1959).
9. R. Nast, *ibid.*, pp. 103-113 (1959).

The Effect of Gaseous Impurities on the High-Temperature Oxidation of Magnesium

J. E. Castle,[1] S. J. Gregg, and W. B. Jepson[2]

Department of Chemistry, University of Exeter, England

ABSTRACT

The kinetics of the oxidation of magnesium in oxygen at temperatures between 475° and 570°C have been investigated. It is found that the course of the oxidation is grossly different according to whether the oxidation is carried out on a vacuum microbalance in static oxygen at 10 cm pressure or on a thermal balance in flowing oxygen at 76 cm pressure. This discrepancy cannot be attributed to different surface pretreatments. It is shown that the ready film breakdown (and subsequent nonprotective oxidation) in flowing oxygen is brought about by the reaction of the impurities in the oxygen with the magnesium. If these impurities are removed from the oxygen by gettering, either with magnesium itself or with a mixture of copper and iron oxides, before the magnesium is oxidized on the microbalance, then the amount of oxidation is very small, *e.g.*, at 525°C only 3 $\mu g/cm^2$ after 50 hr. The impurities are thought to be hydrocarbons which are catalytically cracked on the oxide surface to deposit carbon which becomes incorporated in the growing oxide layer. The rate of film thickening is dependent on the partial pressure of impurities in the oxygen, and as a consequence the rate of oxidation shows an apparent dependence on the pressure of oxygen.

The oxidation of magnesium has been the subject of a number of investigations (1-3); it is generally recognized that if magnesium is heated in flowing oxygen on a thermal balance at a temperature such as 550°C, "breakaway" occurs after several hours; as the white oxide scale extends over the sample surface so the rate of oxidation continuously increases with time until the whole of the specimen surface is covered (3). The metal then oxidizes at a constant or linear rate (*e.g.*, 0.18 $mg/cm^2/hr$ at 550°C). If the oxidation is continued for a sufficiently long time, the rate may increase to a second constant value, some tenfold greater than the first and "second breakaway" is said to have occurred; the oxide formed over this second linear branch is buff in color and different in texture from the white oxide scale.

During the course of an investigation (4, 5) of the oxidation of a number of magnesium alloys in oxygen with a vacuum microbalance, it became necessary to obtain reference data for magnesium itself. Rather surprisingly it was found that when a magnesium sample was oxidized at 550°C in the same batch of oxygen as that used on the thermal balance, but under static conditions and at a reduced pressure (100 mm), the inception of breakaway was delayed for several hundred hours.

This discrepancy has led to a reinvestigation of the oxidation of magnesium in oxygen which has established that traces of organic impurity (probably hydrocarbon in nature) play a fundamental role in promoting breakaway. If the impurity is removed from the oxygen, either by gettering or by catalytic oxidation, the weight gained by the magnesium is extremely small, *e.g.*, 3 $\mu g/cm^2$ after 50 hr at 525°C.

[1] Present address: C.E.R.L., Leatherhead, Surrey, England.

[2] Present address: Metallurgy Division, A.E.R.E., Harwell, Didcot, Berks, England.

Experimental

The magnesium, supplied by Magnesium Elektron Ltd. (England), was in the form of 1.6 mm thick sheet and was of the same stock (batch 2) as that used in previous work (3); the impurities amounted to 500 ppm (Table I). The major portion of the work was carried out with samples whose surfaces had been abraded to 4/0 emery and then electropolished according to the method of Jacquet (6) in a bath of phosphoric acid and ethyl alcohol.

Several grades of oxygen, all from B.O.C. Ltd. (England) were used; *viz.*, batch A, medical grade; batch B, spectroscopically standardized; and batch C, spectroscopically standardized which unlike batch B had been prepared in a single run and contained smaller amounts of impurity. Analyses are given in Table II.

The oxidation of magnesium was followed on a vacuum microbalance (7, 8) sensitive to 2.5 μg (*i.e.*,

Table I. Analysis of magnesium, in ppm

Zn	<200	Al	<100
Si	<50	Cu	<10
Mn	<100	Fe	<100
Ni	<20	Zr	Tr

Table II. Analysis of oxygen, in ppm

Batch	CO	CO_2	Other carbon cpds. as CO_2	Ar	N_2	H_2
A	0	<7	approx. 7	<0.4%	Tr	—
B	0	<4	—	—	<570	<15
C	0	<4	—	—	<57	<15

0.2 $\mu g/cm^2$ of the sample used). The normal practice with experiments in the microbalance is to outgas the sample before the start of the run at the proposed reaction temperature; with magnesium, such a procedure was not desirable however because evaporation of the metal readily occurred [saturation vapor pressure of magnesium (9) at 525°C is 0.15 mm], and the following method was therefore adopted. At the start of an experiment, the sample was first outgassed at room temperature, then a furnace, preset to 450°C, was raised around the balance limb, and outgassing was continued for a further hour. Under these conditions, no evaporation of the metal could be detected. Next the furnace was replaced by a second furnace preset to the desired run temperature, and oxygen was admitted to a pressure of 100 mm; the zero of time was taken as the instant when oxygen was admitted, and the first reading was taken after about 3 min, subsequent readings being taken at suitable intervals.

The normal practice of obtaining the "balance correction"[3] by evacuating the balance case at the end of the run led to evaporation of magnesium and a consequent weight loss; a standard correction was therefore applied to data obtained in each run and was determined in several preliminary runs using an aluminum sample of the same dimensions as the magnesium samples. A useful check of the balance correction was provided by the fact that little oxidation occurred over the first few minutes of each run so that the first reading of the balance after admission of oxygen corresponded essentially to zero weight gain.

Results

Runs were carried out at 500°, 525°, and 550°C in oxygen of batch A. As is seen from Fig. 1, the rate of oxidation at 550°C at first decreases with time (OA) to become almost constant along AB until at C breakaway occurs and the rate increases along CD: by visual examination the breakaway was found to be associated with the formation of small mounds of buff-colored oxide, particularly along the edges of the sample (Fig. 2). At 500° and 525°C, breakaway was absent within the period of the experiments, and the weight gains after a given time were smaller than at 550°C. Comparison with a run on a thermal balance in flowing oxygen of commercial quality and at atmospheric pressure showed the weight gains to be lower by several orders of magnitude in the microbalance experiments, *e.g.*, 50 $\mu g/cm^2$ compared with 10 mg/cm^2 at 550°C on the thermal balance, after 30 hr. Furthermore, after breakaway, the oxide was white in the thermal balance runs and buff-colored in the microbalance experiments.

Possible reasons for the differences are: (*a*) in the runs on the microbalance the magnesium underwent a vacuum anneal at 450°C for 1 hr before oxygen was admitted, whereas in those on the thermal balance the furnace, already at temperature, was raised into position around the reaction chamber through which oxygen was already flowing; (*b*) the pressure of oxygen was 100 mm in the microbalance experiments compared with 1 atm in the thermal balance runs; and (*c*) oxidation may be promoted by some impurity in the oxygen which in the thermal balance runs would be both continuously supplied and present at a larger partial pressure than in the microbalance experiments.

To test possibility (*a*), the normal procedure of starting a run on the vacuum microbalance was carried through up to the point at which oxygen would have been admitted; the furnace was then removed, and after the sample had cooled to room temperature, it was transferred to the thermal balance and heated at 550°C in flowing oxygen. The oxidation followed the same course as that of a freshly abraded sample so that the vacuum anneal has negligible influence in retarding breakaway.

A further set of experiments gave results which, although not eliminating (*b*), favored the third possibility (c), *viz.*, that an impurity in the oxygen is responsible for the higher rate of oxidation in the thermal balance experiments; three runs were carried out on the microbalance at 525°C but at the different pressures of 1 mm, 10 mm, and 100 mm, respectively. As is seen from Fig. 3, the curves are all similar in shape, but the weight gain at a common ordinate along the branch AB is some threefold greater at 100 mm than at 1 mm. Since it was considered unlikely that the pressure of oxygen *per se* would account for these large differences it was inferred that the increase in weight gain with increasing pressure of oxygen is in fact caused by a corre-

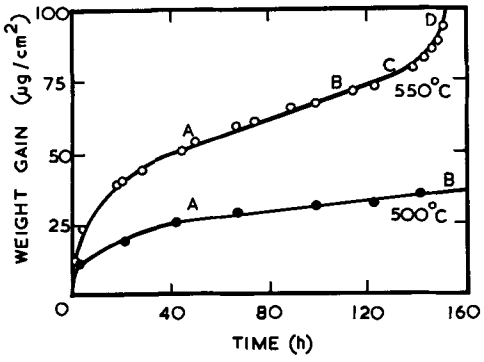

Fig. 1. Oxidation of magnesium at 500° and at 550°C in static oxygen (batch A) at 100 mm pressure. The magnesium had been abraded.

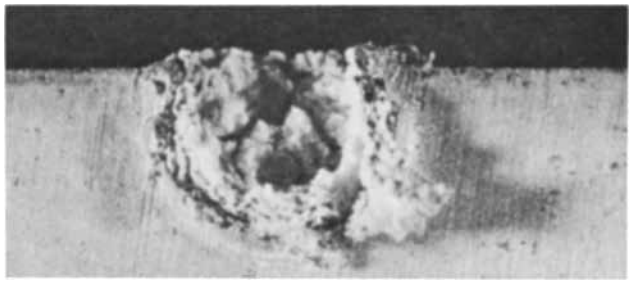

Fig. 2. Characteristic pit on the edge of a magnesium specimen which had undergone breakaway during oxidation at 550°C in static oxygen (batch A) at 100 mm pressure. Magnification approximately 32X.

[3] The balance correction is the change in deflection of the beam when the pressure of gas within the balance case is raised from 10^{-6} mm to 100 mm, the mass of the sample remaining constant. The magnitude of the balance correction is a function of pressure and is mainly due to the thermomolecular flow of gas molecules along the suspension wire (8).

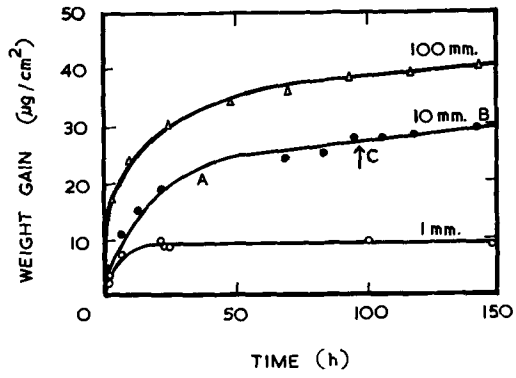

Fig. 3. Oxidation of magnesium at 525°C in static oxygen (batch B) at pressures of 1 mm, 10 mm, and 100 mm, respectively. The magnesium had been electropolished.

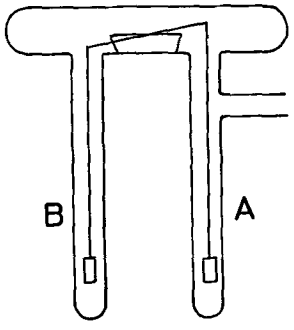

Fig. 4. Microbalance case in its modified form with the limb B extended to accommodate the second magnesium sample which was used to getter the oxygen.

sponding increase in the quantity of impurity, which being proportional to the pressure of oxygen would in the experiment at 100 mm be present in an amount one-hundredfold greater than in the experiment at 1 mm.

This conclusion was confirmed by experiments in which the suspected impurity was removed from the oxygen by "gettering" it with a sample of magnesium suspended in limb B of the microbalance case (Fig. 4) which was lengthened for the purpose. The sample under test was suspended in limb A in the usual way, and both samples were outgassed for 1 hr at 450°C in the standard manner, when the sample in limb A was allowed to cool to room temperature. Oxygen of batch B was then admitted to a pressure of 100 mm, and the temperature of the furnace around limb B was raised to 575°C and held there for 70 hr, in the expectation that the magnesium in the course of its oxidation would getter the impurity. After limb B had cooled to room temperature, a furnace preset to 525°C was raised into position around limb A, and the second magnesium sample oxidized. The resultant weight gain was very small (Fig. 5, curve 1) being only 3 $\mu g/cm^2$ after 50 hr; this strongly suggests that some impurity which can be gettered by magnesium is able to promote oxidation.

It now remained to attempt the identification of the impurity. Nitrogen and water vapor were obvious possibilities, but were eliminated from consideration by the following experiments. A number of runs were carried out at 525°C with oxygen of batch C containing a partial pressure of 0.05 mm (500 ppm) of nitrogen as an addendum, but the curves of weight

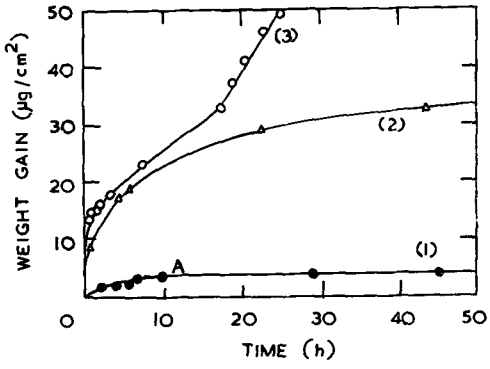

Fig. 5. Oxidation of magnesium at 525°C in static oxygen (batch C) at 100 mm pressure. Curve 1, gettered oxygen; curve 2, ungettered oxygen; curve 3, oxygen + 500 ppm of *n*-nonane. The magnesium had been electropolished.

gain against time did not differ appreciably from those obtained with batch C oxygen itself. In some further experiments, the oxygen (batch C) was thoroughly dried by leaving it in contact with a surface immersed in liquid oxygen for 24 hr, before starting the oxidation run at 525°C. Again the curves of weight gain against time did not differ appreciably from those obtained with batch C oxygen itself.

For various reasons it was suspected that the impurity might be organic in nature. A run was accordingly carried out in which an oxidizing catalyst, commercially available, consisting of a mixture of iron and copper oxides supported on kaolin, replaced the magnesium getter in limb B (Fig. 4). The catalyst was outgassed *in situ* at 620°C (the highest temperature it could withstand) until the vacuum was 10^{-6} mm, and the magnesium in limb A then outgassed at 450°C. The furnace was then removed from A and the sample allowed to cool to room temperature, oxygen of batch C was admitted to a pressure of 100 mm, and was left for 20 hr with the catalyst still at 620°C so as to allow ample time for oxidation of the impurity; a furnace preset to 525°C was then raised into position around the limb A. The resultant curve of weight gain against time (for the sample in A) closely resembled that obtained with magnesium as getter (curve 1, Fig. 5), strongly indicating that the relevant impurity is organic.

On general grounds it seemed that the impurity might be hydrocarbon in nature and was perhaps introduced during manufacture of the oxygen by leakage of lubricating oil from the compressors. In a further experiment therefore 500 ppm of a hydrocarbon, nonane ($n\text{-}C_9H_{20}$), was deliberately introduced into the oxygen (batch C). A run at 525°C (Fig. 5, curve 3) gave a curve which lies above that for oxygen of batch C containing no added hydrocarbon (curve 2); moreover signs of breakaway are present, the curve becomes convex to the time axis, and some white oxide scale was formed along the edges of the sample in a manner characteristic of oxidation in flowing oxygen.

The partial pressure and not merely the absolute amount of the impurity is important. This is evident from a comparison of two parallel experiments carried out with flowing oxygen of batch A, one on the microbalance at 100 mm pressure and the other

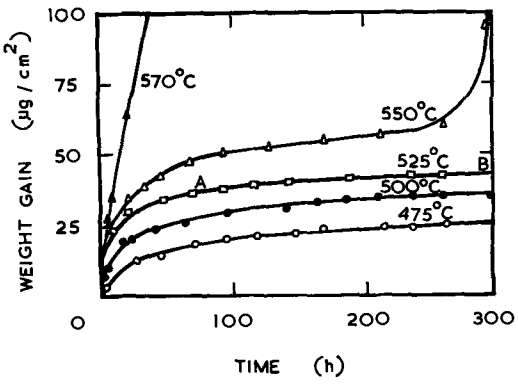

Fig. 6. Oxidation of magnesium at 475°, 500°, 550°, and 570°C in static oxygen (batch C) at 100 mm pressure. The magnesium had been electropolished.

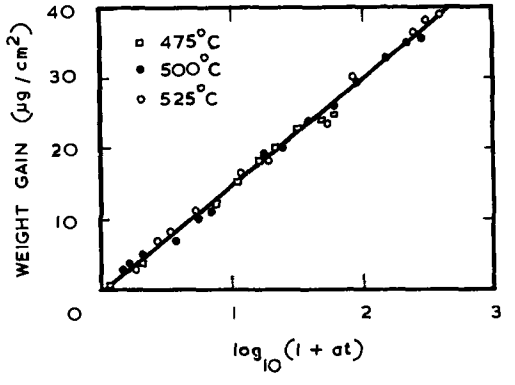

Fig. 7. Oxidation of magnesium at 475°, 500°, and 525°C in static oxygen (batch C) at 100 mm pressure. Data are tested for conformity to the logarithmic rate law by plotting w against log $(1 + at)$. Values of a were 0.22 hr^{-1}, 0.9 hr^{-1}, and 3.8 hr^{-1} at 475°, 500°, and 525°C, respectively.

on the thermal balance at atmospheric pressure, the mass of oxygen passed (equivalent to 6.6 liters at NTP/hr) and therefore the total quantity of impurity being the same in each case. In the run at atmospheric pressure breakaway commenced after only 10 min and was accompanied by the formation of the usual white oxide scale, whereas in the run at 100 mm the inception of breakaway was delayed for 11 hr and the oxide was buff in color.

Once a film has been formed in a closed system, *i.e.*, in the presence of a small and fixed amount of impurity, it confers protection on the metal when this is subsequently exposed to flowing oxygen with its more plentiful supply of impurity. This was demonstrated by oxidizing a sample of magnesium on the microbalance for 30 min at 550°C in oxygen of batch C at 100 mm pressure, then transferring it to the thermal balance and continuing the run there at the same temperature. Breakaway was now delayed for 19 hr as compared with the 10 min of a normal run on the thermal balance at this temperature.

It was thought desirable to study systematically the detailed kinetics of oxidation; untreated oxygen of batch C was used at a pressure of 100 mm. Three runs were carried out at each of the temperatures 500°, 525°, and 550°C; of these, two runs were continued for at least 25 hr and the third for at least 250 hr, the reproducibility as judged by the weight gain at 25 hr being ±7%, ±3%, and ±2% at 500°, 525°, and 550°C, respectively. Single runs were also carried out at 475° (250 hr) and at 570°C (23 hr).

The curves obtained (Fig. 6) fall into a regular sequence. At 475°, 500°, and 525°C the rate of oxidation continually decreased with time, whereas at 550°C in two out of the three runs the rate of oxidation increased after the initial protective stage, indicating breakaway, and at 570°C, breakaway occurred only after 15 hr. Visual examination of the oxidized samples showed that breakaway was associated with film breakdown at isolated points on the metal surface followed by the formation of buff-colored oxide. Samples which had been oxidized at 525°C and below showed a slight loss of luster, but no interference colors were discernible. At the three lower temperatures (although not at 550° and 570°C) the data conformed fairly well (Fig. 7), over the first 150 hr at least, to the logarithmic law

$$w = k \log (1 + at) \qquad [1]$$

where w is the weight gain at time t. The value of k was the same at all three temperatures, *viz.*, 15 $\mu g/cm^2$, but a varied with temperature from 0.22 hr^{-1} at 475°C to 0.90 hr^{-1} at 500°C and 3.8 hr^{-1} at 525°C.

At the longer times (branch AB, 525°C curve, Fig. 6) the rate, which was very small (*e.g.*, 0.02 $\mu g/cm^2$/hr at 525°C), was almost independent of temperature. This is a necessary consequence of the fact that the parameter k is independent of temperature, for from Eq. [1] we have

$$\frac{dw}{dt} = \frac{ak}{1 + at} \qquad [2]$$

which for values of t such that $at >> 1$ becomes

$$\frac{dw}{dt} = \frac{k}{t} \qquad [3]$$

and this for a given value of t is the same at all three temperatures.

Finally, information was sought as to the texture of the oxide film; the surface area of a sample of magnesium, oxidized for 268 hr at 525°C on the microbalance to a weight gain of 42 $\mu g/cm^2$ was measured by krypton sorption (10, 11). A value of 111 cm^2 was obtained, as compared with 68 cm^2 for a freshly polished sample. Both values contain a not negligible contribution for adsorption on the glass walls of the container, but the difference of 43 cm^2 should not be very different from the area of the oxide; it is equivalent to 3 cm^2 per cm^2 of geometrical area of the sample and suggests a degree of roughness which is inconsistent with the model of a uniformly thick oxide layer. Electron microscopic examination of a few representative samples by the replica technique unfortunately gave no clear evidence as to the texture of the oxide film.

Discussion

The present results strongly suggest that the well-known breakaway and subsequent nonprotective oxidation of magnesium, which occur at temperatures of 475°C and above in flowing oxygen, are promoted by an organic impurity, probably hydrocarbon in nature, present in the oxygen. When mag-

nesium is heated in oxygen the impurity must either be oxidized or consumed in some way, as evidenced by the successful use of magnesium at 570°C as a getter. Nevertheless the pronounced diminution in rate which occurs after a period of time (as at A on the 10 mm curve in Fig. 3) is not a simple consequence of the complete removal of the impurity; for when a further charge of oxygen, and with it more impurity, was admitted at B (Fig. 3) to increase the pressure to 100 mm there was no detectable change in the rate of oxidation. Thus while the rate of thickening of the oxide layer up to the 'knee' at A is dependent on the partial pressure p of impurity, the rate of oxidation beyond the knee is insensitive to p. These conclusions are supported by the experiment at 550°C in which it was shown that an oxide layer preformed in static oxygen is able to retard breakaway on subsequent oxidation in flowing oxygen.

If, as seems likely, the impurity is present as a complex mixture of hydrocarbons, the fates of the separate constituents could only be fully elucidated by a series of detailed studies. There is some evidence for decomposition resulting in carbon deposition on the oxide surface; a specimen of magnesium was oxidized at 525°C in gettered oxygen at 100 mm pressure containing C^{14}-labelled decane ($C^{14}H_3$ $(C_2H)_8$ CH_3) at a partial pressure of 0.035 mm. A "count" (12) of the surface of the specimen after 40-hr oxidation indicated the presence of 0.15 μg of carbon per cm^2, a value far in excess of that which could be attributed to chemisorbed carbon dioxide (from oxidation of the hydrocarbon).

Turning now to the kinetics of the oxidation, these can be regarded as proceeding in two stages: (*a*) the growth of a continuous oxide film which under certain conditions is followed by (*b*), the actual breakdown of this film (breakaway) and subsequent nonprotective oxidation.

The preceding discussion leads to the tentative conclusion that the enhanced rate of growth of the protective film, stage (*a*), in oxygen containing the hydrocarbon impurity is brought about by deposition of carbon on the oxide surface and its incorporation in the oxide. As to the mechanism by which this carbon promotes the outward diffusion of Mg^{++} ions and their electrons [it is generally agreed (3) that magnesium oxidizes by cationic diffusion] one can at present only speculate: possible factors are an increase in the electrical conductivity of the oxide film [experiments at 1000°-1500°C show (13) that magnesium oxide is a mixed ionic and electronic conductor], and the production of mechanical defects in the film. Regarding the kinetics of stage (*a*), it needs to be emphasized that the extant theories of oxidation refer by implication to systems free of impurity, and only the curve obtained with gettered oxygen (curve 1 of Fig. 5) fulfills this condition sufficiently well. Unfortunately the weight gains in this experiment were too small for detailed discussion, but it is obvious from casual inspection that the curve cannot be represented by a parabolic or cubic equation (the rate falls off too sharply in the region of A); it appears to be logarithmic in form, but unfortunately, even if conformity to a logarithmic law could be confirmed, this would be of little help in elucidating the mechanism of oxidation, since at least six derivations of this type of law have appeared in the literature (14).

When present in sufficient amounts, the hydrocarbon impurity is also able to promote breakaway and subsequent nonprotective oxidation with the production of a white, brittle oxide scale. If however the conditions are such that the supply of impurity is limited (as in the microbalance experiments with batch C oxygen at 100 mm), breakaway does not occur within 300 hr at 525°C. Breakaway was in fact only observed at 550°C and above and was associated with the formation of the powdery, buff-colored oxide in isolated regions on the specimen surface (Fig. 2); what probably occurs is that magnesium vapor erupts through mechanically weak areas in the oxide film (the saturated vapor pressure of magnesium (9) at 550°C is 0.29 mm) and reacts with oxygen in the vapor phase. The buff color is probably due to traces of metallic magnesium in the oxide, and if the latter is exposed to the laboratory atmosphere for several months, it becomes white (3).

The type of breakaway associated with lateral growth of the familiar white oxide thus seems to be attributable to the presence of hydrocarbon impurity in the oxygen; oxidation in "pure" oxygen, free of the impurity, is characterized by localized breakaway which results in buff-colored oxide.

Conclusions

The oxidation of magnesium in flowing oxygen at temperatures of 500°C and above is promoted by traces of an impurity, probably a mixture of hydrocarbons, but under "static" conditions and at 100 mm pressure of oxygen, *i.e.*, in a strictly limited supply of the impurity, the oxidation remains protective for at least 300 hr at 525°C. In oxygen from which the impurity has been removed, either by gettering or by catalytic oxidation, the oxidation is still protective and is very slight, a mere 3 μg/cm^2, or so, after 50 hr at 525°C.

Acknowledgments

The authors are grateful to Dr. J. E. Antill for several helpful discussions and to the U.K. Atomic Energy Authority for the financial support which they have given to this work.

Manuscript received April 18, 1962; revised manuscript received July 17, 1962.

Any discussion of this paper will appear in a Discussion Section to be published in the June 1963 JOURNAL.

REFERENCES

1. E. A. Gulbransen, *Trans. Electrochem. Soc.*, **87**, 589 (1945).
2. T. E. Leontis and F. N. Rhines, *Trans. AIME*, **166**, 265 (1946).
3. S. J. Gregg and W. B. Jepson, *J. Inst. Metals*, **87**, 187 (1958-59).
4. J. E. Castle and S. J. Gregg, To be published.
5. J. E. Castle, S. J. Gregg, J. E. Antill, and W. B. Jepson, *J. Nucl. Mat.*, **5**, 254 (1962).
6. P. A. Jacquet, "Le Polissage Electrolytique des Surfaces Mètalliques et Ses Applications." I "Aluminium, Magnésium, Alliages légers," 1948: Paris (Editions Métaux).

7. D. W. Aylmore, S. J. Gregg, and W. B. Jepson, *J. Inst. Metals*, **88**, 205 (1959-60).
8. "Vacuum Microbalance Techniques," M. J. Katz, Editor, Plenum Press, New York (1961).
9. F. F. Coleman and A. Egerton, *Phil. Trans. Roy. Soc.*, **234A**, 177 (1935).
10. R. A. Beebe, J. B. Beckwith, and J. M. Honig, *J. Am. Chem. Soc.*, **67**, 1554 (1954).
11. D. W. Aylmore and W. B. Jepson, *J. Sci. Inst.*, **38**, 156 (1961).
12. S. J. Gregg, R. J. Hussey, and W. B. Jepson, *J. Nucl. Mat.*, **3**, 175 (1961).
13. S. P. Mitoff, *J. Chem. Phys.*, **36**, 1383 (1962).
14. See for example, W. E. Boggs, *This Journal*, **108**, 124 (1961).

The Oxidation of an Iron-5 Per Cent Chromium Alloy in the Temperature Range 600°-850°C

J. M. Perrow[1] and W. W. Smeltzer

Department of Metallurgy and Metallurgical Engineering, McMaster University, Hamilton, Ontario, Canada

ABSTRACT

An investigation is reported on the oxidation of an iron-5% chromium alloy over the temperature range 600°-850°C. The film on abraded specimens underwent transformation by nodular-type growths to produce a scale containing iron chromite and ferric-chromic oxide. The alloy underlying iron chromite was susceptible to internal oxidation. These phenomena combined with mechanical breakdown of oxides gave rise to nonreproducible oxidation rate curves.

Despite the considerable number of investigations, an understanding has not been obtained of the complex oxidation behavior of iron-chromium steels at high temperatures. Scales may contain one or both of the rhombohedral sesquioxide, $Fe_2O_3 \cdot XCr_2O_3$ or of the spinel, $FeO \cdot XCr_2O_3$ depending on the exposure conditions. Yearian, Randell, and Longo (1) have characterized a single phase type, which consists of chromium oxide with some dissolved hematite, to be found at low oxidation rates, at low temperatures and/or high chromium content alloys, and a duplex type, which consists of an outer layer of hematite with a small amount of dissolved chromium oxide and an inner layer of iron chromite, to be found at high rates of attack. At long exposure times, both scales undergo breakdown by cracking.

Utilizing electron microscopic observations, Yearian, Derbyshire, and Radavich (2) have demonstrated that the transformation of a ferric-chromic oxide film to one containing iron chromite proceeds in localized oxide growths at randomly distributed positions on the surface. This behavior is typical of both abraded and electropolished specimens. Since the kinetics for formation of films undergoing this transformation have not been demonstrated, this study was designed to investigate the oxidation kinetics of an Fe-5% Cr alloy over the temperature range 600°-850°C. Such an investigation should lead to a further insight into the underlying causes of the poor reproducibility in the kinetic data found for these alloys (3-5).

Experimental

A vacuum microbalance assembly similar to that described by Gulbransen (6) was employed for the kinetic measurements. The sensitivity of quartz microbalance was 1 division (0.001 cm) of the microscopic micrometer per 11 μg for a sample of 0.6900g. The system, capable of maintaining a vacuum of 10^{-6} mm Hg, consisted of a mechanical pump, a three-stage oil diffusion pump, oxygen storage flasks, and a number of traps to protect the metal specimens and oxygen from moisture, oil, and mercury vapors. Temperatures were controlled to ±2°C.

All specimens were subjected to a standard annealing exposure before oxidation. Once a specimen was placed on the microbalance, the system was evacuated to 10^{-6} mm Hg. The temperature was brought to 800°C over a period of 1½ hr and the specimen was annealed for 2 hr at this temperature. Upon adjustment of the furnace to the desired temperature, oxidation was carried out in an oxygen atmosphere at 200 mm Hg pressure. After an oxidation test, the system was evacuated to allow the specimen to cool in vacuum. Oxidized specimens were vacuum mounted in a cold-setting polyester resin for metallographic examinations. The alloy grain structure could be determined after etching specimens for 40 sec in a 5% Nital solution.

The alloy contained 5.0% chromium with impurity contents of 0.01, 0.004, 0.04, 0.04% sulfur, phosphor, silicon, and manganese, respectively. Specimens with surface areas of approximately 2.0 cm^2 were cut from the as-received 0.035 in. thick sheet. A 1/64 in. suspension hole was drilled near one end of a specimen which was then abraded to 4/0 grade silicon carbide paper, degreased in acetone, and suspended in the reaction tube from the microbalance.

Results

Results are presented for the kinetic tests over the temperature range 600°-850°C in conjunction with metallographic examinations of the oxide scales. Since the transformation temperature of the alloy from the alpha to gamma structure is 855°C

[1] Present address: Metallurgy Division, Atomic Energy of Canada Ltd., Chalk River, Ontario, Canada.

(7), the oxidation phenomena are characteristic of a ferritic alloy.

Of the five initial tests for exposures of 3 hr at 800°C, Fig. 1, two rate curves (1 and 2) were similar, whereas the others were different in form and magnitude. The oxide topographies revealed features associated with these phenomena. Small nodular oxide growths were distributed over the surface of the specimen exhibiting the least oxidation, test 5, while the specimens which had undergone larger degrees of oxidation displayed larger nodules. To illustrate these localized growths, a photomicrograph of the nodules on specimen of test 1 is shown in Fig. 2. A series of oxidation tests was carried out at 700° and 850°C to determine the influence of temperature on these phenomena. As illustrated by the curves in Fig. 1, these kinetics were also nonreproducible. As before, oxidation proceeded via nodular growths. On the heavily oxidized specimens at 700°C, these growths had coalesced to a less protective scale. It was apparent from a correlation of the results from the kinetic tests with microscopic observations that the extent of nodular growths at a specific temperature was more important in determining the degree of oxidation than the absolute magnitude of temperature.

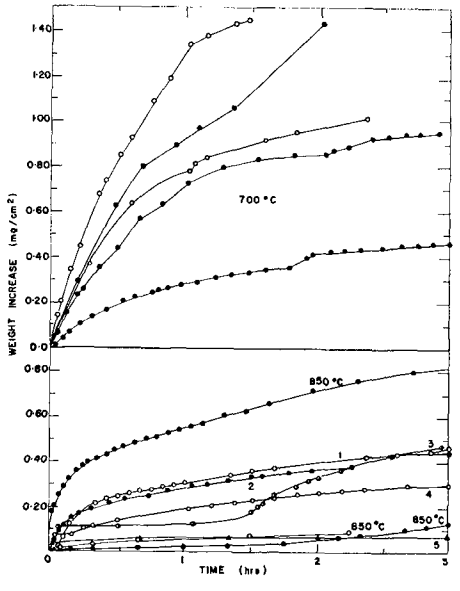

Fig. 1. Oxidation rate curves over the temperature range 700°-850°C (800°C: curves 1-5).

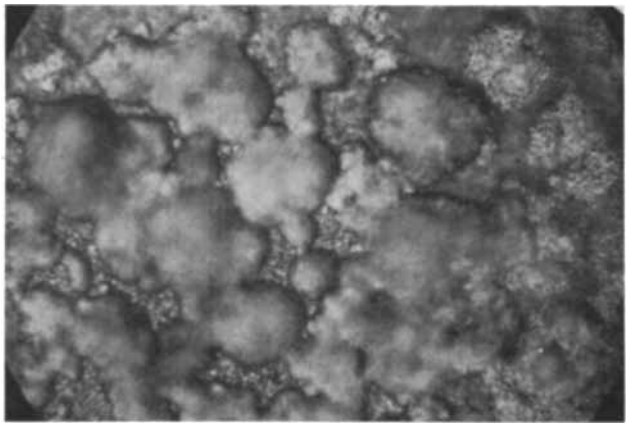

Fig. 2. Surface topography of specimen oxidized for 3 hr at 800°C (test 1, Fig. 1). Magnification approximately 250X.

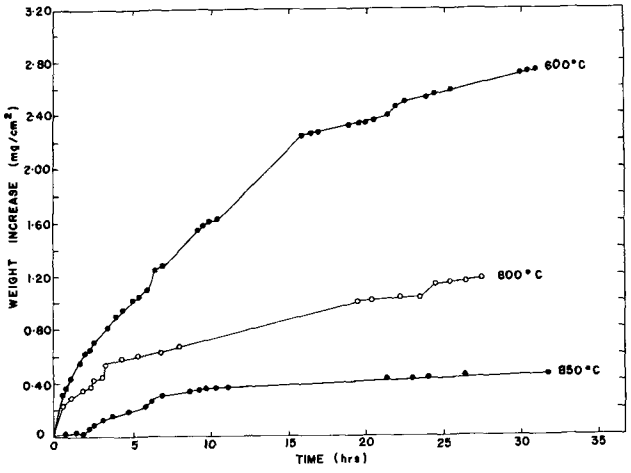

Fig. 3. Oxidation rate curves over the temperature range 600°-850°C.

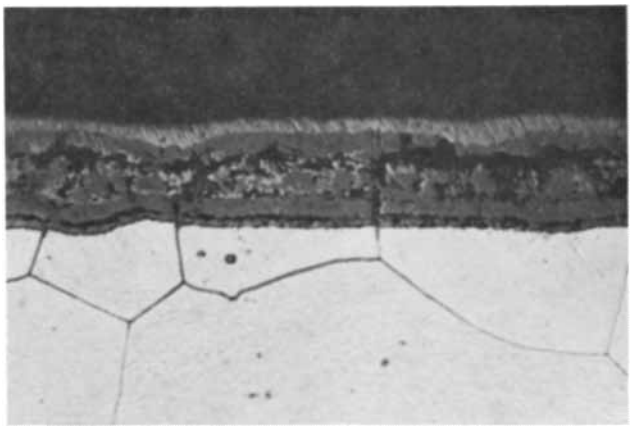

Fig. 4. Cross-section of specimen oxidized at 600°C for 31 hr, etched in 5% Nital. Magnification approximately 575X.

In order to examine the effect of exposure time at several temperatures on oxidation behavior, tests were carried out for exposures to 30 hr at 600°, 800°, and 850°C. These results are illustrated in Fig. 3. The curves were irregular; the specimen exhibiting the lowest initial oxidation rate at 850°C maintained this characteristic even though this temperature was of highest value.

Examination of scale cross sections illustrated features associated with this behavior. Photomicrographs are presented in Fig. 4-6 of the scales on the specimens of the three above tests. Iron chromite is distinguishable from ferric-chromic oxide by its darker color. At the lowest temperature of 600°C, the scale, which consisted predominately of iron chromite, was severely cracked. Voids in this oxide layer were encased by ferric-chromic oxide. On the other hand, the scale consisted predominately of this latter oxide at 800° and 850°C with large amounts of iron chromite occurring only in the nodular growths. Detailed examination of cross sections demonstrated that specimens whose scales contained the smaller amounts of iron chromite exhibited the less rapid oxidation rates in the temperature range 600°-850°C.

Internal oxidation of the alloy proceeded predominantly intergranularly at temperatures below 700°C

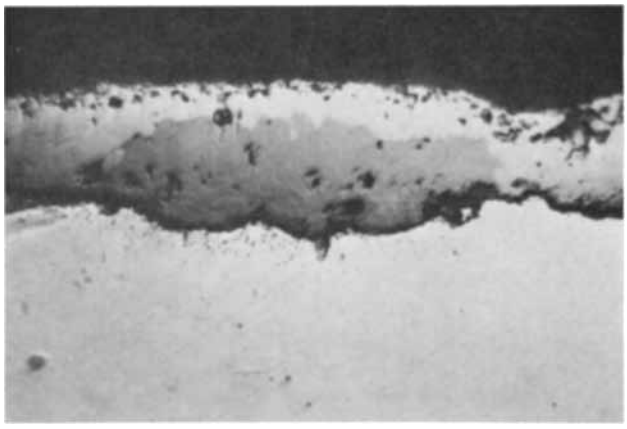

Fig. 5. Cross section of specimen oxidized for 51 hr at 800°C. Magnification approximately 575X.

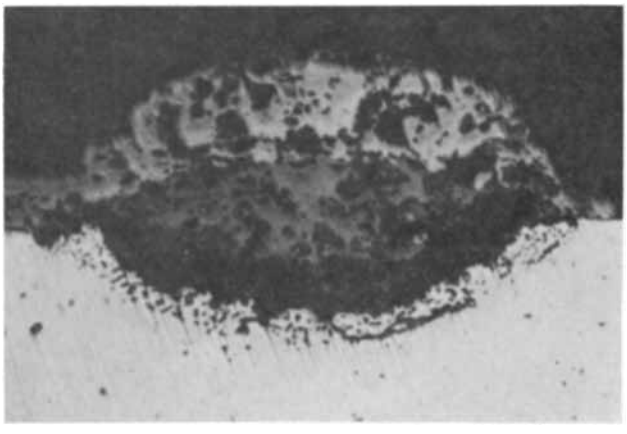

Fig. 6. Cross section of a localized oxide growth on specimen after 43 hr oxidation at 850°C. Magnification approximately 250X.

and predominantly intragranularly at temperatures above 800°C. These phenomena are illustrated in the photomicrographs of Fig. 4-6. Moreover, highly localized external and internal oxidation in the temperature range 800°-850°C gave rise to the unusual growths depicted in Fig. 6. These growths, which exhibited porosity, contained large amounts of both iron chromite and ferric-chromic oxide. It was possible to show by etching experiments that alloy grains had been completely converted to oxide by these growths.

Discussion

In this section, the salient oxidation characteristics are correlated insofar as possible with the mobilities of the reactants in the alloy and oxide phases and the Fe-Cr-O phase diagram.

The correlation of the results from the kinetic experiments with metallographic examinations has demonstrated that the degree of oxidation at constant temperature was dependent on the extent of nodular oxide growths from the metastable film on the abraded specimens. These findings substantiate the electron microscopic observations of Yearian, Derbyshire, and Radavich (2). They also demonstrate that a ferric-chromic oxide film on an Fe-5% Cr steel was stable for exposures to at least 30 min at 625°C. For the experimental conditions of this investigation, this oxide was extremely protective in the temperature range 800°-850°C and only transformed to localized growths containing large

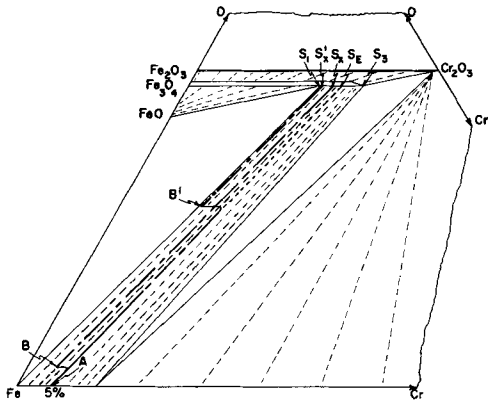

Fig. 7. Qualitative ternary phase diagram for the ferritic iron-chromium solid solution and oxides at temperatures higher than 600°C. ABS_x, hypothetical path for small degree of internal oxidation in 5% Cr alloy underlying iron chromite at 800°C. $AB'S'_x$, hypothetical path for large degree of internal oxidation in 5% Cr alloy underlying localized oxide growths at 850°C.

amounts of iron chromite for exposures in the order of 30 hr.

This transformation of ferric-chromic oxide to iron chromite is brought about by a simple chemical displacement reaction. As illustrated by the tentative Fe-Cr-O phase diagram for temperatures greater than 600°C in Fig. 7 (8), ferric-chromic oxide may exist only in stable equilibrium with alloys containing greater than 12% chromium. When this oxide exists in contact with a 5% Cr alloy, iron and oxygen react to transform this initial metastable film to one containing spinel and a rhombohedral oxide richer in iron

$$2O_2 + 3Fe + xFe_2O_3 \cdot 2Cr_2O_3 \rightarrow FeCr_2O_4 + (1 + x)\, Fe_2O_3 \cdot Cr_2O_3$$

For heavily oxidized specimens, this reaction leads progressively to formation of a scale containing distinct layers of the two oxides (Fig. 4).

The alloy beneath the localized oxide growths containing iron chromite was subjected to severe internal oxidation. Chromium was sufficiently depleted for oxide precipitation because the diffusion constant of metal in the spinel oxide is of the relatively large magnitude (9) (10^{-11} cm²/sec at 800°C). On the other hand, chromium was not depleted from the alloy beneath rhombohedral oxide because the diffusion constant for this oxide is relatively small (9) (10^{-16} cm²/sec at 800°C). The composition paths in the internally oxidized regions of the alloy at 800° and 850°C are qualitatively represented in the phase diagram of Fig. 7. Iron chromite which would exist in equilibrium with a 5% chromium alloy is designated S_E. Its composition lies within the range S_1-S_3 ($Fe_{1.5}Cr_{1.5}O_4$ to $FeCr_2O_4$). Since chromium may be depleted from 5% to as little as 2% by oxidation at 800°C (4), the oxide of the scale S_x, lies on the iron rich side of S_E. Consequently, a composition path ABS_x in the two phase field represents the depletion of chromium in the internally oxidized regions of the alloy. The position of B on the tie-line between the 2% alloy and spinel S_x is determined by the degree of internal oxidation (Fig. 5). This degree of oxidation was much larger beneath the

localized oxide growths at 850°C, where the pronounced depletion of chromium lead to complete conversion of alloy grains to oxide. Consequently, the composition of the spinel oxide would approximate closely to the composition S_1 for the spinel of smallest chromium concentration. The composition in the internally oxidized region may then be presented by the path $AB^1S_x^1$ where the position of B^1 represents the large degree of oxide precipitation (Fig. 6).

The irregular, nonreproducible oxidation rate curves are similar to those from previous investigations. Because the initial rates were not representative of uniform oxide growth, a distinction could not be made between the acting chemical and physical processes. We could only conclude that oxidation proceeded in the early exposure stages by localized external and internal oxidation. The large variations of such oxidation over the alloy surface at a specific temperature were more important than the absolute value of temperature in determining the magnitudes of oxidation in the range 600°-850°C. Since oxygen could also penetrate inwards through cracks in the localized oxide growths, spinel oxide growth and its cracking to more pervious oxide played effective roles in the occurrence of irregular transitions to more rapid rates in the oxidation curves. These results emphasize that reproducible curves for a ferritic alloy of low chromium composition will be obtained only under conditions where the initial metastable film is uniformly converted to the stable duplex film of iron chromite and ferric-chromic oxide prior to oxidation.

Acknowledgments

This contribution is based on a thesis submitted by J. M. Perrow to the School of Graduate Studies, McMaster University in partial fulfillment of the requirements for the M.Sc. degree. He wishes to acknowledge the award of the Steel Company of Canada Research Fellowship. The authors were indebted to Dr. J. S. Kirkaldy for helpful discussions.

This work forms part of a research project sponsored by the U. S. Air Force Office of Scientific Research, Office of Aerospace Research, and the Defence Research Board, Ottawa, Canada.

Manuscript received Nov. 1, 1961; revised manuscript received July 2, 1962.

Any discussion of this paper will appear in a Discussion Section to be published in the June 1963 JOURNAL.

REFERENCES

1. H. J. Yearian, E. C. Randell, and T. A. Longo, *Corrosion*, **12**, 515t (1956).
2. H. J. Yearian, W. D. Derbyshire, and R. F. Radavich, *ibid.*, **13**, 597t (1957).
3. D. Caplan and M. Cohen, *ibid.*, **15**, 141t (1959).
4. D. Lai, R. J. Borg, M. J. Brabers, J. D. Mackenzie, and C. E. Birchenall, *ibid.*, **17**, 357t (1961).
5. W. W. Smeltzer, *Acta Met.*, **8**, 268 (1960).
6. E. A. Gulbransen, *Rev. Sci. Instr.*, **15**, 201 (1944).
7. F. Adcock, *J. Iron Steel Inst. (London)*, **124**, 99 (1931).
8. A. U. Seybolt, *This Journal*, **107**, 147 (1960).
9. L. Himmel, R. F. Mehl, and C. E. Birchenall, *AIME Trans.*, **197**, 827 (1953).

The Anodic Dissolution of Binary Alloys

R. F. Steigerwald[1] and N. D. Greene

Corrosion Research Laboratory, Interdisciplinary Materials Research Center, Rensselaer Polytechnic Institute, Troy, New York

ABSTRACT

A method for calculating the anodic polarization curves of binary alloys from those of their components is presented. Heterogeneous alloys can be treated as simple galvanic couples, but homogeneous alloys are subject to a modification of Tammann's concept of surface enrichment. Potentiostatic anodic polarization curves are used to compare the calculated and experimental curves. Data are presented for the tin-zinc, cadmium-zinc, iron-chromium, titanium-chromium, and iron-titanium systems.

The practical and commercial importance of alloys has made their corrosion and dissolution the subject of numerous experimental investigations (1-7); however, no general, quantitative theory has been presented for the dissolution of alloys.

The recent application of potentiostatic polarization techniques to metallographic etching (8, 9) has shown that the phases of a heterogeneous alloy probably dissolve independently of one another, but only limited experimental evidence has been presented (10). The theory for homogeneous alloys has been largely an extension of Tammann's (11) explanation of parting limits in gold alloys.

[1] Present address: Research Division, Electrochemicals Department, Experimental Station, E. I. du Pont de Nemours and Company, Wilmington, Delaware.

Theory

General.—The homogeneous or mixed potential theory of electrode kinetics was stated by Wagner and Traud (12) and extensively applied to corroding systems by Stern and Geary (13, 14). The basic assumptions are that electrochemical reactions may be treated as sums of partial reactions (usually considered as independent of one another) and that no net current flows at an electrode which is in equilibrium or at steady state. Thus the net rate of oxidation equals the net rate of reduction at steady

state; any polarizing current will be the difference between the oxidation and reduction rates at the polarized potential.

$$\vec{i}\ \text{applied} = \vec{i} - \overleftarrow{i} \qquad [1]$$

where $\vec{i}$ is the oxidation current and $\overleftarrow{i}$ the reduction current.

For the present discussion, consider an electrode corroding under activation control (13)

$$\epsilon = \vec{\beta} \log \vec{i}/i_{cor} = -\overleftarrow{\beta} \log \overleftarrow{i}/i_{corr} \qquad [2]$$

where ϵ equals $E - E_{cor}$ and $\vec{\beta}$, $\overleftarrow{\beta}$ are Tafel slopes, constants of the system.

Combining Eq. [1] and [2]

$$\vec{i}_{applied} = i_{corr}(10^{\epsilon/\beta} - 10^{-\epsilon/\beta}) \qquad [3]$$

Taking $\vec{\beta} = \overleftarrow{\beta}$ 0.10 volt/decade (typical for a corroding electrode), $\vec{i}/\overleftarrow{i} = 10$ at $\epsilon = 0.05$v. Thus at 50 mv noble to the corrosion potential, the applied current is approximately equal to the dissolution current. It is this fact that makes the polarization curve such a useful tool for studying the dissolution of metals.

For completeness, note that dissolution current, like any other rate process, can be expressed by a typical exponential equation

$$\vec{i} = A \exp\left(-\frac{\Delta G^*}{RT}\right)\exp\left(\frac{\alpha Z\mathbf{F}}{RT}\right)\epsilon \qquad [4]$$

where A is a constant, ΔG^* the free energy of activation, α the distribution coefficient, Z the oxidation number, and **F** equals 1 Faraday. Detailed discussions of electrochemical currents as rate processes can be found elsewhere (15, 16).

Dissolution of heterogeneous alloys.—Stern (17) studied the cathodic polarization of galvanic couples and found both theoretically and experimentally that at any potential E

$$i_T = i_A f_A + i_B f_B \qquad [5]$$

where the subscript T stands for total, A, B for the couple components, and f_A, f_B are area fractions of the components.

A heterogeneous alloy can be regarded as a galvanic couple in which electrical connection is made by direct contact. If the polarization curve for each phase is known, the polarization curve of the alloy can be calculated from Eq. [5]. The area fractions needed in Eq. [5] can be calculated from the composition of the alloy since a section through an alloy (in this case the exposed surface) has an area composition equal to the volume composition of the alloy. The volume composition is easily calculated from the weight composition and the specific gravity of the components.

Although Eq. [5] is generally applicable to dissolution of multiphase alloys, some exceptions must occur. Applicability of Eq. [5] depends on the fact that area fractions of each phase can be calculated from the alloy composition. Under some conditions, the surface composition of the alloy may not equal its volume composition. Consider a heterogeneous alloy containing an active phase dispersed as small isolated colonies in a relatively inert matrix. Under these conditions, the area fraction of the matrix would be greater than the one calculated from the composition since the rapid dissolution of the second phase exposes the matrix, not more of itself. However if the colonies are large or the active phase continuous, the surface composition would not be affected by the disparity of dissolution rates, and the area fractions could be calculated accurately. The occurrence of surface enrichment in heterogeneous alloys is determined by the relative and absolute dissolution rates and the dispersion of the phases. A large difference in rates, of course, is necessary for surface enrichment, and unless the dissolution rate of the active phase is relatively high deviations from Eq. [5] would not be observed in finite times. Because of the dispersion effects noted above, surface enrichment should be expected only in relatively dilute heterogeneous alloys; however, as the dispersion of the phases becomes finer, the possibility of surface enrichment extends to less dilute alloys.

This application of the mixed potential theory to a heterogeneous alloy surface extends it beyond Wagner and Traud's (12) original assumption that anodic and cathodic reactions occur randomly on the electrode surface. Equation [5] implies that the cathodic reaction may occur almost entirely on one phase and the anodic on the other. This localization of the partial reactions is the principle underlying the addition of noble metals to Ti and Cr (18-20). The high exchange current density for hydrogen ion reduction on the platinum rich areas of the surface leads to the passivation of the base metal.

The mixed potential theory is based on the conservation of charge and the existence of partial processes. Neither of these principles is concerned with the distribution of reaction sites, and therefore the character of the electrode surface is not basic to the theory.

Dissolution of Homogeneous alloys.—Equation [5] is applicable to the dissolution of any alloy; the problem is determining the proper area fractions and component current densities at any point in the dissolution process. In the previous section, the values of these parameters were set by assuming that each phase dissolved independently of the others. However, as the dispersion of the phases in the alloy becomes finer and finer, the possibility of surface enrichment, discussed above, becomes proportionately greater. Finally when the dispersion reaches atomic dimensions, a solid solution, surface enrichment controls the dissolution rate of the alloy. By considering surface enrichment as the rate-determining factor, Mueller (21) has derived an expression for the steady-state dissolution rate of a homogeneous alloy. A slight modification of this derivation follows:

If all possible solid-state interactions and interfacial energies are neglected, the current density for each component of a homogeneous alloy at any potential E would be that of the component as a

pure metal. Furthermore, if the dissolution is uniform (as opposed to dezincification where one component is removed selectively), the ratio of A to B is the same in the solution as the alloy. Hence it follows that surface enrichment of the more noble component occurs. This may be expressed

$$\frac{N_A}{N_B} = \frac{Z_B i_A f_A}{Z_A i_B f_B} \quad [6]$$

where N_A, N_B are the mole fractions in the alloy, Z_A, Z_B are the oxidation numbers of the ions, i_A, i_B are dissolution current densities of the components A and B at a given potential, and f_A, f_B are the area fractions of A and B.

By definition

$$f_A + f_B = 1 \quad [7]$$

Combining Eq. [6] and [7]

$$f_A = \frac{Z_A N_A i_B}{Z_A N_A i_B + Z_B N_B i_A}, f_B = \frac{Z_B N_B i_A}{Z_A N_A i_B + Z_B N_B i_A} \quad [8]$$

Substituting Eq. [8] into Eq. [5]

$$i_T = \frac{i_A i_B (Z_A N_A + Z_B N_B)}{Z_A N_A i_B + Z_B N_B i_A} \quad [9]$$

i_T is now the alloy dissolution current density. Equation [9] is Mueller's final expression for dissolution rate written in terms of current density.

When Eq. [9] was applied to experimental data measured in this study, it was found that even in systems in which there were negligible free energy changes on alloying the calculated and experimental steady-state dissolution rates were in agreement only when corrosion potentials of the pure components were nearly the same.

Equation [9] was derived on the basis that the components are independent on each other, that the atoms of the alloy are joined as minute galvanic couples. Even in an ideal solid solution this is not true; an A atom cannot dissolve without affecting both A and B neighbors. It is obvious that the effect of solid-state interactions on dissolution, a kinetic process, cannot be adequately evaluated on the basis of equilibrium thermodynamic data. It is, however, difficult to assess the magnitude of these kinetic interactions theoretically.

If the surface of a corroding alloy is enriched in the noble component, the polarization behavior of the alloy should be controlled by the polarization behavior of this component. Although Eq. [9] describes this kind of control, it does not take into account possible interactions between the components.

If dissolution is considered as an activated process (Eq. [2] and [4]), the rate is determined not by the potential E but by the overvoltage ϵ. Therefore, one correction that could be applied to Eq. [9] is to take currents at constant overvoltage rather than constant potential. This condition of constant overvoltage is most easily met by shifting the polarization curves of the components along the potential axis until their corrosion potentials coincide with that of the alloy and then calculating the curve for the alloy from Eq. [9].

Just as Eq. [5] is expected to fail in describing the behavior of heterogeneous alloys under certain conditions, Eq. [9] will fail for certain homogeneous alloys. Mueller (21) has pointed out that deviations are more likely when an alloy contains an excess of the active component. The principle underlying Eq. [9] is the surface enrichment of the more noble component. If the active component is in the majority, surface enrichment can occur only by the removal of a large number of atom layers from the surface of the electrode (*e.g.*, nine atom layers have to be removed from the alloy where the mole fraction of the noble component is 0.1). If the difference in the dissolution rates is large ($i_A/i_B > 10^3$), surface enrichment is probably hindered by the removal of loosely bound noble atoms by the rapidly dissolving active atoms of succeeding monolayers. In the extreme case, the dissolution current of the alloy would be given by Eq. [5]. It is worth noting that the limiting case for the dissolution of a homogeneous alloy is the normal case for a heterogeneous one and *vice versa*. The two alloy types are thus not as different as they seem.

Ideally, this discussion might include the calculation of the corrosion potentials of solid solutions. This very complex problem has been treated in detail by Akimov (22) and will not be considered here. Two points should be made about the corrosion potential, however: (i) considering the above discussions, the corrosion potential does not affect the shape of the calculated polarization curve, only its position on the potential axis. It should be noted that surface enrichment precludes any simple treatment of the corrosion potential; (ii) in many actual cases, the corrosion potential of a single phase varies almost linearly with composition (23-25). Therefore, when experimental values are not available, a straight line relationship can be used as an approximation.

Dissolution of intermetallic compounds and other intermediate phases.—Intermetallic compounds and intermediate phases are homogeneous alloys, but differ from the ordinary (terminal) solid solutions discussed above since they may have different crystal structures, ordered structures, and/or stronger solid-state binding. Since they are homogeneous, the general features of their dissolution behavior should be same as solid solutions; the principle of surface enrichment should apply, but the solid-state differences between the intermediate phase and its components may cause displacement of the calculated polarization curve along either the current or potential axis. Since the type and magnitude of these interactions differ greatly in the various alloy systems, and since little is known about the interfacial effects of different crystal structures, it is difficult to make predictions about the kinds and magnitudes of displacements which would occur. If the dissolution rate is controlled by surface enrichment, however, the shapes of calculated and experimental curves will be similar.

To summarize, the rules for calculating anodic polarization curves of alloys are:

1. Polarization curves of heterogeneous alloys can be calculated by Eq. [5]. The area fractions used are equal to the volume fractions calculated from the composition of the alloy. Care must be used in applying this method when the rapidly dissolving phase is present in very small amounts.

2. The polarization curves for homogeneous alloys can be calculated from Eq. [9] after the polarization curves of the components have been shifted along the potential axis until their corrosion potentials are at the corrosion potential of the alloy. If the corrosion potential of the alloy is not known, as a first approximation it can be assumed to vary linearly between those of the two components. Some caution should be used in applying these calculations to alloys in which the noble component is present in small amounts.

3. Intermetallic compounds and intermediate phases are treated in the same manner as other homogeneous alloys, but the stronger interactions in these materials may lead to displacements of their polarization curves along either axis.

Procedure

The experimental part of this investigation involved measuring the anodic polarization of a number of alloy systems. The systems chosen all exhibited active-passive transitions (26-28). Although the polarization curves of active-passive metals are much harder to reproduce than those of normal metals, their characteristic shapes provide points at which unambiguous comparisons can be made between theory and experiment. Simple dissolution curves have no such singularities.

Materials.—The difficulty in reproducing anodic polarization curves reported in the literature is probably the result of trace impurities in the metals under study (29). To minimize this difficulty, the alloys used in this study were prepared from very high-purity metals, and all alloys of a given series were prepared under identical conditions. Table I lists the component metals and their purity, Table II the alloys studied.

In general, buttons of the high melting alloys were prepared by arc melting in an argon atmosphere and machined into specimen electrodes. Low melting alloys were melted in Pyrex tubes under argon. The alloys were used in the as-cast condition unless heat treatment was needed to insure a particular structure (Table II).

All solutions were prepared from reagent grade chemicals and triply distilled water.

Experimental.—The dissolution studies employed conventional potentiostatic anodic polarization techniques. The greater part of the measurements were made with a classical potentiostat as described by Greene (28); in the later stages of the work, a transistorized electronic potentiostat[2] was used. Control in both cases was within 1 mv, and potentials were measured relative to a saturated calomel electrode using a Luggin probe and high impedance circuitry.

The polarization cell was similar to those described by Stern and Greene (28, 30). Two platinized platinum electrodes on opposite sides of the cell were used as cathodes. Electrodes of alloys that could be machined were cylinders of approximately 1 cm² surface area mounted on the electrode holder described by Stern and Makrides (31). The hardness and brittleness of the intermetallic compounds studied made it necessary to mount them in Bakelite or epoxy resin in order to make connections to them. Unwanted area and exposed portions of the connectors were masked with glytal paint. Control experiments showed that the presence of these materials did not affect the dissolution curves.

[2] Duffer's Associates, Inc., Troy, N. Y.

Table I. Pure metals

Metal	Nominal purity, w/o	Supplier
Sn	99.9999	Vulcan Detinning Co.
Zn	99.999	American Smelting & Refining Co.
Cd	99.999	American Smelting & Refining Co.
Fe	99.94	Purchased Commercially
Cr	99.94	Union Carbide Metals Co.
Ti	99.90	Union Carbide Metals Co.

Table II. Alloy compositions studies

A	B	w/o B in alloy
Sn	Zn	0.0, 6.5, 10.5, 15.7, 51.0, 73.3, 100.0
Cd	Zn	0.0, 10.0, 30.0, 100.0
Fe	Cr	0.0, 5.5, 10.5, 13.6, 20.6, 25.0, 100.0
Ti	Cr	0.0, 10.0, 20.4, 49.5, 65.0*, 100.0
Fe	Ti	0.0, 30.0*, 46.0*, 100.0

* Intermetallic compound.

Polarization curves were measured in either normal sulfuric acid or normal sodium hydroxide depending on the alloy system. All solutions were hydrogen-saturated to simplify the reduction kinetics. Prior to polarization the specimens were exposed to the test solution for several hours to insure that a stable corrosion potential was attained.

At most potentials, the current reached steady-state values in a short time (less than 5 min), and these steady-state values are reported. In the passive region, however, current is time dependent (29, 32-34). Experiments showed that even after three or four days the passive current was still decreasing on some metals. Therefore, it is a practical impossibility to wait for steady state at each point on the polarization curve. As partial solution to this problem, it was decided to report the currents at these time-dependent points, usually 10 min. It must be emphasized that in the alloys studied only the passive current had this pronounced time-dependence. All other currents reported are steady-state values; the onset of passivity and the shapes of the polarization curves are not affected by this method of waiting stated intervals in the passive region.

All polarization measurements were made at room temperature which was 25° ± 2°C.

Results

Similar to all rate processes, dissolution is a logarithmic function of its driving force (cf. Eq. [4]). Current is expected to vary exponentially with overvoltage, and for this reason electrode po-

tential is plotted as a function of the logarithm of the applied current in this presentation, and agreement between calculated and experimental results is discussed in terms of these curves. In addition to the logarithmic nature of the processes involved, one other point should be made in favor of semi-log plotting of these data. The difference between the active and passive currents is usually from two to five orders of magnitude. Simple linear plotting could not reveal all the pertinent features of curves which contain such large changes in one of the variables.

Dissolution of heterogeneous alloys.—The tin-zinc system is a simple eutectic with no solid solubility in either component at room temperature (35). Alloys of this system are therefore simple mixtures, and their dissolution behavior should conform to Eq. [5].

Figure 1 shows the anodic polarization curves of tin and zinc in normal sodium hydroxide. Figures 2 through 5 compare the measured and calculated curves for several of their alloys. The curves for tin and the alloys were quite reproducible, but that of zinc varied by as much as a factor of three. The dashed lines indicate loss of potentiostatic control.

The agreement between the calculated and experimental curves is generally quite good. Although current values sometimes differ by as much as a factor of ten, the curves generally coincide, and their shapes are always the same. Note particularly the agreement between potentials for the calculated and experimental current maxima or "noses."

The calculations show that the polarization curves for each of the alloys should have two noses, one for tin, the other for zinc. Only in the absence of the more active nose in the 10.5 w/o Zn alloy (Fig. 2) is there serious disagreement between the calculated and experimental curves. This disagreement occurs under the circumstances which were discussed above, that is when the active component is present in small amounts. If this hypothesis is correct, refining the dispersion of the phases should extend this surface enrichment to alloys with higher zinc contents. To test the idea, the dispersion of a sample of the 15.7 w/o Zn alloy shown in Fig. 3 was refined by cold work and heat treatment and its anodic polarization curve was measured. As predicted, the curve shown in Fig. 6 was unchanged except that the more active nose was replaced by cathodic current.

Alloys of the cadmium-zinc system are also simple eutectic mixtures (36), and their polarization behavior can be described by Eq. [5]. Table III records the important parameters for the anodic polarization

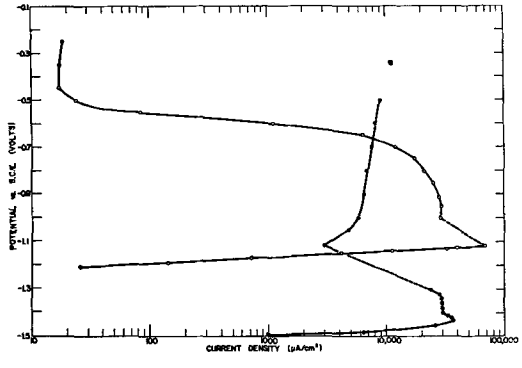

Fig. 1. Anodic polarization of tin and zinc in normal sodium hydroxide: ○, tin; ●, zinc.

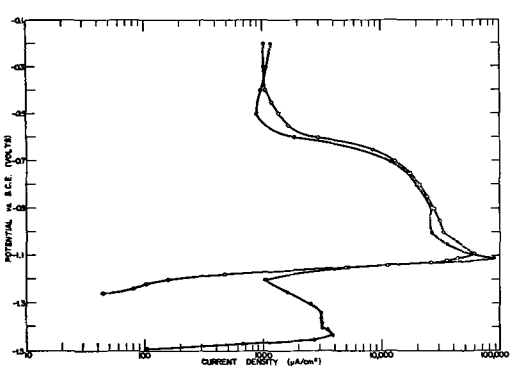

Fig. 2. Anodic polarization of a Sn-10.5 w/o Zn alloy in normal sodium hydroxide: ○, experimental; ●, calculated.

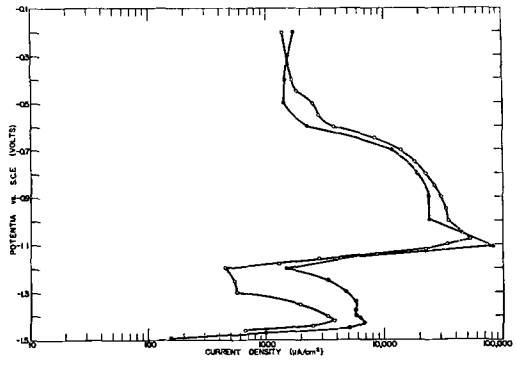

Fig. 3. Anodic polarization of a Sn-15.7 w/o Zn alloy in normal sodium hydroxide: ○, experimental; ●, calculated.

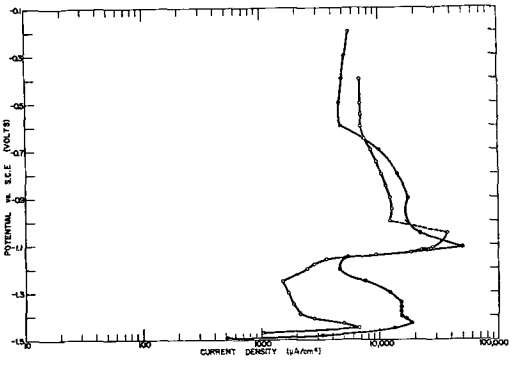

Fig. 4. Anodic polarization of a Sn-51 w/o Zn alloy in normal sodium hydroxide: ○, experimental; ●, calculated.

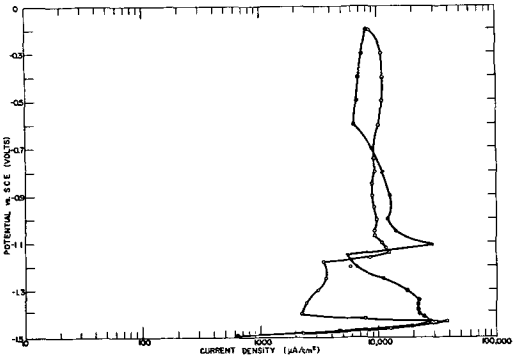

Fig. 5. Anodic polarization of a Sn-73.3 w/o Zn alloy in normal sodium hydroxide: ○, experimental; ●, calculated.

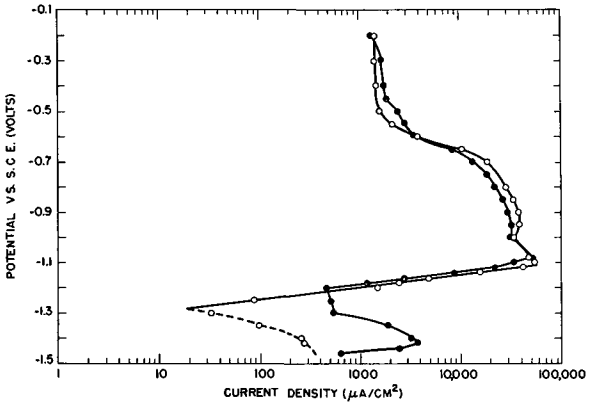

Fig. 6. Effect of cold work on the anodic polarization behavior of the Sn-15.7 w/o Zn alloy in normal sodium hydroxide: •, as cast; ⊙ cold worked; ——— cathodic current.

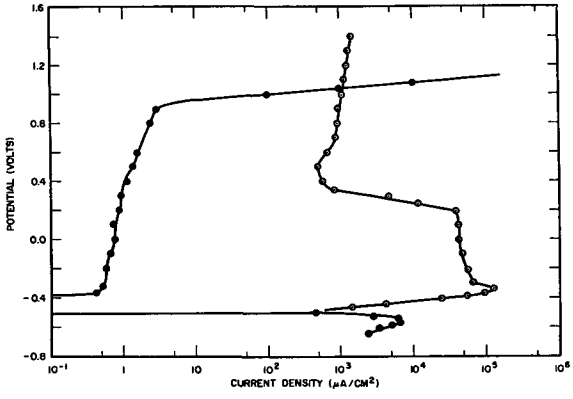

Fig. 7. Anodic polarization of iron and chromium in normal sulfuric acid: ⊙, Fe; •, Cr.

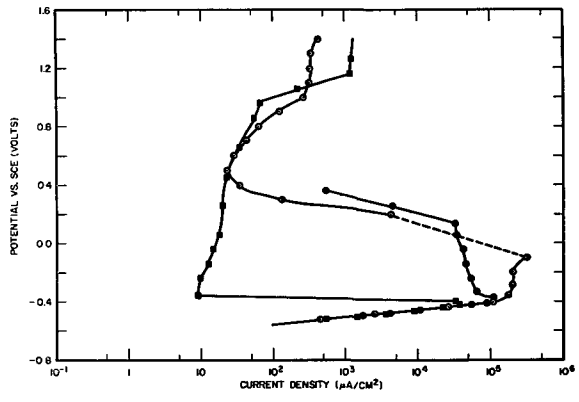

Fig. 8. Anodic polarization of an Fe-5.48 w/o Cr alloy in normal sulfuric acid: ⊙, exp; •, calc (Eq. [5]); ■, calc (Eq. [9]).

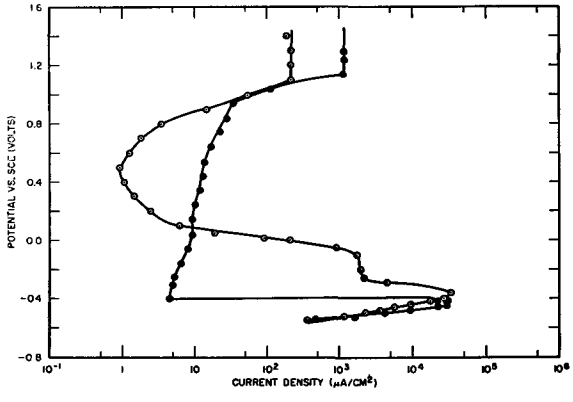

Fig. 9. Anodic polarization of an Fe-10.5 w/o Cr alloy in normal sulfuric acid: ⊙, exp; •, calc.

of some Cd-Zn alloys. The critical current *Ic* is the current maximum; and the primary passive potential *Epp* is the potential corresponding to this maximum. *Ip* is the passive current measured at −0.2v *vs.* S. C. E. As noted above, there is some scatter in the polarization data of zinc; Table III shows this scatter. The agreement between the calculated and experimental values is generally within the limits of experimental reproducibility.

Dissolution of solid solutions.—The iron-chromium system is essentially a continuous solid solution (interrupted only by the sigma phase near 50% Cr); this solid solution approaches ideality (37), and it is of considerable practical interest. These factors make it a logical choice as the principle subject for an investigation of the dissolution of solid solution alloys. Although the polarization behavior of this system has been studied previously (38, 39), none of the data were complete enough to allow their analysis in terms of the present discussion.

Figure 7 shows the anodic polarization of iron and chromium[3] in normal sulfuric acid. Figures 8 through 11 compare experimental and calculated polarization curves for some Fe-Cr alloys. The curves were calculated according to the procedure outlined above:[4] the polarization curves of the pure components were shifted so that their corrosion potentials were at the corrosion potential of the alloy, and Eq. [9] was used to calculate the polarization curve of the alloy. It must be remembered that Eq. [9] can be applied only after the polarization curves of the components have been shifted.

The experimental results are consistent with the general rules described above. In the case of the dilute 5.48 w/o Cr alloy (Fig. 8), that portion of the curve where the rates differ widely, *e.g.*, at $E = -0.4$v $i_{Fe}/i_{Cr} = 3.3 \times 10^6$, follows Eq. [5] more closely than Eq. [9]. This is consistent with earlier discus-

[3] The negative loop (40), the region where the reduction current exceeds the passive current, was not shown for chromium or the 25 w/o Cr alloy.

[4] Z_{Cr}/Z_{Fe} was taken as 3/2.

Table III. Anodic dissolution of Cd-Zn alloys in N/NaOH

Alloy	Critical current, I_c, μa/cm²		Primary passive potential, E_{pp}, v *vs.* S.C.E.		Passive current, I_p, μa/cm² at −0.2v	
	Exp.	Calc.	Exp.	Cacl.	Exp.	Calc.
Cd	20.6	—	−1.000	—	20.6	—
Cd-10 w/o Zn	1,000-2,500	1,250-4,000	−1.400	−1.420 −1.400	100-200	350-1,070
Cd-30 w/o Zn	9,000-11,000	4,500-12,000	−1.430 −1.400	−1.420 −1.400	1,100-1,400	1,000-3,100
Zn	12,200-37,000	—	−1.420 −1.400	—	2,290-9,000	—

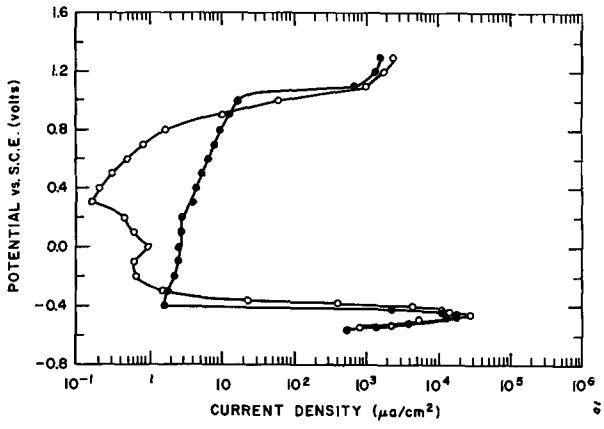

Fig. 10. Anodic polarization of an Fe-20.6 w/o Cr alloy in normal sulfuric acid: ○, exp; ●, calc.

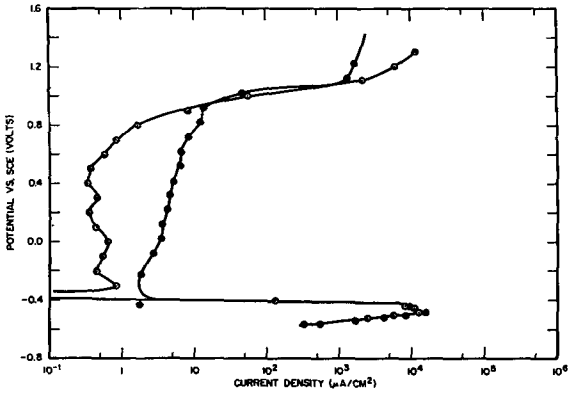

Fig. 11. Anodic polarization of an Fe-25.0 w/o alloy in normal sulfuric acid: ⊙, exp; ●, calc.

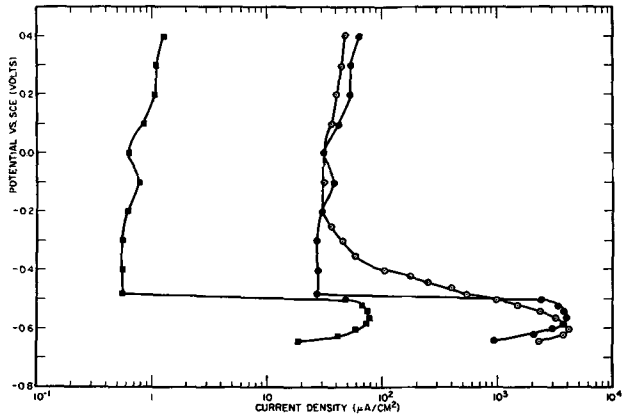

Fig. 12. Anodic polarization of $TiCr_2$ in normal sulfuric acid: ⊙, exp; ■, calc; ●, calc with correction.

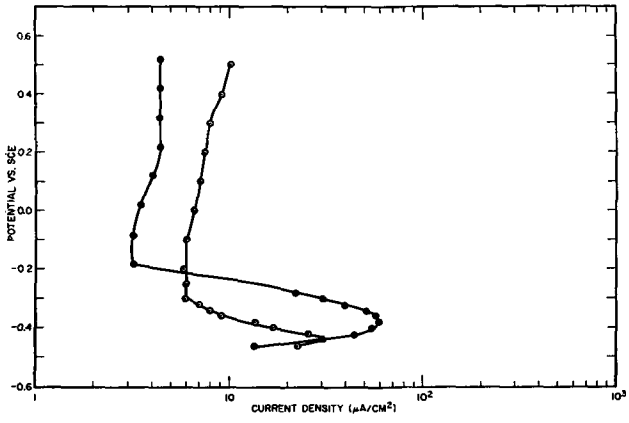

Fig. 13. Anodic polarization of TiFe in normal sulfuric acid: ⊙, exp; ●, calc.

sions of the behavior of dilute alloys. In the 10.5 w/o Cr alloy, only the relatively wide current maximum remains as evidence of the effect of greatly different dissolution rates on the polarization curves of relatively dilute alloys. Except for the magnitude of the passive currents, the experimental and calculated curves for the 20.6 and 25 w/o alloys agree quite well.

In Table IV, calculated and experimental values of the parameters for the anodic dissolution of some metastable solid solutions of titanium and chromium are listed. Again, calculated and experimental results compare favorably.

In both of the alloy systems discussed above, there is a noticeable difference between calculated and observed passive currents.[5] It should be noted that due to the large change in current during the transition from the active to the passive state, the differences observed in the passive currents are not significant in relation to the over-all polarization behavior of these alloys. Furthermore, these differences are no greater than would be expected in the values of passive currents reported by independent investigations on the same metal.

Dissolution of intermetallic compounds.—It was postulated above that the dissolution of intermetallic compounds should be controlled by the enrichment of the noble component on the surface, but it was also noted that the strong interactions that are characteristic of these alloys might lead to displacement of the polarization curve along either the current or potential axis. Figures 12 and 13 show the calculated and experimental polarization curves for $TiCr_2$ and TiFe. The experimental and calculated curves have the same shapes but are displaced from one another along the current axis. In general

$$i_{exp} = C i_{calc}$$

[5] Work in this laboratory has shown that the time-dependence of the passive current is different for different elements. Although discussion of this phenomenon is beyond the scope of this paper, it is natural that the behavior of alloys would be intermediate to that of their components. Such behavior could lead to the differences observed.
Mueller (21) has suggested that the formation of mixed oxides or spinels may lead to passive films on alloys which are less soluble than those of either component. Such reactions also could explain the observed differences.

Table IV. Anodic polarization of Ti-Cr alloys in NH_2SO_4

Alloy	Critical current, I_c, μa/cm²		Primary passive potential, E_{pp}, v vs. S.C.E.		Passive current, μa/cm² at 0.2v	
	Exp.	Calc.	Exp.	Calc.	Exp.	Calc.
Ti	29.1	—	−0.520	—	2.18	—
Ti-10 w/o Cr	26	33	−0.520	−0.520	1.4	2.0
Ti-20.4 w/o Cr	42	35	−0.520	−0.540	1.2	1.8
Cr	3,700	—	−0.560	—	1.25	—

Table V. Correction factors for the dissolution of some intermetallic compounds

Compound	C
$TiCr_2$	50
TiFe	2
$TiFe_2$	15

where C is an experimentally determined constant. Values from 2 to 50 have been found for C (Table V), but there is no method of predicting the constant for a particular compound.

The experimental results show that the polarization of these complex alloys is apparently determined by that of their most noble component, but the position of the curve is influenced to varying degrees by the fact that these compounds have characteristics which are usually quite different from their pure components.

Discussion

For the most part, the experimental results have been discussed in relation to the theory in the previous section; however, some general points merit further discussion.

The results of metallographic etching (8, 9) and the quantitative agreement between theory and experiment in this study make physical interpretation of the dissolution of heterogeneous alloys relatively sure. The dissolution behavior of the phases of a heterogeneous alloy are unaffected by the fact that they are in an alloy. Electrochemically, such an alloy is a galvanic couple in which the necessary electrical connections are made by physical contact between phases. It was noted above that this fact extends the mixed potential theory beyond its original assumption and requirement of randomly distributed anodic and cathodic sites.

Considerable care must be taken in attaching physical significance to the fact that the dissolution of homogeneous alloys can be treated by assuming that the noble component enriches on the surface of the alloy. The polarization curves of alloys are apparently controlled by surface enrichment or at least some surface enrichment-like effect, but there is no evidence that this enrichment is a gross effect like the dezincification of brass. On the contrary, the behavior of intermetallic compounds and the necessity of the potential shift in applying Eq. [9] make enrichment at only the active dissolution sites a much more likely explanation. If the noble component covered the entire electrode surface to any thickness, the behavior of the electrode would be independent of solid-state interactions in the alloy, yet allowance for these interactions had to be made in this study. Although the present theory is undoubtedly only an approximation of a very complex process, the quantitative agreement between it and experiment show that the approximation is generally valid.

Summary

1. A general quantitative theory has been presented for the anodic dissolution of binary alloys.

2. Experimental verification of the theory has been presented.

3. The rules for calculating the polarization curves of alloys can be summarized:

(*A*) Heterogeneous alloys behave as simple galvanic couples. If the polarization curve for each phase in the alloy is known

$$i = i_A f_A + i_B f_B \qquad [5]$$

The area fractions f_A, f_B can be calculated from the composition of the alloy. i is the total alloy current density at a potential E; i_A, i_B are the current densities of the components at this potential.

(*B*) Homogeneous alloys must be treated by extending Tammann's concept of surface enrichment. To compensate for interactions in the alloy, the polarization curves of the components are shifted along the potential axis until their corrosion potentials are at the corrosion potential of the alloy. The current at any potential can then be calculated

$$i = \frac{i_A i_B (Z_A N_A + Z_B N_B)}{Z_A i_B N_A + Z_B i_A N_B} \qquad [9]$$

N_A, N_B are the mole fractions of the components in the alloy; Z_A, Z_B are the oxidation numbers of the ions. The other symbols are as in (*A*).

(*C*) Intermetallic compounds and intermediate phases behave in general like other homogeneous alloys, but stronger solid-state interactions may shift their polarization curves along the current axis.

Acknowledgment

This work was partially supported by research grants from the Monsanto Chemical Company and the National Science Foundation. One of the authors (R. F. Steigerwald) wishes to thank the Union Carbide Metals Company for financial support under a Union Carbide Metals Company Fellowship.

The pure metals listed in Table I were gifts of the suppliers.

The authors wish to thank Messrs. H. L. Andrews, A. P. Lee, and J. C. Uy for their help in preparing the experimental alloys.

Manuscript received May 2, 1962. This paper was prepared for delivery at the Detroit Meeting, Oct. 1-5, 1961.

Any discussion of this paper will appear in a Discussion Section to be published in the June 1963 JOURNAL.

REFERENCES

1. F. R. Morral and J. L. Bray, *Trans. Electrochem. Soc.*, **75**, 427 (1939).
2. R. Landau and C. S. Oldach, *ibid.*, **81**, 521 (1942); R. Landau, *ibid.*, 559.
3. A. P. Bond and H. H. Uhlig, *This Journal*, **107**, 488 (1960).
4. H. G. Feller and H. H. Uhlig, *ibid.*, **107**, 864 (1960).
5. J. Osterwald and H. H. Uhlig, *ibid.*, **108**, 515 (1961).
6. G. M. Florianovich, Y. M. Kolotrykin, and N. K. Smirnova, *Doklady Akad. Nauk. S.S.S.R.*, **120**, 845 (1958).
7. N. Ohtani, *J. Inst. Metals* (Japan), **19**, 674 (1955); **19**, 677 (1955); **19**, 726 (1955); **19**, 729 (1955); **20**, 20 (1956); **20**, 158 (1956); **20**, 162 (1956); **20**, 468 (1956).
8. C. Edeleanu, *J. Iron Steel Inst. (London)*, **185**, 482 (1957).
9. V. Cihal and M. Prazak, *J. Iron Steel Inst.*, **193**, 360 (1959).

10. M. Prazak, *Collect. Czeck. Chem. Comm.*, **25**, 1126 (1960).
11. G. Tammann, "A Textbook of Metallography," The Chemical Catalog Company, New York (1925). *Z. anorg. u. allegem. Chem.*, **107** (1919).
12. C. Wagner and W. Traud, *Z. Elektrochem.*, **44**, 391 (1938).
13. M. Stern and A. L. Geary, *This Journal*, **104**, 56 (1957).
14. See also *e.g.*, A. C. Makrides, *ibid.*, **107**, 864 (1960).
15. E. Mattson, "The Electrode Process in Metal Deposition from Aqueous Solution," p. 31, Elandeis Boktryckeri Aktiebolog, Goteberg (1955).
16. J. O. Bockris, "Modern Aspects of Electrochemistry," Academic Press, Inc., New York (1954).
17. M. Stern, *Corrosion*, **14**, 329t (1958).
18. M. Stern and H. Wissenberg. *This Journal*, **106**, 759 (1959).
19. N. D. Greene, C. R. Bishop, and M. Stern, *ibid.*, **108**, 836 (1961).
20. N. D. Tomashov, R. M. Altobsky, and C. P. Chernova, *ibid.*, **108**, 113 (1961).
21. W. A. Mueller, *Corrosion*, **18**, 73t (1962).
22. G. V. Akimov, *ibid.*, **11**, 474t, 515t (1955).
23. S. Morioka and K. Sakiyama, *Technol. Repts. Tohoku Univ.*, **17**, 176 (1953).
24. S. Morioka and K. Sakiyama, *J. Inst. Metals (Japan)*, **19**, 31 (1955); **19**, 438 (1955); **19**, 598 (1955); **19**, 732 (1955).
25. G. Economy, R. Speiser, F. H. Beck, and M. G. Fontana, *This Journal*, **108**, 337 (1961).
26. C. Edeleanu, *Nature*, **173**, 739 (1954).
27. N. Y. Bune and Y. M. Kolotrykin, *Doklady Akad. Nauk, S.S.S.R.*, **111**, 1050 (1956).
28. N. D. Greene, *Corrosion*, **15**, 369t (1959).
29. N. D. Greene, "Proceedings of the First International Congress on Metallic Corrosion," Butterworth's, London, in press.
30. M. Stern, *This Journal*, **102**, 609 (1955).
31. M. Stern and A. C. Makrides, *ibid.*, **107**, 782 (1960).
32. M. Stern, *ibid.*, **106**, 376 (1959).
33. A. Rahmel and W. Shwenk, *Arch. Eisenhuttenw.*, **31**, 189 (1960).
34. Y. M. Kolotrykin, *Z. Elektrochem.*, **62**, (1958).
35. Metals Handbook, p. 1240, ASM, Cleveland (1948).
36. *Ibid.*, p. 1190.
37. H. W. Paxton and T. Kunitake, *Trans. AIME*, **218**, 1003 (1960).
38. P. F. King and H. H. Uhlig, *J. Phys. Chem.*, **63**, 2026 (1959).
39. R. Olivier, Dissertation, Leiden (1955).
40. C. Edeleanu, *J. Iron Steel Inst. (London)*, **188**, 122 (1958).

Darkening Speed Tests with Reversible Electroplating Shutters

S. Zaromb[1] and J. Y. Chang[2]

Philco Scientific Laboratory, Blue Bell, Pennsylvania

ABSTRACT

The design and construction of experimental reversible electroplating light shutters are described, and their preliminary evaluation by means of resistance measurements is outlined. Oscilloscope traces of simultaneous light transmission changes and plating pulses are presented and interpreted. An observed better-than-expected darkening efficiency may be attributed either to an anomalously high absorption coefficient of the very thin Ag films deposited by an unusually fast plating procedure or to increased turbidity and/or increased multiple light reflections. The maximum achieved plating speeds corresponded to average current densities of up to 80 amp/cm^2 for 250 to 400 μsec over an area of up to 16 cm^2. No damage in the tin oxide coating was observed after more than 13 such pulses with a plating solution of 3M AgI plus 8M NaI at a neutral *p*H. The maximum plating speeds expected from first order estimates of diffusion rate limitations were approached in five tests.

Preliminary experiments (1) with a Reversible Electroplating Light Modulator (RELM) of small area (0.2 cm^2) showed excellent resistance of transparent tin oxide-coated glass electrodes in alkaline AgI-NaI solutions to numerous plating-deplating cycles and fair general agreement with theory (2). The present work was aimed at demonstrating the feasibility of a RELM of increased area and plating speed. Furthermore, the experimental conditions used were much more drastic, the cells being subjected to high voltage and current pulses ($\simeq$200v and $\simeq$1000 amp), and the electrolyte being not strongly alkaline but rather acidic or neutral, and, therefore, more likely to damage the conductive tin oxide coating via formation of nascent hydrogen.

[1] Present address: Research and Advanced Technology Department, Electronic Systems & Products Division, Martin-Marietta Corporation, Baltimore, Maryland.

[2] Present address: Research Division, New York University, Bronx, New York.

Shutter Design, Construction, and Evaluation

The shutter design was based on arrangement 6 of Fig. 2 of ref. (2) consisting of parallel (nonalternating) electrical connections between line-symmetric subelements of width *b* ($\simeq$0.3 cm). The contacts to each subelement were made by sawing parallel, narrow grooves (approximately 0.03 cm wide and 0.15 cm deep) in flat lime-glass plates, with a distance 2*b* between adjacent grooves, applying a conductive tin oxide coating over the entire grooved surface, and introducing Ag paint and Cu leads into the grooves so as to form good electrical contacts between the leads and the conductive coating within the grooves, as shown in Fig. 1. A protective insulating layer of Kimble CV 137 solder glass was formed in the upper half of the grooves by repeated filling with the solder glass frit, heating to 425°C at a rate of 10°C/min, sintering for 1 hr at 425°C, and cooling at a rate of 5°C/min. In order to allow for differ-

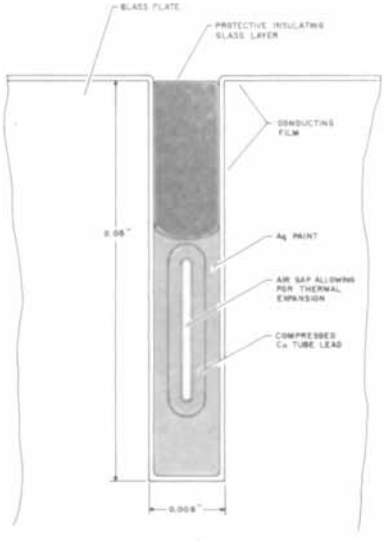

Fig. 1. Schematic cross-sectional drawing of groove, contacting lead, and protective layer.

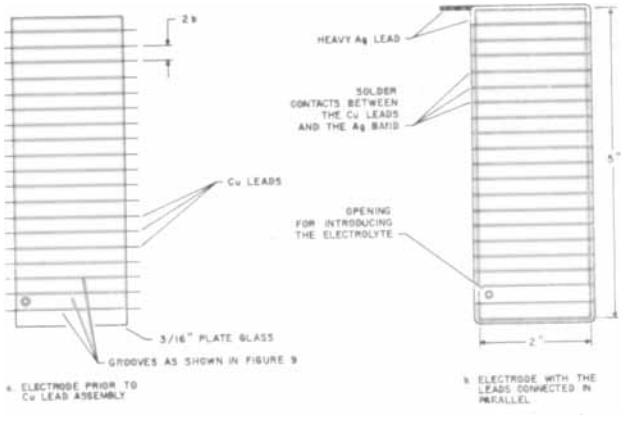

Fig. 2. Construction of the transparent electrodes

ential thermal expansion during the sintering process, the Cu leads were made of Cu tubing, 0.04 cm OD and 0.005 cm wall thickness, compressed into ribbons 0.012 cm thick and 0.05 cm wide so as to leave the narrow air hole shown in Fig. 1. The parallel connection of the Cu leads to a heavy Ag

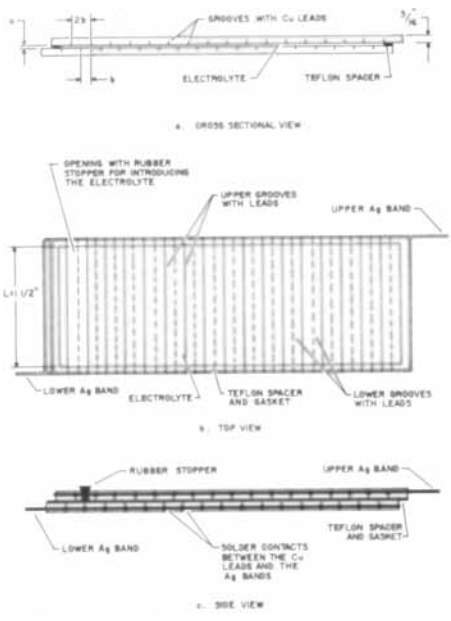

Fig. 3. Assembled reversible electroplating light shutter

band surrounding each plate is shown in Fig. 2. The dimensions of Fig. 2 correspond to those of the original plating cell design of Fig. 3. However, most of the actual plating cells used in the present experiments had a smaller shutter area, as listed in Tables I and II.

For maximum plating speeds, a low cell resistance was desired. Hence, special efforts were made during the tin oxide coating step to render the glass surface as highly conducting as possible. The grooved glass plates were cleaned with laboratory detergent (Alconox or Calgonite), rinsed with alcohol, air dried, etched for at least 1 min in a solution of 1.5:3:0.9 volume ratio of concentrated HF, H_2SO_4, and H_2O, rinsed with distilled water, placed on graphite holders, and preheated in a muffle furnace to 650°C. Holders and plates were then placed in front of several hot propane burners within a firebrick enclosure arranged so as to yield fairly uniform and intense heating of the entire glass plate and

Table I. Pertinent data and interpretation of the oscilloscope traces of tests I-XVII.

Test No.	Plate spacing a, cm	Plated area A, cm²	Cell resistance, ohms	Series resistance, ohms	Capacitance C, μfd	Voltage V, v	Time constant from RC product μsec	Time constant from V-trace μsec	τ_1, μsec	Q, coul	q_d, coul/cm²	δ final calc.	Q_1/Q	q_{at}, coul/cm²	δ_1 calc.	$(\tau_1)_{min}$, μsec
I	0.09	6	0.40	0.2	1575	135	1000	600	600	0.21	0.035	1.3	0.65	0.023	0.8	260
II	0.038	6	0.25	0.2	1575	135	700	600	400	0.21	0.035	1.3	0.55	0.019	0.7	180
III	0.043	6	0.25	0.2	1575	135	700	400	300	0.21	0.035	1.3	0.5	0.018	0.65	160
IV	0.043	6	0.28	0.2	1575	135	700	400	250	0.21	0.035	1.3	0.45	0.016	0.6	130
V	0.043	6	0.28	0.2	1575	135	700	400	400	0.21	0.035	1.3	0.65	0.023	0.9	260
VI	0.06	15	0.15	0.14	2625	180	800	400	400	0.47	0.031	1.2	0.65	0.020	0.8	200
VII	0.06	15	0.15	0.12	2625	300	700	500	400	0.79	0.053	2.0	0.5	0.027	1.0	370
VIII	0.045	16	0.16	0.12	2625	300	700	500	300	0.79	0.049	1.9	0.5	0.025	1.0	310
IX	0.045	16	0.15	0.12	1575	135	500	300	400	0.21	0.013	0.5	0.7	0.009	0.4	40
X	0.045	16	0.14	0.12	1575	200	500	300	400	0.31	0.016	0.6	0.7	0.010	0.4	50
XI	0.045	16	0.14	0.12	1575	300	500	300	300	0.47	0.029	1.1	0.6	0.017	0.7	140
XII	0.045	16	0.14	0.12	1575	400	500	300	250	0.63	0.039	1.5	0.5	0.020	0.8	200
XIII	0.045	16	0.14	0.12	1050	400	300	200	250	0.42	0.026	1.0	0.7	0.018	0.7	160
XIV	0.045	16	0.14	0.12	2100	135	600	400	500	0.28	0.018	0.7	0.7	0.012	0.5	70
XV	0.043	16	0.25	0.12	1575	135	600	350	500	0.21	0.013	0.5	0.75	0.010	0.4	50
XVI	0.043	16	0.20	0.12	1575	182	600	350	400	0.29	0.018	0.7	0.7	0.013	0.5	80
XVII	0.043	16	0.19	0.12	1575	250	600	300	300	0.39	0.024	0.9	0.6	0.014	0.5	100

Table II. Data and calculations pertaining to the oscilloscope traces of tests XVIII-XXIX.

Test No.	Plated area A, cm²	Cell resistance, ohms	Series resistance, ohms	Capacitance C, μfd	Voltage V, v	Time constant from RC product μsec	Time constant from V-trace μsec	τ_1, μsec	Q, coul	q_s, coul/cm²	δ final calc.	δ final measured	Q_1/Q	q_{s1}, coul/cm²	(δ_1), calc.
XVIII	6			4725	67				0.32	0.053	2.0	2.0			
XIX	3	0.44	0.12	2625	70	1600			0.18	0.060	2.3	2.4			
XX	13.3	0.28	0.5	5250	180	4100	3500	5000	0.94	0.071	2.7		0.7	0.05	1.9
XXI	13.3	0.20	0.4	5250	180	3100	3500	1500	0.94	0.071	2.7		0.4	0.03	1.1
XXII	13.3	0.18	0.3	5250	180	2500	3000	1300	0.94	0.071	2.7		0.3	0.02	0.8
XXIII	16.2	0.18	0.5	5250	180	3600	4000	1000	0.94	0.058	2.2		0.2	0.012	0.5
XXIV	16.2	0.16	0.4	5250	200	2900	3000	600	1.05	0.058	2.2		0.2	0.012	0.5
XXV	16.2	0.16	0.3	5250	200	2400		400	1.05	0.058	2.2		0.15	0.009	0.3
XXVI	16.2	0.16	0.3	5250	200	2400		400	1.05	0.058	2.2	>2.0	0.15	0.009	0.3
XXVII	16.2	0.16	0.3	5250	200	2400		350	1.05	0.058	2.2	>2.0	0.15	0.009	0.3
XXVIII	16.2	0.16	0.3	5250	200	2400		400	1.05	0.058	2.2	3.0	0.15	0.009	0.3
XXIX	16.2	0.16	0.3	5250	200	2400		400	1.05	0.058	2.2	3.0	0.15	0.009	0.3

holder. Dull-red heat, corresponding to the softening temperature of the glass, was reached within 10 to 20 min, at which time a fine spray of $SnCl_4$ solution was immediately directed at the grooved glass surface.

The spraying solution was made up by slowly adding anhydrous $SnCl_4$ to a solution of 100g $SnCl_4 \cdot 5H_2O$ in 50g distilled water plus 10g concentrated HCl and 1.0 or 1.5g $SbCl_3$ until a slight supersaturation was observed, and then adding a tenth part of the same solution to render the solution slightly undersaturated. The spray gun was constructed entirely of Pyrex glass. The spray was triggered by the passage of compressed O_2 through a gas inlet tube. The spray nozzle was held at a distance of 10 cm from the glass plate and the spray applied for 10- to 15-sec periods with a continuous horizontal and/or vertical motion of the nozzle aimed at obtaining a uniformly conductive coating. After allowing a few minutes for the glass to regain its softening temperature, the spraying was resumed; this was repeated 4-10 times depending on the desired conductivity and light transmission. The plates were then placed in an annealing furnace and allowed to cool slowly (in >2 hr) to room temperature.

Although the resistivity of the glass on the flat plate surface could readily be brought down to 5 ohms/sq by the above procedure, the resistivity inside the grooves usually tended to be much higher, especially when the groove widths were less than 0.025 cm. With grooves 0.03 cm wide, a satisfactory groove surface resistivity of approximately 20 ohms/sq was obtained in the best plates.

The average resistivity in the grooves was estimated in the following way: Let r be the ratio of the surface resistivities ρ_G and ρ_g of the conductive film inside and outside the grooves, respectively,

$$r = \rho_G/\rho_g \quad [1]$$

n_g the number of grooves or conductive strips between grooves, w_g and w_G the respective perimeters of a strip and groove cross section, and l_g the length of each groove or strip. Then the resistances R_{gl} and R_{Gl} between the long edges of each strip and groove, respectively, are

$$R_{gl} = \rho_g w_g/l_g \quad [2]$$

and

$$R_{Gl} = \rho_G w_G/l_g \quad [3]$$

whereas the respective resistances R_{gs} and R_{Gs} between the shorter edges are

$$R_{gs} = \rho_g l_g/w_g \quad [4]$$

and

$$R_{Gs} = \rho_G l_g/w_G \quad [5]$$

The total series resistance R_l between n_g alternating resistors $(R_{gl} + R_{Gl})$ is

$$R_l = n_g (R_{gl} + R_{Gl}) = (\rho_g w_g + \rho_G w_G)\, n_g/l_g \quad [6]$$

whereas the total conductance $(1/R_s)$ of n_g conductors $(1/R_{gs} + 1/R_{Gs})$ connected in parallel is

$$1/R_s = (n_g/R_{gs}) + (n_g/R_{Gs}) = \frac{n_g}{l_g}\left(\frac{w_g}{\rho_g} + \frac{w_G}{\rho_G}\right) \quad [7]$$

The ratio

$$\frac{R_l}{R_s} = \frac{n_g^2}{l_g^2}\,\frac{(\rho_g w_g + \rho_G w_G)(\rho_G w_g + \rho_g w_G)}{\rho_g \rho_G} \quad [8]$$

was measured readily by clamping two parallel soft-copper contacting strips first along the shorter and then along the longer edges of each conductive plate. Setting $w_G \simeq 2 \times 0.15$ cm $= 0.3$ cm and $w_g = 2b = 0.6$ cm one obtains

$$R_l/R_s \simeq n_g^2 w_g^2 (1 + 0.5r)(r + 0.5)/r l_g^2$$
$$\simeq w^2(1 + 0.5r)(r + 0.5)/l_g^2 r \quad \text{for } b \simeq 0.3 \text{ cm} \quad [9]$$

where

$$w \cong n_g w_g \quad [10]$$

is the total length (or width of the plate along the direction perpendicular to the grooves. The values of R_l/R_s corresponding to various resistivity ratios r were tabulated for $w^2/l_g^2 = 1$ (square plates). Multiplication of the actually measured ratios R_l/R_s by the dimensional correction factor l_g^2/w^2 and comparison with the tabulated values gave a direct estimate of r. Furthermore, since usually $w_g/\rho_g >> w_G/\rho_G$, the value of R_s gave an approximate estimate of ρ_g

$$\rho_g \simeq l_g R_s/w \quad [7']$$

As seen from Fig. 1, the contact resistance r_c between a Cu lead and the conductive film layer near the top of the groove may be written as

$$r_c = r_{Ag} + r_{tg} \quad [11]$$

where r_{Ag} is the resistance of the Ag paint layer and r_{tg} is that of the conductive film in the upper half

of the groove. If ρ_G is the surface resistivity of the latter film, then

$$r_{tg} \simeq \rho_G \times (0.05 \text{ cm}/5 \text{ cm}) \simeq 0.01\, \rho_G \quad [12]$$

where the factor 0.05 cm/5 cm corresponds to the approximate width and length of the top half groove wall. Considering that the resistance of each subelement must be at least

$$\rho_g b/2L \simeq 0.04\, \rho_g \quad [13]$$

where L ($\simeq$4 cm) is the length of each subelement (cf. Eq. [13'] of ref. (2)), and that there are two contacts per subelement [cf. Fig. 3], then the total resistance due to the r_{tg} component would be less than ½ of the theoretical cell resistance given by Eq. [24'] of ref. (2), if ρ_G were not larger than ρ_g. On the other hand, the r_{Ag} component should be negligible if no serious cracks, air gaps, or other sources of spurious resistance are present between the Cu lead, the Ag paint, and the conductive film at the lower half of the groove surface. Furthermore, the resistance of a Cu lead 2 cm long and 500 x 10^{-6} cm^2 in cross section is less than 0.01 ohm which is negligible, *i.e.*, less than 10% of $\rho_g\, b/2L$. Hence, according to the design of Fig. 1, the total resistance due to contacts would be nearly half the minimum theoretical cell resistance.

With the Cu leads and Ag paint imbedded in the lower part of the groove, the resistance R_{Cu} between two neighboring Cu leads was

$$\begin{aligned} R_{Cu} &= 2r_c + R_{gl} \\ &\simeq 2r_{tg} + \rho_g w_g/l_g \\ &\simeq 0.02\, \rho_G + 0.12\, \rho_g \text{ for } b \simeq 0.3 \text{ cm} \end{aligned} \quad [14]$$

Thus, for $b \simeq 0.3$ cm, $\rho_g \simeq 5$ ohms/sq, and $\rho_G = 20$ ohms/sq, one obtains $R_{Cu} \simeq 1.0$ ohm. The actual values of R_{Cu} measured in most of the plates subsequently found to be unsatisfactory were usually higher than 1.0 ohm. On the other hand, those plates which yielded the best experimental cells actually showed R_{Cu} values of 0.4-0.9 ohm suggesting higher conductivities or values of ρ_G even lower than 20 ohms/sq in the upper parts of the grooves.

The cells were assembled as shown in Fig. 3 and filled with an aqueous solution of 3M AgI plus 8M NaI and pH values ranging from 3 to 9 (usually approximately 8), in accordance with the recommendations of ref. (2).

These cells could be partly evaluated even without actual plating experiments by simply comparing their resistances with the theoretical values predicted by Eq. [24'] of ref. (2)

$$R_p \simeq (a\rho_e + 0.5\, \rho_g b^2)/A \quad [15]$$

Setting $\rho_e \simeq 10$ ohm-cm, $a \simeq 0.05$ cm (a rather high value usually necessitated by the warping of the plates), $\rho_g \simeq 6$ ohms/sq, $b \simeq 0.3$ cm, and $A \simeq 16$ cm^2, one would expect $R_p \simeq 0.05$ ohm.

The cell resistances were measured by the Cahan-Rüetschi square wave pulse method (3). The 100-kc square wave calibrator output V_s (50 or 100v) of a Tektronix 535 oscilloscope was connected to a series circuit comprising a 10 μfd condenser, a large current determining resistance $R_{c.d.}$ (10,000 ohms or 100,000 ohms), and the plating cell. The amplitude i_s of the square wave current pulse through the plating cell was then approximately

$$i_s \simeq V_s/R_{c.d.} \quad [16]$$

i.e., 1-10 ma, and the plating cell resistance R_p was given by the instantaneous voltage changes ΔV_p across the cell at the beginning or end of each pulse

$$R_p \simeq \Delta V_p/i_s \simeq R_{c.d.}\, \Delta V_p/V_s \quad [17]$$

The cells listed in Tables I and II actually had areas A of 3-16 cm^2 and resistances of only 0.14-0.4 ohm, in tolerable agreement with the minimum theoretical values of approximately 0.05-0.25 ohm (cf. Eq. [15]). These cells also yielded the best results (highest measured plating speeds as given in Table I).

Measurement of Plating Current and Optical Density Changes

Several 525 μfd-450v electrolytic capacitors connected in parallel were charged to the desired voltage and then discharged rapidly through the plating cell and a 0.1-ohm precision series resistor upon closing of an EM-1 Hg plunger-type relay (manufactured by Ebert Electronics Corp., Queens Village, New York). The voltage across the 0.1-ohm resistor connected to one trace input of a Tektronix 502 oscilloscope gave the instantaneous current through the plating cell (cf. Fig. 4). The second trace of the same oscilloscope showed the output of a photomultiplier tube circuit measuring the light transmitted through the shutter. Both simultaneous traces were photographed with a Polaroid camera. The data for the best experimental cells are listed and interpreted in Table I and typical oscilloscope traces are shown in Fig. 5 under the same test numbers (in Roman numerals). In each graph, the time coordinate is horizontal, starting at the second line from the right and increasing from right to left, whereas the vertical coordinate refers either to the current or voltage, increasing upward, in those traces which show an initial maximum followed by a typical downward capacitor discharge curve (V-trace) or to the light transmission, decreasing upward, in curves showing a steady upward climb towards an asymptotic value on the left-hand side. In test V, the (upper) light transmission curve shows an initial maximum followed by a slow decrease due either to partial spontaneous clearing of the shutter

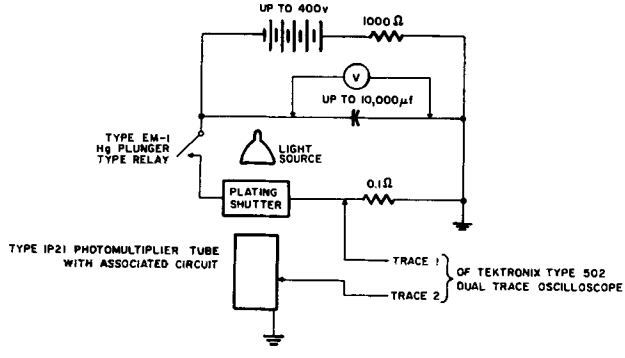

Fig. 4. Experimental arrangement for simultaneous measurements of plating current and optical density.

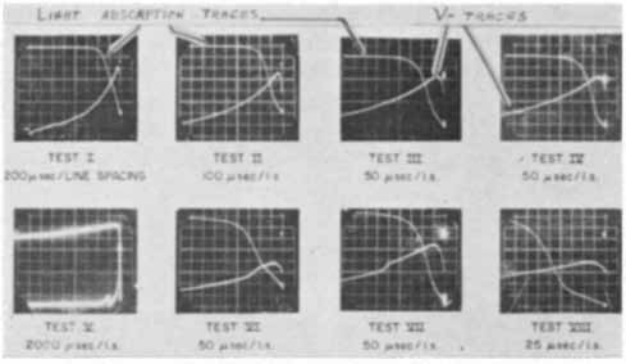

Fig. 5. Applied current pulses and light absorption changes in typical shutter closing experiments of less than 1000 μsec duration.

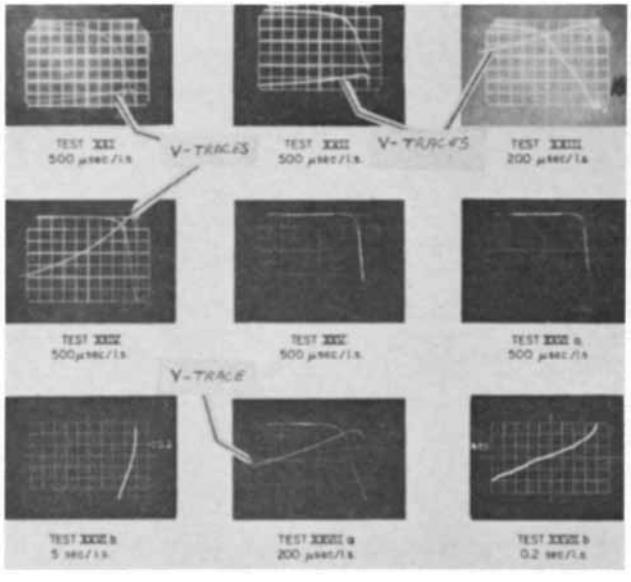

Fig. 6. Light absorption measurements of improved accuracy and, where indicated, current pulse shapes in shutter closing experiments of up to 10 μsec duration.

similar to that observed in tests XXVIb and XXVIIb of Fig. 6, or to a partial recovery of the photomultiplier circuit output from an initial "overshoot." The upper bright spots (near the second vertical line from the right and between the second and fourth lines from the top) mark the steady state output of the photomultiplier circuit when the light source was turned off. Hence, the asymptotes of the light transmission curves should all be located below the level of these upper bright spots. The actual upward displacement of the asymptotes was attributed at first to absorption of stray light upon closing the shutter, but was finally traced to an actual transient overshooting by the photomultiplier circuit. Because of this defect and partly also because of the inaccuracy of the ordinate scale, light absorption values of more than 90% (or optical densities exceeding 1.0) are unfortunately uncertain in the tests of Table I and Fig. 5. However, the times τ_1 corresponding to an optical density change δ of at least 1.0 could still be estimated from these curves and are listed in the tenth column of Table I. Comparison of the time values in columns 8, 9, and 10 shows a close parallelism and near equality of τ_1 and the time constant of the capacitor discharge circuit. The higher values of column 8 are probably due to nonlinear resistances in the circuit arising from a breakdown of spurious resistances under a high voltage. Because of the spurious and nonlinear circuit resistances, the current and voltage traces are also subject to uncertainties. Hence, the actual charge Q_1 passed through the cell up to the time τ_1 was estimated by means of the relation

$$Q_1/Q = 1 - e^{-\tau_1/\tau_c} \qquad [18]$$

where Q is the total capacitor charge (column 11) deduced from the product CV of columns 6 and 7, and τ_c is the time constant of column 9. Division of Q by the area A of column 3 yielded the total charge density q_d of column 12, and multiplication of q_d by the Q_1/Q ratio (column 14) yielded the charge density q_{d1} passed up to the time τ_1.

According to Fig. 1 of ref. (2), the actual optical density change δ_1 corresponding to a charge density q_{d1} should be

$$\delta_1 = 38q_{d1} \qquad [19]$$

and similarly, for δ corresponding to 100% capacitor discharge

$$\delta \simeq 38q_d \qquad [19']$$

The calculated values of δ_1 (column 16) are usually less than the estimated actual value of at least 1.0. This may be due either to a higher actual absorption coefficient of the very thin films produced by the rapid plating process, or to marked local refractive index changes giving rise to increased reflections and increased turbidity.

The last column $(\tau_1)_{min}$ gives the minimum values of τ_1 allowed according to Eq. [33] of ref. (2)

$$(\tau_1)_{min} \simeq 5 \times 10^{-6} q_d^2/c_p^2 \simeq 0.5 q_{d1}^2 \qquad [20]$$

the concentration c_p of platable ions being 0.003 mole/cc. Comparison of columns 10 and 17 shows that $(\tau_1)_{min}$ was barely approached only in tests V, VII,VIII, XII, and XIII, and was exceeded by a factor of 2-10 in all the other tests. Since the actual speed limitations in all these tests were due to circuit RC time constants rather than to electrochemical limiting factors, the results of Table I do not give any indication of the actual applicability of Eq. [33] of ref. (2), but they do at least suggest the absence of any more severe intrinsic speed limitation.

To check the accuracy of the τ_1 and q_{d1} values of Table I, measurements were made with a corrected photomultiplier tube circuit and more sensitive scales obtained with a Tektronix 535 oscilloscope and a type Z differential pre-amplifier. The data and interpretation are given in Table II and typical traces shown in Fig. 6. In tests XVIII, XIX, XXV, XXVI, XXVIII, and XXIX, the V-trace (current or voltage-time curve) was not recorded. Tests XXVIb and XXVIIb in Fig. 6 are simultaneous recordings of the same photomultiplier outputs as in the respective tests XXVIa and XXVIIa, but on more compressed time scales and a more sensitive (expanded) vertical (light transmission) scale. The downward slope in test XXVIb and XXVIIb shows the slow partial clearing in the absence of a continuous plating current following the initial charge pulse.

The time constants and τ_1 values in Table II are usually much longer than those in Table I due to

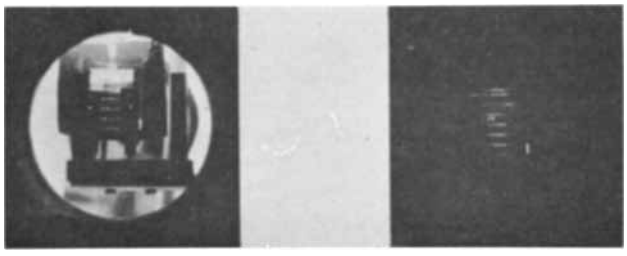

Fig. 7. Photographs of irregular incandescent lines resulting from a nonuniform distribution of high current pulses through an unsatisfactory plating cell.

breakage of the best experimental cells by the time the photomultiplier circuit was improved. However, the q_{d1} and $(\delta_1)_{calc.}$ values of Table II (columns 15 and 16) are usually comparable with, and thereby indirectly confirming, those of Table I. The unusually high value of $(\delta_1)_{calc.}$ in test XX is probably due to a nonuniformity of plating in the area directly in front of the photomultiplier tube.

As mentioned above, the cells used in tests XVIII through XXIX were generally poorer and less uniform than the earlier cells. Attempts to increase their plating speed by reducing the number of capacitors and charging to higher voltages invariably resulted in an incandescence of the grooves (cf. Fig. 7) probably due to an excessive value of ρ_G and associated I^2R power dissipation in the conductive film in the groove walls. Furthermore, a nonuniform current distribution could result in permanently damaged spots in the conductive film adjacent to the electrolyte in areas where the current densities were at a maximum. Since any such damage would tend to enhance subsequent plating nonuniformities, a single passage of an excessive current pulse would usually be followed by incandescence and further deterioration even with lower (previously acceptable) current pulses. These effects were especially serious in the larger area cells ($A \simeq 40$ cm^2) not listed in Table I and II.

In view of the extreme sensitivity of parallel circuits to imbalance under very high loads, it is almost surprising that the relatively high plating speeds of Table I could have been obtained. The average currents and current densities in tests VII, VIII, XII, and XIII correspond to between 1000 and 1300 amp and 70-80 amp/cm^2 for 250 to 400 μsec over a relatively large area of 15-16 cm^2. It should be noted that tests II through XIV were all performed with the same pair of matched plates, and that no damage due to the high current pulses was observed in these plates.

However, even these best plates had the serious shortcomings of (*a*) relatively poor light transmissivity (40-60%), resulting in an over-all light transmission of only 20% for the assembled cell; and (*b*) excessive warping, necessitating cell spacings of 0.04-0.09 cm, *i.e.*, 4-9 times the original design value of 0.01 cm.

Rate of Unplating

The time required for clearing of the light shutter was highly irreproducible and could vary from less than 10 sec to more than 5 min depending on cell structure. Since the gap widths a in most of the cells studied were 4-10 times larger than the design value

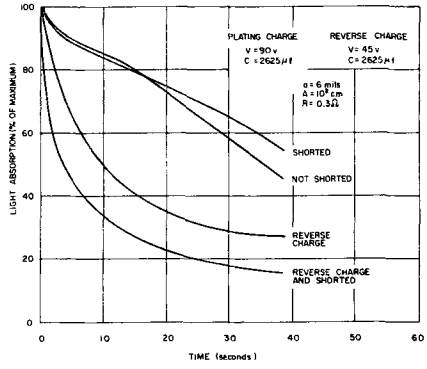

Fig. 8. Effect of a reverse charge pulse and/or shorting the cell terminals on the rate of clearing of a 6-mil gap width light shutter.

of 0.01 cm (required to revert to 78% of the original transmission in 1 sec or 90% in 3 sec), and since the clearing time is proportional to a^2, one would indeed expect the observed "clearing times" to range from 16 to 300 sec in cases where the proper reverse charge has been applied, and about fourfold longer "clearing times" without the reverse charge, in agreement with the actual observations. However, in addition to the effect of the spacing a, the following factors may further reduce the clearing rate: (*A*) Any loss of the oxidizing component (I_3^- or IO_3^-) via a reaction with the insulating material or with the metal leads would result in incomplete clearing. Hence, faulty insulation may be partly responsible for some observed irreproducibilities. (*B*) In cases where reversed charge pulses were applied, current density nonuniformities different in two pulse directions may produce an excess of Ag in some areas and of I_2 in others. Since the motion of I_3^- ions in directions parallel to the electrodes is extremely slow (considering the low a/L and a/w ratios), such areas of excess Ag and excess I_2 may remain dark for a very long time.

These last two factors may explain the type of discrepancy shown in Fig. 8. The nominal gap width a being only 0.015 cm, one would expect a return to 78% of the original transmission in 2 sec rather than the 20 sec shown by the lowest curve. However, the actual gap width in the cell must have fluctuated by at least ±50%, each of the two plates having a surface uneveness of about 0.01 cm. Hence, a reverse charge pulse was likely to result in separate areas of excess Ag and excess I_2. Shorting the cell terminals following the reverse charge pulse would then be expected to accelerate the rate of clearing of the Ag and I_2 spots via a type of battery discharge mechanism, as shown by the lower two curves of Fig. 8, whereas no marked effect resulted from shorting when a reverse charge had not been applied, as shown by the upper two curves.

Summarizing, then, the observed rate of deplating usually agreed in first order of magnitude with theoretical expectations. Occasional cases of irreproducibility or of marked discrepancy appear attributable to faulty cell structures.

Conclusions

The experimental results are usually in fair agreement with theory. Discrepancies in rate of unplating are obviously related to the following main devia-

tions from the design prescriptions of ref. (2): (*a*) uneven spacing between the electrodes; and (*b*) nonuniform electrode surface resistivities and the presence of spurious resistances in the contacts to the individual subelements.

These deviations were also responsible for: (*a*) the nonuniformities in plating density observed with unsatisfactory cells; (*b*) circuit imbalances associated with these nonuniformities, resulting in overloading of some of the parallel subelements; and (c) irreparable damage of the overloaded subelements or of the contacts due to excessive local I^2R heat generation on passage of excessive current pulses.

With satisfactory cells having negligible spurious contact resistances, the tin oxide coating was able to withstand average current densities as high as 80 amp/cm^2 for 250 to 400 μsec over an area of up to 16 cm^2 in solutions of neutral pH. No damage in the coating was observed even after more than 13 such high current pulses. The maximum plating speed expected on the basis of a first order estimate of diffusion rate limitations (Eq. [33] of ref. (2)) were approached but not exceeded in five of the tests listed in Table I. Since the plating speed in all these tests was limited by the RC time constant of the circuit used, no conclusion can be drawn as to the actual importance of diffusion limited mechanisms.

Optical density changes of 1.0 or higher were obtained with an average charge density q_{av} of 0.016 coul/cm^2 (in tests of both Tables I and II), *i.e.*, 60-70% of the charge density calculated on the basis of the absorption constant of thick Ag layers. This better-than-expected darkening efficiency may be due either to variation of absorption constant with film thickness and method of formation (possibly related to defect and impurity concentration in the film), or to increased turbidity and/or multiple light reflections. A more thorough investigation of these results should have an important bearing both on the optimization of the performance of the light shutter and on the understanding of the effect of growth parameters on the properties of very thin films.

Acknowledgments

Thanks are due to J. O'M. Bockris, B. D. Cahan, V. de Maria, F. Johnson, R. R. Kegg, and E. Kostyk for useful suggestions and/or assistance in the performance of the experiments. This work was sponsored by the Aerospace Medical Laboratory, Aeronautical Systems Division, Wright-Patterson Air Force Base under contract AF 33(616)-7928.

Manuscript received February 12, 1962; revised manuscript received Feb. 12, 1962.

Any discussion of this paper will appear in a Discussion Section to be published in the June 1963 JOURNAL.

REFERENCES

1. J. Mantell and S. Zaromb, *This Journal*, **109**, 992 (1962).
2. S. Zaromb, *ibid.*, **109**, 903 (1962).
3. B.D. Cahan and P. Ruetschi, *ibid.*, **106**, 543 (1959).

Magnetic Electrodeposits of Cobalt-Phosphorus

J. S. Sallo and J. M. Carr

Research Center, Minneapolis-Honeywell Regulator Company, Hopkins, Minnesota

ABSTRACT

Means of preparing Co-P electrodeposits having a wide range of magnetic properties are discussed. X-ray diffraction data, electron micrographs, and Bitter patterns are presented. An explanation of the origin of the high coercivity is presented. Low flux density of the material is described, and a possible explanation is presented.

For many years there has been interest in magnetic electrodeposits having high coercivity for use in serial storage devices. Most of the electrodeposits used for this purpose have been Co-Ni alloys. These materials usually have coercivities of 200-300 oe, although recently a Co-Ni alloy having a coercive force of 500 oe has been reported (1). A coercive force of 810 oe has been previously reported from a Co-Ni-P system (2). This system has been shown to consist of clusters of small single domain platelets, thus explaining the high coercive force (3).

The Co-Ni-P material is prepared from a system containing hypophosphite ion. Since the total products of the electrolysis exceed a 100% cathode efficiency, the original workers (2) concluded that the material is formed through a combination of chemical (electroless) deposition and electrodeposition. Since the system operates at a pH of about 4, and since chemical deposition of cobalt does not take place from acid systems, it can be concluded that the nickel is essential for the occurrence of chemical deposition and that removal of the nickel ion from the system will eliminate the phosphorus from the deposit. Despite these conclusions, Co-P deposits are formed from such a system, and modifications of this system lead to a series of deposits having a wide range of magnetic properties. Figure 1 shows the effect of removing the nickel from the Co-Ni-P system. The mechanism by which these deposits are formed is not fully understood.

Experimental

The electrodeposition was done on flat 0.003 in. Be-Cu or phosphor bronze foil. Temperature control was provided by a "Glascol" heating mantle surrounding a 1-l beaker which served as a plating chamber. A d-c power supply was used as a current source. The standard system was a 1-l bath containing 100 g/l

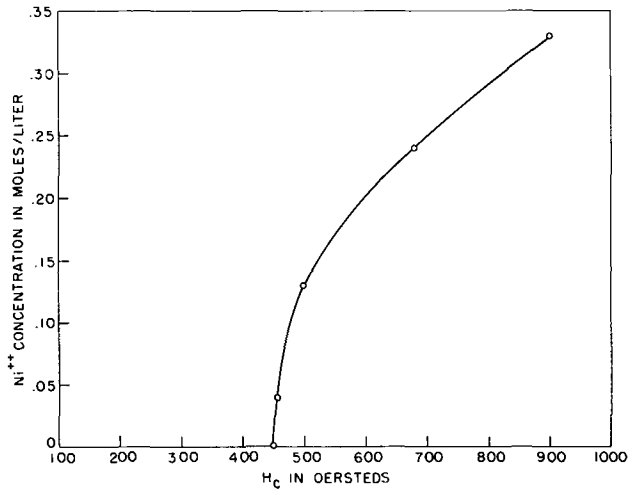

Fig. 1. Nickel ion concentrations vs. Hc of deposit in oersteds

$CoCl_2 \cdot 6H_2O$, 100 g/l NH_4Cl, and 15 g/l $NaH_2PO_2 \cdot H_2O$ at 50°C and operated at 60 amp/ft². This system produces a deposit having a coercive force of about 400 oe. Other coercivities are obtained by varying the concentration of bath constituents and the plating parameters of the system such as current density, temperature, and pH.

The phosphorous analysis was done with a "Spectronic 20" Colorimeter by the molybdovanadophosphoric acid method. The ethylenediamine tetraacetic acid (EDTA) titration method was used to determine cobalt with dithizone as indicator.

Magnetic measurements were obtained with a conventional 60-cycle hysteresis loop tester (4). Direct current measurements were obtained by the "moving coil method" by use of a ballistic galvanometer and a 6 in. Varian Magnet capable of producing fields of 10,000 gauss.

Electron microscopy was performed using an RCA model EMU3 by conventional collodian replication techniques using carbon shadowing and by the Craik technique (5) with an extension of this technique (3).

X-ray diffraction studies were performed using a North American Philips Norelco with a wide angle automatic Diffractometer.

All chemicals were reagent grade and were used without further purification. All solutions were prepared using distilled water.

Results

Under suitable conditions the coercive force of these deposits can be varied from 50 oe to 1300 oe. Under certain conditions a stepped hysteresis loop can be obtained.

The 400-oe material obtained from this system has shown good capabilities as a high density storage media. Results obtained from a conventional fixed head drum system show the deposit to have a packing density capability of about twice that of conventional magnetic oxide. Recording data will be published at a later date.

The coercive force of these materials is dependent on the crystal orientation of the deposit which, in turn, is dependent on the plating parameters of the system. The 50-oe coercivity material exhibits an uncertain crystal orientation and some samples appear to be amorphous. The 400-oe material has the 110 plane parallel to the substrate. The 1300-oe material has the 002 plane strongly orientated in the plane of the deposit. The nature of the latter material is described elsewhere (6).

The 60-cycle hysteresis loop of the deposit at all coercivities within the test range (50-2000 oe) shows a squareness (Br/Bm) of about 0.5. Remanence values are about 5500 gauss for a 400-oe deposit; however, full saturation may not have been attained. The properties are independent of the thickness of the deposit over the range studied (1-30μ).

The magnetic properties of the deposit are not dependent on an epitaxial growth from the substrate. Although most test samples were prepared on 0.003 in. Be-Cu and phosphor bronze foils, any substrate may be used which is used in normal electrodeposition techniques. The deposit may be plated on aluminum through use of the zincate method or by using electroless nickel-clad aluminum. Plastics can also be used as the substrate after being made conductive by one of the conventional techniques. In either of these cases, the magnetic properties are equivalent to those obtained on a copper based substrate.

The most significant factor influencing the coercive force of the deposited material is the pH of the system. A pH of 2 or less yields a deposit having a coercive force of about 50 oe. At pH of 3-4.5 a deposit having a coercivity of 400 oe is obtained. Increasing the pH to the precipitation point of the system, about 4.7, produces a deposit whose coercive force is 800 oe or higher. In all cases studied, the phosphorous content of the deposit remained in the range of 2-3%.

The concentrations of the bath constituents also have an effect on the coercive force of the deposit. Figure 2 shows the effect of varying the $CoCl_2$, NH_4Cl, and NaH_2PO_2 concentrations. Excluding the hypophosphite from the system produces an unsound deposit having a coercive force of about 100 oe. Replacing the ammonium ion with sodium ion also produces an unsound deposit. Small amounts of common impurities with the exception of iron have

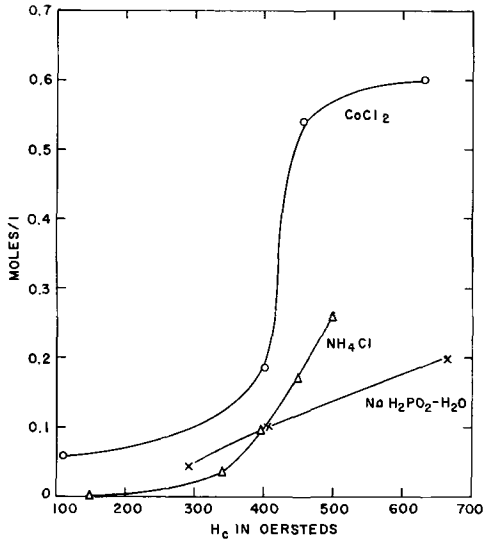

Fig. 2. Concentrations of Co^{++}, NH_4^+, $H_2PO_2^-$, vs Hc of deposit in oersteds.

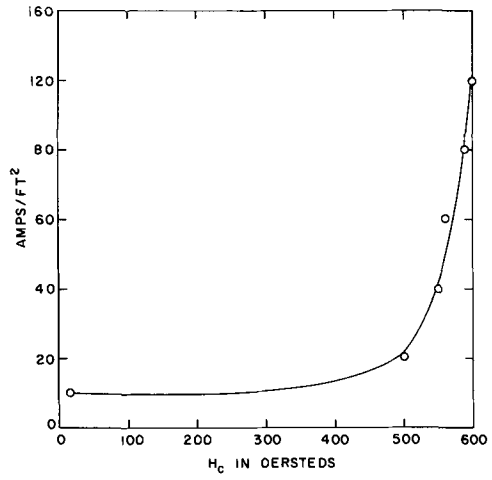

Fig. 3. Current density vs. Hc of deposit in oersteds

little or no effect on the deposit. Relatively large quantities of phosphite do not alter the properties of the deposit. Figure 3 shows the effect of varying the current density. The maximum coercivity obtainable by increasing the current is about 600 oe. In a still system current densities above 120 amp/ft^2 give an unsound deposit. As the temperature of the system is increased, the coercive force of the deposit increases. The highest coercive force deposit is obtained at 65°C. Further increases in temperature result in a decrease in the coercive force of the deposit until the deposit becomes unsound at a temperature of about 95°C.

When an inert anode is used, a rapid decrease in *p*H occurs. This leads to a change in the magnetic properties of the deposit as discussed previously. Replacement of the inert anode with a soluble cobalt anode minimizes the decrease in *p*H and results in a very stable system. By using the soluble cobalt anode and making periodic additions of hypophosphite, plating of a particular coercive force deposit can be continued almost indefinitely without an appreciable change in the *p*H of the system or the magnetic properties of the deposit.

Discusssion

The coercivity of these Co-P deposits is high enough to suggest single domain particle behavior. A very similar situation has been studied previously for Co-Ni-P electrodeposits (3). Figure 4a is an electron micrograph showing the platelet like structure of the Co-P deposit which is similar to the Co-Ni-P electrodeposit. These platelets differ from the Co-Ni-P platelets. They appear to be larger in the smallest dimension. The larger size of the platelet may explain the lower coercive force observed in the Co-P system. Figure 4b is an electron micrograph of the Co-P platelets in the demagnetized state with the use of the modified Craik techniques. The collection of magnetite shows flux leaving the plane of the film at cluster boundaries. The same technique applied to a magnetized sample shows no magnetite pattern.

These results can best be explained by use of Fig. 5. Each set of vectors represents a cluster of single domain platelets with the boundary between them

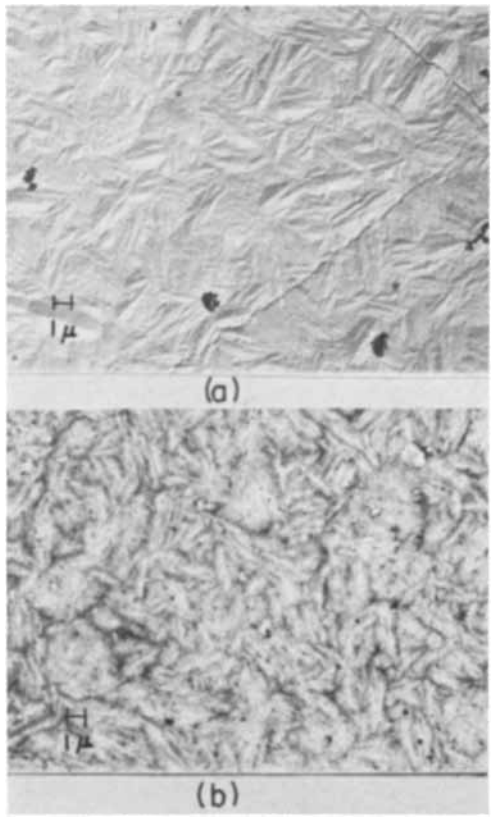

Fig. 4a. Electron micrograph of surface of Co-P deposit; magnification 3000X. Fig. 4b. Bitter pattern of demagnetized surface of Co-P deposit (Craik technique); magnification 3000X.

considered a cluster boundary. In the demagnetized state (a) each platelet has its magnetic vector at 180° to the platelet adjacent to it. Since all of these vectors are in the plane of the deposit (the uniaxial easy direction) there are no fields out of the plane of the film and no magnetite is collected within the

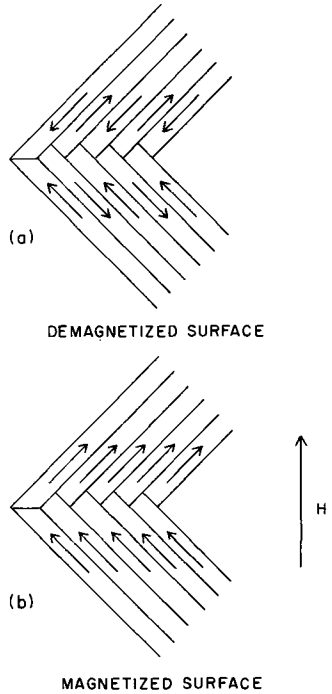

Fig. 5. Representation of flux state in (a) demagnetized state and (b) magnetized state.

clusters. At cluster boundaries each platelet may attempt to obtain closure with itself, with an adjacent platelet, or with a similarly oriented platelet in a neighboring cluster. Closure cannot be entirely between adjacent platelets as mismatching of the magnetic polarity of the platelets must occur to some extent. Self closure or closure between adjacent platelets will lead to some flux leaving the plane of the film at cluster boundaries particularly since the neighboring cluster may be attempting closure in the same area. This closure flux explains the magnetite pattern shown in Fig. 4b.

In the case of a magnetized sample, as shown in Fig. 5b, the platelets within the cluster have parallel magnetic vectors. In the remanent state of the material, all magnetic vectors will return to the easy direction of magnetization. Even so, each cluster has a component of magnetization in the direction of the previously applied field. Closure at cluster boundaries can take place between neighboring clusters and in the plane of the film, since mismatching of the magnetic polarities of the platelets cannot occur.

Smaller flux outputs were obtained from both the Co-Ni-P and Co-P deposits than would be expected from the chemical composition. A possible explanation for this is that the metal in the deposit is in the form of the phosphide. A lower saturation magnetization value is obtained for the Co-P deposit than for the Co-Ni-P. This is contrary to the expected value as cobalt has a much higher saturation magnetization value than nickel. This may be explained by assuming Ni to be in the form of the phosphide in the Co-Ni-P deposit and cobalt in the form of the phosphide in the Co-P deposit. Further studies of the saturation magnetization may reveal the nature of the phosphides in this type of deposit.

Conclusions

The magnetic properties of cobalt phosphorous electrodeposits have been determined. An extremely wide range of magnetic properties are available in this system. Studies of the crystalline structure of the deposit are presented along with an interpretation of the origin of the coercivity. Possible applications exist for this material in the field of hard magnetic materials. High density magnetic storage capabilities seem to exist.

Acknowledgment

The Celacol used in the Craik technique studies was kindly provided by J. M. Steel and Company, Limited.

Manuscript received April 11, 1962; revised manuscript received July 1, 1962. This paper was prepared for delivery before the Detroit Meeting, Oct. 1-5, 1961.

Any discussion of this paper will appear in a Discussion Section to be published in the June 1963 JOURNAL.

REFERENCES

1. I. Tsu, *Plating*, **48**, 379 (1961).
2. T. H. Bonn and D. C. Wendell, Jr., U. S. Pat. 2,655,787.
3. J. S. Sallo and K. H. Olsen, *J. Appl. Phys.*, **32**, 203S (1961).
4. D. H. Howling, *Rev. Sci. Instr.*, **27**, 952 (1956).
5. D. J. Craik and P. M. Griffiths, *Brit. J. Appl. Phys.*, **9**, 279 (1958).
6. J. S. Sallo and J. M. Carr, *J. Appl. Phys.*, **33**, 1316 (1962).

Electroluminescent Lines in ZnS Powder Particles

I. Embedding Media and Basic Observations

Albrecht G. Fischer

RCA Laboratories, Radio Corporation of America, Princeton, New Jersey

ABSTRACT

Several new embedding media of the same refractive index as ZnS are described which make possible the microscopic examination of the interior of electroluminescent particles taken from efficient industrial lots. Light is emitted in form of lines or striations extending through most of the diameter of the particles. The brightness of single lines has been measured in dependence of applied voltage, frequency, phase, and position along the line. Evidence is presented that the EL lines are associated with invisible copper-sulfide-decorated, conducting imperfection lines of submicroscopic diameter, and that coarse, visible imperfections are not the cause of EL.

Most studies of the electroluminescence (EL) of ZnS-type powders have been carried out on macroscopic cells containing a great number of particles. The study of the individual light-emitting elements in single particles, which alone can give reliable clues as for the acting mechanism, is difficult, and hence little has been done. There are several reports (1-3) that light emission takes place at the surfaces or tips of the particles or at contacts between grains. Due to the high refractive index of the irregularly shaped ZnS particles such observations are quite unreliable because of possible deceptions by multiply-reflected light.

To evade these difficulties, several authors have studied the EL of single crystals grown by sublimation. Light emission exclusively in front of the cathode (4, 5), or light emission in the bulk in the form of striations or dotted lines parallel to the field

(3, 6, 7) has been reported. Recently, and when the present work was already concluded (25), Gillson and Darnell (8) published results very similar to those to be reported here. They found light emission in the form of striations in insulatingly-embedded, small single crystals grown by sublimation from EL powder, similar to the method used by Zalm (3). Their crystals were embedded in a dark resin and had a ground and polished flat surface through which viewing of the interior without disturbance by scattered light was possible. In view of the importance of these findings for the theoretical interpretation of EL in ZnS powder, which may lead to improvements of brightness and efficiency, and since several different forms of EL are possible in ZnS so that conclusions by analogy may lead to errors, it is justified to confirm these results on particles taken from efficient industrial powders,[1] and to measure the properties of these striations.

Matched Embedding Media for EL Particles

If ZnS particles ($n = 2.37$) are immersed in the conventional immersion liquid with the highest refractive index, methylene iodide ($n = 1.75$), the Becke fringes (9) are so thick that microscopic observation reveals no details of the bulk. A mixture of sulfur, white phosphorus, and methylene iodide (10) of index 2.08, which was used for the same task by Lehmann (11), gives better but still unsatisfactory results and is unpleasant to handle. In a search for matched embedding media for ZnS, several new materials were found to be described in the following.

Sulfur-Selenium Glass and Cell Preparation Technique

A red-orange mixture of sulfur [26 w/o (weight per cent)] and selenium (74 w/o), which can be easily prepared by fusing the elements together in a test tube, matches the index of ZnS. Samples for optical observation can be prepared by melting a small piece of the S-Se glass on a microscope slide on a hot plate (180°C). The EL powder is mixed into the viscous liquid and squeezed as flat as possible under a cover slide. The cell is cooled to room temperature slowly to prevent peeling.

For the observations, a Leitz Panphot microscope with oil immersion objective was used, giving a total magnification of 1200.

The exact matching of refractive indices can be accomplished by using the method of disappearing Becke fringes, or the method of oblique illumination (9). Small amounts of S or Se have to be added to the main charge, melted, and mixed, and new test cells have to be prepared and checked under the microscope until the surfaces of the particles disappear completely. The crystallites can then be discerned only by the difference in color, provided the embedding layer is not much thicker than the particle diameter. It is advantageous to have a slight remaining mismatch so that the fringe of the largest diameter of the particle appears as a faint dark line. Any larger mismatch can lead to misinterpretations due to multiple scattering.

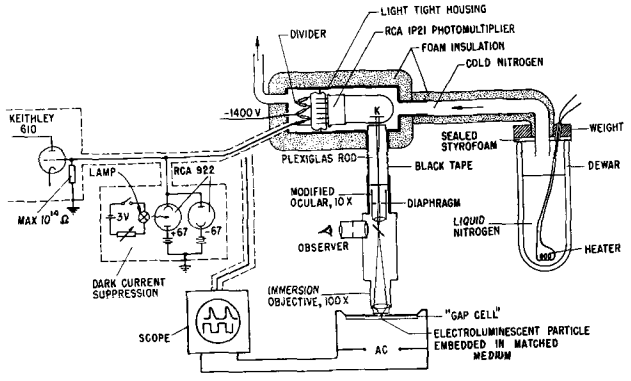

Fig. 1. Apparatus used to observe and measure EL lines. For most of the measurements, cooling of the photomultiplier is unnecessary. Vertical sensitivity of dual-sweep oscilloscope 50 mv/cm. Leitz Panphot microscope with immersion objective. Upper lens of ocular removed and replaced by adjustable diaphragm. Audiofrequency generator and amplifier not shown.

It is unfortunate that the findings of visual microscopic observations are difficult to document by photographs. Due to the shallow focal depth it is necessary to move the focus up and down through the volume of the particles to see all the details.

For the observation of EL emission, a "gap cell" has to be prepared, which consists of a microscope slide with an evaporated aluminum film. A gap of 1 mil width is produced by the shadow of a 1 mil wire strung across the slide under spring tension prior to evaporation. EL powder is mixed into the molten embedding medium, spread across the gap, squeezed as thin as possible with a cover slide, and cooled. In the center of the gap, the alternating electrical field is perpendicular to the optical axis. It is supplied by a generator giving up to 1000 v, 25 kc of a sinusoidal voltage. The experimental setup is indicated in Fig. 1.

The specific electrical resistance of this S-Se glass is in the order of 10^{14} ohm-cm. The optical absorption edge is at 6100Å. Observation of EL emission is only possible for orange-emitting phosphors like ZnS-Cu, Mn. Other ZnS-phosphors can be examined for imperfections with external illumination.

Thallium Bromide-Thallium Chloride Mixtures

For the examination of green and blue emitting phosphors, and in order to see inclusions which have a body color which is only slightly off white, an embedding medium with a wider transmission range is desirable.

It was found that a mixture of about 70/30 w/o TlBr-TlCl has the refractive index of ZnS. TlCl alone has an index of $n = 2.2$; TlBr has an index of $n = 2.4$. Both materials are white, of cubic crystal structure, and completely miscible as liquids and solids. In pure state their melts solidify without air inclusions, completely transparent in areas large enough for microscopical examination. The melting point of the mixture is about 450°C. At that temperature, chemical reactions between the EL powder and the TlBr-TlCl take place, resulting in a slight

[1] Gillson and Darnell (8) state that they were able to find powder particles with flat surfaces into which viewing was possible, and that they found the same results as in larger crystals. The author was unable to find such flat powder particles. In the work presented here, a more convenient method is described, as well as physical measurements on EL lines. An interpretation of the mechanism is presented which, though containing elements of former models, is different from previous theories.

discoloration. Nevertheless, the EL properties of the powder are preserved; only the photoluminescent response is quenched due to absorption of the exciting light.

Since the molten mixture etches away the evaporated metal film, it is difficult to prepare gap cells with this mixture. Iridium or platinum films have to be used. Conductive, transparent tin oxide coatings on glass also withstand the corrosive effect so that plate capacitor cells consisting of two conductive cover slides, with the electric field parallel to the optical axis, can be made.

Arsenic-Chalcogen-Halogen Glasses

It is known that molten arsenic sulfides solidify as yellow glasses of high refractive index. It was found that a mixture having a refractive index of 2.4 has a very high viscosity even at temperatures beyond 400°C. This glass is not very suitable.

In the older literature on highly refractive immersion media for mineralogical purposes (12) it is reported that arsenic tribromide (mp 28°C) can dissolve large amounts of arsenic sulfide. It was found that with increasing sulfide content the solutions become more viscous and finally solid at room temperature. Due to impurities in the chemicals, these glasses were dark brown, so that synthesis from spectroscopically pure elements had to be used. This can be accomplished by first melting arsenic and sulfur together in a test tube, and then adding small increments of liquid bromine until the desired refractive index has been reached. The synthesis is very simple and can be carried out in a chemical hood without difficulty. The mixture which matches ZnS has a composition of 33/30/37 w/o As, S, and Br, as determined by chemical analysis. The thermal expansion coefficient of this glass is similar to that of aluminum. The softening point is at 140°C; at 180°C the glass is liquid enough for cell preparation. The resistivity is 10^{13} ohm-cm, the dielectric constant is 7.5. The optical absorption edge is situated at 5000Å, and the glass is transparent in the infrared up to 13μ. The glass has excellent stability and imperviousness against moisture. This glass is the most suitable and convenient embedding medium for ZnS and was used in most of this work (13).

The existence of an extended range of arsenic-sulfur-iodine glasses has been recently reported; however no data on refractive indices and optical transmission were given (14). It was found that these glasses have a pink body color, with absorption edges around 5500Å. They can be made with indices higher than 2.4 which makes them suitable for red-emitting ZnS-CdS, ZnS-ZnSe-ZnTe, and GaP phosphors. The melting points of some of the mixtures are below 100°C. The resistance to moisture is poor.

Other glasses in this system, with absorption edges in the red and infrared and still higher refractive indices, are As-Se-Br and As-Se-I glasses. Glasses containing tellurium are p-type semiconductors (15). Glasses of this group are also of interest as optical cements to reduce reflection losses in combinations of EL and photoconducting crystals.

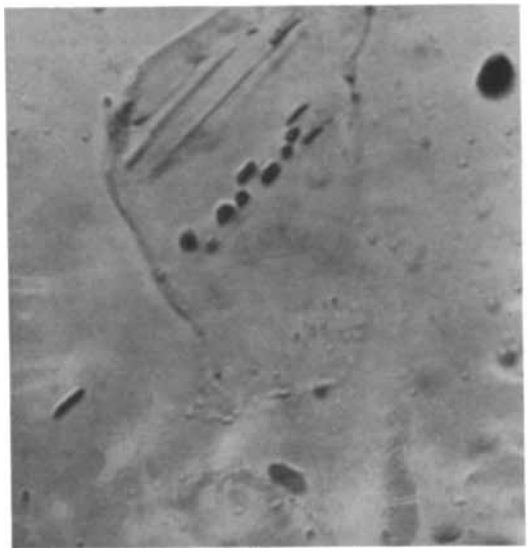

Fig. 2. Cavities in EL particles. The particle (about 15μ diameter) is embedded in matched As-Br-S glass. Illumination from below. The striations in the upper part are probably decorated imperfection lines.

It was ascertained that the inorganic polymers described above do not appreciably impair the EL properties of the powder. This was assured by dissolving the glass with methylene iodide or alkaline solution and comparing the recovered powder with fresh powder in castor oil cells.

Due to trapping of light in matched layers in the absence of scattering, the apparent brightness of ideally matched cells is only about 1/22 of that of unmatched cells.

Visual Microscopic Observations

In most of this work, green-emitting ZnS-Cu,Al phosphors of various United States manufacturers were used. It was ascertained, however, that halogen-coactivated and manganese-containing materials show the same features.

With external illumination the finding of Lehmann (11) was confirmed that EL particles contain numerous round spots (Fig. 2). It could be established that these "inclusions" are not filled with copper sulfide, as Lehmann assumed, but are voids which look black only because of their strong Becke fringes. The same spots, often in clusters of up to 10, occur in powders which were prepared like EL powders but without copper doping. Most probably these cavities are caused by rapid, disorderly growth in the presence of volatile flux. The presence of these coarse imperfections, which makes it likely that submicroscopic imperfections are also present in large numbers, seems to be a necessary (but not sufficient) condition for efficient EL, since all EL particles, active and inert ones from the same preparation, contain them, whereas particles of comparable size taken from commercial photoluminescent and cathodoluminescent powders show fewer voids.

It is most likely that the walls of these voids are coated with copper sulfide layers which are thin enough to be transparent. As is well known, EL phosphors have to be prepared with an excess of copper which precipitates at the surfaces during cooling. The following cyanide washing process re-

moves the precipitated excess copper sulfide from external surfaces, but does not reach the internal surfaces. Only if the EL powder is reheated in halogen-containing atmosphere (16) or in molten KCN (17) can the internally precipitated copper sulfide be removed, but then the EL properties are destroyed. The photo-and cathodoluminescence, which are due to dissolved copper, remain and change only their color due to secondary effects.

That such thin, conducting, and transparent copper sulfide layers can indeed exist was established by washing a large, polished wafer of melt-grown ZnS (18) in copper nitrate solution. After careful rinsing and drying, this crystal, which now looked yellowish, had a conducting surface layer with a square resistance of 500 ohms, which gave a p-type signal with thermoelectric probes. It could be easily removed with cyanide solution. The same treatment of the crystal with silver or gold solutions gave layers whose resistance was higher by at least three orders of magnitude. The high conductivity of the copper precipitates may serve as an explanation why only copper doping produces efficient EL in ZnS.

The voids are never associated with EL emission. In some cases, especially in inefficient phosphors with higher than optimum copper doping levels, the black spots are associated in lines or strings (Fig. 3a). Parallel to these dotted lines one finds, by observation with polarized light, birefringent striations (Fig. 3b). When the field is applied, electroluminescent striations can be found along these birefringent striations (Fig. 3c). This indicates that the occurrence of EL is closely connected with crystal imperfections (imperfection lines), a finding that has been expressed in the literature repeatedly (8, 19-24).

In efficient EL particles, however, observation with crossed nicols shows that the particles are isotropic and that the sites of EL lines are indistinguishable from the bulk. Some hexagonal particles are present, but these are usually inert. With intense x-ray excitation, the particles luminesce uniformly throughout the volume. It must be concluded that in efficient EL particles the imperfection lines have submicroscopic diameters.

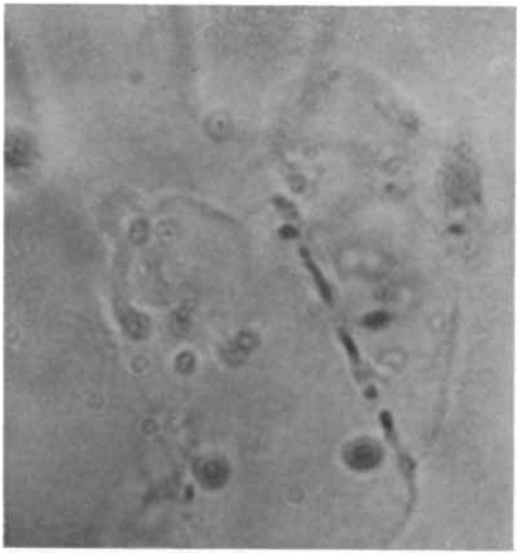

Fig. 3a. External illumination: Long hollow channel (cavity) in EL particle. Fig. 3a-c show the same particle.

Fig. 3b. External illumination, crossed nicols. Birefringent lines extending parallel to long cavity. Bright areas: Strained glass.

Fig. 3c. A-C field applied. Electroluminescent double-line at site of birefringent striation.

With a-c excitation, light is emitted in long lines along those orientations fixed within the crystals which form an acute angle (usually less than 45°) to the field. If, in a specially constructed cell, the direction of the field was rotated, the EL lines faded away as they became more perpendicular to the field, whereas new ones lighted up and became brighter as they became more parallel to the field.

The lines start with a bright, thick "head" near one surface and extend far into the bulk, forming a thinner and dimmer tail. In many cases, in straight continuation of the tail of one line, the tail of a new line starts which has its head at the opposite end of the particle (Fig. 4 and 5). It is therefore a natural conclusion, which was also independently drawn by Gillson and Darnell, that the two lines which have the form of two comets fleeing each other, are actually one unit. The dark interspace in the center shortens with increasing voltage.

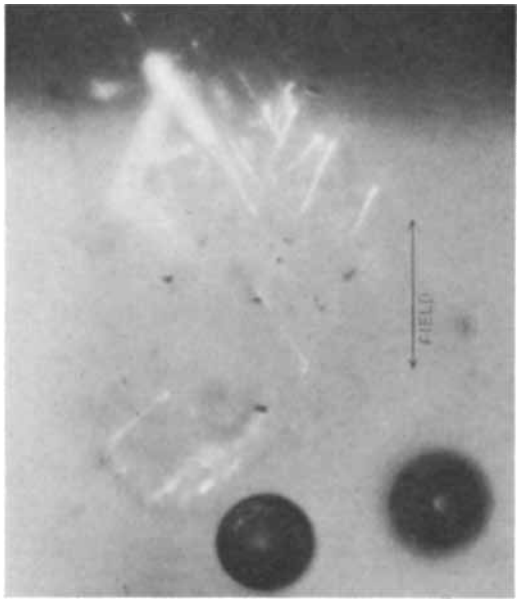

Fig. 4. EL lines in single particle. Due to the shallow focal depth of the microscope at high magnification (up to 2000X) most of the lines are slightly out of focus. With visual observation and continuous accommodation, the lines appear much sharper.

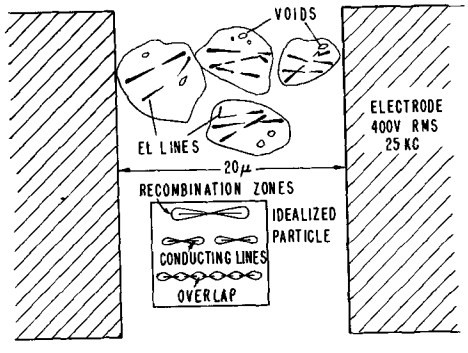

Fig. 5. EL lines drawn from visual observation. Some rather round, non-EL cavities are also shown. In the "idealized particle" below, several possible interactions of EL lines are indicated. The upper case is the most frequent one.

In well-crystallized, efficient powders, the EL lines are coherent; they do not consist of series of fine dots. (The resolution of the microscope is about 0.1μ.) The slow, time-dependent movements of EL lines which Lehmann reports (11) could not be observed.

Thus, our observations on powder particles are in complete accord with the findings of Gillson and Darnell on larger crystallites.

Brightness Measurements

Waymouth and Bitter (1) and Gillson and Darnell (8) state that the time-integrated light output of single particles or lines has a threshold and then rises linearly, whereas Zalm, Diemer, and Klasens (2) and Lehmann (26) report that it follows about the same exponential relation as holds for the light output of a complete cell. This situation requires clarification.

The various brightness measurements to be described here were carried out with the setup shown in Fig. 1. Since most particles have many (up to 30) EL lines so that it is difficult to measure the

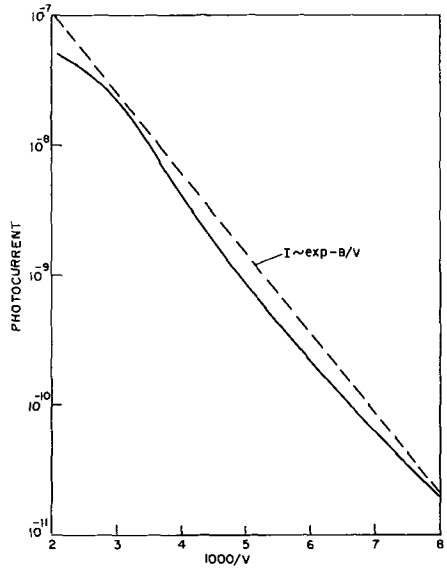

Fig. 6. Log brightness vs. (voltage)$^{-1}$ for a single line. Very long, bright lines show deviations towards linear dependence near breakdown. There is no threshold voltage. The fit to the equation $I \sim \exp - C/V$ is not too good.

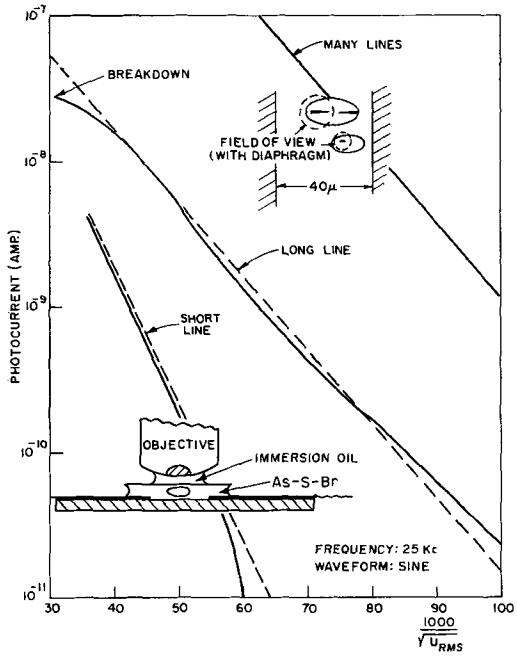

Fig. 7. Log brightness vs (voltage)$^{-1/2}$ for single lines. Short, dim lines rise faster than long, bright lines and have no linear range. The fit to the equation $I \sim \exp - C/V^{1/2}$ is good only for measurements which integrate over many lines.

light from one line without interference from other lines, it was necessary to inspect a great number of particles to find some with isolated, single lines of typical shape. To eliminate light from neighboring lines, a diaphragm with a fine slot was inserted into the ocular of the microscope.

The measurements of brightness *vs.* voltage indicate (Fig. 6-8) that there is no apparent voltage threshold, but that the light emission of a single line rises exponentially. The points do not yield a good straight line either for a plot of log I *vs.* $1/V$ (I = brightness, V = voltage) or for the plot of log I *vs.* $V^{-1/2}$. This could have been caused by the nonhomo-

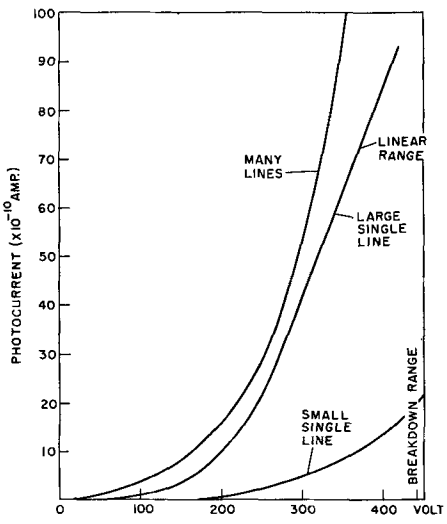

Fig. 8. Brightness *vs.* voltage. Some very bright, long lines show a linear range.

geneous field in the gap cell; however, a measurement integrating over about 100 single lines yields an excellent straight line on the plot log I *vs.* $V^{-1/2}$. The slope of short, dim lines, which require higher voltages to reach the same brightness as long lines, is steeper than that of long lines. Some very bright, long lines were found which showed a linear increase of brightness with voltage in the last half decade of brightness before electric breakdown. This linear range at high voltage is of significance for the theoretical interpretation.

By moving the EL line under the microscope with the microscope stage, the brightness of a line *vs.* its length could be measured. For this purpose, the slotted diaphragm was arranged with the slot perpendicularly to the EL line. The brightness increases from "tail" to "head" in a strongly superlinear fashion.

By displaying the signal of the photomultiplier, which was focused on one or the other half of a double-comet line, on a dual-trace oscilloscope together with the a-c voltage which excited the gap cell, the phase relation of the light bursts or "brightness waves" of a single line could be obtained. (Fig. 9). At 100 cps the light waves extend only over a fraction of the cycle, whereas at higher frequencies the decay time becomes longer than the cycle so that a background develops. For all phosphors examined, the phase relation of light emission is such that light is emitted at that half of a line which points to the electrode which is becoming less negative or more positive. Both halves of a line go on and off alternatingly with a phase shift of 180° (6). The primary and secondary peaks observed in the emission of complete cells exist also at the elementary level in green-emitting particles (not in manganese-containing ones). With sine-wave excitation, the peaks of the brightness waves of Mn-doped phosphors coincide exactly with the voltage peaks. In contrast, the brightness waves of phosphors not doped with Mn lead the voltage slightly. The study of these elementary brightness waves may yield better insight into the mechanism than the study of integrated light waves.

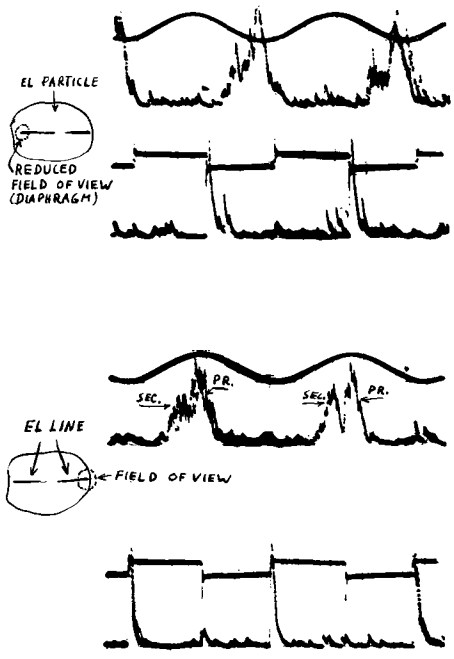

Fig. 9. Brightness waves of single lines, ZnS-Cu,Al particle. Above: photomultiplier focused on left half of "double-comet" line, sine and square-wave excitation, 100 cps. Below: Photomultiplier focused on right half. With sine excitation, the "primary" and "secondary" peaks are recognizable. In all phosphors light is emitted at that half which points to the electrode which is turning positive.

By counting the number of perceptible lines in a given field of observation, which exceed the threshold of visibility, *vs.* the applied voltage, the plot of Fig. 10 was obtained, which differs from the linear increase reported by Zalm (3).

The approximate brightness of single lines at 10 kc near breakdown voltage was measured by raising the external illumination of the microscope (green light) to such a level that the EL line just disappeared against the bright background. The

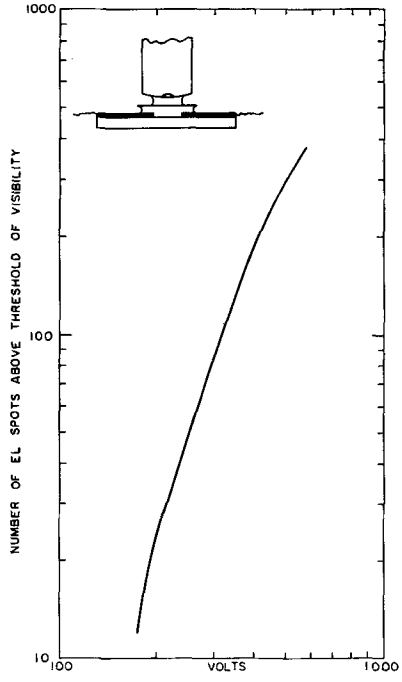

Fig. 10. Number of spots above threshold of perceptibility of dark-adapted eye in a constant viewing area, *vs.* voltage (7 kc).

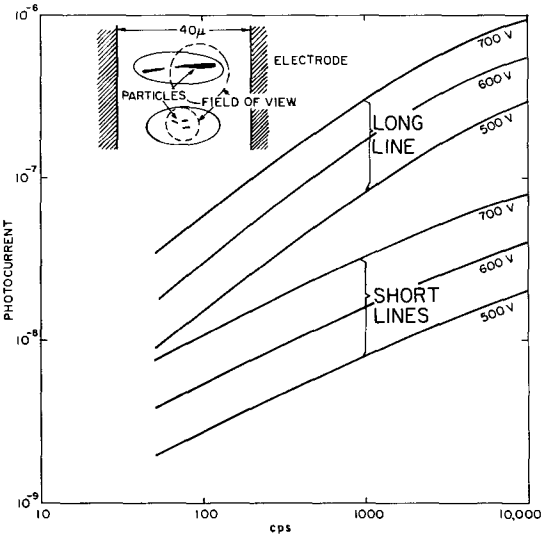

Fig. 11. Log brightness vs. log frequency at constant voltage for short and long lines.

brightness of the background was then measured with a brightness meter. A value of about 5.10^3 ft-L was obtained.

The brightness of single lines *vs.* frequency of the applied voltage, which is kept constant, is plotted in Fig. 11. Whereas the brightness of complete cells increases with a power only slightly less than one at low frequencies (3), the brightness of short lines increases with a power of about 0.6. Long bright lines show a steeper rise.

Conclusion

Microscopic observation of the interior of EL particles which are embedded in the matched-refractive-index-media described, is a new, convenient tool for studying the active elements of the EL process, which heretofore have been almost inaccessible. Electroluminescence is by no means a surface process, as previously believed, but is associated with crystal imperfections in the bulk. Previous theories do not describe the real situation.

In a separate article, a new model (25) will be treated in which it is assumed that insulating luminescent ZnS particles contain conductive, copper-sulfide-decorated imperfection lines, which, by means of geometrical field intensification at their ends, are capable of field-emitting both holes and electrons from opposite ends into the crystal. The injected holes become trapped in luminescent centers and recombine radiatively with field-injected electrons and electrons returning through the bulk at field-reversal.

Acknowledgment

The author received invaluable help by Allen S. Mason during several phases of this work, especially in the preparation of the As-S-Br glass. Gratitude is expressed to Dr. R. E. Shrader for valuable discussions and criticism and suggestion of the dark-current bucking circuit. Dr. S. M. Thomsen supplied several samples and stimulating discussions. Special thanks are due to Dr. S. Larach for his continuing interest in this work.

Manuscript received June 11, 1962. This paper was prepared for delivery before the Los Angeles Meeting, May 6-10, 1962. The research in this paper was sponsored by the Electronic Research Directorate, Air Force Cambridge Research Laboratories, Office of Aerospace Research, U. S. Air Force, under Contract AF 19(604) 8018. It is contained in reports AFCRL 360,721,979, and 62-142.

Any discussion of this paper will appear in a Discussion Section to be published in the June 1963 JOURNAL.

REFERENCES

1. J. F. Waymouth and F. Bitter, *Phys. Rev.*, **95**, 941 (1954).
2. P. Zalm, G. Diemer, and H. A. Klasens, *Philips Research Repts.*, **10**, 205 (1955).
3. P. Zalm, *ibid.*, **11**, 353, 417 (1956).
4. W. W. Piper and F. E. Williams, *Phys. Rev.*, **81**, 151 (1952).
5. D. R. Frankl, *ibid.*, **111**, 1540 (1958).
6. E. E. Loebner and H. Freund, *Bull. Am. Phys. Soc.*, **30**, 22 (1955).
7. V. E. Oranovskii and B. A. Khmelinin, *Optics and Spectroscopy*, **7**, 336 (1959).
8. J. L. Gillson, Jr. and F. J. Darnell, *Phys. Rev.*, **125**, 149 (1962).
9. M. Chamot and C. S. Mason, "Handbook of Chemical Microscopy," 2nd edition, Vol. I, p. 360, John Wiley & Sons, New York (1951).
10. C. West, *Am. Mineral.*, **21**, 245 (1936).
11. W. Lehmann, *This Journal*, **107**, 657 (1960), **108**, 607 (1961).
12. R. Meyrowitz, *Am. Mineral.*, **40**, 398 (1955).
13. A. G. Fischer and A. S. Mason, *J. Opt. Soc. Am.*, **52**, 721 (1962).
14. S. S. Flaschen, A. D. Pearson, and W. R. Northover, *J. Appl. Phys.*, **31**, 219 (1960).
15. J. F. Dewald, A. D. Pearson, W. R. Northover, and W. F. Peck, ECS Meeting Los Angeles, May 1962, Electronics Div., Enlarged Abstracts, p. 258.
16. S. Larach and R. E. Shrader, *J. Phys. Chem. Solids*, **3**, 159 (1957).
17. W. Lehmann, Personal communication.
18. A. G. Fischer, *Z. Naturforsch.*, **13a**, 105 (1958).
19. A. H. McKeag and E. G. Steward, *This Journal*, **104**, 41 (1957).
20. L. W. Strock, *Illum. Eng.*, **55**, 24 (1960).
21. M. A. Short, E. G. Steward, and T. B. Tomlinson, *Nature*, **177**, 240 (1956).
22. D. W. Ballentyne, *J. Phys. Chem. Solids*, **10**, 242 (1959); *This Journal*, **107**, 807 (1960).
23. P. Goldberg, *J. Appl. Phys.* **32**, 1520 (1961).
24. W. Lehmann, *This Journal*, **104**, 45 (1957).
25. A. G. Fischer and A. S. Mason, ECS Meeting Los Angeles, May 1962, Electronics Div., Enlarged Abstract. No. 44, p. 55.
26. W. Lehmann, *This Journal*, **107**, 20 (1960).

Luminescence in the System Al_2O_3-AlN

I. Adams,[1] T. R. AuCoin, and G. A. Wolff[2]

U.S. Army Signal Research and Development Laboratory, Fort Monmouth, New Jersey

ABSTRACT

Aluminum nitride and aluminum oxide are mutually soluble at high temperatures. A number of solid solutions and reaction products of various compositions in the system AlN-Al_2O_3 have been prepared at about 2000°C, which can be described by one general formula

$$Al_{(2+x/3)}O_{(3-x)}N_x$$

where x represents the number of nitrogen atoms.

Five phases were observed: (i) Al_2O_3 of corundum structure with negligible solubility of AlN; (ii) a phase similar to δ-alumina, found when the AlN content was about 5.5 mole %; (iii) a spinel phase with an AlN content up to 50 mole %; (iv) a phase obtained when the AlN content was between 50 and 67 mole % (this phase always occurred mixed with phase iii); (v) AlN of wurtzite structure with up to about 17 mole % Al_2O_3.

Phases (ii) to (v) show no observable fluorescence, but broad band phosphorescence in the blue when excited with 2537Å radiation. Manganese activation produces a green or a red luminescence which is attributed to transitions of Mn^{2+} and Mn^{4+} at different lattice sites. Electroluminescence in the visible is observed in all phases when suitably activated.

The similarity of the crystal structures of α-Fe_2O_3 and α-Al_2O_3 (1) has long led to conjecture concerning the formation of an aluminum spinel similar to Fe_3O_4. The metastable γ-form of Al_2O_3 has a spinel-like structure with a deficiency of metal ions with respect to the hypothetical spinel Al_3O_4. In 1957 Filonenko *et al.* (2) reported an aluminum spinel to which they assigned the formula $AlO \cdot Al_2O_3$. This product was formed by the reduction of Al_2O_3 with carbon according to the formula

$$3Al_2O_3 + C \rightarrow 2Al_3O_4 + CO$$

In the same year, Vert *et al.* (3) reported the formation of an aluminum spinel by firing a mixture of Al_2O_3 and carbon at 1500°-1900°C. Long and Foster (4) reported formation of a δ-Al_2O_3 and a phase similar to the spinel-type lithium-ξ-alumina when AlN and Al_2O_3 mixtures were fused in an argon atmosphere, but did not explain the mechanism of the phase transformations involved. The formation of a spinel phase was found (5) during the preparation of AlN in an Al_2O_3 crucible. This phase was described as a solid solution of AlN in Al_2O_3 with a maximum AlN:Al_2O_3 ratio of 1:1 corresponding to the formula Al_3O_3N. Recently Yamaguchi and Yanagida (6) revised their previous Al_3O_4 formulation for the spinel phase to the formula $AlN \cdot Al_2O_3$.

Electroluminescence has been reported for AlN (7, 8). As early as 1934, Guntherschulze and Gerlach (9) reported a faint red emission when a thin film of pulverized ruby was subjected to an alternating field in a high vacuum. A bright emission has recently been observed in specially treated Al_2O_3 excited by an electric field (10, 11).

[1] Present address: Airtron, Division of Litton Industries, Morris Plains, New Jersey.

[2] Present address: Solid State Research Laboratory, The Harshaw Chemical Company, Cleveland, Ohio.

In the present study, the reaction products of various compositions, heated to 2000°C, are identified, and a comparison of their luminescent properties is presented. An Al_2O_3-AlN phase, not previously reported in the literature, was detected.

Experimental Procedure

The AlN used for this study was prepared in an autoclave, similar to that shown schematically in Fig. 1, by reacting high-purity aluminum powder with nitrogen at 1000°C and 1000 psi in AlN or Al_2O_3 crucibles. Solid solutions containing more than 50 mole % AlN were also prepared in the autoclave by mixing aluminum powder with Al_2O_3 powder (ALCOA A-14) and firing in nitrogen at 1000°C and 1000 psi. The reaction of nitrogen with aluminum is exothermic and served to increase the temperature to about 2000°C as indicated by the beginning of melting of the container when an Al_2O_3 (melting point 2050°C) crucible was used. Samples

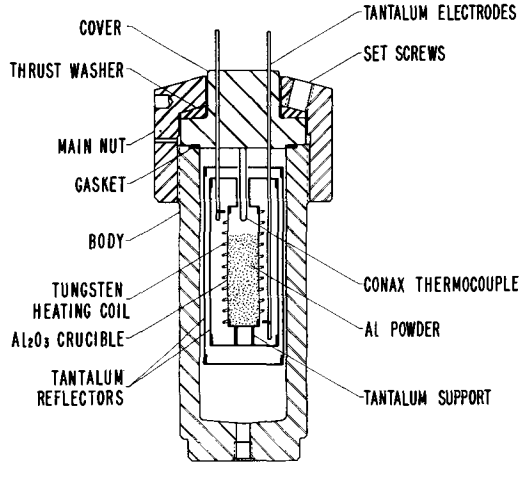

Fig. 1. Autoclave pressure reactor

containing less than 50 mole % AlN could not be prepared in the autoclave, since the heat generated by the reaction of small amounts of aluminum with nitrogen was insufficient to increase the temperature to the required 2000°C; therefore these samples were prepared by fusing mixtures of Al_2O_3 and AlN in an arc image furnace at 2000°C or above for 5 min, the raw mix serving as its own container. An argon atmosphere of 5 psi was admitted into a previously evacuated reaction flask, and the temperature was measured pyrometrically.

Unreacted aluminum was removed by treating the fused material with a hot dilute solution of sodium hydroxide. Nitrogen was then determined by a modified Kjeldahl procedure (12) in which 1-5 mg samples in 10 cm^3 of 50% NaOH were heated to 200°C. This served to decompose aluminum nitride quantitatively. The reaction was carried out in a specially designed apparatus made of quartz which contained a nickel reaction tube. The ammonia was entrained in a stream of wet nitrogen and determined by acidimetric procedures.

Doping was achieved by two methods. One method consisted of mixing the dopant (as a salt or oxide in amounts of fractions of a per cent to several per cent) with the compound to be activated and placing the mixture in an alumina boat. A large number of different dopants were used, but only a few will be discussed here. The boat was then fired in a quartz tube at 600°-1000°C in nitrogen for ½ hr followed by a similar treatment in chlorine which removed unreacted aluminum (and, incidentally, was responsible for producing the electroluminescent response property). Generally, it also removed most of the added activators such that only a small fraction of the amount added was retained in the finished phosphor.

The second method, used to produce red luminescent Mn-doped AlN, consisted of firing a mixture of the dopant (salt or metal) powder and aluminum powder in the autoclave at 2000° under nitrogen pressure. The sample was then reacted as described before.

For luminescence studies, the samples were excited using two mercury lamps, one rich in 2537Å and one rich in 3650Å. Electroluminescence was excited by applying a d-c potential of 500v across the powdered sample, about ½ mm thick, between a metal base plate and a conducting glass plate. Spectra were measured as described in ref. (7) and (13).

A square wave generator was built to study the effect of square voltage pulses on light output. It consisted of a motor-driven commutator to control the frequency, a high voltage thyratron circuit for switching, and a rotating brush assembly for selecting pulse width. The unit was designed to produce the very low frequency range of 0.2-2000 cycles/min, an output pulse width of between 1.0 and 99.0% of the period, and output pulse amplitudes of ± 1000v. The operation was such that, after a part of each cycle, the applied voltage was reversed in sign for the rest of the cycle.

Results

Four crystalline phases were identified in the products obtained in the reaction between Al_2O_3 and AlN at 2000°C. A tetragonal phase similar to δ-alumina (14) was found when mixtures consisting of 40 to 1 and 18 to 1 molar ratio of Al_2O_3 and AlN were fused. As the concentration of AlN was increased beyond $18Al_2O_3$ to 1AlN a spinel phase appeared. When the molar amount of AlN exceeded that of Al_2O_3 a new phase was observed. This new phase was the only one which could not be obtained as a single phase. It was always found mixed with the spinel and could not be separated from it. For a molar ratio of Al_2O_3:AlN of less than 1 to 6, only a wurtzite-like phase was detected. The nitrogen content of some of the phases is shown in Table I. X-ray powder diffraction patterns of the dominant phases are shown in Fig. 2.

A comparison of the fluorescence, phosphorescence, and electroluminescence of these phases doped with Mn, Cr, and Eu is presented in Table II. The observed intensity of the electroluminescence varied from 1 to 10 ft-L. About 10 ft-L were observed for Mn-doped AlN of green electroluminescence, and about 5 ft-L for Mn-doped AlN of red electroluminescence. The intensity of the electroluminescence of the various undoped materials was below 1 ft-L. The strongest phosphorescence intensity of about ½ ft-L was found on the Mn-doped red emitting AlN when it was irradiated with filtered u.v. from a Hanovia lamp at a distance of about 5 cm. Electroluminescence in these materials is observed only after the addition of an activator as

Table I. Weight per cent nitrogen in crystal phases detected in the Al_2O_3-AlN system

Sample	Molar ratio Al_2O_3 : AlN	Wt. % N theoretical, in starting material	Wt. % N by analysis	Major phase-type	
1.	1 : 0	0.00	0.00	α-Alumina	(phase 1)
2.*	40 : 1	0.34	—	α-Alumina and δ-alumina	(phase 1 and 2)
3.*	18 : 1	0.75	0.95	δ-Alumina	(phase 2)
4.*	2 : 1	5.72	7.15	Spinel	(phase 3)
5.*	1 : 1	9.79	10.20	Spinel	(phase 3)
6.**	1 : 2	15.10	13.10	Spinel and new phase	(phase 3 and 4)
7.**	1 : 5	22.82	—	Wurtzite	(phase 5)
8.**	1 : 6	24.16	24.70	Wurtzite	(phase 5)
9.**	0 : 1	34.19	34.60	Wurtzite	(phase 5)

* Samples fused in arc image furnace.
** Samples prepared in pressure reactor.

Table II. Comparison of fluorescence, phosphorescence, and electroluminescence of phases in the Al_2O_3-AlN system

Activator	Major phase-type	3650A Hg Fl	3650A Hg Ph	2537A Hg Fl	2537A Hg Ph	El
Cl treated no dopant	α-Al_2O_3 (phase 1)	no*	no	no*	no	blue (N_2)
	δ-Al_2O_3 (phase 2)	no*	no	no*	blue	blue (N_2)
	spinel (phase 3)	no*	no	no*	blue	blue (N_2)
	spinel + new phase (phase 3 and 4)	no*	no	no*	blue	blue (N_2)
	AlN (phase 5)	no*	no	no*	blue	blue (N_2)
Manganese	α-Al_2O_3 (phase 1)	no*	no	no*	no	blue (N_2)
	δ-Al_2O_3 (phase 2)	no*	no	pink	no	pink
	spinel (phase 3)	no*	no	yellow	green	green
	spinel + new phase (phase 4)	no*	no	red	no	pink
	AlN (Mn^{2+}) (phase 5)	no*	no	no*	blue	green
	AlN (Mn^{4+}) (phase 5)	no*	no	red	red	red
Europium	α-Al_2O_3 (phase 1)	red	no	no*	no	red
	δ-Al_2O_3 (phase 2)	no*	no	red	blue	red
	spinel (phase 3)	no*	no	pink	blue	red
	spinel + new phase (phase 4)	no*	no	green	blue	red
	AlN (phase 5)	no*	no	no*	blue	red
Chromium	α-Al_2O_3 (phase 1)	red	no	red	no	red
	δ-Al_2O_3 (phase 2)	no*	no	pink	no	red
	spinel (phase 3)	no*	no	yellow	blue	red
	spinel + new phase (phase 4)	no*	no	red	blue	red
	AlN (phase 5)	no*	no	no*	blue	blue (N_2)

* Fluorescence could not be observed because of insufficient filtering of visible light from the existing u.v. source.

a chloride and subsequent heat treatment, or after heat treatment with chlorine gas. The chlorine treatment was not necessary, however, to obtain fluorescence and phosphorescence. The materials that were treated with chlorine, but prepared without an activator, emitted only the N_2 band systems during d-c excitation as reported previously (7, 8). In suitably activated materials, an emission characteristic of the activator was observed in addition to the N_2 bands.

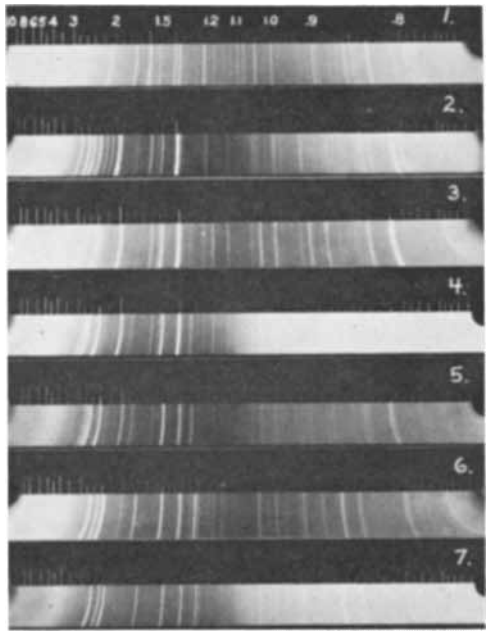

Fig. 2. X-ray powder diffraction patterns (Cu K_α) of the dominant phases in the Al_2O_3-AlN system. 1, α-Al_2O_3; 2, 18 Al_2O_3-AlN; 3, $2Al_2O_3 \cdot AlN$; 4, $Al_2O_3 \cdot AlN$; 5, $2AlN \cdot Al_2O_3$; 6, $6AlN \cdot Al_2O_3$; 7, AlN.

During electroluminescence excitation, chlorine-treated samples exhibited increased conductivity over the untreated material as measured by a microammeter, and the current was proportional to the light intensity. Figure 3 shows characteristic light wave forms from an AlN sample using square wave voltage excitation. Similar behavior is exhibited by the other phases 1 to 4 as defined above. The voltage was varied from positive (with respect to the metal electrode) to negative with a frequency of 60 cycles/min. When the pulse was positive less than 60% per cycle, no light was emitted from the powder. For positive pulse durations greater than 60% of the cycle (Fig. 3a), a slow increase in light was seen. This light intensity increase on the oscilloscope was followed by a fast decrease to zero and a very intense and short burst of light at the moment of polarity reversal. When the pulse width was 75% (Fig. 3b) the intensity was much greater and the light reached its maximum much more rapidly. On field reversal the decay no longer reached zero. The subsequent increase was still rapid, but the decay extended over the full period of field reversal. At 78% positive pulse, (Fig. 3c) the decay of the light burst is seen to be slower still and falls to zero only on field reversal. Using a.c., light output was obtained for frequencies as high as 25 kc; the light intensity increased with decreasing frequency down to 20 cps, which was the low-frequency limit of our a-c amplifier.

Discussion

An oxide spinel with only one cation species is formulated as R_3O_4. The defect spinel γ-Al_2O_3, which can also be written as $Al_{8/3}O_4$, has one-ninth of the

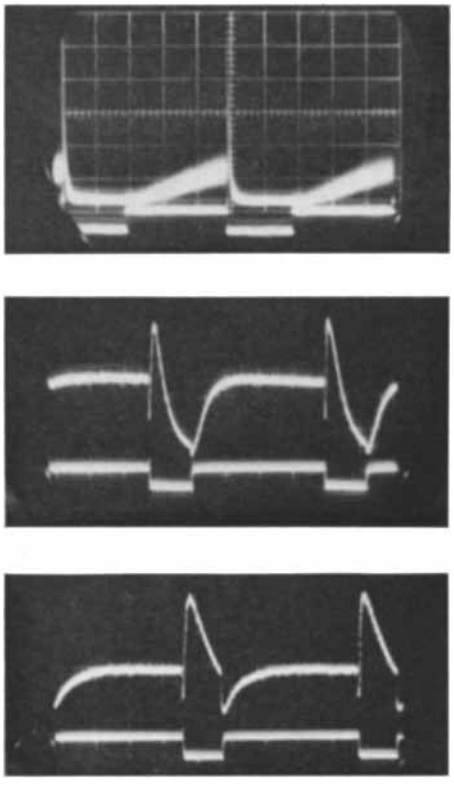

Fig. 3. Light wave forms emitted from AlN when applying square waves at 60 cycles/min: (a) (top) 62% pulse width; (b) (center) 75% pulse width; (c) (bottom) 78% pulse width.

total number of spinel cation sites vacant. This can be represented as

$$Al_{8/3}\boxed{S}_{1/3}O_4 \qquad [1]$$

where $\boxed{S}$ represents spinel cation vacancies. For every aluminum atom added to fill a vacancy $\boxed{S}$ in formula [1], charge compensation can be achieved by three nitrogen atoms replacing three oxygen atoms. Thus the spinel Al_3O_3N is obtained by adding one third of an aluminum to formula [1] and compensating with the substitution of one nitrogen for one oxygen. Consider the formula

$$Al_{\left(2+\frac{x}{3}\right)}\boxed{S}_{\left(\frac{3-4x}{12}\right)}O_{(3-x)}N_x \qquad [2]$$

where x represents the number of nitrogen atoms. Setting $x = 0$ and multiplying through by 4/3, formula [2] reverts to $Al_{8/3}\boxed{S}_{1/3}O_4$. When $x = 3/4$, implying that all spinel sites are occupied, formula [2] becomes

$$Al_{9/4}O_{9/4}N_{3/4}\ (\text{or } Al_3O_3N) \qquad [3]$$

This corresponds to one mole of AlN for one mole of Al_2O_3. Thus formula [2] is an empirical formula describing the solid solution series Al_2O_3-$Al_2O_3 \cdot AlN$ with $O \leq x \leq 3/4$.

From stability considerations it appears plausible that very small values of x will yield a γ-type spinel which, like γ-Al_2O_3, is probably unstable at high temperatures, changing into a structure which resembles δ-alumina. For larger values of x, enough additional aluminum and nitrogen atoms have entered the structure to stabilize it as a spinel at high temperatures. The spinel vacancy sites are then filled, and further addition of AlN yields a wurtzite-type phase with substantial oxygen impurity and cation wurtzite vacancies.

A wurtzite-type phase requires a 1:1 ratio of anion to cation, *e.g.*, AlN. Formula [3] formulated from the point of view of a wurtzite structure, appears as

$$Al_{9/4}\boxed{W}_{3/4}O_{9/4}N_{3/4} \qquad [4]$$

where $\boxed{W}$ represents wurtzite cation vacancies. Again, the introduction of one aluminum atom in a vacancy can be compensated by substituting three nitrogens for three oxygens. Thus AlN of wurtzite structure is obtained by adding three-fourths of an aluminum to formula [4] and compensating by substituting nine-fourths oxygen. Consider the formula

$$Al_{\left(2+\frac{x}{3}\right)}\boxed{W}_{\left(\frac{3-x}{3}\right)}O_{(3-x)}N_x \qquad [5]$$

When $x = 3$, the wurtzite structure is filled, oxygen disappears, and we have Al_3N_3 (or AlN). Formula [5], with $3/4 \leq x \leq 3$, is thus an empirical formula for describing the solid solution series $Al_2O_3 \cdot AlN$-AlN.

Disregarding cation vacancies in considering the series $Al_2O_3 \rightarrow Al_3O_3N \rightarrow AlN$, it follows that all the phases in this series can be described by the general formula

$$Al_{\left(2+\frac{x}{3}\right)}O_{(3-x)}N_x \qquad [6]$$

with $O \leq x \leq 3$.

In α-Al_2O_3 it is apparently possible to replace aluminum atoms with other cations, but not to introduce additional cations toward R_3O_4, although one third of the octahedral sites and all the tetrahedral sites are unfilled. To accommodate more Al atoms when nitrogen is introduced, the spinel phase appears which accommodates three cations for every four anions present. When still more cations are added, the wurtzite-type phase appears which can accommodate one cation for every anion present. If aluminum could exist in a divalent as well as a trivalent state, as does iron, then increasing aluminum concentration would form α-$Al_2O_3 \rightarrow \gamma$-$Al_2O_3 \rightarrow Al_3O_4 \rightarrow AlO$. Since this sequence would entail a valence change of aluminum, it cannot occur in a solid. The following sequence is observed, however; α-$Al_2O_3 \rightarrow \gamma$-$Al_2O_3 \rightarrow Al_3O_3N \rightarrow AlN$. In the process the anion close packing changes from hexagonal to cubic and back to hexagonal.

The action of Cl_2 gas on these materials is complex. The effects are possibly (*a*) incorporation of Cl into the lattice causing an apparent increase in the electrical conductivity, and (*b*) increase in the diffusion velocity of impurities into these materials. For instance, doping of Al_2O_3 with Cr^{3+} occurs at substantially lower temperatures than is possible in the absence of Cl.

Since Cr^{3+} shows a strong octahedral site preference, it therefore readily replaces Al atoms in corundum and in the spinel Al_3O_3N, where two-thirds of the Al occupy octahedral sites. In AlN where only

tetrahedral sites are occupied, no substitutional Cr doping is possible. Manganese, on the other hand, produces a characteristic green electroluminescent emission in AlN and Al_3O_3N which is attributed to Mn^{2+}. No green emission was observed in α-Al_2O_3. Red emission has been reported in Al_2O_3 doped with Mn (15, 16), but we were unable to duplicate these findings. Red emission was observed only in AlN when the latter was fired in the autoclave, not by simple doping followed by the Cl treatment. However, some spinel may have been present in this material causing the red emission. In fact, with Mn activation the spinel and the new phase did produce a red luminescence as well as a green one. Kröger (16) reported green emission from Al compounds of structures other than α-Al_2O_3. This is most likely only when Al (or some other cation) is displaced from tetrahedral sites. It would appear then that green emission is observed in these materials only when Mn^{2+} replaces Al^{3+} in tetrahedral sites (AlN, Al_2O_3-AlN spinel), and red emission only when Mn^{4+} replaces Al^{3+} in octahedral sites (α-Al_2O_3, Al_2O_3-AlN spinel). More extensive investigation of Mn substitution in these structures must be undertaken to substantiate the valence states and activator coordination in crystals which give rise to the emission observed and the position of Mn in the structures. The results of a chemical analysis cannot be considered as conclusive proof of the valence state of Mn; disproportionation, decoration of dislocations and segregation of small undetectable amounts of a Mn-containing second phase could interfere with its proper identification. A physical determination, *e.g.*, ESR, must therefore supplement the chemical analysis. In particular, a rigorous proof is required before one can say with certainty that the red emission is due to Mn^{4+}, *i.e.*, until the absence of oxide in solid solution or as a second phase in AlN is ascertained. A red luminescence can be produced in AlN by Mn-doping, yet no octahedral sites are available in AlN except interstitial sites. It is also not quite understood why a red Mn-luminescence is difficult to obtain in α-Al_2O_3, since an octahedral Mn^{4+} site is available by Al^{3+} substitution.

The luminescence and electroluminescence observed in the system Al_2O_3-AlN are radiations characteristic of the activators. Both emissions, the activator and the nitrogen band system emission, are observed in all Al_2O_3-AlN samples after chlorine heat treatment. The N_2 band emission might be explained by electron emission and/or by the energy transfer of the electron-hole recombination at the surface to adsorbed or impinging N_2 molecules. The latter process would be the reverse of the excitation of luminescence in solids by impinging excited gases as investigated by Sancier, Fredericks, and Wise (17). Ultraviolet light is available from the emission of the N_2 systems and could secondarily excite fluorescence in the phosphors. Further work on the effects of nonsinusoidal voltage pulses on the light wave forms and measurements of the electrical conductivity under these conditions is needed to obtain a clear picture of the exact mechanism involved in the electroluminescence observed.

Acknowledgments

The authors wish to express their appreciation to R. K. Buder and R. O. Savage for spectrochemical analysis, to Joseph Locicero and D. Larson for construction of various devices, and to J. W. Mellichamp, J. A. Kohn, and H. H. Kedesdy for stimulating discussions.

Manuscript received Feb. 28, 1962; revised manuscript received July 5, 1962. This paper was prepared for delivery before the Los Angeles Meeting, May 6-10, 1962.

Any discussion of this paper will appear in a Discussion Section to be published in the June 1963 JOURNAL.

REFERENCES

1. A. F. Wells, "Structural Inorganic Chemistry," Clarendon Press, Oxford.
2. N. E. Filonenko, I. V. Lavrov, O. V. Andreeva, and R. L. Pevzner, *Doklady Akad. Nauk. S.S.S.R.*, **115**, 583 (1957).
3. Z. L. Vert, M. V. Kamentsev, V. I. Kudryastsev, and M. I. Sokhor, *ibid.*, **116**, 834 (1957).
4. G. Long and L. M. Foster, *J. Am. Ceram. Soc.*, **44**, 255 (1961).
5. I. Adams, T. R. AuCoin, and G. A. Wolff, "Preparation of Luminescent Aluminum Nitride," Proceedings of the Conference on Ultra Purification of Semiconductor Materials, April 1961, The MacMillan Co., N. Y.
6. G. Yamaguchi and H. Yanagida, *J. Chem. Soc. Japan*, **32**, 1264 (1959).
7. G. A. Wolff, I. Adams, and J. W. Mellichamp, *Phys. Rev.*, **114**, 1262 (1959).
8. I. Adams, J. W. Mellichamp, and G. A. Wolff, Electrochemical Soc., Electronic Div., Enlarged Abstracts, **9**, 55 (1960).
9. A. Guntherschulze and M. Gerlach, *Z. Physik*, **88**, 355 (1934).
10. I. Adams, T. R. AuCoin, and J. W. Mellichamp, *J. Appl. Phys.*, **33**, 245 (1962).
11. I. Adams and J. W. Mellichamp, *J. Chem. Phys.*, **36**, 2456 (1962).
12. Otto Schwarzkopf, Private communication.
13. J. W. Mellichamp, I. Adams, and G. A. Wolff, *Appl. Spectroscopy*, **15**, 52 (1961).
14. R. C. Stumpf, A. S. Russel, J. W. Newsome, and C. M. Tucker, *Ind. Eng. Chem.*, **42**, 1398 (1950).
15. Frank Pallila, Private communication.
16. F. A. Kröger, "Some Aspects of the Luminescence of Solids," Elsevier Publishing Co., New York (1948).
17. K. M. Sancier, W. J. Fredericks, and H. Wise, *J. Chem. Phys.*, **30**, 1355 (1959).

Impurity Distribution in Epitaxial Silicon Films

C. O. Thomas, D. Kahng, and R. C. Manz

Bell Telephone Laboratories, Incorporated, Murray Hill, New Jersey

ABSTRACT

A differential capacitance-voltage method for determining doping profiles in depth in epitaxial semiconductor films is described. Experimental profiles, in which the doping level generally is not flat but decreases with film thickness, are shown for several film growth conditions. A possible explanation for the observed distribution is discussed.

The measurement, understanding, and control of doping distribution in depth is necessary for proper utilization of epitaxial semiconductor films in device fabrication, especially for very thin films, for structures in which the substrate-film interface is a functional part of a device, or for structures in which the profile must be tailored (as with grown junctions).

The impurity distribution in epitaxial semiconductor films is determined by two factors: (i) that related to the growth method *per se*, and (ii) that related to diffusion, especially from the substrate into the film. The first of these is dealt with in this paper. The diffusion effects are considered in a separate paper (1).

Experimental Methods

The epitaxial films were grown by means of the hydrogen reduction of silicon tetrachloride. The method is standard at this point and has been reported in detail by a number of investigators (2-5). For these experiments, the substrate slice in every case was subjected to a 30-min preheat treatment (cleaning) at 1240°-1250°C in flowing dry hydrogen immediately before film growth. The film growth temperatures were selected in the range 1060°-1220°C. All temperatures have been corrected for emissivity and for wall transmission losses and are measured by means of an optical pyrometer viewing the upper surface of the slice.

The silicon tetrachloride saturator temperature was stabilized at -40°C (±0.2°C) which gives a calculated mole fraction of 0.01 in the vapor. The hydrogen flow rate was 2.5 liters min^{-1} through a 1¼-in. ID chamber. The apparatus was a single slice, vertical, RF heated system with a silicon pedestal. The pedestals were preheated with projection lamps to facilitate RF coupling and did not contain doped inserts. Both purified and doped silicon tetrachloride, as well as lightly and heavily doped pedestals, were used in these experiments.

Unless specifically stated otherwise, all of the substrate slices were from the same, arsenic-doped, pulled ingot, 0.004-0.006 ohm-cm and about ⅝-in. diameter. The slices were cut to a (111) orientation and electrochemically polished (6). Each slice was cleaned immediately prior to use by means of a 1-min room temperature etch in 250 cc HNO_3, 50 cc HF, and 220 cc (I_2 saturated) HAc followed by a deionized water rinse in a counter-current flow system. The samples were dried in a continuously purged nitrogen atmosphere oven and immediately placed in the deposition chamber.

Diodes were fabricated by a ¼μ boron diffusion through a photoresist oxide mask.[1] A 10 by 10 array of 18 mil diameter dots was prepared on each slice. Six to eight diodes were measured on each slice. Comparable results have been found using aluminum alloy diodes. However, the percentage yield of good diodes was better with the shallow boron diffusion, and consequently it was used for the major portion of this investigation.

Growth temperatures of 1200°C or higher have been widely reported in the past as necessary for the preparation of good electrical quality films. Figure 1 shows the forward and reverse characteristics of a typical diode (¼μ boron diffused, 18 mil diameter) in one of the low-temperature films of about 7μ thickness. The current just before breakdown is about 10^{-7} amp. Diode characteristics as shown in Fig. 1 are quite adequate for the electrical measurements described below. The essential point for preparation of good device material at this temperature appears to be scrupulous attention to the substrate and system cleanness.

The measurement method is based on the fact that for a junction between a heavily doped and a

[1] Oxidation at 1100°C for 30 min, diffusion at 900°C for 70 min.

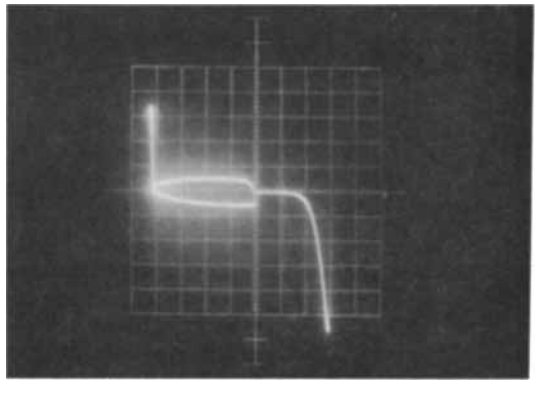

Fig. 1. Diode characteristics for film grown at 1060°C. Boron diffused 18 mil diameter dots, ¼μ depth; measured current just before breakdown about 10^{-7} amp.

← Reverse — Forward →

10 v/cm H, 10 μa/cm V — 0.2 v/cm H, 10 μa/cm V

more lightly doped semiconductor, the slope of $1/C^2$ *vs.* the applied reverse voltage (V) is a simple function of the doping concentration at the edge of the space-charge, (N_s) (7). The basic equations are as follows

$$d\,(1/C^2)/dV = 2/\epsilon q N_s \qquad [1]$$

$$C = dQ/dV = \epsilon/s \qquad [2]$$

$$d(1/C^2)/dV = -2C^{-3}(dC/dV) \qquad [3]$$

A nomograph based on these equations is shown in Fig. 2.[2] The measurement method is as follows. Capacitance is measured at a given voltage. Then the capacitance bridge dial setting is changed by a small increment, roughly 1%. The applied reverse voltage is changed to rebalance the capacitance bridge. This gives $\Delta C/\Delta V$ ($\sim dC/dV$) at the given values of C and V. After suitable correction for diode area, the doping concentration, the depth at which the measurement is made, and the resistivity in ohm-cm (for n-type silicon) may be determined directly from the nomograph. Thus, a doping profile in depth may be determined by multipoint measurements on each diode.

Experimental Results

Figure 3 shows the point-to-point measurements in depth for six diodes on a typical epitaxial silicon film grown at 1220°C. A 70-90 ohm-cm arsenic-doped pedestal was used. The saturator contained purified silicon tetrachloride (8) at -40°C. The film thickness is measured from the junction. Angle-lap and staining indicate that the interface is approximately 6.85μ below the junction.

The main body of the curve approximates a straight line which may be extrapolated to give an "effective" initial doping concentration at the apparent interface, which is labeled as N^*_o. Near the interface, there is also a diffusion tail. In some instances, it has been possible near the junction to see the compensation effect of the boron diffusion.

[2] This specific measurement method was first suggested by M. M. Atalla and D. Kahng who constructed the nomograph.

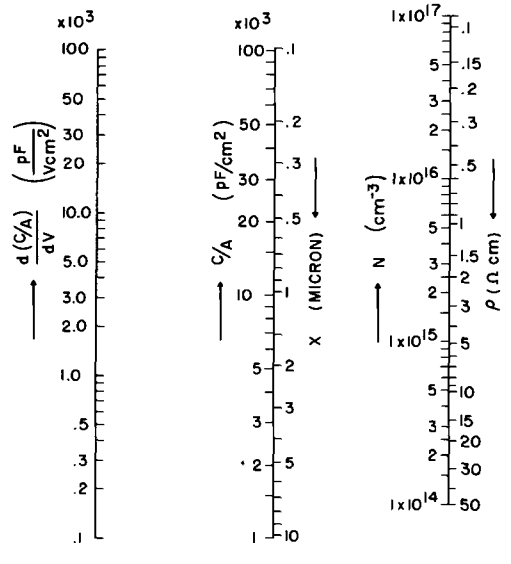

Fig. 2. Nomograph for use in resistivity profile determination

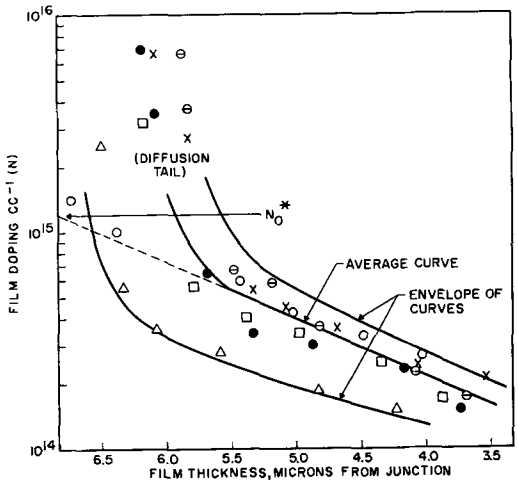

Fig. 3. Diode data for an epitaxial silicon doping profile. Substrate (As-doped) 0.004 ohm-cm; $SiCl_4$ (purified) saturator at —40°C; pedestal (As-doped) 70-90 ohm-cm silicon; growth temperature 1220°C; growth rate 2.5μ min^{-1}; interface estimated at 6.85μ below junction.

Since the doping is not uniform with depth, some of the spread between the diodes may be caused by film thickness variations across the sample. Figure 4 shows the effect of making a lateral adjustment in the points from Fig. 3 to bring the diffusion tails to a common level. The maximum adjustment required is about 0.5μ which is within the range of normally observed thickness variations. The result is to significantly reduce the data spread without changing the slope or the intercept by any appreciable amount. However, the adjustment introduces a degree of approximation in the film thickness coordinate. In like manner, some of the vertical data spread probably is related to variations in diode area. Average curves shown throughout this paper are based on the unadjusted data as shown in Fig. 3. Figure 5 shows a composite profile for three films of different thicknesses grown with a doped saturator under otherwise identical conditions. The points are mean values, and the vertical lines indicate the maximum spread in the measurements. Five to six

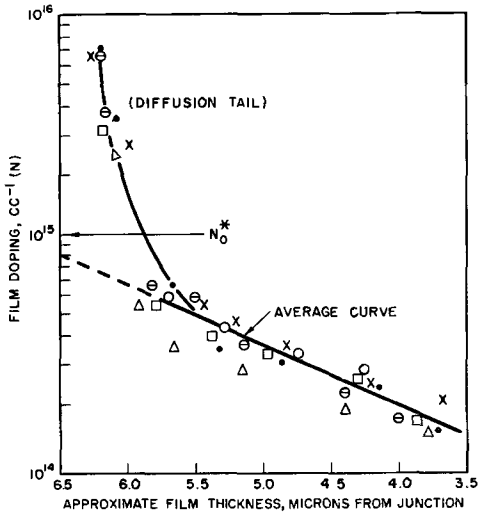

Fig. 4. Data from Fig. 3 adjusted for presumed thickness variations by bringing diffusion tails to a common line.

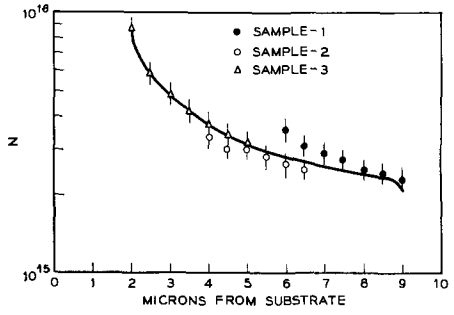

Fig. 5. Composite curve for three films of different thicknesses grown with the same doped saturator.

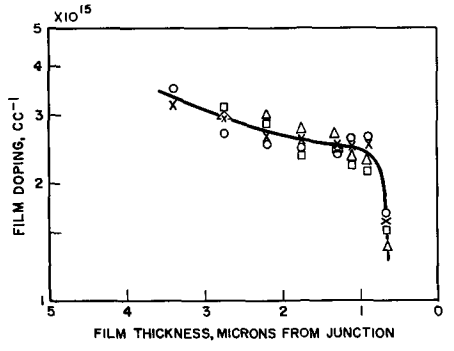

Fig. 6. Point data for sample-1 of Fig. 5 showing compensation effect near junction.

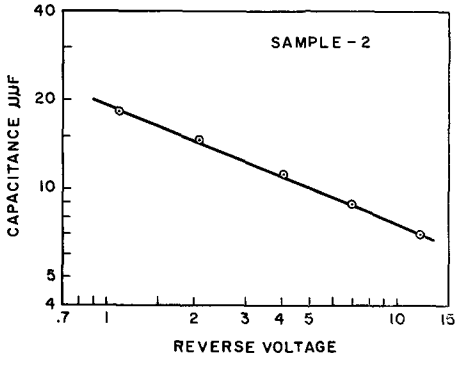

Fig. 7. Customary capacitance vs. voltage plot for sample 2 (Fig. 5) with boron diffused diodes; slope —0.4.

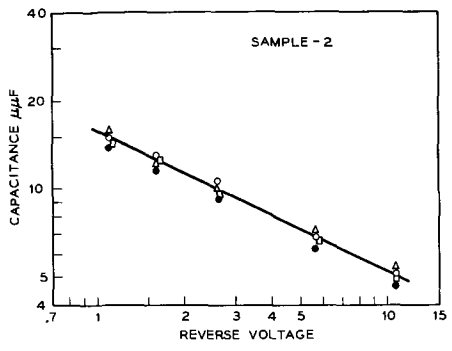

Fig. 8. Customary capacitance vs. voltage plot for sample 2 A(Fig. 5) with aluminum alloy diodes; slope —0.45.

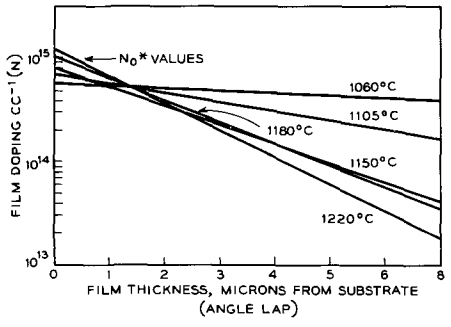

Fig. 9. Straight-line portions of doping profiles at several growth temperatures. Diffusion tails not shown; substrates (As-doped) 0.004 ohm-cm; purified $SiCl_4$; pedestal (As-doped) 70-90 ohm-cm silicon.

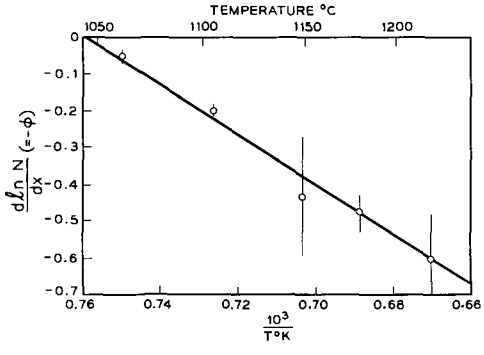

Fig. 10. Film growth temperature dependence of profile slopes

diodes selected at random were measured on each sample. The three films were grown at 1180°C using a doped saturator. Figure 6 shows the detailed diode data for sample 1 and clearly illustrates the compensation effect near the junction. Figure 7 shows the usual capacitance vs. reverse voltage plot for the boron diodes on sample 2. This is the same raw data as above, but is merely plotted differently. Figure 8 shows capacitance vs. reverse voltage data for aluminum alloy diodes (15 mil diameter dots) prepared on a portion of sample 2. Four diodes selected at random were measured. There is a reasonable resistivity check between the four plots in Fig. 5, 6, 7, and 8.[8] However, the advantage of the differential method for determining the detailed profile shape is clearly shown. On sample-2 the differential method indicates a profile shape that cannot readily be determined from the capacitance *vs.* reverse voltage plots.

[8] Obtained by treating the data of Fig. 7 and 8 as if the slopes were −0.5.

Figure 9 shows the variation in the slope of the straight line portion of the profiles as a function of the temperature at which the film is grown (using purified $SiCl_4$). There will, of course, be a diffusion tail (not shown here) near the interface for each of the profiles. The profiles extrapolated to the apparent interface give an "effective" interface concentration labelled as N^*_0. The profile at each growth temperature is a composite for three to eight slices.

There are several important points in Fig. 9: (i) the semilog plots are straight over a rather wide thickness range; (ii) flat profiles are approached only at the lower growth temperature; and (iii) there appears to be a common intercept or pivotal point somewhere near the interface. These points will be considered in more detail in the Discussion section. The temperature dependence of the profile slopes, ϕ, is shown in Fig. 10.

Figure 11 shows the shift in N^*_0 produced by a shift in substrate resistivity. However, the ratio of N^*_0 to substrate resistivity is not constant. This point

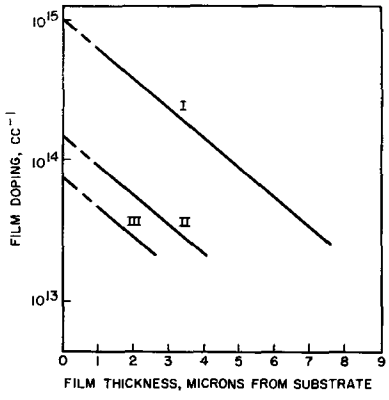

Fig. 11. Effect of substrate resistivity on profiles. I, Substrate 0.004 ohm-cm ($2x10^{19}$); II, substrate 1 ohm-cm ($5.5x10^{15}$); III, substrate 15 ohm-cm ($3x10^{14}$); All substrates As-doped; growth temperature 1180°C with purified $SiCl_4$.

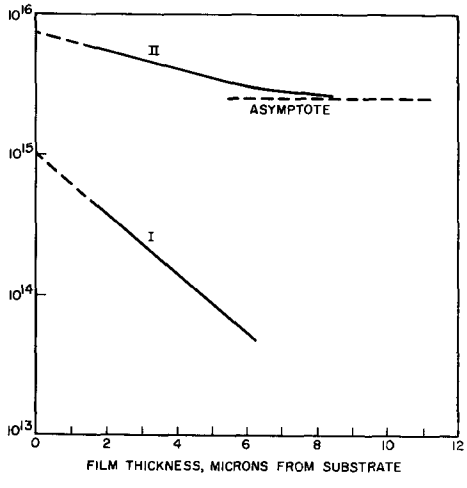

Fig. 12. Effect of gas-phase doping on profiles. I, Purified $SiCl_4$, 70-90 ohm-cm pedestal; II, doped $SiCl_4$, 2000-3000 ohm-cm pedestal. Substrates 0.004 ohm-cm; growth temperature 1150°C.

will be considered further in the Discussion section. The slopes remain identical within the sensitivity limits of the measurement method.

Figure 12 shows the effect of heavy gas phase doping. In thick films (10-14μ) grown with this doped saturator, there is an asymptote of about 2.5×10^{15} which is approached at a distance of 10-11μ from the substrate.

Model

It has been shown above that the experimentally measured doping level in a given epitaxial silicon film (grown by the hydrogen reduction of silicon tetrachloride in a flow system) generally decreases as a function of distance into the film from the substrate. This distribution is distinct from and in addition to diffusion from the substrate into the film. In addition, the doping level in the film is affected both by the ambient gas-phase doping level and by the substrate doping level.

At present, there is insufficient data for an analysis of the kinetics of the system. However, there is considerable evidence that dopant is transferred from the silicon pedestal and from the backside of the substrate slice to the growing film through the gas phase (2). We propose here that a similar transfer from the upper surface of the substrate (or the film after it has begun to grow) into the working gas phase is a major factor in determining the shape of the doping profile in the film. Since the mechanism is not understood, we merely write

$$(\text{silicon, dopant})_{gas} \rightleftarrows (\text{silicon, dopant})_{solid}$$

Distribution expressions which appear to agree in form with the measured profiles (n-type) have been derived by treating the film growth as a discontinuous process in which the sequential steps are:

1. Silicon and dopant are removed from the solid in the ratio in which they are found at the solid surface, *i.e.*, the step involves an "etch" phenomenon with no preferential leaching of either silicon or dopant.
2. The working gas-phase composition is modified by mixing with the incoming gas ambient which contains $SiCl_4$ and may or may not contain dopant.
3. Silicon and dopant are deposited in the ratio in which they are now present in the modified working gas phase. These steps constitute a complete cycle in which there is a net increase in film thickness. Thus, some dopant from the substrate (as well as that supplied by the incoming gas ambient) is available for redistribution in the film.

The discontinuous model is used here on the grounds of mathematical convenience, reasonable agreement with the measured profiles, and the absence of adequate kinetic data at present. It is not intended to imply that the actual process is discontinuous.

In developing the model, we ignore diffusion from the substrate into the film or diffusion within the body of the film. These effects are considered in a separate paper (1).

In the first step, material is removed from the solid phase in the dopant-to-silicon ratio.

$$(\text{dopant/silicon})_s = (N/N^\circ) \qquad [4]$$

This material mixes with the incoming gas phase to give a working gas concentration near the surface

$$(\text{dopant/silicon})_g = (N + bn)/(N^\circ + bn^\circ) \qquad [5][4]$$

On the deposition half of the cycle, the dopant and silicon deposit in the ratio shown in [5] with a net increase in film thickness

$$y = ax = 1, 2, 3, \ldots . \qquad [6]$$

The value of x for $y = ax = 1$ is analogous to the HETP (height equivalent to a theoretical plate) in distillation and extraction theory and defines the incremental thickness in microns equivalent to one theoretical cycle. From the above considerations it follows that

$$(N_1/N^\circ) = (N_o + bn)/(N^\circ + bn^\circ) \qquad [7]$$

$$N_1 = N^\circ(N_o + bn)/(N^\circ + bn^\circ) = \alpha(N_o + bn) \qquad [8]$$

where

$$\alpha = N^\circ/(N^\circ + bn^\circ)$$

[4] The dimensions of N and N° are atoms-cc^{-1}(s), and of n and n° are atoms-cc^{-1}(g). Therefore the exact form of [5] is

$$(\text{dopant/silicon})_g = (wN + Bn)/(wN^\circ + Bn^\circ)$$

where

$$w = d_g/d_s \text{ and } b = B/w$$

$$N_2 = \alpha^2 N_o + \alpha^2 bn + \alpha bn \quad [9]$$

$$N_y = N_o\alpha^y + \alpha bn(1 + \alpha) + \ldots + \alpha^{y-1} \quad [10]$$

Rewriting the geometrical progression in exact terms gives

$$N_y = N_o\alpha^y + \alpha bn(1-\alpha^y)/(1-\alpha) \quad [11]$$

or

$$N_x + N^*_o\alpha^{ax} + \alpha bn(1-\alpha^{ax})/(1-\alpha) \quad [12]$$

where N^*_o is the effective N_o at the interface between the film and the substrate.

Equation [12] is the generalized expression for the case where dopant is present both in the substrate and in the gas phase. The ambient gas-phase doping may originate with the silicon tetrachloride, the system contamination, the pedestal, or even from the backside of the substrate by a transfer mechanism discussed elsewhere (2).

For a pure gas phase, $n = 0$ and [12] reduces to

$$N_x = N^*_o\alpha^{ax} = N^*_o e^{-\phi x} \quad [13]$$

since by definition, $0 < \alpha < 1$. Also for an intrinsic substrate and doped gas, the expression reduces to

$$N_x = \alpha bn(1-\alpha^{ax})/(1-\alpha) = [\alpha bn/(1-\alpha)](1-e^{-\phi x}) \quad [14]$$

For larger values of x, (*i.e.*, thick layers)

$$N_{x\to\infty} = \alpha bn/(1-\alpha) = A, \text{ (an asymptote)} \quad [15]$$

The various derived equations are summarized in Table I. The physical significance of these expressions is shown in Fig. 13 where log N_x is plotted against x. The several curves are discussed below.

Curve I.—This is the asymptotic limit for a system in which gas doping occurs, *i.e.*

$$N_x = Kn = n(N^\circ/n^\circ) = A \quad [16]$$

This is obvious from the fact that the exponential term $N^*_o e^{-\phi x}$ becomes vanishingly small for large x-values, while the summation term approaches a constant value. The absolute position of the asymptote will depend on the gas-doping concentration, n, as shown in Table I.

Curve II.—This is the exponential profile for a doped substrate with an intrinsic gas phase. The diffusion tail is not shown. The slope of this curve is given by ϕ and will be discussed later.

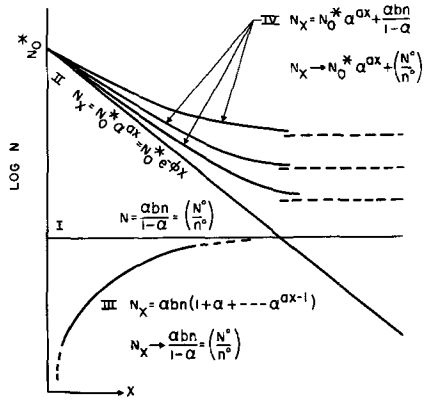

Fig. 13. Theoretical doping profiles derived from model discussed in text; diffusion effects not shown. I. Hypothetical profile for process with no etch-back; also determines the asymptote at a given doping level in the gas phase; II, profile for doped substrate and pure gas; III, profile for pure substrate and doped gas; IV, profiles for doped substrate and doped gas showing the approach to an asymptote.

Curve III.—This is the profile for a gas-doped system with an intrinsic substrate. N_x theoretically approaches zero at the interface. This profile will approach the asymptotic limit defined earlier for thick films.

Curve IV.—This is the generalized profile for the case where both the substrate and the gas phase are doped. As the gas doping contribution increases, the asymptote moves up. It is apparent that the gas-phase doping contribution will alter the slope of the curve and also affect its straightness on the semilog plots.

There are only two constants involved in these expressions. They are b, the gas-phase mixing constant, and a, the constant involved in the HETP. If the gas-phase concentration is known accurately, then b may be determined by an analysis of the curves, and α may then be calculated. Unfortunately, the gas-phase concentrations generally are not known with sufficient accuracy and, in fact, are usually adjusted by trial-and-error to give a specified film resistivity. Also, there is the added difficulty that the desired gas-phase concentration is that of the working gas near the surface rather than the ambient supplied by the saturator. The working gas may contain miscellaneous contributions

Table I. Doping profile equations for hypothetical epitaxial growth process

Case	For any x-value	For large x-values
Substrate and gas doping (general)	$N_x = N^*_o\alpha^{ax} + \alpha bn\left(\frac{1-\alpha^{ax}}{1-\alpha}\right)$	$N_x = N^*_o\alpha^{ax} + \alpha bn\left(\frac{1}{1-\alpha}\right) = N^*_o\alpha^{ax} + \left(\frac{N^\circ}{n^\circ}\right)n$
Substrate doping only	$N_x = N^*_o\alpha^{ax} = N^*_o e^{-\phi x}$	$N_x = N^*_o\alpha^{ax} = N^*_o e^{-\phi x}$
Gas doping only	$N_x = \alpha bn(1-\alpha^{ax})/(1-\alpha) = [\alpha bn/(1-\alpha)](1-e^{-\phi x})$	$N_x = \alpha bn\left(\frac{1}{1-\alpha}\right) = \left(\frac{N^\circ}{n^\circ}\right)n$

from the system, the pedestal, and the slice backside (2).

Discussion

Experimentally it is found that substrate dominated (*i.e.*, purified gas phase) profiles appear to decrease exponentially with distance from the substrate. Also, it is found that, with sufficiently thick films, the profiles approach an asymptotic limit defined by the gas-phase doping level. For purified silicon tetrachloride, the asymptote is below about $5 \times 10^{13} cc^{-1}$. As the gas-phase doping level is increased, the asymptote moves up, and the shape and slope of the profile are modified accordingly. These observations are consistent in form with predictions which derive from the counter-current model.

The model suggests that the profile slopes should be temperature dependent. However, neither the quantitative dependence of the slopes nor the location of the interfacial intercepts may be predicted from the model. Experimentally it is found that the slopes decrease with temperature and that the exponential portion of the profile pivots about a point in the vicinity of the interface. A practical consequence is that flattening the profile by decreasing the growth temperature also produces a lower film resistivity at a given thickness level. This effect is opposite to that which would be produced by a diffusion phenomenon. This problem may be offset somewhat by increasing the substrate resistivity and thus shifting the location of N^*_o. The ultimate limitation will be that of device specifications on substrate resistivity since a very large shift in substrate resistivity is necessary to produce a factor-of-ten shift in N^*_o.

We have found that for given experimental conditions the mean film resistivity generally increases with film thickness. This observation also is consistent with the preceding points.

The position of the gas-phase mixing constant b in the profile expressions indicates that a higher dilution factor in the working gas volume should produce a more rapid approach to the asymptote and, consequently, a more nearly flat profile. If the working gas volume extends sufficiently far into the gas phase, this might be accomplished by higher gas velocity, etc.

For the counter-current model, as stated, the amount of substrate dopant involved in the initial etch-back step is the total amount available for redistribution throughout the film. Table II shows the integration of the profiles in Fig. 9 from N^*_o to 10^{13}. For the lower growth temperatures this, of course, requires a considerable extrapolation of the profiles. The dimension of the third column is atoms-cc^{-1}-micron. If we assume etch back into a substrate with a uniform doping level at 2×10^{19} then the required etch-back distance is about 1-6Å. The calculations in Table II are based on experimental data from runs with purified $SiCl_4$, where the ambient gas-phase contribution to the integrated value is negligible. The etch-back concept has been discussed elsewhere (9, 10).

Table II. Computed etch back distance based on a substrate surface concentration of 2×10^{19}

Temp, °C	x at 10^{13}, μ	$\frac{N^*_o}{\phi}(1 - e^{-\phi x})$	Etch back distance, Å
1060	66.5	1.16×10^{16}	5.77
1105	20.7	2.48×10^{15}	1.74
1150	10.1	2.11×10^{15}	1.05
1180	9.5	2.08×10^{15}	1.04
1220	7.9	2.01×10^{15}	1.01

A second point not explained by the model is the fact that N^*_o is about $N_{sub} \times 10^{-4}$ for heavily doped substrates and about $N_{sub} \times 10^{-1}$ for lightly doped substrates. These two points indicate that the nature of the process at the boundary layer is not clearly understood and that the counter-current model should not be interpreted in a literal mechanistic sense. Infrared and electron microscope studies of surfaces of n-type silicon (doped in the range of 2×10^{19}) show considerable changes in the surface properties of the starting substrate material as a function of the heat treatment given the substrate prior to film deposition (11). Furthermore, the numerical value of N^*_o has been found to be sensitive to the heat treatment conducted prior to film deposition.

Equation [5] indicates the nature of the dopant/silicon ratio in the working gas phase. It was assumed that, on the deposition half of a cycle, the deposit occurs in this ratio. If this is not true, then the effect will be to modify the value of the term α (and consequently ϕ) without changing the form of the equation. Earlier work by Theuerer (3) indicates that the assumption is reasonable for n-type doping (phosphorus), but that for p-type doping (boron) α should be reduced by a factor of about 10.

Summary

An experimental method for determining doping distribution along the thickness coordinate in epitaxial semiconductor films has been described. The doping concentration generally is found to decrease with distance from the substrate. A model has been described which leads to a distribution expression which is in reasonable agreement with the experimental data. The model has obvious pragmatic value. However, additional information will be necessary before the kinetics and mechanism of the film growth process are clearly understood.

Acknowledgments

The authors are indebted to M. M. Atalla for valuable discussions related to the measurement method, to C. E. Shoemaker for providing the purified silicon tetrachloride, and to A. Loya for assistance with the electrical measurements.

Manuscript received April 5, 1962; revised manuscript received June 26, 1962. This paper was prepared for delivery before the Detroit Meeting, Oct. 1-5, 1961.

Any discussion of this paper will appear in a Discussion Section to be published in the June 1963 JOURNAL.

REFERENCES

1. D. Kahng, C. O. Thomas, and R. C. Manz, *This Journal*, **109**, 1106 (1962).
2. H. Basseches, R. C. Manz, C. O. Thomas, and S. K. Tung, AIME Semiconductor Metallurgy Conference, Los Angeles, August 30-September 1, 1961.

3. H. C. Theuerer, *This Journal*, **108**, 649 (1961).
4. H. C. Theuerer and H. Christensen, Semiconductor Symposium, Electrochemical Society, Houston, October 1960.
5. K. J. Miller and R. C. Manz, Semiconductor Symposium, Electrochemical Society, Detroit, October 1961.
6. D. L. Klein, G. A. Kolb, L. A. Pompliano, and M. V. Sullivan, Semiconductor Symposium, Electrochemical Society, Indianapolis, May 1961.
7. W. Schottky, *Z. Physik*, **118**, 539 (1942).
8. H. C. Theuerer, *This Journal*, **107**, 29 (1960).
9. E. Matovich and R. J. Andres, Semiconductor Symposium, Electrochemical Society, Detroit, October 1961.
10. J. J. Grossman, Private communication.
11. W. G. Spitzer and G. W. Gobeli, Private communication.

SYMBOLS

N	atoms-cc^{-1} of dopant in the solid phase
N°	atoms-cc^{-1} of silicon in the solid phase
N^*_o	"effective" dopant concentration at the interface, atoms-cc^{-1}
n	atoms-cc^{-1} of dopant in the ambient gas phase
n°	atoms-cc^{-1} of silicon in the ambient gas phase
b	gas mixing factor
B	gas dilution factor
w	d_g/d_s
d_s	density of solid
d_g	density of gas
y	index number of the theoretical cycle
x	distance in microns from the substrate
s	space charge thickness, or distance between the junction and the edge of the space charge
a	y/x = a constant
A	asymptotic limit of doping profile $= abn(1/1-\alpha) = n(N^\circ/n^\circ)$
ϕ	$d(\ln N)/dx$, μ^{-1}
C	pfd/cm^2
V	volts
Q	coulombs/cm^2
q	electronic charge $=1.6 \times 10^{-19}$ coulombs
ϵ	permittivity of silicon $\cong$ 1 pfd/cm

Preparation of Epitaxial GaAs and GaP Films by Vapor Phase Reaction

R. R. Moest and B. R. Shupp

Bell Telephone Laboratories, Incorporated, Murray Hill, New Jersey

ABSTRACT

Single crystal films of GaAs and GaP have been grown from the vapor phase on several substrates in a closed system containing source material and hydrogen chloride. The GaAs and GaP source material reacts with HCl to form gallium chlorides and elemental arsenic or phosphorus. These are transported along a temperature gradient in the ampoule and deposited at the cooler end as GaAs or GaP, several hundred degrees below their melting points. Epitaxial GaAs films have been grown on monocrystalline Ge and GaAs substrates of various crystallographic orientations and GaP epitaxial films on GaAs and GaP. The conductivity type of the films was controlled by appropriate doping of the source material. The growth rates were determined as a function of temperature and intial HCl pressure.

The successful growth of Si and Ge epitaxial films has stimulated considerable interest in methods for growing epitaxial films of III-V compound semiconductors from the vapor phase, in particular of GaAs and GaP. An inherent problem to the growth of compound semiconductors is the stoichiometry of the material. Experiments to grow some III-V compound films by simultaneous evaporation of the constituents from separate containers have been reported (1, 2). This technique, however, is for all practical purposes limited to constituents with a relatively high vapor pressure at moderate temperatures and cannot be readily applied to the controlled growth of substantial GaAs and GaP films. A more promising method appears to be the vapor growth of these compounds by a chemical reaction. Deposition from the vapor phase by a chemical reaction was first reported by Antell and Effer (3). They reacted iodides and chlorides of gallium and indium with arsenic or phosphorus in a sealed tube at elevated temperatures and grew small crystals of GaAs, GaP, InAs, and InP in the cooler end of the ampoules. The chemical methods for the preparation of III-V compounds were further investigated by Effer and Antell (4). Lyons and Silvestri (5) and Hagenlocher (6) described the growth of GaAs films in a sealed tube using iodine as transfer agent. Holonyak (7) disclosed methods for the growth of III-V compound films with halogen or metal halides as transfer agents, also in a closed system. Another approach to the growth of III-V compounds from the vapor phase is the open flow method in which a steady flow of a suitable carrier gas with a reacting agent, mostly hydrogen halides, reacts with some source material at higher temperature and redeposits the compound at a cooler region of the reaction tube. Reactions of this type have been reported by Effer and Antell (4), Williams and Ruehrwein (8), and Newman and Goldsmith (9). Frosch (10) reported the evaporation of GaAs and GaP at elevated temperatures in a flow of hydrogen gas and the subsequent redeposition of the compound in a cooler zone of the system.

This communication describes the epitaxial growth of GaAs or GaP on an appropriate substrate from the vapor phase in a sealed tube initially containing HCl. These compounds were transferred from GaAs or GaP sources and deposited on a substrate at a somewhat lower temperature. Gallium arsenide or germanium substrates were used for

GaAs growth and GaP or GaAs substrates for GaP growth. The effects of growth rate on source and substrate temperatures and initial HCl pressure were determined.

Experimental

Epitaxial GaAs or GaP films were grown in sealed quartz ampoules with an ID of 9 mm and 10 to 15 cm long. One end of the ampoule was flattened so that its cross section was semicircular. After adding the source and substrate the ampoule was evacuated to 10^{-4} torr, outgassed by heating with a torch, cooled, backfilled with HCl, and sealed off. The ampoule containing the substrate at the flattened end of the tube and the source at the opposite end was heated in a furnace shown schematically in Fig. 1. Growth was restricted to the substrate by introducing a local cold spot on the ampoule directly beneath the substrate. Either a metal wire or strip extending from the substrate to outside the furnace is a satisfactory heat sink. A silver wire 1 mm in diameter with a flat button at one end was generally used. Thermocouples located beneath the source and substrate were used to measure their temperatures. The quartz tube shown on the left side of Fig. 1 supported the substrate thermocouple and cold sink. The furnace was either a 12-in. cylindrical microcombustion type or a 10-in. hinged microcombustion type. The latter proved to be very convenient with respect to ease of loading in addition to its short heat-up time. Typical temperature profiles are indicated in Fig. 1. The dotted curves show schematically the temperature profile along the bottom of the ampoule beneath the substrate. Failure to make this region the minimum temperature of the ampoule results in spurious growth (generally whiskers) on the wall.

After growth for a desired time the ampoule was cooled locally with wet asbestos and then quenched in water. Monocrystallinity and epitaxy of the deposited films were demonstrated by Laue back reflection and electron diffraction analyses.

Growth of GaAs *Films*

Epitaxial GaAs films 1μ to 2 mm thick have been grown on GaAs substrates. These films were

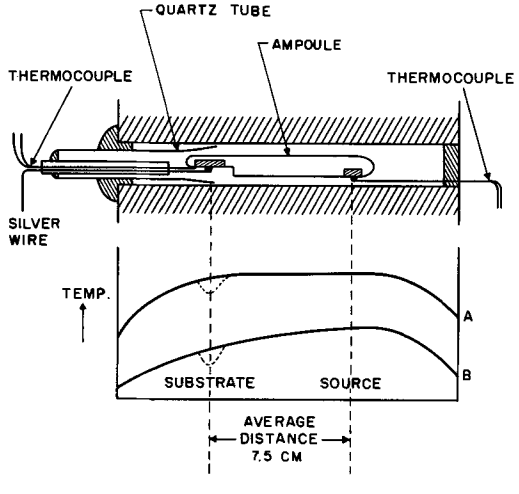

Fig. 1. Furnace arrangement for epitaxial growth and typical temperature profiles.

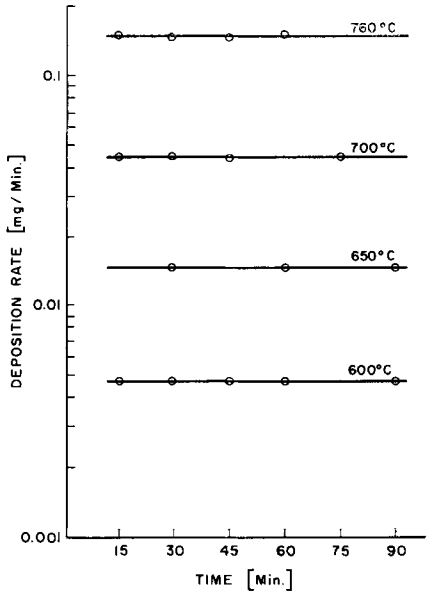

Fig. 2. Deposition rates of GaAs at various time intervals and source temperatures. Initial HCl pressure, 240 torr.

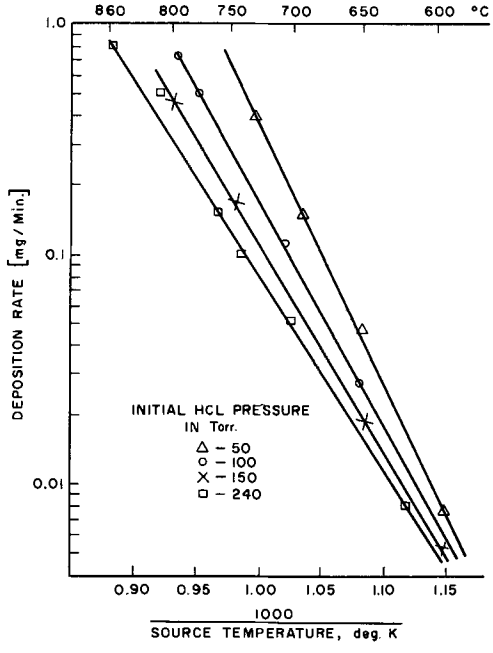

Fig. 3. Deposition rates of GaAs as a function of source temperature and HCl pressure.

either n- or p-type, depending on the conductivity type of the source. They were grown over the temperature range 550°-750°C. Source temperatures varied from 600° to 850°C. Films were grown at temperatures 20°-150°C below the source temperature. The initial HCl pressure varied from 50 to 240 torr. Within the above limits, the growth rates of the films depended only on the source temperature and the initial HCl pressure. As mentioned earlier, growth was restricted to the substrate so that the growth and transfer rates are identical. Independence of the rate on the substrate temperature is illustrated by the data in Table I. It remained constant well within experimental error when the substrate was 67°-125°C below the source temperature, 700°-707°C, and was independent of the substrate size.

Table I. Growth rate for GaAs films on GaAs substrates at various substrate temperatures. Initial HCl pressure in ampoules, 240 torr

Exp. No.	Temperatures in °C Source	Substrate	Δ Temp, °C	Growth rate, mg/min
1	707	640	67	0.054
2	700	623	77	0.045
3	700	610	90	0.049
4	700	600	100	0.048
5	700	595	105	0.049
6	700	584	116	0.048
7	703	578	125	0.049

Substrate wafers of different crystallographic orientations were used to determine possible effects on the growth rate. No variation was found for deposition on {100}, {110}, {111}, or $\{\overline{111}\}$ planes. Spherical or polycrystalline substrates may show preferential deposition on one plane. However, the over-all transfer rate is independent of orientation within the experimental conditions described above.

The growth rate is independent of time for a given source temperature and HCl pressure except for an initial starting period of less than 15 min required to establish steady-state conditions. These observations are summarized in Fig. 2.

Four different initial HCl pressures were used. The effects on growth rate are shown in Fig. 3, where the log of the growth rate is plotted *vs.* the reciprocal of the source temperature for the different initial HCl pressures. The growth rate increases with increasing source temperature and decreasing HCl pressures. Since the growth rates were found to be independent of substrate temperature, the slopes of the curves in Fig. 3 may be related to average activation energies for reactions at the source. These are 85 and 39 kcal for initial HCl pressures of 50 and 240 torr, respectively. These relatively high values indicate that the process is not diffusion limited. A strong dependence of the activation energy on the initial HCl pressure justifies an assumption that competing reactions take place at the source. Upon cooling the ampoules condensation of arsenic and gallium trichloride could be observed. Melting point determinations (77°-79°C) and chemical analyses indicated that the condensed chloride was essentially gallium trichloride. Within the analytical limits of accuracy, approximately 10%, there was no evidence of unreacted HCl.

Smooth uniform films were obtained with thickness variations of less than 10% over 60-80% of the total substrate area. Figure 4 shows interferometric microphotographs of a polished GaAs substrate and of a uniform epitaxial film approximately 2μ thick. Over the viewing field of the surface, diameter 2.1 mm, the average thickness variation was less than 0.27μ, the wavelength of the thallium light used with the interferometer. The substrate slices were generally flatlapped with Carborundum 1800 and chemically polished on a rotating Teflon plastic block in a solution of 70% sulfuric acid, 15% hydrogen peroxide, and 15% water to a mirrorlike finish (11). It was observed that the smoothness and film uniformity depended mainly on the preparation and cleanliness of the original substrate surface, and not on the crystallographic substrate orientation. Microphotographs of typical films grown by this method are shown in Fig. 5. The film surfaces are essentially free of growth patterns.

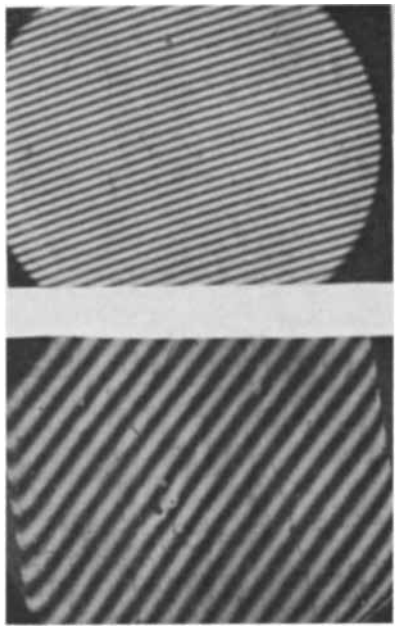

Fig. 4. Interferometric microphotographs of GaAs substrate (top) and film surface (bottom). Explanation in text. Magnification 34X.

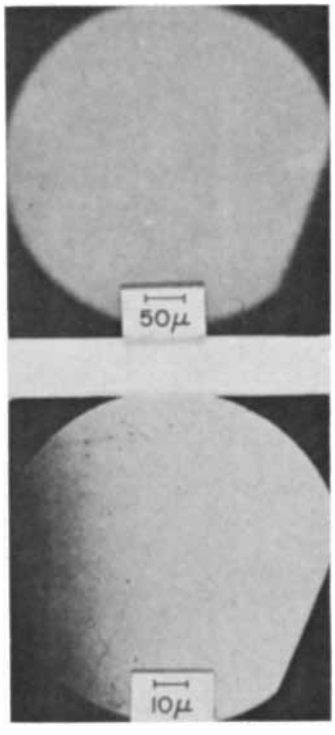

Fig. 5. Microphotographs of typical surfaces of epitaxial GaAs films. Magnification 100X.

As mentioned earlier, the conductivity type and resistivity of the films were determined primarily by the conductivity type and resistivity of the source material. Epitaxial p-n junctions have been grown with this method. Figure 6 shows a section of a typical p-n junction after angle lapping and staining. The sharpness of the junction is noteworthy. Since the sample was beveled in a 10° angle, the scale of

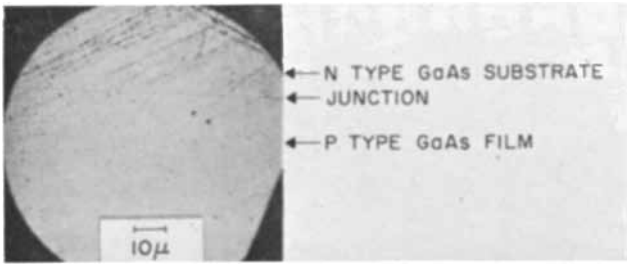

Fig. 6. Microphotograph of GaAs p-n junction. Magnification 100X

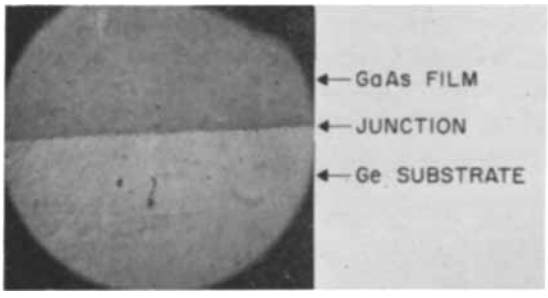

Fig. 7. Microphotograph of GaAs-Ge junction. Magnification 100X

1 cm on the photomicrograph plane perpendicular to the junction corresponds to a thickness difference of 1.7μ of substrate or film. Thus the apparent width of the junction is less than 0.1μ.

Epitaxial films of GaAs have also been grown on germanium substrate wafers. The temperature of the GaAs source material was between 680° and 780°C whereas the Ge substrate temperature was between 550°-600°C. Figure 7 shows part of an angle lapped heterojunction of a GaAs film grown epitaxially on a Ge substrate.

Growth of GaP Films

Epitaxial GaP films with thicknesses from 1μ to 100μ have been grown on GaAs substrate wafers. The temperatures in these experiments varied from 750° to 900°C for the GaP source material. The GaAs substrate wafers were generally 100°-200°C below the source temperature. Within these limits the deposition rate was independent of the substrate temperature.

Growth rates of GaP were measured as a function of source temperature at an initial HCl pressure of 240 torr. The dependence on source temperature is shown in Fig. 8. From the slope of the curve we estimate the average activation energy of the source reaction(s) to be 45 kcal. This compares with 39 kcal found for GaAs under similar conditions.

Film smoothness and uniformity were again found to depend mainly on the initial surface preparation and cleanliness of the substrate wafer. A section of a heterojunction with a GaP film on a GaAs substrate after 10° angle lapping and staining is shown in Fig. 9.

Summary

A method is described for the growth from the vapor phase of epitaxial films of GaAs and GaP on several substrates. The reaction products of either GaAs or GaP source material and HCl constitute the vapor phase. Gallium arsenide substrates were used for both GaAs and GaP film growth; Ge substrates

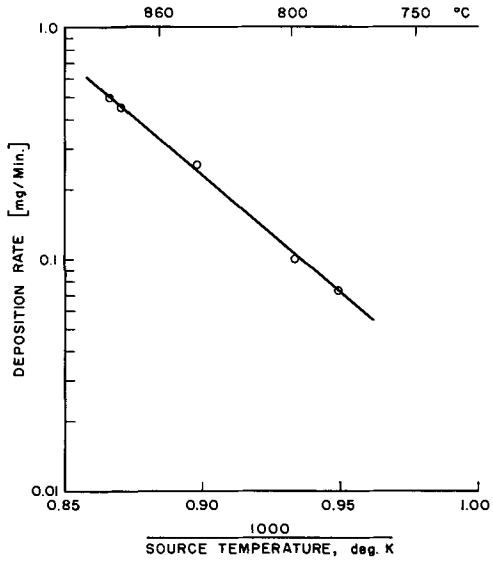

Fig. 8. Deposition rate of GaP as function of source temperature at constant HCl pressure.

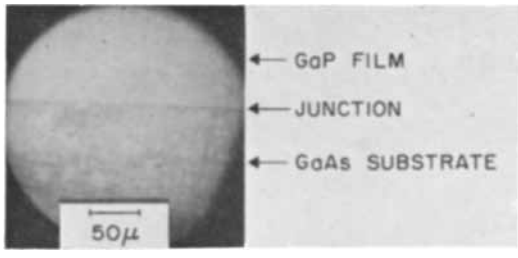

Fig. 9. Microphotograph of GaAs-Ge junction

were also used for GaAs growth. Deposition from the vapor phases was in all cases restricted to the substrate located at a cold spot in the system.

The growth rate of GaAs was dependent on source temperature and initial HCl pressure and independent of the substrate temperature or orientation. Source and substrate temperatures were in the ranges 600°-850°C and 550°-750°C, respectively. Initial HCl pressures varied from 50 to 240 torr. The growth rates were proportional to exp $(-\Delta H/RT)$ where T °K is the source temperature, R the gas constant, and ΔH is interpreted to be the average activation energy for reactions at the source. The value of ΔH was 39 and 85 kcal for initial HCl pressures of 240 and 50 torr, respectively. The strong dependence of ΔH on pressure is taken as evidence for competing source reactions. Growth rates for GaP exhibited the same general dependences as for GaAs.

The physical qualities, smoothness, and uniformity of epitaxial GaAs and GaP films were independent of substrate orientation, but dependent on the substrate surface preparation prior to deposition.

Acknowledgment

The authors wish to express their thanks to J. M. Whelan and C. D. Thurmond for helpful advice and discussions.

Manuscript received April 23, 1962; revised manuscript received July 11, 1962. This paper was prepared for delivery before the Detroit Meeting, Oct. 1-5, 1961.

Any discussion of this paper will appear in a Discussion Section to be published in the June 1963 JOURNAL.

REFERENCES

1. K. G. Günther and H. Freller, *Z. Naturforsch.*, **16a**, 279 (1961); further references to be found there.
2. V. A. Presnov and V. F. Synorov, *Soviet Physics, Techn. Physics*, **2** [1], (January, 1957).
3. G. R. Antell and D. Effer, *This Journal*, **106**, 509 (1959).
4. D. Effer and G. R. Antell, *ibid.*, **107**, 252 (1960).
5. V. J. Lyons and V. J. Silvestri, *ibid.*, **108**, 177C (1961).
6. A. Hagenlocher, *ibid.*, **108**, 213C (1961).
7. N. Holonyak, Jr., D. C. Jillson, and S. F. Bevacqua, AIME, Techn. Conf., Los Angeles, Aug. 31, 1961.
8. F. V. Williams and R. A. Ruehrwein, *This Journal*, **108**, 177C (1961).
9. R. L. Newman and N. Goldsmith, *ibid.*, **108**, 127 (1961).
10. C. J. Frosch and P. W. Foy, *ibid.*, **108**, 177C (1961).
11. M. V. Sullivan and L. A. Pompliano, *ibid.*, **108**, 60C (1961).

The Diffusivity of Arsenic in Silicon

W. J. Armstrong

Components Division, International Business Machines Corporation, Poughkeepsie, New York

ABSTRACT

The diffusion coefficient of arsenic in silicon has been investigated over the temperature range of 1100°-1350°C using the formation of p-n junctions to determine diffusion depths and concentrations. Diffusion coefficients are in good agreement with previously published data, but the diffusion equation

$$D = 68.6 \exp\left(\frac{-97{,}600}{RT}\right)$$

has a higher D_o and activation energy. Surface concentrations of arsenic were in the 10^{17} to 10^{19} range.

The use of arsenic as an impurity for making diffused silicon devices has received little attention compared to boron and phosphorus. Only two references to this diffusant are known: the work of Frosch and Derrick (1), and that of Fuller and Ditzenberger (2). The former paper reports a scattering of open tube experiments with no attempt to calculate a diffusion constant. The latter paper gives data obtained from experiments carried out in sealed capsules. The present work is concerned with diffusion of arsenic from the vapor phase over the temperature range of 1100°-1350°C in an open tube system. The experimental results are consistent with a diffusion model exhibiting a complimentary error function distribution of diffusant in the bulk material.

Experimental Procedure

Three-quarter inch diameter slices were cut parallel to the (111) crystallographic direction from approximately 0.35 ohm-cm boron doped silicon. The slices were lapped with 12μ alumina, then with 5μ alumina, cleaned ultrasonically in distilled water, and polished to a mirror finish on one side with 0.3μ alumina powder on Pellon Pan-W cloth. Final sample thickness was approximately 7-9 mils. After degreasing, cleaning, and etching in HF acid the resistivity of each slice was measured on the lapped side using a four-point probe.

The arsenic diffusion was carried out in a 1¾ in. ID Zirco tube which was fitted with ground Pyrex taper joints cemented to each end. The As_2O_3 source material was placed in a Pyrex tube which was immersed in a constant temperature bath and connected to the Zirco tube via the ground joint. The Pyrex tube joining the source with the Zirco tube was maintained at a rising temperature gradient from source to silicon through the use of a glass-covered resistance-heated wire. Automatic controllers and Pt-Pt 10% Rd thermocouples maintained the SiC heated sample furnace at ±3°C while the constant temperature bath held the As_2O_3 at ±1°C. A carrier gas of 99.4% nitrogen-0.6% oxygen was dried to less than 1.5 ppm H_2O, mixed by volume, and passed into the diffusion tube at 1.5 l/m. Water vapor content was continuously scanned on a CEC Model 26-301 Moisture Monitor.

Due to the slow sublimation rate of As_2O_3 it was necessary to replenish the source supply only once in this entire group of experiments. A constant source area of about 1140 mm² was maintained, and reagent special grade As_2O_3 was used as source material. The silicon slices were diffused two or three at a time on a flat quartz slab which was removed from the furnace only long enough (5-10 sec) to place the slices.

After removing the As_2O_3 glassy layer in concentrated HF acid, the diffused slices were measured with a four-point probe to determine sheet resistivity. The samples were then beveled on a 1° block, stained with a HF, H_2O_2, H_2O etch, and photographed. Interference fringes produced with sodium light were used to determine the junction depth on the samples. Surface concentrations were calculated using curves of Irvin (6).

Results and Discussion

Junction depth as a function of time.—To determine if the surface concentration was constant as a function of time, diffusion runs were made at 1100°, 1150°, 1200°, 1225°, 1240°, 1300°, and 1350°C for

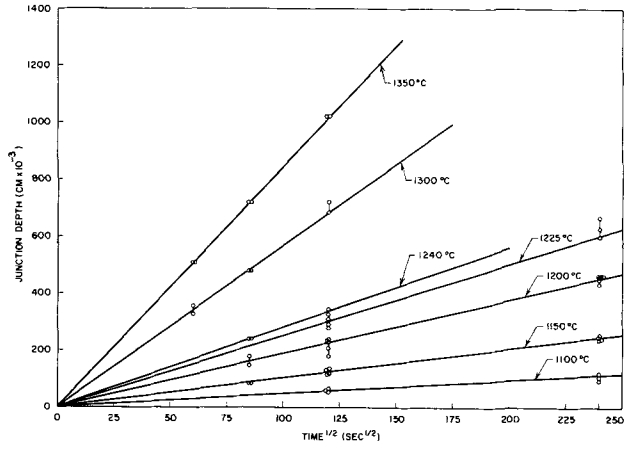

Fig. 1. Junction depth as a function of the square root of time

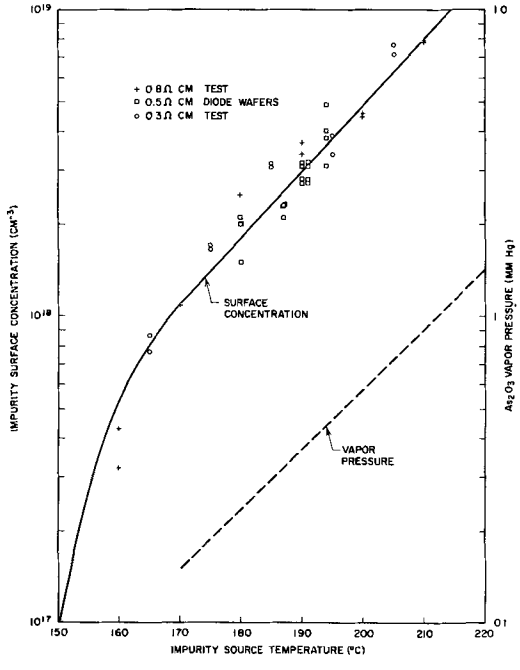

Fig. 2. Surface configuration and vapor pressure as functions of arsenic trioxide source temperature.

times ranging from 1 to 16 hr. A source temperature of 180° was used for all experiments. Results are presented graphically in Fig. 1. The junction depth is proportional to the square root of time indicating that the surface concentration is constant for the duration of the experiments.

Surface concentration as a function of source temperature.—Solution of the differential diffusion equation for these boundary conditions of constant diffusant surface concentration and a semi-infinite solid give a complementary error function distribution of diffusant. Under these conditions the measurement of junction depth, sheet resistivity, and bulk doping level permits calculation of surface concentrations from the previously mentioned curves. The results of the experiments to determine the effect of source temperature on arsenic surface concentration are shown in Fig. 2. All experiments were done at a silicon temperature of 1300°C, and carrier gas conditions were as described earlier. As expected, differences in silicon resistivity of 0.3-

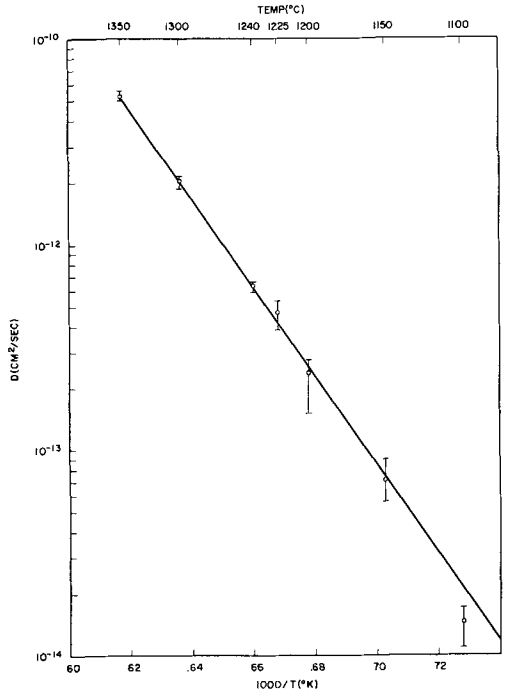

Fig. 3. Diffusion constant as a function of reciprocal absolute temperature.

0.8 ohm-cm did not appear to affect the surface concentration results.

For arsenic surface concentrations greater than 10^{18}, the natural logarithm of the impurity surface concentration is linear with the source temperature and has a slope of 0.050. A curve for the natural logarithm of As_2O_3 vapor pressure as a function of temperature is shown in the same figure. This curve is based on data from several authors given in the "Handbook of Physics and Chemistry" and extrapolated below 212°C. This curve, which also approximates a straight line in the region of interest, has a slope of 0.049. Thus, the two curves are in excellent agreement over the 170°-200°C range, demonstrating the direct relationship between impurity surface concentration and vapor pressure.

Determination of diffusion constant.—The diffusion equation solution for these boundary conditions may be written

$$C_x = C_o \operatorname{erfc}\left(\frac{x}{2\sqrt{Dt}}\right)$$

where C_o is the surface concentration, C_x the concentration at a distance x from the surface, erfc the error function complement, t the time of diffusion, and D the diffusion constant. For each diffusion, C_x, C_o, x and t are known and D may be calculated. A plot of ln D *vs.* the reciprocal of absolute temperature is shown in Fig. 3. The slope of this curve is the activation energy for arsenic diffusion in silicon and has been determined to be 97,600 cal/mole. D_o has been calculated as 68.6 cm²/sec; the diffusion equation for arsenic in silicon is then

$$D = 68.6 \exp\left(\frac{-97{,}600}{RT}\right)$$

The paper of Fuller and Ditzenberger gives a value of:

$$D = 0.32 \exp\left(\frac{-82{,}000}{RT}\right)$$

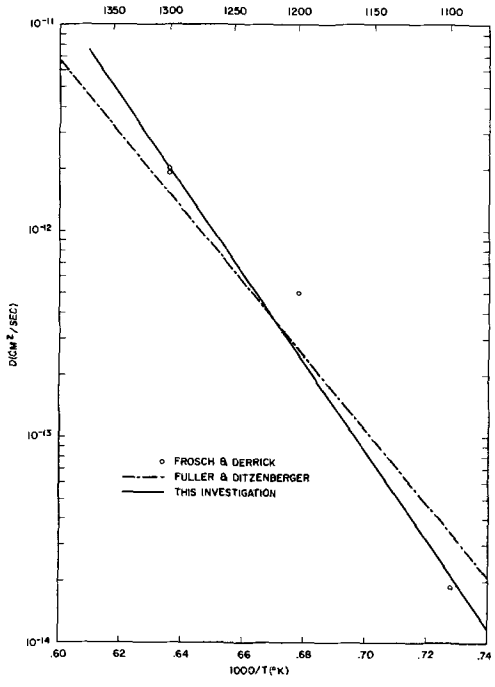

Fig. 4. A comparison of diffusion curves from this investigation with other published data.

for diffusion in sealed capsules. Not enough data are given in the paper of Frosch and Derrick to permit calculation of the activation energy; however, the diffusivity data agree much better with this investigation than with the work of Fuller as can be seen from Fig. 4.

The reason for the discrepancy in the values of ΔH and D_o between this investigation and that of Fuller is not readily apparent. It is evident from their data, however, that some irregularity with regard to arsenic diffusion is present. Fuller and Ditzenberger's classic investigation covers the elements boron, phosphorus, aluminum, gallium, indium, tellurium, antimony, and bismuth as well as arsenic. All diffusions were done in sealed capsules where the source material is maintained at the same temperature as the silicon. Thus, one would expect the surface concentration in each case to be near the solid solubility of the impurity in silicon at the temperature of diffusion. Table I gives a comparison of the surface concentrations obtained by Fuller and the solid solubilities as given by Trumbore (3).

Of the seven elements for which data are available, there is gross discrepancy for two, aluminum and arsenic. Results from the investigation described herein have shown that higher arsenic surface concentrations are obtainable than those reported by Fuller. These facts could indicate some anomaly which would effect the value of D as reported in the earlier investigation.

Table I. Comparison of surface concentration and solid solubility data for various elements in silicon

Element	Temperature	Solid solubility (Trumbore) cm^{-3}	C_o (Fuller *et al.*) cm^{-3}
Al	1300	1.7×10^{19}	5×10^{16}
	1085	2×10^{19}	3×10^{16}
Ga	1320	3.5×10^{19}	6.7×10^{19}
	1105	3.5×10^{19}	5.8×10^{19}
As	1380	10^{20}	4.5×10^{18}
	1200	1.5×10^{21}	5.8×10^{17}
Sb	1200	3×10^{19}	5.7×10^{19}
	1095	5×10^{19}	1.4×10^{18}
Bi	1305	8×10^{17}	5.4×10^{17}
	1220	5×10^{17}	1.0×10^{17}
B	1275	5.5×10^{20}	1.0×10^{21}
	1122	4.5×10^{20}	1.0×10^{22}
P	1235	1.4×10^{21}	6.0×10^{20}
	1030	1.2×10^{21}	3.0×10^{21}

A good estimate of the activation energy for arsenic diffusion can be obtained through a method suggested by Nowick (4). This estimate utilizes the value of D_o for self-diffusion which can be estimated from entropy data (5). An estimate of this type has been made for silicon by Fuller who reports a value of 0.8 cm^2/sec. It should be borne in mind that this is probably a minimum D_o and the introduction of foreign atoms will result in a change in its value. Using 0.8 cm^2/sec for D_o and the experimental value of D at the highest temperature of diffusion to minimize effects of internal surfaces, ΔH can be calculated from

$$D = D_o \exp\left(\frac{-\Delta H}{RT}\right)$$

giving a result of $\Delta H = 85$ kcal. Since this should be a minimum value, the agreement with this investigation is good.

Acknowledgments

It is a pleasure to acknowledge the contribution of T. Nagasaki who carried out many of the experiments from which data for this paper were gathered.

Manuscript received April 25, 1962; revised manuscript received July 10, 1962. This paper was prepared for delivery before the Boston Meeting, Sept. 16-20, 1962.

Any discussion of this paper will appear in a Discussion Section to be published in the June 1963 JOURNAL.

REFERENCES

1. C. S. Fuller and J. A. Ditzenberger, *J. Appl. Phys.*, **27**, 544 (1956).
2. C. J. Frosch and L. Derrick, *This Journal*, **104**, 547 (1957).
3. F. A. Trumbore, *Bell System Tech. J.*, 205 (1960).
4. A. S. Nowick, *J. Appl. Phys.*, **22**, 1182 (1951).
5. C. Zener, *ibid.*, **22**, 372 (1951).
6. J. C. Irvin, *Bell System Tech. J.*, 387 (1962).

Growth of Silicon Bicrystals by the Dash Pedestal-Method

R. Gereth

Shockley Transistor, Unit of Clevite Transistor, Palo Alto, California

ABSTRACT

Silicon bicrystals are grown in an inert atmosphere avoiding quartz crucibles. The oxygen content of the bicrystals is below the limit of detection with the 9μ absorption line. The Dash pedestal method is modified, and the bicrystals are pulled from the melt by means of a "bi-seed" which contains a small angle grain boundary. A float zone scanner is converted into a crystal grower. A "drill press"-etching apparatus facilitates the etching of the seed crystals to a needle-like shape with the grain boundary in the center of the 0.1 mm diameter of the tip.

Small angle grain boundaries consist of a regular array of edge dislocations (1-3). Bicrystals with such boundaries are an excellent tool to investigate dislocations. From the result of grain boundary experiments one can draw conclusions about the behavior of isolated dislocations.

Silicon bicrystals have been studied in the past (4-8). Enhanced diffusion along small angle grain boundaries in silicon has been found in this laboratory (5). Phonon drag measurements in silicon grain boundary specimens have been carried out by Hubner and Shockley (6), and light emission at high voltage from a grain boundary junction has been observed by Goetzberger and Stephens (7). All these experiments were made with oxygen-rich bicrystals grown from a quartz crucible by the Czrochralski method (9). It is, however, not well known what role oxygen plays in the behavior of silicon crystals together with dislocations. Hooper and Queisser (8) recently found a strong influence of heat treatment on the photoresponse of Si bicrystals. They assumed that oxygen particularly accounts for these effects. For further studies it is, therefore, desirable to have both oxygen-rich and oxygen-free silicon grain boundary crystals available. All bicrystals obtained by the standard crucible procedure are contaminated with oxygen. This paper describes a method and an apparatus for growing oxygen-free silicon bicrystals.

Method of Growing Dash Bicrystals

Dash (10-12) describes a method of growing silicon monocrystals free of dislocations and oxygen. This procedure does not employ the quartz (SiO_2) crucible necessary with the well-known Czochralski method (9). The use of quartz crucibles gives rise to high oxygen content in the pulled crystals. With the Dash method, the crystal is pulled from the molten top of a silicon rod, commonly called the "pedestal." A seed consisting of material of low dislocation density is used. It is tapered at the tip to a diameter of approximately 0.1 mm. The crystal is pulled in an inert argon atmosphere to avoid contamination and oxidation.

For these experiments, a Dash crystal-growing apparatus was constructed. After many perfect silicon monocrystals had been grown, the equipment was used to grow grain boundary crystals with low oxygen content. Silicon material containing grain boundaries was chosen for the seeds, instead of the dislocation-free bars employed in the conventional Dash method.

Crystal grower.—A Lindberg float zone scanner (Model LA-VSE-24 ZR) was converted into a crystal grower. The basic arrangement is shown in Fig. 1.

The quartz tube, L, contains the main components of the crystal grower. The tube (35 mm OD) is

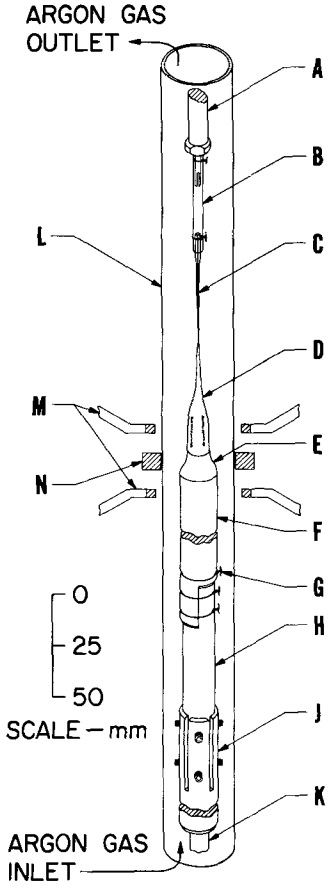

Fig. 1. Schematic drawing of the Dash crystal grower

aligned inside the heating coil, N, and shading coils, M, of the Lindberg RF generator (Model LI-10-C-1, 4MC, 10 KW). During growth, argon gas containing less than 0.1 ppm of oxygen flows through the quartz tube.

The pedestal, F, is connected to the quartz chuck, H, (15 mm diameter, 100 mm length). A slotted steel tube, J, with centering screws supports the quartz rod. The top of the rod is cut to a step shape to fit a corresponding step on the pedestal material. The parts are connected by tantalum wires. One of these wires, G, establishes the coupling of the RF field before the silicon pedestal is heated. The quartz chuck, H, insulates the hot parts of the grower. It also helps to reduce contamination of the pedestal, and improves the ease of aligning the whole assembly. The supporting shaft, K, is mechanically connected to a motor unit. Thus the operator is able to rotate and move all parts, F-K, according to any desired program.

A small quartz tube, B, is used as a "seed holder." It is connected to the elevator shaft A. The crystal, D, is pulled from the melt, E, by moving the seed, C, upward. At the same time it rotates with a constant speed of 6 rpm. The solid liquid interface is kept at a constant level by feeding the pedestal upward to compensate for the removed material.

Preparation of silicon starting material.—Czochralski-grown crystals (25-500 ohm-cm, n-type and 7-15 ohm-cm, p-type) with a diameter of about 18 mm were used as pedestal materials. The top portions of all these rods were tapered to a cone with a SiC-abrasive, while the lower parts were cut to fit the quartz chuck. Subsequently, the pedestal was etched in a solution consisting of 1 part HF (49%) and 3 parts of HNO_3 (70%).

The seed was prepared in the following way: A bicrystal containing a 10.5° grain boundary was grown by the Czochralski method using two seeds disoriented with respect to each other [as described by Mataré and Wegener (13)]. From this crystal a rectangular piece, containing the grain boundary (14) was cut (2 x 2 x 60 mm). It was lapped by hand

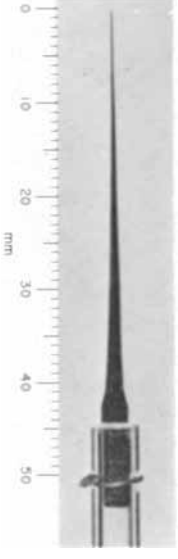

Fig. 2. Etched bi-seed containing a 10.5° grain boundary (diameter of the tip is about 0.1 mm).

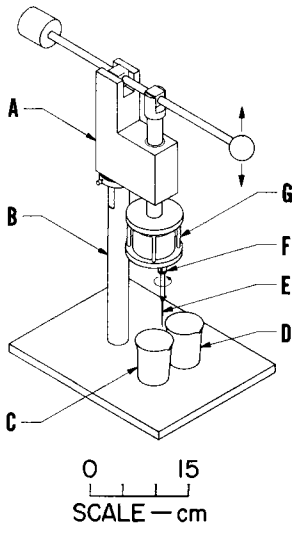

Fig. 3. Etching apparatus

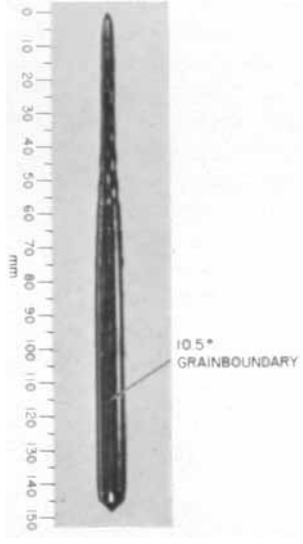

Fig. 4. Oxygen free, 10.5° grain boundary crystal with [100] pull axis.

until the grain boundary was equidistant from both sides parallel to the grain boundary plane. This "bi-seed" was etched to a needlelike shape (see Fig. 2) with the grain boundary still remaining in the center of the tip. The bi-seed must have a small diameter (approximately 0.1 mm) at the tip in order to avoid freezing of the molten silicon on top of the pedestal when the seed is lowered into the melt.

An apparatus for facilitating the etching of the seed crystals was constructed (see Fig. 3). The etching apparatus moves the seed vertically, while simultaneously rotating it at 10 rpm. This way, seed crystals can be etched very accurately to the desired concentric geometry. The etching apparatus is similar to a drill press. The supporting block, A, can be turned about the column, B, so that the seed, E, may be alternatively dipped into the etching solution, C, [1 part HF (49%), 3 parts HNO_3 (70%)] or cooling water, D. The seed is connected to the synchronous motor G, by means of the Teflon chuck, F.

Experimental Results

Figure 4 is a photograph of a Dash grain boundary crystal. The 10.5° grain boundary is seen on the

crystal surface as a fine, sharp line which is not completely parallel to the growth lines. This is caused by inaccurate orientation of the grain boundary with respect to the bi-seed. The crystal is 147 mm long and has a nearly constant diameter of 9 mm over a length of approximately 80 mm. It was grown with a starting pull rate of 4 mm/min and a final pull rate of 1.4 mm/min. The output energy of the RF generator was manually controlled to achieve optimum growing conditions, and the temperature of the molten Si was determined using an optical pyrometer.

Earlier infrared transmission measurements had indicated that Dash crystals grown from unrefined normal Czochralski crystals or from float zone refined silicon bars showed the same absorption peak height at 9μ. The absorption coefficient of all these slices was calculated to be in the order of 0.8 cm^{-1}. This value is known to be the background absorption of silicon itself (15). All measurements were carried out with a Beckman spectrophotometer (Model IR4). Since this instrument has a double-beam arrangement, the test slices cut from crystals grown by the Dash-method could be directly compared with equivalent float zone material placed in the reference path. A slice taken from the bicrystal shown in Fig. 4 was checked in this manner. No oxygen content could be detected by the 9μ absorption line.

Acknowledgments

The author wishes to express his thanks to Dr. W. Shockley and Dr. H. J. Queisser for valuable advice and stimulating discussions. He also is very obliged to K. E. Alvin who assisted in the experimental work. The help of the Stanford Research Institute in making the infrared measurements possible is gratefully acknowledged.

Manuscript received May 9, 1962. Research was supported in part by Rome Air Development Center under Contract AF30(602)-2556.

Any discussion of this paper will appear in a Discussion Section to be published in the June 1963 JOURNAL.

REFERENCES

1. W. L. Bragg, *Proc. Phys. Soc.*, (London), **52**, 54 (1940).
2. J. M. Burgers, *ibid.*, **52**, 23 (1940).
3. Summary of experimental results, S. Amelinckx and W. Dekeyser, in "Solid State Physics," F. Seitz and D. Turnbull, Vol. 8, p. 420, Academic Press, New York and London, (1959).
4. Y. Matukura, *J. Phys. Soc. Japan*, **16**, 842 (1961).
5. H. J. Queisser, K. Hubner, and W. Shockley, *Phys. Rev.*, **123**, 1245 (1961).
6. K. Hubner and W. Shockley, "Advanced Energy Conversion," Vol. 1, p. 93, Pergamon Press, Great Britain (1962).
7. A. Goetzberger and C. Stephens, *J. Appl. Phys.*, **32**, 2646 (1961).
8. W. Hooper and H. J. Queisser, *Bull. Am. Phys. Soc.*, **7**, 211 (1962).
9. J. Czochralski, *Z. physik. Chem.* **92**, 219 (1917).
10. W. C. Dash, *J. Appl. Phys.*, **29**, 736 (1958).
11. W. C. Dash, *ibid.*, **30**, 459 (1959).
12. W. C. Dash, *ibid.*, **31**, 736 (1960).
13. H. F. Mataré and H. A. R. Wegener, *Z. Physik*, **148**, 631 (1957).
14. H. J. Queisser, Unpublished work.
15. W. Kaiser and P. H. Keck, *J. Appl. Phys.*, **28**, 882 (1957).

The Effect of Hydrogen Reduction on the Morphology of Copper Oxide Whiskers

William R. Lasko and Warren K. Tice

Research Laboratories, United Aircraft Corporation, East Hartford, Connecticut

ABSTRACT

A series of closely controlled experiments was conducted to determine the effect of hydrogen reduction on the morphology of oxide whiskers formed on unannealed and preannealed copper. Initial reduction occurred along random sites at the whisker surface. No preferential reduction at the whisker tip was observed. During the reduction cycle, the whiskers collapsed to form small irregularly shaped high-opacity nodes. Some differences were observed in the rate and manner in which the whiskers reduced on the unannealed and preannealed samples which were attributed to initial variations in size and shape of the whiskers. Selected area diffraction analyses of the reduced products revealed that the whiskers changed from CuO to Cu_2O and then to Cu. Cu_2O appeared to form adjacent to the metal surface.

Replica examinations of the oxidized-reduced surfaces when compared with replicas of the original surface revealed considerable surface rearrangement with the formation of subgrain-type structure. The size of the subgrains formed on the preannealed sample appeared to be smaller than that obtained on the unannealed sample. In most cases, the reduced oxide whisker growth products appeared to emanate from subgrain boundary intersections rather than from subboundary interiors.

Unusual growth products resembling needles, blades, serrated blades, etc., have been observed by many workers in the oxidation of metals (1-3). In most cases the growths have been identified by x-ray and electron diffraction techniques to be oxides of the base metal. The whisker shape, in some instances, has been related to the pretreatment given the metal (4) and the environment (5). The exact mechanism

by which this growth occurs is still quite obscure. Some investigators have postulated growth from the base (6) while others have indicated that growth occurs from the tip (7). To date, not too much work has been done on the effect of a reducing atmosphere on whisker morphology, particularly to determine how and where the reduction process is initiated on the whisker surface. A common assumption, although infrequently supported by experimental evidence, is that reaction occurs at dislocation sites. Unquestionably, whiskers grow by many different mechanisms and may even grow at both ends at once.

Since copper oxide is readily reduced by hydrogen at relatively low temperatures, a systematic series of experiments was conducted to determine the effect of hydrogen on the morphology of the oxide growth products. Particular emphasis in this study was directed toward determining the site or sites of initial reduction. In addition, an attempt was made to detect differences in reactivity between the whiskers formed on the cold-rolled and preannealed samples, since previous studies (8) have indicated that whiskers formed on cold-rolled copper are somewhat different in size and shape from whiskers grown on preannealed copper. Electron transmission replication and diffraction techniques were employed to evaluate the various reaction products critically.

Experimental Procedure

The copper oxide whiskers used in the reduction experiments were grown by a technique previously described (4). Briefly, high-purity (99.999%) cold-rolled and preannealed slotted copper disks (0.3 cm diameter) were oxidized in air. The disks were held in porcelain boats at a temperature of 400°C for 1 hr and whiskers were formed in the area of the slot. The annealed specimens were prepared by heat treating the cleaned, slotted disks at 450°C for 4 hr. In order to insure that the copper disks were not oxidized during the annealing step, standard precautions such as flowing argon gas over the disks prior to reaching the annealing temperature and maintaining the gas flow while the specimens were being cooled to room temperature were exercised.

Chemical reduction of the oxide growths was conducted in a specially designed tubular furnace. The whisker-coated disks were held in porcelain boats and reduced by flowing dry high-purity (99.995%) hydrogen over the boats at a rate of ~0.98 l/min. The hydrogen was dried by flowing the gas through a drying column containing indicating-type Drierite. The reaction time was varied from 1 min to 2 hr while the reaction temperature was maintained at 200° ± 2°C. Examinations were made of various specimens at various phases of reduction, but only micrographs necessary for clarity are illustrated in this paper.

Electron optical studies were performed to detect the reaction products in the area of the slot as well as the top surface of the disk as shown in Fig. 1 for both the unannealed and preannealed samples. Transmission techniques were employed primarily to detect the effect of hydrogen reduction on whisker morphology during reduction and, in particular, to determine the site or sites of initial reaction. Negatives were taken at electronic magnifications of 3000X. Prints were made by optical enlargement to 5000X and 25,000X.

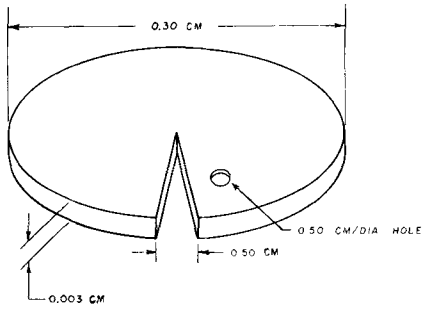

Fig. 1. V-slot copper specimen. (Not to scale)

Replicas were made of the unannealed and preannealed disk surfaces prior to oxidation and after reduction of the oxidized surface using the direct carbon-chromium, post-shadowed, and preshadowed replica techniques. High-purity, reagent-grade nitric acid was employed as the solvent for copper. Both negative and positive replicas of the oxidized-reduced surfaces were prepared. All replica micrographs were processed to the negative print stage in an attempt to simplify the interpretation of the various surface features.

Selected area diffraction analyses were conducted at various stages of the reduction cycle to ascertain the structure of the reduction products. In order to improve the accuracy of determining the lattice constants of the reduced products utilizing the selected area diffraction attachment, a method was devised for incorporating an internal standard. A small hole was punched in the area of the slot as shown in Fig. 1. After the disks were oxidized and reduced, Mg ribbon was ignited and the MgO smoke was collected along the sides of the holes. An appropriate mask was employed to restrict the deposition of the smoke to the region of the hole only. Selected area diffraction patterns were taken of the reduced products formed in the area of the slot. Without changing any of the instrumental dial settings (intermediate current, high voltage, objective current, etc.), the specimen stage was moved into the MgO-coated area and the diffraction pattern was photographed in an identical manner. The lattice constants of the oxidized-reduced products were then determined in terms of the instrumental correction factor established from the MgO standard as was previously described in ref (9).

Results and Discussion

Three methods (transmission, replication, and selected area diffraction) were used to evaluate the effect of hydrogen on the morphology of the oxide whiskers formed on unannealed and preannealed copper. Particularly, it was of interest to determine by high magnification microscopy the site or sites of initial reduction on the oxide whiskers. In addition, an attempt was made through the application of replication techniques to determine the whisker growth site as well as to determine differences in surface rearrangement produced by the oxidation-reduction

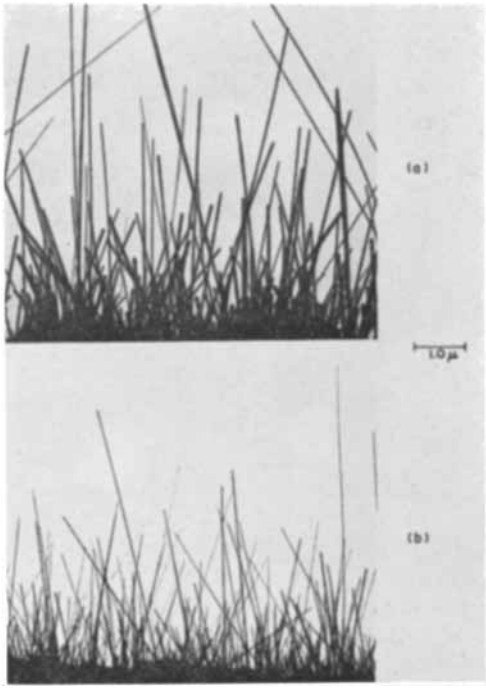

Fig. 2. Copper oxide whiskers grown in dry air for 1½ hr at 400°C: (a) unannealed; (b) preannealed. Magnification 5000X.

treatment on copper samples which were unannealed and preannealed.

Transmission.—Typical whisker growths induced on unannealed and preannealed copper after exposure to dry air for 1½ hr at 400°C are shown in Fig. 2a and 2b. The oxide whiskers formed at this temperature on the unannealed sample are normally thicker than the whiskers obtained on the preannealed samples as indicated in the electron micrographs. After exposure to dry hydrogen for 1 min at 200°C (Fig. 3a and 3b), the oxide whiskers show

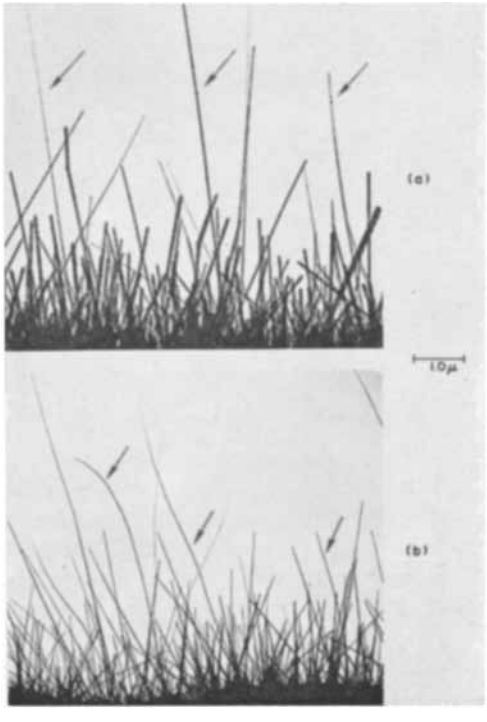

Fig. 3. Copper oxide whiskers reduced in hydrogen for 1 min at 200°C: (a) unannealed; (b) preannealed. Magnification 5000X.

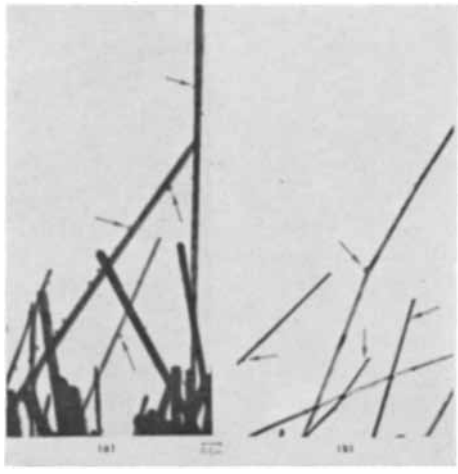

Fig. 4. Copper oxide whiskers reduced in hydrogen for 1 min at 200°C: (a) unannealed; (b) preannealed. Magnification 25,000X.

some evidence of attack at the whisker sides (revealed by untailed arrows). The attack apparently occurs more or less randomly along the whisker sides, and no preferential attack at the tip was indicated. Further examination (Fig. 4a and 4b) of some specimens at higher magnifications (25,000X) revealed that the attack proceeds with the formation of small high-capacity nodules (shown by untailed arrows) of varying size and shape along the whisker sides. No difference could be detected between the unannealed and preannealed samples, particularly in the degree of surface attack.

The micrographs in Fig. 5 illustrate the change in whisker morphology after exposure in hydrogen from 16 min to 2 hr. The amount of whisker collapse is shown to increase with time of exposure to hydrogen for both the whiskers formed on the unannealed and preannealed samples. However, the oxide whiskers grown on the preannealed sample appeared to collapse faster than the whiskers formed on the unannealed specimens. This observation is to be expected since the whiskers grown on the former are

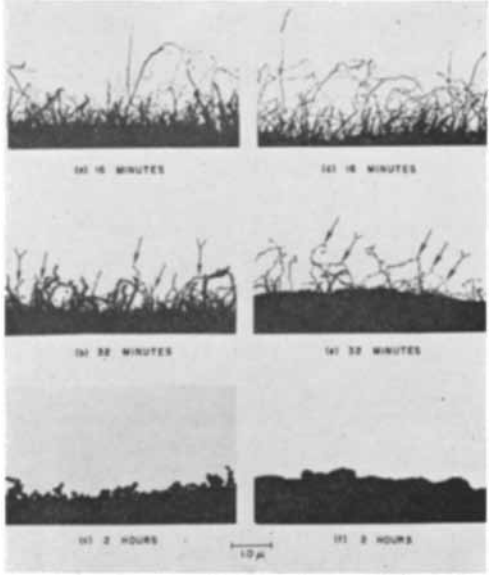

Fig. 5. Copper oxide whiskers reduced in hydrogen at 200°C for varying periods of time: (a-c) unannealed; (d-f) preannealed. Magnification 5000X.

Table I. Electron diffraction analysis of reduction products

Lattice spacings (dA) of products formed on unannealed samples for the indicated times					Literature spacings from ASTM Card File		
Prior to reduction	1 min	16 min	32 min	2 hr	CuO	Cu_2O	Cu
		3.03-S	2.98			3.02	
2.73-S	2.76-S	2.79			2.75		
2.52-S	2.54-S				2.52-S		
		2.50-S	2.46-S			2.47-S	
2.33-S	2.34-S	2.33			2.33-S		
	2.12	2.12-S				2.13-S	
			2.07-S	2.10-S			2.09-S
1.89	1.91	1.88			1.86-S		
			1.81	1.79-S			1.81-S
1.74		1.74				1.74	
	1.67				1.71		
1.58	1.55				1.58		
				1.55		1.51	
1.50-S	1.52	1.50-S	1.50-S		1.50-S		
1.41-S	1.42-S				1.42		
1.35	1.37				1.35		
1.30	1.32				1.30		
1.25	1.26	1.28-S	1.27-S	1.28	1.26	1.28	1.28-S
1.14	1.16				1.15		
	1.08		1.07	1.09			1.09
1.03			1.01		1.04		1.04
0.92					0.92		
CuO	CuO + Cu_2O	Cu_2O + CuO + Cu	Cu_2O + Cu	Cu + Cu_2O			

normally thinner and longer than those grown on the latter. Further evidence of some difference in reactivity between the unannealed and preannealed samples is shown in Fig. 5c and 5f where the reduction time was increased to 2 hr. The unannealed sample still reveals small, irregular, high-opacity nodules projecting out from the surface while the preannealed sample reveals only minor variations in surface roughness.

Selected area diffraction.—Tables I and II contain lattice spacing data obtained by application of the selected area diffraction technique to the various oxidized-reduced products at different stages of the reduction cycle. The tables also list the literature *d* spacings for CuO, Cu_2O, and Cu obtained from the ASTM card file. To simplify the interpretation of the data, all high intensity lines are designated by the letter "S". In all the diffraction analyses, the selected area diffraction leaves were kept relatively close together to insure that the resulting pattern was restricted to the whisker reaction products rather than to the base oxide. In the sample that was reduced for

Table II. Electron diffraction analysis of reduction products

Lattice spacings (dA) of products formed on preannealed sample for the indicated times					Literature spacings from ASTM Card File		
Prior to reduction	1 min	16 min	32 min	2 hr	CuO	Cu_2O	Cu
		3.04-S	3.04			3.02	
2.73-S	2.73-S				2.75		
2.52-S	2.52-S				2.52-S		
		2.50-S	2.48-S			2.47-S	
2.33-S	2.32-S		2.32		2.33-S		
	2.14	2.15-S	2.14-S	2.15		2.13-S	
1.88	1.88				1.86-S		
	1.78	1.78		1.80-S			1.81-S
			1.75			1.74	
1.73	1.73				1.71		
1.58					1.58		
			1.51-S	1.55		1.51	
1.52-S	1.52-S	1.52-S			1.50-S		
1.42-S	1.43-S		1.40		1.42		
1.36					1.35		
		1.29-S	1.28-S	1.29-S		1.28	1.28-S
		1.24			1.26		
			1.13		1.15		
		1.09		1.10			1.09
			1.04	1.04	1.04		1.04
			0.95	0.96		0.95	
		0.91	0.93		0.92		
CuO	CuO + Cu_2O	Cu_2O + CuO + Cu	Cu_2O + Cu	Cu + Cu_2O			

2 hr (Fig. 5c and 5f), the reduced products were quite small; consequently, some of the base surface was also included in the field made available by the diffraction leaves.

Prior to reduction, the whiskers show primarily the CuO structure. After reduction for 1 min, trace amounts of Cu_2O were observed, while after 16 min the intensity of the Cu_2O lines became more pronounced. However, no strict comparison between the observed and literature intensities can be made since anomalous intensities are encountered in electron diffraction. Further reduction for 32 min resulted in a mixture of CuO, Cu_2O, and Cu, with Cu_2O being the predominant oxide. Final reduction for 2 hr showed copper as the major constituent with only trace amounts of Cu_2O. No differences in structure could be detected in the reduced products formed on either the unannealed or preannealed samples.

From these diffraction results, it would appear that the oxide whisker growths initially reduce from CuO to form Cu_2O and then ultimately from Cu_2O to Cu. It is suspected that the small spherical opaque-shaped droplets (shown by untailed arrows in Fig. 5b and 5e) are Cu, with the remaining portion of the collapsed whisker (shown by tailed arrows) being a mixture of Cu_2O and CuO. Since trace amounts of Cu_2O were present even after 2 hr of reduction, it would appear that in the reduction process of the mixed oxides (CuO and Cu_2O), Cu_2O is the final oxide to be reduced to Cu. CuO is the principal oxide component in the whiskers.

Replication.—In electron transmission studies of specimens of the type shown in Fig. 1, particularly in the area of the slot which exhibits considerable depth to the electron beam, it is possible to obtain a false impression of the over-all product distribution. This is attributed to the large depth of field in the electron microscope where the maximum thickness permissible for specimens in electron microscopy is normally less than the depth of field. As a result, relatively sharp images of the reduced-oxide products will be obtained regardless as to where the products are situated in relation to the object plane of the specimen. In order to offset this problem, particularly in determining the manner in which the oxidized-reduced products are distributed, a direct carbon replica technique was utilized. Typical electron micrographs of the unannealed and preannealed surfaces prior to the oxidation-reduction treatment prepared by the positive replica technique are shown in Fig. 6. The unannealed sample (Fig. 6a) reveals considerable surface roughness such as striations and pitting possibly instituted by the cold-rolling process. On the other hand, the preannealed surface (Fig. 6b) is relatively free of pits, but numerous surface striations are still evident. The formation of what appear to be subgrains (shown by untailed arrows) is also revealed.

After subsequent oxidation at 400°C in air for 1½ hr and reduction in hydrogen for 2 hr at 200°C, considerable alteration of the surface topography had occurred for both the unannealed and preannealed samples, Fig. 7. The hydrogen-reduced topography of the unannealed sample shown in Fig. 7a no longer resembles the surface prior to oxidation (Fig. 6a). Large grain boundaries as well as surface striations are no longer evident. Instead "patch-like" areas which may be subgrains ranging in size from ~0.1 to 1.0μ are readily visible. Metal-coated carbon shells (light areas on the micrograph) of the reduced oxide whisker growth products are distributed randomly over the surface. From the size of the shells it would appear these represent clusters of reduced-oxide whisker growths (Fig. 5c) rather than individual whiskers. In some instances the shells cast shadows (illustrated by an untailed arrow) indicating these regions are elevations. In other areas the shadows are on opposite sides of the shells indicating that some of the shells may represent depressions. It is more probable that these shells are located in the valleys between two subgrains and consequently receive no metal during shadow casting. Similar type structures can be observed in the reduced oxidized surface of the preannealed sample (Fig. 7b). However, the size of the subgrains on the preannealed sample appears somewhat smaller. Close inspection of the micrograph also reveals that the shells appear to emanate from subgrain boundary intersections. Fur-

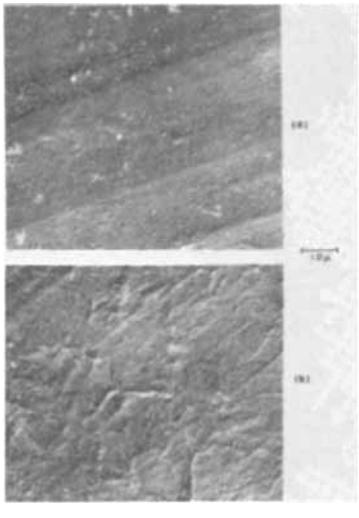

Fig. 6. Positive carbon replicas of copper surfaces prior to oxidation-reduction treatment: (a) unannealed; (b) preannealed. Magnification 5000X.

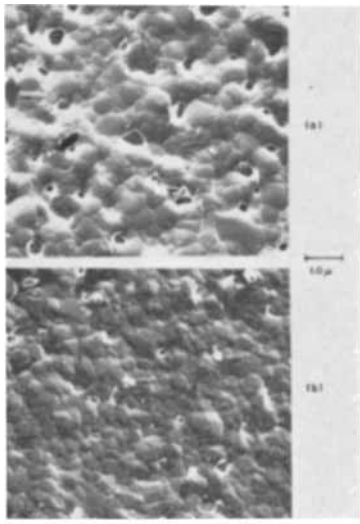

Fig. 7. Positive carbon replicas of oxidized-reduced copper surfaces: (a) unannealed; (b) preannealed. Magnification 5000X.

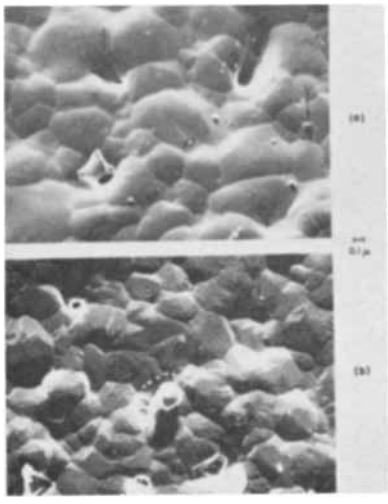

Fig. 8. Positive carbon replicas of oxidized-reduced copper surfaces: (a) unannealed; (b) preannealed. Magnification 13,300X.

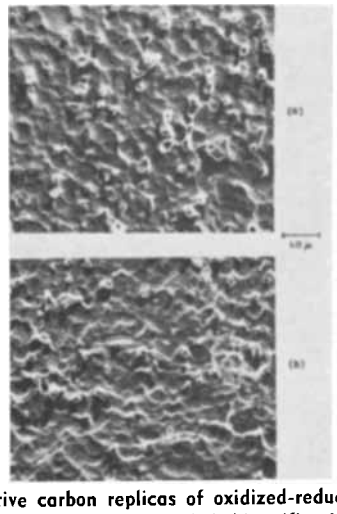

Fig. 9. Negative carbon replicas of oxidized-reduced copper surfaces: (a) unannealed; (b) preannealed. Magnification 5000X.

ther examination of the micrographs particularly at the shell-subgrain interfaces reveals that the subgrains appear to form around the reduced whisker growth products and definite interface boundaries are formed. It is not conclusively known whether the whiskers and the base oxide reduce in a similar manner. However, it is suspected that the physical processes (liberation of copper from the lattice of the oxide and subsequent condensation of the copper atoms to produce the rearrangement of the surface) occurring in the reduction rearrangement of the whiskers are somewhat different from those occurring in the base oxide. Otherwise, if the physical processes of reduction were similar for both the whiskers and base oxide, it would be reasonable to expect that there would be no resolvable differences in topography between the reduced-oxide whisker sites and the base oxide subgrain boundaries.

High magnification examinations (Fig. 8) (13,300X) of the same surfaces further reveal the extent of the surface rearrangement resulting from the reduction treatment. At this magnification the characteristic subgrain structure with the carbon shells of the reduced whisker products is clearly revealed. Projections (shown by tailed arrows) are easily distinguished from the depressions (shown by untailed arrows). Some subboundary migration is also indicated (open untailed arrows). Close examination of the shell-type structures also reveals that the carbon layer around the depressions and elevations has partially collapsed accounting to some extent for the unusual shapes. The lack of shadows behind some of the shells (shown by untailed arrows) is believed to be caused by the variation in topography of the subgrains. The reduced oxide whisker products in this case are emanating from a valley between a cluster of subgrains whose faces are relatively normal to the electron beam. As a result, during the preshadowing step employed in the preparation of the direct positive carbon replica, these areas would receive no metal and appear as depressions.

To substantiate these observations, negative replicas were prepared of the same specimens. In this technique, since it represents a reverse of the true surface, the low regions between subgrains should cast shadows while the narrow valleys would appear as wavy white lines. From the micrographs shown in Fig. 9, it would appear that these observations have been substantiated. The white outlines surrounding the reduced-oxide whisker products represents a long dimension of carbon or carbon and metal to the electron beam. At these regions on the replica, increased inelastic scattering occurs accounting for the abrupt change in photographic density observed on the micrographs. In addition, when comparing the distribution of reduced-oxide products (Fig. 5c and 5f with Fig. 7a and 7b), it would appear that product distribution shown by the shadow images in Fig. 5c and 5f are somewhat exaggerated.

Conclusions

From these studies it has been demonstrated that both transmission and replication electron microscopy are required to define completely the manner in which the oxide growth products reduced on copper. The studies have shown that the oxide whiskers reduce more or less randomly at the sides with no indication of preferential reduction at the tip. On this basis, one could perhaps conclude, if the assumption is made that the reaction occurs more readily at a dislocation site, that the mechanism of growth in this case was basal growth rather than growth from the tip. This assumption is based on the proposition that a growth step exists at the whisker tip. In order for the tip growth mechanism to be operable, it is required that the whisker tip be a much better heat sink for the oxidation products than the whisker sides or the base oxide layer. However, this is purely a qualitative assumption which is difficult to prove experimentally. There is also some probability that the oxidation growth and reduction processes are not morphologically equivalent. On this basis the transport mechanisms for the oxidation and reduction processes would be dissimilar, and no quantitative conclusions for the failure to observe reduction at the tip can be made.

The observation that reduction occurred along the whisker sides may indicate the formation of defects, such as growth steps, whereby reduction occurs preferentially. However, transmission and replication examinations of individual whiskers revealed rela-

tively smooth surfaces. It is interesting to note in the replica examinations of the oxidized-reduced surfaces that the reduced products appeared to emanate from subgrain boundary intersections rather than from the interior. This is understandable since a greater concentration of dislocations is expected at the boundaries than at the interior of the grains. It is hoped through the controlled oxidation and reduction of thin metallic foils, planned for the future, that the role of specific dislocations in the whisker growth process and the nature of the growth site will be more clearly defined.

Manuscript received April 27, 1962; revised manuscript received July 18, 1962.

Any discussion of this paper will appear in a Discussion Section to be published in the June 1963 JOURNAL.

REFERENCES

1. S. E. Koonce and S. M. Arnold, *J. Appl. Phys.*, **25**, 365 (1953).
2. E. A. Gulbransen, T. P. Copan, and K. F. Andrew, *This Journal*, **108**, 119 (1961).
3. E. A. Gulbransen and T. P. Copan, *Discussions Faraday Soc.*, **28**, 229 (1960).
4. W. R. Lasko, *J. Electron Micros.*, **10** (1961).
5. W. R. Lasko and W. K. Tice, *Corrosion*, **18**, 116 (1962).
6. S. E. Koonce and S. M. Arnold, *J. of Appl. Phys.*, **25**, 134 (1954).
7. G. W. Sears and R. V. Coleman, *J. Chem. Phys.*, **25**, 635 (1956).
8. W. R. Lasko and W. K. Tice, *This Journal*, **109**, 211 (1962).
9. G. R. Grieger, ASTM Special Technical Publication No. 262, 77 (1959).

High-Temperature Electrical Conduction in the System UO_2-ZrO_2

H. A. Johansen and J. G. Cleary

Research Laboratories, Westinghouse Electric Corporation, Pittsburgh, Pennsylvania

ABSTRACT

A method for determining the a-c electrical conductivity of ceramic oxides to 2000°C in neutral atmosphere is described. The electrical conduction of the system UO_2-ZrO_2 is investigated. All compositions of $(UO_2)_x$ $(ZrO_2)_{1-x}$, where $0.1 \leq x \leq 0.9$, show two modes of conduction: a low-temperature region below about 1100°C with an activation energy of 0.26 ev, and a high-temperature region with an activation energy of about 1.59 ev.

The property of electrical conduction in refractory ceramic oxides has been a relatively neglected study until recent years. High-temperature measurements, in particular, have been scanty and the results frequently conflicting.

It was the purpose of the present investigation to develop a technique for measuring electrical conductivity to 2000°C and to use this technique to examine the electrical behavior of a ceramic oxide system which combined both wholly ionic and wholly electronic type conduction. The system UO_2-ZrO_2 was chosen because no previous high-temperature conductivity data were available for this system, and recent published work on UO_2 and on CaO stabilized ZrO_2 afforded a convenient starting point.

The high-temperature electrical conductivity of $(CaO)_{0.15}(ZrO_2)_{0.85}$ has been measured by Kingery, Pappis, Doty, and Hill (1), and their results indicated that over the range 700°-1725°C the conductivity, σ, could be represented by the relation

$$\sigma = 1.50 \times 10^8 \exp\left(\frac{-1.26}{kT}\right) \qquad [1]$$

where k is the Boltzmann constant and T the absolute temperature. Measurements of the conductivity under varying partial pressures of oxygen indicated no dependence on oxygen pressure; hence conduction in $(CaO)_{0.15}(ZrO_2)_{0.85}$ was judged to be due to the presence of oxygen ion vacancies, the number of which is fixed by the composition.

The case for the conductivity of UO_2 is less clear. Willardson, Moody, and Goering (2) have summarized the more recent data on the electrical conductivity of UO_2. The electrical properties of nonstoichiometric UO_2 have been studied in a recent paper by Aronson, Rulli, and Schaner (3). The material behaves as an amphoteric semiconductor; that is, the sign of the current carrier may be plus or minus depending on the composition. Nonstoichiometric UO_2 is therefore an electronic conductor. The sensitivity of the electrical conductivity to a variety of factors is attested to by the wide variations in conductivity values reported in the literature.

Experimental

Material.—Materials used were a commercial grade ZrO_2 with an analysis of 99.8% $ZrO_2 + HfO_2$ with Cu, Ti, and Fe as principal impurities. Hafnium was determined to be about 1%. The UO_2 was prepared from U_3O_8 by hydrogen reduction. Analysis showed UO_2 to be 99.9% with Si as chief impurity. No special attempt was made to avoid the slight oxidation of UO_2 attending the mixing and briquetting operations prior to the firing of the UO_2-ZrO_2 specimens in argon. However, there is no question that some slight oxidation occurred so that the initial firing composition of urania should properly be referred to as UO_{2+x}. X-ray diffraction patterns for the UO_2 showed only the cubic phase and an $a_o = 5.466$Å.

Preparation of specimens.—The mixed powders were pressed in carbide dies at approximately 50,000

psi with no binder, and the briquets were fired in argon in a split graphite resistor furnace to 1900°C for approximately 15 min. The fired briquet was then ground, re-pressed, and refired as before. This procedure produced a well-sintered cylinder 1 x 2 cm with densities between 65% and 70% of theoretical.

The sintered briquets were then coated on the ends to obtain a low ohmic contact. This was done in two ways, either of which appeared to be satisfactory: a coating of $TaSi_2$ was applied by means of an argon plasma jet, or a coating of platinum could be obtained by painting on platinum paste.

X-ray diffraction.—X-ray powder diffraction patterns were obtained for all compositions of $(UO_2)_x(ZrO_2)_{1-x}$ prepared. The pattern for $x = 0.1$ showed what appeared to be a cubic phase plus traces of monoclinic ZrO_2. At $x = 0.15$ only the cubic phase was obtained. However, published phase diagrams indicate that the first phase formed is actually a face-centered tetragonal phase with c/a ratio nearly equal to one. At $x = 0.2$ a second phase was detected by the presence of a slight splitting of the lines. This indicated the phase boundary between the face-centered tetragonal and the face-centered cubic plus face-centered tetragonal region. The two phase region then continued to about 70 mole % UO_2. From $x = 0.7$ to 1 the patterns showed the face-centered cubic structure of UO_2.

Electrical conductivity measurements.—Measurements were carried out from room temperature to 2000°C. The range from room temperature to 1000°C was obtained using a conventional split tube furnace and argon atmosphere. The range from 800° to 2000°C was obtained by use of a split graphite resistor furnace with argon atmosphere. Temperature in the lower range was measured by thermocouple and in the higher range by optical pyrometer.

Alternating current conductivity measurements were made using a General Radio Impedance Bridge, Type 1650-A. This instrument gave satisfactory readings on the oxides down to approximately 0.2 ohm-cm.

In order to establish the reliability of the measuring apparatus, the conductivity of $(CaO)_{0.15}(ZrO_2)_{0.85}$ was determined to 2000°C. The plot of the logarithm of the electrical conductivity *vs.* the reciprocal temperature gave a straight line which was represented by the relation

$$\sigma = 1.27 \times 10^3 \exp \frac{-1.26}{kT} \qquad [2]$$

Our value for the activation energy, 1.26 ev, agrees directly with the value of Kingery, Pappis, Doty, and Hill (1) as shown in Eq. [1]. Our somewhat lower pre-exponential term probably reflects the lower density of the specimens. Since quite similar results were obtained using different methods of preparation, the apparatus and techniques were considered provisionally satisfactory.

Results and Discussion

Figure 1 shows the plot of the logarithm of the conductivity *vs.* the reciprocal temperature for the composition $(UO_2)_{0.1}(ZrO_2)_{0.9}$, and for comparison, the composition $(CaO)_{0.15}(ZrO_2)_{0.85}$. The curve for

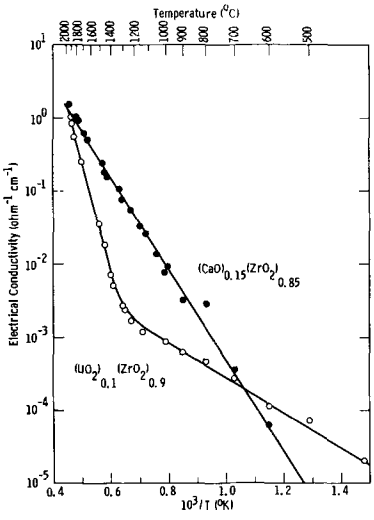

Fig. 1. Electrical conductivity for $(UO_2)_{0.1}(ZrO_2)_{0.9}$ and $(CaO)_{0.15}(ZrO_2)_{0.85}$.

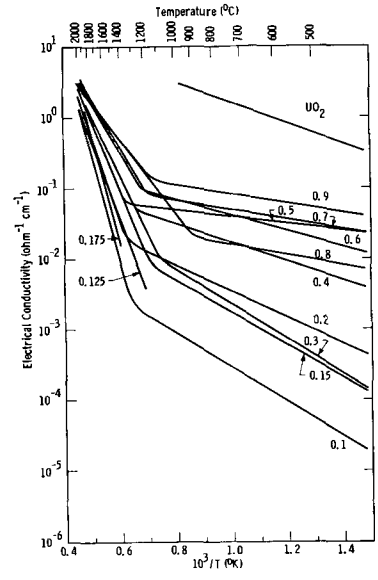

Fig. 2. Electrical conductivity for $(UO_2)_x(ZrO_2)_{1-x}$

$(UO_2)_{0.1}(ZrO_2)_{0.9}$ is seen to consist of two straight line portions which intersect near 1200°C. This behavior is typical for all compositions $(UO_2)_x(ZrO_2)_{1-x}$ where $0.1 \leq x \leq 0.9$.

Figure 2 shows the straight lines from the plot of the log conductivity *vs.* reciprocal temperature for the curves for $(UO_2)_x(ZrO_2)_{1-x}$ for x values of 0.1 to 1. While the progression is not perfect, it can be seen that the conductivity in the lower temperature region ranges steadily upward with increasing x. Conduction in the high-temperature region is also higher with increasing x. The variations from a direct progression in both high- and low-temperature regions may possibly be ascribed to variations in oxygen stoichiometry in UO_2, which are reported (2, 3) to influence profoundly the electrical properties.

From the slopes of the straight line portions of the data plotted in Fig. 2, the activation energy for each composition was calculated and the results are shown in Fig. 3 where the activation energy and logarithm of the conductivity at two temperatures are plotted *vs.* the composition. With increasing UO_2 content the

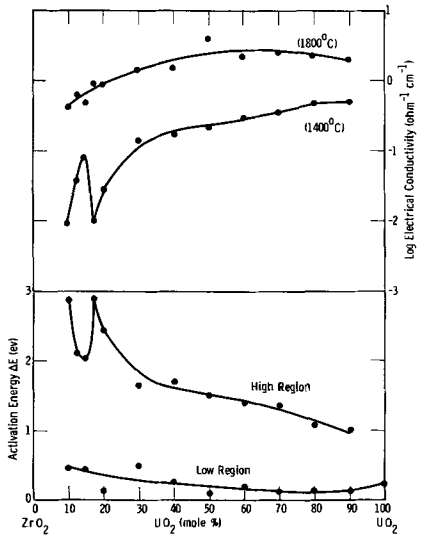

Fig. 3. Results of calculation of activation energy for each composition, from data plotted in Fig. 2.

activation energy in the high region falls sharply from 2.9 ev to a minimum of about 2 ev at 15 mole % UO_2, rises sharply again to another maximum 2.9 ev at 17.5 mole %, then falls steadily to a value of 1 ev at 90 mole % UO_2. In the low region the activation energy falls off gradually from about 0.5 ev at 10 mole % UO_2 to 0.26 ev for pure UO_2. This value for the activation energy of UO_2, 0.26 ev, agrees reasonably well with the 0.30 ev activation energy in the single phase UO_{2+x} region found by Aronson, Rulli, and Schaner (3).

The plot of the logarithm of the conductivity at 1400°C *vs.* composition in Fig. 3 shows corresponding changes with the changes in the activation energy, *i.e.*, the conductivity rises to a maximum simultaneous with the fall to a minimum in the activation energy at 15 mole % UO_2, then falls to a minimum, again corresponding to the maximum in the activation energy at 17.5 mole % UO_2. The conductivity then steadily rises to its highest value at 90 mole % UO_2. At 1800°C, the conductivity curve is much smoother, rising to an apparent maximum at about 50 mole % of UO_2, and without the pronounced maximum-minimum in the 15 mole % UO_2 region at 1400°C.

The problem of the abrupt change in slope often observed in plots of log conductivity *vs.* reciprocal absolute temperature has been examined in detail by Mitoff (4) for the case of the electronic conductor NiO. It is possible that the argument for the abruptly changing slope in NiO applied as well to the UO_2-ZrO_2 system. Our results for UO_2 (in argon), however, do not show an abrupt change in slope up to 1400°C, nor is a change in slope observed in the system CeO_2-ZrO_2 up to 1200°C as reported by Pal'guev and Volchenkova (5). However, time-temperature dependent effects in the UO_2-ZrO_2 system may be a factor and should be considered.

Considering the data as presented in Fig. 2, the tendency is very strong to believe the conduction mode in the high-temperature region, with its high activation energy, to be principally ionic. However, if the mode of conduction in the high-temperature region is ionic and proceeds by oxygen vacancy, then some other mechanism of producing oxygen vacancies in the ZrO_2 fluorite lattice must be found than the mechanism proposed for $(CaO)_{0.15}(ZrO_2)_{0.85}$: that is, oxygen vacancy production by substitution of divalent Ca ions in the zirconium lattice, thus upsetting the charge balance. In the case of UO_2, the substitution of tetravalent U in the zirconium lattice would produce no charge imbalance.

However, we may consider that the total conductivity, σ, in $(UO_2)_x(ZrO_2)_{1-x}$, $(0.1 \leq x \leq 0.9)$ is composed of the low-temperature conductivity, σ_L, where

$$\sigma_L = A_L \exp -\frac{\Delta E_L}{kT} \qquad [3]$$

and the high-temperature conductivity σ_H, where

$$\sigma_H = A_H \exp -\frac{\Delta E_H}{kT} \qquad [4]$$

In these equations A_L, A_H, ΔE_L, and ΔE_H are constants, k is the Boltzmann constant, and T is the absolute temperature. For Eq. [3] the average value for ΔE_L is found to be 0.26 ev, which is also the identical value found for UO_2. This also corresponds to the activation energy for electronic conduction in UO_{2+x} (3), but there is no indication as to the possible contribution from the ionic mode. The pre-exponential term A_L is found to be between 1 and 10^{-1}, in fair agreement with values determined from ref. (2).

For Eq. [4] an average value for ΔE_H is found to be 1.59 ev. While this corresponds to the activation energy for ionic conduction in calcia stabilized ZrO_2, again we have no indication as to the possible contribution from the electronic mode. The pre-exponential term A_H is found to show a wide scatter with values between 10^3 and 10^6, and thus is higher than the value of about 10^3 found for $(CaO)_{0.15}(ZrO_2)_{0.85}$.

The peculiar behavior of the conductivity at 1400°C in the 15 mole % UO_2 region as shown in Fig. 3 cannot as yet be explained. Repeated measurements in this region indicate, however, that the pronounced maximum-minimum at 15 and 17.5 mole % UO_2, respectively, are real. It may be possible that the variations at 1400°C are associated with phase changes, or ordering. Such a maximum-minimum in the conductivity is also shown in the systems CaO-ZrO_2 and La_2O_3-ZrO_2 as reported by Trombe and Foex (6, 7) and at the same 15 mole %. However, it cannot yet be decided whether the maximum at 15 mole % UO_2 at 1400°C in the UO_2-ZrO_2 system is associated with the stabilization of the tetragonal phase, or with the appearance of the two phase region at $x = 0.2$, or with an ordering phenomenon. The same fluctuations do not appear at 1800°C, and this may indicate that the upper consolute phase boundary suggested by Wolten (8) has been exceeded.

In summary, a method has been described for obtaining the a-c electrical conductivity to 2000°C in inert atmosphere for various ceramic oxides. The method gave good agreement with values obtained by other investigators for CaO stabilized ZrO_2.

The system $(UO_2)_x(ZrO_2)_{1-x}$ ($0.1 \leq x \leq 0.9$) has been found to exhibit two modes of electrical conduction: a low-temperature region (below about 1200°C) which obeys approximately the relation

$$\sigma_L = 5 \times 10^{-1} \exp - \frac{0.26}{kT}$$

and a high-temperature region (1200°-2000°C) which obeys approximately the relation

$$\sigma_H = (10^3 \text{ to } 10^6) \exp - \frac{1.59}{kT}.$$

Acknowledgment

Acknowledgment for helpful discussions is made to J. Weissbart and R. Hooke.

Manuscript received Jan. 15, 1962; revised manuscript received May 31, 1962. This paper was prepared for delivery before the Detroit Meeting, Oct. 1-5, 1961.

Any discussion of this paper will appear in a Discussion Section to be published in the June 1963 JOURNAL.

REFERENCES

1. W. Kingery, J. Pappis, M. Doty, and D. Hill, *J. Am. Ceram. Soc.*, **42**, 393 (1959).
2. R. Willardson, J. Moody, and H. Goering, *J. Inorg. Nucl. Chem.*, **6**, 19 (1958).
3. S. Aronson, J. Rulli, and B. Schaner, *J. Chem. Phys.*, **35**, 1382 (1961).
4. S. Mitoff, *ibid.*, **35**, 882 (1961).
5. S. Pal'guev and Z. Volchenkova, *Russian J. Phys. Chem.*, **34**, 211 (1960).
6. F. Trombe and M. Foex, *Comptes rend.*, 1783 (1953).
7. F. Trombe and M. Foex, *J. Recherches CNRS*, 1 (1951).
8. G. Wolten, *J. Am. Chem. Soc.*, **80**, 4772 (1958).

The Existence and Formation of the Solid B_6O

H. F. Rizzo, W. C. Simmons, and H. O. Bielstein

Aeronautical Research Laboratories, Office of Aerospace Research, United States Air Force, Wright-Patterson Air Force Base, Ohio

ABSTRACT

The suboxide of boron, B_6O, has been prepared as a pure crystalline powder and in dense solid masses. The existence of B_6O was substantiated from crystallographic, chemical, and density data. Information on x-ray diffraction, chemical formation, oxidation resistance, and stability is also described. B_6O was found to have a greater diamond pyramid hardness than boron carbide.

Studies in this Laboratory on the oxidation of boron and the reactions in the Si-B-O system have revealed the existence of a crystalline suboxide of boron which has been identified as B_6O.

A number of investigations on the B-O system have been on the detection and identification of vapor species. Inghram, Chupka, and Porter (1) reported that between 1300° and 1500°K the major gaseous species above $B_2O_3 + B$ was $B_2O_{2(g)}$. Another gaseous species recently reported on by Kaskan, Mackenzie, and Millikan (2) is $BO_{2(g)}$. Although the condensed suboxides of boron, B_7O, B_6O, B_5O, B_3O, and BO, have been mentioned briefly in the literature only the existence of BO has been established. Wartik and Apple (3) prepared $BO_{(s)}$ by dehydration of $B_2(OH)_4$ *in vacuo*, and Kanda *et al.* (4) prepared it by reacting $B_2O_3 + B$ at 1050°C *in vacuo*. This solid amorphous suboxide was reported to decompose at 450°C. The other suboxide of boron mentioned frequently in the literature is B_7O which was reported some fifty years ago by Weintraub (5). He prepared the suboxide by the reduction of B_2O_3 with Mg. This suboxide was frequently referred to as "Moissan's boron" since Moissan prepared his boron by the Mg reduction of B_2O_3. Kahlenberg (6) produced evidence that the B_7O was a mixture of B_3O and B. Chemical analysis of a similar material by Pasternak (7) had a composition $B_{6.6}O$ which he concluded to be the compound B_7O. Pasternak also determined the structure of B_7O to be orthorhombic with $a = 8.21$, $b = 5.35$, $c = 5.13$Å, and a density of 2.64 g/cm³. One of the difficulties in establishing the correct composition for this oxide is that only boron was determined with the difference assumed to be oxygen. Thus no consideration was given to the possible solution of Mg in the suboxide or the presence of small amounts of MgB_6 or MgB_{12}. In a study of the Si-B-O system (8) it was found very difficult to prepare B_6O free from SiB_6 unless the composition, temperature, and particle size of the reactants were all controlled. A series of papers by Mikheeva and co-workers (9) elaborate on the problem of producing boron by the reduction of boron oxide and show the effect of various methods of preparation on the amount of bound boron (in suboxides or boride).

Formation

We have observed the presence of B_6O after the oxidation of boron in air and O_2 above 1100°C (10), as a reaction product between B and B_2O_3, and as a reaction product between Si and B_2O_3. It was determined, by reacting mixtures of B_2O_3 and boron in oxidizing and inert atmospheres, that the major reaction was the reduction of liquid B_2O_3 by B. The formation of B_6O from $B_2O_3 + B$ questions the validity of the thermodynamic data on B_2O_2 of Inghram *et al.* (1). However, the free energy of formation of $B_2O_{2(g)}$ from $B_2O_3 + C$ by White *et al.* (11) and the reduction of MgO by B, by Searcy and Meyers (12) were in moderately good agreement with Inghram's

data indicating that B_6O was not a major reaction product under their experimental conditions.

In studying the possible effects of $B_2O_{2(g)}$ and other gaseous oxides of boron on the kinetics of the formation of B_6O the following reactions may be considered:

$$5B_{(s)} + B_2O_{3(l)} \rightarrow B_6O + BO_{2(g)} \quad [1]$$

$$6B_{(s)} + B_2O_{3(l)} \rightarrow B_6O + B_2O_{2(g)} \quad [2]$$

$$6B_{(s)} + B_2O_{3(l)} \rightarrow B_6O + 2BO_{(g)} \quad [3]$$

$$2B_{(s)} + 2B_2O_{3(l)} \rightarrow B_6O + 3O_{2(g)} \quad [4]$$

$$5\text{-}1/3B_{(s)} + 1/3B_2O_{3(l)} \rightarrow B_6O_{(s)} \quad [5]$$

Although no thermodynamic data exist for B_6O, it is possible by considering the effect of the gaseous products to select the reactions which would be more likely to occur. Thermodynamically $BO_{(g)}$, $BO_{2(g)}$, and $O_{2(g)}$ would be most difficult to form so that the most favorable reactions are [2] and [5]. From existing thermodynamic data the calculated pressure of $B_2O_{2(g)}$ at 1500°K in an inert atmosphere is 2×10^{-5} atm; however, in air at 1 atm the partial pressure is 10^{-16} atm. The indication is, then, that at 1500°K a much smaller amount of $B_2O_{2(g)}$ would be formed in air than in an inert atmosphere. Correspondingly, there would be a greater yield of B_6O in He than in air. This was found not to be the case. Reactions between B_2O_3 + B in flowing atmospheres of air and helium produced comparable amounts of B_6O, thus ruling out reaction [2]. Reaction [5] was further substantiated when a molecular mixture of B_2O_3 and B corresponding to B_6O was heated at 1500°C for 1 hr in 2 atm of He. The reacted material contained B_6O and a small amount of unreacted B. The small weight loss (9%) coupled with the high concentration of B_6O clearly points out that reaction [5] is the controlling and major reaction for the formation of B_6O.

Discussion

The establishment of the composition of the suboxide has been difficult due to analytical problems and the lack of pure material. These problems would be further compounded if the suboxide was found to be merely a solution of oxygen in boron. With the method of producing pure B_6O by the B reduction of B_2O_3, the effects of the formation temperature of the suboxide on the chemical composition and lattice parameters were studied. The lattice constants of the suboxide, B_6O, prepared at 1200°, 1300°, 1400°, 1500° and partially decomposed at 1850°C were initially determined, based on Pasternak's (7) assignment of an orthorhombic cell. The data indicated a rather poor fit and a greater degree of inaccuracy than would be expected. This has recently been clarified by La Placa and Post (13) who have found that the powder pattern data of Pasternak could be indexed more satisfactorily on the basis of a rhombohedral cell with hexagonal cell constants $a = 5.37$ and $c = 12.31$Å. They also applied the formula $B_{12}O_2$ to the suboxide which would require a calculated density of 2.80 compared to Pasternak's observed value of 2.64 g/cm³ (7). La Placa and Post indicated that the discrepancy in these densities could be explained on the basis that a small amount of B_2O_3 was present. However, the presence of B_2O_3 would indicate that Pasternak's composition of $B_{6.6}O$ determined by chemical analysis would be low and thus favor a composition B_7O.

Table I. Chemical analyses of B_6O compositions

Source of B_6O*	B, w/o	O, w/o	Si, w/o	Total
B_2O_3 + 15 w/o B, 1300°C, 72 hr, air	79.50	21.2		100.7
B_2O_3 + 15 w/o B, 1400°C, 24 hr, argon	80.10	20.5		100.6
B_2O_3 + 15 w/o B, 1400°C, 24 hr, argon	80.30	20.6		100.7
	(0.017%H, 0.018% N, <0.001% Si)			
Hot-pressed B_6O (HP-21)**	79.43	20.0		99.4
Hot-pressed B_6O (HP-22)**	80.06	19.5		99.6
Hot-pressed B_6O (HP-23)**	79.85	19.9		99.8
Hot-pressed B_6O + 5 w/o Si**			2.32	
B_2O_3 + Si, 1315°C, 75 hr, air	79.1		5.28	
B_2O_3 + Si, 1370°C, 4 hr, air	77.12		5.30	

Chemical analyses reported by Paul Close, Owens-Illinois Glass Co., Air Force Contract No. AF 33(616)-7431.
* The crucible materials for B_2O_3 melts were BN for inert atmospheres and Si-B-O refractory material (8, 16) for reactions carried out in inert and oxidizing atmospheres.
** Solid samples, others are fine powders.

In the present investigation density measurements on the powdered suboxide never exceeded 2.62, and the highest density of hot pressed B_6O was 2.588 g/cc. This hot pressed sample contained less than 3% free boron. Thus it is highly unlikely that the true density is 2.80 as calculated by La Placa and Post. Assuming two molecules per unit cell and a composition $B_{12}O_2$ with the hexagonal cell constants determined for this hot pressed B_6O sample of $a = 5.395$ and $c = 12.342$Å, the calculated density was 2.59. The possibility of $B_{12}O_2$ structure with unoccupied B sites in the lattice appears unlikely in that no density above 2.64 g/cm³ was ever observed and no significant changes in lattice parameters and chemical analyses were observed in this study. From the chemical analyses shown in Table I, it can be seen that the first three entries, which are high-purity powders, fall very close to the theoretical boron content for B_6O of 80.23 w/o. It can also be seen that the boron and oxygen content totals 100.7% which indicates good accuracy and the absence of substantial impurities. The boron analysis was accomplished by conventional methods following the fusion with sodium potassium carbonate-sodium nitrate mixture as described by Close (14) and Bielstein (15). The accuracy is considered to be ± 0.15%. Boron values from three different laboratories for sample three of Table I were 80.30, 80.30, and 80.33, respectively. Oxygen content was found by the fluorination method (14) and is considered to be accurate within ±0.5%. It appears that nitrogen, if present, is carried along and reported as oxygen. However, sample three of Table I was found to contain only 0.018% nitrogen, and of course a higher nitrogen concentration would be expected on the surfaces of the hot-pressed samples. No free boron was observed in the first three samples reported in Table I, either by x-ray diffraction or microscopic examination of the powders. The presence of free crystalline boron as low as 3 w/o could be detected in samples of B_6O by x-ray diffraction techniques. For example, hot-pressed samples HP-21 and HP-22 contained

in the order of 3 w/o free boron while no boron could be detected in HP-23. These observations were confirmed by metallographic examination of these samples. In the hot pressed samples containing 3% free boron, one would expect the total boron content to increase from 80.23 w/o to 80.8 w/o. From Table I it is seen that the boron content is somewhat low, as is the oxygen content and, consequently, the total analyzed content. This indicates that approximately 1% impurity, other than boron and oxygen, has been introduced possibly during hot pressing, *i.e.*, nitrogen from BN die, or during crushing for chemical analysis, *i.e.*, iron from steel mortar. Therefore, the composition B_6O is the most reasonable one to assume.

The interplanar spacings and relative diffraction intensities were determined on powder samples using a spectrogoniometer and are presented in Table II. Lattice parameter data on B_6O prepared at 1200°, 1300°, 1400°, 1500°C and hot pressed B_6O (small amount of free boron present) indicated only slight changes such that the volume of the unit cell remained practically constant. In addition, chemical analyses of B_6O prepared at various temperatures and presented in Table I indicate no significant changes in composition. Thus the solubility of oxygen and boron in this compound must be small. Evidence of oxygen deficiency was noted when the reddish-brown B_6O powder turned black upon heating in a vacuum in a tungsten crucible or hot pressing in BN dies to temperatures between 1850° and 1950°C. The hot-pressing cycle usually included heating to temperature within 15 min with 1-5 min soak time at maximum temperature. Chemical analysis of B_6O prepared by reacting Si + B_2O_3 mixtures (Table I) indicated a solubility of Si or the presence of SiB_6 (which could not be removed by chemical treatment). Since B_6O prepared in this manner did not conform to equilibrium conditions it would be expected that SiB_6 would be present. The possibility of Si solubility in B_6O was tested by hot pressing a mixture of 5 w/o Si and B_6O. The resulting sample was a single phase by x-ray analysis, and chemical analysis indicated 2.32 w/o Si. The extent of Si solubility and its effect on the structure and properties of B_6O are currently being investigated.

Table II. X-ray powder diffraction data for B_6O

Hexagonal, hkl	d, A	Intensity, I/I_0
101	4.378	10
003	4.129	50
012	3.740	17
110	2.696	11
104	2.580	100
021	2.297	80
113	2.261	5
015	2.188	8
024	1.861	7
211	1.748	<2
205	1.698	5
107	1.651	7
116	1.637	3
300	1.555	<2
018	1.464	23
303	1.457	19
125	1.436	26
027	1.408	3
009	1.386	<2
220	1.347	17
208	1.283	16
223	1.278	20
312	1.264	4
217	1.247	10
119	1.223	<2
134	1.194	3
401	1.161	5
042	1.145	7
01(11)	1.092	<2
039	1.028	7
21(10)	1.011	8

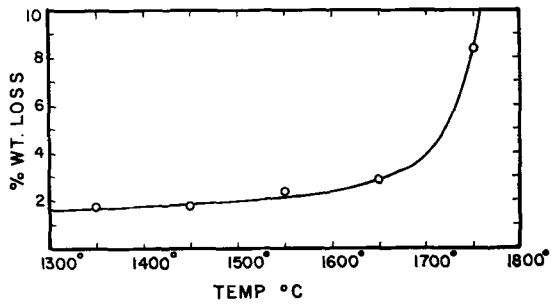

Fig. 1. Decomposition of B_6O in helium atmosphere after 1 hr

Properties

The chemical and physical properties of B_6O have not been completely established. The compound decomposes above 1760°C into crystalline boron and presumably oxygen. Figure 1 presents the weight loss, presumably oxygen, at temperatures up to 1750°C in helium. Decomposition temperature was determined by heating pressed pellets of B_6O powder in an inert atmosphere for 1-hr periods until free boron was detected. The compound is not attacked by HF, HCl, or dilute nitric acid. It can be oxidized by concentrated nitric acid if heated vigorously, and its oxidation resistance is slightly better than boron. However, it suffers from the same problems as boron in that the oxidation product B_2O_3 is a glass whose viscosity and vapor pressure at high temperatures result in a nonprotective coating. The oxidation rates of rectangular slabs (approximately 0.5 x 1.5 x 0.2 cm) of dense boron and hot pressed B_6O were comparable at 700°, 800°, 900°C. The per cent boron of the samples oxidized was, in both cases, determined to be 2.2, 4.0, and 7.4%, respectively, on weight gain and the weight loss of B_2O_3 from the oxidized sample when treated with a HF solution. The only physical property that has been explored is its hardness which was found to be greater than all commercially available materials except diamond and Borazon. The average Vickers hardness (100-g load) of B_6O was 3820 kg/mm^2 as compared to 3450 for B_4C and 3100 for TiB_2 which were also tested.

Manuscript received Nov. 29, 1961; revised manuscript received May 15, 1962.

Any discussion of this paper will appear in a Discussion Section to be published in the June 1963 JOURNAL.

REFERENCES

1. M. G. Inghram, R. F. Porter, and W. A. Chupka, J. *Chem. Phys.*, **25**, 498 (1956).
2. W. E. Kaskan, J. D. Mackenzie, and R. C. Millikan, *ibid.*, **34**, 2, 570 (1961).

3. Thomas Wartik and E. F. Apple, *J. Am. Chem. Soc.*, **77** (23), 6400 (1955).
4. F. A. Kanda, A. J. King, V. A. Russell, and Walter Katz, *ibid.*, **78** (7), 1509 (1956).
5. E. Weintraub, *Trans. Am. Electrochem Soc.*, **16**, 165 (1909).
6. H. Kahlenberg, *ibid.*, **47**, 23 (1926).
7. R. A. Pasternak, *Acta Cryst.*, **12** (8), 612 (1959).
8. H. F. Rizzo, M. P. Davis, and W. R. Foster, "Reactions in the Si-B-O System," to be published.
9. a, V. I. Mikheeva, F. I. Shamrai, and E. Ya. Krylova, *Zhur. Neorg. Khim*, **2**, 1223 (1957); b, V. I. Mikheeva, V. Yu. Markina, and O. N. Kryukova, *ibid.*, **2**, 1232 (1957); c, F. I. Shamrai, V. I. Mikheeva, and E. Ya. Krylova, *ibid.*, **2**, 1242 (1957); d, V. I. Mikheeva, F. I. Shamrai, and E. Ya. Krylova, *ibid.*, **2**, 1248 (1957).
10. H. F. Rizzo, "Oxidation of Boron at Temperatures between 400°C and 1300°C in Air," pp. 175-189, Proceedings of Conference on Boron, J. A. Kohn, W. F. Nye, G. K. Gaule', Editors, Plenum Press, Inc., New York (1960).
11. D. White, D. E. Mann, P. N. Walsh, and A. Sommer, *J. Chem. Phys.*, **32**, 381 (1960).
12. A. W. Search and C. E. Myers, *J. Phys. Chem.*, **61**, 957 (1957).
13. S. La Place and B. Post, *Planseeber. Pulvermet.*, Bd. **9**, 109 (1961).
14. P. Close, "Investigation of Analytical Methods for Determination of Various Chemical Components in Refractory Systems" Air Force Contract No. AF 33(616)7431, ARL 180 Tech Report, W-P AFB, Ohio.
15. H. Bielstein, "Analytical Methods of Investigating Some Highly Refractory Carbides and Nitrides (SiC, B_4C, BN) Technical Report No. F-TR-1154-ND GS-AAF, Wright Field, No. 34, August 1947.
16. H. F. Rizzo, B. C. Weber and M. A. Schwartz, *J. Am. Cer. Soc.*, **43** (10), 497 (1960).

Ionic Movement during the Growth of Anodic Oxide Films on Aluminum

W. J. Bernard

Sprague Electric Company, North Adams, Massachusetts

ABSTRACT

Anodic oxide films formed on aluminum in aqueous phosphate solutions resist hydration, whereas those formed in conventional borate solutions react readily with water. This property has been used to determine the mode of ion movement during the growth of duplex films. The results show that both cations and anions move through the films, but that the metal ion motion predominates.

During the growth of anodic films on aluminum, tantalum, zirconium, and similar metals the current, exclusive of electronic current, must be transported by metal ions, by oxide ions (or other anions in the film), or by a combination of both. Although it has not yet been definitely established which of the three possibilities is the correct one, the bulk of the work to date has favored the idea that growth is due almost entirely to cationic motion. Vermilyea's work with tantalum (1) presents a strong argument for the belief that the metal ion is the mobile species in the formation of films on that metal. In his experiments, anodic films were formed successively on the same specimen in two electrolytes which were known to give films of different chemical characteristics. The spatial relationship between the films, which were assumed to remain discrete, was then deduced by their known difference in solubility in HF solution. An objection which may be raised to this procedure is that small differences in rates of solubility of a pure film and one present in the composite film may go unobserved. Young (2) has arrived at the same conclusion as Vermilyea by establishing the relationship between the anodic film on tantalum and the residual layer on the metal (an extremely thin film of what is presumed to be an oxyfluoride of tantalum) created during the chemical polishing of the metal prior to electrochemical oxidation. However, as was recognized, the oxyfluoride layer is not a barrier layer (in the sense of the anodic oxide film) and although it may not impede the passage of tantalum ions to the electrolyte-oxyfluoride interface, there is no evidence that establishes the subsequent motion of ions once the oxyfluoride layer has been traversed. The work of Bernard and Randall (3) on aluminum is subject to somewhat the same criticism, even though in that case the existing film before anodization consisted of an air-formed oxide having barrier properties. The experiments showed only that the pre-existing oxide was covered by an anodic film, not that the original layer retained its identity throughout the course of oxidation. In other work with aluminum, Lewis and Plumb (4) used a multiple layer method in which one of the layers was tagged with sulfur-35 and its position identified by the rate of loss of radioactivity during a chemical stripping process. The results were interpreted to favor the theory of metal ion mobility, but these results are obscured to some extent because of the formation of one of the films in an electrolyte (dilute sulfuric acid) which normally gives rise to a porous film on aluminum.

On the other hand, the observations of Flint and Varley (5, 6) on the thermal and anodic oxidation of zirconium indicate that, depending on the surface condition of the metal and applied field strength, both cations and anions can demonstrate mobility during film growth. Haas and Bradford (7) have also

shown that in the formation of multiple layers of Al_2O_3 and TiO_2 oxygen must be the mobile species at least during some part of the anodic process.

The work reported here supports the idea that cationic motion is the major contributor to the growth of barrier oxides, but also indicates that there is a nonnegligible contribution from anion movement.

Experimental

Films of different compositions may be laid down on aluminum by anodic oxidation in suitable electrolytes. Plumb (8) has shown that appreciable deviation from stoichiometric aluminum oxide is obtained in films formed in aqueous solutions of potassium phosphate. The work of Hunter *et al.* (9) with sodium phosphate solutions has been interpreted in the same way. Plumb has found that films formed in a neutral solution of dilute potassium phosphate contained phosphorous equivalent to about 8% $AlPO_4$ distributed uniformly throughout the film; we have since made measurements which are in essential agreement with this. On the other hand, nearly stoichiometric Al_2O_3 may be formed in solutions of ammonium pentaborate in ethylene glycol (10). These two types of films have somewhat different chemical characteristics, among them being their relative resistance to hydration. The stoichiometric oxide becomes hydrated readily in boiling water (9, 11), whereas the phosphate-containing oxide resists attack. Hydration, if it occurs at all, does so at a very slow rate (9). This property was utilized to observe the manner of growth of the anodic films, since the degree to which a barrier oxide film has been attacked by water may be determined by the change in the capacity of the film after reaction. The procedure for this has been described in an earlier paper (11). Thus, by successively forming films of different composition on the same specimen of aluminum and comparing the rate of hydration of such composite films with the known reactions of the individual films, the position of the two oxide layers with respect to each other and to the underlying metal may be deduced, assuming that discrete layers persist under these conditions. If the individual layers lose their identity, then this also should be recognized through the hydration data.

Films were prepared in two different sequences: one set was formed in 0.1M NaH_2PO_4 solution, followed by formation in a 30% solution of ammonium pentaborate in ethylene glycol, and a second set was formed by reversing the order of electrolytes. Anodic oxidation was carried out at 25°C at an initial current density of 1.0 ma/cm² and a final current density of 0.1 ma/cm². Specimens were scrupulously washed with distilled water between formations in order to remove adsorbed electrolyte as much as possible. Electropolished aluminum of 99.986% purity was used for all experiments. After treatment with boiling water, capacitance of the specimens was measured at 25°C. The values of reciprocal capacitance are then used as a measure of the thickness of the unhydrated oxide. The data may also be expressed in terms of the equivalent barrier voltage of the films. Pertinent experimental details have been described earlier (11).

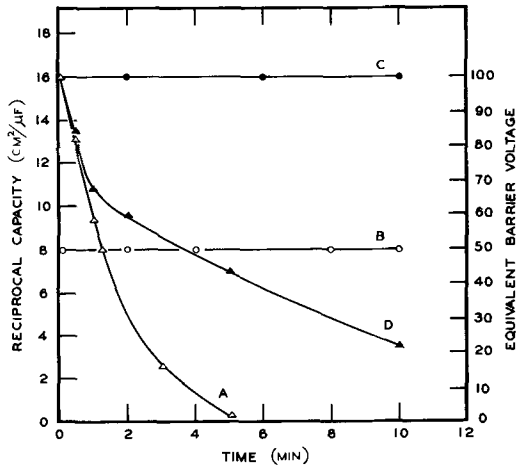

Fig. 1. Reciprocal capacitance and barrier voltage vs. hydration time at 100° for anodic oxide films: A, 100v in borate electrolyte; B, 50v in phosphate electrolyte; C, 50v in borate electrolyte and then to 100v in phosphate electrolyte; D, 50v in phosphate electrolyte and then to 100v in borate electrolyte.

Results and Discussion

In Fig. 1, curves A and B show the hydration rate at 100° of films formed to 100v in ammonium pentaborate solution and to 50v in NaH_2PO_4 solution, respectively. Over the range of reaction time considered here, the phosphate-containing film is completely unaffected by water whereas the comparatively pure oxide film is converted entirely to a nonbarrier hydrated oxide. The behavior of a film formed first in the borate solution to 50v and then in the phosphate solution to a final value of 100v is shown in curve C. It is quite clear from this plot that the outermost portion of the film must contain phosphate; this would suggest cation movement during film growth since the film has grown at the oxide-electrolyte interface. However, curve D shows that film growth cannot be attributed only to the mobility of cations. In this case the film was first formed in the phosphate solution and then in the borate solution. The rate of hydration of this duplex film at first closely follows that of the stoichiometric oxide, but begins to show an appreciable deviation from that rate at a remaining barrier voltage of about 70v. This reduction in rate can only be explained by the presence of phosphate ion in the outermost oxide layer. Furthermore, the originally formed layer is shown to be depleted of phosphate by the fact that hydration of this portion of the film can now proceed at a measurable rate. If the two layers had remained completely discrete, hydration would have ceased entirely at a remaining barrier voltage of 50v. However, it should be noted that hydration of the original phosphate-formed layer occurs at a far slower rate than with normal oxide layers, indicating that the amount of phosphate lost from this layer to the subsequently formed film probably is not very great.

The relative thickness of the two films has no effect on the results. For comparison, the curves in Fig. 2 show the behavior of films in which the nor-

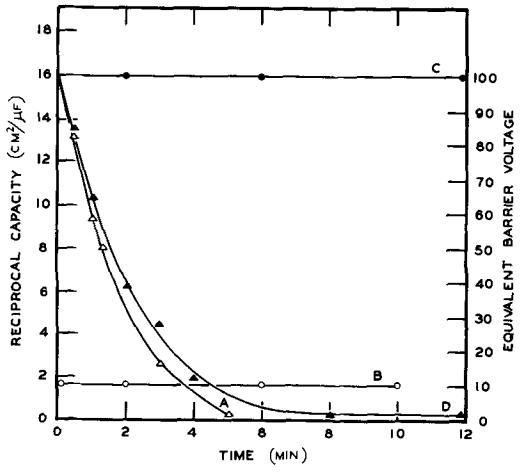

Fig. 2. Reciprocal capacitance and barrier voltage vs. hydration time at 100° for anodic oxide films: A, 100v in borate electrolyte; B, 10v in phosphate electrolyte; C, 90v in borate electrolyte and then to 100v in phosphate electrolyte; D, 10v in phosphate electrolyte and then to 100v in borate electrolyte.

mal oxide was nine times as thick as the phosphate-formed layer. In this case, in curve D, the composition of the outermost portion of the film is even more clearly shown to be that of a phosphate-free oxide. An appreciable fraction of the film must be penetrated before the mixed nature of the underlying oxide, and thus the movement of anions, is manifested.

Although these experiments show that both ions move during formation, the relative mobilities under these conditions cannot be determined. However, it is reasonable to believe that metal ion motion predominates. The work of Lewis and Plumb (4) to some extent substantiates this view since an examination of their data shows that it can be used to demonstrate a partial contribution of anion movement to film growth.

Manuscript received Jan. 31, 1962; revised manuscript received May 31, 1962.

Any discussion of this paper will appear in a Discussion Section to be published in the June 1963 JOURNAL.

REFERENCES

1. D. Vermilyea, *Acta Met.*, **2**, 482 (1954).
2. L. Young, *Trans. Faraday Soc.*, **53**, 841 (1957).
3. W. J. Bernard and J. J. Randall, Jr., *This Journal*, **107**, 483 (1960).
4. J. E. Lewis and R. C. Plumb, *ibid.*, **105**, 496 (1958).
5. O. Flint and J. H. O. Varley, *Nature*, **179**, 145 (1957).
6. O. Flint and J. H. O. Varley, *Phys. and Chem. Solids*, **6**, 213 (1958).
7. G. Haas and A. P. Bradford, *J. Opt. Soc. Am.*, **44**, 810 (1954).
8. R. C. Plumb, *This Journal*, **105**, 498 (1958).
9. M. S. Hunter, P. F. Towner, and D. L. Robinson, *Tech. Proc. Am. Electroplaters Soc.*, 46th Ann. Con., **1959**, 3.
10. W. J. Bernard and J. W. Cook, *This Journal*, **106**, 643 (1959).
11. W. J. Bernard and J. J. Randall, Jr., *ibid.*, **108**, 822 (1961).

Electrochemical Measurements at High Pressures

A. Distèche

Laboratory of General Biology, University of Liège, Liège, Belgium

ABSTRACT

*p*H measurements with a glass electrode at 1000 kg cm^{-2} give direct evidence of the pressure induced ionization constant shift and permit calculation of the corresponding volume change for the reaction $HA \rightarrow A^- + H^+$. Extrapolation at zero ionic strength and zero acid concentration is used to determine log K_{1000}/K_1 for formic acid, phosphoric acid, and phosphate buffer (step 1). Data concerning phosphate buffer (step 2), acetic acid, acetate buffer, carbonic acid, bicarbonate buffer, sodium bicarbonate, sodium acetate, and ammonia are given together with the results of direct *p*H measurements at great ocean depth (2350m). Work done in the same field but based on conductivity determinations is briefly reviewed.

The field of application of electrochemical technique in high-pressure chemistry is almost completely restricted to electrolytic conductance and galvanic cell emf measurements, the former receiving much more attention.

Conductance Measurements

New cell design [Teflon-Pt (1)] has made it possible to obtain more accurate results over a wide pressure range (1-12,000 atm) in the last 10 years. The subject has been fully reviewed by Hamann (2) and co-workers (3, 4), Ellis (5), Clark and Ellis (6), and is briefly dealt with here.

The results show that the limiting conductance of strongly dissociated salts first increases slightly up to 1000-2000 atm, but decreases at higher pressures. The effect is related to viscosity and dielectric constant changes in the solvent. HCl and KOH behave differently, their conductance being reduced much less by high pressures.

In contrast, the molal conductance of weak acids and bases increases steadily with pressure. This is due to enhanced ionization and is best demonstrated by the shift of the ionization constants (K) computed from conductivity measurements. Formic acid, acetic acid, propionic acid, carbonic acid, benzoic

acid, o-, m-, p-nitrobenzoic, salicylic, and 3-5 dimethyl-4-nitrobenzoic acid, ammonia, mono-, di, trimethyl amine (2-7) in water have been thoroughly studied, and some results are reported in nonaqueous solvents (2, 6).

Log K_p/K_1 varies almost linearly with pressure between 0 and 3000 atm. In this range, at 25°C, log K_{1000}/K_1 lies between 0.1 and 0.25 for organic acids, is equal to 0.4 for carbonic acid, and amounts to ~ 0.45 for ammonia and amines.

The basic ionization constant of ammonia at 45°C is increased from 1.9 10^{-5} mole kg^{-1} at 1 atm to 1010 x 10^{-5} mole kg^{-1} at 12,000 atm (7). David and Hamann (3, 4) have measured the conductivity of water and several liquids at shock pressures between 33,000 and 127,000 atm. The ionic product of water increases by a factor as great as 10^{12} at 127,000 atm. In these spectacular experiments, the pressures are produced by Schall's method (8) of using an explosion to drive an intense shock wave into the water. The cell is made from polyethylene and has platinum electrodes.

Some polarographic measurements at high pressure have been made by Ewald and Lim (9) and by Hayashi and Kono (10); the results are consistent with the fact that pressure shifts chemical equilibria in the direction of the more ionic species.

Galvanic Cell emf Measurements

The effect of pressure (p) on the emf (E) of a galvanic cell can be predicted from the classical relations

$$\left(\frac{\partial \Delta G}{\partial p}\right)_{m,T} = \Delta V \qquad [1]$$

$$\left(\frac{\partial E}{\partial p}\right)_{m,T} = \frac{-\Delta V}{n\mathbf{F}} \qquad [2]$$

where ΔG represents the free energy, ΔV the volume change when n Faraday ($\mathbf{F}$) are passed through the cell at constant molal concentration (m) and temperature (T).

$$\text{If } \Delta V = 1 \text{ cm}^3,\ n = 1,\ \left(\frac{\Delta E}{\Delta p}\right)_{m,T} = \frac{1 \text{ x } 0.10133}{96.500}$$

= 1.05 10^{-6} volt/atm or 1.016 10^{-6} volt/kg cm^{-2}; 0.10133 is the factor which converts cubic centimeter-atmospheres into joules.

Cohen and Piepenbroek (12) showed that ΔV can be considered independent of pressure for the cell Tl-amalgam-TlCNS, KCNS | KCl, TlCl-Tl-amalgam. Hainsworth, Rowley, and MacInnes (13) have given an integrated form of Eq. [2] for the cell Pt-H_2 | HCl 0.1N | HgCl-Hg up to 1000 atm. pH values for some standard buffers are given by Le Peintre (15) at 150 atm between 20° and 250°C, using a symmetrical Pt-H_2 cell with liquid junction (quartz cell).

In a paper published in 1959, Distèche (14) showed that the symmetrical glass electrode cell: Ag-AgCl | HCl 0.1N | glass | X, KCl 0.1M | AgCl-Ag, where X stands for various electrolytes, can be used for precise pH measurements up to 1500 atm. A similar cell has been tested for industrial use in the 0-150 atm range by Le Peintre (15). The cell assembly (whole glass) is reported to have been patented in 1957, and a few preliminary results up to 150°C are given (Pb-amalgam is used for the inner electrode), but glass corrosion very much reduces the reliability of the electrode at high temperature. Marburger, Anderson, and Wigle (16) described a glass cell capable of withstanding pressure, where one of the junction electrodes is made of lead, apparently directly deposited on the active glass (U tube).

A conventional glass electrode easily can be made to withstand 1500 kg cm^{-2} simply by applying the pressure to a layer of silicone oil, which acts as a liquid piston on the inner and outer solutions of the electrode (Fig. 1).

Figure 2 represents a cross section through part of a cell designed for laboratory work, which has some advantages compared with the apparatus described in 1959 (14). The use of araldite (potting resin) for making highly insulated pressure resisting seals around the electrical connections has been avoided. Crevices appear in this type of seal after prolonged use. The electrical connections shown in Fig 2. is a variant of that described by Poulter (17). Low-pressure leakage is avoided by the use of "O"

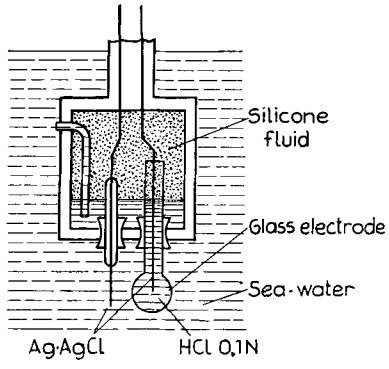

Fig. 1. Schematic drawing showing how a glass electrode can be made to withstand high pressure. From Distèche (14).

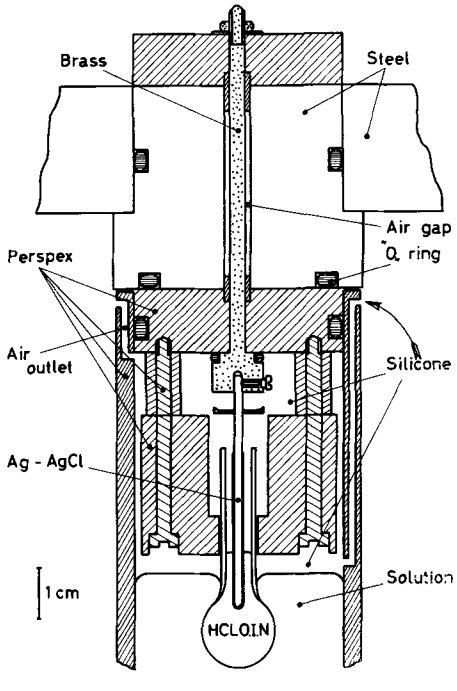

Fig. 2. Cross section through part of the glass electrode assembly

rings. The connector, which can be taken to pieces in a few minutes, is easy to build, and the insulating resistance is extremely high (>10^4 meg).

The glass electrode is blown from a Corning 015 glass tube and fits into a Perspex mounting block which occupies a volume as large as possible compared to the volume filled with silicone oil. This is to minimize heat transfer between the silicone and the solution.

The Ag-AgCl electrodes are made from pure silver wire, and the surface separating the two liquid phases falls on the AgCl coating. Silvered Pt wire, first sealed at the extremity of a glass tube, is to be avoided. The glass seal seldom stands repeated pressure application and short circuits appear at the junction between the AgCl coating and the glass stem. In fact, the greatest difficulty in these experiments lies in the Ag-AgCl electrodes. The slightest scratch or irregularity in the coating makes the electrodes behave erratically, and the defect is greatly emphasized at high pressure. Care also should be taken to eliminate dust deposits which generally gather at the liquid interface. Carefully made electrodes generally stand a week or more of intensive experimental work before showing some sign of aging. An emf hysteresis loop is observed when pressure is applied and suppressed. The Ag-AgCl electrodes then have to be replaced which means that the whole cell must be designed to be taken to pieces quickly and easily. Glass electrodes last indefinitely and, when carefuly washed and wiped, never show any defects.

The silicone oil has a viscosity of 1 cS at 25°C. The use of a liquid of low viscosity makes filling easier and air bubbles escape quickly. One disadvantage is the rather high compressibility, which means that positive or negative heat is generated in the silicone layer. It can be shown that, with a pressure step of 1000 kg cm^{-2} applied in 40 sec, the rise of temperature is 3°C in the silicone fluid, and never exceeds 1°C in the solution.

With 250 kg cm^{-2} increments applied every 5 or 10 min, it is estimated that the total temperature rise is less than 0.25°C when the final pressure is reached. The effect can be minimized further by the use of a water-jacket at constant temperature around the pressure bomb.

The results obtained with pressure resisting glass electrodes show that the hydrogen electrode constant (2.303 $RT/\mathbf{F}$) of the glass electrode is not affected by pressure. The asymmetry potential measured with 0.1M HCl or any buffer solution on both sides of the membrane varies slightly, but linearly with pressure in the investigated range (0-1000 kg cm^{-2}). The variation generally does not exceed 1 mv and is carefully determined to correct the pH measurements.

Weak Acids and Buffers

The effect of pressure on the dissociation constant (K) of a weak acid and on the activity coefficient (γ_i) of an ion species i is given by

$$\left(\frac{\partial \ln K}{\partial p}\right)_{m,T} = \frac{-\Delta V^\circ}{RT} \text{ and } \left(\frac{\partial \ln \gamma_i}{\partial p}\right)_{m,T} = \frac{V_i - V^\circ_i}{RT} \quad [3]$$

where ΔV° is the algebraic difference between the partial molal volumes of the products and the reactants of the chemical equilibrium in their standard states and V_i the partial molal volume of the ion species i.

For acetic acid, acetate buffer, phosphate buffer (step 2), carbonic acid, and bicarbonate buffer, at concentrations where H^+ is negligible compared with the stoichiometric acid or salt concentrations, it is easy to show that log K_p/K_1 can be calculated from Eq. [4] and [5], valid respectively for acids and buffers at 22°C

$$E_1 - E_p = 0.0293 \log K_p/K_1 + 0.0293 \log \frac{\gamma_{A^-1}\,\gamma_{H^+P}}{\gamma_{A^-P}\,\gamma_{H^+1}} \quad [4]$$

$$E_1 - E_p = 0.0585 \log K_p/K_1 + 0.0585 \log \frac{\gamma_{A^-1}}{\gamma_{A^-P}} \quad [5]$$

where A^- = acid anion, E_1 and E_p the emf of the glass electrode assembly at pressure 1 and P.

Figure 3 (14) shows a plot of $E_1 - E_p$ against pressure from which ΔV_1 corresponding to the reaction $HA \rightarrow H^+ + A^-$ at 1 atm in 0.1M KCl (reference electrode HCl 0.1M) can be estimated. The values are given in Table I (column 1) together with ΔV°_1 (columns 3 and 4) obtained from density and conductivity determinations ($E_1 - E_{1000\text{ kg cm}^{-2}} = 1$ mv, corresponds almost exactly to $\Delta V_{1\text{ atm}} = 1$ cm^3 (see page 1085); $E_{1000\text{ kg cm}^{-2}}$ is obtained from the slope of $E_1 - E_p = f(P)$ at 1 atm and generally coincides with the reading at 1000 kg cm^{-2}).

Except for carbonic acid ΔV_1 is always lower than ΔV°_1. Part of the difference lies in the contribution of the activity coefficient term in Eq. [4] and [5] ($\gamma_p > \gamma_1$). The data necessary to calculate log γ_1/γ_p generally are not available, but the effect of this

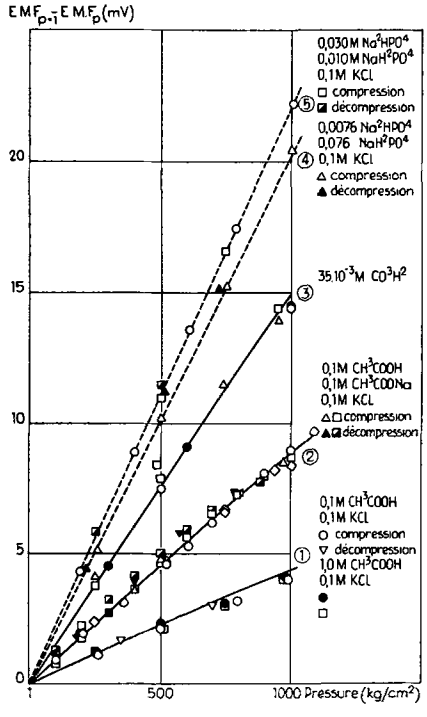

Fig. 3. Variation of the glass electrode potential with pressure for various acid and buffer solutions in 0.1M KCl (reference half-cell: 0.1M HCl). Solid lines are calculated from the data of Owen and Brinkley (11). From Distèche (14).

Table I. Volume change for ionization of some weak acids at 1 atm and 22°C

Acids	$-\Delta V_1$ (0.1M KCl), cm³ mole⁻¹ Glass electrode ref. 0.1M HCl[14] (( ) = molarities)	$-\Delta V°_1$, cm³ mole⁻¹ Glass electrode	$-\Delta V°_1$, cm³ mole⁻¹ Density	$-\Delta V°_1$, cm³ mole⁻¹ Conductivity
Acetic	8.2-9.3* (0.1-1.0)	10.8-11.5*	12.5[2]-11.5[19] 9.2[11]	12.2[7]
Formic		8.8-9.1	8.0[2]	8.8[2]
Phosphoric (K_1)		17.5	16.2[21]	
Carbonic (K_1)	29.0-30.0 ($3.5.10^{-2}$)		29.0[11]	24.9[5]
Buffers				
Acetate	8.7-9.7* (HA 0.1-NaA 0.1)	10.3-10.8*		
Phosphate (K_1)		14.6-15.2		
Phosphate (K_2)	22.0 (NaH_2 0.03-Na_2H 0.01) 20.3 (NaH_2 0.0076-Na_2H 0.076)	23.0	28.1[21]**	
Bicarbonate	22.7-20.7 (NaH 2.10^{-3}-$3.5.10^{-2}$ HA 2.10^{-4}-$3.5.10^{-2}$)			

* The lower values are read from the curves of Fig. 3 and similar ones at 1000 kg cm⁻²; the higher values are obtained from the slope of the curves at 1 atm.

** $\Delta V^1 = -24.1$ cm³ is reported from dilatometric experiments by Linderstrom-Lang and Jacobsen (22).

factor is expected to be small (18). It also should be noticed that we have assumed so far that the pH of the reference half-cell (0.1M HCl) is not affected by pressure and that the effects of pressure on the specific electrode reactions cancel out. ΔV_1 corresponds in fact to the total volume change in the observed cell at 1000 kg cm^{-2}.

We will now describe how the $\Delta V°_1$ values listed in column 2 of Table I have been obtained.

When $[H^+]$ is no longer negligible compared to the stoichiometric concentrations, K_p and K_1 must be calculated using the classical methods to determine dissociation constants from electromotive force data.

For acids (formic acid, phosphoric acid (step 1), $E_1 - E_p$ is then given by

$$E_1 - E_p = 0.0293 \log \frac{K_p}{K_1} + 0.0293 \log \frac{(m_{HA} - m_{H^+})_p}{(m_{HA} - m_{H^+})_1} + f(\sqrt{\mu}) \quad [6]$$

where $f(\sqrt{\mu})$ stands for the activity coefficient term and m for the stoichiometric acid and H^+ concentrations on the molal scale [$m_1 = m_p = (M_1/\rho_1)_1 = (M_1/\rho_1)_p$ in diluted solutions; M_1 is the corresponding concentration on the molar scale, ρ_1 the density of water at 1 atm; the approximation $m_1 = m_p \simeq M_1$ has been used throughout this paper].

Figure 4 shows how $E_1 - E_p$ varies with the concentration M_1 of formic acid in 0.1M, 0.01M, and 0.001M KCl, the corresponding reference half-cells containing 0.1M, 0.01M, and 0.001M HCl.

Figure 4 also gives $\Delta pK' = -\log k'_1 + \sqrt{\mu_1} + \log k'_p - \sqrt{\mu_p}$ where $k' = m'^2_{H^+}/(m_{HA} - m'_{H^+})$ and $\sqrt{\mu}$ is the usual estimate for the activity coefficient term. The primes indicate the uncertainty introduced by the values of γ_{H^+} used to calculate m'_{H^+}. They correspond to the mean activity coefficient for HCl in KCl solutions, used by Harned and Owen (20) in their determinations of the dissociation constant of formic acid. As a first approximation it has been assumed that the activity coefficients do not change with pressure.

Values for $\Delta pK'$ in 0.001M KCl agree fairly well with the expected one which lies between 0.137 [$\Delta V°_1 = -8.0$ cm³ (2, 7)] and 0.150 [$\Delta V°_1 = -8.8$ cm³ (7)].

In 0.1M KCl, $\Delta pK'$ drops unexpectedly at low acid concentrations, with 0.1M HCl as reference. It is easy to show that the anomaly disappears when a small constant is added to the observed emf shifts, and there exists experimental evidence to give a meaning

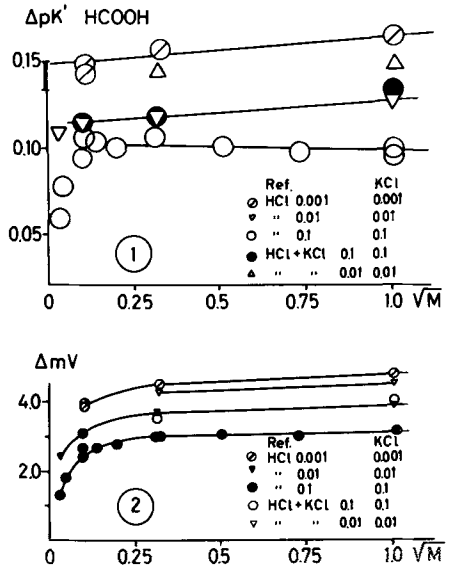

Fig. 4. Formic acid in KCl solutions. Top: $\Delta pK' = -\log k'_1 + \sqrt{\mu_1} + \log k'_p - \sqrt{\mu_p}$ (p = 1000 kg cm^{-2}) as a function of the acid concentration. Bottom: observed emf shifts (Δmv). (HCl + KCl 0.1 and 0.001 is simplified for HCl 0.01M + KCl 0.09M and HCl 0.001M + KCl 0.009M).

to this constant increment. If 0.01*M* KCl + 0.09*M* KCl is used as reference, the observed Δ mv values for formic acid in 0.1*M* KCl are about 0.8-0.9 mv greater than with 0.1*M* HCl. Similarly a 0.6 mv shift is obtained when 0.001*M* HCl + 0.009*M* KCl is used instead of 0.01*M* HCl. A further tenfold dilution of the reference solution indicates that the differences with 0.001*M* HCl are within the experimental errors (±0.1 mv), but the emf of the reference electrode shows then a slow linear drift which makes the determination of the absolute *pK* values impossible, although pressure induced emf changes are still measurable.

It is to be expected that with HCl + KCl as reference solution, the effect of pressure on the activity coefficient γ_{H^+} almost or completely cancels on both sides of the glass membrane. This might not be the case with HCl alone, except at high dilutions, but there remains the difficulty that the activity coefficient in pure HCl solutions than appears to be more affected by pressure then when KCl is present. The pH of 0.1*M* HCl would have to decrease from 1.09 to 1.075 to explain the observed shift, if γ_{H^+} in presence of KCl is supposed to remain constant. Such a large change is rather unexpected (18). Another explanation is that the asymmetry potential of the glass electrode changes with pressure when KCl is absent in one of the half-cells which might imply that the glass membrane under pressure would become slightly sensitive to K ions also. The phenomenon might also take place at the Ag-AgCl electrodes or more likely, represent the net effect of pressure on the protode reaction ($H_3O^+ \rightarrow H_2O + p$) on both sides of the glass membrane. A complete analysis of this problem needs more experiments and is beyond the scope of this paper.

Figure 5 is a plot of $-\log k'$ as a function of $\sqrt{\mu}$ to attempt to extrapolate the results both at $\mu = 0$ and zero acid concentration. The general aspect of this diagram is in reasonable agreement with the results of Harned and Owen (20) regarding the ionic strength and medium (undissociated acid) effects.

Great accuracy is not claimed for the absolute value of the dissociation constant ($pK_1 = 3.71$ instead of 3.75); it can be seen that a better value (3.74) is obtained when the results in 0.1*M* KCl

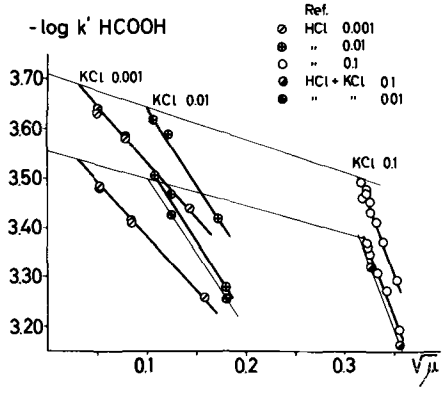

Fig. 5. Formic acid in KCl solutions. Extrapolation of $-\log k'_1$ and $-\log k'_p$ at $\mu = 0$ and zero acid concentration (HCl + KCl 0.1 and 0.01 is simplified for HCl 0.01M + KCl 0.09M and HCl 0.001M + KCl 0.009M; $-\log k'_1 > -\log k'_p$).

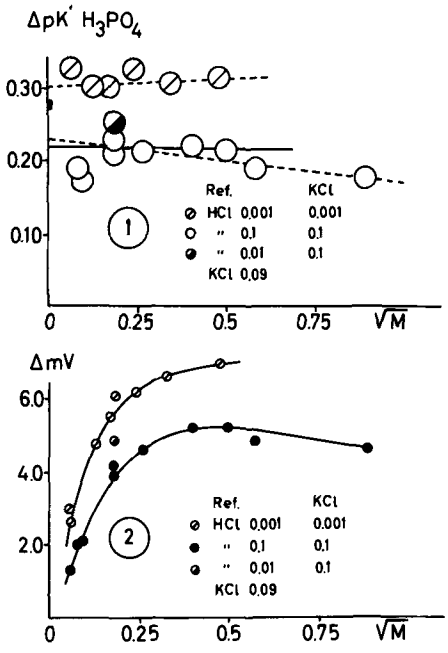

Fig. 6. Phosphoric acid (step 1) in KCl solutions. Top: $\Delta pK' = -\log k'_1 + \sqrt{\mu_1} + \log k'_p - \sqrt{\mu_p}$ (p = 1000 kg cm^{-2}) as a function of the acid concentration ($\sqrt{M}$). Bottom: observed emf shifts (Δ mv).

and 0.01*M* KCl alone are considered. More data are needed in 0.01*M* and 0.001*M* KCl, but those available are sufficient to determine ΔpK with some accuracy. The linear extrapolation of $-\log k'_p$ from $\mu = 0.1$ to $\mu = 0.001$ through $-\log k'_p$ at $\mu = 0.01$ is seen to be possible only when HCl + KCl is used in the reference half-cell instead of 0.1 and 0.01*M* HCl. The diagram shows that the activity coefficient term ($\sqrt{\mu}$) used to calculate $\Delta pK'$ in Fig. 4 is an overestimate. The corrected values are: $-0.66\sqrt{\mu_1}$ and $-0.52\sqrt{\mu_p}$ at $\mu = 0.1$, in agreement with the value at 1 atm given by Harned and Owen (20) and derived from the equation

$$-\sqrt{\mu_1}/(1 + 1.175\sqrt{\mu_1}) + 0.19\mu_1 = \log \gamma_{H^+}\gamma_{A^-}/\gamma_{HA}$$

Pressure mainly affects the coefficient of the term in μ_1.

The most probable value for ΔV°_1, 8.8-9.1 cm^3, corresponding to $\Delta pK = 0.150 - 0.155$ is in good agreement with the density and conductivity data (2, 7). The contribution of the activity coefficient change is about 1.5 cm^3 at $\mu = 0.1$.

The effect of pressure on the ionization constant of phosphoric acid (step 1) has also been studied.

Figure 6 shows $E_1 - E_p$ as a function of $\sqrt{M_1}$ in 0.1*M* and 0.001*M* KCl, using 0.1*M* and 0.001*M* HCl as reference. As for formic acid, a shift of about 0.9 mv is observed when 0.01*M* HCl + 0.09*M* KCl is used. The corresponding $\Delta pK'$ values calculated in the same way as for formic acid are shown in the upper part of Fig. 6. Again $\Delta pK'$ drops too much at high dilution in 0.1*M* KCl and the same explanation holds.

The contribution of the second term on the right side of Eq. [6] is very important in the case of H_3PO_4 and makes the $\Delta pK'$ values much more sensitive to experimental errors. $\Delta pK'$ extrapolates around 0.300 ($\Delta V^\circ_1 = -17.5$ cm^3) in 0.001*M* KCl, which is rather

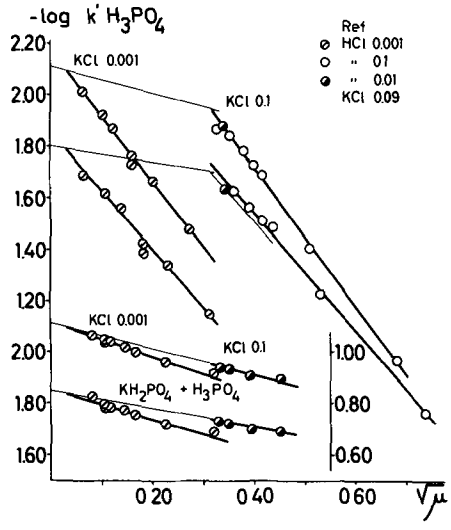

Fig. 7. Phosphoric acid (step 1) and phosphate buffer (buffer ratio $[A^-]/[HA] \simeq 10/1$) in KCl solutions. Extrapolation of $-\log k'_1$ and $-\log k'_p$ at $\mu = 0$ and zero acid and buffer concentration ($-\log k'_1 > -\log k'_p$; the upper left hand scale is continued on the right below).

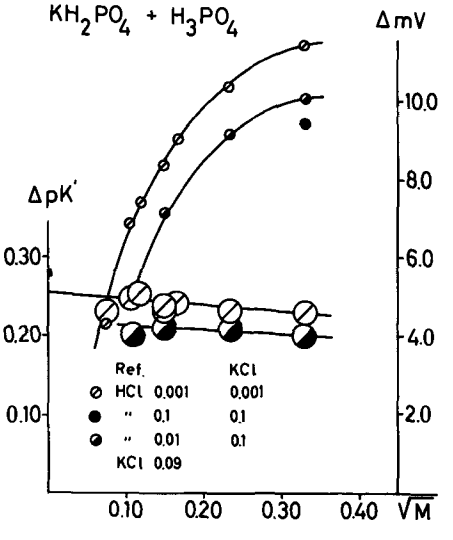

Fig. 8. Phosphate buffer (step 1) in KCl solutions. $\Delta pK' = -\log k'_1 + \sqrt{\mu_1} + \log k'_p - \sqrt{\mu_p}$ (p = 1000 kg cm^{-2}) and Δ mv observed (emf shifts) as a function of the buffer concentration ($[HA] + [A^-] = M$).

too high compared to the −16.2 cm³ obtained by Smith (21) from density measurements.

Figure 7 gives $-\log k'_1$ and $-\log k'_p = f(\sqrt{\mu})$ and may be extrapolated to $\mu = 0$ and zero acid concentration. The absolute value of pK_1 (2, 11) is in agreement with the value 2.13 given by Bates (23); the most probable value for ΔpK is again 0.300, and the contribution of the activity term at $\mu = 0.1$ is equal to 1.03 cm³ which is somewhat less than for formic acid.

The results gathered for phosphate buffer (step 1) are given in Fig. 7, 8, and 9. The stock buffer solutions contained 0.1M KH_2PO_4, 0.011M H_3PO_4, and KCl, and were diluted with corresponding KCl solutions. This buffer ratio explains why the medium effect of undissociated H_3PO_4 is very much reduced, compared with pure H_3PO_4 solutions. The extrapolated value of ΔpK lies around 0.260 ($\Delta V°_1 = -15.2$

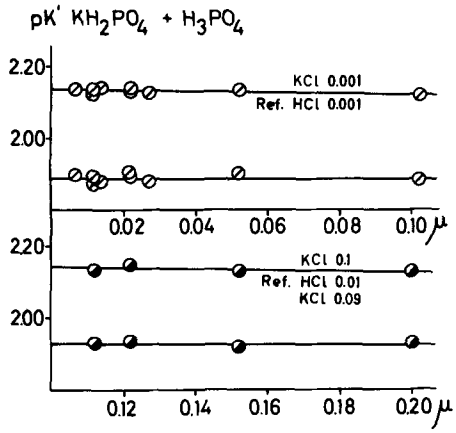

Fig. 9. Phosphate buffer (step 1) in KCl solutions. Extrapolation of $pK' = pk' + \sqrt{\mu}/(1 + 1.96\sqrt{\mu})$ at 1 and 1000 kg cm^{-2} on the μ scale ($pK'_1 > pK'_p$).

cm³) on both Fig. 7 and 8. The contribution of the activity coefficient term is $\simeq 0.7$ cm³ at $\mu = 0.1$. Figure 9 indicates that the results are better represented on the μ scale. $pK' = pk' + \dfrac{\sqrt{\mu}}{1 + 1.96\sqrt{\mu}}$ is then used to extrapolate at $\mu = 0$ (23), again assuming that pressure has no effect on the activity coefficients. ΔpK seems now to be closer to 0.250 ($\Delta V°_1 = -14.6$ cm³), whereas the absolute value of pK_1 is in excellent agreement with the data of Bates.

We have so far no explanation for the fact that $\Delta V°_1$ for phosphate buffer is about 2 or 3 cm³ smaller than $\Delta V°_1$ for H_3PO_4 alone. It should be noticed however that extrapolation at nearly equal buffer ratios on the $\sqrt{\mu}$ scale (Fig. 8) yields values for ΔpK between 0.280 and 0.270 (−16.4 and −15.8 cm³) in much better agreement with the density data of Smith (21).

Preliminary results for acetic acid in 0.001 KCl lead to $\Delta pK = 0.180$ ($\Delta V°_1 = -10.8$ cm³); for acetate buffer, $\Delta pK = 0.175$ ($\Delta V°_1 = -10.3$ cm³). Some uncertainty arises from the slight curvature of $E_1 - E_p = f(P)$ which is generally absent in the other investigated media. The emf values at 500 kg cm^{-2} give for $\Delta V°_1$ −11.5 and −10.8 cm³ for the acid and the buffer, respectively. The agreement with the results obtained from conductivity and density measurements is satisfactory (see Table I).

The effect of the ionic strength on ΔpK in phosphate buffer (step 2) seems to be quite small. The importance of the buffer ratio will have to be investigated carefully, but the observed shifts in 0.001M KCl point toward $\Delta pK = 0.390$ or $\Delta V°_1 = -23.0$ cm³, a value which is still about 5 cm³ too small compared to the one obtained from density measurements (21).

We have not reinvestigated (14) the effect of pressure on H_2CO_3 and bicarbonate buffer in dilute KCl solutions. Taking into account the apparent reference cell shift (0.8–0.9 mv) for 0.1M HCl and a reasonable estimate of 0.5 mv for the activity coefficient contribution, would lead to $\Delta V°_1$ values for bicarbonate buffer between −22.0 and −24.0 cm³, not too far from the value (−24.9 cm³) proposed

recently by Ellis (5) from conductivity measurements. These ΔV°_1 values are however much lower than the figure given by Owen and Brinkley (11) (29.0 cm³) and are in disagreement with the pH shift observed in H_2CO_3 solutions, which lies between 14.5 and 15.0 mv in 0.1*M* KCl (reference 0.1*M* HCl) ($\Delta V_1 = -30.6$ and -31.8 cm³, after correction for the reference shift).

The increase of the second dissociation constant of carbonic acid is not measurable with a glass electrode without careful investigation of the effect of pressure on the alkaline error at pH > 9. The shift can be computed however from the emf change observed in $NaHCO_3$ solutions, the pH of which is known to be given by

$$pH = \tfrac{1}{2}\, pK_1 + \tfrac{1}{2}\, pK_2$$

The observed value, with 0.1*M* HCl as reference, is 22.6 mv at 1000 kg cm^{-2} for a 0.1*M* solution in 0.1*M* KCl. It is close to the 22.7 mv change obtained for bicarbonate buffer. This gives, after correction for the reference half-cell shift, a corresponding value of ΔV_1 equal to -23.6 cm³. The expected ΔV°_1 is -27.8 cm³ (11).

It appears from Table I, which summarizes our findings, that the observed pH shifts induced by pressure in acetic acid, formic acid, phosphoric acid (step 1), and perhaps carbonic acid are in reasonable agreement with the *pK* decrease or ΔV°_1 values calculated from density and conductivity data. However, the recorded emf changes in buffer solutions appear to be systematically too small and the difference is too great to be accounted for in terms of activity coefficient contributions or reference cell shifts. On the other hand, the experiments described in the next section tend to show that the behavior of the glass electrode under pressure is normal in the alkaline region, so that the cause of the observed discrepancy will have to be sought elsewhere (ionic association, hydration, incompletely dissociated salts, etc.).

Sodium Acetate, Ammonia (Ionic Product of Water)

The ionic product of water K_w increases by a factor of 2.36 at 1000 atm according to the calculation of Owen and Brinkley (11). Several experiments can be carried out with a glass electrode to obtain experimental data about this shift. The pH of a sodium acetate solution is known to be given by

$$pH = \tfrac{1}{2}\, pK_w + \tfrac{1}{2}\, pK_{HA} + \tfrac{1}{2} \log M$$

The *pK* decrease observed from pH measurements for acetic acid lies between 0.180 and 0.195 at 1000 atm, the pK_w shift is expected to be 0.373. The observed pH change for Na-acetate should thus be equal to 0.277-0.284 pH, or 16.2-16.6 mv at 21°C. The experimental values in four successive experiments with 0.1*M* HCl as reference are: 16.0, 16.5, 16.7, 17.2 mv. The mean value corrected for the reference shift is 17.4 mv. The agreement is acceptable despite the fact that the pH of Na-acetate solutions is somewhat unstable. The solution should be prepared from acetic acid and CO_2-free NaOH, and very carefully adjusted at the neutralization point (pH = 8.4). At lower pH values, the observed shifts fall between that for acetate buffer and Na-acetate.

The pH of ammonia solutions is given by

$$pH = pK_w - \tfrac{1}{2}\, pK_{NH_4OH} + \tfrac{1}{2} \log M$$

The expected pH shift estimated from the data of Hamann and co-workers (24, 7) ($\log Kp/K_1 = 0.465$) can be shown to be 0.140 pH or 8.2 mv. The observed values for a $10^{-4}M$ solution in 0.1*M* KCl, with 0.1*M* HCl as reference, are 9.2 and 8.4 mv at pH 9.64. However, the glass electrode is known to present an alkaline error above pH 9, and the effect of pressure in this region has not been investigated. Further, Ag-AgI electrodes should be substituted to the Ag-AgCl electrodes, AgCl being soluble in NH_4OH. The agreement is thus to be accepted with caution, although no change in the asymmetry potential shift could be detected before and after 20-min treatment in $10^{-4}M$ NH_4OH.

Sea Water

The effect of pressure on the pH of sea water reveals a linear pH decrease which amounts to 0.3 pH at 1000 kg cm^{-2} (14).

The pressure resisting glass electrode has been adapted for deep sea investigations, and Distèche and Dubuisson (25) have been able to record the pH of the water of the Mediterranean Sea from the French Bathyscaphe to 2.350m depth.

The electrode cell is shown on Fig. 10 which is self-explanatory. The cell assembly is attached to

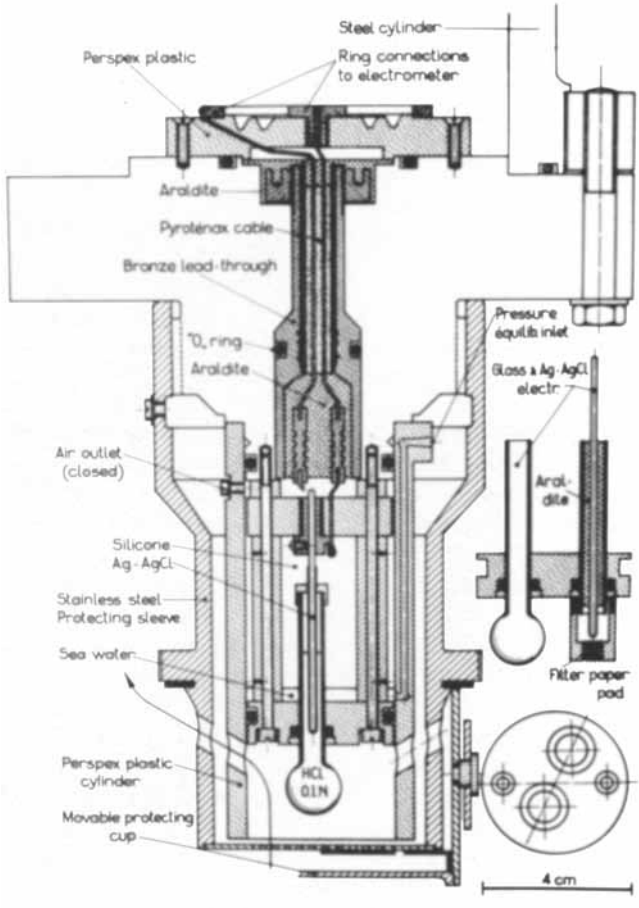

Fig. 10. Glass electrode assembly for deep sea investigations. From Distèche and Dubuisson (25).

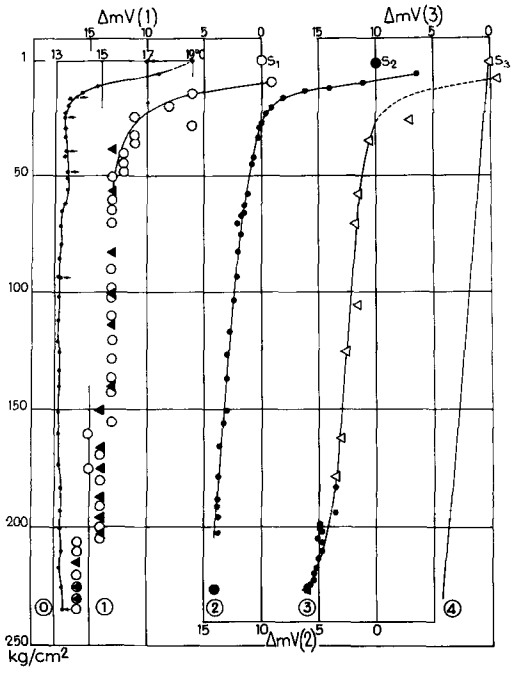

Fig. 11. pH changes recorded from the Bathyscaphe FNRS III between 0 and 2350m in the Mediterranean Sea. Curves 1, 2, 3 give $E_1 - E_p = f(P)$, E_1 corresponding to the pH values at the surface (S_1, S_2, S_3). Curve 4 gives $E_1 - E_p = f(P)$ for sea water of constant composition. Curve 0 represents the simultaneous temperature record. From Distèche and Dubuisson (25).

the lower end of a pressure resisting steel cylinder containing a d-c amplifier with cathode follower output, driving a pen recorder, on which the pH shifts are observed as the distance between two traces, one of which represents the zero drift of the apparatus. The error on ΔpH is certainly less than 0.01 pH unit and very close to 0.005 pH unit.

The curves on Fig. 11 were obtained during two dives. They represent direct manual measurements (large dots) with a precision potentiometer circuit and the data taken from the recorded curves (small dots). After a small increase near the surface, the pH is seen to decrease exponentially (~0.15 pH unit) from 0 to 400m. From 400m to 2350m, the bicarbonate/CO_2 ratio remains constant since the observed pH change corresponds to the effect of pressure on water of constant composition. A slight acid gradient is found near the bottom. The results obtained from the surface to the sea bottom agree with those recorded during the return to the surface, and there is a distinct correlation between the temperature curve and the pH curve.

Conclusion

The author is fully aware that his investigations on the behavior of a glass electrode at high pressure in various electrolytes cover only an extremely small portion of a very wide field. The important fact is that the reproducibility and the precision of the pH measurements with a glass electrode are affected by pressure but little or not at all. This statement is not a proof that the electrode gives, under all circumstances, the value of the hydrogen ion activity, but considering as a whole the results which have been obtained so far, makes one feel confident, since many results agree well with what is known from conductance and density data.

Further instrumental development is possible. A bright gold electrode can be added to the glass electrode cell for rH measurements[1] and it is planned to try glass electrodes sensitive to Na^+ and K^+ (26, 27).

The use of multielectrode cells, including a conductivity cell, would certainly broaden the field of electrochemical investigation at high pressures (properties of electrolytes, protein chemistry, kinetics, oceanography, and industrial technology).

Acknowledgment

The author wishes to express his gratitude to Professor B. B. Owen, Yale University, U.S.A., Dr. R. Bates and Dr. W. Hamer, National Bureau of Standards, U.S.A., for very helpful discussions and suggestions. Part of this work was supported by the "Centre Belge d'Océanographie."

Manuscript received Jan. 15, 1962; revised manuscript received May 1, 1962. This paper was prepared for delivery before the Indianapolis Meeting, April 30-May 3, 1961.

Any discussion of this paper will appear in a Discussion Section to be published in the June 1963 JOURNAL.

REFERENCES

1. J. C. Jamieson, *Chem. Phys.*, **21**, 1385 (1953).
2. S. D. Hamann, "Physico-chemical Effects of Pressure," Butterworths Scientific Publication (1957).
3. H. G. David and S. D. Hamann, *Trans. Faraday Soc.*, **55**, 72 (1959).
4. H. G. David and S. D. Hamann, *ibid.*, **56**, 1043 (1960).
5. A. J. Ellis, *J. Chem. Soc.*, **1959**, 3689.
6. R. J. H. Clark and A. J. Ellis, *ibid.*, **1960**, 247.
7. S. D. Hamann and W. Strauss, *Trans. Faraday Soc.*, **51**, 1684 (1955).
8. R. Schall, *Z. angew, Physik*, **2**, 252 (1950).
9. A. H. Ewald and S. C. Lim, Unpublished experiments, see ref. (2).
10. K. Hayashi and I. Kono, *Japan J. Physiol.*, **8**, 246 (1958).
11. B. B. Owen and S. R. Brinkley, *Chem. Rev.*, **29**, 461 (1941).
12. E. Cohen and K. Piepenbroek, *Z. Physik. Chem.*, **170A**, 145 (1934).
13. W. R. Hainsworth, H. J. Rowley, and D. A. MacInnes, *J. Am. Chem. Soc.*, **46**, 1437 (1924).
14. A. Distèche, *Rev. Sci. Instruments*, **30**, 474 (1959).
15. M. Le Peintre, *Bull. soc. franc. elec.*, 8ième série, **1** [9], 1 (1960).
16. W. H. Marburger, K. Anderson, and G. L. Wigle, A.N.L. 5298 Tech. Inf. Serv., Oak Ridge, Tenn. See ref. (15).
17. T. C. Poulter, *Phys. Rev.*, **40**, 860 (1932).
18. H. S. Harned and B. B. Owen, "The Physical Chemistry of Electrolytic Solutions," 2d ed., Reinhold Publishing Corp., New York (1958).
19. O. Redlick and J. Bigeleisen, *Chem. Rev.*, **30**, 171 (1942), see ref. (18).
20. S. Harned and B. B. Owen, *J. Am. Chem. Soc.*, **52**, 5079 (1930).
21. J. S. Smith, Dissertation, Yale University (1943), see ref. (18).
22. F. K. Johnson, H. Eyring, and M. J. Polissar, "The Kinetic Basis of Molecular Biology," John Wiley & Sons, New York (1954).

[1] The potential of the cell Au-$FeSO_4$ 0.05*M*, $Fe_2(SO_4)_3$ 0.025*M*, HCl 0.1*M*, AgCl-Ag changes very little with pressure in the range 0-1000 atm, and it might be interesting to replace the internal Ag-AgCl electrode of the glass electrode by a redox half cell; for the use of a glass electrode and an external redox half cell for rH determinations in oceanographic research, see ref. (28) and (29).

23. R. G. Bates, *J. Res. Nat. Bur. Standards*, **47**, 127 (1951).
24. J. Buchanan and S. D. Hamann, *Trans. Faraday Soc.*, **49**, 1425 (1953).
25. A. Distèche and M. Dubuisson, *Bull. Inst. Océanogr. Monaco*, No. 1174, p. 1-8 (1960).
26. S. H. Friedman and C. L. Friedman, *Anat. Rec.*, **138**, 129 (1960).
27. C. H. Townes, Cation Selective Glasses. Internat. Biophysics Congress, Stockholm, 1961.
28. A. Riviere, *C. R. Acad. Sci. France*, **248**, 717 (1959).
29. F. Manheim, *Acta Univ. Stockholmiensis*, Stockholm Contributions in Geology, **VIII:3**, 27 (1961).

The Performance of Hydrocarbons in Ion Exchange Membrane Fuel Cells

L. W. Niedrach

Research Laboratory, General Electric Company, Schenectady, New York

ABSTRACT

Exploratory work has been performed on the behavior of hydrocarbons and carbon monoxide in acidic ion-exchange membrane fuel cells having platinum and palladium black electrodes. Electrical output was obtained from such cells when propane, propylene, ethylene, methane, and carbon monoxide were used as fuels. In all cases qualitative tests indicated at least partial oxidation to CO_2. All of the gases performed better on platinum than palladium. In all cases the performance improved with increasing temperature in the range 27°-85°C. None of the fuels tested performed as well as pure hydrogen in the same cells.

In the development of the ion-exchange membrane fuel cell, the greatest emphasis to date has been placed on its utilization as a hydrogen-oxygen cell. Detailed accounts of the construction, operation, and performance of such cells operating on hydrogen have been given elsewhere (1-3). Some exploratory work on the performance of hydrocarbons has now been done using the platinum and palladium black electrodes that have been regularly employed in the studies with hydrogen. Only cells with acidic electrolytes were used. While it was recognized that such catalysts had little chance of proving optimum for the desired oxidations, it seemed likely that their performance would be illustrative of some of the general effects which will be encountered during the electrolytic oxidation of hydrocarbons. This paper presents the results of the experimental work.

Experimental

A diagram showing the cell construction appears in Fig. 1. The heart of the unit is the membrane-electrode structure. A reinforced sulfonated phenol formaldehyde casting resin in its acidic form was used for the electrolyte. Thin layers of the electrode materials (platinum or palladium black) were bonded on the surfaces of the membrane electrolyte. These layers had a thickness of about a mil and a circular area of 11.4 cm^2. The thickness of the electrolyte was approximately 0.06 cm. Since the catalyst layers are relatively poor electronic conductors, platinum gauzes (80 mesh) were buried in the electrolyte surfaces to serve as current collectors. Tabs on the gauzes served as terminals for the cells.

The membrane-electrode structure was mounted in a Lucite housing having a diameter of 3 in. Neoprene rubber gaskets (1/64 in. thick) were used for all seals. Stainless steel backing plates were used to prevent warping of the Lucite during operation at elevated temperatures.

Experiments at room temperature were performed with the cells mounted in air. For operation at temperatures above room ambient, they were mounted in a water bath containing distilled water. The gases that were fed to the cells were then preheated and saturated with water by passing them through coils of copper tubing followed by glass saturators that were also immersed in the bath. A schematic diagram of the arrangement is shown in Fig. 2.

To facilitate handling, individual cell assemblies were prepared as modules which could be inserted

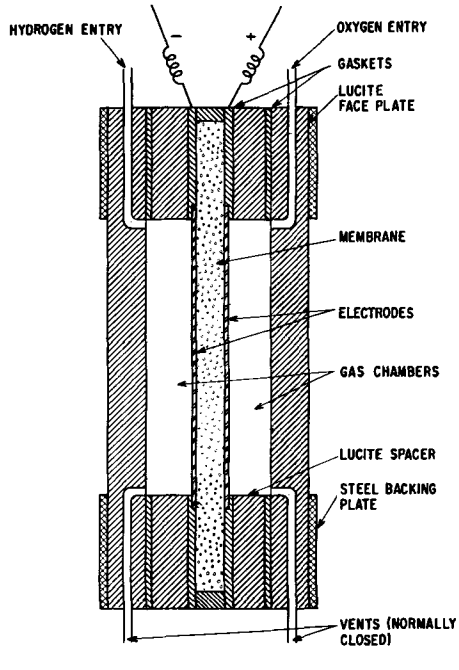

Fig. 1. Cell structure

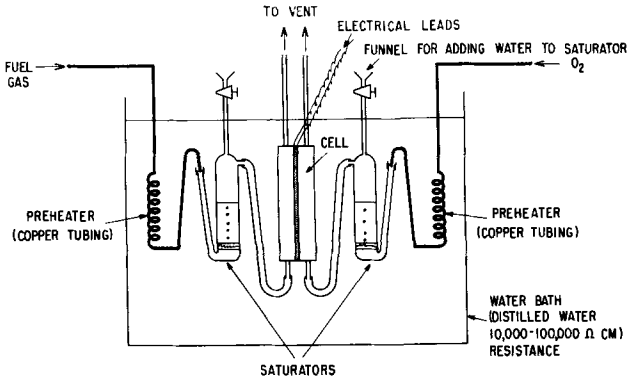

Fig. 2. Diagram showing arrangement for experiments at elevated temperatures.

through openings in the lid used on the water bath. In preparing the modules a cell housing was fastened to a rod extending down from a Bakelite cover which fitted a hole in the lid of the water bath. Leads from a terminal jack on the cover were connected to the cell terminals. The vent lines from the cell were led through holes in the cover.

By using distilled water in the thermostat bath the leakage path across the cell terminals could be maintained at reasonable values even at 85°C. Actual leakage resistances measured with the aid of a dummy cell housing were 15,000 ohms at 55°C and 6000 ohms at 85°C. Under these conditions the effect of the leakage current was negligible when the cell was operating under load. Leakage through the bath, however, prevented the measurement of true "open-circuit" potentials.

Performance measurements were made at three temperatures: 27°, 55°, and 85°C. At each temperature a reference polarization curve was first obtained with the cell operating on hydrogen and oxygen in order to insure that the units were functioning properly. Then successive runs at a given temperature were made with the various test gases. Immediately after changing the fuel gas the cells were placed on 1-ohm loads and permitted to operate with a gas flow of a few milliliters per minute until a steady state was established. In some cases this took as long as 1 hr. This procedure was employed in order to remove remaining traces of the previous fuel from the catalyst surface as well as from the feed lines and saturators. During operation a continuous slow flow of gas was used. The exhaust gases were bubbled through $Ba(OH)_2$ to test for CO_2.

Electrolytic oxygen was used as the oxidant in all cases. Electrolytic hydrogen was also used. With the exception of the natural gas, which was obtained from the house line, all of the remaining gases were Matheson C.P. grade. While all are reported to be low in hydrogen, the tank gases were checked mass spectrographically with the results shown in Table I.

Table I. Amount of hydrogen in test gases

Gas	Vol. % H_2
Propylene	<0.00010
Propane	<0.00002
Ethylene	0.033
CO	<0.015

While the gases were not analyzed quantitatively for carbon dioxide, qualitative tests were performed by bubbling through $Ba(OH)_2$ solutions under conditions simulating those later used during cell operation. No precipitates developed from the tank gases during periods exceeding those used in testing the operating cells. All gases were used without further purification.

Polarization curves were obtained by measuring the current with a Sensitive Research Instrument Company milliammeter and the cell potential with a Rubicon potentiometer. To aid in following slow changes in the voltage with time, a Varian recorder was connected across the cells during measurements. The time required to establish a steady state varied from a few seconds to over an hour.

Normally potentials were followed for a minimum of 10-15 min before final measurements were taken; however, in extreme cases over an hour was required to reach a steady state. Recordings showing time effects in such extreme cases appear in Fig. 6 and are discussed later. In no case were voltage oscillations observed.

The reproducibility of the data varied considerably among the fuels and was somewhat dependent on the temperature and current density. With the more reactive fuels, potentials could generally be reproduced to within 15-20 mv in the current density region under 2 ma/cm^2. As current densities increased, larger uncertainties were incurred so that above 5 ma/cm^2 they were of the order of 100 mv. In the case of propane two regions of operation were found with the transition between them being temperature dependent. At low current densities (no greater than 1 ma/cm^2) potentials could be reproduced to within 15-20 mv; however, conditions became very unstable at higher current densities as discussed below.

Results and Discussion

Figure 3 shows the performance of a number of fuels at room temperature in a cell having platinum electrodes. The curve for the hydrogen fuel serves as a reference. It is to be noted that the per-

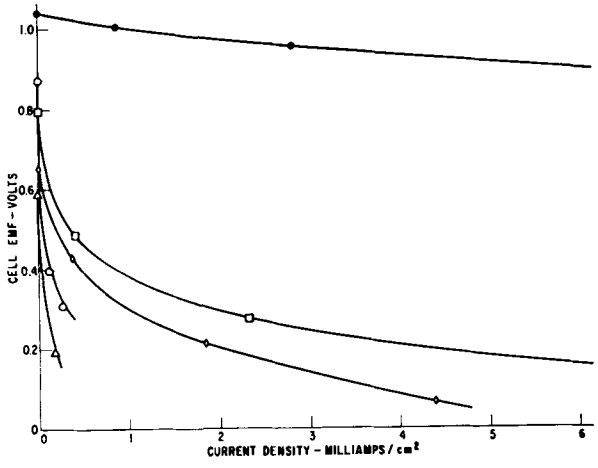

Fig. 3. Performance of several fuels in a membrane cell with platinum electrodes, sulfonated phenol formaldehyde resin; 0.018 g/cm^2 Pt/electrode; room temperature; • H_2; □ CO; ◇ C_2H_4; ○ C_3H_8; △ natural gas.

formance of the natural gas, which was 95% methane, was the poorest among the hydrocarbons, as is to be expected.

In this case it is possible that small traces of sulfur-containing impurities had some influence on its performance. Subsequent tests with hydrogen and the pure hydrocarbons, however, indicated that if such were the case the effect was not a permanent poisoning of the catalyst.

When a cell was run on a gas that contained a carbon compound, a continuous flow was employed, and the effluent fuel gas was bubbled through a $Ba(OH)_2$ solution. In all cases white precipitates of $BaCO_3$ indicated that at least partial oxidation to CO_2 occurred. No attempts were made to identify other products of the oxidations.

A cell operating on ethylene, one of the more reactive hydrocarbons, was used to obtain more quantitative information about the extent of oxidation at room temperature. For this purpose the fuel cell chamber was connected to a small gas buret, and the cell was operated on the fuel within the system. The net rate of change in volume of the gas phase was then followed at several current densities. The data, both volumetric and analytical, indicated that a minimum of 50% of the ethylene was oxidized completely to CO_2.

Performance data for the hydrocarbons in a cell having palladium electrodes are shown in Fig. 4. In general, the performance paralleled, but was inferior to, that of the cell having platinum electrodes. In part, at least, the poorer performance may have resulted from a somewhat lower surface area (12 m^2/g *vs.* 36 m^2/g for Pt as determined by krypton adsorption).

Data were also obtained for a number of gases at elevated temperatures, 55° and 85°C. For illustration the data obtained with cells having platinum electrodes are shown in Fig. 5 (for propane), Fig. 7 (for propylene), and Fig. 8 (for CO). Just as at room temperature, the corresponding data (not shown) for cells with palladium electrodes paralleled, but were inferior to, those for the cells having platinum electrodes.

The data in Fig. 5 for the cell operating on propane show the typical improvement in performance with temperature associated with an activated process. On each curve the points are numbered to indicate the order in which they were taken. From the clustering of points 3, 5, and 7 at 55° and 85°C it is seen that reasonable reproducibility is obtained independent of whether a point is approached from a previous operating point on a higher or lower load.

Up to currents of the order of 1 ma/cm^2 the curves are concave upward as is normal for activated electrode processes. At currents greater than 1 ma/cm^2 the polarization curves become concave downward, and indications of an approach to a limiting current are evident. This type of behavior is indicative of concentration polarization and could be associated with diffusion control. It could also be associated with slow adsorption or desorption kinetics, if, as is likely, adsorption of the hydrocarbon on the electrode is a prerequisite to reaction. Because the effect occurs at relatively low current densities, it appears more likely to be associated with slow sorption kinetics.

Eventually still another effect becomes apparent when on higher loads both the current and potential fall. This is most clearly shown by point 11 at 85°C. When a steady state is attained the current and

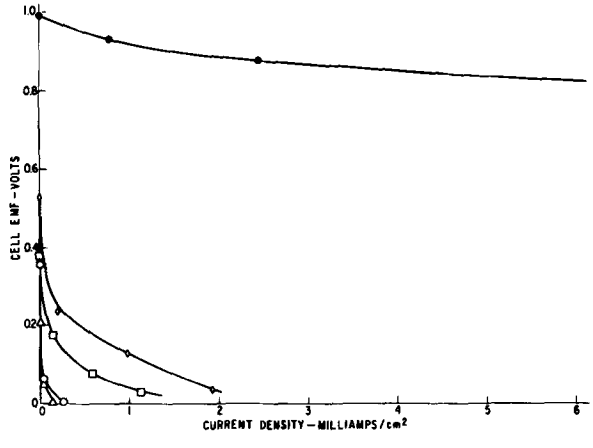

Fig. 4. Performance of several fuels in a membrane cell with palladium electrodes, sulfonated phenol formaldehyde resin, 0.0088 g/cm^2 Pd/electrode; room temperature; • H_2; □ CO; ◇ C_2H_4; ○ C_3H_8; △ natural gas.

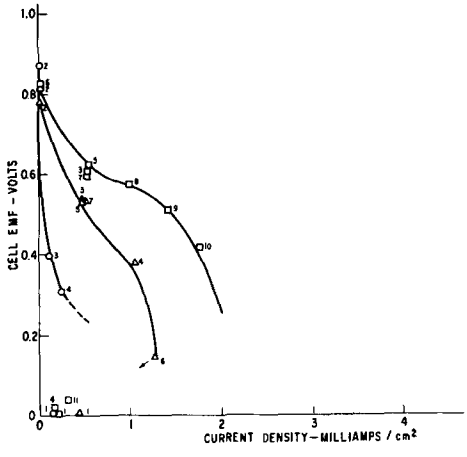

Fig. 5. Performance of propane at several temperatures, sulfonated phenol formaldehyde resin; 0.018 g/cm^2 Pt/electrode; ○ 27°C; △ 55°C; □ 85°C.

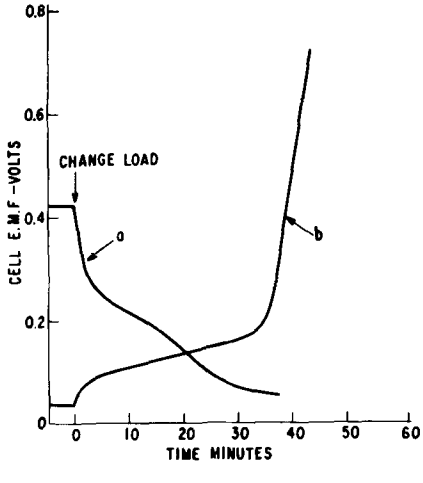

Fig. 6. Change in potential of a propane cell with time, sulfonated phenol formaldehyde resin; 0.018 g/cm^2 Pt/electrode; 85°C; a, 20-10 ohm load; b, 10-100 ohm load.

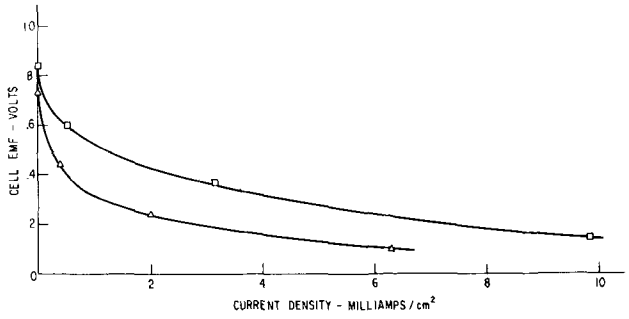

Fig. 7. Performance of propylene at two temperatures, sulfonated phenol formaldehyde resin; 0.018 g/cm² Pt/electrode; △ 55°C; □ 85°C.

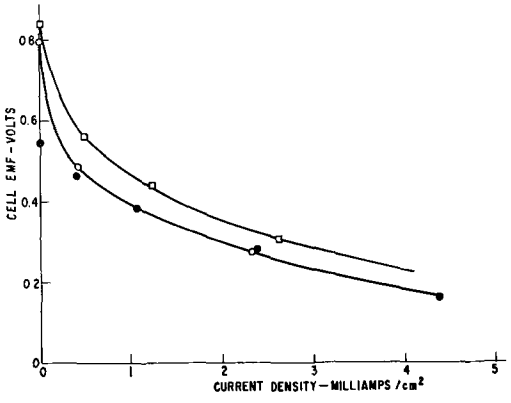

Fig. 8. Performance of carbon monoxide at two temperatures, sulfonated phenol formaldehyde resin; 0.018 g/cm² Pt/electrode; ○ 27°C; ● 27°C (a second cell); □ 85°C.

voltage relationship shows a marked transition in the performance. The changes in potential with time as the cell approached a steady state on point 11 are shown by the potential-time plot in Fig. 6.

From previous experience with the ion-exchange membrane fuel cell it is known that the observed behavior is not associated with the oxygen electrode. This means, then, that the potential of the fuel electrode finally reaches a value approximating that of the oxygen electrode so that the net voltage across the cell is close to zero. It is therefore felt that the break in the current-time curve of Fig. 6 is associated with the formation of an adsorbed oxygen (oxide) layer on the platinum electrode and that the gradual change in performance on point 11 represents a shift in the kinetics from those on a clean metal electrode to those on an oxide film electrode. It is likely that this transition would have been observed on points prior to 11 had sufficient time been allowed. However, it is also clear that, below some critical load, operation is stable under conditions that result in moderate cell potentials, cf. points 3, 5, 7 in Fig. 5 and curve b in Fig. 6 which shows the change in potential with time when the cell was shifted from a 10-ohm load to 100 ohms. In this case the prolonged pause in the potential corresponds to the destruction of the oxide film on the electrode.

This behavior is by no means unique and has been observed in the electrolysis of such substances as formic acid (4), methyl alcohol (5, 6) and formaldehyde (7). In all these cases the potentials at which the change in performance has occurred has also been consistent with the formation of an oxide film on the metal surface and has resulted in this explanation having been invoked in the past.

As already noted, it seems likely that adsorption of propane on the electrode surface is a prerequisite for reaction. It is also probable that this adsorption step results in the dehydrogenation of the propane to propylene or beyond as a preliminary step in the reaction chain. For this reason it was felt of interest to test the behavior of propylene in the cell. Performance data are shown in Fig. 7.

It is to be noted that at current densities less than 1 ma/cm² the cells operating on propane seem to be slightly better than those operating on propylene. While the data are not adequate to assure that this is a real difference, it is quite possible that the hydrogen that would be split from the propane could account for this effect.

The absence of the limiting current from the polarization curves for propylene is of interest. An implication is that the sorption kinetics are more favorable in the case of the unsaturated molecule. Preliminary adsorption measurements with ethane and ethylene using related cell structures tend to confirm that it is actually the rate of adsorption of a saturated hydrocarbon that is limiting. It was found that the unsaturated molecule adsorbed at a much greater rate on clean electrode surfaces than the corresponding saturated species (8).

Another point of interest in connection with the propylene is the absence of the transition in performance to that on an oxide surface during operation on high loads. While probably relating to a higher rate of adsorption, it also appears to be related directly to the rate of reduction of oxide films on platinum by the various materials. In separate tests it was found that propane reacts with such a film extremely slowly and, when an oxidized electrode is exposed to propane, the time required for the potential to reach that of a fuel electrode is of the order of an hour. In addition a prolonged break is observed in the transition curve at a potential of about 0.1v *vs.* the oxygen electrode. The same reduction with propylene is rapid (a few minutes) and, for comparison, the reaction with hydrogen occurs in seconds. With the propylene, therefore, the direct reduction of the oxide film by the fuel gas is sufficiently rapid that the film is not encountered under the usual operating conditions.

The behavior of carbon monoxide at two temperatures is shown in Fig. 8. Its performance is analogous to that of propylene. Again no indication of a limiting current is evident. In this case, of course, the number of products is much more limited than in the case of the higher molecular weight hydrocarbons and the product, CO_2, is not tightly adsorbed. Furthermore CO, like propylene, reacts rapidly with surface oxides on the platinum electrode.

Summary and Conclusions

The ion-exchange membrane fuel cell employing platinum and palladium black electrodes has been shown to be operable on hydrocarbons and carbon

monoxide. Performance of the cells with these fuels is inferior to that obtained with hydrogen as the fuel. The performance of the cells with the present electrode materials is probably illustrative of the general type of effects which will be encountered during the electrolytic oxidation of hydrocarbons.

Acknowledgments

The author is indebted to F. J. Norton and P. D. Zemany for mass spectrographic analyses of gas samples. He also acknowledges helpful discussions with S. Gilman and W. T. Grubb.

Manuscript received Dec. 7, 1961; revised manuscript received May 28, 1962. This work was performed in part under Contract No. DA 44-009 ENG-3771 with the U. S. Army Engineer Research and Development Laboratories.

Any discussion of this paper will appear in a Discussion Section to be published in the June 1963 JOURNAL.

REFERENCES

1. W. T. Grubb, U. S. Pat. No. 2,913,511, assigned to the General Electric Co., Nov. 17, 1959.
2. W. T. Grubb and L. W. Niedrach, *This Journal*, **107**, 131 (1960).
3. E. J. Cairns, D. L. Douglas, L. W. Niedrach, *A.I.Ch.E. Journal*, **7**, 551 (1961).
4. E. Müller, *Z. Elektrochem.*, **29**, 264 (1923).
5. S. Tanaka, *ibid.*, **35**, 38 (1929).
6. T. O. Pavela, *Ann. Acad. Sci. Fennicae, Ser A. II.*, No. 59 (1954).
7. E. Müller and S. Takegami, *Z. Elektrochem.*, **34**, 704 (1928).
8. L. W. Niedrach, Unpublished results.

Electrical Double Layer Capacities of Iron During Forced Cathodic Decay of Passivity

G. M. Schmid and Norman Hackerman

Department of Chemistry, The University of Texas, Austin, Texas

ABSTRACT

A study of the behavior of the differential capacity of the electrical double layer of high-purity, zone-refined iron in 0.1N Na_2SO_4, pH 2.3-6.5 has been made during forced cathodic decay of passivity using a fast single pulse technique. The capacity-time curve shows a maximum >22 $\mu f/cm^2$ (but <35 $\mu f/cm^2$) at the end of the Flade plateau. This is explained on the basis of a desorption step of an as yet undefined charged particle. The capacity at O_2 evolution potentials is 6-8 $\mu f/cm^2$, compatible with an oxide film; at H_2 evolution potentials it is 19 $\mu f/cm^2$, independent of pH in both cases. The charge involved in the Flade plateau is 550-850 $\mu coul/cm^2$ with an average 680 $\mu coul/cm^2$.

The exact causes for the electrochemical passivity of metals, and especially that of iron, are still largely in dispute. One school of thought suggests that the responsible agent is a stoichiometric, three-dimensional oxide film (1), or a sandwich type film consisting of different oxides (2). Oxide films with a defect structure, n-type at the metal-film and p-type at the film-electrolyte junction, have also been proposed (3). A second school assumes the sorption of oxygen or some oxygen-containing species as the reason for passivity (4). Ample experimental evidence for both points of view can be found. A postulate reconciling both standpoints has been proposed by one of us (5). It suggests that the immediate cause of passivity is the rapid sorption of a monolayer of some oxygen-containing species. In time this monolayer grows into a three-dimensional oxide film, self-limiting in thickness and responsible for "longlived" passivity. The sorbed monolayer accounts for the rapid potential changes associated with passivity.

The usefulness of measurements of the differential capacity of the electrical double layer (edl) in the study of adsorption on metal-solution interfaces has been demonstrated (6). On solid electrodes in the region of their nearly ideal polarizability empirical calibration of edl capacity *vs.* amount adsorbed seems to be possible in some cases (7). The potential region in which the adsorption, or desorption, occurs is characterized by a maximum in the capacity-potential curve. For nonideally polarizable electrodes the difficulties in obtaining "true" edl capacities free of the influence of faradaic processes have been solved recently with the aid of high-frequency bridge techniques (8) and short risetime single pulses (9). These techniques have made possible a study of the behavior of the edl of iron during forced cathodic decay of passivity, especially during the course of the Flade plateau.

Experimental

The electrodes consisted of zone-refined, high-purity iron containing $<$ 10 ppm C, 28 ppm O_2, 2 ppm N_2 (10). This was kindly provided by Battelle Memorial Institute as a billet. The electrodes were cut into cylinders topped by a hemisphere, approximately 0.3 cm^2 in projected area, thoroughly electropolished and base mounted on Pyrex glass using Teflon washers. Pretreatment consisted of polishing with No. 4/0 emery paper, etching with concentrated HCl, and degreasing with acetone. It was estimated that the roughness factor was about two. The electrolytes were made up with thrice recrystallized Na_2SO_4 and conductivity water obtained from a Barnstead conductivity still ($\sim 2 \times 10^{-7}$ ohm^{-1} cm^{-1}), to 0.1*N*. The pH was adjusted with

H_2SO_4 to values between 2.3 and 6.5. The electrolytes were pre-electrolyzed for 48 hr at 80 ma between Pt electrodes. The conventional type all-Pyrex cell had a water jacket and was thermostated at 5°C. Grade A helium was bubbled through the electrolyte at all times. Immediately after immersion the electrodes were either cathodically protected with 5 ma/cm² or were made passive.

Differential capacities were measured with a single pulse method described in detail elsewhere (9). The method consists of calculating the capacity from the initial slope of the potential-time curve produced by the pulse under the assumption that the slope of the potential-time function just before onset of the pulse is zero. This is not true here. The slope before onset of the pulse (< 0.01 v/sec) can however be neglected as compared to the slope produced by the pulse (> 5 v/sec), with the exception of the steep transition from O_2 evolution potentials to the Flade plateau and from the Flade plateau to H_2 evolution potentials, of about 1 sec duration each. The electrical circuit used in the experiments is shown in Fig. 1. The test electrode was passivated from a negative potential corresponding to a polarizing current of 5 ma/cm² cathodic with a strong (~ 200 ma/cm²) anodic pulse from an auxiliary battery. The electrode was then kept passive with a constant anodic current of 80-160 μa/cm² drawn from the pulse generator (9) through a large area platinized Pt wire gauze. The potential of the test electrode was measured with respect to a saturated calomel electrode (SCE) through a Haber Luggin capillary by feeding the output of this cell through a type-L preamplifier into the lower beam of a Tektronix type 555 oscilloscope used on single sweep push button triggered operation.

In addition to the steady anodic current the pulse generator delivered cathodic pulses at the regular rate of 1 pulse every 3.5 sec. Pulse risetime was 0.1 μsec, duration 100 μsec, height 0.211 ma. The potential changes of the test electrode caused by these pulses were displayed using a type-D preamplifier and the upper beam of the oscilloscope, triggered by the pulse itself. The gate output of the lower beam was also fed into test electrode and polarizing electrode. The scope delivers + 30v to the gate as long as the beam is in motion. This results in a cathodic current at the test electrode which is superimposed on the anodic steady-state current delivered by the pulse generator and with a suitable series resistor gives an over-all cathodic decay current of 30-100 μa/cm². With this circuit, manually starting the lower beam simultaneously initiates cathodic decay of passivity. A limited number of pulses displayed by the upper beam, and occurring during this decay, could be identified by changing the vertical and horizontal control settings between pulses. Figure 2 shows a schematic of the type of photographs obtained with a Dumont Polaroid Oscilloscope camera. These allowed calculation of capacity-time curves, which should not be confused with the more familiar capacity-potential curves. The accuracy of the capacity measurement was limited by the nonlinearity of the oscilloscope amplifiers to 3%.

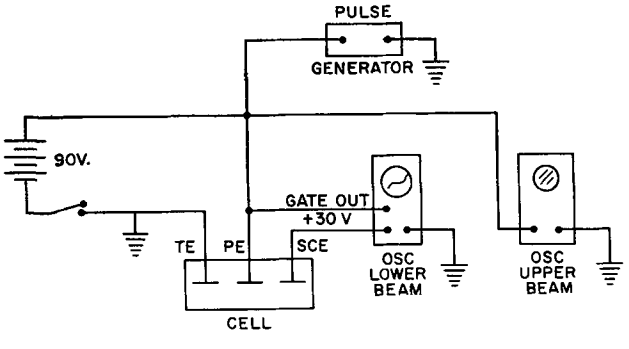

Fig. 1. Experimental arrangement, circuit diagram: TE, test electrode; PE polarizing electrode; SCE saturated calomel electrode.

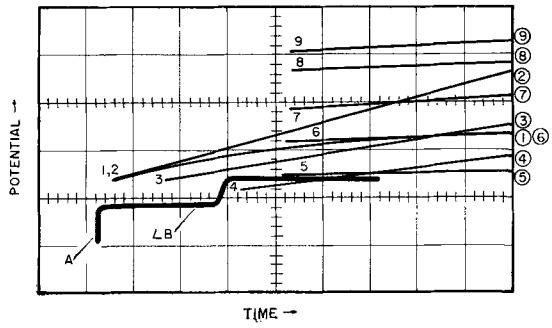

Fig. 2. Oscilloscope tracing: LB, lower beam displaying cell potential, 1 v/cm, 5 sec/cm, 55 μa/cm² cathodic; 1-9, upper beam displaying variations in cell potential due to the pulse, 2 mv/cm, 10 μsec/cm, 0.211 ma pulse current. Traces are numbered in their sequence and correspond to points on the lower beam 3.5 sec apart starting at A.

Results

The first capacity value on the capacity-time curves (Fig. 3) represents the capacity of the passive electrode. This value is established shortly after the electrode is passivated and is independent of the time during which the electrode is kept passive up to 24 hr. It is also independent of the applied anodic current density (80-160 μa/cm²), the *p*H between 2.3 and 6.5, and the potential between + 0.9 and + 1.1v *vs.* SCE. It is reasonably reproducible, varying between 6.0 and 8.0 μf/cm².

After the initial low value, the capacity rises to a maximum during the course of the Flade plateau,

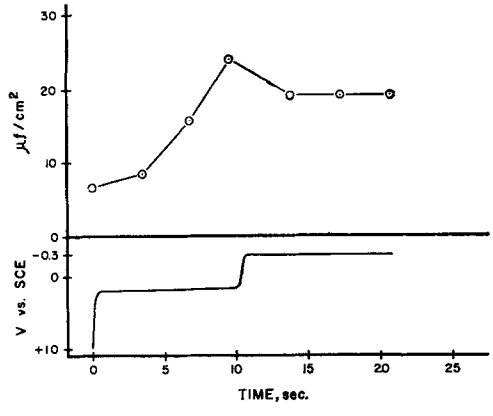

Fig. 3. Capacity-time (upper) and potential-time (lower) curves; 65 μa/cm² cathodic, pH = 4.5. The time-potential plateau at about +0.3v vs. SCE is the Flade plateau; the other plateau at —0.3v is hydrogen evolution.

culminating right at the breakdown of passivity within the limit of timing error of ± 1 sec. With the method used in this investigation, the values of the maximum could not be determined precisely. The value is > 22 μf/cm^2 in all cases, sometimes as high as 35 μf/cm^2.

After the passivity has broken down and H_2 evolution potentials have been reached, the capacity rapidly assumes a constant value of 19 μf/cm^2. This is independent of *p*H in the investigated region of the cathodic current (30-100 μa/cm^2) and of the potential between —0.3 and —0.5v *vs.* SCE, within the limit of experimental error.

The amount of charge involved in the Flade plateau varied from 550 to 850 μcoul/cm^2 with an average value of 680 μcoul/cm^2. Within these limits no influence could be detected of the time during which the electrode was kept passive prior to decay (up to 24 hr), of the magnitude of the cathodic decay current, or of the *p*H between 2.3 and 6.5.

Discussion

Various attempts have been made to measure the steady-state differential capacity of the edl on iron. Alternating current methods with frequencies up to 10 kcps were used by Engell and Ilschner (11) and by Prazak and co-workers (12); low-frequency measurements were reported by Franke, Knorr, and Breiter (13). It has already been pointed out (9, 14) that the use of these methods entails the danger of measuring some part of the faradaic capacity together with the "true" edl capacity. Correspondingly, the reported values are rather high and show frequency dependence, as would be expected if faradaic phenomena are involved. The dynamic method used by Sukhotin and Kartashova (15) and the square wave method as used by Popat and Hackerman (16) seem to suffer from the same faults. The "steady-state" values reported here, 6-8 μf/cm^2 for O_2 evolution potentials and 19 μf/cm^2 for H_2 evolution potentials, agree well with data obtained in this laboratory with a potentiostatic technique using a square wave signal and a method of calculation similar to the one used in this paper (17).

Low capacity values, especially on the oxygen evolution side, have frequently been associated with the presence of oxide films (18). This interpretation is certainly correct in some cases. However, one should allow from the definition of the differential capacity,

$$C = \delta q/\delta E$$

that small capacity values indicate primarily that the surface in question is in a quiescent state, that is, in a state and a potential region where little variation of charge with potential occurs, a region where adsorption and desorption processes are absent. Correspondingly, high-capacity values indicate an "active" surface, one which is in a potential region where adsorption processes do take place.

In these experiments the capacity shows a rapid rise immediately after the cathodic decay current is switched on. Whereas the presence of well-defined three-dimensional oxide films at actual oxygen evolution potentials cannot be ruled out, the behavior of the capacity-time curve does not support the presence of an oxide film at the Flade plateau, but rather the occurrence of a desorption (or adsorption) process. As would be expected, the iron surface is most "active" at the point where the passivity breakdown actually occurs.

As can be seen from Fig. 3, it is not possible in this case to relate capacity values directly with the amount of coverage on the electrode as was done on Pt (7). The constant cathodic current should lead to a linear decrease of coverage with time. Moreover there is a possibility of chemical dissolution of the film, as is suggested by the poor reproducibility of the amount of charge associated with this coverage. Evidence to the same effect was also obtained by Bonhoeffer (19).

Both neutral and charged particles are expected to exhibit a maximum in the capacity-potential curve when the capacity is measured by a low or intermediate frequency a-c technique. In the case of adsorption of neutral molecules one measures an adsorption capacity in the sense of Bockris (20), the magnitude of which is caused by the accompanying charge transfer into the adsorbed layer. High-frequency measurements show that the peaks caused by neutral substances disappear with increasing frequency (8). What remains is a step in the capacity function which can be explained by the difference in the geometrical and dielectric properties of the edl before and after the adsorption step. No sudden changes in the charge of the metal with potential occur. High-frequency data on the adsorption of charged particles are not available at present (21). It would be expected that the peaks do not disappear in this case since the charge of the adsorption layer causes an increase in charge on the metal side and with it an increase in capacity in the potential region of adsorption.

The single pulse technique as used in this paper is equivalent to a-c measurements at high frequencies (> 500 kcps). This leads to the conclusion that the high-capacity region the electrode exhibits when going through the Flade plateau is caused by the desorption of charged particles. Obviously capacity data alone do not allow firm conclusions as to the nature of these particles. We may be dealing with OH^- or HO_2^- ions, created by the reductive action of the cathodic current.

The nondependence of the capacity values on the *p*H is not surprising if it is kept in mind that the data reported here are "dynamic" rather than steady-state values and should be influenced primarily by the structure of the surface and not by the properties of the electrolyte.

Summary

The differential capacity of high-purity, zone-refined iron has been measured during cathodic decay of passivity with a single pulse technique in 0.1*N* Na_2SO_4 solutions of *p*H 2.3-6.5 (with H_2SO_4).

The capacity-time function during this decay exhibits a maximum at the end of the Flade plateau. It is shown that high-capacity values when meas-

ured with a fast single pulse method coincide with the surface being in an "active" state and that adsorption and desorption phenomena of charged rather than neutral particles are involved. It is concluded that the desorption of an undefined charged particle is part of the reaction sequence occurring during the regime of the Flade plateau.

The capacity during O_2 evolution (80-160 $\mu a/cm^2$) was found to be 6-8 $\mu f/cm^2$, during H_2 evolution (30-100 $\mu a/cm^2$) 19 $\mu f/cm^2$. No dependence on pH in the investigated region could be detected. The charge involved in the Flade plateau was calculated to be 550-850 $\mu coul/cm^2$ with an average value of 680 $\mu coul/cm^2$.

Acknowledgment

The authors take this opportunity to express their sincere appreciation for support of this research by a grant from the Robert A. Welch Foundation of Houston, Texas, and by Contract Nonr 375(15) with the Office of Naval Research. They also are pleased to acknowledge their appreciation for the sample of zone-refined iron provided by the Battelle Memorial Institute.

Manuscript received April 26, 1962; revised manuscript received July 3, 1962.

Any discussion of this paper will appear in a Discussion Section to be published in the June 1963 JOURNAL.

REFERENCES

1. U. R. Evans, "Metallic Corrosion, Passivity and Protection," 2nd ed., Arnold, London (1948).
2. H. Goehr and E. Lange, *Naturwissenschaften*, **43**, 12 (1956).
3. M. J. Pryor, *This Journal*, **106**, 557 (1959).
4. H. H. Uhlig, *Z. Elektrochem.*, **62**, 626 (1958); Y. M. Kolotyrkin, *ibid.*, **62**, 664 (1958).
5. Norman Hackerman, *ibid.*, **62**, 632 (1958).
6. D. C. Grahame, *Chem. Revs.*, **41**, 441 (1947).
7. H. A. Laitinen and C. G. Enke, *This Journal*, **107**, 773 (1960).
8. W. Lorenz, *Z. Physik. Chem.*, (NF), **26**, 424 (1960).
9. J. S. Riney, G. M. Schmid, and Norman Hackerman, *Rev. Sci. Instr.*, **32**, 588 (1961).
10. G. W. P. Rengstorff and A. B. Goodwin, *J. Metals*, **7**, 467 (1955).
11. W. J. Engell and B. Ilschner, *Z. Elektrochem.*, **59**, 716 (1955).
12. M. Prazak, V. Prazak, and Vl Cihal, *ibid.*, **62**, 739 (1958).
13. K. Franke, C. A. Knorr, and M. Breiter, *ibid.*, **63**, 226 (1959).
14. G. M. Schmid and Norman Hackerman, *This Journal*, **109**, 243 (1962).
15. A. M. Sukhotin and K. M. Kartashova, *Russ. J. Phys. Chem.* (English Transl.), **33**, 562 (1959).
16. P. V. Popat and Norman Hackerman, *J. Phys. Chem.*, **65**, 1201 (1961).
17. N. E. Wisdom and Norman Hackerman, To be published; G. A. Aronowitz and Norman Hackerman, To be published.
18. J. J. McMullen and Norman Hackerman, *This Journal*, **106**, 341 (1959).
19. K. F. Bonhoeffer, "Activation of Passive Iron," in *Soviet Electrochemistry II* (Consultants Bureau, New York, 1961), 210.
20. J. O'M. Bockris and Hideaki Kita, *This Journal*, **108**, 676 (1961).
21. See however, M. Senda and P. Delahay, *J. Am. Chem. Soc.*, **83**, 3763 (1961).

Anodic Oxidation of Methanol on Platinum

II. Interpretation of Potentiostatic Current-Potential Curves in Acidic Solution

S. Gilman and M. W. Breiter

Research Laboratory, General Electric Company, Schenectady, New York

ABSTRACT

The shape of periodic potentiostatic current-potential curves at low sweep rate in 1*N* $HClO_4$ at different methanol concentrations is discussed on the basis of the methanol and oxygen coverage of the surface. At the foot of the first oxidation wave the current is due solely to the oxidation of adsorbed methanol molecules for $0.3 \leq \theta_M < 0.9$. Adsorption and the subsequent discharge step are rate-determining. For $\theta_M < 0.3$ methanol oxidation occurs at a larger rate. Two possible interpretations are suggested. The decrease of the current after the first peak is attributed to the blocking action of adsorbed oxygen atoms. The shape of anodic current-potential curves which were taken with single sweeps of different sweep rate in 1*N* $HClO_4$ + 1M CH_3OH is interpreted on the basis of a concept of two partial currents of methanol oxidation.

The characteristic shape of current-potential curves and the results of the analysis of reaction products have been widely reported as evidence for theories of the oxidation mechanism of fuels such as CH_2O, CHOOH, CH_3OH, etc., in alkaline and acidic solutions (1-13). Potentiostatic current-potential curves show current peaks which divide the whole oxidation range into two or more parts. The occurrence and the potential of the peaks depend on many parameters (nature and concentration of the fuel and of the electrolyte, pretreatment of the electrode, temperature, electrode material).

As the knowledge of the adsorption of fuel and oxygen in the potential range of fuel oxidation has been inadequate, the interpretation of the shapes of the current-potential curves and, even to a greater extent, the theories of the oxidation mechanism have remained of a more or less speculative nature. Results on the adsorption of methanol and oxygen under the conditions of quasistationary

potentiostatic current-potential curves were reported in the first paper of this series (14). An interpretation of the current-potential curve of methanol oxidation at low sweep rate which is based on the results of the first paper and additional investigations is attempted in this paper. The shape of potentiostatic current-potential curves which were obtained with single potential sweeps of different sweep rate is discussed. The approach is suggestive for further studies which could lead to the complete elucidation of the reaction mechanism.

Experimental

All measurements were made at 30°C using the equipment and chemicals previously described (14). All recorded potentials are referred to a hydrogen electrode in the same solution as the test electrode. The technique by Will and Knorr (15) was used for the measurement of the *I-U* curves.

Periodic potentiostatic I-U curves at low speed in unstirred solutions.—The anodic and the cathodic part of a potentiostatic *I-U* curve on smooth platinum in 1*N* $HClO_4$ + 1M CH_3OH at 30°C are shown in Fig. 1a and 1b. The sweep rate was 30 mv/sec. The *I-U* curve is fairly reproducible in unstirred solutions which are saturated with argon. It was obtained after a few cycles had been performed in the quiet solution. The coverage (14) with methanol (θ_M) and oxygen (θ_O) is plotted as a function of potential below the *I-U* curve. An oxygen monolayer was attributed (16) to $Q_O = 2_sQ_H$ where $_sQ_H$ is the number of coulombs per square centimeter for the formation of a monolayer of hydrogen atoms on the same electrode in 1*N* $HClO_4$ at 30°C.

The *I-U* curve during the anodic and cathodic cycle has the characteristic form described in earlier work (1-13). High resolution at small sweep rates shows the existence of a prewave at the foot of the first wave. The peak of the first wave appears at +0.9v in 1*N* $HClO_4$ + 1M CH_3OH at 30°C. The peak is shifted toward less positive potentials with decreasing methanol concentration. The first wave is narrow in 1*N* $HClO_4$ + 1M CH_3OH. The current decreases rapidly with increasing potential on the right side of the peak. The first wave becomes broader with decreasing methanol concentration. A current minimum is reached practically independent of the methanol concentration at about +1.1v. Then a second, relatively broad wave with a peak current at about 1.4v is observed. The location of the second peak is less defined than that of the first one. The current decreases only slightly with potential after the peak at +1.4v because O_2 evolution and methanol oxidation on top of the oxygen layer (7) increase rapidly with potential above +1.5v. During the cathodic sweep the current is small between +1.4 and +0.9v in 1*N* $HClO_4$ + 1M CH_3OH. Oxygen evolution and methanol oxidation on the surface covered with an oxygen monolayer do not occur at a significant rate in this potential range. If the methanol bulk concentration $_oC_M$ is smaller than 0.01M, a small cathodic wave appears between +0.9 and +0.8v. The cathodic wave is due to the reduction of the oxygen coverage. It is too small to be recognizable at larger methanol concentrations

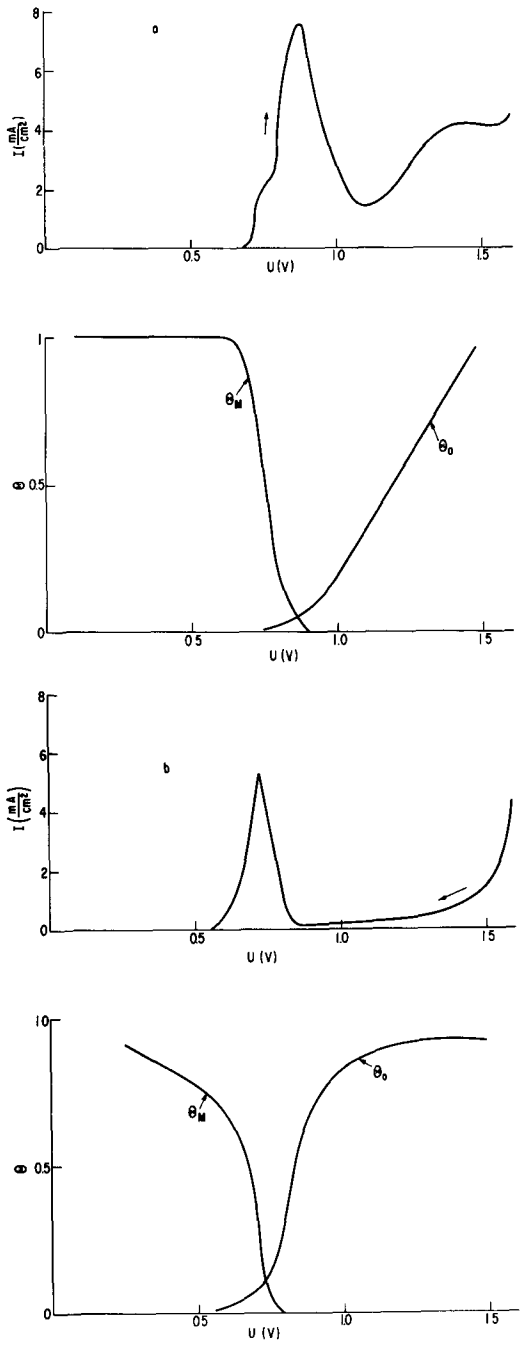

Fig. 1. Anodic (a) and cathodic (b) part of an *I-U* curve in unstirred 1*N* $HClO_4$ + 1M CH_3OH at 30°C. The methanol coverage (θ_M) and the oxygen coverage (θ_O) are plotted as functions of potential below the *I-U* curves.

(see Fig. 1b). The current becomes anodic again after the cathodic wave, reaches a peak, and finally decreases with decreasing potential to a very small value.

The comparison of the *I-U* curve with the θ_M-*U* curve in Fig. 1a shows that part of the methanol oxidation in 1*N* $HClO_4$ + 1M CH_3OH below +0.9v and practically all oxidation between +0.9 and +1.3v takes place on a surface whose coverage with adsorbed methanol or adsorbed intermediates is very small. The coverage is too small ($\theta < 0.1$) to be detected with certainty by the techniques used here. A similar statement holds for the concentration range 0.001M $\leq {}_oC_M \leq$ 1M. It is assumed that the decrease of methanol coverage with poten-

tial is not due to a replacement of adsorbed methanol molecules by water molecules. Such a displacement is formulated in the theories of the electrocapillary curve on mercury (17, 18). The assumption is confirmed by the result of the previous paper (14) that θ_M is independent of potential during the anodic sweep between +0.1 and +0.6 at bulk concentrations $0.001M \leq {}_0C_M \leq 1M$. If a desorption due to an electrostatic effect would occur, θ_M could not be potential-independent in such a broad potential range at moderate and small coverage. Therefore it is concluded that the depletion of the methanol coverage during the anodic sweep is solely caused by the oxidation process.

The current decrease after the peak at +0.9v may result from the blocking action of adsorbed oxygen or intermediates. Initially it can only be a blocking of active centers because the oxygen coverage and the coverage with intermediates are small in the immediate vicinity of the peak. Figure 1a shows that the current decreases while the oxygen coverage increases steadily in the same potential range. Therefore the current decrease after the first peak is attributed to oxygen blocking. This conclusion is confirmed by the shape of *I-U* curves of formaldehyde and formic acid oxidation (1, 3, 5, 8, 11, 12). A current decrease is always observed in a potential range where the formation of the oxygen layer starts in the absence of fuel (19). Müller and co-workers (1-5) have already concluded that the current decrease after the first peak is caused by the surface oxidation of platinum. The fact that these investigators did not observe a sharp drop-off in current and a second maximum above 0.9v (as recorded in Fig. 1a) may be simply explained on the basis of the large internal resistance of their slide-wire device to apply a potential potentiostatically. Recently Giner (20) and Lingane (21) studied similar passivity phenomena during the oxidation of oxalic acid on platinum. Blocking mechanisms of small amounts of adsorbed oxygen were discussed in detail by Ershler (22) in a paper on the passivity of platinum.

It follows from Fig. 1b that methanol oxidation and oxygen evolution are strongly hindered during the cathodic sweep between +1.3 and +0.9v where the surface is covered with practically a monolayer of oxygen atoms. The anodic current of methanol oxidation in 1*N* $HClO_4$ + 1M CH_3OH rises with decreasing potential between +0.9 and +0.75v where most of the oxygen layer is reduced cathodically. Methanol is oxidized at a higher rate between +0.75 and +0.6v during the cathodic sweep than during the anodic sweep. The methanol coverage is larger and the oxygen coverage is smaller at the same potential between +0.6 and +0.9v during the anodic than during the cathodic sweep. A similar statement holds for $0.001M \leq {}_0C_M \leq 1M$. This suggests that methanol is oxidized on the free surface at a larger rate. Another interpretation (11) attributes the current peak to a large oxidation rate on a fresh surface activated by the preceding covering with oxygen. An activation of this type is likely to occur. However, this interpretation

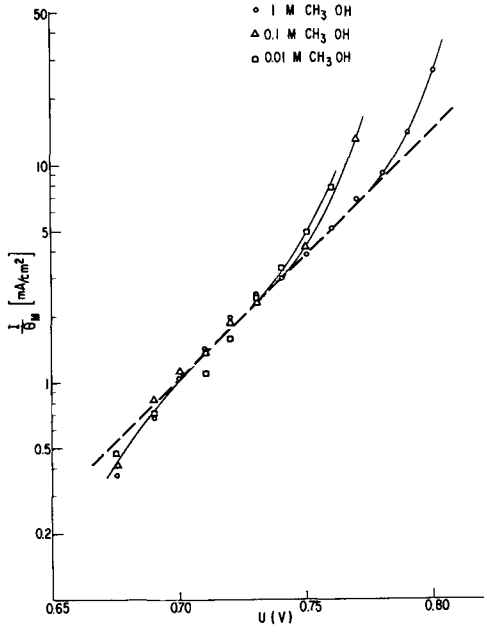

Fig. 2. Semilogarithmic plot of I/θ_M vs. U in the region of the prewave of *I-U* curves at different methanol concentrations in 1*N* $HClO_4$ at 30°C.

cannot explain the higher oxidation rate of formic acid (23) during the cathodic sweep when the potential is reversed at a value between +0.7 and +0.8v where the oxygen coverage is very small.

It was thought that the prewave during the anodic sweep could be due to the oxidation of adsorbed methanol molecules alone. This assumption was tested for three bulk concentrations (see Fig. 2) in the following way. If the rate-determining step after the adsorption is a discharge reaction which involves the adsorbed molecules only, then

$$I \approx I_1 = k_1\theta_M \exp\left(\frac{\alpha nFU}{RT}\right) \qquad [1]$$

Here, I designates the net current density; I_1 is the current density due to the oxidation of adsorbed molecules; k_1 is the rate constant of the discharge step; n is the number of electrons involved in the discharge step; and α is the transfer coefficient. In Fig. 2 I/θ_M is plotted on a logarithmic scale *vs.* U for 0.01M CH_3OH, 0.1M CH_3OH, and 1M CH_3OH. The respective θ_M-values were reported in the previous paper (14). Equation [1] is applicable for $0.3 \leq \theta_M < 0.9$ at ${}_0C_M = 1M$. For $\theta_M < 0.3$ the current rises more rapidly with potential than follows from Eq. [1]. For $\theta_M \geq 0.9$ deviations in the opposite direction are observed. A similar statement holds for ${}_0C_M = 0.1M$. The points of the measurements at ${}_0C_M = 0.01M$ deviate slightly at small current. Equation [1] is in fair agreement with the experiments for $0.3 \leq \theta_M \leq 0.9$. The agreement can be called "fair" if it is considered that the same term "fair" applies to the reproducibility of the *I-U* curves.

The validity of Eq. [1] in the said θ_M-range has another implication. During the sweep

$$F\Gamma \frac{d\theta_M}{dt} = I_a - I_1 \qquad [2]$$

Here $F\Gamma \approx 0.3 \frac{\text{m coulomb}}{\text{cm}^2}$ and I_a is the rate of adsorption. I_a depends on ${}_0C_M$, θ_M and U. Equation [1] can only be fulfilled if

$$F\Gamma \left| \frac{d\theta_M}{dt} \right| << I_1 \approx I \qquad [3]$$

It was found that $F\Gamma \left| \frac{d\theta_M}{dt} \right| < \frac{I}{10}$ holds at $\nu = 30$ mv/sec in the θ_M-range where Eq. [1] is applicable. The coverage θ_M is determined by the difference between I_a and I_1. The decrease of θ_M with increasing potential implies that I_1 is slightly larger than I_a at low speed. Adsorption and a subsequent discharge step are both rate determining in the region of the prewave.

The deviation from Eq. [1] below $\theta_M = 0.3$ can be interpreted in two different ways which do not differ much formally. Below $\theta_M = 0.3$ methanol molecules may be oxidized without previous adsorption with the rate, I_2. The net current, I, is equal to $I_1 + I_2$, and $I_1 >> I_2$ for $\theta_M > 0.3$. This statement holds for the vicinity of the first wave where the partial currents due to the oxygen layer formation, and to methanol oxidation and oxygen evolution on the oxygen covered surface are negligible. It is assumed with the second interpretation that the rate constant k_1 and the rate of adsorption increase with decreasing θ_M for $\theta_M < 0.3$. Methanol adsorption and oxidation occur on the very active sites of the heterogeneous platinum surface. Then I_2 designates the partial current of methanol oxidation on these sites. The active sites are made available by oxidizing off the molecules which are adsorbed in the hydrogen region during the cathodic and subsequent anodic sweep.

The rate constant, k_1, referred to the hydrogen electrode as reference electrode, and the αn-value were determined from Fig. 2. It was found

$$\log k_1 = -8.1, \quad \alpha n = 0.67$$

Here the rate constant is given in the units ma/cm^2. The experimental αn-value suggests a one-electron transfer ($n = 1$). The discharge step is a first order reaction with respect to the adsorbed methanol molecules. This implies that the first discharge step in the over-all reaction is the slowest discharge step. If it were a subsequent discharge step and if the equilibrium of one or more of the subsequent discharge steps were established, αn should be greater than 1. Another possible interpretation is that all the discharge steps are hindered to nearly the same extent. However, this interpretation is discarded because of the low probability of the assumption on the same hindrance of all the discharge steps. It should be noted that rate constants and transfer coefficients calculated without consideration of the change of θ_M at the foot of the first wave are incorrect.

Thus far, the shapes of the first wave during the anodic sweep and of the wave during the cathodic sweep of low-speed periodic I-U-curves have been discussed in detail. A similar discussion would be

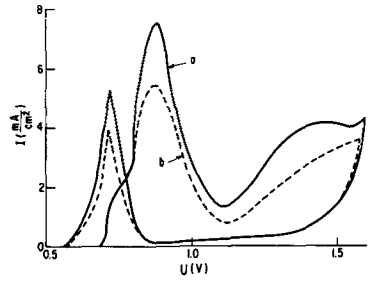

Fig. 3. I-U curve in unstirred (curve a) and stirred (curve b) 1N $HClO_4$ + 1M CH_3OH at 30°C.

desirable for the second wave. However, the analysis of the experimental results did not lead to a conclusion which differs essentially from that of Müller and co-workers (1-5) on the origin of the second wave. Müller and co-workers suggested that another mechanism becomes increasingly effective at higher potentials. It cannot yet be decided if the difference in the two mechanisms is of the specific type postulated by Müller and co-workers. More work is required.

Periodic potentiostatic I-U-curves at low speed with argon-stirring.—Curve b in Fig. 3 represents an I-U-curve with $\nu = 30$ mv/sec in 1N $HClO_4$ + 1M CH_3OH at 30°C when the solution was stirred intensively with argon. Curve a is the I-U-curve in the unstirred solution which had been saturated with argon before. It takes about five cycles before curve a is obtained after interruption of the stirring. The reproducibility of curve b is not good, as the shape of curve b changes slightly with time.

Stirring reduces the current at the same potential U above the region of the anodic prewave during the anodic sweep and in the region of the oxidation wave during the cathodic sweep. The following interpretation is suggested for the stirring effect. Stable intermediates (CH_2O, CHOOH) of methanol oxidation do not exist in a high concentration on the surface between +0.9 and +1.5v during the anodic sweep. After they have been formed, they can either be oxidized or diffuse into the bulk of the electrolyte. A high stirring rate favors diffusion while a low stirring rate is favorable for oxidation. This interpretation has to be considered a tentative one. The relative decrease of the current with stirring at $U > +1.0$v appears rather large and cannot be explained on the basis of the preceding interpretation alone. It indicates the presence of a second hindering effect. It appeared conceivable that the second hindering effect might be caused by a difference in the θ_0-U-curves for the stirred and unstirred solution. However, no difference could be detected in the experimental θ_0-U-curves under the two conditions.

Single I-U curves at different sweep rates in stirred solutions.—The anodic parts of potentiostatic I-U curves at variable voltage speed are shown in Fig. 4 for 1N $HClO_4$ (dotted curves) and 1N $HClO_4$ + 1M CH_3OH (solid curves) at 30°C. The I-U curves were measured by applying a single triangular voltage sweep. The pretreatment consisted of a single triangular sweep extending from 0.4 to 2.0v and returning to 0.4v. This served to

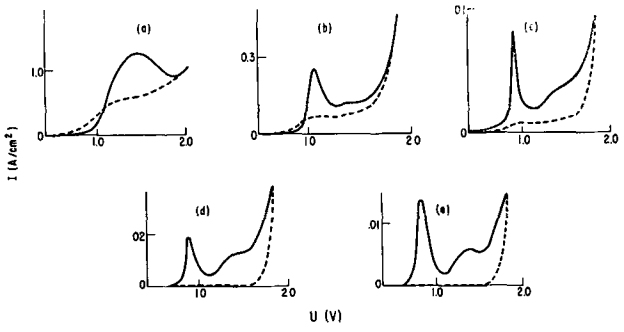

Fig. 4. Anodic parts of *I-U* curves, measured with a single sweep of different sweep rate which started from the open circuit potential: curve a, v = 800 v/sec; curve b, v = 70 v/sec; curve c, v = 7 v/sec; curve d, v = 0.7 v/sec; curve e, v = 0.07 v/sec.

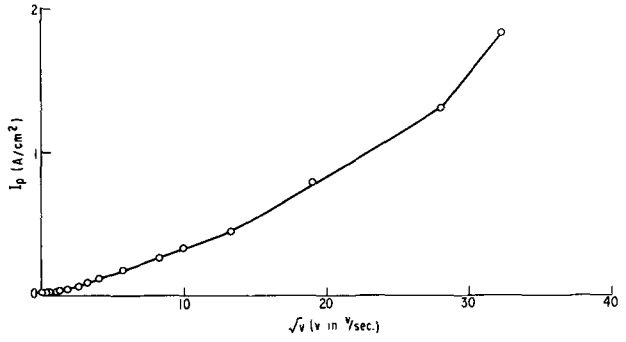

Fig. 5. Peak current density, I_p, of the first anodic wave as a function of the square root of the sweep rate of the single sweep.

clean the electrode surface of adsorbed materials. After 10 msec at 0.4v, the electrode was open-circuited and methanol allowed to adsorb for 1 min with argon flowing. A triangular sweep was then applied and the *I-U* curve recorded. These conditions approximate those used in determining the methanol adsorption isotherm (14).

The *I-U* curves in Fig. 4 can be understood on the basis of the concept developed in the preceding sections. The current density I_M of methanol oxidation is

$$I_M = I_1 + I_2 = I_a - F\Gamma \frac{d\theta_M}{dt} + I_2 \qquad [4]$$

The curves d and e at low speed have the characteristic shape discussed in the preceding sections. They coincide with the *I-U* curves in 1*N* $HClO_4$ at a potential $U < +2.0$v in the region of O_2 evolution. The scale is such that the anodic current due to the formation of the oxygen coverage in 1*N* $HClO_4$ between +0.8 and +1.5v is rarely recognizable. The heights of the first and second peaks increase with the voltage speed (curves e, d, c). The first peak appears at more positive potentials with increasing voltage speed, while the second peak remains at nearly the same potential. Curves d, e, and c show a narrowing of the potential range of the first wave. Above $v = 7$ v/sec the first wave begins to broaden until only one peak is observed at 800 v/sec (curve a). These observations can be interpreted as follows. Methanol molecules which diffuse to the surface and are oxidized there on the free surface with the rate I_2 represent the main contribution to the first peak current in the curves e, d, and c. The term

$F\Gamma_m \frac{d\theta_M}{dt}$ in Eq. [4] begins to contribute more and more with increasing voltage speed above $v = 7$ v/sec (curves a and b). Finally the current I_M results mainly from the oxidation of the initially adsorbed molecules (14). The potential of reversal has to be made more positive with increasing voltage speed so that the *I-U* curves in the electrolyte with and without methanol coincide. The current which is due to the formation of the oxygen layer becomes larger with increasing voltage speed and contributes considerably to the net current (curves a, b, and c).

The above results make the form of the $I_p - \sqrt{v}$ curve in Fig. 5 understandable. There I_p designates the current density at the first peak of the *I-U* curves. Kinetic data are often deducted from $I_p - \sqrt{v}$ curves. Figure 5 shows a nonlinear dependence between I_p and $\sqrt{v}$ which appears linear between 1 v/sec and 100 v/sec. In general a linear dependence is characteristic for a reversible (24) or irreversible (25) electrode process with diffusion control. However, this interpretation does not apply here as the following consideration shows. I_p is smaller for an irreversible process with diffusion control than for a reversible one (25). It is for an irreversible process (25)

$$I_p = 3.01\ 10^5\, n\, (\alpha n_a)^{1/2}\, D^{1/2}\, {}_0c\, v^{1/2} \qquad [5]$$

Here, n designates the number of electrons involved in the net process; α is the transfer coefficient of the discharge step; n_a is the number of electrons involved in the discharge step; D is the diffusion coefficient; ${}_0c$ is the bulk concentration of the reacting species; and v is the sweep rate. By taking $\alpha n_a = 0.5$ (close to the experimental αn-value of Eq. [1]), $D = 10^{-6}$ cm²/sec and $n = 2$ (assuming that the methanol oxidation only goes to the first stable intermediate CH_2O) the I_p-values in Table I are obtained from Eq. [5] as the lowest estimate for I_p at ${}_0c_M = 1$ M. The computed I_p-values in Table I are considerably larger than the observed ones.

It is concluded that the first current peak is caused at $v < 10$ v/sec by a blocking action of adsorbed oxygen on the oxidation mechanism with the partial current density I_2. The partial current due to the surface oxidation and that due to the oxidation of adsorbed methanol contribute considerably to I_p above $v = 10$ v/sec. At $v > 200$ v/sec I is practically equal to $-F\Gamma \frac{d\theta_M}{dt} + F\Gamma \frac{d\theta_0}{dt}$ with $F\Gamma_0 = 0.65$ mcoulomb/cm². The oxidation of the adsorbed molecules occurs at such positive potentials that I_2 is not observed any longer, owing to the considerable oxygen coverage in the respective

Table I. I_p-values from Eq. [5] and from Fig. 4

v	v/sec	0.07	0.70	7	70	800
$I_{p,\,comp}$	A/cm²	0.116	0.35	1.16	3.5	11.8
$I_{p,\,exp}$	A/cm²	0.014	0.019	0.08	0.18	1.27

Table II. Comparison of measured and computed I_p-values

$_oc_M$	M	1	0.1	0.01	0.001
$I_{p,\,comp}$	ma/cm²	76	7.6	0.76	0.076
$I_{p,\,exp}$	ma/cm²	8.3	2.7	0.75	0.20

potential range (compare curves a and c in Fig. 4).

The same conclusions hold for unstirred solutions. The peak current was determined as a function of the concentration at a sweep rate of 0.03 v/sec in 1*N* $HClO_4$ (see Table II). Table II shows clearly that the required linear dependence between $I_{p,\,exp}$ and $_oc_M$ (see Eq. [5]) is not observed. I_p decreases with $_oc_M$ in a way which is indicative for the presence of the postulated adsorption step. The shifting of the peak potential to less positive values at lower methanol concentration is correlated to the depletion of the adsorbed methanol at less positive potentials during the anodic sweep at the smaller bulk concentrations of methanol [see Fig. 6 of the preceding paper (14)].

Manuscript received Jan. 15, 1962; revised manuscript received June 28, 1962.

Any discussion of this paper will appear in a Discussion Section to be published in the June 1963 JOURNAL.

REFERENCES

1. E. Müller, *Z. Elektrochem.*, **29**, 264 (1923).
2. E. Müller, *ibid.*, **33**, 561 (1927).
3. E. Müller and S. Tanaka, *ibid.*, **34**, 256 (1938).
4. E. Müller and S. Takegami, *ibid.*, **34**, 704 (1928).
5. S. Tanaka, *ibid.*, **35**, 38 (1929).
6. A. Hickling and F. J. Rodwell, *J. Chem. Soc.*, **1943**, 90.
7. T. O. Pavela, *Ann. Acad. Sci. Fennicae, Ser. A*, II. *Chem.*, Helsinki **1954** pp. 1-47.
8. A. I. Shlygin and G. A. Bogdanovsky, Proc. 4th Conference on Electrochemistry, Moscow, 1956; Academy of Sciences, Moscow, 1959, pp. 282-286.
9. G. A. Bogdanovskii and A. I. Shlygin, *Zhur. fiz. Khim.*, **34**, 57 (1960).
10. Ye. Skorbets and N. N. Atamenko, Kiev Forestry Institute, Report VII, Zavodskaya Lab. Vol. 15, pp. 1291-1299.
11. W. Vielstich, Extended Abstracts of Papers presented before Battery Division and at Joint Symposia on Fuel Cells with the Corrosion, Industrial Electrolytic and Theoretical Divisions, Detroit Meeting, The Electrochemical Society 1961, Abstr. 113, pp. 149-151.
12. R. P. Buck and L. R. Griffith, *ibid.*, Abstr. 18, pp. 42-44.
13. D. E. Icenhower and A. P. Bond, *ibid.*, Abstr. 19, pp. 45-46.
14. M. W. Breiter and S. Gilman, *This Journal*, **109**, 622 (1962).
15. F. G. Will and C. A. Knorr, *Z. Elektrochem.*, **64**, 258 (1960).
16. M. W. Breiter, C. A. Knorr, and W. Völkl, *ibid.*, **59**, 681 (1955).
17. A. N. Frumkin, *Z. Physik*, **35**, 792 (1926).
18. J. A. V. Butler, *Proc. Royal Soc. (London)*, **A122**, 399 (1929).
19. M. Becker and M. Breiter, *Z. Elektrochem.*, **60**, 1080 (1956).
20. J. Giner, *Electrochim. Acta*, **4**, 42 (1961).
21. J. J. Lingane, *J. Electroanal. Chem.*, **1**, 379 (1961).
22. B. Ershler, *Acta Physicochim. U.R.S.S.*, **19**, 139 (1944).
23. To be published.
24. J. E. B. Randles, *Trans. Faraday Soc.*, **44**, 327 (1948); A. Sevcik, *Collection Czechoslov. Chem. Communs.*, **13**, 349 (1948).
25. P. Delahay, *J. Am. Chem. Soc.*, **75**, 1190 (1953).

Technical Notes

Sodium Borohydride, An Interesting Anodic Fuel (1)

Maurice E. Indig and Richard N. Snyder

Delco-Remy Division, General Motors Corporation, Anderson, Indiana

Sodium borohydride has long been considered as a potential source of limited amounts of hydrogen, based on the work of Schlesinger (2) and co-workers. In an aqueous solution sodium borohydride is a powerful reducing agent. Reactions with metal ions can result in precipitation of a metal (3), precipitation of a metal boride (4), formation of a volatile metal hydride (5), or reduction of the oxidation state of a metal ion (4).

The standard electrode potential of the reaction $BH_4^- + 8\ OH^- \rightarrow BO_2^- + 6\ H_2O + 8e$ has been calculated as 1.23v by Pecsok (6) and 1.24v by Stockmayer (7) and co-workers. Pecsok also indicated that the oxidation of sodium borohydride was highly irreversible.

The possibility of using sodium borohydride as an anodic fuel appeared attractive due to its extremely low equivalent weight of 4.73g, the fact that concentrated solutions of $NaBH_4$ in a highly basic medium can be quite stable, and the favorable electrochemical potential of the oxidation of the borohydride ion.

Experimental Procedure

A series of laboratory experiments were conducted to characterize the properties of the sodium borohydride electrode. Weighed amounts of $NaBH_4$ were dissolved in 30% KOH solutions. Four milliliter aliquots containing 0.12g of $NaBH_4$ were introduced into Lucite cell containers. The cells consisted of a sintered nickel anode of 80% porosity, an auxiliary cathode of silver sheet, and a mercury-mercuric oxide reference electrode located adjacent to the anode. The concentration of potassium and, later, sodium hydroxide were the same in ref-

erence electrodes as in the bulk solution. The reference electrodes were drawn down, and an asbestos wick was sealed into the fine tip. The apparent areas of anode and cathode were 6.45 cm². Current was supplied to the cell by an external d-c power supply. Potential measurements were obtained between the nickel anode and reference electrode with the aid of a potentiometer. Coulombic efficiencies were obtained in the constant current discharge by comparison of the total coulombs passed and the theoretical capacity of the $NaBH_4$, based on the theoretical eight electron oxidation.

In later experiments a commercial 12% solution of $NaBH_4$ in 40% sodium hydroxide was used as the source of borohydride ion. At 21°C these solutions had a decomposition rate of 0.000005% per day (8). In these experiments a 60-cycle interrupter (9) was used in order to determine polarization values without residual IR losses. It should be mentioned that any activation polarization that had a decay time faster than 1/120 of a second would not be measured with the interrupter. A schematic of the cell and discharge circuit are shown in Fig. 1.

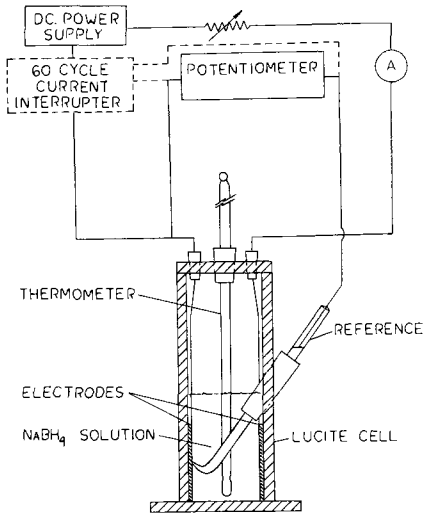

Fig. 1. Schematic of cell and discharge circuit

Results and Discussion

The results of the polarization studies of the sodium borohydride electrodes at three different temperatures are shown in Fig. 2. The curves represent data obtained in the constant direct current discharges and data obtained with the current interrupter technique.

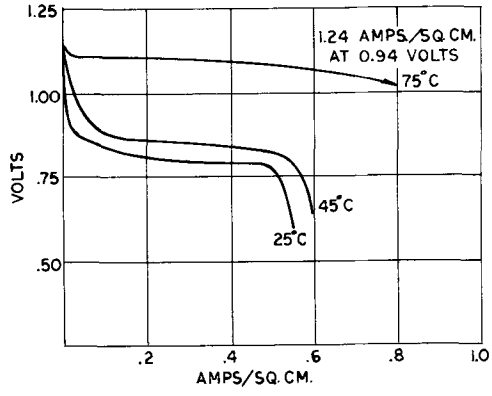

Fig. 2. Polarization of $Ni/NaBH_4$ electrode vs. Hg/HgO reference as a function of current density at three temperatures for electrolyte composition of 20% NaOH, 6% $NaBH_4$.

One of the major problems encountered in the discharges was the formation of large amounts of hydrogen gas. Although the sodium borohydride solutions were quite stable on storage, in contact with the porous nickel electrodes, the solutions gassed slowly. The gassing rate increased with the electrochemical oxidation, and at a rate of 775 ma/cm² much hydrogen was evolved. This indicated that hydrogen was formed as a product of the electrochemical oxidation. This was further substantiated by the coulombic efficiency studies. The coulombic efficiencies in separate discharges varied between 43 and 49% of a possible eight-electron change. At low current densities, 100 ma/cm² and below, the latter figure was approached and the efficiencies dropped as the current density increased. Thus, apparently a four-electron oxidation could be approached. The decomposition of $NaBH_4$ under open-circuit condition was due to a simple hydrolysis reaction, $BH_4^- + 2H_2O \rightarrow BO_2^- + 4H_2$. This reaction is accelerated by sintered nickel and other types of low overvoltage metals (2).

The average measured open-circuit potential of the borohydride electrode was 1.15v *vs.* the mercury-mercuric oxide reference electrode. It was possible to raise the open-circuit and operating potential by 0.075v with the use of platinum metal catalysts, but this caused severe gassing.

Although the observed potential of the nickel-borohydride electrode was almost 0.2v below the calculated reversible borohydride oxidation potential, it certainly could not be mistaken for the lower hydrogen potential in a basic medium, which is 0.926v *vs.* the mercury-mercuric oxide reference electrode. Further evidence of the fact that hydrogen was not contributing to the electrochemical performance was noted in a blank run. A sintered nickel electrode, with hydrogen as a fuel, gave an open-circuit potential of 0.63v *vs.* a mercuric oxide reference electrode. On application of a small load the electrode rapidly polarized to the oxygen evolution potential, thus indicating that the electrode had no activity for hydrogen.

The possibility of achieving a reversible sodium borohydride electrode with an eight-electron oxidation appeared unlikely. One might have to settle for a reaction involving a four-electron change and a lower potential. This reaction may be given as

$$BH_4^- + 4\,OH^- \rightarrow BO_2^- + 2H_2 + 2H_2O + 4e.$$

Manuscript received July 2, 1962.

Any discussion of this paper will appear in a Discussion Section to be published in the June 1963 JOURNAL.

REFERENCES

1. Patent pending.
2. H. I. Schlesinger, H. C. Brown, H. E. Finholt, J. R. Gilbreath, H. R. Hoekstree and E. K. Hyde, *J. Am. Chem. Soc.*, **75**, 215 (1953).
3. H. C. Brown and A. C. Boyd, Jr., *Anal. Chem.*, **27**, 156 (1955).
4. G. W. Schaefer, E. K. Hyde, H. R. Hoekstra, and H. I.

Schlesinger, Div. of Physical and Inorganic Chemistry, 110th Meeting, A.C.S., Chicago, Abstract 24 (1946).
5. G. W. Schaefer, Sister M. Emilius, O.S.B., *J. Am. Chem. Soc.*, **76**, 1203 (1954).
6. R. L. Pecsok, *ibid.*, **75**, 2862 (1953).
7. W. H. Stockmayer, D. W. Rice, and C. C. Stephenson, *ibid.*, **77**, 1980 (1955).
8. Metal Hydrides, Inc., Beverly, Mass., Tech. Bull. 550 (1958).
9. K. Kordesch and H. Marko, *This Journal*, **107**, 480 (1960).

Anomalous Impurity Diffusion in Epitaxial Silicon near the Substrate

D. Kahng, C. O. Thomas, and R. C. Manz

Bell Telephone Laboratories, Incorporated, Murray Hill, New Jersey

Ingham and McDade (1) have reported in epitaxial germanium grown by the closed tube method (2) an interfacial region (up to 100μ thick) which contained a relatively large concentration of imperfections. Figure 1 is a composite photograph which illustrates a similar, but thinner, interfacial region in epitaxial silicon grown on a heavily doped substrate by the hydrogen reduction of silicon tetrachloride in an open tube flow system (3) at 1105°C. The interface was located by beveling and staining. After this the bevel was polished again and etched with a silver etch (4) which revealed the "gross imperfections" at the interfacial region. It was found that such gross imperfections were not revealed when a CP etch was used. When an epitaxial film was grown on a lightly doped (10-20 ohm-cm) substrate neither the silver etch nor the CP etch revealed gross imperfections at the interfacial region. We have found that in the interfacial region immediately above a heavily doped substrate, where the region of gross imperfections is located, the impurity diffusion rate also is anomalously high, while in the remainder of the film the normal diffusion rate found in bulk silicon obtains.

Figure 2 shows impurity concentration profiles as measured by a differential voltage-capacitance method in an epitaxial silicon film grown at 1060°C on an arsenic doped substrate. The measurement method is described elsewhere (5). Note that the abscissa is the distance from the substrate rather than from the surface. Curve 1 is for a film which has been subjected to the normal film growth cycle (3) followed by a diode fabrication step consisting of an oxidation at 1100°C for 30 min, in order to provide an oxide diffusion mask, and a boron diffusion at 900°C for 70 min. One-half of the sample slice was used for curve 1. The other half slice was heat treated at 1200°C in air for 45 min after film growth but before diode fabrication. Curve 2 is the profile measured on the second half slice after the heat treatment at 1200°C and the diode fabrication.

For the film grown at 1060°C, the incremental arsenic diffusion distance (Δ) of about 2μ (at the 10^{15} level) is attributed to the heat treatment at 1200°C, since all the other heat treatments were the same for the two half slices. For films grown at 1105°C the incremental arsenic diffusion distance

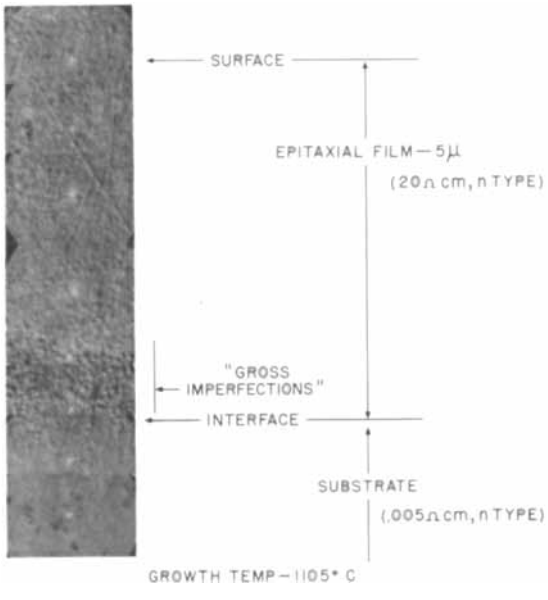

Fig. 1. Cross section of epitaxial silicon film on heavily doped (As) substrate. Interface located by staining. Gross imperfections developed by silver etch. This is a composite photograph.

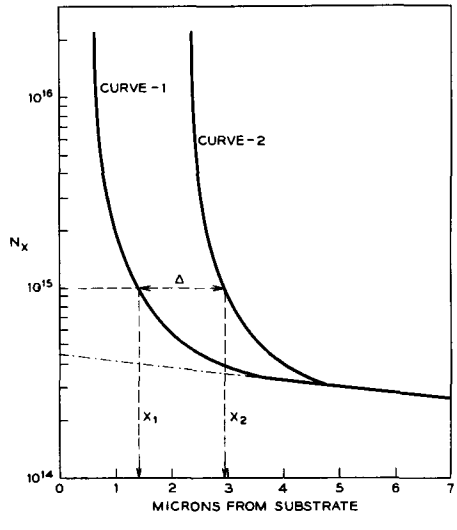

Fig. 2. Impurity profiles for n-type epitaxial silicon film grown on 0.005 ohm-cm (As doped) silicon substrate. Saturator contained purified silicon tetrachloride at —40°C. Film grown at 1060°C for 4 min. Δ = incremental diffusion distance produced by 1200°C heat treatment for 45 min after film growth.

was found to be about 1μ at the 10^{15} level using the same post-growth heat treatment as above.

An effective diffusion rate at the heat treatment temperature, in this case 1200°C, was estimated as follows. Since the diode fabrication involves much more heat treatment than does the film growth one may assume that the impurity distribution near the interface after the diode fabrication has the form

$$N'_x = \frac{N_o}{2} \operatorname{Erfc} \frac{x}{2\sqrt{K}} \qquad [1]$$

where N'_x is the impurity concentration at a distance x from the interface, N_o is the substrate doping level, and K is a constant. Equation [1] is a straightforward consequence of Fick's law where a concentration and position insensitive diffusion constant is assumed. As for curve 2, the distribution can be written as

$$N_x = \frac{N_o}{2} \operatorname{Erfc} \frac{x}{2\sqrt{K + Dt}} \qquad [2]$$

where D is the diffusion constant at the major heat treatment temperature, *i.e.*, 1200°C, and t is the duration of the major heat treatment. It is seen that the initial condition prior to this major heat treatment is simply N'_x given in Eq. [1]. In actuality, the major heat treatment was performed prior to the diode fabrication part which both halves underwent. The order of heat treatments should be interchangeable since simple superposition is expected so far as the final impurity distribution is concerned, aside from possible annealing effects which we ignore for simplicity.

We can now compute the effective diffusion constant as follows. Let x_1 and x_2 denote for the first and for the second half-slice, respectively, the distances from the stained interface at which the impurity concentration is a given value. Then

$$\frac{x_2}{x_1} = \sqrt{1 + \frac{Dt}{K}} \qquad [3]$$

Since N_o is known and x_1 is measurable from curve 1, K can be calculated. Use of this K and x_2 from curve 2 enables one to calculate the effective diffusion constant D from Eq. [3].

When the data in Fig. 2 were analyzed as outlined above, the effective diffusion constant was found to be larger by a factor of five than the published bulk diffusion constant (6). Since x_1 and x_2 are measured from the stained interface, the actual interface where the concentration is $N_o/2$ may not be coincident with the stain. When an allowance of $\pm 0.5\mu$ was made for this ambiguity, the calculation still yielded a value of 3-8 for the ratio of the effective diffusion constant to the published bulk value.

The effective diffusion constant estimated in the manner described above showed a dependence on the film growth temperatures. Higher film growth temperatures in general produced films whose interfacial effective diffusion rate is in better agreement with the bulk value. As the film growth temperature is lowered, the agreement becomes worse and the ratio of the effective diffusion constant to the bulk value reaches a value as high as nine. This suggests that the film structure near the interface has a direct bearing on the diffusion rate. If concentration dependent diffusion rates are responsible for the observed anomaly, the film growth temperatures should have no significant influence on the measured effective diffusion constant.

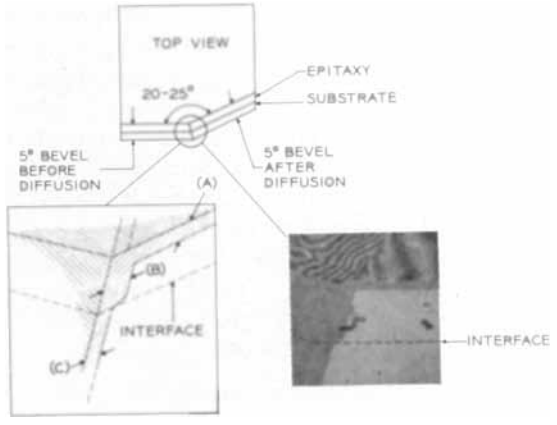

Fig. 3. Relative diffusion depths of boron (15 min at 1200°C) in epitaxial silicon and in substrates. Film resistivity ~ 2 ohm-cm (n-type). Substrate resistivity 0.005 ohm-cm (n-type). Film thickness 25μ. A = 3.25μ, B = 3.25μ, C = 2.5μ.

As illustrated in Fig. 1, the epitaxial film away from the interface shows no gross imperfections. Therefore, a normal diffusion of impurity into this region is expected. The diffusion of boron into the main body of the film and into the substrate has been studied by means of a double bevel technique as illustrated in Fig. 3. An n-type film was grown at 1060°C on an n^+-type substrate. After the film was grown the slice was beveled and polished along one edge at a 5° angle to the surface. It was then given a shallow boron diffusion (1200°C for 15 min) and beveled and polished at 5° again as shown. The intersection of the two bevels was stained and photographed. The junction depths in the film from its upper surface (A) and from the first bevel surface (B) are both 3.25μ as determined by interferometry. The apparent visual difference is an artifact of both the photographic and lapping angles. The junction depth in the substrate (C), also measured by interferometry, is 2.5μ. These junction depths are consistent with the diffusion constant for boron in normal bulk silicon when allowance is made for the background donor concentration in the film and in the substrate.

One might expect an excursion in junction depth to occur near the substrate film interface. However the thickness of the region in which the larger diffusion rate exists is of the same order of the magnitude as the diffusion depth in the sample of Fig. 3. In addition, out-diffusion of the background dopant from the substrate tends to minimize such an excursion. In a similar experiment in which the diffusion depth was smaller than the interfacial region thickness (~2μ), the surface irregularities (strain, lapping damage, etc.) resulted in an irregular junction front obscuring the expected excursion near the interface.

Summary

The interfacial region for epitaxial silicon films grown on heavily doped substrates appears to have unusual and undesirable characteristics as exhibited by characteristic etch patterns and anomalously high diffusion rates. For very thin films this interfacial region may occupy the major portion of the total film thickness and so cause serious problems in device fabrication in such very thin films on highly doped substrates. The diffusion rate of impurities in the main body of the film, however, is consistent with the rate in normal bulk material.

Acknowledgments

The authors are indebted to T. B. Light for assistance with the imperfection studies and to A. Loya for assistance with the electrical measurements.

Manuscript received June 19, 1962. This paper was prepared for delivery before the Detroit Meeting, Oct. 1-5, 1961.

Any discussion of this paper will appear in a Discussion Section to be published in the June 1963 JOURNAL.

REFERENCES

1. H. S. Ingham and P. J. McDade, *IBM Journal*, 302, July 1960.
2. J. C. Marinace, *ibid.*, 248, July 1960.
3. H. Basseches, R. C. Manz, C. O. Thomas, and S. K. Tung, AIME Semiconductor Metallurgy Conference, Los Angeles, Aug. 30-Sept. 1, 1961.
4. R. H. Wynne and C. Goldberg, *Trans. AIME*, **197**, 436 (1953).
5. C. O. Thomas, D. Kahng, and R. C. Manz, *This Journal*, **109**, 1055 (1962).
6. C. S. Fuller and J. A. Ditzenberger, *J. Appl. Phys.*, **27**, 544 (1956).

X-Ray Studies of Twinned GaAs Blades Grown from the Vapor Phase

Roch R. Monchamp, William J. McAleer, and Peter I. Pollak

Electronic Chemicals Research Department, Merck Sharp & Dohme Research Laboratories, Division of Merck & Company, Inc., Rahway, New Jersey

In a recent paper (1) McAleer *et al.* reported on the preparation of GaAs bladelike crystals from the vapor phase. This paper reports on the x-ray studies of these crystals. Using the rotating crystal technique, the major growth axis was determined to be $[\bar{2}11]$ and the major faces were shown to be (111) and $(\bar{1}\bar{1}\bar{1})$ by microscopic examination of etched surfaces and x-ray reflection studies. The same general crystallographic characteristics have been observed in silicon ribbons grown from the vapor (2) and are also found in Ge and Si dendrites grown from supercooled melts (3). The similarities of the GaAs blades to the Si and Ge dendrites, which have been demonstrated to grow via a twin mechanism, suggest that blades may also contain a coherent twin plane. In both the Ge and Si dendrites {111} twin planes were observed by fracture and etch techniques (3). Although twin planes were indicated also in the GaAs blades by these techniques, more positive evidence for the existence of such structures was sought from x-ray examination.

For a twinned crystal belonging to the diamond class geometric considerations require that the crystallographic axes of one section of the twin, when continued across the twin plane, are transformed into a new set of axes having rational indices (4).

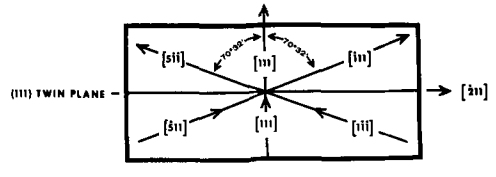

Fig. 1. Transformation of crystallographic directions across a single twin plane.

For twinning in the (111) plane, the $[\bar{1}11]$ direction is transformed into a $[\bar{5}11]$ direction after passing through the twin plane, the [011] is transformed into the $[\bar{4}\bar{1}\bar{1}]$ and the [100] into the $[1\bar{2}\bar{2}]$. Figure 1 illustrates the relationship for a single twin plane and the $[\bar{1}11]$ and $[\bar{5}11]$ case.

When a twinned crystal of the type depicted in Fig. 1 is rotated about the $[\bar{1}11]$ axis or the $[5\bar{1}\bar{1}]$ axis, layer lines characteristic of both $[\bar{1}11]$ and $[5\bar{1}\bar{1}]$ are observed in a rotation photograph and identical patterns are produced (see Fig. 2c). On the other hand, when an untwinned crystal is rotated about the $[\bar{1}11]$ and the $[5\bar{1}\bar{1}]$ axes, clearly distinguishable layer line patterns are obtained (Fig. 2a and 2b). Comparing only the layer lines produced on rotating a single crystal about its $[5\bar{1}\bar{1}]$ axis (Fig. 2b) and those produced by twinned crystals when rotated about $[5\bar{1}\bar{1}]$ and $[\bar{1}11]$ axes, one finds that the layer line structures are indistinguishable. This results from the fact that the $[5\bar{1}\bar{1}]$ rotation yields many more layer lines than the $[\bar{1}11]$ rotation and the 3rd, 6th, and 9th lines produced by [511] rotation are coincident with the $[\bar{1}11]$ layer lines. Thus, on the basis of layer line structure, rotation about the $[5\bar{1}\bar{1}]$ axis does not distinguish between twinned and untwinned crystals.

If it were possible to mount the crystal to clearly rotate about the $[\bar{1}11]$ axis, a single rotation photograph would distinguish between a single crystal and a twinned one. If the crystal is untwinned, it will produce the pattern shown in Fig. 2a, if twinned, a pattern as in Fig. 2c.

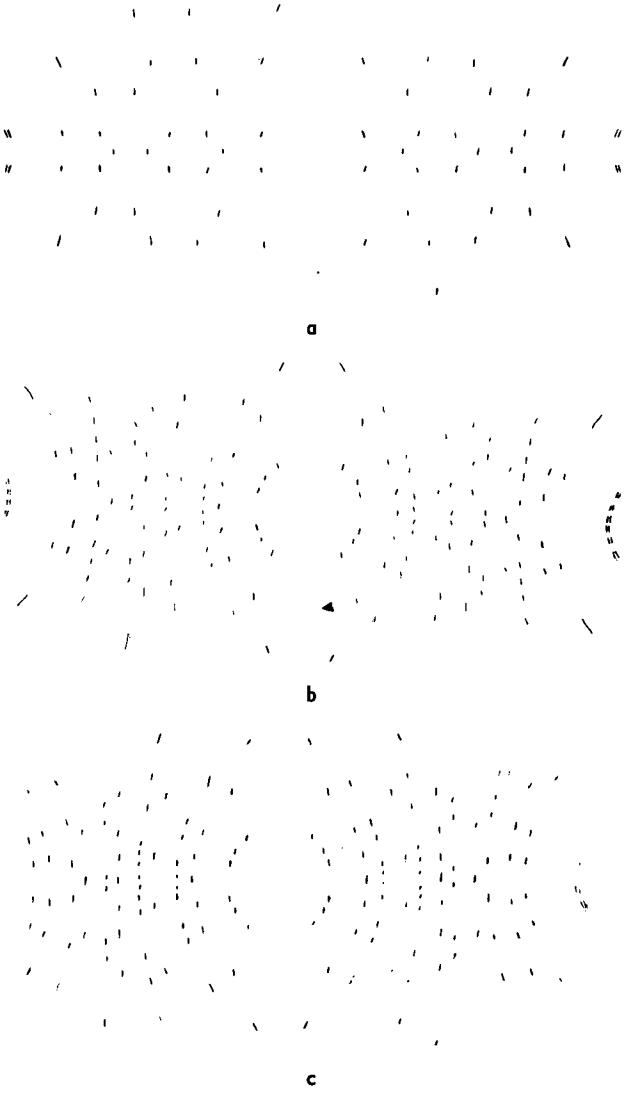

Fig. 2. Reproduction of x-ray film showing layer line structures for (a) (top) [$\bar{1}11$] rotation of a single crystal; (b) (center) [$5\bar{1}\bar{1}$] rotation of a single crystal; and (c) (bottom) [$5\bar{1}\bar{1}$] and [$\bar{1}11$] rotation of a (111) twinned crystal.

The specific selection of the [$\bar{1}11$] axis is possible if the precise orientation of the crystal is established. This step can be avoided, however, by taking two photographs rotating about opposed axis (see Fig. 2a) both 70° 32″ from the [111] axis, thus insuring that the [$\bar{1}11$] axis has been examined. When this was done with the GaAs blades, both photographs were identical, showing that the blade is twinned.

An alternate approach in distinguishing between twinned and untwinned crystals rotated about [$5\bar{1}\bar{1}$] axis resides in the indexing of the individual spots of the photographs (5). For instance a single crystal rotated about the [$5\bar{1}\bar{1}$] would not show any reflection on the zero layer line due to a {422}, whereas

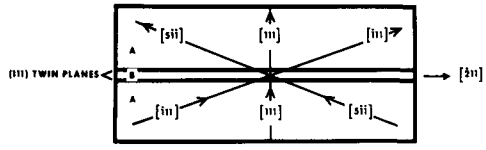

Fig. 3. Transformation of crystallographic directions across two twin planes.

a twinned crystal has this reflection due to the presence of the [$\bar{1}11$] axis.

The same x-ray technique was also applied to silicon and germanium dendrites grown from the melt. For germanium dendrites identical x-ray photographs were obtained when the crystal was rotated about both the [$\bar{1}11$] and the [$5\bar{1}\bar{1}$], which, in accordance with the geometric requirements given above, demonstrated the existence of a twin plane. In the case of a silicon dendrite, rotations about [$\bar{1}11$] and [$5\bar{1}\bar{1}$] produced layer line photographs corresponding to the rotation axis, *e.g.*, Fig. 2a and 2b. Since the presence of twins in this crystal has been demonstrated by other means, it must be concluded that this x-ray method can fail under two conditions: (*a*) if a very narrow B section is present, as in Fig. 3, reflections from this region would not be detected (a limiting value of ~5% of the crystal would be expected), or (*b*) the overlying section is of such a thickness as to prevent penetration of the x-ray beam to the twins.

Considering the limitation cited above for the case of the silicon dendrite, it is clear that all available techniques must be employed in examining a crystal for the presence of twin structures. The ancillary problem of determining the number of twins in these crystals is not amenable to solution by this technique. This aspect of the work may best be handled by fracture and etch techniques described by Faust *et al.* (3).

Acknowledgment

The authors are grateful to Drs. Conn, Price, and Williams for their suggestions and discussions.

Manuscript received March 12, 1962; revised manuscript received June 27, 1962. This paper was prepared for delivery before the Boston Meeting, September 16-20, 1962.

Any discussion of this paper will appear in a Discussion Section to be published in the June 1963 JOURNAL.

REFERENCES

1. W. J. McAleer, H. Barkemeyer, and P. I. Pollak, *This Journal*, **108**, 1168 (1960).
2. R. S. Wagner and R. G. Treuting, *J. App. Phys.*, **32**, 2490 (1961).
3. J. W. Faust, Jr., and H. F. John, *This Journal*, **107**, 562 (1960).
4. C. B. Slawson, *Am. Mineral.*, **41**, 778 (1950).
5. R. S. Wagner and W. Ellis, Private communication.

The Preparation of Single Crystals of Some Rare Earth Tellurides

P. Bro

Research and Advanced Development Division, Avco Corporation, Wilmington, Massachusetts

We report the first preparation of single crystals of some rare earth tellurides which were made by the vapor transport method described by Schäfer and his co-workers (1). Data have been reported (2, 3) on the properties of several rare earth tellurides in polycrystalline form; however, polycrystalline materials are unsatisfactory for the proper electrical and structural characterization of these semiconductors.

The reactions between the rare earth metals and tellurium gave rise to MTe, M_3Te_4, M_2Te_3, MTe_2, and MTe_3 of which the La, Ce, Pr, and Nd compounds have been studied in our laboratories so far. This note is concerned with the growth of single crystals of the sesqui- and di-tellurides. M_2Te_3 was synthesized from the elements in degassed, evacuated quartz tubes at 800°C. The crude product contained a tellurium rich phase near the surface and a metal rich phase in the interior, and it was not suitable for the preparation of single crystals without further treatment. Satisfactory results were obtained with sesquitellurides which had been melted in graphite crucibles at temperatures up to 1800°C in evacuated quartz tubes by means of induction heating. The single crystals were prepared in a bithermal furnace in an evacuated quartz tube containing iodine and sesquitelluride in weight ratios between 0.09 and 0.37. The MTe_2 crystals appeared within 1-2 days in the middle of the tube at temperatures between 700° and 830°C, and the M_2Te_3 crystals formed near the M_2Te_3 source at approximately 900°C. The cooler end of the tube was maintained at approximately 650°C, and a deposit which formed at that end was probably the metal iodide. The MTe_2 crystals grew to various sizes up to 4 x 2 x 1 mm and were suitable for electrical measurements, whereas the M_2Te_3 crystals were too small for any measurements other than x-ray diffraction. Transfer periods of two weeks were required for the growth of large, regular, single crystals.

The crystals were stable in air, except for the formation of a barely noticeable tarnish in a few weeks. The tarnish could be removed by a chemical polishing solution consisting of bromine, acetic acid, and ethanol. The M_2Te_3 compounds possessed a body-centered cubic structure, and the MTe_2 compounds were tetragonal. Some of the compounds in the MTe_2 series exhibited two reversals in their Hall effect and a strongly anisotropic thermoelectric effect.

Manuscript received June 15, 1962.

Any discussion of this paper will appear in a Discussion Section to be published in the June 1963 JOURNAL.

REFERENCES

1. Schafer, Jacob, and Etzel, *Z. Anorg. Chem.*, **286**, 27 (1956).
2. Miller, Reid, and Himes, *This Journal*, **106**, 1043 (1959).
3. Carter, Scientific Paper 23-929-8902-P7, Westinghouse Research Laboratories, Pittsburgh, Pennsylvania, August 9, 1961.

The Rapid Determination of the Conductivity Type of Materials at 4°K

R. C. Bourke[1]

Battelle Memorial Institute, Columbus, Ohio

In a specimen of a semiconductor there may be a "crossover" in conductivity type at some temperature depending on the material parameters and on the acceptor and donor concentrations. Hence, the true extrinsic conductivity type, *i.e.*, the predominance of donors or acceptors, may not be determinable by thermoelectric probing or other means at ordinary temperatures, but may require investigation at liquid-helium temperature, especially in the case of low-band-gap materials. Conventional methods for making quantitative cryogenic measurements of the Seebeck and Hall coefficients are complex and time consuming. Therefore, a simple probing method has been devised for the rapid determination of the sign of the Seebeck coefficient at liquid-helium temperature. Very small specimens of arbitrary geometry may be used, and soldering or welding of leads to the specimen is not necessary.

Several modifications of the system have been devised; Figure 1 shows the one that has been found the most useful. The sample is held in the bottom of an open-ended 8-mm Pyrex guide tube by a slight constriction in the end of the tube. A small-diameter copper wire is wrapped around the bottom end of the specimen and a large-diameter copper wire is placed in contact with the upper end. When the sample is cooled by immersion of the end of the tube in liquid helium, the large-diameter wire becomes a "hot"

[1] Present address: Allison Division, General Motors Corporation, Indianapolis, Indiana.

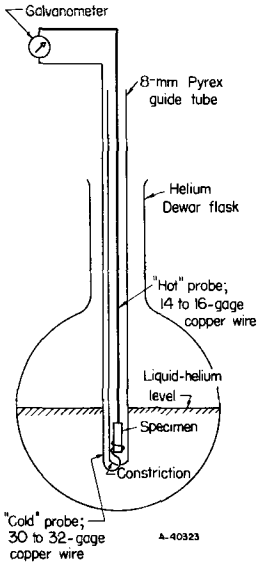

Fig. 1. Details of liquid-helium hot-probe technique

probe because of its greater heat capacity and higher rate of heat conduction from the atmosphere above. As the tube is immersed, the small-wire probe and the sample attain the temperature of liquid helium in a short time, whereas the large probe remains at a higher temperature for a relatively long period of time. Thus, a changeover in conductivity type, indicated by a reversal in the direction of the galvanometer deflection, can easily be detected before the temperature difference between the two probes approaches zero. The determination can be repeated by raising the large-diameter wire above the surface of the liquid helium and allowing it to warm slightly. The probe is then lowered quickly until contact is made with the specimen which is still immersed in the helium. Ice or frozen air on the surface of the specimen can prevent good contact between the hot probe and the sample and, thus, cause erratic galvanometer deflections. Therefore, the tube must be thoroughly flushed with helium prior to immersion This is conveniently done by forcing most of the escaping helium to flow up through the guide tube by the insertion of packing material between the neck of the Dewar flask and the outside of the guide tube.

The method indicates only the sign of the Seebeck coefficient of a specimen and is not quantitative. However, it is quite useful when, for example, a series of doping experiments are being made in an attempt to change the conductivity type of the material being studied. When it has been found that the desired change has been produced, more detailed measurements can be made. The technique has been used successfully on certain specimens of Ag_2Se and Ag_2Te which undergo conductivity-type changes at low temperatures.

Manuscript received June 20, 1962.

Any discussion of this paper will appear in a Discussion Section to be published in the June 1963 JOURNAL.

Impurity Incorporation into CdSe and Equilibria in the System CdSe-$CdCl_2$

A. Reisman and M. Berkenblit

Thomas J. Watson Research Center, International Business Machines, Yorktown Heights, New York

Because of its high melting point, 1239° (1), and high dissociation pressure, approximately 100 mm Hg at 1000° (2), and because of restriction of container and substrate materials to silica or Al_2O_3, CdSe is most conveniently sintered into polycrystalline layers or grown as single crystals from fluxes such as $CdCl_2$. Since the selenide has always been observed to exhibit n-type conductivity, undoubtedly contributed to by a high excess selenium vacancy count (1), one normally compensates the material by addition of acceptors, such as Cu, to the flux. The effectiveness of such doping will be a function of the degree of selenide solution attained at a given temperature and flux concentration, as well as the distribution of the impurity between the flux and semiconductor. The present report describes equilibria in the system CdSe-$CdCl_2$ and discusses the gross manner in which Cu and Ag, another common activator, are incorporated into the lattice using the chlorides of each as dopant sources.

The DTA technique has been described elsewhere as have the x-ray techniques used for phase identification (3, 4).

Results and Discussion

Equilibria in the system CdSe-$CdCl_2$.— Studies were conducted in both closed and open sample holders since each type of arrangement has certain practical advantages. Thus, sintered layer preparation is most easily accomplished in open systems while single crystal growth may be conducted in either type of arrangement. Above 500° however, the vapor pressures of CdSe and $CdCl_2$, the latter particularly, become appreciable, and consequently an open system cannot be considered to conform to the reduced phase rule since composition changes would be occurring in the condensed phases as a function of time. To prevent oxidation of CdSe in the open system, experiments were conducted in an N_2 atmosphere.

Table I presents the results of thermal studies for the closed system experiments, and Fig. 1 depicts the proposed equilibrium diagram in unbroken lines. The results of open system experiments are also presented in Fig. 1 by the dashed lines. In the low-temperature regions, the results of both investigations are essentially the same, the eutectic composi-

Table I. Thermal data for system CdSe-$CdCl_2$ under its equilibrium vapor pressure

Mole % $CdCl_2$	Liquidus temperature	Eutectic temperature[a]
0	1239	520
5	1210	520
10	1165	522
15	1127	522
20	1088	522
25	1054	521
30	1006	521
35	976	521
40	928	519
45	882	522
50	832	522
55	791	524
60	732	523
65	663	521
70	612	521
75	549	523
80	—	521
85	538	521
90	546	521
95	558	521
100	565	

[a] Eutectic temperatures were defined in heating analysis.

tion being detected at about 77.5 mole % $CdCl_2$ in both studies. As higher temperatures become necessary, the open system curve, as expected, becomes displaced to the CdSe-rich side of the system. Thus, the 70 mole % of $CdCl_2$ starting sample in the closed system exhibited a liquidus at 612° while the open system value was 644°. At 40 mole % $CdCl_2$, the respective values were 928 and 963°. While it is evident that the open system value will depend on the sample surface area, the data obtained in closed system experiments should not, within the limits of error involved in measuring liquidus temperatures, 2-3°, since liquidus values will be a function of the sample container volume only. The latter, with respect to vapor-available space, was kept small, about equal to the volume of the condensed phase, so that

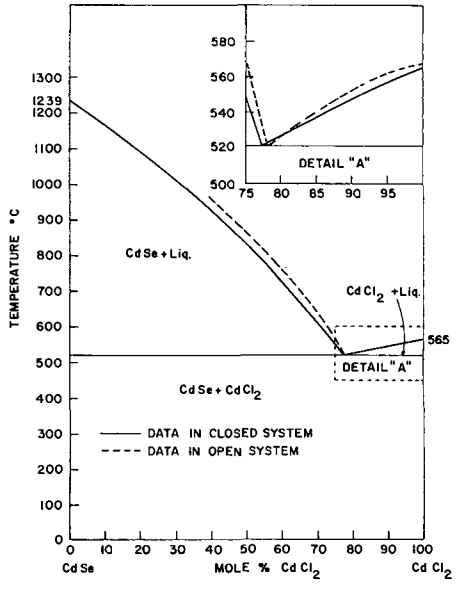

Fig. 1. Phase diagram for the system CdSe-$CdCl_2$ in open and closed systems.

composition variation due to the presence of vapor might be ignored. It is evident that Fig. 1 represents a projection on the T-X plane rather than a constant pressure plane in a T-P-X set of coordinates. Since the pressures developed in the sealed systems are not very great, however, Fig. 1 is probably equivalent within experimental limits to T-P-X representations at 1 atm. Additional experiments were performed to establish an upper limit on the solubility of $CdCl_2$ in CdSe. Quantities of $CdCl_2$ to give 0.5-2.5 mole % of this material were fired in 0.5 mole % steps with CdSe and examined with x-rays. The $CdCl_2$ pattern was detected in the 0.5 mole % sample placing the solubility limit below this value.

Reactions of CdSe *with* $CuCl_2$ *and* AgCl.—Anhydrous $CuCl_2$, 0.1, 1.0, 5.0, and 20 mole %, was mixed with CdSe, and the samples were treated at 550° and 900° in evacuated quartz containers for varying lengths of time. The samples were then either quenched or cooled slowly. In all cases, except one, identical results were obtained. The samples containing 0.1 mole % $CuCl_2$ yielded only the CdSe diffraction pattern while all the others exhibited the pattern of CdSe, CuSe, and $CdCl_2$. Samples were then prepared containing $CuCl_2$, CdSe, and $CdCl_2$ in which the compositions were $CdCl_2$ relative to CdSe, 20 mole %, $CuCl_2$ relative to CdSe 1 and 5 mole %. These were heat treated in open containers under an atmosphere of N_2 at 600° and 700° for 30 min and quenched. X-ray examination again indicated the presence of CuSe in addition to CdSe and $CdCl_2$.

The above data indicate that, rather than incorporation of copper via the mechanism

$$2CuCl_2 \rightleftarrows 2CuCl + Cl_2(v) \qquad [1a]$$

$$(1-x)\ CuCl + x\ CdSe \rightarrow Cd_xCu_{1-x}Se_xCl_{1-x} \qquad [1b]$$

the reaction proceeds via

$$CuCl_2 + CdSe \rightarrow CdCl_2 + CuSe \qquad [2]$$

followed by a partial solution of CuSe in CdSe. The extent of solution is presumably less than 1 mole % on the basis of the x-ray data, and the reaction appears to go to completion.

While the failure to detect Cu_2Se or CuCl, irrespective of firing temperature or cooling cycle, is not proof that copper is initially incorporated in the lattice as a bivalent ion, it is an indication that such is the case. One would, of course, expect that within the lattice an equilibrium between Cu^+ and Cu^{++} would obtain.

Experiments similar to those employed in studying the reactions of $CuCl_2$ with CdSe were conducted with AgCl and CdSe. As with $CuCl_2$, a reaction rather than a simple solution occurred, and Ag_2Se and $CdCl_2$ were products of the reaction according to

$$2AgCl + CdSe \rightarrow Ag_2Se + CdCl_2 \qquad [3]$$

The silver selenide is then incorporated into the selenide lattice with the formation of one selenium vacancy for each two added silver atoms. It appears therefore that when the molar quantity of AgCl is less than that of CdSe, the system AgCl-CdSe is not an equilibrium one under normal ambient or vacuum conditions, being more properly designated by the ternary representation Ag_2Se-CdSe-$CdCl_2$. When

the molar quantity of AgCl exceeds that of CdSe, a binary representation is again invalid, a proper designation being Ag_2Se-AgCl-$CdCl_2$. Similarly, the system $CuCl_2$-CdSe is more properly designated by either CuSe-CdSe-$CdCl_2$ or CuSe-$CuCl_2$-$CdCl_2$.

Reactions of CdSe *with silica, silica-based materials and* Al_2O_3.—In attempts at growing single crystals of CdSe at its melting point in silica containers evacuated with a mechanical pump, the interior of the containers had severely corroded during the experiments, in some instances sufficiently to cause fragmentation of the containers. When the initial pressure was reduced to the 10^{-4} mm region, the container corrosion was greatly reduced. This was evidenced primarily by decreased wetting of the silica surface in contact with the melt. In the 10^{-5}-10^{-6} mm range wetting effects disappeared, the selenide separating cleanly from the silica when the containers were broken open after cooling. These experiments indicated that the apparent reactivity of CdSe with silica is not due to the compound itself but rather to the presence of CdO. To resolve this question, distilled Cd, Se, CdSe, and CdO were each heated in silica. Only the latter gave visual evidence of reaction, so much so that in each attempt fragmentation of the containers resulted.

The product of the reaction of the CdO with SiO_2 gives a very distinct powder pattern which, however, is not listed in the A.S.T.M. card index. In all probability, the pattern is representative of a mixture of two compounds having compositions nominally represented by $xCdO \cdot ySiO_2$ in the system CdO-SiO_2. These results are of some practical concern since, in addition to indicating cautions to be observed in high-temperature handling of CdSe, they indicate a means of obtaining sintered layer adhesion to smooth silica and silica-based substrates. In the preparation of photoconductive polycrystalline sintered layers on such substrates, two processes must be considered. (i) interparticle adhesion and (ii) sintered layer-substrate adhesion. Since cadmium oxide-silica based glues would be expected to exhibit high melting points, they should, on forming, tend to solidify immediately because of the high SiO_2 concentration and not contaminate the sintered layer to any degree. CdSe sintered layers using $CdCl_2$ fluxes were prepared on soft glass substrates in the absence of O_2 and these failed to adhere although sintering of the selenide itself did occur. When prepared in a 1% O_2 atmosphere just above the eutectic temperature in the system CdSe-$CdCl_2$, 522°, the layers did adhere. By treating in higher concentrations of O_2, a quantity of the interlayer between the substrates and sintered layers was formed sufficient to allow x-ray and spectroscopic analysis. These x-ray patterns were distinct, but could not be identified. Spectroscopic analyses showed the normal constituents of the glass employed plus Cd.

Neither CdO nor CdSe was found to exhibit any detectable attack on recrystallized Al_2O_3 even in the presence of $CdCl_2$ flux. Sintered layer adhesion to the latter when serving as a substrate is therefore mechanical. In fact, if the particle size of a sintering CdSe layer is permitted to became too large, the layer flakes off the substrate.

Manuscript received July 24, 1962.

Any discussion of this paper will appear in a Discussion Section to be published in the June 1963 JOURNAL.

REFERENCES

1. A. Reisman, M. Berkenblit, and M. Witzen, To be published.
2. G. Somorjai, *J. Phys. Chem.*, **65**, 1059 (1961).
3. A. Reisman and M. Berkenblit, To be published.
4. See, for example, A. Reisman, Ph.D. Thesis, Univ. Michigan No. 58-2876, Chem. Phys.; A. Reisman, *Anal. Chem.*, **32**, 1566 (1960); A. Reisman and J. Mineo, *J. Phys. Chem.*, **64**, 748 (1960); A. Reisman and J. Karlak, *J. Am. Chem. Soc.*, **80**, 6500 (1958); F. Holtzberg, A. Reisman, M. Berry, and M. Berkenblit, *ibid.*, **79**, 2039 (1957).

Brief Communication

A Dislocation Etch for Lead Selenide Crystals

Marriner K. Norr

United States Naval Ordnance Laboratory, White Oak, Silver Spring, Maryland

The etch recently published for PbSe by Coates *et al.* (1) can be modified to give sharp, square, pyramidal dislocation etch pits at room temperature. This modified etch was found to be an improvement over the one published by Brebrick and Scanlon (2), because their etch required a temperature of 60°C and its pitting action was quite slow.

The modified etch was prepared by dissolving 10g of KOH in 10 ml of distilled water and then adding 1.0 ml of glycerol. After the solution had cooled to room temperature, 0.5 ml of 30% H_2O_2 was added. Reagent grade chemicals were used throughout. Fresh cleavage-surfaces of PbSe were etched in the solution for 2 min at 25°, after which they were rinsed with water and carefully dried on lens paper. It is recommended that the surfaces to be etched should be freshly cleaved because they are very susceptible to mechanical damage and chemical contamination.

The etch produces results (see Fig. 1) qualitatively very similar to those obtained by Gilman and Johnston (3) (using their "A" etch) on LiF and by

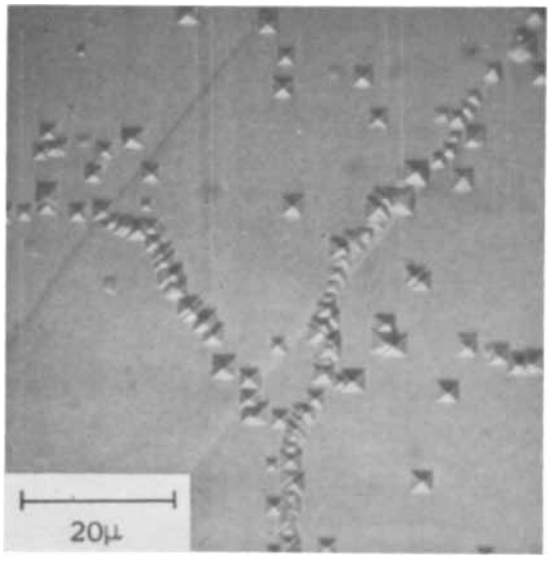

Fig. 1. Dislocation etch pits on a PbSe cleavage surface

Houston and Norr (4) on PbTe. Sharp, square, pyramidal pits were formed on both n- and p-type material. The pits were 2-6μ across, and their edges were parallel to the <100> directions of the crystal. They were obtained along small-angle grain boundaries, along the traces of active slip planes, and at points distributed randomly over the surface. The edges of cleavage steps were attacked. When previously etched material was lightly deformed and etched again, new pits were produced which appeared to be due to dislocations introduced by the deformation. When the two surfaces formed by the cleavage of a crystal were etched, their pit patterns were approximate mirror images of each other, except in areas which showed traces of active slip planes.

The PbSe crystals used above were grown by the Bridgman-Stockbarger technique in silica crucibles. The best material had pit densities (excluding pits along subgrain boundaries) of 1 x $10^6/cm^2$. The angle of tilt between adjoining subgrains, as estimated from the number of pits per unit length along the boundary, was of the order of 1-5 minutes of arc. The subgrains averaged about 0.1 mm across.

Acknowledgment

The author wishes to express thanks to Dr. Bland B. Houston, Jr., for helpful advice, for supplying the PbSe crystals, and particularly for the photograph shown in Fig. 1.

Manuscript received July 16, 1962.

Any discussion of this paper will appear in a Discussion Section to be published in the June 1963 JOURNAL.

REFERENCES

1. D. G. Coates, W. D. Lawson, and A. C. Prior, *This Journal*, **108**, 1038 (1961).
2. R. F. Brebrick and W. W. Scanlon, *J. Chem. Phys.*, **27**, 607 (1957).
3. J. J. Gilman and W. G. Johnston in "Dislocations and Mechanical Properties of Crystals," J. C. Fisher, W. G. Johnston, R. Thomson, and T. Vreeland, Jr., Editors, p. 116, John Wiley & Sons Inc., New York (1957).
4. B. B. Houston and M. K. Norr, *J. Appl. Phys.*, **31**, 615 (1960).

Chemical and Electrical Characteristics of the Alkali Carbonate High-Temperature Fuel Cell

Y. L. Sandler

Research Laboratories, Westinghouse Electric Corporation, Pittsburgh, Pennsylvania

ABSTRACT

When hydrogen is used as a fuel in an alkali carbonate-type fuel cell operating at about 580°C, carbon monoxide and methane are being evolved by formed by secondary reactions with the products H_2O and CO_2, the latter from decomposition of $CO_3^=$. The reactions and resulting emf's under conditions of equilibrium are discussed. With natural gas, the reforming reaction with water was carried out in a separate reactor in contact with the cell. At the temperatures used, the conversion to hydrogen on a nickel-alumina reforming catalyst can be brought to near completion before the gas mixture enters the cell. The experimental cell, a modified version of the cell of Broers and Ketelaar, is leak-proof and gives higher outputs than heretofore obtained (up to 230 ma/cm² at 0.6v with hydrogen at 20% reaction).

This paper deals with a high-temperature fuel cell that employs a fused mixture of alkali carbonates as electrolyte and is operated near 600°C. The reactions taking place at the fuel electrode of the cell, and the effect of these reactions on the electrical characteristics, are discussed. Some performance data are also given.

Experimental

The experimental cell is shown in Fig. 1. It resembles the cell used by Broers (1, 2) in his earlier work. It was, however, developed to be practically leak-proof and to give substantially higher outputs than heretofore obtained. The electrolyte consists of a melt of alkali carbonates contained in a porous magnesia disk. The fuel electrode is a nickel mesh filled with nickel particles, and a silver mesh filled with silver particles serves as the oxygen electrode. The perforated plates in the gas inlet caps serve to admit the gases to the electrodes and to press the electrodes firmly against the electrolyte disk. A strong closing pressure was used to leakproof the cells and to minimize the electrode-electrolyte resistance. An electrode area of 11 cm² was used in all experiments presented in this paper.

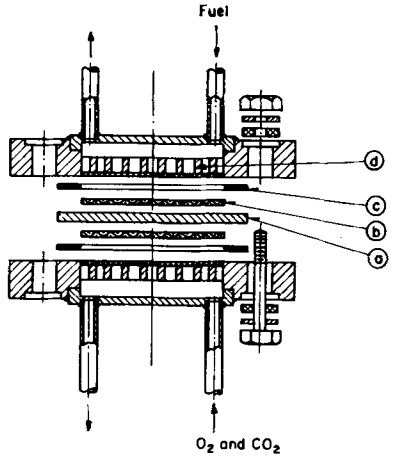

Fig. 1. Blown-up view of the cell. (a) electrolyte disk, (b) electrode, (c) gasket, (d) perforated plate.

The reactions were monitored by mass-spectrometric analysis. They were investigated under realistic flow conditions; this is essential because, at the high flow rates that must be employed in leaking cells, the secondary reactions discussed in this paper may not take place to any appreciable extent. A relatively low temperature of about 580°C was chosen because the life and output of the carbonate type of fuel cell are limited by rate processes such as the evaporation of electrolyte, corrosion reactions, and grain growth of the electrode particles. It will be seen that, despite the low temperature, substantial outputs can be obtained.

When hydrocarbons are used, the electrode has a twofold task: the first is a catalytic one, *via.*, to produce the electrochemically reactive species. In the chosen temperature range, this is essentially hydrogen. The second task is the electrochemical oxidation of the hydrogen. In the following paragraphs, the operation of the cell with hydrogen will first be discussed in greater detail. When hydrocarbons are used, the electrochemical cell functions in essentially the same manner.

Electrode Reactions with Hydrogen as Fuel

Primary reactions.—The primary reactions taking place at the electrodes of a carbonate cell are

$$\text{Anode: } H_2 + CO_3^= = H_2O + CO_2 + 2e \qquad [1]$$

CO_2 is thus liberated at the anode; it must be replaced by adding CO_2 to the oxygen at the cathode.

$$\text{Cathode: } \tfrac{1}{2}O_2 + CO_2 + 2e = CO_3^= \qquad [2]$$

The emf of a pure hydrogen-oxygen cell, as, for example, realized when a solid oxygen ion conductor (3) is used, is given by the Nernst relation

$$E = E^\circ - (RT/2\mathbf{F}) \ln (p_{H_2O} p_{H_2}^{-1} p_{O_2}^{-1/2}) \qquad [3]$$

It is assumed that all concentrations are uniform throughout the gas phase. When st: rting with pure

hydrogen, the degree of electrochemical oxidation of the fuel is: $x = p_{H_2O}/(p_{H_2O} + p_{H_2})$. Then, with $p_{O_2} = 1$ atm, Eq. [3] becomes

$$E = E^\circ - (RT/2\mathbf{F}) \ln [x/(1-x)] \quad [4]$$

In the carbonate cell, CO_2 is in electrochemical equilibrium at both anode and cathode (1, 4). We assume for the present that the primary reaction [1] is the only reaction taking place at the fuel electrode. Then

$$E = E^\circ - (RT/2\mathbf{F}) \ln [(p_{H_2O} p_{H_2}^{-1} p_{CO_2})_{anode} (p_{O_2}^{-1/2} p_{CO_2}^{-1})_{cathode}] \quad [5]$$

A corresponding expression for the emf as a function of the fraction x of hydrogen consumed in the cell is easily derived from [5] and the following three conditions at the anode

(a) $p_{H_2O} = p_{CO_2}$ (one mole of CO_2 is formed from the electrolyte with each mole of H_2 reacted)

(b) $x = p_{H_2O}/(p_{H_2} + p_{H_2O})$

(c) $p_{H_2} + p_{H_2O} + p_{CO_2} = 1$ atm

This leads to

$$E = E^\circ - (RT/2\mathbf{F}) \ln (C x^2/(1-x^2)),$$

$$\text{with } C = (p_{O_2}^{-1/2} p_{CO_2}^{-1})_{cathode} \quad [6]$$

Usually the cells were run with a ratio O_2:CO_2 at the cathode of 1:2 and at 1 atm total pressure. This gives a value of $C = 2.6$.

Secondary reactions.—Actually, when an active electrode is used, the situation is complicated by secondary reactions taking place at the fuel electrode between hydrogen and the reaction products, water and carbon dioxide (the latter being formed by decomposition of the carbonate ion). Carbon monoxide and methane are formed. This appears to have remained unnoticed until now.

The following typical analysis was obtained with a cell run with dry hydrogen at 580°C. The flow rate was 25 cc (STP)/min and a current of 700 ma was drawn. Assuming a current efficiency of 100%, about 20% of the hydrogen must have been electrochemically oxidized. The analysis given in Table I shows that both CO and CH_4 are formed at 580°C.

The chemical reactions to be considered are

$$H_2 + CO_2 = CO + H_2O \quad [7a]$$

(the reverse water-gas shift reaction)

$$4H_2 + CO_2 = CH_4 + 2H_2O \quad [7b]$$

(the reverse methane reforming reaction)

The equations do not necessarily represent the actual course of the reactions; in principle, two more reactions of this type can be written which, however, are not independent. Only two of these four equations together with three mass balance equations for the number of oxygen, hydrogen, and carbon atoms before and after the reaction, determine the equilibrium amounts of the gases H_2, H_2O, CO_2, CO, and CH_4.

Table I. Composition of gases emerging from hydrogen cell

CO_2	CO	H_2O*	H_2	CH_4
18.8%	4.8%	(7.2%)	66.8%	2.4%

* Gas compositions were determined by mass spectrometer. Later tests showed that the H_2O values thus obtained were consistently too low. This explains that the analyses gave somewhat inaccurate material balances. Lack of equilibrium with the electrolyte and carbonyl formation (by reaction of CO with the stainless steel gas exit tube) may also have contributed to this. The present data must be considered preliminary, and discussion of the analytical results is therefore given in a qualitative fashion.

No carbon was found in the cells after cooling the cells to room temperature in an inert gas. After removal of the carbonates, the electrodes were reacted with oxygen. No CO or CO_2 was found in excess of the amount present in the starting material.

It can also be shown from thermodynamic data that no carbon can be formed under equilibrium conditions. At low electrochemical fuel conversion the hydrogen prevents carbon formation; instead, CH_4 is formed. At higher conversions the water formed prevents carbon deposition.

At high electrochemical conversions at 580°C, the concentrations of CH_4 are very small; this is best seen by considering the mass action law for Eq. [7b]. When the concentration of H_2O is large and at the same time the concentration of H_2 is small, then the concentration of CH_4 must be very small. Also, on raising the temperature, the methane rapidly vanishes from the products; reaction [7b] is highly exothermal and, therefore, the equilibrium constant must rapidly decrease with temperature. On the other hand, on lowering the temperature, the methane concentration rapidly increases and this actually may set the lower temperature limit at which the cell can be run effectively.

The formation of CO (reaction [7a]) is endothermal; the amount of CO is thus smaller at lower temperatures.

Figure 2 shows the calculated emf as a function of the degree of fuel conversion in the cell at 580°C for the three different cases: curve 1, the pure hydrogen cell, in accordance with Eq. [3] or [4]; curve 2, for the carbonate cell in absence of secondary reactions, in accordance with Eq. [5] or [6]; and curve 3, for the same cell when a complete chemical equilibrium is established at the fuel electrode. This curve is shown only at higher conversions where

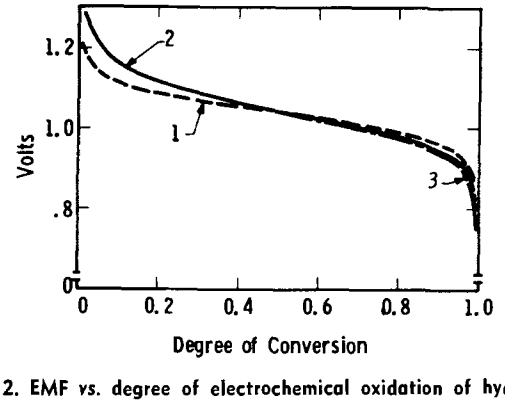

Fig. 2. EMF vs. degree of electrochemical oxidation of hydrogen for: 1, solid oxide cell; 2, carbonate cell, in absence of secondary reactions; 3, carbonate cell, equilibrium established.

only the water-gas shift reaction has to be taken into account.

The equilibrium curve 3 was calculated from the same Eq. [5] which was used for the nonequilibrium curve 2, but using calculated equilibrium values for the partial pressures of H_2, H_2O, and CO_2 at the anode.[1] The difference in emf between curves 2 and 3 is seen to be small.

Results with Hydrocarbon Fuels

When a hydrocarbon like propane is used, the gas undergoes cracking reactions. The hydrogen formed reacts electrochemically; the water thus formed again reacts with the fuel and intermediates to give more hydrogen. Essentially, the function of the hydrocarbon fuel in the present cell is to provide hydrogen to the electrochemical system.

In order to increase the rate of catalytic reactions a separate catalyst can be used. This was found to be of particular advantage when a relatively unreactive fuel like natural gas was used. Outputs with this important fuel as published have thus far been rather low, and higher temperatures (~700°C) have generally been employed (2, 4, 5).

In the case of natural gas, the reforming reaction with water was carried out upstream from the cell. An efficient catalyst made it possible to run the reaction at a temperature low enough to obtain a fairly complete conversion into hydrogen before the gas came in contact with the electrochemical system.

One may distinguish between two different reforming reactions with water

$$CH_4 + 1H_2O = CO + 3H_2 \qquad [8a]$$

and

$$CH_4 + 2H_2O = CO_2 + 4H_2 \qquad [8b]$$

Around 700°C or above, Eq. [8a] is the main equation to be considered. However, at the low temperatures used in the present work (~580°C), Eq. [8b] is the main reaction. This has the advantage that more hydrogen is produced. If an even lower temperature is chosen, the equilibrium will shift to the left and the reaction will be incomplete. The degree of completion of the reaction also depends on the excess of water used in the entering gas mixture. In Table II, analytical results are given of gases emerging from the catalytic reactor containing a nickel-alumina catalyst. Different concentrations of steam were used in the CH_4-steam mixture entering the reactor. The water concentration is again uncertain (cf. footnote to Table I), but the expected trend is clearly visible: the higher the water concentration, the lower is the CH_4 concentration; at high water concentrations practically no methane and little CO are found.

The standard emf's for the direct oxidation of methane and for the oxidation of hydrogen happen to be the same at the chosen temperature, *viz.*, 1.04v. Then even under reversible conditions (strictly, only when all gases are at one atmosphere partial pressure), no additional heat supply is required for the reforming reaction: the heat required is just equal to the heat supplied by the electrochemical oxidation of the hydrogen, as a consequence of the theoretical inefficiency (1) of the latter reaction ($T\Delta S = 11$ kcal/mole of H_2).[2]

Table II. Composition of gas mixtures emerging from reforming reactor at 580°C

CO_2	CO	Mole % H_2O	H_2	CH_4
14.32	4.90	(0.43)	77.81	2.54
13.98	4.91	(0.54)	78.61	1.95
13.82	3.54	(1.20)	80.73	0.70
15.79	2.44	(6.25)	75.34	0.19
8.73	1.21	(50.19)	39.86	0.02

Since methane is the most stable hydrocarbon, the low-temperature reforming method can obviously also be applied to other hydrocarbons. The same equilibria will occur and the same products will be formed, *viz.*, only H_2, H_2O, CO_2, CH_4, and CO. Since the reforming reaction involves a larger free energy change for the higher hydrocarbons, the reaction is practically complete. The natural gas used in the experiments contained 6% higher hydrocarbons and these completely disappeared while passing through the reforming reactor, before entering the cell. Thus, in all the reactions discussed, including the reaction of pure hydrogen in the carbonate cell, the same five species are formed. Only the ratios of C:H:O are different and consequently the relative concentrations will be different.

Cell Performance

In Fig. 3, terminal voltage-current characteristics are shown for reformed natural gas at two different flow rates, and, for comparison, a curve taken with undiluted hydrogen. The percentage conversion is indicated for the end points. The upper natural gas

[2] It can be shown that this is a consequence of the given conditions and the fact that the oxidation of methane involves no entropy change.

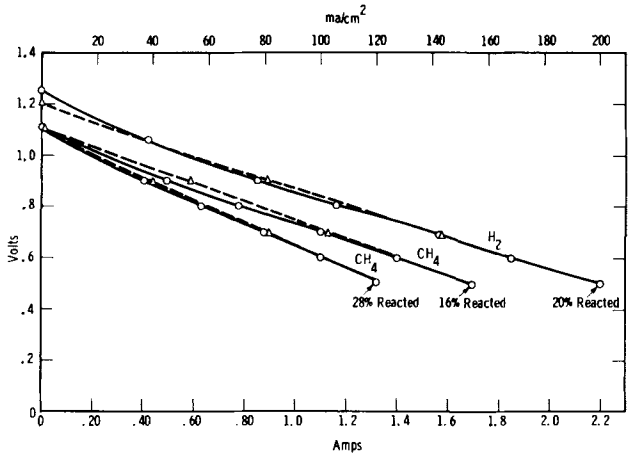

Fig. 3. Terminal voltage vs. current with hydrogen, and with reformed natural gas at two different flow rates. ○, increasing currents, △, decreasing currents; 1½ in. effective ϕ; hydrogen and natural gas (CH_4).

[1] If x is the degree of electrochemical oxidation and y the degree of chemical reaction in accordance with the equation $H_2 + CO_2 = H_2O + CO$, the partial pressures are $(1-x-y)/(1+x)$; $(x-y)/(1+x)$; $(x+y)/(1+x)$; $y/(1+x)$. (Total pressure = 1 atm.)

Then $K = \dfrac{(x+y)\,y}{(1-x-y)\,(x-y)} = 0.35$ at 580°C. This gives y and the partial pressures for any x.

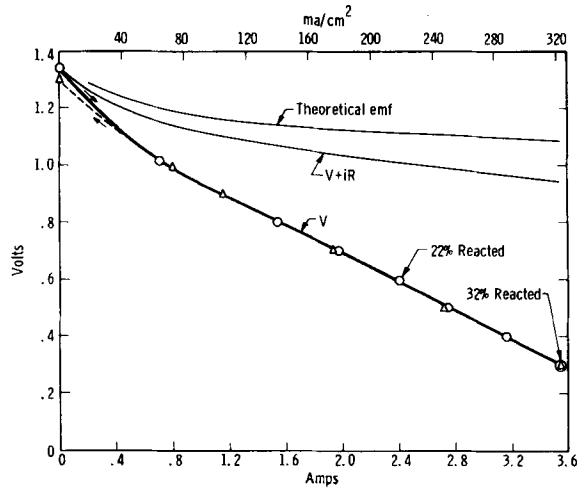

Fig. 4. Terminal voltage V, voltage + iR drop and theoretical emf as a function of current with hydrogen as fuel. ○, Increasing current; △, decreasing current; fuel, H_2; 580°C.

curve gives a current density of 130 ma/cm² at 0.6v. The points were taken at 2-min intervals for increasing and decreasing current. The CH_4 curves lie below the H_2-curve because the hydrogen obtained by reforming is diluted. Similarly, the CH_4-curve obtained at the lower flow rate gives the stronger decline of voltage with current because of the larger change of fuel composition with current. It is seen that, despite the relatively low temperature chosen and the low reactivity of the fuel, a considerable output can be obtained by use of the low temperature reforming reaction.

Cell life was limited to about one week. This is probably a consequence of poor retention of the carbonate melt by the relatively coarse MgO disk. Use of such disks was necessary because of the high clamping pressure employed to leakproof the cells. Characteristically, the voltage declined 5-10% per day during the first days when run at 25 ma/cm². Similar outputs have been obtained with many cells. The ohmic cell resistance, measured at 1000 cps, accounted for 80% of the voltage drop if allowance was made for the change in the theoretical emf with increasing degree of fuel conversion.

Even higher outputs were obtained with one cell. To improve the electrode-electrolyte contact, the MgO disk in this case was machined flat after soaking it with the melt in vacuo. The voltage-current curve for this cell, operated with hydrogen, is shown in Fig. 4, curve V. A current density of 230 ma/cm² was obtained at 0.6v at a gas flow rate giving a 20% reacted mixture at this point. The a-c cell resistance, R, again accounted for 80% of the voltage drop as shown in the same figure. (The theoretical emf curve was calculated from Eq. [6], neglecting the minor decreases in emf caused by secondary reactions.)

The output obtained is close to the maximum achievable with this type of cell for the chosen geometry: the resistivity of the melt by itself, consisting of 30 wt% Li_2CO_3, 30% K_2CO_3, and 40% Na_2CO_3, was 1.1 ohm cm (±20%) at 580°C. Assuming that there was no contact resistance, the resistance of the electrolyte disk of 0.41 cm thickness, 11 cm² electrode area and 45% porosity would be expected to be 1.1 (0.41/11) (1/0.45) q, where q is the "tortuosity factor" (6) of the disk. Comparing this with the measured a-c resistance of the cell of 0.18 ohm, one finds $q = 2.0$ (±20%). This factor accounts for blind alleys in the sintered MgO disk as well as for the tortuosity of the conduction path and is close to the attainable minimum value (6). The electrode-electrolyte contact resistance, usually assumed to limit the performance of this type of cell (1), must have been quite small.

Acknowledgment

The author is indebted to Drs. S. Barnartt, R. J. Ruka, and J. Weissbart for many discussions and to Mr. D. D. Durigon for his efficient help with the experiments.

Manuscript received May 7, 1962; revised manuscript received Aug. 11, 1962. This paper was prepared for delivery at the Detroit Meeting, Oct. 1-5, 1961.

Any discussion of this paper will appear in a Discussion Section to be published in the June 1963 JOURNAL.

REFERENCES

1. G. H. J. Broers, "High Temperature Galvanic Fuel Cells," Thesis, University of Amsterdam (1958).
2. G. H. J. Broers and J. A. A. Ketelaar in "Fuel Cells," G. J. Young, editor, pp. 78-93, Reinhold Publishing Corp. (1960).
3. J. Weissbart and R. J. Ruka, *This Journal*, **109**, 723 (1962).
4. H. H. Chambers and A. D. S. Tantram, ref. (2) pp. 94-100.
5. E. B. Schulz, Jr., L. G. Marianowski, H. R. Linden, and K. S. Vorres, *Am. Gas J.* (May 1961).
6. P. C. Carman, "Flow of Gases Through Porous Media," p. 49 Academic Press, New York (1956).

The Silver-Silver Oxide Electrode

II. Anodization at 0° and 25°C in Alkaline Solutions

Charles P. Wales

United States Naval Research Laboratory, Washington, D. C.

ABSTRACT

Silver electrodes were studied in 20% KOH at 25°C and in 35% or 50% KOH at 0°C. The capacity decreased when an electrode was cycled in 20% KOH at 25° mainly due to loss of active material during current flow. In 35% KOH at 0° the electrode capacity was close to that at 25°, the capacity decreased with increasing charge current similar to results at 25° although polarization had increased, and the charge-discharge efficiency was 100% at low currents but less when using high currents. In 50% KOH at 0° the capacity was much less than at 25°, the charge acceptance was relatively poor, under certain conditions a silver peroxy compound may form, and the electrode discharged even less readily than it charged.

Although silver-zinc storage batteries can discharge readily at high currents, experience has shown that recharging the Ag electrode is more difficult. A 12 to 24 hr rate of charge is usually recommended by the manufacturers of commercial Ag-Zn batteries, but a more rapid charge is highly desirable and in some cases essential from the user's point of view.

The anodic oxidation of Ag electrodes is being examined to find a method of improving their charge characteristics. Results have been reported using 35% and 50% KOH at 25°C (1). The work was extended to 20% KOH and to 0°C as a part of the study of the chargeability of the Ag electrode under various charge currents, electrolyte concentrations, and temperatures.

Experimental Procedure

The Ag electrodes were made by cutting Ag plates taken from an unused commercial Ag-Zn storage battery. The test electrodes were slightly larger than those used previously (1). They averaged 30.5 x 63.5 x 0.8 mm and weighed 8.3-8.4g including the grid. The grid weight was relatively minor, about 0.6g. The capacity theoretically possible was about 3.9 amp-hr if all of the Ag could be fully utilized, but the average actually measured was 2.8 amp-hr in the period of peak capacity. The experimental setup was similar to that previously reported, using the same cell assembly and control equipment (1). Ag electrodes served as both positive and negative electrodes. In order to slow the transfer of active material from an electrode to the bulk of the solution, the electrodes were wrapped with several layers of separator material of a type normally used in commercial Ag-Zn batteries. Potentials were measured with a Ag, Ag_2O/OH^- reference electrode.

Results

The Ag electrodes were cycled in 35% KOH for the first 8 to 16 cycles to ensure electrodes of normal, reproducible capacity. The capacity increased during the initial cycles. The KOH concentration was then changed for the electrodes that were studied in 20% or 50% KOH.

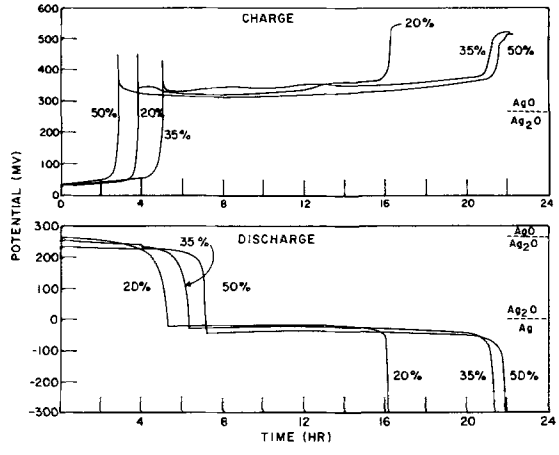

Fig. 1. Typical 100-ma constant current charges and discharges of silver electrodes in 20%, 35% and 50% KOH at 25°C. Potentials are given with respect to a Ag/Ag_2O reference electrode.

20% KOH at 25°C.—The capacity of electrodes cycling in 20% KOH decreased rapidly, a fifth being lost in the first 5-10 cycles. Typical results after the electrodes had been cycled 5-20 times are shown in Fig. 1. Charge and discharge potentials usually were closer to the equilibrium values in 20% KOH than they were in 35% or 50% KOH when using a charge or discharge lasting the same length of time. After 50 cycles the capacity in 20% KOH had dropped to near 60% of its original value. Attempts were then made to improve capacity. An electrode was charged 12.5 hr at 100 ma ending at the gassing potential. After a stand of 5 hr the electrode accepted a further 2.5 hr of charging before the potential made the sharp rise to gassing. Then stands of 15 and 5 hr allowed a total of 0.2 hr of additional charging below gassing potentials. This improved the capacity of the next discharge to 75% of the original value although there was little permanent improvement from this treatment. The decline in capacity when

using 20% KOH contrasted with the results reported earlier using more concentrated KOH at 25°C. The capacity of Ag electrodes had increased gradually with cycling in 35% KOH and although there was a decrease in 50% it was gradual (1).

One Ag electrode lost 0.6 amp-hr after 58 cycles in 20% KOH. Its weight loss was 1.00g which is equivalent to 0.50 amp-hr. Another electrode lost 0.3 amp-hr after 30 cycles in 20% KOH and had a weight loss of 0.65g which is equivalent to 0.32 amp-hr. The rate of loss was reproducible for both electrodes and was on the order of ½% of the original capacity per cycle. This active material loss accounted for most if not all of the capacity decrease. The capacity loss of a Ag electrode cycling in 20% KOH is included in Fig. 2. The slight rise in capacity after cycle 60 was the result of charges followed by stands and additional charges. The capacity was quite low compared to the original capacity in 35% KOH. For clarity Fig. 2 shows only one electrode in the early cycles, but all electrodes were similar during the initial cycling. Although the capacity varied from cycle to cycle the average capacity of each electrode was within 5% of 2.1 amp-hr in the early cycles using 35% KOH at 25°C.

The charge efficiency of the Ag electrodes was below 100% in 20% KOH, in contrast to the results reported for 35% and 50% KOH at 25° (1). There were 34 cycles at 100 ma in 20% KOH in which the charge was stopped before gas evolution (Fig. 3). The straight line fitted to these points in Fig. 3 by the method of least squares shows the tendency for the loss to increase with longer charges in 20% KOH. The scatter of these points can be attributed in part to variation in the length of time between one discharge and the following charge.

35% KOH at 0°C.—The Ag electrode gave good results at 0°C in 35% KOH. Initially the capacity averaged about 10% greater than it had been at 25°C. The capacity increased for over 100 cycles (Fig. 2). This was similar to the results reported at 25°C (1). At cycle 168, after the electrode had cycled

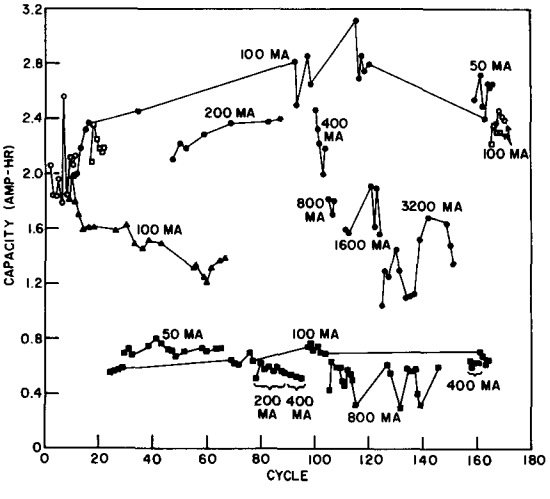

Fig. 2. Changes in electrode capacity with cycling under various conditions. All discharges were at 100 ma to —300 mv. Only discharges that followed a charge to gas evolution are shown. △, 25°, 20% KOH; •, 0°, 35% KOH; ○, 25°, 35% KOH; ■, 0°, 50% KOH; □, 25°, 50% KOH.

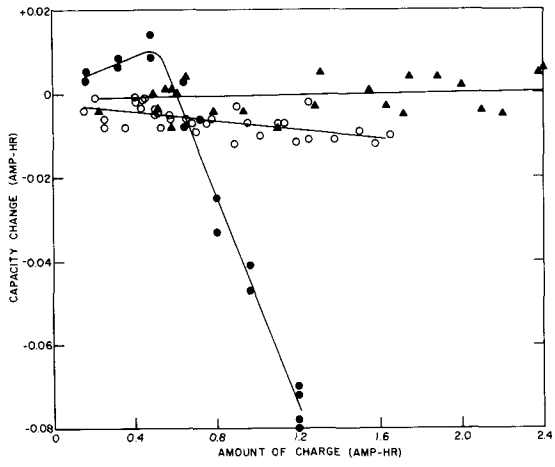

Fig. 3. Loss or gain of capacity for cycles that did not reach gassing. All discharges were at 100 ma. ○, 100 ma, 20% KOH, 25°C; ▲, 100 ma, 35% KOH, 0°C; •, 3200 ma, 35% KOH, 0°C.

156 times at 0°, it was cycled at 25° again. Capacity was then slightly higher than it had been in the early cycles at 25° (Fig. 2). The electrode weight loss at cycle 170 equaled 0.30 amp-hr.

The charge efficiency was 100% at low currents using 35% KOH at 0°C. Efficiency decreased as the electrode became more completely charged using a high current, with very short charges apparently giving over 100% efficiency (Fig. 3).

The electrode was charged at currents from 50 ma to 3200 ma (56 hr to ⅝ hr rates) at 0°C (Fig. 4). The arrows on the charge curves, denoting the capacity of the following 100-ma discharge, indicate that once gassing began there was little additional charge acceptance at the lower currents. At 3200 ma, much of the active material not having been oxidized before gassing began, there was up to 50% charge acceptance after gas evolution had commenced. The capacity using a 3200 ma charge could be increased to 1.9 or 2.0 amp-hr by halting the charge for ¼ to 1 hr after gas evolution had commenced and then charging to gas again. The potential peak between the first and second charge plateaus disappeared as the current was increased to the 2 or 1 hr rate. There

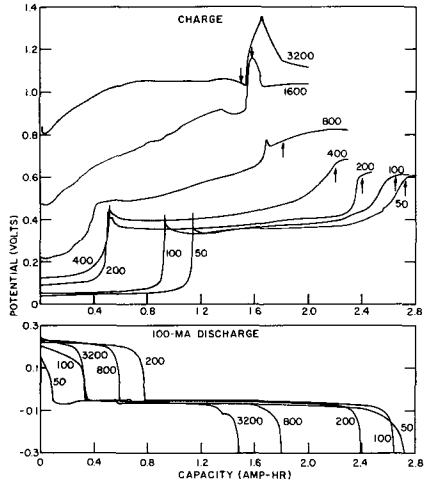

Fig. 4. Results of typical constant-current charges in 35% KOH at 0°C. Arrows on the charge curves indicate the length of the following 100-ma discharge. Numbers indicate the charge rate. Potentials are given with respect to a Ag/Ag_2O electrode.

Table I. Effect of charge current on the upper potential plateau of 100 ma discharges in 35% KOH at 0°C

Charge current, ma	Number of measurements	Ratio of upper discharge plateau length to total discharge length: Mean	Ratio of upper discharge plateau length to total discharge length: Standard deviation of mean
50	3	0.050	0.006
100	14	0.118	0.004
200	7	0.325	0.005
400	5	0.339	0.013
800	3	0.335	0.005
1600	7	0.278	0.007
3200	14	0.203	0.007

was a different peak near the end of the charge at the higher rates.

Discharges following low-rate charges had relatively short plateaus at the AgO/Ag_2O potential. The longest plateau was obtained using 200 ma (the 12-hr charge rate). For clarity Fig. 4 does not include discharges for every charge rate. Table I gives the change in length of the upper discharge potential when varying charge current and indicates the high reproducibility of the measurements under the given experimental conditions. All charges were to gas evolution. For these measurements the end of the upper plateau was taken to be at the end of the sharp drop in potential, which was at about —50 mv.

The decrease in discharge capacity when using higher charge currents was similar to the logarithmic relationship previously reported (1). Figure 5 includes the results at 25° corrected for the small differences in electrode capacity.

50% KOH at 0°C.—The electrolyte is referred to in this paper as being 50% KOH, but after the temperature was lowered to 0°C some crystals precipitated and the actual concentration did not exceed 49.2% at equilibrium (2). The results at 0° were quite different from those obtained at 25°C in 50% KOH. The low temperature gave only a quarter of the normal capacity with 100 ma charge current. High charge currents did not reduce the capacity sharply (Fig. 2) and the rate of decrease was less at 0° than at 25°C (Fig. 5). A comparison of the potentials at 25° and 0° reveals the increased polarization at the lower temperature (Fig. 6).

The lower potential plateau was unusually short during discharges at 0° in 50% KOH. The open-circuit potential rose to above 0 mv after the discharge, indicating that the electrode had not discharged fully. The electrode gave a second discharge of appreciable length after standing on open circuit (Fig. 7). Note in panel VII of Fig. 7 that the electrode sustained a discharge even after three previous discharges and a relatively short stand, and in panel VIII the stand potential still rose. Longer stands gave longer discharges. The relationship was approximately linear for up to one day of stand. One set of these discharges followed a nearly complete charge that went an estimated 95% of the way to gas evolution. The capacity of the discharge shown in panel I of Fig. 7 was 92% of this so-called 95% charge, and the total discharge by panel V was 120%. After the Ag electrode was given a series of discharges and stands the length of the following charge was much longer than the normal 0° charge (after one continuous discharge to —300 mv) although still much shorter than the usual 25° charge.

Charge efficiency varied with the amount of charge at 0° in 50% KOH, with results resembling the curve for 3200 ma shown in Fig. 3 although the points were scattered more widely. The efficiency was above 100% for short charges since the active material not reduced in the previous cycle could be utilized. The excess of discharge capacity over charge capacity gradually decreased to zero during a series of consecutive cycles in which gassing was not reached.

The effect of increasing charge current at 0° in 50% KOH is shown in Fig. 8. The Ag electrode was discharged twice before these charges, with a stand period of 6-20 hr between discharges, to ensure that the electrode was mostly discharged. A borderline

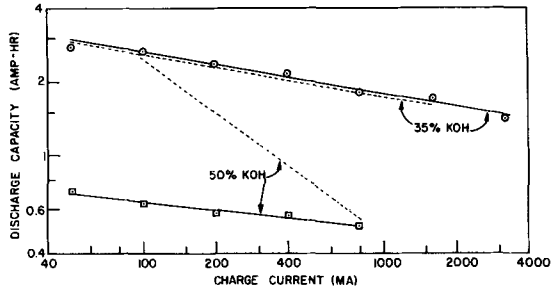

Fig. 5. Dependence of discharge capacity on charging current; ———, 0°C; - - - -, 25°C.

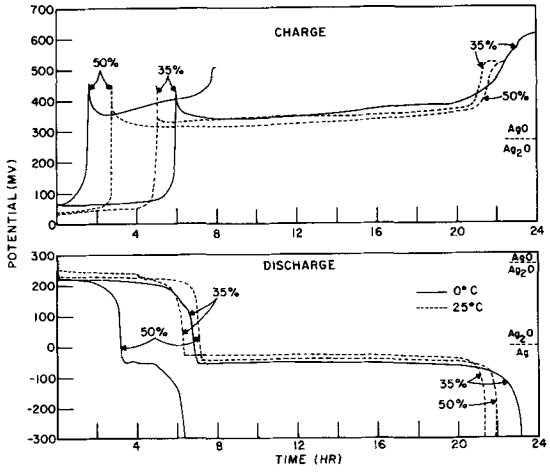

Fig. 6. Effect of temperature and KOH concentration at 100 ma. Potentials are given with respect to a Ag/Ag_2O reference electrode.

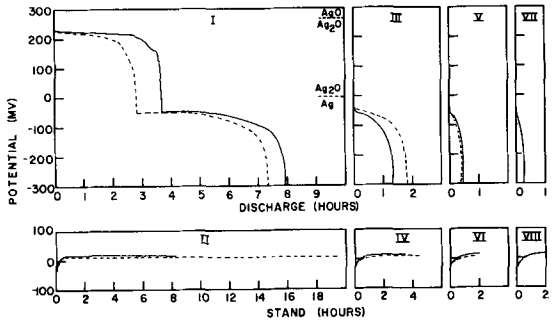

Fig. 7. Effect of stand periods on 100-ma discharges in 50% KOH at 0°C following 50-ma charges; ———, full charge; - - - -, 95% charge.

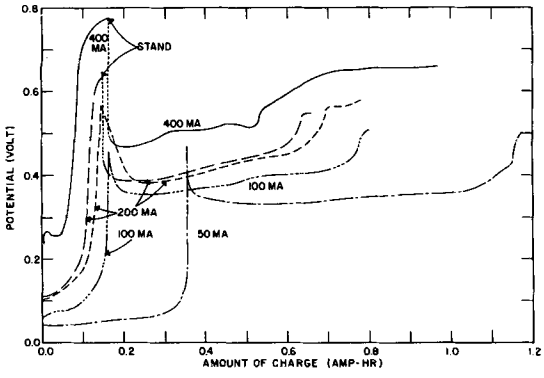

Fig. 8. Constant current charges in 50% KOH at 0°C. Potentials are given with respect to a Ag/Ag_2O electrode.

condition was reached at 200 ma, and occasionally the electrode charged at both plateaus, but at other times the potential rose to a high gassing potential instead of the electrode charging at the second plateau of charge. At 400 ma the potential usually rose to gassing. An open-circuit period at this point changed conditions so that charging could proceed. Charges following these stands are shown for 200 and 400 ma (Fig. 8). When there was no stand the charging potential remained high (although gradually declining) and the following discharge capacity was well below the normal for a given rate unless there had been a long overcharge.

The open-circuit potentials for these stands showed several plateaus (Fig. 9). The potential reported for Ag_2O_3 is shown despite its questionable value. There were three open-circuit plateaus, the first at 0.41-0.42v, the second at 0.26-0.27v, and finally the potentials approached zero. The length of the first plateau depended on the final charge potential (Fig. 10). When the electrode was discharged without a stand period the electrode sustained a few minutes of discharge at this highest plateau. These measurements were made in the first 96 cycles (6 months of cell life). The cell was put into use again after it was one year old (cycle 97, Fig. 2). Capacity had not changed, but the potential seldom rose to gassing at the beginning of the second plateau. After rewrapping the electrode with a new separator, charges at 400 ma rose to gassing at the second plateau more often. Cycles 165 to 168 at 25° indicated a

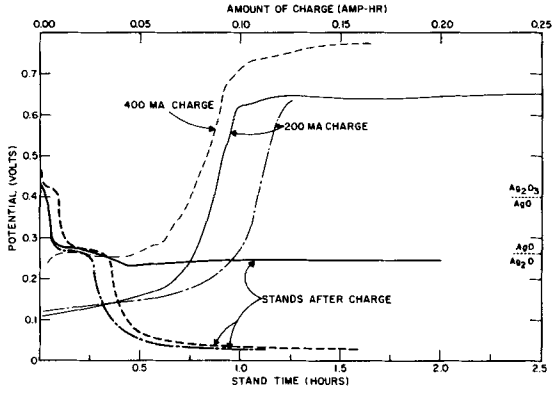

Fig. 9. Constant current charges in 50% KOH at 0°C and the subsequent open-circuit potentials.

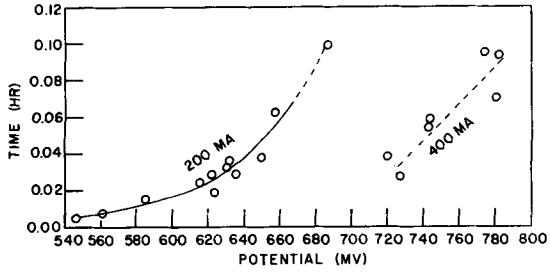

Fig. 10. Relationship between the final charge potential and the length of time the subsequent open-circuit potential takes to reach 390 mv in 50% KOH at 0°C. Potentials are given with respect to a Ag/Ag_2O electrode.

slight gain in capacity compared to cycles 17 to 22 (Fig. 2). The loss in weight of this electrode was equal to 0.31 amp-hr after cycle 168.

Ag electrodes were put in a U-tube containing 50% KOH at 0°. When an electrode was at the high gassing potential attempts were made to detect O_3 in the evolved gas. Filter paper test strips wet with $MnSO_4$ or TlOH solutions were exposed to the gas but did not indicate O_3. Since the fine gas bubbles rise very slowly it seemed possible that any O_3 present may have decomposed before reaching the surface. Another Ag electrode in 50% KOH at 0° was arranged so that air swept through the electrolyte and carried the evolved gas into a buffered 5% KI solution. It is claimed in atmospheric pollution work that 0.06 ppm O_3 can be detected with this indicator, but none was detected in the anodic gas.

Discussion

The slightly decreased polarization that resulted from using 20% KOH was desirable, but this was more than offset by the decrease in capacity with cycling. Capacity was improved by permitting the charged Ag electrode to stand on open circuit for several hours and then recharging. AgO had time to react with remaining metallic Ag during this open-circuit period. Therefore the plate charged more deeply after a stand. The additional capacity was removed readily in the following discharge, indicating that the difficulty was in the oxidation portion of the cycle and not in the reduction. The charging potential during the first hour was lower after a stand than it was during the second plateau before the stand. This raises the question of why the potential of the upper charge plateau is normally so high above the equilibrium potential. The answer is probably connected with the mechanism of the charge reaction at this plateau. It is hoped that work now being carried out at this Laboratory will shed light on this problem.

It was somewhat surprising that the loss in weight correlated so closely with the loss in capacity in 20% KOH since only a little over half of the theoretical capacity was obtained when the electrode was first put into 20% KOH, and the loss of the original surface material should expose more usable material. If the electrode still oxidized to the same depth the surface area must have decreased as the active material left the electrode. From Fig. 3 the loss was 0.008(0) amp-hr for the average charge of 10.9

amp-hr. (This average included 23 charges that reached gassing.) If this rate of loss remained constant, in 58 cycles the total loss would be 0.46 amp-hr. This was close to the value 0.50 amp-hr calculated from the weight loss. Thus the inefficiency was due to loss of oxidized silver from the electrode, and not due to gassing. It was concluded that most or all of the loss of silver occurred during cycling, most likely during the charge, with little or no loss during open-circuit periods. The difference between these results and those in 35% and 50% KOH at 25°C may be an effect of the separator becoming more porous and allowing active material to diffuse away from the electrode. As indicated by figures given earlier, the weight loss per cycle was 5-6 times as great in 20% KOH as in 35% or 50% KOH. The capacity increase when cycling in 35% or 50% KOH (presumably due to forming the plates more deeply) more than made up for the active material loss equivalent to only 0.3 amp-hr.

The inefficiency in 35% KOH at 0° was attributed to slow gas evolution during high rate charges (Fig. 3) although no attempts were made to measure gas. About an eighth of the charging current was lost after the potential reached 1.03v at 3200 ma (Fig. 3 and 4). Efficiency was 100% at low currents. An additional 0.005-0.010 amp-hr was obtained when a discharged electrode was discharged a second time after standing for one day. This residual capacity was probably the cause of the apparent efficiency being slightly over 100% for very short charges at 3200 ma.

The short discharge plateaus at the upper potential which were observed following low-rate charges at 0°, *i.e.*, at the 26 and 54 hr rates in Fig. 4, can be attributed to the reaction of Ag with AgO to form Ag_2O. This reaction is known to decrease the upper discharge plateau when charged Ag electrodes are allowed to stand on open circuit. Although the time required for the charge was long, time alone was insufficient to account for all of the large decrease in length of the upper discharge plateau. Even if the electrode had been converted completely into Ag_2O the maximum discharge at the lower plateau would only have been one half of the theoretical capacity or 1.95 amp-hr. After a 50 ma charge 71% of the theoretical capacity was obtained (Fig. 4). Therefore a minimum of 21% of the theoretical capacity must have been obtained from silver oxidized higher than Ag_2O. Assuming that this oxide was AgO, a minimum of 42% of the electrode must have been oxidized to AgO using 50 ma although less than 3% of the theoretically possible AgO capacity was obtained. Due to the reaction of Ag with AgO the electrode surface probably was not covered completely with AgO to a very great depth when the electrode was charged at a low current at 0°. Ag_2O covered the surface after a relatively short discharge and then the potential reached the lower plateau, although there was considerable AgO remaining in the electrode.

There was a potential peak near the end of the high rate charges at 0°C using 35% KOH (Fig. 4). AgO had been forming, and by the time this late peak was reached its formation was hindered greatly. There was a lack of one or more reactants due to the slow diffusion at this temperature and the need for rapid diffusion at the high current density, therefore passivation increased and the potential rose. A possible explanation of the drop in potential at the end of the charge is that given by Cahan *et al.* (3) for the decrease in resistance measured just as gassing began. They believed this was not rupture of a film, but proposed that further incorporation of oxygen in the AgO film had taken place, producing an unstable film of an oxide higher than AgO having a lower resistance.

There may be a connection between this peak and the potentials that were recorded in 50% KOH at 0°C (Fig. 8). The lower two open-circuit plateaus corresponded to the well-known oxides of silver (Fig. 9). It is possible that the upper plateau corresponded to a higher oxide of Ag, but the existence of trivalent Ag_2O_3 or other higher oxides of Ag has not been proven (4-6). Many of the claims for it could be explained by the presence of a peroxy linkage. Note that the Ag_2O_3/AgO potential measurements cited in the literature use the values of Luther and Pokorny (7) which were obtained with silver peroxysulfate and silver peroxynitrate and not actually with Ag_2O_3.

The open-circuit plateau at the AgO/Ag_2O potential lasted longer after a long charge at 200 ma than after a short charge, although the upper plateau length was the same (Fig. 9). This first plateau could be shortened by interrupting the charge while the potential was still rising. The length of the first plateau did not depend on the amount of charge given the electrode at a high potential, *i.e.*, over 600 mv at 200 ma, but it varied instead with the final charge potential (Fig. 10). The points at 400 ma were too few and scattered to determine whether a curved line should be drawn through them although they gave the same trend as that shown for 200 ma (Fig. 10). It was not surprising that the potentials were higher at 400 ma since the IR drop was higher.

It was mentioned earlier that the electrodes charged poorly after the potential rose to the high values. Conditions changed during a short stand so that the electrode accepted a charge again. Very short stands in which the potential did not fall below about 0.35v did not aid further charging, nor did long stands in which the potential fell to well below the AgO/Ag_2O value. The charge potential usually rose again to high values in these cases. The only beneficial stands were those ending near the AgO/Ag_2O potential.

The presence of a certain amount of AgO was necessary for good charge acceptance above the Ag/Ag_2O potential plateau. This was indicated by the differing results when the stand ended above or below the AgO/Ag_2O plateau. Either AgO was rendered inactive at the beginning of these stands or the necessary AgO was not present until some other compound decomposed. At room temperature the potential peak was reached when the electrode surface was covered with Ag_2O and ohmic resistance

then reached its maximum (3). By using high currents at a low temperature the gradients in the concentrated electrolyte were greater than when using lower charge currents at room temperature. The combination of these factors resulted in an unusually high electrode potential and may have allowed some intermediate material having the peroxy linkage such as O_2^- or HO_2^- to form in larger than normal amounts, in addition to O_2 the final product. The failure to detect any O_3 in the evolved gas does not prove that O_3 was never present since it would be in contact with Ag_2O and Ag_2O catalytically decomposes O_3. Any O_3 remaining could decompose while passing through the alkaline electrolyte, since aqueous alkali decomposes O_3. The potentials measured, however, were low for the formation of O_3.

There is evidence that O_2 forms through a peroxide mechanism in alkaline solution instead of directly according to $4\ OH^- = O_2 + 2H_2O + 4e^-$. Oxygen was reported to establish a reversible equilibrium with HO_2^- ion in alkali (8). It is likely that OH^- goes first to O_2^- and this to HO_2^-, although possibly OH^- goes directly to HO_2^- at high current densities. The low temperature used would tend to stabilize for a longer time any O_2^- or HO_2^- that formed, and these may react with the Ag_2O instead of producing O_2.

Jirsa and Jelinek (9) reported that Ag or Ag_2O oxidized with a mixture of $O_3 + O_2$ gave a compound that in KOH showed the potential reported for Ag_2O_3 (really the potential of silver peroxy compounds) before this compound decomposed into AgO. AgO did not react with O_3, casting some doubt on their report that O_3 was producing trivalent Ag. Schwab and Hartmann (10) reported that Ag with a mixture of $O_3 + O_2$ formed two compounds: AgO and a compound that gave a typical silver peroxy x-ray diffraction pattern. It is postulated that this type of reaction with a substance having the peroxy linkage formed a silver peroxy compound when the high charging potentials were observed to 0° in 50% KOH, and that the silver peroxy compound gave the initial high open-circuit potential plateau (Fig. 9). The reaction may be analogous to the formation of silver peroxysulfate when Ag is anodized in H_2SO_4 (5, 11). The decomposition of the silver peroxy compound produced AgO during the initial part of the open-circuit period. With a longer open-circuit period this AgO reacted with Ag to give highly resistive Ag_2O, and again charging difficulty could occur.

The final potentials at the end of the high-rate charges following the beneficial stands were lower than those reached before the stands (Fig. 8) since the final resistance was less due to the AgO present. An open circuit at this point gave only a very brief period of high potential before the potential dropped to the AgO/Ag_2O plateau.

High potentials at the beginning of the second plateau occurred less often late in the life of the cell before the electrode was rewrapped. By this time the separator was not as effective and diffusion through it was easier. After rewrapping with a new separator high potentials occurred more frequently. Then the cell was cycled without any separator and the high potentials occurred less often. This indicated that the presence of the separator was not essential although it was a factor in the high potentials.

The discharges in 50% KOH at 0°C were unusual in that the Ag_2O/Ag plateau was about the same length as the upper plateau instead of being two or three times as long (Fig. 6). This was not an effect of temperature alone since it was not noted in 35% KOH. The high open-circuit potentials after a discharge indicated that all of the AgO had not been reduced (Fig. 7). Another indication of this was obtained by interrupting a discharge after it was 90% complete. The potential then rose to the AgO/Ag_2O plateau after 1½ days of stand. This indicated that a sizeable quantity of AgO must have remained, since the AgO decreased during a stand as it reacted with Ag. The results suggest that the reaction rate was affected by the concentration of the electrolyte and by temperature. The O^{--} diffused from within the electrode to its surface where it combined with H_2O to give OH^- Increasing the KOH concentration decreased H_2O and increased OH^-, both changes making the reaction with O^{--} more difficult. The low temperature slowed the reaction and the flow of ions, the complete formation of Ag on the electrode surface was inhibited as the O^{--} concentration built up, and the electrode potential fell before the discharge was complete. After a high rate charge at 0°C in 50% KOH a second discharge of appreciable length could be obtained following a shorter stand than after a low rate charge, since the electrode had not formed as deeply. The electrode charged more readily than it discharged under these conditions since there was no shortage of OH^- ions to supply the needed oxygen during the charge.

Many problems were pointed out in the work described above. A further study with experiments designed to clarify these problems is necessary for a full and definite explanation.

Manuscript received May 16, 1962; revised manuscript received July 20, 1962. This paper was prepared for delivery before the Boston Meeting, Sept. 16-20, 1962.

Any discussion of this paper will appear in a Discussion Section to be published in the June 1963 JOURNAL.

REFERENCES

1. C. P. Wales, *This Journal*, **108**, 395 (1961).
2. International Critical Tables, New York: McGraw-Hill Book Co., **4**, 239 (1928).
3. B. D. Cahan, J. B. Ockerman, R. F. Amlie, and P. Rüetschi, *This Journal*, **107**, 725 (1960).
4. T. P. Dirkse, *ibid.*, **106**, 453 (1959).
5. C. P. Wales and J. Burbank, *ibid.*, **106**, 885 (1959).
6. T. P. Dirkse, *ibid.*, **107**, 859 (1960).
7. R. Luther and F. Pokorny, *Z. anorg. Chem.*, **57**, 290 (1908).
8. W. G. Berl, *Trans. Electrochem. Soc.*, **83**, 253 (1943).
9. F. Jirsa and J. Jelinek, *Z. anorg. u. allgem. Chem.*, **158**, 61 (1926).
10. G-M. Schwab and G. Hartmann, *ibid.*, **281**, 183 (1955).
11. G. W. D. Briggs, I. Dugdale, and W. F. K. Wynne-Jones, *Electrochim. Acta*, **4**, 55 (1961).

The Use and Behavior of Aluminum Anodes in Alkaline Primary Batteries

Solomon Zaromb[1]

Scientific Laboratory, Philco Corporation, Blue Bell, Pennsylvania

ABSTRACT

The two- to threefold reduction in over-all theoretical reactant weight (and usually also volume) which results from replacing Zn by Al in alkaline primary batteries could best be preserved in practice with a 3M KOH "self-regenerating" electrolyte in large (>1 kw) Al-air (or $-O_2$) power sources, whereas small Al-air (or $-O_2$ or $-AgO$) reserve cells should function best with a consumable 10M KOH solution. Special attention is given to the use of Al in Al-air cells with porous C or, preferably, porous Ni air cathodes. Anode polarization and current efficiency data are presented for both the self-regenerating and the consumable electrolytes with and without several effective corrosion inhibitors consisting of alkyldimethylbenzylammonium salts and/or Hg with or without ZnO. It is concluded that optimum battery performance would result from the use of some of these inhibitors, as well as from elimination of sulfides and other corrosion accelerators, use of highly pure Al or specially resistant Al-Mg, Al-Zn, or Al-Hg alloys, effective heat removal, operation at high current densities (preferably $\geq$10 ma/cm^2), and anode-electrolyte separation during periods of inaction.

In spite of the highly attractive anode characteristics of Al, all previous attempts (1-8) to utilize it in practical batteries failed (9-11) either because of the formation of passivating, resistive oxide layers in those electrolytes in which Al oxides are not readily soluble (1-6, 12) or because of high rates of corrosion in those electrolytes in which the oxide layers are dissolved, *e.g.*, in concentrated alkali solutions (7, 8). Nevertheless, the author was interested in the possibility of using Al anodes under conditions wherein the corrosive alkaline electrolyte would be in contact with the metal during current drain only.

Thanks to encouraging initial experimental results suggesting the possibility of achieving outputs of 1.0-1.5v at current densities of up to 50 ma/cm^2 (cf. Fig. 3 and the relevant text) and current efficiencies of 60-100% at current densities of 3.5-140 ma/cm^2, a systematic study was initiated toward incorporating Al anodes in practical alkaline primary batteries.

In order to survey and define the most promising applications of Al anodes, a comparison was made of the theoretical reactant requirements in three types of alkaline primary batteries. Table I shows that, in all three types, a reduction by a factor of 2-3 in the minimum reactant weight (and usually also volume) is theoretically achievable by substituting Al for Zn. With an actual output voltage of 1.3v, battery type 1 can thus yield 4 kw-hr/kg Al. Since the O_2 is obtainable from air and H_2O is usually plentiful, the over-all cost of portable electricity would amount to \$0.15-0.20/kw-hr for a battery operating at an optimum achievable current efficiency of 80-100%. This might conceivably be

[1] Present address: The Martin-Marietta Corporation, Baltimore, Maryland.

Table I. Comparative theoretical reactant requirements per Faraday of electricity for alkaline primary batteries with Zn or Al Anodes

Battery Type No.	Over-all reaction	Minimum theoretical: Required reactants	Total Weight, g	Total Volume, cc	Wt, g Without O_2	Vol, cc Without O_2	Wt, g Without O_2 and H_2O	Vol, cc Without O_2 and H_2O
1	$1/3\ Al + 1/4\ O_2 + 1/2\ H_2O \rightarrow 1/3\ Al(OH)_3$	9.0g Al + 9.0g H_2O + 8.0g O_2	26.0		18.0	12.3	9.0	3.3
2	$1/3\ Al + 1/4\ O_2 + 1/3\ OH^- \rightarrow 1/3\ AlO_2^- + 1/6\ H_2O$	9.0g Al + 33.3 cc 10M KOH + 8.0g O_2	63.6		55.2	36.6	27.7	13.1
3	$1/3\ Al + 1/2\ AgO + 1/3\ OH^- \rightarrow 1/3\ AlO_2^- + 1/2\ Ag + 1/6\ H_2O$	9.0g Al + 61.9g AgO + 33.3 cc 10M KOH	117.5	44.9				
4	$1/2\ Zn + 1/4\ O_2 + 1/2\ H_2O \rightarrow 1/2\ Zn(OH)_2$	32.7g Zn + 9.0g H_2O + 8.0g O_2	49.7		41.7	13.5	32.7	4.5
5	$1/2\ Zn + 1/4\ O_2 + OH^- \rightarrow 1/2\ ZnO_2^= + 1/2\ H_2O$	32.7g Zn + 100 cc 10M KOH + 8.0g O_2	180.7		172.7	104.5	88.8	32.1
6	$1/2\ Zn + 1/2\ AgO + OH^- \rightarrow 1/2\ ZnO_2^= + 1/2\ Ag + 1/2\ H_2O$	32.7g Zn + 61.9g AgO + 100 cc 10M KOH	234.6	112.8				

reduced further by recovering the $Al(OH)_3$ product, worth about half the cost of the Al. Partly in view of this promising price estimate, and in view of the high theoretical energy to weight and volume ratios, battery types 1 and 2 were selected specifically for the present studies.

The Aluminum-Oxygen Or-Air Cell

Basic Components and Reactions

The following battery reactions are to be considered

Anode: $(Al + 4OH^- \rightarrow Al(OH)_4^- + 3e^-) \times 4$ $E^\circ = -2.35v$ [1][2]

Cathode: $(O_2 + 2H_2O + 4e^- \rightarrow 4OH^-) \times 3$ $E^\circ = -0.40v$ [2][2]

Over-all: $4Al + 3O_2 + 4OH^- + H_2O \rightarrow 4Al(OH)_4^-$ $E^\circ = -2.75v$ [3][2]

Electrolyte regeneration: $(Al(OH)_4^- \rightarrow Al(OH)_3 + OH^-) \times 4$ [4]

Net over-all reaction [3] + [4]: $4Al + 3O_2 + 6H_2O \rightarrow 4Al(OH)_3$ [5]

The corrosion process can be considered as the sum of reaction [1] and

$$2H_2O + 2e^- \rightarrow 2OH^- + H_2 \quad E^\circ = 0.83v \qquad [6][2]$$

both occurring at the Al electrode, yielding the over-all corrosion reaction

$$2Al + 6H_2O + 2OH^- \rightarrow 2Al(OH)_4^- + 3H_2 \quad E^\circ = -1.5v \qquad [7][2]$$

Thus, the performance of Al-air cells is contingent on: (*a*) a suitable means of supplying the reactants and removing the product of reaction [5] or [3]; (*b*) the occurrence of reactions [1] and [2] and possibly also [4] at sufficiently high rates; and (c) the inhibition of reaction [7].

Although the present paper is concerned mainly with the chemical aspects (*b*) and (c), especially with the study of electrolyte and anode behavior, a brief preliminary discussion of the cathode and over-all battery design features is presented first.

Air Electrodes

At the time of writing, the best commercially available carbon-air cathodes (Eveready type CG-500, manufactured by the National Carbon Company) could deliver current densities of up to 15 ma/cm^2 with reasonably low polarization, but they would be too bulky for practical Al-air cells. However, the author obtained air cathodes by impregnating 0.06 cm thick 60-80% porous sintered Ni sheets first with C and Ag and finally with a Teflon emulsion. With a proper impregnation and heat treatment procedure, the Teflon prevents leakage of the electrolyte through the pores, while allowing atmospheric O_2 to diffuse readily from the ambient atmosphere toward the cathode-electrolyte interface. These porous Ni cathodes have current density-polarization characteristics comparable to those of the above-mentioned Eveready type CG-500 carbon-air electrode (cf. Fig. 1), but with the advantage of a tremendous reduction in thickness and weight. The maximum Ni-air electrode sizes that could be conveniently made with the initially available laboratory facilities were 5 cm x 5 cm. Hence, for most experiments it was found expedient to use the type CG-500 carbon cathodes, sometimes in modified form (as in Fig. 8).

[2] The listed E° values correspond to maximum theoretical energy conversion, and not to actually observed open-circuit voltages.

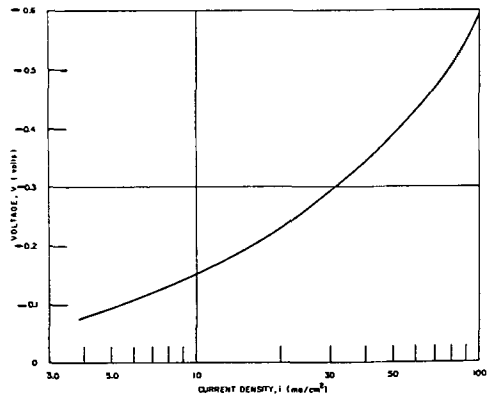

Fig. 1. Polarization curve for a typical 0.06 cm thick sintered Ni air-cathode prepared in January-February 1961. The ordinate V is given relative to the Hg-HgO half-cell.

It is worth noting that the electrode sheets serve also as container walls, as shown in Fig. 8. This arrangement may be adapted to a collapsible accordion-like cell design, which could eliminate the air gaps during periods of inaction and thereby (i) reduce the inactive, portable volume of Al-air (and possibly also Zn-air) batteries to a minimum and (ii) prevent corrosion of Al and slow deterioration of electrolyte by evaporation and CO_2 pick-up on shelf.

Optimum Electrolyte Concentrations for Minimum Volume and Weight Requirements

Self-regenerating electrolyte (type 1 of Table I).—For a battery to maintain its characteristics over prolonged periods of operation and/or storage, the electrolyte composition must remain constant or at least confined within satisfactory concentration ranges. Electrolyte composition may be affected by the following factors: (*a*) absorption of atmospheric carbon dioxide; hence direct contact between the electrolyte and atmospheric air should be prevented by using a properly sealed system; (*b*) loss of water by evaporation, corrosion reaction, and over-all battery reaction [5]; this loss must be compensated for by replenishing the water at various intervals; (c) comparative rates of reactions [3] and [4]. Under conditions of prolonged heavy current drain, marked changes would occur in the concentration of hydroxide ions if the rate of the regeneration reaction [4] were slower than that of the battery reaction [3]. However, the experiments reported in a concurrent paper (13) show that, with 2-3M KOH concentrations, reaction [4] occurs soon and fast enough to permit a continuous heavy current drain far in excess of the maximum charge theoretically achievable without electrolyte regeneration.

The optimum alkali concentrations for the occurrence of reaction [4] are $\leq$3M [cf. ref. (13) and references quoted therein], whereas those yielding high anode current densities are $\geq$3M [cf. Fig. (2)].

Hence, the most suitable alkali concentration for type 1 batteries should be approximately 3M.

Electrolyte in reserve cells (type 2 of Table I).— According to the best available phase equilibrium data (14) the maximum obtainable solubilities of $Al(OH)_3$ in alkali solutions are ≧7.5M in 12.9M NaOH and ≧5M in 10.5M KOH. However, the polarization data of Fig. 2-4 suggest that the 10.5M KOH solution is preferable, yielding satisfactory current densities and voltage outputs for up to 7 moles $Al(OH)_3$ per liter of 10.5M KOH (cf. Table II). This corresponds to a minimum actual reactant requirement of only 3.5 g/w-hr or 2.2 cc/w-hr.

Corrosion Inhibiting Additives

The control of Al corrosion in caustic solutions is discussed extensively in a concurrent paper (15) which lists a number of corrosion inhibitors. Of the most effective ones, those showing no excessive anode polarization in preliminary tests were used for further studies. These include approximately 0.5M ZnO with surface-amalgamated Al anodes and/or "Hyamine" (alkyldimethylbenzyl ammonium salt) surfactants (supplied by the Rohm and Haas Company, Philadelphia).

Anode Polarization and Current Efficiencies

Dilute alkali solutions (type 1).—All anode polarization measurements were performed with small Al strips placed between two large-area air cathodes. Figure 2 shows the current-voltage characteristics of smooth amalgamated Al anodes in solutions saturated with ZnO and containing in addition 0.5M $Al(OH)_3$ and 3 to 5M KOH or NaOH. The current efficiency as function of current density is shown in Fig. 1 of ref. (15).

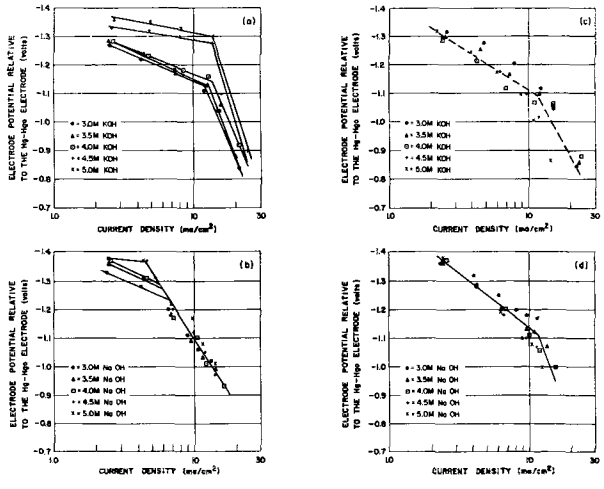

Fig. 2. Room temperature current-voltage characteristics of smooth amalgamated Al anodes in 3.0-5.0M alkali solutions saturated with ZnO and containing 0.5M $Al(OH)_3$. The anodes, with dimensions of 2.9 x 1.7 x 0.01 cm, were contained in a Patterson L-1400 parchment paper bag, dipping in Hg contacts along the shortest (bottom) edge, and suspended between two large area carbon-air cathodes (Eveready type CG-500, manufactured by The National Carbon Co.). (a) Al grade 1145, 3.0-5.0M KOH; (b) Al grade 1145, 3.0-5.0M NaOH; (c) Al grade 2S, 3.0-5.0M KOH; (d) Al grade 2S, 3.0-5.0M NaOH.

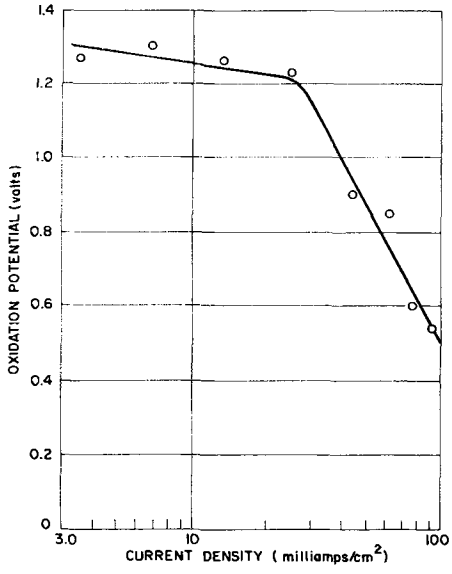

Fig. 3. Room temperature oxidation potential of surface-amalgamated Al anodes relative to the Hg-HgO reference electrode as a function of anode current density. Electrolyte composition: 10M KOH saturated with ZnO.

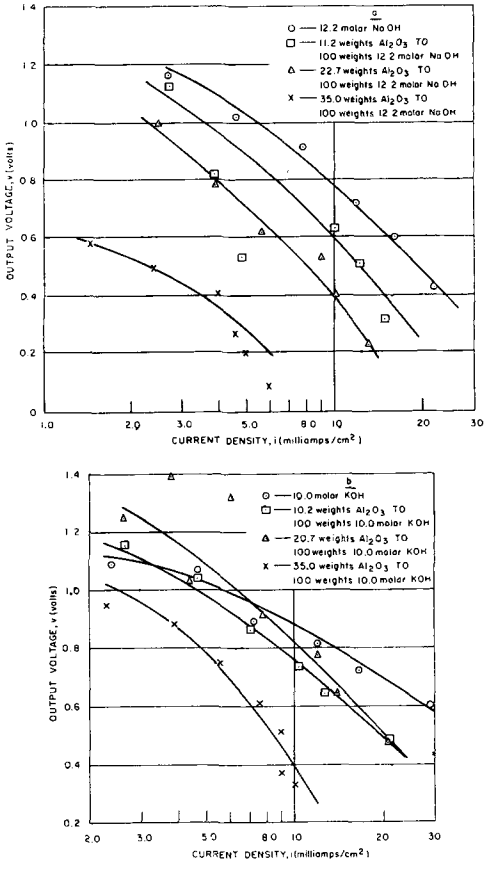

Fig. 4. Room temperature polarization curves for surface-amalgamated Al grade 2S (≧ 99.0% Al) anodes in concentrated alkali solutions containing dissolved Al_2O_3 (the ordinates V are anode oxidation potentials relative to an Hg-HgO reference electrode).

In Fig. 2 (b), (c), and (d) there is no appreciable decrease in allowable current density as the OH^- concentration is reduced from 5M to 3M, and even in Fig. 2 (a), where such a decrease occurs, current densities of 15 ma/cm² produced additional polarization of not more than 0.3v for the lowest OH^- ion concentration. The observed differences between NaOH and KOH solutions and between the two

different grades of Al [grade 1145 containing ≥99.45% Al, ≤0.55% (Si + Fe), ≤0.20% Mn and ≤0.09% other impurities, and grade 2S containing ≥99.0% Al, ≤1.0% (Si + Fe), ≤0.20% Cu, ≤0.05% Mn, ≤0.1% Zn, and ≤0.15% (Be + other impurities)] are interesting and deserve further study.

It is also worth noting that no appreciable increase in the polarization of the unamalgamated high-purity (≥99.99%) Al anodes occurred on supersaturation of the 3M KOH solution with $Al(OH)_3$ in the electrolyte regeneration experiments described in ref. (13).

Concentrated alkali solutions (type 2).—The polarization curve of surface-amalgamated Al grade 1145 anodes in ZnO-saturated 10M KOH solution is shown in Fig. 3. Similar curves were obtained with 10M solutions of both technical and chemically pure KOH grades containing an excess of ZnO or of Zn0.3CaO, and also with 10M NaOH solutions with or without the same additives. All such curves overlapped within a band of ±0.1v. On the other hand, integration of the complete discharge curves of the weighed, surface-amalgamated Al grade 1145 or 2S anodes showed average current efficiencies ≥60% for the following current density ranges in the indicated electrolytes: 10M or saturated NaOH solutions, 30-65 ma/cm²; solutions saturated with both ZnO and NaOH, 5-30 ma/cm²; 10M solutions of NaOH or KOH (chemically pure or technical grades) saturated with ZnO or Zn 0.3CaO, 3.5-140 ma/cm². Thus addition of ZnO definitely helps inhibit the corrosion of surface-amalgamated Al over a very wide current density range without significantly affecting polarization.

Without the ZnO additive, the current density-voltage characteristics of Al anodes in concentrated NaOH and KOH solutions containing various concentrations of dissolved $Al(OH)_3$ (prepared by utilizing the corrosion reaction [7]) are shown in Fig. 4 to 6. The data in Fig. 4 are for surface-amalgamated Al (grade 2S), while those in Fig. 5 and 6 are for high-purity Al (grade 1199 containing at least 99.99% Al) not exposed to Hg. The purer, unamalgamated Al anodes obviously have the better polarization characteristics. The KOH electrolyte is definitely more satisfactory than the NaOH, in spite of the higher solubility of $Al(OH)_3$ in concentrated NaOH solution. The scatter of experimental points in Fig. 5 and 6 appears mainly due to accidental impurities. From the upper curves in Fig. 6 (a) through (d) one obtains Table II in which is shown the variation in output voltage on continued dissolution of $Al(OH)_3$ at a constant current density of 10 ma/cm².

Effect of "Hyamine" inhibitors.—Upon addition of 0.1M "Hyamine 3500" the corrosion rate of surface-amalgamated Al was reduced sufficiently to yield an almost satisfactory cell performance at temperatures of 50° and 70°C [Fig. 7(a)]. However, anode polarization was barely acceptable at these temperatures [Fig. 7(b)] and, at room temperature, proved too high to yield useful current densities even with the KOH concentration increased to 10M.

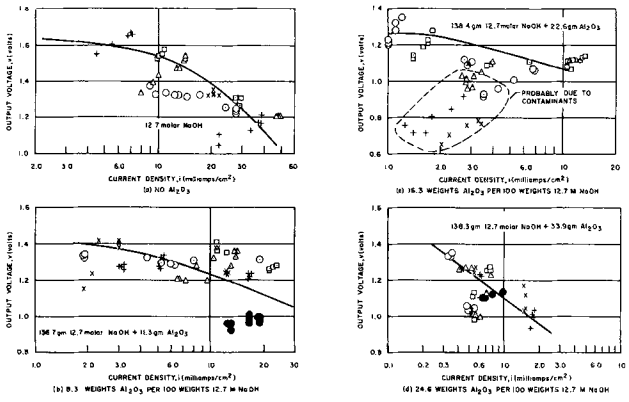

Fig. 5. Room temperature polarization curves for high purity (≥ 99.99%) Al anodes in 12.7M NaOH solutions with various amounts of dissolved Al_2O_3. The anode strips were clamped with rubber gaskets between two large-area Ni-air cathodes.

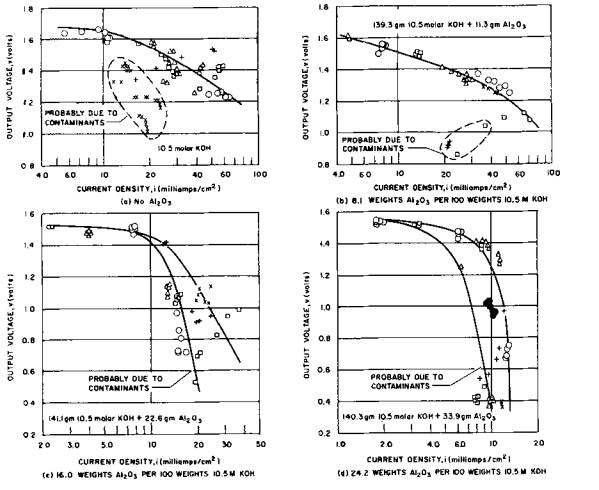

Fig. 6. Room temperature polarization curves for high purity (≥ 99.99%) Al anodes in 10.5M KOH solutions with various amounts of dissolved Al_2O_3.

Table II. Variation in output voltage at a current density of 10 ma/cm² on continued dissolution of aluminum hydroxide

Moles of $Al(OH)_3$ per liter of 10.5M KOH	Anode oxidation potential (volts) relative to the Hg-HgO half-cell
0	1.66
2.3	1.51
4.5	1.45
6.7	1.26

Similar results were obtained with the other Hyamine inhibitors listed in ref. (15).

In experimental cells with unamalgamated high-purity (>99.99%) Al anodes in 10M KOH (Fig. 8), addition of about 0.1M "Hyamine 3500" or "Hyamine 10-X" reduced the maximum rate of H_2 evolution by a factor of 3 at a current density of 4 to 5 ma/cm² (Fig. 9). The corrosion current in the presence of the inhibitors reached maximum steady values of 7-12 ma/cm² after 30-50 min (corresponding to a steady temperature of 40°-50°C) at current densities of both 4-5 ma/cm² and 18-19 ma/cm², with the effect of the additives being most pronounced at the lower current density. On the other hand, the Hyamines showed no adverse effect on the polarization of the unamalgamated anodes, the outputs being

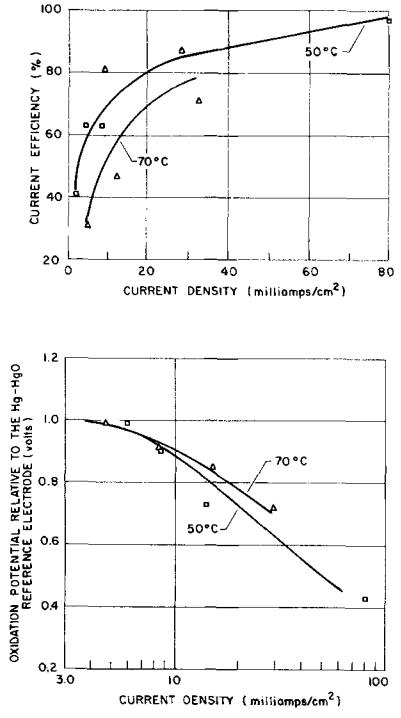

Fig. 7. Current efficiency and oxidation potential (relative to the Hg-HgO reference electrode) as a function of anode current density for surface-amalgamated Al grade 1145 anodes in a ZnO-saturated solution of 2.7M KOH plus 0.5M $Al(OH)_3$ plus 0.15M Hyamine 3500 inhibitor at 50° and 70°C. The experimental procedure was similar to that used for Fig. 2. (a) Current efficiency; (b) oxidation potential.

1.5v for the lower and 1.1v for the higher current densities in all three cases.

Conclusions

Both the current-voltage characteristics and the rate of corrosion of the Al anodes vary with temperature, anode composition, and electrolyte composition. Furthermore, the corrosion rate in alkaline solutions decreases with increasing current density. For a constant anode potential, parallel decreases in current densities and corrosion rates have usually been observed with decreasing temperature, decreasing concentration of hydroxide ions (or other corrosion accelerators), and increasing effectiveness of corrosion inhibitors. Only a few inhibitors such as Hg plus ZnO but no Hyamines or a Hyamine but no Hg would reduce corrosion without seriously decreasing the current density or increasing the anode polarization. With amalgamated Al anodes it may prove possible to develop relatively long-lasting batteries with medium or even low and intermittent current drain by taking proper precautions to eliminate harmful corrosion accelerators.[3] At the present time, however, alkaline Al batteries appear most promising for applications requiring a high energy capacity per unit weight and/or volume and a medium or high power density. For such applications corrosion may be kept under adequate control by: (a) a Hyamine inhibitor; (b) precautions to avoid obvious corrosion accelerators such as sulfides; (c) use of highly pure (>99.99%) Al or a specially resistant Al-Hg, Al-Zn or Al-Mg alloy; (d) an arrangement for effective heat removal by air convection (exposure of the back side of the anode to air) and/or electrolyte circulation; and (e) preferably operation at high current densities and an arrangement for not exposing or for separating the anode(s) from the electrolyte during appreciable periods of inaction.

[3] Such amalgamated anodes will, of course, require precautions to prevent direct contact with air, such as permanent immersion in the electrolyte (or in oil during inactive periods) or use of an air-tight enclosure.

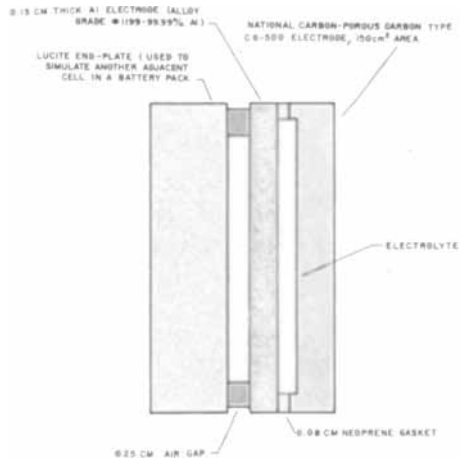

Fig. 8. Experimental Al-air test cell (schematic drawing). Electrolyte volume: 34-38 ml; electrolyte thickness: 0.3 cm.

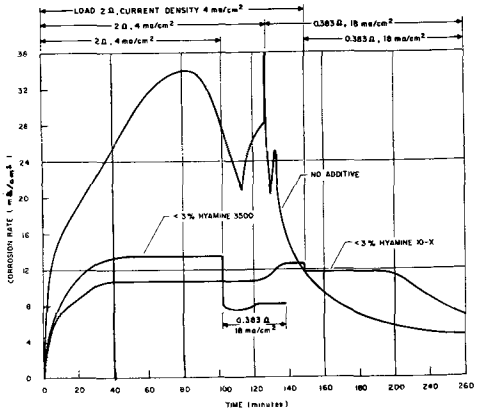

Fig. 9. Effect of Hyamine additives on the anode corrosion rate in the cell of Fig. 8.

For small batteries, a 10.5M KOH solution (with or without 0.1M Hyamine inhibitor) appears most suitable, with the electrolyte being replaced after Al dissolution to a concentration of 6-7 g-moles $Al(OH)_3$ per liter of 10.5M KOH. On the other hand, for larger power supplies (of >1 kw) a 3M KOH solution with auxiliary circulating and $Al(OH)_3$ removing equipment should offer the highest energy to weight and to volume ratios.

Acknowledgment

Thanks are due to J. O'M. Bockris, L. Bockstie, D. Trevethan, R. A. Foust, Jr., P. C. Cholet, and M. E. Lasser for valuable suggestions and/or assistance in the experimental work.

Manuscript received Nov. 28, 1961; revised manuscript received Aug. 25, 1962.

Any discussion of this paper will appear in a Discussion Section to be published in the June 1963 JOURNAL.

Note added in proof: Al-air battery packs based on the results of Fig. 1 and 6 and Table II were recently completed and described by R. A. Foust, Jr. [cf. Abstract No. 49, *This Journal*, **109**, 198C (1962) and in Extended Abstracts of the Battery Division, Boston Meeting, ECS].

REFERENCES

1. C. H. Brown, U. S. Pat. No. 503,567 (1893).
2. J. Sully, U. S. Pat. No. 585,855 (1897).
3. G. Polcich, U. S. Pat. No. 1,771,190 (1926).
4. S. Ruben, U. S. Pat. Nos. 1,920,151 (1933), 2,638,489 (1951), and 2,783,292 (1952).
5. J. J. Stokes, Jr., U. S. Pat. No. 2,796,456 (1955).
6. G. S. Lozier, R. Glicksman, and C. K. Morehouse, U. S. Pat. Nos. 2,874,079 (1959) and 2,976,342 (1961).
7. C. H. Vince, Jr., British Pat. No. 397,475 (1933).
8. D. E. Sargent, U. S. Pat. No. 2,554,447.
9. Q. I. Jorge Grunwaldt Ramasso, *Quimica Industrial (Uruguay)*, **2**, 115 (1951).
10. R. Glicksman, *This Journal*, **106**, 457 (1959).
11. Gerald A. Baum, WADC Technical Report 59-780, Contract No. AF 33(616)-6399, November 1960.
12. J. V. Petrocelli, *This Journal*, **97**, 10 (1950).
13. S. Zaromb and R. A. Foust, Jr., *ibid.*, **109**, 1191 (1962).
14. N. F. Linke and A. Seidell, "Solubilities," pp. 196-8, Van Nostrand, New York (1958).
15. L. Bockstie, D. Trevethan, and S. Zaromb, *This Journal*, submitted for publication.

Dissolution of Brass in Sulfuric Acid Solutions

I. 85/15 Brass

J. Bumbulis[1] and W. F. Graydon

Department of Chemical Engineering and Applied Chemistry, University of Toronto, Toronto, Ontario

ABSTRACT

The dissolution of 85/15 brass from rotating cylindrical samples by aerated dilute sulfuric acid solutions was investigated over the range of 15°-35°C. The reaction was found to proceed in three successive steps, dezincification of the brass surface, dissolution of redeposited copper and etching of the brass surface, and dissolution of the etched, dezincified surface. The dissolution rates of the last two steps were determined by the rate of dissolution of copper, zinc being dissolved as fast as it was uncovered by the dissolved copper.

The mechanism of dissolution of copper from 85/15 brass was found to be similar to that of pure copper, controlled by the rate of oxidation of cuprous ions to cupric. Rate equations are given for the apparent dissolution rate of copper at each stage. Hydrogen peroxide was a reaction product.

Corrosion of metals and alloys is of great importance to industry, and a large amount of work has been devoted to this subject. The main effort has been devoted to the comparison of the resistance of various materials to corroding agents. There are relatively few studies of the kinetics and mechanism of dissolution of pure metals, and even fewer of the effect of alloying on dissolution rate.

The study of the kinetics and mechanism of the dissolution of copper in sulfuric acid (1) prompted a similar study using α-brass, to evaluate the effect of zinc on the dissolution of the base metal. An alloy of 85% copper and 15% zinc was selected, to provide an appreciable amount of zinc, while still maintaining a single metal phase.

Experimental

The apparatus and experimental procedure used were the same as for the study of dissolution of copper reported earlier. A cylindrical brass specimen three quarters of an inch in length and diameter was mounted on a vertical shaft and rotated in aerated dilute sulfuric acid solutions.

The brass samples were cut from bar stock supplied by Anaconda American Brass Limited. Two samples were cut from each of three different bars. The analyses of the bars are shown in Table I. Duplicate experiments with samples from each bar did not show a significant difference in the reaction rates. Therefore, no distinction was made between samples from different bars.

Table I. Analysis of 85/15 brass

Bar No.	1	2	3
Cu, wt %	85.36	84.55	85.26
Pb, wt %	0.005	0.005	<0.005
Sn, wt %	0.04	0.00	0.01
Fe, wt %	0.01	0.02	0.02
Zn, wt %*	14.58	15.42	14.72

* By difference.

All reagents used were of "AnalaR" grade. Water was redistilled in an all glass apparatus. Air was taken from a compressed air line, filtered, dried, and saturated with water at the operating temperature.

The reaction was followed by measuring polarographically the concentrations of copper and zinc at regular intervals. A manual polarograph was used, with a dropping mercury electrode and a saturated calomel half-cell. The copper concentration was measured at −0.5v and zinc at −1.3v against the calomel electrode. Hydrogen peroxide, present in the solution, complicated the zinc measurement, since its half-wave potential is very close to that of zinc. To measure the quantities of zinc and hydrogen peroxides, duplicate samples of the solution were taken. One of these was evaporated to dryness and redissolved in water. The diffusion current at −1.3v for the evaporated sample gave the zinc concentration, while the difference in the diffusion current at −1.3v between the two samples gave the hydrogen peroxide concentration. Duplicate meas-

[1] Present address: Research Department, Imperial Oil Limited, Sarnia, Ontario, Canada.

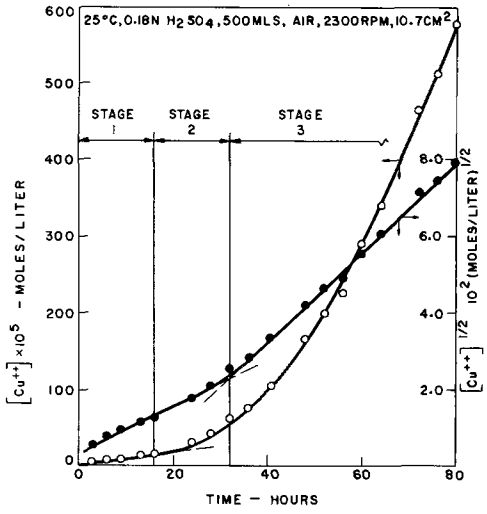

Fig. 1. Typical experimental results. The numbers at the top of the figure refer to temperature, acid strength and volume, composition of gas phase, sample rotational speed and surface area.

urements of the copper concentration on each sample were obtained.

A constant liquid volume was maintained during the experiment by replacing the samples taken with an equivalent volume of the starting solution. The measured concentrations were corrected for this dilution, which usually was very small. At the end of the run the brass sample was dried and weighed. The weight loss was in good agreement with the amount of metal in solution.

Results

The results are presented mainly in terms of dissolution of copper. The zinc data are less accurate due to the low concentration of zinc in the metal.

Reaction Rate Order

The dissolution of 85/15 brass in sulfuric acid proceeded in three distinct, successive stages. For the dissolution of copper, these stages can be best represented by a zero-order reaction, followed by two half-order reactions with respect to cupric ion concentration in solution. Figure 1 shows the three stages for a typical run. The reaction rates for these stages can be represented by the following equations:

$$\text{Stage 1:} \quad \frac{d\,[Cu^{++}]}{dt}\,1 = k_1 \qquad [1]$$

$$\text{Stage 2:} \quad \frac{d\,[Cu^{++}]}{dt}\,2 = k_2\,[Cu^{++}]^{1/2} \qquad [2]$$

$$\text{Stage 3:} \quad \frac{d\,[Cu^{++}]}{dt}\,3 = k_3\,[Cu^{++}]^{1/2} \qquad [3]$$

where $k_2 < k_3$.

The order of the reaction rate with respect to copper ions could not be confirmed by extending the time of reaction because of the several successive stages. Therefore, it was checked by the addition of various concentrations of cupric and/or zinc ions to the starting solution. The results should give a set of parallel straight lines, when plotting the copper ion concentration against time for a zero order reaction, or on a plot of the square root of the copper ion concentration against time for a half-order reaction. A typical set of results, for stage 2 at 25°C is shown in Fig. 2, and results are summarized in Fig. 3.

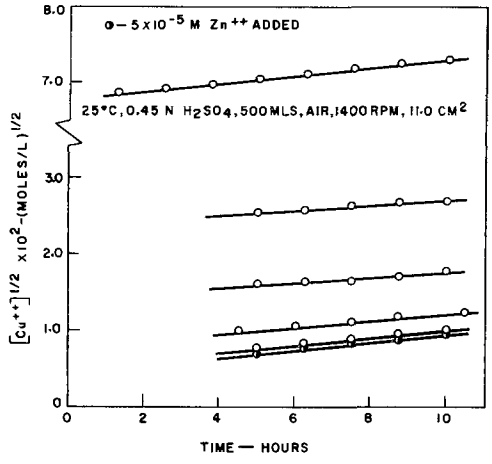

Fig. 2. Addition of copper ions, stage 2

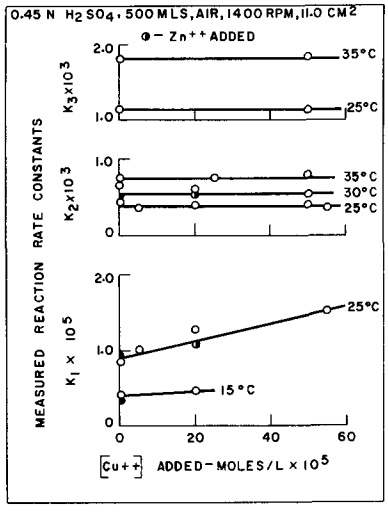

Fig. 3. Effect of copper and zinc ions

The data in Fig. 1 could be interpreted as showing only two half-order reaction rates, because the change in cupric ion concentration during stage 1 gave a straight line both for a zero-order and a half-order reaction. However, addition of cupric ions to the starting solution gave straight lines on a zero-order plot, curves for half-order, indicating a zero-order reaction.

There was no sharp transition from one stage to the next, and the duration of stage 1 and 2 varied with the experimental conditions. The transition from one stage to another could be correlated with the amount of copper dissolved from the brass and appeared to be associated with changes in the brass surface. The change from stage 1 to stage 2 occurred when approximately 0.25 mg/cm^2 of copper had been dissolved, and stage 3 set in after dissolution of approximately 1.07 mg/cm^2 of copper. A brown coating was formed on the surface during stage 1. The brown layer dissolved in stage 2, leaving a greenish, crystalline surface in stage 3.

It was found that the addition of zinc ions had no effect on the rate of dissolution of copper for

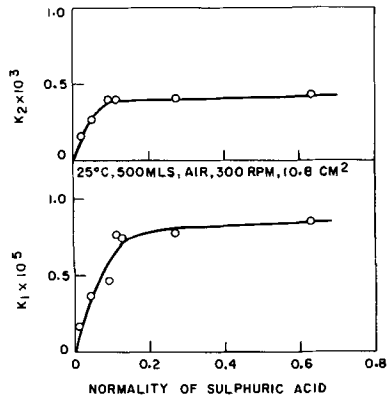

Fig. 4. Effect of acid strength

all stages. The addition of copper ions showed stages 2 and 3 to be of the half-order in copper ion concentration. While stage 1 was best represented by a zero-order reaction at all copper concentrations added, the rate constant increased with increasing copper ion concentration, indicating that at least two different reactions were occurring during stage 1.

Effect of Experimental Variables

Changes of the speed of rotation in the range 300-3500 rpm had no noticeable effect on the rate of reaction of any stage. Therefore diffusion of reagents or products did not control the reaction under the conditions investigated.

The sulfuric acid concentration had no effect on the reaction rates as long as it was above 0.1*N*. The reaction rate decreased at lower acid concentrations (Fig. 4). The acid concentration was maintained above 0.1*N* for all experiments.

The amount of copper dissolved in a given time should be directly proportional to the surface area of the metal sample. Also, when the rate of dissolution is expressed in terms of the metal ion concentration in solution, rather than the amount of metal dissolved, it should be inversely proportional to the volume of the solution, as shown by the relation:

$$\frac{dc}{dt} = \frac{1}{v}\frac{dn}{dt} \qquad [4]$$

where n is moles of metal dissolved. Combining these two effects, the measured reaction rate should be proportioned to A/V. It was found that with changes in the metal surface area from 3.8 to 14.8 cm², and in solution volume from 250 to 750 ml the reaction rates of stages 1 and 2 were directly proportional to A/V up to 25 cm²/l, but there was some deviation at higher values (small solution volumes).

The reaction rates of all three stages were proportioned to the square root of the oxygen partial pressure.

Plots of log k against the inverse of the absolute temperature (Arrhenius' plots) gave an activation energy of approximately 11,000 cal/mole for stages 1 and 2. Limited data for stage 3 indicated an activation energy of 7000-8000 cal/mole. The relatively high values obtained support the conclusion that diffusion effects do not influence the reaction rate.

The presence of hydrogen peroxide as one of the reaction products was detected polarographically, and confirmed by the phenolphthalein method of Schales (2). Addition of hydrogen peroxide to the starting solution indicated that the reaction rate of stage 1 was directly proportional to the hydrogen peroxide concentration. Little change was observed in the rate of stage 3. The addition of hydrogen peroxide shortened stage 2 so that the concentration data indicated a direct transition from stage 1 to stage 3; however, visual observation of the sample showed stage 2 to be present briefly. The concentration of hydrogen peroxide in the solution appeared to have a limiting value of approximately 150-200 $\times$ 10^{-5} moles/l. Higher hydrogen peroxide concentrations decomposed to this limiting value. The existence of a limiting concentration would explain the lack of effect of hydrogen peroxide on stage 3, since essentially constant concentration is reached by the onset of stage 3 regardless of the initial concentration.

The transition between stages appeared to be related to the amount of metal dissolved, accompanied by noticeable changes in the appearance of the metal surface. It was postulated that the transition from stage 1 to stage 2 was caused by changes in the composition of the metal surface, because there was a change in the order of reaction. Stages 2 and 3 had the same order of reaction, but different values of the rate constant. This change could be due to an increase in the surface area. Since dissolution was not diffusion controlled the measured reaction rate should be proportional to the true surface area, and changes in the surface roughness would give a different value of the measured rate constant. To test the latter assumption, samples that had reached stage 3 were washed carefully, to remove all traces of the corroding solution, and placed in fresh solution. In every case, a stage 3 reaction rate was obtained from the start. As a check, freshly polished samples were etched for 15 and 30 min in an acid solution containing 0.035M H_2O_2, when visual appearance of the sample resembled stage 3. The same reaction rate was obtained by both treatments, indicating that the nature of the surface, and not the history of the sample, determine the onset of stage 3. The increase in the surface area must have been the same, regardless of the treatment.

Correlating Equations

The results of these experiments can be summarized by the following general equations

Stage 1:

$$\frac{d[Cu^{++}]}{dt} = 1.93 \times 10^2 \, e^{-\frac{11400}{RT}} \, [P_{O_2}]^{1/2} \, \frac{A}{V} \qquad [5]$$

Stage 2:

$$\frac{d[Cu^{++}]}{dt} = 5.94 \times 10^3 \, e^{-\frac{10700}{RT}} \, [Cu^{++}]^{1/2} \, [P_{O_2}]^{1/2} \, \frac{A}{V} \qquad [6]$$

The limits investigated were:

	Stage 1	Stage 2
Temperature, °C	15-30	25-35
Oxygen partial pressure, atm	0.21-1.00	0.21-1.00
Sample surface area, cm^2	3.8-14.8	10.7-14.8
Solution volume, liters	0.25-0.75	0.50-0.75
Acid concentration	0.2-0.6*N*	0.2-0.6*N*

The standard deviation of the constant in Eq. [5] was 0.19×10^2 (9.8%), calculated from data of 26 individual experiments, and for Eq. [6] 0.28×10^3 (4.7%), determined from 21 experiments. These equations do not include the effect of H_2O_2. Equation [5] is valid until approximately 0.25 mg/cm^2 of copper is dissolved, while Eq. [6] applies for the range of 0.25-1.07 mg/cm^2 of copper dissolution. An equation similar to Eq. [6] should represent stage 3, but enough data were not obtained, to permit an accurate evaluation of the constant term.

A comparison of the relative amounts of copper and zinc in solution, shown in Fig. 5, revealed that at the start of the experiment there was dezincification. The ratio of total zinc to total copper in solution approached that in the metal as the reaction progressed. Therefore, as far as the bulk of the metal is concerned, there was little dezincification.

Discussion

Dissolution of 85/15 brass in sulfuric acid is very similar to the dissolution of pure copper reported by Lu and Graydon (1). The main difference is the existence of an initial stage of relatively slow copper dissolution for brass, caused by the dezincification of the brass surface, which can not exist for pure copper. Both copper and 85/15 brass show an increase in the reaction rate, caused by changes in the surface roughness or surface area (transition from stage 2 to stage 3), without an apparent change in the reaction mechanism.

There is disagreement in the literature on the production of hydrogen peroxide. Traube (3) and Bengough (4) reported the presence of hydrogen peroxide and proposed reaction mechanisms to include its production. There is evidence that hydrogen peroxide is decomposed by the presence of metal ions, particularly copper, in solution (5-8). This would explain why some investigators could not find hydrogen peroxide in measurable quantities. A fairly rapid hydrogen peroxide decomposition is indicated by the present study. The hydrogen peroxide concentration in solution has not exceeded a value of 0.002M. Solutions to which larger concentrations were added showed a loss of hydrogen peroxide.

The standard electrode potential for the reaction $Cu \rightarrow Cu^{++} + 2e^-$ is +0.34v relative to the reaction $H \rightarrow H^+ + e^-$, and copper should not dissolve in air-free acid solutions. In the presence of air copper can dissolve according to the following mechanism:

$Cu \rightarrow Cu^{++} + 2e^-$	anode
$O_2 + 2H^+ + 2e^- \rightarrow H_2O_2$	cathode
$Cu + O_2 + 2H^+ \rightarrow Cu^{++} + H_2O_2$	over-all

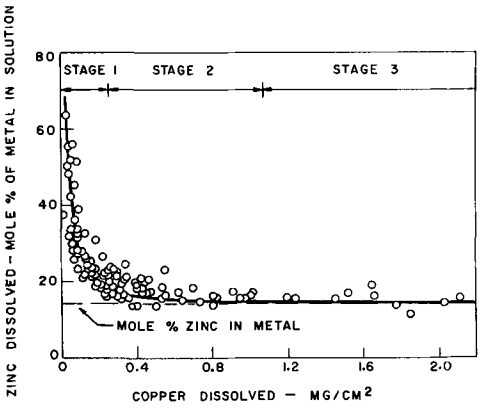

Fig. 5. Zinc content of dissolved brass

The cathode reaction is the same as proposed by Churchill (9), and accounts for the formation of hydrogen peroxide as well as depolarization by oxygen.

Lu and Graydon (1) proposed a mechanism for the dissolution of copper, which accounted for the half-order rate by the following assumptions:

1. The cupric ion concentration in the bulk of the solution is essentially the same as at the copper-solution interface.
2. The cuprous ion, cupric ion equilibrium $Cu + Cu^{++} \rightleftharpoons 2\ Cu^+$ is established at the interface.
3. The rate of dissolution of copper is assumed to be controlled by the removal of cuprous ions from the interface by a reaction which is first order with respect to cuprous ion.

Using the same assumptions the following set of equations represent a possible mechanism for the dissolution of copper from brass:

$O_2(gas) \rightleftharpoons O_2(solution) \rightleftharpoons O_2 i$	equilibrium
$Cu + Cu^{++} \rightleftharpoons 2\ Cu^+$	equilibrium
$2\ Cu^+ + O_2 i + 2H^+ i \rightarrow 2\ Cu^{++} + H_2O_2$	slow
$Cu + O_2 i + 2H^+ i \rightarrow Cu^{++} + H_2O_2$	over-all

The subscript i refers to concentrations at the metal-solution interface. The slow step accounts for the dependence of the dissolution rate on the square root of the oxygen partial pressure, on the hydrogen ion concentration at low acid strength, and, together with the assumed cupric-cuprous ion equilibrium, it also accounts for the dependence on the square root of the cupric ion concentration.

The addition of copper ions to the starting solution showed that the reaction rate order of stage 1 was somewhat higher than zero order, although the latter was the best representation. Since the next stage is of the half-order in copper ion concentrations, it was thought that the measured reaction rate might be the sum of a zero-order reaction for stage 1, and the half-order reaction of stage 2, an attempt was made to relate the experimental data from stage 1 by the equation

$$\frac{d[Cu^{++}]}{dt} 1 = k' + k'' [Cu^{++}]^{1/2} \qquad [7]$$

It was found that the experimental data could be represented reasonably well by the above expression. However, the values of k'' required to produce this agreement were considerably smaller than the rate constants of stage 2 for the same experimental conditions.

Another reaction affecting the concentration of copper ions should also be considered. Studies by Centnerszwer (10, 11) and King (12) indicate that solution of zinc in copper sulfate-sulfuric acid solutions is of the first order in copper ion concentration. The reaction has been shown to proceed by the displacement of copper ions from solution (13). Thus, Eq. [7] should be modified to include the decrease in cupric ion concentration due to displacement by zinc

$$\frac{d[Cu^{++}]}{dt} 1 = k' + k'' [Cu^{++}]^{1/2} - \frac{d[Zn^{++}]}{dt} \text{ displ.} \quad [8]$$

The experimental data do not permit an evaluation of the order of the displacement reaction with respect to cupric ion concentration. If a cupric ion concentration gradient exists at the brass surface, it would be first-order in cupric ion concentration. The existence of a displacement reaction is supported by the formation of a brown surface layer during stage 1.

Little can be said about the mechanism of dissolution of zinc. Comparison of the quantities of copper and zinc in solution (Fig. 5) indicated dezincification of the brass surface during the initial stage. As the reaction progressed, the ratio of zinc to copper in solution approached that in the bulk metal, indicating dissolution of a copper surface followed by dissolution of brass as a unit.

The zinc data from stage 1 showed considerable scatter, and did not permit an evaluation of the dissolution mechanism. In stage 3, where more reliable zinc data were available, the changes in zinc concentration could be predicted from changes in the copper concentration. This agrees with the assumption that in stage 3 the brass dissolves as a unit, controlled by the rate of dissolution of copper.

Addition of zinc ions to the starting solution showed no effect on the rate of copper dissolution in all stages.

Summary

The dissolution of 85/15 brass in sulfuric acid proceeds through three successive stages. There is an initial period of surface dezincification accompanied by some copper redeposition. This is followed by the dissolution of copper by a mechanism similar to that of pure copper. During the later stages, zinc is dissolved from the brass surface as fast as it is uncovered by the dissolution of copper. The copper dissolution proceeds in two stages, depending on the area of surface exposed to solution. The rate controlling step is believed to be the oxidation of cuprous ions to cupric ions at the metal surface. Hydrogen peroxide is found in the corroding solution.

Acknowledgments

The authors gratefuly acknowledge the financial aid received through the School of Engineering Research of the University of Toronto. They are also indebted to the Consolidated Mining and Smelting Company of Canada Ltd. for providing the Cominco Research Fellowship for one of them (J. B.) for the sessions of 1955-1956 and 1956-1957.

Manuscript received May 23, 1962; revised manuscript received Aug. 1, 1962. This paper was prepared for delivery before the Boston Meeting, Sept. 16-20, 1962.

Any discussion of this paper will appear in a Discussion Section to be published in the June 1963 JOURNAL.

REFERENCES

1. B. C-Y Lu and W. F. Graydon, *Can. J. Chem.*, **32**, 153 (1954).
2. O. Schales, *Ber.*, **71**, 447 (1938).
3. M. Traube, *ibid.*, **15**, 2434 (1882).
4. G. D. Bengough, *Engineering*, **91**, 96, 136, 167 (1911).
5. H. T. Barnes and G. W. Shearer, *J. Phys. Chem.*, **12**, 468 (1908).
6. A. V. Kiss and E. Lederer, *C.A.*, **21**, 3532^2 (1927).
7. H. W. Rudel and M. M. Haring, *Ind. Eng. Chem.*, **22**, 1234 (1930).
8. J. Weiss, *Trans. Faraday Soc.*, **31**, 1547 (1935).
9. J. R. Churchill, *Trans. Am. Electrochem. Soc.*, **76**, 341 (1939).
10. M. Centnerszwer and J. Drucker, *J. Chim. Phys.*, **13**, 191 (1915).
11. M. Centnerszwer and W. Heller, *Z. Physik. Chem.*, **A161**, 113 (1932).
12. C. V. King and M. M. Burger, *Trans. Am. Electrochem. Soc.*, **65**, 403 (1934).
13. J. H. Stansbie, *J. Soc. Chem. Ind.*, **32**, 1135 (1913).

Dissolution of Oxygen Layers on Platinum in Chloride Solutions

M. W. Breiter and J. L. Weininger

Research Laboratory, General Electric Company, Schenectady, New York

ABSTRACT

Oxygen layers on platinum are dissolved at open circuit in electrolytes containing chloride ions. The dissolution of layers formed at 1.4 and 1.6v in 1*N* H_2SO_4 was investigated in two solutions with different concentrations of chloride ions at 25° and 85°C, and it is shown that the dissolution occurs by the following mechanism. The electrode is the seat of simultaneous cathodic and anodic reactions, in which the sum of the partial currents of anodic platinum dissolution on the free surface is equal to the cathodic partial current of the oxygen reduction.

The role of oxygen on anodized platinum has received much attention in the past. Oxygen at platinum electrodes was alternately believed to be an oxide film (1-7), or an adsorbed film of oxygen (8-17). The oxide-film hypothesis has gained greater credence even for oxygen layers formed at potentials below oxygen evolution in recent years. We are re-opening this question, however, because the present potentiostatic and potentiometric measurements on the dissolution of oxygen layers from platinum in chloride solutions, as well as the earlier experiments of Anson and Lingane (5), are satisfactorily explained by a mechanism that may involve adsorption of oxygen alone. It is postulated that at the platinum electrode, after anodization, simultaneous reduction and oxidation processes occur.

Generally, the anodic formation of oxygen layers on platinum is retarded in electrolytes containing chloride ions (9, 12, 18). Obrucheva (12) observed that the oxygen branch of cathodic charging curves on smooth platinum was larger after the same anodic polarization in sulfuric acid than in a mixture of H_2SO_4 and HCl. Anson and Lingane (5) studied the dissolution of oxygen layers on smooth platinum at open circuit in a gently boiling solution of 0.2*N* HCl + 0.1M NaCl by determining photometrically the concentration of the ions $PtCl_4^=$ and $PtCl_6^=$ after the oxygen layer had been formed either anodically in 1*N* H_2SO_4 or by chemical oxidation. They found that the chemical analyses of the dissolved platinum corresponded quantitatively with the electrometrically measured charges for the cathodic removal of the oxygen layer from the platinum. From this quantitative agreement it was concluded that the oxygen layer consists of PtO and PtO_2. But the dissolution of the oxygen layer may occur according to the following mechanism

$$Pt - O + 2H^+ + 2e^- \xrightarrow{I_1} Pt + H_2O \qquad [1]$$

$$Pt + 4Cl^- \xrightarrow{I_2} PtCl_4^= + 2e^- \qquad [2]$$

$$Pt + 6Cl^- \xrightarrow{I_3} PtCl_6^= + 4e^- \qquad [3]$$

with the condition that $|I_1| = |I_2 + I_3|$. The oxygen layer is formally denoted by Pt — O above. Reactions [1] to [3] are themselves net reaction. The cathodic reaction [1] takes place on the oxygen layer, the anodic reactions [2] and [3] on the free platinum surface. If the mechanism is correct, then the formation of $PtCl_4^=$ and $PtCl_6^=$ during dissolution is not evidence for the presence of PtO and PtO_2. This would follow only for a purely chemical process without charge transfer across the platinum-solution interface.

The described mechanism can be verified by observing the dissolution of the oxygen layer in a stripping solution at open circuit under the experimental conditions of Anson and Lingane (5) and by taking cathodic charging curves to determine the amount of oxygen in coulombs per square centimeter on the surface after different times of dissolution. This technique was used by one of us (M.W.B.) in a similar problem concerning the reduction of the oxygen layer on platinum by molecular hydrogen (19). Dissolution should only take place in the potential range of the cathodic reaction [1] in the case of the suggested mechanism. The surface area free of oxygen will have another effect on the dissolution rate in case of the above mechanism as in a chemical dissolution process. Processes of the type described by Eq. [1] to [3] are of importance in a recent general theory of passivity advanced by Schwabe (20).

Experimental

The following technique, used to study the dissolution process with time, involves the anodic formation of an oxygen layer on platinum in 1*N* H_2SO_4 in one cell, washing the electrode in double-distilled water, and transferring it to another cell with an electrolyte containing Cl^- ions (5). The stripping solution was the same as that of Anson and Lingane. A periodic voltage of triangular shape was potentiostatically applied to the platinum electrode in 1*N* H_2SO_4 at 25° with helium-stirring in a vessel of conventional design. The electrode potential was changed at 30 mv/sec between 0.05v and 1.62v, the potential U being referred to a hydrogen electrode in the same solution. When the potential reached a suitable value in the oxygen region (+1.4v and 1.6v, respectively), the circuit was interrupted manually. The electrode, now covered with an oxygen layer (4, 16), was taken out of the vessel, washed in double-distilled water, and transferred within a few seconds to a second vessel containing the stripping

solution which was stirred with purified argon to remove molecular oxygen. Little oxygen is gained or lost in this transfer. It is not lost because the rate of self-decomposition of the oxygen layer on platinum is very small in sulfuric acid or other solutions (8, 15). Nor is oxygen gained because the adsorption of molecular oxygen does not even occur at a measurable rate on a free platinum surface immersed in an aqueous solution at open circuit and room temperature (8, 15). Since the method involves the study of the following cathodic charging curves a small change in the concentration of oxygen would not interfere with the subsequent conclusions. On immersion the electrode was quickly connected to the circuit of the second cells and the potential decay was measured with an electrometer (Keithley 610A-input resistance $> 10^{14}$ ohms). When the potential had reached a given value during the open-circuit decay a cathodic charging curve was taken by switching on a current of 10 ma/cm^2 with a mercury relay (Western Electric 275C) and registering the potential-time curves oscillographically (Tektronix 502). The method of connecting the oscilloscope with the electrode by means of the relay was used to avoid current being drawn by the input resistance of 10^6 ohms of the oscilloscope. In the second cell the potential was measured against a calomel electrode in the stripping solution, but all potentials are reported below against a reference hydrogen electrode at 25° and 85°C, respectively, in the stripping solution. The voltage between the calomel and hydrogen electrode was measured at 25° and 85°C, respectively. After the charging curve was obtained, the electrode was washed thoroughly and transferred to the 1N H_2SO_4 solution. In the cell with 1N H_2SO_4 at least one potentiostatic cycle was passed before repeating the above procedure. At the end of a series of charging curves at least three of the initial curves were checked for reproducibility, which was found to be within 10% of the amount of oxygen Q_o in mcoul/cm^2.

Results

The dissolution of oxygen layers formed at 1.4 and 1.6v in 1N H_2SO_4 at 25° was studied under conditions comparable to those of Anson and Lingane (5) at 25° and 85° in 0.2N HCl + 0.1M NaCl (denoted below as the "dilute" chloride solution). To investigate the influence of the chloride ion concentration the same experiments were carried out in 0.2N HCl + 2.8 NaCl ("concentrated" chloride solution).

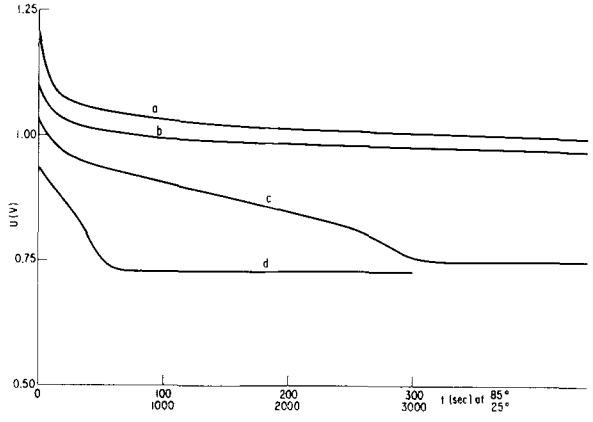

Fig. 1. Potential decay at open circuit in 0.2N HCl + 0.1M NaCl during the dissolution of oxygen layers on smooth platinum. Curve a, layer formed at +1.6v, dissolved at +25°C; curve b, layer formed at +1.4v, dissolved at +25°C; curve c, layer formed at +1.6v, dissolved at +85°C; curve d, layer formed at +1.4v, dissolved at +85°C.

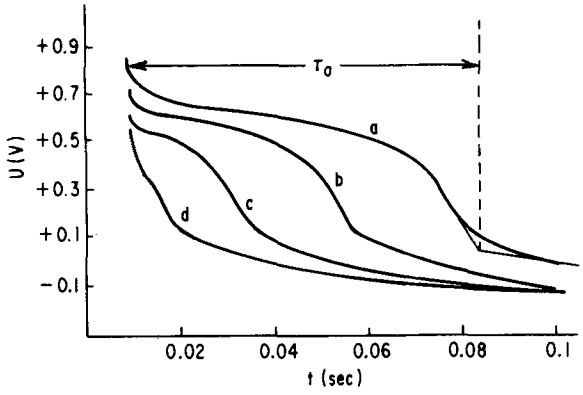

Fig. 2. Cathodic charging curves taken after different times of dissolution of an oxygen layer, formed at +1.6v, in 0.2N HCl + 0.1M NaCl at 85°C. Curve a, taken after 3.8 sec; curve b, taken after 52 sec; curve c, taken after 106 sec; curve d, taken after 195 sec.

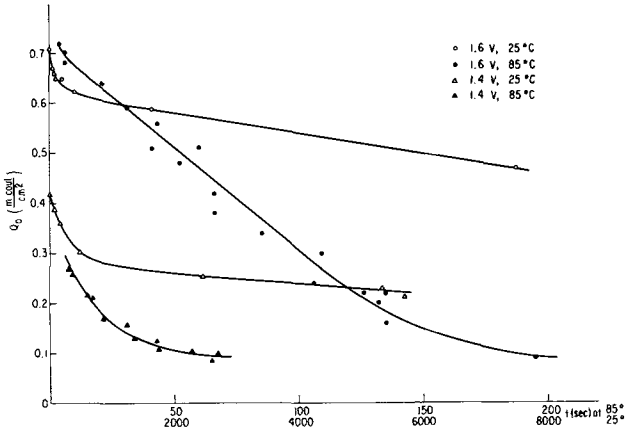

Fig. 3. Amount of oxygen on the surface as a function of time during dissolution in 0.2N HCl + 0.1M NaCl under different conditions.

For convenience the experimental results are arranged graphically in Fig. 1 to 5, which with their legends, and with reference to the above discussion of experimental procedure, are largely self-explanatory. Figure 1 illustrates the potential decay of platinum electrodes, covered with oxygen, at open circuit in the dilute chloride solution. Figure 2 shows cathodic charging curves for one of the platinum electrodes of Fig. 1. Figures 3 and 4 give the amount of oxygen on the surface after different times of dissolution at 25° and 85°, in the dilute and concentrated chloride solutions, for layers formed at 1.4 and 1.6v, respectively. Finally, the potentiostatic current-voltage curves of Fig. 5 show some of the individual electrochemical steps occurring in the dissolution process.

Potential decay of platinum electrodes covered with oxygen.—The potential decay is very slow at room temperature. After 6.5 hr the potential reached a value of 0.95v in the case of curve a of Fig. 1. Ob-

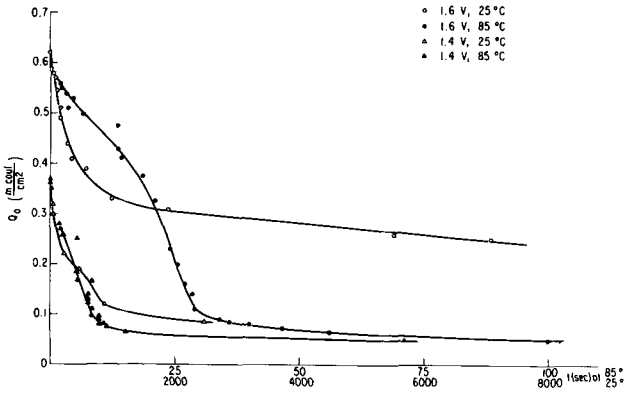

Fig. 4. Amount of oxygen on the surface as a function of time during dissolution in 0.2*N* HCl + 2.8M NaCl under different conditions.

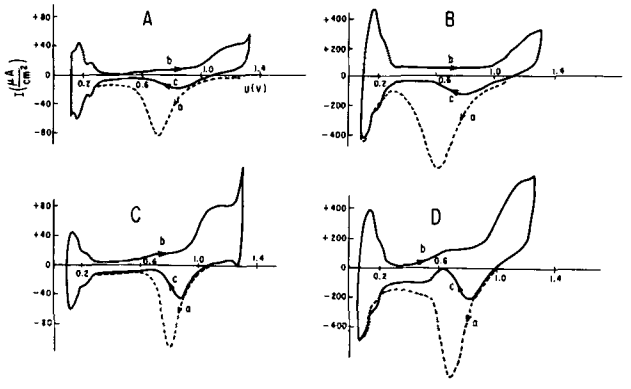

Fig. 5. Potentiostatic current potential curves in 0.2*N* HCl + 0.1M NaCl. Initial oxygen layer formed at +1.6v for 2 min in 1*N* H_2SO_4. Curve A, 0.03v/sec, 25°C; curve B, 0.30 v/sec, 25°C; curve C, 0.03 v/sec, 85°C; curve D, 0.30 v/sec, 85°C. Sweep a, initial reduction; sweep b, anodic wave; sweep c, second reduction wave.

viously the dissolution of the oxygen layer is slow. At 85° the potential decays more rapidly and tends towards a time-independent value at about 0.75v. As may be expected, the final value of the potential is reached more quickly for the oxygen layers formed at 1.4v. Also the initial potential decay is larger at 25° than at 85°.

Cathodic charging curves.—Figure 2 shows four charging curves which were started at different potentials of curve c of Fig. 1. The approximate determination of the transition time τ_o for a cathodic reduction of the oxygen layer is demonstrated for curve a. A correction of the value of τ_o for the charging of the double layer was not applied since this error is smaller than 10%. With increasing time of dissolution τ_o becomes smaller, and the curves are shifted to less positive potentials. Some of the oxygen, having a higher heat of adsorption (17) than that originally being dissolved, requires a higher overvoltage. It was found, similarly to Anson and Lingane, that about 10-15% of the oxygen layer did not dissolve within a reasonable experimental time (cf. Fig. 1). Generally, the dissolution times were shorter under equivalent conditions than those observed by Anson and Lingane. This difference may be attributed to the use of wire electrodes of relatively small apparent surface area (0.5 cm²), which are known to be more active than larger foil electrodes. Figure 2 refers to measurements at 85°. Similar curves are obtained at 25°, but the decrease of τ_o with dissolution time is considerably smaller as expected on the basis of the results of Fig. 1.

Dissolution of oxygen layer.—The dissolution of oxygen layers in the dilute and concentrated chloride solutions is shown respectively in Fig. 3 and 4. The oxygen layer which still exists after the dissolution time t is represented by Q_o, the number of millicoulombs per square centimeter required for its cathodic reduction. At 85° the dissolution proceeds at a reasonable rate until the last part is reached when the slower dissolving oxygen comes off. This occurs about three times faster in the concentrated than in the dilute chloride solution.

Current-voltage curves.—The example of potentiostatic measurements chosen for Fig. 5 is a platinum electrode with an oxygen layer formed at 1.6v in 1*N* H_2SO_4. After the transfer the cathodic sweep a was applied first, followed by an anodic sweep b, and finally another cathodic sweep c. The four curves were taken at two different voltage rates (0.3 and 0.03 v/cm) at the two different temperatures. During sweep a the originally present oxygen layer is reduced (dotted lines). At low speed this reduction takes place between 1.1 and 0.6v. In the hydrogen region, between 0 and +0.3v, the I-U-curves of sweeps a and c coincide. During the anodic sweep b a small wave is observed between 0.6 and 0.9v. This is probably due to reactions [2] and [3], which occur on an electrode not yet completely passivated (18, 21). During sweep b evolution of chlorine (18, 22) takes place for U > 1.4v, as well as reactions [2] and [3], which become increasingly inhibited by the growing oxygen layer (21). Finally sweep c shows the reduction of the oxygen layer formed during sweep b. The potential range for this reduction is between 1.1 and 0.6v, narrower at 85° than at 25°. At 85° the current has a tendency to become anodic between 0.6 and 0.8v during the cathodic sweep c as a result of anodic reactions [2] and [3] setting in when the oxygen layer has been partly removed.

Discussion

The above experiments were performed to see whether one can characterize the oxygen layers formed on platinum electrodes. A mechanism is given to show the "electrochemical" nature of the dissolution process. This is supported by two principal observations. First, dissolution takes place between 1.0 and 0.7v, and second, the rate of dissolution does not have an order to be expected from a purely chemical reaction without charge transfer at the electrode interface. The present mechanism should apply to the dissolution of oxygen layers formed by moderate oxidation processes at platinum, either anodically with voltages at or below 1.6v, or in oxidative solutions. These were also the conditions used by Anson and Lingane; hence their observations are consonant with the present mechanism.

The experiments on the dissolution of the oxygen layer in the dilute chloride solution at 85° (Fig. 1 and 3) show clearly that the process takes place between 1.0 and 0.7v. This is the potential range in

which the oxygen layer formed in 1*N* H_2SO_4 is reduced during the cathodic sweep at low voltage speeds (Fig. 5, branches a and c). At room temperature the same conclusion holds for that part of the oxygen layer which is dissolved within the studied time interval.

The present experiments show that the order of the dissolution reaction cannot be one or higher as would be expected for a chemical reaction. Comparing two platinum electrodes covered by oxygen to a different extent, it can be seen from Fig. 3 that about 0.6 mcoul/cm^2 are removed at 85° within the studied time for the oxygen layer formed at 1.6v and about 0.2 mcoul/cm^2 for that formed at 1.4v. The first half of 0.6 mcoul/cm^2 is dissolved in about 80 sec, half of 0.2 mcoul/cm^2 in about 17 sec. The fact that dissolution is more rapid if Q_o-values are smaller can be understood on the basis of the suggested mechanism. A larger part of the surface is free of oxygen and is available for reactions [2] and [3] in the case of small Q_o-values, when as in the present case, the Q_o-value of the oxygen layer formed at 1.6v corresponds to no more than a monolayer (13). The same conclusion follows from Fig. 4.

Regarding the influence of temperature and the concentration of chloride ions it is difficult to give a quantitative interpretation of the dissolution rates because reactions [2] and [3] are inhibited by the oxygen layer (18, 21). But qualitatively the increase in dissolution rates can be observed by a comparison of Fig. 3 and 4.

In conclusion, the present measurements substantiate a dissolution mechanism of oxygen layers in which the cathodic reduction of oxygen and anodic dissolution of platinum occur simultaneously at the same electrode. The experimental results and the proposed mechanism are consonant with a concept of adsorbed oxygen on the Pt surface, but do not exclude the possibility of oxide formation. Conversely, if such a mechanism is valid, chemical evidence of reaction products is not sufficient proof that an oxide film exists. Oxide films and adsorbed oxygen layers on other metals than platinum should also be approached with the same caution and should be examined for the possibility of complying with a similar mechanism.

Manuscript received May 2, 1962; revised manuscript received July 10, 1962. This paper was prepared for delivery before the Boston Meeting, Sept. 16-20, 1962.

Any discussion of this paper will appear in a Discussion Section to be published in the June 1963 JOURNAL.

REFERENCES

1. F. P. Bowden, *Proc. Roy. Soc.*, **A125**, 446 (1929).
2. A. Hickling, *Trans. Faraday Soc.*, **41**, 333 (1945).
3. S. E. Wakkad and S. H. Amara, *J. Chem. Soc.*, **46**, 461 (1952).
4. I. M. Kolthoff and N. Tanaka, *Anal. Chem.*, **26**, 632 (1954).
5. F. F. Anson and J. J. Lingane, *J. Am. Chem. Soc.*, **79**, 4901 (1957).
6. G. Rädlein, *Z. Elektrochem.*, **61**, 727 (1957).
7. See K. Nagel and H. Dietz, *Electrochim. Acta*, **4**, 141 (1961) for a review of older results.
8. J. A. V. Butler and G. Armstrong, *Proc. Roy. Soc.*, **A137**, 604 (1932); G. Armstrong, F. R. Himsworth, and J. A. V. Butler, *ibid.*, **A143**, 89 (1934).
9. B. V. Ershler, *Discussions Faraday Soc.*, **1**, 269 (1947).
10. Z. F. Salkind and B. V. Ershler, *Zhur. fiz. Khim.*, **25**, 565 (1951).
11. V. I. Nestorova and A. N. Frumkin, *ibid.*, **26**, 1178 (1952).
12. A. D. Obrucheva, *Doklady Akad. Nauk SSSR*, **26**, 1448 (1952).
13. M. Becker and M. Breiter, *Z. Elektrochem.*, **60**, 1080 (1956).
14. K. J. Vetter, *ibid.*, **62**, 378 (1958).
15. J. Giner, *ibid.*, **63**, 386 (1959).
16. F. G. Will and C. A. Knorr, *ibid.*, **64**, 258 (1960).
17. W. Böld and M. Breiter, *Electrochim. Acta*, **5**, 145 (1961).
18. J. Llopis and A. Sancho, *This Journal*, **108**, 720 (1961).
19. M. Breiter, *ibid.*, **109**, 425 (1962).
20. K. Schwabe, *Electrochim. Acta*, **3**, 186 (1960).
21. B. Ershler, *Acta Physicochim. URSS*, **19**, 139 (1944).
22. G. A. Tedoradse, *Zhur. fiz. Khim.*, **33**, 129 (1959).

The Structure of Oxide Films Formed on Aluminum After Exposure to High-Temperature Pure Water

J. H. Greenblatt

Department of National Defence, Defence Research Board, Naval Research Establishment, Dartmouth, Nova Scotia, Canada

ABSTRACT

The structure of the oxide films formed an aluminum after exposure to high-temperature pure water over the temperature range 150-350°C has been examined after periods of exposure varying from 1 min to 7 hr. The technique used to prepare samples for examination shows up the different structural zones in the oxide by intensifying the contrast in refractive index between them. It was observed that the number of distinguishable zones increased as exposure conditions became more extreme and that the time for appearance of more than two zones was minimum with the least corrosion resistant material and maximum with the most corrosion resistant material. Columnar structures joining the outer crystalline layer to the metal surface at the site of second phase particles protruding through the metal interface were also observed. These columns also appeared to be connected to the third layer when such a layer was present.

The structure of oxide films formed on aluminum after exposure to high-temperature water has been investigated by a number of previous workers (1-7). This previous work consisted of electron microscopic examination of the topology of the inner metal-oxide interface and the outer oxide-water interface of the film, as well as examination, in silhouette, of crystals protruding from the surface. In addition considerable work was also done on the optical microscopy of cross sectioned specimens bearing oxide films. As a result of this past work it has been established that: (i) the oxide film is multilayered with two and possibly more zones of differing structure in the film; (ii) that the outer zone is crystalline with the crystalline material being generally Boehmite but under certain conditions may also include diaspore needles; (iii) that the inner surface (oxide-metal interface) is amorphous.

No detailed study on the development of structure in the oxide film with time at various temperature has been published although Biefer (2) and Hart and Ruther (3) have given some values on the variation of the thickness of the outer crystalline layer and remainder of the oxide with time. The work reported here was therefore undertaken to provide more detailed information on how the various zones and structures develop in the oxide film formed on aluminum exposed to high-temperature water. Commercial 2S Aluminum and two special alloys containing iron and nickel were used in the work described, and specimens were exposed for eight different times at five different temperatures.

Experimental

Cylindrical samples of aluminum 3/8 in. in diameter and 5/16 in. long were machined from extruded 1/2 in. diameter rod and then one end was polished down to 0.25μ diamond. Polishing was done in a special jig holding 14 samples. Following this preparation the specimens were degreased in refluxed trichloroethylene for 2 hr and then annealed in argon in the test autoclaves for 2 hr at 340°C. The specimens were then brought to test temperature in argon, and water at the test temperature was added to the system. The apparatus and procedure have been described more fully in an earlier paper (8). The nominal composition of the alloys is given in Table I.

After exposure the samples were coated with a thin film of vacuum-evaporated aluminum to demarcate the boundary between oxide and mounting medium. They were then mounted in diallyl phthalate plastic and cross sectioned by grinding on a polishing wheel. The cross sections were then polished down to 0.25μ diamond with kerosene as a lubricant followed by polishing down to 0.1μ using "Gamal" and water. This phase of specimen preparation was reported in detail earlier (9, 10). The specimens prepared this way showed no detail of oxide structure, but did show excellent detail at the oxide metal interface and the information obtained has also been reported (9).

A further stage of sample preparation revealed detail in the oxide itself, and the results of this further examination of the oxide films form the subject of the present paper. The polished samples prepared as above were then mounted in batches of six

Table I. Composition of the alloys

Alloy	% Ni	% Fe	% Si
10155	0.5	0.5	0.2
10157	2.0	0.5	0.2
2S Commercial aluminum			0.4% for typical material

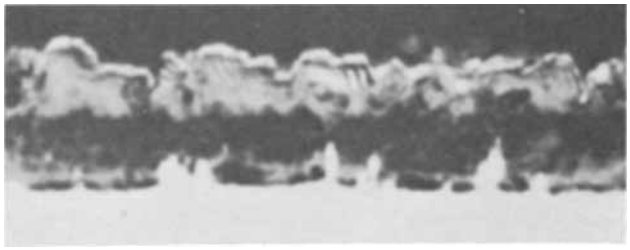

Fig. 1. 10155 alloy after 7 hr of exposure at 350°C. Four layers are evident. Magnification 4000X.

in a special jig in a bell jar so that all samples had the same vertical incidence to the source, and a thin film of aluminum was evaporated over the polished face of the cross section. The thickness of this film was of the order of 400Å, and it showed about 50% transmission. This thin film increases the contrast between zones in the oxide film that have different indices of refraction when viewed by reflected light in the microscope. The first film of aluminum deposited on the specimen before mounting acts as sharp demarcation of the boundary between oxide and mounting plastic. The specimens coated in this way were examined at 1000X.

Results

Examination of cross sections showed that on all alloys the number of discernible zones in the oxide film increases with time. For 10155 at the most extreme exposure condition, 350°C and 7 hr of exposure, four distinct zones could be distinguished below the demarcating aluminum boundary: the outer crystalline layer, a second layer next to this one, a third layer following the second, and a thin band next to the metal surface. These can be seen in Fig. 1. The bright metallic flecks seen protruding into the oxide are unattacked second phase particles. After 2 hr of exposure at 350°C only two zones are definitely present, and the third layer is seen only as a thin discontinuous line, while at shorter times the number of layers decreases to two. After 7 hr and with decreasing temperature a similar trend is observed, and the number of layers observed decreases. Thus at 300°C after 7 hr of exposure the third layer is very thin, and no fourth layer is observed.

With 10157 no more than two distinct zones were distinguishable after the exposure times studied,

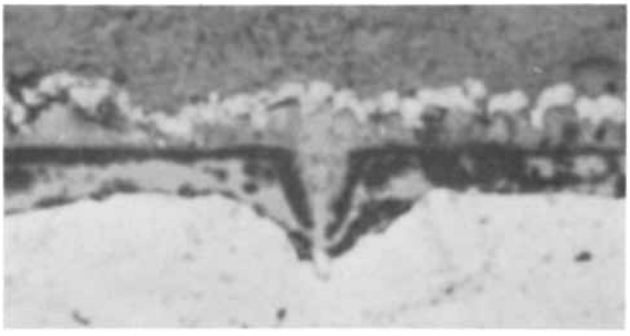

Fig. 2. 2S aluminum after 7 hr exposure at 300°C. Three layers can be seen distinctly and a very thin discontinuous fourth layer. A columnar structure joining the third layer to the outer layer can also be seen. Magnification 4000X.

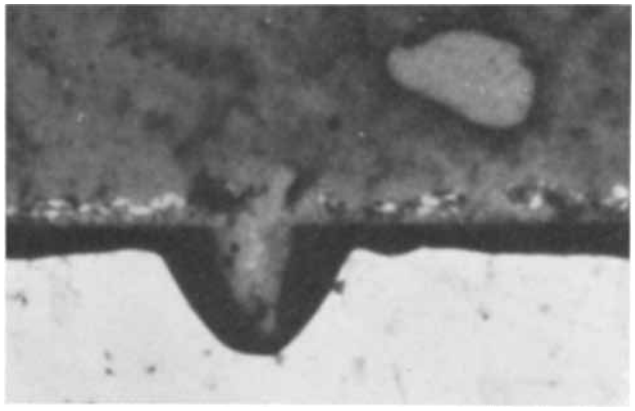

Fig. 3. 2S aluminum after 7 hr of exposure at 250°C. Magnification 4000X.

while with 2S four layers were observed at more extreme conditions. Figures 2 and 3 are photographs showing the layers observable in 2S. The number of layers discernible in the oxide films of the alloys studied is tabulated in Table II. It must be emphasized that the numbers in the table should be accepted as indicating general trends and should not be taken as completely unequivocal. This is due to the fact that the appearance of the film is conditioned to a degree by the thickness of the aluminum layer deposited over the specimens, and contrast may not be great enough in some cases to indicate an additional layer when it is very thin.

Certain structural features were also observed in the oxide cross sections. These were columnar structures between the outer layer and the metal surface. The "columns" appeared to be connected to the third layer when one could be distinguished. They appeared to occur at places where second phase particles were protruding through the metal oxide interface either at the regular metal surface or in pits. Examples of these columns are shown in Fig. 2, 3, 4, and 5. It cannot be stated unequivocally whether

Table II. Number of discernible zones in the oxide film after exposure at the following times and temperatures

Temp, °C	1 Min	5 Min	10 Min	15 Min	30 Min	60 Min	120 Min	420 Min
				2S Alloy				
150	1	1	1	1	2	2	2	2
200	1	1	1	1	2	2	2	2
250	1	1	1	1	2	2	2	2
300	1	1	1	2	2	—	3	4
350	3	3	3	3	3	3	3	4
				10155 Alloy				
150	1	1	1	1	1	1	2	2
200	1	1	1	1	1	2	2	2
250	1	1	1	1	2	2	2	3
300	1	1	1	2	2	2	2	3
350	1	2	2	2	2	2	2*	4
				10157 Alloy				
150	1	1	1	1	1	1	1	1
200	1	1	1	1	2	2	2	2
250	1	1	1	1	2	2	2	2
300	1	1	1	1	2	2	2	2**
350	1	2	2	2	2	2	2	2

* Third layer present discontinuously.
** Some evidence for a discontinuous third layer observed.

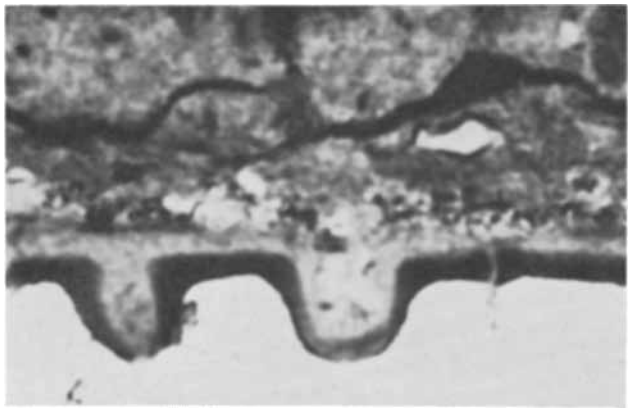

Fig. 4. 2S after 30 min of exposure at 300°C showing columnar structures terminating at the bottom of pits and at protruding second phase particles. Magnification 4000X.

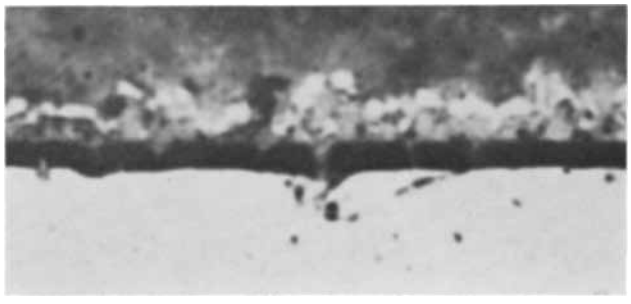

Fig. 5. 10155 alloy after 60 min of exposure at 350°C showing columnar structures terminating at protruding second phase particles. Magnification 4000X.

these columns grow up from the metal or down from the crystalline layer. The general configuration of the columns, thick on top, thin on the bottom, their presence even in very thin films, their lack of penetration beyond the third layer at times, indicates they grow down from the crystalline layer. Their appearance at the site of second phase particles at the surface or in pits could indicate evidence either of downward or upward growth. In Fig. 2 and 3 the columns certainly would seem to be the result of downward growth, but Fig. 4 shows several types of such columns including some very small thread-like ones connecting second phase particles at the metal interface with the crystalline layer that could have grown from the bottom up.

The percentage of total film thickness of the crystalline zone and other zones was also determined by measuring projected images of the photographed cross sections. Over the range of times and temperatures covered in our work the crystalline layer on 10157 constituted 48% of the total film thickness with the smallest value measured being 37% and the largest 61%. For 10155 the average was 48% with the smallest value measured 32% and the largest 66%. For 2S the average was 44% with the minimum being 22% and the maximum 62%. The low minimum for 2S occurred at 350°C. At this temperature the film on 2S appeared to be different than that on the other alloys. The low values measured when determining the average showed no definite pattern of either increasing or decreasing thickness of the crystalline layer with time. With 10155 and 10157 more of the larger values occurred at shorter exposure times than longer ones, but with 2S the reverse was true and more of the lower values occurred at earlier times.

The second layer constituted 41% of the total thickness of the oxide film on 10155 when three zones were visible and 35% when four were. The third layer increased from 8% of total film thickness when only three layers could be detected to 20% when four were detected.

With 2S the second layer averaged 36% of the total with a low of 16% and a high of 61%. The third layer made up 22% on the average with a low of 8% and a high of 35%.

Discussion of Results

The examination of the structural zones in oxide films formed on aluminum exposed to high-temperature water shows that the corrosion film on the alloys examined differs. With 10157 only two distinct zones could be discerned at the most extreme conditions of exposure time and temperature used. With 10155 as many as four zones were observed at the most extreme condition, while with 2S the maximum number of zones observed was four, and three zones were observed after as short an exposure time of 1 min at 350°C compared with 2 hr at 300°C. Since other work has shown that 10157 has better corrosion resistance than the other materials tested, the results indicate that the delay in formation of such structural zones may be tied up with the protective properties of the oxide film. Further evidence for this is the fact that the worst material, 2S, shows the third zone after extremely short exposures at 350°C.

All the films examined showed columnar structures between the crystalline outer layer and the metal surface or a visible third layer. The columns tended to occur at the protruding second phase particles when these were in pits or at the more regular metal-oxide interface. The evidence indicates, although not unequivocally, that they grow down from the crystalline layer. Because the visible third layer appears to spread laterally from such columns, Fig. 2, and appears to be separate and distinct from the metal surface, Fig 1 and 2, this layer could also be a crystalline layer nucleating from the column parallel and close to the metal surface.

Values of percentage of crystalline oxide to total film thickness agree with previously reported ones. Biefer's (2) data show a levelling off in the rate of increase of thickness of the crystalline layer with time after about one week's exposure with 10157 and two week's exposure with 10155. At the bend in Biefer's curves of layer thickness against time the values are 40% for both 10155 and 10157. Over the period three weeks to 30 weeks (1, 2) the values given for both alloys decreased gradually to about 25%. Hart and Ruther's (3) values averaged 33% over the period 24 hr to 32 days where general attack occurred and 50% when local attack occurred. These values all indicate that with times of exposures larger than ours, the outer crystalline layer forms a smaller proportion of total film thickness.

Measurements of Biefer's (1) cross sections after 62 days exposure at 350°C show that the third layer on 10155 constituted 17% of total film thickness while that on 10157 constituted 13%. Although the difference is just significant it adds further support to our finding of the absence of any distinct third zone on 10157 during the exposure times investigated by us as it indicates the slower growth of such a layer on 10157.

Conclusions

The examination of cross-sectioned aluminum oxide corrosion film shows that the number of structural zones observed in the oxide is least for the most resistant material, and that in the least resistant material a third layer appears after very short exposure times at 350°C. The linking of the third zone to the crystalline outer layer by columnar structures through the oxide suggests that this layer may also be crystalline. If this is the case, it could explain spalling and cracking that occurs after longer exposure times.

Acknowledgments

The work reported formed part of Defence Research Board of Canada Project D12-75-10-35. The author acknowledges the Board's permission to publish. The author also acknowledges the work of Mr. C. A. Godden who made the photomicrographs.

Manuscript received June 29, 1962.

Any discussion of this paper will appear in a Discussion Section to be published in the June 1963 JOURNAL.

REFERENCES

1. G. J. Biefer, Atomic Energy of Canada Ltd. Report No. CR Met 796, July 1958.
2. G. J. Biefer, Minutes of a Conference on the Corrosion of Aluminum in Water at High Temperature, held at Chalk River, Dec. 18 and 19, 1956. Atomic Energy of Canada Ltd. Report No. CR Met 700, June 1957, pages 115-119, 1400.
3. R. K. Hart and W. E. Ruther, Argonne National Laboratory Report ANL 6230, April 1961.
4. R. K. Hart and W. E. Ruther, *J. Nuclear Materials*, **4**, 272 (1961).
5. H. Coriou, *et al.*, AEC-Euratom Conference on Aqueous Corrosion of Reactor Materials. Brussels, October 1959, U. S. Atomic Energy Commission Report Tld-7587, pp. 188-210.
6. V. H. Troutner, Atomic Energy Commission Research and Development Report HW 53389.
7. J. H. Greenblatt and T. C. Copps, In press.
8. D. F. MacLennan, *Corrosion*, **17**, 181t (1961).
9. J. H. Greenblatt and J. T. N. Atkinson, *This Journal*, **109**, 771 (1962).
10. C. A. Godden and J. T. N. Atkinson, *Metallurgia*, **151**, 63 (1961).

The Mechanism of the Niobium Reaction with Water Vapor and with Oxygen

P. E. Blackburn[1]

Chemistry Department, Research Laboratory, Westinghouse Electric Corporation, Pittsburgh, Pennsylvania

ABSTRACT

The low-temperature oxidation of niobium in water vapor and in oxygen occurs by diffusion of oxygen into the metal and formation of NbO and NbO_2 on the surface. NbO_2 forms a porous scale on NbO, growing linearly from the oxide-oxide interface. Solution of oxygen in the metal and the growth of NbO on niobium are believed to be diffusion controlled. The so-called breakaway oxidation occurring between 400° and 500°C in oxygen and between 750° and 950°C in water vapor is shown to be caused by nucleation and growth of Nb_2O_5 on NbO_2.

The oxidation of niobium has been the subject of a considerable amount of research over the last 20 years. Niobium is a relatively abundant refractory, and in addition to its high melting point and low vapor pressure, it has good ductility and a low neutron cross section. A major deterrent to its use at high temperatures, however, is its low oxidation resistance above 400°C. The poor oxidation resistance manifests itself between 400° and 500°C where the initially protective film is supplanted by a scale which offers no barrier to rapid oxidation (1). The transition from a protective film to the nonprotective scale is rather abrupt, resulting in a prompt increase in the oxidation rate at an oxygen pickup of around 50-80 $\mu g/cm^2$. This change has been termed breakaway oxidation. Several investigators have proposed a mechanism for the change.

[1] Present address: Arthur D. Little, Inc., Acorn Park, Cambridge, Massachusetts.

Cathcart, Campbell, and Smith (2) on the basis of a microtopographic study, propose that the transition to a high linear rate is due to mechanical stress in the film. These stresses lead to occurrence of cracks and blisters in the film and subsequent breakdown of protection. These authors suggest that the linear oxidation results from continual healing and cracking of the film.

A report published by the author (3) in March 1959 on the reaction between water vapor and niobium proposed a new mechanism for the so-called breakaway oxidation. It was suggested that this phenomenon could be related to the nucleation and growth of Nb_2O_5 on NbO_2. Hurlen, Kjøllesdal, Markali, and Norman (4) in their study of the reaction of oxygen with niobium independently proposed nucleation and growth of Nb_2O_5 as the cause of breakaway oxidation.

There is some disagreement over the oxidation mechanism occurring before the transition to a high linear rate. Gulbransen and Andrew (1), Inoye (5), Cathcart *et al.* (2), and Bridges and Fassell (6) all found protective oxidation (*i.e.*, parabolic rates), while Klopp, Simms, and Jaffee (7) found the low-temperature oxidation to be linear. Klopp *et al.* make no mention of the transition.

An excellent review of the niobium oxidation research through 1958 is contained in the Hurlen *et al.* report (4). It is interesting to note that only Phelps, Gulbransen, and Hickman (8) were able definitely to identify NbO as one of the low-temperature products of oxidation. This compound was found on a specimen oxidized at 400°C for 5 min in 0.1 atm O_2. These conditions are such that the measurement was made well before the transition to the high linear rate. The stripped film showed Nb_2O_5 electron diffraction lines, but Hurlen *et al.* (4) state that the stripping process could have produced the pentoxide.

In all of the studies reviewed by Hurlen, with the above exception and one study at 300°C by Brauer and Müller (9), the oxide scale formed below the transition point was not successfully identified.

Klopp *et al.* (7) found some evidence for NbO above 500°C.

In the Hurlen *et al.* (4) studies which covered the temperature range of 100°-1000°C and 10^{-2} to 760 mm of oxygen, neither NbO, NbO_2, nor Nb_2O_5 were found below the transition point, although in some cases two oxides, designated NbO_x and NbO_y, were detected. Hurlen suggests that the initial reaction is entirely due to solution of oxygen in the metal. At pressures of 1 mm or less, there were some instances where NbO and NbO_2 were found in addition to Nb_2O_5.

The phase designated NbO_x was found earlier by Brauer and Müller (9) on niobium powders oxidized in air at 330°C. These authors suggested the formula Nb_2O for this phase. NbO_y was not identified by Hurlen except to indicate that there were two strong spectral lines which could not be identified as belonging to previously reported phases.

Hurlen *et al.* have shown that the nucleation and growth of Nb_2O_5 can be related to the transition to "breakaway" oxidation. Since there was no x-ray evidence for NbO and NbO_2 before the transition they speculated that the nuclei were formed in NbO_x or in the oxygen saturated metal.

A report by Kofstad, Kjøllesdal, Markali, and Norman (10) covers the oxidation between 500° and 1200°C and at oxygen pressures from 10^{-1} to 760 mm. Their work concerns oxidation above the transition point.

Brewer's survey of thermodynamics of oxides (11) indicates that the stable oxides of niobium are NbO, NbO_2, and Nb_2O_5. In terms of crystal structure, NbO possesses a defective NaCl-type lattice (12), NbO_2 has a rutile structure (13, 14), and Nb_2O_5 occurs in three forms. Brauer (13) reports that the pentoxide exists between 500° and 900°C as an pseudohexagonal phase, γ, between 1000° and 1100°C as an unknown phase, β, and above 1100°C as a monoclinic phase, α. Recently Holtzberg, Reisman, Berry, and Berkenblit (15) investigated the polymorphism of high-purity Nb_2O_5. They found three forms: (i) amorphous to 435°, (ii) γ to 830°, and (iii) α above 830°C. The γ phase, a two-dimensional array, is Brauer's γ and β phases which Holtzberg *et al.* show to be a single phase. They found the α phase to be monoclinic. Brewer (11) also reports that Nb_2O_5 has an oxygen solubility range of $NbO_{2.4-2.5}$. Seybolt's data (16) indicate an oxygen solubility from 5.5 atom per cent (a/o) in niobium at 1100°C to 1.4 a/o at 775°C.

There have not been any studies involving the oxidation of niobium in pure water vapor. However, Inoye (5) found that water vapor mixed with air appeared to accelerate the rate of reaction at temperatures below 400°C.

The purpose of this study is to determine the stability of Nb_2O_5, the rate of reaction of niobium with water vapor, and the mechanism of reaction of niobium with oxygen and with water vapor.

Experimental Procedure

Apparatus.—The apparatus for the thermodynamic and kinetic experiments consists of an all quartz microbalance sealed into a Pyrex glass system. Using this balance, weight changes could be read to ± 2.2 x 10^{-7}g. Alpert (17) valves and all-metal diaphragm valves were used to permit the system to be baked out at 300°C. Pressures were measured with a mercury manometer isolated from the system by a null manometer (18), while vacuums were measured with a Bayard-Alpert (19) gauge. At room temperature, vacuums of about 1 x 10^{-9} mm were obtained, but at high temperatures vacuums were on the order of 1 x 10^{-5} mm.

Thermodynamic equilibrium method.—The CO/CO_2 equilibrium over the Nb_2O_5-NbO_2 two-phase region was measured by suspending a platinum crucible containing niobium oxide with a composition of $Nb_2O_{4.59}$ from one arm of the microbalance into a mullite furnace tube. The system was evacuated. The temperature of the furnace was regulated at a constant value. A measured pressure of spectroscopically analyzed CO containing 0.25% CO_2 was then admitted to the furnace section, the volume of which had been established previously. The weight of oxygen lost from the niobium oxide as a result of reduction by CO gas was measured with the microbalance. The experiment was continued until there was no further change in weight (about 24 hr). The amount of CO_2 formed was calculated from the oxygen weight loss of the niobium oxide.

Kinetic method.—The rate of reaction of niobium with water vapor was measured by suspending a specimen from one arm of the microbalance into the evacuated furnace tube. The temperature of the furnace tube was raised and held constant to ± 0.5°C while the rest of the system was heated to prevent condensation of water vapor. Water vapor was generated into a storage bulb from a container of distilled water which had been thoroughly degassed. These two components were joined to each other and to the rest of the system with metal

valves and Kovar-to-glass seals. Water vapor was admitted to the furnace section and weight change as a function of time was observed.

X-ray diffraction method.—Monochromatic filtered nickel radiation from a fine focus x-ray tube was used with a Guinier camera. Diffraction patterns of powder scraped from oxidized niobium specimens by sapphire and carbide tools were made at room temperature.

Samples.—The Nb_2O_5 was prepared by oxidizing 2 mil sheet manufactured from powder melted by electron bombardment. Oxidation was carried out at 1200°C until there was no further weight gain. The composition of the fully oxidized sample was assumed to be stoichiometric Nb_2O_5. Its resistivity was found to be about 3×10^8 ohm-cm at room temperature.

The above oxide was reduced with hydrogen and from the weight change a composition of $Nb_2O_{4.69}$ was calculated. This material, assumed to be in the two-phase region $Nb_2O_{4.8}$-NbO_2, was used in the CO/CO_2 equilibrium study.

Niobium monoxide and dioxide were prepared by mixing the metal and Nb_2O_5 in the correct ratios and arc melting them in an atmosphere of pure argon. The monoxide was silver and metallic in appearance. This material had a diamond pyramid hardness of 830. Its electrical conductivity was very high, with a room temperature resistance of 5×10^{-4} ohm-cm. Chemical analysis indicated a composition of $NbO_{1.005}$. The dioxide was a black polycrystalline sintered porous solid whose resistivity was about 4000 ohm-cm. The composition of several samples varied from $NbO_{2.01}$ to $NbO_{2.04}$.

Two different types of niobium sheet were used for the kinetic study. The first, employed in the 200° and 225°C measurements, was the electron bombarded metal mentioned above. It had the following impurities as determined by spectroscopic analysis: Al, 0.04; Fe, 0.015; Si, 0.01; Ta, 0.1-0.2; V, 0.05; Na, 0.01; and K, 0.01. The second specimen, used for the remaining studies, was prepared from Fansteel high-purity vacuum sintered Nb sheet which contained the following impurities: C, 0.016; Ta, 0.14; Fe, 0.008; Zr, 0.65; Ti, 0.013; N, 0.028; and O, 0.11. Two types of surface preparation were used: (i) abrading with polishing paper under kerosene, (ii) abrading with a blast of Al_2O_3 powder forced through a nozzle under pressure.

Results

Thermodynamic equilibrium.—Three experiments, performed at 927°, 977°, and 1027°C, were carried out with one CO charge admitted at room temperature before the sample was heated. This method required a correction for the altered balance reading caused by temperature induced variations in convection currents. The convection coefficient was equivalent to 1.1×10^{-7} g/C° at a pressure of 5.9 mm.

In two experiments made at 1077° and 1227°C, the CO charge was added after the sample was at temperature. Here the effect of convection currents on the readings was eliminated by extrapolating the weight *vs.* time curve to zero time.

Factors limiting accuracy of the experiments were thermal diffusion of the lower molecular weight gas to the furnace tube and reaction of CO with the mullite furnace tube. The former effect was believed to be small. The latter circumstance occurred only during the 1227° measurement, when the weight change of the sample with time reached zero and then reversed. The reversal may have occurred in the following manner: (i) the sample loses weight by reaction with CO, *i.e.*,

$$Nb_2O_{4.8} + 4/5CO = 2NbO_2 + 4/5CO_2 \qquad [1]$$

(ii) A second reaction is assumed to occur simultaneously with the first

$$CO + SiO_2(s) \text{ (in mullite)} = CO_2 + SiO(g) \qquad [2]$$

The excess CO_2 produced then reacts with NbO_2 reversing Eq. [1]. Although the calculated pressure of SiO(g) is very low ($10^{-7.1}$ atm at 1227°C), SiO may condense in cooler parts of the apparatus allowing more CO_2 to be produced. Thus the total amount of CO_2 formed may not be entirely accounted for by reaction [2]. This effect could also be caused by diffusion of oxygen through the mullite tube. It is estimated from the weight gain after equilibrium was reached, that 15% of the total CO_2 produced at 1227°C was due to one of these effects. This is equivalent to 0.36 kcal of the free energy change. The 1227° measurement was corrected for this effect.

Table I summarizes the data and gives the calculated free energy of formation of $Nb_2O_{4.8}$ from NbO_2. The composition of the former is the lower limit of the oxygen solubility in the Nb_2O_{5-x} phase.

A least squares fit to the free energies of formation in Table I gives for

$$2NbO_2 + 2/5O_2 = Nb_2O_{4.8} \qquad [3]$$

$\Delta H_{1350} = -56.6$ kcal/mole of the oxide and $\Delta S_{1350} = -13.8$ e.u./mole of the oxide. Brewer (11) calculated the heat of solution of oxygen in $Nb_2O_{4.8}$ for the reaction

$$Nb_2O_{4.8} + 1/10O_2 = Nb_2O_5 \qquad [4]$$

to be $\Delta H_{298} = -15.3$ kcal/mole of oxide. The latter value may be combined with the heat of reaction [3] to give the heat of formation of Nb_2O_5 from NbO_2, $\Delta H_{1350} = -71.9$ kcal/mole of oxide. In the absence of entropy data for the solid solution region, the entropy for reaction [3] is multiplied by 5/4 to give the entropy of formation of Nb_2O_5. from

Table I. Free energy of formation of $Nb_2O_{4.8}$ from NbO_2

Temp, °K	Initial CO press., mm	O_2 wt loss, μg	$PCO_2/PCO \times 10^2$	$-\Delta F_1$[a] kcal/ mole $Nb_2O_{4.8}$	$-\Delta F_2$[b] kcal/ 0.8 mole of CO_2	$-\Delta F_3$[c] kcal/ mole of $Nb_2O_{4.8}$
1200	5.85	293	4.11	6.08	34.01	40.09
1250	5.85	314	4.41	6.21	33.18	39.39
1300	5.85	327	4.59	6.37	32.35	38.72
1350	11.4	631	5.41	6.26	31.53	37.79
1500	8.7	489	5.55	6.92	29.07	35.99

[a] ΔF_1: $2NbO_2 + 4/5CO_2 = Nb_2O_{4.8} + 4/5CO$.
[b] ΔF_2: $4/5CO + 2/5O_2 = 4/5CO_2$ from Coughlin (20).
[c] ΔF_3: $2NbO_2 + 2/5O_2 = Nb_2O_{4.8}$.

Table II. Thermodynamic values for formation of Nb_2O_5 from NbO_2 at 1300°K

	This research	Coughlin's tables (20)
$-\Delta H$ kcal/mole of oxide	71.9	71.9
$-\Delta S$ e.u./mole of oxide	17.2	17.2
$-\Delta F_{1300}$ kcal/mole of oxide	49.5	49.5

NbO_2, $\Delta S = -17.2$ e.u./mole of Nb_2O_5. Table II compares the author's thermodynamic values for formation of Nb_2O_5 from NbO_2 at 1300°K with those from Coughlin's tables (20). The agreement is excellent.

From Coughlin's tables the hydrogen-water vapor ratio may be calculated for the reaction

$$2NbO_2 + H_2O\ (g) = Nb_2O_5 + H_2 \qquad [5]$$

At 225° and 1125°C this ratio is $10^{5.2}$ and $10^{1.1}$, respectively. As long as less than 90% of the water is consumed in these reactions, thermodynamically there is no reason why Nb_2O_5 would not be a stable product of the reaction of water and niobium at temperatures up to 1125°C.

Kinetics of Niobium-Water Vapor Reaction

There are three rate equations which appear to be followed in this study

$$W = k_1 t \qquad [6]$$

$$W^2 = k_2 t \qquad [7]$$

$$W^3 = k_3 t \qquad [8]$$

where W is the weight gained by the sample in time, t, and k_1, k_2, and k_3 are, respectively, the linear, parabolic, and cubic rate constants. To find which equation applies, the logarithm of the weight gain may be plotted against the logarithm of the time.

The linear rate is obeyed by reactions which are controlled by processes occurring at one of the interfaces. Parabolic reactions have been shown by Wagner (21) to apply to an oxidation mechanism governed by the rate of diffusion of either or both the oxygen anion or the metal cation through the oxide film. It is conceivable that a process controlled by gaseous effusion of the reacting gas through a growing porous oxide layer could also result in parabolic oxidation, assuming that the pore diameters remained relatively constant and only their length increased with time. A decrease in the area of the interface at which the reaction takes place would also yield a curve of decreasing slope. Hence a curve of this type alone is not incontrovertible evidence for a diffusion controlled reaction.

The cubic rate has been observed empirically, but except for the case of thin films, has not been explained theoretically. Hurlen (22) suggests that it may be a transition region between inverse logarithmic and parabolic oxidation.

Figures 1, 2, and 3 show the weight gain *vs.* time for the reaction of niobium in 5 cm of water vapor. Figure 4 gives the logarithm of the weight gain *vs.*

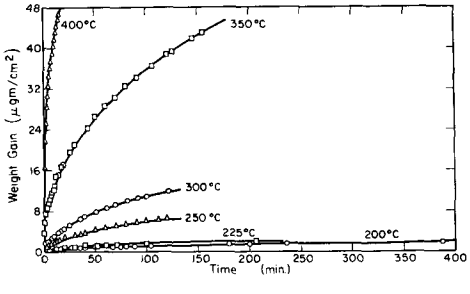

Fig. 1. Niobium oxidized in 5 cm H_2O vapor, weight gain *vs.* time.

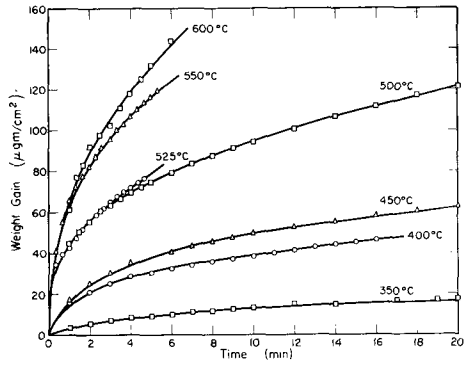

Fig. 2. Niobium oxidized in 5 cm H_2O vapor, weight gain *vs.* time.

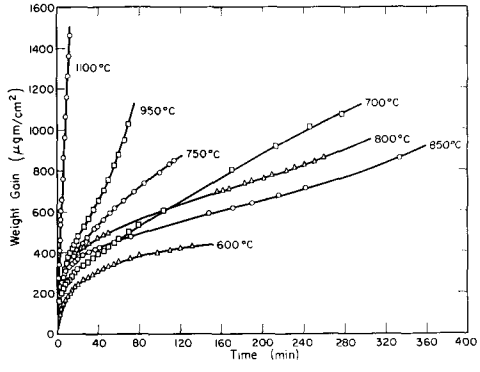

Fig. 3. Niobium oxidized in 5 cm H_2O vapor, weight gain *vs.* time.

time for the reaction of niobium in 5 cm of water vapor. Figure 4 gives the logarithm of the weight gain *vs.*

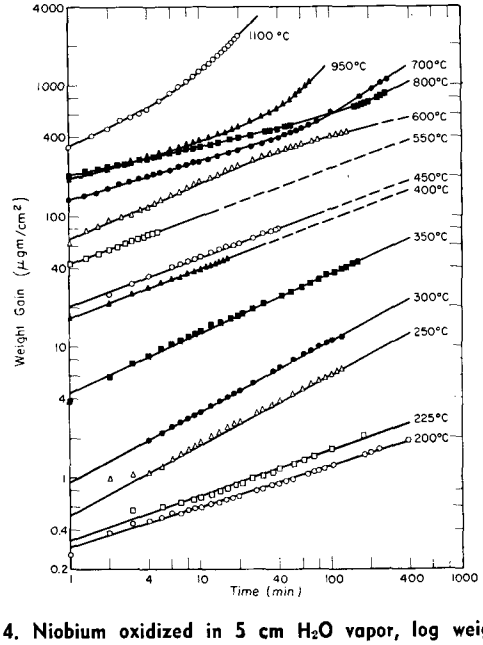

Fig. 4. Niobium oxidized in 5 cm H_2O vapor, log weight gain *vs.* log time.

the logarithm of the time for all the runs from 200° to 1100°C (the 750° and 850° curves are not included for the sake of clarity). The slopes of the curves obtained between 250°-350°C are close to 0.5, while the measurements between 200°-225° and 400°-750°C have slopes of about 0.33. Above 750°C the log-log curves do not fit either category.

Niobium samples for 250°-500°C runs were prepared by abrasion with a blast of Al_2O_3 powder. The remaining experiments were made on samples prepared by polishing specimen through 4/0 emery paper under kerosene.

The effect of surface treatment on reaction rate is clearly demonstrated in Fig. 5, which compares two samples with different surface preparations, each reacted at 200°C. The manually polished metal reacts cubically over the full test time, whereas the blast cleaned sample failed to oxidize for the first 40 min of the run. This behavior was upheld by a second blast-abraded specimen, also measured at 200°C.

When the measurements are plotted by surface treatment of the sample, curves indicating two kinetic rates emerge. The slope for the polished samples is 0.33 for the temperature range 200°-700°C. For the abraded metal a slope of 0.5 was found up to 350°C, but from this temperature to 750°C the samples followed cubic curves.

The upper limit for application of the cubic rate occurs at an approximate weight gain of 400 $\mu g/cm^2$ in 5 cm of water vapor as shown in Fig. 6. This weight gain is from 6 to 8 times as much as that observed for the protective phase of oxygen reacting with niobium. In some of the measurements shown in Fig. 3 an acceleration in the reaction rate may be observed after an oxygen weight gain between 500 and 800 $\mu g/cm^2$. This is believed to correspond to the so-called breakaway oxidation of niobium found between 400° and 500°C. However, in the water vapor experiments, the temperature range for accelerated activity is between 750° and 950°C. The rate of reaction of niobium with 5 cm of water vapor is within a factor of two of the oxidation rate in 0.1 atm oxygen up to 400°C (*i.e.*, the protective oxide scale range) (1).

The specimens varied in color after oxidation from dull gray to dark blue or black. The intensity of the color increased with oxygen pickup.

There was no evidence in these studies for spalling of the oxide film, a factor which has been observed in

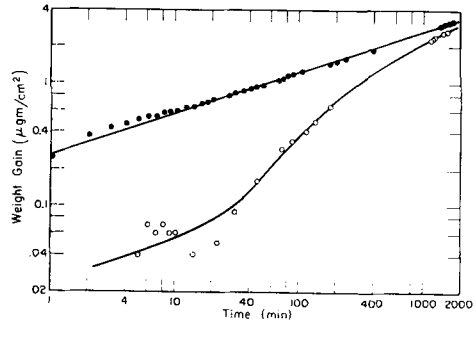

Fig. 5. Effect of surface treatment; niobium oxidized at 200°C in 5 cm H_2O vapor, log weight gain *vs.* log time. •, abraded through 4/0 polishing paper, annealed at 300°C; ○, abraded with Al_2O_3 blast, no anneal.

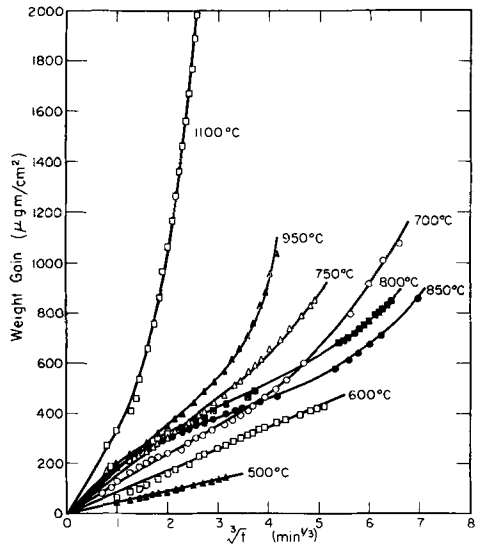

Fig. 6. Cubic plot, niobium oxidized in 5 cm H_2O vapor, weight gain *vs.* $t^{1/3}$; 600°-1100° samples abraded through 4/0 polishing paper, 500° sample abraded with Al_2O_3 blast.

other studies (1, 4, 7) of the niobium-oxygen reactions.

An Arrhenius plot of the cubic rate constant (Eq. [8], *i.e.*, for the reaction occurring before the transition to breakaway oxidation, *vs.* the reciprocal of the temperature is presented in Fig. 7. It is evident that a change in the reaction mechanism occurs above 750°C, where a decrease in the rate constant manifests itself.

Since the pretransition weight gain curves represent the sum of at least three simultaneous processes, *i.e.*, oxygen solution in the metal and formation of NbO and NbO_2, no heat of activation can be assigned to the oxidation of niobium.

In addition to studies on the rate of oxidation of the metal in water vapor, kinetic measurements were made of the reaction of water vapor with two of the niobium oxides. Both samples were heated in a small platinum crucible in 5 cm of water vapor. The NbO

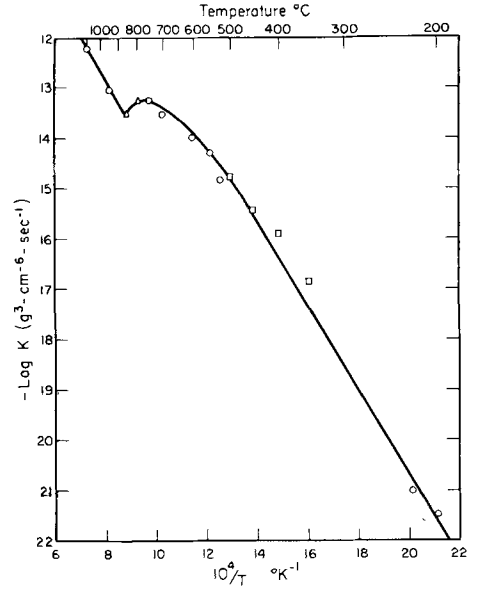

Fig. 7. Oxidation of niobium in 5 cm H_2O, logarithm of cubic rate constant *vs.* 1/T. △, not cubic; △○ abraded through 4/0 polishing paper; □ abraded with Al_2O_3 blast.

Table III. Lattice parameters of oxides and metal reacted with 5 cm of water vapor

Temp, °C	Oxidation time, min	Wt gain, $\mu g/cm^2$	Lattice parameters in Angstroms: Nb a	NbO a	NbO_2 a	NbO_2 c	Nb_2O_5# phase
450-S*	40	80	3.320 ± 6	ND‡	13.75 ± 7	6.00 ± 3	ND
550-S	6	120	3.326 ± 7	4.235 ± 3	13.72 ± 2	6.00 ± 1	Trace γ
700-W	280	1080	3.321 ± 1	4.219 ± 2	13.72 ± 2	5.99 ± 1	γ
850-S	330	860	3.315 ± 4	4.226 ± 1	13.74 ± 2	6.00 ± 1	ND
950-W	70	1030	3.309 ± 1	4.216 ± 1	13.72 ± 1	5.99 ± 1	ND
1100-S	20	2330	ND	ND	Trace?		α

* S, sample surface, W, whole sample.
‡ ND, not detected.
# γ is the low-temperature phase and α the high-temperature phase.

was oxidized at 500°C for 2 days. Oxidation for the first 3 hr was linear, with a rate of 4.2 x 10^{-9} $g/cm^2/sec$. The rate slowly decreased with time to 1.3 x 10^{-9} $g/cm^2/sec$ after 50 hr.

The porous NbO_2 sample was heated for 18 hr at 500°C in 5 cm of water vapor with no apparent change in weight. The temperature was then raised to 900°C, where the sample readily oxidized. During the 40-min measurement the reaction rate was amplified by a factor of 4. Since the sample was exposed to water vapor while being heated from 500° to 900°C, the increase in rate with time was measured after some reaction had already taken place. This oxidation behavior appears to be a nucleation and growth process in the formation of the pentoxide from the dioxide. By comparing the 900° curve with measurements of NbO_2 in air (see below), an induction period of about 100 min could be estimated. This may be compared to 25 min at 950° and 200 min at 850°C for the onset of the high linear rate in the oxidation of the metal. This rate appears to be caused by the nucleation and growth of Nb_2O_5 on NbO_2 in water vapor.

The amount of hydrogen produced in the water vapor-niobium reactions was never greater than 1.4% of the total pressure well below the thermodynamic limit for reduction of Nb_2O_5 to NbO_2 at 1100°C. The pressure of hydrogen produced in all cases was so small compared to the equilibrium pressure over a saturated solution of hydrogen in niobium that the niobium should have dissolved less than 1.6 a/o of hydrogen (220 ppm) during the water vapor reaction. The maximum capacity for hydrogen occurred in the 200°C measurements. The solubility of hydrogen as a function of hydrogen pressure was calculated from Katz and Gulbransen's data (23). Katz's data were extrapolated below the minimum concentration of 3 a/o. It is possible that solution of hydrogen in the metal may have been much less than that calculated, since hydrogen may not be able to diffuse through an oxide layer. The presence of hydrogen gas is not believed to have any effect on the oxidation mechanism. The amount of hydrogen gas present was far too small to prevent the formation of Nb_2O_5 under any of the conditions presented in this study.

X-Ray Diffraction Spectra of Oxides Formed on Niobium

Some of the samples were scraped with carbide and sapphire tools to remove the oxide film. The extreme hardness of NbO (830 DPH) requires diamentine tools to assure its removal. Other samples were completely ground for use as x-ray samples. There was not enough oxide to make an x-ray measurement on specimens oxidized below 450°C. These samples reacted with less than a total of 400 μg of oxygen.

Table III gives the results of the x-ray measurements. Except for the 450° measurement, where only dioxide was observed, both monoxide and dioxide were found on samples up to 950°C. Since no lines were found for niobium in the 1100° sample the absence of the two lower oxides may have been caused by failure to remove the oxide layer to a sufficient depth. The lack of NbO lines at 450° may be due to either small crystal size or low concentration. The lack of pentoxide spectra at 850° and 950°C may perhaps be due to inadequate x-ray exposure time or sample size.

The lattice parameters given here are compared to literature values in Table IV.

Seybolt's data (16) for oxygen dissolved in niobium gives a room temperature niobium lattice parameter of 3.3125Å for niobium saturated with 4.6 a/o oxygen at 1000°C. The room temperature parameters measured here indicate that the saturated metal may expand at least to as much at 3.320Å after oxidizing between 500° and 700°C. This value may be compared to that of Hurlen who found a maximum value of 3.342Å for a sample oxidized at 350°C. It appears that niobium can take up more than 4.6 a/o oxygen at lower temperatures.

With the exception of Hurlen's (4) low oxygen pressure results, the x-ray data for the samples differ from earlier work on the oxygen-niobium reactions in that all three oxide phases were found at higher temperatures. Most of the published results have indicated only Nb_2O_5 as the product of oxidation. It would be very desirable to know what phases are present on the samples oxidized below 450°C.

Contact Resistance of Oxides and Oxidized Niobium

Hurlen (4) has suggested that neither of the two oxides, NbO and NbO_2, forms before the pentoxide

Table IV. Lattice parameters for niobium and its oxides

Author	Nb a	NbO a	NbO_2 a	NbO_2 c
	in Angstroms			
Edwards *et al* (24)	3.3004			
Brauer (13)		4.210		
Magneli (14)			13.71	5.985
This research	3.301 ± 1	4.211 ± 4	13.70 ± 2	5.99 ± 2

Table V. Contact resistance of oxides and oxidized niobium

Temp, °C	Wt gain, μg/cm²	Contact[a] resistance, ohm/cm²
200	2	0.13
200	3	0.2
200	3	0.2
225	2	0.2
250	6	0.2
300	12	0.2
350	40	0.3
350[b]	50	0.3
500	140	0.5
600	100	1.2
Abraded Nb		0.015
Blast abraded Nb		0.002
NbO[c]		0.0024
NbO_2[c]		4×10^3
Nb_2O_5[c]		3×10^6

[a] Two surfaces, each 1 cm².
[b] Sample oxidized in 0.1 atm O_2, all others in 5 cm H_2O.
[c] 1 cm thick, total resistance.

in oxygen pressures greater than 0.1 mm and that oxygen dissolves in the metal initially without forming an oxide film.

In order to test this hypothesis, the contact resistance of the three oxides and the oxidized samples was measured. These data are given in Table V. The values are for two contacts of 1 cm² each. Indium foil was used to improve the electrical contact.

The contact resistance in all cases is at least 10 times greater than that for either the metal or NbO. This is evidence that even the samples oxidized at 200°C have some oxide present, either NbO_2 or Nb_2O_5. The dark gray to black color of the oxide films support this finding, indicating that the oxide is probably NbO_2 or nonstoichiometric Nb_2O_5.

Oxidation of NbO *and* NbO_2 *in Air*

In order to prove the assumed analogy between the oxidation of niobium in water vapor and in oxygen, the kinetics of NbO and NbO_2 oxidation in air were studied. The results of the NbO_2 oxidation between 400° and 500° are shown in Fig. 8 where the oxygen-niobium ratio is plotted against the logarithm of the time. The surface area of the sample was not known, prohibiting the calculation of a quantitative rate of reaction. These curves do demonstrate that NbO_2 oxidizes in a manner which is characteristic of a nucleation and growth controlled reaction. The induction periods agree favorably with the time elapsed before the onset of the high linear oxidation of niobium (breakaway oxidation) observed by other authors.

Figure 9 shows the oxidation of NbO in air between 350° and 450°C. These curves show that NbO oxidizes linearly and that NbO_2 is present before the pentoxide is formed.

Discussion

The thermodynamic study on the NbO_2-$Nb_2O_{4.8}$ phases indicate that the Nb_2O_5 is stable in water vapor, so that its failure to form in water vapor at low temperatures cannot be attributed to this factor. There is excellent agreement between the data obtained here and the tables calculated by Coughlin.

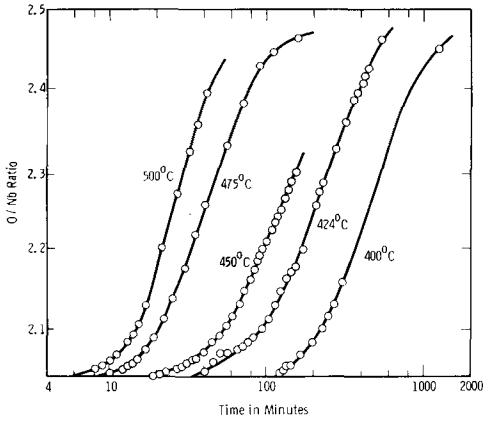

Fig. 8. Oxidation of $NbO_{2.04}$ in air

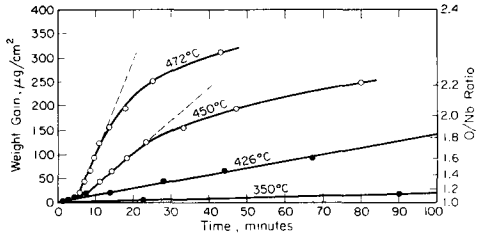

Fig. 9. Oxidation of NbO in 1 atm of air.
○, $NbO + O_2 \rightarrow Nb_2O_5 + NbO_2$; ●, $NbO + \frac{1}{2} O_2 \rightarrow NbO_2$.

The use of a vacuum balance for determining the CO/CO_2 ratio in a static system has the advantage that the equilibrium point may be precisely defined.

The suggestion by earlier authors that the breakdown of protective oxidation is due to a physical mechanism involving stresses and strains in what was assumed to be a protective film of Nb_2O_5 is incompatible with findings in this study. First, it has been shown that a protective oxide film can grow in water vapor to a thickness almost 10 times that of a film grown in oxygen. Thus failure cannot be related to a physical breakdown. Second, there is good evidence that Nb_2O_5 is not present before the breakdown occurs; rather, the breakdown can be directly correlated with the appearance of Nb_2O_5. It seems possible that the cracks and blisters observed by Cathcart *et al.* (2) are due to the formation of a nonprotective film of Nb_2O_5 growing into the underlying films of NbO and NbO_2.

The interference colors observed on pretransition samples oxidized in oxygen and in water vapor must be caused by NbO_2. Optical properties for NbO and NbO_2 have not been found in the literature. However, with regard to the former, it seems very likely that it will behave in a fashion similar to metals, since its electrical conductivity is within an order of magnitude of several metals. Because of their high conductivity, metals are known to be practically opaque (25).

It appears that interference colors observed on oxidized niobium must be due to NbO_2 or Nb_2O_5. Since it has been shown that Nb_2O_5 forms only after temperature dependent induction periods, the interference colors observed before the nucleation and growth of Nb_2O_5 must be due to NbO_2. Hurlen has attributed the interference colors on his samples to an oxide of unspecified composition, NbO_x. This

phase has a cubic lattice parameter slightly greater than niobium (NbO_x, $a_o = 3.384$; Nb, $a_o = 3.300$) and is referred to by Hurlen as a suboxide of niobium. It is presumably more metal rich than NbO. Its electrical conductivity and metallic character should therefore be even greater than NbO. Hence, it would appear to be less likely to cause interference colors than NbO, and there is good reason to doubt that NbO could form the transparent films necessary for the occurrence of interference colors.

Hurlen (4) has observed that niobium oxidizes initially at a linear rate, contrary to several other studies in which a parabolic rate has been reported. He believes that this linear rate corresponds to solution of oxygen in the metal without the formation of an oxide film. Both Gulbransen's work in oxygen and the present work in water vapor give initially higher rates than found by Hurlen. A possible explanation for the difference in the shape of the curves and rates may be found in the surface preparation of the various samples. In this study it was found that the initial low-temperature rate was either parabolic or cubic depending on whether the sample was abraded with a blast of Al_2O_3 or polished with emery paper. At 200°C a more profound effect was found: the blast abraded sample failed to oxidize for the first 40 min. Hurlen, on the other hand, did not observe any differences between samples polished with alumina and electropolished specimens.

The absence of diffraction spectra for NbO and NbO_2 at lower temperatures in Hurlen's study is not unambiguous evidence that these phases are not present. The amount of oxide which can be detected by x-ray diffraction depends on a number of factors, among which are (i) crystallinity and crystallite size, (ii) crystal structure, (iii) atomic number of elements present, and (iv) sensitivity of the measuring instrument. Under the most favorable conditions Cu_2O oxide films as thin as 100Å have been detected by x-ray diffractometer (26). Some studies by Blackburn, Weissbart, and Gulbransen (27) on the oxidation of UO_2 indicated that an oxide layer of cubic U_3O_7 less than 600°-800Å thick could not be detected in a powder camera using a fine focus x-ray beam. Taylor (28) has estimated that an oxide film as much as 10^5Å thick may be needed for effective detection with a diffractometer. Thus, the minimum level for detection cannot be stated categorically. It certainly is finite, and failure to detect x-ray spectra cannot be taken as evidence for complete absence of an oxide film.

The difference in the oxidation behavior of niobium in water vapor and oxygen is pertinent to this problem. It has been shown that the protective layer grown in water vapor is as much as 10 times thicker than that grown in oxygen. This of course gives both more oxide material to analyze and larger crystals. These factors may account for the detection of the lower oxides in this study where they were not found in most cases before. Even though the color and the resistivity of samples reacted with less than 80 μg of H_2O indicated the presence of an oxide film, the amount was inadequate for analysis in the present study.

Contrary to what might be expected, the pretransition rates (*i.e.*, before breakaway oxidation) are not a function of the partial oxygen pressure in equilibrium with water vapor and the hydrogen produced by the reaction. Instead, the water vapor rates at 5 cm pressure appear to be similar to oxidation rates of niobium in 5 cm of oxygen. For example, after 100 min at 350°C; Gulbransen's sample gained 45 $\mu g/cm^2$ in 7.6 cm of oxygen; Hurlen's sample gained 16 $\mu g/cm^2$ in 10 cm of oxygen; the sample in this study gained 35 $\mu g/cm^2$ in 5 cm of water vapor. Unfortunately, data were not obtained over a range of water vapor pressures, and it is therefore not possible to compare rates at other pressures.

The oxidation of NbO to NbO_2 may go at a somewhat faster rate in oxygen than in water vapor. In 1 atm of air or about 15 cm of oxygen the rate at 472°C was around 3×10^{-8} g/cm^2 compared to 4×10^{-9} g/cm^2 for 5 cm of water vapor at 500°C. On the other hand, there is a very significant difference between the nucleation and growth of Nb_2O_5 or NbO_2 in oxygen and water vapor. Whereas detection of this reaction begins at 400°C in 15 cm of oxygen, after 100 min a temperature of 900°C is required with 5 cm of water vapor for a similar induction period.

The data from this research indicate that the mechanism of the low-temperature oxidation of niobium is very similar in both oxygen and water vapor. Before the transition to a high linear rate or to breakaway oxidation, the reaction involves solution of oxygen in the metal and formation of NbO and NbO_2 on the surface. Since NbO_2 grows at a linear rate which is less than the total oxidation rate, it must grow at the NbO-NbO_2 interface offering no barrier to the penetration of gaseous oxygen or water to the NbO surface. If this were not the case, of course, the over-all rate would be controlled by the rate of formation of NbO_2. The cubic or parabolic rate which accounts for the bulk of the low-temperature oxidation involves solution of oxygen by diffusion in the metal and possibly diffusion controlled formation of NbO simultaneously. From the available data it is not possible to tell much about the mechanism for NbO formation since it cannot be separated from the solution of oxygen in the metal. One method which has not been tried to determine the method of NbO formation would be the use of oxygen-saturated niobium as kinetic specimens. If these are oxidized below the temperature at which the pentoxide forms, both NbO and NbO_2 would appear. Subtracting the rate of conversion of NbO to NbO_2 from the total curve would leave the curve for NbO formation.

The mechanism for the breakaway oxidation in both water vapor and oxygen is the nucleation and growth of Nb_2O_5 on NbO_2. By contact resistance measurements, by oxidation of NbO and NbO_2, and by x-ray data it has been shown that NbO_2 is present before the Nb_2O_5 phase appears. The oxidation of NbO_2 to Nb_2O_5 has been shown to occur by nucleation and growth where the induction period agrees favorably with the time elapsed before breakaway oxidation of the metal begins. The principal difference between the water vapor and oxygen reaction with niobium is the much slower nucleation and growth

rate of Nb_2O_5 in water vapor. The result is that protective oxidation proceeds for a longer time at higher temperatures in water vapor.

Conclusions

Niobium reacts in water vapor at low temperatures forming NbO and NbO_2 as well as dissolving oxygen in the metal. That NbO and NbO_2 form in oxygen before Nb_2O_5 may be inferred from (i) contact resistance measurements on an oxygen reacted sample, (ii) interference colors arising most likely from an NbO_2 film, (iii) pretransition films observed microscopically by Cathcart *et al* (2), (iv) induction periods for Nb_2O_5 formation on NbO_2 in good agreement with the time elapsed before breakaway oxidation of the metal, and (v) over-all kinetics quite similar in both oxygen and water vapor. The NbO_2 grows as a porous film on NbO. The solution of oxygen occurs by a diffusion process. The mechanism of NbO growth has not been established although it is suspected that it may also grow by diffusion.

At higher temperatures and after decreasing induction periods, breakaway oxidation occurs by the nucleation and growth of Nb_2O_5 on NbO_2. The over-all rate becomes linear after the pentoxide has grown part way through the protective NbO layer. The rate is controlled by conversion of NbO or NbO_2 to Nb_2O_5. Since the rate of growth for Nb_2O_5 is greater than that for NbO_2, the latter phase should eventually be completely consumed.

Acknowledgment

The author is very grateful to H. A. Johansen for preparing the NbO and NbO_2 samples.

Manuscript received Nov. 6, 1961. Much of the material discussed in this paper was presented before the American Chemical Society Meeting in Boston, April 1959. This study was supported in part by the United States Air Force through a contract with the Wright Air Development Center of the Air Research and Development Command.

Any discussion of this paper will appear in a Discussion Section to be published in the June 1963 JOURNAL.

REFERENCES

1. E. A. Gulbransen and K. F. Andrew, *This Journal*, **96**, 364 (1949); *ibid.*, **105**, 4 (1958); *Trans. AIME*, **188**, 586 (1950).
2. J. V. Cathcart, J. J. Campbell, and G. P. Smith, *This Journal*, **105**, 442 (1958).
3. R. T. Begley, WADC Technical Report 57-344 Part II, ASTIA Document No. 210258, March, 1959, pp. 69-94.
4. T. Hurlen, H. Kjøllesdal, J. Markali, and N. Norman, Technical (Scientific) Note No. 1, Contract No. AF61(052)-90, April, 1959; T. Hurlen, *J. Inst. Metals*, **89**, 273 (1961).
5. H. Inoye, USAEC, ORNL-1565 (1953).
6. D. W. Bridges and W. M. Fassel, Jr., *This Journal*, **103**, 326 (1956).
7. W. D. Klopp, C. T. Sims, and R. I. Jaffee, *Proc. Second United Nations International Conferences on the Peaceful Uses of Atomic Energy*, **6**, 293 (1958).
8. R. T. Phelps, E. A. Gulbransen, and J. W. Hickman, *Ind. Eng. Chem.*, **18**, 391 (1946).
9. G. Brauer and H. Müller, "Proceedings of IUPAC's 16th Congress," p. 63, Butterworth, London (1958).
10. P. Kofstad, H. Kjøllesdal, J. Markali, and N. Norman, Technical (Scientific) Note No. 2, April 1960.
11. L. Brewer, *Chem. Revs.*, **52**, 8 (1953).
12. G. Andersson and A. Magneli, *Acta Chem. Scand.*, **11**, 1065 (1957).
13. G. Brauer, *Z. anorg. u. allgem. Chem.*, **248**, 1 (1941).
14. A. Magneli, G. Andersson, and G. Sundkvist, *Acta Chem. Scand.*, **9**, 1402 (1955).
15. F. Holtzberg, A. Reisman, M. Berry, and M. Berkinblit, *J. Am. Chem. Soc.*, **79**, 2039 (1957).
16. A. U. Seybolt, *J. Metals*, **6**, 774 (1954).
17. D. Alpert, *Rev. Sci. Instr.*, **22**, 536 (1951).
18. D. Alpert, C. G. Matland, and A. O. McCoubrey, *ibid.*, **27**, 569 (1957).
19. R. T. Bayard and D. Alpert, *ibid.*, **21**, 571 (1950).
20. J. P. Coughlin, "Contribution to Data on Theoretical Metallurgy, XII Heats and Free Energies of Formation of Inorganic Oxides," Bureau of Mines Bulletin 542, pp. 54-55.
21. C. Wagner and K. Grunewald, *Z. Physik. Chem.*, **40B**, 455 (1938).
22. T. Hurlen, *Acta Chem. Scand*, **13**, 695 (1959).
23. O. M. Katz and E. A. Gulbransen, "Thermodynamic Functions for the Columbium-Hydrogen System," Metallurgy of Columbium, AIME and Interscience, New York (1961).
24. J. W. Edwards, R. Speiser, and H. L. Johnston, *J. Appl. Phys.*, **22**, 424 (1951).
25. M. Born and E. Wolf, "Principals of Optics," pp. 608-661, Pergamon Press, New York (1959).
26. B. S. Borie, *Acta Cryst.*, **13**, 542 (1960).
27. P. E. Blackburn, J. Weissbart, and E. A. Gulbransen, *J. Am. Chem. Soc.*, **62**, 902 (1958).
28. A. Taylor, Private communication.

Some Factors Controlling Gross Leakage Currents in Sputtered Tantalum-Film Capacitors

N. W. Silcox and L. I. Maissel

Components Division, International Business Machines Corporation, Poughkeepsie, New York

ABSTRACT

Methods for producing sputtered tantalum-film capacitors are described. The breakdown voltage of such capacitors is shown to depend on the type of metal used for the counterelectrode and on the counterelectrode area. This dependency is explained as being due to microfissures (in the oxide), which some metals are more likely to enter than others. Electron micrographs of these fissures are shown. The origin of the microfissures is thought to be lattice mismatch between oxide and metal in those regions where the original tantalum was not sufficiently smooth. It is suggested that anodizing these films in hot solutions will establish a thermal mismatch between metal and oxide, which will partly compensate for the lattice mismatch.

As is well-known in the industry, and as first shown by Berry and Sloan (1) in 1959, excellent capacitors can be made by the anodization of sputtered (or evaporated) tantalum films. These units, unlike capacitors made of sintered or bulk tantalum, exhibit breakdown characteristics that are largely independent of the sign of the applied voltage. The counterelectrodes are applied by vacuum evaporation, but very few metals have proved suitable in this connection. In fact, only gold has been regarded as really satisfactory, although good results have occasionally been reported with other metals, such as aluminum. It has also been widely observed that sputtered counterelectrodes generally yield lower performance than do evaporated counterelectrodes.

Experimental

The tantalum films used in these investigations were all deposited by cathodic sputtering. Films were deposited in an argon glow discharge (3000v at 1 ma/cm^2) at a pressure of 60μ onto microscope slides at the rate of about 10 Å/sec, generally for about 15 min, resulting in sheet resistivities of about 4 ohms/square.

Films were usually anodized to a formation voltage of 100v. A number of anodizing baths, all aqueous, were used in the early stages of the investigation, but no systematic differences were found among the resulting oxide films. For convenience, therefore, a standard bath consisting of a 1% Na_2SO_4 aqueous solution was later adopted. In general, anodization was carried out at room temperature, again for convenience. However, several anodizations in hot solution were also performed, primarily to see if the tantalum-oxide film would recrystallize. No such recrystallization was observed.

Nature of the counterelectrode.—As mentioned earlier, counterelectrodes of evaporated gold generally give better results than electrodes of other metals such as nickel, copper, chromium, etc., which would normally be preferred because of their better adhesion, both to the oxide itself and to the glass substrate. This investigation shows that this superiority of gold is due to the structure of gold films rather than to such things as metal-to-oxide work function, preferential alloying with impurities in the oxide, etc.

Langmuir (2) showed that atoms from a metal vapor condensing onto a substrate do not, in general, remain at the exact location at which they land; instead, they move over the surface with a finite mobility which is a function of, among other things, the substrate temperature. These mobile metal atoms have a limited lifetime on the substrate surface, after which they will return to the vapor phase. If, however, a metal atom meets up with another of its own species during its brief lifetime on the surface, the atom-pair that is formed has both a very much greater probability of remaining on the substrate and a much lower surface mobility. Thus, unless the deposition rate is very high and/or the substrate temperature very low, the film will not grow as a continuous sheet but as a series of discrete globules (nucleated by the original atom-pairs just mentioned) which eventually touch, after which the film grows "normally." Films of this sort, therefore, are in true contact with the surface in only a very limited number of places. On many substrates, gold films are known to be an extreme case of this.

This tendency toward the formation of an agglomerated film is usually determined by two factors, the free energy of formation of the metal oxide and the melting point of the metal. The larger the former and the higher the latter, the more continuous will be the film deposited under a given set of conditions.

If the anodic oxide film contains a number of relatively widely spaced cracks or microfissures, the probability of a gold film penetrating one or more of these fissures will be a great deal less than the probability of penetration by a high-melting-point metal having a large free energy of oxide formation, such as chromium or tantalum. This behavior, which is somewhat analogous to the phe-

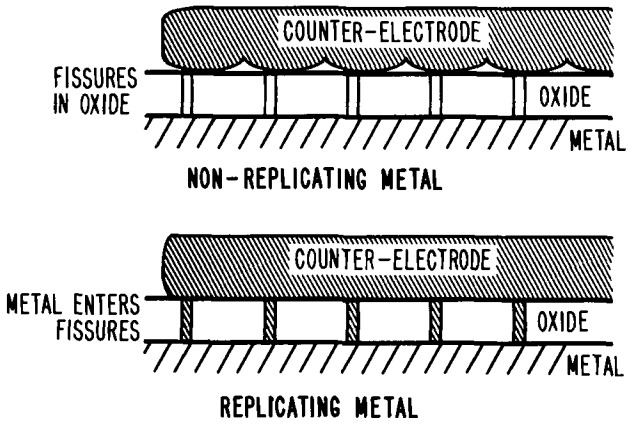

Fig. 1. Tendency for high-mobility (non replicating) metal to stay out of microfissures.

nomenon of liquids keeping out of the capillaries of a porous material that they do not wet, is illustrated diagramatically in Fig. 1.

If this notion is correct, we would expect to find that other metals that tend to agglomerate when deposited would also make good counterelectrodes. Note that this tendency to agglomerate also makes for poor adhesion, so that one would not normally have occasion to investigate these metals as possible counterelectrodes.

In addition, if (as postulated) occurrence of these cracks is relatively rare, the probability of any particular metal penetrating a crack should be a function of the counterelectrode area.

Results

Two criteria have been used for the evaluation of various metals as counterelectrodes. The first is the breakdown voltage, expressed as a percentage of the forming voltage and measured in the anodic direction (tantalum electrode positive). We define breakdown as occurring when the leakage current through the capacitor exceeds 1 ma/cm^2. The second criterion that we have used is the yield of capacitors. For this purpose, the leakage current is measured at 5% of the forming voltage, and units showing leakage currents in excess of 10 ma/cm^2 are defined as "shorts." In practice, leakage currents were found to be either very high or in the vicinity of 10^{-3} amp/cm^2.

Table I shows the range of breakdown voltages observed for a number of counterelectrode materials on tantalum oxide films formed to 100v. Occasional shorts occurred, and these have not been included. Results are given for large- and small-area electrodes. At least 100 capacitors were made of each metal.

The breakdown in the cathodic direction (tantalum electrode negative) was not systematically measured, but was periodically spot-checked. It was consistently found to be between 60 and 80% of the anodic breakdown voltage.

Several interesting facts may be seen in Table I. Perhaps the most noticeable are the much higher breakdown voltages measured for the small-area than for the large-area counterelectrodes in the case of low-mobility metals such as copper, chromium,

Table I. Breakdown voltages of anodized tantalum film capacitors for various counterelectrode materials

Metal	Per cent formation voltage Small electrodes, area, 1 × 10^{-3} cm^2	Large electrodes, area, 200 × 10^{-3} cm^2
Gold	95-98	80-90
Cadmium	95-98	60-65
Lead	80-95	45-55
Zinc	75-90	40-50
Tin	70-75	55-60
Silver	75-85	<0.1
Nickel	70-85	<0.1
Copper	80-90	<0.1
Chromium	60-75	<0.1
Aluminum	50-70	<0.1
Tantalum, sputtered	0-15	<0.1
Gold, sputtered	70-80	<0.1

etc., contrasted with the more nearly equal voltages measured for each electrode area in the case of high-mobility metals such as gold, cadmium, tin, etc. Gold, in particular, has breakdown voltages that are practically independent of electrode area. Although not shown in the table, on one occasion a cadmium unit was observed to have a breakdown voltage of 102% of the forming voltage. This is possible as a consequence of our definition of breakdown; *viz.*, the voltage at which the leakage current is 10^{-3} amp/cm^2. At the termination of anodization, the residual current is in the vicinity of 2 to 3 x 10^{-6} amp/cm^2; hence subsequent application of higher current density at the same temperature results in a greater voltage drop across the dielectric.

The two sets of electrodes deposited by means of sputtering also have the poorest characteristics. Two factors are believed to be responsible for this. First, other things being equal, sputtered thin films are known to be considerably more continuous than evaporated ones. This was shown by Ditchburn (3) and is evidenced, for example, by the better adhesion to glass of sputtered, as opposed to evaporated, films of copper or gold. The other factor believed responsible for the low quality of sputtered counterelectrodes is the very rapid heating of the substrate that occurs during sputtering. As we shall see presently, this would tend to increase both the size and number of the microfissures.

Table II shows the evaluation of various metals as counterelectrodes using the criterion of percent-

Table II. Yield of anodized tantalum film capacitors for various counterelectrode materials

Per cent yield of capacitors (100v)
Electrode area, 15 × 10^{-3} cm^2; capacitor "good" if leakage at 5v (+) <1.5 × 10^{-4} amp

Metal	% Yield
Gold	99
Cadmium	99
Lead	99
Zinc	99
Tin	55
Silver	73
Nickel	20
Copper	15
Chromium	95
Aluminum	97

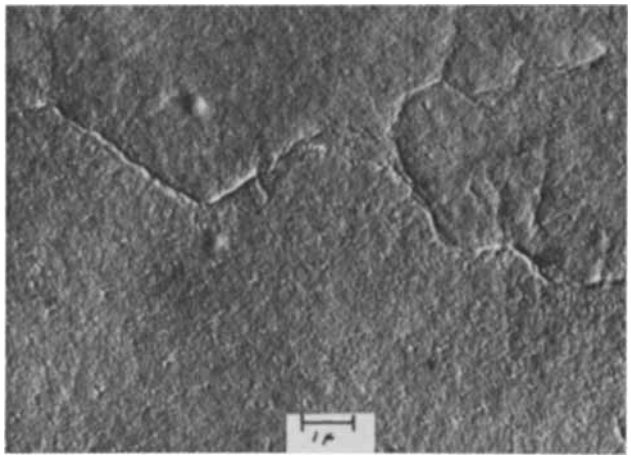

Fig. 2. Microfissure in tantalum oxide film (formed to 100v)

age yield. An electrode area intermediate in size between the two extremes used in Table I was deliberately chosen.

It is apparent from the data given in Table II that electrodes of this size are still too small to discriminate effectively between most counterelectrode materials. However, in two cases, nickel and copper, a significantly low yield was obtained, indicating that these metals are particularly unsuitable for counterelectrodes.

Direct Evidence for the Microfissures

Assuming that at least the widest and deepest of the microfissures should be detectable by electron microscopy, we may estimate from the data in Table II that the largest microfissures, that is, those that represent a complete break in the oxide, are, on the average, 200-300 mils apart. The probability of finding one in a random examination of the oxide surface is therefore quite slight. However, by restricting the electron microscope search to a small region within which one or more fissures are definitely known to be present, this probability may be greatly increased. This was accomplished by examining the oxide underneath a small gold dot which electrical measurements had shown to be a complete short, itself a very rare event. A typical electron micrograph obtained in this manner is shown in Fig. 2.

Origin of the Microfissures

A mechanism for the formation of fissures, such as the one shown in Fig. 2, has been proposed by Young (4). It will be recalled that the ratio of the molar volumes of tantalum pentoxide to tantalum is 2.3. During normal growth of the oxide film on a plane surface, this "lattice mismatch" does not produce any strain since the film is not constrained during its growth; *i.e.*, the ratio of the total thickness of oxide to the depth of the oxide below the metal surface will automatically adjust itself to 2.3. If, however, the surface of the tantalum, prior to anodization, is not perfectly smooth, strain due to lattice mismatch will occur as the oxide forms at a surface irregularity (see Fig. 3). As the oxide grows in thickness, the higher fields at the irregularity cause the oxide to form more rapidly there so that a smooth oxide surface is eventually formed.

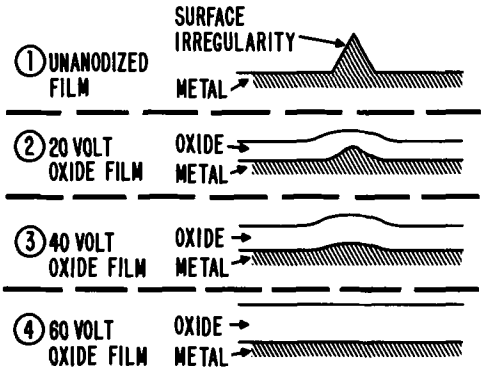

Fig. 3. Effect of anodizing irregular tantalum surface (voltages shown are only approximate).

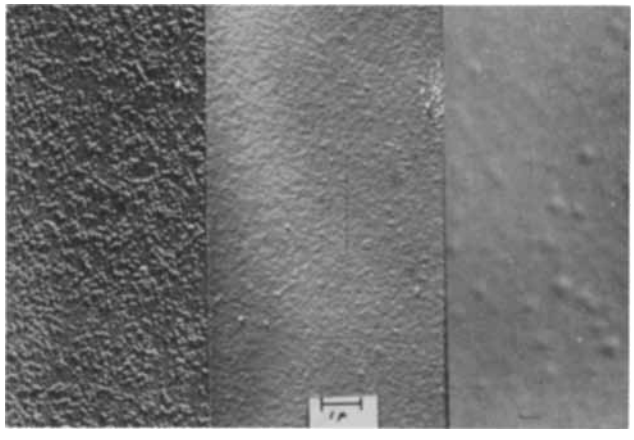

Fig. 4. Smoothing effect of anodization. Left to right, unanodized, as-sputtered film; oxide film formed to 30v; oxide film formed to 100v.

Thus, in the vicinity of the original irregularity, more material than was originally there will have been forced into a given volume, and the oxide in that vicinity will be under tensile stress. This stress can be relieved by cracking. This smoothing effect on an actual oxide surface is illustrated in Fig. 4. From left to right we see an unanodized tantalum-film surface, an oxide surface formed to 30v, and one formed to 100v.

One interesting consequence of this theory of fissure formation is that very thin oxide films should be free of cracks since sufficient strain will not have developed in the oxide to generate them. Experiments confirmed that this was indeed the case; the breakdown voltages of films formed (at room temperature) to 15v or less were no longer a function of the electrode area or of the tendency of the metal to agglomerate.

We believe that the roughness of the metal film cannot be completely eliminated simply by using a sufficiently smooth substrate. This is illustrated in Fig. 5, in which the surface of the tantalum film is compared with that of the clean substrate. Of course, if the substrate surface is itself rough to begin with, we would expect the number of microfissures subsequently occurring in the oxide film to be proportionately greater. The consequences of this, *viz.*, poor quality capacitors on rough substrates, are well-known.

In conclusion, we would like to indicate one method for reducing the incidence of the microfis-

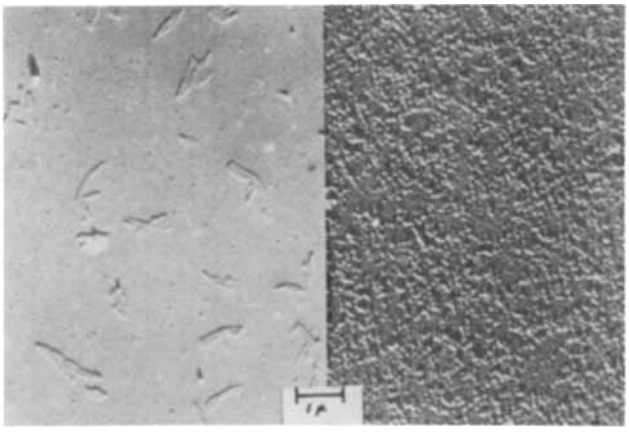

Fig. 5. Comparison of original substrate surface (left) and surface of tantalum film deposited on substrate (right).

sures. In the vicinity of room temperature, the linear coefficients of thermal expansion of tantalum and tantalum pentoxide are, respectively, 64.6 x 10^{-7}/°C and 5.5 x 10^{-7}/°C. If, therefore, the anodic oxide film is formed in a hot solution and then allowed to return to room temperature, it will be under compressive stress, thus relieving the tensile stress in the oxide. The use of solutions at 105°C, as described by Berry (1), is an example of this. Similarly, Ruscetta *et al.* (5) have shown that anodizing in hot solution often leads to superior oxide films. Even higher anodizing temperatures can be and have been achieved through use of pressure bombs. It should also be noted that films formed at room temperature will have their tensile stresses increased still further if subsequently heated. This has already been mentioned as one of the reasons why sputtered counterelectrodes are generally inferior to evaporated ones.

Summary

It has been shown that gross leakage currents in sputtered tantalum-film capacitors are due to the penetration of microfissures or cracks in the oxide film by the counterelectrode material. Some metals, such as gold, cadmium, etc., which do not follow the contours (on an atomic scale) of the surface on which they deposit, are much less likely to enter these microfissures and consequently make better counterelectrodes. The origin of the microfissures is believed to be the microroughness of the as-sputtered (unanodized) tantalum film; this leads to tensile stresses in and eventually cracking of the oxide film. By anodizing in hot solutions, it is possible to create compressive stresses which will partly compensate for this.

Acknowledgments

The authors wish to thank M. H. Whitehill for tantalum sputtering, K. L. Brown and E. E. Pacher for electrical measurements, and D. P. Cameron for the electron micrographs.

Manuscript received June 11, 1962. This paper was prepared for delivery before the Los Angeles Meeting, May 6-10, 1962.

Any discussion of this paper will appear in a Discussion Section to be published in the June 1963 JOURNAL.

REFERENCES

1. R. W. Berry and D. J. Sloan, *Proc. I.R.E.*, **47**, 1070 (1959).
2. I. Langmuir, *Proc. Nat. Acad. Sci.*, **3**, 141 (1917).
3. R. W. Ditchburn, *Proc. Royal Soc.*, **141A**, 169 (1933).
4. L. Young, *Acta Met.*, **5**, 711 (1957).
5. Ruscetta *et al.*, U. S. Pat, 2, 739,110.

Optical Measurements on ZnS:Cu Produced by Neutron Irradiation of ZnS

R. M. Potter, M. Aven,[1] and J. Kastner[2]

Lighting Research and Development Operation, General Electric Company, Cleveland, Ohio

ABSTRACT

ZnS powder, irradiated in a high density thermal neutron flux, was partly converted to radioactive Zn-65, Zn-69, and S-35. These radioisotopes decay to Cu-65, Ga-69, and Cl-35, respectively. One week after removal from the nuclear reactor the sample was fired at 900°C to anneal out radiation damage occurring in the reactor. The brightness and spectral distribution under 3650Å excitation and the diffuse reflectance spectra of the annealed sample were monitored during a period of 600 days. The principal results are interpreted in terms of an increasing concentration of uncompensated copper centers produced by the decay of Zn-65.

The common method of preparing zinc sulfide phosphors is to mix zinc sulfide with the necessary amount of activators and coactivators and to fire the mixture at temperatures above approximately 800°C. When equimolar amounts of activators and coactivators are added one expects a fully compensated material, *i.e.*, one which contains no unpaired electrons. Bowers and Melamed (1) showed, however, that even when activators alone (Cu) or coactivators alone (Cl) are added to zinc sulfide, the material comes out of the firing fully compensated. Evidently it is energetically favorable at the firing temperature to produce physical "self-activator" or "self-coactivator" species in the form of vacancies

[1] Present address: Research Laboratory, General Electric Company, Schenectady, N. Y.

[2] Present address: Argonne National Laboratories, Lamont, Ill.

or interstitials which compensate the added chemical coactivators and activators. For this reason there exists very little information about the optical properties of uncompensated zinc sulfide.[3]

The objective of the present work was to prepare uncompensated copper-activated zinc sulfide by introducing the activator through the decay of a radioactive isotope of zinc, Zn*-65, which becomes Cu-65, and to study the optical properties of the material as a function of the concentration of the newly formed Cu-65. This method of introducing copper was also found useful in another connection. In a series of publications Prener and Williams (7-9) have advanced a theory which contends that a definite spacial relationship must exist between activators and coactivators in zinc sulfide phosphors in order for them to function as efficient recombination centers. According to this theory, only activator atoms with a coactivator atom at a second, third, etc., to approximately 10th or 15th nearest neighbor position are active in luminescence recombination. First nearest neighbors are excluded because too great an overlapping of wave functions causes the activator and coactivator levels to recede to within a few hundredths of an electron volt from the valence and conduction bands, respectively. Too distant neighbors are excluded because of insufficient overlap of wave functions which results in a low transition probability.

In phosphors prepared by conventional techniques, the distribution of distances between activators and coactivators is determined by the balance between their mutual coulombic attraction and the thermal randomizing effect. At a relatively high firing temperature, say 1200°C, the thermal agitation is probably strong enough to keep singly charged activators and coactivators randomly distributed. As the phosphor is cooled to room temperature the activators and coactivators start associating due to their mutual attraction. The degree of completion which this process will attain depends on how effectively the necessary diffusion processes can take place. As a result, the phosphor will contain activators and coactivators in a wide variety of associations. It is therefore difficult to verify the concepts of the ion association theory by working with conventional phosphors. The degree of association can be controlled to a certain extent by varying the concentration of activators and coactivators and by using thermal treatments like annealing and quenching. A more effective way to obtain at least one extreme type of association, namely a random distribution, is to introduce either the activator or the coactivator through the process of radioactive decay of one of the base lattice components.

Such a method was used for the first time by Prener and Williams (8). They irradiated a sample of zinc oxide with a flux of neutrons which produced about 50 ppm[4] of Zn*-65. They subsequently converted the zinc oxide to zinc sulfide by firing in hydrogen sulfide mixed with some hydrogen chloride. During the ensuing two years, as the Zn*-65 was decaying to Cu-65, they monitored the green-to-blue luminescence emission ratio of their sample and found that it stayed constant within approximately 10%. From this they concluded that the newly formed copper, appearing at random sites with respect to the chlorine coactivators, did not produce luminescence centers.

In the present work copper was introduced into zinc sulfide also through the radioactive decay of Zn*-65. The preparation of the sample and the optical measurements were, however, different from those carried out by Prener and Williams. It will be evident from the discussion below that this made it possible to obtain new information bearing on the problem of ion association and the position of the level introduced by substitutional copper into zinc sulfide.

Experimental

A 0.12g sample of luminescence grade zinc sulfide was fired at 900°C in purified hydrogen sulfide. It contained ~2 ppm copper, ~2 ppm combined iron, cobalt, and nickel, and a very small concentration of halogens. It showed practically no luminescence response under 3650Å excitation at room temperature. The sample was placed in a spectroscopically pure graphite crucible which was inserted into a quartz tube. Hydrogen sulfide was passed through the quartz tube for 1 hr at 1000°C, and the tube was sealed off while hot. The sealed sample was then irradiated for 15 days at the Idaho Falls Materials Testing Reactor. About four days after removal from the pile, the sample was refired for 3 hr at 900°C, removed from the graphite crucible, and placed in a brass sample container provided with a "nonbrowning"[5] quartz window. The sample container could be attached to a slide which fit into a track fastened to the spectrometer used for optical measurements. The sample was removed from the brass container 326 days after the firing and divided between two quartz capillaries. One was used for the annealing experiments to be described later, and the other was used for the continuation of the luminescence response versus time measurements.

Optical measurements were performed with a Perkin-Elmer Model 99 Spectrophotometer. As the experiment was originally conceived, it was desired to measure the ratio of the luminescence emission in the green to that in the blue band as a function of time. To obviate measuring the complete spectrum each time, most luminescence intensity measurements were made only at two energies: in the blue at 2.82 ev and in the green at 2.44 ev. The actual peak intensities of the resolved bands were calculated from these data by a formula derived from comparing complete resolved[6] emission spectra measured initially and at 235 days with simultaneously taken intensity measurements at 2.82 ev and 2.44 ev. Complete spectra were also obtained at 378, 413, and 604 days.

[3] Since this experiment was started a number of publications have appeared in literature describing optical properties of materials which probably contain uncoactivated copper (2-7).

[4] Throughout this paper ppm (parts per million) will signify atom fraction × 10^6.

[5] Supplied by W. A. Graff of Glass Technology Laboratory, General Electric Lamp Glass Department, Cleveland, Ohio, this quartz was designed to show minimal discoloration under high energy irradiation.

[6] See section: Fluorescence Spectra.

In order to assure approximately constant excitation intensity the ultraviolet source (an AH4 mercury lamp mounted in a microscope illuminator housing, with a 7-37 Corning filter) was calibrated before each run. This was accomplished by precisely reproducing the settings of the photomultiplier voltage, spectrometer slits and wavelength (3650Å), and amplifier gain. The intensity of the source was then adjusted so as always to obtain the same recorder deflection when the 3650Å was diffusely reflected from a placque of powdered magnesium carbonate mounted on the same slide as the radioactive sample. To afford a further check, the brightness of a standard green ZnS:Cu,Al phosphor held in a brass container identical with the one holding the radioactive sample was measured before each reading of the response of the radioactive sample. Due to these precautions it is believed that the green luminescence intensities obtained during the first 326 days are precise to ±1%. The reproduction of these conditions was considerably more difficult after the sample was transferred to the quartz capillary. Therefore the accuracy of the measurements at times longer than 326 days was approximately ±5%. The 3650Å excitation intensity during all luminescence measurements was of the order of 5×10^{13} photons/cm² sec.

Diffuse reflectance spectra were obtained by dividing the reflectance of the sample by the reflectance of the standard at each spectral energy. Magnesium oxide was used as standard in the visible and ZnS:Cu,Al phosphor in the infrared.

Nuclear Reactions

When a compound such as zinc sulfide is placed in a nuclear reactor and irradiated with slow and fast neutrons, gamma rays, etc., certain reactions take place, introducing several types of defects. As noted above, the sample of zinc sulfide powder was refired after neutron irradiation, for 3 hr at 900°C. As Smith and Turkevich (10) were able to repair neutron damage to zinc sulfide by heating for only a few minutes at 900°C, it can be safely assumed that all the annealable damage, *e.g.*, displaced atoms, existing in the present sample after irradiation, was repaired by this annealing. The only nuclear reactions to be considered therefore are those which occur or contribute to effects in the period since the firing.

Of the postfiring defects, those of major interest are impurity atoms and displaced atoms. The creation of impurity atoms as a result of radioactive decay of such nuclides as Zn*-65, S*-35, etc., is the basis of the whole experiment. Displaced atoms are produced when a nucleus ejects mass and/or electromagnetic radiation and the recoil energy is sufficient to cause permanent displacement. Thus a very pertinent question is whether, for example, the impurity daughter atom, Cu-65, ends up in an interstitial or in a substitutional position. This problem will be discussed later. The identities, the abundance, and the decay rates of the produced isotopes will be detailed below.

The zinc sulfide sample used in this study was irradiated for 15 days in a position where the thermal neutron flux was 1.3×10^{14} (±20%) neutrons per cm² sec associated with a fast neutron flux of about 1.5×10^{13} neutrons/cm² sec. After capturing a neutron the target nucleus forms a different atomic species which in turn transforms to new products by radioactive decay. The rates of formation of these new products and the resultant concentration of new elements can be calculated from the well-known laws of radioactive decay. This was done for the present sample of zinc sulfide which was composed of several isotopes of zinc and sulfur each with known relative abundances. Each of these isotopes can absorb neutrons to a certain degree, with resonance absorption occurring for neutrons of a particular energy. The most important nuclear reactions from the point of view of the described experiment are those involving the transmutations listed in Table I.

Table I. Neutron reactions with zinc sulfide

Target, % abundance	Product nuclide	Half-life	Daughter
Zn-64 (49%)	→ Zn*-65	245 days	Cu-65
	→ Cu*-64	12.8 hours	Ni-64
Zn-68 (19%)	→ Zn*-69	14 hours	Ga-69
S-32 (95%)	→ P*-32	14.3 days	S-32
S-33 (0.8%)	→ P*-33	24.4 days	S-33
S-34 (4.2%)	→ S*-35	87.1 days	Cl-35

Of the radioisotopes listed in Table I, Cu*-64, P*-32, and P*-33 are present in sufficiently low concentrations, ~0.6 ppm, ~1 ppm, and ~0.01 ppm, respectively, to be neglected. The fate of the remaining radioisotopes, Zn*-65, Zn*-69, and S*-35, is summarized in the chart in Fig. 1, which also illustrates the complete course of the experiment.

As shown, the irradiation produced approximately 49 ppm Zn*-65, 37 ppm Zn*-69, and 2 ppm S*-35. While in the reactor and on the way from the reactor to this laboratory all the 37 ppm of Zn*-69 had decayed to Ga-69, and 2 ppm of Zn*-65 had decayed to Cu-65. In the ensuing firing process the 2 ppm of Cu-65 presumably was coactivated by an equivalent amount of Ga-69 and formed 2 ppm of "ordinary" green copper centers. The remaining 35 ppm of Ga-69 formed self-activated blue centers ($V_{Zn}Ga^-$ . . Ga^+),[7] in a concentration corresponding to its (unknown) equilibrium solubility at or near the firing temperature, the excess diffusing out of the zinc sulfide lattice.

The last box in the chart shows the census after a 600-day decay period. Practically all S*-35 had then decayed to Cl-35, and 39 additional ppm of Zn*-65 had decayed to Cu-65. Since chlorine acts as a donor in zinc sulfide, and copper as an acceptor, 2 ppm of the copper formed in this period will accept electrons from the 2 ppm of newly formed chlorine, leaving 37 ppm of copper acceptor states empty. The effect of these transmutations on the optical properties of the sample will be described below.

Fluorescence Spectra

The room temperature emission spectra of the sample under 3650Å excitation shortly after the

[7] The self-activated blue center will be represented by the model proposed by Prener and Weil (11), *i.e.*, $(V_{Zn}Ga)^-$ . . Ga^+. This model indicates that the activator is a zinc vacancy in close association with a gallium, and the coactivator is another gallium two or more lattice distances apart.

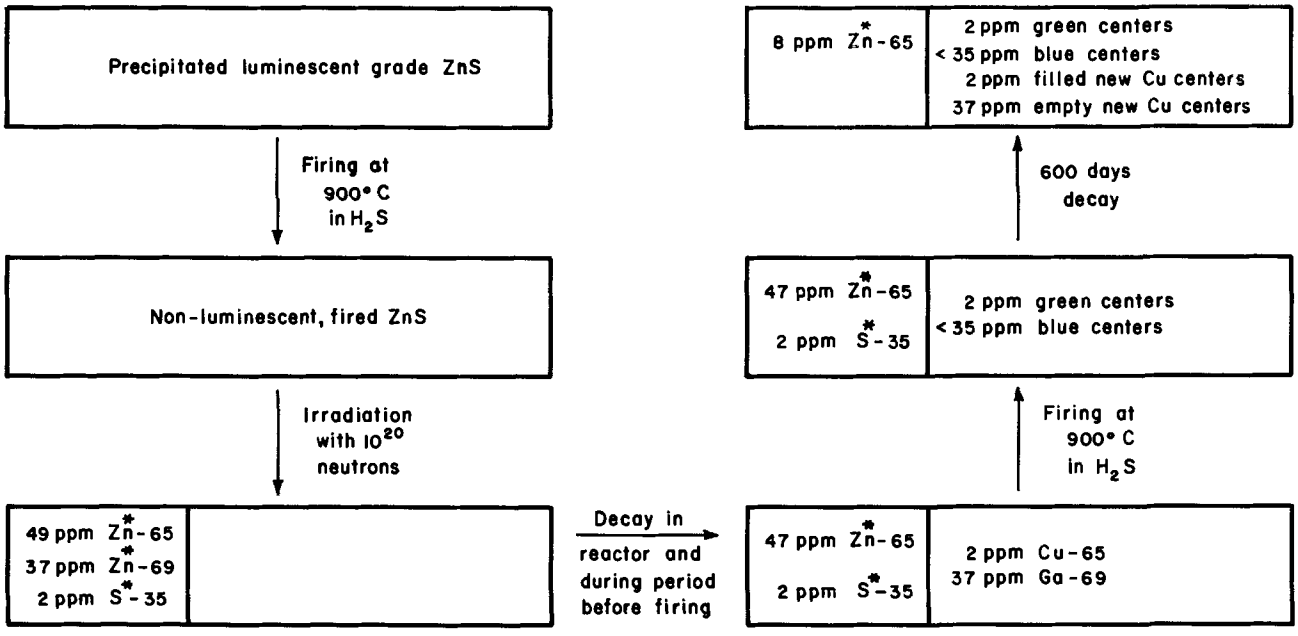

Fig. 1. Sequence of operations in preparing radioactivated zinc sulfide (the radioactive species appear in the left-hand side of the divided boxes).

900°C annealing and at 378 days are shown in Fig. 2 and 3, respectively. These spectra, plotted as energy emitted per unit photon energy interval, were resolved into three approximately Gaussian subbands peaking at 2.72 ev, 2.36 ev, and about 2.06 ev. The first two bands are identified as the "self-activated" blue band, due to zinc vacancies promoted by gallium, and the "copper green" band. The yellow band is probably identical with the one described by Apple and Williams (12) as due to copper-gallium associated pairs.

The green-to-blue ratio, expressed in terms of photons corresponding to the resolved green and blue bands, is plotted in Fig. 4. The ratio increased by a factor of two in the first 180 days and thereafter decreased asymptotically to about 60% of the initial value. The figure also shows the trend of behavior of the green-to-yellow and yellow-to-blue photon emission ratios. The dashed parts of the curves is an interpolation between the initial and the 235 day points.

The dependence of the ratio of emission in the green to that in the blue on intensity of 3650Å excitation was measured initially and at 182 days. The results are shown in Fig. 5. It can be seen that initially the green-to-blue ratio of the radioactive

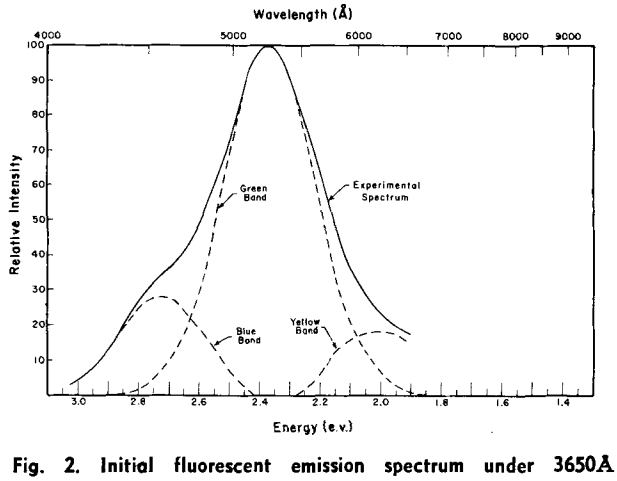

Fig. 2. Initial fluorescent emission spectrum under 3650Å excitation.

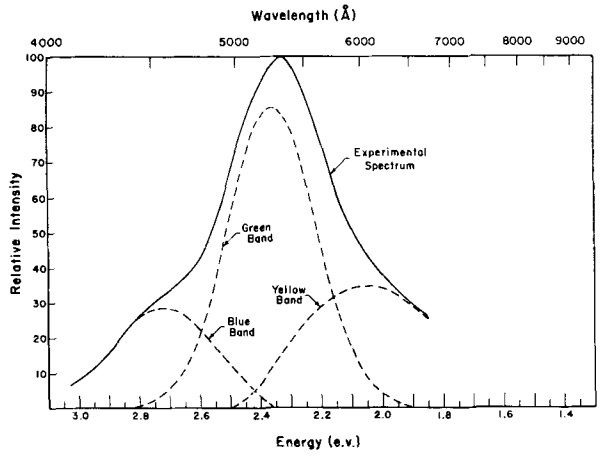

Fig. 3. Fluorescent emission spectrum under 3650Å excitation at 378 days.

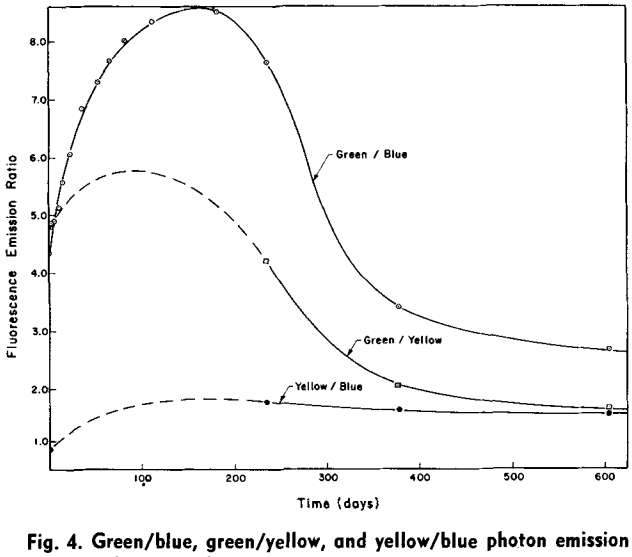

Fig. 4. Green/blue, green/yellow, and yellow/blue photon emission ratios as a function of time.

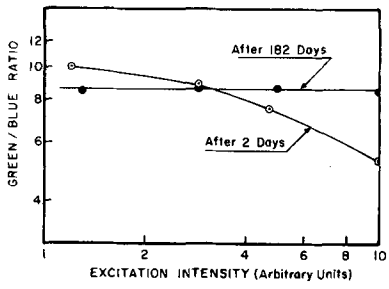

Fig. 5. Green/blue emission ratios of neutron-irradiated ZnS as a function of excitation intensity.

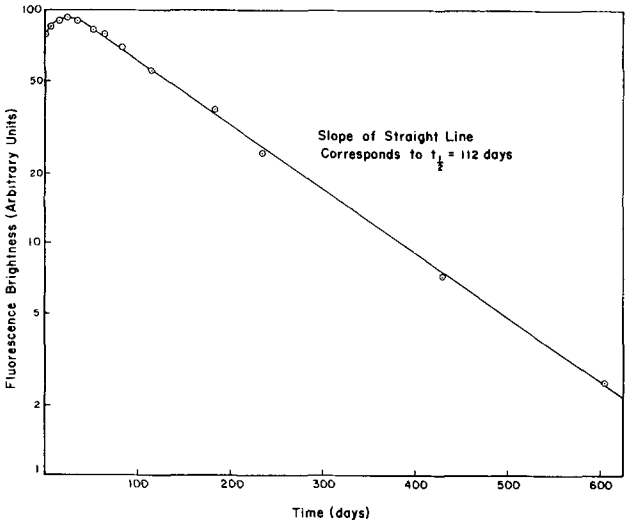

Fig. 6. Brightness of green fluorescence as a function of time

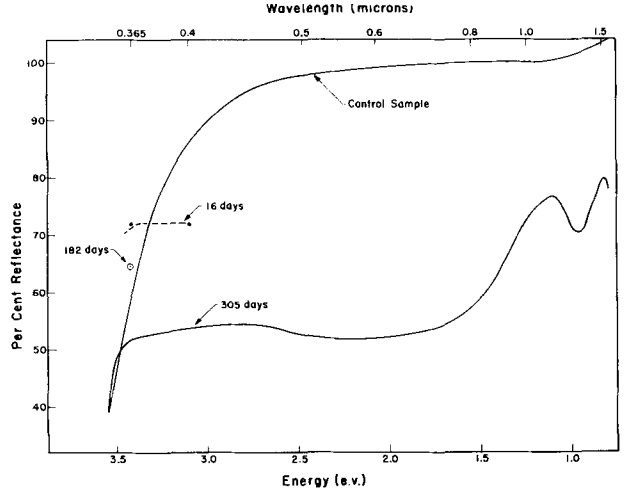

Fig. 7. Diffuse reflectance of the radioactivated sample and the the control sample.

sample showed a fairly strong dependence on the excitation intensity; at 182 days, however, the green-to-blue ratio was almost independent of the excitation intensity.

The green luminescence brightness of the sample increased slightly initially and thereafter decreased exponentially without limit. Figure 6 shows a semilog plot of the relative intensity at 2.44 ev as a function of time.

Diffuse Reflectance and Infrared Fluorescence

The diffuse reflectance spectrum of the sample was measured at 305 days. In Fig. 7 the spectrum of the sample is shown along with that of a control sample containing about the same concentration of impurities as the radioactive sample did initially. Two absorption bands are present, a broad one extending from about 1.2 ev to the zinc sulfide fundamental absorption edge and a narrow one peaking at 0.95 ev. Diffuse reflectance readings at 3.13 ev and 3.42 ev were taken at 16 days, and at 3.42 ev at 182 days. These readings in conjunction with the complete diffuse reflectance spectra of the control and of the radioactive sample at 305 days show that the strength of the absorption band extending from 1.2 ev to the fundamental absorption edge increased with increasing concentration of Cu-65.

It was possible to detect infrared fluorescence in the sample by exciting with visible or near infrared light. The fluorescence appeared to peak in the energy range found by Browne (2) in zinc sulfide which had been fired in sulfur vapor and which presumably contained uncoactivated copper, and by Halsted *et al.* (4) and Potter and Aven (5) for ZnS:Cu fired in sulfur vapor to promote incorporation of copper without coactivation.

Annealing Experiments

It was suspected that part of the Cu-65 produced by decay of Zn*-65 might be ejected into interstitial sites because of the 10-16 ev recoil energy of the nuclear reaction. Two experiments designed to give evidence of displaced copper were carried out. In the first experiment (performed at 326 days) part of the sample was placed in a quartz tube, and annealed at 200°C. The fluorescence in the blue and green (2.82 ev and 2.44 ev) was measured after each heating period. The intensity in both the blue and green bands increased with annealing, but the blue showed a greater increase, which led to a decrease in the green-to-blue ratio. A similar annealing experiment was done on the same sample at 413 days. Again both the green and the blue luminescence intensity increased after annealing and the green-to-blue ratio decreased. In a series of control experiments it was found that copper could diffuse into a ZnS:Ga powder phosphor (*i.e.*, one containing zinc vacancies) in 5 hr at 200°C, and change the luminescence response from blue to green. At this temperature, the copper probably diffuses by an interstitial mechanism. There was no change, however, in the luminescence response of a green-emitting ZnS:Cu,Ga phosphor (which presumably had all copper and gallium in substitutional sites) when it was annealed at 200°C for the same period of time.

In the second experiment, a sample of neutron-irradiated zinc sulfide was obtained from Dr. J. S. Prener which had decayed for about 4 years. The diffuse reflectance spectrum of this sample was measured before and after a 5-hr annealing at 200°C. The spectrum was qualitatively similar to that obtained on the present sample (see Fig. 1) and showed no significant change after annealing.

Discussion

The purpose of this work was (i) to prepare and measure certain optical properties of zinc sulfide containing "uncoactivated" substitutional copper;

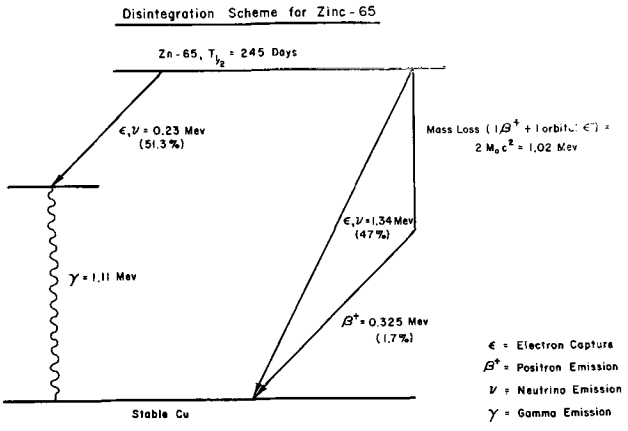

Fig. 8. Disintegration scheme of Zn-65

and (ii) to obtain evidence on the question of whether copper green centers must have coactivators associated with them in order to be luminescence-active. The first purpose was largely accomplished. The evidence obtained from the experiment, however, does not allow an unambiguous answer to the question in the second purpose.

For the first purpose, it was necessary to show that most of the Cu-65 produced by decay of Zn*-65 remained in substitutional sites and that the properties measured were due to this majority of the copper, and not to the minority which was ejected into metastable sites.

Zn*-65 has a rather complex decay scheme as shown in Fig. 8. Forty-seven per cent of the disintegrations occur by pure electron capture where the complete excess energy is removed by the ejection of a neutrino. The recoil energy may be computed to a good approximation by treating the neutrino as a photon (13). Thus the recoil energy is given by

$$E_r = E^2/2Mc^2 = 15 \text{ ev}$$

Similarly, for the 51.3% of the disintegrations giving rise to the 1.1 Mev gamma ray, the important recoil energy is approximately 10 ev.

To evaluate the recoil energy for the positron emission the relativistic relation should be used (14).

$$E_r = E(E + 2mc^2)/2Mc^2$$

For $E = 0.325$ Mev this yields only about 3.5 ev.

Whether any of these recoil energy values are sufficient to cause displacement will depend on the threshold energy for such a process, E_d. This parameter has been studied theoretically and experimentally for a number of materials (15). Unfortunately, there are few specific references to zinc sulfide, and so one can only make a reasonable estimate based on materials of similar structure. Seitz and Koehler (16) derived the value of $E_d = 25$ ev for tightly bound solids on theoretical grounds. This value is borne out in the case of germanium as most of the experiments yielded displacement energies of about 30 ev (17, 18) although special types of displacements requiring lower energies could be produced with a small probability (19, 20). Kohn (21) calculated a value for germanium of $E_d = 10$ ev, but suggests that the interstitials arising this way would be very unstable and would recombine spontaneously. This type of recombination probably accounts for the annealing which is stated to occur at room temperature (22).

It is admittedly difficult to extrapolate from germanium to zinc sulfide. There is a clue, fortunately, in a report by Czyzak *et al.* (23) on a radiation damage study of single crystals of zinc sulfide, cadmium sulfide, germanium, and silicon. They used a 2 Mev electron beam of about 1 μa and could observe no significant damage in either cadmium or zinc sulfide whereas the germanium and silicon crystals were badly damaged. The average energy transferred to a zinc or germanium atom struck by a 2 Mev electron is of the order of 100 ev, and thus one would expect that the germanium would be damaged. On the other hand, the implication from these data is that the threshold energy for displacement of zinc in zinc sulfide is greater than 100 ev, and therefore neither the emitted gamma-ray nor the neutrino should displace the nucleus by recoil. Experiments have been carried out in this laboratory in which zinc sulfide single crystals have been irradiated with beta-rays of a maximum energy of 2 Mev with no significant changes in the transmission spectrum.

There is one piece of information which seems to be in disagreement with these observations. The United States Radium Corporation reports (24), without amplification, that cadmium sulfide is damaged by electrons of energy greater than 0.23 Mev. As no details are available one must explain the discrepancy by assuming either that the U.S.R.C. method of observing radiation damage was much more sensitive or that the much greater specific ionization of 0.23 Mev electrons compared to the more penetrating 2 Mev electrons can account for the difference in results. The possibility of displacement by electronic excitation can be eliminated in the case of the emission of a gamma ray or a neutrino because the latter are not charged particles. The threshold energy in cadmium sulfide corresponding to 0.23 Mev electrons is about 19 ev. Thus if one assumes that sulfur displacement would show up as radiation damage and extrapolates to zinc sulfide (by considering E_d to be roughly proportional to the heat of formation) one arrives at a value for displacement of sulfur in zinc sulfide of about 27 ev. This is still greater than the maximum recoil energy for any disintegration of Zn*-65.

On the basis of the evidence available at present, therefore, it is likely that the majority of the copper atoms resulting from decay of Zn*-65 in ZnS will remain in substitutional positions.

A similar conclusion can be reached by analyzing the changes in optical properties of the present as well as the Prener-Williams sample during annealing. The change in the green-to-blue ratio of the radioactive sample during annealing at 200°C is definitely suggestive of rearrangements involving interstitial migration, as this temperature is too low for appreciable substitutional or vacancy diffusion. The conclusion is supported by the control experiments mentioned earlier. The 900°C firing after neu-

tron irradiation should have stabilized the phosphor structure with respect to imperfections then present, so that initially the sample should not have contained any metastable interstitials. Therefore, it follows that the interstitials must have been formed during the ensuing radioactive decay of Zn*-65. As this isotope is a part of the zinc sulfide base lattice, the Cu-65 formed from it must also be substitutional, unless it is ejected by recoil. Hence one is forced to conclude that at least a part of the Zn*-65 was ejected from its substitutional position while decaying to Cu-65. It is likely that the interstitial copper exists as Cu_i^+, the compensating negative charge residing on the lattice position from which it was ejected. Such Cu_i^+ would be coulombically attracted to any negative charges present in the crystal. Besides the lattice position from which the Cu_i^+ was ejected, such negative charges are located on initially present coactivated (substitutional) copper centers and on gallium-coactivated zinc vacancies (created during the firing). It is impossible to be certain to which of these sites the Cu_i^+ was migrating. Because of this uncertainty and because of the complicated nature of the equilibrium involved, the blue-to-green ratio changes cannot be used for a quantitative estimate of the fraction of ejected copper.

However, one can obtain a rough estimate of the maximum fraction of ejected Cu-65 from the annealing experiment performed on the Prener-Williams sample. It will be recalled that, within experimental error, no change in the strength of the absorption bands was detected. The probable error in this measurement was 0-3%. Using the approximate expression $n \propto (1-R)^2/R$ for the relation between the diffuse reflectance R and the number of absorbing centers n, gives 0 to 0.23 as the fraction of ejected Cu-65 which could go undetected due to experimental uncertainty. It should be noted that whatever the true value for the fraction of ejected copper, it is clear from the constancy of diffuse reflectance that the copper remaining in substitutional sites was responsible for the observed absorption.

Diffuse Reflectance Spectrum

The significant conclusion of the preceding section was that the appearance of uncoactivated substitutional copper at the Zn sites was accompanied by the appearance of absorption bands in the diffuse reflectance spectrum. The same absorption bands have also been found in conventionally prepared zinc and cadmium sulfide by many workers (25-29) as stimulation or quenching bands in measurements of fluorescence or photoconductivity. In these cases, simultaneous or previous excitation with light of energy near that necessary to excite across the band gap was necessary. These bands have also been found in ZnS:Cu relatively free of coactivator in infrared excitation (2) and in photoconduction (3) without simultaneous or previous excitation of higher energy. Some of these workers ascribed these bands to electron transitions to the conduction band (25, 29) and some to hole transitions to the valence band (2, 3, 26-28). In the present work, the latter explanation is strongly supported.

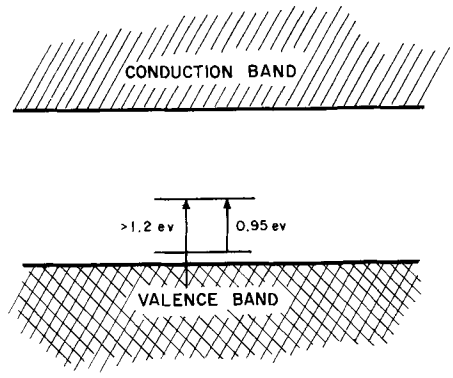

Fig. 9. Energy level diagram for copper in zinc sulfide

In the first place, because the same bands are found in conventionally prepared ZnS:Cu and in the radioactivated ZnS:Cu, it can be concluded that the copper is the same environment in both cases. Since in this work it has been shown that the copper responsible for the absorption bands in radioactivated ZnS:Cu is substitutional, copper must also be at substitutional sites in conventionally prepared ZnS:Cu.

The transitions responsible for the absorption bands are indicated in Fig. 9. According to this model, in the radioactivated sample, the absorption in the broad band corresponds to exciting an electron from the valence band into an empty level about 1.2 ev[8] above the valence band. The 0.95 ev band is ascribed to excitation of an electron from a state about 0.25 ev from the top of the valence band into the empty level. This assignment is based on the observation that infrared quenching or stimulation in fully coactivated phosphors takes place at room temperature by absorption of light in this band. At lower temperatures, where the hole ionization from the lower level into the valence band is negligible, only absorption in the broad band is effective (27).

In conventionally prepared, coactivated phosphors, four models are possible to account for the broad stimulation or quenching band: a discrete level about 1.2 ev above the valence band or 1.2 ev below the conduction band, with or without an electron in it. The models involving an empty level near the valence band or a filled level near the conduction band can be ruled out because, for these models, absorption would be observed in the broad band without simultaneous short wavelength excitation. The choice between the remaining two models is made on the following basis: If the model with a filled level near the valence band is correct for fully coactivated ZnS:Cu, then in radioactivated (uncoactivated) ZnS:Cu, with one less electron available for each copper, the level would be empty, and the observed absorption is readily understood. If the model with an empty level near the conduction band (for fully coactivated ZnS:Cu) is correct, it is difficult to understand how in the radioactivated ZnS:Cu, with one less electron for each copper, this level could have been filled by an electron. Thus the location of

[8] 1.2 ev is the approximate minimum energy for this transition at room temperature. This figure is used because the absorption band does not show a clear maximum. Quenching and stimulation spectra show a maximum at about 1.65 ev.

the level about 1.2 ev from the top of the valence band can be made without any other supporting evidence, such as electrical measurements demonstrating hole conduction (5, 30).

Kinetics of Luminescence

The second purpose of this work, to obtain evidence on the question of whether copper green centers must have associated coactivators in order to be luminescence-active, was not fulfilled unambiguously. The experimental results pertaining to this aspect are that: (i) the over-all brightness, after a brief rise, decayed exponentially without limit, (ii) the green-to-blue and probably green-to-yellow ratio went through a maximum and then tended asymptotically to a value below the initial values, and (iii) the green-to-blue ratio, initially sensitive to excitation intensity, became independent of it later.

The first result can be partially explained by (*a*) the increasing absorption of 3650Å exciting light and fluorescence emission in the broad absorption band due to uncompensated copper and (*b*) possible killer center formation associated with migration of ejected copper.

Result (iii) can be understood as a change from the kinetics of a compensated phosphor to a p-type phosphor. The initial dependence of green-to-blue ratio on excitation intensity is predicted by the Schön-Klasens (31, 32) model for compensated phosphors. As the concentration of uncompensated copper increases, the rate of thermal ionization of holes from copper centers increases and eventually exceeds the excitation intensity. The distribution of holes between green and blue centers (and therefore the green-to-blue ratio) is then determined by thermal equilibrium and is independent of excitation intensity.

It should be possible to explain result (ii) by setting up a number of models for the steady-state kinetics of luminescence. Unfortunately, any realistic model would have to be rather complicated because of the presence of three emitting states and probably a killer state. Also the 3650Å exciting light can be absorbed strongly at both filled and unfilled Cu centers.

An attempt was made to fit the observed data on blue-to-green ratio with two models which considered only blue and green emitting states and a single trapping level. In the first model, it was assumed that all substitutional Cu centers were active in luminescence recombination; in the second, that only Cu centers with coactivator centers within a certain distance were active. It turned out that neither model could be made to fit the data with reasonable assumptions for the kinetic constants, but the second model looked more promising than the first. It is felt that this slightly better agreement of the experimental data with the associated center model is not sufficiently clear-cut to be regarded as evidence in favor of one model or the other. In the opinion of the authors, further work on kinetic models is not justified by the present experimental data.

Comparison to the Prener-Williams Experiment

It was mentioned in the preceding text that Prener and Williams (8) had performed an experiment which also involved the decay of Zn^*-65 to Cu-65 in zinc sulfide. They employed a different preparative technique, and their results were different in some respects. The green-to-blue ratio *vs.* time relationship of their sample exhibited no initial strong increase and no subsequent drop. The fluorescent spectrum after approximately four years of decay was very nearly identical with the initial spectrum. The luminescence brightness-time relationship of the sample was not measured, which makes it impossible to compare this feature of the two experiments. However, diffuse reflectance measurements on the Prener-Williams sample (which they kindly made available to us) revealed the presence of the same absorption bands as found in our sample.

Visual inspection under ultraviolet light of the Prener-Williams sample showed bright green particles scattered throughout a nonluminous background (the sample was thoroughly mixed in the course of transfer from the original container to the quartz tube used for examination). A rough particle count under the microscope indicated that the green particles comprised about 2-3% of the total. On the basis of this observation it is suggested that the Prener-Williams sample was not homogeneous, but consisted of two different kinds of materials. The bulk, which after four years of decay became practically nonluminescent, corresponds closely to this laboratory's sample. The latter exhibited an approximately tenfold decrease in brightness in one year. Based on the logarithmic relationship between brightness and time, four years of decay should then have reduced the brightness of the Prener-Williams sample to approximately 10^{-4} of the initial, accounting for the experimentally observed practically nonluminescent appearance of the bulk of their sample. By the same reasoning, since the loss of brightness was interpreted at least partly on the basis of the appearance of empty copper levels near the valence band, this part of the sample ought to have exhibited more prominent infrared absorption bands than this laboratory's sample, as it in fact did. The smaller part of the Prener-Williams sample had different properties. Its brightness had not decayed, and its most recently measured spectral response corresponded to the initial spectral response of the whole sample.

This is not the place to speculate as to what the cause of the heterogeneity of the sample could be. The above arguments do, however, present one way to explain the different behavior of the Prener-Williams and this laboratory's sample. The small portion of the strongly luminescent green particles can account for the constancy of the green-to-blue ratio of the whole sample between, say, the end of the first year of decay (*i.e.*, when the brightness of the bulk was down by a factor of 10) and now. Not knowing the relative brightness of the two components of the sample, it is hard to say whether this also could account for the constancy of the green-to-blue ratio during the first year of decay. It is

conceivable that the presence of a small amount of a bright component, which stayed constant in its spectral distribution, would partly mask the changes occurring in a less bright but more abundant component. In fact, a closer look at Fig. 2 on page 343 of the quoted reference (8) will reveal that this curve may have a weak maximum somewhere between the 20th and 50th day of decay.

Manuscript received March 16, 1962; revised manuscript received July 17, 1962. This paper was prepared for delivery before the New York Meeting, April 27-May 1, 1958.

Any discussion of this paper will appear in a Discussion Section to be published in the June 1963 JOURNAL.

REFERENCES

1. R. Bowers and N. T. Melamed, *Phys. Rev.*, **99**, 1781 (1955).
2. P. F. Browne, *J. Electronics*, **2**, 1 (1956-57).
3. F. G. Ullman and J. F. Dropkin, Enlarged Abstracts Electrochemical Society, New York, 1958, p. 66.
4. R. E. Halsted, E. F. Apple, and J. S. Prener, *Phys. Rev. Letters*, **1**, 134 (1958).
5. R. M. Potter and M. Aven, *Bull. Am. Phys. Soc.*, Ser. II, **4**, 227 (1959).
6. J. S. Prener, E. F. Apple, and D. J. Weil, Enlarged Abstracts Electrochemical Society, Philadelphia, 1959, p. 54.
7. J. S. Prener, *J. Chem. Phys.*, **25**, 1294 (1956).
8. J. S. Prener and F. E. Williams, *This Journal*, **103**, 342 (1956).
9. F. E. Williams, *J. Opt. Soc. Am.*, **47**, 869 (1957).
10. A. W. Smith and T. Turkevich, *Phys. Rev.*, **94**, 857 (1954).
11. J. S. Prener and D. J. Weil, *This Journal*, **106**, 409 (1959).
12. E. F. Apple and F. E. Williams, *ibid.*, **106**, 224 (1959).
13. D. Halliday, "Introductory Nuclear Physics," p. 107, J. Wiley and Sons, Inc., New York.
14. F. Seitz and J. S. Koehler, *Solid State Physics*, **2**, 329, 1956.
15. G. J. Dienes, "The Effects of Radiation on Materials," chap. 3, Reinhold Publishing Corp., New York (1958).
16. F. Seitz and J. S. Koehler, ref. (14), p. 311; F. Seitz, *Discussions Faraday Soc.*, **5**, 271 (1949).
17. E. E. Klontz and K. Lark-Horowitz, *Phys. Rev.*, **82**, 763 (1951).
18. E. E. Klontz and K. Lark-Horowitz, *ibid.*, **86**, 643 (1952).
19. P. Rappaport and J. J. Toferski, *Bull. Am. Phys. Soc.*, **30**, 34 (1955).
20. W. L. Brown and W. M. Augustymak, *Bull. Am. Phys. Soc.*, **2**, 156 (1957).
21. W. Kohn, ref. (15).
22. F. Seitz and J. S. Koehler, ref. (14), p. 440.
23. S. J. Czyzak *et al.*, U. S. Dept. of Commerce, PB 121537 (1955).
24. Private communication.
25. N. T. Melamed, *This Journal*, **97**, 33 (1950).
26. E. A. Taft and M. H. Hebb, *J. Opt. Soc. Am.*, **42**, 249 (1952).
27. H. Kallman, B. Kramer, and A. Perlmutter, *Phys. Rev.*, **99**, 391 (1955).
28. R. H. Bube, *ibid.*, **99**, 1105 (1955).
29. G. Garlick and D. Mason, *J. (and Trans.) Electrochem. Soc.*, **96**, 90 (1949).
30. M. Aven, *This Journal*, **109**, 66C (1962); Enlarged Abstracts Electrochemical Society, Los Angeles, 1962, p. 46.
31. M. Schön, *Z. Phys.*, **119**, 463 (1942).
32. H. A. Klasens, *Nature*, **158**, 306 (1946).

Red-Emitting (Zn,Cd)(S,Se) Electroluminescent Phosphors

F. C. Palilla and D. H. Baird

General Telephone & Electronics Laboratories, Inc., Bayside, New York

ABSTRACT

Red electroluminescence at 60 cps has been obtained with copper-activated, bromine co-activated, $Zn_{1-x}Cd_xS_{1-y}Se_y$ systems at field strengths as low as 50 v/mil. Emission color depends on the Cd and/or Se contents. Electroluminescence sensitivity depends on crystal structure. The ratio of host lattice components, together with the conditions of firing, etablishes the crystallographic nature of the matrix. The results suggest a similarity to the structural features associated with optimum electroluminescence in ZnS. Details of phosphor preparation and performance are discussed.

In recent years, considerable progress has been made in the preparation of phosphor systems suitable for use in electroluminescent lighting sources. Synthesis techniques are available for green-, blue-, and yellow-emitting electroluminescent phosphors of good quality, and appropriate mixtures of these phosphors yield white emission at practically useful levels. Comparable performance has not yet been achieved with red-emitting electroluminescent phosphor systems. The investigations described in this paper form part of an effort directed toward that end.

Investigations in the synthesis of electroluminescent phosphors have been most extensive and successful for materials based on zinc sulfide as the host and activated with copper. Experience in this laboratory and elsewhere (1-3) has indicated that optimum electroluminescence in ZnS is obtained when the crystallites exist as a complex structure consisting of faulted hexagonal and/or cubic modifications. It is probable that the peculiar excellence of ZnS as host in electroluminescent phosphors is due in part to its susceptibility to forming such complex structures. In seeking a host material for effective red-emitting electroluminescent phosphors, we therefore felt it desirable to select systems chemically and structurally related to ZnS, but with suitable lattice substitutions to shift the emission to longer wavelengths. Two binary systems are well known which produce this desired shift in emission: ZnS-CdS and ZnS-ZnSe. In neither case, however, is the desired degree of structural similarity to ZnS maintained in

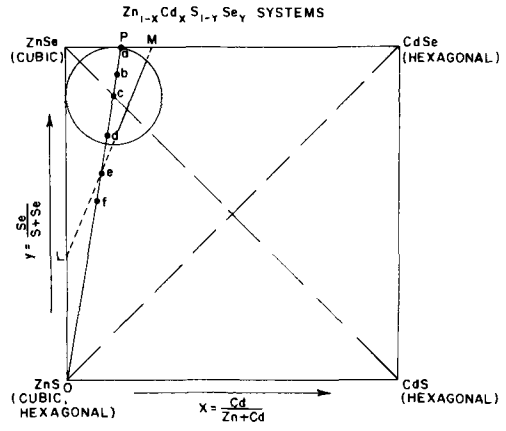

Fig. 1. Composition diagram for the $Zn_{1-x}Cd_xS_{1-y}Se_y$ system

the composition ranges which yield red emission. Substitution of cadmium for zinc in ZnS rapidly stabilizes the hexagonal modification and, at the same time, the electroluminescent sensitivity obtainable by synthesis methods employed to date diminishes (4). Thus, with sufficient Cd substitution to give red emission, little if any, electroluminescent sensitivity remains. Substitution of selenium for sulfur stabilizes the cubic modification (5). The electroluminescent sensitivity also falls, particularly at the low frequencies of excitation which are the most important for practical applications.

The structural characteristics of the binary systems described above suggest that, in the more general family of materials, (Zn,Cd) (S,Se), compositions exist that are characterized by the desired long-wavelength emission, and which are also close to a region of transition between stable hexagonal and stable cubic structures. Such materials might be expected to show some of the structural features characteristic of ZnS. The approach to the delineation of this compositional region and the investigation of the luminescent properties of materials within it is conveniently described in terms of the diagram of Fig. 1. Here composition is plotted as a function of x and y, where x represents the fraction of Cd substitution for Zn, and y the Se substitution for S. On this diagram, departures in any direction from ZnS ($x = y = 0$) may be expected to produce increases in the wavelength of emission. Compositions near the lower right corner may be expected to be hexagonal in structure, those near the upper left cubic. In order to define the region of structural transition and also to determine the dependence of emission color on composition in the central part of the diagram, preparations were made initially of compositions along the diagonals, *i.e.*, in the binary systems ZnS-CdSe and ZnSe-CdS. These served to focus attention on the circled region as being of primary interest in terms both of emission color and structural characteristics. Synthesis was then carried out of compositions along the line OP, a line possibly representing a division between cubic structures on the left and hexagonal materials on the right. These syntheses resulted in the best red-emitting electroluminescent phosphors obtained. It should be noted that Wachtel (6) has obtained red electroluminescence by a route essentially similar in principle, namely the incorporation of HgS in suitable (Zn, Cd)S compositions in order to bring the product from the range of hexagonal to that of cubic stability. In this case the high volatility of HgS necessitates special techniques of phosphor preparation. Lasof, Shrader, and Leverenz (7), as part of an investigation of the photo- and cathodoluminescence of (Zn,Cd) (S,Se) phosphors, also determined the structures of a number of compositions of this family, most of them predominantly comprising ZnS. Their preparations were carried out at temperatures below 900°C where the cubic phase of ZnS is stable, while ours were carried out at 1000°C and above where the hexagonal phase is stable so that the results are not directly comparable.

Experimental

Evaluation procedures.—A 1x1x0.006 in. demountable cell was used with one brass and one transparent conductive glass electrode. A phosphor volume fraction of 0.32 was used with castor oil as the dielectric medium.

The phosphor emittance was determined in terms of the surface brightness of the demountable cell measured with a 1P21 photomultiplier corrected to yield the eye response with a Wratten 106 filter and calibrated against a regulated brightness source.

It should be noted that because of problems inherent in the photometry in the red region of the spectrum (detector response and approximate correction to eye response with the Wratten 106 filter), the emittance values presented herein should be considered on a relative, rather than on an absolute, basis.

The spectral energy distribution was measured with a General Electric Automatic Recording Spectroradiometer, modified according to Hardy & Kirkpatrick, for increased sensitivity (8).

Phosphor preparation.—The synthesis of all phosphors described in the succeeding sections involves blending the mixture of host materials with 0.06-0.2% Cu as $CuSO_4$, and with 5-20% NH_4Br. Within these ranges no significant changes in emittance were observed. The luminescent grade ZnSe and CdSe used were obtained from Merck and the ZnS and CdS from Sylvania Electric Products, Inc. From 40 to 60g of the blend, contained in a quartz boat, is then fired in a lightly plugged quartz tube at 1000°-1200°C for a period of from 20 to 60 min. A self-generated atmosphere is thereby established. The tube is next removed from the furnace for cooling. After washing with hot solutions of 50% HAc, H_2O, 5% KCN and H_2O, the final product is dried at 160°C and sieved through a 400-mesh sieve.

Results

Binary system ZnS-CdSe.—In the case of the ZnS-CdSe system, increasing the amount of CdSe from 0 to 100% results in a progressive shift of the photoluminescence color under 3650Å excitation from blue-green to yellow to red and finally to no emission in the visible region. The electroluminescence color goes through a similar transition and the photoconductive sensitivity increases. In all cases, the host composition was fired with

Table I. Summary of results

Mole % CdSe	Body color	Photoluminescence under 3650A excitation	Electroluminescence, 60-6000 cps, 30-100 v/mil
0	White	Blue-green	Blue-green
25	Yellow	Yellow	Yellow
50	Red	Deep red	Red (weak)
75	Black	None	None
100	Black	None	None

0.1% Cu (as $CuSO_4$) and 10% NH_4Br at 1000°C for 40 min. The results are summarized in Table I. The crystal structure of these compositions is hexagonal in every case and the hexagonal lattice parameter a_o increases linearly with increase in CdSe content in accordance with Vegard's law.

Binary System ZnSe-CdS.—In the case of the ZnSe-CdS system, increasing the amount of CdS from 0 to 100% results in a transition of emitted color under 3650Å excitation from orange-red, to red, and finally to no emission in the visible region. Again the electroluminescence color goes through a similar transition and the photoconductive sensitivity increases. The preparative procedure here was the same as with the previous binary system. The results are summarized in Table II. These results indicate the compositional region of interest to be near 25 mole % CdS, both since it is the region of phase transition and since is corresponds to the desired red emission color. To define the compositional range of interest more closely, additional syntheses were made of phosphors of this binary system in the range of 0 to 25 mole % CdS. In these syntheses, the host composition was fired with 0.1% Cu as $CuSO_4$ and 10% NH_4Br at 1200°C for 20 min, conditions which earlier experience indicated gave the most satisfactory results with ZnSe itself. The results of these experiments are summarized in Table III.

It will be noted that the region of stability of the hexagonal structure appears to be larger at the higher firing temperature used in these experiments: the product with 25 mole % CdS contains only the hexagonal phase in this case, whereas the earlier product of this composition, fired at 1000°C, contains both cubic and hexagonal phases. In the 1200° preparations, the region of phase transition occurs at 15 mole % CdS. There is clearly indicated a maximum in electroluminescent brightness near this composition. Increasing the content of CdS shifts the peak of the spectral energy distribution

Table III. Summary of results

Mole % CdS	Structure	Electroluminescent brightness (ft-L), 400 cps, 600v	Peak of spectral energy distribution, Å
0	Cubic	0.03	6350
5	Cubic	0.07	6550
10	Cubic	0.07	6700
15	Hexagonal-cubic	0.12	6900
25	Hexagonal	0.01	7000

to progressively longer wavelengths, from 6350Å for 0 mole % CdS to more than 7000Å for 25 mole % CdS. Since luminosity decreases with wavelength in this range, it is clear that up to 15 mole % CdS, the emitted power is increasing with CdS content more rapidly than is the brightness. In the case of the product containing 25 mole % CdS, a substantial part of the emission, probably most of it, lies beyond 7000Å, the limit of detection of the spectroradiometer used. For this reason, no measurement is available of the power emitted by this phosphor and hence the question of whether there is a maximum in emitted power in the vicinity of the phase transition is not resolved. Thus the present results are in accord with the hypothesis concerning the desirability of mixed structures in that they show substantial increase in electroluminescent sensitivity as the composition of the host lattice is changed from the region of high stability of the cubic phase to the region of phase transition. However, they do not serve to show whether or not a corresponding decrease takes place as the composition is changed to a region of high stability of the hexagonal phase. From the point of view of obtaining improved red electroluminescent phosphors in the ZnSe-CdS system, they indicate that the region of the phase transition is most promising, although this may be coincidentally due to the fact that the emission of hexagonal materials in this system is primarily in the infrared.

Ternary system ZnSe-ZnS-CdSe.—From the results in terms of brightness, emission color, and structure obtained with the binary system ZnSe-CdS above, the composition range represented by the circled area of Fig. 1 was selected for further study in order to obtain further improvement. Syntheses were carried out of the compositions a through f along the line OP which was taken as a first approximation to the line separating the

Table II. Summary of results

Mole % CdS	Body color	Photo-luminescence under 3650A excitation	Electro-luminescence, 60-6000 cps, 30-100 v/mil	Structure
0	Yellow	Orange-red	Orange-red	Cubic
25	Orange-red	Deep red	Deep red	Cubic with some hexagonal
50	Red	Deep red	Deep red (weak)	Hexagonal
75	Red-brown	Deep red	None	Hexagonal
100	Brown	Deep red (faint)	None	Hexagonal

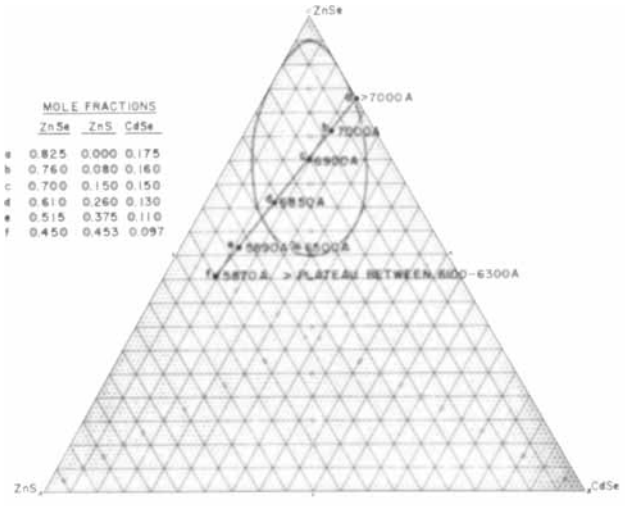

Fig. 2. Ternary composition diagram for ZnS, ZnSe, CdSe

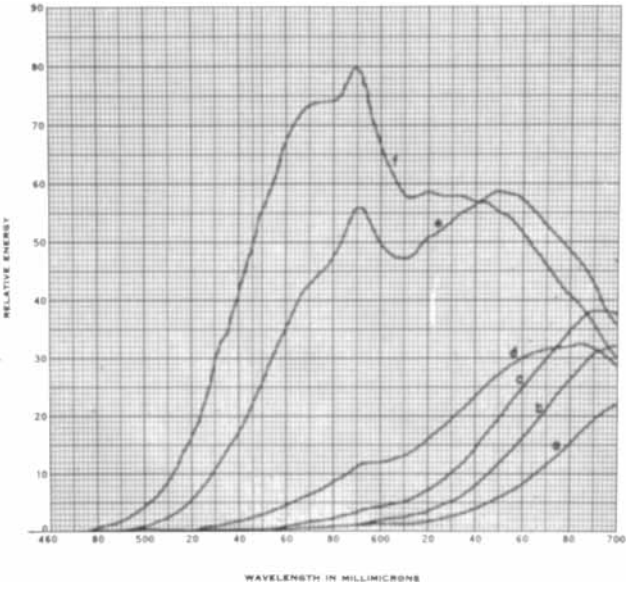

Fig. 3. Spectral energy distributions of phosphors in Fig. 1 and 2

regions of cubic and hexagonal stability. These compositions all fall in the ternary system ZnSe-ZnS-CdSe and are shown in Fig. 2 on the conventional triangular coordinate composition diagram of this system. Also listed are the wavelengths of peak emission of the phosphors which will be discussed further below. The enclosed area corresponds to the circle of Fig. 1. The samples were all prepared by firing at 1200°C for 20 min the appropriate blends of ZnSe, ZnS, and CdSe with 0.06% Cu as $CuSO_4$ and 10% NH_4Br.

The spectral energy distributions of these phosphors under 6000 cps electroluminescent excitation are shown in Fig. 3. The curves have not been normalized and therefore indicate the relative emitted energies of the phosphors. As we progress from sample f to a, there is a shift in peak emission of a red band from 6200 to above 7000Å with decreasing ZnS content. In the same sequence, there is the gradual disappearance of a yellow-orange band, which peaks at about 5770Å, but which does not shift its peak position appreciably with variation of composition. This is analogous to the shifts observed with increasing ZnSe in the Zn(S, Se) system where there is observed a decrease in intensity of a short wavelength band and a simultaneous shift in emission peak of a long wavelength band. In Table IV are listed the compositions and the structural characteristics of this series.

Table IV. Compositions and structural characteristics

Sample	ZnSe	ZnS	CdSe	Solid-solution structure	Lattice constant, A
a	0.825	0	0.175	Cubic	5.742 (Cubic)
b	0.760	0.080	0.160	Cubic	5.716 (Cubic)
c	0.700	0.150	0.150	Cubic	5.690 (Cubic)
d	0.610	0.260	0.130	Cubic with some hexagonal	5.658 (Cubic) 4.826 (Hex. a_o)
e	0.515	0.375	0.110	Hexagonal-cubic	5.611 (Cubic) 4.772 (Hex. a_o)
f	0.450	0.453	0.097	Hexagonal	4.656 (Hex. a_o)

There is observed a structural shift from the cubic modification in the low ZnS samples (a, b, and c) to the hexagonal modification in the highest ZnS sample (f) with concomitant decrease in lattice constants of both the cubic and hexagonal solid-solution structures. This implies that the line representing the transition between materials of cubic and hexagonal structures, under these conditions of preparation, passes through the lower portion of the circled area as possibly indicated by the line LM in Fig. 1. It is probable, however, that the entire series lies in a compositional region in which the energy difference between the two structures is relatively small. This factor is probably responsible for the relatively high level of brightness displayed by the phosphors of this series in that it is conducive to the formation of mixed and faulted structures in spite of the apparent existence of only single phases in some of these materials.

On the basis of emission colors of the phosphors of this series, composition d was selected for investigation of the effects on electroluminescent brightness of varying the temperature and time of firing. The results are given in Table V. These data are presented here for illustrative purposes only, without implication as to the optimized conditions for other compositions. It is probable that, with the complex mixtures involved in such a system, optimized thermal conditions may be different for different compositions.

In Fig. 4 and 5, the brightness-frequency and brightness-voltage characteristics of a phosphor of composition d, prepared by firing for 20 min at 1200°C, are compared with those of a ZnSe phos-

Table V. Results

$ZnSe_{0.610}$, $ZnS_{0.260}$, $CdSe_{0.130}$:Cu, Br			
		Brightness (ft-L)	
Firing temperature, °C	Firing time, min	60 cps, 600v	6000 cps, 600v
1200	20	0.16	10.0
1200	60	0.07	6.1
1100	20	0.07	5.3
1100	40	0.08	5.7
1100	60	0.10	8.4

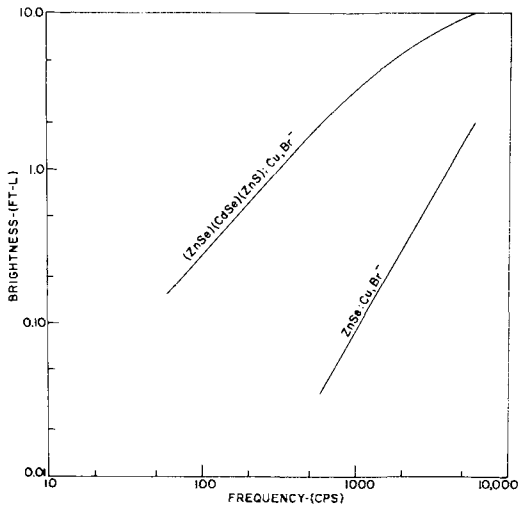

Fig. 4. Brightness vs. frequency for $ZnS_{(0.260)}$ and $ZnSe_{(0.610)}CdSe_{(0.130)}$:Cu,Br (composition d) and ZnSe:Cu,Br.

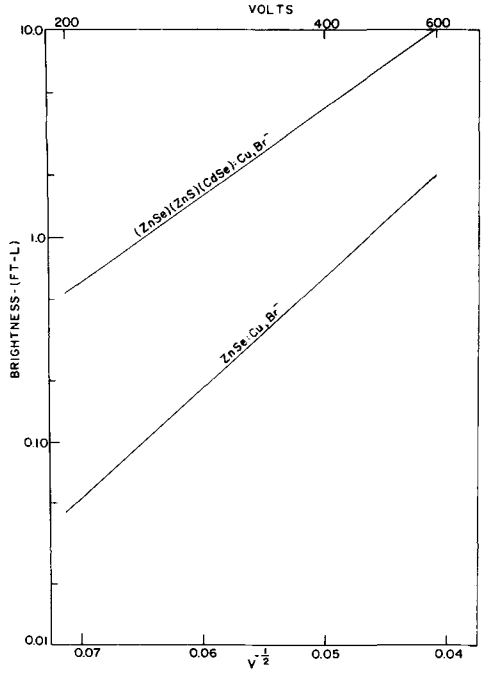

Fig. 5. Brightness vs. voltage for $ZnS_{(0.260)}ZnSe_{(0.610)}CdSe_{(0.130)}$: Cu,Br (composition d) and ZnSe:Cu,Br.

phor for which the preparative conditions were identical. Emission of the former peaks at 6850Å while that of the latter peaks at 6350Å. The most striking feature of these figures is the superiority they show in the brightness of the ternary phosphor over that of the selenide phosphor. Figure 4 shows this to be particularly the case at low frequencies. At 60 cps the brightness of the selenide phosphor is too low for measurement, but extrapolation from higher frequencies indicates the factor of superiority of the ternary phosphor to be at least two orders of magnitude. Figure 5 shows that both systems display the same brightness-voltage relationship commonly observed for electroluminescent phosphors.

Summary and Conclusions

In seeking improved red-emitting electroluminescent phosphors, investigation has been carried out of the system (Zn,Cd) (S,Se):Cu,Br. Increases in the content of either Cd or Se serve to shift the emission from the blue-green of ZnS to longer wavelengths. In addition, Cd serves to stabilize the hexagonal modification, Se the cubic. By suitably balancing these two substituents, it has been shown to be possible to produce a series of electroluminescent phosphors with emission peaks ranging from the yellow to near infrared, each close to a region of transition between the hexagonal and cubic modifications. These are thus to some extent the structural analogues of electroluminescent ZnS itself. Detailed evaluation of the brightness characteristics of a red-emitting member of this series shows it to represent a large improvement over those displayed by ZnSe:Cu,Br electroluminescent phosphors. This tends to confirm earlier speculation concerning the significance of mixed structures in achieving high-level electroluminescence in ZnS. It suggests that more detailed investigations of the present system of phosphors will lead to a better understanding of the role of such structures.

Acknowledgments

It is a pleasure to express thanks to Drs. P. Goldberg and A. K. Levine for many helpful discussions and for their encouragement. Grateful acknowledgment is made to J. Ragusin for his assistance in the preparation of the phosphors, and to C. Creter and P. Lublin for the x-ray analyses.

Manuscript received May 19, 1962; revised manuscript received Aug. 8, 1962. This paper was prepared for delivery before the Los Angeles Meeting, May 6-10, 1962.

Any discussion of this paper will appear in a Discussion Section to be published in the June 1963 JOURNAL.

REFERENCES

1. A. H. McKeag and E. G. Steward, *This Journal*, **104**, 41 (1957).
2. D. W. G. Ballentyne, *ibid.*, **107**, 807 (1960).
3. T. E. Peters, J. Singer, V. A. Brophy, and J. L. Birman, *Bull. Amer. Phys. Soc., Series II*, **7**, 211 (1962).
4. A. Wachtel, *This Journal*, **107**, 602 (1960).
5. I. J. Hegyi, S. Larach, and R. E. Shrader, *ibid.*, **104**, 717 (1957).
6. A. Wachtel, *ibid.*, **107**, 682 (1960).
7. S. Lasof, R. E. Shrader, and H. W. Leverenz, "Solid Luminescent Materials," Cornell Symposium 1946, p. 223, John Wiley & Sons, New York (1948).
8. A. E. Hardy and G. P. Kirkpatrick, *Rev. Sci. Instr.*, **27**, 417 (1956).

Large-Area "Jet" Electrolytic Polishing of Ge and Si

G. R. Booker and R. Stickler

Research Laboratories, Westinghouse Electric Corporation, Pittsburgh, Pennsylvania

ABSTRACT

Germanium and silicon specimens have been electrolytically polished by scanning the surface of the specimen in a systematic manner with a narrow diameter jet of electrolyte. A comprehensive examination showed that the surfaces of p-type Ge specimens polished in this manner are smooth, flat, and strain-free. Brief examinations indicated that the method is probably also satisfactory for polishing n-type Ge and p-type Si specimens.

Highly polished, flat, strain-free semiconductor surfaces, particularly Ge and Si, are frequently required for semiconductor device fabrication purposes. For example, such surfaces would be valuable for epitaxial layer and shallow diffused devices. However, such surfaces are difficult to prepare. A procedure frequently adopted is first to polish the specimen mechanically to obtain a highly polished, flat surface, and then to polish the specimen chemically to remove the strained surface layers formed during the mechanical polishing. However, the removal of the strained surface layers by chemical polishing usually causes a significant deterioration in the high polish and/or flatness of the surface (see later).

An alternative procedure is mechanical polishing followed by electrolytic polishing, the latter being performed by either a 'bath' method, the rotating disk method (1, 2), or a "jet" method (3-5). Bath methods are not entirely satisfactory and are not often used.

In the rotating disk method, recently introduced by Sullivan and his colleagues (1, 2), a flat disk is rotated close to the surface of the specimen to be polished, thereby intensively stirring an electrolyte introduced between the two surfaces. High points on the specimen surface are preferentially removed, and the resulting surface is highly polished and strain-free. The surface is slightly convex owing to different stirring rates at different distances from the center of rotation, the deviation from flatness over an area 25x25 mm being 2.5μ. The surface roughness is 25Å. The method loses some of its simplicity when applied to n-type specimens. This is because with such specimens it is necessary to produce holes at the surface being electropolished, and the standard procedure for doing this (to shine strong illumination directly onto the surface) is complicated by the closeness of the rotating disk. Sullivan *et al.* (1, 2) overcome the difficulty by shining light through the disk, various procedures being devised for making the disk both transparent and conducting. Polishing rates for p-type Ge specimens are 0.3 to 33μ/min, and for n-type Ge, p-type Si, and n-type Si specimens are of the order of 1.5μ/min.

In the jet method (3-5) a nozzle sprays a narrow circular jet of electrolyte onto the specimen, and polishing occurs over the area of impingement. Extremely fast polishing rates (100-500μ/min) can be obtained, and the resulting surfaces are highly polished and strain-free. However, the surfaces are not flat, a circular depression being formed on the surface opposite the jet.

The possibility of scanning a jet across the surface of a specimen so that the polished surface is also flat does not appear to have been investigated for semiconductor materials. The method is, however, used for metals. Thus, Farmer and Glaysher (6) used a scanning jet method to polish cylindrical iron tensile specimens in order to obtain smooth strain-free surfaces, while Nutting and Kelly (7) used a scanning jet method to thin metal specimens as a preliminary stage in the production of metal foils approximately 1000Å thick for transmission electron microscope studies. For both of these applications the complete surface of the specimen was scanned in a systematic manner by combining a rapid scan in one direction with a slow scan in a perpendicular direction.

The rate of removal of material (g/min) for a scanning jet is similar to the rate of removal of material (g/min) for a stationary jet. However, the average polishing rate (μ/min) for a scanning jet is very much less than the polishing rate (μ/min) for a stationary jet. This is because with a scanning jet the material is removed from a much larger area. If a jet with a cross-sectional area A_s and a stationary polishing rate (μ/min) R_s is scanned over an area A_m, then the average scanning polishing rate (μ/min) R_m is given approximately by $R_m = (A_s/A_m)\,R_s$. For a jet 2 mm in diameter and an area of scan 25x25mm the reduction factor A_m/A_s is approximately 200 times. This gives for semiconductor specimens polishing rates in the range 0.5-2.5 μ/min, *i.e.*, rates still adequate for most of the likely semiconductor applications. Moreover, the apparatus used for the electropolishing can be made fully automatic so that it can be run for several hours if necessary with little or no attention.

In order to investigate the possibility of applying the scanning jet method to semiconductor specimens we have used a scanning jet apparatus originally constructed for polishing metal specimens. The

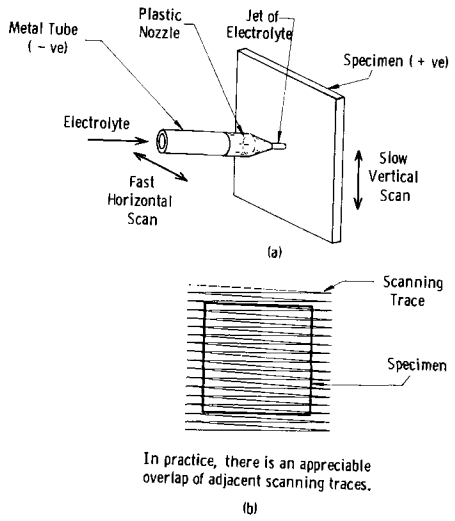

Fig. 1. Diagrammatic illustration of the apparatus used for large-area jet electropolishing.

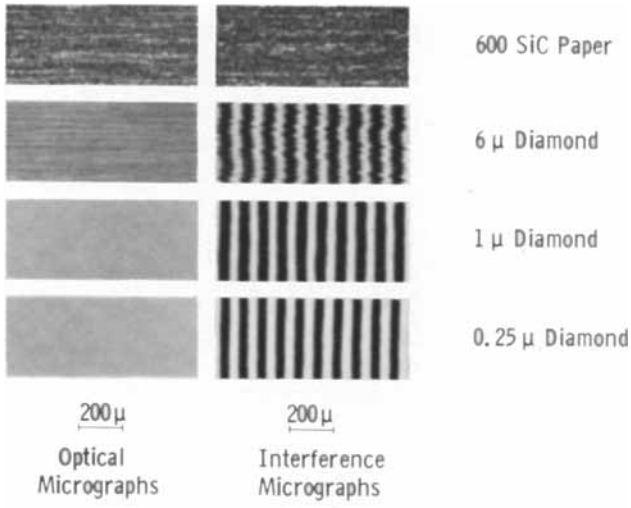

Fig. 2. Single-crystal Czochralski-grown p-type Ge at progressive stages during mechanical polishing. Micrographs show typical random areas.

present paper describes some results obtained for p-type Ge, n-type Ge, and p-type Si specimens.

Electropolishing Method

A slice approximately 25x25x1 mm thick was cut from the semiconductor material, and the two main faces were ground flat. One of the faces was then mechanically polished with progressively finer abrasives, the final abrasive being 0.25μ diamond. The resulting specimen was placed on a flat plastic plate with the mechanically polished side uppermost; lacquer was applied around the edges of the specimen and allowed to dry. In this manner the specimen was held in position and electrolyte was prevented from reaching the back surface. The specimen was mounted vertically opposite a plastic nozzle attached to a horizontal metal (platinum) tube (Fig. 1a). The nozzle contained a hole 2 mm in diameter, and the distance between the end of the nozzle and the specimen surface was 3 mm. The specimen was the anode, the metal tube was the cathode, and the anode to cathode distance was 15 mm. The electrical lead for the anode passed through a hole in the plastic plate and was soldered to the back surface of the specimen. This surface previously had been completely coated with solder so that during the subsequent electropolishing there would be no variation in the electrical polishing conditions from a point to point on the front surface of the specimen. However, other less permanent methods for making the electrical contact would also no doubt have been satisfactory.

The nozzle moved horizontally backwards and forwards at a uniform rate across the specimen, while the specimen had a similar but slower movement in the vertical direction (Fig. 1a and b). The scanning speeds were: horizontal, 25 mm/sec; vertical, 0.083 mm/sec. The jet thus scanned the specimen horizontally 300 times during the course of one vertical scan. The amplitudes of the scans were both 25 mm so that a specimen surface up to 25x25 mm could be polished. The scanning movements were obtained with the aid of two synchronous electric motors, gear-wheels, and two eccentric cams.

The electrolyte after impinging on the specimen was collected and pumped up to a reservoir, from whence it returned to the nozzle via a gravity feed. The pressure head was 60 cm and the jet had a flow rate of 0.4 liters/min and a flow speed of 200 cm/sec. The total amount of electrolyte circulated was 2 liters so that polishing could be continued for long periods without significant deterioration or heating of the electrolyte.

Mechanical and Chemical Polishing

Before describing the electropolishing results some observations on the mechanical polishing and subsequent chemical polishing of Ge and Si specimens are given. These observations enable the electropolishing results to be more clearly followed.

A single-crystal p-type Ge specimen was mechanically polished, the final abrasive being 0.25μ diamond, and examined at progressive stages with the optical and interference microscopes (Fig. 2). Details of the polishing procedure are given in Table I. As the polishing proceeded the abrasive

Table I. Mechanical polishing procedure

Stage	Abrasive	Particle size, μ	Lubricant	Method
1	No. 600 SiC paper	25	Water	Rotating wheel
2	Diamond powder in slurry	6	Kerosene	Rotating wheel, cloth pad
3	Diamond powder in slurry	1	Kerosene	Rotating wheel, cloth pad
4	Diamond powder in slurry	0.25	Kerosene	Rotating wheel, cloth pad

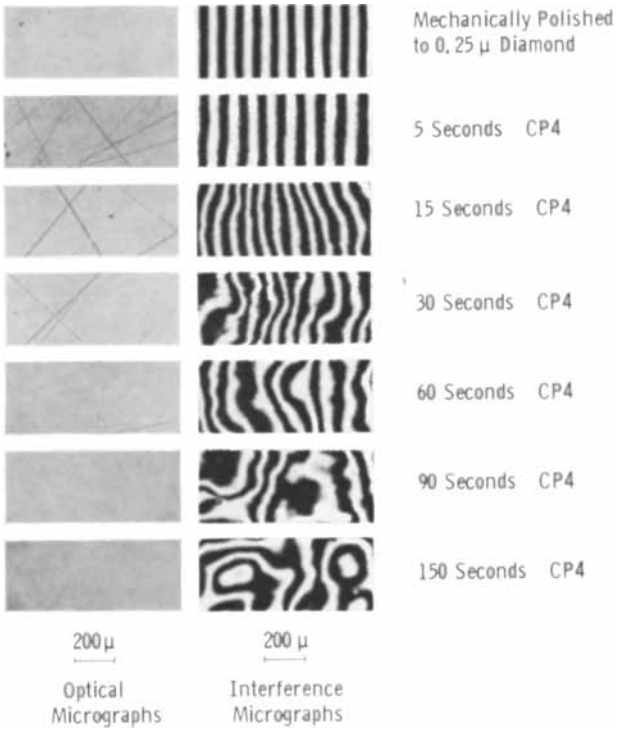

Fig. 3. Mechanically polished single-crystal Czochralski-grown p-type Ge at progressive stages during subsequent chemical polishing with CP4. Micrographs show typical random areas.

marks became less pronounced. After the 0.25μ diamond polish the specimen possessed a highly polished, very flat surface.

This mechanically polished specimen was then chemically polished with a modified CP4 solution[1] and similarly examined (Fig. 3). After a polishing time of 5 sec a dense array of sharply defined "scratch marks" was observed. After 15 sec the scratch marks were shallower, and after 30 sec still shallower. After 60 sec the trend continued, but a number of clear areas were now visible. After 90 sec all the fine scratch marks were eliminated, broad scratch marks only remaining. After 150 sec only a few broad scratch marks were still present. Moreover, during the chemical polishing the surface progressively lost its flatness and became wavy on a coarse scale. The waviness was slight after a polishing time of 5 sec, was pronounced after 30 sec, and very pronounced after 90 and 150 sec. The total thickness of the specimen removed during the chemical polishing was approximately 60μ, corresponding to an average chemical polishing rate of 24μ/min.

A single-crystal p-type Si specimen was then prepared and examined in the same manner. The chemical polishing proved to be similar to that of the p-type Ge specimen. In particular, scratch marks were rapidly revealed and then slowly removed, and the surface became progressively wavy. However, the scratch marks were much less pronounced on the Si specimen than on the Ge specimen.

[1] 200 ml HNO_3 : 120 ml HF : 120 ml CH_3COOH : 1.6g Ge : 1.2 ml liquid Br_2. The addition of Ge to CP4 introduces reaction products which improve the reliability of the etch by reducing the induction period to essentially zero (8). The action of CP4 on Si is reliable without the addition of Si (8).

These observations are interpreted (8) as follows. When Ge and Si specimens are mechanically polished in the manner described, a 'damaged layer' extending no more than a few microns below the surface is formed.[2] Chemical polishing with CP4 for approximately 5 sec removes this layer. The scratch marks then covering the surface result from nonuniform chemical polishing occurring while the damaged layer is being removed. This nonuniform polishing arises because of local differences in chemical polishing rates due to local differences in damage. After the damaged layer has been removed, further chemical polishing gradually smooths over the scratch marks but does not eliminate them until much later. During the chemical polishing the surface becomes progressively wavy on a coarse scale. This waviness is characteristic of the chemical polishing process and is not related to the damaged layer. The scratch marks are more pronounced on Ge than Si specimens because the damaged layer extends further below the surface of Ge than Si specimens.

Electropolishing

p-Type Ge.—Single-crystal p-type Ge specimens were electropolished using an electrolyte of composition 0.1*N* H_2SO_4 plus a few ml of HF (48%) per liter. The electrical polishing conditions were not critical, 150v and 200 ma[3] being typical. The electropolishing was similar to the chemical polishing in that scratch marks were revealed and later eliminated (Fig. 4). However, the electropolishing differed in that the initially flat condition of the surface was not significantly altered. The polishing times were longer than the corresponding times for the chemical polishing, the final electropolished surface being obtained after 120 min. The total thickness of the specimen removed was again approximately 60μ, corresponding to an average electropolishing rate of 0.5μ/min.

The final electropolished surface possessed a high-quality mirror-like finish. Optical micrographs at 1000X did not reveal any structure (Fig. 5a), while electron micrographs at 20,000X of shadow-cast replicas indicated only a slight granular structure (Fig 5b). The surface roughness was estimated from the electron micrographs to be approximately 25Å. Thtis value was subsequently confirmed by multiple-beam interference microscopy. The flatness of the final electropolished surface over an area 25x25 mm was in general equivalent to approximately 1 to 2 interference fringes, *i.e.*, approximately 0.5μ.

A p-type Ge specimen possessing numerous gross crystallographic imperfections, *e.g.*, twin planes and irregular boundaries, was electropolished as

[2] It is emphasized that the damage associated with the final mechanically polished specimens arose from the final 0.25μ diamond polishing treatment. No damage remained from the previous coarser abrasive treatments. This was established as follows. Similar specimens were cut, lapped, chemically polished to remove all the damage, and mechanically polished with 0.25μ diamond. When these specimens were chemically polished with the modified CP4 solution, the results obtained were precisely the same as those shown in Fig. 3.

[3] A current of 200 ma corresponds to a current density of approximately 6 amp/cm^2 when referred to the cross-sectional area of the 2 mm diameter jet used. The current density at the surface of the specimen is somewhat lower because of the spreading of the electrolyte on impingement.

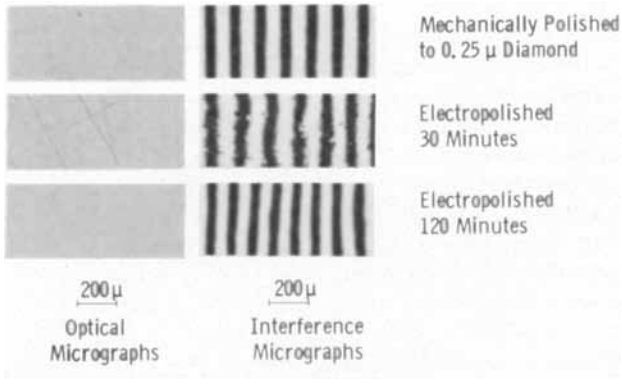

Fig. 4. Mechanically polished single-crystal Czochralski-grown p-type Ge at progressive stages during subsequent electrolytic polishing. Micrographs show typical random areas.

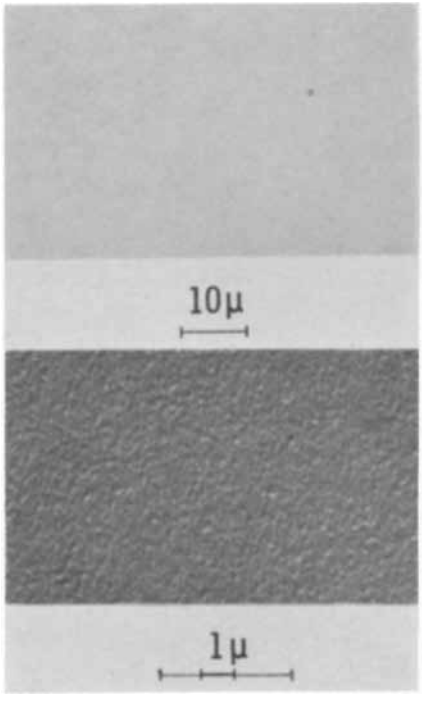

Fig. 5. Final electropolished surface of p-type Ge specimen of Fig. 4. a, (top) Optical micrograph; b, (bottom) electron micrograph of a shadow-cast replica. The shadow-casting angle was $\cot^{-1} 2$.

above. Examination of the final electropolished surface with the optical microscope showed that the imperfections were delineated in an extremely sharp manner (Fig. 6) (without etching the surface), while the remainder of the surface was structureless. The surface deviated slightly from flatness in the areas of the imperfections and was flat in the areas away from the imperfections.

n-Type Ge.—When single-crystal n-type Ge specimens were electropolished as above, the surface of the specimens became covered with a white film. However, if the electropolishing was performed while the surface was strongly illuminated, *e.g.*, by focusing the light beam from a high intensity lamp onto the surface, polishing occurred over the area illuminated. Moreover, if the small circular area of the jet only was illuminated then, owing to the vertical movement of the specimen, a narrow vertical strip was polished. The electrical polishing

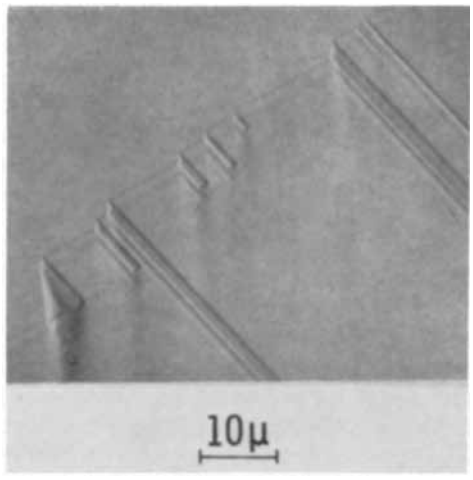

Fig. 6. Final electropolished surface of p-type Ge specimen similar to that of Fig. 4. but containing gross crystallographic imperfections.

conditions were somewhat critical, 90v and 100 ma being typical. Although polishing was effected in this manner, the polished surfaces were not always of the high quality of the p-type Ge specimens. However, highly polished surfaces could usually be obtained if, before electropolishing, the specimens were chemically polished for 5 sec with CP4.

p-Type Si.—Single-crystal p-type Si specimens were electropolished in a similar manner to the p-type Ge specimens but using an electrolyte of composition 0.2*N* HF. The electrical polishing conditions were not critical and highly polished surfaces were obtained.

Discussion

The large-area jet electropolishing method has been applied to p-type Ge, n-type Ge, and p-type Si specimens: all three types of specimen were satisfactorily polished. A comprehensive investigation of p-type Ge specimens showed that the method is capable of producing a final electropolished surface which possesses a surface roughness of approximately 25Å, is flat to approximately 0.5μ over an area 25x25 mm, and is strain-free.[4]

In order to obtain such high-quality electropolished surfaces, the specimens were initially mechanically polished, the final abrasive being 0.25μ diamond. This was necessary because the electropolishing method only slowly preferentially removes high points from irregular surfaces. Moreover, the electropolishing was continued appreciably beyond the stage at which the damaged layer arising from the mechanical polishing was removed, at least in the case of Ge.

For p-type Ge specimens 25x25 mm the electropolishing rate was 0.5μ/min and the electropolishing time was 120 min. Although the polishing time was relatively long, the apparatus required little or no attention during this period, except occasional observation of the specimen surface to see how the polishing was proceeding. Moreover, a reduction in the polishing time by a factor of 2 or 3 could prob-

[4] By "strain-free" is meant that no strains are present in the surface of the specimen due to the surface preparation method. Strains in the surface arising from strains previously present in the bulk material may, presumably, exist.

ably have been obtained by increasing the jet flow speed.

The method is directly applicable to n-type specimens because the surface of the specimen can readily be illuminated during electropolishing. For n-type Ge specimens electropolishing occurred as long as the light intensity exceeded a certain minimum value. However, a highly polished surface was often obtained only if, after mechanical polishing, the specimen was chemically polished for 5 sec with CP4 and then electropolished. The reason for this behavior is not definitely known. It is thought to be in some way associated with local variations in the lifetimes of the induced electron-hole pairs due to local variations of strain within the damaged layer. The difficulty might not have arisen if higher intensity illumination had been used during the electropolishing.

When the method is applied to n-type specimens, it would be advantageous if the jet remained stationary, and the two scanning movements were applied to the specimen. It is then only necessary to illuminate the area of the jet, *i.e.*, an area a few millimeters in diameter, in order to electropolish the complete area of the specimen, and several advantages result. First, by using a suitable optical system to focus the illumination, sufficient intensity can be obtained from a standard light source. Second, any nonuniformity in the intensity of the light over the area illuminated, a possible source of nonuniform polishing, is automatically compensated by the two scanning movements. Third, heating of the specimen, and hence the electrolyte, by the light beam is minimized. Consequently, any variations in the electrical polishing conditions resulting from an increase in the temperature of the electrolyte are also minimized. Fourth, by suitable modulation of the intensity of the light beam, selected areas of the specimen surface can be polished, *i.e.*, specific geometric areas can be isolated. However, the resolution which could be obtained in this way has not been ascertained. The same result could, of course, be obtained by placing the light on the same support as the jet. However, it is simpler practically to apply both scanning movements to the specimen.

Summary and Conclusions

A scanning jet electrolytic polishing method has been applied to Ge and Si specimens. A comprehensive examination showed that the surfaces of p-type Ge specimens polished in this manner were smooth, flat, and strain-free. Brief examinations indicated that the method is probably also satisfactory for polishing n-type Ge and p-type Si specimens.

Acknowledgments

The authors wish to thank Doctors J. W. Faust, H. F. John, and P. F. Schmidt for useful discussions, and Mr. R. Engle for assistance with the experimental work. The work was sponsored in part by the Wright Patterson Air Force Base.

Manuscript received June 18, 1962. This paper was prepared for delivery before the Los Angeles Meeting, May 6-10, 1962.

Any discussion of this paper will appear in a Discussion Section to be published in the June 1963 JOURNAL.

REFERENCES

1. M. V. Sullivan and R. M. Finne, Abstract No. 156, Electrochemical Society Meeting, Houston, 1960.
2. D. L. Klein, G. A. Kolb, L. A. Pompliano, and M. V. Sullivan, Electronics Division of Electrochemical Society, Abstracts, **10**, [46], 72 (1961).
3. J. W. Tiley and R. A. Williams, *Proc. I.R.E.*, **41**, 1706 (1953).
4. P. F. Schmidt and M. Blomgren, *This Journal*, **106**, 694 (1959).
5. P. F. Schmidt and D. A. Keiper, *ibid.*, **106**, 592 (1959).
6. M. H. Farmer and G. H. Glaysher, *J. Sci. Inst.*, **30**, 9 (1953).
7. J. Nutting and P. Kelly, *J. Iron and Steel Inst.*, **192**, 246 (1959).
8. J. W. Faust, Private communication.

Kinetics of Silicon Crystal Growth from $SiCl_4$ Decomposition

E. G. Bylander[1]

Texas Instruments, Inc., Dallas, Texas

ABSTRACT

The relationship of silicon epitaxial growth, following $SiCl_4$ decomposition in hydrogen, to classical heterogeneous reaction theory is discussed. The expected behavior of mass transfer control which shifts to a surface effect rate control is found to fit the observations. No conclusion is made whether the surface rate control is, say, due to reaction rate or adsorption rate, but the results appear to favor the adsorption rate of $SiCl_4$. Experimentally a competing etching reaction is found which appears to explain $SiHCl_3$ and $(SiCl_2)_n$ production. The diffusion of a reactant away from the surface appears to play the role of reducing the deposition reaction rate, and at high halide concentrations may be responsible for the etching reaction predominating. The variation of the surface morphology with substrate temperature appears to be explainable from the kinetics. The low temperature morphologies of etched and deposited slices were found to be similar.

Methods for epitaxial growth of silicon on silicon have been of recent interest (1-4). The purpose of this study was to explore the morphologies and growth rates of single crystal silicon films formed by $SiCl_4$ decomposition in hydrogen. A by-product of the investigation was the reaction kinetics data. Since the investigation was mainly ex-

[1] Present address: Melpar, Inc., Falls Church, Virginia.

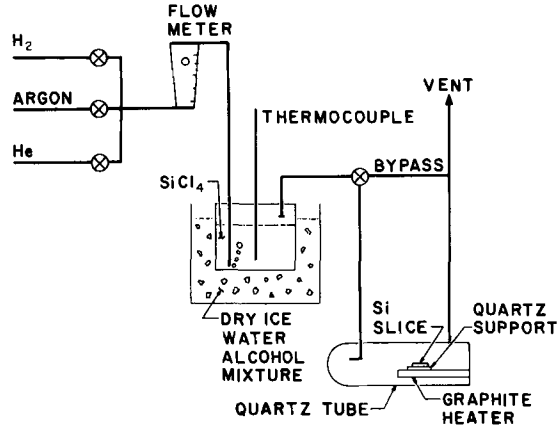

Fig. 1. Deposition apparatus

ploratory, no attempt was made to use a special kinetic reactor design. During the course of the work an etching reaction was found to be a part of the decomposition process, a fact which led to complications in the crystal growth study.

Experimental

The experimental arrangement was similar to that used earlier by Theuerer (3) and is shown in Fig. 1. Either hydrogen, helium, or argon was arranged to bubble through cooled $SiCl_4$ whose temperature was monitored directly with a thermocouple. Before a run was made, the bypass valve was opened until the $SiCl_4$ temperature reached steady state at the desired temperature with the gas flowing, and at which time the vapor was switched to blow over the slice.

Although the actual concentration will depart from that calculated using the vapor pressure because of the change in residence time of the gas with flow rate and possibly droplet entrainment, these factors are unimportant at the flow rates of interest and for concentrations up to at least 8%. This result was established from the close agreement which was obtained between growth rates using the bubbler and average rates using an evaporator in which the above items were not a factor. In the evaporator, halide was metered onto heated quartz chips and subsequently the vapor was picked up by the hydrogen. The bubbler was used in preference to the evaporator because of better reproducibility of results at low concentrations. The flow meter was calibrated for hydrogen flow rate. The slices were generally of (111) orientation and were placed in the center of a quartz carrier plate which in turn rested on a graphite heater. The slice temperature was measured pyrometrically, and an emissivity correction was applied. Deposit thicknesses were measured by measuring the slice thickness before and after deposition (5). Questionable results were checked by interferometry. The halide concentration was calculated from its vapor pressure. It is to be noted that the $SiCl_4$ concentration varied with position along the 4 in. hot zone and is some 40% less at the reactor exit than at the inlet for a 6% halide concentration at 1250°C and 10 liters/min. Also reaction product concentrations

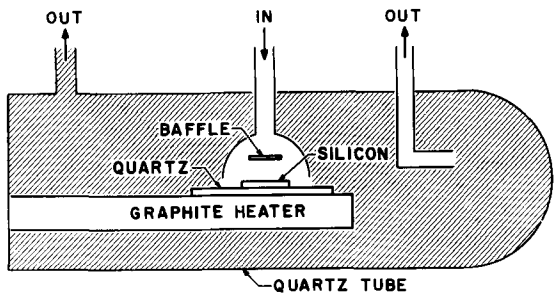

Fig. 2. Vertical reactor geometry

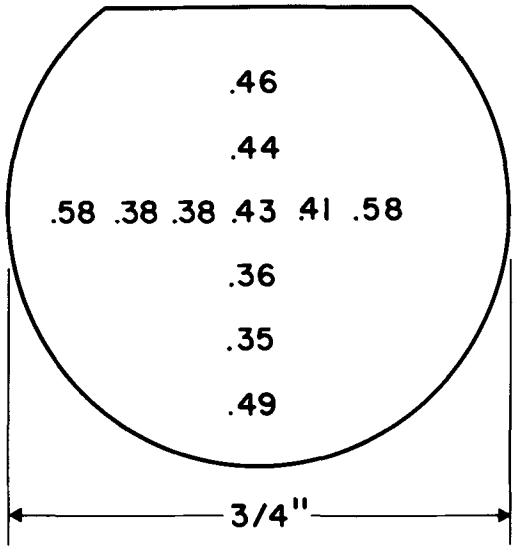

Fig. 3. Slice thickness variation for a slice deposited in the vertical reactor for a flow of 2 liters/min and halide concentration of 2%. Numbers are thickness in mils.

built up along the reaction zone as determined from quite rough gas chromatograph results. At high flow rates or low temperatures this perturbation should have little effect on the results, whereas under other conditions it may give rise to misleading results.

Two reactor arrangements were used. Either the gas was blown across the slice as in Fig. 1 (horizontal reactor) or it was blown down on the slice as in Fig. 2 (vertical reactor). The same 50 mm diameter quartz envelope was used in both cases. In the latter, a 4-cm diameter bell housing directed the gas down on the slice over a 1½ cm diameter baffle. The baffle was positioned for the best flow pattern by blowing smoke across it. Slice thickness variation for the horizontal reactor was only about 10% front to back at a 2% concentration and 10 liters/min flow, whereas under similar conditions it was much greater for the vertical reactor. A result from one vertical reactor run is shown in Fig. 3. The numbers on the slice are film thickness in mils. It is thought from this result that measurements made near the center would be meaningful within ± 20%, and the data seem to bear this out.

Flow patterns in the reactors were observed by blowing air through a lighted cigar in the feed line. Quite large convection currents were observed above the hot regions. In both cases a stagnant layer formed along the bottom of the tube and below the heater strip. Convection currents around the strip

were found not to affect the horizontal reactor results, since the slice was far enough away from the heater edge. It is thought that a similar situation held for the vertical reactor.

Results

The observed morphologies for (111) oriented slices are (i) whisker growth around 900°C; (ii) triangle growth 950°-1100°C; (iii) rippled growth 1150°C up. At $SiCl_4/H_2$ concentrations of $> 6\%$ and around 1250°C localized dimpling occurs.

Figures similar to etch figures were observed for the other orientations for step (ii). No systematic measurements of growth rate *vs.* orientation were made, but (110) oriented slices grew faster than (111) when the deposition conditions were such that there was an orientation dependence of growth.

During the course of the experiments the behavior of $SiCl_4$ in helium and argon was investigated. It was found in every case that material was removed, and there was no evidence of deposition (on the quartz support boat for example). In addition large amounts of the yellow, waxy polymer[2] were formed. Qualitatively more of it appeared to be formed during etching than was observed to be formed during similar deposition runs. The etching rates for helium flows of roughly 8 liters/min are also shown in Fig. 4, 5, and 8. The morphology of a slice etched at 1050°C is shown in Fig. 9. Figure 10 is a micrograph of a slice deposited under conditions similar to those for the slice of Fig. 9. As mentioned earlier, the concentrations in Fig. 5 and 8 above 8% are expected to be only relative because of departures from halide saturation of the gas.

Discussion

Although there is some controversy as to whether the $SiCl_4$ decomposes on the silicon surface or just near it,[3] it will be convenient to discuss the results in terms of heterogeneous reaction theory (8). A classical heterogeneous reaction is supposed to follow the steps:

1. Mass transfer of the reactant to the surface.
2. Adsorption onto the surface.
3. The reaction or series of reactions which take place on the surface.
4. Desorption of product molecules.
5. Mass transfer of the product molecules to the main gas stream, and for a growing crystal.
6. Addition of atoms to growth steps.[4]

If one of the above steps is much slower than the others, it will control the growth rate. In addition,

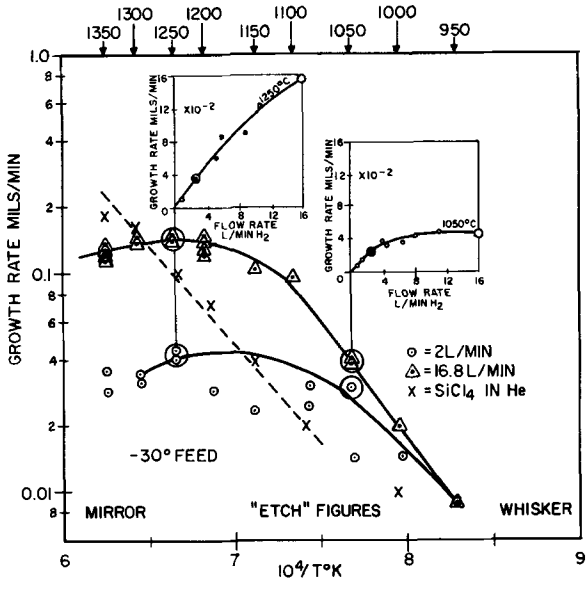

Fig. 4. Horizontal reactor: temperature and flow dependence of deposition and etch rates. The upper curves are the flow rate dependence of growth rate at 1250° and 1050°C. The large open circles are not data points but correspond to equivalent conditions. The lower curves are the temperature dependences of both the deposition and the etching rates.

the mass transfer step will be influenced by the gas flow rate yet be relatively temperature independent (10). The surface controlled steps 2, 3, 4, or 6, are expected to be quite temperature dependent and flow rate independent. The 950°-1100°C region (hereafter referred to as region I) of Fig. 4 is seen to be quite temperature dependent but relatively flow rate independent. The slope is about the same as reported by Theuerer for a different reactor (3). The surfaces observed for slices deposited in this region are quite rough and uneven; apparently this is due to surface rate control and the resulting independence of the various regions on the surface. That it is not due to mean free path effects of silicon may be seen by reference to Fig. 9 and 10. Since the morphology is the same in both cases, it must arise from localized etching.

The etching rate in helium, for a flow rate of about 8 liters/min,[5] is much slower, but it has the same slope. This result suggests that the etching rate is governed by the same mechanism as is the growth, either as a competing reaction or as that and a growth initiating reaction. These possibilities would rule out a hydrogen process as a limiting factor, but rather would suggest a $SiCl_4$ process. It is hypothesized that the etching reaction is

$$SiCl_4 + Si \rightarrow 2\,SiCl_2$$

based on the $(SiCl_2)_n$ polymer observed and on the $SiHCl_3$ which is observed to be formed in the growth plus etching reaction as follows

$$SiCl_4 + 2H_2 \rightarrow Si + 4HCl \quad \text{(major growth reaction)}$$

$$SiCl_2 + HCl \rightarrow SiHCl_3$$

One would expect orientation independent growth in the mass transfer control region, but orientation

[2] Early wax samples taken from a similar process here were identified as the polymer $(SiCl_2)_n H_2$, $n \approx 10$, when formed under deposition conditions (6).

[3] Kurov (7) supposes from the morphology change with distance in a $GeCl_4$ reaction tube and arguments based on the heating times of H_2 that the germanium reacts in the gas and is carried as supercooled liquid droplets. Others (unpublished) have supposed that similar arguments apply to $SiCl_4$ decomposition. However, Kurov does not examine the effect of concentration changes with distance on the morphology, or the differences in the heating time of $SiCl_4$, with its different mass and viscosity, over that of H_2. In addition, he supposes the supersaturation of germanium is around 10^4. Similar "supersaturations" would obtain during $SiCl_4$ decomposition in the gas phase and one wonders how whiskers could grow under these circumstances.

[4] Some investigators have considered the possibility that for a similar reaction that the reaction and growth take place at the same site, i.e., steps 3 and 6 would be combined. See for example reference (9).

[5] Estimated from an indicated flow rate of 17 liters (H_2)/min. Note from Fig. 4 that this flow rate is still well into the surface reaction rate-controlled region, provided that $SiCl_4$ diffusion in helium is similar to that in hydrogen. Unpublished results of others for growth rates in $He-H_2$ and $A-H_2$ mixture indicate that it is.

dependence in region I. No systematic observations of this point have been made, but polycrystalline substrates which were inadvertently run in early tests were reinspected. Marked rate differences for slices deposited under region I conditions were found, but little if any difference was found for the regions of mass transfer control. The marked temperature and orientation dependence and the similarity of the etching and the growth rate activation energies make it not unreasonable to suggest that $SiCl_4$ adsorption is the rate-controlling step. These arguments would not, of course, rule out a step with similar features such as $SiCl_4$ bonding at a growth step.

At the higher temperature (region II), the rate is seen to be mass transfer controlled. The lower curve of Fig. 4, taken for flow rates of 2 liters/min, is seen to shift gradually from surface rate to mass transfer rate control. Note that if the two high temperature etching rate points of Fig. 4 are reliable (also see footnote 5) the growth is not $SiCl_4$ mass transfer rate limited but suggests that reaction product mass transfer limits the rate. Also the predominance of the etching curve leads to a greater than expected temperature dependence for the region II deposition rate. A mirror surface was obtained here and is apparently due to mass transfer control of the growth rate.

In Fig. 5 is shown the concentration dependence of the etching and growth rates. The growth curve has the same general shape as previously observed elsewhere (3). The etching curve appears to level out although the data is sketchy and suggests either an adsorption isotherm or a fractional order reaction. The etching behavior for low concentrations is not known in detail. It seems nearly certain that the etching is a competing reaction since localized dimpling of slices is observed at 1250°C and at concentrations greater than 6%. Also in another experiment, for a room temperature $SiCl_4$-H_2 source, etching and deposition on a thin, hot silicon film deposited on a quartz window were observed microscopically to occur adjacent to one another.

In Fig. 6 is shown the temperature dependence of growth rate for the vertical reactor and two concentrations. The growth rate is seen to have the

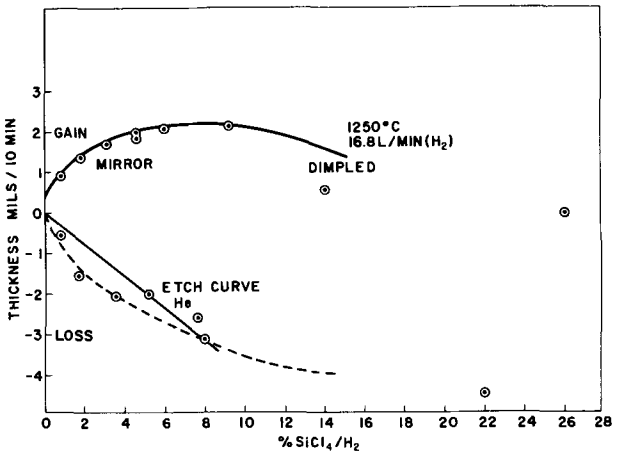

Fig. 5. Horizontal reactor: concentration dependence of silicon deposition rate and etch rate.

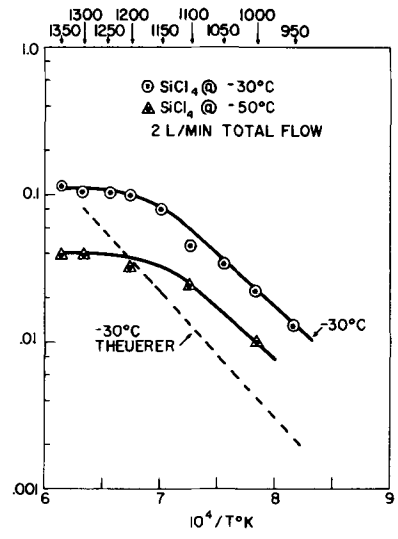

Fig. 6. Vertical reactor: temperature dependence of growth and etch rates.

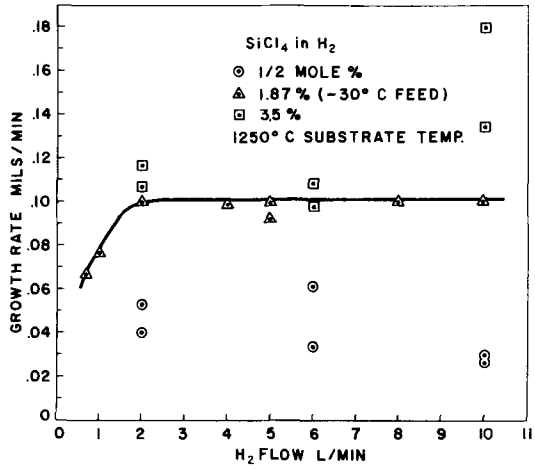

Fig. 7. Vertical reactor: flow rate dependence of the deposition rate for a 1250°C slice temperature. The data points shown for the highest and lowest halide concentrations were taken before the thermocouple was installed. The spread shows the importance of temperature control of the halide source.

same form at low temperatures as for the horizontal reactor. The higher rate than observed by Theuerer (3) is attributed to reactor geometry differences. The fact that a constancy of rate is observed for the higher temperatures here but not in ref. 3 is attributed to a high-temperature rate-limiting mechanism which was not reached for the lower rates. Interestingly enough the high temperature rate mechanism is flow rate independent (Fig. 7) and suggests that a low activation energy, surface rate controlling mechanism is operating.

The highest and lowest rates of Fig. 7 were run before a thermocouple was installed to aid temperature control of the source, and the variability seen emphasizes the importance of source temperature control. There is also an indication of a shift to mass transfer control at the higher concentration.

Figure 8 shows the concentration dependence of etching and growth rate for the vertical reactor and 1250°C slice temperature. The curve's behavior is similar to that of the horizontal reactor. Although

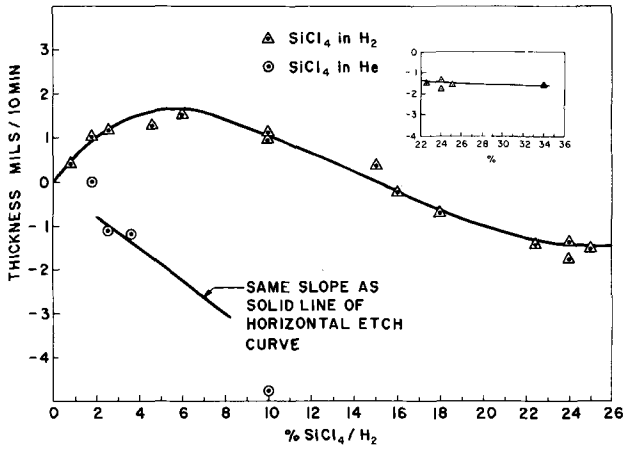

Fig. 8. Vertical reactor: concentration dependence of growth and etch rates.

the growth is constant above about 20% out to above 30% as pointed out earlier, there is some suspicion attached to the concentrations since they were measured indirectly. It would be preferable to repeat the experiment and measure them directly near the reaction point. Etching rates were not measured at high halide concentrations for the vertical reactor because about that time the work was shifted to a study of slice polishing by $SiCl_4$ etching. Polishing was found to be feasible. One is tempted to analyze the reaction by combining the growth plus etching and the etching rate curves to obtain a growth rate curve, but the data does not warrant it. Also it would be useful to fully identify the reactants and products in order to continue.

Figures 9 and 10 were taken for slices etched and deposited under similar conditions. Figure 9 is an etched slice. Figure 10 is of a deposited slice which, of course, was both deposited and etched during the course of the deposition. Although etching and growth are the same to the first order, the complication introduced by the etching reaction, which operates during growth, makes the interpretation of morphologies and growth rates difficult.

To summarize, $SiCl_4$ decomposition and etching have been observed in horizontal and vertical reactors. The reactions in both the horizontal and vertical reactors seem to be surface reaction rate controlled at low temperatures. Reasoning from high activation energy, orientation dependence, flattening of rates with concentration, and similarity of growth and etching rate slopes, it is suggested that $SiCl_4$ adsorption rate controls here. The horizontal growth rate was found to shift to mass transfer control at the higher temperatures while the etching rate did not. It is suggested that reaction product mass transfer governs the growth rate here. The vertical reactor behaved somewhat differently at these temperatures. An etching reaction of $SiCl_4$ on Si was observed which complicated the study. Where it was studied it appeared to always be surface reaction rate dependent and possibly involves the same rate limiting mechanism as low temperature growth, *i.e.*, $SiCl_4$ adsorption. The morphologies appear to be explainable from the kinetics. A suggested next step is to identify all of the reactants and products.

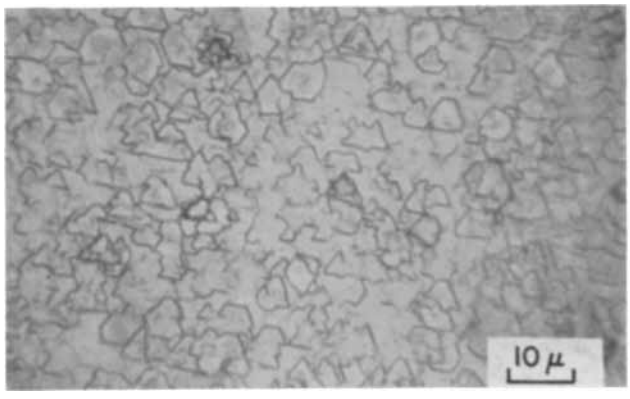

Fig. 9. Etched slice: slice was etched in 2% $SiCl_4$ + He at 1050°C and 0.6 liter/min in the vertical reactor.

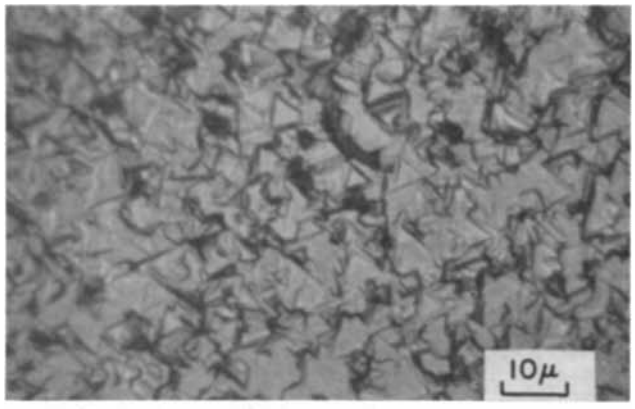

Fig. 10. Deposited slice. Slice was deposited from $SiCl_4$ + H_2 under the same conditions as the slice of Fig. 9.

Acknowledgments

It is a pleasure to acknowledge the help of colleagues at Texas Instruments, especially helpful discussions with J. Fischer and J. Short. Thanks go to Ervin Duncan for data taking and Fred Kennedy for quartz work. Discussions with and suggestions from W. Rice, S. Craig, and W. R. Runyan are also appreciated.

Manuscript received June 28, 1962. This paper was prepared for delivery before the Los Angeles Meeting, May 6-10, 1962. A partial account of this work was reported previously before the American Physical Society, *Bull. APS Series II*, **7**, 2, 115 (1962).

Any discussion of this paper will appear in a Discussion Section to be published in the June 1963 JOURNAL.

REFERENCES

1. G. Teal *et al.*, *J. Appl. Phys.*, **17**, 879 (1946).
2. R. C. Sangater *et al.*, *This Journal*, **104**, 317 (1957).
3. H. C. Theuerer, *ibid.*, **108**, 649 (1961).
4. A. Mark, *ibid.*, **108**, 880 (1961).
5. C. C. Allen and E. G. Bylander, *Proc. 1961 AIME Conf. Metallurgy Semiconductor Material.* To be published.
6. A. J. Barry, Down-Corning Corp., Private communication. *See also* R. Schwarz and R. Thiel, *Z. anorg u. allgem Chem.*, **235**, 247 (1938).
7. G. A. Kurov, *Sov. Phys., Solid State*, **3**, 1512 (1962).
8. See for example, A. van Hook, "Crystallization," p. 22, Rheinhold Publishing Corp., New York (1962).
9. S. S. Brenner, *Acta Met*, **7**, 519 (1959).
10. See for example, F. L. Walker, Jr., *et al.*, in "Advances in Catalysis," Vol. 11, p. 171, Academic Press, New York (1959).

Aluminum Nitride Containers for the Synthesis of GaAs

G. Long and L. M. Foster

Alcoa Research Laboratories, Physical Chemistry Division,
Aluminum Company of America, New Kensington, Pennsylvania

ABSTRACT

High-purity aluminum nitride refractory ware has been produced for use as containers in the synthesis of semiconductor gallium arsenide. Use of these containers essentially eliminates contamination of the GaAs with silicon, as is usually encountered when the synthesis is carried out in quartz. The principal problem encountered in the use of this material is wetting by the molten gallium and GaAs, which results in sticking of the solidified ingot. This problem is circumvented if synthesis is carried out in crucibles from which the charge is subsequently drawn by Czochralski techniques. Room temperature mobilities of 7000-8000 cm^2/volt-sec have been reported in GaAs synthesized in these crucibles.

Progress in gallium arsenide semiconductor technology has been disappointing in some areas, and a number of the desirable characteristics that were early predicted for this material have not been fully realized. In general, electron mobilities, although frequently obtainable at sufficiently high levels for some applications, could not be obtained consistently and correlated poorly with known impurity levels. Minority carrier lifetime has been several orders of magnitude below that determined by radiative recombination. Whereas this has had other tentative explanations, it has also been suspected of originating with unidentified impurities.

Gallium arsenide synthesis is generally carried out in quartz systems; certainly in quartz outer envelopes and, with few exceptions, in quartz boats or crucibles. Silicon almost invariably occurs in GaAs and, since it is absent in gallium and probably very low or absent in arsenic, its pickup from the synthesis system is assumed.

Cochran and Foster (1) described the nature of the attack of gallium and GaAs on quartz and demonstrated that silicon pickup is not only possible but unavoidable in the usual synthesis. That work could not treat the possible contamination by oxygen because of the absence of information on the solubility of the oxygen species, Ga_2O and SiO, in gallium and GaAs, but the possibility of oxygen pickup cannot be excluded.

Few alternative container materials can be considered. A refractory material consisting of elements from Groups III and V of the periodic table would, of course, be ideal for gallium arsenide synthesis. Boron nitride ware was an obvious early choice because of its commercial availability. However, it was found to suffer from problems attributable to the binder used in fabrication and to chalking and dusting of the surface when the binder was largely removed.

Aluminum nitride, AlN, also a III-V compound, emerges as a promising container material since it can be fabricated into refractory ware without objectionable binder material. Its suitability for this purpose was demonstrated by Blum, Weiser, and Ainslie, who reported obtaining room temperature electron mobilities from 7000 to 8000 cm^2/volt-sec consistently in GaAs synthesized in and drawn from AlN crucibles (2). The present report describes the properties of this new material, particularly as related to gallium arsenide synthesis.

Preparation of Ware

A method of preparation of AlN sintered bodies was described by Long and Foster (3). Modifications of that preparation to result in a more pure product were made. These modifications were in the nature of use of higher purity starting materials, better cleanliness throughout all operations, selection of grinding media to minimize contamination, use of diamond machining tools, etc., and will not be described in detail.

Both crucibles and boats have been evaluated in GaAs synthesis. The crucibles are 38 mm OD by 30 mm high and 33 mm OD by 26 mm high, with capacities of 25 and 16 ml, respectively. Both have 2 mm wall and bottom and a very slight taper on the side walls. The boat is 100 mm inside length by 25 mm inside width, hemicylindrical in shape, with 2 mm wall. The capacity of the boat is about 40 ml.

Articles with thinner walls could be produced, but the loss of pieces due to breakage during fabrication would be appreciable. Other shapes could be produced as long as suitable draft could be provided for removal from the mandrels on which the pieces are formed, and no re-entry surfaces are required.

Properties of AlN

Several properties determined in ref. (3) have implications in the synthesis of GaAs. Being electrically insulating, the material cannot be used as its own susceptor in heating by RF induction. Either a graphite susceptor must be employed or it is necessary to induce directly in the gallium or GaAs.

The coefficient of expansion of 5.7×10^{-6}/°C is identical to that reported by Welker and Weiss for GaAs (4). It is possible, therefore, to freeze GaAs in a crucible and remelt it without cracking the crucible, although, if coupling is directly to the

gallium arsenide, heating must be carried out with great care to avoid setting up steep temperature gradients.

The AlN ware that has been evaluated in GaAs synthesis is blue in color. Completely pure, single crystal AlN is water white. The blue color results from very carefully controlled addition of a trace of aluminum oxycarbide, Al_2OC, to the crystal. Al_2OC is also water white, but its solution in AlN is blue. The nature of the color is not known. It is obviously a color center situation since the color can be radiation bleached. The oxycarbide is isomorphous with AlN (5) and is in complete solid solution. This addition affects the nature of crystal growth during sintering, and a strong, impervious body results that cannot be obtained in pure AlN itself.[1]

It is interesting to speculate on the effect of contamination by Al_2OC on the GaAs crystal. Although an oversimplification, Al_2OC can be regarded as resulting from two nitrogen atoms in the AlN lattice being replaced by one oxygen (—2 charge) and one carbon (—4 charge). The average charge is thus —3. The average radius (carbon = 2.6Å and oxygen = 1.4Å) is just that of nitrogen (2.0Å) in AlN, and the substitution occurs with very little parameter shift. The oxygen and carbon thus are an internally compensated pair that should contribute neither carriers nor scattering centers to the crystal. This view is supported by the insensitivity of the electrical conductivity of AlN single crystals to their Al_2OC content.

Conceivably this favorable situation might exist as well in GaAs that picks up traces of oxygen and carbon in equal atomic amounts from the Al_2OC in the refractory.

Chemical Stability

Aluminum nitride is completely stable in contact with graphite to very high temperatures, and outer graphite susceptor crucibles have been employed. It is also stable in contact with tungsten and molybdenum up to about 1800°C, but the use of these materials in GaAs synthesis systems presents other problems.

Highly sintered AlN is very stable in almost all chemical environments at room temperature. It is insoluble in acids and bases and shows no evidence of hydrolysis in water over extended times. Nevertheless, since there is always some inherent porosity in a sintered body, cleaning in aqueous media should be strictly avoided if the article is intended for use in semiconductor synthesis.

Sintered aluminum nitride begins to react with chlorine at about 600°-700°C to form nitrogen and aluminum chloride. This treatment should not contaminate the AlN since aluminum chloride is volatile. A chalkiness develops on the surface during this treatment, however, that could interfere with crystal pulling, and in general, such cleaning treatments should be avoided.

It is possible to clean small amounts of GaAs from a crucible by first pumping off the arsenic at 1000°-1100°C, then removing the gallium as $GaCl_3$ in a stream of chlorine at about 300°C. Obviously this will be a laborious operation if considerable quantities of gallium arsenide must be removed.

[1] Patent applied for.

Thermal Stability

The usefulness of aluminum nitride ware in GaAs synthesis is contingent on a high stability at the synthesis temperature. Previous thermodynamic data for AlN have differed widely. For example, Neugebauer and Margrave (6), in a survey of the literature, found values for the heat of formation ranging from —55 to —80 kcal/mole. The uncertainty of this value reflected similar uncertainties in other thermodynamic data for AlN.

The heat of formation was redetermined recently by Neugebauer and Margrave (6), and by Mah *et al.* (7), using opposite approaches. The former used the nitridation of aluminum powder to obtain —76.47 ± 0.20 kcal/mole, and the latter used combustion calorimetry to obtain —75.6 ± 0.4 kcal/mole, using aluminum nitride supplied by the authors. Mah *et al.* also obtained heat content and entropy functions, using the same material.

The calculated equilibrium nitrogen partial pressures for the reaction

$$AlN_{(c)} \rightarrow Al_{(g)} + \tfrac{1}{2} N_{2(g)}$$

are shown in Table I for the temperature range 1000°-1600°K. These are equilibrium values which will not be achieved in practice because of kinetic effects. In particular, gas-producing reactions at a surface proceed slowly if there is no intermediate liquid phase because of the difficulty in transporting heat to or from the reaction site (8). Margrave (9) studied the decomposition in vacuum of massive, sintered AlN, supplied by the authors, in the temperature range 1450°-1870°K, and found the rates to be only 2.5×10^{-8} of the thermodynamically calculated values. Thus, at 1500°K, the observed nitrogen partial pressure would be about 2.5×10^{-7} mm instead of the equilibrium value of 1×10^{-4} mm. Moreover, vaporization should be even further suppressed in an atmosphere of arsenic.

Purity of Sintered AlN

Very pure single crystals of AlN have been produced, usually as accidental growths in high-temperature furnaces in which AlN was being employed. In high-pressure bomb reactions between aluminum and nitrogen gas, AlN can be prepared whose purity is presumably determined entirely by the purity of the reactants. Experience has shown, however, that the purity of the final sintered shape is determined more by procedures used in grinding, milling, shaping, and sintering than by the purity of the starting materials.

Table I. Calculated equilibrium nitrogen partial pressures from decomposition of AlN

$AlN_{(c)} \rightarrow Al_{(g)} + \tfrac{1}{2}N_{2(g)}$

T, °K	N_2 pressure, mm
1000	5×10^{-12}
1200	2×10^{-8}
1400	1×10^{-5}
1500	1×10^{-4}
1600	9×10^{-4}

Sintered ware that has been evaluated in GaAs synthesis shows the following "typical" spectrographic analysis

Si	0.005-0.03 %
Mg	0.001-0.005
Cu	0.001
Ti	0.001
Fe	0.001
Ga	0.001
All others	<0.01

Preparation of a sample for analysis is made difficult by the extremely hard, abrasive nature of the material, and absence of suitable standards in an AlN matrix limits the sensitivity of detection of many elements. Consequently, the analysis is only semiquantitative and serves principally to indicate the high purity of this product. The silicon figure is probably real as it is known that there is some silicon pickup during a grinding operation.

It is significant that because of the extremely high temperature employed for sintering (2200°C), many impurities will be volatilized, and the rest must certainly be in solid solution in the crystal. It is unlikely that they could be selectively extracted by the GaAs without a corresponding pickup of aluminum. Thus, for every ppm of aluminum pickup there should be no more than 0.0003 ppm of silicon, and substantially less of the other metallic impurities.

GaAs that has been drawn from AlN crucibles is reported to contain 10-20 ppm aluminum (2). Thus, about 0.005 ppm of silicon pickup is all that would be expected from the AlN container. Higher pickup must be attributed to remaining quartz components of the apparatus. There are several possible mechanisms for transporting silicon through the vapor phase. The most likely appears to be through the action of water vapor. Water vapor will react with gallium or gallium arsenide to produce hydrogen and Ga_2O. The reaction can reverse at the quartz surface to deposit gallium and regenerate the water. The gallium can subsequently reduce SiO_2 to volatile SiO, which can condense back into the ingot (1). Great care in baking out all of the quartz parts of a synthesis system is recommended, even when the synthesis itself is not carried out in quartz. Moreover, if a graphite susceptor is employed, and this rests on a quartz support, the reaction

$$SiO_2 + C \rightarrow SiO + CO$$

can occur to also generate SiO, which can dissolve in the ingot.

GaAs Synthesis in AlN Ware

The electrical properties of GaAs synthesized in and drawn from AlN crucibles have recently been described by Blum (2). Effort in the authors' laboratory has been directed toward the general aspects of the physical and chemical stability of AlN in the synthesis environment.

The AlN ware is not completely dense. How much of the porosity communicates with the surface is not known. It has been a practice to outgas the containers at 750°C overnight in a quartz vacuum system with oil diffusion pumping and a liquid nitrogen trap. A noticeable improvement in vacuum is observed over this pumping period, and 10^{-6} mm pressure is ultimately attained. The nature of the gases that are evolved during this period has not been established. If the crucibles are not to be used in synthesis immediately, vacuum is broken with helium and the articles are hermetically sealed in polyethylene containers. They are stored over a desiccant until required. It has been observed that only superficial outgassing of the crucible is subsequently required in the synthesis system.

The stability of AlN toward gallium and arsenic could have been predicted from thermodynamic considerations. Arsenic does not form a nitride, and GaN loses its stability at low temperatures (10).

In one experiment, ALCOA Ga-6 grade gallium (99.9999+%) was heated by induction in an AlN crucible for 1 hr at about 1200°C in a few centimeters of helium pressure to suppress volatilization of the gallium. The residual resistivity ratio of the gallium

$$\frac{\rho 4.2°K}{\rho 298°K}$$

between helium and room temperature was determined. The ratios were $2.6 \times 10^{-5} \pm 0.1 \times 10^{-5}$ before heating and $2.7 \times 10^{-5} \pm 0.1 \times 10^{-5}$ after heating. From previous calibration of the contribution to the resistance at 4.2°K of known amounts of impurities (11) it is estimated that less than 0.1 ppm total impurities was picked up by the gallium.

Most of the gallium was poured out of the crucible, and the remainder was volatilized as $GaCl_3$ in a stream of chlorine at 300°C. The crucible regained its original appearance and showed no weight change within the sensitivity of the analytical balance. AlN similarly shows no change in appearance or weight when heated in an atmosphere of arsenic vapor at 1250°C.

The principal problem that has been encountered in the synthesis of GaAs in AlN is partial or complete wetting of the container by the molten GaAs, and subsequent sticking of the ingot. For this reason evaluation of AlN as crucible material in Czochralski crystal pulling, rather than boat synthesis, has been encouraged. Here, sticking presents no problem other than possibly precluding the reuse of crucibles. Actually, a crucible can be reused if most of the previous charge is pulled out and care is exercised in remelting the remaining heel.

GaAs can be removed from AlN boats and, with somewhat greater difficulty from crucibles, by freezing it rapidly in 1 atm of arsenic. This is slightly in excess of the equilibrium arsenic pressure at the freezing point, and some of the excess dissolved arsenic comes out of solution as small bubbles at the interface between the charge and the container. These tend to release the GaAs from the wall so that it will fall out. It is not possible, of course, to obtain large crystal ingots in this way, but it does offer a possible procedure for preparing GaAs in a boat for subsequent crystal pulling, or for removing

the heel from a crucible so that the latter can be reused.

The manner in which GaAs adheres to AlN containers is not known. There is undoubtedly considerable mechanical keying in of the GaAs to the surface, which cannot be produced completely smooth. In addition, however, both gallium metal and molten GaAs appear to wet the AlN surface truly at the synthesis temperature. In the case of other III-V compounds it has been observed that there is a sharp maximum in viscosity at the stoichiometric composition just above the melting point (12). It would be expected that there would also be a maximum in the surface tension. Similar measurements have not been made on GaAs, but it is expected that it follows the same pattern. It would seem, therefore, that if stoichiometric gallium arsenide could be melted carefully in aluminum nitride, or if a molten stoichiometric charge could be poured into an AlN container, the wetting and sticking problem might be minimized.

This has been confirmed to a degree. Synthesis has been carried out in a double boat arrangement where one boat was inverted to serve as a cover for another similar boat. After outgassing of the boats, gallium was introduced into the bottom boat through a 1-mm bore Teflon tube inserted through a hole in the end formed by a depression in the ends of the boats at the parting line. These same holes permit access of the arsenic vapor to the gallium. The usual horizontal synthesis was carried out, maintaining an arsenic boiler at 605°C, then the GaAs was allowed to solidify in the boat in which it was produced. When cold, the tube was rotated about 180° so that the cover boat was on the bottom. The charge was then carefully reheated in the arsenic atmosphere so that it melted out of the top boat and drained into the bottom. It was then carefully solidified through a gradient freeze technique. There was a greater tendency for the ingot thus produced to free itself from the boat than in cases where the synthesis and freezing were carried out entirely in a single boat. Nevertheless, there was still sufficient sticking to preclude the formation of single crystals, and, at best, this procedure might again serve only as a means of recovering the GaAs from a boat for subsequent crystal pulling.

It has been observed that the tendency to wet and stick to an AlN boat is very temperature sensitive, and actual soaking of the GaAs into the aluminum nitride structure has been observed when it is considerably superheated. Synthesis as close to the melting point as possible is recommended, but even then complete freedom from sticking cannot be assured. Other aspects of this problem are being investigated.

Manuscript received May 15, 1962; revised manuscript received July 17, 1962. This paper was prepared for delivery before the Los Angeles Meeting, May 6-10, 1962.

Any discussion of this paper will appear in a Discussion Section to be published in the June 1963 JOURNAL.

REFERENCES

1. C. N. Cochran and L. M. Foster, *This Journal*, **109**, 149 (1962).
2. S. E. Blum, K. Weiser, and N. G. Ainslie, Paper presented at The Electrochemical Society Meeting, May, 1962, Los Angeles.
3. G. Long and L. M. Foster, *J. Am. Ceram. Soc.*, **42**, 53 (1959).
4. "Solid State Physics," F. Seitz and D. Turnbull, Editors, Chapter Group III-Group V Compounds by H. Welker and H. Weiss, Academic Press, New York (1955).
5. L. M. Foster, G. Long, and M. S. Hunter, *J. Am. Ceram. Soc.*, **39**, 1 (1956).
6. C. A. Neugebauer and J. L. Margrave, *Z. anorg. u. allgem. Chem.*, **290**, 82 (1957).
7. A. D. Mah, E. G. King, W. W. Weller, and A. U. Christensen, "Thermodynamic Properties of Aluminum Nitride," U. S. Bureau of Mines, R. I. 5716 (1961).
8. L. M. Foster, *J. Am. Chem. Soc.*, **72**, 1902 (1950).
9. J. L. Margrave, Private communication.
10. M. R. Lorenz and B. B. Binkowski, General Electric Company Research Lab. Report No. 61-RL-2799G, August (1961).
11. R. A. Kramer and L. M. Foster, "Compound Semiconductors," McGraw-Hill Book Co., New York, Chapter on Residual Resistivity. (In Press.)
12. V. M. Glazov, *Izvest. Akad. Naak. SSSR, Met i Topl*, No. 5, 190 (1960).

The Dehydration of Ammonium Metatungstate

R. W. Mooney, V. Chiola, C. W. W. Hoffman, and C. D. Vanderpool

Chemical and Metallurgical Division, Sylvania Electric Products Inc., Towanda, Pennsylvania

ABSTRACT

Ammonium metatungstate was allowed to reach equilibrium at temperatures between 55° and 450°C. The products were characterized by chemical analyses, thermogravimetric analyses, and x-ray diffraction patterns. The data confirm the association of one constitutional water molecule with the metatungstate ion. The x-ray diffraction patterns of ammonium metatungstate varied with the water content.

The isomorphism of the metatungstates and the heteropoly tungstates was first suggested by Copaux (1). The determination of the structure of the heteropoly anion, $PW_{12}O_{40}^{3-}$, by Keggin (2-4) provided a basis for more definitive studies, and he suggested that metatungstates contained $H_2W_{12}O_{40}^{6-}$ ions. Subsequent studies confirmed the isomorphism of metatungstic acid with phosphotungstic acid by the aid of x-ray powder photographs (5, 6). The central group in the metatungstates corresponding

to the PO_4 group in phosphotungstic acid was thought by Signer and Gross (5) to be an H_2O_4 group. Jahr (7) contested their hypothesis and instead claimed that the WO_6 octahedra were grouped about an empty hole.

More recent work by Schott and Harzdorf (8) on the metatungstates of lithium, sodium, and potassium confirmed Keggin's hypothesis that two hydrogen atoms were associated with each metatungstate ion, thus favoring the $H_2W_{12}O_{40}^{6-}$ ion rather than the $W_{12}O_{40}^{8-}$ or $(OH_4W_{12}O_{40})^{6-}$ ions. In contrast to the dehydration studies of Schott and Harzdorf who found no distinct chemical hydrates in their metatungstates, Kolli, Pirogova, and Spitsyn (9) in a study of the dehydration of sodium metatungstate reported the existence of hydrates containing 10, 4.5, 2.5, 2, 1.5, 1, and 0.2-0.3 moles water per mole of the anhydrous salt.

The present study of ammonium metatungstate was undertaken to compare the dehydration of this salt to the previous studies of dehydration of alkali metal metatungstates and to determine whether the water associated with ammonium metatungstate at various temperatures was in the form of discreet hydrates or was zeolitic.

Experimental

Preparation.—Ammonium metatungstate was prepared by the digestion of hydrated tungstic oxide with ammonium hydroxide solution. A slurry of 908g of tungstic acid in 2.4 liters of deionized water was agitated and heated to 80°-90°C. While maintaining temperature, 105 ml of reagent grade ammonium hydroxide solution (28%) was added during a period of 1 hr. Digestion was continued for 2 hr, and the mother liquor, ammonium metatungstate solution, was separated by filtration. The yield of ammonium metatungstate crystals was 50-55% of theoretical based on WO_3. The crystalline product was dried at approximately 35°C for 4 hr to get the starting material required for equilibration studies.

Equilibration.—The ammonium metatungstate samples were equilibrated at various temperatures by placing them in an Abderhalden drying apparatus, Fig. 1, for periods of approximately 24, 72, and 128 hr. The temperature of equilibration ranged from 55° to 200°C and was characteristic of the liquid used in the distilling flask of the apparatus. The specific liquids used and the temperatures obtained in the drying chamber of the apparatus were acetone (55°), ethyl alcohol (75°), water (91°), acetic acid (115°), 2-ethoxyethyl acetate (150°), and 2,2-diethoxy ethyl acetate (200°). Differences between the equilibration temperatures and the boiling points of the various liquids as given in the literature were attributed to heat losses in the apparatus. The drying chamber was wrapped with insulating tape to reduce heat losses at temperatures above 100°C. Equilibration temperatures were measured by a thermometer placed in the inner tube of the drying chamber.

For equilibration, two silica boats, 100 x 18 x 11 mm high, and containing 10g of ammonium metatungstate each, were placed inside the inner tube

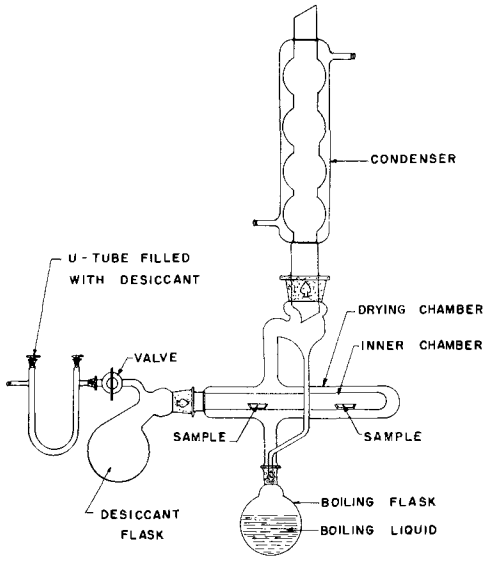

Fig. 1. Abderhalden drying apparatus used for the equilibration experiments.

of the drying chamber. Vapors from the boiling liquid in the distilling flask heated the drying chamber and sample to constant temperature. The moisture released from ammonium metatungstate was absorbed by calcium sulfate (Drierite) drying agent contained in the desiccant flask. The drying chamber and the desiccant flask were open to the atmosphere through a U-tube which also contained drying agent.

From 200° to 450°C the samples were equilibrated at 50°C intervals for 24 hr in a Stanton thermobalance. The weight loss after 24 hr was negligible.

The equilibrated samples were stored in sealed glass tubes until measurements could be made.

Analyses.—To determine the amount of tungsten, the tungstates were ignited at 800°C and the residue weighed as WO_3. Ammonia was determined by the Kjeldahl distillation method. The per cent water was obtained by difference. Thermogravimetric analyses were made on a Stanton thermogravimetric balance at a heating rate of 3°C/min. The sample was contained in a covered quartz crucible in order to employ the "self-generated atmosphere" technique (10) to emphasize changes in rate of weight loss.

The x-ray diffraction patterns were taken on a Philips Norelco unit with a Geiger-counter diffractometer using nickel-filtered CuKα radiation of 1.542Å wavelength. Sample preparations and intensity measurements followed the procedure adopted by the National Bureau of Standards (11). The intensity values of each pattern were measured as peak height above background and expressed as percentages of the strongest line.

Results and Discussion

Crystals formed at room temperature.—Large transparent crystals several centimeters in size were grown from saturated solution. After removal from solution, the crystals lost water rapidly and

Table I. Characteristic low angle diffraction lines of the ammonium metatungstates

	d(A)	I		d(A)	I
AMT 22-24			AMT-1		
	10.4	100		12.5	10
	9.0	20		9.1	100
AMT 12-15				8.8	70
	10.7	10		8.6	60
	9.8	40	AMT-0		
	9.3	100		8.7	100
	8.6	10		5.0	50
AMT 2-6			X		
	12.8	25		6.3	70
	9.3	100		3.82	80
	8.9	95		3.66	25
	8.5	30		3.28	20
				3.17	100

became translucent. Therefore, x-ray and thermogravimetric analyses (TGA) were carried out as soon as possible after removal. The crystals were surface-dried with filter paper for the TGA measurements since any heating changed the water content and structure. The water content varied from 22 to 24 waters of hydration per mole of $(NH_4)_6H_2W_{12}O_{40}$. In view of the rapid dehydration the equilibrium form in saturated solution is believed to contain 24 waters of hydration as represented by the formula $(NH_4)_6H_2W_{12}O_{40}\cdot 24H_2O$. Reliable NH_3 analyses could not be obtained on this form. Characteristic low angle x-ray diffraction lines of the 24-hydrate designated AMT22-24, and the other less hydrated metatungstates are given in Table I.

When the evaporation was continued until all of the ammonium metatungstate had crystallized from solution, the product was reduced in water content to between 12.6 and 14.3 waters of hydration by air drying. A typical weight loss curve on this product is shown in Fig. 2. Chemical analyses are given in Table II.

All of the thermogravimetric analysis curves showed a temperature region of little or no weight loss corresponding to the formation of the anhydrous $(NH_4)_6H_2W_{12}O_{40}$. In addition, certain runs including the data of Fig. 2 showed an inflexion point in the curve at a weight corresponding approximately to $(NH_4)_6H_2W_{12}O_{40}\cdot H_2O$. The weight loss above 350°C was relatively slow.

Equilibration results.—The results of equilibration experiments with samples of AMT 12-15 in the Abderhalden drying apparatus are tabulated in Table III. The moles of water were calculated from the thermogravimetric data. A change in structure to the AMT 2-6 form was observed at temperatures from 55° to 91°C with water contents which varied from 1.8 to 5.6 moles of H_2O per mole of $(NH_4)_6H_2W_{12}O_{40}$. A fourth pattern, designated AMT-1, was found on the sample equilibrated at 75°C for 168 hr, which had a H_2O content of 1.1 moles. This latter form is undoubtedly the monohydrate, $(NH_4)_6H_2W_{12}O_{40}\cdot H_2O$ whose presence was indicated by the inflexion point on several TGA curves (see, for example, Fig. 2).

Table II. Quantitative analyses of ammonium metatungstate

	% WO_3	% NH_3	% H_2O
Theoretical for $(NH_4)_6H_2W_{12}O_{40}\cdot 14H_2O$	86.71	3.18	10.11
Found	86.51	3.20	10.29

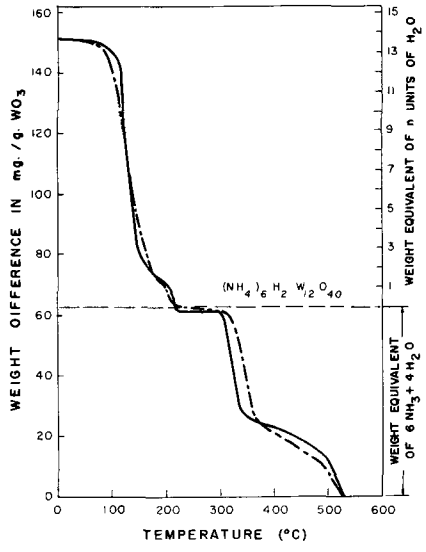

Fig. 2. Thermogravimetric analyses of ammonium metatungstate: solid line, covered crucible technique; dotted line, uncovered crucible.

The sample equilibrated at 91°C for 120 hr and all samples equilibrated at higher temperatures (115°, 150°, and 200°C) in the Abderhalden apparatus were essentially nonhydrated and displayed a common pattern, designated AMT-0, which is characteristic of unhydrated ammonium metatungstate, *i.e.*, $(NH_4)_6H_2W_{12}O_{40}$. The wide region of temperature stability of this unhydrated form is in agreement with the observance of a region of negligible weight loss on the TGA curves at a weight corresponding to the compound $(NH_4)_6H_2W_{12}O_{40}$. This AMT-0 form was very easily hydrated as evidenced by the fact that, if left in the normally humid atmosphere of the laboratory, it hydrated at room temperature changing from AMT-0 to AMT-1 and finally to AMT 2-6, as shown by several series of x-ray experiments.

Above 250°C anhydrous $(NH_4)_6H_2W_{12}O_{40}$ decomposed rapidly to a material of variable composition with respect to both water and ammonia. The x-ray diffraction pattern of this material is designated as X, since it could not be identified as any of the known oxides of tungsten. The pattern was identical to that of material formed at high temperatures from ammonium paratungstates. Finally, at 450°C ammonium metatungstate was completely transformed to tungsten trioxide.

The results are readily seen by a plot of NH_3 and total H_2O content *vs.* temperature of equilibration (Fig. 3). The NH_3 contents were essentially independent of time of equilibration, and therefore average values were calculated (Table III) and used (Fig. 3). On the other hand, the H_2O contents were dependent on time indicating that none of the data represent true equilibrium. It is apparent that from room temperature up to 250°C the NH_3 content is essentially constant at $6NH_3$ per $12WO_3$, de-

Table III. Equilibration analyses and identification

Equilibration Temp, °C	Time, hr	Analyses % WO_3	% NH_3	Calculated moles NH_3 per $12WO_3$	Moles H_2O over anhydrous per $12WO_3$	X-ray identification
55	25	90.72	3.19	5.75	5.6	AMT 2-6
55	64	92.34	3.37	5.96	3.1	AMT 2-6
55	123	92.49	3.33	5.91	2.5	AMT 2-6
				Avg. 5.86		
75	24	92.39	3.32	5.87	2.9	AMT 2-6
75	120	93.07	3.32	5.83	1.8	AMT 2-6
75	168	93.30	3.34	5.85	1.1	AMT-1
				Avg. 5.85		
91	24	93.10	3.36	5.90	1.8	AMT 2-6
91	65	93.10	3.33	5.85	1.8	AMT 2-6
91	120	93.47	3.44	6.01	0.8	AMT-0
				Avg. 5.92		
115	24	93.73	3.42	5.96	0.8	AMT-0
115	72	94.08	3.36	5.84	0.2	AMT-0
115	128	94.03	3.37	5.86	0.1	AMT-0
				Avg. 5.89		
150	24	93.53	3.36	5.87	0.9	AMT-0
150	72	94.04	3.36	5.84	0	AMT-0
150	128	94.09	3.40	5.91	—0.2	AMT-0
				Avg. 5.87		
200	24	94.23	3.15	5.46	—0.1	AMT-0
200	72	94.14	3.27	5.68	—0.4	AMT-0
200	127	94.27	3.25	5.63	—0.3	AMT-0
			Avg. (last 2)	5.66		
					Total Moles H_2O	
200	24	93.99	3.27	5.69	4.1	AMT-0
250	24	94.13	3.29	5.71	3.7	AMT-0
300	24	98.03	1.27	2.12	1.1	X
350	24	98.45	0.95	1.58	0.9	X
400	24	99.04	0.51	0.84	0.7	X
450	24	100.00	0	0	0	WO_3

creasing only slightly with temperature. The water content, however, decreases steadily with increasing temperature approaching a value of $4H_2O$ per $12WO_3$, which is characteristic of the anhydrous metatungstate $(NH_4)_6H_2W_{12}O_{40}$. Since only three waters are contributed from the six ammonium ions and oxygen, the fourth must be associated with the metatungstate ion itself. Thus the association of two hydrogens with the metatungstate ion is found with the ammonium metatungstates as well as the alkali metal metatungstates (8). A further corroboration of this conclusion and an indication of the tenacity with which that one water is bound are indicated by the fact that when the anhydrous form starts to decompose above 250°C it still retains the one molecule of water up to 400°C until WO_3 is formed.

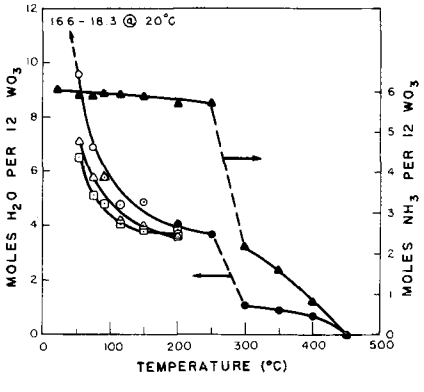

Fig. 3. Water and ammonia content of ammonium metatungstate as a function of equilibration temperature. Equilibrated in Abderhalden apparatus for 24 hr (○), 72 hr (△) and 128 hr (□); equilibrated 24 hr on Stanton thermobalance (●); average ammonia values (▲).

The analytical results as illustrated by Fig. 3 suggest that the water content of the hydrated metatungstates is zeolitic, *i.e.*, the amount of water associated with the structure varies continuously with temperature and relative humidity. Such a finding would be in agreement with Schott and Harzdorf (8). However, evidence for a lattice transition in the anion at 75°C, postulated by them was not observed from the water content *vs.* temperature curve (Fig. 3), although the x-ray data of Table III indicate the possibility of a transition from AMT 2-6 to AMT-1 at that temperature.

These results suggest a fixed anionic structure into which water molecules may be absorbed continuously depending on the relative vapor pressure. Such a model is consistent with the findings of Spitsyn and co-workers (12) who reported no change in the structure of the metatungstate ion or in the coordination of water in a study of the infrared absorption spectra of sodium metatungstates.

The model suggesting zeolitic water is not consistent, however, with the detection of specific x-ray diffraction patterns as a function of water content as found herein or with the existence of specific hydrates of sodium metatungstates reported in the earlier paper (9) by Spitsyn and co-workers. It is suggested that different hydrates of ammonium metatungstate exist and are readily transformed into one another depending on the relative water vapor pressure. The transitions between hydrates proceed so readily, however, that the water content varies continuously with temperature or relative humidity behaving in a manner suggestive of zeolitic water.

Manuscript received March 26, 1962; revised manuscript received Aug. 8, 1962.

Any discussion of this paper will appear in a Discussion Section to be published in the June 1963 JOURNAL.

REFERENCES

1. H. Copaux, *Ann. chim. phys.*, **17**, 245 (1909).
2. J. F. Keggin, *Nature*, **131**, 908 (1933).
3. J. F. Keggin, *ibid.*, **132**, 351 (1933).
4. J. F. Keggin, *Proc. Roy. Soc. (London)*, **144A**, 75 (1934).
5. R. Signer and H. Gross, *Helv. chim. Acta*, **17**, 1076 (1934).
6. J. W. Illingworth and J. F. Keggin, *J. Chem. Soc.*, **1935**, 575.
7. K. F. Jahr, *Naturwiss.*, **29**, 528 (1941).
8. G. Schott and C. Harzdorf, *Z. anorg. u. allgem. Chem.*, **288**, 15 (1956).
9. I. D. Kolli, G. N. Pirogova, and V. I. Spitsyn, *Zhur. Neorg. Khim.*, **1**, 470 (1956).
10. P. D. Garn and J. E. Kessler, *Anal. Chem.*, **32**, 1563 (1960).
11. H. E. Swanson and E. Tatge, *Natl. Bur. Standards (U.S.) Cir. 539* (1953).
12. A. A. Babushkin, G. V. Yukhnevich, Yu. F. Berezkina, and V. I. Spitsyn, *Zhur. Neorg. Khim.*, **4**, 823 (1959).

Theoretical Analysis of Current Distribution in Porous Electrodes

John S. Newman and Charles W. Tobias

Department of Chemical Engineering, University of California, Berkeley, California

ABSTRACT

General equations describing the behavior of porous electrodes are developed. These equations are used to determine the initial and the steady-state conditions in one-dimensional porous electrodes of uniform geometry and polarization parameters. In particular, it is shown that the current and reaction distributions in the depth of the electrode are strongly influenced by the type of activation polarization and by mass transport of the reacting ionic species, in addition to the effective conductivities of the two phases. It is found that a linear approximation to a Tafel curve leads to an inadequate description of actual behavior when the reaction is distributed nonuniformly in the depth of the electrode.

A simple electrode has a well-defined interface between the metal electrode and the adjacent electrolytic solution, and the electrode reaction is restricted to this interface, which is often a plane surface. A large class of industrially important electrochemical reactions, however, involves the use of electrodes consisting of porous matrices of a single reactive electronic conductor, or mixtures of solids which include essentially nonconducting, reactive materials in addition to inactive electronic conductors. An electrolytic solution penetrates the void spaces of the porous matrix. This paper is restricted to cases where this penetration by electrolyte is complete or nearly complete. Thus the results are not directly applicable when the penetration by electrolyte is deliberately kept partial, as in most fuel-cell electrodes where the electrode reaction occurs mainly at the three-phase contact between the solid electrode, the electrolyte, and a gaseous reactant.

Relative to solid electrodes, porous electrodes provide much larger contact areas per unit volume between electrolyte, solid (or gaseous) reactant, and electronic conductor. Their use is widespread in primary and secondary batteries and in continuous-feed galvanic cells. At any given time, there will be a large range of reaction rates within the pores. The distribution of these rates will depend on physical structure, conductivity of the matrix and of the electrolyte, and on parameters characterizing overpotential phenomena (1). In galvanic cells this rate distribution directly influences the net power available for external use. A rational understanding of the processes that determine the distribution of reaction rates within porous electrodes is therefore of prime importance, basic to any design or optimization of electrochemical conversion or storage devices.

In order to perform a theoretical analysis of such a complex problem, it is necessary to establish a model which accounts for the essential features of an actual electrode without going into exact geometric detail. Further, the model should be described by parameters which can be obtained by suitably simply physical measurements. For example, a porous material of arbitrary, random structure can be characterized by its porosity, average surface area per unit volume, volume-average resistivity, etc. Similarly, one can use a volume-average resistivity to describe the electrolytic phase in the voids. A suitable model would involve averages of various variables over a region of the electrode small with respect to the over-all dimensions but large compared to the pore structure. In such a model, rates of reactions in the pores will have to be defined in terms of transferred current per unit volume.

Analyses of this type have been developed by Euler and Nonnenmacher (1) and by Ksenzhek and Stender (2). Euler and Nonnenmacher considered the case of a porous electrode flooded with electrolyte and backed by a solid metallic conductor of negligible resistivity (Fig. 1). Solving the equations for a one-dimensional field, uniform concentration, and an assumed linear polarization, these authors showed that, depending on the relative conductivities of the two phases, the current tends to

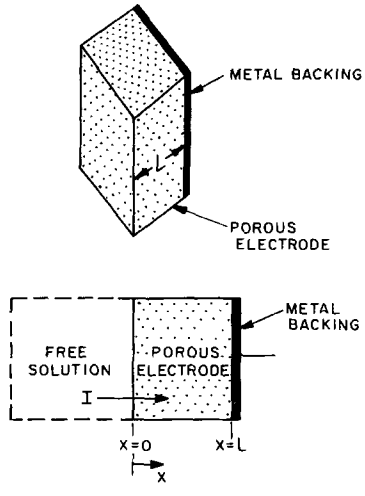

Fig. 1. One-dimensional porous electrode

pass from one phase to the other preferentially near the electrolyte-electrode interface or the electrode-metal backing interface. Although these conclusions represent a significant step forward in our understanding the phenomena occurring in porous electrodes, the model does not adequately resemble real systems. Except in regions of low overpotential, linear polarization is an unrealistic assumption if there is a large range of current densities, that is, if the reaction distribution is quite nonuniform, and, furthermore, concentrations of reacting species may not be regarded as constant except at the instant of closing the circuit.

We next present a general model of porous electrodes which reduces to that of Euler and Nonnenmacher as a special case. However, the subsequent application of the general model takes into account Tafel-type polarization and incorporates concentration variations caused by the charge transfer across phase boundaries.

Macroscopic Description of Porous Electrodes

In this macroscopic treatment of porous electrodes, we shall disregard the actual geometric detail of the pores. The model is an extension of the concepts of conventional electrochemical systems, specifically those of transport phenomena in electrolytic solutions and of the kinetics of electrode reactions. Thus we can define a potential in the solid matrix material, Φ_1, and another in the pore-filling electrolyte, Φ_2. Similarly, two current densities may be defined: $\bar{i}_1$ referring to the current density in the matrix phase and $\bar{i}_2$ to the one in the pore-electrolyte. These current densities will be referred to the projected area of the electrode, rather than to the areas of the individual phases. The flux $\bar{N}_i$ and the concentration C_i of a species will also be expressed relative to this superficial area and to the over-all unit volume of the electrode, respectively. The quantities enumerated are assumed to be continuous functions of time and space coordinates.

The set of equations describing the changes occurring during the passage of current in the porous electrode are as follows:[1]

We apply Ohm's law to the matrix

$$\bar{i}_1 = -\sigma \nabla \Phi_1 \qquad [1]$$

The flux of a mobile ionic species is due to migration, diffusion, and convection

$$\bar{N}_i = -z_i U_i e C_i \nabla \Phi_2 - D_i \nabla C_i + \bar{v} C_i \qquad [2]$$

The fluxes of charged species, when appropriately summed, yield an expression for the current density in the pores

$$\bar{i}_2 = \mathbf{F} \sum_i z_i \bar{N}_i \qquad [3]$$

For expressing the electrochemical reaction occurring in the electrode, we adopt the convention

$$\sum_i s_i M_i^{z_i} \rightarrow n e^- \qquad [4]$$

where s_i may be called the stoichiometric coefficient of species i. Then the conservation law for species i becomes

$$\frac{\partial C_i}{\partial t} = -\nabla \cdot \bar{N}_i + \frac{s_i}{n\mathbf{F}} \nabla \cdot \bar{i}_1 \qquad [5]$$

This equation states that the concentration can change at a point because the species moves away from the point (divergence of the flux $\bar{N}_i$) or because the species is involved in the electrochemical reaction (since $\nabla \cdot \bar{i}_1$ is proportional to the rate of the electrode reaction). We make the reasonable assumption of electroneutrality

$$\sum_i z_i C_i = 0 \qquad [6]$$

The polarization equation

$$\nabla \cdot \bar{i}_1 = af(\Phi_1 - \Phi_2, C_i) \qquad [7]$$

is necessary to express the dependence of the local rate of reaction on the various concentrations and on the potential jump at the matrix-solution interface. This equation, as written, really doesn't help us very much. The appropriate analytic expression depends on the particular chemical system and reaction mechanism involved, and the reader is referred to the specialized literature (3) for details. Since our purpose is not to consider the problems of electrode kinetics in detail, we seek a specific polarization equation which indicates expected behavior and is sufficiently general to cover many cases of practical interest. As an example, we may write

$$\nabla \cdot \bar{i}_1 = a i_o \left[\frac{C_1}{C_1^\circ} \exp\left\{ -\frac{\alpha n \mathbf{F}}{RT} (\Phi_1 - \Phi_2) \right\} - \frac{C_2}{C_2^\circ} \exp\left\{ \frac{(1-\alpha) n \mathbf{F}}{RT} (\Phi_1 - \Phi_2) \right\} \right] \qquad [8]$$

for an "oxidation-reduction" reaction. Here, the forward and reverse reactions are first order with respect to the reactant and product and depend exponentially on the matrix-solution potential jump.

Finally, the equation of conservation of charge is

$$\nabla \cdot \bar{i}_1 + \nabla \cdot \bar{i}_2 = 0 \qquad [9]$$

It should be noted that Eq. [1] to [7] are sufficient to describe the porous electrode, if $\bar{v}$ is specified. Equation [9] can be derived from the preceding equations. However, one may occasionally wish to abandon the assumption of electroneutrality, in which case Eq. [9] should be retained.

Application to One-Dimensional Porous Electrodes

In the following analysis, we consider a one-dimensional porous electrode (Fig. 1), bounded on one side by a metal "electron collector" and on the other by a free electrolytic solution. By "one dimensional" we mean that quantities such as potentials, current densities, and concentrations vary only with depth within the electrode and not with lateral position. This is a worthwhile simplification since it yields results indicative of the general behavior of porous electrodes and since many practical porous electrodes have this geometry.

[1] These equations have been written in vector notation for generality and for brevity.

We shall assume that the shape characteristics and volume percentage of pores are uniform throughout the thickness of the electrode and that the fluid velocity $\bar{v}$ is zero in the electrode. Furthermore, the problems will be posed in such a way that time does not enter in an explicit manner.

Concentration-Independent Polarization Equation

Ordinarily the concentration of species in the pore electrolyte will depend on the position, x, in the electrode. Let us first consider the conditions at the instant of closing the circuit so that the concentrations are uniform and have not had time to change. Then, Eq. [2] becomes

$$\bar{i}_2 = -\kappa \nabla \Phi_2$$

where

$$\kappa = \mathbf{F}e \sum_i z_i^2 U_i C_i$$

is the effective conductivity of the pore electrolyte and is constant. Since the concentrations have been assumed uniform, the polarization equation is essentially independent of concentration, and we may write the problem in one dimension as

$$i_2 = -\kappa \frac{d\Phi_2}{dx}, \quad i_1 = -\sigma \frac{d\Phi_1}{dx}, \quad \frac{di_1}{dx} + \frac{di_2}{dx} = 0, \qquad [10, 11, 12]$$

$$\frac{di_1}{dx} = af(\Phi_1 - \Phi_2) \qquad [13]$$

Here the subscript, x, for components of vector quantities has been omitted. The following boundary conditions are suggested.

At $x = 0, i_2 = I, i_1 = 0, \Phi_2 = 0.$

At $x = L, i_2 = 0.$

These state that at the electrode-solution interface the current is carried entirely by the pore electrolyte while at the metal backing, the current is carried entirely by the matrix. As an arbitrary reference of potential, we choose $\Phi_2 = 0$ at $x = 0$. Somewhere inside the electrode, between $x = 0$ and $x = L$, the current is transferred from the solution to the matrix, and the local rate of the reaction is proportional to di_1/dx.

This problem may be solved analytically for either a linear or a Tafel polarization equation. For Tafel polarization, Eq. [8] becomes in the anodic case ($I < 0$)

$$\frac{di_2}{dx} = ai_o \exp\{\beta(\Phi_1 - \Phi_2)\} \qquad [14]$$

where

$$\beta = (1-\alpha)\frac{n\mathbf{F}}{RT}$$

The cathodic case $I > 0$ can be handled in a completely analogous fashion. By integrating Eq. [12], differentiating Eq. [14], and eliminating Φ_1, Φ_2, and i_2, one obtains

$$\frac{d^2 i_1}{dx^2} = \frac{di_1}{dx}\beta\left[\frac{I}{\kappa} - i_1\left(\frac{1}{\kappa} + \frac{1}{\sigma}\right)\right] \qquad [15]$$

Upon the introduction of the quantities

$$y = \frac{x}{L}, \quad j = \frac{i_1}{I}, \quad \delta = L|I|\beta\left(\frac{1}{\kappa} + \frac{1}{\sigma}\right), \text{ and } \epsilon = \frac{L|I|\beta}{\kappa}$$

a dimensionless, nonlinear differential equation for the current is finally obtained,

$$\boxed{\frac{d^2 j}{dy^2} = \frac{dj}{dy}(\delta j - \epsilon)} \qquad [16]$$

with the boundary conditions

$$j = 0 \text{ at } y = 0 \text{ and } j = 1 \text{ at } y = 1.$$

Since the variable y does not appear in this equation, the latter can be reduced to a first-order equation by introducing

$$p = \frac{dj}{dy}, \text{ so that } \frac{d^2 j}{dy^2} = p\frac{dp}{dj}$$

Then, the first integration is straightforward, and the second integration, somewhat more involved, may be found in standard mathematical tables. The solution is

$$j = \frac{\tan(\theta y - \psi) + \tan\psi}{\tan(\theta - \psi) + \tan\psi} = \frac{2\theta}{\delta}\tan(\theta y - \psi) + \frac{\epsilon}{\delta} \qquad [17]$$

where

$$\tan\theta = \frac{2\delta\theta}{4\theta^2 - \epsilon(\delta - \epsilon)} \text{ and } \tan\psi = \frac{\epsilon}{2\theta}$$

The integration constants θ and ψ cannot be simply related to the parameters δ and ϵ but must be calculated by a trial and error procedure. For a finite current density in the electrode, $0 < \theta < \pi$.

The dimensionless reaction rate is found to be

$$\frac{dj}{dy} = \frac{2\theta^2}{\delta}\sec^2(\theta y - \psi) \qquad [18]$$

and the potential of the metal backing plate is

$$\beta\Phi_1(L) = (\delta - \epsilon)\left[\frac{\epsilon}{\delta} + \frac{2}{\delta}\ln\sec(\theta - \psi)\right] + \frac{2\epsilon}{\delta}\ln\sec\psi + \ln\left(\frac{2|I|\theta^2}{ai_o L\delta}\right) \qquad [19]$$

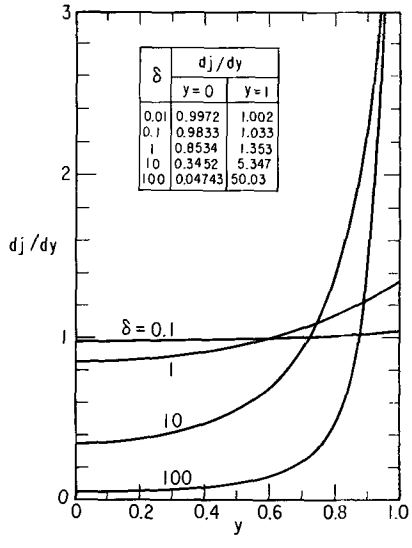

Fig. 2. Reduced current distributions for Tafel polarization with $\epsilon = 0$.

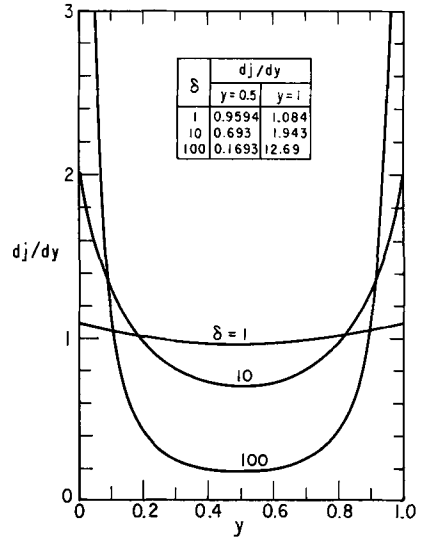

Fig. 3. Reduced current distributions for Tafel polarization with $\epsilon = \frac{1}{2}\delta$.

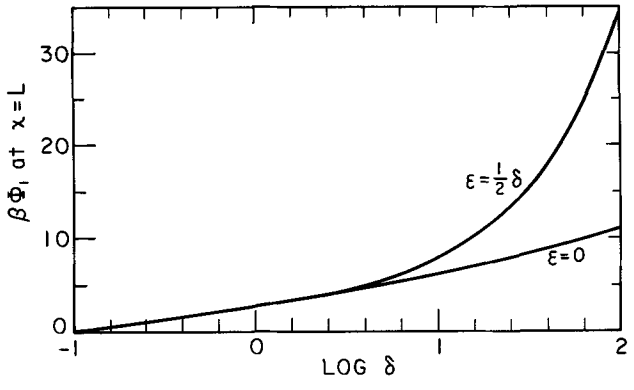

Fig. 4. Potential of the metal backing plate as it depends on δ

Figures 2 and 3 show the reduced reaction rate for $\epsilon = 0$ and $\epsilon = \frac{1}{2}\delta$, while Fig. 4 shows the potential of the metal backing plate when

$$\frac{2\kappa\sigma}{ai_oL\beta(\kappa+\sigma)} = 20$$

From the graphs, we see that for a small value of δ the reaction is uniform, but for large values of δ the reaction takes place mainly at the interfaces. Figure 4 corresponds to a Tafel polarization curve for a plane electrode since δ and ε are both proportional to $|I|$ at fixed thickness, conductivities, and other parameters. The ordinate actually represents the overpotential and should approach zero at small current densities. Instead it approaches ln $|I|/ai_oL$, reflecting the fact that, in using the Tafel polarization curve [14], we have dropped a term in Eq. [8]. This gives us a quantitative criterion for the applicability of the Tafel approximation in porous electrodes, $|I| > ai_oL$.

Euler and Nonnenmacher (4) have solved the constant concentration problem for a linear polarization equation. In this case, Eq. [13] becomes

$$\frac{di_2}{dx} = c\,(\Phi_1 - \Phi_2) \qquad [20]$$

where c is a constant. The solution for the current and the reaction rate is

$$\frac{i_2}{I} = \frac{\kappa}{\kappa+\sigma}\left[1 + \frac{\sigma/\kappa \sinh \nu(1-y) - \sinh \nu y}{\sinh \nu}\right] \qquad [21]$$

and

$$\frac{dj}{dy} = \frac{\nu\kappa}{(\kappa+\sigma)\sinh\nu}\left[\frac{\sigma}{\kappa}\cosh\nu(1-y) + \cosh\nu y\right] \qquad [22]$$

where

$$j = \frac{i_1}{I},\ y = \frac{x}{L},\ \nu = L\sqrt{c\,\frac{\kappa+\sigma}{\kappa\sigma}}$$

For small overpotentials or small current densities, both terms of Eq. [8] must be retained, but under this condition of low polarization, the equation may be linearized to give

$$\frac{di_2}{dx} = ai_o\frac{n\mathbf{F}}{RT}(\Phi_1 - \Phi_2)$$

so that

$$c = \frac{ai_on\mathbf{F}}{RT}$$

Thus, for $|I| < ai_oL$, the linear analysis is better than the Tafel analysis.

However, for $|I| > ai_oL$, the linear analysis requires linearization of the polarization equation. Thus the parameter c is a function of the over-all current density, $c = c(I)$. In order to find the connection between the two models, it is necessary to choose the point about which the Tafel equation is to be linearized. If we choose the midpoint between the extreme rates of reaction (as predicted by the Tafel analysis), we obtain

$$\nu = \theta\sqrt{1+\sec^2(\theta-\psi)} \quad \text{if } \epsilon \leq \tfrac{1}{2}\delta$$

$$\nu = \theta\sqrt{1+\sec^2\psi} \quad \text{if } \epsilon \geq \tfrac{1}{2}\delta$$

On the other hand, if we choose the average reaction rate, we obtain

$$\nu = \sqrt{\delta}$$

The results of the two models are compared in Fig. 5 for $\delta = 2$, $\epsilon = 0.1$ and in Fig. 6 for $\delta = 20$, $\epsilon = 1$. A

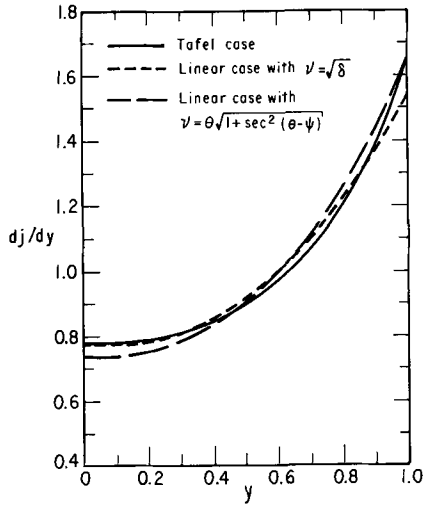

Fig. 5. Comparison of linear and Tafel results for $\delta = 2$, $\epsilon = 0.1$.

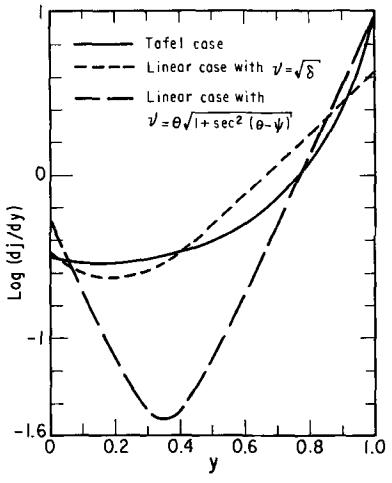

Fig. 6. Comparison of linear and Tafel results for $\delta = 20$, $\epsilon = 1$.

straight line can approximate a curve well over only a short distance compared with the curvature. Therefore the linear case would serve quite adequately where the reaction rate is fairly uniform through the porous electrode. But in Fig. 6 the reaction rate varies by a factor of about 33, and the linear model is not a very good approximation (note the logarithmic ordinate).

Effect of Concentration Variation

The previous analytic results have been obtained by considering concentrations to be constant. Qualitatively, the effect of variations of concentration of the electrolyte would be expected to be the following: The species which react will become depleted in the electrode; this will have the effect of shifting the reaction zone toward the electrode-solution interface where the concentration of the reacting species is greater. With some approximations we may obtain a more quantitative idea of the effect of concentration.

We again consider the one-dimensional, steady-state system described above, and we ignore the structural changes in the electrode as the reaction proceeds. Let us say that the reaction is

$$M_1^{z_1} + ne^- \rightarrow M_2^{z_2}$$

so that $I > 0$. Then we may write the polarization Eq. [8] as

$$\frac{di_1}{dx} = ai_o \frac{C_1}{C_1^\circ} \exp\{-\beta(\Phi_1 - \Phi_2)\} \qquad [23]$$

where $\beta = \alpha n\mathbf{F}/RT$. From the more complete polarization equation we have selected the more important term, both because di_1/dx is positive and because this term contains the concentration of the critical species. We shall assume that the conductivity of the pore electrolyte is unaffected by the concentration of the reacting species. This assumption is well approximated when a large excess of supporting electrolyte is present.

If we neglect ionic migration for the reacting species, then Eq. [2] gives

$$N_1 = -D_1 \frac{dC_1}{dx} \qquad [24]$$

and the continuity Eq. [5] becomes

$$D_1 \frac{d^2C_1}{dx^2} = \frac{1}{n\mathbf{F}} \frac{di_1}{dx} \qquad [25]$$

In addition, we need Eq. [10], [11], and [12]. The boundary conditions are

$$\text{at } x = 0,\ i_1 = 0,\ i_2 = I,\ \Phi_2 = 0,\ C_1 = C_1^\circ$$
$$\text{at } x = L,\ i_2 = 0,\ dC_1/dx = 0$$

The two new boundary conditions on the concentration state that at the solution-electrode interface, the concentration is maintained constant, while at the metal backing the flux is zero. By integrating Eq. [12] and [25], differentiating Eq. [23], eliminating i_2, Φ_1 and Φ_2, and introducing the additional dimensionless quantities

$$\xi = \frac{C_1}{C_1^\circ}, \quad \gamma = \frac{|I|L}{n\mathbf{F}D_1C_1^\circ}$$

we obtain

$$\boxed{\frac{d^2j}{dy^2} = \frac{dj}{dy}\left(\delta j - \epsilon + \frac{d\ln\xi}{dy}\right), \quad \frac{d\xi}{dy} = \gamma(j-1)} \qquad [26], [27]$$

with boundary conditions

$$\text{at } y = 0,\ j = 0,\ \xi = 1, \text{ and at } y = 1,\ j = 1.$$

An exact solution to this problem has not been obtained. Instead, as a first approximation we let

$$\xi^\circ = e^{-Ay} \qquad [28]$$

This reduces Eq. [26] to the form of Eq. [16], which we have already solved. Then Eq. [27] is used to obtain a second approximation for ξ and to select the best value of A. This was done by requiring that the average concentration in the electrode be the same for the two approximations. This is a somewhat involved calculation, for which we shall not give the details here (5). The effect of concentration variations is shown in Fig. 7 for $\delta = 2$, $\epsilon = 0.1$. The results in the form of dj/dy and ξ are given for $\gamma = 1$ and $\gamma = 2.8$, while the corresponding results

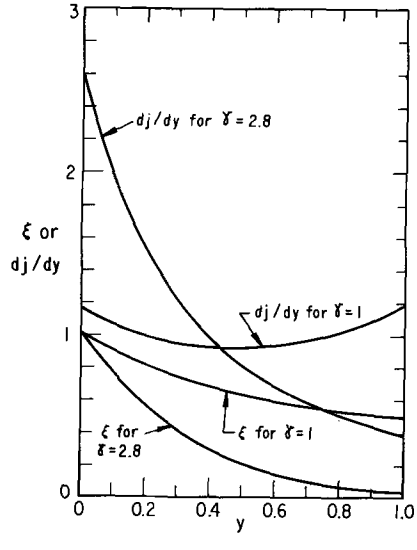

Fig. 7. Effect of concentration variations for $\delta = 2$, $\epsilon = 0.1$

Table I. Comparison of approximate solution of varying concentration problem with numerical results for $\delta = 2$, $\epsilon = 0.1, \gamma = 1$

	Approximation		Numerical calculations	
y	dj/dy	ξ	dj/dy	ξ
0.0	1.155	1.0	1.1577	1.0
0.09	1.0685	0.9145	1.0589	0.9145
0.21	0.9894	0.8140	0.9678	0.8139
0.3	0.9516	0.7480	0.9239	0.7476
0.39	0.9295	0.6898	0.8978	0.6888
0.51	0.9222	0.6238	0.8901	0.6217
0.6	0.9329	0.5830	0.9058	0.5798
0.69	0.9581	0.5499	0.9432	0.5452
0.81	1.0717	0.5177	1.0378	0.5112
0.9	1.0845	0.5032	1.1564	0.4954
1.0	1.1888	0.4975	1.3626	0.4890

for $\gamma = 0$ have already been presented in Fig. 5. Indeed, we see that the depletion effect does shift the reaction toward the electrode-solution interface. Table I shows how the approximate results compare with a numerical solution of Eq. [26] and [27], in the case $\gamma = 1$. This approximation probably becomes less accurate at higher values of γ.

Deposition from a Binary Electrolyte

A problem involving deposition from a binary electrolyte can be handled in a manner similar to that of the preceding section. From the treatment of the binary electrolyte in an electrolytic solution (6), we can expect some simplification here. This manifests itself in two ways. It is not necessary to assume that the conductivity of the electrolyte is constant, and migration of the reacting species can be accounted for. The assumptions which are retained are that one term of the exponential polarization equation is sufficient and that the approximate method of solution used in the last section is accurate enough. Although the diffusion coefficients and transference numbers vary with concentration, they are taken to be constant in the following treatment.

The electrode reaction may be written

$$M_+^{z+} + ne^- \rightarrow M_o^\circ$$

When the solution concentration

$$C = -\frac{C_+}{z_-} = \frac{C_-}{z_+}$$

is used, the equations describing the binary electrolyte in the porous electrode are

$$\overline{N_+} = z_+z_-U_+eC\nabla\Phi_2 + z_-D_+\nabla C$$

$$\overline{N_-} = -z_-z_+U_-eC\nabla\Phi_2 - z_+D_-\nabla C$$

$$\frac{\bar{i}_2}{z_+z_-\mathbf{F}} = (z_+U_+ - z_-U_-)eC\nabla\Phi_2 + (D_+ - D_-)\nabla C \quad [29]$$

$$\frac{\partial C}{\partial t} = D\nabla^2 C - \frac{t_-}{z_+z_-\mathbf{F}}\nabla\cdot\bar{i}_2 \quad [30]$$

where

$$D = \frac{z_+U_+D_- - z_-U_-D_+}{z_+U_+ - z_-U_-} \quad \text{and} \quad t_- = \frac{-z_-U_-}{z_+U_+ - z_-U_-}$$

Now the one dimensional, steady-state problem becomes

$$D\frac{d^2C}{dx^2} = \frac{t_-}{z_+z_-\mathbf{F}}\frac{di_2}{dx} \quad [31]$$

$$\frac{i_2}{z_+z_-\mathbf{F}} = (z_+U_+ - z_-U_-)eC\frac{d\Phi_2}{dx} + (D_+ - D_-)\frac{dC}{dx} \quad [32]$$

$$i_1 = -\sigma\frac{d\Phi_1}{dx}. \quad \frac{di_1}{dx} + \frac{di_2}{dx} = 0 \quad [33], [34]$$

$$\frac{di_1}{dx} = ai_o\frac{C}{C^\circ}\exp\{-\beta(\Phi_1 - \Phi_2)\} \quad [35]$$

where $\beta = \alpha n\mathbf{F}/RT$ and where the second term in the polarization equation has been dropped ($I > 0$). The boundary conditions are

$$\text{at } x = 0,\ i_1 = 0,\ i_2 = I,\ C = C^\circ,\ \Phi_2 = 0$$

$$\text{and at } x = L,\ dC/dx = 0,\ i_2 = 0$$

The condition that dC/dx is zero at $x = L$ is implied by the requirements that $N_+ = N_- = 0$ at $x = L$.

By integrating Eq. [31] and substituting the result into Eq. [32], we obtain

$$\frac{d\Phi_2}{dx} = -\frac{D_-}{z_-U_-e}\frac{d\ln C}{dx} \quad \text{or} \quad \Phi_2 = -\frac{D_-}{z_-U_-e}\ln\frac{C}{C^\circ}$$

By integrating Eq. [34], differentiating Eq. [35], and eliminating i_2, Φ_1, and Φ_2, the problem is reduced to

$$\frac{d^2i_1}{dx^2} = \frac{di_1}{dx}\left[\frac{\beta}{\sigma}i_1 + \left(1 - \frac{D_-\beta}{z_-U_-e}\right)\frac{d\ln C}{dx}\right],$$

$$\frac{dC}{dx} = \frac{t_-}{z_+z_-\mathbf{F}D}(I - i_1)$$

By defining $j = i_1/I$, $\xi = C/C^\circ$, $y = x/L$, $\delta = \beta IL/\sigma$

$\epsilon = 1 - \dfrac{D_-\beta}{z_-U_-e}$, $\gamma = -\dfrac{t_-IL}{z_+z_-\mathbf{F}DC^\circ}$, one obtains

$$\frac{d^2j}{dy^2} = \frac{dj}{dy}\left[\delta j + \epsilon\frac{d\ln\xi}{dy}\right], \quad \frac{d\xi}{dy} = \gamma(j - 1) \quad [36], [37]$$

with boundary conditions

$$\text{at } y = 0,\ j = 0,\ \xi = 1, \text{ and at } y = 1,\ j = 1.$$

This binary electrolyte problem is similar to problems treated earlier. We can obtain an approximate solution by assuming that

$$\xi = e^{-Ay}$$

Then with $f = \epsilon A/\delta$ we have

$$\frac{d^2j}{dy^2} = \frac{dj}{dy}[\delta j - \epsilon A] = \delta(j - f)\frac{dj}{dy} \quad [38]$$

whose solution has been discussed before. The adjustment of A will not be significantly different.

Although this problem has been stated in terms of deposition processes, the binary electrolyte treatment applies to many reactions occurring in batteries. For example, in the lead-acid battery, lead sulfate is quite insoluble and the electrolyte is essen-

tially a solution of sulfuric acid in water, *i.e.*, a binary electrolyte.

Limitations and Interpretation of the Basic Equations

For a plane electrode, the electrode reaction is restricted to the plane interface between the metal and the solution. In a porous electrode, on the other hand, the interface between the solid and the solution is not so simple, but extends throughout the depth of the electrode. Thus one is interested in the rate of reaction per unit volume rather than the rate of reaction per unit of surface area. To be sure, there is still a well-defined interface between the solution and the solid, but now the geometry is quite complicated.

One might begin an analysis of porous electrodes with exact considerations of this geometry. This would become extremely complicated, necessitating crude approximations, and one would probably be forced to consider several specific geometrical arrangements. This could be designated a microscopic approach. Another point of view has been adopted here. In order to obtain results which might be of practical significance, a model is proposed which describes the macroscopic features of porous electrodes. It represents, then, some average over the random and complicated geometry of the porous electrode. Accordingly, it contains parameters which are difficult to predict, but which could perhaps be estimated satisfactorily from a more detailed consideration of a specific system or more likely from some cleverly devised experimental methods. (Among such parameters we find σ, D_i, and U_i, which are the effective conductivity of the matrix material and the effective diffusion coefficients and mobilities of species in the pore electrolyte. Also there are the parameters in the polarization equation.)

Thus, the equations presented at the beginning of this paper should describe reasonably well the macroscopic features of a porous electrode in which there is no gas evolution. This model assumes that, while the porous electrode consists of two phases, it may be described by a combination of equations which treat the porous electrode as a continuum or a superposition of two continua. The microstructure of the electrode is assumed to be sufficiently fine that the various functions, such as the potentials, may be considered to be continuous. If, on a microscopic level, one were in a particular phase, the corresponding potential would be assumed to exist there, so that the actual variation of potential across a pore is not described. This means that the length of a pore is assumed to be long compared to its diameter. The superficial current densities and species fluxes must be corrected for the areas involved in order to obtain the current density or flux in a particular phase. The concentrations must be corrected for the volumes involved, but, as with the potential, concentration variations across the diameter of a pore are not accounted for. From this, we should expect the model to fail when a length characteristic of the microstructure, say the diameter of a pore or of a matrix particle, becomes comparable to a length characteristic of the size of the electrode, say its thickness.

Let us interject a few comments here about the structure of the general Eq. [1] to [9]. Equation [1] describes the matrix phase while Eq. [2], [3], and [6] describe the solution phase. Equations [7] and [9] represent boundary conditions between the phases, although Eq. [9] can be derived from the preceding equations, just as, in the case of a free electrolytic solution, the analogous equation $\nabla \cdot \bar{i} = 0$ follows from the electroneutrality assumption. Equation [5] describes the solution phase, but, while in a free electrolytic solution the bulk production of a species is normally zero, here we have a term from the electrode reaction. It is interesting that relationships like Eq. [7] and [9] are no longer boundary conditions, but, in the macroscopic model, apply throughout the volume of the electrode.

We shall now cite some limitations of the model. There is no consideration of the capacitive effects of the double layer, which means that certain time dependent processes, such as alternating current behavior and interruptor techniques, may not be accurately explained by the model.

More serious is the failure to discuss the complicated phenomena in the solid phase. In the discharge of a battery, the reactant is consumed, products may be deposited, and there are changes in the structure and properties of the electrode. The framework of Eq. [1] to [9] is sufficiently general to describe such processes. The amount of nonmobile reactants and products is already given by the continuity equation. The parameters in the polarization equation and in Eq. [1] and [2] will depend in some complicated way on the local electrode structure or, equivalently, on the local extent of reaction. Before we can satisfactorily predict the discharge curves of batteries, we must obtain a better understanding of this dependence and of the phenomena occurring. It is already quite difficult to determine the values of these parameters at the beginning of the discharge.

Thus, the special cases considered earlier were idealized. The first could apply to any uniform electrode at the beginning of discharge. That involving concentration effects corresponds to the steady state of a redox reaction in a porous metal. The results do not apply strictly to a primary or storage battery since no steady state is possible in these cases.

Finally we should note that Eq. [1] to [9] are limited to dilute solutions of the reactant in the electrolyte phase. In the special cases we have set $\bar{v} = 0$ which would not be the case if there were an appreciable flux of the reactant. In more concentrated solutions we must be more careful in defining the "mass average" velocity. We may also note that fuel cells often use porous electrodes. In one type, a gaseous fuel is dissolved in the electrolytic solution, which is then forced to circulate through the electrode. Here, of course, we should not set $\bar{v} = 0$. If the circulation is sufficiently rapid, concentrations may be uniform through the electrode, and the first special case would apply.

Discussion

Let us now consider the more positive significance of the results obtained. In general, the reaction rate

is not uniformly distributed in the electrode. In fact, with no polarization, that is, when $\Phi_1 - \Phi_2$ is independent of $\nabla \cdot \bar{i}_2$ and of the concentrations, the reaction occurs only at the surfaces of the electrode and is divided between the two interfaces according to the ratio of the effective conductivities of the two phases. Thus, the reaction rate at the electrode-solution interface is $I\sigma/(\kappa + \sigma)$. In this limiting case, the current entering the electrode immediately distributes itself between the phases so that the ohmic drop is the same in each phase.

The effect of polarization is to distribute the reaction more uniformly through the electrode. In the absence of concentration effects, the nonuniformity of the reaction distribution is determined by the parameter $\delta = L|I|\beta(1/\kappa + 1/\sigma)$ for the Tafel case. Increasing the value of this parameter increases the nonuniformity. An interesting feature of this Tafel analysis is that the reaction distribution is independent of the exchange current density i_o and of the specific interfacial area a.

In order to investigate the limit approached at low current densities, it is necessary to use the linear analysis. Here the nonuniformity of the reaction increases with increasing values of the parameter

$$\nu^2 = L^2 c \left(\frac{1}{\kappa} + \frac{1}{\sigma} \right)$$

The linearization of the polarization equation in this region yields

$$c = \frac{a i_o n \mathbf{F}}{RT}$$

or

$$\nu^2 = \frac{L^2 a i_o n \mathbf{F}}{RT} \left(\frac{1}{\kappa} + \frac{1}{\sigma} \right)$$

Now, in the Tafel range we found that the relationship between the parameters of nonuniformity could be expressed as

$$\nu^2 = \delta$$

and since $|I| > a i_o L$ in the Tafel range, we find

$$\nu^2 > L^2 a i_o \beta \left(\frac{1}{\kappa} + \frac{1}{\sigma} \right) \approx \frac{\alpha L^2 a i_o n \mathbf{F}}{RT} \left(\frac{1}{\kappa} + \frac{1}{\sigma} \right)$$

Closer analysis reveals that the reaction distribution is the most uniform when

$$I \approx a i_o L \frac{1 - 2\alpha}{\alpha^{2\alpha} (1 - \alpha)^{(2-2\alpha)}}$$

In this way, we can arrive at a fairly general conclusion. For uniform concentration, the reaction distribution becomes less uniform as one increases the magnitude of the current density, the thickness of the electrode, or the sum of the effective resistivities of the two phases, but the point of most uniform distribution will not occur at zero current unless $\alpha = \frac{1}{2}$.

Mass transport of a reacting mobile species has a significant effect on the steady-state reaction distribution. In the analysis given here, this effect is measured by the value of the additional parameter

$$\gamma = \frac{|I|L}{n\mathbf{F}D_1 C_1^o}$$

which indicates the magnitude of the consumption rate relative to the mass-transfer rate. Here we conclude that the steady-state reaction distribution will be shifted more or less strongly toward the electrode-solution interface as a result of hindered movement of the reactant. The generality of this conclusion is indicated by the following considerations: For a redox reaction, reversing the current means that the other species will become critical, and the other term in the polarization equation will be retained. We have shown that this conclusion holds for deposition, while, for dissolution, the higher concentration will suppress the reaction in the depth of the electrode. However, the effect will be small compared to the cathodic case and would not show up in the Tafel analysis since we retain the other term of the polarization equation.

There are many problems which must still be solved. For a given system it is necessary to determine the parameters in the porous-electrode models. Euler and Nonnenmacher (1) have indicated procedures for measuring several of these. Methods of experimental measurement and theoretical prediction of these parameters should be improved.

Experimental verification of porous-electrode analyses will be attempted in this laboratory. There are great difficulties, but a direct determination of current distribution by using sectioned electrodes shows promise. Some quite crude measurements of this type have been made by Coleman (7). It should also be mentioned that Daniel'-Bek (8) has tried to measure potential distributions in porous electrodes by using probes. However, these probes destroy the pore structure and would require a double differentiation of experimental data in order to obtain the reaction distribution.

In this laboratory, the validity of the macroscopic approach will also be tested theoretically and experimentally by considering models of the pores themselves.

Another important area for further work is in transient phenomena, that is, the transition from the initial conditions to the steady state. It may be necessary to rely on numerical solutions here. However, approximations could yield useful analytic results. First note that time enters explicitly into only the continuity equation. In many cases this can be written as

$$\frac{\partial C}{\partial t} = D\nabla^2 C + B\nabla \cdot \bar{i}_2 \qquad [39]$$

where $B = 1/n\mathbf{F}$ for the supporting electrolyte case.

$$B = \frac{1}{z_+ z_- \mathbf{F}} \left(t_+ + \frac{z_+ s_+}{n} \right)$$ for a binary electrolyte.

Thus the potential can often be removed from the continuity equation.

This equation is of the form of the heat conduction equation, which has been studied extensively in mathematical physics. Furthermore, the last term

representing sources or sinks is known initially and at steady state. Thus, since the total current density I is specified, it should be possible to guess a first approximation for the reaction distribution and to solve Eq. [39]. Then the potential across the electrode (and a second approximation to the reaction distribution) can be calculated for any particular time from the concentration distribution.

Finally, for practical systems it will be necessary to account for changes in the electrode properties as the reaction proceeds (see preceding section) and to combine the analytic description of detailed processes in order to allow the prediction of the dynamic performance of complete systems.

Acknowledgment

This work was supported in part by the Electrochemistry Branch, Naval Ordnance Laboratory, Corona.

Manuscript received April 16, 1962; revised manuscript received Aug. 14, 1962. This paper was prepared for delivery before the Boston Meeting, Sept. 16-20, 1962.

Any discussion of this paper will appear in a Discussion Section to be published in the June 1963 JOURNAL.

REFERENCES

1. J. Euler and W. Nonnenmacher, *Electrochim. Acta*, **2**, 268 (1960).
2. O. S. Ksenzhek and V. V. Stender, *Doklady Akad. Nauk S.S.S.R.*, **106**, 487 (1956); **107**, 280 (1956); *Zhur. Priklad. Khim.*, **32**, 110 (1959).
3. K. J. Vetter *Elektrochemische Kinetic*, Springer-Verlag, Berlin (1961).
4. J. Euler and W. Nonnenmacher, *op. cit.*, pp. 280-282.
5. John Newman, Masters thesis, University of California, Berkeley, December, 1961, p. 39.
6. V. G. Levich, *Acta Physicochim. U.R.S.S.*, **17**, 260 (1942). One should also read *Fiziko-khimicheskaya Gidrodinamika* (Moscow, 1959), or the English translation *Physicochemical Hydrodynamics*, Prentice-Hall, 1962. Chapter VI, §§ 50, 51, and 53, is of particular interest for this paper.
7. J. J. Coleman, *This Journal*, **98**, 26 (1951).
8. V. S. Daniel'-Bek, *Zhur. Fiz. Khim.*, **22**, 697 (1948).

SYMBOLS

a	specific interfacial area per unit volume, cm^{-1}.
A	constant used in approximation to concentration distribution.
c	slope of polarization curve in linear model, mho/cm^3.
C_i	concentration of species i, g-mole/cm^3.
C_i°	reference concentration.
D	molecular diffusion coefficient of binary electrolyte.
D_i	diffusion coefficient of species i, cm^2/sec.
e	magnitude of the electronic charge, coulomb.
e^-	symbol for electron.
f	used to denote function in polarization equation.
F	Faraday's constant, coulomb/g-equivalent.
i_o	exchange current density in Tafel polarization, amp/cm^2.
$\bar{i}_1$	current density in matrix phase, amp/cm^2.
$\bar{i}_2$	current density in pore electrolyte, amp/cm^2.
I	over-all current density in one-dimensional porous electrode.
j	i_1/I.
L	thickness of one-dimensional porous electrode, cm.
M_i	symbol for chemical formula of species i.
n	number of electrons in equation for electrode reaction.
$\bar{N}_i$	flux of species i, g-mole/cm^2-sec.
R	universal gas constant, joule/mole-deg.
s_i	stoichiometric coefficient in equation for electrode reaction.
t	time, sec.
t_-	transference number of negative species in binary electrolyte.
T	temperature, degrees absolute.
U_i	mobility of species i, cm/sec-dyne or cm^2/m-sec-newton.
$\bar{v}$	fluid velocity, cm/sec.
x	distance through the one-dimensional porous electrode, cm.
y	x/L.
z_i	valence of species i.
α	transfer coefficient in Tafel polarization equation.
β	convenient reciprocal potential, *e.g.*, $\alpha n\mathbf{F}/RT$.
γ	$\lvert I\rvert L/n\mathbf{F}D_1C_1^\circ$ or $-t_-IL/z_+z_-\mathbf{F}DC^\circ$ for binary electrolyte.
δ	$\beta\lvert I\rvert L(\kappa+\sigma)/\kappa\sigma$ or $\beta IL/\sigma$ for binary electrolyte.
ϵ	$\beta\lvert I\rvert L/\kappa$ or $1 - D_-\beta/z_-U_-e$ for binary electrolyte.
θ	integration constant for Tafel polarization.
κ	conductivity of pore electrolyte, mho/cm.
ν	$L\sqrt{c(\kappa+\sigma)/\kappa\sigma}$ for linear polarization.
ξ	C_1/C_1°.
σ	conductivity of matrix, mho/cm.
ϕ_1	potential of matrix phase, volts.
ϕ_2	potential of pore electrolyte, volts.
ψ	integration constant for Tafel polarization.

Technical Notes

Feasibility of Electrolyte Regeneration in Al Batteries

S. Zaromb[1] and R. A. Foust, Jr.

Scientific Laboratory, Philco Corporation, Blue Bell, Pennsylvania

In a concurrent paper (1) an Al battery is discussed, based on the reaction

$$Al + \tfrac{3}{4}O_2 + OH^- + \tfrac{1}{4}H_2O \rightarrow Al(OH)_4^- \quad [1]$$

followed by an electrolyte regeneration reaction

$$Al(OH)_4^- \rightarrow Al(OH)_3\,(solid) + OH^- \quad [2]$$

The occurrence of reaction [2] at a sufficiently fast rate is, of course, an essential requirement for maintaining the electrolyte concentration within a satisfactory range over prolonged periods of heavy current drain.

Reaction [2] has already been studied exhaustively in connection with the Bayer process for the manufacture of purified Al_2O_3 for use in the production of Al (2-5). However, these experiments involved various fixed initial starting conditions (temperature, NaOH and $NaAl(OH)_4$ concentrations, and $Al(OH)_3$ seed surface) with the experiments completed upon decomposition of the excess concentration of $Al(OH)_4^-$ ions.

In Al-air batteries, on the other hand, the $Al(OH)_4^-$ ions are to be continuously replenished by reaction [1] and removed by reaction [2] over

[1] Present address: Research and Advanced Technology Department, Electronic Systems and Products Division, Martin-Marietta Corporation, Baltimore, Maryland.

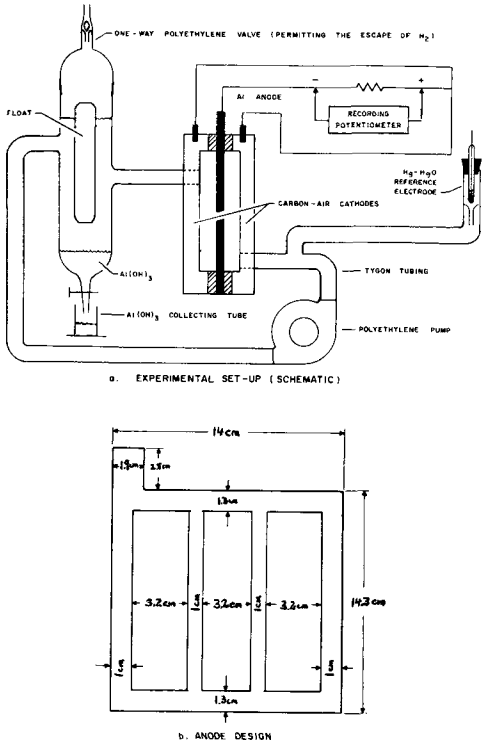

Fig. 1. Experimental setup for the electrolyte regeneration experiment. The cell components (cathodes, gaskets, and anode) were clamped together between two 0.6 cm steel plates (not shown).

long periods of time. These processes introduce a number of favorable and unfavorable factors.

Continuous current drain experiments aimed at proving spontaneous self-regeneration of the electrolyte had been impeded initially by accumulation of the $Al(OH)_3$ reaction product near the Al electrodes. The formation of this product is, in itself, a proof of the fast occurrence of the desired reaction [2]. However, to prove the feasibility of long lasting Al-air cells, it still remained necessary to achieve continuous satisfactory current and voltage outputs for longer periods of time. Utilizing an improved circulating and $Al(OH)_3$ collecting system, a steady current of about 2 amp (corresponding to a current density of at least 20 ma/cm^2) at approximately 1½v was withdrawn from an experimental cell for a period of 30 hr. Clogging of the anodes by the $Al(OH)_3$ product was again responsible for the subsequent decrease in current voltage outputs. This clogging was further reduced by the improved anode design and $Al(OH)_3$ collecting setup shown in Fig. 1 .

Finally, the feasibility of electrolyte regeneration was conclusively proved by a continuous current-drain experiment of more than 100-hr duration. The initial electrolyte consisted of 120 cc 3.0M KOH solution. The total current-drain amounted to more than 80 amp-hr (at around 1.5v and 20 ma/cm^2), which is equivalent to more than 3 times the discharge expected without electrolyte regeneration.

To make up for appreciable accidental losses of electrolyte at several stages of the experiment, a total of 330 cc of H_2O was added. This resulted in dilution of the remaining electrolyte to less than 0.5M total KOH. Nevertheless, appreciable current could still be drawn for a number of hours even with this low alkali concentration thanks to continuous circulation of the electrolyte. However, with the lowest alkali concentrations, a slow build-up of an adherent $Al(OH)_3$ layer at the anodes gradually reduced the current and voltage outputs to nearly zero. Addition of H_2O should therefore be confined to KOH concentrations exceeding 2-3M.

Manuscript received Nov. 28, 1961; revised manuscript received Aug. 25, 1962.

Any discussion of this paper will appear in a Discussion Section to be published in the June 1963 JOURNAL.

REFERENCES

1. S. Zaromb, *This Journal*, **109**, 1125 (1962).
2. T. G. Pearson, "The Chemical Background of the Aluminum Industry," pp. 22-33, Royal Institute of Chemistry, London (Reprinted Sept. 1957).
3. T. Vrbaski, J. Ivekovic, and D. Pavlovic, *Can. J. Chem.*, **36**, 1410 (1958); *Croatica Chem. Acta*, **28**, 41 (1956).
4. E. Herrmann, *Arhiv za Kemiju*, **25**, 71 (1953); *Z. anorg. u. allegem. Chem.*, **274**, 81 (1953).
5. S. I. Kuznetsov and V. A. Derevyankin, *Croatica Chem. Acta*, **31**, 141 (1959).

Silicon Dioxide as Dielectric in Solid Electrolyte Capacitors

W. Haas

Philco Scientific Laboratory, Blue Bell, Pennsylvania

The present work is a preliminary study of silicon as a new candidate as basic material for solid electrolyte capacitors. Such a capacitor consists of the following functioning parts: (*a*) an anode of silicon doped to achieve the necessary conductivity; (*b*) a film of silicon dioxide covering the anode and serving as dielectric; and (*c*) a coating of conducting MnO_2 (1), making contact over the outer surface of silicon dioxide. In order to produce the high capacity per unit volume which characterizes solid electrolyte capacitors, pellets of sintered silicon powder were used as anodes. Such structures provide the necessary large available surface area for dielectric and counterelectrode.

The dielectric is formed on the pellets by a step of thermal oxidation. This step, usually performed in moist O_2 at 1200°C for 16 min, produces an oxide about 1500Å thick, yielding a clear interference color. Silicon is capable of being oxidized anodically, but it is recognized that the thermally produced oxide is electrically superior (2).

Experimental

It was initially determined that the surface treatment of the silicon is of great importance in achiev-

Table I. Leakage in NMA after 10 min bias at 150v

V	Acetone cleaned I, μa/cm²	Etched I, μa/cm²
150	50.0	1.6
125	6.6	0.12
100	2.5	0.053
75	0.66	0.025
50	0.18	0.0083

Table II. Leakage parameters of thermally oxidized silicon measured in NMA

Leakage current μa/μf, after thermal oxidation, at 150v		Leakage current μa/μf, at 150v, remeasured after 48 hr without bias	
3 min	276	3 min	1.56
5 min	168	5 min	1.20
10 min	86.4	10 min	0.96
16½ hr	1.68		

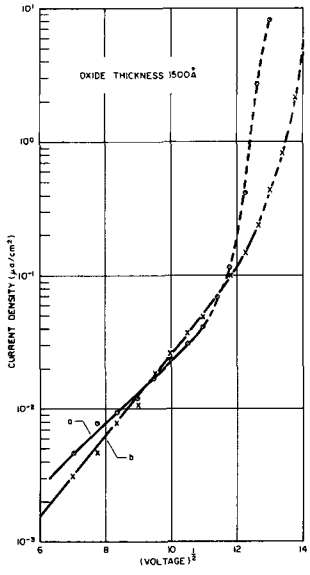

Fig. 1. I-V characteristics of an oxidized silicon crystal in NMA

ing high insulation resistance of a thermally grown oxide, and that the insulation resistance could be improved by anodically biasing the oxidized silicon in an electrolyte of NMA (a solution of 0.04*N* KNO_3 in N-methylacetamide (3).

The importance of the surface treatment is illustrated in Table I by the leakage values of the same silicon crystal (oxidized under the same conditions), first after a brief cleaning with acetone and then after an etch with 1:2 of $HF:HNO_3$.

In Table II, leakage values of a thermally oxidized silicon crystal (oxide thickness about 1500Å) after different lengths of time under bias are recorded along with the values obtained after 48 hr without bias. The insulation resistance was increased by a factor greater than 100 by the anodic bias.

The mechanism of this improvement is not clearly understood but we think that pores, channels, or fissures are plugged during the process. The oxide thickness does not increase under the chosen bias. If a sufficiently higher voltage is applied, the oxide starts to increase in thickness; at the same time, the current increases drastically, and luminescence of the anode can be observed in a darkened room.

As said before, the leakage current through thermal oxides decays under anodic bias. The precise effect of bias was illustrated on a polished crystal slab (n-type, 6 ohm-cm) covered with a thermal oxide of 1500Å thickness. After 2-hr bias at 150v in NMA, a I-V plot was taken (plot a, Fig. 1). The bias was varied by 10-v steps and current measured after 1 min. After a further hour bias at 200v a second I-V plot was recorded (plot b, Fig. 1). Clearly, the linear range on a log I *vs.* $\sqrt{V}$ plot extends to higher voltages as observed also with anodic oxides (3).

The absolute leakage values for silicon dioxide are, in fact, lower than leakage current densities reported for tantalum (4) and niobium (5) pentoxides at equal field strengths (Table III).

The leakage values depend to a certain extent on the testing electrolyte as already pointed out by Hand *et al.* (5); to illustrate this better we compared the I-V characteristics taken in NMA and in 10% H_3PO_4 of a silicon crystal which had been oxidized and subsequently biased for 30 min in NMA (Fig. 2).

It should be noted that the ratio of leakage values of silicon dioxide in H_3PO_4 and NMA is higher at lower voltages. This trend is still more pronounced on sintered pellets, as also shown in Fig. 2. For oxide thicknesses of 1500Å measurements had to be carried out below 200v in H_3PO_4 because of the onset of violent sparking at this voltage.

Planar Capacitors

Several sample capacitors were prepared on single crystal silicon wafers by thermal oxidation

Table III. Leakage values

	Leakage, μa/cm²	Electrolyte	Field strength, v/cm	ε
Ta_2O_5 on Ta foil (4)	≈0.24	H_3PO_4 10% 7% ammonium pentaborate	5.6×10^6	27.6 (6)
Nb_2O_5 on Nb foil (5)	≈0.05-0.42	56% ethylene glycol 37% H_2O	3.6×10^6	41.0 (6)
SiO_2 on Si crystal	0.015	NMA	5.7×10^6	3.82 (7)
	0.0071	NMA	3.8×10^6	
	0.12	H_3PO_4 10% 7% ammonium pentaborate	5.6×10^6	
	0.011	56% ethylene glycol 37% H_2O	3.6×10^6	

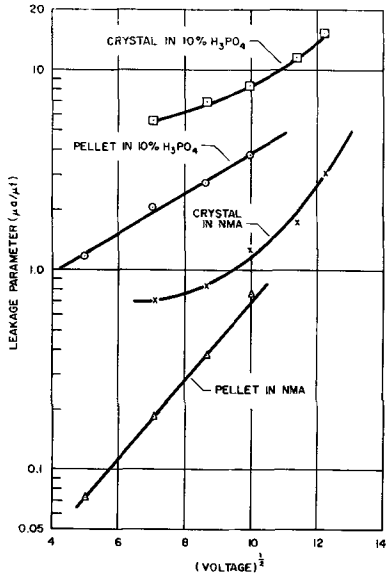

Fig. 2. Comparison of the I-V characteristics in H_3PO_4 and NMA of an oxidized silicon crystal and an oxidized silicon pellet.

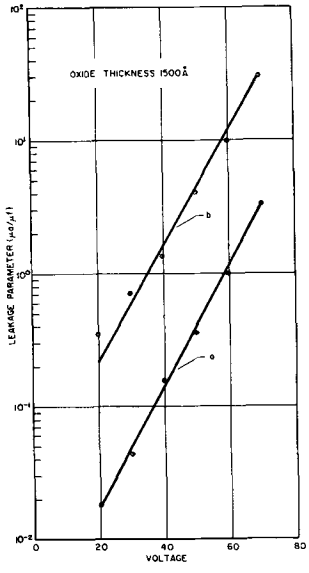

Fig. 3. I-V characteristics of two planar silicon capacitors

and subsequent anodic bias at 150v in NMA. Manganese dioxide counterelectrodes were applied by pyrolysis of $Mn(NO_3)_2$, reformed in NMA, and capacitors were finished with Aquadag and silver paste. The area varied from 3-8 cm² (capacitance between 65-175 nf).

To achieve low leakage values, as said before, the preoxidation treatment is very important. In Fig. 3, line (a) illustrates the leakage values of a finished capacitor using a mechanically polished silicon crystal etched in HF for a short time; line (b) shows the leakage values of another sample, not previously polished, and only cleaned with acetone. Even though the values differ by a factor of 10, the slope of both lines is the same.

The capacitance of the finished samples corresponded to the values calculated from the oxide thickness. The dissipation factor of all capacitors was high (0.1 at 1000 cps) due to high series resistance of the silicon tabs. Low resistivity crystals only became available later and were used for the preparation of pellets.

Preliminary life tests still in progress show that a bias of 47v, at room temperature decreases the leakage current from ≈ 0.7 to ≈ 0.08 μa/μf after 500 hr.

Sintered Pellets

Silicon powder of mesh −100 +200 for the preparation of pellets was prepared from n-type silicon crystals (ρ = 0.006-0.010 ohm-cm). Using benzene as lubricant disks ¾ in. in diameter and ⅛ in. thick were pressed with a single-action single-punch press at 6.8 tsi. The green strength was just sufficient to allow careful handling. Each pellet was cut into smaller pieces of about ⅛ x ⅛ x ¼ in. Pellets were sintered in an argon atmosphere for 60 min at 1300°C or 1400°C. After sintering, the pellets had a density of ≈ 1.4 g/cc, *i.e.*, about 60% of the bulk value.

Since it was necessary to attach an integral lead to the pellets, as a first approach, tabs 1/16 x 1/16 x 1/2 in. were cut from crystals of the same type used for the powder preparation. These tabs were welded to the sintered pellet using an oxy-hydrogen flame.

The surface area of the pellets was calculated from the weight increase after oxidation since the oxide thickness was known approximately from its refraction index (1.46 for amorphous silica) and interference color. Values of about 1100 cm²/cm³ were obtained.

The wet capacitance measured in dilute H_2SO_4, however, was about 25% lower than expected from the calculated surface area and assumed oxide thickness.

It is possible that this discrepancy is explained by cumulative errors in the oxide thickness and small weight increases recorded. The possibility that the pores were incompletely contacted was ruled out by remeasuring the capacitance after removing any air bubbles by a low-pressure treatment.

After thermal oxidation, samples were biased at 125v and the leakage current allowed to decay at room temperature for 17 hr (Table IV). Leakage current characteristics were subsequently improved by the use of certain techniques prior to the thermal oxidation. Table V shows results obtained with two different cleaning techniques (A and B) and

Table IV. Parameters of silicon pellets measured in 8N H_2SO_4

Pellets were pressed at 6.8 tsi using benzene as lubricant and sintered in argon for 60 min

No.	Sinter. temp, °C	Oxidation temp, °C	Oxidation time, min	Leakage, μa/μf at 125v
6	1300	1200	16	140
7	1300	1400	10	129
9	1300	1400	10	195
10	1400	1200	16	190
11	1400	1200	16	83
12	1400	1400	10	50
13	1400	1400	10	159
14	1400	1400	10	53
16	1400	1400	10	54
17	1400	1400	10	74
18	1400	1400	10	108

Table V. Leakage parameters of silicon pellets measured in NMA after different cleaning techniques

No.	Leakage, $\mu a/\mu f$ at 150v	Treatment
19	4.2	A
20	1.6	A
21	7.1	B
22	7.5	B
25	8.5	A
26	46.0	*
27	86.0	*
28	6.5	A

* No treatment.

for comparison the results obtained at 150v with two nontreated pellets.

Technique A consisted in dipping the sintered pellets with silicon contact for 5-10 sec in a 2:1 mixture of HNO_3 and HF. The reaction is violent and rapidly reduces the size of the pellet. Technique B consisted in oxidizing the sintered pellet for 16 hr in air and removing the thick oxide with HF.

The average leakage value of chemically treated pellets was 5.9 $\mu a/\mu f$ at 150v against 113 $\mu a/\mu f$ at 125v for pellets described in Table IV. Leakage values could be further improved by the use of pellets prepared from powder etched in a mixture of 5% HF 95% HNO_3, prior to the sintering.

So far, we were only concerned with oxide thicknesses of 1500Å. Some pellets were oxidized for longer periods and, in consequence, voltages well over 400v could be applied in NMA without excessively high leakage currents. From capacitance *vs.* time measurements, we suspected, however, that the oxidation did not proceed uniformly throughout the pellet. This suspicion was confirmed by the appearance of different interference colors inside the pellet.

Several sample capacitors were finished by application of two coats of MnO_2 and an outer electrode of Aquadag and silver paste applied after the last reforming step. Typically, such units have at room temperature a capacitance per unit volume of 270 $\mu f\text{-}v/cm^3$ (calculated on the basis of anode volume), a leakage parameter of about 0.1 $\mu a/\mu f$ at 20v and a dissipation factor of 0.15 at 1000 cps.

Conclusions

Thermally formed silicon dioxide improved by anodic bias is a dielectric film which can be used in solid electrolytic capacitors. Judging from the low leakage currents at high field strengths of single crystals in NMA, the relatively low dielectric constant might be partially compensated by using thinner oxides for a given working voltage. Therefore, a better capacitance-to-volume ratio than the one given by the dielectric constants can ultimately be expected for sintered pellets. The preoxidation treatment is of utmost importance in achieving good results.

Acknowledgments

The author wishes to express thanks to Dr. Basil J. Nicholson for many useful discussions and to Dr. Paul F. Schmidt for suggesting a method of improving thermally formed silicon dioxide.

Manuscript received May 23, 1962; revised manuscript received Sept. 6, 1962.

Any discussion of this paper will appear in a Discussion Section to be published in the June 1963 JOURNAL.

REFERENCES

1. R. L. Taylor and H. E. Haring, *This Journal*, **103**, 611 (1956).
2. M. M. Atalla, E. Tannenbaum, and E. J. Scheibner, *Bell System Tech. J.*, **38**, 749 (1959).
3. P. F. Schmidt and W. Michel, *This Journal*, **104**, 230 (1957).
4. L. H. Belz, *ibid.*, **108**, 229 (1961).
5. R. B. Hand, H. W. Ling, and T. Kolski, *ibid.*, **108**, 1023 (1961).
6. L. Young, *Can. J. Chem.*, **38**, 1141 (1960).
7. J. L. Sprague, J. A. Minahan, and O. J. Wied, *This Journal*, **109**, 94 (1962).

Surface Photovoltage Studies of Silicon-Electrolyte Systems

Richard S. Muller[1]

Pacific Semiconductors Inc., Lawndale, California

The space-charge region at the surface of a semiconductor will, if illuminated, be the seat of a photovoltaic effect. This photovoltage may be detected by measurements made between a nonrectifying contact, affixed to the semiconductor, and an electrode having a potential difference with the semiconductor surface that is independent of illumination.

The theoretical behavior of the surface photovoltage has been analyzed by Garrett and Brattain (1). The feasibility of the determination of surface potential through measurements of the surface photovoltage was demonstrated for germanium in gaseous ambients by Johnson (2) and for germanium in liquid ambients by Garrett and Brattain (3). Harten has reported some use of the technique for silicon in Na_2SO_4 solutions (4, 5). In the work to be reported here, surface photovoltage measurements were employed to test the effects of electrolytic environment on both n- and p-type silicon having a range of resistivity values. The electrolytes chosen were those used in various phases of the chemical processing of silicon for commercial use.

[1] Present address: Department of Electrical Engineering, University of California, Berkeley, California.

Experimental Technique

The experimental apparatus used to make the photovoltage measurements is sketched in Fig. 1. Light from a 300w tungsten filament lamp was passed through a crossed polaroid modulator and a rotating disk shutter. It was then partially deflected by a mirror to shine through a specified depth of

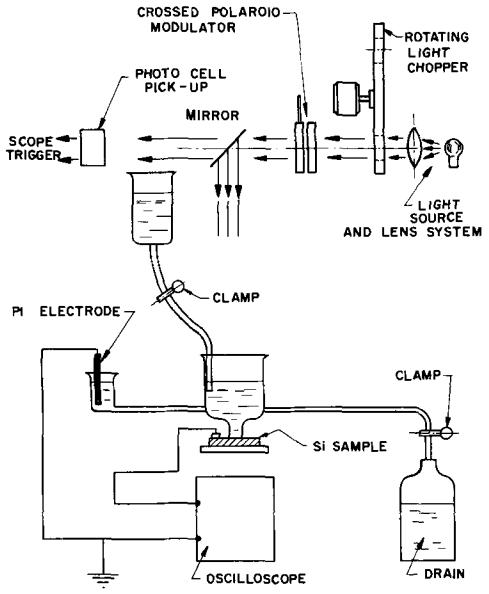

Fig. 1. Apparatus used to measure the surface photovoltage. The reservoir and drain system permit holding the silicon surface in a continuously liquid ambient.

liquid onto the surface of the test specimen. A portion of the light was gathered at a photocell, which served as a synchronizing trigger for the oscilloscope used to measure the photovoltage. The photocell also served to calibrate the light source.

The silicon specimens were cut in the (100) plane and lapped, chemically polished in a CP-4 solution, and dried in air. The over-all thickness of each wafer was about 10 mils. The specimens were then glued with an epoxy cement to the lip of an inverted polyethylene bottle, the bottom of which had been removed. Clamp arrangements between electrolyte reservoir and drain facilitated flushing the sample surface with distilled water between changes of the electrolyte. The photovoltage was measured between an ohmic contact made to the silicon sample and a platinum counter-electrode situated in a remote reservoir which was connected by a liquid-filled tube to the test sample bottle. The platinum electrode was used after trials showed it to give readings consistent with those of a calomel standard which had been used initially. The photovoltage was detected in a-c fashion by an oscilloscope (one megohm input impedance) and its polarity checked by comparison with the synchronizing trigger from the photocell.

Table I lists the resistivity values of the three p-type and three n-type specimens which were used in the experiments. To check the consistency of the results, some of the measurements were duplicated on a second set of three n-type samples which had resistivities equal to those of the first set.

Table I. Resistivity values

Sample	Resistivity, ohm-cm
N-1	0.56
N-2	19.5
N-3	48.0
P-1	2.8
P-2	26.0
P-3	58.0

The photovoltage was measured first in three different solutions which are fairly inactive with the silicon surface: these were 0.1M solutions of $PdCl_2$, $SnCl_2$, and NaCl. A solution of 0.5M NaH_2PO_2, which was capable of a partial reduction in the silicon surface oxide, was used next. Finally, readings were taken in a 0.1M HF solution. The HF was sufficient to remove all the silicon surface oxide coating.

Results

Typical behavior of the photovoltage in the absence of HF is shown in Fig. 2 for three n-type samples. The electrolyte used for the data in this figure was 0.5M NaH_2PO_2. The data for p-type material in the same electrolyte plot as a reflection of the curves of Fig. 2 in the $y = 0$ plane, with the measurements showing the same relative dependence on resistivity as does the n-type. Actual magnitudes of the photovoltage in p-type material were, however, less than 0.25 kT/e. In the electrolytic environments not containing hydrofluoric acid, the silicon consistently became the positive terminal for p-type material and the negative terminal for n-type material in the measured surface photovoltaic effect. Consistency with the data trend of Fig. 2 was obtained with a series of identical resistivity-value silicon samples, measured under the same conditions. Actual photovoltage values did, however, differ by about 10% of the magnitudes given in Fig. 2 in the second set of data.

Figure 3 indicates the dependence of the photovoltage on the electrolytes tested. The data for this curve were taken for sample N-3 (19-ohm-cm material); qualitatively similar curves were obtained for all other n-type samples. An HF environment is seen in Fig. 3 to reverse the polarity of the observed photovoltage, as well as to change the character of the illumination dependence. For p-type samples, an HF solution maintained the positive polarity of the photovoltage, while increasing its magnitude by a tenfold factor. About 30 sec in the HF solution were necessary to reach an equilibrium condition for the

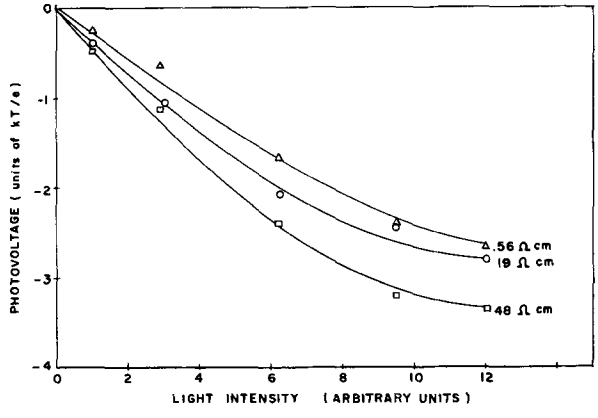

Fig. 2. Measured photovoltage vs. light intensity for three samples of n-type silicon in 0.5M NaH_2PO_2 solution. An intensity of 12 corresponds approximately to one lumen. The polarity of the photovoltage is that of the silicon with respect to the Pt electrode immersed in the electrolyte.

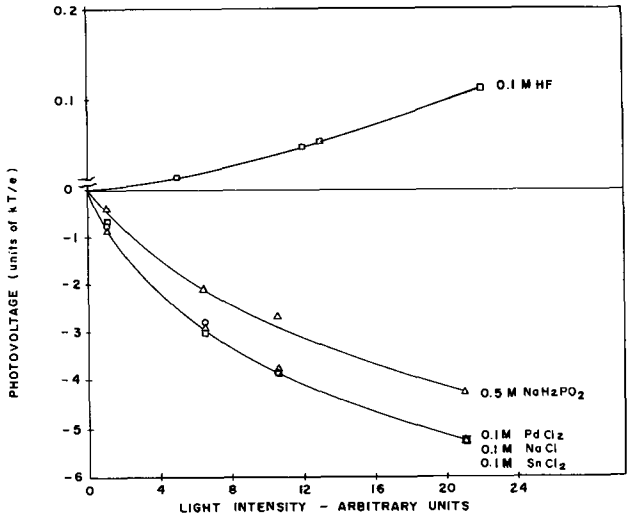

Fig. 3. Measured photovoltage vs. light intensity of sample N-3 (19 ohm-cm resistivity) in three electrolytes. Note the change in the ordinate scale for positive photovoltages.

photovoltage. The *p*H of the HF solution was varied over a wide range. The only effect on the photovoltage was a shortened time to reach an equilibrium as *p*H was decreased. In solutions other than HF, the p-type samples showed a low value for the positive photovoltage, which increased slightly in changing from a NaCl electrolytic environment to a NaH_2PO_2 environment.

The apparent source resistance for the photovoltage measurements was monitored by observing the loading resistor which halved the output voltage. This resistance was always less than 100 kilohms and varied in a way which was not directly related to the silicon resistivity.

Discussion

The polarity of the measured photovoltage indicates that both n- and p-type silicon assume a depletion-layer surface in an electrolytic environment free of HF. Thus, the immobile surface charge is negative for n-type material and positive for p-type material. The addition of NaH_2PO_2, which partially removes the surface oxide layer, tends to make both surfaces increasingly positive. This suggests that the oxide complexes formed in the dissolution carry off surface electrons. A completion of the oxide stripping of n-type material results in an accumulation-layer surface. For p-type silicon, HF acts to increase the magnitude of the depletion layer at the surface and thereby to increase the photovoltage. The dependence of photovoltage on material resistivity is not a very strong one, as is evident in Fig. 2.

The difference in the photovoltage polarity in a given electrolyte with a change in conductivity type suggests that a predominant part of the energy interchange resulting in an equilibrium at the liquid-silicon interface is through electron transfers. The other possible mechanism for this energy transfer, ionic adsorption and dissolution, would not depend on the position of the Fermi level in the material, or, therefore, on conductivity type (6).

An independent measurement of the photon-injected carrier density would be necessary to make a quantitative comparison of the general theory of the surface photovoltage as developed by Johnson (2) with the results described here. Following the suggestion of Harten (5), an attempt was made to obtain this quantity by monitoring the change in sample resistance with illumination. This technique led to nonreproducible results apparently due to variations in the current flow through the electrolyte in parallel with the surface. In Harten's work this component of current was considered to be negligible.

Qualitatively, the rapidly rising curve followed by a saturation for the depletion-layer photovoltage and the slowly rising curve for an accumulation-layer photovoltage, as seen in Fig. 3, match the predictions of Johnson's theoretical analysis. However, Johnson's theory predicts a stronger dependence on material resistivity and a smaller light sensitivity than is actually observed.

Manuscript received June 12, 1962; revised manuscript received Aug. 16, 1962.

Any discussion of this paper will appear in a Discussion Section to be published in the June 1963 JOURNAL.

REFERENCES

1. C. G. B. Garrett and W. Brattain, *Phys. Rev.*, **99**, 376 (1955).
2. E. O. Johnson, *ibid.*, **111**, 153 (1958).
3. C. G. B. Garrett and W. Brattain, *Bell System Tech. J.*, **34**, 129 (1955).
4. H. U. Harten, *J. Phys. Chem. Solids*, **14**, (1960).
5. H. U. Harten, *Z. f. Naturforschung*, **16a**, 459 (1961).
6. R. W. Gurney, "Ions in Solution" (1936).

Dislocation Cracks in Abraded Germanium Surfaces

E. N. Pugh and L. E. Samuels

Defence Standards Laboratories, Australian Defence Scientific Service, Sydney, Australia

Dislocation cracks were first reported by Allen in indium antimonide (1); they are dislocation arrays which usually occur as extensions to true cracks and which have the same morphology. The present authors have shown that dislocation cracks can be produced in germanium by local impact and have suggested that their formation is an intermediate stage in the fracture process (2). If this is so, dislocation cracks should be associated with cracking irrespective of the method of stressing. However, while damaged layers in abraded germanium surfaces have been shown to contain large numbers of true cracks, no dislocations were detected (3, 4). Abraded surfaces were therefore re-examined in the light of the more recent observations.

The problem of distinguishing between fine cracks and arrays of closely spaced dislocations when both have the same morphology arises from the fact that

etching reagents which reveal dislocations also attack cracks. This difficulty can be overcome by using the ferricyanide reagent developed by Billig (5), which has been shown to make fine cracks readily visible in short etching treatments (2-3 sec) whereas longer times (5 min) are required to reveal dislocations (3).

Experimental

Studies were confined to {111} surfaces of germanium single crystals which were abraded unidirectionally with silicon carbide particles, used both in abrasive papers and as slurries on a glass plate. Etching studies with the ferricyanide reagent require flat surfaces. Accordingly, the abraded surfaces were polished with a relatively fine diamond abrasive used on a napless cloth, polishing being continued to the stage when the surface irregularities were just removed; damage cracks then still remained. The surfaces were finally polished metallographically using fine magnesia abrasive. The polishing operation itself produced some damage, and on etching this gave rise to background "scratches." These scratches were visible at high magnifications (see Fig. 3), but could readily be distinguished from the damage introduced by the original abrasion process.

Observations and Conclusions

Etching with the ferricyanide reagent for short times (less than 10 sec) resulted in attack at the damage cracks. Figure 1 illustrates these cracks in a surface abraded with 220-grade papers. It must be emphasized that these features are true cracks which could be detected before etching. Further etching caused the cracks to become more pronounced and produced a number of additional markings (cf. Figs. 1 and 2) which have the characteristics of dislocation cracks, as described in the earlier paper (2). The dislocation cracks are shown at higher magnification in Fig. 3; they can be readily distinguished from the fissures formed at true cracks (indicated by arrows in Fig. 3) since the closely spaced dislocations give rise to shallow v-sectioned grooves. Dislocation cracks were observed to accompany cracking in all the abrasive treatments investigated.

Fig. 1. Surface originally abraded with 220 grade paper (abrasion direction horizontal) after etching for 3 sec with the ferricyanide reagent. Magnification 250X.

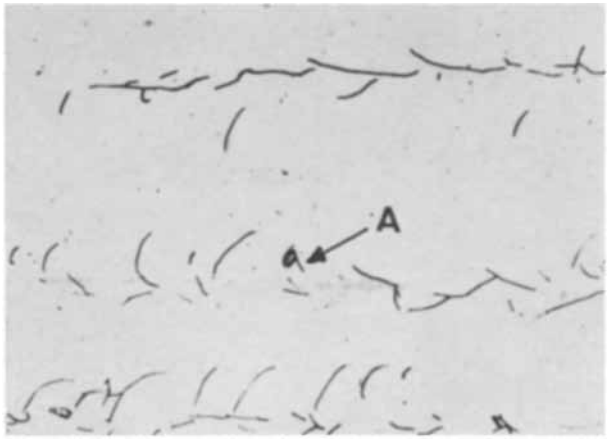

Fig. 2. Same field as in Fig. 1 after etching 5 min. Magnification 250X.

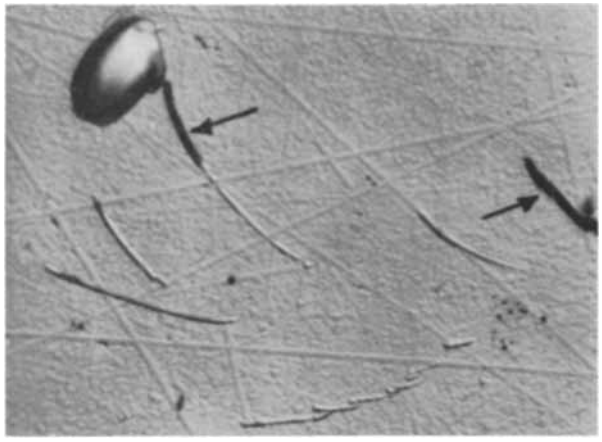

Fig. 3. Region A of Fig. 2 showing two cracks (marked with arrows) and several dislocation cracks. Magnification 1500X.

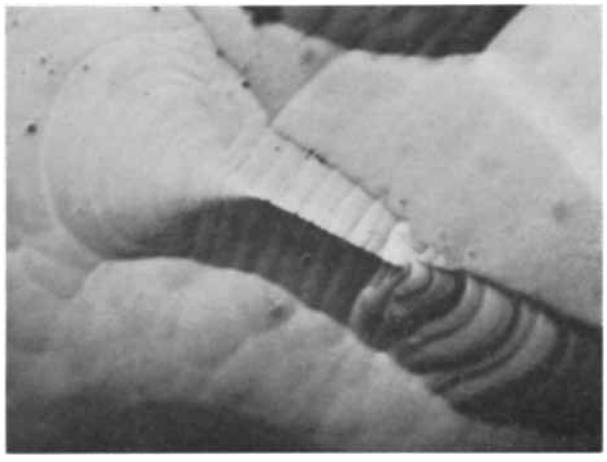

Fig. 4. Dislocation crack in a surface abraded with 220 grade silicon carbide slurry and etched with CP4. Magnification 750X.

Etching with CP4 has previously been shown to produce characteristic grooves at dislocation cracks (2). When abraded surfaces were etched with this reagent dislocation cracks were detected. Figure 4 illustrates a typical example. However, they were observed only in specimens in which the dislocation cracks were relatively large, *i.e.*, in surfaces treated with coarse abrasives. Further, the number of dislocation cracks revealed in these specimens was small compared to the number produced by the ferricyanide reagent. This suggests that the difference between the rate of etching along dislocations

and the rate normal to the surface is small, so that the smaller dislocation cracks were removed before they produced detectable grooves.

It is concluded that arrays of dislocations, in the form of dislocation cracks, are present in damaged layers in abraded germanium surfaces. However, the dislocation cracks are minor features of the damaged layers, their area being less than 10% of that of the true cracks which constitute the bulk of the damage.

Acknowledgments

The authors are indebted to Mr. A. Connellan for the metallographic preparation. This paper is published by permission of the Chief Scientist, Department of Supply, Australia.

Manuscript received Aug. 27, 1962.

Any discussion of this paper will appear in a Discussion Section to be published in the June 1963 JOURNAL.

REFERENCES

1. J. W. Allen, *Phil. Mag.*, **2**, 1475 (1957); *ibid.*, **4**, 1046 (1959).
2. E. N. Pugh and L. E. Samuels, submitted to *Phil. Mag.*
3. E. N. Pugh and L. E. Samuels, *This Journal*, **108**, 1043 (1961).
4. E. N. Pugh and L. E. Samuels, *ibid.*, **109**, 409 (1962).
5. E. Billig, *Proc. Roy. Soc.*, **235**, 37 (1956).

The Effect of Dissolved Germanium on the Surface Tension of Molten Indium

A. A. Bergh

Bell Telephone Laboratories, Incorporated, Allentown, Pennsylvania

Molten indium has been observed to spread and contract during alloying on (111) oriented single crystal germanium (1). This was explained by the variations in the surface tension of the melt during alloying (2). The surface tension of indium was assumed to decrease with the temperature rise and to increase with the concentration of the dissolved germanium, the two competing forces thus resulting in spreading and contraction. While the first assumption is substantiated by experimental data (3, 4), the second is contradictory to the generally observed behavior of mixtures. In general, the surface tension of liquid metals follows approximately a linear mixture law (linear in the surface fraction) unless the components form intermetallic compounds, and the surface tension of the liquid is likely to be dominated by the component with the lower value of γ (5). No intermetallic compounds are formed between germanium and indium (6) and Table I shows how close the respective surface tension values are, those of the indium being smaller by about 20%. Hence, in view of the empirical rules, very little effect of the dissolved germanium can be expected on the surface tension of indium. In order to resolve the above contradiction, experiments were carried out to collect quantitative data on the effect of dissolved germanium on the surface tension of molten indium.

Experimental

All surface tension values were measured by the maximum bubble pressure method. The principle of the method along with an application for a liquid metal system is given, *e.g.*, in Taylor's paper (9). A schematic diagram of the apparatus is shown in Fig. 1. A quartz or alundum crucible (A) contained the indium or indium-germanium sample of about 10 ml in volume; 99.999% pure indium and 5 ohm-cm n-type germanium were heated to 800°C in a hydrogen furnace for 30 min and then rapidly cooled to about 100°C to establish a nearly homogeneous distribution of germanium composed of small crystallites within the indium. Next the crucible was placed into a stainless steel vessel (B) equipped with bellows to lift or lower the sample with respect to capillary (D). Quartz cylinder (G) was connected to the stainless steel vessel with the help of a Buna gasket. Coaxial with the capillary was tube (C) to protect the orifice tube during handling. The pressure was affected by means of a polyethylene bellows compressed by a micrometer screw, and it was measured by following the change of the meniscus in the smaller limb of the manometer with a high precision

Table I. Surface tension of molten indium and germanium

	γ, dynes/cm	Temp, °C	Method of determination	Atmosphere	Ref.
In	515	600	Max. bubble pressure	H_2	(3)
	518	600	Drop volume	H_2	(4)
	514 ± 4	600	Max. bubble pressure	H_2	Present work
Ge	600	Mp	Drop weight	Ar	(7)
	600	1000	Sessile drop	Vac	(8)

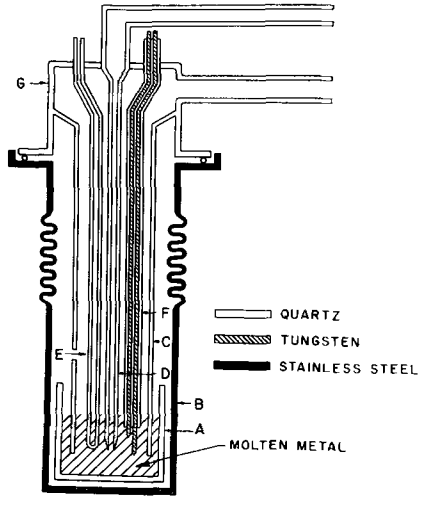

Fig. 1. Schematic diagram of the maximum bubble pressure apparatus.

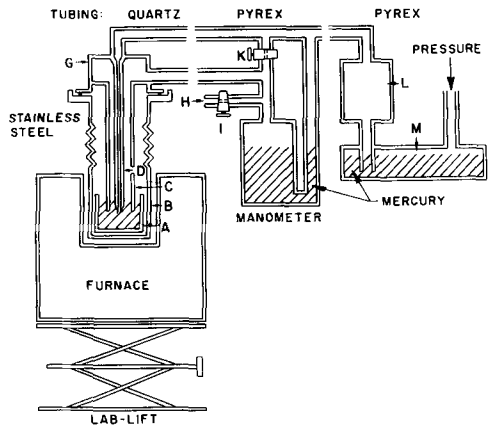

Fig. 2. Part of the maximum bubble pressure apparatus containing the capillary.

cathetometer. The system was flushed with hydrogen through tube (H) for 30 min when stopcock (I) was closed and stopcock (K) was opened and the sample heated to the desired temperature. The accurate positioning of the orifice in the liquid was facilitated by a simple electrical circuit. An indicator lamp was turned on when the upper tungsten wire (Fig. 2, F) got into contact with the liquid metal surface. The orifice at this point was immersed 4.07 mm deep. The bath temperature was recorded by a thermocouple carried in sheath (E).

Since the contact angle of indium on quartz is unknown, the orifice of the capillary was ground extremely thin (less than 0.1 mm) thus equalizing the internal and external radii for any practical conditions. For the effect of the gravitational distortion, Sugden's correction method was applied making use of the Bashforth's and Adam's tables as shown, *e.g.*, in Taylor's paper (9).

Results

The surface tension of pure indium and that of alloys containing different atomic per cents of germanium has been determined at 600°C. Each value in Table II represents the average of at least five measurements with the corresponding mean deviations.

Table II. Surface tension of indium-germanium alloys at 600°C in hydrogen atmosphere

Atomic % In	Atomic % Ge	γ, dynes/cm
100	0	514 ± 4
96.54	3.46	511 ± 3
91.98	8.02	510 ± 6
83.02	16.98	516 ± 5

Measurements are in good agreement with the generally observed behavior of mixtures and lead to the conclusion that the dissolved germanium does not affect the surface tension of indium to any greater extent than the accuracy of our measurements and can by no means be responsible for the contraction of the indium at higher temperatures.

Acknowledgment

The author wishes to acknowledge the help rendered by Mr. T. S. Miller in carrying out surface tension measurements.

Manuscript received Aug. 8, 1962.

Any discussion of this paper will appear in a Discussion Section to be published in the June 1963 JOURNAL.

REFERENCES

1. A. S. Rose, *R.C.A. Review*, **19**, 423 (1958).
2. J. I. Pankove, *J. Appl. Phys.*, **28**, 1054 (1957).
3. D. A. Melford and T. P. Hoar, *J. Inst. Metals*, **85**, 197 (1957).
4. O. A. Timofecvicheva and P. P. Pugachevich, *Akad. Nauk. SSSR Dokl.*, **124**, 1043 (1959).
5. F. Sauerwald, *Z. Metallkunde*, **35**, 105 (1943); A. Bondi, *Chem. Rev.*, **52**, 417 (1953).
6. F. A. Trumbore, *Bell System Tech. J.*, **39**, 205 (1960).
7. P. H. Keck and W. Van Horn, *Phys. Rev.*, **91**, 512 (1953).
8. T. P. Kolesmikova *Isvest. Vysshikk Ucheb Zavadenii Chernaya, Met.*, [9], 14 (1960).
9. J. W. Taylor, *J. Inst. Metals*, **83**, 143 (1955).

Brief Communication

Structure of Electroless Nickel

A. H. Graham, R. W. Lindsay, and H. J. Read

Department of Metallurgy, Pennsylvania State University, University Park, Pennsylvania

Ever since the first extensive studies of electroless nickel were published in 1944, the as-plated deposits have been regarded as amorphous because of the appearance of only one broad diffraction peak in their x-ray spectra. This belief, supported by intensive investigations by Goldenstein *et al.* (1), has posed difficulties in understanding the hardening of the deposits when they are heat-treated at temperatures above 200°C. Explanations such as one by Ziehlke, Dritt, and Mahoney (2) attributing the first stage of hardening to the formation of "an interim crystal lattice in the initially amorphous deposit" are not attractive because all the hardening mechanisms familiar to metallurgists are based on the existence of a crystalline structure at the start of the hardening process.

The x-ray evidence for the amorphous structure reported in the literature does not exclude the possibility that the as-plated deposits may be extremely fine-grained, supersaturated, solid solutions of phosphorus in crystalline nickel. The transmission electron diffraction pattern that we offer in Fig. 1 for a

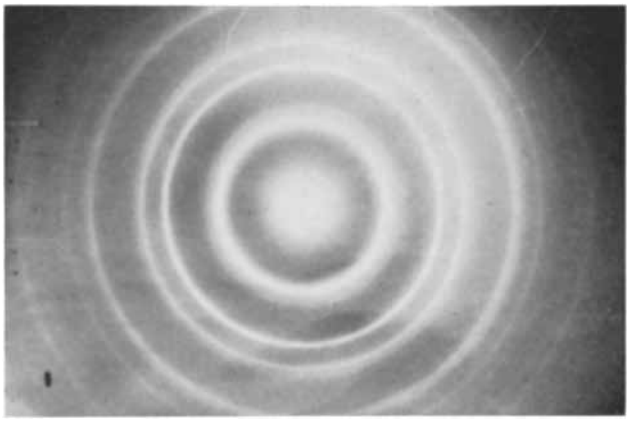

Fig. 1. Transmission electron diffraction pattern of as-plated electroless nickel, 5 weight per cent phosphorus; accelerating voltage 75 kv.

specimen plated on a thin copper substrate in a conventional alkaline nickel-chloride bath and thinned by electropolishing is one of many patterns that appear to us to be convincing evidence that as-plated electroless nickel is crystalline. On the negative for this pattern eleven rings were distinct enough that their diameters could be measured.

The composition and operating conditions for the bath used in making the specimen for Fig. 1 are as follows: nickel chloride hexahydrate, 45 g/l; ammonium chloride, 50 g/l; sodium citrate dihydrate, 82 g/l; sodium hypophosphite, 16 g/l; pH, 8.5; temperature, 90°C; agitation, stirrer. The as-deposited film was about 25μ thick on copper foil and had the lustrous matte appearance typical of deposits from this bath. Phosphorus content was determined by wet chemical analysis. A solution of chromic acid (500 g/l) and sulfuric acid (50 g/l) served for removal of the copper substrate. Extensive experience with this stripping solution has shown that there is neither chemical attack nor mechanical disturbance of nickel or nickel-phosphorus films. The deposit was thinned by electropolishing until it would transmit an electron beam. Although the exact thickness was not determined, it must have been less than 0.1μ. Diffraction patterns were produced by impinging the electron beam vertically on the plane of the film, and appropriate precautions were taken to prevent heating by the electron beam that could have caused crystallization of an initially amorphous deposit.

Although difficulties were encountered in the determination of the lattice type and in the indexing of the pattern, all the reflections could be attributed to nickel regardless of the lattice type assumed. Therefore it is probable that the deposit is primarily a supersaturated solid solution.

Figure 1 can be reasonably indexed according to either a hexagonal-close-packed (hcp) or a face-centered-cubic (fcc) structure. The most important factor in attempting to distinguish between the two possible structures is the {200} reflection for the fcc structure. The presence of this reflection would be indicative of a fcc structure, whereas its absence would indicate a hcp structure. In the large majority of the electron transmission diffraction patterns observed, the {200} reflection was either absent

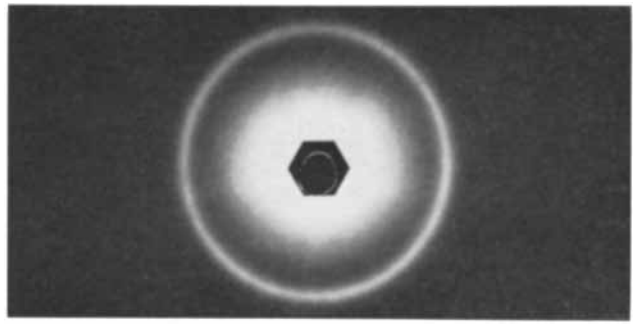

Fig. 2. Transmission x-ray diffraction pattern of as-deposited electroless nickel, 5 weight per cent phosphorus; unfiltered copper radiation.

or extremely weak. The difficulties in indexing can be attributed to stacking faults in the structure of fcc nickel. Paterson (3) has shown that stacking faults not only shift the {200} reflection toward a lower Bragg angle, but also greatly diminish its intensity. The diffraction pattern in Fig. 1 is compatible with the effects of stacking faults on the other reflections.

The fact that x-ray diffractometer patterns and x-ray transmission photographs of electroless nickel (see Fig. 2) give a definite indication of an amorphous structure was confirmed for the same specimens that yielded electron diffraction patterns that were evidence for a crystalline structure. This apparent contradiction between electron and x-ray results can be explained by a consideration of the effect of grain size. Lines in x-ray patterns are broadened and become less intense as the grain size decreases to diameters less than 10^{-3} cm. In electroless nickel the apparent grain size as indicated by transmission electron micrographs is of the order of 10^{-6} cm; therefore, only the most intense x-ray lines would appear. The amount of broadening of diffracted radiation from a fine-grained material is directly proportional to the wavelength of the radiation. Because the wavelength of electrons accelerated through a potential of 75 kv is almost two orders of magnitude smaller than the wavelengths of x-rays used in diffraction work, the fine grain size of electroless nickel does not preclude the production of electron diffraction lines. Although the x-ray spectrum of a crystalline material with a particle size of 10^{-6} cm should probably contain more than one line, the added effects of internal stress, solid solution, and stacking faults on diminishing the intensities of reflections can reasonably account for the destruction of all but the most intense x-ray reflection from electroless nickel.

It is anticipated that a future contribution will contain a detailed account of this and other work on the metallurgical properties and structure of electroless nickel.

Manuscript received July 9, 1962; revised manuscript received Sept. 26, 1962.

Any discussion of this paper will appear in a Discussion Section to be published in the June 1963 JOURNAL.

REFERENCES

1. A. W. Goldenstein, W. Rostaker, F. Schossberger, and G. Gutzeit, *This Journal*, **104**, 104 (1957).
2. K. J. Ziehlke, W. S. Dritt, and C. H. Mahoney, *Metal Progr.*, **77** [2], 84 (1960).
3. M. S. Paterson, *J. Appl. Phys.*, **23**, 499 (1952).

Oxidation of Iron-Nickel Alloys

VI. A Survey of Kinetics and Mechanism

R. T. Foley[1]

General Electric Company, Schenectady, New York

ABSTRACT

The oxidation of Fe-Ni alloys in the 500°-1100°C range has been the subject of many investigations. These observations are summarized, and an attempt is made to generalize on the kinetics and mechanism of oxidation. The composition of the oxide film over the entire composition range can be explained in terms of the thermodynamic stability of the oxides of Fe, of NiO, and of $Ni_xFe_{3-x}O_4$. In alloys of all compositions that have been investigated the first reaction is one of selective oxidation, creating a Ni-rich metal layer at the alloy-oxide interface. The growth of a Ni-containing spinel is promoted and formation of FeO is suppressed. This explains the reduction of oxidation rate to about 1000 times less than that of pure iron. The short-time kinetics of oxidation appears to be governed by diffusion through this Ni-rich metal layer or by diffusion through the Ni-containing spinel. Only at the Ni-rich end of the Fe-Ni system is NiO observed, and this exists next to the alloy interface under a layer of spinel. The reaction between NiO and Fe_2O_3 is rapid at these temperatures, thus explaining why these two oxides are not observed together. On prolonged reaction, subscale oxidation and intergranular attack is observed. Because of the stratification of oxide layers and these secondary effects, the development of a general rate law would be difficult.

Since 1916 and particularly during the last decade, a number of investigations have been carried out on the kinetics and mechanism of oxidation of Fe-Ni alloys. From the practical standpoint the need to acquire knowledge of the high-temperature behavior of these alloys is obvious, as various compositions are used in industry because of their magnetic behavior, their thermal expansion properties, their ability to participate in glass-to-metal seals, and their corrosion resistance. From the theoretical viewpoint the Fe-Ni system is of significance. Thermodynamically the system, consisting of a continuous series of solid solutions, is almost ideal (1) in the sense of obeying Raoult's law. Both Fe and Ni are oxidizable, and in addition, the oxides of iron are known to undergo solid state reactions with nickel oxide.

The investigations carried out in a number of laboratories have dealt with compositions over the entire phase diagram, varying from high-purity vacuum-melted preparations to commercial alloys containing several per cent of various alloying elements. The oxidizing atmospheres have included laboratory air of unknown moisture content as well as rigorously controlled atmospheres. The duration of the experiments have been such as to produce, in some cases, thin films, while in others thick scales and considerable subscale formation.

[1] Present address: Melpar, Inc., A Subsidiary of Westinghouse Air Erake Company, Falls Church, Virginia.

The objective of this paper is to organize these rather extensive observations and to develop the generalizations that would summarize the oxidation behavior of Fe-Ni alloys. This report will restrict itself to film formation beyond the nucleation stage. The concepts that the reaction product appears first at special points on the metal surface and that the number and form of these nuclei is related to the crystallographic orientation (2) of the surface, will be accepted.

For the sake of organization the whole Fe-Ni system is divided into three parts: the Fe-rich part of the system, 0-30% Ni; the intermediate section, 30-75% Ni; the Ni-rich part of the system, 75-100% Ni. The observations relative to kinetics of oxidation, composition, and nature of oxide film, as well as secondary effects, *e.g.*, subscale oxidation, will be discussed on this basis.

Oxidation of Fe-Rich Alloys (0-30% Ni)

In interpreting some of the results reported in the literature distinction should be made between "equilibrium" compositions and those compositions actually observed during an oxidation at elevated temperature. The oxide species observed on the alloys in the latter case are those growing under the particular conditions of temperature and gaseous environment that exist during the experiment. The "equilibrium" results were achieved (3, 4) by a technique involving strenuously oxidizing the alloy

Table I. Fe-Rich alloys (0-30% Ni)

Composition, % Ni	Temperature range, °C	Duration investigated	Kinetics	Film composition	Comments	Ref.
2.08, 6.40, 10.36, 15.06	1050-1095	7-20 days (equilibrium)	Reaction decreases considerably with increase in Ni content.	External layer of wüstite free of Ni.	"Equilibrium" studies. No spinel is found on alloys containing 15% or less Ni. Magnetite does form on cooling.	(3)
5.10	675-950	5-100 hr (in some cases 300 hr)	$y^n = kt$ (y = total O_2 picked up) where $n \neq 2$ always	Fe_2O_3 Fe_3O_4 FeO + Fe_3O_4 (alloy)	High-purity alloys. Extensive internal oxidation in low nickel range.	(6)
20	675	up to 14 hr	$n \cong 2$. (parabolic)			
	800	up to 5 hr	$n = 2.4$			
		5-14 hr	$n = 1.6$			
	900	up to 2 hr	$n = 2.6$			
		2-8 hr	$n = 1.22$			
30	850-1050	1 hr			Studied Ni enrichment of alloy surface	(5)
4.89	500	1-60 min		Fe_3O_4 on surface.	1 mm O_2 pressure; electron diffraction	(7)
				Spinel with a = 8.34A agrees with $NiFe_2O_4$ in body of film	X-ray transmision	
25	871	100 hr		40% Spinel $Ni_{0.05}Fe_{0.95}Fe_2O_4$ 60% αFe_2O_3	Alloy oxidized in air saturated with H_2O at 90°F	(8)
25	982	100 hr		50% $Ni_{0.53}Fe_{0.47}Fe_2O_4$	X-ray diffraction of oxide layers	
25	1093	100 hr		40-60% Spinel with $Ni_{0.4}$-$Ni_{0.6}$ 60-40% αFe_2O_3 spinel with a = 8.340-8.356 kx*		
25.6	800	up to 400 hr	Generally outer layers grew parabolically	Outer Fe_2O_3 up to 50% of total thickness. Spinel phase mixed with a small portion of NiO + FeO near the metal. NiO more evident in severely oxidized specimens.	X-ray diffraction at temperature of formation. Measured kinetics of oxidation of each phase in O_2 (atm pressure). Extensive internal oxidation in low nickel range.	(9)
29.6	600	0-60 min	$k_p = 1.27 \times 10^{-12}$**	Spinel and Fe_2O_3 (on atmosphere side)		(10, 11)
29.6	700	0-60 min	$k_p = 1.46 \times 10^{-11}$	Spinel and Fe_2O_3 (on atmosphere side)		
29.6	800	0-60 min	$k_p = 8.5 \times 10^{-11}$	Spinel and Fe_2O_3 (on atmosphere side)		
29.6	900	0-60 min	$k_p = 5.2 \times 10^{-10}$	Spinel and Fe_2O_3 (on atmosphere side)		
29.6	1000	0-60 min	$k_p = 3.3 \times 10^{-9}$			
1.53 (commercial steel)	1250	8-36 hr		Scale next to metal contained appreciable amount of Ni.	Oxidized in sulfur-containing atmosphere.	(22, 23)
2.92 (commercial steel)	1250			Scale next to metal contained appreciable amount of Ni.	Oxidized in sulfur-containing atmosphere.	(22, 23)
7	1000	24 hr		Zone of unoxidized Ni and oxide next to metal		(21)
25	~1000	oxidized to brittle scale		Scale contained unoxidized Ni		
2.75 (commercial steel)	1000	6 days		Outer layer = 0% Ni Middle layer = 0.16% Ni Inner layer = 7.07% Ni		(20)
					Intercrystalline attack and external oxidation	

* 1 kx unit = 1.00202Å.
** k_p = parabolic rate constant in $y^2 = k_p t$.

and then equilibrating the sample for an extended period of time (about 1000 hr) in an inert atmosphere. In this way sections of the equilibrium diagram for the Fe-Ni-O system were obtained. The kinetic tests would reach this end point if the reaction were allowed to proceed indefinitely in an oxygen partial pressure equal to the dissociation pressure of the oxide with the lowest dissociation pressure.

The experimental investigations bearing on the oxidation of the Fe-rich alloys are summarized in Table I.

In the oxidation of these alloys the first reaction involves selective oxidation of Fe, and in the very thin layers it appears that no Ni is contained in the oxide. The fact that the surface is enriched with Ni seems well established for all alloys in this region. Moreau and Bénard (5) measured this Ni enrichment occurring on the surface of the 30% Ni alloy. After a 1-hr oxidation time the Ni content of the surface approximates 50% at 850°C, 60% at 950°C, and 82% at 1050°C. As oxidation proceeds there is developed a composite layer with Fe_2O_3 (on the atmosphere side), a spinel structure, and FeO (in contact with the metal). FeO, which represents the "equilibrium" oxide (3), is found only with the very low Ni content alloys and probably exists in a layer mixed with Fe_3O_4 as observed metallographically (6). At oxygen pressures of about 0.2 atm Fe_2O_3 is a major reaction product at these temperatures (600°-1000°C). At 1 mm O_2 pressure no Fe_2O_3 was observed on the 4.89% alloy (7). The spinel observed even on the low Ni alloys contains appreciable Ni. Thus Gulbransen, Phelps, and Hickman (7) reported a spinel with a = 8.34Å, which conforms to $NiFe_2O_4$, in the body of the oxide film formed by oxidizing at 4.89% Ni alloy at 500° for up to 60 min in 1 mm O_2 pressure. The existence of a high Ni content in films grown on alloys containing 25% Ni is well established (8). It has also been noted (8) that when an alloy contains a few per cent of Mn, this Mn appears to concentrate in the spinel. The concentration of Ni dissolved in the Fe_3O_4 structure exists in a gradient with the high concentration next to the alloy, which itself is nickel rich at this interface.

The phenomenon of nickel enrichment either on the metal surface or in the innermost layer was observed during metallographic investigations of

specimens which had been severely oxidized (21-23). These studies revealed that metallic Ni was segregated during these extended oxidations as a result of the alloy-oxide interface moving into the sample.

Usually the oxidation rate of these alloys approximates a parabolic law for short periods of time (1-2 hr), and the rate seems to be determined by diffusion of cations, either through the Ni-rich metallic zone or through the Ni-containing spinel. The Ni has the outstanding effect of suppressing the formation of FeO, probably by decreasing the thermodynamic activity of Fe at the alloy surface (3). FeO is the fastest growing phase of the three possible oxides; it is the major oxide formed on pure Fe and accounts for the high oxidation rate of Fe. The effect of Ni on the oxidation rate appears at very low contents of Ni in the alloy. Thus, the rate of oxidation of a 2.08% alloy is appreciably less than that of pure Fe, and the rate of a 10.38% alloy is less by many orders of magnitude. The early part of the oxidation is made complex by continual change in alloy composition at the surface. After oxidation times of several hours and the build-up of appreciable scale it is likely that the rate-determining step is diffusion across the oxide film. At these longer times the growth law deviates from a simple parabolic relationship because layers of different composition are growing. Actually there is not a great deal of quantitative data available to evaluate the effect of small percentages of Ni on the oxidation rate. However, it is apparent that the Ni effect is considerable, reducing the oxidation rate of Fe by a factor of 10^2-10^3 as measured by parabolic rate constants determined for 1 hr oxidations. At 30% Ni the effect is established in the sense that further addition of Ni has little effect on the rate. The oxidation rate of the 30% alloy is approximately the same as that of the 40.9%, and the activation energy is about the same, 40.5 kcal/mole inferring a similar mechanism.

Oxidation of Fe-Ni Alloys Containing 30-75% Ni

The first-formed film on alloys in this intermediate range is an oxide of Fe which results from selective oxidation. Thus lines for FeO (12) and Fe_2O_3 (11) are observed in the vacuum of the high-temperature electron diffraction camera. As a consequence there is an early enrichment of Ni at the alloy-oxide interface. However, upon oxidation at times longer than 1 min at 600°C, a spinel structure is obtained. This spinel has a formula $Ni_xFe_{3-x}O_4$ wherein x approaches unity close to the alloy-oxide surface, as established by lattice parameter measurements and chemical analysis (13, 14). For example, the oxide produced on the 41% alloy after 1 min at 800°C contained 31.8% Ni (average value) (13). For oxidation times up to about 3 hr at temperatures in the 500°-1100°C range the predominant oxide was this nickel-containing spinel. In addition a layer of Fe_2O_3 was formed at the oxide-atmosphere interface. Continued oxidation followed by equilibration in an inert atmosphere (4) yields external scales composed of nickel-containing spinel with wüstite. In addition there is extensive subscale formation, the product in this case being wüstite and spinel. While this subscale would penetrate completely a normal oxidation strip during runs of several hundred hours, for runs up to 1 or 2 hr this secondary phenomenon does not appear to play an important part in the kinetics, at least insofar as quantitative data are available to us. During the extended equilibration periods hematite disappears and FeO appears. The equilibrium procedure is carried out at the oxygen pressure established by the dissociation pressure of FeO.

The enrichment with respect to Ni at the alloy-oxide interface is observed for long time oxidations (13 days at 1000°C). The development of an "inner layer" containing 52% Ni on an original 36% Ni alloy was interpreted by Pfeil as due to the movement outward of Fe through the Fe-Ni metallic zone in contact with the oxidizing atmosphere (20).

The kinetics of reaction for alloys in this range is governed primarily by the formation and growth of the Ni-containing spinel. As has been pointed out (4), the high Ni content of the alloy has made the fastest growing phase on Fe, namely FeO, thermodynamically unstable. The growth rate of magnetite on Fe is only about one-twentieth that of FeO on

Table II. Fe-Ni alloys (30-75% Ni)

Composition, % Ni	Temperature range, °C	Duration investigated	Kinetics	Film composition	Comments	Ref.
48.5	1050	1000 hr equilibrium		Spinel + wüstite with spinel containing up to 10% Ni	"Equilibrium" studies—Extensive subscale composed of wüstite and spinel	(4)
37.13	1050	1000 hr equilibrium		Wüstite + spinel, 8.72% Ni in external scale	Subscale of wüstite + a little spinel	
49 Ni, 2 Mn	500	up to 60 min		Fe_3O_4 (a = 8.42Å) (probably contained Mn)	This alloy was Hipernik; 1 mm O_2; electron diffraction at temperature	(12)
49 Ni, 2 Mn	600	1, 5 min		Fe_3O_4 (a = 8.43Å)		
49 Ni, 2 Mn	600	30, 60 min		Fe_3O_4 + Fe_2O_3		
49 Ni, 2 Mn	700	0 (oxidized in vacuum of electron diffraction instrument)		FeO		
		1-60 min		Fe_3O_4 (a = 8.43Å)		
36 (commercial alloy)	1000	13 days		Outer layer = 1.46% Ni Middle layer = 2.29% Ni Inner layer = 52.08% Ni	Nickel in inner layer in metallic form	(20)
50 Ni	1093	3 hr		Strong spinel, a = 8.36Å and weak Fe_2O_3 patterns	X-ray fluorescence	(14)
40.9	600	up to 60 min	$k_p = 1.27 \times 10^{-12}$*	Both Ni-containing spinel and Fe_2O_3 with spinel present in larger proportion.	These alloys contained Mn and Si which were not detected in film	(10, 11)
40.9	700	up to 60 min	$k_p = 9.8 \times 10^{-12}$			
40.9	800	up to 60 min	$k_p = 9.3 \times 10^{-11}$			
40.9	900	up to 60 min	$k_p = 4.05 \times 10^{-11}$			
40.9	1000	up to 60 min	$k_p = 3.51 \times 10^{-9}$			

* k_p = parabolic rate constant (see footnote, Table I).

Table III. Ni-rich alloys (75-100% Ni)

Composition, % Ni	Temperature range, °C	Duration investigated	Kinetics	Film composition	Comments	Ref.
79%	1093	1 hr		Only spinel lines, a = 8.37Å, obs.	Severe oxidation with scale continuously spalling	(14)
75.4	800	up to 400 hr	Parabolic growth of individual layers	Thin layer of Fe_2O_3; compact layer of spinel phase; porous NiO occupying up to 50% of scale thickness. Spinel with a = 8.356-8.367Å	Extensive intergranular and subscale oxidation	(9)
84.2	800	up to 400 hr	Parabolic growth of individual layers	Only thin skin of Fe_2O_3 (barely detectable metallographically); Ni containing spinel; NiO, 50% of scale thickness		(9)
80%	700 900	2, 12, 32 min		Ni containing spinel	High purity alloy	(17)
78% Ni 3.8% Mo	600 700 800 900 1000	0-60 min 0-60 min 0-60 min 0-60 min 0-60 min	$k_p = 7.2 \times 10^{-13}$ $k_p = 3.01 \times 10^{-12}$ $k_p = 1.70 \times 10^{-11}$ $k_p = 7.5 \times 10^{-11}$ $k_p = 6.4 \times 10^{-10}$	Spinel NiO (MoO_3) NiO (MoO_3)		(10, 11)

Fe. The diffusion rate in the Ni-containing spinel is still lower as evidenced by the rate data given in Table II. Because of differences in testing atmospheres, surface preparation, and other factors, a comparison of rate data in the literature can only be semiquantitative. However, with this limitation in mind, a comparison with data on the oxidation of pure Fe (15) yields a factor of improvement from alloying of 10^2-10^3. The apparent energy of activation for the rate-determining diffusion process in the spinel structure is about 41,000 cal/mole (10). This value does not hold at elevated temperatures or in atmospheres that contain H_2O vapor, presumably because of solid-state reactions influencing the morphology of the oxide film (16).

Oxidation of Nickel-Rich Alloys, 75-100% Ni

The oxide film formed on an 80% Ni alloy during the first hour of oxidation in the 600°-1100°C range is essentially the nickel-containing spinel with a lattice parameter 8.35-8.37Å (14, 17) (Table III). The result of the preferential oxidation is a composition closer to $NiFe_2O_4$ than to Fe_3O_4. FeO is not observed as it was on the alloys of lower nickel content. On extended oxidation the system Fe_2O_3: Spinel: NiO (traversing the scale from the outside to the inside) is developed. The thermodynamic activity of Fe is low, and thus only a thin layer of Fe_2O_3 is observed. Fe_2O_3 should not exist in contact with NiO at temperatures of 800°C and above because of the tendency for solid-state reaction to occur as previously discussed (16), and where these two species are observed in the oxide scales they are separated by a layer of spinel. Following depletion of Fe at the surface because of outward diffusion and reaction, the surface, which is essentially Ni, reacts to form NiO which occupies about 50% of the scale after oxidation for 1 hr at 800°C. The only short-time data available for high nickel alloys (10) approximate the oxidation rate data for Ni (18), which presumably is controlled by the diffusion of Ni cations through the NiO layer (19).

Discussion

The composition of the oxide films developed over the whole range of Fe-Ni alloys in the 500°-1100°C range may be explained by consideration of the thermodynamic stability of the oxides of Fe, of NiO and $NiFe_2O_4$ (actually $Ni_xFe_{3-x}O_4$). The dissociation pressure of NiO is large compared with that of the Fe oxides. Above 600°C, Fe_2O_3 and NiO react rapidly to form the spinel.

In the Fe-rich part of the system the first reaction involves the selective oxidation of Fe. The alloy-oxide interface is enriched in Ni, and Fe must diffuse through this metallic layer for further reaction. The concentration and hence the thermodynamic activity of Fe at the interface is greatly reduced; the growth of Fe_3O_4 is promoted and that of FeO is suppressed. This directly bears on the kinetics of reaction as the oxidation rate is reduced by a factor of 1000 as the Ni content increases to 30% Ni. Fe_2O_3 is produced at the atmosphere interface on prolonged oxidation. As the nickel content of the alloy increases, the kinetics and the mechanism of reaction are governed by the formation and growth of the Ni-containing spinel in contact with an alloy interface which has become enriched in Ni. A definite concentration gradient of Ni exists in this spinel, which approaches stoichiometric $NiFe_2O_4$ next to the alloy and Fe_3O_4 in contact with Fe_2O_3 or the oxidizing atmosphere.

The Ni-containing spinel is observed in thin films produced on alloys containing as much as 80% Ni. As oxidation continues, the alloy adjacent to the reaction interface is depleted in Fe and the Ni activity rises; NiO then grows next to the alloy. The fact that NiO and Fe_2O_3 are not seen in contact is due to the rapid rate of reaction of these two species at elevated temperatures.

With oxidation times of many hours there is a considerable subscale formation and grain boundary attack as viewed metallographically. In addition, the usual situation involves stratification of various oxide layers. Therefore, the formulation of a general rate law covering all alloy concentrations would be difficult. For short periods of time (less than 60 min) a single parabolic relationship appears to represent adequately the experimental observations. The kinetics suggest diffusion through the Ni-containing spinel or through the metallic layer enriched with Ni as the rate-determining step. A simple rate law does not hold for longer times or even for shorter times if there is a change in the morphology of the oxide film as a result of solid-state reaction.

Manuscript received Nov. 11, 1961; revised manuscript received June 2, 1962.

Any discussion of this paper will appear in a Discussion Section to be published in the June 1963 JOURNAL.

REFERENCES

1. O. Kubaschewski and O. von Goldbeck, *Trans. Faraday Soc.*, **45**, 948 (1949).
2. J. Bardolle and J. Bénard, *Compt. rend.*, **232**, 231, 2217 (1951).
3. M. J. Brabers, W. J. Heideger, and C. E. Birchenall, *Chim. Phys.*, **53**, 810 (1956).
4. M. J. Brabers and C. E. Birchenall, *Corrosion*, **14**, 179t (1958).
5. J. Moreau and J. Bénard, *Compt. rend.*, **232**, 1842 (1951).
6. J. Bénard and J. Moreau, *Rev. met.*, **47**, 317 (1950).
7. E. A. Gulbransen, R. T. Phelps, and J. W. Hickman, *Ind. Eng. Chem. (Anal. Ed.)*, **18**, 640 (1946).
8. H. J. Yearian, H. E. Boren, Jr., and W. E. Warr, *Corrosion*, **12**, 561t (1956).
9. S. W. Kennedy, L. D. Calvert and M. Cohen, *Trans. AIME*, **215**, 64 (1959).
10. R. T. Foley and C. J. Guare, *This Journal*, **106**, 936 (1959).
11. R. T. Foley, C. J. Guare, and H. R. Schmidt, *ibid.*, **104**, 413 (1957).
12. J. W. Hickman and E. A. Gulbransen, *Trans. AIME*, **171**, 344 (1947).
13. R. T. Foley, J. U. Druck, and R. E. Fryxell, *This Journal*, **102**, 440 (1955).
14. P. K. Koh and B. Caugherty, *J. Appl. Phys.*, **23**, 427 (1952).
15. J. K. Stanley, J. von Hoene, and R. T. Huntoon, *Trans. Am. Soc. Metals*, **43**, 426 (1951).
16. R. T. Foley, *This Journal*, **109**, 278 (1962).
17. R. T. Foley, *ibid.*, **108**, 216 (1961).
18. E. A. Gulbransen and K. F. Andrew, *ibid.*, **104**, 451 (1957).
19. M. T. Shim and W. J. Moore, *J. Chem. Phys.*, **26**, 802 (1957).
20. L. B. Pfeil, *J. Iron Steel Inst.*, **119**, 501 (1929).
21. J. E. Stead, *ibid.*, **94**, 243 (1916).
22. K. Sachs, *ibid.*, **185**, 348 (1957).
23. K. Sachs, *Metallurgia*, **54**, 109 (1956).

Measurement of Thickness and Refractive Index of Oxide Films on Silicon

G. R. Booker and C. E. Benjamin

Research Laboratories, Westinghouse Electric Corporation, Pittsburgh, Pennsylvania

ABSTRACT

Optical interference methods for determining the thickness and refractive index of oxide films on silicon are described. The treatment is confined to those methods in which a portion of the film is dissolved with HF, and measurements are made on the height of the step thus created. For thick films (>3000Å) two-beam interference is used, and for thin films (<3000Å) multiple-beam interference is used. The different types of fringes are explained, and the accuracies of the methods are given. The emphasis is on the development of simple, practical procedures which can be applied in a routine manner.

Oxide films on silicon surfaces are widely employed during the fabrication of semiconductor devices. Relatively thick films (3000-20,000Å) are used for masking against epitaxial growth and certain elements during diffusion, while thin films (50-1000Å) are useful in other device fabrication operations. These thicknesses are equivalent to a few wavelengths of light or less, and hence it is not surprising that the two standard methods used to measure such thicknesses are optical methods.

In the first of these methods the specimen is viewed by reflected white light, and the film thickness is deduced from the color of the film. The color arises because of interference occurring between the light beams reflected from the upper and lower surfaces of the oxide film. Reflections of specific wavelengths interfere destructively, and the remaining wavelengths combine to give a characteristic color. The method consists of comparing the color of the unknown film with the colors of a set of standard films of different thicknesses. However, this method can be applied only to films in the thickness range of approximately 500-4000Å and hence does not fully cover either of the above practical thickness ranges. Moreover the accuracy is limited to approximately ±200Å.

In the second of these methods the film is completely removed from a portion of the specimen so that a step is created equal in height to the film thickness. The step height is then determined by measuring the displacement of monochromatic light interference fringes on crossing the step. The method is direct and can be applied to films of any thickness. The accuracy is dependent on the particular procedure used to obtain the interference fringes. For thick films the two-beam interference technique, which produces relatively broad fringes, is generally sufficiently accurate. A commercial two-beam interference microscope is often used for such measurements because of its convenience and versatility. On

the other hand, the multiple-beam interference technique, which produces narrow sharp fringes, is almost essential for reasonable accuracy with thin films. A noncommercial type of apparatus is usually employed for this purpose.

The present paper is concerned with the second, *i.e.*, step height, method of measurement. In particular, the various types of interference fringes associated with a step or a wedge in a surface oxide film on silicon are demonstrated, the methods used to obtain such fringes are described, and the equations for calculating the film thicknesses are given. In many practical applications of both white light and monochromatic light interference methods of measurement the refractive index of the surface film enters directly into the step-height calculation. A simple technique is described for determining this index with satisfactory accuracy.

The principles underlying the methods described are not new. The purpose of the paper is rather to explain the methods briefly and to indicate how they may be used in a practical manner.

Thick Films

The following procedure is convenient for forming shallow wedge-shaped steps in surface oxide films on silicon. A solution of Apiezon W wax in toluene is applied with a brush to a portion of the silicon specimen surface possessing the oxide film (Fig. 1a). The toluene rapidly evaporates, leaving a hard wax surface film. The specimen is immersed for 60 sec in HF (48%) to dissolve the unprotected portion of the oxide film (Fig. 1b). The specimen is then thoroughly rinsed, and the wax is removed (Fig. 1c) with trichloroethylene. Undercutting of the wax layer by the HF produces a relatively uniform wedge-shaped oxide film step, the angle of the wedge being approximately 1°.

The different types of interference fringes associated with such a specimen can readily be demonstrated if a portion of a specimen possessing a relatively thick oxide film is metallized (Fig. 1d), and the specimen is examined with a two-beam interference microscope (Fig. 2). This instrument produces interference fringes which may be considered as occurring between the surface of the specimen and a nearby image of the surface of a reference plane. Typical fringes for such a specimen which was oxidized in wet argon at 1200°C are shown in Fig. 3. The fringes have been adjusted to be perpendicular to the wedge and of a convenient spacing. This occurs when the reference plane of the interference microscope intersects the plane of the silicon surface along a line perpendicular to the wedge and at a suitable angle. Monochromatic thallium green light ($\lambda = 5350$Å) was used throughout the investigation.

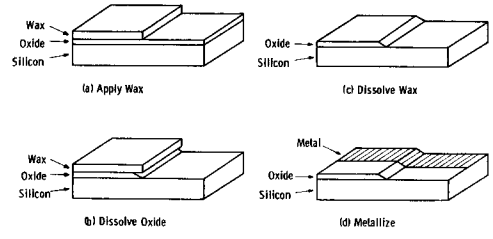

Fig. 1. Preparation of the oxide film step and subsequent metallizing.

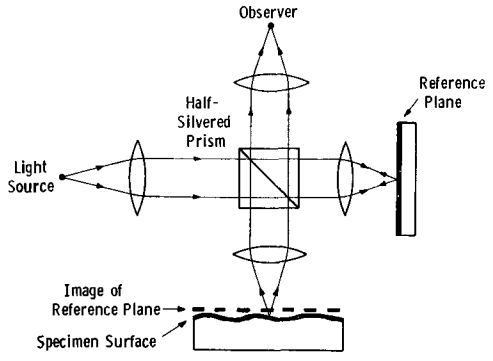

Fig. 2. Optical system of the interference microscope for forming two-beam interference fringes.

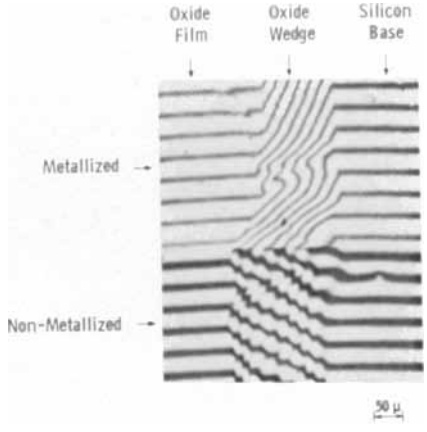

Fig. 3. Interference fringes associated with a relatively thick oxide film on silicon. The specimen was prepared as in Fig. 1 and examined with a two-beam interference microscope.

In the metallized portion of the specimen (Fig. 3, top) a single fringe system occurs, and the displacement of the fringes on going from the silicon base to the oxide film corresponds to a step up. In the nonmetallized portion of the specimen (Fig. 3, bottom), the fringes are more complex. Thus, in the oxide wedge area more than one fringe system occurs. However, a single fringe system predominates, and the displacement of these fringes on going from the silicon base to the oxide film corresponds to a step down.

The origin of these fringe systems is as follows. In the metallized portion (Fig. 4) the interference takes place between the beam reflected from the reference plane of the interference microscope and the beams reflected from the metallized surface of the silicon base, the metallized upper surface of the oxide wedge, and the metallized upper surface of the oxide film in their respective areas. The film thickness d is given by

$$d = p\frac{\lambda}{2} \qquad [1]$$

where p is the fringe displacement and λ is the wavelength of the light. Hence, measurement of fringe displacement on a metallized specimen provides an absolute determination of the film thickness. The

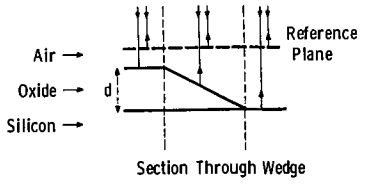

Fig. 4. Origin of the interference fringes in the metallized portion of Fig. 3.

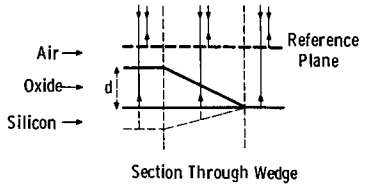

Fig. 5. Origin of the main interference fringes in the nonmetallized portion of Fig. 3.

accuracy is estimated to be ±0.1 fringe, corresponding to ±270Å. The displacement for the film of Fig. 3 is 6.0 fringes, corresponding to a film thickness of 16,000Å.

In the nonmetallized portion (Fig. 5) the interference mainly takes place between the beam reflected from the reference plane of the interference microscope and the beams reflected from the surface of the silicon base, the lower surface of the oxide wedge, and the lower surface of the oxide film in their respective regions. The oxide film of refractive index n has the effect of increasing the optical path length in the film, the oxide/silicon interface thereby being apparently lowered. The amount of lowering in the oxide film area is $d(n-1)$, and the film thickness is given by

$$d = q\frac{\lambda}{2(n-1)} \qquad [2]$$

where q is the fringe displacement. Hence, measurement of fringe displacement on a nonmetallized specimen enables the film thickness to be determined if the refractive index of the film material is known. The accuracy is again estimated to be ±0.1 fringe, but this now corresponds (assuming $n = 1.50$) to ±540Å.

If measurements are made on metallized and nonmetallized portions of the same specimen, then equations [1] and [2] hold simultaneously and so

$$n = 1 + q/p \qquad [3]$$

Hence, the refractive index of the oxide film can be determined simply by measuring the two fringe displacements q and p. The accuracy for a 15,000Å film is estimated to be 1-2%. The values obtained to date for oxide films on silicon have been in the range 1.48-1.50. This method for determining the refractive index of surface oxide films can presumably be applied to materials other than silicon.

Returning to Fig. 3, the wedge area in the nonmetallized portion of the specimen exhibits a complicated fringe array.[1] In addition to the main fringe system crossing the wedge obliquely, there is a weaker system crossing the wedge obliquely in the opposite direction. Comparison with the metallized portion of the specimen identifies this system as being associated with the reference plane of the interference microscope and the upper surface of the oxide film. There is also a third system, seen as a perturbation associated with the main system, running in a direction parallel to the wedge. This system arises from interference occurring between the upper surface and lower surface of the oxide wedge. Hence, it should be possible to examine this latter system without using an interference microscope. The result of removing the reference plane of the interference microscope, equivalent to using a metallurgical microscope equipped with a monochromatic light source, is shown in Fig. 6. In the metallized portion of the specimen no fringes occur, while in the nonmetallized portion of the specimen the third fringe system occurs alone. The origin of this fringe system is shown in Fig. 7. The film thickness is given by

$$d = r\frac{\lambda}{2n} \qquad [4]$$

where r is the number of fringes within the wedge area. The number of fringes r is counted from the silicon base toward the oxide film, the silicon base being considered as the center of a bright fringe. The fractional fringe is estimated by interpolation assuming the slope of the wedge to be uniform. When the wedge terminates with a dark fringe, as for example in Fig. 8b, d, and f, the fractional fringe can also be estimated from the degree of grayness of the oxide film away from the wedge area. Hence, counting the number of wedge fringes on a nonmetallized specimen enables the film thickness to be determined if the refractive index of the film is

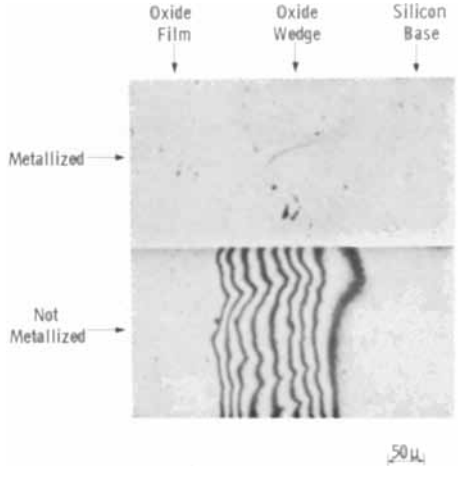

Fig. 6. Result of removing the reference plane of the interference microscope while observing the fringes of Fig. 3. Only wedge fringes in the nonmetallized portion remain.

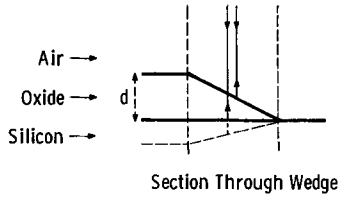

Fig. 7. Origin of the wedge fringes of Fig. 6

[1] A somewhat similar array associated with oxide films on uranium was recently reported by Stebbins and Shreir (1). However, no photographs of the fringes were shown.

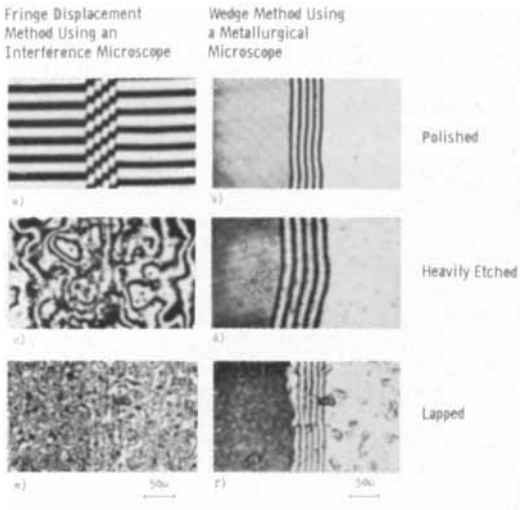

Fig. 8. Influence of surface finish on the fringe displacement and wedge methods for determining film thickness. The wedge method can be used for smooth and rough surfaces.

known. The accuracy is estimated to be ± 0.2 fringe, corresponding (assuming $n = 1.50$) to ± 350Å. Alternatively, by making measurements on metallized and nonmetallized portions of the same specimen according to Eq. [1] and [4], respectively, the refractive index of the oxide film can be calculated from

$$n = r/p \qquad [5]$$

For the derivation of Eq. [3] and [4] it was assumed that any phase changes occurring at the air/silicon, oxide/silicon, and air/oxide interfaces could be disregarded. The assumption is justified by the following. Referring to the nonmetallized portion of Fig. 3, the fringe system associated with the silicon base is dependent on a phase change occurring at the air/silicon interface. On reaching the oxide wedge this fringe system splits into two systems. The main system, proceeding toward the top of the photograph, is dependent on a phase change occurring at the oxide/silicon interface. The secondary system, proceeding toward the bottom of the photograph, is dependent on a phase change occurring at the air/oxide interface. Figure 3 and other similar photographs show that these three fringe systems all meet without any abrupt discontinuities at the boundary where the oxide wedge begins. Hence, it can be deduced that these phase changes are all the same, at least within the accuracy of the measurements discussed here, and can therefore be disregarded. The assumption is further supported by the good agreement obtained in measuring thicknesses by more than one of the interference methods described above.

In the calculation of the accuracies from Eq. [2] and [4], no account was taken of possible errors due to uncertainty in the value assumed for the refractive index n. The additional error which would result may be readily calculated. For example, for Eq. [4] a 1% error in n corresponds to an additional 1% error in d, and for a film 10,000Å thick this amounts to a further ±100Å. This error is small compared with the error given above arising from the fringe measurement, ±350Å, indicating that a knowledge of n to 1% is usually adequate for such measurements.

The wedge method for determining film thickness has a number of practical advantages over the fringe displacement method. The time and equipment involved in metallizing are eliminated. The fringes can be observed readily with a standard metallurgical microscope equipped with a monochromatic light source, so that an interference microscope is not required. Moreover, the only adjustment necessary in order to see the fringes is to focus the microscope.

The wedge method has a further practical advantage, namely, that measurements can be made equally well on specimens whose original surfaces are relatively uneven. This has been demonstrated by applying the fringe displacement and the wedge methods to specimens with three different types of surface finish: polished, heavily etched, and lapped (Fig. 8). The photographs in column 1 were obtained using the interference microscope, and fringe displacements can only be measured on the polished specimen. On the other hand, the photographs in column 2 were obtained using a metallurgical microscope, and the fringes are uniform and clearly discernible for all three specimens. The polished and etched specimens were thermally oxidized at the same time, and it can be seen that the number of fringes within each of these two wedge areas are the same even though the angles of the two wedges are slightly different. The number of fringes for the films of Fig. 8b, d, and f are 4.7, 4.7, and 5.5, respectively, corresponding (assuming $n = 1.50$) to film thicknesses of 8400Å, 8400Å, and 9800Å, respectively. For an additional check on the film thickness of the polished specimen, the fringe displacement of Fig. 8a is 1.6 fringes. Substituting this value into Eq. [2] gives (assuming $n = 1.50$) $d = 8500$Å, in good agreement with the value obtained by the wedge method.

It may be noted that many of the surface irregularities associated with the lapped specimen (Fig. 8e) are of the same order of magnitude as the thickness of the oxide film (Fig. 8f), and yet relatively uniform wedge fringes are still obtained (Fig. 8f). The reason for this is that during the oxidation process an oxide film of uniform thickness is formed, the upper surface of the film following the irregularities of the surface of the silicon specimen. During the step-forming process a certain proportion of this thickness is dissolved depending on its distance from the edge of the wax coating. Hence, although the upper surface of the oxide wedge is also irregular, the thickness of the wedge still varies in a relatively uniform manner.

Because of the simplicity and practicability of the wedge method, it has been found advantageous to use the method as a routine laboratory procedure for determining the thickness of oxide films on silicon. In particular, the method has been extensively applied to films thicker than 3000Å with an accuracy of ±350Å.

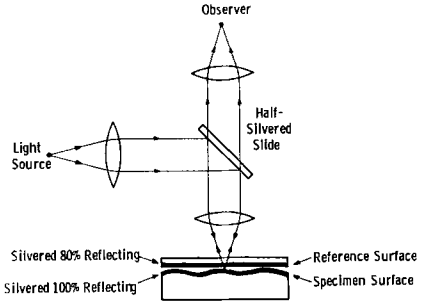

Fig. 9. Optical system using a silvered glass slide for forming multiple-beam interference fringes.

Thin Films

In order to determine the thickness of thin oxide films on silicon, such as those produced by anodic techniques, the methods described in the last section are not sufficiently accurate, and it is necessary to use multiple-beam interference (2). The standard method for obtaining multiple-beam fringes is shown in Fig. 9. One surface of a glass slide is silvered to be approximately 80% reflecting, and the surface of the specimen is silvered to be approximately 100% reflecting. The two silvered surfaces are placed close together with the glass slide uppermost, and the combination is examined with a metallurgical microscope equipped with a monochromatic light source. Light entering the combination undergoes a series of multiple reflections, giving rise to narrow sharp fringes. The silvered surface of the glass slide acts as a reference plane, and the fringes reveal the irregularities associated with the surface of the specimen. The orientation and spacing of the fringes are adjusted by slightly altering the position of the glass slide. Silver is generally used for the metallizing because of its low absorption of light. The value of 80% reflection given above for the glass slide surface is a practical value, being relatively easy to achieve and not critical. Good quality fringes occur only if the two silvered surfaces are very close together.

Multiple-beam fringes obtained by this method for a silicon specimen with a thin oxide film are shown in Fig. 10. The wedge-shaped step in the oxide film was formed by the standard procedure. In this instance the silvered surface of the glass slide was placed directly in contact with the silvered surface of the specimen, and the orientation and spacing of the fringes were adjusted by moving three small weights resting on top of the glass slide. Since the material between the two silvered surfaces is air, the film thickness is given by Eq. [1], where p is the fringe displacement. However, because of the narrowness of the fringes the accuracy here is estimated to be 0.02 fringe, corresponding to ±55Å. The displacement for the film of Fig. 10 is 0.14 fringe, corresponding to a film thickness of 370Å. However, it is difficult when using this method to achieve a routine accuracy much better than ±55Å. This is because of difficulties in positioning the reference surface at an appropriate angle only a few wavelengths away from the specimen surface, and in maintaining the silvered surfaces in good condition, *i.e.*, free from tarnish and surface damage.

Fig. 10. Multiple-beam interference fringes obtained by the silvered glass slide method. The specimen is a step in a thin oxide film on silicon.

A multiple-beam method capable of greater accuracy than the standard technique given above was recently described by Tolansky (3), and Joshi and Tolansky (4). In this method the specimen surface is silvered to be 100% reflecting, and a dilute solution of collodion in amyl acetate is applied to the surface. The specimen is held vertically so that the solution drains and subsequently dries to give a thin wedge-shaped collodion film. The upper surface of the collodion film is then silvered to be approximately 80% reflecting and acts as the reference plane, and the combination is examined in the standard manner.

This method has several advantages compared with the standard technique. First, extremely thin collodion films with very small wedge angles can be formed. Second, the two silvered surfaces between which the reflections occur are protected from the atmosphere, and so do not tarnish. Third, no mechanical adjustment of the two silvered surfaces is performed, so that no surface damage results. Hence, the conditions are ideal for multiple-beam interference, and extremely high quality fringes result. On the other hand, the orientation and spacing of the fringes cannot be adjusted after the collodion film has been formed. Consequently, it is necessary to apply the collodion solution and allow it to drain in such a way that the resulting fringes possess the required configuration.

Fringes obtained using this method for a specimen with a relatively smooth surface are shown in Fig. 11. The fringes are extremely narrow compared with the fringe spacing. If this method were used to measure oxide film thicknesses, the thickness would be given by Eq. [4] where r is the fringe displacement and n is the refractive index of collodion (1.40). It is estimated that fringe displacements could be measured to ±0.002 fringe, corresponding to ±4Å. However, for the method to be successful it is nescessary that the upper surface of the collodion film be smooth.

Fig. 11. Multiple-beam interference fringes obtained by the collodion film method. The specimen is a glass slide with a relatively smooth surface.

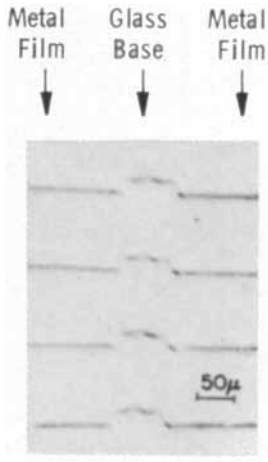

Fig. 12. Multiple-beam interference fringes obtained by the resin film method. The specimen is a double step in an evaporated metal film.

When this method was used to determine the thickness of a number of surface films by measuring step heights, the results were unsatisfactory because the upper surface of the collodion film tended to follow the contour of the step rather than remain smooth. This was ascertained by examining the metallized upper surface of the collodion film with a two-beam interference microscope. Consequently, the indicated fringe displacement was not a true measurement of the film thickness.

The lack of smoothness of the upper surface of the collodion film on crossing the step is thought to arise from the following mechanism. When the collodion solution is applied, the lower surface of the liquid film closely follows the contour of the specimen surface, and the upper surface of the liquid film is smooth. As the solvent evaporates the film becomes thinner and more viscous, and before solidification is complete the film is so viscous that no further lateral movement of the liquid is possible. Consequently, the remaining solidification occurs by a fractional reduction of the remaining liquid film thickness, with the result that the upper surface of the final collodion film follows to some extent the contour of the specimen surface. This behavior presumably occurs whenever a film is formed by a method in which a volume change occurs during solidification.

In order to overcome this difficulty a number of films were prepared using materials exhibiting an insignificant volume change during solidification, *e.g.,* resins which solidify by polymerization and waxes. In all instances the upper surfaces of these films remained smooth on crossing steps on the specimen surface. Consequently, if such materials are used instead of collodion to form the required film, the measured fringe displacement correctly corresponds to the step height.

However, when clear resins with such properties were used to form the wedge-shaped films, the films tended to possess large wedge angles and to be thick. Consequently, the fringes were closely spaced and not of the high quality obtainable with a collodion film. The reason for this is that the viscosities of the liquid resins were approximately the same as the viscosity of the collodion solution. Hence, the liquid films formed on draining a surface vertically using the resins exhibited approximately the same profile as the liquid film formed using collodion. However, after solidification the resin films had substantially the same form, whereas the collodion film possessed a much shallower wedge angle and was much thinner because of the appreciable volume reduction caused by the evaporation of the solvent. Consequently, although a film material which does not significantly change in volume on solidification is required to give valid step height measurements, such a material is less suitable for forming the wedge-shaped films.

A practical application of this method using an epoxy film is shown in Fig. 12. The specimen is a metal film evaporated onto glass rather than an oxide film on silicon, but nevertheless serves to illustrate the method. A strip of the metal film approximately 0.1 mm wide was in this instance removed by lightly scribing the surface with a needle point; the specimen was then silvered to be 100% reflecting. An epoxy resin was applied with a small brush, one stroke being made perpendicular to the strip. When the resin had solidified the upper surface was silvered to be 80% reflecting, and the combination was examined in the standard manner. In the area shown in Fig. 12 uniformly spaced fringes cross the strip approximately perpendicularly and undergo symmetrical displacements at the two steps. The straight part of the displaced fringe corresponds to the thickness of the metal film, while the central V-shaped part corresponds to the depth of the scratch mark made on the glass by the needle point. The film thickness is given by Eq. [4], where r is the fringe displacement and n is the refractive index of the epoxy resin (1.49). The accuracy of measurement is estimated to be 0.02 fringe, corresponding to ±35Å. The displacement is 0.18 fringe, corresponding to a film thickness of 320Å. Accuracies as good as ±20Å have been obtained occasionally by this method.

Summary and Conclusions

Optical interference methods for determining the thickness of oxide films on silicon have been investigated. In all instances a portion of the film was dissolved with HF, and the height of the step thus created was measured. For thick films (>3000Å) two-beam interference was used, and for thin films (<3000Å) multiple-beam interference was used.

Three different methods were employed for the thick films. First, the specimen was metallized and the fringe displacement on crossing the step was measured. Second, the procedure was the same, except that the specimen was not metallized. Third, a shallow wedge-shaped step was formed, the specimen was not metallized, and the number of fringes within the wedge area was counted. The routine accuracies of the three methods were approximately ±270, ±540, and ±350Å, respectively. The first and third methods are the most important. Thus, the first method is an absolute method, *i.e.*, is independent of the refractive index of the oxide film, and is most accurate. The third method has a number of practical advantages that make it valuable as a routine laboratory procedure, and it is only slightly less accurate than the first method. For those oxide films whose refractive index is not known, the refractive index can be deduced simply from fringe measurements made on any particular film by either the first and second methods, or the first and third methods. The accuracy is ±1-2% for a film 15,000Å thick.

Two different methods were used for the thin films. First, the specimen was silvered to be 100% reflecting, a glass slide was silvered to be 80% reflecting, and the slide was placed close to the surface of the specimen (2). The routine accuracy was approximately ±55Å, and the method is an absolute method. Second, the specimen was silvered to be 100% reflecting, a thin liquid film was applied to the specimen surface and allowed to solidify, and the upper surface of the film was silvered to be 80% reflecting. When solutions which dried by evaporation of a solvent were used for the liquid films, *e.g.*, collodion in amyl acetate (3, 4), extremely high-quality fringes were obtained. However, step height measurements were not valid because the upper (reference) surface of the dry collodion film tended to follow the contour of the specimen surface rather than remain flat. When clear resins which solidified by polymerization were used for the liquid film the fringes were not of such high quality. However, step height measurements were valid because the upper surface of the solidified resin was flat. The routine accuracy using resins was approximately ±35Å. Further development of this method, and in particular procedures for applying thin resin films to specimens, should enable this accuracy to be significantly increased.

Acknowledgments

The authors wish to thank Doctors H. F. John, G. Mott, and R. Stickler for useful discussions, and Mr. D. Sealer and Mrs. E. M. Black for valuable assistance with the experimental work. The work was sponsored in part by The Wright Patterson Air Force Base.

Manuscript received June 11, 1962. This paper was prepared for delivery before the Detroit Meeting, Oct. 1-5, 1961.

Any discussion of this paper will appear in a Discussion Section to be published in the June 1963 JOURNAL.

REFERENCES

1. A. E. Stebbins and L. L. Shreir, *This Journal*, **108**, 30 (1961).
2. S. Tolansky, "Multiple-Beam Interferometry of Surfaces and Films," Clarendon Press, Oxford (1948).
3. S. Tolansky, "Surface Microtopography," p. 288, Interscience Publishers, New York (1960).
4. M. S. Joshi and S. Tolansky, *Proc. Roy. Soc.*, **A260**, 475 (1961).

Discussion Section

This Discussion Section includes discussion of papers appearing in the JOURNAL of The Electrochemical Society, Vol. 108, No. 11 (November 1961), and Vol. 109, No. 1-6 (January-June 1962). Discussion not available for this issue will appear in the Discussion Section of the June 1963 JOURNAL.

Hydrogen Absorption by Zircaloy-2 and Some Other Alloys during Corrosion in Steam

B. Cox (pp. 6-12, Vol. 109, No. 1)

H. A. Fisch[1]: Tests have been made in this laboratory using both annealed and heat treated zirconium-2 atom % Sn-2 atom % Nb alloy in 316° and 360°C neutral water at saturation pressure and in 400-, 440-, and 482°C-1500 psi steam. Some results of these tests are shown in Fig. 1 and 2 and Tables I and II of this

[1] Knolls Atomic Power Lab., General Electric Co., Schenectady, N. Y. (Operated for the U.S.A.E.C.)

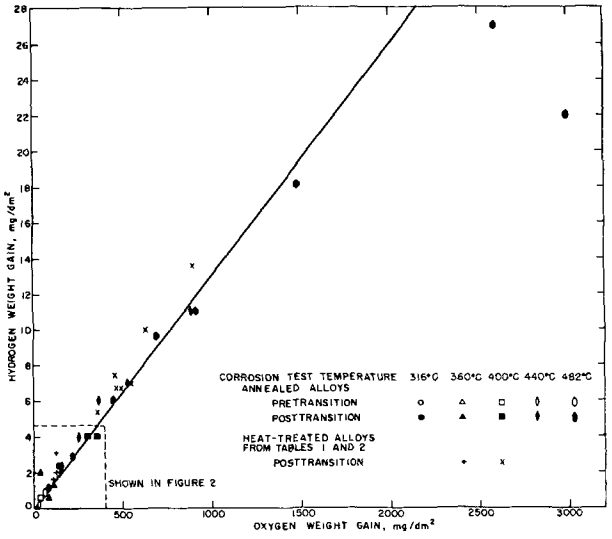

Fig. 1. Relationship between absorbed hydrogen and oxygen weight gains.

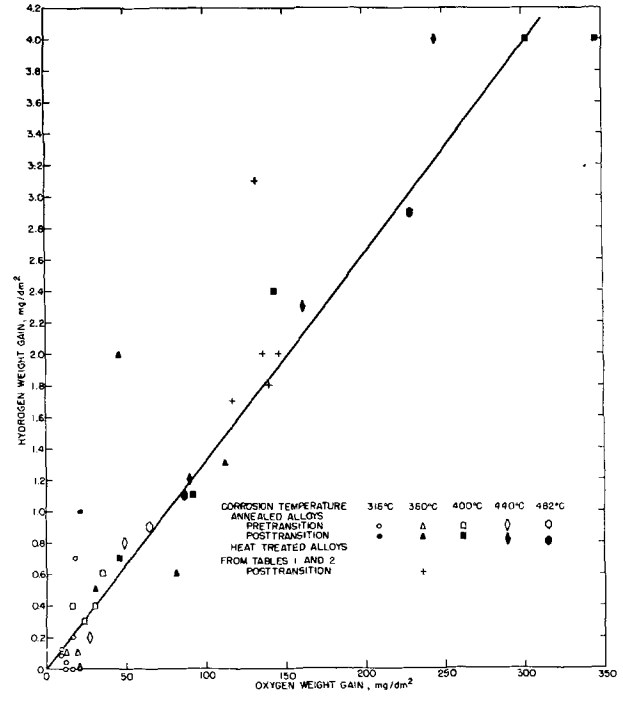

Fig. 2. Relationship between absorbed hydrogen and oxygen weight gains.

Table I. Effect of heat treatment on hydrogen absorption by zirconium-2 at. % tin-2 at. % niobium after 98 days exposure in 360°C, neutral water

Heat treatment	Oxygen, mg/dm²	Hydrogen mg/dm²	Hydrogen % theoretical	Hydrogen H:O ratio
Betatized at 950°C, 24 hr,				
Furnace-cooled	139	1.8	10.2	0.013
Air-cooled	136	2.0	11.8	0.015
Water-quenched				
Aged at 500°C, 100 hr, furnace-cooled	132	3.1	18.9	0.023
Aged at 700°C, 100 hr, furnace-cooled	146	2.0	11.1	0.014
Cold-worked approximately 30%	117	1.7	11.9	0.015

Table II. Effect of heat treatment on hydrogen absorption by zirconium-2 at. % tin-2 at. % niobium after 98 days exposure in 400°C-1500 psi steam

Heat treatment	Oxygen, mg/dm²	Hydrogen mg/dm²	Hydrogen % theoretical	Hydrogen H:O ratio
Betatized at 950°C, 24 hr,				
Furnace-cooled	495	6.7	10.9	0.014
Air-cooled	471	6.7	11.5	0.014
Water-quenched	900	13.6	12.2	0.015
Aged at 500°C, 100 hr, furnace-cooled	634	10.0	12.7	0.016
Aged at 600°C, 100 hr, furnace-cooled	459	7.4	12.9	0.016
Aged at 700°C, 100 hr, furnace-cooled	551	7.0	10.1	0.013
Cold-worked approximately 30%	357	5.4	12.2	0.015

discussion. It was found that the ratio of hydrogen to oxygen uptake was essentially constant over both the pretransition and post-transition corrosion region and independent of heat treatment conditions.

It would be of interest to know if the plateau in the hydrogen to oxygen uptake ratio for Zr-2 Nb-0.5 Sn in 500°C-1 atm steam (Fig. 12 of the discussed paper) has been observed at lower temperatures and/or higher pressures or for other Zr-Nb-Sn alloys.

B. Cox: The primary difference between the results obtained at A.E.R.E.[2] and those of Fisch[3] was the observance at A.E.R.E. of an increased rate of hydrogen uptake by a Zr-Nb-Sn alloy in the post-transition oxidation region at 500°C, and not the occurrence of a "plateau" (since the results at low weight gains, if extrapolated, give a line of similar gradient to that through the K.A.P.L. results). More recent results of hydrogen absorption by Zr-Nb(-Sn) alloys have been presented in an A.E.R.E. report,[4] and the difference

[2] B. Cox, *This Journal*, **109**, 6 (1962).

[3] H. A. Fisch, K.A.P.L., 2149.

[4] B. Cox, P. G. Chadd, and J. F. Short, AERE-R 4134, Aug. 1962.

between these results and those obtained at K.A.P.L. has been discussed. At temperatures of 400°C and below, results obtained here for a range of Zr-Nb (-Sn) alloys were in good agreement with those reported from K.A.P.L.; at higher temperatures, however, an increase in the rate of hydrogen uptake during post-transition oxidation was generally observed.

Rösler[5] and Klepfer[6] have also observed increases in the hydrogen uptake rate following transition, whereas Dalgaard[7] and Boulton[8] have not. In many instances, the alloys used in these experiments differ somewhat in composition and heat treatment, and it is not possible to eliminate either of these as the cause of the divergence of results. However, both Boulton and ourselves have used specimens from the same billet, in the same metallurgical condition, with different results. Thus, the observed differences result, probably, from small variations in experimental technique, the oxygen content of the steam being the most likely variable to affect the results. Recent work at Hanford[9] has shown that even small variations in the oxygen content of the steam can result in profound changes in the hydrogen uptake behavior of Zircaloy-2 and Zircaloy-4. We currently are performing experiments to test this hypothesis, with respect to Zr-Nb alloys.

Electrodeposition of Gallium on Liquid and Solid Gallium Electrodes in Alkaline Solutions

J. O'M. Bockris and E. Enyo
(pp. 48-54, Vol. 109, No. 1)

J. D. Corbett[10]: The authors' purpose and technique for studying the electrolysis of basic gallate solutions at gallium electrodes are well taken. However, the suggested electrode mechanisms should be made compatible with more recent knowledge of the solution chemistry of gallium. The principal evidence cited regarding the stability of lower oxidation states of gallium in aqueous solution is Latimer's[11] conclusion that $Ga_2O(s)$ is unstable with respect to disproportionation into gallium metal and Ga_2O_3. However, the evidence for this is tenuous and, moreover, it is stated to apply to *acidic* systems. The same source also estimates that the gallium (II) state is similarly unstable in *alkaline* solutions, the evidence in this case being the behavior of the so-called gallous chloride $GaCl_2$. It is now known that neither statement is entirely correct. First, the gallium dichloride has amply been shown to be a salt of gallium (I), $Ga^+(GaCl_4^-)$,[12,13] and there is no evidence for salts of Ga^{2+}. Secondly, the principal reaction of such gallium(I) salts with aqueous acid or base is the formation of hydrogen [plus gallium (III)] and not disproportionation,[12,14] contrary to Latimer and to Eq. [7] of this paper.

Equally pertinent to this discussion is the observation in this laboratory[15] that alkaline solutions of gallium(I) salts are relatively stable, in contrast to the rapid reaction found with acids. Solutions of Ga ($GaCl_4$) in aqueous NaOH decompose solely *via* the homogeneous reduction of water in a reaction that is first order in both gallium(I) and hydroxide concentrations over the range of 1 to 4M OH^-; a maximum of −1.39v for the Ga(I)—Ga reduction potential can be derived from the reducing capabilities of such solutions. Since the half life of the decomposition reaction is 5.2 hr in 1M OH^-, the possible formation of this intermediate should certainly be considered in the oxidation of gallium metal or in the reduction of alkaline galate(III) solution. It is difficult to assess the rate of the subsequent, nonelectrolytic oxidation of gallium(I) by solvent in the present paper, however, as the concentration of free (or total) hydroxide utilized does not appear to be given.

Insofar as macroscopic reactions can be related to the mechanisms under consideration here, the production of significant amounts of gallium(I), either by equilibration of 0.05M $Ga(OH)^-_4$ in 1M OH^- with the liquid metal or as a by-product of the deposition of the metal by electrolysis of gallate (III) solutions 1 to 3M in OH^-, has not been detected. On the other hand, the anodic oxidation of metal into 1M NaOH has been found to yield reduced gallium as well as the normal gallate at least in the range of 17-170 ma/cm². Although the authors note that the anodic overpotential-current density relationship (Fig. 7 of discussed paper) shows deviations suggestive of Ga(I), the mechanism applied still involves the unknown disproportionation reaction. It would seem more appropriate to consider instead either the disproportionation of or a rapid reduction of water by the less stable gallium(II) in both the anodic and the cathodic processes.

Anodic Polarization Studies in Neutral and Alkaline Solutions Containing Corrosion Inhibitors

K. S. Rajagopalan, K. Venu, and K. Balakrishnan
(pp. 81-87, Vol. 109, No. 2)

J. E. O. Mayne[16]: The authors conclude from the current density/NaCl conc relationship, Fig. 3, that a current density of 290 μa/cm² should distinguish between a corrosive and inhibitive solution. However, this conclusion is not in accordance with their experimental results since the correlation between the polarization tests given in Fig. 5 and the results of the corrosion tests recorded in Table III cannot be regarded as satisfactory. The bias toward passivity shown in the anodic polarization test carried out at 290 μa/cm², Fig. 5, is to be expected at such a high current density; much better correlation has been obtained in similar solutions at 10 μa/cm², although a similar bias toward passivation in the polarization experiments has been experienced at this low current density in the presence of certain corrosive ions such as perchlorate.[17]

It is felt that in order for anodic polarization to be of use in making predictions the current density should be kept low; furthermore, the period of immersion in the solution before the application of the current should be carefully controlled.[18]

K. S. Rajagopalan, K. Venu, and K. Balakrishnan: We have shown that when one plots the current density required to reach the desired potential (of oxide film formation or oxygen evolution) against concentration of sodium chloride, a very sharp increase in the current requirement is observed after a given chloride concentration is reached. This would indicate that at higher chloride concentrations there is little likelihood of the oxide film being kept in repair by local

[5] U. Rösler, Paper presented at the Symposium on Corrosion in Nuclear Energy, Paris, Oct. 1961.

[6] H. H. Klepfer, W. V. Cummings, and R. E. Blood, GEAP-3729.

[7] S. B. Dalgaard, AECL-1308 and AECL-1513.

[8] J. Boulton, Paper presented at I.A.E.A. Conference on Corrosion of Reactor Materials, Salzburg, June 1962.

[9] H. P. Maffei and D. W. Shannon, HW-67437 and HW-72266.

[10] Institute for Atomic Research and Dept. of Chemistry, Iowa State University, Ames, Iowa.

[11] W. M. Latimer, "Oxidation Potentials," 2nd Ed., pp. 160-161, Prentice-Hall, Inc., New York (1952).

[12] J. D. Corbett and R. K. McMullan, *J. Am. Chem. Soc.*, **78**, 2906 (1956); R. K. McMullan and J. D. Corbett, *ibid.*, **80**, 4761 (1958).

[13] L. A. Woodward, G. Garton, and H. Roberts, *J. Chem. Soc.*, 3623 (1956); G. Garton and H. M. Powell, *J. Inorg. & Nuclear Chem.*, **4**, 84 (1957).

[14] J. D. Corbett and R. K. McMullan, *J. Am. Chem. Soc.*, **77**, 4217 (1955).

[15] J. D. Corbett, To be published.

[16] Dept. of Metallurgy, University of Cambridge, Cambridge, England.

[17] P. Hancock and J. E. O. Mayne, *J. Appl. Chem. (London)*, **7**, 700 (1957).

[18] H. F. Lorking and J. E. O. Mayne, *J. Appl. Chem. (London)*, **10**, 264 (1960).

action. The choice of 290 μa/cm^2 was made as it was rational to take the current represented by the region where the change in the current density requirement was steepest with respect to sodium chloride concentration. In other words, experiments were carried out under the most favorable conditions of repair of oxide film that can at all be met with in the actual system to study the inimical effect of aggressive anions. The authors have shown later in the paper that a study of the time taken for potential to fall back to a corroding potential in relation to concentration of sodium chloride would be more significant than an experiment based on the criterion of a rise in potential on application of current as suggested by Dr. Mayne. It appears to be quite reasonable to carry out such a study under the most favorable conditions, as failure under these conditions may be taken to be a clear indication of failure in natural conditions.

A more detailed investigation may reveal the exact relationship that exists between the time of breakdown and concentration of sodium chloride. This would help in defining the conditions for breakdown of the oxide film. Even then the conditions for breakdown of an oxide film that is not kept under efficient repair would differ somewhat from those inferred in this way. The lack of complete correlation between results obtained in direct tests (Table III) and the conclusions drawn earlier from polarization measurements is, therefore, not unexpected. But the point to be remembered here is that the actual system is a more difficult system for making predictions about the Cl: OH concentration ratio which will cause breakdown of the oxide film.

The Effective Duration of a Linear Slow-Cool

D. R. Killoran (pp. 170-171, Vol. 109, No. 2)

E. D. Fabricius[19]: There are two major types of impurity diffusion mechanisms, interstitial and substitutional. Impurities that diffuse interstitially are characterized by a small diffusion activation-energy, and a very temperature-dependent solid solubility; while those that diffuse substitutionally exhibit a large diffusion activation-energy and a relatively temperature-insensitive solid solubility. Below the maximum solid solubility of impurities in germanium and silicon, the temperature dependence of the solid solubility may be approximated quite closely by an expression of the form[20]:

$$C_s = A \exp(BT) \qquad [1]$$

Table I

Diffusion type	Element	B (°K^{-1})[a]	H/k (°K)
Interstitial	Ag	0.0100	14,300[b]
Interstitial	Li	0.0100	5,800[b]
Substitutional	Sb	0.0020	28,600[c]
Substitutional	In	0.0011	42,400[c]

[a] Calculated from Solid Solubility graphs of: F. A. Trumbore, *B.S.T.J.*, 39, No. 1, 208 (1960).
[b] B. I. Boltaks, *Zhur. Tekh. Fiz.*, 28, 996 (1958), and G. A. Ratcliff, Private communication.
[c] W. C. Dunlap, *J. Phys. Rev.*, 94, 1531 (1954).

Table I of this discussion lists some representative values of the activation energies of diffusion and the approximation of Eq. [1] for impurities in germanium.

On cooling, a material will tend to reject impurities in excess of the solid solubility, thus forcing the diffusion near the surface where the concentration of impurities is greatest.

The general equation for a slow-cool when both the solid solubility and the diffusion coefficient are changing with temperature cannot be solved in a closed analytical manner. However, an arbitrary distribution of impurities, $C_1(x)$, in an infinite slab of material, if allowed to redistribute itself by diffusion, will diffuse according to the following equation[21]:

$$C(x,t) = \int_{-\infty}^{\infty} (4\pi Dt)^{-1/2} C_1(\xi) \exp[-(x-\xi)^2/4Dt]\, d\xi \qquad [2]$$

where D is the diffusion coefficient, and t is the time of diffusion. Eq. [2] can be approximated for a slow-cool by replacing the integral by a series and using the constant-temperature diffusion data for the initial profile, yielding:

$$C(x,t) \approx \sum_i (4\pi Dt)^{-1/2} C_1(\xi_i) \exp[-(x-\xi_i)^2/4Dt]\, \Delta\xi \qquad [3]$$

Due to a lack of data on both rate limitations at surfaces[22,23] and the reactions involved when the concentration at the surface exceeds the solid solubility of a material, one approach would be to assume that the material rejects everything in excess of the solid solubility, limited by the rate of diffusion, and that on the vapor side of the interface the concentration is given by the solid solubility.

Eq. [3] has been programmed on an IBM 650 digital computor under the above assumptions, for the case of an interstitial diffusor, Ag, and a substitutional diffusor, Sb, with the results as shown in Fig. 1 and 2 of this discussion. A comparison with Killoran's equation shows that, except very near the surface, both methods yield almost the same concentration profile for substitutionals. Thus, due to its simplicity, Killoran's approach is the more useful.

For interstitials, a better solution would be to calculate Eq. 3, assuming $[D]$ is a constant, given by the mean value over the temperature interval. While tedious, the equation can be calculated in a reasonable time in this manner, with an accuracy within about 5% of the programmed values. This is due to the fact that, since D appears in the argument of an exponent and under a radical sign, Eq. [3] is relatively insensitive to small change in D.

The validity of Eq. [3] has been verified by measurements of sheet resistivity (yielding the area under the curve), and junction-depth measurements [yielding the value of $C(x)$ at various depths] for several impurities in germanium, the calculated values being within the limits of error in measurement in all cases.

Acknowledgments.—The discussor is indebted to Fred Barson of IBM for directly suggesting this method of attack, to Ray Zachary for arranging the equation in a manner amenable to programming, to Charles Ratliff for programming the equation, and to Gordon Ratcliff for data on the diffusion coefficient of Ag in Ge, as well as many valuable discussions of the problem.

Daniel R. Killoran[24]: The validity of the method used in my paper depends on the assumption that all other parameters remain the same during the slow-cool as during the previous diffusion. However, these results are applicable to the problem considered by Fabricius in the sense that they constitute a limiting case. In particular, it will be shown that

$$U(x,\tau) = C_o \operatorname{erfco}\left[\frac{x}{\sqrt{4\lambda}}\right] - |\epsilon| \qquad [1]$$

where C_o is the initial surface concentration, x is the distance from the surface, $U(x,\tau)$ is the exact solution of the problem when the surface concentration is allowed to decrease during the slow-cool, and

$$\lambda = D(\theta_o)\{\text{duration of initial diffusion}\} \qquad [2]$$

[19] Giannini Controls Corp., 55 North Vernon Ave., Pasadena, Calif.

[20] *See* reference *a*, Table I of this discussion.

[21] I. N. Sneddon, "Elements of Partial Differential Equations," p. 282, McGraw-Hill Book Co., New York (1957).

[22] R. C. Miller and F. M. Smits, *Phys. Rev.*, 107, 65 (1957).

[23] F. M. Smits and R. C. Miller, *Phys. Rev.*, 104, 1242 (1956).

[24] Present address: Sagamore Farm Rd., Hamilton, Mass.

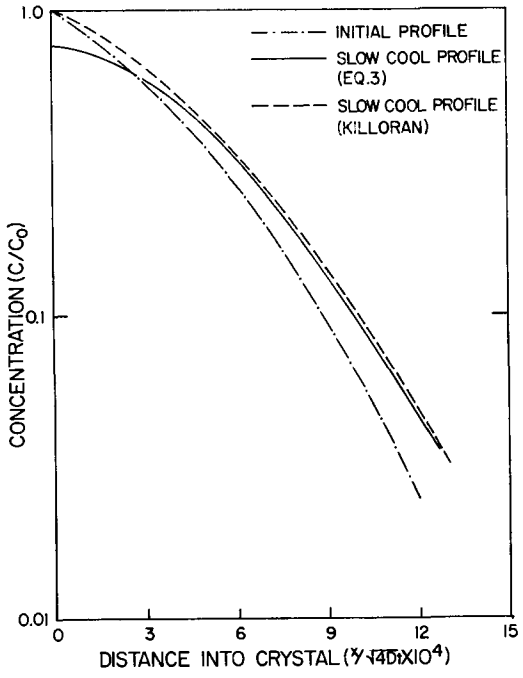

Fig. 1. Concentration profile of Sb in Ge, before and after slow-cool, comparing Eq. [3] with Killoran's equation.

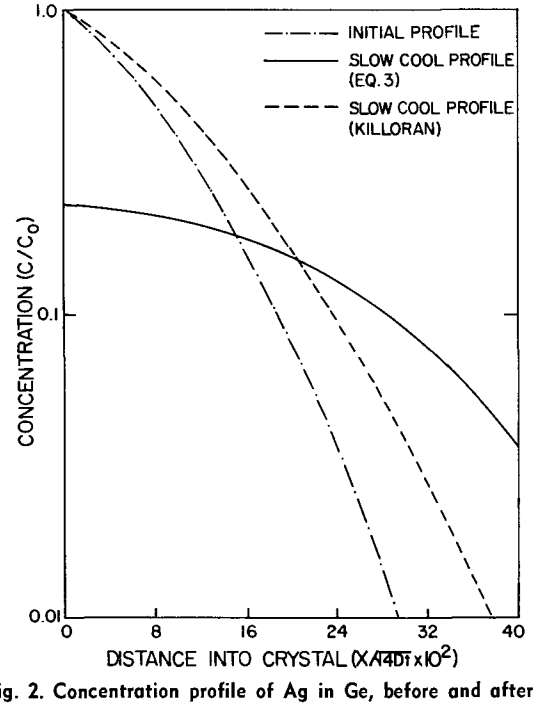

Fig. 2. Concentration profile of Ag in Ge, before and after slow-cool, comparing Eq. [3] with Killoran's equation.

Throughout the analysis we will use the effective time (τ) defined by the equation

$$\tau = \int_0^t D(t)\,dt \qquad [3]$$

where $D(t)$ is the diffusion constant expressed as a function of time.

The expression for the surface concentration as a function of tau is exceedingly complicated, but we only need to know that it is everywhere positive, differentiable, of exponential order, and monotonic decreasing. These facts can be verified by inspection.

Let

$$\frac{\partial^2 C}{\partial x^2} = \frac{\partial C}{\partial \tau} \qquad [4]$$

subject to the boundary conditions

$$C(O,O) = C_o \qquad [5]$$

$$C(x,O) = C_o \operatorname{erfco}\left[\frac{x}{\sqrt{4\lambda}}\right] \qquad [6]$$

$$C(\infty,\tau) = 0 \qquad [7]$$

$$C(O,\tau) = F(\tau) \qquad [8]$$

where $\mathbf{F}(\tau)$ is to satisfy the stated conditions on the surface concentration.

Then, by Duhamel's Theorem

$$C(x,\tau) = \int_0^\tau F(\tau-s)\frac{\partial}{\partial s}\left[\operatorname{erfco}\left(\frac{x}{\sqrt{4(\lambda+s)}}\right)\right] ds \qquad [9]$$

Integrating by parts

$$C(x,\tau) = F(O)\operatorname{erfco}\left[\frac{x}{\sqrt{4(\lambda+\tau)}}\right] - F(\tau)\operatorname{erfco}\left[\frac{x}{4\sqrt{\lambda}}\right] - \int_0^\tau \operatorname{erfco}\left\{\frac{x}{\sqrt{4(\lambda+s)}}\right\}\frac{\partial}{\partial s}F(\tau-s)\,ds \qquad [10]$$

But $F(O) = C_o$ by condition [5] and

$$F(\tau) > 0 \text{ for all } \tau$$

$$\operatorname{erfco}\left\{\frac{x}{\sqrt{4\lambda}}\right\} > 0 \text{ for all } x$$

$$\operatorname{erfco}\frac{x}{\sqrt{4(\lambda+s)}} > 0 \text{ for } x \text{ and } s$$

$$\frac{\partial F(\tau-s)}{\partial s} > 0 \text{ for all } s \text{ and } \tau$$

Therefore,

$$F(\tau)\operatorname{erfco}\left\{\frac{x}{\sqrt{4\lambda}}\right\} > 0 \text{ for all } x \text{ and } \tau \qquad [11]$$

and

$$\int_0^\tau \operatorname{erfco}\left\{\frac{x}{\sqrt{4(\lambda+s)}}\right\}\frac{\partial}{\partial s}F(\tau-s)\,ds > 0 \qquad [12]$$

for all x and τ. It then follows that

$$C(x,\tau) = C_o \operatorname{erfco}\left\{\frac{x}{\sqrt{4(\lambda+\tau)}}\right\} - |\epsilon| \qquad [13]$$

which was to be shown. This means that the solution obtained by ignoring the decrease in surface is an upper bound for the exact solution, as physical intuition would suggest. In particular, the exact solution cannot cross the curve

$$C(x,\tau) = C_o \operatorname{erfco}\left[\frac{x}{\sqrt{4(\lambda+\tau)}}\right] \qquad [14]$$

and, consequently, Fabricius' equation is not valid for large values of $\left(\frac{x}{\sqrt{4\,Dt}}\right)$ in his Fig. 2.

The reason for this is not quite obvious, but the assumption that D is constant is certainly suspect.

By expanding the error functions in Eq. [10] in asymptotic series in x, it can also be shown that

$$\frac{|\epsilon|}{\operatorname{erfco}\left[\frac{x}{\sqrt{4(\lambda+\tau)}}\right]} \to O \text{ as } x \to \infty \qquad [15]$$

and therefore Eq. [14] is also the asymptote for the exact solution for large values of x.

It is interesting to compare these results to those obtained by Waring,[25] although his problem is slightly different.

[25] W. Waring, *This Journal*, 105, 702 (1958).

Solution and Diffusion of Corrosion Oxide Film in Zircaloy

R. M. Treco (pp. 208-211, Vol. 109, No. 3)

Richard E. Westerman[26]: The author states (p. 209) that "if the entire weight gain of the oxygen in the film were to be dissolved and diffused uniformly throughout the Zircaloy-2, it would increase the oxygen concentration by 270 ppm."

The increase in oxygen concentration must depend on the geometry of the Zircaloy-2 piece, yet this is nowhere specified. In any case, the system is implied to be finite.

The author has calculated the time required to dissolve completely and uniformly distribute the film throughout the Zircaloy-2 (Eq. [7], p. 209). This equation, as derived by Barrer, gives the time dependence of the solute concentration existing at the surface of a *semi-infinite solid*. The equation has been applied to a finite system, where $C_f = 1270$ ppm. Infinite time is required in a classical diffusion system to effect uniform distribution of a solute, yet an answer of 7.8 days has been obtained by specifying $(C_f - Co)$ and Q in a dimensionless yet finite system, using an equation developed for semi-infinite media. What has been found is simply the approximate time required to attain an arbitrary surface concentration of 1270 ppm oxygen for a Zircaloy-2 specimen of reasonable thickness. A uniform distribution of oxygen throughout the specimen cannot be implied.

The author then applies the same relation to determine the time required to make the corrosion film just disappear from the surface of the specimen, and obtains a value of 1.8 min (p. 210). This time is erroneously short, as the equation does not take into account the terminal solubility of the solute, which will interfere with the establishment of the predicted concentration gradients during solute redistribution. A rigorous method of finding the time required makes use of Pemsler's formulas[27]:

$$X' = 0.676\,\Delta L \qquad [1]$$

where ΔL = decrease in ZrO_2 film thickness

X' = displacement of oxide-metal boundary during solution of ZrO_2 film.

$$t = \frac{X'^2}{4b^2D} \qquad [2]$$

where $b = 0.126$

D = diffusivity of oxygen in Zircaloy-2

t = time

Substituting $\Delta L = 6.180 \times 10^{-5}$ cm, we obtain a value of 3.8 min for film disappearance.

Use of Pemsler's formulas requires that the oxygen initially present in the Zircaloy-2 is initially uniformly distributed or negligible; the latter is a good assumption under the conditions cited in the paper, and the value of the constant "b" has been derived for these conditions. Though it may appear that the difference between 1.8 min and 3.8 min is trivial, only the (fortuitously) high terminal solubility of oxygen in Zircaloy-2 allows Eq. [7] to yield an approximately correct answer. The author states that the time of 1.8 min has been experimentally verified for complete film dissolution. It would be interesting to know if the limits of experimental error are such that the time of 3.8 would be satisfactory also.

In Eq. [9], $\sqrt{X}$ should be replaced with $\sqrt{t}$.

[26] Chemical Metallurgy, Hanford Labs. Operation, General Electric Co., Richland, Wash.

[27] J. P. Pemsler, "The Diffusion of Oxygen in Zirconium and Its Relation to Oxidation and Corrosion," NMI-1177 (May 1957).

R. M. Treco: Correction is to be noted for Eq. [9] on p. 210 as follows:

$$C - C_o = \left(\frac{0.7}{\sqrt{t}}\right) \exp\left(-1.32 \times 10^{+10} X^2_{\text{in.}}/t\right)$$

Respecting Mr. Westerman's first comment, it should be stated that the original work for this paper was based on a finite section which would lead to a concentration of 270 ppm oxygen for that section. Unfortunately, it was necessary to delete actual dimensions from the paper but this in no way alters the diffusion equations presented. The application of Eq. [7], p. 209, was in fact to a semi-infinite solid, the semi-infinite referring to the diffusion path rather than the time for diffusion. In considering the terminal solubility of the solute, it is also necessary to take into account the classical problem of the moving boundary condition. This has also been pointed out in a private communication of J. P. Pemsler who has derived a relationship which is theoretically correct. When this relation is applied to the present problems, *e.g.*, diffusion during corrosion, the calculated results are very similar. Experimentally, the difference between 1.8 and 3.8 min is difficult to rectify on the basis of experimental error, and for the work described was not significant.

An Electron Optical Study of the Effect of Temperature and Environment on the Growth of Oxide Whiskers on Cold-Rolled and Annealed Copper

W. R. Lasko and W. K. Tice (pp. 211-215, Vol. 109, No. 3)

Axel Rönnquist[28]: In the paper of Lasko and Tice it is shown that the lower temperature limit for the appearance of whiskers is about 300°C and that the number of whiskers per unit area in the temperature range 300°-500°C is higher on the preannealed samples than on the cold-rolled ones. This is also in good agreement with the results obtained by the discussor in a kinetic and morphological study of the initial stages of the oxidation of copper.[29]

Lasko and Tice explain their results by assuming that the whiskers are nucelated at dislocations in the base metal. However, another plausible explanation is that the nucleation of whiskers takes place at stress-induced dislocations in the oxide layer. With this assumption the appearance of oxide whiskers at 300°C is readily explained, since at this temperature the ratio CuO/Cu_2O in the outer oxide layer increases[29, 31] sharply, favoring a high stress—the stress in the outer layer will be larger, the larger the proportion of this less dense oxide.[30]

The higher density of whiskers on the preannealed samples than on the cold-rolled ones in the range 300°-500°C is explained by the authors as differences in the movement of dislocations in the metal. A more attractive explanation which favors a higher stress in the oxide layer may be based on the higher oxidation rate of the preannealed samples. The higher oxidation rate depends upon the anisotropic oxidation of copper and the crystallographic transformation taking part during annealing.

Copper when strongly cold-rolled has the well-defined texture (110) $<111>$—the $<111>$ direction of the face-centered cubic crystals is aligned approximately in the cross-rolling direction and the (110)-faces lie approximately in the rolling plane. When the rolled copper has been completely annealed, the preferred orientation changes to (100) $<100>$.[32] Many

[28] Swedish Institute for Metal Research, Stockholm, Sweden.

[29] A. Rönnquist, *J. Inst. Metals*, In press.

[30] W. Jaenicke and S. Leistikow, *Z. physik. Chem. (Frankfurt)*, 15, 175 (1958).

[31] R. F. Tylecote, *Metallurgia*, 53, 191 (1956).

[32] B. F. Decker and D. Harker, *Trans. Am. Inst. Mining, Met. Petrol. Engrs.*, 188, 887 (1950).

authors[33] have pointed out the high oxidation rate of the (100)-face or the preannealed copper sheets.[29]

At temperatures of 500°C and above, it seems somewhat difficult to give an explanation of the higher density of whiskers on the cold-rolled copper. The situation will be rather complicated because of not only oxidation going on, but even recrystallization and grain growth of the metal.

W. R. Lasko and W. K. Tice: The proposed explanation by Dr. Rönnquist that whisker growth takes place at stress-induced dislocation sites in the base oxide layer, although plausible, has not been confirmed experimentally. In order to demonstrate that whiskers originate at defect sites, as proposed in the paper, either in the oxide layer or base metal, it is suggested that the thin foil technique be adopted. Through the controlled oxidation of thin foils it should be possible to establish a correlation between the nature of the growth site and the points at which dislocation lines emerge.

Similarly, Dr. Rönnquist's explanation might be tested by removing the oxide layer from the base metal by means of selective etchants and subsequently observing it, using standard transmission microscopy. If the hypothesis proposed in the paper is correct then one might see structural detail from the whisker continue through the basal oxide. Conversely, if whisker growth emerges from dislocation sites in the basal oxide layer then one may observe the relationship between dislocations and whiskers using "dark field" techniques. Further emphasis using this approach is under way.

Dr. Rönnquist further indicates that the higher density of whiskers observed on the preannealed sample than on the cold-worked material can be accounted for by the higher stresses setup in the oxide layer, the higher oxidation rate depending on the anisotropic oxidation of the copper and the changes in crystallography resulting from the annealing step. This is an interesting hypothesis and one we have previously considered. In fact, we have made studies using the direct carbon replica technique and have observed the anisotropic oxidation of copper. The results of this study will be published shortly.

Transport Numbers in Pure Fused Zinc Chloride

Arnold Lundén (pp. 260-267, Vol. 109, No. 3)

Richard C. Pinkerton[34]: In order to assign transport numbers in the manner described by the author it was assumed that the rates of association and dissociation of the possible complex ions were very small when compared with the time of transit of an ionic species through the membrane. One would expect that the opposite is true, both because the length of the diffusion path must necessarily be large (10^6 times the average interatomic distance), and because any ionic equilibria should be reached very rapidly. The temperature is high. Exchange studies of zinc complexes at room temperature show that over 90% exchange is complete within the time of separation, which is less than a minute in many cases.[35]

After finding that t_c^+ and t_c^- are apparently very small, the author concludes that "no transport by complex ions has been detected in any part of the investigated temperature range" (p. 265). Rather, it should be concluded that, if complex ions are present, equilibrium is reached rapidly. Large proportions of these ions could be present, without affecting the values as they are assigned by the author.

For experiments of Type I (p. 262), tagged M is placed in the anolyte. The catholyte is examined after the run for activity. Assuming that equilibrium is slow, the author concludes that the sum of t^+ and t_c^+ is obtained, corresponding to transport by M^{2+} and MX^+. If the equilibrium is rapid, on the other hand, one should obtain $t^+ + t_c^+ - t_c^-$. This accrues because any M finding itself in the transport region, or membrane, by virtue of being in the cationic state, will eventually spend a fraction of its life as MX_3^-. While in that state, it will be transported in the reverse direction. This can be shown in more detail by defining the transport numbers in terms of the velocities of the individual ions and their mole fractions. As a result, one observes transport which depends on an averaged velocity.

In experiments of Type II, the author finds t_c^-, whereas the rapid equilibrium case would give $t_c^- - t^+ - t_c^+$. This is seen to be just the negative of the value obtained in Type I. However, for the radiotracer experiments performed, a negative value could not possibly be expected. By definition, no tracer is placed in the anolyte in Type II experiments. Instead, it can only be observed that the net transport of M tracer is not positive. Similarly, for the rapid equilibrium case in experiments of Type III and IV, one should obtain $t_c^+ - t^- - t_c^-$ instead of t_c^+, and $t^- + t_c^- - t_c^+$ instead of $t^- + t_c^-$.

Since the results of experiments of Types II and III indicated to the author that the values of t_c^+ and t_c^- would be small, a value for the sum of t^+ and t^- was found by adding the results from experimental Types I and IV. In the fast equilibrium case, this operation would still give $t^+ + t^-$, but it is also seen that this sum is

$$(t^+ + t_c^+ - t_c^-) + (t^- + t_c^- - t_c^+) = t^+ + t^- + t_c^+ + t_c^- - t_c^+ - t_c^- = 1 - t_c^+ - t_c^-.$$

The author is surprised that the sum of t^+ and t^- is not unity. However, the significant result obtained from this very carefully performed series of experiments is precisely that this sum is less than unity. It may be taken to mean that complexed ionic forms do indeed transport a measureable fraction of the current in molten zinc chloride.

Arnold Lundén: In the original paper it was concluded (p. 265) that "if complex ions exist in molten $ZnCl_2$, their lifetime must be considerably less than the time it takes for an ion to traverse the membrane." Dr. Pinkerton has shown that it should be possible to estimate the contribution to transport also from complex ions with lifetimes of the order of 1 sec or less, since $t_c^+ + t_c^- = 1 - t^+ - t^-$, which would give $t_m^+ + t_m^- < 1$. He suggests that the existence of such short-lived complex ions is the cause of the apparently low values of t_m^+ and t_m^-. However, in this case the obtained transport numbers would be independent of the duration of the runs, and the spread in the results should not be larger than corresponding to a probable error of about ± 0.02. There remains a discrepancy with the experimental results in these two respects, unless diffusion inside the disk as well as in the surface layer is taken into account, as was done in the original communication.

While the results for the runs below the melting point of zinc (420°C) are too uncertain for this purpose, the measurements at higher temperatures can be used to estimate an upper limit for Pinkerton's $t_c^+ + t_c^-$. An extrapolation of t^+ and t^- to "infinite running time" gives a sum that might well be unity as stated in the original communication, but if the experimental error is considered there might instead be a slight deficit, and one might write $t_c^+ + t_c^- = 0.03 \pm 0.03$. Thus the existence of short-lived complex ions is neither proved nor excluded, and it seems difficult to do this with the present type of experiment.

Mechanism of Stress Corrosion Cracking in Stainless Steels

R. Stickler and S. Barnartt (pp. 343-344, Vol. 109, No. 4)

J. C. Scully[36]: The work reported by Stickler and Barnartt represents a most welcome extension of

[33] A. Rönnquist and H. Fischmeister, *J. Inst. Metals*, 89, 65 (1960-1961).

[34] Dept. of Chemistry, North Carolina State College, Raleigh, N. C.

[35] F. Basolo and R. G. Pearson, "Mechanisms of Inorganic Reactions," pp. 402-403, John Wiley & Sons, Inc., New York (1958).

[36] Metals Research Labs., Olin Mathieson Chemical Corp., P. O. Box 906, New Haven 4, Conn.

studies of the stress corrosion of stainless steel by use of electron microscopy. The results, however, must be interpreted with care.

The observation, that nonsusceptible stainless steels exhibit a "cell structure" of dislocations while susceptible stainless steels do not, does not necessarily mean that the restricted slip theory of Forty[37] is applicable. He did not originally propose it for austenitic stainless steels, and what evidence there is suggests that it does not apply to them.

Although the rapid mechanical/slow chemical type of propagation has been reported for other systems of stress corrosion, *e.g.*, Cu 4% Al/NaCl + $NaHCO_3$,[38] mild steel in nitrate,[39] the same experimental techniques have failed to indicate that this type of propagation occurs in stainless steel. Nor is this surprising. Austenitic stainless steel is a highly ductile material and it is difficult to see how it can sustain a stage of brittle crack propagation. When 18-8 is strained at 10^6%/sec at −193°C, brittle failure does not occur.[40] For a brittle crack to run under stress corrosion conditions, the strain-rate at the tip of the crack must be higher than this, yet simple calculation shows that it is several orders of magnitude lower.

In a face-centered cubic lattice there are 12 slip directions. A brittle crack will propagate only if the initial tensile stress in the notch is applied in a shorter time than it takes for the critical resolved shear stress of the material to be reached on the nearest conveniently oriented slip plane. It must be pointed out that no time delay has been detected in stainless steel between the application of a stress and the production of a stress.[41] Furthermore, since the postulated chemical embrittling stage is a slow one, a very sharp notch will probably never form since there will be adequate time for plastic relaxation to occur at the tip.

While an alternating mechanism of propagation can explain certain types of intergranular cracking or transgranular cracking associated with precipitates, I fail to see how it can be applied to the transgranular cracking of austenitic stainless steels.

R. Stickler and S. Barnartt: It is true that some of the attempts to detect sudden fracture steps during crack propagation in 18-8 stainless steels have been negative. Sudden jumps in the potential or elongation of wire specimens were not observed in 42% $MgCl_2$ solutions,[42,43] and acoustic detection of mechanical fracture steps was also negative.[43] Only one positive detection (direct microscopic observation) has been reported [Ref. (4) of the paper]. It is possible that, where negative results were obtained, the sensitivity of the method used was not sufficiently high to show up very short fracture steps.

We do not agree that sharp notches would not occur when the over-all anodic reaction which reinitiates the brittle fracture step is slow. The reinitiation process may be pictured as one in which slow anodic metal dissolution takes place over a relatively large area along the edge of the arrested crack; the brittle step does not occur until a small active area is uncovered, at which both the rate and direction of metal dissolution are favorable for development of a microcrack capable of brittle propagation. The latter propagation takes place immediately, but soon stops when the nearest soft region (such as a slip band) is encountered. Meanwhile, there may have been a large number of embryo microcracks developed by the anodic dissolution process. These would be inactive if they were misoriented or if they developed too slowly, so that as Dr. Scully indicated there would be adequate time for plastic relaxation to take place. A more detailed review of the evidence favoring the restricted-slip model, and of related factors such as stacking fault energy, has been given recently by one of the authors.[44]

[37] A. J. Forty, "Physical Metallurgy of Stress Corrosion Failure," T. N. Rhodin, Editor, p. 99, Interscience Publishers, New York (1959).

[38] D. van Rooyen, *Corrosion*, **16**, 421t (1960).

[39] H. J. Engell and A. Bäumel, Ref. 1, p. 341.

[40] G. Meyrick and H. W. Paxton, *J. Metals*, **13**, 87 (1961).

[41] W. D. Briggs, "The Brittle Fracture of Steel," p. 97, MacDonald and Evans, London (1960).

[42] T. P. Hoar and J. G. Hines, *J. Iron Steel Inst. (London)*, **177**, 248 (1954); *ibid.*, **182**, 124 (1956).

[43] D. van Rooyen, *Corrosion*, **16**, 421t (1960).

[44] S. Barnartt, *Corrosion*, **18**, 322t (1962).

The Effect of Pressure on the Electroless Deposition Process

J. S. Sallo, J. I. Swenson, and J. M. Carr
(pp. 389-392, Vol. 109, No. 5)

G. Gutzeit[45]: The authors of this paper appear to have neglected the effect of *p*H decrease inherent in the chemical ("electroless") nickel deposition process, and, consequently, to have misunderstood the reasons for the modification of the Brenner and Riddell bath[46] as reported by Gutzeit[47]—which had precisely for its main purpose the elimination of *p*H variations.[48]

The gross equation for chemical nickel deposition has been written[46] as follows:

$$Ni^{++} + (H_2PO_2)^- + H\,O \rightarrow Ni^{\circ} + 2H^+ + H(HPO_3)^-$$

Obviously, a high concentration of hydrogen ions in the bath favors the formation of nickel ions and will, therefore, slow down or stop the reaction from left to right.[49]

The following test data[47] show the effect of initial *p*H in a moderately buffered plating solution (optimum buffering range *p*H 4.0) on the rate of deposition, specifically the weight of the coating deposited in 15 min.

Initial *p*H	Final *p*H (after 15 min)	Avg wt of deposit (3 tests)
5.5	4.55	0.1047
5.0	4.45	0.0918
4.5	4.21	0.0858
4.0	3.90	0.0448
3.5	3.45	0.0223

Furthermore, regardless of the initial *p*H of the plating bath, the hydrogen ion concentration constantly increases as the reaction proceeds, due to the fact that, for each mole of nickel deposited, two hydrogen ions are formed. As a result, the rate of deposition steadily declines while deposition takes place.

As the hydrogen ions are formed at the catalytic surface, the *apparent* reaction rate in an unbuffered or moderately buffered bath is primarily controlled by a diffusion process (*i.e.*, the transfer of H^+ away from said surface). This masks the effect of any other rate determining factors.

Unpublished data[50] show that by increasing the velocity of turbulent agitation in the bath, the rate of nickel deposition is also increased up to a maximum (roughly equal to twice the original rate), then starts decreasing steadily. The first phase is interpreted in relation to hydrogen ion transfer; while the second phase is believed to be due to the rapid translation of the nickel ions past the catalytic surface.

However, if, in order to study the mechanism of reduction of nickel ions by hypophosphite anions, experimental conditions are selected so that the *p*H remains substantially constant (*i.e.*, a strongly buffered

[45] General American Transportation Corp., 131 South Wabash Ave., Chicago 3, Ill.

[46] A. Brenner and G. Riddell, *J. Res. Nat. Bur. Standards*, **37**, 1 (1946); *ibid.*, **39**, 385 (1947).

[47] G. Gutzeit, *Plating*, **46** (1959) and **47** (1960).

[48] The experimental work for this kinetic study was carried out by Dr. Warren G. Lee, Research Associate, in General American Transportation Corp.'s Research & Testing Lab., East Chicago, Ind.

[49] G. Gutzeit and A. Krieg, U.S. Pat. 2,658,841, Nov. 10, 1953.

[50] Obtained several years ago by D. E. Metheny in General American Transportation's Research & Testing Lab.

bath with a large liquid volume to solid area ratio), it has been shown that the reduction rate (and, consequently, the rate of deposition) is essentially a function of hypophosphite concentration. Thus, we agree that the data reported by Gutzeit[47] indicate a pseudo-first-order reaction in a static system, *i.e.*, in a batch operation.

The practical value of these findings resides in the fact that, in modern industrial "electroless" plating systems (KANIGEN® process), the pH shift is continuously corrected by addition of hydroxyl ions to the buffered bath; in other words, the pH value is kept practically a constant, so that the rate of deposition becomes only a function of hypophosphite anion concentration.

In the light of these remarks, the results obtained by the authors of the above captioned paper could have been expected.

J. S. Sallo, J. I. Swenson, and J. M. Carr: We find the comments by Dr. Gutzeit to be in general agreement with the findings and conclusions reported in our paper. It is of particular interest to note that his unpublished data on the effect of agitation agree with our data.

Although this paper was not concerned with the practical aspect of electroless deposition we do not feel that we neglected the effect of pH decrease inherent in the process, or misunderstood the reasons for the modification of the Brenner and Riddell bath. In the text of the paper we state, "It is probable that the main difference between the systems studied in this work is that bath 2 is highly buffered and bath 1 is not."

It is true that certain of our theoretical conclusions could have been anticipated, particularly since Brenner had previously suggested that in his system the rate is controlled by diffusion of hydrogen ions from the active surface. We have attempted to supply experimental data to support these previous conclusions. Our conclusions dealing with the interplay of active surface area and hydrogen gas, and with the effect of the evolved gas, are results of our new data and, to the best of our knowledge, had not been anticipated in the literature.

We do not believe that any available data, including the discussion presented here, could have led to an anticipation of our experimental results. The fact that small applied pressures can alter the rate of the process was completely unanticipated and unexpected.

Etching of Abraded Germanium Surfaces with CP-4 Reagent

E. N. Pugh and L. E. Samuels (pp. 409-412, Vol. 109, No. 5)

A Metallographic Investigation of the Damaged Layer in Abraded Germanium Surfaces

E. N. Pugh and L. E. Samuels (pp. 1043-1047, Vol. 108, No. 11)

T. M. Buck[51]: The two recent papers by Pugh and Samuels[52,53] have presented an interesting metallographic study of the nature of abrasion damage in germanium. In the more recent paper[53] the microscopic observations are used as a means of determining the depth of damage, and it is concluded that the microscopic method is more reliable than the photomagnetoelectric (PME) method[54] and a number of other methods[55,57] which have agreed essentially with the PME method.

While agreeing that the metallographic method appears to be a convenient and useful one, I do not feel that the published information leads to the conclusion that it is the most reliable method. This conclusion was drawn from measurements reported by Pugh and Samuels[52] in which depth values for three different abrasive treatments were obtained by the metallographic method and by the PME method; the depth values by the PME measurements were about 10% smaller in two cases, and 30% smaller in the third case for every deep damage produced by a coarse abrasive, 220-mesh silicon carbide. These discrepancies do not seem very serious since one does not expect great precision in this type of work and is usually able to leave some safety margin in a practical application, such as etching of devices or research specimens. But, beyond this, it should be noted that comparisons with some of the other data in the literature might lead to the opposite conclusion regarding reliability of the methods, if larger depth

[51] Bell Telephone Labs., Inc., Murray Hill, N. J.

[52] E. N. Pugh and L. E. Samuels, *This Journal*, **108**, 1043 (1961).

[53] E. N. Pugh and L. E. Samuels, *This Journal*, **109**, 409 (1962).

[54] T. M. Buck and F. S. McKim, *This Journal*, **103**, 593 (1956).

[55] T. M. Buck, "The Surface Chemistry of Methods and Semiconductors," H. C. Gatos, Editor, p. 107, John Wiley & Sons, Inc., New York (1960).

[56] P. R. Camp, *This Journal*, **102**, 586 (1955).

[57] J. W. Faust, Jr., American Society for Testing Materials Symposium on Cleaning of Electronic Device Components and Materials, Special Tech. Publ. 246 (1959).

Table I

Abrasive & nominal particle size	Mtd. of treatment (done with water slurry on glass plate unless otherwise noted)	Mtd. of meas. of depth of damage	Depth of damage in microns	Footnote Reference
220-Mesh SiC	Unidirectional abrasion	Metallographic	85	Pugh & Samuels (52, 53)
68μ (avg)	Unidirectional abrasion	PME	60	Pugh & Samuels (52, 53)
220-Mesh abrasion paper	Unidirectional	Metallographic	22	Pugh & Samuels (52, 53)
220-Mesh abrasion paper	Unidirectional	PME	20	Pugh & Samuels (52, 53)
600-Mesh SiC	Unidirectional abrasion	Metallographic	11.5	Pugh & Samuels (52)
25μ (avg)	Unidirectional abrasion	PME	10	Pugh & Samuels (52)
	Random motion abrasion	Metallographic	8.7	Pugh & Samuels (52)
	Random motion abrasion	PME	17-18	Buck & Mckim (54)
	Random motion abrasion	Photocond. decay	15	Buck (55)
	Random motion abrasion	Etch-rate	18-19	Faust (57)
1200-Mesh alumina				
12.5μ (avg)	Unidirectional abrasion	Metallographic	5.5	Pugh & Samuels (52)
3200-Mesh alumina				
5μ (avg)	Random motion abrasion	PME	6-7	Buck & Mckim (54)
		Photocond. decay	5-6	Buck (55)
		Field effect mobility	5	Buck (55)
		Etch-rate	5-7	Camp (56)
		Etch-rate	8-10	Faust (57)

values, *i.e.*, sensitivity, are to be taken as the criterion of reliability. It may be that the PME method was not used with its greatest possible sensitivity in the results of Pugh and Samuels. Thus, in Table I of this discussion, it can be seen that for 600-mesh SiC depths of damage obtained in earlier work by three different methods range from 15 to 19μ as compared with values of 8.7-11.5μ obtained from Pugh and Samuels. For abrasion with 305 alumina (3200 mesh) we obtained values of 5-7μ by the PME, photoconductivity decay (PCD), and field-effect mobility measurements; by the etch-rate method Camp[56] got 5-7μ, and Faust reported 8-10μ. But Pugh and Samuels reported a depth of only 5.5μ for 303-½ (1200 mesh) alumina which is a coarser abrasive than 305. It might be argued that we used a rougher method of application but we do not believe this to be the case. As we pointed out[55], our values refer to very gentle hand lapping; rougher methods of application can cause deeper damage, but the values quoted represent the smallest obtained for a given abrasive.

The largest discrepancy found by Pugh and Samuels was for deep damage, with 220-mesh SiC. For very deep damage the slope of the curve of PME response vs. depth removed is more gradual and there is, of course, more uncertainty in choosing the point or region where the response ceases to change. Greater sensitivity might have been obtained with the PME method than apparently was achieved in the work of Pugh and Samuels, by using a thinner specimen with higher resistivity. Their highest PME responses were only 7-8 mv, whereas we had values of 100-240 mv which would afford greater sensitivity in the region where response levels off.

The criteria for reliability and sensitivity, and the definition of "damage" itself, are of course related to the properties of the material in which one is interested. We have always been primarily interested in the electrical properties and have, therefore, used the most sensitive electrical property we could find—the surface recombination velocity, measured by both the PME and PCD methods—to estimate the "depth of damage." The etch-rate methods[56, 57] agree well with the electrical methods. The metallographic method now also seems to correlate reasonably well with surface recombination velocity. It is true that the metallographic method would seem to offer the advantage of detecting isolated spots of damage whereas the other methods measure an average property over a large area, as we have pointed out before.[55] However, this advantage does not seem to have resulted in greater sensitivity for the finer abrasive treatments which are of the greatest interest in semiconductor technology.

The metallographic method certainly provides a nice way of studying the nature of surface abrasion damage. At least two models for this damage have been considered in the past. One[58, 59] involves a cracked layer plus a deeper layer containing a high dislocation density. In another study[55] only the cracked layer was found; no evidence for dislocations was found, nor were cracks found as deep as the electrical effects were felt. Pugh and Samuels now find deeper cracks, extending well below the surface irregularities, and it appears that the damage consists of many fine cracks rather than a high density of dislocations. This still seems to leave an unanswered question about the nature of the recombination centers. Why are recombination centers associated with a crack? If it is just a case of a freshly cracked surface having a high density of recombination centers, then it is rather surprising but true that chemical treatments which lower S on an etched surface but which do not dissolve germanium have no apparent effect on the minority carrier lifetime at an abraded surface. It might be interesting to forcing nonetching solutions or gases into the cracks under pressure to see if this would lower the recombination velocity by acting on more of the cracked surface area.

In summary, it is suggested that the differences in sensitivity between the metallographic method and the lifetime methods are small and probably insignificant, but that if a comparison is to be made most of the data in the literature seems to favor the lifetime methods.

E. N. Pugh and L. E. Samuels: We thank Dr. Buck for his comments and for his interest in the work. However, we cannot accept his arguments on the relative sensitivities of the metallographic method and other methods. Our conclusions that the metallographic method was the most reliable were based on comparative tests carried out on specimens abraded under the same conditions. We do not consider that measurements made by different methods on surfaces abraded in different laboratories can be compared. Thus, the differences discussed by Buck could be due simply to differences in the abrasion conditions. This view is supported by the observations reported in our first paper that the depth of damage was greater in specimens abraded unidirectionally than in those abraded with a random motion.

The Influence of Residual Stress on the Magnetic Characteristics of Electrodeposited Nickel and Cobalt

R. D. Fisher (pp. 479-485, Vol. 109, No. 6)

V. Zentner[60]: The author states that "very little attention has been given to the effects of the internal stress on the magnetic characteristics of electrodeposits."

In 1952 we published a report[61] which contains significant information on this subject, thus anticipating Mr. Fisher's recent contribution. Figure 53 of our publication shows a general relation between stress on the one hand and the magnetic properties of coercive force and maximum permeability on the other for 15 nickel deposits obtained from eight different baths. This figure contains essentially the same information as Fisher's Fig. 7. The latter's Fig. 6, showing the effect of the nickel chloride concentration on stress and on the coercive force, is covered in our Fig. 18 and 46.

Table II of Fisher's paper shows that heat treatment at 440°C causes the coercive force of nickel deposits to decrease and the ratio B_r/B_m to increase. Our Table XXI shows the same effects for deposits from five different types of baths; our heat treatment temperature was 400°C.

The effect of stress on the magnetic properties of nickel was also discussed from a different angle on p. 915 of our publication, and data were given in Table XVIII. It was shown that simply removing the basis metal from a nickel deposit relieved the stress and changed the magnetic properties.

Mr. Fisher's paper is of value since it contains information on the magnetic properties of electrodeposited cobalt in addition to nickel coatings. Furthermore, the latter were not deposited under the same conditions as those used by us. However, the conclusions are very similar. If the author had been familiar with our work, he could have used his efforts to enlarge the general knowledge of the magnetic properties of these coatings, rather than to reconfirm data previously published.

R. D. Fisher: I would like to thank Dr. Zentner for calling my attention to his most comprehensive report on the physical properties of electrodeposited metals.

[58] J. W. Faust, Jr., Paper presented before the Buffalo Meeting of The Electrochemical Society, October 1957.

[59] J. W. Faust, Jr., "The Surface Chemistry of Metals and Semiconductors," H. C. Gatos, Editor, p. 130, John Wiley & Sons, Inc., New York (1960).

[60] Materials Technology Dept., Hughes Aircraft Co., Culver City, Calif.

[61] V. Zentner, A. Brenner, and C. W. Jennings, *Plating*, 39, 865 (1952).

Dr. Zentner's results in regard to nickel deposits are similar to mine despite the difference in solution composition, deposition conditions, and methods of measurement. It is significant to note that the influence of the internal stress on the hysteresis properties of nickel deposits appears to be independent of the solution composition and deposition conditions.

The cobalt deposits were heat-treated at 440°C in an attempt to convert some of the cubic cobalt obtained from solutions at low salt concentration to hexagonal cobalt. This was partially successful as indicated in the paper on page 481. Consequently, the nickel deposits were also heat-treated at 440°C.

Diagrammatic Representation of the Thermodynamics of Metal-Fused Chloride Systems

R. Littlewood (pp. 525-534, Vol. 109, No. 6)

K. E. Johnson[62]: The idea of potential $-pO^{2-}$ diagrams for fused salt systems is attractive in principle. However, the significance of the numbers given by Littlewood is questionable because they are determined solely from free energy data for pure chlorides and oxides (some liquid and some solid). For example, the solubility product of NiO in KCl is really given by:

$$\log K_{sp} = \frac{\Delta G_s}{2.303\,RT}$$

and not

$$\log S \frac{\Delta G^\circ}{2.303\,RT}$$

where ΔG_s and ΔG° are the free energy changes accompanying the reactions

$$NiO\ (s) + KCl\ (l) \rightarrow (NiCl_2 + K_2O)$$

in KCl solution and

$$NiO\ (s) + KCl\ (l) \rightarrow (NiCl_2\ (S) + K_2O\ (?)$$

respectively.

The difference, $|\Delta G_s - \Delta G^\circ|$ represents the free energy of solution of the products. Some measure of this quantity has been given for solutions in NaCl-KCl[63] but the problem arises of an appropriate definition of a standard state. For solution (*e.g.*, $NiCl_2$ in KCl) it seems preferable to define the standard state of the solute as when it is at infinite dilution, whereas for a mixed solvent (*e.g.*, $NiCl_2$-KCl) it is appropriate to refer to the pure salt ($NiCl_2$) as the standard state.

If $|\Delta G_s - \Delta G^\circ|$ is small compared with ΔG° then the author's conclusions regarding solubility products would be qualitatively correct and, indeed, there is some further experimental evidence in support of them.[64] However, the author's data[65] give $S = 10^{-4.46}$ for Na_2O in KCl at 800°, yet he prepared a 5% solution of Na_2O in NaCl-KCl at 700°! Would he elaborate on this point.

R. Littlewood: I thank Dr. Johnson for his comments. He is quite correct in saying that the formal treatment presented in this paper makes the assumption that the free energies of solution of oxides in chlorides are negligible. This fact is not mentioned specifically in the paper but, from the expressions used, it should have been clear that this was an implicit assumption. Its validity has not yet been directly established experimentally, and the scant data available are somewhat conflicting. There is now some evidence that the activity solubility products calculated by the methods suggested in the paper have some physical significance, but, on the other hand, the behavior of the oxygen (on platinum) electrode in contact with chloride melts containing oxide ions cannot at present be explained quantitatively. The latter effects might be due to irreversibility of the electrode processes (in which case the subject is not relevant to the present discussion), or they might indicate that hydroxide ions are important.

In his remarks about the solubility of Na_2O, Dr. Johnson has fallen into the common physicochemical trap of confusing activities with concentrations. It should be emphasized that the parameters "*S*" is an *activity* solubility product and the standard states must always be borne in mind. The activity solubility product of Na_2O in KCl at 700°C may be calculated to be about $10^{-5.67}$, relative to K_2O as standard state for oxide ions. This means that for Na_2O at unit activity in contact with a chloride melt we have the expression:

$$S = (Na^+)^2(O^{2-}) = 10^{-5.67}$$

For example, in equimolar NaCl-KCl (writing ion fraction of Na^+ as activity of Na^+, after Temkin), this gives $(O^{2-}) = 10^{-5.67}$ or $pO^{2-} = 5.07$. The meaning of these figures is that if we immersed a reversible oxygen electrode half-cell in the melt, its potential *vs.* a reference electrode would be about 0.6v higher than a similar electrode immersed in pure K_2O. The figure of $10^{-5.67}$ alone does not tell us what concentrations to expect, unless we know something about the ideality of the system.

On the question of standard states it is pertinent to point out that in fused salt solutions a standard state for solutes of infinite dilution does not have the same significance as in aqueous solutions. Infinite dilution in water is equivalent to isolated ions in a dielectric medium, predominantly molecular in character; in fused salts the mixture is still ionic, even at infinite dilution. Standard states referred to infinite dilution in fused salts thus appear to be both cumbersome and irrelevant; where difficulties arise when the pure salt is taken as a standard state, an arbitrary concentration, say 1 mole %, might be used, as is already common in many systems of metallurgical interest. (For references pertinent to this discussion, *see* Footnotes 66-68.)

[62] Dept. of Chemistry, Sir John Cass College, Aldgate, London E.C. 3, England.

[63] S. N. Flengas and T. R. Ingraham, *This Journal*, **106**, 714 (1959).

[64] H. A. Laitinen and B. B. Bhatia, *This Journal*, **107**, 705 (1960).

[65] R. Littlewood and E. J. Argent, *Electrochimica Acta*, 4, 114 (1961).

[66] H. A. Laitinen and B. B. Bhatia, *This Journal*, **107**, 705 (1960).

[67] K. H. Stern, *J. Phys. Chem.*, **66**, 1311 (1962).

[68] R. Littlewood and E. J. Argent, *Electrochimica Acta*, 4, 114 (1961).

June 1963 Discussion Section

A Discussion Section, covering papers published in the July-December 1962 JOURNALS, is scheduled for publication in the June 1963 issue. Any discussion which did not reach the Editor in time for inclusion in the December 1962 Discussion Section will be included in the June 1963 issue.

Those who plan to contribute remarks for this Discussion Section should submit their comments or questions in triplicate to the Managing Editor of the JOURNAL, 30 East 42 St., New York 17, N. Y., *not later than March 1, 1963*. All discussion will be forwarded to the author(s) for reply before being printed in the JOURNAL.

that the problems confronting the world today desperately need the broad outlook of the natural philosopher with his familiarity with many fields of knowledge, including the physical, life, and social sciences. In the professional area he posed the question: "Dos Industry want Electrochemists?" Now, eleven years later, greatly needing electrochemically trained people for fuel-cell research and industrial electrolytic operations, many companies wish they had had the foresight to have given encouragement and support to the teaching of electrochemistry.

In his address as the Society's president Professor Uhlig has treated the subject of creativity. He attributes the progress of science to the emphasis placed on creative thinking and intellectual honesty and suggests that the problems of diplomacy and international relations would be greatly benefited by emphasis on these same qualities.

Professional Society Activities

Professor Uhlig is a member of ten professional societies. His participation in the affairs of The Electrochemical Society has been continuous since he became a member in 1937. He is a past chairman of both the Corrosion and Theoretical Divisions. He was for two years editor of the "Journal" and during that time established the high standards that characterize this publication and that have led to its wide acceptance in the scientific world. He has been chairman of the Publication Committee, vice-president, and in 1955-1956 was President of the Society. He helped organize and served as the Society's representative at the First International Conference on Passivity held at Jugenheim, Germany in 1957, and is now assisting in the organization of the Second International meeting on this subject to be held in Toronto next September.

Uhlig has been chairman of the Gordon Research Conference on Corrosion and of the Intersociety Corrosion Committee. He has been a member of the Advisory Committee for the Prevention of Deterioration Center of the National Research Council and of the Corrosion Research Council.

Professor Uhlig is a member of Sigma Xi and of Tau Beta Pi. In 1951 he received the Willis R. Whitney Award of the National Association of Corrosion Engineers given in recognition of outstanding scientific contributions to corrosion knowledge.

The foregoing account has given some evidence of the manner of man we honor this evening. It should be added that he is soft-spoken and considerate of the views of others, yet firm and persistent in his own opinions; that he is unassuming and reserved, yet articulate and convincing, and finally, that he is gentle, gracious, and an altogether delightful human being.

Ladies and gentlemen: I give you Herbert Henry Uhlig, scientist, scholar, and dedicated teacher who has enriched the lives of his fellow men!

Conquering the Outer Space of Corrosion Science[2]

Herbert H. Uhlig

To attempt to tell you about the outer space of corrosion science is somewhat optimistic, as you well realize, because no one knows the details of outer space, real or imagined. Yet we have some concept of the great expanse of the physical universe, and also in the figurative sense of our subject. And the challenge of exploring what we do not know is equally real in either rocket experiments or corrosion studies.

The value of space exploration of any kind is sometimes questioned on economic grounds. This should be less a factor in evaluating corrosion experiments than in launching rockets which are extremely costly per unit, but perhaps we should remind ourselves that the value of all basic investigations including rocket research lies in the facts which are made available and the use of such facts to fulfill the varied needs of mankind. Not to be overlooked is the additional value of such facts interacting with the minds and attitudes of men. In the long range, accumulated truth of whatever kind elevates mental horizons and provides background and preparation for greater things that lie ahead. The world was first proved round before Newton achieved an audience who appreciated his new ideas regarding the solar system. And only after Newton's ideas were digested did Einstein succeed in presenting his concept of relativity. Purely on the side, as a result of logical deductions concerning relativity, he also concluded that mass and energy are equivalent. It was not many years later that we were brought into the nuclear age. One has the impression that if we succeed in solving all the problems which this age has thrust forth, we shall be strong indeed. And succeed we must.

The greatest things that lie ahead in corrosion science on the short range view are the savings of billions of dollars now lost annually by interaction of metal structures with their environments, plus the avoidance of accidents by sudden failure through stress corrosion cracking or corrosion fatigue. Considering the long-range view, our metal resources, of which there is only a limited supply, will be conserved. Purely on the side, our fuller understanding of the corrosion process itself will raise our mental horizons with regard to the nature of metal surfaces and metal fracture, the kinetics of heterogeneous reactions, the basic electrochemistry of composite electrodes in contact with liquid or solid electrolytes, and the structure of semiconductors at metal- or electrolyte-semiconductor interfaces. What more in addition might result from a well thought-out fundamental program is not predictable; the outer space of corrosion science is a vast area, and undoubtedly many surprises await us as we send man-guided rockets farther and farther into the unknown.

Anode and Cathode Reactions

The basic reactions that occur when a metal corrodes in an aqueous electrolyte involve a simultaneous oxidation and reduction reaction on different sites of the surface. Ions of the metal lattice are not soluble, but they become so if they first interact with water thereby acquiring a sheath of water molecules in accord with

$$M^+(s) + nH_2O(l) \rightarrow M(H_2O)^+_n(l) \qquad [1]$$

where n is not well defined; for the alkali metal ions n apparently ranges from 3 to 5 (1). The solvated complex $M(H_2O)_n^+$ still cannot easily escape the metal surface, however, unless the attracting force between the positive ion and a corresponding free negative electron of the metal is neutralized. This neutralization can occur by a reduction reaction elsewhere on the metal surface (cathodic site) which absorbs the elec-

[2] Palladium Medal Address delivered on Oct. 3, 1961, at the Detroit Meeting of The Electrochemical Society.

tron belonging originally to the positive ion of the metal. Typical reactions at cathodic sites are

$$2H^+ \rightarrow H_2 - 2e \quad [2]$$

and

$$1/2\ O_2 + 2H^+ \rightarrow H_2O - 2e \quad [3]$$

supplemented in many instances by

$$O_2 + 2H^+ \rightarrow H_2O_2 - 2e$$

Because of the neutralization process, or stated another way, because electric charge cannot accumulate anywhere in the system without tremendous energy imbalance, both anode and cathode reactions proceed at the same rate. The slower reaction of the two determines the over-all rate of corrosion. If H^+ discharge controls, for example, the corrosion rate becomes sensitive to factors which catalyze or impede H^+ discharge. Good catalysts correspond to values of low hydrogen overvoltage, whereas poor catalysts correspond to high hydrogen overvoltage. Bonhoeffer (2) showed some time ago that catalytic properties of a metal for the reaction $H + H \rightarrow H_2$ approximately parallel hydrogen overvoltage values (Table I). His experiment consisted of measuring the temperature rise of a thermometer, the bulb of which was coated with one of various metals, on exposure to a stream of gaseous hydrogen atoms. He noted that the temperature rise accompanying combination of H atoms in presence of a good catalyst like Pt was higher than for a poor catalyst like Hg. The parallel behavior of temperature rise with hydrogen overvoltage does not mean that the slow step of H^+ discharge is always H atom combination on the cathode surface, but it does indicate that the controlling reaction, whatever it may be, is sensitive to catalytic properties of the electrode material. We find in fact that many corrosion reactions, and also the so-called passive properties of metals and alloys, are frequently related to catalytic properties. This suggests that the detailed electron transfer steps accompanying formation of adsorbed films entering catalytic properties may also occur in corrosion reactions and in establishing passive films (3).

Platinum is a good catalyst for either reaction [2] or [3], and Cu or Ni is effective for reaction [3]. Other metals may behave less effectively for O_2 reduction because of either inherently poor catalytic properties, or because of interposing surface films. Along these lines, copper when coupled to iron in sea water accelerates corrosion of iron by favoring the O_2 reduction reaction and absorbing electrons which otherwise prevent hydrated Fe^{++} from leaving the iron lattice. The reduction of O_2 proceeds so rapidly that within wide limits all dissolved oxygen reaching the copper surface is reduced, and the increased corrosion is proportional to the total surface of copper exposed. Expressed quantitatively, the penetration rate p through corrosion of iron having area A coupled to copper of area B is

$$p = p_o\left(1 + \frac{B}{A}\right) \quad [4]$$

where p_o is the penetration rate of iron uncoupled. Note that if the ratio B/A is large as when iron rivets are placed in a copper sheet, the ensuing corrosion rate of iron in a good conducting medium can be very large. This equation holds in addition for platinum, nickel, and other good catalysts, but for metals such as titanium or lead, which are poor catalysts, the increased corrosion of iron by reason of galvanic coupling is less than the calculated value. Many data have been published which illustrate this point. LaQue (4), for example, reported values in flowing sea water for various iron couples which show greater galvanic corrosion using Ni and Cu compared to Ti and 18-8 (Fig. 1). These results correlate with parallel data on cathodic polarization of the more noble component of the couple in sea water, good catalysts polarizing less than poor catalysts. Tomashov (5) and Delahay (6) also reported polarization data for the O_2-reduction reaction on various metals which can be interpreted in the same way.

Table I. Relation of catalytic activity for $H + H \rightarrow H_2$ to hydrogen overvoltage

Decreasing catalytic activity (Bonhoeffer)	H_2 overvoltage, v 1N HCl, 10^{-3} amp/cm^2
Pt	0.09
Pd	0.12
W	0.27
Fe	0.40
Cr	—
Ag	0.46
Cu	0.50
Pb	0.67
Hg	1.04

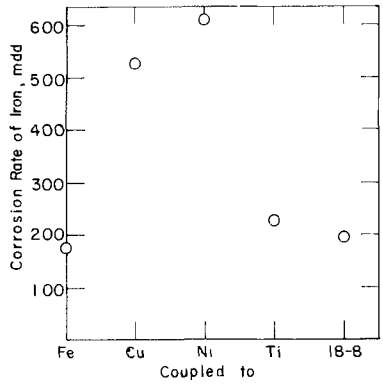

Fig. 1. Corrosion rate of iron coupled to various metals in flowing sea water (LaQue).

Passivity

When an uncoupled metal corrodes, reaction [3] proceeds quantitatively at cathodic sites up to an O_2 concentration at the metal surface which reaches or exceeds a critical value. At such a concentration, particularly for transition metal, excess O_2 forms a monolayer of oxygen atoms adsorbed on the surface, resulting in an expanding cathodic and a shrinking anodic area. A layer of this kind excludes H_2O molecules from the metal surface and hence reaction [1] corresponding to dissolution of metal ions is impeded except at residual exposed anodic sites. Hence metal ions no longer enter solution at their usual rate and the metal is said to become passive. Looked at in other terms, adsorbed oxygen decreases the exchange current density i_o (increases anodic overvoltage, O.V.) attending metal ion dissolution in accordance with the Tafel equation

$$O.V. = \beta \log \frac{i}{i_o}$$

Passivity of metal M can also result from anodic polarization at current densities sufficiently high to discharge OH^- or oxidize H_2O in accord with the reactions:

$$M + OH^- \rightarrow O(\text{adsorbed on M}) + H^+ + e \quad [5]$$

$$M + H_2O \rightarrow O(\text{adsorbed on M}) + 2H^+ + 2e \quad [6]$$

where O(adsorbed on M) represents chemisorbed oxygen on the metal surface. The amount of oxygen adsorbed corresponds in some measurements, *e.g.*, stainless steels, to a monolayer of atoms over which a layer of O_2 molecules is chemisorbed (7-9). The critical current density at which reactions [5] and [6] take place is a function of H^+ activity in accord with the following relation:

$$i(\text{crit.}) = K(H^+)^\lambda \quad [7]$$

where λ and K are constants. This relation is derived (10) from first principles and is confirmed by experiment.

Hence for a metal exposed to an aerated solution, the mechanism of passivation may involve a cathodic current in accord with Eq. [3] equal to or in excess of the critical current required for passivity. Since i(crit.) usually increases with H^+ activity (λ is positive), the critical partial pressure of O_2 for passivity also increases with H^+ activity. The quantitative relation between the critical oxygen concentration c for passivity of a metal and *p*H of the solution in which the metal is immersed is obtained by equating the diffusion current for dissolved O_2 to Eq. [7]

$$p\text{H} = \frac{1}{\lambda}\log\left(\frac{K\delta}{4D\mathbf{F}}\right)\frac{1}{c} \quad [8]$$

where D is the diffusion constant of O_2, δ is the thickness of the stagnant liquid diffusion layer at the metal surface (about 0.05 cm), and **F** is the Faraday.

Consequently iron, for example, becomes passive in air-saturated alkaline solutions (*p*H > 10), but only at higher partial pressures of O_2 in neutral water. For chromium or the stainless steels, which have higher affinity for oxygen than does iron and for which i(crit.) is much lower, the passive film forms at a lower critical partial pressure of oxygen, and hence these metals become passive in air-saturated water, or even in dilute acids. For 14% Cr-Fe alloy, as an example, the critical *p*H above which passivity can establish itself in aerated sulfuric acid is 3-4.

For nontransition metals, *e.g.*, Zn, Sn, Pb, which escape from the metal lattice more readily than the transition metals having characteristically higher sublimation energies, excess dissolved oxygen at the cathode, or alternatively anodic polarization beyond i(crit.) may lead to immediate formation of an oxide film instead of an adsorbed film. The oxide film then impedes further corrosion and accounts for passivity by the mechanism of a relatively thick surface diffusion barrier rather than by the mechanism described above. Since chemisorbed films are only metastable intermediates in the formation of surface compounds, an oxide forms eventually on all metals, both transition and nontransition, and hence in many instances of passivity both kinds of films act jointly.

Critical experiments in this area are very difficult to devise, and for this reason investigators of passive phenomena continue to debate whether the adsorbed films described here are really nothing more than thin oxide films. The vast literature on properties of metal surfaces in contact with gases, beginning with the classic investigations of Langmuir, and continued by many investigators more recently (11), speak against this possibility. The evidence is quite clear to anyone willing to look into the matter that adsorbed films have properties distinct from those of thin oxide films. In addition, it can be said that supposed oxide films equivalent in thickness to a measured 0.003-0.01 coulomb/cm² of apparent surface for passive Cr, Fe, and the stainless steels can be no more than 5-20Å thick based on true surface area, and films of this thickness are not likely to be effective diffusion barrier layers. Thermodynamic interpretation of the Flade potential particularly for iron (8) indicates that oxygen comprising the passive film is adsorbed and is not part of any known iron oxide. Furthermore, capacitance and resistance measurements of Kolotyrkin (12) support the view that the passive film on iron is similar to the oxygen film on Pt which is known to be adsorbed.

Effect of Complexing Agents

Returning to reaction [1], the rate at which this reaction proceeds appears to be sensitive to surface complex formation probably involving OH^-. The overvoltage for the anodic dissolution reaction, therefore, is found in the case of iron to increase with decrease in *p*H (13). The details and quantitative relations, however, are not well understood, and much more information is needed, particularly for the transition metals. The complexity of the problem has been discussed by several investigators (14-17). Complexing agents in general, of course, are known to play a part in the tendency for reaction [1] to go. Any complexing agent which reduces the activity of Fe^{++}, for example, simultaneously changes the potential for the reaction $Fe \rightarrow Fe^{++} + 2e$ in the more active direction. Accordingly, under these circumstances, the potential difference between anodes and cathodes of a corroding metal increases, accounting for an increase in the corrosion current. Iron therefore, corrodes much more rapidly than is normal in ammonium salts, in sodium ethylene diamine tetra-acetates, or in concentrated sodium polyphosphate solutions, all of which form complexes with Fe^{++}. When a good oxidizing anion is also present to stimulate the cathodic reaction, as in the case of NH_4NO_3, the rate can be catastrophically high as is well known to those handling fertilizer solutions. Unusually high rates of corrosion for iron in NH_4NO_3 solutions have been measured by several investigators including Heyn and Bauer (18), and still higher rates in concentrated solutions containing excess NH_3 by Weitz and Muller (19), Libinson, Kukushkin, and Morozova (20) and by Hackerman, Hurd, and Snavely (21). Typical examples of such rates obtained recently by Schick at the M.I.T. Corrosion Laboratory (22) for mild steel in an aqueous solution of 44.4% NH_4NO_3, 5.9% NH_3 at room temper-

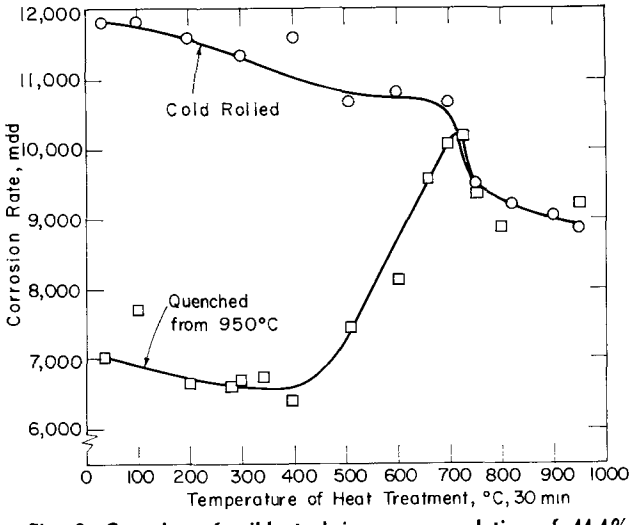

Fig. 2. Corrosion of mild steel in aqueous solution of 44.4% NH_4NO_3, 5.9% NH_3, room temperature.

ature are given in Fig. 2. The highest rates correspond to a penetration of over 2 in. (5 cm) per year. By chemical analysis it was shown that the complex forming in this case has the structure $[Fe(NH_3)_6](NO_3)_2$. Since coupling iron to an equal area of Pt has no effect on the rate, control of the reaction is assumed to be at anodic sites. The rate of dissolution at the anode is sensitive to metallurgical structure as shown by data of Fig. 2, a cold-worked steel corroding more rapidly than one that is quenched from 950°C. However, increased residual energy of the cold-worked metal is not the cause as shown by additional experiments in which cold-worked pure iron, zone refined, corroded at a somewhat lower rate than the same iron quenched from 950°C. Instead, the state of subdivision of carbides and the grain orientation appear to be important, both factors reaching comparable states on heat treatment of mild steel, either cold worked or quenched, for ½ hr at 700°C or above. The corrosion rate can be retarded to the extent of 99 or more % by small additions of SCN^- or various high molecular weight organic substances. These inhibitors probably adsorb on the metal surface interfering with either complex formation, NO_3^- reduction, or both. We have already seen how effectively an adsorbed oxygen film on a passive metal surface can interfere with dissolution of metal ions.

Unusual Valence States

Reaction [1] is complicated for some metals by the tendency to form ions of more than one valence. Which particular valence ion predominates is determined in the usual case by the equilibrium existing at the metal-solution interface. For example for copper, which forms both Cu^{++} and Cu^+, the equilibrium is $Cu + Cu^{++} \rightleftarrows 2Cu^+$ and the corresponding equilibrium constant $(Cu^+)^2/(Cu^{++})$ as calculated from thermodynamic data equals 6×10^{-7}. This value indicates, as observed, that copper usually dissolves predominantly as the divalent ion, Cu^{++}. In a solution which complexes Cu^+, *e.g.*, in HCl, the situation may, of course, change. For other metals, particularly those active in the emf series, it has been proposed that an ion of lower valence may predominate initially, even though it is unstable in water. Unstable ions of this kind are reported to form, for example, during anodic dissolution of Al (23), Mg (24, 25), and Be (26, 27). For Mg, the initially dominant ion, Mg^+, quickly reduces water, one possible reaction being the following

$$2Mg^+ + 2H_2O \rightarrow Mg^{++} + Mg(OH)_2 + H_2 \qquad [9]$$

Additional lesser side reactions may also take place at the same time. In any event, when Mg is polarized anodically, it is observed that hydrogen is evolved at the anode to the extent of about half that at the cathode, and the electrochemical equivalent for magnesium is almost half that usually assigned to magnesium based on formation of Mg^{++} ions. It is not surprising, therefore, that magnesium anodes used for cathodic protection produce only about 500 amp-hr/lb, whereas calculated on the basis of Mg^{++} they should produce 1000 amp-hr/lb instead. The actual output is altered somewhat by local action cells operating on the metal surface, and hence the current efficiency of a magnesium anode also depends to some extent on composition of environment and on the alloy or impurity content of the metal. Some investigators believe that the output of magnesium anodes, so much lower than the calculated value based on Mg^{++}, is accounted for entirely by local action currents. Others (28, 29) propose that a contributing factor resides in metal particles dislodged during the anodic dissolution process. Metallic residues, in fact, are sometimes detected by x-ray as a constituent of anodic reaction products. Other than the possibility that they may also form by dissociation of lower valence ions to a mixture of metal and normal valence ions, it is not yet clear to what extent metallic particles are released during anodic dissolution of metals. For metals like Ag and Cu, some metallic product is detectable, but the total amount is very small and Faraday's law applies, by and large. The fact is significant that the calculated apparent valence of magnesium ions in anodic dissolution experiments for varying current density, temperature, and electrolyte within wide limits always falls between 1 and 2, and that analogous relations are noted for Al and Be. This plus the fact that portions of anolyte obtained from these metals while current flows, temporarily reduce various substances, *e.g.*, $KMnO_4$, lends weight to the conclusion that a state of unusual lower valence exists. After all, multiple valence ions are well known for most of the transition metals, and it is perhaps to be expected that similar ions although unstable may occur in the case of some nontransition metals. But more experiments are undoubtedly necessary to bring this matter into proper focus. Should the existence of lower valence ions receive further confirmation as seems likely, it will probably become necessary to revise the present standard potentials of metals like Al, Mg, and Be as listed in the emf series to bring them into line with equilibria involving the valence of ions actually present at the metal surface.

Oxidation and Tarnish

In presence of a reactive environment but in absence of excess water, metal ions may escape from the metal lattice to form the new lattice of a surface oxide or other type compound such as chloride or sulfide. In this event, electrons enter the film substance along with ions, but along different paths. The initial rate of oxidation, therefore, is controlled either by metallic ion escape, or by electron transfer. In the general case, because of differing electron affinities of metal and film substance, a space charge builds up within the film first forming, which greatly influences the rate of both processes (Fig. 3). The space charge density, in turn, is sensitive to the density of defects within the film substance at which electrons are trapped, and hence impurities and other factors which affect defect density influence the reaction rate.

Under conditions of continuing growth of space charge, the logarithmic equation usually expresses the rate of oxidation, such that thickness of surface film substance y is a linear function of the logarithm of oxidation time t or: $y = k \log (t/\tau + 1)$ where τ and k are constants (30, 31). Under some conditions, the inverse logarithmic equation $1/y = k \log (t/\tau + 1)$ has

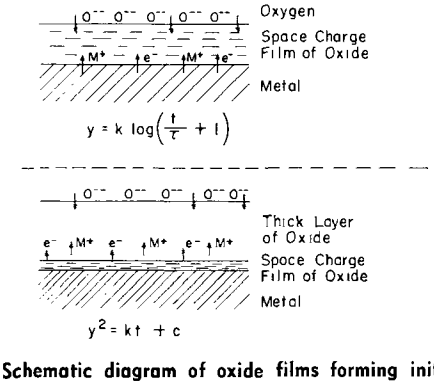

Fig. 3. Schematic diagram of oxide films forming initially (top) and during thick film conditions (bottom).

been found to apply (32, 30) indicating that the mechanism of initial reaction rate is not always the same.

Beyond thin film thickness, the oxidation rate is controlled by diffusion of cations or anions, as described by Wagner (33), and the so-called parabolic equation $y^2 = kt + \text{constant}$ holds. The rate of diffusion, in turn, is now dependent on concentration of lattice defect sites within the film substance. Impurity atoms, in line with semiconductor theory, influence defect concentration; hence impurities also sensitively affect the rate of reaction. Indeed several experiments have demonstrated, in accord with expectation, a major effect of impurities in surface oxides on the oxidation rate of zinc (34) and of nickel (35, 36).

There are many questions that remain regarding the general relationship of kinds of impurities, their concentration and their position within the lattice to initial and thick film oxidation of metals. Also, heat treatment and quenching, for example, which alter the defect structure of semiconductors should have an effect on oxidation rate. An interesting phenomenon as yet unexplored concerns the general properties of surface films in contact with metals accounting for the tendency of protective films to spall off during cooling and heating cycles. In this way, otherwise protective films are destroyed, and the oxidation process continues at higher rates than are normal. Tendency to spalling is an important factor in the general application of all oxidation resistant metals and alloys.

Effect of Stress

The effect of stress on corrosion is important because of catastrophic failures that continue to take place through fretting corrosion, corrosion fatigue, and stress corrosion cracking. Fretting corrosion is damage that occurs when two surfaces, one or both of which are metals, rub against each other. Corrosion products form which in the case of mild steel consist mostly of αFe_2O_3 accompanied by deep pitting at the interface. The pitting is a result of the large volume of oxide compared to the metal from which it forms exerting extra stress at local areas of the surface and accelerating damage. Ultimately, these pits act as nuclei for fatigue or corrosion fatigue cracks. In practice, fretting corrosion causes failure of bearings including jewel bearings, riveted flanges, variable pitch propellers on planes, shrink-fits, steering knuckles of automobiles, and various metal parts subject to vibration in high-speed machinery. The mechanism is not electrochemical; both moisture and higher temperatures reduce fretting damage of steel instead of increasing it. The mechanism appears to be one of mechanical activation of a chemical reaction between the metal and adsorbed oxygen on its surface to form an oxide which is rubbed off by further relative motion. Damage is supplemented by a mechanical wear process, but the latter is not always important as shown by experiments in a nitrogen atmosphere in which a much smaller amount of metal damage results compared to damage in air (37). The assumption that chemical damage and mechanical wear are additive is in reasonable agreement with a limited number of experiments that have been reported so far using mild steel (38). The question arises as to whether the same situation applies to other metals as well. Is the increased damage at lower temperatures caused by more rapid or more complete adsorption of gases on tracks of metal rubbed clean by abrasion? Some investigators propose that the increased damage results from freezing of moisture thereby removing a source of natural lubricant. But this is unlikely in view of the increased damage observed in our experiments at low temperatures using dried air. Does moisture lubricate in any case, or does it soften abrasive metal oxide by forming hydrates? Does the increased damage by fretting noted for stainless steels or titanium result from their increased affinity for oxygen? Is there support in any metal system for the proposal that all the damage is in the form of wear and that small wear particles subsequently oxidize? Considering the importance of this problem to the aircraft, railroad, automotive, and to all industry using high-speed machinery, it is surprising that so little research has been supported aimed at understanding the nature of the damage. Large amounts of money have been spent on empirical approaches to the problem which have provided only temporary relief or which have proved wholly inadequate.

The same situation prevails more or less in the subject of corrosion fatigue. Very little is known at present about the mechanism of metal fatigue itself, and still less is known about corrosion fatigue. In the meantime, airplanes crash, axles break, and machines grind to a halt when components crack. The mechanical engineer redesigns the failed part, but is this the only or the best approach? No one knows. Fundamental factors of metal and environment entering the corrosion fatigue of metals are known to only a limited extent. D. J. McAdam, Jr., at the National Bureau of Standards appears to be one of the few investigators who has systematically surveyed the field, but his excellent work appeared 20-35 years ago, and many unanswered questions remain. The mechanism appears to be at least in part electrochemical, as shown for example by the fact that cathodic protection and corrosion inhibitors reduce damage. But how does the mechanism of corrosion fatigue using repeated or alternate stresses compare with that of stress corrosion cracking requiring a constant stress? Is the effect of metal composition and interstitial impurities the same? Present data indicate they are not, but why? Also why are specific ions required for stress corrosion cracking but presumably not for corrosion fatigue? Some present theories are based on rupture of protective films at the base of cracks in both types of failure. But metals on which naturally formed films are not particularly protective, such as copper or brass, are more resistant to corrosion fatigue than metals with highly protective films such as the stainless steels, which in turn are more resistant than carbon steels, again having less protective films. Also pure metals whether naturally covered or not by protective films do not stress corrosion crack.

Dr. Z. Foroulis recently showed in my laboratory that zone-refined iron corrodes in deaerated hydrochloric acid at the same rate whether cold worked or annealed. Only when small amounts of nitrogen or carbon are present does cold work increase rate of attack, and the effect is then large. Polarization measurements show that the reaction is cathodically controlled. We have interpreted these facts to mean that cold working of iron produces lattice defect arrays at which nitrogen or carbon segregates, and that these areas have lower hydrogen overvoltage than iron itself. Any increased energy of a disarrayed lattice has apparently little effect, contrary to intuitive statements appearing in various textbooks and in the literature. But why do such arrays of interstitial atoms have lower hydrogen overvoltage? What other alloyed elements behave similarly? How does iron differ in this respect from other metals, if indeed it does differ?

Significantly, zone-refined iron does not stress corrosion crack in hot nitrate solutions, whereas iron containing small amounts of nitrogen or carbon is very susceptible. The attack is along grain boundaries. It is

reasonable to suppose that nitrogen or carbon atoms segregate at grain boundaries and thus form the paths along which high corrosion rates prevail. But why are NO_3^- or OH^-, which are specific in causing stress corrosion cracking, the only anions to increase corrosion along such paths? Certainly Cl^-, SO_4^{--}, ClO_4^-, or acetate ions, which do not cause cracking, form good conducting salts and should provide equal local action at the apex of any crack that forms. Is the cracking phenomenon one of surface energy reduction? Do metal atoms at the crack apex, the mutual affinities of which are reduced through adsorption of NO_3^- or OH^-, no longer have the ability to hold on to each other, allowing the metal to separate under stress? This seems to be a reasonable interpretation of the experimental evidence (39). And does the responsible adsorption depend on potential difference between metal at the apex and at the walls of the crack? Is the increased concentration of nitrogen or carbon atoms diffusing to the highly deformed metal at the apex sufficient to account for preferential adsorption of ions? Or the absence of preferential adsorption in the case of pure iron?

In the stable austenitic stainless steels, our experiments (40, 41) show that nitrogen is the major impurity accounting for susceptibility to stress corrosion cracking in boiling $MgCl_2$ solutions. Carbon, to the contrary, decreases susceptibility. Why is this? Susceptibility to cracking is also decreased by alloying nickel with Cr-Fe austenitic stainless steels in the amount of 45-50% or more (42). There have been suggestions that perhaps the dislocation arrays of high-Ni alloys differ from those of other metals, but recent measurements by J. Sava in my laboratory indicate that increasing the nickel content is accompanied by a continuously decreasing solubility of the alloy for nitrogen. Perhaps the critical nitrogen content below which stress corrosion cracking does not occur is reached at about 50% nickel. But additional questions similar to those that were raised regarding carbon steels also enter here. For example, for austenitic stainless steels only Cl^- or OH^- are specific in causing cracking, all other ions apparently having no effect, and it would seem that here too reduction of surface energy through adsorption of specific anions is a likely contribution to failure.

Outlined Program of Fundamental Corrosion Research

It is fair to state, I believe, that we have barely gotten off the ground in our initial search for basic facts in the outer space of corrosion science. For many reasons, fundamental information has accumulated only slowly during the past 10 years, despite the tremendous gains that are promised by any well-directed, adequately supported corrosion program. One of the difficulties is that fundamental corrosion research requires the best scientific talent available among those well trained in both chemistry and in metallurgy. Students having aptitudes in both fields are found only among our best students.

The several questions I have touched on during my discussion in themselves suggest the outline of a serious basic research program in corrosion science. With the thought that a summary of these questions may be worthwhile, I have also included a few subjects deserving of attention, but for which time and space do not permit further discussion.

Outline of Basic Research Program in Corrosion Science

1. Electrochemical problems.
   - A. Anodic overvoltage constants; effect of pH, temperature, nature of anion.
   - B. Unusual valence ions.
   - C. Ratio of anodic to cathodic areas; how to measure them, their values for typical cases.
2. Kinetics of tarnish and oxidation.
   - A. Relation of space charge to initial reaction. Effect of deficit structure, including heat treatment and impurity content of surface films.
   - B. Effect of specific trace impurities and heat treatment of surface films on thick film rates. Effect of impurities on path of oxidation. (For example, Ca additions to 20% Cr, 80% Ni alloy allegedly avoid preferential grain boundary attack.)
   - C. Factors of metal and film substance accounting for spalling of protective films.
3. Mechanism of stress corrosion cracking.
   - A. Relative importance of electrochemical action within cracks compared to specific adsorption of ions and accompanying reduction of surface energy (stress sorption cracking). Effect of potential on specific adsorption within cracks.
   - B. Effect of dislocation patterns and resultant segregation of impurities or alloying components as source of crack paths.
   - C. Factors affecting intermetallic compound formation and rate of formation at grain boundaries and at slip planes as sources of crack paths.
   - D. Effect of metal heat treatment on susceptibility. Similarly effect of impurities and metal composition.
4. Mechanism of corrosion fatigue.
   - A. Effect of metal composition and heat treatment; relative susceptibility of zone-refined metals.
   - B. Effect of environment, (pH, anions, dissolved O_2, etc).
   - C. Effect of temperature.
5. Mechanism of fretting corrosion.
   - A. Effect of frequency and temperature on fretting corrosion of typical metals.
   - B. Relation of susceptibility to rate at which gases adsorb on metal surfaces.
   - C. Effect of magnitude of relative slip.
6. Mechanism of corrosion inhibition, *e.g.*, polyphosphates, benzoates.
7. Mechanism of protective $CaCO_3$ deposition from potable waters. Effect of natural colloids, temperature, and flow rate.

Many other subjects could be added. A small part of the above program is already underway in various laboratories but most of it still waits for attention by those competent to undertake programs of this kind. The above outline does not include service tests nor engineering programs which are also extremely important to progress in corrosion control but which have different objectives. It has already been stated many times by others that engineering programs soon reach a dead end as basic information is used up, and no attempt is made to replenish such information. As a consequence, more than one applied program currently underway stares at a blank wall. New ideas are needed, and although these are sometimes stumbled on, there is merit in paying the price for searching them out systematically. In addition, new ideas often become available through research in understanding corrosion reactions which are wholly unexpected, and which may have even greater importance than the initial program itself. Finally, not least of the benefits to be derived from carrying out a fundamental research program is the training of young minds in the basic sciences and in research techniques. Such minds represent the most

valuable asset of any university, of any industry, or of any nation. Climbing on the shoulders of those who have gone before, young men and women adequately trained can see far more of outer space than do any of us. To them belong the future and it behooves us to give them a good start.

REFERENCES

1. J. Bockris and B. Conway, "Modern Aspects of Electrochemistry," p. 71, Academic Press, New York (1954).
2. K. Bonhoeffer, *Z. physik. Chem.*, **113**, 119 (1924).
3. H. H. Uhlig, *Z. Elektrochem.*, **62**, 700 (1958).
4. F. L. LaQue, *Proc. A. S. T. M.*, **51**, 495 (1951).
5. N. Tomashov, "Theory of Corrosion and Protection of Metals," (in Russian) Acad. of Sciences, Moscow (1959).
6. P. Delahay, *This Journal*, **97**, 198 (1950).
7. H. Uhlig and S. Lord, *ibid.*, **100**, 216 (1953).
8. H. H. Uhlig, *Z. Elektrochem.*, **62**, 626 (1958).
9. P. King and H. Uhlig, *J. Phys. Chem.*, **63**, 2026 (1959).
10. H. H. Uhlig, *This Journal*, **108**, 327 (1961).
11. B. Trapnell, "Chemisorption," Academic Press, New York (1955).
12. Y. Kolotyrkin, *Z. Elektrochem.*, **62**, 664 (1958).
13. K. Heusler, *ibid.*, **62**, 582 (1958).
14. T. Hoar, "Modern Aspects of Electrochemistry," No. 2, p. 262, J. O'M. Bockris, Editor, Butterworths, London (1958).
15. T. Hurlen, *Acta Chem. Scand.*, **14**, 1533, 1555, 1564 (1960).
16. K. Christiansen, H. Hoeg, K. Michelsen, G. Nielsen, and H. Nord, *ibid.*, **15**, 300 (1961).
17. J. O'M. Bockris and H. Kita, *This Journal*, **108**, 676 (1961).
18. G. Heyn and D. Bauer, "Mitteilungen aus dem Königlichen Materialprüfungsamt," p. 1-104 (1908).
19. E. Weitz and H. Muller, *Ber. Deutsch. Chem. Ges.*, **58**, 363 (1925).
20. I. Libinson, I. Kukushkin, and A. Morozova, *Zhur. Khim. Prom.*, **12** [6], 590 (1935).
21. N. Hackerman, H. Hurd, and E. Snavely, *Corrosion*, **14**, 203t (1958).
22. G. Schick, Thesis, Department of Metallurgy, M.I.T. (1961).
23. E. Raijola and A. Davidson, *J. Am. Chem. Soc.*, **78**, 556 (1956).
24. J. Greenblatt, *This Journal*, **103**, 539 (1956).
25. M. Rausch, W. McEwen, and J. Kleinberg, *Chem. Revs.*, **57**, 417 (1957).
26. B. Laughlin, J. Kleinberg, and A. Davidson, *J. Am. Chem. Soc.*, **78**, 559 (1956).
27. K. Heusler, *Z. Elektrochem.*, **65**, 192 (1961).
28. G. Marsh and E. Schaschl, *This Journal*, **107**, 960 (1960).
29. G. Hoey and M. Cohen, *ibid.*, **105**, 245 (1958).
30. H. H. Uhlig, *Acta Met.*, **4**, 541 (1956).
31. E. Williams and P. Hayfield, "Vacancies and Point Defects in Metals and Alloys," Inst. of Metals Report No. 23, p. 131, London (1958).
32. N. Cabrera and N. Mott, *Repts. Prog. Phys.*, **12**, 163 (1949).
33. C. Wagner, *Z. Physik. Chem.*, **21B**, 25 (1933); **32B**, 447 (1936); **40B**, 455 (1938); with K. Grünwald, *Trans. Faraday Soc.*, **34**, 851 (1938); "Atom Movements," pp. 153-73, A.S.M., Cleveland (1951).
34. G. Gensch and H. Hauffe, *Z. physik. Chem.*, **196**, 427 (1950).
35. C. Wagner and K. Zimens, *Acta Chem. Scand.*, **1**, 547 (1947).
36. K. Hauffe and H. Pfeiffer, *Z. Elektrochem.*, **56**, 390 (1952).
37. I. Ming Feng and H. Uhlig, *Trans. A.S.M.E.*, **76**, 395 (1954).
38. H. H. Uhlig, *ibid.*, **76**, 401 (1954).
39. H. H. Uhlig, "Physical Metallurgy of Stress Corrosion Fracture," pp. 1-17, T. Rhodin, Editor, Interscience Publishers, New York (1959).
40. H. Uhlig, R. White, and J. Lincoln, *Acta Met.*, **5**, 473 (1957).
41. H. Uhlig and R. White, *Trans. A.S.M.*, **52**, 830 (1960).
42. H. Copson, "Physical Metallurgy of Stress Corrosion Fracture," T. Rhodin, Editor, p. 247, Interscience Publishers, New York (1959).